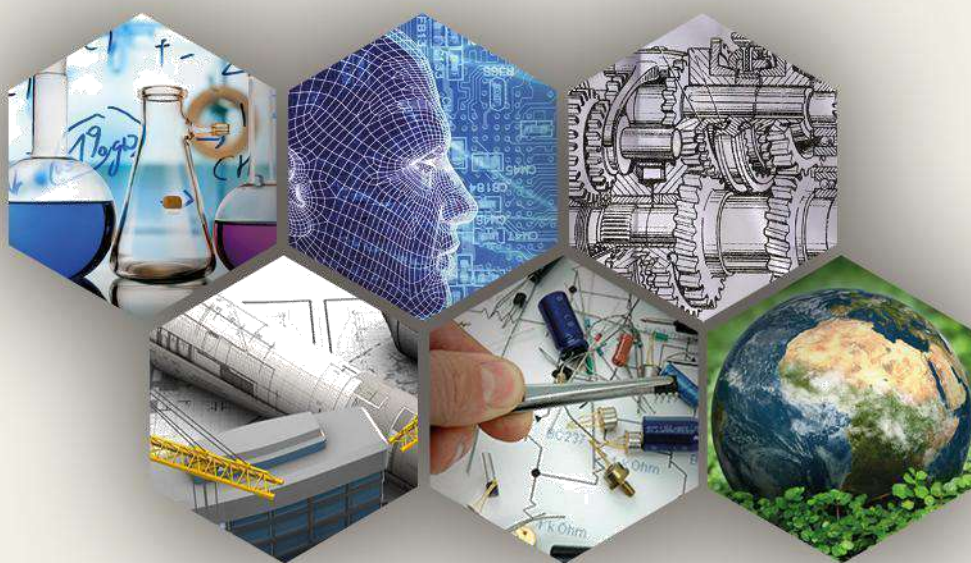




ICAIE



International Conference on Advances and Innovations in Engineering



Conference Proceedings

10-12 May / Elazığ

Fırat University



ICAIE

International Conference on Advances and Innovations in Engineering

Oral Submissions Book

10-12th MAY 2017

Fırat University Engineering Faculty /
ELAZIĞ

Editor in Chief

Ahmet Bedri ÖZER

Editor

Onur ALKAÇ

Barbaros DURMUŞ



Fırat University

Honour Committee of the ICAIE

Prof. Dr. Hasan MANDAL, Executive Board Member at Council of Higher Education (CoHE)

Prof. Dr. Kutbeddin DEMİRDAĞ, Rector

Prof. Dr. Mehmet CEBECİ, Vice Rector

Prof. Dr. Halil HASAR, Vice Rector

Prof. Dr. Ahmet ÖZER, Dean

Scientific and Technical Committee of the ICAIE

A. Feyzi BİNGÖL, Fırat University, Turkey

A. Yadigar DURSUN, Fırat University, Turkey

Abdülkadir ERDEN, Atılım University, Turkey

Abdullah Hilmi LAV, İstanbul Technical University, Turkey

Abdullah ÖZTÜRK, Middle East Technical University, Turkey

Abuzer ÇALIŞKAN, Fırat University, Turkey

Adil BAYKASOĞLU, Dokuz Eylül University, Turkey

Adnan DERDİYOK, Sakarya University, Turkey

Ahmet BALDAN, Mersin University, Turkey

Ahmet CİHAN, Beykent University, Turkey

Ahmet ÇINAR, Fırat University, Turkey

Ahmet DEMİR, Yıldız Technical University, Turkey

Ahmet EKERİM, Yıldız Technical University, Turkey

Ahmet FENERCİOĞLU, Gaziosmanpaşa University, Turkey

Ahmet KARAASLAN, Yıldız Technical University, Turkey

Ahmet KOYUN, Yıldız Technical University, Turkey

Ahmet ORHAN, Fırat University, Turkey

Ahmet ÖZER, Fırat University, Turkey

Ahmet SAĞIROĞLU, Fırat University, Turkey

Ahmet ŞAŞMAZ, Fırat University, Turkey

Ahmet TUNA, Fırat University, Turkey

Ahmet TÜRK, Manisa Celal Bayar University, Turkey

Ahmet ÜNAL, Yıldız Technical University, Turkey
Ahu ÇELEBİ, Manisa Celal Bayar University, Turkey
Aino-Maija LAKANIEMI, Tampere University of Technology, Finland
Akın ODABAŞI, Fırat University, Turkey
Ali Arslan KAYA, Muğla Sıtkı Kocman University, Turkey
Ali Bülent UŞAKLI, Karatay University, Turkey
Ali Erçin ERSUNDU, Yıldız Technical University, Turkey
Ali Savaş KOPARAL, Anadolu University, Turkey
Ali Sinan DİKE, Adana Science and Technology University, Turkey
Ali GÜNGÖR, Ege University, Turkey
Ali TOPAL, Dokuz Eylül University, Turkey
Ali YARAŞ, Bartın University, Turkey
Ali Yurdun ORBAK, Uludağ University, Turkey
Alper İLKİ, İstanbul Technical University, Turkey
Alvaro Garcia HERNANDES, Nottingham University, UK
Andrzej SOLECLU, Wrocław University, Poland
Anna KAKSONEN, Commonwealth Scientific and Industrial Research
Organisation (CSIRO), Australia
Aqeel Al-ADILI, University of Technology, Iraq
Aral OKAY, İstanbul Teknik University, Turkey
Arif GÜLTEN, Fırat University, Turkey
Atike NAZİK, Cukurova University, Turkey
Atilla EVCİN, Afyon Kocatepe University, Turkey
Aydın ÇİTLAK, Fırat University, Turkey
Aydın DURMUŞ, Ondokuz Mayıs University, Turkey
Aydın YEŞİLDİREK, Yıldız Technical University, Turkey
Ayhan AKBAL, Fırat University, Turkey
Ayhan ÜNLÜ, Fırat University, Turkey
Aykut TOPDEMİR, Fırat University, Turkey
Ayla ÖZER, Mersin University, Turkey
Aylin DELİORMANLI, Manisa Celal Bayar University, Turkey
Aynur UÇAR, Fırat University, Turkey

Ayşe DALOĞLU, Karadeniz Technical University, Turkey
Ayşe Didem KILIÇ, Fırat University, Turkey
Ayşe Şükran DEMİRKİRAN, Sakarya University, Turkey
Ayşegül UÇAR, Fırat University, Turkey
Ayşen DAVRAZ, Suleyman Demirel University, Turkey
Ayten ÖZTÜFEKÇİ ÖNAL, Munzur University, Turkey
Azize AYOL, Dokuz Eylül University, Turkey
Baha Vural KÖK, Fırat University, Turkey
Bahattin ÇETİNDAG, Fırat University, Turkey
Bahman GHİASSİ, TU Delft University of Technology, Netherlands
Barış SEVİM, Yıldız Technical University, Turkey
Barış YÜKSEKKAYA, Hacettepe University, Turkey
Bekir KARASU, Anadolu University, Turkey
Bekir Zühtü UYSAL, Gazi University, Turkey
Bestamin ÖZKAYA, Yıldız Technical University, Turkey
Betül BILGIN, University of Illinois at Chicago, USA
Bilal ALATAŞ, Fırat University, Turkey
Bilge YAMAN, Eskişehir Osmangazi University, Turkey
Burak BİRGÖREN, Kirikkale University, Turkey
Burak ŞENGÖZ, Dokuz Eylül University, Turkey
Burak YÖN, Munzur University, Turkey
Burhan ERGEN, Fırat University, Turkey
Bülent KESKİNLER, Gebze Technical University, Turkey
Bülent ÖZTÜRK, Karadeniz Technical University, Turkey
Bülent TOPKAYA, Akdeniz University, Turkey
Bünyamin AKGÜL, Fırat University, Turkey
Bünyamin AKSAKAL, Yıldız Technical University, Turkey
Calibe KOÇ TAŞGIN, Fırat University, Turkey
Can ÇOĞUN, Çankaya University, Turkey
Candan GÖKÇEOĞLU, Hacettepe University, Turkey
Cemal BÖLÜCEK, Balıkesir University, Turkey
Cengiz KAHRAMAN, Istanbul Technical University, Turkey

Cengiz SOYKAN, Usak University, Turkey
Cengiz YILDIZ, Firat University, Turkey
Cevdet AKOSMAN, Firat University, Turkey
Chung Hak LEE, Seoul National University, Korea
Cihan ÖZEL, Firat University, Turkey
Cumali KINACI, Istanbul Technical University, Turkey
Cüneyt GÜLER, Mersin University, Turkey
Çiğdem GÜLDUR, Gazi University, Turkey
D. Lucian GORGAN, Alexandru Ioan Cuza University, Romania
Dan STAN, Technical University of Cluj-Napoca, Romania
Darius ANDRIUKAITIS, Kaunas University of Technology, Lithuania
Delia Teresa SPONZA, Dokuz Eylul University, Turkey
Deniz UZUNSOY, Bursa Technical University, Turkey
Deniz ÜNER, Middle East Technical University, Turkey
Derya DIŞPINAR, Istanbul University, Turkey
Dicle BAL AKKOCA, Firat University, Turkey
Dilek SANİN, Middle East Technical University, Turkey
Diyi CHEN, Northwest A & F University, China
Durmuş KARAYEL, Sakarya University, Turkey
Dursun ÖZER, Firat University, Turkey
Dursun PEHLİVAN, Firat University, Turkey
Duygu EVİN, Firat University, Turkey
Ebru K. AKPINAR, Firat University, Turkey
Ebru Devrim ŞAM PARMAK, Bursa Technical University, Turkey
Ebubekir ERDEM, Firat University, Turkey
Elabed SOUMYA, University Sidi Mohamed Ben Abdellah, Morocco
Engin GÜRTEKİN, Firat University, Turkey
Eoin CASEY, University Collage Dublin,
Ireland Ercan AKSOY, Firat University, Turkey
Erdal ÇELİK, Dokuz Eylul University, Turkey
Erdal ÖBEK, Firat University, Turkey
Erdin BOZKURT, Middle East Technical University, Turkey

Ergin TAŞKAN, Firat University, Turkey
Ergün YILDIZ, Ataturk University, Turkey
Erhan AKDOĞAN, Yıldız Technical University, Turkey
Erhan AKIN, Firat University, Turkey
Erhan ALTUNEL, Eskisehir Osmangazi University, Turkey
Erkan BAHÇE, Inonu University, Turkey
Erkan DOĞAN, Manisa Celal Bayar University, Turkey
Erkan DUMAN, Firat University, Turkey
Erkan KÖSE, Aksaray University, Turkey
Erkan ŞAHİNKAYA, Istanbul Medeniyet University, Turkey
Erkut SAYIN, Firat University, Turkey
Errol HASSAN, School of Agriculture and Food Sciences The University of
Queensland, Australia
Ertan EVİN, Firat University, Turkey
Ertan GÖKALP, Karadeniz Technical University, Turkey
Ersin ARSLAN, Ataturk University, Turkey
Esra YILDIRIM, Firat University, Turkey
Eşref ADALI, Istanbul Technical University, Turkey
Fatih CETİŞLİ, Pamukkale University, Turkey
Faruk YİĞİT, Yıldız Technical University, Turkey
Fazilet VARDAR SUKAN, Ege University, Turkey
Ferda MUTLU, Gazi University, Turkey
Fethi KAMIŞLI, Firat University, Turkey
Fevzi KARSLI, Karadeniz Technical University, Turkey
Figen BALO, Firat University, Turkey
Figen KAYA, Yıldız Technical University, Turkey
Fikret TÜMEN, Firat University, Turkey
Fikret ATA, Firat University, Turkey
Fikret KAÇAROĞLU, Muğla Sıtkı Koçman University, Turkey
Filiz KAR, Firat University, Turkey
Francesco ITALIANO, INGV (National Institute of Geophysics and Volcanology), Italy
Fuat YAVUZ, Istanbul Technical University, Turkey

Gabriel Ovidiu LANCU, Alexandru Ion Cuza University, Romania
Galip AYDIN, Firat University, Turkey
Gamze DOĞAN TETİK, Usak University, Turkey
Gökhan GÖKMEN, Marmara University, Turkey
Gülbeyi DURSUN, Firat University, Turkey
Gülcan BOZKAYA, Pamukkale University, Turkey
Gülen GÜLLÜ, Hacettepe University, Turkey
Gülfem BİNAL, Bartın University, Turkey
Gülşad USLU, Firat University, Turkey
Gülşah ÇAKMAK, Firat University, Turkey
H. Cenk ÖZMUTLU, Uludag University, Turkey
H. İbrahim EKİZ, Mersin University, Turkey
H. Soner ALTUNDOĞAN, Firat University, Turkey
H. Suha AKSOY, Firat University, Turkey
Hacer GÜNER GÖREN, Pamukkale University, Turkey
Hadi Shafaii MOGHADAM, Macquarie University, Australia
Hakan ÇELİK, Firat University, Turkey
Hakan KALENDER, Firat University, Turkey
Halil AKINCI, Artvin Coruh University, Turkey
Halil HASAR, Firat University, Turkey
Halit L. YÜCEL, Firat University, Turkey
Haluk KÜÇÜK, Marmara University, Turkey
Hanzade AÇMA, Istanbul Technical University, Turkey
Hasan ÇELİK, Firat University, Turkey
Hasan GÜLER, Firat University, Turkey
Hasan SELİM, Dokuz Eylül University, Turkey
Hasan TOĞRUL, Eskisehir Osmangazi University, Turkey
Haşim PIHTILI, Firat University, Turkey
Haşmet TÜRKOĞLU, Gazi University, Turkey
Haydar EREN, Firat University, Turkey
Haydar LİVATYALI, Yıldız Technical University, Turkey
Hayrettin CAN, Firat University, Turkey

Hilmi Berk ÇELİKOĞLU, Istanbul Technical University, Turkey
Hilmi Cenk BAYRAKÇI, Suleyman Demirel University, Turkey
Hulusi KARGI, Pamukkale University, Turkey
Hükmü ORHAN, Selcuk University, Turkey
Hülya KAFTELEN ODABAŞI, Karadeniz Technical
University, Turkey
Hümeysra ŞAHİN, Firat University, Turkey
Hüseyin Metin ERTUNÇ, Kocaeli University, Turkey
Hüseyin KARACA, Inonu University, Turkey
Hüseyin KURT, Selcuk University, Turkey
Imamoto KEI-ICHI, Tokyo University of Science, Japan
Imre Benkő, BME, FME, Hungary
Ismail HOSSAIN, Rajshahi University, Bangladesh
Işık KABDAŞLI, Istanbul Technical University, Turkey
Işıl ARSLAN TOPAL, Firat University, Turkey
İ. Kuban ALTINEL, Bogazici University, Turkey
İbrahim ÇOPUROĞLU, Omer Halisdemir University, Turkey
İbrahim TÜRKMEN, Balıkesir University, Turkey
İbrahim UYSAL, Karadeniz Technical University, Turkey
İhsan DAĞTEKİN, Firat University, Turkey
İlhan AYDIN, Firat University, Turkey
İnanç ÖZGEN, Firat University, Turkey
İsmail KOYUNCU, Istanbul Technical University, Turkey
İsmail TORÖZ, Istanbul Technical University, Turkey
Jaakko PUHAKKA, University of Eastern, Finland
Jacek GURWIN, Wroclaw University, Poland
Jan OLEK, Purdue University, USA
Jayantha KODĪKARA, Monash University, Australia
Jianfu ZHANG, Tsinghua University, China
Jon C. CLARE, University of Nottingham,
UK Kadir BİLEN, Ataturk University, Turkey
Kadir GÜLER, Istanbul Technical University, Turkey
Kahraman ALBAYRAK, Middle East Technical University, Turkey

Korhan ÖZGAN, Karadeniz Technical University, Turkey
Kouzou ABDELLAH, Djelfa University, Algeria
Kürşat Esat ALYAMAÇ, Fırat University, Turkey
Latif ÖZLER, Fırat University, Turkey
Levent TAŞÇI, Fırat University, Turkey
Leyla KALENDER, Fırat University, Turkey
Luna LU, Purdue University, USA
Lütfi ARDA, Bahcesehir University, Turkey
Lütfü ŞAĞBANŞUA, Fırat University, Turkey
M. Ayşen LAV, Istanbul Technical University, Turkey
M. Cihan AYDIN, Bitlis Eren University, Turkey
M. Cihat TUNA, Fırat University, Turkey
M. Emin EMİROĞLU, Fırat University, Turkey
M. Emin ÖNCÜ, Dicle University, Turkey
M. Salih KESKİN, Dicle University, Turkey
M. Sara TUNÇ, Fırat University, Turkey
M. Şaban TANYILDIZI, Fırat University, Turkey
Mahmut Temel ÖZDEMİR, Fırat University, Turkey
Marika KOKKO, Tampere University of Technology, Finland
Massimo MORETTI, Studi di Bari University, Italy
Mehmet ALTUNBEY, Fırat University, Turkey
Mehmet CEBECİ, Fırat University, Turkey
Mehmet ÇAKMAKÇI, Yıldız Technical University, Turkey
Mehmet DURANAY, Fırat University, Turkey
Mehmet Deniz TURAN, Fırat University, Turkey
Mehmet ERDEM, Fırat University, Turkey
Mehmet EROĞLU, Fırat University, Turkey
Mehmet KALENDER, Fırat University, Turkey
Mehmet KARAKÖSE, Fırat University, Turkey
Mehmet KARATAŞ, Fırat University, Turkey
Mehmet KAYA, Fırat University, Turkey
Mehmet KİTİŞ, Suleyman Demirel University, Turkey

Mehmet ÖZDEMİR, Fırat University, Turkey
Mehmet ÖZKUL, Pamukkale University, Turkey
Mehmet POLAT, Fırat University, Turkey
Mehmet SALTAN, Suleyman Demirel University, Turkey
Mehmet TURAN, Karadeniz Technical University, Turkey
Mehmet ÜLKER, Fırat University, Turkey
Mehmet YILMAZ, Fırat University, Turkey
Mehmet YÜCEER, Inonu University, Turkey
Mehtap MURATOĞLU, Fırat University, Turkey
Melahat BEYARSLAN, Fırat University, Turkey
Melek URAL, Fırat University, Turkey
Melek YILGIN, Fırat University, Turkey
Meral ÖZEL, Fırat University, Turkey
Merve AÇIKGENÇ ULAŞ, Fırat University, Turkey
Mete O. KAMAN, Fırat University, Turkey
Metin AYDOĞAN, Istanbul Technical University, Turkey
Metin GÜRÜ, Gazi University, Turkey
Miray ÇELİKBİLEK ERSUNDU, Yıldız Technical University, Turkey
Mircea NICOARA, Alexandru Ioan Cuza University, Romania
Mohammed Y. FATTAH, University of Technology, Iraq
Mualla ÖZTÜRK, Fırat University, Turkey
Muhammet KARATON, Fırat University, Turkey
Muhsin Tunay GENÇOĞLU, Fırat University, Turkey
Murat BASKAK, Istanbul Technical University, Turkey
Murat ELİBOL, Ege University, Turkey
Murat KARACASU, Eskisehir Osmangazi University, Turkey
Murat ÖZTÜRK, Suleyman Demirel University, Turkey
Murat Y. SOLMAZ, Fırat University, Turkey
Musa ARTAR, Bayburt University, Turkey
Mustafa AFŞİN, Aksaray University, Turkey
Mustafa BOYRAZLI, Fırat University, Turkey
Mustafa GÜR, Fırat University, Turkey

Mustafa İNALLI, Fırat University, Turkey
Mustafa KARASHAHİN, Istanbul University, Turkey
Mustafa POYRAZ, Fırat University, Turkey
Mustafa TÜRİK, Fırat University, Turkey
Mustafa ULAŞ, Fırat University, Turkey
Nalan KABAY, Ege University, Turkey
Nazire ÖZGEN ERDEM, Cumhuriyet University, Turkey
Nazmi GÜR, Fırat University, Turkey
Necati KULOĞLU, Fırat University, Turkey
Neslihan DURANAY, Fırat University, Turkey
Neşe ÖZTÜRK, Eskişehir Osmangazi University, Turkey
Nevin ÇELİK, Fırat University, Turkey
Nihat AKKUŞ, Marmara University, Turkey
Nihat KAYA, Fırat University, Turkey
Nihat TOSUN, Fırat University, Turkey
Nilgün KUŞKONMAZ, Yıldız Technical University, Turkey
Nilüfer NACAR KOÇER, Fırat University, Turkey
Nizamettin KAZANCI, Ankara University, Turkey
Nurhan CANSEVER, Yıldız Technical University, Turkey
Nurettin ARSLAN, Manisa Celal Bayar University, Turkey
Nurhan ARSLAN, Fırat University, Turkey
Nusret ŞEKERDAĞ, Fırat University, Turkey
O. Sermet KABASAKAL, Eskişehir Osmangazi University, Turkey
Oğuz GÜNGÖR, Karadeniz Technical University, Turkey
Olli TUOVINEN, Ohio State University, USA
Onur ONAT, Munzur University, Turkey
Orhan ÇAKAR, Fırat University, Turkey
Orhan TATAR, Cumhuriyet University, Turkey
Oscar CASTILLO, Tijuana Institute of Technology, Mexico
Osman ELDOĞAN, Sakarya University, Turkey
Ö. Murat DOĞAN, Gazi University, Turkey
Ömer AKGİRAY, Marmara University, Turkey

Ömer BİLHAN, Nevsehir Hacı Bektas Veli University, Turkey
Ömer GÜLER, Firat University, Turkey
Ömer MUNZUROĞLU, Firat University, Turkey
Ömer ŞAHİN, Siirt University, Turkey
Özge HANAY, Firat University, Turkey
Özgür DEĞERTEKİN, Dicle University, Turkey
Özgür KARADUMAN, Firat University, Turkey
Özlem ÖZTEKİN OKAN, Firat University, Turkey
Özlem TEPE, Firat University, Turkey
Paul TIBULEAC, Alexandru Ioan Cuza University, Romania
Paulo B. LOURENÇO, University of Minho, Portugal
Pranshoo SOLANKİ, Illinois State University, USA
Ragıp İNCE, Firat University, Turkey
Rahmat ELLAHI, California University, USA
Raif BAYIR, Karabuk University, Turkey
Rakesh Kumar KATARE, APS University, India
Ramazan ORHAN, Firat University, Turkey
Ray Y. CHUANG, National Taiwan University, Taiwan
Recep ARTIR, Marmara University, Turkey
Rengin ELTEM, Ege University, Turkey
Saadet YAPAR, Ege University, Turkey
Sadettin KAPUCU, Gaziantep University, Turkey
Saeid POURNADERİ, Karadeniz Technical University, Turkey
Sandor KELE, Institute for Geological and Geochemical
Research, Hungary
Seda ARSLAN TUNCER, Firat University, Turkey
Seda ÖZMUTLU, Uludag University, Turkey
Sedat SAVAŞ, Firat University, Turkey
Sedat SÜNTER, Firat University, Turkey
Sefa TARHAN, Gaziosmanpasa University, Turkey
Sefer Cem OKUMUŞ, Sakarya University, Turkey
Selma Ayaz / TÜBİTAK MAM ÇTEÜ Enstitüsü , Turkey
Sema SALGIN, Cumhuriyet University,

Sencer ÜNAL, Firat University, Turkey
Serdar AKYÜZ, Istanbul Technical University, Turkey
Serhan TANYEL, Dokuz Eylul University, Turkey
Serhat ELÇİÇEK, Firat University, Turkey
Serkan DAĞ, Middle East Technical University, Turkey
Servet SOYGÜDER, Firat University, Turkey
Servet TİMUR, Istanbul Technical University, Turkey
Seval Hale GÜLER, Mersin University, Turkey
Sevcan KÜRÜM, Firat University, Turkey
Sevgi ŞENGÖZ, Eskisehir Osmangazi University, Turkey
Sevil ÇETİNKAYA, Cumhuriyet University, Turkey
Sevil YÜCEL, Yildiz Technical University, Turkey
Sezgin ERSOY, Marmara University, Turkey
Sibel ASLAN, Firat University, Turkey
Sinan Serdar ÖZKAN, Sakarya University, Turkey
Siqing XIA, Tongji University, China
Sorin Silviu UDUBASA, Bucarest University, Romania
Suheyda ATALAY, Ege University Turkey
Sultan ÖZTÜRK, Karadeniz Technical University, Turkey
Sun-Lin CHUNG, National Taiwan University, Taiwan
Şahin GÜLABOĞLU, Ataturk University, Turkey
Şahin YILDIRIM, Erciyes University, Turkey
Tacettin GEÇKİL, Inonu University, Turkey
Tacibaht TUREL, Youngstown State University, USA
Taner ALATAŞ, Firat University, Turkey
Taner DERBENTLİ, Emeritus in Istanbul Technical
University, Turkey
Taner TUNCER, Firat University, Turkey
Tanmay BASAK, Indian Institute of Technology Madras, India
Tareq Salih AL-ATTAR, University of Technology, Iraq
Terin ADALI, Near East University, TRNC
Tolga ELBİR, Dokuz Eylul University, Turkey
Tuğba KARAHAN, Istanbul Gedik University, Turkey

Turan PAKSOY, Selcuk University, Turkey
Turgay KAYA, Fırat University, Turkey
Ubeyde İPEK, Munzur University, Turkey
Ufuk ALKAN, Uludag University, Turkey
Ufuk BÖLÜKBAŞI, Middle East Technical University, Turkey
Uğur SALGIN, Cumhuriyet University, Turkey
Ülkü YETİŞ, Middle East Technical University, Turkey
Ünal AKDAĞ, Aksaray University, Turkey
Vedat ÇELİK, Fırat University, Turkey ,
Vedat TANYILDIZI, Fırat University, Turkey
Vedat UYAK, Pamukkale University, Turkey
Venhar ÇELİK, Fırat University, Turkey
Veyis SELEN, Fırat University, Turkey
Volkan PATOĞLU, Sabanci University, Turkey
Yaghoob FARNAM, Drexel University, USA
Yakup DEMİR, Fırat University, Turkey
Yavuz EROL, Fırat University, Turkey
Yetiş Şazi MURAT, Pamukkale University, Turkey
Yetkin TATAR, Fırat University, Turkey
Youcef SOUFI, Larbi Tebessi University, Algeria
Yunus Emre BENKLİ, Ataturk University, Turkey
Yusuf CALAYIR, Fırat University, Turkey
Yücel GENÇER, Gebze Technical University, Turkey
Zafer BİNGÜL, Kocaeli University, Turkey
Zehra Semra CAN, Marmara University, Turkey
Zeki ÇİZMECİOĞLU, Istanbul Commerce University, Turkey
Zerrin ALADAĞ, Kocaeli University, Turkey
Zülfü GÜROCAK, Fırat University, Turkey
Zülfü Çınar ULUCAN, Fırat University, Turkey
Zümriye AKSU, Hacettepe University, Turkey

Organizing Committee of the ICAIE

Chair of Conference
Prof. Dr. Hasan KÜRÜM

A. Bedri ÖZER, Firat University, Turkey

A. Burak TATAR, Firat University, Turkey

Abdullah Gökhan TUĞAN, Firat University, Turkey

Ahmad B. RAD, Simon Fraser University, Canada

Ahmet MÜNGEN, Firat University, Turkey Ahmet

YAZICIOĞLU, Firat University, Turkey

Aino-Maija LAKANIEMI, Tampere University of Technology, Finland

Akın ODABAŞI, Firat University, Turkey

Alvaro Garcia HERNANDES, Nottingham University, UK

Anna KAKSONEN, Commonwealth Scientific and Industrial Research Organisation
(CSIRO), Australia

Baha Vural KÖK, Firat University, Turkey

Barbaros DURMUŞ, Firat University, Turkey

Betül AY, Firat University, Turkey

Bircan KAMIŞLIOĞLU, Firat University, Turkey

Calibe KOÇ TAŞKIN, Firat University, Turkey

Celal KISTAK, Firat University, Turkey

Cenk YANEN, Firat University, Turkey

Çağrı KAYMAK, Firat University, Turkey

Elabed SOUMYA, University Sidi Mohamed Ben Abdellah , Morocco

Elif ARANCI ÖZTÜRK, Firat University, Turkey

Ercan AYDOĞMUŞ, Firat University, Turkey

Erdal ÖBEK, Firat University, Turkey

Erdal ÖZBAY, Firat University, Turkey

Fatih KAYA, Firat University, Turkey

Filiz KAR, Firat University, Turkey

Gökhan ALBAYRAK, Firat University, Turkey

Hakan ALTUNAY, Firat University, Turkey

Hakan ÇELİK, Firat University, Turkey Hakan

TUTUMLU, Firat University, Turkey Hasan

ARSLANOĞLU, Firat University, Turkey İbrahim

Rıza HALLAÇ, Firat University, Turkey Jaakko

PUHAKKA, University of Eastern, Finland Jon C.

CLARE, University of Nottingham, UK Kainat

ÖZPOLAT, Firat University, Turkey

M. Ali UYGUT, Firat University, Turkey

M. Çağrı ŞAHİN, Firat University, Turkey

M. Ertuğrul ÇELOĞLU, Firat University, Turkey Marika

KOKKO, Tampere University of Technology, Finland

Mehmet ERDEM, Firat University, Turkey

Mehmet KÖKÜM, Firat University, Turkey

Mehmet Erbil ÖZCAN, Firat University,

Turkey Mehmet ŞAHİN, Firat University,

Turkey Mehmet YILMAZ, Firat University,

Turkey Merve YILDIRIM, Firat University,

Turkey Mesut GÖR, Firat University, Turkey

Murat ŞEN, Firat University, Turkey

Musab COŞKUN, Firat University, Turkey

Mustafa KAPTANOĞLU, Firat University, Turkey

Mustafa Eren RİZELİ, Fırat University, Turkey

Nevin ÇELİK, Fırat University, Turkey

Olli TUOVINEN, Ohio State University, USA

Onur ALKAÇ, Fırat University, Turkey Özlem

ÖZTEKİN OKAN, Fırat University, Turkey Rakesh

Kumar KATARE, APS University, India Seda

ARSLAN TUNCER, Fırat University, Turkey

Selen GÜRBÜZ, Fırat University, Turkey

Tanveer SALEH, International Islamic University, Malaysia

Veyis SELEN, Fırat University, Turkey

Yaghoob FARNAM, Drexel University, USA

Session Chairmans

Bioengineering

H.Soner ALTUNDOĞAN
M. Şaban TANYILDIZI
Hakan KALENDER
İnanç ÖZGEN
Nazmi GÜR
Venhar ÇELİK
Mehmet KALENDER

Chemical Engineering

Cevdet AKOSMAN
Dursun PEHLİVAN
Fethi KAMIŞLI

Civil Engineering

Muhammet KARATON
Mehmet ÜLKER
Yusuf CALAYIR
Zülfü Çınar ULUCAN
Mehmet KARATAŞ
Ragıp İNCE
M. Emin EMİROĞLU
Baha Vural KÖK
Taner ALATAŞ

Computer Engineering

Burhan ERGEN
Yetkin TATAR
İlhan AYDIN
Taner TUNCER
Bilal ALATAŞ
Mehmet KARAKÖSE

Electrical-Electronic Engineering

Hasan GÜLER
Adnan CORA
Mustafa TÜRK
Tunay GENÇOĞLU
Sedat SUNTER
Ayhan AKBAL
Kouzou ABDELLAH
Turgay KAYA

Environmental Engineering

Gülşad USLU
Özge HANAY
Azize AYOL

Food Engineering

Zehra GÜLER
Gülbeyi DURSUN
Cevdet AKOSMAN

Geological Engineering

A.Feyzi BİNGÖL
Ercan AKSOY
Bahattin ÇETİNDAG
Dicle BAL AKKOCA

Geomatic Engineering

Erhan KÖSE

Industrial Engineering

Ağca AKTUNÇ
H.Cenk ÖZMUTLU
Seda ÖZMUTLU
Burcu FELEKOĞLU
Seren ÖZMEHMET TAŞAN

Mechanical Engineering

Oktay HACIHAFIZOĞLU
İhsan DAĞTEKİN Nevin
ÇELİK
Şefika KASMAN
Ahmet SARI Onur
KAMAN Vedat
TANYILDIZI

Mechatronic Engineering

Hakan AKPOLAT

Metalurgical and Materials Engineering

Mehmet EROĞLU
Mehtap MURATOĞLU
Deniz TURAN
Ertan EVİN

Other Engineering

A.Bedri ÖZER

INTRODUCTION

Dear Distinguished Delegate,

International Conference on Advances and Innovations in Engineering (ICAIE) is held at Firat University, Faculty of Engineering in Elazığ, Turkey during May 10-12, 2017 in honor of the 50th anniversary of the establishment of the faculty.

International Conference on Advances and Innovations in Engineering is an international scientific forum of distinguished scholars engaged in scientific, engineering and technological research, dedicated to the furtherance of science, engineering and technology. The academic research conference since its inception is at the cutting edge of international nonprofit scientific, engineering and technological progress to promoting excellence in science.

The conference plays an influential role in science and promotes developments in science, engineering and technology in a wide range of ways. The conference aims to foster research in the area of science and technology and its impact to mainstream human activities. Specifically, it serves as a venue for discussions and exchange of ideas in current issues in science and technology.

All full paper and abstract submissions to the conference are peer reviewed and refereed and evaluated based on originality, research content and correctness, relevance to contributions, and readability. In this content the full paper and abstract submissions are chosen based on technical merit, interest, applicability and how well they fit a coherent and balanced technical program. The accepted papers after rigorous peer reviewing process have been published in the refereed international conference proceedings

Chair of ICAIE Committee
Prof. Hasan KÜRÜM

CONTENTS

Scientific and Technical Committee of the ICAIE	i
Honour Committee of The ICAIE	i
Organizing Committee of the ICAIE	xiv
Session Chairmans	xvii
Introduction	xix
Bioengineering Oral Submissions	1
Geological Engineering Oral Submissions	59
Industrial Engineering Oral Submissions	90
Environmental Engineering Oral Submissions	140
Mechatronics Engineering Oral Submissions	170
Electrical-Electronic Engineering Oral Submissions	185
Mechanical Engineering Oral Submissions	335
Civil Engineering Oral Submissions	609
Other Engineerings Oral Submissions	904
Computer Engineering Oral Submissions	920
Metalurgical and Materials Engineering Oral Submissions	1056
Chemical Engineering Oral Submissions	1105
Food Engineering Oral Submissions	1207

BIOENGINEERING

ORAL SUBMISSIONS



Performance of Some Soil Bacteria on Ethalfluralin Biodegradation

Gökhan Önder ERGÜVEN

Department of Environmental Engineering,
Faculty of Engineering,
Munzur University,
Tunceli, Turkey
gokhanondererguven@gmail.com

Abstract— *The aim of this study is investigate the efficiency of *Bacillus thuringiensis* and *Fusarium fujikuroi* soil bacteria on ethalfluralin biodegradation with chemical oxygen demand (COD) and reveal the population dynamics of these bacteria during biodegradation process under agitated culture conditions with turbidity. Bacteria samples were firstly isolated from agricultural soil in agar media taken from Thrace region of Turkey and these bacteria were stocked. These stocked cultures were used in experimental studies. COD experiments were done according to standard methods 5220C closed reflux titrimetric method and turbidity experiments were performed by Photolab 6600 UV-VIS Spectrophotometer. All experiments were performed triplicate. As a result; COD removal efficiency of *Bacillus thuringiensis* was determined as 83% and *Fusarium fujikuroi* as 53%, at the end of the 120th hour. According to the results; COD removal efficiency showed some differences depend on the bacteria species. It was also observed that *Bacillus thuringiensis* had more removal efficiency on COD and it was a suitable bacteria species for bioremediation contaminated waters by ethalfluralin against *Fusarium fujikuroi*.*

Keywords— *bacteria; ethalfluralin; biodegradation; chemical oxygen demand; removal efficiency.*

*An Experimental Study on Determination of Optimal Growth Conditions of *Physisporinus vitreus* for Biotechnology*

Davut BAKIR

Department of Forest Industrial Engineering
Faculty of Forestry,
Istanbul University
Istanbul, TURKEY
davut.bakir@istanbul.edu.tr

Evren TERZİ

Department of Forest Industrial Engineering
Faculty of Forestry,
Istanbul University
Istanbul, TURKEY

S. Nami KARTAL

Department of Forest Industrial Engineering
Faculty of Forestry,
Istanbul University
Istanbul, TURKEY

Abstract— Wood is a natural material that can be deteriorated and decomposed by both biotic (fungi, insects, bacteria, etc.) and abiotic factors (UV radiation, fire, chemicals, mechanical effects, etc.). Impregnation by various chemical agents is a common application to protect and extend service life of wood and wood products against such factors. High permeability of wood is a required feature for successful impregnation process in terms of better penetration and high retention level of preservative chemical. For refractory wood species, various attempts to increase permeability and treatability i.e. immersion in water, steaming, solvent application, enzyme treatment, mechanical incising and incubation with fungi or bacteria are available. Among those applications, bio-incising by organisms is a process that aims at increasing the permeability of wood without affecting its desired properties in a negative way. *Physisporinus vitreus* is a fungal species having an ability to penetrate the sealed pits of wood microstructure that are important cell elements for fluid flow. This species is a well-know fungal species for bio-incising attempts in refractory woods. In this study, we evaluated various practices for applicability of *P. vitreus* to *Picea orientalis* wood (spruce), which is difficult to impregnate and less durable. The main goal of this study is to increase the service life of wood from *P. orientalis*, one of the refractory wood species in Turkey by improving its ability to impregnate by bio-incising procedures. Within the scope of the study, ten different strains of *P. vitreus* were obtained from various research laboratories and augmented in laboratory conditions in Petri dishes containing 4% of malt-agar nutrient medium.

The Petri plates inoculated with the strains were periodically observed and the strain that showed the fastest development was preferred as a basic test strain. Three different growth media were used during the experiments and the EN 113 standard test method was used for each test medium. Only glass jars were used during the tests as they provided larger usage volume for wood specimens rather than standard Kolle flasks. In the first set of the experiments, wood specimens previously dipped into 2% malt extract emulsion were inoculated by *P. vitreus* strains. Wood specimens were dipped into glucose-pepton malt extract emulsion in the second set. Wood specimens in the third experiments were directly placed into glass jars containing 4% malt extract agar nutrient medium previously inoculated with the fungal strains. The methods were evaluated according to the ability of the fungal mycelium to envelop the entire wood surfaces. The key point is the necessity of ensuring the homogeneous penetration of fungal hyphae into the wood structure. As a result of macroscopic and microscopic evaluations, the best development was provided by the third test set, which is simpler than the other methods followed. The best fungal growth in the third test set was provided at the conditions of $24\pm 2^{\circ}\text{C}$ and $70\pm 5\%$ relative humidity and by using a growth medium where wet vermiculite was added under sterile conditions.

Keywords— *Physisporinus vitreus*, bio-incising, permeability, impregnation, wood, optimum growth conditions.

Screening and Isolation of Enzyme-Producing Bacteria for Biotechnology

Fatma MATPAN BEKLER

Department of Molecular Biology and Genetics,
Faculty of Science,
Dicle University,
Diyarbakir, Turkey

Zindar ASLAN

Department of Molecular Biology and Genetics,
Faculty of Science,
Dicle University,
Diyarbakir, Turkey

Reyhan G. GÜVEN

Science Teaching Section,
Faculty of Education,
Dicle University,
Diyarbakir, Turkey

Kemal GÜVEN

Science Teaching Section,
Faculty of Education,
Dicle University,
Diyarbakir, Turkey

Abstract— *In this study, Bacillus subtilis 4NK isolated from Bingöl Binkap hot spring in Turkey. The isolate was identified based on different by morphological, physiological, biochemical and 16S rRNA gene sequencing. The strain 4NK was found to be an aerobic, Gram-positive and rod shaped. The optimum temperature, pH and incubation period for bacterial growth were 40 oC, 6.0-7.0 and 24 h, respectively. The result of 16S rRNA gene sequence analysis showed that, the strain 4NK related to the Bacillus subtilis (98% similarity). This strain was found to produce biotechnologically important enzymes for industrial application.*

Keywords— *16S rRNA, hot spring, isolation, enzyme.*

Investigation of α -Amylase Production in Novel Rotating Drum Bioreactor

Muhammet Şaban TANYILDIZI

Bioengineering Department
Firat University
Elazig, Turkey
mtanyildizi@firat.edu.tr

Muhammet Ali UYGUT

Bioengineering Department
Firat University
Elazig, Turkey
muygut@firat.edu.tr

Abstract— Alpha amylase are extracellular endo enzymes that randomly cleave the 1,4- α linkage between adjacent glucose units in the linear amylose chain and ultimately generate glucose, maltose and maltotriose units. Amylases are one of the most important industrial enzymes and their annual production volume is 25-30% of the total manufacturing of enzyme production [1]. Solid substrate fermentation (SSF) that is a good alternative to produce cheaper enzyme was known as a fermentation process in which microorganism grown in the absence of free water media. Solid particles distributed in a liquid phase are defined as slurry state fermentation (SLSF) [2]. SLSF merges advantages of other fermentation modes that SSF (higher yield, lower cost) and submerged fermentation (easy control and measurement of fermentation conditions). Rotating drum bioreactor (RDB) that is one of main solid state bioreactors types has gained great attention from researchers. Although conventional RDB is an important microbial production system in terms of preventing heat accumulation and having less severe shear stress on microorganisms, it isn't completely adequate in larger-scale RDB due to high levels in temperature gradient.

In this study, RDB was designed by adapting for SLSF and the effects of bioreactor operating parameters on α -amylase production was screened by experimental design with enzyme production system (Fig. 1). Ceramic micro diffuser was used to increase oxygen transfer efficiency in the RDB design. *Bacillus amyloliquefaciens* NRRL B-645 that is a commercial bacterial α -amylase producer was used. In the α -amylase production studies was used optimum conditions (25 g/l corn bran, 10 g/l yeast extract and 1 g/l KH_2PO_4) that determined earlier obtained α -amylase production studies in erlenmeyer flasks. Dissolved oxygen, pH, temperature, oxygen and carbon dioxide at gas outlet were followed online during fermentation. Dinitrosalicylic acid method [3] was used for determination of α -amylase activity.

Effects of operating parameters, rotation speed, aeration rate, working volume, diffuser's pore diameter, baffle size, temperature and inoculum size, on the α -amylase production in the RDB were determined with Plackett-Burman design. According to ANOVA results, Model is significant as it is seen Model F value (17,46) and very low probability value (0,0075). The enzyme production in erlenmeyer scale was applied to laboratory scale RDB and an important step was taken for production on commercial scale.

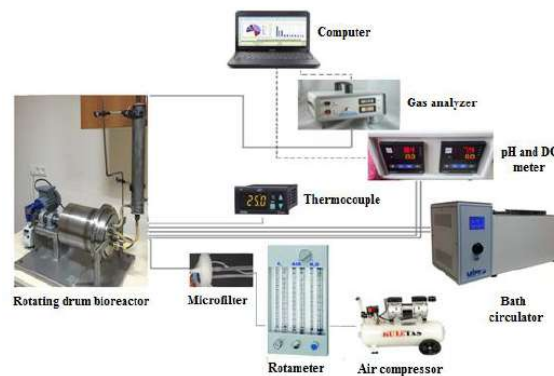


Figure 2. Enzyme production system.

When the results are compared, the enzyme production in RDB was about 2-fold higher specific productivity (50,86 U/g corn bran.h), with higher activity and shorter time, according to the erlenmayer scale production (25,36 U/g corn bran.h) and a cheaper enzyme production system by using agricultural wastes has been created.

Keywords - *Slurry state fermentation, Rotating drum bioreactor, α -Amylase, Plackett-Burman design*

ACKNOWLEDGMENT

This study was financially supported by the The Scientific and Technological Research Council of TURKEY (TUBITAK no. 115M502).

REFERENCES

- [1] Deb P, Talukdar SA, Mohsina K, Sarker PK, Sayem SA (2013) Production and partial characterization of extracellular amylase enzyme from *Bacillus amyloliquefaciens* P-001. Springer Plus 154:1-12.
- [2] Glover, K. and Benno, K.: Theoretical Characterization of Slurry Fermentation. Eng. in life sci. 5, 237-241 (2003)
- [3] Bernfeld P (1955) Amylases, α and β . Methods in enzymology 1:149-158.

α -Amylase Production by Submerged Fermentation in Novel Rotating Drum Bioreactor

Muhammet Şaban TANYILDIZI

Bioengineering Department
Firat University
Elazig, Turkey
mtanyildizi@firat.edu.tr

Muhammet Ali UYGUT

Bioengineering Department
Firat University
Elazig, Turkey
muygut@firat.edu.tr

Abstract— In the present study, α -amylase production and microbial growth by SmF was investigated in the novel rotating drum bioreactor that has micro air diffuser. Ceramic micro air diffuser was used for minimization of mass transfer limitations by increasing oxygen transfer efficiency in addition to the conventional RDB design. *Bacillus amyloliquefaciens* NRRL B-645 was used as α -amylase producer. In rotating drum bioreactor studies, optimum conditions (15 g/l starch, 2,5 g/l peptone, 1 g/l yeast extract, 1 g/l $\text{MgSO}_4 \cdot 7\text{H}_2\text{O}$, 1 g/l KH_2PO_4 and 0,1 g/l CaCl_2) that determined from earlier erlenmayer flasks was used. Dissolved oxygen, pH, temperature, oxygen and carbon dioxide at gas outlet, starch concentration, growth and total weight of bacteria was followed during fermentation. Dinitrosalicylic acid method [3] was used for determination of α -amylase activity. The highest enzyme activity (24,84 U/ml) was measured for the incubation time (14 h) in the conditions that are rotation speed (18 rpm), aeration rate (1 lpm) and baffle size (4 cm).

Keywords— Rotating drum bioreactor, Ceramic micro diffuser, α -Amylase, Submerged fermentation.

I. INTRODUCTION

Enzyme production has grown rapidly and is a vital sector. According to Grand View Research report, the global industrial enzyme market was \$8.18 billion in 2015 and it is forecasted that the market will reach \$17.50 billion by 2024 [1]. Amylases are one of the most important industrial enzymes and their annual production volume is 25-30% of the total manufacturing of enzyme production [2]. Alpha-amylases catalyze the hydrolysis of the 1,4- α -linkage between adjacent glucose units in the amylose chain of starch.

Submerged fermentation (SmF) has important advantages and it has commonly been preferred thanks to greater control of process parameters that has great significance about yield such as pH, dissolved oxygen and temperature and easier sterilization. Despite of its high cost, approximately 90% of fermentation products has been produced by SmF.

Rotating drum bioreactor (RDB) is an important microbial production system in terms of having less severe shear stress and researchers have explored applications of RDB in a plant cell culture, solid substrate fermentation, bioleaching and bioremediation. Although conventional RDB is an important microbial production system in terms of preventing heat accumulation [3,4] and having less severe shear stress on microorganisms [5], it is not completely adequate in terms of heat and mass transfer due to the absence of an effective air diffuser and free water. Therefore, biomass or enzyme production yield decreases in larger-scale RDB due to high levels in temperature and concentration gradient [6]. In addition to, on account of liquid-gas mass transfer, a drum reactor should be operated in lower working volumes ($\leq 50\%$) to keep a thinner film to provide the effective gas-liquid contact [7].

Studies have shown that the size of the air bubbles is effective on the cells and air bubbles in large diameters are damaged by the shear stress of the cell, on the other hand the bubbles in micron size cause less damage to the cell [8, 9, 10]. Michaels et al. (1996) have shown that the clustering and dispersion problems of bubbles can be minimized by microbubbles supplied to the system at low rotational speeds [11]. Nehring et al. (2004) compared a ceramic micro air diffuser producing bubbles with a diameter of 100-500 μm and a stainless steel air diffuser producing bubbles with a diameter of 800-3000 μm in a cell culture bioreactor [12]. Ceramic micro air diffuser has proven to 3 times more high oxygen transfer. Czermark et al. (2005) compared ceramic, stainless steel and silicone air diffusers in another study of cell culture and reported that the ceramic micro-air diffuser has a distinct advantage over other air diffusers in terms of oxygen transfer, ease of design and operating parameters at large scales [13].

Problems of RDB are mainly the lack of free water and the efficiency of mixing, especially for large scale production. For minimization of the problems in RDB,

ceramic micro air diffuser with proven effectiveness [12, 13, 14] can be used in addition to the conventional RDB design in liquid phase.

In the present study, α -amylase production and microbial growth by SmF was investigated in the novel rotating drum bioreactor that has micro air diffuser.

II. MATERIALS AND METHODS

A. Microorganism and Inoculation

For α -amylase production, *Bacillus amyloliquefaciens* NRRL B-645 (kindly provided by ARS Culture Collection) that is a commercial strain was preferred. The strain was maintained on an agar slant at 4°C. Inoculum culture was produced by using medium that contains (g/l) glucose 10, CaCl₂ 0.1, MgSO₄ 0.5, KH₂PO₄ 0.5, NaCl 1.5, yeast extract 2.0 and peptone 2.5. Inoculum was cultivated in 50 ml liquid medium at 150 rpm and 37°C for 18. All enzyme production studies were done with the production medium that was determined as optimum conditions in earlier studies [15].

B. Rotating drum bioreactor and fermentation

The enzyme production experiments were conducted in a RDB, which is a stainless steel tank of 5 mm thickness, 205 mm diameter, and 225 mm length. The technical drawing of the designed RDB is given in Fig. 1.

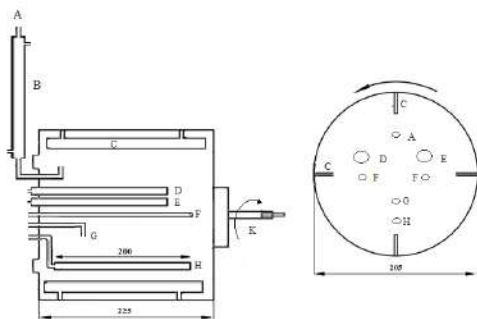


Figure 1. The technical drawing of the designed DTB. A gas outlet; B condenser; C Buffer; D dissolved oxygen probe; E pH probe; F heat exchanger; G thermocouple; H ceramic micro air diffuser; K stationary shaft.

The total volume of the bioreactor is 7 L. The bioreactor and its condenser, which is designed to prevent water losses, are shown in Fig. 2. The bioreactor is equipped with a 0.5 hp motor and inverter with adjustable rotation rate of 3-18 rpm. The bioreactor top cap can be demountable for loading substrate and installation of equipments. A micro air diffuser, a heat exchanger tube, a thermocouple, a DO probe (Hamilton, Visiform Arc 120) and a pH probe (Hamilton, Easyform Plus Arc 120) were attached to the stationary surface on the cap. The static top cap was mounted with autoclavable sealed bearings while the drum rotates around its axis.

Four straight baffles were placed to the bioreactor's inner surface for increasing mixing efficiency. For improving the

gas-liquid mass transfer efficiency of the RDB, a 200-mm ceramic micro air diffuser (Refractron, USA) with a pore size about 6-25 μ m was used as a sparger. An air compressor equipped with a rotameter was used to adjust the inlet air velocity and a water bath with external circulation was used to control the reactor temperature with heat exchange tube. After substrate loading and equipped with ceramic micro air diffuser, DO and pH probes and gas inlet and outlet line, the RDB was sterilized in an autoclave (Lab Companion, ST-65G) at 121°C for 30 min. Gas analyzer (Quantek, Model 902P) was used to determine concentration of O₂ and CO₂ at gas outlet. When the foaming in fermentation is observed, a simethicone based antifoam was added. Enzyme production system is shown in Fig. 2.



Figure 2. Enzyme production system.

C. α -Amylase Assay

Sampling was conducted at regular intervals and supernatant was obtained by centrifuge at 4100 rpm for 10 min. The supernatant was used as crude enzyme extract for activity assay. 0.5 ml enzyme was added to 1 ml soluble starch (1% (w/v)) in phosphate buffer (0.02 M, pH=6.9) and incubation was carried out at 37°C for 3 min. The reaction was stopped by using 3,5-dinitrosalicylic acid and reducing sugar was determined by Bernfeld method [16].

D. Bacterial Growth and Starch Analysis

Bacterial growth during fermentation was measured by turbidity meter followed by measurement of absorbance at 600 nm wavelength. For starch analysis, 0.1 ml of cell-free fermentation medium, was added to the tube containing 1 ml of KI-I₂-HCl solution and 10 ml of distilled water were added. This solution is read at 600 nm wavelength against the blind sample which does not contain the fermentation medium. The starch concentration is determined in g/l by calibration graph.

III. RESULTS AND DISCUSSION

The highest enzyme activity (24,84 U/ml) was measured for the incubation time (14 h) in the conditions that are rotation speed (18 rpm), aeration rate (1 lpm) and baffle size (4 cm). The change of investigated physical parameters with time in the validation experiment is shown in Figure 3 and 4. The maximum enzyme activity (24.84 U / mL) were reached in 14 h. The maximum activity was reached in the end of the logarithmic phase can be interpreted according to analysis of DO and CO₂ value at gas outlet.

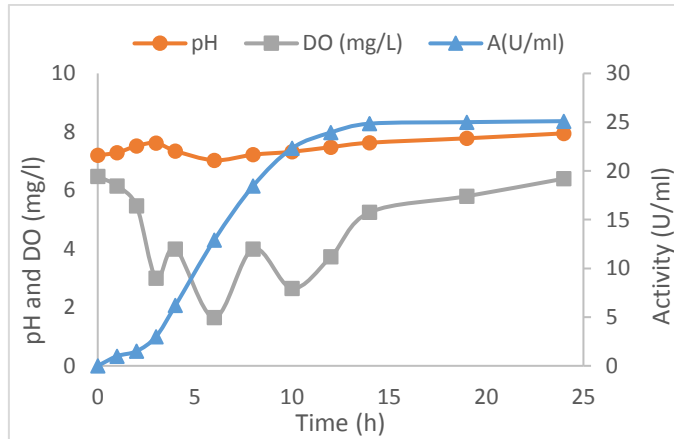


Figure 3. The change of α -amylase activity, DO and pH with time.

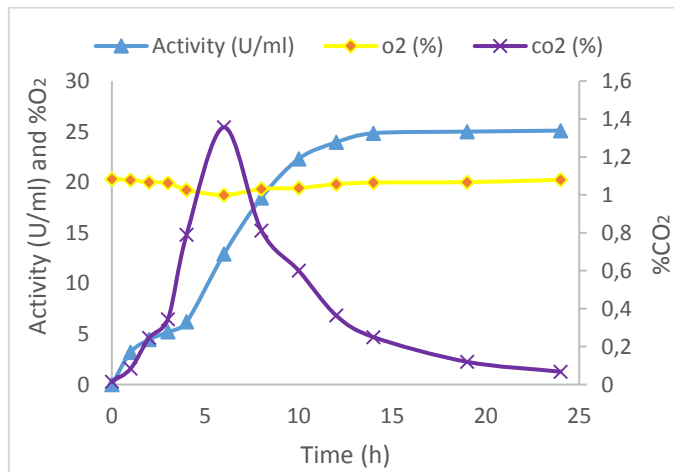


Figure 4. The change of α -amylase activity, O₂% and CO₂% with time.

The change of bacterial growth, amylase production and starch concentration with time is shown in Fig 5. The enzyme production started from mid-log phase and continued in the stationary phase. After starch is completely consumed, there is a noticeable increase in enzyme production. This increase can be explained by the induction of enzyme production by hydrolysis products formed by the catalysis of starch by the enzyme. It is seen that the enzyme production reaching

maximum in the stationary phase has remained constant after this period.

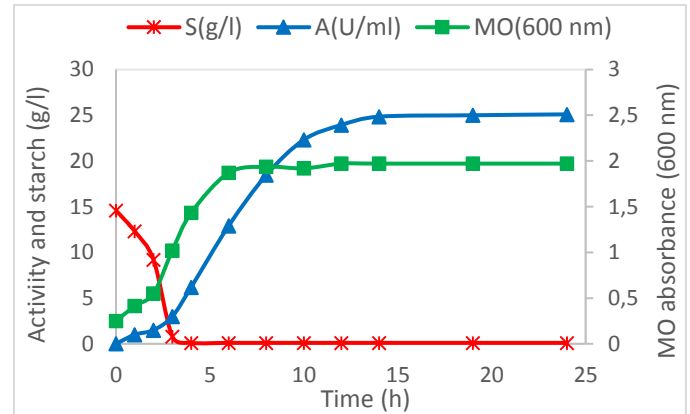


Figure 5. The change of starch and mo absorbance with time.

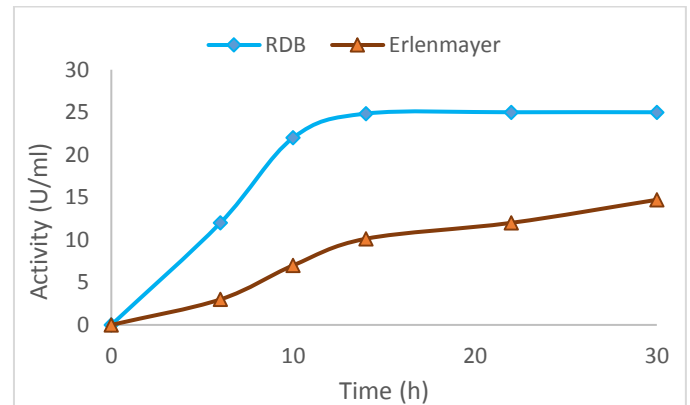


Figure 6. The change of enzyme production in RDB and erlenmeyer with time.

When results compared, enzyme production in RDB (24,84) was performed with approximately 2-fold higher enzyme activity than erlenmeyer scale study (14,72 U/ml) in shorter time as shown in Fig. 6.

As a result, enzyme production by SmF was successfully applied to novel RDB that can be operated at higher working volumes and an alternative bioprocess has been created to produce enzyme efficiently without dissolved oxygen limitation thanks to ceramic micro diffuser.

ACKNOWLEDGMENT

This study was financially supported by the The Scientific and Technological Research Council of TURKEY (TUBITAK no. 115M502).

REFERENCES

- [1] Global Enzymes Market Report (2016) US Grand View Research, San Francisco. <http://www.grandviewresearch.com/press-release/global-enzymes-market>. Accessed 14 Feb 2017
- [2] Deb P, Talukdar SA, Mohsina K, Sarker PK, Sayem SA, "Production and partial characterization of extracellular amylase enzyme from *Bacillus amyloliquefaciens* P-001," Springer Plus, vol 154, pp. 1-12, 2013.
- [3] Fung, C.J., Mitchell, D.A, "Baffles increase performance of solid-state fermentation in rotating drum bioreactors," Biotechnol. Techniq., vol. 9, pp. 295-298, 1995.
- [4] Stuart, D.M, "Solid-state fermentation in rotating drum bioreactors," Ph.D. thesis, The University of Queensland, Australia, 1996.
- [5] Wang, Z., Wen, Q., Zhang, Q., Liu, G., Wu, X., Cong, W, "Power consumption of liquid and liquid/solid systems in a rotating-drum bioreactor," Chem. Eng. and Technol., vol. 36, pp. 1395-1401, 2013.
- [6] Hardin, M. T., Howes, T., Mitchell, D.A, "Mass transfer correlations for rotating drum bioreactors," Journal of Biotechnology. Vol. 1, pp. 89-101, 2002.
- [7] Mitchell, D.A., Berovič, M., Krieger, N., "Solid-state fermentation bioreactor: Fundamentals of design and operation," Springer, Berlin, 2006.
- [8] Kunas, K.T., Papoutsakis, E.T., "Damage mechanisms of suspended animal cells in agitated bioreactors with and without bubble entrainment," Biotechnology and bioengineering., vol 5, pp. 476-483, 1990.
- [9] Wu, J., "Mechanisms of animal cell damage associated with gas bubbles and cell protection by medium additives," Journal of Biotechnology., vol. 2, pp. 81-94, 1995
- [10] Meier, S.J., Hatton, T.A., Wang, D.I., "Cell death from bursting bubbles: role of cell attachment to rising bubbles in sparged reactors," Biotechnology and bioengineering., vol. 4, pp. 468-478, 1999.
- [11] Michaels, J.D., Mallik, A.K., Papoutsakis, E.T., "Sparging and agitation-induced injury of cultured animals cells: Do cell-to-bubble interactions in the bulk liquid injure cells,". Biotechnology and bioengineering. vol. 4, pp. 399-409, 1996.
- [12] Nehring, D., Czermak, P., Vorlop, J., Lübben, H., "Experimental Study of a Ceramic Microsparging Aeration System in a Pilot-Scale Animal Cell Culture," Biotech. Progress., vol. 20, pp. 1710-1717, 2004.
- [13] Czermak, P., Weber, C., Nehring, D., Hall, D., "A ceramic microsparging aeration system for cell culture reactors," Pub Series of IBPT Uni of App Sci Giessen-Friedberg, vol.1, pp. 1-6, 2005.
- [14] Jin, J., Liu, G.L., Shi, S.Y., Cong, W., "Studies on the performance of a rotating drum bioreactor for bioleaching processes. Oxygen transfer, solids distribution and power consumption," Hydrometallurgy, vol. 103, pp. 30-34, 2010.
- [15] Tanyildizi, M., Özer, D., "An Investigation of α -amylase production in semi solid substrate fermentation by using corn bran with *Bacillus amyloliquefaciens*," Turkish J. of Sci. & Technol., vol. 6, pp. 47-52, 2011.
- [16] Bernfeld P, "Amylases, α and β . Methods in enzymology," vol. 1, pp. 149-158, 1955.

Isolation, Identification and characterization of Cave Bacteria

Yağmur ATAĞAV
Bioengineering Department,
Adana Science and Technology University,
Adana, Turkey

Rozelin AYDIN
Bioengineering Department,
Adana Science and Technology University,
Adana, Turkey

Abstract— Caves are formed by rocks such as gypsum, granite, quartzite, and talus but most commonly by calcareous rocks such as limestone and defined as a type of natural, rocky cavity under the ground that receives little to no light and also accessible to humans. Especially deep of the caves are usually considered to be extremely nutrient poor environments because of the absence of photosynthetic activity due to the lack of sunlight; nevertheless the cave environment presents variety of other potential energy sources for microbial growth. Firmicutes, Actinobacteria and α - β - and γ - Proteobacteria stated as three dominant phyla that can be found in such environments.[1] Furthermore, recent studies suggest bacteria may also have a role in cave formations such as carbonate precipitation in speleothem formations or moonmilk depositions. [2,3] In addition to that, the number of cave studies increase rapidly due to its potential to host microorganisms that can secrete secondary metabolites that may be of value to humans eg. enzyme, antibiotic and biofuel production. [4]

In this study bacterial load of a Cave located in Mersin was investigated by using culture dependent and culture independent methods. Samples were taken by sterile swaps and submersed in distilled and stored in +4°C degrees until culturing. For culturing the water that samples were submersed in was diluted 103 fold before plating. First, the bacteria were cultured on R2A media which is widely used for cave microbiology research and distinct looking colonies were picked from the petri dishes and isolated. After isolation, 16S rRNA PCR analysis was performed and PCR products were sent to a company for identification. As a result of this study, the bacterial load of the related cave is unveiled. The further results will be discussed in the oral presentation.

Keywords— Cave Microbiology; Microbial Isolation; Characterization.

ACKNOWLEDGMENT

This project has been funded by the Scientific Research Projects Department of Adana Science and Technology University with the 16303003 project number.

REFERENCES

- [4] Ortiz, M., Neilson Julia, W., Legatzki, A., & Maier Raina, M. "Bacterial and Archaeal Diversity on Cave Speleothem and Rock Surfaces: A Carbonate Cave Case Study from Kartchner Caverns" Microbial Life of Cave Systems. (2015).
- [5] Baskar, S., Baskar, R., Mauclaire, L., and McKenzie, J. A. "Role of microbial community in stalctite formation, Sahastradhara caves, Dehradun, India", Current Science, 88, 1305–1308, 2005.
- [6] Northup E., Diana. K. H. L., "Geomicrobiology of caves: a review." Geomicrobiology Journal, 18(3), 199-222, 2001.
- [7] Barton, H. A. "Introduction to cave Microbiology: A review for the non-specialist." Journal of Cave and Karst Studies, 68(2), 43-54, 2006.

Crystal Structure of Myofibrils

Murat AYAZ

Selcuk University, Medical Faculty,
Departments of Biophysics
Selcuklu, Konya 42130 Turkey
ayaz72@yahoo.com

Sırma Başak YANARDAĞ

Selcuk University, Medical Faculty,
Departments of Biophysics
Selcuklu, Konya 42130 Turkey
sirmabasak@gmail.com

Abstract—Crystal structure of myofibril resembles a graphene like structure, which looks interesting, moreover it can be useful in myofibril modeling.

Solid state physics deals with the electrical behavior of the solids. The conductive properties depend on the properties of electron and on the arrangement of the atoms [1]. It is well known that crystals are built with a periodic array of single atom or groups of atoms. An ideal crystal can be defined as the infinite repetition of the identical groups of atoms called a lattice. Lattice, atomic planes and atomic directions determine not only the mechanical properties of crystals, such as ductility and strength but also its electrical properties [2].

The micrograph of a cross section of the myofibril, can be found in any undergraduate level physiology book, is given in figure 1. Hexagonal arrangements of the thick and thin filament can be seen in a myofibril, in which six thin filaments surround each thick filament whereas three thick filaments surround each thin filament [3]. Flexibility of the myofibril can be related to the graphene like structure of it, moreover the nearest neighbors of the crystal structure determine the mechanical properties, thus the flexibility of the myofibril can be written as a function of the lattice space.

In such crystal structures packing efficiency is also important parameter, which characterizes the structure. It is well known that hexagonal close-packed structure has the highest packing fraction (0.74). In nature, it is impossible to find a structure –regular or not- with a packing fraction higher than 0.74.

Most of the solids can be found in crystal form and the property of it is known in detail. This knowledge can be used to understand myofibril structure better and may connect two unrelated disciplines: solid state physics and biology.

Keywords— crystal structure; hexagonal lattice; myofibril

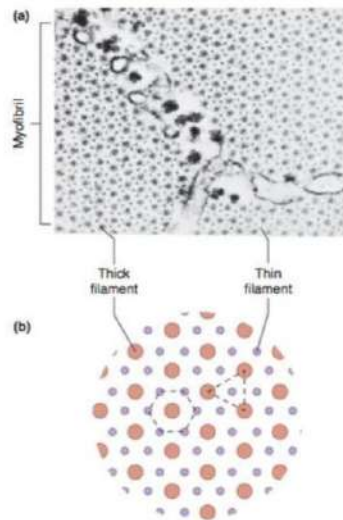


Figure 1. Micrograph of a single muscle fiber [4]

REFERENCES

- [1] B. Streetman, S. Banarjee, Solid State Electronic Devices, 6th ed, USA: Prentice Hall; 2000, pp. 1-22.
- [2] C. Kittel, Introduction to Solid State Physics, 8th ed, USA: Wiley, 2005, pp. 1-22.
- [3] B. Koeppe, B. Statnton, Physiology, 6th ed, USA: Elsevier, 2010, pp. 233-256.
- [4] E. Widmaier, H. Raff, K. Strang, Human Physiology, 13th ed, USA: Mc Graw Hill, 2014, pp. 257-300.

Nanoantimicrobials and Nanopropolis

Pınar Tatlı Seven

Department of Animal Nutrition and Nutritional Diseases,
Faculty of Veterinary Medicine, University of Firat
Elazığ, TURKEY

Ismail Seven

Department of Plant and Animal Production
Vocational School of Sivrice, University of Firat
Elazığ, TURKEY
E-mail: iseven@firat.edu.tr

Burcu Gul Baykalir

Faculty of Health Sciences
University of Firat
Elazığ, TURKEY

Seda Iflazoglu Mutlu

Department of Animal Nutrition and Nutritional Diseases,
Faculty of Veterinary Medicine, University of Firat
Elazığ, TURKEY

Abstract—Nanotechnology is effective in almost every area of concern to human and animal health. Nanomedicines against various pathogens in veterinary medicine could be developed. Antimicrobials are being placed into polymer-coated crystalline nanoparticles, cholesterol-conjugated amphiphilic peptide self-assembled particles, homogenized particulate suspensions, liposomes, composite hydrogel/glass particles, poly lactic-co-glycolic acid, cationic and pDNA coated gold nanoparticles. Liposome-based therapeutics have been accepted by the FDA for fungal infections, for instance, liposomal amphotericin B. Probiotics, prebiotics and immunomodulators can be used as growing promoter in animals. Recently, natural products which have antibacterial effects are preferred. Because, the use of antibiotics as growing promoter in animals brings out problems associated with microbial resistance and antibiotic residue. These nanostructures have indicated perfect results, particularly in life-threatening. In recent years for this aim, the alternative solution including natural antibacteria as propolis. It was reported that propolis has an efficacy against the inhibitory effects of free radicals and as an antibacterial (Hasan et al., 2014; Kothai and Jayanthi, 2014; Schmidt et al., 2014). Barud et al. (2013) determined that the ethanol extract of propolis is 70% effective at inhibiting the growth of microorganisms.

Epecially, natural nano antimicrobials such as nanopropolis are useful to veterinary medicine in terms of health, performance, and reliable food production. Propolis does not have a good solubility in water. Nanopropolis expected to supply a better antibacterial activity compared to propolis. Nanopropolis would raise the ability to dissolve a substance achieving better solubility compared to propolis. Nanopropolis can more easily enter through the outer membrane of bacteria in order that the active antibacterial compounds can harm bacterial cell walls. (Hasan et al., 2014). Also, the antimicrobial activity of nanopropolis was determined to be more effective against gram-positive bacteria than yeast. It is assumed that the causes for being more effective in antibacterial activity from antifungal activity of nanopropolis can be due to the characteristic of cell walls, differences present in membranes of bacteria and yeast, the antibacterial activity, and the thickness of the peptidoglycan layer (Afrouzan et al., 2012). As a result, nanomedicines against various pathogens in veterinary medicine could be developed. Especially, natural nano antimicrobials such as nanopropolis are useful to veterinary medicine in terms of health, performance, and reliable food production. But, there is a need to increase research because of the paucity of research currently being done on this topic.

Keywords—Antimicrobials; Nanopropolis; Nanotechnology

References

1. Afrouzan, H., Amirinia, C., Mirhadi, S.A., Ebadollahi, A., Vaseji, N. and Tahmasbi, G. 2012. Evaluation of antimicrobial activity of propolis and nanopropolis against *Staphylococcus aureus* and *Candida albicans*. *African Journal of Microbiology Research*, 6: 421-425.
2. Barud, H.S., Junior, A.M.A., Saska, S., Mestieri, L.B., Campos, J.A.D.B., Freitas, R.M., Ferreira, N.U., Nascimento, A.P., Miguel, F.G., Vaz, M.M.O.L.L., Barizon, E.A., Marquele-Oliveira, F., Gaspar, A.M.M., Ribeiro, S.J.L. and Berretta, A.A. 2013. Antimicrobial Brazilian propolis (EEP-AF) containing biocellulose membranes as promising biomaterial for skin wound healing. *Evidence-Based Complementary and Alternative Medicine*, 1-10.
3. Hasan, A.E.Z., Ambarsari, L., Widjaja, W.K. and Prasetyo, R. 2014. Potency of Nanopropolis Stinglessbee *Trigona* spp Indonesia as Antibacterial Agent. *IOSR Journal of Pharmacy*, 4: 1-9.
4. Kothai, S. and Jayanthi, B. 2014. Evaluation of antioxidant and antimicrobial activity of stingless bee propolis (*Tetragonula iridipennis*) of Tamilnadu, India. *Int J Pharm Pharm Sci*, 6: 81-85.
5. Schmidt, E.M., Stock, D., Chada, F.J.G., Finger, D., Sawaya A.C.H.F., Eberlin, M.N., Felsner, M.L., Quináia, S.P., Monteiro, M.C. and Torres, Y.R. 2014. A comparison between characterization and biological properties of Brazilian fresh and aged propolis. *BioMed Research International*, 1-10.

Determination of the effect of 3,3'-bisindole derivatives on rat erythrocyte 6PGD: an in vitro and in silico study

Adnan AYNA

Department of Chemistry,
Faculty of Sciences and Arts,
Bingöl University,
Bingöl, 12000, Turkey
aaayna@bingol.edu.tr

Sinan BAYINDIR

Department of Chemistry,
Faculty of Sciences and Arts,
Bingöl University,
Bingöl, 12000, Turkey
sbayindir@bingol.edu.tr

Yusuf TEMEL

Department of Health Services,
Vocational Schools,
Bingöl University,
Bingöl, 12000, Turkey
ytemel@bingol.edu.tr

Abstract— 6-Phosphogluconate dehydrogenase (6PGD; E.C.1.1.1.44) is an enzyme in the pentose phosphate pathway. It is a well-known oxidative carboxylase that catalyses conversion of 6-phosphogluconate into ribulose 5-phosphate [1]. It was reported that suppression of 6PGD decreased lipogenesis and RNA biosynthesis and increased reactive oxygen levels in cancer cells, lessening cell proliferation and tumour growth implying that 6PGD could be an anticancer target [2]. The aim of this study was to investigate whether biologically active organic indole derivatives alters the enzymatic activity 6PGD of rat erythrocytes in vitro. In order to do that, the 3,3'-bisindole derivatives 1 and 2 were synthesized, the enzyme was purified from rat blood and its activity was spectrophotometrically measured. The studies of the effect of these compounds on the activity of rat 6PGD revealed that while the 3,3'-bisindole derivatives 1 inhibited the activity with an IC₅₀ of 115.8 μ M, the activity was increased in the presence of 3,3'-bisindole derivative 2. To understand the mechanism of inhibition/activation, in silico docking experiments were performed.

Keywords— erythrocyte, docking, indole.

REFERENCES

- [1] a) Beutler, E. (1971). Red Cell Metabolism Manuel of Biochemical Methods. Academic Press, 68-70. b) Beutler, E. (1991). Glucose-6-Phosphate Dehydrogenase Deficiency. *N Engl J Med*, 324, 169-174.
[2] Wood, T. (1986). Distribution of the pentose phosphate pathway in living organisms. *Cell Biochem Funct.* 4, 235-40.

New amide derivatives as inhibitors of glucose 6-phosphate dehydrogenase and docking studies

Yusuf TEMEL

Department of Health Services,
Vocational Schools,
Bingöl University
Bingöl, Turkey
ytemel@bingol.edu.tr

Sinan BAYINDIR

Department of Chemistry,
Faculty of Sciences and Arts,
Bingöl University,
Bingöl, Turkey
sbayindir@bingol.edu.tr

Adnan AYNA

Department of Chemistry,
Faculty of Sciences and Arts,
Bingöl University,
Bingöl, Turkey
aayna@bingol.edu.tr

Abstract— Glucose 6-phosphate dehydrogenase (G6PD, E.C. 1.1.1.49) is one of the key enzymes that involves in the catalysis of a rate-limiting reaction in the pentose phosphate pathway (PPP), providing reducing power to all cells in the form of NADPH and ribose 5 phosphate [1,2]. Recently, the corresponding enzyme, G6PD, has been revealed to be involved in apoptosis, and the efficacy to anti-cancer therapy, making it as a important target in cancer treatment as one of the final products of the PPP, ribose-5-phosphate, is necessary for nucleic acid synthesis and tumour progression[3]. In this study we reported the synthesis of some biologically active indomethacin derivatives and studied their effects on the activity of corresponding enzyme obtained from rat erythrocytes. Among ten heterocyclic compound we found that the inhibition was most potent in the presence of 5 and 6 with an IC₅₀ of 3.85 μ M and 3.39 μ M respectively while compound 2 and 10 did not alter the activity. In silico docking studies of 5 and 6 were also carried out to understand binding mechanism in detail.

REFERENCES

- [1] Luzzatto L, Testa U. Human erythrocyte glucose 6-phosphate dehydrogenase: structure and function in normal and mutant subjects. *Curr Top Hematol* 1978;1:1–70.
- [2] Ying W. NAD⁺/NADH and NADP⁺/NADPH in cellular functions and cell death: regulation and biological consequences. *Antioxid Redox Signal* 2008;10:179–206.
- [3] Zhang C, Zhang Z, Zhu Y, Qin S1. Glucose-6-phosphate dehydrogenase: a biomarker and potential therapeutic target for cancer. *Anticancer Agents Med Chem*. 2014 Feb;14(2):280-9.

Investigation the effects of hetero aromatic compounds on rat erythrocyte 6PGD and in silico molecular docking experiments

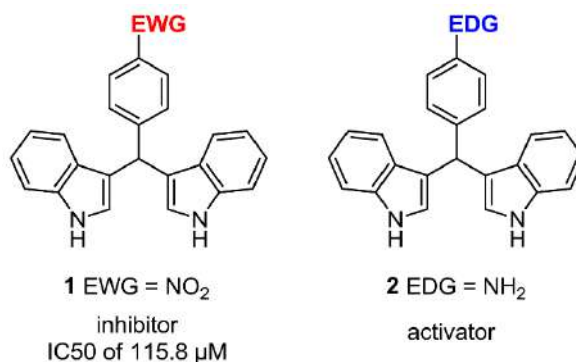
Sinan BAYINDIR
Department of Chemistry,
Faculty of Sciences and Arts,
Bingöl University,
Bingöl, Turkey
sbayindir@bingol.edu.tr

Adnan AYNA
Department of Chemistry,
Faculty of Sciences and Arts,
Bingöl University,
Bingöl, Turkey
aayna@bingol.edu.tr

Yusuf TEMEL
Department of Health Services,
Vocational Schools,
Bingöl University
Bingöl, Turkey
ytemel@bingol.edu.tr

Abstract— The pentose phosphate pathway (PPP) is an anabolic pathway that utilizes glucose to generate molecular building blocks of nucleic acids and reducing equivalents in the form of NADPH through 6-phosphogluconolactone dehydrogenase (6PGD). Recently, it was reported that 6PGD is implicated in cancer disease which makes designing 6PGD inhibitors in cancer treatment a necessity [1- 3]. Herein we reported the synthesis of 3,3'-bisindole derivatives and studied their effects on the corresponding enzyme. The studies demonstrated that o bisindole derivative 1 inhibited the activity of 6PGD with an IC50 of 115.8 μ M, while the activity was increased in the presence of 2. In silico docking studies were also performed to clarify the mechanism of inhibition/activation.

Keywords—component; Glucose-6-phosphate dehydrogenase (G6PD) indole, indole derivatives, in silico docking



References

- [1] Beutler, E. (1971). Red Cell Metabolism Manuel of Biochemical Methods. Academic Press, 68-70.
- [2] Beutler, E. (1991). Glucose-6-Phosphate Dehydrogenase Deficiency. *N Engl J Med*, 324, 169-174.
- [3] Wood, T. (1986). Distribution of the pentose phosphate pathway in living organisms. *Cell Biochem Funct.* 4, 235-40.

Optimization of Thermostable α -Amylase Production by Statistical Modeling

Fatma MATPAN BEKLER

Department of Molecular Biology and Genetics,
Faculty of Science,
Dicle University,
Diyarbakir, Turkey

Seçil YALAZ

Department of Molecular Biology and Genetics,
Faculty of Science,
Dicle University,
Diyarbakir, Turkey

Kemal GÜVEN

Science Teaching Section,
Faculty of Education,
Dicle University,
Diyarbakir, Turkey

Reyhan G. GÜVEN

Science Teaching Section,
Faculty of Education,
Dicle University,
Diyarbakir, Turkey

Abstract—*Thermophilic bacteria are well known to be of great importance, since they are the source of industrially used enzymes. Therefore a novel amylolytic enzyme producing thermophilic bacterial strain FMB2 from the Sorgun hot spring water in Yozgat, Turkey, was isolated in the present study. Phylogenetic analysis based on the partial 16S rRNA gene, biochemical and physiological tests revealed that the strain FMB1 belongs to the genus Bacillus licheniformis. Optimal growth was obtained at pH 9.0–10.0 and 55-60 °C. The optimum pH and temperature for the enzyme activity were determined. Out of six variables in the α -amylase production medium, pH and temperature were screened and optimized through response surface methodology (RSM) for higher α -amylase production. These methods have proven suitable to optimize α -amylase production by a thermophilic Bacillus licheniformis.*

Keywords—*component; Bacillus licheniformis, α -amylase, optimization, response surface methodology*

New heterocyclic compounds as inhibitors of rat erythrocytes G6PD and 6PGD and docking studies

Adnan AYNA

Department of Chemistry,
Faculty of Sciences and Arts,
Bingöl University,
Bingöl, 12000, Turkey
aaayna@bingol.edu.tr

Sinan BAYINDIR

Department of Chemistry,
Faculty of Sciences and Arts,
Bingöl University,
Bingöl, 12000, Turkey
sbayindir@bingol.edu.tr

Yusuf TEMEL

Department of Health Services,
Vocational Schools,
Bingöl University,
Bingöl, 12000, Turkey
ytemel@bingol.edu.tr

Abstract— Glucose-6-phosphate Dehydrogenase (G6PD) is the rate-limiting enzyme of the pentose phosphate pathway. It catalyses the irreversible conversion of glucose 6-phosphate to 6-phosphoglucono- δ -lactone in the presence of NADP⁺ [1]. 6-phosphogluconolacton Dehydrogenase (6PGD) is the third enzyme in the pentose phosphate pathway. It is a well-known oxidative carboxylase that catalyses conversion of 6-phosphogluconate into ribulose 5-phosphate. In the absence of these enzymes the erythrocyte is susceptible to oxidative damage. G6PD is associated with some human diseases including cancer, metabolic disorders and cardiovascular diseases. It was also reported that suppression of 6PGD decreased lipogenesis and RNA biosynthesis and increased reactive oxygen levels in cancer cells, lessening cell proliferation and tumour growth suggesting that 6PGD could be an anticancer target. Therefore one aim of the work described in this paper is to investigate the effect of some biologically active indole derivatives on the activity of corresponding enzymes. The studies revealed that while the bisindole derivatives 1, 2 and 3 inhibited the activity of G6PD with an IC₅₀ of 138 μ M, 231 μ M and 304 μ M respectively, the studies of rat erythrocyte 6PGD indicated that the activity was increased in the presence of 1 and 2 and was inhibited in the presence of 3. Molecular docking studies were also carried out to understand the mechanism of inhibition/activation.

Keywords— carboxylase, heterocyclic, inhibition.

REFERENCES

- [1] Gupte SA (2008) Glucose-6-phosphate dehydrogenase: a novel therapeutic target in cardiovascular diseases. *Curr Opin Investig Drugs* 9, 993–1000.

Design and synthesis of indole derivatives for the inhibition of G6PD and detailed in silico studies

Sinan BAYINDIR

Department of Chemistry,
Faculty of Sciences and Arts,
Bingöl University,
Bingöl, 12000, Turkey
sbayindir@bingol.edu.tr

Adnan AYNA

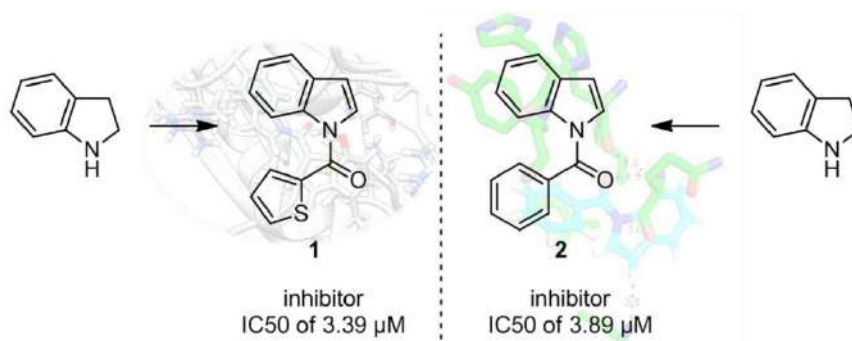
Department of Chemistry,
Faculty of Sciences and Arts,
Bingöl University,
Bingöl, 12000, Turkey
aayna@bingol.edu.tr

Yusuf TEMEL

Department of Health Services,
Vocational Schools,
Bingöl University,
Bingöl, 12000, Turkey
ytemel@bingol.edu.tr

Abstract— Glucose-6-phosphate dehydrogenase (G6PD) is an enzyme participates in the pentose phosphate pathway, a metabolic pathway that supplies reducing energy to cells (such as erythrocytes). G6PD reduces NADP⁺ to NADPH while oxidizing glucose-6-phosphate [1]. In last decade, the role of G6PD in apoptosis and the efficacy to anti-cancer therapy has been reported which makes it a promising target for cancer treatment. The aim of the work described in this study was to synthesise potent inhibitors of G6PD and investigate their effects on the enzyme along with in silico molecular docking studies. Among two derivatives tested we found that the compounds 1 and 2 inhibited the activity with an IC₅₀ of 3.39 and 3.89 μ M respectively. In silico docking studies of 1 and 2 were also carried out to understand binding mechanism in detail.

Keywords—component; Glucose-6-phosphate dehydro-genase (G6PD) indole, indole derivatives, in silico docking



References

- [1] Gupte SA, "Glucose-6-phosphate dehydrogenase: a novel therapeutic target in cardiovascular diseases," Curr. Opin. Inv. Drugs, 9, 993–1000, 2008.

Some Antibiotics As Inhibitors And Activators Of Rat Erythrocyte 6PGD And G6PD

Yusuf TEMEL

Department Of Health Services, Vocational Schools
Bingöl University
Bingöl, 12000, Turkey
ytemel@bingol.edu.tr

Adnan AYNA

Department of Chemistry, Faculty of Sciences and Arts
Bingöl University
Bingöl, 12000, Turkey
aayna@bingol.edu.tr

Mehmet ÇİFTÇİ

Department of Chemistry, Faculty of Sciences and Arts
Bingöl University
Bingöl, 12000, Turkey
mciftci@bingol.edu.tr

Abstract—Glucose-6-phosphate dehydrogenase (G6PD) and 6-phosphogluconate dehydrogenase (6PGD) are the two important enzymes of the pentose phosphate pathway which provides reducing power to the cell. G6PD, the rate-limiting enzyme of the pentose phosphate pathway, catalyzes the irreversible conversion of glucose 6-phosphate to 6-phosphoglucono- δ -lactone in the presence of NADP [1]. 6PGD is the third enzyme in the pentose phosphate pathway. G6PD is associated with some human diseases including cancer [2]. It was also reported that suppression of 6PGD decreased lipogenesis and RNA biosynthesis and increased reactive oxygen levels in cancer cells, lessening cell proliferation and tumor growth suggesting that 6PGD could be an anticancer target. In this study, G6PD and 6PGD were purified with 2'5' ADP-sepharose 4B affinity chromatography in single step. Following purification, we investigated the in vitro effects furosemide, cefazolin, gentamicin and cefuroxime on the activity of rat erythrocyte G6PD and 6PGD. It was determined that gentamicin and furosemide inhibited 6PGD with an IC₅₀ of 13.86 mM and 0.775 mM respectively while cefuroxime and cefazolin increased the activity of the enzyme. On the other hand, gentamicin and furosemide inhibited the activity of the G6PD with an IC₅₀ of 1.75 mM, 0.526 mM respectively whereas cefuroxime and cefazolin increased the activity of the enzyme.

Keywords— G6PD, 6PGD, Antibiotics, Inhibitors, Activators, Rat Erythrocyte

REFERENCES

- [1] Ciftci, M., Beydemir, S., Yilmaz, H., Bakan, E.: Effects of some drugs on rat erythrocyte 6-phosphogluconate dehydrogenase: an in vitro and in vivo Polish J. Pharmacol., 2002, 54: 275.
- [2] Zhang C, Zhang Z, Zhu Y and Qin S (2014) Glucose-6-phosphate dehydrogenase: a biomarker and potential therapeutic target for cancer. Anticancer Agents Med Chem 14, 280–289

Does Hypovolemia Effect Contraction Kinetics?

Murat AYAZ

Selçuk University Faculty of Medicine Department of
Biophysics
Konya, Turkey
ayaz72@yahoo.com

Nilüfer AKGÜN

Selçuk University Faculty of Medicine Department of
Biophysics
Konya, Turkey

Abstract— An inadequate volume condition that develops with any loss of volume in the body is called hypovolemia. This loss of volume is wrong to evaluate as a blood loss only. Hypovolemia can be caused by blood loss due to external and internal blood vessels in the body, extracellular fluid loss, vomiting and dehydration. Hypovolaemia is a serious problem with electrolyte impairments due to both direct effects of loss of fluid and loss of dense electrolyte. Hypovolemic disorders occur when these reduced circulating fluid volume. Even though at hypovolemia is reduced the volume of extracellular fluid, actually plasma sodium concentration is reduced. This study aims to reveal the effects of hypovolemia on the cardiac contraction with computer simulation of a rabbit ventricular cardiomyocyte. As a result of maximum reduction was seen in contraction kinetics (CT50) period with 8.3%.

The disturbance of water-electrolyte balance may cause hypovolemia, is the most common fluid disorder, especially seen in postoperative and elderly patients in which the findings are all related to the reduction of tissue perfusion [1]. In such cases, restoration of the water-electrolyte balance is vitally important [2,3]. Since sodium ions have an important role in the water balance of the extracellular fluid, regulation must be done via sodium-rich fluids [4]. The amount and the rate of fluid administration are adjusted according to the clinical response of the patient in the treatment of hypovolemia [5].

Simulation programs are an extremely powerful aid in the solution of the biological problems that's why they are widely used. Indeed, following the construction of the simulation of the biological system it is so easy to produce data that has been similar to biological systems. It also removes the experiments that have been used by the animals. Indeed the cost of the experiments decreased dramatically when we use the simulations. Besides their advantages due to the nature of the calculation mistakes the results of the simulation should be double checked. [6]. For the production of the data we used the modified version of the non-commercial software program of Lab Heart 5.3. The contraction parameters were analyzed by the home made excel program. The physiological parameters were established by the ionic concentrations of mM: extracellular; Na:142, K:4 intracellular; Na:10, K:120. For the simulations of the hypovolumetric situation Na:110 mM were used and comparison to physiological case was done.

There is a connection between action potential and muscle contraction, which known as excitation contraction coupling. This study aims to investigate the effects of hypovolemia on the rabbit ventricular cardiomyocyte contractions. It is well known that heart works as a pump, which sends deoxygenated blood to the lung and oxygenated blood to the body, thus the troubles in the contraction of it is a key parameter in several pathophysiology. It was shown that hypovolemia (110 mM) results in a 12.66% decrease in the maximum contraction value. Furthermore both the contraction and the relaxation kinetic values of contraction were also affected. To reveal the effects of it on the kinetics 50% of the contraction time, 50% and 90% of the relaxation time are measured and a reduction of 8.3%, 3.2% and 0.3% is observed respectively, maximum reduction was seen in CT50 period with 8.3%. Our simulation results show that the modifications observed in excitation-contraction coupling are serious effects on hypovolemic conditions.

Keywords— Contraction kinetics; excitation-contraction coupling; hypovolaemia; water-electrolyte balance

References

- [1] J.L. Incent, "Perioperative cardiovascular monitoring of high-risk patients: A consensus of 12", Crit Care. 19:224, 2015.
- [2] L.H. Avarro, "Perioperative fluid therapy: A statement from the international fluid optimization group. Perioper Med (Lond)". April 2015.
- [3] F. Michard, J.L. Teboul, "Using heart-lung interactions to assess fluid responsiveness during mechanical ventilation", Crit Care. 4(5):282-9, 2000.
- [4] J.W. Lee, "Fluid and Electrolyte Disturbances in Critically Ill Patients," Electrolyte Blood Press.8(2):72-81, December 2010.
- [5] A. Friedman, "Fluid and electrolyte therapy: a primer", Pediatr Nephrol. 25(5):843-6, 2010 May.
- [6] E. Ayaz, S.B. Yanardag, H. Karabagli, M. Ayaz, "Effects of the Experiment Conditions on the Nerve Action Potential", A Model Study. Journal of Advanced Neuroscience Research, 3, 61-69,2016.

The Role of Alkali Metals on Nerve Action Potential

Murat AYAZ

Selcuk University, Medical Faculty,
Departments of Biophysics Selcuklu,
Konya 42130 Turkey
ayaz72@yahoo.com

Abstract— Sodium and potassium are the major ions of the extracellular matrix, moreover they have key role in nerve excitability. It is found that changes in the extracellular ion concentration (Na^+ and K^+) affect not only axonal action potential parameters but also conductance of the ion channels.

Since 1700s scientists have been trying to understand the electricity in living organisms. As far as we know today, similar to electrical wire information is delivered through the body in the form of electricity. Living organism produce electrical energy from the ion concentration gradient across the membrane, and the measured current is the flow of the ions, both inside and outside of the excitable cell and controlled by the ion channels in the membrane, thus transmission is tightly dependent on the ionic concentrations. Unlike pH or temperature there is not a tight control mechanism for the extracellular sodium and potassium concentration, thus, dysnatremia and dyskalemia are frequently seen in the clinic especially in hospitalized, postoperative and elderly patients [1].

Sodium ions abundant in the blood and extracellular fluid, and it have a key role in osmotic pressure regulation and excitation of the nerve and muscle cells. Sodium is obtained through nutrients and excreted via sweat and urine. If the intake and excretion are not in balance dysnatremia occurs. Potassium is the major ion of the intracellular matrix. Like sodium intake is done by nutrients, excretion is seen through the digestive tract and in sweat, urine; moreover imbalance causes dyskalemia. It is vital to keep extracellular potassium concentration in a tight range otherwise it may have serious consequences such as abnormal heart rhythm or cardiac arrest. Ionic changes in the plasma level can be seen, but if the change is dramatic and persistent it may have many effects on the body, for instance, it may affect prognosis and even the survival rates of the patients with cancer, brain trauma and in many pathophysiology [2,3]. Macroscopic effects of the ionic changes, are well known, however the research on the molecular level is still missing.

In a microscopic point of view, the change in the ionic content affects the conductivity of the extracellular and intracellular matrix, so the transmission is very much dependent on the ions around their membranes. In this research, the effect of change in extracellular ion concentration on the single nerve fiber action potential is studied by using action potential simulation. The experimental conditions are built to simulate hypo/hyperkalemic and hypo/hyponatremic conditions and, it is found that the sodium ion channel conductivity is much more susceptible to the changes in the extracellular ion concentrations. Due to the susceptibility of the sodium channel conductivity, hypo/hyperkalemic conditions are much more dangerous for patients at least for neuronal conduction.

Keywords—axonal action potential; ion channel; ion concentration; simulation.

References

- [1] H.D. Humes, Kelley's Essentials of Internal Medicine, USA: Lippincott Williams & Wilkins, 2001.
- [2] M. Biswas, J.S. Davies, "Hyponatraemia in clinical practice," Postgrad Med J, vol. 83, pp.373–378, 2007.
- [3] M. Darmon, M. Pichon, C. Schwebel, et al, "Influence of early dysnatremia correction on survival of critically ill patients," Shock vol. 41(5), pp. 394-399, 2014.

A Biological Example of Avalanche Multiplication: Hodgkin Cycle

Murat AYAZ

Selcuk University, Medical Faculty, Departments of Biophysics
Selcuklu, Konya 42130 Turkey
ayaz72@yahoo.com

Sırma Başak YANARDAĞ

Selcuk University, Medical Faculty, Departments of Biophysics
Selcuklu, Konya 42130 Turkey
sirmabasak@gmail.com

Abstract— Voltage gated Na⁺ channels, has a key role in the excitable cells, is one of the few examples of positive feedback mechanism, and opening of it exhibits an avalanche-like multiplication which can be used to understand nature and the kinetics of the voltage –gated sodium channels.

In a manner of excitation sodium is the most important ion, and it is abundant in the extracellular matrix. In comparison with the extracellular matrix, intracellular matrix is characterized with lower sodium concentration. Since sodium is roughly 15-fold larger than inside, with the opening of voltage gated sodium ions a large current is measured across the membrane, it is usually high enough to saturate the electronic equipment, so ion replacement is necessary [1].

The cell membrane is composed of lipids, proteins and carbon hydrates, which houses organelles. Lipid bilayer is a perfect insulator for the ions, thus ion movement is only observed through, protein component of the membrane, ion channels [2].

Modeling of the biological mechanism is used in educational purposes and helps us to reveal the unknown phenomena, to develop new therapeutic approaches.

Axonal membranes can be modeled as a p-n junction, in which the application of reverse or forward bias results in an electron flow from p to n or vice versa. In its resting state the extracellular matrix is p-doped (has an excessive positive charge) whereas the intracellular matrix is n-doped (has an excessive negative charge), and the lipid bilayer, the depletion region, is lack of free charges in the absence of an applied external electric field [3].

Voltage-gated Na⁺ channels, has a key role in the excitable cells, and is one of the few examples of positive feedback mechanism in living organisms. The opening of sodium channel triggers the rest, which is called as Hodgkin circle. The avalanche-like opening can be modeled with avalanche multiplication seen in p-n junctions. In the presence of a large electric field an electron entering from the p side may be accelerated high enough kinetic energy, and the interaction of with the lattice creates carrier multiplication. By using the probability of carrier to create carrier multiplication P, total multiplication can be calculated as follows. For n_{in} entering from the p side will create Pn_{in} electron hole pairs (secondary carriers) for each collision. Likewise the collision of secondary carriers will create P²n_{in} electron hole pairs and summation gives

$$\begin{aligned}n_{out} &= n_{in} (1 + P + P^2 + P^3 + \dots) \\n_{out}/n_{in} &= 1 + P + P^2 + P^3 + \dots \\M &= n_{out}/n_{in} = 1/(1-P).\end{aligned}$$

It should be noted that the ionization probability depends on the reverse bias. The empirical relation near breakdown voltage is given in the following formula

$$M = 1/(1 - V/V_{br})^n$$

where M is the carrier multiplication, V_{br} is the breakdown voltage, and n is the exponent varies from 3 to 6 which depends on the material [3].

Keywords— avalanche multiplication; p-n junction; voltage-gated sodium channel

REFERENCES

- [1] A.L. Hodgkin, A.F. Huxley "Quantitative description of membrane current and its application to conduction and excitation in nerve," J Physiol, vol. 117, pp. 500-544, 1952.
- [2] D. Goldfarb, Zar Biyofizigi. In: M Ayaz, editor. Biyofizik sirlari cozulmus. 1st ed. Konya: Nobel Tip Kitabevleri 2013; p. 265-291.
- [3] B. Streetman, S. Banarjee, Solid State Electronic Devices, 6th ed, USA: Prentice Hall; 2000, pp. 61-108.

The Using of Nanotechnology in Animals

Pınar TATLI SEVEN

Department of Animal Nutrition and Nutritional Diseases,
Faculty of Veterinary Medicine,
University of Firat
Elazig, TURKEY

İsmail SEVEN

Department of Plant and Animal Production
Vocational School of Sivrice,
University of Firat
Elazig, TURKEY
iseven@firat.edu.tr

Burcu Gul BAYKALIR

Faculty of Health Sciences
University of Firat
Elazig, TURKEY

Seda IFLAZOĞLU MUTLU

Department of Animal Nutrition and Nutritional Diseases,
Faculty of Veterinary Medicine,
University of Firat
Elazig, TURKEY

Abstract—Nanotechnology has a significant potency to solve the problems in the animal health field, since likely applications of the technology to veterinary practices are almost mind-boggling. Lately, studies related to nanotechnology have been on the agenda. In particular, they have focused on drugs used in human health. To develop improvements in techniques of animal production, it is necessary to enforce this knowledge for animal health. Nanotechnology can solve lots of mysteries related to animal health, reproduction, production, good hygienic practices during rearing and maintaining of food animals. Nanotechnologies can be used for constitute nanostructures of food ingredients that can improve taste, texture and stiffness or provide the formation of emulsions. Also, nanotechnology has been utilized to improve finding of a range of chemical and microbial contaminants in feeds. Nanotechnology offers scientific advantage with its rapid and specific moves, besides high bioavailability, and biodegradability properties. All these advantages have significant effects on both fewer production and economic losses in livestock animals and more healthy food and feed production. The technology application is usable especially with livestock. But, much more research and company development are needed before this research can be used widely in veterinary medicine and the animal science field of nanotechnology.

Keywords—Nanotechnology; Animal Health; Nanodrug; Food; Nutrition

Effects of Hypovolemia on Action Potential Parameters

Murat AYAZ

Selcuk University Faculty of Medicine
Department of Biophysics
Konya, Turkey
ayaz72@yahoo.com

Nilüfer AKGÜN

Selcuk University Faculty of Medicine
Department of Biophysics
Konya, Turkey

Abstract—Liquid loss is not just water loss also electrolytes are lost. Depending on the severity of fluid loss hypovolemia creates different clinical signs. Cardiovascular manifestations involve reduction of central venous pressure and it varies from resting tachycardia to hypotension. The aim of this study is to reveal the effects of extracellular sodium concentration on the duration of action potential with computer simulation of a rabbit ventricular cardiomyocyte. As it is expected, sodium concentration is effective on these measured currents. As a result, it shows that the potassium ion channels which are the major responsible for APD 90 is also associated with the concentration of extracellular sodium.

Hypovolemia is a serious problem with electrolyte impairments due to the direct effects of fluid and dense electrolyte loss [1,2,3]. Since sodium is the major extracellular cation, when the volume of extracellular fluid is reduced, the plasma sodium concentration is reduced as well. Depending on the severity of fluid loss, hypovolemia shows different clinical symptoms [4,5]. Cardiovascular manifestations involve reduction of central venous pressure and it varies from resting tachycardia to hypotension [6].

Simulation is the process of creating a model that represents a real system. Simulation studies are extremely effective in problem solving issue [7].

For the production of the data we used the modified version of the non-commercial software program of Lab Heart 5.3. The contraction parameters were analyzed by the home made excel program. The physiological parameters were established by the ionic concentrations of mM: extracellular; Na:142, K:4 intracellular; Na:10, K:120. For the simulations of the hypovolumetric situation Na:110 mM were used and comparison to physiological case was done.

The aim of this study is to reveal the effects of hypovolemia on the duration of action potential and ionic currents with a simulation program of a rabbit ventricular cardiomyocyte. In its physiological range, plasma sodium concentration varies between 138-145 mM. When this value is lowered to 110 mM, the action potential duration at 25%, 50%, 75% and 90% repolarization is decreased 18.5%, 39.2%, 30.5% and 29.2% respectively; furthermore, the decrease is more significant APD 90 values. As a result, it shows that the potassium ion channels which are the major responsible for APD 90 is also associated with the concentration of extracellular sodium. Moreover the results of simulations are use to investigate the ionic mechanism underlying these changes in action potential. In comparison with the physiological value, the decrease of extracellular sodium concentration results in a 6.6% decrease in the peak value of the sodium current, thus decline in the external sodium ion concentration generates less current. As it is expected, sodium concentration is effective on these measured currents. Our simulation results show that hypovolemic conditions caused significant changes in the APD 90 of the simulated action potentials. In addition, the peak sodium current was found to be depressed.

As a result, treatment should be performed with liquids containing sodium, which are the most important elements of the extracellular fluid space. To have a successful outcome in cardiac arrest it is necessary to evaluate the causes of it such as hypovolemia, underestimation of may cause serious results such as death.

Keywords— action potential; hypovolemia; ionic currents; plasma sodium concentration; simulation

References

- [1] L.H. Avarro, "Perioperative fluid therapy: A statement from the international fluid optimization group. *Perioper Med (Lond)*". April 2015.
- [2] J.W. Lee, "Fluid and Electrolyte Disturbances in Critically Ill Patients," *Electrolyte Blood Press.*8(2):72-81, December 2010.
- [3] A. Friedman, "Fluid and electrolyte therapy: a primer", *Pediatr Nephrol.* 25(5):843-6, 2010 May.
- [4] S.M. Bagshaw, D.R. Townsend, R.C. McDermid, "Disorders of sodium and water balance in hospitalized patients", *Can J Anaesth.* 56(2):151-67, 2009 Feb.
- [5] K. Holte, H. Kehlet, "Fluid therapy and surgical outcomes in elective surgery: a need for reassessment in fast-track surgery", *J Am Coll Surg.* 2006;202:971-89.
- [6] M. Sedlacek, A.C. Schoolwerth, B.D. Remillard, "Electrolyte disturbances in the intensive care unit", *Semin Dial* 19(6): 496-501, 2006 Nov-Dec.
- [7] E. Ayaz, S.B. Yanardag, H. Karabagli, M. Ayaz, "Effects of the Experiment Conditions on the Nerve Action Potential", *A Model Study. Journal of Advanced Neuroscience Research*, 3, 61-69,2016

The Effects of the Potassium Channel Conductivity on the Cardiac Action Potential and Contraction

Murat AYAZ

Selcuk University, Medical Faculty,
Departments of Biophysics
Selcuklu, Konya 42130 Turkey
ayaz72@yahoo.com

Abstract— *In cardiac tissue action potential not only initiates the contraction but also, with its presence along the contraction, it regulates contraction, thus it is more sophisticated than nerve action potential. This study aims to reveal the effects of potassium channel conductivity on the action potential and contraction parameters.*

Since Galvani and Volta, electricity in the living tissue is one of the hottest subjects of science; furthermore, generation, conduction and creation of it still have some blanks and many scientists tries to fill them. One fact we are sure of is that, living system generates electrical energy from the ion gradient present across the cell membrane, which can be visualized in excitable cells as action potential, membrane potential change that is the result of the flow of the ions through channels. The molecular mechanism of action potential must be studied in detail to cure any pathophysiology, which results in alterations in action potential parameters.

In comparison with the other excitable tissues cardiac action potential is more complex, and since in every cycle it pumps deoxygenated blood to the lung and oxygenated blood to the body alterations in cardiac action potential is vitally important. It is well known that in cardiac tissue action potential not only initiates the contraction but also, with its presence along the contraction, it regulates contraction [1].

Although there are a group of ion channels which all together make the pumping function more controllable, this work contains the effect of the conductivity changes of the I_{to} s, I_{to} f and IK_1 , which are the well marked ion channels in the literature [2,3]. As expected the conductivity changes affected the action potential parameters, but surprisingly degree of change in increase and in decrease are not same, somehow channels resembles a rectification-like behavior. Likewise, in contraction parameters a rectification-like behavior is observed too.

It has been shown that I_{to} , which is the responsible for the early repolarization, has two types in which the slow type is more dominant, whereas at the determination of the maximum depolarization of the action potential IK_1 is more prominent. Additionally, this channel has an important role in the regulation of intracellular free calcium concentration mechanism.

Keywords—cardiac action potential; channel conductivity; ion channel; simulation

REFERENCES

- [1] D.M. Bers, "Cardiac excitation-contraction coupling," Nature, vol. 415, pp. 198-205, 2002.
- [2] J. Liu, K.H. Kim, B. London, M.J. Morales, P.H. Backx, "Dissection of the voltage-activated potassium outward currents in adult mouse ventricular myocytes: I_{to} , I_{to} s, IK_{slow1} , IK_{slow2} and I_{ss} ," Basic Res Cardiol, vol. 106, pp. 189-204, 2011.
- [3] H. Xu, W. Guo, J.M. Nerbonne, "Four kinetically distinct depolarization-activated K^+ currents in adult mouse ventricular myocytes", J Gen Physiol, vol. 113, 661-78, 1999.

Electrospinning of Hydroxyapatite/Poly(lactic acid)/Polyurethane Based Nanocomposites for Multi-Purpose Biomedical Applications

Yeşim Müge ŞAHİN

Biomedical Engineering Department
Faculty of Engineering & Architecture,
ArelPOTKAM(Polymer Technologies and Composite
Materials Research and Development Center),
Istanbul Arel University
Istanbul, Turkey
ymugesahin@arel.edu.tr

Erdi BULUŞ

ArelPOTKAM) (Polymer Technologies and Composite
Materials Research and Development Center),
Istanbul Arel University
Istanbul, Turkey.
Mechanical Engineering Department
Faculty of Technology, Firat University
Elazığ, Turkey
erdibulus@arel.edu.tr

Gül TOSUN

Mechanical Engineering Department
Faculty of Technology,
Firat University
Elazığ, Turkey
gultosun@firat.edu.tr

Abstract— HA demonstrates greater hydrophobic property, and possesses lower resorption rate than TCP. There have been advantageous in pairing HA with TCP, as some designed parameters such as degradability and surface characteristics of the engineered scaffold have been improved [1]. By using a simple chemical method, it is possible to synthesize such biphasic nanoceramics from natural marine shells [2,3]. Marine sourced hydroxyapatite (HA) is a natural ceramic and is used as the most preferred implant material in orthopedics and dentistry due to their chemical similarity to bone scaffold. A relatively new process known as “electrospinning” has received considerable attention in the production of porous scaffolds [4]. In the present study, biocomposites having different compositions were prepared from bioceramics and biocompatible, biodegradable polymers. Solution of Poly(lactic acid) (PLA), a Polyurethane (PU), HA with different concentrations were used for electrospinning technique to prepare nanofiber based biocomposite. Physical measurements such as viscosity, electrical conductivity and density were conducted to optimize the system. Structural analysis were performed with fourier transform infrared spectroscopy (FTIR) and the crystalline structure were analyzed with x-ray diffraction (XRD) measurements. Morphological properties of the formed nanotopographic fibrous mat were investigated in terms of fiber structure, size and diameter range. by scanning electron microscopy (SEM). Mechanical tests were carried out after production of nanobiocomposites.

Keywords— Hydroxyapatite; β -Tricalcium Phosphate; Biodegradable; Poly(lactic acid); Polyurethane; Electrospinning; Nanobiocomposite; Tissue Engineering

REFERENCES

- [1] Kwon SH, Jun YK, Hong SH, Lee IS, Kim HF. “Calcium phosphate bioceramics with various porosities and dissolution rate” J. Am. Ceram. Soc. 2002;85:3129–3131.
- [2] Sahin Y. M., Gündüz O., Bulut B., Özyeğin L. S., Gökçe H., Ağaoğullar D., Chou J., Kayalı E. S., Ben-Nissan B., Oktar F. N., “Nano-Bio ceramic Synthesis from Tropical Sea Snail Shells (Tiger Cowrie Cypraea Tigris) with Simple Chemical Treatment” Acta. Phys. Pol.A 2015:127(4), 1055-1058.
- [3] Gunduz, O., Sahin, Y. M., Agathopoulos, S., Ben-Nissan, B., & Oktar, F. N. (2014). “A new method for fabrication of nanohydroxyapatite and TCP from the sea snail Cerithium vulgatum”. J. Nanomater. 2014: 1.
- [4] J. M. Deitzel, J. Kleinmeyer, D. Harris and N. C. Beck Tan, Polymer 42 (2001) 261-272.

Effects of the pneumatic gait assist system on the lower extremity muscles during walking using superficial EMG

İbrahim MUTLU

Department of Biomedical Engineering
Kocaeli University
Kocaeli, TURKEY
mutluibrahim@gmail.com

Fatih TEZEL

Department of Biomedical Engineering
Kocaeli University
Kocaeli, TURKEY
fatihtezel@gmail.com

Abstract—Pneumatic wearable walking support device (PWWS) is especially designed to increase performance in repetitive gaiters such as factory workers. The support of the device in the lower extremities was measured by evaluating myoelectric signals obtained from the EMG measurement on leg muscles during the gait cycle swing phase. Twelve male volunteers were measured three times from right side of the body on the treadmill, at the speed of 2.5 km/h for 2 minutes, without/with device, device-off and device-on. When the device was running – in device-on mode- , there was a decrease in Rectus Femoris (RF) muscle mean amplitude of 3 volunteers as a result of superficial EMG, an increase in mean amplitude in the remaining 9 volunteers, a decrease in 7 volunteers in the mean amplitude of Vastus lateralis (VL) muscle, and an increase in 5 volunteers. In 2 volunteers, the mean amplitudes of both muscles measured were reduced during instrument use (device-on mode). It was seen that the PWWS supported these two muscles, which play a key role in movement the thighs and legs, in the swing phase of the gait cycle during device-on mode. In conclusion, the performance can be maintained constantly by adjusting such as thigh-leg size, person weight, and thigh-leg thickness parameters or considering walking habits of the person in the design of such devices and providing the necessary ergonomics by using a flexible and light material in the structure of the device.

Keywords—Wearable walking helper; Pneumatic system; EMG measurement)

I. INTRODUCTION

Nowadays, auxiliary mechanisms are gaining importance due to the increase of the elderly population and the current working conditions. Especially, gait ability is the most necessary functional movement during life. For this reason, except for wheeled systems, systems which will make it easier to step are needed. Many researchers have invented and developed walker-type support system. In this study, A PWWS is specially designed to increase efficiency for the factory walkers during the swing phase of walking and measured the efficiency of PWWS on the subjects. The main aim of this study is to evaluate the myoelectric signals obtained by superficial EMG measurement during walking and to have knowledge about the support of PWWS to the lower extremity muscles, to create the groundwork for new studies to be done in this topic.

II. MATERIAL AND METHODS

A pneumatic cylinder and its valves were mounted on a post-op knee brace with aluminum bar. Then the device was fitted to the subjects. Three measurements from the volunteers were performed from VL and RF muscles in the right thigh region for 2 minutes on the treadmill. In all measurements, the walking speed was set at 2.5 km/h to provide pneumatic piston activation of the PWWS. The first measurement was performed without the PWWS, while the second measurement was performed with device attached, but pneumatic piston was inactive in device-off mode in order to observe the effect of the weight of the apparatus and the adjustment points of the volunteer. The third measurement was made while the device was active in device-on mode. Superficial EMG measurements were performed by a 4-channel Biopac MP36R instrument and the results obtained by comparing the mean amplitudes of the myoelectric signals produced by the muscles using the Biopac Student Lab 4.0 software were evaluated.

III. RESULTS AND DISCUSSION

The myoelectric signals of RF and VL muscles of the 3 volunteers resulted in a reduction in the mean amplitude of RF and an increase in mean amplitude of the remaining 9 volunteers. In the mean amplitude of VL, a decrease was seen in 7 volunteers and an increase was seen in 5 volunteers. During the use of the PWWS in 2 volunteers, the mean amplitudes measured in both muscles decreased together. The PWWS supports the RF in 4 volunteers and the VL in 5 volunteers in device-off mode. That means the average amplitudes of the muscles decreased in both muscles of these 4 volunteers. In device-on mode, RF muscle of 2 volunteers and VL muscle of 5 volunteers were supported by the PWWS. It was seen that there was no device support in the remaining measurements. The severity of PWWS is thought to result in different outcomes in different volunteers due to restricting hip-knee movements during the walking cycle. So, it is considered that the necessary ergonomics should be provided.

2D and 3D Drug-Testing Platforms for Glioma Cell Line

Seda Ceylan
Bioengineering Department
Adana Science and Technology University
Adana, Turkey
sceylan@adanabtu.edu.tr

Dilek Göktürk
Bioengineering Department
Adana Science and Technology University
Adana, Turkey
dgokturk@adanabtu.edu.tr

M. Damla Özdemir
Bioengineering Department
Adana Science and Technology University
Adana, Turkey
md_ozdemir@hotmail.com

Didem Demir
Chemical Engineering Department
Mersin University
Mersin, Turkey
didemdemir@mersin.edu.tr

Nimet Bölgen Karagülle
Chemical Engineering Department
Mersin University
Mersin, Turkey
nimet@mersin.edu.tr

Abstract— Tissue engineering focuses on clinical applications in regenerative medicine. Tissue engineering scaffolds can be used as matrices for three dimensional (3D) cancer cell cultures to imitate the tumors and better understand tumor development and metastasis. The purpose of this study was to reveal the effects of Etoposide (chemotherapy drug) on the two dimensional (2D) and 3D culture models. In this study, PVA/Starch cryogel scaffolds were produced with different ratios (90:10;70:30;50:50) and prepared scaffolds were analysed by FTIR and SEM. Swelling ratio and degradation profile of the scaffolds were also determined. 3D culture was established by culturing Human U-87 MG glioma cancer cells within highly porous PVA/Starch cryogel scaffolds. MTT assay and SEM was used to investigate the biocompatibility of the scaffolds and cell morphology. To investigate the drug resistance, cytotoxic effects of Etoposide were compared in 2D and 3D cell culture models. Results show that, in addition to tissue engineering applications, scaffolds can be potentially used as 3D model systems to better simulate the in vivo tumor microenvironment.

Keywords—3D tumor engineering, Scaffolds, Drug resistance, Polyvinyl alcohol, Starch

DWT and Descriptive Features based Mammogram Classification for Breast Cancer Detection

M. MOHSIN JADOON, IHSAN UL HAQ

Department of Electronic Engineering, Faculty of Engineering & Technology, International Islamic University Islamabad, Pakistan.

mohsin.khan@iiu.edu.pk

Rizwan sadiq

Department of Electronic Engineering, Faculty of Engineering & Technology, KOC University Istanbul, Turkey.

rsadiq13@ku.edu.tr

Abstract—The World Health Organization (WHO) has indicated breast cancer as the second most lethal leading cause of cancer in women. In the advanced computerized era, computer aided diagnosis (CAD) systems framework are generally developed to detect and characterize the breast cancer in light of screening mammography test. Various techniques have been developed for mammogram screening examination to get high accuracy, robustness and exactness. The three class classification is still an open research area because the tumor can be benign, malignant or normal. In this paper, a novel scheme for three class classification study is presented. Mammogram patches are filtered by the Columnwise neighborhood operations filter (COLFILT). Discrete Wavelet Transform (DWT) is used to decompose the enhanced patches into sub-band images. Six rotation and scale invariant features are extracted by using the Dense Scale Invariant Feature Transform (DSIFT). In last step a features matrix is generated that is used as input to Multi Layer Perceptron (MLP). Image Retrieval in Medical Application (IRMA) database is used to test the proposed scheme. Simulation results have verified the importance of the proposed idea in comparison to the existing schemes in the literature

Keywords—Mammography, Detection, cancer, Multi-Layer Perceptron

I. INTRODUCTION

According to breast cancer care, United Kingdom (UK) facts and statistic for year 2015 shows that the breast cancer is the second most regular reason for death from disease in ladies in the UK. Consistently around 55,000 are analysed for the breast cancer in UK, which is like one individual in every 600 seconds interval. In UK one women out of eight in her life time have a chance to be diagnosed as a patient of breast cancer [1]. Breast cancer usually takes time to develop and symptoms are shown very late. As there is no effective way to cure later stage breast cancer, many lives can be saved if it can be detect at early stage. Therefore for the early detection of breast cancer it is recommended by America Cancer Society (ACS) that every women who have risk factor of breast cancer should take screening test once in a year [2].

In modern technological era, CAD system widely use mammogram screening method to classify the breast tumour. CAD system typically rely on machine learning classifier (MLC) to classify the tumour. It needs discriminant descriptive feature that can help MLC to classify the image into multiple classes. In past decade various schemes have been proposed for mammogram screen methods to get high characterization precision, robustness and efficiency. However it is still an open area of research.

Many researchers have studied mammogram images for two class classification and achieved significant results. Mazurowski et al. [3] proposed a template based a recognition algorithm for breast masses. Their data set is based on 1,852 Digital Database for Screening Mammography (DDSM) images and it achieved accuracy up to 83%. Lesniak et al. [4] compared the performance of Support vector machine (SVM) based classification with nearest neighbor algorithms. They have used a private data set of mammography patches containing 10,397 images. The accuracy of their model is up to 67%. Wei et al. [5] present relevance feedback learning method and performed classification using SVM radial kernel with a data set of 2,563 DDSM images. Tao et al. [16] has compared the performance of two classifier named curvature scale space, and local linear embedded matric using a database of 476 and 415, and the accuracy of the two classifiers are 75% and 80% respectively. Bovis & Sing [6] and in [9] Elter & Hasslmer performed classification using Artificial Neural Network (ANN) and Euclidean metric classifier respectively and achieved a performance over 85 %. All of the above mentioned researchers have used two class classification but two class classification is not enough to avoid unnecessary biopsy because the tumour can be either benign or malignant. Vani et al. [12] proposed Extreme Learning Machine (ELM) method to classify mammograms of the Mammographic Images Analysis Society (MIAS) [13] database. Performance results of the algorithm out performed other techniques with same database. Jasmine et al. [14] performed two class classification with his proposed method based on wavelet analysis using ANN. This experiment is performed using MIAS database of 322 images and has achieved accuracy up to 87%. In [15] Xu, et al. compared the performance of three NN and has suggested that improved performance through



Figure 1: Sample images of mammogram patches

From literature, it can be seen that significant results have been achieved for two-class classification. However, for three-class classification, either data set is small or it has not achieved very promising results. ANN have been widely used for the classification of biomedical images. ANN is capable of precision for classification particularly for biomedical problems [11]. Standard MLP use back propagation methods techniques, which train feed forward ANN. They are supervised networks so they also need training. In this work, a novel classification technique is proposed for large dataset of mammograms using feed forward MLP. At first, a two-class classification is carried out. The features regarding scale invariant and rotation are extracted by using DSIFT descriptor. Then same procedure is followed for the three-class classification study for the malignant, benign and normal. The patches of mammogram are filtered by the column wise filter. DWT is used to decompose the enhanced patches into four sub- band images. Six scale invariant and rotation features are extracted by using the DSIFT descriptor. In the end a features matrix is generated that process as input to MLP. Results have verified the importance of the proposed scheme in comparison to the existing schemes in the literature. A flow diagram of the proposed scheme is given in Figure 2. The rest of the paper is sorted out as follows: Section 2 explain the feature extraction and representation. Section 3 describes the MLP. Section 4 and 5 comprises the simulation / results and conclusion respectively.

IV. FEATURE EXTRACTION AND REPRESENTATION

Enhancement technique is used to enhance the possibly degraded contrast in some of mammogram images; therefore as pre-processing step we have applied a contrast enhancement technique i.e.

$$I \leftarrow \text{COLFILT} (E, 3) \quad (1)$$

Where column wise filter enhances the image E depending upon the global mean and global variance of the image [29].

A. Two - Dimensional Discrete Wavelet Transform

In the next step enhanced mammogram patch I is decomposed into four sub groups by utilizing DWT. It is the combination of digital filter banks and down-samplers. It consist of high-pass (h) and low-pass (l). The quantity of banks is set according to the desired resolution of the architect [27]. As the mammogram image is a 2D signal, separable wavelet functions are used to compute the DWT. The columns and rows of the image are independently process through the 1D WT to obtain the 2D-DWT. In frequency domain, the mammogram patch I is subdivided into four sub-band images at resolution 2^{j+1} . B^a is the approximation image. B^h , B^v and B^d are three detailed sub-band images in horizontal, vertical, and diagonal directions respectively at resolution 2^{j+1} .

As the result of wavelet decomposition the enhanced image I decomposed into four sub-band components like igh - High (HH), High - Low (HL), Low - High (LH) and Low - Low (LL), that correspond to sub images are B^a , B^d , B^v and B^h , respectively.

B. Dense Scale Invariant Feature Transform

Next, DSIFT descriptor is applied to all the sub-bands components. DSIFT used Difference-of-Gaussian (DOG) function to distinguish potential interest focuses points [25], which were invariant to orientation and scale.

$$D(x, y, \sigma) = (G(x, y, \alpha\sigma) - G(x, y, \sigma)) * I(x, y) \quad (2)$$

Where α a constant multiplier and variable scale is is Gaussian, which is represented by $G(x, y, \sigma)$ i.e.

$$G(x, y, \sigma) = \frac{1}{2\pi\sigma^2} e^{-\left(x^2+y^2/2\sigma^2\right)} \quad (3)$$

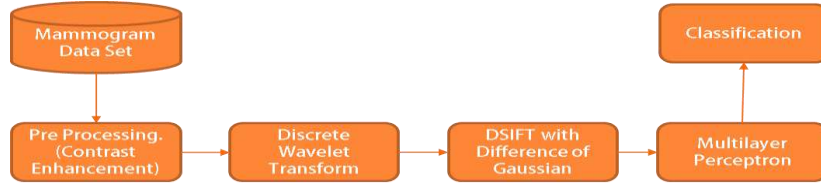


Figure 1: Block Diagram

$$D(x, y, \sigma) = G(x, y, \alpha\sigma) * I(x, y) - G(x, y, \sigma) * I(x, y) \quad (4)$$

$$= L(x, y, \alpha\sigma) - L(x, y, \sigma)$$

Where scale space of an image $L(x, y, \alpha\sigma)$ is the convolution of G with an input image $I(x, y)$. DOG was utilized here rather than gaussian to enhance the computation speed.

In keypoint localization stage, hessian matrix is utilized to compute key curvatures that eliminate the edges by rejecting the low contrast point [25]. Keypoint descriptors were found out by using a three dimensional histogram. Here the first two dimensions correspond to image spatial dimensions and the third dimension corresponds to the image gradient direction and it is computed centred at the keypoints.

The DSIFT descriptor is applied to all the sub-bands with step size 4 and radius size 5; while feature matrix having dimension (128 x 400) are extracted for all the sub bands.

From the columns of this matrix, six statistical features (kurtosis, mean, skewness, energy, maximum and standard deviation) are extracted for each sub-band. The resultant feature matrix is of the shape of (128 x 6), which is reshaped into a vector form of (1 x 768). Coefficient weights are apply to the sub band images according to the equation 5.

$$Feature\ vector = (3 * LL + 2 * LH + 2 * HL) \quad (5)$$

Equal zero padding is performed on start and end columns such that feature vector as (1 x 784). Enhancement and feature extraction steps are performed on all the data set so that we have a data matrix Y of the shape (2796 x 785), where 2796 are the sample images and 784 features of the each sample. Every sample has a last column label, which belongs to its receptive patch class

V. MULTI LAYER PERCEPTRON

In the last step, the features set Y is used as input to ANN. ANN are mostly used in classification due to significant success in nonlinear mapping among the input features and

desired output [26]. MLP is an ANN consist of an input layer, hidden layer and an output layer. The number of hidden layers depend upon the designer and application. Each node in MLP

performs two function. At first step, it computes the weighted sum of the input along with the bias.

$$s_j = \sum_{i=1}^n (W_{ij} X_i) - \theta_j, \quad j = a, a1, a2, \dots, z \quad (6)$$

Where X_i shows the i^{th} input, W_{ij} indicates the connection weight from input i to j^{th} hidden layer, θ_j is bias of j^{th} hidden layer and n is number of input neuron.

Activated function is used to generate the output of each neuron, i.e.

$$S_j = f(s_j) \quad (7)$$

$f(s_j) = \text{sigmoid}(s_j)$ and is defined as:

$$\text{sigmoid}(s_j) = \frac{1}{1 + \exp(-s_j)}, \quad j = a, a1, a2, \dots, z \quad (8)$$

The final output are defined as:

$$o_l = \sum_{j=1}^z (W_{jl} S_j) - \tilde{\theta}_l, \quad l = a, a1, a2, \dots, m \quad (9)$$

Where W_{jl} indicates the connection weight from j^{th} hidden layer to output l , $\tilde{\theta}_l$ is bias of l^{th} hidden layer and l is the output neuron. In output layer each neuron use activated function to generate the output, i.e.

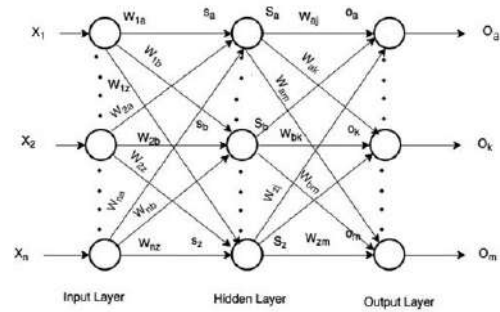


Figure 3: Multi layer perceptron model

$$O_l = f(o_l) \quad (10)$$

Where $f(o_l) = \text{sigmoid}(o_l)$ and is defined as:

$$\text{sigmoid}(o_l) = \frac{1}{1 + \exp(-o_l)}, \quad l = a, a1, a2, \dots, n1$$

In this experiment, we use MLP to classify this data set into three classes. To train the MLP optimal values of weights and bias are required for desirable output. In our experiment, we have used MLP with 500 hidden units and one hidden layer. Figure 3 presents the basic concept of MLP.

VI. SIMULATION / RESULTS

A. Database

We have used IRMA dataset [28] for this study. Total 2796 patches of original mammogram images are used for this experiment. Selected IRMA patches consist of four different sources including 2,576 images from DDSM. 150 images from MIAS, Lawrence Livermore National Laboratory (LLNL) and Rheinisch-Westfälische Technische Hochschule (RWTH) contribute 1 and 69 images respectively. The selected images are further divided into two classes (normal and cancerous) and three Classes (malignant, benign and normal) as prescribed in IRMA dataset. The final size of mammogram images patches are 128 x 128.

Initially a two-class classification is done by using DSIFT, Local Configuration Pattern (LCP) and Histogram Oriented Gradient (HOG) methods. Figure 4 shows the result of two-class classification. It can be observed that in two-class classification HOG method performs better with accuracy rate 83.2 %. The other two schemes LCP and DSIFT have accuracy rates of 82.26% and 74.6% respectively. Then three-class classification is performed by using the same methods. In three-class classification with large dataset of mammogram images, results from all three state of the art techniques are not very promising so we proposed our scheme. We initially train our model with MLP and then used the output of MLP as input for the classifier. In this research, SVM with linear kernel is used for classification.

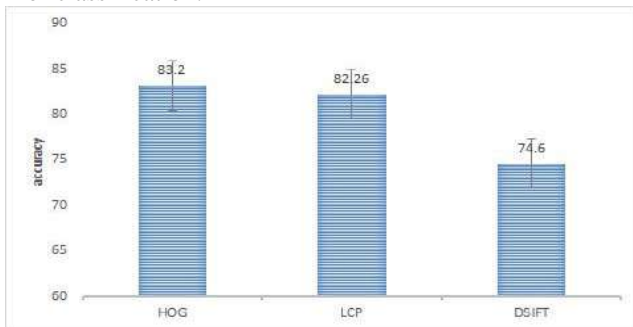


Figure 4: Two class classification accuracy rate for different methods

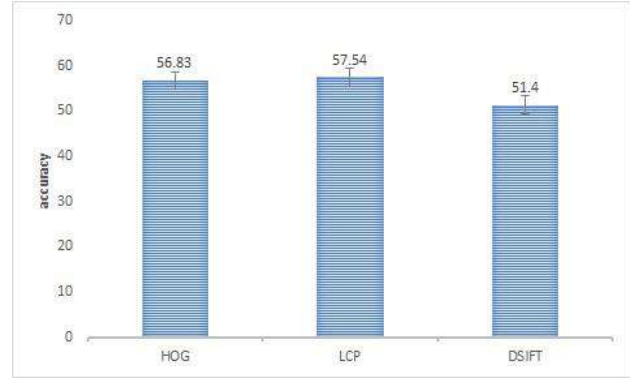


Figure 5: Three class classification accuracy rate for different methods

Figure 5 shows the result of three-class classification. Here LCP method performs better than the other two schemes but the results is not so promising, with the best result accuracy of 57.54%.

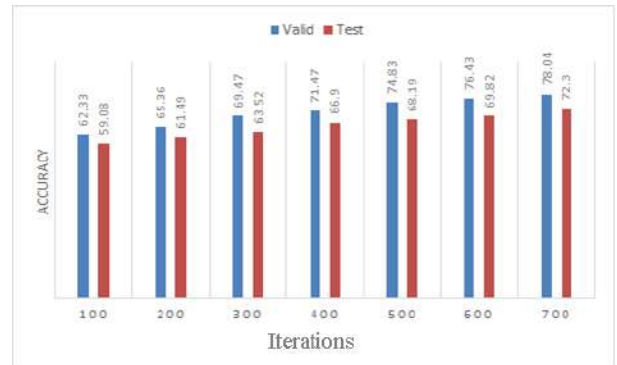


Figure 6: Accuracy rate of proposed method for test and validation data set

Figure 6 shows the results of proposed method. Note that the classification results for three-class category obtained by proposed scheme is more pleasing as compared to the existing schemes in Figure 5. Proposed method achieved the accuracy of 72.3% and 78.04% on test data set and validation dataset respectively.

VII. CONCLUSION

Novel mammograms classification method for breast cancer detection based on MLP is proposed. Result shows the significance of our proposed method for large amount of mammogram data as compared to other state of art techniques. In future, this method can be used with the combination of deep neural networks techniques for more accuracy.

ACKNOWLEDGMENT

The data set used for this experimental study is provided by the IRMA group, Aachen, Germany, <http://irma-project.org.cknowledgment>

REFERENCES

- [1] <https://www.breastcancercare.org.uk/about-us/media/press-pack-breastcancer-awareness-month-2015/facts-statistics-2015>.
- [2] American Cancer Society, <http://www.cancer.org/cancer/breastcancer/detailedguide/breast-cancer-detection>
- [3] M.A. Mazurowski, Lo. JY, B.P. Harrawood and G.D. Tourassi, "Mutual information-based template matching scheme for detection of breast masses mammography to digital breast tomosynthesis," *Journal of biomedical informatics*, 2011, vol. 44, no.5, pp. 815-23.
- [4] Lesniak, Jan, R. Hupse, M. Kallenberg, M. Samulski, R. Blanc, N. Karssemeijer and G. Szekely, "Computer aided detection of breast masses in mammography using support vector machine classification," *SPIE Medical Imaging*, 2011.
- [5] W. CH, Y. Li and P.J. Huang, "Mammogram retrieval through machine learning," *BI-RADS standards. Journal of biomedical informatics*, 2011, vol. 44, no.4, pp. 607-14.
- [6] K. Bovis and S. Singh, "Classification of mammographic breast density using a combined classifier paradigm," *medical image understanding and analysis (MIUA) conference Portsmouth*, 2002.
- [7] A. Tagliafico, G. Tagliafico, S. Tosto, F. Chiesa, C. Martinoli, LE. Derchi and M. Calabrese, "Mammographic density estimation: comparison among BI-RADS categories a semi-automated software and a fully automated one," *The Breast*, 2009, vol. 18, no.1, pp. 35-40.
- [8] T.S. Subashini, V. Ramalingam and S. Palanivel, "Automated assessment of breast tissue density in digital mammograms," *Computer Vision and Image Understanding*, 2010, vol. 114, no.1, pp. 33-43.
- [9] M. Elter and E. Hablmeyer, "A knowledge-based approach to the CADx of mammographic masses," *Medical imaging*, 2008.
- [10] T.M. Deserno, M. Soiron, JEE. de Oliveira, A. de and A. Araujo, "Towards computer-aided diagnostics of screening mammography using content-based image retrieval," *Proceedings SIBGRAPHI*, 2011, pp. 211-9.
- [11] A. Pinkus, "Approximation theory of the MLP model in neural networks," 1999, vol. 8, no. 1, 143-195.
- [12] G. Vani, R. Savitha, and N. Sundararajan, "Classification of abnormalities in digitized mammograms using Extreme Learning Machine," *Control Automation Robotics and Vision*, 2010, pp. 2114-211.
- [13] J. Suckling, "The Mammographic Image Analysis Society Digital Mammogram Database," *Excerpta Medica. International Congress Series*, 1994, pp. 375-378.
- [14] J. A. Jasmine, A. Govardhan, and S. Baskaran, "Microcalcification detection in digital mammograms based on wavelet analysis and neural networks," *Control, Automation, Communication and Energy Conservation*, 2009, pp. 1-6.
- [15] W. Xu, W. Liu, L. Li, G. Shao, and J. Zhang, "Identification of Masses and Microcalcifications in the Mammograms Based on Three Neural Networks: Comparison and Discussion," *Bioinformatics and Biomedical Engineering*, 2008, pp. 2299-2302.
- [16] Y. Tao, S.C.B. Lo, L. Hadjiiski, H.P. Chan and T.M. Freedman, "Birads guided mammographic mass retrieval," *Medical imaging*, 2011.
- [17] J. Ge, B. Sahiner, L. M. Hadjiiski, H.P. Chan, J. Wei, M. A. Helvie and C. Zhou, "Computer aided detection of clusters of microcalcifications on full field digital mammograms," *Medical Physics*, 2006, vol. 33, no. 8, pp. 2975-2988.
- [18] A. Krizhevsky, I. Sutskever and G.E. Hinton, "Imagenet classification with deep convolutional neural networks," *Advances in neural information processing systems*, 2012, pp. 1097-1105.
- [19] A.R. Jamieson, K. Drukker and M.L. Giger, "Breast image feature learning with adaptive deconvolutional networks," *SPIE Medical Imaging*, 2012.
- [20] J. Arevalo, F.A. Gonzalez, R. Ramos-Pollan, J.L. Oliveira and M.A. Guevara Lopez, "Convolutional neural networks for mammography mass lesion classification," *Engineering in Medicine and Biology Society (EMBC)*, 2015, vol. 25, pp. 797-800.
- [21] A. Mert, E. Bilgili and A. Akan, "Breast cancer detection with reduced feature set," *Computational and mathematical methods in medicine*, 2015, pp. 1-11.
- [22] J. Dheeba, N.A. Singh and ST. Selvi, "Computer-aided detection of breast cancer on mammograms: A swarm intelligence optimized wavelet neural network approach," *Journal of biomedical informatics*, 2014, vol. 49, pp. 45-52.
- [23] A.M. Abdel-Zaher and M. Eldeib, "Breast cancer classification using deep belief networks," *Expert Systems with Applications*, 2016, vol. 46, pp. 139-44.
- [24] M.J. Islam, M. Ahmadi and M.A. Sid-Ahmed, "An Efficient Automatic Mass Classification Method in Digitized Mammograms Using Artificial Neural Network," *International Journal of Artificial Intelligence & Applications (IJAIA)*, 2010, vol. 1, no. 3, pp. 1-13.
- [25] D.G. Lowe, "Distinctive image features from scale-invariant keypoints," *International journal of computer vision*, 2004 vol.60, no. 2, pp. 91-110.
- [26] J. Shi, B.D. Sekar, M.C Dong and W.K. Lei, "Fuzzy neural networks to detect cardiovascular diseases hierarchically," *Computer and Information Technology (CIT), IEEE 10th International Conference*, 2010, pp. 703708
- [27] S. Mallat, "A Wavelet Tour of Signal Processing," *Academic Press*, 1999.
- [28] J.E. Oliveira, M.O. Gueld, A.D. Araujo, B. Ott and T.M. Deserno, "Toward a standard reference database for computer-aided mammography," *Medical Imaging*, 2008.
- [29] R.C. Gonzalez and R.E. Woods. "Digital Image Processing," *3rd Edition*, 2006.

Analysis of Limbic System Volume with Atlas Based Volume Measurement Pipeline on Alzheimer Disease

Muhammet Üsame ÖZİÇ

Department of Electrical-Electronics Engineering
Selcuk University
Konya, TURKEY
muozic@selcuk.edu.tr

Seral ÖZŞEN

Department of Electrical-Electronics Engineering
Selcuk University
Konya, TURKEY
seral@selcuk.edu.tr

Abstract— Segmentation of any region of interest in three-dimensional structural MR images is a difficult and laborious process. Manual segmentation of these regions is relative to user dependence and experience. Electronic brain atlases, which have been accepted by international standards and have proven to be reliable, are used in the literature to address these challenges. There are very few studies on how to use the brain atlas as a pipeline. In this study, a pipeline was developed to measure the volume of the brain limbic system using the atlas based segmentation technique. Calculated volumes were statistically compared between Alzheimer's and Normal images from the Open Access Series of Imaging Studies database. Statistical analysis revealed that the limbic system volume was significantly different between Alzheimer's Patient and Normal Control, and decreased in average. At the same time, the ratio of limbic system volume to total brain volume was discussed in terms of its effect on the analysis result. SPM8 and MRICro programs were used in the study.

Keywords— Brain Atlas, Alzheimer, MRI, Volume Measure

I. INTRODUCTION

The human brain is divided into three main parts: gray matter (GM), white matter (WM), cerebrospinal fluid (CSF). The GM forms the cortex layer that surrounds the outside of brain, and subcortical regions are also present in the brain's inner parts. The CSF is a fluid that protects the brain from impulses and the BM is a kind of communication cables that provide communication between GM and body functions. If any of the body functions have lost their function because of the brain, this is a problem caused by the degeneration of the relevant functional center on GM. This problem is caused by the occurrence of volumetric losses or textural defects [1].

Alzheimer's Disease (AD) is a neurodegenerative disease that usually starts with age and is not reversible. As the AD phases begin with mild forgetfulness, it makes it impossible for the person to do daily work. The degeneration that begin in the hippocampus and amygdala regions, which are memory centers in the brain, then spread to other regions, especially the limbic system. In addition to volumetric loss, the neurofibrillary tangles and senile plaques wrap around the brain structures on

a micro basis. The alteration of the amount of some proteins in CSF is another biomarker in AD [2]. Rapid and accurate segmentation of brain regions in AD and volume analysis are important in terms of diagnosis of the disease. If the volumes of biomarkers in AD are adequate and are followed up gradually over time in a strong population, the stages of newcomers can be statistically determined. The delaying medication needed to prolong the interval of the phase can be given in time. Volume studies done for this purpose are divided into manual and automatic methods. Manual methods are volume calculations by peripheral drawings of areas of interest by a specialist radiologist, neurologist or anatomist. This method can give relative results in terms of user dependency and inexperience. Auto-based methods are computer programs based on brain atlases [3]. In this study, a brain atlas based volume measurement pipeline of the limbic system, one of the basic lobes is initiated by AD, was developed and statistical analysis of volume differences between AD and Normal Control (NC) was performed.

II. ATLAS BASED VOLUME MEASUREMENT

Atlas based approach is the mapping of the MR image to the corresponding regions by overlapping a predefined template image. Brain labeling studies are based on very ancient histories. One of the first studies to be used today was made by German scientist Korbanian Broadmann in 1909. Korbanian Broadmann labeled the brains in 52 different regions and defined "Broadmann Fields", which are still used in his own name [4]. In 1988, scientists named Talairach and Tourneux identified the Anterior Commissure (AC) as $x, y, z = 0$ and designated the brain center. With reference to this point, the line leading to the front and the back of the brain is accepted as y -axis, the line leading to the ears is accepted as x -axis, and the line leading to the head and neck is accepted as the z -axis. These axes have made it practical to assign coordinates to the brain regions according to a reference system. Talairach did this work at the age of 60 a right-handed dominant French female cadaveric brain. The brain is parceled with images showing the sagittal, axial and coronal axes with high resolution [5]. Three dimensional stereotactic space was created from the parceled

regions and a brain mask database named "Volume Occupancy Talairach Labels" consisting of 148 regions was produced [6]. This study has been criticized because it does not represent the general population, mapping from a single individual. To overcome this shortcoming, the Montreal Neurological Institute (MNI) has continued to work for the general population, again referring to the axis of the Talairach. The template, which is formed by taking 305 healthy MR averages and developed by MNI, is often used in normalization processes because it is a representative image of all brains. The MNI and Talairach coordinate systems differ from the points they represent, even though the AC point is centralized. Therefore, a point in the Talairach coordinate system may not compatible with the same point in MNI. To avoid this incompatibility, MATLAB code scripts such as "mni2tal" and "tal2mni" are used [7]. Developed by Wake Forest University, the WFU Pick Atlas is a collection of different atlases and provides the masks of the respective regions in a practical way. The program maps the Talairach Deamon (TD) tags (TD Broadmnn areas, TD Lobes, TD Hemipheres, TD Labels, TD Type), Automated Anatomical Labeling (AAL), IBASPM116, IBASPM71 atlas. The mask of a selected region can be obtained as converted into MNI space. These generated masks can be easily used in MNI space-aligned structural MR images [8].

III. MATERIAL AND METHODS

The data used in the application consist of structural MR images labeled with the Clinical Dementia Rating (CDR) from the Open Access Series of Imaging Studies (OASIS) database. CDR is a psychological test used to measure the degree of illness in AD. CDR0: Normal CDR0.5: Mild Cognitive Impairment CDR1: mild stage, CDR2: modarete stage, CDR3: severe stage. Dementia and normal over 60 years of age were obtained from the database and only CDR labeled data were taken [11]. 99 AD and 97 NC MR images were taken in three dimensional .* nii format. 030 and 031 MR images were removed from the work because they failed in the MRIcro program. The imaging protocol of the structural MR images are 1.25 mm slice thickness, pixel resolution 1x1 mm without any gap between the cross sections, the imaging protocol of TR = 9.7 ms, TE = 4.0 ms, Flip angle = 10, TI = 20 ms, T1-weighted MP-RAGE (Magnetization-Prepared Rapid Gradient Echo) with a 256x256 matrix sized 1.5 T Siemens device. The demographic structure of the population set used is given in Table 1.

Table 1. Demographic features of the data used

	NC	AD
Mean Age	76.03	76.64
M/F	26/71	40/59
CDR	0	0.5(70)/1(27)/2(2)

From the database, raw MR images with image size of 256*256*160, voxel size of 1*1*1, prefixed with "OAS1_xxxx_MRy_mpr_ni_anon_sbj_111" were taken. Since the

limbic system is a part of GM, it must be segmented into MNI space by preserving the GM's volume from the raw MR images. For this, Voxel Based Morphometry toolbox (VBM8) (<http://www.neuro.uni-jena.de/Vbm/>) [9], working under Statistical Parametric Mapping (SPM8) [10] (<http://www.fil.ion.ucl.ac.uk/spm/>) library was used. VBM8 offers a practical application since it performs noise reduction, normalization and segmentation in one interface in one operation. The DARTEL method, which has proven to be better than many methods for registration, has been chosen [12]. In the study, modulated normalized GM used the "affine + nonlinear" option, which preserves the volume after normalization. Although the VBM8 normalizes to the MNI space, the coordinate shift originates because of the default Tissue Probability Map (TPM) in VBM8. This shift is corrected by performing "Coregister" operation on the TPM with the AC point (x,y,z)=0 so that the modulated GMs exactly register with the AC point (x,y,z)=0. There is no interpolation during this process, only the image is shifted axially. The limbic system mask created with Wfu Pick Atlas was produced in the MNI space, with AC points (x,y,z)=0. However, since the voxel size is incompatible with GM, the masks are resliced using the "coregister" operation and the "nearest neighbor" interpolation method. As a result of this process, the GM and the mask were placed on the same coordinate plane with the same voxel size. The volume calculator was implemented with the "get_totals.m" script developed by Ged Ridgway (http://www.cs.ucl.ac.uk/staff/g.ridgway/vbm/get_totals.m). This script offers practical use in the volume calculation of the GM images that have been specially Jacobian determinants and the masks overlapping under GM. The preprocessing and volume calculations performed in Figure 1 are shown on the patient flow diagram with OASIS 028. Significance of Limbic system volume difference between AD and NC was analyzed by using MATLAB statistical tool.

IV. EVALUATION

All images taken from the OASIS database were processed through the operations shown in Figure 1 one by one. The total brain volume was summing up by calculating the volumes of GM, BM, BOS images modulated by VBM8 library with "get_totals.m" script. Differences between the two groups were examined by t-test in MATLAB. The statistical results and some descriptive statistics obtained in Table 2 are given.

Table 2. Statistical results and some descriptive statistics

	AD		NC		Stats
	Mean	Std	Mean	Std	
Limbic Lobe(ml)	53.148	6.092	56.087	5.443	5E-04
Limbic Lobe/TIV	0.0391	0.003	0.0416	0.002	2E-11

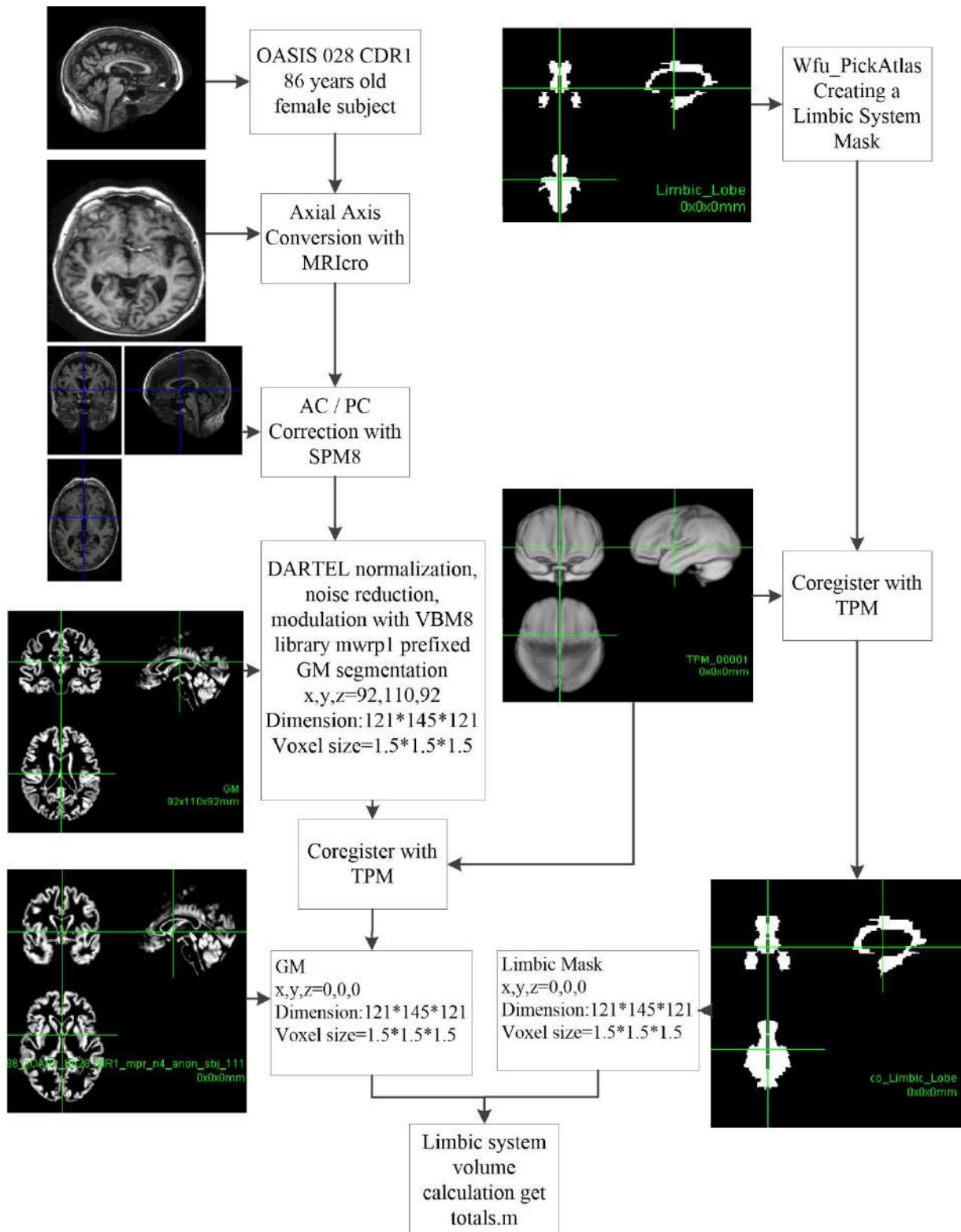


Fig 1. Atlas Based Volume Measurement Pipeline

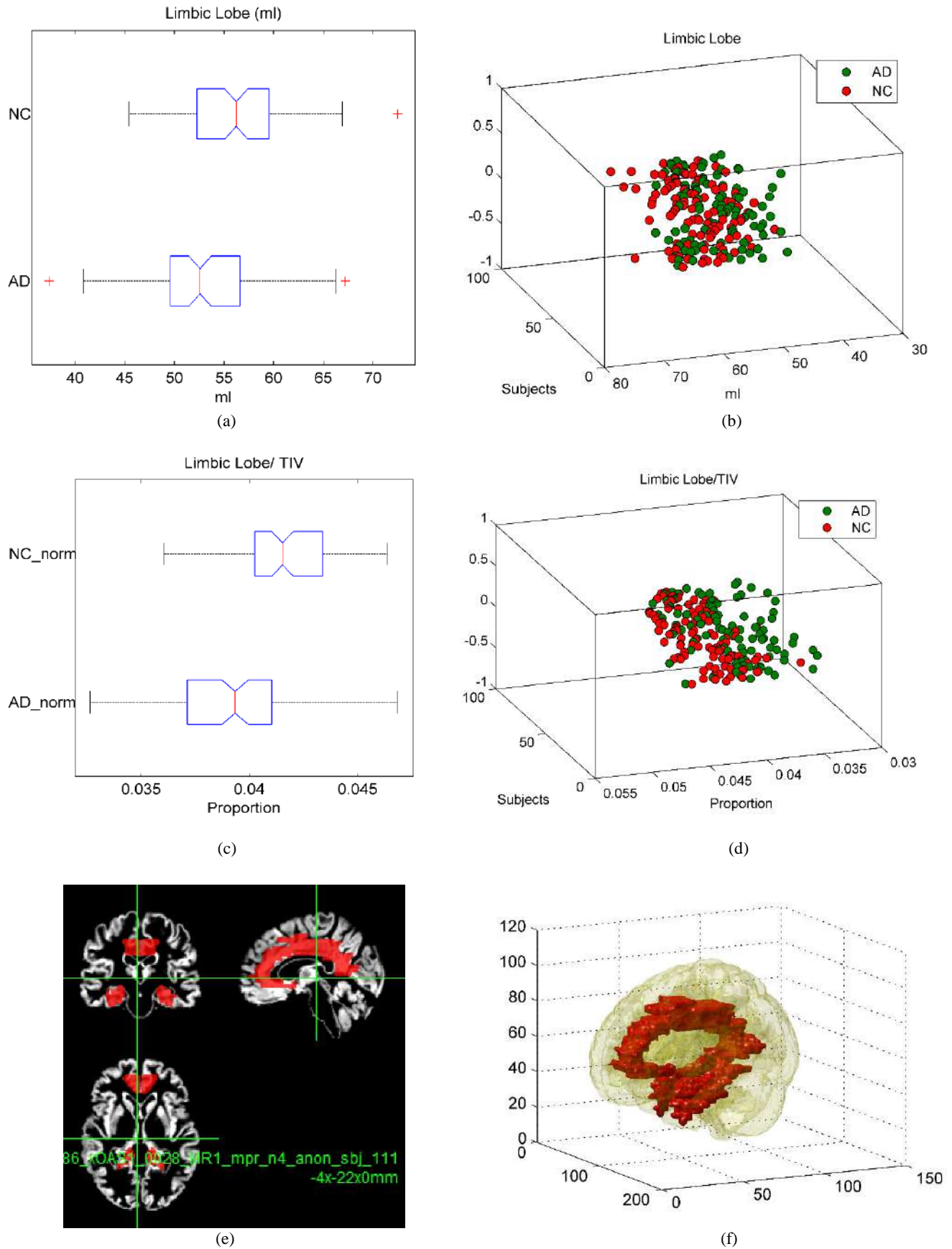


Fig. 2. (a) Box-plot for AD and NC Limbic Lobe Volume (b) Scatter diagram AD and NC Limbic Lobe Volume (c) Box-plot for AD and NC TIV normalized Limbic Lobe Volume (d) Scatter diagram AD and NC TIV normalized Limbic Lobe Volume (e) Superimposing Limbic Lobe mask and normalized segmented modulated image (f) 3D model Limbic Lobe inside brain

As shown in Table 2, the Limbic system volumes were higher in NC than in all brain normalization and non-normalization measurements with respect to AD. The limbic lobe volume and TIV ratio between AD and NC were statistically significant ($p < 0.05$). However, the ratio of the limbic system to the TIV was statistically more significant. Because each person's brain size is different, volume measurements differ from person to person. However, this bias can be corrected by normalizing any region volume to TIV as proven in this study.

When looked at the box-plot graph shown in Fig 2a, it shows outliers. This discrepancy is due to the fact that the total brain volume of each person is different. Even if the disease progresses, the total brain volume does not change, but the ratio of the functional regions in the brain to the total brain volume changes. Because of this, the brain regions measured in the literature are often normalized to the total brain volume. In Fig 2c, the outliers are moved together with the other outputs due to this normalization. In both box-plot charts, the median volume of the limbic system of NC is higher than the AD as expected. Fig 2b and 2d show the distribution of raw limbic lobe volume and TIV normalized limbic lobe, respectively. Fig 2d shows the normalized segmented modulated GM image with the superimpose of the limbic lobe mask and Fig 2e shows the three-dimensional shape of the limbic system mask in the brain. The limbic systems shown in both figures are very similar to the limbic system in the real brain.

V. CONCLUSION

In three-dimensional MR images, segmentation and volume calculation of the corresponding region is a difficult and laborious process. Since the boundaries of the corresponding regions are not clear in the MR images, it is almost impossible to find the transition regions by image processing methods. GM, WM and CSF volumes can be easily calculated after the segmentation process. However, brain atlases must be used to calculate the subcortical zone volumes of the gray matter. There are programs such as FSL [13] and Freesurfer [14] that calculate automatic volume in the literature. However, since analysis with Freesurfer takes a lot of time for an MR image and FSL may not offer practical use because it only calculates certain subcortical regions.

In this study, a practical pipeline for atlas based volume calculation of three dimensional MR images was proposed. The volume calculation for the limbic system in which the most volume loss occurred in AD was realized. A statistically significant difference was found when the limbic system volume was analyzed statistically between AD and NC. This significant difference is consistent with the literature. The masks and borders produced are discussed with an anatomist. The size inconsistency between the MR image and the atlas generated mask has been removed with some preprocessing. With this pipeline, statistical differences can be analyzed by calculating brain volume not only for limbic system but other lobe volumes. At the same time, subregions belonging to the lobe regions can be calculated with the pipeline developed by creating masks with Wfu Pick Atlas. These values will be calculated in other neurodegenerative diseases such as Parkinson, Frontotemporal dementia and used in future studies for pattern recognition and artificial intelligence.

REFERENCES

- [1] Seeley, W. W., Crawford, R. K., Zhou, J., Miller, B. L., & Greicius, M. D., "Neurodegenerative diseases target large-scale human brain networks", *Neuron*, 62(1), 42-52, 2009
- [2] Musiek, E. S., & Holtzman, D. M., "Origins of Alzheimer's Disease: Reconciling CSF biomarker and neuropathology data regarding the temporal sequence of A β and tau involvement", *Current opinion in neurology*, 25(6), 715, 2012
- [3] Wenger, E., Mårtensson, J., Noack, H., Bodammer, N. C., Kühn, S., Schaefer, S., ... & Lövdén, M., "Comparing manual and automatic segmentation of hippocampal volumes: reliability and validity issues in younger and older brains", *Human brain mapping*, 35(8), 4236-4248, 2014.
- [4] Brodmann, K., "Brodmann's: Localisation in the cerebral cortex.", *Springer Science & Business Media*, 2007
- [5] Talairach, J., & Tournoux, P., "Co-planar stereotaxic atlas of the human brain. 3-Dimensional proportional system: an approach to cerebral imaging", Thieme Medical Publishers, New York, 1988
- [6] Bazin, P. L., Pham, D. L., Gandler, W., & McAuliffe, M., "Free software tools for atlas-based volumetric neuroimage analysis." In *Medical Imaging* (pp. 1824-1833). International Society for Optics and Photonics, 2005
- [7] Lancaster, J. L., Tordesillas-Gutiérrez, D., Martinez, M., Salinas, F., Evans, A., Zilles, K., ... & Fox, P. T., "Bias between MNI and Talairach coordinates analyzed using the ICBM-152 brain template", *Human brain mapping*, 28(11), 1194-1205, 2007
- [8] Maldjian, J. A., Laurienti, P. J., Kraft, R. A., & Burdette, J. H., "An automated method for neuroanatomic and cytoarchitectonic atlas-based interrogation of fMRI data sets", *Neuroimage*, 19(3), 1233-1239, 2003
- [9] Kurth, F., E. Luders, and C. Gaser. "VBM8 toolbox manual." *Jena: University of Jena* (2010).
- [10] Penny, W. D., Friston, K. J., Ashburner, J. T., Kiebel, S. J., & Nichols, T. E. (Eds.). (2011). *Statistical parametric mapping: the analysis of functional brain images*. Academic press.
- [11] Marcus, D. S., Wang, T. H., Parker, J., Csernansky, J. G., Morris, J. C., & Buckner, R. L., "Open Access Series of Imaging Studies (OASIS): cross-sectional MRI data in young, middle aged, nondemented, and demented older adults", *Journal of cognitive neuroscience*, 19(9), 1498-1507, 2007
- [12] Klein, A., Andersson, J., Ardekani, B. A., Ashburner, J., Avants, B., Chiang, M. C., ... & Song, J. H. (2009). Evaluation of 14 nonlinear deformation algorithms applied to human brain MRI registration. *Neuroimage*, 46(3), 786-802.
- [13] Jenkinson, M., Beckmann, C. F., Behrens, T. E., Woolrich, M. W., & Smith, S. M. (2012). Fsl. *Neuroimage*, 62(2), 782-790.
- [14] Fischl, B. (2012). FreeSurfer. *Neuroimage*, 62(2), 774

Finite Element Analysis of Biomechanical Performance of Spinal Rods In Different Geometries

Yusuf Burak BOZKURT

Department of Mechanical Engineering,
Ataturk University,
Erzurum, Turkey

Mevra ASLAN

Department of Mechanical Engineering,
Ataturk University,
Erzurum, Turkey

Halim KOVACI

Department of Mechanical Engineering,
Ataturk University,
Erzurum, Turkey

A. Fatih YETİM

Department of Mechanical Engineering,
Faculty of Engineering and Architecture,
Erzurum Technical University,
Erzurum, Turkey

Ayhan ÇELİK

Department of Mechanical Engineering,
Faculty of Engineering,
Ataturk University,
Erzurum, Turkey

Abstract—*In situations such as congenital spinal defects, degenerations, tumors, spinal trauma, it is often necessary to use an implant to re-establish stability and bring the vertebrae in line. Any operation with a higher degree of difficulty contributes to the development of next generation equipment. It has become compulsory to work on modifying or completely replacing old systems due to the difficulties or deficiencies identified by the surgeon.*

Studies on modern biomechanics have made considerable progress in terms of understanding the mechanism of musculoskeletal movement. Innovative spinal implants have begun to offer a variety of internal fixation concepts for spinal stabilization. In this context new types of materials and designs have emerged, more successful surgical interventions and treatment methods have been developed. Nowadays, many similar principles are presented in pedicle screw / rod systems in different designs. The advantages and disadvantages of these systems, especially in terms of biomechanics, are the subject of this extensive work.

Spinal systems are implants commonly used in vertebral injuries and spinal injuries that require surgical intervention. It is very important that spinal systems are implanted correctly in diseases such as scoliosis, which makes the daily activities of people difficult. Thus, the so-called rod, which directly affects the spinal curve in the implant system, is an important part of this system. The geometric changes in the rods directly affect the biomechanical performance of the spinal implant. At the same time, less rigid rods increase patient comfort and this geometry improves the mechanical performance of the system. In this context, the literature includes rod designs with different geometric properties.

In this study, rods with three different geometries were designed and their effects on the dynamic rod structure were investigated. Solid models of parts were obtained using SolidWorks 2014 software. The mechanical tests of the obtained models were analyzed by ANSYS Workbench 17.0 software. These analyzes consist of tensile, compression, bending, torsion and fatigue tests. In this study, it was aimed to increase the fatigue life and strain value of the models subjected to biomechanical tests. Models that designed under the same load are expected to be less rigid than standard models and therefore they are more suitable for dynamic rod construction.

Keywords—*Spinal implant; dynamic rod; scoliosis; biomechanical testing; finite element analysis*

In Vitro Corm Regeneration from Saffron (Crocus sativus L.) sprout

Ayça ŞAHİNALP
Bioengineering Department
Faculty of Engineering
Firat University
Elazığ, Turkey

Nazmi GÜR
Bioengineering Department
Faculty of Engineering
Firat University
Elazığ, Turkey

Abstract— Saffron is one of the highly prized spices known since ancient times for its color, taste and disease treatment. Saffron spices obtain from stigma of Saffron plant (*Crocus sativus*). This plant is a sterile geophyte. The natural propagation rate of most geophytes including saffron is relatively low. The aim of this study determination of corm forming capacity of saffron sprout. The saffron corms obtained from a farmer from Safranbolu in Karabük province of Turkey. The corms were descaled and thoroughly washed under running tap water for 1h and then cleaned with the detergent Tween-20. These corms were then surface-disinfected with PPM. Murashige Skoog media [1] supplemented with 3% sucrose, 0.8% agar and different concentration and combination of PGR (BAP, NAA, 2,4D) used for in vitro corm regeneration from saffron sprout.

The cultures were incubated at 24 °C under 16/8 h (light/darkness) photoperiod with a light intensity approximately 3000 lux. 1 0.5 mg l⁻¹ BAP + 0.5 0.5 mg l⁻¹ NAA resulted in maximum corm regeneration [2].

Keywords: Saffron, corm regeneration, sprout

REFERENCES

- [1] Murashige, T., and Skoog, F., A Revised Medium for Rapid Growth and Bioassays with Tobacco Tissue Cultures. *Physiol. Plant.* 15, 473-497, 1962.
- [2] Smith, R.H., *Plant Tissue Culture: Techniques and Experiments*. Third edition. Academic Press, pp 208, 2013.

Investigation of the Cytotoxic Effect of *Lavandula dentata* on Glioblastoma Cell Line

M.Damla ÖZDEMİR

Nanotechnology & Engineering Sciences Department
Adana Science and Technology University
Adana, Turkey
md_ozdemir@hotmail.com

Dilek GÖKTÜRK

Bioengineering Department
Adana Science and Technology University
Adana, Turkey
dgokturk@adanabtu.edu.tr

Abstract— Glioblastoma multiforme (GBM) is the IV grade of glioma which is the most aggressive and the most frequent of the primary brain tumor. This highly invasive tumor has very poor prognosis and the lifespan of the patients generally couldn't be more than 15 months after the diagnosis. In many cases, the tumor can gain resistance against the treatment. Therefore, developing new therapy strategies, finding new approaches and combining them with the existing methods have importance to be able to prolong the lifespan of patients and fighting with this lethal tumor. In this study it was aimed to investigate the cytotoxic effect of *Lavandula dentata*, an aromatic Mediterranean plant in the glioblastoma and fibroblast cell cultures. Inspired by the traditional medicine, the plant was prepared as an infusion solution. Studies were carried out with the Glioblastoma (GBM) (U87 MG) and Mouse Embryonic Fibroblast (MEF) cell lines. Cytotoxic effects were determined by the neutral red cell viability assay

Keywords— Glioblastoma multiforme; U87MG; *Lavandula dentata*; Lavender

[5] Introduction

Glioblastoma multiforme (GBM) is an aggressive and invasive type of primary brain tumor [1–3]. GBM is a vascular tumor with very poor prognosis [4]. The usual treatment of the GBM is surgical resection, radio- and chemotherapy. Despite the important advances in treatment strategies, the lifespan of the patients generally couldn't be more than 15 months after diagnosis [5–9]. There are so many molecular alterations which involve in the development of GBM and cause to gain resistance to radio- and chemotherapies [10].

Lavender (*Lavandula*) is an aromatic, evergreen Mediterranean plant belongs to Lamiaceae family [11]. Like many plants belonging to the Lamiaceae family, lavender has served traditional medicine for hundreds of years. Nowadays it is greatly used in aromatherapy as a relaxant and widely used in cosmetic and food industries [11], [12]. In addition to that, many studies have shown that the various species of lavender including *Lavandula angustifolia*, *Lavandula stoeches* and *Lavandula dentata*, possess antibacterial, anti-inflammatory and anticancer properties [13]–[15]. One of the lavender species used in traditional medicine for various purposes is *Lavandula dentata* [16]. *Lavandula dentata* also has cytotoxic and antioxidant activity [17]. Besides, it was observed that *Lavandula dentata* had the highest anticancer

potential among different plants against human breast adenocarcinoma (MCF7) cells [18].

[6] METHOD

A. Cells and Culture Conditions

The study was constructed using Glioblastoma (GBM, U87 MG (ATCC® HTB-14™)) and Mouse Embryonic Fibroblast (MEF, (CF-1) (ATCC® SCRC-1040™)) cell lines. The GBM cells were provided by Asst. Prof. Tuba Bağcı Önder (Koç University, Faculty of Medicine, Bağcı Onder Laboratory) and the MEF cells were provided by Assoc. Prof. Devrim Gözüaçık (Sabancı University, Gozuacık Laboratory). The cells were seeded into 24 well plates (40000 GBM cells and 10000 MEF cells/well), and cultured with Dulbecco's Modified Eagle's medium (DMEM, Lonza, Belgium) which was supplemented with 10% fetal bovine serum (FBS, South America) in a humidified incubator at 37 °C in which the CO₂ level was kept constant at 5%.

B. Preparation of the *Lavandula dentata* Infusion

Lavandula dentata was collected from Adana, Turkey and the infusion solution was prepared as indicated below;

1,5 grams of the herbal were added to 50 ml of double distilled hot water (90°C). After ten minutes it was sterilized by a 22 µm pore sized filter.

C. Cytotoxic Effect of *Lavandula dentata* on GBM and MEF cells

On the second day of the culture, *Lavandula dentata* infusion solutions were given to cell cultures, except the control group, in the proportions equivalent to 1/25, 1/15, 1/10 (v/v) and only ddH₂O was given to the control group in the equivalent volume of infusion solutions. GBM cells have exposed the infusion solution 3 and 5 days. MEF cells have exposed the infusion solution for 5 days. Each day the culture mediums were refreshed. At the end of the incubation periods, cytotoxic effects were measured by the neutral red cell viability assay.

D. Cytotoxicity Assay

Cell viabilities were tested by neutral red assay. As regards the neutral red assay, firstly the growth medium was removed after the incubation period, and 500 µL of neutral red solution was added to each well. Cells were incubated for nearly 2

hours until the red precipitates became visible. Following the growth of visible red precipitates, 1000 μ L of neutral red solubilization solution (50% absolute ethanol, %1 acetic acid and % 49 ddH₂O mixtures) was added to each well. Plates were incubated for nearly 1 hour until the red precipitate completely dissolved. Absorbance values of each well were measured at 540 nm using a spectrophotometer (Shimadzu UV-VIS, UVmini-1240, Japan). All tests were performed in triplicate. Cell viability percentages were calculated with respect to control groups.

[7] RESULTS AND DISCUSSIONS

Neutral red assay results indicated that increased quantities of *Lavandula dentata* inhibited the survival of GBM cells (Figure 1). However, the most significant result was observed in the fifth day of the GBM culture with 1/10 (v/v) *Lavandula dentata*. The viability of GBM cells was reduced by nearly 46%. The results showed that *Lavandula dentata* has cytotoxic and antiproliferative activity for the GBM cells.

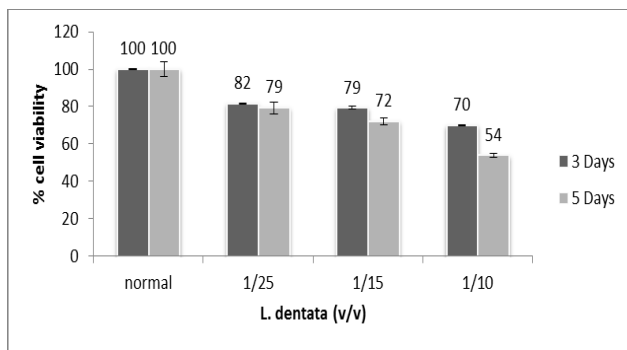


Fig. 1. The neutral red cell viability assay results of 3 and 5 days cultured U87MG cells.

According to neutral red assays, it was also observed that the viability of MEF cells were reduced in the *Lavandula dentata* added cultures (Figure 2). But the antiproliferative effects in the MEF cell cultures were less than that of the GBM cell cultures.

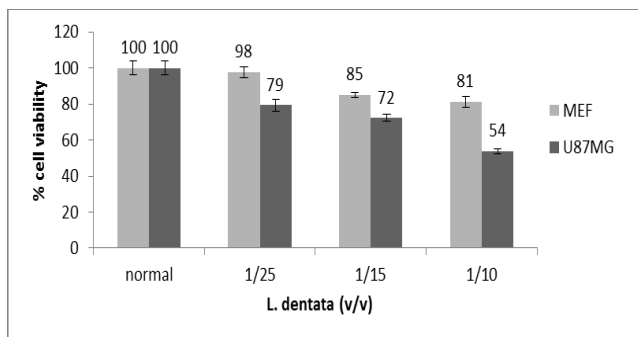


Fig. 2. The neutral red cell viability assay results of 5 days cultured U87MG and MEF cells.

[8] CONCLUSION

This study indicated that *Lavandula dentata* has cytotoxic effect for the GBM cells. It may contribute to researches that aim to develop new strategies for the treatment of GBM.

Moreover in the future as the continuation of this study, it is planning to investigate the effect of *Lavandula dentata* in combination with the several chemotherapeutic agents in different cell lines to be able to develop new approaches.

REFERENCES

- [1] Van Meir, E. G, Hadjipanayis, C. G, Norden, A. D, Shu, H. K, Wen, P. Y, Olson, J. J, "Exciting new advances in neuro-oncology: the avenue to a cure for malignant glioma," *CA. Cancer J. Clin.*, 60(3), 166–193, 2010.
- [2] Logun, M. T, Bisel, N, Tanasse, E, *et al.*, "Glioma cell invasion is significantly enhanced in composite hydrogel matrices composed of chondroitin 4- and 4,6-sulfated glycosaminoglycans," *J. Mater. Chem. B*, 4(36), 6052–6064, 2016.
- [3] Cerami, E, Demir, E, Schultz, N, Taylor, B. S, Sander, C, "Automated Network Analysis Identifies Core Pathways in Glioblastoma," *PLoS One*, 5(2), e8918, 2010.
- [4] Caspani, E. M, Crossley, P. H, Redondo-Garcia, C, Martinez, S, "Glioblastoma: A Pathogenic Crosstalk between Tumor Cells and Pericytes," *PLoS One*, 9(7), e101402, 2014.
- [5] Kuo, L. T, Tsai, S. Y, Yang, C. Y, Lin, L. W, "Meningeal seeding from glioblastoma multiforme treated with radiotherapy and temozolomide," *Asian J. Surg.*, 40(1), 61–65, 2017.
- [6] Hanif, F, Muzaffar, K, Perveen, K, Malhi, S. M, Simjee, S. U, "Glioblastoma Multiforme: A Review of its Epidemiology and Pathogenesis through Clinical Presentation and Treatment," *Asian Pacific J. Cancer Prev.*, 18, 3–9, 2017.
- [7] Zarkoob, H, Taube, J. H, Singh, S. K, Mani, S. A, Kohandel, M, "Investigating the Link between Molecular Subtypes of Glioblastoma, Epithelial-Mesenchymal Transition, and CD133 Cell Surface Protein," *PLoS One*, 8(5), e64169, 2013.
- [8] Sweeney, K. J, Jarzabek, M, Dicker, P, *et al.*, "Validation of an imageable surgical resection animal model of Glioblastoma (GBM)," *J. Neurosci. Methods*, vol. 233(2014), 99–104, 2014.
- [9] Schijns, V. E. J. C, Pretto, C, Devillers, L, *et al.*, "First clinical results of a personalized immunotherapeutic vaccine against recurrent, incompletely resected, treatment-resistant glioblastoma multiforme (GBM) tumors, based on combined allo- and auto-immune tumor reactivity," *Vaccine*, 33(23), 2690–2696, 2015.
- [10] Elkamhawy, A, Viswanath, A, Pae, A, *et al.*, "Discovery of potent and selective cytotoxic activity of new quinazoline-ureas against TMZ-resistant glioblastoma multiforme (GBM)," *Eur. J. Med. Chem.*, 103(2015), 210–22, 2015.
- [11] Cavanagh, H. M. A, Wilkinson, J. M, "Biological activities of lavender essential oil," *Phyther. Res.*, 16(4), 301–308, 2002.
- [12] Imelouane, B, Elbachiri, A, Ankit, M, Benzeid, H, Khedid, K, "Physico-chemical compositions and antimicrobial activity of essential oil of eastern moroccan *Lavandula dentata*," *Int. J. Agric. Biol.*, 11(2), 113–118, 2009.
- [13] Zhao, Y, Chen, R, Wang, Y, Qing, C, Wang, W, Yang, Y, "In vitro and in vivo efficacy studies of *Lavender angustifolia* essential oil and its active constituents on the proliferation of human prostate cancer," *Integr. Cancer Ther.*, April-June, 1–12, 2016.
- [14] Donadu, M. G, Usai, D, Mazzarello, V, *et al.*, "Change in Caco-2 cells following treatment with various lavender essential oils," *Nat. Prod. Res.*, Jan, 1–4, 2017.
- [15] Algieri, F, Rodríguez-Nogales, A, Vezza, T, *et al.*, "Anti-inflammatory activity of hydroalcoholic extracts of *Lavandula dentata* L. and *Lavandula stoechas* L.," *J. Ethnopharmacol.*, 190, 142–158, 2016.
- [16] do Rocio Duarte, M, Carvalho de Souza, D, "Microscopic characters of the leaf and stem of *Lavandula dentata* L. (Lamiaceae)," *Microsc. Res. Tech.*, 77(8), 647–652, 2014.

- [17] Imelouane, B, Elbachiri, A, Wathelet, J-P, Dubois, J, Amhamdi, H, "Chemical Composition, Cytotoxic and Antioxidant Activity of the Essential Oil of *Lavandula dentata*," *world J. Chem.*, 5(2), 103–110, 2010.
- [18] Ali, M. A, Abul Farah, M, Al-Hemaid, F. A, Abou-Tarboush, F. M, "In vitro cytotoxicity screening of wild plant extracts from Saudi Arabia on human breast adenocarcinoma cells," *Genet. Mol. Res.*, 13(2), 3981–3990, 2014.

Studies on the In Vitro Micropropagation of *Fritillaria minuta*

Ayşegül ÇELİK
Bioengineering Department
Firat University
Elazığ, Turkey
141132103@firat.edu.tr

Ömer MUNZUROĞLU
Bioengineering Department
Firat University
Elazığ, Turkey
omunzuruglu@firat.edu.tr

Abstract— *Fritillaria* is represented World wide by 7 subgenera, 2 sections, and 165 taxa. In Turkey is showing a wide distribution area there are 45 taxa *Fritillaria* genus is that 19 of them endemic to Turkey [1]. *Fritillaria minuta* which is an endangered species shows distribution in Eastern Anatolia and South East Anatolia. The plant has very showy red and brown-orange flowers [2].

This study was carried out with aim to determine in vitro micropropagation potential of *F. minuta* bulbs of the plant that were cultivated at the Department of Bioengineering, Firat University, Elazığ, Turkey, at 2015. For in vitro tissue culture, the bulbs were carefully selected from disease free material without any injury on the them. At tissue culture studies, parts of bulb scales which is obtained *Fritillaria minuta*, petals of not open flowers and stems of flowers were used as the explant source. Murashige and Skoog medium as the primary food (MS) was used [3]. Murashige and Skoog was used as the primary nutrient medium. As plant growth regulators, different combinations of 6-Benzyl amino purine (BAP), indole acetic acid (IAA) and α -naphthalene acetic acid (NAA) was added to nutrient medium. At sterilization of surface process, to ensure the best sterilization, considering literature, it was prepared preliminary various protocols.

The best results in carried out the preliminary experiments for sterilization were taken from treated explants in Tween 20 was added dropwise 30% sodium hypochlorite (20 min), 70% ethyl alcohol (1 min) and sterile distilled water. At two different concentrations of sucrose (30% and 60%); Plant growth regulator (PGR Plant Growth Regulator = PRG) free, 1 mg / l BAP + 0.6 mg / L NAA + 0.4 mg / L IAA containing, 0.1 mg / L BAP + 0.6 mg / L NAA + 0.4 mg / L containing media were prepared. Plates completely wrapped with stretch film are incubated at $20 \pm 1^\circ \text{C}$ under 16 hours white fluorescent light ($30 \mu\text{mol m}^{-2}\text{s}^{-1}$) and 8-hour dark photoperiod. The most effective culture medium was containing %30 sukroz, 1 mg / l BAP + 0.6 mg / l NAA + 0.4 mg / l IAA. It was observed that the cultures induced excessive somatic embryos were formed from bulbs of *F. minuta* at culture medium. In this study was obtained direct organogenesis, callus and indirect organogenesis from pieces of bulb scales. The results showed that *F. minuta* could be successfully propagated using in vitro techniques.

Keywords— *Fritillaria minuta*, in vitro micropropagation, bulblet

- [1] Tekşen M. and Aytaç Z. 2011. The Revision of The Genus *Fritillaria* L. (Liliaceae) in The Mediterranean Region (Turkey). Turkish Journal of Botany, 35, 447-478.
- [2] Koyuncu, M. (2000). *Fritillaria minuta* Boiss. & Noe (Liliaceae). (*Fritillaria minima* Boiss. & Noe [Zambakgiller]). Karaca Arboretum Magazine 5(4): 185-188.
- [3] Murashige, T. and Skoog, F. 1962. A revised medium for rapid growth and bio assays with tobacco tissue cultures. Physiol. Plant. 15: 473-497.

Evaluating Household Water Filtration Systems

Rozelin AYDIN
Bioengineering Department,
Adana Science and Technology University,
Adana, Turkey

Yağmur ATAKAV
Bioengineering Department,
Adana Science and Technology University,
Adana, Turkey

Sema ŞİRİN
Bioengineering Department,
Adana Science and Technology University,
Adana, Turkey

Abstract— Accessing to clean water is very important in order to protect human health. Realization of minor changes in parameters such as smell, color or taste or misdirected news on the visual/written media led public to use bottled water or residential water filtration systems in the cases of crowded households for economical reasons to clean the tap water instead of buying bottled water. The aim of this study was to investigate public awareness on the residential water filtration systems.

A total of 5139 people participated the survey according to simple random sampling method. The survey was completed by using face to face interview and computer aided telephone interview (CATI) methods. The collected data were analyzed by using SPSS V11.5.

For the research, a total of 5139 people were surveyed. 29% of the respondents stated that they prefer not to use municipal water as drinking water while 53,9% stated they do not prefer drinking municipal water as drinking water because they do not believe it is clean enough to drink. It is determined that of all the respondents 13,4% were using residential water filtration systems(WFS) while the main purpose of the usage was to clean the water from pathogenic microorganisms.

The respondents (82%) stated that they knew the proper frequency to replace water filter cartridges. When definition of the WFS were asked 34,4% of them said “a sanitation process to remove all of the harmful substances and impurities as well as living microorganisms, or decrease them in number”.

The behavior of the use of WFS showed statistically significant relationships with the variables age ($\chi^2= 30,75$; $P<0,05$), education level ($\chi^2= 6,17$; $P<0,05$) and income ($\chi^2= 6,17$; $P<0,05$). Also profession of the household head ($\chi^2= 24,29$; $P<0,05$) variable showed statistically significant relationship with the behavior of the use of WFS. Similar findings were observed that consumption of municipal water was decrease, when age-earnings profile and education level were increase.

One of the most important outcome of the research is that the tendency to use WFS increase with age. Because of the parameters income, education level, profession of household head is related with the age, an increase in these parameters lead to an increase in WFS usage frequency.

In conclusion of the survey, even though people were aware of the replacement of filter cartridges, one of the most important aspects of the water filter devices, and get warned about this replacement by the vendors; the importance of the replacement is not fully understood by the public.

Keywords— Clean water, public health, residential water filtration systems, public awareness.

Elliptic Filter Based Noninvasive Blood Pressure Analyze with LabVIEW

Duygu Kaya

Firat University

Department of Electrical and Electronics Engineering

Elazig, Turkey

dgur@firat.edu.tr

Mustafa Türk

Firat University

Department of Electrical and Electronics Engineering

Elazig, Turkey

mturk@firat.edu.tr

Turgay Kaya

Firat University

Department of Electrical and Electronics Engineering

Elazig, Turkey

tkaya@firat.edu.tr

Abstract— The blood in the vein is called blood pressure or tension. It depends on the amount of blood pumped by the heart and the resistance of the vessels to this flow and the flexibility of the arterial walls. Very low values than optimum blood pressure and very high values than normal blood pressure are important. With this aim, Noninvasive Blood Pressure Analyze with LabVIEW offers an insight into us. LabVIEW is a graphical programming language that uses a Dataflow model instead of sequential lines of text code. LabVIEW runs principle of Data flow programming that allows multiple operations to work in parallel. So, designers spend less time than a text based programming language. Application areas such as signal processing, image processing and Data analysis are available. In this paper, LabVIEW- based Noninvasive Blood Pressure Analyze (NIBP) using different Data and to obtain systolic/diastolic pressure. As a result of this, the current data are divided into optimum blood pressure, normal blood pressure and prehypertension.

Keywords—LabVIEW; blood pressure; elliptic filter.

I. INTRODUCTION

Blood Pressure (BP) is the pressure that the blood in the vein bed makes to the vein walls during the flow. It depends on the amount of blood pumped by the heart and the resistance of the vessels to this flow and the flexibility of the arterial walls [1]. As the heart contracts, blood is pumped into the arteries. This increases the pressure in the arteries, while the pressure decreases in the heartbeats. As a consequence of this, the BP is indicated by two values, namely systolic pressure and diastolic pressure and the unit is millimeters of mercury (mmHg) [2]. In general, systolic pressure is known as hypertension, while diastolic pressure is known as hypotension. With BP measurement, it is decided which characteristics the person exhibits from optimum, normal, hypertension, hypotension and prehypertension. The optimum BP is below 120/80 mmHg. The normal BP is below 130/85 mmHg. Hypertension is higher than normal accepted values and one of the most important health problems. The BP is above 140/90 mmHg. Hypertension can lead to headache, dizziness, and can lead to heart-kidney disorders, paralysis and visual disturbances if not noticed.

Hypotension is abnormally low BP that is 90/60 mmHg below. It can occur due to many reasons such as sadness, stress, long-term hunger and vitamin deficiency. But every low BP not indicate a health problem. Prehypertension is used to describe patients whose BP is elevated but still within normal limits. The BP is between 120-139 mmHg systolic and 80-89 mmHg diastolic [3]. BP monitors should be considered to prevent serious illnesses and situations that could cause life-threatening injuries. The aim of this paper to investigate LabVIEW- based Noninvasive Blood Pressure Analyze (NIBP) using different Data and to obtain systolic/diastolic pressure. As a result of this, the current Data are divided into optimum pressure, normal pressure and prehypertension.

The structure of this paper is as follows: Second section includes preprocessing of signals, database signals taken from LabVIEW. Third section includes evaluation of results. The last section includes conclusion and future works.

II. MATERIAL AND METHODS

A. Database

Signals required for paper are taken from the LabVIEW own Database. Signals of three Databases that are NIBP_Data_1, NIBP_Data_2, NIBP_Data_3 were used to examine. Each signal is sampled at intervals of 0.002 for 31, 32, 27 seconds, respectively. These signals correspond to prehypertension, normal and optimal respectively.

B. LabVIEW

LabVIEW is a graphical programming language that uses a Dataflow model instead of sequential lines of text code. Comparison of the other language, LabVIEW runs principle of Data flow programming that allows multiple operations to work in parallel [4,5]. It provides that acquires of bioelectrical signal, preprocesses and analyzes them.

LabVIEW is a software based graphical programming language that consists of front panel and block diagram. The sections where the user interface prepares and the code is written correspond to front panel and block diagram, respectively. The

block diagram of designed system is shown in Figure 1. LabVIEW is called a Virtual Instrument (VI) because it resembles the physical instruments used in the laboratory with the way it works [6]. The biomedical workbench toolkit in LabVIEW allows applications such as recording, by sensor with DAQ hardware, and viewing bioelectrical signal, heart rate

variability (HRV) analysis, ECG Feature Extracture and Noninvasive Blood Pressure Analyze By file format converter, the files are converted into different types of file formats for the various applications. For instance, it supports .hea, .tdms, .mat, .rec extensions file [7]. In this paper, .tdms extensions file was used.

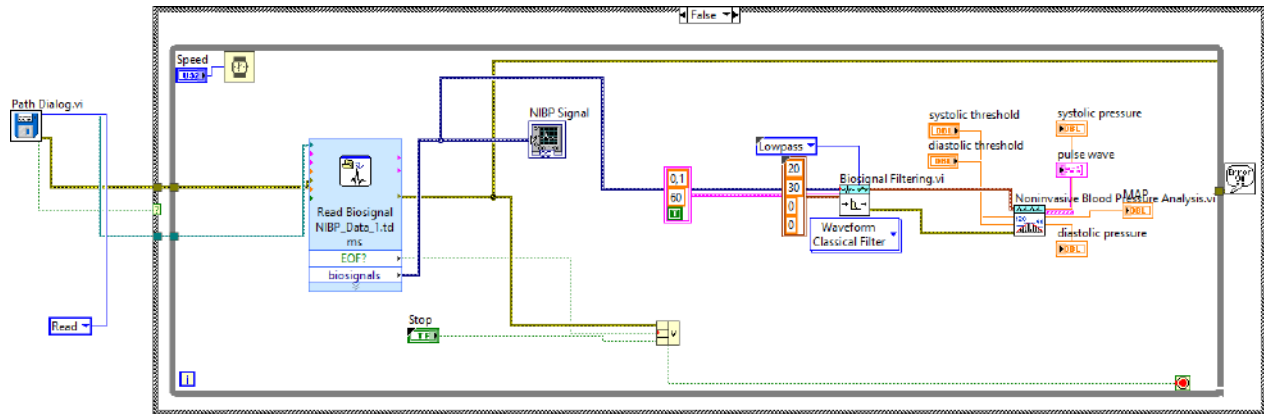


Fig 1. Block diagram of designed system

C. Preprocessing

Used signals are recorded with many low frequency undesired noise caused by the circulatory system. Filtering should be done to suppress them. For this, lowpass elliptic filter was chosen. An elliptic filter is a signal processing filter with equalized ripple behavior in both the passband and the stopband [8]. The level of ripple on each band is a configurable filter. As the ripple in the pass-band approaches zero, the filter becomes a Chebyshev type I filter, as the ripple in the stop-band approaches zero, it becomes a Chebyshev type II filter and both band approaches zero, filter becomes a Butterworth filter. Although this filter has ripple both band, it has a rapid decline from the pass band to the stop band. With this filter, undesired signals removed then with BP analyzer systolic/diastolic and mean arterial pressure (MAP) were obtained.

[9] RESULTS AND DISCUSSION

Mentioned techniques have been applied to BP signals to obtain systolic/diastolic BP and MAP value. In order to interpret the results obtained, the values that the World Health Organization (WHO) prescribes for BP limit values are taken as references. The classification of BP by the World Health Organization International Hypertension Committee is given in Table 1. Obtained BP results are shown in Table 2.

Figure 2 shows NIBP_Data_1, Figure 3 shows the result of the analysis, Figure 4 shows the NIBP_Data_2, Figure 5 shows the analysis result, Figure 6 shows the NIBP_Data_3, and Figure 7 shows the analysis result.

TABLE 1 CLASSIFICATION OF BP

Category	systolic, mmHg	diastolic, mmHg
Hypotension	< 90	< 60
Normal	< 130	< 85
Optimal	< 120	< 80
Prehypertension	130-139	85-89
Stage 1 hypertension	140- 159	90-99
Stage 2 hypertension	160-169	100-109

TABLE 2 OBTAINED BP RESULTS

Category	systolic, mmHg	diastolic, mmHg	MAP mmHg
NIBP_Data_1	131	86	93
NIBP_Data_2	122	72	83
NIBP_Data_3	107	64	72

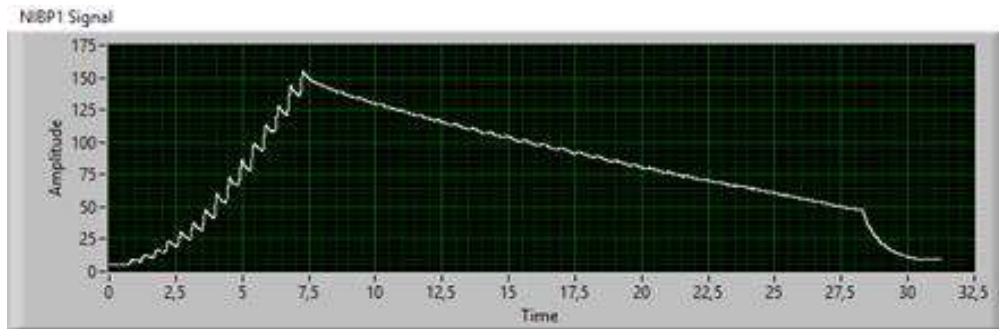


Fig.2 NIBP_Data_1 Signals

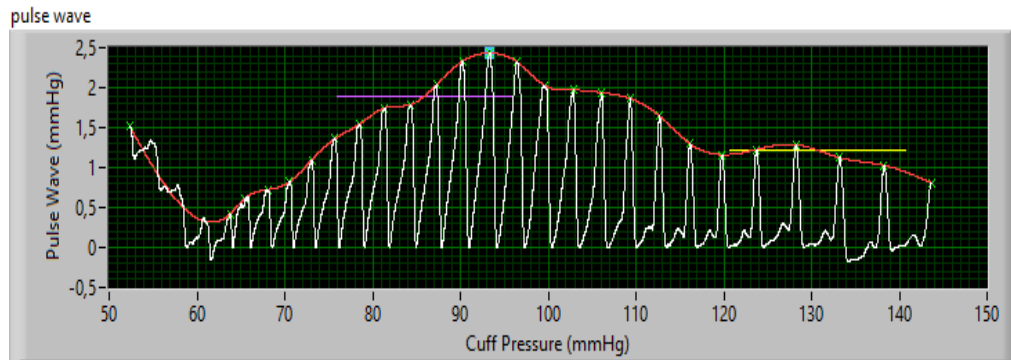


Fig.3 Analyze results of NIBP_Data_1 Signals

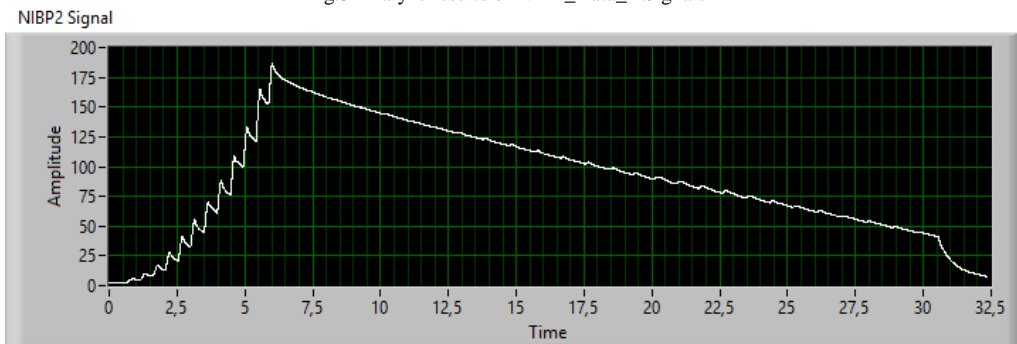


Fig.4 NIBP_Data_2 Signals

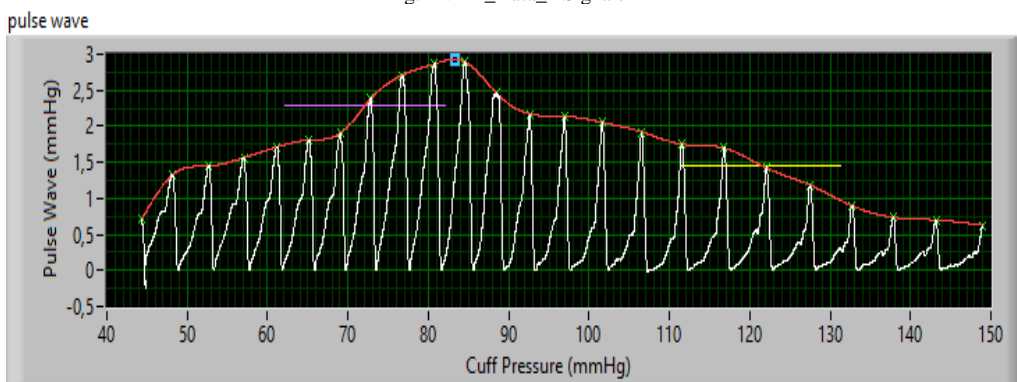


Fig.5 Analyze results of NIBP_Data_2 Signals

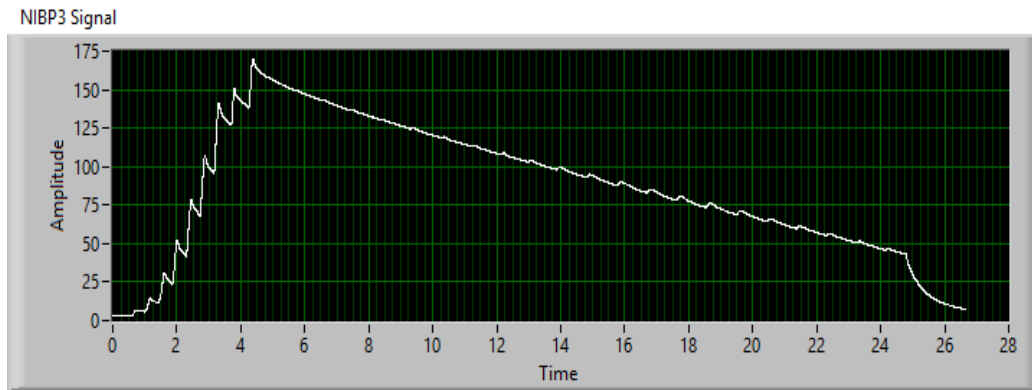


Fig.6 NIBP_Data_3 Signals

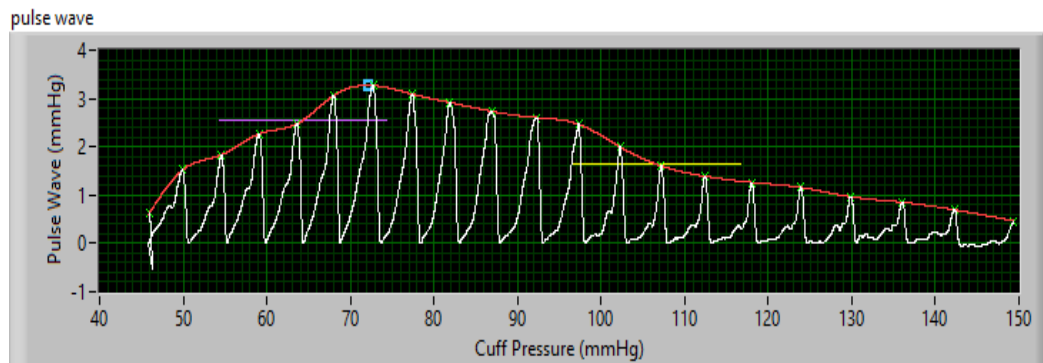


Fig. 7 Analyze results of NIBP_Data_3 Signals

Obtained results show that NIBP_Data_1 corresponds to prehypertension, NIBP_Data_2 corresponds to normal BP and NIBP_Data_3 corresponds to optimal BP.

[10] CONCLUSIONS

Low BP and high BP are important health problems. Especially, hypertension is one of the most important health problems in the world that requires regular checking. Prehypertension is used to describe patients whose BP is elevated but still within normal limits. The optimum BP is below 120/80 mmHg. People with pre-hypertension are more likely to have a risk of myocardial infarction and fallacies than people with normal BP. The normal BP is below 130/85 mmHg. Hypotension is abnormally low BP that is 90/60 mmHg below. It can occur due to many reasons such as sadness, stress, long-term hunger and vitamin deficiency.

So, in this study, it is provided to measure BP level with the developed LabVIEW algorithm. Simple usage of graphical structure allows to observe BP level to the doctor or the patients.

In future studies, classification models will be tried to be improved.

REFERENCES

- [1] Ogedegbe, Gbenga; Pickering, Thomas, "Principles and techniques of blood pressure measurement". *Cardiology Clinics*. (2010-11-01). 28 (4): 571–586.
- [2] O'Brien, Eoin, "Blood pressure measurement is changing!". *Heart*. 85 (1): 3–5. doi:10
- [3] "Understanding blood pressure readings". American Heart Association. 11 January 2011.S.
- [4] N. Kehtarnavaz and S. Mahotra, "Digital Signal Processing Laboratory: LabVIEW-Based FPGA Implementation", pp.7
- [5] S.G. Aydın, T. Kaya, H. Güler, "Wavelet-based study of valence–arousal model of emotions on EEG signals with LabVIEW", *Brain Informatics*, vol.3, pp.1-9.
- [6] <http://www.ni.com/white-paper/4752/en/>
- [7] A. Deshmukh and Y. Gandole "ECG Feature Extraction Using NI Lab-View Biomedical Workbench", *International Journal of Recent Scientific Research* 6(8), pp.5603-5607, August, 2015.
- [8] R. W. Daniels, *Approximation Methods for Electronic Filter Design*. New York: McGraw-Hill. (1974). ISBN 0-07-015308-6.R.

TDZ and Zeatin Effects on In Vitro Corm Production in Saffron (*Crocus sativus* L.)

Nazmi GÜR
Bioengineering Department
Faculty of Engineering
Firat University
Elazig, Turkey

Ayça ŞAHİNALP
Bioengineering Department
Faculty of Engineering
Firat University
Elazig, Turkey

Abstract— *Saffron (*Crocus sativus* L.) is a monocotyledonous plant of the Iridaceae family that produces annual renewal corms which are indispensable for their propagation, since the plant is triploid and sterile (1). Saffron is a cormous plant which is one of the most economic valuable plants as medicinal and aromatic ingredients world wide. Saffron is used mainly dye, food, drug and pharmacology industries. It has analgesic and sedative properties so folk herbal medicines have used for some diseases. Saffron consumption is rising but production is not well-proportional. Plant tissue culture technique like micropropagation has been used for the propagation of saffron. In our study, sprout explants were culture Murashige Skoog media (2) supplemented with various concentration of TDZ (Thidiazuron) or Zeatin. Explants incubated in dark at 25°C. The best corm production was achieved at 4 mg/l TDZ.*

Keywords— *Saffron, TDZ, Zeatin, Corm production.*

REFERENCES

- [1] Ebrahimzadeh, H., Karamian, R., Noori-Daloii, R., Somatic Embryogenesis and Regeneration of Plantlet in Saffron, *Crocus Sativus* L. J. Sci. I. R. Iran. 11, 169-173.
- [2] Murashige, T., and Skoog, F., A Revised Medium for Rapid Growth and Bioassays with Tobacco Tissue Cultures. *Physiol. Plant.* 15, 473-497, 1962.

Investigation of Infrared Drying of Mixed Algae Culture

Mehmet KALENDER
Bioengineering Department
Faculty of Engineering
Firat University
Elazig, Turkey

Ahmet YAZICIOĞLU
Bioengineering Department
Faculty of Engineering
Firat University
Elazig, Turkey

Abstract—Alga species compose are around approximately 127.000 in the world. Some of these are macro alga which include 9000 species, and others are named as micro alg. *Spirulina*, which is a microalga consists of chemically moisture (76.7 %), protein (17.2 %), carbohydrates (2.4 %), lipids (2 %), and ash (1.7 %) [1]. Alga has a high nutritional value with contents of protein and vitamins (A, B1, B2, B6, B12, E, and K), minerals (Fe, Ca, Zn, K, P, Mn, Cu, and Mg) [2]. Due to anti-oxidant and anti-inflammatory properties, alga is used in cosmetic industry [3]. Also, alga is a good resource in order to produce biofuel [4, 5]. One of the important production stages of algae technology is drying because of high moisture content. Algae drying techniques could affect algal quality and process economics [6]. Thus, drying phenomena of algal biomass should be examined.

In this study, mix algae culture was cultivated in a laboratory scale airlift photobioreactor with volume of 50 L, light intensity of 100 lux during 24 hours, and at room temperature. Zarrouk medium (per L of H₂O: 16.0 g NaHCO₃, 0.5 g K₂HPO₄, 2.5 g NaNO₃, 1.0 g K₂SO₄, 1.0 g NaCl, 0.2 g MgSO₄·7H₂O, 0.04 g CaCl₂, 0.01 g FeSO₄·7H₂O and 0.08 g EDTA.) was used for culture growth [7]. At the end of 10 days, the algal cells that came to the collapsing phase in the photobioreactor were filtered. All wet algae sludges were stored at +4 °C until used in the drying experiments.

Drying experiments were carried out with the infrared dryer (Shimadzu, MOC63u). The drying experiments were performed at the temperature between 50-105 °C. Drying and drying rate curves were obtained from the experimental data. The drying periods of the algae culture for all temperatures studied were generally the falling rate period. Also, effective diffusion coefficients were determined by the experimental data.

Keywords— Drying of algae, Mixed algae, Infrared drying.

REFERENCES

- [1] Bennamoun, L.; Afzal, M.T.; Léonard, A. Drying of alga as a source of bioenergy feedstock and food supplement—A review. *Renewable and Sustainable Energy Reviews* 2015, 50, 1203-1212.
- [2] Oliveira, E.G.; Duarte, J.H.; Moraes, K.; Crexi, V.T.; Pinto, L.A. Optimisation of *Spirulina platensis* convective drying: evaluation of phycocyanin loss and lipid oxidation. *International journal of food science & technology* 2010, 45, 1572-1578.
- [3] Dissa, A.; Desmorieux, H.; Savadogo, P.; Segda, B.; Koulidiati, J. Shrinkage, porosity and density behaviour during convective drying of spirulina. *Journal of food Engineering* 2010, 97, 410-418.
- [4] Sumprasit, N.; Wagle, N.; Glanpracha, N.; Annachhatre, A.P. Biodiesel and biogas recovery from *Spirulina platensis*. *International Biodeterioration & Biodegradation* 2016,
- [5] Brennan, L.; Owende, P. Biofuels from microalgae—a review of technologies for production, processing, and extractions of biofuels and co-products. *Renewable and sustainable energy reviews* 2010, 14, 557-577.
- [6] Show, K.-Y., D.-J. Lee, and J.-S. Chang. Algal biomass dehydration. *Bioresource technology*, 2013. 135: p. 720-729.
- [7] Tedesco, M.A. and E.O. Duerr, Light, temperature and nitrogen starvation effects on the total lipid and fatty acid content and composition of *Spirulina platensis* UTEX 1928. *Journal of Applied Phycology*, 1989. 1(3): p. 201-209.

Dye Removing from Waters by Using Pyrolysis Residue of Activated Sludge

Kübra GÖLEBATMAZ

Bioengineering Department, Faculty of Engineering,
University of Firat,
Elazığ, Turkey
kubra211@gmail.com

Hamdi Soner ALTUNDOĞAN

Bioengineering Department, Faculty of Engineering,
University of Firat,
Elazığ, Turkey
saltundogan@firat.edu.tr

Muhammet Şaban TANYILDIZI

Bioengineering Department, Faculty of Engineering,
University of Firat,
Elazığ, Turkey
mtanyildizi@firat.edu.tr

Abstract— Activated sludge is a main waste coming from biological water treatment facilities. This waste can be evaluated either for biogas production by an anaerobic fermentation process or as a fertilizer for agricultural areas. On the other hand, in general, it is not preferred as fertilizer due to ethical reasons in Turkey. For that reasons, it is disposed to wide lands and it can cause some environmental problems. Therefore, it is needed to enhance new processes to evaluate this residue. In fact, activated sludge contains significant amount of organic and inorganic matters. Due to high organic matter content, the pyrolysis of the activated sludge is widely investigated to convert some secondary useful products such as some gas and liquid fuels and activated carbon [1]. Also, there are some studies about the using of activated carbon obtained during pyrolysis process in water treatment. Activated carbon obtained from the sewage sludge can be used to remove some pollutants from waters such as heavy metals [2] and dyes [3].

In this study, firstly, it was investigated that the pyrolysis of activated sludge in a fixed bed pyrolysis reactor. Then, dye removal properties of the solid pyrolysis residue obtained at optimum conditions from waste sludge was investigated. The waste sludge was obtained from a municipal waste treatment plant (Elazığ, Turkey). The proximate analysis of the materials showed that it contains 47.1 % of ash, 11.8 % of fixed carbon, 2.9 % of moisture and 38.2 % of volatile matter. Gas, liquid and solid pyrolysis product yields were investigated depending on pyrolysis temperature (200-500°C) and heating time (30-120 min). So, the optimum conditions were determined as to the maximize liquid product yield. Optimum pyrolysis conditions were determined as 400°C of pyrolysis temperature and 90 min of heating time. The liquid, gas and solid product yields were 28.9 %, 12.5 % and 58.6 %, respectively. As seen from the results, it can be said that the solid pyrolysis residue of waste sludge contains significant amount of inorganic constituents. For that reason, it can be said that this residue is not suitable for evaluation as a fuel. Since it contains significant amount of metal oxides and carbon, it can be evaluated for pollutant removal from waters. Therefore, waste sludge pyrolysis residue was used in a dye removing study. The golden yellow was selected as a model dye. In dye removing study, effect of some parameters such as dye concentration, contact time and temperature were investigated. The results obtained were evaluated by using some kinetic and adsorption isotherm models. Also, some thermodynamic evaluations were made. The results of the study showed that the most suitable kinetic models for golden yellow adsorption onto pyrolysis residue is pseudo-second order model and the data best fits to Langmuir adsorption isotherm. Thermodynamic evaluations showed that the sorption process has exothermic and spontaneous nature.

Keywords—Activated sludge; pyrolysis; adsorption; dye removing; water treatment

REFERENCES

- [1] Hadi, P., Xu, M., Ning, C., Lin, C.S.K., McKay, G., 2015, A critical review on preparation, characterization and utilization of sludge-derived activated carbons for wastewater treatment, Chemical Engineering Journal, 260, 895-906.
- [2] Tao, H.-C., Zhang, H.-R., Li, J.-B., Ding, W.-Y., 2015, Biomass based activated carbon obtained from sludge and sugarcane bagasse for removing lead ion from wastewater, Bioresource Technology, 192, 611-617.
- [3] Rozada, F., Calvo, F.L., García, A.I., Martín-Villacorta, J., Otero, M., 2003, Dye adsorption by sewage sludge-based activated carbons in batch and fixed-bed systems, Bioresource Technology, 87, 221-230.

Gluconic Acid Production from Sugar Beet Molasses by Submerged Fermentation with *Aspergillus niger*

Kübra GÖLEBATMAZ

Bioengineering Department, Faculty of Engineering,
University of Firat,
Elazığ, Turkey
kubra211@gmail.com

Hamdi Soner ALTUNDOĞAN

Bioengineering Department, Faculty of Engineering,
University of Firat,
Elazığ, Turkey
saltundogan@firat.edu.tr

Muhammet Şaban TANYILDIZI

Bioengineering Department, Faculty of Engineering,
University of Firat,
Elazığ, Turkey
mtanyildizi@firat.edu.tr

Abstract— Gluconic acid is mainly produced by oxidation of glucose. This oxidation process can be realized by microbial fermentation, chemical catalysis, enzymatic catalysis, electrochemical and bio-electrochemical methods [1]. Microbial fermentation is most widely used method due to its cost efficiency. Some fungus and bacteria are used for microbial fermentation. Most important microorganisms used in gluconic acid production are *Gluconobacter* and *Aspergillus niger* as bacteria and fungus, respectively. In earlier studies, gluconic acid production from glucose by using *A. niger* has been investigated widely [2]. Also, there are some studies about the production from sugar cane molasses. But, there are not sufficient studies about production from sugar beet molasses. Also, *A. niger* is capable to metabolize disaccharides (sucrose) due to it has invertase enzyme [3]. This paper is first part of the study on gluconic acid production by fermentation with *A. niger* from sugar beet molasses and pulp, which are by-products obtained during the sugar production. The results of submerged fermentation study are given in this paper.

In this part of the study, sugar beet molasses obtained from a domestic sugar plant was characterized and then submerged fermentation conditions for gluconic acid production by using *A. niger* were optimized. It was determined that the sugar beet molasses contains about 49.4 % of sucrose and 1.5 % of invert sugars (glucose and fructose). Also, it was determined that it contains about 20 % water and the about 29 % of sugar free dry matter. As well known, sugar beet molasses also contains phosphorus, nitrogen and some metal ions such as calcium and iron. For that reason, it can be said that the sugar beet molasses is a good fermentation media which is not needed addition of any nutrient. The response surface methodology (RSM) was used to the design of experiments. For this purpose, central composite design (CCD) route was selected as design method. The investigated parameters were sugar beet molasses concentration, CaCO_3 amount, temperature and shaking speed. All experiments designed by CCD were conducted depending on the fermentation time. The samples taken on different periods were analyzed by HPLC to determining gluconic acid, oxalic acid, citric acid, sucrose, glucose and fructose concentrations. Optimum conditions for gluconic acid productions from sugar beet molasses by using *A. niger* were determined as 257.8 g/L of molasses concentration, 30.1 g/L of CaCO_3 amount, 31.8 °C of temperature and 135.2 rpm of shaking speed and the maximum gluconic acid concentration was obtained as 57.6 g/L under these conditions for 192 h of fermentation period. Also, a model equation was obtained for the gluconic acid production as below:

$$\text{Gluconic Acid Conc. (g/L)} = -636.865 + 0.823xA + 4.589xB + 20.854xC + 2.776xD + 0.001xAxB + 0.003xAxC - 0.001xAxD - 0.032xCxD - 0.002xA^2 - 0.081xB^2 - 0.272xC^2 - 0.006xD^2$$

Where A is molasses concentration (g/L), B is CaCO_3 amount (g/L), C is temperature (°C) and D is shaking speed (rpm).

It has been determined that citric and oxalic acid productions together with gluconic acid are being occurred in the significant levels. For that reason, it can be said that the *A. niger* can perform citric acid and oxalic acid production by phosphofructokinase and oxaloacetate acetylhydrolase enzymes, respectively [4].

Keywords—Gluconic acid; *Aspergillus niger*; fermentation; sugar beet molasses; response surface methodology

REFERENCES

- [1] Hustede H., Haberstroth H.J., Schinzig E. 1989. Gluconic acid, Ullmann's Encyclopedia of Industrial Chemistry, 449–56.
- [2] Stubbs J.J., Lockwood L.B., Roe E.T., Tabenkin B., Ward G.E. 1940. Ketogluconic acids from glucose, Industrial Engineering and Chemical, 32, 1626–1630.
- [3] Vargas L.H.M., Sdomingos. R.N., Carmona E.C. 2004. Ultrasound effects on invertase from *Aspergillus niger*, World Journal of Microbiology and Biotechnology, 20, 137–142, 200.
- [4] Cameselle C., Bohlmann J.T., Núñez M.J., Lema J.M. 1998. Oxalic acid production by *Aspergillus niger* Part I: Influence of sucrose and milk whey as carbon source, Bioprocess Engineering, 19, 4, 247–252.

Diagnosis of Dysmorphic Syndromes From Facial Photographs Based on Machine Learning Techniques

Merve Erkinay Özdemir
Electrical and Electronics Engineering
Iskenderun Technical University
Iskenderun/Hatay, Turkey
merve.erkinyozdemir@iste.edu.tr

Ziya Telatar
Electrical and Electronics Engineering
Ankara University
Ankara, Turkey
telatar@ankara.edu.tr

Osman Eroğul
Biomedical Engineering
TOBB University of Economics and Technology
Ankara, Turkey
erogul@etu.edu.tr

Yusuf Tunca
Medical Genetics
Gülhane Training and Research Hospital
Ankara, Turkey
ytunca@gata.edu.tr

Abstract— Clinically, facial appearance is an important indicator in diagnosing dysmorphic syndromes and it paves the way for computer-aided diagnosis based on facial image analysis. The initial clinical diagnosis of dysmorphic syndromes carried out by clinical geneticists using the comparison method. In this method the specialists compares physical properties of patients with physical properties of who was definite diagnosed patients in the books and databases. This process may take a long time and this method is subjective so the diagnosis success depends on experience of the by clinical geneticists. The early diagnosis of dysmorphic syndromes is crucial for the timely management of patients and disease. To speed up pre-diagnosis and eliminate subjectivity, computer-assisted objective methods are needed. The fast development of image processing and machine learning techniques facilitates the detection of facial dysmorphic features. In this study, we propose a novel method based on machine learning techniques to detect Fragile X, Hurler, Prader Willi, Down, Wolf Hirschhorn syndromes and healthy group automatically. The image database consists of 130 frontal photographs from dysmorphic syndromes and healthy groups. We define the particular facial characteristics of patient affected by each syndrome, after that the reference points are marked on the face images and ratios between the points' distances are taken into consideration as features. Then k-Nearest Neighbor (kNN) and Artificial Neural Network (ANN) classifiers are used to detect syndrome types. k-NN and ANN classifiers are trained by 130 samples and leave-one-out method are used for training and tests. Euclidean distance metric is used for the kNN method. Different k values are implemented and the best results are obtained for k=4. For ANN classifier we used multi layered feed forward ANN. Our method achieved 55% and 75% accuracy with kNN, ANN respectively. The promising results indicate that our method can detect dysmorphic syndromes effectively in a simple, non-invasive imaging data and can be used for pre-diagnosis of the dysmorphic syndromes by clinical experts.

Keywords— dysmorphic syndromes; diagnosis; machine learning techniques; k-nearest neighbor; artificial neural network

Comparison of structure and tribological properties of titanium oxide films fabricated by thermal oxidation, DC plasma oxidation, and the sol-gel

Onur ÇOMAKLI

Department of Mechanical Engineering,
Faculty of Engineering,
Ataturk University,
Erzurum, Turkey
onur.comakli@atauni.edu.tr

Mustafa YAZICI

High Technology Research Centre,
Erzurum Technical University,
Erzurum, Turkey

Tuba YETİM

Department of Chemical Engineering,
Faculty of Engineering and Architecture,
Erzurum Technical University,
Erzurum, Turkey

A. Fatih YETİM

Department of Mechanical Engineering,
Faculty of Engineering and Architecture,
Erzurum Technical University,
Erzurum, Turkey

Ayhan ÇELİK

Department of Mechanical Engineering,
Faculty of Engineering,
Ataturk University,
Erzurum, Turkey

Abstract— Titanium oxide films were produced on commercially pure titanium (Cp-Ti) by thermal oxidation, DC plasma oxidation and by the sol-gel. The structural properties of samples were analyzed by X-ray diffraction, scanning electron microscopy (SEM). Mechanical and tribological properties of untreated and treated samples were observed by microhardness, profilometer and pin-on-disc tribo-tester. Wear tests were performed under both drying and in simulated fluid body (SBF) condition. The results showed that the oxide films produced under three different treatments at 500°C consist of TiO₂ in the anatase structure. Although the XRD pattern obtain from treated samples at 700°C demonstrates the coexistence of anatase and rutile phases. Also, it was seen that the plasma oxidated samples at 700°C have higher intensities of rutile compared to other samples. Test results indicated that the hardness and wear resistance values of treated all samples were higher than the untreated CP-Ti values. Furthermore, the highest hardness and wear resistance values were attained at the plasma oxidated sample at 700°C both in drying and SBF condition. Since, rutile-TiO₂ structure exhibited self-lubrication like behavior.

Keywords— TiO₂; CP-Ti; Wear properties; Thermal oxidation; Plasma oxidation; Sol-gel

Population Development of *Zygina rhamni* (Ferrari, 1882) (Hemiptera: Cicadellidae) on vineyard in the Diyarbakır, Elazığ and Mardin provinces in Turkey

İnanç ÖZGEN
Bioengineering Department,
Fırat University,
Elazığ, Turkey
inancozgen@gmail.com

Yusuf KARSAVURAN
Plant Protection Department,
Ege University,
İzmir, Turkey
yusuf.karsavuran@ege.edu.tr

Abstract: This species was found in Diyarbakır and Elazığ provinces. It has been made to follow the populations in the vineyards of *Z. rhamni*. Each of the vineyard made of population 8.th month between 10. th months. In this study will be contribute vineyard IPM Studies

Keywords—*Zygina rhamni*, Diyarbakır, Elazığ, Mardin, population development, IPM

INTRODUCTION

Zygina rhamni Ferrari (Hemiptera: Cicadellidae: Typhlocybinae) is a mesophyll-feeding leafhopper on *Vitis vinifera* L. This species is facultative heteroecious species of their life cycle. In autumn, it migrates from vineyards to *Rubus* sp and rose, *Rosa* sp (Mazzoni et al., 2008). Females lay eggs at the end of March on these host plants in Italy. Adults that developed on bramble colonize grapevines beginning in May; the leaf fall of rose, which takes place during the first half of April. In Italy; (May–early July) with following, progressive spread through the vineyards, with concentration in areas of high vegetative density (Mazzoni et al., 2008). *Z. rhamni* Ferr. had been listed from Turkey by Metcalf (1968) from Turkey. In additionally; This species was distributed in İzmir, Tekirdağ and Elazığ province of Turkey (Altınçağ, 1987, Karagöz, 1988, Özgen and Karsavuran, 2009). In this study, that have been aimed in *Z. rhamni* population development in Elazığ, Diyarbakır and Mardin provinces.

MATERIAL AND METHODS

In this study, yellow sticky traps work population dynamics of pests methods were applied. Study was carried out a total of twelve vineyard location in Diyarbakır, Elazığ, Mardin cities. maintaining the integrity of the specifications. These locations are Diyarbakır (Ergani, Çermik, Çüngüş 1 and Çüngüş 2), Elazığ (Altınçevre, Akçakiraz Yurtbaşı and Center), Mardin (Mazıdağı, Derik 1, Derik 2 and Ömerli). In each vineyards were collected

specimens on five sticky traps and taken to average to weekly.

RESULTS AND DISCUSSIONS

Population development were summarized in Fig.1, Fig 2, Fig, 3, Fig 4 of *Z rhamni*.

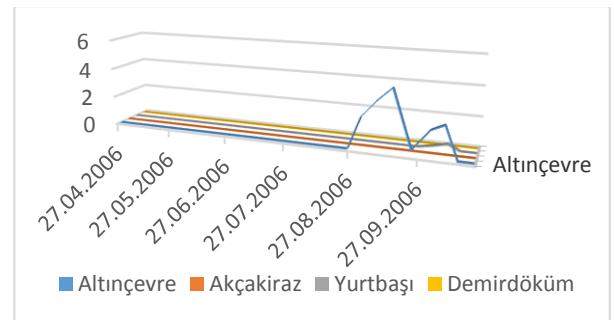


Figure 1. Population Development of *Z. rhamni* in Elazığ city in 2016 years

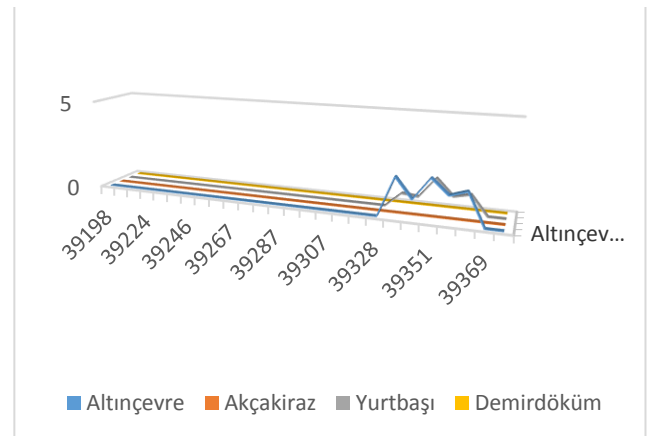


Figure 2. Population Development of *Z. rhamni* in Elazığ city in 2017 years.

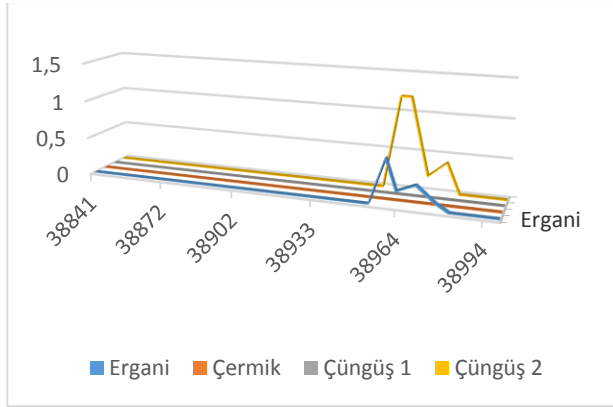


Figure 3. Population Development of *Z. rhamni* in Diyarbakır city in 2016 years.

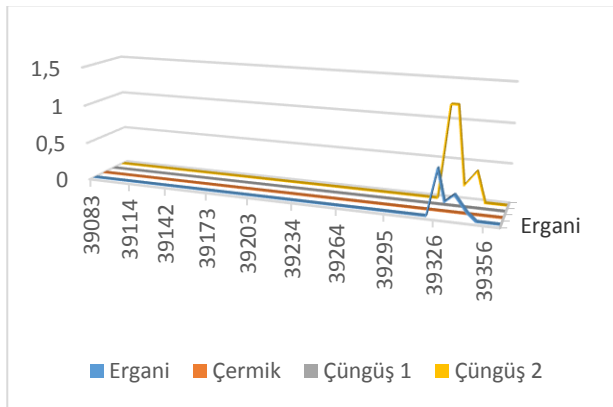


Figure 4. Population Development of *Z. rhamni* in Diyarbakır city in 2017 years.

Z. rhamni was firstly determined Diyarbakır province. In this location; was distributed commonly white varieties. It was determined that the average population formed with the end of the 8th month and the middle of the 10 th month in each location. It were seen commonly that the Tahannebi, Sireli, Boğazkere grape varieties. This species was found Bois noir infected vineyard in Europe. Bois Noir makes it crucial that phytoplasmic disease be found in vineyards where it is found in vineyards. Since this disease has been detected in the

Aegean, Central Anatolia and Eastern Anatolian vineyards of our country, it is important to prevent the spread of the disease.

REFERENCES

- [1] Mazzoni, V., Anfora, G., Ioriatti, C. and A. Lucchi, 2008. Role of winter Host Plants in Vineyard Colonization and Phenology of *Zygina rhamni* (Hemiptera: Cicadellidae: Typhlocybinae). *Annals of Entomological Society of America*. 101 (6): 1003-1009.
- [2] Mettcalfe, Z.P., 1968. General Catalogue of the Homoptera. Fas. VI. Cicadelloidea. Pt. 17 Cicadellidae. ARS., USDA. Washington, D.C., 1513 pp.
- [3] Altınçağ, R., 1987. İzmir, Manisa ve Çevresindeki Bağlarda Zarar Yapan Böcek Türleri, Önemlilerinin Tanınmaları ve Özellikle Empoasca decedens Paoli, Arboridia adanae (Dlabola) ve Zygina sp.'nin Biyokolojileri ve Zararları Üzerinde Araştırmalar. E. Ü. Ziraat Fakültesi Bitki Koruma Bölümü'nde hazırlanmış doktora tezi. 165 s. (Yayımlanmamış)
- [4] Karagöz, M., 1988. Trakya bölgesinde bağlarda zarar yapan böcek türleri, önemlilerinin tanımları, yayılışları, zarar şekilleri ve ekonomik önemleri üzerinde incelemeler. Türkiye III. Bağıcılık Simpozyumu Özetleri, Bursa, 66.s.
- [5] Özgen, İ. ve Y. Karsavuran, 2009. Diyarbakır, Elazığ ve Mardin İlleri Bağ Alanlarında Bulunan Cicadellidae (Homoptera Türleri. Türk entomol derg., 33 (3): 217-240.
- [6] R. Nicole, "Title of paper with only first word capitalized," J. Name Stand. Abbrev., in press.
- [7] Y. Yorozu, M. Hirano, K. Oka, and Y. Tagawa, "Electron spectroscopy studies on magneto-optical media and plastic substrate interface," IEEE Transl. J. Magn. Japan, vol. 2, pp. 740-741, August 1987 [Digests 9th Annual Conf. Magnetics Japan, p. 301, 1982].
- [8] M. Young, The Technical Writer's Handbook. Mill Valley, CA: University Science, 1989.

Internal Diseases Diagnosis Using Artificial Neural Networks

Merve Erkinay Özdemir
Electrical and Electronics Engineering
İskenderun Technical University
İskenderun/Hatay, Turkey
merve.erkinyozdemir@iste.edu.tr

Harun Geçirgen
Electrical and Electronics Engineering
İskenderun Technical University
İskenderun/Hatay, Turkey
harunngrcn@gmail.com

Abstract— *Internal diseases are common to adults. Physicians diagnose of internal diseases according to their experimental knowledge and laboratory results. Laboratory tests such as blood analysis, urine analysis are very important for diagnosis of internal diseases. Diagnosis of most internal diseases can be done by evaluating the blood test results. Health care workers and patients have gained great convenience with the implementation of technological developments in the field of medicine. Besides the personal information of the patient, diagnostic information such as laboratory results are started to save electronically in health care units in recent decades. The stored data is analyzed with modern techniques and then served to the doctors and managers. The use of artificial neural network structures for classification systems in medical diagnosis are increasing. In this study, a system based on artificial neural network is developed for diagnosis of anemia, liver disease, kidney failure, B12 vitamin deficiency, diabetes and thyroid disease. The data obtained from blood analysis results of state hospital's database. The blood analysis results are obtained from 62 patients. Multi layered feed forward artificial neural network is used as a classifier to distinguish between internal diseases. Our method achieved 95% accuracy. The promising results indicate that our method can detect internal diseases effectively. Based on this result our method can serve as important and useful method in diagnosis for physicians to avoid unnecessary medical waste and enhance healthcare quality.*

Keywords— *internal diseases; diagnosis; artificial neural network*

GEOLOGICAL ENGINEERING

ORAL SUBMISSIONS



Provenance Investigation From Sedimentary Petrography Of The Upper Cretaceous Deep Marine Low Density Turbidites Of Tanjero Formation Around Arbat, Northern Iraq

Tavan Muhammad Hama Salih

Ministry of Higher Education and Scientific-
Research-KGR, KISSR Sulaimani, Northern Iraq.
tavan.hamasalih@gmail.com

Hasan Çelik

Fırat University Engineering Faculty Department of
Geological Engineering, 23119, Elazığ, Turkey.
hasancelik@firat.edu.tr

Abstract—Deep marine low density turbidites of Upper Cretaceous Tanjero Formation were studied to present petrographic composition and provenance of the unit in Arbat area. Petrographic works based on modal analysis of the clastic rock fragments and released single minerals in silt, fine to coarse grained sandstone and, in very small quantities pebbly sandstone show that these turbidites are mainly composed of sedimentary rock fragments such as carbonate, microcrystalline and cryptocrystalline quartz bearing siliceous sedimentary cherts, radiolarian bearing cherts, and released radiolarians from the cherts during a short distance transportations. Quartz and feldspar ratios in the whole thin sections are below three percent. The turbidite siltstones and sandstones are litharenite in composition indicating sedimentary source rocks mainly consisting of carbonate rocks and radiolarian and chert rich limestones.

The composition of the clastics suggests a recycled sedimentary sources. Likewise, the QtFL ternary diagram suggests that the sediments are derived lithic recycled provenance which may be the Lower Cretaceous Qulqula Formation.

Keywords— Tanjero Formation, petrography, provenance, Northern Iraq.

Microfacies Analysis of Kocaçay Formation (Middle Eocene) Around Şefaati Township of Yozgat, Central Turkey

Emrah Erdem

Ahimesut Mahallesi 1782 Sokak No:1/6 Etimesgut,
Ankara, Turkey
emraherdem2@gmail.com

Hasan Çelik

Fırat University Engineering Faculty Department of
Geological Engineering, 23119, Elazığ, Turkey.
hasancelik@firat.edu.tr

Abstract—This study based on biostratigraphic micro facies characteristics of Middle Eocene Kocaçay Formation consisting of layered fossiliferous limestone outcropping at 1,5 km to the east of Deliler Village in Şefaati township, southern Yozgat, central Turkey, show the existence of three main faunal microfaciesses. The measured section of this study was taken on the only clearest outcrop of the unit in a vacated limestone quarry as no any open and suitable section of the limestones exist around the township.

According to the biostratigraphic evidences obtained from thin to medium bedded limestone layers show existence of Miliolidae facies, Alveolina facies and Nummulite facies. These three faunal microfaciesses were interpreted as internal shelfal carbonate and shallow marine for palaeo environment of the formation during Middle Eocene. At the evidences obtained from work place and verifications from works of slim-mid layer limestone with stratigraphic section, three main facies are much in evidence as Miliolide Facies, Alveolina Facies, Nummulite Facies in this forms.

Keywords— Middle Eocene, Kocaçay Formation, microfacies, benthic foraminifers, Yozgat, Central Turkey.

Sedimentary Facies Analysis And Depositional Model Of the Upper Cretaceous Turbidites To The Northwest Of Sulaimani, Northern Iraq

Hemin Muhammad Hama Salih

Ministry of Higher Education and Scientific- Research-
KGR, KISSR Sulaimani, Northern Iraq.
hemin.hamasaleh@gmail.com

Hasan Çelik

Firat University Engineering Faculty
Department of Geological Engineering, 23119,
Elazığ, Turkey.
hasancelik@firat.edu.tr

Abstract— *This study outlines a lithofacies analysis of the Upper Cretaceous deep marine turbidites of Tanjero Formation outcropping in the close northwest of Sulaimani area. The outcrops of the unit are seen throughout of the northern Iraq more or less parallel to the Iranian border. This study will trigger further studies on lithofacies analysis of the formation to establish a complete work for depositional model of the unit in the meaning of lobe hierarchy. The turbidites represent a large submarine distal fan depositional system related to the described lithofacies as the lateral continuations of the turbidite beds are visible along tens of kilometers in the area.*

Seven distinctive main lithofacies groups were identified from seven measured sections. Each of them is more than one hundred meters in thickness consisting of fourtyeight subfacies. The groups classified as grain size are coarse grain sandstone beds (CGSB: includes four subfacies), medium grain sandstone beds (MGSB: includes twelve subfacies), fine grain sandstone beds (FGSB: includes eighteen subfacies), very fine grain sandstone beds (VFGSB: includes two subfacies), shale and silt sized thin bedded turbidites (STBT: includes five subfacies), fine sand thin bedded turbidites (FSTBT: includes four subfacies) and medium sand thin bedded turbidites (MSTBT: includes three subfacies). The subdivisions of the groups are seperated according to their internal sedimentary structures. All facies groups represent low density turbidites composed of some divisions of Bouma sequence.

These facies represent about middle part of outer fan and lobe fringe to lobe distal fringe sand rich depositional system for the turbidites outcropping around Sulaimani.

Keywords— *Facies analysis, Upper Cretaceous turbidites, lobe fringe, outer fan, Sulaimani, northern Iraq*

Slip Rates Contradiction Between Geologic And Geodetic Data Along The North Anatolian Fault

Mehmet Köküm

Firat University, Engineering Faculty, Geological
Engineering, 23119, Elazığ, Turkey.
mkokum@firat.edu.tr

Kaj M. Johnson

Geological Science Indiana University Bloomington, USA.
kajjohns@indiana.edu.tr

Abstract— Modeling studies for slip rate along the North Anatolian Fault (NAF) indicate a contradiction between the geologic and geodetic slip rates along the fault segments. Previously published geodetic slip rates are higher than geological long-term slip rates along the NAF. An apparent contradiction between the geologic and geodetic slip rates along the faults is quite common problem for the modeling studies. In this work, we address on this contradiction in order to find out reasons of the different slip rates estimates. There are three potential scenarios to clarify this remarkable difference on slip rate estimates. The first and second scenarios could be that either geodetic slip rates or geologic slip rates are incorrect. There are some limitations to estimate slip rates both on geodetic data and geologic rates. Insufficient geodetic data along the fault zone (e.g., Reilinger et al., 2006) and insufficiency of the model (e.g., sudden change in deformation such as mantle flow, misplaced block boundaries, poor locking depth estimates) or poorly constrained geometry of the submarine faults, which is not defined well (e.g., Ching and Johnson, 2011) could be examples for the limitation of geodetic studies. Large uncertainties on geologic estimates (e.g., Allen et al., 2004) could be examples for the limitations of the geologic slip rate estimates. The third scenario could be that both geodetic slip rates and geologic slip rates are correct. Polonia et al. (2004), hypothesis is that geodetic estimates might represent a recent increase or decrease in slip rate; in this case the geodetic result does not represent the long-term geological motion. Modeling studies reveal the locking depth estimates with slip rates for the major fault system that is very useful information for the earthquake hazard studies. Geodetically determined locking depth estimates are rather deeper than depth of background seismicity along the NAF. We cannot answer of this question ‘which data should be taken into account for slip rate estimates’; however, we may suggest using both geodetic and geologic slip rates as data to have better slip rates estimates. Because slip rates estimates using both data set to build a model are consistent with the depth of background seismicity along the NAF. The question may reach the solution by improving modeling and having more data in the near future.

Keywords— North Anatolian fault; geodetic slip rate, geologic slip rate, contradiction

Lithofacies And Architectural Elements Of The Deep Marine Calciclastic Low Density Turbidites Of Upper Cretaceous Tanjero Formation, Around Arbat, Northern Iraq

Tavan Muhammad Hama Salih

Ministry of Higher Education and Scientific- Research-
KGR, KISSR Sulaimani, Northern Iraq.
tavan.hamasalih@gmail.com

Hasan Çelik

Fırat University Engineering Faculty Department of
Geological Engineering, 23119, Elazığ, Turkey.
hasancelik@firat.edu.tr

Abstract— *The calciclastic low density turbidites of the Upper Cretaceous Tanjero Formation widely crop out throughout of Northern Iraq. In order to interpret the sedimentary environment of the turbidite cropping out around Arbat six detail measured sections taken from eastern side of a hill oriented about NW-SE direction have been studied. The equated thickness of the measured sections is 45m. The analysis of lithofacies and architectural elements, leads to recognition of three main lithofaciesses and fourtynine total subfaciesses of the turbidites in the location. The main faciesses represent the grain size from fine to coarse grain sandstone. The subfaciesses are consisting of many types of combinations of complete Bouma sequence associated with thin bedded turbidites. These faciesses point out that the environment of the turbidites is inner part of outer fan. In the meaning of lobe hierarchy the turbidite beds in thin and medium thicknesses represent lobe fringe. Only one architectural element recognised in the section is small sandy channel fills in about ten metres lenght and a few metres thick representing beginning of outhter fan or in lobe fringe. The composition of the clastics suggests a recycled sedimentary sources. Likewise, the QtFL ternary diagram suggests that the sediments are derived lithic recycled provenance which may be the Lower Cretaceous Qulqula Formation.*

Keywords— *Tanjero Formation, petrography, provenance, Northern Iraq.*

Reservoir Characterization Of The Deep Marine Calciclastic Turbidites Of Tanjero Formation Northwestern Sulaimani, (Northern Iraq)

Hemin Muhammad Hama Salih

Ministry of Higher Education and Scientific- Research-
KGR, KISSR Sulaimani, Northern Iraq.
hemin.hamasaleh@gmail.com

Hasan Çelik

Fırat University Engineering Faculty Department of
Geological Engineering, 23119, Elazığ, Turkey.
hasancelik@firat.edu.tr

Abstract—In this study reservoir characterization of the Upper Cretaceous low density calciclastic turbidite sandstones of Tanjero Formation were analysed. The sandstone portion of the unit have been examined through field and laboratory based studies. 7 were measured and described in detail. Average thickness of the measured sections is 158 m. The field logs start from the contact between underlying Shiranish Formation to more than 150 metres in thickness in the turbidite unit. 44 rock samples were taken for petrographic analysis, porosity and permeability tests from the logs for laboratory analyses. The turbidites represent distal fan and low density deep marine depositional sand rich system. The sandstones are litharenite (sedarenite), very fine to coarse and pebbly coarse grained in size consisting of chert, siltstone, mudstone, radiolarian chert and radiolarian mudstone fragments, angular to subangular in shape, and moderately sorted, transported over short distances and submature. Porosity of the studied sandstones range from 5,51 to 11,59 % which is poor to beginning of fair with an average value of 7,11%. The obtained permeability varies between 10,71-2315,65 md and their mean value is 866,35 md representing high permeability. As the modal components of the sandstones are made up of 97 % sedimentary rock fragments (average and mainly reworked carbonate fragments) and calcite minerals, the reservoir quality of the turbidite sandstones was strongly negatively influenced by the alteration of these elements creating mainly calcite and some clay cementations. The combined effect of calcite and clay occurrences and the plugging of pores by these cements causes a final reduced porosity. As a result the turbidite sandstones of the Tanjero Formation cropping out to the northwest of Sulaimani have general poor porosity and a very good permeability.

Keywords: Tanjero Formation, turbidite sandstone, reservoir characterization, Sulaimani, Northern Iraq

Investigation Of Fly Ash Effect On Rheological And Filtration Properties Of Drilling Muds

Abdullah Özkan

Iskenderun Technical University, Department of Petroleum
and Natural Gas Engineering, Hatay, 31200

Vildan Özkan

Iskenderun Technical University, Department of Petroleum
and Natural Gas Engineering, Hatay, 31200

Sitki Ekrem Turan

Iskenderun Technical University, Department of Petroleum
and Natural Gas Engineering, Hatay, 312

Behlül Merve Kaplan

Iskenderun Technical University, Department of Petroleum
and Natural Gas Engineering, Hatay, 31200.
behlulmervekaplan@gmail.com

Abstract—Drilling fluids are used in drilling operation for many reasons such as lubricating and cooling the drill bits, elimination of cuttings from wellbore, ensuring the stability of the hole and preventing crossflow of fluids between borehole and formation. Therefore selection of a convenient drilling fluid makes drilling operations easier and economical. For this purpose, researches have been concentrated on improving the related properties of drilling fluids by adding additives different in composition and size. In this study ultra fine micro-sized fly ash, which is the combustion product of coal fired power plants, is combined with drilling fluids in order to investigate the changes on rheologic and filtration properties of drilling fluids. Fly ash is mostly consists oxides of Silica (SiO_2), Alumina (Al_2O_3), Iron (Fe_2O_3), Calcium (CaO), Magnesium (MgO) and Sodium (Na_2O) respectively. Chemical composition of fly ash is determined by X-Ray Fluorescence (XRF) and X-Ray Diffraction (XRD). Fly ash is added to water based bentonite clay drilling mud in different concentrations (% 0.05, % 0.1, % 0.5, % 1, % 2, % 3, % 4, % 5 and % 10) (%w/v). Plastic viscosity (PV), yield point (YP), visible viscosity (AV) and gel strength are examined with Fann Viscometer as rheological properties, filtrate loss and filter cake thickness are examined with API fluid loss testing equipment as filtration properties.

Result of this study show that addition of fly ash into water based drilling fluids improve filtration and rheological properties of drilling fluids. Use of fly ash provides benefits both in environmentally and economically since a waste combustion by product is utilized and circulating fluid amount is saved by decreasing fluid loss to formations.

Keywords—Fly Ash, Drilling Muds, Rheological Properties, Filtration Properties.

The Evaluation Of Hydrochemical, Geothermal Energy Potential And Balneotherapy Of The Some Important Geothermal Waters, Central Anatolia, Turkey

Mustafa Afşin

Aksaray University, Department of Geological Engineering.
mafsinbaglum@gmail.com

Murat Kavurmacı

Aksaray University, Department of Geological Engineering.
mkavurmaci@aksaray.edu.tr

Ali Gürel

Nigde University, Geological Engineering Department, Campus,
Nigde, Turkey agurel_1999@yahoo.com

Macit Karadağlar

General Directorate of Mineral Research and Exploration (MTA) Department of Energy Raw Material Research and Exploration, Ankara

Ümmühan Gökçen Duru

Ministry of Environmental and Urbanisation,
Eskisehir Devlet Yolu, Çankaya
gokcenduru@hotmail.com

Hatice Gürdal

Istanbul University, Istanbul Medical Faculty, Medical Ecology and Hydroclimatology Dept, Istanbul, Turkey

Abstract— *There are many geothermal waters with low-middle enthalpy in central Anatolia. In this study, some important geothermal waters in Nevşehir, Kırşehir, Aksaray, Nigde, Kayseri geothermal fields were evaluated for origin, geothermal energy potential and balneotherapy point of view.*

The basement of the fields forms metamorphics which comprise marble, gneiss and quartzites in ages Paleozoic. These units are overlaid by different units from Cenozoic to Quaternary age. Occurrence of the waters is mainly related to tectonism and volcanism. The primary and secondary aquifers of the geothermal waters are of marbles (Paleozoic in age) and limestones (Tertiary in age), respectively.

Types of waters are Na-Cl-HCO₃ for the long circulating groundwaters (Kemerhisar, Incesu, Kozakli, Ziga) and Ca-Na-HCO₃-Cl for relatively shorter circulating groundwaters (Bayramhaci, Terme, Narligöl). The sources of dominant ions of Ca²⁺ and HCO₃⁻ in the waters are mainly related to the high CO₂ contents resulting from interactions with the carbonate rocks; whereas, the high Na⁺ concentration is derived from the increasing of albites in volcanic rocks, by ion exchange occurred between the tuff, clay, sandstone and granites/syenites. Na⁺ and Cl⁻ in some geothermal waters are increased as a result of short contact time with evaporitic sequences (halite etc.) and also paleowaters in the old basins.

All the waters are of meteoric origin according to isotope analyses (18O, 2H, 3H), and cold waters have shallow and fast circulation, and geothermal waters have relatively deep and low circulation. The deviation of some waters from global meteoric water line is mainly due to the high CO₂ contents and increase the δ18O values as a result of water-rock interaction. 14C ages of the waters are not real ages of the waters, but they are the measures of contribution of modern biogenic carbon in total dissolved carbonate or bicarbonate. 14C apparent values of the waters are increasing from young waters to old waters, whereas per cent modern (pmc) carbon and 3H values are decreased in the same order. The sources of CO₂ in the waters may suggest freshwater carbonate, marine carbonate and metamorphic according to the results of δ13C. The origins of δ34S in the waters may atmospheric, evaporitic, volcanic and/or carbonate rocks.

The estimated reservoir temperatures (50-123°C) of the rock of the geothermal waters by silica geothermometers denote the higher geothermal energy potential of these waters. Heat sources of these geothermal systems are geothermal gradient, volcanism and granite/syenite intrusions in the areas.

This region has the natural possibilities for the human health protection and treatment of diseases. These geothermal waters have capacity for specific applications in balneoclimatherapy; Aksaray city having the highest open air curative summer day with 175.5 days over 20°C. Kayseri city is favorable for healthy persons and sportsmans due to the high actinic stimulant. In this connection, all the geothermal waters comprising dominant ions such as Na, Cl, HCO₃ and CO₂ are also useful for the treatment of psoriasis, some gastrointestinal, metabolic, urinary trac, some rheumatological and dermatological disorders in balneotherapy-climatherapy. Controlled clinical studies are required especially for long-lasting benefits.

Acknowledgement: *This study was granted by The Scientific and Technological Research Council of Turkey (TUBITAK) by Project No. CAYDAG 104Y197.*

Keywords— *Geothermal water, groundwater circulation, , isotope, geothermal system, balneoclimatherapy, central Anatolia*

Effect Of Nano Zeolite Addition In Drilling Fluid

Abdullah Özkan

Iskenderun Technical University, Department of Petroleum
and Natural Gas Engineering, Hatay, 31200

Vildan Özkan

Iskenderun Technical University, Department of Petroleum
and Natural Gas Engineering, Hatay, 31200

Behlül Merve Kaplan

Iskenderun Technical University, Department of Petroleum
and Natural Gas Engineering, Hatay, 31200.
behlulmervekaplan@gmail.com

Sıtkı Ekrem Turan

Iskenderun Technical University, Department of Petroleum
and Natural Gas Engineering, Hatay, 312

Abstract—Wellbore instability is the most important problem in drilling operation, especially in high temperature and pressured shale formations. This problem can be accomplished in drilling industry with the help of nano particules like that nano zeolites. Nano zeolites can bring benefit to the industry in various manners such as improving the quality of mud cake, decreasing the frictional resistance in the well, minimizing the risk of pipe sticking, improving rheological properties, preventing reservoir from formation damage. For this purpose, in this study, effect of nano zeolite addition to drilling fluid is investigated in terms of rheological and filtration properties. Nano zeolites that planned to be added to drilling fluids, are the alumino silicate members of the family of microporous solids known as "molecular sieves" mainly consisting of Si, Al, O, and metals including Ti, Sn, Zn, and so on. Additionally, nano zeolites at different concentrations (% w/v) to improve the drilling fluid of water based bentonite added. The rheological behavior, the filtration loss property, pH and density test of each drilling fluid developed is measured using API recommended standard procedures. The rheological properties like that visible viscosities (AV), plastic viscosity (PV), flow-point (YP), gel strength, of the nano-zeolite-added mud were measured using with fann viscometer. Also, the filtration, pH and density test were also carried out using an API Filter Press, pH meter and mud balancer respectively.

As a result of this study; it was found that the nano-drilling fluid has better rheological properties when compared to the results of the water-based bentonite drilling fluid and the nano-zeolite-added drilling fluids. It was also observed that the loss of filtrate was reduced and the filtrate cake thickness decreased.

Keywords—Nano Zeolite, Drilling Fluids, Rheological Properties, Filtration Properties.

Inversion of fracture spatial distribution for micro-seismic based on Genetic Algorithm

Yinting Wu

Department of Geological Engineering and Surveying
Chang'an University
Xi'an, China

National Engineering Lab for Offshore Oil Exploration
Xi'an Jiaotong University
Xi'an, China

Abstract—Genetic Algorithm (GA) is an effective nonlinear inversion method. In this paper, we combine the micro-seismic and GA to inverse the acoustic emission locations. A 3D synthetic model is set and solutions are achieved through the establishment of two objective functions. Contrast their accuracy and convergence speed, we find that their differences of error ratio can be about 2.7 times and the one of time costing can be triple times. Basing on the result, we chose objective function II for field data. From the application of a certain curve well, we clearly know about the crack growth direction. The spatial distributions of three fracturing sections are demonstrated in different views. The fractures are all concentrated at corresponding perforations, but form to different directions. We believe it can provide the basis for evaluation and adjustment of fracturing schemes.

Keywords—GA; hydraulic frecturing; inversion; micro-seismic

I. INTRODUCTION

Genetic algorithm (GA) is an adaptive technology, of which probabilistic search approach increases the flexibility of computing process, and also a progressive global search method. From 1960s, Professor J. Holland and his students from the University of Michigan began a series of studies [1]. Then into the 1990s, GA ushered in a prosperous period of development. Since it does not need to calculate the derivative of objective functions in the optimization search process with GA, especially for the discrete problem, nonlinear problem and optimization of complex issues which cannot be explicitly represented by functions, so in various fields GA has been widely used [2]. Since 1995, researchers began to use GA for solving the problems of Geophysics as follows [3]: residual statics in the seismic survey [4-5], parameters inversion in the multi-layer density interface [6], anisotropic elastic parameters calculation [7], speed parameters inversion [8-9], wave impedances inversion [10], Amplitude Versus Offset (AVO) [11], bending ray imaging [12], multi-electrode resistivity logging and 2D magneto-telluric [13], estimation of logging interpretation parameters [14-17] and so on. Wang discussed the effect of GA used in micro-seismic [18].

On the other hand, the micro-seismic monitoring began from the mining industry in the 1940s and in the 1990s, the data processing has made great progress. Theoretically, with the observation and analysis of small seismic events, the source location of micro-seismic and causative events can be determined, thus the spatial distribution and geometry of

fracture in the fracturing process can be described. In the process of exploration and development of oil and gas reservoirs, using micro-seismic monitoring technology can optimize the low permeability injection and production programs, reduce the development costs and increase the oil and gas production. It has become an effective way to solve the short supply problem of oil and gas production at present.

Based on the above, this paper combines the GA and micro-seismic to portray the hydraulic fracture

II. SYNTHETIC DATA INVERSION

The ultimate goal of hydraulic fracturing micro-seismic is to determine the spatial distribution and development of fractures, which is a nonlinear inversion problem. GA is used to calculate the source distribution of a three-dimensional layered medium model as follows.

A 3D layered micro-seismic model is shown in Figure 1. Where, the (x_s, y_s, z_s) is the micro-seismic source location; t_s is the event's break time; (x_i, y_i, z_i) , $i=1, \dots, n$ is the coordinate of the i th detector respectively; t_i indicates the time when the event is monitored at all levels of detectors; t_{si} is the theoretical value, which represents the travel time between the layers from the micro-seismic source to the i th detector computed with the piecewise Ray Tracing method.

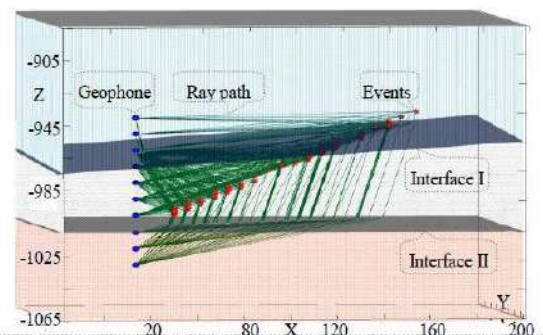


Fig. 1. 3D layered micro-seismic model

The fracture parameters are: the fracture development azimuth angle is 30 degrees and the dip angle is 5 degrees; the speed of the fracture developing in the reservoir is 1m/s. The fracture center is (100, 200, -1,000); the focal complex distribution is the range of 5m at the fracture surface. The

detector parameters are: the plane coordinates are all (20, 219); the Z-axis of the first detector is -940 and that of the tenth one is -1,030, as the interval is 10m. There are 5,000 sampling points in the forward micro-seismic record and the sampling rate is 500ms; the location and origin time of each event generate randomly. In order to be more realistic, the random noise is added to the forward modeling process. One event is shown in Fig. 2. X, Y, Z component are shown on the left, center and right side, respectively.

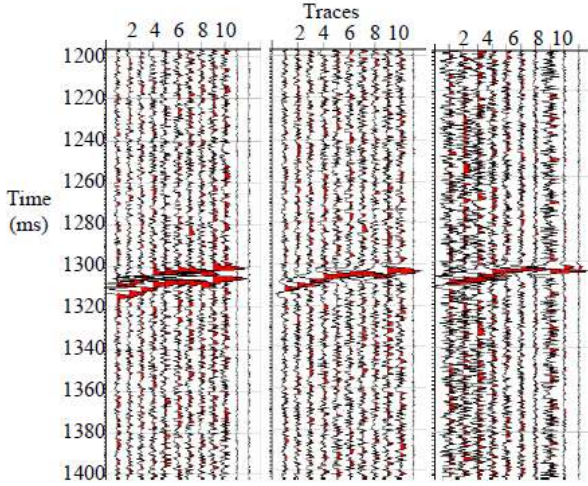


Fig.2. One event of hydraulic fracturing (Left: X component; Center: Y component; Right: Z component)

To one micro-seismic event, there is the following relationship between time parameters:

$$\Delta t_i = t_i - t_{si} - t_s \quad (1)$$

And the theoretical traveling time can be written as:

$$t_{si} = \sum_{j=1}^{m-1} \frac{\sqrt{(x_i - x_{ij})^2 + (y_i - y_{ij})^2 + (z_i - z_{ij})^2}}{v_j} + \frac{\sqrt{(x_m - x_s)^2 + (y_m - y_s)^2 + (z_m - z_s)^2}}{v_m} \quad (2)$$

Where x_{ij} , y_{ij} , z_{ij} are the coordinates of the j th ray path between the i th detector and source, v_j is the formation velocity where j th ray is traveling in; and m is the number of layers where the rays pass through

The nonlinear equation (objective function I) of the seismic source and the origin time can be presented as follows:

$$\max : F(x_s, y_s, z_s, t_s) = \sum_{i=1}^{10} |\Delta t_i| = \sum_{i=1}^{10} |t_i - t_{si} - t_s| \quad (3)$$

The amounts to be solved in (3) are the coordinates of micro-seismic source and the origin time. They can be gotten when the known parameters are brought into this Formula.

On the other hand, taking into account the negative impact of the origin time on the results, by minimizing the time between the adjacent detectors, we establish the objective function II:

$$\begin{aligned} tt_i &= \Delta t_{2i} - \Delta t_{2i-1} \\ &= (t_{2i} - t_{s2i} - t_s) - (t_{2i-1} - t_{s2i-1} - t_s) \\ &= (t_{2i} - t_{2i-1}) - (t_{s2i} - t_{s2i-1}) \end{aligned} \quad (4)$$

GA is used to make optimization. The calculation process and parameter settings are shown as below, respectively:

Population: 5

Crossover way: Single-point;

Crossover probability: 0.8;

Mutation probability: 0.05;

Range of X offset (m): $0 \leq x \leq 200$;

Range of Y offset (m): $0 \leq y \leq 300$

Range of Z offset (m): $-800 \leq z \leq -1200$;

Range of $t_s \in$ (Automatic picking time ± 20)

Remarks: Phase Only Corresponding method is applied for Automatic time picking.

For the established objective function I, the optimal fitness function change curve can be gotten after 600 iterations with GA, as shown in Fig. 3. While, for objective function II, the optimal fitness curve can be gotten with 200 iterations (Fig. 4). It can be seen that, the objective function II is convergent only after 50 iterations, so the convergence rate is 3 times faster than that of the objective function I.

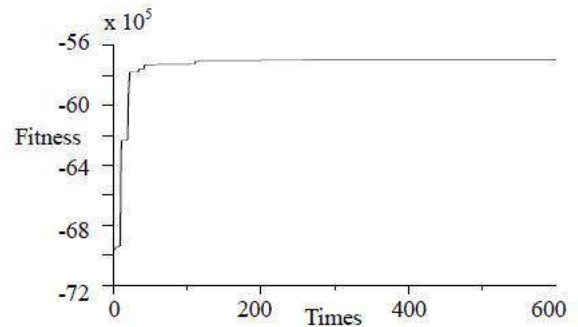


Fig. 3. Fitness curve of objective function I

What is worth mentioning is that, due to the model using a single vertical monitoring well, it is unable to determine the real plane coordinates (x, y) of seismic sources. Therefore, in the inversion, X and Y components are directed by the Covariance Matrix method. Therefore, the optimal solution can be obtained finally. Take the fracturing center (100, 200, -1,003) as an example, the output results of objective function I and II are (98.8623, 201.8541, -1,003.2147) and (100.1324, 200.7530, -1,003.2639), respectively, both with less calculation errors. However, the objective function I has a 3D spatial error of 2.1858m, and the latter one is 0.8088m. The error ratio is 2.7025.

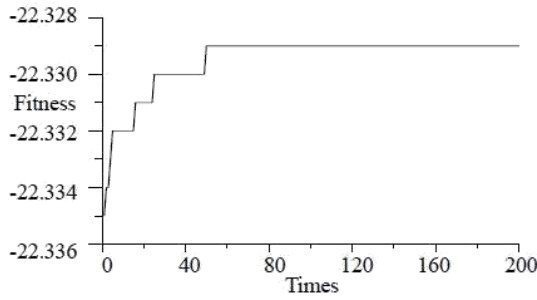


Fig. 4. Fitness curve of objective function II

Comparing the inversion values between the above two objective functions, we can see that the positioning results of the objective function II is closer to the theoretical value with a higher accuracy and a faster convergence rate. And the origin time of the seismic can be solved with known data and calculated source value. Therefore, the establishment and selection of the objective function should be considered, and this paper will choose the objective function II to do the inversion of source location for the real micro-seismic.

III. APPLICATION IN FIELD DATA

In order to check the effectiveness of GA to field micro-seismic data, we chose a certain area. There are two wells, one is for fracturing and the other one is for monitoring. Both of their depths are more than 2,200m. And the wellhead distance between fracturing well and monitor well is 713m, while, the target distance is 219m, because the wells are not vertical. In the fracturing well, three fracturing sections are designed as 2,187-2,191m, 2,176-2,179m, and 2,159-2,163m, respectively. Ten geophones are set in the monitoring well from 2,173 to 2,083m, with the interval of 10m.

The initial layered medium model is built based on logging data and the times of events are automatically gained based on Phase Only Correlation method. Then, according to the objective function II (seen in (4)), the fracture spatial distribution of fracturing section I is inverted. We demonstrate different plane pictures: the top view (X-Y direction) is in Fig. 5, the lateral view of (X-Z direction) can be seen in Fig. 6, and the lateral view of (Y-Z direction) is shown in Fig. 7. Meanwhile, the total events are calibrated in the 3D graph of Fig. 8. With respect to the results, we can see that, the fracture has a specific direction, with the azimuth of 32 degrees north by west. Most of the events are concentrated nearby the corresponding fracturing section.

Then, the positions of the other two fracturing sections are solved as the same as the section I. The total fracture positions are gained. Fig. 9 represents the plane view of fracture spatial distribution of three fracturing sections, which is along the direction of the two wells connection. This is a good evidence to evaluate the effect of hydraulic fracturing. According as the distribution, we could say that the construction meets the original expectations. Otherwise, the total positions of fracturing events can be seen from Fig.10. It's a comprehensive top view. Through observation we know that all the three fracture are happened around perforated intervals. Each fracture development has specific direction.

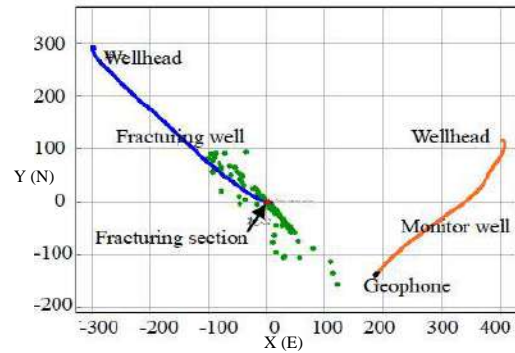


Fig. 5. Top view of inversion for fracturing section I (X-Y direction: X axis points to the east direction of the geography, and Y axis represents the north direction of the geography)

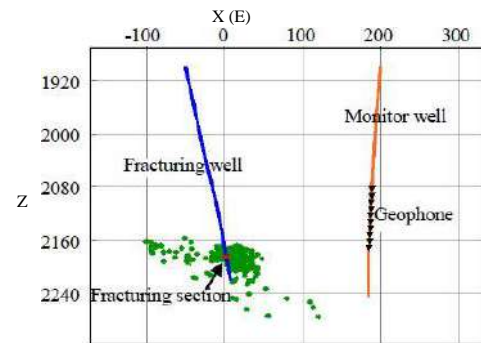


Fig. 6. Lateral view of inversion for fracturing section I (X-Z direction: Z axis is the depth)

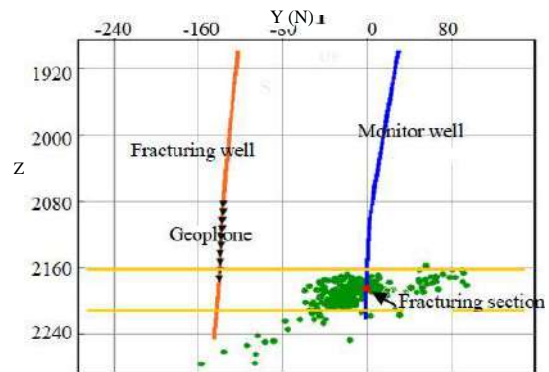


Fig. 7. Lateral view of inversion for fracturing section I (Y-Z direction: Y-north direction; Z-depth)

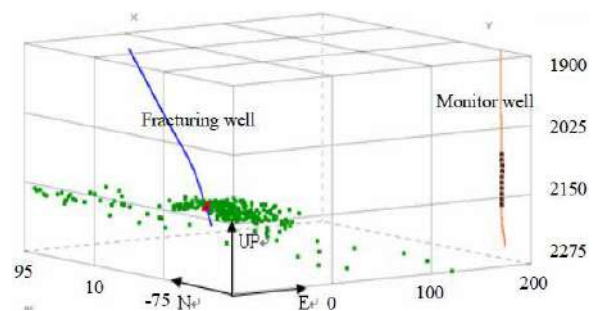


Fig. 8. 3D graph of fracture spatial distribution of fracturing section I

According to the positions of all acoustic events, we can get the fracturing parameters. And the total solutions are summarized and shown in Tab. 1. The accuracy of the fracturing parameters is proved by the subsequent mining process.

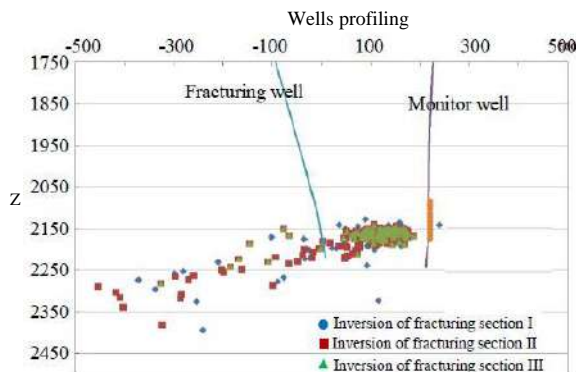


Fig. 9. Plane view of fracture spatial distribution of three fracturing sections (Along the direction of the two wells connection)

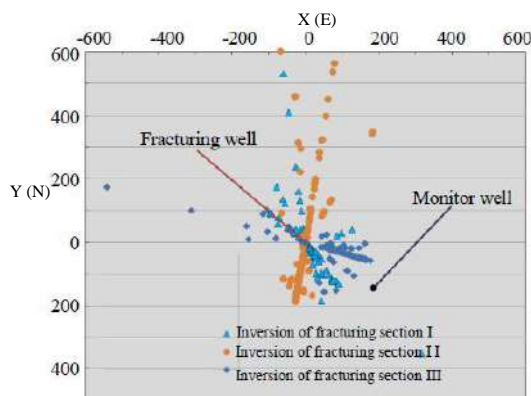


Fig. 10. Comprehensive top view of fracture spatial distribution of three fracturing sections

Tab. 1. Summarized fracturing parameters of three sections

Fracturing Section			I	II	III
Fracture azimuth			32° N by W	8° N by E	72° N by W
Depth domain	Thickness (m)	maximum	250	260	160
		average	175	100	85
Plane domain	Length (m)	maximum	250	125	250
		average	150	75	100
	Width (m)	maximum	40	20	35
		average	20	15	25

IV. CONCLUSIONS

This paper is focused on fixing positions of micro-seismic events during hydraulic fracturing based on GA.

We establish two different objective functions and inverse sources for a 3D layered synthetic data. Comparison results show that differences are produced not only in the accuracy but also the convolution speed. In this example, the error ratio could run up to 2.7025, and time-costing reaches a difference of 3 times. So, we should consider and choose the reasonable one even for the same question. After that, a field micro-

seismic data is also processed. From a series of different views and the total solutions, we could evaluate the fracturing effect. While, it should be pointed out that, the inversion progress is somewhat too simple. As the properties of hydraulic fracturing mediums are often unknown and not elastic, but exist attenuation or porous, the corresponding wave-fields are complex. Therefore, more parameters should be introduced to describe reservoirs more accurately. And wave equation should be combined. Taking these as the basis and establishing suitable objective function is the future subject.

ACKNOWLEDGMENT

This work is supported by the National Natural Science Foundation (Grant No. 41204076), Postdoctoral Science Foundation (Grant No. 2013M540756, 2014T70925) and the Shaanxi Natural Science Foundation (Grant No. 2014JQ2-4019). The author wishes to acknowledge the support and contributions of the project sponsors, other participating institutions and their personnel. The author also thanks the anonymous referees who reviewed an earlier version of this manuscript for their constructive and helpful comments.

REFERENCES

- [1] J. H. Holland, "Adaptation in natural and artificial systems", Ann Arbor, Michigan: The University of Michigan Press, 1975; Cambridge, MA: The MIT Press, 1992.
- [2] De, Jong K. A., "Genetic Algorithms: a 25 years perspective: Computational Intelligence Imitating Life", New York: IEEE Press, 1994.
- [3] L. S. Hu, J. L. Wang and J. S. Wu, "The application process of the Genetic Algorithm in geophysics", Progress in Geophysics, vol. 17, 2002, pp. 598-604.
- [4] C. Yin, Zhou X. X., B. S. Zhong, Y. L. Jiang, and C. L. He, "Hybrid parallel-search strategies and their applications to residual statics", Journal of Chengdu University of Technology, vol. 24, 1997, pp.75-80.
- [5] Y. Yao, "Automatic static correction by nonlinear genetic inverse method", Earth Science-Journal of China University of Geoscience, Vol. 21, 1996, pp. 90-92.
- [6] J. Chen, J. L. Wang, J. S. Wu, B. Chen, G. Chen and Y. J. Chen, "Application of improved Genetic Algorithm to inversion of multi-layer density interface", Earth Science-Journal of China University of Geosciences, vol. 25, 2000, pp. 651-655.
- [7] W. S. Zhang, Q. D. He and F. Wu, "Inversion of elastic parameter in transversely isotropic media using Genetic Algorithms", Computing Techniques for Geophysical and Geochemical Exploration, vol. 20, 1998, pp. 293-298.
- [8] S. X. Luo and L. M. Li, "Inversion of velocity parameters using the Genetic Algorithms", Computing Techniques for Geophysical and Geochemical Exploration, vol. 17, 1995, pp. 30-35.
- [9] H. Z. Zhang, H. Z. Yang and B. Y. Xu, "Interval velocity inversion by Genetic Algorithms", OGP, vol. 30, 1995, pp. 633-644.
- [10] B. Z. Wang and W. C. Yang, "Seismic wave impedance inversion using improved hereditary algorithm", OGP, vol. 33, 1998, pp. 258-264.
- [11] K. S. Mrinal, X. Y. Yang (translator) and W. Li (collator), "Genetic inversion of AVO", World's Oil Science, 1995, pp. 38-41.
- [12] S. Z. Chen, Q. H. Xie and H. L. Liu, "Bending-rays imaging based on Genetic Algorithm", Chinese Journal of Engineering Geophysics, vol. 1, 2004, pp. 102-105.
- [13] Y. J. Tan and J. L. Wang, "Calculate the geophysical inverse problems using Genetic Algorithm", Chinese Journal of Engineering Mathematics, vol. 22, 2005, pp. 427-434.
- [14] J. H. Fang, C. L. Karr and D. A. Standley, "Genetic Algorithm and its application to petrophysics", Society of Petroleum Engineers, 1992.

-
- [15] J. H. Fang, C. L. Karr and D. A. Stanley, "Transformation of geochemical log data to mineralogy using Genetic Algorithms", *The Log Analyst*, vol. 37, 1996, pp. 26-31.
- [16] C. C. Zou, Z. L. Wei, X. Y. Chai, C. Han and H. Y. Zhang, "Optimization of log interpretation using Genetic Algorithm", *WLT*, vol. 23, 1999, pp. 361-365.
- [17] G. J. Yan and B. Z. Pan, "The application of Genetic Algorithm to the parameter estimation in well logging interpretation", *Computing Techniques for Geophysical and Geochemical Exploration*, vol. 23, 2001, pp. 43-47.
- [18] L. F. Wang, "Research on positioning technology of fracturing micro-seismic source place of oil well based on the Genetic Algorithm", Thesis (Master), Changchun: Jilin University, 2012.

Organic matter-major-trace elements relationship of the Derindere–1 area, from Dadaş Formation , Bismil, Diyarbakır, Southeastern Turkey

Dicle Bal Akkoca

Firat University, Engineering Faculty, Geological Engineering, 23119, Elazığ, Turkey.
dbal@firat.edu.tr

Ümit Işık

Firat University, Engineering Faculty, Geological Engineering, 23119, Elazığ, Turkey.

Abstract—The study area is located in the Derindere drill hole, around Bismil, Diyarbakır, southeast of Turkey. Investigated Early Silurian-Early Devonian organic rich Dadas Formation is one of the main source rocks for oil. Formation consists of grayish-green, organic-matter rich dark colored shales, limestones, mudstones and sandstones. Samples were collected from the Derindere drill hole. Element analysis of 20 representative samples were carried out, using ICP-AES for the determination of major and trace elements. 20 total organic carbon (TOC) analysis was performed by the pyrolysis method using the Rock-Eval 6 analyzer. Al_2O_3 , Fe_2O_3 , Na_2O , TiO_2 and Cr_2O_3 , Sc, Ba, Co, Cs, Ga, Hf, Rb, Nb, Ta, Th decrease at the between 3000-3020 m. showing lower detritic contribution at these levels. On the other hand CaO is higher at these levels show carbonate occurrences. Cu, Pb, Zn, As sulphophile elements are lower at the 3060. meter showing lower sulphide minerals at these level. TOC values increase between 2890–3070 meters. These variations in elements and TOC concentrations reflect changes in paleoclimate, paleoredox and paleoproductivity in Paleozoic sedimentation. The positive correlations between SiO_2 , Al_2O_3 , Cs, Ga, Nb, Rb, Ta, Th, Sc reflect silicates and, positive correlations between Cu, Pb, Zn, Ni show sulphide occurrences. Negative correlations of TOC and SiO_2 , Al_2O_3 , Fe_2O_3 reflect that these elements depend on silicates than organic materials. The correlations between Ga, Rb, Ta, Th and TOC show detritic silicate- organic material discriminations.

Keywords—organic matter; major element, trace element, Dadaş , Eastern Turkey

Bioaccumulator Characteristic for Cu of *Euphorbia Cyparissias* Plants Growing in Red-Bed Type Cu Deposits, Yozgat, Turkey

Güllü Kırat

Bozok University, Faculty of Engineering and Architecture,
Department of Geological Engineering, Yozgat, Turkey
e-mail: gullu.kirat@bozok.edu.tr

Leyla Kalender

Firat University, Faculty of Engineering and Architecture,
Department of Geological Engineering, Elazığ, Turkey
e-mail: leyla.kalender@firat.edu.tr

Nasuh Aydin

Balikesir University, Faculty of Engineering and
Architecture, Department of Geological Engineering,
Balikesir, Turkey e-mail: nasuhaydin@hotmail.com.tr

Abstract— Red-bed type Cu deposit between Delice and Terzili villagers is associated with stratiform sedimentary basin (Oligo-Miocene) and co-existing with evaporites. The red-bed type Cu deposits are in the form of layers and lenses and formed in red, brown, purple sandstones, mudstones, conglomerates and shale layers. The color of the ore zones is green, gray and greenish grid.

For the biogeochemical studies around the Delice and Terzili Cu mineralizations, collected samples of *Euphorbia cyparissias* (sparrow) which grows naturally in the region and analyzed by ICP-MS. The obtained results were evaluated statistically. The mean Cu value of this plant in the stems, leaves and associated soil are 413.6 mg/kg, 123.3 mg/kg and 70.4 mg/kg.

In this study, it was determined that there is a positive correlation between Cu concentrations in the leaves of *Euphorbia cyparissias* (*E. cyparissias*) plant and Cu concentrations in the soils ($n = 10$, $r = 0.42$) for Cu concentrations. Accordingly, it can be said that the leaves of *E. Cyparissias* plant may be the indicator plant for Cu. The mean enrichment coefficient of this plant stems and leaves is 0.48 and 0.27 and is less than 1. This coefficient indicates that the plant may be a medium-bioaccumulator plant for Cu. It can be said that *E. cyparissias* plant can be used for ore exploration by biogeochemical method, for improving contaminated areas by Cu (phytoremediation) and environmental pollution.

Keywords— biogeochemistry; bioaccumulator; indicator; Red-bed; soil

I. INTRODUCTION

Oligo-Miocene aged Red-Bed copper (Cu) deposits are a type of stratiform sedimentary beds [1], [2], which are associated with evaporites. In Turkey, red-bed type Cu deposits are located around and in the Yozgat, Çorum, Çankırı, Sivas [2]. In these beds, the ore is in the form of lenses and thin plates in red-colored levels [3].

Red-bed type Cu deposits are formed in red, brown, and gray sandstones, mudstones and shale layers. The red color of the side rocks of these deposits is due to the deposition of hematite and limonite around the grains as a result of the oxidation of $Fe + 2$ to $Fe + 3$. The color of the lens and layer of the ore in the reductive environment is green and greenish grid. The thickness of these ore deposits varies from mm to meters and the width is extended for kilometers [4].

There are three different views on the formation of red-bed type copper deposits: syngenetic, diagenetic and epigenetic. According to the synergetic view, mineralization has taken the form of stratiform [5], [6], [7], [2]. According to the epigenetic view, the mineralization has taken place after precipitation due to diagenesis [4], [8], [9], [3]. Some researchers [10] suggest that this mineralization is similar to the formation of "roll-type" uranium deposits. According to the diagenetic view, the ore melts are found in the sedimentary environment. Because, as a result of the melt and gases filling the space between pre-deposited materials, ore minerals have formed.

In this study, elemental analysis of collected *E. cyparissias* plant (stem and leaf) and soil samples related to this plant were done. By statistically evaluating the analysis results the correlation coefficient between the elements, plant organs with high accumulation of metal in the structure, indicator plants and biogeochemical relationships between plant and mineralization were determined.

II. GEOLOGY

The age of the Red-bed type Cu deposits ranges from Precambrian to Pliocene (probably Quaternary). Especially Precambrian aged have metamorphism in these deposit. However, the deposits in Turkey were not affected by metamorphism since the original sedimentary features and structures were not damaged. Delice – Yerköy Cu deposit (Fig. 1) is located in Bayat Formation in Çankırı Basin. In Fig. 2, Bayat Formation (Middle-Upper Eocene), Kocaçay Formation

(Upper Eocene), İncik Formation (Upper Eocene-Middle Miocene), Kızılırmak Formation (Upper Miocene), Bozkır Formation (Middle Miocene), Yoncalı Formation (Late Paleocene - Middle Eocene) and Yozgat magmatics (Late Cretaceous) [12]. [13] named Bayat Volcanics as Yozgat Volcanics. These researchers have suggested that andesites, basalts, basaltic andesites and dacites are volcanic.



Fig. 1. Location map of the study area and its surroundings.

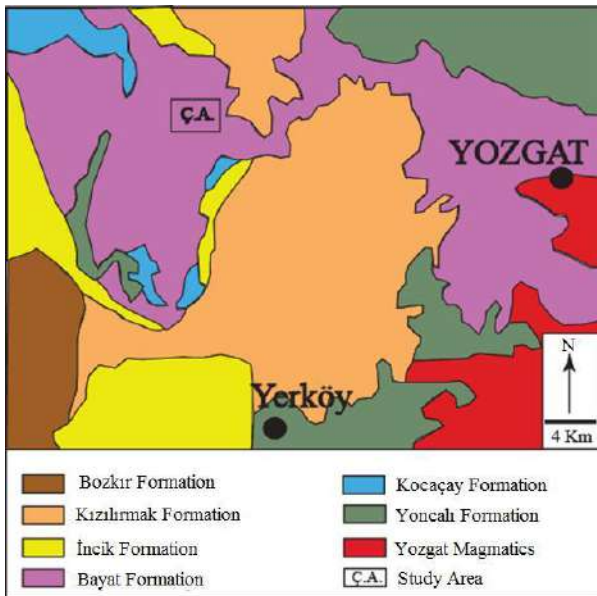


Fig. 2. The geological map of the study area ([11])

III. MINERALIZATION

The mineralizations in the study area are in the form of thin beddings and a wide field survey, indicating that these deposits are semi-economic deposits [3]. The samples taken from ore zones between Delice and Terzili indicate that these deposits originate from Lutetian volcanic rocks. The high concentration of Ag and Cu in these rocks, such as andesite and basalt, and the high U in rocks such as rhyolite, support this view [3]. It is known that such deposits are closely related to the evaporites. For this reason, evaporites occur along with mineralization and around the mineralization [14]. The main minerals in these beds are; Pyrite, chalcopryrite, chalcocite, bornite, native copper, native silver and uraninite. In addition, the secondary minerals are azurite, malachite, covellite and cuprite. Gangue

minerals are iron oxide minerals, gypsum, anhydrite, dolomite, quartz, feldspar, chlorite, illite and barite [3].

IV. SAMPLING AND ANALYSIS METHODS

Samples of *E. cyparissias* plants were collected from the study area (Fig. 3) and brought to the laboratory. The collected samples were separated into their branches and leaves and washed first with tap water and then with distilled water. The plant samples dried at room temperature are then completely dried by recovering from moisture the sample at 95 °C for 24 hours. From these dried samples, ash was obtained by burning flamelessly up to 550 °C, starting at a temperature of 50 °C and increasing a temperature of 50 °C per hour.



Fig. 3. A view from the plant cyperissias (a) Example no: 1 and (b) Example no: 3

Samples from the soil associated with the plant of *E. cyparissias* were taken from the study area and bagged. The samples brought to the laboratory were dried at room temperature by passing through a 2 mm sieve. 0.10 g of ash and 2 ml of concentrated HNO₃ were added to the soil samples and dried by heating at 95 °C in microwave for 1 hour. The dried samples were added after cooling to a mixture of 2 ml of HNO₃ and the prepared HCl-HNO₃-H₂O (6 ml of each 1: 1: 1 mixture and 0.10 gr of ash and soil sample). The resulting mixture was diluted with pure water to 50 ml and the calculations were made according to the final volume.

BILTEM (Bozok University, Science and Technology Application and Research Center) with elemental analysis of Cu, Ag, Co, Mo, Ni, Se, Pb, U, V and Zn of soil and plant samples, Inductively Coupled Plasma Mass Spectrophotometer (ICP- MS), Yozgat, Turkey.

V. CONCLUSIONS AND DISCUSSION

The results of the analysis obtained from samples of *E. cyparissias* planted and its surroundings and in the Delice-Terzili related soil samples were evaluated statistically and the results are given in Table 1.

The elemental concentrations of soil samples were Sb: 941.08 mg/kg (mean), As: 37.43 mg/kg (mean), Cu: 403.25 mg/kg (mean), Pb: 21.09 mg/kg (mean), Mn: 922.6 mg/kg (mean), Ni: 101.34 mg/kg (mean), Se: 133.96 mg/kg (mean), Ag: 2.51 mg/kg (mean), Th: 7.51 mg/kg (mean), U: 1.88 mg/kg (mean), V: 90.8 mg/kg (mean) ve Zn: 170.99 mg/kg (mean) (Table 1)

TABLE I. Statistical values of the elements of *E. cyparissias* plant

	Ag	Al	As	Ca	Co	Cr	Cu	Fe	Mg	Mn	Ni	Pb	Sb	Se	Th	U	V	Zn
	Soil																	
Minimum	1.04	1.27	31.98	2.32	21.46	30.56	116.40	1.72	1.82	808.36	95.45	19.14	870.99	122.65	6.30	1.11	53.75	129.71
Maximum	3.81	1.69	41.23	5.02	27.05	59.16	794.80	2.19	2.92	1122.25	117.74	23.55	1010.04	147.82	8.95	2.68	115.79	187.69
A.Mean	2.29	1.51	37.18	3.22	23.86	45.58	413.58	1.93	2.25	936.54	104.25	21.10	941.08	133.93	7.51	1.88	88.18	164.67
Std. Deviation	0.96	0.13	3.22	0.84	1.80	9.95	228.82	0.16	0.40	90.63	7.59	1.50	42.94	8.53	0.82	0.48	18.40	22.18
	Stem																	
Minimum	0.98	0.16	19.14	10.02	3.75	3.35	84.50	0.31	3.60	118.94	27.31	5.59	505.35	63.59	0.39	0.21	12.42	46.21
Maximum	4.25	0.50	40.52	12.47	12.93	8.86	150.80	0.68	5.09	704.40	97.65	8.35	797.85	80.70	1.95	0.83	27.01	210.14
A.Mean	2.23	0.31	28.70	11.16	7.82	6.33	123.32	0.56	4.56	329.65	56.61	6.65	645.12	69.73	1.04	0.44	16.95	116.91
Std. Deviation	1.12	0.14	7.96	0.92	3.09	1.54	22.46	0.11	0.39	192.39	22.74	0.94	98.67	5.28	0.39	0.17	4.38	51.45
	Leaf																	
Minimum	8.89	0.20	12.99	13.51	4.09	19.40	54.50	0.40	3.54	234.12	97.10	3.00	490.20	62.66	0.26	0.12	5.38	97.35
Maximum	32.65	0.68	25.65	15.85	6.98	181.60	89.60	0.78	5.00	848.07	546.66	5.78	910.76	79.96	1.93	0.81	44.87	138.84
A.Mean	14.77	0.45	17.78	14.73	5.52	76.03	70.41	0.62	4.13	532.79	342.50	4.42	726.22	73.72	1.22	0.50	26.45	116.46
Std. Deviation	7.37	0.15	4.09	0.81	1.01	46.39	12.23	0.12	0.49	227.48	177.20	0.91	135.19	5.55	0.67	0.25	14.46	13.75

In soil samples indicated by [9] Sb: 2 mg / kg, As: 7.5 mg / kg, Cu: 15 mg/kg (mean), Pb: 17 mg / kg (mean), Mn: 320 mg/kg, Ni: 17 mg/kg (mean), Se: 0.31 mg/kg (mean), Ag: 0.1 mg/kg (carbonated rock), 0.25 mg/kg (sandstone), 0.19 mg/kg (shale) (mean), Th: 13 mg/kg (mean), U: 1 mg/kg (mean), V: 57 mg/kg (mean) ve Zn: 36 mg/kg (mean). In the case of soil samples specified by WHO (World Health Organization) Ni: 0.15-1.03 mg / kg, Cr: 4.12-6.74 mg / kg, Cu: 0.54-1.50 mg / kg, Pb: 0.06-0.46 mg / kg, Fe: 0.0143-0.0313 mg / kg, Zn: 0.03-0.35 Mg / kg [15].

Element values of soil samples in the surrounding and Delice-Terzili according to the specified element values can be considered as anomalous values (except for Th; according to [9]).

In plant ash samples specified by [9] Sb: 1 mg / kg, As: 0.25 mg / kg, Cr: 6.3 mg / kg, Co: 5 mg / kg, Cu: 130 mg / (mean), Fe: 0.16% (mean), Pb: 30 mg / kg, Mn: 6700 mg / kg, Ni: 18 mg / (mean), V: 5 mg / kg (mean) and Zn: 570 mg / kg (mean): 0.1-1 mg / kg, Th: 20 µg /kg. The maximum amount of Ni: 10 mg / kg [16], Cr: 1.30 mg / kg, Cu: 10 mg / kg [16], Pb: 2 mg / kg, Fe: 0.0020% [17], Zn: 50 mg / kg [17] [15].

While it is found in the stem of *E. Cyparissias* plant (mean) Sb: 645.12 mg / kg, As: 28.16 mg / kg, Cr: 6.22 mg / kg, Co: 6.56 mg / kg, Cu: 125.1 mg /kg, Fe: 0.57%, Pb: 6.61 mg / kg, Mn: 258.97 mg / kg, Ni: 52.12 mg / kg, Se: 68.64 mg /kg, V: 15.54 mg / kg and Zn: 111.87 mg / kg in the range of Ag: 0.98-4.25 mg / kg, Th: 1.04 mg /kg, in the leaf of this plant (mean) Sb: 726.22 mg / kg, As: 16.56 mg / kg, Cr: 68.26 mg / kg, Co: 5.39 mg / kg, Cu: 69.95 mg /kg, Fe: 0.66% (mean), Pb: 4.49 mg / kg, Mn: 483.61 mg / kg, Ni: 408.36 mg / kg, Se: 75.48 mg/kg, Ag:8.89-32.65 mg/kg (range), Th: 1.22 mg/kg, U: 0.50 mg/kg, V: 25.69 mg/kg ve Zn: 13.75 mg/kg (Table 1).

In the stem of the plant samples taken in the study area (maximum) Ni: 97.65 mg/kg, Cr: 8.86 mg/kg, Cu: 150.8

mg/kg, Pb: 8.35 mg/kg, Fe: 0.68 %, Zn: 210.14 mg/kg and in the leaf Ni: 546.66 mg/kg, Cr: 181.6 mg/kg, Cu: 89.6 mg/kg, Pb: 5.78 mg/kg, Fe: 0.78 %, Zn: 138.84 mg/kg (Table 1).

In the stem of the plant taken from the study area Sb, As, Co, Fe, Ni, Se, Ag and V (according to [9]), elemental values in the leaf Sb, As, Cr, Co, Fe, Ni, Se, Ag, Th and V (according to [9]) and the values of Ni, Cr, Cu, Pb, Fe and Zn in both the stem and the leaf (according to [15]) show anomaly values according to the above values. It is thought that these elements, which show anomalies in the soil, stem and leaf, have similar dissolution, migration and sedimentation.

Sperman Correlation Coefficients (rs) show similar behavior of element pairs in ore deposits. Correlation coefficient values are negative in some element pairs in some element pairs. These movements can also have meaning as origin. Positive correlation values indicate that element pairs increase or decrease together, that is, they move together, while negative correlation values indicate that an element increases while the other decreases, that is, they move in opposite directions [17].

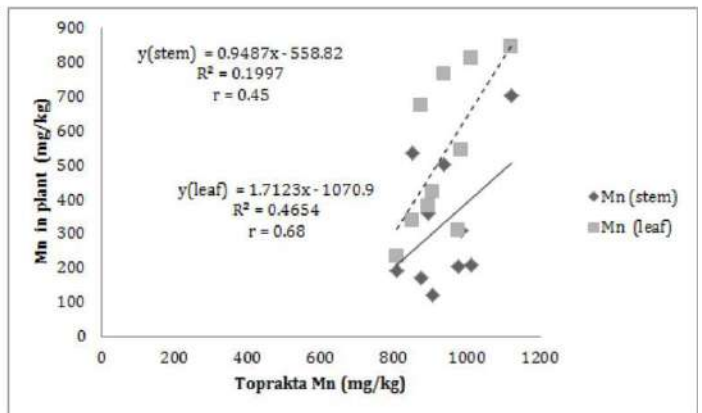
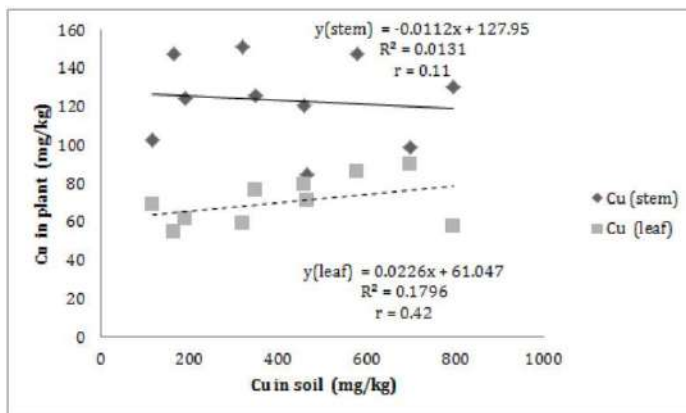
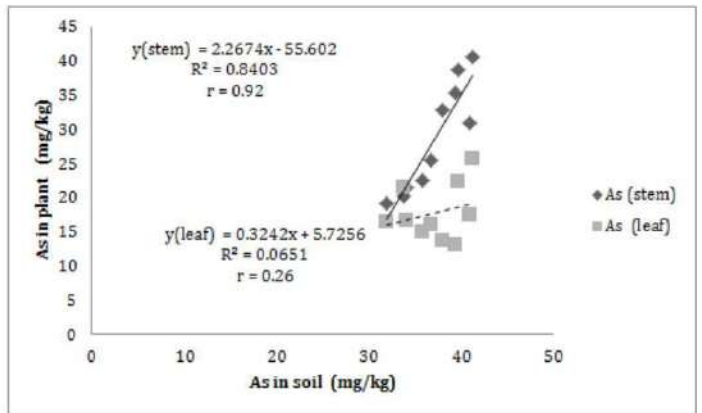
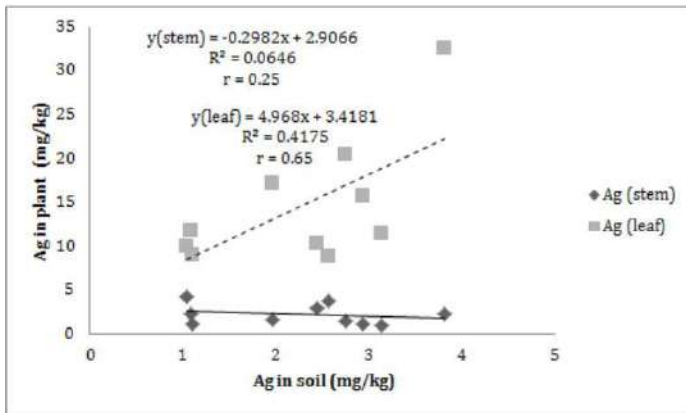
When we look at Sperman correlation relations among the elements in the soil samples collected in Terzili and its surroundings; a high positive correlation was observed between the two groups, Al-Cr (rs:0.77, p<0.01, % 99 confidence), Co-Ni: (rs:0.89, p<0.01, % 99 confidence), Cu-Fe (rs:0.89, p<0.01, % 99 confidence), Mn-Sb (rs:0.87, p<0.01, % 99 confidence); Al-Mn (rs:0.66, p<0.05, % 95 confidence), Al-Sb (rs:0.75, p<0.05, % 95 confidence), Co-Se (rs:0.71, p<0.05, % 95 confidence). There was a high negative correlation between Ag-Th (rs:-0.82, p<0.01, % 99 confidence), Fe-Pb (rs:-0.92, p<0.01, % 99 confidence); Cu-Pb (rs:-0.76, p<0.05, % 95 confidence), Th-U (rs:-0.71, p<0.05, % 95 confidence).

TABLE II. Correlation of the elements in soil samples (* p <0.05 and ** p <0.01)

	Ag	Al	As	Cu	Co	Cr	Cu	Fe	Mg	Mn	Ni	Pb	Sb	Se	Th	U	V	Zn
Ag	1																	
Al	-0.04	1																
As	-0.07	-0.55	1															
Ca	-0.53	0.43	-0.10	1														
Co	-0.55	-0.12	0.06	-0.03	1													
Cr	0.49	.766(**)	-0.27	-0.02	-0.22	1												
Cu	0.20	-0.09	0.46	0.30	0.02	0.18	1											
Fe	0.35	0.09	0.21	0.21	-0.14	0.31	.888(**)	1										
Mg	0.24	0.21	-0.06	-0.01	0.33	0.41	0.33	0.25	1									
Mn	-0.24	.66(*)	-0.22	.661(*)	-0.22	0.30	-0.12	-0.11	0.10	1								
Ni	-0.47	0.22	0.21	.891(**)	-0.22	-0.13	0.43	0.34	-0.26	0.48	1							
Pb	-0.16	-0.05	-0.22	-0.09	-0.02	-0.20	-.758(*)	-.918(**)	-0.02	0.26	-0.29	1						
Sb	-0.08	.748(*)	-0.32	0.36	-0.42	0.46	-0.38	-0.25	-0.13	.867(**)	0.26	0.30	1					
Se	-0.38	-0.28	0.52	-0.02	.709(*)	-0.24	0.39	0.27	0.05	-0.19	0.04	-0.46	-0.37	1				
Th	-.818(**)	0.01	-0.09	0.47	0.20	-0.58	-0.27	-0.22	-0.38	0.15	0.49	0.03	0.09	0.08	1			
U	0.55	0.28	-0.30	0.10	-0.18	0.54	0.24	0.14	0.60	0.24	-0.15	0.20	0.08	-0.38	-.709(*)	1		
V	.709(*)	0.03	0.14	-0.08	-0.36	0.47	0.59	0.61	0.57	-0.18	-0.04	-0.33	-0.25	-0.30	-0.56	0.60	1	
Zn	0.10	-0.20	-0.22	-0.31	0.24	-0.16	0.08	0.30	-0.29	-0.41	-0.27	-0.52	-0.33	0.44	-0.01	-0.30	-0.29	1

Correlation coefficients between the soil-stem and the soil-leaf of the *E. cyparissias* plant growing in the surrounding and Terzili are shown in Fig. 4. In this study, positive correlation was found between values in the stem of *E. Cyparissias* plant

and values of soil for As, (n = 10, r = 0.92, P <0.01, 99% confidence), Sb (n = 10, r = 0.76, P < 0.01, % 99 confidence) and Pb (n = 10, r = 0.53, P < 0.05, % 95 confidence). Accordingly, it can be said that the stem of *E. cyparissias* plant may be the indicator plant for As, Sb and Pb.



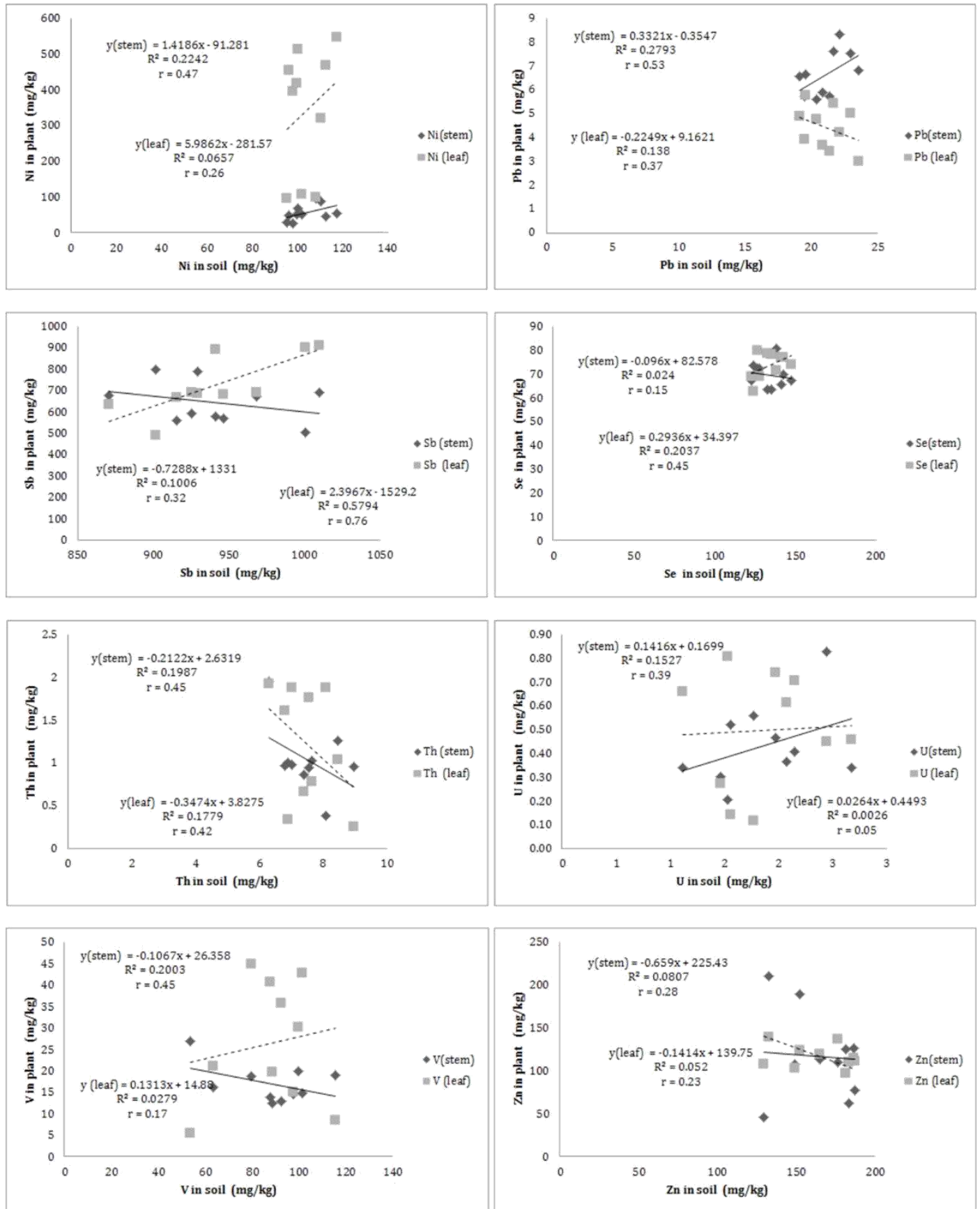


Fig. 4. Correlation between soil-stem and soil-leaf of elements of *E.Ciparissias* plant

ACKNOWLEDGMENT

This work was supported by the project BAP Unit 2015 MMF / A181. Analyses of plant and soil samples were carried out at BILTEM (Bozok University, Science and Technology Application and Research Center) (Yozgat, Turkey).

REFERENCES

- [1] LB. Gustafson and N. Williams, "Sediment-hosted stratiform deposits of copper, lead and zinc": Econ.Geol., 75th Anniv., 139-178, 1981.
- [2] H. Aral, "Red Bed" Tipi Bakır Yatakları ve Türkiye'den Örnekler. Madencilik, Cilt Xxx, Sayı 2, 1990.
- [3] H. Aral, "Orta Anadolu'da Delice-Yerköy Arasında Yer Alan Sedimanter Bakır (Gümüş- Uranyum) Yataklarının Stratigrafisi, Sedimentolojik Özellikleri ve Oluşumu". MTA Dergisi, 110, 55-76, 1990
- [4] DW. Haynes, "Stratiform copper deposits hosted by low-energy sediments. I. Timing of sulfide precipitation - An hypothesis" Econ.Geol., 81, 250-265, 1986a.
- [5] KC. Dunham, "Neptunist concepts in ore genesis" Econ. Geol., 59, 1-21 1964.
- [6] C. Haranczyk, "Zechstein lead-bearing shales in the Fore-Sudetic monocline in Poland" Econ. Geol., 65, 481-495, 1970.
- [7] WG. Garlick, "Depositional and diagenetic environments related to sulfide mineralization. Mufulira, Zambia- a discussion": Econ. Geol., 69, 1344-1351, 1974.
- [8] PN. Shockey, AR. Renfro, RJ. Peterson, "Copper-sulfide solution fronts at Paoli, Oklahoma" Econ. Geol., 69, 266-268, 1974.
- [9] AW. Rose, "The effect of cuprous chloride complexes in the origin of red-bed copper and related deposits" Econ. Geol., 71, 1036-1048, 1976.
- [10] PN. Schockey, AR. Renfro, R.J. Peterson, "Copper Sulfide Solution Fronts at Paoli, Oklahoma", Economic Geology, v., 69, s. 266, 1974.
- [11] Erdoğan B, Akay E, Uğur MS. Geology of the Yozgat region and evolution of the collisional Çankırı Basin. International Geology Review, 38, 788-806, 1996.
- [12] N. Çevik, "Yozgat-Yerköy-Belkavak Köyü Civarı Kalsedon ve Ametist Oluşumlarının İncelenmesi". Yüksek Lisans Tezi, Ankara Üniversitesi Fen Bilimleri Enstitüsü, Ankara, Türkiye, 2009.
- [13] M. Alpaslan, A. Temel, "Petrographic and geochemical evidence for magma mixing and crustal contamination in the Post-Collisional calcalkaline Yozgat Volcanics, Central Anatolia, Turkey". International Geology, 42, 850-863, 2000.
- [14] A. Gümüş, "Metalik Maden Yatakları", Karadeniz Teknik Üniversitesi Yayınları, Trabzon, Türkiye, 1974.
- [15] R. Nazır, M. Khan, M. Masab, HU. Rehman, NU. Rauf, S. Shahab, N. Ameer, M. Sajed, M. Ullah, M. Rafeeq, Z. Shaheen, "Accumulation of Heavy Metals (Ni, Cu, Cd, Cr, Pb, Zn, Fe) in the soil, water and plants and analysis of physico-chemical parameters of soil and water Collected from Tanda Dam kohat". J. Pharm. Sci. and Res. 7(3), 89-97, 2015.
- [16] Hassan Z, Anwar Z, Khattak KU, Islam M, Khan RU, Zaman J, Khattak K; et al. "Civic Pollution and Its Effect on Water Quality of River Toi at District Kohat, NWFP" , Research Journal of Environmental and Earth Sciences, 4, 5, 2012
- [17] A. Shah, A. Niaz, N. Ullah, A. Rehman, M. Akhlaq, M. Zakir, MS. Khan, "Comparative Study of Heavy Metals in Soil and Selected Medicinal Plants" , Journal of Chemistry, 5, 2013
- [18] Ünlü T, Stendal H. "Divriği Bölgesi Demir Yataklarının Element Korelasyonu ve Jeokimyası; Orta Anadolu, Türkiye". Jeoloji Mühendisliği. 28, 5 – 19, 1986.

Occupational Health And Safety Issues In Layout Design Problem Of a Marble Processing Plant

Yaşar Can Özbel

Dokuz Eylül University,
The Graduate School of Natural and Applied Sciences
Izmir, Turkey
yasarcan.ozbel@gmail.com

Muharrem Kemal Özfirat

Dokuz Eylül University,
Department of Mining Engineering
Izmir, Turkey
kemal.ozfirat@deu.edu.tr

Abstract –Designing the occupational health and safety management system for the small-scale industries is more challenging due to their limited plant space and other constraints. The essential for the proper implementation of occupational health and safety management system in any of the industry is based on risk identification process in relation to the overall system. Therefore, occupational health and safety management process depends upon the scope of the industry as it varies according to the functions and scale. In this study, the application field has been chosen small-scale marble factory which state in Turkey that have been exposed to different types of occupational hazards in the workplace. The risks in considering marble plant can be determined by failure mode and effects analysis (FMEA) method, since FMEA is a widely used engineering technique for designing, identifying and eliminating known and/or potential failures. For this purpose, firstly, the general information and methodology are given, then the risk priority indicator has been calculated and all failure types have been ranked according to the risk priority. The purpose of this study is to propose an alternative layout by considering the determined risks and their priority. Finally, current layout and proposed layout are compared in terms of the requirements of worker health and safety regulation. As a result, it is found that “current layout” is more risky than “proposed layout” for the marble factory. In this way, the hazards and risks in terms of layout occupational health and safety management can reduce at acceptable levels by applying the proposed layout.

Keywords –Marble factory; Facility layout; Occupational health and safety; Risk analysis

Finite Impulse Response (FIR) For Chaotic Applications Of Soil Radon Gas (^{222}Rn)

Miraç Kamışlıoğlu
Firat University Faculty of Science,
Department of Physics
Elazığ, Turkey
mkamislioglu@gmail.com

Fatih Külahcı
Firat University Faculty of Science,
Department of Physics
Elazığ, Turkey
fatihkulahci@firat.edu.tr

Abstract — The different chaotic methodologies are applied to identify possible chaotic behaviors of soil radon gas and related earthquake magnitudes. Relations between magnitudes of earthquakes and the radon concentrations are non-linear, and therefore, the radon emissions exhibit chaotic behaviors. In order to depict the nonlinear relationship between the radon concentrations and earthquake qualitative and quantitative chaotic time series analysis methodologies are employed including Lyapunov exponent and power spectrum analyses by using FIR (Finite Impulse Response). This study used that signal process techniques and showed nonlinear behavior of ^{222}Rn gas.

Keywords—Chaos Analyses, Radon, Earthquake, Radon time series, Lyapunov exponent, FIR (Finite Impulse Response).

I. INTRODUCTION

Earthquakes are complex natural events and their generation mechanism's explanation is one of the most difficult problems in geophysical sciences. In order to understand dynamical, mechanical, chemical and other aspects of earthquakes is important on the one hand for scientific developments and on the other hand for the society alert Earthquake behaviors are, in general, among the non-linear topics of physics. Unfortunately, researches could not yet propose a complete mathematical model for earthquake behavior prediction, due to the non-linear behavior of earthquakes under a set of dependent factors [1]. Among such factors are strain, fault creep, tilt, foreshocks sequences, underground water, seismic wave velocity changes and oil flow, earth currents, radon variations, and geomagnetic effects [2,3].

Soil gas radon concentration measurement are the most commonly used indicator in earthquake prediction studies. The most significant isotope of radon gas is ^{222}Rn , which has half-life 3.82 days. It is produced in the radioactive decay series of ^{238}U and tends to migrate from its source mainly upwards in the earth crust [4].

Chaotic systems cannot be estimated by random variability, because they are the deterministic factors. The reason why the chaotic systems are unique is due to their sensitive dependence on the initial conditions. Even a slight change in the initial

parameters of the system may cause entirely different trajectories [5]. There are various methodologies for detecting the chaotic behavior of any system.

II. MATERIAL AND METHODS

A- FINITE IMPULSE RESPONSE (FIR)

The time series obtained from a nonlinear dynamic system can be used to reconstruct the phase space of the system, but if the time series obtained from the nonlinear dynamic system is passed through a linear filter, the phase space of the system can be reconstructed [6]. Noise is the dispersion of the signal to be transmitted by the obstacles or other effects that is encountered in the transmission channel, and getting the signal weaker in the other side in out of the desired range. It is obvious that it is produced by a kind of physical system showing noisy chaotic behavior. In order to eliminate the effect of these unwanted components on the mark, the so-called filters are used. Filtering is the process of intensifying the desired frequency values of the sign, undermining the unwanted frequency values. Finite impulse response (FIR) filters; It is a simple and effective structure in digital filter design, it gives fix results constantly in non-repetitive applications, it is easy to get results in linear phase.

They are often preferred due to their efficient use for multiple / fast and adaptive filter designs, the ability to specifically match amplitude responses to obtain easy-to-understand designs, the availability of some software and hardware specifically with FIR filters, and the low sensitivity of the quantization effect [7].

FIR, the sign in the filter bank applied to the input is divided into lower bands at different speeds. These markings are obtained after the signal processing techniques have been applied at different frequencies (at speeds). The use of window functions for FIR digital filter design is also well known, quite efficient and very convenient for processing digital signs. FIR filters with "Kaiser Windows" are user-friendly because of their adjustable parameters [7].

FIR filters have been shown in studies that do not alter the size and chaotic properties of the time-series signals. In support of this study, the ^{222}Rn signals were filtered using a FIR filter that passes the signals at a 10-degree-high frequency with a sharp cut-off frequency of 100 Hz to remove the noises.

B- TIME SERIES ANALYSIS AND CHAOTIC APPLICATION METHODS

Time series analysis is the most useful method of providing information about data. This method is used for visible of data. In this study were used Lyapunov exponent method and power spectrum method. Further, time series graphics are allowing us to see the trend of data [8].

While performing chaotic application the most frequently used qualitative methods power spectrum analysis and Maximum Lyapunov exponents. Power spectrum is used that a statistical based approach among quantitative methods. Also, Maximum Lyapunov exponent calculating is that determining the non-linearity.

Lyapunov exponents are defined as the exponential increase or decrease of minor perturbations on an attractor. Maximum Lyapunov exponent is one of the most descriptive methods. To define is used chaotic behavior in a system. Lyapunov exponent is very close to each other to monitor both the starting point that is based in different trajectories [9, 10]. Its sign gives information about the system dynamics. If exponential value is positive then system indicates chaotic behaviors [11]. Maximum Lyapunov exponent is calculated according to the following expression Equation (1).

$$L_{\max} = \lim \left[\ln \left[\frac{d(t)}{d(0)} \right] \right], \quad (1)$$

The Fourier power spectrum analysis is used for decomposition of a given time series into a set of regular orthogonal sine and cosine signal combinations at different frequencies. Fourier power spectrum is obtained by making use of the fast Fourier transform procedure [12]. If the system is chaotic then there is continuity in the power spectrum. Otherwise, there are jumps at a set of definite frequencies. In any time series existence of a wide band power spectrum indicates a definite peak implying chaotic behavior. Entirely random signals have random fluctuations around a constant level in the power spectrum. In Equation 2, for a given time series, the power spectrum is defined as,

$$\tilde{s}(f) = \frac{1}{\sqrt{2\pi}} \int_{-\infty}^{+\infty} s(t) e^{2\pi i f t} dt \quad (2)$$

where $s(t)$ is a function, Equation 3 is defined squared modules.

$$\tilde{s}_k = \frac{1}{\sqrt{N}} \sum_{j=1}^N s_j e^{2\pi i k n / N} \quad (3)$$

The power spectrum of a process is defined as the squared

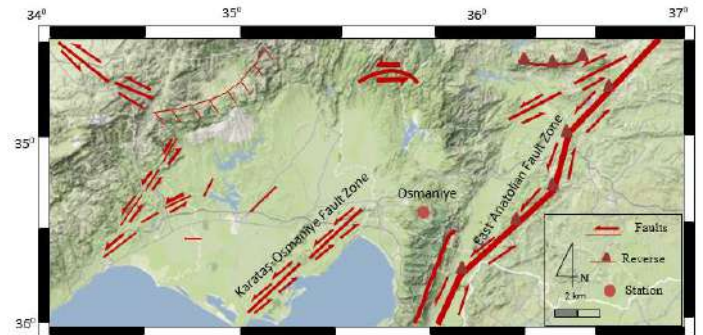
modulus of the continuous Fourier transform $S(f) = |\tilde{s}(f)|^2$. It is helpful for understanding the basic frequencies in the dynamical system, because it will yield broader peaks at dominant frequencies and frequency of signal is described in Equation (4).

$$S(f) = (1/f^\alpha) \quad (4)$$

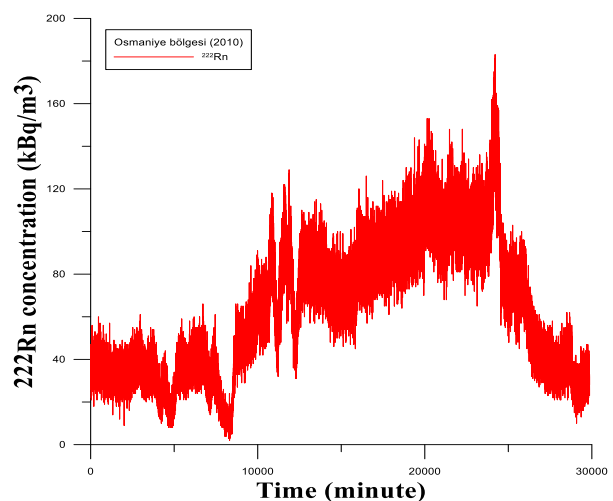
where $S(f)$ is the system's power spectral density f is the frequency and α is a positive real number. Commonly, the dynamics systems that are under dynamic equilibrium having noise capture the signature of uncorrelated or white noise [13].

III.RESULT AND DISCUSSION

This section presents analysis of the ^{222}Rn gas in Osmaniye region for 2009 year (Figure 1). Time series for ^{222}Rn values given in counts per 15 min recording interval (Figure 2).

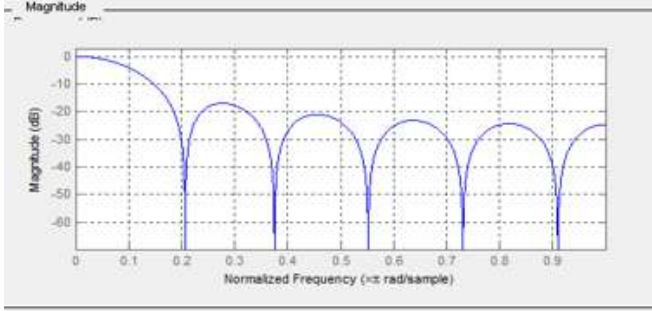


Location map of radon monitoring sites and EAFZ

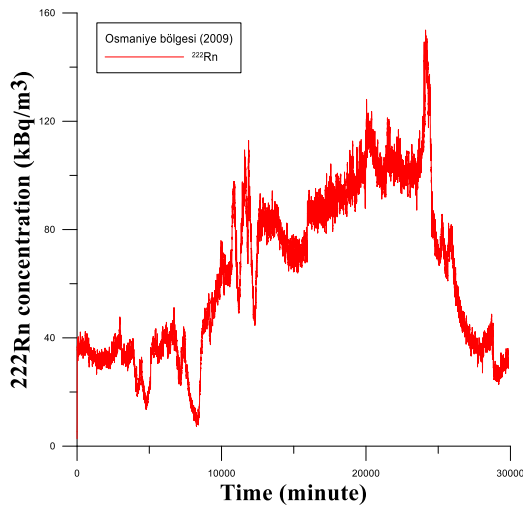


Time series for ^{222}Rn in Osmaniye region (2009 year)

Figure 3 is showed filter designed. Figure 4 present the time series generated from one-year 10. degrees filter for ^{222}Rn data.

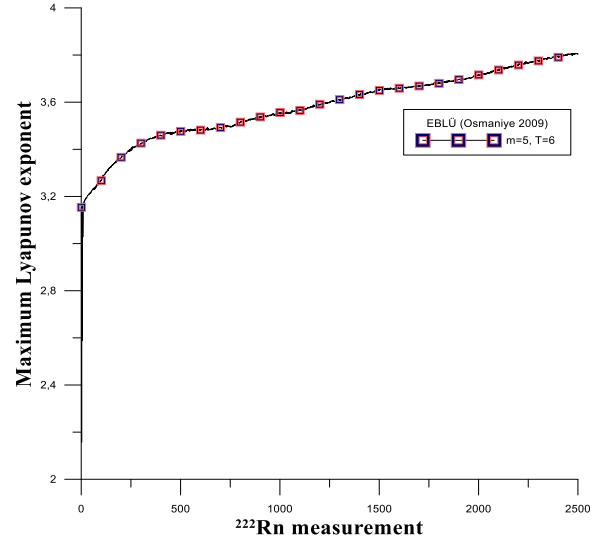


Matlab filter design for ^{222}Rn in Osmaniye region (2009 year) 10. degrees filter



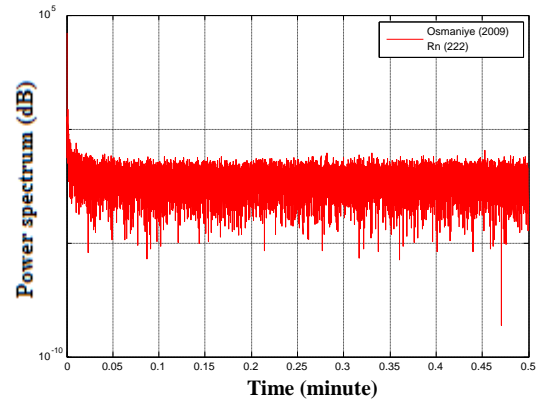
10. degrees FIR Kaiser window for ^{222}Rn concentration in Osmaniye region (2009 year)

Figure 5 present the time series generated from one-year maximum Lyapunov exponent for ^{222}Rn in Osmaniye region (2009).



The maximum Lyapuniv exponent for ^{222}Rn (m :embedding dimension, τ : delay time)

Power spectrum is used for chosen random peak into broad band. Figure 6 indicates the power spectrum of chaotic behavior Osmaniye region.



Power spectrum for ^{222}Rn data Osmaniye region

IV.CONCLUSION

Geophysical observations and indicators showed nonlinear periodic behavior. Chaotic measurements are offers an opportunity to detect irregularities behaviors. For measurements data filter was applied to prepare for signal processing methods and smoothing of measurements taken from the soil. Chaotic applications have been used to implement ^{222}Rn data taken from the Osmaniye Region on the East Anatolian Fault Line. In this study, has been proved that show non-linear behavior of ^{222}Rn gas.

ACKNOWLEDGMENT

This work was supported by TUBITAK, Project number and Scholarship Program. Also, this research is supported by Republic of Turkey Prime Ministry Disaster & Emergency Management Presidency (AFAD).

REFERENCES

- [1] H. Friedmann, K. Aric, R. Gutdeutsch, C.Y. King, C. Altay, H. Sav, Tectonophysics. 152, 209-214 1988. 2. J. Janssen and R. Manca. Semi-Markov risk models for finance, insurance and reliability, Springer, New York, 2007.
- [2] C. Y. King, J. Geophys. Res. 91-B12, 12269-12281 1986.
- [3] F. K lahcı, M.  nce z, M. Dođru, E. Aksoy, O Baykara. Appl Radiat Isotop 67, 212-219, 2009.
- [4] V. Planinić, Radolić, B. Vuković. Radon as an earthquake precursor. Nucl Instrum Methods vol. 530, 568-574, 2004.
- [5] H.S. Virk, B. Singh. Radon anomalies in soil gas and groundwater as earthquake precursor phenomena. Tectonophysics vol. 227, 215-224, 1993.
- [6] D.S., Broomhead, Huke, J.P., and Potts, M.A.S., 1996. Cancelling deterministic noise by constructing nonlinear inverse to linear filters, Physica D, 89, 439-458.
- [7] B., Kamışlıođlu, 2014. Yeni  eyrek ayna s zge  bankası tasarımı ve uygulamaları. Y ksek Lisans Tezi, Erciyes  niversitesi, Fen Bilimleri Enstit s , Kayseri.
- [8] H., Kantz, and Schreiber, T., 1997. Nonlinear time series analysis, Cambridge University Press, Cambridge.
- [9] A. Wolf, et al. Determining Lyapunov exponents from a time series. Phys D, vol. 16, 285-317, 1985.
- [10] N.K., Das, P. Sen, R.K. Bhandari, and B. Sinha (2009), Nonlinear response of radon and its progeny in spring emission, Appl. Radiat. Isotopes 67, 2, 313-318, DOI: 10.1016/j.apradiso.2008.09.016.
- [11] M., Sano, and Sawada, Y., 1985. Measurement of the Lyapunov spectrum from a chaotic time series, Phys. Rev. Lett., 55, 1082-1085.
- [12] M.N., Islam, Sivakumar, B., 2002. Characterization and prediction of run off dynamics: a nonlinear dynamical view. Adv. Water Resour. 25, 179-190.
- [13] S., Sakata, Hayano, J., Mukai, S., Okada, A., Galdrikian, B., and Farmeret, J.D., 1999. Aging and spectral characteristic of the nonharmonic component of 24-h heart rate variability, Amer. J. Phys.-Reg. Interative Comp. Physiol., 276, 1724-1731.

name: 2211-C Priority Areas Related to Domestic Doctoral

Geochemical Characteristics Of Kesikköprü Granitoid (Central, Turkey) And Comparison With Skarn Related Granitoids

Mustafa Haydar Terzi

Department of Geological Engineering Aksaray University
Aksaray, Turkey.
mhaydarterzi@aksaray.edu.tr

Erkan Yilmazer

Department of Geological Engineering Aksaray University
Aksaray, Turkey..
eyilmazer@eng.ankara.edu.tr

Abstract— Kesikköprü iron skarn deposit, located in the northwestern part of Central Anatolian Crystalline Complex (CACC), occurred at the contact between marble, and mafic-ultramafic rocks composed of gabbro and pyroxenite, and granitoids defined as granite, granodiorite and monzonite. The skarns are characterized by local endoskarn and widespread exoskarn zones in granitoid and marble/mafic-ultramafic rocks, respectively. Alteration in Kesikköprü iron deposit is defined as dominantly calcic, rich in garnet, pyroxene, epidote in marble, and partially magnesian described with formation of phlogopite at the contacts with mafic-ultramafic rocks. Iron comes from exoskarn zones as massive, bands and lenses, and total reserve of which is 12,7 Mt with grades of average 39-61 % Fe. The aim of this study is to compare with the geochemistry of Kesikköprü granitoid, and the geochemistry of granitoids associated with skarns worldwide, and in order to reveal the potential for different types of mineralization associated with the Kesikköprü granitoid.

The Kesikköprü granitoid are geochemically calc-alkaline, and shoshonitic in character, and has metaluminous-partly peraluminous features. The granitoid is especially characterized by enrichment in Large Ion Lithophile Elements (LILE) relative to High Field Strength Elements (HFSE) with significant depletion in Ta, Nb, P, Ti and Y. In the tectonic classification diagrams, granitoids plot in volcanic arc field, and close to the boundary between syncollisional, within plate granite and volcanic arc granite. The major element composition of the Kesikköprü granitoid is compared with both the worldwide average compositions of granitoids associated with Fe, Au, Cu, Zn, W, Mo and Sn skarns, and some of skarn related granitoids such as Ertsberg (Irian Jaya) Cu-Au, and Edong (China) Cu-Fe, and Çelebi (Turkey) Fe-W. As a result, geochemical characteristics of Kesikköprü granitoid resemble the geochemistry of plutons associated with Cu, and Cu-Fe skarn, suggesting new exploration possibilities for copper in the region.

Keywords— Iron skarn, granitoid, geochemistry, Kesikköprü, CACC.

Petrographic And Geochemical Properties Of Sarıcakaya (Eskişehir) Magmatic Mass

Hacer Bilgilioğlu

Aksaray University Geological Engineering, Turkey
bilgiliogluhacer@gmail.com

Bahattin Güllü

Aksaray University Geological Engineering, Turkey
bahattinogullu@gmail.com

Abstract—The study field is approximately an area of 150 km² which includes the settlement of Sarıcakaya in the north of Eskişehir province. The Paleozoic rocks composed of blueschist, gneiss and amphibolites in the region are cut by Carboniferous age Sarıcakaya Magmatic Mass. The basement units are covered by lithostratigraphic units in range of ages from Jurassic to Quaternary.

According to modal mineralogical datas, the magmatic mass have different compositions such as gabbro, diorite, granodiorite and granite. They are cutted by felsic and mafic units with several directions varying from K20D to K40B (longitude?).

Hypidiomorphic granular textured Sarıcakaya magmatic mass has contains oval-rounded shaped and holocrystalline textured mafic microgranular enclaves which diorite and quartz diorite in composition and range from 1 cm to 50 cm in sizes.

The geochemical analysis datas indicate that, Sarıcakaya Magmatic Mass have sub-alkaline, ranging from tholeiitic to calc-alkaline and metaluminous character

The primitive mantle normalized to trace element distributions of the mass show generally enrichment in terms of, large ion lithophile elements (LILE) and high field strength elements (HFSE) Similarly, The chondrite normalized rare earth element diagrams of the rocks show enrichent of light rare earth elements (LREE) showing depletion of heavy rare earth elements (HREE).

All petrographic and petrological datas of the Magmatic Mass of Sarıcakaya are interpreted as reflecting the enrichment of the subduction derived magma and the crustal contamination is effective during the rise of the mantle.

Contribution Specification This work was supported by Aksaray University Scientific Research Coordination Unit with BAP project no 2015-77. The authors would like to thank Aksaray University for their contributions.

Keywords— Sarıcakaya Magmatic Mass, Eskişehir, Granitoid, Geochemistry, Petrography

Petrographic and Geochronologic investigation of Neogene volcanites in Kınık (İzmir) area, NE Aegean (Turkey)

Onur ALKAÇ

Firat University Engineering Faculty Department of
Geological Engineering, 23119, Elazığ, Turkey.
.hemin.hamasaleh@gmail.com

Hayrettin KORAL

İstanbul University Engineering Faculty Department of
Geological Engineering, İstanbul, Turkey.

Abstract— Continental volcanism accompanies lacustrine sedimentary units (Soma and Deniz Formation) in the large basins at Miocene Periods divided into two subgroups in Kınık district of NE Aegean. Adilköy Volcanites settled by magmatic intrusion in Soma Formation units and Kalemköy Volcanites interfinger and/or overlapping with Deniz Formation units. In this study, geochemical and petrographic features of Kalemköy and Adilköy Volcanites have been examined and their stratigraphic relationship investigated together with other sedimentary units. Adilköy Volcanites are defined by calc-alkaline basaltic andesite rocks whereas according to K_2O and SiO_2 compounds, Kalemköy volcanites are generally defined by dacite, rhyolite, rhyodacite, trachydacite, andesite type rocks which formed by high potassium and shoshonitic series in base. According to petrographic data on polarizing microscope, Adilköy Volcanites defined to Andesite, basalt, basaltic andesite whereas Kalemköy Volcanites have different composition which dacite, rhyolite, rhyodacite, trachyandesite and andesite.

According to $^{40}K/^{40}Ar$ age analysis in Neogene aged volcanites, First volcanism at Upper Oligocene time started 25.5 my ago (Chattian) in area. On the other hand, Adilköy Volcanites show 22.2 my age (Aquitian), whereas Kalemköy Volcanites are 17 my age (Burdigalian).

Geochemical studies refer to decreasing Ta, Nb, P, Ti elements in trace element diagrams of both magmatic phase and presence of the loser component in magmatic reservoir area or contamination of continental crust in Adilköy and Kalemköy Volcanites. High content of Fe, Mg, Cr, Ni and Co elements in Adilköy Volcanites showed aged mantle materials are located by intrusion on the surface. Adilköy Volcanites located in mantle fractional part on tectonic discrimination diagrams and contains mantle derived materials. Kalemköy Volcanites refer to develop from a subduction-influenced source and derived from a magma by continental crust assimilation at syn- collisional and post-collisional setting.

Keywords— Neogene Volcanites, Petrography, Geochronology, Kınık (İzmir).

Comparison Of The Interpolation Methods For Evaluation And Presentation Of The Geochemical Data: Sarıcakaya Granitoidi (Eskişehir-Türkiye)

Hacer Bilgilioğlu

Aksaray University, Department of Geological Engineering.
bilgiliogluhacer@gmail.com

Süleyman Sefa Bilgilioğlu

Aksaray University, Department of Geomatics Engineering.
sefa.bilgilioğlu@gmail.com

Bahattin Güllü

Aksaray University, Department of Geological Engineering.

Abstract—Sarıcakaya granitoid is located to the north of the Sakarya River and approximately 50 km north of Eskişehir province, consists of gabbro, diorite, granodiorite and granite types of rocks. The general mineralogical composition of the granitoid is composed of quartz, plagioclase, orthoclase, hornblende, biotite, \pm microcline \pm zircon, \pm apatite minerals. The geochemistry shows changes according to the defined rock type. In this context, geochemical data that taken from geochemical analysis of geochemistry data should transform into surfaces covering the entire study area. Spatial interpolation methods have been developed for the purpose of expressing the point data on the spatial basis. These methods calculate the values of the areas between these points based on the reference data of the referenced point geometry, and express the results as raster surfaces.

In this study spatial interpolation methods used for the evaluation and presentation of the geochemical data of the Sarıcakaya granitoid. The method with optimal performance for mapping geochemical data were determined based on spatial distribution of data sources within the study area and characteristics of the data. The accuracy of distributions produced by different interpolation methods (IDW, Kriging, Natural Neighbor) had been calculated. It turns out that the Kriging method is more useful when it comes to generate geochemical distribution maps. Considering the petrographic properties and generated geochemical distribution maps of the Sarıcakaya granitoid, it is revealed that SiO_2 distributions controlled by quartz mineral. MgO distributions controlled by amphibole and pyroxenes. $\text{CaO-Na}_2\text{O}$ distributions controlled by plagioclase and K_2O distributions controlled by presence of orthoclase minerals.

Keywords: Keywords: Geographic Information Systems, Spatial Interpolation, Geochemistry, IDW, Kriging, Sarıcakaya, Granitoid

INDUSTRIAL ENGINEERING

ORAL SUBMISSIONS



Ring Planning for University Campus by Using Set Covering Problem

Eren ÖZCEYLAN
Industrial Engineering Department
Gaziantep University
Gaziantep, Turkey
erenozceylan@gmail.com

Cihan ÇETİNKAYA
Industrial Engineering Department
Gaziantep University
Gaziantep, Turkey
cihancetinkaya@gantep.edu.tr

Abstract— Gaziantep University has over than 40 thousands of students, 1500 academic and 1200 administrative staff who spend most of their time in 30 different facilities. To prevent traffic congestion and decrease the amount of personnel vehicles, an efficient ring planning is essential inside the campus. To do so, a study to design the ring services in Gaziantep University campus is considered. First of all, 15 bus-stop and 30 demand points are determined. Then, a set covering problem is applied to assign the bus-stop points to each demand point under different accessible distances. Finally, different ring plans which minimize the number of bus-stops and maximize the coverage are generated. Results show that all the demand points can be reached within 12 minutes. Since the existing route cannot cover all demand points, proposed four different routes are better than the existing route.

Keywords—ring planning; set covering problem; campus; case study

Internal and External Factors Affecting Open Innovation

Gül OZKAN

The Graduate School of Natural and Applied Sciences,
Dokuz Eylül University,
Izmir, Turkey
gulozkanozdag@gmail.com

Burcu FELEKOGLU

Industrial Engineering Department, Faculty of Engineering,
Dokuz Eylül University,
Izmir, Turkey
burcu.felegoklu@deu.edu.tr

Abstract— Open innovation refers to an innovation approach where there are no boundaries for the knowledge inflow and outflow and additionally, risk and reward are shared by two or more sides. Open innovation is becoming a widely used approach since it provides agility, flexibility, concentration on core competencies, identifying and diversifying risk and sharing uncertainty. Identifying factors which affect open innovation performance is important to be better manage this approach. In literature there are limited number of studies investigating facilitators of open innovation for only SMEs (small medium sized enterprises) (Brunswick & Vanhaverbeke, 2015), (Güzel, Sağ & Sezen, 2016) and science park companies (Şimşek, 2015). Yet, there has not been any comprehensive and elaborate study identifying both external and internal facilitators and impediments of open innovation for various sectors and company sizes (small, medium or large sized).

The aim of this study is to identify the internal and external facilitator factors of open innovation from a comprehensive review of the literature. Considering the meaning of facilitator, it encompasses the acceleration, benefit, usefulness and systematic operations for open innovation activities. Moreover, this study also indicates and focuses out the impediment factors that obstruct the operation of OI activities.

A structured methodology is followed in this study. First of all, literature is reviewed and analyzed rigorously. In reviewing the literature, the studies are investigated according to the relationship between various factors and open innovation. Studies are identified and analyzed according to the factor name in publication, construct measures, effect on open innovation performance, data collection method, conceptual framework and data analysis method. Then the factors are separated, if they facilitate or prevent OI. Facilitating factors of OI are divided into two groups: external facilitator factors of OI and internal facilitator factors of OI. For all of these two groups main heading, subheading factors and other lower level heading factors are determined.

Findings indicate that there are various factors which have positive or negative effect on open innovation. Four external main factors are identified that have positive effect on open innovation. These are environment outside the company, OI funding, OI technological resources and OI network connections. Three internal main factors are identified that have positive effect on open innovation. These are integrative organizational practices, time management and company's culture. For each main factor, sub-factors are also identified. Some of the identified factors have both positive and negative effects on OI mechanisms. The main headings of the impeding factors are: OI technological resources, OI network connections, environment outside the company, some subheadings of integrative organizational practices and company's culture.

This study contributes to the literature by determining facilitating and impeding factors for open innovation. There are several implications for the practitioners. For instance, existing business owners or new entrepreneurs can easily analyze market conditions, accomplish main goals and destinations of their companies, decrease risk and decrease uncertainty while implementing and managing open innovation approaches and activities by considering the findings of this study.

Keywords—open innovation; facilitators; impeditors

REFERENCES

- Brunswick, S., & Vanhaverbeke, W. (2015). Open innovation in small and medium-sized enterprises (SMEs): External knowledge sourcing strategies and internal organizational facilitators. *Journal of Small Business Management*, 53 (4), 1241-1263.
- Güzel, M., Sağ, S., & Sezen, B. (2016). Factors That Motivate or Prevent Adoption of Open Innovation by SMEs in Developing Countries and Policy Suggestions. *Procedia - Social and Behavioral Sciences* 235 756 – 763.
- Şimşek, K. (2015). Open innovation practices in science park firms in Turkey. M.Sc. Thesis, Istanbul Technical University, İstanbul.

A Data Mining Application on Sales Data of A Cable Factory in Kayseri

Nuh Mehmet Oskaybaş

Department of Industrial Engineering
Erciyes University
Kayseri, Turkey
nmoskaybas@gmail.com

Sinem Kulluk

Department of Industrial Engineering
Erciyes University
Kayseri, Turkey
skulluk@erciyes.edu.tr

Abstract—Data mining is the process of extracting useful information from large databases. Today, data mining is used in many areas such as marketing, banking and finance, health, telecommunications, tourism, education and transportation successfully. In this study, a data mining application is done in order to estimate the sales values of the future years by using the sales data of a company operating in Kayseri. For obtaining future forecasts, firstly the factors affecting the sales values are determined and then function estimation function of data mining is performed with the help of five different models appropriate for the structure of the problem. The study is aimed to reach the critical information and significant points related with the company's sales.

Keywords—data mining; sales data; sales forecasting

I. INTRODUCTION

Today, there are quite a lot of raw data in the databases of big companies. The amounts of raw data are increasing day by day, but using these data is not very convenient. Raw data plays an important role in moving companies forward, especially in marketing, manufacturing, management and investment. Therefore, processing these data and extracting useful information from them is very important. Data Mining (DM) methods are very helpful in processing huge amounts of data.

Data mining has been defined as the nontrivial extraction of implicit, previously unknown and potentially useful information from data [1]. The general goal of DM is to discover knowledge that is not only correct, but also comprehensible and interesting for the user. DM encompasses a number of different technical approaches such as clustering, data summarization, learning classification rules, finding dependency networks and detecting anomalies [2]. Among the various data mining tasks function estimation is popularly used to estimate the target variable in many areas. In function estimation the target variable is continuous in contrast to the classification which has discrete outputs.

Function estimation function of data mining to sales forecasting has been widely studied in the literature. Among these studies Krause-Traudes et al. [3] presented a use case of spatial data mining for aggregate sales forecasting in retail

location planning. Özsağlam [4] forecasted the sales of a Turkish consumer electronics store company by using regression and naïve bayes classifier methods. Huang et al. [5] proposed a novel trigger model for sales prediction with data mining techniques. Beheshti-Kashi et al. [6] presented state-of-the-art methods in the sales forecasting research with a focus on fashion and new product forecasting. İşlek and Ögüdücü [7] addressed the problem of forecasting various product demands of main distribution warehouses and provided an appropriate methodology for demand forecasting. Wu et al. [8] developed and compared different models to forecast new product sales data with increasing sales trend and multiple predictor inputs. Zhang and Li [9] presented the retail commodity sale forecast model based on data mining. They firstly selected the profit ratio which was on behalf of commodity profit element and several other key sale attributes including the season ratio and the sale volume to establish the SPV Model, secondly done commodity sale state segmentation based on the SPV Model with ID3 decision tree algorithm, and on this basis they predicted the sale state of the commodity at some future time. Gahirwal and Vijayalakshmi [10] focused on how the best models of one series can be applied to similar frequency pattern series for forecasting using association mining.

Sales forecasting can have a crucial impact on the success and performance of companies. Motivated by this situation, future sales of a cable factory is estimated by using data mining algorithms in this study. Simple linear regression, Multi-Layer Perceptron (MLP), Sequential Minimal Optimization for regression (SMOreg), Gaussian functions and REPTree, M5P, RandomTree, RandomForest algorithms are used to estimate the future sales of the factory. SMOreg function outperforms the other algorithms in terms of error rates.

II. DATA MINING

A. What is Data?

Data is a set of values of qualitative or quantitative variables. Pieces of data are individual pieces of information. While the

concept of data is commonly associated with scientific research, data is collected by a huge range of organizations and institutions, including businesses (e.g., sales data, revenue, profits, stock price), governments (e.g., crime rates, unemployment rates, literacy rates) and non-governmental organizations (e.g., censuses of the number of homeless people by non-profit organizations) [11].

B. What is Data Mining?

Data mining, the science of extracting useful knowledge from such huge data repositories, has emerged as a young and interdisciplinary field in computer science. Data mining techniques have been widely applied to problems in industry, science, engineering and government, and it is widely believed that data mining will have profound impact on the society [12].

The actual data mining task is the automatic or semi-automatic analysis of large quantities of data to extract previously unknown, interesting patterns such as groups of data records (cluster analysis), unusual records (anomaly detection), and dependencies (association rule mining, sequential pattern mining). This usually involves using database techniques such as spatial indices. These patterns can then be seen as a kind of summary of the input data, and may be used in further analysis or, for example, in machine learning and predictive analytics. For example, the data mining step might identify multiple groups in the data, which can then be used to obtain more accurate prediction results by a decision support system. Neither the data collection and data preparation, nor result interpretation and reporting is part of the data mining step, but do belong to the overall knowledge discovery in databases process as additional steps as shown in Fig. 1.[13].

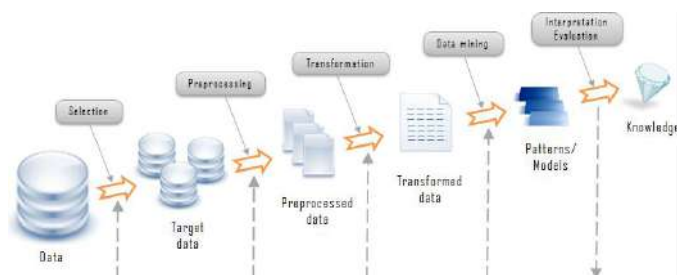


Fig. 1. Knowledge discovery process

III. DATA MINING ON SALES DATA

A cable manufacturer operating in Kayseri wants to know the monthly sales for 2017 according to the past 9 year sales data of the firm. Company executives determined the variables that will affect the sales quantity as follows:

- Months: 12 months of the year is taken as first input variable.
- Types of Cables: Five different types of cables as A, B, C, D and E are manufactured in the factory and taken as input to the problem.

- Constantly changing USD / TL exchange rate which is effective in raw material purchasing is another input variable that affects the sale quantities.
- The price of copper on LME (London Metal Exchange), which is also effective in purchasing raw material, is the last variable affecting the sales.

So there are totally four input variables for the sale forecasting problem. The first two variables are nominal and the remaining variables are continuous attributes. The output variable, sales quantity is also a continuous attributes leading us to the regression model. Looking at the structure of the problem, it is obvious that it will be solved by the regression method. In this context, function estimation is performed by using 8 different models/algorithms using Weka 3.9.1 data mining software. According to the results, the probabilistic suitability of the models/algorithms is examined.

A. Methods

Four function-based methods and four tree-based algorithms that use regression logic from Weka data mining software are used for the sales forecasting problem. Brief description of the methods and algorithms used in this study are as follows:

Simple Linear Regression; is a technique that aims to identify the relationship between two continuous variables (the dependent variable and the independent variable being estimated). It aims to form a state equation using technical data. When this state equation is established, it is ensured that the rectification is optimized by minimizing the squares of the distance, which is estimated from all the data points [14].

A multilayer perceptron is a feed forward artificial neural network model that maps sets of input data onto a set of appropriate outputs. An MLP consists of multiple layers of nodes in a directed graph, with each layer fully connected to the next one. Except for the input nodes, each node is a neuron (or processing element) with a nonlinear activation function. MLP utilizes a supervised learning technique called back-propagation for training the network [15, 16].

Sequential Minimization Optimization for regression - SMOreg is a new algorithm for training Support Vector Machines (SVM). This implementation globally replaced all missing values, transformed nominal attributes into binary ones and also normalized all attributes by default. SMOreg is a support vector machine for regression problems linear regression. It's beyond the scope of these forums to discuss the theory behind kernel methods like SVMs [17].

In probability theory and statistics, a Gaussian process is a statistical model where observations occur in a continuous domain, e.g. time or space. In a Gaussian process, every point in some continuous input space is associated with a normally distributed random variable. Moreover, every finite collection of those random variables has a multivariate normal distribution. The distribution of a Gaussian process is the joint distribution of all those (infinitely many) random variables, and as such, it is a distribution over functions with a

continuous domain, e.g. time or space [18]. Viewed as a machine-learning algorithm, a Gaussian process uses lazy learning and a measure of the similarity between points (this is the kernel function) to predict the value for an unseen point from training data. The prediction is not just an estimate for that point, but also has uncertainty information -- it is a one-dimensional Gaussian distribution (which is the marginal distribution at that point) [19]. Gaussian method in Weka implements Gaussian processes for regression without hyper parameter-tuning.

REPTree uses the regression tree logic and creates multiple trees in different iterations. After that it selects best one from all generated trees. That will be considered as the representative. In pruning the tree the measure used is the mean square error on the predictions made by the tree [20].

M5P model tree is used for numeric prediction and at each leaf it stores a linear regression model that predicts the class value of instances that reach the leaf [21].

Random trees have been introduced by Leo Breiman and Adele Cutler. The algorithm can deal with both classification and regression problems. Random tree is a collection (ensemble) of tree predictors that is called *forest* (the term has been also introduced by L. Breiman). The classification works as follows: the random trees classifier takes the input feature vector, classifies it with every tree in the forest, and outputs the class label that received the majority of "votes". In case of a regression, the classifier response is the average of the responses over all the trees in the forest [22].

Random forest is an ensemble learning method for classification, regression and other tasks, that operate by constructing a multitude of decision trees at training time and outputting the class that is the mode of the classes (classification) or mean prediction (regression) of the individual trees [23].

B. Data set and Partitioning

As mentioned before the sales data has two nominal, two continuous inputs and a continuous outputs. The dataset totally has 540 instances.

For partitioning the dataset into training and testing sets a well-known ten-fold cross-validation procedure is applied to the dataset. Dataset is partitioned into ten data subsets and algorithms/methods are executed once for each partition. Each time a different partition is used as testing set and the remaining 9 are grouped together to build training set. The training set is used to train the algorithm for good learning capability, while the testing set is applied to evaluate the generalization capability of the algorithm/method.

C. Performance metrics

Correlation Coefficient: A correlation coefficient (*corr*) is a number that quantifies a type of correlation and dependence, meaning statistical relationships between two or more values in fundamental statistics.

$$corr(x, y) = \frac{\sum_{i=1}^n (x_i - \bar{x})(y_i - \bar{y})}{(\sum_{i=1}^n (x_i - \bar{x})^2 \sum_{i=1}^n (y_i - \bar{y})^2)^{1/2}} \quad (1)$$

Mean absolute error: In statistics, the mean absolute error (MAE) is a quantity used to measure how close forecasts or predictions are to the eventual outcomes. The mean absolute error is an average of the absolute errors.

$$MAE = \frac{1}{n} \sum_{i=1}^n |forecast_i - sales_i| = \frac{1}{n} \sum_{i=1}^n |e_i| \quad (2)$$

Root Mean Squared Error: The root-mean-square deviation (RMSD) or root-mean-square error (RMSE) is a frequently used measure of the differences between values (sample and population values) predicted by a model or an estimator and the values actually observed. The RMSD represents the sample standard deviation of the differences between predicted values and observed values. The RMSD serves to aggregate the magnitudes of the errors in predictions for various times into a single measure of predictive power.

$$RMSE = \sqrt{\frac{\sum_{t=1}^n (\hat{y}_t - y_t)^2}{n}} \quad (3)$$

Relative Absolute Error: The relative absolute error (RAE) is very similar to the relative squared error in the sense that it is also relative to a simple predictor, which is just the average of the actual values. In this case, though, the error is just the total absolute error instead of the total squared error. Thus, the relative absolute error takes the total absolute error and normalizes it by dividing by the total absolute error of the simple predictor.

$$RAE = \frac{\sum_{t=1}^n |\hat{y}_t - y_t|}{\sum_{t=1}^n |\bar{y} - y_t|} \quad (4)$$

Root Relative Squared Error: The root relative squared error (RRSE) is relative to what it would have been if a simple predictor had been used. More specifically, this simple predictor is just the average of the actual values. Thus, the relative squared error takes the total squared error and normalizes it by dividing by the total squared error of the simple predictor. By taking the square root of the relative squared error one reduces the error to the same dimensions as the quantity being predicted.

$$RRSE = \sqrt{\frac{\sum_{t=1}^n (\hat{y}_t - y_t)^2}{\sum_{t=1}^n (\bar{y} - y_t)^2}} \quad (5)$$

IV. PERFORMANCE ANALYSIS

Before applying function-based methods and tree-based algorithms the sales dataset is randomized in order to balance the learning. Tables 1 and 2 show the error rates of the ten-fold-cross-validation results of function-based methods and tree-based algorithms respectively.

TABLE I. ERROR RATES OF FUNCTION-BASED METHODS

	Linear Regression	MLP	SMOreg	Gaussian
Correlation Coefficient (R)	0,9349	0,8559	0,9355	0,9348
R ²	0,8740	0,7326	0,8752	0,8739
Mean Absolute Error	363141,47	569479,66	323192,41	367062,94
Root Mean Squared Error	665264,45	1000190,2	663310,73	665626,69
Relative Absolute Error	25,4526 %	39,9148%	22,6525%	25,7274%
Root Relative Squared Error	35,4004 %	53,2226%	35,2964%	35,4197%

According to Table 1, it is clear that the MLP method has the smallest correlation coefficient, mean absolute error and largest relative absolute error even though all of the models have very close error values. MLP is the model that gives the worst result to this problem.

R², the square of the correlation coefficient indicates the degree of linear relationship between the variables. Therefore, reliability of the model increases by the increase of the R² value. It is easy to see that the values of R² in the table are very close to each other. As seen in the table, the highest value of R² is the SMOreg method. Also, if we look at the values obtained by the SMOreg method, we can see that it has the lowest rate of both error rates. As a result, we can clearly say that the SMOreg method gives the best result for this problem.

TABLE II. ERROR RATES OF TREE-BASED MODELS

	REPTree	M5P	Random Tree	Random Forest
Correlation Coefficient (R)	0,9342	0,9323	0,8782	0,9287
R ²	0,8727	0,8692	0,7712	0,8625
Mean Absolute Error	287747,25	326924,33	405270,24	311759,83
Root Mean Squared Error	668977,27	678182,78	937621,41	699480,31
Relative Absolute Error	20,1682 %	22,9141 %	28,4054 %	21,8512 %
Root Relative Squared Error	35,5980 %	36,0878 %	49,8932 %	37,2211 %

When the tree-based algorithms given in Table 2 analyzed and compared with each other, RandomTree is the function that gives the worst result to this problem. REPTree algorithm gives the highest R² value and smallest error rates.

If both function-based methods and tree-based algorithms compared altogether, SMOreg algorithm outperforms the other algorithms in terms of error rates and R² values. The firm can use the SMOreg algorithm to estimate their future sales.

Multi-layer perceptron method gives the worst rates among the eight algorithms. Remaining algorithms give near values to each other.

V. CONCLUSION

In this study, a cable manufacturer sales potential is estimated by using eight function-based methods and tree-based regression focused algorithms. The dataset consists of four inputs and a continuous output for the last nine years. Ten-fold-cross-validation procedure is used to partition the datasets into training and testing sets. Correlation coefficient, R² and some error rates are used as performance metrics for analyzing the performance of the algorithms. SMOreg algorithm outperforms the compared algorithms and can be used to predict the sales of the cable manufacturer.

References

- [1] W. Frawley, G. Piatetsky-Shapiro, C. W. Matheus, "Knowledge discovery in databases: An overview", *AI Magazine* (1992), pp. 213-228.
- [2] A. Baykasoğlu, L. Özbakır, "MEPAR-miner: Multi-expression programming for classification rule mining", *European Journal of Operational Research*, vol. 183(2), pp. 767-784, 2007.
- [3] M. Krause-Traudes, S. Scheider, S. Süping, H. Mebner, "Spatial data mining for retail sales forecasting", *11th Agile International Conference on Geographic Information Science*, University of Grona, Spain, pp. 1-11, 2008.
- [4] M. Y. Özsağlam, "Data mining techniques for sales forecasting", *International Journal of Technical Research and Applications*, Special Issue 34, pp. 6-9, 2015.
- [5] W. Huang, Q. Zhang, W. Xu, H. Fu, X. Liang, "A novel trigger model for sales prediction with data mining techniques", *Data Science Journal*, vol. 14:15, pp. 1-8, 2015.
- [6] S. Beheshti-Kashi, H. R. Karimi, K.-D. Thoben, M. Lütjen, M. Teucke, "A survey on retail sales forecasting and prediction in fashion markets", *Systems Science & Control Engineering*, vol. 3(1), 154161, 2015.
- [7] İ. İşlek, Ş. G. Öğüdücü, "A retail demand forecasting model based on data mining techniques", *Industrial Electronics (ISIE)*, 2015 IEEE 24th International Symposium on Industrial Electronics, 3-5 June 2015.
- [8] L. Wu, J. Y. Yan, Y. J. Fan, "Data mining algorithms and statistical analysis for sales data forecast", *Computational Sciences and Optimization (CSO)*, 5th International Joint Conference on Computational Sciences and Optimization, 23-26 June 20123.
- [9] J. Zhang, J. Li, "Retail commodity sale forecast model based on data mining", *Intelligent Networking and Collaborative Systems (INCoS)*, International Conference on Intelligent Networking and Collaborative Systems, 7-9 September, 2016.
- [10] M. Gahirwal, M. Vijayalakshmi, "Inter time series sales forecasting", *arXiv: 1303.0117*, 2013.
- [11] https://en.wikipedia.org/wiki/Data#cite_note-1 Access date: 18.02.2017.
- [12] S. Chakrabarti, M. Ester, U. Fayyad, J. Gehrke, J. Han, S. Morishita, G. Piatetsky-Shapiro, W. Wang, "Data Mining Curriculum: A Proposal (Version 1.0)", April 30, 2006.
- [13] https://en.wikipedia.org/wiki/Data_mining#cite_ref-acm_1-2 Access Date: 25.02.2017

- [14] Y. Argüden, B. Erşahin, “ Veri Madenciliği – Veriden Bilgiye, Masraftan Değere” Arge Danışmanlık Yayınları No: 10 ISBN: 978-975-93641-9-9 1. Publication Date: November 2008.
- [15] Rosenblatt, Frank. x. Principles of Neurodynamics: Perceptrons and the Theory of Brain Mechanisms. Spartan Books, Washington DC, 1961.
- [16] Rumelhart, E. David, E. Geoffrey, Hinton, and R. J. Williams, "Learning Internal Representations by Error Propagation". David E. Rumelhart, James L. McClelland, and the PDP research group. (editors), Parallel distributed processing: Explorations in the microstructure of cognition, Volume 1: Foundations. MIT Press, 1986.
- [17] S. Vitkar, “Trend Analysis and Prediction of Air and Water Pollutants using Regression algorithm SMOreg” Journal of Information, Knowledge and Research in Computer Engineering, ISSN: 0975 – 6760| Nov 12 TO Oct 13 | Volume – 02, Issue – 02.
- [18] https://en.wikipedia.org/wiki/Gaussian_process Access Date: 24.02.2017.
- [19] <http://platypusinnovation.blogspot.com.tr/> "Platypus Innovation: A Simple Intro to Gaussian Processes (a great data modelling tool)" Access Date: 25.02.2017.
- [20] S. Kalmegh, “Analysis of WEKA Data Mining Algorithm REPTree, Simple Cart and RandomTree for Classification of Indian News”, IJISSET - International Journal of Innovative Science, Engineering & Technology, Vol. 2 Issue 2, February 2015.
- [21] E. K. Onyari, F. M. Ilunga, “Application of MLP Neural Network and MSP Model Tree in Predicting Streamflow: A Case Study of Luvuvhu Catchment, South Africa”, International Journal of Innovation, Management and Technology, Vol. 4, No. 1, February 2013.
- [22] http://docs.opencv.org/2.4/modules/ml/doc/random_trees.html, Access Date: 25.02.2017.
- [23] https://en.wikipedia.org/wiki/Random_forest Access Date: 24.02.2017.

Cost Minimizing Fuel-Coal Selection for Power Plants under Operational Constraints

Ahmet Yücekaya
Department of Industrial Engineering,
Faculty of Engineering,
Kadir Has University
İstanbul, TURKEY
E-mail: ahmety@khas.edu.tr

Abstract— Power companies require sophisticated tools to manage fuel-coal supply chains which include multiple suppliers, coal contracts, and multimode transportation routes. In this research, an integrated multi-objective model for supplier, transportation, and coal order is developed for the coal supply network in which multiple suppliers, coal contracts, and multimode transportation routes exist. The model simultaneously optimizes multiple objectives such as minimizing purchase costs and transportation costs and it also presents a decision framework on the selection of suppliers, transportation routes, and coal products that will achieve these objectives. The network and capacity constraints of suppliers and transportation routes are included in the model. The methodology for the solution is illustrated via a case study and an alternative evaluation process is presented. The study demonstrates that the model can be used by power companies to find desired solutions and has the potential to apply to other industries.

Keywords— fuel coal supply; supply chain; supplier mix; transportation optimization

I. INTRODUCTION

Coal is the most abundant and commonly used energy resource in the generation of electricity. Since it is readily available, flexible to use, and accessible all around the world, it is one of the most reliable resources. However, coal as a product has different characteristics and each coal type differs. The heat content ranges from low to high, which affects the amount of energy gained when it is burned. Power producers tend to purchase coal with high heat content as it generates more electric power in comparison with the same amount of coal with lower heat content. Also, not all coal products can be burned in a power plant, and it is necessary to purchase the right coal product to most efficiently use plant resources and minimize costs.

Although coal is crucial for the industrialized world, the environmental impacts should be carefully handled. The land where coal is mined becomes temporarily unavailable for other uses such as agriculture, and it makes the land susceptible

to soil erosion in addition to creating noise, water pollution, and dust. Moreover, coal mines are a source of methane gas which is harmful to the environment, and the gas is released during mining. Also, coal has environmental impacts when it is burned, which is its major challenge. The oxides of sulphur (SO_2) and nitrogen (NO_x), CO_2 , particulate, and trace elements such as mercury can have serious impacts on nature. It has been found that the release of greenhouse gas emissions derived from human activities is related to global warming, and increasing amounts of sulphur and nitrogen oxides lead to acid rain. For these reasons, coal-fired power plants are known to be a major source of air pollution [1]. If a coal resource is not carefully chosen, the cost of power generation and the environmental hazards can be higher for power producers.

Suppliers provide coal contracts for each coal type which are sold via a merchandise exchange to power companies. A coal contract includes the amount, type, price, heat content, ash content, sulfur content, and chemical structure of the coal that will be delivered to the power company. The price for each contract is different and often times the mine mouth-price does not include transportation costs. Suppliers issue different coal contracts each of which has its own price and related product descriptions. Power companies must contend with the problem of choosing the best coal contracts that will meet the demand in a cost-effective way given that there may be multiple power plants at different locations.

It is best to locate a coal-fired power plant near to a coal mine, but this is not usually the case as a generation point should also be in close proximity to where power is consumed. Coal then must be transported from where it is blended or mined to its final destination plant, and it is usually shipped by professional transportation companies; it is also common, however, for power companies to have their own fleet for coal transportation. In the US, railway companies have the largest share of coal transportation as they have their own railroads and specialized transport cars. Other methods of transportation include coal barges on waterways and trucks on highways, and with these, coal can be transported directly to the power plants. Coal can also be transported to a trans-load location where it is loaded to another vehicle at a hub point for further shipment to

power plants or to another trans-load location. While the final destination is the power plant, transportation costs differ based on the method, the distance, and selected route mix. Also, the transportation capacity of each route is limited and the tariff to ship coal can differ. For these reasons, power companies must ensure that effective transportation methodologies are chosen at a minimum cost.

Power companies are required to make decisions about suppliers, transportation, and order mix selection in a supply chain where suppliers, products, and a diversity of transportation possibilities exist. The overall objective can be classified in two different ways. The first is related with suppliers and coal selection, and the aim is to minimize the purchase cost of orders. The second is related with transportation, and the aim is minimal costs and the reliable transportation of coal resources.

A limited amount of research exists in the literature that integrates suppliers, transportation, and order diversity for the power industry. Author presents a fuzzy multiple-objective linear programming model for production-transportation planning problems in a supply chain in [2]. The proposed model attempts to simultaneously minimize many objectives like total production and transportation costs along with the number of rejected items, total delivery time, and labor level. The fuzzy data is in a modifiable format so that a decision-maker can develop a satisfactory solution that will improve the supplier-distributor relationship. Authors develop a model for a manufacturer's supply network in which there are numerous suppliers with capacity limitations, numerous products, and uncertain demand in [3]. The model considers market demand uncertainty, costs, and product characteristics, and the main objective is to find how much of each material to order from each supplier given that supplier and manufacturing companies have a limited capacity. Author develops a model to select the best routes in international intermodal networks where multiple commodities and multimode transportation opportunities exist [4]. The objectives are to minimize the total flow cost and the total travel time where a time window constraint is imposed. The problem is NP-hard and hence Lagrangian relaxation and a decomposition method with a heuristics method is used to solve the problem. The existing research considers supplier-transportation, supplier capacity-product and multiple products-transportation, and it develops methods to solve problems for a supply chain. However, these studies do not respond to problems when they involve multiple products, multimode transportation, order diversity, and supplier diversity with capacity constraints. Furthermore, the operational constraints in coal-fired plants impose new limitations on coal, such as energy content and non-homogeneity. This body of knowledge assumes that products are identical and do not have operational constraints.

Authors develop a method to optimize a regional railroad network in [5]. The main objective is the minimization of total costs in transportation when there is increased coal shipment traffic and resources are allocated among demand

points. In [6], Shih (1997) proposes a mixed integer programming method for the planning of fuel-coal imports for power plants. A diversity of supply sources for power companies that have more than one plant complicates coal logistics. The main objective is the minimization of total inventory costs and holding costs, and the constraints are harbor unloading capacity, demand balance, and inventory balance. The model is developed for the central coal logistics system of a Taiwanese power company to demonstrate its validity. In [7] authors present a model for coal blending and cleaning silos for supplies of coal from different resources and delivery to customer locations to meet demand. In [8], a model is developed for a coal loading port in China. The coal is first transported to the port via trains and then barges are used to deliver the coal to the final destinations. They develop a Markov decision model that minimizes holding costs, shortages, and transportation costs by integrating ordering and delivery decisions. The study briefly considers product and route diversities which are usually the decision variables that make the problem challenging.

Authors provide a simulation methodology for coal shipment from mines in western Canada to power stations in the east [9]. The transportation cost for such distances becomes increasingly important as it is a major component of final coal prices. They simulate alternative routes across Canada and present the possible outcomes of each scenario for strategic route planning. A research is presented on the existing coal distribution infrastructure and four scenarios are developed lasting until 2050 to analyze coal consumption and possible problems for meeting coal demand [10]. Tu and Guldman (2001) develop a model and a tool called the Geographic Information System to identify coal transportation routes considering coal production sites, power plants, and costs of transportation [11]. They visualize the transportation process and validate the model in a case study developed for Ohio. The author in [12] presents a comprehensive study on coal transportation to power plants and its reliability in the US. He explores major coal resources and discusses transportation reliability issues while noting the importance of coal for energy supplies. In [13] a model is proposed for coal blending and transportation in which an inter-model transportation network for coal import exists. The coal supply, quality, price, and demand at the power plant are included in the model, and it is a mix-integer zero-one programming problem in which the main objective is overall cost minimization.

In this research, a linear model that considers multimode transportation alternatives, multiple products, and multiple suppliers is developed for the efficient management of the coal supply of an electric power company with more than one plant at different locations. The methodology is able to optimize the supply of fuel-coal over the network and also able to help configure the supply chain. Capacity limitations on transportation routes, supplier capacity for a particular product, and plant burn capability constraints are also considered in the model. The remainder of the paper is organized as follows:

Section 2 formulates the problem Section 3 provides a case study developed for a power company in the Midwestern USA. Conclusions are given in section 4.

II. FUEL-COAL SELECTION PROBLEM

The coal is first mined and transported to a silo where the stones and refuse are removed at the supplier's site. The next step is to crush the coal and sort it before the washing process. Then it is ready to be blended to get the desired level of physical specifications. The last step is to load the coal onto trains, barges or trucks to ship it to its next destination. The coal transportation network is heavily dominated by private railroad companies as they have their own fleet with specialized coal transportation cars and railroads for transportation. Barges on waterways are also used, especially for large power companies that have their own coal transportation fleet. The coal is transported directly to the power plant or often times it is transported to a trans-load location where it is loaded to another vehicle of a supplier or another company. The trans-load location is a hub point that is used to efficiently manage the transportation network.

The coal supply chain can be represented as a network in which suppliers, transportation routes, trans-load locations and power plants are natural entities. Fig. 1 gives a description of a coal supply network. The coal $q \in Q$ is supplied at supplier $i \in I$, and it is transported to power plant $j \in J$ directly or via trans-loading at trans-load location $t \in T$. The coal can also be shipped from a trans-load location t to another trans-load location $t' \in T$ where $t' \neq t$. The decision variable that should be found for each power plant is $X_{i,j,q}$, the total amount of coal q transported from supplier i to power plant j , where

$$X_{i,j,q} = X_{i,j,q} + X_{i,t,q} + X_{t,j,q} + X_{t,t',q} + X_{t',j,q}.$$

The decision variable includes the total coal q transported directly to plant j , the coal transported to a trans-load location t then transported to plant j , and the coal further transported to other trans-load locations t' then transported to plant j .

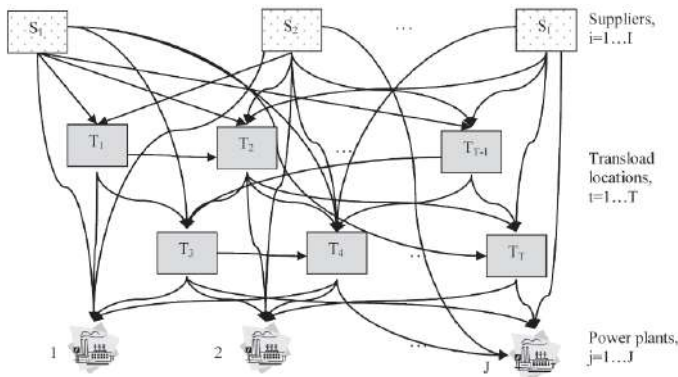


Fig. 1. Coal transportation network

The main components of the objective are the cost of purchase and the cost of transportation to the destination power

plant which are related with supplier selection, the transportation route, and coal type. Accordingly, the main objective of the problem is the minimization of purchase and transportation cost. Selection of coal suppliers depends on their location and the specifications of their product, and whether they offer different price ranges for coal contracts. However, the availability of alternative transportation routes, trans-loading locations, and associated costs also force power companies to optimize the coal delivery process. The detailed formulations are as follow:

- Purchase cost: This objective function finds purchase cost by multiplying the price of coal q with the total amount of coal q transported from supplier i whether directly to plant j or trans-load location t .

$$f_1 = \sum_{i \in I} \left(\sum_{j \in J} \sum_{q \in Q} X_{i,j,q} P_{i,q} + \sum_{t \in T} \sum_{q \in Q} X_{i,t,q} P_{i,q} \right) \quad (1)$$

$P_{i,q}$ is the given price of coal q at supplier i . The first part of the objective function is the cost of purchased coal that is transported directly to the plant without trans-loading. The second part calculates the purchase cost of coal q that it is transported to a trans-load location t .

- Transportation cost: The cost of transportation over the transportation network is minimized in this objective.

$$f_2 = \sum_{q \in Q} \left(\sum_{i \in I} \sum_{j \in J} X_{i,j,q} TC_{i,j} + \sum_{i \in I} \sum_{t \in T} X_{i,t,q} TC_{i,t} + \sum_{t \in T} \sum_{t' \in T, t' \neq t} X_{t,t',q} TC_{t,t'} + \sum_{t \in T} \sum_{j \in J} X_{t,j,q} TC_{t,j} \right) \quad (2)$$

$TC_{i,j}$, $TC_{i,t}$, $TC_{t,j}$, and $TC_{t,t'}$ represents the transportation cost of coal from supplier i to plant j , from supplier i to trans-load location t , from trans-load location t to plant j and from trans-load location t to trans-load location t' ($t' \neq t$), respectively.

Electricity is a non-storable commodity that must be produced and consumed in real-time. The power plant j keeps a coal inventory that is sufficient to meet F_j (days) of power demand and orders coal that is sufficient to meet D_j (days) of power demand assuming that the plant would work at its maximum capacity. The heat content of coal q , H_q (BTU/lb) is released during the burning process and is converted into electric power. The total power amount that can be gained from coal q is H_q multiplied with the reserve of coal q at plant j (ton), which is the accumulation of the current inventory of coal q , $I_{j,q}$ (tons), and the coal inflow of coal q from suppliers and trans-load locations. As a result of the energy release process, the total BTU units of energy can be derived from coal q at power plant j to meet demand. However, the efficiency of a power plant in converting the potential energy output into electricity should be considered. The power generated from a coal-fired power plant is approximated with its heat rate R_j (mmBTU/MWh). Note that in order to generate M_j (MWh) of power for each hour, $R_j \times M_j$ (mmBTU) units of energy is needed. Hence, the necessary

condition is that the potential power output in terms of BTUs should be higher than the required BTUs to generate M_j amount of power for $D_j + F_j$ days. After necessary unit conversions, the equation can be represented as:

$$\sum_{q \in Q} \left(I_{j,q} + \sum_{i \in I} X_{i,j,q} + \sum_{t \in T} X_{t,j,q} \right) H_q \geq (D_j + F_j) (24 M_j) (R_j / 500) \quad \text{for all } j \in J \quad (3)$$

The amount of coal that is processed and blended at each supplier i is limited and usually determined by market conditions. The total amount of coal q transported to trans-load locations and power plants from supplier i is limited to its capacity. Note that $X_{i,t,q}$ is the amount of coal q that is transported to a trans-load location from supplier i , and it can be further transported to another trans-load location or to a power plant. On the other hand, $X_{i,j,q}$ is the amount of coal q that is directly transported to power plant j . Since both of them were sent from supplier i , the total should sum up the amount of coal q that is provided by supplier i which has a limited capacity.

$$\sum_{t \in T} X_{i,t,q} + \sum_{j \in J} X_{i,j,q} \leq O_{i,q} \quad \text{for all } i \in I, q \in Q \quad (4)$$

Not all coal types can be burned in a coal fired power plant. Technological infrastructure, environmental constraints, and regulations require plants to burn pre-defined coal types. Additionally, the grindability index (size) of coal q , gi_q , should be in an interval of minimum grindability permitted in plant j , $gi_{j,min}$, and maximum grindability permitted in plant j , $gi_{j,max}$. Similarly the percentage of moisture content in coal q , mc_q , should be in an interval of $mc_{j,min}$ and $mc_{j,max}$ which are the minimum and maximum percentage of moisture allowed at plant j . To lower the SO_2 outputs from coal it is desirable to keep the sulfur content in coal q , S_q , within the limit of maximum and minimum sulfur percentage permitted at plant j , which are $S_{j,min}$ and $S_{j,max}$ respectively. The equations can be gathered in a single representing formula as given below:

$$X_{i,j,q} = \begin{cases} 0 & \text{if coal } q \text{ cannot be burned at plant } j \\ & \text{and/or if } gi_q \notin [gi_{j,min}, gi_{j,max}] \\ & \text{and/or if } mc_q \notin [mc_{j,min}, mc_{j,max}] \\ & \text{and/or if } S_q \notin [S_{j,min}, S_{j,max}] \\ X_{i,j,q} & \text{Otherwise} \end{cases} \quad \text{for all } q \in Q, i \in I \quad (5)$$

$$X_{t,j,q} = \begin{cases} 0 & \text{if coal } q \text{ cannot be burned at plant } j \\ & \text{and/or if } gi_q \notin [gi_{j,min}, gi_{j,max}] \\ & \text{and/or if } mc_q \notin [mc_{j,min}, mc_{j,max}] \\ & \text{and/or if } S_q \notin [S_{j,min}, S_{j,max}] \\ X_{t,j,q} & \text{Otherwise} \end{cases} \quad \text{for all } q \in Q, t \in T \quad (6)$$

The coal transportation network has multiple transportation routes that are used if they are more economical. The total coal amount that can be transported on a route is limited to the transportation capacity of the arc in the network.

$$\sum_{q \in Q} X_{i,t,q} \leq U_{i,t} \quad \text{for all } i \in I, t \in T$$

$$\sum_{q \in Q} X_{t,j,q} \leq U_{t,j} \quad \text{for all } j \in J, t \in T \quad (7)$$

$$\sum_{q \in Q} X_{t,t',q} \leq U_{t,t'} \quad \text{for all } t, t' \in T, t \neq t' \quad (8)$$

$$\sum_{q \in Q} X_{i,j,q} \leq U_{i,j} \quad \text{for all } i \in I, j \in J \quad (9)$$

Total coal transportation between supplier i to trans-load location t is limited with that of arc capacity in eq. 7. Eq. 8 gives the capacity constraint of transportation between trans-load location t and plant j , eq. 9 gives the transportation limit between trans-load location t to another trans-load location t' , and eq. 10 gives the direct transportation capacity from supplier i to plant j .

Total coal transported to a trans-load location t is transported either to another trans-load location t' or power plant j .

$$\sum_{t \in T} X_{i,t,q} - \sum_{t \in T, t \neq t'} X_{t,t',q} - \sum_{j \in J} X_{t,j,q} = 0 \quad \text{for all } i \in I, q \in Q, j \in J \quad (10)$$

The non-negativity constraints are also included to ensure non-feasible solutions.

$$X_{i,j,q}, X_{i,t,q}, X_{t,t',q}, X_{t,j,q} \geq 0 \quad \text{for all } i \in I, q \in Q, j \in J, t, t' \in T, t \neq t' \quad (11)$$

Let

$$X = \{X_{i,j,q}, X_{i,t,q}, X_{t,t',q}, X_{t,j,q}\} \quad \text{for all } i \in I, q \in Q, j \in J, t, t' \in T, t \neq t'$$

be a feasible solution set for the linear fuel coal supply problem, and the objective of the problem is to determine the optimum

suppliers, coal products, and transportation routes that will minimize total purchase and transportation cost.

It is important for power companies to report operational expenses in their financial reports. Each cost item has to be explained in the report and they affect the financial performance of the company, which is released to shareholders. As a result, they need to be careful to separate the cost of coal and the cost of transportation. The price of coal is determined by market conditions and it can thus be explained. However, a high cost of transportation decreases the performance of the company. For this reason, these costs have to be treated with different weights and have to be separated.

III. CASE STUDY

The proposed methodology is illustrated for a case study for the Midwestern USA. The electric power supply in the region is dominated by coal-fired generation. 4 suppliers (S_1, S_2, S_3, S_4), 9 alternative contracts (q_1, q_2, \dots, q_9), 4 trans-load locations (T_1, T_2, T_3, T_4) and 3 power plants (Plant 1, 2 and 3) are taken into consideration. The power company has 3 coal-fired power plants located in Indiana, Ohio, and Kentucky. Table I provides the coal contract specifications.

Table 1 Coal contracts and specifications

Product	Contract	Heat Content (BTU)	S (%)	GI	MC(%)	Ash (%)
q_1	CAPP	12500	0.90	41	10	13.50
q_2	CSX Compliance	12500	0.80	43	7	12.00
q_3	CSX	12500	1.00	43	7	12.00
q_4	NS Compliance	12500	0.75	44	7	12.50
q_5	NS Rail	12500	1.00	44	7	12.90
q_6	NYMEX Big Sandy	12000	1.00	41	10	13.00
q_7	PRB 8800	8800	0.80	51	27	5.50
q_8	PRB 8400	8400	0.80	51	30	5.50
q_9	Pittsburgh Seam	13000	3.00	55	8	8.00

The fuel supply department contacted suppliers and was offered the following coal contracts. The supplier price and daily capacity for each product are provided in Table II.

Table 2 Supplier prices and capacities

Supplier	Price & Capacity	Coal Products								
		q_1	q_2	q_3	q_4	q_5	q_6	q_7	q_8	q_9
S_1	Price (\$/ton)	63.5	57.1	67.5	65.5	64.8	28.1	15.0	14.9	41.0
	Capacity (ton)	8640	13440	25920	0	0	0	0	0	11520
S_2	Price (\$/ton)	62.4	56.2	66.4	63.2	63.1	26.8	15.2	15.1	42.1
	Capacity (ton)	13440	11520	0	17280	0	0	0	0	13440
S_3	Price (\$/ton)	63.8	56.8	68.0	64.6	64.2	25.5	14.5	14.0	40.8
	Capacity (ton)	0	0	19200	10560	13440	18240	11520	17280	0
S_4	Price (\$/ton)	64.1	54.8	65.2	66.7	66.3	27.1	15.8	15.8	42.9
	Capacity (ton)	0	0	10560	11520	9600	12480	13440	11520	0

The power company also has the data given in Table III for its coal fired power plants. Note that not all plants are able to burn the available coal products provided from suppliers, and those are represented with a 0.

Table 3 Plant specifications

Plant	Demand (MWh)	Heat Rate (mmBTU/MWh)	q_1	q_2	q_3	q_4	q_5	q_6	q_7	q_8	q_9
Plant 1	2862	9.2	1	0	1	0	1	0	1	1	0
Plant 2	1185	9.8	0	1	0	1	0	1	0	0	1
Plant 3	820	10.2	1	0	0	1	0	0	1	1	0

Table IV gives the coal specific plant constraints which include grindability index, moisture content, and permitted maximum and minimum sulfur rate at the plants.

Table 4 Plant constraints

Plant	GI	MC (%)	S_{min} (%)	S_{max} (%)
Plant 1	[40-60]	[5-35]	0	1.2
Plant 2	[39-58]	[6-33]	0	1.9
Plant 3	[39-57]	[5.5-32]	0	3.8

Each power plant has a current inventory that is a mix of available products. Table V shows the current inventory level at each power plant. As a policy, power companies would like to keep a safety stock that is sufficient to provide three days of energy. On the other hand, in addition to current inventory and safety stock levels, companies seek to maintain fuel that is sufficient to meet two days of power demand.

Table 5 Plant coal inventories

Plant	q_1	q_2	q_3	q_4	q_5	q_6	q_7	q_8	q_9
Plant 1	29432	0	2000	0	0	0	37440	29823	0
Plant 2	0	4000	0	2450	0	34839	0	0	450
Plant 3	8000	0	0	15100	0	0	0	13376	0

In addition to coal offers, the company has to decide about transportation routes. It is possible to deliver the coal directly from the supplier to the power plant; however, the transportation cost is usually higher. Coal is shipped via train-cars on railways, barges on waterways, trucks, or by using a multimode that utilizes a trans-load location. For the multimode alternative, there are 4 trans-load locations where the coal can be transferred to another form of transportation for further shipment. The transportation costs and capacities between each point are given in Table VI and Table VII, respectively. Note that the trans-loading cost is included in transportation costs.

Table 6 Transportation costs (\$/Ton)

Location	Destination						
	T_1	T_2	T_3	T_4	Plant 1	Plant 2	Plant 3
S_1	6.95	9.65	15.68	13.47	21.75	23.52	24.60
S_2	8.25	4.50	9.20	12.35	24.48	20.45	19.40
S_3	7.32	8.85	11.45	12.25	23.43	18.26	23.16
S_4	4.60	4.20	10.25	10.10	19.45	17.26	18.06
T_1	0.00	8.46	7.99	6.11	13.72	12.21	14.49
T_2	10.92	0.00	4.53	10.17	15.06	12.47	13.58
T_3	6.79	4.19	0.00	3.24	7.13	4.65	5.77
T_4	7.79	9.66	2.86	0.00	5.40	5.87	6.74

Table 7 Transportation capacities (Ton)

Location	Destination						
	T ₁	T ₂	T ₃	T ₄	Plant 1	Plant 2	Plant 3
S ₁	7392	17040	19344	24576	19440	24720	17856
S ₂	11616	25680	18720	22128	27696	23280	16560
S ₃	10512	11232	13008	11424	26736	18240	11424
S ₄	9744	9696	9168	12096	26736	18768	9840
T ₁	0	30000	25392	33216	21984	25056	26016
T ₂	20784	0	20832	23712	29040	28608	30048
T ₃	21936	21264	0	20640	17040	25776	26688
T ₄	29424	34704	35856	0	29424	34704	35856

The transportation and coal specification data has been gathered from EIA [1] and verified in [14]. The data for the coal fired power plants has also been gathered from the same sources; however, they have been slightly modified for confidentiality reasons in the market. The illustrated case is coded in GAMS (General Algebraic Modeling System), a high level modeling and optimization tool. The solutions were obtained using a CPLEX 12.1. The computations were performed on a computer with an Intel Core 2 duo 2 Ghz CPU with 4 GB RAM. Table VIII provides the a solution to presented case study.

Table 8 Solutions for suppliers and transportation

supplier	First Trans-load Location	Second Trans-load Location	Plant	Coal Type	Amount (ton)	Transportation Cost (\$/ton)	Transportation Cost /Final Price
S ₁	-	-	1	q ₁	3472	21.75	58%
S ₂	-	-	1	q ₈	11520	19.45	55%
S ₃	T ₁	-	1	q ₇	7056	18.58	56%
S ₃	T ₁	T ₁	1	q ₁	5616	22.07	26%
S ₃	T ₂	T ₂	1	q ₇	4368	20.51	58%
S ₃	T ₂	T ₁	1	q ₁	13440	20.07	24%
S ₃	T ₁	T ₄	1	q ₁	632	18.46	22%
S ₄	T ₁	T ₁	1	q ₇	9372	16.11	50%
S ₄	T ₁	-	1	q ₇	595	15.50	49%
S ₄	T ₂	T ₄	1	q ₇	96	24.42	63%
S ₄	T ₁	T ₄	1	q ₈	5288	18.83	57%
S ₄	T ₁	T ₃	2	q ₈	372	17.24	39%
S ₄	T ₂	T ₁	2	q ₈	9696	13.38	33%
S ₄	T ₂	-	2	q ₈	5952	16.10	39%
S ₄	T ₁	T ₃	3	q ₈	5224	21.08	60%
S ₄	T ₂	T ₁	3	q ₈	6768	19.15	52%

The transportation route is represented in such a way that the first column is the beginning point (supplier), the second column is the first trans-load location, the third column is the second trans-load location, and the fourth column is the destination power plant. Notice that usage of more than two trans-load locations is also possible but no solution was found for such a case.

Based on the results shown, the demand of plant 1 is supplied from 4 suppliers in different amounts. S₁ and S₂ supply q₁, S₃ supplies q₇ and S₄ supplies q₇ and q₈. A mixed strategy for transportation seems optimum for plant 1 as all the transportation is made via different routes.

The coal demand of plant 2 is provided by S₃ and S₄ with coal type q₆. Trans-load locations T₁, T₂ and T₃ are used for transportation of coal. All of the coal demand for plant 3 is provided from S₃ with coal type q₈. Two different transportation routes using T₁, T₂ and T₃ are preferred. The total transportation cost and its ratio on final cost are also provided. Notice that when the purchase price is low, the ratio of transportation on total cost becomes higher.

The amount of coal supplied from each supplier is different. Fig.2. shows the percentage of total coal supplied by each supplier. Ignoring the coal types, a large amount of coal is supplied by S₃ and S₄, whereas a small amount of coal is supplied by S₁. Also, the decision-maker can apply a coal-type analysis for each supplier to make further comparisons.

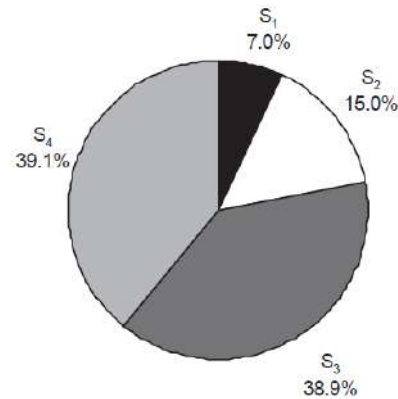


Fig. 2. Comparisons of Supplier by Total Coal Supplied

It is also useful to do a comparison for the procured coal types. Fig.3. shows the percentages of each coal type transported to the plants. It is shown that q₂, q₃, q₄, and q₅ are not preferred coal types at this time. On the other hand, the range of preferences for four coal types is relatively close, with q₈ being the most preferred and q₁ being a lesser preferred coal.

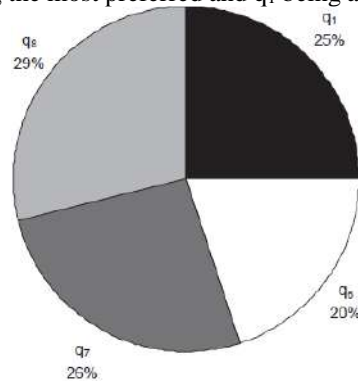


Fig. 3. Supplied Coal Types by Percentage

The results show that the coal price is more important as regards product selection than its heat content, as q₈ and q₇ have lower prices and lower heat and ash contents whereas q₆ has a moderate price and a higher heat and ash content. q₁ on the other hand has a higher price, heat and ash content, and it is less preferred while the other coal products are not preferred. The amount of coal transported via each trans-load location should also be evaluated. Fig.4. shows the usage of trans-load locations, indicating that most of the coal is trans-loaded at T₃, followed by T₂, T₃, and T₁.

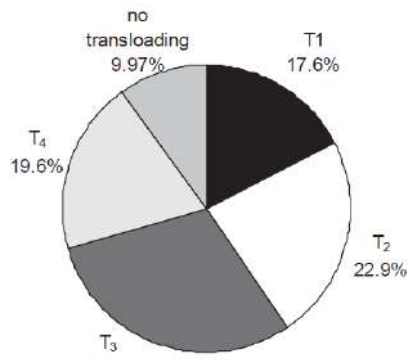


Fig. 4. Usage of Trans-Load Locations

IV. CONCLUSION

In this paper, a method is developed for the selection of the best supplier, transportation alternative, and coal orders given multiple suppliers, contracts, and multimode transportation routes in a fuel-coal supply chain. The solution method is applied to a case study for a power company located in the Midwestern USA. The results provide a mix of suppliers, transportation routes, and coal products for the power company to meet its needs. For the presented case, it is possible to do a benefit/cost analysis based on the results and this is considered for future extensions of the research. The ratio of the transportation cost in terms of the final price is presented for comparison purposes. The output analyses of the presented results are required to help the fuel supply department with future decisions. The methodology can be implemented as an integrated software using a graphical user interface (GUI) and it has the potential to be used by managers. Although the model is validated for a particular case study, the proposed methodology is applicable to manage any supply chain as it includes network constraints, demand constraints, and product characteristics. The model is especially suitable for commodities such as oil, liquefied natural gas, wheat, corn, wood, and metallic materials, with some required modifications due to the nature of the material.

REFERENCES

- [1] EIA, International Energy Outlook, Energy Information Administration report, USA, 2009, received from: <http://www.eia.doe.gov/oiaf/ieo/electricity.html>
- [2] Liang, Tien-Fu, "Integrating production-transportation planning decision with fuzzy multiple goals in supply chains", International Journal of Production Research, <http://www.informaworld.com/smpp/title~db=all~content=t713696255~tab=issueslist~branches=46-v4646:6>, (March 2008), pp.1477-1494.
- [3] Kim, Bowon, Janny Leung, Kwang Tae Park, Guoqing Zhang, and Seugnchul Lee, "Configuring a manufacturing firm's supply network with multiple suppliers", IIE Transactions, 34:8, (January 2002), pp.663-677.
- [4] Chang, Tsung-Sheng, "Best routes selection in international intermodal networks", Computers & Operations Research, 35, (2008), pp. 2877 - 2891.

- [5] Chang, Chia-Juch, Robert D. Miles and Kumares C. Sinha, "A regional railroad network optimization model for coal transportation", Transportation Research Part B: Methodological, 15:4, (1981), pp. 227-238.
- [6] Shih, Li-Hsing, "Planning of fuel coal imports using a mixed integer programming method", International Journal of Production Economics, 51:3, (1997), pp.243-249.
- [7] Sherali, H.D., R. Puri, "Models for a coal blending and distribution problem", Omega, 21:2, (1993), pp. 235-243.
- [8] Zhao, Qiu Hong, Shuang Chen, Stephen Leung, K.K. Lai, "Integration of inventory and transportation decisions in a logistics system", Transportation Research Part E: Logistics and Transportation Review, 46:6, (2010), pp. 913-925.
- [9] Ash, L., and Donald Waters, "Simulating the Transport of Coal across Canada -- Strategic Route Planning", Journal of Operations Research Society, 42:3, (1991), pp. 195-203.
- [10] McCollum, David L., "Future Impacts of Coal Distribution Constraints on Coal Cost", Institute of Transportation Studies, University of California, Davis, Research Report, 2007, UCD-ITS-RR-07-26
- [11] Tu, Hamming, Jean-Michel Guldmann, "GIS in Coal Transportation Modeling: Case Study of Ohio", Geographic Information Sciences, 7:1, (2001), pp.24-34.
- [12] Kaplan, See Stan Mark, "Rail Transportation of Coal to Power Plants: Reliability Issues", CRS Report for Congress RL34186, 2007, received from: <http://ncseonline.org/nle/crs/abstract.cfm?NLEid=1916>
- [13] Liu, Chiun-ming, "A Blending and Inter-Modal Transportation Model for the Coal Distribution Problem", International Journal of Operations Research, 5:2, (2008), pp.107-116.
- [14] Nymex, New York Merchandise Exchange, 2010, <http://www.cmegroup.com>

Modeling and Solving a Closed-Loop Reverse Supply Chain Problem in Marble Industry

Adil BAYKASOĞLU
Industrial Department, Faculty of Engineering,
University of Dokuz Eylül,
Izmir, Turkey
adil.baykasoglu@deu.edu.tr

Burcu KUBUR ÖZBEL
Industrial Department, Faculty of Engineering,
University of Dokuz Eylül,
Izmir, Turkey
burcu.kubur@deu.edu.tr

Abstract—Today, we are faced with a growing need for recycling strategies in many industries as a result of limited capacity of reserves of natural sources and rising population which leads to increasing amount of consumption and waste. Marble is one of these industries. Since considerable amount of waste materials are produced in the mining, processing and polishing stages which also have a serious impact on the environment. Therefore, companies have a social responsibility to protect the environment and ensure the sustainable use of the natural resources. Marble wastes from the processing plant can be divided into two main product groups. The first product group is large-sized pieces of marble waste and the second product group is dust waste. Large-sized piece of marble wastes are stored in marble waste storage area for reusing in plants or selling to other small firms. On the other hand, marble dust wastes are sent to recycling centers for using in different industries such as cement production, glass production etc. In this paper, a linear programming (LP) model is proposed for a remanufacturing system of marble industry, which includes both forward and reverse flows. The objective of the model is to minimize the transportation, recycling, cutting operation, holding and fixed opening costs in a reverse logistics network. Revenues obtained from selling the reused parts and solid dust wastes are also considered in the proposed model. Application of the proposed model is illustrated by a numerical example. Several closed-loop supply chain scenarios are discussed on this example in order to show the performance and applicability of the proposed model in the marble industry.

Keywords—closed-loop chains; mathematical modeling; marble industry

An Integrated Approach to the Vehicle Routing and Container Loading Problems

Adil BAYKASOĞLU
Industrial Department, Faculty of Engineering,
University of Dokuz Eylül,
Izmir, Turkey
adil.baykasoglu@deu.edu.tr

Burcu KUBUR ÖZBEL
Industrial Department, Faculty of Engineering,
University of Dokuz Eylül,
Izmir, Turkey
burcu.kubur@deu.edu.tr

Abstract—This work studies a problem of integrated three-dimensional loading and vehicle routing problem which consists of some practical thoughts related to vehicle capacity such as physical feasibility of arrangements. Despite their practical importance in transportation operations, these cases usually do not considered in a realistic way in the previous studies. This is mainly due to the fact that adding these constraints increase combinatorial complexity of problem considerably. This work aims to present a mathematical model that strengthen the formulation of these two combinatorial optimization problems (“Vehicle Routing Problem with Time Windows” and “Container Loading Problem”) in an integrated way. In order to test the quality and efficiency of the proposed mathematical model a sample problem is solved. The result of the integrated approach is also compared with the separate solution of these two problems. The test results demonstrate that the proposed approach has a potential to solve this complex problem.

Keywords—vehicle routing problem with time windows, container loading problem, mathematical modeling

Investigation of the companies' perspective on occupational health and safety culture in scope of joint health and safety agencies

Seren OZMEHMET TASAN

Industrial Engineering Department, Faculty of Engineering,
Dokuz Eylül University,
İzmir, Turkey
seren.ozmehmet@deu.edu.tr

Berkay TUNALI

The Graduate School of Natural and Applied Sciences
Dokuz Eylül University
İzmir, Turkey

Abstract— In the globalizing world; technological, scientific, artistic, and cultural developments, regardless of industry, nowadays require the need for businesses to become structured with innovative ideas, sustainability conscious developments while attending the workers' health and safety. Businesses are now obliged to ensure that employees are in a healthy and safe working environment before, during and after work within the scope of occupational health and safety (OHS) regulations. The provision of this environment is possible through the establishment and dissemination of OHS culture. With the employment law no. 6331 enacted on 2012 and the further legislations enacted due to the EU harmonization, Turkish companies are obliged to attend these issues on their own or with the help of a joint health and safety agency (JHSA). As stated by legislation No: 28512, JHSA acts as a private establishments comprised of work health and safety professionals who are authorized by the Ministry of Employment and Social Security, established to provide businesses with work health and safety services and possess the physical and medical capability required by the regulation. In this study, perspectives of companies on OHS culture were investigated.

In the scope of this study, a survey is conducted to businesses operating in Western Marmara Region that work with JHSAs to receive services for the obligations required to be fulfilled in terms of OHS. The purpose of the survey is to determine whether or not the OHS culture varies according to the demographic features of employees and reveal whether or not there is a connection between the OHS applications of the JHSAs in workplaces and the safety communication perception. The survey results are analyzed with the SPSS 21.0 program. This analysis provides a an insight of OHS culture from eight different views; i.e. procedures/policies, accidents, ergonomics, personal protective equipment, physico-social factors, awareness, training/attitude, the usage of control list that were developed by the Ministry of Labor and Social Security, especially to be used in these kinds of businesses. In this context, the results clearly show that businesses that fulfill their OHS obligations with the help of JHSAs do not fully comprehend the importance of the OHS culture and as a result they cannot internalize the concept of OHS. Inevitably, the businesses do not consider this culture as a part of their management system. Using the detailed analysis of the results, it can be clearly stated that while providing all the work health and safety services, JHSAs should also carry out awareness activities to increase businesses' understanding of the OHS concepts and implement sector specific training programs. Additionally, business should not let the agencies to provide the services but also they have to take active part in OHS management during agencies' services to form an interactive relationship and communication structure. Specifically, to overcome these types of problems, there is a greater need for conjoint attempts including both sides of the relationship.

Keywords—occupational health and safety; joint health and safety agencies; perspective investigation

Development and Implementation of Social Innovation

Burcu FELEKOGLU

Industrial Engineering Department, Faculty of Engineering,
Dokuz Eylül University,
Izmir, Turkey
burcu.felekoglu@deu.edu.tr

Seren OZMEHMET TASAN

Industrial Engineering Department, Faculty of Engineering,
Dokuz Eylül University,
Izmir, Turkey
seren.ozmehmet@deu.edu.tr

Abstract— Social innovation is finding and implementing new solutions, strategies to social problems in order to create social value and provide a sustainable life for people, society and the planet. Social entrepreneurs can either be an individual, a group/team or a firm/company who are willing to contribute to the solution of the problems we face today with social innovation projects. Every project realized by social entrepreneurs does not only contribute to the solution of the problem discussed but at the same time changes the attitudes, perceptions, behaviors and methods that cause the problem to arise. Institutions engaged in social innovation do not consist only of public institutions, foundations, associations and non-profit-making companies. Profit-oriented companies may also conduct projects for social innovation, and their gathering can make a significant contribution to a sustainable life. Since innovative social projects require multilateral work, a variety of projects have recently been produced by public, private and non-governmental organizations. In actualizing these projects usually organizational, sectoral or disciplinary boundaries need to be spanned.

The main difference that distinguishes social innovation from other innovations is that the main purpose of the innovation process is not to achieve financial gain but to aim for generating social value. The purpose of a good social innovation project depends on for whom it is done. For this reason, social innovation has been explored as the main method in solving problems such as the lack of communication emerging in the society and the coming generations and conflicts between communities, with the rapid technological development, rapid city experience and the social media entering more to our lives.

This paper focuses on successful examples of social innovation development and implementation to identify the main success factors. First, the definition of social innovation is given. Then the scope and characteristics of social innovation are discussed. Following this, main actors involved in solving social issues and their roles are mentioned. Additionally, main success factors are derived based on successful examples of social innovation development and implementation.

The case study research method, which is an empirical inquiry that investigates a contemporary phenomenon using multiple sources of evidence within its real-life context when the boundaries between phenomenon and context are not clearly evident, is used in this study. First of all, a literature review about related topics are made. Then, the appropriate cases are selected. The secondary data are gathered for each case. Then the data is evaluated and interpreted in order to find linkages between the research object and the outcomes with reference to the research questions. When examining case studies on social innovation, the reasons for the emergence of the problem in the society, the actors involved in the solution of the problem, the aim and way of their involvement, factors that affect the success are examined.

Findings demonstrate that various actors can be involved in social innovations such as government, international organizations, civil society organizations, private companies, social enterprises, social entrepreneurs, social movements, social media, universities and there is a mission and method diversity on social innovation actors. Based on the major contributions of different actors, social innovation can be considered to have two main phases, development and implementation. Main factors for successfully implementing social innovation include awareness about social issues, good problem definition, availability of resources, use of technology, having different viewpoints, collaboration with inquisitive and creative organizations for effective presentation, number of voluntaries involved, developing a strategic policy for social innovation.

Keywords— social innovation; implementation; case study; success factors

Customer Perception of Social Innovation Activities: An Investigation on Brand Image, Firm Performance and Customer Loyalty

Yasemin POLAT
Department of Industrial Engineering
Dokuz Eylül University
İzmir, Turkey
yasemin.polat@deu.edu.tr

Burcu FELEKOĞLU
Department of Industrial Engineering
Dokuz Eylül University
İzmir, Turkey
burcu.felegoglu@deu.edu.tr

A. Serdar TAŞAN
Department of Industrial Engineering
Dokuz Eylül University
İzmir, Turkey
serdar.tasan@deu.edu.tr

Abstract – Creating sustainable business success cannot be achieved only through maximizing short-term profits. Beside the economic missions, there are also social missions of businesses. Customers expect social benefits from the firms that also provides sustainability. One of the most important tools to create a positive image is social innovation activity. Consequently, social innovation is becoming important for corporations. Today's companies focus on the social and environmental problems to obtain business success to be competitive. Resource allocation in the social fields such as arts, culture, education, environmental protection, health care etc., to create a social investment strategy for it, set up partnerships with non-governmental organizations, to launch innovative initiatives to solve social problems/needs, allocating employees to the social projects are increasingly adopted strategies for social innovations by companies.

The aim of this study is to evaluate the customer perception of social innovations on brand image, firm performance and customer loyalty. A web-based survey is developed and conducted. Survey was applied to 129 people. 109 surveys were valid. In the first part of the survey, information about social innovation is provided and a sample project is mentioned. The second part contains demographic information. The third part consists of the social innovation perception questions. The data obtained from the survey have been tested using SPSS 22. Explanatory factor analysis was used in this study to identify the main factors related to customer perception of social innovation effects. Responses are also analyzed to understand whether perceived social innovation effects differ according to a number of demographic variables. T-test was used for bivariate variable (gender) and ANOVA test was performed for multivariate groups such as (income, age) and results were evaluated.

Findings demonstrate that social innovations positively impact customer beliefs and attitudes. Demographic factors make a significant difference on customer perception. Two factors explain the %55.975 of the total variance which are named as firm performance and customer loyalty. Beside the social innovation activities, customers consider other factors (such as price, quality, past experience) for buying product or service. Research indicate that the main objectives of social innovation activities in firms are creating an image that is sensitive to social issues, working for social issues and making advertisement.

Keywords— *social innovation; customer perception; brand image; firm performance and customer loyalty*

Metaheuristic Approach to Joint Preventive Maintenance and Dynamic Flexible Job Shop Scheduling

Adil BAYKASOĞLU

Industrial Engineering Department, Faculty of Engineering,
University of Dokuz Eylül,
İzmir, Turkey
adil.baykasoglu@deu.edu.tr

Fatma Selen KARASLAN

Industrial Engineering Department, Faculty of Engineering,
University of Abdullah Gül,
Kayseri, Turkey
selen.karaslan@agu.edu.tr

Abstract—A metaheuristic approach is proposed to solve joint dynamic flexible job shop scheduling (DFJSS) and maintenance scheduling problem in this study. An event-driven DFJSS with dynamic events is studied under sequence-dependent setup times. Moreover, order acceptance/rejection decision and Order Review Release (ORR) mechanism are adapted to the proposed approach in order to execute capacity adjustments regarding to customer due date requirements. A greedy randomized adaptive search procedure (GRASP) is proposed to deal with DFJSS with preventive maintenance. A preemptive goal programming based logic is considered with four objectives: mean tardiness, schedule instability, makespan and mean flow time. Benchmark problems are composed for different problem scales under dynamic events with preventive maintenance to emphasize real scheduling environment better. Fixed completion time of the preventive maintenance and non-fixed completion time of the preventive maintenance cases are considered. The results of the two preventive maintenance approaches are analyzed. Extensive computational tests are presented that the proposed GRASP algorithm can improve the job shop performance in comparison to employing basic dispatching rule based approaches for scheduling/rescheduling problems with maintenance activities.

Keywords—dynamic flexible job shop scheduling; maintenance scheduling; GRASP; combinatorial optimization; rescheduling

Analyzing the Effect of Machine Flexibility on the Scheduling Performance through Dynamic Job Shop Scheduling System

Adil BAYKASOĞLU

Industrial Engineering Department, Faculty of Engineering,
University of Dokuz Eylül,
İzmir, Turkey
adil.baykasoglu@deu.edu.tr

Fatma Selen KARASLAN

Industrial Engineering Department, Faculty of Engineering,
University of Abdullah Gül,
Kayseri, Turkey
selen.karaslan@agu.edu.tr

Abstract—The effect of machine flexibility on the scheduling performance of dynamic job shops with different flexibility levels are analyzed in this study. Four different flexibility levels are defined for operations. A greedy randomized adaptive search procedure is proposed for event-driven dynamic flexible job shop scheduling problem under sequence-dependent setup times with order acceptance/rejection decision and order review release mechanism. In order to depict the performance of the proposed algorithm, six dispatching rules are evaluated according to mean tardiness as the performance criteria for the scheduling system. Benchmark problems are presented for different problem scales under dynamic events. Performance variations of the proposed algorithm and dispatching rules among different flexibility levels are determined and analyzed statistically. It is found out after the analysis that the effect of machine flexibility on dynamic job shop performance increases as the machine flexibility increases. The results are showed that the proposed algorithm is very effective and able to provide good schedules under event-driven scheduling scenarios.

Keywords—dynamic flexible job shop scheduling; GRASP; flexibility; combinatorial optimization; rescheduling

Multi-Objective Nurse Scheduling with Preferences in a Surgical Suite

Esra Ağca Aktunç and Elif Tekin

Department of Industrial Engineering

Kadir Has University

İstanbul, Turkey

esra.agca@khas.edu.tr, elif.tekin@khas.edu.tr

Abstract— Nurse scheduling is a crucial part of hospital personnel scheduling. For effective nurse scheduling, fair workload and job satisfaction should be taken into account, because these factors directly affect the quality of service in healthcare systems. In this study, nurse scheduling constraints for a surgical suite are determined according to government regulations, hospital management requirements, and nurse preferences. First, the nurses can determine their preference for off days based on the priority of importance; for example, for their own planned surgeries, wedding day, or birthday. Then, shifts are assigned subject to the constraints that ensure fair workload in addition to the regulatory constraints. To generate an optimal nurse schedule which provides fair workload and satisfies nurse preferences for off days, a multi-objective integer program with hard and soft constraints is formulated in GAMS and solved using CPLEX as a goal programming model. Our main goal is increasing nurse motivation in order to help reduce the mistakes caused by fatigue as a result of working too many shifts. Therefore, service quality can improve in terms of patient care while optimizing the work schedule of nurses. The optimal schedules under various scenarios are compared to show the improvement in the schedule quality in terms of performance measures such as the proportion of nurse preferences met and distribution of unmet preferences.

Keywords—nurse scheduling; multi-objective optimization; integer program; goal programming; nurse preferences; fair workload distribution

I. INTRODUCTION

Healthcare systems have experienced drastic changes in the last few decades as a result of increasing population and technological developments that both increased life expectancy and incurred additional costs. There have also been budget cuts that force hospitals to use their resources more efficiently. Healthcare organizations have to work twenty-four hours a day for every day of the year and shift work is used in healthcare organizations in order to provide continuous service for patients. An important resource of a hospital is its surgical suite of operating rooms where nurse scheduling is one of the most challenging workforce planning problems since the quality of care provided by nurses depends greatly on their shift assignments and, thus, job satisfaction. Compared to the globally increasing demand for healthcare, the supply and retention of

qualified nursing staff has been insufficient [1]. This makes nurse scheduling one of the most significant issues in terms of hospital managements' expectations to use their budget wisely, patient expectations of continuous high quality care, and nurses' expectations of fair workload distribution.

Nurse scheduling is the task of specifying the work pattern for individual nurses and it can be generated manually by a head nurse or using software systems for scheduling. In most hospital units, nurse schedules are still manually developed by experienced head nurses who have to gather information from nurses about their time conflicts and have to adjust schedules as needed. However, developing a fair schedule manually is time consuming and difficult because of the vast number of possible schedules and all the constraints to consider. In practice, nurse schedules are typically developed for a period of four weeks. These schedules can be flexible, changing every period, or fixed. Fixed (or cyclical) schedules generally provide good solutions, but they cannot easily address staff preferences or fluctuating demand [2]. While generating nurse schedules, significant constraints should be considered such as observing work regulations, distinguishing between permanent and temporary staff, ensuring that night and weekend shifts are distributed fairly, allowing for leave and days off, and accommodating a range of employee preferences [3]. In this study, we address the flexible scheduling of nurses in a surgical suite where the nurse preferences for shifts are used as input to generate fair shift assignments.

The remainder of this paper is organized as follows. In section II, we review relevant work from the nurse scheduling literature. In section III, we present our integer programming model for nurse scheduling. We describe the solution methodology by formulating the goal programming model in section IV and demonstrate the use of this model with a case study in section V. We conclude the paper with our discussion of the study results and possible extensions of this work in section VI.

II. LITERATURE REVIEW

In this section, we provide an overview of existing literature on nurse scheduling, which is a special case of personnel scheduling. Personnel scheduling can be defined as generating

and arranging duty timetables for employees while considering certain work regulations, coverage constraints, or personnel preferences in order to satisfy the demand for the goods and services of organizations. Personnel scheduling has been studied widely for several decades in various application areas such as transportation systems, healthcare systems, call centers, emergency services, restaurants, hotels, and retail stores [3-8].

Our paper focuses on the nurse scheduling problem in a surgical suite (or operating theatre) that consists of operating rooms (ORs) and recovery rooms. This is especially a significant issue since the surgical suite has high operating costs and workforce planning directly impacts the efficiency of not only this unit, but also other units of the hospital that are related to the surgical suite [9]. According to Health Care Financial Management Association Report, ORs have been estimated to account for more than 40% of a hospital's total revenues, and it is both the greatest source of revenues and the largest cost center for hospitals [10]. Therefore, management of the workforce of a surgical suit is a crucial and complex issue for hospital administration. Nurse scheduling plays an important role in the efficiency of surgical suites.

In order to develop a nurse schedule, first of all, the required number of qualified nurses from various skill sets should be determined for each shift to meet the demand based on the number of patients in the wards or a predetermined patient-to-nurse ratio. Then, adequate nurses should be assigned to shifts in order to meet the service needs. The quality of nurse scheduling directly affects the quality of healthcare and job satisfaction of nurses [11]. Therefore, the schedule must strive to satisfy nurse preferences, distribute shifts fairly among nurses, and distinguish between full-time and part-time staff, in addition to abiding by work regulations determined by governments or other authorities and other hospital-specific constraints. These constraints can be classified as hard constraints, that cannot be violated, and soft constraints, that can be violated at a cost. Finding an optimal solution that minimizes the costs can be complicated regarding all these constraints at the same time. A wide range of solution methods are used to solve these complex problems, such as mathematical programming, simulation, queueing, constraint programming, and metaheuristics [3, 8].

Several studies have been published since the 1960s on various aspects of computerized healthcare personnel scheduling. Mathematical programming methods such as linear and integer programming are widely used for solving nurse scheduling problems [11]. While most of the mathematical programs have a single objective function subject to a restricted set of constraints as a result of oversimplifying assumptions, there are also several studies that use goal programming or multi-objective decision making. The most commonly used objectives of nurse scheduling problems are versions of cost minimization, that may either directly consider recruitment costs, nurse wages, and overtime costs or consider penalty costs for violating a set of soft constraints. Ozkarahan and Bailey [12] defined three goals to avoid understaffing while maximizing coverage and the utilization of nurses, then solved the problem

using a two-phase approach that first determines the day-of-week schedules and then the time-of-day schedules. Arthur and Ravindran [13] proposed a goal programming model solved similarly in two phases, first by assigning day-on/day-off patterns using goal programming and then by assigning shifts using a heuristic. Berrada et al. [14] treated the problem as a multi-objective model with hard and soft constraints, where soft constraints are used to define goals, and they solved the problem by goal programming and tabu search. Azaiez and Al Sharif [15] developed a 0-1 goal program with five goals and solved the monthly scheduling problem by subgrouping the nurses and workloads into manageable sizes. Wright and Mahar [16] compare centralized and decentralized nurse scheduling across two multi-unit hospitals and show that the centralized model performs better in terms of scheduling cost and schedule desirability.

The literature on nurse scheduling in surgical suites can be considered scarce compared to nurse scheduling in other hospital units. Belien and Demeulemeester [17] solve an integrated nurse and surgery scheduling problem using column generation. The daily surgery assignment of nurses is modeled as a multi-objective integer programming model and solved using a solution pool method and a variant of goal programming in [18]. Similarly, a nurse scheduling model with the objectives of minimizing labor costs, patient dissatisfaction, nurse idle time, and maximizing job satisfaction is presented in [19].

Although there is a considerable amount of literature on nurse scheduling, there are only a few studies that are based on nurse preferences to improve job satisfaction and that have multiple goals for equitable shift assignment among nurses. In this study, we give nurse preferences the highest priority after the demand-related hard constraints and consider multiple goals to ensure fair workload distribution. Next, we introduce our multi-objective integer programming model.

III. MODEL DEVELOPMENT

The nurse scheduling model proposed in this study is an integer programming model with the objectives of minimizing schedule cost and maximizing job satisfaction for nurses. The assumptions of our mathematical model for our multi-objective nurse scheduling problem are as follows:

1. Minimum number of required nurses in each shift is deterministic and known based on experience of demand since mostly elective surgeries are performed in the surgical suite.
2. There are two 12-hour shifts in a day: (1) from 7:00-19:00 and (2) from 19:00-7:00 (day and night shifts for 7 days a week, and 24 hours a day).
3. There are two skill classes of nurses: regular nurses and intern nurses.
4. Minimum staff level requirements must be satisfied.
5. Each nurse has to work at least 24 hours and at most 72 hours per week.

6. Nurses cannot work for more than 6 consecutive working days.
7. A nurse should not work more than 3 consecutive night shifts.
8. Each nurse works at most one shift a day. This is especially a necessary constraint for a surgical suite because of the high service level expectations and more arduous workload than other hospital units.

The notation used in the model formulation are explained below.

Sets

I	the set of nurses
J	the set of shifts in a day, where $j = 1$ for day shift and $j = 2$ for night shift
T	the set of days in the scheduling period
W	the set of weeks in the scheduling period

Parameters

p_{it}	$\begin{cases} 1, & \text{if nurse } i \in I \text{ prefers to work on day } t \in T \\ 0, & \text{otherwise} \end{cases}$
R	the number of regular nurses
NR_{jt}	the number of regular nurses required for shift $j \in J$ on day $t \in T$
NI_{jt}	the number of intern nurses required for shift $j \in J$ on day $t \in T$
h_L	lower limit on the number of hours that a nurse can work per week
h_U	upper limit on the number of hours that a nurse can work per week
cr_i	cost of regular nurse $i \in \{1, 2, \dots, R\}$ per shift
c_i	cost of intern nurse $i \in \{R + 1, \dots, I \}$ per shift

Decision Variables

$$x_{ijt} = \begin{cases} 1, & \text{if nurse } i \in I \text{ is assigned to shift } j \in J \\ & \text{of day } t \in T \\ 0, & \text{otherwise} \end{cases}$$

The mathematical model for the nurse scheduling problem is presented as follows.

Model Formulation

$$\text{Min } cr_i \left(\sum_{i=1}^R \sum_{j \in J} \sum_{t \in T} x_{ijt} \right) + c_i \left(\sum_{i=R+1}^{|I|} \sum_{j \in J} \sum_{t \in T} x_{ijt} \right) \quad (1)$$

Subject to

$$\sum_{i \in I} x_{ijt} \geq NR_{jt}, \quad \forall j \in J, t \in T \quad (2)$$

$$\sum_{i \in I} x_{ijt} \geq NI_{jt}, \quad \forall j \in J, t \in T \quad (3)$$

$$\sum_{t=7(w-1)+1}^{7w} \sum_{j \in J} x_{ijt} \geq h_L/12 \quad \forall i \in I, w \in W \quad (4)$$

$$\sum_{t=7(w-1)+1}^{7w} \sum_{j \in J} x_{ijt} \leq h_U/12 \quad \forall i \in I, w \in W \quad (5)$$

$$\sum_{j \in J} x_{ijt} \leq 1 \quad \forall i \in I, t \in T \quad (6)$$

$$x_{i2t} + x_{i1(t+1)} \leq 1 \quad \forall i \in I, t \in T \quad (7)$$

$$\sum_{j \in J} \sum_{t=k}^{k+6} x_{ijt} \leq 6 \quad \forall i \in I, k = 1, 2, \dots, |T| - 6 \quad (8)$$

$$\sum_{t=k}^{k+3} x_{i2t} \leq 3 \quad \forall i \in I, k = 1, 2, \dots, |T| - 3 \quad (9)$$

$$\sum_{t \in T} x_{i2t} \geq 3 \quad \forall i \in I \quad (10)$$

$$\sum_{j \in J} x_{ijt} - p_{it} \leq 0, \quad \forall i \in I, t \in T \quad (11)$$

$$\sum_{t \in T} x_{i2t} - \sum_{t \in T} x_{i1t} \leq 0 \quad \forall i \in I \quad (12)$$

$$\left(1 - \sum_{j \in J} x_{ijt} \right) + \sum_{j \in J} x_{ij(t+1)} + \left(1 - \sum_{j \in J} x_{ij(t+2)} \right) \leq 2 \quad \forall i \in I, t = 1, 2, \dots, |T| - 2 \quad (13)$$

$$\sum_{j \in J} x_{ijt} + \left(1 - \sum_{j \in J} x_{ij(t+1)} \right) + \sum_{j \in J} x_{ij(t+2)} \leq 2 \quad \forall i \in I, t = 1, 2, \dots, |T| - 2 \quad (14)$$

$$x_{ijt} \in \{0, 1\}, \forall i \in I, j \in J, t \in T \quad (15)$$

The initial objective function (1) minimizes the total cost of nurses assigned to shifts. Constraints (2) and (3) ensure that the required numbers of regular nurses and intern nurses are met, respectively, for each shift on each day. Constraints (4) and (5) bound the total weekly hours assigned to a nurse using the minimum and maximum allowed working hours, respectively. Constraint (6) avoids the assignment of more than one shift per day to a nurse. Assigning a day shift followed by a night shift or a night shift right before a day shift is prevented by constraint (7). According to constraints (8) and (9), a nurse can work for at most 6 consecutive days and can be assigned at most 3 consecutive night shifts, respectively. Constraint (10) ensures that each nurse is assigned at least 3 night shifts over the scheduling period. Constraint (11) avoids shift assignments on days that are not preferred by a nurse, in other words, over-assignment. Constraint (12) requires the total night shifts assigned to be at most as many as the total day shifts assigned to a nurse. Constraints (13) and (14) avoid the “0-1-0” or “1-0-1” types of assignments where a day on would be between two days off or a day off would be between two days on, which are both undesired cases from the nurse’s perspective. Constraint (15) defines the binary decision variables.

In this model, hard constraints that cannot be violated are (2)-(10) and soft constraints are (11)-(14). In the following section, the goal programming model is formulated by incorporating the penalty of violating these soft constraints in the objective function.

IV. SOLUTION METHODOLOGY

In the proposed model, soft constraints are (11)-(14). Therefore, in order to penalize the violation of these soft constraints, appropriate decision variables should be added to the model as explained below.

Goal 1: We modify the soft constraint (11) as follows:

$$\sum_{j \in J} x_{ijt} - p_{ijt} - o_{it} + u_{it} = 0, \quad \forall i \in I, t \in T \quad (16)$$

where the binary decision variables $o_{it} \in \{0, 1\}, \forall i \in I, t \in T$, and $u_{it} \in \{0, 1\}, \forall i \in I, t \in T$, represent the over- and under-assignment of shifts based on nurse preferences, respectively. It would be undesirable if a nurse is assigned to a shift on a day the nurse does not prefer as well as if a nurse is not assigned a shift

on a day the nurse prefers to work. Therefore, both of these variables are penalized using the following objective function:

$$\text{Minimize} \quad \sum_{i \in I} \sum_{t \in T} (\alpha o_{it} + \beta u_{it}) \quad (17)$$

where α is the penalty cost for assignment of a shift that a nurse does not prefer and β is the penalty cost for not assigning a shift that a nurse prefers, such that $\alpha > \beta$ because over-assignment is even more undesirable than under-assignment.

Goal 2: Soft constraint (12) is modified as follows to allow for deviations:

$$\sum_{t \in T} x_{i2t} - \sum_{t \in T} x_{i1t} - d_i^+ + d_i^- = 0 \quad \forall i \in I \quad (18)$$

where $d_i^+ \in \{0,1\}, \forall i \in I$, and $d_i^- \in \{0,1\}, \forall i \in I$, are the positive and negative deviations from the goal of assigning more day shifts than night shifts in total. The positive deviations from this goal is penalized by adding the following objective function:

$$\text{Minimize} \quad \sum_{i \in I} d_i^+ \quad (19)$$

Goal 3: Soft constraint (13) is modified as follows to allow for deviations:

$$\left(1 - \sum_{j \in J} x_{ijt}\right) + \sum_{j \in J} x_{ij(t+1)} + \left(1 - \sum_{j \in J} x_{ij(t+2)}\right) - da_{it}^+ + da_{it}^- = 2 \quad \forall i \in I, t = 1, 2, \dots, |T| - 2 \quad (20)$$

where $da_{it}^+ \in \{0,1\}, \forall i \in I, t \in T$, and $da_{it}^- \in \{0,1\}, \forall i \in I, t \in T$, are the positive and negative deviations from the goal of avoiding isolated days on. Only the positive deviations from this goal is penalized by adding the following objective function:

$$\text{Minimize} \quad \sum_{i \in I} \sum_{t \in T} da_{it}^+ \quad (21)$$

Goal 4: Soft constraint (14) is modified as follows to allow for deviations:

$$\sum_{j \in J} x_{ijt} + \left(1 - \sum_{j \in J} x_{ij(t+1)}\right) + \sum_{j \in J} x_{ij(t+2)} - db_{it}^+ + db_{it}^- = 2 \quad \forall i \in I, t = 1, 2, \dots, |T| - 2 \quad (22)$$

where $db_{it}^+ \in \{0,1\}, \forall i \in I, t \in T$ and $db_{it}^- \in \{0,1\}, \forall i \in I, t \in T$ are the positive and negative deviations from the goal of avoiding isolated days off. Only the positive deviations from this goal is penalized by adding the following objective function:

$$\text{Minimize} \quad \sum_{i \in I} \sum_{t \in T} db_{it}^+ \quad (23)$$

As a result of these goal formulations, the initial objective function is modified as follows.

$$\begin{aligned} \text{Min } z = & cr_i \left(\sum_{i=1}^R \sum_{j \in J} \sum_{t \in T} x_{ijt} \right) + c_i \left(\sum_{i=R+1}^{|I|} \sum_{j \in J} \sum_{t \in T} x_{ijt} \right) \\ & + \sum_{i \in I} \sum_{t \in T} (\alpha o_{it} + \beta u_{it}) + \sum_{i \in I} d_i^+ \\ & + \sum_{i \in I} \sum_{t \in T} da_{it}^+ + \sum_{i \in I} \sum_{t \in T} db_{it}^+ \end{aligned} \quad (24)$$

The objective function (24) is weighted sum of five different objectives: (i) minimizing the total cost of nurses assigned to shifts as in (1), (ii) minimizing the total penalty cost for the

undesired shift assignments according to nurse preferences as shown in (17), (iii-v) minimizing the total violation of soft constraints as shown in (19), (21), and (23), respectively.

Next, we describe our case study and present the computational results of our proposed model in terms of various performance measures.

V. COMPUTATIONAL RESULTS

In this section, we provide a numeric example for illustrating the nurse scheduling model presented above. Consider a surgical suite in which 30 nurses are employed in total. 8 of these nurses are intern nurses who are still in training. The other 22 regular nurses are more experienced and they have higher priority in terms of shift preferences and taking time off work. The planning horizon is four weeks (28 days, including the weekends). The minimum required number of nurses in each shift are generated based on the work regulations and are provided in Table I. The cost of a regular nurse per shift $cr_i = 3, i = 1, 2, \dots, 22$ and the cost of an intern per shift $c_i = 2, i = 23, 24, \dots, 30$.

TABLE I. MINIMUM NURSE REQUIREMENTS

	$j = 1$	$j = 2$
NR_{jt}	10	3
NI_{jt}	4	1

In order to measure the performance of the model solutions, we define the following terms (25) and (26).

Let ω be the number of nurses who are over-assigned, i.e., that are assigned a shift on a day they did not prefer to work, as shown below.

$$\omega = \sum_{i \in I: o_{it}=1} 1 \quad (25)$$

Let ρ be the ratio of the total number of over-assigned shifts to the maximum possible number of over-assigned shifts, i.e., the total number of days that nurses do not prefer to work on, as shown below.

$$\rho = \frac{\sum_{i,t} o_{it}}{|I|*|T| - \sum_{i,t} p_{it}} \quad (26)$$

The optimization model is formulated using GAMS 24.6 and solved using CPLEX 12.6 software on a 2.20GHz Windows laptop computer with 6GB RAM.

Base Case Scenario 1:

In our Base Case Scenario 1 all nurses are available on all days over the planning horizon, i.e., $p_{it} = 1, \forall i \in I, t \in T$. Assuming that $\alpha = \beta = 1$, the optimal value for the objective function (24) is $z^* = 1708$, $\sum_{i,j,t} x_{ijt} = 504$, which is exactly the total minimum required number of nurses (18 nurses/day*28 days=504 nurses), and $\sum_{i,t} u_{it} = 336$. In this case, since there cannot be any over-assignment, $\rho = 0\%$.

Base Case Scenario 2:

The other extreme is having all preferences set to zero, i.e., $p_{it} = 0, \forall i \in I, t \in T$. Assuming that $\alpha = \beta = 1$, the optimal value for the objective function (24) in this scenario is $z^* = 1895$, $\sum_{i,j,t} x_{ijt} = \sum_{i,t} o_{it} = 505$. In this case, $\rho = 60.11\%$.

These base case scenarios show us the limits on the objective function value and the limits on the quantity $\sum_{i,t} o_{it}$, as well as ρ , when $\alpha = \beta = 1$ at the two extreme nurse preference values.

Two different Preference Scenarios (PS) are developed to test the performance of the scheduling model. The first scenario, PS1, is designed such that 4 regular nurses each take a week off consecutively and all the other nurses have a preference of taking one weekday and one weekend day off. The preference matrix in this scenario results in the total number of undesired days by nurses to be $|I| * |T| - \sum_{i,t} p_{it} = 260$. In the second scenario, PS2, 4 more regular nurses each take a week off in addition to the PS1 preferences. Therefore, PS2 is a more restrictive scenario in terms of nurse availability. The total number of undesired days by nurses are $|I| * |T| - \sum_{i,t} p_{it} = 280$ in PS2. The problem is solved for these scenarios with different penalty cost α values for not meeting nurse preferences and all the problem instances are solved to optimality within at most 2 seconds. We present the optimal solutions of the proposed model for the two scenarios for various α values in Table II and Table III below.

When PS1 is used, the best possible schedule in terms of the total number of over-assignments is achieved for $\alpha \geq 5$ and at least 28 over-assignments can be made for at least 14 nurses as can be seen from Table II. There is a cost of 112 units for reducing the number of nurses over-assigned, ω , from 17 to 14.

According to the results shown in Table III, when the more restrictive PS2 is used, the best possible schedule in terms of the total number of over-assignments is achieved for $\alpha \geq 8$ and at least 32 over-assignments can be made for at least 17 nurses. PS2 is resulting in less under-assignment as expected, because the maximum possible under-assignments is less than that in PS1

TABLE II. RESULTS FOR PS1

α	z^*	$\sum_{i,t} o_{it}$	$\sum_{i,t} u_{it}$	da_{it}^+	db_{it}^+	ω	ρ
1	1551	9	14	6	17	25	0.0346
2	1566	32	108	2	20	20	0.1231
3	1597	30	106	4	25	16	0.1154
4	1630	30	106	5	27	17	0.1154
5	1655	28	104	8	31	17	0.1077
6	1683	28	104	8	31	15	0.1077
7	1711	28	104	8	31	15	0.1077
8	1739	28	104	8	31	16	0.1077
9	1767	28	104	8	31	14	0.1077
10	1795	28	104	8	31	15	0.1077

TABLE III. RESULTS FOR PS2

α	z^*	$\sum_{i,t} o_{it}$	$\sum_{i,t} u_{it}$	da_{it}^+	db_{it}^+	ω	ρ
1	1534	44	100	3	15	21	0.1571
2	1570	40	96	1	21	22	0.1429
3	1609	37	93	4	29	19	0.1321
4	1643	34	90	7	38	17	0.1214
5	1678	32	87	11	46	17	0.1143
6	1746	32	88	11	44	17	0.1143
7	1771	32	87	13	48	17	0.1143
8	1746	32	88	11	44	17	0.1143
9	1803	32	88	11	44	17	0.1143
10	1835	32	88	11	44	17	0.1143

due to regular nurses having more days off preferred.

The positive slack variable for constraint (18), d_i^+ , is almost always zero, which means that the total day shift assignments almost never exceed the total night shift assignments.

In Fig. 1, the effect of increasing the penalty cost for over-assignment (α) on the proportion of over-assignments (ρ) is shown. Increasing α not only reduces ρ and the total over-assignments, but also the number of over-assigned nurses. This results in higher nurse satisfaction in terms of their shift preferences.

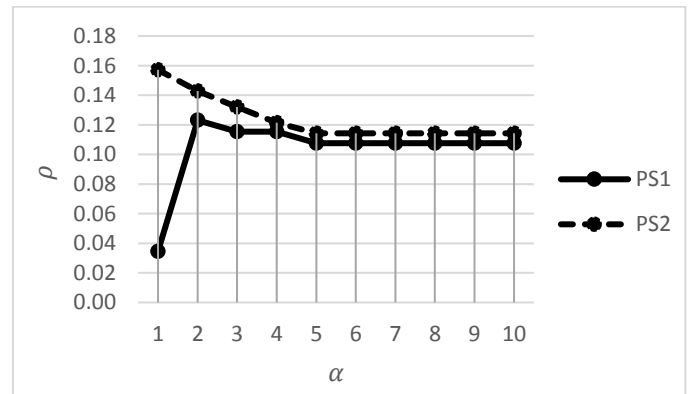


Fig. 1. The proportion of over-assigned shifts, ρ , for various α levels for the two preference scenarios, PS1 and PS2.

VI. CONCLUSIONS

In this study, we focus on the nurse scheduling problem where nurse preferences are given the highest priority after meeting the demand-related constraints that cannot be violated. We develop a multi-objective integer programming model with

hard and soft constraints and solve the model using goal programming. The model is designed to produce the best possible schedule in terms of meeting the shift preferences of nurses and fair distribution of workload. We illustrate the performance of the proposed model with an example under two different nurse preference scenarios. Computational results show that the multi-objective nature of the model leads to higher job satisfaction for nurses by avoiding the assignment of shifts that are not preferred, by avoiding isolated days on or off, and by avoiding unbalanced night shift assignments.

This model can be extended to allow more shifts per day, express the workforce requirements by surgery types, and to consider multiple skill sets for nurses based on these surgery types. Another extension could be using stochastic demand as input rather than deterministic demand so as to include emergency surgeries. Our model considers a wide set of constraints already, however, there are other scheduling constraints in the literature that can easily be added to this model such as constraints dealing with annual vacations or minimum number of weekend days off.

REFERENCES

- [1] J.E. Oulton, "The global nursing shortage: An overview of issues and actions," *Policy, Politics, & Nursing Practice*, vol. 7(3), pp. 34S-39S, 2016.
- [2] E.K. Burke, P. De Causmaecker, G.V. Berghe, and H. Van Landeghem, "The state of the art of nurse rostering," *Journal of Scheduling*, vol. 7(6), pp. 441-499, 2004.
- [3] A.T. Ernst, H. Jiang, M. Krishnamoorthy, and D. Sier, "Staff scheduling and rostering: a review of applications, methods and models," *European Journal of Operational Research*, vol. 153(1), pp.3-27, 2004.
- [4] K.R. Baker, "Workforce allocation in cyclical scheduling problems: A survey," *Operational Research Quarterly* (1970-1977), vol. 27(1), pp. 155-167, 1976.
- [5] J.M. Tien, and A. Kamiyama, "On manpower scheduling algorithms," *Siam Review*, vol. 24(3), pp. 275-287, 1982.
- [6] D. Bradley and J. Martin, "Continuous personnel scheduling algorithms: A literature review," *Journal of the Society for Health Systems*, vol. 2(2), pp. 8-23, 1991.
- [7] S. Bechtold, M. Brusco, and M. Showalter, "A comparative evaluation of labor tour scheduling methods," *Decision Sciences*, vol. 22(4), pp. 683-699, 1991.
- [8] J. Van den Bergh, J. Beliën, P. De Bruecker, and E. Demeulemeester, "Personnel scheduling: A literature review," *European Journal of Operational Research*, vol. 226(3), pp. 367-385, 2013.
- [9] I. Marques, M.E. Captivo, and M. Vaz Pato, "A bicriteria heuristic for an elective surgery scheduling problem," *Health Care Management Science*, vol. 18(3), pp. 251-266, 2015.
- [10] D. Sitompul and S. Radhawa, "Nurse scheduling: a state-of-the-art review," *Journal of the Society for Health Systems*, vol. 2(1), pp. 62-72, 1990.
- [11] B. Cheang, H. Li, A. Lim, and B. Rodrigues, "Nurse rostering problems - a bibliographic survey," *European Journal of Operational Research*, vol. 151(3), pp. 447-460, 2003.
- [12] I. Ozkarahan and J.E. Bailey, "Goal programming model subsystem of a flexible nurse scheduling support system," *IIE Transactions*, vol 20(3), pp. 306-316, 1988.
- [13] J.L. Arthur and A. Ravindran, "A multiple objective nurse scheduling model," *AIIE Transactions*, vol. 13(1), pp. 55-60, 2015.
- [14] I. Berrada, J.A. Ferland, and P. Michelon, "A multi-objective approach to nurse scheduling with both hard and soft constraints," *Socio-Economic Planning Sciences*, vol. 30(3), pp. 183-193, 1996.
- [15] M.N. Azaiez and S.S. Al Sharif, "A 0-1 goal programming model for nurse scheduling," *Computers and Operations Research*, vol. 32(3), pp. 491-507, 2005.
- [16] D.P. Wright and S. Mahar, "Centralized nurse scheduling to simultaneously improve schedule cost and nurse satisfaction," *Omega*, vol. 41(6), pp. 1042-1052, 2013.
- [17] J. Belien and E. Demeulemeester, "A branch-and-price approach for integrating nurse and surgery scheduling," *European Journal of Operational Research*, vol. 189(3), pp. 652-668, 2008.
- [18] A. Mobasher, G. Lim, J.F. Bard, and V. Jordan, "Daily scheduling of nurses in operating suites," *IIE Transactions on Healthcare Systems Engineering*, vol. 1(4), pp. 232-246, 2011.
- [19] G.J. Lim, A. Mobasher, and M.J. Côté, "Multi-objective nurse scheduling models with patient workload and nurse preferences," *Management*, vol. 2(5), pp. 149-160, 2012.

Class-Based Warehouse Location Allocation for Homeware Products

Esra Ağca Aktunç, Halil Argun, Erkin Gökçe

Department of Industrial Engineering

Kadir Has University

İstanbul, Turkey

esra.agca@khas.edu.tr, halil.argun@stu.khas.edu.tr, erkin.gokce@stu.khas.edu.tr

Abstract— This study focuses on building a layout plan by allocating storage space to products in a warehouse of a homeware retailer which allows for the minimum total travel distance of operators for order picking or placing. The study is carried out by (1) performing regression analysis for sales forecasting for each product class, (2) applying Analytical Hierarchy Process (AHP) for determining product class weights, and (3) formulating and solving an integer programming model to minimize the weighted total distance between storage locations, collecting area, and loading dock using GAMS. Optimal solution results in 26.8% less distance required for order picking than the previous layout.

Keywords—warehouse planning; storage location allocation; integer programming; AHP

I. INTRODUCTION

Storage of goods in warehouses has emerged with the purpose of protection of basic necessities from environment and climate conditions. Warehouse systems have changed and improved in terms of scope, purpose, and implementation with the improvement of industrial systems. Warehouses have become essential components of the supply chain of companies in the increasingly globalized and competitive world market. Nowadays, warehousing is commonly utilized in an attempt to not only store and protect goods but also to provide continuous raw material or product flow, to fulfill customer orders, and to carry out other relevant tasks such as packaging or inspection [1]. Producers purchase vast amounts of raw materials to be used in production to minimize the cost and time spent for raw material supply and they store them in their warehouses for later use at the expense of inventory holding cost. In order to reduce inventory holding costs, warehouse operations should be controlled such that deliveries are timely and storage space is available when needed. Well-designed storage systems, selection of appropriate storage policy and methods, and determination of the order in which the goods are stored increase the efficiency of warehouses and the whole supply chain [2].

The main areas in a warehouse are loading and unloading docks and storage area. Warehouses can be designed to use different levels of automation for storing and picking items. Operations can be manual (picker-to-product), automated

(product-to-picker), or completely automatic [3]. In a manual warehouse system, products need to be stored or distributed by operators and the location allocation of products affects the time and effort spent for order picking, thus, the performance of warehouse operations significantly. There are several storage location allocation policies such as randomized, dedicated, or class-based storage and the optimal policy can be different for each warehouse depending on the products and operations involved. This work focuses on building a layout plan by allocating storage space to classes of products in a distribution warehouse of a homeware company where manual order picking policy is practiced. The main issue that the company faces is late deliveries of items due to the time picking randomly stored products requires after an order is received. The goals of this study are (1) to determine the best location of different classes of products in a warehouse, (2) to minimize total weighted travel distance and order picking time, and (3) to maximize warehouse utilization.

The remainder of this paper is organized as follows. In section II, we provide a review of the relevant warehouse management literature. In section III, we present our integer programming model for storage location allocation. We describe our solution methodology in section IV and demonstrate the use of this model for a textile products warehouse in section V. We conclude the paper with our discussion of the study results and possible extensions of this work in section VI.

II. LITERATURE REVIEW

Order picking is the task of collecting items requested by customers from their storage locations and it is the most expensive operation in a warehouse, especially when the system is manual, in terms of the time and labor it requires. The cost of order picking is estimated to be almost 55% of the total warehouse expenses [4]. In our study we consider a distribution warehouse that operates with manual order picking policy. The time and labor spent for order picking depends on the layout, location of the goods, classification of the goods, and picking method. Considering the vast number of times that warehouse employees need to pick orders, even a small improvement of these factors would have a remarkable effect on the performance of warehouse operations.

Storage location assignment can be made by forward-reserve allocation, separating the bulk stock in a reserve area and the pick stock in a forward area [4]. Most frequently used storage policies are random storage, closest open storage, dedicated storage, full-turnover storage, and class-based storage. Random storage may increase space utilization, but causes long travel distance. At the other extreme, dedicated storage can result in low space utilization, but order picking is easier. In full-turnover storage, products with highest turnover rates are located in easier to reach areas. Class-based storage combines mainly dedicated storage and full-turnover storage. Products can be classified using ABC analysis where the fastest moving products are in class A.

Retail stores also require efficient location allocation of products to improve product visibility and accessibility. Hwang, Choi, and Lee develop a model for shelf space allocation and inventory control with an objective to maximize the retailer's profit [5]. Chen and Lin apply the multi-level association rule mining to the problem of product assortment and shelf space allocation for a retailer [6].

Making decisions based on the distances in the warehouse and product classifications are common features of warehouse storage allocation studies. Roodbergen and Vis study travel length expressions for two different route heuristics and they use these expressions for optimization of the warehouse layout [7]. Ng developed a weighted linear optimization model for solution of ABC stock classification model. All criteria are converted to a single scalar score and stock classification is performed with the ABC method with the evaluated score [8]. Bragg emphasized the ABC classification to be an effective method in the majority of research done in this area [9]. He recommended the assignment of location codes to all inventory locations. Öñüt et al. planned a particle swarm optimization algorithm to design a multi-level unit load warehouse employing class-based storage where classification is made in terms of effectiveness [10]. Heragu et al. develop a mathematical model for product allocation and determining the functional area size simultaneously with a heuristic algorithm that minimizes handling and storage costs [1].

The relevant research on order picking and storage allocation suggests that class-based storage results in a better warehouse performance. We present our mathematical model in the next section.

III. MODEL DEVELOPMENT

We develop an integer linear programming model that will find the storage location allocation that has the minimum weighted distance from loading dock and collecting area for all products. Assumptions of the model are as follows:

- Storage locations are represented on a two dimensional space such that the vertical racks are merged into one storage location.
- Storage locations have equal space and are identical, i.e., any product class can be stored in any storage location.

- The minimum unit of products is called a *pallet* which is equivalent to the capacity of a single storage location.
- Distances are measured from the center of each storage location to the center of the collecting area or the loading dock.
- Euclidean-distances are used considering the shortest (straight) path from the storage location to the end of an aisle and the shortest path from the end of an aisle to the destination (collecting area or loading dock).
- Even though demand is stochastic, the maximum number of pallets of products of each class that needs to be stored in the warehouse can be determined based on historical sales data.

The notation used in model formulation is defined below.

Sets

- I the set of product types stored in the warehouse
 J the set of storage locations in the warehouse

Parameters

- d_j distance between storage location $j \in J$ and loading dock of the warehouse
 k_j distance between storage location $j \in J$ and the collecting area
 W_i AHP-based weight of product type $i \in I$
 P_i total number of pallets of product type $i \in I$ to be stored in the warehouse

Decision Variables

- x_{ij} binary variable that is equal to 1 if product type $i \in I$ is stored in storage location $j \in J$

The model formulation is shown below.

$$\text{Min } z = \sum_{i \in I} \sum_{j \in J} W_i (d_j + k_j) x_{ij} \quad (1)$$

Subject to

$$\sum_{i \in I} x_{ij} \leq 1 \quad \forall j \in J \quad (2)$$

$$\sum_{j \in J} x_{ij} \geq P_i \quad \forall i \in I \quad (3)$$

$$x_{ij} \in \{0,1\} \quad \forall i \in I, j \in J \quad (4)$$

The objective function (1) is to minimize the total weighted distance to loading dock and collecting area for each product with the product weights. Constraint (2) ensures that there has to be one pallet in one cell. Constraint (3), uses the total amount of each product type as the lower bound on the number of pallets placed. Constraint (4) is for the binary decision variables.

Next, we discuss the methods used for obtaining the required input parameters and the solution of the optimization model.

IV. SOLUTION METHODOLOGY

In order to find the optimal storage location allocation of product classes, first we need to determine (1) the sales forecast for each product class, and (2) weights for each product class based on the share of a product class in total sales. Below we explain the procedure used to obtain the aforementioned values.

A. Regression Analysis

Regression analysis is used for estimating relationships between two or more variables. The knowledge of the existence of relationship between variables, and if exists its strength can be acquired with regression analysis. Linear regression demonstrates the relationship between variables as dependent and independent variables with a linear equation. In the general multiple linear regression model, there are p independent variables and the regression model is $Y_i = \beta_0 + \beta_1 x_{i1} + \beta_2 x_{i2} + \dots + \beta_p x_{ip} + \varepsilon_i$, where x_{ij} is the i^{th} observation on the j^{th} independent variable, and where the first independent variable takes the value 1 for all i (so β_1 is the regression intercept). The least squares parameter estimates are obtained by solving the system of p linear equations. We use linear regression to forecast sales of product classes so that the maximum number of pallets to be stored in the warehouse can be determined. We demonstrate sales forecasting for our case study in section V.

B. Analytic Hierarchy Process

Analytical Hierarchy Process (AHP) is a decision making method that involves pairwise comparisons of criteria and relies on expert judgement to prioritize these criteria [11]. At the top of the hierarchy, there is the goal of the decision. At the lower levels of hierarchy the elements that contribute to the goal exist. Details of these elements can be increased at the lower levels. At the lowest level of the hierarchy, decision alternatives or options exist. Based on the decision hierarchy, pairwise comparison matrices are constructed. Upper level elements are used to compare the elements in the level below. Priorities for each element are found and finally the overall priority of each element is obtained. AHP is used for finding the weights of homeware product types based on the quantity, income, and volumetric weight criteria in section V.

V. CASE STUDY AND COMPUTATIONAL RESULTS

Our case study is based on one of the most popular textile companies in Turkey that entered the Turkish market in 2008. As of the end of 2016, the company has more than 280 stores in Turkey and more than 70 stores in other countries such as Bulgaria and Ukraine. The company has two warehouses. One of them is located in Gebze, Kocaeli. It is used for products which are shipped to stores. This warehouse has 11,300 m² and up to 130,000 products can be stored here. There are 110 employees that can collect or load approximately 18,000 pallets within their daily operations. The second warehouse is located in Akyazı, Sakarya. It is used for products of the online store and returned products. This warehouse has 5,000 m² and up to 60,000 products can be stored here. There are 55 employees that can process approximately 9,000 pallets per day. Both of these

warehouses operate with a randomized storage method and manual order picking. In our case study, we focus on the Akyazı warehouse since online shopping has recently increased and timely delivery of products purchased online is deemed more important at this point in terms of customer satisfaction.

Necessary inputs are the physical distance between each storage location and the order collecting area, k_j , the distance between each storage location and the loading dock, d_j , and the AHP-based weight of each product class, W_i . These input data are determined and the integer programming model is solved as explained in the following subsections.

A. Distances

The physical layout of the warehouse consists of 46 rows of storage space with five racks vertically. In order to work on a two-dimensional layout, five racks in one column are considered as a single storage location that can contain one pallet of products. In each row there are 68 columns, therefore, our storage area can be represented as a 46-by-68 matrix with 3128 cells where each cell represents a storage area, i.e., $J = \{1, 2, \dots, 3128\}$.

We calculate the distance for each cell to the loading dock and to the collecting area in the warehouse, therefore we created two matrices for distance. For example, we calculate the distance between cells and the collecting area using Euclidean distances as shown in Fig. 1. A storage location $j \in J$ can have a distance of $k_j = a$ or $k_j = x + y$ depending on its location in the aisle.

B. Sales Forecast

The products are grouped in 17 classes, i.e., $I = \{1, 2, \dots, 17\}$, such as “Accessories”, “Blankets”, or “Carpet & Rugs”. The number of products in each class sold in each month between 2010 and 2015 are obtained and converted to the number of pallets by dividing the number of products by the pallet capacity for each product class. By using linear regression, we performed the sales forecast for each month in 2016 based on the same month's sales in the past six years such that the seasonal changes in sales are accounted for. The results of the linear regression are adjusted according to expert opinion about the sales of each product class and the warehouse capacity that can be used for these products. The sales forecast in terms of pallets is used for choosing the maximum number of pallets for each product class as parameter P_i , $i \in I$, as shown in Fig. 2.

C. Product Class Weights

The weight for each product class is determined through AHP using Super Decision software. First, a goal node is created in the program and three criteria are added: (1) quantity expected to be stored, (2) income obtained from sales, and (3) volumetric weight. The alternatives are defined as the product classes. The goal node is connected to criteria and criteria is connected to alternatives as can be seen in Fig. 3.



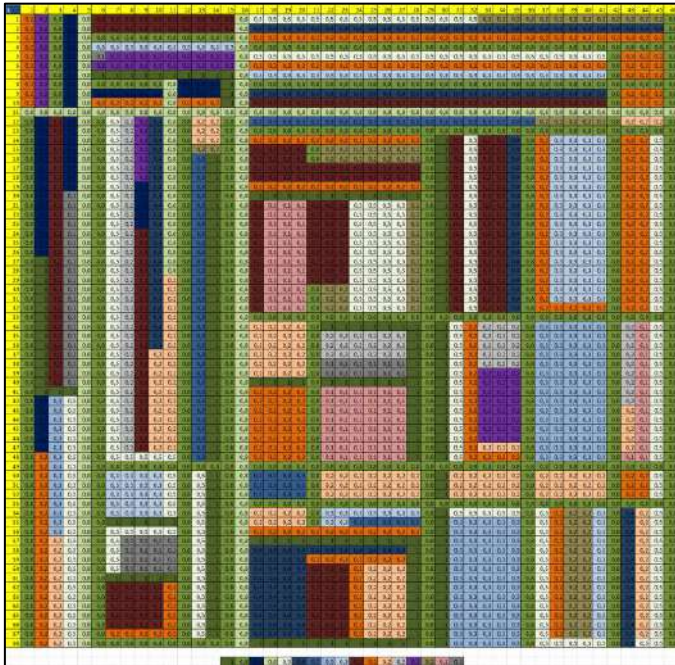


Fig. 6. Optimal randomized location allocation in the warehouse.

When the proposed class-based storage policy is used, the optimal objective function value for the proposed model with the class-based storage policy is 177,121 m. This is the sum of distances of each product from the dock and collecting area multiplied by the product class weights. The optimal solution leads to a location allocation for the 17 product classes as shown in Fig. 7, placing more demanded product classes in closer locations to the collecting area and the loading dock.

Comparison of the two policies shows that the proposed class-based storage decreases the total weighted distance by 26.8%. By using this model, warehouse employees will take fewer steps and they will collect products and prepare the orders faster than in the randomized model. In the long run, if the company uses this model they may not need as many as 55 employees in a single warehouse to maintain the same level of service. As this warehouse is mostly for online store products, the company can improve customers' online shopping experiences by implementing a product class-based storage.

VI. CONCLUSIONS

The main objective of our project was to construct a model to allocate storage locations for products to improve the order picking performance. An integer programming model is used to minimize a distance measure weighted by product class priorities. Linear regression is used to forecast sales and AHP is used to determine product class priorities or weights. The results show that the class-based product locations result in shorter travel distances and, thus, time. As stated in the comparison section, results are 26.8% more effective than the randomized product storage. Model results are satisfying and this work is suggested to be applied at the company warehouse.

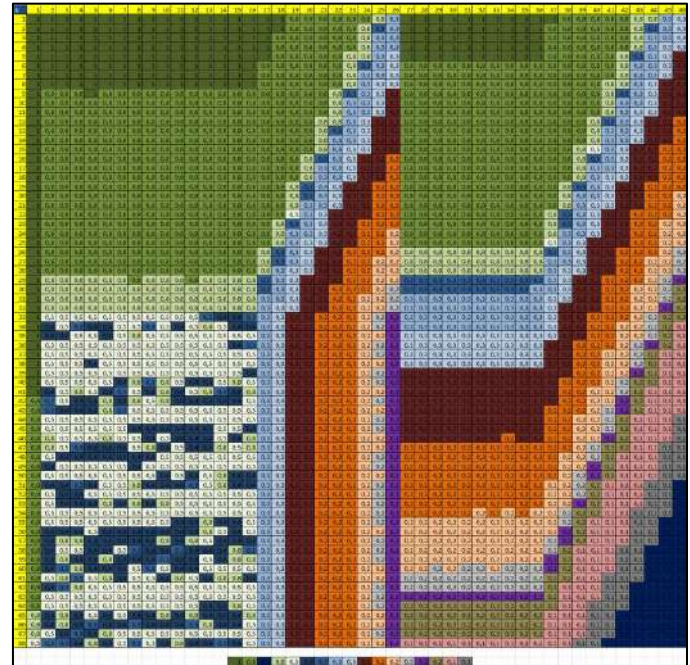


Fig. 7. Optimal class-based location allocation in the warehouse.

However the model has some limitations. The model can be improved by considering the specific order picking algorithm to evaluate distance travelled more accurately. Besides, five racks of items are assumed as one pallet to achieve a reasonable problem size in a two dimensional system, so, the model can be expanded to a three dimensional model. Additionally, more store constraints can be added on volume and weight of products, for example, heavy products are better stored in lower racks than higher racks.

Warehouses are vital elements of a supply chain and any improvement of the warehouse affects the supply chain performance. The proposed product storage location allocation model in this study is shown to have a strong potential to improve the order picking process and lead to more timely deliveries.

REFERENCES

- [1] S.S. Heragu, L. Du, R.J. Mantel, and P.C. Schuur, "Mathematical model for warehouse design and product allocation," *International Journal of Production Research*, vol. 43(2), pp. 327–338, 2005.
- [2] B. Özyörük and S. Ak, "A model to arrange warehouse layout effectively: Application in an electronic firm," *Türkiye Bilim Araştırma Vakfı Bilim Dergisi*, vol. 5(1), pp. 21–29, 2012.
- [3] J.P. van den Berg and W.H.M. Zijm, "Models for warehouse management: Classification and examples," *International Journal of Production Economics*, vol. 59, pp. 519–528, 1999.
- [4] R. de Koster, T. Le-Duc, and K.J. Roodbergen, "Design and control of warehouse order picking: A literature review," *European Journal of Operational Research*, vol. 182(2), pp. 481–501, 2007.
- [5] H. Hwang, B. Choi, and M.J. Lee, "A model for shelf space allocation and inventory control considering location and inventory level effects on

- demand," International Journal of Production Economics, vol. 97, pp. 185-195, 2005.
- [6] M.C. Chen and C.P. Lin, "A data mining approach to product assortment and shelf space allocation," Expert Systems with Applications, pp. 976-986, 2007.
- [7] K.J. Roodbergen and I.F. Vis, "A model for warehouse layout," IIE Transactions, vol. 38(10), pp. 799-811, 2006.
- [8] W.L. Ng, "A simple classifier for multiple criteria ABC analysis," European Journal of Operational Research, pp. 344-353, 2007.
- [9] S. Bragg, Inventory Best Practices, 2nd ed., Hoboken, New Jersey: John Wiley & Sons, Inc, 2004.
- [10] S. Öntüt, U.R. Tuzkaya, and B. Doğaç, "A particle swarm optimization algorithm for the multiple-level warehouse layout design problem," Computers & Industrial Engineering, vol. 54(4), pp. 783-799, 2008.
- [11] T.L. Saaty, Decision Making for Leaders: The Analytic Hierarchy Process for Decisions in a Complex World, 2008.

A Study of Adopter Categories among Healthcare Personnel in a Hospital in Turkey

Çiğdem SİCAKYÜZ

Industrial Department, Faculty of Engineering,
University of Çukurova,
Adana, Turkey
csicakyuz@live.de

Oya Hacıre YÜREĞİR

Industrial Department, Faculty of Engineering,
University of Çukurova,
Adana, Turkey,
oyuregir@yahoo.com

Abstract— Diffusion of innovations is a theory developed by Rogers that examines to explain how, why, and at what rate new ideas and technology disperse. Rogers suggests that the innovation itself, communication channels, time, and a social system are the main elements of generating new idea, and humans are the key for spreading the innovation.

Any idea, practice, process or technology that is perceived as new by people or organization can be considered as innovation. Adopters are individuals, but can also be organizations such as firms, hospitals or schools. Rogers offers five categories of adopters in order to systematize the usage of adopter classes in diffusion research. Adopter categories are defined as pioneers, early adopters, early majority, late majority, and laggards according to the degree of accepting a new idea.

The purpose of this study is to classify healthcare personnel in hospitals in Turkey according to their acceptability of new technology (information systems) based on Roger's Diffusion of innovation theory. With this framework, hospital management can have the opportunity to predict the risks of innovation by evaluating their own personnel in an implementation of new technology or idea. Thus the management can manage the change easily.

The survey has been applied on a total of 149 health personnel from the hospitals called "Adana Numune" in Adana and the results are compared with Roger's innovation categories. The individual innovation measurement model of Hurt et al. (2013) was used to evaluate the degree of innovativeness of health staff. First, the data were compiled and formulated for each category based on the categories of Rogers with the help of MS Excel (2007). Then the data were analyzed with SPSS 21 software program and descriptive statistics were generated.

As a result, while Roger's innovation categories were constructed from five classes, four classes emerged in this study. There were no pioneers among the adopters of health personnel in the hospital. The class of traditionalists known as "Laggards" was only 7% in this study. According to Roger, this value is 16%. Late Majority (34%) category defined by Roger is greater than the results of this study (21.5%). The percentage of the personnel in the Early Majority group is more than half (61.1%) of the respondents while it was mentioned as 34% according to Rogers. Only 16.8% respondents belong to the Early Adopters category.

In conclusion, the hospital has the most personnel from the category of Early Majority. This means that these employees adopt the innovation longer time later than pioneers and early adopters. Their social statuses are above the average, they are both cost sensitive and also risk averse. The management of the hospital has to support them by convincing the benefits of innovation since seldom they behave as opinion leaders in the system and they prefer to interact frequently with peers.

Keywords— *diffusion theory; innovation; adopter categories; healthcare*

A Decision Support System for the Optimum Log Transportation

Ahmet Yücekaya

Department of Industrial Engineering, Faculty of Engineering,

Kadir Has University

İstanbul, TURKEY

E-mail: ahmety@khas.edu.tr

Abstract— Forest product industries deal with loggers, sometimes directly with wood dealers, to cut, shape and transport logs from different locations to different regions. The number of trucks are limited and the drivers have defined work hours and they have to return to hub at the end of their travel. The problem is a variant of truck scheduling problem and it includes time windows, demand constraints and multiple visits. The objective is to determine the most efficient route for given number of trucks, mills, loggers and load demand from the mills. In this paper, the problem is formulated as an integer programming model and a spreadsheet based decision support system is designed to help operation managers to schedule the deliveries. The proposed approach is validated using a real case study and the results are implemented in a Decision Support System for the operation managers

Keywords—log transport; vehicle routing; integer programming; decision support system

I. INTRODUCTION

Especially in the southern US, trees are harvested and processed using what is termed a ‘Tree-length’ approach. The felled trees are first processed (removal of remaining limbs and tops) either manually by capable log makers or by using sophisticated machines. Then the logs are transported to the specific mills such as saw mills and paper mills which are already established in a certain location.

Forest product industries deal with loggers, sometimes directly with wood dealers, to cut, to shape and transport from different locations to different regions. The main problem is that the locations that woods being cut are far away from the actual factories or the regions, so trucks are assigned to make transportations. Most of the time trucks transport the loggers and woods from one location to other and return back as empty; so it causes lots of time consumption and cost increases. In order to make this process efficient and cut the cost and time consumptions, optimal routes and truck transportations method should be found.

Forest industry is forced to be more careful about their costs. The industry in other countries have invested in logging technology and lowered delivered wood costs through

innovation in logistics and the Forest industry need to be decrease their cost in order to compete. Loggers are looking for ways to lower their operating costs.

Currently the scheduling of trucks to loggers and mills is done manually and they do not utilize any solution method to solve the problem efficiently.

The problem is to find optimal route for given number of trucks, mills, loggers and load demand from the mills from loggers. Each truck will be scheduled to some routes and the demand will be met along with the minimized cost.

There are some researches about the log truck scheduling problem that are considered in the literatures of transportation and routing management. Road planning and transportation operations in forestry gets 40% of the costs. Any improvement can help save money in current logistics system.

As the log-truck scheduling problem is a subset of vehicle-routing problem, the researches are classified in vehicle routing studies. Relevant literatures are being reviewed in this chapter.

Gerdesson [1] has made an attempt to solve the vehicle-routing problem with trailers. The problem is solved in two phases. Construction heuristics are first used to obtain a feasible solution and then improvement heuristics are used to obtain an improved solution from the initial solution.

Chao [2] models a truck and trailer routing problem and uses the tabu search heuristic to solve the problem. The customers are assigned to the trucks by relaxing the integrality constraint and obtaining a linear initial solution. Sumichrast et al. [3] have compared the solutions obtained by a heuristic algorithm with that of a lower bound integer programming solution from a commercial solver. The problem size used in the paper was small in terms of demand met for the day and in the number of trucks used to meet the demand.

Thangiah et al. [4] have developed a heuristic algorithm for the vehicle routing problem with backhauls and time windows. The loading time, unloading time and waiting time were exclusively accounted for when calculating the total route time of the trucks. Czech et al. [5] have used parallel simulated annealing algorithm to solve a vehicle routing problem with time window without any backhauling. The objective function minimized the number of vehicles used as

well as the total distance traveled. The truck could only serve customers whose total demand is less than the total capacity of the truck in one trip.

Ronnquist [6] describes the scope for optimization in various stages of forestry beginning with harvesting, bulking, crew scheduling, road building, fleet management, truck scheduling and ending with production planning. Solution methods such as dynamic programming, linear programming methods, branch and bound methods, heuristics and column generation were used for the optimization. Bent et al. [7] have modeled the dynamic vehicle routing with stochastic service times and customer locations using the Multiple Plan Approach and Multiple Scenario Approach. The Multiple Plan approach's main idea is to generate and maintain all possible sets of routing plans along with the main routing plan. Weintraub et al. [8] discusses the need to centralize ownership of the trucks in order to schedule the trips efficiently. The paper explains that the trucks should start and end the day from a place which is very near to the driver's home. The paper mainly aims at meeting the demand and did not take into consideration any optimization or heuristic approach to reduce the unloaded miles traveled. Palmgren et al. [9] proposed a solution approach based on column generation and pseudo branch and price for the log-truck scheduling problem. The solution approach starts with generating an initial set of feasible routes followed by pricing using dual variables in order to reduce the cost of the routes. Hirsch et al. [10] have used four different tabu search approaches and a few post optimization heuristics to solve the timber transport vehicle routing problem. One standard tabu search approach searches a large neighborhood whereas the tabu search with limited neighborhood approach searches a very limited neighborhood, and the third approach is a combination of the above two approaches. Valenzuela et al. [11] have designed a transportation scheduling system for silvicultural projects considering project due dates, precedence relationship and transportation costs. They considered five different classes of resources. The solution approach consists of two stages starting with simulating the network and then improving the solution using a search heuristic. Haridass et al. [12] use simulated annealing for scheduling a log transport system. They have modified operators and they return better results comparing the the existing system.

In this research, an integer model that considers time windows, speed limit, trip constraints and demand requirements developed for the efficient management of a log transport system. Then the model is integrated with a Decision Support System to help operations management decisions. The remainder of the paper is organized as follows: Section 2 formulates the problem, Section 3 provides a case study developed for a company in Luisiana, USA. Conclusions are given in section 4.

II. LOG TRANSPORTATION PROBLEM

In the pooled transport management system, trucking resources are distributed among a group of loggers. The trucking resources are dispatched by a centralized operator.

In order to find the solution to the problem, a 0-1 Linear / Integer Programming has been developed to find the set of routes that minimizes total traveled unloaded distance.

The objective is to minimize the total unloaded miles traveled. In other words, we will minimize the cost by minimizing total unloaded miles traveled. The notation for the model is given in Appendix A.

$$\text{Min } F = \sum_{i=1}^T \sum_{l=1}^L \sum_{m=1}^M \sum_{j=1}^N Y_{ilmj} D_{lm}$$

Decision Variable (0, 1)

Distance (Miles)

The model has some constraints related with trucks and related with loading. A truck can make at the most one trip at a time to a mill which can be represented as below:

$$\sum_{l=1}^L \sum_{m=1}^M X_{ilmj} \leq 1 \quad i = 1 \dots T, j = 1 \dots N$$

A truck also can make at the most one trip at a time to a logger.

$$\sum_{l=1}^L \sum_{m=1}^M Y_{ilmj} \leq 1 \quad i = 1 \dots T, j = 1 \dots N$$

If a truck travels from any logger to mill m , then it must travel from mill m to any logger in the next trip. This is because the unloaded truck in the mill should go to a logger to get loaded.

$$\sum_{k=1}^L Y_{imkj} \leq \sum_{k=1}^L X_{ikmj} \quad i = 1 \dots T, m = 1 \dots M, j = 1 \dots N$$

If a truck travels from any mill to logger l , then it must go to any mill in the next trip. This is because the loaded truck in the logger should go to a mill to get unloaded.

$$\sum_{k=1}^M X_{ilkj+1} \leq \sum_{k=1}^M Y_{iklj} \quad i = 1 \dots T, l = 1 \dots L, j = 1 \dots N-1$$

Total number of loads transported from logger l to mill m by all trucks must be equal to the number of loads at logger l with destination m . This is the demand constraint.

$$\sum_{i=1}^T \sum_{j=1}^N X_{ilmj} = S_{lm} \quad l = 1 \dots L, m = 1 \dots M$$

A driver drives no more than 8 hours at an average speed of 45 Mph and 360 miles totally. This is the driver's constraints.

$$\sum_{l=1}^L \sum_{m=1}^M \sum_{j=1}^N (X_{ilmj} + Y_{imlj}) d_{lm} \leq 360 \quad i = 1 \dots T$$

X and Y are binary variables since we do use integer programming.

$$X_{ilmj}, Y_{imlj} \in (0,1)$$

The Problem is a variant of classic truck routing problem which is The truck routing problem is a complex combinatorial problem and few approaches to solve the problem have been proposed in literature. There are many heuristic approaches like tabu search, column generation, branch and bound heuristics to solve the general vehicle routing problem where the destinations are visited only once. But in case of the log truck scheduling problem multiple visits to a single mill or logger are required to meet the demand. Since this involves repeated visits to the customer sites, it can't be easily solved using the existing heuristic approaches. A schematic view of the system is given Fig. 1.

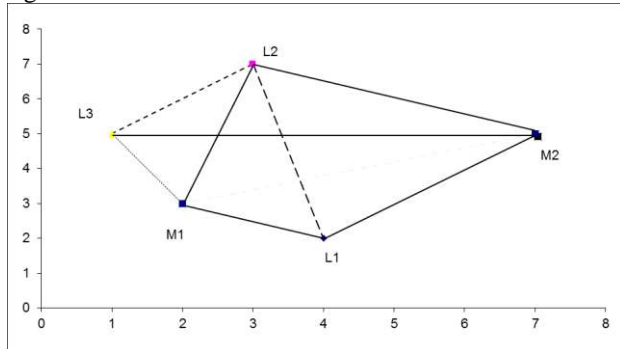


Fig. 1. A Log transport system

III. CASE STUDY

The proposed methodology is illustrated for a case study for a company in Luisiana, USA. For the illustration of the solution approach, a real data-set from the company is provided and checked with the classical method. In a typical day the company has T=4 trucks, M=2 mills, L=3 loggers and N=4 trips. In this case of the log truck scheduling problem with multiple visits to a single mill or logger, there are 192 variables and 146 constraints. The distances between loggers and mills are provided in Table 1 whereas daily demand from mills are provided in Table 2.

Table 1. Distances Between Mills and Logs (Miles)

Logging sites	Mills
---------------	-------

	M1	M2
L1	70	67
L2	65	76
L3	45	51

Table 2. Daily demands from mills

Logging sites	Mills	
	M1	M2
L1	1	2
L2	2	3
L3	2	1

The problem is a complex combinatorial problem and the number of iterations increases as the number of trucks, mills, loggers and trips increase. A problem with a data-set given above can still be solved in a spreadsheet. The problem is modeled in a spreadsheet and it is designed as a decision support system. Basically, the decision support system converts the solution to a more acceptable information. A solution for the Truck 1 is given in Fig.2. the information from the provides the information

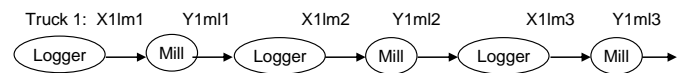


Fig. 2. A Solution for Truck1

The decision support system solves the problem for 4 trucks and determine a daily schedule for the trucks. The solution to log truck scheduling problem with 4 trucks, 2 mill, 3 loggers and 4 trips is given in Table 3.

Table 3 Daily Trip demands from mills

Truck #	Logger	Mill	Logger	Mill	Logger	Mill	Travel (Mil)
T1	L2	M2	L1	M2			207
T2	L2	M1	L3	M1	L3	M2	287
T3	L2	M1	L2	M2	L1	M2	332
T4	L1	M1	L3	M1	L2	M2	336

Note that the schedule also includes the travel distance. The objective of the model is to minimize the total unloaded mileage traveled from mills to logger. The total unloaded travel to this solution is 399 miles. The DSS is in modifiable format and can be used to solve the problems with different data-sets. The detailed screens for the DSS is provided in Appendix B.

IV. CONCLUSION

In this paper, a method is developed for the log transport optimization of a logger company. The problem is a variant of truck scheduling problem and it includes time windows, demand constraints, multiple visits and limited rest times. The problem is formulated as an integer programming model and a DSS is developed for the logger transport company.

The model successfully reaches to an optimal solution in an acceptable time for the given problem. All of the constraints are met and decision variables deliver the routes which then are converted as schedules by DSS. A spreadsheet, however, is limited with certain number of constraints and variables so a larger problem needs more sophisticated computation and solution methods.

REFERENCES

- [1] Johanna C. Gerdessen 1996, "Theory and Methodology Vehicle routing problem with trailers", European Journal of Operational Research 93 (1996) 135-147
- [2] I-Ming Chao 2002, "A tabu search method for the truck and trailer routing problem", Computers & Operations Research 29 (2002) 33-51
- [3] Robert T. Sumichrast and Ina S. Markham 1995, "A heuristic and lower bound for a multi-depot routing problem", Computers Ops Res. Vol.22, No.10, pp.1047-1056, 1995
- [4] Sam R. Thangiah, Jean-Yves Potvin and Tong Sun 1996, "Heuristic approaches to vehicle routing with backhauls and time windows", Computers Ops Res. Vol.23, No.11, pp.1043-1057, 1996
- [5] Zbigniew J. Czech and Piotr Czarnas 2001, "Parallel simulated annealing for the vehicle routing problem with time windows", Research grant BK-280-Rau2-2001
- [6] Mikael Ronnqvist 2003, "Optimization in forestry", Math. Program., Ser. B 97:267-284 (2003)
- [7] Russell Bent and Pascal Van Hentenryck, "Dynamic vehicle routing with stochastic requests"
- [8] Andres Weintraub, Rafael Epstein, Ramiro Morales, Jorge Seron and Pier Traverso, 1996, "A truck scheduling system improves efficiency in the forest industries", Institute for Operations Research and the Management Sciences, Interfaces 26: 4 July- August 1996 (pp.1-12)
- [9] M.Palmgren, M.Ronnqvist and P.Varbrand 2004, "A near-exact method for solving the log-truck scheduling problem", International Transactions in Operations Research 11(2004) 447-464
- [10] Patrick Hirsch and Manfred Gronalt, "Tabu search based solution methods for scheduling log-trucks"
- [11] Jorge F.Valenzuela, H.Hakan Balci and Timothy McDonald 2003, "A Transportation-scheduling system for managing silvicultural projects" Journal of Forest Engineering 2003
- [12] Karunakaran Haridass, Jorge F.Valenzuela, Ahmet Yucekaya and Timothy McDonald 2014, "Scheduling a Log Transport System using Simulated Annealing", Information Sciences, Vol.264, pp. 302-316

APPENDIX A: NOTATION

T : Number of Trucks
M : Number of Mills
L : Number of Logger
N : Number of Trips
i : Denotes truck i ($i=1, \dots, T$)
m : Denotes Mill m ($m=1, \dots, M$)
l : Denotes Logger l ($l=1, \dots, L$)
j : Denotes trip j ($j=1, \dots, N$)
 D_{lm} : Distance from logger l to mill m
 S_{lm} : Number of loads going from logger l to mill m (Demand)
 X_{ilmj} : Equal to 1 when truck "i" goes from logger "l" to mill "m" during trip "j"
 Y_{imlj} : Equal to 1 when truck "i" goes back from mill "m" to logger "l" during trip "j"

APPENDIX B : DECISION SUPPORT SYSTEM

Welcome Workbook

There is an explanation about the problem and company history. Then it will continue to the main menu.

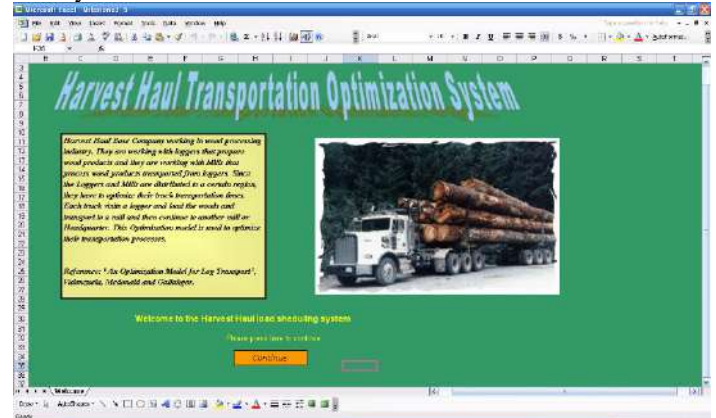


Fig. 3. Welcome workbook

Main Menu

There will be links to other workbooks and solution to the problem.

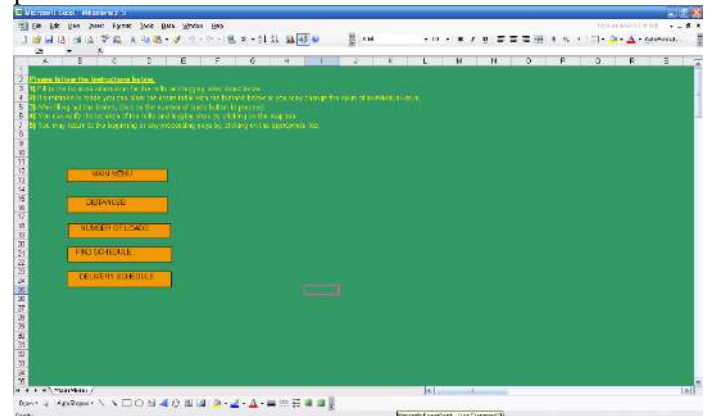


Fig. 4. Main menu workbook

Distances

In this workbook, the matrix shows the distances between mills and loggers. A user will be able to input and change the distances.

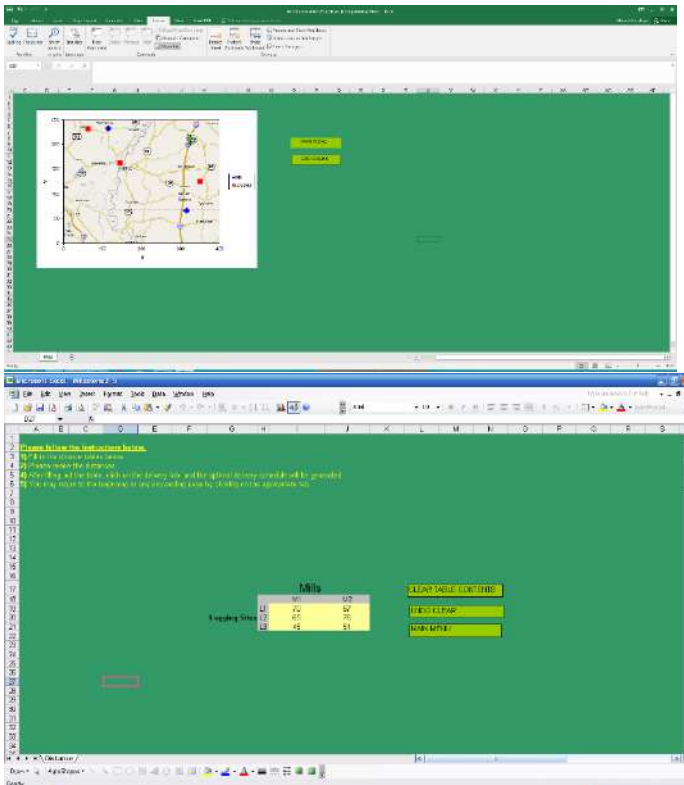


Fig. 5. Distance workbook and distance matrix

Load Information

In this workbook, the matrix shows the loads to mills from each logger. A user will be able to input and change the loads.

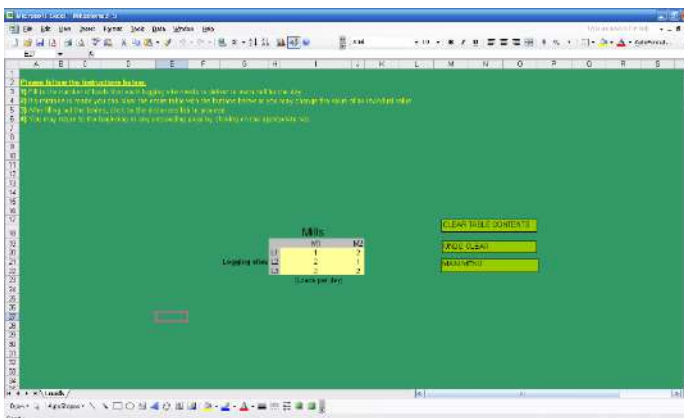


Fig. 6. Loads workbook and load matrix

Find schedule and model

This button will run the excel solver in the model section. This is a macro that is run in background.

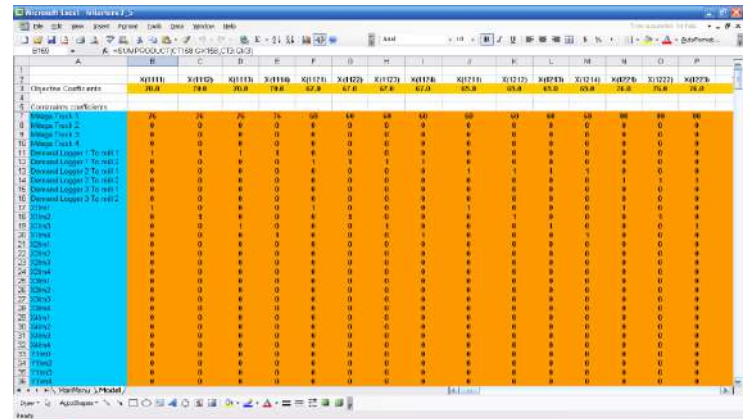


Fig. 7. Model workbook that include constraints and variables

Delivery schedule

The workbook shows the routes of the trucks that will optimize the transportation and meet all of the demand. The workbook also shows the total mileage of each truck.

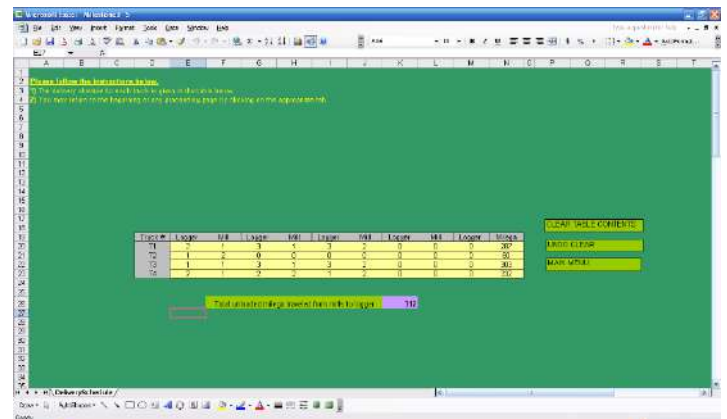


Fig. 8. Delivery schedule workbook that shows the route of the each truck

Determination Student's Profiles of Engineering Faculty with Data Mining Method: A Sample of Kocaeli University

Zerrin Aladağ
Department of Industrial Engineering
Kocaeli University
Kocaeli, Turkey
zaladag@kocaeli.edu.tr

Atakan Alkan
Department of Industrial Engineering
Kocaeli University
Kocaeli, Turkey
aalkan@kocaeli.edu.tr

Elif Ecem Çeltek
Department of Industrial Engineering
Kocaeli University
Kocaeli, Turkey
elifecem.celtek@gmail.com

Ayşegül Dinç
Department of Industrial Engineering
Kocaeli University
Kocaeli, Turkey
aysgl_dnc@ymail.com

Abstract—In this article, it is aimed to reveal the profile of the students of Kocaeli University Engineering Faculty by means of data mining method for making future deductions in the light of this information by extracting valuable information from large amount of data. In this study, the relationship between the variables such as gender, birth place, registered province, high school graduation type, high school grade-point average, university entrance scores and university grade-point average of students which have registered in Kocaeli University Faculty of Engineering in 2017 were examined by data mining techniques. In the study, a decision tree was created with the help of entropy-based algorithms, a concept that measures the uncertainty in the dataset using related variables. In addition, the number of branches is determined for the problem when decision trees are constructed so that the decision tree can be easily interpreted and easily integrated with the database systems. The results of the study decision tree will shed light on not only determining the current profiles of the students, but also determining the academic achievement status of the students who will be newly enrolled at the university. For this reason, the decision tree that will be created in the study will be used to facilitate decision-making at the election stage for students who will be selected as future scholarships or part-time employees.

Keywords—educational data mining; classification; decision tree

Introduction to Grey Systems

Erkan KÖSE

Nuh Naci Yazgan University

Industrial Engineering Department, Kayseri, Turkey,
erkankose93@gmail.com

Abstract-In the natural world, uncertain systems with small samples and poor information exist commonly. The grey systems theory, established by Julong Deng in 1982, is a methodology that focuses on the study of problems involving small samples and poor information. It deals with uncertain systems with partially known information through generating, excavating, and extracting useful information from what is available. Research and its application covered by grey theory include systems analysis, data processing, prediction, decision-making and control. In this study we intend to introduce main concepts of grey system theory and emphasize its differences between other nondeterministic methodologies.

Keywords-grey system; black system; white system; uncertainty

I. INTRODUCTION

Many systems, such as those that are social, economic, agricultural, industrial, ecological, or biological in nature, are named based on the fields and ranges to which the research subjects belong. In contrast, the name grey systems was chosen based on the colors of the subjects under investigation. For example, in control theory, the darkness of colors has been commonly used to indicate the degree of clarity of information. One of the most well accepted representations is the so-called “black box.” It stands for an object with its internal relations or structure totally unknown to the investigator. Here, we use the word “black” to represent unknown information, “white” for completely known information, and “grey” for that information which is partially known and partially unknown. Accordingly, we name systems with completely known information as white systems, systems with completely unknown information as black systems, and systems with partially known and partially unknown information as grey systems, respectively. Having “incomplete information” is the fundamental meaning of being “grey”. In different circumstances and from different angles comparison between black, grey and white systems can be summarized as in Table 1 [1].

TABLE I. Comparison between black, grey and white systems [1]

	Black	Grey	White
Information	Unknown	Incomplete	Known
Appearance	Dark	Grey	Bright
Process	New	Replace old with new	Old
Property	Chaos	Complexity	Order
Methodology	Negative	Transition	Positive
Attitude	Indulgence	Tolerance	Serity
Conclusion	No result	Multiple solution	Unique solution

Grey system theory is an interdisciplinary scientific area that was first introduced in early 1980s by Deng [2]. Since then, the theory has become quite popular with its ability to deal with the systems that have partially unknown parameters. As superiority to conventional statistical models, grey models require only a limited amount of data to estimate the behavior of unknown systems [3].

One characteristic of grey systems theory is that it makes the most and best use of the available “minimal amount of information.” The “principle of minimal information” can be seen as a dialectic unification of “a little” and “a lot.” One advantage of grey systems theory is its ability to handle such uncertain problems with “small samples” and/or “poor information.” Its foundation of study is the concept of “spaces of limited information.” “Minimal amount of information” is the basic territory for grey systems theory to show its power. The amount of information acquirable is the dividing line between “grey” and “not grey”. Making sufficient discovery and application of any available “minimal amount of information” is the basic thinking logic of problem-solving used in grey systems theory [4].

II. COMPARISON BETWEEN NONDETERMINISTIC METHODS

Probability and statistics, fuzzy mathematics, and grey systems theory have been the three most- often applied theories and methods employed in studies of non-deterministic systems. Even though they study objects with different uncertainties, the commonality of these theories is their ability to make meaningful sense out of incompleteness and uncertainties. It is the differences among the uncertainties studied in these theories that three areas of scientific study, each of which has its

own characteristics, on uncertainties have been established.

The power of fuzzy mathematics lies in its capability to find solutions for the problems with cognitive uncertainties. All objects studied by fuzzy mathematics, has the clear interiority and recessive extension characteristics. For example, “young man” is a fuzzy concept. When a young man is considered everybody know what is being implied, however it is quite difficult to say which age groups are addressed to. Different from the fuzzy mathematics, objects studied through grey system theory, has got clear extension and recessive interiority characteristics. For example in the statement of “T.C Republic is planning to maintain its population till 2050 at the numbers of 90 to 100 million” the 90 to 100 million interval is a grey concept which we do not know the exact number but we know the borders clearly [5].

Probability and statistics are used in the solutions of stochastically uncertain problems. In the solution quest, most of its ambitions are used to make out statistic course existent in the past data. This theory, in order to produce reliable solutions needs a great sampling which is considered to be coming from the same distribution.

The characteristics of grey systems can hardly be described by fuzzy mathematics or probability and statistics. Technically, fuzzy mathematics mainly deals with problems of the phenomenon with cognitive uncertainty by experience with the help of affiliation functions. Probability and statistics need special distributions and samples of reasonable size to draw valid inferences. Different from the two theories, grey system theory has been developed to find solutions for the problems where there is small sampling and lack of data. At the following table, the differences between three theories have been summarized [6].

TABLE II. Comparison between nondeterministic methods [6]

	Grey System Theory	Probability & Statistics	Fuzzy Mathematics
Objects of study	Poor information uncertainty	Stochastic uncertainty	Cognitive uncertainty
Basic sets	Grey hazy sets	Cantor sets	Fuzzy sets
Methods	Information coverage	Probability distribution	Function of affiliation
Procedure	Grey series generation	Frequency distribution	Marginal sampling
Requirement	Any distribution	Typical distribution	Experience
Emphasis	Intention	Intention	Extension
Objective	Laws of reality	Laws of statistics	Cognitive expression
Characteristics	Small samples	Large samples	Experience

III. MAIN CONTENTS IN GREY SYSTEMS THEORY

The grey theory is a feasible mathematical means to deal with systems analysis characterized by poor information. Grey system theory is applied to an uncertain system, for which information is insufficient to build a relational analysis or to construct a model to characterize the system. Grey theory considers each stochastic variable as a grey quantity that change within a given range. The theory does not rely on a statistical method to handle grey quantities. Rather, it deals directly with original data, and searches for the intrinsic regularity therein.

Through nearly thirty years of development, grey systems theory has been built up as a newly emerging scientific discipline with its very own theoretical structure consisting of systems analysis, evaluation, modeling, prediction, decision-making, control, and techniques of optimization. Its main contents contain [7]:

- Grey numbers and algebraic system, grey matrices, grey equations, etc., constitute the foundation of grey systems theory. In terms of the theoretical beauty and completeness of the theory, there are still a lot of problems left open in this area.
- The sequence operators mainly include buffer operators (weakening buffer operators, strengthening operators), mean generation operators, stepwise ratio generators, accumulating generators, inverse accumulating generators, etc.
- Grey incidence analysis refers such materials as grey incidence axioms, degree of grey incidence, generalized degree of grey incidence (absolute degree, relative degree, synthetic degree), the degrees of grey incidence based on either similar visual angles or nearness visual angles, grey incidence order, superiority analysis, and others.
- Grey cluster evaluation focuses on such contents as grey variable weight clustering, grey fixed weight clustering, cluster evaluations based on (center-point or end-point) triangular whitenization weight functions, and other related materials.
- Through grey generations or the effect of sequence operators to weaken the randomness, grey prediction models are designed to excavate the hidden laws; and through the interchange between difference equations and differential equations, a practical jump of using discrete data sequences to establish continuous dynamic differential equations is

materialized. Here, GM(1, 1) is the central model that has been most widely employed.

- In terms of grey predictions, they produce quantitative forecasts on the basis of the GM model. Based on their functions and characteristics, grey predictions can be grouped into sequence predictions, interval predictions, disaster predictions, seasonal disaster predictions, stock-market-like predictions, and system predictions, etc.
- The grey combined models include grey econometric models (G-E), grey Cobb-Douglass models (G-C-D), grey Markov models (G-M), grey-rough mixed models, etc.
- Grey decision-making involves multi-attribute weighted grey target models, grey incidence decision-making, grey cluster decision-making, grey situation decisions, grey stratified decisions, etc.
- The main contents of grey control cover the control problems of essential grey systems, the controls composed of grey systems methods, such as grey incidence control, GM(1, 1) prediction control, etc.

Grey numbers, grey elements, and grey relations are the main subjects of research in grey systems theory. So, the entire theory of grey systems lies on the foundation of grey numbers and their operations, grey matrices, and grey equations. In this part, we briefly review some relevant definitions and the calculation process in grey theory [4].

Definition 1. A grey number is a number whose exact value is unknown, but a range which comprises its value is known. Following are the several classes of grey numbers.

(1) Grey numbers with only lower limits are denoted as $\otimes \in [\underline{a}, \infty)$ or $\otimes(\underline{a})$ where \underline{a} , a fixed real value, represents the lower limit of the grey number \otimes .

(2) Grey numbers with only the upper limits are denoted as $\otimes \in (-\infty, \bar{a}]$ or $\otimes(\bar{a})$ where \bar{a} , a fixed real number, stands for the upper limit of the grey number \otimes .

(3) Interval grey numbers are the numbers with both lower limit \underline{a} and upper limit \bar{a} , denoted as $\otimes \in [\underline{a}, \bar{a}]$.

(4) Black and white numbers. When $\otimes \in (-\infty, +\infty)$ or $\otimes \in (\otimes_1, \otimes_2)$, i.e. when \otimes has neither upper nor

lower limits, or the upper and the lower limits are all grey numbers, \otimes is called a black number. When

$\otimes \in [\underline{a}, \bar{a}]$ and $\underline{a} = \bar{a}$, \otimes is called a white number.

Definition 2. Grey number operation is an operation defined on sets of intervals, rather than real numbers. Assume that we have grey numbers $\otimes_1 \in [a, b]$, $a < b$, and $\otimes_2 \in [c, d]$, $c < d$. The operations between grey numbers are as below:

(1) The sum of \otimes_1 and \otimes_2 : $\otimes_1 + \otimes_2 = [a+c, b+d]$

(2) The difference between \otimes_1 and \otimes_2 : $\otimes_1 - \otimes_2 = [a-c, b-d]$

(3) The product of \otimes_1 and \otimes_2 : $\otimes_1 \times \otimes_2 = [\min(ac, ad, bc, bd), \max(ac, ad, bc, bd)]$

(4) The division of \otimes_1 and \otimes_2 : $\otimes_1 \div \otimes_2 = [\min(\frac{a}{c}, \frac{a}{d}, \frac{b}{c}, \frac{b}{d}), \max(\frac{a}{c}, \frac{a}{d}, \frac{b}{c}, \frac{b}{d})]$

(5) The scalar multiplication of k and \otimes_1 : $k \times \otimes_1 = [ka, kb]$

(6) The reciprocal of \otimes_1 : $\otimes_1^{-1} = [\frac{1}{\bar{a}}, \frac{1}{\underline{a}}]$

Definition 3. The length of grey number $\otimes \in [\underline{a}, \bar{a}]$ is defined as $L(\otimes) = [\bar{a} - \underline{a}]$.

Definition 4. For two grey numbers $\otimes_1 \in [a, b]$, $a < b$, and $\otimes_2 \in [c, d]$, $c < d$ the possibility degree of $\otimes_1 \leq \otimes_2$ can be expressed as follows:

$$P\{\otimes_1 \leq \otimes_2\} = \frac{\max(0, L^* - \max(0, b - c))}{L^*}$$

where $L^* = L(\otimes_1) + L(\otimes_2)$.

For the position relationship between \otimes_1 and \otimes_2 , there exist four possible cases on the real number axis. The relationship between \otimes_1 and \otimes_2 is determined as follows:

(1) If $a=c$ and $b=d$, we say that \otimes_1 is equal to \otimes_2 , denoted as $\otimes_1 = \otimes_2$. Then $P\{\otimes_1 \leq \otimes_2\} = 0.5$.

(2) If $c > b$, we say that \otimes_2 is larger than \otimes_1 , denoted as $\otimes_1 > \otimes_2$. Then $P\{\otimes_1 \leq \otimes_2\} = 1$.

(3) If $d < a$, we say that \otimes_2 is smaller than \otimes_1 , denoted as $\otimes_2 < \otimes_1$. Then $P\{\otimes_1 \leq \otimes_2\} = 0$.

(4) If there is an intercrossing part in them, when $P\{\otimes_1 \leq \otimes_2\} > 0.5$, we say that \otimes_2 is larger than \otimes_1 , denoted as $\otimes_2 > \otimes_1$. When $P\{\otimes_1 \leq \otimes_2\} < 0.5$, we say that \otimes_2 is smaller than \otimes_1 , denoted as $\otimes_2 < \otimes_1$.

IV. CONCLUSIONS

Grey theory is one of the methods used to study uncertainty, being superior in the mathematical analysis of systems with uncertain information. In grey theory, according to the degree of information, if the system information is fully known, the system is called a white system; if the information is unknown, it is called a black system. A system with information known partially is called a grey system. In reality, many processes of interest in environmental management are in the grey stage due to inadequate and fuzzy information.

Grey system theory is relatively a new theory in the solution of uncertain systems. In this study we try to introduce main concept of grey systems. We mentioned comparison between grey system theory, probability, statistics and fuzzy mathematics. It is our hope that a reader who does not know anything about this branch of scientific exploration will gain an understanding of the basics of the grey system theory.

REFERENCES

- [1] Lin, Y., Chen, M.Y., and Liu, S. Theory of grey systems: capturing uncertainties of grey information. *Kybernetes* Vol. 33 No. 2, pp. 196-218, 2004.
- [2] Deng, J.L., Control problems of grey system. *Systems & Control Letters* 1, 288–294, 1982.
- [3] Deng, J.L., Introduction to grey system theory. *The Journal of Grey System* 1, 1–24, 1989.
- [4] Liu, S. and Lin, Y. *Grey Information: Theory and Practical Applications*. Springer, London, 2006.
- [5] Kose, E., Temiz, I., Erol, S. Grey system approach for economic order quantity models under uncertainty. *The Journal of Grey System*, 1, 71-82, 2011.
- [6] Liu, S. and Lin, Y. *Grey Systems: Theory and Practical Applications*. Springer, London, 2010.

[7] Liu, S., Forrest, J., Yingjiel, Y. A brief introduction to grey systems theory. *Grey Systems: Theory and Application*, Vol. 2 Iss: 2, pp.89 – 104, 2012.

Multi-site and multi-method forecasting modelling of hospital emergency room patient arrivals

Muhammet Gul

Department of Industrial Engineering
Munzur University
Tunceli, TURKEY
muhammetgul@munzur.edu.tr

Melih Yucesan

Department of Mechanical Engineering
Munzur University
Tunceli, TURKEY
melihiyucesan@munzur.edu.tr

Erkan Celik

Department of Industrial Engineering
Munzur University
Tunceli, TURKEY
erkancelik@munzur.edu.tr

Abstract— Emergency rooms (ERs) are the sole subsystems of a hospital system that provide patients nonstop emergency care at any time of the day. Owing to the changing demand in the number of arrivals at these units, accurate forecasting gains vital importance in order to arrange staffing and scheduling policies. Therefore, we deal with forecasting modelling of patient arrivals from three different hospital ERs located in Istanbul using autoregressive integrated moving average (ARIMA) and exponential smoothing (ES) methods. The daily patient arrivals from each hospital ER were gathered by the hospital information management system. Results of the study show that ARIMA models developed for each ER give better accuracy values than ES models in terms of mean absolute percentage of error (MAPE). ARIMA model of ER-2 is found to be the best model for the data under study (MAPE is 6.51%, 5.42%, 8.27% for each ER, respectively). This study contributes to the knowledge from two aspects: (1) Usage of statistical forecasting tools in planning of hospital environments against the increased city population has become compulsory by decision makers. (2) This study includes forecasting results of multi ER daily patient demand in terms of two methods that is, enables decision makers making comparison between these tools.

Keywords—emergency room; patient arrival; exponential smoothing

I. INTRODUCTION

Emergency room (ER) is one of the most important units of a hospital system and is considered as the most crowding department [1]. These units provide non-stop emergency care for patients at any time of the day. In times of a patient surge, ED medical staff and treatment areas may become insufficient and this situation may cause overcrowding [2-5]. Therefore, accurate forecasting of patient demand, in other words patient arrivals, has vital importance in order to set ER resource planning. Key performance indicators for service quality through ERs are relating with length of stay (LOS) and waiting times, which are affected by high levels of ED arrivals [6-8]. According to the numbers of Turkish Ministry of Health, ER arrivals are increasing rapidly which reflects a

worse condition compared to the countries such as USA and UK [9].

Increased patient arrivals may lead to prolonged waits and overcrowding. In order to enhance ER processes, a better balance between ER resources (doctors, nurses, beds, medical equipment and etc.) and demand (patient arrivals) is required. Accurate forecasting of ER patient demand can provide managerial implications on long and short term staffing policies so that the ERs can be better prepared for the coming demand variations [8]. Regarding the theme of ER patient arrival forecasting, several investigations were carried out.

However, the knowledge is satisfied enough with the work done up to now, the current works on ER patient arrival forecasting cover mostly single site and single method based models. But in our study, ER patient arrivals have been forecasted based on a collection of related data obtained from three different public hospital ERs. We used two separate methods namely, ARIMA and ES to make a daily analysis of the data. By comparing these two methods in terms of forecasting patient demand using MAPE, we aim to determine the optimum method in order to plan hospital ERs.

In the lights of above mentioned points, this study aims to present multi-site and multi-method forecasting modelling of patient arrivals providing case studies performed in three public hospital ERs in Istanbul. It contributes to the literature providing usage of statistical forecasting tools in planning of hospital environments against the increased city population especially for metropolitans such as Istanbul.

The remaining of the study are organized as follows: In section II, a short literature review is given within the concept of ER patient demand forecasting. The data and forecasting methods used in the study are introduced in Section III. In section IV, application of the methods using the related data is provided. In the final section, the conclusion and discussion about the models are presented.

II. LITERATURE REVIEW

Although studies on developing patient demand forecasting were many, we do not have enough space here to discuss all of them in details. Wargon et al. [10] presented a systematic review study that covers nine ER and walk-in clinic visit forecasting models. Researchers applied various methods to forecast ER patient demand such as regression, time series and data mining. The first method is regression, which may be investigated under linear, logistics and Poisson and consisted of looking for correlations between patient demand and a series of independent variables, such as calendar or meteorological variables. The second method is time series based forecasting models that view patient demand as a time series and predict future values from past values [10]. The last method is concerned data mining based forecasting models. Within the context of this class, artificial neural networks (ANNs), support vector machine (SVM), decision trees and Bayesian networks can be mentioned.

Among the studies, many variants of regression models exist as linear [5,8,12-14], logistic [15-16] and Poisson [17]. LR models are used in ER patient demand forecasting as in Eq. (1):

$$y_i = \alpha_i + \beta_1 x_{i1} + \dots + \beta_p x_{ip} + \varepsilon_i \quad (i = 1, \dots, n) \quad (1)$$

where y_i is the number of patients per time period estimated by the model, α_i is a constant, $x_{i1} + \dots + x_{ip}$ are independent variables or input variables (e.g., day of the week, month of the year, temperature), β is a p-dimensional parameter vector and it is also called weighting coefficient of each of these variables and ε_i is called the error term.

In a logistic regression model, the dependent variable is categorical. Logistic regression is divided into the classes as binomial, ordinal or multinomial. Poisson regression models are based upon the assumption that the events in one time period are independent of the events in another time period [17].

Except from regression based models, several authors or investigators proposed time series methods to forecast ER patient demand. In the literature of ER patient arrival forecasting, different time series models were applied. ARIMA model is the most widely used time series method proposed by [13,18-21].

ES is also one of the most important time series method applied mostly by researchers in the field of ER patient demand forecasting. Calegari et al. [22], Aboagye-Sarfo et al. [23], Bergs et al. [24], Jones et al. [20] and Champion et al. [25] used and successfully applied ES method to their data regarding ER patient arrivals.

The data mining based models used to forecast ER patient demand include ANNs, SVM and decision trees. ANNs are applied to several practices such as forecasting. For ER operations, ANNs are frequently applied to forecasting ER patient arrivals [5,8,13,26].

III. MATERIAL AND METHODS

A. Data

The daily data for each ER used in this study consist of 275, 642 and 707 patient records in the calendar years of 2011-2013. The data are obtained from each hospital information management system database. We study on appropriate time units to create time series, make daily forecasts. The data used in the analyses are collected in the related ER, in which arrivals are time-stamped and electronically recorded. Much of the effort to generate the ER arrival forecasts includes organizing the raw data in a way that it can be used to forecast the suitable ARIMA and ES models. The time series used for the models are shown in Fig. 1.

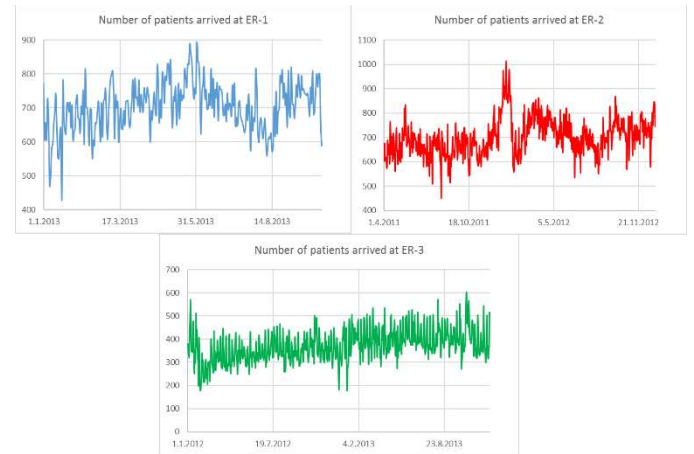


Fig. 1. ER arrivals used for each ARIMA and ES models

B. Forecasting methods

In this section, the explanation of the ARIMA and ES are given in details. autoregressive model is considered one of the simplest time series [11]. In this process model, understandings are assumed to result from a linear combination of past understandings.

A first order AR model, symbolized as AR (1), can be presented as

$$y_t = \hat{\phi} + \phi_1 y_{t-1} + \varepsilon_t \quad (2)$$

where ϕ_1 and $\hat{\phi}$ present unknown, “to-be-forecasted” parameters and ε_t presents error component.

The moving average (MA) model, in which actualizations are stated as linear combinations of shocks. MA (1) presented of a first order moving average model as follows [11]:

$$y_t = \mu + \varepsilon_t - \theta \varepsilon_{t-1} \quad (3)$$

The autoregressive moving average model (ARMA) contains merging the AR() and MA() model into combined method. ARMA (1,1) presented model of first order in both components model as follows:

$$y_t = \hat{\phi} + \phi_1 y_{t-1} - \theta \varepsilon_{t-1} + \varepsilon_t \quad (4)$$

ARIMA models stated notation as p, d, q; for example, the notation ARIMA (4,3,2) assign to a fourth order autoregressive component, third order differencing, and a second order moving average component.

Exponential smoothing is developed by Robert G. Brown's work as an operation research analyst for the US Navy during World War II [27]. It can be very useful for forecasting [28] if the weights decline exponentially when the observations get elder.

Considering that f_t is the forecasted data at some point of the time series and y_t is the actual data, hence the errors is obtained as follows:

$$e_t = y_t - f_t \quad (5)$$

The single exponential smoothing method (SES) takes the forecasted for the previous period and regulates it using the forecasted error. Thus, the forecasted for the next period is:

$$f_{t+1} = f_t + \alpha(y_t - f_t) \quad (6)$$

where α is a constant between 0 and 1.

When α close to 1 means that the new forecast will contain a considerable modification for the error in the previous forecast. On the contrary, if α is close to 0 means that the new forecast will contain very slight modification.

IV. APPLICATION

This study was conducted in three public hospital ERs in Istanbul which is Turkey's largest and most advanced city and used a dataset extracted from *HBYS* databases. The ER-1 data utilized for analysis includes 275 days' data of patients who visited the ER from January, 1 2013 to October, 10 2013. The ER-2 data similarly provides 642 days' data of patients who arrived at the ER from April, 1 2011 to December, 31 2012. The data of ER-3 presents 707 days' data from January, 1 2012 to December, 12 2013. The daily number of patients arrived at the ERs was considered as a dependent variable for each of the models. The daily number of patients arriving at the ERs was calculated by counting the number of visiting patients from 12 a.m. to the following 12 a.m. For this study, ARIMA and SES models were applied, from other models relating to the time series analysis methodology. Firstly, in order to examine the stationary of the data used, Augmented Dickey-Fuller Test was carried out as shown in TABLE I. It is observed that each ER data used through the study is stationary in its level (see the last column of TABLE I).

TABLE I. ARIMA DIFFERENCE TESTS

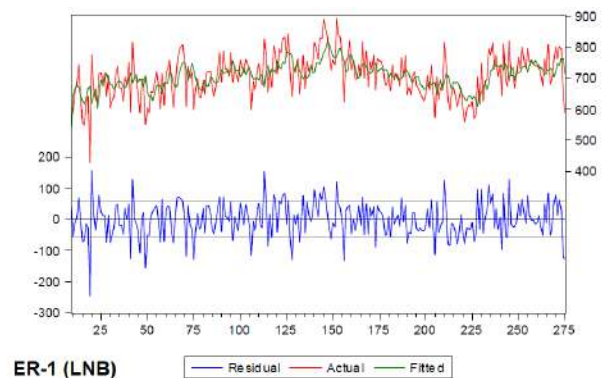
Augmented Dickey-Fuller Test (Exogenous: Constant, Linear Trend) Null Hypothesis: Number of Patience has a unit root			
Hospital ER	Lag Length Automatic-based on SIC	t-Statistic	Prob
LNB (ER-1)	1	-6.563808	0.0000
BAY (ER-2)	7	-4.125858	0.0060
ARN (ER-3)	13	-4.763412	0.0006

To make a comparison between built ER models in terms of accuracy and performance, R^2 and MAPE values are calculated. MAPE values show the relative measure of the forecasting error between the forecasted value, which is a series variable, and the observed actual value. The smaller the error, the more accurate the forecasting model is. In TABLE II, it is seen that among ARIMA models developed for each ER, ER-2 results in better accuracy values than other models in terms of MAPE. According to the R^2 values, ER-3 has a higher value than the others (65%).

The figures that include comparison between the forecasted and actual values in the three ER sites represents that the ER-3's forecast visually demonstrates the mean of the observed value, hence reflecting its insufficiency as a prediction model (Fig. 2). In contrast, the ER-2 ARIMA model displays a pattern of change similar to the observed values.

TABLE II. STATISTICAL VALIDATION MEASURES APPLIED TO DATA

ER	LNB (ER-1)	BAY (ER-2)	ARN (ER-3)
ARIMA	(8,0,2)	(4,0,3)	(14,0,8)
R^2	0.3272	0.5968	0.6549
MAPE	6.513	5.417	8.273



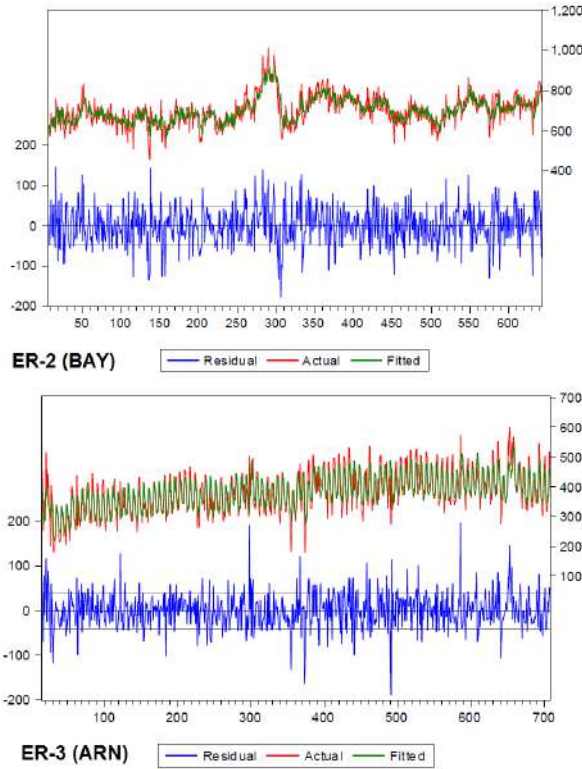


Fig. 2. Actual vs. forecasted ER arrivals

A MAPE comparison of the accuracy of each SES model's forecasting ability shows that ER-2 model scored a 5.81%, the ER-1 model scored 6.89%, and the ER-3 model scored 13.3%, thus identifying the ER-2 SES model as the most accurate forecasting model among others (Table III). Also, a comparison of the actual and forecasted values for the best SES model in terms of MAPE (ER-2 model) were given in Fig. 3.

TABLE III. COMPARISON MEASURES IN TERMS OF TWO METHODS

MAPE (%)	ARIMA	SES
ER-1 (LNB)	6.51	6.89
ER-2 (BAY)	5.42	5.81
ER-3(ARN)	8.27	13.13

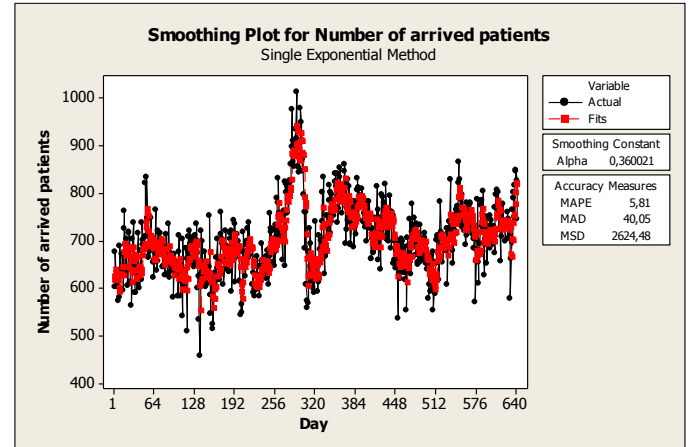


Fig. 3. Actual vs. forecasted ER-2 arrivals according to SES modeling

V. CONCLUSION

In this study, a multi-site and multi-method forecasting modelling of hospital emergency room patient arrivals was taken into consider in order to show applicability of these methods and contribute to the observed ERs. Two methods were assessed to forecast ER arrivals of three public hospitals in Istanbul, Turkey: autoregressive integrated moving average and single exponential smoothing. The historical data of ER arrivals were collected from the information management system of the hospitals. ARIMA(4,0,3) was found to be the best model for the ER data used for the study. The results of this study show that among ERs, ER-2 had the best model performance (MAPE is 6.51%, 5.42%, 8.27% for each ER, respectively). As a creative contribution to the knowledge, accurate forecasting modeling of ER arrivals enable stakeholders arranging appropriate staff levels at the ER and other inpatient units and reducing boarding times.

ACKNOWLEDGMENT

We thank the General Secretary of Istanbul Fatih Association of Public Hospitals and the emergency departments' staff for their guidance and help in gathering daily patient demand data.

REFERENCES

- [1] Aladeemy, M. Chou, C-A. Shan, X. Khasawneh, M. Srihari, K., & Poranki, S. (2016). Forecasting Daily Patient Arrivals at Emergency Department: A Comparative Study. Proceedings of the 2016 Industrial and Systems Engineering Research Conference, May 2016.
- [2] Gul, M., & Guneri, A. F. (2012). A computer simulation model to reduce patient length of stay and to improve resource utilization rate in an emergency department service system. *International Journal of Industrial Engineering*, 19(5), 221-231.
- [3] Gul, M., & Guneri, A. F. (2015). A comprehensive review of emergency department simulation applications for normal and disaster conditions. *Computers & Industrial Engineering*, 83, 327-344.

- [4] Gul, M., & Guneri, A. F. (2015). Forecasting patient length of stay in an emergency department by artificial neural networks. *Journal of Aeronautics and Space Technologies*, 8(2), 43-48.
- [5] Gul, M., & Guneri, A. F. (2016). Planning the future of emergency departments: Forecasting ED patient arrivals by using regression and neural network models. *International Journal of Industrial Engineering*, 23(2), 137-154.
- [6] Akoğlu, H. Acil servis kalabalığını önleme başarılı yurtdışı protokoller, http://file.atuder.org.tr/_atuder.org/fileUpload/zbe9EcYpr43t.pdf.
- [7] Au-Yeung, S. W. M., Harder, U., McCoy, E. J., & Knottenbelt, W. J. (2009). Predicting patient arrivals to an accident and emergency department. *Emergency Medicine Journal*, 26(4), 241-244.
- [8] Xu, M., Wong, T. C., & Chin, K. S. (2013). Modeling daily patient arrivals at Emergency Department and quantifying the relative importance of contributing variables using artificial neural network. *Decision Support Systems*, 54(3), 1488-1498.
- [9] Arslanhan, S. (2010). Does an increase in the examination number represent a significant increase in access?. *Economic Policy Research Foundation of Turkey (EPRFT) Policy Topic*.
- [10] Wargon, M., Guidet, B., Hoang, T. D., & Hejblum, G. (2009). A systematic review of models for forecasting the number of emergency department visits. *Emergency Medicine Journal*, 26(6), 395-399.
- [11] Elias, R. J., Montgomery, D. C., & Kulahci, M. (2006). An overview of short-term statistical forecasting methods. *International Journal of Management Science and Engineering Management*, 1(1), 17-36.
- [12] Cote, M. J., Smith, M. A., Eitel, D. R., & Akçali, E. (2013). Forecasting emergency department arrivals: A tutorial for emergency department directors. *Hospital topics*, 91(1), 9-19.
- [13] Jones, S. S., Thomas, A., Evans, R. S., Welch, S. J., Haug, P. J., & Snow, G. L. (2008). Forecasting daily patient volumes in the emergency department. *Academic Emergency Medicine*, 15(2), 159-170.
- [14] Batal, H., Tench, J., McMillan, S., Adams, J., & Mehler, P. S. (2001). Predicting patient visits to an urgent care clinic using calendar variables. *Academic Emergency Medicine*, 8(1), 48-53.
- [15] Chase, V. J., Cohn, A. E., Peterson, T. A., & Lavieri, M. S. (2012). Predicting emergency department volume using forecasting methods to create a "surge response" for noncrisis events. *Academic Emergency Medicine*, 19(5), 569-576.
- [16] Schonwetter, R. S., Clark, L. D., Leedy, S. A., Quinn, M. J., Azer, M., & Kim, S. (2008). Predicting emergency room visits and hospitalizations among hospice patients with cardiac disease. *Journal of palliative medicine*, 11(8), 1142-1150.
- [17] McCarthy, M. L., Zeger, S. L., Ding, R., Aronsky, D., Hoot, N. R., & Kelen, G. D. (2008). The challenge of predicting demand for emergency department services. *Academic Emergency Medicine*, 15(4), 337-346.
- [18] Xu, Q., Tsui, K. L., Jiang, W., & Guo, H. (2016). A hybrid approach for forecasting patient visits in emergency department. *Quality and Reliability Engineering International*, 32(8), 2751-2759.
- [19] Kadri, F., Harrou, F., Chaabane, S., & Tahon, C. (2014). Time series modelling and forecasting of emergency department overcrowding. *Journal of medical systems*, 38(9), 107-127.
- [20] Jones, S. S., Evans, R. S., Allen, T. L., Thomas, A., Haug, P. J., Welch, S. J., & Snow, G. L. (2009). A multivariate time series approach to modeling and forecasting demand in the emergency department. *Journal of biomedical informatics*, 42(1), 123-139.
- [21] Zibners, L. M., Bonsu, B. K., Hayes, J. R., & Cohen, D. M. (2006). Local weather effects on emergency department visits: a time series and regression analysis. *Pediatric emergency care*, 22(2), 104-106.
- [22] Calegari, R., Fogliatto, F. S., Lucini, F. R., Neyeloff, J., Kuchenbecker, R. S., & Schaan, B. D. (2016). Forecasting Daily Volume and Acuity of Patients in the Emergency Department. *Computational and Mathematical Methods in Medicine*, 2016.
- [23] Aboagye-Sarfo, P., Mai, Q., Sanfilippo, F. M., Preen, D. B., Stewart, L. M., & Fatovich, D. M. (2015). A comparison of multivariate and univariate time series approaches to modelling and forecasting emergency department demand in Western Australia. *Journal of Biomedical Informatics*, 57, 62-73.
- [24] Bergs, J., Heerincx, P., & Verelst, S. (2014). Knowing what to expect, forecasting monthly emergency department visits: A time-series analysis. *International Emergency Nursing*, 22(2), 112-115.
- [25] Champion, R., Kinsman, L. D., Lee, G. A., Masman, K. A., May, E. A., Mills, T. M., ...& Williams, R. J. (2007). Forecasting emergency department presentations. *Australian Health Review*, 31(1), 83-90.
- [26] Menke, N. B., Caputo, N., Fraser, R., Haber, J., Shields, C., & Menke, M. N. (2014). A retrospective analysis of the utility of an artificial neural network to predict ED volume. *The American journal of emergency medicine*, 32(6), 614-617.
- [27] S.I. Gass, C.M. Harris (Eds.), *Encyclopedia of operations research and management science* (Centennial edition), Kluwer, Dordrecht, The Netherlands (2000).
- [28] Cadenas, E., Jaramillo, O. A., & Rivera, W. (2010). Analysis and forecasting of wind velocity in chetumal, quintana roo, using the single exponential smoothing method. *Renewable Energy*, 35(5), 925-930.

Assembly Line Balancing with Task Parallelizing Approach and a Case Study

Hakan Altunay
Department of Industrial Engineering
Firat University
Elazığ, Turkey
haltunay@firat.edu.tr

H. Cenk Özmutlu
Department of Industrial Engineering
Uludağ University
Bursa, Turkey

Seda Özmutlu
Department of Industrial Engineering
Uludağ University
Bursa, Turkey

Abstract—An assembly line is a manufacturing process which consist of a set of workstations connected together by transfer mechanisms such as conveyor systems. The problem of assigning tasks to workstations so that the total time required at each station is nearly the same by considering some constraints about cycle time or precedence relationships is known as the assembly line balancing problem. In this study, single model assembly line balancing problem with task parallelizing is considered. Firstly, a new mathematical model is presented to solve the problem. Then, the proposed model is tested with a case study. Finally, some computational analysis are conducted to assess the performance of the proposed mathematical model.

Keywords—task parallelizing; assembly line balancing; mathematical programming; operations research

ENVIRONMENTAL ENGINEERING

ORAL SUBMISSIONS



Ground State Nuclear Properties Determination for Heavy Even-Even Nuclei

Serkan AKKOYUN
University of Cumhuriyet,
Sivas, Turkey
serkan.akkoyun@gmail.com

Tuncay BAYRAM
University of Sinop,
Sinop, Turkey
t.bayram@ymail.com

Abstract— The ground state nuclear properties of the heavy nuclei between $Z=80-100$ region have been determined by using Hartree Fock Bogolibov (HFB) and Relativistic Mean Field (RMF) models. The results were compared with each other and experimental values in the literature. The ground state binding energies, two-neutron and two-proton separation energies, neutron, proton and charge radii, electric quadrupole moments and deformation parameters of these nuclei were calculated. In HFB method, Sly5 Skyrme forces and in RMF model, DEFNE interaction parameter sets were used for determination of the nuclear properties.

Keywords— Ground state properties; Heavy nuclei; HFB; RMF

Biological Selectors

Engin GÜRTEKİN

Enviromental Department, Faculty of Engineering,
University of Firat,
Elazığ, Turkey
egurtekin@firat.edu.tr

Ergin TAŞKAN

Enviromental Department, Faculty of Engineering,
University of Firat,
Elazığ, Turkey
etaskan@firat.edu.tr

***Abstract—** The activated sludge process has found wide application as one of effective methods in wastewater treatment. The performance of the activated sludge process depends largely on the balance between filamentous and flocking bacteria. Excessive growth of filamentous bacteria causes various problems. Bulking and foaming phenomena are the major problems referred usually resulting in poor sedimentation of sludge and low-quality final effluents. The application of biological selector reactor technology has become one of the promoted methods for the control of filament proliferation, enhancing sludge settleability in activated sludge systems. In this study, the biological selector reactor technology used to control the sludge bulking was examined.*

***Keywords—** Filamentous bacteria; sludge bulking; biological selectors; settleability.*

Biodegradation of Malathion by Phanerochaete chrysosporium (ME446) under Submerged Culture Conditions: Monitoring by COD reduction and Laccase Activity in Medium

Numan YILDIRIM
University of Munzur,
Tunceli, Turkey
numanyildirim@gmail.com

Gökhan Önder ERGÜVEN
University of Munzur,
Tunceli, Turkey
gokhanondererguven@gmail.com

Elanur ADALAR
University of Yildiz Technical,
İstanbul, Turkey
cm.elanur@gmail.com

Abstract— *This present study aims at evaluating the efficiency of *P. chrysosporium* to degrade the different concentration of malathion (50, 100 and 150 mgL⁻¹) under agitated (130 rpm) submerged culture conditions with reduction of chemical oxygen demand (COD). We have previously screening the growth of fungus in Saboroud Dextrose Agar medium for 10 days. We have also determined the laccase activity during degradation process for 15 days. According to our results the fungus have achieved 99.6, 98.8 and 98.7 % COD reduction at concentration of 50, 100 and 150 mgL⁻¹ respectively the end of the 15 days. The highest laccase activity (180±5,69 U/L) was measured at concentration of 50 mgL⁻¹ the end of the 15 days and the lowest activity (36±3,26) was determined at concentration of 150 mgL⁻¹ the end of the 15 days. The dried biomass of fungus was weighted at end of the 15 days and we have determined that malathion in culture medium reduced the biomass production compared the control group (SDB + P.c). Our results showed that, *P. chrysosporium* could be an effective bioremediation tool for treatment of malathion containing wastewater*

Keywords— *P. chrysosporium; Malathion; COD reduction; Laccase activity.*

Bacillus subtilis ATCC 6051 and MgO nanoparticles for Reactive Orange from Wastewater

Besi SERİN

Biology Department, Faculty of Science,
University of Dicle,
Diyarbakır, Turkey
beserin@hotmail.com

Nurullah AKCAN

High Health School Department,
University of Siirt,
Siirt, Turkey
nurullah.akcan@gmail.com

Serhat UZAN

Chemistry Department, Faculty of Science,
University of Dicle,
Diyarbakır, Turkey
serhatuzan21@gmail.com

Fikret UYAR

Biology Department, Faculty of Science,
University of Dicle,
Diyarbakır, Turkey
fuyar@dicle.edu.tr

Abstract— With the development of society and scientific technology, more attentions have been paid to environmental issues which were caused by the discharge of wastewater. Metal nanoparticles (NPs) with controlled size and shape are of great interest because of their morphology dependent properties and potential applications in a lot of fields. Metal NPs have attracted considerable interest because of their novel properties and their potential application. Binding capacity of noble metal NPs with dyes are more when compared with other NPs. Novel metal crystallites provide a more interesting research field due to their close lying conduction and valence bands in which electrons move freely. The free electrons give rise to a surface plasmon absorption band, which depends on both the particle size and chemical surrounding. Right now, shape-controlled synthesis of NPs has been achieved either by using geometric templates, or by using some additive, such as polymers, or inorganic anions, to regulate the particle growth. Accurate controls of size, composition, morphology and stability, and the use of environment-friendly procedures are highly desirable for the synthesis of NPs. Biosorption is rather difficult to define because many mechanisms may contribute to the overall process depending on the substance to be sorbed, the biosorbent used, environmental factors and the presence or absence of metabolic processes in the case of living organisms. Biosorption may be simply defined as the removal of substances from solution by biological material. Such substances can be organic and inorganic, and in soluble or insoluble forms. Biosorption is a physico-chemical process and includes such mechanisms as absorption, adsorption, ion exchange, surface complexation and precipitation. It is a property of living and dead biomass (as well as excreted and derived products): metabolic processes in living organisms may affect physico-chemical biosorption mechanisms, as well as pollutant bioavailability, chemical speciation and accumulation or transformation by metabolism-dependent properties. This work we use *Bacillus subtilis* ATCC 6051 (BS) and MgO (n-MgO) nanoparticles. This work deals with the preparation, characterization and dye adsorption properties of novel biocomposite composite (*Bacillus subtilis* ATCC 6051–magnesium oxide nanoparticle) (BS/n-MgO). Physical characteristics of BS/n-MgO were investigated. The textile dye reactive orange was used as model compound. The isotherm and kinetics of dye adsorption were studied.

Keywords— *Bacillus subtilis* ATCC 6051; MgO; reactive orange; nanoparticle

*Effect of Oxytetracycline on Serum Response of Rainbow Trout, *Oncorhynchus Mykiss**

Muammer KIRICI
University of Bingöl,
Bingöl, Turkey
muammerkirici@hotmail.com

M. Enis YONAR
University of Fırat,
Elazığ, Turkey

Unal ISPIR
University of Inönü,
Malatya, Turkey

Serpil MISE YONAR
University of Fırat,
Elazığ, Turkey

Abstract— *In this study, effect of oxytetracycline (OTC), which is widely used in the treatment of fish diseases, on serum response was investigated. We conducted two experiments, the first with intraperitoneal (IP) injection and the second with immersion (IM) bath administration of OTC. For this purpose, fish was injected IP 20 mg/kg fish weight dose of OTC every day for 4 days. After 24 hours the last treatment serum were collected. In trial second, fish were exposed to 50 mg/L concentration of OTC for 48 hours. The several immune parameters (lysozyme, myeloperoxidase and total protein activities) and bactericidal activity against *Yersinia ruckeri* were studied. The present results demonstrate that immune parameters (lysozyme and myeloperoxidase activities) slightly decreased after the injection administration of OTC. But, The immersion administration of OTC in fish had no effect on this parameters. The serum bactericidal activity of all groups showed a increase in comparison with control untreated group.*

Keywords— *Oxytetracycline; *Oncorhynchus mykiss*; immune parameters; bactericidal activity*

Toxic Impact of Carbamazepine on Protein, Fat and Glycogen Levels of Carp *Cyprinus Carpio*, Fry

Muammer KIRICI
University of Bingöl,
Bingöl, Turkey
muammerkirici@hotmail.com

M. Enis YONAR
University of Firat,
Elazığ, Turkey

Unal ISPIR
University of Inonu,
Malatya, Turkey

Serpil MISE YONAR
University of Firat,
Elazığ, Turkey

Abstract— Carbamazepine (CBZ) is widely used to help people with epilepsy control seizures. CBZ have been detected in many environmental samples. The present study was conducted to investigate the biochemical effects of CBZ on whole body of carp fry (*Cyprinus carpio*). The fish used in this study were an average weight of 0.65 g. Fishes were treated with 0, 1, 10 and 100 µg/L of CBZ during 96 hours and 14 days. Total protein, fat and glycogen levels were measured after of CBZ treatment. The immersion administration of CBZ in fish had no effect on all the parameters in 96 h. But, the showed that in fish significantly decreased total protein, fat and glycogen levels in 14d of CBZ administration ($P<0.05$). In conclusion, administration of CBZ up to 1 and 10 µg/L has no toxic effect on whole body biochemical parameters of fishes. However, dose of 100 µg/L of CBZ caused toxicity biochemical parameters of fish.

Keywords— Carbamazepine; *Cyprinus carpio*; fry; toxicity; biochemical parameters

Recent Progress in Design and Applications of Electrode Materials for Microbial Fuel Cells

Ergin TAŞKAN

Enviromental Department, Faculty of Engineering,
University of Fırat,
Elazığ, Turkey
etaskan@firat.edu.tr

Halil HASAR

Enviromental Department, Faculty of Engineering,
University of Fırat,
Elazığ, Turkey
hhasar@firat.edu.tr

Abstract— *Microbial fuel cells (MFCs) are bioreactors that convert organic matter into the electricity by using microorganisms. In MFC reactor, microorganisms on the surface of anode electrode generate electrons and transfer them to the anode electrode. However, the electricity generated from MFC is relatively low for practical applications. The performance of MFCs is directly related to efficiency of anode compartment. In a MFC reactor, the most important part of the anode compartment is the anode electrode. Studies so far have widely used carbon materials as anode and cathode electrodes in MFCs. In the past ten years, there has been significant new developments in electrode materials which has resulted in several-fold increase in achievable electricity. This paper reviews, recent advances in the construction of novel electrode materials for MFCs*

Keywords— *Microbial fuel cell; electrode; electricity*

Removal of Phenol from Aqueous Solution by using Carbonized Peanut Hull

Gülşad USLU ŞENEL

Enviromental Department, Faculty of Engineering,
University of Firat,
Elazığ, Turkey
guslu@firat.edu.tr

Evren ÇAKIROĞLU

Firat University
Elazığ, Turkey,

Abstract— The peanut hull was used to prepare carbon in this study. It was produced by carbonization in carbon dioxide atmosphere at 500 °C for 1.0 h. The adsorption of phenol onto peanut hull carbon (PHC) was studied as a function of initial pH, temperature, initial phenol concentration and adsorbent dosage. The maximum phenol adsorption capacity was obtained as 23.10 mg g⁻¹ for 300 mg dm⁻³ initial phenol concentration at the temperature of 35 °C at pH = 8.0. The Freundlich and Langmuir adsorption models were used for the mathematical description of the adsorption equilibrium and isotherm constants were evaluated at different temperatures. The adsorption equilibrium was well described by the Langmuir model, although they could be modeled by the Freundlich equation. Batch adsorption models, based on the assumption of the pseudo-first order and pseudo-second order mechanism, were applied to examine the kinetics of the adsorption. The results showed that kinetic data were followed more closely the pseudo-second order model than the pseudo-first order. The thermodynamics constants of the adsorption process: ΔH^0 , ΔS^0 and ΔG^0 were evaluated. The results show that adsorption of phenol on PHC is an endothermic and spontaneous in nature

Keywords— peanub hull, phenol adsorption, adsorption models

Performance, Kinetics, and Equilibrium of Methylene Blue Adsorption From Wastewater on Herbal-Based Modified Biochar

Hasan SAYGILI

Department of Petroleum and Natural Gas Engineering
Faculty of Engineering and Architecture, Batman
University, 72100 Batman, Turkey
hasan.saygili33@gmail.com

Fuat GÜZEL

Department of Chemistry, Faculty of Education, Dicle
University, 21280 Diyarbakır, Turkey
guzelfuat@gmail.com

Gülbahar AKKAYA SAYGILI

Department of Chemistry, Faculty of Education, Dicle
University, 21280 Diyarbakır, Turkey
gb.akkaya@gmail.com

Filiz KOYUNCU

Department of Chemistry, Faculty of Education, Dicle
University, 21280 Diyarbakır, Turkey
flkync@gmail.com

Cumali YILMAZ

Department of Chemistry,
Faculty of Education, Dicle University, 21280
Diyarbakır, Turkey
ylmazcumali0@gmail.com

Abstract— Biochar derived from weeds modified with nitric acid (HNO_3) at optimum condition was utilized as adsorbent to remove methylene blue (MB) from aqueous solutions. The effects of solution pH, initial dye concentration, agitation time and solution temperature on MB adsorption were investigated by the optimal oxidized weeds char (OWC). The kinetic data followed the pseudo-second order kinetic model. The equilibrium data were best represented by the Langmuir isotherm model. The maximum MB sorption capacities of WC and optimal OWC were determined as 39.68 and 161.29 mg/g, respectively, under detected optimum conditions (pH 7.4, OWC dosage 0.1 g/50 mL, agitation time 480 min and temperature 50 °C).

Keywords—biochar; modification; methylene blue; adsorption

I. INTRODUCTION

Biochar is a stabilized, recalcitrant organic carbon compound obtained when biomass is heated to temperatures between 300 °C and 1000 °C under low (preferably zero) oxygen concentrations [1]. Biochar is an effective adsorbent derived from agricultural and industrial solid wastes [2] and is frequently applied to remove various pollutants, including dyes, pesticides, and heavy metals, from aqueous solutions [3].

The presence of dyes in wastewater has become a significant source of water pollution, due to textile, paper and printing industries. Methylene blue (MB) is one of the most commonly used azo dyes in industry [4], having various detrimental effects on human and aquatic

life when released into the environment [5].

Until now, the study on methylene blue (MB) desorption using biochar and its oxidized form produced from weeds has not been reported in literature. The weeds hinder the efficient agricultural production. Therefore, these bio-wastes are removed from their millions of tons of fertile soil, and discarded into the environment.

This work aims to (i) prepare OWC from weeds (W), (ii) to optimize the MB sorption onto the OWC according to the process parameter such as solution pH, sorbent dosage, initial concentration, agitation time and solution temperature, (iii) to evaluate in terms of kinetic and

equilibrium isotherm parameters to explain the MB sorption mechanisms of the OWC.

II. MATERIALS AND METHODS

Synthesis of modified (WC-HNO₃) adsorbent

The biochar was prepared by pyrolyzing the weeds were supplied. The herbal-based biochar named WC was obtained by slow-pyrolyzing from weeds at 500 °C for 1 h under oxygen-limited conditions. HNO₃ modified biochar was made by the following steps: 1.0 g of dried WC powder was treated

with 25 mL of 20, 40, and 65% of HNO₃ solution for 1 h in the 80 °C (reflux under continuous stirring).

From surface chemical analysis results, the WC65 was selected as optimal OWC sample. It was used in the sorption experiment of MB dye from the aqueous phase in this study.

Batch aqueous MB adsorption

To optimize the sorption conditions, the effects of various operating parameters such as initial solution pH (2-10), sorbent dosage (0.1-0.5

g), initial MB concentration (50-400 mg/L), agitation time (5-480 min) and solution temperature (20-50 °C) were studied. After each process, the samples were centrifuged (5000 rpm, 10 min) for solid-liquid separation and the residual MB concentration in solution was analyzed by a UV-vis spectrophotometer (Perkin Elmer-Lambda 25) at its λ_{max} (665 nm).

III. RESULTS AND DISCUSSION

Effect of various operating parameters on the Methylene blue dye adsorption

The optimum pH for MB adsorption onto WC65 was found to be 7.4. Optimum dosage of WC65 was found to be 0.1 g/50 mL. The amount of MB adsorbed onto WC65 increased from 27.21 to 77.77 mg/g with increase in initial MB concentration from 50 to 400 mg/L. This may be caused to an increase in the driving force between the aqueous and solid phases and increase the number of collisions between MB dye ions and WC65. The sorbed amount of MB with increase from 20 to 50 °C of temperature was found to increase from 67.57 to 161.29 mg/g. The increase in the adsorption capacity might be due to the possibility of increase

in the number of active sites for the adsorption with the increase of temperature.

Removal of Lambda Cyhalothrin by Ralstonia eutropha in a Batch System: Effect of Carbon Starvation and Some Growth Conditions

Gülşad USLU ŞENEL

Environmental Department, Faculty of Engineering,
University of Firat,
Elazığ, Turkey
guslu@firat.edu.tr

İrem ÖZDEMİR ATAY

Environmental Department, Faculty of Engineering,
University of Firat,
Elazığ, Turkey,

Abstract— In this study, biodegradation of Lambda C by free *Ralstonia eutropha* was performed in batch system. Glucose was used as carbon source in addition to pesticides. The effects of initial pH, temperature and initial pesticides concentrations on the substrate removal and specific growth rates and yields were investigated. Optimum initial lambda c concentrations, initial pH and temperature were determined as 2 mg-1, 6 and 20 °C, respectively for free cells. In these optimum conditions, the maximum microorganism's specific growth and pesticide removal rates were determined as 0,0878 h-1 and 0,0408 mg/g dry cell/h for lambda c., respectively.

Lambda C had a strong inhibitory effect on the microbial growth. substrate inhibition was observed at concentrations higher pesticide concentrations than 2 mg/L. At experiments, where substrate inhibition was not observed, microorganism's specific growth was implied with Monod Equality depending on substrate concentration. In these conditions, microorganisma inhibition constant values was determined as $K_s = 0,8540$ for lambda c. The results show that the growth of *R. eutropha* was not effective for biodegradation of Lambda C.

Keywords— Biodegradation, Lambada cyholothrin, Microbial growth

Pb(II) Adsorption from Aqueous Solution by Low Cost Agro-Based Adsorbent – Grape Stalk

Mehmet ERDEM

Environmental Department, Faculty of Engineering,
University of Firat,
Elazığ, Turkey
guslu@firat.edu.tr

Halime DURAN

Firat University
Elazığ, Turkey,

Abstract— Lots of the heavy metals and their salts are widely used in the industrial applications. As a result of their widespread use, heavy metal pollution in waters is an important environmental problem encountered at industrial areas. Heavy metals are extremely toxic and their adverse effects can last for a long time in nature. Therefore, the wastewater containing heavy metals must be treated with an effective treatment method such as chemical precipitation, ion exchange, membrane processes and adsorption before the discharging [1]. Among these methods, adsorption is recognized as a promising method owing to the properties of high adsorption capacity, easy operation, low-cost and eco-friendly nature.

Usages of the low-cost adsorbents such as agricultural wastes and residuals, metallurgical slags, fly ashes and different minerals have been used or tested for heavy metal removal from the wastewaters recently [2-6]. Agricultural wastes or residues have become the subject of considerable interest due to their low cost, abundant and readily available. Starting from this information, in this study; effects of the some parameters such as pH, adsorbent dosage, contact time, particle size, initial Pb(II) concentration and temperature on Pb(II) removal from aqueous solutions by agro-based adsorbent prepared from grape stalk were investigated. The data was analyzed with first and second-order kinetics models and Langmuir and Freundlich adsorption isotherms. It was found that the adsorption kinetics followed the second-order rate law and adsorption fitted to the Langmuir isotherm. The Pb(II) maximum adsorption capacity of the grape stalk was calculated to be 32.8947 mg/g at 25°C.

Keywords— Grepe Stalk, Adsorbent, Lead, Adsorption

Compacted Geolayer Design from Coal Boiler Bottom Ash, Fly Ash and Geosynthethics- Bottom Seal Layer for Municipal Waste Landfill

Yıldırım Tosun

Şırnak University, Engineering Faculty

Şırnak, Turkey

yildirimismailtosun@gmail.com

Abstract— The stability analysis has been made in terms of geotechnical points at the potential and active landslide areas at Şırnak Province. By making engineering geology map in 1/10.000 scale of an area of 2 km² at the research area of Waste Fill Dumping and surrounding it, the mechanical characteristics of the outcropped soil and sub soil units have been defined. By the topographical maps of 1/5000 scale of the dumping slopes, the landfill areas of S2, S3 and S4 were investigated. Bottom layer units on the local small scale sections have been made. By laboratory tests the physical and mechanical characteristics of the slope have been made on the samples taken from the land.

Keywords—landfill; municipal slurry; bottom layer; geolayer; permeability

I. INTRODUCTION

The main factors affecting the gravitational mass movements as well as the geology of the rock material, precipitation, erosion, earthquakes and the vegetation can be classified as withdrawal. In determining the risk of slipping and possible future limits its ability to estimate the dynamic tension and equilibrium analysis gives accurate results (Hoek and Bray, 1977; Lamb and Whitman, 1969).

Heavy rainfall, seismic, and changes in the level of groundwater, erosion, climate processes such as decomposition, topography creates a natural slope parameters for triggering the shift in critical areas. These effects increase the shear stress or reduce the shear strength of the slope material (Bishop, 1955; Hoek, 1970). The growing urbanization brought on the landfills, housing, trade, the creation of social and infrastructure activities can disrupt stability, such as the realization of the implementation of urban land use.

According to appropriately measured and weighted factors of each GEO5 hazardous cross-sections, A landfill susceptibility map for each data layer is developed using an algorithm that combines factors in weighted linear combinations. To verify the practicality of the susceptibility map was compared with a landfill map containing few active landslide zones. The outcome was that the active critical zones do not completely fit into the high and very high susceptibility class. But 33% of these zones fall into the high and very high susceptibility zones.

The area shown in Figure 1 was chosen as municipal landfill area and concluded that 54 and 63.1% areas of the province are close to ground water sources with regard to landfills hazard, respectively. In conclusion, we can say that this basin suffers from a relatively high

potential of instability to make us largely hesitate to develop the basin for urban use.

The city province may develop in future so that we have to know the mechanism and the properties of the landfill in the future, is important basic information to assess landfills may develop in similar or adjacent areas, geotechnical. Especially in developing countries, land is used according to the topology and improper land use in mountainous areas increases the likelihood of water drainage development. Therefore, the physical environment of the relevant fields, exchange and sustainability cannot be achieved in terms of efficiency (Bishop, 1955; Hoek, 1970).

A geological map of the provinces of Şırnak and the surrounding area has been identified geotechnical engineering unit of surface features (Anonymous, 2012). The slope, was one of the first large-scale topographic maps of the bottom preparation work in the region on the geological map processing. The determination of the engineering properties of slope, is intended to draw attention to the critical importance of geotechnical and municipal development plans in the future in the construction field.

It was examined as potential criteria for waste storage piles stability of slopes in static challenges. Mass of the examined parameters affecting slope stability is indicated on the map possible anomalous situations and risk analysis. Something that will not threaten the environment of coal waste piles and construction will be put into operation shortage in size is recommended. Seismic design of the static properties of materials characterization and solid waste storage is a difficult task. Due to the heterogeneity of the batch material must be made large static and dynamic analysis. In this direction, in the province of Şırnak area, waste heaps of the coal mines in the south and 7 km from the city center (Figure 1) is evaluated within the city. The study area and an area of around 3 km² 1 / 1,000 scale topographic map made of engineering, also performed drilling and laboratory engineering properties of materials are determined by geotechnical tests (c Anonymous 2011). Close accordance with the settlement, the bottom of the stream and pond design will save the nature and condition of the masses slope stability analysis was performed by examining the geotechnical characteristics of the program GEO5 programs in different ways. This project covers whole part of urbanization area, a 7 km² area covering the work area and the environment, which will be open to urban use. The general scale engineering map of 1/15,000 of the field and laboratory studies has been prepared as a result has also generated topographic map of every four slopes with field studies using the polar coordinate system.

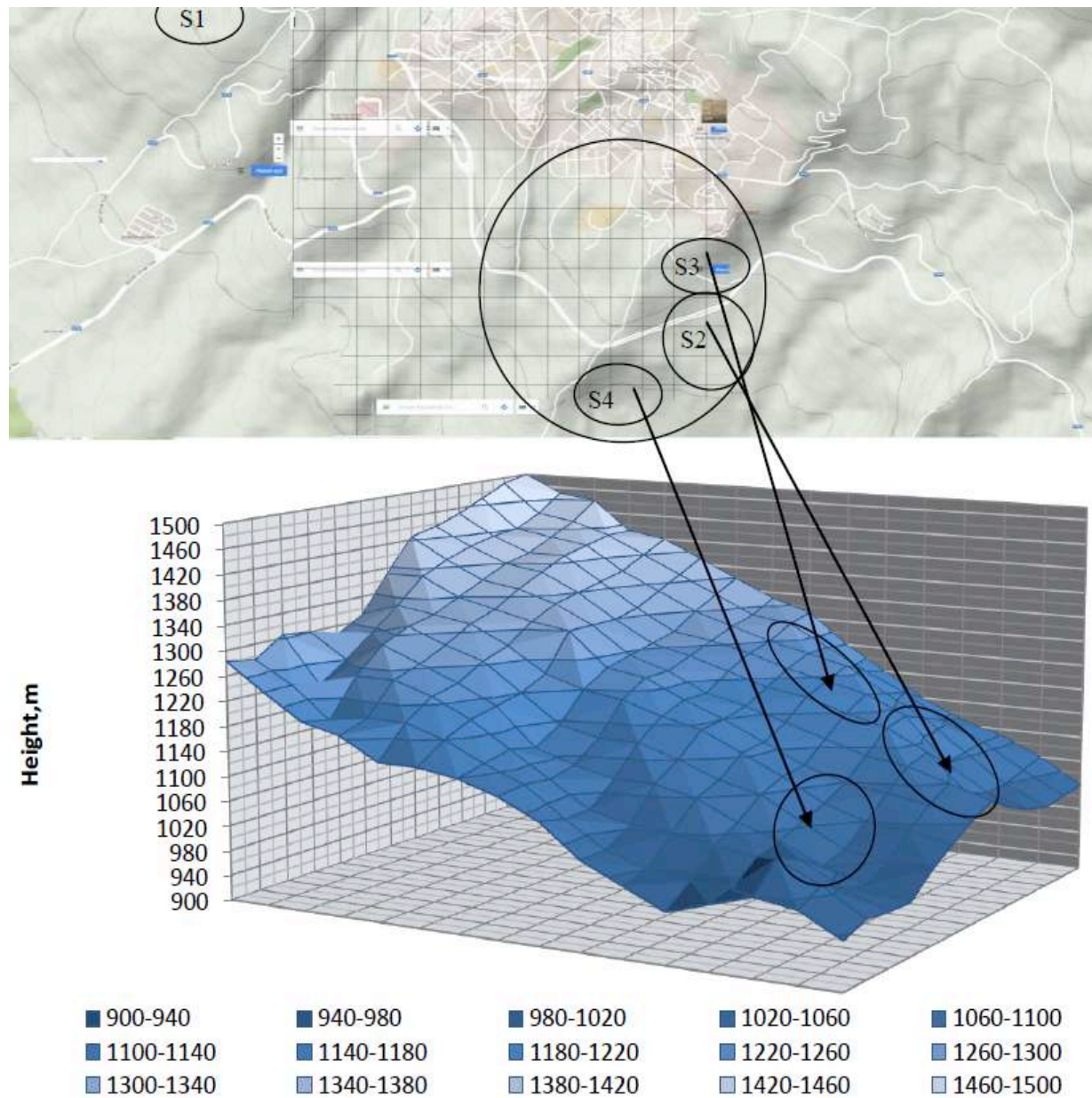


Fig 1. A scale of 1/15,000 engineering map of the field and topographic image

Table 1. chemical composition values of Sirnak province boiler bottom slag, volcanic slag and Tatvan pumice

Component%	Sirnak boiler bottom ash-slag	Volcanic slag	Tatvan pumice	Şırnak Fly Ash	
SiO ₂	43,48	50,50	60,13	41,48	
Al ₂ O ₃	16,10	14,61	17,22	18,10	
Fe ₂ O ₃	10,52	24,30	4,59	4,52	
CaO	8,48	2,30	2,48	18,48	
MgO	3,80	1,28	2,17	4,20	
K ₂ O	2,51	2,51	3,51	2,71	
Na ₂ O	1,35	1,35	4,35	1,95	
Ign.Loss.	10,9	0,21	4,12	1,9	
SO ₃	0,32	0,12	0,52	0,22	

II. METHOD

A. Physical Quality of Geomaterials

American Standard (ASTM 3080) experiments were carried out in the fill area. The specimens were tested to determine the geotechnical properties based on the representative masses in the study area, where the soundings of content are given in Table 1. S2, S3 and S4 fields of investigation were made in 2013. The micro pictures of used bottom ash-slag and volcanic cinder and pumice are seen from Figure 2 and grain size distributions of the material used as bottom layer in the landfill are shown in Figure 3.



Figure 2. The macro and micro images of Boiler slag, volcanic slag, Tatvan Pumice.

B. Quality the Geobottom Layer

Municipal waste heaps in the study area (Figure 1) showed gray marl, shale outcrops of new alluvial deposits observed to the south. Some parts of this section are generally covered by silty soil consists of sandy and clayey zones. The investigations in the area of the landfill to the south located the grain size of coarse sand and fine clay was observed as soil. By sorting and grading, the thickness of the soil ranged from 10-35 cm.

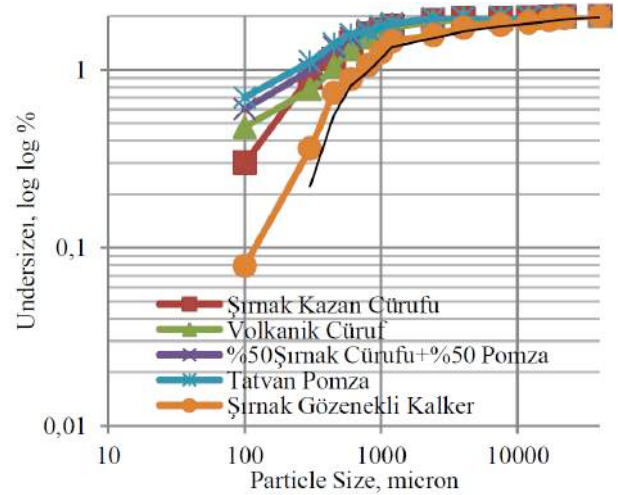


Figure 3. Particle Size Distribution of Bottom Layer Clay and Slag

III. RESULTS AND DISCUSSIONS

The free dumping of municipal waste were carried on the slopes of landfill bottom layer of slag-fly ash, such as compacted fine-grained parts-upper geotextile and disturbed samples of bottom layer were taken. The experiments were conducted on compacted layer. The grain size distribution curves of the samples showed fine grains unit weight over 80% which limited consistency of coarse was less.

By the cutting box test effective cohesion (c) the effective shear strength and friction angle (ϕ°) of bottom layer and soils were determined.

Water content in the ground, the ratio of clay and fly ash affected significantly. As the evaluated according to the percentage of clay and fly ash in the samples showed cohesive or low cohesive property. The saturated unit weight is given in Table 2. Fixed level permeability test instrument is used to determine the permeability of the ground. Degree of permeability of the soil was determined by evaluating the test results (Table 3). As examined in Table 3, S2, S3 and S4 floors were permeable ground. Proctor tests showed the slag-fly ash effect on compaction,

IV. CONCLUSION

The bond between the grains at geolayer and the compaction was critical in strength. The weathering of rocks in the study area is weakening quickly change the height and tilt angle of the slopes to erosion and slope. Dissociation seen in geolayer materials in the study area also offers a negative contribution to permeability problems. The compression strength could be easily tested by indentation on the landfill as shown in Figure 2. The durability of the landfill bottom layer was tested easily on the chart of fly ash and slag mixture content as given in the Table 2.

As a result of the geotechnical analysis performed in the study area should be considered in the future danger of very large stacks and site reclamation methods are suitable to be determined. In addition, the working area of the project due to be opened to urban use contraceptive methods studied and developed instability poses a special importance.

REFERENCES

- [1] Anonim, c 2011, “Türkiye Deprem Bölgeleri Haritası”, Afet ve Acil durum Yönetimi Başkanlığı Deprem Dairesi Başkanlığı, Ankara
- [2] Anonim, d 2011, Şırnak İl Özel İdare Raporları
- [3] ASTM, 1990 “Standard Test Method for Direct Shear Test of Soils Under Consolidated Drained Condition”, D3080-90,
- [4] Bishop, A.W., 1955, The use of the slip circle in the stability analysis of earth slopes, *Geotechnique*, Vol. 5, 7-17.
- [5] Dramis, F., Sorriso-Valvo, M., 1994 “Deep-Seated gravitational slope deformations, related landslides and tectonics”, *Engineering Geology* 38, 231- 243,
- [6] Erguvanlı, K, ve Erdoğan, Y., “Yeraltı Suları Jeolojisi”, İTÜ yayınları No: 23, Maçka İstanbul, Nisan 1987
- [7] Görög P & Török Á, 2007 Slope stability assessment of weathered clay by using field data and computer modelling: a case study from Budapest ,*Natural Hazards and Earth System Sciences*, 7, 417–422, www.nat-hazards-earth-syst-sci.net
- [8] Görög P & Török Á, 2006, Stability problems of abandoned clay pits in Budapest, IAE2006 Paper number 295 , The Geological Society of London
- [9] Güz, H , 1987, “Geoteknikte Gelişmeler”, DSİ Yamaç ve Şevlerin Stabilitesi ve Dayanma Yapıları Semineri, Samsun
- [10] Höek, E., 1970, Estimating the stability of excavated slopes in opencast mines, *Institution of Mining and Metallurgy*, A105, A132
- [11] Höek, E. ve Bray, J.W., 1977, *Rock slope engineering*, Stephen Austin and Sons Ltd, Hertford, 402 s.
- [12] Hoek, E., 2013, *Practical Rock Engineering*, Hoek notes by Evert Hoek. <http://www.rocksience.com>
- [13] Hutchinson, JN., 1995”Landslide hazard assessment. Keynote paper. In: Bell DH (ed) *Landslides, Proceeding of 6th international symposium on landslides*, Christchurch, New Zealand, vol 1. Balkema, Rotterdam, pp 1805–1841,
- [14] Lambe, W.T. ve Whitman, R.V., 1969, *Soil mechanics*, John Wiley and Sons, New York

A Relationship Between Physico-Chemical Properties of The Soil and Selenium Speciation

Abdullah ÖZKAN
University of Iskenderun Technical,
Hatay, Turkey

Şana SUNGUR
University of Mustafa Kemal,
Hatay, Turkey

Vildan ÖZKAN
University of Iskenderun Technical,
Hatay, Turkey

Abstract—elenium is both essential and toxic for biological and environment system. There is a very sensitive balance between the toxic and beneficial state of selenium species that depending on the element concentration. So it is very important to determine of amount of selenium speciation in soil.

This study aimed to determine relations to between selenium species that different geochemical fractions (soluble, exchangeable and carbonate-bound, iron / manganese oxide bound, organic matter bound and residual) with physico-chemical properties in soil series Amik Plain.

Selenium analyzes were performed according to the method that described by Wang and Liang, (2012) using the high resolution continuous atomic absorption spectrophotometer (HR-CS AAS) hydride system. Routine soil parameters which the exchangeable cations by the ammonium acetate method, organic matter by the Walkley Black method, available phosphorus by sodium bicarbonate method, pH and EC in soil-water suspensions, lime equivalent by Scheibler calsimeter and texture analyzes by hydrometer were determined to soil samples. The data were subjected to correlation and regression analysis with SPSS programme. The statistical analyzes show that no significant relations between selenium species with soil physico-chemical properties. But there is a significant relationship between total selenium with total of exchangeable cations and organic matters.

Keywords— Soil Physico-Chemical Properties; Selenium Speciation; HR-CS AAS, SM&T; Amik Plain

Productivity Parameters of Agricultural Lands of Hatay Province

Abdullah ÖZKAN
University of Iskenderun Technical,
Hatay, Turkey

Vildan ÖZKAN
University of Iskenderun Technical,
Hatay, Turkey

Şana SUNGUR
University of Iskenderun Technical,
Hatay, Turkey

***Abstract—** The present study were aimed to determine some productivity parameters of soil belong to Amik plain, which is located in Hatay province, Turkey. For this purpose, 179 soil samples were collected at 2 km intervals in 0 – 30 cm depth of the agricultural lands. pH, EC, lime, organic matter, useful phosphorus, total exchangeable cations and structure (Sand, Silt and Clay) of the soil samples were analysed.*

The study results were determined as pH: 7.00-8.90, EC: 78-1188 (μ S), lime:0-43.9 (%), organic matter: 0.095-4.0 (%), useful phosphorus: 0.010-71.4 (mg.kg-1), total variable cations: 53-140.9 (mmol), clay: 0.010-58.8 (%), sand: 4.60-70.9 (%), silt: 15.6-88.8 (%).

In conclusion, the current data suggested that the use of unnecessary fertilization could be decrease with agricultural activities more consciously of the local people. The results will provide an important contribution to our national economy in future.

***Keywords—** Hatay province; Amik plain; productivity; soil.*

Arsenic Removal from Aqueous Solution by Using Magnetic Activated Carbon Prepared from the Mixture of Almond Shell, Apricot and Peach Stones by Chemical Activation

Hawraz Luqman RAHMAN

Environmental Department, Faculty of Engineering,
University of Firat,
Elazığ, Turkey
hawraz.luqman@gmail.com

Hatice ERDEM

Environmental Department, Faculty of Engineering,
University of Firat,
Elazığ, Turkey
erdemhatice23@gmail.com

Özlem AKÇAKAL

Environmental Department, Faculty of Engineering,
University of Firat,
Elazığ, Turkey
akcakalozlem@gmail.com

Mehmet ŞAHİN

Environmental Department, Faculty of Engineering,
University of Firat,
Elazığ, Turkey
msahin230@gmail.com

Mehmet ERDEM

Environmental Department, Faculty of Engineering,
University of Firat,
Elazığ, Turkey
merdem@firat.edu.tr

Abstract— Arsenic is creating potentially serious environmental problems for humans and other living organisms. Arsenic contamination is caused by natural processes such as mineral weathering and dissolution resulting from a change in the geo-chemical environment to a reductive condition and by human activities such as mining wastes, petroleum refining, sewage sludge, agricultural chemicals, ceramic manufacturing industries and coal fly ash. Arsenic occurs in the forms of organic and inorganic in waters. The organic arsenic usually occurs less than 1 µg/L in natural conditions. Arsenate (as $H_2AsO_4^-$ and $HAsO_4^{2-}$) is the predominant and stable inorganic arsenic form in the oxygen-rich aerobic environments, while arsenite occurs primarily as H_3AsO_3 and $H_2AsO_3^-$ (above pH 9.3) in reducing anaerobic environments. Owing to epidemiological evidence linking arsenic and cancer, maximum concentration level in drinking water has been limited to 10 µg/L by WHO.

Many treatment technologies have been developed such as lime precipitation, oxidation, coagulation/filtration, adsorption, ion exchange and membrane processes to remove arsenic from water. Among these methods, adsorption method seems to be promising. Activated carbon is the most widely used adsorbent. Particularly, it can be obtained the most suitable adsorbents for different pollutants by modifying its surface properties. In this study; a magnetic activated carbon prepared from almond shell, apricot and peach stones mixture with $FeSO_4$ chemical activation was used as an adsorbent to remove the arsenic and effects of the some parameters such as adsorbent dosage, contact time and initial arsenic concentration on the arsenic adsorption were examined. It was found that whole arsenic in the solution (10 mg/l) was removed by using 2 g/l of magnetic activated carbon at the pH range of 2-9 at 25°C for 60 min.

Keywords— Magnetic activated carbon; Arsenic; Adsorption; Almond shell; Apricot stone; Peach Stone.

Acknowledgment— The authors thank Firat University, Scientific Research Project Funding (FUBAP) for their financial support [Project number: MF.16.56].

Investigation on The Water Source Change by Using GIS Relationship Between Climate and Hydrology of Batman Province Site Turkey

Yıldırım TOSUN
University of Şırnak,
Şırnak, Turkey
yildirimismailtosun@gmail.com

Vahap YONTEN
University of Munzur,
Tunceli, Turkey
vyonten@hotmail.com

Abstract— *The parameters and data controlling hydrologic processes by Geographic Information Systems (GIS) have become an integral part of hydrologic studies. The main management is to bring together the use GIS to model s and hydrologic data. The general distribution of the inputs and parameters can control the surface sources or underground loss. GIS maps commonly describe topography, land use and cover, soils, rainfall, and meteorological variables may become model parameters or inputs in the simulation of hydrologic processes.*

This investigation of water logging can be extremely useful in suitable water management strategies by reclaiming existing water logged areas. The problems of water logging and quality mostly exist in the irrigated areas like in South Eastern rocky plains of Batman, Turkey. The climate change and ground water changes generally results in over irrigation, seepage losses through channel and distributions, poor water management practices and inadequate control of drainage system. Analysis of high water table in water logged areas and drainage of irrigated areas have not been paid adequate attention in the planning and management of water resources, partly due to lack of requisite data and partly due to flood and rainfall in the country. In order to develop suitable water management strategies and controlling the extent of water logging in the area. GIS may facilitate the reconstruction of the ecological environment but also to accommodate the sustainable development of the water resources and waste water.

In this study, the hydrological characteristics of the Batman city were explained and the effect of these characteristics on the the city was examined. In the investigation, hydrological features and the urbanization with new settlements needs modeling regarding available water source. The hydrological property of settlement areas with dense populated areas in the model was determined by Geographic Information Systems (GIS) techniques. The main purpose of this study is to investigate the effect of settlement on the basic hydrological structure by studying the characteristics of the ground topography, ground water elevation, slope and viewing. GIS techniques were used in the creation of the thematic maps and in the analysis of the parameters. Finally, the GIS study models created , the available water source change and a stream network model was provided sufficient source control at the Batman province. The presence of this stream network structure in the Batman province reveals the potential flood scale and flood risk. This study produced more systematic data with hydrological studies carried out with GIS support. GIS has made it possible to obtain more qualified data by enabling the use of multi-criteria decision making method in this research.

Keywords— *Water resource; GIS; hydrology; clean water; water management; Batman*

IV. CONCLUSIONS

Based on the obtained results, the following conclusions can be drawn: The kinetic and equilibrium data were well represented by the pseudo-second order kinetic and Langmuir isotherm models, respectively. The maximum sorption capacities for MB onto WC and WC65 were found to be 39.68 and 161.29 mg/g at 50 °C, respectively.

Consequently, this study shows that WC65 acts as a potential and low-cost sorbent for the removal of hazardous dye MB from aqueous medium.

REFERENCES

- [1] T. Xie, K.R. Reddy, C. Wang, E.Yargicoglu, K. Spokas, "Characteristics and applications of biochar for environmental remediation: a review." *Crit. Rev. Environ. Sci. Technol.*, vol. 45 (9), pp. 939-969, 2015.
- [2] M. Rafatullah, O. Sulaiman, R. Hashim, A. Ahmad, "Adsorption of methylene blue on low-cost adsorbents: a review." *J. Hazard. Mater.*, vol. 177 (1-3), pp. 70-80, 2010.
- [3] D. Mohan, A. Sarswat, Y.S. Ok, C.U. Pittman Jr., "Organic and inorganic contaminants removal from water with biochar, a renewable, low cost and sustainable adsorbent: a critical review." *Bioresour. Technol.*, vol. 160, pp. 191-202, 2014.
- [4] J. Fu, Z. Xu, Q.S. Li, S. Chen, S.Q. An, Q.F. Zeng, H.L. Zhu, "Treatment of simulated wastewater containing Reactive Red 195 by zero-valent iron/activated carbon combined with microwave discharge electrodeless lamp/sodium hypochlorite." *J. Environ. Sci.*, vol. 22, pp. 512-518, 2010.
- [5] R. Reid, "Go green – a sound business decision." *J. Soc. Dye. Colour.*, vol. 112, pp. 103-105, 1996.

Electricity Generation from Meat Processing Industry Sludge: Double Chamber Microbial Fuel Cell (Mfc) Application

İdris BIRYOL
University of Dokuz Eylul,
İzmir, Turkey
idrisbiryol88@hotmail.com

Azize AYOL
University of Dokuz Eylul,
İzmir, Turkey
azize.ayol@deu.edu.tr

Abstract— *The microbial fuel cell (MFC) production from biodegradable organic wastes is considered as a new concept based on the recent molecular discovery of specific microbes capable of catalyzing efficient half reactions at electrode surfaces. Typical double chamber MFCs consist of two separate chambers which can be inoculated with any type of liquid. These two chamber reactors have an anaerobic anode chamber and an aerobic cathode chamber, generally separated by a PEM such as Nafion (Oh and Logan, 2004). MFC is the possibility of combining waste degradation with energy generation. This technology uses microorganisms to catalyze the direct production of electricity from organic materials (Rezaei et al., 2007, Logan and Regan, 2006). This study has investigated the electricity production from waste activated sludge taken from meat processing industry wastewater treatment plant. The double chamber MFC reactors were designed at laboratory scale and different electrodes as Pt/C carbon paper and carbon cloth were used during experiments. Sludge characterization studies were first done before feeding the reactors. Maximum power, maximum current, power and current densities were calculated for all experimental series. Double chamber MFC- Pt/C carbon paper reactor has 33.80 mW/m² and 12.99 μ A/cm² maximum power and current densities while double chamber MFC-carbon reactor has 60.30 mW/m² and 17.36 μ A/cm² maximum power and current densities. Double chamber MFC Pt/C gave a positive reaction to NaCl additions. This paper debugs the experimental results in details.*

Keywords— *Meat processing industry treatment plant sludge; microbial fuel cell; energy recovery; waste degradation*

Effect of polymer additives on the structure and gas transfer performance of polyvinylidene fluoride (PVDF) hollow fiber membranes by wet spinning

Yunus AKSOY

Department of Environmental Engineering, Faculty
of Engineering, Firat University
23119- Elazig, Turkey
yaksoy@firat.edu.tr

Halil HASAR

Department of Environmental Engineering, Faculty
of Engineering, Firat University
23119- Elazig, Turkey
hhasar@firat.edu.tr

Abstract—The objective of this study was to investigate the effect of polyvinylpyrrolidone (PVP) and propionic acid (PA) on the structure and gas transfer performance of polyvinylidene (PVDF) hollow fiber membranes by wet spinning. PVDF hollow fiber membranes were fabricated using wet spinning process.

Keywords—Hollow fiber membrane, wet spinning, polymer additives, gas transfer.

I. INTRODUCTION

By changing the regulations on drinking water quality and wastewater discharge standards and decrease in available fresh water supplies in all over the world, this situation has prompted researchers to find and develop new technologies in water and wastewater treatment. Due to membrane technologies can produce high quality reusable water from wastewater for irrigation, reuse and agricultural purpose water, researchers have

focused on the development of this technology. The membrane biofilm reactor (MBfR) is developing technology for water and wastewater treatment. It is composed of hydrophobic membranes that provide gas transfer [1]. Certain gaseous diffuse from the inside of membrane fibers to the biofilm located on the outer surface of each fiber [2]. This system appears to be more advantageous than conventional biofilm systems. One of the most important advantages of MBfRs is that the gas, which may vary according to contaminant species desired to be removed from wastewater, delivered to each membrane fiber is diffused from the inside to the outside without bubble formation. The manufacturing of gas transfer membrane has crucial potential in the development of this technology. In this study, we tried to produce gas transfer hollow fiber membranes by wet spinning process.

II. MATERIALS and METHODS

Polyvinylidene fluoride (Solef 6010 homopolymer) was purchased from Solvay was used as the polymer in the dope solutions. N-Methylpyrrolidone (NMP) was used as solvent and bore liquid component supplied from Asland. Polyvinylpyrrolidone (PVP K10) and propionic acid (PA) were used as a polymer additive supplied from ISP and Merck respectively. Chemicals used other than PVDF have not undergone any pretreatment. Hollow fiber membranes were fabricated by wet spinning. Based on study, polymer material wt. %20 of PVDF was used in dope solutions. N-Methylpyrrolidone (NMP) with

wt. %77,5 and %80 was used as a solvent. PVP K10 and PA were used with wt. %2,5 as a polymer additives. Mixture of water and NMP (10 wt. % water and 90 wt. % NMP) was used as a bore liquid. Tap water was used in the coagulation bath and the air gap distance was zero. Spinning parameters (dope and bore flow rate, take-up speed etc.) were kept constant. PVDF was dried for 1 day at 60°C, NMP was added to the dope solution after being sure that PVDF dissolved in NMP, polymer additive (PVP K10 or PA) was slowly added into the dope solution and dope solution mixed for 2 days at 70°C. To remove air bubbles from the dope solution before spinning, the solution was sealed under vacuum. Pressurized nitrogen gas (2 atm) pumped the dope and bore solutions to the spinneret where all solutions were combined. From the

spinneret, the solution immediately immersed into the first coagulation bath and formed fibers moved from the first coagulation bath to the second coagulation bath. Ultimately fibers were collected on the take up roll. The produced membranes were room temperature. Morphology of hollow fibers membranes was characterized by using scanning electron microscope (SEM). Surface functionalization of hollow fiber membranes was characterized using FTIR Spectrophotometer. Hydrophilicity of hollow fiber membranes was found by conducting contact angle measurements. For mechanical testing of hollow fiber membranes

stored in distilled water in a container for minimum 3 days to remove solvent and additives. After this process, the membranes were dried to determine the characterization and gas transfer performance at

DMS instrument was used. The produced membranes were made into modules to determine gas transfer performance. Oxygen concentrations values were recorded versus time at constant 2 psi. Spinning parameters and the contents of dope and bore liquid solutions are given in Tables I and II, respectively.

Table I. Contents of solutions

Membranes	Dope solutions			Bore solutions	
	<i>PVDF</i> (wt. %)	<i>Solvent</i> <i>NMP</i> (wt. %)	Additive (wt. %)	Solvent (wt. %)	Water (wt. %)
HF1	20	80	-	90	10
HF2	20	77,5	2,5 (PVP K10)	90	10
HF3	20	77,5	2,5 (PA)	90	10

Spinning parameters	M1	M2	M3
Dope solution velocity (mL/min)	6	6	6
Bore liquid velocity (mL/min)	3	3	3
Take-up speed (m/s)	0,1	0,1	0,1
Air gap (cm)	-	-	-
Coagulation baths temperature (°C)	25	25	25

Table II. Spinning parameters

III. RESULTS and CONCLUSIONS

SEM images of the produced hollow fiber membranes are shown in Figure I. It can be observed by scanning electron microscope (SEM)

that pristine (HF1) and containing PVP K10 (HF2) hollow fiber membranes have thin and long finger-like cavities, containing PA (HF3) hollow fiber membrane has macrovoid defects.

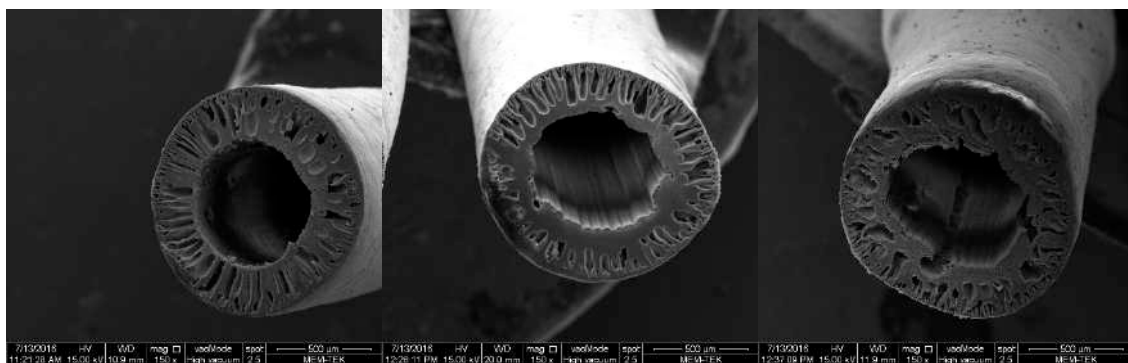


Figure I. SEM images of hollow fiber membranes from left to right HF1, HF2, and HF3 respectively.

The graphs of contact angle, mechanical strength and diffusion coefficient values of the produced hollow fibers are given in Fig. II, Fig. III and Fig. IV, respectively. As can be seen that with the addition of PVP K10 and PA in the dope solution, contact angles of the hollow fibers decreased. According to the results, the highest Young's Modulus of hollow fiber was dope solution contained wt. %2,5 of PVP K10. Diffusion coefficients of hollow fiber membranes were

decreased with the addition of PVP K10 and PA in the dope solution. Pristine hollow fiber membrane was the highest. Due to same peaks were observed between three hollow fiber type only pristine hollow fiber membrane FTIR-ATR measurement is given in Fig V. 762, 796, 858, 975, 1070, 1178 cm^{-1} peaks (α -phase) and 839, 1275 and 1401 cm^{-1} peaks (β -phase) were observed from FTIR-ATR measurements.

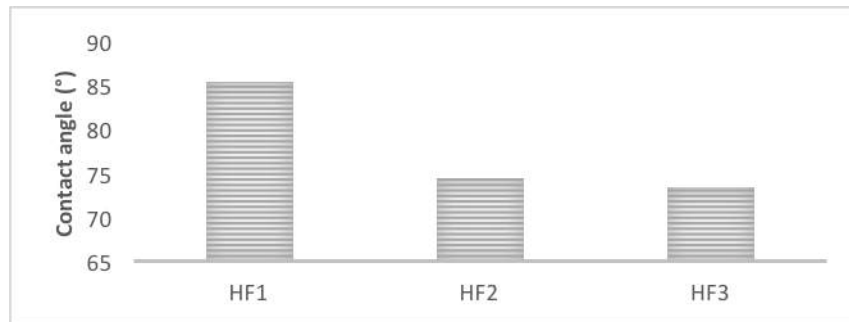


Figure II. Contact angles of the produced hollow fibers.

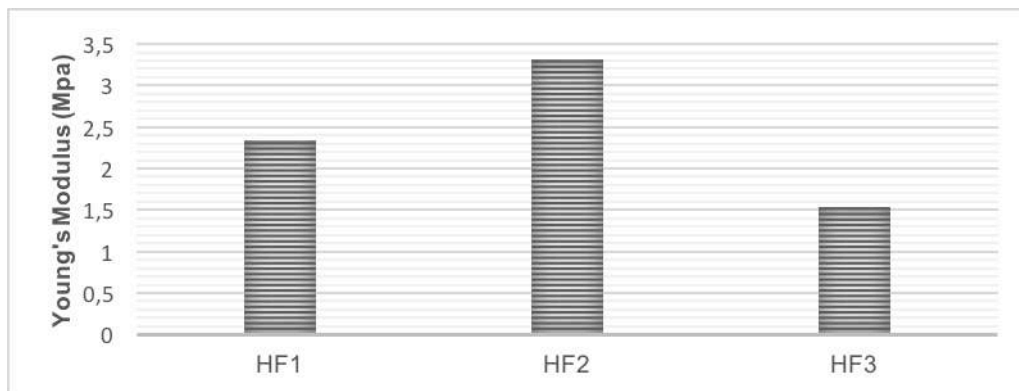


Figure II. Young's Modulus of the produced hollow fibers.

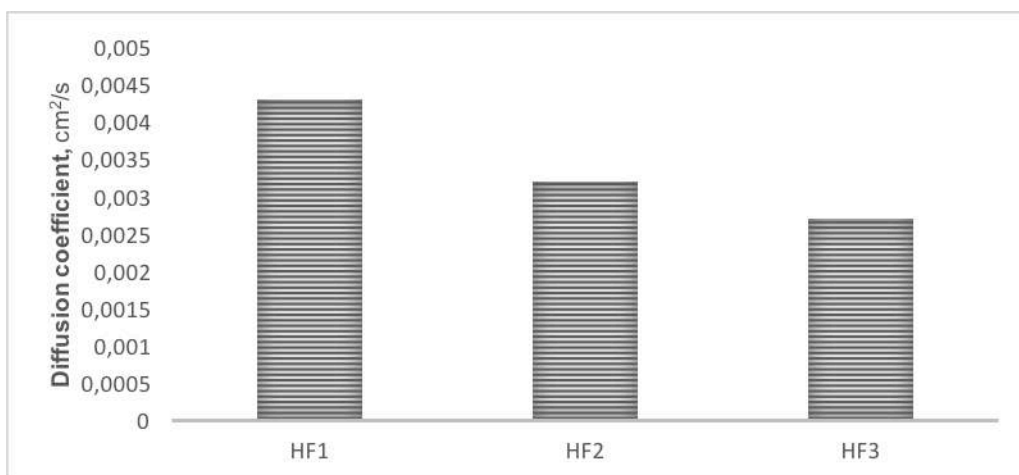


Figure IV. Diffusion coefficients of the produced hollow fibers.

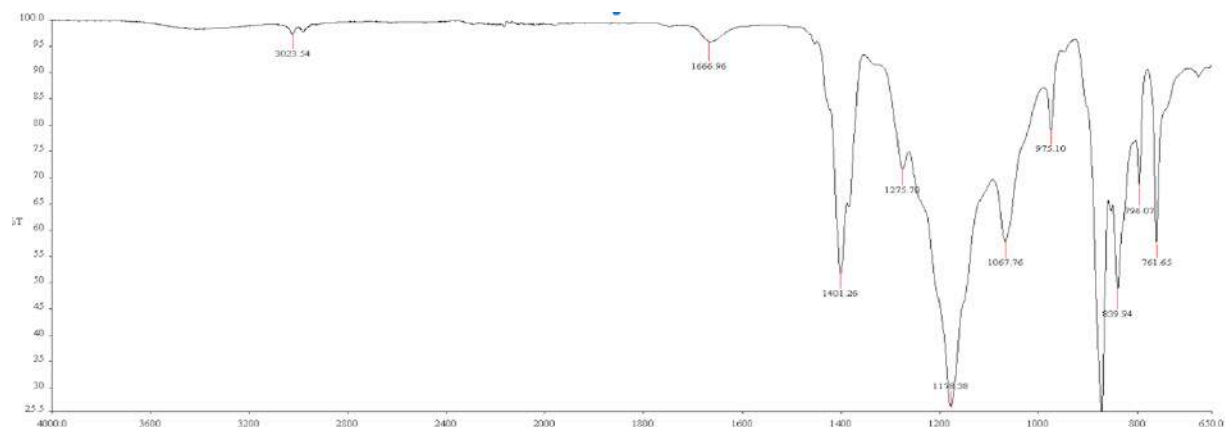


Figure V. FTIR-ATR of the pristine hollow fiber.

ACKNOWLEDGMENT

This paper includes Ph.D thesis data of MSc. Yunus AKSOY. Authors graceful acknowledge the financial support from The Scientific and Technological Research Council of Turkey (TUBITAK) with the project number of 115Y106.

REFERENCES

- [1] Hasar, H., Xia, S., Ahn, C. H., Rittmann, B.E. (2008). Total Nitrogen Removal of Organic Matter and Nitrogen Compounds by an Aerobic\Anoxic Membrane Biofilm Reactor, *Water Res.* 42, 409-411.
- [2] Taskan, E., Hanay, O., and Hasar, H. (2015), Energy-Efficient Nitrification and Microbial Community in a Completely Stirred Membrane Biofilm Reactor. *Environmental Engineering Science.* 32, 179-184.

Investigation Of Gasification Potential Of Leather Indusrty Treatment Plant Sludge

Özgun TEZER
University of Dokuz Eylul,
İzmir, Turkey
ozguntezer@gmail.com

Alim GURGEN
University of Dokuz Eylul,
İzmir, Turkey
alimgurgen@hotmail.com

Azize AYOL
University of Dokuz Eylul,
İzmir, Turkey
azize.ayol@deu.edu.tr

Abstract— Sludges produced at different treatment stages in biological wastewater treatment plants have rich organic materials in their characteristics. Recent research studies dealing with the sludge related problems have focused on the energy recovery from sludge due to its high organic content. Gasification process is a thermal conversion technology transforming the chemical energy contained in a solid fuel into thermal energy and electricity (Bruno, 2006, Arena and Mastellone, 2005). The inspiration point of the study is based on the successful gasification applications by using different organic materials like coal, walnut, wood chips, etc. The sludge produced from the wastewater treatment plants has a fuel merit with its high calorific value for usage of supplementary fuel as in the cement factories or recovery of energy from sludge while it is processing with the different valorization processes like gasification. Using the insight that sludge gasification may also be admitted as an energy resource, new and fundamental research approaches can be presented that are likely to produce syngas or combined heat and power production in a cost effective way and to minimize the ultimate waste amount to be landfilled.

The most important by-product of the gasification process is syngas including a mixture of CO, CH₄, H₂ and other gases to be used as fuel. In this study, the energy recovery from leather industry sludge taken from a leather industry wastewater treatment plant located in İzmir, Turkey by means of gasification process was investigated. A pilot scale downdraft type gasifier was used during the experimental studies. The produced syngas was converted to electrical power by using a gas engine. According to the experimental results, leather industry sludge was found as an appropriate material for gasification studies and remarkable energy recovery was obtained interims of power production by using syngas in an engine. This paper presents on the research results in detail.

Keywords— Leather industry treatment plant sludge; gasification; renewable energy; energy recovery; syngas

Adsorption Properties *Paenobacillus barcionensis* (PB) and MgO (n-MgO) nanoparticles for Reactive Black 5 from Wastewater

Nurullah AKCAN
High HealthSchool Department,
University of Siirt,
Siirt, Turkey
nurullah.akcan@gmail.com

Besi SERİN
Biology Department, Faculty of Science,
University of Dicle,
Diyarbakır, Turkey
beserin@hotmail.com

Serhat UZAN
Chemistry Department, Faculty of Science,
University of Dicle,
Diyarbakır, Turkey
serhatuzan21@gmail.com

Fikret UYAR
Biology Department, Faculty of Science,
University of Dicle,
Diyarbakır, Turkey
fuyar@dicle.edu.tr

Abstract— Various kinds of synthetic dyes appear in the effluent of industries such as textiles, leather, paper, plastics, etc. The textile dyeing industry consumes large quantities of water at its different steps of dyeing and finishing, among other processes. Since a very small amount of dye in water is highly visible and can be toxic to creatures in water, the removal of dye from wastewater becomes environmentally important. Among several chemical and physical methods, the adsorption process is one of the effective techniques that have been successfully employed for dye removal from wastewater. The use of microorganism for biosorption of arsenic ions from water is an enormously effective process, due to which it is becoming widespread day by day. Biosorption plays an important role in the removal of dyes from aqueous solutions to control water pollution. Low operating cost, reusability of biomaterial and improved selectivity for specific metals of interest, removal of heavy metals from wastewater irrespective of toxicity, short operation time and minimal sludge generation convinced many environmental managers in the mining and dyes smelting industry to attempt biological systems. Biosorption is a passive process which uses the cell wall of biomass for sequestering the metal ions from wastewater. It is a metabolism independent process and so can be done by both living and dead cells. The mechanisms of biosorption may be categorized into three types: (1) cell surface sorption/precipitation (2) extracellular accumulation/precipitation and (3) intracellular accumulation. This can take place by adsorption, coordination, complexation, ionexchange, chelation and microprecipitation. The cell wall of a microorganism mostly contains proteins, polysaccharides and lipids that deliver predominantly profuse dye binding functional groups for example hydroxyl, phosphate, carboxylate, sulphate, sulfhydryl, amino, amido and imidazole groups. This work we use *Paenobacillus barcionensis* (PB) and MgO (n-MgO) nanoparticles. This work deals with the preparation, characterization and dye adsorption properties of novel biocomposite composite (*Paenobacillus barcionensis*–magnesium oxide nanoparticle) (PB/n-MgO). Physical characteristics of PB/n-MgO were investigated. The textile dye reactive black 5 was used as model compound. The isotherm and kinetics of dye adsorption were studied.

Keywords— *Paenobacillus barcionensis*; MgO; reactive black 5; nanoparticle

The Influence of Water Salt Content on Desalination Performance

Ali ZOUNGRANA
Environmental Department,
University of Yildiz Technical,
Istanbul, Turkey
zoungson1@gmail.com

İsmail H. ZENGİN
Environmental Department,
University of Yildiz Technical,
Istanbul, Turkey
ismailhakkizengin@gmail.com

Doğan KARADAĞ
Environmental Department,
University of Yildiz Technical,
Istanbul, Turkey
dkaradag@yildiz.edu.tr

Mehmet ÇAKMAKCI
Environmental Department,
University of Yildiz Technical,
Istanbul, Turkey
cakmakci1974@gmail.com

Abstract— Membrane distillation (MD) is a well-known process for its application with high performance in desalination. However, the quality of the treated solution, as well as high transmembrane flux (TMF) and low membrane fouling, depend on many parameters including the feed solution salt content. In the present study, the salt content of the permeate solution and the TMF flux of a direct contact membrane distillation (DCMD) were evaluated during the desalination of various saline solution with different salt concentration. The treatment was performed using two hydrophobic membranes made of polytetrafluoroethylene (PTFE) and Polyvinylidene Fluoride (PVDF) 0.45 μm pore sizes, at 60 $^{\circ}\text{C}$ feed temperature. The results showed that at moderate salinity, the salt participated to increasing the TMF, and very high salt rejection took place as well. But at very high salt concentration, the flux dropped, and the effluent quality was reduced. The highest flux (around 12.89 $\text{L}/\text{m}^2\cdot\text{h}$) was obtained with 40 mS/cm conductivity of the feed solution when using PTFE membrane and the salt rejection reached 99.84% in the same condition. Similarly, with a higher salt content of the feed solution (60 mS/cm conductivity), the TMF reduced to 9.8 $\text{L}/\text{m}^2\cdot\text{h}$, however, the salt rejection was still high. It is obvious that an efficient control of salt concentration in real scale desalination can lead to a cost-effective MD for clean water supply from sea water.

Keywords— Conductivity; Desalination; Hydrophobic Membrane; Membrane distillation

Properties of Elazığ Organized Industrial District Wastewaters and Physicochemical Treatability

Merva GÖRGÜLÜ

Enviromental Department, Faculty of Engineering,
University of Firat,
Elazığ, Turkey
mervagorgulu@gmail.com

Ayhan ÜNLÜ

Enviromental Department, Faculty of Engineering,
University of Firat,
Elazığ, Turkey
aunlu@firat.edu.tr

Abstract— *Organized Industrial Districts (OID), are models that purpose to minimize and/or to remove environmental problems originating from industries. The Elazığ OID is located on an area of 322 hectares, 11 km east of the Elazığ province center. Industrial and domestic wastewaters of the OID are discharged to Elazığ Wastewater Treatment Plant via common channel. In this study, a trial work was carried out to determine the properties of wastewater taken from the OID common channel and its physico-chemical treatability. In the study, the pollution parameters expressed as chemical oxygen demand (COD), biological oxygen demand (BOD5) and suspended solids (SS) were determined as average 720 mg/L, 290 mg/L and 270 mg/L, respectively. In physico-chemical treatability studies; COD, SS and Total Nitrogen (TN) removal yield was around 50-70 %, 90- 95 % and 30-60 %, respectively. It was suggested to use $Al_2(SO_4)_3 \cdot 18H_2O$ for chemical treatment as a result of physico- chemical preliminary treatability tests using $Al_2(SO_4)_3 \cdot 18H_2O$ and $FeCl_3 \cdot 6H_2O$ with wastewater from OID common channel.*

Keywords— *Organized industrial districts; physico-chemical treatability; wastewater; preliminary treatability*

MECHATRONICS

ORAL SUBMISSIONS



Sliding Mode Based Control of a Triaxial MEMS Gyroscope

Zeynep ILKILIC

Dept. of Mechatronics,
Ondokuz Mayıs University,
Samsun, Turkey
zeynepilkilic00@hotmail.com

Zuhtu Hakan AKPOLAT*

Dept. of Mechatronics Engineering,
Faculty of Technology,
Firat University,
Elazig, Turkey
z.h.akpolat@gmail.com

*Corresponding Author

Gonca OZMEN KOCA

Dept. of Mechatronics Engineering,
Faculty of Technology,
Firat University,
Elazig, Turkey
gonca.ozmen@gmail.com

Abstract— Gyroscopes are devices that use rotational motion and balance for finding direction and measuring velocity. Gyroscopes, which were initially in normal size, have been transformed into gyroscopes created by Micro Electro-Mechanical Systems (MEMS), which have been progressively smaller in size with advances in technology over the years. The gyroscope consists of two axes perpendicular to each other and to the axis of rotation around an axis. It is made in such a way that it can freely turn around one or both of its axes and its mass center is fixed. Unlike other rotary sensors, gyroscopes have the ability to measure the motion of an object without an external signal. In this study, two control methods for tracking sinusoidal trajectories of triaxial MEMS gyroscopes have been investigated. Mathematical model of a triaxial MEMS gyroscope has been presented and modeled in MATLAB / Simulink environment. The proportional-integral-derivative controller and the Sliding Mode Control based approach have been implemented to control the system with the generated block diagrams. Both control methods have enabled triaxial MEMS gyroscopes to follow the desired sinusoidal references. The results obtained by both control methods have been examined.

Keywords—Triaxial Gyroscope; Micro Electro-Mechanical Systems; Robust Control; Sliding Mode Control.

I. INTRODUCTION

The gyroscope consists of two axes perpendicular to each other and to the axis of rotation around an axis. Gyroscopes can rotate freely around one or both axes. They have the ability to measure the motion of an object without an external signal [1]. Gyroscope examples can be found in a variety of forms, and although it has been around for a long time, little is known about this device until the 19th century. Jean Bernard Leon Foucault in 1852 gave the name of the gyroscope that he made to show the world's return. However, the gyroscope has remained the game of scientists for about 60 years since the rotational motion cannot be sustained continuously. As steel is used in ships, the confidence in the magnetic compass is reduced and the gyroscopic compass becomes more important. Gyroscopic instruments have been developed to control the movement of ships and aircraft. Gyroscopes that inhibit roll motion in ships are also used to give direction to the torpedo. In 1943, a gyroscope was used to direct sea vessels and with the emergence

of the Second World War, the gyroscope began to develop rapidly [2].

Fei et al. have developed an adaptive drive mode control strategy that combines the benefits of drive mode control and indirect adaptive fuzzy control to regulate the triaxial MEMS gyroscope against outer disturbances, uncertainties and nonlinearities. This control strategy has helped the model in the presence of external disturbances and uncertainties and in controlling position of MEMS gyroscope. Adaptive fuzzy systems in both the equivalent control circuit and the switching control circuit are used approximately in the control of drive mode. Then the switching control has become continuous and the noise disturbances are weakened. Numerical simulations have been investigated to verify the effectiveness of the proposed adaptive fuzzy control schemes [3].

Fang et al. constructed a MIMO Takagi-Sugeno (T-S) fuzzy model based on the nonlinear model of MEMS gyroscope [4]. A robust adaptive drive mode control is proposed for the estimation of the uncertainty parameters of the model and for the upper limits of the external distributions. Based on the Lyapunov methods, these adaptive laws can guarantee asymptotic stability and robust mass force in x and y directions for oscillation in the given amplitude and frequency. The controller was also implemented on the MEMS gyroscope nonlinear model. Numerical simulations have been investigated to verify the effectiveness of the proposed control scheme on T-S and nonlinear models [4].

Park et al. has provided an adaptive control method for a MEMS gyroscope that can carry out both vibration axes and controls in all applications of the gyroscopes [5]. Leland has proposed an adaptive control method for a MEMS gyroscope using rebalancing force [6]. John et al. has proposed a new concept for adaptive control of a triaxial angular velocity sensor device [7]. Fazlyab et al. have designed an intelligent controller for applications in mono-axial vibrating MEMS gyroscopes [8]. First, a micro-gyroscope unknown parameters with unknown time constants of angular velocity are estimated continuously through the least quadruple algorithm. Then, the two fuzzy sliding-mode control ranges are added to match the resonance frequency and compensate for unwanted mechanical

connections. The main purpose of this control strategy is to increase the robustness against gyroscope parameter changes, external disturbances and noise measurements. Consistent estimates of the parameters can be guaranteed and the stability of the closed-loop system is ensured through Lyapunov stability theory. In order to validate the effectiveness of this proposed method, a number of simulations, both fixed and time-varying, have been performed [5].

The performance of MEMS gyroscopes is determined by time-varying parameters, external disturbances caused by quadrature errors and oscillation incompatibility between two oscillating axes. In recent years, the application area of triaxial angular velocity sensors has increased considerably with the rapid development of MEMS production technology. Control methods such as intelligent control or adaptive control are adaptable control methods for MEMS gyroscope control. Various control approaches have been proposed to control the triaxial MEMS gyroscope [9].

Leland, produced two adaptive controllers in a vibrating gyroscope to adjust the frequency of the drive axis to a specified frequency and to reduce the vibration of the detection axis to zero to rebalance the force [6]. Batur et al. have developed a Sliding Mode Controller for a MEMS gyroscope [10]. Sung et al. have developed a phase-space design to work on mode adaptive control of the gyroscope [11]. Antonello et al. have studied extreme values search control to automatically match the vibration mode on vibrating MEMS gyroscopes [12]. Park et al. proposed an adaptive controller that controls both the vibration axis and entire performance of the gyroscope [5]. John et al. developed a new control concept to adaptively control the triaxial angular velocity sensor device [7]. In other studies, Sliding Mode Control approach has been used in adaptive control scheme to control MEMS gyroscopes, [13-14].

This study includes the mathematical model of a triaxial MEMS gyroscope in order to provide sinusoidal trajectory tracking. In order to improve tracking performance two methods: tuned PID and SMC-based control approaches are implemented in the MATLAB/Simulink environment. The effectiveness of the controllers to track sinusoidal trajectory is demonstrated with the simulation results in x , y and z axes.

The paper is organized in six sections. In the Section I, literature review about basic gyroscopes is included. Studies related with triaxial MEMS gyroscopes and their controls are given in Section II. Dynamic model of the triaxial MEMS gyroscope is also obtained in Section III. PID and SMC based control of the system are presented in the Section IV and V, respectively. Finally, simulation results are given in Section VI.

II. DYNAMIC MODEL OF THE TRIAXIAL MEMS GYROSCOPE

Let assume that the gyroscope moves at a constant linear velocity, then it rotates at a constant angular velocity. If the centrifugal forces are neglected and the gyroscope is thought to move along the x , y , z axes, then the triaxial MEMS gyroscope dynamic equations can be given with (1-3) as [9]:

$$\begin{aligned} m\ddot{x} + d_{xx}\dot{x} + d_{xy}\dot{y} + d_{xz}\dot{z} + k_{xx}x + k_{xy}y + k_{xz}z \\ = u_x + 2m\Omega_z\dot{y} - 2m\Omega_y\dot{z} \end{aligned} \quad (1)$$

$$\begin{aligned} m\ddot{y} + d_{xy}\dot{x} + d_{yy}\dot{y} + d_{yz}\dot{z} + k_{xy}x + k_{yy}y + k_{yz}z \\ = u_y + 2m\Omega_z\dot{x} - 2m\Omega_x\dot{z} \end{aligned} \quad (2)$$

$$\begin{aligned} m\ddot{z} + d_{xz}\dot{x} + d_{yz}\dot{y} + d_{zz}\dot{z} + k_{xz}x + k_{zy}y + k_{zz}z \\ = u_z + 2m\Omega_y\dot{x} - 2m\Omega_x\dot{y} \end{aligned} \quad (3)$$

In these equations, m represents the mass. The production errors mainly affect the asymmetric spring coefficients ω_{xy} , ω_{xz} , ω_{yz} .

d_{xy} , d_{yz} , d_{xz} are asymmetric damping coefficients. ω_x , ω_y , ω_z are the spring coefficients and d_{xx} , d_{yy} , d_{zz} are the damping terms in the x , y , z axes. Ω_x , Ω_y , Ω_z are the angular velocities and u_x , u_y , u_z are the control forces in the x , y , z axes.

Our control objective on the triaxial MEMS gyroscope is to force the system outputs in the x , y , and z axes sinusoidally to track the desired trajectories. Table I [9] presents desired parameters. In the table, (x_m, y_m, z_m) indicate desired sinusoidal trajectories and $(\omega_1, \omega_2, \omega_3)$ also indicates frequency of trajectories.

TABLE I. DESIRED PARAMETERS

x_m	$\sin(\omega_1 t)$
y_m	$1.2 \sin(\omega_2 t)$
z_m	$1.5 \sin(\omega_3 t)$
ω_1	6.71 kHz
ω_2	5.11 kHz
ω_3	4.17 kHz

System parameters of the MEMS gyroscope is given in Table II [9]. Since the settlement range is at micrometer levels, the reference length q_0 is selected as 1 μm and the expressions we use in kHz are assumed to be Hz in this study, so ω_0 is taken as 1000 Hz.

TABLE II. SYSTEM PARAMETERS OF THE TRIAXIAL MEMS GYROSCOPE

Parameters	Values
m	0.57e-8 kg
ω_0	1000 Hz
d_{xx}	0.429e-6 Ns/m
d_{yy}	0.0429e-6 Ns/m
d_{zz}	0.895e-6 Ns/m
d_{xy}	0.0429e-6 Ns/m
d_{xz}	0.0687e-6 Ns/m
d_{yz}	0.0895e-6 Ns/m
Ω_z	5 rad/sn
Ω_x	3 rad/sn
Ω_y	2 rad/sn
λ	1000
K	20
τ_i	0.001

III. PID CONTROL OF THE TRIAXIAL MEMS GYROSCOPE

The system is controlled with the help of the PID controller in continuous time. The MATLAB / SIMULINK block diagram of the entire system is illustrated in Fig.1. Table III shows the PID controller parameters applied to the system. These parameters are obtained from the "auto tuning option" of the PID block.

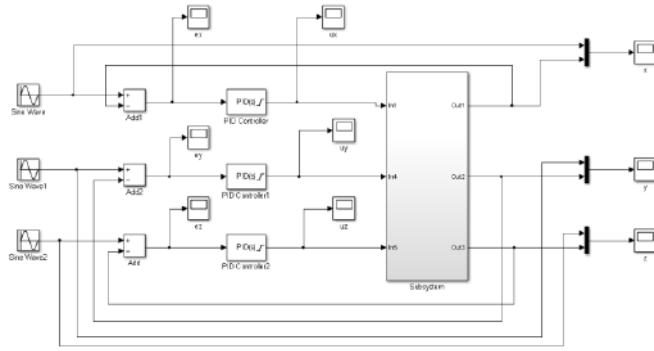


Fig. 1. Block diagram created with MATLAB / Simulink of PID control of the triaxial MEMS gyroscope

TABLE III. PID CONTROL PARAMETERS

Axes	Coefficients		
	K_p	K_i	K_d
x axis	962	15898055	8.2×10^{-4}
y axis	836	8333102	7.6×10^{-4}
z axis	731	6810265	7.103×10^{-6}

IV. SMC-BASED CONTROL OF THE TRIAXIAL MEMS GYROSCOPE

SMC is a robust control technique with many attractive features such as sensitivity to external disturbances and robustness to parameter changes [15, 16]. In SMC, the phase trajectories formed by the system curves are provided with the help of the switching function on the tangent line passing through the equilibrium point, and the variables are kept on this line. Therefore, the switching function has a great importance. Switching function directly affects performance and robustness of the control [16].

In this study, a control structure based on the SMC as well as the PID controller is used for the same system dynamics and reference inputs for a triaxial MEMS gyroscope. In this control structure, the control signal can be described as [17]:

$$u = KS \quad (4)$$

here K is the constant gain value and switching function S can be given with;

$$S = \lambda e + \dot{e} \quad (5)$$

Slope of the sliding surface is represented by λ . In Fig. 2, a MATLAB / Simulink block diagram is shown in which a control structure based on a SMC is implemented to triaxial MEMS gyroscope.

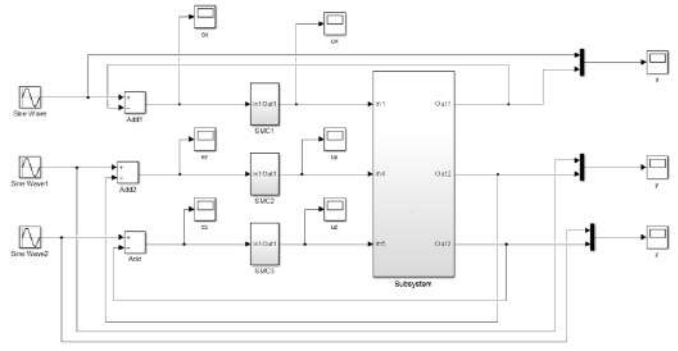


Fig. 2. MATLAB / Simulink block diagram of the system using SMC

The coefficients for the x, y and z axes are chosen as 1000, 20 for λ and K, respectively. The saturation value is also preferred as [100 -100]. Fig. 3a shows the SMC-based control structure, Fig. 3b shows the internal structure of the controller.

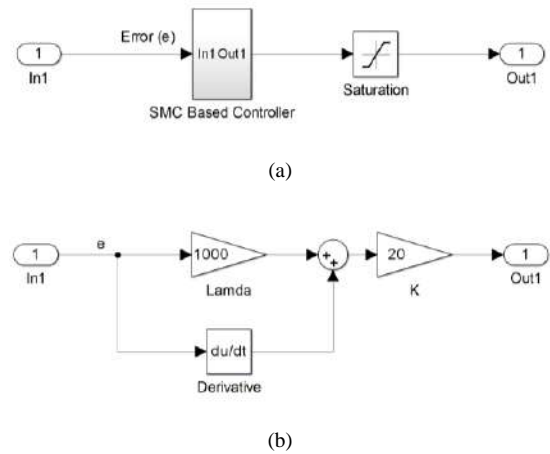
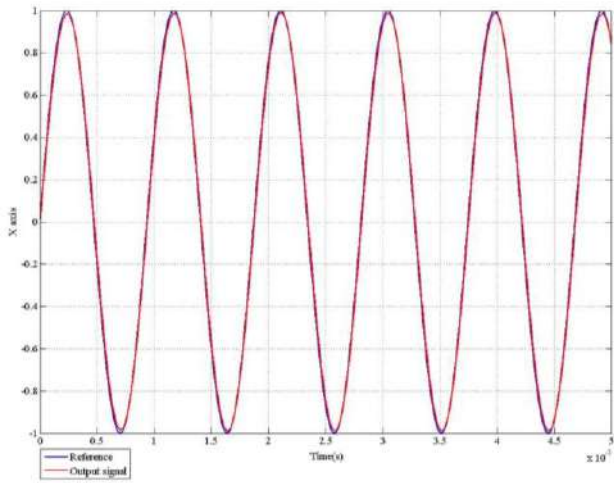


Fig. 3. a) SMC-based control structure b) internal structure of the controller.

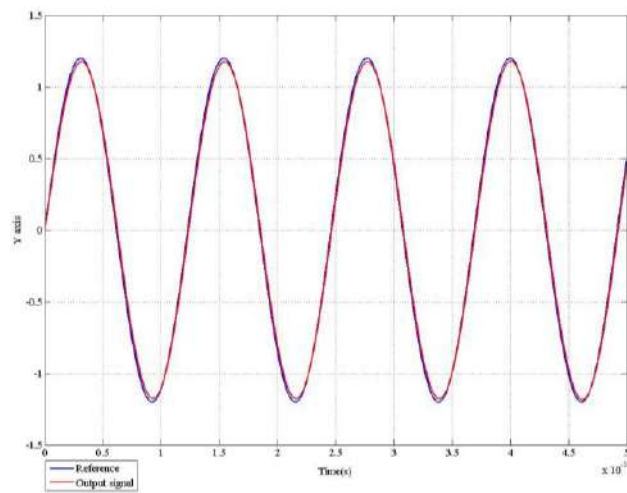
V. RESULTS

A triaxial MEMS gyroscope is constructed by using dynamic equations and the system is controlled by PID and SMC-based control method. The triaxial MEMS gyroscope system has sinusoidal reference inputs with amplitude 1 at x axis and frequency 6710 Hz, amplitude 1.2 at y axis, frequency 5110 Hz, amplitude 1.5 at z axis and frequency 4170 Hz.

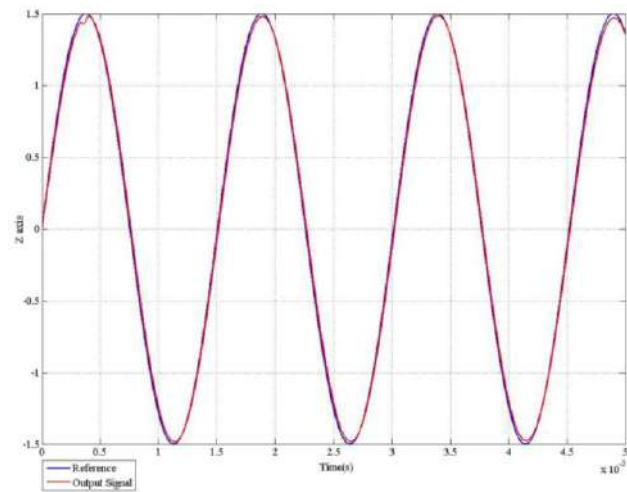
The simulation results obtained in the x, y and z axes with PID are shown in Fig. 4. The SMC-based controller is also implemented to obtain more robust control output on the x, y and z axes for the triaxial MEMs gyroscope as illustrated in Fig. 5. The error signals in the x, y, and z axes are also illustrated in Fig.6 in order to compare the results obtained with the PID controller and SMC-based controller.



(a)

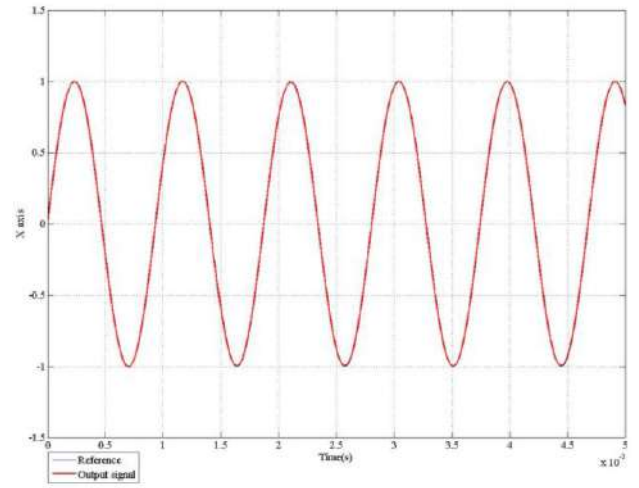


(b)

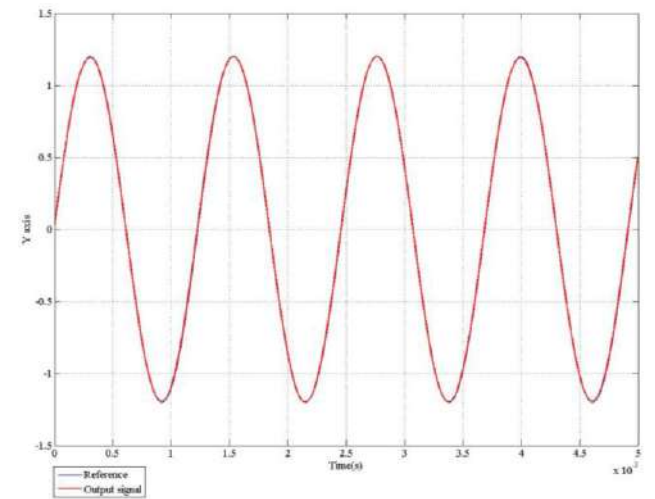


(c)

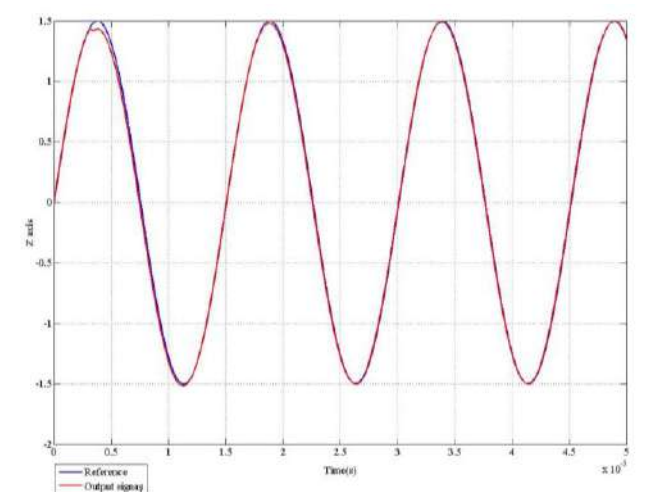
Fig. 4. The simulation results for PID controller in the a) x b) y c) z axes



(a)



(b)



(c)

Fig. 5. The simulation results for SMC-based controller in the a) x b) y c) z axes

VI. CONCLUSION

In this study, dynamic model of a triaxial MEMS gyroscope is investigated to perform sinusoidal trajectory tracking. System is modeled in MATLAB/Simulink environment to illustrate trajectory performance by using two methods: PID tuned with auto tuning option of the PID block and SMC-based control approach which uses switching function to reach the minimum error faster with a very simple control structure.

The error signals in the x , y and z axes, obtained from the SMC-based controller have a smaller value than the tuned PID controller for the same conditions as can be seen from the figures.

REFERENCES

- [1] A. A. Trusov, Ph.D., "Overview of MEMS Gyroscopes: History, Principles of Operations, Types of Measurements", MicroSystems Laboratory, Mechanical and Aerospace Engineering University of California, Irvine, CA, 92697, USA, 2011.
- [2] <http://www.turkcebilgi.com/jiroskop>, Jiroskop, 29 Kasım 2016.
- [3] J. Fei and M. Xin, "Adaptive Fuzzy Sliding Mode Control of MEMS Gyroscope Sensor Using Fuzzy Switching Approach", SICE Annual Conference, pp. 14-17, 2013.
- [4] Y. Fang, S. Wang, and J. Fei, "Adaptive T-S Fuzzy Sliding Mode Control of MEMS Gyroscope", IEEE International Conference on Fuzzy Systems (FUZZY-IEEE), pp. 6-11, 2014.
- [5] R. Park, R. Horowitz, S. Hong, and Y. Nam, "Trajectory-switching algorithm for a MEMS gyroscope," IEEE Trans. Instrum. Meas., vol. 56, no. 6, pp. 2561–2569, 2007.
- [6] R. Leland, "Adaptive control of a MEMS gyroscope using Lyapunov methods," IEEE Trans. Control Syst. Technol., vol. 14, no. 2, pp. 278–283, 2006.
- [7] J. John and T. Vinay, "Novel concept of a single mass adaptively controlled triaxial angular velocity sensor," IEEE Sensors J., vol. 6, no. 3, pp. 588–595, 2006.
- [8] M. Fazlyab, M. Z. Pedram, H. Salarieh, and A. Alasty, "Parameter estimation and interval type-2 fuzzy sliding mode control of a z-axis MEMS gyroscope", ISA Transactions 52, pp. 900–911, 2013.
- [9] J. Fei and J. Zhou, "Robust Adaptive Control of MEMS Triaxial Gyroscope Using Fuzzy Compensator", IEEE Transactions On Systems, Man, And Cybernetics—Part B: Cybernetics, vol. 42, no. 6, December, pp. 1599-1607, 2012.
- [10] C. Batur, T. Sreeramreddy, and Q. Khasawneh, "Sliding mode control of a simulated MEMS gyroscope", ISA Transactions, vol. 45, no. 1, pp. 99–108, 2006.
- [11] W. Sung and Y. Lee, "On the mode-matched control of MEMS vibratory gyroscope via phase-domain analysis and design," IEEE/ASME Trans. Mechatron., vol. 14, no. 4, pp. 446–455, 2009.
- [12] R. Antonello, L. Oboe, F. Prandi, and F. Biganzoli, "Automatic modematching in MEMS vibrating gyroscopes using extremum-seeking control," IEEE Trans. Ind. Electron., vol. 56, no. 10, pp. 3880–3891, 2009.
- [13] J. Fei and C. Batur, "A novel adaptive sliding mode control with application to MEMS gyroscope," ISA Trans., vol. 48, no. 1, pp. 73–78, 2009.
- [14] J. Fei and F. Chowdhury, "Robust adaptive controller for triaxial angular velocity sensor," Int. J. Innov. Comput., Inf. Control, vol. 7, no. 6, pp. 2439–2448, 2010.
- [15] J. Fei and Ding H., 2012. "Adaptive Neural Sliding Mode Control of MEMS Triaxial Gyroscope Based on Feedback Linearization Approach", SICE Annual Conference Akita University, Akita, Japan, pp. 1271-1276, August 2012.
- [16] M. S. Fadali, "Sliding Mode Control", Lecture Notes, 2005

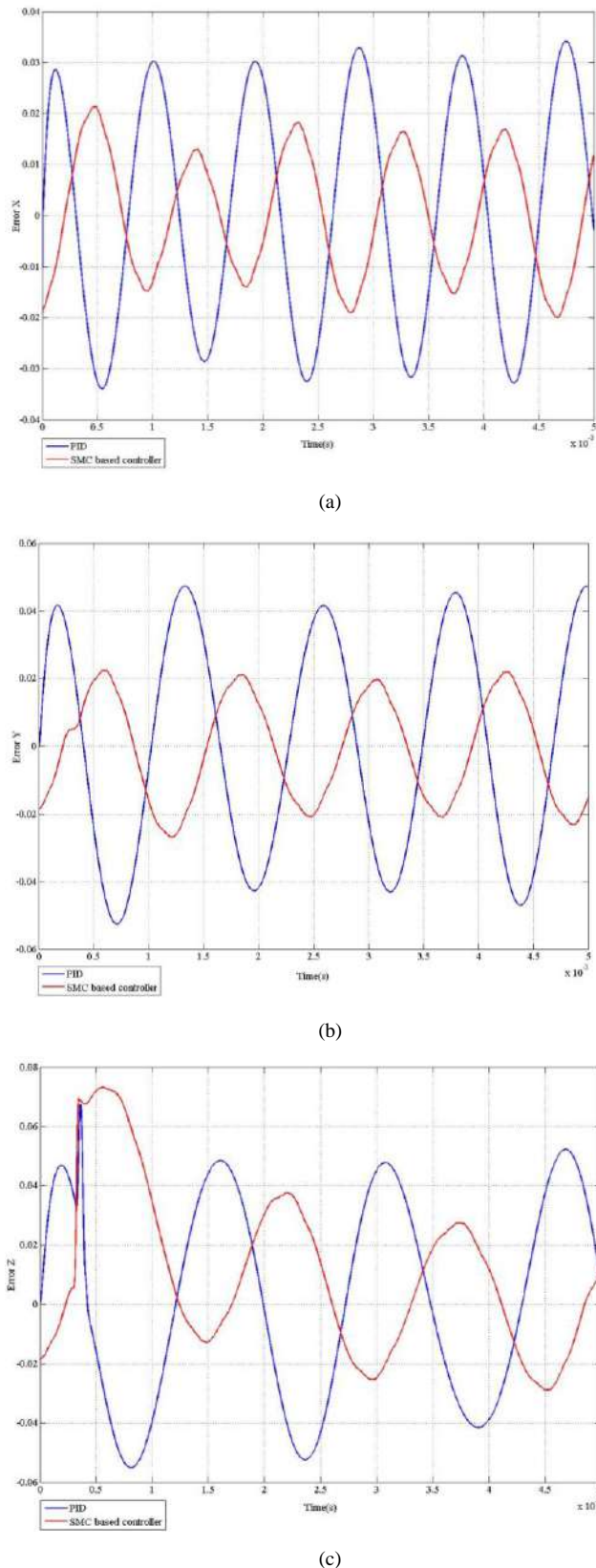


Fig. 6. The simulation results of errors for SMC-based and PID controller in the a) x b) y c) z axes

- [17] Z. H. Akpolat and H. Guldemir, "Trajectory following sliding mode control of induction motors," *Electrical Engineering*, vol. 85, pp. 205–209, 2003.

2 DOF Vehicle Simulator

H. Emre Güner, Bora Demirci, İsmail Doğan, Yalçın Sabiha, C. Efe Yıldırım, H. Metin Ertunc

Department of Mechatronics Engineering

Kocaeli University, Izmit / Kocaeli

emre.guner @kocaeli.edu.tr

hmertunc@kocaeli.edu.tr

Abstract— Today, driving simulators are used in many fields. However, vehicle driving simulators are expensive to use driving evaluation or education. The aim of this study is that to design and control 2-DOF low cost vehicle simulator. This system is designed using SOLIDWORKS program. Finite element and structural analysis of the system is analyzed using ANSYS program. Also, kinematics equations are delivered of the system and PID control is applied to this kinematic model in MATLAB environment. SOLIDWORKS model of the system is imported to SimMechanics. Therefore, Mass, inertia, and center of gravity coordinate system of each part is automatically transferred to body blocks in SimMechanics. PID control parameters is applied to SimMechanics model of the system. Physical system is mechanically robust and controlled successfully due to the SimMechanics simulation results. This approach can be applied to design low cost vehicle driving simulator systems.

Keywords—ANSYS, driving simulator, SimMechanics and Solidworks

I. INTRODUCTION

Vehicle simulators are the mechanisms which provide to feel like moving a real vehicle platform. Nowadays, vehicle simulator systems are used in many fields such as educational, driving evaluation and aerospace industry. Traffic accidents is dramatically increased in Turkey over the past ten years. A major current focus on vehicle simulators are how to decrease traffic accidents in Turkey. In the literature, Vehicle simulators are designed to use commercial or educational. The first studies on this study begin with ‘Stewart Platform’ in 1965 for flight simulator [1]. Stewart Platform consisted of 6 DOF parallel mechanisms and has been named from D. Stewart. This platform used many researches such as robotic and industrial areas. The first model of the Stewart platform is shown in Fig. 1.

Parallel robots and mechanisms have been used for various applications. These systems have high carrying capacity, suitable dynamic, kinematic performance and precision. If degree of the freedom increases, then the precision of the system will increase [2]. Thus, 6 DOF system is the best solution for simulation but controlling the platform will be more complicated. On the other hand, 2 DOF systems has not better precision when they compared 6 DOF systems.

Driving simulators are used effectively for vehicle system development and other purposes by enabling to reproduce actual driving conditions in a safe and tightly controlled.

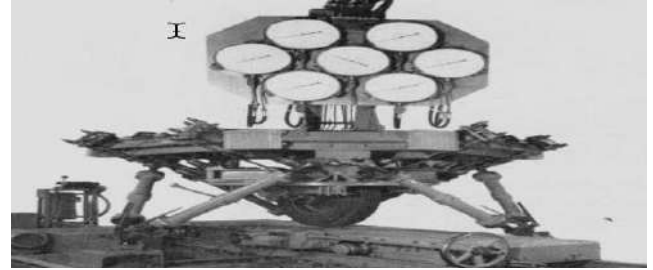


Fig 1. Stewart Platform

A low-cost motion platform has two degree of freedom (2 DOF) that is designed and built. The main aim of this project is that to design low-cost fully functional driving simulator for education and driving evaluation. This system is useful for the driver's behavior study in related driving exams as shown in Fig. 2 [7-9].

Like other related studies this project consist of steering wheel, gear shift and pedal, driving seat, components of a computer system of a motion platform.



Fig 2. Driving simulator in use

According to chronological order Volkswagen, IFAS, VTI, Daimler-Benz, Mazda, Ford, BMW, JARI, Nissan and WIVW, NADS-1, SimuSYS, Renault, Katech, SimCar, UoLDS, Toyota such as many companies have managed to become a global giant technology with produced motion simulators [3-6]. These are more expensive and complicated systems then our project. This

system as mentioned above has low cost, good calibration and dynamics and optimal solution for simulation [10].

The remainder of this paper organizes Section 2 discusses how to design mechanically to the system Section 3 examines SimMechanics model of the system and in Section 4 consists of the conclusion and discussion part of the system.

II. MECHANICAL DESIGN

The current design involved mechanical analysis part and SimMechanics part to control low-cost 2-DOF vehicle simulator. In mechanical analysis part, Solidworks model of the system was designed. Motion analysis was carried out using Solidworks Motion Analyze. Statics and rigid analyze is done using ANSYS program. Mechanical design of the system is shown in Fig. 3 and Fig. 4.



Fig 3. Mechanic Design of the System

The simulator will consist of two main parts: mechanical and electronic modules.

Mechanical parts will be part of the general movement of the user's location that will be transferred to the mechanical system.

Electronic system is the control and processing part of the project. This part is processed using a computer program, the data will be transferred to the motors to move the system. Thus, when the steering control program set by the computer in the control synchronously. Computer, Microprocessors, Motor Driver, Motors motion simulation environment will be designed providing the platform.



Fig 4. Mechanic Design of the System

Static, transient and rigid analyzes are examined using ANSYS environment. Revolute joint is used all revolute links. In static analyze 1000 N force is given to the system. Stress of the system maximum reaches 23.9 MPa value shown as in Fig. 6.

When using the transient analyze, giving 15-degree rotation to the system transient analyze is obtained. Maximum total deflection of the system is 0.28m as shown in Fig.7.

Using rigid method results is compared to nonlinear finite elements solution methods as shown in Figure 8. Also Maximum velocity prob. is tested 0,044 m/s.

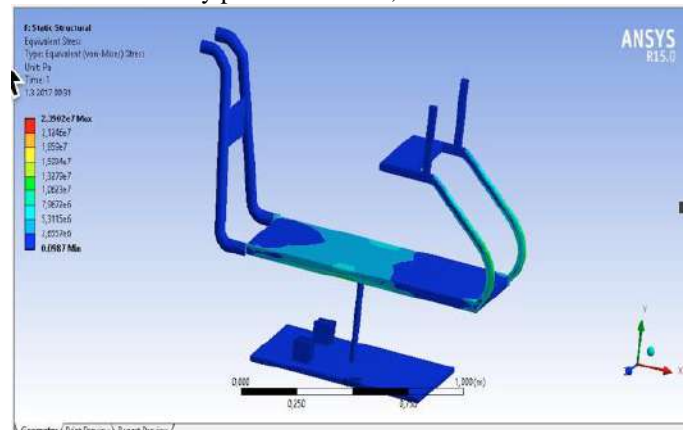


Fig 5. Stress analyze of the system

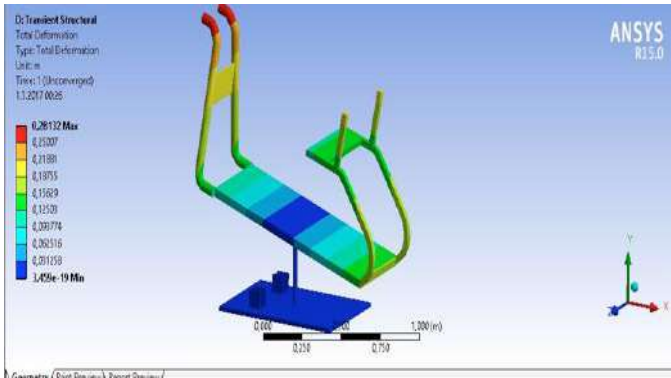


Fig 6. Total Deformation Results

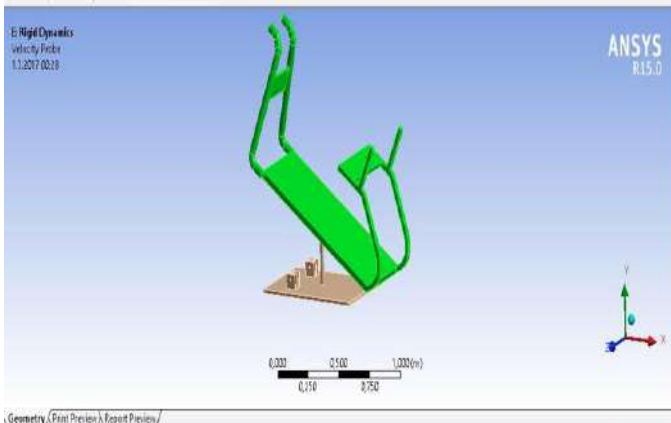


Fig 7. Rigid Dynamics Results

Motion analyze is applied to our Low-cost 2 DOF vehicle simulator using SolidWorks. Three different motion analyze is examined to the system. They are angular displacement, angular velocity and angular acceleration. 90 degrees with 1Hz oscillation frequency is carried out to system. Motor power is 2A at rated current and 10 A at under load. Due to the test results, Motor works with 12V DC supply and 240W power that carry 100kg load. The results shown in Fig. 8.

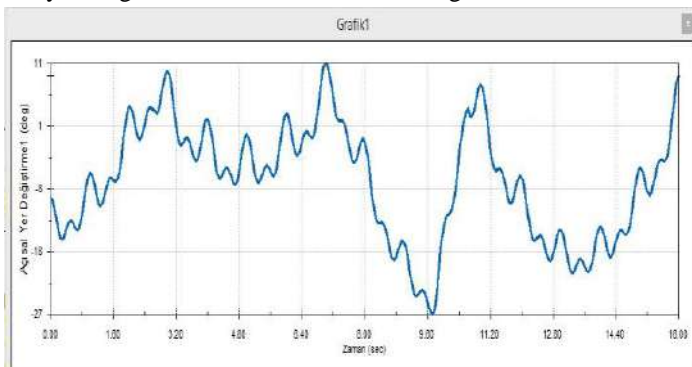


Fig 8. Angular Displacement of the System

The motors scan an angle of 40 degrees in both axes for 16 seconds. This gives us the angular positions required for the planned simulator. An angular displacement relationship between the motor shaft and the platform was monitored. It is

observed that the output is sinusoidal because the applied motor speed is oscillatory.

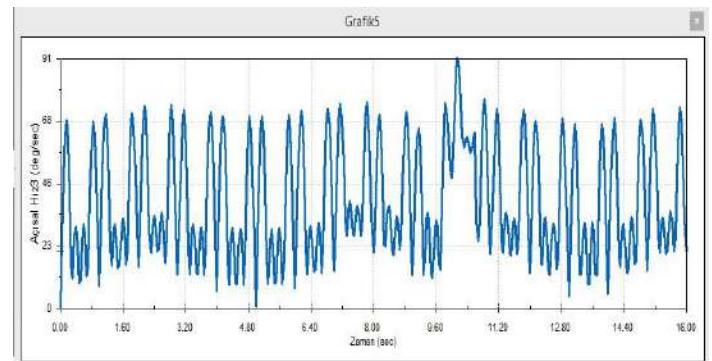


Fig 9. Angular Velocity of the System

When the motors were rotated and oscillated at a 90-degree angle for 16 seconds, a 90-degree sinusoidal motion was seen between the motor shaft and the platform. The results of this graph and the angular displacement graph are similar.

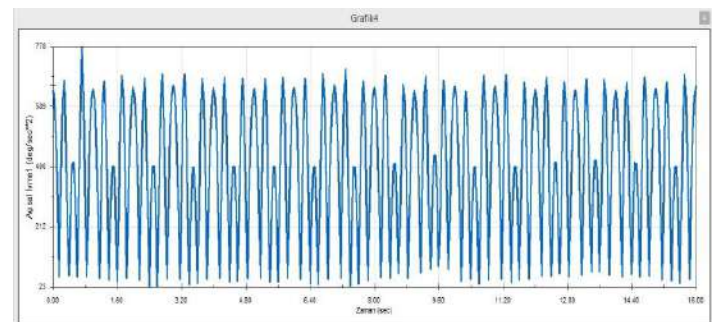


Fig 10. Angular acceleration Results of the System

We have also obtained a synchronous motion graph similar to the angular velocity and displacement graphs in the direction of motion when we apply the angular acceleration-time graph to the motor mills.

III. CONTROLLING OF THE SYSTEM

Solidworks Assembly design is imported to MATLAB SimMechanics environment. The main advantage of the SimMechanics is that automatically generate MATLAB model using SolidWorks files. The SimMechanics model consists of the joints, actuators, sensors and links of the system. PID control parameters is determined MATLAB control toolbox using SimMechanics model. In Fig. 12 SimMechanics model is shown.

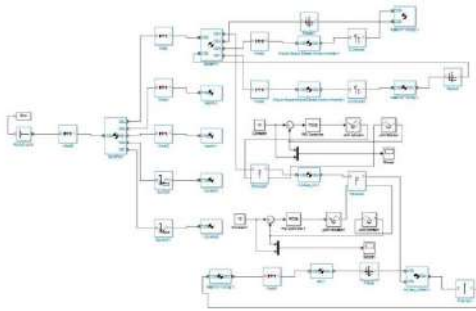


Fig 11. SimMechanics Model of the System

PID control response graphics are shown in Fig. 13 and Fig. 14. System is two degree of freedom therefore two angle called as theta and Fi that is controlled using SimMechanics PID. Desired position of the system is set to reference position of the system effectively. SimMechanics 3-D model is shown in Fig 15.

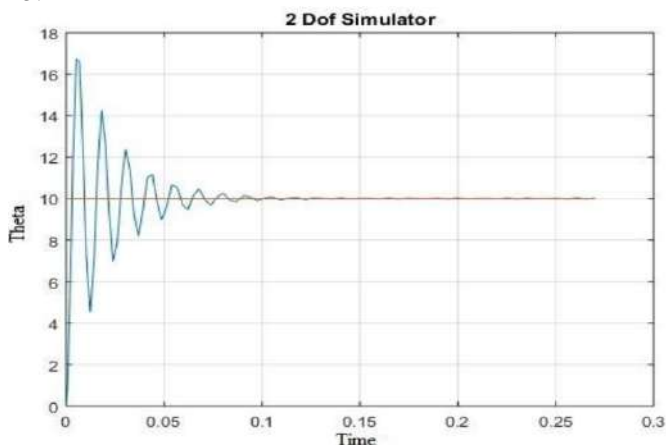


Fig 12. theta angle of the system

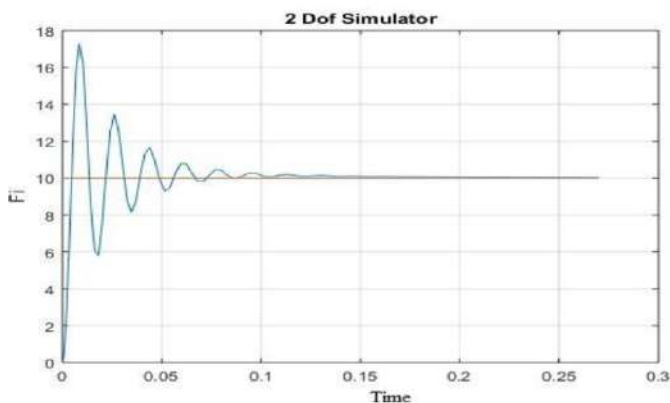


Fig 13. Fi angle of the system

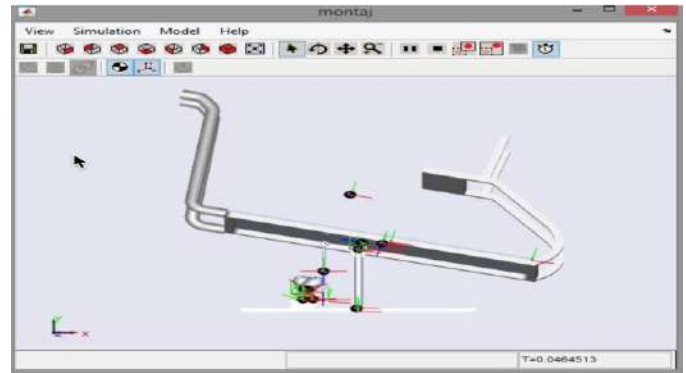


Fig 14. 3-D SimMechanics Model

IV. CONCLLUCION

In this study, low cost 2 DOF vehicle simulator is designed and controlled. Solidworks and ANSYS programs are used for mechanical design of the system. SimMechanics model is used for controlling the vehicle simulator. Due to the test results, the simulator controlled effectively. It is observed that Low cost vehicle simulator model is very useful for education and driving evaluation. In the future work, fuzzy logic control algorithm will be applied to the system.

ACKNOWLEDGMENT

The work presented in this paper has been done at Sensor Laboratory of Mechatronics Engineering Department.

REFERENCES

- [1] " <http://www.cncexpo.com/DegreesOfFreedom.aspx>", .
- [2] J.C. Popieul, "Automobile Driving: SHERPA simulator ", <http://www.univ-valenciennes.fr/LAMIH/en/hybrid-simulator-automotive-studies-and-research>"
- [3] B. Howard , " Inside Virttex, Ford's amazing driver distraction simulator", Extreme Tech Journal , August 1st 2012 , from: "<http://www.extremetech.com/extreme/133549-inside-virttex-fords-amazing-driver-distraction-simulator>"
- [4] D. Newcumb, "BMW Connected Drive First Look", March 18th 2011, from: "<http://www.edmunds.com/car-reviews/features/bmw-connecteddrive-first-look.html>",
- [5] D. Stewart, "A platform with six degrees of freedom", Proc. Inst. Mech. Engrs, Part I 180 (15) (1965) 371–386.
- [6] F.Gao, W. Li, X. Zhao, Z. Jin, H. Zhao, " New kinematic structures for 2-, 3-, 4-, and 5- DOF parallel manipulator designs ", Mechanism and Machine Theory, 2012
- [7] W.S. Lee, J.H. Kim, J.H. Cho, " A Driving Simulator as a Virtual Reality Tool ", Kookmin University, IEEE International Conference on Robotics & Automation Leuven, Belgium May 1998
- [8] L. Nehaoua, H. Mohellebi, A. Amouri, H. Arioui, S. Espié, and A. Kheddar, " Design and Control of a Small-Clearance Driving Simulator ", IEEE Transactions on Vehicular Technology, Vol. 57, No. 2, March 2008
- [9] H. Arioui, S. Hima, L. Nehaoua, R.J. Bertin, S. Espié, " From Design to Experiments of a 2-DOF Vehicle Driving Simulator ", IEEE Transactions on Vehicular Technology, Vol. 60, No. 2, February 2011
- [10] J. Jelmer, "State-of-the-Art Driving Simulators, a Literature Survey Slob", Document o:2008.10

Closed Loop Control of a Landing Gear System

Mustafa Can BINGOL

Dept. of Mechatronics Engineering
Faculty of Technology
Firat University
Elazig, Turkey
mustafacanbingol@gmail.com

Zuhtu Hakan AKPOLAT*

Dept. of Mechatronics Engineering
Faculty of Technology
Firat University
Elazig, Turkey
z.h.akpolat@gmail.com
*Corresponding Author

Gonca OZMEN KOCA

Dept. of Mechatronics Engineering
Faculty of Technology
Firat University
Elazig, Turkey
gonca.ozmen@gmail.com

Abstract— Researchers have placed great emphasis on controlling and modeling of landing gear systems since these systems are very essential tools for aircraft. In this paper, a landing gear system is modeled to analyze and control by using general modeling method. The closed loop control performance is provided by adding zeros to cancel the poles affecting stability and a simple proportional control is implemented to obtain reduction on vibration of the gear system. The root locus curve is presented to observe stability of the system. Zeros are assigned very close to the poles to prevent the branches of the root locus curve passing through the right half s plane and a very simple proportional controller ensures the distinctive reduction on vibration of the gear system.

Keywords—Landing Gear System, Root Locus Design, Close Loop Control.

I. INTRODUCTION

An aircraft consists of many different parts such as fuselage, wing, winglet, and landing gear. These parts have been subject to a lot of work from maintenance to control [1]–[5]. For example, Fard and Melachrinoudis have examined maintenance span of airplane parts for reducing repairing cost and early detection of error in their own study [2]. In the other work, Currey has talked about what the landing gear is and how to designing [1]. Landing gear is one of the most important aircraft pieces due to landing, taxiing, and taking off aircraft. There are many different landing gear systems such as helicopter landing gear system or plane landing gear system [3], [4], but they have been usually consisted of three parts as mechanics, electronic and hydraulic [5]. Therefore, the systems are very complex and nonlinear.

This complex and nonlinear issue has attracted the attention of many scientists and engineers. While Yin and his team have investigated crosswind velocity, oil leak, liquid capacity, etc. effect on a landing gear system, Sivakumar and Haran have generated dynamic model of the system and then controlled via proportional integral derivative (PID) controller, which is one of traditional control methods [5], [6]. In another study, Li et.al has modeled the system using state space model and controlled by using Fuzzy PID controller, one of the adaptive control methods [7]. Zhu et.al have followed up same trace in 2012 [8]. The system model has been generated and controlled by

using the same controller in this study. Li et.al has controlled different from to other work by using Model Opredictive Control (MPC) [9].

It is very important to obtain the dynamic model of the system in order to predict the behavior of the system. There are many different methods to obtain system dynamic model. These methods are separated two main parts as simulation and analytic methods. First method is the way to obtain a dynamic model using simulation programs such as MATLAB/SimMechanics. Akpolat et.al have obtain dynamic model of robotic fish by using SimMechanics environment [10]. Second method depends on mathematical identification of physical facts. The analytic methods are divided into many ways like Hamiltonian, Lagrange, and Newton Mechanics. Newton Mechanics uses forces while the other mechanics methods use energies to obtain the mathematical model of the system. Applied forces are certain at the landing gear system. Hence, Newton Mechanics is preferred when the landing gear system is modeled.

The system is also controlled to track desired behavior. For this purpose, there are many algorithms such as PID, MPC, and Fuzzy Logic. If a system is wanted to be controlled by using traditional control methods, root locus curves may be benefited to set parameters of the controller. Root locus curves give a lot of information, such as stability, transient, and steady state of a system, so root locus curves are very necessary tools to analyze and control a system. The curves generally are obtained for single input single output (SISO) linear time invariant (LTI) systems [11]. The SISO LTI system block is given Fig 1.

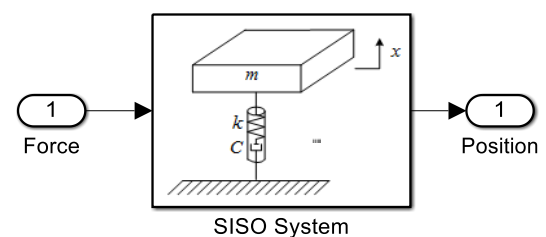


Figure 1. Single Input Single Output (SISO) System Block

Many researchers have studied root locus curves in order to control various systems. In 2016, Kwon and Chang examined root locus curves so as to design PI controller [12]. At another study, buck and boost converters have been designed by using root locus method [13]. In this study, two models of converters have been transformed discrete time model and controllers have been designed. Then, experimental results have been compared to each other. Iranian scientists have developed root locus curves of the fractional order systems [14]. Wellman and Hoagg generated quadratic root locus curves as different perspective [15]. At this approach, unlike the general root locus curves, there are gain and gain square.

In this study, Newton Mechanics is preferred to create the mathematical model of the landing gear system since applied forces are certain at the system. The mathematical model of the system is examined by using root locus curve and the closed loop roots of the system are provided at the left half s plane to ensure stability of the system by adding two zeros very close to poles. Thus, the system can be controlled by using very simple proportional controller.

The paper is organized as follows. Section II presents problem description. Then, the controller design is given in Section III. Section IV illustrates simulation results of the system. Finally, conclusion is presented in Section V.

II. PROBLEM DESCRIPTION

As soon as a plane lands on airport, vibrations are formed, due to sudden shock effect. The vibrations distribute to the plane passenger and crew. In order to understand this discomfort state, dynamic model of the landing gear system ought to be generated. For this aim, the structure of the system illustrated in Fig. 2 is used in order to obtain mathematical model of the system. At the figure, m_p and m_s indicate plane and wheel structure mass, respectively.

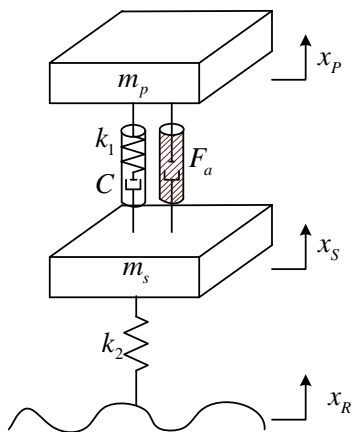


Figure 2. Landing gear system

Where, x_p , x_s and x_R are plane, wheel structure and way position with order. k_1 and k_2 are spring coefficient system.

C is passive damping coefficient and F_a is active adjustable damping force. To easier analyses, the system is converted free body diagram as Fig 3.

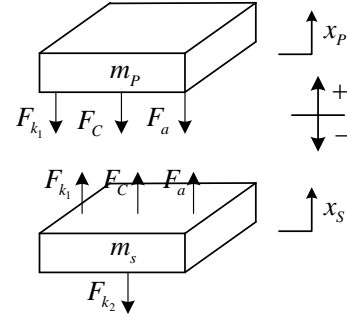


Figure 3. Free body diagram of landing gear system

In this figure, F_{k_1} , F_{k_2} and F_C are force of k_1 , k_2 spring and C damping elements, respectively. The sums of net forces of m_s and m_p are shown with Eq. (1), (2).

$$\sum F_{m_s} = F_{k_1} + F_C + F_a - F_{k_2} \quad (1)$$

$$\sum F_{m_p} = -(F_{k_1} + F_C + F_a) \quad (2)$$

If these equations are extended, dynamic equations are obtained as below.

$$\ddot{x}_s = (k_1(x_p - x_s) + C(\dot{x}_p - \dot{x}_s) + F_a - k_2(x_s - x_R)) / m_s \quad (3)$$

$$\ddot{x}_p = -(k_1(x_p - x_s) + C(\dot{x}_p - \dot{x}_s) + F_a) / m_p \quad (4)$$

Newton's second law is proved that the sum of forces equals to multiply of the mass and acceleration and it is known that the acceleration is second order derivative of the position. Parameters in Eq. (3) and Eq. (4) are given in Table I [7].

TABLE I. SYSTEM PARAMETERS

Symbol	Value	Unit
m_p	250000	kg

m_s	800	kg
k_1	600000	N/m
k_2	3200000	N/m
C	50000	Ns/m

III. CONTROLLER DESIGN

Usually, root locus curves are drawn so as to analyze steady state and transient performance of a system. Hence, root locus curves inform about stability state such as stable or unstable. This method also gives information about the performance specifications.

In order to draw root locus curve of the landing gear system, the system transfer function is obtained from Eq. (3) and (4) as:

$$G_p(s) = \frac{X_p(s)}{X_R(s)} = \frac{800(s+12)}{(s-0.07 \pm 1.42i)(s-31.28 \pm 61.34i)} \quad (5)$$

for active adjustable damping force (output of the controller) $F_a = 0$. Root locus of Eq. (5) is illustrated in Fig.4.

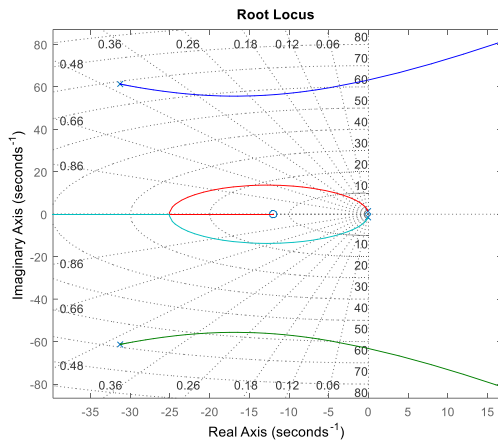


Figure 4. Root locus curve of landing gear system

It can be seen from the figure that the system can be controlled by a proportional controller. A tuned gain value of the proportional controller is found approximately as $K_p = 100$. The step response of the closed loop landing gear system given in Fig. 5 is presented in Fig.6.

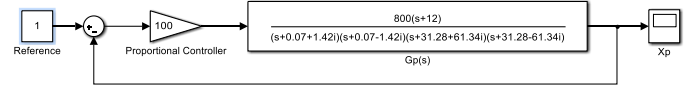


Figure 5. The block diagram of the closed loop landing gear system with proportional controller

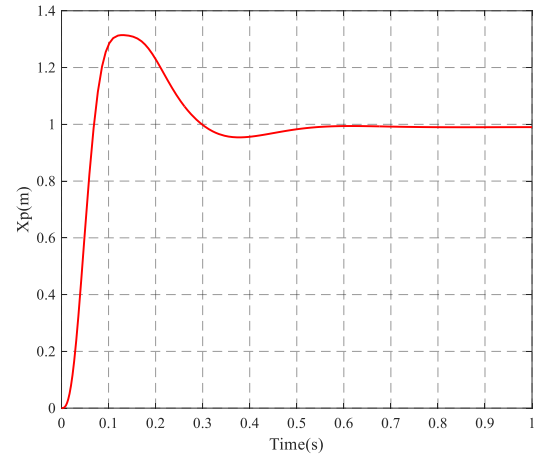


Figure 6. The step response of the closed loop system

In order to improve the control performance of the system, a controller is proposed as:

$$G_c(s) = K \frac{(s+30 \pm 60i)}{(s+300 \pm 400i)} \quad (6)$$

Zeros and poles of the controller are chosen such that the root locus moves to the left half s plane and the system response becomes faster owing to the new dominant roots of the characteristic equation. The root locus of the system with proposed controller is shown in Fig.7.

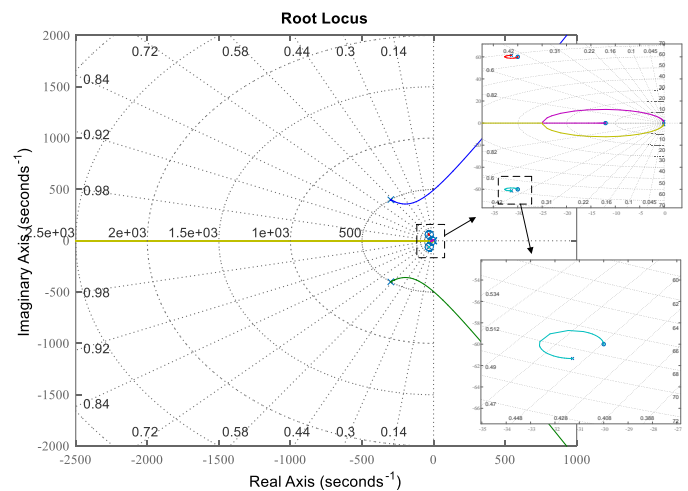


Figure 7. The root locus of the system with proposed controller

The gain value K of the controller given in Eq. (6) is determined as 40177 from the root locus shown in Fig.7 to obtain faster and more robust control performance.

IV. SIMULATION RESULTS

The system is simulated by using *MATLAB/Simulink* toolbox. So as to simulate the system, parameters given in Table 1 are used. These parameters are provided from the study of Hua-Lin et.al [7].

The step response of the open loop system shown in Fig. 8 is presented in Fig.9.

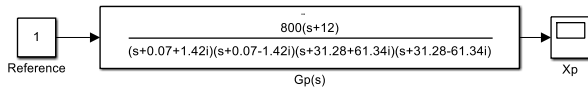


Figure 8. The block diagram of the open loop system

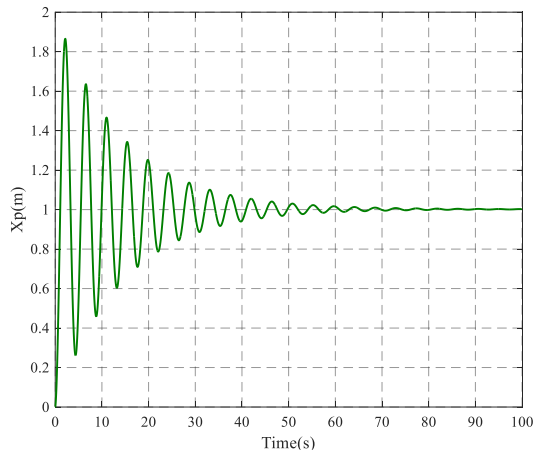


Figure 9. The step response of the open loop system

In order to show the performance of the proposed controller the Simulink block diagram, involving proportional controlled system and the system with proposed controller, is constructed for comparison as shown in Fig.10.

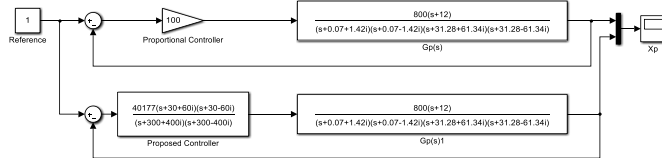


Figure 10. The simulink block diagram for comparison

Step responses of the closed loop systems are illustrated in Fig.11.

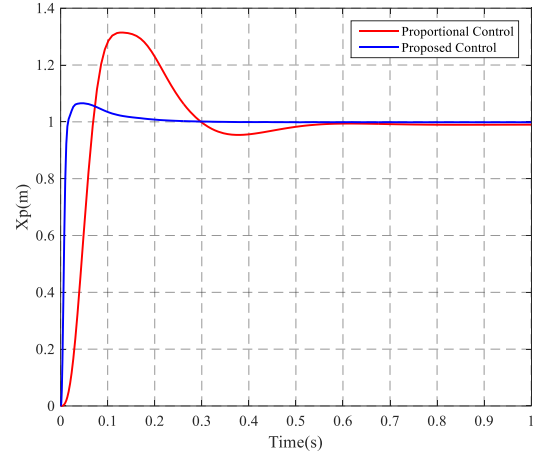


Figure 11. Step responses of the closed loop systems

In order to show the performance of the controllers against external disturbance and practical road condition, external inputs are included in the block diagram as shown in Fig.12.

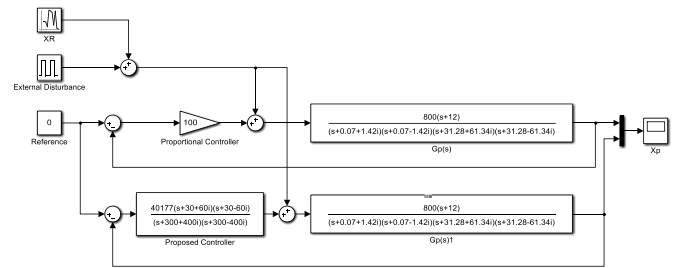


Figure 12. The simulink block diagram for comparison

Note that x_R represents the practical road condition and external disturbance corresponds to an obstacle on the road such as a small stone. Amplitudes of the external inputs are exaggerated to show the difference between control performances of the controllers. Fig.13 shows the responses to external inputs for zero reference.

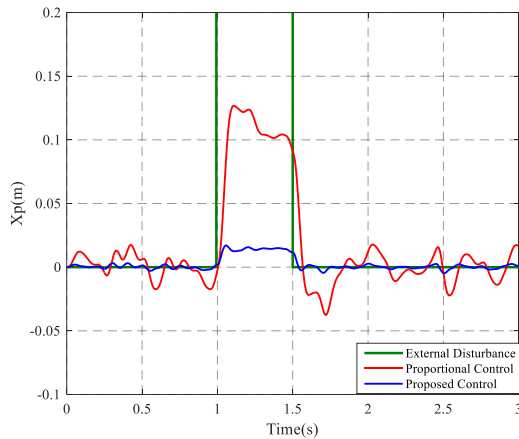


Figure 13. Responses to external inputs for zero reference

Fig. 11 and 13 show the superior performance of the purposed controller. This is achieved by adding zeros at $-30 \pm 60i$ very close to the poles of the open loop transfer function at $-31.28 \pm 61.34i$ and adding poles far away from the origin at $-300 \pm 400i$ resulting a faster and better control performance.

V. CONCLUSION

In this study, landing gear system is studied in order to reduce vibration during the landing span. A landing gear system is modeled by using Newton method. The control system analysis and design are realized using root locus of the system. When the root locus of the open loop system is examined, it can be easily seen that a proportional controller is suitable for this system. However, control performance of the proportionally controlled system does not seem to be satisfactory. Therefore, a new controller is introduced in order to achieve better control performance. The proposed controller includes pairs of complex zeros and complex poles. In addition, the proposed controller performance against external disturbance and practical road condition is also investigated and simulation results showing the effectiveness of the controller are presented.

In the future work, the system may be modeled for more degree of freedom with nonlinear dynamics and the nonlinear

model can be controlled by using intelligent and robust control methods.

REFERENCES

- [1] N. S. Currey, "Aircraft Landing Gear Design: Principles and Practices", *Aiaa*, s. 373, 1988.
- [2] N. S. Fard ve E. Melachrinoudis, "Maintenance scheduling for critical parts of aircraft", *1991 Annu. Reliab. Maintainab. Symp.* 29-31 Jan. 1991, ss. 44-47, 1991.
- [3] L. Heirendt, H. H. T. Liu, ve P. Wang, "Aircraft landing gear greased slider bearing steady-state thermo-elastohydrodynamic concept model", *Tribol. Int.*, c. 82, sayı PB, ss. 453-463, 2015.
- [4] B. Krstic vd., "Investigation into recurring military helicopter landing gear failure", *Eng. Fail. Anal.*, c. 63, ss. 121-130, 2016.
- [5] Y. Yin, N. Hong, N. Huajin, ve Z. Ming, "Reliability Analysis of Landing Gear Retraction System Influenced by Multifactors", *J. Aircr.*, c. 53, sayı 3, ss. 713-724, 2016.
- [6] S. Sivakumar ve a. Haran, "Mathematical model and vibration analysis of aircraft with active landing gears", *J. Vib. Control*, c. 21, sayı 2, ss. 229-245, 2013.
- [7] H. L. Li, C. Yong, H. Qi, ve L. I. Jian, "Fuzzy pid control for landing gear based on magneto-rheological (MR) Damper", *2009 Int. Conf. Apperceiving Comput. Intell. Anal. ICACIA 2009*, ss. 22-25, 2009.
- [8] S. X. Zhu ve C. J. Chen, "Study on Variable Universe Fuzzy PID Control for Landing Gear Based on MRF (Magneto-Rheological Fluid) Damper", *Appl. Mech. Mater.*, c. 233, ss. 66-71, 2012.
- [9] F. Li, G. Wei, W. Qi, ve X. Xinhe, "Modeling and adaptive control of magneto-rheological buffer system for aircraft landing gear", *Appl. Math. Model.*, c. 39, sayı 9, ss. 2509-2517, 2015.
- [10] Z. H. Akpolat, M. Bingöl, M. Ay, G. Özmen Koca, C. Bal, ve D. Korkmaz, "Dynamic Model and Simulation of One Active Joint Robotic Fish", *e-Journal New World Sci. Acad.*, c. 12, sayı 1, ss. 29-39, 2017.
- [11] K. Ogata, *Modern Contro Engineering*. 2002.
- [12] M. Kwon ve H. Chang, "Extended Root-Locus Technique Applied to Pole-Placement for PI Controller Design", 2016.
- [13] L. Guo, J. Y. Hung, ve R. M. Nelms, "Digital controller design for buck and boost converters using root locus techniques", *Ind. Electron. Soc. 2003. IECON '03. 29th Annu. Conf. IEEE*, c. 2, s. 1864-1869 Vol.2, 2003.
- [14] F. Merrikh-bayat, M. Afshar, ve M. Karimi-ghartemani, "Extension of the root-locus method to a certain class of fractional-order systems", c. 48, ss. 48-53, 2009.
- [15] B. J. Wellman ve J. B. Hoagg, "Quadratically Parameterized Root Locus Analysis", c. 59, sayı 7, ss. 1803-1817, 2014.

ELECTRIC-ELECTRONIC ENGINEERING

ORAL SUBMISSIONS



Performance analysis of 20 Gb/s QPSK modulated dual polarization coherent optical OFDM systems

Ahmet Güner

Bingöl University, Faculty of Engineering and Architecture

Bingöl, Turkey

aguner@bingol.edu.tr

Abstract— In this study, 20 Gb/s Dual Polarization Coherent Optical Orthogonal Frequency Division Multiplexing (DP-CO-OFDM) system is studied to obtain the relation between the Bit Error Rate (BER) and launch power for different transmission length and polarization mode dispersion (PMD) coefficient. DP-CO-OFDM system is simulated by designing a Monte Carlo simulation. In this simulation, the effects of chromatic dispersion, launch power and PMD coefficient on received signals are demonstrated with constellation diagrams and results are given in form of BER-Launch Power variations.

Keywords— OFDM; optical communication; dual polarization; launch power

I. INTRODUCTION

OFDM is a suitable solution due to its many advantages known in wireless communications. Moreover, it is also used to transmit and receive large data rates in optical communications.

In 2005, the demonstration of the coherent receivers has been caused the increase of interest in coherent optical communications [1]. The main point of coherent communications is to improve sensitivity of the receiver. In addition, it allows the detection of both amplitude and phase increasing the detection capabilities, and combined with advance modulations formats [2].

Recently, the coherent optical communication and OFDM method are combined to obtain both advantages in a communication link. CO-OFDM technique is proposed for long haul transmission to remove inter-symbol interference (ISI) caused by chromatic dispersion in optical communication [3]. CO-OFDM systems allow for equalization of dispersive effects of optical channel.

The first CO-OFDM transmission was reported in 2006 [4, 5]. Dual polarization CO-OFDM has been experimentally demonstrated at 1 Tb/s over 600 km transmission [6]. In conventional coherent optical OFDM systems, training symbols (TSs) are added at the transmitter to facilitate channel estimation, which provides crucial channel information and enables efficient digital compensation of linear fiber impairments such as chromatic dispersion (CD) and polarization mode dispersion (PMD) [7].

In this study, the bit error rate (BER) performance of DP-CO-OFDM system is investigated for different launch powers with the increase in the transmission length under the effect of CD, PMD and the fiber nonlinearity. Also it is shown in constellation diagram the effect of CD, PMD and the higher launch power on optical signals before or after the conventional TS based channel equalization. In section 2, a general dual polarization coherent optical OFDM system is described. In section 3, the TS based channel equalization is described. In section 4, the results of simulated system are reported and finally in section 5, the conclusion is made.

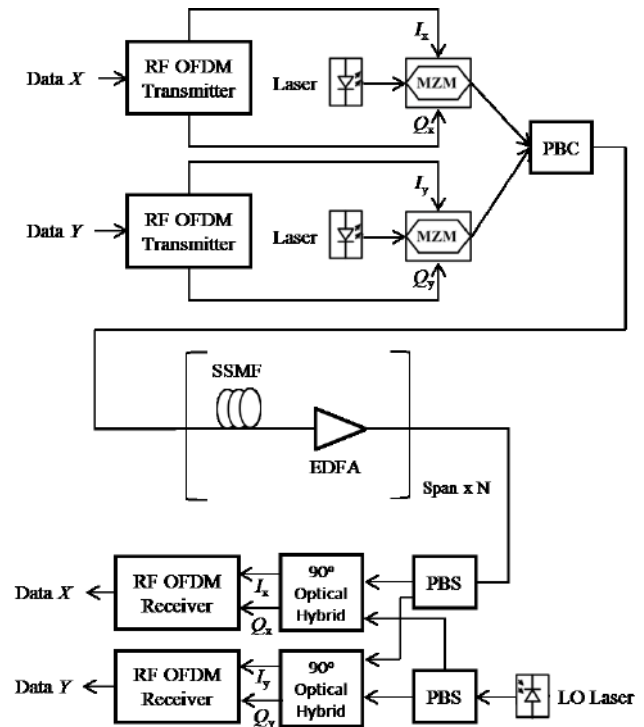


Fig. 1. Block diagram of a DP-CO-OFDM system. PBC : polarization beam combiner, PBS : polarization beam splitter, LO : local oscillator.

II. DUAL POLARIZATION COHERENT OPTICAL OFDM SYSTEM

In Fig. 1, it is shown a general dual polarization coherent optical OFDM system. At the transmitter, the data sets are first mapped to QPSK symbols. Then, training symbols are added into OFDM symbol before IFFT. Two optical IQ modulators are used to convert the electrical signals to the optical signals and a polarization beam combiner combines the two optical signals.

The optical channel consists of many standard single mode fiber (SSMF) spans with CD, PMD, fiber nonlinearity and attenuation. In optical channel, the erbium-doped fiber amplifier (EDFA) for gain is used in line amplification of signal.

In the receiver, two polarization beam splitters are used for mapping X polarization and Y polarization of the optical signal onto optical carrier. The polarized optical signals are passed through 90° optical hybrids that converting the optical signals to an electrical signals along with light of LO laser. Then, the data symbols on each subcarrier are obtained by FFT. The channel estimation is implemented to compensate for the inter-subcarrier interference caused by CD and PMD.

III. CHANNEL ESTIMATION AND EQUALIZATION

The linear fiber impairments in DP-CO-OFDM system can be described by a 2×2 multiple-input multiple-output (MIMO)-OFDM model in frequency domain on subcarrier basis as follows [7]:

$$\begin{bmatrix} R_x^i \\ R_y^i \end{bmatrix} = \begin{bmatrix} H_{xx}^i & H_{xy}^i \\ H_{yx}^i & H_{yy}^i \end{bmatrix} \begin{bmatrix} T_x^i \\ T_y^i \end{bmatrix} \quad (1)$$

Where T and R are the transmitted data and the received data. i is subcarrier index, x and y are polarization indexes. H_{xy}^i is channel frequency response of the i th subcarrier from X polarization to Y polarization. In (1), the noise term is omitted for simplicity.

In CO-OFDM systems, the training symbols (TS) using for estimation of the channel are added at the transmitter. Thanks to the training symbols are orthogonal, all coefficient of H matrix are estimated as follows,

$$H_{xx}^i = \frac{R_x^i}{TS_x^i}, H_{xy}^i = \frac{R_y^i}{TS_x^i}, H_{yx}^i = \frac{R_x^i}{TS_y^i}, H_{yy}^i = \frac{R_y^i}{TS_y^i}, \quad (2)$$

In TS based channel equalizer, the value of \hat{H}_{xy}^i can be obtained by the inverse of H_{xy}^i in (2). Then the signal at the i th subcarrier can be recovered by,

$$\begin{bmatrix} T_x^i \\ T_y^i \end{bmatrix} = \begin{bmatrix} H_{xx}^i & H_{xy}^i \\ H_{yx}^i & H_{yy}^i \end{bmatrix}^{-1} \begin{bmatrix} R_x^i \\ R_y^i \end{bmatrix} = \begin{bmatrix} \hat{H}_{xx}^i & \hat{H}_{xy}^i \\ \hat{H}_{yx}^i & \hat{H}_{yy}^i \end{bmatrix} \begin{bmatrix} R_x^i \\ R_y^i \end{bmatrix} \quad (3)$$

IV. SIMULATIONS RESULTS

In order to get the results of performance analysis, a simulation of DP-CO-OFDM systems was developed by using MATLAB. Optical fiber parameters and basic OFDM parameters are given Table 1 and Table 2 respectively. The data transmission bit rate is 10 Gp/s on each polarization.

TABLE I. FIBER OPTICAL PARAMETERS

Parameter	Value
Wavelength	1550 nm
Velocity of light	200000 km/s
Fiber optical cable length	100 – 1000 km
Chromatic dispersion parameter	16 ps/(nm.km)
PMD coefficient	0.1 – 0.6 ps/km
Nonlinearity coefficient	$1.32 (W.km)^{-1}$
Attenuation	0.2 dB/km
Gain of EDFA	12 dB
Noise figure of EDFA	5 dB
Length of spans	100 km

TABLE II. OFDM PARAMETERS

Parameter	Value
FFT/IFFT length (N_{FFT})	256
Number of subcarriers	128
Cyclic prefix	% 6.25
Modulation	QPSK
OFDM symbol rate	39.06 MHz

In Fig. 2, it is shown output signal constellation diagram before the channel equalization after transmission length 10 km, 50 km, 200 km and 500 km respectively for 0.1 ps/km PMD coefficient. The constellation points increase as the circumference and scatter due to the chromatic dispersion as a function of the transmission length.

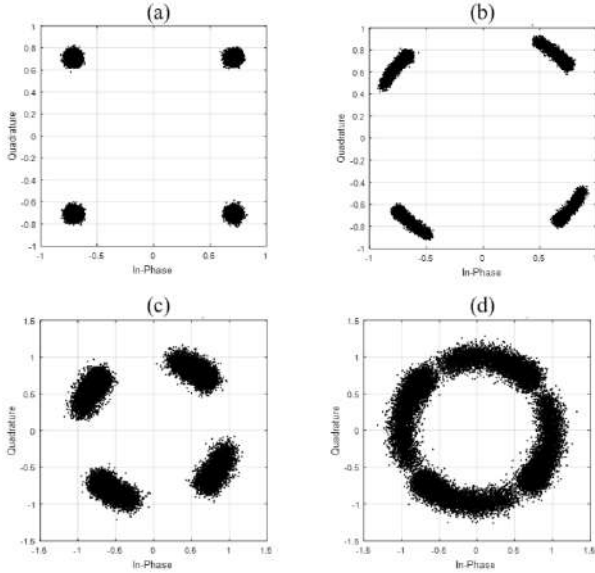


Fig. 2. Output signal constellation of X polarization of QPSK OFDM systems with Launch power -2 dBm for different transmission length, (a) $L = 10$ km, (b) $L = 50$ km, (c) $L = 200$ km (d) $L = 500$ km

In Fig. 3, it is shown output signal constellation diagram after the channel equalization by keeping launch power -6 dBm, -2 dBm, 0 dBm and 2 dBm respectively for 0.1 ps/km PMD coefficient after 900 km transmission length. As the launch power increases, the constellation points scatter as a function of the launch power because a higher launch powers lead to a larger nonlinear distortion.

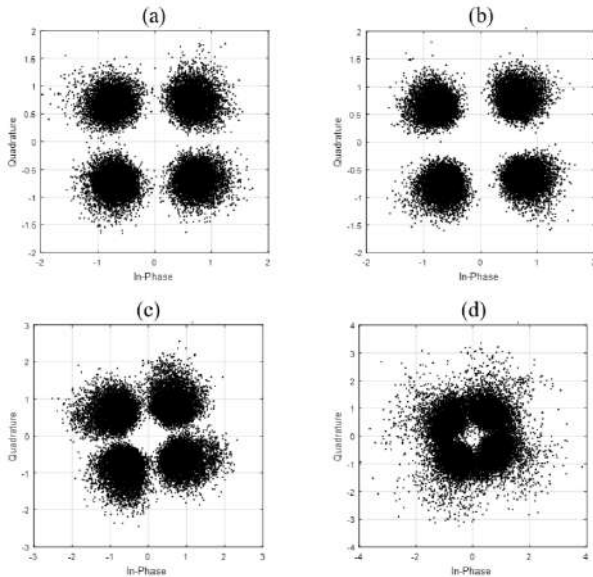


Fig. 3. Output signal constellation of X polarization of QPSK OFDM systems after 900 km transmission for different launch power, (a) -6 dBm (b) -2 dBm (c) 0 dBm (d) 2 dBm

As shown in Fig. 4, the bit error rate (BER) as a function of the launch power decreases initially up to -1 dBm after 800 km

transmission length as the launch power increases. However, at higher launch powers, BER increases due to distortions caused by the fiber nonlinearity.

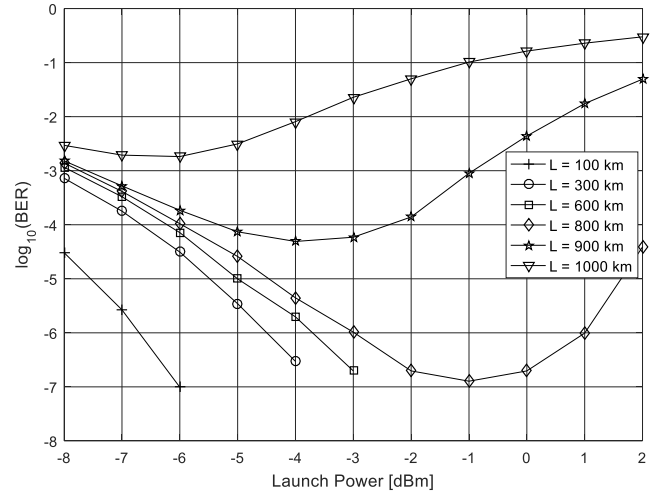


Fig. 4. BER of DP-CO-OFDM systems versus launch power for different transmission length

As also shown in Fig. 4, as the transmission length increases, value of the launch power at which BER begins to increase varies as a function of the transmission length.

In Fig. 5, it is shown output signal constellation diagram before the channel equalization by keeping PMD coefficient 0.1 ps/km and 0.3 ps/km respectively after 100 km transmission length. The circumference of the constellation points increase due to PMD as shown with red line in Fig. 5

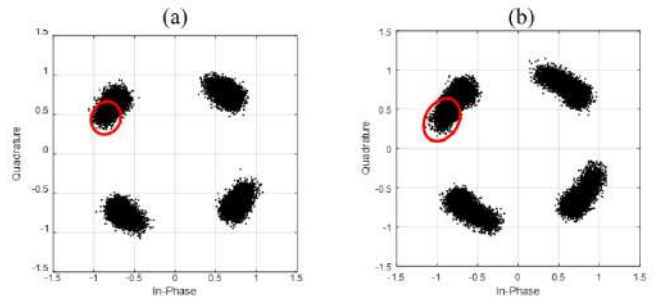


Fig. 5. Output signal constellation of X polarization of QPSK OFDM systems with Launch Power -2 dBm after 100 km transmission for (a) PMD = 0.1 ps/km (b) PMD = 0.3 ps/km

As shown in Fig. 6, the PMD coefficient changes from 0 ps/km to 0.6 ps/km at a step of 0.2 ps/km and BER as a function of the PMD coefficient increases due to the degradation caused by PMD.

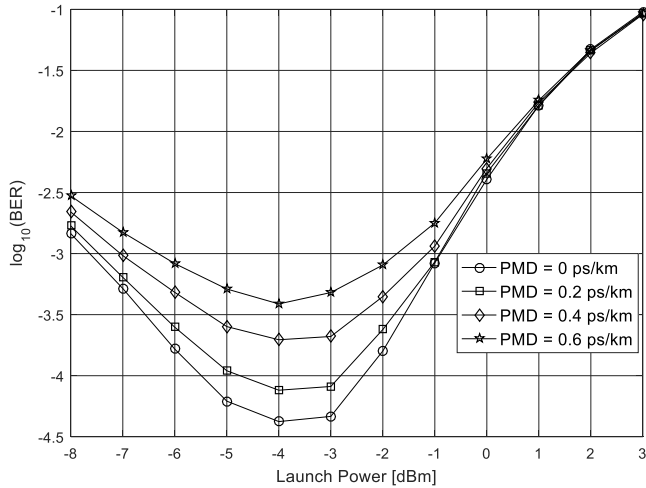


Fig. 6. BER of DP-CO-OFDM systems versus launch power after 900 km transmission for different PMD coefficient

V. CONCLUSIONS

We have analyzed performance of DP-CO-OFDM system against transmission impairments such as CD, PMD and fiber nonlinearity through simulations. The simulations are designed by QPSK modulated OFDM signals with dual polarization each with 10 Gb/s. The results of simulation show that at higher launch powers, BER increases due to the fiber nonlinearity and distortions caused by CD and PMD with the

increase of the transmission length. Also the results of simulation are supported by constellation diagrams at fixed launch power and fixed transmission length.

REFERENCES

- [1] K. Kikuchi, "Fundamentals of coherent optical fiber communications," J. Lightw. Technol.34(1),pp. 157-179, 2016.
- [2] J. Torres-Zugaide, I. Aldaya, G. Campuzano and G. Castano, "Hammerstein-based equalizer for nonlinear compensation in coherent OFDM long-reach PONs", International Conference on Transparent Optical Networks (ICTON), pp. 1-3, 2016.
- [3] A. Yazgan and İ.H. Çavdar "Optimum link distance determination for a constant signal to noise ratio in M-ary PSK modulated coherent optical OFDM systems", TELECOMMUNICATION SYSTEMS, vol.55, pp.461-470, 2014.
- [4] I.B Djordjevic and B. Vasic, "Orthogonal frequency division multiplexing for high-speed optical transmission", Optics Express, 14, 3767-3775, 2006.
- [5] W. Shieh, and C. Athaudage, "Coherent optical orthogonal frequency division multiplexing", Electronics Letters, 42, 5-589, 2006.
- [6] Y. Ma, Q. Yang, S. Chen, and W. Shieh, "1-Tb/s single-channel coherent optical OFDM transmission with orthogonal-band multiplexing and subwavelength bandwidth access," J. Lightw. Technol., vol. 28, no. 4, pp. 308-315, 2010.
- [7] X. Li, W.D. Zhong, A. Alphones, C. Yu, and Z. Xu, "Channel Equalization in Optical OFDM Systems Using Independent Component Analysis," IEEE/OSA Journal of Lightwave Technology, vol. 32, no. 18, pp. 3206-3214, 2014.

Selection of Fiber Optic Fabry-Perot Interferometer Parameter for Acoustic Sensing Applications

Şekip Esat Hayber

Ahi Evran University, Electronic and
Automotion Dep.
Kırşehir, Turkey
sehayber@ahievran.edu.tr

Timuçin Emre Tabaru

Erciyes University, Clinic Eng. Research
and App. Cen.
Kayseri, TURKEY
etabaru@erciyes.edu.tr

Ömer Galip Saraçoğlu

Erciyes University, Electrical&Electronic
Engineering Dep.
Kayseri, TURKEY
saracog@erciyes.edu.tr

Abstract— Optic interference theory and diaphragm dynamic vibration analysis compose the two principle units of diaphragm based fiber optic interferometric acoustic sensors. The two theories should be analyzed together for a sensor system to operate in linear zone. The sensitivity to acoustic pressure, the linearity and frequency response of the sensor system which combines these two principles can be analyzed quantitatively and these analysis results can be used for choosing the suitable sensor system parameters. With the improved calculation approach, more than one condition is evaluated and most suitable result is calculated easily. Because the software permits multiple calculations the relationship between the parameters can be seen easily in a wide range. In addition, the most suitable dimensions for the measuring conditions can be calculated. In this work, we calculated diaphragm diameter regarding the other mechanical and corresponding optical design parameters of Fabry-Perot interferometric sensor system.

Keywords—*Fabry-Perot interferometer (FPI); optical fiber sensors; acoustic detection*

I. INTRODUCTION

Acoustic detection is now an important area in modern life with its applications ranging from structural health monitoring to medical imaging. The detection and analysis of acoustic waves has become an interesting research area with a wide range of applications over the last few decades. Acoustic methods have proven to be highly informative for understanding of the structures of the materials, their features and different physical processes within them, and consequently the importance of acoustic wave technology has rapidly increased in both modern science and engineering applications [1, 2]. Piezoelectric sensors have been used in many acoustic applications for many years with a reasonable number of success. These sensors are sensitive to small size and different input parameters and also they are cost effective, but despite all these advantages, they have some problems when they are exposed to heavy environments because of their low resistance to chemical factors and high temperatures and they are affected by electromagnetic interference. These systems consist of many electronic components and electrical cabling which can weaken the electronic signals much. This makes them less useful in many conditions where long structures and remote

control are required [2]. Sensors with fiber optics have proven to be much better than conventional sensors based on piezoelectric transducers. Fiber optic sensors have many abilities like multiplexing capacities, direct access to optical transmission lines that classical piezoelectric sensors are unfavorable. These sensors also bring many advantages like having broadband range, no limits on size and shape, and being able to be firmly connected [3-5]. Fiber optic interferometric sensors realize the detection mechanism by means of phase change; that's why these sensors are much more necessary for applications requiring high resolution. Sensitivity and resolution of optical interferometric sensors are better than other sensors based on intensity and polarization [6]. Unlike other interferometers (Mach-Zehnder, Michelson, Sagnac) used in detection, the Fabry-Perot Interferometer (FPI) does not have complex structures. For this reason, FPI is the most preferred method for advanced interferometric sensor applications and a good transducer for many smart sensor applications [7].

In this work, we developed a MATLAB code for calculation of a key design parameter regarding mechanical and corresponding optical design parameters of an FPI sensor system.

II. OPERATING PRINCIPLE OF THE SENSOR SYSTEM

A. Components of the sensor system

Fig. 1 shows the general structure of the FPI optical detection system, which has a single or multimode fiber transmission medium. This system consists of a sensor tip, a semiconductor light emitter capable of operating in different wave lengths, an optical receiver and fibers providing the connection between the components. A 3dB fiber coupler is used to receive the reflected signal and reduce the optical feedback which comes back to the source. The light emitted from the light source is firstly reflected from the end of the fiber. The remaining light passes through the air gap and is partially reflected back by hitting the diaphragm surface. These multiple reflections reach the optical receiver through the same fiber. The general operating principle of the system is that the light from the light source is reflected from two separate layers

and is perceived again, the system is based on measuring the phase difference between the transmitted light and the detected [8].

Optical interference theory and diaphragm dynamic vibration analysis constitute the two basic principles of fiber optic interferometric acoustic sensors with diaphragm base [9]. The acoustic sensor which combines these two principles can quantitatively analyses system's sensitivity to acoustic pressure and system's frequency response. These analysis results are used to determine the sensor system parameters such as geometric dimensions of the diaphragm, the FPI cavity length etc.

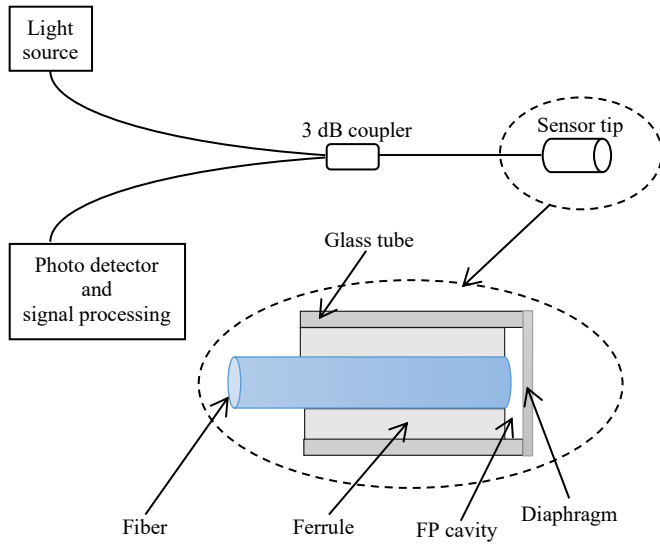


Fig. 7. The structure of diaphragm based fiber optic FPI sensor system.

B. Optic Interference Theory

The schematic representation of the Fabry-Perot (FP) cavity and the typical reflection spectrum are shown in Fig. 2. The incident light leaves the cavity after the reflections and refractions between two parallel reflective surfaces. The reflected light is not taken into consideration. The spectrum of the transmitted light will be symmetrical with respect to the horizontal axis.

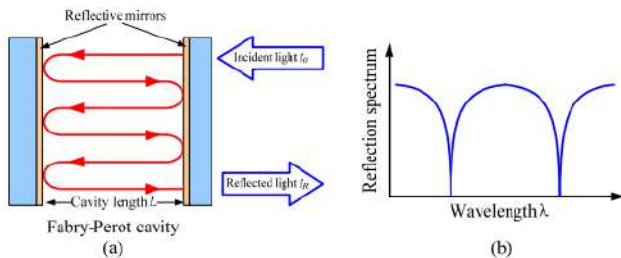


Fig. 8. (a) Schematic representation of FP cavity; (b) Typical reflection spectrum of FPI [10].

The intensity of reflected light, I_r in FPI is defined as follows [11].

$$I_r(L, \lambda) = \alpha_0 I_0(\lambda) \frac{R_1 + \eta R_2 - 2\sqrt{\eta R_1 R_2} \cos \phi}{1 + \eta R_1 R_2 - 2\sqrt{\eta R_1 R_2} \cos \phi} \quad (1)$$

Where L is FP cavity length, $I_0(\lambda)$ is the optical density of the incident light which has the λ wavelength, α_0 is a constant that identifies the optical losses in the system. These optical losses consist of couplings in the input / output fibers, optic coupler, connector and so on. R_1 and R_2 are the reflectivity in the fiber-to-space and space-to-diaphragm interface, respectively. ϕ indicates the optical phase and defined as follows,

$$\phi = \frac{4\pi n_m L}{\lambda} \quad (2)$$

where n_m is the refractive index of the medium in the FP cavity η denotes the transmission coefficient of the light coming to and going from in the cavity [12],

$$\eta = \frac{1}{1 + \left(\frac{\lambda L}{\pi n_m w^2}\right)^2} \quad (3)$$

where w is the mode-field radius (spot size) of the fiber used in the system. The analytical definition of a single mode step index fiber with w Gaussian distribution is as follows [10],

$$\frac{w}{a} \approx 0.65 + \frac{1.619}{V^{3/2}} + \frac{2.879}{V^6} \quad (4)$$

V is the normalized frequency of fiber. It is given as follows,

$$V = \frac{2\pi a}{\lambda} \sqrt{n_f^2 - n_c^2} \quad (5)$$

where a is the radius of the fiber core, n_f represents the refractive index of the fiber core, n_c represents the refractive index of the fiber cladding.

The expressions R_1 and R_2 in (1) are given in (6a) and (6b), respectively depending on fiber core refractive index n_f , refraction index of the medium in FP cavity n_m and refraction Index of the diaphragm n_d ,

$$R_1 = \left(\frac{n_f - n_m}{n_f + n_m}\right)^2 \quad (6a)$$

$$R_2 = \left(\frac{n_m - n_d}{n_m + n_d}\right)^2 \quad (6b)$$

When all parameters between (1) and (6) are taken into consideration with regard to their typical values, the spectrum of the reflected light depending on the change of FP cavity length is shown in Fig. 3.

The light intensity measured by the optical detector decreases as the cavity length increase. There must be a linear relationship between the change of cavity length and the optical signal at the output for the operation of the sensor system. Fig. 4. shows the reflection spectrum in three different wavelengths according to FP cavity length. The half of the difference between the cavity lengths corresponding to the successive maximum and minimum values of the reflected signal in a determined narrow region can be evaluated as the maximum amount of the change of FP cavity length. It can be seen in (7). FPI is outside the linear region when values are above this value. This limitation is because of optic interference theory, it is called as optic limitation.

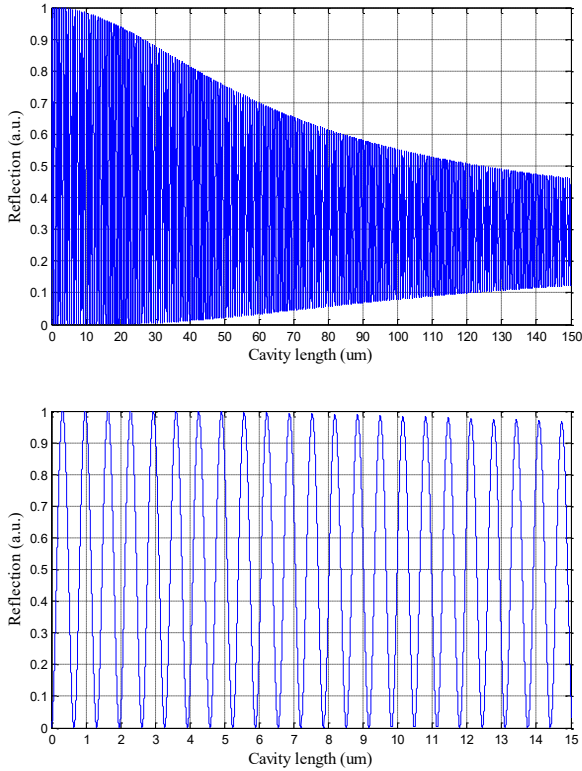


Fig. 9. Calculated reflection spectra of the FPIs. In the calculation, the refractive indices of the fiber core $n_f=1.4492$, $n_c=1.444$, $n_m=1$ (air), and $n_d=1.45$ (silica), fiber radius $a=4.5 \mu\text{m}$, center wavelength of source $\lambda=1310 \text{ nm}$; cavity length is (a) 0-150 μm (b) 0-15 μm .

$$(\Delta L)_{\max} = \frac{L@I_{\max} - L@I_{\min}}{2} \quad (7)$$

Where $L@I_{\max}$ and $L@I_{\min}$ are the FP cavity lengths corresponding to the maximum and minimum points of the output optic power.

The maximum change of FP cavity length can be calculated for different wavelengths from (7) and Fig. 4. These values are given in Table I.

TABLE III. MAXIMUM VARIATION AMOUNT OF FPI CAVITY

Center Wavelength h (nm)	$L@I_{\max}$ (μm)	$L@I_{\min}$ (μm)	$(\Delta L)_{\max}$ (nm)
850	49.9374	49.7250	106.20
1310	50.1073	49.7800	163.65
1550	49.9872	49.6000	193.60

As shown in Table I, as the wavelength of the optic source increases, larger variations are allowed in the FP cavity. The ratio of maximum length variation to wavelength of optical source is determined as a value of 1/8 [13]. In that case, limit value of the maximum amount of diaphragm expansion which will be discussed in the next section is determined here.

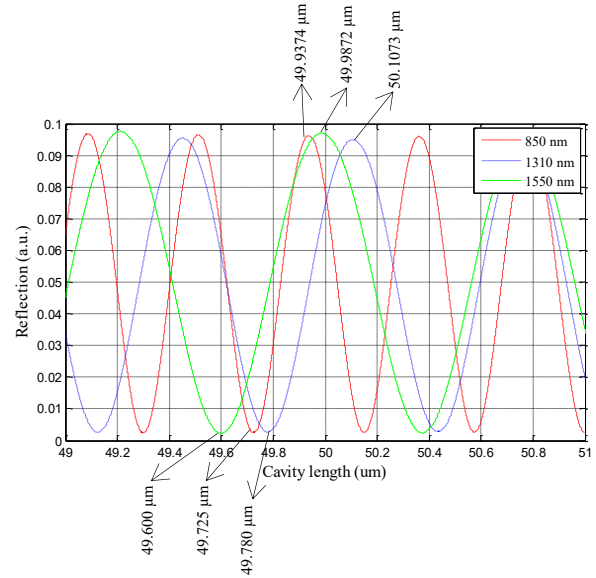


Fig. 10. Calculated reflection spectra of the FPIs. In the calculation, the refractive indexes of the fiber core $n_f=1.4492$, $n_c=1.444$, $n_m=1$ (air), and $n_d=1.45$ (silica), fiber radius $a=4.5 \mu\text{m}$, center wavelength of source $\lambda=850, 1310, \text{ and } 1550 \text{ nm}$; cavity length is 49 to 51 μm .

The other sensor-performance parameter which is used for the determination of the FP cavity length is the source coherence length and it stands for L_c . This parameter depends on the central wavelength and the full-width at half maximum (FWHM) of the optic source. L_c is defined as in [10],

$$L_c = \frac{\lambda^2}{\Delta\lambda} \quad (8)$$

where $\Delta\lambda$,

$$\Delta\lambda = \frac{\lambda_{FWHM}}{\sqrt{8 \ln 2}}. \quad (9)$$



$$\xi = 0.6689 \frac{\rho' r}{\rho t} . \quad (12)$$

TABLE IV. THE SELECTION OF FP CAVITY ACCORDING TO OPTIC SOURCE FEATURES

Center Wavelength (nm)	FWHM (nm)	$\Delta\lambda$ (nm)	L_c (μm)
850 (LED)	105	44.590	16.203
1300 (LED)	130	55.206	30.613
1308 (LED)	147	62.425	27.407
1310 (LD)	7.1	3.015	569.187
1550 (LD)	12	5.096	471.448

Providing $L < L_c$ relation between FP cavity length and source coherence length is important for the sensitivity of the sensor system [10]. As shown in Table II, when compared to spectral width values, the laser diodes (LD) exhibit better performances than the LEDs and this enable them to provide larger FP cavity-lengths.

C. The Diaphragm Dynamic Vibration Analysis

The signal that dynamically modulates the cavity length of FPI signal (e.g. acoustic wave) causes a vibration in the diaphragm. The deflection of the diaphragm caused by the acoustic wave can be determined theoretically by the load-deflection method and is given by [14],

$$d = \frac{3(1-\nu^2)Pr^4}{16Et^3}. \quad (10)$$

By using (10), the deflection of a circular diaphragm under a pressure value of P is calculated. Where ν is Poisson's ratio, E is Young's modulus of the diaphragm material, r is the radius of the diaphragm defined by the inner diameter of the cylindrical glass tube, and t is the thickness of the diaphragm. Generally, in order to ensure the linearity of the deflection at the center point, the deflection amount should be less than 30% of the diaphragm thickness [14]. This limitation is similar to the maximum value of the FP cavity length in the optical interference theory. Whichever smaller parameter is taken into account, two conditions will be provided. Therefore, we start our calculation by taking into account this fundamental principle.

The last parameter that must be determined is the frequency band. Depending on the material properties and the geometrical dimensions of the diaphragm (thickness and radius), the resonance frequency is determined from (11) and (12) [14],

$$f = \frac{\varphi_{mn}^2}{2\pi r^2 \sqrt{1+\xi}} \sqrt{\frac{Et^2}{12\rho(1-\nu^2)}} \quad (11)$$

The parameters ρ and ρ' represent the density (kg/m^3) of diaphragm material and the surrounding medium, respectively. φ_{mn} is the roots of the vibration equation for different mode orders ($m = 0, 1, 2, 3, \dots$ and $n = 0, 1, 2, 3, \dots$). The values of φ_{mn} are listed in Table III [14].

TABLE V. VALUES OF φ_{mn} .

$m \backslash n$	0	1	2	3
0	3.196	4.611	5.906	7.143
1	6.306	7.799	9.917	10.537
2	9.44	10.958	12.402	13.795
3	12.577	14.108	15.579	17.005

In Fig. 5, the frequency response of a circular diaphragm that is made of silica is shown for the first 16 resonance frequencies.

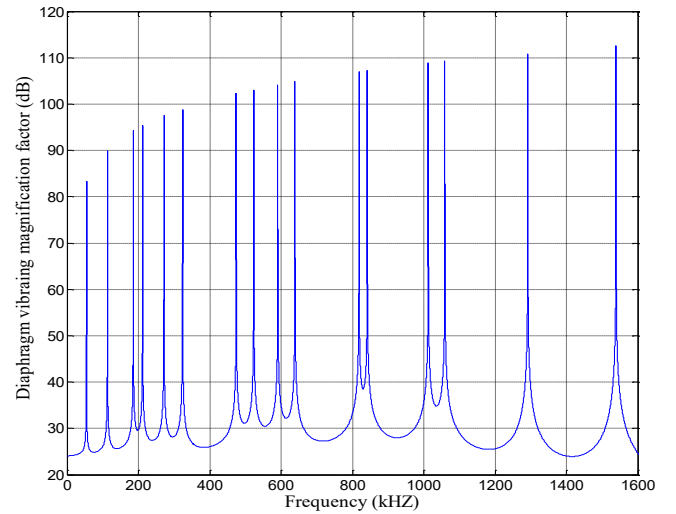


Fig. 11. Calculated frequency response of the diaphragm with the radius $r=1500 \mu\text{m}$ and the thickness $t=20 \mu\text{m}$, $E=73\text{GPa}$, $\nu=0.17$, $\rho=2200 \text{ kg}/\text{m}^3$, $\rho'=1.225 \text{ kg}/\text{m}^3$ (air), $f=0-1600\text{kHz}$.

In Fig. 6. the response of the diaphragm around the lowest resonance frequency is shown. The frequency response of the sensor system can be decomposed into two regions which are broad- and narrow-band spectra. The system is defined as a narrow-band sensor in the case of the detection of the signals that are very close to the resonance frequency. On the other hand it is specified as a broad-band sensor in the case of the detection of the signals which have a frequency value lower than the 1/3 of the resonance frequency; additionally a straight response is obtained for a wide frequency range. In this situation, the desired properties for a sensor system can be obtained according to the chosen material and geometric dimensions of diaphragm.

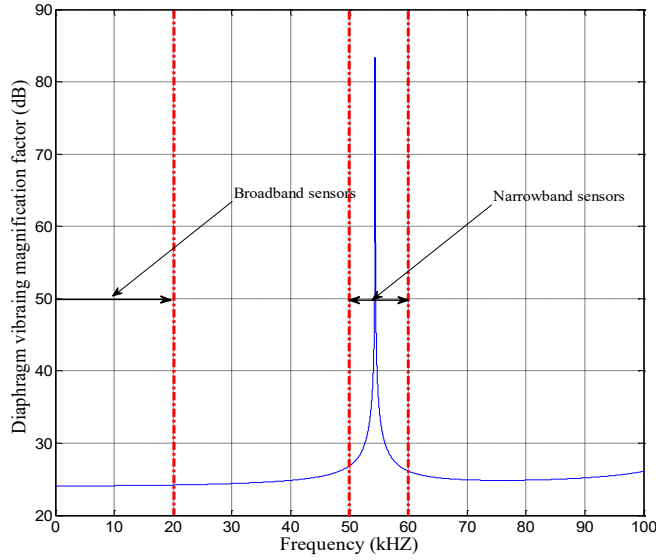


Fig. 12. Calculated frequency response of the diaphragm with the radius $r=1500 \mu\text{m}$ and the thickness $t=20 \mu\text{m}$, $E=73\text{GPa}$, $\nu=0.17$, $\rho=2200 \text{ kg/m}^3$, $\rho'=1.225 \text{ kg/m}^3$ (air), $f=0\text{-}100\text{kHz}$.

III. NUMERIC ANALYSIS RESULTS

A. Optimum Radius Selection

The resonance frequency of the acoustic waveguide and the amount of deflection of the diaphragm depend on the radius of the diaphragm when the other parameters are kept constant (E, ν, ρ, t, ρ'). This relationship was given in (10) and (11). The amount of deflection in this relationship is directly related to the maximum amount of variation in the FP cavity in the optical interference theory. There are two limit values in determining the amount of deflection of the diaphragm. One of them is $\lambda/8$ (optic limit) and the other is $0.3t$ (mechanical limit). The radius value is calculated by considering the smallest of these limits but in this situation the amount of pressure must be taken into consideration. A second radius value is calculated from the frequency value by taking broadband or narrow-band into account. The value which is calculated smaller is considered as a solution because it provides all conditions. The radius value in the calculation result shows the largest value that can be chosen. The diaphragms created under this value will provide the desired conditions. Selection of optimum radius can be explained a flow chart given in Fig. 7.

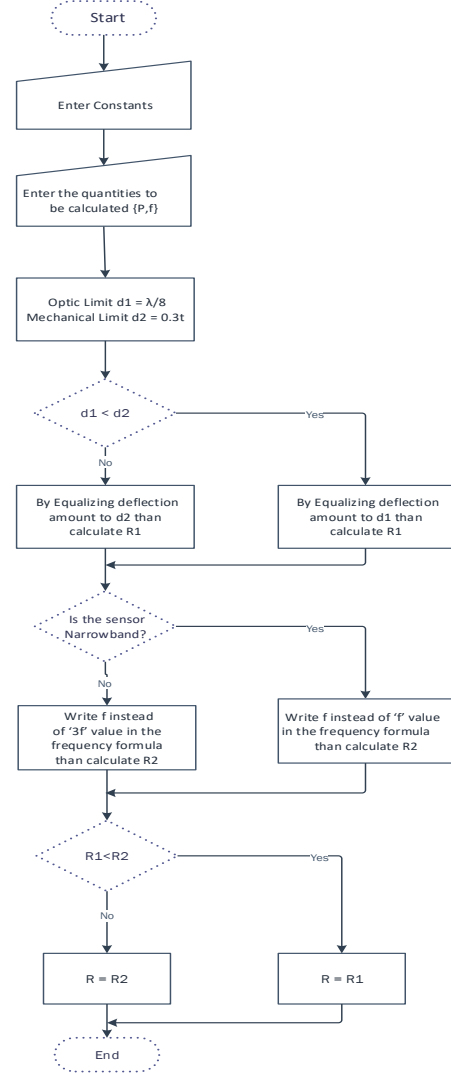


Fig. 13. The flow chart is shown to calculate the most appropriate radius value.

B. Computational Results

In this work, we developed a MATLAB code for calculation of diaphragm diameter. The silica was selected as the diaphragm material. Because it is compatible with the fiber parameters. Properties of Silicon Dioxide (Silica, SiO_2) material, which is used frequently in diaphragm-based FP pressure sensors, are given in Table IV [15]. The center wavelength of the optical source was taken as 1310 nm. Diameter values calculated according to pressure and frequency values to be measured are given in Table V-VIII. By keeping constant the pressure value, the variation of the diaphragm diameter in water is shown in Table V. The same calculations in Table V were applied in the air environment in Table VI. By keeping the frequency value constant, the variation of diaphragm diameter in water is shown in Table VII. The same calculations in Table VII were applied in the air environment in Table VIII.



TABLE VI. VALUES OF SILICA.

Parameter	Symbol	Value	Units
Density	ρ	2200	kg/m^3
Young's Modulus	E	73	GPa
Poisson's Ratio	ν	0.17	-

TABLE VII. VALUES OF DIAMETER IN WATER.

f 15 kHz-100 MHz	Diameter (μm)
$P=10$ kPa $f=15$ kHz broadband	957.4400
$P=10$ kPa $f=50$ kHz broadband	751.4770
$P=10$ kPa $f=100$ kHz broadband	564.0353
$P=10$ kPa $f=500$ kHz broadband	286.4866
$P=10$ kPa $f=1$ MHz broadband	212.6603
$P=10$ kPa $f=10$ MHz broadband	76.2885
$P=10$ kPa $f=50$ MHz broadband	36.0052
$P=10$ kPa $f=100$ MHz broadband	25.8601

TABLE VIII. VALUES OF DIAMETER IN AIR

f 15 kHz-100 MHz	Diameter (μm)
$P=10$ kPa $f=15$ kHz broadband	957.4400
$P=10$ kPa $f=50$ kHz broadband	957.4400
$P=10$ kPa $f=100$ kHz broadband	853.6019
$P=10$ kPa $f=500$ kHz broadband	382.1592
$P=10$ kPa $f=1$ MHz broadband	270.2975
$P=10$ kPa $f=10$ MHz broadband	85.5123
$P=10$ kPa $f=50$ MHz broadband	38.2465

$P=10$ kPa $f=100$ MHz broadband	27.0450
--	---------

TABLE IX. VALUES OF DIAMETER IN WATER.

P 10 Pa-100 GPa	Diameter (μm)
$P=10$ Pa $f=100$ kHz broadband	564.0353
$P=100$ Pa $f=100$ kHz broadband	564.0353
$P=1$ kPa $f=100$ kHz broadband	564.0353
$P=10$ kPa $f=100$ kHz broadband	564.0353
$P=100$ kPa $f=100$ kHz broadband	538.4000
$P=500$ kPa $f=100$ kHz broadband	360.0600
$P=1$ MPa $f=100$ kHz broadband	302.7600
$P=10$ MPa $f=100$ kHz broadband	170.2600
$P=100$ MPa $f=100$ kHz broadband	95.7440
$P=1$ GPa $f=100$ kHz broadband	53.8400
$P=10$ GPa $f=100$ kHz broadband	30.2760
$P=100$ GPa $f=100$ kHz broadband	17.0260



TABLE X. VALUES OF DIAMETER IN AIR

P 10 Pa-100 GPa	Diameter (μm)
$P=10\text{ Pa}$ $f=100\text{ kHz}$ broadband	853.6019
$P=100\text{ Pa}$ $f=100\text{ kHz}$ broadband	853.6019
$P=1\text{ kPa}$ $f=100\text{ kHz}$ broadband	853.6019
$P=10\text{ kPa}$ $f=100\text{ kHz}$ broadband	853.6019
$P=100\text{ kPa}$ $f=100\text{ kHz}$ broadband	538.4000
$P=500\text{ kPa}$ $f=100\text{ kHz}$ broadband	360.0600
$P=1\text{ MPa}$ $f=100\text{ kHz}$ broadband	302.7600
$P=10\text{ MPa}$ $f=100\text{ kHz}$ broadband	170.2600
$P=100\text{ MPa}$ $f=100\text{ kHz}$ broadband	95.7440
$P=1\text{ GPa}$ $f=100\text{ kHz}$ broadband	53.8400
$P=10\text{ GPa}$ $f=100\text{ kHz}$ broadband	30.2760
$P=100\text{ GPa}$ $f=100\text{ kHz}$ broadband	17.0260

IV. CONCLUSION

In this work, we calculated an important design parameter for FP interferometer that can be used for acoustic sensing applications. It is concluded in this work that the diaphragm diameters remain constant for some calculation results in the tables than they start to change because of the limitations used in calculations precedes the other. This is actually the aim of the developed software. Evaluating more than one parameter at the same time and studying all of them in the limit values are difficult because they must be calculated separately. More than one condition is evaluated thanks to the software and the most appropriate result is calculated quickly. Since the software allows multiple calculations, the relationship between the parameters in a wide range can be easily seen. Most suitable geometric dimensions for measuring conditions can be calculated. By changing diaphragm materials, detection medium, wavelength which is used as a light source, and thickness of the diaphragm materials, any system designer can see how these parameters affect the frequency and the pressure value to be measured.

ACKNOWLEDGMENT

This work was supported by the Research Fund of the Erciyes University. Project numbers FDK-2016-6811 and FDK-2016-6815. The authors would like to thank Erciyes University Clinical Engineering Research and Application Center for their supports in the research activities among the staffs.

REFERENCES

- [1] G. Wild, and S. Hinckley, "Acousto-ultrasonic optical fiber sensors: overview and state-of-the-art," *IEEE Sensors Journal*, vol. 8(7), pp. 1184-1193, 2008.
- [2] J. G. Teixeira, I. T. Leite, S. Silva, and O. Frazão, "Advanced fiber-optic acoustic sensors," *Photonic Sensors*, vol. 4(3), pp. 198-208, 2014.
- [3] E. Cibula, S. Pevec, B. Lenardič, E. Pinet, and D. Đonlagić, "Miniature all-glass robust pressure sensor," *Optics Express*, vol. 17(7), pp. 5098-5106, 2009.
- [4] F. Guo, T. Fink, M. Han, L. Koester, J. Turner, and J. Huang, "High-sensitivity, high-frequency extrinsic Fabry-Pérot interferometric fiber-tip sensor based on a thin silver diaphragm," *Optics letters*, vol. 37(9), pp. 1505-1507, 2012.
- [5] W. Wang, N. Wu, Y. Tian, C. Niezrecki, and X. Wang, "Miniature all-silica optical fiber pressure sensor with an ultrathin uniform diaphragm," *Optics Express*, vol. 18(9), pp. 9006-9014, 2010.
- [6] E. Udd, and B. William, Jr. W. B. Spillman, (Eds.), *Fiber optic sensors: an introduction for engineers and scientists*, 2nd ed., John Wiley & Sons, 2011.
- [7] S. S. Yin, and P. Ruffin, *Fiber optic sensors*, 2nd ed., John Wiley & Sons, Inc., 2002, pp. 36.
- [8] J. Deng, H. Xiao, W. Huo, M. Luo, R. May, A. Wang, and, Y. Liu, "Optical fiber sensor-based detection of partial discharges in power transformers," *Optics & Laser Technology*, vol. 33(5), pp. 305-311, 2001.
- [9] A. K. Lazarevich, *Partial discharge detection and localization in high voltage transformers using an optical acoustic sensor*, Doctoral dissertation, Virginia Tech, 2003.
- [10] J. Ma, *Miniature fiber-tip Fabry-Pérot interferometric sensors for pressure and acoustic detection*, Doctoral dissertation, The Hong Kong Polytechnic University, 2014.
- [11] B. Yu, A. Wang, and G. R. Pickrell, "Analysis of fiber Fabry-Pérot interferometric sensors using low-coherence light sources," *Journal of lightwave technology*, vol. 24(4), pp. 1758, 2006.
- [12] B. Yu, D. W. Kim, J. Deng, H. Xiao, and A. Wang, "Fiber Fabry-Pérot sensors for detection of partial discharges in power transformers," *Applied optics*, vol. 42(16), pp. 3241-3250, 2003.
- [13] J. Deng, *Development of novel optical fiber interferometric sensors with high sensitivity for acoustic emission detection*, Doctoral dissertation, Virginia Polytechnic Institute and State University, 2004.
- [14] D. Giovanni, *Flat and corrugated diaphragm design handbook*, 1st ed., vol. 11. CRC Press, 1982.
- [15] J. Xu, *High temperature high bandwidth fiber optic pressure sensors*, Doctoral dissertation, Virginia Polytechnic Institute and State University, 2005.



LSE Channel Estimation and Performance Analysis of OFDM Systems

Bircan Kamislioglu
Ayhan Akbal
Firat University Engineering Faculty
Electric-Electronic Engineering
Elazığ, Turkey
bkamislioglu@firat.edu.tr
ayhan_akbal@firat.edu.tr

Abstract —Orthogonal frequency division multiplex (OFDM) is one of the best approach to overcome frequency selectivity of channels. In multiple-input multiple-output (MIMO) orthogonal frequency division multiplexing (OFDM) systems, we purposed channel estimation with least squares (LS) estimation method in this paper. To improve channel estimation achievement a LS algorithm is developed, so we obtain Bit Error Rate (BER) performance of channel. Mean Square Error (MSE) of LS estimation calculated and depicted in figure. Signal to noise ratio (SNR) indicated notable efficacy in this paper that obtained by using the LS algorithm, in particular channels with variation in time.

Keywords— *Estimation of Channel with LSE, MIMO System, BER, SNR, OFDM.*

I. INTRODUCTION

In recent years in communication systems data rate is getting high and researchers have notable interest on rapid modulation techniques. As a multicarrier modulation technique OFDM is fairly interested by researchers. Because of its basic application and stability, frequency-fading channels are transformed the channel into flat-fading sub channels. OFDM has been performed for a lot of applications, such as high speed telephone line communication, digital audio broadcasting, wireless local area network digital television broadcasting and lines of digital subscriber. In recent communication systems we can realize a remarkable increased capacity OFDM and multiple antennas together and this enhancement obtained due to diversity of transmit and receive sides. [1]. Adding training pilot symbols at the transmitter in practice implementations, CSI is effective estimated at the receiver. Channel estimation with pilot symbol is especially attractive for wireless communication systems in the channel with varying time [2].

Meanwhile a lot channel estimators use for OFDM, error probability examination availability of channel estimation errors has taken notionally less care. In recent days phase shift keying and quadrature amplitude modulation approximations were progressed about BER performance for channel estimation errors of OFDM [3, 4].

OFDM systems consist completely of pilot symbols because of identifying the multiple training channels. This approach for single input and single output (SISO) systems is showed in [5-7], whereas MIMO systems is detailed described in [8]. Like this application firstly any transmission of data we compute estimation of the CSI. When remarkably changes exist for CSI, reobtaining pilot symbols is transmitted. To estimate the CSI in fast time varying surroundings, we must continuously retrain for such systems. About retraining, these systems are experienced an incremented BER because of their antiquated channel estimates. Wiener filter method as based on a known channel correlation function can be used to advance the estimation of channel parameters [9, 10].

MSE of the channel estimation with LS technique is recommended the pilot symbols have an optimum location for SISO OFDM systems. If this channel estimation technique wanted to length to MIMO OFDM systems, seeing that either the location of the pilot symbol or the pilot sequence must be optimized to enhance the MSE value minimum with channel estimation method with LS [11].

In this paper, based on pilot tones MIMO OFDM system is described with a LS channel estimation scheme. MSE of the channel estimation with LS technique is computed, optimum pilot tones of the pilot subcarriers are supplied. LS channel estimation design for multiple OFDM symbols is debated. LS channel estimation algorithm is proposed to advance estimation application.

The organization of this paper is regulated as trace. In chapter II OFDM technique is explained, LSE channel estimation steps are given in chapter III. Analysis of channel estimation is introduced in chapter IV and conclusions are offered in chapter V.

II. OFDM TECHNIQUE

Transmission system of the OFDM about account is depicted in Figure 1. High data rate streams of the random

input signal are transformed into low data rate streams. The low data rate streams are modulated in parallel subcarriers in the OFDM. This parallel stream is dedicated input to the IFFT block structure. The data is transformed from frequency to time before the data accessed the channel by the IFFT block structure. The data is encoded with adding the cyclic prefix as the guard interval and transmission is successful at receiver [12]. Binary source generator produced the digital input data like as BPSK, QPSK and QAM modulation approach are used to modulate the binary data with several different constellations. The data is transformed frequency domain to time domain by the IFFT block in Figure 2. To insert guard interval known as CP succeed the problems like ICI/ISI with acquiring the delay connected problems at the channel. Before the symbols transmitting to the channel, firstly the symbols of OFDM are in the time domain available length. After that all the operations enforced in the inverse direction and obtained OFDM signal as the output of receiver block. CP insertion in the OFDM modulation is the most extensive technique among all the multicarrier modulations because of its facility and its stability across to multipath fading using the cyclic prefix. Even so this technique caused a decrement of spectral efficiency owing to the CP. Also the OFDM spectrum is not dense because of the large side lobe levels resulting from the rectangular pulse [13].

OFDM is a typical multiple channel modulation technique that used to separate to the channel numerous of parallel sub channels and the parallel channels transmit multiple symbols. OFDM has an attractive feature that is considered efficient spectral and also applications of OFDM cope with equalization of dispersive slowly fading channels which is a perfect way. OFDM is used by multiuser systems that exhibited perfect schemes for multiple accesses such as transmission systems with single carrier. When we compared to carrier systems with each other, as a variable modulation technique for multiple access systems OFDM is in that case intrinsically make easy multiple access both time domain and frequency domain.

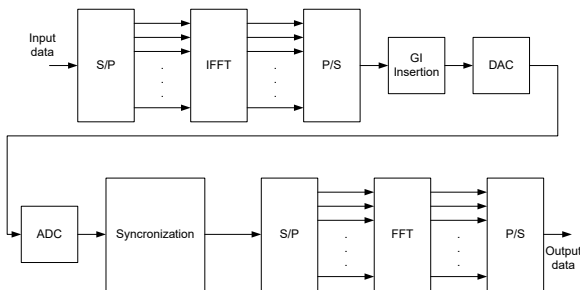


Fig. 14. OFDM transmitter and receiver block diagram.

OFDM also has some imperfections properties. OFDM is sensitive errors of carrier frequency, because a given spectral assignment divides into many narrow subcarriers by OFDM structure with small spacing for

subcarriers inherently. Furthermore, to obtain the orthogonality about subcarriers, it needs linear amplifiers. Because of OFDM systems own a high peak to average power ratio the systems require a large amplifier power back off and a many of bits in the analog to digital (A/D) and digital to analog (D/A) designs. So high requirement is available transmitter and receiver sides in OFDM [14].

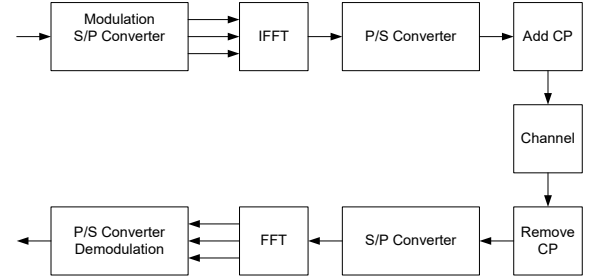


Fig. 15. OFDM block diagram.

OFDM modulation and demodulation block diagram is given in Figure 2. Guard interval is transformed CP in this figure.

III. CHANNEL ESTIMATION WITH LEAST SQUARE METHOD

In this part, channel estimation with LS design is clarified. Data vector is formulated as $X_r(n)$ in Equation 1.

$$X_r(n) = S_r(n) + B_r(n) \quad (1)$$

In Equation 1, $S_r(n)$ is some optional $K \times 1$ data vector, $B_r(n)$ is some optional $K \times 1$ pilot sequence vector and demodulated signal is described in Equation (2).

$$Y_q(n) = \sum_{r=1}^{N_r} \text{diag}\{X_r(n)\} Fh_{q,r} + \Xi_q(n) \quad (2)$$

$$= \sum_{r=1}^{N_r} (\text{diag}\{S_r(n)\} + \text{diag}\{B_r(n)\}) * Fh_{q,r} + \Xi_q(n) \quad (3)$$

Taking to FFT of $Y_q(n)$ in Equation (3) we obtained finally as Equation (4).

$$Y_q(n) = \sum_{r=1}^{N_r} S_{r, \text{diag}}(n) Fh_{q,r} + \sum_{r=1}^{N_r} B_{r, \text{diag}}(n) Fh_{q,r} + \Xi_q(n) \quad (4)$$

We consider the data model as Equation (5).

$$Y_q = Th_q + Ah_q + \Xi_q \quad (5)$$

LS estimate of h_q can obtained as \hat{h}_q and formulated in Equation (6).

$$\hat{h}_q = A^T Y_q \quad (6)$$

Note that equation (6) shows that \hat{h}_q is a composition of the true channel vector h_q and noise vector in the system. We can see whether or not the pilot tones are the same for each ofdm symbol. Namely, same set of pilot tones in ofdm structure is not compulsory.

IV. CHANNEL ESTIMATION PERFORMANCE AND SIMULATIONS

This section presents enhancement of the MSE of the channel estimation with LS. Results of applications are provided to have optimal pilot sequences and optimal placement of the pilot tones in point of the MSE. In Equation 7, L describes the maximum channel length. MSE calculation of the channel estimation with LS is formulated in Equation 7.

$$MSE = \frac{1}{LNt} \mathcal{E} \left\{ \left\| \hat{h}_q - h_q \right\|^2 \right\} \quad (7)$$

Because of obtaining the minimum MSE of the channel estimation with LS linked to a fixed power ρ given for training and zero mean white noise is σ_n^2 in Equation 8.

$$MSE_{\min} = \frac{\sigma_n^2}{\rho} \quad (8)$$

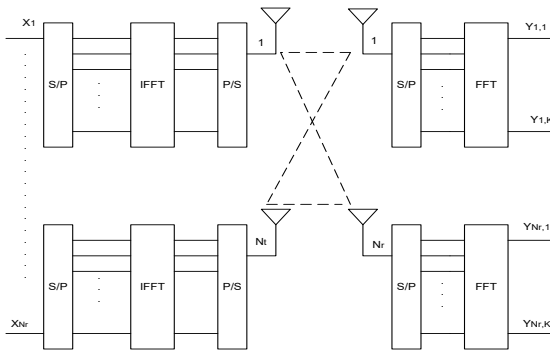


Fig. 16. MIMO-OFDM block diagram.

Figure 3 is depicted block diagram of MIMO-OFDM. In Figure 3 number of transmit antennas is N_t , number of receive antennas is N_r and number of subcarriers is K . Each transmit or receive antenna is utilized in conventional

OFDM modulator or demodulator. Take for the OFDM symbol that is transmitted from the r th antenna at time index n is denoted by $K \times 1$ the vector $X_r(n)$. Before transmission, IFFT is processed to this vector, and v lengthed a cyclic prefix is added. If all channels maximum length is L we obtain that $v \geq L - 1$, which is common practice in wireless communications. Since we extracted the cyclic prefix from the q th receive antenna, $Y_q(n)$ is obtained as $K \times 1$ vector length.

To channel estimation in OFDM is used pilot symbols. OFDM is directly practicable to techniques from single carrier flat fading systems when each subcarrier is flat fading. The sparse insertion of known pilot symbols is found in pilot symbol assisted modulation (PSAM) on channels with flat fading that is in a stream of data symbols in such systems. When the pilot symbols attenuation is calculated the data symbols attenuations among the pilot symbols are characteristically predicted with the fading channel on time correlation features.

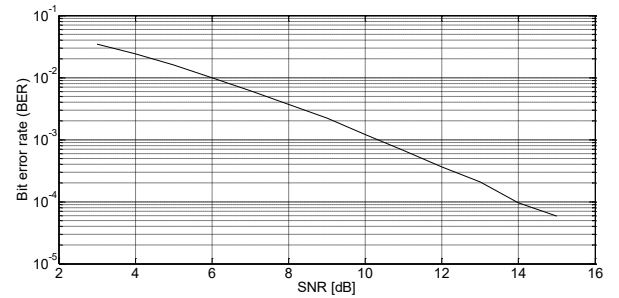


Fig. 17. BER versus SNR in LS channel estimation for MIMO OFDM

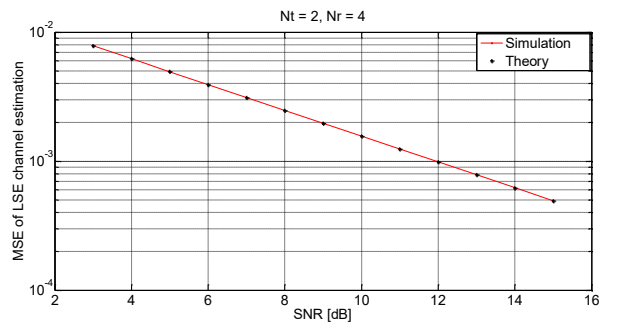


Fig. 18. MSE of LSE channel estimation for MIMO OFDM

BER versus SNR in LS channel estimation for MIMO OFDM system application is shown in Figure 4. MSE of LS channel estimation in simulation and theory for MIMO OFDM system is depicted in Figure 5. In application we selected that $N_t=2$, $N_r=4$, number of subcarriers is 128 and percentage of guard interval is 0.25. Number of pilot

symbols is 64 plus number of the data symbols is 64 we get all of subcarriers.

In literature most of document explains that channel estimation impressions consist of two steps using the channel correlation property. First, correlation of channel technique is used to measure and smooth the attenuations at the pilot positions. Then complex valued attenuations of the data symbols is estimated by these measurements in the second step. Channel correlation properties are used in this second step by filters interpolation technique or a decision directed technique. [15].

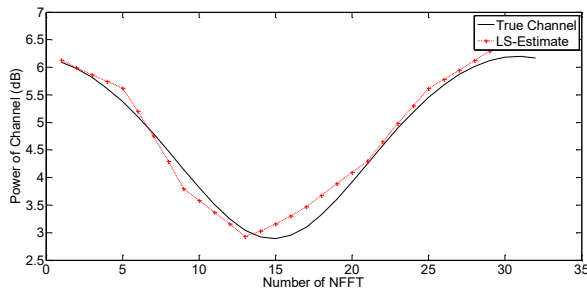


Fig. 19. Power of channel with LSE channel estimation and true channel.

In Figure 6 power of estimated channel and true channel with LSE is depicted. Estimated channel power is fairly close to true channel. So this result shows that LS estimation is appropriate for MIMO OFDM channel estimate.

V.

CONCLUSIONS

This study focused channel estimation with LS method based on pilot tones approach has been evaluated for application of MIMO OFDM systems. The pilot sequences must be equal powered, equal spaced, and obtained orthogonal phase shift to enhance the channel estimation with the minimum MSE. Our results indicates that purposed method about pilot tones the number of transmit antennas are increased so pilot tones for training require more and decreases the efficiency of application. When the channel is slowly time-varying, estimating the channel parameters can reduce this effect over multiple OFDM symbols. Also in next organizations, BER performance will be improve with different from LS estimation method about of MMSE estimation method.

REFERENCES

- [1] H. Bölcskei, D. Gesbert, and A. J. Paulraj, "On the capacity of OFDMbased spatial multiplexing systems," *IEEE Trans. Commun.*, vol. 50, pp. 225–234, Feb. 2002.
- [2] J. K. Cavers, "An analysis of pilot symbol assisted modulation for Rayleigh fading channels," *IEEE Trans. Veh. Technol.*, vol. 40, pp. 686–693, Nov. 1991.
- [3] M.X. Chang and Y. T. Su, "Performance analysis of equalized OFDM system in Rayleigh fading," *IEEE Trans. Wireless Commun.*, vol. 1, pp. 721–732, Oct. 2002.
- [4] H. Cheon and D. Hong, "Effect of channel estimation error in OFDMbased WLAN," *IEEE Commun. Lett.*, vol. 6, pp. 190–192, May 2002.
- [5] L. Deneire, P. Vandenameele, L. Van der Perre, B. Gyselinckx, and M. Engels, "A low complexity ML channel estimator for OFDM," in *Proc. IEEE Int. Conf. Commun., Helsinki, Finland*, June 11–14, 2001.
- [6] O. Edfors, M. Sandell, J.J. van de Beek, S. K. Wilson, and P. O. Borjesson, "OFDM channel estimation by singular value decomposition," *IEEE Trans. Commun.*, vol. 46, pp. 931–939, July 1998.
- [7] J.J. van de Beek, O. Edfors, M. Sandell, S. K. Wilson, and P. O. Brjesson, "On channel estimation in OFDM systems," in *Proc. IEEE Vehic. Technol. Conf.*, vol. 2, Chicago, IL, July 1995, pp. 815–819.
- [8] W. G. Jeon, K. H. Paik, and Y. S. Cho, "An efficient channel estimation technique for OFDM systems with transmitter diversity," in *Proc. IEEE Int. Symp. Pers., Indoor Mobile*, vol. 2, 2000, pp. 1246–1250.
- [9] Y. Li, N. Seshadri, and S. Ariyavisitakul, "Channel estimation for OFDM systems with transmitter diversity in mobile wireless channels," *IEEE J. Select. Areas Commun.*, vol. 17, pp. 461–471, Mar. 1999.
- [10] Y. G. Li, L. J. Cimini, and N. R. Sollenberger, "Robust channel estimation for OFDM systems with rapid dispersive fading channels," *IEEE Trans. Commun.*, vol. 46, pp. 902–915, July 1998.
- [11] S. Ohno, G. B. Giannakis, "Optimal training and redundant precoding for block transmissions with applications to wireless OFDM," in *Proc. IEEE ICASSP, Salt Lake City, UT*, May 2001, pp. 2389–2392.
- [12] C. Veerananarayanareddy, K. Prabhakar "A Novel BER Analytical Performance of DWT based ofdm using various channel over dft based ofdm" *International journal of engineering and computer science* ISSN: 2319-7242 Volume: 4 pp. 14313-14318 Issue 9 Sep 2015.
- [13] B. Le Floch, M. Alard, and C. Berrou, "Coded orthogonal frequency division multiplex," *Proc. IEEE*, vol. 83, no. 6, pp. 982–996, June 1995.
- [14] J.J. Beek, "Channel Estimation in OFDM Systems", Lulea University of Technology, 1402-1544, 1998.
- [15] J.J. van de Beek, "Synchronization and Channel Estimation in OFDM Systems", Lulea University of Technology, Division of Signal Processing, 1998.

Implementation Of Two Cell Non-Autonomous Cnn Model On FPGA

Bariş Karakaya, Vedat Çelik and Arif Gülten
Department of Electrical – Electronics Engineering
Faculty of Engineering, Firat University
Elazig, Turkey
{bkarakaya, celik, agulten}@firat.edu.tr

Abstract— This paper presents implementation of a chaotic Cellular Neural Network (CNN) on field programmable gate array (FPGA). The network has two non-autonomous cells and exhibits chaotic behaviour. In the implementation stage, Verilog Hardware Description Language (HDL) is used and discrete time model of the network is coded on Xilinx ISE Design Suite 13.2. It seems that the chaotic attractor can be used as entropy source or short key (seed) of chaos based random number generator design.

Keywords— Cellular Neural Network, Chaos, FPGA, Random Number Generator

I. INTRODUCTION

Chaos can be defined as unpredictable behaviors that are sensitive to initial conditions in a nonlinear deterministic system [1]. As chaotic behavior can be undesirable in some applications, there are a lot of application areas which use the chaotic behavior in their structures. In [2], the use of the Field Programmable Gate Array (FPGA) as a controller of a DC-DC boost converter, controlling the output current of a photovoltaic cells and minimizing the effect of the boost converter chaotic behavior on the output voltage are discussed. Micro controllers, Digital Signal Processors (DSP) and FPGAs can be used to design implementations of chaotic systems [3-6]. FPGA realizations of chaotic systems are studied in [7, 8] by using Euler algorithm with both integer arithmetic and floating-point number format. Especially, the Lorenz's chaotic system is implemented onto a FPGA with the help of the fourth order Runge Kutta (RK4) algorithm in [9]. The chaotic behavior can be used in Random Number Generator (RNG) applications in order to generate exactly true random number series which are required for secure communication systems. In literature, the realizations of chaotic systems are proposed by using the Xilinx System Generator technology in order to have the HDL code. In [10], the Lorenz's chaotic system is implemented onto FPGA to obtain chaotic sequence for information security issue and in this design the Xilinx System Generator technology is also used. As Cellular Neural Network (CNN) proposed by Chua [11, 12] has complex dynamics, chaotic behaviour can occur in the CNN structures [13]. In this paper, a chaotic attractor is observed with two non-autonomous cell CNN using opposite-

sign template. This network is reported in [14] and solved with Runge-Kutta iterative solution method.

In recent years, many chaotic CNN applications are implemented on the FPGA. Main advantage of the usage of the FPGA is that it can be programmed with more flexibility during implementation of design. Furthermore, development of any design on FPGA is easier and faster than other microprocessors [15]. Implementation of CNN structure on FPGA platform presents all advantages in the meaning of higher operating frequency, minimum resource utilization, reconfigurable systems and more secure applications.

Herewith this introduction, CNN structure and its mathematical model which exhibits chaotic behavior, are presented in Section 2. In Section 3, the implementation of discrete time chaotic CNN model on FPGA platform is also presented. At the end, final section concludes the paper.

II. THE CHAOTIC CNN STRUCTURE

The two-cell non-autonomous CNN model given in [14] is described by state equations as follow:

$$\dot{x}_1 = -x_1 + pf(x_1) - sf(x_2) + g(t) \quad (1)$$

$$\dot{x}_2 = -x_2 + sf(x_1) + pf(x_2)$$

$$f(x_i(t)) = \frac{1}{2}(|x_i(t) + 1| - |x_i(t) - 1|), \quad i = 1, 2 \quad (2)$$

$$g(t) = A \sin\left(\frac{2\pi t}{T}\right) \quad (3)$$

where $p > 1$, $s > 0$; x_1, x_2 are state variables of each cell and $f(\cdot)$ is an odd piecewise-linear function as defined in Eq. (2). For the CNN parameters $p = 2$, $s = 1.2$, initial condition $x(0) = (0.14, -0.1)$ and a sinusoidal input signal parameters $A = 4.04$ and $T = 4$, the non-autonomous CNN with two-cell given in [14] and chaotic portrait of the system are shown in Fig.1 and Fig.2, respectively.

In Fig 2, the chaotic behavior is observed. It is clearly appeared that the attractor has a roughly point symmetric property. If the Poincaré map of (x_1, x_2) -plane is obtained, it can be seen that the attractor possesses the horseshoe structure [14].

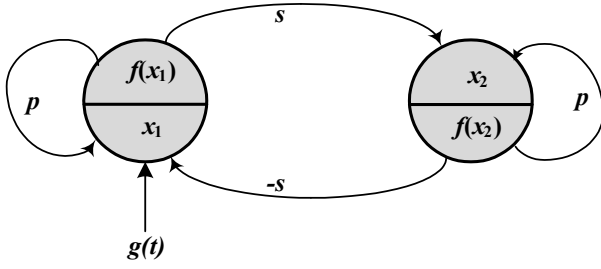


Fig. 1. The non-autonomous CNN with two-cell.

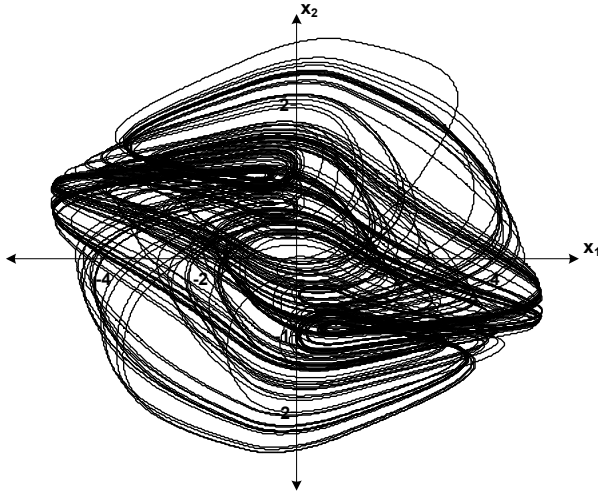


Fig. 2. Phase plane portrait of system with initial condition of $x(0) = (0.14, -0.1)$.

III. IMPLEMENTATION OF DISCRETE TIME CHAOTIC CNN MODEL

In order to implement the model on microprocessor, state equations must be discretized. Discrete time model of the CNN based chaotic system is determined as below.

$$x_1[n+1] = \frac{1}{a} \left[\left(\frac{x_1[n]}{T} \right) + pf(x_1[n]) - sf(x_2[n]) + g[n] \right] \quad (4)$$

$$x_2[n+1] = \frac{1}{a} \left[\left(\frac{x_2[n]}{T} \right) + sf(x_1[n]) + pf(x_2[n]) \right]$$

$$f(x_i[n]) = \frac{1}{2} (|x_i[n] + 1| - |x_i[n] - 1|), \quad i = 1, 2 \quad (5)$$

$$g[n] = 4.04 \sin(\pi n / 2) \quad (6)$$

Discrete time response of the model can be acquired by using CNN parameters as $p = 2$, $s = 1.2$, initial conditions $x(0) = (0.14, -0.1)$, $T = 0.005$, $a = 1 + (1/T) = 201$.

In arithmetic operations, fractional numbers are used as well as integers. There are two types of binary number representation format which are floating-point and fixed-point

format. Any of them can be chosen to represent a fractional number as a fractional binary number. A fractional number representation format should be considered that it represents the fractional number as a decimal and then converts it to a fractional binary number by multiplying the decimal number by 0.5 repeatedly. A binary coded number can be defined by equation,

$$\dots b_2 b_1 b_0 . b_{-1} b_{-2} \dots = \sum_i b_i 2^i \quad (7)$$

where there is a binary radix point in the above equation before b_{-1} [16].

In this study, the fixed-point number format is chosen because of advantages on easy coding. In this format, a signed/unsigned number is stored and this number is scaled by a fixed factor which is determined by user with respect to format parameters. This method implies shifting operation the radix point to the left side [16].

$Qm.n$ is the representation of fixed-point number format that has m bit for integer part and n bit for fractional part as shown in Fig. 3.. As we use signed numbers in discrete time model of our network, $Qm.n$ format has to be arranged as it contains signed two's complement fixed-point fractional binary number [16].

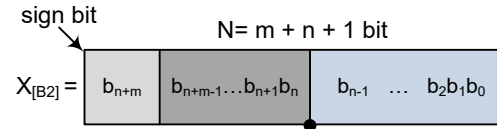


Fig. 3. Structure of the $Qm.n$ fixed-point signed number format.

Since initial values of state variables and parameters are chosen signed numbers as 16-bits in width, the format is arranged to $Q3.12$ and 1 bit is reserved for the sign.

$$x_{[B10]} = \frac{1}{2^n} \left[-2^{N-1} b_{N-1} + \sum_{i=0}^{N-2} 2^i b_i \right] \quad (8)$$

Regarding to equation above (8) where $x_{[B10]}$ represents fractional number in decimal, $N=16$, $x_{min} = -2^m = -8$, $x_{max} = 2^m - 2^{-n} = 7.99975$ and $resolution = 2^{-n} = 2.4414.10^{-3}$ are determined for $Q3.12$ signed two's complement format.

In the implementation stage, three peripheral circuits are used in the CNN core design. These are Clock Generator, CNN Circuit and CNN Cache.

The Clock Generator generates the low frequency clock signal by using the 50 MHz clock signal on FPGA chip. Generated low frequency clock signal is used for iterative solution of model. In FPGA applications, instead of *for loop* operation, a counter module is arranged in order to calculate the next value of state variables repeatedly. Each increment of counter value is admitted as the beginning of the new loop.

The CNN circuit has two state variables, four parameters for state variables, sampling period register and external sinusoidal input register which are all in 16 bit width. The CNN circuit solves the equations (4), (5) and (6) iteratively by using the clock pulse of the Clock Generator circuit. The model requires previous values of the state variables in order to determine the current values. Therefore, the CNN Cache circuit is used.

The CNN Cache needs 20 KB of total memory in order to emulate the discrete time chaotic CNN model. Since FPGA chip has enough memory in BlockRAM, no external memory is needed. 2 BlockRAM modules are defined for this implementation each one of module has 10 KB capacity. Defined BlockRAM modules have a dual-port interface. Therefore, the values at different addresses can be accessible at the same time.

The CNN core is designed, implemented on Spartan 3e XC3S1600e FPGA development board and programmed by Xilinx ISE Design Suite 13.2. When core is programmed, initial values of state variables and parameters are transferred to the core by using built-in communication interfaces and functions in MATLAB. The whole system is illustrated in Fig.4. Table 1 illustrates resource utilization of the CNN core design.

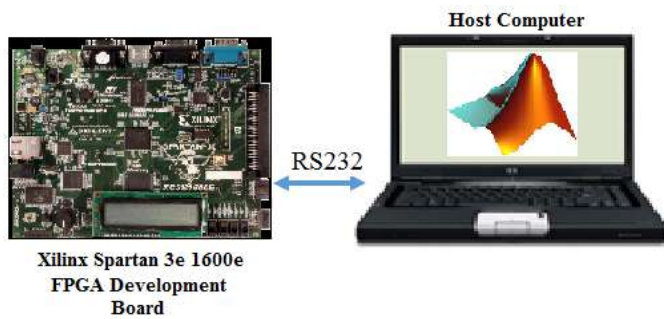


Fig. 4. The scheme of the CNN Core Design.

TABLE XI. RESOURCE UTILIZATIONS OF THE DESIGN

Arithmetic Unit	Number of Used Resource		
	Used Slices	Used FFs	Used LUTs
Clock Generator Circuit	24	33	47
CNN Core Design	4013	5214	6589

After the whole design is implemented, the programming bit stream of the design is generated and FPGA chip is programmed by Xilinx ISE Design Suite. The maximum operating frequency is obtained as 24.67 MHz from Xilinx ISE Design Suite. Fig. 5 shows the discrete time response of

the model, which is very similar to the continuous time response given in Fig. 2. Also, Fig.6 illustrates the discrete time response of each cell. Fig. 5 and Fig. 6 are plotted in MATLAB and the data are obtained from implementation results on Xilinx ISE Design Suite for FPGA of the chaotic discrete time CNN model.

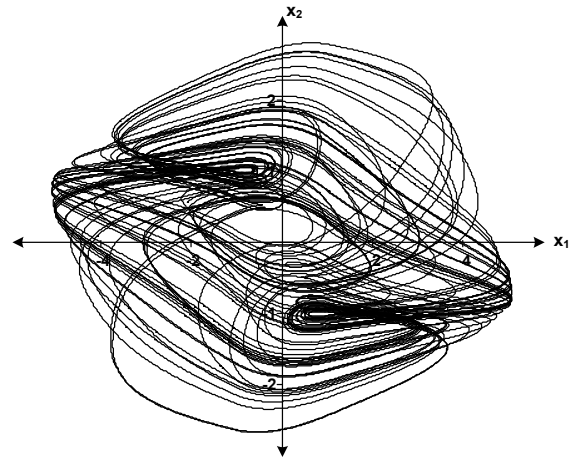


Fig. 5. Discrete time response of the model with given parameters.

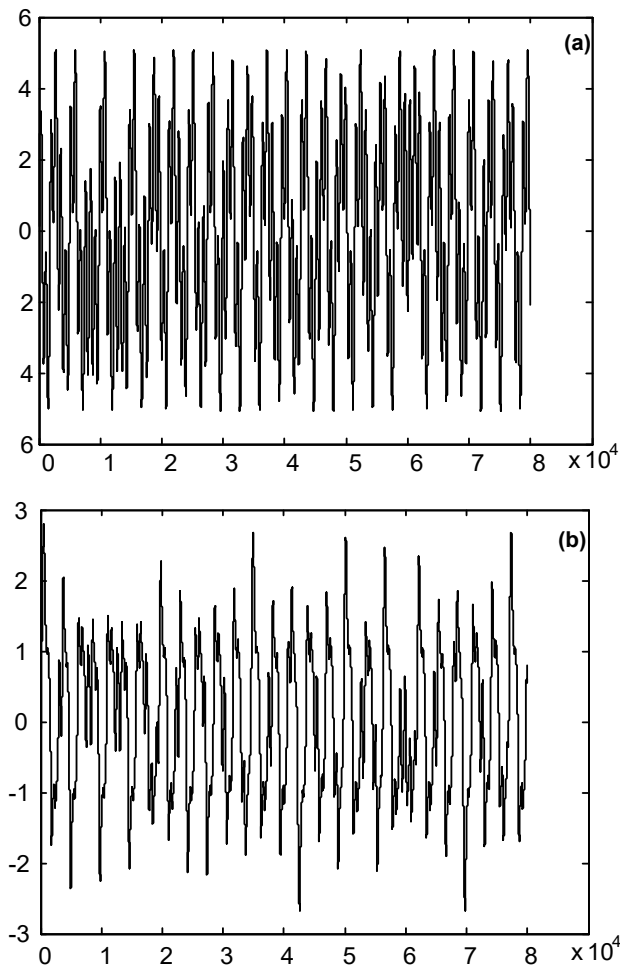


Fig. 6. Discrete time response of a) $x_1[n]$, b) $x_2[n]$.

IV. CONCLUSION

In this study, we have presented the implementation of two cell non-autonomous CNN model on FPGA. This study shows that the implemented CNN model have chaotic behaviors and model can be easily adapted to RNG applications using FPGA not only the entropy source of RNG but also the seed of pseudo random number generator application.

REFERENCES

- [1] S.H. Strogatz and D.E. Herbert, "Nonlinear dynamics and chaos," Medical Physics-New York-Institute of Physics vol. 23, no. 6, pp. 993-995, 1996.
- [2] A.N. Natsheh and E.M.S. Al-Habibah, "Chaos control DC-DC boost converter by FPGA," 2015 IEEE 42nd Photovoltaic Specialist Conference (PVSC), New Orleans, LA, 2015, pp. 1-6. doi: 10.1109/PVSC.2015.7356278LS.
- [3] R. M. Hidalgo, J. G. Fernández, R. R. Rivera, and H. A. Larrondo, "Versatile dsp-based chaotic communication system," Electronic Letters, vol. 37, pp. 1204-1205, 2001.
- [4] A. Ali-Pacha, N. H. Said, A. M'Hamed and A. Belgoraf, "Lorenz's attractor applied to the stream cipher (alipacha generator)," Chaos, Solitons and Fractals, vol. 33, no. 5, pp. 1762 - 1766, 2007. [Online]. Available: <http://www.sciencedirect.com/science/article/B6TJ44JYKMN1-1/2/7b1aa936c2c11a007b8967c3121d393a>.
- [5] G. Mazzini, G. Setti, and R. Rovatti, "Chaotic complex spreading sequences for aynchrous ds-cdma-part 1: System modeling and results," IEEE Trans. Circuits Syst. 1, vol. 44, no. 10, pp. 937-947, 1997.
- [6] G. Setti, M. Balestra, and R. Rovatti, "Experimental verification of enhanced electromagnetic compatibility in chaotic fm clock signals," in Proceedings of ISCAS'00. IEEE Circuits and Systems Society, 2000, pp. III-229-232.
- [7] C. M. González, H. A. Larrondo, C. A. Gayoso, and L. J. Arnone, "Generación de secuencias binarias pseudo aleatorias por medio de un mapa caótico 3d," in Proceedings del IX Workshop de IBERCHIP, 2003.
- [8] L. De Micco, O. G. Zabaleta, C. M. González, C. M. Arizmendi, and H. A. Larrondo, "Estocasticidad de un atractor caótico determinista implementado en fpga," Proceedings Iberchip 2010, Febrero 2010.
- [9] L. De Micco and H. A. Larrondo, "FPGA implementation of a chaotic oscillator using RK4 method," 2011 VII Southern Conference on Programmable Logic (SPL), Cordoba, 2011, pp. 185-190. doi: 10.1109/SPL.2011.5782646
- [10] L. Merah, A. Ali-Pacha, N. H. Said and M. Mamat, "Design and FPGA implementation of Lorenz chaotic system for information security issues," Applied Mathematical Sciences, vol. 7, no. 5, pp. 237-246, 2013.
- [11] L. O. Chua and L. Yang, "Cellular neural networks: Theory," IEEE Trans. Circuits Syst., vol. 35, pp. 1257-1272, 1988.
- [12] L. O. Chua and L. Yang, "Cellular neural networks: applications," IEEE Transactions on Circuits and Systems, vol. 35, no. 10, pp. 1273-1290, 1988.
- [13] F. Zou and J.A. Nossek, "Bifurcation and chaos in cellular neural networks," IEEE Transactions on Circuits and Systems I: Fundamental Theory and Applications, vol. 40, no. 3, pp. 166-173, 1993.
- [14] F. Zou and J. A. Nossek, "A chaotic attractor with cellular neural networks," in IEEE Transactions on Circuits and Systems, vol. 38, no. 7, pp. 811-812, Jul 1991.
- [15] A. Gerosa, R. Bernardini and S. Pietri, "A fully integrated 8-bit, 20MHz, truly random numbers generator, based on a chaotic system," In: Proceedings of the Southwest Symposium on Mixed-Signal Design, SSMSD, pp. 87-92, 2001.
- [16] B. Karakaya, R. Yeniceri and M.E. Yalcin, "Wave computer core using fixed-point arithmetic", 2015 IEEE International Symposium on Circuits and Systems (ISCAS), Lisbon, pp. 1514-1517, 2015.



PWM Control of AC Chopper Fed by Unbalanced 3-Phase Voltage Source

Nurbanu Macit

Electrical and Electronic Engineering
Faculty of Engineering, Firat University
Elazig, Turkey
nmacit@firat.edu.tr

Sedat Sünter

Electrical and Electronic Engineering
Faculty of Engineering, Firat University
Elazig, Turkey
ssunter@firat.edu.tr

Abstract—In recent years, power electronic has become even more popular with the development of semiconductor switching devices. Power electronics applications can be found almost in all systems related to electrical and electronic fields. With the power electronic circuits, ac or dc voltages at various amplitudes can be obtained from constant voltage sources. Ac voltage with constant frequency and variable amplitude with high power factor can be provided by an ac chopper. Purpose of these power electronic circuits is to make the system more efficient, provide output waveforms with higher quality (less harmonics) and prevent power loss in large power systems. In this study, a three-phase PWM controlled ac chopper circuit has been modelled and simulated in MATLAB / Simulink package program. In this simulation, the output statements obtained for the switching devices by a different control method are discussed. Various operating conditions have been examined where a three-phase unbalanced voltage source without and with having the 5th and 7th harmonics was applied to the input side of the chopper. As a result, superiority of the control system used in the PWM controlled ac chopper has been demonstrated by the simulation results.

Keywords—Three-phase PWM ac chopper, Hysteresis band current controller (HBCC), Harmonic analysis, Pulse width modulation (PWM).

I. INTRODUCTION

Along with the developing technology, the amount of energy consumed all over the world has also increased. Due to the amount of energy consumed, new ways have been sought to meet this energy demand. More efficient systems with smaller structures and circuits designed to consume less power loss despite adverse conditions are required. The most popular circuit is the power electronics circuits, which are still being developed. Power electronic circuits reduce energy loss on the earth with renewable energy processing and create efficient systems for it. Power electronic circuits

transform electrical power by using the switching characteristics of semiconductor elements.

Ac chopper circuits of the power electronic family are the basic concept of this study. Ac choppers are, at its most basic definition, a power circuit which can convert a constant frequency ac voltage to another voltage at a desired amplitude [1,2]. Single-phase and three-phase versions of the ac chopper are available. Ac choppers with natural commutation have negative features such as high harmonics on the mains or load sides. Ac choppers are used in many industrial areas. Frequent use of such power electronic circuits has led to poor quality in energy systems [2]. It is possible to further improve ac choppers by eliminating these undesirable features. With the use of power electronic devices which can operate at high switching frequencies, the PWM method has begun to be used in the chopper circuits [3]. PWM ac chopping circuits have reduced side effects of the natural commutated ones as well as have become a special application of these circuits [3,4].

In this study, it is aimed to obtain load current with less harmonics by applying Hysteresis Band Current Controller (HBCC) technique for three-phase PWM ac chopper. The HBCC technique is preferred because of its dynamic response and simplicity [5]. Thanks to this controller, whatever the input voltage of the system is, a load current with very low harmonics at the output is obtained. The results will be quite advantageous for all power electronics-based systems.

II. HYSTERESIS BAND CURRENT CONTROLLER FOR A THREE PHASE AC CHOPPER

Fig.1 shows the circuit schema of the three-phase ac chopper [6]. The simulation model of this circuit using MATLAB / Simulink is shown in Fig. 2 [6]. IGBTs are used as switching semiconductor devices and a three-phase $R-L$ load is used at the output. Depending on the nature of the load used, there will be a load phase angle between the voltage and current space vectors of the source. The reference currents in the ac chopper must have the same frequency as the source voltage and the same phase angle as

that of the load [6]. With the HBCC technique, the reference currents are obtained and the continuity of the load current paths is ensured [6].

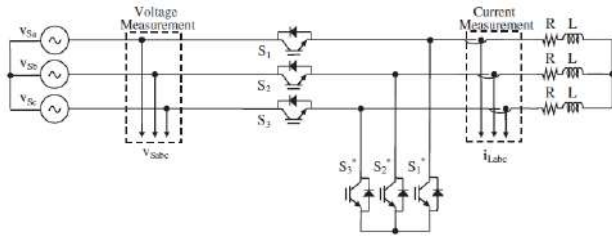


Fig. 1. The power scheme of the three-phase PWM ac chopper [6]

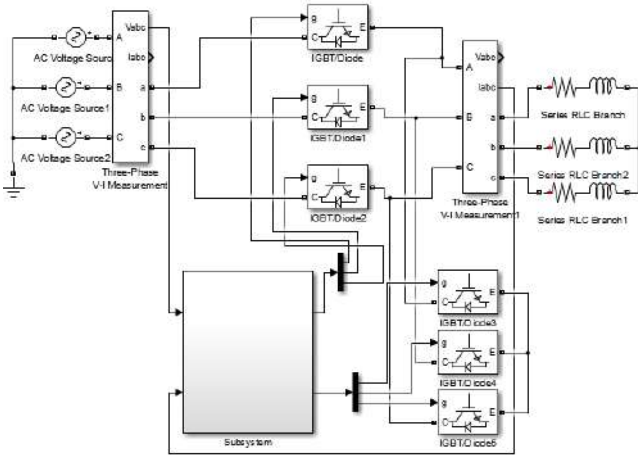


Fig. 2. The Simulink model of the three-phase PWM ac chopper

The reference currents can be obtained using phase locked loop (PLL) or using abc/dq transformations called Park Transform. The continuity of the load current conduction paths is also provided using the technique called the minimum voltage algorithm [3,6]. The minimum voltage algorithm ensures the continuity of the resulting current paths by triggering the correct switch according to the instantaneous values of the source voltage [3,6].

In the proposed model, the on and off states of the switches are provided using specific switching states. The goal is to obtain high quality waveforms at the output whatever the input voltage source is. In order to demonstrate the superiority of the control system, three-phase voltage source having harmonics or unbalanced voltage waveforms are applied to the system input. Undesirable changes in the source voltage (such as noise or harmonic distortion) will directly affect the output voltage and hence the amplitude of the output current. To analyze this situation, the fifth and seventh harmonics of the input voltage source are added to the input with certain amplitude ratios [7].

A. Analysis of HBCC Technique Applied to Ac Chopper

Any kind of load can be controlled with the PWM ac chopper connected to the three-phase source. The PLL block shown in Fig. 3 is used to set the source frequency [6]. The abc/dq transform block is also used to set the load phase. Only the amplitudes of the generated reference currents are input to the control system depending on the demand.

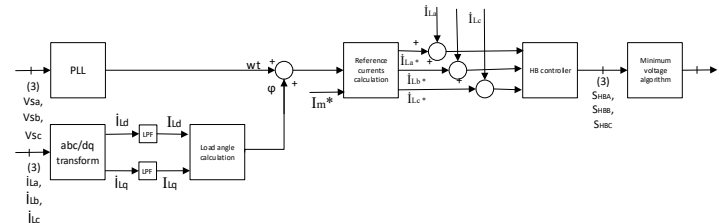


Fig. 3. The application of the HBCC theory [6]

The minimum voltage algorithm can be used in various systems. For instance, in a 3-phase inverter as the 3-phase chopping operation is made independent of each other, the current flow is continuous. In the proposed topology, the chopping procedures depend on each other and the flow paths are separated from each other during the phase chopping operation. The minimum voltage algorithm is used to prevent such undesirable situations. Depending on the instance, the switch with the minimum voltage is kept off while the chopper continues to operate in the other two phases and the sum of these currents returns from the phase with the minimum voltage.

B. Switching States

Besides the values in Table 1, four different switching states have been performed.

TABLE I. SYSTEM PARAMETERS USED IN SIMULATION

Parameters	Values
Source	$V_{SA} = 220$ V (rms)
	$f = 50$ Hz
Load	$L = 20$ mH
	$R = 10$ Ω

By referring to Fig.1, the following switching situations exist:

TABLE II. SWITCHING SITUATIONS

Switching States	ON	OFF
1	S_1, S_1^*, S_2^* and S_3^*	S_2 and S_3
2	S_1, S_3, S_1^* and S_2^*	S_2 and S_3^*
3	S_1, S_2, S_1^* and S_3^*	S_3 and S_2^*
4	S_1, S_2, S_3 and S_1^*	-

III. ANALYZES

In the simulation, two different conditions were performed. The first condition is used to observe the effect of the distorted three-phase input supply on a three-phase $R-L$ load where no power electronic circuit was used and the load is directly connected to the input supply as shown in Fig. 4. The second condition is to observe the effect of the same source voltage on $R-L$ load using HBCC technique applied to PWM ac chopper.

A. Analysis of the Proposed System Fed By 3-Phase Input Supply

In this application, a balanced and undistorted three phase voltage set is applied to the system input. In this case, the wave form of the load current of the system is observed to be smooth. The waveforms obtained are as follows for a complete period:

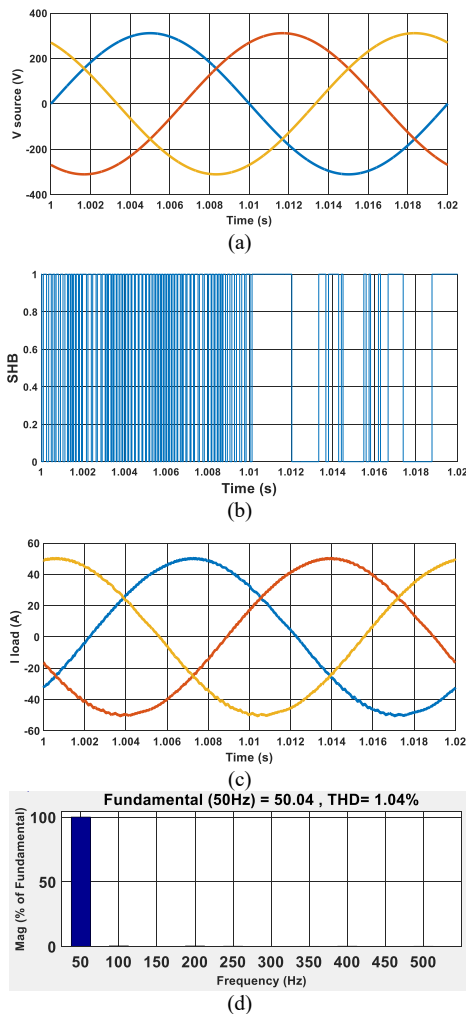


Fig.4. Simulation results of the PWM ac chopper fed by a distorted 3-phase supply and feeding a three-phase star connected $R-L$ load. (a) Voltage

source, (b) Switching signal, (c) Load current, (d) The harmonic spectrum of the load current.

In the Fig.4, 1-1.02 s is selected as a full period interval to see more clearly the waveform and harmonic analysis of the load current. Since the circuit is still in transient state at 0-0.02 s, the waveforms are harmonic. Therefore, the period of 1-1.02 s reached the permanent status has been taken into account. In this range, reference current is $I=50$ A. With the obtained waveforms and FFT analysis, it can be said that the harmonics are at an acceptable level.

In this application, Total Harmonic Distortion (THD) of the load voltage waveform is 1.04%. These results show us how reasonable and feasible the controller proposed for the three-phase PWM chopper.

B. Analysis of 3-Phase Star-Connected $R-L$ Load Fed By A Distorted Three-Phase Input Supply

Undesirable changes in the source voltage such as noise or harmonic distortion will directly affect the output voltage and hence amplitude of the output current. To demonstrate these effects, the fifth and seventh harmonics of the input voltage set are added at certain amplitude ratios in the simulation model.

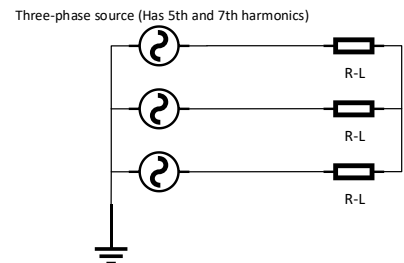


Fig. 5. A star-connected 3-phase system with harmonic voltage applied to the input

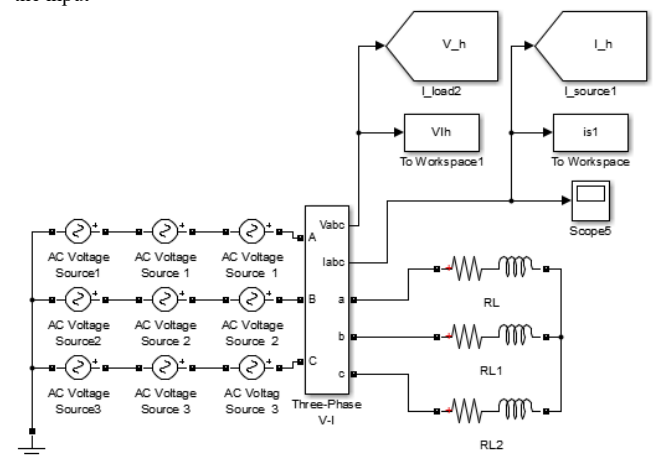


Fig. 6. Simulation Model of the star-connected 3-phase system with harmonic voltage applied to the input

In order to demonstrate the superiority of the ac chopper system used in this work, a distorted supply voltage model is

created in Simulink/Matlab to be used as input to the system. The three-phase sinusoidal voltage source with harmonics is defined as follows:

$$V_{1h} = k_1 \cos(5\omega t) + k_2 \cos(7\omega t) \quad (1)$$

$$V_{2h} = k_1 \cos\left(5\omega t - \frac{2\pi}{3}\right) + k_2 \cos\left(7\omega t + \frac{2\pi}{3}\right) \quad (2)$$

$$V_{3h} = k_1 \cos\left(5\omega t + \frac{2\pi}{3}\right) + k_2 \cos\left(7\omega t - \frac{2\pi}{3}\right) \quad (3)$$

The k_1 and k_2 values in Eq.(1-3) are set to be about 10% of the supply voltages [7]. V_{1h} , V_{2h} and V_{3h} are the harmonic voltages of A, B and C phases, respectively. The resulting simulation waveforms are given in Fig. 6 for a full period.

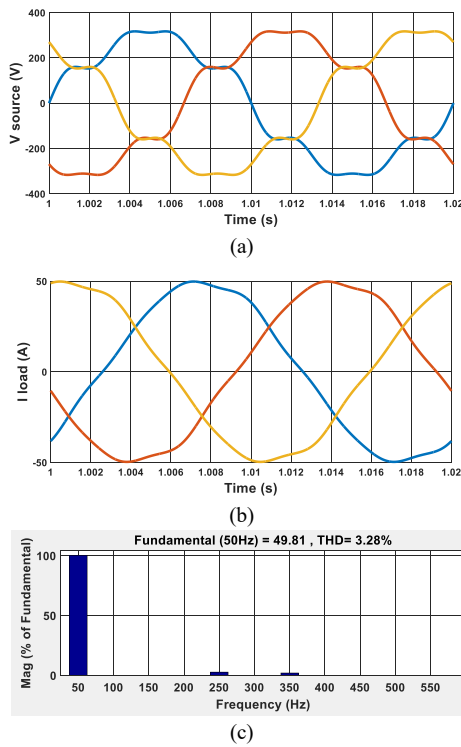


Fig.7. Simulation results of star-connected 3-phase load fed by a distorted 3-phase supply, (a) Distorted source voltages, (b) Load currents, (c) The harmonic spectrum of the load current.

As can be seen in Fig.7, when a voltage source with harmonics is applied directly to the R - L load, all harmonics of the supply are reflected to the output. THD of the load current waveform is 3.28%.

C. Analysis of the Proposed System Fed By A Distorted 3-Phase Input Supply

In this case, three-phase voltage supply with 5th and 7th harmonics used in the previous system was also applied to the input of the PWM ac chopper circuit controlled by the HBCC. The Simulink model of the system including the

distorted voltage supply source is illustrated in Fig.8. Comparing to the previous system, the superiority of the proposed method in [6] is confirmed by the simulation results in Fig.9. It is observed that the system gives successful results, that is, the waveforms of the load currents and voltages have sufficient quality. The simulation results taken for a complete period are shown in Fig. 9.

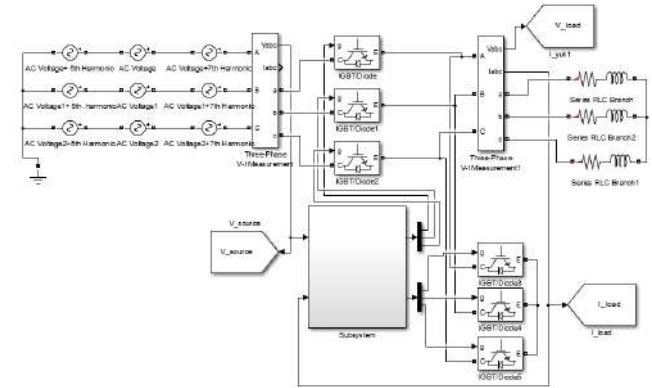


Fig. 8. Simulink model for 3-phase PWM ac chopper fed by a distorted input supply

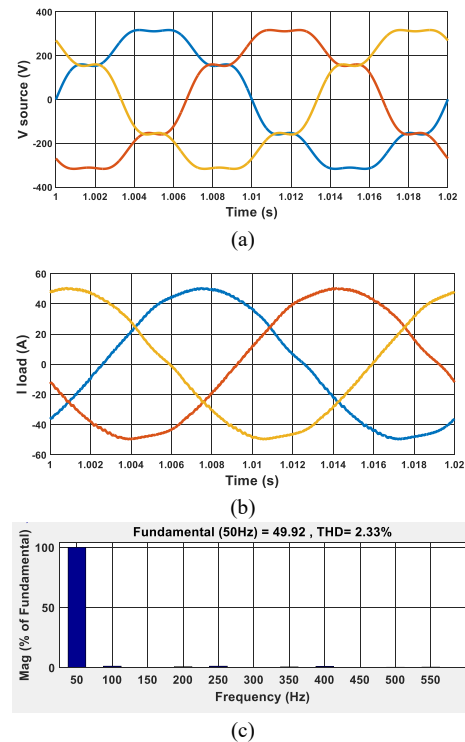


Fig.9. Simulation results of the PWM ac chopper fed by a distorted 3-phase supply and feeding a three-phase star connected R - L load. (a) Voltage source, (b) Load current, (c) The harmonic spectrum of the load current.

As can be seen in the Fig.9 (b), the resulting load current waveforms have less harmonics than expected and their shapes are almost pure sinusoidal waveforms. As seen in



Fig.9 (c), main harmonics are much dominant. This is why the hysteresis band controller is used in the simulation and proposed in [6]. Thanks to this controller the switches used in the chopper are controlled in a manner to have less harmonics at the output. The controller in simulation are designed for analysing the parameter of voltage and current. In general, it has features such as reducing the harmonic components and increasing the power factor of a particular circuit.

In this study, Total Harmonic Distortion (THD) of the load voltage waveform is 2.33%. These results show us how reasonable and feasible the controller proposed for the three-phase PWM chopper.

IV. CONCLUSIONS

In this study, a PWM ac chopper with hysteresis band controller has been modelled and simulated with the Simulink/MATLAB package program. It is aimed to have more efficient chopper comparing to the traditional 3-phase ac chopper. Although, the traditional phase controlled ac chopper has not been simulated in this work, its waveforms are well known. Therefore, it could be easily stated that the performance of the proposed system would be much better than that of the traditional ac chopper. In addition, operating conditions of the PWM ac chopper have been made much worst by adding the 5th and 7th harmonics to the input voltage waveforms. Even so promising simulation results have been obtained. The simulation results show that the proposed control algorithm minimizes the amount of THD at the output currents. Despite of the voltages with harmonics applied to the input, three-phase currents at the output are stable and they consist of very low amount of harmonics because of the HBCC used. As a result, the ratio of harmonics is reduced significantly with the switching control algorithm. These results have been supported by the harmonic analysis.

V. REFERENCES

- [1] Rashid, H. M., Power Electronics Devices, Circuits and Applications (4th Edition), England.
- [2] Bodur, H., Güç Elektronik I, http://afguven.com/depo/ESM312/guc_elektronigi.pdf, (Access: 16.08.2016)
- [3] Kwon BH, Min BD, Kim JH. 'Novel topologies of AA choppers', IEE Proc Electr Power; 143(4):323–30, Appl 1996.
- [4] Kim JH, Min BD, Kwon BH, Won SC. A PWM buck–boost AC chopper solving the commutation problem. IEEE Trans Ind Electron 1998;45(5):832–5.
- [5] Chun, T., and Choi, M., 'Development of Adaptive Hysteresis Band Current Control Strategy of PWM Inverter with Constant Switching Frequency', Conference Proceedings of Applied Power Electronics Conference and Exposition, San Jose CA, Vol. 1, pp. 194-199, 3-7 March 1996.
- [6] Kale, M., Karabacak, M., and Saracaoglu, B., 'A Novel Hysteresis Band Current Controller Scheme for Three Phase AA chopper', Electrical Power and Energy Systems 44, pp. 219–226, 2013.
- [7] Sunter, S., Altun, H., and Clare, J. C., 'A Control Technique for Compensating the Effects of Input Voltage Variations on Matrix Converter Modulation Algorithms', Electric Power Components and Systems, pp. 807-822, 2010.



A Study of Experimental Efficiency of PV-Hydrogen Generation Hybrid Energy System

Mahir ÇEVİK

Kilis 7 Aralık University, Faculty of Engineering,
Department of Electricity and Electronics,
Kilis, Turkey
mahir_407@windowslive.com

Abdulkadir YILDIZ

Kahramanmaraş Sutcu Imam University, Faculty of
Science & Arts, Department of Physics,

Abstract

The exploring of new energy resources using renewable energy resources is essential both for environmental impact and for sustainable clean energy. In this study, we present a hydrogen production method using photovoltaic energy as a renewable energy via electrolysis system in Kahramanmaraş city conditions-Turkey. An electrolyser system that we designed for H₂ is introduced, and the efficiency and feasibility are discussed. The efficiency of simple system gives 72%, and it can be used safely in rural areas or the places where city network cannot reach.

Keywords: Hydrogen energy; Photovoltaic; solar energy; photoelectrolysis by electrolysis of water using the electricity produced by the photovoltaic cells

I.

INTRODUCTION

It has been widely recognized that the primary energy sources such as petroleum, coal and natural gas consuming mostly in developed and developing countries have been causing air pollution/green house effect which leads inevitably to the global climate changes and bring about other many problems such as adverse effects on the human's life, rising CO₂, melting of glaciers and floods, etc.. Such reasons challenged the scientists in the field both energy and other disciplines to focus on sustainable and environmentally clean and renewable alternative energy sources and the technologies in the last three decades. In other words, interest in the connection between energy utilization and the environment from the past to the present became more pronounced and so that there has been increasing attention to this connection. However, there is no doubt that the researches on new alternative energy sources are not related only to the environmental effects of the fossil sources, but also the fluctuations of energy market and the truth of limited reserve of conventional energy sources consuming rapidly day by day. Although renewable energy

Kahramanmaraş, Turkey
ayildiz@ksu.edu.tr

Kemal DELİHACIOĞLU

Kilis 7 Aralık University, Faculty of Engineering,
Department of Electricity and Electronics, Kilis, Turkey
kemal@kilis.edu.tr

sources like solar, wind, biomass, etc. have a great potential, their efficient utilization is still difficult task due to their fluctuating and intermittent nature.

Nonetheless, to assure the present and future generations demands, we have to seek and discover environmentally clean/benign and sustainable energy sources combined with the growing concerns of global warming. For example, hydrogen production is, recently, of great significance in seeking a better way to use natural gas resources. Hydrogen is a clean and sustainable alternative to fossil fuels. It has no carbon emissions and offers important improvements in health and quality of life. It is the most economical synthetic fuel to produce environmentally friendly energy source, and can be converted to other forms of energy more efficiently than other fuels. In an overview of Ngoh and Njomo [1] have examined hydrogen production from solar energy and stated that solar energy as a renewable energy is, in particular, seen as a strong driving force capable of maintaining the availability of energy with hydrogen as energy carrier and is an emissions-free way to produce hydrogen, and, conversely, hydrogen offers a way for renewable to generate transportation fuel and reliable power. It is also argued that the future conjunction of hydrogen and renewable energy technology is a promising one if we put together positive and negative aspects of hydrogen energy. These are only a few of the many beneficial possibilities of a hydrogen economy. Clarke *et al.* [2] have discussed a complete stand-alone electrolyser system and indicated that hydrogen as an energy carrier and storage media is expected to play a key role in future power generation and with the development of the fuel cell technology as a transport fuel. There exists various types of hydrogen production methods such as solar thermal (high temperature and low temperature), photovoltaic, photoelectrolysis, biophotolysis, etc. as discussed in detail by Joshi *et al.* [3], but it is still produced

mainly by fossil fuel sources which release green house gases. As it has also been discussed in the recent studies that there are several environmentally benign hydrogen production processes using solar energy such as hybrid-sulphur cycle, metal oxide based cycle and electrolysis of water [3,4,5,6]. Hence, utilizing from solar energy in any processes involving energy is of great importance for protecting environment from green house effects and the other adverse effects.

Turkey is a developing country and dependent considerably on the important energy although it possesses an abundant solar energy potential. In an overview report by IEA [7], the current energy case of Turkey is well analysed and reported that more than 87% of total liquid fuels are important from foreign countries and crude oil imports are expected to double over the next decade. Turkey is also increasingly dependent on natural gas imports, and consumption has increased rapidly over the past decade and reached a new high of 1.7 trillion cubic feet in 2014. Consumption growth is expected to remain strong as industrial sector growth and rising electricity consumption continue to encourage demand day by day. However, it is stated that Turkey's natural gas demand is not flat over the duration of the year, but peaks in the winter months as the detail given in the report. If we superpose all these and the energy crisis experienced in the mid of 1970 plus regional problems going on nowadays, it is apparent how important for any country to develop its sustainable energy resources. Hence, Turkey dependence on foreign oil would be curtailed, and providing establishments with their own power generation capability would reduce the demand on the electric grid.

The goal of this article is to investigate the performance of a photovoltaic –hydrogen production hybrid energy system designed as an example for a stand-alone house system in city of Kahramanmaras, Turkey. The study is also aimed to stimulate in an extent both production of hydrogen energy from renewable energy as a benign alternative energy and encourage using abundant renewable energy potential sources, particularly solar energy for a liveable and clean environment. The study describes the design and feasibility of a 6 kW PV energy system. Hybrid energy system design is site specific, and depends on the resources available and the load demand. Three months recorded solar radiation and estimation of the hydrogen load are used for the design of a hybrid energy system. To pick an optimum hybrid hydrogen energy system, National Renewable Energy Laboratory's HOMER software was used to select an optimum hybrid hydrogen energy system.

II. METHOD

A. Hydrogen production methods

There are several well known hydrogen production methods from non-renewable and renewable energy

resources. Since use of non-renewable energy causes negative impacts on environment and also is not sustainable, the recent studies are focused mostly on renewable energy resources such as solar photovoltaic, geothermal, wind and hydropower. The development of the methods of hydrogen production based on renewable energy sources takes place as much as possible without releasing the greenhouse effect. These methods represent alternative ways for hydrogen production through fossil combustibles [5]. In particular, solar energy are used more extensively in many purposes. For example, hydrogen production from solar energy is outlined under four groups as [5];

- Photovoltaic (PV)
- Photoelectrochemical
- Photobiological
- Solar thermal energy

B. Solar photovoltaic based electrolysis

In this section, we will discuss and illustrate one of hydrogen production methods using PV panels via electrolysis method. In the early of 70s the PV panels were utilized to produce hydrogen by electrolysis of water using the electricity produced by the photovoltaic cells [2,13–15]. The electrolysis of water can be carried out by a current generated by the photovoltaic cells. It needs a higher and extensive research in this area as the hydrogen produced by this technology is not cost effective as the PV technology is costly. The end product of the electrolysis was also oxygen. Fig.1. shows a schematic diagram of hydrogen production system that uses photovoltaic technology [7].

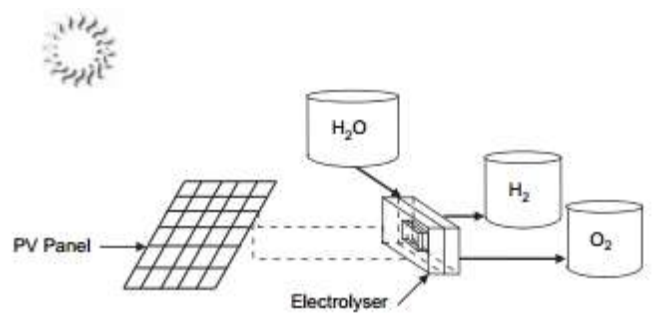
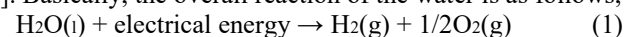


Figure 1. Schematic diagram of photovoltaic hydrogen production system [7].

C. Production of hydrogen via electrolysis method

Electrolysis method, which is the process of separation of H₂O to H₂ and O₂ using DC current, is one of the simplest methods for hydrogen production among the other methods [8]. Basically, the overall reaction of the water is as follows;



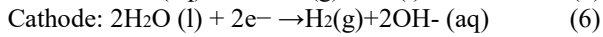
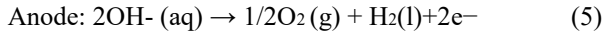
Based on the chemical equation (1), a minimum electric voltage (reversible voltage) must be applied to both electrodes for the reaction, and this can be determined from Gibbs equation [8],

$$\Delta G = zFV_{rev} \quad (2)$$

$$V_{rev} = \Delta G / zF \quad (3)$$

$$V_{rev} = \frac{237.2 \text{ kJ/Kmole}}{2 \times 96485 \text{ C/mole}} = 1.229 \text{ V} \quad (4)$$

Where V is the required minimum voltage, ΔG is Gibbs Energy, z is the number of electron, F is Faraday's Constant. On the other hand, the reactions for the alkaline anode and cathode are given, respectively, showing the hydroxyl (OH^-) ion transport [9].



D. Experimental procedure and Results

In the experimental the materials of system are solar cell, battery, charge controller, Pulse Width Modulation (PWM) circuit for adjusting current-voltage, electrolyser which are consisting of 21 plate/cell (15x15 cm size and 1.5cm thickness made from 304L steel), hydrogen flow-meter and KOH compound, which is an alkaline base, to provide conductivity in the electrolyser.

The system works as follows: solar PV panels converts solar energy to DC current that charges battery via the charge controller. The PWM (Pulse Width Modulation) circuit connected to the battery supplied power to the electrolyser at the desired current -voltage level. The amount of hydrogen obtained according to the amount of power supplied to the system has been determined and accordingly the efficiency of system has been carried out. Tommatech trademark solar panels are used for the designed system and the properties of PV panel are given in table 1.

Table 1: PV Power Parameters

Standard Test Conditions Power Parameters	
P(max)	TT250P-60P
Voc	36.3V
ISC	8.71A
Vmp	30.6 V
Imp	8.17A
operating temperature	-40 ⁰ C to +85 ⁰ C

STC: Radiaton 1000W/m² temperature 25⁰C

Moreover, as seen in Fig.2, the electrolyser is consisting of 20 cells and 4 sections connected in parallel and 21 plates of 304L steel as seen in Fig.2 (left hand side). The plates arrangement scheme of electrolyser device are shown in Fig.3



Figure 2. Electrolyzer (left side) and 304L steel plate (right side)

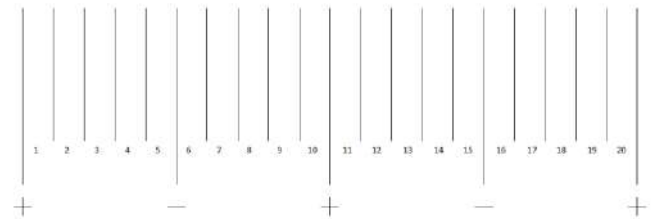


Figure 3. Plates Arrangement Scheme of Electrolysis Device

Theoretically, water separates into ions at 1.229V. Due to the slow response and other reasons, it was given an average of about 2 volts to the cells. It was observed that the measured input voltage at the site during the experiment was around 10.4 Volts and the measured current value was about 18.7 A. The electrolyte used in the system is KOH and the electrolyte solution was prepared at a concentration of 2.13 mol / dm³. The measured voltage values between the cells at 10.4 volts input voltage are shown in Fig.4. As seen in the figure the voltage values are not flat which are expected values.

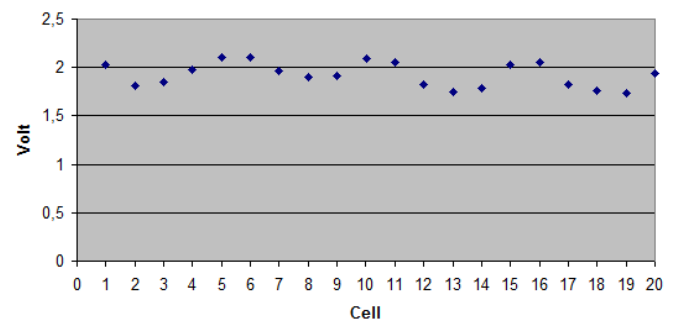


Figure 4. The voltage values measured between cells

It was obtained that the electrolyser produced 666.66 ml/minutes of H₂ at 18.7 A and 10.4 volts. Hence, the amount of H₂ per minutes is 5.99x10⁻⁵ kg using the density value $\rho = 0.08988 \text{ kg/m}^3$ [10]. If one takes the upper heat value of hydrogen as 140,9 MJ/kg [11], the amount of production energy is then 8442,719 joule. On the other hand, the amount of consumed energy in a minute at 10.4 volt and 18.7 A corresponds to 11668.8 joule. Moreover, the

efficiency of the system, η , has also been carried out from the following equation [10].

$$\eta = \frac{\text{produced energy}}{\text{The energy consumed}} \quad (7)$$

and using the obtained results above, the efficiency is

$$\eta = \frac{8442,643}{11668,8} = 0,722 = \% 72,2 \quad (8)$$

III. RESULTS AND DISCUSSIONS

In this work, a solar energy supported hybrid energy system design was made considering the sunshine amounts of Kahramanmaraş radiation. The designed PEM type electrolyzer produced $0.04 \text{ m}^3 \cdot \text{h}^{-1}$ H_2 at 10.4 volts at 18.7 A current. For production of $1 \text{ m}^3 \text{ H}_2$, 4.86 kWh^{-1} electricity is consumed. The amount of solar radiation in Kahramanmaraş province is seen in figure 5.

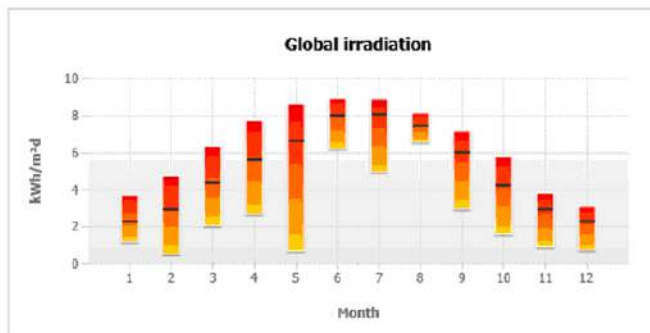


Figure 5. Annual amounts of solar radiation of Kahramanmaraş

The amount of photovoltaic energy produced according to these radiation values is also seen in figure 6.

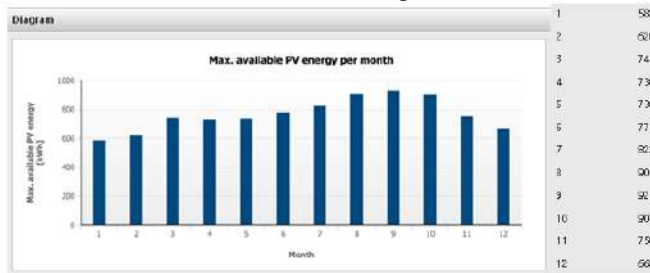


Figure 6. Amount of energy produced per month

The amount of hydrogen produced according to these energy values is shown in Figure 7.

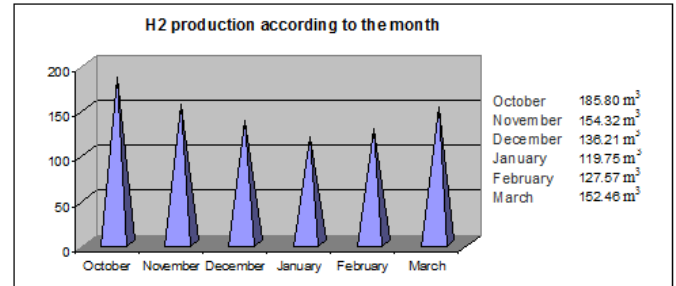


Figure 7. The amounts of hydrogen produced to warm up in the winter months

Energy consumption values are also increased rapidly according to development levels of countries and fossil fuel reserves are also declining day by day. Our country has a very convenient geographical position for insolation. However, since solar energy is not an uninterrupted energy source, solar energy need to be stored in order to be used as a constant energy source. In this case, hydrogen is of great importance for the sun to be stored and used as an uninterrupted energy source. In addition, hydrogen is an environmentally friendly fuel that is stronger than fossil fuels and has no pollutant properties when burned.

The goal of this study was to assess the production and use of H_2 from renewable energy (i.e solar PV systems) in the sectors which are, in particular, depending on imported gasoil/fuel and firewood in rural areas in Turkey since such project will save declining forests in rural areas day by day and reduce important energy dependence and also encourage sustainable clean, diversible, economic and benign energy. In order to achieve this goal, we have evaluated H_2 production by electrolysis method from solar PV energy system. It was achieved the result that the electrolysis system was very simple and cheap although it was argued in literature that H_2 production from solar photovoltaic via electrolysis was one of the most costly methods, which is due to the cost of PV system. However, the cost of production H_2 will go down and the system amortizes its own cost in a couple of years if the low cost equipments are used and a PV system life time is considered as 20-25 years. As a result, it is hoped that photovoltaic supported hydrogen production systems will become even more important in the solar-rich countries in the future.

REFERENCES

- [1] Ngoh S. K., Njomo, D. An overview of hydrogen gas production from solar energy. *Renewable and Sustainable Energy Reviews* 2012; 16: 6782–6792.
- [2] Clarke, R.E., Giddey, S., Badwal, S.P.S. Stand-alone PEM water electrolysis system for fail safe operation with a renewable energy source. *Int. J. of hydrogen energy* 2010; 35: 925-935.
- [3] Joshi, A.S., Dincer, I., Reddy, B. V. Exergetic assessment of solar hydrogen production methods. *Int. J. of hydrogen energy* 2010; 35: 4901-4908.



- [4] Gahleitner, G. Hydrogen from renewable electricity: An international review of power-to-gas pilot plants for stationary applications. *Int. J. of hydrogen energy* 2013; 38: 2039-2061.
- [5] Yilanci, A., Dincer I, Oztürk H.K. Performance analysis of a PEM fuel cell unit in a solar-hydrogen system. *Int. J. of hydrogen energy* 2008; 33: 7538-7552.
- [6] Joshi, A.S., Dincer, I., Reddy, B. V. Performance analysis of photovoltaic systems: A review. *Renewable and Sustainable Energy Reviews* 2009; 13: 1884-1897.
- [7] https://www.eia.gov/beta/international/analysis_includes/countries_long/Turkey/turkey.pdf, International Energy Agency (IEA), Monthly Oil Data Service, accessed June 10, 2015.
- [8] M. Öztürk, A. Elbir, N. Özek, A.K. Yakut "Examination of Solar Hydrogen Production Methods", 6th International Advanced Technologies Symposium (IATS'11), 16-18 May 2011, Elazığ, Turkey
- [9] Tijani AS, Yusup NAB, Rahim AHA. Mathematical modelling and simulation analysis of advanced alkaline electrolyzer system for hydrogen production. *Procedia Technol* 2014;15:799e807
- [10] http://www.engineeringtoolbox.com/gas-density-d_158.html
- [11] Prentis, M., "Energy Revolution: The Physics and the Promise of Efficient Technology" 233s

Speech based Gender Classification with 1D Local Binary Patterns

Abdulkadir Şengür
Elec.-Electronic Eng.
Firat University
Elazig, Turkey
ksengur@gmail.com

Sami Ekici
Energy Systems Eng.
Firat University
Elazig, Turkey
sami.ekici@gmail.com

Yaman Akbulut
Dept. of Informatics
Firat University
Elazig, Turkey
yamanakbulut@gmail.com

Ömer Faruk Alçın
Elec.-Electronic Eng.
Bingol University
Bingol, Turkey
ofalcin@gmail.com

Turgut Kavas
Elazig Vocational
Educational Center
Elazig, Turkey
turgutkavas@gmail.com

Abstract—In this paper, texture descriptors of speaker's speech are used for gender recognition. More specifically, Local Binary pattern (LBP) based features are employed for gender classification. LBP is known as a powerful tool for texture image characterization. To directly apply the LBP on speech, a straightforward transformation is needed. Therefore, 1D LBP is considered. After several pre-processing stages, which are considered for normalization and noise removal, LBP coding is applied to all input speech signals. Then, histogram of the LBP descriptors is constructed and is used as features. Support Vector Machines (SVM) and Extreme Learning Machines (ELM) classifiers are used to classify the obtained features as female or male. In experiments, a dataset, which contains 55 female and 41 male speaker's speeches, is considered. With both classifiers an average classification accuracy that are greater than 95% are obtained. Moreover, the obtained sensitivity and specificity values are greater than 95%.

Keywords—gender classification; LBP; speech signals; SVM; ELM.

I. INTRODUCTION

Speech based gender classification has important applications in machine learning and pattern recognition communities. Especially, some of the artificial intelligence based systems may need to detect the gender of interacted persons for various reasons. For instance, a machine learning based advertisement system can be specialized based on the gender of the interacted person or a phone based fortune teller system's persuasiveness can be augmented by the gender recognition. In addition, in a digital forensic view, speech based gender recognition may help to get more clues about the suspicions.

In the reviewed literature, it is seen that so many works have been proposed so far for speech based gender classification [1-8]. In [1], the author firstly extracted the Mel Frequency Cepstral Coefficient (MFCC) and Shifted Delta Cepstral (SDC) features from the speech signals and Support Vector Machine (SVM) classifier was used for detection of the age and gender. Kotti et al. [2] proposed a methodology for gender classification from the emotional speech. Authors firstly extracted a large number of features and a feature selection mechanism was employed to detect the efficient features.

Finally, SVM classifier was adopted to classify the features as man or woman. In [3], a Gaussian mixture model (GMM) was used for speech based gender classification. The authors extracted various features, which were based on the pitch and spectral perceptual linear predictive coefficients. The reported accuracies are in the 95% and 98% interval. In [4], the authors proposed a new method for speech based gender classification. The presented approach was leveraged from pitch feature trajectories. In addition, the authors achieved high classification performance with as little speech as possible. Zourmand et al. [5] explored the fundamental and formant frequencies in speech signal to recognize the gender of Malay children. Distance based classifier and artificial neural nets were used in the classification of the gender of 360 Malay Children. In [6], authors investigated the usage of ensemble based techniques for decision fusion for efficient recognition of gender from speech signals. Each member of ensemble structure was generated via a feature selection mechanism. In [7], authors measured CPP, HNR and $H_2^*-H_4^*$ in conjunction with F0 and formant values for automatic gender recognition. An Acoustic measure based gender classification system was proposed by Shue et al. [8]. The considered acoustic measures were the vocal tract and the voice source. The SVM classifier was adopted for efficient classification.

In this paper, different from the reviewed literature, an image texture based method namely local binary pattern (LBP) is adopted for gender classification from speech signals. LBP, which was original proposed by Ojala et al. [9], is known as a powerful method for texture image characterization. LBP method produces a binary code for a pixel position by comparing its value with its 8 neighbor pixel values. Binary 1 value is assigned a neighbor if its gray scale value is higher than the center pixel gray scale value; otherwise binary 0 value is assigned. Thus, eight bits binary code is produced which is then converted to the decimal value. The adaptation of the 2D LBP to 1D LBP is straightforward [10] and will be described in next section. After obtaining the 1D LBP scheme of the input speech signal, histogram of the coded speech signal is calculated. Different bin numbers for histogram calculation is considered. SVM, Extreme learning machine (ELM) classifiers are used in the classification stage. The experimental works are carried out with a real life dataset containing courtroom

dialogue recordings of 120 people [12]. Almost 70% of the dataset was randomly used in the training, with the remainder used in testing the efficiency of the proposed method. For 100 times run, average 96.46% accuracy is obtained with SVM, and ELM gets 98.91% accuracy.

The paper has been organized as follows: In the next section, a brief review of the theory of LBP is given. In Section 3, the experimental works, related parameter settings and results are given, with the paper concluding in Section 4.

II. LOCAL BINARY PATTERN

As we mentioned earlier, LBP is an important and efficient method for texture characterization. It reveals the local repetitive patterns which are further used for classification purposes. Generally, LBP works on a 3×3 image patches. The center pixel is coded according to its 8 nearest neighbors. An illustrative example is given in Fig. 1. As seen in Fig.1, the center pixel gray scale value is 7. After LBP coding, its new value becomes 103. The first-order neighbor pixels of the center pixel are coded as 0 or 1. This coding is handled by considering the gray scale values of the neighbor pixels. If a neighbor pixel gray scale value is greater than or equal to the center pixel gray scale value, binary 1 is assigned otherwise binary 0 is assigned to that neighbor pixel. The obtained binary numbers are aligned starting from the up-left pixel position in a circular trajectory as shown in Fig. 1. Thus, an eight bits binary sequence is obtained. Finally, the procedure is ended with the converting binary sequence to decimal number.

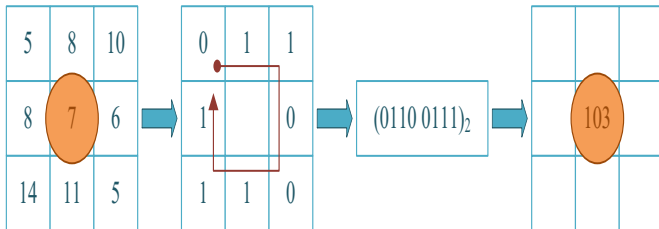


Fig. 20. 2D LBP code of an image patch.

The adaptation of the 2D LBP to 1D case is straightforward [11]. A sliding window with 9 samples length is employed for 1D LBP coding of input signal. An illustrative example is given in Fig. 2. As seen in Fig. 2(a), the samples of the input signal indicated with P_0 to P_7 are in the sliding window coverage. P_C is the interested sample which is in the center of the sliding window.

In Fig. 2(b), all samples in the sliding window coverage are given and the related coding is given in Fig. 2(c). The samples, which have greater value than the center sample, are coded as binary 1 and others are coded as 0. The coded samples are collected from left to right to obtain the 8 bits binary code as shown in Fig.2(c). The last step is converting the binary sequence to decimal number as shown in Fig. 2(d).

III. EXPERIMENTAL WORKS

The dataset, which was used in the experimental works, was collected by Pères-Rosas et al. [12]. The dataset was recorded in courtrooms and contains totally 120 trial video clips. The average length of each video clips in the dataset is 28.0 seconds. 55 video clips contain just female speeches and 41 video clips contain male speeches. The rest video clips, which contain both female and male speeches, are not used in the experiments. The speakers are with ages ranging from 16 to 60 years. Video files were converted into audio files, with a frequency value of 16,000 Hz, a bit rate of 128 kbps, and mono channel specified. Fig. 3 presents a sample time domain speech signal from the dataset.

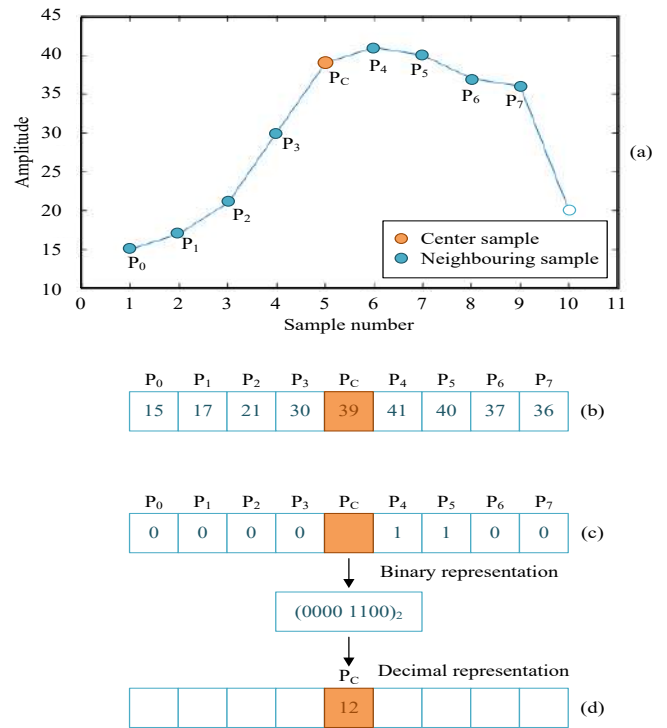


Fig. 21. 1D LBP code of an image patch.

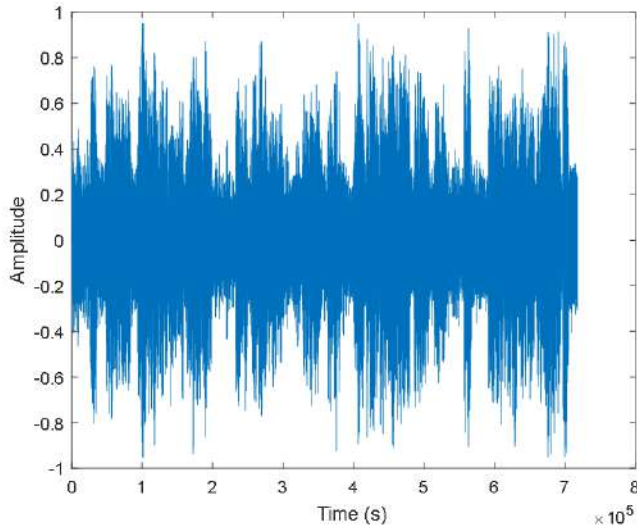


Fig. 22. A sample speech signal from dataset.

A sequence of pre-processing steps was applied to the input speech signals for normalization and noise removal. In this context, min-max magnitude normalization and hamming filtering was applied for noise removal. The hamming window length was selected to 15 ms.

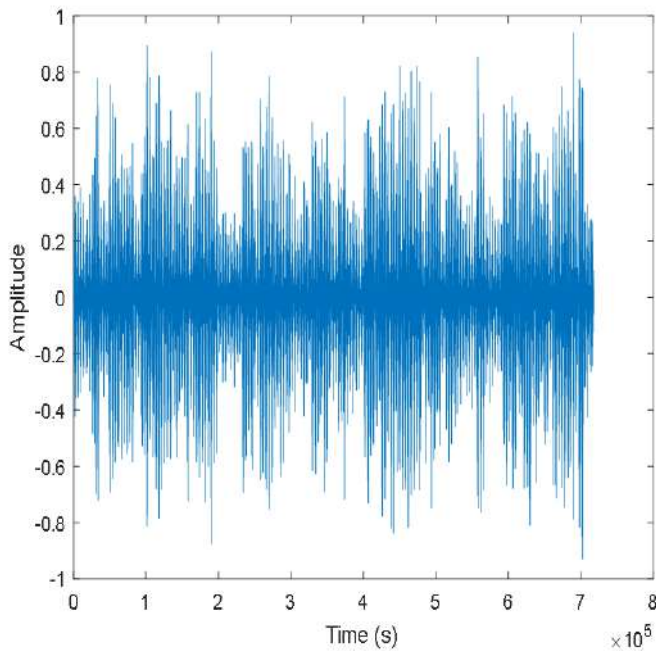


Fig. 23. A sample speech signal after pre-processing.

After pre-processing steps, we applied the 1D LPB to the pre-processed speech signals and histogram of the LPB codes were used as features. The bin size of the histogram was chosen as 50. A sample histogram is depicted in Fig. 5.

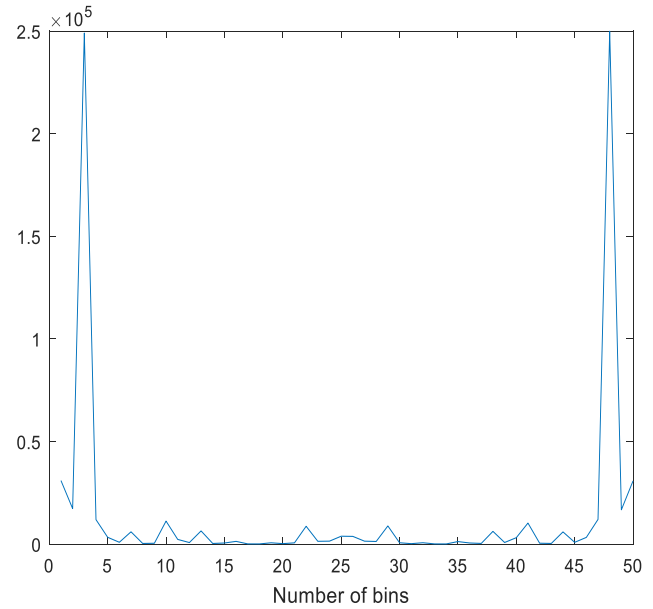


Fig. 24. 1D LBP histogram bins.

As we had 96 speakers and for each speaker 50 dimensional feature vector was constructed, totally a 96x50 feature matrix was obtained before classification stage. 70% of the dataset was used for training and the rest was used for performance test of the proposed method. For performance evaluation, the experiments were run 100 times for each classifier and average classification accuracies were recorded for each classifier. For SVM classifier, linear kernel was selected and the C parameter was assigned as 0.1. For ELM, the sigmoid activation function was selected and the number of neurons in hidden layer was chosen as 1,000. The obtained results are tabulated in Table 1.

TABLE III. OBTAINED RESULTS

Classifier	Accuracy	Sensitivity	Specificity
SVM	96.57%	97.28%	95.61%
ELM	98.03%	98.87%	96.95%

The results show that the best accuracy is obtained with ELM. The classification accuracy is 98.08%. In addition, the sensitivity and specificity values are 98.87% and 96.95%, respectively. In addition, SVM yielded the 96.57% accuracy. Sensitivity and specificity values for SVM classifier are 97.28% and 95.61%, respectively. According to the obtained results, ELM classifier highly increases the performance of the proposed scheme. ELM classifier is almost 1.5% better than SVM.

IV. CONCLUSIONS

In this paper, we proposed texture descriptors for efficient classification of gender of a speaker. In other words, speech based gender classification was carried out by LBP. In this



context, 1D LBP structure was employed to extract meaningful features from the speech signals. The histogram of the 1D LBP was used as feature and two classifiers namely, SVM and ELM was adopted. Obtained results are quite good where both classifiers achieved classification accuracy greater than 95%. In addition, both classifiers sensitivity and specificity values were greater than 95%.

REFERENCES

- [1] H. Erokyar, Age and Gender Recognition for Speech Applications based on Support Vector Machines, Graduate Theses and Dissertations, University of South Florida, 2014.
- [2] M. Kotti, and K. Constantine, "Gender classification in two emotional speech databases," IEEE 19th International Conference on Pattern Recognition, USA, pp. 1-4, December 2008.
- [3] Y-M. Zeng, Z. Y. Wu, T. Falk, W.Y. Chan, "Robust GMM based gender classification using pitch and RASTA-PLP parameters of speech," IEEE International Conference on Machine Learning and Cybernetics, Dalian, pp. 3376-3379, August 2006.
- [4] S.I. Levitan, T. Mishra, and S. Bangalore, "Automatic identification of gender from speech," in Proceeding of Speech Prosody, pp.84-88, 2016.
- [5] A. Zourmand, H.N. Ting, and S. M. Mirhassani. "Gender classification in children based on speech characteristics: using fundamental and formant frequencies of Malay vowels," Journal of Voice, vol. 27(2), pp. 201-209, 2013.
- [6] F. Lingenfelser, J. Wagner, T. Vogt, J. Kim, and E. André, "Age and gender classification from speech using decision level fusion and ensemble based techniques," In Interspeech, vol. 10, pp. 2798-2801, 2010.
- [7] G. Chen, X. Feng, Y. L. Shue, and A. Alwan, "On using voice source measures in automatic gender classification of children's speech," In Interspeech, pp. 673-676, 2010.
- [8] Y. L. Shue, and M. Iseli, "The role of voice source measures on automatic gender classification," IEEE International Conference on Acoustics, Speech and Signal Processing, Las Vegas, pp. 4493-4496, May 2008.
- [9] T. Ojala, M. Pietikäinen, and D. Harwood, "A comparative study of texture measures with classification based on feature distributions," Pattern Recognition, vol. 29 (1), pp. 51-59, 1996.
- [10] N. Chatlani, J.J. Soraghan, "Local binary patterns for 1-D signal processing," 18th European Signal Processing Conference (EUSIPCO), Denmark, pp. 95-99, August 2010.
- [11] Y. Kaya, M. Uyar, R. Tekin, S. Yıldırım, "1D-local binary pattern based feature extraction for classification of epileptic EEG signals," Applied Mathematics and Computation, vol. 243, pp. 209-219, 2014.
- [12] V. Pérez-Rosas, M. Abouelenien, R. Mihalcea, and M. Burzo, "Deception detection using real-life trial data," ACM on International Conference on Multimodal Interaction, USA, pp. 59-66, November 2015. ACM.



Design and Implementation of PID Controller System Based on Android Platform For an Espresso Machine

Ender Oguz and M.Zeki Bilgin
Kocaeli University, Faculty of Engineering,
Kocaeli, Turkey
ender.oguz@gmail.com, bilgin@kocaeli.edu.tr

Abstract – This article suggests an espresso machine design with PID controller and operating principles of the machine. Smart devices are commonly used in daily routine as connectable devices become wider and automation systems are more developed. Especially home control systems and smart home appliances are the main application areas of this field. Coffee machines are widely preferred among fast consumption devices and users choose coffee for their own taste. The high-sensitive cooking process of Espresso is a distinctive property of this coffee type among others. To provide this level of sensitivity, PID control is proposed in this study. Android based operating system is proposed with various criteria for Espresso cooking systems to provide a taste for user preferences. Connectivity is added to the developed control and communication system so that user specific espresso cooking systems can be achieved by connecting this proposed system to common espresso machines in the market. System stages and control methods are stated and experimental results are presented.

Keywords – smart home appliances; PID control; espresso brewing; TDS; Android OS; mobile applications; IoT

I. INTRODUCTION

One of the sectors that is effected by the development of automation systems is smart home appliances. With the increasing number of coffee shops, almost each house has its own coffee machines. The most important proof is that by the year of 2015 more than 76 million coffee machines were sold worldwide and it is expected that the sales figures will exceed 100 million by 2021 [1]. Twelve Turkish coffee machine that has innovation award in 2015 in Turkey has reached over 500.000 sales [2]. Although general structure of coffee machines are similar, factors such as coffee bean, cooking method, brewing time and cooking time can differ. In addition to these factors, personal preferences are the most important factor effecting the coffee devices. In recent years, espresso is one of the widely consumed coffee type. The espresso brewing, originating from Italy, is making hot and pressured water pour over the coffee [3]. Coffee particles dissolves with temperature and pressure, gives the aroma to espresso. The most distinctive property of espresso brewing method is the

balanced and controlled cooking method. Temperature, pressure and flow duration in brewing process increases the quality of espresso. The best way to obtain optimized espresso with bean type, bean grinding and roasting, and personal preferences are empirical methods. If it is considered that each person has different preferences, individual configuration of an espresso machine is a distinctive advantage. Factors such as determining, setting, and saving personal preferences in smart home appliances respond the need of users. Also, the users' involved to the process and this positively contributes to efficiency of coffee and the machine by creating a new experience and increasing product-user interaction. Devices with automation system should also have the connectivity property to commonly use customization option. The largest contribution comes from widely use of internet of things concepts with improved internet and network structures. As the number of connectable objects in the market increase rapidly, application areas have become wider and approximately 500 billion dollar market share is formed [4]. It is inevitable that coffee machines are oriented in this market.

In this paper, design and control method of a smart and connectable espresso machine is proposed. Coffee machine control systems in the literature mainly use fuzzy logic, PID and proportional control methods [5], [6], [7]. PID control system is applied to provide stable and high precision cooking. Thus, according to preferences from smart and Android operating system based device, pressure, temperature, and flow duration is set and brewing process is managed by the user. Suggested reference values are recorded to form user profile. To evaluate the acceptability of the coffee after brewing process, TDS (Total Dissolved Solids) measurement method is used [6]. Thus, TDS method can measure how many coffee particles are dissolved.

Section II of the proposed paper states operating principle of espresso machine. Section III shows design and experimental studies. Section IV indicates the obtained results.

II. OPERATING PRINCIPLE OF PROPOSED ESPRESSO COFFEE MACHINE

Configuration options that can be selected by users for their espresso preferences is shown in Fig. 1. As a result of this configuration options, control system sets temperature, pressure, and cooking time with high-precision and stability.

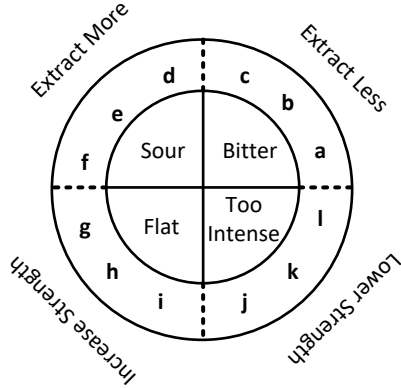


Fig. 1. Espresso balancing chart (a: lower temperature, b: grind coarser, c: stop the shorter i.e. lower target weight, d: allow the shot to run longer i.e. increase target weight, e: grind finer, f: increase temperature, g: tamp harder, h: stop the shot shorter i.e. lower target weight, i: use fresh coffee ground on demand, j, k: allow the shot to run longer i.e. increase target weight) [8].

Espresso machines fundamentally operate as shown in Fig.2. Water heated in the chamber is poured on milled coffee from portal filter mounted on ground head with a pump and coffee particles are dissolved in hot water. When operating system of espresso machine is considered, pressure and flow duration are the main steps of brewing process. Control of these steps affects the taste of coffee. Since temperature, pressure, and flow duration effects the taste of the coffee, certain control algorithm should be used on these variables to provide the customized tastes for individual users. Fig.4 shows cooking diagrams for different aroma and stiffness. When ideal duration and high precision is changed according to the diagram, the taste of the coffee will improve. To enhance this improvement and to obtain a high-performance device, proposed system implemented a PID control structure. Effects of PID parameters are stated in Fig.4 and Appendix for the given flow.

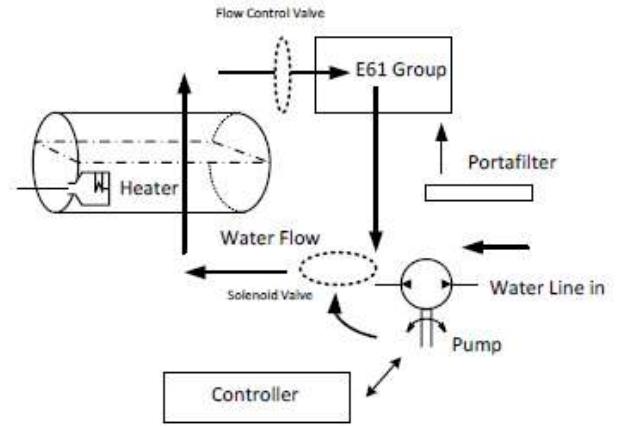


Fig. 2. Espresso machine working principle.

PID control system measures error between feedback and reference value and aims to provide a stable improvement [9]. Both applicability and fast adjustment for the process and time constants, this type of controller is selected in the study.

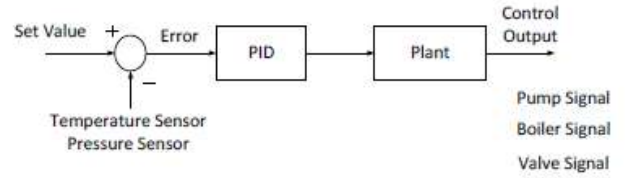


Fig. 3. Espresso control diagram.

In the control method with proportional, integral and derivative effects, proportional gain, integrator and derivative coefficients can be adjusted and control system can be arranged for cooking method. Control method in Fig.3 is separately applied for temperature, pressure, and flow duration. Transfer function of PID controller is shown in Eq. (1).

$$G(s) = K_p \left(1 + \frac{1}{T_i s} + T_d s \right) \quad (1)$$

Equation shows K_p proportional gain, T_i as integral time constant, and T_d as derivative time constant. Integral gain $K_i = K_p / T_i$ Integral gain is stated as $K_i = K_p / T_i$, derivative gain is stated as $K_p T_d$ [9].

$$e(t) = r(t) - x(t) \quad (2)$$

When the effects of the component on the system are investigated, these effects are shown in Eq. (2) - (4) separately. Where Eq. (2), $e(t)$ is error shows the difference between reference value $r(t)$ and sensor feedback value $x(t)$.

$$P = K_p e \quad (3)$$

$$I = K_I \int_0^t e(t) dt \quad (4)$$

$$D = K_D \frac{de(t)}{dt} \quad (5)$$

Proportional (P) expression in Eq. (3) provides a proportional decrease of error. Integral (I) expression decreases steady-state error. In this study, a low frequency integrator is selected. Derivative (D) expression controls the transient state response. Control algorithm with D uses high frequency differentiator.

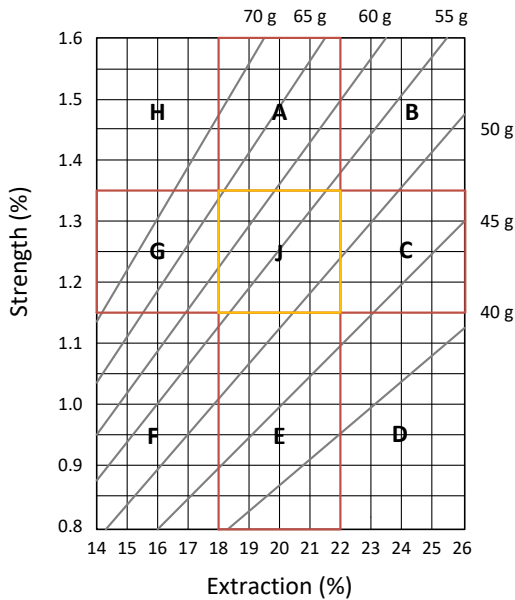


Fig. 4. Coffee brewing control chart (A: strong, B: strong bitter, C: bitter, D: weak bitter, E: weak, F: weak underdeveloped, G: underdeveloped, H: strong underdeveloped, I: ideal) [10]

III. DESIGN & EXPERIMENTAL STUDIES

Control block diagram of designed espresso machine is shown in Fig. 6. The designed system should brew 10 glass of espresso with 1500 Watt power and 1.3 L volume. Prototype device is selected as a product on the market. This product and experiment mechanism is shown in Fig.5. Control strategy of the machine consists of three main parts. Selection and placement of sensors, communication and addition of IoT properties and forming control algorithm. The application has a database and user-friendly interface for Android based control. General control structure of the system is shown in Fig.6. User can adjust related interface parameters as shown in Fig.7. These parameters are transferred to coffee machine using Bluetooth communication protocol. The references are arranged with embedded PID control algorithm in microcontroller and data from the sensors provide feedback. If the coffee has the desired taste after brewing process, user records the data and a personal coffee taste archive is obtained.

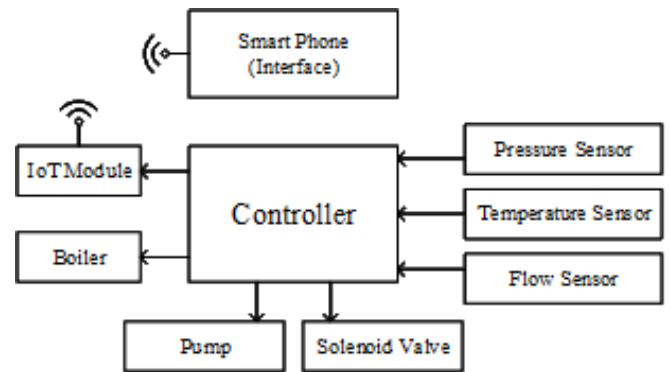


Fig. 5. Overall block diagram.



Fig. 6. Prototype coffee machine.

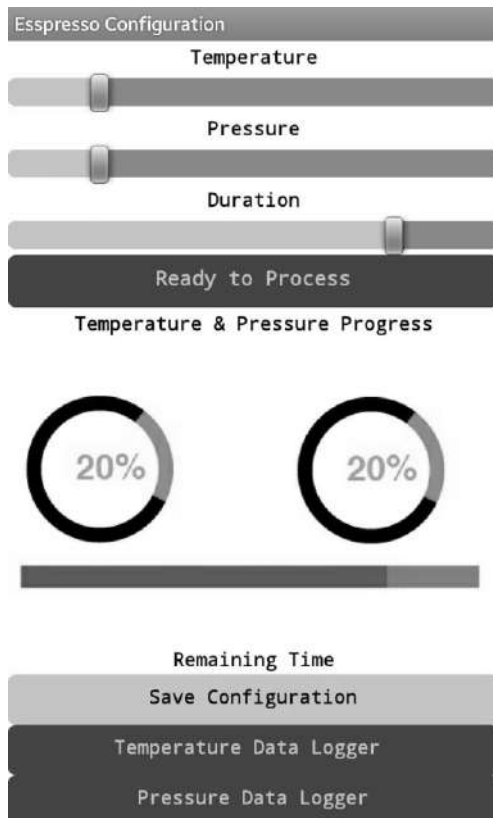


Fig. 7. Android based application's user interface.

Proposed device consists of Atmel Mega 2560 processor, YF-S201 pressure sensor, 100k NTC temperature sensor and HC-05 Bluetooth module. Tests for developed system are conducted according to ideal espresso settings. Fig. 8 and Fig. 9 shows the test results. To show the device performance in the experiments, temperature and pressure change and stability are presented. Fig.8 shows change of temperature and pressure by sampling period. Temperature value is set to 94 °C and pressure reference value is set to 9 Bar. In Fig.9 using an oscilloscope, integrated reference value tracking is presented. Here each noise and disturbance effects are considered and changes in temperature, pressure and cooking duration are monitored. The results show that a control algorithm with desired stability is achieved.

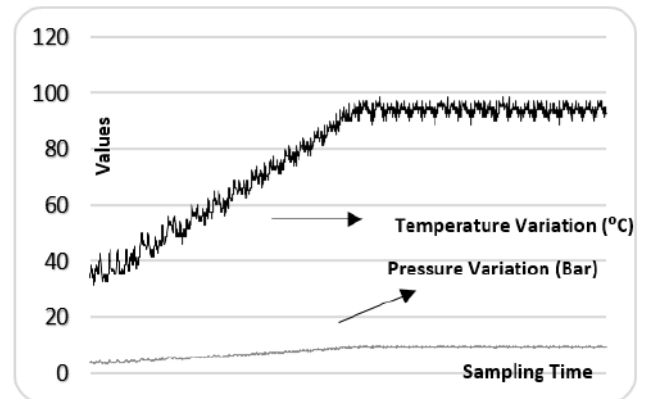


Fig. 8. Heat and pressure variation of cooking process.

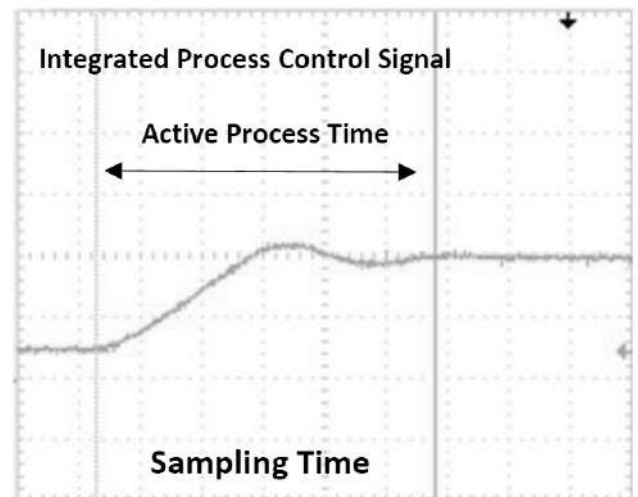


Fig. 9. Integrated settlement graphic of cooking process.



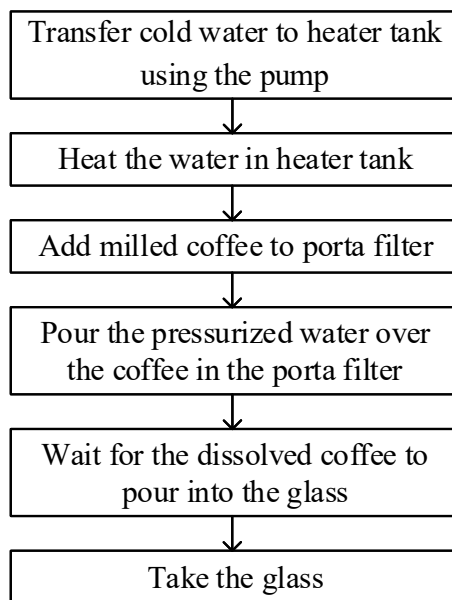
IV.

CONCLUSION

As connectivity properties are added to smart devices in fast moving consumer goods sector, high level of sales figures are achieved in the market. The most important reason is that these devices provide manufacturing custom products for the preference of the user. In this study, customized Android controlled espresso machine is designed. Precise temperature and pressure control are the distinctive properties of espresso. To provide this level of sensitivity, PID control method is applied in this study. Ideal level of espresso is prepared with obtained results and design process and experimental results are presented in the study.

APPENDIX

Proposed System Operation Flow Diagram



REFERENCES

- [1] QYResearch, 2016, Global Coffee Machine Industry 2016 Market Research Report, Brooklyn, NY, United States.
- [2] Ödüller ve Başarılar(n.d.). Retrieved from http://www.arcelikas.com/sayfa/58/Oduller__Basarilar
- [3] How an Espresso Machine Works: What's Really Inside? (n.d.). Retrieved from <http://www.thecoffeebrewers.com/howesmawo.html>
- [4] Adiono T. "Challenges and Opportunities in Designing Internet of Things," 1st International Conference on Information Technology, Computer and Electrical Engineering (ICITACEE), pp 11-12, 2014
- [5] Benefits of a Coffee Machine with a Temperature Control System (TCS),(2014, July 8). Retrieved from <http://www.casaespresso.co.uk/temperature-control-systems/>.
- [6] Vanderpool N.J. 2007. Autonomous Home Coffee Maker Using Fuzzy Logic, M.Sc. Thesis, Wright State University, Ohio
- [7] A Brief History of the PID (2015, Oct. 15). Retrieved from <https://home.lamarzoccousa.com/history-of-the-pid/>
- [8] Diagnosing Espresso for Better Extraction(2015, May 13). Retrieved from <http://ww2.handloom.co.uk/blogs/blog/17901792-diagnosing-espresso-for-better-extraction>
- [9] Karl J. Åström and Richard M. Murray, 2016. Feedback Systems: An Introduction for Scientists and Engineers. Retrieved from http://www.cds.caltech.edu/~murray/amwiki/index.php/Main_Page
- [10] Brewing Fundamentals(April, 23 2015). Retrieved from <https://www.coffeechemistry.com/quality/brewing/brewing-fundamentals>



DSP Controlled Single Phase Bridgeless PFC Buck Converter

Harun Ozbay

Bilecik Seyh Edebali University, Vocational High School
Bilecik, Turkey
harun.ozbay@bilecik.edu.tr

Yasemin Onal

Bilecik Seyh Edebali University, Engineering Faculty
Bilecik, Turkey
yasemin.onal@bilecik.edu.tr

Akif Karafil

Bilecik Seyh Edebali University, Vocational High School
Bilecik, Turkey
akif.karafil@bilecik.edu.tr

Metin Kesler

Bilecik Seyh Edebali University, Engineering Faculty
Bilecik, Turkey
metin.keslerl@bilecik.edu.tr

Abstract— In this study, DSP controlled a single-phase bridgeless AC-DC rectifier with low total harmonic distortion (THD) and high power factor (PF) is proposed. Bridgeless converters remove the input bridge the conventional Buck PFC converters to reduce complexity and improve overall efficiency. Moreover, some additional advantages such as zero-voltage cutoff in power switches, zero-voltage conduction in the output diode, and continuous input current are provided by the proposed system. Therefore, electromagnetic noise (EMI) emissions are minimized and high power factor is obtained with low total harmonic distortion (THD) in the input current. The performance of the proposed system is evaluated using simulation studies performed with PSIM and embedded codes are obtained for the TMS320F28335 DSP processor.

Keywords— Power factor correction (PFC); total harmonics distortion (THD); DSP; PSIM

I. INTRODUCTION

Electronic devices cause harmonic currents in power systems. Non-sinusoidal magnitudes occur when passive components such as inductors and capacitors are connected to the power system. However, these harmonics cause various problems such as voltage distortion, heating and noise as well as reducing the line capacity to provide energy [1]. To improve the PF, to decrease the AC current harmonics, to reduce noise and electromagnetic pollution, to use the minimum number of components and to increase the current efficiency are required [2].

The converters used to obtain the enhanced power factor are called power factor correctors (PFC). PFCs are divided into two classes as active or passive. Using active PFC converters, the power factor of the grid is approached to 1 and the power quality can be corrected by drawing currents close to the sinus with reduced harmonic content from the grid. In the world, any device connected to the grid must provide input line current harmonic limit values given in EN 61000-3-2.

According to this standard, the limitation of the input current harmonics is sufficient, so it is not necessary to provide the unit power factor. However, it is important to understand the standard, to evaluate the PFC techniques in accordance with the standard, and to optimize the total cost and performance by some changes in the standard [3].

In this respect, the standards force PFC circuits to be used as rectifiers in power systems. Single phase PFC circuits are widely used in applications ranging from low to moderate power due to simple circuit construction, low current and voltage stresses, low number of components, ease of control, etc. [4]. The commonly used PFC converters are Boost [5], Buck [6], Boost-Buck [7]. Boost PFC converters are often preferred in practical applications, such that the input current can be brought to a sinusoidal waveform in a suitable manner to obtain a unit power factor. However, the Boost PFC converter has a limited capacity because it requires a higher voltage than the AC input of the DC output [8]. Moreover, high voltage stress is produced by Boost PFC converters in wide input voltage range for adjustable electronic devices especially for high voltage input condition. As a result, it becomes very difficult to choose the circuit elements and the energy storage capacitor.

On the other hand, the Buck converter's DC output voltage is lower than the peak value of the AC input voltage, thereby reducing component values and cost [9]. A Buck PFC converter appears as an alternative to lower voltage applications such as 48V DC bus. In addition, when the Buck PFC exceeds the limits specified in IEC 61000-3-2, high efficiency can be achieved in the entire input voltage range [10].

In this study, to evaluate the performance of the proposed control, simulation studies were performed with PSIM software and embedded codes were obtained for the TMS320F28335 DSP processor.

II. BRIDGELESS CONVERTER TOPOLOGY

The output voltage of a Buck PFC is always lower than the grid voltage. The output voltage for 220V grid voltage is usually set to 48 VDC. Figure 1 (a) shows the conventional Buck PFC. The conventional Buck PFC consists of a full bridge diode rectifier and a buck converter. When the switch is closed, the energy is stored in the inductor and the capacitor is discharged through the resistor. By controlling the duty ratio of the output voltage to the desired value, a value lower than the input voltage can be obtained. The disadvantage of this circuit is the occurrence of high conduction losses in the direction of the bridge [11].

The Buck topology of the two active switched bridgeless (Q1 and Q2) is shown in Figure 1 (b).

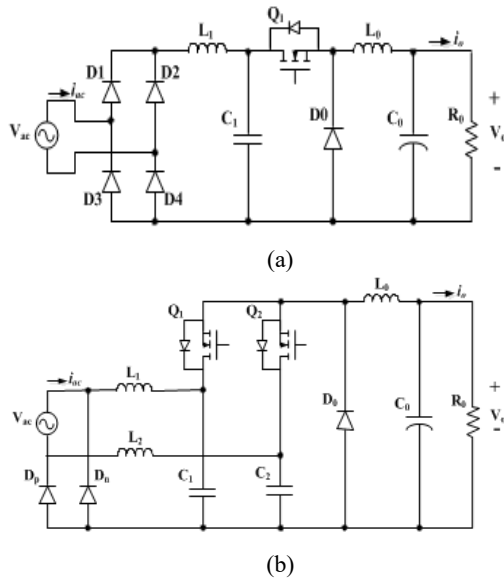


Figure. 1.(a) Conventional Buck PFC (b) Bridgeless Buck PFC.

L_1 and L_2 inductors must be small enough to reduce the phase shift between the line voltage and the input current to be minimum. Furthermore, L_1 and L_2 inductors must be large enough not to resonate with the input capacitors C_1 and C_2 ;

$$L_1 = L_2 < \frac{(1-D)^2 T_s}{4\pi C_1 f_l} \quad (3)$$

$$L_1 = L_2 > \frac{1}{C_1} \left(\frac{(1-D) T_s}{2\pi} \right)^2 \quad (4)$$

where; f_l represents the line frequency. L_0 coil in the output must be chosen in accordance with the maximum point (peak) I_m of the converter input current;

The same control signal can be controlled by both switches. As a result, the control cycle becomes simpler. During the positive half-line cycle, L_1 , C_1 , Q_1 , L_0 , D_0 and D_p are active. During the negative half-line cycle, L_2 , C_2 , Q_2 , L_0 , D_0 , and D_n are active.

Compared with a conventional buck PFC converter, the bridgeless topology uses an additional inductor and a capacitor and this causes disadvantage because of size and cost. However, compared to a single inductor, better heat performance can be achieved with two inductors. In addition, the return diodes D_p and D_n always provide a low impedance current path for the return current. Thus, higher efficiency is achieved compared to conventional Buck PFC converter by reducing conduction and heat losses [12].

Multi loop fashion as the inner current loop and outer voltage loop are used at the proposed control. The reference current through innovative filtering and signal processing is calculated to outer control loop. PWM switching signals through the PI controller are generated to inner control loop.

III. DESIGN OF BRIDGELESS BUCK CONVERTER

There are many factors in the design of single-phase bridgeless PFC [13]. Input capacitors C_1 and C_2 can be calculated from Equation 1;

$$C_1 = C_2 = \frac{KT_s}{2R_l} \quad (1)$$

where, T_s represents the switching period. K constant should be chosen as follows;

$$K < \frac{D^2(1-D)}{\eta} \quad (2)$$

where, D is the switching rate, η is the efficiency.

$$L_0 = \frac{1}{2I_m f_s} (V_m - V_o) \frac{V_o}{V_m} \quad (5)$$

where; V_m is the maximum value of the converter input voltage, V_o is the output voltage, f_s is the switching frequency and I_m is the maximum value of the input current. On the other hand, output compensator is chosen in accordance with the desired frequency fluctuation value ($\theta\%$) of the output voltage.

$$\alpha + \beta = \chi. \quad (1) \quad (1)$$

$$\theta\% = 2 \cos^{-1} \left(\frac{V_{des}}{V_m} \right) \frac{1}{\pi} \quad (6)$$

$$C_o = \frac{P_L(1-\theta\%)}{V_o^2 \Delta V_{des\%} 2f_L} \quad (7)$$

where V_{des} is the desired output voltage, P_L is the output power of the converter, $\Delta V_{des\%}$ is the fluctuation frequency of the output voltage.

IV. PSIM SIMULATION RESULTS

Two active switched bridgeless buck PFCs are simulated using the parameters shown in Table 1. In the simulation, one voltage control loop and one current control loop are used. Higher PF and lower THD values are obtained by using the current and voltage control loop in the control of the proposed PFC system. The controller can control the output voltage at the desired value.

Table 1. Parameters of Simulation

Parameters		Value
Input Inductors	L_1, L_2	3 mH
Output Inductor	L_o	50 μ H
Input Capacitors	C_1, C_2	47 nF
Output Capacitor	C_o	3000 μ F
Input Voltage	V_{rms}	220 V
Output Power	P_o	100 W
Output Voltage	V_o	48 V
Grid Frequency	f_L	50 Hz
Switching Frequency	f_s	75 kHz

Figure 2 shows the simulation circuit for current and voltage control of the two active switched bridgeless PFCs. Figure 3 shows the simulation results for the input current and voltage of the proposed system. The input current is in the same phase as the input voltage. The output voltage is regulated around 48 V with a frequency fluctuation of 100 Hz. PFC is operated at 75 kHz switching frequency, 220V input voltage and 100 W output power. The PF and THD values were measured as 0.9993 and 4.0195%, respectively.

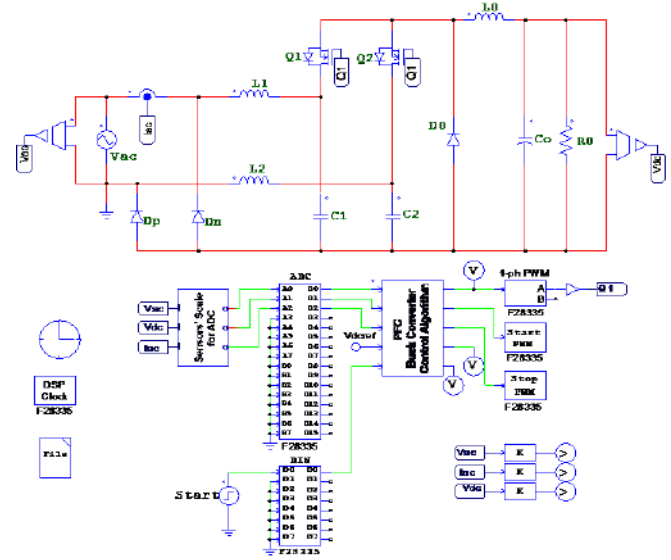


Figure 2. The simulation circuit of the two active switched bridgeless buck PFC

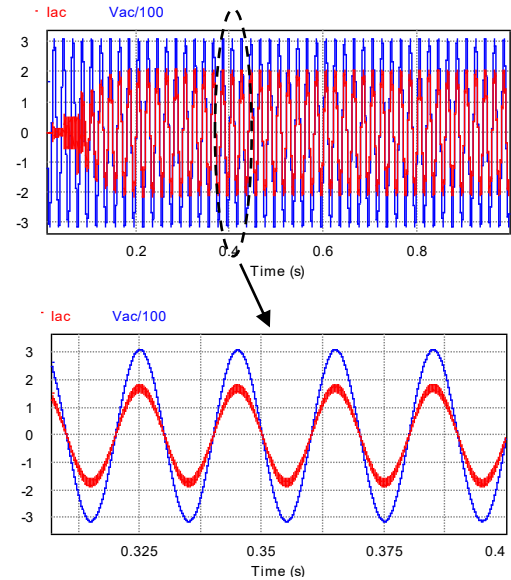


Figure 3. Simulation results of the input current and input voltage

The voltage stress on the capacitor and the switch is around 560V as shown in Figure. 4. Therefore, when selecting the capacitor and the switch, it is necessary to take these voltage values into consideration.

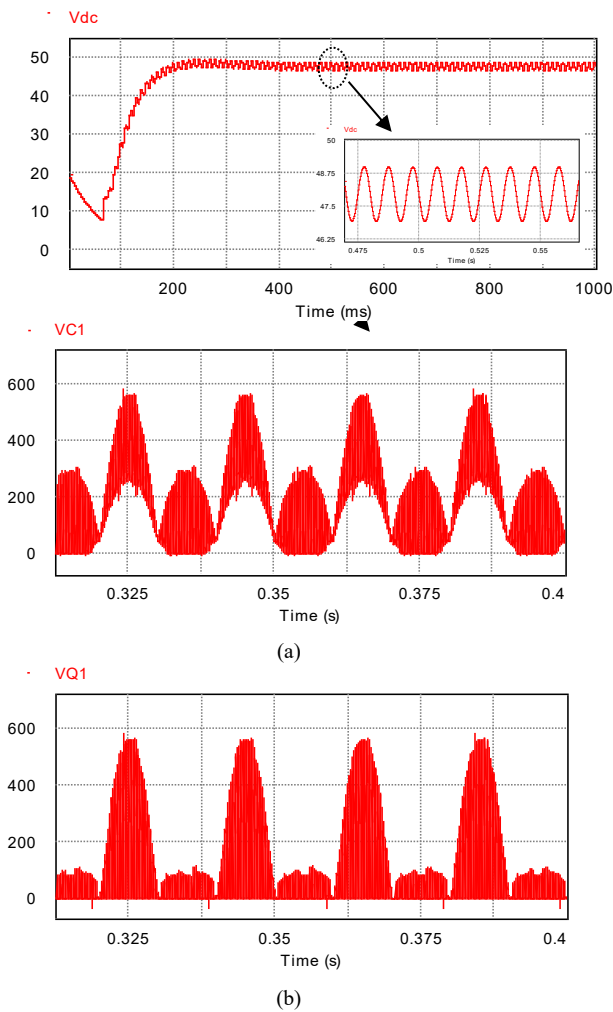


Figure 4. Simulation results of (a) the capacitor (C1) voltage and (b) the switch (Q1) voltage

As it is seen in Figure 5, the output voltage oscillates from 47 V to 49 V at a frequency of 100 Hz, fixing at the desired value of 48 V in a short period of time. The amount of oscillation can be adjusted with the output capacitor.

Figure 5. Simulation results of the output voltage (Vdc)

V. CONCLUSION

In this study, the control of the proposed single phase bridgeless PFC buck converter system is implemented using DSP control. Electromagnetic interference noise emissions are minimized by continuous input current and switching at zero voltage. In addition, total low harmonic distortion and high power factor are obtained by the current and voltage control loop. Therefore, EN61000-3-2 international standards have been provided in the proposed system. To evaluate the performance of the system, simulation studies were performed with PSIM software and embedded codes

were obtained for the TMS320F28335 DSP processor. As a result, the application studies of the proposed system will be more practical in the future.

ACKNOWLEDGMENT

This research was supported by TUBITAK Research Fund (No: 115E104) and Bilecik Seyh Edebali University Research Fund (No: 2015-02.BŞEÜ.03-09).

REFERENCES

- [1] O. Garcia , J. A. Cobos , R. Prieto , P. Alouand J. Uceda, "Power factor correction: A survey", Proc IEEE Power Electronics Specialists Conf. (PESC 01), pp. 8-13, 2001
- [2] B. Singh and S. Singh, "Single-phase power factor controller topologies for permanent magnet brushless dc motor drives", IET Power Electron., vol. 3, no. 2, pp. 147-175, 2010
- [3] EPSMA, "Harmonic Current Emissions Guidelines to the Standard EN 61000-3-2", European Power Supply Manufacturers Association, www.epsma.org., 5-7, 2010.
- [4] Mao, Hengchun, et al. "Review of high-performance three-phase power-factor correction circuits." IEEE Transactions on Industrial Electronics 44.4 (1997): 437-446.
- [5] Bhaskar, Atla, and U. Ramesh Babu. "FLC-FPGA based digital controller for boost PFC SMPS without current measurement." India Conference (INDICON), 2016 IEEE Annual. IEEE, 2016.
- [6] Vahedi, Hani, and Kamal Al-Haddad. "A novel multilevel multioutput bidirectional active buck pfc rectifier." IEEE Transactions on Industrial Electronics 63.9 (2016): 5442-5450.
- [7] Zhao, Ben, Alexander Abramovitz, and Keyue Smedley. "Family of bridgeless buck-boost pfc rectifiers." IEEE Transactions on Power Electronics 30.12 (2015): 6524-6527.
- [8] Zhang, Junda, et al. "Research on a novel bridgeless boost PFC converter." Power Electronics Conference (SPEC), IEEE Annual Southern. IEEE, 2016.
- [9] Gao Chao, Luo Shiguo, "Research of alleviating switch voltage stress in single stage PFC converters," Acta Scientiarum Universitatis Sunyatseni, 2002, vol. 41, no. 5, pp. 34-37.
- [10] Marei M I, El-Saadany E F, Salama M M A "Flexible distributed generation: (FDG)", Power Engineering Society Summer Meeting, IEEE vol.1, pp.49-53, Chicago USA, 2002.
- [11] N. S. Kurian, F. Mohan, "Performance Evaluation of Bridgeless High Power factor Buck Front End", International Journal of Engineering Research & Technology, vol. 3, April 2014.
- [12] Y. Jang and M. M. Jovanović, "Bridgeless Buck PFC Rectifier," in Proc. IEEE Applied Power Electronics Conf., 2010, pp. 23-29.
- [13] N. Mohan, T. Undeland, and W. Robbins, "Power Electronics: Converters, Applications and Design, Hoboken", NJ: Wiley, 1995.

Protection Analysis of Surge Arresters and Isolators Against Overvoltages Caused by Lightning Electromagnetic Pulses

Turan Cakıl

Akdeniz University Engineering Faculty
Electrical and Electronic Engineering Department
Antalya, Turkey

H. Feza Carlak

Akdeniz University Engineering Faculty
Electrical and Electronic Engineering Department
Antalya, Turkey

fezacarlak@akdeniz.edu.tr

Sukru Ozen

Akdeniz University Engineering Faculty
Electrical and Electronic Engineering Department
Antalya, Turkey

sukruozen@akdeniz.edu.tr

Abstract— the characteristic parameters of the lightning electromagnetic pulse (LEMP) current have been investigated for many years on the basis of the isolation coordination by scientists studying in the field of electricity and physics. The necessity of studying in this area has arisen in order to protect the electrical and electronic equipment inside the power transmission lines and electrical installations against the harmful effects of the harmonic current of the lightning electromagnetic pulse. The Heidler function is used as the LEMP model used in this study. Analyses of the over-voltages that occur because of the lightning strike to the protection conductor on the top of a grounded pole or one of the pole conductors of the pylon are carried out. In this study, the voltage insulators of the power transmission lines used in Turkey were tested. Furthermore, the behavior of surge arresters against LEMP induced surges and currents of surge arresters used in low voltage (LV) systems was investigated.

Keywords—Lemp, Isolator Protection, Surge Arrester Protection, Voltage Distribution

I. INTRODUCTION

The energy breakdowns and interruptions in power transmission lines and power plants have mainly emerged from research conducted by weather conditions. Currents flowing in the direction of lightning electromagnetic pulses

(LEMP) can lead to high pulsating voltages in power plants [1]. In power transmission lines, when the LEMP strikes on the protection conductor and the phase conductors, the voltage on the insulators may rise due to the voltage increase. This causes the breakdown of the isolators, the deterioration of the insulation of the transformers, and the explosion of the surge arresters in the power plants [2].

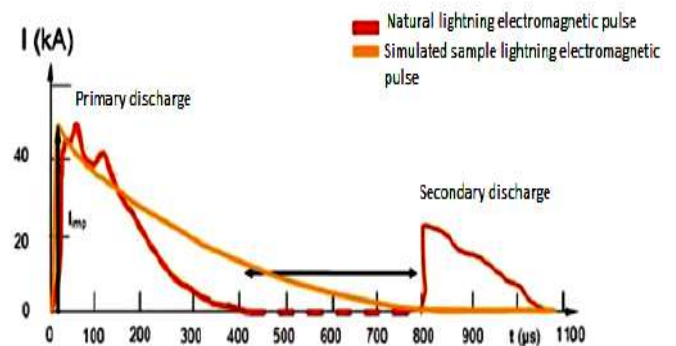


Fig. 25. Lightning electromagnetic pulse and time relation [1]

(Fig. 1), the natural lightning LEMP runs at about 1000-1100 μ s, while the simulated orange curve at the LEMP discharge shows that the LEMP of 50 kA reaches its peak value in the time of 0-10 μ s and the time of 10-350 μ s it falls to half the value in my language. The LEMP current resistance characteristics of the protection elements are determined by the discharge current capacity in the range of 10-350 μ s [3]. In this study, the absorber test simulation programs performed the over voltages of the LEMP insulators used in poles and the surge arresters in the power plants, which are used as the result of dropping to the protection conductor of the power transmission lines. Since these tests are expensive in practice and experiments are difficult to repeat, programs such as MATLAB and ATP-Draw, which are designed with numerical methods using modern electronic technology, are used [4].

Many studies have been carried out to investigate the model of surge arresters on 150 kV Hellenic transmission lines, protection against over voltages in low voltage transmission lines, analysis of over voltages generated by LEMP due to type of the utility pole, and modeling of energy systems in simulation programs [5- 6-7].

II. MODELING AND THEORETICAL ANALYSIS OF THE SYSTEM

Using the appropriate mathematical equations that make up the LEMP, a voltage test was performed in MATLAB depending on the breakdown voltage of the isolators at the high voltage (HV) level and the change of the breakdown voltage of the isolators and phase angle. Furthermore, the protection behavior of surge arresters used at the low voltage (LV) level has been examined. 380 kV energy transmission lines prototype models were created and the insulators were tested for voltage. In another analysis, prototypical models of surge arresters were constructed in places with LV level such as workplaces, dwellings, and the behavior of surge arresters against over voltages and currents caused by LEMP was investigated.

A. LEMP Model:

LEMP is modeled as parallel resistance and current source with lightning path impedance in ATP model (Fig. 2). In numerical analysis, Heidler function (Equation 1) is used as LEMP numerical model [8].

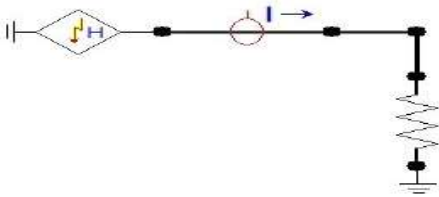


Fig. 26. The current waveform of the LEMP used in the studies

$$i(t) = \frac{I_0}{\eta} \frac{(t - \tau_1)}{(t / \tau_2)^n + 1} e^{-t/\tau_2} \quad (1)$$

$$\eta = e^{\left[(\tau_1 - \tau_2) \left(\frac{\tau_2}{\tau_1} \right)^n \right]^{\frac{1}{n}}} \quad (2)$$

Where,

I_0 : Peak value of LEMP current,

τ_1 : Time constant dependent on current rise time,

τ_2 : Time constant dependent on the current delay time,

N : The steepness factor of the current.

The parameters of the Heidler function used in the study are $V = 800$ kV, $\tau_1 = 1.6$ μ s, $\tau_2 = 50$ μ s and $n = 4$, respectively. For the analysis made for the surge arrester, $I_0 = 10$ kA, $\tau_1 = 8$ μ s, $\tau_2 = 20$ μ s and $n = 2$ respectively.

B. Voltage Distribution and Protection Method on Isolators in Power Transmission Lines

In power transmission lines, in case insulators acting as insulation do not have protection armatures, the voltage distribution is not smooth.

$$U_x = \frac{U_n}{C'_E + C'_H} \left[C'_E + C'_H \cdot \frac{sh \gamma x}{sh \gamma h} - C'_H \cdot \frac{sh \gamma (h - x)}{sh \gamma h} \right] \quad (3)$$

Where,

C'_E : Capacity against soil,

C'_H : Capacity against transmission line,

U_n : The voltage at the ends of the conductor-connected isolator element,

H : Isolator height

The voltage distribution for an isolator below a certain voltage level is shown in (Equation 3). If the LEMP pulse is in a falling energy transmission line, the impact voltage will jump back to the conductors via the pole jump when the HV isolator reaches a value greater than 170 kV, which is the impact resisting voltage, causing the insulators to be damaged. That is why the grounding resistance of the poles must be reduced to the point that prevents this backlash. In the case of a voltage drop across the isolators, if the voltage that is blown during the passage of the LEMP current through the grounding conductor is smaller than the breakdown voltage of the isolators used in the overhead lines.

Insulators used in the study have a voltage lower than the voltage level of 170 kV. Therefore, it is determined that they are suitable for the line [9].

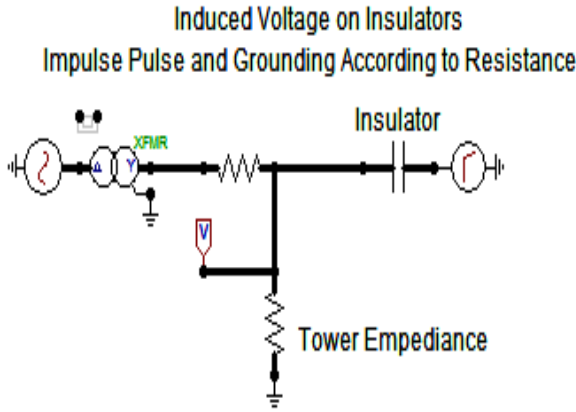


Fig. 27. Isolator voltage test circuit

The structure of the isolators and the angle between the conductor and the conductor (Fig. 4).

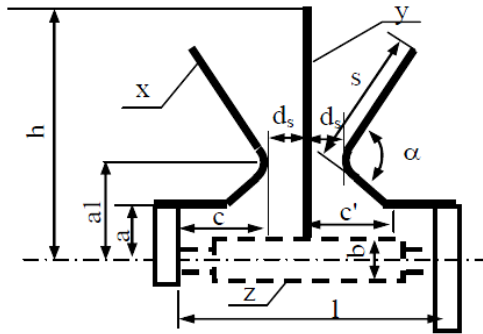


Fig. 28. Structure of isolators

In this study, the voltage test for the insulators was performed using the ATP model shown in Fig. 3. In a further analysis, the load voltage at the isolators due to the different openings occurring when the impulse voltage is lowered is calculated according to the form shown in (Equation 4) [10].

$$U_{load} = U_m \cdot \sin(\theta) \quad (4)$$

C. Voltage Surge Protection in Low Voltage Systems

The surge arresters are made according to the pulse discharge current of 5-10 kA. In areas where the atmospheric discharges are intensive, 10 kA, where the

lightning currents are infrequent, 5 kA paraphrase selection is appropriate. When the low voltage windings exposed to impulses, the tests showed that the low voltage windings have been damaged under the surge exceeding 34.5 kV level [11-12]. The other occasion was that the high voltage windings have been damaged under weak impulses (as low as 3 kV) but with long duration applied on low voltage windings. For the transformer connected to the overhead line with length more than 100 m, it is recommended to fit surge arrester with the transformer. However, in case of overhead line less than 100 m, there is no need for fitting the surge arrester. Under the condition that the line length is less than 100m, the applied voltage on the low voltage windings is decreased in addition to the frequency is decreased by factor 10 where in this case the overhead line capacitance is less than the winding capacitance. The surge arrester is as any device has a definite lifetime where it is impossible for its life to be infinity. The lifetime of metal oxide varistor depends on the magnitude and number of strokes. The lifetime can increase other factors by increasing the number of varistors, the varistor size or these two factors together. The surge arrester can be damaged when it is subjected to surge strokes exceeding the maximum voltage or current rating. The ideal surge arrester has the same lifetime of the power distribution network where it is installed [13].

The required conditions for any used surge arrester are [14]:

- Not to absorb current (energy) at the power frequency voltage,
- To operate correctly based on its setting designed based on the electric power system rating,
- To work in the same environment of the protected equipment.

In the study, surge arrester type is selected according to the following data:

Continuous operating voltage (U_c): 280 V,
Nominal discharge current (I_n) 8/20 μ s: 5 kA,
Maximum discharge current (I_{max}) 8/20 μ s: 25 kA,
Voltage protection level (U_p) at I_n : 1100 V,
Voltage protection level (U_p) at I_{max} : 1500 V,
Voltage protection level at long lasting surge 2ms: 850 V

This selected surge arrester is modeled and simulated in the ATP-Draw environment where the above mentioned data in accordance with Pinceti et al. model are used in order to verify the model parameters as discussed in the following section.

$$L_1 = 0.03 \cdot U_n \quad (5)$$

$$L_2 = 0.01 \cdot U_n \quad (6)$$

In this work, Pinceti et al. model is used because of its simplicity. However, its inductance parameters are calculated using relations (Equation 5) and (Equation 6) [14], where U_{r1}/T_2 is not available in the data sheet. So, L_1 and L_0 are found equal to $0.0084 \mu H$ and $0.0028 \mu H$ respectively. The nonlinear characteristics of the two elements A_0 and A_1 are given as the per-unit data (Table I).

TABLE IV. SURGE ARRESTER CHARACTERISTICS OF A_0 AND A_1 [15]

V-I Characteristics of A_0 and A_1		
$I (kA)$	$A_0 (PU)$	$A_1 (PU)$
2×10^{-6}	0.81	0.623
0.1	0.974	0.788
1	1.052	0.866
3	1.108	0.922
10	1.195	1.009
20	1.277	1.091

The surge arrester model is simulated and tested using ATPDraw circuit shown in (Fig. 5). A discharge current $8/20 \mu s$, 5 kA and 25 kA for nominal and maximum conditions respectively are injected to the surge arrester that its parameters are defined above. Adding $1 M\Omega$ resistance is used parallel with the current source in order to avoid the numerical instability of the combination of the current source and non-linear elements. Regularly, it is recommended to add high resistance parallel with the current source in the field of EMTP or ATP/Draw programs [10].

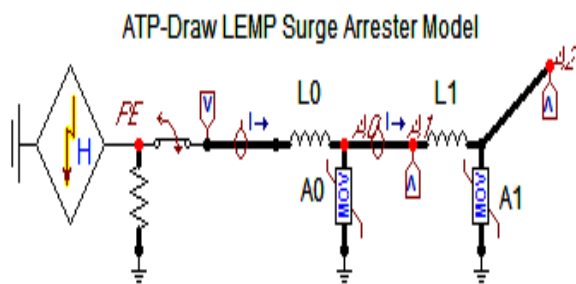


Fig. 29. ATP-Draw circuit model for the surge arrester.

III. RESULTS

In this study, the voltage test of the isolators was done in ATP and Matlab programs. In this analysis, the insulators are represented as capacitors in the analysis performed in the ATP draw program (Fig. 3). These capacitors have a capacitance value of $500 pF$, which is equivalent to the value chain insulators.

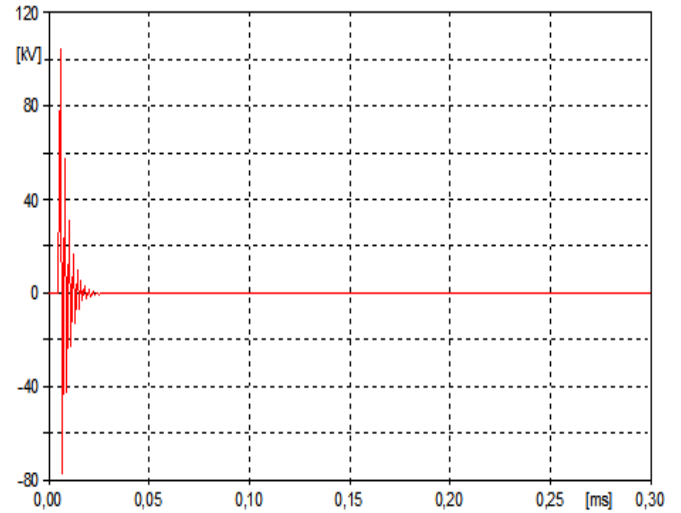


Fig. 30. ATP-Draw Voltage test on insulators

The instantaneous voltage rise in L1 phase in an isolator with a LEMP pulse is shown in (Fig. 6). In the surge analysis, the Heidler wave model was used as the voltage type. One of the surge models of low voltage systems was used for analysis. This simulation test was also implemented in the ATP program Fig. 5 and Fig. 7.

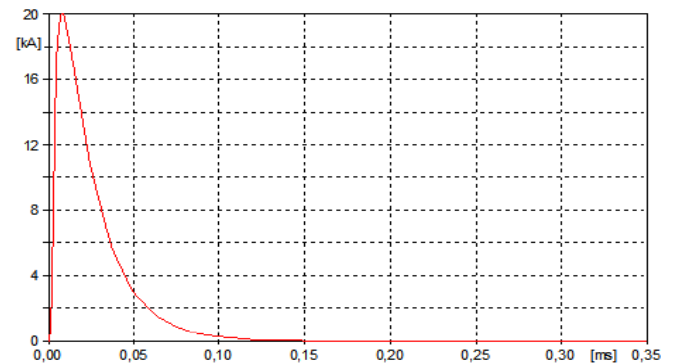


Fig. 31. ATP-Draw surge arrester type injected current (maximum discharge current).

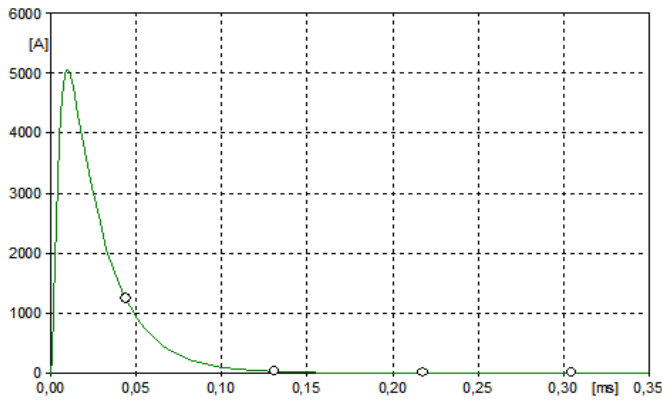


Fig. 32. ATP-Draw Surge arrester type injected current (nominal discharge current).

In the same model, the measured current value between the A_0 and A_1 surge arresters is shown in Fig. 8.

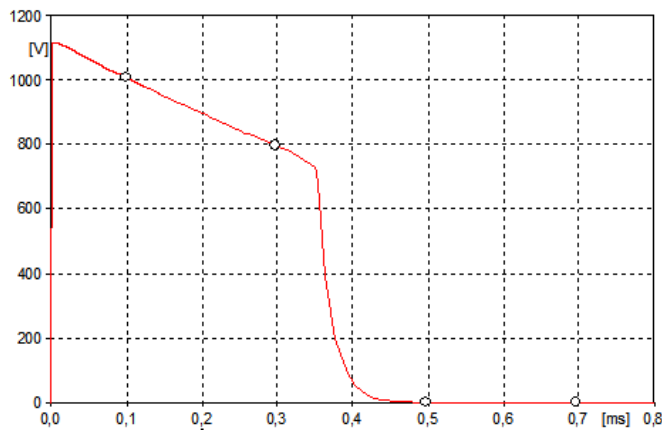


Fig. 33. ATP-Draw Model surge arrester type residual voltage.

The model shown in Fig. 5 is also shown in the voltage value measured at point A_2 (see Fig. 9). In the Matlab analysis, the voltage distribution in the isolators (see Fig. 10) is denoted as a result of the LEMP pulse striking to the L1 phase due to the angle change in the L1 phase.

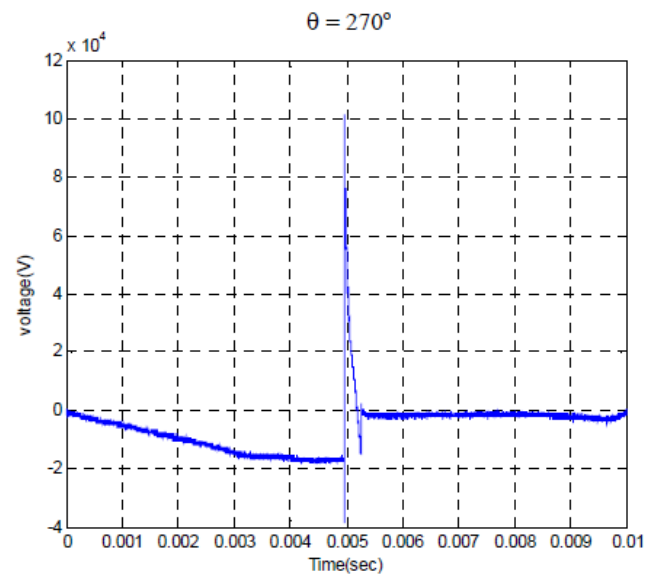
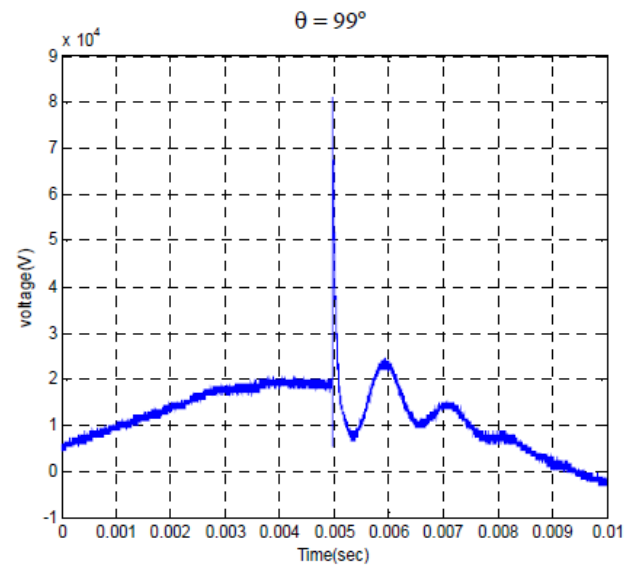


Fig. 34. Voltage waveforms measured at different inception angles θ .

IV. CONCLUSION AND DISCUSSION

Overvoltages due to LEMP, damage power transmission lines, underground cables, distribution transformers, isolators, cable glands, and even AG receivers. In this study, the analysis of the ATP application leads to investigate the overvoltages on the isolator and the protection conductors in the case of LEMP strokes in the energy transmission lines. The proper isolator was specified for energy transmission lines. The phase shifts due to lightning electromagnetic pulses and the corresponding voltage distributions on each isolator were determined. Moreover, the surge arrester behaviors in LV systems were analyzed. The results of the



LEMP analysis may lead to use more realistic pole models and may help to determine the degree of protection and isolation against overvoltages in power transmission systems. If the construction and operation of the facilities are carried out by taking into consideration the existence of LEMP's and corresponding overvoltages which cause short or long term interruptions in the electricity facilities, the uninterrupted and economical high quality power network can be maintained continuously.

ACKNOWLEDGMENT

This study was supported by Akdeniz University, Scientific Research Projects Supporting Unit (BAPYB).

REFERENCES

- [1] N.Cahit Gençer Effects of Lightning and Overvoltages on High Voltage Lines-The Relationship Between the Poles of the Poles and the Isolation of the Isolators - The Activity of the Parafudors Transformer Adders, TMMOB EMO 2015/1
- [2] Shaida, N., Jamoshid, B.T., Lightning Simulation Study on Line Surge Arresters and Protection Design of Simple Structures, Degree Of Master Of Engineering Faculty of Electrical Engineering Tech., Malaysia, 2008.
- [3] S. Ersin Özdemir, Lightning and Surge Suppression Systems Damages and Preventive Measures. Turkish Parafudr Association.
- [4] Ishii, M., Vedig., Multistory Transmission Tower Model for Lightning Surge Analysis, IEEE Trans. on Power Del., vol. 6, No.3, pp. 1327-1335, 1991.
- [5] Ueda, T., and Diğ., A Comparison between Two Tower Models for Lightning Surge Analysis of 77 kV System, IEEE Trans., 2000.
- [6] Comparison of Simulation Tools ATP-EMTP and MATLAB-Simulink for Time Domain Power System Transient Studies, M. Danyek, P. Handl, D. Raisz, Budapest Univ. of Technology and Economics Hungary
- [7] Cakıl T, Carlak H F, Özen S, 2015. Modeling of Power Network System of the High Voltage Substation: A Simulation Study. International Journal of Engineering and Applied Sciences, 7(3), pp. 39-57.
- [8] K. Fekete, S. Nikolovski, G. Knezevic, M. Stojkov, Z. Kovac. (2010). Simulation of Lightning Transients on 110kV Overhead- Cable Transmission Line using ATP- EMTP. MELECON 2010- 2010 15th IEEE Mediterranean Electrotechnical Conference. pp. 856- 861.
- [9] Kemal Üçleröğlü, Protection in High Voltage Electrical Installations. SEGEM.
- [10] Nehmdoh A. Sabiha, Lightning-Induced Overvoltages in Medium Voltage Distribution Systems and Customer Experienced Voltage Spikes, 2009, Finland.
- [11] M. Darveniza and D. R. Mercer, "Lightning Protection of Pole Mounted Transformers", IEEE Transactions on Power Delivery, Vol. 4, No. 2, pp. 1087-1095, April 1989.
- [12] J. F. Carter, M. Darveniza, N. Logothetis and T. M. Parneli, "Investigations of Selected High Voltage Tests on the Windings of 11 kV Transformers", ibid. Vol 6612. pp 89-97, 1976.
- [13] IEEE Std C62.72™-2007, IEEE Guide for the Application of Surge-Protective Devices for Low-Voltage (1000 V or Less) AC Power Circuits.
- [14] S. S. Kershaw, G. L. Gaibrois and K.B. Stump, "Applying Metal-Oxide Surge Arresters on Distribution Systems", IEEE Transactions on Power delivery, Vol. 4, pp. 301-307, Jan. 1989.
- [15] M. C. Magro, M. Giannettoni and P. Pinceti, "Validation of ZnO Surge Arresters Model for Overvoltage Studies", IEEE Transactions on Power Delivery, Vol. 19, No. 4, Oct. 2004.

TiO₂ Memristor Modelling With LabVIEW

Muhammet Emin SAHIN, Hasan GULER
Firat University, Turkey
memnshn@gmail.com, hasanguler23@gmail.com

Abstract— The fourth fundamental circuit element-Memristor, was mathematically modelled by Prof. Leon Chua in 1971. After about four decade, researchers at the Hewlett-Packard (HP) laboratories submitted the development of a new basic circuit element that completes the missing link between charge and flux linkage, which was suggested by Chua. Though a physical memristor device was not discovered then, many unique simulation applications are executed totake advantage of memristor feature which is different from other circuit elements by many researchers. In this paper, we use TiO₂ memristor model which has different mathematical equations in literature on account of its simplified expressions and the same ideal physical behaviors. Firstly, we obtained the mathematical equations of TiO₂ memristor. Then, this equations are created with LabVIEW and results are submitted. Finally, results of this system's behavior and stability analysis of are submitted.

Keywords— *Memristor, LabVIEW, modelling and simulation, physical behavior*

I. INTRODUCTION

Leon O. Chua published his work where the fourth passive two-terminal electrical component – memristor was described in 1970s [1]. Current, voltage and magnetic flux are the basic elements in circuit theory. There is a relationship between them. Three of them define the three basic devices which are resistor, capacitor, and inductor. They showed that memristor should represent the relation between electric, charge (q) and magnetic flux (φ),

$$d\phi = M dq \quad (1)$$

Memristor was developed for several times, but the scientists did not realised, that they developed a new component– memristor [2]. R. S. Williams who is leader of HP team invented this item, while they have been searching for a device which is a resistor with a state and not for a device, which has charge – magnetic flux relation. This work was published in [3] and it include the first relations for memristor modeling. Memristor has drawn the worldwide attention after HP released its invention. After then many researchers focus on this element. Owing to different properties, memristors are being found out for many potential applications in the areas of nonvolatile memory very-large-scale integrated (VLSI) circuit, digital image processing, artificial neural networks, and pattern recognition and signal processing [4].

In this paper, we focalize the memristor modeling with LabVIEW. We submitted memristor model with different mathematical statement. Similar works have not founds up to, thus we assume that this is a different publications of the models and simulations described below. In methods, our nonlinear model of the memristor is presented and a formula is given in order to infer model parameters used physical parameters. In methods, measurements of simulation are defined. Final part of methods contributions of this paper are summarized.

II. MEMRISTOR

A. HP TiO₂ Memristor Model

In 2008, R. Stanley Williams of Hewlett Packard was submitted an experimental solid state version. A semiconductor device was either use magmatic field as flux or keeps charge as capacitor, memristor which has memory feature used chemical mechanism. One of the film slide depletion of oxygen atoms. The absence oxygen act as carriers it mean that the depleted layer has lower resistance than the non-depleted layer. Meanwhile the resistance of the film as all is dependent on how much charge has been went through it, in a particular direction, which is convertible by changing the direction of current. [5-7]

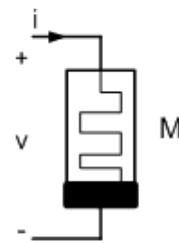


Figure 1. Memristor

A memristor device is essentially a two-terminal passive electronic element with memory capacity. Its memristance state is affected from amplitude, polarity, and duration of the external applied power. The physical model of the HP memristor from [7], shown in Figure 1, consists of a two layer thin film (thickness $D \approx 10\text{nm}$) of TiO₂ sandwiched between two platinum electrodes. One of the layers, which is described

as TiO_2-x , is doped with oxygen vacancies and thus it exhibits high conductivity. The width w of the doped region is modulated depending on the amount of electric charge passing through the memristor.

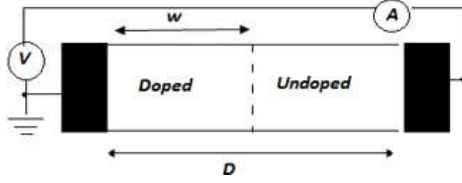


Figure 2. HP's memristor model

Fig. 2 exhibits HP's memristor model. We see that total memristance is made of w and D regions. The total resistance of the memristor,

M , is a sum of the resistances of the doped and undoped regions:

$$M(t) = R_{on} \left(\frac{w(t)}{D} \right) + R_{off} \left(1 - \frac{w(t)}{D} \right) \quad (2)$$

where R_{on} and R_{off} are the limited values of memristance for $w=D$ and $w=0$. We selected internal state as $x = w/D \in [0,1]$ then we rewritten as

$$M(t) = R_{off} + (R_{on} - R_{off})x(t) \quad (3)$$

When $t=0$, the initial memristance is

$$M_0 = R_{off} + (R_{on} - R_{off})x_0 \quad (4)$$

Resistance of doped area affects the movement speed of the boundary between the doped and undoped regions.

$$\frac{dx}{dt} = ki(t)f(x), \quad k = \mu_V R_{on} / D^2 \quad (5)$$

where $\mu_V \approx 10^{-14} \text{ m}^2 \text{ s}^{-1} \text{ V}^{-1}$ is the average ionic mobility parameter. As for a memristive device, these nonlinearities are manifested particularly at the thin film edges, especially at the two boundaries [8].

This phenomenon, called nonlinear dopant drift, can be simulated by multiplying a proper window function (x) on the right side of (5). We use this window function for increasing the nonlinearity.

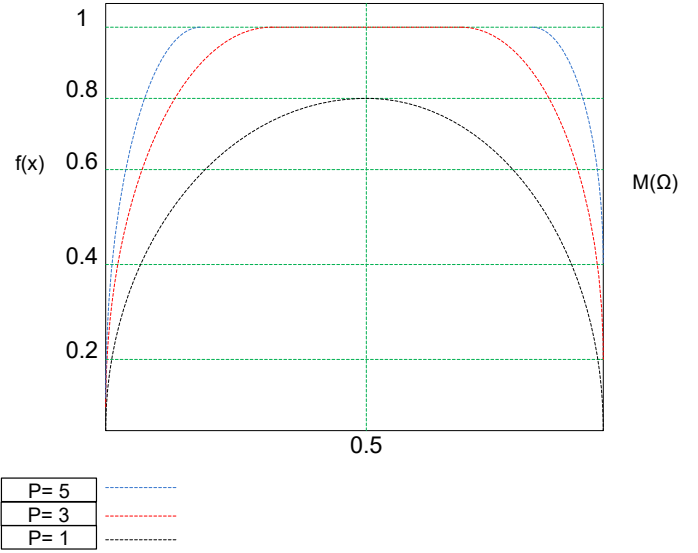


Figure 3. Joglekar window function for $P=1$, $P=3$ and $P=5$

$$f(x) = 1 - (2x - 1)^{2P} \quad (6)$$

where P is a positive integer called the control parameter. Fig. 3 shows the behaviour of the Joglekar window function for different values. Nonlinearity changes with value of P integer. As the integer P increases, the model tends to the linear. Based upon this, we selected $P=1$.

$$f(x) = 4x - 4x^2 \quad (7)$$

Substituting (7) into (5),

$$\int_{x_0}^{x(t)} \left(\frac{1}{x(\tau)} - \frac{1}{1-x(\tau)} \right) dx(\tau) = \int_0^t 4ki(\tau) d\tau \quad (8)$$

Where the internal state variable satisfies $x(\tau) \in [x_0, x(t)]$ and the integration time is $0 \leq \tau \leq t$.

Assume $q_0=0$; we can get

$$\frac{x(t)}{1-x(t)} = \frac{x_0}{1-x_0} * e^{4kq(t)} \quad (9)$$

Then the expression of $x(t)$ can be calculated as

$$x_0 = \frac{R_{off} - R_0}{\Delta R} \quad (10)$$

Then, the expression of (t) can be calculated as

$$x(t) = 1 - \frac{1}{Ae^{4kq(t)} + 1} \quad (11)$$

where A is a constant and its value is determined by R_{off} , R_{on} , and R_0 :

$$A = \frac{R_{off} - R_0}{R_0 - R_{on}} \quad (12)$$

This mathematical statements are used for modelling memristor. They are made control and simulation block in LabVIEW.

III. MEMRISTOR MODEL WITH LABVIEW

We developed a behavioral model of a memristor at device level using the LabVIEW programme by following the mathematical equations presented before. The reason of preferring the LabVIEW program is its graphic based structure and the ease provided to user in constituting interface. [9] We examined TiO_2 memristor model to make it easy to comprehend and ready to be used in memristive systems.

We used LabVIEW programme which is a graphics-based software platform. The usage of program is going up in engineering applications for making this model [9]. We used mathematical equations which are given previous part. Model depicted control and simulation block in LabVIEW. Fig.4 shows the memristor model of LabVIEW front panel.

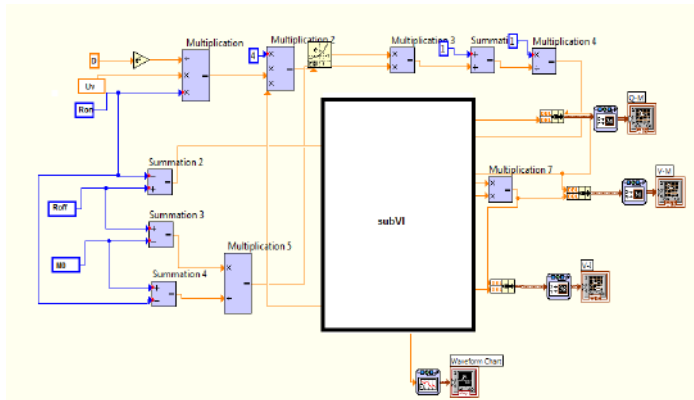


Figure 4. Memristor model of LabVIEW

The parameters of the model are $R_{on} = 100\Omega$, $R_{off} = 20\text{k}\Omega$, $M_0 = 10\text{k}\Omega$, $D = 10\text{nm}$ and $\mu v \approx 10^{-14} \text{ m}^2 \text{ s}^{-1} \text{ V}^{-1}$. [7-8] Moreover, the simulation results in Figure 6.

IV. RESULTS

In order to show memristor characteristics, values of passive elements, and, are chosen to work firstly 0.5mA input current at 5 Hz . Memristor model was simulated to examine the behavior via using LabVIEW program. The simulation results are exhibited in Fig. 5, 6, 7 and 8.

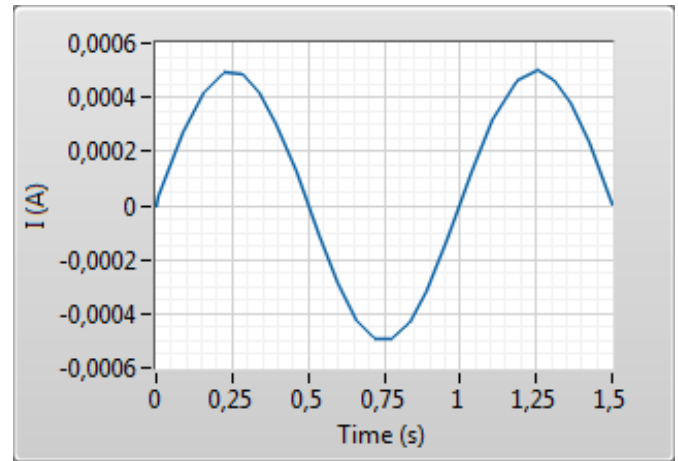


Figure 5. Memristor's current graph

Fig. 5. shows that input current graph to time. The value of this is 0.5 mA sinus flowing through the memristor in this model.

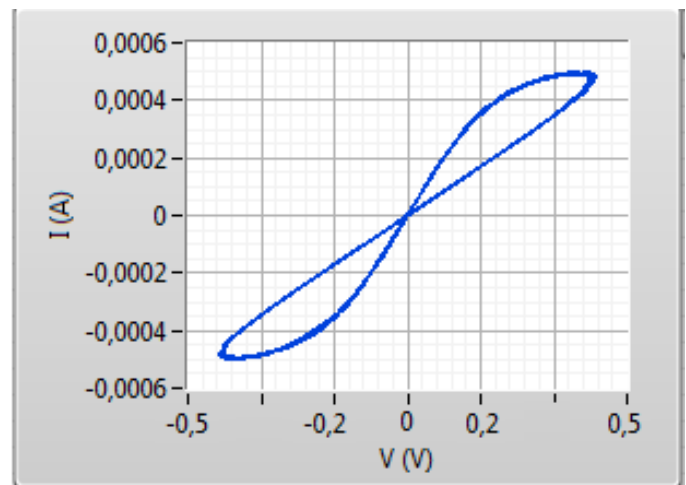


Figure 6. Relationship between memristor's current (I) and voltage (V)

The typical hysteresis loop in figure 6 shows its switching characteristic; that is, the memristance can switch between low resistance and high resistance.

One of the most important memristors' observed specialty is the existence of a pinched hysteresis that effect could be represented by the $i-v$ pinched hysteresis loop characteristic, as Chua highlighted that 'If it's pinched, it's a memristor' [11].

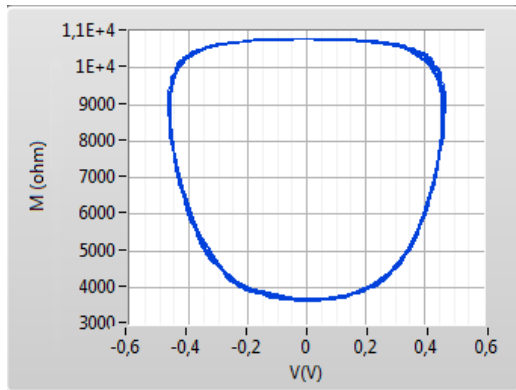


Figure 7. Relationship between memristor's voltage and memristance

Figure 7 illustrates that the memristance is a nonlinear function of the flow of charge. Figure 8 shows the relationship between the memristance M and the charge q . Especially, in the part of the higher memristance state, the change ratio of the memristance is low, while, in the part of the lower memristance state, the change ratio of the memristance is high.

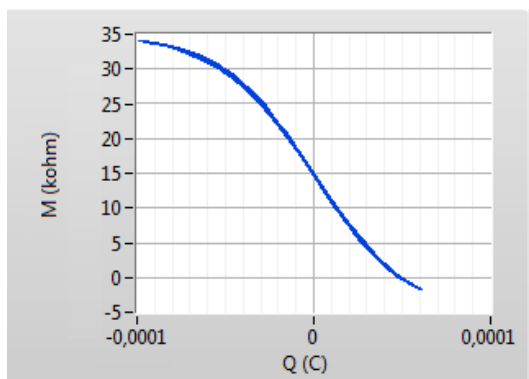


Figure 8. Relationship between memristor's charge and memristance

If we increase input signal frequency, memristor behave as linear resistor. Fig.9 shows signal frequency is at 20Hz and fig.10 shows that memristor's loop turns the line chart at 200 Hz.

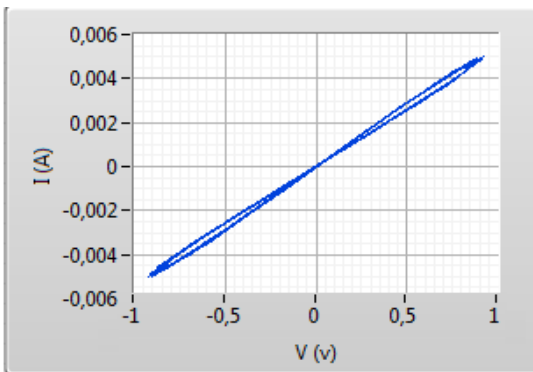


Figure 9. Relationship between memristor's current (I) and voltage (V)

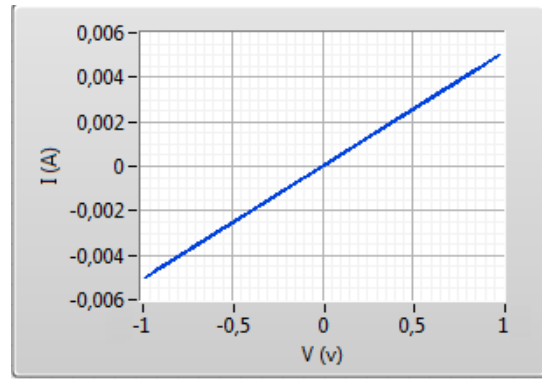


Figure 10. Relationship between memristor's current (I) and voltage (V)

V. CONCLUSION

Although HP workers has invited to memristor physically, it is not submitted to the market yet and it will be probably not available for at least some years. Hence, memristor studies are still going on theoretically and based simulation. This paper is one of them. Since memristors have a natural nonlinear behaviour, they can be used in chaotic circuit systems and other different systems such as secure communication and cryptology. The main aim of this study is to show the possibility of application of memristor based circuits. LabVIEW environments were used to achieve simulation and real time application.

REFERENCES

- [1] L. Chua, "Memristor-the missing circuit element," *Circuit Theory, IEEE*
- [2] G. Dearnaley, A. M. Stoneham, and D. V. Morgan, "Electrical phenomena in amorphous oxide films," *Reports on Progress in Physics*, vol. 33, no. 3, p. 1129, 1970. [Online]. Available: <http://stacks.iop.org/0034-4885/33/i=3/a=306>
- [3] D. B. Strukov, G. S. Snider, D. R. Stewart, and R. S. Williams, "The missing memristor found," *Nature*, vol. 453, pp. 80–83, 2008.
- [4] ME Sahin, H Guler, T Kaya, LabVIEW Model Of Memristor With Nonlinear Dopant Drift, *European Journal of Technic* 6 (2), 124-130,2016
- [5] Mazumder, P., Kang, S. M., & Waser, R. (2012). Memristors: devices, models, and applications. *Proceedings of the IEEE*, 100(6), 1911-1919.
- [6] Biolek, Z., Biolek, D., & Biolkova, V. (2009). SPICE Model of Memristor with Nonlinear Dopant Drift. *Radioengineering*(18), 210-214.
- [7] Zhang, Y., Xuliang, Z., & Juebang, Y. (2009). Approximated SPICE model for memristor. In *Communications, Circuits and Systems, ICCAS 2009. International Conference* (pp. 928-931). IEEE.
- [8] Dong, Zhekang, et al. "A novel memristive multilayer feedforward small-world neural network with its applications in PID control." *The Scientific World Journal* 2014 (2014).
- [9] Guler, H., & Ata, F. (2014). The Comparison of Manual and LabVIEW Based-Fuzzy Control on Mechanical Ventilation. *Journal of Engineering in Medicine*, 916-925.
- [10] Aydin, S. G., Turgay, K., & Hasan, G. (2016). Wavelet-based study of valence-arousal model of emotions on EEG signals with LabVIEW. *Brain Informatics*, 3(2), 109-117.
- [11] Chua, L. (2011). Resistance switching memories are memristors. *Applied Physics A*, 102(4), 765-783.



Reflection Based Smartphone Spectrometer for Detection of Harmful Dyes in Water

Volkan Kılıç¹, Ali Y. Mutlu¹, Abdullah Bayram², Nesrin Horzum³, Mehmet E. Solmaz^{1*}

¹Department of Electrical and Electronics Engineering, Izmir Katip Celebi University, Izmir, Turkey

²Department of Material Science and Engineering, Izmir Katip Celebi University, Izmir, Turkey

³Department of Engineering Sciences, Izmir Katip Celebi University, Izmir, Turkey

*mehmete.solmaz@ikc.edu.tr

Abstract— We report a low cost, field-deployable, reflection based smartphone spectrometer to detect dyes in a body of water. Exploiting built-in flash and camera of smartphones, a customized cradle is fabricated for reflectance based spectroscopy with no requirement for additional electrical parts. First, we evaluated the success rate of the designed spectrometer in identifying methylene blue (MB) reflectance in water with a limit of 0.1 ppm. Then we contrasted our design with that of a commercial spectrometer for reflectance spectra. The resulting condensed, less-costly and high-speed platform could facilitate remodeling the science of measurement for sustainable water management.

Keywords—*smartphone spectrometer; reflection spectroscopy; environmental sustainability.*

I. INTRODUCTION

Dye accumulation in water is harmful to humans and environment and optical spectroscopy is a major measurement method for detection of dyes [1, 2]. Field portable measurement devices offer great advantage to their bulky laboratory counterparts due to similar performance and ability to detect at the location of interest. Smartphones with their embedded hardware are great candidates for spectroscopy instrumentation [3]. By using the flexibility of 3D printing, smartphones can be converted to colorimetric plate readers for ELISA (enzyme-linked immunosorbent assay) immunoassays [4], to absorbance spectrometers for biomarker analysis [5], or to a fluorimeter to detect mRNA sequences [6]. On the other hand, a smartphone without a 3D apparatus is enough to analytically analyze color test strips [7, 8]. For smartphone based spectroscopy, the wavelength range is limited to visible range (400-700nm) owing to the simple optical filters for ultraviolet and near-infrared. A dispersive element placed at a certain angle is used right before the camera to obtain color spectrum image, which is later used to extract absorbance value. Recent work on smartphone spectrometers integrating fiber optical cables aimed to monitor food quality [9]. Moreover, smartphone spectrometers with no external active components (i.e. LEDs, lasers, incandescent sources) were reported for

surface plasmon resonance based refractive index sensing [10], and simultaneous glucose and troponin I detection [11].

Recently, an ultra-low cost plastic fiber based smartphone spectroscopy system was proposed for detection of dyes in water and contribute to environmental sustainability [12]. It requires no extra optical and electrical components, uses camera flash for optical source and camera for spectrometric detection. Here we report an improved version of the plastic fiber based system in the form of reflection spectroscopy integrated onto a smartphone. To enable reflection measurements, a custom cradle was designed to align plastic optical fibers onto the phone camera and flash. A bifurcated fiber design on a dipping apparatus was used along with a small mirror to allow reflection measurements. The system can be used without any liquid extraction from the water source of interest. Our design is very low cost, ultra-stable and enables smartphone based detection of dyes in water using reflection.

II. EXPERIMENTAL METHODS

A. Spectrometer system for smartphone

The smartphone spectrometer was designed by using LG G4 (1/2.6" sensor size with 5312x2988 resolution, 1.12 μm pixel size). The rear-facing camera of the phone was used in capturing to get high resolution images and to be able to use flash of the smartphone. The cradle design includes a hot-plug apparatus holding a diffraction grating, and a smartphone case holder keeping the whole part compact with reflection measurement apparatus were fabricated from the Acrylonitrile Butadiene Styrene (ABS) polymer using a 3D printer (Zortrax M200). The total polymer usage was about 120 g.

In the cradle design, two pieces of plastic (PMMA) fibers were used as one is a 1.5 mm diameter fiber couples the light from the cellphone flash to the reflection measurement apparatus while the other is a 0.25 mm diameter fiber collects the transmitted light, which passes through a linear

diffraction grating (1000 lines per mm, Rainbow Symphony) at an angle of $\sim 42^\circ$ to the normal to reach the smartphone camera. A photographic image of the dipping apparatus is shown in **Hata! Başvuru kaynağı bulunamadı.** To make the design cost-effective, it was simplified by avoiding usage of any collimating lens or mirror components in the light pathway. The alignment of the smartphone flash and camera was implemented mechanically. The total cost of design is less than \$10 which significant part of it caused by 3D printer material. Besides the cost, the plastic optical fibers have an advantage, as compared with glass-based optical fibers, because of its ability to use them without any special tools for stripping and cutting.

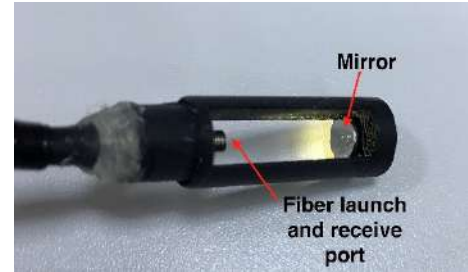
B. Image processing

An image is recorded by a digital camera using a two-dimensional array of pixels. When a pixel receives a light, intensity value increases with the number of photons stored in the pixel. Earlier cameras were designed to generate only grayscale images as the pixels cannot classify the photons with respect to color. After each pixel is covered by the color filter array which allows only red (R), green (G) or blue (B) primary colors, then a color image can be captured since the pixel stores only filtered photons which give the intensity value for the respective color. When light passes through the color filter, each pixel contains one of R, G or B color information. By knowing only one color value of each pixel, a RAW image can be created. However, other two color values are unknown for each pixel. To address this issue, demosaicing method was proposed which calculates missing two color values by interpolating from nearby neighbors where those colors are known. Many methods have been proposed such as white-balance, gamma correction, color space correction and compression to obtain viewable image like JPEG.

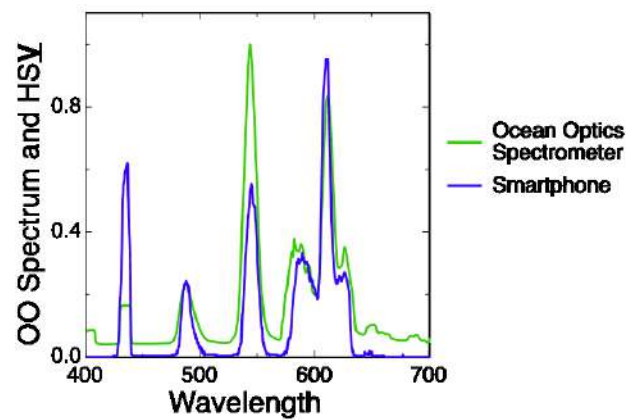
Conversion of RAW images into JPEG image formats offers some advantages such as occupying a small size and being instantly displayable. However, this conversion causes loss of information due to the compression, having a non-linear RGB color space [13]. In addition, JPEG image formats provide an 8-bit color depth while RAW images have 10–14 bits color information. RAW images do not have any post-processing and contain original image data. If the post-processing steps are applied to the RAW image, it causes corruption of linearity information. Linear images keep the linear relation between the intensity value and the number of received photons which is essential for quantitative scientific data acquisition as a linear relationship with scene radiance is maintained.

Although the RAW images keep the linearity, the issue with this format is difficulty in using the images. Therefore, there are many attempts to approximate raw (linear) RGB from nonlinear RGB images. In that sense, a series of training images captured under different settings and light conditions as well as ground-truth raw images to model a relation between RAW and nonlinear RGB images [14]. To

simplify this approximation process, it is reported to use just gamma correction [15] to overcome nonlinearity problem which has not been verified by other researchers yet. Here, the images were captured and processed in RAW format due to the limitations of the JPEG format. In addition, using raw



(a)



(b)

Fig. 1 (a) The launch and receive port reflectance based sensor when the camera flash is ON; b) The output spectrum comparing smartphone and commercial spectrometer for fluorescent light. (HSV) means the Value is plotted.

data allows to make precise image analysis in our experiments. The problem arises capturing a RAW image with smartphone. It is usually available to get a RAW image from semi-professional and professional cameras.

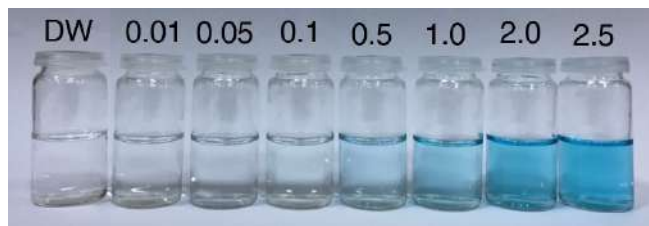
Recently, smartphone companies produce the smartphones which provide access to raw image data free from postprocessing. One of three RAW file formats can be chosen to work with RAW data. Nikon and Canon companies released their RAW file formats which are “.NEF” and “.CR2”, respectively. In this study, “.DNG” raw file format was chosen since it is a common open format. After the images were captured using smartphone, they were transferred to a computer to process in Matlab environment. The reliability of the camera was tested by capturing five consecutive images and checked normalized values of the images. It was found $\pm 2.73\%$ difference with respect to the average. To improve the reliability of the results, it was decided to use the average of five consecutive images in processing and analyzing the experiments. In addition, same conditions such as the same shutter speed and ISO were set,

and to avoid any possible post-processing performed by the smartphone, manual mode was selected when the images were captured. After that, they were processed with freely available DCRAW software [16] to convert them to tagged image file format (TIFF) for easier extraction of the R, G, B values. Main advantage of using DCRAW is to keep the linear relationship between RAW images and the radiance scene even after conversion. Then, these RGB values were converted to HSV (Hue–Saturation–Value) due to its robustness to the illumination change. For the further processing steps of the image, the V (value) was employed as it was defined, for this study, the amount of the transmitted light through the solution.

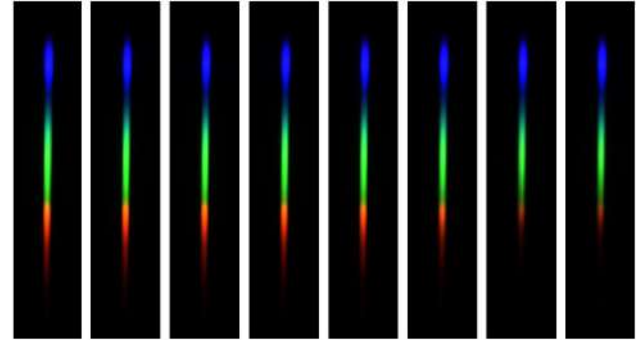
A calibrated fiber-optic spectrometer (HR2000; Ocean Optics, FL, USA) was used with a fluorescent lamp to convert each pixel index in the image into its corresponding wavelength value. The detail description of this method is given in [17] which assumes that there is a linear relationship between the wavelength value and pixel index, and extracted spectral resolution values for different size plastic fibers. A resolution of 0.26 nm per pixel is obtained using a 0.25 mm plastic fiber while larger diameter 0.5 and 1.0 mm fibers gives spectral resolutions of 0.265 nm per pixel and 0.27 nm per pixel, respectively. **Hata! Başvuru kaynağı bulunamadı.b** shows the spectrum with the 0.25 mm plastic fiber which closely resembles the spectrum of the calibrated spectrometer, even though the spectral line shapes obtained from different sized fibers show fluorescent light characteristics with 4 peaks between 400 and 700 nm. It is also noted that the spectral resolution and signal-to-noise ratio are directly related to the fiber diameter.

III. RESULTS AND DISCUSSION

We measured different concentrations of MB solution using the developed reflectance based spectrometer. A stock solution of MB dye (50 ppm) was prepared and diluted to the required initial concentrations from 10.0 ppb to 2.5 ppm.



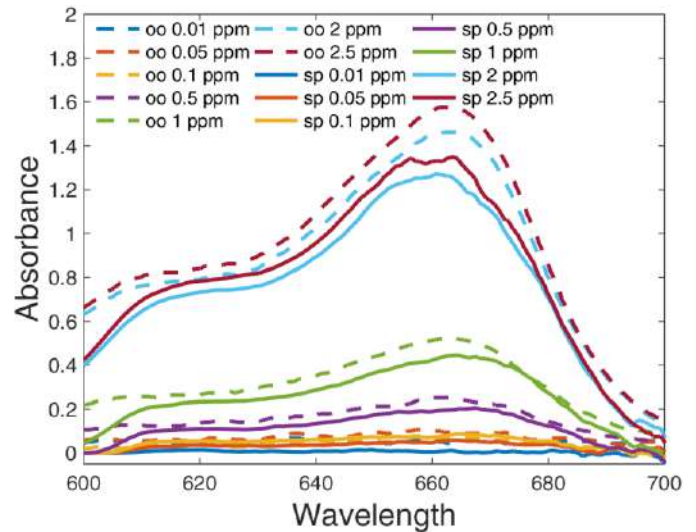
(a)



(b)

Fig. 2 (a) The photograph of MB solutions from 0.01 to 2.5 ppm. (b) The spectral images of the MB solutions.

The concentration range was designed to achieve a high dynamic range and to observe if we can reach a much smaller limit of detection. The solution color gets darker with concentration and the solutions with PPB concentration are almost transparent color (**Hata! Başvuru kaynağı bulunamadı.a**). Although the color of MB is blue, the absorption band is around 664nm, which corresponds to red spectrum. The **Hata! Başvuru kaynağı bulunamadı.b** shows the spectral images of the MB solutions. The red portion of the spectrum starts to lose intensity (8-bit pixel value) as the concentration gets bigger. The green and blue portions of the spectrum are saturated due to high intensity of light.



(a)

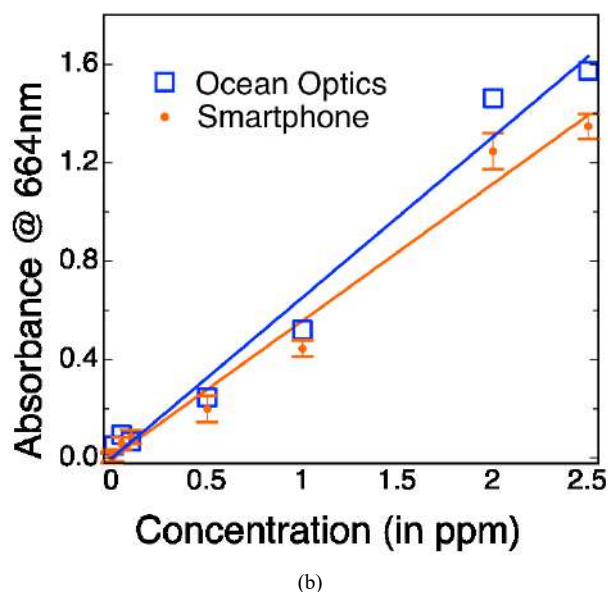


Fig. 3 (a) Absorbance spectra obtained from smartphone and commercial (b) The absorbance at 664 nm with standard deviation.

The calibrated spectrum of smartphone spectral images for MB solutions and the spectrum of commercial optical spectrometer (Ocean Optics) with reflection measurement apparatus are shown in **Hata! Başvuru kaynağı bulunamadı.a**, respectively, with solid line with abbreviation of smartphone (sp) and dashed line with “oo” abbreviation. There is a good agreement between the spectrums. It is important to note that the smartphone spectrometer dipping apparatus has an opening of 1.4cm for liquid entrance while the commercial spectrometer has 0.5cm. Hence, the values obtained from commercial spectrometer were multiplied by a value of 2.8 for all the spectrum data.

The absorbance vs. concentration plots show linear relationship for both systems and the coefficients of determination (R^2) are 0.981 and 0.978 for smartphone and commercial spectrometer, respectively (**Hata! Başvuru kaynağı bulunamadı.b**). The limit of detection (LOD) for smartphone based spectrometer is 109ppb that is 3 standard deviations above the distilled water measurement.

By increasing the optical path length by 1.4 times, we were able to reduce the LOD from ~500ppb in our previous report [12]. The sensitivity of the system was increased from 0.1817 ppm^{-1} to 0.5574 ppm^{-1} . The different slope between the commercial and smartphone spectrometer suggests that the analytes should be characterized by the same smartphone instrument.

IV. CONCLUSIONS

In this paper, we proposed a new smartphone spectrometer in the form of reflection spectroscopy integrated onto a smartphone, which is produced from plastic fiber and therefore has ultra-low cost, to examine MB dye reflection.

The reflection measurements were obtained with a custom designed cradle and the influence of fiber size on the spatial and spectral resolution is evaluated. Images were captured in RAW format to obtain more information about the measurements. With proposed system, we obtain significant reduction in the LOD which leads to an increased sensitivity for detection of dye in the water. Another contribution of our proposed system is to prove that it is not necessary to take a water sample to detect dye; instead it can be measured by simply dipping apparatus.

REFERENCES

- [1] Alver, E. and A.Ü. Metin, *Anionic dye removal from aqueous solutions using modified zeolite: Adsorption kinetics and isotherm studies*. Chemical Engineering Journal, 2012. **200**: p. 59-67
- [2] Ayad, M.M. and A.A. El-Nasr, *Adsorption of cationic dye (methylene blue) from water using polyaniline nanotubes base*. The Journal of Physical Chemistry C, 2010. **114**(34): p. 14377-14383.
- [3] Contreras-Naranjo, J.C., Q. Wei, and A. Ozcan, *Mobile Phone-Based Microscopy, Sensing, and Diagnostics*. IEEE Journal of Selected Topics in Quantum Electronics, 2016. **22**(3): p. 1-14.
- [4] Berg, B., et al., *Cellphone-based hand-held microplate reader for point-of-care testing of enzyme-linked immunosorbent assays*. ACS nano, 2015. **9**(8): p. 7857-7866.
- [5] Long, K.D., H. Yu, and B.T. Cunningham, *Smartphone instrument for portable enzyme-linked immunosorbent assays*. Biomedical optics express, 2014. **5**(11): p. 3792-3806.
- [6] Yu, H., Y. Tan, and B.T. Cunningham, *Smartphone fluorescence spectroscopy*. Analytical chemistry, 2014. **86**(17): p. 8805-8813.
- [7] Shen, L., J.A. Hagen, and I. Papautsky, *Point-of-care colorimetric detection with a smartphone*. Lab on a Chip, 2012. **12**(21): p. 4240-4243.
- [8] 8Hong, J.I. and B.-Y. Chang, *Development of the smartphone-based colorimetry for multi-analyte sensing arrays*. Lab on a Chip, 2014. **14**(10): p. 1725-1732.
- [9] Hossain, M.A., et al., *Optical fiber smartphone spectrometer*. Optics letters, 2016. **41**(10): p. 2237-2240.
- [10] Bremer, K. and B. Roth, *Fibre optic surface plasmon resonance sensor system designed for smartphones*. Optics express, 2015. **23**(13): p. 17179-17184.
- [11] Wang, Y., et al., *Smartphone spectrometer for colorimetric biosensing*. Analyst, 2016. **141**(11): p. 3233-3238.
- [12] Kocakusak, G., et al., *Smartphone-based detection of dyes in water for environmental sustainability*. Analytical Methods, 2016.
- [13] Akkaynak, D., et al., *Use of commercial off-the-shelf digital cameras for scientific data acquisition and scene-specific color calibration*. JOSA A, 2014. **31**(2): p. 312-321.
- [14] Kim, S.J., et al., *A new in-camera imaging model for color computer vision and its application*. IEEE Transactions on Pattern Analysis and Machine Intelligence, 2012. **34**(12): p. 2289-2302.
- [15] Yetisen, A.K., et al., *A smartphone algorithm with inter-phone repeatability for the analysis of colorimetric tests*. Sensors and Actuators B: Chemical, 2014. **196**: p. 156-160.
- [16] Coffin, D. *Decoding raw digital photos in Linux*. [cited 2016 1 st October]; Available from: <https://www.cybercom.net/~dcoffin/dcraw/>.
- [17] Grasse, E.K., M.H. Torcasio, and A.W. Smith, *Teaching UV-Vis Spectroscopy with a 3D-Printable Smartphone Spectrophotometer*. Journal of Chemical Education, 2015. **93**(1): p. 146-151.



Multifunctional Smart White Cane

Okan Bingöl

Department of Electrical-Electronics Engineering
Suleyman Demirel University
Isparta, Turkey
okanbingol@sdu.edu.tr

Burçin Özkaya

Department of Electrical-Electronics Engineering
Suleyman Demirel University
Isparta, Turkey
burcinozkaya@sdu.edu.tr

Onur Mahmut Pişirir

Department of Computer Technologies
Suleyman Demirel University
Isparta, Turkey
onurpisirir@sdu.edu.tr

Semih Topsakal

Department of Electrical-Electronics Engineering
Suleyman Demirel University
Isparta, Turkey
11112706044@stud.sdu.edu.tr

Abstract— The studies for the visually impaired have slightly progressed with development of technology, even so previously mentioned studies are not yet at the desired level. At the present time, visually impaired persons keep continue to use white cane. When taking into consideration of the complaints and the difficulties encountered of these persons, it is not possible to ignore that situations.

In this study, an electronic smart walking stick has been designed for visually impaired persons. Creating a structure that is for visually impaired persons make themselves feel safe via assembled components which are on the cane has been intended. With this purpose, increasing of their movement ability without being in need an additional component, determining their location and easily contact with them in required situation has been provided via microcontroller. On the whole, this mentioned walking stick has been designed as like giving a warning when detect obstacle, providing them to being noticed when the environment is getting dark, if necessary carrying out process which are calling and sending message via GSM and determining location. In consequence of these features, roaming autonomously and ensuring that they may be more adaptable to society has been intended for visually impaired persons.

Keywords—Disabled People, Visual Impairment, GPS, GSM, Arduino, RF, Walking Stick, Voice Recognition, Pulse, Obstacle Detection

I. INTRODUCTION

Finding direction and mobility is important for both children and adults in terms of changing place in their own world safely and effectively. Mobility is a big problem for people who are visually impaired. According to reports of World Health Organization(WHO), 285 million people are visually impaired and 39 million people are totally blind. Vision defect has a significant influence on life quality and the ability of working and developing individual relationships of people. Although some people make improvement for

those people to go on their daily lives, this is not enough. An obstacle may not be dangerous for everyman, but it endangers for visually impaired people. They hardly perceive ambient conditions, thus they have difficulties while moving [1], [2]. Today many blind people rely on other people, dogs or walking sticks to enter the buildings. The handicapped prefer to sort their works out independently instead of relying others [3]. As the technologies, which are used by everyone, improved, solutions, which are user centered, can be more easily found. Innovative devices become sufficient for the cases which people face around them.

According to World Health Organization, Assistive Technology (AT) is defined as product, tool, equipment, or technology to improve the life of disabled person. AT aims to help disabled people for their needs of special training and rehabilitation, cope with daily troubles and get a better quality of life [4]–[6]. At the same time, to develop devices to support the old people is really important. That provides to demand devices which expand the length of life and improve the health. [7].

Historically, walking sticks and cabinet accessories help and protect the disabled people. Walking sticks are guide to visually impaired people and thanks to them, those people can find their way easily. These rescuers also help the old people while they are walking or working. That they fall is one of the cause of physical injury. Falling causes bone fracture and brain injury [8].

In this study, it is provided that blind or old people's ability of mobility have been increased, so they can feel better while doing something without need of anyone. Also, their location can be found by competent authority in case of any injury via more than one microcontroller.

Determination of obstacle and ability of direction are carried out with various distance sensors, GSM and GPS modules, voice recognition and voice command, MP3 module, micro SD card, RF technology, LDR and LED, sensors of pulse and beat, and Ion and LiPo batteries to provide power to the system.

II. METHODS

A. Assistive Technology

In terms of assistive technology, there are various definitions. All of these definitions, the one, which is the most common, is that a tool or a piece of tool provides the disabled people to include in a society. Among traditional support techniques, there are white canes, narrators, leading strings and something like that. White canes give information about the environment, but they are not to be such as to define the obstacle which is one meter ahead of the level of underbelly. Fig. 1 shows the characteristic movement of a white cane [9].

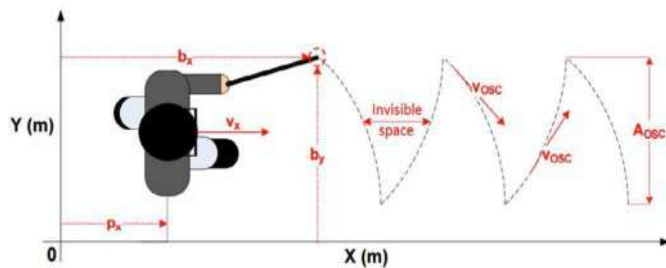


Fig. 35. The characteristic movement of a white cane [9]

Assistive technologies have the potential that they increase the quality of lives of the disabled people with secure. Also these technologies, which encourage them to go out of their normal environment and direct them to interaction with other people, decrease their fear of social isolation [2].

Assistive technology devices, which visually impaired people use to be warned, are portable electronic devices which are held and worn. Many technology devices use ultrasound techniques to measure the items in terms of their distance. Some of them use an infrared light giver or laser technology to find and warn the obstacle. These devices demonstrate some problems. The most important ones are about the interface which transmits the data of obstacle to the user. Each module of the devices should work independently [10].

B. Arduino Mega 2560

Arduino Mega 2560 is an improving card which is based on ATmega2560 microcontroller. It consists of 54 digital inputs / output pins, 4 UART 16 MHz crystal oscillator, USB connection, power jack, offline serial programming header and reset button. They can be used to improve

interactive tools, to get the inputs from the various toggles and sensors and to control other physical outputs. Table 1 shows specification of the Arduino Mega 2560 [1], [11]. Arduino Mega is shown in Fig. 2.

TABLE I. ARDUINO MEGA SPECIFICATIONS [1]

Microcontroller	Atmega2560	Analog Input Pins	16
Operating Voltage	5V	DC Current for 3.3V output	50 mA
Input Voltage	7-12V	Flash Memory	256 KB
Input Voltage (limit)	6-20V	SRAM	8 KB
Digital I/O Pins	54 (15 PWM)	EEPROM	4 KB
DC Current for Each I/O Pin	40 mA	Clock	16 MHz

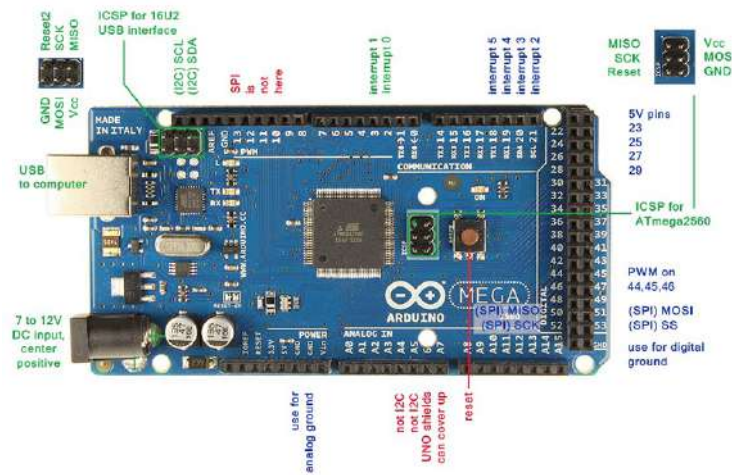


Fig. 36. Arduino Mega [12]

C. MP3 Player Shield

In the mold of MP3 Player Shield, there is VS1053B voice handler and that provides decoder for voice folders. VS1053, OGG/MP3/AAC/WMA/MIDI support the types of data and it connects to the microcontroller via SPI. The card gets 5V over Arduino and it reduces 3.3V and 1.8V with regulator and gives energy to VS1053B. On it, there is a socket of 3.5mm headphone and micro SD memory card. Track files, which are downloaded to the micro SD card, are transmitted by decoding by card. Fig. 3 shows MP3 Player Shield [12].



Fig. 37. MP3 Player Shield [12]

D. Voice Recognition Module

Voice Recognition Module is an electronic module used to control anything by using voice. In voice recognition module, 15 voice command can be recorded. Voice recognition module is connected to speaker. After the voice is recorded, the command with the voice of anybody else can not be applied. Operating voltage is between 4.5V-5.5V and operating current is lower than 40mA. Digital interface is about 5V TTL, UART is GPIO. Analog interface is 3.5mm mono channel microphone connector. Fig. 4 shows Voice Recognition Module [13].

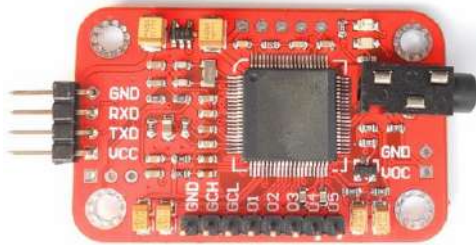


Fig. 38. MP3 Player Shield [13]

E. GSM/GPS Module

GSM is an open, digital, raster technology used to transmit voice and data. The module of GSM use the technique of TDMA [11]. The module of GGS01 GSM/GPS consists of Simcom with quad-band and SIM900 GSM module matching to RoHS and SIM28 GPS module. Fig. 5 shows GSM/GPS Module.

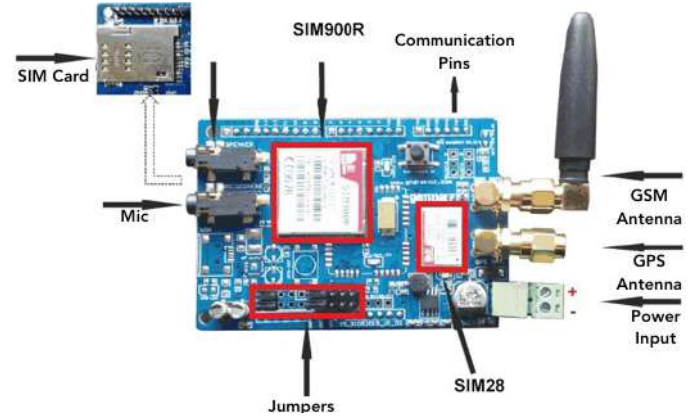


Fig. 39. GSM/GPS Module

F. E18-D80NK IR Digital Distance Sensor

It is an adjustable, distance sensor. When it perceives an obstacle, its velocity is 0V, if there isn't any obstacle, then it is 5V. Also in logic level, it can be seen as 1 or 0. Its distance can be adjusted between 3-80 cm by an adjusting button. Output current is 100Ma, and reaction time is 2ms. Fig. 6 shows sensor and working principle [14].

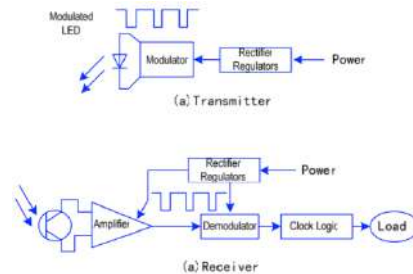


Fig. 40. E18-D80NK IR Digital Distance Sensor [14]

III. RESULTS AND DISCUSSION

The system consists of two main molds as mechanic and electronic. In the part of mechanic, there is a plastic box keeping walking stick, electronic component and equipment. In electronic part, there is LDR, LED, resistor, Arduino Mega, jumper wires, MP3 Player Shield, voice recognition module, NRF24L01 RF module, GSM/GPS module, E18-D80NK infrared digital distance, pulse sensor, LIPO and Li-Ion battery, micro SD memory card, SIM card, on/off switch, microphone and headphone, PL2303HX USB-TTL converter. To carry out software operations, computer, Access Port serial port communication program, C and C++ based software scripts, AVR-GCC compiler, Java based IDE (Arduino IDE) and RF protocol

implementation. Fig. 7 shows a blind user walking with a smart stick.

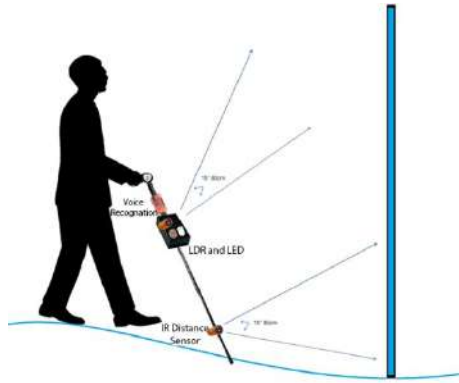


Fig. 41. Blind user walking with a smart stick.

Seven basic function such as lighting, communication, power supply, determination of obstacle and finding direction, searching, sending of SMS in optional case or in accord with the pulse data and learning location data are observed. In the study, the processing lining up below, are obtained;

-Lighting system composed of LED and LDR steps in, when the Sun sets and gives a warning in the shape of a flasher.

-The system of communication is provided with the model of NRF.

The system of power supply is provided with 7.4V 3000mAh featured Li-Ion battery and 3S 25C 1050m featured LiPo battery. The function of determination of obstacle and finding direction is perceived by IR sensor, a type of E18-D80NK, which has a definite range sensor and it is implemented to give warning with headphone via MP3 module. Searching processing is practiced via GSM module after the voice command is practiced over the voice recognition module. Sending of location SMS in optional case or in accord with the pulse data is practiced, when the obtained location data is transmitted with GSM module via GPS module after filtering the pulse sensor used or voice command is practiced over the voice recognition module. As for learning the data, it is practiced to give warning with headphone via MP3 module after the voice command is practiced over the voice recognition module. Components that used in system are shown in Fig. 8.

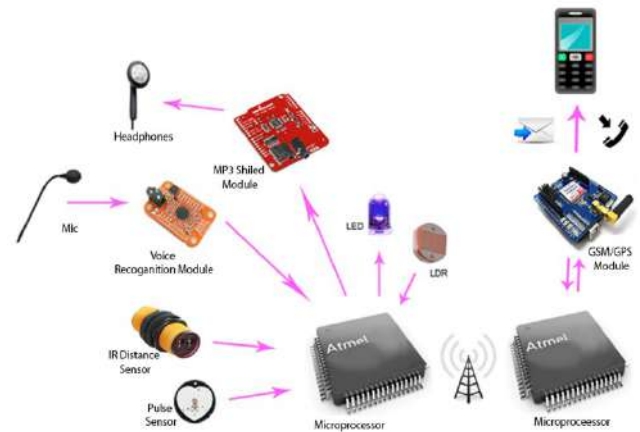


Fig. 42. System components

One of the most important characteristics of the study is that visually impaired people use the functions on walking stick by only talking under normal conditions or in any emergency case and that the notification is sent vocally. Use of sensor, which is not sensitive, remain incapable in terms of determination of direction. To prevent that visually impaired person is warned with buzzer system by being determined with the help of sensors in the system. Hence, the accidents, which is possible to occur, are stopped and those people can find their ways more easily. To reduce the conflict of wires, communication is carried out with RF communication without any wire between two Arduino in the system. Because of the fact that there is the system of voice command, no need for any control circuit. If the individuals are thought to use the mechanism in a dark place, a lighting system associated with walking stick, which is to step in, provides the individuals to be recognized by others more easily. Pulse data is used for the purpose of sending the SMS including location data to necessary people, when the pulse endangers. That there are sound control and notifications for all functions provides people convenience in terms of using the walking stick.

After the place of components (sensors, modules, electronic coponents, battery, and plastic box, etc.) has been detected, connections are made by being carried out cabling function. Figure 9 has demonstrated the walking stick, the sensors placed on walking stick, modules, electronic componenets, plastic box in which equipment is placed.

Fig. 43. Smart walking stick and components

TABLE II. ARDUINO MEGA SPECIFICATIONS [1]

1	Pulse Sensor	7	GSM Antenna
2	Voice Recognition Module	8	Arduino Mega
3	Mic	9	NRF24L01 Module
4	IR Distance Sensor	10	LDR
5	LiPo Battery	11	LED
6	GPS Antenna	12	On/Off Switch

The ability of the disabled person who is a walking stick user uses the voice command to learn, search and send the location as a message by the functions of the system. Fig. 10 shows the location notifications that system sends. Functions such as the illumination system for the awareness, the detection of the obstacles and the warning of the user, the acquisition of the pulse data (the user's finger must touch the sensor in order to be able to receive the pulse data) and an automatic location notification message is sent with an indication of the dangerous situation, work without expecting any command from the user [15].

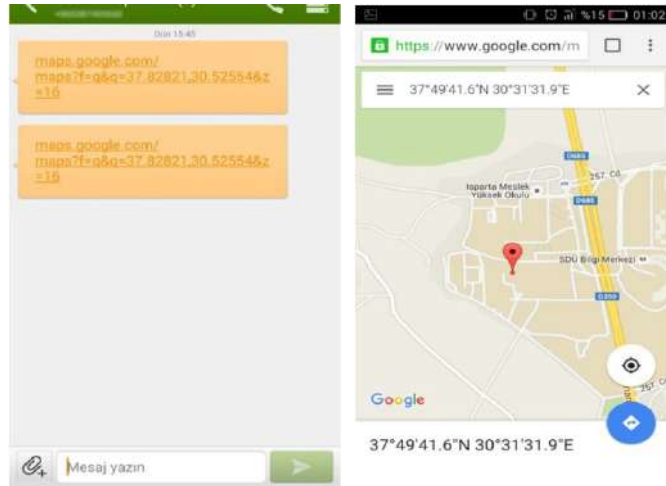
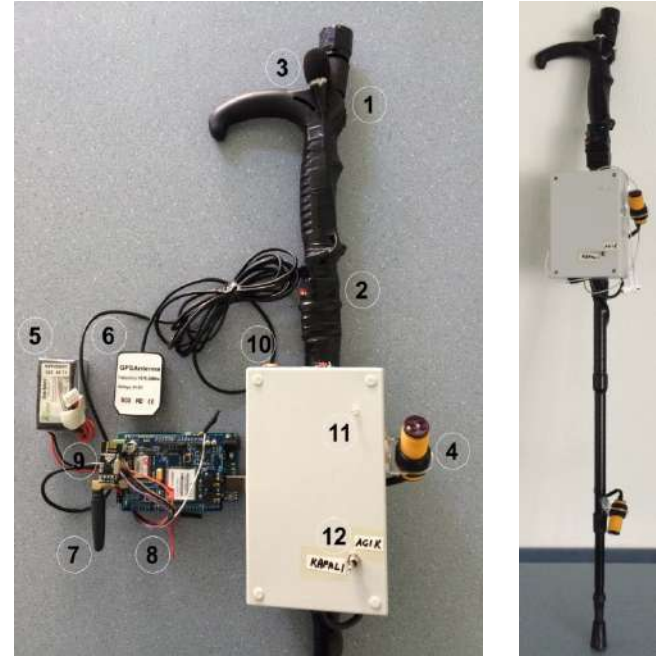


Fig. 44. Send location SMS and Google Maps screen

IV. CONCLUSION

In this study, some problems of visually impaired and elderly people are solved. It is aimed to increase the activities in business and social life of visually impaired people. Visually impaired people are provided with the ability to detect the direction through a walking stick, feel safe, be protected against any danger, find out if they can achieve their goal. It is also aimed to remind them that we have not forgotten the visually impaired people and increase the sensitivity of the society to a certain extent. Considering researchs and experiences in the next years, will increase and develop for the disabled and elderly people.

REFERENCES

- [1] N. Agarwal, A. Iyer, S. Naidu, and S. Rodrigues, "Electronic guidance system for the visually impaired - A framework," *2015 Int. Conf. Technol. Sustain. Dev.*, pp. 1–5, 2015.
- [2] L. Hakobyan, J. Lumsden, D. O'Sullivan, and H. Bartlett, "Mobile assistive technologies for the visually impaired," *Surv. Ophthalmol.*, vol. 58, no. 6, pp. 513–528, 2013.
- [3] M. A. Hussain, M. G. Ullah, A. Fareed, and B. Sohail, "The Smartcane for Blind People An Electronically Smart Stick to Aid Mobility The Smartcane for Blind People An Electronically Smart Stick to Aid Mobility," vol. 14, no. May, pp. 276–285, 2016.
- [4] G. Kbar, A. Al-Daraiseh, S. H. Mian, and M. H. Abidi, "Utilizing sensors networks to develop a smart and context-aware solution for people with disabilities at the workplace (design and implementation)," *Int. J. Distrib. Sens. Networks*, vol. 12, no. 9, 2016.
- [5] T. Ito, "Preliminary study on gesture recognition for walking-stick interface," *ISMS 2010 - UKSim/AMSS 1st Int. Conf. Intell. Syst. Model. Simul.*, pp. 65–70, 2010.
- [6] M. Leo, G. Medioni, M. Trivedi, T. Kanade, and G. M. Farinella, "Computer vision for assistive technologies," *Comput. Vis. Image Underst.*, vol. 154, pp. 1–15, 2015.
- [7] M. M. Martins, C. P. Santos, A. Frizzera-Neto, and R. Ceres, "Assistive mobility devices focusing on



- Smart Walkers: Classification and review,” *Rob. Auton. Syst.*, vol. 60, no. 4, pp. 548–562, 2012.
- [8] O. Almeida, M. Zhang, and J. C. Liu, “Dynamic fall detection and pace measurement in walking sticks,” *Proc. - 2007 Jt. Work. High Confid. Med. Devices, Software, Syst. Med. Device Plug-and-Play Interoperability, HCMDSS/MDPnP 2007*, pp. 204–206, 2007.
- [9] C. S. S. Guimares, R. V. B. Henriques, and C. E. Pereira, “Tracking System Proposal of Walking Sticks Aiming the Orientation and Mobility of the Visually Impaired,” *IFAC-PapersOnLine*, vol. 49, no. 30, pp. 161–166, 2016.
- [10] D. J. Calder, “Assistive technology interfaces for the blind,” *2009 3rd IEEE Int. Conf. Digit. Ecosyst. Technol. DEST '09*, pp. 318–323, 2009.
- [11] S. Chaurasia and K. V. N. Kavitha, “An electronic walking stick for blinds,” *2014 Int. Conf. Inf. Commun. Embed. Syst. ICICES 2014*, no. 978, pp. 1–5, 2015.
- [12] “Spark Fun Electronics,” 2017. [Online]. Available: <https://www.sparkfun.com/products/12660>. [Accessed: 20-Feb-2017].
- [13] “Elechouse,” 2017. [Online]. Available: http://www.elechouse.com/elechouse/index.php?main_page=product_info&products_id=2151. [Accessed: 20-Feb-2017].
- [14] E. Estudio, “Adjustable Infrared Sensor Switch,” 2016. [Online]. Available: <http://www.mindkits.co.nz/store/sensors/adjustable-infrared-sensor-switch>. [Accessed: 20-Feb-2016].
- [15] S. Topsakal, “Yol Arkadaşım” Bachelor Thesis, Electrical and Electronics Engineering, Faculty of Technology, Suleyman Demirel University, Isparta, 2016.



Smart Playground Lighting with Solar Energy System

Okan Bingöl

Department of Electrical-Electronics Engineering
Suleyman Demirel University
Isparta, Turkey
okanbingol@sdu.edu.tr

Burçin Özkaya

Department of Electrical-Electronics Engineering
Suleyman Demirel University
Isparta, Turkey
burcinozkaya@sdu.edu.tr

Onur Mahmut Pişirir

Department of Computer Technologies
Suleyman Demirel University
Isparta, Turkey
onurpisirir@sdu.edu.tr

Hamza Mert Dirik

Department of Electrical-Electronics Engineering
Suleyman Demirel University
Isparta, Turkey
11112706014@stud.sdu.edu.tr

Abstract— The methods which are used for the production of electrical energy contaminate our nature. Fossil energy sources (coal, oil, natural gas) thermal reactor, hydroelectric power station are commonly used and they are methods which damage our nature so eco-friendly systems should be developed and expanded for a better world. One of the eco-friendly systems which are commonly used is PV (photovoltaic) systems in recent years.

Maximum Power Point Trackers (MPPT) are used to get potential maximum power from Photovoltaic Source Energy Production Systems. Using MPPT, it is aimed to reduce minimal levels the situation of not able to take electric energy which is taken from photovoltaic panels because of load and environmental conditions. In this study, smart playground lighting which powered with solar energy was carried out. Perturb & Observe algorithm which is used to find maximum power point was used. A lighting system which works with solar energy was used to test created Photovoltaic system.

Keywords— MPPT, DC-DC Converters, Energy Efficiency, Photovoltaic Systems, LED lighting.

I. INTRODUCTION

Alternative energy sources are being searched because of the rapid depletion of fossil fuels, and they are also being searched to meet energy demand worldwide. Solar energy technologies are sustainable and clean energy which are important components of the future [1]. Solar energy has an important role to meet the growing demand for electricity with a reduced environmental impact [2]. In recent years, the use of photovoltaic power increased significantly which supports electricity network. Reduction of the cost of photovoltaic solar panels caused development of the big scaled solar energy plants which are connected to medium and high voltage electricity networks [3]. Personal interest in the

photovoltaic solar panels has risen quickly in recent years even the consumers don't abandon using energy by old traditional fossil fuels [4]. Even after obtaining energy from photovoltaic solar panels, green houses which can be combined with agricultural production has started to emerge [5].

Photovoltaic systems convert solar energy directly into electrical energy. Photovoltaic cell is the most important component of a PV system which converts solar energy into electrical energy. PV cells combine to create PV modules. Inverter, battery, electrical elements, installations elements are the most important component of PV modules. PV modules are connected each other in series and parallel configurations because of getting high power. The efficiency of solar panels depend on parameters such as internal resistance, contact patterns, the material that they produced, temperature and solar intensity changes [6]–[8]. In the world, photovoltaic panels, solar energy applications and investments are increasing. Photovoltaic energy trading and the production of photovoltaic cells are promoting [9].

In this study, smart playground lighting which powered with solar energy was done. Perturb & Observe algorithm was used to find maximum power point. The energy stored by this method has been spent using LED lighting elements in places such as parks, walkways, and bicycle paths. The brightness of these LED luminaries was adjusted according to the signal from the ultrasonic distance sensors placed on poles.

The authors acknowledges TUBITAK for the realization of this study, providing financial support within the "2209-A College Students Domestic/Abroad Research Projects Support Program".

II. METHODS

A. Photovoltaic Modules

A solar cell is a p-n junction fabricated in a thin layer of semiconductor. Electricity is being generated by converting the electromagnetic radiation of solar energy through photovoltaic effect. Being exposed to the sunlight, photons with energy greater than the band-gap energy of the semiconductor creates some electron-hole pairs proportional to the incident irradiation. The equivalent circuit of PV cell is shown in Fig. 1 [1].

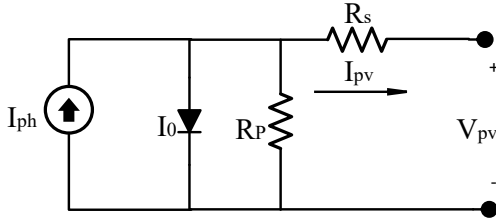


Fig. 45. The equivalent circuit of PV cell

The total output current and power equation of the parallel and series connected PV modules are expressed in equations (1) and (2) [2]. Parameters in equations (1) and (2) are explained in Table 1.

$$I_{pv} = N_p \left(I_{ph} - I_0 \left[\exp \left(\frac{q(V_{pv} + R_s I_{pv})}{N_s A k T} \right) - 1 \right] - \frac{(V_{pv} + R_s I_{pv})}{N_s R_p} \right) \quad (1)$$

In equation (1), the series resistance R_s value is extremely low and the parallel resistance R_p value is extremely high for silicon in idyllic state. Therefore, the value of R_s and R_p can be neglected and the generated power by PV is calculated with V_{pv} and the simplified I_{pv} in equation (2) [2].

$$P_{pv} = V_{pv} \times N_p \left(I_{ph} - I_0 \exp \left(\frac{q V_{pv}}{N_s A k T} \right) - \frac{V_{pv}}{N_s} \right) \quad (2)$$

TABLE I. EQUATIONS' PARAMETERS

Symbol	Explanation
I_{pv} and V_{pv}	Output current and voltage
R_s and R_p	Series and parallel resistances
N_p and N_s	Number of modules connected in parallel and series
A	P-N junction ideality factor
k	Boltzmann's constant (1.38×10^{-23} J/K)
T	Temperature in Kelvin
I_{ph}	Photon current
q	Electron charge (1.6×10^{-19} C)
I_0	Reverse saturation current

B. DC-DC Converters

DC-DC conversion technology is an important research area in the field of power electronics and has been under development for decades. DC-DC converters are commonly used in applications requiring regulated DC power such as computers, communication devices, battery chargers, switched mode power supplies, and DC machine drive applications [10]. Therewithal, DC-DC converters are being used for applications of smooth speed control of engines applications and have advantages such as high efficiency and dynamic response [11]. DC-DC converters are circuits that generally give steady output and convert DC voltage to another voltage level. DC-DC converters are being used for obtaining stabilized or changing DC voltage(s) by increasing, decreasing or multiplexing from any DC source [12].

Commonly, rectified and unregulated DC voltage obtained from line voltage is used as an input to these converters. So that step-up and step-down processes are being handled a priori as an input to these converters. Unregulated DC voltage levels are regulated by using DC-DC converters [10].

Three fundamental structures of DC-DC converter circuits are buck, boost and buck-boost converters. Other converters are developed from these three main structures [10]. In Fig. 2, DC-DC converter block diagram is shown.

In this system, buck converter was used. Buck or step-down converter regulates the average DC output voltage at a level lower than the input voltage. The circuit diagram of the buck converter is shown in Fig. 2.

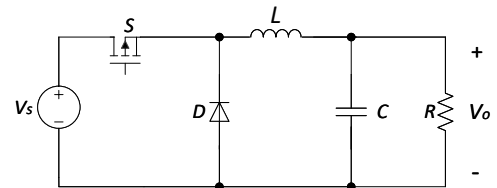


Fig. 46. Circuit diagram of buck converter

The circuit diagram of buck converter consists of a controlled switch S , a diode D , a filter inductor L , a filter capacitor C and a load resistance R . In the circuit, V_o is output voltage and V_s is input voltage [11], [12].

The relationship between the output voltage, the input voltage and the duty ratio (D) is given in equation (3).

$$V_o = V_s D \quad (3)$$

C. MPPT Algorithms

Enhancing the performance of the PV installation economically is to consider the balance of system components, particularly the power converter. Researchers developed many MPPT algorithms such as Perturb and Observe method (P&O), incremental conductance method (INC), feedback voltage or current, fuzzy logic method and neural network method. Increasing the efficiency of the MPPT algorithm makes the performance better. MPPT contains software codes that can be embedded within the power converter firmware. The MPPT automatically locates the maximum power point (MPP) that is the desired operating voltage (V_{MPP}) or current (I_{MPP}) in order to achieve the maximum output power (P_{MPP}). Most popular MPPT technique is the perturb and observe (P&O) in literature [13], [14]. The flowchart of the perturbation and observation algorithm is shown in Fig. 3 [15].

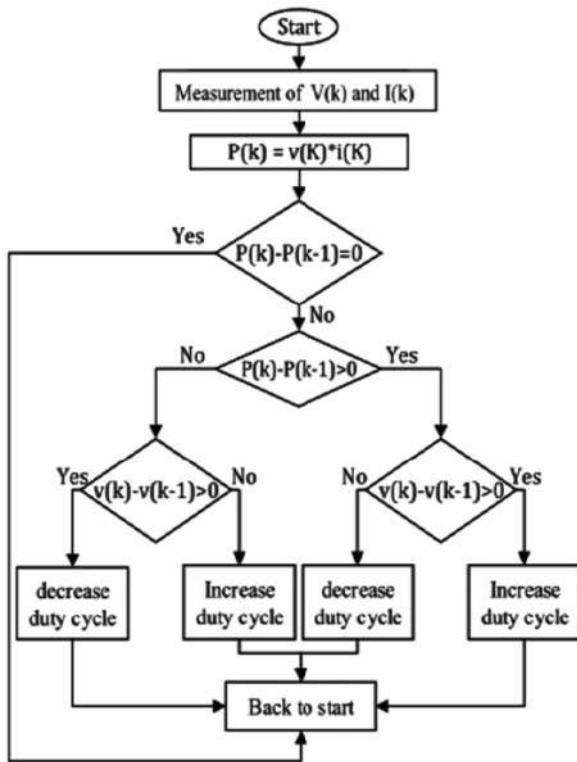


Fig. 47. P&O algorithm [15].

III. RESULTS AND DISCUSSION

DC-DC converter circuits are being used to eliminate the incoordination of the power transfer between the photovoltaic systems and the load or the battery. DC-DC converters have types of buck, boost and buck-boost. The system block diagram is shown in Fig. 4.

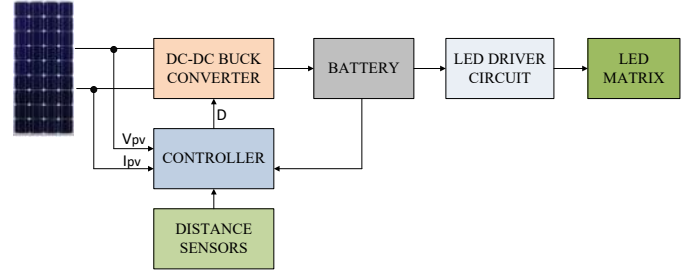


Fig. 48. System block diagram

The PWM signal required by the voltage-down converter must be low enough to reduce the effects of parasitic inductances on the load and must be high enough to provide undervoltage fluctuation without having filter elements in extreme sizes. As a result of the experiments, 50 kHz switching frequency is sufficient[16].

In addition to the main components of the DC-DC converter, there are several other elements in the circuit that allow to drive MOSFET, to measure output voltage and current. TLP 250 optocoupler is used to drive the MOSFET. The power circuit and the ground of the control card are separated at the measuring circuit so that the noise generation is prevented and in case of any short circuit, the controller is protected. Power circuit with MPPT and the battery charge circuit were implemented on the printed circuit by using at least several circuit elements. The power circuit for the system is shown in Fig. 5.

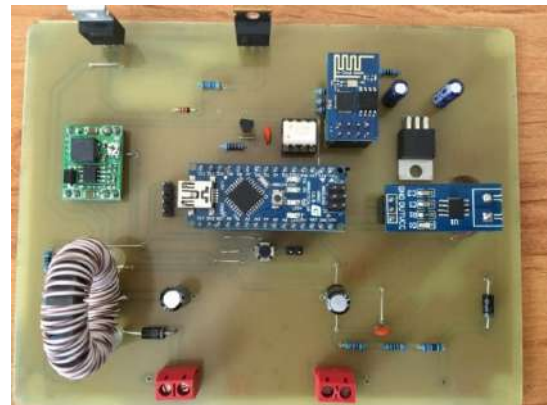


Fig. 49. Power circuit

The Arduino Nano development card with ATmega328p microprocessor, voltage and current sensors to measure voltage and current that MPPT needs for required functions, are used in this study. The voltage sensor is also used for the battery in the system. In addition, an ultra-sonic distance sensor capable of measuring up to 6.5 meters is used to measure the distance of the lighting poles [16].



Armature height connected to poles in the area that needed to be illuminated and the required amount of lighting is calculated in lighting system design.

The MPPT software calculates current power in every 20 μ s and compares it with the previous power. By adjusting the PWM signal according to the power it increases and decreases the voltage and finds the maximum power points. This software runs on Arduino.

Lighting poles were taken out at night to observe and test the operation of the designed system. It has been observed how the LED lighting system works. The amount of light flux obtained for each armature is approximately 5000 lumens(lm). The light flux will change according to the change of light brightness. LED light flux is approximately 1250lm at 25% brightness , %50 2500lm at 50% brightness and 5000lm at 100% brightness.

As coming near to the lighting pole A, the brightness of A armature will be 100% and the brightness B armature will be 50% and the lighting pole C will be at 25% brightness as the distance sensors are out of the detection range [16]. The intensity of the illuminations is shown in Fig. 6. Photographs of the running system are shown in Fig. 7 and Fig. 8.

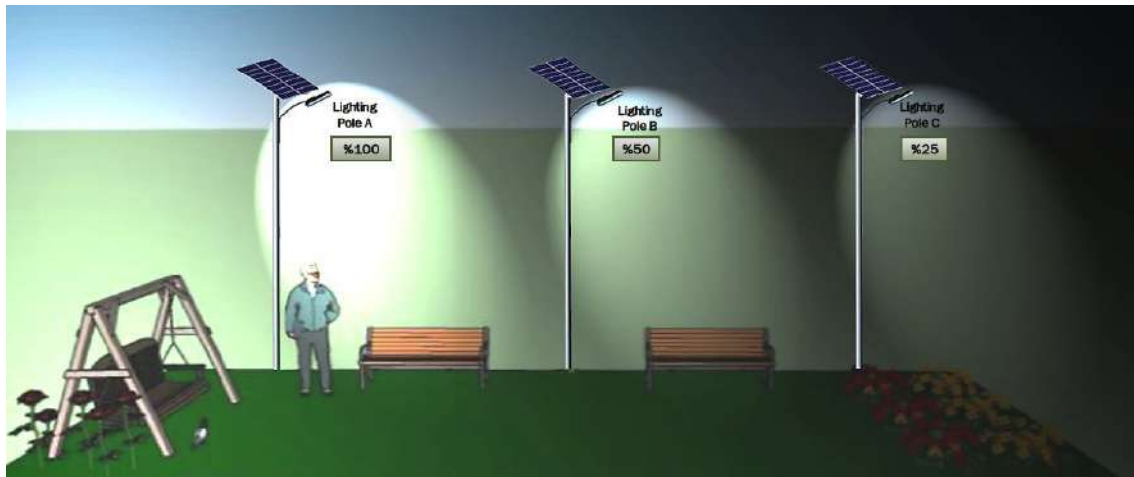


Fig. 50. Working system illustration



Fig. 51. 25% and 50% Lighting intensity



Fig. 52. 100% and 50% Lighting intensity



IV. CONCLUSION

In this study, an MPPT converter is designed and implemented for effective application of energy conversion in photovoltaic systems, and this application is used in playground lighting. Another advantage of using MPPT is increasing the lifetime of the load that connected to the system by preventing fluctuations in output voltage. The cost of using MPPT in photovoltaic systems is very low as well as the profit generated by increasing the yield and the service life of the loads. The perturb and observe (P&O) algorithm is used in this MPPT. This algorithm seems to have been used in many studies because of its simplicity.

The efficiency of the system can be increased by adding solar tracking system beside MPPT to get more efficiency than solar panels. In addition to the solar tracking system, the efficiency can be further increased by using special coatings that focus the sunlight. By using faster microcontrollers and MPPT algorithms, maximum power points can be found faster. A system can be added to the system that monitors the solar radiation and temperature and a module to estimate the maximum power points. Artificial intelligence techniques can be used by saving the power points, air temperature, panel temperature, solar radiation, etc. to find the maximum power points more quickly.

REFERENCES

- [1] Z. Wissem, K. Gueorgui, and K. Hédi, "Modeling and technical-economic optimization of an autonomous photovoltaic system," *Energy*, vol. 37, no. 1, pp. 263–272, 2012.
- [2] R. Rajesh and M. Carolin Mabel, "A comprehensive review of photovoltaic systems," *Renew. Sustain. Energy Rev.*, vol. 51, pp. 231–248, 2015.
- [3] A. Cabrera-Tobar, E. Bullich-Massagué, M. Aragüés-Peñalba, and O. Gomis-Bellmunt, "Topologies for large scale photovoltaic power plants," *Renew. Sustain. Energy Rev.*, vol. 59, pp. 309–319, 2016.
- [4] Q. Wu, X. Zhang, J. Sun, Z. Ma, and C. Zhou, "Locked post-fossil consumption of urban decentralized solar photovoltaic energy: A case study of an on-grid photovoltaic power supply community in Nanjing, China," *Appl. Energy*, vol. 172, pp. 1–11, 2016.
- [5] A. Marucci and A. Cappuccini, "Dynamic photovoltaic greenhouse: Energy efficiency in clear sky conditions," *Appl. Energy*, vol. 170, pp. 362–376, 2016.
- [6] O. Ellabban, H. Abu-Rub, and F. Blaabjerg, "Renewable energy resources: Current status, future prospects and their enabling technology," *Renew. Sustain. Energy Rev.*, vol. 39, pp. 748–764, 2014.
- [7] M. E. Şahin, H. İ. Okumuş, R. T. E. University, Electrical and Electronics Engineering, Faculty of Engineering, "Güneş Pili Modülünün Matlab / Simulink ile Modellenmesi ve Simülasyonu Modeling and Simulation of Solar Cell Module in Matlab / Simulink," pp. 17–25, 2013.
- [8] I. Kotciolu, "Clean and sustainable energy policies in Turkey," *Renew. Sustain. Energy Rev.*, vol. 15, no. 9, pp. 5111–5119, 2011.
- [9] F. Dinçer, "Overview of the photovoltaic technology status and perspective in Turkey," *Renew. Sustain. Energy Rev.*, vol. 15, no. 8, pp. 3768–3779, 2011.
- [10] K. Kayisli, S. Tuncer, and M. Poyraz, "An educational tool for fundamental DC-DC converter circuits and active power factor correction applications," *Comput. Appl. Eng. Educ.*, vol. 21, no. 1, pp. 113–134, 2013.
- [11] Ö. Ferenczi, *Power Supplies: Linear power supplies, DC-DC converters*. Elsevier, 1987.
- [12] D. Hart, *Power Electronics*. McGraw-Hill Education, 2010.
- [13] H. Bounechba, A. Bouzid, K. Nabti, and H. Benalla, "Comparison of perturb & observe and fuzzy logic in maximum power point tracker for PV systems," *Energy Procedia*, vol. 50, pp. 677–684, 2014.
- [14] J. Ahmed and Z. Salam, "An improved perturb and observe (P&O) maximum power point tracking (MPPT) algorithm for higher efficiency," *Appl. Energy*, vol. 150, pp. 97–108, 2015.
- [15] S. Messalti, A. Harrag, and A. Loukriz, "A new variable step size neural networks MPPT controller: Review, simulation and hardware implementation," *Renew. Sustain. Energy Rev.*, vol. 68, no. October 2016, pp. 221–233, 2017.
- [16] H. M. Dirik, "Smart Playground Lighting with Solar Energy System," Bachelor Thesis, Electrical and Electronics Engineering, Faculty of Technology, Suleyman Demirel University, Isparta, 2016.

PI and Fuzzy Logic Control of Photovoltaic Panel Powered Synchronous Boost Converter

Ahmet Yuksel

Dept. of Electrical and Electronics Engineering
Karadeniz Technical University
Trabzon, Turkey
ahmetyuksel@ktu.edu.tr

Adnan Cora

Dept. of Electrical and Electronics Engineering
Karadeniz Technical University
Trabzon, Turkey
cora@ktu.edu.tr

Abstract—In this paper, control of DC/DC synchronous boost converter for photovoltaic panels with different controllers is simulated in the Matlab/SIMULINK software. Firstly, synchronous boost converter is simulated, and then regarding to the changes in reference and source voltages traditional PI and Fuzzy Logic control is achieved. Results obtained are analyzed and compared.

Keywords—Synchronous; Boost Converter; PI; Fuzzy Logic; Control

I. INTRODUCTION

As the usage of electrical energy continuously increasing this also brings so many problems in together. Problems in providing fossil energy resources, environmental disasters, increasing in energy consumption, in order to stay away from nuclear energy disputes are being the reason of global disagreements and even the wars. Therefore in recent years financial losses as the result of not to providing energy demand properly, regional electricity cut-offs directed people to the renewable energy sources for their clean and reliable energy needs [1].

Approximately 20 % of the energy needs is being provided from renewable energy sources in the world, in Turkey this figure is almost in the rate of 9 % only [2-3]. Electrical energy generated from sun as one of those energy sources is usually obtained by using photovoltaic (PV) panels. While total generated energy from this type of energy was 177 GW in 2014, at the beginning of 2016 this figure reached 227 GW. As in January 2017 in Turkey, this figure has exceeded 860 MW [3]. With regard to the installed power, respectively China, Germany and Japan are the leader countries in this sector [2]. According to the load or systems energy to be provided, whether they are DC or AC, power electronic circuits differ from one to another[4-5].

In order to meet the needs of DC sources, PV systems are in need of boost, buck or buck-boost converters. According

to their circuit structures these converters increase or decrease input voltages, at the same time if they include a diode in their circuit, they are called asynchronous converter, or if they include a switch instead of the diode are called synchronous converters (Figure 1-a and -b).

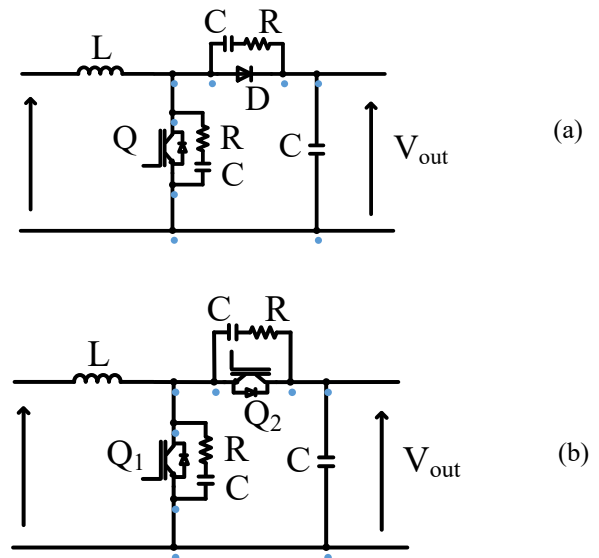


Fig. 1. (a) Asynchronous Boost Converter
(b) Synchronous Boost Converter

In the synchronous converters using a switch instead of diode, as there will not be a voltage drop in forward direction their efficiencies are higher than asynchronous converters[5,6]. Another advantage of synchronous converters output voltage is constant when it is controlled even in no load case. Output voltage in both converter types will be changed with the solar irradiance, temperature and load. In order to fix this output voltage it must be controlled. In the literature there are papers in controlling of

synchronous converter [6,7]. Beside these works, in [8] maximum power point tracking in distributed grids, cost and efficiency analysis are verified for asynchronous and synchronous converters. Efficiency of synchronous type converters reached up to 98 %.

In the controlling of converters are implemented in different ways based on current or voltage. Aims of controlling can be sequenced as maximum power transfer, reactive power control, bus voltage stability and providing load with the quality power supply[9,10]. In [11] fuzzy logic control of buck converter is done for water electrolysis. Beside this in [12], radiant control of synchronous converter is done in case of changing LEDs' status ON or OFF.

In this study, design of a PV panel powered synchronous boost converter is made and then fuzzy logic and PI control under varying source and reference voltage cases, the results obtained are compared and proper control method is proposed.

II. GENERAL DESCRIPTION OF THE SYSTEM

General block diagram of a PV panel powered converter is in Figure 2. System structure includes a PV panel, a synchronous converter, a filter and a control unit.

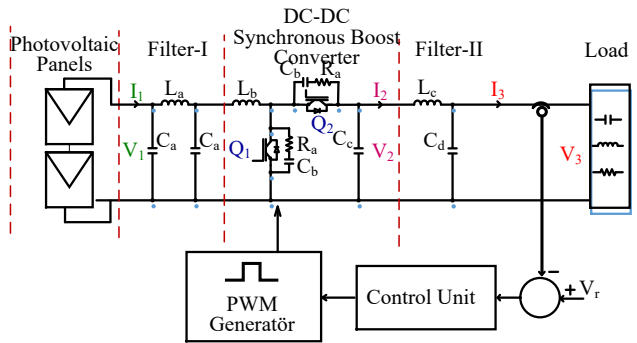


Fig.2. Systems' General Diagram

A. Synchronous Boost Converter

Synchronous boost converter transfer D.C. voltages applied to their inputs by boosting to their outputs according to duty-cycle of switches (Figure 1-b). DC voltage that is generated PV panel will be boosted by synchronous boost converter. Then filtering output filter, this voltage will supply to load

$$\frac{V_{out}}{V_{in}} = \frac{1}{1-D} \quad (1)$$

Where, V_{out} : output voltage, V_{in} : input voltage and D is the duty-cycle.

Output voltage of a synchronous boost converter is basically determined by the duty-cycle of Q_1 switch. Q_1 and Q_2 are opposite switches. When one is ON, the other is OFF. Switching frequencies are 100-1000 times higher than asynchronous converter. Despite in such high frequencies

switching causes to be smaller passive circuit components in greater power systems causes more losses. Therefore faster semiconductor materials and better switching actions are needed.

B. Controller Structure

System controlling depends on synchronous converter control. Classical PI controller and fuzzy logic controllers will be used to stabilize the voltage at the output of converter. Output voltage readings will be compared with reference voltage, the difference between those is the error. In both controllers to decrease the error to the Q_1 and Q_2 switches of converter, Pulse Width Modulation (PWM) will be produced.

$$e(k) = r(k) - y(k) \quad (2)$$

Where, $e(k)$: error signal, $r(k)$: reference signal and $y(k)$: output signal.

1) Fuzzy Logic

Fuzzy logic controller without being in need of a mathematical model adjusts the input signal according to the output signal. System variables is designed for system control. Output voltage of boost converter can be controlled by changing the duty-cycle of switch used. The error in equation (2) and the changing error in equation (3) are inputs of fuzzy logic controller

$$de(k) = e(k) - e(k-1) \quad (3)$$

Where, $de(k)$ change in error is obtained from subtracting previous value of error.

Fuzzy Logic Controller as it is seen in Figure 3 becomes combination of three parts as fuzzification, rule base and defuzzification. Input and output membership functions chosen as a triangle. Two inputs signals, five membership functions by using Positive Greater (PG), Positive Smaller (PS), Zero (Z), Negative Smaller (NS) and Negative Greater (NG).

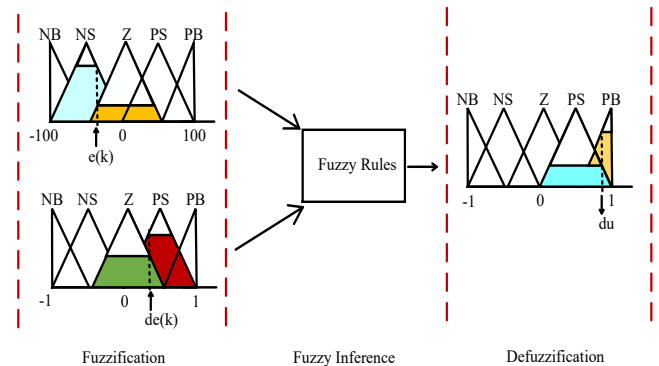


Fig.3. Fuzzy Main Diagram

After the fuzzification process, rules in Table.1 is applied to determine fuzzy memberships of equalized output signal.

Finally, by using the max-min method definite results is obtained. In order to confirm Fuzzy Logic Parameters a better control can be provided by the trial and error method.

TABLE V. RULE BASE

		de				
		NB	NS	ZZ	PS	PB
e	NB	NB	NB	NS	NS	ZZ
	NS	NB	NS	NS	ZZ	PS
	ZZ	NS	NS	ZZ	PS	PS
	PS	NS	ZZ	PS	ZZ	NS
	PB	ZZ	PS	PS	PB	PB

These definite values will be given PWM generator, and according to the duty cycle values PWM will generate two signals inverse of each other, at high frequencies that will be applied to the switches by this mean error will approach to zero.

Fuzzy Logic can be applied to different control systems with fundamental alterations, for detailed information refer to [13,14].

2) PI Controller

In the PI controller, a PI controller is designed to approach to zero the error between the output voltage and the reference voltage such as fuzzy logic controller. In figure 4, a PI controller block diagram is seen.

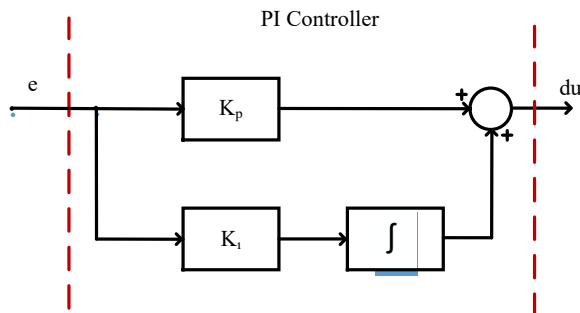


Fig.4. PI Controller Block Diagram

Output of the PI controller like fuzzy logic controller generates PWM signal according to du signal at its output, so the error becomes zero.

III. SIMULATION WORK

In this section, system simulation of a PV panel powered synchronous boost converter with DC loads is done in Matlab/SIMULINK software. Simulation works are accomplished under variable reference and source voltages. Output voltage is controlled by PI and Fuzzy Logic Controllers. Used system parameters are given in Table.II.

TABLE VI. PARAMETERS OF THE SYSTEM

Photovoltaic Panel		Synchronous Boost Converter	
V _{open-circuit}	37.6 V	L _b	2.55 uH
I _{short-circuit}	8.55 A	R _a	33 Ohm
N _{serial}	1	C _b	300 pF
N _{parallel}	2	C _c	1 mF
T _{ambient}	25 °C	f _s	100 kHz
S _{ambient}	1000W/m ²		
Filter-I		Filter-II	
L _a	16.2 uH	L _c	0.338 uH
C _a	33 uF	C _d	10 mF
Load			
P	0.5kW		

Control results of a PV powered high frequency switching synchronous boost converters' PI and Fuzzy Logic controls are shown in Figure 5 and 6 respectively. In the case of synchronous boost converter output voltage changes with a defined reference voltage and changing of source voltage with the light intensity. Therefore indirectly changing in the source voltage, output voltage did not change are shown. In Figure 6 similar situations for Fuzzy Logic controller are valid.

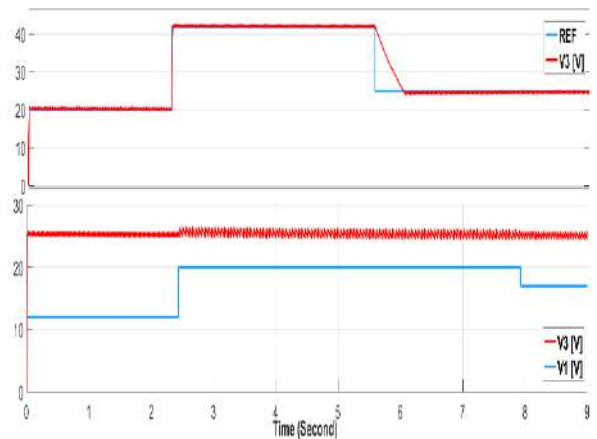


Fig.5. PI Control Results of the System

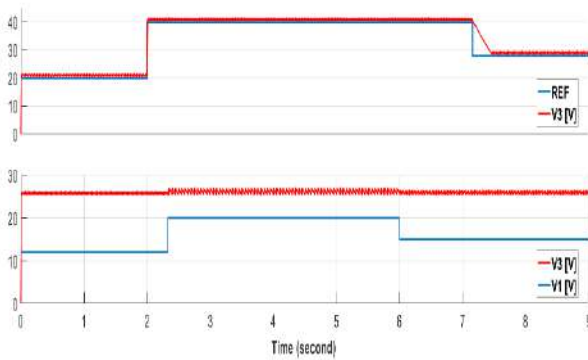


Fig.6. Results of Fuzzy Logic Control of the System

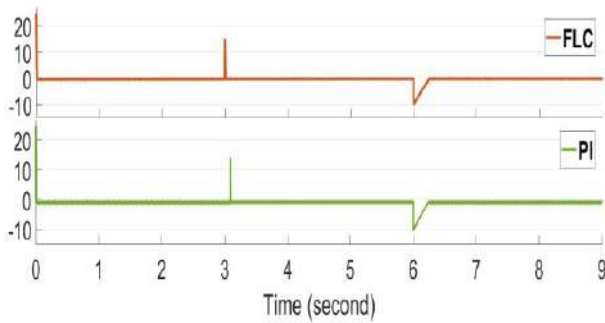


Fig.7. the Change of the Error in Variable Reference Voltage for Both Controller

Where, V1: PV output voltage, V3: Synchronous boost converter output voltage, REF: Reference Voltage. FLC: Fuzzy Logic Controller

IV. RESULTS

In this study, output voltage of a PV panel powered synchronous boost converter PI and Fuzzy logic control is done. In the simulation work, in case of changing in source voltage and reference voltage, PI and Fuzzy Logic control of output voltage show that it is precisely stabilized. When Fuzzy Logic controller gives faster response to the changings in reference voltage, lesser overshoot rate with respect to PI controller are observed. Both control methods give faster response to any increases in reference voltage but in case of any decrease in reference voltage both methods give slow response. In accordance with these results it is observed that fuzzy logic control is better than PI control.

Because of the developments in power electronics in recent years when switches working at high frequencies will

be commercially available, it is expected that usage of high power synchronous converters will increase, also their efficiencies are higher.

REFERENCES

- [1] Tsengenes G. and Adamidis G., "Investigation of The Behavior of a Three phase Grid-Connected Photovoltaic System to control active and Reactive Power", *Electric Power Systems Research*, Vol. 81, pp. 177-184, 2011.
- [2] *Renewables 2016: Global Status Report*, REN21, 2016, ISBN 978-3-9815934-7-1-4.
- [3] Carrasco J. M et al., "Power-Electronic Systems for the Grid Integration of Renewable Energy Sources: A Survey", *IEEE Transactions on Industrial Electronics*, Vol. 53, No. 4, pp. 1002-1016, June 2006.
- [4] Li Q. and Wolfs P., "A Review of the Single Phase Photovoltaic Module Integrated Converter Topologies with Three Different DC Link Configurations", *IEEE Transactions on Power Electronics*, Vol. 23, No. 3, pp. 1320-1333, May 2008.
- [5] Bansal, Sudha, Lalit Mohan Saini, and Dheeraj Joshi. "Design of a DC-DC converter for photovoltaic solar system." *Power Electronics (IICPE), 2012 IEEE 5th India International Conference on*. IEEE, 2012.
- [6] C. G. Wilson, J. Y. Hung and R. N. Dean, "A sliding mode controller two-phase synchronous buck converters," *IECON 2012 - 38th Annual Conference on IEEE Industrial Electronics Society*, Montreal, QC, 2012, pp. 2150-2155.
- [7] Y. Yuan, Y. Lv and G. Tong, "Study on the digitally controlled system of ZCS-QRC synchronous buck converter," *Control Conference (CCC), 2011 30th Chinese*, Yantai, 2011, pp. 4486-4491.
- [8] Graditi, G., et al. "Comparative analysis of synchronous rectification boost and diode rectification boost converter for DMPPT applications." *Industrial Electronics (ISIE), 2011 IEEE International Symposium on*. IEEE, 2011.
- [9] Yu W., Lai J. S. J., Qian H. and Hutchens C., "High-Efficiency MOSFET Inverter with H6-Type Configuration for Photovoltaic Nonisolated AC-Module Applications", *IEEE Transactions on Power Electronics*, Vol. 26, No. 4, pp. 1253-1260, April 2011
- [10] Altas, Ismail H., Ozkop E, Adel M. Sharaf. "A Novel PV-Powered Standalone Village Electricity Utilization Fuzzy Logic Dynamic Controller Strategy." *INISTA 2009* 5: 47.
- [11] Sahin, Mustafa Ergin, and Halil Ibrahim Okumus. "Fuzzy logic controlled parallel connected synchronous buck DC-DC converter for water electrolysis." *IETE Journal of Research* 59.3 (2013): 280-288.
- [12] Pirci Baris, Bilgin M. Zeki, Erfidan Tank " Seri Bağlı Led Armatürlerin Senkron DC-DC Dönüştürücü Kullanarak Işık Şiddeti Kontrolü ", *Elektrik - Elektronik ve Biyomedikal Mühendisliği Konferansı(ELECO2014)*, BURSA, TÜRKİYE, 27-29 Kasım 2014, ss.288-292
- [13] Altas, I. H., and A. M. Sharaf. "A novel maximum power fuzzy logic controller for photovoltaic solar energy systems." *Renewable Energy* 33.3 (2008): 388-399.
- [14] Altas, Ismail H., and Adel M. Sharaf. "A generalized direct approach for designing fuzzy logic controllers in Matlab/Simulink GUI environment." *International journal of information technology and intelligent computing* 1.4 (2007): 1

Smart Eyes for Monitoring and Analysis of Human Interactions in Smart Cities

Orhan Yaman, Mehmet Karakose
Firat University, Department of Computer Engineering
Elazig, Turkey
{orhanyaman, mkarakose}@firat.edu.tr

Abstract— Developments in technology are changing the whole area of life. They have led to some changes also in city life and changed people's lives. The concept of smart city has emerged along with the use of developing technological products in city life. In smart cities, applications that will facilitate people's lives in many areas such as transportation and energy consumption have been developed. In recent years, it has become even more difficult to live in cities along with the migrations to large cities. Many conveniences have been provided in many areas such as transportation and energy consumption along with smart city applications. In this study, a vision-based method was proposed to facilitate transportation in large cities. It is aimed to plan public transportation vehicles according to the intensity of use of them by people. The numbers of using public transportation vehicles by people will be observed using cameras. A vision-based method is proposed for the planning of the numbers of service by taking into account the bus stations where there is a great number of people using public transportation vehicles, and the intensity hours. Thus, the transportation of people using public transportation vehicles will be carried out in a more controlled way. With this method, it is aimed to reduce the time people spend in transportation.

Keywords— *computer vision; image processing; smart city; smart cameras; smart devices.*

I. INTRODUCTION

Transportation in smart cities is associated with the buses, rail systems, traffic systems, cameras, traffic lights, road information systems, traffic signal optimization systems, electronic communication systems and car navigation systems that are used in the city's public transportation systems [1-2].

Smart cities should have integrated systems that provide infrastructure and transportation convenience, protect energy, increase water and air quality, quickly identify the problems and provide solutions [3-4]. The purpose of a smart city, in a sense, is to ensure that the systems that can produce effective projects work in an integrated structure by taking into account the city's demands and resources. In this process, infrastructural issues such as transportation infrastructure systems, water resources viewers, energy saving buildings are the key issues in which city

managements invest. Applications are performed in basic study areas needed for smart city management and liveable cities. Issues like transportation, energy, water and security are addressed as smart city solutions.

Traffic problems arise in cities along with transportation, today's increasing population and increasing number of cars. Due to the lack of existing transportation structure, the time of people's daily basic journeys increases and this negatively affects the quality of life. Besides, transportation expenses and environmental pollution are also increasing. It is aimed to facilitate people's transportation by developing many applications for transportation in smart cities.

Luca et al. [1] carried out a study by establishing a smart camera network to monitor traffic in cities. The density of traffic was determined by placing cameras on the electricity lines in the city. Mustafa [2], in his master's thesis study, developed a public transportation information system for transportation in Istanbul. The data kept in public transportation institutions were combined in a standard format and on a common platform and made accessible to mobile devices. The developed method was written as an android application. In the application, users get the most appropriate directions by choosing the location information of the places they want to go and the type of transportation. In addition, the developed application contains information such as times of services of transportation vehicles. It also contains information about station locations of transportation vehicles.

Narol [4] developed an application for public transportation vehicles using NFC technology. In the study, a business model was proposed for a safe and practical ticketing system by giving examples from the projects where NFC technology was used.

Saglam [5], in his thesis study, developed positional decision support tools for transportation services in smart city management. Within the scope of the thesis, the legislative analysis was performed for the city information system and the relevant responsibilities were examined. Maria et al. [6] proposed drone-based image processing system for vehicle identification in smart transportation infrastructure. The aim is to provide useful information automatically, such as available parking spaces and level of

vehicle intensity on the street. The system was tested both on a desktop computer and on an embedded system. A cascade classification was used in the vehicle identification method. The block diagram of the system architecture is presented in Figure 1.

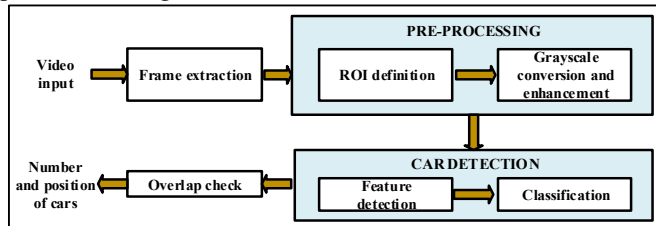


Figure 1. Block diagram of the system architecture [6]

Robin et al. [7] developed a smart parking system, which is a parking occupancy monitoring and imaging system, for smart cities. A prototype for smart parking system using wireless sensor technology and networks is presented in this study. By using a wireless Sensor network, full or available space in the parking space are determined and transmitted to a database. Then, this information is reached by the users through the website or mobile application to get real-time updates. Along with the successful implementation of smart parking, economic and time costs associated with traffic congestion and the costs associated with wasted fuel are decreased. In addition, the time elapsed to search for free parking space will significantly be reduced. A general system model for the smart parking system is presented in Figure 2.

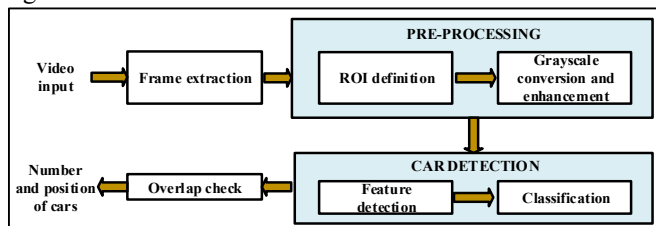


Figure 2. A general system model for the smart parking system [7]

Energy sources have become a symbol of power for countries at the present time. The emission rate of toxic gases is also very high in cities with high energy consumption over the world. Today, it is known that half of the world's population lives in cities. This rate is expected to increase further within the next years [8]. Smart methods are developed to carry out energy consumption in a planned way.

Kiral [9], in his thesis study, developed a smart power socket for energy management in smart networks. A wireless sensor network was created using wireless communication devices. The existing power sockets in the house are remotely controlled. All power sockets are monitored and controlled by the central unit used. In this

study, it is aimed to ensure the efficient and economic use of energy by taking into account the consumers' demands.

Nowadays, water resources are one of the most important life sources for people. Water consumption is increasing rapidly along with the increase in population. Drinking water and wastewater infrastructures are not only insufficient in cities but also cause energy consumption. Water transportation and recycling should be performed using environmentally friendly systems. Studies have been carried out for the efficient use of water in recent years. These studies have become a part of smart cities.

Celik [10], in his thesis study, carried out a study for the modeling of e-management process in the water management administrations of smart cities. In this thesis study, general information about e-applications in water and sewage administrations in Turkey has been given in smart city managements. Studies that would speed up the citizens' transactions were proposed in the light of the existing e-applications that Istanbul water and sewerage administrations have.

First aid and security services are very important concepts for a smart city. First aid services should work concurrently with infrastructure services to be carried out effectively. Today, the increasing population problems as well as the crime scene response services are also affected. Therefore, databases with a dynamic infrastructure and transportation vehicles supported by decision-making tools should be used. More rapid intervention can be performed by using geographical information systems based products in crime scene response. In addition, cameras can also be used in follow-up and investigations. Tokta [11], in his thesis study, developed abnormal situation detection in the crowds through security systems. People's movements were monitored using image processing methods in cameras placed in crowded environments. The abnormal situation detection was performed by taking into account the behaviors of the people identified. In this thesis study, algorithms were developed using optical flow and effect map approach.

In this study, human detection is performed using image processing based methods. The arrangement of service plans is ensured by taking into account the density of people using public transportation vehicles, the hours of use and the locations of stations. It is aimed that the people using public transportation vehicles will be able to travel more easily.

II. DATA SHARING AND MANAGEMENT IN SMART CITIES

A lot of information about our daily life can be reached by means of the information technology that has further increased in recent years. For instance, satellite images and aerial photographs can be obtained and can be used in smart city applications. Nowadays, dynamic vehicle tracking can be performed by GPS systems in vehicles and on the phones thanks to geographic information systems and satellites. The lives of people are made easier with the applications such as

driving directions as well as vehicle tracking. In particular, directions are given by taking into account traffic density with the applications developed on mobile phones.

Millions of data are gathered in a single center using sensors, and real-time traffic, temperature and moisture data are obtained and used in smart city managements. In recent years, there have been developments within the scope of transforming the data obtained using many sensors into open data serving the public. While data production and management studies are carried out in cooperation with the private sector, studies are carried out for the development of internet based software providing open services to the public with these data. The private sector provides information about services to cities, traffic and navigation directly to the users with dynamic data as in official institutions. In applications provided to people, location-based information sharing can be performed through cloud-based systems where users are stakeholders. The relationship between data management and sharing in smart cities is presented in Figure 3.

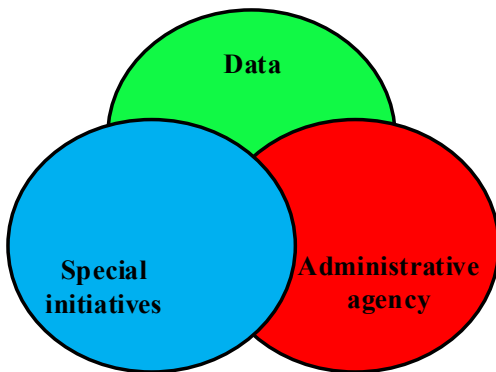


Figure 3. Data management in smart cities [5]

The management and sharing of data obtained for smart cities is very important in terms of data accuracy. Nowadays, numerical data of almost every place in daily life are obtained using many sensors. Many network structures are used to store the obtained data in specific centers. Information obtained from the sensors are transmitted to base stations using wireless modules or to certain data centers via internet line. A sample wireless configuration developed for a smart city is presented in Figure 4.

III. THE PROPOSED APPROACH

It is aimed to implement the method proposed in this study in many public transportation vehicles. Timetable planning can be made by placing the structure developed for the proposed method in the desired public transportation vehicles. Camera and GPS sensor are used to obtain the necessary information. The cameras are placed on the doors of public transportation vehicles and images are received. The placement of the cameras in a sample public transportation vehicle is presented in Figure 5.

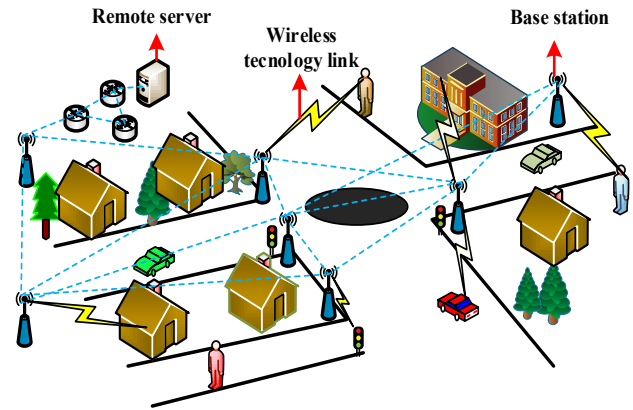


Figure 4. Smart wireless systems [5]

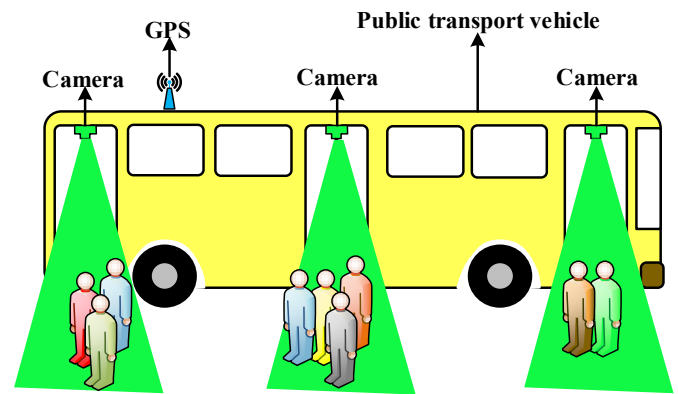


Figure 5. Placement of the cameras in a sample public transportation vehicle

The placement of cameras in a bus is presented in Figure 5. Transportation vehicles for the proposed method are not different. The same system can also be used in public transportation vehicles such as metrobus, tramway and metro. Human detection is performed by using image processing methods on the images received from the cameras. Today, image processing methods are used in almost everywhere [12-21]. An optimization was made by taking into account the number of passengers getting on and getting off public transportation vehicles and the locations of public transportation vehicles. The general architecture of the proposed method is presented in Figure 6.

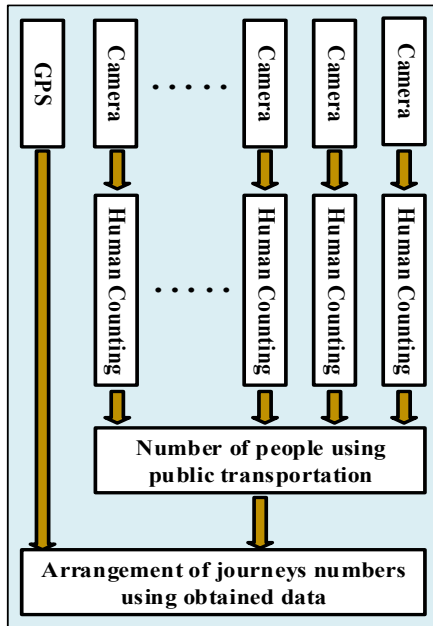


Figure 6. General architecture of the proposed method

According to the architecture in Figure 6, cameras are placed on all the doors of the public transportation vehicle. The cameras placed are connected to an embedded system. The images received from the cameras are used for human detection with algorithms developed on the embedded system. The flow chart of the proposed algorithm for human detection and counting is presented in Figure 7.

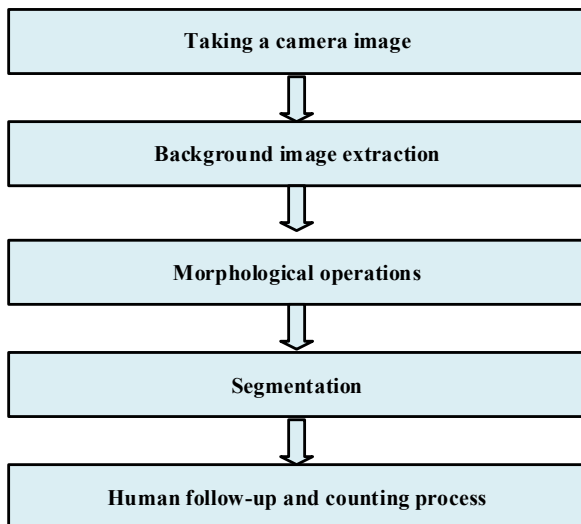


Figure 7. Flow chart of the algorithm proposed for human detection and counting

After the human detection process, it calculates the number of people who get on and get off transportation vehicles by monitoring people's movements. The number of people at all doors is combined on a single module. The

obtained data are combined with the position information received from the GPS device and transmitted to the data collection center. The data collected from public transportation vehicles throughout the day are analyzed using an optimization method. As a result of the analyses, arrangements can be made on the timetable by detecting the hours of intensity in the bus stations. Thus, people using public transportation vehicles will be able to travel faster.

In this study, a sample test data was created to clarify the proposed method. In the sample test data created, the numbers of people who get on and get off a public transportation vehicle going from 1st to the 10th stop are presented in Table 1.

When the test data presented in Table 1 are examined, there were greater numbers of passengers especially between the 1st and 4th stop in the services performed at 07:00, 08:00 and 09:00. It can be concluded that the passengers waited for the public transportation vehicle for more hours. When the numbers of passengers are taken into account, 50 passengers, 66 passengers, 115 passengers and 81 passengers used this vehicle in the services at 06:00, 07:00, 08:00 and 09:00, respectively.

As it can be understood from the numbers of passengers, the number of passengers is quite high in the services at 07:00 and 08:00. In this case, the problem can be solved in the case of increasing the number of services at 07:30 and 8:30 or it is possible to plan different public transportation lines that pass by 1st and 4th stops.

IV. CONCLUSIONS

In this study, a method was proposed for the smart transportation system, which is the most important part of smart cities. In the proposed method, the use of cameras and GPS modules was planned and the number of passengers carried by public transportation vehicles and the information that passengers get on and get off was obtained. The numbers of services or hours of public transportation vehicles can be rearranged by using these data obtained. Image processing methods were used to detect passengers who get on and get off public transportation vehicles. Many applications can be developed for smart cities by using these methods. People at certain points can be counted using cameras. Traffic intensity can be calculated by counting the vehicles in the traffic. The quality of life of people can be increased by using image processing methods in many similar applications. Cameras are indispensable devices for people. Effective applications can be developed for smart cities using cameras and image processing methods.

Table 1. Sample test data used in the study

	Number of passengers descending and arriving via public transportation from 1st stop to 10th stop (Getting on: Getting off)									
	1	2	3	4	5	6	7	8	9	10
06:00	9:0	7:0	6:2	3:4	11:6	7:7	5:4	1:10	1:3	0:14
07:00	19:0	21:1	11:7	6:3	3:3	2:6	1:9	3:7	0:8	0:22
08:00	17:0	34:3	9:4	11:7	9:6	19:9	8:13	6:5	1:29	0:38
09:00	16:0	22:5	16:3	17:3	1:22	3:9	1:15	3:8	2:5	0:11
10:00	9:0	10:3	9:4	6:7	8:5	3:8	1:2	4:10	0:7	0:4
11:00	3:0	11:3	8:5	7:7	4:9	12:7	2:4	1:8	6:8	0:3
12:00	8:0	10:3	9:6	9:7	8:0	7:9	6:8	4:7	1:6	0:16
13:00	7:0	3:8	11:7	9:9	7:8	5:7	6:1	3:4	2:7	0:1
14:00	5:0	4:8	13:6	6:4	7:7	4:9	8:5	7:7	1:9	0:0
15:00	9:0	9:8	11:4	7:9	6:8	4:7	8:5	3:8	1:2	0:9
16:00	4:0	11:1	10:7	5:7	6:1	3:4	9:4	6:16	8:5	0:17
17:00	5:0	4:7	11:7	9:6	1:2	4:10	8:5	7:7	4:9	0:0
18:00	8:0	8:8	17:3	1:22	12:4	1:8	9:6	9:7	2:1	0:8
19:00	3:0	7:4	6:7	8:5	9:4	6:7	11:7	9:9	7:8	0:15
20:00	6:0	6:3	7:7	4:9	8:5	7:7	4:9	12:7	9:7	0:9
21:00	2:0	13:5	9:7	8:0	9:6	9:7	8:10	1:9	5:9	0:11
22:00	1:0	4:1	9:9	7:9	6:8	14:7	7:8	5:7	6:4	0:6
23:00	0:0	7:4	5:2	5:7	6:1	3:4	11:6	7:7	5:4	0:14

REFERENCES

- [1] Calderoni, L., Maio, D., Rovis, S., 2014 "Deploying a network of smart cameras for traffic monitoring on a "city kernel", Expert Systems with Applications, vol. 41(2), pp. 502-507.
- [2] Özcan, M., 2013 "A model of Android application: Istanbul public transportation information system," Computer Engineering and Computer Science and Control, pp 97.
- [3] Moss, R.M., Litow, S.S., 2009. "Manifesto for Smarter Cities," Harvard Business School Working Paper 09-141.
- [4] Narol, T., 2014 "NFC teknolojisinin toplu ulaşımında uygulanması", Yıldız Teknik Üniversitesi, Fen bilimleri enstitüsü, bilgisayar mühendisliği anabilim dalı, pp. 80.
- [5] Sağlam, D., 2014 "Developing spatial decision support tools regarding transportation services in smart city management: Istanbul case," İstanbul Teknik Üniversitesi, bilişim enstitüsü, bilişim uygulamaları anabilim dalı, Coğrafi bilgi teknolojileri bilim dalı, pp. 125.
- [6] Maria, G., Baccaglini, E., Brevi, D., Gavelli, M., Scopigno, R., 2016 "A drone-based image processing system for car detection in a smart transport infrastructure", In Electrotechnical Conference (MELECON), 2016 18th Mediterranean, pp. 1-5.
- [7] Grodi, R., Rawat, D.B., Rios-Gutierrez, F., 2016 "Smart parking: Parking occupancy monitoring and visualization system for smart cities", In SoutheastCon, pp. 1-5.
- [8] Provoost, R., "Smart cities: innovation in energy will drive sustainable cities," Guardian Sustainable Business Blog.
- [9] Kırıl, G.E., 2014 "Development of smart plug for energy management system in smart grid" Yıldız Teknik Üniversitesi, Fen Bilimleri Enstitüsü, Elektrik Mühendisliği Anabilim Dalı, Elektrik Tesisleri Bilim Dalı, pp. 83.
- [10] Celik, V., 2016 "Modelling of e-application process at the water management" İstanbul Sabahattin Zaim Üniversitesi, Fen Bilimleri Enstitüsü Mimarlık Anabilim Dalı, Kent Çalışmaları ve Yönetimi Bilim Dalı, pp. 147.
- [11] Tokta, A., 2016 "Abnormal behavior detection in surveillance systems" Gebze Teknik Üniversitesi, Fen Bilimleri Enstitüsü, Elektronik Mühendisliği Anabilim Dalı, pp.73.
- [12] Yaman, O., Karakose, M., Akin, E., 2016 "PSO Based Diagnosis Approach for Surface and Components Faults in Railways," International Journal of Computer Science and Software Engineering (IJCSSE), 5(5), pp. 89-96.
- [13] Suranjan, G., Bhattacharjee, D., Nasipuri, M., 2016 "Fuzzy matching of edge and curvature based features from range images for 3D face recognition," Intelligent Automation & Soft Computing pp. 1-12.
- [14] Wang, K., Zhao, Y., Xiong, Q., Shen, X., Fan, M., Gao, M., 2016 "Video Recognition of Human Fall Based on Spatiotemporal Features," Intelligent Automation & Soft Computing, vol. 22(2), pp. 303-309.
- [15] Baygin, M., Karakose, M., 2015 "A new image stitching approach for resolution enhancement in camera arrays," IEEE 9th International Conference on Electrical and Electronics Engineering (ELECO), pp. 1186-1190.
- [16] Smereka, M., Duleba, I., 2008 "Circular Object Detection Using a Modified Hough Transform," Applied Mathematics and Computer Science, vol. 18(1), pp. 85-91.
- [17] Karakose, M., 2013 "Reinforcement learning based artificial immune classifier," The Scientific World Journal, pp. 1-7.
- [18] Tastimur, C., Karaköse, M., Celik, Y., Akin, E., 2016 "Image processing based traffic sign detection and recognition with fuzzy integral," International Conference on Systems, Signals and Image Processing (IWSSIP), pp. 1-4.
- [19] Yetis, H., Baygin, M., Karakose, M., 2016 "An investigation for benefits of cyber-physical systems in higher education courses," 15th International Conference on Information Technology Based Higher Education and Training (ITHET), pp. 1-5.
- [20] Karakose, M., Yaman, O., Baygin, M., Murat, K., Akin, E., 2017 "A New Computer Vision Based Method for Rail Track Detection and Fault Diagnosis in Railways," International Journal of Mechanical Engineering and Robotics Research vol. 6(1), pp. 22-27, (doi: 10.18178/ijmerr.6.1.22-27).
- [21] Karhan, M., Oktay, M. O., Karhan, Z., Demir, H., 2011 "Morfolojik Görüntü İşleme Yöntemleri ile Kayısılarda Yaprak Delen Hastalığı Sonucu Oluşan Lekelerin Tespiti," In 6 th International Advanced Technologies Symposium, pp. 172-176.

FPGA implementation of a chaotic Quadratic map for cryptographic applications

Hidayet Oğraş

Batman University, Technical Education Faculty
Batman, Turkey
hidayet.ogras@batman.edu.tr

Mustafa Türk

Firat University, Engineering Faculty
Elazığ, Turkey
mturk@firat.edu.tr

Abstract— A hardware implementation of a quadratic map through FPGA platform is proposed in this paper. Firstly, a chaotic quadratic map is modeled by using Matlab/Simulink programming and then implemented into the FPGA (Field Programmable Gate Array) to be used for key generation for cryptographic applications. When the quadratic map is in chaotic mode, its output is unpredictable and aperiodic. Besides this, the map has a uniform output distribution and sufficient randomness. These characteristics make the chaotic quadratic map a suitable key generator for cryptography. This paper also reveals the successful real-time implementation of the quadratic map using FPGA for practical applications. Experimental results confirm that the feasibility of the quadratic map is verified under a digital hardware environment.

Keywords— chaos; quadratic map; implementation; FPGA

I. INTRODUCTION

Chaos theory in complex systems has been cited increasingly in several different scientific areas especially in engineering science such as secure communication and cryptography. For example, chaos is used for analog and digital communication systems in [1-6]; for image cryptosystems in [7-12] and is applied in electrical power systems in [13-16]. Chaotic systems have similar properties such as sensitivity to initial conditions and control parameters, pseudo-random behavior and mixing with modern cryptography. These fundamentals characteristics can make the chaotic systems a good candidate for the key generation in data encryption algorithms. Many cryptosystems based on the generation of pseudo-random sequences using chaos have been proposed recently for mixing clear messages in information security [17].

Chaos generation in discrete time systems is very easy and simple due to the low complexity, but having high efficiency comparing with analog chaos generators [18]. In fact,

analogue chaotic systems typically exhibit some practical difficulties since the component conditions are varying with age, temperature, etc. Furthermore, analog circuit implementations generally require a large chip area for realization. Hence, hardware implementations of the discrete chaotic systems can be a solution to overcome these problems. Many digital realizations of chaotic systems have been reported to be used as key generators in cryptographic applications. For instance, in [19], Henon map as a chaotic generator is implemented in real-time on a FPGA to obtain high frequency at output for chaotic communication. In other study [20], a chaotic map is used as a bit generator and its FPGA implementation is performed successfully for cryptographic applications. Generally, chaotic system is used to generate pseudo-random sequences as key streams to mask information. Key streams should be generated randomly and contain enough entropy in order to prevent the key from being guessed. Key sensitivity is also required by secure cryptosystems [21].

In this paper, we consider a quadratic map and present direct real-time implementation into the FPGA as well as hardware co-simulation structure in Simulink. Xilinx ISE (Integrated Synthesis Environment) design software including system generator tool is one of the efficient software technologies, is used to design and implement the chaotic Quadratic map. Firstly, the map equation is modeled by using Xilinx blocks in MATLAB/Simulink and then Xilinx system generator (XSG) performs the compilation of the design.

The rest of the paper is structured as follows: Section II briefly introduces the Quadratic map with its dynamical behaviors and some statistical analyses of the map are performed. In Section III, we realize the digital implementation and hardware-co simulation of the Quadratic map on FPGA. Finally, Section IV concludes the whole paper.

II. CHAOTIC QUADRATIC SYSTEM

A. Quadratic Map

Quadratic map is a simple discrete system exhibiting chaos and defined by [22],

$$x_{n+1} = r - x_n^2 \quad (1)$$

where $0 < r \leq 2$ is called control parameter and $x_n \in (-2, 2)$ is the state variable of the system. Quadratic map can show rich dynamic behaviors from a stationary system to a chaotic state. When $r \in (0, 0.74)$, the map behaves in steady state and if $r \in [0.74, 1.5)$, then the map has periodic behavior. When $r \in [1.5, 2]$, the Quadratic map is capable of very complicated behavior which means that the output of the map is aperiodic, non-convergent and very sensitive to initial conditions. Hence, the value of the control parameter specifies the dynamical behavior of the system.

B. Lyapunov and Bifurcation Analyses

Lyapunov exponent checks a sensitivity criterion of the initial condition for a nonlinear dynamical system [23]. In discrete systems, Lyapunov values are given by the following equation.

$$\lambda = \lim_{n \rightarrow \infty} \frac{1}{n} \sum_{i=0}^{n-1} \ln |f'(x_i)| \quad (2)$$

A positive Lyapunov exponent indicates that the orbit of a dynamical system is unstable and chaotic. The dynamical behaviors of a system from a fixed point to a chaos as a function of its control parameter are shown by a bifurcation diagram. Fig. 1 shows the Lyapunov spectrum and the bifurcation diagram of the Quadratic map.

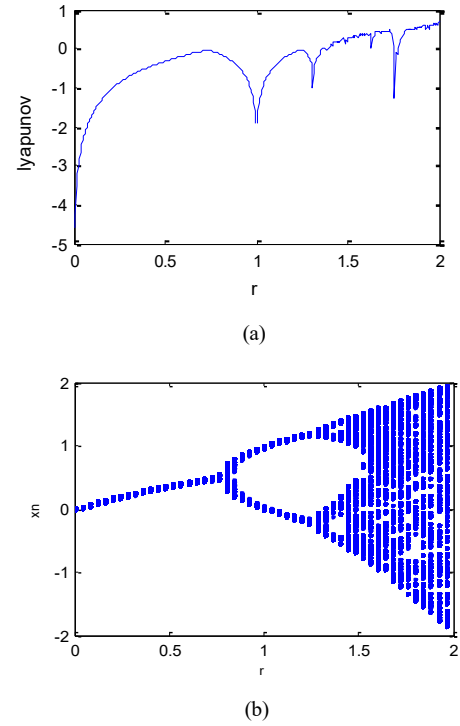
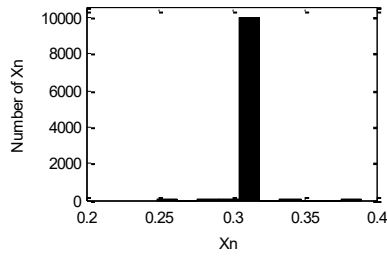


Figure 1. (a) Lyapunov spectrum of the Quadratic map
(b) Bifurcation diagram of the Quadratic map
 $\alpha + \beta = \chi$. (1) (1)

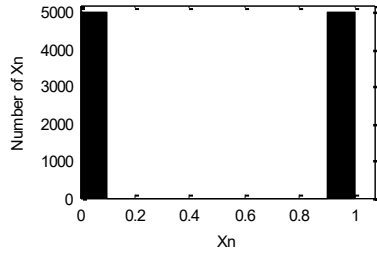
As it is easily observed that when the control parameter is close to 2, then the Lyapunov values are positive and the bifurcation diagram displays complex behavior resulting chaos.

C. Histogram Analysis

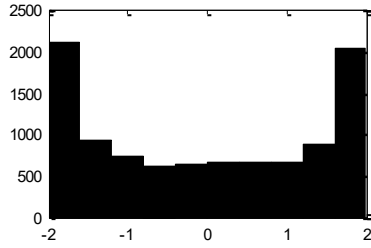
Histogram is a graphical display for the frequency distribution of a set of data. A distribution having constant probability for each data is known as uniform distribution. Fig. 2 shows the histogram distribution of the x_n series generated from the Quadratic map with different control parameters. From the graphical results, Fig. 2(a), Fig. 2(b) and Fig. 2(c) demonstrate steady, periodic and chaotic behavior of the Quadratic map, respectively. It is obvious that the histogram has an excellent symmetric property and better uniform distribution when the map behaves chaotically as in Fig. 2(c).



(a) $r = 0.4$



(b) $r = 1$



(c) $r = 2$

Figure 2. Histogram of x_n series with different control parameter (a) $r=0.4$ (b) $r=1$ (c) $r=2$

D. Checking chaotic output

When the Quadratic map is in chaos state, it exhibits complex behavior and generates chaotic sequences at output. Firstly, chaotic output will be checked for homogeneity through central tendency analysis and then the randomness of these sequences will be evaluated by using NIST test. Finally, the entropy of the Quadratic map as a number generator will be determined to measure its uncertainty. If a key generator is used in a cryptosystem, these properties need to be confirmed. In this paper, we chose as $r=2$ to make the system chaotic and perform the following statistical analyses by using Matlab programming.

a) Homogeneity Analysis

In order to check the chaotic output of the Quadratic map, the following two propositions are considered. First of all, the mean value of the output sequences spreading between $(-2,2)$ should be

$$x_{mean} = \lim_{N \rightarrow \infty} \frac{1}{N} \sum_{k=1}^N x_k = 0 \quad (3)$$

and second, the self-correlation of these sequences should be zero as given in the following equation.

$$s(\beta) = \lim_{N \rightarrow \infty} \frac{1}{N} \sum_{k=1}^N (x_k - x_{mean}) \cdot (x_{k+\beta} - x_{mean}) = 0 \quad (4)$$

According to the above equations, based on 50 simulations with different initial conditions, we have performed 10^6 iterations to get sufficient number of chaotic sequences from the Quadratic map. Then, we got the average mean value 0.000174 and the self-correlation is calculated to be 0.001598. These results are quite good, because both are very close to zero.

b) Randomness Analysis

Randomness means unpredictability and does not follow an intelligible pattern in a sequence of symbols [24]. NIST test is used to determine the degree of randomness of the Quadratic map outputs. NIST includes fifteen tests [25] and each test produces a real p -value in $[0,1]$. If the p -value is greater than a significance predefined level such as $\alpha = 0.01$, then the test is passed successfully. When the all statistical tests are passed, then the map is considered as random generator with 99% confidence. NIST uses binary series to test the randomness, but the output of the chaotic Quadratic map is floating-point value. Therefore, the following transformation is used for the output of the map in order to get sequential bit streams.

$$b_n = \begin{cases} 1, & x_n \geq 0 \\ 0, & x_n < 0 \end{cases} \quad (5)$$

Here, a threshold level of 0 is selected to produce a bit value "1" or "0" from x_n . We preferred the initial value as $x_0 = 0.123$ to obtain 1,000,000 bits to proceed NIST suite. The results are listed in Table 1.

Table 1. Results of the NIST test

Test Name	p-value	Result
Frequency	0.8524	Passed
Block frequency	0.3093	Passed
Runs	0.4939	Passed
Long runs of ones	0.7852	Passed
Rank	0.9912	Passed
Spectral DFT	0.7204	Passed
Non-overlapping templates (m=9; B=000000001)	0.7659	Passed
Overlapping templates (m=9)	0.7819	Passed
Universal (L=7; Q=1280)	0.1201	Passed
Liner complexity	0.9138	Passed
Serial-1 (m=5)	0.5875	Passed
Serial-2 (m=5)	0.6469	Passed
Approximate entropy (m=5)	0.4142	Passed
Cumulative sums forward	0.4086	Passed
Cumulative sums reverse	0.5553	Passed
Random excursions (x=+1)	0.3511	Passed
Random excursions variant (x=-1)	0.8741	Passed

It is concluded that the chaotic Quadratic map is very stochastic that represents random process and generates output sequences having enough randomness according to the NIST results.

c) Uncertainty Analysis

We use information entropy to determine the uncertainty or disorder of the Quadratic map. Entropy is a measure of uncertainty related to a random event [24, 26]. If $H(X)$ is a random source with N length, then its entropy is

$$H(X) = -\sum_{i=1}^N p(x_i) \cdot \log_2 p(x_i) \quad (6)$$

where $p(x_i)$ represents the probability of x_i . For instance, in a uniform bit stream having equal probability '0' and '1', the entropy will be 1 which is a theoretical result. When the output is certain, then the entropy is zero. The entropy of an practical information source is smaller than the ideal one. Generally, the more uncertain or random the event is, the more entropy it will contain [11].

We have used different initial values and number of iterations in order to generate bit streams using the Eqn. (5) from the chaotic Quadratic map. The entropy results for different conditions of the map are listed in Table 2.

Table 2. Entropy results

Initial value	Iterations	# of '0'	# of '1'	p(0)	p(1)	Entropy
0.2	100	52	48	0.52	0.48	0.9988455
-0.315	1000	490	510	0.49	0.51	0.9997114
1.27	10,000	4,967	5,033	0.4967	0.5033	0.9999685
-0.88354	100,000	49,829	50,171	0.4982	0.5017	0.9999916

From the results, when the number of iteration is increased, then the entropy value closes to 1 which means that the uncertainty of the map is becoming greater. Generated for all bit streams, number of zeros and ones are very close to each other resulting uniform distribution in the sequences.

d) Sensitivity Analysis

Quadratic map is highly sensitive to initial value. Thus, arbitrarily small change in the initial value will cause significantly different future output. This property is also acceptable while the map is used as a bit generator. To perform the sensitivity analysis, firstly, we randomly choose an initial value $x_0 = 0.123456788$ and iteration of $n = 50$ to generate a bit sequence (b_1) from the map. Then, a very slight change of 10^{-9} is applied to the first initial value, such as $x_0 = 0.123456789$ to generate another bit sequence (b_2). The last ten elements for both sequences are shown in Fig. 3.

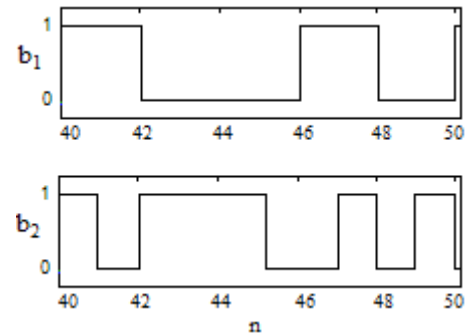


Figure 3. Generated different bit sequences with a slight change of initial value

Fig. 3 states that when a tiny change occurs in the initial value of the chaotic Quadratic map, generated bit sequences are completely different.

III. DIGITAL IMPLEMENTATION

This section describes an approach to the real-time implementation as well as hardware simulation of the chaotic Quadratic map on FPGA. FPGA is a type of programmable chip that can be completely reconfigured for various field applications. Using prebuilt logic blocks and programmable routing resources, FPGAs can be reprogrammed to the required functionality and customized by loading the related configuration data into its internal memory cells. The stored data in these cells determine the logic blocks and reconfigurable interconnects in FPGA. We have used Spartan 3E-XC3S1600E family from Xilinx for the hardware simulation and implementation of the Quadratic map.

Xilinx System Generator (XSG) is a high-level design tool and fully integrated in MATLAB/Simulink that enables the use of the model-based Simulink environment for FPGA design. It allows compilation of the design that is captured using Xilinx blocks and generates synthesizable VHDL (Very High speed integrated circuit Hardware Description Language) codes for FPGA programming. All of the downstream implementation steps including synthesis, place and root processes are automatically performed to generate the programming file via XSG. The Quadratic map model has been designed by Matlab/Simulink with XSG which offers the library of fixed-point arithmetic blocks that can be directly implemented into the FPGA. Fig. 4 shows the Quadratic map model created by Xilinx blocks under the Simulink.

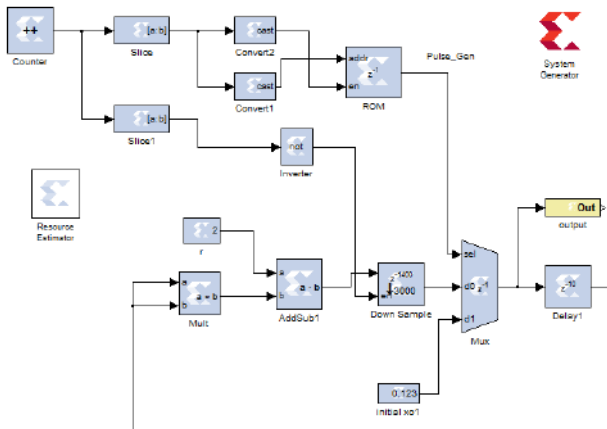


Figure 4. Chaotic Quadratic map model using Xilinx blocks

XSG enables hardware into a simulation, called hardware co-simulation structure that allows incorporating a design running in an FPGA directly into a simulation. Hardware co-simulation compilation targets automatically generate a bit streams and associate it to a block. When this block is simulated in Simulink, then the results for the compiled part are calculated in the hardware. Hence, hardware co-

simulation is used to verify that the design actually works in FPGA platform.

The bitstream download step is performed by using a JTAG cable. We performed the real-time implementation with a fixed-point data type and the real data are represented on 128 bits. Fig. 5 shows the simulation results of the chaotic Quadratic map design with hardware and software in Simulink. It is observed that the hardware-co simulation result is same to the Simulink simulation which means that the realization of the map is performed successfully and the map design actually works in FPGA.

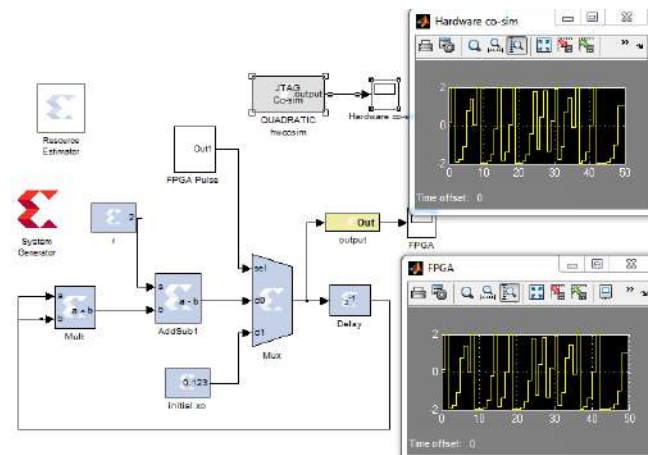


Figure 5. Hardware co-simulation of the Quadratic map

The generated output depends on the initial value of the map that can be directly entered into the design model before the generator starts. We randomly chose the initial value as $x_0 = 0.123$ for the real-time FPGA implementation.

XSG tool automatically generates a synthesizable VHDL codes associated with the design and the created file can be opened with the Xilinx ISE software. PlanAhead tool in ISE is used to assign input and output pin locations in the design. After assigning pins for input and output, then the design is ready to be synthesized in ISE. Successful synthesis creates the programming file of the design. IMPACT tool is used to load the programming file into the FPGA. For real-time implementation of our design, we use the chaotic Quadratic map as an 8-bit number generator to observe the numbers at LED output of the FPGA. First, the output of the map needs to be converted to 8-bit decimal number between 0 and 255. Hence, the following equation is applied to the output of the map.

$$number = \text{mod}(\text{round}(x_n \times 10^9), 256) \quad (7)$$

Here, *round* operation is used to get the nearest integer value and *mod* limits the output between 0 and 255. We assigned 8-bit number for the implementation because our FPGA has

eight LEDs at output. Transformation module is also added to the Quadratic map design. For example, if the initial value of the map is 0.123, then the second number generated from the Eqn. (7) will be 88 in decimal or 01011000 in binary. Fig. 6 shows this value at LED output of the FPGA.



Figure 6. Display of 88 in binary at LED output of the FPGA

Table 3 shows the numbers generated from the chaotic Quadratic system by using MATLAB and FPGA with the same initial value of the map.

Table 3. Generated 8-bit numbers from MATLAB and FPGA

MATLAB (Software)	FPGA (Hardware)
192	192
88	88
137	137
189	189
57	57
133	133
12	12
220	220

The amount of FPGA resources and the required by the Quadratic map can be determined by using Resource Estimator block. They are listed in Table 4.

Table 4. Mapping report of the Quadratic map design

Device	Spartan3E-XC3S1600E				
Resource Type	Slices	Flip-Flops	RAMB 16S	LUTs	IOBS
Available	14,752	29,504	36	29,504	250
Used	10,160	10,922	1	18,843	9

IV. CONCLUSION

This paper presents a chaotic Quadratic map and its implementation on a digital hardware. The results of the statistical analyses confirm that the output of Quadratic map can be used as cryptographic keys when the map behaves

chaotically. In practice, chaotic Quadratic map can be used as a generator in all scientific fields where the pseudo-randomness and chaos are required. The design of the map as well as hardware co-simulation and real-time implementation are successfully applied to the FPGA platform that encourages its usage for practical applications. This paper can be used as a good guide for anyone who wants to implement digital designs on FPGA without knowing VHDL codes.

REFERENCES

- [1] Z. Kang, J. Sun, L. Ma, Y. Qi and S. Jian, "Multimode synchronization of chaotic semiconductor ring laser and its potential in chaos communication," *IEEE journal of Quantum Electronics*, vol. 50, pp. 148-157, 2014.
- [2] J. Yang, Y. Chen and F. Zhu, "Associated observer-based synchronization for uncertain chaotic systems subject to channel noise and chaos-based secure communication," *Neurocomputing*, vol. 167, pp. 587-595, 2015.
- [3] M. Eisencraft, et al., "Chaos-based communication systems in non-ideal channels," *Communications in Nonlinear Science and Numerical Simulation*, vol. 17, pp. 4707-4718, 2012.
- [4] G. Kaddoum, M. Coulon, D. Roviras and P. Charge, "Theoretical performance for asynchronous multi-user chaos-based communication systems on fading channels," *Signal Processing*, vol. 90, pp. 2923-2933, 2010.
- [5] A. A. Zaher and A. Abu-Rezq, "On the design of chaos-based secure communication systems," *Communications in Nonlinear Science and Numerical Simulation*, vol. 16, pp. 3721-3737, 2011.
- [6] M. Turk and H. Ogras, "Classification of chaos-based digital modulation techniques using wavelet neural networks and performance comparison of wavelet families," *Expert Systems with Applications*, vol. 38, pp. 2557-2565, 2011.
- [7] Z. L. Zhu, W. Zhang, K. W. Wong and H. Yu, "A Chaos-based symmetric image encryption scheme using a bit-level permutation," *Information Sciences*, vol. 181, pp. 1171-1186, 2011.
- [8] V. Patidar, N. K. Pareek, G. Purohit and K. K. Sud, "A Robust and secure chaotic standard map based pseudorandom permutation-substitution scheme for image encryption," *Optics Communications*, vol. 284, pp. 4331-4339, 2011.
- [9] M. A. Murillo-Escobar, et al., "A RGB image encryption algorithm based on total plain image characteristics and chaos," *Signal Processing*, vol. 109, pp. 119-131, 2015.
- [10] R. Ye and W. Guo, "An image encryption scheme Multimode synchronization of chaotic semicon based on chaotic systems with changeable parameters," *I. J. Computer Network and Information Security*, vol. 4, pp. 37-45, 2014.
- [11] H. Zhu, C. Zhao and X. Zhang, "A Novel image encryption-compression scheme using hyper-chaos and Chinese remainder theorem," *Signal Processing: Image Communication*, vol. 28, pp. 670-680, 2013.
- [12] H. Ogras and M. Turk, "A Robust chaos-based image cryptosystem with an improved key generator and plain image sensitivity mechanism," *Journal of Information Security*, vol. 8, pp. 23-41, 2017.
- [13] W. Yibei, L. Man, X. Yanting and C. Hougui, "Research on chaos phenomena in power systems," *Power engineering and automation conference*, vol. 2, pp. 453-456, 2011.
- [14] H. T. Yau, M. H. Wang, T. Y. Wang and G. Chen, "Signal clustering of power disturbance by using chaos synchronization," *Int. J. Electr. Power Energy System*, vol. 64, pp. 112-120, 2015.
- [15] M. Ghasemi, S. Ghavidel, J. Aghaei, M. Gitizadeh and H. Falah, "Application of chaos-based chaotic invasive weed optimization



- techniques for environmental OPF problems in the power systems,” *Chaos, Solitons Fract.*, vol. 69, pp. 271-284, 2014.
- [16] Q. Chen, X. Ren and J. Na, “Robust finite-time chaos synchronization of uncertain permanent magnet synchronous motors,” *ISA Trans.*, vol. 58, pp. 262-269, 2015.
- [17] L. Merah, A. Ali-Pacha, N. H. Said and M. Mamat, “Design and FPGA implementation of Lorenz chaotic system for information security issues,” *Applied Mathematical Sciences*, vol. 7, pp. 237-246, 2013.
- [18] H. Xue, S. Wang and X. Meng, “Study on one modified chaotic system based on Logistic map,” *Res. J. Appl. Sci. Eng. Technol.*, vol. 5, pp. 898-904, 2013.
- [19] M. A. Aseeri and M. I. Sobhy, “A New approach to implement Chaotic generators based on Field Programmable Gate Array (FPGA),” *Proc. 3rd. Int. Conf. Discrete Chaotic Dynam. Nature Soc.*, September 2002.
- [20] Y. Mao, L. Cao and W. Liu, “Design and FPGA implementation of a pseudo-random bit sequence generator using spatiotemporal chaos,” *IEEE Proceedings of International Conference on Communications, Circuits and Systems*, pp. 2114-2118, 2006.
- [21] S. Lian, J. Sun and Z. Wang, “Security analysis of a chaos-based image encryption algorithm,” *Physica A: Statistical Mechanics and its Applications*, vol. 351, pp. 645-661, 2005.
- [22] N. Ramadan, H. E. H. Ahmed, S. E. Elkhamy and F. E. Abd El-Samie, “Chaos-based image encryption using an improved quadratic chaotic map,” *American Journal of Signal Processing*, vol. 6, pp. 1-13, 2016.
- [23] H. M. Hathal, R. A. Abdulhussein and S. K. Ibrahim, “Lyapunov exponent testing for AWGN generator system,” *Communications and Network*, vol. 6, pp. 201-208, 2014.
- [24] K. Marton, A. Suciu, C. Sacarea and O. Cret, “Generation and testing of random numbers for cryptographic applications,” *Proceedings of the Romanian Academy*, vol. 13, pp. 368-377, 2012.
- [25] A. Rukhin, J. Soto, J. Nechvatal and M. Smid, “A Statistical Test for random and pseudorandom number generators for cryptographic applications,” *NIST Special Publication 800-22 rev1*, pp. 2-40, 2010.
- [26] J. X. Chen, Z. L. Zhu, C. Fu, H. Yu and L. B. Zhang, “A Fast chaos-based image encryption scheme with a dynamic state variables selection mechanism,” *Communications in Nonlinear Science and Numerical Simulation*, vol. 20, pp. 846-860, 2015.



Visible Light Communication: A Tool For Addressing Radio Frequency Spectrum Congestion

Mahmud Mustapha

Institute of Natural and Applied Sciences
Erciyes University
Kayseri, Turkey
mahmudmustapha1@gmail.com

Ibrahim Develi

Department of Electrical and Electronics Engineering
Erciyes University
Kayseri, Turkey
develi@erciyes.edu.tr

Abstract— The rapid increase in data traffic exposes the limitations of using only radio frequency (RF)-based mobile communications whose spectrum became so much congested and scarce. The advances made in solid-state lighting technology in the past few years witnessed a growing research in visible light communication (VLC) that can supplement the RF-based mobile communication. Visible light spectrum made up of hundreds of terahertz bandwidth capacity that is licensed free and relatively unexploited. This paper reviews the advent of VLC technology, its transceiver structure, some important challenges and the recent advances made by researchers to address some of these challenges.

Keywords— *Visible light communication, radio frequency, solid-state lighting, spectrum, transceiver and challenges.*

I. INTRODUCTION

The interior lighting in our buildings is undergoing a dramatic change. The widely used incandescent bulb for lighting since its invention about a hundred years ago is becoming obsolete. This is due to the inefficiency of the product as only about 10% of the electrical energy is being converted to light [1] while the remaining 90% is dissipated as heat. In the 1990s compact fluorescent bulbs were introduced. These bulbs provide better efficiency in terms of lighting compared to incandescent bulbs. Although the fluorescent bulbs performs relatively well, but recent advancement in solid state technology gave rise to the introduction of light emitting diodes (LEDs). LEDs prove to have excellent efficiency and longer lifespan. On the average, LEDs luminous efficacy was observed to be as high as 113 lumens/watt in 2015 [2] and it is expected by the year 2020 to be around 200 lumens/watt. These values by far exceed the luminous efficacy of the fluorescent and incandescent bulbs of 60 and 15 lumens/watt respectively [2]. In addition, the longer lifespan of LEDs is of the order of 25,000 to 50,000 hours compared to about 10,000 hours of the compact fluorescent bulb. The LEDs have other advantages apart from high efficiency and longer lifespan of lower heat generation even after excessive usage, low power consumption, non-physiological effects as usage of harmful materials in the design is reduced. Owing to the

forementioned benefits, the adoption of LED luminaries is on the increase and it has been projected that by the year 2030 nearly all lightings will be LEDs [2].

The most important advantage of the LED is its fast switching ability to different levels of light intensity. The rate at which the LED switches is very fast that a human eye cannot notice. This unique characteristic enable LED to have dual purpose, that is, to be used for communication in addition to lighting. The dual ability of LEDs to provide lighting and communication gave rise to interesting applications in home networking, high speed data transfer using the luminaries in offices, traffic light management, communications in airplane cabins and trains and other applications too numerous to mention [3]. VLC researches have shown that very high data rates can be achieved (about 100Mbps in IEEE 802.15.7 standard and up to multiple Gbps in research) [2]. VLC utilizes LED luminaries as transmitters and photodiode or image sensor (a matrix of photodiodes) as a receiver. VLC communication is regarded an emerging area that possesses important characteristics in comparison to other existing wireless communications. Although the history of visible light communication can be traced back to 1880 with the invention of photo-phone by Alexander Graham Bell, the idea of using LEDs for communication in addition to lighting started in the year 2000 by Japanese researchers from Keio University [2]. Japan is therefore regarded as the pioneer hub for research in VLC. Researches in VLC were further ignited as a result of the success recorded in Japan with the formation of visible light communication consortium (VLCC) in 2003 [4]. In 2006, a proposal was made by the center for information communication technology research (CICTR) which is based in the United States to come up with a novel indoor broadband access by combining power line communication (PLC) with LED [4]. The most interesting of all these findings as far as VLC technology is concerned over the past years is that of Herald Haas from the University of Edinburgh United Kingdom referred to as Light Fidelity (Li-Fi). These activities witnessed a growing research in VLC with researchers all over the world paying attention to different aspects of the technology such as light source arrangements (transmitter) to reduce signal to noise ratio (SNR) fluctuations, the receiver position and

orientation, handoff strategies, multiple input multiple output (MIMO) systems, single input single output (SISO) systems and others too numerous to mention.

The rest of the paper is organized as follows: Section II dealt with the transceiver structure, channel models and

modulation techniques. Some important challenges were discussed in section III. Advances made by researchers to address these challenges were discussed in section IV. This is followed by conclusion in section V.

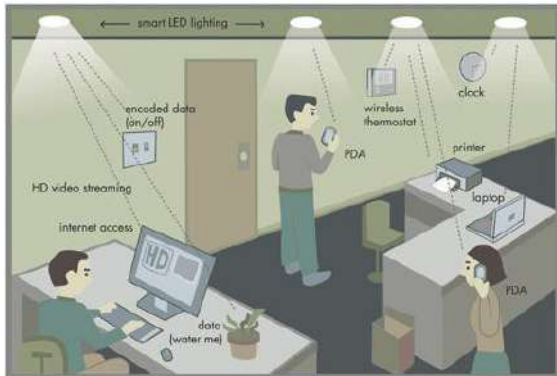


Figure 1. LEDs used for lighting and communication [5].

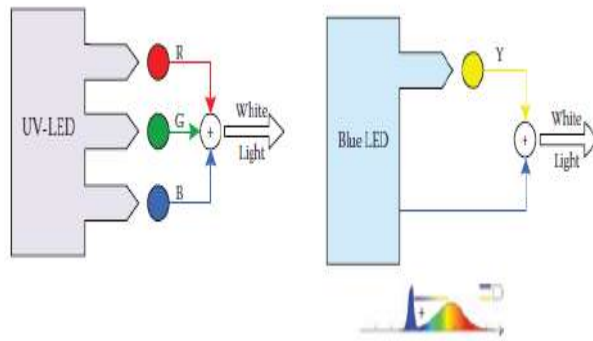


Figure 2. Methods of producing white light [3].

II. VLC TRANSCEIVER STRUCTURE

A. Transmitter

A VLC system employs LED luminaire as transmitter. The LED bulb can contain one or more LEDs to form an array usually used for lighting purposes. Apart from the LED lamps the bulb also contains the driver circuit which controls the amount of current flowing which in turn controls the brightness. For communication purpose the driver has to be modified to use two different intensity levels of light. It should be noted that the primary purpose of the LED lamp is the provision of lighting, therefore designing an LED luminaire to serve the function of communication without compromising the lighting requirement in addition to the ability to mitigate any noticeable flickering by the users is the most crucial design requirement. VLC transmitters should be able to meet these two requirements simultaneously as depicted in Fig.1. In practice, white light is the most commonly used for both indoor and outdoor illumination as a result of its excellent color rendering. The white light is usually produced by either combining blue LED with a Phosphor layer or via a mixture of red, blue and green light referred to as RGB combination. This is illustrated in Fig. 2. Although, the first method is cheaper to implement and the most widely used, but has a switching limitation to few MHz due to the phosphor coating. The RGB combination is the most preferred for communication.

B. Receiver

Two types of receivers are employed for VLC systems. The photo-detector (PD) (also called photodiode) referred to as non-imaging receiver and the imaging sensor which is essentially a matrix of photodiodes used as camera sensor. The imaging sensor is a good device used for VLC signal reception which is readily available on smart phones, tablets and laptops even though the frames per second (fps) on smart

devices is limited due to the control number of photo detectors that is commonly not more than 40 fps [2]. The basic architecture of a VLC receiver consists of a concentrator, optical filter, amplifier and an equalizer. The rays initially pass through the concentrator and optical filter before being captured by the detector. The complete architecture is shown in fig 3.

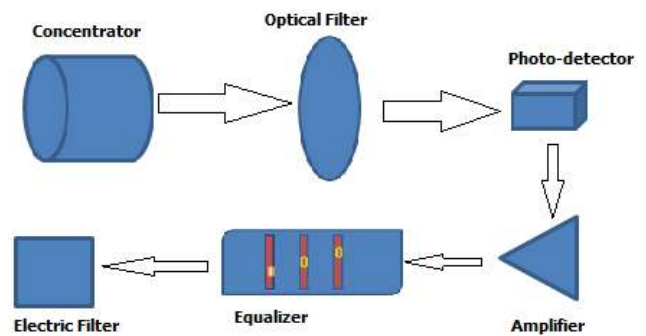


Figure 3. VLC receiver configuration

C. VLC Channel Model

The space between the transmitter and the receiver is referred to as the channel in communication. A measure of performance of any communication channel is its ability to transmit the carrier signal under the influence of many factors that includes attenuation, interference and noise. The space between the LED transmitter and Photo detector in VLC is the channel, mathematically represented as the response H . Two major types of channels are considered in VLC. The single VLC channel involving single transmitter and a single receiver referred to as single-input single-output (SISO) system, and a multichannel VLC referred to as multiple-input multiple-output (MIMO) system where there are multiple transmitters and

multiple detectors. In any case, the channel model is either line-of-sight (LOS) or non-line of sight (NLOS).

LOS

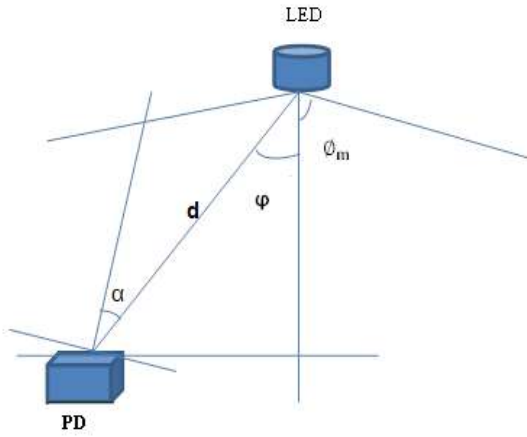


Figure 4. Line-of-sight (LOS) propagation

In an optical wireless communication, the DC channel gain due to the directed light propagation as studied in the literatures [5], [6], [7] and [8] as shown in Fig.4 can be written as:

$$H(0) = \left[\frac{(m+1)A}{2\pi d^2} \right] \cdot \cos^m(\varphi) \cdot T_f(\alpha) \cdot g(\alpha) \cdot \cos(\alpha) \quad (1)$$

Where the incident angle φ takes the values: $0 \leq \varphi \leq FOV$. It should be noted that the gain $H(0)$ will be null when $\varphi \geq FOV$. $T_f(\alpha)$ is the transmission filter while $g(\alpha)$ is the concentrator gain. The distance between the transmitter and receiver is d and A stands for the physical area of the detector. The concentrator gain is expressed as:

$$g(\alpha) = \frac{n^2}{\sin^2(FOV)} \quad , \quad 0 \leq \varphi \leq FOV \quad (2)$$

$$0, \quad 0 \geq FOV$$

Where n is the index of refraction.

The power received P_r can be derived from the transmitted power P_t as:

$$P_r = H(0) \cdot P_t \quad (3)$$

NLOS

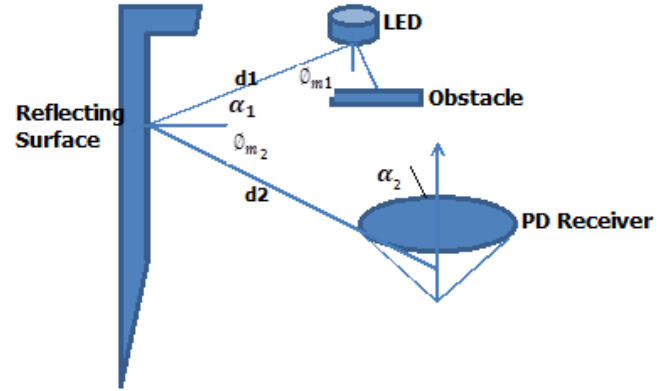


Figure 5. Non Line-of-sight (NLOS) propagation

Fig.5 shows the NLOS configuration where the effect of reflections due to the walls is taking into consideration. In this case the received power is computed from the DC channel gain of the directed path (LOS) $H(0)$ and that of the reflected paths (NLOS) $H_{ref}(0)$.

$$P_r = \sum_{LEDs} \{ H(0) \cdot P_t + \int_{walls} H_{ref}(0) \cdot P_t \} \quad (4)$$

Where $H_{ref}(0)$, is the DC channel gain due to reflections.

D. Modulation Techniques

Presently, four modulation techniques are adopted for VLC in the literatures. These techniques are (1) On-Off Keying (OOK), (2) Orthogonal Frequency Division Modulation (OFDM), (3) Pulse position modulation (PPM) and (4) Color shift keying (CSK). Of these techniques OOK is the simplest and most widely utilized but only suitable for a single light source [9]. Table I gives the characteristics of these modulation techniques.

TABLE I: MODULATION TECHNIQUES USED IN VLC

	Techniques			
	OOK	PPM	OFDM	CSK
Data Rate	Low	Moderate	High	High
Dimming Support	Yes	Yes	No	Yes
Flickering	High	Low	Low	Low
Comment	Simple Design	Max. spectral Efficiency with MEPPM	Complex design, support MIMO system	Utilizes RGB LED enhanced multi-user access

III. CHALLENGES

For effective deployment and commercialization of VLC technology a number of challenges need to be addressed. The visible light spectrum needs to be organized and the standardization of this novel discovery needs to be given the required attention in order to move the technology forward.



Although, the working group IEEE 802.15.7 provides a set of rules guiding the technology and the consortium in Japan, VLCC provides few working standards that can support VLC deployment but a number of issues need to be addressed for effective deployment and commercialization of this technology.

Based on reviews of some current literatures on VLC, some important challenges that required attention are outlined as follows:

A. LED Arrangement in VLC

It was observed that indoor LED arrangement has a direct effect on SNR variations in a room which affects the performance of a VLC system. Most studies provide a suitable LED arrangement for square layouts that minimizes the fluctuations of received power and luminance distribution in the layout. Further research is necessary to design LED arrangement that can optimize communication performance while meeting the illumination constraints for different layouts such as Hospitals, Shopping malls, etc.

B. Shadowing

Although there was a preliminary study on shadowing effect on the performance of a VLC system, however, shadowing in VLC has not been studied separately in the literatures. Since VLC exhibits different characteristics than Radio Frequency signals, it is therefore desirable to model VLC shadowing in indoor environment in order to fully understand how to mitigate its effect.

C. Optical Beam-forming

Optical beam-forming can significantly improve the performance of a VLC system, but unfortunately there are a very limited number of studies done towards that. Performing beam-forming while meeting the illumination constraints is an important direction for future research in VLC MIMO systems.

D. Inter-cell Interference and Hand-over Issues

Since the primary function of an LED luminaire is to provide illumination, it is not clear whether the resultant cell topology in use is interference optimal for communication purposes or not. Further research is needed to determine interference optimal cell topology by efficient hand-over strategies.

E. Receiver Position and Orientation

Because of users movement within a room there are cases where LOS propagation cannot be collected by the receiver. In such cases reflected light has to be taken into consideration during channel modeling. Most studies consider static receiver situation and does not account for receiver orientations and positions.

F. LED to internet connectivity

Most present literatures consider the downlink design only. Connecting the large number of LEDs to internet via wired infrastructure (E.g. Ethernet etc.) will attract huge additional cost which may cancel the expected benefit of reusing the

LEDs for communication. Uplink design consideration for VLC is therefore another area for future research.

IV. SOME ADVANCES IN VLC TECHNOLOGY

A. Light source Arrangement

Authors in [10] successfully analyzed the performance of a new light sources arrangement for indoor VLC. In the study, the authors proposes a new light sources arrangement which involves placing individual LEDs spaced at 0.5m apart as against the traditional LED arrays typically used in buildings. A total of 121 LEDs were used in the research and the performance of this new arrangement shows significant improvement in the luminance and SNR fluctuations in the room as compared with that of a four (4) LED arrays centered on the ceilings. The illumination in the room also met the ISO standard of 300lx – 1500lx. A novel LED arrangement that is applicable to a square layout was proposed in [11]. The authors compare the performance of 16 LEDs placed in the center of a square layout (5m*5m*3m) with that of a 12 LEDs arranged in a circle of radius 2.2m + 4 LEDs one at each corner of the room. The proposed arrangement significantly reduced the SNR fluctuation in the room and the Q-factor was also improved.

B. Hand-Over Strategies

Hand-over strategies is another aspect that is directly linked to LED configuration in an indoor layout. In an effort to address hand-over issues Thai-Chien Bui et al [12] in 2014 proposed a configuration for supporting hand-over in a rectangular layout. The study suggested that to deal with mobility issues in indoor VLC the overlap area between two adjacent LEDs must be large for a successful handover while maximizing illumination and SNR distribution. To overcome ISI the research suggested that the various LEDs should be modulated using different frequencies and the receiver should be a photo-detector with multiple lenses to distinguish between signals.

C. Receiver Position and Orientation

In order to maximize signal reception in an indoor VLC system, the receiver position and orientation needs to be taken into account. The receiver might not necessarily be stationary but mobile as in the case of a smart phone or a tablet being carried by a user in the room. Also, the orientation of the receiver changes with time, it is not always perpendicular as previous studies assume. To deal with such situations authors in [13] demonstrated the impact of receiver orientation and position on VLC link performance. The study considers a square layout with four LEDs as transmitters and analyses a scenario where the receiver is assumed to be a smart phone or a tablet being carried within the room. Although the analysis uses only four transmitters but result shows that the ISI contribution due to receiver orientation variation has a stronger impact compare to the case where the receiver is perpendicular which shows that ISI needs to be taken into consideration for channel modeling.



D. Shadowing

The effect of shadowing is directly linked to the user carrying the receiver in an indoor VLC; this depends on the body posture and varies according to the data rate. In a study carried out by [14], where the performance of two body models having different reflectivity were investigated using a mobile receiver with random orientation to account for varying body postures. The result shows that under the assumption of low data rate, a 2D body model with perpendicular receiver orientation provides a suitable performance. But for high data rates when the 2D body model was used, the result shows link-efficiency deterioration depending on the receiver orientation variation.

V. CONCLUSION

Visible light Communication technology is a novel research area with potential to compete with other existing optical wireless communication systems. In this review a general overview of the technology with emphasis on the transceiver structure, modulation techniques and some important challenges were presented. It should be noted that for effective implementation of VLC technology, the existence of appropriate regulations is paramount. And these regulations and standards are lacking. Also, most of the researches on VLC are simulations based; therefore further research needs to be done on practical implementation of various aspect of the technology. In order to address some of the VLC technology challenges such as Uplink internet connectivity more studies need to be conducted, this further portrays VLC technology as a hot research area with a lot of future scope and potentials.

ACKNOWLEDGMENTS

This work was supported by the Scientific Research Projects Coordinating Office of Erciyes University under project grant FYL-2017-7310.

REFERENCES

- [1] P. H. Pathak et al "Visible light communication, networking and sensing: A survey, potential and challenges" IEEE communications surveys & tutorials vol. 17 No. 4, 2015, pp. 2047 – 2077.
- [2] United States Department of Energy. Energy Savings Forecast of Solid-State Lighting in General Illumination Applications. [Online]. Available:http://apps1.eere.energy.gov/building/publications/pdf/ssl/energy_savings_forecast14.pdf
- [3] Z. Ghassemloooy, W. Popoola and S. Rajbhandari "Optical Wireless Communication: System and channel modeling with Matlab" CRC Press, pp. 443
- [4] A. R. Ndjongue, H.C. Ferreira and T.M.N. Ngatched "Visible light communications (VLC) technology" Wiley Encyclopedia of Electrical and Electronics Engineering, June 2015, pp. 1- 24
- [5] N. Kumar "Visible light communication: concept, technology, challenges and possibilities" WCNC 2013, pp. 1 – 99
- [6] T. Komine, M. Nakagawa "Fundamental Analysis for Visible Light communication system using LED light," IEEE Trans. Consum. Electron. Vol. 50, pp. 100-107 (2004).
- [7] H. Q. Nguyen et al "A MATLAB-based simulation program for indoor visible light communication" International symposium on communication systems, networks and digital signal processing, 2010, pp. 537 – 541
- [8] L. Zeng et al "Improvement of data rate by using equalization in an indoor visible light communication system" 4th IEEE International conference for circuits and systems for communications, 2008, pp. 678 - 682
- [9] N. Yadav and P. Kundu "Literature study of the visible light communication techniques" International journal of innovations in engineering and technology (IJJET), Vol. 7 Issue 1, 2016, pp. 275 – 280
- [10] Yung Wang et al "A new design of light source arrangements for indoor visible light communication" The 3rd International Conference on Systems and Informatics, (ICSAI 2016), pp. 705 – 709
- [11] Z. Wang, C. Yu, W-D. Zhong, and J. Chen, "A novel LED arrangement to reduce SNR fluctuation for multi-user in visible light communication systems," International Conference on Information, Communication and Signal Processing, (ICICS 2011)
- [12] T. Chien Bui et al "LEDs configuration method for supporting hand-over in visible light communication" 2014 IEEE Region 10 conference (TENCON 2014), pp. 1 – 6
- [13] C. Le Bas et al "Impact of receiver orientation and position on visible light communication link performance" International Workshop on Optical Wireless communication (IWOW) 2015, pp. 1 – 5
- [14] C. Le Bas et al "Human body impact on mobile visible light communication link" 10th International Symposium on Communication Systems, Networks and Digital Signal Processing (CSNDSP), 2016, pp. 1 - 6

Development of Smart Security System for Remote Control Using Small Computer

Huda Al-saffar

Gaziantep University, Electrical and Electronics Engineering
Gaziantep, Turkey
msc.computereng89@gmail.com

Ergun Ercelebi

Gaziantep University, Electrical and Electronics Engineering
Gaziantep, Turkey
ercelebi@gantep.edu.tr

Abstract— The aim of this paper is to develop a smart security system for remote control using a small computer. In this paper, it has been proposed a comparatively inexpensive security system which has the capability to automatically initiate capture a picture by Raspberry Pi Camera Module when any movement is detected by PIR sensor and the Raspberry Pi device will send that picture to the user's smartphone device via Wi-Fi using application. Also, the system will light up the light bulb and LEDs when motion is detected. In addition, this system can be counted the number of moving objects located with the help of the infrared PIR sensor and will be sent that number with notification message "Motion Detection" to smartphone alongside the picture. The proposed system is very effective and crucial choice for energy save and security for home or service buildings. Nowadays, in electronic markets, there are many expensive solutions. However, low-cost solutions are very important for spreading between all people. Knowing that the Raspberry Pi 3 device and Telegram application were used in this proposed system.

Keywords—Raspberry Pi 3; PIR Sensor; Raspberry Pi Camera Module; Relay; Smartphone

I. INTRODUCTION

Security is the first attention in everywhere, every time and for everyone. Each person who wishes to be his home and service buildings in safety (PRIYANKA and REDDY, 2015). The heart-dominant in this system is the small computer is Raspberry Pi 3. Obviously, Raspberry Pi 3 is a single board which, when it is interfaced with the screen, keyboard, mouse and installed the operating system to be able to achieve the functions for any computer. The Operating System (OS) is the collection of programs and instructions that make the Raspberry Pi 3 run. In addition, the operating system whose works in Raspberry Pi 3 based only on Linux operating systems such as Raspbian OS and NOOBs (Narkhede and Khadke, 2016). It is worth to mention that, in this system, Raspbian OS version Jessie with PIXEL is installed in the Raspberry Pi 3 and the python programming language was

used to programming the project program. This project describes a smart security system for all homes and service buildings that can monitor any place. The system has been able to detect any object movement, turn ON/OFF light bulb and LEDs when an object moving in light day or darkness, take a picture, count the object moving number and automatically send the data to a smartphone via Wi-Fi using Telegram application. The data include the picture and notification message "Motion Detection" with moving object number located. The advantage of using this system is very crucial choice for energy save and home security. Also, another advantage is that it is a simple circuit and able to work at any time in the light day or darkness (Ahmad, Studiawan and Ramadhan, 2014). The other major advantage is that it is very economic system and it can be placed anywhere (Zafar and Carranza, no date).

II. DESIGN AND IMPLEMENTATION OF PROPOSED SYSTEM

The design and implementation of a low-cost system monitoring based on Raspberry Pi 3, a single board computer which interfaced with PIR Sensor, Raspberry Pi Camera Module, LEDs and relay and controlling them by implementing program written in python language in software implementation. The block diagram of this system is illustrated in Figure 1 below.

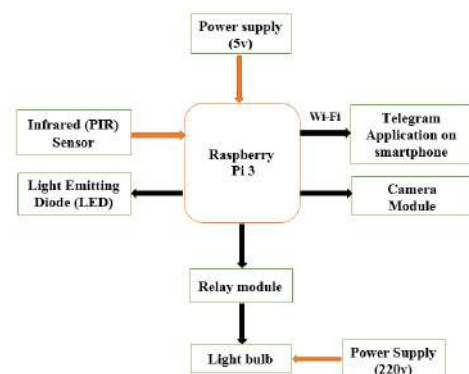


Figure 1. Block Diagram for the proposed system

To improve and facility the algorithm for the proposed system, the algorithm is separate into two parts which are motion detection part and lighting part. The system implementation begins when connecting the Raspberry Pi 3 and relay to the power supply. Knowing that the starting number for image counter is 1. Firstly, if there is no motion detected by the PIR sensor, the program will turn OFF the LEDs and suspends the program for 1 second and directly return back to check the motion detection. Secondly, if the motion is detected by PIR sensor the program will turn ON the lighting part and then the camera module will capture the picture and stores it in micro SD card. After that, the program will send the picture taken and notification message "Motion Detection" with the object number located directly to smartphone by Telegram application every time a motion is detected to alert the owner which having a smartphone and then the program will increment the counter image by 1 and subsequently turn OFF light bulb to energy save after that the program will suspend for 10 seconds before return one more time to check the object movement. The lighting part consists of LEDs and light bulb. Besides that, the security system will stop when separating the power supply. The flowchart for the proposed system is shown in the Figure 2 and the block diagram of the lighting part is shown in Figure 3.

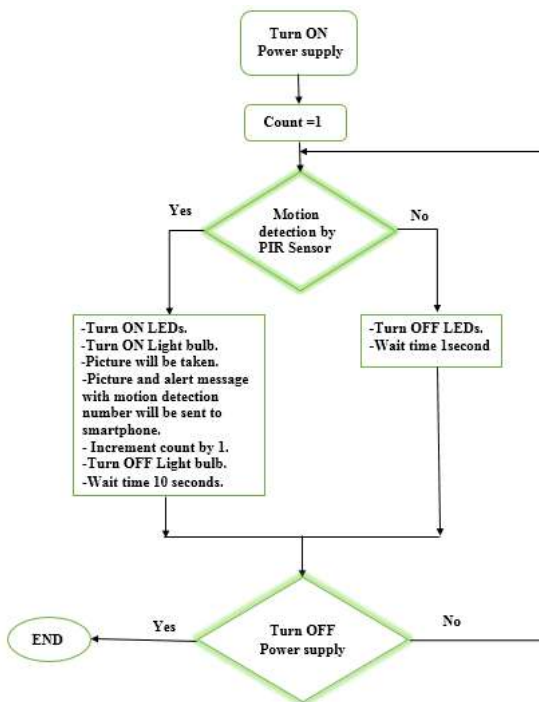


Figure 2. Flow Chart of proposed system.

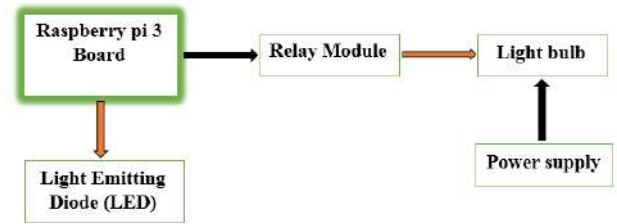


Figure 3. Lighting part

III. SYSTEM COMPONENT DESCRIPTION

The major components of the proposed system are Raspberry Pi 3 Model B, Passive Infrared (PIR) Sensor, Raspberry Pi Camera Module, Relay, Power supply, LED (Light Emitted Diode), Telegram Application on smartphone and GPIO pins configuration. The block diagram for the proposed system illustrated in Figure 1.

A. Raspberry Pi 3 Model B

Raspberry Pi is a small credit card sized, single-board computer. It was more useful for projects which require very low power and used for computer science education. The amazing new version of raspberry pi is Raspberry Pi 3 Model B. This third generation model developed by the Raspberry Pi Foundation Company in the UK (Chandana, Jilani and Javeed Hussain, 2015).

The proposed system used Raspberry Pi 3 Model B that consists of the key specifications as illustrated in Table 1 and Raspberry Pi 3 board in Figure 4.

Table 1. Specifications of Raspberry Pi3 Model B

Specification	Description
SoC (System on Chip)	Broadcom BCM2837
CPU	64-bit, ARMv7, Quad cortex A53 @ 1.2GHz
GPU	400 MHz video Core IV 3D graphics Core
RAM	1GB SDRAM
SD Card Slot	Micro SD Card Slot (Push-Pull)
GPIO	40 Pin
USB 2.0	4 Ports
Bluetooth	Bluetooth 4.1, BLE(Bluetooth Low Energy)
Wireless LAN	802.11n Wi-Fi
Ethernet Port	10/100 LAN Port
HDMI Output	Full-Size HDMI Video Output
Power Supply	5V and Up to 2.5 Amps
Audio Output	3.5 mm, 4-track composite video and audio output jack
Dimensions	85.6mm x56mm x21mm
Price	35\$

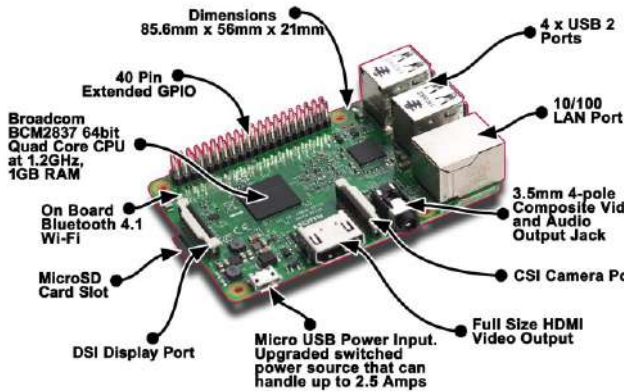


Figure 4. Raspberry Pi 3 Model B board

B. Passive Infrared (PIR) Sensor

PIR sensor is an essential part of this proposed system. The object will emit infrared (IR) radiation through his movement. PIR is an electronic sensor that used to detect the object motion by receiving the infrared (IR) radiates light from the external environment. Hence, the sensor compares the intensity of the infrared radiation from time to time. If there is an object movement in the room, then the intensity changes, it causes detecting the object movement. Knowing that the range for PIR sensor can up to 5-7 meters (Ahmad, Studiawan and Ramadhan, 2014). The PIR Sensor is small in size, inexpensive in price, used low-power, easy in use and connectivity. They are often referred to as PIR, Passive Infrared, Pyroelectric, or IR motion sensors (Patel *et al.*, 2016). In this proposed system the HC-SR501 PIR Sensor Module is used.



Figure 5. PIR Sensor

C. Raspberry Pi Camera Module

The Camera Module Rev 1.3 is a camera that created specifically for Raspberry Pi model A and B. It is manufactured by the Sunny company. It provides high sensitivity, very small PCB design, price almost 25\$, lightweight design and 5-megapixel resolution image. The camera module connects to Raspberry Pi 3 by CSI (Camera Serial Interface) connector using a 15cm ribbon cable to the 15 pin CSI connector (Million, 2013).



Figure 6. Raspberrv Pi Camera Module

D. Relay Card

A relay is an electrical switch that is used to control high voltage by using very low voltage and as an input (GPIO pins). It is used to control several circuits by one signal (Vigneswari *et al.*, 2015). The relay card consists of two parts. The first part of the right side in Figure 7 below, it consists of a ground, a control pin to switch ON/OFF depending on the state and a 5V power pin for the relay card itself. The second part on the left side, will be connected to the load device, it contains 3 cards:

- NC means (Normally Closed): this indicate to that when the relay card has 0 on the control pin (no input signal), the connected circuit active COM is connected to this thing when the relay coil is off.
- NO means (Normally Open): this indicate to that, on the reverse, when the relay card has 1 on the control pin (value of 5V applied to the relay card) will switch off the circuit and vice versa. COM is connected to this thing when the relay coil is on.
- COM means (Common): always connected, it is the moving point of the switch.

Besides that, only two relay plugs will be used in accordance with the selected operating mode. The Raspberry Pi sends a low current on its GPIO pins whether at 0 or 1. This a weak current is enough to excite the relay. In this proposed system the SRD-05VDC-SL-C sainsmart 2 relay module are used and the light bulb is load used for relay card. The light bulb was worked like the flashlight for the camera module



Figure 7. Relay Card

E. Power supply

The proposed system needs of two power supplies. The first one used for Raspberry Pi3 board is Micro USB connector that supplied at least 5V at up to 2.5Amps is main for the proposed system. It is worth to mention that, many smartphone chargers are appropriate for Raspberry Pi (Pi, 2012) as shown in Figure 8 below. The second one used for the light bulb is 220V.



Figure 8. Power supply adapter for Raspberry Pi

F. LED (Light Emittied Diode)

Electronic pieces resemble small lamps work to convert electricity to light and are available in different colors. In this system, the 5MM white LEDs are used to improve lighting for an image which captured by the camera module.



Figure 9. White LED

G. Telegram Application on a Smartphone

The telegram is a cloud-based mobile and computer messaging application with a focus on security and speed. The telegram-cli is a private library for telegram application which provides a possibility to send any file type from Raspberry Pi to smartphone and from the smartphone to the Raspberry Pi.



Figure 10. Telegram Application on Smartphone

H. GPIO Pins Configuration

The Raspberry Pi 3 has two rows of pins that called General Purpose Input Output (GPIO) connector which includes 40 pin connector.



Figure 11. GPIO pins layout for proposed system

The Raspberry Pi 3 allows the peripheral devices such as sensors, LEDs...etc to connect directly to GPIO pins. Also, the GPIO pins allow control and interact directly with the Raspberry Pi processor (Antony and Gidveer, no date). In addition, the Raspberry Pi 3 needs to install the libraries such as Rpi.GPIO that allows access to the GPIO pins using a programming language such as python. Besides that, the Rpi.GPIO library is used to install these pins as an input or output. The GPIO pins which used in the proposed system are mentioned in Figure 11.

IV. RESULTS

The security system is developed which result is represented in Figure 12 and Figure 13.

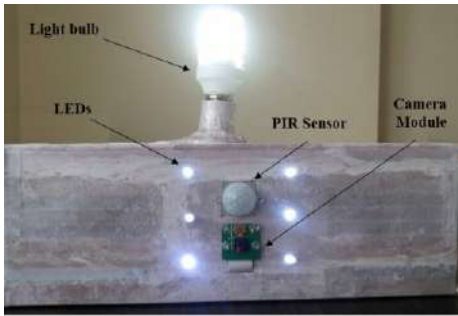


Figure 12. The security system at the moment of take the picture if motion is detected.

Transmission of Image, Message and The number of persons located via Wi-Fi internet to a smartphone.



Figure 13. The result of proposed security system in smartphone.

V. CONCLUSION

This paper presents a new smart security system that able to monitor any movement in the room .Besides that, this movement will be detected by using PIR sensor. The smart security system able to give monitoring information (image, a notification message with the numbers of people sites) in real time to alert the user through Telegram Application .Hence, the Raspberry Pi 3 has two basic components interacting with each other: one is the Telegram Application that executes on

the smartphone device's browser and server side scripts that run by the Raspberry Pi 3 Hardware tool component. This security system works immediately when turning ON the power supply for the system and no need for the user to execute the smart security system .Additionally, this system is the very effective and crucial system choice for several reasons belong to inexpensive, consumes low power, simple circuit, and advanced system.

REFERENCES

- [1] Ahmad, T., Studiawan, H. and Ramadhan, T. T. (2014) 'Developing a Raspberry Pi-based Monitoring System for Detecting and Securing an Object', International Electronics Symposium (IES).
- [2] Antony, A. and Gidveer, G. R. (no date) 'LIVE STREAMING MOTION DETECTION CAMERA SECURITY SYSTEM WITH EMAIL NOTIFICATION USING RASPBERRY PI', IOSR Journal of Electronics and Communication Engineering (IOSR-JECE), (AETM'16), pp. 142–147.
- [3] Chandana, R., Jilani, S. and Javeed Hussain, S. (2015) 'Smart Surveillance system using Think Speak and Raspberry Pi', International Journal of Advanced Research in Computer and Communication Engineering, 4(7), pp. 214–218.
- [4] Million, R. P. S. P. F. (2013) 'The MagPi Magazine', Edition, 31(14), p. 6.
- [5] Narkhede, Y. V. and Khadke, S. G. (2016) 'Application of Raspberry Pi and PIR Sensor for Monitoring of Smart Surveillance System', International Journal of Electronics, Electrical and Computational System IJEECS, 5(5), pp. 145–148.
- [6] Patel, P. B., Bhatt, K. R., Choksi, V. M. and Potdar, M. B. (2016) 'Smart Surveillance and Monitoring System using Raspberry Pi And Android', International Journal of Enhanced Research in Science, Technology & Engineering, 5(5).
- [7] Pi, R. (2012) 'Quick start guide'.
- [8] PRIYANKA, Vp. and REDDY, D. R. K. S. (2015) 'PIR Based Security Home Automation System with Exclusive Video Transmission', international journal of Scientific Engineering and Technology Research, 4(18).
- [9] Vigneswari, P., Indhu, V., Narmatha, R. R., Sathinisha, A. and Subashini, J. M. (2015) 'Automated security system using surveillance', International journal of current engineering and technology, 5(2), pp. 882–884.
- [10] Zafar, S. and Carranza, A. (no date) 'Motion Detecting Camera Security System with Email Notifications and Live Streaming Using Raspberry Pi', in Conference of the American Society for Engineering Education, pp. 1–5.



A Study of Multistage Network Expansion Planning by Using DC-Lossy and Linearized-AC Models

Mehmet Fatih Cankurtaran, Engin Karatepe
Department of Electrical-Electronics Engineering,
Engineering Faculty, Dokuz Eylul University
Izmir, Turkey

mfatih.cankurtaran@gmail.com, engin.karatepe@deu.edu.tr

Abstract

— As the world's electrical consumption increases rapidly, the network expansion planning becomes a crucial issue for power system planners. In that manner, the transmission expansion planning (TEP) and the reactive power planning (RPP) should be performed in order to meet the growing demand in economically and securely. This paper presents a multistage network expansion planning; in the first stage the TEP is performed by using DC-lossy network model, in the second stage the RPP is performed by using linearized-AC network model in order to improve the voltage profile. Finally, the obtained network in planning stages is tested for long term performance by using Power World Simulator. The effectiveness of proposed method is demonstrated by using IEEE 24-bus reliability test system.

Keywords — *Transmission Expansion Planning, Reactive Power Planning, Multistage Network Expansion Planning, Voltage Profile*

I. INTRODUCTION

Over the last decade, network expansion planning has gained great importance due to the fact that the consumption of electricity in the world has been increasing rapidly [1], because the generated power should be transmitted to the loads in economically and securely. In that manner, transmission expansion planning (TEP) and reactive power planning (RPP) are of capital importance for power system planners [2].

In literature, the different network models have been developed for TEP problems [3-6]. In general, the DC network model is used because of its simplicity and less computational burden [3-4]. On the other hand, the AC network models have been introduced in power planning problems [5-6]. But in this case, the problem becomes more complex because of increasing variables and constraints. In addition, although the reactive power issue and voltage

magnitudes can be included in AC network models, it can be result in oversized investment on transmission lines [7] for maintaining the voltage levels within allowable range by adding more lines. Due to these reasons, the RPP is usually performed after the TEP problem where the main aim is to allocate the reactive resources with a minimum cost in order to improve the voltage profile.

In this paper, a multistage network expansion planning is performed. In the first stage, the TEP is performed by using DC-lossy network model. In the second stage, the RPP is performed by using linearized-AC network model in order to improve the voltage profile. The annual peak load is considered during the planning stages. In order to demonstrate the effectiveness of the planning results for a long term performance, the AC optimal power flow (OPF) including voltage and line constraints is performed under the hourly test load profile of a year. Thanks to ability of Power World Simulator (PWS) program [8], the IEEE 24-bus system is constructed with obtained expansion planning and then the long term simulation is performed through this environment.

This paper is organized as follows. In Section II, the planning procedures and the mathematical formulation of TEP and RPP are given. Section III presents the results of the planning stages using IEEE 24-bus test. In Section IV, the long term performance of the planning results is investigated by using PWS program. Finally, some concluding remarks are presented in Section V.

II. PLANNING PROCEDURE AND FORMULATION

In this paper, the planning procedure consists of two stages. In the first stage, TEP is applied by using DC-lossy network model for the purpose of dealing with the congestion on the lines. In the second stage, RPP is

This study was supported by the Scientific and Technological Research Council of Turkey, TUBITAK-114E514.

performed by using linearized-AC network model and it is aimed to find the location and size of capacitors by using the obtained network in the first stage in order to get the voltage levels in acceptable range and enhance voltage profile of system.

A. Transmission Expansion Planning

The DC network model considering power loss is used to solve TEP problem and the formulation is given as follows;

$$\text{Min} \quad C_{line} = \sum_{(i,j) \in \Omega^c} c_{ij} n_{ij} \quad (1)$$

Subject to

$$\sum_{(i,j) \in \Omega^o \cup \Omega^c} P_{ij} + PG_i = \sum_{(i,j) \in \Omega^o \cup \Omega^c} PL_{ij} + PD_i \quad (2)$$

$$PL_{ij} = g_{ij} \theta_{ij}^{sqr} \quad \forall (i,j) \in \Omega^o \quad (3)$$

$$0 \leq PL_{ij} - g_{ij} \theta_{ij}^{sqr} \leq (1 - n_{ij})M \quad \forall (i,j) \in \Omega^c \quad (4)$$

$$0 \leq PL_{ij} \leq n_{ij} g_{ij} (\bar{\theta}_{ij})^2 \quad \forall (i,j) \in \Omega^c \quad (5)$$

$$P_{ij} = b_{ij} \theta_{ij} \quad \forall (i,j) \in \Omega^o \quad (6)$$

$$-\bar{P}_{ij} \leq P_{ij} \leq \bar{P}_{ij} \quad \forall (i,j) \in \Omega^o \quad (7)$$

$$-(1 - n_{ij})M \leq P_{ij} - b_{ij} \theta_{ij} \leq (1 - n_{ij})M \quad \forall (i,j) \in \Omega^c \quad (8)$$

$$-n_{ij} \bar{P}_{ij} \leq P_{ij} \leq n_{ij} \bar{P}_{ij} \quad \forall (i,j) \in \Omega^c \quad (9)$$

$$\underline{PG}_i \leq PG_i \leq \bar{PG}_i \quad (10)$$

$$\theta_{ij}^{sqr} = \sum_{l=1}^L s(l) \Delta \theta_{ij}(l) \quad \forall (i,j) \in \Omega^o \cup \Omega^c \quad (11)$$

$$\theta_{ij} = \theta_{ij}^+ - \theta_{ij}^- \quad \forall (i,j) \in \Omega^o \cup \Omega^c \quad (12)$$

$$\sum_{l=1}^L \Delta \theta_{ij}(l) = \theta_{ij}^+ + \theta_{ij}^- \quad \forall (i,j) \in \Omega^o \cup \Omega^c \quad (13)$$

$$0 \leq \theta_{ij}^+ \leq \sigma_{ij} \bar{\theta}_{ij} \quad \forall (i,j) \in \Omega^o \cup \Omega^c \quad (14)$$

$$0 \leq \theta_{ij}^- \leq (1 - \sigma_{ij}) \bar{\theta}_{ij} \quad \forall (i,j) \in \Omega^o \cup \Omega^c \quad (15)$$

$$-\bar{\theta}_{ij} \leq \theta_{ij} \leq \bar{\theta}_{ij} \quad \forall (i,j) \in \Omega^o \cup \Omega^c \quad (16)$$

$$0 \leq \Delta \theta_{ij}(l) \leq \frac{\bar{\theta}_{ij}}{L} \quad \forall (i,j) \in \Omega^o \cup \Omega^c \quad (17)$$

$$\Delta \theta_{ij}(l+1) \leq \Delta \theta_{ij}(l) \quad \forall (i,j) \in \Omega^o \cup \Omega^c \quad (18)$$

$$\frac{\bar{\theta}_{ij}}{L} - \Delta \theta_{ij}(l) \leq [1 - \varepsilon_{ij}(l)] \frac{\bar{\theta}_{ij}}{L} \quad \forall (i,j) \in \Omega^o \cup \Omega^c \quad (19)$$

$$\Delta \theta_{ij}(l+1) \leq [1 - \varepsilon_{ij}(l)] \frac{\bar{\theta}_{ij}}{L} \quad \forall (i,j) \in \Omega^o \cup \Omega^c \quad (20)$$

$$s(l) = (2l-1) \frac{\bar{\theta}_{ij}}{L} \quad \forall (i,j) \in \Omega^o \cup \Omega^c \quad (21)$$

Ω^o and Ω^c denote the set of existing and candidate lines, respectively. The objective function is presented in (1) which includes total line investment cost. In (2), the real power balance equation is given. While the real power loss for existing lines is represented in (3), constraints (4) and (5) represent the real power loss for candidate lines where θ_{ij}^{sqr} denotes the square of bus voltage angle difference. In order to represent this quadratic term as in linear form, the piece-wise linearization technique [9] is used and corresponding equations are given in (11)-(21). In (6) and (7), the real power flows and its limits for existing lines are presented, respectively. In (8) and (9), to calculate the real power flows for candidate lines, disjunctive method is used in order to overcome the nonlinearity term which come from product of binary variable and continuous variable. The real power limits of generators are given in (10).

B. Reactive Power Planning

The linearized-AC network model is used to solve RPP problem by using obtained network in first stage. The formulation of this problem is given as follows.

$$\text{Min} \quad C = \sum_{i \in \Omega^L} (\Delta V_i^{set} - \Delta V_i)^2 \quad (22)$$

Subject to

$$\left\{ \begin{array}{l} \text{Constraints (1), (7), (10)-(21)} \end{array} \right.$$

$$\sum_{(i,j) \in \Omega^{up}} Q_{ij} + \sum_{k \in \Omega^{cap}} QC_i^k + QG_i = \sum_{(i,j) \in \Omega^{up}} QL_{ij} + QD_i \quad (23)$$

$$P_{ij} = (\Delta V_i - \Delta V_j) g_{ij} - b_{ij} \theta_{ij} \quad \forall (i,j) \in \Omega^{up} \quad (24)$$

$$PL_{ij} = g_{ij} \sum_{l=1}^L s(l) \Delta \theta_{ij}(l) \quad \forall (i,j) \in \Omega^{up} \quad (25)$$

$$Q_{ij} = -(\Delta V_i - \Delta V_j) b_{ij} - g_{ij} \theta_{ij} \quad \forall (i,j) \in \Omega^{up} \quad (26)$$

$$QL_{ij} = -b_{ij} \sum_{l=1}^L s(l) \Delta \theta_{ij}(l) \quad \forall (i,j) \in \Omega^{up} \quad (27)$$

$$(1 - d_i^k) \underline{QC}_i^k \leq QC_i^k - (1 + 2\Delta V_i) b_i^{cap} \leq (1 - d_i^k) \bar{QC}_i^k \quad \forall i \in \Omega^L \quad (28)$$

$$d_i^k \underline{QC}_i^k \leq QC_i^k \leq d_i^k \bar{QC}_i^k \quad \forall i \in \Omega^L \quad (29)$$

$$\sum_{k \in \Omega^{cap}} d_i^k \leq \bar{d}_i \quad \forall i \in \Omega^L \quad (30)$$

$$\underline{\Delta V}_i \leq \Delta V_i \leq \overline{\Delta V}_i \quad (31)$$

$$\underline{QG}_i \leq QG_i \leq \overline{QG}_i \quad (32)$$

The objective function is given in (22) where the aim is to improve the voltage profile and ΔV_i is the voltage deviation. Ω^u and Ω^L denote the set of updating network lines (obtained from TEP result) and set of load buses, respectively. The reactive power balance equation is given in (23). The real power flow and power loss are presented in (24) and (25), respectively. Similarly, the reactive power flow and power losses are presented in (26) and (27). In (29), the installation of capacitor k at bus i is determined by d_i^k which is binary variable, i.e. when d_i^k is equal to 1, capacitor k is installed at bus i , otherwise it is not installed. When the capacitor k is connected at bus i , the value of reactive power injection is calculated in (28). In this equation, the linear approximation technique is used to linearize the square of voltage (i.e. $V_i^2 \approx 1 + 2\Delta V_i$). The installation limits of capacitors at bus i is given in (30). In (31) and (32), upper and lower limits of voltage magnitude and reactive power limits of generators are given, respectively.

III. CASE STUDY

The presented method is performed on the IEEE-24 bus reliability test system (RTS) which has 24 buses, 35 existing lines, 32 generators at 10 buses, and 21 loads. The system parameters and line investment cost can be found in [10]. In order to create contingency, the total system load is increased by 50% and the maximum power flow limit of line is decreased by 50%. The system peak load which is at the 51th week on Tuesday from 5 to 6 P.M. is used for TEP and RPP stages. The capacitor used in this paper has 0.2 per unit susceptance value with a cost M\$ 0.05 each [11].

All results are obtained on the computer which has Intel(R) Xeon(R) CPU E5-2650 @ 2.3 GHz with 64 GB of RAM by using CPLEX under GAMS. While the mixed integer linear programming (MILP) is used to solve TEP problem, the mixed integer quadratic programming (MIQCP) is used to solve RPP problem.

TABLE VII. TEP RESULTS FOR THE IEEE-24 BUS SYSTEM

Candidate Lines	Expansion Plan
3-9	
3-24	
7-8	1
6-10	2
10-12	

10-11	1
11-13	1
11-14	
12-13	
14-16	1
15-21	
15-24	
16-17	1
17-22	
20-23	1
Investment Cost (M\$)	202.65

The candidate lines and expansion plan of TEP problem are given in Table I. There are 15 candidate lines and as an expansion plan, totally 8 lines are required to be built with a cost M\$ 202.65 in order to run the system in efficient manner. Then, the RPP is performed to find the location and number of capacitors by using the updated network and the results are given in Table II.

As seen in Table II, the all load buses are selected as a candidate bus and totally 6 capacitors are required to be connected at 4 buses. The IEEE-24 bus test system has two regions considering voltage levels which are lower region with 132kV and the upper region with 230kV. At upper region of system, there are strong buses because the bulk generators are placed and there are generation surplus. On the other hand, the buses at the lower region of system are weak buses because of the generation deficits. Thus, as it is expected, the locations of the capacitors were found at lower region of system in the RPP stage.

TABLE VIII. RPP RESULTS FOR THE IEEE-24 BUS SYSTEM

Candidate Buses	Expansion Plan
3, 4, 5, 6, 8, 9, 10, 11, 12, 17, 19, 20, 24	3(1), 6(2), 9(2), 10(1)
Investment Cost (M\$)	0.3

To demonstrate the effectiveness of the RPP, the voltage levels of load buses before and after RPP are illustrated in Fig. 1. These values are obtained from AC power flow solution for annual peak load. As seen in this figure, the voltage violations are observed at some buses before the RPP. After the RPP, the voltage magnitudes can be maintained within the range of required levels and the voltage profile of system is improved.

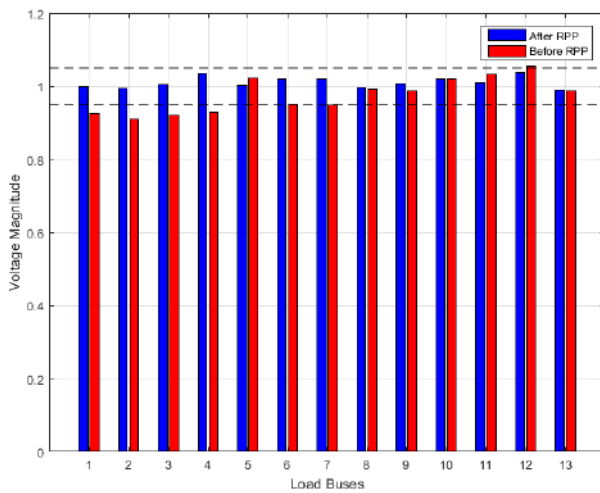


Fig. 1. The voltage levels for before and after performed RPP stage

IV. LONG TERM PERFORMANCE OF PLANNING RESULTS

The results of TEP and RPP stages are obtained according to maximum load condition. In this section, the long term performance of obtained expansion plan by using proposed method is investigated. In that manner, the hourly 8736 real and reactive load data are generated as seen in Fig. 2 according to annual peak load for IEEE 24-bus system [12].

Power World Simulator (PWS) is a user friendly program and it facilitates to understand what happens in the power system visually. Moreover, it is an interactive simulation program designed to simulate the power system operation on a time frame ranging from several minutes to several days [8]. Thus, PWS is used in order to perform AC-OPF for 8736 hours and the IEEE 24-bus test system is shown in Fig. 3.

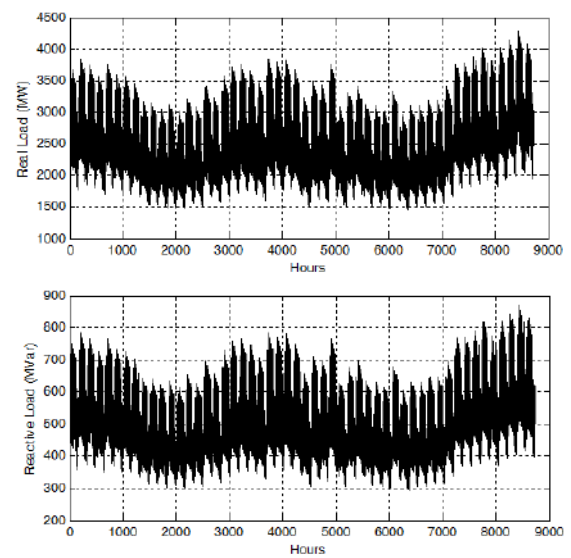


Fig. 2. The generated hourly real and reactive load data

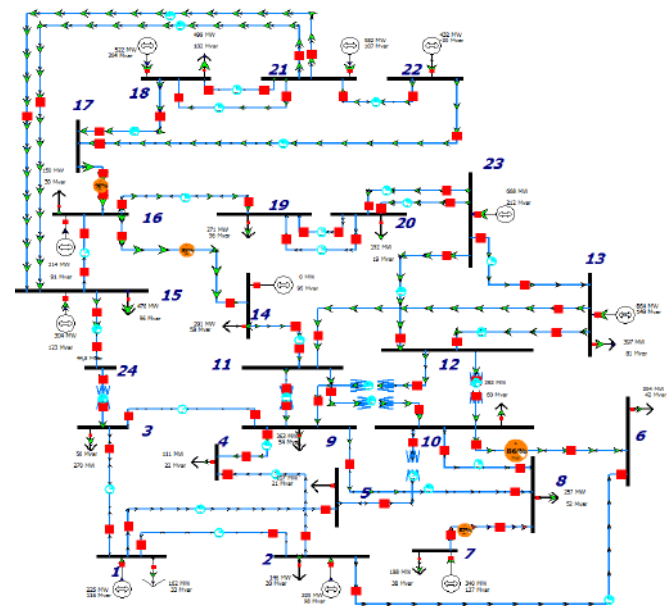


Fig. 3. The IEEE 24-bus test system in PWS

The IEEE 24-bus test system is constructed according to planning results in order to investigate the long term system performance. Voltage levels and line flows for each hour are obtained and it is observed that there is no violation on lines and voltage limits. The mean and standard deviation of the voltage at load buses are given in Table III for 8736 hours. As seen in table, the mean of the most of bus voltages are around 1 per unit and the standard deviations are within acceptable range. As a result, besides no violation, a good voltage profile is obtained for long term load profile by using presented planning procedure.



TABLE IX. LONG TERM PERFORMANCE OF VOLTAGE PROFILE

Load Buses	Mean	Standard Deviation
3	1,0098	0,0159
4	1,0001	0,0132
5	0,9997	0,0129
6	0,9949	0,0126
8	0,9845	0,0151
9	1,0049	0,0116
10	0,9909	0,0126
11	0,9745	0,0105
12	0,9851	0,0135
17	1,0400	0
19	1,0200	0
20	1,0388	0,0012
24	1,0079	0,0102

V. CONCLUSION

In this paper, a multistage network expansion planning is presented. In the first stage, DC-lossy network model is used in TEP problem for minimizing line investment cost. Then, in the second stage, the linearized-AC network model is used in RPP problem to improve the voltage profile of system. The effectiveness of the proposed method is demonstrated by using IEEE 24-bus reliability test system. The planning results are tested for long term operation by using Power World Simulator. The results show that the planning procedure is capable of long term operation without any violation and also improvement on voltage profile.

ACKNOWLEDGMENT

We thank to the Scientific and Technological Research Council of Turkey (TUBITAK) for their financial support as a grant with project number "114E514".

REFERENCES

- [1] E. G. Brown Jr, "California Energy Demand Updated Forecast 2015-2025," staff draft report, California Energy Commission, December 2014.
- [2] A. Hajebrahimi, A. Abdollahi, M. Rashidinejad, "Probabilistic Multiobjective Transmission Expansion Planning Incorporating Demand Response Resources and Large-Scale Distant Wind Farms," *IEEE Systems Journal*, vol. PP, no. 99, pp. 1-1, 2015.
- [3] L. Bahiense, G. C. Oliveira, M. Pereira, S. Granville, "A mixed integer disjunctive model for transmission network expansion," *IEEE Trans. Power Syst.*, vol. 16, no. 3, pp. 560-565, Aug. 2001.
- [4] F. Zhang, Y. Song, Z. Hu, "Mixed-integer linear model for transmission expansion planning with line losses and energy storage systems," *IET Gener. Transm. Distrib.*, vol. 7, no. 8, pp. 919-928, 2013.
- [5] H. Zhang, G. T. Heydt, V. Vittal, H. D. Mittelmann, "Transmission expansion planning using an AC model: formulations and possible relaxations," *Proc. IEEE PES General Meeting*, July 2012.
- [6] M. J. Rider, A. V. Garcia, R. Romero, "Power system transmission network expansion planning using AC model," *IET Gener. Transm. Distrib.*, vol. 1, no. 5, pp. 731-742, Sep. 2007.
- [7] A. Mahmoudabadi and M. Rashidinejad, "An application of hybrid heuristic method to solve concurrent transmission network expansion and reactive power planning," *Int. J. Electr. Power Energy Syst.*, vol. 45, no. 1, pp.71-77, February 2013.
- [8] "Power World Corporation Homepage", *PowerWorld Corporation*, accessed on Feb. 2017. [online] Available: <http://www.powerworld.com>.
- [9] H. Zhang, G. T. Heydt, V. Vittal, and J. Quintero, "An improved network model for transmission expansion planning considering reactive power and network losses," *IEEE Trans. Power Syst.*, vol. 28, no. 3, pp. 3471-3479, 2013.
- [10] N. Alguacil, A. L. Motto, and A. J. Conejo, "Transmission expansion planning: A mixed-integer LP approach," *IEEE Trans. Power Syst.*, vol. 18, no. 3, pp. 1070-1077, August 2003.
- [11] H. Macedo, C. V. Montes, J. F. Franco, M. J. Rider, and R. Romero, "MILP branch flow model for concurrent AC multistage transmission expansion and reactive power planning with security constraints," *IET Gener. Transm. Distrib.*, vol. 10, pp. 3023-3032, 2016.
- [12] R. D. Christie, IEEE Power Systems Test Case Archive, accessed on Feb. 28, 2017. [Online]. Available: <http://www2.ee.washington.edu/research/pstca/rts/rts79/ieeerts79.txt>.

Classification of Short Circuit Faults Occurring in Transmission Lines by Using Transient Current Signals, J48 And Naïve Bayes Machine Learning Algorithms

Düzgün Akmaz
Munzur University, Engineering Faculty
Tunceli, Turkey
dakmaz@munzur.edu.tr

Mehmet Salih Mamiş
Inonu University, Engineering Faculty
Malatya, Turkey
mehmet.mamis@inonu.edu.tr

Abstract— In this study, a method has been used to classify the short circuit faults. In this method, the current values of three phases and zero, positive, and negative sequence current component values obtained through the application of modal transformation on the line currents have been used in order to obtain the classification features. In each case of fault, in order to ensure that the classification features remain within specific range of values, the current values of the three phases for one cycle after fault occurrence are reduced being divided by the biggest peak value among the current values of again these three phases. Similarly for each case of fault, the sequence current components for one cycle after fault occurrence are reduced being divided by the biggest peak value among the sequence current components. After the signals are reduced, the classification features are obtained using Root Mean Square (RMS) values of the three phase current signals, RMS values of the sequence current component signals and the proportions of these RMS values to each other. The classification features obtained are used with Naive Bayes and J48 machine learning methods to classify the short circuit faults occurring in transmission lines. While the Alternative Transients Program (ATP/EMTP) is used to model the transmission lines, the Waikato Environment for Knowledge Analysis (WEKA) program is used for Naive Bayes and J48 machine learning algorithms.

Keywords—*fault classification; naïve bayes; j48; root mean square; transient current signals*

I. INTRODUCTION

With several literature studies, fault classification is one of the significant issues worked on in order to treat short circuit faults faster and better. Half Cycle Discrete Fourier Transform (HCDFT), Full Cycle Discrete Fourier Transform (FCDFT) and Fuzzy Logic (FL) are used in order to define different types of faults (Das and Reddy, 2005). HCDFT and FCDFT are applied on current signals to obtain different features for classification. Although in the study it is emphasized that the use of FCDFT will bring about better

classification features, HCDFT and FL combination is recommended for fault classification as HCDFT is faster (Das and Reddy, 2005). Multi Resolution Analysis (MRA) and Fuzzy Interference System (FIS) are used in order to develop a method to determine the location and type of fault in transmission lines (Reddy and Mohanta, 2007). Wavelet transform is applied on line currents in order to obtain MRA coefficients, then the type of fault is determined by applying the sum of these MRA coefficients on a certain rule base. In the study, fault types have been determined for approximately 1000 individual cases and phase angle at fault instant has been claimed to have a significant influence on line currents and phase angle at fault instant has been kept between (0-180°) degrees (Reddy and Mohanta, 2007). Discrete Wavelet Transform (DWT) and Multiclass Support Vector Machine (MCSVM) are used in order to develop a method to determine the type of fault in transmission lines (Ekici, 2012). Consisting of half cycle before and half cycle after fault a total one cycle of current and voltage signals have been used for DWT feature extraction (Ekici, 2012).

In this study, one-cycle current signals have been used in order to obtain classification features. Modal transformation has been applied on current signals in order to increase the number of features to be used in classification. Each line current is divided by the biggest peak value among the line currents of the three phases in order to ensure that the classification features in various fault cases remain within the specific range of values. Similarly, each of the three sequence components are divided by the biggest peak value of the three sequence current components. Then, RMS values of the line currents, RMS values of the sequence current components and the proportions of these RMS values to each other are used in order to obtain classification features. After the classification features are obtained, Naive Bayes (NB) and J48 machine learning algorithms are used in order to classify short

circuit faults. While the ATPDraw (Meyer and Liu, 1987) program is used to model the transmission lines and to obtain transient current, WEKA (Hall, Frank, Holmes,

II. OBTAINMENT OF CLASSIFICATION FEATURES

Extraction of classification feature from current or voltage signals has mostly been one of the most significant issues in the studies conducted. Varying line and fault parameters might influence the classification features obtained. Consequently, classification features must be clear and consistent for several states of faults. In this study, RMS values of one-cycle line currents occurring after fault, RMS values of zero, positive and negative sequence current components obtained after modal transformation of these line currents and the proportions of these RMS values to each other are used in order to obtain the classification features.

Equation 1 is used in order to apply modal transformation to line currents. Here, I_m indicates the modal current vector and I_p indicates the phase domain current vector. Transformation matrix T and T^{-1} is given in Equation 2.

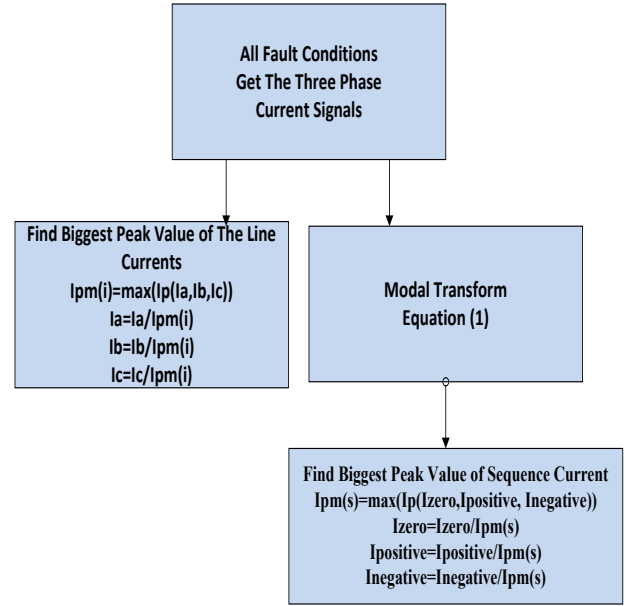
$$I_m = T^{-1}I_p \quad (1)$$

$$T = \begin{bmatrix} 1 & 1 & 0 \\ 1 & 0 & 1 \\ 1 & -1 & -1 \end{bmatrix} \text{ and } T^{-1} = \frac{1}{3} \begin{bmatrix} 1 & 1 & 1 \\ 2 & -1 & -1 \\ -1 & 2 & -1 \end{bmatrix} \quad (2)$$

RMS values of line current signals are affected by different states of faults. In order to minimize this effect, line current signals and sequence components of current signals at each case of fault are reduced through a certain method before getting RMS values. To do this, each line current is divided by the biggest peak value of the three phase currents and so the line current signals are reduced. Similarly, each of the three sequence current components is divided by the biggest peak value of these components to reduce the sequence current component signals. Figure 1 presents the method used to reduce the signals at each case of short circuit fault.

Figure 2 presents the wave forms obtained after the reduction of the line currents formed by the Symmetrical Three-Phase Fault (LLL) occurring in the middle of the 600 km long transmission line with 25 mH source inductance. As it can be seen here, the biggest peak value of the three phase line current is +1 A. Figure 3 presents the wave forms obtained after the reduction of the sequence current components for the same fault. As it can be seen in this figure, the biggest peak value of the sequence current components is +1 A. With this method, the signals are reduced in such a way that the peak values of the biggest

Pfahringner, Reutemann, Witten, 2009) program is used for classification algorithms.



line current and the biggest sequence current component will be either -1 A or +1 A in each case of faults.

Figure. 1. The method used for each case of short circuit fault to reduce three phase currents and sequence components of the currents

In this study, 12 features in total have been used for classification after reducing signal. While RMS values of each line current (RMS (Phase (A)), RMS (Phase (B)), RMS (Phase (C))) and the proportions of these values to each other (RMS (Phase (A))/RMS (Phase (B)), RMS (Phase (B))/RMS (Phase (C)), RMS (Phase (C))/RMS (Phase (A))) are used in the first six features; RMS values of the zero, positive and negative sequence current components obtained after the application of modal transformation on current signals (RMS (Zero), RMS (Positive), RMS (Negative) and the proportions of these values to each other (RMS (Zero)/RMS (Positive), RMS (Positive)/RMS (Negative), RMS (Negative)/RMS (Zero)) are used in the other six features.

Here, the RMS value of a vector is calculated as;

$$X_{RMS} = \sqrt{\frac{1}{N} \sum_{n=1}^N [X_n^2]}$$

(3)

The Bayes Theorem determines the probability of the occurrence of an event by considering the probability of another event that occurred in the past (Vijayarani and Muthulakshmi, 2013; Khoshgoftaar, Golawala and Hulse, 2007). NP classifiers are very fast for learning and applying. The classifier is called “naïve” as all predictor variables are assumed to be conditionally independent. Although the assumption of independence is typically inaccurate for the real world data, the classifier is reported to have shown

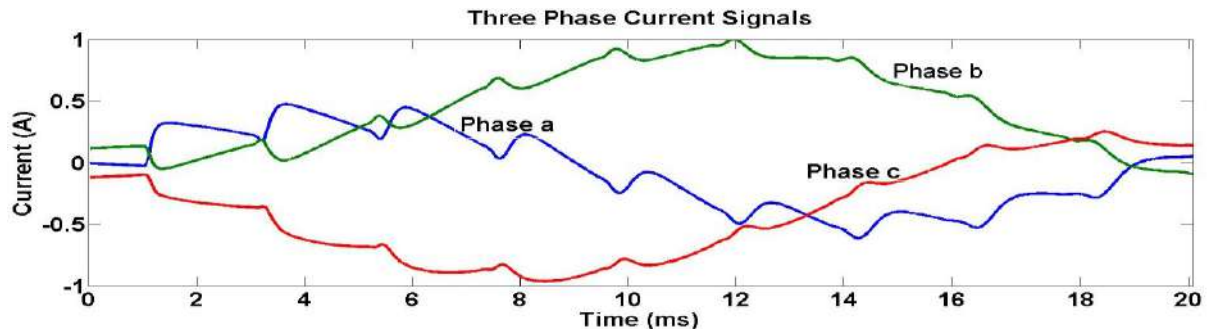


Figure. 2. The wave forms obtained after the reduction of the three phase line currents

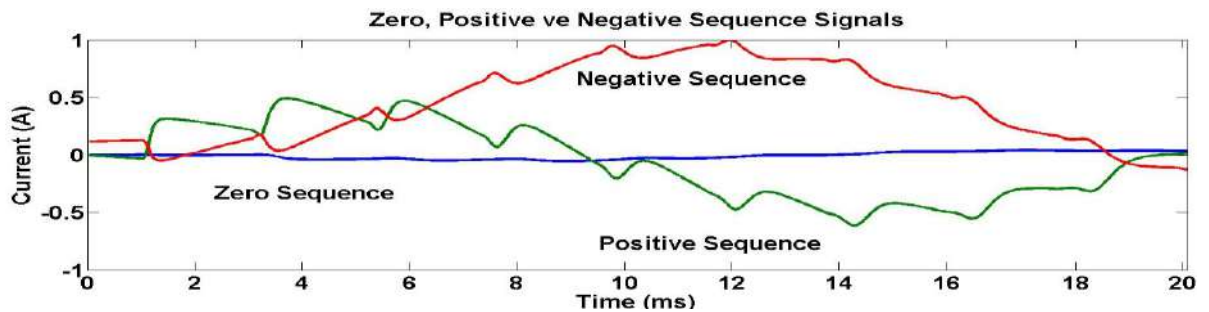


Figure. 3. The wave forms obtained after the reduction of the sequence current components

III. NAÏVE BAYES AND J48 MACHINE LEARNING ALGORITHMS

After the classification features are obtained, NB and J48 machine learning algorithms are used in order to classify the types of faults. WEKA program is used in order to apply NB and J48 algorithms. WEKA is a JAVA program having graphical tools and algorithms necessary for data analysis. WEKA is able to perform several standard data mining applications such as pre-processing, clustering, classification, integration, visualization and feature selection (Aher and Lobo, 2011).

A. Naïve Bayes

NB algorithm depends on conditional probabilities. This machine learning method uses the Bayes Theorem, which is a formula that calculates a probability by counting the frequency of the past data values and value combinations.

good performance even in the presence of strong feature dependencies (Khoshgoftaar, Golawala and Hulse, 2007).

B. J48

Ross Quinlan (Quinlan, 1993) developed C4.5 algorithm which is used to create a decision tree. In this technique, a tree is created in order to model the classification process. Once the tree is created, the method is applied to each data group inside the database and that data group is classified. When creating a tree, J48 ignores the missing values. The value of that matter can be predicted based on the feature values of other records. J48 allows for classification through decision trees or through rules that are made depending on those (Patil and Sherekar, 2013)

IV. SIMULATION STUDY

Transmission line parameters selected in the study are presented in Table 1. Figure 4 presents the ATPDraw model of LLL fault.

Table 1. transmission line parameters

Line length	600km
Voltage	380kV
Frequency	50Hz

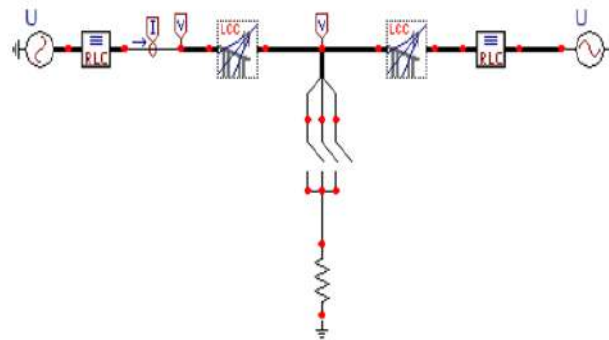


Figure. 4. ATPDraw model used in the simulation for LLL fault

Table 2. short circuit fault parameters used in the simulation

	Database 1	Database 2	Database 3
Fault Distance (km)	20,40,60,80...580	30,50,70,90...570	100,200,300...500
Fault Resistance (Ω)	1,25,50	15,30,45	15,30,45
Source Inductance (mH)	1,25,50	15,30,45	15,30,45
Phase Angle (Degree)	0	0	30,90,150,210,270,330
Number of Fault Types	10	10	10
Number of Different Fault Types	10	10	10
Total Data	7830		

Table 2 presents the short circuit fault parameters selected for creating the faults in different conditions. As it can be seen from this table, 7830 individual short circuit faults were created using ATPDraw program. 10 different types of fault, namely, Line-to-Ground-(LG)(a), Line-to-Ground-(LG)(b), Line-to-Ground-(LG)(c), Line-to-Line-(LL)(a-b), Line-to-Line-(LL)(a-c), Line-to-Line-(LL)(b-c), Double Line-to-Ground fault (LLG)(a-b-g), Double Line-to-Ground fault (LLG)(a-c-g), Double Line-to-Ground fault (LLG)(b-c-g) and LLL short circuit fault, were used in this study. 10 different types of classification were appointed in NB and J48 classification algorithms for these 10 different types of faults.

In the study, the classification method created in three different ways was tested using WEKA program. First, randomly chosen 20% of the database (1556 data) was used

for training and 80% (6264 data) was used for testing. Then, randomly chosen 30% of the same database (2349 data) was used for training and 70% (5481 data) was used for testing. Finally, k=10 cross-validation was made in database in order to test the classification success of the method. Table 3 presents the results of the simulation.

Table 3 shows that J48 machine learning algorithm ($S \geq 98.83\%$), which is based on tree structure, is more successful in fault classification compared to the NB machine learning method ($S=90.93$) which is based on probability. This is similar to the results of [10]. In study [10], NB and J48 algorithms were compared in terms of

classification in certain datasets and J48 algorithm was reported to be more successful in classification. In Table 4, literature studies and the recommended method are compared in terms of certain aspects. Values given in the Table 4 show that, the recommended method ($S \geq 98.83\%$) is as successful as the methods used in literature. However, number of test data used (6264) in this study is more than

Table 4. fault classification studies completed in literature

	The signal used	Feature extraction	Classifier	Number of tests	Success %
Das and Reddy	Line Currents	MRA, FIS	Some detected rules	T \approx 1000	100
Reddy and Mohanta	Line Currents	HCDFT	Fuzzy Rule Base	T=2400	97.41
Ekici	Line Currents Line Voltages	DWT	MCSVM	T=100	99
Rec.	Line Currents	RMS	J48	T=6264	98.83

Table 3. simulation results for naive bayes and j48 classification algorithms

Classifier	Database 20% Training 80% Testing	Database 30% Training 70% Testing	k=10 Cross Validation
Naive Bayes	90.93	94.98	94.40
J48	98.83	99.41	99.77



number of test data used in literature.

V. CONCLUSIONS

Fault classification is one of the significant issues worked on in transmission lines. In this study, several different short circuit faults were created using ATPDraw program in order to obtain transient current signals. In order to ensure that the classification features remain within certain value range in different fault conditions, three phase currents of after-fault were divided by the biggest peak values of three phase current. Similarly, sequence components of line currents were divided by the biggest peak values of sequence components of line currents. Then, RMS values of the line current signals, RMS values of sequence current component signals and the proportions of RMS values to each other were used in order to obtain classification features. Once the features were obtained, Naive Bayes and J48 machine learning algorithms were used in order to classify the types of short circuit faults. Results of the simulation showed that J48 machine learning algorithm based on the tree structure was more successful for the database used in classification. Similarly, these simulated results show that combination of the classification feature extraction method used in the study and the J48 classification algorithm are successful for determining the short circuit faults.

REFERENCES

- [1] Aher, S.B., Lobo, L., 2011''Data mining in educational system using Weka, IJCA Proceedings on International Conference on Emerging Technology Trends (ICETT)'', pp 20-25.
- [2] Das, B., Reddy, J.V., 2005, Fuzzy-logic-based fault classification scheme for digital distance protection, IEEE T. Power. Deliver, Vol. 20, 609-616.
- [3] Ekici, S., 2012, Support Vector Machines for classification and locating faults on transmission lines, Appl Soft Comput, Vol. 12, 1650-1658.
- [4] Hall, M., Frank, E., Holmes, G., Pfahringer, B., Reutemann, P., Witten, I. H., 2009, The WEKA data mining software: an update, ACM SIGKDD explorations newsletter, Vol. 11, 10-18.
- [5] Khoshgoftaar, T. M., Golawala, M., Hulse, J. V., 2007''An Empirical Study of Learning from Imbalanced Data Using Random Forest, in 19th IEEE International Conference on Tools with Artificial Intelligence(ICTAI 2007)'', pp. 310-317.
- [6] Meyer, W. S. ve Liu,T.-h., 1987, Alternative transients program (ATP) rule book, Canadian/American EMTP User Group.
- [7] Patil. T. R., Sherekar, S., 2013, Performance analysis of Naive Bayes and J48 classification algorithm for data classification, International Journal of Computer Science and Applications, Vol. 6, 256-261.
- [8] Reddy, M.J., Mohanta ,D. K., 2007, A wavelet-fuzzy combined approach for classification and location of transmission line faults, Int. J. Elec. Power, Vol. 29, 669-678.
- [9] Vijayarani, S., Muthulakshmi, M., 2013, Comparative analysis of bayes and lazy classification algorithms, International Journal of Advanced Research in Computer and Communication Engineering, Vol. 2, 3118-3124.
- [10] Quinlan J., C4.5: Programs for Machine Learning. Morgan Kaufmann Publishers, 1993.

Microfluidic Chemical Sensor Applications by Using a Metamaterial Based Sensor

Olcay Altintas, Oguzhan Akgol, Emin Unal, Muharrem Karaaslan
Department of Electrical and Electronics Engineering
Iskenderun Technical University
Iskenderun, Hatay, 31200, Turkey.

Murat Aksoy
Department of Electrical and Electronics Engineering
Cukurova University
Saricam, Adana, 01330, Turkey

Abstract—A metamaterial based sensor is designed and demonstrated numerically and experimentally for the detection of microfluids. The structure consisting of a single circular split ring resonator (CSRR) has a simple geometry and can be adjusted to any desired frequency depending on the material to be characterized. In this study, two different chemical liquid sensor applications have been investigated. First, a liquid sensor application which can successfully achieve the alcohol content of the ethanol water mixture. Second, application of chemical liquid sensor to distinguish branded and unbranded diesel samples from each other are designed. The results show that the proposed structure is especially applicable to liquid sensor applications in biochemistry.

Keywords—metamaterial; biochemical sensor; liquid sensor; microwave

I. INTRODUCTION

Sensor applications have always attracted the attention of many scientists. In this work, a novel sensor technology recently interested by many scientists is being investigated. This technology is based on metamaterials (MTM) exhibiting unusual electromagnetic behaviors. Using these extraordinary materials, it is possible to achieve negative permeability and permittivity at the same time. MTMs [1]-[3] have great potential and wide application prospects in perfect absorber [4], perfect lenses [5], invisible cloaks [6], chirality [7], and super definition [8] and so on.

Recently, many MTM-based sensor structures have been investigated in microwave frequencies. Characterization and applications of various sensing devices such as liquid sensing based on a discrete ring resonator was performed by Withayachumnankul et al [9]-[10]. The operating principle of such microfluidic sensing devices depends on the interaction between the samples placed in the sensing layer and the electric field provided by the microstrip lines. A chiral MTM sensor structure has been designed by Karaaslan et al [11] to determine the properties of samples with chiral properties.

Various MTM-based strain sensor applications have been implemented by Melik et al [12] to detect mechanical deformation in microwave frequencies.

In this work, we proposed a metamaterial sensor with the ability to detect ethanol-alcohol mixed liquid detection and branded-unbranded diesel fuels in microwave frequency regime theoretically and experimentally. The proposed structure has a simple circular split ring resonator (CSRR) topology coupled with a microstrip transmission line to investigate the transmitted signal. First, the operating frequency of the structure was investigated numerically and experimentally, assuming that the sensor layer was empty. To perform the liquid sensing application, the dielectric constant and dielectric loss values of the ethanol-water mixture and the diesel samples were measured using the dielectric probe kit at the operating frequency band. The sensing ability of the proposed structure according to the obtained dielectric properties of the fluids was analyzed numerically and experimentally with a simulation program and a vector network analyzer.

II. NUMERICAL AND EXPERIMENTAL DESIGN

The proposed sensor structure is designed and fabricated as a circular split ring resonator (CSRR). A microstrip transmission line, which forms the magnetic coupling effect with the CSRR, is integrated on the structure to observe the shifts in resonance frequency as shown in Fig. 1 (d). The back side of the structure is covered with a metallic plate, which is set as the ground plane. A radial gap was created in the CSRR to measure the sensitivity of the samples by monitoring the shifts in resonance frequency, which is an important parameter for the sensor applications. Typical dimensions of the CSRR and microstrip line obtained from parametric studies are given in Table 1.

Table 1. Typical dimensions of the proposed structure

r1	r2	sr1	sr2	rg	rd
7.0 mm	5.0 mm	4.35 mm	3.85 mm	2.0 mm	7.30 mm

Numerical studies were carried out with electromagnetic simulator software based on finite integration technique. As shown in Fig. 1 (c), two separate connection points are integrated at both ends of the microstrip transmission line to monitor the transmission coefficient S_{12} . Electromagnetic properties of the ethanol water mixtures and diesel samples were measured with the Agilent 85070E dielectric probe kit and these mixtures and diesel samples are defined as new materials according to the values measured in the simulation program.

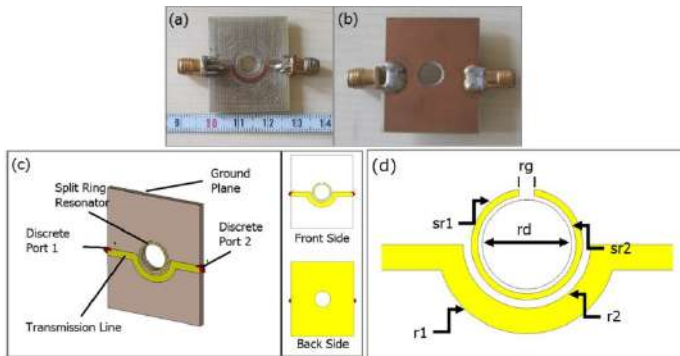


Figure 1. (a) The front side of the proposed structure, (b) the back side of the proposed structure, (c) The simulation model of the sensor structure, and (d) the geometrical dimensions of the proposed structure.

The metamaterial-based sensor structure was fabricated by the LKPF E33 Protomat PCB prototyping machine as shown in Fig. 1 (a) and (b). The dielectric substrate used in simulation and production is FR4 with a thickness of 1.6 mm, relative permittivity of $\epsilon_r = 4.3$ and loss tangent of $\tan \delta = 0.02$. The metal plates on the dielectric substrate is copper with a thickness of 35 μm and an electrical conductivity of $\sigma = 5.80001 \times 10^7 \text{ S/m}$. In addition, 50 Ω connectors are soldered on both sides of the transmission lines.

Experimental study of the sensor was performed with the PNA-L Agilent vector network analyzer (VNA) with operating frequency up to 43.5 GHz. The experimental setup is shown in Fig. 2. Before connecting the sensor structure for measurement, the VNA was calibrated using the appropriate calibration kit.



Figure 2. The experimental setup

The structure was then connected to the VNA and measured without the sample to be measured in the sensing layer. The corresponding simulation and test results for the sensor structure without any sample placed in the sensing layer are shown in Fig. 3. It is observed that the proposed sensor structure has a resonance frequency of about 4 GHz. There was a slight difference between the measurement and simulation results, due to calibration errors and manufacturing errors.

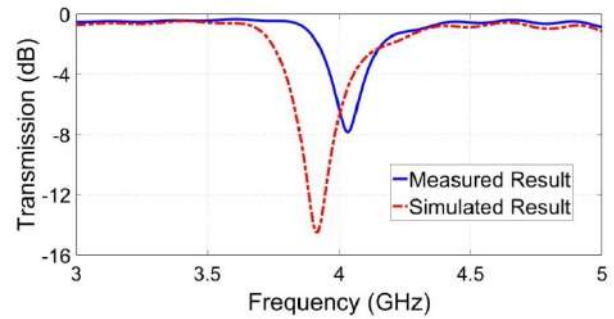


Figure 3. Simulation and experimental results of the transmission coefficient

III. ETHANOL-WATER MIXTURE SENSING APPLICATION

An ethanol water mixture was used for liquid detection application. The dielectric constant and dielectric loss factor values of the mixtures were determined with Agilent 85070E dielectric probe kit based on the percentage of ethanol in the mixture. After the dielectric probe kit was calibrated, the ethanol ratio of the mixture was increased by 20% each time, and the measurements are carried out at the operating frequency of 4.1 GHz. Table 2 shows the dielectric properties of the alcohol content in purified water measured at 4.1 GHz by means of a dielectric probe connected to the network analyzer. The dielectric properties given in Table 2 are those obtained at 4.1 GHz.

Table 2. Dielectric and loss tangent values of the ethanol-water mixture at 4.1 GHz

Ethanol Content (%)	ϵ'	ϵ''	Loss Tan.	Sim. Res. Freq. (GHz)
0	78,64	11,34	0,144	3,897
20	69,42	11,03	0,159	3,911
40	52,85	10,03	0,190	3,924
50	45,03	9,27	0,206	3,930
60	37,66	8,16	0,217	3,943
80	25,35	6,99	0,276	3,987
100	8,96	5,22	0,583	4,057

In this section, the application of liquid sensor for specific ethanol and water mixture ratios of the CSSR sensor structure has been investigated. The observed transmission coefficient values are obtained numerically and experimentally as shown in Fig. 4. Examining the simulation results given in Fig. 4 (a), the resonance frequency is found to be at about 3.897 GHz for pure water content. When the percentage of ethanol in the mixture increases by 20%, the resonance frequency shifts to the right to new value of 3.911 GHz. As the amount of ethanol content in the mixture increases, the shift in the resonance frequency of the proposed sensor appears to be approximately linear as shown in the simulation results in Fig. 4 (a). Such linear variation is also observed in the experimental results as seen in Fig. 4 (b). The experimental results have the resonance frequencies obtained for 0%, 20%, 40%, 50%, 60%, 80% and 100% of the ethanol content of the mixture at 4.024 GHz, 4.029 GHz, 4.033 GHz, 4.035 GHz, 4.038 GHz, 4.043 GHz, and 4.0, respectively. Numerical and experimental results demonstrate that the proposed CSSR based sensor structure has the potential to be used as a liquid sensor.

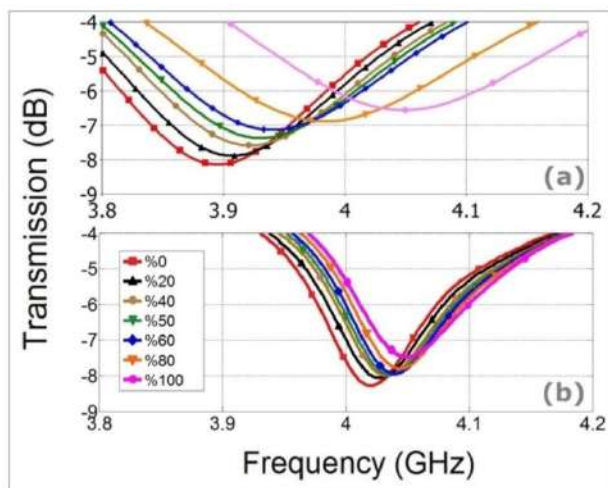


Figure 4. (a) simulation and (b) test results for the liquid sensor with respect to ethanol content

IV. BRANDED AND UNBRANDED DIESEL SENSING APPLICATION

In this section, an experimental study was conducted to distinguish branded and unbranded diesel fuels. First, the dielectric properties of the diesel samples were determined with the Agilent 85070E dielectric probe kit as shown in Table 3. Although the values are close to each other, the sensor structure of the proposed sensor has different capacitive effects on the sensor layer.

Table 3. Dielectric and loss tangent values of branded and unbranded diesel samples at 4.1 GHz

	ϵ'	ϵ''	Loss Tan.	Meas. Res. Freq. (GHz)
Branded Diesel	2.642	0.584	0.221	4.082

Unbranded Diesel	2.689	0.614	0.228	4.091
-------------------------	-------	-------	-------	-------

The experimentally obtained resonance frequencies for branded and unbranded diesel samples are shown in Fig. 5. It has been observed that the branded and unbranded diesel samples placed in the sensor layer shift the resonance frequency of the CSRR. The resonance frequency was obtained at 4.082 GHz for the branded diesel sample and 4.091 GHz for the unbranded diesel sample. A difference of about 9 MHz has occurred between the resonance frequencies of the two samples. When the results are examined, it is understood that the proposed sensor structure has the ability to separate two samples from each other.

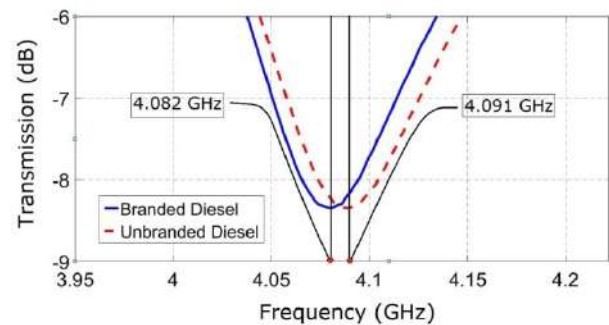


Figure 5. Experimental results for branded and unbranded diesel samples

V. CONCLUSION

A CSRR type sensor structure with a metamaterial base exhibiting chemical liquid sensor characteristics has been analyzed both numerically and experimentally at microwave frequencies. In the study, first, the dielectric properties of the ethanol water mixture and diesel samples were determined. The samples are then tested both experimentally and numerically. When the findings are examined, it is understood that the proposed sensor structure works well as a chemical liquid sensor.

REFERENCES

- [1] D. R. Smith and N. Kroll, "Negative Refractive Index in Left-Handed Materials," *Phys. Rev. Lett.*, vol. 85(14), pp. 2933-2936, 2000.
- [2] R. A. Shelby, D. R. Smith and S. Schultz, "Experimental Verification of a Negative Index of Refraction," *Science*, vol. 292(5514), pp. 77-79, 2001.
- [3] D. R. Smith, J. B. Pendry and M. C. K. Wiltshire, "Metamaterials and Negative Refractive Index," *Science*, vol. 305(5685), pp. 788-792, 2004.
- [4] F. Dincer, M. Karaaslan, E. Unal, O. Akgol and C. Sabah "Multi-Band Metamaterial Absorber: Design, Experiment and Physical Interpretation" *ACES Journal*, vol. 29(3), pp. 197-202, 2014.
- [5] N. Fang and X. Zhang, "Imaging properties of a metamaterial superlens," *Applied Physics Letters*, vol. 82, pp. 161, 2016.
- [6] S. Maci, "A Cloaking Metamaterial Based on an Inhomogeneous Linear Field Transformation," *IEEE Antennas and Wireless Propagation Letters*, vol. 58(4), pp. 1136-1143, 2010.



- [7] F Dincer, M Karaaslan, O Akgol, E. Unal and C Sabah "Asymmetric transmission of linearly polarized electromagnetic waves using chiral metamaterials with constant chirality over a certain frequency band," *Modern Physics Letters B*, vol. 28 (32), pp. 1450250, 2014.
- [8] J. Helsing, R. C. McPhedran and G. W. Milton "Spectral super-resolution in metamaterial composites," *New Journal of Physics*, vol. 13, pp. 115005, 2011.
- [9] W. Withayachumnankul, K. Jaruwongrungsee, C. Fumeaux and D. Abbott, "Metamaterial-Inspired Multichannel Thin-Film Sensor," *IEEE Sensors Journal*, vol. 12(5), pp. 1455-1458, 2012.
- [10] W. Withayachumnankul, K. Jaruwongrungsee, A. Tuantranont, C.Fumeaux and D. Abbott "Metamaterial-based microfluidic sensor for dielectric characterization," *Sensors and Actuators A*, vol. 189, pp. 233-237, 2013.
- [11] M Karaaslan and M Bakir, "Chiral metamaterial based multifunctional sensor applications," *Progress In Electromagnetics Research*, vol. 149, pp. 55-67, 2014.
- [12] R. Melik, E. Unal, N. K. Perkgoz, C. Puttlitz, and H. V. Demir, "Metamaterial-based wireless strain sensors," *Applied Physics Letters*, vol. 95, pp. 011106, 2009.

A Metasurface Polarization Converter Designed by Two Metallic Patches Placed in the Cross Corner of a Rectangular Loop

Olca Altintas, Oguzhan Akgol, Emin Unal, Muharrem Karaaslan
Department of Electrical and Electronics Engineering
Iskenderun Technical University
Iskenderun, Hatay, 31200, Turkey.

Murat Aksoy
Department of Electrical and Electronics Engineering
Cukurova University
Saricam, Adana, 01330, Turkey

Abstract—We present a Metasurface (MS) polarization converter to transform linearly polarized signals into circularly polarized signals. The unit cell of the proposed structure consists of two metallic patches placed in the cross corners of a rectangular loop. Polarization conversion quality referred to axial ratio is kept below 3 dB. The axial ratio is obtained numerically and experimentally by the division of cross-polar and co-polar responses of the antennas. Quite good axial ratio bandwidth, 260 MHz, is achieved experimentally which supports the simulation results. The proposed MS structure can be fabricated and configured easily for any desired frequency range due to its simple design. It can be used efficiently in many applications such as weather radar, airport surveillance radar and satellite communications.

Keywords—axial ratio; axial ratio bandwidth; metasurface; polarization conversion

I. INTRODUCTION

Metamaterials (MTMs) are artificial materials having unusual electromagnetic properties which cannot be found in nature. First theoretical study about double negative material (DNG) was carried out by Veselago in 1968 [1]. In the late 20th century, Pendry et. al. produced materials which have negative value of dielectric permittivity [2] in 1996 and magnetic permeability [3] in 1999. In 2000, Smith et al. realized the first DNG material which consists of a split ring and wires providing negative permittivity and negative permeability, simultaneously [4]. In recent years, many researchers study MTMs and its application areas and this attention gradually increases [5]–[7].

Metasurfaces (MSs) are the two dimensional equivalent of MTMs. MSs take up less volume and they can be less lossy structures comparing to the three dimensional MTMs [9]. There are many potential application areas concerning MS structures such as controllable smart surfaces [10], wave guide

structures [11] and absorbers [12]. In addition to these topics, MSs are also configured as polarization converter structures. Many radar and satellite systems need circularly polarized signals rather than linearly polarized ones, because circular polarization keeps signal constant at bad weather conditions.

In this study, we present a polarization converter MS structure to transform linearly polarized signal into circularly polarized one, numerically and experimentally. In order to show the conversion feature, the axial ratio (AR) of the proposed MS is calculated by dividing cross and co-pol responses. In the design, metallic patches placed in cross corners of rectangular loops are provide phase difference to obtain circular polarization. The proposed MS has two dip points which provide perfect polarization conversion activity at 2.85 GHz and 3.10 GHz. It has also 260 MHz of axial ratio bandwidth (ARBW) at two separate frequency ranges. The polarization converter can be efficiently used in S-band applications such as weather radar, airport surveillance radar, and satellite communications and so on.

Furthermore, in antenna industry, you must design two separate antennas if you need both linear and circular polarization. It is not only costly and time consuming but it also requires more physical space which is extremely important in the sector. Physical space for the antenna integration is generally limited meaning that the engineers mostly faced up the problem shrinking the antenna to fit the limited space on the radio transmitter or receiver structures. Therefore, there are many studies and researches concerning about the miniaturization of antennas. This problem can be overcome by using the proposed structure, having an antenna which is capable of radiating both linearly and circularly polarized waves will be possible. In other words, designing a linear polarized antenna will be enough to work with in any application requiring both linearly and circularly polarized

signals. In addition, the structure only contains a single layer which makes it possible for us to integrate the structure on any traditional radomes of antennas. Thus, no extra space will be used and radiation in a desired polarization can be achieved by a simple radome change which can be considered another advantage of the proposed model. Using multilayer structures may give good results in polarization conversion but it will most probably ruin the radiation pattern as well as the gain and directivity.

II. DESIGNING OF THE METASURFACE POLARIZATION CONVERTER

The unit cell of the proposed MS polarization converter consists of two metallic patches placed in crossed corners of a rectangular loop. The construction of MS structure is arranged by 16 unit cell in 4X4 layout. Rogers RT 5870 is used in the structure substrate with a thickness, loss tangent and relative permittivity of 1.575 mm, 0.012 and 2.33, respectively as shown in Fig. 1(a). The unit cell of the periodic structure is shown in Fig. 1(b) with a strip line whose thickness is $w = 0.48$ mm while the width and length are $x = 14.68$ mm $y = 14.90$ mm, respectively connecting the metallic patches. Dimensions of each metallic patches are $R_x = 4.90$ mm, $R_y = 4.64$ mm.

The goal of the study is to obtain circularly polarized signals from linearly polarized signals that can be investigated by the axial ratio (AR) which can be simply written in dB as;

$$AR(dB) = \text{Mag}(20 \log(AR(\omega))) \quad (1)$$

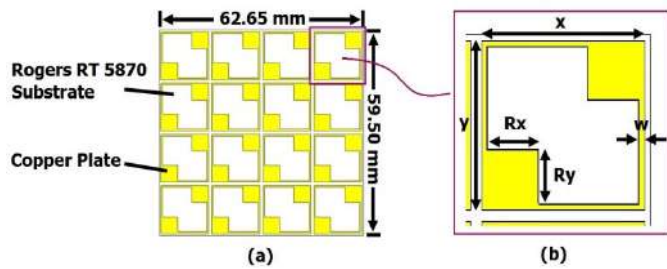


Figure 1. (a) Linear to circular polarization converter MS (b) unit cell dimensions of MS

AR is;

$$AR(\omega) = \frac{T(\omega)_{cross-polar}}{T(\omega)_{co-polar}} \quad (2)$$

III. NUMERICAL AND EXPERIMENTAL STUDY

Numerical study of the proposed MS structure is realized by CST Microwave Studio which is a commercial simulation software and 3D full wave electromagnetic solver based on finite integration technique. Periodic boundary conditions and floquet port mode are chosen for this study. To obtain efficient

circular polarization, AR is kept below 3 dB. The proposed MS has two dip points at 2.95 GHz and 3.15 GHz which give perfect polarization activity in the simulation results of AR as shown in Fig. 2(b). About 300 MHz of ARBW is also obtained between the frequencies of 2.92 GHz and 3.22 GHz.

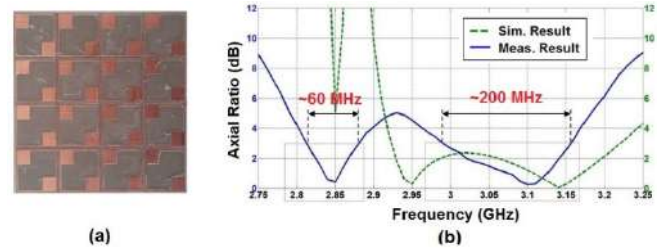


Figure 2. (a) Fabricated MS sample (b) simulated and measured AR results of proposed structure

Experimental study is achieved by Rohde & Schwarz ZVL6 vector network analyzer (VNA) with two linearly polarized microwave horn antennas. Fabrication of MS is realized by using LPKF E33 Protomat as shown in Fig. 2(a).

To obtain transmission values ($T(\omega)$), VNA is calibrated by using free space measurement. Both co-pol and cr-pol responses should be measured in order to obtain AR for the working frequencies. To measure co-polar response, the MS is placed between two horn antennas whose E-fields are in the same direction and for cross-polar response measurement, one of the horn antennas is simply rotated by 90° and the scattering parameters for the transmission (S_{21}) is measured and recorded. Finally, AR is calculated by the division of these two responses as in Eq. (2). There are two frequency bands below 3 dB which is optional to choose operating frequency range of MS as shown in Fig. 2(b). First band is between at 2.82 GHz and 2.88 GHz with a ARBW of 60 MHz. The second one is occurred between at 2.98 GHz and 3.16 GHz with a ARBW of 200 MHz. Since we have dual working frequency band, the proposed MS polarization rotator can be used with dual band antennas, either. Another dip points are also obtained at 2.85 GHz and 3.10 GHz for the proposed structure.

Although there is a small mismatch between numerical and experimental results as shown in Fig. 2(b), AR dip points and ARBW of these results are almost at the same level and agree well with each other. The deficiencies are originated by not having ideal measurement conditions in the laboratory and the manufacturing defects of MS sample.

IV. CONCLUSION

A metasurface polarization converter which transforms linearly polarized signals into circularly polarized one is realized in this study. Simulated and measured results are compared to each other and it shows that the results are in a good agreement. AR is kept below 3 dB for polarization



conversion quality. The perfect polarization conversion activities are obtained at frequencies of 2.83 GHz and 3.10 GHz and the ARBW of 260 MHz is also obtained at two frequency bands when the measured results are considered. Since circularly polarized signals are not affected by the weather conditions, the proposed MS can be used effectively in S-band radar and satellite systems. In addition, this design can be used on the existing linearly polarized antennas without using any extra space on the enclosures on which antennas are mounted. Furthermore, the proposed MS structure can be easily fabricated, integrated and reconfigured for any desired frequency range.

REFERENCES

- [1] V.G. Veselago, "The electrodynamics of substances with simultaneously negative values of ϵ and μ ," *Sov. Phys. Usp.*, vol. 10, no. 4, p. 509–514, 1968.
- [2] J.B. Pendry, W.J. Stewart and I. Youngs, "Extremely low frequency plasmons in metallic mesostructures," *Physical Review Letters*, vol. 76, p. 4773–4776, 1996.
- [3] J.B. Pendry, A.J. Holden, D.J. Robbins and W.J. Stewart, "Magnetism from conductors and enhanced nonlinear phenomena," *IEEE Transactions on Microwave Theory and Techniques*, vol. 47, p. 2075–2084, 1999.
- [4] D.R. Smith, W.J. Padilla, D.C. Vier, S.C. Nemat-Nasser and S. Schultz, "Composite medium with simultaneously negative permeability and permittivity," *Physical Review Letters*, vol. 84, p. 4184–4187, 2000.
- [5] M. Karaaslan and M. Bakir, "Chiral metamaterial based multifunctional sensor applications," *Progress In Electromagnetics Research*, vol. 149, p. 55–67, 2014.
- [6] F. Dincer, M. Karaaslan, S. Colak, E. Tetik, O. Akgol, O. Altintas, C. Sabah, "Multi-band polarization independent cylindrical metamaterial absorber and sensor application", *Modern Physics Letter B*, vol. 30, p. 1650095, 2016.
- [7] H.L. Zhu, S.W. Cheung, K.L. Chung and T.I. Yuk, "Linear-to-circular polarization conversion using metasurface," *IEEE Transactions on Antennas and Propagation*, vol. 61, no. 9, p. 4615–4623, 2013.
- [8] C.L. Holloway, E.F., Kuester, J.A. Gordon, J.F. O'hara, J. Booth and D.R. Smith, "An overview of the theory and applications of metasurfaces: The two-dimensional equivalents of metamaterials," *IEEE Antennas Propag. Mag.*, vol. 54, No. 2, p. 10–35, 2012.
- [9] C.L. Holloway, M.A. Mohamed, E. F. Kuester and A. Dienstfrey, "Reflection and transmission properties of a metafilm: with an application to a controllable surface composed of resonant particles," *IEEE Trans. Electromag. Compat.*, vol. 47, no. 4, p. 853–865, 2005.
- [10] S. Sajuyigbe, M. Ross, P. Geren, S.A. Cummer, M. H. Tanielian and D.R. Smith, "Wide angle impedance matching metamaterials for waveguide-fed phased-array antenna," *IET Microwaves, Antennas, and Propagation*, vol. 4, no. 8, pp. 1063–1072, 2010.
- [11] Y. Kotsuka, K. Murano, M. Amano and S. Sugiyama, "Novel right-handed metamaterial based on the concept of 'autonomous control system of living cells,' and its absorber applications," *IEEE Trans. Electromag. Compat.*, vol. 52, no. 3, p. 556–565, 2010.



A Comparative Study between Matrix Converter Fed Induction Machine and Dual-Matrix Converter Fed Open-End Winding Induction Machine

Beladel Abdelkader
Applied Automation and
Industrial Diagnostics Laboratory
(LAADI), Faculty of Sciences and
Technology, Djelfa University,
Algeria
Beladel_abdelkader@yahoo.fr

Kouzou Abdellah
Applied Automation and
Industrial Diagnostics
Laboratory (LAADI), Faculty
of Sciences and Technology,
Djelfa University, Algeria
kouzouabdellah@yahoo.fr

Hafaifa Ahmed
Applied Automation
and Industrial
Diagnostics
Laboratory (LAADI),
Faculty of Sciences
and Technology,
Djelfa University,
Algeria

Sedat Sünter
Firat
University,
Elazig, Turkey

Mahi Djilali
University
Amar Telidji
of Laghouat,
Algeria

Abstract—This paper deals with a comparative study between the control of three to three phase matrix converter feeding a star-connected three phase induction machine and the control of three to three phase dual matrix converter feeding an open-end winding induction machine. The control strategy used in both cases is based on a proposed direct transfer function control approach of Venturini algorithm which allows to obtain a unity power factor at the input side to boost the output phase voltage up to 150% compared to the input phase voltage, while keeping the main advantage of the matrix converter by providing a fully bidirectional power flow operation. The main objective of using the open-end winding topology is to ensure the minimization of the common mode voltage which is clearly observed in the case of star-connected winding. Simulation results are presented under both control strategies, where both matrix converters are supplied from the same three-phase power source. Whereas; the two output voltage system of the dual matrix converter are shifted with 180 degrees. Based on the obtained results the performances of the both control approaches are technically discussed.

Keywords: Matrix converter, Dual matrix converter, Direct transfer function approach, Simulation Model, Open-End Induction Machine Drive.

I. INTRODUCTION

Recently, dual-matrix converter feeding open-end winding induction motor drives have attracted great interest due to their inherent advantages compared to the standard star or delta connected induction machine drives. The main characteristics of open-end winding induction machine are [1,2]: Since the machine is powered from both ends of the winding, each matrix converter has half of the machine power rating and therefore each stator phase current can be controlled individually. Consequently, depending on the modulation strategy, possibility of doubling the effective switching frequency is caught. The matrix converter (MC) is

a forced commutated converter which can achieve varying amplitude and frequency at the output side. Indeed in recent years, significant research efforts have focused on direct matrix converter where it is increasingly used in several applications due to some implicit advantages comparing to their analogue indirect power electronics conversion using two stages power conversion, DC-AC and AC-AC. Main outstanding advantages of the matrix converter can be summarized as follows [2,3]:

1. Direct conversion (no dc link);
2. Sinusoidal input and output currents can be achieved;
3. The easiness of the input power factor control for any kind of load;
4. Bi-directional power flow capability;
5. Simple and compact design;

On the other side, due to the high integration capability of the semiconductor structures, the matrix converter topology is being recommended for several extreme and critical applications. However, the topology of the matrix converter itself has pushed the researchers to run after more favorable control strategies. In this context several modulation techniques have been developed to fulfil the requirement of the matrix converter control. Among these techniques two main control approaches are being used, the scalar approach such as; the direct transfer function approach (DTF) proposed by Venturini [4,5], and the space vector approach such as; direct and indirect space vector modulation (DSVM and ISVM) [6,7].

In this paper, the direct transfer function control approach is applied to the matrix converter for feeding an

open-end three-phase load topology to overcome the main problem of the common mode voltage and to achieve a more flexible control and the operation reliability [8,9]. The both sides of the three-phase load are supplied using dual three-phase to three-phase matrix converters. The dual matrix converter has the same topology as shown in Fig. 1. The load is an open-end winding induction machine supplied by a dual matrix converter.

In this paper, a comparison between the applications of the same induction machine supplied by a single matrix converter and a dual-matrix converter is presented. Simulation tests were performed to demonstrate the effectiveness of the used topology and control approach for both single and dual matrix converter applications for the same induction machine.

C_f limits the voltage distortion between the terminals of the converter.

L_f limits the current distortion of the supply.

R_f limits the overshoot on turn-on and avoids the resonance excitation by the supply or converter.

II. THE MATRIX CONVERTER TOPOLOGY

The topology of a three-phase input - three-phase output matrix converter is presented in Fig.1. The voltages V_{i1} , V_{i2} and V_{i3} are the input-voltages and V_{o1} , V_{o2} and V_{o3} are the output voltages. Each leg has three bidirectional power switches to ensure the connection between one phase of the input and one phase of the output at any instant [8]. These switches are operating under the two main constraints which are: The input side is not short-circuited and the output side cannot present an open-circuit at any instant. These are the two main important constraints that they are imposed by the normal operation of matrix converter to protect both of the matrix converter and the load [9-11].

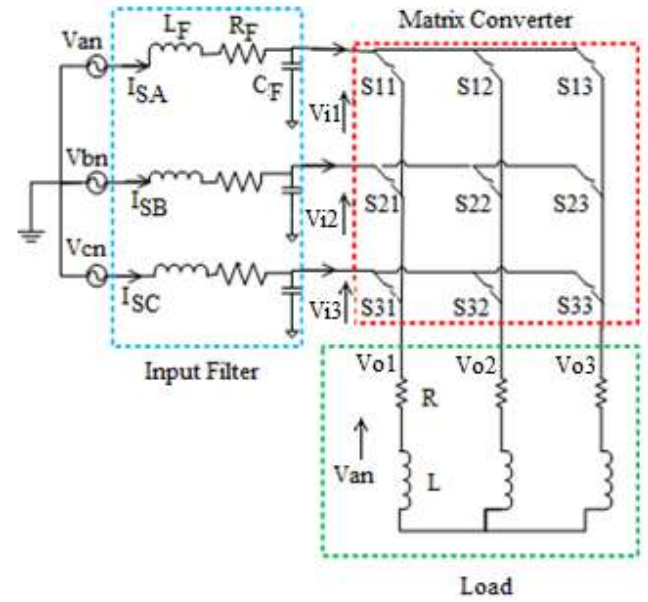


Fig.1 Three-phase matrix converter with input filter

The vector of the input voltages is given as follows:

$$\begin{bmatrix} V_{i1} \\ V_{i2} \\ V_{i3} \end{bmatrix} = V_{im} \begin{bmatrix} \cos(\omega_i t) \\ \cos(\omega_i t + 2\pi/3) \\ \cos(\omega_i t + 4\pi/3) \end{bmatrix} \quad (1)$$

The vector of the output voltages is given as follows:

$$\begin{bmatrix} V_{o1} \\ V_{o2} \\ V_{o3} \end{bmatrix} = V_{om} \begin{bmatrix} \cos(\omega_o t) \\ \cos(\omega_o t + 2\pi/3) \\ \cos(\omega_o t + 4\pi/3) \end{bmatrix} \quad (2)$$

A. The Switching Equations

The symbol S_{ij} represents the ideal bidirectional switches, where i ($=1, 2, 3$) represents the index of the output side and j ($=1, 2, 3$) represents the index of the input side. The relation between the output voltages and the input voltages can be achieved via an intermediate matrix M , which is known as the modulation matrix, hence the relation between the input and output voltages can be expressed as follows:

$$[V_o] = [M] \cdot [V_i] \quad (3)$$

The relation between the input current $[I_i]$ and output current $[I_o]$ can be deduced:

$$[I_i] = [M]^T \cdot [I_o] \quad (4)$$

Where $[M]^T$ represents the transposed matrix of $[M]$.

Equation (3) can be presented in a developed manner as follows:

$$\begin{bmatrix} V_{o1} \\ V_{o2} \\ V_{o3} \end{bmatrix} = \begin{bmatrix} m_{11} & m_{12} & m_{13} \\ m_{21} & m_{22} & m_{23} \\ m_{31} & m_{32} & m_{33} \end{bmatrix} \begin{bmatrix} V_{i1} \\ V_{i2} \\ V_{i3} \end{bmatrix} \quad (5)$$

where the elements of the modulation matrix representing the modulation coefficients are expressed as follows:

$$m_{ij} = \frac{t_{ij}^k}{T_s} \quad (6)$$



During the switching process, the bidirectional switches can connect or disconnect the phase i of the input to the phase j of the output which is connected to the load. In general, the modulation coefficient must provide the following rules [12]:

- At any instant, only one switch S_{ij} ($i = 1, 2, 3$) conducts in order to avoid short-circuit between the input phases.

$$\sum_{i=1,2,3} S_{ij}(t) = 1; j = \{1, 2, 3\} \quad \forall t \quad (7)$$

- At any instant, at least two switches S_{ij} ($j = 1, 2, 3$) conduct to ensure a way to the inductive load current.
- The switching frequency $f_s = \omega_s / 2\pi$ must have a higher value than the maximum of f_i, f_o ($f_s \gg \max f_i, f_o$).
- During the period, T_s which is known as the sequential period, the sum of the conduction times of switches being used to synthesize the same output phase, must be equal to T_s .

The time t_{ij} , which is called the time of modulation, can be defined as:

$$t_{ij} = m_{ij} \cdot T_s \quad (8)$$

III. MODIFIED DIRECT TRANSFER FUNCTION APPROACH

The modified direct transfer function approach [4,5] permits to control the switch, S_{ij} , whereas the output voltage, V_{oij} and the input current, i_{ij} are sinusoidal with the same values of the output frequency, the input amplitude, the input frequency and the displacement factor.

The maximum voltage output is obtained by the injection of the third harmonic of the output and input waveforms. The mean values of the output voltage over the sequence K^{th} are then given by:

$$\begin{aligned} v_{o1}^{(k)} &= v_{i1}^{(k)} \frac{t_{11}}{T_s} + v_{i2}^{(k)} \frac{t_{12}}{T_s} + v_{i3}^{(k)} \frac{t_{13}}{T_s} \\ v_{o2}^{(k)} &= v_{i1}^{(k)} \frac{t_{21}}{T_s} + v_{i2}^{(k)} \frac{t_{22}}{T_s} + v_{i3}^{(k)} \frac{t_{23}}{T_s} \\ v_{o3}^{(k)} &= v_{i1}^{(k)} \frac{t_{31}}{T_s} + v_{i2}^{(k)} \frac{t_{32}}{T_s} + v_{i3}^{(k)} \frac{t_{33}}{T_s} \end{aligned} \quad (9)$$

The conduction time is modulated with the ω_m while T_s is constant, such as $\omega_m = \omega_o - \omega_i$, these times are defined as follows:

1. In the first phase, we have:

$$\begin{aligned} t_{11} &= \frac{T_s}{3} (1 + 2q \cos(\omega_m t + \theta)) \\ t_{12} &= \frac{T_s}{3} \left(1 + 2q \cos(\omega_m t + \theta - \frac{2\pi}{3}) \right) \\ t_{13} &= \frac{T_s}{3} \left(1 + 2q \cos(\omega_m t + \theta - \frac{4\pi}{3}) \right) \end{aligned} \quad (10)$$

2. In the second phase, we have:

$$\begin{aligned} t_{21} &= \frac{T_s}{3} \left(1 + 2q \cos(\omega_m t + \theta - \frac{4\pi}{3}) \right) \\ t_{22} &= \frac{T_s}{3} (1 + 2q \cos(\omega_m t + \theta)) \\ t_{23} &= \frac{T_s}{3} \left(1 + 2q \cos(\omega_m t + \theta - \frac{2\pi}{3}) \right) \end{aligned} \quad (11)$$

3. In the third phase, we have:

$$\begin{aligned} t_{31} &= \frac{T_s}{3} \left(1 + 2q \cos(\omega_m t + \theta - \frac{2\pi}{3}) \right) \\ t_{32} &= \frac{T_s}{3} \left(1 + 2q \cos(\omega_m t + \theta - \frac{4\pi}{3}) \right) \\ t_{33} &= \frac{T_s}{3} (1 + 2q \cos(\omega_m t + \theta)) \end{aligned} \quad (12)$$

Where θ is initial phase angle.

The output voltage is:

$$[V_o^{(k)}] = [M^{(k)}] \cdot [V_i^{(k)}] \quad (13)$$

$$[M^{(k)}] =$$

$$\begin{bmatrix} 1 + 2q \cos(A) & 1 + 2q \cos\left(A - \frac{2\pi}{3}\right) & 1 + 2q \cos\left(A - \frac{4\pi}{3}\right) \\ 1 + 2q \cos\left(A - \frac{4\pi}{3}\right) & 1 + 2q \cos(A) & 1 + 2q \cos\left(A - \frac{2\pi}{3}\right) \\ 1 + 2q \cos\left(A - \frac{2\pi}{3}\right) & 1 + 2q \cos\left(A - \frac{4\pi}{3}\right) & 1 + 2q \cos(A) \end{bmatrix} \quad (14)$$

Where:

$$\begin{cases} A = \omega_m t + \theta \\ \omega_m = \omega_o - \omega_i \end{cases} \quad (15)$$

This mathematical development shows that the matrix converter with modified direct transfer function approach generates three-phase sinusoidal voltage waveforms at the output.

IV. MODELLING OF THE OPEN-END WINDING INDUCTION MACHINE

The open-end stator winding induction machine presented in Fig. 2 is supplied by two three-phase voltage systems and these systems are defined as:

The three-phase systems supplied by the first matrix converter: $[V_{s1}] = [V_{s11} \ V_{s12} \ V_{s13}]^T$;

The three-phase systems supplied by the second matrix converter: $[V_{s2}] = [V_{s21} \ V_{s22} \ V_{s23}]^T$;

Hence, the voltage vector applied on the stator winding of the machine is:

$$[V_s] = [V_{s11} - V_{s21} \ V_{s12} - V_{s22} \ V_{s13} - V_{s23}]^T$$

The mathematical flux model is defined in (d-q) reference frame, and described by the following state equations representation:

$$\frac{dX(t)}{dt} = [A(\omega, \omega_{dq})][X(t)] + [B] \cdot U(t) \quad (16)$$

$$Y(t) = [C] \cdot Y(t) \quad (17)$$

where:

$X(t) = [\phi_{sd} \ \phi_{sq} \ \phi_{rd} \ \phi_{rq}]$ is the state vector;

$U(t) = U_1(t) - U_2(t) = [V_{sd1} - V_{sd2} \ V_{sq1} - V_{sq2}]$ is the control vector;

$Y(t) = [I_{sd} \ I_{sq} \ I_{rd} \ I_{rq}]$ is the output vector;

The principle diagram of the system is shown in Fig. 2:

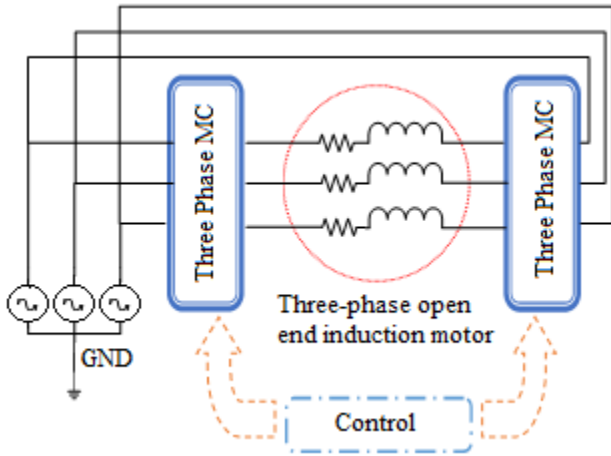


Fig.2 Three phase open-end winding induction motor fed by dual matrix converter

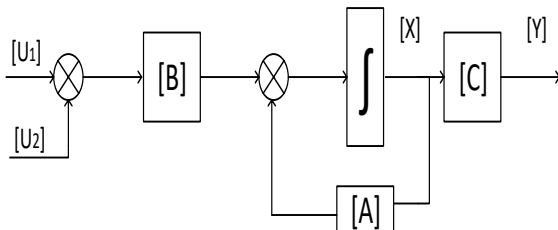


Fig.3 Block diagram of the open-end winding machine

On the other side the following parameters are taken into account:

$\tau_s = \frac{L_s}{R_s}$ is the stator constant time

$\tau_r = \frac{L_r}{R_r}$ is the rotor constant time

$\sigma = 1 - \frac{M_{sr}^2}{L_s L_r}$ is the coefficient of dispersion of Blondel

R_r is the rotor resistance, R_s is the stator resistance, L_r is the rotor inductance, L_s is the stator inductance, M_{sr} is the mutual inductance between stator and rotor.

The equation for current vector is:

$$[I] = [L]^{-1}[\phi] \quad (18)$$

The matrices [A], [B] and [C] are defined as follows:

$$[A] = \begin{bmatrix} -\frac{1}{\sigma\tau_s} & \omega_{dq} & \frac{M_{sr}}{\sigma\tau_s L_r} & 0 \\ -\omega_{dq} & -\frac{1}{\sigma\tau_s} & 0 & \frac{M_{sr}}{\sigma\tau_s L_r} \\ \frac{M_{sr}}{\sigma\tau_r L_s} & 0 & -\frac{1}{\sigma\tau_r} & \omega_{dq} - \omega \\ 0 & \frac{M_{sr}}{\sigma\tau_r L_s} & -(\omega_{dq} - \omega) & -\frac{1}{\sigma\tau_r} \end{bmatrix} \quad (19)$$

$$[B] = \begin{bmatrix} 1 & 0 & 0 & 0 \\ 0 & 1 & 0 & 0 \\ 0 & 0 & 1 & 0 \\ 0 & 0 & 0 & 1 \end{bmatrix}$$

$$[C] = [L]^{-1} = \begin{bmatrix} \frac{1}{\sigma L_s} & 0 & \frac{M_{sr}}{\sigma L_s L_r} & 0 \\ 0 & -\frac{1}{\sigma\tau_s} & 0 & \frac{M_{sr}}{\sigma L_s L_r} \\ -\frac{M_{sr}}{\sigma L_r L_s} & 0 & -\frac{1}{\sigma L_r} & 0 \\ 0 & -\frac{M_{sr}}{\sigma L_r L_s} & 0 & \frac{1}{\sigma L_r} \end{bmatrix} \quad (20)$$

The mechanical equation is given as follows:

$$T_{em} - T_r = j \frac{d\omega}{dt} + f\omega \quad (21)$$

$$T_{em} = \frac{3}{2} p (\phi_{s\alpha} I_{s\beta} - \phi_{s\beta} I_{s\alpha}) \quad (22)$$

where, T_{em} is the electromagnetic torque; T_r is the load torque.

V. SIMULATION

In this work, two simulation tests were performed to prove the advantage of the use of the open-end winding induction machine fed by a dual matrix converter having the same

topology and characteristic. The first simulation presents the induction machine fed by only one matrix converter, where the output voltage is characterized by a fundamental frequency of $f_0=50$ Hz and a magnitude of $V_0=350$ V. The parameters of the input voltage source and the induction machine are presented in Table 1. On the other side, due to the distortion which may occur in the input current and to avoid the propagation of this kind of harmonics pollution toward the source, an LC input filter is inserted as shown in Fig.2 where its parameters can be found in Table 1. [13-15].

A. Induction Motor Fed by A Three-Phase Matrix Converter

In this case, a single three-phase matrix converter is used to feed a three-phase induction motor. The output voltage and the output current of the matrix converter are presented in Fig. 4 and 6, respectively. Total Harmonic Distortion (THD) of the output voltage and current waveforms, which is defined in Eq. (23), are presented in Fig. 5 and 7, respectively. It can be concluded that the harmonic rays are around the switching frequencies ($n \times f_s$) where it is taken as $f_s=10$ kHz

$$THD = \sqrt{\frac{V_2^2 + V_3^2 + \dots + V_n^2}{V_1^2}} \quad (23)$$

The fundamental harmonic amplitude of the output voltage is 344.4 V with THD of 99.36% as shown in Fig. 5 and harmonics rays can be remarked clearly around the switching frequency. However, due to the inductive nature of the induction motor, the output current posses a low THD as 2.77%. Figs. 8 and 9 show the decoupling carried out between the flux and the electromagnetic torque. The decoupling between torque and machine speed is remarked clearly especially at the interval between 1.5 s and 2.5 s. The supply current waveform is shown in Fig.10. The result shows great effect of the input filter where the high order harmonics are eliminated by the input filter.

Table 1 Simulation parameters

V_s	Input voltage	350 V
f_s	Input frequency	50 Hz
L_f	Filter inductance	0.03 H
R_f	Filter Resistance	0.5 Ω
C_f	Filter Capacitance	25 μ F
R_s	Stator resistance	4.85 Ω
R_r	Rotor resistance	3.81 Ω
L_s	Stator inductance	0.274 H
L_r	Rotor inductance	0.274 H
L_m	Mutual inductance	0.258 H

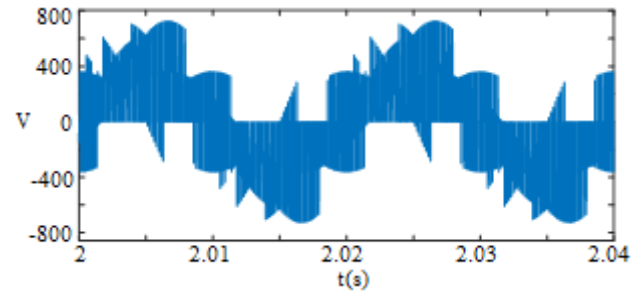


Fig.4 Output line voltage waveform of the matrix converter

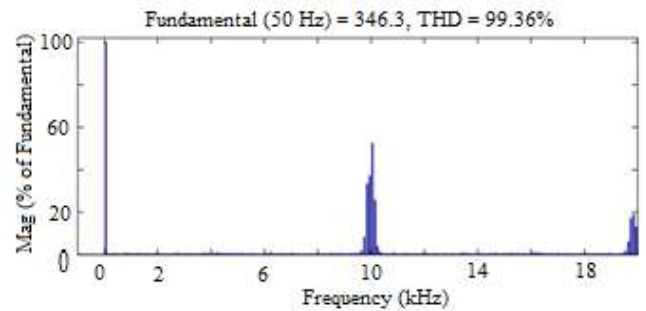


Fig.5 Harmonic spectrum of the matrix converter output voltage waveform

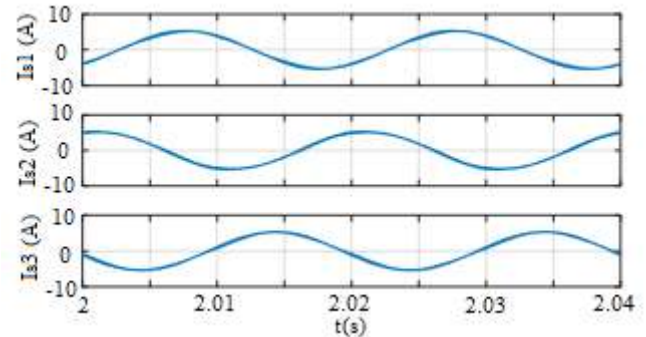


Fig.6 Three-phase motor currents

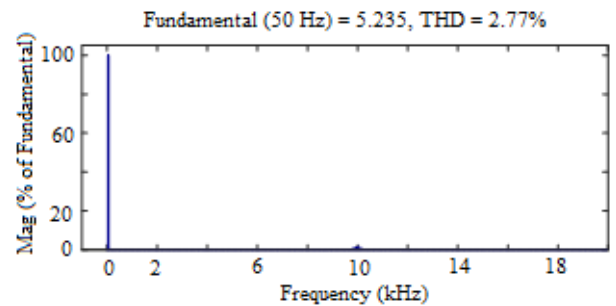


Fig.7 Harmonic spectrum of the matrix converter output current

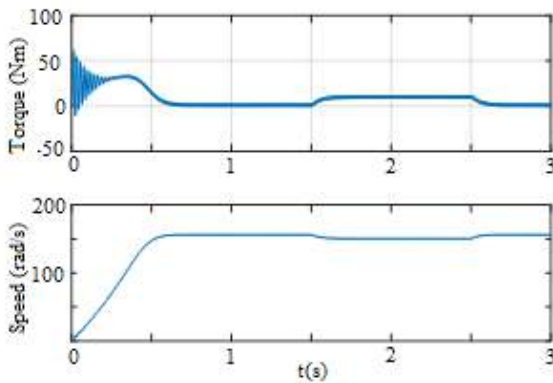


Fig.8 Torque (up) and speed(bottom) of the induction motor

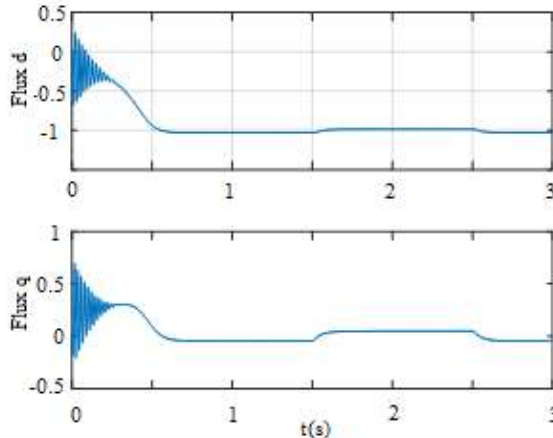


Fig.9 Flux flowing rotor axis "d" (up) and flux flowing rotor axis "q" (bottom)

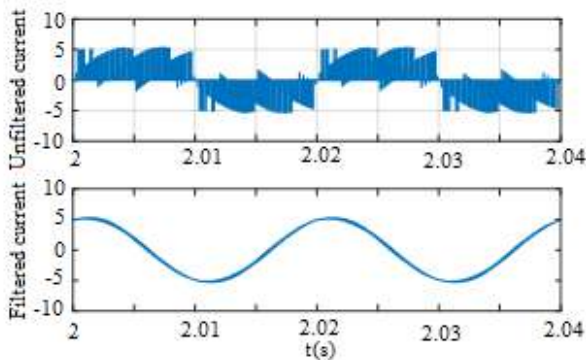


Fig.10 The supply current without and with filtering, respectively

B. Dual Matrix Converter Feeding Open-End Winding Induction Motor

In this case, two of three-phase matrix converter feed the both sides of the open-end winding of the same induction machine stated previously. Under this topology the common mode voltage (CMV) will be totally removed and the three-phase load can be controlled independently. Due to the balanced nature of the load, the voltage applied at each load phase is the same except for the eventual required phase shift. Figs.11 and 12 illustrate the voltages between the two

terminals of the three-phase load and the load currents, respectively. It is obvious that the fundamental magnitude of the voltage is 348.5 V with a THD of 75.12 % whereas, the fundamental current is 4.636 A with THD of 3.36 % which means that there is an improved voltage and current quality in comparison with the situation where the machine is fed by a single three-phase matrix converter (Fig. 13 and Fig. 14). In the same time a less harmonic rays can be remarked clearly near the switching frequency $f_s = 10$ kHz. The two level voltage is clearly observed and the three-level voltage at the load terminals is also obviously observed. The effect of the input filter can be seen clearly in Fig. 17. Figs.15 and 16 show the decoupling carried out between the flux and the electromagnetic torque. In the same time, the decoupling between the torque and the speed of the machine can be seen especially at the interval between 1.5 s and 2.5 s.

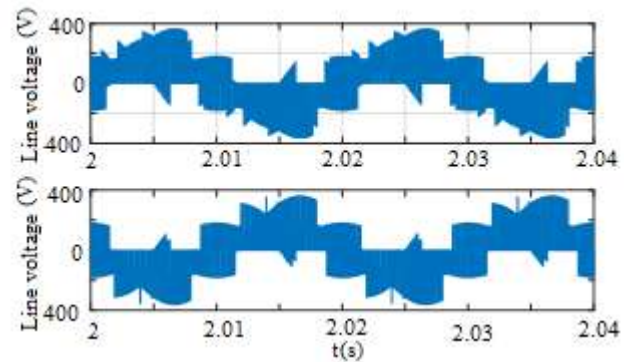


Fig.11 Output line voltage waveforms of MC1 (up) and MC2 (bottom)

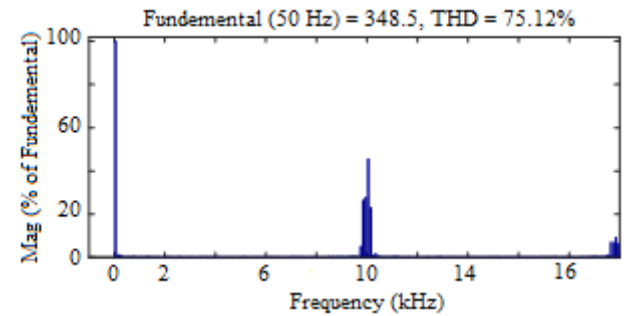


Fig.12 The Harmonic spectrum of the output voltage applied to one phase of the induction motor

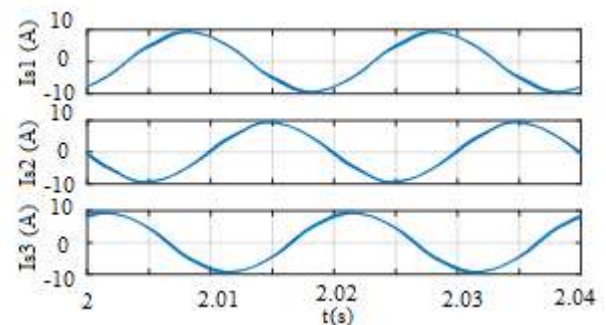


Fig.13 Three-phase motor currents

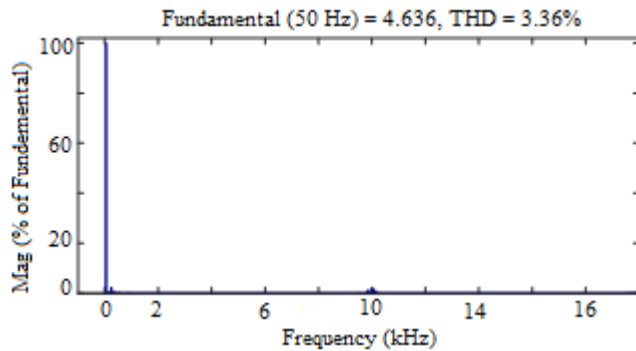


Fig.14 Harmonic spectrum of the output current

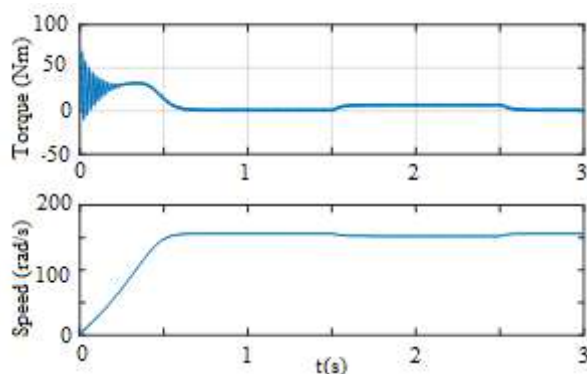


Fig.15 Torque (up) and speed (bottom) of the induction motor

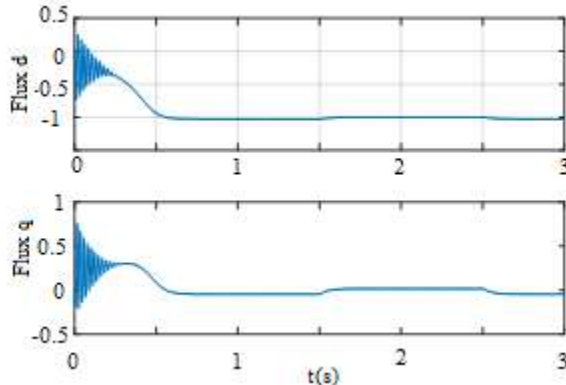


Fig.16 Flux flowing rotor axis "d" (up) and flux flowing rotor axis "q" (bottom)

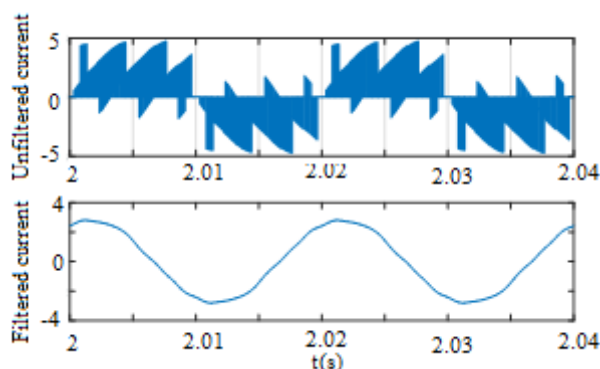


Fig.17 The supply current without and with filtering, respectively

VI. CONCLUSIONS

In this paper, the main advantages of the dual matrix converter used in open-end structure is proved by simulation results. The results show clear improvement on quality of the voltages enforced to the induction machine drive and elimination of the common mode voltage which is major problem in all three-phase load applications, especially in three-phase electrical machines. On the other side, due to the multilevel nature of the voltage applied at the terminal of the open-end load, the current quality is also improved, where the THD is decreased at nearly 48% compared to the classical topology based on one matrix converter. An important issue is that the use of a dual matrix converter is more reliable in case of fault on one or more switches. This problem can be solved by easily adjusting control signals of the switches. Finally, it can be said that the presented topology can have a large use in electric machines application in industry based on the afore mentioned advantages.

REFERENCES

- [1] Javier Riedemann, Iván Andrade, Rubén Peñab, Ramón Blasco-Gimenez, Jon Clare, P. Melin, M. Rivera, "Modulation strategies for an open-end winding induction machine fed by a two-output indirect matrix converter", *Mathematics and Computers in Simulation*, 31 May 2016, pp. 144-152.
- [2] P.W. Wheeler, P.W., Rodriguez, J.C. Clare, L. Empringham, and A. Weinstein: "Matrix Converters: A Technology Review", *IEEE Trans. On Ind. Elect.* Vol. 49, no. 2, Apr, 2002, pp. 276-288.
- [3] René Vargas, José Rodríguez, Ulrich Ammann, and Patrick W. Wheeler, "Predictive Current Control of an Induction Machine Fed by a Matrix Converter With Reactive Power Control", *IEEE Tran. On Ind. Electronics*, Vol. 55, No. 12, Dec. 2008, pp. 4362-4371.
- [4] M. Venturini, "A new sine wave in sine wave out, conversion technique which eliminates reactive elements," in *POWERCON 7*, 1980, pp. E3-1-E3-15.
- [5] A. Alesina, and M. Venturini, "Analysis and design of optimum amplitude nine-switch direct ac-ac converters", *IEEE Trans. Power Elect.* Vol. PE-4, No. 1, 1989, pp. 101-112.
- [6] S. Moin Ahmed, Haitham Abu-Rub, Abdellah Kouzou, "Predictive Simultaneous Power and Current Control in a Three-phase Direct Matrix Converter", *International Conference on Power Electronics and Their Applications (ICPEA)*, Djefia- Algeria, 2013.
- [7] G. Bachir, A. Bendiabdellah, "A Comparative Study between Two Control Strategies for Matrix Converter", *Advances in Electrical and Computer Engineering*, Vol. 9, No. 2, 2009.
- [8] A. Beladel, A. Kouzou, A. Hafaifa, D. Mahia, "Dual matrix converter feeding an open-end winding load based on modified direct transfer approach", *International Scientific Conference on Engineering, Technologies and Systems, TECHSYS 2016*, Technical University – Sofia, Plovdiv branch 26 – 28 May 2016, Plovdiv, Bulgaria.
- [9] H. Altun, S. Sunter, "Matrix converter induction motor drives: Modelling simulation and control", *Electrical Engineering*, Dec 2003, Vol. 86, Issue 1, pp 25-33.
- [10] J. Rodriguez, E. Silva, and P. Wheeler "Matrix converter controlled with the direct transfer function approach: Analysis, modelling and simulation", *International journal of electronics*, 2013, pp. 63-85.
- [11] A. Djahbar, B. Mazari, "High performance motor drive using matrix converter" *Acta Electrotechnica et Informatica*, No.2, Vol.7, 2007.



- [12] S. Guizana, F. Ben Ammar, "Dual open-end stator winding induction machine fed by redundant voltage source inverters", Turkish Journal of Electrical Engineering & Computer Sciences, Vol.92, No.2, Feb. 2005, pp. 2171-2181.
- [13] J. Riedemann, J.C. Clare, P.W. Wheeler, R. Blasco-Gimenez, M. Rivera, R. Peña, "Open-End Winding Induction Machine Fed by a Dual-Output Indirect Matrix Converter", IEEE Transaction on Industrial Electronics, Vol. 63, No. 7, July 2016.
- [14] M. Gopal, K. Gopakumar, P.N. Tekwani, L.A. Emil, "Reduced-Switch-count five-level inverter with common-mode voltage elimination for an open-end winding induction motor drive", IEEE Transactions on Industrial electronics, Vol. 54, No.4, 2007.
- [15] M. Elbar, M.O. Mahmoudi, B. Naas, "A Carrier-Based PWM Techniques Applied to a Three-Level Four-Leg Inverter For Use as a Shunt Active Power Filter", J. Electrical Systems, Special Issue No.2,2010, pp.47-57.

Microwave Metamaterial Absorber For Sensing Applications

M. Bakır¹

¹Department of Computer Engineering, Faculty of Engineering and Architecture, Bozok University
Yozgat / Turkey

M. Karaaslan², O. Akgo², E. Unal², C. Sabah³

²Electrical and Electronics Engineering, Iskenderun Technical University, Iskenderun, Hatay, Turkey

³Department of Electrical and Electronics Engineering, Middle East Technical University - Northern Cyprus Campus, Kalkanli, Guzelyurt, 99738, TRNC / Mersin 10, Turkey

Abstract— A metamaterial absorber (MA) based sensor is designed and analyzed for various important applications including pressure and density sensing. After obtaining a perfect absorption (PA) at around 5.5 GHz and 7.7 GHz, we have achieved 130 MHz bandwidth for the pressure sensing depending on the thickness of the sample, 200 MHz bandwidth for density sensing in different type of materials Arlon type AD 300, AD 350 and AD 450 and 200 MHz bandwidth in the working frequency band. The proposed structure uses the changes on the overall system resonance frequency caused by the sensor layer's dielectric constant which varies depending on the electromagnetic behavior of the sample placed in. This model can be adapted to be used in industrial, medical and agricultural product for sensor applications.

Keywords— *metamaterial, absorber, sensor*

I. INTRODUCTION

Metamaterials (MTMs) are such engineered structures that possessing extraordinary features as backward propagation, negative permittivity and/or permeability. They allow researchers to explore many interesting areas [1-6]. MTM sensors offer higher sensitivity and resolution compared to the traditional structures due to their strong localization of fields. They also reduce the sensor size compared to a regular structure that is less proportional to the operating frequency. For this reasons, For the past decade, MTMs have been extensively used in sensor applications. For example, Schueler et al. [7] reviewed the MTM inspired composite right/left-handed transmission line microwave sensors. Chen et al. [8] examined MTMs application in sensing with an emphasis on split ring resonator-based sensors. Niu et al. [9] investigated an optical waveguide sensor application. Yang et al. [10] developed a high sensitive sensor based on split ring resonators. In this manuscript, we want to develop a concept study which is covering both MA and MTM sensor studies in C band to provide high resolution sensing in temperature, humidity, pressure and density.

II. NUMERICAL DESIGN AND EXPERIMENTAL SETUP

Proposed MTM The main subject of the study is to design a MA, therefore, firstly absorption configuration of the proposed structure is introduced and investigated. Designed MTM as introduced in Fig.1 composed from consists of two resonators; one of them is a square and the other one is a ring shaped inclusion which incorporates two splits. There are dual splits placed on both of them as shown in Figure 1.a. Resonators are made of copper elements with the conductivity of $5.8 \times 10^7 S/m$, Arlon DiClad 5.27 type material is used as a substrate whose thickness is 1.6mm and dielectric constant is 2.50. Square and ring resonators have a thickness of 0.8 mm and the distance between the square resonator and the unit cell edge is also 0.8 mm. split width on the resonators The gap width were chosen as 1.6mm to ensure the best numerical results. The proper dimensions of the unit cell are evaluated by using parametric studies. Design is produced by using CNC controlled machine and experimental tests are realized by using horn antennas and a 42.5 GHz VNA as shown in Figure 1.b As it is explained in the following sections, proposed design is tested numerically and experimentally for absorber and sensor applications. For absorber configuration, copper plate is used behind the dielectric substrate that supports resonators. For sensor configuration copper plate is not used behind the resonators' substrate and sensor layer is put behind the substrate. In order to show the absorption characteristics, a dielectric substrate (DiClad 5.27) which is backed by copper is placed behind the sensor layer as shown in Figure 1.a and Figure 1.b.

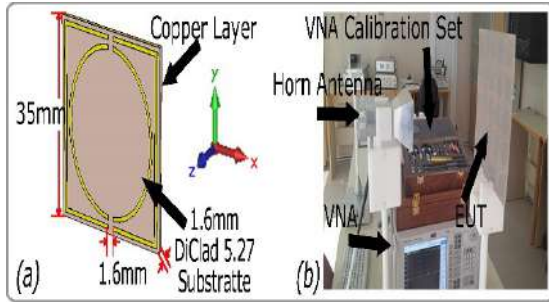


Fig. 1. (a) 35mm x 35mm unit Cell of the proposed MA based sensor structure which is composed from square and ring resonators cell, (b) experimental setup for absorber

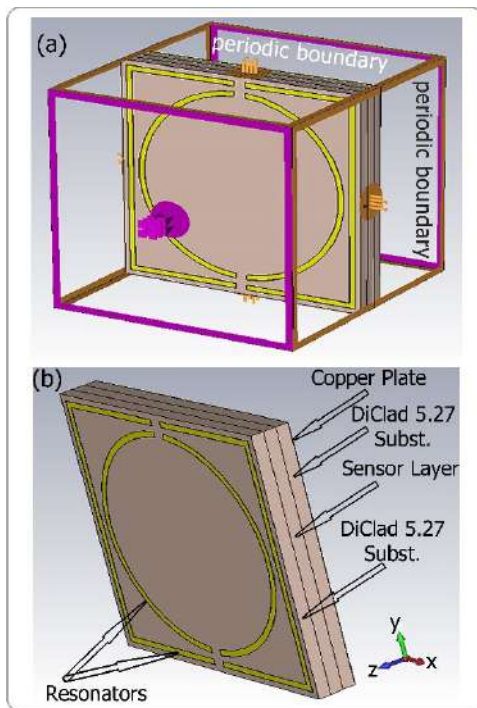


Fig. 2 (a) Profile view of the proposed structure for sensing configuration showing layers and boundary conditions in X, Y axis (b) explanation of layers in the sensor configuration of the proposed structure.

III. METAMATERIAL ABSORBER AND SENSOR APPLICATIONS

Since proposed MTM sensor application based on an absorber, we physically produced, numerically and experimentally verified the absorber application. For absorber application, copper plate is placed behind the dielectric back of resonators and by using horn antennas experimental verification is of absorber is tested. Numerical verification is realized by using CST microwave studio under periodic boundary conditions. It is known that the essential

requirement of an absorber is to confine the penetrated energy in the structure. The reflected and transmitted waves have to be minimized ($R(\omega) \& T(\omega) \rightarrow 0$) so that these waves should be as small as possible in order to realize perfect absorption. Numerical and experimental results obtained for the mentioned dimensions of the structure are given in Fig. 3. As shown in figure, there are two resonances that occur at 6.46 GHz and 7.68 GHz which are resulted from two coupled resonators. Resonant frequencies are located in the upper half of the C-band and dual resonance characteristics are good for absorbing electromagnetic energy. When numerical results are compared with the experimental results, a tiny shift is seen in the resonant frequency which is due to calibration, fabrication errors and non-ideal measurement conditions. Measured absorption level is also smaller than that of the simulation due to the same reasons.

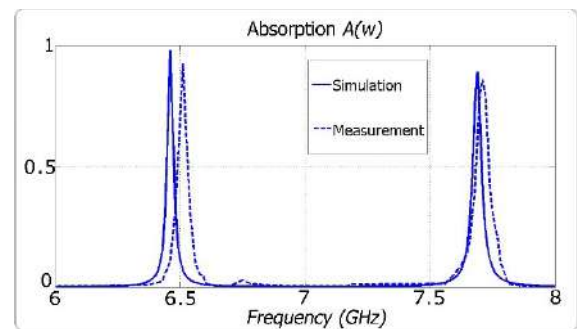


Fig. 3 Numerical and experimental results for absorber configuration of the proposed structure showing double resonances around 6.5 and 7.7 GHz.

First sensor application by using the sensor configuration defined in Fig. 2 is pressure sensor. It is simulated and experimentally tested by changing the sensor layer's thickness up and down which correspond a pressure increase and decrease. gives the opportunity to build different sensor applications. One of these sensors is a pressure sensor. This type of sensor is realized by changing the sensor layer thickness. It should be noted that as the pressure decreases, the thickness of the layer expands. On the other hand, an increase in the pressure leads to a decrease in the thickness of the sensor layer. Three different air cushion have been taken as sample which are 1mm, 1.5mm and 2mm to show reflection coefficient both numerically and experimentally as compared in Fig.4. In this application, a sensor layer which is composed of air having a relative dielectric constant of 1 is used. Numerical and experimental results for three different sensor layer thicknesses (1, 1.5, 2 mm) are presented in Fig.5. Three different air cushions are especially chosen to show linearity. This is because of the fact that, resonance frequency behaves according to $1/\sqrt{LC}$ formula, capacitance is inversely proportional with plate distances as the distance increases capacitance value decreases and resonance frequency increases. When the thickness

decreases, the resonance frequency shifts downwards as shown in Figure 4 due to the coupling effects of the sensor layer. Capacitive effect is responsible for this shift, because it is inversely proportional to the layer thickness. Absorption ($A(w)$) term is the main criteria for all sensor applications in this study, since air is an isolating material, its' thickness is affecting $A(w)$ term. Figure 4 shows that the absorption frequencies for sensor layer with the thicknesses of 1, 1.5, 2 mm sensor layer are 5.92 GHz, 6.00 GHz and 6.05 GHz, respectively. The corresponding absorption values are 0.77, 0.97, 0.99 at 5.92, 6.00 and 6.05 GHz respectively. As shown in Figure 4, the best results for absorption values are obtained when the layer thicknesses are 1.5 and 2 mm. Fig. 4 also shows that 1mm change in the sensor layer thickness results in a shift of 130 MHz in the resonance frequency which proves that the sensor application based on this absorber is very sensitive to the changes in the sensor layer thickness

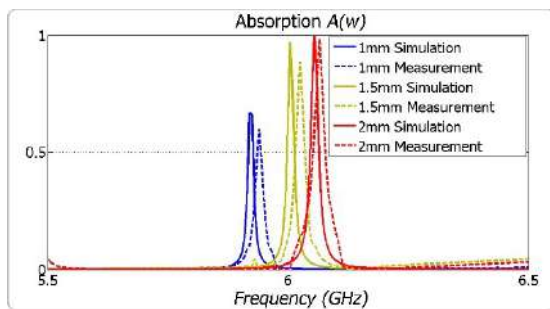


Fig.4 MA Based pressure sensor application for 1mm, 1.5mm and 2mm.

Sensor layer can be used to detect the density of a material if it is properly configured. In this part of numerical and experimental study, sensor layer is assumed to be filled with such materials that have different density values. Sensor layer thickness is again 1.6mm for numerical and experimental parts of this illustrations. As a beginning, Since the resonance frequency of the absorber based sensor changes with respect to the capacitance of the structure, sensor layer is assumed to be compromised of a material having different dielectric constant permittivity with respect to the density. Inductance term of the absorber based sensor is kept constant during the density sensor application, since it is only affected by metallic path dimensions and wavelength of the incident electromagnetic wave. Mutual inductance between the front and back side structures does not change due to the constant substrate and sensor layer thicknesses. Three different materials known as Arlon AD300, Arlon AD350 and Arlon AD 450 are used in the sensor layer for simulation and experimental validation. Sensor layer thickness is also 1.6 mm as in the previous study. Numerical and experimental results are presented in Figure 5. Resonance frequencies are 8.44, 8.36, 8.23 GHz for

AD 300, AD350 and AD450, respectively. When AD450 type material is used in the sensor layer, as the sensor layer, the maximum absorption value of 0.97 is obtained. The dielectric constants are 3.3, 5.4, 5 for AD 300, AD350 and AD450, respectively. As seen from Figure 8, when the dielectric constant of the material used in the sensor layer as a sensor layer increases, the resonance frequency of the absorber based sensor shifts downward. The total shift is about 210MHz which shows that the absorber based sensor is very sensitive to the changes in the dielectric constant of the sensor layer.

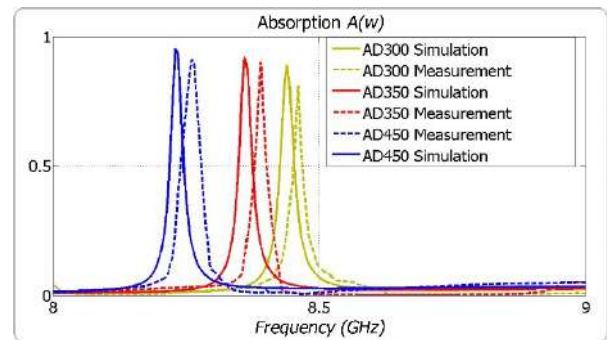


Fig. 5 MA Based density sensor numerical and experimental result comparison for Arlon type AD300, AD 350 and AD450 materials.

IV. CONCLUSION

This study focuses on multi-functional sensor applications based on MA. The sensing properties of the suggested sensor design are presented for pressure and density. In order to show the sensor quality of the proposed design, pressure and density sensor applications are also experimentally tested. It can be seen that the numerical results are in a good agreement with the experimental ones. The linearity of the sensing frequency changes depending on the dielectric constant of the proposed structure. For this reason, more applications can be developed.

REFERENCES

- [1] D.R. Smith, and N. Kroll, "Negative refraction index in left-handed materials," *Phys. Rev. Lett.*, Vol. 85, 2933-2936, 2000.
- [2] D. Schurig, J. J. Mock, B. J. Justice, S. A. Cummer, J. B. Pendry, A. F. Starr and D. R. Smith. "Metamaterial Electromagnetic Cloak at Microwave Frequencies." *Science* 314, 977-980 (2006).
- [3] J.B. Pendry, "Negative Refraction Makes a Perfect Lens," *Physical Review Letters*, vol. 85, no. 18, 3966-3975, 2000.
- [4] J.J. Yang, J. J., Huang, M., Sun, J., "Double negative metamaterial sensor based on micro ring resonator," *IEEE Sensor*, vol. 11, 2254-2259, 2011.
- [5] F. Dincer, M. Karaaslan, O. Akgol, E. Unal, C. Sabah, "Design of polarization- and incident angle-independent perfect metamaterial absorber with interference theory" *J of Elect. Mat.* 43, 3949 (2014).
- [6] N.I. Landy, S. Sajuyigbe, J. J. Mock, D.R. Smith, W.J. Padilla, "Perfect Metamaterial Absorber" *Phys. Rev. Lett.* 100, 207402 (2008).



- [7] [M. Schueler, C. Mandel, M. Puentes, and R. Jakoby, "Metamaterial inspired microwave sensors," IEEE Microwave Magazine, vol. 13, no. 2, pp. 57–68, 2012
- [8] T. Chen, S. Li, and H. Sun, "Metamaterials application in sensing," Sensors, vol. 12, no. 3, pp. 2742–2765, 2012T. Chen, S. Li, and H. Sun, Sensors 12, 2742(2012).
- [9] W. Niu, M. Huang, Z. Xiao, and J. Yang, "Sensitivity enhancement in TE mode nonlinear planar optical waveguide sensor with metamaterial layer," Opt. Adv. Mat.5, 1039(2011).
- [10] J. J. Yang, M. Huang, and J. Sun, "Double negative metamaterial sensor based on microring resonator," IEEE Sens. J.11, 2254(2011).

Multifunctional Sensor Applications in X Band

M. Bakır¹

¹Department of Computer Engineering, Faculty of Engineering and Architecture, Bozok University
Yozgat / Turkey

M. Karaaslan², O. Akgöl², E. Unal²

Electrical and Electronics Engineering, Iskenderun Technical University,
Iskenderun, Hatay, Turkey

Abstract— Metamaterials are attractive media for scientific society for their potential multi-functional and a wide range of applications due to their unusual electromagnetic properties. In this paper, we present pressure and bulk material type sensing applications with different permittivity values. Pressure and material sensing applications are carried out experimentally and numerically. The model is based on a split ring resonator (SRR) topology and the sensing layer sandwiched between the SRR and a rectangular copper layer located at the background. . Since sensor layer affects the resonance frequency of the system, the proposed model can be used for chemical, agricultural, medical and biological sensing applications in the microwave frequency band

Keywords— metamaterial, absorber, sensor

I. INTRODUCTION

Metamaterials with their extraordinary electrical and magnetic behaviors offer a wide range of application areas, such as sensing, absorption, polarization rotation, source shifting or imaging, perfect lenses and many more applications attracting an increasing number of researchers in this field [1-5]. In the case of sensing applications, micro and nano size metamaterial structures started to be built with the new and continuously growing technology. For example, Schueler et al. [6] worked with metamaterial inspired composite right/left-handed transmission line microwave sensors. Chen et al. [7] developed a sensor application by using split ring resonator. In this study, we have proposed a sensor based on metamaterial absorber which is different from traditional sensor designs. This is realized by placing sensor layer between resonator and metallic layers as an absorber which is explained in the next section. Although changing resonant frequency due to the environment has been studied previously by different scientists. Difference of the proposed study from the others is being metamaterial absorber based study for X band waveguide operation and having unique design features. Sensor layer's thickness and permittivity value of material inside the layer affects the resonance frequency of sensor system. Several sensor applications can be developed by this design approach from medical to food industry.

II. NUMERICAL DESIGN AND EXPERIMENTAL SETUP

In this study, we created a MA based sensor. The proposed design consists of a Roger RT 5870 type dielectric material which has a thickness of 0.76 mm and a dielectric constant of 2.33 which is chosen as a substrate as seen from Fig. 1. The suggested structure has five parts, resonators, a substrate, sensor layer, another substrate and a copper plate, respectively. Back side of this sensor design is completely plated with copper type metal which is supported by an RT 5870 material. In numerical analysis, PEC boundary conditions for x- and y-directions and open boundary condition for z-direction are applied to simulate waveguide measurements. Sensor layer is realized in order to use for multi-functional applications. It can be adapted for different sensor applications such as density, pressure, temperature and humidity sensing. In this study, density and pressure sensor applications are numerically and experimentally realized and discussed. In Fig.1, the proposed MA based sensor design and waveguide boundary conditions are given.

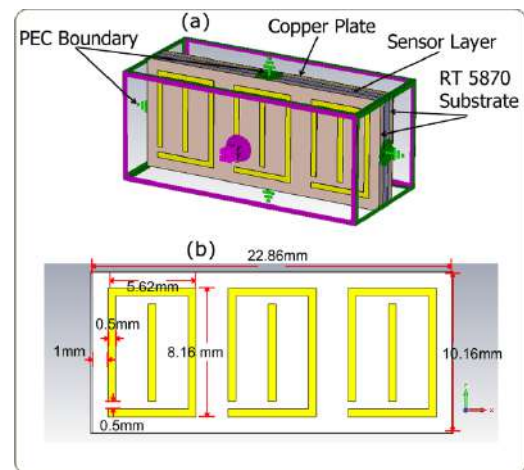


Fig. 1. (a) The proposed MA based sensor design, (b) Dimensions of the suggested MA based sensor design.

III. SENSOR APPLICATIONS

Different materials together with different version of the same materials have different density values and different permittivity values. In this part of the study, change in the permittivity used for density sensing. In the first part of density sensing demonstration, three different samples which are Roger RT5870, Arlon AD350 and Arlon AD450 are used for numerical simulation and experimental testing. Other density sensor applications are realized numerically by using published data about density and permittivity values because of the laboratory possibilities.

In this part of the study, sensor layer thickness is 0.76mm which is same as substrate thicknesses. When one of the given materials are placed in the sensor layer, overall reflection coefficient of the unit cell reacts according to the placed materials' properties. Densities of RT 5870, AD 350 and AD 450 are 2.2 g/cm³, 2.40 g/cm³ and 2.45 g/cm³, respectively. Absorption which is related to the angular frequency can be represented as $A(\omega)$ and it can be defined as $A(\omega) = 1 - |S_{11}|^2 - |S_{22}|^2$ and the absorption values of different materials are given in Fig. 2. The term (ω) given here refers to the angular frequency. As it can be seen from Fig. 2(a), the resonance frequencies shift depending on the material densities to the resonance frequencies of 9.68, 9.46 and 9.33 GHz, respectively. Furthermore, the resonance frequencies are measured experimentally as 9.70, 9.44 and 9.34 GHz for the materials of RT5870, AD 450 and AD 350, respectively as shown in Fig. 2. Linear relation between the material densities and the resonance frequencies is presented in Fig. 2. One can see from Fig. 2. that the absorption level is decreasing according to the material densities. Obtained results show that the numerical values of the sample are in a good agreement with the measured ones. According to Fig. 2, resonance frequency shifts backward as the permittivity values of the material inside the sensor layer increases. Because, capacitance and permittivity are directly proportional with each other, resonance frequency shifts backward according to $1/2\pi\sqrt{LC}$.

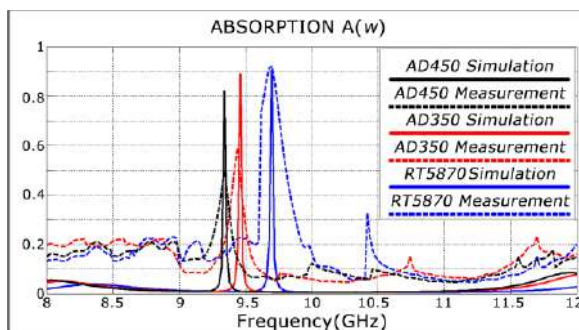


Fig. 2. Simulated and measured absorption values for density sensor application based on MA design,

One of the other important sensor parameters of MA based sensor design is the pressure sensor application which is realized both numerically and experimentally. In this part, the suggested sensor layer is assumed to be filled with air and the thickness is assumed to be loosened or tightened according to the pressure as seen from Fig. 3. Pressure is affecting the system resonance directly due to the capacitive effect which is directly related with the thickness of the air gap. Numerical simulation and experimental test results are compliant with each other, there are small resonance frequency and absorption level differences due to calibration and configuration errors as testing. As shown in Fig. 3, when sensor layer leaves empty (only air placed inside), and thickness of sensor layer has been changed, resonance frequency of the metamaterial absorber based sensor system changes accordingly. As generally known, capacitance of the parallel plates is inversely proportional with plate distance, as it shown in Fig. 3, when the distance increases, resonance frequency of the split ring resonator increases according to $1/2\pi\sqrt{LC}$. Three distance values have been taken as sample which are 0.4, 0.8, 1.2mm to show pressure increase and decrease application, resonance frequency of them 10.04, 10.24 and 10.32 GHz, respectively. According to figure, every 0.1mm change, in the pressure results with 35MHz change in the resonance frequency which can be noticed by vector network analyzers easily.

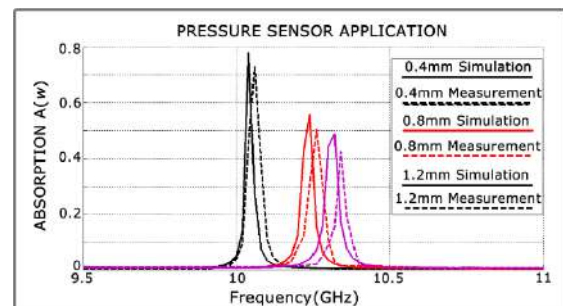


Fig. 3. Pressure sensor application of MA based density sensor

IV. CONCLUSION

This study focuses on the multi-functional sensor applications in X band. Unique design is obtained by numerical study which also experimentally tested to obtain sensitive metamaterial absorber based sensor. The sensing properties of the suggested sensor design are presented for different material and pressure sensor applications. It can be seen that the numerical results are in a good agreement with the experimental ones.



REFERENCES

- [1] F. Dincer, M. Karaaslan, O. Akgol, E. Unal, C. Sabah, "Asymmetric Transmission of Linearly Polarized Electromagnetic Waves Using Chiral Metamaterials with Constant Chirality Over a Certain Frequency Band", *Modern Physics Letters B*, 28, 2014, pp. 1450250-10.
- [2] F. Dincer, M. Karaaslan, O. Akgol, E. Unal, C. Sabah, "Design of Polarization- and Incident Angle-Independent Perfect Metamaterial Absorber with Interference Theory", *Journal of Electronic Materials*, 43, 2014, pp. 3949-3953.
- [3] Y. Ye and S. He, "90° polarization rotator using a bilayered chiral metamaterial with giant optical activity", *Appl Phys Lett*, vol. 96, 2010, pp. 203501
- [4] C. Sabah and H. G. Roskos, "Design of a terahertz polarization rotator based on a periodic sequence of chiral-metamaterial and dielectric slabs", *Prog. Electromag. Res*, vol. 124, 2012, pp. 301-314,
- [5] F. Dincer, M. Karaaslan, O. Akgol, E. Unal, C. Sabah, "Polarization-Insensitive FSS based Perfect Metamaterial Absorbers in GHz and THz Frequencies", *Radio Science*, 49, 2014, pp. 306-314.
- [6] M. Schueler, C. Mandel, M. Puentes, and R. Jakoby, "Metamaterial inspired microwave sensors," *IEEE Microwave Magazine*, vol. 13, no. 2, pp. 57-68, 2012.
- [7] T. Chen, S. Li, and H. Sun, "Metamaterials application in sensing," *Sensors*, vol. 12, no. 3, pp. 2742-2765, 2012.

SINGLE PHASE FIVE- LEVEL INVERTER BASED STATCOM FOR REACTIVE POWER COMPENSATION

Ahmet Mete Vural

*Electrical and Electronics Engineering Department
University of Gaziantep*

27310 Şahinbey / Gaziantep, Turkey

E-mail: mete.vural@gaziantep.edu.tr

Hamed Atyia Soodi

*Electrical and Electronics Engineering Department
University of Gaziantep*

27310 Şahinbey / Gaziantep, Turkey

E-mail: hs45149@mail2.gantep.edu.tr

Abstract— This paper details a Single-Phase Multilevel Inverter based STATCOM for reactive power compensation. STATCOM is very important in any generation and distribution system because it plays a major role in supporting the reactive power, whenever the reactive power compensation takes place. Two controllers PI and Fuzzy Logic are used in this paper, PI controller for producing the modulation index and fuzzy controller for getting the delta(which is used to generate the reference signals from the change in phase angle). Sinusoidal Pulse Width Modulation then uses the modulation index and delta for producing the switching signals for the inverters. In this research we used two full H-bridges.

Keywords— STATCOM; PI controller; Fuzzy Logic controller; Sinusoidal Pulse Width Modulation; H-bridge Multilevel Inverter

I. INTRODUCTION

In every power system, the reactive power improvement and harmonic compensation have always been very important areas of discussion. This is because of the fact that it has a very strong impact on the power loss, voltage stability and power quality of the power system. As we know that the total power in any power system is the sum of the active and the reactive power and therefore the improvements in the reactive power means improvements in the overall power of the system. Many methods (Peng and Adams, 1998) have been employed in the past for the compensation of the reactive power which includes the use of reactors and capacitors. But these methods are not very good and efficient as they tend to become more complicated when non-linear loads are applied which leads to higher implementation and maintenance cost. Therefore, extensive research has been going on in this area and new techniques are developed in order to get better results. These techniques make use of Active Power Filter (APF), Static Synchronous Compensator (STATCOM) and other Flexible AC Transmission System (FACTS) devices which shows a quite fast response and good performance for harmonic compensation and reactive power improvement (Prakash, Mahalakshmi and Karpagam, 2016). There are a variety of control techniques in electronics which can be used for this purpose with their own merits and demerits.

STATCOM is used for injecting and absorbing reactive power, so it will improve the power system. It belongs to the FACTS device family. The basic aim of a STATCOM is to absorb or inject reactive-power in the power system and the output of the converter is controlled by changing the amplitude of the output voltage (Cheng, Qian, Crow, Pekarek and Atcity, 2006). The cascaded H-bridge multilevel topology for inverter is used here and the cascaded H-bridge multilevel topology offers several advantages over other inverter topologies in such cases (Paserba, Reed, Takeda and Aritsuka, 2000). There are many different cascaded topologies for STATCOM application and the one which is implemented in this work is the cascaded transformer multilevel topology. The inverter in this work consists of two full H-bridges and two capacitors are used, i.e. one for each bridge. Also, two controllers are used, fuzzy logic controller produces change in phase angle by comparing the reference DC voltage with the obtained DC voltage and the other PI controller outputs the modulation index from the inputs which is the reference reactive power and the obtained reactive power. These two parameters along with the capacitor voltages, carrier signals and current are given to the Sinusoidal Pulse Width Modulation as an input and the switching or gating signals are generated by the Sinusoidal Pulse Width Modulation as the output which is used to drive the inverters.

II. STATIC SYNCHRONOUS COMPENSATOR (STATCOM)

In power systems to compensate reactive power STATCOM device is often used. The basic purpose of STATCOM is to maintain stable reactive power to the power system by absorbing or supplying reactive power as required. STATCOM is the member of FACTS controller's family. A typical STATCOM contains following components such as voltage source converter with capacitor on DC side as energy storage element, a coupling transformer and an inductor for AC side. A basic STATCOM configuration is shown in (Figure 1) which is directly connected to the main power line.

A. Components of STATCOM

A STATCOM consists of following components:

a). Voltage Source Converter (VSC)

i. Square Wave Inverters

In square wave inverters, the output waveform usually contains multilevel steps. The inverter's fundamental component is directly related to DC voltage. The inverters generally use insulated gate bipolar thyristor for switching. The IGBTs are used because of its high frequency switching and high power rating. Furthermore, to reduce the harmonic contents of square waves generated by each inverter a transformer is used along with passive filter.

ii. PWM Inverters

The most prevalent method of controlling cascaded h-bridge multilevel inverter is sinusoidal pulse width modulation (SPWM). The main working principle of sinusoidal PWM modulation scheme is to compare a reference sine wave signal with a triangular waveform in order to produce the controlling signals for switches

The pulse width modulation (PWM) scheme is used by voltage source converter (VSC) to convert a dc voltage at the input into sinusoidal waveform at the output. The frequency of PWM is few kHz used to drive the IGBTs. There is a difference between these types of inverters as compared to the GTO type. These inverters rely on modulation index to change their ac output voltages. Also, a shunt filter is employed on the AC side to reduce the harmonic content in the output waveform.

b). Coupling transformer

STATCOMs cannot be linked directly with the high voltage power systems. These high voltages can damage the system components. Therefore, a transformer is needed to reduce these voltage levels. Transformer steps down the high grid voltages to appropriate levels for further processing by the system. But there is a drawback related to the use of transformer; the power losses are increased mainly due to reactance.

c). DC Capacitor

DC capacitor is an essential component of STATCOM as it provides the necessary voltage for inverters and also stores energy.

d). Inductive Reactance

This inductive reactance is due to the leakage inductance of coupling transformer. It is connected with the output of inverter and power system.

e). Harmonic Filter

The harmonic filter is located at the AC side. It is mainly used for removing harmonic content present in the output waveforms of each inverter. To remove the harmonics we used inductor.

B. Operation Modes of STATCOM

Following are the two ways to operate STATCOM.

a). Voltage Regulation mode

In voltage regulation mode, the main operation of STATCOM is to compensate for reactive power in the power system. It will either absorb or supply the reactive power using voltage source converter. A DC capacitor is used for voltage regulation. At point of Common Coupling, multiple electric loads are connected. Following are some of the functions performed by the STATCOM during reactive power compensation:

When PCC voltage is higher than its reference, STATCOM absorbs reactive power from PCC.

When PCC voltage is lower than its reference, STATCOM injects reactive power into PCC.

b). VAR Control mode

In this mode, irrespective of other system parameters the reactive output of STATCOM remains constant. In VAR control, reactive power of the STATCOM injected or absorbed is controlled. Generally a closed loop control scheme is used to control the reactive power generated or absorbed by STATCOM.

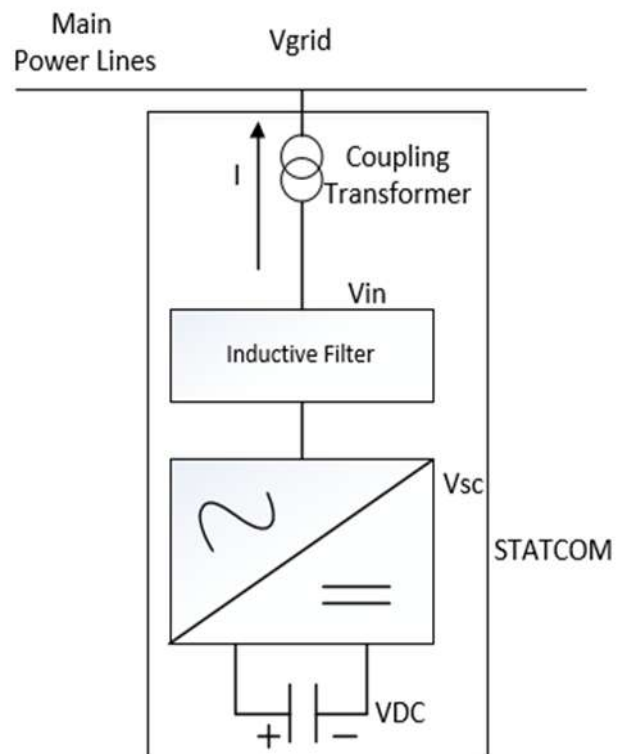


Fig.1 The Grid Connection of STATCOM with power line

III. MODELLING OF SINGLE PHASE CASCADED H-BRIDGE MULTILEVEL INVERTER

The basic construction of five level ($2N+1=5$) cascaded H-bridge inverter consisted of two ($N=2$) full-bridges is shown in Fig. 2. Since there are two capacitors, there usually happens a voltage imbalance between capacitor voltages that should be minimized or practically eliminated with a number of techniques. Furthermore, capacitor voltage ripples can be reduced by active power control for each bridge (Lipo, 2000). Various methods are discussed in to remove the ripples in DC voltages. This topology involving cascaded H-bridge multilevel inverters is used in many applications for reactive power compensation. Low-frequency modulation scheme is used in (Haque, 2004). Due to the switching losses of IGBTs. According to (El-Moursi and Sharaf, 2005). The frequency of line and commutation are almost similar.

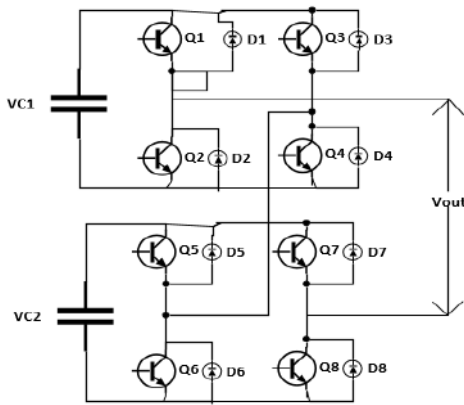


Fig.2 A basic construction of H-Bridge Multilevel Inverter

Each h-bridge consists of four switches and four diodes connected in parallel with switches. These diodes which are connected in anti-parallel fashion act as full-bridge rectifier and together they are used for charging the DC capacitor. The charging energy comes from the coupling inductor. The output of h-bridge contains three levels namely positive, negative and zero level. These voltage levels when summed up form a sinusoidal waveform. The AC output of h-bridge is given as:

$$V_{ca} = V_{ca1} + V_{ca2} + V_{ca3} + \dots + V_{caM} \quad (1)$$

Where: M represents the number of inverters per phase.

The proposed topology of cascaded multilevel inverter is modular meaning the output AC waveform can be improved by simply adding more h-bridges in the circuit. The conduction time for each h-bridge varies for example, for the first level the DC capacitor will charge less and discharge more and for the last level the DC capacitor charges more and discharges less. To solve this problem, we select suitable switch pattern swapping method which will

swap the angles of switching for every half cycle as mentioned in (Shukla, Ghosh and Joshi, 2007). The rectified energy accumulated in the inductor is stored in a capacitor that is linked on the DC side of the h-bridge multilevel inverter. The circulation of current and non-stop charging and discharging of inductor can cause voltage ripples. To remove these ripples and smoothing the voltage DC capacitor is used. Below figure further demonstrates the process:

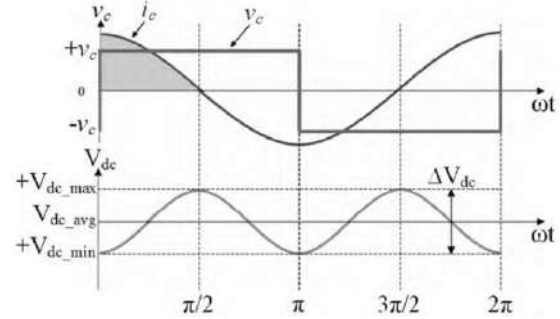


Fig.3 Fundamental components DC voltage, Capacitor current and capacitor voltage

As can be seen in the figure above the VDC is either maximum or minimum at $\pi/2$. The area under the I_c gives us the total reactive power. Capacitance is calculated as given by the equation:

$$C = \frac{i_c}{f_{rp} * \Delta V_{Dc}} \quad (2)$$

Where: f_{rp} here represents the ripples frequency which is twice the fundamental frequency

The RMS value of I_c is:

$$i_c = \frac{Q}{V_{pcc}} \quad (3)$$

Where Q: maximum power (reactive) produced by STATCOM

The voltage ripples can be further reduced by using a high value capacitor as given by the equation for capacitance. But increasing the value of capacitor will also increase the time constant RC. With increase in value of time constant it may lead to large current flows from the switches. The large current flows in on state can damage the switching devices. For coupling of reactive power between STATCOM and PCC an inductor is used. Its inductance depends on the modulation index of multilevel inverter and harmonic content. The inductance is calculated using the following equation:

$$L_{fmax} = \frac{V_{pcc}}{2 * \pi * f * i_c} \quad (4)$$

Where: V_{PCC} is the voltage at PCC and f represents the fundamental frequency

i_c : maximum current that inverter can produce or absorb

Using the above equation, we can calculate the maximum size of inductor to be used. Using a large size inductor will improve harmonics at PCC and will help minimize current ripples. But it will also lead to less current flows through capacitors. To solve this issue phase shift between the V_{pcc} and V_c is increased which results in active current flows through capacitor but it also increases the V_L across the inductor. This effect is reduced by increasing the voltage produced by multilevel inverter. It is accomplished by increasing the h-bridges or size of DC capacitors.

In (Mynavathi, Chinnaiyan, Venkatesh and Balamurugan, 2015) on the electric transmission lines STATCOM was utilized for the reactive power compensation. It discusses the compensation and its conventional way using STATCOM. Its implementation, the circuit configuration, switching technology along with the operating principle has been discussed.

The reactive power control has been presented in (Gultekin and Ermis, 2013) of an Autonomous Wind-Diesel Hybrid Power Systems (AWDHPS) with a real time environment in which the STATCOM helps supplies and absorbs the reactive power which has been controlled by the proportional plus integral controller.

A proposed design has been discussed in (Singh, Murthy and Chilipi, 2014) for a STATCOM which is for the cascaded multilevel converter (CMC) based transmission. It discusses the details of the system along with the number H-bridges used in the CMC for each of the phase along with its voltage ratings and other important aspects.

(Rao and Yang, 2000). Proposes a system which uses a 3-phase induction generator which is self-excited (SEIG) which is being utilized by a power generation of a single phase. They both work in conjunction with a STATCOM (3-phase). The single-phase loads which create the unbalanced currents are compensated by the STATCOM.

The distinct feedback control strategies have been compared with the PI control conventional method in (Mosobi, Chichi and Gao, 2014). The LQR control is discussed along with its superior terms (control effort and the response profile) which has been used in order to be applied on the voltage control applications of the power systems.

IV. SINUSOIDAL PWM MODULATION SCHEME

In determining the harmonic content and efficiency of a multilevel inverter, choosing the modulation scheme used for the semiconductor switching plays a major role. The sinusoidal pulse width modulation (SPWM) is the most prevalent modulation scheme for cascaded H-bridge multilevel inverter. The working principle of Sinusoidal pulse width modulation is to compare a reference sine wave

with a triangular waveform in order to produce the control or gating signals of semiconductor switches. The phase shifted SPWM modulation scheme has several advantages such as easier implementation, reduced switching loss and lower level of harmonics. The magnitude of the output inverter voltage is controlled by the modulation index m

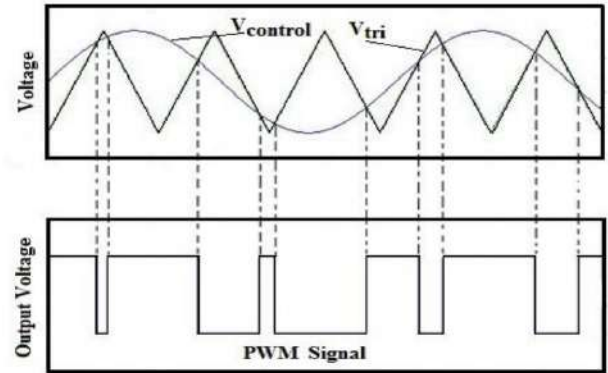


Fig.4 Sinusoidal Pulse width modulation

V. CONTROL SCHEME OF STATCOM

The PI and fuzzy controllers are used in this research work. Fuzzy controller is used to get the phase angle or delta. PI controller is used to get the modulation index. The single-phase STATCOM designed in this work is based on two cascaded H-bridges that produce five voltage levels at the output. STATCOM is proposed to be operated under VAR control mode in which the reactive power of the STATCOM is expected to follow its reference value with a high dynamic performance both in inductive and capacitive modes of operation.

The block diagram of the STATCOM location is shown in (Figure 5).

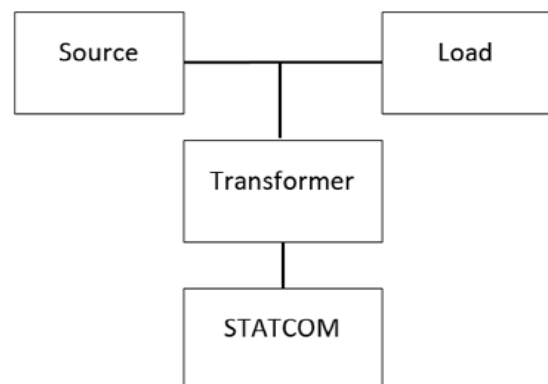


Fig.5 Block diagram of the proposed system

The control method presented here consists of two controllers namely fuzzy logic and PI. The delta (δ) or change in phase angle is generated using fuzzy controller from DC voltage. The PI controller is used for generating modulation index using the difference between measured and reference reactive powers. The delta, modulation index, capacitor voltages and carrier signals are then fed to the modulator which produces control signals for driving IGBTs. The block diagram of the overall control method is shown in (Figure 6):

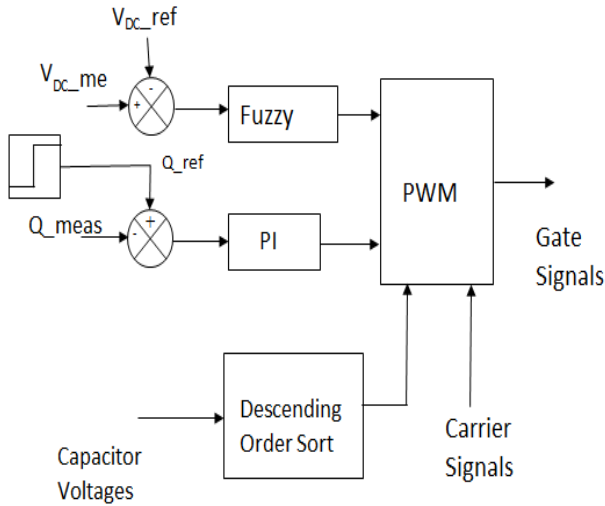


Fig.6 Control Scheme using Fuzzy Logic and PI Controllers

The reactive power is given by the following equation.

$$Q_s = \frac{E_c^2 - E_c E_s \cos \delta}{X} \quad (5)$$

This is the reactive power which STATCOM transfers to the line.

Where

X: represent the modeled reactance

E_s: is the RMS Voltage of line

E_c: is the RMS voltage of STATCOM

By changing the voltage level of STATCOM the reactive power can be controlled. Following is the relation between the STATCOM voltage and DC voltage.

$$\frac{V_{out}}{E_{Dc}} = m \quad (6)$$

Equation for reactive power is now

$$Q_s = \frac{E_s^2 - m E_{Dc} E_L \cos \delta}{X} \quad (7)$$

This equation represents the working of STATCOM. Modulation index is changed in order to control the reactive power of STATCOM. It is the main manager of STATCOM.

The control block contains two controllers PI and Fuzzy Logic. PI controller generates the modulation index. It takes difference of measured and reference reactive power as an input. Reactive power is controlled using this modulation index. Fuzzy logic controller is used for producing delta (δ). It takes difference of reference and measured DC voltage as an input.

In a fuzzy logic system, there are three stages namely; Fuzzification, Rule assessment and De-fuzzification. The first stage or fuzzification involves the mapping of variables between 0 and 1. This is done using the membership functions at the input. The rule assessment is important stage where all the processing takes place. Each rule is evaluated and then result is compiled which is then used in next stage. In last stage of de-fuzzification crisp variables are obtained by converting the fuzzy variables into non-fuzzy. As a membership function we have used triangular function. The rules used are negative big, negative medium, negative small, zero, positive big, positive medium and positive small. In the figures below the input error, change of error and output is shown separately.

The control block Simulink diagram is shown below:

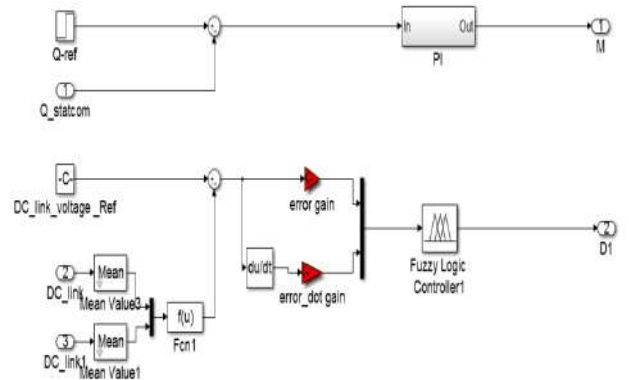


Fig.7 PI Control block diagram in Simulink

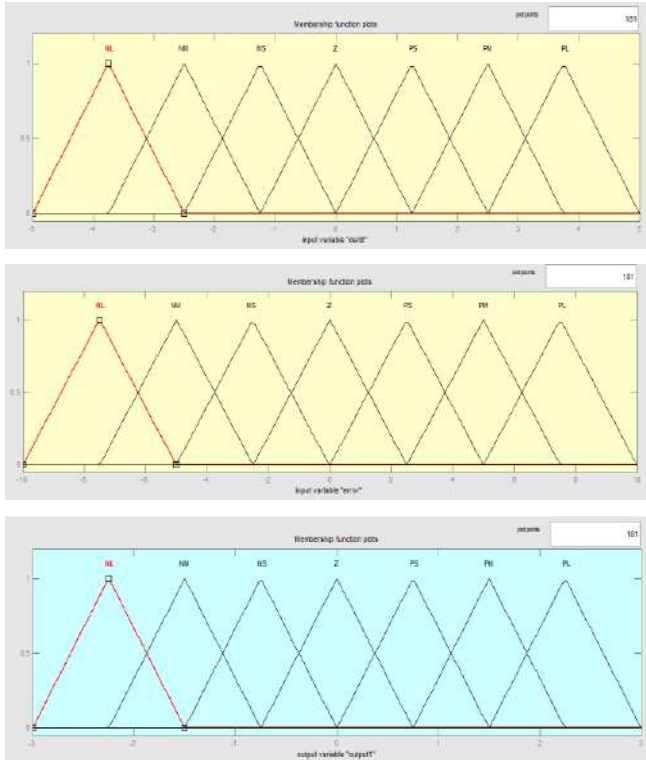


Fig.8 Membership functions for error (Top), change in error (Middle) and change in output (Bottom)

a. Phase Locked Loop Block

Shown below is the block diagram of phase lock loop or PLL. It is used for tracking of voltage. The PLL outputs the angle as it tracks the voltage signal.

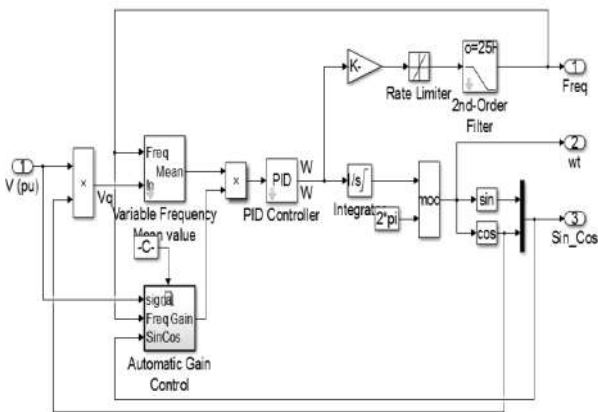


Fig.9 Simulink block diagram of PLL

A. Modulation Block

The modulation block is used for producing control pulses to drive the switches of inverter. The inputs given are carrier signal, delta and modulation index. Shown below is the Simulink block diagram of modulation scheme.

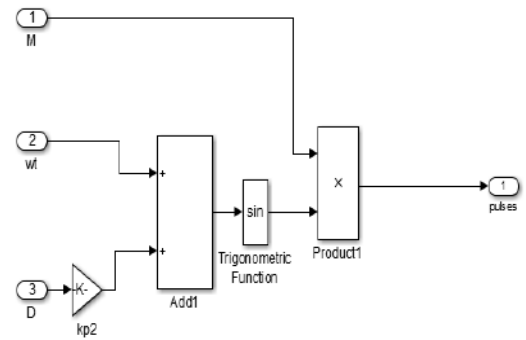


Fig.10 Modulation block in Simulink

The output of this block generates the pulses to drive switches. Equation (5) is used for the calculation of reactive power of STATCOM. Equation (6) is used for calculation of the modulation index. It is deduced from above equations that it is possible to control reactive power by varying the voltage levels of STATCOM. Using this relation of modulation index in the equation for reactive power we get equation (7) as shown, we can directly control the reactive power by varying the modulation index.

B. Inverter Block

Following block consists of the inverter and switching circuitry. The modulation block produces the control pulses which are compared with triangular wave to give a resultant pulse signal. This pulse is then inverted and given to h-bridges to perform switching. Shown below is the diagram for inverter block:

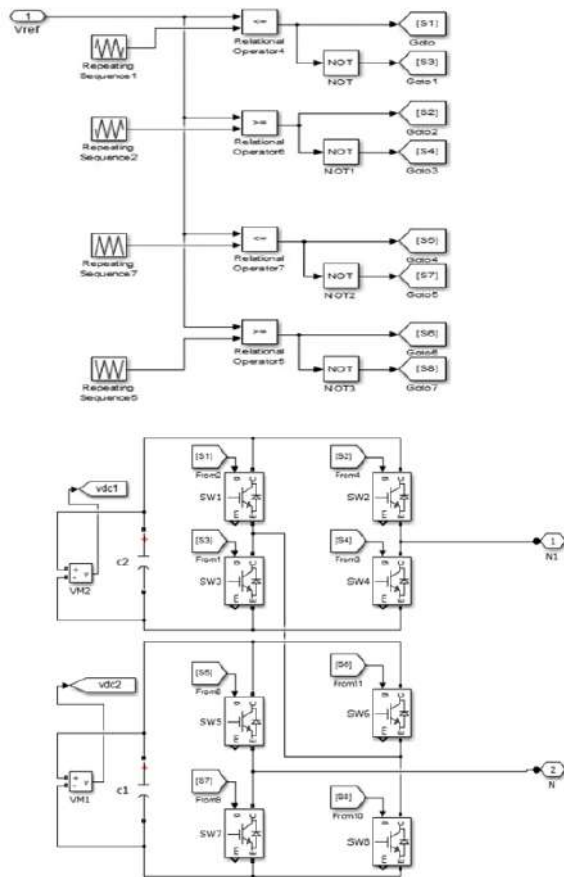


Fig.11 Simulink block diagram of inverter

There is no need for extra STATCOM or capacitor for the power factor regulation on feeders.

VI. SIMULATION RESULTS

The proposed system is designed and simulated using software with libraries for electrical components and systems. The block presented in software of complete system is shown in the following figure:

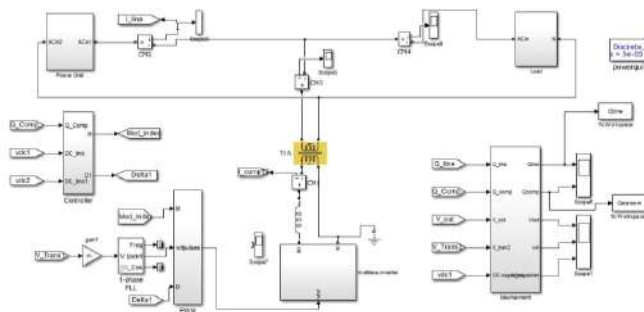


Fig.12 Simulink block diagram of complete system

In this case, we have considered a purely sinusoidal waveform as source voltage and a non-linear load. The IGBTs are used as switching devices in the h-bridge circuit. The system is simulated for 10 sec. During the first five seconds the system supplies 200 VAR reactive power and in the next five seconds it absorbs 200 VAR reactive power.

Table 1. Detail of System Parameters

	Parameters	Values
Source	Peak Amplitude (Volts)	311.12 V
	Frequency (Hz)	50 Hz
	Phase (Degree)	0 °
Load	Nominal Voltage (Volts)	220 Vrms
	Nominal Frequency (Hz)	50 Hz
	Active Power (Watts)	100 W
	Reactive Power Inductive (+Var)	300 Var
	Reactive Power Capacitive (-Var)	0 Var
Dc Link volt	Reference DC Link Voltage (Volts)	77.5 V
One Phase PLL	Phase Input (Degrees)	0 °
	Frequency Input (Hz)	50 Hz
	Regulator Gain (Kp)	180
	Regulator Gain (Ki)	32000
	Regulator Gain (Kd)	1
Coupling Transformer	Nominal Power (Volt-ampere)	5000 VA
	Nominal Frequency (Hz)	50 Hz
Winding 1 Parameters	Voltage (Volts)	220 Vrms
	Resistance (per unit)	0.0005 pu
	Inductance (per unit)	0.0005 pu
Winding 2 Parameters	Voltage (Volts)	110 Vrms
	Resistance (per unit)	0.0005pu
	Inductance (per unit)	0.0005 pu

A. The Simulation Results

Given below are the results obtained in Simulink by simulating the presented system.

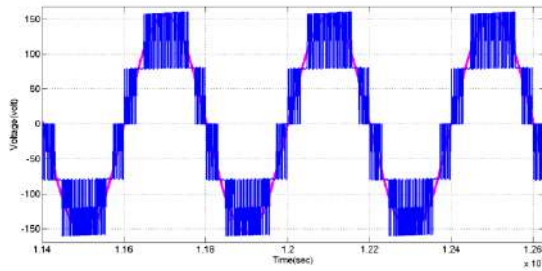


Fig.13 Reference Signal against the inverter voltage

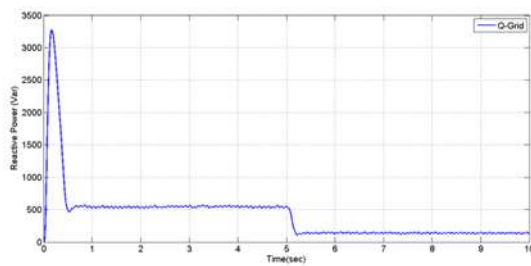


Fig. 14 Reactive power of Grid

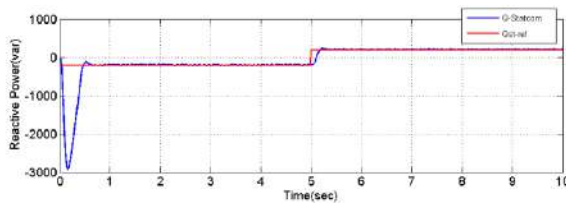


Fig.15 Reactive power of STATCOM

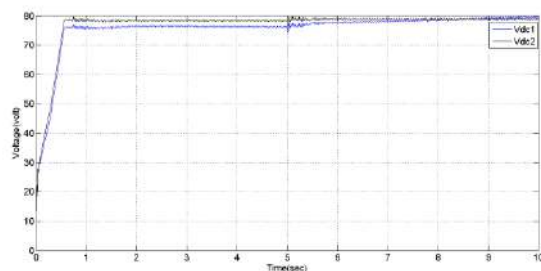


Fig.16 DC link capacitor voltage

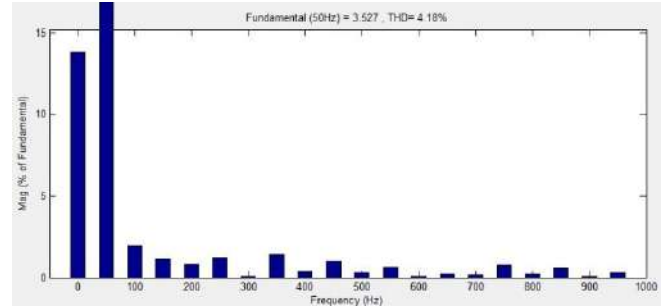


Fig.17 THD Value for Source Current

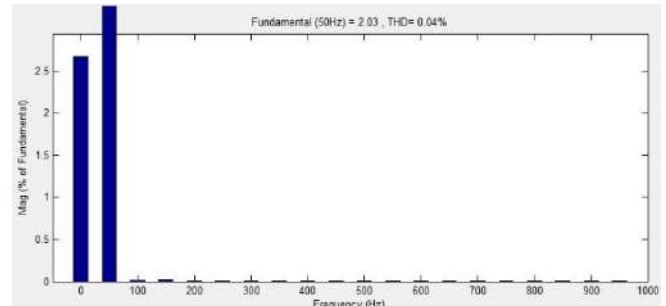


Fig.18 THD Value for Load Current

VII. CONCLUSION

In this study, we designed and simulated two effective techniques to compensate for reactive power. The results suggest that using PI and Fuzzy Logic controllers together can maintain the reactive power flow in the power system. This is done with the help of STATCOM which is connected with the grid for controlling the reactive power. The proposed system is able to supply and absorb the reactive power in inductive and capacitive mode respectively. The simulation ran for 10 s. providing reactive power for 5 s and absorbing for the next 5 s.

REFERENCES

- [1] Peng, F. Z., Ott, G. W., & Adams, D. J. (1998). Harmonic and reactive power compensation based on the generalized instantaneous reactive power theory for three-phase four-wire systems. *IEEE Transactions on Power Electronics*, 13(6), 1174-1181.
- [2] Prakash, D., Mahalakshmi, R., & Karpagam, M. (2016). SVM PWM based STATCOM for Voltage Transient Stability. *Asian Journal of Research in Social Sciences and Humanities*, 6(11), 492-506.
- [3] Cheng, Y., Qian, C., Crow, M. L., Pekarek, S., & Atcitty, S. (2006). A comparison of diode-clamped and cascaded multilevel converters for a STATCOM with energy storage. *IEEE Transactions on Industrial Electronics*, 53(5), 1512-1521.
- [4] Paserba, J. J., Reed, G. F., Takeda, M., & Aritsuka, T. (2000, May). FACTS and custom power equipment for the enhancement of power transmission system performance and power quality. In *SEPOE Conference*.



- [5] Lipo, Q. J. T. A. (2000). Switching angles and DC link voltages optimization for multilevel cascade inverters. *Electric Machines & Power Systems*, 28(7), 605-612.
- [6] Haque, M. H. (2004). Use of energy function to evaluate the additional damping provided by a STATCOM. *Electric Power Systems Research*, 72(2), 195-202..
- [7] El-Moursi, M. S., & Sharaf, A. M. (2005). Novel controllers for the 48-pulse VSC STATCOM and SSSC for voltage regulation and reactive power compensation. *IEEE Transactions on Power systems*, 20(4), 1985-1997.
- [8] Barrena, J. A., Marroyo, L., Vidal, M. Á. R., & Apraiz, J. R. T. (2008). Individual voltage balancing strategy for PWM cascaded H-bridge converter-based STATCOM. *IEEE Transactions on Industrial Electronics*, 55(1), 21-29..
- [9] Patil, K. V., Mathur, R. M., Jiang, J., & Hosseini, S. H. (1999). Distribution system compensation using a new binary multilevel voltage source inverter. *IEEE transactions on power delivery*, 14(2), 459-464.
- [10] Shukla, A., Ghosh, A., & Joshi, A. (2007). Hysteresis current control operation of flying capacitor multilevel inverter and its application in shunt compensation of distribution systems. *IEEE Transactions on power delivery*, 22(1), 396-405.
- [11] Mosobi, R. W., Chichi, T., & Gao, S. (2014, December). Modeling and power quality analysis of integrated renewable energy system. In *Power Systems Conference (NPSC), 2014 Eighteenth National* (pp. 1-6). IEEE..
- [12] Mynavathi, M., Chinnaiyan, V. K., Venkatesh, P., & Balamurugan, S. (2015). A New Real Time Approach for Reactive Power Control by STATCOM in Autonomous Wind-Diesel Hybrid Power System. In *Power Electronics and Renewable Energy Systems* (pp. 91-99). Springer India..
- [13] Gultekin, B., & Ermis, M. (2013). Cascaded multilevel converter-based transmission STATCOM: System design methodology and development of a 12 kV±12 MVar power stage. *IEEE transactions on power electronics*, 28(11), 4930-4950.
- [14] Singh, B., Murthy, S. S., & Chilipi, R. S. R. (2014). STATCOM-based controller for a three-phase SEIG feeding single-phase loads. *IEEE transactions on energy conversion*, 29(2), 320-331.
- [15] Rao, P., Crow, M. L., & Yang, Z. (2000). STATCOM control for power system voltage control applications. *IEEE Transactions on powerdelivery*, 15(4), 1311-1317.

Employing Adaptive-Biasing Technique and New Drivers to Upgrade the Folded Cascode Amplifier

Meysam Akbari

Microelectronic Laboratory, Shahid Beheshti University,
G.C., Tehran, Iran
Me_akbari@sbu.ac.ir

Omid Hashemipour

Faculty of Electrical Engineering, Shahid Beheshti University,
G.C., Tehran, Iran
Hashemipour@sbu.ac.ir

Abstract—This paper presents a class AB amplifier with enhanced transconductance and slew rate using adaptive biasing technique and new drivers. Adaptive biasing configuration provides a tail current dependent on the input signal to increase the slew rate during slewing phase. In addition, the new structure benefits from new drivers to enhance the transconductance which are supported by adaptive biasing configuration. These enhancement techniques lead to the input and output class AB structures for fast settling applications. The proposed structure is simulated in 65-nm CMOS technology which shows a 16.2-dB enhancement in DC gain and a 72% reduction in settling time compared to the conventional structure.

Keywords—landfill; municipal slurry; bottom layer; geolayer; permeability

I. INTRODUCTION

Development of data converters and analog filters lead circuit designers to improve operational transconductance amplifiers (OTAs) as the block that consumes the most power. The accuracy, speed and input noise of such circuits are directly dependent on specifications of the OTAs [1, 2]. Therefore, enhancing their specifications is still one of the important design challenges. Folded cascode (FC) structure is the most commonly used owing to its advantages over the other structures [1, 3]. The FC structure provides more output voltage swing and it does not have the input to output connection problem in comparison to the telescopic structure, besides, the FC amplifier consumes more power. Therefore, to optimize the power consumption, the recycling folded cascode (RFC) structure has been presented in [1, 2]. This structure employs load transistors as new drivers to enhance transconductance and consequently enhance the specifications of the amplifier. Besides, some transconductance enhancing techniques such as current shunt [4, 5], extra paths [5, 6], positive feedback [6], additional drivers [6, 7] and self-biasing configurations [8, 9] have been recently applied on the RFC structure to get more efficiency. In addition, a design methodology based on Gm/Id characteristics to reach the maximum efficiency and decrease the input referred noise has been reported in [3] that is dedicated to the FC structures.

There are other techniques which their main objective is increasing the slew rate to get smaller settling time. Adaptive biasing technique presents a structure that its tail current is

dependent on the input common mode voltage [10-12]. Therefore, such structures can provide more DC current to charge and discharge load capacitors during slewing phase when the input voltage has a large swing. Moreover, creating extra paths from the input node to the output node transfer more DC current into the load capacitors to charge and discharge them in a shorter time [13, 14]. In the most cases, in addition to increase the slew rate, the extra paths will also result an enhancement in the transconductance [5]. Therefore, to reach higher speed (smaller settling time) and higher accuracy (larger DC gain) employing such enhancing techniques are necessary in the FC structures.

In this paper, the conventional FC structure is somehow re-configured to provide a class AB structure with enhanced transconductance and slew rate. The proposed structure uses new input to output paths and adaptive biasing technique to increase the slew rate and transconductance. The paper is organized as follows: Section 2 illustrates the enhanced structure and compares it with the conventional structures based on mathematical analyses for frequency and transient characteristics. Section 3 reports the simulation results of the designed amplifiers and finally, the conclusions are given in Section 4.

II. ENHANCED RFC

Fig. 1 shows the conventional FC amplifier. In this figure, transistors M3a and M4a play role of the load in a cascode structure. To improve its efficiency, load transistors can be employed as common source amplifiers. The RFC structure which uses transistors M3a and M4a as new drivers is shown in Fig. 2. In this structure, the input signal is applied to the gate terminals of the new drivers through transistors M1b-M6b [1, 2]. Therefore, the RFC structure includes two different amplifiers: one folded cascode amplifier (M1a-M6a) and one current mirror amplifier (M1b-M6b) with a current gain of (k). Thus, the transconductance of the RFC structure is summation of gm_{1a} and $k(gm_{1b})$ [2, 3]. To have the same current consumption for the FC and RFC structures, the current gain factor k is typically set equal to 3 or less. Note that the DC current through M1a_{RFC} is half of that through M1_{FC}, the transconductance of the RFC is two times over the FC that leads to higher DC gain and gain bandwidth (GBW). In addition, due to the existence of the extra paths from the

input node to the output node, the RFC structure charges and discharges load capacitors by more DC current compared to the FC during slewing phase [1, 5]. Besides, both of the FC and RFC amplifiers include a flipped voltage follower (FVF) cell as the tail current to have an internal class AB operation.

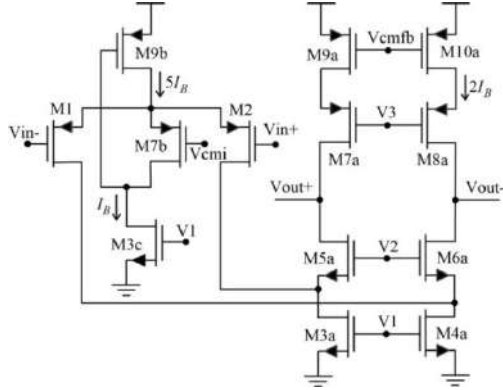


Fig. 1. The conventional FC amplifier

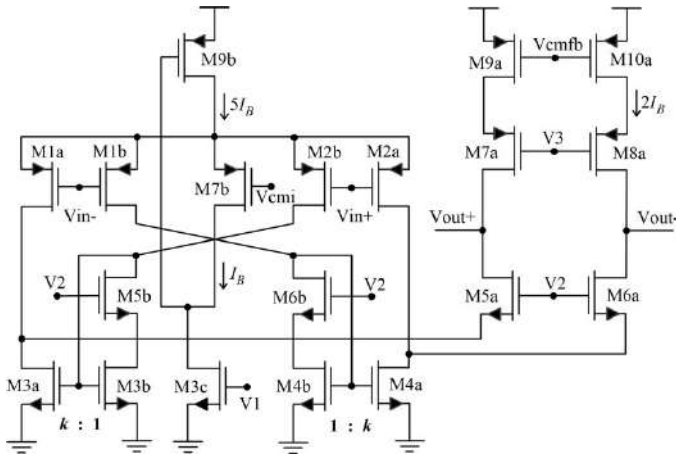


Fig. 2. The RFC amplifier

A. Small Signal Analysis

Fig. 3 shows the enhanced recycling folded cascode (ERFC) structure. By adding the adaptive biasing technique and employing new drivers (M9a and M10a), the RFC structure in Fig. 2 is re-configured in Fig. 3. To implement the adaptive biasing technique in the enhanced structure, two FVF cells (M7b-M10b) are employed as two matched tail currents [8, 15]. In the small signal operation, the input signal applies to the source terminals of the input drivers (M1a-M2b) through adaptive transistors M7b/M9b and M8b/M10b. On the other hand, the input signal is connected to the gate terminals of the input drivers. Based on the superposition theorem and analysis in [11], the total transconductance of these transistors is concluded from two amplifiers: one common source amplifier and one common gate amplifier. In addition, load transistors (M9a and M10a) in the cascode structure are employed as new drivers similar to M3a and M4a. The input

signal which passes through the adaptive biasing transistors (M9b and M10b) is applied to the gates of M9a and M10a to enhance transconductance. The transistors M3d and M4d with smaller current than M3a and M4a are used to control output common mode voltage by using a simple switched-capacitor common mode feedback. According to the above discussions, and also $gm_{1,FC} = 2gm_{1a,RFC}$, $gm_{9a} = 2gm_{1a}$, $k=3$ and $m=2.5$ the small signal transconductance of three structures can be given by

$$Gm_{FC} = gm_1 \quad (1)$$

$$Gm_{RFC} = (1+k) gm_{1a} = 2Gm_{FC} \quad (2)$$

$$Gm_{ERFC} \approx 2(1+m) gm_{1a} + gm_{9a} = 4.5Gm_{FC} \quad (3)$$

Equation (3) shows a 350% and 125% enhancement in the transconductance of the ERFC structure compared to the FC and RFC structures, respectively, which leads to the DC gain and GBW improvement. However, because of the added transistors to implement the adaptive biasing technique, the enhanced transconductance will not significantly decrease the total input referred noise in comparison with the RFC amplifier.

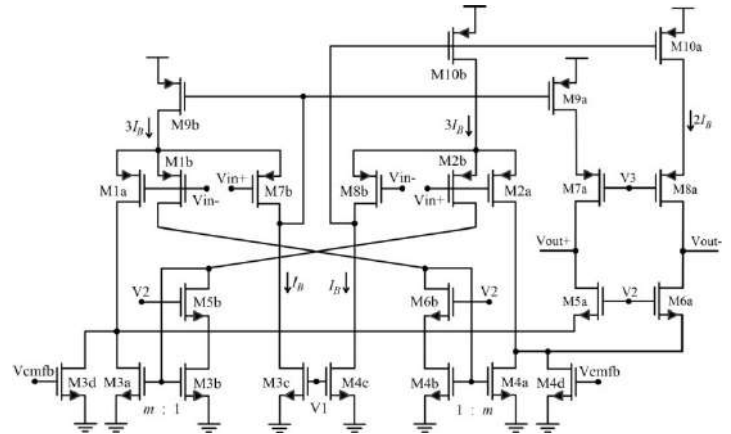


Fig. 3. The enhanced RFC amplifier

B. Large Signal Analysis

The adaptive transistors (M9b and M10b) perform as variable tail currents that their gate voltages are dependent on the amplitude of the input signal. On the other words, the DC current of these transistors will significantly change for a large input signal. Therefore, the DC current of all transistors that charge and discharge load capacitors will increase. In addition, the new drivers (M9a and M10a) are biased by adaptive transistors (M9b and M10b) and their gate voltages and consequently their DC currents can change during slewing phase to enhance the slew rate. Therefore, the adaptive biasing technique and new drivers provide an input and output class AB operation for the ERFC amplifier that leads to a significant enhancement in the slew rate.

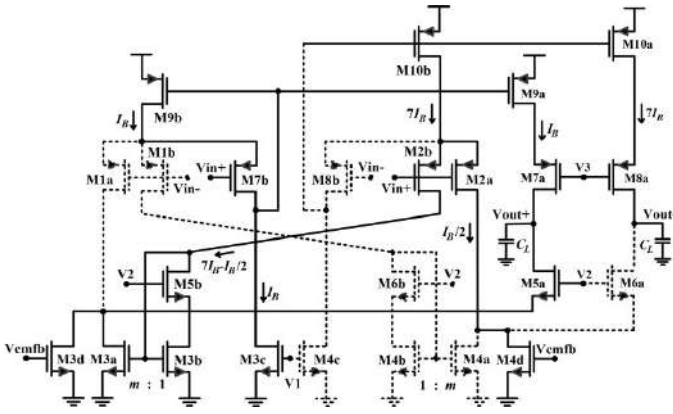


Fig. 4. The large signal model of the ERFC structure during slewing phase

Fig. 4 shows the enhanced structure during slewing phase when a large positive voltage is applied to the v_{in-} . Therefore, transistors M1a and M1b enter the cut-off region that force M4b, M4a and M6b to cut-off and M6a to deep triode region. Under this situation, M9b wants to pass a large DC current through M7b, but this current is limited by M3c. Consequently, the drain voltage of M7b rises to set the DC current through M9a and M9b equal to (I_B) . On the other hand, transistor M8b turns off which forces M4c to deep triode region by decreasing its drain voltage. Given that the gate voltages of M10b and M10a are connected to the drain voltage of M4c, the drain currents of M10b and M10a increase approximately to $(7I_B)$ for an input amplitude equal to the maximum output swing.

The gate voltage of M4d is controlled by a constant voltage which sets the drain current of M2a equal to $(I_B/2)$. For better illustration, the turned off transistors are shown in Fig. 4 by dash lines. It can be seen that the load capacitor at the negative output is charged by $(7I_B)$ and the load capacitor at the positive output is discharged by $[m \times (7I_B - I_B/2) - I_B/2]$. By considering $k=3$ and $m=2.5$, the differential slew rate ($SR_{Diff} = SR^+ + SR^-$) of three structures can be calculated by

$$SR_{FC} = \frac{4I_B}{C_L} \quad (4)$$

$$SR_{RFC} = \frac{k(4I_B)}{C_L} = 3(SR_{FC}) \quad (5)$$

$$SR_{ERFC} = \frac{(13I_B/2) \times (m+1)}{C_L} = 5.7(SR_{FC}) \quad (6)$$

Equation (6) shows a 470% and 90% enhancement in the slew rate of the ERFC structure compared to the FC and RFC structures, respectively, which leads to the settling time reduction.

III. SIMULATION RESULTS

Three structures FC, RFC and ERFC are designed in 65-nm CMOS technology while drive a $2 \times (2\text{pF})$ load at 1.2V supply voltage. Table 1 reports the transistor sizes of the three

structures. To obtain high DC gain and low input referred noise, the channel length of all transistors are chosen to be $0.3\mu\text{m}$. Fig. 5 presents the open loop frequency response of the designed amplifiers which shows a better performance for the ERFC amplifier over the others. The DC gain of the FC, RFC and ERFC are 39.9dB, 48dB and 56.1dB, and their GBWs are 32.6MHz, 82.6MHz and 180.5MHz, respectively. Therefore, the ERFC amplifier shows a 154% and 118% improvement in the DC gain and GBW over the RFC, respectively, which confirm theoretical analyses. Besides, the added new transistors as adaptive biasing technique and the new drivers lead to more poles and consequently worse phase margin. The ERFC amplifier has a phase margin about 62.5° that shows a reduction of 26.5° and 22.5° compared to the FC and RFC amplifiers, respectively.

Table 1. Transistor sizes (μm)

Parameters	FC	RFC	ERFC
$(W/L)_{1,2}$	$2 \times 6.2/0.3$	-	-
$(W/L)_{1a,2a}$	-	$1 \times 6.2/0.3$	$1 \times 6.2/0.3$
$(W/L)_{1b,2b}$	-	$1 \times 6.9/0.3$	$1 \times 6.9/0.3$
$(W/L)_{3a,4a}$	$4 \times 2.5/0.3$	$3 \times 2.5/0.3$	$3 \times 2.1/0.3$
$(W/L)_{3b,4b}$	-	$1 \times 2.5/0.3$	$1 \times 2.5/0.3$
$(W/L)_{3c,4c}$	$1 \times 2.1/0.3$	$1 \times 2.1/0.3$	$1 \times 2.1/0.3$
$(W/L)_{3d,4d}$	-	-	$1 \times 1.2/0.3$
$(W/L)_{5a,6a}$	$2 \times 2.1/0.3$	$2 \times 2.1/0.3$	$2 \times 2.1/0.3$
$(W/L)_{5b,6b}$	-	$1 \times 2.1/0.3$	$1 \times 2.1/0.3$
$(W/L)_{7a,8a}$	$2 \times 7/0.3$	$2 \times 7/0.3$	$2 \times 7/0.3$
$(W/L)_{7b,8b}$	$1 \times 6.9/0.3$	$1 \times 6.9/0.3$	$1 \times 6.9/0.3$
$(W/L)_{9a,10a}$	$2 \times 8.4/0.3$	$2 \times 8.4/0.3$	$2 \times 8.4/0.3$
$(W/L)_{9b,10b}$	$5 \times 8.4/0.3$	$5 \times 8.4/0.3$	$6 \times 8.4/0.3$

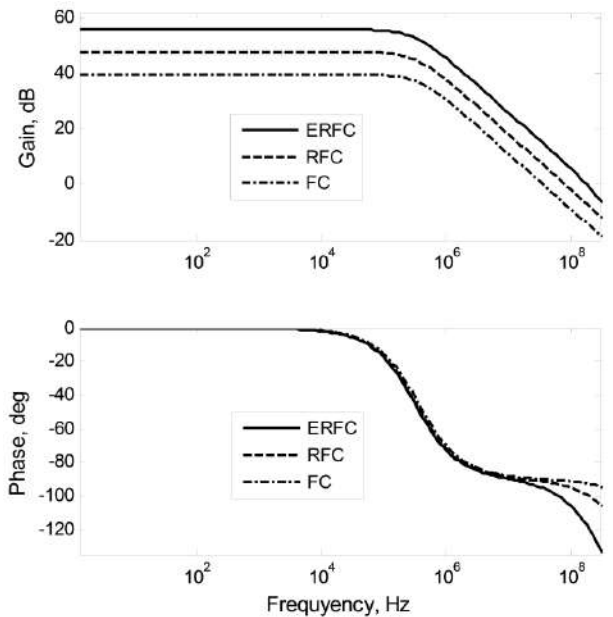


Fig. 5. Open loop frequency response of the designed amplifiers

Fig. 6 shows the total input referred noise versus frequency for designed amplifiers. The input referred noise of the FC, RFC and ERFC at 100kHz are respectively 17.9nV/ $\sqrt{\text{Hz}}$, 14.1nV/ $\sqrt{\text{Hz}}$ and 13.6nV/ $\sqrt{\text{Hz}}$ that ERFC shows a 4.3nV/ $\sqrt{\text{Hz}}$ reduction compared to the FC. Besides, the ERFC does not show a significant input noise reduction in comparison with the RFC due to the existence of more elements.

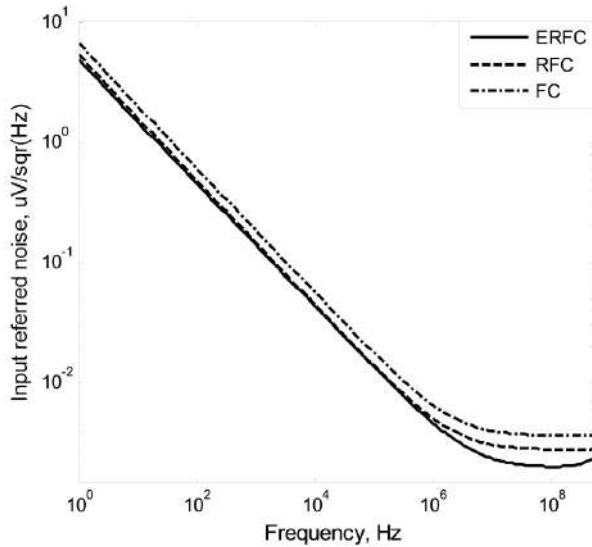


Fig. 6. Input referred noise for designed amplifiers

In order to consider the settling time and the slew rate, three structures are configured as a unity gain capacitive buffer that has been presented in [1]. A large step of 1V at 10MHz is applied and the results are shown in Fig. 7. It indicates that the average slew rate of the FC, RFC and ERFC are respectively 25.9V/ μs , 60V/ μs and 128V/ μs . The ERFC shows an enhancement of 102.1V/ μs and 68V/ μs over the FC and RFC. The enhanced slew rate and GBW of the ERFC result a 72% and 46% reduction in the 0.1% settling time compared to the FC and RFC, respectively. In addition, this figure shows a better final value for the ERFC due to its higher DC gain.

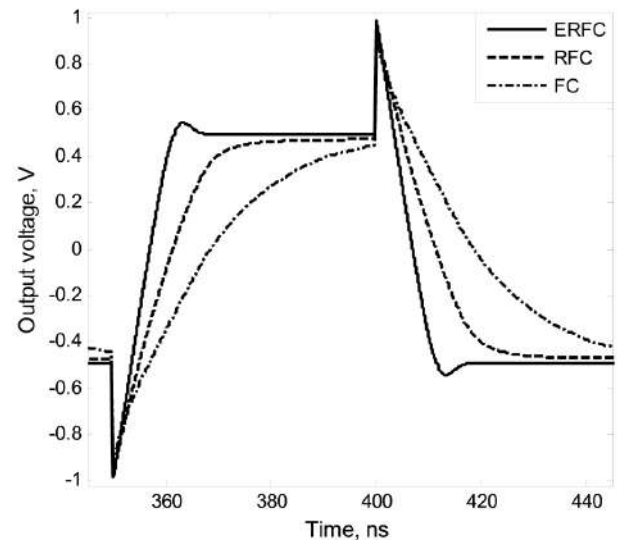


Fig. 7. The large step response of the designed amplifiers

During fabrication process the mismatch and variations directly effect on the specifications of the circuit. Monte-Carlo and corner analyses are considered to show their influence on the important specifications of the ERFC amplifier. The results are reported in Table 2 that shows the considered factors of the ERFC amplifier do not experience substantial changes over process variations. The Monte-Carlo analysis was performed for 1000 runs.

Two figures of merit (FOM) are defined by equations (7) and (8) for better comparison between ERFC amplifier and the others. Finally, the comparison results are summarized in Table 3.

$$FoM_1 = \frac{(GBW)(C_L)}{(Power\ dissipation)} \quad (7)$$

$$FoM_2 = \frac{(SR)(C_L)}{(Power\ dissipation)} \quad (8)$$

Table 2. Important specifications of the ERFC amplifier in Monte-Carlo and corner analyses

Parameter	Corner analysis					Monte-Carlo analysis	
	TT	SS	FF	SF	FS	Average	Standard deviation
Unity-gain bandwidth [MHz]	180.5	176	186.5	182.7	179.7	181.5	0.44
Phase margin [°]	62.5	63.3	61.6	62.3	62.6	62.48	0.087
Open loop DC gain [dB]	56.1	57.1	54.6	55.9	56	55.7	0.46
Average slew-rate [V/ μs]	128	121.5	130.5	129.9	125.1	127.9	0.51
0.1 % settling times [ns]	20.7	26	16.4	16.6	23.4	20.8	0.48
Power dissipation (including bias circuitry) [μW]	380	378	392	384	376	381	0.87
Input voltage noise @ 100 kHz [nV/ $\sqrt{\text{Hz}}$]	13.6	13.9	13.5	13.7	13.5	13.65	0.012



Table 3. Specifications of the ERFC amplifier in comparison with other works

Parameters	FC	RFC	ERFC	[4]	[7]	[8]	[14]
Power supply [V]	1.2	1.2	1.2	1.2	3	1.8	1.8
Technology [nm]	65	65	65	130	250	180	180
Power dissipation (including bias circuitry) [μ W]	0.35	0.35	0.38	0.312	4.33	0.318	1.476
Capacitive load [pF]	2 \times 2	2 \times 2	2 \times 2	7	2 \times 5	2 \times 1	2 \times 1
Unity-gain bandwidth [MHz]	36.2	82.6	180.5	83	94.3	24.8	300
Phase margin [$^{\circ}$]	89	85	62.5	70	68.8	64.8	81
Open loop DC gain [dB]	39.9	48	56.1	70.2	73.6	87.7	53
Average slew-rate [V/ μ s]	25.9	60	128	29.8	197	53.8	1280
0.1 % settling times [ns]	73.3	38.3	20.7	-	7.2	-	6.6
Input voltage noise @ 100 kHz [nV/ \sqrt Hz]	17.9	14.1	13.6	-	-	-	-
FOM ₁ [MHz \times pF/ μ W]	0.41	0.94	1.9	1.86	0.21	0.16	0.4
FOM ₂ [(V/ μ s) \times pF/ μ W]	0.3	0.69	1.35	0.67	0.45	0.34	1.73



IV. CONCLUSION

In this paper, an enhanced class AB amplifier based on the RFC structure is presented. The enhanced structure uses the adaptive biasing technique and new input to output paths to enhance transconductance and slew rate. Simulation results in 65-nm CMOS technology show 16.2dB, 144.3MHz and 102.1V/ μ s improvement in the open loop DC gain, GBW and slew rate over the conventional one, respectively, with just 8% expense in power dissipation.

REFERENCES

- [1] R. S. Assaad and J. Silva-Martinez, "The recycling folded cascode: a general enhancement of the folded cascode amplifier," *Solid-State Circuits, IEEE Journal of*, vol. 44, pp. 2535-2542, 2009.
- [2] R. Assaad and J. Silva-Martinez, "Enhancing general performance of folded cascode amplifier by recycling current," *Electronics Letters*, vol. 43, pp. 1243-1244, 2007.
- [3] M. Akbari and O. Hashemipour, "Design and analysis of folded cascode OTAs using Gm/Id methodology based on flicker noise reduction," *Analog Integrated Circuits and Signal Processing*, vol. 83, pp. 343-352, 2015.
- [4] Y. L. Li, K. F. Han, X. Tan, N. Yan, and H. Min, "Transconductance enhancement method for operational transconductance amplifiers," *Electronics Letters*, vol. 46, pp. 1321-1323, 2010.
- [5] Akbari M. Single-stage fully recycling folded cascode OTA for switched-capacitor circuits. *Electronics Letters*. 2015 Jun 4;51(13):977-9.
- [6] M. Akbari, S. Biabanifard, S. Asadi, and M. E. Yagoub, "High performance folded cascode OTA using positive feedback and recycling structure," *Analog Integrated Circuits and Signal Processing*, vol. 82, pp. 217-227, 2015.
- [7] M. Yavari and O. Shoaee, "A novel fully-differential class AB folded-cascode OTA," *IEICE Electronics Express*, vol. 1, pp. 358-362, 2004.
- [8] A. Sarkar and S. S. Panda, "Design of a power efficient, high slew rate and gain boosted improved recycling folded cascode amplifier with adaptive biasing technique," *Microsystem Technologies*, pp. 1-8, 2016.
- [9] J. Torrifard and A. K. B. A'ain, "A power-efficient CMOS adaptive biasing operational transconductance amplifier," *ETRI Journal*, vol. 35, pp. 226-233, 2013.
- [10] S. Baswa, A. J. Lopez-Martin, J. Ramirez-Angulo, and R. G. Carvajal, "Low-voltage micro-power super class AB CMOS OTA," *Electronics Letters*, vol. 40, pp. 216-217, 2004.
- [11] A. J. López-Martín, S. Baswa, J. Ramirez-Angulo, and R. G. Carvajal, "Low-voltage super class AB CMOS OTA cells with very high slew rate and power efficiency," *IEEE Journal of Solid-State Circuits*, vol. 40, pp. 1068-1077, 2005.
- [12] Akbari M, Hashemipour O. A 63-dB gain OTA operating in subthreshold with 20-nW power consumption. *International Journal of Circuit Theory and Applications*. 2016 Jan 1.
- [13] Akbari M, Nazari M, Sharifi L, Hashemipour O. Improving power efficiency of a two-stage operational amplifier for biomedical applications. *Analog Integrated Circuits and Signal Processing*. 2015 Aug 1;84(2):173-83.
- [14] Akbari M, Hassanzadeh A, Hashemipour O. Slew rate boosting technique for an upgraded transconductance amplifier. *Analog Integrated Circuits and Signal Processing*. 2016 Jul 1;88(1):57-63.
- [15] R. G. Carvajal, J. Ramirez-Angulo, A. J. López-Martín, A. Torralba, J. A. G. Galán, A. Carlosena, and F. M. Chavero, "The flipped voltage follower: A useful cell for low-voltage low-power circuit design," *Circuits and Systems I: Regular Papers, IEEE Transactions on*, vol. 52, pp. 1276-1291, 2005.

Handwriting Character Recognition by Using Fuzzy Logic

Enes Vardar¹, Kaplan Kaplan², H. Metin Ertunc³

^{1, 2, 3} Mechatronics Engineering Department

Kocaeli University, Izmit / Kocaeli

enes_vdr@hotmail.com

kaplan.kaplan@kocaeli.edu.tr

hmertunc@kocaeli.edu.tr

Abstract- Handwriting character recognition can be used to seek texts in big documents, take notes on tablet or decide whether or not internet user is a human or a computer in terms of Web security. In this study, a handwriting recognition system is studied by using fuzzy rules. The system includes 4 parts, namely image processing, feature extraction, fuzzification of the inputs, and defuzzification. In the first stage, image processing based on morphological operations are used to perform the handwriting recognition under the same conditions. The feature extraction process is employed to find the total number of white pixels in each column. Then these pixel numbers are assigned to arrays. The next step is to find the local maximum and minimum values by considering this arrays as an increasing-decreasing mathematical function. Therefore, it is observed that the handwritten letters of these values are divided into various groups. In the next operation, fuzzy classification membership functions and rule tables of text groups are generated by using extracted feature data. For a better recognition performance, the letters group have to be known in order to use image fuzzy logic algorithm. Consequently, this group of letters was successfully classified with fuzzy logic rules.

Keywords — Handwriting recognition, character recognition, fuzzy logic approach, image processing algorithms.

I. INTRODUCTION

Nowadays, studies on handwriting recognition have found numerous application area in technological development. Handwriting recognition systems can greatly facilitate human life by speeding up many operations such as reading tax statements, directing mail, reading bank checks and so on and so forth. On the other hands, these systems may reduce the need for human interaction. Therefore, the academics and commercial studies about handwriting characters have recently become an important research topic in pattern recognition. The human handwritings have been tried to be recognized by many artificial intelligence methods such as Artificial Neural Networks (ANN) [1], K-Nearest Neighbors (KNN) [2], and Linear Differential Analysis (LDA) [3]. One of the methods in application is Fuzzy Logic approach. Fuzzy logic is very suitable for handwriting recognition systems because of its capability for processing of uncertain data. The difficulty in handwriting recognition systems is that handwriting characteristic varies greatly from person to person. For this reason, handwriting recognition systems are quite complex.

In this study, we have studied on the set of images containing big handwritten letters with straight lines. Image processing and feature extraction algorithms in the system were coded in C++ environment. Fuzzy logic algorithms have been constructed and tested in MATLAB environment for handwritten letters. Once the fuzzy logic algorithms were tested in MATLAB to check the recognition performance, then they are written in C++. In the final stage, all the algorithms are combined in a single software, and, therefore handwritten characters are recognized with a reliable performance.

II. IMAGE PROCESSING

Most of the images require preliminary image processing algorithms before applying any recognition technique. In order to increase the accuracy of the classification, it is very important to include descriptive features

when extracting features. The steps of image processing algorithms used in this study are explained as in the following subsections.

A. Convert the Image into a Binary Image

The image to be classified in this section is converted from RGB space to gray space by using *OpenCV* in C++ environment. The grayscale histogram density is automatically calculated and converted to a binary image with the applied threshold value. In the obtained binary image, all the pixel values above the threshold value are assigned to 1 (white) value and all the pixel values below the threshold value are assigned to 0 (black) value. Thus, the image to be classified is divided into two parts that are 1 and 0 with the threshold value. Since feature extraction is related to the number of pixels that have value of 1, the division of parts must be done properly. For this, the Otsu Method, which has a library on *OpenCV* that automatically calculates the threshold value, is used. This method assumes that the image is composed of only two color classes, namely, the background and the foreground. The variance values for all threshold values for these two color class is calculated. The threshold value, which has the smallest variance value, is determined as the optimum threshold value

B. Finding More than One Character in the Image

In this section, binary image applied with threshold value is used as input. The binary image can have more than one character. Firstly, the characters must be separated from the whole image and considered as single image, and each process referred to in this work must be applied. As a first step, the boundary lines is found by the *findContours* function in *OpenCV* library [7]. The boundary lines are stored in an array with two memory files. The first memory of the array is the object and the second is the point of the object boundary line. The object boundaries are dropped to an array by using a simple for loop. Then, the smallest rectangles surrounding these boundary lines are found with the help of *OpenCV* rectangle as in Fig. 1 [7]. This rectangular image is cropped sequentially from the left of the image, and each cropped rectangle is regarded as an image to be classified.



Figure 1. The handwriting image divided into character groups

C. Image Standardization

The last step of image processing procedure is the size standardization of the image characters. Since character images are in different sizes from each other, they need to be reduced to the same size for comparison and recognition of images adequately. By means of this algorithm, the images to be classified in different sizes are standardized to (40 × 30) pixel dimensions.

D. Feature Extraction

In feature extraction stage, the approach is to scan all the columns of the digitized image respectively and keep the total number of white pixels in each column in a string form. Then classification of the characters is performed by comparing the total number of white pixels in this column. Figure 2 shows the 'A' letters drawn with different handwriting and Table 1 lists the column pixel data after image processing procedure is applied to these characters. Note that the pixel values of the characters are different according to each column in Table 1. The main reason of the characters' difference is that they are written by different handwritings.

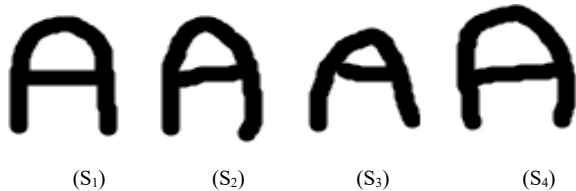


Figure 2. The characters 'A' written by different handwriting

As the columns are observed carefully, even if the characters look like in the form of a different character, the Table 1 gives a hint about classification scheme. In all four cases, the column data shows that the values of pixels increase to nearly 21, decrease to nearly 11, increase nearly 39 again, and finally decrease to 0, respectively. For this reason, a mathematical function can be evaluated according to the local maximum and local minimum values of the data in Table 1. The difference between the current local maximum (or minimum) and the previous local minimum (or maximum) gives us the transition values. These transition values will form the inputs of the fuzzy system. It is possible to verbalize these pixel values in the column with fuzzy logic. Then, the characters can be defined by these verbal statements with fuzzy rules.

TABLE I. S₁, S₂, S₃ and S₄ PIXEL DATA

Column	S ₁	S ₂	S ₃	S ₄
1	5	8	0	0
2	14	14	9	11
3	20	19	14	17
4	23	16	17	24
5	22	16	20	19
6	15	16	17	15
7	13	14	14	13
8	11	13	12	12
9	12	14	13	13
10	13	14	14	13
11	13	14	15	12
12	14	15	32	12
13	14	32	32	11
14	14	38	30	12
15	38	39	29	13
16	39	22	25	38
17	39	16	13	40
18	14	13	13	40
19	14	14	13	27
20	14	14	13	13
21	14	14	14	13
22	14	14	14	12
23	14	14	13	12
24	14	14	13	12
25	14	14	13	12
26	14	13	12	13
27	14	13	12	12
28	12	10	10	11
29	8	5	5	9
30	0	0	0	0

1) *Finding extreme values:* In this process, the program takes into account the data in the column and compares it with the previous data set in order to see whether or not it extracts a local maximum or local minimum

point. Figure 3 shows the flow diagram of the algorithm for computing the extremum (transition) values written in C++. In Table 2, the transition values are listed for the letter 'A' with this block diagram. In the diagram, CD is the current state data and PD is the data in the previous column. Outputs of this algorithm is a transition number and a transition value associated with it. For instance, the parameters $T_1 = 23$ indicates that the transition number is 1 and the transition size is 23. The algorithm also includes determining directional change. When a directional change (transition value) is determined, there must be more difference than ± 3 value between CD and PD. Negative DIT (-DIT) (Direction of transition) means incrementation and positive DIT (+DIT) means the decrementation. If there is a difference equal to 2 or less between CD and PD, the big one is selected. If CD is big, the direction sign is considered. If the direction sign is positive, then L_{max} is equal to CD, otherwise the algorithm will search the next column. If PD is big and the direction sign is negative, then L_{min} becomes as CD. If the direction sign is positive, the other column is passed.

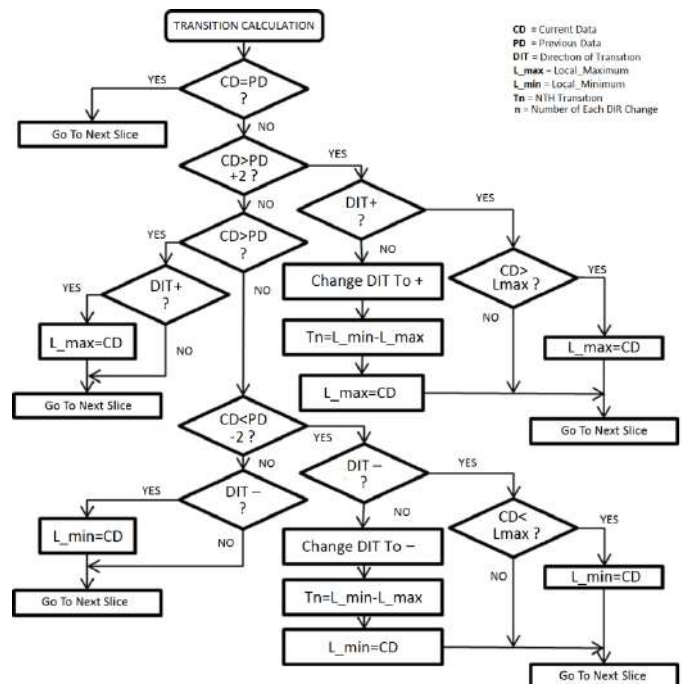


Figure 3. Transition value calculation algorithm

The transition values of the character A (S₁) found using the algorithm in Fig. 3 are shown in Table 2. As shown in Table 2, there are 4 transition points of character A ($T_1 = 23$, $T_2 = -12$, $T_3 = 28$, $T_4 = -39$). The feature extraction in order to characterize each character is applied to all the letters. In feature extraction operations, characters are divided into 3 character sets with 2, 4, or 6 transition values. B, E, G, S have six transition values; A, C, F, J, O, P, R, Z, D have four transition values and H, I, K, L, M, N, T, U, V, Y letters have two transition values character sets, respectively. Firstly, the character to be recognized is determined by which of these letter class, and so this operation facilitates decision of classes with and also flow of the system. These transition values can not provide sufficient accuracy in each character set in order to recognize the characters. For this reason, the total number of pixels, the first maximum and minimum column number, and the characteristic length specific for the character set are extracted by the software to increase the accuracy of the program.

2) *Finding total pixel data:* In this process, the pixel of images that are standardized and considered to be drawn in certain dimensions are scanned in C++ in order to find the total number of white pixels. The total number of pixels is not used because it does not vary much in the class which has only 4 transition values. The total number of pixels found is written in the fuzzy logic rule table and in the membership functions with TPS abbreviation.

3) *Finding the first maximum and minimum points:* It was observed that the column numbers in which the first and maximum transition values were found during the observation of the data differ between the letters and that the same letter has close values even in different handwritten letters.

The first maximum and minimum column numbers found differ in letter sets with 2 transition and 4 transition values. They are not used since these values do not vary sufficiently in the 6-pass value set.

TABLE II: DISPLAY OF TRANSITION VARIABLES

Coloumn	CR	PR	DIR	T	L min	L max	Tn
0	0	0	+		0	0	0
1	5	0	+		0	5	0
2	14	5	+		0	14	0
3	20	14	+		0	20	0
4	23	20	+		0	23	0
5	22	23	+		0	23	0
6	15	22	-	T ₁	15	23	23
7	13	15	-		13	23	0
8	11	13	-		11	23	0
9	12	11	-		11	23	0
10	13	12	-		11	23	0
11	13	13	-		11	23	0
12	14	13	-		11	23	0
13	14	14	-		11	23	0
14	14	14	-		11	23	0
15	38	14	+	T ₂	11	23	-12
16	39	38	+		11	39	0
17	39	39	+		11	39	0
18	14	39	-	T ₃	11	39	28
19	14	14	-		14	39	0
20	14	14	-		14	39	0
21	14	14	-		14	39	0
22	14	14	-		14	39	0
23	14	14	-		14	39	0
24	14	14	-		14	39	0
25	14	14	-		14	39	0
26	14	14	-		14	39	0
27	14	14	-		14	39	0
27	12	14	-		14	39	0
29	8	12	-		8	39	0
30	0	8	-	T ₄	0	39	-39

4) *Feature extraction of a set of letters with four transition values:* In this process, the character lengths of this set of letters shown in Fig. 4 are determined to increase the accuracy of the system. The logic of the written algorithm is to count the number of black pixels remaining between the first white pixel and the next white pixel. To find the length between the vertical and horizontal red lines, the scan operation is performed from (20,0) to (20,30), and from (0,28) to (40,28), respectively. The accuracy of recognizing letters has been increased thanks to differences in letters (C, F, J, P, Z) that do not have horizontal length (HU), and the letters (C, F, J, P, Z) do not have vertical length (VU).

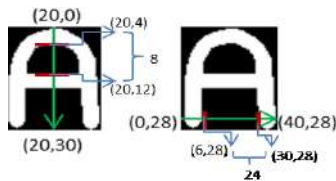


Figure 4. The characteristic length extraction

5) *Feature extraction of a set of letters with two transition values:* Characteristic length extraction in the case of two transition values is to determine the length between the horizontal and vertical red lines shown in Fig. 5. The reason for obtaining these lengths is the same as in the previous feature extraction process. The difference only in the scanning process is that the scanning direction is from (33,0) to (33,30) for the vertical lengths, from (12,3) to (28,3) for horizontal lengths. In this letter set, only the letter K is recognized by using fuzzy logic with the length of the letter K in the vertical direction, the differences in the horizontal length between the letters with the transition values, the first maximum column number, and the total pixel values.

E. Fuzzification of Data

Fuzzification is the process of converting information received from the system into symbolic values, which are linguistic qualifiers. By taking advantage of the membership process, it determines the fuzzy set and membership level to which the input information belongs, and assigns numerical values to the entered numerical values such as "small, smallest". In order to determine each verbal expression, firstly the intervals where the values of the data change must be found. In this study, many different handwritten characters have been evaluated for each character; feature data were examined, and variation intervals of values were found. Each variable interval is divided into sub-regions and each sub-region is labeled with verbal expression. The rule tables of each character group are determined via the MATLAB FIS Editor interface by using the variable data found in C++ software in order to find the membership level of these verbal expressions. Then the variable data are labeled as verbal expressions; fuzzy clusters and membership functions are created in the most accurate way by trial and error method. The fuzzy clusters and membership functions that have been verified by MATLAB program are created in C++ and integrated into image processing and fuzzy logic software. The fuzzy sets in the system consist of 3 membership functions that are small (S), medium (M) and large (L). These membership functions are defined as triangular and trapezoidal functions as shown in Fig. 6. The trapezoid membership function consists of 4 points, n_1, n_2, n_3 and n_4 , and the triangular membership function consists of 3 points, n_1, n_2 ve n_3 . Points of triangular and trapezoidal functions of all letter sets are given in Table 3, Table 4 and Table 5.

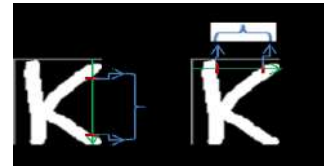


Figure 5. The characteristic length extraction

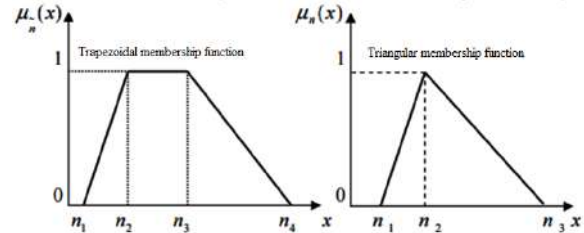


Figure 6. Trapezoidal and triangular membership functions

TABLE III: MEMBERSHIP FUNCTIONS OF LETTERS WITH 6 TRANSITION VALUES

	T ₁	T ₂	T ₃	T ₄	T ₅	T ₆	TPS
S	[0 0 23 30]	[0 0 17 23]	[0 0 15 22]	[0 0 15 22]	[0 0 15 22]	[0 0 20 30]	[0,300,449,500]
M	[23 30 40 40]	[17 23 30]	[15 22 25 30]	[15 22 25 30]	[15 22 27 30]	[20 30 40 40]	[449 500 536 600]
L	-----	[23 30 40 40]	[25 30 40 40]	[25 30 40 40]	[27 30 40 40]	-----	[536 600 775 800]

TABLE IV. MEMBERSHIP FUNCTIONS OF LETTERS WITH 4 TRANSITION VALUES

	T ₁	T ₂	T ₃	T ₄	HU	VU	Min1
S	[0 0 20 31]	[0 0 15 20]	[0 0 14 23,5]	[0 0 22 33]	[0 0 2 3]	[0 0 18 20]	[0 0 10 18]
M	[20 31 40 40]	[15 20 25 30]	[14 23,5 25 30]	[22 33 40 40]	[2 3 40 40]	[18 20 40 40]	[10 18 30 30]
L	-----	[25 30 40 40]	[25 30 40 40]	-----	-----	-----	-----

TABLE V. MEMBERSHIP FUNCTIONS OF LETTERS WITH 2 TRANSITION VALUES

	T ₁	T ₂	VU	HU	Max1	TPS
S	[0 0 15 20]	[0 0 14 20]	[0 0 2 5]	[0 0 15 20]	[0 0 5 10]	[0 0 300 400]
M	[15 20 24 30]	[14 20 24 30]	[2 5 25 40]	[15 20 40 40]	[5 10 13 21]	[300 400 500 600]
L	[24 30 40 40]	[24 30 40 40]	[25 30 40 40]	-----	[13 21 25 40]	[500 600 700 800]

TABLE VI. FUZZY RULE TABLES OF LETTERS WITH 6 TRANSITION VALUES

Letter	T1	T2	T3	T4	T5	T6	TPS
S	Medium	Medium	Small	Small	Medium	Medium	Small
B	Medium	Small	Small	Small	Medium	Medium	Large
G	Medium	Medium	Large	Medium	Small	Medium	Medium
E	Medium	Medium	Medium	Medium	Large	Medium	Medium

TABLO VII. FUZZY RULE TABLES OF LETTERS WITH 4 TRANSITION VALUES

Letter	T1	T2	T3	T4	HU	VU	Min1
A	Medium	Small	Medium	Large	Medium	Small	Small
J	Large	Large	Medium	Medium	Small	Medium	Medium
F	Large	Large	Medium	Large	Small	Small	Small
O	Medium	Small	Small	Medium	Medium	Medium	Medium
P	Large	Small	Small	Large	Small	Small	Small
R	Medium	Small	Small	Large	Medium	Small	Small
Z	Large	Medium	Large	Large	Small	Small	Medium
C	Medium	Medium	Medium	Medium	Small	Medium	Medium
D	Medium	Small	Small	Medium	Small	Medium	Medium

TABLE VII. FUZZY RULE TABLES OF LETTERS WITH 2 TRANSITION VALUES

Letter	T1	T2	VU	HU	Max1	TPS
H	Large	Large	Small	Medium	Medium	Medium
I	Large	Large	Small	Small	Large	Large
K	Medium	Medium	Medium	Small	Medium	Medium
M	Large	Large	Small	Small	Medium	Large
N	Medium	Medium	Small	Medium	Large	Medium
T	Large	Large	Small	Small	Small	Small
U	Large	Large	Small	Medium	Large	Medium
V	Small	Small	Small	Medium	Large	Small
Y	Small	Small	Small	Medium	Medium	Small
L	Large	Large	Small	Small	Large	Small

F. Fuzzy Inference

Fuzzy inference is the process and inference of the fuzzy concepts in a way similar to the ability of people to make decisions and make inference. In fuzzy inference, there are several methods such as min-max, max-prod and Tsukamoto. Min-max was used in this study. The number of transition values of the letter and the letter set given above will be evaluated according to in the rule table. In the rule table, the number of the transition values of the image to be recognized and the character set of letters given above is found. For each letter rule in the rule table, the membership function value of the fuzzy set which the letter is the member is found, respectively. The minimum values of the membership degree of each rule found are stored in an array. The maximum value obtained between these minimum ratings specifies which letter is the image.

III. TESTING OF HANDWRITING RECOGNITION SYSTEM

Figure 7 shows the output of the program with the image of the letter S handwritten to be classified. The letter S image was first converted to binary image by thresholding method, and then the boundary points were found in the OpenCV library. The character to be recognized is regarded as a separate image by the smallest rectangle formed by these boundary points, and this image has been translated into (40 × 30) pixel dimensions for standardization data in the program. As shown in the program output, this character is a member of a set of letters with 6 transition value. The fuzzy logic inputs in this set of letters are the transition values and the total number of pixels. The total pixel values and transition values found and the membership degree of the fuzzy clusters are calculated. In the next step, the membership degrees as shown in Figure 8 are placed in each letter rule table as in Table 6. The minimum membership degree between the membership degrees listed in rule table is found. As shown in Figure 8, S character has 0.2, B character has 0, the character G has 0 and the character E has a membership rate of 0.1. based on taking into account the maximum membership level between these minimum membership degree, it can be determined which letter rule is the Max degree member of the image to be classified. As seen from the Min values, this character belongs to two rules. The letter E is a member with a membership level of 0.14 and the letter S is also a member with a membership level of 0.2. As mentioned before, the

maximum value (0,2) between these two membership levels indicate the letter S.

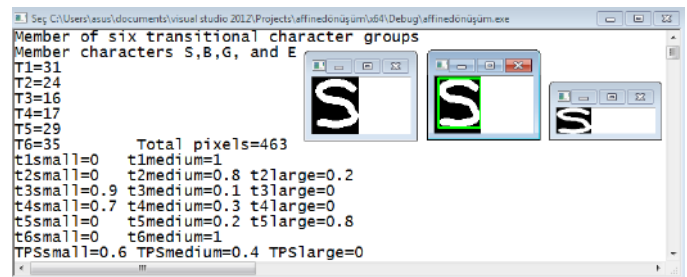


Figure 7. C++ program output

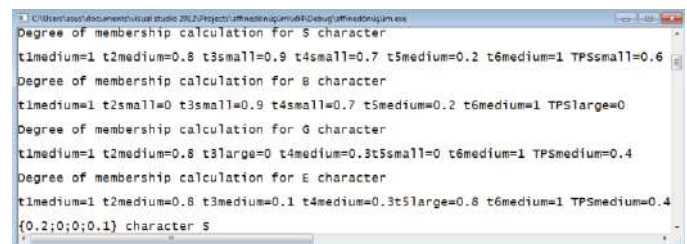


Figure 8. C++ program output

IV. CONCLUSION

In this study, a handwriting recognition system is realized by using image processing, feature extraction and fuzzy logic algorithms in C++ environment. Character images written in different handwriting, image processing algorithms, feature extraction are examined. The accuracy of the system has been increased by examining more than one samples for each letter. As a result of this examination, it is found that the same data in each letter does not vary, that each letter does not have the same number of variable data numbers, and that each letter does not contain the same variable data. Therefore, letters are separated into character groups and fuzzy logic algorithm is created by using variable data of each group of letters. Handwritten letters are successfully classified by using fuzzy logic algorithm. In this study, the dotted letters (ö, ü, i) were not classified due to the uncertainties of the data. In future work, the authors will be concentrated on a recognition system based on more advanced intelligent algorithms such as artificial neural networks, neuro-fuzzy inference system and support vector machines.

REFERENCES

- [1] O. A. Erdem and E. Uzun, "Turkish Times New Roman, Arial, And Handwriting Characters Recognition By Neural Network", Journal of the Faculty of Engineering and Architecture of Gazi University, Ankara, vol. 20, 2005, pp. 13-19.
- [2] S. Weijie, and X. Jin, "Hidden Markov Model with Parameter-Optimized K-Means Clustering for Handwriting Recognition", IEE E2011 International Conference on Internet Computing & Information Services (ICICIS), Hong Kong, 2011.
- [3] M. Mahadeva, Prasad, M. Sukumar. "2D-LDA based online handwritten kannada character recognition." Int. J. of Computer Science and Telecommunications, vol. 4, 2013, pp. 14-18.
- [4] M. K. Jasim, A. M. Al-Saleh, A. Aljanaby, "A Fuzzy Based Feature Extraction Approach for Handwritten Characters", International Journal of Computer Science Issues (IJCSI), vol. 10, 2013, pp. 208-2015.
- [5] W. A. Gowan, "Optical character recognition using fuzzy logic", Microprocessors and Microsystems, vol. 19, 1995, pp. 423-434.



Classification of Bearing Fault Size by Using Support Vector Machines

Kaplan Kaplan¹, Melih Kuncan², H. Metin Ertunç³

^{1, 2, 3} Department of Mechatronics Engineering
Kocaeli University, Izmit / Kocaeli
kaplan.kaplan@kocaeli.edu.tr
melih.kuncan@kocaeli.edu.tr
hmertunc@kocaeli.edu.tr

Abstract — Bearings are generally used as rolling elements in rotation machines. Faults in the rolling elements causes breakdown, and this may lead downtime and huge damages in rotating machines. On the other hand, bearings are often employed under high load and high running speed conditions. In this study, artificial faults are created on bearing inner rings by a laser beam in certain size namely 0.15 cm, 0.5 cm, 0.9 cm diameter. Vibration signals are collected by a data acquisition device in a shaft-bearing test setup. Before classifying the data, feature extraction is performed to characterize the signal. Statistical features are calculated and they are used as input to classification method. SVM classification model is employed to diagnose the size of the faults. The SVM model developed in this study classify the size of bearings faults with no prediction error. In addition, 0.1 mm error band is determined to eliminate minor bugs.

Keywords- Support vector machines; bearings; diagnosing

I. INTRODUCTION

A bearing element is composed of an inner ring, an outer ring and certain number of rolling balls. Bearings are also one of the most important elements of mechanisms such as motor-shaft which is rotating with the least friction. Nowadays, there are usually bearings on the wheel and on the hub of everything that turns. The first manufacturer of bearings is the FAG Company and its founder Friedrich Fisher invented the first bearing in 1883. There are nearly three hundred thousand types of roller bearings used in the industrial applications. Hence, the usage areas of the bearings are a lot. They are used in many different areas and sectors as a transitional element between mechanisms such as aircrafts, subways, coaches, buses, trains, engines, conveyor lines, gears, patters, washing machines, microscopes, telescopes, wind power plants, pumps [1].

A fault on the roller bearings may cause damage in the whole mechanical system. Moreover, faulty bearings can lead to downtime in whole plant. This is undesirable case especially for the big and expensive systems. For this reason, the bearings must be checked at periodic intervals; and repair or replacement must be carried out before fault occurs. To prevent these faults, many diagnostic studies carried out.

There are numerous research studies in the literature related to diagnosing of bearing elements. For example, Liu

et al. [2] developed an expert system that can detect faulty conditions by examining the vibration signals measured in the radial direction before bearing faults occur. This system can classify bearing faults by using fuzzy logic model with various time domain features such as kurtosis. The authors also calculated the success of the diagnosis methods and they claimed that the fuzzy logic method can detect fault with 100% success. The developments in fault diagnosis by using artificial intelligence strategies are summarized by Frank and Koppen –Seliger [3]. They pointed out that the artificial intelligence methods play an important role in the control of faults together with analytical methods.

Along with the developing classification methods, Abdulshahed et al. [4] employed ANN and ANFIS model to detect warming points by friction, corrosion etc. They recorded the thermal warming areas that occurred during spindle motor rotation on the CNC machine tools. The correctness of the positioning of these thermal faults that is very important in terms of machine stability. ANN and improved c-averages fuzzy method achieved valid classification rate. Under different operating conditions, the ANFIS model carried out 98.6% successful classification rate.

Zhang X. et al. [5] performed fault detection and classification of motor bearing by using a hybrid model. The authors calculated permutation entropy (PE) from the vibration signal. They employed the support vector machines (SVM) optimized by inter-cluster distance (ICD) in the feature space in order to classify the fault type and fault severity. They noticed that the developed model obtained effective and robust detection and classification results for motor bearing fault. Fernandez-Francos D. et al. [6] studied on an automatic method for bearing fault detection and diagnosis. They employed a one-class v-SVM to classify normal and faulty conditions. The authors used band-pass filters and Hilbert Transform to obtain the envelope spectrum of the original raw signal. To compare the performance of the method, they used two different data sets are used that are real data from a laboratory test setup and a fault-seeded bearing test setup. They claimed they determined not only the failure in an incipient stage but also the location of the defect.

In this study, a classification method based on Support Vector Machine (SVM) was developed for various faulty bearing elements. For this, bearing faults were created by a laser beam artificially in different sizes. The faulty bearing elements were made run in the experimental setup under various operating conditions. Vibration data was collected from a shaft-bearing setup, then time domain statistical features were calculated. These features were employed as input parameters to a SVM classification method to predict the different fault sizes of the bearings.

II. SUPPORT VECTOR MACHINES

The aim of Support Vector Machines is to estimate the most appropriate function for separating two classes with the help of the optimal hyperplane by the binary classification logic. Since multiple planes can be calculated when the data are classified, it is necessary to obtain the most appropriate hyperplane. The optimal hyperplane is obtained by maximizing the distance between the support vectors of the different classes with the separation of the state of interest. The Support Vectors are the closest vectors on either side of the hyperplane. SVM minimizes the empirical classification error while classifying.

Burgess noted that he needs to maximize the distance from the boundary of the hyperplane which passes through the two classes for a good classification in his studies. SVM classifiers are basically separate two groups according to the linearity of the data set [7].

Let $\{x_i, y_i\}$ $i = 1, 2, \dots, N$ the set of N elements is used for training of Support Vector Machines. Where $x_i \in R^p$ p is the input vector number and $y_i \in \{-1, 1\}$ is output values. In case of linear separation, the two field output values can be separated by a direct hyperplane.

When $S = \{(x_1, y_1), (x_2, y_2), \dots, (x_n, y_n)\}$ is given to training set consisting of $\{x_i, y_i\}$ pairs, the appropriate weight vector w and threshold value b for this training set will determine whether the training set is linearly separated.

$$Y_i (wx_i + b) \geq 1 \quad i = 1, 2, \dots, N \quad (1)$$

If the (1) is generalized, $w x + b = 0$ is obtained. With the help of this equation, the bounds are determined in order to obtain the most appropriate hyperplane between the two vectors.

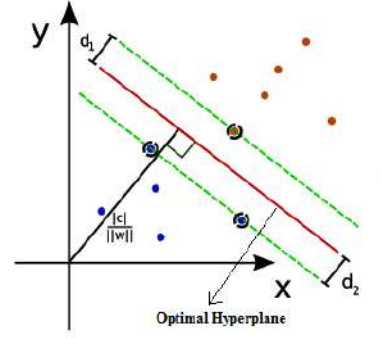


Figure 1. Optimal hyperplane and support vectors [8]

In Fig. 1, the green lines and the red line represent border and the most appropriate hyperplane, respectively. The marked points on the green lines indicate the support vectors. The most appropriate hyper polarity is located at the midpoint of the boundary lines. The distance between these boundary lines is called d distance [8].

The main philosophy of Support Vector Machines is to maximize the d distance. The distance between two sample classes, namely the distance between the boundaries can be calculated from $d = 2/\|w\|$ formula. The maximum distance between these two bounds is obtained by minimizing the $\|w\|^2$ value.

$$\text{Objective Function} = \text{Min} \frac{1}{2} \|w\|^2 \quad (2)$$

$$\text{Constraint} = y_i (wx_i + b) \geq 1 \quad (3)$$

To find the maximum limit, the nonlinear optimization problem must be solved by the objective function as in (2) with the constraint in (3). The Lagrange Multipliers method should be used to solve this problem. The Lagrange function found in Cortes, Vapnik and later Burgess's work is used in

$$(4) \cdot L_p(w, b, \alpha) = \frac{1}{2} \|w\|^2 - \sum_{i=1}^n \alpha_i [y_i (wx_i + b)] + \sum_{i=1}^n \alpha_i \quad (4)$$

In (4), each $\alpha_i \geq 0$ is a Lagrange multiplier.

L_p is a function that maximizes the Lagrange multipliers, w is the weight vector, and b constant is a function that is minimized. According to this method, the derivatives of the function w and b are obtained and equalized to zero. Karush-Kuhn-Tucker (KKT) conditions are calculated as seen in (5) and (6).

$$w = \sum_{i=1}^n y_i \alpha_i x_i \quad (5)$$

$$\sum_{i=1}^n y_i \alpha_i = 0 \quad (6)$$

The obtained KKT conditions are substituted in (4) and the optimization problem becomes dual problem of the maximization type.

$$L_D(w, \alpha, b) = \sum_{i=1}^n \alpha_i + \frac{1}{2} \sum_{i=1}^n \sum_{j=1}^n \alpha_i \alpha_j y_i y_j (x_i x_j) \quad (7)$$

$$\sum_{i=1}^n \alpha_i y_i = 0 \quad (8)$$

When the model in (7) is solved under the constraint given in (8), one Lagrange multiplier is obtained for each training data. Gunn named his support vectors as Lagrange multipliers which values greater than zero in his studies in 1998. Those that are non-zero are those that are above the borders, and those that are equal to zero are those that remain on the other side of the borders. These non-zero Lagrange multipliers are located above the boundaries and those equal to zero remain on the other side of the bounds.

III. METHOD

A. The Test Platform

The experimental data used in this study is collected from a bearing-shaft assembly which is consist of an AC servo motor as shown in Fig. 2.



Figure 2. The experimental setup

The data is collected by National Instruments 6211 data acquisition card (DAQ) via MATLAB environment. The piezoelectric vibration sensor (352C65) is used for transmitting vibration signals to electrical signals. Signal conditioners is employed in order to eliminate noise and to amplify the vibration signal.

Bearing faults in specific size are formed by laser beam artificially on inner ring for this study. Faults are formed in

micron precision to inner ring for this experiment in the size of 0.15 mm, 0.5 mm and 0.9 mm diameter. Fig. 3 a microscopic fault formed by laser beam can be seen. Laser beam is very sensitive in terms of diameter size error.

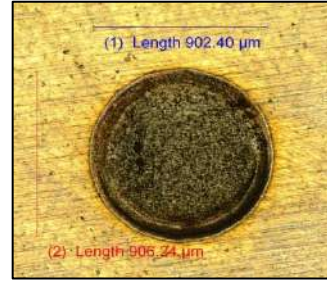


Figure 3. A sample microscopic fault image

B. Raw Vibration Data and Feature Extraction

Vibration data at a sampling frequency of 24 kHz is separated into 20 pieces with 1 second. These data packet are calculated and stored in computer environment. A sample raw vibration data can be seen in Fig. 4.

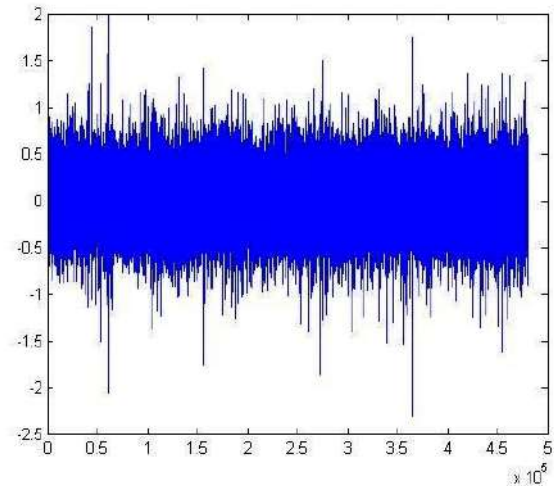


Figure 4. Raw vibration data

Time domain statistical features are obtained from data packets. The features must represent data packets accurately. Otherwise, it is very hard to classify the fault size. 9 different feature are utilized to create feature data. That are:

- RMS
- Kurtosis
- Standard Deviation
- Skewness
- Maximum
- Minimum
- Average
- Median
- Crest Factor

C. Building of Support Vector Machine Model

The 9 type feature is extracted from the data packets divided into 20 part. This procedure is applied for each data in different size. Therefore, the feature matrixes were stored in 9x60 sizes. These feature matrixes are given as input to developed SVM model. As in Fig. 5, SVM model and its feature inputs can be seen.

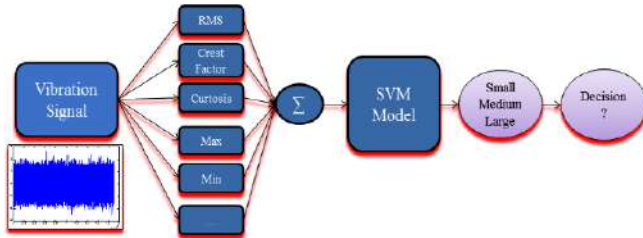


Figure 5. Bearing fault size classification model

A target output matrix of 1x60 that meets the input matrix was created. The target matrix consists of 3 different matrices that are 1x20 small size, 1x20 medium size, 1x20 large size. The hypothetical values that are 0.15, 0.5, and 0.9 mm are determined as small, medium and large size, respectively. In Table I, faults size and target output size are illustrated.

TABLE I. FAULT TYPES

Fault Types	Target Output (mm)
Small	0.15
Medium	0.5
Large	0.9

The SVM model actually distinguishes objects into 2 groups. Thus, the classification process is performed in the form of steps as in Fig. 6. First, the small faulty bearing was separated from the other faulty bearing. In the remaining group, medium and large defective bearings were distinguished from each other by the 2nd stage classification process.

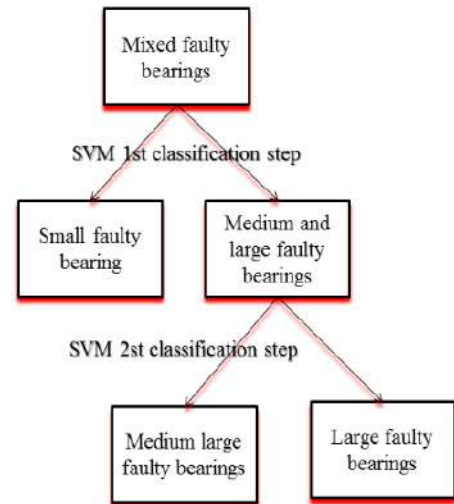


Figure 6. SVM classification model steps

IV. EXPERIMENTAL RESULTS

The simulation results obtained were evaluated according to two different performance criterion. Equation (9) and (10) were taken into consideration when evaluating the results.

$$Actual\ Error\ (\%) = \frac{1}{N} \times \sum_{i=1}^n \left| 100 \times \frac{(a_i - p_i)}{a_i} \right|$$

$$(9) \text{ Error Band Success } (\%) = \frac{1}{N} \left(\sum_{i=1}^n \left(\left| (a_i - p_i) \right| > 0.1 \right) \right) \times 100$$

(10)

a and p values are respectively the actual and predicted values. n is the number of output values not included in the error band, and N is the total number of inputs used. The actual error equation indicates how far the prediction results of the classification models from the actual test data. It is aimed to estimate the bearing fault dimensions more precisely by observing the small faults by the 0.1 mm error band.

For classification via Support Vector Machine, MATLAB Statistics and Machine Learning Toolbox is used. The Radial Basis Function (RBF) was selected as the appropriate kernel function. These parameters were selected by trial and error according to their accuracy performance. In addition, quadratic programming was selected as a solver algorithm, subsampling heuristic procedure is used.

50% of the data set were used to train the SVM network, and remaining 50% were used for testing. The train and test data is randomly assigned for each trial. As the SVM classifies the classes according to the assignment process, the results of the classification process are estimated as exact 0.15, 0.5 and 0.9 values. Therefore, deviations from the average were not observed.

A successful classification was achieved in the SVM model thanks to the hyperplane technique. The classification is performed by the assignment between them according to hyperbolic lines. In Fig. 7, blue points are target output and the red values show estimated results by an SVM model. By the SVM model, the bearing fault dimensions are classified correctly and the bearing error dimensions are determined with 100 % success.

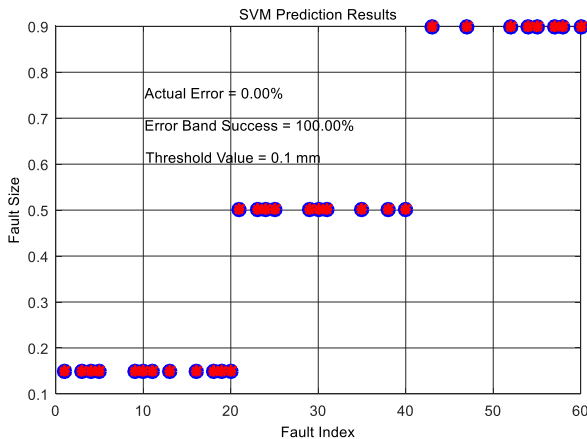


Figure 7. The predicted and the target output

V. CONCLUSIONS

In this study, artificial faults on bearing were created by laser beam on inner ring. The vibration signal was acquired from the experimental setup. The features were extracted through raw vibration data in the time domain and they were given as input to SVM model for classifying fault sizes in the bearings. In order to avoid small classification errors, an error band function was employed in the diagnosing approach. The fault sizes are determined with a %100

success by the classification model. It is observed that SVM model is very useful for detection fault size. In the future work, a multi-decision algorithm will be employed for inner, outer and ball faulty bearings.

ACKNOWLEDGEMENT

The work presented in this paper has been done at Sensor Laboratory of Mechatronics Engineering Department and was supported by TÜBİTAK under the project code 106M280. Authors of this paper thank to the Middle East Bearing Industry (ORS) for granting bearings. They also thank to Laser Technologies Research and Application Center (LATARIUM) for contributing to make the artificial defects on bearings.

REFERENCES

- [1] <http://www.teknikport.com/2012/03/rulman-2/>
- [2] Li B., Chow M., Tipsuwan Y., Hung J.C., "Neural-Network- Based Motor Rolling Bearing Fault Diagnosis", *Industrial Electronics*, 2000, vol. 47, pp. 1060-1069.
- [3] Frank P. M., Köppen-Seliger B., "Fuzzy Logic and Neural Network Applications to Fault Diagnosis", *International Journal of Approximate Reasoning*, vol. 16, 1997, pp. 67-88.
- [4] Abdulshahed A. M., Longstaff A. P., Fletcher S., Myers A., "Thermal Error Modelling of Machine Tools Based on ANFIS With Fuzzy C-Means Clustering Using a Thermal Imaging Camera", *Applied Mathematical Modelling*, vol. 19, 2015, pp. 1837-1852.
- [5] Zhang, X., Liang, Y., & Zhou, J., "A novel bearing fault diagnosis model integrated permutation entropy, ensemble empirical mode decomposition and optimized SVM", *Measurement*, vol. 69, 2015, pp. 164-179.
- [6] Fernández-Francos, D., Martínez-Rego, D., Fontenla-Romero, O., & Alonso-Betanzos, A., "Automatic bearing fault diagnosis based on one-class v-SVM. *Computers & Industrial Engineering*", vol. 64, 2013, 357-365.
- [7] Burges, C. J., "A tutorial on support vector machines for pattern recognition", *Data mining and knowledge discovery*, vol. 2, 1998, pp. 121-167.
- [8] www.math.cornell.edu/~numb3rs/kostyuk/num219.htm

MECHANICAL ENGINEERING

POSTER SUBMISSIONS



Detailed FGM Modelling using Dummy Thermal Loads using ANSYS APDL

Ahmed Hassan

Department of Mechanical Engineering,

Ondokuz Mayıs University, 55139 Samsun, Turkey

Tel: +905388652306 Email: ahah432@yahoo.com

Ibrahim Keleş

Department of Mechanical Engineering,

Ondokuz Mayıs University, 55139 Samsun, Turkey

Email: ibrahimkeles@omu.edu.tr

Abstract—This work reports a modelling method of functionally graded materials (FGM) using ANSYS APDL. ANSYS, as many other analysis software packages, does not provide a direct way to model variation in material properties as a function of position. However, ANSYS offers the option of temperature dependent properties; and ANSYS also offers the ability of assigning temperature values according to the position; joining these two abilities offered by ANSYS, the material properties would be position dependent. In this work, using ANSYS APDL, dummy thermal loads are used to obtain FGM distributed properties. The presented modelling method is explained and then applied to some case study of static analysis to verify its accuracy by comparing its results with the analytical solution from the case study source. The main advantage of such a method is its simplicity and ease; it does not require deep knowledge of mathematical models of FGM and delivers high accuracy. Although in this study ANSYS APDL is used, one can apply it in ANSYS Workbench Mechanical or any other analysis package that has coupling capabilities of structural and thermal studies. The presented method is already mentioned in the literature, but no single documentation about it is found. This paper presents a complete representation of the method.

Keywords—Functionally graded material; ANSYS; modeling; Dummy thermal loads method.

I. INTRODUCTION

Functionally graded materials FGMs are defined as “materials that comprise a spatial gradation in structure and/or composition, tailored for specific performance or function” [1]; i.e. functionally graded material properties at any point at the structure differ according to the position of the point. So we can say that Functionally Graded Material (FGM), a revolutionary material, belongs to a class of advanced materials with varying properties over a changing dimension [2]. This distributed properties are achieved by composing the microstructure using different materials, at least two. The microstructure is designed in such a way that leads to gain certain desired properties for the whole structure. For example, ceramics have high strength and high thermal properties, but lack toughness, so they could be

compounded with metals as FGM to gain the desired toughness.

As in FIG-01, the structure is ranging from one material phase, i.e. ceramic to another material phase, i.e. metal. The properties transition from one phase to another occurs gradually according to the design equation of the microstructure. Typically, properties variation could be linear, exponential, some power equation, etc. as a function of some dimension i.e. position.

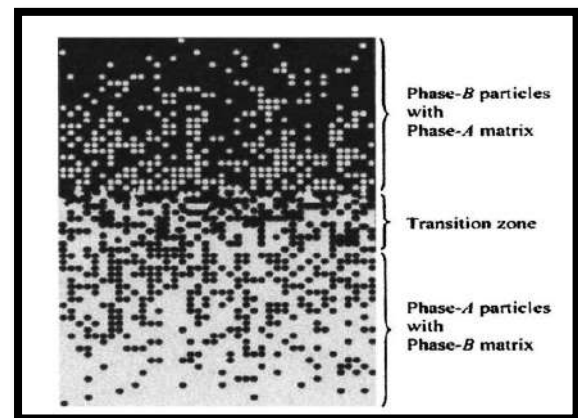


Figure 1 FGM microstructure. [3]

FGM properties variation could be modeled as microstructure changes, layers change, continuous changing, as shown in FIG-2.

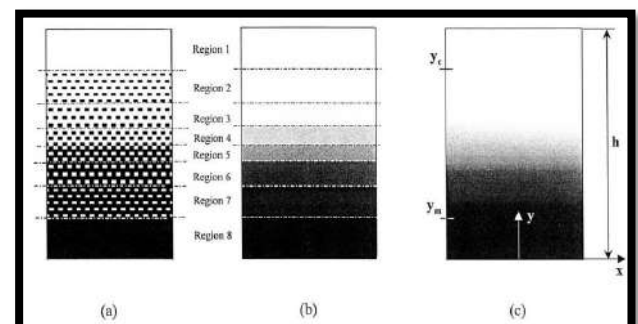


Figure 2 FGM modeled by: (a) micro-structure, (b) layers and (c) a continuously changing structure. [4]

The three models have the same concept of dimension dependent microstructure, and so the properties. The microstructure change and layer change models have

additional concept of intervals for properties (regions). The selection of one model represents the manufacturing technique, i.e. the design of the microstructure, or the simplicity level desired in the model.

These models have been the subject of many studies.[3] It requires a solid knowledge of mathematics, elasticity, mechanics, etc. to model, solve, or even use these models.

ANSYS and analysis packages offer obtaining solutions and results without the must of neither the knowledge of mathematical model nor the solution methods of them. The only requirement is to express the problem correctly to the software. ANSYS has wide range options and capabilities that makes it easy to communicate with it; i.e. express the problem and extract results.

II. THE CASE PROBLEM DESCRIPTION

An application problem is selected to illustrate the presented modelling way. It is a static analysis problem of FGM solid cylinder with radius (b) m, subjected to external pressure (P₀) Pa. The goal is to obtain the normalized radial displacements, radial stresses and hoop stresses. There are two material properties in concern here, Elasticity modulus (E) and Poisson's ratio (ν). Poisson's ratio is considered fixed in this problem, while elasticity modulus of the cylinder varies exponentially through its radius according to the following equations:

$$E(r) = E_0 e^{-nR^n}, \quad n = \ln\left(\frac{E_0}{E_{out}}\right), \quad R = \frac{r}{b}$$

where,

r = radius at given point.

E(r) = the elasticity modulus at points at radius r.

E₀ = Elasticity modulus at the cylinder center.

n, η = material parameters.

E_{out} = Elasticity modulus at the cylinder outer surface.

R = rational radius.

b = Radius of the cylinder.

Radial displacements, radial stresses and hoop stresses are obtained for different values of (n) and (η), while the values of (b) and (E₀) are arbitrary assumed; their values has no importance because the comparison is between the normalized outputs. (E_{out}) is directly related to (E) through the value of (n). Normalized outputs follows the following equations:

$$U = \frac{uE_0}{bP_0}, \quad \sigma' = \frac{\sigma}{P_0}$$

where:

U = normalized radial displacement.

u = obtained radial displacement (m).

σ' = normalized stress, applicable to the radial and hoop stresses.

σ = obtained stress, radial or hoop stresses (N/m²).

For this particular problem, it can be modelled as 2D plane strain problem. Due to the symmetry of the cylinder cross

section shape (circle) and the symmetry of the load, only quarter of the cross section is needed.

The following values are used:

B = 200 mm

E₀ = 120 GPa

P₀ = 1000 Pa

n = [-1.0, -0.5, 0.0, 0.5, 1.0]

ν = 0.3

η = 0.9

III. METHOD OVERVIEW

The main goal is to obtain dimensional dependent properties, which is not directly available in ANSYS. The idea is to make the desired distributed property as a function of other value which is a function of position only; which makes the desired property depends only on dimensions.

ANSYS offers the ability of temperature dependent properties; and ANSYS offers the ability of assigning temperature value at any point (node) according to the point's position; joining these two abilities offered by ANSYS, the material properties would be position dependent.

The general steps can be summarized as:

- Define the material properties as a function of temperature; and make sure the expansion is set to zero to eliminate any thermal stresses.
- Create and mesh the geometry to obtain the nodes (points).
- Apply thermal loads, i.e. temperature values, for each node of the structure as a function of position (dimension). This makes material properties depend only on temperature, and temperature depends only on position, so material properties depends only on position. The temperature value will represent the dimension; i.e. replace the dimension.
- Apply problem's loads and constraints
- Run the simulation and obtain results.

IV. METHOD APPLICATION BY STEPS

Here is the detailed step-by-step illustration:

A. Selection of GUI filtering:

This case problem is about static analysis, so select structural analysis filter. In addition, thermal loads are used in this method; so thermal analysis has to be selected as well. Selection of GUI filters is at:

Main Menu > Preferences

B. Selection of the element type and its options

i. Element Type

Selection of the element type depends on the specific problem as it may be planer 2D elements or solid 3D. Since the problem includes thermal and structural studies and since it is decided to be a 2D analysis, a coupled field element could be selected. Exactly "Quad 8 nodes 223" is selected as the element type. It is a planer 2D element which has the ability of performing coupled thermo-structural analysis. Select element type at:

Main Menu > Preprocessor > Element Type > Add/Edit/Delete > Add..

ii. Element Options

Since this is a plane strain problem, element behavior has to be set as plane strain. Set element options at:

Main Menu > Preprocessor > Element Type > Add/Edit/Delete > Options...

C. Create part geometry

Create the problem geometry. Here for this example case study, create an area of a circle quarter, with radius of 200 which its center is at (0,0).

Main Menu > Modelling > Areas > Circle > Partial Annulus

D. Meshing

Main Menu > Preprocessor > Meshing > Mesh tool

Modify meshing options as to have a fine mesh, which leads to more real representation of the FGM material. Here Smart Size is used, and its value is set as 1 (Fine Mesh).

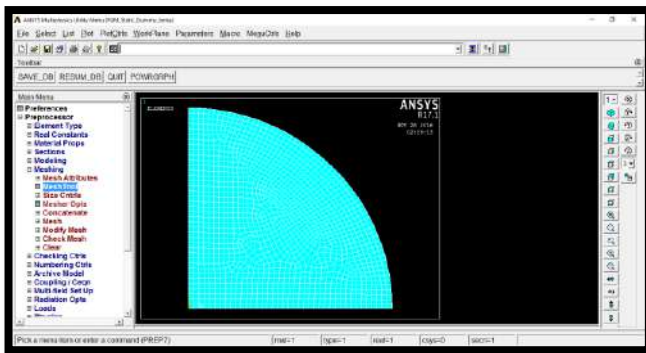


Figure 3 Meshed Shape

E. Material properties

We want to distribute the elasticity modulus across the cross section as a function of the radius, using a linear distribution of nodes temperatures. ANSYS allows us to express the elasticity as a function of temperature by assigning points of (Temp, Elasticity) in the material model window.

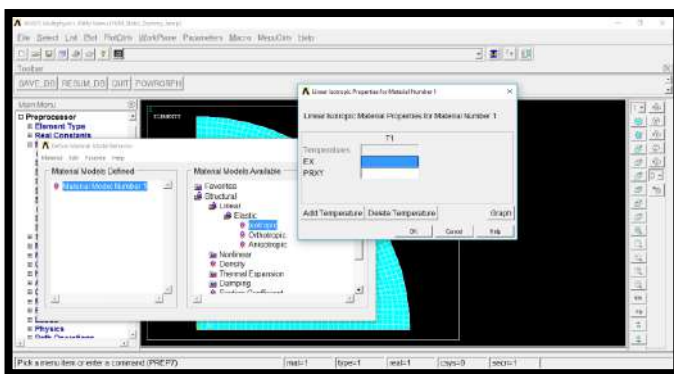


Figure 4 Material Properties

If the material property varies linearly, we have to put only two points to express the straight line. But with nonlinear variation of the property, as in this case problem (exponential distribution) we have to assign more the two points; and it is better to have as much points as possible to present the curve of distribution. ANSYS allows up to 100 points to be assigned to express the curve. This is tedious to

be achieved manually. We can use other program like MS Excel to obtain these points, or we can use MACRO. MACRO is the name of subroutines in ANSYS. We can make a MACRO that automates the process of assigning these points of temperature-Elasticity relationship. Here MACRO is used.

From: Pull Down Menu > Macro > Create Macro, give it a name end with (.mac).

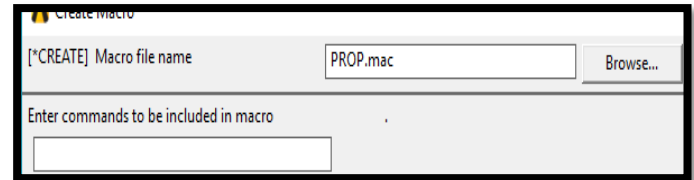


Figure 5 MACRO Creating

Then open it from the directory using any text editor. In the .mac file write this command series; i.e. program:

```

PREP7                                ! allows preprocessor commands
E0 = 120                              ! GPa
n = -0.5                              ! v = 0.3 constant ... Poisson's ratio
mu = 0. 3
*DO,j,1,100,1                         ! loop of 100 points
  R = (j-1)/99                        ! R ranges from 0 to 1
  T = 0 + (100-0)*(j-1)/99            ! T ranges from 0 to 100
  Er = 1000*E0*exp(-n*R**mu)          ! E(r) ranges from E0 to Eout
  MPTEMP,j,T                          ! assign the (j)th temperature
  MPDATA,EX,1,,Er                     ! assign the (j)th Elasticity (E)
  MPDATA,PRXY,1,,0.3                  ! assign the (j)th v, Poisson's ratio
*ENDDO
!the following lines of code: Assign expansion to zero,
!conductivity to arbitrary value i.e. 60
MPTEMP,,,,,,,,
MPTEMP,1,0
UIMP,1,REFT,,
MPDATA,ALPX,1,,0
MPTEMP,,,,,,,,
MPTEMP,1,0

```

This MACRO loops through temperature and calculates E(r) as a function of R and T, finally in each loop it assign the calculated values to the material properties.

Run this macro by calling it with its name from the command line

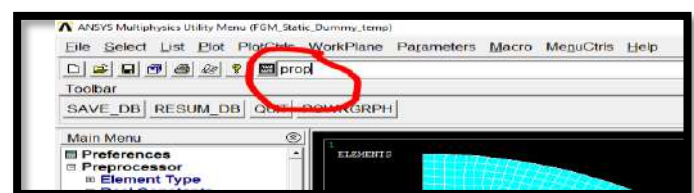


Figure 6 Calling created MACRO

Then check the material properties. The material properties should be filled with points.



Figure 7 Checking Material Properties

We can check the variation of elasticity modulus through the temperature range by clicking on “Graph” button in the above figure

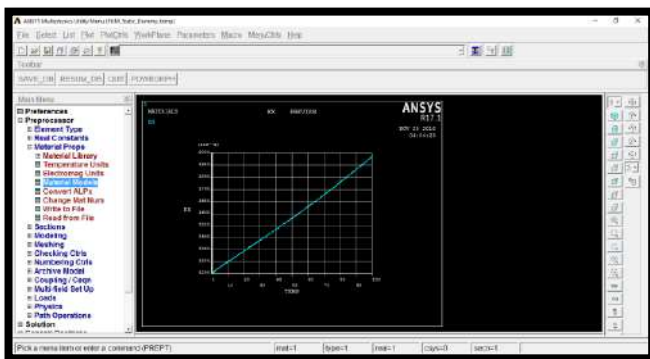


Figure 8 Graph material properties

F. Loads

In this step we will apply the thermal loads, and for this case problem we have to apply the external pressure. So we have two loads to apply. In addition we will express the symmetry of the shape.

i. Thermal loads

Thermal loads are applied as assigning temperature value at each node. The range of temperature has to be the same as the temperature range used in assign properties in Step 5. The range of 0-100C was selected, as the center point has 0C and the outer radius has 100C. Temperature varies linearly across the radius. To assign these values of temperature we use Function capability offered by ANSYS.

Pull Down menu > Parameters > Functions > Define/Edit..

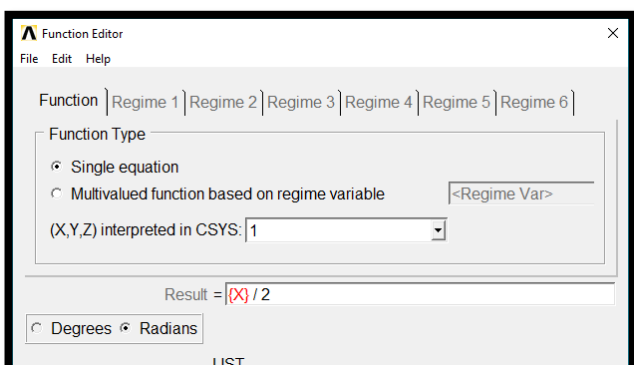


Figure 9 Function Creating

- Modify the coordinate system (CSYS) to be polar system (value 1); now (X) means the radius. Since we want to range the temperature between 0C and 100C, and our radius range from 0 to 200, so the result must output the value of $(X / 2)$. Save the function; and then call it from:

Pull Down menu > Parameters > Functions > Read From File

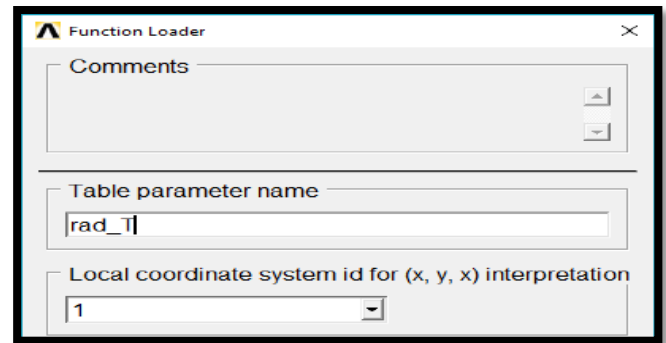


Figure 10 Creating table from function

- Give it a name at “table parameter name”. Here we named it as “rad_T”. Now we can finally apply the thermal load.

Main Menu > Preprocessor > loads > Define Loads > Apply > Temperature > On Nodes

Select all nodes by choosing “pick all” in the selection window. Select TEMP as DOF to be constrained, and apply as “existing table”

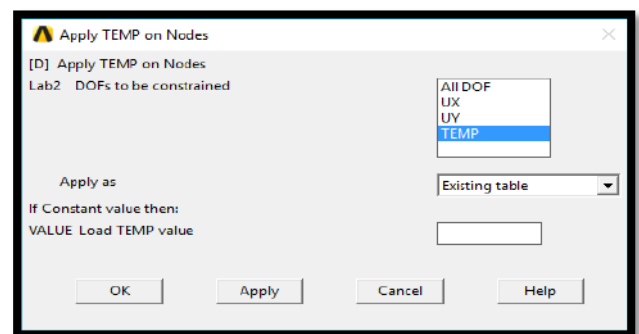


Figure 11 Apply TEMP on Nodes using existing table option

- Select the table name previously created “RAD_T”

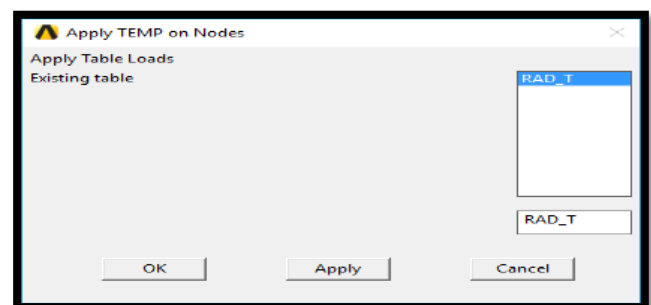


Figure 12 Calling The created Table

The temperature load applied, and will appear as follows:

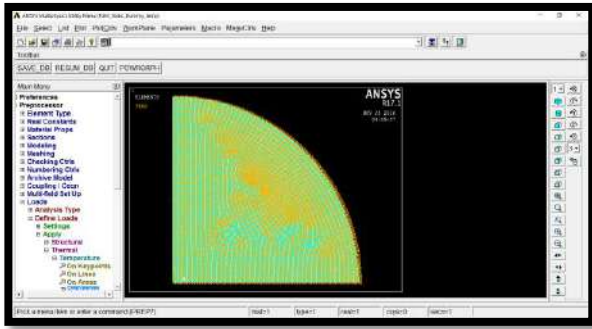


Figure 13 Temperature applied to nodes

ii. Structural load

Apply the external pressure at the outer radius of the quarter. Main Menu> Preprocessor > Loads> Structural > Pressure > On Lines, and select the outer arc line of the shape. Assign the value of the pressure as given 1000 Pa.

iii. Symmetry boundary condition

From: Main Menu> Preprocessor > Loads> Structural > Displacement > Symmetry B.C. > On Lines, select the two straight lines of the circle quarter.

G. Solve

Run the analysis from: Main Menu> Solution > solve > Current L.S

V. RESULTS

The analysis has been done with different values of proposed material constant (n). The output files of our ANSYS analysis are then processed in Excel to obtain the normalized values, and compared with the analytical solutions. The obtained values from ANSYS are compared to those obtained by the formulae in [5]. The comparison plots are shown in figures 14,15 and 16. The obtained values from analytical solution and ANSYS are shown in tables 1 and 2 respectively. Table 2 also contains in its last column a comparison between the analytical and ANSYS solution expressed as percentage relative error (ERROR%).

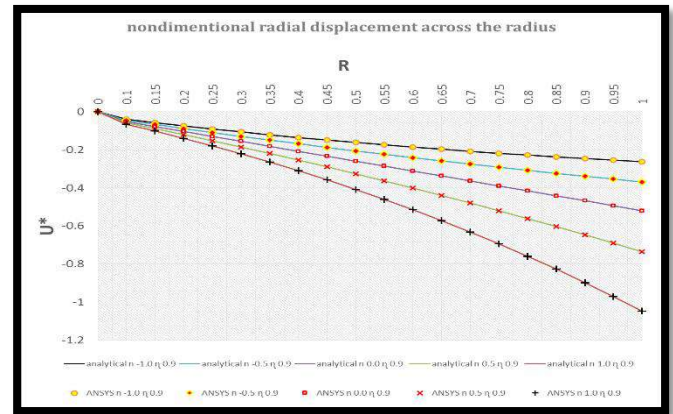


Figure 14 Normalized Radial Displacement $n=-0.5$, $\eta=0.9$

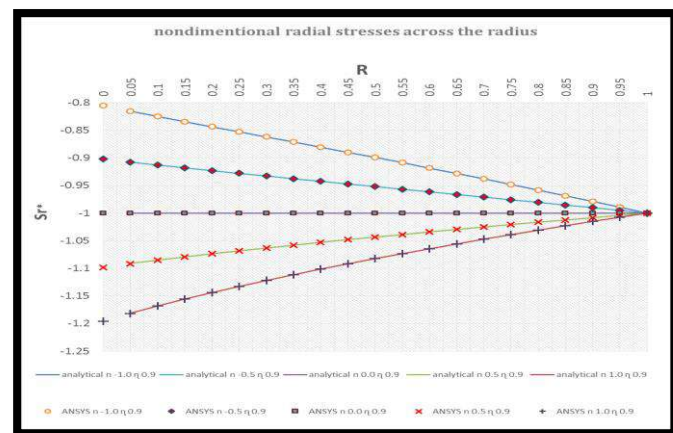


Figure 15 Normalized Radial Stresses $n=-0.5$, $\eta=0.9$

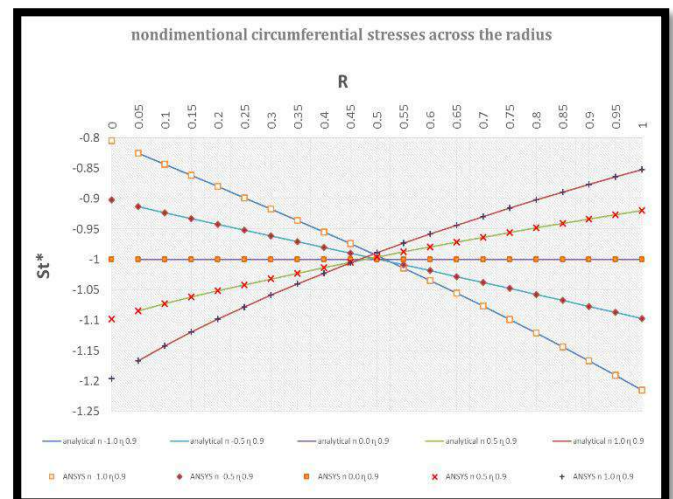


Figure 16 Normalized Hoop Stresses $n=-0.5$, $\eta=0.9$

Analytical Solutions																								
n	η 0.9	R	0	0.05	0.1	0.15	0.2	0.25	0.3	0.35	0.4	0.45	0.5	0.55	0.6	0.65	0.7	0.75	0.8	0.85	0.9	0.95	1	
analytical n=1.0n 0.9 n=1.0n 0.9																								
-1	0.9	0	0	-0.020241301 -0.015490292 -0.004523761	-0.039471371 -0.025108633 -0.084039722	-0.057495959 -0.034504871 -0.085225623	-0.074669591 -0.047374564 -0.088048928	-0.09034022 -0.062905417 -0.089793988	-0.106620064 -0.071311663 -0.091278637	-0.121474236 -0.087131663 -0.096027328	-0.136638871 -0.088931877 -0.095045983	-0.149517333 -0.099300168 -0.097439614	-0.162090068 -0.103608188 -0.094042057	-0.174365717 -0.105629845 -0.117461799	-0.186218882 -0.093502945 -0.107646069	-0.197480036 -0.092042024 -0.087663226	-0.208610619 -0.08091461 -0.08663326	-0.218770522 -0.05817613 -0.120020257	-0.228182612 -0.05827613 -0.114368267	-0.237563683 -0.05842078 -0.11669599	-0.246533468 -0.07973486 -0.190766995	-0.255114346 -0.08821091 -0.125124663	-0.26331466 -0.08542078 -0.125124663	
analytical n=0.5n 0.9 n=0.5n 0.9	0.9	0	0	-0.023060545 -0.907808149 -0.912373669	-0.045460933 -0.913097068 -0.923813321	-0.06728235 -0.918172814 -0.931839346	-0.088548096 -0.923130903 -0.942795783	-0.109291816 -0.928015694 -0.961760198	-0.129537049 -0.932852086 -0.976050084	-0.149304032 -0.937650084 -0.983438825	-0.168610743 -0.942388482 -0.990067195	-0.187473236 -0.947204899 -0.995958729	-0.205906613 -0.951971383 -0.101862507	-0.223924304 -0.95672345 -0.100910689	-0.241539165 -0.96149573 -0.100862507	-0.258763167 -0.966246031 -0.103280853	-0.27607559 -0.971041879 -0.104774464	-0.290083111 -0.97583012 -0.107364167	-0.308198665 -0.980631123 -0.108746416	-0.323967506 -0.985447087 -0.109746416	-0.339395247 -0.990279574 -0.12742315	-0.354891905 -0.99513009 -0.12742315	-0.369269505 -0.999700005 -0.12742315	
analytical n=0.0n 0.9 n=0.0n 0.9	0.9	0	0	-0.026 -1 -1	-0.052 -1 -1	-0.078 -1 -1	-0.104 -1 -1	-0.13 -1 -1	-0.156 -1 -1	-0.182 -1 -1	-0.208 -1 -1	-0.234 -1 -1	-0.26 -1 -1	-0.286 -1 -1	-0.312 -1 -1	-0.338 -1 -1	-0.364 -1 -1	-0.39 -1 -1	-0.416 -1 -1	-0.442 -1 -1	-0.468 -1 -1	-0.494 -1 -1	-0.52 -1 -1	
analytical n=0.5n 0.9 n=0.5n 0.9	0.9	0	0	-0.029042579 -1.091322804 -1.068483618	-0.058932046 -1.08511575 -1.073146673	-0.089624795 -1.079298983 -1.066232188	-0.121107471 -1.073717539 -1.058184211	-0.153376158 -1.068338836 -1.041854668	-0.186431732 -1.0603119047 -1.022272115	-0.220077991 -1.050370899 -1.008229868	-0.254920718 -1.040345457 -0.996312511	-0.290037615 -1.03678494 -0.98780138	-0.326625672 -1.034198912 -0.979645126	-0.363705553 -1.029600991 -0.97157038	-0.401616846 -1.025256573 -0.963670008	-0.440370362 -1.020891669 -0.959219413	-0.479977096 -1.016592778 -0.94832163	-0.520494169 -1.012356801 -0.940863854	-0.561798788 -1.008180669 -0.933541962	-0.604038707 -1.00062789 -0.926350402	-0.647812107 -1.00062789 -0.918284016	-0.691254272 -1.00062789 -0.918284016	-0.736230472 -1.00062789 -0.918284016	
analytical n=1.0n 0.9 n=1.0n 0.9	1	0	0	-0.032174299 -1.181157065 -1.167880743	-0.066249774 -1.167880743 -1.147427096	-0.102577663 -1.147427096 -1.116648919	-0.139973602 -1.143882845 -1.106826934	-0.179674025 -1.132777209 -1.090826114	-0.221267166 -1.122004402 -1.06830316	-0.264987132 -1.111656472 -1.050414965	-0.310716635 -1.101643301 -1.038416095	-0.358851542 -1.091932057 -1.028498225	-0.408662585 -1.079320722 -1.016438204	-0.460046592 -1.064035972 -1.005667191	-0.51571631 -1.04761313 -1.000888378	-0.56748617 -1.03172962 -0.995261636	-0.61579642 -1.01179642 -0.97946163	-0.6645282 -0.99246163 -0.95868352	-0.71492947 -0.97024947 -0.93882473	-0.766295947 -0.94280669 -0.90280929	-0.819842985 -0.91528289 -0.87528161	-0.87428818 -0.88242699 -0.83943523	-0.92848695 -0.84755623 -0.80342469	

		ANSYS Solutions and Normalization																																																																																																																																																																																																																																																																																																																																																																																																																																																																																																																																																																																																																																																																																																																																																																																																																																																																																																																																																																																																																																																																																																																																																																																																																																																																																																																																																																																																																																																									
--	--	-----------------------------------	--	--	--	--	--	--	--	--	--	--	--	--	--	--	--	--	--	--	--	--	--	--	--	--	--	--	--	--	--	--	--	--	--	--	--	--	--	--	--	--	--	--	--	--	--	--	--	--	--	--	--	--	--	--	--	--	--	--	--	--	--	--	--	--	--	--	--	--	--	--	--	--	--	--	--	--	--	--	--	--	--	--	--	--	--	--	--	--	--	--	--	--	--	--	--	--	--	--	--	--	--	--	--	--	--	--	--	--	--	--	--	--	--	--	--	--	--	--	--	--	--	--	--	--	--	--	--	--	--	--	--	--	--	--	--	--	--	--	--	--	--	--	--	--	--	--	--	--	--	--	--	--	--	--	--	--	--	--	--	--	--	--	--	--	--	--	--	--	--	--	--	--	--	--	--	--	--	--	--	--	--	--	--	--	--	--	--	--	--	--	--	--	--	--	--	--	--	--	--	--	--	--	--	--	--	--	--	--	--	--	--	--	--	--	--	--	--	--	--	--	--	--	--	--	--	--	--	--	--	--	--	--	--	--	--	--	--	--	--	--	--	--	--	--	--	--	--	--	--	--	--	--	--	--	--	--	--	--	--	--	--	--	--	--	--	--	--	--	--	--	--	--	--	--	--	--	--	--	--	--	--	--	--	--	--	--	--	--	--	--	--	--	--	--	--	--	--	--	--	--	--	--	--	--	--	--	--	--	--	--	--	--	--	--	--	--	--	--	--	--	--	--	--	--	--	--	--	--	--	--	--	--	--	--	--	--	--	--	--	--	--	--	--	--	--	--	--	--	--	--	--	--	--	--	--	--	--	--	--	--	--	--	--	--	--	--	--	--	--	--	--	--	--	--	--	--	--	--	--	--	--	--	--	--	--	--	--	--	--	--	--	--	--	--	--	--	--	--	--	--	--	--	--	--	--	--	--	--	--	--	--	--	--	--	--	--	--	--	--	--	--	--	--	--	--	--	--	--	--	--	--	--	--	--	--	--	--	--	--	--	--	--	--	--	--	--	--	--	--	--	--	--	--	--	--	--	--	--	--	--	--	--	--	--	--	--	--	--	--	--	--	--	--	--	--	--	--	--	--	--	--	--	--	--	--	--	--	--	--	--	--	--	--	--	--	--	--	--	--	--	--	--	--	--	--	--	--	--	--	--	--	--	--	--	--	--	--	--	--	--	--	--	--	--	--	--	--	--	--	--	--	--	--	--	--	--	--	--	--	--	--	--	--	--	--	--	--	--	--	--	--	--	--	--	--	--	--	--	--	--	--	--	--	--	--	--	--	--	--	--	--	--	--	--	--	--	--	--	--	--	--	--	--	--	--	--	--	--	--	--	--	--	--	--	--	--	--	--	--	--	--	--	--	--	--	--	--	--	--	--	--	--	--	--	--	--	--	--	--	--	--	--	--	--	--	--	--	--	--	--	--	--	--	--	--	--	--	--	--	--	--	--	--	--	--	--	--	--	--	--	--	--	--	--	--	--	--	--	--	--	--	--	--	--	--	--	--	--	--	--	--	--	--	--	--	--	--	--	--	--	--	--	--	--	--	--	--	--	--	--	--	--	--	--	--	--	--	--	--	--	--	--	--	--	--	--	--	--	--	--	--	--	--	--	--	--	--	--	--	--	--	--	--	--	--	--	--	--	--	--	--	--	--	--	--	--	--	--	--	--	--	--	--	--	--	--	--	--	--	--	--	--	--	--	--	--	--	--	--	--	--	--	--	--	--	--	--	--	--	--	--	--	--	--	--	--	--	--	--	--	--	--	--	--	--	--	--	--	--	--	--	--	--	--	--	--	--	--	--	--	--	--	--	--	--	--	--	--	--	--	--	--	--	--	--	--	--	--	--	--	--	--	--	--	--	--	--	--	--	--	--	--	--	--	--	--	--	--	--	--	--	--	--	--	--	--	--	--	--	--	--	--	--	--	--	--	--	--	--	--	--	--	--	--	--	--	--	--	--	--	--	--	--	--	--	--	--	--	--	--	--	--	--	--	--	--	--	--	--	--	--	--	--	--	--	--	--	--	--	--	--	--	--	--	--	--	--	--	--	--	--	--	--	--	--	--	--	--	--	--	--	--	--	--	--	--	--	--	--	--	--	--	--	--	--	--	--	--	--	--	--	--	--	--	--	--	--	--	--	--	--	--	--	--	--	--	--	--	--	--	--	--	--	--	--	--	--	--	--	--	--	--	--	--	--	--	--	--	--	--	--	--	--	--	--	--	--	--	--	--	--	--	--	--	--	--	--	--	--	--	--	--	--	--	--	--	--	--	--	--	--	--	--	--	--	--	--	--	--	--	--	--	--	--	--	--	--	--	--	--	--	--	--	--	--	--	--	--	--	--	--	--	--	--	--	--	--	--	--	--	--	--	--	--	--	--	--	--	--	--	--	--	--	--	--	--	--	--	--	--	--	--	--	--	--	--	--	--	--	--	--	--	--	--	--	--	--	--	--	--	--	--	--	--	--	--	--	--	--	--	--	--	--	--	--	--	--	--	--	--	--	--	--	--	--	--	--	--	--	--	--	--	--	--	--	--	--	--	--	--	--	--	--	--	--	--	--	--	--	--	--	--	--	--	--	--	--	--	--	--	--	--	--	--	--	--	--	--	--	--	--	--	--	--	--	--	--	--	--	--	--	--	--	--	--	--	--	--	--	--	--	--	--	--	--	--	--	--	--	--	--	--	--	--	--	--	--	--	--	--	--	--	--	--	--	--	--	--	--	--	--	--	--	--	--	--	--	--	--	--	--	--	--	--	--	--	--	--	--	--	--	--	--	--	--	--	--	--	--	--	--	--	--	--	--	--	--	--	--	--	--	--	--	--	--	--	--	--	--	--	--	--	--	--	--	--	--	--	--	--	--	--	--	--	--	--	--	--	--	--	--	--	--	--	--	--	--	--	--	--	--	--	--	--	--	--	--	--	--	--	--	--	--	--	--	--	--	--	--	--	--	--	--	--	--	--	--	--	--	--	--	--	--	--	--	--	--	--	--	--	--	--	--	--	--	--	--	--	--	--	--	--	--	--	--	--	--	--	--	--	--	--	--	--	--	--	--	--	--	--	--	--	--	--	--	--	--	--	--	--	--	--	--	--	--	--	--	--	--	--	--	--	--	--	--	--	--	--	--	--	--	--	--	--	--	--	--	--	--	--	--

VI. CONCLUSIONS AND COMMENTS

From the obtained results comparison with the analytical results the validity of this method is justified. As seen in the results section in Table-2, there is a very small relative error in the results; sometimes the error vanishes to zero. The main advantage of such a method is its simplicity and ease; it does not require deep knowledge of mathematical models of FGM and delivers high accuracy.

In this paper a static loads problem is solved successfully but other certain types of analysis will not work. The first problem with the illustrated method is the lack of ability of performing thermal studies on FGM. Because thermal properties and loads are already used to present the dimension change. So, if thermal study is needed other methods of modelling FGM in ANSYS have to be used. The second problem is that it cannot be applied to obtain normal modes, since this kind of studies simply ignores the thermal and all other loads.

This method is not the only method to model FGM in ANSYS; i.e. one can build the model as layers stacked in the changing dimension, then assign different properties to each layer while making sure each adjacent layers are somehow connected i.e. glued. This later method is also effective and can solve all kinds of analysis but it will need much more MACRO programming skills especially if the change in properties is in more than one dimension.

H. REFERENCES

1. Reimanis, I.E., Functionally graded materials. Handbook of advanced materials, 2004: p. 465.
2. Mahamood, R.M., E.T. Akinlabi, M. Shukla, and S. Pityana. Functionally Graded Material: An Overview. in Proceedings of the World Congress on Engineering. 2012.
3. Birman, V. and L.W. Byrd, Modeling and analysis of functionally graded materials and structures. Applied mechanics reviews, 2007. 60(5): p. 195-216.
4. Banks-Sills, L., R. Eliasi, and Y. Berlin, Modeling of functionally graded materials in dynamic analyses. Composites Part B: Engineering, 2002. 33(1): p. 7-15.
5. Abedi, M., M.Z. Nejad, M.H. Lotfian, and H. Sabouri, Effects of Exponential Varying Moduli on Stress Distribution of Solid Shafts. American Journal of Scientific Research, 2011. ISSN 1450-223X(37): p. 68-74.

Cfd Modeling On Performance Comparison Of PEM Fuel Cell With A Serpentine And A Straight Flow Channel

Elif Eker Kahveci*

Engineering Faculty, Mechanical Engineering Department
Sakarya University
Sakarya, Turkey
eeker@sakarya.edu.tr

Imdat Taymaz

Engineering Faculty, Mechanical Engineering Department
Sakarya University
Sakarya, Turkey
taymaz@sakarya.edu.tr

Abstract— In this investigation, a three dimensional, single-phase proton exchange membrane (PEM) fuel cells with triple-serpentine and straight flow channel was studied numerically, evaluating reactant gas humidification, water management and cell performance. The structured grid scheme was employed which was built with a pre-processing software, GAMBIT 2.4.6. Then, the grid was imported into finite volume based commercial software, ANSYS-FLUENT 16.2. The PEMFC Module is an add-on module based on FLUENT CFD package for computations. These 3-D models with $19 \times 50 \text{ mm}^2$ same active layer used to investigate the performance of fuel cell by determining the current density, oxygen, hydrogen and water molar concentration distributions took into account the mass, momentum, energy, species, charge conservation equation as well as combines electrochemistry reaction inside the fuel cell. The simulation results of comparison of triple-serpentine and straight channels were illustrated polarization curves including I-V and I-P curves which were obtained by varying the cell potential with a 0.1 V steps. From the results, analyzing the polarization curve of the different flow field design it can be said that maximum current and power density was obtained from straight channel. For lower operating voltages, as the cathode and anode relative humidity increases, the cell performance is enhanced because the cell performance is mainly dependent on the cathode mass transport limitations due to the liquid water blockage effect. As decreases, the oxygen concentration in the reactants increases and the water concentration on the cathode side decreases, this reduces flooding and improves the cell performance.

Keywords— Fluent; PEM fuel cell; performance; simulation

I. INTRODUCTION

PEM fuel cells are one of the most promising clean energy technologies in many applications like portable, automotive and stationary due to their high power density at low operating temperatures. Besides, flow field design is one of the most important considerations in the development of PEM fuel cell components. A good flow field design cannot only provide optimum reactant gas supply but also reduce the overall cell weight and cost. Generally; modelling is preferred instead of

costly experimental works in order to reduce project costs, to try different working conditions more quickly and to be able to make the necessary corrections in a much shorter time by seeing the negativities that may occur. Therefore, modeling plays a very significant role in determining the way the new materials developed, the best configuration for the reactant transport and the optimum operating conditions of the fuel cell in order to improve the performance.

The proton exchange membrane fuel cell (PEMFC) is considered one of the most promising alternative clean power generators for mobile and stationary applications because of its low to zero emissions, low-temperature operation and high power density. The performance of PEMFC depends on material characteristics, mechanical design (particularly the flow-field design in bipolar plates) and operating conditions [1–6].

The flow plates are an important component in PEM fuel cell. Flow plates contain either a few very long channels or a large number of channels referred to as the flow field. These flow plates account for the bulk of the stack generally between 80% and 90% of the total weight of the stack. For this reason, an optimal flow plate design is critical for obtaining high power density in fuel cell. Since the early development of PEM fuel cells there have been many varieties of flow field designs. Early designs of flow fields generally consisted of parallel or straight channels. In literature, several modelling and experimental work has been investigated in order to understand the effect of channel geometries in bipolar plate including, serpentine flow channels, parallel flow channels, interdigitated flow field, flow field with pins and the influence of these parameters to the fuel cell performance.

Ionescu [1] studied gas flow velocity influence on the cell performance at first then investigated the effect of channel width and channel height on the current density at various cathode gas flow velocities based on Comsol Multiphysics which is a commercial solver. He found that the most uniform variation of local current density was achieved at $0.8 \times 3 \text{ mm}^2$, $1.2 \times 3 \text{ mm}^2$ and $1.6 \times 3 \text{ mm}^2$ gas channel geometries due to more amount of oxygen entering the channel.

Lim et al. [2] investigated a conventional and modified parallel flow field designs split flow into variant channel widths to facilitate even reactant distribution using computational fluid dynamic modeling at their study. They found that multiple stages of flow distribution can achieve an evenly distributed pressure drop with an ideal distribution of reactant among channels.

Xing et al. [3] developed a fully coupled 2D, along-the-channel, two-phase flow, non-isothermal, CFD model. In their results thinner GDL could result in more non-uniform and more significant temperature rise at high current densities. Also a new channel design featured with multi-inlets and outlets is proposed to reduce water flooding improve the cell performance.

Rahimi-Esbo et al. [4] in their paper seven flow fields were analyzed and their performances were investigated at the optimum channel to rib ratio. A novel serpentine flow field design aimed at effective water removal is introduced and examined. The results showed that 2-1-serpentine flow field has the highest performance especially at high current densities. It was founded that for operating voltages over 0.5 V, the geometry of the flow channels did not have a significant effect on performance.

Saco et al. [5] carried out a numerical analysis on scaled up model of PEM fuel cell (225 cm²) with four flow channel models. The study was mainly conducted to find the impact of flow field design on the performance of PEM fuel cell. From the results it was found that the current and power density of the straight zigzag flow channel was quite high compared to all other flow channels due to better consumption of hydrogen and oxygen molecules, better water removal rate in the flow channels.

Rostami et al. [6] studied a three-dimensional numerical model to understand the effect of bend sizes on a PEM (polymer electrolyte membrane) fuel cell in this work. The obtained results showed that as bend size increases from 1 mm to 1.2 mm, not only did the over potential reduce significantly but temperature gradient was also alleviated. Moreover, it was shown that the serpentine flow channels with 1.2 mm square bend size acted successfully in preventing secondary flows internal thereby decreasing pressure drop about 90.6% compared to serpentine flow channels with a bend size of 0.8 mm.

For the objective of this paper, a three-dimensional, single-phase, steady-state model that resolves coupled transport processes in membrane, catalyst layers, gas diffusion layers ,single and double serpentine channel of PEM models which have 70x70 mm² active layer have been developed to investigate performance of fuel cell by determining the current density with different humidity conditions.

II. MODELLING

The PEMFC module is an add-on module based on ANSYS-FLUENT for computations. While the basic governing

equations related to the mass, momentum and energy transport are solved by FLUENT solver as usual, the other constitutive relations unique to fuel cell application, related to electric potential and current as well as electrochemical reactions are computed with additional equations coming with the add-on module.

After the geometry and mesh are generated in GAMBIT 2.4.6, the relevant zones for the modeling domains which are current collectors(bipolar plate) , flow channels, gas diffusion layers, catalyst layers and membrane can be identified easily by using this module

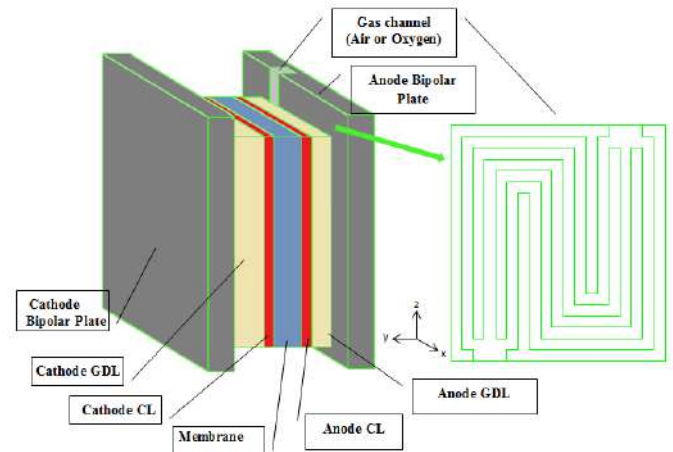


Fig. 1. Example of a figure caption.

TABLE I. GEOMETRICAL PROPERTIES OF MODELS

Parameters	Value	Units
Channel width	1	mm
Channel length	50	mm
Gas diffusion layer thickness	0.2232	mm
Catalyst layer thickness	0.0287	mm
Membrane thickness	0.23	mm
Active area	0.00095	m ²
Number of channels(for two types of PEMFC)	9	-

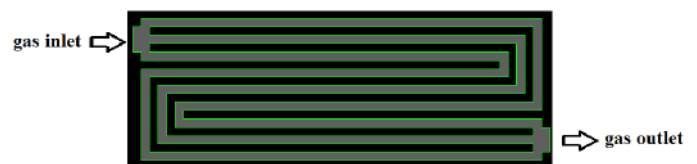
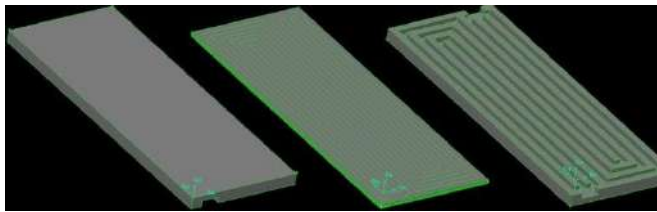


Fig. 2. Triple serpentine bipolar plate flow channel pattern

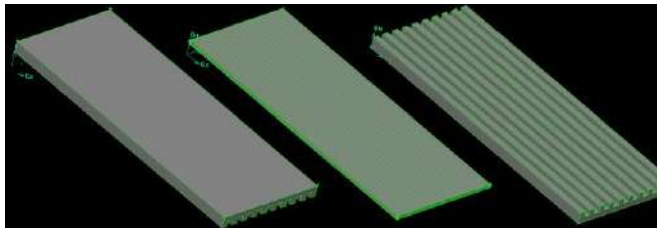
Assumptions of the study;

- The PEM fuel cell operates under steady-state conditions.
- Operating temperature is assumed to be 343 K.
- The reactants are hydrogen and air.
- The gas flow is laminar, incompressible.
- The gas diffusion layers, catalyst layers and membrane layer are isotropic materials.

- Therefore gas flow of the anode and cathode channels is in the same directions



(a)



(b)

Fig. 3. Solid model of fuel cells, (a) serpentine ,(b) straight.

III. RESULTS AND DISCUSSIONS

Before you begin to format your paper, first write and save the content as a separate text file. Keep your text and graphic files separate until after the text has been formatted and styled.

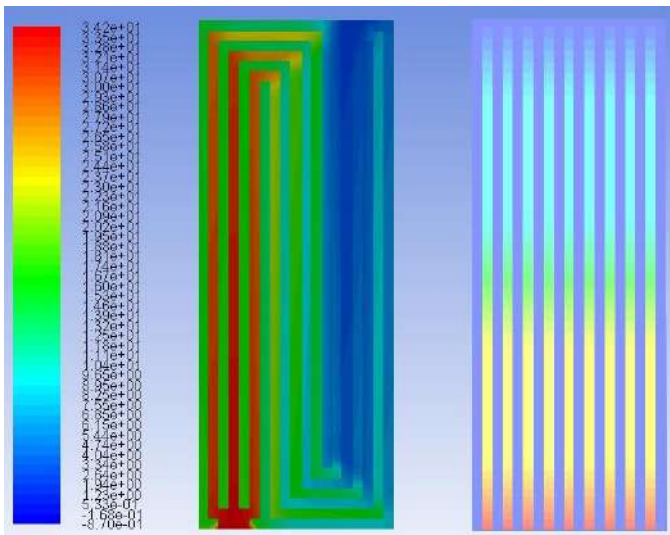


Fig. 4. Pressure drop of cathode channel at x-y plane for 0.6 V

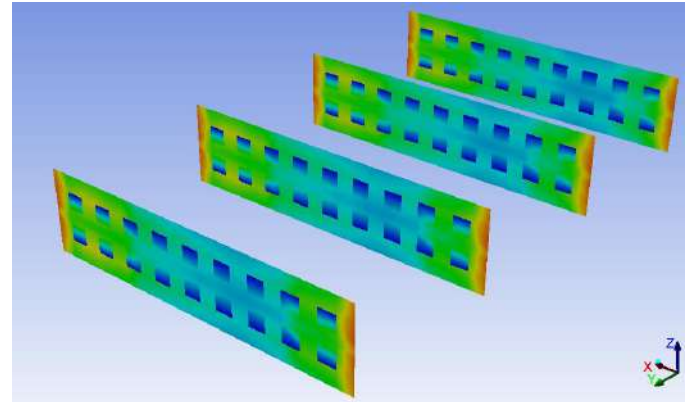


Fig. 5. Current density distribution of serpentine channel model at 0.6 V

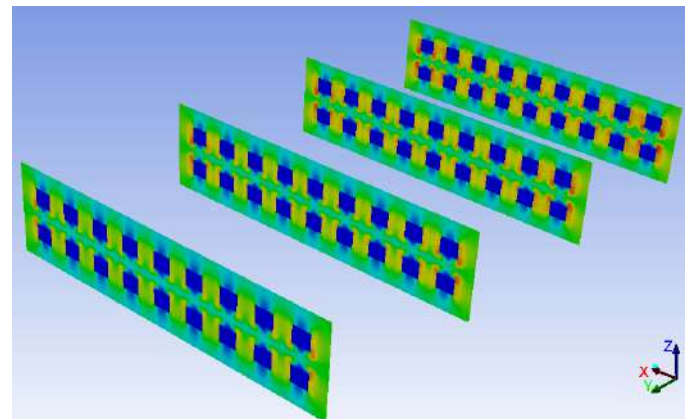


Fig. 6. Current density distribution of straight channel model at 0.6 V

REFERENCES

- [1] V. Ionescu, "Simulating the effect of gas channel geometry on PEM fuel cell performance by finite element method" *Procedia Technology*, vol.22, pp. 713-719, 2016.
- [2] B.H. Lim, E.H. Majlan, W.R.W. Daud, M.I. Rosli and T. Husaini., "Numerical analysis of modified parallel flow field designs for fuel cells", *International Journal of Hydrogen Energy*, vol.XX, pp. 1 – 9, April 2016.
- [3] L. Xing, Q. Cai, X. Liu, C. Liu, K. Scott and Y. Yan , "Anode partial flooding modelling of proton exchange membrane fuel cells: Optimisation of electrode properties and channel geometries," *Chemical Engineering Science*, vol.146, pp.88–103, Jun. 2016.
- [4] M. Rahimi-Esbo, A.A. Ranjbar, A. Ramiar, E. Alizadeh and M. Aghaei, "Improving PEM fuel cell performance and effective water removal by using a novel gas flow field," *International Journal of Hydrogen Energy*, vol.41, pp. 3023–3037, Jan. 2016.
- [5] S. Arun Saco , R. Thundil Karuppa Raj and P. Karthikeyan, " A study on scaled up proton exchange membrane fuel cell with various flow channels for optimizing power output by effective water management using numerical technique ," *Energy*, vol.113, pp. 558–573, Oct. 2016.
- [6] L. Rostami, P. M. G. Nejad and A. Vatani, "A numerical investigation of serpentine flow channel with different bend sizes in polymer electrolyte membrane fuel cells," *Energy*, vol.97, pp. 400–410, Feb. 201

Thermal energy storage performance of gypsum based composite phase change material for thermoregulation of building envelopes

Alper BİÇER^{*,a}, Ahmet SARI^{b,c}, Ali KARAİPEKLİ^d

^aDepartment of Chemistry, Gaziosmanpaşa University, 60240 Tokat, Turkey

^bKaradeniz Technical University, Metallurgical and Material Engineering, 61080, Trabzon, Turkey ^cCenters of Research Excellence, Renewable Energy Research Institute, KFUPM, 31261, Dhahran, KSA ^dÇankırı Karatekin University, Department of Chemistry, 18100, Çankırı, Turkey

* alper.bicer@gop.edu.tr

The building sector is the leading energy consumer in the worldwide in terms of primary energy consumption. According to the energy technology perspectives 2015 report, 40% of total final energy was consumed by the building sector for the activities such as heating, cooling, air conditioning, and lighting [1]. Up to now, several organic PCMs have been examined as a TES material in buildings due to their desired thermodynamic, kinetic and chemical characteristics. Among the organic phase change materials (PCMs), paraffins are the most recommended PCMs because of their advantages of high heat storage capacity, chemical and thermal stability, lowcost, non-subcooling, congruently melting, non-corrosiveness, odorlessness, chemically inertness and good thermal reliability after repeated thermal cycles [2,3]. However, the high phase-transition temperature of most paraffins limits their use in building TES applications such as energy conservation and indoor temperature regulation. Fortunately, the eutectic mixtures of paraffins can be easily formed and thereby providing PCMs with a proper temperature for their use in building applications. In this work, a gypsum-based composite with the paraffin eutectic mixture was prepared via direct impregnation method to form a novel energy storing composite building material. The structure and thermal energy storage properties of the form-stable composite PCM (FSCPCM) were investigated by The Fourier Transform Infrared (FT-IR) and Differential Scanning Calorimetry (DSC) analysis techniques. The thermal regulating performance of the gypsum plaster prepared with this composite was also evaluated in a small test chamber. The maximum mass percentage of C18–C24 absorbed in gypsum was determined as 18% without the leakage of C18–C24 in liquid state. The FT-IR spectroscopy and DSC techniques were used to characterize the FSCPCM. The FT-IR spectra confirmed that any chemical interaction did not occur among the components of the composite during the impregnation. Besides, DSC analysis showed that the FSCPCM had reversible melting and freezing behavior and quite satisfying thermal properties for building applications. The composite maintained its chemical structure and thermal energy storage characteristics after 1000 melting/freezing cycles. In addition, the gypsum plaster with FSCPCM exhibited excellent thermal regulating performance when compared to that of only gypsum plaster under the same conditions. From all results, it can be deduced that the obtained gypsum based composite plaster is a promising material to control room temperature and to conserve energy in buildings.

Key words: Phase change material, Form-stable PCM, Thermal properties, Thermal performance

References:

- [1] Energy Technology Perspectives, 2015. <<http://www.iea.org/etp/etp2015/>>.
- [2] B. Zalba, J.M. Mari'n, L.F. Cabeza, H. Mehling, Review on thermal energy storage with phase change: materials, heat transfer analysis and applications, Appl. Therm. Eng. 23 (2003) 251–283.
- [3] A. Sharma, V. Tyagi, C. Chen, D. Buddhi, Review on thermal energy storage with phase change materials and applications, Renew. Sustain. Energy Rev. 13 (2009) 318–345.

Preparation, morphology and thermal energy storage characteristic of polystyrene/(capric-stearic acid) micro/nano capsules

Ahmet SARI^{a,b}, Alper BİÇER^c, Cemil ALKAN^c, Ayşe ALTINTAŞ^c

^aKaradeniz Technical University, Metallurgical and Material Engineering, 61080, Trabzon, Turkey ^bCenters of Research Excellence, Renewable Energy Research Institute, KFUPM, 31261, Dhahran, KSA ^cDepartment of Chemistry, Gaziosmanpaşa University, 60240 Tokat, Turkey

* ahmet.sari@ktu.edu.tr OR asari061@hotmail.com

Latent heat thermal energy storage (LHTES) using phase change materials (PCMs) is one of the best solar passive techniques used for different type of applications such as thermoregulation of medical and textile products, cooling electronic and medical equipments and space heating/cooling of buildings. The main problem regarding the usage of PCMs is their leakage behavior during phase change from solid to liquid phase. This problem of the PCMs can be solved by encapsulating of them within a capsule with polymeric shell in micro or nano sizes. Moreover, the encapsulation case provides much more surface/volume ratio for heat transfer and also gained direct utility function in actual LHTES systems [1,2]. Fatty acids have been used as solid-liquid PCMs for solar passive heating and cooling purposes due to their good LHTES characteristics [3]. However, the leakage problem mentioned above significantly restricts the usage potential of them. In this sense, the present study is focused on preparation, chemical and morphological characterization and determination of LHTES properties of the micro-nano encapsulated capric acid (CA)-stearic acid (SA) by using polystyrene (PS) shell. For this aim, the eutectic mixture of CA-SA was prepared to decrease the melting temperature of SA and thus expand its practice effectiveness in LHTES applications. PS/(CA-SA) micro/nano capsules were prepared successfully by using emulsion polymerization method. In the fabricated capsules, the CA-SA eutectic mixture as a PCM has LHTES function while the PS has shell action around the eutectic mixture. The experimental parameters, monomer(styrene)/PCM ratio, homogenization rate, temperature, type and amount of surfactant and cross-linking agent were optimized systemically. The styrene polymerization reaction around the eutectic PCM was characterized by FT-IR spectroscopy analysis. The morphology and the particle size distribution of the capsules were investigated by SEM, POM and PSD analysis techniques. The SEM and POM results showed that the prepared capsules were consisted of almost smooth micro and nano sized spheres. However, some of spheres with especially nano-sized were partially agglomerated. The PSD analysis results indicated that the capsules had almost uniform PSD value in the range of 0.01 - 125 μm and the mean diameter of them was 7.6 μm . The DSC analysis results indicated that the fabricated capsules, PS/(CA-SA)Ö(2:1), PS/(CA-SA)(1:1) and PS/(CA-SA)(1:2) had a melting temperature of 16.19, 17.33 and 22.29 °C and a latent heat of 56.21, 77.31 and 114.25 J/g, respectively. The thermal cycling test revealed that the prepared capsules had long-term LHTES performance after 5000 melting/freezing process. Moreover, The TGA results exhibited that the prepared capsules had good thermal stability until 200 °C. Furthermore, based on all findings, it was concluded that the synthesized PS/(CA-SA) micro/nano capsules were considered as promising PCM for solar passive LHTES applications for heating and cooling targets.

Acknowledgement: The author would like to acknowledge by Scientific and Technological Research Council of Turkey (TÜBİTAK) for financial support (Project No:112T864).

References

- [1] Alkan C., Sarı A., Karaipekli A. 2011. Preparation, thermal properties and thermal reliability of microencapsulated n-eicosane as novel phase change material for thermal energy storage, *Energy Conversion and Management*, 52, 687–692.
- [2] Li, W., Zhang, X., Xue-chen W., Tang, G., Hai-feng S. 2012. Fabrication and morphological characterization of microencapsulated phase change materials (MicroPCMs) and macrocapsules containing MicroPCMs for thermal energy storage, *Energy*, 38, 249-254.
- [3] Feldman, D., Banu, D., Hawes, D., 1995a. Low chain esters of stearic acid as phase change materials for thermal energy storage in buildings, *Solar Energy Materials And Solar Cells*, 36, 311-322.

Investigation of the Effects of CAD/CAM Parameters on the Machining Times of Cycloidal Gears in CNC Milling Machines

Cihan ÖZEL¹

Firat University

Mechanical Engineering Departmet
Elazığ/TURKEY
cozel@firat.edu.tr

Yunus ORTAÇ²

Firat University

Mechanical Engineering Departmet
Elazığ/TURKEY
Yunusortac23@gmail.com

Turan GÜRGENÇ³

Firat University

Automotive Engineering Departmet
Elazığ/TURKEY
tgurgenc@firat.edu.tr

Abstract—In this study, the machining times of the cycloidal gears in a CNC milling machine were examined according to the radial machining method. In order to determine these times, the CAM program, which was prepared according to the parametric tool path equations of the cycloidal gear in the previous studies of the authors, was taken into account. In this program, the design and cutting parameters of the gear were changed and simulations of the cycloidal gears were performed for final machining. Then, gears with different numbers of teeth were manufactured in Dyna 4M CNC machine and their manufacturing times were determined. As a result, it was observed that the CAD/CAM parameters of the cycloidal gear significantly affected the production times of the gear.

Keywords—cycloidal gear; CAD/CAM parameters; CNC milling machine; machining times

IV. INTRODUCTION

There is a great deal of manufacturing data involved in process planning, such as the identification of machines, tools, features, parameters and operations [1-3]. All this data has to be evaluated in order to select the sequence of operations that will make up what is known as the route sheet. The sequence is generally obtained to conform to particular objectives, such as, the shortest time and /or the minimum cost.

A method is described for calculating the optimum cutting conditions, in turning for objective criteria such as maximum production rate. The method uses empirical models for tool life, roughness and cutting forces. The method consists on explaining the feed in relation to the roughness which depends on the cutting speed. Then, the cutting speed which gives the minimum production times was calculated [4]. To minimize the cost of workpiece machining, cutting parameters must permit to minimize production time and obtain specified specifications such as roughness [5,6]. In another work was discussed the

influence of the tool path strategy on the cycle time of high-speed milling operations. Experiments and predictions were focused on pocketing operations with a zig-zag tool path, quantifying the significant discrepancy between the programmed feed rate and the actual average feed rate [7, 8]. Maropoulos, P.G. et al. was discussed the estimation of machining times necessary to assess the tools selected using machining performance related criteria [9]. Boogret et al. was designed reliable NC programs to generate tool path and cutting condition algorithm [10]. An alternative method devised by Ou-Yang and Lin uses assumptions about the operations carried out and the likely cutting conditions of the tool in order to determine machining times of common milling features such as those implemented within VITool [11]. Malakooti and Deviprasad formulate at metal cutting operation, specifically for a turning operation, as a discrete multiple objective problems. The objectives are to minimize cost per part, production time per part, and roughness of the work surface, simultaneously [12]. Panwalkar and Rajagopalan consider the static single machine sequencing problem with a common due date for all jobs in which job processing times are controllable with linear costs. They develop a method to find optimal processing times and an optimal sequence to minimize a cost function [13].

The effects of the CAD parameters on the tooth profile errors of the cycloidal gears manufactured with an end mill in CNC milling machines were examined [14]. In other studies, spur and bevel gears were manufactured in CNC milling machines and then, the manufacturing times and tooth profile errors of these gears were examined [15-17].

In this study, while cycloidal gears were machined in a vertical machining centered CNC milling machine according to

the radial machining method, the effects of the parameters in the tool path equations of the gear on the machining times were examined.

II. RADIAL MACHINING OF CYCLOIDAL GEARS IN CNC MILLING MACHINE

For machining the cycloidal gear in a vertical-machining-centered CNC milling machine, the gear blank was connected to the machine table with the help of bolts and wedges as follows (Figure 1) [14]:

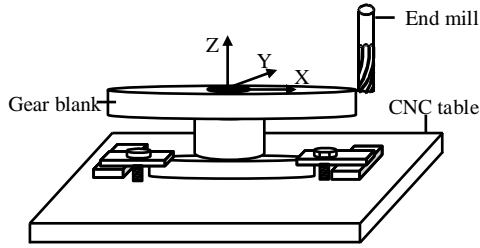


Figure 1. The clamping of the cycloidal gear blank

In the previous study, it was stated that the end mill cut the gear blank along the Z-axis, in the planes parallel to the X-Y plane as follows (Figure 2) [14].

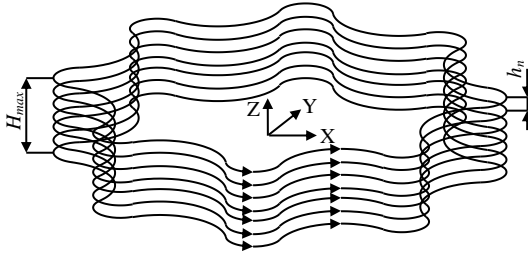


Figure 2. Tool paths for radial machining

Where, h_n and H_{max} heights show the chip cutting thickness and tooth length of the gear, respectively.

A. Tool Path Equations for the Tooth Profiles of the Cycloidal Gear

As is known, the tooth upper profile of a cycloidal gear is an epicycloid curve. The epicycloid curve is a curve formed by any point P on a circle (roulette) that rolls on another circle without slipping (Figure 3).

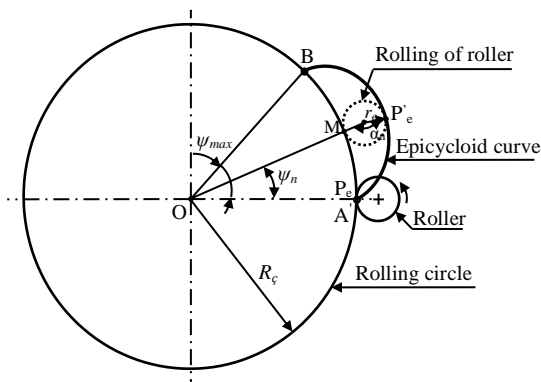


Figure 3. The formation of an epicycloid curve (top view)

While the end mill cuts the gear in a CNC milling machine, the trajectory followed by the center of the cutter is the equidistant curve of the epicycloid curve. An equidistant curve is expressed as the geometric location of the points at equal and perpendicular distances from a curve (Figure 4).

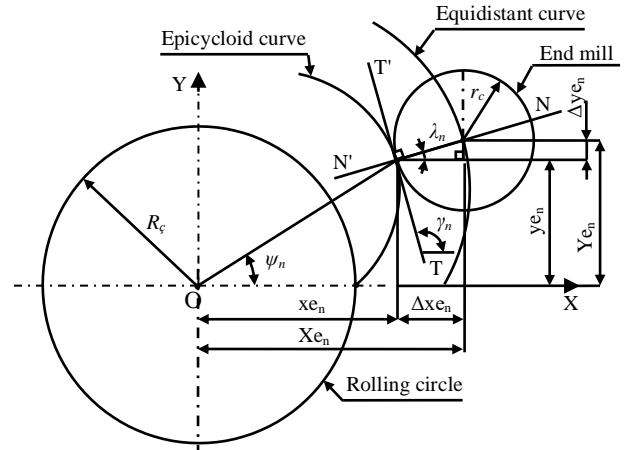


Figure 4. The relation between the end mill and epicycloid curve (top view)

The tool path equations for the epicycloid tooth profile were derived as follows by taking the location of the cutter centre according to the X and Y axes (Figure 4).

$$X_{e_n} = x_{e_n} + \Delta x_{e_n} \quad (1)$$

$$Y_{e_n} = y_{e_n} + \Delta y_{e_n} \quad (2)$$

Where, x_{e_n} and y_{e_n} were defined as the coordinates of any point on the epicycloid curve. The coordinates of this point were written as follows (Figure 3 and 4) [14].

$$x_{e_n} = (R_c + r_e) \cdot \cos \psi_n - r_e \cdot \cos \left[\frac{(R_c + r_e)}{r_e} \cdot \psi_n \right] \quad (3)$$

$$y_{e_n} = (R_c + r_e) \cdot \sin \psi_n - r_e \cdot \sin \left[\frac{(R_c + r_e)}{r_e} \cdot \psi_n \right] \quad (4)$$

Where, r_e and R_c are the radii of the roulette and rolling circle, respectively. Δx_{e_n} and Δy_{e_n} were derived as follows (Figure 4).

$$\Delta x_{e_n} = r_c \cdot \cos \lambda_n \quad (5)$$

$$\Delta y_{e_n} = r_c \cdot \sin \lambda_n \quad (6)$$

λ_n and γ_n are defined as the normal and tangent curves, respectively. Where, slope of the tangent was written as follows.

$$m_t = \tan \gamma_n = \frac{dy_{en}}{dx_{en}} \quad (7)$$

The relation between the curves can be written as follows.

$$m_t \cdot m_n = -1 \quad (8)$$

In this case, λ_n angle is derived as follows.

$$m_n = \lambda_n = \tan^{-1} \left(-\frac{dx_{en}}{dy_{en}} \right) \quad (9)$$

Where, the derivatives of dX_n and dY_n (3) and (4) equations were taken according to ψ_n angle and were calculated as follows.

$$\frac{dX_n}{d\psi_n} = -(R_\zeta + r_e) \cdot \sin \psi_n + (R_\zeta + r_e) \cdot \sin \left(\frac{R_\zeta + r_e}{r_e} \cdot \psi_n \right) \quad (10)$$

$$\frac{dY_n}{d\psi_n} = (R_\zeta + r_e) \cdot \cos \psi_n - (R_\zeta + r_e) \cdot \cos \left(\frac{R_\zeta + r_e}{r_e} \cdot \psi_n \right) \quad (11)$$

λ_n angle was derived as follows.

$$\lambda_n = \tan^{-1} \left(\frac{-(R_\zeta + r_e) \cdot \sin \psi_n + (R_\zeta + r_e) \cdot \sin \left(\frac{R_\zeta + r_e}{r_e} \cdot \psi_n \right)}{(R_\zeta + r_e) \cdot \cos \psi_n - (R_\zeta + r_e) \cdot \cos \left(\frac{R_\zeta + r_e}{r_e} \cdot \psi_n \right)} \right) \quad (12)$$

As a result, the tool path equations for the epicycloid tooth profile were derived as follows.

$$Xe_n = xe_n + r_c \cdot \cos \left[\tan^{-1} \left(\frac{-(R_\zeta + r_e) \cdot \sin \psi_n + (R_\zeta + r_e) \cdot \sin \left(\frac{R_\zeta + r_e}{r_e} \cdot \psi_n \right)}{(R_\zeta + r_e) \cdot \cos \psi_n - (R_\zeta + r_e) \cdot \cos \left(\frac{R_\zeta + r_e}{r_e} \cdot \psi_n \right)} \right) \right] \quad (13)$$

$$Ye_n = ye_n + r_c \cdot \sin \left[\tan^{-1} \left(\frac{-(R_\zeta + r_e) \cdot \sin \psi_n + (R_\zeta + r_e) \cdot \sin \left(\frac{R_\zeta + r_e}{r_e} \cdot \psi_n \right)}{(R_\zeta + r_e) \cdot \cos \psi_n - (R_\zeta + r_e) \cdot \cos \left(\frac{R_\zeta + r_e}{r_e} \cdot \psi_n \right)} \right) \right] \quad (14)$$

$$Ze_n = H_{\max} \text{ (constant)} \quad (15)$$

Similarly, the tooth bottom profile of the cycloid gear is a hypocycloid curve. The hypocycloid curve is a curve formed on the inner side of the rolling circle by any point on the roulette rolling without slipping. Where, r_h is defined as the radius of the roulette (Figure 5).

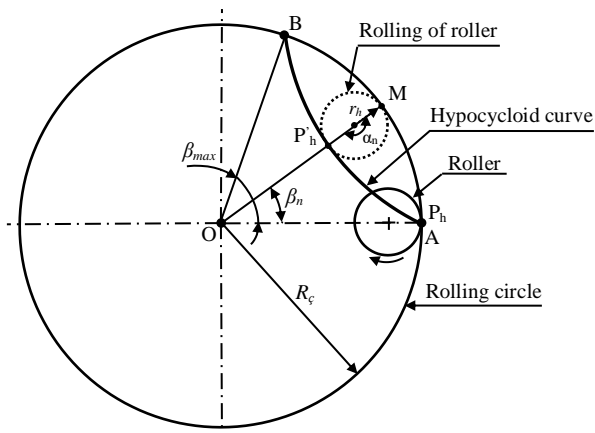


Figure 5. Formation of the hypocycloid curve (top view)

Similarly, while the end mill cuts the hypocycloid profile, the trajectory followed by the centre of the cutter is the equidistant curve of the hypocycloid curve (Figure 6).

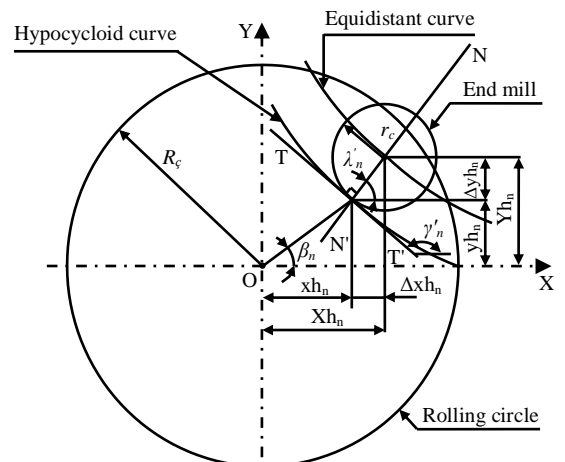


Figure 6. The relation between the end mill and hypocycloid curve (top view)

The tool path equations for the hypocycloid tooth profile were also derived similarly to those of the epicycloid profile as follows (Figure 5 and 6) [14].

$$Xh_n = xh_n + r_c \cdot \cos \left[\tan^{-1} \left(\frac{-(R_\zeta - r_h) \cdot \sin \beta_n - (R_\zeta - r_h) \cdot \sin \left(\frac{R_\zeta - r_h}{r_h} \cdot \beta_n \right)}{(R_\zeta - r_h) \cdot \cos \beta_n - (R_\zeta - r_h) \cdot \cos \left(\frac{R_\zeta - r_h}{r_h} \cdot \beta_n \right)} \right) \right] \quad (16)$$

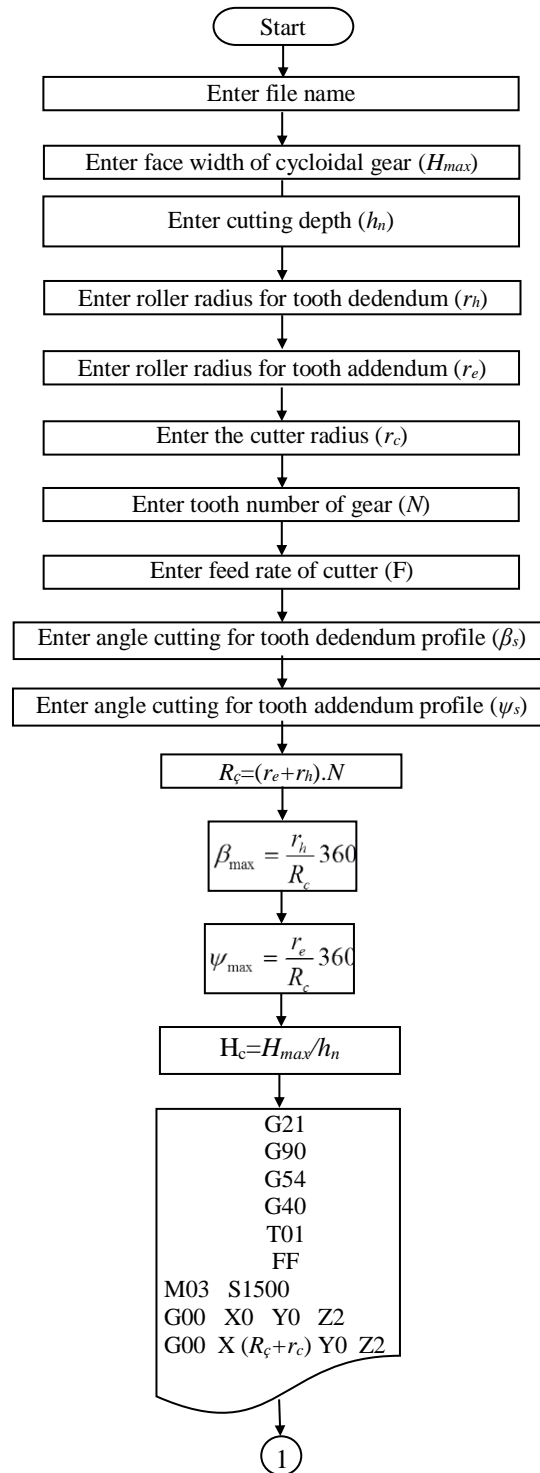
$$Yh_n = yh_n + r_c \cdot \sin \left[\tan^{-1} \left(\frac{-(R_\zeta - r_h) \cdot \sin \beta_n - (R_\zeta - r_h) \cdot \sin \left(\frac{R_\zeta - r_h}{r_h} \cdot \beta_n \right)}{(R_\zeta - r_h) \cdot \cos \beta_n - (R_\zeta - r_h) \cdot \cos \left(\frac{R_\zeta - r_h}{r_h} \cdot \beta_n \right)} \right) \right] \quad (17)$$

$$Zh_n = H_{\max} \text{ (constant)} \quad (18)$$

It is observed that while the end mill machines the cycloidal gear according to all these equations written above, parameters such as β_n , ψ_n , R_ζ , r_e , r_h and H_{\max} in the equations will affect the machining times of the gear.

III. CAD/CAM PARAMETERS OF THE CYCLOIDAL GEAR AND MACHINING TIMES

According to the equations written above, the C++ program prepared to derive the CAM codes of the cycloidal gear works according to the CAD/CAM parameters such as the sensitivity of hypocycloid profile cutting (β_s), sensitivity of epicycloid profile cutting (ψ_s), feed rate of the end mill (F), tooth number of the cycloidal gear (N), roulette radius of the tooth addendum (r_e), roulette radius of the tooth dedendum (r_h), and cutting depth (h_n) (Figure 7) [14].



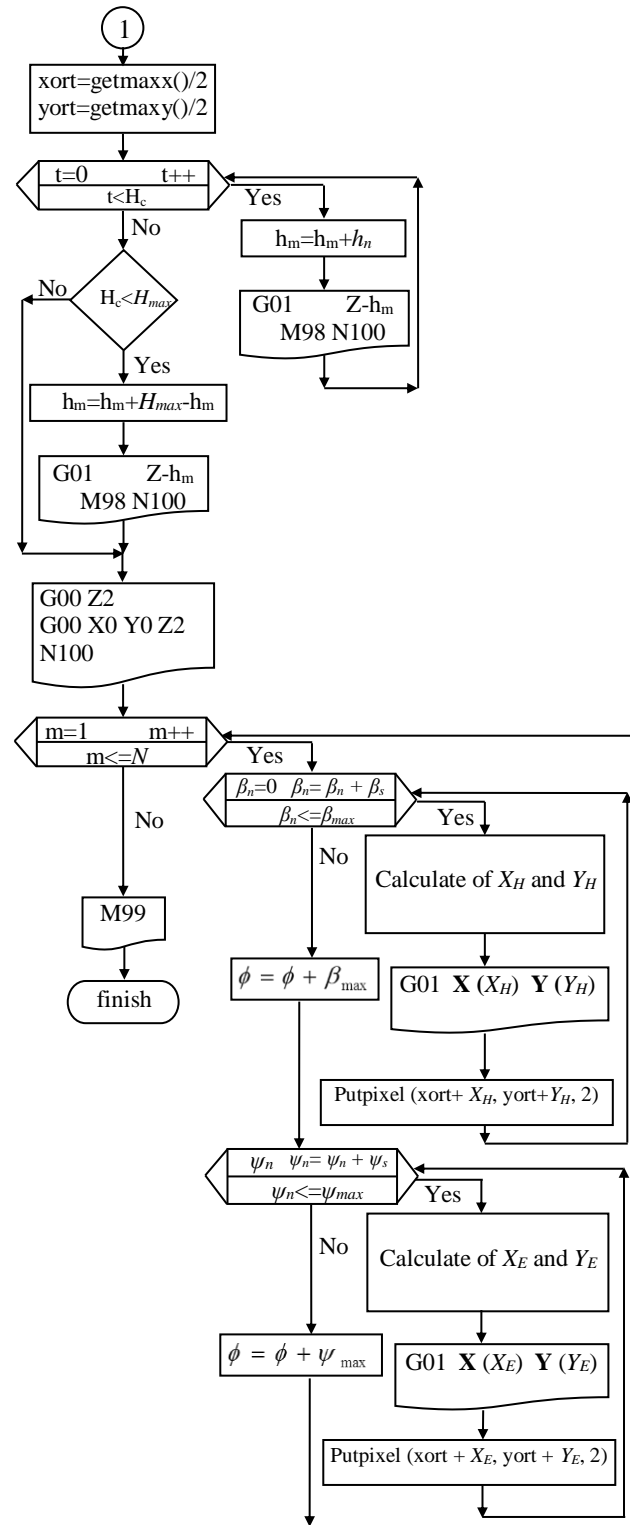


Figure 7. The algorithm used to derive CAM codes

In this study, C++ program was operated according to various values of these parameters and the CNC codes were derived for the cycloidal gears. The simulation of the gears was performed using these codes in Dyna 4M CNC program (Figure 8).

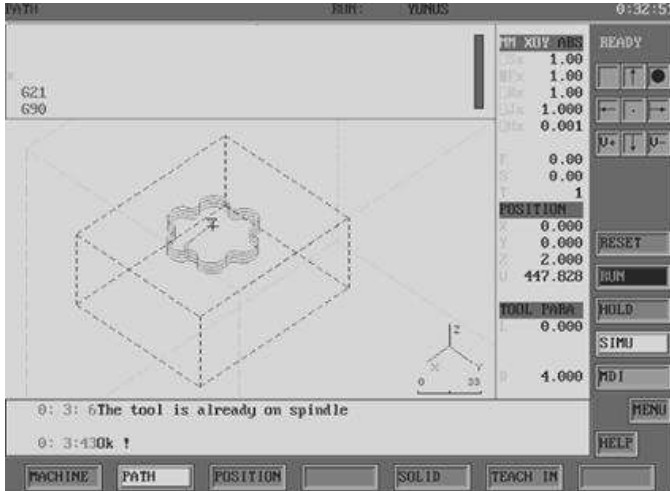


Figure 8. Simulation of a cycloidal gear

Then, cycloidal gears with different tooth numbers were manufactured (Figure 9) and the manufacturing times of the gears were determined.

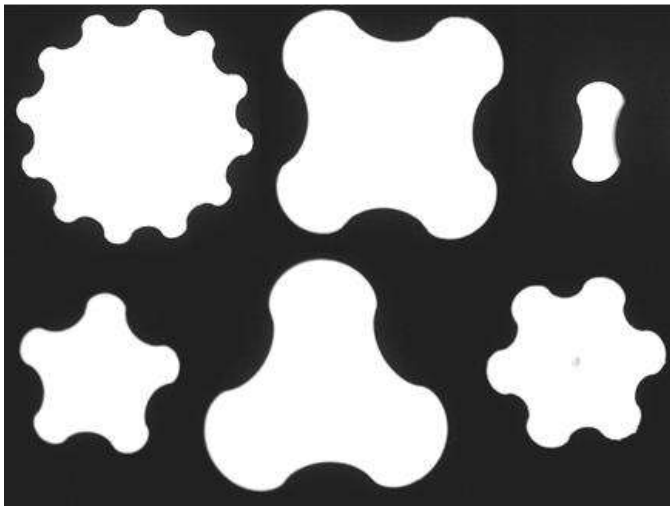
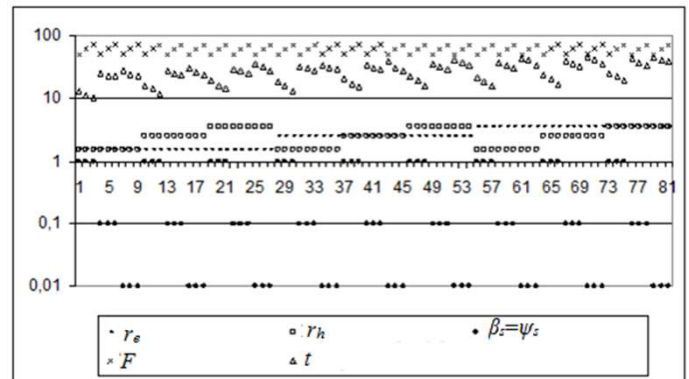


Figure 9. Manufactured cycloidal gears

These times were determined for the $H_{max}=1$ and $h_n=1$ values of the cycloidal gear. To find the actual machining times of the cycloidal gear, the values in Table 1 can be obtained by

multiplying by the number of layers (H_{max}/h_n) in the X-Y plane along the Z-axis (Figure 2). In this study, the machining times (t) for the cycloidal gear with $N=4$ teeth are given in Table 1.

In this study, the machining times were also determined for a cycloidal gear with 8 teeth. However, these results were not presented in the form of a table so that the paper would not be too long. These results are shown in the graphical form only (Figure 10 and 11).



Figures 10. Machining times for $N=4$ teeth

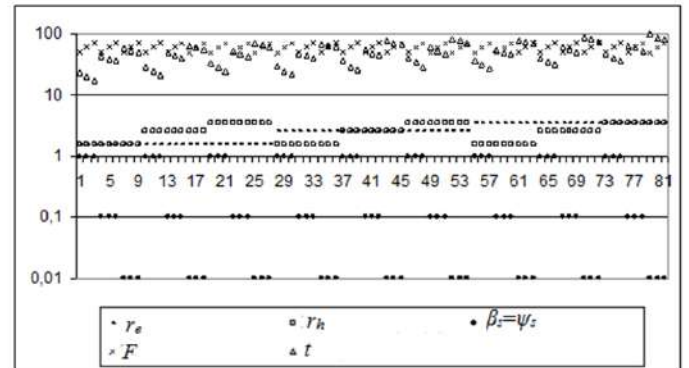


Figure 11. Machining times for $N=8$ teeth

In order to read the graphs in Figure 10 and 11, three of the machining parameters are kept stable and the change in the machining time is examined depending on the change in the fourth parameter. For example, in Figure 10, it is observed that the machining time of the cycloidal gear in the CNC milling machine decreases with the increase in the feed rate of the end mill if the sensitivity of machining, minor roulette radius and major roulette radius are kept stable (Table 1). In the graphs, the section scaled from 1 to 81 shows the number of experiments.

TABLE I. FINISHING MACHINING TIMES OF THE CYCLOIDAL GEAR ACCORDING TO THE CAD/CAM PARAMETERS

Experiment Number	N	r_e (mm)	r_h (mm)	$\psi_s=\beta_s$ (degree)	F (m/min)	t (sec)	41	4	2.5	2.5	0.1	60	31
1	4	1.5	1.5	1	50	13	42	4	2.5	2.5	0.1	70	29
2	4	1.5	1.5	1	60	11	43	4	2.5	2.5	0.01	50	38
3	4	1.5	1.5	1	70	10	44	4	2.5	2.5	0.01	60	31
4	4	1.5	1.5	0.1	50	25	45	4	2.5	2.5	0.01	70	27
5	4	1.5	1.5	0.1	60	23	46	4	2.5	3.5	1	50	23
6	4	1.5	1.5	0.1	70	22	47	4	2.5	3.5	1	60	19
7	4	1.5	1.5	0.01	50	28	48	4	2.5	3.5	1	70	16
8	4	1.5	1.5	0.01	60	24	49	4	2.5	3.5	0.1	50	35
9	4	1.5	1.5	0.01	70	22	50	4	2.5	3.5	0.1	60	32
10	4	1.5	2.5	1	50	16	51	4	2.5	3.5	0.1	70	29
11	4	1.5	2.5	1	60	14	52	4	2.5	3.5	0.01	50	40
12	4	1.5	2.5	1	70	12	53	4	2.5	3.5	0.01	60	37
13	4	1.5	2.5	0.1	50	27	54	4	2.5	3.5	0.01	70	33
14	4	1.5	2.5	0.1	60	25	55	4	3.5	1.5	1	50	21
15	4	1.5	2.5	0.1	70	24	56	4	3.5	1.5	1	60	18
16	4	1.5	2.5	0.01	50	30	57	4	3.5	1.5	1	70	16
17	4	1.5	2.5	0.01	60	26	58	4	3.5	1.5	0.1	50	37
18	4	1.5	2.5	0.01	70	24	59	4	3.5	1.5	0.1	60	33
19	4	1.5	3.5	1	50	19	60	4	3.5	1.5	0.1	70	31
20	4	1.5	3.5	1	60	16	61	4	3.5	1.5	0.01	50	43
21	4	1.5	3.5	1	70	14	62	4	3.5	1.5	0.01	60	40
22	4	1.5	3.5	0.1	50	29	63	4	3.5	1.5	0.01	70	34
23	4	1.5	3.5	0.1	60	27	64	4	3.5	2.5	1	50	24
24	4	1.5	3.5	0.1	70	25	65	4	3.5	2.5	1	60	20
25	4	1.5	3.5	0.01	50	35	66	4	3.5	2.5	1	70	17
26	4	1.5	3.5	0.01	60	32	67	4	3.5	2.5	0.1	50	39
27	4	1.5	3.5	0.01	70	27	68	4	3.5	2.5	0.1	60	35
28	4	2.5	1.5	1	50	18	69	4	3.5	2.5	0.1	70	32
29	4	2.5	1.5	1	60	16	70	4	3.5	2.5	0.01	50	44
30	4	2.5	1.5	1	70	13	71	4	3.5	2.5	0.01	60	40
31	4	2.5	1.5	0.1	50	32	72	4	3.5	2.5	0.01	70	36
32	4	2.5	1.5	0.1	60	30	73	4	3.5	3.5	1	50	25
33	4	2.5	1.5	0.1	70	28	74	4	3.5	3.5	1	60	22
34	4	2.5	1.5	0.01	50	34	75	4	3.5	3.5	1	70	19
35	4	2.5	1.5	0.01	60	31	76	4	3.5	3.5	0.1	50	42
36	4	2.5	1.5	0.01	70	29	77	4	3.5	3.5	0.1	60	37
37	4	2.5	2.5	1	50	20	78	4	3.5	3.5	0.1	70	34
38	4	2.5	2.5	1	60	17	79	4	3.5	3.5	0.01	50	46
39	4	2.5	2.5	1	70	15	80	4	3.5	3.5	0.01	60	40
40	4	2.5	2.5	0.1	50	34	81	4	3.5	3.5	0.01	70	38

IV. RESULTS AND DISCUSSION

The high values of the cycloidal gear such as N , r_e and r_h prolong the manufacturing time of the gear (Figures 10 and 11). On the other hand, the high values of h_n and F shorten the manufacturing time of the gear. However, in this case, the cutting efficiency of the cutter may decrease. In the case that these values are selected as too small, the manufacturing time prolongs considerably (Figures 10 and 11). The very high values of β_s and ψ_s also shorten the manufacturing time of the cycloidal gear. However, in this case, the amount of error of the tooth profiles (epicycloid and hypocycloid profiles) will also increase. The very low values of β_s and ψ_s prolong the manufacturing time of the cycloidal gear (Table 1).

CNC milling machine," *Journal of Manufacturing Science and Engineering, Transaction of the ASME*, vol. 127, 503-511, 2005.

- [17] C. Özel, "A study on cutting errors in the tooth profiles of the spur gears manufactured in CNC milling machine," *The International Journal of Advanced Manufacturing Technology*, vol. 59, num. 1-4, 243-251, 2012.

REFERENCES

- [1] P. Gu, D.H. Norrie, *Intelligent Manufacturing Planning*, Chapman & Hall, 1995.
- [2] C. Granville, "Computer-aided Process planning," *Comput.-Aided Eng.*, vol.8, num. 8, 46-48, 1989.
- [3] G. Ulusoy and R. Uzsoy, "Computer-aided process planning and material requirements planning: first steps towards computer-integrated manufacturing," *Interfaces*, vol. 22, num. 2, 76-86, 1992.
- [4] B. Wassila, "Cutting Parameter Optimization to Minimize Production Time in High Speed Turning," *Journal of Materials Processing Technology*, vol. 161, 388-395, 2005.
- [5] B. Arezoo, K. Ridgway and A. M. AlAhmari, "Selection of Cutting Tools and Conditions of Machining Operations Using an Expert System," *Comput. Ind.*, vol. 42, 43-58, 2000.
- [6] P. J. Davim, "A note on the determination of optimal cutting conditions for surface finish in turning using design of experiments," *JMPT*, vol. 116, 305-308, 2001.
- [7] M. Manuel and A. R. Cido, "Influence of tool path strategy on the cycle time of high-speed milling," *Comput. Aided Des.*, vol. 35, 395-401, 2003.
- [8] R. I. King, *Handbook of High Speed Machining Technology*, Chapman & Hall, 1985.
- [9] P. G. Maropoulos, R. P. Baker and K. Y. G. Paramor, "Integration of tool selection with design Part 2: Aggregate machining time estimation," *Journal of Materials Processing Technology*, vol. 107, 135-142, 2000.
- [10] R. M. Boogret, H. J. Kals and F. J. V. Houten, "Tool paths and cutting technology in computer-aided process planning," *Int. J. Adv. Manuf. Technol.*, vol. 11, 186-197, 1996.
- [11] C. Ou-Yang and T. S. Lin, "Developing an integrated framework for feature-based early manufacturing cost estimation," *Int. J. Adv. Manuf. Technol.*, vol. 13, 618-629, 1997.
- [12] B. Malakooti and J. Deviprasad, "An interactive multiple criteria approach for parameter selection in metal cutting," *Operations Research*, vol. 37, 805-818, 1989.
- [13] S. S. Panwalkar and R. Rajagopalan, "Single-machine sequencing with controllable processing times," *European Journal of Operational Research*, vol. 59, 298-302, 1992.
- [14] C. Özel and Y. Ortaç, "A study on the cutting errors of the tooth profiles of the cycloidal gears manufactured in CNC milling machine," *International Journal of Materials and Product Technology*, vol. 53, num. 1, 42-60, 2016.
- [15] C. Özel, "Research of production times and cutting of the spur gears by end mill in CNC milling machine," *Int. J. Adv. Manuf. Technol.*, vol. 54, 203-213, 2010.
- [16] C. Özel, A. İnan and L. Özler, "An investigation on manufacturing of the straight bevel gear using end mill by

Robust and Gain Scheduling PI Control of Varying Time Delay Systems

Cem ONAT
Mechanical Engineering
Inonu University
Malatya, TURKEY
cem.onat@inonu.edu.tr

Abdullah TURAN
Mechanical Engineering
Inonu University
Malatya, TURKEY
abdullah.turan@inonu.edu.tr

Abstract— In this study, a gain scheduling PI controller for variable time delay systems is designed. The design is based on finding the weighted geometric center of stabilizing control parameters area and valid for the systems in which variable time delay is measurable or observable. Each of the control parameters of proposed gain scheduling PI controller is a function of variable time delay. These functions are obtained through matching of weighted geometric center points corresponded to different time delays by means of curve fitting method. The simulation results show that the designed gain scheduling PI controller presents good transient responses through overcoming the variable time delay in the system.

Keywords— Gain scheduling; PI control; weighted geometrical center; variable time delay

V. INTRODUCTION

VARIABLE time delay processes pose a challenging problem in control engineering. A time delay of the order of the time constant of the system, combined with a variation of it, requires an inventive control strategy to fulfill certain performance requirements. As there are many practical problems involving variable time delay in industry (e.g. steel rolling processes, paper manufacturing, fuel-air ratio control systems at engines, thermal plants, nuclear reactors), it would be interesting to develop new control strategies on it.

Although several advanced control strategies have been developed, structurally simple proportional-integral (PI) and proportional-integral-derivative (PID) controllers are still widely used in industrial control systems because of their robust performance and simplicity. Because of these reasons, developing better PI/PID design methods still attracts the interest of researchers [1-5]. One of the PI design methods reported in recent years is weighted geometrical center (WGC) method which is presented in [6]. The method is based on calculating the weighted geometric center of stabilizing controller parameters area.

In this study, WGC method was adapted to control of a variable time delay system. Proposed scheduling method is valid in the systems where variable time delay directly measured or observed. For example, variable time delay in fuel-air ratio control systems of engines can be observed by means of their rotation speed [7-11]. The design is based on

calculating the WGC controllers corresponding to different values of variable time delay and following this, associating these values to variable time delay by means of curve fitting method and obtaining the controller parameters (k_p, k_i) as a function of time delay. The simulation results show that the gain scheduling PI controller guarantees the stability of the system against the variable time delay existing in the system and exhibits a good performance.

The paper is organized as follows. The next section represents considered varying time delay system. In Section 3, design of the gain scheduling PI controller is presented. Simulations are considered in Section 4 to illustrate the wisdom of the designed controller. Finally, concluding remarks are given in Section 5.

VI. MODEL

For the method is explained, a FAR control system given in [12] is used. In this system, variable time delay (T_D) can be obtained by using (1) [7-11].

$$T_D = \frac{120}{n} \quad (1)$$

Where n is the rotation speed of the engine. Accordingly, if it is considered that engine speeds typically vary from 600 to 6000 rpm, the time delay in the system will also vary by at least 10:1 [12].

The considered system is a second order system with variable time delay. The transfer function of this system is given in (2), and the controller block with PI controller is shown in Fig. 1. Where, r , y , $C(s)$ and $H(s)$ represents the reference input, system output, transfer function of the PI controller and sensor dynamics respectively. $C(s)$ and $H(s)$ are given in (3) and (4) respectively.

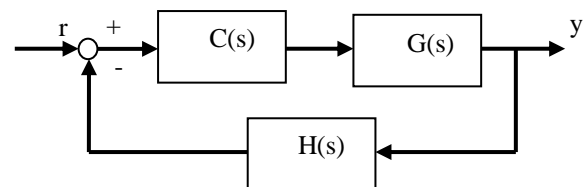


Fig. 7. Control blok diagram

$$G(s) = \frac{25.5 \cdot s + 50}{s^2 + 51 \cdot s + 50} \cdot e^{-T_D s} \quad (2)$$

$$C(s) = k_p + \frac{k_i}{s} \quad (3)$$

$$H(s) = \frac{1}{0.1 \cdot s + 1} \quad (4)$$

VII. GAIN SCHEDULING PI CONTROLLER

Calculating the stabilizing controller parameters area was obtained from the joint solution of (5) and (6) through the stability boundary locus approach [11] according to the variable time delay. The (5) and (6) were obtained respectively, through the separation of imaginary and reel terms of the characteristic equation of the system shown at Figure 1. In these equations, ω is frequency. It was considered that the time delay changed between the range of [0.2, 2] s. The stabilizing controller parameter areas and obtained for ten different values in this value range, are shown at Figure 2.

$$\begin{aligned} &2.04 \cdot k_p \cdot \omega^2 \cdot \sin(T_D \cdot \omega) + 4 \cdot k_p \cdot \omega \cdot \cos(T_D \cdot \omega) \\ &- 4 \cdot k_i \cdot \sin(T_D \cdot \omega) + 2.04 \cdot k_i \cdot \omega \cdot \cos(T_D \cdot \omega) \\ &= 0.488 \cdot \omega^3 - 4 \cdot \omega \end{aligned} \quad (5)$$

$$\begin{aligned} &-2.04 \cdot k_p \cdot \omega^2 \cdot \cos(T_D \cdot \omega) + 4 \cdot k_p \cdot \omega \cdot \sin(T_D \cdot \omega) \\ &+ 4 \cdot k_i \cdot \cos(T_D \cdot \omega) + 2.04 \cdot k_i \cdot \omega \cdot \sin(T_D \cdot \omega) \\ &= 0.896 \cdot \omega^2 - 0.008 \cdot \omega^4 \end{aligned} \quad (6)$$

As it is expected, increase in time delay, limits the stabilizing controller parameter area. It is presented at [11] that, the WGC of the stability region is a special point for the time delay systems with regards to trade-off of the transient response characteristics. The controller parameter values corresponding to WGC of the stability areas obtained at Figure 2 are given in Table 1.

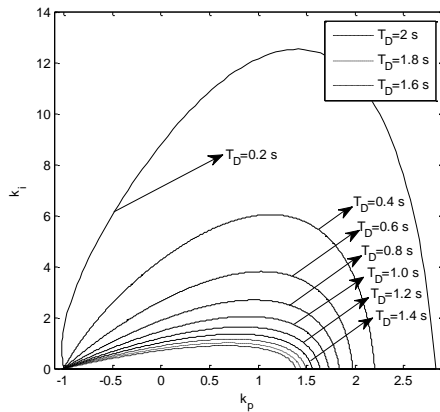


Fig. 8. Stability regions in accordance with different time delay values

TABLE II.
THE WGC
CONTROLLER PARAMETERS CORRESPONDING TO
DIFFERENT TIME DELAY VALUES

T_D	k_p	k_i
0.2	0.6322	3.4710
0.4	0.4644	1.6700
0.6	0.4063	1.0450
0.8	0.3557	0.7358
1.0	0.3060	0.5584
1.2	0.2675	0.4443
1.4	0.2270	0.3693
1.6	0.1976	0.3148
1.8	0.1747	0.2739
2.0	0.1526	0.2432

To obtain the gain scheduling PI controller, by using the values given at Table 1, the controller parameters are obtained as the third degree function of time delay. In (7) and (8), the expressions of controller parameters of k_p and k_i according to time delay are given respectively. In Fig. 3, the change of fitted $k_p(T_D)$ and $k_i(T_D)$ functions corresponding to time delay is shown. In Fig. 3, it is seen that curve fitting at third degree provides enough precision.

$$k_p(T_D) = -0.089T_D^3 + 0.403T_D^2 - 0.738T_D + 0.720 \quad (7)$$

$$k_i(T_D) = -1.874T_D^3 + 7.780T_D^2 - 10.495T_D + 4.993 \quad (8)$$

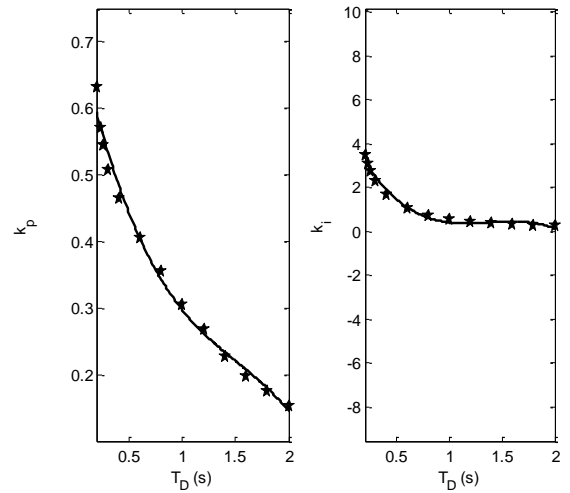


Fig. 9. Change of controller parameters with time delay

VIII. SIMULATIONS

The simulations performed for two different time delay cases for the efficiency of the proposed gain scheduling PI controller is showed. The Matlab-Simulink block used in simulations is given at Fig. 4. The change of time delay in first case in the different trapeze form, as seen at Fig. 5 and the change of time delay in second case in the sinusoidal form, as seen at Fig. 6 were taken into consideration.

Moreover the closed loop system with classical PI controller was used in the simulations in order to

provide a comparing opportunity. For this purpose, the WGC controller of most interior area remaining in the entire stability areas between the considered time delay value ranges was used as classical PI controller (see Fig. 2). The parameters of this controller are $k_p=0.1526$ and $k_i=0.2432$ (for $T_D=2s$).

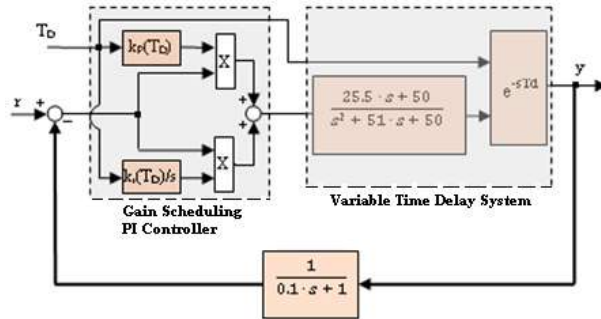


Fig. 10. Simulation block diagram

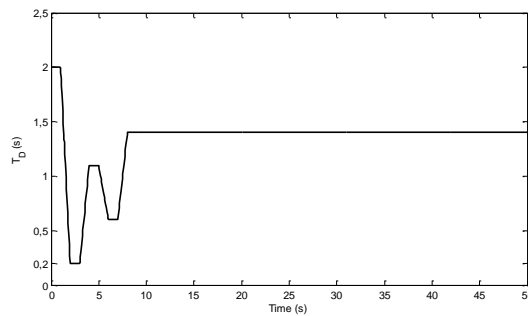


Fig. 11. Change of time delay in trapeze form

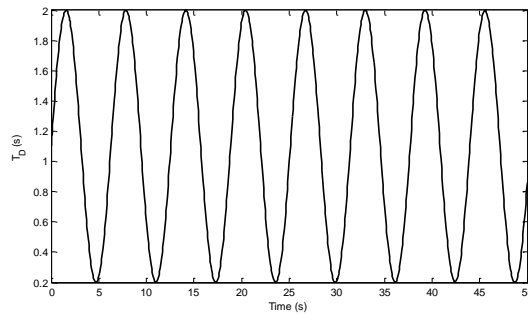


Fig. 12. Change of time delay in sinusoidal form

The unit step responses corresponding to the change in time delay of proposed controller in first and second case are given at Fig. 7 and 8. Numerical values of transient state response characteristics performances of the closed loops are given in Table 2 for comparison. Here, it is seen that the proposed gain scheduling PI controller against the time delay change in the system, provides the system to be stable continuously and presents better transient state responses comparing with classical PI controller. In addition to this, it is seen that the selected classical PI controller for comparison is robust against variable time delay, because it is

WGC controller of area providing joint stability for all values of the time delay value range.

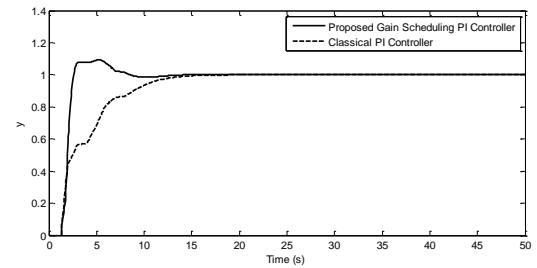


Fig. 13. The unit step reply for the first case

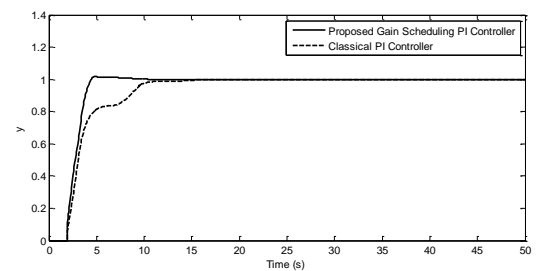


Fig. 14. The unit step reply for the second case

TABLE III. NUMERICAL VALUES OF TRANSIENT STATE PERFORMANCES OF THE CONTROLLERS

	Cases	Rising Time (s)	Settling Time for %2 (s)	Overshoot (%)
Gain Scheduling PI Controller	Case 1	0.94	7.41	9.37
	Case 2	1.84	4.26	1.65
Classical PI Controller	Case 1	7.48	12.65	0
	Case 2	6.46	10.25	0

IX. CONCLUSION

In this study, a new gain scheduling PI controller design method for a second degree system with variable time delay was presented. This method, is based on calculating the weighted geometric center controllers corresponding to different values of variable time delay and following this, associating these values to variable time delay by means of curve fitting method and obtaining the controller parameters as a function of time delay. The proposed system's assuring system steady against the variable time delays in the system is the most important characteristic of the method. But requirement for one more sensor for sensing or observing the varying time delay is a disadvantageous. The results of the simulation show that the proposed method will provide successful results for systems where variable time delay can be observed.

X. REFERENCES

- [1] J. P. Richard, "Time-delay systems: an overview of some recent advances and open problems," *Automatica*, Vol. 39, pp. 1667-1694, Oct. 2003.
- [2] E. Fridman, U. Shaked, "An improved stabilization method for linear time-delay systems," *IEEE Transactions on Automatic Control*, Vol. 47, pp. 1931-1937, Nov. 2002.
- [3] S. Xu, J. Lam, "Improved delay dependent stability criteria for time delay systems," *IEEE Transactions on Automatic Control*, Vol. 50, pp. 384-387, March 2005.
- [4] Q. L. Han, "Absolute stability of time delay systems with sector bounded nonlinearity," *Automatica*, Vol. 41, pp. 2171-2176, December 2005.
- [5] C. Onat, "A new concept on PI design for time delay systems: weighted geometrical center," *International Journal of Innovative Computing, Information and Control*, Vol. 9, pp. 1539-1556, 2003.
- [6] C. Onat, "WGC based robust and gain scheduling PI controller design for condensing boilers," *Advances in mechanical engineering*, SAGE Publications Sage UK: London, England, May. 2014.
- [7] Y. Yildiz, A. M. Annaswamy, D. Yanakiev, I. Kolmanovsky, "Spark ignition engine fuel to air ratio control: An adaptive control approach," *Control engineering practice*, Vol. 8, pp. 1369-1378, Dec. 2010.
- [8] Y. Yildiz, A. M. Annaswamy, D. Yanakiev, I. Kolmanovsky, "Adaptive air fuel ratio control for internal combustion engines," *IEEE, American control conference*, 11-13 June 2008.
- [9] S. Pace, G. G. Zhu, "Transient air to fuel ratio control of an spark ignited engine using linear quadratic tracking," *J. Dyn. Sys. Meas. Control*, 136 (2) Dec. 2013.
- [10] A. Ghaffari, A. H. Shamekhi, A. Saki, E. Kamrani, "Adaptive fuzzy control for air-fuel ratio of automobile spark ignition engine," *World academy of science press, International journal of engineering and technology*, Vol. 48, pp. 284-292, 2008.
- [11] J. Lauber, T. M. Guerra, M. Dambrine, "Air fuel ratio control in a gasoline engine" *International journal of systems science*, Vol. 42, pp. 277-286. 2010.
- [12] G. F. Franklin, J. D. Powell, A. E. Naeini, "Feedback Control of Dynamic Systems" 6th edition, Pearson, 2014.

Impact Performance of Intraply-Woven Carbon/Aramid Hybrid Composites with Nano-Clay Particles

Mehmet BULUT

*Mechanical Engineering Department,
Gaziantep University, Engineering Department,
27310 Gaziantep, Turkey*

Ahmet ERKLİĞ

*Mechanical Engineering Department,
Gaziantep University, Engineering Department,
27310 Gaziantep, Turkey*

Ömer Yavuz BOZKURT

*Mechanical Engineering Department,
Gaziantep University, Engineering Department,
27310 Gaziantep, Turkey*

Abstract— Present study explores the impact resistance and energy absorption capacity of intraply Carbon/Aramid/epoxy composite laminates with nano-clay particles. Impact performance of samples was evaluated by assisting charpy impact tests in accordance with ISO 179 international standards. Nano clay particles were used as additive material within the epoxy resin by the weight ratios of 0, 2, 4, 6, 8 and 10. Failure characteristics after the impact tests will be studied over the surface of the samples. Results from this study will be analyzed according to incorporation of nano-clay particles in intraply Carbon/Aramid/epoxy composite in terms of impact and energy absorption capacity according to full samples.

Keywords— Impact, Nano-clay, Carbon, Aramid

XI. INTRODUCTION

Although carbon fiber reinforced composites have high strength and modulus in recent years, their low fracture energy and impact resistance are their limitations due to brittle nature of carbon fiber [1], and impact resistance properties of carbon fiber reinforced composites can be increased by hybridization of aramid fibers [2-3]. Dorey et al. [4] showed that hybridization of Aramid fibers with carbon or glass fibers significantly improved the energy absorption and impact resistance of materials.

Hybrid composites are composed of two or more different types of fibers, and they are extensively used in many engineering applications as like aviation, marine and automotive in order to design the structures as desired specifications. In addition, hybrid type and structure are major parameters influencing load bearing and impact resistance of

hybrid composites [5], and two different hybrid composites are existing in terms of weaving architectures, namely, interplay and intraply, respectively. Even though many studies are available about impact behavior of interplay woven hybrid composites in literature, studies on impact behavior of intraply woven hybrid composites are limited. Pegoretti et al. [6] investigated interplay and intraply woven E-glass and polyvinyl alcohol composite laminates. It was asserted that intraply woven composites exhibited greater mechanical and impact resistance as compared with interplay one. Researchers [7] studied impact behavior of 3D woven hybrid composites, indicating their superior impact resistance compared with 2D woven composites. Besides hybridization of fibers with different weaving architectures, another one of increasing impact resistance of composite materials is incorporation of nano particles within the epoxy. In nano particles, nano clay is one of the best particle that is utilized and is considered one of the multiple functions of clay materials, which are widely utilized in many areas. Several studies [8-10] performed on mechanical characterization of composite laminates with addition on nano clay particles. It was indicated that mechanical performance of the materials was increased at the small amount of nanoclay inclusions by weight ratio. Shishavan et al. [11] explored the influence of nano clay addition and temperature on the tensile strength and toughness of nano-composites using the (Taguchi) mode of design of experiences. Results showed that tensile strength and stiffness of nano clay reinforced composites were significantly affected by injection temperature. Chowdary and Kumar [12] investigated the effect of Nano-clay content on the mechanical and morphological behavior of the S-glass

fiber/polyester resin. Nano-clay contents were 1, 3, 5, and 7 % by weight in polyester resin. The results suggested that the inclusion of Nano-clay has a significant effect on the mechanical behavior of composite materials, resulting highest improvement in addition of Nano clay by 3 wt %.

Results from above studies prove that limited studies are existing about impact and mechanical properties of intraply woven hybrid composites investigating nano particle effects. Present study experimentally investigated the tensile and charpy impact resistance of intraply woven carbon/aramid hybrid composites reinforced with nano clay particles. Tensile, energy absorption and impact resistance of samples were characterized different amount of nanoclay particle loading within the epoxy resin. Their failure mechanisms after impact tests were also recorded.

XII. MATERIALS AND METHODS

A. Production materials

The epoxy (MOMENTIVE-MGS L285), hardener (MOMENTIVE-MGS H285), twill intraply Kevlar/carbon woven fabrics (190 g/m²) were supplied from Dostkimya Company, Tuzla, Istanbul, Turkey. Montmorillonite (NM-MMT) Nano clay was bought from Grafen Chemical Industries in Turkey.

Kevlar/carbon fabric has weight of 190 g/m², weave of 2/2 twill, width of 1000 - 1200 mm and thickness: 0.23 mm. Nano clay particles have lateral width of 0.5-2 μ m, thickness of 1-10 nm and bulk density of 200-500 kg/m.

B. Production of test samples

The laminates were manufactured using hand layup technique with application the epoxy/nanoclay particle mixture on fibers. Samples were prepared 10 layers impregnating fabrics layer by layer. Then, they are subjected to (120 kPa) pressure for 1 h curing time at 80°C temperature, and cooled to room temperature under constant pressure for three hours. Production process and some of produced samples were illustrated in Figure 1.

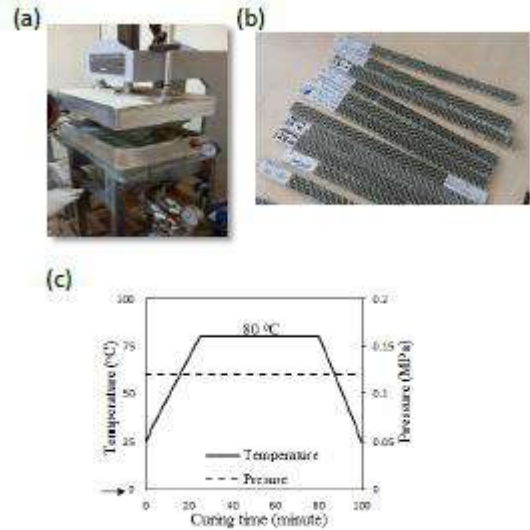


Fig. 15. Production process and test samples. (a) Hot-mold press, (b) Test samples with bulk shapes, (c) Curing procedure

C. Tensile tests

The tensile properties of the composite samples were determined at room temperature utilizing the AG-X series-Shimadzu testing machine (Kyoto, Japan) as illustrated in Fig. 2 (a). After the production process, test specimens were prepared from bulk sheets by cutting to meet desired size as per ASTM standards (D638-00). Fig. 2(b) illustrates the produced tensile test samples. The thickness of tensile specimens was in the range of 2.5 \pm 0.1 mm depending on variation of Nano-clay content. The crosshead speed was set to 2 mm/min for tensile test. Three samples were tested at least for each group, and their average values were recorded.

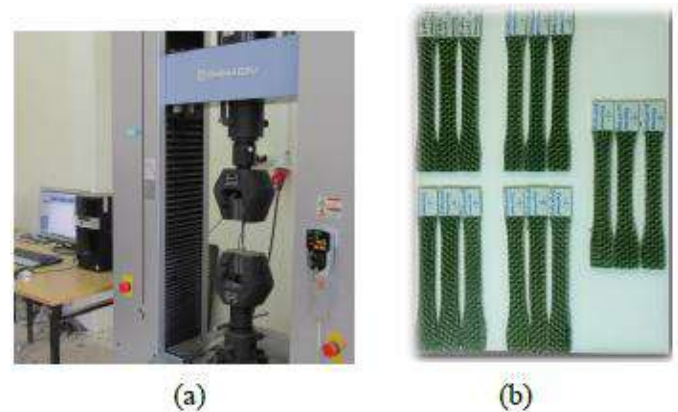


Fig. 16. Tensile test measurements. (a) Tensile test machine, (b) Tensile test specimens.

D. Impact tests

Charpy impact tests were performed by a Köger 3/70 Charpy impact tester with 15 J hammer (Köger, Germany) (Fig. 3 (a)). Absorbed energy and impact strength of composite samples were calculated using equations 1 and 2 from energy differences after (E_2) and before (E_1) impact tests as illustrated in Fig 3 (b)

$$E = E_1 - E_2 \quad (1)$$

$$U = \frac{E}{bh} \quad (2)$$

where E is the absorbed energy after impact, E_1 is the impact strength, and E_2 are initial and final potential energies, b and h are width and thickness of the samples, respectively. Multiply of b and h shows impacted area of the samples by impact hammer.

Composite samples have rectangular shapes with dimensions of 55×10 mm for impact tests according to the prescriptions of the ISO 179/92 standard [13].

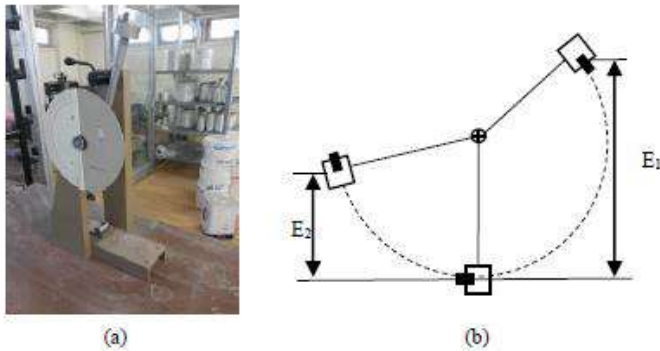


Fig. 17. Impact tests. (a) Charpy impact machine, (b) Illustration of impact mechanism

XIII. RESULTS AND DISCUSSIONS

A. Tensile tests

Fig. 4 shows the variation of tensile properties of test samples according to nanoclay content by weight. From Fig.4, it is observed that Kevlar/carbon/epoxy composite (pure) exhibits a tensile strength of 371 MPa, while Kevlar/carbon/epoxy at 1wt % of Nano clay showed the highest tensile strength as 421 MPa. After the critical value of 1wt %, tensile strength values were decreased while strain values were increasing. This is attributed the agglomeration of nanoparticles after the critical value of 0.1 wt %, leading to decrease mechanical properties of composites. In addition, all the specimens were broken without any necking and the fracture in intra-layered samples, (Fig. 5) which means that specimens fail in a brittle fashion during a tensile test.

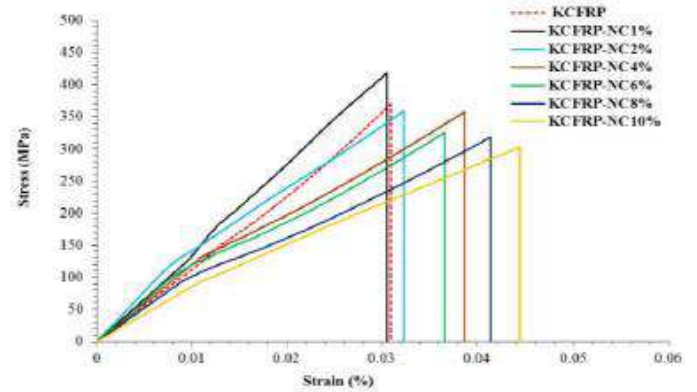


Fig. 18. Tensile properties of test samples

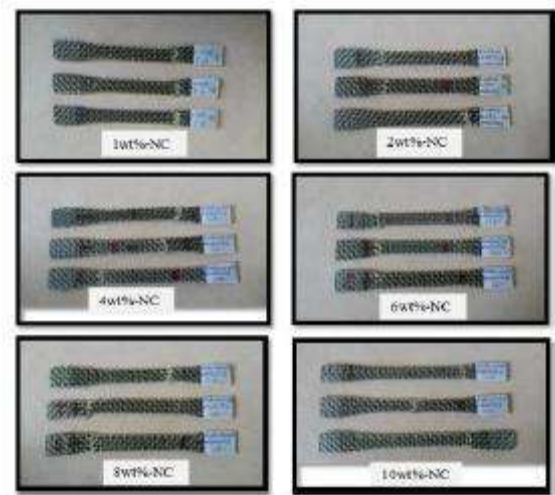


Fig. 19. Fractured tensile test samples after tests

B. Impact tests

Impact tests were performed using energy lost by charpy impact tests. Table 1 presents the results on impact tests in terms of absorbed energy and impact strength, and their variations were displayed in Fig. 6. It is observed that impact strength was gradually increased from KFRP to KFRP-NC6%, then decreased as addition of nanoclay content in the epoxy. The increase in impact strength was attributed the good adhesion between fiber and nanoclay particles, providing composite samples efficiently to withstand impact loadings, and usage of nanoclay filler at 6 wt % increases the impact strength by 19.84 % compared to unfilled composite sample (KFRP).

TABLE I. IMPACT TEST RESULTS

Specimen	Absorbed Energy (J)	Impact strength (kJ/m ²)
KFRP	1.23	51.25
KCFRP-NC2%	1.42	57.49
KCFRP-NC4%	1.56	61.42
KCFRP-NC6%	1.64	60.97
KCFRP-NC8%	1.62	57.14
KCFRP-NC10%	1.52	52.65

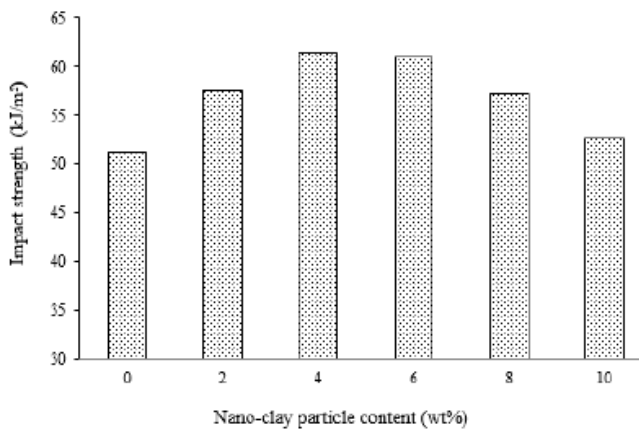


Fig. 20. Variation of impact test results

Failure surfaces of test samples were displayed in Fig. 7. It is noted here that fiber ruptures and delaminations are observed over the rear side of the samples, and amount of the damages for sample of KFRP-NC6% is much more than those of other samples due to the enhancement of brittle nature as increasing nanoclay content in the epoxy resin.

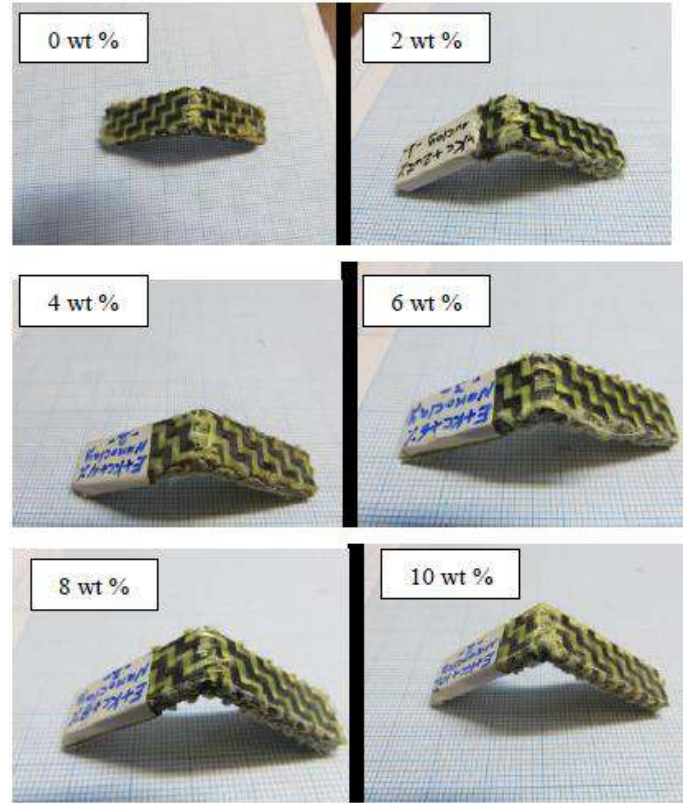


Fig. 21. Fractured test samples after impact tests

XIV.CONCLUSION

Tensile and impact properties of intraply woven hybrid composites were investigated incorporating different weight content of nanoclay particles in the epoxy resin. It is concluded that incorporation of nanoclay filler at 1 wt % and 4 wt % revealed the highest tensile and impact performances, respectively. Further increase in content of nanoclay in the epoxy resin caused the decrease of the mechanical performances due to the poor interphase bonding between nanoclay particle-fibers-epoxy, suggesting the usage of nanoclay particles at the small amounts for enhancement of structural performances during the services.

REFERENCES

- [1] M. Karahan and N. Karahan "Effect of weaving structure and hybridization on the low-velocity impact behavior of woven carbon-epoxy composites" *Fib. Text. East Europe* vol. 22, pp. 109–115, 2014.
- [2] X. Wang, B. Hu and Y. Feng "Low velocity impact properties of 3D woven basalt/aramid hybrid composites", *Compos. Sci. Technol.*, vol. 68, pp. 444–450, 2008,
- [3] J. Gustin, A. Joneson and M. Mahinfalah "Low velocity impact of combination Kevlar/carbon fiber sandwich composites", *Compos. Struct.* Vol. 69, pp. 396–406, 2005

- [4] G. Dorey, G.R. Sidey and J. Hutching, *Composites*, 1978, January 25-32. In: *Composite materials-Vol. 2.*, editors. Kelly I, Zweben C, Elsevier Science Ltd., Oxford, UK, 2000. p 216
- [5] D. Zhang, Y. Sun and L. Chen “A comparative study on low-velocity impact response of fabric composite laminates” *Mater Design* vol. 50, pp. 750–756, 2013.
- [6] P.A. Pegoretti, E. Fabbri and C. Migliaresi “Intraply and interply hybrid composites based on E-glass and polyvinyl alcohol woven fabrics: tensile and impact properties”, *Poly Int*, vol. 53, pp. 1290–1297, 2004,
- [7] S. Chou, H.C. Chen and H.E. Chen “Effect of weave structure on mechanical fracture behavior of three-dimensional carbon fiber fabric reinforced epoxy resin composites”, *Compos Sci Technol*, vol 45, pp. 23–35, 1992.
- [8] A. Yasmin, J.J. Luo, J. L. Abot and I. M. Daniel “Mechanical and thermal behavior of clay/epoxy Nano composites. *Composites Science and technology*”, vol. 66, pp. 2415-2422., 2006.
- [9] C. Mahesha, R. Shivarudraiah, N. Mohan, R. Suprabha “Erosive wear behavior of nano clay filled basalt - epoxy hybrid composite” *International journal of modern engineering research (ijmer)*, vol. 4(6), pp. 92-97, 2014.
- [10] J. J Karippal, H. N. Murthy, K. S. Rai, M. Sreejith and M. Krishna “Study of mechanical properties of epoxy/glass/Nano clay hybrid composites”, *Journal of Composite Materials*, vol. 45(18), pp. 1893-1899, 2011
- [11] S. M. Shishavan, T. Azdast and S. R. Ahmadi, “Investigation of the effect of nanoclay and processing parameters on the tensile strength and hardness of injection molded Acrylonitrile Butadiene Styrene–organoclay Nano composites”, *Materials & Design*, vol. 58, pp. 527-534, 2014.
- [12] M. S. Chowdary and M. N. Kumar, “Effect of nano clay on the mechanical properties of polyester and S-glass fiber (Al)”, *International Journal of Advanced Science and Technology*, vol. 74, pp. 35-42, 2015.
- [13] ISO 179-1:2010. *Plastics – Determination of charpy impact properties – Part 1: Non instrumented impact test*

An Investigation on the Low Velocity Impact Damage of GFRP Composite Materials Interleaved with Nylon 6,6 Nanofiber Mats

Murat YILDIZ
Mechanical Eng. Dep.
Iskenderun Technical
University
Hatay, TURKEY

Vildan ÖZKAN
Petroleum and Natural Gas
Eng. Dep.
Iskenderun Technical
University
Hatay, TURKEY

Ahmet YAPICI
Mechanical Eng. Dep.
Iskenderun Technical
University,
Hatay, TURKEY
ahmet.yapici@iste.edu.tr

Ömer Sinan ŞAHİN
Mechanical Eng. Dep.
Selçuk University
Konya, TURKEY

Abstract—In the past many studies proved that when polymers are laminated with nanofibers there are positive gains in regard of their mechanical properties such as improved impact resistance, ductility, less delamination, less debonding and more. In this work Glass Fiber Reinforced Polymer (GFRP) composite materials have been developed and interleaved with non-woven Nylon 6,6 nanofiber mats which are produced by the electrospinning technique and compared with a corresponding virgin sample by using the Low Velocity Impact tests. Three kind of polymer configurations are generated for the specimens; one virgin configuration where two glass fiber layers are placed in epoxy and two kind of nanofiber interleaved configurations in which one and three Nylon 6,6 nanofiber mats are interleaved in the two glass fiber layered epoxy composition specimens. Then those specimens are considered for their impact resistance and energy absorption capabilities after Low Velocity Impact experiments. The results showed that while nylon 6,6 nanofiber mats resulted in decrease of load carrying capacities of the composite laminates and improved the energy absorption capabilities.

Keywords—GFRP; Nylon 6,6; Low Velocity Impact

XV. INTRODUCTION

In today's world, Fiber Reinforced Polymers (FRP) composites have found themselves many application areas. Glass, Carbon, Aramid and Basalt are among the fibers that are used as reinforcements [1]. Those fibers are often used in polymers. Epoxy resin is one of the most frequently used polymer for composite manufacturing due to its superior abilities and being relatively cheap than other alternatives. FRPs can be used in aerospace, automotive, marine, and construction industries [2].

Glass Fiber Reinforced Polymer (GFRP) is a strong and not so weight material that has many application areas such as aircraft, boats, automobiles, bath tubs and enclosures, swimming pools, hot tubs, water tanks, roofing, pipes, cladding, casts, etc. Compared to Carbon Fiber Reinforced Polymer (CFRP), it might be not so strong still but is less brittle, and its raw materials are cheaper [3,4].

In laminated composite structures, physical disunities and mismatches can cause problems like debonding and/or delaminations. Delamination means separation of laminated plies that stuck together in a composite structure. If one takes into consideration that composites are of anisotropic character and how they performance during external impact forces, even a weak blow might cause enough damage the composite material to fracture thus rendering it defected. To minimize this problem, many methods are developed [5-11] and interleaving nanofiber mats in the composites is one of them [11-16].

Nowadays electrospinning is one of the most frequently used method to produce nanofiber mats [17-19]. Materials like Polyamides, PVC, Chitosan etc. can be electrospun to produce nanofibers as well. [20-26]. Nylon 6,6 is a thermoplastic polyamide that has a high elastic module and also has a compatibility with epoxy so it is often used for generating nanofibers for composite materials [27, 28].

In literature, there are studies that focused on mechanical performances of virgin [29-34] and the nanofiber modified [12-15,36,37] GFRP laminated composite structures as well. Modifying the epoxy resin of the GFRP is also investigated [38]. Some researchers also used Carbon Fiber in studies and by interleaving nanofiber mats to see their effects on the impact resistance of their specimens [13,15,22,27,39]. Modifying the epoxy resin of the CFRPs with interleaved nanofiber mats is also investigated [40].

In this work, Nylon 6,6 nanofiber mats were electrospun and placed into GFRP laminated composite structures in three different configurations. The virgin specimens were also manufactured and Low Velocity Impact tests at an energy value of 6,3 Joule were conducted on the specimens. A comparison was made to determine the effects of the nanofiber mats on delamination as well as impact resistance and energy absorption capabilities of the specimens.

XVI. MATERIALS AND METHODS

The specimens are generated by placing two E-glass fiber layers into epoxy and then interleaving the nylon 6,6 nanofiber mats for the nanofiber modified configurations.

The epoxy resin codenamed H160 which was provided from Dostkimya company was used. Its properties can be found on their website [41]. Epoxy resin and hardness were mixed together in a weight ratio of 60% and 40%, respectively. Dry E-Glass fiber layers were cut in $150 \times 100 \text{ mm}^2$ proportions and the fiber orientations being; $[0^\circ, 90^\circ]$. The specimens were produced in dimensions proposed in ASTM-D-7136 standards [42] by using the hand lay-up method where the iron molds were used for the manufacturing.

Electrospin device was used to generate nanofibers. Nylon 6,6 pellets were provided from Sigma Aldrich and their properties can be found on their website [43]. The pellets were dissolved in a mix of two different acids with a concentration of 10% w/w. The acids were Formic Acid and Dichloromethane and they were put together in 1:1 weight ratio. To assure homogeneity of the solution, it was put in an ultrasonic bath device for about 8 hours. Afterwards the solution was drawn into a 10 mL syringe and then it was placed into a syringe pump system. The electrospinning process was performed in those following conditions: applied voltage 30 kV, distance between the cylindrical collector and the needle 20 cm, feed rate 0,65 mL/hour, temperature 25°C and relative humidity 50-60%. The electrospun nanofiber mats were left in a room for a few days to make sure they were dry enough before used in the specimens. Fig. 1 shows the SEM image of the electrospun nanofibers.

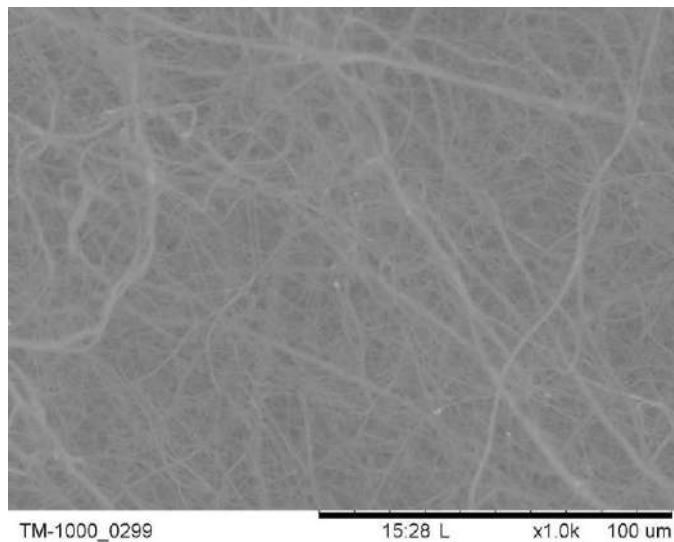


Fig. 1. SEM images of Nylon 6,6 Nanofiber Mats

The laminated composite specimens were produced by the hand lay-up method. Three kind of configurations for the specimens were considered; one kind of virgin one and two kind of nanofiber modified ones. For the virgin one; only two glass fiber layers were placed in epoxy and their simplified cross-

sections are presented in Fig. 2. For the nanofiber modified ones; one nanofiber mat was interleaved in two glass fiber layers and then placed into epoxy and three nanofiber mats were interleaved in two glass fiber layers and then placed into epoxy as well, whose simplified cross-sections are presented in Fig. 3, and Fig. 4, respectively. The nylon 6,6 nanofibers mats are notated as NF mats in those figures.

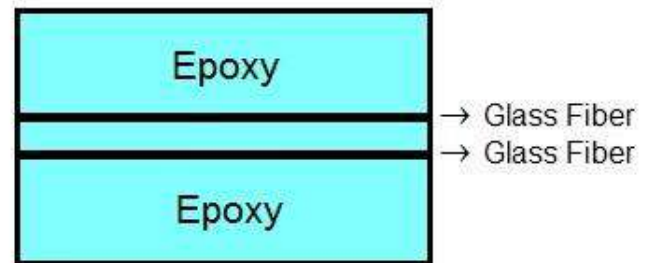


Fig. 2. Cross-section of the specimens codenamed "G"

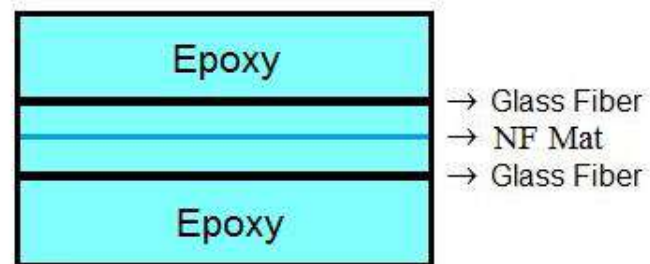


Fig. 3. Cross-section of the specimens codenamed "1N"

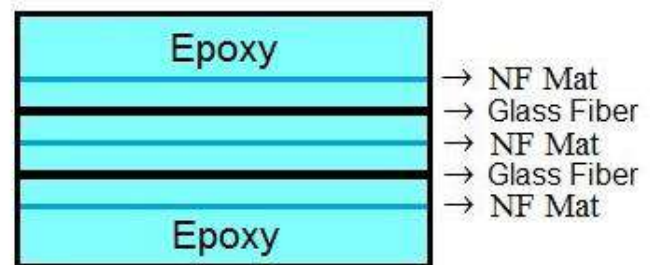


Fig. 4. Cross-section of the specimens codenamed "3N"

The specimens were left to cure for 24 hours and removed from the mold eventually.

The virgin specimens are codenamed with the suffix G. The nanofiber mat modified ones are codenamed with the 1N and 3N suffixes; 1N is indicating one nylon 6,6 nanofiber mat interleaved two glass fiber layered specimens while 3N is indicating three Nylon 6,6 nanofiber mat interleaved two glass fiber layered specimens.

Afterwards the produced composite laminates have been subjected to Low Velocity Impact tests in accordance with

ASTM-D-7136 standards. Impact tests were conducted with a drop tower in which the impactor has a hemispherical tip with a mass of 5,6 kg and a diameter of 12 mm diameter. The test specimens were placed into a fixture produced for placing and holding the test specimens at the point of impact. The test specimens were tested under impact velocity of 1,5 m/sec which corresponds to impact energy of 6,3 Joules.

The force signals were measured by a force sensor in mili volts scale. The signals were first amplified and filtered by a signal processor and transmitted to the data acquisition card. The variations of interaction force between the impactor and the sample versus time were obtained using NI Signal Express software. The sampling rate of data acquisition system is 25 kHz. As described in the regarding standard, the Newton's second law of motion was used to express the velocity and displacement of impactor versus time. When the impactor first hits the material, the kinetic energy of the impactor is partly transferred to the material. The remaining kinetic energy is used for rebound which makes the impactor to rise. This process continues until the kinetic energy of the impactor is fully consumed. During this process the material is generally subjected to 12-15 impacts. However, the testing machine has an anti-rebound system which allows us to get only one impact.

XVII. RESULTS AND DISCUSSION

Fig. 5 shows the variation of contact force with time for different specimens. It is seen in this figure that the addition of Nylon 6,6 nano fiber mats has resulted in decrease of maximum contact force. This can be explained due to the delaminations that occurred in the specimens. While the nylon 6,6 nanofiber mat modified specimens had the delamination problem, the virgin specimens were better in that aspect.

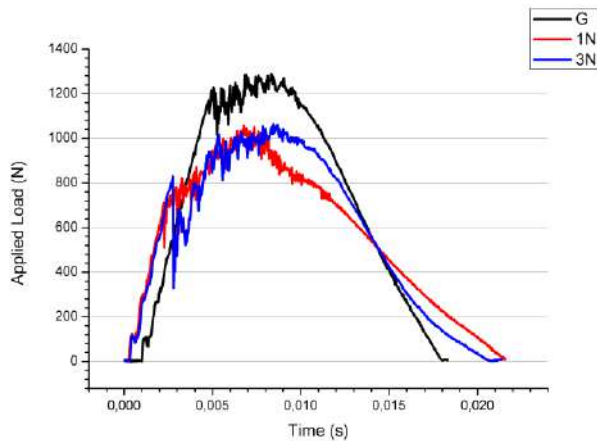


Fig. 5. Load-Time graphs of the specimens

Fig. 6 shows the load-deflection curves for different specimens. In Fig. 6 it can be observed that the specimens showed tendency to create closed curves which are typical of the load-deflection graphs. Due to the failures (delaminations, penetrations, fiber detachments etc.), the curves weren't fully closed.

It is seen in this figure that delamination take place when contact force reaches to 650-720 N. After that point, a clear decrease in bending stiffness is observed. It is clear that when delamination takes place, the bending stiffness considerable decreases. The virgin specimens do not show a damage formation until contact force reaches about 1200 N. After that point delamination takes plate. So, it can be concluded that nylon nano mats has clearly resulted in decrease of delamination threshold.

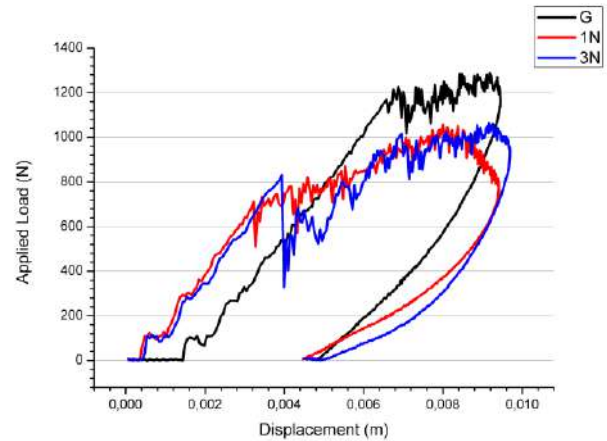


Fig. 6. Load-Displacement graphs of the specimens

Fig. 7 shows the variation of energy during contact. It is clearly seen that specimens with nylon 6,6 nano fiber mats absorb much more energy than virgin specimens. It is seen in this figure that all specimens started to consume the kinetic energy of impactor until it is fully consumed at 6,3 Joules. After that rebound period has started. It is clear that rebound energy for virgin specimen is considerably high that that for modified specimens.

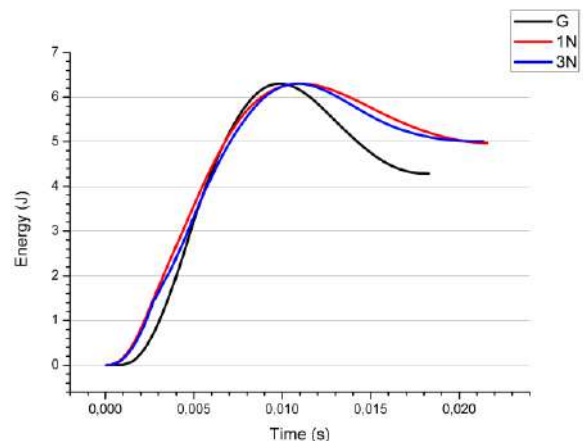


Fig. 7. Energy-Time graphs of the specimens

Table I shows the total energy distributions for the specimens. 1N and 3N specimens perform pretty similar in their

energy absorption capabilities. While the absorbed energy of the G specimens was about 68% the total energy, 1N and 3N ones managed to absorb almost 80% of the total energy which correspond to an enhancement about 12% with respect to virgin specimens.

TABLE I. ENERGY DISTRIBUTIONS ON THE SPECIMENS

Specimen Codenames	G	1N	3N
Total absorbed energy (J)	4,29	4,972	5,009
Total rebound energy (J)	2,009	1,327	1,29
Total Energy (J)	6,3	6,3	6,3
Total absorbed energy (%)	68,10	78,92	79,51
Total rebound energy (%)	31,89	21,06	20,48
Total Energy (%)	100,0	100,0	100,0

XVIII. CONCLUSION

In this work, three kind of laminated composite specimen configurations were considered. The first one was the virgin configuration where only two glass fiber layers placed into epoxy. The other two was about nanofiber mat modified configurations where one nylon 6,6 nanofiber mat was interleaved in two glass fiber layers then placed into epoxy for one configuration and three nylon 6,6 nanofiber mats were interleaved in two glass fiber layers then placed into epoxy for the other one to generate laminated composite specimens. The specimens were manufactured with the hand lay-up method and the relationships between them were investigated by putting them through the Low Velocity Impact tests. The results are as follows:

- It has been observed that adding nylon 6,6 nanofiber mats into the specimens caused premature delamination and a decrease in the load capacity.
- There wasn't a significant difference between one and three nylon 6,6 interleaved nanofiber mats in regard to their influence on the load and absorbed energy capabilities and the damage resistance.
- Still specimens with nylon 6,6 interleaved nanofiber mats absorbed more energy than the virgin specimens; absorbing about 12% energy than their corresponding virgin specimens.

REFERENCES

- [14] O. Hag-Elsafi, S. Alampalli, and J. Kunin, "Application of FRP laminates for strengthening of a reinforced concrete T-beam bridge structure," *Compos. Struct.*, vol. 52, no. 3-4, pp. 453-466, 2001.
- [15] L. Eimde, H. F. Naguib, and R. Elsayed, "Use of FRP composites in civil structural applications," *Constr. Build. Mater.*, vol. 17, no. 6-7, pp. 389-403, 2003.
- [16] L. C. Hollaway, "A review of the present and future utilisation of FRP composites in the civil infrastructure with reference to their important in-service properties," *Constr. Build. Mater.*, vol. 24, no. 12, pp. 2419-2445, 2010.S
- [17] S. N. A. Safri, M. T. H. Sultan, N. Yidris, and F. Mustapha, "Low Velocity and High Velocity Impact Test on Composite Materials – A review," *Int. J. Eng. Sci.*, pp. 50-60, 2014.S
- [18] M. Hojo, S. Matsuda, M. Tanaka, S. Ochiai, and A. Murakami, "Mode I delamination fatigue properties of interlayer-toughened CF/epoxy laminates," *Compos. Sci. Technol.*, vol. 66, no. 5, pp. 665-675, 2006.S
- [19] I. K. Partridge and D. D. R. Cartié, "Delamination resistant laminates by Z-Fiber® pinning: Part I manufacture and fracture performance," *Compos. Part A Appl. Sci. Manuf.*, vol. 36, no. 1, pp. 55-64, 2005.S
- [20] E. Fuoss, P. V. Straznicki, and C. Poon, "Effects of stacking sequence on the impact resistance in composite laminates. Part 1: parametric study," *Compos. Struct.*, vol. 41, no. 1, pp. 67-77, 1998.S
- [21] T. Yang, C. H. Wang, J. Zhang, S. He, and A. P. Mouritz, "Toughening and self-healing of epoxy matrix laminates using mendable polymer stitching," *Compos. Sci. Technol.*, vol. 72, no. 12, pp. 1396-1401, 2012.
- [22] G. Tang, Y. Yan, X. Chen, J. Zhang, B. Xu, and Z. Feng, "Dynamic damage and fracture mechanism of three-dimensional braided carbon fiber/epoxy resin composites," *Mater. Des.*, vol. 22, pp. 21-25, 2001.
- [23] C. Marieta, E. Schulz, L. Irusta, N. Gabilondo, A. Tercjak, and I. Mondragon, "Evaluation of fiber surface treatment and toughening of thermoset matrix on the interfacial behaviour of carbon fiber-reinforced cyanate matrix composites," *Compos. Sci. Technol.*, vol. 65, no. 14, pp. 2189-2197, 2005.
- [24] A. Zucchelli, M. L. Focarete, C. Gualandi, and S. Ramakrishna, "Electrospun nanofibers for enhancing structural performance of composite materials," *Polym. Adv. Technol.*, vol. 22, no. 3, pp. 339-349, 2011.
- [25] H. Saghaei, R. Palazzetti, A. Zucchelli, and G. Minak, "Influence of electrospun nanofibers on the interlaminar properties of unidirectional epoxy resin/glass fiber composite laminates," *J. Reinf. Plast. Compos.*, vol. 34, no. 11, pp. 907-914, 2015.
- [26] P. Akangah, S. Lingaiah, and K. Shivakumar, "Effect of Nylon-66 nanofiber interleaving on impact damage resistance of epoxy/carbon fiber composite laminates," *Compos. Struct.*, vol. 92, no. 6, pp. 1432-1439, 2010.
- [27] H. Saghaei, A. Zucchelli, R. Palazzetti, and G. Minak, "The effect of interleaved composite nanofibrous mats on delamination behavior of polymeric composite materials," *Compos. Struct.*, vol. 109, no. 1, pp. 41-47, 2014.
- [28] R. Palazzetti, "Flexural behavior of carbon and glass fiber composite laminates reinforced with Nylon 6,6 electrospun nanofibers," *J. Compos. Mater.*, vol. 49, no. 27, pp. 3407-3413, 2015.
- [29] S. Jiang, H. Hou, A. Greiner, and S. Agarwal, "Tough and Transparent Nylon-6 Electrospun Nano fiber Reinforced Melamine – Formaldehyde Composites," pp. 4-10, 2012.
- [30] N. Bhardwaj and S. C. Kundu, "Electrospinning: A fascinating fiber fabrication technique," *Biotechnol. Adv.*, vol. 28, no. 3, pp. 325-347, 2010.
- [31] C. J. Thompson, G. G. Chase, A. L. Yarin, and D. H. Reneker, "Effects of parameters on nanofiber diameter determined from electrospinning model," *Polymer (Guildf.)*, vol. 48, no. 23, pp. 6913-6922, 2007.
- [32] Z. M. Huang, Y. Z. Zhang, M. Kotaki, and S. Ramakrishna, "A review on polymer nanofibers by electrospinning and their applications in nanocomposites," *Compos. Sci. Technol.*, vol. 63, no. 15, pp. 2223-2253, 2003.
- [33] K. Behler, M. Havel, and Y. Gogotsi, "New solvent for polyamides and its application to the electrospinning of polyamides 11 and 12," *Polymer (Guildf.)*, vol. 48, no. 22, pp. 6617-6621, 2007.
- [34] M. Z. Elsayed, H. F. Naguib, and R. E. Morsi, "Chitosan based nanofibers, review," *Mater. Sci. Eng. C*, vol. 32, no. 7, pp. 1711-1726, 2012.

- [35] J. Zhang, T. Yang, T. Lin, and C. H. Wang, "Phase morphology of nanofibre interlayers: Critical factor for toughening carbon/epoxy composites," *Compos. Sci. Technol.*, vol. 72, no. 2, pp. 256–262, 2012.
- [36] H. Fong, W. Liu, C. S. Wang, and R. A. Vaia, "Generation of electrospun fibers of nylon 6 and nylon 6-montmorillonite nanocomposite," *Polymer (Guildf)*, vol. 43, no. 3, pp. 775–780, 2001.
- [37] F. Croisier et al., "Mechanical testing of electrospun PCL fibers," *Acta Biomater.*, vol. 8, no. 1, pp. 218–224, 2012.
- [38] C. Carrizales et al., "Thermal and mechanical properties of electrospun PMMA, PVC, Nylon 6, and Nylon 6,6," *Polym. Adv. Technol.*, vol. 19, no. 2, pp. 124–130, 2008.
- [39] Y. Li, Z. Huang, and Y. Lü, "Electrospinning of nylon-6,6,1010 terpolymer," *Eur. Polym. J.*, vol. 42, no. 7, pp. 1696–1704, 2006.
- [40] R. Palazzetti, A. Zucchelli, and I. Trendafilova, "The self-reinforcing effect of Nylon 6,6 nano-fibres on CFRP laminates subjected to low velocity impact," *Compos. Struct.*, vol. 106, pp. 661–671, 2013.
- [41] T. Skourlis, T. Duvis, and C. Papaspyrides, "The role of a polyamide interphase on carbon fibres reinforcing an epoxy matrix," *Compos. Sci. Technol.*, vol. 48, no. 1–4, pp. 119–125, 1993.
- [42] Y. Wang, J. Li, and D. Zhao, "Mechanical properties of fiber glass and Kevlar woven fabric reinforced composites," *Compos. Eng.*, vol. 5, no. 9, pp. 1159–1175, 1995.
- [43] L. M. Nunes, S. Paciornik, and J. R. M. d'Almeida, "Evaluation of the damaged area of glass-fiber-reinforced epoxy-matrix composite materials submitted to ballistic impacts," *Compos. Sci. Technol.*, vol. 64, no. 7–8, pp. 945–954, 2004.
- [44] B. Yang, V. Kozey, S. Adanur, and S. Kumar, "Bending, compression, and shear behavior of woven glass fiber-epoxy composites," *Compos. Part B Eng.*, vol. 31, no. 8, pp. 715–721, 2000.
- [45] Z. Aslan, R. Karakuzu, and B. Okutan, "The response of laminated composite plates under low-velocity impact loading," *Compos. Struct.*, vol. 59, no. 1, pp. 119–127, 2003.
- [46] S. N. A. Safri, M. T. H. Sultan, and F. Cardona, "Impact damage evaluation of Glass-Fiber Reinforced Polymer (GFRP) using the drop test rig - An experimental based approach," *ARPN J. Eng. Appl. Sci.*, vol. 10, no. 20, pp. 9916–9928, 2015.
- [47] G. Belingardi and R. Vadori, "Low velocity impact tests of laminate glass-fiber-epoxy matrix composite material plates," *Int. J. Impact Eng.*, vol. 27, no. 2, pp. 213–229, 2002.
- [48] L. Liu, Z. M. Huang, C. L. He, and X. J. Han, "Mechanical performance of laminated composites incorporated with nanofibrous membranes," *Mater. Sci. Eng. A*, vol. 435–436, pp. 309–317, 2006.
- [49] A. D. Kelkar, R. Mohan, R. Bolick, and S. Shendekar, "Effect of nanoparticles and nanofibers on Mode I fracture toughness of fiber glass reinforced polymeric matrix composites," *Mater. Sci. Eng. B Solid-State Mater. Adv. Technol.*, vol. 168, no. 1, pp. 85–89, 2010.
- [50] H. Zarei, T. Brugo, J. Belcari, H. Bisadi, G. Minak, and A. Zucchelli, "Low Velocity Impact Damage Assessment of GLARE Fiber-Metal Laminates Interleaved by Nylon 6,6 Nanofiber Mats," *Compos. Struct.*, vol. 167, pp. 123–131, 2017.
- [51] I. Papa, M. R. Ricciardi, V. Antonucci, V. Lopresto, and A. Langella, "Impact performance of GFRP laminates with modified epoxy resin," *Procedia Eng.*, vol. 167, pp. 160–167, 2016.
- [52] T. Brugo et al., "Study on Mode I fatigue behaviour of Nylon 6,6 nanoreinforced CFRP laminates," *Compos. Struct.*, vol. 164, pp. 51–57, 2016.
- [53] E. Stelldinger, A. Kühhorn, and M. Kober, "Experimental evaluation of the low-velocity impact damage resistance of CFRP tubes with integrated rubber layer," *Compos. Struct.*, vol. 139, pp. 30–35, 2016.
- [54] "Epoxy Systems / Lamination Epoxy, HEXION MGS L160 System," 2010, accessed 20.03.2017, <<http://www.dostkimya.com/en/product-browser/lamination-epoxy-hexion-mgs-l160-system/51>>
- [55] ASTM D7136, "Standard test method for measuring the damage resistance of a fibre-reinforced polymer matrix composite to a drop-weight impact event," 1. Annual book of ASTM standards; 2007.
- [56] "Nylon 6/6 pellets", 2017, accessed 20.03.2017 <<http://www.sigmaaldrich.com/catalog/product/aldrich/429171>>

Effect of Constant Magnetic Field to the Hydrogen Evolution Reactions Under Acidic Medium

Mehmet Fatih KAYA

Dept. of Energy Systems Engineering,
Erciyes University,
Kayseri, TURKEY

e-mail: kayamehmetfatih@erciyes.edu.tr

Nesrin KAYATAŞ DEMİR

Dept. of Energy Systems Engineering,
Erciyes University,
Kayseri, TURKEY

e-mail: nkayatas@erciyes.edu.tr

Abstract—Water electrolysis is an efficient method to produce hydrogen efficiently. It can be applied to a clean energy storage and conversion system for sustainability of energy production. Especially Proton Exchange Membrane (PEM) water electrolysis which has acidic media, commonly used to produce the big amount of hydrogen in the industry. However, in water electrolysis, there are some obstacles to overcome. Mass transport limitations and bubble coverage on the electrode surface are some examples of these problems. It is aimed that to increase electrolysis performance using the constant magnetic field. When magnetic field positioned with the electric field in a perpendicular direction velocity of the particles enhances remarkably. This effect can be called as “magnetohydrodynamic(MHD)”. In the literature, there are several applications of the MHD. Some of these are related to the observation of the fluids and metallic particles under magnetic field [1, 2]. Shail et.al. [3] investigated laminar two-phase flow using MHD effects. Another important application is in electrochemistry. MHD maintains in an electrochemical cell to the convective movement of the hydrogen and oxygen bubbles and other species from the electrode surface [4, 5] thanks to Lorentz Force. Effect of Lorentz force to the hydrogen production is investigated by many researchers. They generally about the observation of the mass transport effect to the water electrolysis. Matsushima et al. [6-8] investigated water electrolysis under a magnetic field to show how they affect the convection in several electrochemical cells. Lin et al. [4, 9] showed that magnetic field enhances the separation of bubbles to the electrode surface and decreasing the sticking of species to the electrode. Kaya et al. [10] used cost effective electrodes in alkaline solutions to show possibilities of the using lower concentration water electrolysis to produce economical hydrogen production. There is remarkable interest this issue to improve the electrolysis performance using different parameters. In this study, it is investigated that low concentration acidic solutions (0.5 M H₂SO₄) with the Pt anode and cathode electrodes under magnetic field. Two magnets are positioned to these Pt electrodes perpendicularly in the electrolyte solution to obtain upward direction Lorentz Force. Magnetic flux density of the magnets is nearly 0.8 T in this experiment. For the solution bath, acidic resistant Delrin® Polyoxymethylene (POM) material is used and it is specially designed to position magnets, solution and electrodes for water electrolysis. Neodymium magnets are used to produce constant magnetic field. Experiments are conducted using magnetic field and non-magnetic field condition. Electrode distance between anode and cathode is selected the same (25 mm) for both electrochemical cell. Hydrogen production is measured using gas accumulation tubes. In the experiment section; firstly, stability of the Pt electrodes are investigated in 4 V. Afterward, at the same voltage, current density of the cell is investigated with time in magnetic and the non-magnetic cells. During these experiments, 11% increase of current density is observed in magnetic cell. Approximately, 8% increase the rate of hydrogen production is investigated in the magnetic cell. It can be concluded that using Pt electrode and magnetic field; lower energy consumption to produce per mole of hydrogen can be possible during water electrolysis process. Thanks to the constant magnetic field it will be possible to study lower solution concentration and lower current density value. Results of this study can be apply to the other application of the electrochemistry.

Keywords—Water electrolysis; Magnetohydrodynamic(MHD); Lorentz Force.

The authors would like to thank the Scientific Research Projects Unit of Erciyes University(ERU-BAP) for funding and supporting the project under the contract no: FBA-2016-6704, FDK-2016-6705 and FYL-2017-7279. The first named author (M.F.K.) thanks to The Scientific and Technological Research Council of Turkey (TÜBİTAK) “Priority Areas PhD Scholarship Program (2211-C)” for their scholarship with the grant number: 1649B031501867.

REFERENCES

- [1] J. A. Shercliff, "Textbook of magnetohydrodynamics," 1965.
- [2] S. Chen, H. Chen, D. Martnez, and W. Matthaeus, "Lattice Boltzmann model for simulation of magnetohydrodynamics," *Physical Review Letters*, vol. 67, p. 3776, 1991.
- [3] R. Shail, "On laminar two-phase flows in magnetohydrodynamics," *International Journal of Engineering Science*, vol. 11, pp. 1103-1108, 1973.
- [4] M.-Y. Lin, L.-W. Hourng, and C.-W. Kuo, "The effect of magnetic force on hydrogen production efficiency in water electrolysis," *international journal of hydrogen energy*, vol. 37, pp. 1311-1320, 2012.
- [5] K. M. Grant, J. W. Hemmert, and H. S. White, "Magnetic field- controlled microfluidic transport," *Journal of the American Chemical Society*, vol. 124, pp. 462-467, 2002.

- [6] T. Iida, H. Matsushima, and Y. Fukunaka, "Water electrolysis under a magnetic field," *Journal of the electrochemical society*, vol. 154, pp. E112-E115, 2007.
- [7] H. Matsushima, T. Iida, and Y. Fukunaka, "Gas bubble evolution on transparent electrode during water electrolysis in a magnetic field," *Electrochimica Acta*, vol. 100, pp. 261-264, 2013.
- [8] H. Matsushima, T. Iida, and Y. Fukunaka, "Observation of bubble layer formed on hydrogen and oxygen gas-evolving electrode in a magnetic field," *Journal of Solid State Electrochemistry*, vol. 16, pp. 617-623, 2012.
- [9] M. Y. Lin and L. W. Hourng, "Effects of magnetic field and pulse potential on hydrogen production via water electrolysis," *International Journal of Energy Research*, vol. 38, pp. 106-116, 2014.
- [10] M. F. Kaya, N. Demir, M. S. Albawabiji, and M. Taş, "Investigation of alkaline water electrolysis performance for different cost effective electrodes under magnetic field," *International Journal of Hydrogen Energy*, 2017.tr

Numerical Modeling of Magnetohydrodynamic Effect of Lorentz Force to the Water Electrolysis Performance

NESRİN KAYATAŞ DEMİR

Dept. of Energy Systems Engineering,
Erciyes University,
Kayseri, TURKEY
e-mail: nkayatas@erciyes.edu.tr

Mehmet Fatih KAYA

Dept. of Energy Systems Engineering,
Erciyes University,
Kayseri, TURKEY
e-mail: kayamehmetfatih@erciyes.edu.tr

Abstract— Hydrogen energy systems are one of the best alternatives to overcome global warming effects from the environment. Because of their energy conversion by fuel cells, they attract researchers to improve this technology. There is a big interest to produce hydrogen and oxygen gasses efficiently in the electrolysis systems. However, there are some challenges to overcome in water electrolysis systems. Mass transport limitations and concentration losses decrease the cell voltage during hydrogen production. This affects the stability of gas outputs and the durability of the system. There is some field effect to overcome these problems. Supergravity field, ultrasonic field and magnetic field. These effects reduce the voltage drop, reaction overvoltage and transferring of bubbles through the electrolyte and electrode surface [1-4]. Under a magnetic field, it is possible to overcome gas bubble separation and convection problems. To provide this, a constant magnetic field should be positioned to the electrical field perpendicularly. This effect called as magnetohydrodynamic (MHD) due to Lorentz Force. It sustains convective movement of water electrolysis species through the electrolyte bath and electrodes. Gas bubbles sticking at the electrode surface and mass transport limitations are the challenging topic to produce hydrogen efficiently. Kaya et al. [5] investigated alkaline water electrolysis under magnetic field and they concluded that magnetic field decrease the sticking of gas bubbles on the electrode surface due to Lorentz Force and that causes the more current density and hydrogen production via time. In the literature, there is very much interest for magnetic field study in electrochemical applications [6-8]. In the experimental studies, it is hard to use bigger than 1 T magnetic flux density in constant magnets due to the working area. It is possible to make a numerical simulation for magnetohydrodynamics to observe different magnetic flux density effects to the water electrolysis. Moreover, numerical studies related with electrolysis are one of the important research tools to show species distribution in an electrochemical cell. But, there is very limited research about the numerical investigation of the MHD phenomena in electrochemistry. In this study, the magnetohydrodynamic effect to the water electrolysis numerically simulated using Comsol Multiphysics software. Firstly, solution bath and electrodes are modeled and electrochemical model is created using the Butler-Volmer equations. Fluid flow in the cell is selected laminar and transport of diluted species phenomena is used to model transport of species in the electrochemical cell. Current density change with different Lorentz force direction and velocity value change of species are studied.

Keywords— Lorentz Force; Magnetohydrodynamic (MHD); Numerical Modeling; Water Electrolysis.

The authors would like to thank the Scientific Research Projects Unit of Erciyes University (ERU-BAP) for funding and supporting the project under the contract no: FBA-2016-6704, FDK-2016-6705 and FYL-2017-7279. The second named author (M.F.K.) thanks to The Scientific and Technological Research Council of Turkey (TUBITAK) "Priority Areas PhD Scholarship Program (2211-C)" for their scholarship with the grant number: 1649B031501867.

REFERENCES

- [1] M. Wang, Z. Wang, and Z. Guo, "Water electrolysis enhanced by super gravity field for hydrogen production," *International Journal of Hydrogen Energy*, vol. 35, pp. 3198-3205, 2010.
- [2] H. Cheng, K. Scott, and C. Ramshaw, "Intensification of water electrolysis in a centrifugal field," *Journal of The Electrochemical Society*, vol. 149, pp. D172-D177, 2002.
- [3] C.-C. Wang and C.-Y. Chen, "Water electrolysis in the presence of an ultrasonic field," *Electrochimica Acta*, vol. 54, pp. 3877-3883, 2009.
- [4] H. Matsushima, T. Iida, and Y. Fukunaka, "Gas bubble evolution on the transparent electrode during water electrolysis in a magnetic field," *Electrochimica Acta*, vol. 100, pp. 261-264, 2013.
- [5] M. F. Kaya, N. Demir, M. S. Albawabji, and M. Taş, "Investigation of alkaline water electrolysis performance for different cost effective electrodes under magnetic field," *International Journal of Hydrogen Energy*, 2017.

- [6] D. Baczyzmalski, F. Karnbach, X. Yang, G. Mutschke, M. Uhlemann, K. Eckert, et al., "On the Electrolyte Convection around a Hydrogen Bubble Evolving at a Microelectrode under the Influence of a Magnetic Field," *Journal of The Electrochemical Society*, vol. 163, pp. E248-E257, 2016.
- [7] G. Hinds, J. Coey, and M. Lyons, "Influence of magnetic forces on electrochemical mass transport," *Electrochemistry Communications*, vol. 3, pp. 215-218, 2001.
- [8] T. Okada, N. I. Wakayama, L. Wang, H. Shingu, J.-i. Okano, and T. Ozawa, "The effect of magnetic field on the oxygen reduction reaction and its application in polymer electrolyte fuel cells," *Electrochimica Acta*, vol. 48, pp. 531-539, 2003.

Vibration Properties of Intraply Woven Carbon/Aramid Fiber Reinforced Composites with Nanoclay Particles

Ahmet ERKLİĞ

*Mechanical Engineering Department,
Gaziantep University, Engineering Department,
27310 Gaziantep, Turkey*

Mehmet BULUT

*Mechanical Engineering Department,
Gaziantep University, Engineering Department,
27310 Gaziantep, Turkey*

Nurettin Furkan DOĞAN

*Mechanical Engineering Department,
Gaziantep University, Engineering Department,
27310 Gaziantep, Turkey*

Abstract— Damping and vibration properties of Carbon/Kevlar/epoxy composite laminates were investigated incorporated nanoclay particles in the epoxy resin. Test samples were prepared woven intraply carbon/epoxy fabrics following by hand lay-up procedures. During the production process, different weight content of nanoclay fillers were included in the epoxy resin in the ratios of 0, 1, 2, 4, 6, 8 and 10 % by weight. Results showed that samples have shown the highest damping and vibration responses at the nanoclay ratios of 4% wt and 10 % wt, respectively.

Keywords—Vibration, damping, nanoclay, carbon, aramid

I. INTRODUCTION

In recent years, damping and vibration properties of the structures have become the important issue for fiber reinforced composites since structures of aerospace, automobile and ships may subject to dynamic loadings resulting to vibrate the system. Thus, it is needed to predict the vibration properties of the structures for safety of the structures during the service. Hybridization of fibers is one way of designing of structures as desired properties. For example, carbon fiber has high stiffness and strength properties as well as its brittle nature, and Kevlar fiber has good toughness and impact properties. It is possible to make a new material by hybridization of carbon and Kevlar to obtain good toughness and high strength properties. Several researchers [1-3] investigated the hybridization of different fibers influencing mechanical properties of composite laminates. Two different hybrid composites are existing in terms of weaving architectures, namely, interplay and intraply, respectively. Pegoretti et al. [4] indicated that intraply woven

composites exhibited greater mechanical and impact resistance as compared with interplay one.

One way of another method to increase mechanical properties of composites is inclusion of nanofiller in the epoxy resin. Kireitsey et al. [5] indicated that nanoscale carbon fibers significantly increase the structural damping and stiffness of the materials. Jiua et al. [6] showed that damping ratio of the nanocomposite beams may increase in 200–700% at higher frequencies. Chandradas et al. [7] examined that the vibration behavior in glass fabric/vinyl ester composites with different weight contents (0, 1, 3 and 5 wt%). The highest improvements in damping ratio was obtained with Nano-clay content of 3 wt%. Chowdary and Kumar [8] suggested that the inclusion of Nano-clay had a considerable effects on the mechanical behavior of composite materials, and highest improvement was obtained with 3 wt% addition of Nano clay.

In this study, the influence of nanoclay addition on damping and vibration properties of woven Kevlar/carbon/epoxy composite laminates. Natural frequency and damping properties of test samples were characterized dynamic modal analysis experimentally, and result were compared with each other.

II. MATERIALS AND METHODS

A. Production materials

The epoxy (MOMENTIVE-MGS L285), hardener (MOMENTIVE-MGS H285), twill intraply Kevlar/carbon woven fabrics (190 g/m²) were supplied from Dostkimya Company, Tuzla, Istanbul, Turkey. Montmorillonite (NM-

MMT) Nano clay was bought from Grafen Chemical Industries in Turkey.

Kevlar/carbon fabric has weight of 190 g/m², weave of 2/2 twill, width of 1000 - 1200 mm and thickness: 0.23 mm. Nano clay particles have lateral width of 0.5-2 μm , thickness of 1-10 nm and bulk density of 200-500 kg/m.

B. Production of test samples

The laminates were manufactured using hand layup technique with application the epoxy/nanoclay particle mixture on fibers. Samples were prepared 10 layers impregnating fabrics layer by layer. Then, they are subjected to (120 KPa) pressure for 1 h curing time at 80°C temperature, and cooled to room temperature under constant pressure for three hours. Production process and some of produced samples were illustrated in Figure 1.

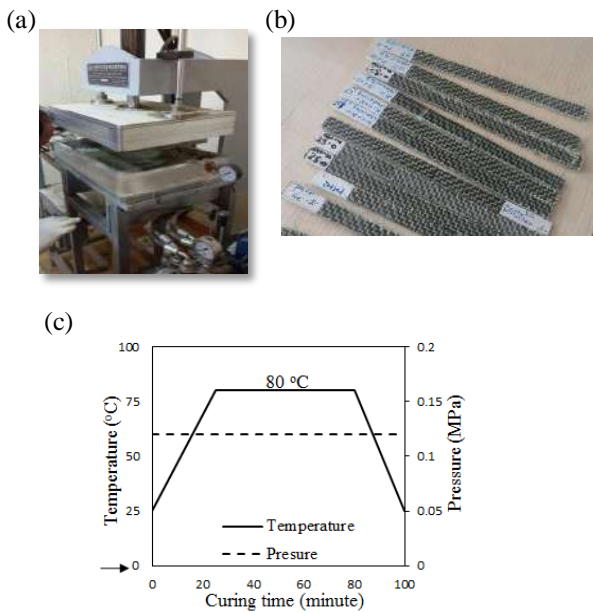


Fig. 1. Production process and test samples. (a) Hot-mold press, (b) Test samples for vibration tests, (c) Curing procedure

C. Vibration tests

Vibration and damping properties of Nano-clay modified CKFRE composite laminates were obtained utilizing test set-up according to ASTM E756 as shown in Figure 2. (Figure 3.12a). In the vibration testing, National Instrument product NI 9234 with LABVIEW software with a general aim PCB 352C03 ceramic shear ICP[®] accelerometer and a PCB 086C03 general purpose modal effect hammer were utilized for output signal acquisition, information acquisition and stimulus force signal, respectively.



Fig. 2. Experimental set-up for vibration tests

Half power bandwidth method was performed to evaluate damping responses of first natural frequency modes of the composite samples using equation 1. Figure 3 illustrates the schematic illustration of half-power method.

$$\xi = \frac{\omega_2 - \omega_1}{2\omega_n} \quad (1)$$

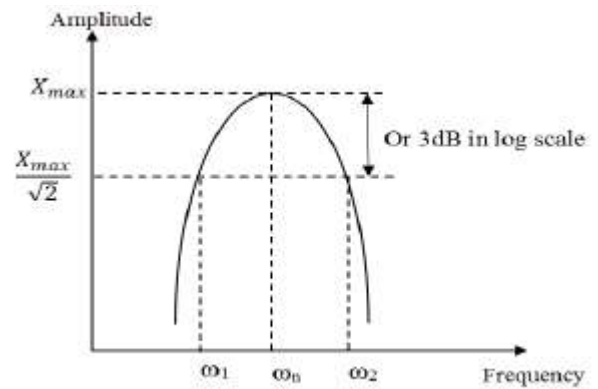


Fig. 3. Schematic illustration of half-power method

The loss modulus (E'') and storage modulus (E') are calculated from in equations (2) and (3).

$$\omega_1 = \frac{1.875^2}{2\pi L^2} \sqrt{\frac{E'I}{\rho A}} \quad (2)$$

$$E''(\omega) = 2E'(\omega)\xi(\omega) \quad (3)$$

Where ω_1 Is the natural frequency of the first mode, L is the free length of the beam, I is the moment of inertia for the given cross-section of the beam, ρ is the density of the beam and A is the cross-section of the beam.

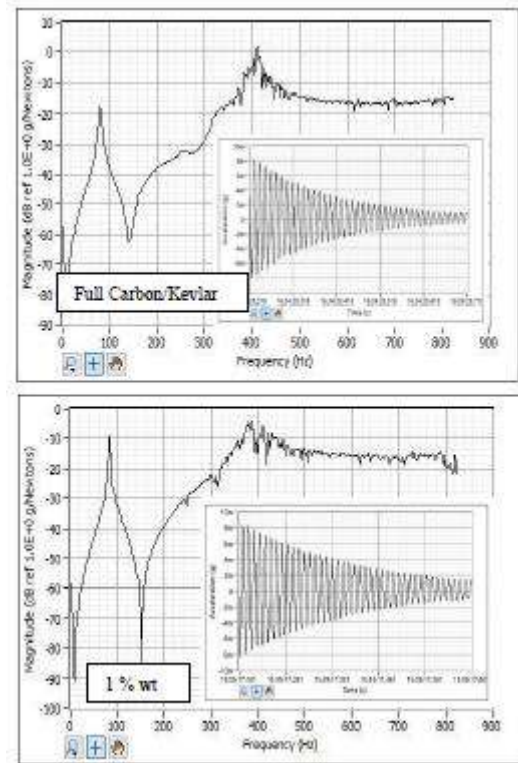
III. RESULTS AND DISCUSSIONS

The results for vibration properties of test samples were presented in Table 1, and their frequency response curves were illustrated in Figure 4. . It is noted here that first mode of natural frequency of the sample is dominantly seen for all Nano-clay particle loadings. The highest increment in maximum amplitude and natural frequency are obtained with 22.7 % at Nano-clay particle content of 10 % wt. The specimens having 1% wt of Nano-clay content exhibited the maximum storage modulus with enhancement of 24.5 %, while specimens with Nano-clay content of 4 wt% have the highest loss modulus with enhancement of 70.0 % compared to full composites composite. Stiffness and natural frequency are directly proportional to each other, suggesting that stiffness of the sample increased while increasing nanoclay content in the epoxy resin. However, further increasing in nanoclay content in epoxy resin resulted the reverse effect decreasing the damping ratio and loss/storage modulus. This may be explained the poor bonding between nanoclay-matrix-fibers interphases.

TABLE I.

TABLE 1. VIBRATION TEST RESULTS

NanoclayC ontent (wt%)	Natural Frequency (Hz)	Damping ratio,	Storage Modulus (GPa)	Loss modulus (GPa)
0	77.62	0.200	30.2	12.1
1	84.23	0.220	36.5	16.0
2	82.58	0.230	36.3	16.7
4	84.99	0.370	31.9	23.6
6	82.58	0.350	30.8	21.5
8	90.83	0.240	27.1	13.1
10	95.23	0.220	25.1	11.2



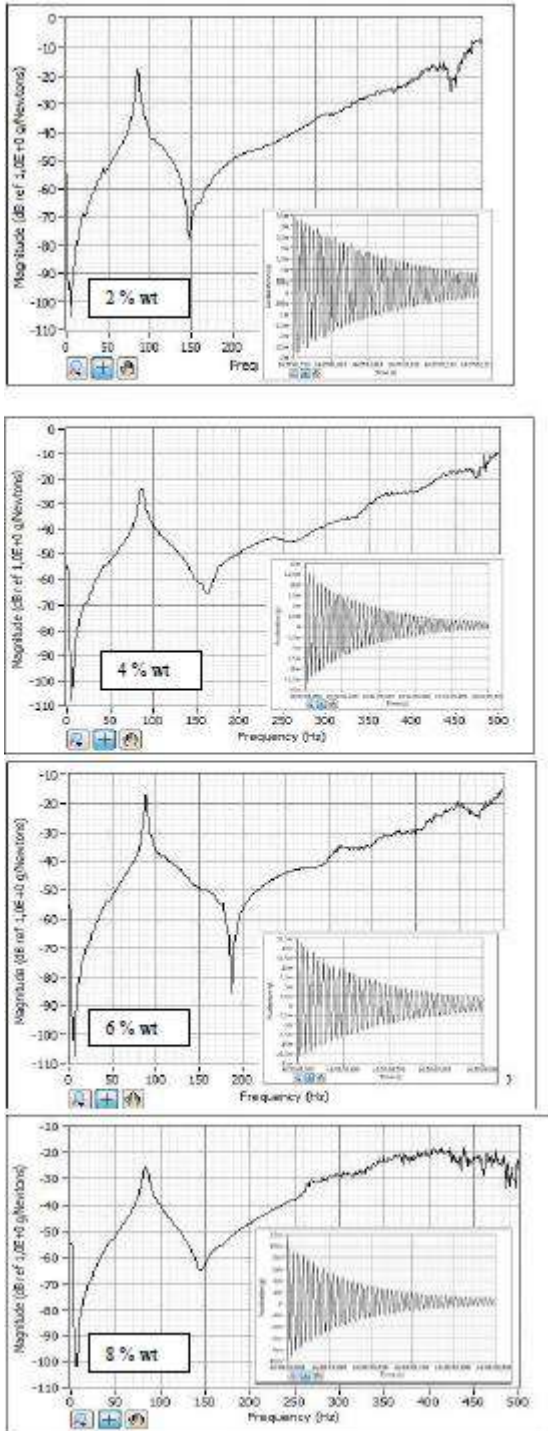


Fig. 4. Schematic illustration of half-power method

IV. CONCLUSION

Damping and vibration properties of woven kevlar/carbon/epoxy composite laminates were inspected incorporating nanoclay inclusion in the epoxy resin. It is shown that incorporation of Nano-clay particles were improved damping ratio for all Nano-clay contents and reached maximum at 4 weight% with increment of 72.0 % compared to unmodified full composites. In addition, natural frequency values were increased with increase of nanoclay content. The first mode frequency and natural frequency were maximum at the Nano-clay content of 10% wt.

REFERENCES

- [57] G. Marom, E. Drukker, A. Weinberg and J. Banbaji, "Impact behaviour of carbon/Kevlar hybrid composites", *Composites*, Vol. 17, pp. 150-153., 1986.
- [58] S.C Woo and T.W Kim, "High strain-rate failure in carbon/Kevlar hybrid woven composites via a novel SHPB-AE coupled test", *Composites Part B: Engineering*, Vol. 97, pp. 317-328, 2016.
- [59] M.T. Isa, A.S. Ahmed, B.O. Aderemi, R.M Taib and I. A Mohammed-Dabo, "Effect of fiber type and combinations on the mechanical, physical and thermal stability properties of polyester hybrid composites", *Composites Part B: Engineering*, Vol. 52, pp. 217-223, 2013.
- [60] P.A. Pegoretti, E. Fabbri and C. Migliaresi, "Intraply and interply hybrid composites based on E-glass and polyvinyl alcohol woven fabrics: tensile and impact properties", *Poly Int*, Vol. 53, pp. 1290-1297, 2004.
- [61] M. Kireitsey, D. Hui, and G. Tomlinson, "Advanced shock-resistant and vibration damping of nano particle-reinforced composite material", *Composite: Part B*, Vol. 39, pp. 128-138, 2008.
- [62] J. Gou, S. O'Briant, H. Gu, and G. Song, "Damping augmentation of nano composites using carbon nano fiber paper", *Journal of Nano Materials*, Vol. 2006, pp.1-7, 2006.
- [63] J. Chandradass, M. R. Kumar and R. Velmurugan, "Effect of clay dispersion on mechanical, thermal and vibration properties of glass fiber-reinforced vinyl ester composites", *Journal of Reinforced Plastics and Composites*, Vol. 27, pp. 1585-1601, 2008.
- [64] M.S. Chowdary and M.N. Kumar, "Effect of nano clay on the mechanical properties of polyester and S-glass fiber (AI)", *International Journal of Advanced Science and Technology*, Vol. 74, pp. 35-42, 2015.

Convective Heat Transfer of Nanofluids in Elliptic Channel with Different Aspect-Ratios

Selma Akcay*

Aksaray University
Institute of Science and Technology
Aksaray, Turkey
selma.352@hotmail.com

Unal Akdag

Aksaray University
Mechanical Engineering Department
Aksaray, Turkey
uakdag@gmail.com

Abstract— In present study, the convective heat transfer and friction factor with using nanofluids in an elliptic channel is investigated numerically in the three-dimensional steady laminar flow conditions. Numerical procedure is solved by SIMPLE algorithm. In the studies, the Reynolds (Re) number, the aspect ratio of elliptic channel (AR), nanoparticle types and volume fraction (ϕ) parameters are changed and the other parameters kept constant for all cases. The change of aspect ratio for elliptic channel effected slightly the heat transfer. Comparison of Nusselt (Nu) number for different nanofluids under the steady flow conditions is presented and numerical results showed that heat transfer significantly increases also due to improve thermal conductivity the use of nanoparticles. It is observed that the heat transfer enhances significantly with increase in nanoparticle concentration at high Reynolds number, but also friction factor increases. The highest thermal performance and friction factor are found for SiO_2 -water nanofluid compared with tested other nanofluids. The obtained results are given as a function of dimensionless parameters.

Keywords—elliptic channel; convection; nanofluids; skin friction; CFD

I. INTRODUCTION

Alternative ways have been investigated to enhance the thermal performance of devices such as refrigeration, compact heat exchangers and air-conditioning applications, one of the most important of these is the use of nanofluids instead of traditional working fluids. It is known that nanofluids have the potential to improve thermal performance. Many researchers have investigated on heat transfer and hydrodynamic characteristics of nanofluids and the results of this researches demonstrated that the nanofluids enhanced the heat transfer performance according to base fluid [1-3]. The single phase fluid model [4-7] and two phase fluid model [8-11] were studied to examine the flow and heat transfer characteristics of the nanofluids for different channel geometries. Beheshti *et al.* [12], investigated numerically turbulent convective heat transfer of Al_2O_3 -water and TiO_2 -water nanofluids inside an annular duct for single phase and two phase fluid models. Findings demonstrated that the Nu number enhanced with increase in nanoparticle concentration and Re number for both nanofluids. Narrein *et al.* [13], performed a numerical study to examine the effect of flow and heat transfer on pulsating laminar flow in a

three-dimensional helical microchannel using Al_2O_3 -water nanofluid for the two phase fluid model. Numerical simulations indicated that the thermal performance enhanced for the pulsating inlet flow condition compared with steady flow conditions and the Nu number increased with increasing the amplitude, frequency and particle volume fraction at high Re numbers.

It is well known that the pressure drop in the elliptical channels is less compared with other circular cross-section channels. Therefore, in the production of heat exchangers is preferred elliptical tubes. There are a lot of studies by using nanofluids for different aspect ratio of elliptic channel. It has been declared that using nanoparticles to the traditional base fluids can lead to heat transfer enhancement with together increase in pressure drop [14].

Rao *et al.* [15], numerically studied the convection heat transfer for laminar flow in short elliptical channels with uniform wall temperature and determined wall heat flux. The Nusselt number for constant wall heat flux was found than constant wall temperature. Velusamy *et al.* [16], numerically examined the heat transfer characteristics for laminar regime in channel of semi-elliptical cross section. They investigated both an isothermal and uniform heat flux conditions on the channel walls for different aspect ratio. Numerical results indicated that the friction and heat transfer coefficients for the uniform heat flux condition increased as the aspect ratio of channel decreased. Sivakumar *et al.* [17], examined numerically the flow characteristics of the two-dimensional steady flow of incompressible power-law fluids over an elliptical cylinder for the different Reynolds number ($0.01 \leq Re \leq 40$), power-law index ($0.2 \leq n \leq 1.8$) and the aspect ratio ($0.2 \leq E \leq 5$). The streamlines and vorticity profiles were obtained and the pressure distribution on the wall of the cylinder was obtained to explain flow kinematics. The results shown that the pressure drop coefficient always decreased with an increase in the power law index, at all events the value of Reynolds number, fluid behaviour, or shape of the cylinder.

Shariat *et al.* [18], investigated effects of the aspect ratio (AR) on the nanofluid flow in elliptic tube. Findings shown that in the elliptic tube with $AR = 0.75$ was obtained the highest heat transfer performance and the lowest friction factor. For this reason, they recommended the usage of the elliptic ducts with

$AR = 0.75$ instead of the circular ducts. Shariat *et al.* [14], in their other studies, researched the effects of volume concentration of nanofluid Al_2O_3 /water under laminar mixed convection flow in an elliptic channel with uniform heat flux for two phase fluid model using the finite volume method (FVM). It was declared that at the constant Reynolds number with increasing of nanoparticles volume fraction heat transfer improved but shear stress increased. Huminic and Huminic [19], effects of parameters such as particle volume fraction, Brownian motions of particles, and Re number on heat transfer coefficient were analyzed by using the flattened tube. Numerical simulations shown that the heat transfer performance enhanced with increase in the particle volume concentration and flattened tubes enhanced significantly the heat transfer coefficients compared to that of the circular and elliptic tubes for the same flow conditions. Dawood *et al.* [20], investigated for three dimensional laminar flow and heat transfer through for different nanofluids in an elliptic annulus channel with uniform heat flux using SIMPLE algorithm. At simulations were performed, four different types of nanofluids Al_2O_3 , CuO , SiO_2 and ZnO , with different nanoparticles size 20, 40, 60 and 80 nm and different volume fractions ranged from 0% to 4% for Re number in the range of 200 to 1000. The effects of particle type, volume fraction, particle diameter, Reynolds number and different base fluids on the Nu number and friction factor were analyzed. The findings indicated that SiO_2 -water nanofluid had the highest Nu number and the Nu number increased with increasing the particle volume fraction and Reynolds number.

In this study, the heat transfer performance and friction factor in an elliptic channel with uniform heat flux by using different types of nanofluids, different nanoparticle volume fractions, different Re numbers and different aspect ratios are analyzed. Differently from previous study [21], in present study the effects on convective heat transfer and friction factor for each aspect ratio of different Re numbers and nanofluids are investigated.

II. NUMERICAL STUDY

The geometry of elliptic channel used in this study is illustrated in Fig.1. The geometry is accepted minor axis of elliptic channel as b , major axis of elliptic channel as a . The length (L) and hydraulic diameter (D_h) of the elliptic channel are 1000 mm and 12 mm, respectively. The problem is considered three dimensional.

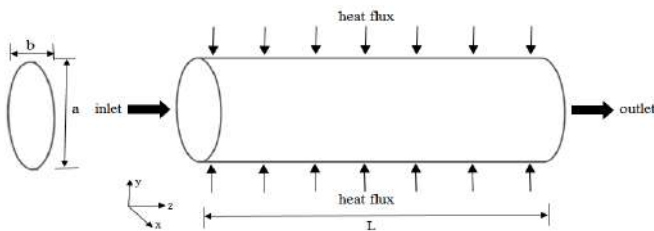


Fig.1. The geometry of the elliptic channel used in this study

A. Governing Equations

It can be assumed that the flow is fully developed, laminar, incompressible, three-dimensional and steady. Additionally, nanofluid is considered as a Newtonian fluid. The single phase flow is assumed. The mixture of water and nanoparticles is homogenous and enters the channel at the same flow and thermal conditions. Gravity and radiation heat transfer are negligible. Therefore the governing equations based on these assumptions are as follows: continuity, momentum and energy equations ($i, j \in \{1, 2, 3\}$):

$$\frac{\partial}{\partial x_i} (\rho u_i) = 0 \quad (1)$$

$$\frac{\partial}{\partial x_i} (\rho u_i u_j) = -\frac{\partial p}{\partial x_j} + \frac{\partial}{\partial x_i} \left(\mu \left(\frac{\partial u_j}{\partial x_i} \right) \right) \quad (2)$$

$$\frac{\partial}{\partial x_i} (\rho C_p u_i T) = \frac{\partial}{\partial x_i} \left(k \left(\frac{\partial T_i}{\partial x_i} \right) \right) \quad (3)$$

B. Numerical Solution and Grid Independence

For the solutions of present problem are used the CFD code Fluent 6.3 [22]. A finite volume method is applied for discretizing the governing equations and they are solved by using the SIMPLE algorithm. The convergence criterion for energy equation is determined to 10^{-8} , for each variable is determined to 10^{-6} . The different cell numbers are applied to the geometry and simulated by calculating the Nusselt number at $Re=700$. The number of cells varied as 845000, 1528000, 1864000 and 1528000 cell and it shown no much difference in the values of Nusselt number. Thus, the cell number of 1528000 is chosen in present study to grid independent solution. In Table 1. is given the numerical solution parameters.

TABLE II. THE NUMERICAL SOLUTION PARAMETERS

Nanofluid	Volume fraction: (ϕ %)	Reynolds Number: Re	Aspect Ratio: (b/a) AR
Al_2O_3 - water	1, 3, 5	100, 400, 700	0.25, 0.5, 0.75, 1
CuO -water	1, 3, 5	100, 400, 700	0.25, 0.5, 0.75, 1
TiO_2 -water	1, 3, 5	100, 400, 700	0.25, 0.5, 0.75, 1
SiO_2 -water	1, 3, 5	100, 400, 700	0.25, 0.5, 0.75, 1

The fluid enters to channel with uniform temperature $T_o=300K$. At the inlet of channel is given uniform "velocity inlet" boundary condition. The flow at the outlet of channel is accepted fully developed and is performed "outflow" boundary condition. The constant heat flux condition is applied for all walls of elliptic channel. The channel walls are kept at a uniform heat flux (q'') of $2000 W/m^2$. At the channel walls are used the usual no-slip boundary conditions. For these boundary conditions, Nusselt number and friction factor are calculated.

C. Physical Properties of the Nanofluids

In order to obtain reliable numerical results, the most proper correlations must choose available in the literature. These properties include thermal conductivity, viscosity, density and heat capacitance depending on what form the governing equations are written. By assuming the nanoparticles are well dispersed within the base fluid, the effective thermo-physical properties of the nanofluids can be evaluated using some classical appropriate formulas. The following equations are used in this study.

$$\rho_{nf} = (1-\phi)\rho_{bf} + \phi\rho_{pt} \quad (4)$$

$$C_{nf} = (1-\phi)C_{bf} + \phi C_{pt} \quad (5)$$

$$k_{nf} = \frac{k_{np} + 2k_{bf} - 2\phi(k_{bf} - 2k_{np})}{k_{np} + 2k_{bf} + 2\phi(k_{bf} - 2k_{np})} \quad (6)$$

$$\mu_{nf} = \mu_{bf}(1 + 1.25\phi) \quad (7)$$

Where the subscript pt and bf is indicates the nanoparticle and base fluids, respectively. In this study, the single phase fluid model is considered. Different equations applied in literature studies are tested especially to calculate thermal conductivity, viscosity and heat capacitance values from thermo-physical properties of the nanofluids. It was observed that there was not so much changed values of this thermo-physical properties. Further details about the thermo-physical properties of nanofluids are available in literature [12, 23-28].

III. RESULTS AND DISCUSSIONS

The this study is validated by comparing the results obtained for different aspect ratios with uniform heat flux in an elliptic channel with the numerical results of Shariat *et al.* [14]. In Fig. 2 is indicated accordance between the calculated Nusselt numbers.

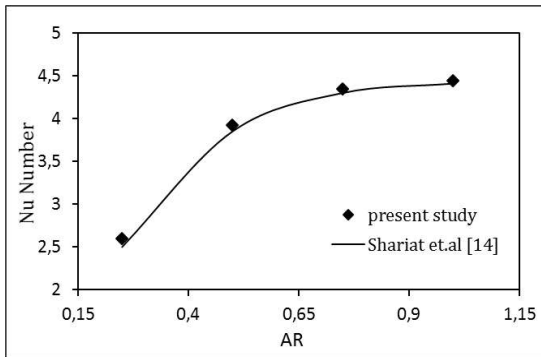


Fig. 2. Validation of present study with Ref. [14].

In present study, laminar forced convection of Al_2O_3 , CuO , TiO_2 and SiO_2 nanofluids with base fluid water in an elliptic channel under steady flow conditions is examined numerically. Nanoparticle type, nanoparticle volume fraction ($1 \leq \phi \leq 5$), aspect ratio of channel elliptic ($0.25 \leq AR \leq 1$) and the Reynolds number are changed. The Re number is considered as 100, 400 and 700.

The local and average Nu number is calculated from Eq. (8) and Eq. (9), respectively;

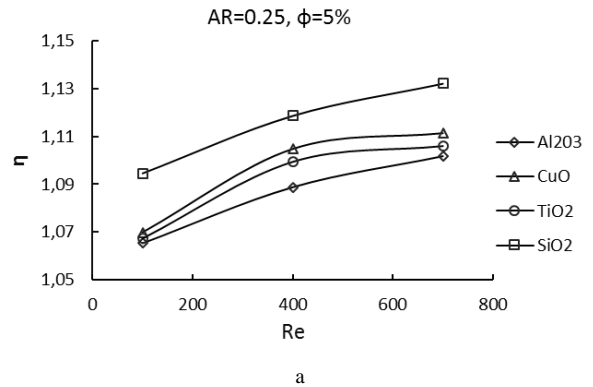
$$Nu_z = \frac{q'' D_h}{k(\bar{T}_{w,z} - \bar{T}_{b,z})} \quad (8)$$

$$Nu = \frac{1}{L} \int_0^L Nu_z dz \quad (9)$$

where, k is thermal conductivity of the nanofluid, D_h is hydraulic diameter, T_w is wall temperature of channel and T_b is bulk temperature of nanofluid. The effectiveness of the heat transfer is obtained by the heat transfer performance η , which is defined by Eq. (10).

$$\eta = \frac{Nu_n}{Nu_w} \quad (10)$$

Where Nu_n is Nu number calculated for each of nanofluids, Nu_w is Nu number calculated for base fluid (pure water).



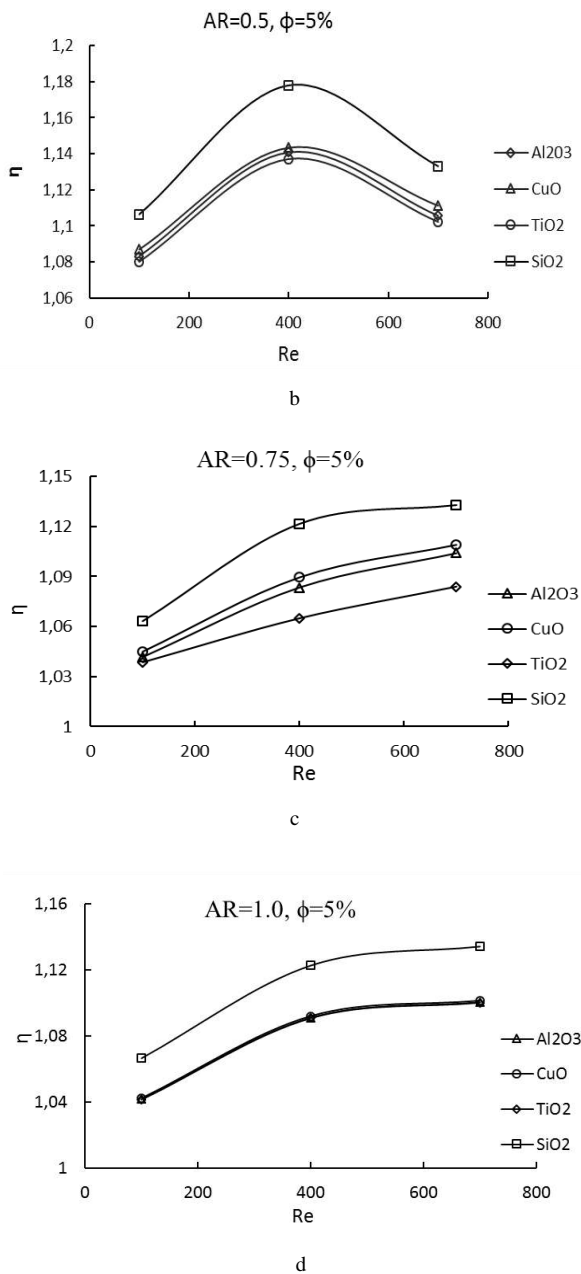


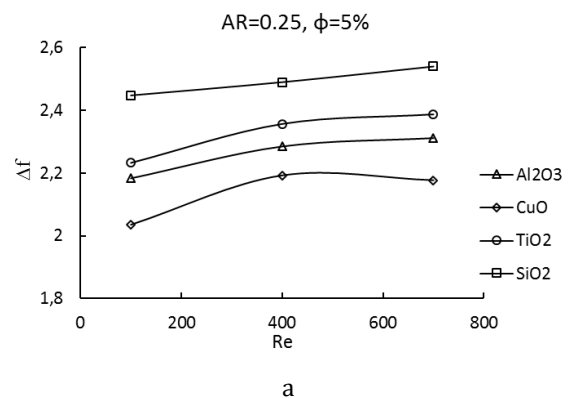
Fig.3 The heat transfer performance varying with Re number and nanoparticle type (a: $AR=0.25$, b: $AR=0.5$, c: $AR=0.75$, d: $AR=1$)

In Fig. 3, heat transfer performance versus Re number with varying nanoparticle type is presented for four different aspect ratio (AR) at fixed concentration ratio ($\phi=5\%$). It is observed that the heat transfer performance increases as Re number increases at $AR=0.25$, 0.75 and 1 for each of nanoparticle type, A peak occurs at a specific value of Re number for each of nanoparticle type at $AR=0.5$ and the maximum heat transfer enhancement is take place at $Re=400$. The heat transfer performance (η) decreases with increasing the Re number after

a specific value. At $AR=1$, the same heat transfer performance is obtained for other tested nanofluids at all Re number excluding SiO_2 -water nanofluid. The results revealed that SiO_2 -water nanofluid has the highest the heat transfer enhancement at $Re=700$, at $\phi=5\%$ for all aspect ratio compared with other nanofluids in the elliptic channel.

The results reveal that the heat transfer is significantly affected by nanofluid type and Reynolds number. There is an enhancement in heat transfer for all of tested nanofluids compared with only base fluid flow. Although there have been satisfactory results for heat transfer enhancement, the effects of shear stress (pressure drop) are an important subject in channel flow. The nanoparticle type and particle concentration contributes to a significant increase in the shear stress because of the interaction and collision among particles, fluid and the flow passage surfaces. The nanoparticles increases the viscosity of the suspension. This is due to the nanofluids have a higher viscosity value in comparison with base fluids. For the evaluation of pressure drop in present elliptic channel, the friction factor is defined as $\Delta f = f_n / f_w$. Where f_n is skin friction of nanofluid and the f_w is skin friction of pure water.

In Fig. 4, the friction factor versus Re number with varying nanoparticle type and aspect ratios is indicated for nanoparticle volume concentration of 5% . It is observed that the friction factor increases as Re number increases at $AR=0.25$, 0.75 and 1 for each of nanoparticle type. A peak occurs at a specific value of Re number for each of nanoparticle type at $AR=0.5$ and the maximum friction factor is take place at $Re=400$. The friction factor (Δf) decreases, with increasing the Re number after a specific value. Also, the friction factor increases as aspect ratio decreases at for each of nanoparticle type. The results revealed that SiO_2 -water nanofluid has the highest the friciton factor at $Re=700$, $AR=0.25$, for $\phi=5\%$ compared with other nanofluids in the elliptic channel.



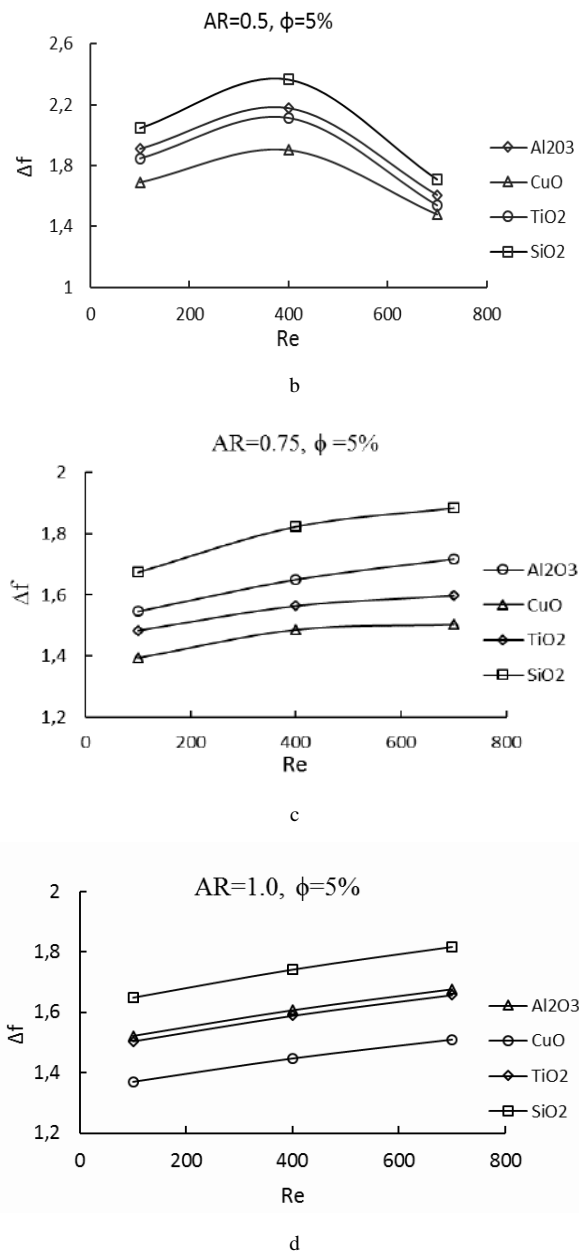


Fig.4 The friction factor varying with Re number and nanoparticle type ($AR=0.25$, b: $AR=0.5$, c: $AR=0.75$, d: $AR=1$)

SiO_2 -water nanofluid has the highest the heat transfer enhancement and friction factor compared with other nanofluids. Because SiO_2 has the lowest thermal conductivity among other nanofluids (but higher than base fluid) and has the highest average velocity due to its lowest density compared with the other nanofluids.

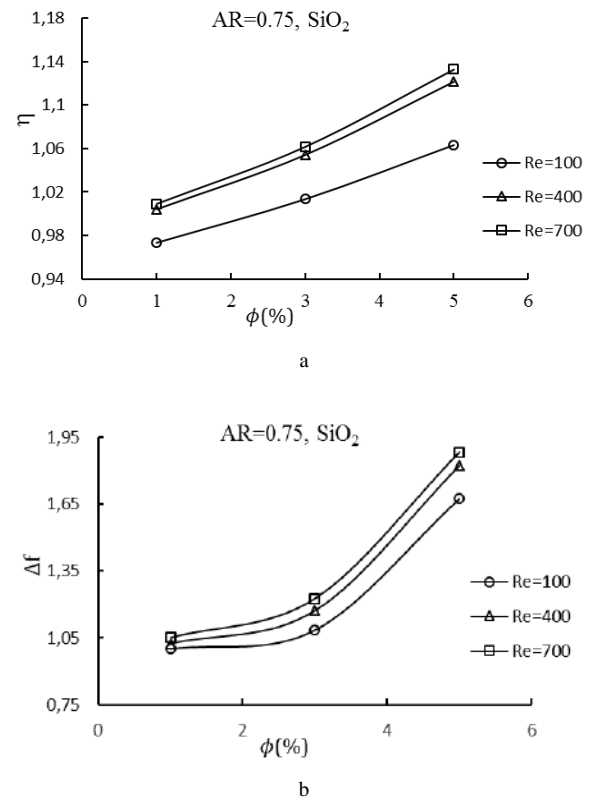


Fig.5 The heat transfer performance (a) and friction factor (b) varying with Re number and particle volume fractions of SiO_2 -water nanofluid at $AR=0.75$.

In Fig. 5a, the heat transfer performance and in Fig.5b, friction factor versus nanoparticle volume fracture with varying Re numbers are shown for SiO_2 - water nanofluid at $AR=0.75$. It is observed that the heat transfer performance and friction factor increased as Re number and nanoparticle volume fraction increases for SiO_2 - water nanofluid at $AR=0.75$.

IV. CONCLUSION

In this study, the heat transfer performance and friction factor of nanofluids in an elliptical channel have been studied numerically in the three-dimensional with uniform heat flux, steady under laminar flow conditions. The effects of aspect ratio, Re number and nanoparticle volume fraction using four different nanofluids of Al_2O_3 , CuO , TiO_2 and SiO_2 as base fluid water are analyzed. The numerical results indicated that the heat transfer performance increases significantly with increase in nanoparticle volume fraction and Re number but the other hand friction factor increases. The highest heat transfer performance and friction factor are obtained at SiO_2 -water nanofluid compared with other nanofluids. The heat transfer performance and friction factor are affected from varying aspect ratio. An elliptical channel having aspect ratio of 0.75 can be used to obtain maximum heat transfer enhancement and minimum friction factor.

REFERENCES

- [1] S.U.S. Choi, and J. A. Eastman "Enhancing Thermal Conductivity of Fluids with Nanoparticles", ASME International Mechanical Engineering Congress & Exposition, San Francisco, CA, November 12-17, 1995.
- [2] Y. Xuan, and Q. Li, "Investigation Convective Heat Transfer and Flow Features of Nanofluids", J. Heat Transfer, vol. 125, pp. 151-155, 2003.
- [3] H.U. Kang, S.H. Kim, and J.M. Oh, "Estimation of Thermal Conductivity of Nanofluid using Experimental Effective Particle Volume", Exp. Heat Transfer, vol. 19, pp. 181-191, 2006.
- [4] A. Akbarinia, "Impacts of Nanofluid Flow on Skin Friction Factor and Nusselt Number in Curved Tubes with Constant Mass Flow", Int. J. Heat Fluid Flow, vol. 29, pp. 229-241, 2008.
- [5] A.R. Sajadi, and M.H. Kazemi, "Investigation of Turbulent Convective Heat Transfer and Pressure Drop of TiO_2 /Water Nanofluid in Circular Tube", Int. Commun. Heat Mass Transfer, vol. 38, pp. 1474-1478, 2011.
- [6] U. Akdag, S. Akcay and D. Demiral, "Heat Transfer Enhancement With Laminar Pulsating Nanofluid Flow in a Wavy Channel", International Communications in Heat and Mass Transfer, vol. 59, pp. 17-23, 2014.
- [7] U. Akdag, S. Akcay and D. Demiral, "Numerical Investigation of Heat Transfer Enhancement with Nanofluids under Laminar Pulsating Flow in a Trapezoidal-Corrugated Channel", Int. Conference on Advances in Mechanical Engineering, (ICAME'15), Istanbul, Turkey, 13-15 May 2015.
- [8] O. Ghaffari, A. Behzadmehr, and H. Ajam, "Turbulent Mixed Convection of a Nanofluid in a Horizontal Curved Tube using a Two-Phase Approach", Int. Commun. Heat Mass Transfer, vol. 37, pp. 1551-1558, 2010.
- [9] M. Alinia, D.D. Ganji, and M. Gorji-Bandpy, "Numerical Study of Mixed Convection in an Inclined Two Sided Lid Driven Cavity Filled with Nanofluid using Two-Phase Mixture Model". Int. Commun. Heat Mass Transfer, vol. 38, pp. 1428-1435, 2011.
- [10] R. MokhtariMoghari, A. Akbarinia, M. Shariat, F. Talebi, and R. Laur, "Two Phase Mixed Convection Al_2O_3 -Water Nanofluid Flow in an Annulus", Int. J. Multiphase Flow, vol. 37, pp. 585-595, 2011.
- [11] A. Behzadmehr, M. Saffar-Avval, and N. Galanis, "Prediction of Turbulent Forced Convection of a Nanofluid in a Tube with Uniform Heat Flux Using a Two Phase Approach", Int. J. Heat Fluid Flow, vol. 28, pp. 211-219, 2007.
- [12] A. Beheshti, M.K. Moraveji., and M. Hejazian, "Comparative Numerical Study of Nanofluid Heat Transfer Through an Annular Channel", Numerical Heat Transfer, Part A, vol. 67, pp. 100-117, 2015.
- [13] K. Narrein, S. Sivasankaran, and P. Ganesan, "Numerical Investigation of Two-Phase Laminar Pulsating Nanofluid Flow in a Helical Microchannel", Numerical Heat Transfer, Part A, vol. 69, (8), pp. 921-930, 2016.
- [14] M. Shariat, R.M. Moghari, S.M. Sajjadi, and M. Khojamli, "Numerical Investigation of Al_2O_3 /Water Nanofluid in Horizontal Elliptic Ducts Using Two Phase Mixture Model", Journal of Computational and Theoretical Nanoscience, vol. 10, pp. 1-9, 2012.
- [15] S.S. Rao, N.C.P. Ramacharyulu, and V.V.G. Krishnamurty, "Laminar Forced Convection in Elliptic Ducts", [Applied Scientific Research](#), vol. 21, (1), pp. 185-193, January 1969.
- [16] K. Velusamy, V.K. Garg, and G. Vaidyanathan, "Fully Developed Flow and Heat Transfer in Semi-Elliptical Ducts", Int.Jour.Heat and Fluid Flow, vol. 16, pp. 145-152, 1995.
- [17] P. Sivakumar, R.B. Prakash, and R.P. Chhabra, "Steady Flow of Power-Law Fluids Across an Unconfined Elliptical Cylinder", Chemical Engineering Science, vol. 62, pp. 1682 - 1702, 2007.
- [18] M. Shariat, A. Akbarinia, A.H. Nezhad, A. Behzadmehr, and R. Laur, "Numerical Study of Two Phase Laminar Mixed Convection Nanofluid in Elliptic Ducts", Applied Thermal Engineering, vol. 31, pp. 2348-2359, 2011.
- [19] G. Huminic, and A. Huminic, "Numerical Analysis of Laminar Flow Heat Transfer of Nanofluids in a Flattened Tube", International Communications in Heat and Mass Transfer, vol.44, pp. 52-57, 2013.
- [20] H.K. Dawood, H.A. Mohammed, and K.M. Munisamy, "Heat Transfer Augmentation Using Nanofluids in an Elliptic Annulus with Constant Heat Flux Boundary Condition", Case Studies in Thermal Engineering,; vol. 4, pp. 32-41, 2014.
- [21] U.Akdag, and S. Akcay, "Heat Transfer Enhancement with Nanofluids in an Elliptic Channel under Laminar Flow", 8th International Energy Symposium and Exhibition, Afyonkarahisar, Turkey, June 12th 2016.
- [22] Fluent 6.3. FLUENT user's guide. Fluent, Inc., Lebanon, NH. 03766, USA, 2006.
- [23] B.C. Pak, and Y.I. Cho, "Hydrodynamic and Heat Transfer Study of Dispersed Fluids with Submicron Metallic Oxide Particles", Experimental Heat Transfer, vol. 11, (2), pp. 151-170, 1998.
- [24] H.C. Brinkman, "The Viscosity of Concentrated Suspensions and Solutions", J. Chem. Phys., vol. 20, pp. 571-581, 1952.
- [25] M. HaghshenasFard, M. Nasr Esfahany, and M.R. Talaie, "Numerical Study of Convective Heat Transfer of Nanofluids in a Circular Tube Two-Phase Model Versus Single-Phase Model", Int. Commun. Heat Mass Transfer, vol. 37, pp. 91-97, 2010.
- [26] M. Nasiri, S.Gh. Etemad, and R. Bagheri, "Experimental Heat Transfer of Nanofluid Through an Annular Duct", Int. Commun. Heat Mass Transfer, vol. 38, pp. 958-963, 2011.
- [27] A.A. Minea, "Effect of Microtube Length on Heat Transfer Enhancement of a Water/ Al_2O_3 Nanofluid at High Reynolds Numbers", Int. J. Heat Mass Transfer, vol. 6, pp. 22-30, 2013.
- [28] S. Kakac, and A. Pramuanjaroenkij, "Review of Convective Heat Transfer Enhancement with Nanofluids", Int. J. Heat Mass Transfer, vol. 52, pp. 3187-3196, 2009.

The Obtaining of Inonu University Electric Demand with Solar-Wind Renewable Energy Systems and Cost Analysis

Apdulmutalip SAHİNASLAN

Mechanical Engineering
Inonu University
Malatya/TURKEY
asahinaslan@inonu.edu.tr

Engin Eren KORKMAZ

Mechanical Engineering
Inonu University
Malatya/TURKEY
engin.korkmaz@inonu.edu.tr

Abstract— In this study it is investigated to find the ways to meet the electric demand (2966 kWh/day) of Inonu University with off-grid and on-grid optimum wind turbine and photovoltaic panel and to generate cost-effective electric energy. Homer software was used for simulations and four different energy system scenarios were carried out. Equipment consisting of energy system are wind turbine, PV panel, battery and converter. In the study annual energy production, annual energy consumption, costs of energy, total net cost of the systems designed were analyzed. It was seen that the costs of energy of off-grid wind and PV energy systems exceeded grid power price and total net costs were quite high according to the simulations results. The cost of energy of on-grid wind energy system was lower than grid power price and cost values of this system were negative sign meaning that incomes were more than expenses. It was also seen that cost values increased when wind turbine number and photovoltaic panel capacity decreased and battery number and converter capacity increased.

Keywords—Solar energy; wind energy; homer software; energy simulation; cost analysis

I. INTRODUCTION

Nowadays, energy has been considerably affecting people's life, health and welfare and hence the economic independence of the countries and their welfares. At present the world's energy demand is essentially and largely met by the fossil fuel which causes critical environmental pollution concerns [1]. Utilization of fossil fuels for energy systems causes many problems including air pollution and global warming. Moreover, this trend has been reinforced since the oil crises in 1970s [2, 3]. These problems can be overcome by using renewable energy sources like solar, wind, and biomass. These energy sources also exist relatively in a broad range contrary to conventional fuels limited in comparison with renewable energy sources. In literature there are many studies about renewable energy and cost analysis by using Homer program. Some examples are presented below.

Prasetyaningsari and his colleagues designed a solar-powered ventilation system for a fish pond in Sleman regency

via HOMER program. They modeled a system and endeavoured to obtain daily 2 kWh load with hybrid energy system. They also indicated that the optimal system which could be implemented according to the optimization result had consisted of 1 kW PV panel, 8 batteries with 200 Ah and 0.2 kW inverter. Initial investment cost and cost of energy of hybrid energy system were calculated respectively 4960 \$ and 0.769 \$ [4]. Shaahid and his colleagues analyzed wind speed and solar radiation data of Rafha, KSA, and assessed the technical and economic potential of hybrid wind-PV-diesel power systems to meet the load requirements of a typical remote village Rawdhat Bin Hab-bas (RBH) with annual electrical energy demand of 15,943 MWh, using HOMER software [5].

II. HOMER SOFTWARE AND ELECTRIC LOAD

A. What is Homer?

HOMER (Hybrid Optimization Model for Electric Renewable), is computer software developed by U.S. National Renewable Energy Laboratory to compare all technologies helping energy generation in a wide range and back up for micro energy system designs. The micro power optimization model, simplifies the task of evaluating designs of both off-grid and grid-connected power systems for a variety of applications. The large number of technology options and the variation in technology costs and availability of energy resources make these decisions difficult. HOMER's optimization and sensitivity analysis algorithms make it easier to evaluate the many possible system configurations. The users can design many energy systems with photovoltaic panels, wind turbines, boilers, hydro, electrolyzers, flywheels, batteries, invertors via Homer program by adding thermal load or electrical load. There can be seen Homer methodology in fig. 1.

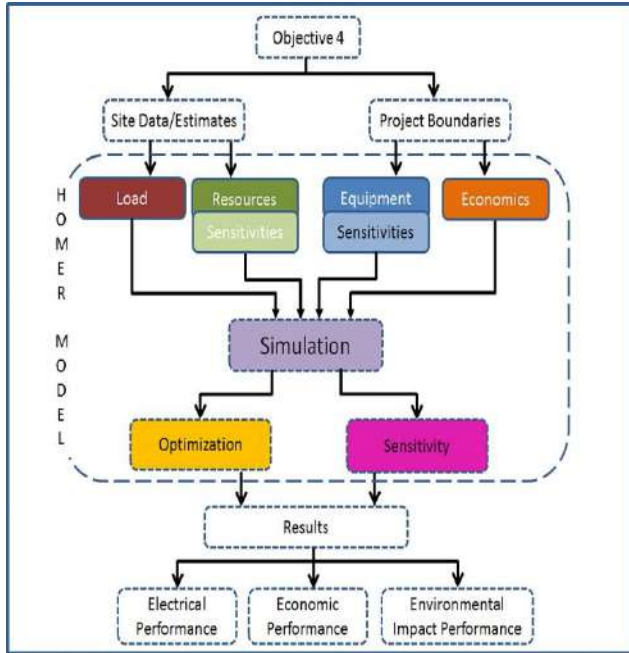


Figure 1. Schematics of HOMER Methodology [6]

B. Electric Load

The monthly electricity consumption amount of Inonu University is 890000 kWh. Electric load which will be supplied is %10. It corresponds to monthly 89000 kWh. Load data was transferred to program as daily 2966 kWh. Day to day and step to step randomness variable are respectively %10 and %15. The daily load profile was given in fig. 2.

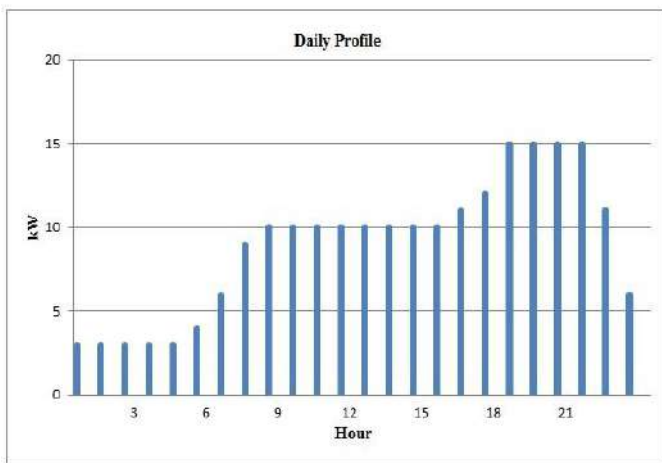


Figure 2. The daily load profile

III. ENERGY RESOURCES

A. Solar Energy Resource

Malatya has quite high solar energy potential. But Inonu University average solar energy level is low. This value extracted from Homer database is approximately 4.83

kWh/m²/day. Malatya global solar radiation and average solar radiation data for Inonu University can be seen respectively in fig. 3 and in table 1.

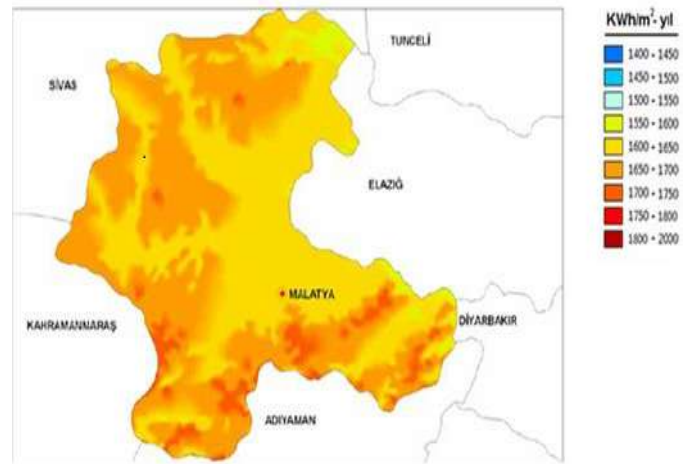


Figure 3. Malatya global solar radiation [7]

TABLE 1. Inonu University average solar radiation data

Months	Clearness Index	Daily Radiation (kWh/m ² /day)
January	0,455	2,060
February	0,490	2,907
March	0,545	4,302
April	0,542	5,307
May	0,580	6,433
June	0,665	7,706
July	0,701	7,899
August	0,701	7,115
September	0,712	5,980
October	0,594	3,796
November	0,530	2,534
December	0,461	1,887

B. Wind Energy and Temperature Resources

Wind energy is a necessary energy resource to specify wind speeds affecting wind turbines all the year round. Inonu University average wind speed extracted from Homer database like solar energy resource is 3.89 m/s. Altitude above sea level is 998 m in program. Anemometer height was chosen 50 m. Weibull K factor, autocorrelation factors, diurnal pattern strength, hour of peak wind speed were used respectively as 1.8, 0.86, 0.2, 15 h. Average wind speed data and temperature values for Inonu University can be seen in table 2. Temperature values of region were taken from Malatya regional directorate of

meteorology. Annual average temperature was specified as 15.93 °C.

TABLE 2. Inonu University average wind speed and temperature

Months	Average Wind Speed (m/s)	Temperature Values (°C)
January	4,070	4,1
February	4,110	4,9
March	3,620	10,4
April	3,550	15,4
May	3,460	19,6
June	3,740	23,9
July	4,220	30,3
August	4,320	30,8
September	4,180	22,7
October	3,620	15,3
November	3,790	7,3
December	3,960	6,4

IV. USED EQUIPMENT

A. Photovoltaic Panel

The PV window allows you to enter the cost, performance characteristics and orientation of an array of photovoltaic (PV) panels as well as choose the sizes you want HOMER to consider as it searches for the optimal system. Both flat panel and concentrating PV technologies can be represented by the PV component. Photovoltaic cells are semiconducting materials used to turn into electricity the sunbeams. Many solar cells generate DC power generally. In this study, the output current was taken DC and powersolar 250 Wp photovoltaic module consisting of monocrystalline silicium technology was used. In table 3, technical specifications of photovoltaic module were given. In the study temperature influence on photovoltaic panels was taken into account. In equation (1) the output power of photovoltaic array was given.

Table 3. Powersolar 250 Wp technical specifications [8]

Rated power	250 W
Open circuit voltage (V_{oc})	59,8 V
Rated power voltage (V_{pm})	48,6 V
Short-circuit current (I_{sc})	5,38 A
Maximum electric current (I_{pm})	5,15 A
Module efficiency	14,7 %
Nominal cell operating temp.	46 °C
Power temperature coefficient	-0,45%/°C
Capital cost	6.500 \$/kW
Replacement cost	6.500 \$/kW
Operating and maintenance cost	65 \$/year
Lifetime	25 year
Lowest and highest kW capacity	100 - 5000

$$P_{PV} = f_{PV} Y_{PV} \left(\frac{I_T}{I_S} \right) [1 + \alpha_P (T_c - T_{c,STC})] \quad (1)$$

where Y_{PV} is the rated capacity of the PV array, meaning its power output under standard test condition (STC); f_{PV} is the PV derating factor; I_T is the solar radiation incident on the PV array; I_S is the incident radiation at STC; α_P is the temperature coefficient of power; T_c is the PV cell temperature and $T_{c,STC}$ is the PV cell temperature under STC.

B. Wind Turbine

The wind turbine window allows you to choose the type of wind turbine you want to model, specify its costs, and tell HOMER how many to consider as it searches for the optimal system. A specified power curve that is a graphic belonging to the output power involving the wind speed in hub height is based and wind turbines are created in Homer. Homer assumes that this power curve is performed in standard air density (1,225 kg/m³) including standard temperature and pressure conditions. In this study E33 wind turbine model pertaining Enercon firm was used. Wind speeds and output powers were taken from firm catalog and power curve was constituted. In table 4, technical specifications of E33 wind turbine were given.

Table 4. E33 wind turbine technical specifications [9]

Rated power	330 kW
Rotor diameter	33,4 m
Hub height	50 m
Number of blades	3
Blade sweep area	876 m ²
Cut-in speed	3 m/s
Cut-out speed	25 m/s
Rotational speed	Variable 18-45 d/d
Capital cost	3.500 \$/number
Replacement cost	2.800 \$/number
Operating and maintenance cost	95 \$/year
Lifetime	25 year
Lowest and highest wind turbine number	1 - 15

C. Battery

Batteries store electric generated and back up the system when necessary. Homer assumes that battery properties are stable throughout batteries lifetime and don't be affected from external effects. In this study Surrette 6CS25P batteries which have 1186 Ah capacity with 6 V were used. One battery capital cost, replacement cost and operating and maintenance cost are respectively 1100 \$, 1000 \$, 10 \$/year [10]. While battery number data for off-grid systems were entered 0, 640, 1280, 2560, 5120, 10240 in search space, data for on-grid systems were entered 0, 80, 160, 320, 640, 1280, 2560 and 5120.

D. Converter

While an inverter converts DC electricity to AC electricity, a rectifier converts AC electricity to DC electricity. These two parameters are examined under converter section in Homer

software. Converter capital cost, replacement cost and operating and maintenance cost are respectively 900 \$/kW, 900 \$/kW, 0 \$/year [10]. While converter capacity for off-grid systems were entered 0 kW and 6000 kW, capacity for on-grid systems were entered 0 kW and 5000 kW.

turbine number, photovoltaic panel capacity, battery number and converter size as a result of simulations. Grid power price and grid sellback price were taken into account respectively 0.17 \$/kWh and 0.089 \$/kWh [11]. Costs of energy were evaluated in comparison with these prices.

a. Wind Energy System

In this scenario the electric load of Inonu University was obtained from off-grid wind energy system and system model was given in fig. 4. The system was consisted of wind turbine, battery and converter.

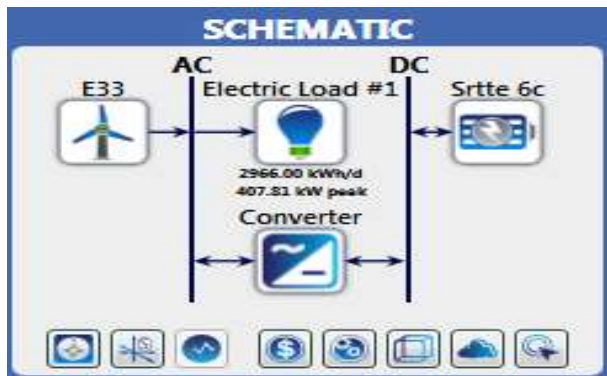


Figure 4. Off-grid wind energy system

Optimum wind energy system consisted of 15 wind turbines, 5120 batteries and 400 kW converters. Total net cost (NPC) and cost of energy (COE) were respectively 11.014.623 \$ and 0.913 \$/kWh according to simulation results. While electric consumption value was 1.082.593 kWh/year, electric generate value was 3.623.266 kWh/year. So, excess electricity meaning surplus electric energy was %63.3. When 7 wind turbines, 20480 batteries and 2000 kW converters were used instead of optimum system, electric generate value was 1.690.859 kWh/year. Therefore, much more batteries stored more energy and excess electricity was %17.3. But, when battery number and converter capacity increase, the costs augment depending parameters.

b. Photovoltaic Energy System

In this scenario the electric load of Inonu University was obtained from off-grid photovoltaic energy system and system model was given in fig. 5. The system was consisted of photovoltaic panel, battery and converter.

V. SCENARIO RESULTS

A. Off-grid Scenarios

In these scenarios two energy systems (wind and photovoltaic) were analyzed. Energy systems were investigated according to the optimum total net cost, cost of energy, wind

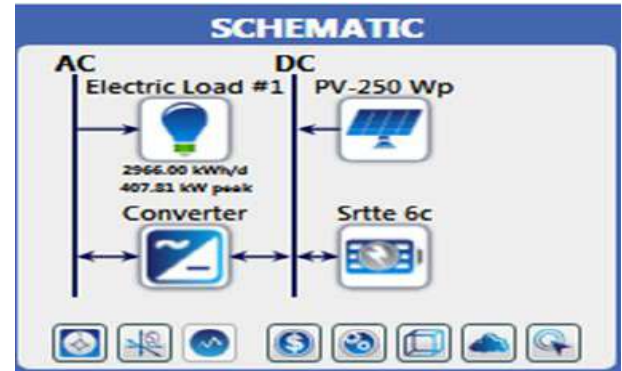


Figure 5. Off-grid photovoltaic energy system

Optimum photovoltaic energy system consisted of 1446 kW photovoltaic panel, 5120 batteries and 400 kW converters. Total net cost (NPC) and cost of energy (COE) were respectively 24.719.907 \$ and 2.05 \$/kWh according to simulation results. While electric consumption value was 1.082.593 kWh/year, electric generate value was 2.196.378 kWh/year. So, excess electricity meaning surplus electric energy was %38.9. When 945 kW photovoltaic panel, 20480 batteries and 400 kW converters were used instead of optimum system, electric generate value was 1.465.308 kWh/year. Therefore, much more batteries stored more energy and excess electricity was %12.8. But, likewise wind energy system when battery number and converter capacity increase, the costs augment depending parameters.

B. On-grid Scenarios

In these scenarios two energy systems (wind and photovoltaic) were analyzed. Energy systems were investigated according to the optimum total net cost, cost of energy, wind turbine number, photovoltaic panel capacity, battery number and converter size as a result of simulations. Grid power price and grid sellback price were taken into account respectively 0.17 \$/kWh and 0.089 \$/kWh [11]. Costs of energy were evaluated in comparison with these prices. While grid sale capacity was entered to the program as 10.000 kW, annual purchase capacity was entered as 0 kW and 1000 kW.

a. Wind Energy System

In this scenario the electric load of Inonu University was obtained from on-grid wind energy system and system model was given in fig. 6. The system was consisted of wind turbine, grid, battery and converter.

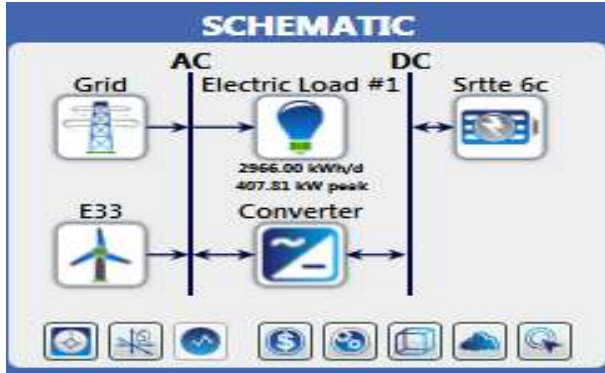


Figure 6. On-grid wind energy system

Optimum wind energy system consisted of 15 wind turbines and 1000 kW electric grid. Total net cost (NPC) and cost of energy (COE) were respectively -2.192.215 \$ and -0.0478\$/kWh according to simulation results. Negative sign means that revenues are more than expenses. While electric consumption value was 1.082.593 kWh/year, electric generate value was 3.721.256 kWh/year and electric grid sale was 3.034.149 kWh/year. When battery and converter were added to the system, cost values increased.

b. Photovoltaic Energy System

In this scenario the electric load of Inönü University was obtained from on-grid photovoltaic energy system and system model was given in fig. 7. The system was consisted of photovoltaic panel, grid, battery and converter.

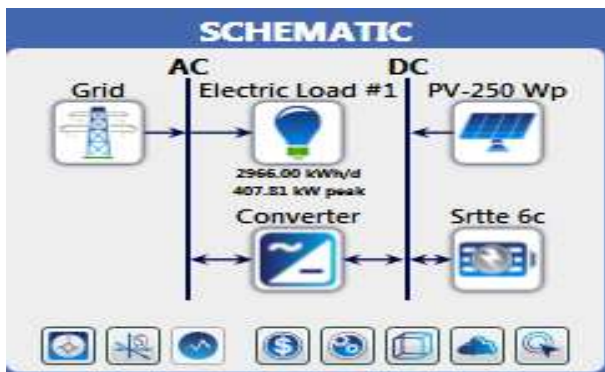


Figure 7. On-grid photovoltaic energy system

Optimum photovoltaic energy system consisted of 3500 kW photovoltaic panel, 1000 kW electric grid, 320 batteries and 3000 kW converters. Total net cost (NPC) and cost of energy (COE) were respectively 25.998.800 \$ and 0.437 \$/kWh according to simulation results. While electric consumption value was 1.082.593 kWh/year, electric generate value was 5.316.885 kWh/year and electric grid sale was 4.253.506 kWh/year. When lower PV capacity is used

for systems, grid sales will decrease and at the same time cost values will diminish, too.

VI. CONCLUSIONS

In this study, Inönü University which is located in Eastern Anatolia region electrical energy demand was supplied with off-grid and on-grid wind and photovoltaic energy systems via Homer software and optimum cost analysis were carried out. According to the simulations, results are listed as follows;

- The optimum energy system for off-grid systems is wind energy (0.913 \$/kWh). But this value is quite higher than grid power price (0.17 \$/kWh).
- Higher battery number and converter capacity and lower wind turbine number and photovoltaic capacity change the costs and enhance for off-grid systems.
- Excess electricity meaning surplus energy occurs for off-grid systems, because more wind turbines or photovoltaic panels produce redundant energy. So much more batteries are necessary to store this energy and to decrease excess electricity.
- The costs of photovoltaic energy system are very high because, photovoltaic panels used in Homer software are expensive in comparison with wind turbines.
- Off-grid energy systems are not suggested for this study.
- The optimum energy system for on-grid systems is wind energy (-0.0478 \$/kWh). Cost of energy has negative value as all revenues are more than expenses. Surplus energy are sold to the grid in this system.
- On-grid energy systems can be suggested to the users according to the study.

Wind speed and solar radiation of selected district are generally low. Equipment installation like wind turbine and PV panel will increase in this case. If wind speed and solar radiation of selected district are high and equipment costs become cheaper in time, renewable energy usage can be more productive.

ACKNOWLEDGMENT

We owe special thanks to Inönü University Scientific Research Projects Coordination Unit for their financial support about Homer software.

REFERENCES

- [1] Y. Kalinci, I. Dincer, A. Hepbasli, "Energy and exergy analyses of a hybrid hydrogen energy system: A case study for Bozcaada," International Journal of Hydrogen Energy, 2016

- [2] F. Fazelpour, N. Soltani, M.A. Rosen, "Feasibility of satisfying electrical energy needs with hybrid systems for a medium size hotel on Kish Island, Iran," *Energy*, August 2014, 73, pp. 856-65.
- [3] Fazelpour F, Soltani N, Rosen MA. "An assessment of wind energy potential as a power generation source for the city of Ardabil, Iran," In: *Colloque Francophone sur l'Energie, Environment, Economie et Thermodynamique*, Paris, 2014.
- [4] I. Prasetyaningsari, A. Setiawan, A. A. Setiawan, "Design optimization of solar powered aeration system for fish pond in Sleman Regency, Yogyakarta by HOMER software," *Energy Procedia*, vol 32, pp. 90-98, 2013
- [5] S.M. Shaahid, I. El-Amin, S. Rehman, A. Al-Shehri, "Techno-economic potential of retrofitting diesel power systems with hybrid wind/photovoltaic/diesel systems for off-grid electrification of remote villages of Saudi Arabia," *International Journal of Green Energy*, vol 7, pp. 632-646, 2010.
- [6] P. R. Bhattarai, "Optimizing an Off-Grid Electrical System in Brochet, Manitoba, Canada," Master Thesis, August 2013
- [7] <http://www.eie.gov.tr/eieweb/duyurular/YEK/gepa/MALATYA-GEPA.pdf> (on-line access on 28 December, 2016).
- [8] Powersolar. Mono-christal 250 Wp solar panel. www.solarpower.com. (on-line access on 20 February, 2014).
- [9] Enercon. WindTurbinesE33. www.enercon.de. (on-line access on 25 February, 2014).
- [10] Gokcol, C., Dursun, B., A comprehensive economical and environmental analysis of the renewable power generating systems for Kırklareli University, Turkey, *Energy and Buildings*, 64, 249-257, 2013.
- [11] Enerji Piyasası Düzenleme Kurumu. <http://www.epdk.gov.tr/index.php/elektrik/piyasaki/tarifeler?id=133>. (Erişim tarihi Mart 5, 2014).

Examination of Locked and Unlocked Fixation Plates Used in Tibia Diaphysis Fractures Produced by Different Materials; a Finite Element Study

Hojjat Ghahramanzadeh Asl

Mechanical Engineering Department
Erzincan University
Erzincan, Turkey
hojjat.g@erzincan.edu.tr

Osman Orhan

Mechanical Engineering
Erzincan University
Erzincan, Turkey

Mustafa Can Irhan

Mechanical Engineering
Erzincan University
Erzincan, Turkey

Özgü Bayrak

Mechanical Engineering
Erzincan University
Erzincan, Turkey

Abstract—Plate-screw fixation is frequently used in treatment of tibia diaphysis fractures. However, design of implants depends on biomechanical behaviors of bone-implant structures, whether they are used locked or unlocked plate-screw systems. In this study, mechanical effects of locked and unlocked plate-screw fixation methods, which are used in treatment of tibial diaphysal fractures. In addition, changes on callus structure, which depend on plate material for first week, were examined by using finite element methods. For this purpose, 3D fractured tibia models with a callus structure consisting of 90 ° fracture angle were established and plate-screw fixations were performed. Obtained models were analyzed by using ANSYS 15.0 software under axial force. When plate material was changed from Ti6Al4V to 316L material, stresses and displacements occurred in the models decreased. As a result of analyzes; it has been determined that locked plate systems provide higher stabilization than unlocked plate systems in terms of stresses and displacements occurring in bone-implant structures.

Keywords— *Tibia diaphysis; Callus; Finite element method; Stress; Deformation*

VII. INTRODUCTION

Bones that are located in limbs are more fragile than other parts of body related to either external forces such as strikes, sprains, falls, accidents or other factors such as ageing and osteoporosis. In order to fix these fractures, several methods are used in medicine. While some of them use nonsurgical treatment as is cast, others uses surgical treatments such as intramedullary necrosis or plate fixations. As a result of developing new techniques and materials, plate fixation become more convenient for these kinds of bone cracks [18].

Quality and time consumption of bone recovery highly depends on variety of materials and plate types. Two main plate types, which are unlocked and locked plate systems, are commonly used in treatments. Unlocked plates contain screws to keep together plate and bone with using traditional non-threaded screw head. This screw type tends to higher pressure on plate and lead to irrevocable damage on bone tissue

especially on osteoporotic bones. Conversely, locked plates are provided directly with screws by plate contact. Locked plates therefore expedite the healing process by contributing to callus formation and provide more flexible structure than unlocked plate systems. Despite all, there is no certain result for superiority of one system. Researches show that although locked plate systems are more reliable than unlocked alternatives, different opinions are still being proposed regarding using of locked and unlocked plate systems. In addition to these, latest studies on using locked, and hybrid plate systems have been proposed by [3, 6-12, 15-17].

In this study, effects of locked and unlocked plate fixation methods on bone-implant structures were investigated. For this purpose, a bone-plate-screw three-dimensional model (3D) was created taking into account of 90° fracture angle and callus structure (0-1 Week). Created models were analyzed with ANSYS 15.0 software under axial load conditions. As a result of analyzes, both mechanical effects of bone-implant structures and callus formation in the healing process have been investigated.

VIII. MATERIAL AND METHOD

In this study, methods of treatment were theoretically examined by using locked and unlocked plates. Biomechanical studies on the tibial bone have been examined and Kim et al.'s plate-screw-bone-callus 3D model has been selected as main model [12]. In modeling, the bone structure was separated as a cortical-trabecular bone and then callus, which formed during the healing process, was placed in the middle part of the obtained models to simulate fractured bone structure. The callus models were designed and modeled with 90 ° fracture angles. After this step, the bone structures were fixed with 6 screws and plates from the middle part (Fig. 1).

Modeling and assembling operations were performed using SolidWorks 2017 software. The models have been transferred to ANSYS Workbench 15.0 software for analysis. At this stage, locked and unlocked models were made of mesh. As a result, the models with 90 ° crack angle was

divided into 176254 elements. Table 1 shows the material properties of bone, implants and callus structures formed at different stages of healing process from obtained finite element models.

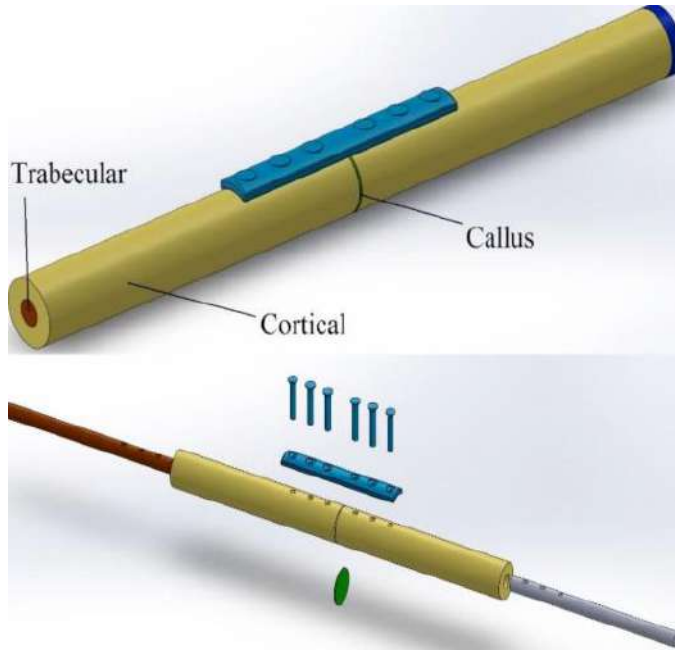


Fig. 5. Plate-screw-bone-callus 3D model

TABLE III. MATERIAL PROPERTIES [9]

Materials	Modulus of Elasticity (MPa)	Poisson Ratio
Ti-6Al-4V	113800	0,340
316L Stainless Steel	191000	0,3
Cortical Bone	17000	0,3
Trabecular Bone	1,061	0,225
Callus 0-1 Weeks	0,02	0,3

Axial loads acting on the tibia bone were taken into account as a boundary condition in analyzes [9]. At this point, distal part of the obtained 3D model was fixed in each direction and a compressive force of 600 N was applied from the proximal part (Fig.2).

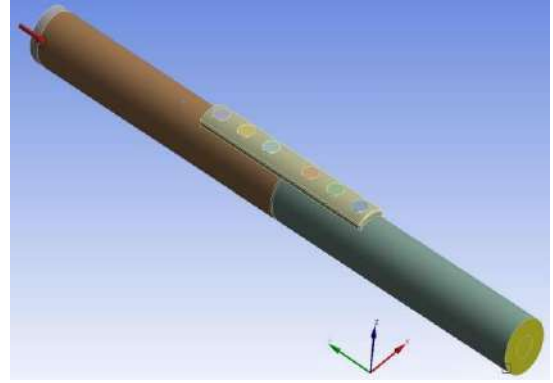


Fig. 6. Axial load and boundary condition acting on the tibia bone

Finally, different contact types have been defined in order to define unlocked and locked plate systems. In unlocked plates, contact type is defined to allow screw-plate contact but also allows the axial and rotational movement of the screws. In locked plates, contact type is defined not to allow movement between the plate and the threads. Plates used in the study are numbered with material and type of plate system. Also, the model used in the study is shown as meshed at Fig. 3.

TABLE IV. NUMBERING OF THE PLATES USED IN THE STUDY

Plate No	Material and type of plate
1	Ti6Al4V- Locked
2	Ti6Al4V- Unlocked
3	316L- Locked
4	316L- Unlocked

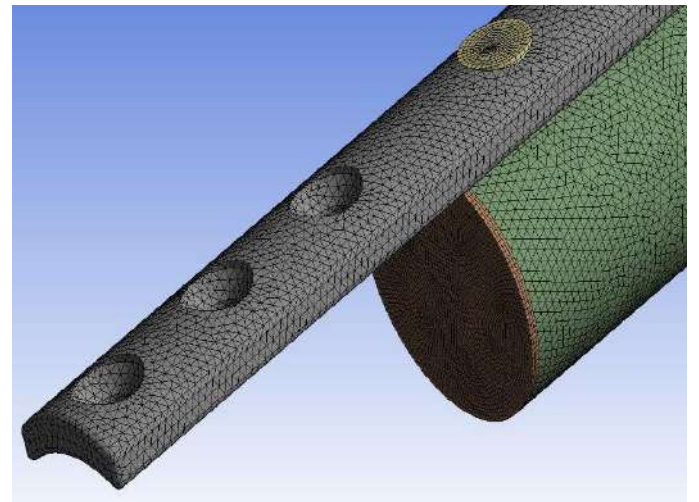
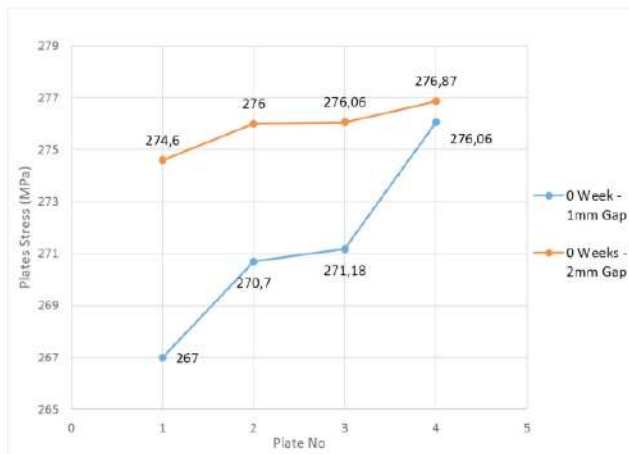


Fig. 7. Mesh structure of the model used in the study

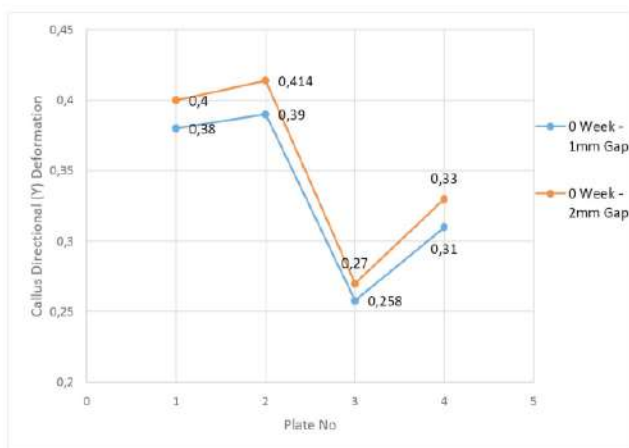
IX. RESULT AND DISCUSSION

A. Stresses in bone-implant structures

Bone-callus-implant models were analysis and divided into 3 groups depending upon stresses and deformations related to these. First, stresses in the plate, then stresses on the cortical bone, and finally, the amount of deformation in the callus structure. Stresses occurring in the bone and plate play an important role in the bone healing process. It is recommended in the literature that the elasticity modulus of the plate materials should be closer to the bone. The reason for this is to prevent the bone from becoming lazy during the healing process. However, when the first week of bone fractures is considered, it is desired that forces should be undertaken by cortical bone and plates. Because of this reason, stress occurring in the cortical bone and plates become more important [13]. Mean von Mises stresses obtained from the 1 mm and 2 mm gap sizes of the Ti6Al4V and 316L unlocked and locked plate models used at 90° fracture angles are given in Fig 4.



(a)



(b)

Fig. 8. Stresses on the plates (a), Stresses on the cortical bone (b)

As seen in the graphs, the stress on the locked plates are lower than in the unlocked equivalents. This is valid for both plates which are made from Ti6Al4V and 316L materials. It is caused by connection between the plate and the screw. In contrast to unlocked plates, locked plates exhibits more rigidity because plate and screw have threaded joint. Due to this reason, load applied to plate is guided to center of plate by means of screws. While cross sectional area increase, behavior of plates display more rigidity.

On unlocked plates, because of the flat contact between the plate and the screw, the applied load concentrates on the contact areas of the plate and the screws. This causes high stress at the screw countersinks and also yield larger stresses on the plates. In addition, 316L plates are exposed to higher stresses than Ti6Al4V plates. This has led to different behaviors depending on the modulus of elasticity of the material due to analyzes are made in the elastic zone. Due to the high modulus of elasticity of 316L material compared to Ti6Al4V, it absorbs more energy under constant load and exhibits less deformation. When the stress in the cortical bone were examined, there was a decrease in the fixation with locked plates in comparison with unlocked plates. Furthermore, analyzes using 316L exhibited lower stress results than Ti6Al4V. As can be seen in the figures above, while locked Ti6Al4V was caused as 44.67 MPa stress, 316L was resulted as 32.57 MPa in the bone. This is about 23% decrease, which is considered to be a high value for the stresses in the bones. The reason for this is that 316L plates have more elasticity due to the modulus of elasticity and prevents stress on the bones.

In our study, fractured regions were examined at two different distances. From results, 2 mm gap size between plate and bone caused more stresses than 1 mm gap size alternatives. The reason for this is that the load applied in the case of axial loading is distributed to the bones and plates through screws. As the distance between the bones increases, more torque is applied to the region between the bones from the other screws on the side where the load is applied and this is increased stresses on the plates. The loads carried by the plates caused less stress on the bones with less load on the bones. Due to this reason, lower stresses in bones and higher stresses in plates occurred in 1mm gap sizes than 2mm gap size. Stresses occurring in 1 mm and 2 mm gap sizes, in plates and cortical bones are shown in Fig. 5.

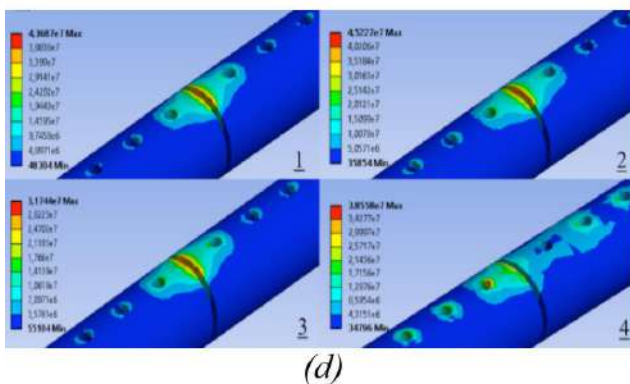
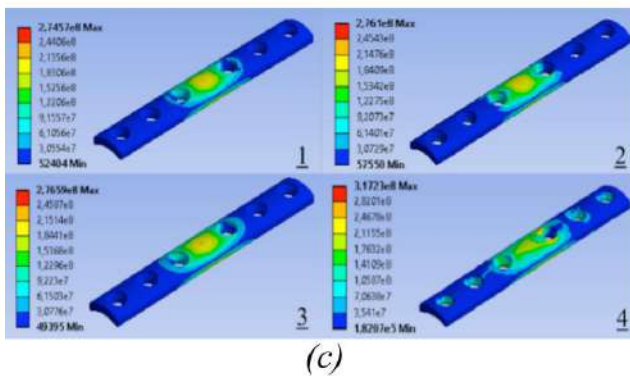
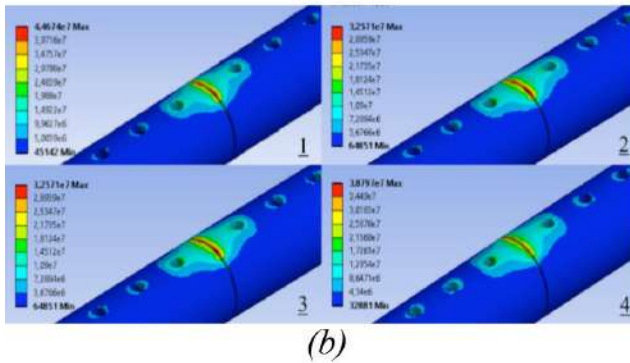
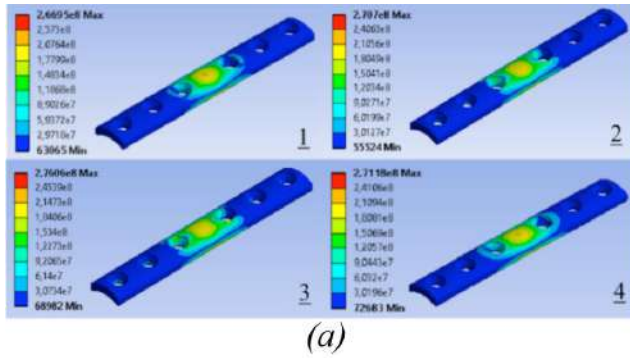


Fig. 9. Stresses in plates in 1 mm gap size (a), cortical bones in 1 mm gap size (b) plates in 2 mm gap size (c), and 2 mm gap size in cortical bones (d)

B. Directional Deformations in Callus Structure

Deformations on the callus structures under axial load in Y direction for different fixation types are given in Fig. 6. From these values, it is seen that the displacements in locked plates are lower for both 1 mm and 2 mm gap sizes compared to unlocked plates. While displacement of the callus structure for Ti6Al4V with 1 mm gap size is 0.38 mm, it reaches 0.39 mm for unlocked equivalent. In addition to this, displacements of the callus structures exhibited different values for the plates for two different materials. The displacement of Ti6Al4V locked plate is 0.38 mm while that of 316L locked plate is reduced to 0.25 mm. These values indicate that the difference between two different materials is about 50%, which is a significant value for first week of callus constructions. Displacement of Ti6Al4V unlocked plate was 0.39 mm when the 316L unlocked plate was 0.31 mm. Since the first week of the healing period for callus structure is taken into account in our study, it is not desirable that callus structures are over deformed. Because of this reason, locked plates give better results.

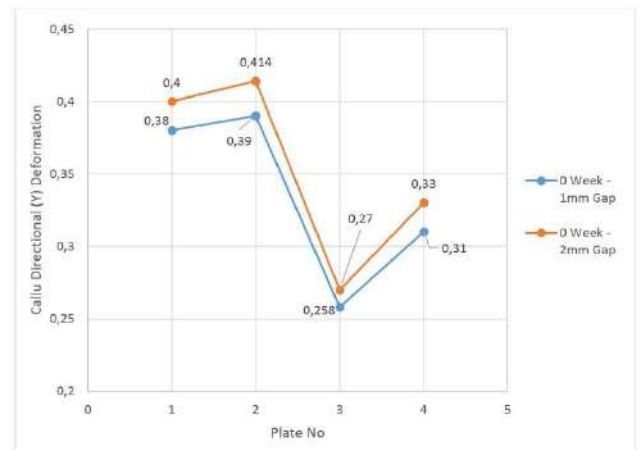


Fig. 10. Deformations in callus structures

The most important phase in the treatment of bone fractures is to remove stress shielding effect [4]. After fixation, implant undertake load from bone and load is bypassed from callus structure. This called as stress shielding effect [1, 4, 14, 19]. In order to prevent long healing times, this effect must be kept at a minimum level. However, in the first stages of the healing process, contrary to this situation, it is desired that the bone-implant structure is sufficiently stable [4, 5, 8, 13, 19]. For this reason, analyzes were carried out taking into consideration of mechanical properties of callus structures for first stage of healing process.

Results that shows callus motions are shown in Fig. 7. When Fig. 7 is examined, it appears that using of locked plate system reduces callus motility during the healing process. In addition, callus motility value is reduced in plates made from 316L material. From literature studies, it has been concluded that fixation system must provide a higher stabilization at the early stages of healing process.

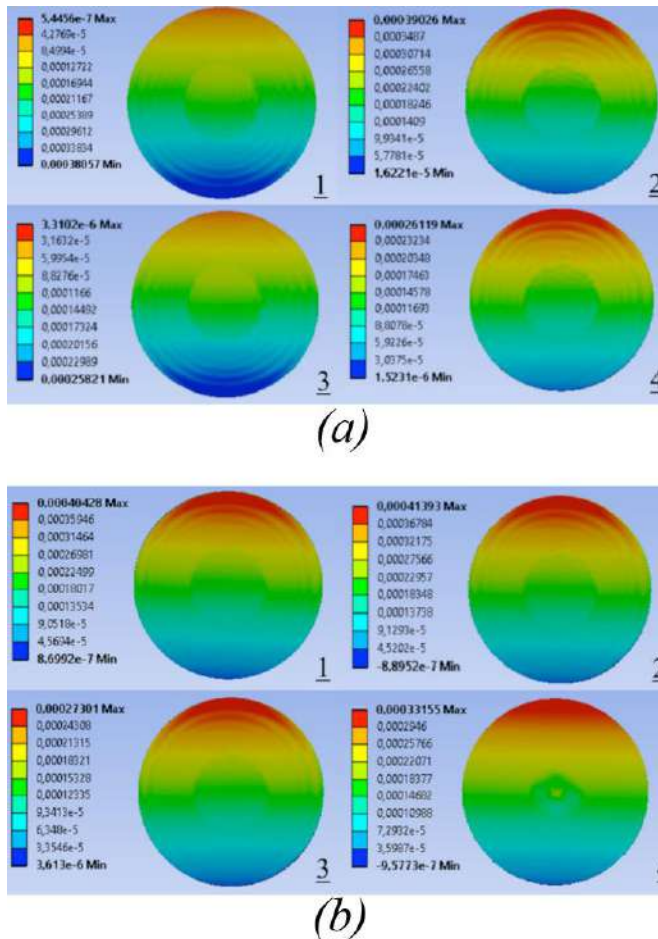


Fig. 11. 1 mm gap size (a) 2 mm gap size (b) Y-direction displacements in callus structures

Considering first stages of treatment of tibial fractures, it is seen that locked plate-screw systems are more convenient than unlocked plate-screw systems in terms of mobility. In addition to this, considering the amount of deformation of callus, 316L material can be selected as plate material.

X. CONCLUSION

In this study, in which locked and unlocked plate fixation methods were theoretically investigated, it was concluded that average plate stress in the bone-callus-implant models with 90° fracture angle for Ti6Al4V material was higher than 316L material. However, it has been observed that using of locked plates considerably reduces the stresses in the bone. When the individual pieces (Bone-callus-plate) are examined, the stresses are obtained from the locked plate made from the 316L material. When stresses on the plate are inspected, the lowest stress value is obtained from the fixation with the locked plate that is made from Ti6Al4V material. According to the amount of callus deformation in the Y direction, the lowest value was obtained from locked plate fixation system that is made of 316L material with a gap size of 1 mm.

Locked plate-screw systems have proven to be a more suitable method for the treatment of tibial fractures than unlocked plate-screw systems in that they provide higher stabilization at the beginning of the recovery process and higher mobility at later stages of the healing process.

REFERENCES

- [1] G. Cheung, P. Zalzal, M. Bhandari, J. Spelt and M. Papini, "Finite element analysis of a femoral retrograde intramedullary nail subject to gait loading," *Medical engineering & physics*, 26 (2), pp. 93-108, 2004.
- [2] P. Cronier, G. Pietu, C. Dujardin, N. Bigorre, F. Ducellier and R. Gerard, "The concept of locking plates," *Orthopaedics & Traumatology, Surgery & Research*, 96 (4), pp. 17-36, 2010.
- [3] A. Cuadrado, A. Yanez, J. Carta and G. Garces, "Suitability of DCPs with Screw Locking Elements to allow sufficient interfragmentary motion to promote secondary bone healing of osteoporotic fractures," *Medical engineering & physics*, 35 (6), pp. 852-859, 2013.
- [4] A. Celik, H. Kovaci, G. Saka and I. Kaymaz, "Numerical investigation of mechanical effects caused by various fixation positions on a new radius intramedullary nail," *Computer methods in biomechanics and biomedical engineering*, pp. 1-9, 2013.
- [5] G.N. Duda, S. Sporrer, M. Sollmann, J.E. Hoffmann, J.-P. Kassi, C. Khodadadyan and M. Raschke, "Interfragmentary movements in the early phase of healing in distraction and correction osteotomies stabilized with ring fixators," *Langenbeck's Archives of Surgery*, 387 (11-12), pp. 433-440, 2003.
- [6] D.C. Fitzpatrick, J. Doornink, S.M. Madey and M. Bottlang, "Relative stability of conventional and locked plating fixation in a model of the osteoporotic femoral diaphysis," *Clinical Biomechanics*, 24 (2), pp. 203-209, 2009.
- [7] M.J. Gardner, M.H. Griffith, D. Demetrakopoulos, R.H. Brophy, A. Grose, D.L. Helfet and D.G. Lorch, "Hybrid locked plating of osteoporotic fractures of the humerus," *The Journal of Bone & Joint Surgery*, 88 (9), pp. 1962-1967, 2006.
- [8] K. Kaspar, H. Schell, P. Seebeck, M.S. Thompson, M. Schutz, N. Haas and G.N. Duda, "Angle Stable Locking Reduces Interfragmentary Movements and Promotes Healing After Unreamed Nailing Study of a Displaced Osteotomy Model in Sheep Tibiae," *The Journal of Bone & Joint Surgery*, 87 (9), pp. 2028-2037, 2005.
- [9] S.H. Kim, S.H. Chang and H.J. Jung, "The finite element analysis of a fractured tibia applied by composite bone plates considering contact conditions and time-varying properties of curing tissues," *Composite Structures*, 92, pp. 2109-2118, 2010.
- [10] H.-J. Kim, S.-H. Kim and S.-H. Chang, "Biomechanical analysis of a fractured tibia with composite bone plates according to the diaphyseal oblique fracture angle," *Composites Part B: Engineering*, 42 (4), pp. 666-674, 2011.
- [11] H.-J. Kim, S.-H. Kim and S.-H. Chang, "Finite element analysis using interfragmentary strain theory for the fracture healing process to which composite bone plates are applied," *Composite Structures*, 93 (11), pp. 2953-2962, 2011.
- [12] S.-H. Kim, S.-H. Chang and D.-S. Son, "Finite element analysis of the effect of bending stiffness and contact condition of composite bone plates with simple rectangular cross-section on the biomechanical behaviour of fractured long bones," *Composites Part B: Engineering*, 42 (6), pp. 1731-1738, 2011.
- [13] H. Kovaci, H.G. Asl, I. Kaymaz, A. Alsaran, A. Celik and G. Saka, "Radius kırıklarında Plak Fiksasyonu ve İntrameduller Cevileme Yöntemlerinin Teorik Olarak İncelenmesi," *Sakarya University Journal of science*, pp. 330-336, 2012.
- [14] S. Kujala, J. Ryhanen, T. Jamsa, A. Danilov, J. Saaranen, A. Pramila and J. Tuukkanen, "Bone modeling controlled by a nickel-titanium

- shape memory alloy intramedullary nail,” *Biomaterials*, 23 (12), pp. 2535- 2543, 2002.
- [15] D.L. Miller and T. Goswami, “A review of locking compression plate biomechanics and their advantages as internal fixators in fracture healing” *Clinical Biomechanics*, 22 (10), pp. 1049-1062, 2007.
- [16] M. Moazen, J.H. Mak, L.W. Etchels, Z. Jin, R.K. Wilcox, A.C. Jones and E. Tsiridis, “The effect of fracture stability on the performance of locking plate fixation in periprosthetic femoral fractures,” *The Journal of arthroplasty*, 28 (9), pp. 1589-1595, 2013.
- [17] K. Seide, J. Triebe, M. Faschingbauer, A. Schulz, K. Puschel, G. Mehrtens and C. Jurgens, “Locked vs. uunlocked plate osteosynthesis of the proximal humerus—a biomechanical study,” *Clinical Biomechanics*, 22 (2), pp. 176-182, 2007.
- [18] P. Szypryt and D. Forward, “The use and abuse of locking plates” *Orthopaedics and Trauma*, 23 (4), pp. 81-290, 2009.
- [19] H. Ghahramanzadeh Asl, H. Kovacı, A. Alsaran, A. Çelik, İ. Kaymaz and Ö.S. Yıldırım, “Finite Element Analysis of Locked and Unlocked Plate Fixation Methods in Tibial Diaphyseal Fractures,” *Suleyman Demirel University Journal of Natural and Applied Science*, 18, pp. 167-174, 2014.

Innovative Analyze Of Operator Viewpoint With Camera System On Single Jaw Vertical Coil Tong

Erhan DÜZGÜN, Mechanical Engineer,

M.Sc. Student, Management of Technology and Innovation Amasya University, Institute of Science and Technology
Amasya, Turkey
e-mail: erhanduzgun06@gmail.com

Arif GÖK, Assoc. Prof. Dr.

Department of Mechanical Engineering Amasya University, Faculty of Technology Amasya, Turkey
e-mail: arif.gok@amasya.edu.tr

Abstract: At the present time, significant improvements have been made in the iron-steel industry and investments in technology have become important. Hoisting and handling appliances are typical devices in order to transport the iron-steel products, especially steel plates and round bars. It is for sure that hoisting and handling appliances have to be used while manipulating the iron-steel products due to their heavy weights.

In this study, it has been mentioned about an innovative approach for preventing coil edge deformation problem arising from the poor viewpoint of the crane operator while manipulating the single jaw vertical coil tong which is used for the lifting of steel plate coils vertically. For this reason, the inner jaw of the vertical coil tong was provided to enter into the coil inner diameter properly by the crane operator by means of making good viewpoint with the camera system for helping to the crane operator.

In conclusion; the problem causing the loss of material was reduced to a minimum level in general and therefore a reasonable benefit was provided by means of the innovative system developed for the single jaw vertical coil tong.

Keywords—Innovation; Innovative; Crane; Tong; Single Jaw Vertical Coil Tong; Camera System;

Optimization of a Perforated Diffuser by Taguchi Methods

Ekrem TAÇGÜN

Mechanical Engineering

Inonu University

Malatya, TURKEY

ekrem.tacgun@inonu.edu.tr

Ahmet ERDOĞAN

Mechanical Engineering

Inonu University

Malatya, TURKEY

muh.ahmeterdogan@gmail.com

İ. Gökhan AKSOY

Mechanical Engineering

Inonu University

Malatya, TURKEY

gokhan.aksoy@inonu.edu.tr

Abstract— Cross-sectional area of air exiting of fans used in air handling units (AHU) is smaller than cross-sectional area of chambers which are located next to the fan such as heating/cooling coils, silencer (muffler), filter or heat recovery elements. To make the air handling unit work efficiently, it is required that the air is blown through fan diffuses with as low as possible pressure loss and homogeneous velocity distribution. Empty chambers with perforated diffuser is used to diffuse air from small cross-sectional area to large cross sectional area. In this concept, diffusion of air and pressure loss through the empty chamber with perforated diffuser are modelled and analyzed numerically. Using Taguchi Method, the effect of five parameters with different levels on the pressure drop is determined. These parameters are namely porosity, angle, diffuser thickness, diffuser distance and hole geometry.

Keywords — AHU; Diffuser; Pressure Drop; Taguchi Method; Air Flow

XI. INTRODUCTION

Average air velocities at discharge section of suction and/or supply fan is in the order of 8-15 m/s and velocity distribution of turbulent flow is much different from that of the fully-developed flow [1]. Exiting air from fans contacts with the certain surface sections of the heating/cooling coils, silencer (muffler), filter or heat recovery elements inside the chamber which are located after the fan if there is not any sufficient chamber length. The efficient chamber length which is approximately 3.5-3.7 times of fan impeller diameter or a shorter chamber including a perforated diffuser must be provided for effective air diffusing to the surfaces inside the chamber after the fan. Therefore, the chambers with perforated diffuser having the length of approximately 0.8-1.5 times of fan impeller diameter which are facilitated the air diffusion are used to efficiently working the chambers such as heating/cooling coils, silencer, mixing and filter or heat recovery element located after the fan exit [2]. Using a chamber with perforated diffuser in air handling

unit (AHU), to increase working efficiency of these chambers following the fan chamber by creating an uniform air flow from fan to following chambers such as heating/cooling coils, silencer, filter or heat recovery element and therefore decreasing of total internal pressure losses for central station AHU are possible [3, 4]. Decreasing of internal pressure losses in AHU and diffusing homogenously to chambers after fan is very important with respect to energy efficiency.

According to marketing investigation carried out among AHU manufacturers, it is determined that they cannot sufficiently ensure flow performance as expected due to the fact that there is not sufficient data on flow structure in chamber with perforated diffuser. According to literature review, it was seen that only one preview CFD (computational fluid dynamics) study for a chamber with truncated pyramid diffuser in was carried out and velocities at chamber exit was investigated [3, 4]. Any scientific study related with flow structure in a chamber having perforated diffuser geometry of V-profile shaped, which is often used in central station AHU applications because it has a simple geometric structure and manufacturing simplicity, has not found. Energy efficiency in AHUs is very important and it is seen that the ratio of electric energy operation costs of fans in their life cycle cost is at the order of 40-50 % approximately [5]. Therefore, even small reduction in internal pressure losses in AHUs is very important.

XII. MATERIAL AND METHOD

Numerical analyses were performed by ANSYS-Fluent 14.5 software. Five variable parameters were considered in numerical analysis. The effect of these parameters on pressure loss in the chamber was investigated. To reduce the numerical simulation number, Taguchi Method was used.

A. Geometry

Solid model of the AHU chamber is illustrated Fig. 1. Perforated diffuser is located in this chamber.

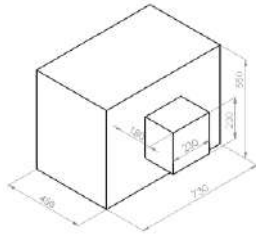


Fig. 12. Solid model of AHU chamber

Top view of the chamber with perforated diffuser with some geometrical details is shown in Fig. 2. The cross-sectional dimensions of the chamber of 730 mm x 550 mm with 450 mm in length and cross-sectional dimensions of air inlet section of 230 mm x 230 mm are considered for the numerical analysis. Diffuser distance in the chamber from the air inlet section is shown with L_0 ;

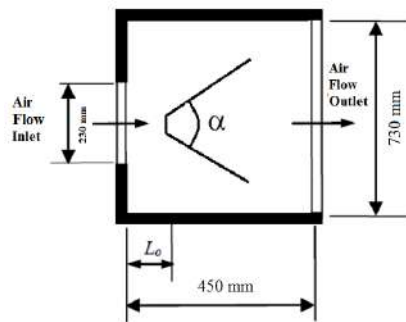


Fig. 13. Geometrical details of the chamber with perforated diffuser

B. Parameters

In this study, five parameters was determined as porosity, angle, thickness, diffuser distance (L_0), hole geometry. Porosity characterizes the void spaces on the diffuser plate surface. Angle is defined as the angle between V – profile diffuser side plates. Thickness is the perforated diffuser plate thickness. Diffuser distance is defined as length from the fan exit to diffuser inside the chamber. And hole geometry is shape of hole on perforated diffuser. Parameters and their levels are given in Table 1.

TABLE V. PARAMETERS AND LEVELS

Parameters	Units	Level 1	Level 2	Level 3
1 Porosity (ϵ)	-	0.4	0.5	-
2 Angle (α)	°	60	90	120
3 Thickness (t)	mm	2	3	5
4 Diffuser Distance (L_0)	mm	50	75	100
5 Hole Geometry	-	Square	Circle	Hexagonal

C. Numerical Model

The numerical calculations were performed by using ANSYS Fluent 14.5 based on finite volume method. The fluid and the solid were described as air and aluminum, respectively. The boundary conditions were defined as following; for the air inlet surface having sizes of 230 mm x 230 mm as “velocity-inlet”, for the back surface of the chamber having sizes of 730 mm x 550 mm as “pressure-outlet” and for other surfaces as “wall”. Static pressure values of pressure-outlet were assumed as 400 Pa and wall roughness value as 0.0032 mm. Depending on geometrical details, About 10^6 tetrahedral cells are generated finely mesh. Three dimensional steady-state flow is assumed and standard k- ϵ turbulence model is chosen as turbulence model. Generated solid model with different viewpoints is given Fig. 3.

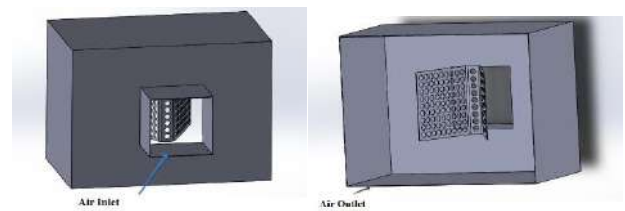


Fig. 14. Solid model for numerical analysis

Mesh form of half symmetric model what generated for numerical analysis is shown in Fig. 4. Symmetric model is considered for reducing computational time.

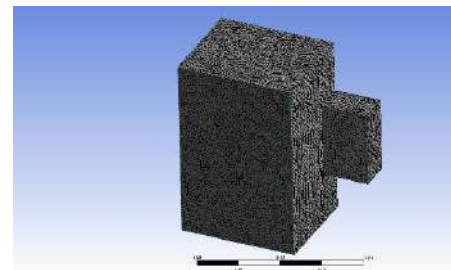


Fig. 15. Mesh form of the numeric model

D. Taguchi Method

Taguchi has developed this statistical method to investigate the effects of different parameters to the process that they are in. The number of tests that will be formed by the combination of different parameters and levels is quite high. Taguchi Method reduces these test numbers drastically. The main trust of Taguchi's techniques is the use of parameter design, which is an engineering method for product or process design that focuses on determining the parameter settings producing the best levels of quality characteristic with minimum variation [6]. With this method proposed by Taguchi, orthogonal arrays are used to define the effects of parameters and each level of parameters that are determined for a process. [7]. L18 orthogonal array is chosen from the orthogonal array option table given in Table II for eight parameters defined in this study.

TABLE VI. SELECTING OF ORTHOGONAL ARRAYS

		Number of Parameters								
		2	3	4	5	6	7	8	9	10
Number of Levels	2	L4	L4	L8	L8	L8	L8	L12	L12	L12
	3	L9	L9	L9	L18	L18	L18	L18	L27	L27
	4	L16	L16	L16	L16	L32	L32	L32	L32	L32
	5	L25	L25	L25	L25	L25	L50	L50	L50	L50

L18 orthogonal array is given in Table III together with the number of tests to be done and levels of parameters that will be used in the model to be analyzed for each test.

TABLE VII. L18 ORTHOGONAL ARRAY

Number of Analyses	Porosity	Angle	Thickness	Diffuser Distance	Hole Geometry
1	1	1	1	1	1
2	1	1	2	2	2
3	1	1	3	3	3
4	1	2	1	1	2
5	1	2	2	2	3
6	1	2	3	3	1
7	1	3	1	2	1
8	1	3	2	3	2
9	1	3	3	1	3
10	2	1	1	3	3
11	2	1	2	1	1
12	2	1	3	2	2
13	2	2	1	2	3
14	2	2	2	3	1
15	2	2	3	1	2
16	2	3	1	3	2
17	2	3	2	1	3
18	2	3	3	2	1

XIII. NUMERICAL ANALYSIS

Pressure loss that is calculated in each one of 18 models determined by Taguchi Method in results of analyses from ANSYS 14.5 program is given in Table IV.

TABLE VIII. PRESSURE DROP OF EACH ANALYSIS

Number of Analysis	Pressure Drop (Pa)
1	44.78
2	52.45
3	62.26
4	60.68
5	39.43
6	64.25
7	76.70
8	41.83
9	48.53
10	42.07
11	54.14
12	66.79
13	49.34
14	81.63

15	39.58
16	58.84
17	61.07
18	42.10

According to variable parameters given in Table III, total 18 model analysis were done numerically. Each of parameters which effects on pressure drop was observed. Statistics of parameters performance graphic is given in Fig. 5. It is seen that, diffuser distance from the variable parameters has a significant effect on pressure drop.

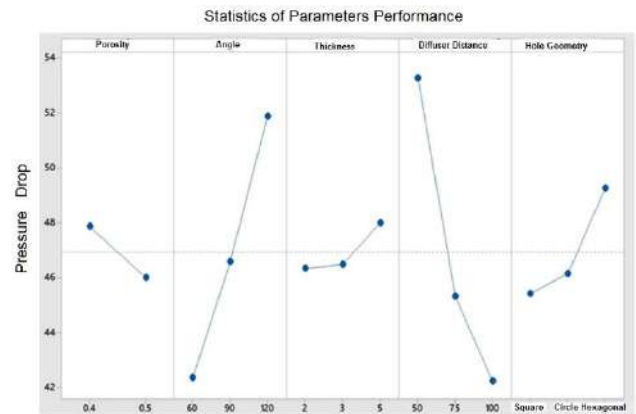


Fig. 16. Statistic of parameters performance

Optimum levels of the variable parameters were determined by Taguchi Method. It is seen that ideal design array caused by minimum pressure loss is in the form of 2-1-1-3-1. These array means that, porosity, angle, thickness, diffuser distance and hole geometry levels are respectively 0.5, 60°, 2 mm, 100 mm and square. When a model is generated with this ideal design array, optimum (lowest) pressure loss is calculated as 38.16 Pa.

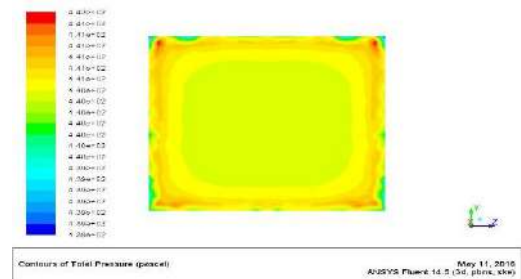


Fig. 17. Contours of total pressure in air inlet

Contours of total pressure distribution which is obtained for optimum model analysis is shown in Fig.6. Also velocity streamlines of optimum model analysis is demonstrated in Fig. 7.

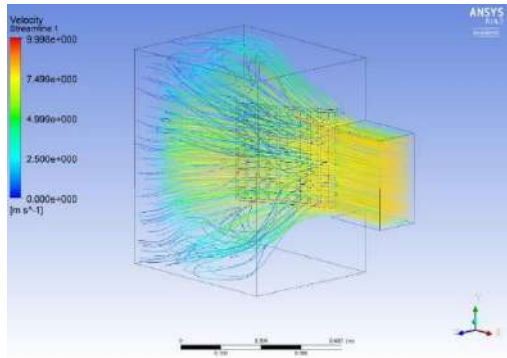


Fig. 18. Velocity streamline for optimum analysis

XIV.CONCLUSION

The following main findings from the numerical results can be given as:

- Pressure loss decreases as diffuser distance and porosity increase.
- Pressure loss increases as angle and thickness increase.
- Square hole geometry causes low pressure loss as regards other geometry types.

- To obtain minimum pressure loss, it is seen that optimum porosity value is 0.50.

ACKNOWLEDGMENT

This study was supported by Turkish Scientific and Technological Research Council of Turkey (Project No: 114M748). This study was also supported by Scientific Research Foundation of Inonu University (Project No: 2013/63).

REFERENCES

- [1] HVAC Systems Duct Design, Fourth Edition, Chapter 6, SMACNA, 2006.
- [2] M. Bilge, Klima Santralleri, ISKAV Teknik Kitaplar Dizisi, No: 01, İstanbul, 2010.
- [3] S. Bulut, M. Ünveren, A. Arisoy, and Y.E. Böke, "CFD Analiz Yöntemiyle Klima Santrallerinde İç Kayıpların Azaltılması", T.M.M.O.B., X. Ulusal Tesisat Mühendisliği Kongresi ve Sergisi, İzmir, p. 291-326, 2011.
- [4] İ. Tanyol, "Klima Santrallerinde Enerji Tasarrufu ve CFD Analizi İle İç Dirençlerin Azaltılması", I. Ulusal İklimlendirme Soğutma Eğitimi Sempozyumu, Çağrılı Konuşma, Balıkesir, 2012.
- [5] Technical and General Product Catalog of AHUs.
- [6] S.K. Karna, R.V. Singh, R. Sahai, "Application of Taguchi Method in Indian Industry", International Journal of Emerging Thecnology and Advanced Engineering, vol. 2, pp. 387-391, Nov. 2012.
- [7] https://controls.engin.umich.edu/wiki/index.php/Design_of_experiments_via_taguchi_methods:_orthogonal_arrays.

Thermal Aging Effect On The Failure Loads Of V-Notched Composite Plates

Experimental Study

Kadir TURAN

Dicle University

Department of Mechanical

Engineering

Diyarbakır, TÜRKİYE

E-mail: kturan@dicle.edu.tr

Mete Onur KAMAN

Firat University

Department of Mechanical

Engineering

Elazığ, TÜRKİYE

E-mail: mkaman@firat.edu.tr

Nihat TOSUN

Firat University

Department of Mechanical

Engineering

Elazığ, TÜRKİYE

E-mail: ntosun@firat.edu.tr

Abstract— In this study, the thermal aging effect on the failure loads of V-notched composite plates were investigated with static tensile tests. The notched and un-notched composite plates were exposed to temperature with changed time. In addition to, the thermally aged composite plates results were compared with un-aged composite plates results. Two different study was realized. In the first study the temperature was changed as 80, 120 and 160 °C and the time was constant as 4 hours. In the second study, the time was changed as 2, 4 and 6 hours and the temperature was constant as 80 °C. The notch width (a) was changed as 5, 10 and 15 mm and notch depth was constant as 10 mm. The results were showed that the time and temperature increasing were lead to decrease of failure loads of composite plates as 19.9% and 25.4%, respectively.

Keywords— Thermo-aging, V notch, Composite plates, Failure analysis. *Introduction*

XV. INTRODUCTION

First, The fiber reinforced composite materials are a combination of continued fibers and resin matrix. Especially, the thermoset based composite plates, which are manufactured glass fiber and epoxy resin, are showed a linear elastic behavior. Because of this behavior, failure to these materials occurs suddenly. When the external objects impact to these materials or due to some structural requirements in the manufacturing process can cause small micro cracks and then the notches can appear with the growth of these cracks on the composite plates. In the traditional materials, the notches generally lead to local stress concentration at the tip of notch. Generally, the failure starts at this location. However, this is a different meaning for composite materials. The fiber orientation angle of composite materials can occur different stress concentration behavior. Thus, the failure propagates with fiber orientation angle of composite plates.

The notch effect on the composite materials were investigated lots of studies [1-5]. Khashaba et al. investigated bending behaviors of notched and un-notched glass fiber/epoxy composite plates with experimental study [1]. Fiber volume fraction effect on the tensile behavior of notched unidirectional

carbon fiber/epoxy composite plates were researched by Tomita et al [2]. They observed that, the failure propagated to the direction of fiber-reinforced angle. Bouiadjra et al. analyzed stress intensity factor at the crack tip with finite element method [3]. They determined that, the crack propagation resistance decreased with increasing fiber direction angle. Kannan et al. and Çelik et al. researched failure behaviors of central circular cut-out composite plates by using finite element method and static tensile test, respectively [4,5].

The temperature can change material properties and generally, increasing of temperature decreases mechanical properties of materials. The composite materials have lower thermal expansion coefficient; this situation prevents the increased temperature from being easily removed from the composite material.

Belaid et al. researched the thermo-aging effect on the mechanical properties of glass fiber/polyester composite plates [6]. The composite plates were kept at 80 oC constant temperature during 30, 60, 90 and 120 days. Ray investigated that the temperature and humidity effect on the interfacial shear strength of glass fiber/epoxy and carbon/epoxy composite plates [7]. The interfacial shear strength of composite materials was determined by short beam shear test methods. They observed that the interfacial shear strength decreased with increasing temperature and absorbed moisture [7]. Allock et al. researched the mechanical properties of composite plates which exposed to temperature [8]. The composite plates exposed to temperature interval (from -40 ° C to 140 ° C) and the dynamic and static tensile tests were realized. Péreza et al. investigated the short-term temperature effect on the mechanical properties of composite plates with experimentally [9]. Mouzakis et al. analyzed mechanical properties of composite materials which exposed to temperature, moisture and UV radiation [10]. In this study, the mechanical properties were determined with static tensile test and three-point bending test [10]. Turan researched the buckling behavior of thermo-aged woven glass fiber/epoxy composite plates [11].

The major aim of this study was investigated failure behavior of V-notched composite plates, which were exposed temperature at different times. The thermal aging effect were analyzed with two studies. In the first, the V-notched composite plates were exposed to 80, 120 and 160 °C temperature with constant time at 4 hours and the second, the V-notched composite plates were exposed to 2, 4 and 6 hours with constant temperature at 80 °C. In addition, obtained results were compared to un-aged specimens. The results were presented as tables and graphs.

XVI. EXPERIMENTAL STUDY

In the experimental study, the eight layered woven glass/epoxy matrix composite plates were used as materials. The composite plates were provide from *Izoreel Composite Production Company*. The V notched were opened to the half-length of composite plates with using milling cutter. The dimension of problem was presented in Figure 1.

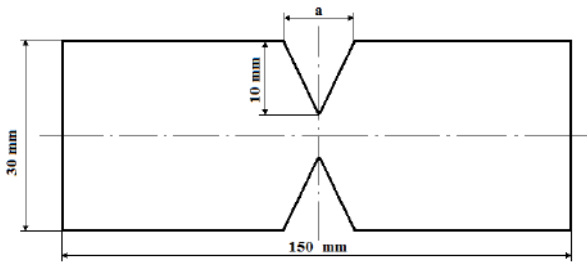


FIGURE 1. THE GEOMETRY OF PROBLEM.

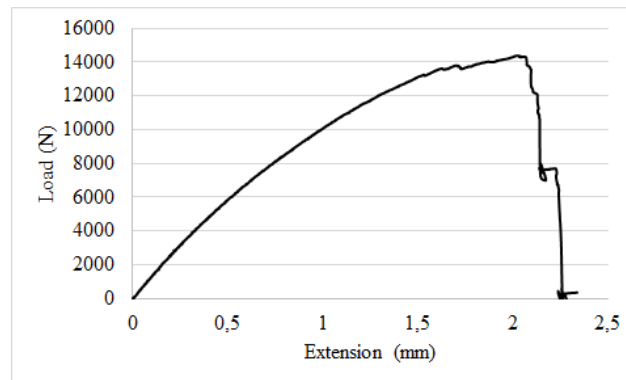
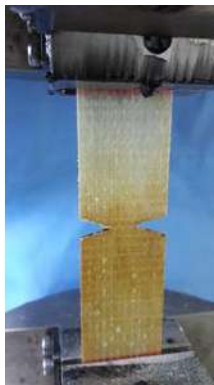


FIGURE 2. EXPERIMENTAL SET-UP AND LOAD-EXTENSION GRAPH (FOR A= 5MM, TEMPERATURE 80°C AND WAITING TIME 6 HOUR).

III. RESULTS AND DISCUSSIONS

The results of experiments were evaluated at two stages. First of these; the time was changed as 2, 4 and 6 hours for constant temperature at 80 °C. The second of these, the temperature was changed as 80, 120 and 160 °C for constant time at 4 hours. In addition, these results were compared with un-aged specimens, which were stayed in room temperature conditions.

The notch width (a) was changed as 5, 10 and 15 mm and notch height (h) was constant at 10 mm. The prepared samples were kept in the electric oven at the prescribed temperatures and times. The variations of time, temperature and notch geometry were given in Table 1.

TABLE IX. THE VARIATIONS OF TIME, TEMPERATURE AND NOTCH GEOMETRY.

Notch width (a) mm	Time (Hour)	Temperature (°C)
5	0, 2, 4 ,6	25, 80, 120, 160
10	4	25, 80, 120, 160
15	4	25, 80, 120, 160

All of tests were repeated three times for reliability of failure loads. The failure loads were obtained from arithmetic average of maximum load for these tests. As a result of thermal aging process, the samples were waited in room temperature and then statically tensile tests were conducted. The tensile tests were realized in 100 kN capacity Instron BS8801 tensile testing machine with 1 mm/min tensile speed. The loads were applied to the samples until the ultimate failure was observed. The load and extension values, which were obtained from tensile testing machine, were recorded into the computer. At the end of experiments, the plotted graphs were obtained from these records. The experimental set-up and typical load-extension behavior of notched specimens were presented in Figure 2.

III.A. THE TIME CHANGING EFFECT ON THE FAILURE LOADS

The time changing effect on the failure loads were studied as 2, 4 and 6 hours for constant temperature at 80 °C. The failure loads of aged specimens were compared with un-aged specimens. The average maximum loads of composites were presented in figure 3.

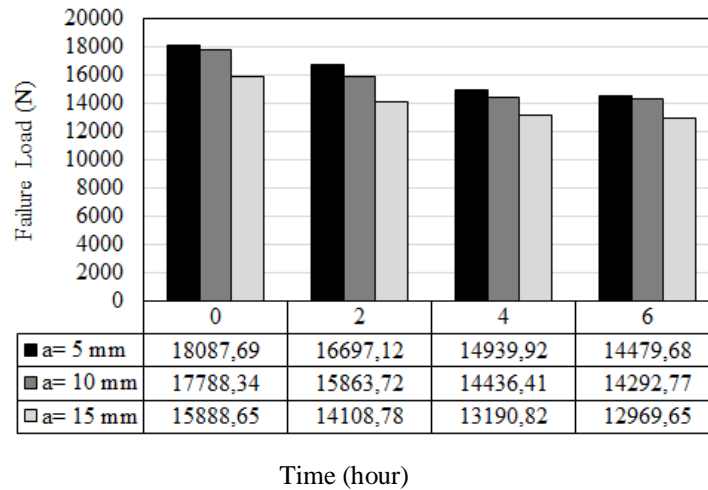


FIGURE 3. THE AGING TIME EFFECT ON THE FAILURE LOADS FOR 80 °C CONSTANT TEMPERATURE VALUE.

It can be seen from Figure 3, the failure loads were decreased with increasing aging-time. The maximum failure load was obtained for a=5 mm and un-aged specimen (stayed in room temperature) as 18087.69 N. The minimum failure load was obtained for a=15 mm and aged specimen in 6 hours at 80°C temperature as 12969.65 N. When the aged specimen's results are compared with un-aged specimen's results, it is observed that the decreasing rates of failure loads vary in a certain interval as 7.7% - 19.9% . The all decreasing rates obtained from tensile test are presented in Table 2. It was observed from Table 2, aging time is an effective parameter on failure load for glass fiber reinforced composites. On the other hand, it can be said that notch width is not important for maximum damage behavior as far as thermal aging.

TABLE II. THE VARIATIONS OF TIME, TEMPERATURE AND NOTCH GEOMETRY.

Time	2 hour	4 hour	6 hour
a=5 mm	7.7	17.4	19.9
a=10 mm	10.8	18.8	19.6
a=15 mm	11.2	16.9	18.4

III.B. THE TEMPERATURE CHANGING EFFECT ON THE FAILURE LOADS

The temperature changing effect on the failure loads were studied as 80, 120 and 160 °C for constant time at 4 hours. The failure loads were presented in figure 4.

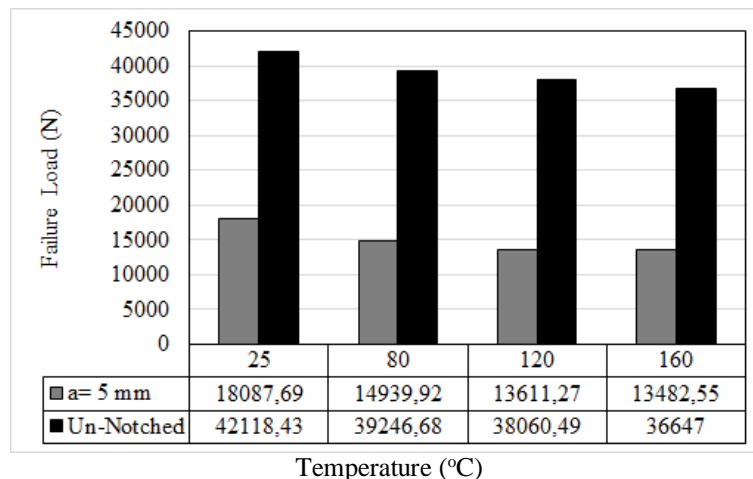


FIGURE 4. THE AGING TEMPERATURE EFFECT ON THE FAILURE LOADS FOR 4 HOURS CONSTANT AGING TIME.

The increasing of temperature leads to decrease both a=5 mm notched and un-notched specimen's failure loads as seen in

Figure 4. The maximum failure load was obtained for un-aged and un-notched specimen as 42118.43 N. The minimum failure

load was obtained as 13482.55 N for notched and aged specimen in 160 °C. The failure loads of thermo-aged specimens were compared to un-aged specimens.

The calculated decreasing rates were presented in Table 3.

TABLE III. DECREASING RATES (%) OF THE FAILURE LOADS FOR TIME CHANGING IN AGING PROCESS AT 4 HOURS.

Temperature	80 °C	120 °C	160 °C
Notched (a=5 mm)	17.4	24.7	25.4
Un-Notched	6.8	9.6	12.9

It can be said that, the V notch were decreased the failure loads of composite plates in figure 4. The failure loads of notched and aged specimens were compared with un-notched and un-aged

specimens. The failure loads of notched composite plates (a=5mm) for 0, 80, 120 and 160 °C were decreased as 57.1%, 62.4%, 64.2% and 63.2% rates, respectively.

III.C. THE FAILURE STARTING AND PROPAGATING IN V-NOTCHED SPECIMENS

In the experimental study, the failure starting and propagating were observed, additionally. The failure mechanisms are showed in Figure 5. Stress concentrations at the tip of notch occur because of the notches. This situation leads to failure starting at this location. When the ultimate failure is realized, it is expected that the composite plate can cracked and breaking occurred. But, in the experimental analysis, it was observed that the matrix failure (epoxy resin) was obtained and fibers fractured. The failure started and propagated along the fiber direction.

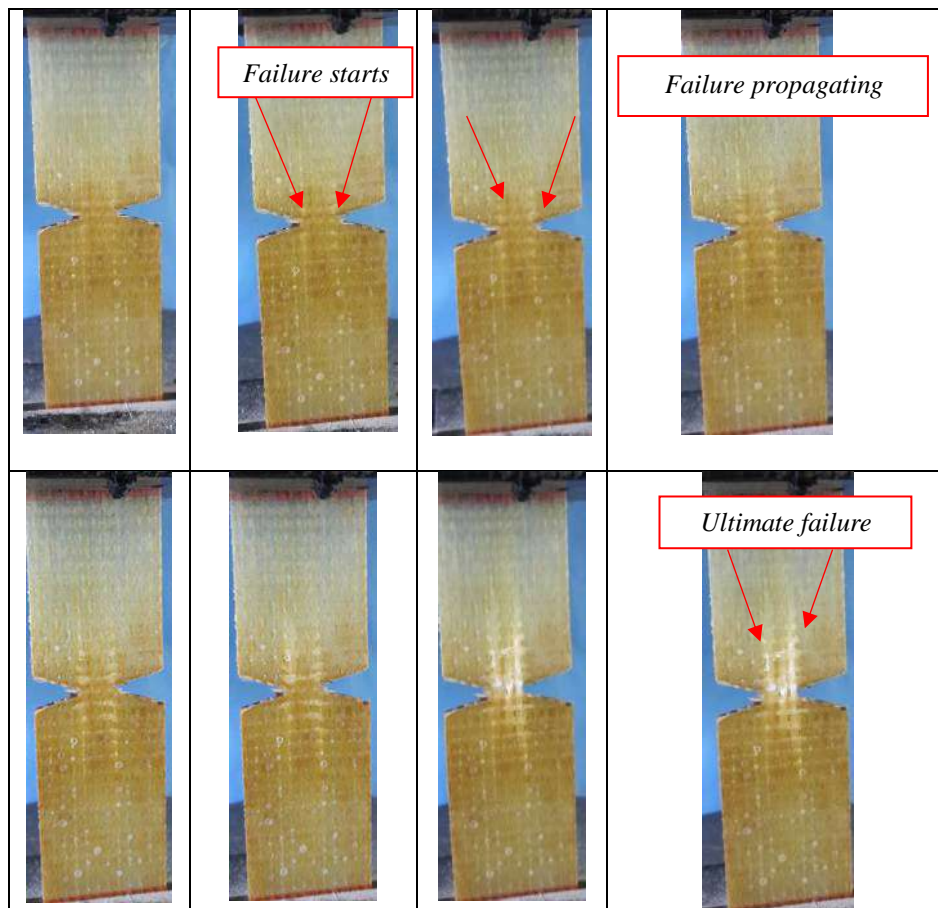


FIGURE 4. THE FAILURE STARTING AND PROPAGATING IN V NOTCHED COMPOSITE PLATES. (TEMPERATURE 120 °C, TIME 4 HOURS, A= 5 MM).

IV. CONCLUSIONS

In this study, the thermo-aging effect on the V-notched glass/epoxy laminated composite plates was investigated experimentally and some of aspects are concluded as follows:

- The failure loads were decreased with opened notch as 57.1%-64.2% rates according to the un-notched composite plates. It is expected situation for failure analysis.
- The increasing of temperature was decreased the failure load for un-notched composite plates as 6.8%-12.9% rates.
- The increasing of temperature was decreased the failure loads of V notched composite plates ($a=5\text{mm}$) as 17.4%-25.4% rates. So, it can be said that variation of temperature is more important parameter on maximum failure load for notched composites
- The increasing of exposure time was decreased the failure loads of V notched composite plates 7.7% - 19.9% rates.
- Variation rates of maximum failure loads remains constant ($\sim 18\%$) for 4 and 6 hours for all notch width. It is seen from results that high curing time does not change variation rates.
- Generally, obtained results shows that thermal aging effect on maximum failure load is independent from notch length and thermal aging is more important effect that reduces the strength for composite materials. Designers of laminated composite plates should choose material and product composites considering this effect in the manufacturing stages.

V. REFERENCES

- [1] Khashaba, U.A., Selmy, A.I., Sonbaty I.A.E., Megahed, M., "Behavior of Notched and Unnotched $[0/\pm 30/\pm 60/90]_s$ GFR/EPOXY Composites Under Static and Fatigue Loads", *Composite Structures*, vol.81, pp: 606-613, 2007.
- [2] Tomita, Y., Tempaku, M., "Effect of Fiber Strength on Tensile Fracture of Unidirectional Long Carbon Fiber-Reinforced Epoxy Matrix Composites", *Materials Characterization*, vol.38, pp: 91-96, 1997.
- [3] Bouiadjra, B.B., Rezgani, L., Ouinas, D., Belhouari, M., Ziadi, A., "Numerical Analysis of the Notch effect and the Behaviour of Notch Crack in Adhesively Bonded Composite Laminates", *Computational Materials Science*, vol.38, pp: 759-764, 2007.
- [4] Kannan, V.K., Murali, V., Rajadural, a., Rao, N., "Finite Element Analysis and Notched Tensile Strength Evaluation of Center-Hole 2D Carbon/Carbon Laminates", *Advanced Composite Materials*, vol.20, pp: 289-300, 2011.
- [5] Çelik A, Turan K., "Investigation of Failure Behaviors of Notched Composite Plates", *Dicle University Journal of Engineering*, vol.6, pp: 73-82, 2015.
- [6] Belaid, S., Chabira, S.F., Balland, P., Sebaal, M., Belhouideg, S., "Thermal Aging Effect on the Mechanical Properties of Polyester Fiberglass Composites", *J. Mater. Environ. Sci.*, vol.6, pp: 2795-2803, 2015.
- [7] Ray, B.C., "Temperature Effect During Humid Ageing on Interfaces of Glass And Carbon Fibers Reinforced Epoxy Composites", *Journal of Colloid and Interface Science*, vol.298, pp: 111-117, 2006.
- [8] Alcock, B., Cabrera, N.O., Barkoula, M., Reynolds, C.T., Govaert, L.E., Peijs, T., "The Effect of Temperature and Strain Rate on the Mechanical Properties of Highly Oriented Polypropylene Tapes and All-Polypropylene Composites", *Composites Science and Technology*, vol.67, pp: 2061-2070, 2007.
- [9] Merino-Pérez, J. L., Ayvar-Soberanis, S., Mersonc, E., Hodzica, A., "The Influence of Heat During Short Ageing Periods on the Mechanical Properties of Cfrp Composites", *ECCM16*, vol.4, pp: 1-8, 2014.
- [10] Mouzakis D.E., Zoga H., Galiotis C., "Accelerated Environmental Ageing Study of Polyester/Glass Fiber Reinforced Composites (GFRPCs)", *Composites: Part B*, vol.39, pp: 467-475, 2008.
- [11] Turan K., "Thermo-Aging Effect on The Buckling Behaviors of U-Notched Composites", *European Journal of Technic*, Vol.6, pp: 9-15, 2016.

MHD Mixed Convection of Nanofluid Flow over a Backward-Facing Step: Effects of Electrical Conductivity Models

Fatih Selimefendigil

Department of Mechanical Engineering,
Celal Bayar University,
Manisa, Turkey
fatih.selimefendigil@cbu.edu.tr

Seda Özcan Çoban

Department of Mechanical Engineering,
Celal Bayar University,
Manisa, Turkey
sedaozcan82@hotmail.com

Abstract—In this study, magneto-hydrodynamic mixed convection of alumina-water nanofluid over a backward-facing step was numerically investigated for various electrical conductivity models. The bottom and top wall of the channel are heated and cooled isothermally while other walls assumed to be adiabatic. Finite element method was used to solve the governing equations. Effects of Hartmann numbers, inclination angles of magnetic field and solid volume fraction of nanoparticles are numerically investigated for three different electrical conductivity models. It was observed that the convective heat transfer characteristics are affected by the variation of these parameters and there exists discrepancy between different electrical conductivity models.

Keywords—nanofluids, electrical conductivity, backward-facing step, mixed convection

XVII. INTRODUCTION

Flow separation and reattachment is of importance in many engineering applications such as flow around buildings, MEMs, airfoils and many others. This phenomenon occurs also for flow over backward/forward facing step geometry [1–11]. The mixed convection studies deals with the complicated interaction between the forced and natural convection effects. Various geometrical configurations and boundary conditions for the mixed convection case has been studied extensively. To increase the convective heat transfer coefficients, convective heat transfer fluids are replaced by nanofluids. Nanofluids are known as new type of heat transfer fluids which consist of nanometer sized particles (nanoparticles sizes 1-100 nm) suspended in the base fluids. They were proved to perform better for heat transfer applications as compared to base fluids. The size, shape and type of nano-particles are effective for the heat transfer enhancement of the base fluid [12, 13]. The influence of magnetic field on electrical conductivity and heat transfer with nanofluids is important for the engineering applications such as coolers of nuclear reactors, purification of molten metals and many other systems. Nanoparticles could be added to the base fluid to affect the thermal conductivity of the

base fluid. In the literature, there are various electrical conductivity models for the nanofluids. In this study, we numerically examined the MHD mixed convection of nanofluid over a backward-facing step for various electrical conductivity models. Effects of various pertinent parameters such as Hartmann number, magnetic inclination angle, solid particle volume fraction on the flow and heat transfer characteristics over a backward-facing step geometry where flow separation and reattachment occurs were analyzed for different electrical conductivity models.

XVIII. MATHEMATICAL FORMULATION

A schematic description of the geometry is shown in Fig 1. The backward step size is H and the height of channel is $3H$. At the inlet of the channel velocity is imposed as parabolic and the temperature is uniform. The channel has a length of $40H$. The walls of the channel are assumed to be adiabatic, except the bottom wall downstream of the channel and the top wall. The working fluid is alumina-water nanofluid under the influence of an oriented magnetic field. The thermophysical properties of the fluid are assumed to be constant. The flow is assumed to be laminar and 2D. Table 1 presents the thermophysical properties of water and alumina nanoparticles at reference temperature.

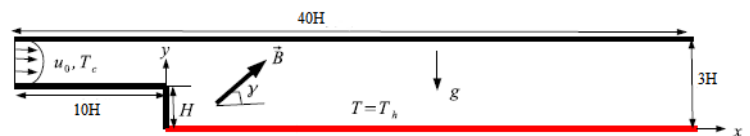


Fig.1. Schematic diagram of the physical model with boundary conditions

TABLE 1: THERMOPHYSICAL PROPERTIES

Property	Water	Al ₂ O ₃
$\rho(\text{kg/m}^3)$	997.1	3970
$C_p(\text{J/kgK})$	4179	765

K (W/mK)	0.6	25
B (1/K)	2.1×10^{-4}	0.85×10^{-5}

Conservation equation of mass, momentum and energy in a 2D Cartesian coordinate system can be written in dimensional form.

$$\frac{\partial u}{\partial x} + \frac{\partial v}{\partial y} = 0 \quad (1)$$

$$\frac{\partial u}{\partial t} + u \frac{\partial u}{\partial x} + v \frac{\partial u}{\partial y} = -\frac{1}{\rho_{nf}} \frac{\partial p}{\partial x} - v_{nf} \left(\frac{\partial^2 u}{\partial x^2} + \frac{\partial^2 u}{\partial y^2} \right) + \frac{\sigma_{nf} B_0^2}{\rho_{nf}} (\sin(\gamma) \cos(\gamma) - \sin^2(\gamma)) \quad (2)$$

$$\frac{\partial u}{\partial t} + u \frac{\partial u}{\partial x} + v \frac{\partial u}{\partial y} = -\frac{1}{\rho_{nf}} \frac{\partial p}{\partial x} - v_{nf} \left(\frac{\partial^2 u}{\partial x^2} + \frac{\partial^2 u}{\partial y^2} \right) + \beta_{nf} g (T - T_c) + \frac{\sigma_{nf} B_0^2}{\rho_{nf}} (\sin(\gamma) \cos(\gamma) - \sin^2(\gamma)) \quad (3)$$

$$\frac{\partial T}{\partial t} + u \frac{\partial T}{\partial x} + v \frac{\partial T}{\partial y} = \alpha_{nf} \left(\frac{\partial^2 T}{\partial x^2} + \frac{\partial^2 T}{\partial y^2} \right) \quad (4)$$

Following parameters can be used to non-dimensionalize the governing equations:

$$X = \frac{x}{H}, Y = \frac{y}{H}, U = \frac{u}{u_0}, V = \frac{v}{u_0}, P = \frac{p}{\rho_f u_0^2}, \theta = \frac{T - T_c}{T_h - T_c}, Gr = \frac{g \beta_f (T_h - T_c) H^3}{\nu_f^2}, Pr = \frac{\nu_f}{\alpha_f}, Ra = Gr Pr \quad (5)$$

$$Ha = B_0 H \sqrt{\frac{\sigma_f}{\mu_f}}, Re = \frac{u_0 H}{\nu_f}, Ri = \frac{Gr}{Re^2}$$

A. Nanofluid effective thermo-physical properties

The effective thermophysical properties of nanofluids are defined by using the following formulas:

$$\rho_{nf} = (1 - \phi) \rho_{bf} + \phi \quad (6)$$

$$(\rho c_p)_{nf} = (1 - \phi) (\rho c_p)_{bf} + \phi (\rho c_p)_p \quad (7)$$

Thermal expansion coefficient of the nanofluid is;

$$(\rho \beta)_{nf} = (1 - \phi) (\rho \beta)_{nf} + \phi (\rho \beta)_p \quad (8)$$

The effective thermal conductivity of the nanofluid includes the effect of Brownian motion. Effects of particle size, particle volume fraction and temperature are taken into account :

$$k_{nf} = k_{st} + k_{Brownian} \quad (9)$$

where k_{st} is the static thermal conductivity.

$$k_{st} = k_f \left[\frac{(k_p + 2k_f) - 2\phi(k_f + k_p)}{(k_p + 2k_f) + \phi(k_f + k_p)} \right] \quad (10)$$

The interaction between the nanoparticles and the effect of temperature are;

$$k_{Brownian} = 5 \times 10^4 \phi \rho_f c_{p,f} \sqrt{\frac{k_b T}{\rho_p d_p}} f(T, \phi, d_p) \quad (11)$$

$$\mu_{nf} = \mu_{st} + \mu_{Brownian} = \mu_f (1 - \phi)^{-0.25} + \frac{k_{Brownian}}{k_f} \times \frac{\mu_f}{Pr_f} \quad (12)$$

B. Electrical conductivity models for alumina-water nanofluid

In this study, three different electrical conductivity models for alumina-water nanofluids were considered. The first model was Maxwell's model which was developed for calculating the electrical conductivity for random suspension of spherical particles. For Maxwell model (M1 model), electrical conductivity of nanofluid is written as [14]:

$$\sigma_{nf} = \sigma_f \left(1 + \frac{3(f-1)\phi}{(f+2) - (f-1)\phi} \right) \quad (13)$$

The second model (M2) is an experimental study for alumina-water nanofluid effective electrical conductivity was obtained by Ganguly et al. [15]

$$\sigma_{nf} = \sigma_f (3679.049\phi - 1.085779T - 42.6384) \quad (14)$$

The electrical conductivity of the nanofluid enhances linearly with volume fraction and temperature.

The third model (M3) used in the study was the experimental correlation from Minea and Luciu [16]:

$$\begin{aligned} \sigma_{nf} = & 176.69 + 588.41(\phi \times 100) - 13.64T - 86.31(\phi \times 100)^2 + \\ & 0.36T^2 + 1.07(\phi \times 100)T + 11.06(\phi \times 100)^3 - 0.03T^3 + 0.18T^2 - \\ & 1.01T(\phi \times 100)^2 \end{aligned} \quad (15)$$

XIX. SOLUTION METHODOLOGY

To solve the governing equations, Galerkin weighted residual finite element method was used. In this method, computational domain was divided into non-overlapping regions and the field variables are approximated by using the Lagrange polynomials of different orders. The convergence of the solution is assumed when the relative error is less than 10^{-6} . The grid independence of the solution is assured and the code is validated by using various sources in the open literature (results are not shown here).

Local Nusselt number is calculated by using the following given equation:

$$Nu_x = -\frac{k_{nf}}{k_f} \left(\frac{\partial \theta}{\partial n} \right)_{wall} \quad (16)$$

Average Nusselt number is calculated along the hot wall of the bottom wall downstream of the step by using:

$$Nu_m = \frac{1}{L} \int_0^L Nu_x dx \quad (17)$$

where L denotes the length of the bottom wall downstream of the step.

IV. RESULTS AND DISCUSSION

Numerical study of nanofluid flow over a backward facing step for the mixed convection under the effect of oriented magnetic field for various electrical conductivity models is performed. It is expected that the variations of the flow conditions and by change of the thermo-physical properties, the transfer and fluid flow characteristics are changed. It is also expected different electrical conductivity models results in variations of heat transfer rates.

In the simulation, Richardson number was fixed to 0.5. In this regime, both forced and natural convective effects are important. Effects of Hartmann number on the streamline and isotherm distributions are demonstrated in Figure 2 for Maxwell model (M1 model). Flow separates at the edge and a recirculation region is formed behind the step. As the value of Hartmann number increases, the length of the separation reduces and it is restricted to a small zone near the step. Steep thermal gradients are seen near the reattachment point and it is getting denser for higher Hartmann values. Table 2 presents the results of average Nusselt number for various Hartmann number and electrical conductivity models. For higher values of Hartmann number, average Nusselt number becomes higher for model 1, but for M2 and M3 model, at the highest value of Hartmann number its value becomes lower which is due to the different electrical conductivity of the models. The sensitivity of M2 and M3 models for changes in Nusselt number with respect to a change in Hartmann number is higher as compared to M1 model.

Effects of varying magnetic inclination angle on the streamline and isotherm distributions are demonstrated Figure 3. There are some small variations in the flow and isotherm structures behind the step. Table 3 presents the results of average Nusselt numbers for different inclination angles and different electrical conductivity models. Average heat transfer rate enhances with magnetic inclination angle which is due to the effect of Lorentz forces caused by magnetic field in the x and y momentum. There are variations in different models (M1, M2 and M3) and the rate of change is lower for Maxwell model (M1) as compared to other models.

Adding nanoparticles to the water results in thermal conductivity enhancement. In this study, alumina solid particle volume fraction up to 0.03 was used. As it is seen in Table 4, the average heat transfer rate increases with nanoparticle addition for all considered models. Average heat transfer enhancement is lowest for M1 model while it is highest for M2 model. For M1 model only 4.36% heat transfer enhancement was obtained while 8.04% was achieved for M2 model at the highest volume fraction as compared to solid volume fraction of 1%.

TABLE II.AVERAGE NUSSELT NUMBER FOR VARIOUS HARTMANN NUMBERS AND ELECTRICAL CONDUCTIVITY MODELS (M1,M2,M3)

Hartman Number	Averaged Nusselt Number		
	Model 1	Model2	Model3
0	7.365	7.365	7.365
20	7.784	8.045	7.719
40	8.080	7.594	6.216

TABLE III.AVERAGE NUSSELT NUMBER FOR VARIOUS MAGNETIC INCLINATION ANGLES AND ELECTRICAL CONDUCTIVITY MODELS (M1,M2,M3)

Inclination angle	Averaged Nusselt Number		
	Model 1	Model2	Model3
0°	7.364	7.349	7.314
45°	7.480	8.049	8.099
90°	7.587	8.226	8.164

TABLE IV.AVERAGE NUSSELT NUMBER FOR NANOPARTICLE VOLUME FRACTION AND ELECTRICAL CONDUCTIVITY MODELS (M1,M2,M3)

Volume Fraction	Averaged Nusselt Number		
	Model 1	Model2	Model3
0.01	7.399	7.831	8.014
0.02	7.561	8.206	8.167
0.03	7.722	8.461	8.479

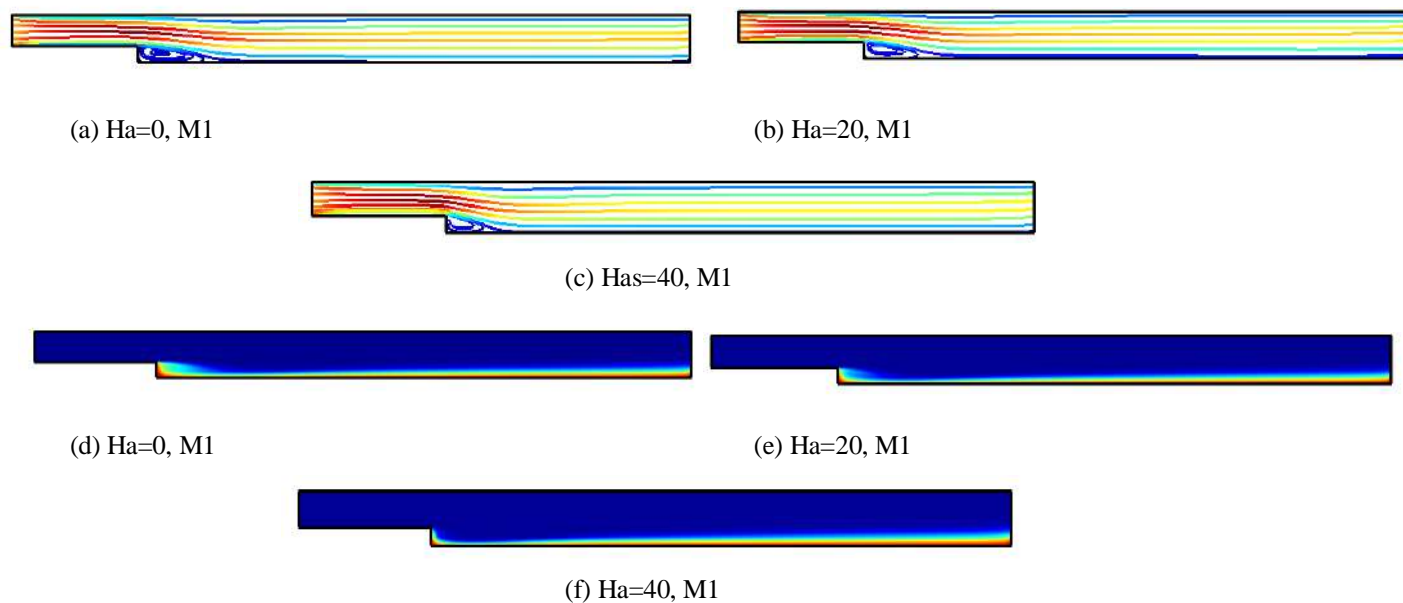


Fig.2.Effects of various Hartmann number on the streamline and isotherm distribution for M1 model ($\eta = 45^\circ$, $Ri=0.5$, $\Phi=0.015$)

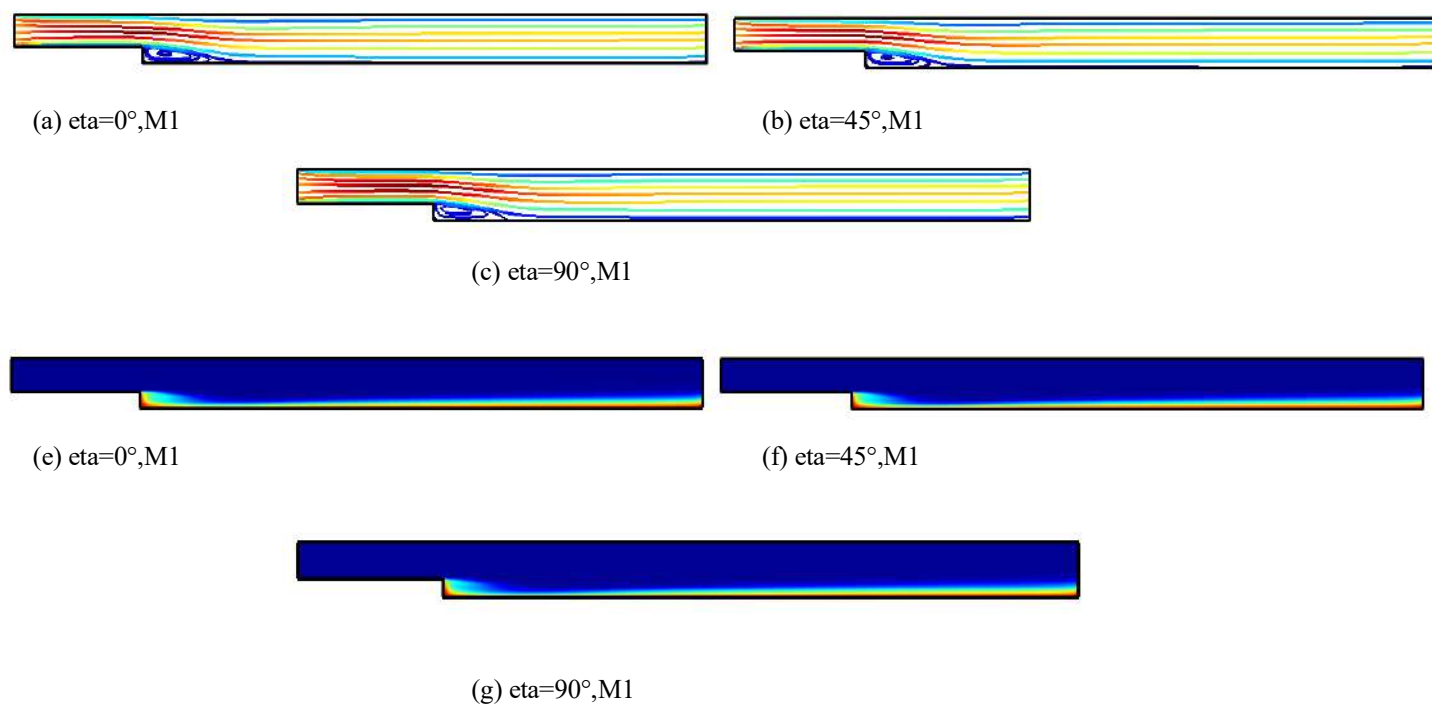


Fig.3. Effects of various magnetic inclination angle on the streamline and isotherm distribution for M1 model ($Ha=10$, $Ri=0.5$, $\Phi=0.015$)

REFERENCES

- [1] E. Erturk, "Numerical solutions of 2-d steady incompressible flow over a backward-facing step, part i: high reynolds number solutions", *Comput. Fluids*, vol. 37, pp.633–655, 2008
- [2] J.G.B. Saldana, and N.K. Anand," Flow over a three-dimensional horizontal forwardfacing Step", *Numer. Heat Transfer, Part A*, vol. 5, pp. 1–17, 2008
- [3] F. Selimefendigil, and H.F. Oztop," Numerical analysis of laminar pulsating flow at abackward facing step with an upper wall mounted adiabatic thin fin", *Comput. Fluids* vol. 88 , pp. 93–107, 2013
- [4] J.G.B. Saldana, N.K. Anand, and V. Sarin," Numerical simulation of mixed convective flow over a three-dimensional horizontal backward facing step", *J. Heat Transfer* ,vol.127, pp.1027–1036, 2005
- [5] H. Iwai, K. Nakabe, and K. Suzuki, "Flow and heat transfer characteristics of backward-facing step laminar flow in a rectangular duct", *Int. J. Heat Mass Transfer* 43, vol. 457–471, 2000
- [6] J. Nie, and B. Armaly , "Convection in laminar three-dimensional separated flow", *Int. J. Heat Mass Transfer* , vol.47 , pp.5407–5416, 2004
- [7] F. Selimefendigil, and H.F. Oztop, "Control of laminar pulsating flow and heat transfer in backward-facing step by using a square obstacle", *J. Heat Transfer* vol.136 pp. 081701, 2014
- [8] D. Barkley, M.G.M. Gomes, and R.D. Henderson," Three-dimensional instability in flow over a backward-facing step", *J. Fluid Mech.* Vol.473, pp. 167–190, 2002.
- [9] H. Abu-Mulaweh," A review of research on laminar mixed convection flow over backward- and forward facing steps", *Int. J. Thermal Sci.* Vol.42, pp. 897–909, 2004
- [10] M. Sherry, D. LoJacono, and J. Sheridan," An experimental investigation of the recirculation zone formed downstream of a forward facing step", *J. Wind Eng. Ind. Aerodyn*, vol. 98, pp. 888–894, 2010.
- [11] H. Abu-Mulaweh, "Turbulent mixed convection flow over a forward-facing step – the effect of step heights", *Int. J. Thermal Sci.* vol. 44, pp.155–162, 2005.
- [12] F. Selimefendigil, and H.F. Oztop, "Pulsating nanofluids jet impingement cooling of a heated horizontal surface", *International Journal of Heat and Mass Transfer* , vol.6, pp. 54-65, 2014
- [13] F. Selimefendigil, and H.F. Oztop, " Mixed convection in a two-sided elastic walled and SiO₂ nanofluid filled cavity with internal heat generation: Effects of inner rotating cylinder and nanoparticle's shape", *Journal of Molecular Liquids*, vol.212, pp. 509-516, 2015
- [14] J. Maxwell, *A Treatise on Electricity and Magnetism*, Oxford University Press, 1873.
- [15] S. Ganguly, S. Sikdar, S. Basu, "Experimental investigation of the effective electrical conductivity of aluminum oxide nanofluids", *Powder Technology*, vol. 196 pp.326-330, 2009
- [16] A. A. Minea, R. S. Luciu, Investigations on electrical conductivity of stabilized water based Al₂O₃- nanofluids, *Microfluid Nanofluid*, vol. 13, pp. 977-985, 2012

Numerical Simulation of Mixed Convection of Nanofluid Flow over a Backward-Facing Step

Fatih Selimefendigil

Department of Mechanical Engineering,
Celal Bayar University,
Manisa, Turkey
fatih.selimefendigil@cbu.edu.tr

Seda Özcan Çoban

Department of Mechanical Engineering,
Celal Bayar University,
Manisa, Turkey
sedaozcan82@hotmail.com

Abstract—In this study, mixed convection of alumina-water nanofluid over a backward-facing step was numerically studied. The bottom wall of the channel is kept at constant hot temperature while the top wall is at isothermal cold temperature. The governing equations were solved with Galerkin residual finite element method. Effects of various parameters such as Richardson number (between 0.01 and 20) and solid volume fraction of nanoparticles (between 0 and 0.04) on the convective heat transfer characteristics are numerically studied. Average Nusselt numbers increases with increasing solid volume fraction of nanoparticle and decreases with Richardson number. The rate of the enhancement is about 8.5% at the highest volume fraction.

Keywords- backward-facing step, nanofluids, fem

I. INTRODUCTION

There are many various engineering applications such as flow around buildings, electronic devices, combustors, airfoils and collectors of power systems where flow separation and reattachment occurs as in flow over backward/forward facing step geometry [1–11]. The complex interaction between the natural and forced convection is very complicated in practical engineering systems and various studies have been performed for different geometries and boundary conditions. In convective heat transfer, nanofluids offer a great advantage to enhance the heat transfer coefficients [12, 13]. Nanofluids are known as new generation heat transfer fluids which consist of nanometer sized particles (nanoparticles sizes 1-100 nm) suspended in the base fluids. Nanofluids have been proved that they are better heat transfer fluids than base fluids. The size, shape and type of metallic or non-metallic nano-sized particles are effective for the heat transfer enhancement of the base fluid.

In this study, we study the mixed convective heat transfer for a backward facing step geometry with nanofluids. The aim was to numerically analyze the effects of various pertinent parameters such as solid particle volume fraction on the flow and heat transfer characteristics over a backward-facing step geometry where flow separation and reattachment occurs.

II. MATHEMATICAL FORMALISM

Fig 1 depicts a schematic description of the physical problem for a channel with a backward facing step. The backward step size is H and the height of channel is $3H$. At the inlet of the channel velocity defined as parabolic and the temperature ($T=T_c$) is uniform. The downstream length of the channel beginning from the step to the outlet is $40H$. The bottom wall downstream of the channel is maintained at ($T = T_h$). The channel is filled with alumina-water nanofluid for different solid particle volume fraction. The flow is assumed to be laminar and 2D. Thermophysical properties of water and alumina is given in Table 1.

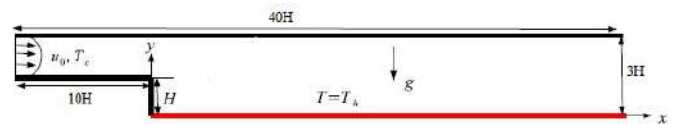


Fig.1. Schematic diagram of the physical model with boundary conditions

TABLE 1: THERMOPHYSICAL PROPERTIES

Property	Water	Alumina
$\rho(\text{kg/m}^3)$	997.1	3970
$C_p(\text{J/kgK})$	4179	765
$K(\text{W/mK})$	0.6	25
$\beta(1/\text{K})$	2.1×10^{-4}	0.85×10^{-5}

Conservation equations of mass, momentum and energy in a two dimensional Cartesian coordinate system can be written in dimensional form as follows:

$$\frac{\partial u}{\partial x} + \frac{\partial v}{\partial y} = 0 \quad (1)$$

$$u \frac{\partial u}{\partial x} + v \frac{\partial u}{\partial y} = -\frac{1}{\rho_{nf}} \frac{\partial p}{\partial x} + \nu_{nf} \left(\frac{\partial^2 u}{\partial x^2} + \frac{\partial^2 u}{\partial y^2} \right) \quad (2)$$

$$u \frac{\partial v}{\partial x} + v \frac{\partial v}{\partial y} = -\frac{1}{\rho_{nf}} \frac{\partial p}{\partial y} + \nu_{nf} \left(\frac{\partial^2 v}{\partial x^2} + \frac{\partial^2 v}{\partial y^2} \right) + \beta_{nf} g (T - T_c) \quad (3)$$

$$\frac{\partial T}{\partial t} + u \frac{\partial T}{\partial x} + v \frac{\partial T}{\partial y} = \alpha_{nf} \left(\frac{\partial^2 T}{\partial x^2} + \frac{\partial^2 T}{\partial y^2} \right) \quad (4)$$

Non-dimensional form of the above equations can be obtained by using the following parameters:

$$X = \frac{x}{H}, Y = \frac{y}{H}, U = \frac{u}{u_0}, V = \frac{v}{u_0}, P = \frac{p}{\rho_f u_0^2}$$

$$\theta = \frac{T - T_c}{T_h - T_c}, Gr = \frac{g \beta_f (T_h - T_c) H^3}{\nu_f^2}, Pr = \frac{\nu_f}{\alpha_f}, Ra = Gr Pr$$

$$Re = \frac{u_0 H}{\nu_f}, Ri = \frac{Gr}{Re^2} \quad (5)$$

A. Nanofluid effective thermo-physical properties

The effective thermo-physical properties of nanofluids are defined by using the following formulas:

$$\rho_{nf} = (1 - \phi) \rho_{bf} + \phi \rho_p \quad (6)$$

$$(\rho c_p)_{nf} = (1 - \phi) (\rho c_p)_{bf} + \phi (\rho c_p)_p \quad (7)$$

Thermal expansion coefficient of the nanofluid is;

$$(\rho \beta)_{nf} = (1 - \phi) (\rho \beta)_{nf} + \phi (\rho \beta)_p \quad (8)$$

The subscript 'bf' denotes the base fluid, 'nf' is nanofluid, 'p' is the solid particle. The effective thermal conductivity of the nanofluid includes the effect of Brownian motion. Effects of particle size, particle volume fraction and temperature are taken into account :

$$k_{nf} = k_s + k_{Brownian} \quad (9)$$

where k_s is the static thermal conductivity,

$$k_{st} = k_f \left[\frac{(k_p + 2k_f) - 2\phi(k_f + k_p)}{(k_p + 2k_f) + \phi(k_f + k_p)} \right] \quad (10)$$

The interaction between the nanoparticles and the effect of temperature are;

$$k_{Brownian} = 5 \times 10^4 \phi \rho_f c_{p,f} \sqrt{\frac{k_b T}{\rho_p d_p}} f'(T, \phi, d_p) \quad (11)$$

$$\mu_{nf} = \mu_{st} + \mu_{Brownian} = \mu_f (1 - \phi)^{-0.25} + \frac{k_{Brownian}}{k_f} \times \frac{\mu_f}{Pr_f} \quad (12)$$

III. SOLUTION METHODOLOGY

Galerkin weighted residual finite element method was used to solve the governing equations. The computational domain was divided into non-overlapping regions and the field variables are approximated by using the Lagrange polynomials of different orders. The convergence of the solution is assumed when the relative error is less than 10^{-6} . The grid independence of the solution is assured and the code is validated by using various sources in the open literature (results are not shown here).

Local Nusselt number is calculated by using the following given equation:

$$Nu_x = - \frac{k_{nf}}{k_f} \left(\frac{\partial \theta}{\partial n} \right)_{wall} \quad (13)$$

Average Nusselt number is calculated along the hot wall of the bottom wall downstream of the step by using:

$$Nu_m = \frac{1}{L} \int_0^L Nu_x dx \quad (14)$$

IV. RESULTS AND DISCUSSION

In this study, a numerical study of nanofluid flow over a backward facing step for the mixed convection is presented. It is expected that the variations of the flow conditions and by change of the thermo-physical properties, the transfer and fluid flow characteristics are changed.

Effects of Richardson number on the streamline and isotherm distributions are demonstrated in Figure 2. Richardson number is the ratio of the natural convection to the forced convection. Ri number was varied by changing the Reynolds number while keeping the Grashof number fixed. Therefore, an increment in the Ri number results in reducing the incoming velocity. The length of the recirculation zone behind the step reduces in size for higher Ri values which is due to the reduction of the x-velocity component and the effects of natural convection becomes important. Steep thermal gradients are seen near the reattachment point. Variations of the local and average heat transfer rates are given in Figure 3 and Figure 4. The location where the highest heat transfer rates are seen becomes closer to the step for higher values of Ri number. Average Nusselt number decreases with Ri number. Average heat transfer rate is reduced by about 56.13% at the highest value of Ri when compared to value for Ri=0.01.

Adding nanoparticles to the water results in thermal conductivity enhancement. In this study, solid particle volume fraction up to 0.04 was used. As it is seen in Figure 5, local Nusselt number increases for higher particle volume fraction. The rate of the enhancement is higher for the location away from the step after the maximum in the local Nusselt number is seen. Average Nusselt number increases linearly with solid particle volume fraction (Figure 6). Average heat transfer rate increases by about 8.5% at the highest volume fraction as compared to the base fluid.

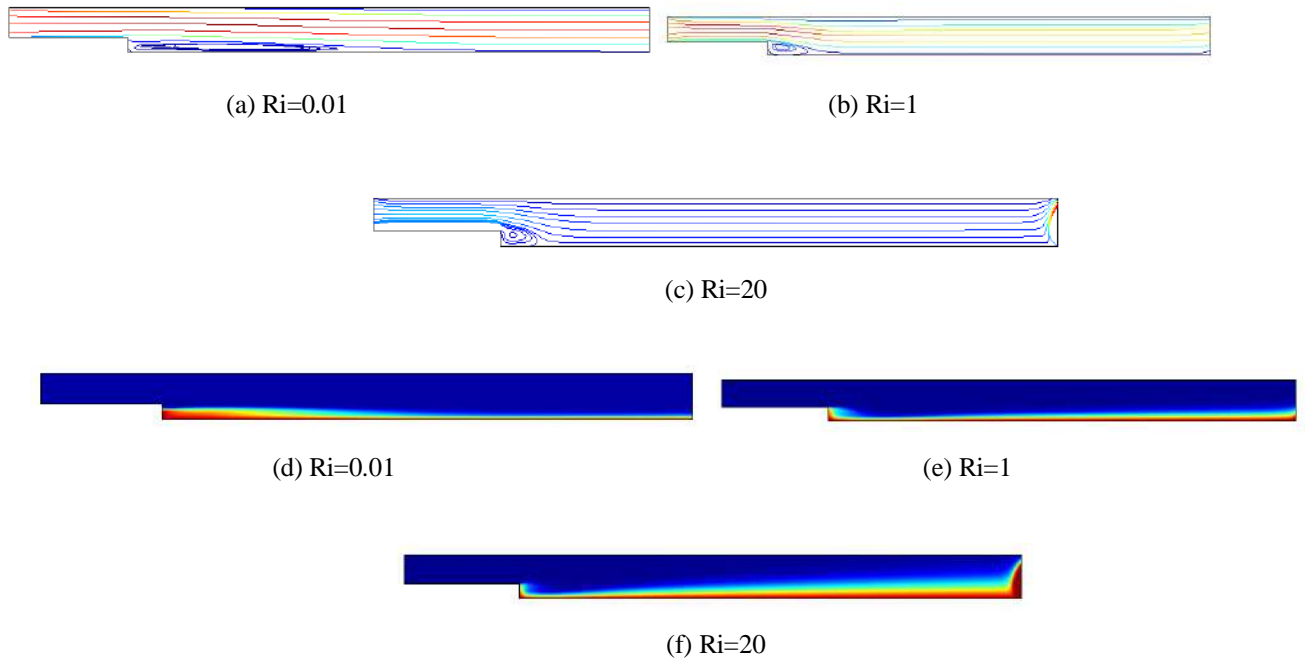


Fig.2.Effects of Richardson number on the streamline and isotherm distributions ($\phi=0.02$)

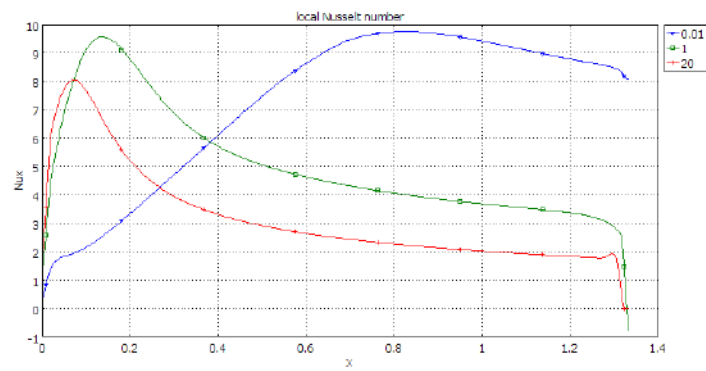


Fig. 3.Effects of Richardson number on the local Nusselt number variations ($\phi=0.02$)

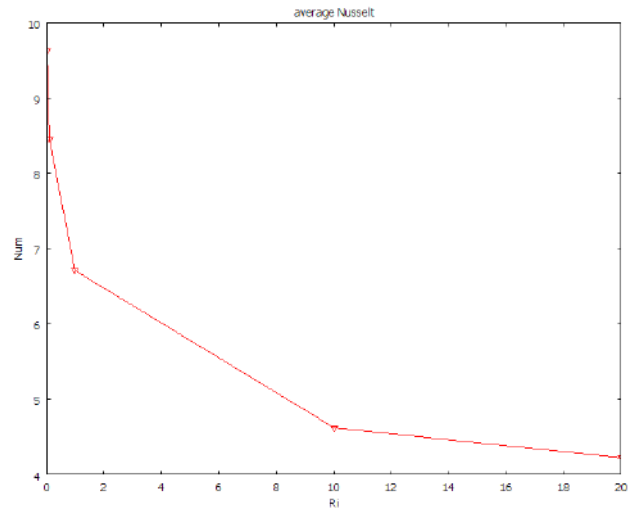


Fig. 4. Effects of Richardson number on the average Nusselt number distributions along the hot wall ($\phi=0.02$)

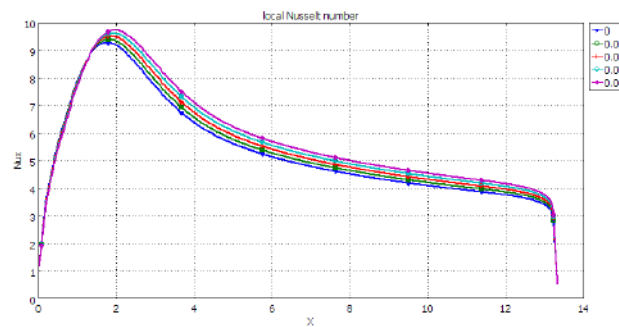


Fig. 5. Effects of solid particle volume fractions on the local Nusselt number distributions along the hot wall ($Ri=1$)

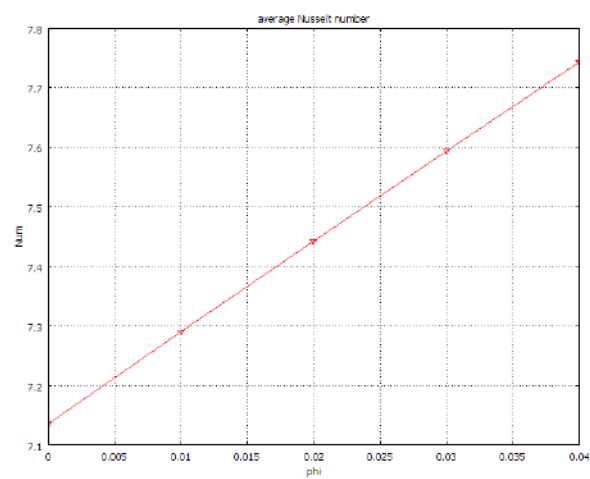


Fig. 6. Effects of solid particle volume fractions on the average Nusselt number distributions along the hot wall ($Ri=1$)

REFERENCES

- [1] E. Erturk, "Numerical solutions of 2-d steady incompressible flow over a backward-facing step, part i: high reynolds number solutions", *Comput. Fluids*, vol. 37, pp.633–655, 2008
- [2] J.G.B. Saldana, and N.K. Anand," Flow over a three-dimensional horizontal forwardfacing Step", *Numer. Heat Transfer, Part A*, vol. 5, pp. 1–17, 2008
- [3] F. Selimefendigil, and H.F. Oztop," Numerical analysis of laminar pulsating flow at abackward facing step with an upper wall mounted adiabatic thin fin", *Comput. Fluids* vol. 88 , pp. 93–107, 2013
- [4] J.G.B. Saldana, N.K. Anand, and V. Sarin," Numerical simulation of mixed convective flow over a three-dimensional horizontal backward facing step", *J. Heat Transfer* ,vol.127, pp.1027–1036, 2005
- [5] H. Iwai, K. Nakabe, and K. Suzuki, "Flow and heat transfer characteristics of backward-facing step laminar flow in a rectangular duct", *Int. J. Heat Mass Transfer* 43, vol. 457–471, 2000
- [6] J. Nie, and B. Armaly, "Convection in laminar three-dimensional separated flow", *Int. J. Heat Mass Transfer* , vol.47 , pp.5407–5416, 2004
- [7] F. Selimefendigil, and H.F. Oztop, "Control of laminar pulsating flow and heat transfer in backward-facing step by using a square obstacle", *J. Heat Transfer* vol.136 pp. 081701, 2014
- [8] D. Barkley, M.G.M. Gomes, and R.D. Henderson," Three-dimensional instability in flow over a backward-facing step", *J. Fluid Mech.* Vol.473, pp. 167–190, 2002.
- [9] H. Abu-Mulaweh," A review of research on laminar mixed convection flow over backward- and forward facing steps", *Int. J. Thermal Sci.* Vol.42, pp. 897–909, 2004
- [10] M. Sherry, D. LoJacono, and J. Sheridan," An experimental investigation of the recirculation zone formed downstream of a forward facing step", *J. Wind Eng. Ind. Aerodyn*, vol . 98, pp. 888–894, 2010.
- [11] H. Abu-Mulaweh, "Turbulent mixed convection flow over a forward-facing step – the effect of step heights", *Int. J. Thermal Sci.* vol. 44, pp.155–162, 2005.
- [12] F. Selimefendigil, and H.F. Oztop, "Pulsating nanofluids jet impingement cooling of a heated horizontal surface", *International Journal of Heat and Mass Transfer* , vol.6, pp. 54–65, 2014
- [13] F. Selimefendigil, and H.F. Oztop, " Mixed convection in a two-sided elastic walled and SiO₂ nanofluid filled cavity with internal heat generation: Effects of inner rotating cylinder and nanoparticle's shape", *Journal of Molecular Liquids*, vol.212, pp. 509–516, 2015

Carbon Footprint and Energy Payback Time of a 2 Megawatt Wind Turbine

Nesrin KAYATAŞ DEMİR

Dept. of Energy Systems Engineering
Erciyes University
Kayseri, Turkey
nkayatas@erciyes.edu.tr

Akif TAŞKIN

Graduate School of Natural and Applied Sciences
Erciyes University
Kayseri, Turkey
taskinakif@yahoo.com

Abstract— Electricity generation from renewable energy sources has a significant presence in Turkey's energy mix in recent years. In 2016, wind energy has 21.2% share among the new installed renewable power sources in Turkey. Wind energy accepted as one of the clean energy sources, but during manufacturing, construction, utilization and decommissioning stages wind turbine power plants have some adverse effects on environment. In this study carbon footprint and energy payback time of a 2 megawatt wind turbine, which is assumed to be installed on Develi/Kayseri, are calculated by using life cycle assessment approach. Life cycle assessment methodology is used to determine the environmental impacts of a system or product by compiling inputs and outputs from raw material extraction to recycling. Firstly, measured annual hourly wind velocities are processed to determine the wind potential of Develi and by using the power curve of selected wind turbine annual electricity production is predicted. In life cycle assessment stage, selected wind turbine's material and energy inputs are collected from manufacturers, literature, field research and assumptions. Functional unit is selected as 1kWh electricity production and lifetime of wind turbine is selected as 20 years. Collected data are entered the GaBi life cycle assessment software to obtain life cycle model and to determine the system descriptions. Results showed that carbon footprint of selected wind turbine is calculated as 3.93E-2 kg- CO₂/kWh and energy payback time of selected wind turbine is calculated as 37 months.

Keywords— carbon footprint; energy payback time; life cycle assessment; renewable energy, wind turbine.

I. INTRODUCTION

Renewable and non-renewable energy sources can be used to produce useful energy such as heat or electricity. Renewable energy sources (wind, hydropower, geothermal, biomass, solar energy) can replenish themselves in a short span of time. Non-renewable energy sources (coal, oil, natural gas, nuclear) can take to form thousands of years and they use up much faster than they are produced [1]. At present, besides the energy production affairs both from renewables and non-renewables, some environmental effects became current issues. Energy conversion from wind power into electricity is one of the cleanest and most

sustainable ways to produce electricity. Wind is caused by variable heating and cooling of the earth's surface. Windmills were using for water pumping and wheat processing in ancient times, but since twentieth century they have been using to generate electricity. Nowadays, wind energy is the fastest growing source of electricity together with hydro. Wind energy is accepted as emission-free source of energy. But they have some harmful effects on the environment. Today, to determine the environmental effects of electricity generation from wind power during the lifetime such as carbon footprint, life cycle assessment methodology is used. The aim of this study, to determine the carbon footprint of a 2 megawatt capacity wind turbine which is assumed to be installed on Develi. Moreover, energy payback time of selected wind turbine is calculated [2-4].

II. WIND ENERGY POTENTIAL OF DEVELI

Generated energy from a wind turbine is based on the wind potential of operation area and characteristics of selected wind turbine in general. Before installing of a wind turbine on a region, wind characteristics of selected area must be estimated. In this work, wind potential of Develi is analyzed. Develi is located at 38°23' latitude (N) and 35°29' longitude (E) with 1330 m altitude. Firstly, annual hourly wind speed and wind direction data, which were observed by Turkish State Meteorological Service at 10 m altitude, is processed on computer, so methodical wind data are obtained. Wind is exposed to some obstacles and surface roughness on the surface of the earth. So, wind velocity changes with height. Therefore, wind speed at 100 m altitude must be calculated. To calculate the wind speed at 100 m height, log law which is given in the following equation is used [5-7].

$$v = v_0 \left(\frac{\ln z/z_s}{\ln z_0/z_s} \right) \quad (1)$$

where, v is the wind velocity at the altitude of z , z_0 is wind speed at the height of z_0 and z_s is selected as 0.15 which is surface the roughness factor and depends on region. By using (1) annual wind speed data at 100 m height are calculated. Results show that mean and maximum wind speeds are 4.32 and 26.84 m/s, respectively. Annual mean wind speed data are given in “Fig. 1”. The graph shows that monthly mean wind speeds reach to the highest levels in April, March and June.

In this study, 2050 kW rated power capacity Enercon E82 brand wind turbine is selected for calculations with 2 m/s cut-in speed, 25 m/s cut-out speed, 100 m hub height and 82 m rotor diameter. To obtain the generated power at 100 m height from the selected wind turbine, power curve is used. “Fig. 2” shows the output power of selected wind turbine that varies with the wind speed. The graph shows that turbine starts to generate power the wind speed of 2 m/s and this point is called cut-in speed. The generated power reaches the maximum at the 13 m/s and this point is called rated output speed.

Moreover, to obtain the power for a given wind speed, 6th degree polynomial equation is derived by using curve fitting method applying on power curve. By substituting the annual hourly wind speed data into the 6th degree polynomial equation hourly generated power ($P_i(v)$) for a given speed is calculated. Annual total amount of generated power (E_p) is calculated by summing the hourly generated powers and defined in the following equation:

$$E_p = \sum_{t=1}^n P_i(v) t \quad (2)$$

where t is defined as one hour period and n is defined as the total number of hours. In this work n is selected as 8760, which is the total number of hours in a year.

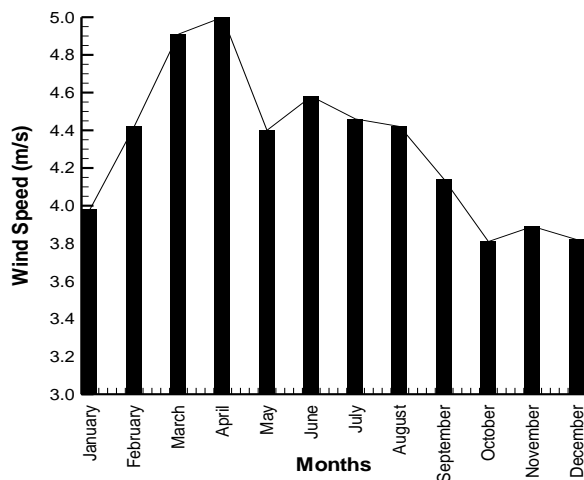


Fig. 1. Monthly wind speed of Develi

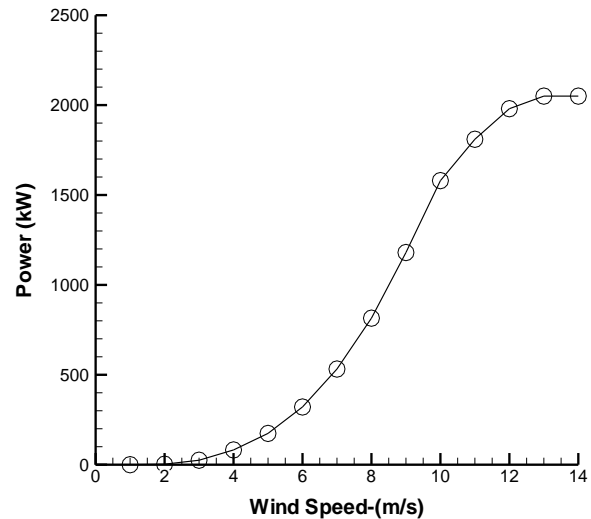


Fig 2. Power curve of 2 megawatt wind turbine

III. LIFE CYCLE ASSESSMENT OF A 2 MEGAWATT WIND TURBINE

Life cycle assessment is defined as the methodology to evaluate the environmental impacts related to raw material extraction, production, assembly, use, dismantling and recycling stages of a system or product. Life cycle assessment consists of 4 stages and each stage interact with each other [8-9].

In goal and scope definition stage, purpose of the work, functional unit, system boundary, assumptions and target groups must be defined clearly. In this study, functional unit, which is used to compare the results, is selected as 1 kWh electricity generation by 2 megawatt wind turbine, system boundary consists of raw material extraction throughout dismantling and recycling, target groups defined as private sector, universities, ministries, decision makers and local governments. The lifetime of the wind turbine is selected as 20 years. GaBi life cycle assessment software tool is used for evaluations [10]. During inventory analysis stage, material and energy inputs must be gathered in accordance with system boundary to calculate the environmental impacts by using GaBi software. For this study, input data are gathered from wind turbine manufacturers, literature and active wind power plants. Selected wind turbine is assumed to be consist of foundation, nacelle, rotor, tower and other components [11-13]. Material input mass percentages are given in “Fig. 3”. The graph shows that foundation of wind turbine shares the maximum amount of material input by mass.

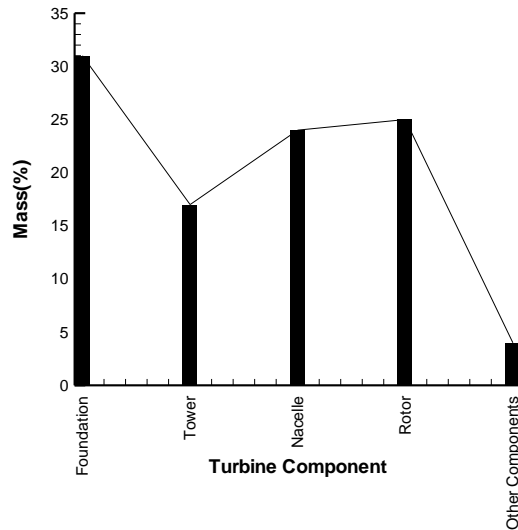


Fig. 3. Material mass inputs by turbine component

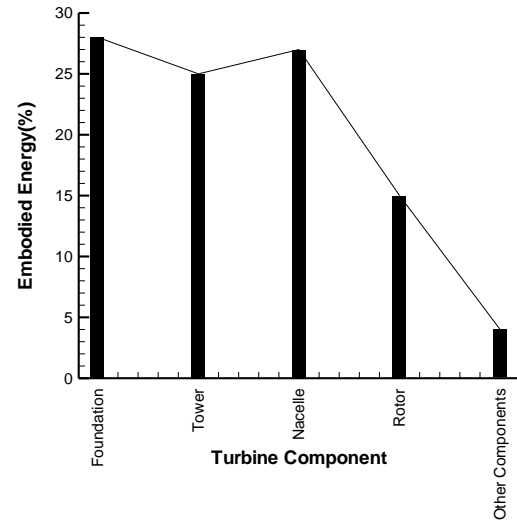


Fig. 4. Embodied energy by turbine component

Impact categories must be selected at impact assessment phase. For this study carbon footprint (kg CO₂-equivalent) is selected as impact category and CML2001 is selected as impact assessment method for calculations. Interpretation stage is the last stage of a life cycle assessment work and results are evaluated at this stage.

IV. RESULTS

Embodied energy (E_{Embodied}) is defined as consumed energy by a wind turbine's whole life cycle and calculated as $4.04\text{E}+6$. Also, energy payback time (E_{PT}) of selected wind turbine is defined as the consumed energy over produced energy (E_{Produced}) in a year and given in the following equation:

$$E_{\text{PT}} = \frac{E_{\text{Embodied}}}{E_{\text{Produced}}} \quad (3)$$

Embodied energies consumed by turbine components are given in the "Fig. 4" and the graph shows that foundation, nacelle and tower consume more energy during the whole life cycle of selected wind turbine.

Carbon footprint of 2 megawatt wind turbine is calculated by compiling the collected material and energy data into GaBi software. Results show that carbon foot print of selected wind turbine is $1.01\text{E}+6$ kg CO₂-mass. Effects of wind turbine components on carbon footprint are given in "Fig. 5". According to the graph amount of contribution on carbon footprint is higher for foundation with the 37 percentage.

By applying the (2), the total amount of energy E_p is calculated as $1.28\text{E}+6$ kWh. Life time of the wind turbine is selected as 20 years so the total amount of energy generated is calculated as $2.56\text{E}+7$ kWh. Carbon footprint of the selected turbine per kWh defined as the ratio of carbon footprint to the total amount of energy generated over 20 years and calculated as $3.93\text{E}-2$ kg-CO₂/kWh. By using (2) and (3) energy payback time is calculated as 37 months.

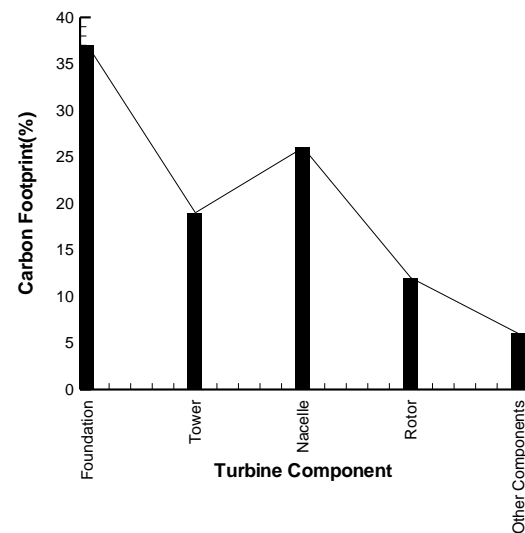


Fig. 5. Carbon footprint by turbine component

V. CONCLUSION

2 megawatt wind turbine assumed to be installed on Develi is selected to evaluate the carbon footprint per kWh and energy payback time. For this purpose, wind energy potential of Develi is analyzed and by using annual hourly actual wind speed data electricity production of selected wind turbine are calculated. Moreover, life cycle analyses of selected wind turbine are carried out by using GaBi software, functional unit is selected 1kWh electricity production and life time is assumed to be 20 years.

Main carbon footprint contribution of turbine components is caused by foundation and nacelle with 37% and 26%, respectively. Embodied energy of turbine components mainly originates from the foundation and nacelle with 28% and 27%, respectively. New developments on manufacturing processes of turbine components or material selection processes of wind

turbine components such as carbon fiber usage can reduce the contributions on carbon footprint and embodied energy in order to maintain the sustainability.

Energy payback time is crucial parameter for energy production facilities. It depends mainly on material used and manufacturing techniques also wind power characteristics of the turbine installed site. In this study, it is calculated as 37 months. Energy payback times of some other energy production techniques are specified as 49 months, 8 to 36 months and 10 to 40 months for solar photovoltaic power plants, wind turbines and geothermal power plants, respectively [14, 15].

Results of this study can be used by environment concerning institution, decision makers or investors who intend to install wind power plant in Develi.

Meteorological Organization (WMO) and the United Nations Environment Programme (UNEP), 2012.

REFERENCES

- [1] M. Ozoemena, R. Hasan, and W. M. Cheung, "Analysis of technology improvement opportunities for a 1.5 MW wind turbine using a hybrid stochastic approach in life cycle assessment," *Renewable Energy*, vol. 93, pp. 369–382, August 2016.
- [2] A.V. Vargas, E. Zenón, U. Oswald, J.M. Islas, L.P. Güereca, F.L. Manzini, "Life cycle assessment: A case study of two wind turbines used in Mexico," *Applied Thermal Engineering*, vol. 75, pp. 1210–1216, January 2015.
- [3] J.K. Kaldellis and D. Apostolou, "Life cycle energy and carbon footprint of offshore wind energy. Comparison with onshore counterpart," *Renewable Energy*, vol. 108, pp. 72–84, August 2017.
- [4] Md. S. Uddin and S. Kumar, "Energy, emissions and environmental impact analysis of wind turbine using life cycle assessment technique," *Journal of Cleaner Production*, vol. 69, pp. 153–164, April 2014.
- [5] M. S. Genç and M. Gökçek, "Evaluation of wind characteristics and energy potential in Kayseri, Turkey," *J Energy Engineering*, vol. 135, pp. 33–43, 2009.
- [6] M. Gökçek and M.S. Genç, "Evaluation of electricity generation and energy cost of wind energy conversion systems (WECs) in Central Turkey," *Applied Energy*, vol. 86, pp. 2731–2739, December 2009.
- [7] M.S. Genç, "Economic analysis of large-scale wind energy conversion systems in central Anatolian Turkey," *Clean energy systems and experiences*, pp. 131–54, 2010.
- [8] ISO 14040, "Environmental Management-Life Cycle Assessment-Principles Framework," International Organization for Standardization, 2006.
- [9] ISO 14044, "Environmental Management-Life Cycle Assessment-Requirements and Guidelines," International Organization for Standardization, 2006.
- [10] GaBi software, (Web Page: <http://www.gabi-software.com/turkey/index/>), Accessed February 2017.
- [11] Enercon, (Web Page: <http://www.enercon.de/en/products/ep-2/e-82/>), Accessed February 2017.
- [12] E. Martinez, F. Sanz, S. Pellegrini, E. Jimenez and J. Blanco, "Life cycle assessment of a multi-megawatt wind turbine," *Renewable Energy*, vol. 34, pp. 667–673, March 2009.
- [13] B. Guezuraga, R. Zauner and W. Polz, "Life cycle assessment of two different 2 MW class wind turbines," *Renewable Energy*, vol. 37, pp. 37–44, January 2012.
- [14] C. Marimuthu, V. Kirubakaran and R. Rajasekaran, "Energy Pay Back Period and Carbon Pay Back Period for Solar Photovoltaic Power Plant," vol. 12, pp. 293-305, 2014.
- [15] O. Edenhofer, R. P. Madruga and Y. Sokona, "Special Report on Renewable Energy Sources and Climate Change Mitigation," World

Numerical Investigation of Active Vibration Control of Composite Plate Using PID Controller

Bendine Kouider

Université de Sidi Bel Abbès

Laboratoire de Mécanique des Solides et des Structures

Sidi Bel Abbès, Algérie

kouider84@live.com

Alper Polat

Munzur University

Tunceli/Turkey

alperpolat@munzur.edu.tr

Abstract— in the present paper, a numerical investigation is carried out using Ansys APDL for the active vibration reduction of smart composite plate. The structure composed of composite plate with three piezoelectric actuators bounded on their upper surface. PID algorithm code is developed and integrated in Ansys to provide damping to the smart composite plate.

Keywords—composite; vibraion; PID controller

Introduction (Heading 1)

Active vibration reducing techniques turn out to be a reality in wide range of applications. Motivated by the piezoelectricity phenomena, the active vibration technique require, bonding piezoelectric patches in a conventional structures to make a kind of smart structure which have the ability of self-control. Recently large numbers of research papers were focused on the mathematical modeling of smart structures using finite element method. [1] developed a finite element model based on third order laminate theory for the active vibration control of composite beams with distributed piezoelectric sensors and actuators. [2] developed a finite element formulation for modeling and analysis of isotropic as well as orthotropic composite beams with distributed piezoelectric actuators subjected to both mechanical and electrical loads. [3] suggested a finite element method (FEM) of to study the active vibration control smart FGM beam based on higher-order shear deformation theory. Piezoelectric sensors and actuators distribution on the structure disturb the control performance, hence many researchers were interested by the search of the most appropriate location that lead to cost and weight reduction. [4] presented an approach based on the Rayleigh–Ritz (RR) assumed mode shape method to predict the behavior of a thin plate with piezoelectric patches bonded to its surface. [5] proposed optimization technique of the placement and size and the feedback control gains of the control system for vibration damping of beam structures. [6] studied the optimization of the size and location of piezoelectric actuators/sensors, and the controller parameters of composite beam by using the particle swarm optimization algorithm. Moreover, extra research papers are used commercially software such Ansys has the ability to model piezoelectric materials and perform the investigation of

the active vibration control. [7] proposed a performance criterion for the optimization of piezoelectric patch actuator locations on flexible plate structures using Ansys and genetic algorithm. [8] dealt with the active control of a smart laminate composite structure (SLCS) by using type of controllers direct velocity feedback (DVF) and displacement feedback (DF) controls with constant gain are used. [9] proposed prototype developed in Ansys for the active vibration control of lightly damped cantilever aluminum using a linear quadratic controller (LQ). [10] coupled Ansys and Matlab to study the active vibration control of a cantilever beam by means piezoelectric patch and PID controller.. In the present work, numerical study of active vibration control of composite plate using PID control algorithm is carried out. The structure was accomplished in the commercial finite element software Ansys, and then a PID control law is designed and integrated in Ansys to perform closed loop simulations.

VI. MODELING OF SMART COMPOSITE PLATE

A. Modal analysis

Consider a smart composite plate bonded by three piezoelectric actuators. It must be noted that the location of the piezoelectric actuator is determined based on [7], [11].. The host plate is made of four graphite–epoxy (carbon-fiber reinforced) layers. Each layer is of thickness 3/4 mm, while the orientations is take as (0 45 -45 90), the piezoelectric actuator is made of PZT5A fiber composite. The material properties of the considered structure are given in table 1. The simulation process has been carried out using Ansys and it's depicted in the flowchart given in Fig. 1.

In the present section, the proposed model is subjected to a modal analysis .The Block Lanczos method is used for performing modal analysis in ANSYS to find the frequencies and mode shape of the composite plate with piezoelectric actuator. First four frequencies are given in Table 2. Fig. 2 presents the first four mode shape

TABLE 1. MATERIAL PROPERTIES

Proprieties	Graphite/epoxy	PZT G-1195
Poisson's ratio	0.31	0.3
Density ρ (kg/m ³)	1550	7600
Elastic stiffness matrix (GPa)		
E11	119	63.0
E22	8.67	63.0
E33	8.67	63.0
G12	5.18	24.2
G13	3.29	24.2
G23	3.29	24.2
Piezoelectric strain matrix	-	
e31		12.5
e33		12.5
e15		12.5
Dielectric matrix (F/m)		
g11		1.53×10^{-8}
g22		1.53×10^{-8}
g33		1.53×10^{-8}

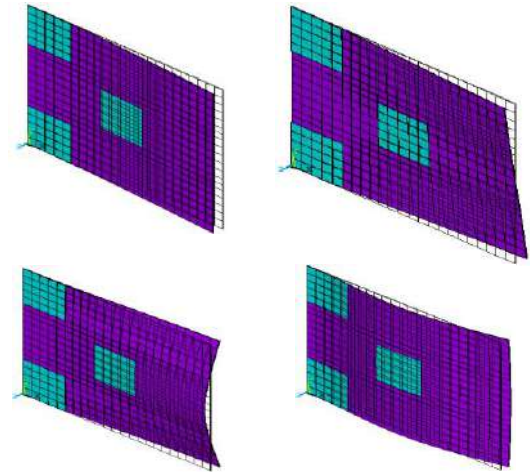


Fig. 2. First four mode shape

TABLE 2. FIRST FOUR FREQUENCIES

Mode	frequency
1	24.790
2	37.071
3	86.681
4	149.27

B. Active vibration control analysis

The vibrations reducing of the smart composite plate is aimed of this section. In order to implement the PID controller in ANSYS parametric design (APDL), a macro has been designed by means of a programming cycle, realized using the *DO *ENDDO command. The whole macro is given as follow [12]

```

Kp=-1500          !PROPORTIONAL GAIN
Ki=-150           !INTEGRAL GAIN
Kd=-100           !DERIVATIVE GAIN
integ1=0
integ2=0
integ3=0
dzp1=0
dzp2=0
dzp3=0
*SET,NSA,3
*SET,STIPNODE1,2676 ! !NODE AT SENS1
*SET,STIPNODE2,2571 ! !NODE AT SENS2
*SET,STIPNODE3,3339 ! !NODE AT SENS3
*do,t,2*Tres,Tstop,Tres
time,t
*GET,SDIS1,NODE,STIPNODE1,UZ
*GET,SDIS2,NODE,STIPNODE2,UZ
*GET,SDIS3,NODE,STIPNODE3,UZ
*set,x1,SDIS1
*set,integ1,integ1+x1*dt
*set,diff1,(x1-dzp1)/dt
*set,va1,kp*x1+ki*integ1+kd*diff1

```

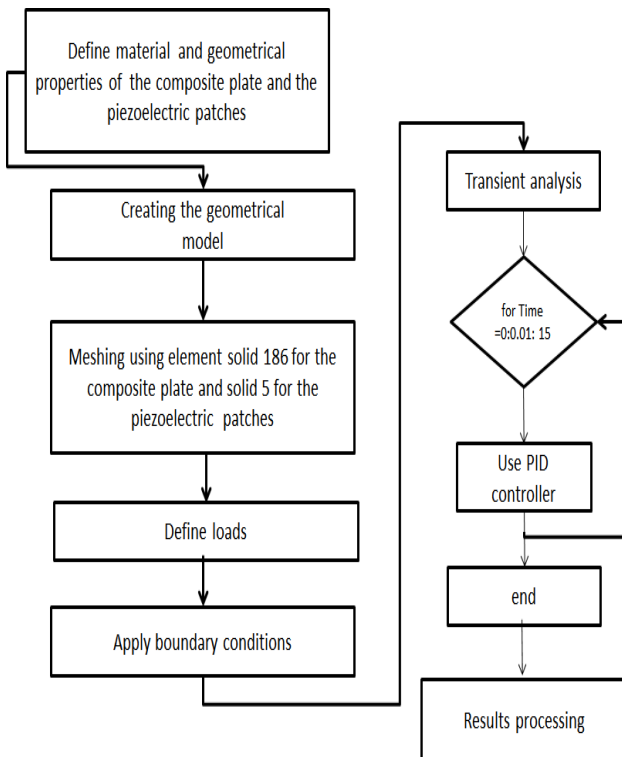


Fig. 1. Flowchart of the Ansys APDL code

```
*set,x2,SDIS2
*set,integ22,integ2+x2*dt
*set,diff2,(x2-dzp2)/dt
*set,va2,kp*x2+ki*integ22+kd*diff2
*set,x3,SDIS3
*set,integ33,integ3+x3*dt
*set,diff3,(x3-dzp3)/dt
*set,va3,kp*x3+ki*integ33+kd*diff3
d,ANTOP1,VOLT,va1 ! VOLTAGE ON ACTUATOR1
d,ANTOP2,VOLT,va2 ! VOLTAGE ON ACTUATOR2
d,ANTOP3,VOLT,va3 ! VOLTAGE ON ACTUATOR3
*set,dzp1,x1
*set,dzp2,x2
*set,dzp3,x3
SOLVE
*enddo
```

The model has been loaded with a nominal force of -2 N with an impulse lasting 0.01 s modeling the effect of deflection of the plate away from the equilibrium position and letting it go without any further force interactions. The displacement of the composite plate with and without PID controller is presented in Fig. 3. It can be noticed that the PID controller is successfully reduced the vibrations. The figure showed that the vibrations attenuated quickly in terms of amplitude and time. The input control voltage for each actuator is presented in Fig. 4.

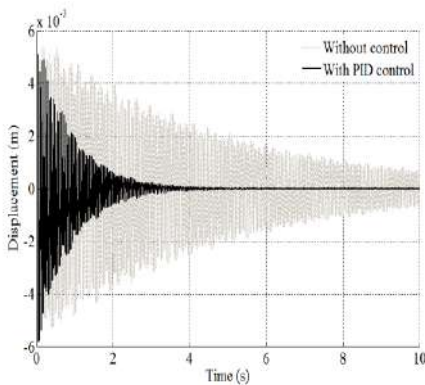


Fig. 3. Tip deflection of the composite plate with and without PID controller.

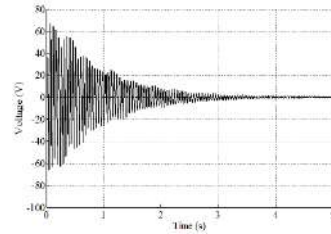
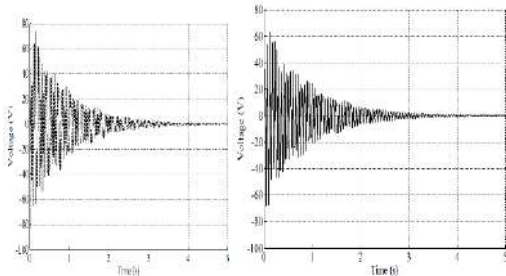


Fig 4. Applied voltage on the three actuators.

CONCLUSION

In this study, we present an approach to Integrate PID control algorithm into the finite element commercial software Ansys to investigate the active vibration control of composite plate with surface bounded piezoelectric actuators. The benefit behind this technique is it does not require any mathematical model. Some macros that are combined with finite element solutions are developed to design a proper controller. Assumptions assigned in a simulation should be tested with analytical solutions and experiments. The results prove that the technique is efficient for the study of active vibration control and it motivated us to use it in more complex structures.

REFERENCES

- [1] X. Q. Peng, K. Y. Lam, and G. R. Liu, "Active vibration control of composite beams with piezoelectrics: a finite element model with third order theory," *J. Sound Vib.*, vol. 209, no. 4, pp. 635–650, 1998.
- [2] M. A. Elshafei and F. Alraies, "Modeling and analysis of smart piezoelectric beams using simple higher order shear deformation theory," *Smart Mater. Struct.*, vol. 22, no. 3, p. 35006, 2013.
- [3] K. Bendine, F. B. Boukhoulida, M. Nouari, and Z. Satla, "Active vibration control of functionally graded beams with piezoelectric layers based on higher order shear deformation theory," *Earthq. Eng. Eng. Vib.*, vol. 15, no. 4, pp. 611–620, 2016.
- [4] A. M. Sadri, J. R. Wright, and R. J. Wynne, "Modelling and optimal placement of piezoelectric actuators in isotropic plates using genetic algorithms," *Smart Mater. Struct.*, vol. 8, no. 4, p. 490, 1999.
- [5] Y. Yang, Z. Jin, and C. K. Soh, "Integrated optimal design of vibration control system for smart beams using genetic algorithms," *J. Sound Vib.*, vol. 282, no. 3, pp. 1293–1307, 2005.
- [6] N. D. Zorić, A. M. Simonović, Z. S. Mitrović, and S. N. Stupar, "Optimal vibration control of smart composite beams with optimal size and location of piezoelectric sensing and actuation," *J. Intell. Mater. Syst. Struct.*, p. 1045389X12463465, 2012.
- [7] F. Peng, A. Ng, and Y.-R. Hu, "Actuator placement optimization and adaptive vibration control of plate smart structures," *J. Intell. Mater. Syst. Struct.*, vol. 16, no. 3, pp. 263–271, 2005.
- [8] L. Malgaca, "Integration of active vibration control methods with finite element models of smart laminated composite structures," *Compos. Struct.*, vol. 92, no. 7, pp. 1651–1663, 2010.
- [9] G. Takacs and B. Rohal-Ilkiv, "Direct closed-loop active vibration control system prototype in ANSYS," in *INTER-NOISE and NOISE-CON Congress and Conference Proceedings*, 2012, vol. 244, pp. 1–12.
- [10] S. M. Khot, N. P. Yelve, R. Tomar, S. Desai, and S. Vittal, "Active vibration control of cantilever beam by using PID based output feedback controller," *J. Vib. Control*, vol. 18, no. 3, pp. 366–372, 2012.
- [11] A. H. A. Daraji, "Active vibration control of flexible structures by optimally placed sensors and actuators," 2013.
- [12] K. Bendine, B. F. Boukhoulida, M. Nouari, and Z. Satla, "Structural Modeling and Active Vibration Control of Smart FGM Plate through ANSYS," *Int. J. Comput. Methods*, p. 1750042, 2016.

Geothermal Energy Integrated Resource Management In Turkey

Orkun TEKE

Iskenderun Technical University Petroleum And Natural Gas Department orkunteke@gmail.com

Ergül YAŞAR

Iskenderun Technical University Petroleum And Natural Gas Department ergul.yasar@iste.edu.tr

Countries steps to change our energy habits while are willing to fight against the problem of global warming, one of the most important hazards our world faces, which is the result of the greenhouse effect created by the a lot carbon dioxide gas from heavy fossil fuel use. Geothermal energy has important role in Increasing Renewable Energy using that the most important way. Source management is really important for using source efficiently, it must be considered. With Integrated Source Management, main point of this study is provided some benefits with solutions for national and field based regulations. Integrated Source Management described clearly after Introduction part of study. Following part, applications for national and field based regulations presented. Kızıldere II Geothermal Power Plant presents as “Well Application Story”. Conclusion part contains general assessment and study’s

Key Words: Integrated Resource Management, Global Warming, Renewable Energy, Geothermal Energy

Investigation of the Effect of Partial Shadowing with Solar Array Simulator

Akif Karafil

Department of Energy, Vocational High School
Bilecik Seyh Edebali University
Bilecik, Turkey
akif.karafil@bilecik.edu.tr

Harun Ozbay

Department of Electric, Vocational High School
Bilecik Seyh Edebali University
Bilecik, Turkey
harun.ozbay@bilecik.edu.tr

Abstract—Sunlight is converted into electrical energy by the help of photovoltaic (PV) panels obtained by semiconductor materials. However, the power values obtained from the PV panels varies continuously due to low efficiency of the panels and the atmospheric conditions changing throughout the day. This is the main drawback of the PV energy systems. Therefore, the output power obtained from PV panels must be at maximum level all the time. However, PV panels, which are subject to partial shadowing due to various reasons such as clouds, buildings, trees, are getting weaker and many maximum power points appear in the system. In this study, the mathematical model of the PV panel in the 100 Watt power plant was developed and the partial shading condition of one of the six series PV panels was examined with the solar array simulator (SAS). It has been observed that different maximum power points occur by obtaining current-voltage (I-V) and power-voltage (P-V) curves according to different shading ratios. The most appropriate maximum power point (MPP) for the system is determined by the conducted analyses.

Keywords—*partial shading; maximum power point; PV panel; solar array simulator*

VII. INTRODUCTION

After the introduction of the mechanized industry emerged from Industrial Revolution, fossil-based resources such as coal and oil have begun to be used as energy sources. Although oil-derived resources are mostly used today, the search for energy sources that can be an alternative to these sources has also been continuing rapidly as a result of the fact that the gases resulting when the fossil fuels burn pollute the environment and these fuels will run out in the future. As a result, renewable energy sources such as wind, solar, geothermal and biomass have gained a great importance. The use of wind and solar energy, especially in the production of electricity has been more prominent among the other renewable energy sources. With the incentives and investments made in this area, it has become able to compete with other energy sources [1-3].

Among the existing alternative energy sources, PV energy is one of the most important renewable energy sources. The most important advantages of these energy sources are that the PV energy is clean and simple to install, not needing too much maintenance and providing power to megawatts. Moreover, the

PV energy has gained an increasing demand since it has been widely used in many areas such as water pumps, solar home systems, and remote buildings from the grid. However, the low efficiency of the PV panels, the variation of the atmospheric conditions during the day, and therefore the continuous change of the power values obtained from the PV panels occur the most important disadvantages of the PV energy systems. Therefore, in recent years, the recent studies have aimed at maximizing the energy level of the PV energy [4-7]. However, partial shadowing occurs when any part of the PV panel is shaded for various reasons such as clouds, buildings, chimneys and trees. This significantly affects the output power of the PV panel and therefore many MPPs occur. Particularly serial PV panels are very influenced by this situation. When one of the serial PV panels is subjected to partial shadowing in order to increase the voltage, the output power of the system decreases considerably. Moreover, hot spots are formed in the cells exposed to the shadow effect, which causes damage to the cells and causes power losses. Bypass diodes are connected parallel to the PV panels to eliminate these adverse effects [8-11].

In this study, Perlite brand PLM-100P/12 100 Watt polycrystalline structured PV panels are used and the mathematical model was formed in Matlab program by using the catalogue data of the panel. Six PV panels were connected to the system in serial and the power of the system was increased to 600W. The current and voltage information of the PV panels modeled in the Matlab program is loaded on the Chroma 62150H-600S brand SAS. The partial shadows of the PV panels with SAS and bypass diodes are examined at different ratios and the P-V curves of the panels are analyzed.

VIII. MATHEMATICAL ANALYSIS

A. The Analysis of the Photovoltaic Cell

In order to determine the values such as current, voltage and power obtained from the PV panels, it is necessary to determine the equivalent circuit model of the PV cell. The solar cell is produced by p-n semiconducting materials. Therefore, it is symbolized by a diode which is one of the basic elements electronics and a current source connected parallel to it. PV cell losses are represented by parallel-series resistance. The equivalent circuit model of the PV cell is shown in Fig. 1.

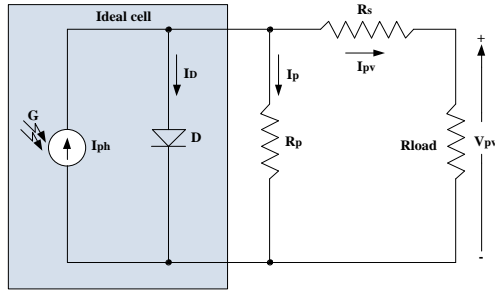


Fig. 4. Equivalent circuit model of PV cell.

Equation (1) obtained according to the circuit model in Fig. 1 [12].

$$I_{pv} = I_{ph} - \left[e^{\left(\frac{q(V_{pv} + I_{pv} \cdot R_s)}{A \cdot k \cdot T_c} \right)} - 1 \right] - \frac{V_{pv} + I_{pv} \cdot R_s}{R_p} \quad (1)$$

Where;

I_{ph} : Photovoltaic current of the PV cell

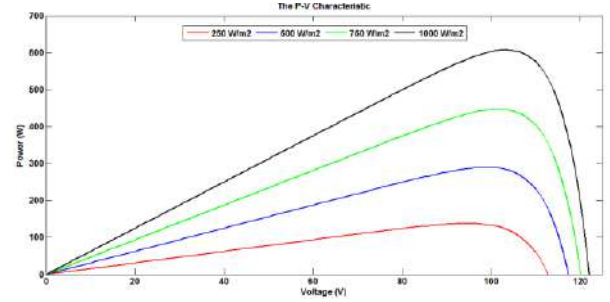
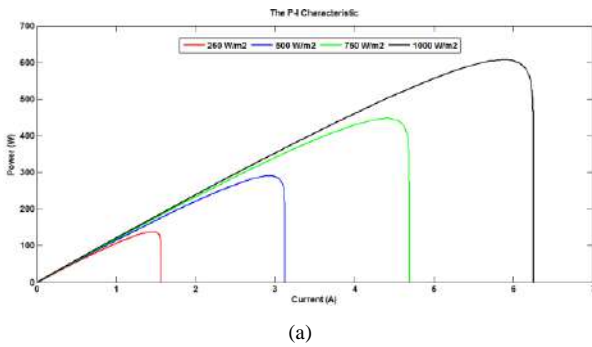
q : Electric charge (1.602×10^{-19} C)

A : Quality factor of diode

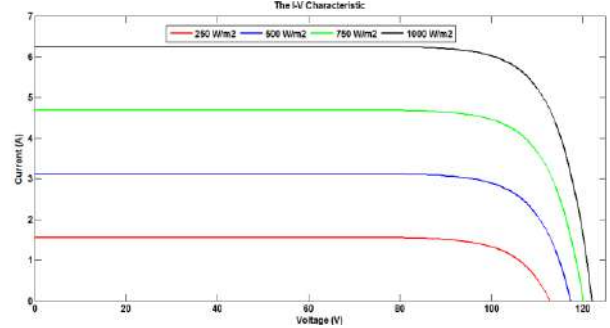
k : Boltzman constant ($1.3806505 \times 10^{-23}$ J/K)

T_c : PV cell temperature (in Kelvin)

The power-current (P-I), power-voltage (P-V), and current-voltage (I-V) characteristics for six series-connected PV panels are analyzed at 25 °C temperature and solar radiation changes under 250, 500, 750 and 1000 W/m² using the mathematical equivalent circuit model.



(b)



(c)

Fig. 5. The (a) P-I, (b) P-V and (c) I-V characteristics of panel.

B. Analysis of the Shaded PV Panel

In Fig. 3, six serial PV panels and a partially shaded panel are given.

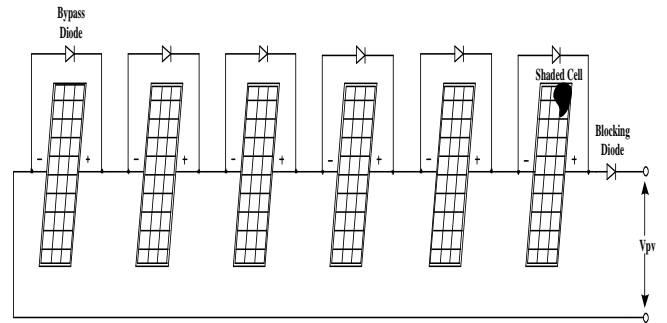


Fig. 6. Series connected PV panels and partial shaded condition.

The short circuit current ($I_{sc}=0$) of the panel is zero in case of partial shading. In this case, the current passing through the circuit passes through the parallel resistance in the cells. The voltage of the shaded panel decreases since the value of the parallel resistor value is higher than the series resistance. This reduces the total voltage and power of the series connected PV panels. If the voltage of the PV panel is V_{pvn} while all the cells of the panel with the cell number n are under the sunlight, and the voltage of the single PV cell is V_{pvs} , then the voltage of the shaded panel is calculated as in Equation (2).

$$V_{pvs} = V_{pvn} - (R_p + R_s) \cdot I_{pv} - \frac{V_{pvn}}{n} \quad (2)$$

Shaded cells are also damaged by heat. To overcome these drawbacks, active bypass diodes are used in the event of shading. Bypass diodes are connected in parallel to the panel to allow current to flow through the diode and prevent damage to the panel [13].

IX. SAS RESULTS

In Fig. 4, six series-connected PV panels are shown in the simulator with I-V and P-V variations under 1000 W/m^2 of solar irradiance. The red dot of the simulator shows 600 W which is the maximum power rating of the panels.

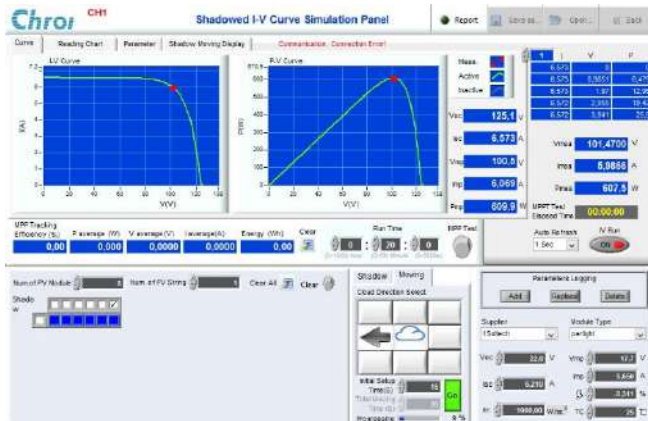


Fig. 7. I-V and P-V changes of the panels under 1000 W/m^2 solar irradiance.

When a panel is subjected to partial shadowing (shadow irradiation 400 W/m^2), the I-V and P-V characteristics shown in Fig. 5 are obtained.

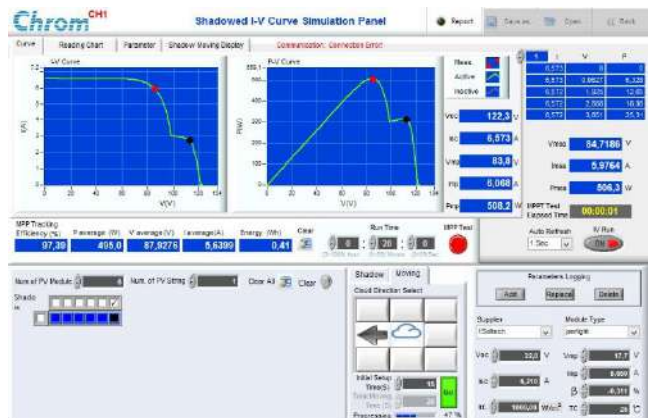
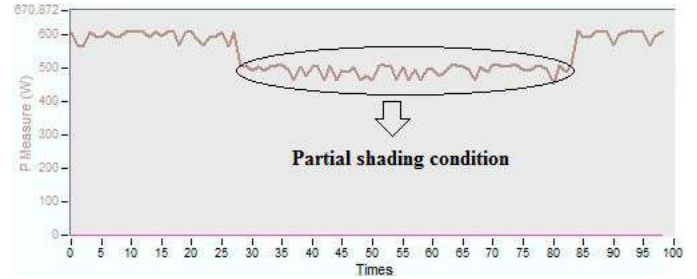
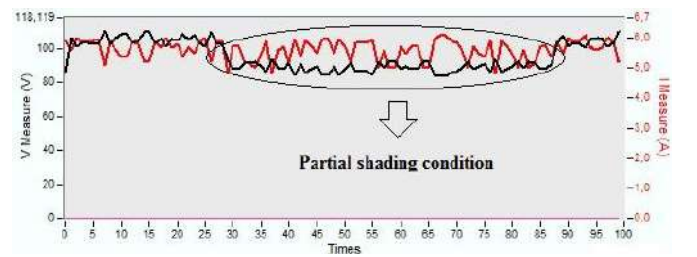


Fig. 8. I-V and P-V changes of one of the panels under 400 W/m^2 shadow irradiance.

When I-V and P-V characteristics shown in Fig. 5 are examined, it is seen that the total power is decreased to 500 W the same time, there are two maximum points due to partial shadowing. The dot in red is the global MPP, and the black dot is the local MPP. Fig. 6 shows the power, voltage, and current variations of the system subjected to the partial shadowing in the global MPP mode.



(a)



(b)

Fig. 9. (a) Power and (b) voltage-current changes of the system subjected to the partial shadowing operating at global MPP.

When the system is operating under the local MPP, the power decreases to approximately 300 W . In this case, the power of the system decreases even further. Fig. 7 shows the I-V and P-V variations obtained when one of the panels has a shadow irradiance of 600 W/m^2 .

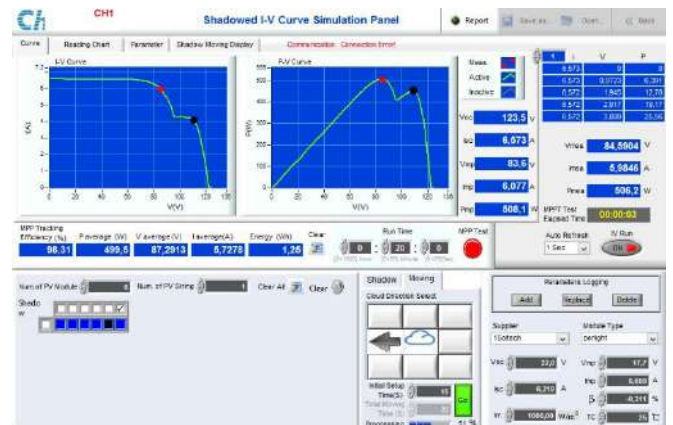


Fig. 10. I-V and P-V changes of one of the panels under 600 W/m^2 shadow irradiance.

When Fig. 7 is examined, it is seen that the global MPP value is 500 W and the local MPP value is about 450 W . In this case it can be said that when the value of the shadow irradiance increases, the local MPP value increases.

X. RESULTS AND DISCUSSION

It is seen that when one of the bypass diode series connected PV panels is subjected to partial shading for any reason, there are two maximum points in the system. One of them is the global and the other is local MPP. According to the simulator analyses, global MPP value is seen to be greater than the local MPP

value. Therefore, more power will be obtained when the PV systems subjected to partial shadowing operates in the global MPP. Therefore, it will be more convenient for the systems especially using the maximum power point tracking (MPPT) algorithm to operate in the global MPP rather than in the local MPP. Thus, more power will be obtained and utilized effectively in PV systems.

REFERENCES

- [1] Á.-A. Bayod-Rújula, and J.-A. Cebollero-Abián, "A novel MPPT method for PV systems with irradiance measurement," *Solar Energy*, vol. 109, pp. 95-104, 2014.
- [2] A. Karafil, H. Ozbay, M. Kesler, and H. Parmaksiz, "Calculation of optimum fixed tilt angle of PV panels depending on solar angles and comparison of the results with experimental study conducted in summer in Bilecik, Turkey," in *Electrical and Electronics Engineering (ELECO)*, 2015 9th International Conference on. IEEE, pp. 971-976, November 2015.
- [3] S. F. Hosseini, B. M. Goortani, and M. Niroomand, "Instantaneous responses of on-grid PV plants to changes in environmental and weather conditions," *International Journal of Renewable Energy Research (IJRER)*, vol. 6, no. 4, pp. 1296-1306, 2016.
- [4] J.-Y. Shi et al., "Improved global maximum power point tracking for photovoltaic system via cuckoo search under partial shaded conditions," *Journal of Power Electronics*, vol. 16, no. 1, pp. 287-296, 2016.
- [5] J. P. Ram, and N. Rajasekar, "A new global maximum power point tracking technique for solar photovoltaic (PV) system under partial shading conditions (PSC)," *Energy*, vol. 118, pp. 512-525, 2016.
- [6] M. Abdulazeez, and I. Iskender, "Simulation and experimental study of shading effect on series and parallel connected photovoltaic PV modules," in *Electrical and Electronics Engineering (ELECO)*, 2011 7th International Conference on. IEEE, pp. 1-28-I-32, 2011.
- [7] S. Khatoon, and M. F. Jalil, "Feasibility analysis of solar photovoltaic array configurations under partial shading conditions," in *India Conference (INDICON)*, 2015 Annual IEEE, pp. 1-6, December 2015.
- [8] J. Ahmed, and Z. Salam, "A critical evaluation on maximum power point tracking methods for partial shading in PV systems," *Renewable and Sustainable Energy Reviews*, vol. 47, pp. 933-953, 2015.
- [9] H. Patel, and V. Agarwal, "MATLAB-based modeling to study the effects of partial shading on PV array characteristics," *IEEE Transactions on Energy Conversion*, vol. 23, no. 1, pp. 302-310, 2008.
- [10] B. A. Alsaid, S. Y. Alsadi, J. S. Jallad, and M. H. Dradi, "Partial shading of pv system simulation with experimental results," *Smart Grid and Renewable Energy*, vol. 4, pp. 429-435, 2013.
- [11] M. Pikutis, D. Vasarevicius, and R. Martavicius, "Maximum power point tracking in solar power plants under partially shaded condition," *Elektronika Ir Elektrotechnika*, vol. 20, no. 4, pp. 49-52, 2014.
- [12] A. Karafil, H. Ozbay, and M. Kesler, "Temperature and solar radiation effects on photovoltaic panel power," *Journal of New Results in Science*, vol. 5, no. 12, pp. 48-58, 2016.
- [13] R. Ramaprabha, and B. L. Mathur, "Impact of partial shading on solar PV module containing series connected cells," *International Journal of Recent Trends in Engineering*, vol 2, no. 7, pp. 56-60, November 2009.

Numerical Investigation of Heat Transfer and Pressure Drop Characteristic of Wire Coil Insert in a Square Duct

Taha Tuna GÖKSU

University of Muş Alparslan, Dept. of Mechanical Engineering
Muş, Turkey

tt.goksu@alparslan.edu.tr, taha_022@hotmail.com

Fuat YILMAZ

University of Gaziantep, Dept. of Mechanical Engineering
Gaziantep, Turkey

fuatyilmaz@gantep.edu.tr

Abstract—The thermohydraulic behavior of equilateral triangular wire coil insert in a square duct is investigated by using ANSYS FLUENT v17. The results of Nusselt number and friction are compared with smooth pipe. Three different pitches ($P=54, 72$, and 90 mm) were examined in the range of Reynolds numbers between 4504 and 18415 . The Renormalized Group (RNG) $k-\epsilon$ turbulence model is used to evaluate the fluid domain. The testing fluid is selected as air and its thermal properties are considered temperature dependent in order to obtain actual fluid properties through the fluid domain. The results showed that Nusselt number increases with increasing Reynolds number and with decreasing the pitch ratio. The friction decreases with increasing Reynolds number and with increasing the pitch ratio. Nusselt number and friction factor raised around 37 to 93% and 82 to 266% . The Nusselt number of 54 mm pitch is higher than 72 and 90 mm around 4.5 and 6.9% , respectively. The friction of 54 mm pitch greater than 72 and 90 mm around 22 and 48% , respectively. The heat transfer performance of 90 mm pitch is around 30% compared with smooth pipe.

Keywords—heat transfer enhancement; wire coil; ANSYS

XI. INTRODUCTION

Heat exchanger uses in industry to cool or heat a system. In the past century, many studies have been done to enhance heat transfer in heat exchanger systems. Passive heat transfer technique is one of the popular examples of heat enhancement techniques. The passive techniques are required no external power for the system. In passive techniques, inserts are generally used to enhance heat transfer. The heat-transfer enhancements of these inserts are related with interconnection between their geometrical parameters and fluid domain. The wire coils are one of the popular ways for this purpose.

Gunes et al. [1] investigated the equilateral cross sectional wire coil inserted in a pipe. In this study, wire coils were separated from the wall to prevent the contamination formation. The effects of three different pitch ratios ($p/D=1, 2$, and 3) and the length side of triangle wire thickness to diameter ratios ($a/D, 0.0714$ and 0.0892) were investigated in the range of Reynolds number between 3500 and 27000 . Uniform heat-flux boundary

condition at the wall was applied. Results showed that the insert with high a/D and lower p/D had the best in the thermal performance factor which is around 36.5% compared with smooth pipe.

Garcia et al. [2] investigated the heat transfer and friction factor characteristics for laminar, transition, and turbulent regimes in circular tubes with helical wire coils having six different characteristic dimensions. The water and water-propylene glycol mixtures were used as the working fluids. The range of the pitch ratio was between 1.17 and 2.68 and the range of wire thickness to the diameter ratio (e/D) was between 0.07 and 0.10 . Results showed that when Reynold numbers smaller than 500 (in the pure laminar regime) wire coil effect on heat transfer enhancement was found very low, however, when the Reynolds number range was between 500 and 3000 (in transition region), there was considerable variation in heat transfer enhancement. In this region, the enhancement was strongly bounded on Prandtl number. Over 3000 Reynolds, Prandtl effect on the enhancement was observed as a negligible. Transition region was found the most effective region for the heat-transfer enhancement. For wire inserts with lower pitch ratio, heat transfer enhancement reached 200% in transition region. In another work of Garcia et al. [3], wire coil inserts having pitch ratios of $1.25, 1.72$ and 3.37 in a horizontal pipe were investigated. Reynolds number range was between 10 and 2500 and Prandtl range was between 200 and 700 . Wire coil effect on heat transfer enhancement was found negligible when Reynolds number was smaller than 200 , however, the results showed that the best performance was in the Reynolds number region between 200 and 1000 . Heat transfer coefficient of a pipe with wire coil was up to eight times more effective than the smooth pipe at $Re=1000$.

Promvonge [4] experimentally investigated heat transfer augmentation by using square cross sectional wire coil turbulators in a pipe. The effects of two different pitch ratios (0.315 and 0.421) were applied in the range of Reynolds numbers between 5000 and 25000 . The working fluid was air. Results showed that wire coil had a good performance in the

Reynold number range between 5000 and 9000. Square wire coil showed better performance than a circular wire coil about 10 % at low Reynolds number.

Shoji et al. [5] investigated the effect of the ratio of the wire coil length in a pipe. Pitch ratio was equal to 10 and wire diameter was 1.5 mm. The full length of wire coil turbulators showed better heat transfer enhancement than others.

Akhavan-Behabadi et al. [6] studied the inserted wire coil in a double pipe heat exchanger. The pitch of wire coil was in the range of 12 to 69 mm, and the two thickness of the wire coils were 2 and 3.5 mm. Results showed that 3.2 fold enhancement in Nusselt number was observed for the wire coil of 3.5 mm thickness.

Eiamsa-ard et al. [7] investigated the effect of tandem wire coil insert in a square duct with under uniform heat flux conditions in the range of Reynolds numbers between 4000 and 25000. Results showed that full-length wire coil turbulators had better heat transfer enhancement than tandem short length one.

Wang and Sunden [8] compared the heat-transfer enhancement and friction factor penalty of the twisted tape and wire coil in laminar and turbulent regimes. Results showed that wire coil and twisted tape were more effective in case of the laminar region. A twisted tape insertion was found better than a wire coil at both regions when the friction factor was neglected.

Xing et al. [9] experimentally investigated the effect of rotating double wire coil turbulators with a thickness of 4 mm in a pipe on heat transfer performance in the turbulent regime. The length of wire coils was 1520 mm in a pipe with a length of 1975 mm. Pitch ratio was equal to 2.654. The results indicated that the 1.3 fold enhancement in the heat transfer the 5 fold penalty compared with those in the plain tube was observed.

Gunes et al. [10] experimentally investigated the heat transfer characteristic of equilateral triangle cross sectioned wire coil. The pipe test length of the study was 3.1 m and each length of equilateral triangle was 6 mm. Three pitch ratios (1, 2, and 3) were applied on the wire coil. The inner diameter of the pipe was 56 mm. The Reynolds number range between 4105 and 26400. In this numerical study, Gunes et al. [10] study was used for validation. Pitch ratio 3 or 168 mm pitch was selected for this purpose.

In this study, the thermohydraulic behavior of equilateral triangular wire coil with 54, 72 and 90 mm inserts separated from the square duct wall is examined by using ANSYS FLUENT v17.

XII. NOMENCLATURE

- A: area (m²)
- C_p: fluid specific heat (J.kg⁻¹. °C⁻¹)
- d: diameter of pipe (m)
- D_h: hydraulic diameter (m)
- f: friction factor
- h: heat transfer coefficient (W.m⁻².K⁻¹)
- k: fluid thermal conductivity (W.m⁻¹.K⁻¹)

- L: length of pipe (m)
- l: length of wire coil (m)
- \dot{m} : mass flow rate
- Nu: Nusselt number
- p: pitch (m)
- PEC: heat transfer enhancement efficiency, performance evaluation factor
- p/D: pitch ratio
- ΔP : pressure drop (Pa)
- Re: Reynolds number
- Pr: Prandtl number
- T_o: outside temperature (K)
- TT: twisted tape
- U_{mean}: mean velocity (m/s)
- Y: twist ratio
- WC: wire coil
- Greek Symbols*
- ρ : density
- μ : viscosity (kg/ms)
- Subscript*
- a: augmented
- b: bulk
- h: hydraulic diameter
- i: inlet
- o: smooth pipe
- w: wall

XIII. CFD MODELLING

A. Numerical Solution

The commercial CFD solver ANSYS FLUENT 17 is used to carry out the analysis, to solve the governing equations with a pressure-based solver. Semi-implicit pressure linked equation method (SIMPLE) algorithm for pressure velocity coupling and RNG k-ε for modeling turbulence are used. The convergence criterion of 10⁻⁶ for energy and of 10⁻⁴ for momentum, continuity, k, and ε is selected. The numerical modeling involves numerical solutions of the conservation equations for mass, momentum, and energy. These can be written as follows.

Mass conservation

$$\frac{\partial \rho}{\partial t} + \nabla(\rho \bar{u}) = 0 \quad (1)$$

Momentum conservation

$$\frac{\partial(\rho \bar{u})}{\partial t} + \nabla \cdot (\rho u \bar{u}) = \rho g - \nabla \cdot P + \nabla \cdot (\bar{\tau}) \quad (2)$$

where

$$\bar{\tau} = \mu \left((+\nabla \bar{u} + \nabla \bar{u}^T) - \frac{2}{3} \nabla \cdot \bar{u} I \right) \quad (3)$$

Energy conservation

$$\frac{\partial(\rho e)}{\partial t} + \nabla \cdot (\bar{u}(\rho e + P)) = \nabla \cdot (K_{\text{eff}} \nabla T + (\bar{\tau}_{\text{eff}} \cdot \bar{u})) \quad (4)$$

B. Geometry

The length of the square duct was 1.25 m and each side of duct was 18 mm. Equilateral triangular cross sectional wire coil (TWC) was assumed separately from the wall in a square duct. The each side of TWC was 2 mm. Figures 1 show geometry of TWC inserted in a square duct. Three different pitches (54, 72, and 90 mm) were examined.

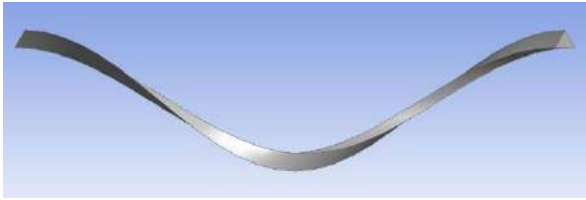


Fig. 1. Triangular cross sectional wire coil

C. Mesh for Validation

Mesh was produced by using Ansys Meshing v17. Four different meshes were applied for the mesh independency. The number of mesh elements were 3535477, 8937123, and 13184499. The number of mesh elements was chosen 8937123, however after this point Nusselt number and friction deviation were lower than 1 percent. Figure 2 and 3 shows the longitudinal section mesh of triangular cross sectional wire coil, inlet and wall mesh of the wire coil insert.

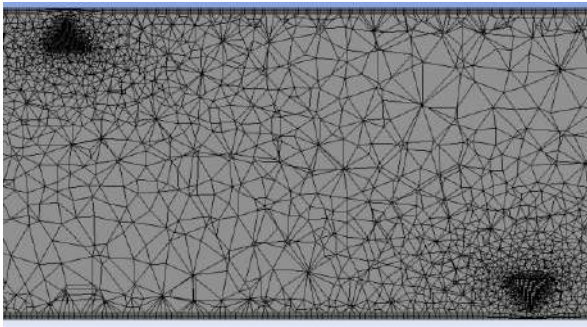


Fig. 2. The longitudinal section mesh

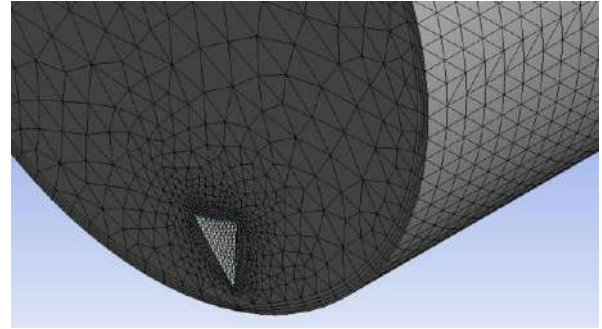


Fig. 3. The inlet and wall mesh of the wire coil inserted pipe

D. Mesh for the Study

Table 1 shows the mesh independency of the triangular wire coil insert in square duct. 7648959, 7570517, and 6051072 mesh elements were used for triangular wire coil with 54, 72, and 90 mm respectively. Mesh independency procedure of TWC insert in square duct were applied the changing of Nusselt number and friction. When deviation is lower than 1%, mesh elements were chosen. The mesh quality of the three study for skewness and orthogonal quality were equal to 0.84 and 0.19, respectively. Figure 4 shows the inlet section mesh for TWC insertion in square duct.

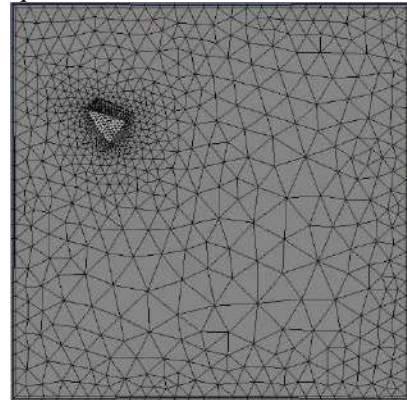


Fig. 4. The inlet section of mesh for TWC insert in square duct

Table I. Mesh independency of the study

Mesh	Re	Nu	f
Mesh independency of TWC for P=54 mm			
4854852	4511,77	23,859	0,141
7648959	4506,51	24,059	0,14
11362117	4505,43	24,077	0,14
Mesh independency of TWC for P=72 mm			
4925983	8235,12	35,297	0,075
7570517	8240,4	34,911	0,074
11745660	8240,66	34,927	0,074
Mesh independency of TWC for P=90 mm			
3982837	9301,27	37,886	0,060
6051072	9304,53	37,523	0,061
8235559	9307,61	37,467	0,061

E. Boundary Condition

The working fluid of the present study was air. The boundary condition of the inlet section was 25°C. The study was carried out under uniform heat flux condition. Reynolds number was in the range of 4504 to 18415.

XIV. DATA REDUCTION

In the present study, Reynolds number (Re), friction (f), and convective heat transfer coefficient (h), Nusselt number (Nu) were calculated by using equation 1, 2, 3, and 4, respectively. Blasius equation (5) for turbulence regime was used for smooth pipe friction calculation.

$$Re = \frac{\rho \cdot U_{mean} \cdot D_{hydraulic}}{\mu} \quad (1)$$

$$f = \frac{2 \cdot \Delta P \cdot D}{\rho \cdot U_{mean}^2 L} \quad (2)$$

$$h = \frac{m \cdot C_p (T_o - T_i)}{A (T_w - T_b)} \quad (3)$$

$$Nu = \frac{h \cdot D_{hydraulic}}{k} \quad (4)$$

$$f = \frac{0.316}{Re^{0.25}} \quad (5)$$

Heat transfer enhancement efficiency or Performance evaluation factor (PEC) show the efficiency of the study. PEC is calculated by equation 6. Nu_a and Nu_0 express the Nusselt number of wire coil insert and smooth pipe, respectively. f_a and f_0 express the friction of wire coil insert and smooth pipe, respectively.

$$PEC = \frac{Nu_a}{Nu_0} \left(\frac{f_a}{f_0} \right)^{1/3} \quad (6)$$

Nusselt number of smooth pipe was calculated by using Glienski equation (7). This equation can be written such as

$$Nu = \frac{\left(\frac{f}{8} \right) (Re - 1000) Pr}{1 + 12.7 \left(\frac{f}{8} \right)^{1/2} (Pr^{2/3} - 1)} \quad (7)$$

XV. RESULTS AND DISCUSSION

A. Numerical Results of Validation

The experimental study of Gunes et al. [10] was used for validation. Figure 5 shows the numerical and experimental results of Nusselt number versus Reynolds number and Figure 6 shows the numerical and experimental results of friction versus

Reynolds number. The Nusselt number was calculated by using equation (4) and friction calculated by using equation (2). Validation results show that Nusselt number deviation band is between 2.43 to 9.56 % and friction deviation band is between 1.87 to 15.59 %. In the experimental study of Gunes et al. [10], teflon rings were used to wire coil separate from the wall and so the deviation of friction may be affected by teflon rings.

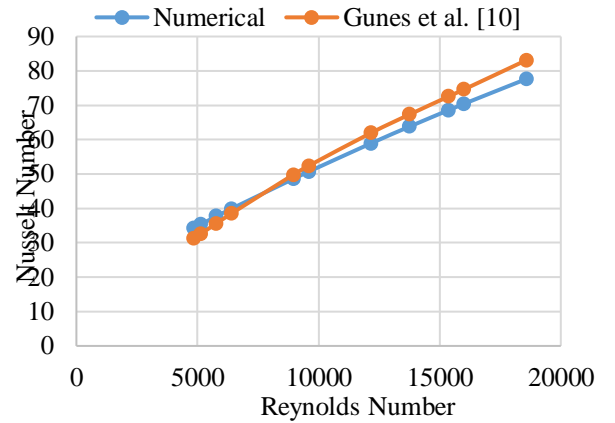


Fig. 5. Nusselt number results of numerical and Gunes et al. [10] studies versus Reynolds number

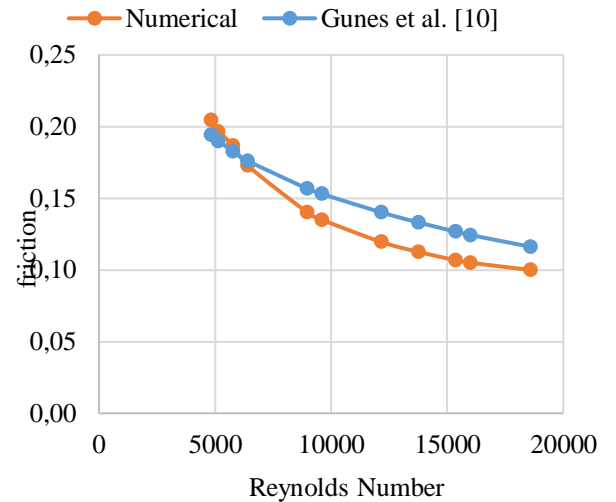


Fig.6. The friction results of numerical and Gunes et al. [10] studies versus Reynolds number

B. Numerical results for TWC insert in square duct

In the present study, TWC was fitted into a square duct. Three types of pitch were used. These pitches were equal to 54 mm, 72 mm, and 90 mm. Wire coil is assumed separated from the duct wall (s=2 mm). The Reynolds number range of was between 4831 and 18578. Figures 7 and 8 shows the Nusselt number and friction versus Reynolds number for different pitches.

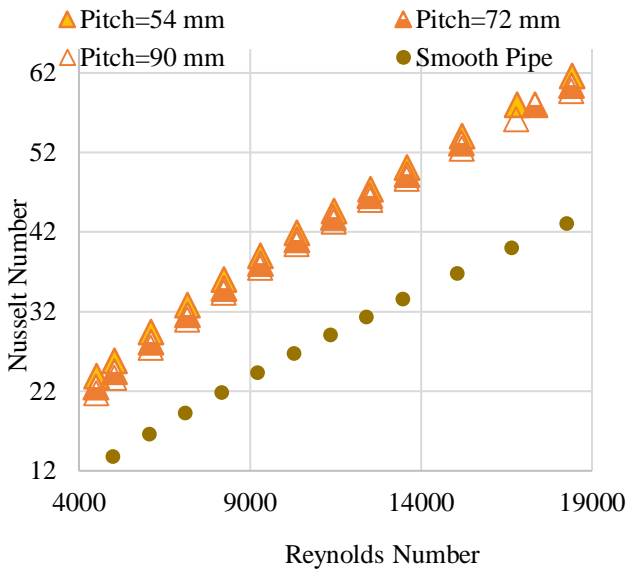


Fig. 7. Results of Nusselt number versus Reynolds number for TWC inserts

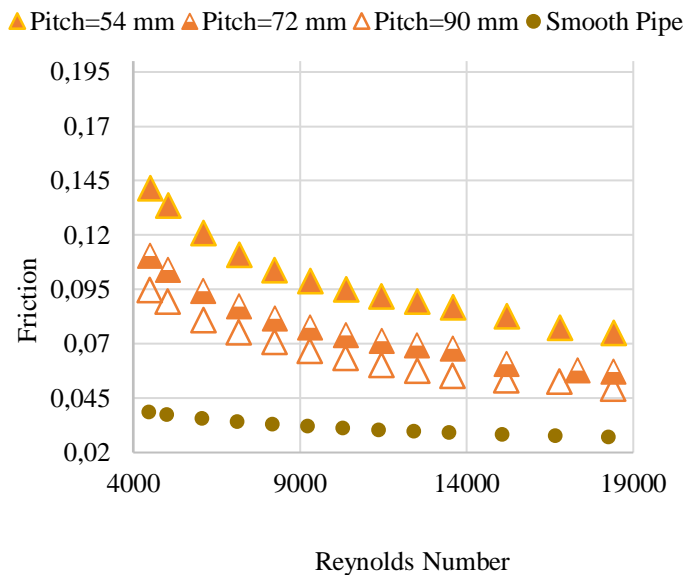


Fig. 8. Results of friction versus Reynolds number for TWC inserts

As understanding from Figure 7, Nusselt number increased with decreasing pitch and increasing Reynolds number. At lower Reynolds number, the Nusselt number of 54 mm pitch is higher than 72 mm and 90 mm approximately 4.5 and 6.9 %, respectively. At higher Reynolds number, Nusselt number of 54 mm pitch is higher than 72 mm and 90 mm approximately 1.56 and 1.75 %, respectively. The Nusselt number of smooth pipe was calculated by using Glienski equation (7). Results showed that Nusselt number increased with increasing Reynolds number

for smooth pipe. However, the Nusselt number of wire coil insert for any pitch is higher than smooth pipe.

As understanding from Figure 8, friction decreased with increasing pitch and Reynolds number. At lower Reynolds number, the friction of 54 mm pitch is higher than 72 mm and 90 mm approximately 21 and 45 %, respectively. At higher Reynolds number, friction of 54 mm pitch is higher than 72 mm and 90 mm approximately 22 and 48 %, respectively. The friction of the smooth pipe was calculated from Blasius equation (5). The friction of the smooth pipe was lower than all pitches in the range of Reynolds number. The negative effect was observed on friction. However, the friction of TWC insertion for any pitch was higher than smooth pipe in the range of Reynolds number. Results showed that the Nusselt number and friction increased with decreasing pitch such as in literature.

Figure 9 shows the PEC versus Reynolds number. PEC was calculated by using equation (6). Results showed that heat transfer enhancement was achieved around 30.46% for 90 mm pitch.

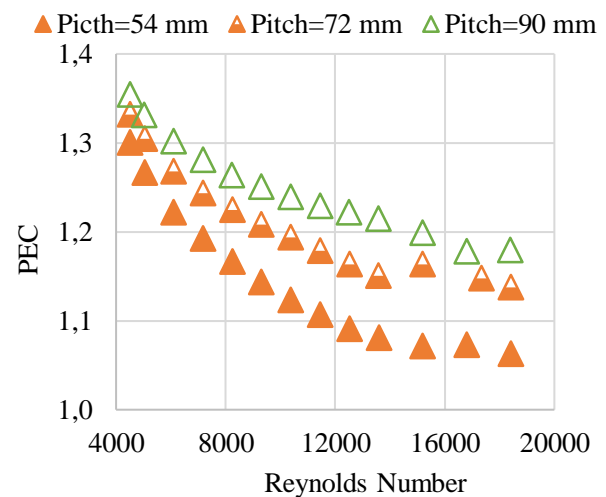


Fig. 9. Results of PEC versus Reynolds number

As understanding from Figure 9, PEC increased with decreasing Reynolds number and increasing pitch. The maximum point of PEC (1.3) was obtained at Reynold number around 4500. The lowest PEC (1.01) was obtained at Reynold number around 18415.

XVI. CONCLUSION

In the present study, triangular wire coils with varying pitches inserted in square duct were investigated. The aim of the study was to numerically understand the effects of wire coil inserts on heat transfer enhancement. Wire coil produces the secondary flow and it effects the retention time of the fluid. Secondary flow effect on convective heat transfer and Nusselt number increases with wire coil insertion. The negative effect of wire coil insert was observed pressure drop. However, the friction of TWC insertion for any pitch was higher than smooth pipe in the range of Reynolds number. The result of study was compared

with smooth pipe. The Nusselt number increased with increasing Reynolds number. The higher Nusselt number was obtained at lower pitches. The friction raised up with decreasing pitch and Reynolds number. The highest PEC was obtained at lower Reynolds numbers and higher pitch ratios.

REFERENCES

- [1] Gunes, S., Ozceyhan, V., & Buyukalaca, O. (2010). "Heat transfer enhancement in a tube with equilateral triangle cross sectioned coiled wire inserts" *Experimental Thermal and Fluid Science*, 34(6), 684-691.
- [2] Garcia, A., Vicente, P. G., & Viedma, A. (2005). "Experimental study of heat transfer enhancement with wire coil inserts in laminar-transition-turbulent regimes at different Prandtl numbers" *International Journal of Heat and Mass Transfer*, 48(21), 4640-4651.
- [3] Garcia, A., Solano, J. P., Vicente, P. G., & Viedma, A. (2007). "Enhancement of laminar and transitional flow heat transfer in tubes by means of wire coil inserts" *International Journal of Heat and Mass Transfer*, 50(15), 3176-3189.
- [4] Promvonge, P. (2008). "Thermal performance in circular tube fitted with coiled square wires" *Energy Conversion and Management*, 49(5), 980-987.
- [5] Shoji, Y., Sato, K., & Oliver, D. R. (2003). "Heat transfer enhancement in round tube using wire coil: influence of length and segmentation" *Heat Transfer-Asian Research*, 32(2), 99-107.
- [6] Akhavan-Behabadi, M. A., Kumar, R., Salimpour, M. R., & Azimi, R. (2010). "Pressure drop and heat transfer augmentation due to coiled wire inserts during laminar flow of oil inside a horizontal tube" *International Journal of Thermal Sciences*, 49(2), 373-379.
- [7] Eiamsa-ard, S., Koolnapadol, N., & Promvonge, P. (2012). "Heat transfer behavior in a square duct with tandem wire coil element insert" *Chinese Journal of Chemical Engineering*, 20(5), 863-869.
- [8] Wang, L., & Sunden, B. (2002). "Performance comparison of some tube inserts" *International Communications in Heat and Mass Transfer*, 29(1), 45-56.
- [9] Xing, C., Meng, J. A., & Li, ZX (2010). "Heat transfer and rotating features of inserted spring rotors" *Journal of Engineering Thermophysics*, 31, 2105-2108.
- [10] Gunes, S., Ozceyhan, V., & Buyukalaca, O. (2010). "The experimental investigation of heat transfer and pressure drop in a tube with coiled wire inserts placed separately from the tube wall" *Applied Thermal Engineering*, 30 (13), 1719-1725.

Numerical Investigation of Heat Transfer and Fluid Flow of Nanofluids with Impinging Jets

Mustafa Kilic

Mechanical Engineering Department
Adana Science and Technology University
Adana, Turkey mkilic@adanabtu.edu.tr

Okan Ozcan

Mechanical Engineering Department
Adana Science and Technology University
Adana, Turkey
okanozcan@outlook.com

Abstract—Present study is focused on numerical investigation of heat enhancement and fluid flow from a heated surface by using nanofluids with three impinging jets. Effects of volume fraction, different heat flux and different types of nanofluids (NiO-water, CuO-water, Cu-water) on heat transfer and fluid flow were studied numerically. NiO-water nanofluid was used as a coolant. Three impinging jets were used to cool the surface. Low Re k- ϵ turbulent model of PHONEICS CFD code was used for numerical analysis. It is obtained that increasing volume fraction from 1% to 4% causes an increase of 8.6% on average Nusselt number. Increasing surface heat flux can not cause any significant increase on local Nusselt number. Using Cu-Water nanofluid can cause an increase of 4.4% on local Nusselt number according to the water.

Keywords—Heat transfer; Nanofluids; Volume fraction; Impinging jets

I. INTRODUCTION

A nanofluid is defined as a suspension of solid particles which have 1-100 nm size in a base fluid. In heat transfer applications using nanofluid, the particles suspended in the base fluid, expand thermal capacity of the fluid. Interactions and collisions between particles cause to increase in turbulence and turbulence intensity of the transition surface. Turbulence intensity and large surface area enables more heat transfer. Nanoparticles carry 20% of their atoms at the surface that makes them ready to heat transfer. Another advantage of using nanofluids is the particle agitation cause micro-convection in the fluid due to its very small size and therefore increases the heat transfer. For this reasons nanofluids can be applied to many heat transfer applications, in particular heat transfer from surfaces with high heat flux, as well as industry, medicine and space research. One of the optimum heat management techniques that provide high cooling efficiency in the industry is the jet impinging technique. The jet impinging technique is used to intensify heating, cooling or drying processes on a surface. The factor that makes the jet impinging technique attractive is that a high heat transfer is can be achieved on a narrow surface. In this method solid surfaces are cooled by means of fluid jets. Thus, at

a very high rate heat transfer can be acquired with a minimum flow rate. The jet impinging is used to obtain a high local heat transfer coefficient between the fluid and the surface, resulting in considerable increases in heat transfer as well as energy savings.

Many studies on nanofluids or impinging jets can be found in the literature. Teamah et al. [1] investigated heat transfer and flow structure formed by Al_2O_3 nanofluid to flat plate by experimentally and numerically with various Re number ($\text{Re}=3000-32000$) and different volume fraction of nanofluids ($\phi=0-10\%$). As the nanoparticles in the base fluid increases, the heat transfer from the surface increases and heat transfer coefficient can be enhanced by 62% according to the water is used base fluid only. They observed that heat transfer can be increased of 8.9% by using CuO-water with respect to Al_2O_3 -water. Manca et al. [2] surveyed the effect of impinging jets on heat transfer from a flat plate with a constant heat flux when pure water and Al_2O_3 -water nanofluids were used as a working fluid. Jet Reynolds number ($\text{Re}=100-400$) and dimensionless channel height ($H/W=4-10$) are the parameters used in operation. It has been stated that as the Reynolds number and the concentration of the particles in the fluid increases, the local heat transfer coefficient and the Nusselt number increase. The highest increase (36%) in the average heat transfer coefficient was obtained when $H/W=10$ and the nanoparticle volume ratios are $\phi=5\%$. Sun et al. [3] researched the effect of a single impinging jet using CuO-water nanofluids as working fluid on heat transfer. It has been determined that when the nanofluid is used, important advance can be achieved in heat transfer with respect to the use of water only, no significant change in pressure drop, a higher heat transfer coefficient is obtained when a circular nozzle is used, and a higher heat transfer coefficient is obtained when the jet angle is 90° . Çakır M.T. [4] experimentally evaluated the thermal performance of the system by using a nanofluid with 2% Al_2O_3 nanoparticles as a working fluid in a thermosyphon type heat pipe. As a result, the thermal resistance was significantly reduced however the thermal performance was not fully stabilized. Chien et al. [5] experimentally investigate the application of nanofluid in the flat plate heat pipe. It was obtained that the use of nanofluid achieves 40% reduction in thermal resistance compared to pure water utilization. Kang et al. [6] operated a nanofluid formed with silver nanoparticles and pure water. It was determined that when 10 nm and 35 nm sized particles used, thermal resistance diminished by 50% and 80% compared to pure water respectively. Xuan Y., Li Q., [7] studied the effect of Cu-water nanofluid, prepared at varied volume ratios, on heat transfer for different volume ratios, particle sizes, particle shapes and nanoparticle properties. As a result, it has

been found that an increase of 2.5% to 7.5% in the volume fraction causes 1.24 to 1.78 proportional increases in the coefficient of thermal conductivity of nanofluids. Shang et al [8] studied the heat transfer characteristics of a closed-loop vibrating heat pipe system with Cu-water nanofluid. When nanofluid was used heat transfer capacity of the system increases by 83% compared with pure water. Umar et al. [9] investigated the heat transfer from constant heat flux surface in laminar flow condition using varied ratios of Cu-Water nanofluid. As a result, it was found that as the particle volume ratio increased and the Reynolds number increased, the heat transfer coefficient increases, the highest increase in heat transfer coefficient (61%) occurred at a particle volume ratio of 4% and Reynolds number $Re = 605$. Qu et al. [10] investigated the thermal performance of a closed-loop vibrating heat pipe utilizing Al_2O_3 -water as a nanofluid. As a result, they found that the thermal resistance of the system decreased by 32.5% in proportion to pure water. Naphon et al. [11] investigated the heat transfer between the nanofluids (titanium-ethanol) and the closed two-phase thermosyphon. It was found that achieving a 10.6% improvement in evaporation heat transfer coefficient in the case of using nanofluid compared to only ethanol. Kilic et al. [12] surveyed the cooling of a flat plate with the support of the impinging fluid air jet for different Reynolds numbers and dimensionless channel heights. The mean Nusselt number was found to increase by 49.5% in $Re = 4000-10000$ and 17.9% in $H/Dh = 4-10$. Lin Z.H. Et al. [13] experimentally investigated heat transfer in confined fluid jets. The effects of Reynolds number and jet-target plate spacing on heat transfer were studied in this study. As a result of local and average Nusselt numbers at the stagnation point, it has been found that effect of the change in jet-target plate distance is not very important on the heat transfer, but the increase in Reynolds number increases heat transfer. Two experimental correlations were determined for mean Nu number and Nu number at the stagnation point in the range of $190 \leq Re \leq 1537$ and $1 \leq H/W \leq 8$. Nada S.A. [14] experimentally investigated the jet flow from the slits in different geometries to the cylinder surface. Two different jet / cylinder configurations have been tried. In the first application jet flow was applied so that the slit length was equal to the cylinder length. In the second application jet flow was applied to the cylinder from three separate slots so that the slit length would be equal to the cylinder diameter. Reynolds number range was taken between 1000 and 10000. The ratio of the slit width (w) to the cylinder diameter (d) is between 0.125 and 0.5. The effect of these widths on the local Nusselt number has been investigated as the width of the slit (w), the distance from the cylinder (z) ratio between 1 and 12. As a result, cooling of the cylinder with multiple slits provides more efficient cooling than cooling with a single slit. In both cases the Nusselt number increases as the Re number increases. Again, in both cases, the average Nusselt number is the maximum at $4 < z/w < 6$. Khudheyer S. M. [15] studied heat transfer numerically in different jet widths, different jet counts, different fin counts and different Reynolds number flows. In this study, surface was heated and tried to cool with channel flow and jet flow. It was

observed that the vortex formation region and local Nusselt number is greatly influenced by jet and flap width, jet spacing, flap thickness and jet Reynolds number. In addition, it has been found that the variation of the position of the fins relative to the jet significantly influences the heat transfer. Choo K. and Kim S. [16] experimentally surveyed the effect of confined and unconfined impinging jet on heat transfer. Air and water used as a fluid. It has been found that confined jet flow performance is similar to unconfined jet flow at constant pump power. At the constant flow rate, the confined jet flow thermal performance was found to be 20% to 30% less than the unconfined jet flow thermal performance. McGuinn A. et al. [17] numerically and experimentally investigated the heat transfer of the flow from the nozzle with two separate output geometries (straight out and shaped). The jet flow is applied to a copper plate representing uniform temperature. The variation of Nusselt number for different flow frequencies and different nozzle-plate distances was investigated. Frequency variation and surface distance hydraulic diameter ratio was investigated in the range of 40 Hz-160 Hz and (H/D) 1-6 respectively. As a result, it has been observed that the shaped nozzle provides more efficient heat transfer than straight nozzle. At the same time, it has been found that uniform flow from the shaped nozzle delays flow disturbances causing turbulent flow. Consequently, it was acquired that the heat transfer in the surface is not only depends on the turbulence formed but also depends on the flow geometry of the surface.

II. PRELIMINARY DEFINITIONS

The heat transfer from the surface will take place by convection, conduction and radiation.

$$Q_{convection} = Q_{total} - Q_{conduction} - Q_{radiation} \quad (1)$$

The total amount of heat to be given to the plate is;

$$Q_{total} = \frac{V^2}{R} \quad (2)$$

$$\alpha + \beta = \chi. \quad (1)$$

Where V is the voltage value of the power unit and R is the resistance of the heater. Here, the heat generated by the heater placed under the copper plate will be transmitted to the upper surface of the plate through the copper plate thickness by conduction, and as a result, the plate surface will be cooled by using nanofluid with impinging jet. Heat transfer by conduction along the plate;

$$Q_{conduction} = \frac{-k_c \cdot A_c \cdot (T_{bottom} - T_{upper})}{L_c} \quad (3)$$

$$\alpha + \beta = \chi. \quad (1)$$

here, k_c is the heat transfer coefficient of the copper plate, A_c is the copper plate surface area, and L_c is the copper plate thickness.

Thermal losses due to radiation;

$$Q_{radiation} = \varepsilon \cdot \sigma \cdot A \cdot F \cdot (T_s^4 - T_{bulk}^4) \quad (4)$$

$$\alpha + \beta = \chi. \quad (1)$$

Where ε is the copper plate emissivity, σ is the Stefan-Boltzmann constant, A is the radiation surface area, T_s is the surface temperature, and T_{bulk} is the mean fluid temperature.

$$T_{bulk} = \frac{T_{in} + T_{out}}{2} \quad (5)$$

It is assumed that heat transfer with radiation is negligible in this study because surface temperature is under 573.15°K.

Heat transfer from surface with convection;

$$Q_{convection} = h \cdot A \cdot \Delta T \quad (6)$$

$$\alpha + \beta = \chi. \quad (1)$$

Where h is the heat transfer coefficient, A is the convection surface area, ΔT ($\Delta T = T_s - T_{bulk}$) is the difference between the measured surface temperature and the fluid mean temperature.

Nusselt number (Nu) is a dimensionless parameter indicating the ratio of heat transfer with conduction to heat transfer with convection.

$$Nu = \frac{(Q_{convection} \cdot D_h)}{(T_s - T_{jet}) \cdot k_{nf}} \quad (7)$$

$$\alpha + \beta = \chi. \quad (1)$$

Where T_s is the measured surface temperature, D_h is the hydraulic diameter, and k_{nf} is the coefficient of thermal conductivity of the nanofluid. Reynolds number (Re) is used to determine for forced convection whether the flow is laminar or turbulent. Reynolds number based on turbulent flow;

$$Re = \frac{(\rho_{nf} \cdot V_{jet} \cdot D_h)}{(\mu_{nf})} \quad (8)$$

$$\alpha + \beta = \chi. \quad (1)$$

Where ρ_{nf} is the nanofluid density, V_{jet} is the jet velocity, and μ_{nf} is the nanofluid dynamic viscosity. The density of nanofluids is;

$$\rho_{nf} = (1 - \varphi) \cdot \rho_{bf} + \varphi \cdot \rho_p \quad (9)$$

$$\alpha + \beta = \chi. \quad (1)$$

Where ρ_{bf} is the base fluid (water) density, φ is the volumetric ratio of the nanofluid, and ρ_p is the density of the solid particles in the nanofluid. The volumetric ratio of nanoparticles is;

$$\varphi = \frac{1}{(1/\omega) \cdot (\rho_p - \rho_{bf})} \quad (10)$$

$$\alpha + \beta = \chi. \quad (1)$$

Where ω is the density difference between the fluid and the main fluid (water). The nanofluid specific heat is calculated from;

$$C_{p_{nf}} = \frac{\varphi \cdot (\rho \cdot C_p)_p + (1 - \varphi) \cdot (\rho \cdot C_p)_f}{(\rho_{nf})} \quad (11)$$

Where $C_{p(p)}$ is specific heat of particle, $C_{p(f)}$ is specific heat of base fluid. The effective thermal conductivity of nanofluid is calculated according to Massimo [18];

$$\frac{k_{eff}}{k_f} = 1 + 4.4 Re^{0.4} Pr^{0.66} \left(\frac{T}{T_{fr}} \right)^{10} \left(\frac{k_p}{k_f} \right)^{0.03} \varphi^{0.66} \quad (12)$$

$$\alpha + \beta = \chi. \quad (1)$$

Where Re is the nanoparticle Reynolds number, Pr is the Prandtl number of the base liquid. k_p is the nanoparticle thermal conductivity, φ is the volume fraction of the suspended nanoparticles, T is the nanofluid temperature (°K), T_{fr} is the freezing point of the base liquid. The effective dynamic viscosity of nanofluids;

$$\mu_{nf} = \mu_{bf} (1 + 2.5 \varphi + 4.698 \varphi^2) \quad (13)$$

III. NUMERICAL MODEL

Low Re k-ε turbulence model of PHOENICS CFD code was used for this numerical analysis. CFD simulation domain is shown in Fig 1. Mesh structure is shown in Fig.2.

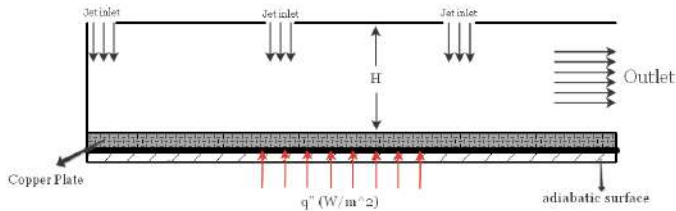


Fig. 1. CFD simulation domain

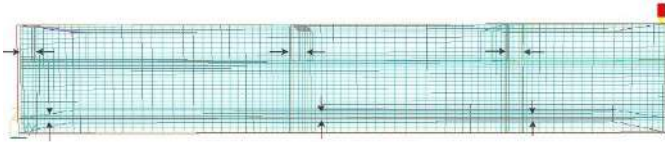


Fig. 2. Mesh structure

The continuity, Reynolds averaged momentum and time averaged energy equations governing 3-dimensional steady, flow of air with constant properties used for turbulent solutions can be written in the Cartesian coordinate system as follows:

Continuity equation:

$$\frac{\partial U_i}{\partial x_i} = 0 \quad (14)$$

Momentum equation:

$$\rho U_i \frac{\partial U_j}{\partial x_i} = -\frac{\partial P}{\partial x_j} + \frac{\partial}{\partial x_i} \left[\mu \left(\frac{\partial U_i}{\partial x_j} + \frac{\partial U_j}{\partial x_i} \right) - \rho \overline{u'_i u'_j} \right] \quad (15)$$

(11)

Energy equation:

$$\rho c_p U_i \frac{\partial T}{\partial x_i} = \frac{\partial}{\partial x_i} \left[k \frac{\partial T}{\partial x_i} - \rho c_p \overline{u'_i T'} \right] \quad (16)$$

All the boundary conditions used in the study are summarized in Table 1. It was used 96x15x34 (48960 elements) meshes for this application. Mesh structure was prepared according to flow conditions. In order to get more precise numerical results, we intensified mesh numbers in some region as jet inlet, surface of copper plate. Sweep number was studied between 400 and 2500 and cell number was also studied between 24 and 44. It is observed that numerical geometry was independent from sweep number and cell number when sweep number was 600 and cell number was 96x15x34.

TABLE X. BOUNDARY CONDITIONS

	$U(m/s)$	$V(m/s)$	$W(m/s)$	$T(^{\circ}K)$	k	ε
Nanofluid jet 1	$U=0$	$V=0$	$W=W_{inlet}$	$T=T_{inlet}$	$(T_1 W_{jet})^2$	$(C_p C_d)^{3/4} \frac{k^{3/2}}{L}$
Nanofluid jet 2	$U=0$	$V=0$	$W=W_{inlet}$	$T=T_{inlet}$	$(T_1 W_{jet})^2$	$(C_p C_d)^{3/4} \frac{k^{3/2}}{L}$
Nanofluid jet 3	$U=0$	$V=0$	$W=W_{inlet}$	$T=T_{inlet}$	$(T_1 W_{jet})^2$	$(C_p C_d)^{3/4} \frac{k^{3/2}}{L}$
Copper Plate	$U=0$	$V=0$	$W=0$	$q''=q''_{inlet}$	$k=0$	$\frac{\partial \varepsilon}{\partial z} = 0$
Outlet	$\frac{\partial U}{\partial x} = 0$	$\frac{\partial V}{\partial x} = 0$	$\frac{\partial W}{\partial x} = 0$	$T=T_{out}$	$\frac{\partial k}{\partial x} = 0$	$\frac{\partial \varepsilon}{\partial x} = 0$
Front and Back wall	$U=0$	$V=0$	$W=0$	$\frac{\partial T}{\partial y} = 0$	-	-
Top wall	$U=0$	$V=0$	$W=0$	$\frac{\partial U}{\partial z} = 0$	-	-

IV. RESULTS AND DISCUSSIONS

In this section, numerical results were prepared for three parameters.

- Effect of NiO-water nanofluid with 25 nm sized particles for different volume fractions on heat transfer ($\phi=1\%$, 2% , 4% , 5%),
- Effect of different heat flux of copper plate with NiO-water nanofluid on heat transfer ($q''=111111W/m^2$, $148148W/m^2$, $185185W/m^2$, $222222W/m^2$).
- Effect of different type of nanofluids on heat transfer (CuO-water, Cu-Water, NiO-Water).

A. Effect of different volume fraction of NiO nanofluid

Fig 3 shows temperature of heated surface when cooled with different volume fractions ($\phi=1\%$, 2% , 4% , 5%) of NiO-water nanofluid;

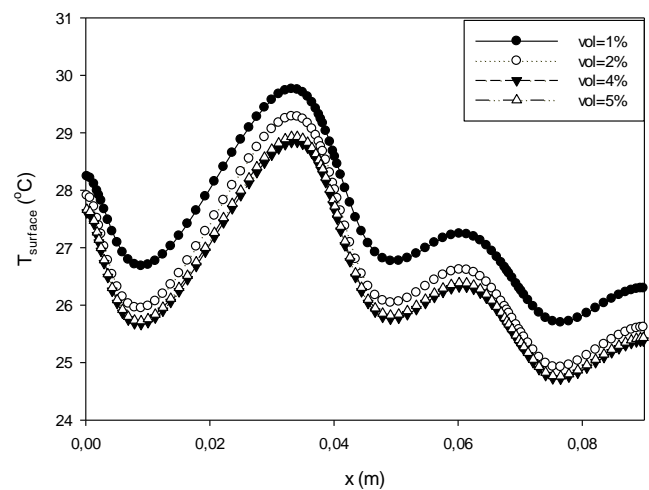


Fig 3. Temperature distribution on surface

It can be seen that the surface temperature decreases on stagnation point of first impinging jet. There is a temperature

increase before the stagnation point of second jet. The reason of this is decreasing of the fluid velocity with effects of second jet. So location of stagnation point of second jet goes upward. When velocity of the fluid decreases, thermal boundary layer thickness increases again. In impact region of the second jet, boundary layer thickness is decreased and heat transfer increases. Effect of third jet reduced because of the channel flow of first and second jet. Jet effect and channel flow effect can also be seen at this region. Therefore, heat transfer rate has the highest level at this region.

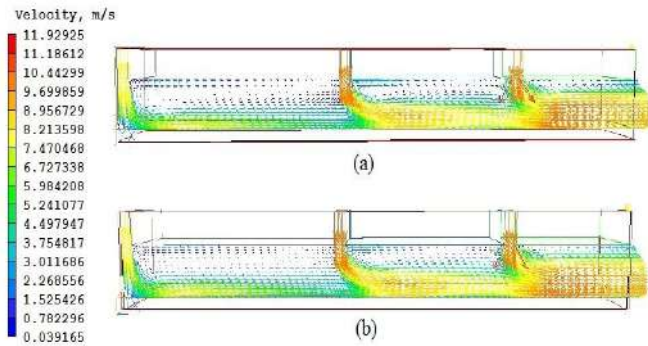


Fig 4. (a) Velocity vectors of 1% NiO-water nanofluid
(b) Velocity vectors of 4% NiO-water nanofluid

Fig 4 shows velocity vectors of NiO-water nanofluid for $\phi=1\%$ and 4% respectively.

Fig 5 shows the analysis of change in Nusselt number when different volume fractions of NiO used as a heat transfer fluid.

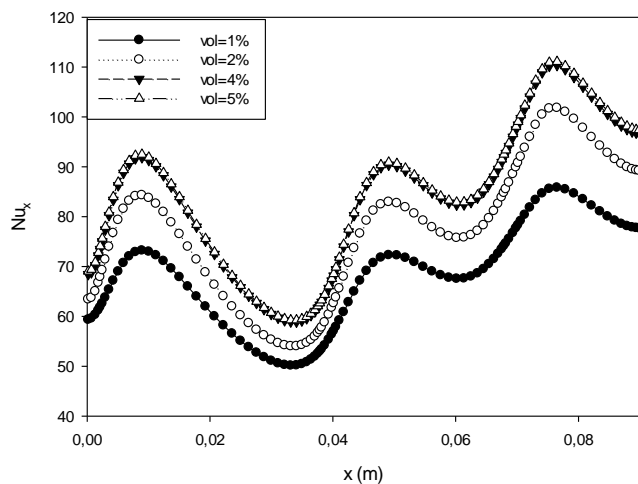


Fig 5. Local Nusselt numbers for different volume fractions

It can be seen that increasing volume fraction of NiO from $\phi=1\%$ to 4% causes an increase of 8.5% on average Nusselt number. But there is not a prominent difference on average Nusselt number between $\phi=4\%$ and $\phi=5\%$.

B. Effect of heat flux of copper plate on heat transfer

Fig 6 shows Nusselt number for NiO-water nanofluid for different heat flux ($q''=111111\text{ W/m}^2$, 148148 W/m^2 , 185185 W/m^2 , 222222 W/m^2).

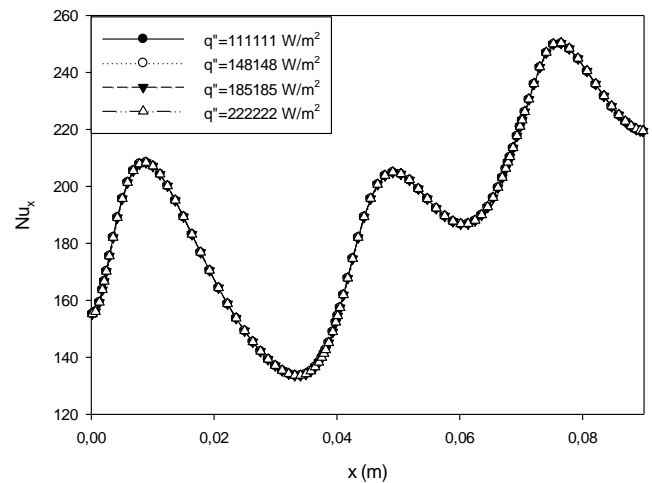


Fig 6. Local Nusselt numbers of nanofluid for different heat fluxes

It was seen that increasing heat flux two times has not a considerable effect on local Nusselt number.

C. Effect of different type of nanofluids

Numerical analysis is conducted for different type of nanofluids (Cu-water, CuO-water and NiO-water) with 25 nm particle size and volume fraction 4%. Properties of nanofluids were calculated at 293K.

TABLE XI. THERMO-PHYSICAL PROPERTIES OF NANOFLUIDS AT 293K.

Nanofluid	ρ (kg/m ³)	C_p (J/kgK)	μ (Pa.s)	Kinematic	k (W/mK)	β (m ² /2)
CuO-water	1218,272	3403,881	0,001099764	9,02725E-07	0,662101313	0,0001597
NiO-water	1230,672	3389,813	0,001099764	8,93629E-07	0,663961878	0,0001592
Cu-water	1316,672	3148,451	0,001099764	8,35261E-07	0,66843348	0,0001612

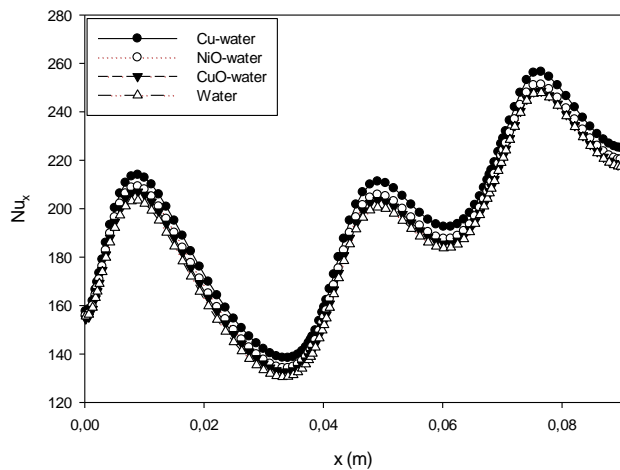


Fig 7. Nusselt numbers for nanofluids

Fig 7 shows variation in Nusselt number for water, CuO-water, NiO-water and Cu-water. It was acquired that using Cu-water nanofluid causes an increase of 3.5%, 2.4%, 4.4% on average Nusselt number with respect to CuO-water, NiO-water and water. Fig 8 and Fig 9 shows surface temperature contours for water and Cu-water nanofluid. It can be seen that using Cu-water nanofluids shows better heat transfer performance.

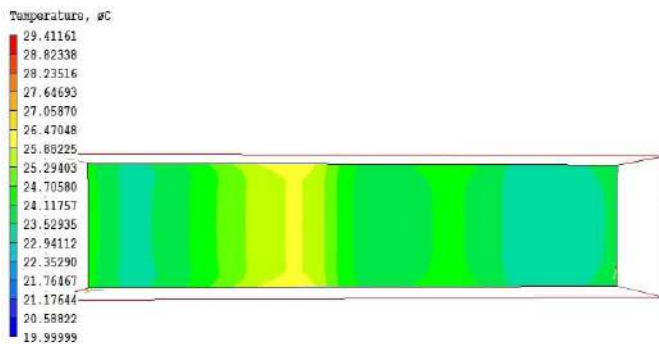


Fig 8. Surface temperature contours for water

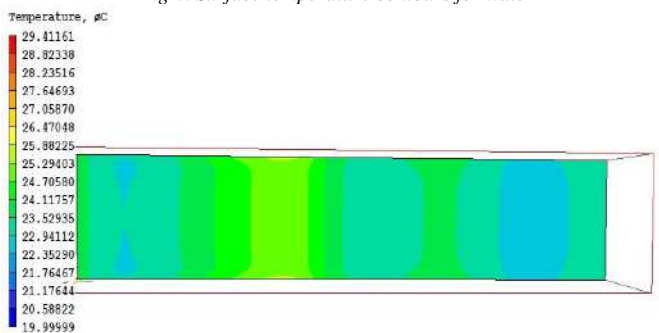


Fig 9. Surface temperature contours for Cu-water nanofluid

V. CONCLUSION

The main goal of the current study was to examine heat enhancement and fluid flow from a heated surface by using nanofluids and three impinging jets numerically. Effect of

volume fraction, different heat flux and different types of nanofluids (Water, NiO-water, CuO-water, Cu-water) were on heat transfer and fluid flow were studied numerically. According to our constraints the result of this study indicate that increasing volume fraction from $\phi=1\%$ to 4% causes an increase of 8.6% on average Nusselt number. But there is not a slight difference between $\phi=4\%$ and 5% . Increasing heat flux two times has not a significant effect on heat transfer. Using Cu-water nanofluid causes an increase of 3.5%, 2.8%, 4.5% on average Nusselt number with respect to CuO-water, NiO-water and water. Using Cu-water nanofluid shows better heat transfer performance. Research areas for future investigations can be investigation of effect of hybrid nanofluids on heat transfer.

ACKNOWLEDGMENT

The financial support of this study by Scientific Research Project (16103021) of Adana Science and Technology University is gratefully acknowledge.

Nomenclature	
C_p	Specific Heat (J/kgK)
ρ	Density (kg/m ³)
ϕ	Nanoparticle volume fraction
μ	Dynamic viscosity (Pa.s)
bf	Base fluid
nf	Nanofluid
p	Particle
Pr	Prandtl Number, $Pr = \frac{C_p \cdot \mu}{k}$
Re	Reynolds number $Re = \frac{(\rho_{nf} \cdot V_{jet} \cdot D_h)}{(\mu_{nf})}$
Nu_x	Local Nusselt number $Nu = \frac{(Q_{convection} \cdot D_h)}{(T_s - T_{jet}) \cdot k_{nf}}$
k_{eff}	Effective Thermal Conductivity (W/mK)

REFERENCES

- [1] Teamah, M.A., Dawood M.M., Shehata A., "Numerical and experimental investigation of flow structure and behavior of nanofluids flow impingement on horizontal flat plate", Experimental Thermal and Fluid Science, vol 74, 235-246, 2016.
- [2] Manca, O., Ricci, D., Nardini S., Lorenzo, G., "Thermal and fluid dynamics behaviors of confined laminar impinging slot jets with nanofluids", International Communications in Heat and Mass Transfer, vol 70, 15-26, 2016.

- [3] Sun, B., Qu, Y., Yang, D., "Heat transfer of Single Impinging jet with Cu nanofluids", *Applied Thermal Engineering*, vol 102, 701-707, 2016.
- [4] Cakır M.T., "Alamünaiçeren Nnaokışkankullanarakısıborularınınperformanslarını iyileştirilmesi", *Journal of The Faculty of Engineering and Architecture of Gazi University*, vol 30, 547-556, 2015.
- [5] Chien, H.T., Tsia C.Y., Chen P.H., Chen P.Y., "Improvement on thermal performance of a disk-shape miniature heat pipe with nanofluid", *Proceedings of the fifth International Conference on Electric Packaging Technology, IEEE*, 389-391, 2003.
- [6] Kang S.W., Wei, W.C., Tsia S.H., Yang S.H., "Experimental Investigation of silver nano-Fluid on heat pipe thermal performance", *Applied Thermal Engineering*, vol 26, 2377-2382, 2006.
- [7] Xuan Y., Li Q., "Heat transfer enhancement of nanofluids", *Int. Journal of Heat and Fluid Flow*, vol 21, 58-64, 2000.
- [8] Shang F.M., Liu D.Y., Xian H.Z., Yang Y.P., Du X.Z., "Flow and heat transfer characteristics of different forms of nanometer particles in oscillating heat pipe", *Journal of Chemical Industry*, vol 58, 2200-2204, 2007.
- [9] Umer A., Naveed S., Ramzan N., "Experimental Study of laminar forced convection heat transfer of deionized water based copper (I) oxide nanofluids in tube with constant wall heat flux", *Heat Mass Transfer*, vol 52, 2015-225, 2015.
- [10] Qu j., Wu H.Y., Cheng P., "Thermal performance of an oscillating heat pipe with Al₂O₃-water nanofluids", *International Communication Heat and Mass Transfer*, vol 37, 111-115, 2010.
- [11] Naphon P., Asssdamongkol P., Borirak T., "Experimental investigation of titanium nanofluids on the heat pipe thermal efficiency", *International Communication Heat and Mass Transfer*, vol 35, 1316-1319, 2008.
- [12] Kilic, M., Çalışır, T., Başkaya, Ş., "Experimental and numerical study of heat transfer from a heated flat plate in a rectangular channel with an impinging Jet", *Journal of the Brazilian Society of Mechanical Sciences and Engineering*, vol 48:1-16, 2016.
- [13] Lin, Z.H., Chou, Y.J., Hung, Y.H., "Heat transfer behaviors of a confined slot jet impingement", *Int Jour. of Heat and Mass Transfer*, 49:2760-2780, 1999.
- [14] Nada, S.A. "Slot/slots air jet impinging cooling of a cylinder for different jets-cylinder configuration", *Department of Mechanical Engineering Technology Benha University, Egypt*, 2006.
- [15] Khudheyer, S., Oztop, F., Yılmaz, I., "Analysis of turbulent flow and heat transfer over a double forward facing step with obstacles", *Heat and Mass Transfer*, 39:1395-1403, 2012.
- [16] Choo, K., Kim, S., "Comparison of thermal characteristics of confined and unconfined impinging jets", *School of Mechanical, Aerospace and Systems Engineering Korea Institute of Science and Technology, South Korea*, 2010.
- [17] McGuinn, A., Persoons, T., O'donovan T., Murray, D., "Surface Heat Transfer From an Impinging Synthetic Air Jet", *Int. Jour. of Heat and Mass Transfer*, 20: 1333-1338, 2005.
- [18] Corcione M., Empirical correlating equations for predicting the effective thermal conductivity and dynamic viscosity of nanofluids. *Energy Convers. Manag.* 2011;52(1):789-93.

Vibration Study of Functionally Graded Beam

BOUAMAMA Mohamed

Université de Sidi Bel Abbès

Laboratoire de Mécanique des Solides et des Structures

Sidi Bel Abbès, Algérie

bouamamamohameddoc@gmail.com

REFASSI Kaddour

Université de Sidi Bel Abbès

Laboratoire de Mécanique des Solides et des Structures

Sidi Bel Abbès, Algérie

Refassi_kaddour@yahoo.fr

Abstract—This work present, a study of the vibration behavior of clamped-clamped functionally graded beam (FGB). The aim of this paper is to investigate the influence of the skin of the sandwich beam on the natural frequencies of the system using Euler-Bernoulli classical theory (CLBT) taking into account that the material properties of the FGM layer in continually graded in the thickness direction with power law distribution.

Keywords—vibration; sandwich; FGM; beam; frequencies

Introduction

Functionally graded (FG) materials are a type of composite composed of two or more materials which are designed to have a spatial continuity of properties. These materials are used in many engineering candidates such as nuclear reactors and high-speed satellite industries.

FGM are produced by continuously changing of the volume fractions in the thickness direction to obtain a well-defined profile. Generally, these materials are made from a mixture of ceramic and metal or a combination of different materials [1].

The beam is considered as the structural element most responded, as an integral part in most of the construction works or machinery parts [2], which made necessary the study of their static / dynamic behavior. The beams are used as structural component in several construction applications and a large number of studies can be found in the literature about the transverse vibration of the uniform isotropic beams [3]. The importance of developing an analysis of the vibration behavior of the beams is related to the use of the beams as a basic element in achieving the structures, and to determine the effects of changes in boundary conditions, and changes of the material on the natural frequencies and natural modes of vibration.

FGM sandwich can mitigate a concentration of shear stress between the faces because of the gradual change in material properties at the interface -Coeur skins. The effects of FGM nucleus have been studied by Venkataraman and Sankar [4] and Anderson [5] on the shear stresses at the skin interface of a beam -Coeur sandwich FGM. Pan and Han [6] analyzed the static response of the rectangular plate made of several functionally graded layers, anisotropic, Shen [7] studied two types of laminated hybrid plates, one with FGM

core and piezoelectric skins ceramic and the other is with FGMs skins and piezoelectric ceramic core. In the present paper we investigate the influence of volume fraction index on the frequency response of a clamped-clamped FG sandwich beam.

I. MATHEMATIC MODELS

Considering a clamped - clamped sandwich FGM beam with uniform thickness composed of three heterogeneous layers relative to a Cartesian coordinate system (x,y,z). Upper and lower faces are located at $Z = \pm h/2$ and the sides of the beam are parallel to the x and y axes fig 1.

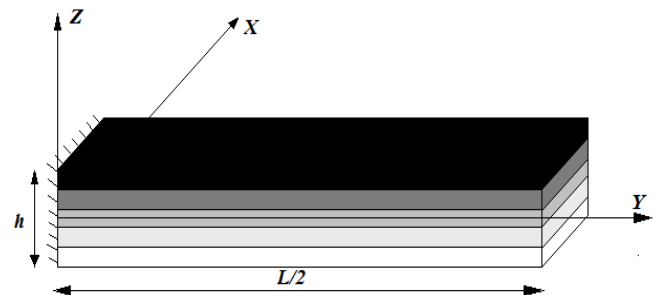


Fig. 11. FGM rectangular sandwich beam (c-c) in Cartesian coordinates

The FGM beam, is composed of three elastic layers, named; layer "1", layer "2" and layer "3" on the front ,lower and the top of the beam. The vertical coordinates of the lower face, the two interfaces, and the upper sides are denoted by $h_1 = -h/2$, h_2 , h_3 , and $h_4 = +h/2$, respectively. On the front, lower and the top of the beam. The vertical coordinates of the lower face, the two interfaces, and the upper sides are denoted by $h_1 = -h/2$, h_2 , h_3 , and $h_4 = +h/2$, respectively.

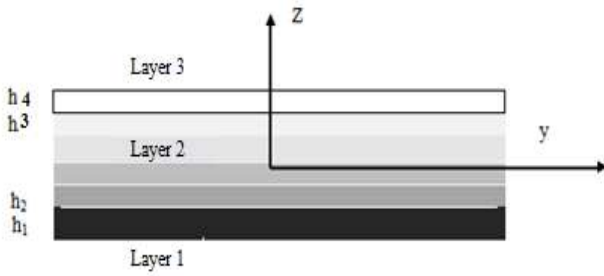


Fig. 12. Geometry of FGM rectangular sandwich beam in Cartesian coordinates.

The properties of the FGM vary continuously as a function of the volume fraction of the material in the direction of the thickness. A function of power law is commonly used to describe this variation in material properties. The sandwich structures FGMs is discussed as follows.

The volume fraction in the P-FGM is provided by a power law depending on the thickness:

$$V^{(1)} = 0 \quad z \in [h_1, h_2] \quad (1)$$

$$V^{(2)} = \left(\frac{z - h_2}{h_3 - h_2} \right)^p \quad z \in [h_2, h_3] \quad (2)$$

$$V^{(3)} = 1 \quad z \in [h_3, h_4] \quad (3)$$

Where $V(n)$ ($n=1,2,3,\dots$) denotes a function of the volume fraction of the layer n ; p is the index of the volume fraction ($0 \leq p \leq +\infty$), which indicates the physical change through thickness.

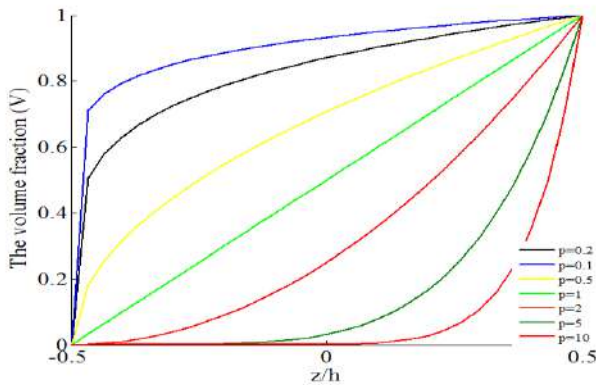


Fig. 13. Distribution of ceramic material through the beam depth according to the power-law form

Actual material properties such as Young's modulus E , and Poisson's ratio ν and bulk density ρ can be expressed by the law of mixtures [8] as:

$$P^{(n)}(z) = P_2 + (P_1 - P_2)V^{(n)} \quad (4)$$

Or $P^{(n)}$ is the actual physical ownership of FGM layer n . P_1 and P_2 are the physical properties of the upper and lower surfaces of the layer 3 and 1, respectively, in this study, it is assumed that the Poisson's ratio is constant [9]

II. RESULTS AND DISCUSSIONS

Considering Clamped-Clamped sandwich beam composed of two rigid homogeneous in its upper and lower surface and FGM in its heart, As the top facet is made of 100% ceramic Al_2O_3 (Alumina), while the lower facet is made of 100% metal Al (Aluminum). The material properties of the considered structure are given in table 1.

Table 1. Material properties

properties	Ceramic (Al_2O_3)	Aluminum (Al)
Poisson's ratio ν	0.33	0.33
Density ρ (Kg/m^3)	3800	2708
Young's Modulus (Gpa)	380	70

Table 2. The natural frequencies for Clamped-clamped (C-C) beam with the power low index

scheme	frequency		
	$P=0.1$	$P=1$	$P=10$
2-1-2	29.425	29.807	30.488
	81.112	82.164	84.043
	159.01	161.07	164.75
1-1-1	29.635	30.178	31.466
	81.707	83.160	86.739
	160.14	163.02	170.04
1-2-1	30.048	30.869	33.217
	82.828	85.093	91.564
	162.37	166.81	179.50
1-3-1	30.216	31.381	34.484
	83.291	86.504	95.059
	163.28	169.58	186.35
1-8-1	29.763	32.558	37.500
	82.042	89.750	103.37
	160.83	175.94	202.64
0-1-0	26.368	33.830	41.073
	72.684	93.254	113.22
	142.49	182.82	221.95

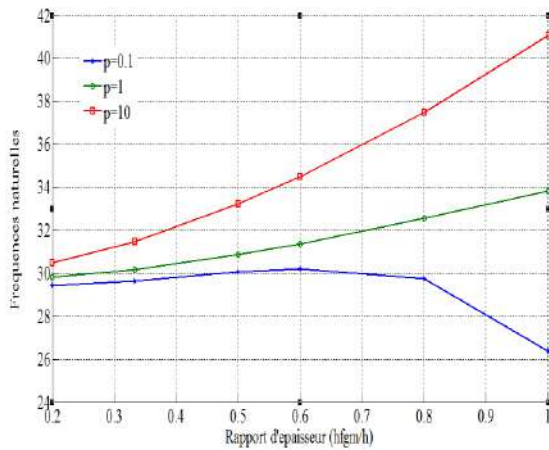


Fig. 14. Natural frequencies versus volume fraction index ($p=0.1, p=1, p=10$) for a clamped-clamped sandwich FGM beams

The tab.1 and Fig. 4 show that for the power law index $p=0.1$, the frequency is more important when the thickness of the FGM layer take 60% of the total thickness; and its less important when rapport between the FGM layer and the total thickness is 1; elsewhere for $p=1$ and $p=10$ the frequency response is maximum when $h_{fgm}=h$ and minimum when the $h_{fgm}=0.2h$.

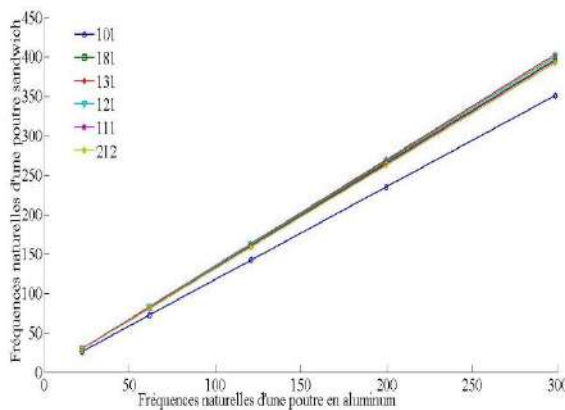


Fig. 15. Natural frequencies of a clamped - clamped In sandwich beam compared to the natural frequencies of an aluminum for beam for $p=0.1$

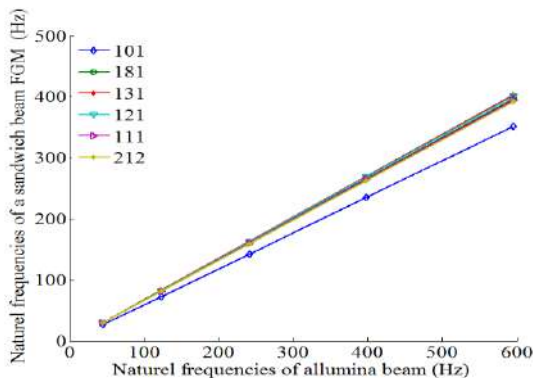


Fig. 16. Natural frequencies of a clamped - clamped In sandwich beam compared to the natural frequencies of an alumina for beam for $p=0.1$

Fig.5 and Fig.6 show that the natural frequencies of a sandwich beam FGM are proportional to the natural frequency of the base materials (ceramics, metal). The plot of the beam with combination "0-1-0" has the smallest frequencies value while that corresponding to "1-3-1" has the largest value.

CONCLUSION

In this study, the free vibrations of sandwich beams FGM assuming that the material properties vary depending on the thickness with a power distribution (P-FGM) is examined. The main purpose of this work is to study the influence of the volume fractions of base materials on the frequencies and modes. The variation in the thickness of the FGM material on the natural frequencies is also studied for various boundary conditions. The results show that the frequencies are proportional to the FGM ratio and getting larger when the structure has a superior ceramic percentage.

REFERENCES

- [1] N. Zouatnia, H. Lazreg, A. Kassoul, "Revue sur les différentes théories de cisaillement applicables aux structures FGM," 2eme Workshop sur le comportement Non Linéaire des structures, Université Hassiba Benbouali de Chlef, 28 février 2016.
- [2] S. Kessas, "Etude de l'effet de cisaillement transverse sur le comportement des poutres composites," Thèse de Magister en Génie civil Université Mentouri de Constantine, 2010.
- [3] D.J. Gorman, "free vibration analysis of beams and shafts," John Wiley and Sons New York .1975.
- [4] S.Venkataraman, and B.V.Sankar, "Analysis of sandwich beams with functionally graded core," Proceedings of the 42nd AIAA/ASME/ASCE/AHS/ASC Structures, Structural Dynamics, and Materials Conference, Seattle, AIAA-1281, pp.16-19, 2001.
- [5] T.A.Anderson, "A 3-D elasticity solution for a sandwich composite with functionally graded core subjected to transverse loading by a rigid sphere," Composite Structures., vol. 60, no. 3, pp. 265-274, 2003.
- [6] E.Pan, F.Han, "Exact solution for functionally graded and layered magneto-electro-elastic plates," International Journal of Engineering Science., vol. 43, pp. 321-339, 2005.
- [7] H.S.Shen, "Postbuckling of FGM plates with piezoelectric actuators under thermo-electromechanical loadings," International Journal of Solids and Structures., vol. 42, pp. 6101-6121, 2005.
- [8] P.R.Marur, "Fracture Behaviour of Functionally Graded Materials," PhD, dissertation. Auburn University, Alabama. 1999.
- [9] F. Delale, F.Erdogan, "The crack problem for a non homogeneous plane," ASME Journal of Applied Mechanics., vol. 50, pp. 609-614, 1983.

Dynamic Analysis of UAV Wings

SATLA Zouaoui

Department of mechanical

Laboratory of mechanic of structures and solids

P.B. 89Ben M'hidi city- Sid Bel Abbas 22000 Algeria

satlazouaoui@hotmail.fr

ELAJRAMI Mohamed

Department of mechanical

Laboratory of mechanic of structures and solids

P.B. 89Ben M'hidi city- Sid Bel Abbas 22000 Algeria

eladjrami_mohamed@yahoo.fr

Abstract— This work is a simulation study to determine the modes shapes and natural frequency in first plate then we do a harmonic vibration of an inflatable wing of drone (fixed wing UAV), to achieve this a wing constructed of an external restraint made of Kapton coated Kevlar fabric encasing a bladder is considered for internal pressures ranging from 3 to 15 psig. The simulation study was driven by Ansys APDL.

Keywords— Inflatable Wing, UAV drone, Natural Frequency, Internal Pressure, Harmonic Vibration.

I. INTRODUCTION

Inflatable wings provide a new solution to unmanned aerial vehicles requiring small cramped volumes, such as those used for military reconnaissance or extra-planetary exploration. There is desire to implement warping actuation forces to change the shape of the wing during flight to allow for greater control of the aircraft. In order to quickly and effectively analyze the effects of wing warping strategies on an inflatable wing. With the ever-expanding technology in the aviation (uav) industry. The inflatable wing, which is produced by using lightweight flexible composite materials made of Kapton coated Kevlar fabric [1], is a new modality of structure with advantages of lowcost, small volume, light weight, high reliability etc. Therefore, for variety of types of UAV, it has wide application and research prospects [2, 3]. The goal of this work is to calculate the natural frequency at different internal pressure then determinate the harmonic response of the wing by using Ansys code.

The paper is organized as follows: In Section 2, we describe the model of wing chosen for this study with principal dimensional and adaptive type of profile. In Section 3 and 4, we present the fundamentals simulation results. In Section 5 concludes the paper.

II. DESIGN OF THE INFLATABLE WING

In this work we choose a model of inflatable wing as clarifier in Fig.3. NACA 4318[4, 5] wing profile was selected as a target in this study.

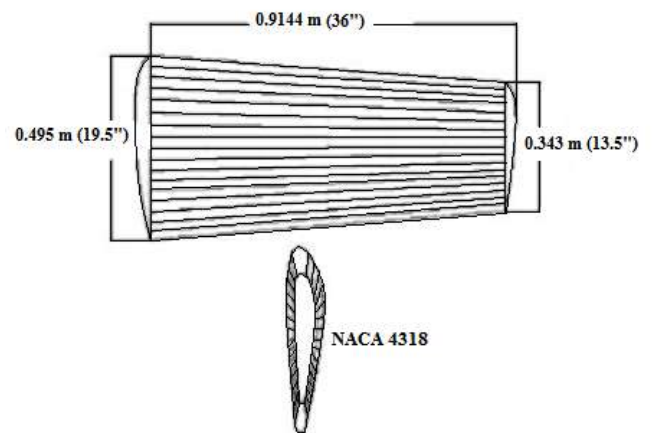


Fig. 1. Geometry of inflatable wings, 36-inch semi-span [4].

III. FINITE ELEMENT ANALYSES

A. Description of Model

The finite element (FE) model of the wing was created using ANSYS FE software. The wing geometry was created in ProEngineer from wing dimensions provided by the manufacturer [1]. For simplicity of modeling [3], the wing tip was modeled as a flat vertical surface, rather than the tip seam seen in Fig.1. Once the geometry was created, the model was meshed with SHELL181 elements, which are 4-node shell elements with 6 DOF at each node. An element thickness of $3.302 \times 10^{-5} \text{ m}$ (0.013 inches) was used, corresponding to the thickness of the Kapton coated Kevlar material.

The model was containing 17,697 elements after meshing of wing and 16,911 nodes. The final model mesh is shown in Fig.2.

A linear orthotropic material model was used in the analysis, with material properties obtained from [1]. The Kapton coated Kevlar is presently under examination for use in construction of double-walled structures show Tab.1.

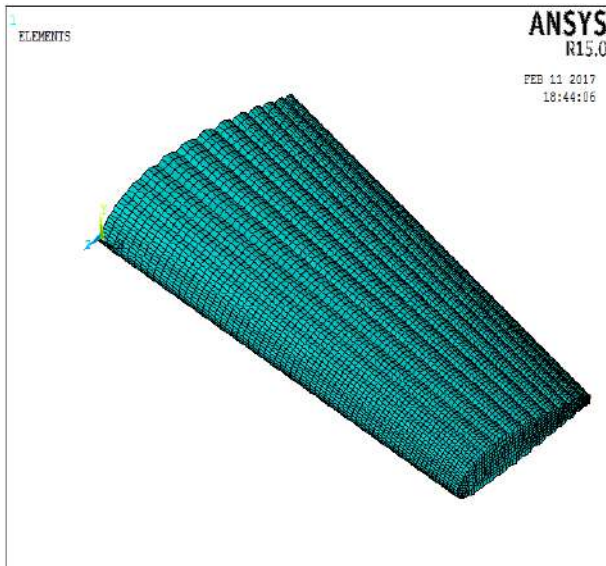


Fig.2. Finite element model of inflatable wing.

TABLE I STIFFNESS RESULTS FOR THE DIFFERENT MATERIALS FROM UNIAXIAL TESTING.

Material	Direction	Young's modulus	Uniaxial (MPa)	Estimated Biaxial (MPa)
PAIDAE	Warp	E_1	13375.83 ± 482.63	8273.71 ± 551.58
	Fill	E_2	13306.88 ± 689.47	8204.76 ± 482.63
IRVE	Warp	E_1	9307.92 ± 413.68	7101.6 ± 1103.16
	Fill	E_2	8411.6 ± 275.79	4757.38 ± 68.94

B. Results

The finite element solution process consisted of multiple steps. First, internal pressure loadings were applied to the "restraint" areas of the model show Fig.3, and the solution was computed using the standard linear sparse solver in ANSYS. Subsequently, a modal analysis was performed using the Block-Lanczos solver, including pre-stress effects from the pressure application solution.

Tab.2 and Fig.4 summarizes the mode shapes and frequencies obtained from the simpler modeling process in which the pressure solution was obtained using a linear solver in ANSYS. For this simpler solution process, results were obtained for all pressure cases considered, though results do not fully follow expected trends. Most notably, the wing stiffness should increase with pressure. In general, this is the case; however, the first bending mode of the 0.02 and 0.08 MPa (3 and 12 psi) cases proves higher than the 0.04, 0.06

and 0.1 MPa (6, 9 and 15 psi) cases show Fig.5. In fact for many of the linearly-solved pressure cases, there were many localized large deflections, which sometimes made identifying wing mode shapes difficult.

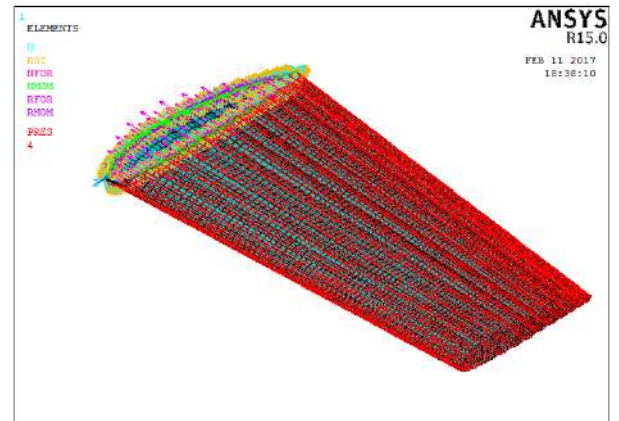


Fig 3. Internal pressure loadings

TABLE XII. FINITE ELEMENTS PREDICTIONS OF WING FREQUENCIES (Hz).

Mode	0.02 MPa	0.04 MPa	0.06 MPa	0.08 MPa	0.1 MPa
First bending mode	10.011	9.4984	8.7210	10.894	7.8075
First torsional mode	26.528	27.085	27.424	28.316	26.869
*Mode in chord direction (Figure 6)	33.789	33.837	33.852	33.642	33.623
Second bending mode	45.775	46.743	46.990	47.488	47.136
Second torsional mode	53.841	60.961	65.634	66.223	70.617

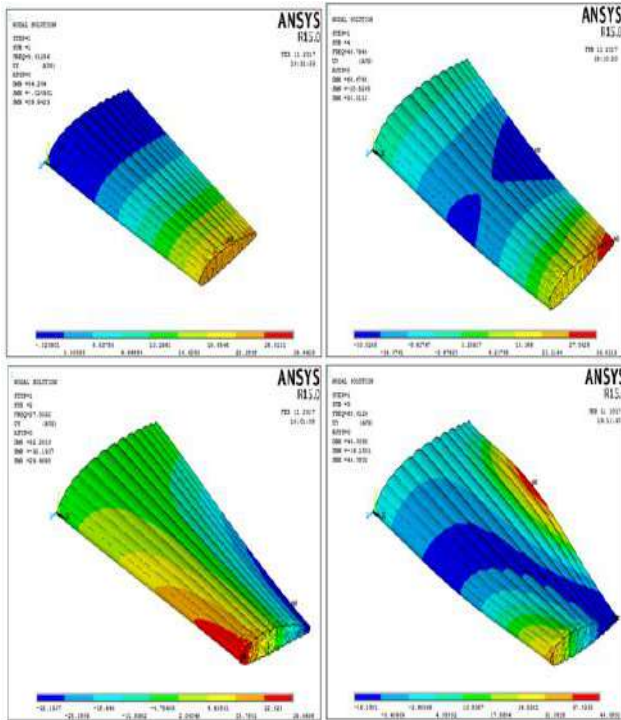


Fig. 4. First four mode shapes of inflatable wing

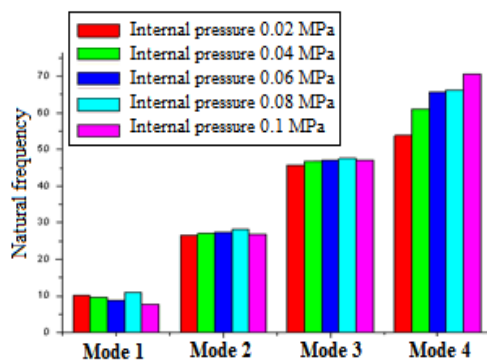


Fig.5. Natural frequency of bending and torsional for different internal pressure.

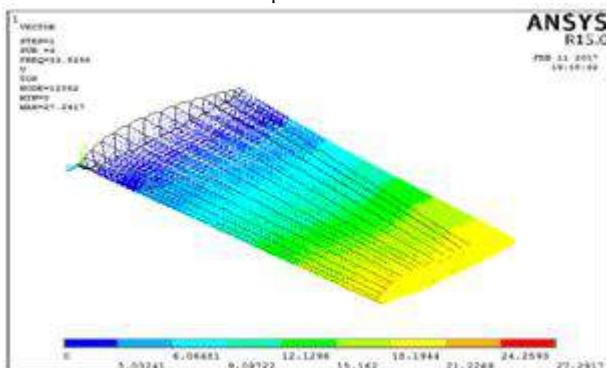


Fig.6. Mode in chord direction

IV.HARMONIC RESPONSE:

This study evaluates the response to aerodynamic forces [6], in the form of graphs illustrating the signal amplitude as a function of frequency according to the different internal pressure. We suppose that the vector of excitation forces of frequency response Fig.7.

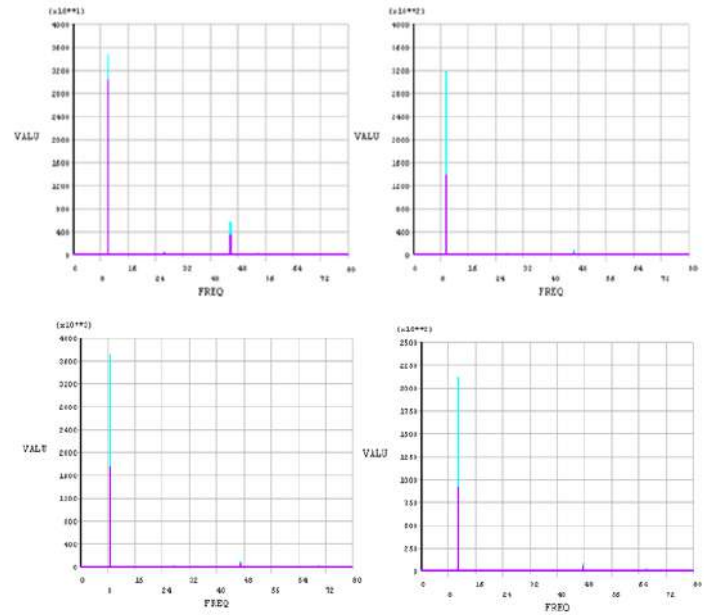


Fig. 7. Harmonic response for different internal pressure 0.02, 0.04, 0.06, and 0.08 MPa respectively X (cyan), Z (purple).

V.CONCLUSIONS

Modal parameter estimation was performed using finite elements method for determined frequency response functions, to determine resonant frequencies, damping, and mode shapes of the wing. We can conclude from these numerical modeling approaches that the dynamic behavior of the inflatable wing of different internal pressure, as frequencies of the internal pressure 0.02 and 0.08 MPa (3 and 12 psi) in this case proves higher than the 0.04, 0.06 and 0.1 MPa (6, 9 and 15 psi) for first bending mode. The visualization of modes shows that the end of the inflatable wing is the area most highly stressed whatever the lag, flapping or twisting. And finally for performance Flight must select tow internal pressure 0.02 and 0.08 MPa (3 and 12 psi) one for flexible wing and second for rigid wing respectively.

REFERENCES

- [1] Allison L. Hutchings: "Experimental Determination of Material Properties for Inflatable Aeroshell Structures", AE8900 MS Special Problems Report Space Systems Design Lab (SSDL) Guggenheim School of Aerospace Engineering Georgia Institute of Technology Atlanta, GA May 26, 2009.

- [2] Johnathan Rowe, Andrew Simpson, and Jamey Jacob: "Preliminary Modal Analysis of Inflatable Wings", Oklahoma State University Mechanical & Aerospace Engineering Dept., Stillwater, Oklahoma, 74078.
- [3] Rowe, J.M., "Finite Element Modeling of an Inflatable Wing," M.S. Thesis, Dept. of Mechanical Engineering, University of Kentucky, Lexington, KY, August 2007.
- [4] Jacob, Stephen Scarborough, and David Cadogan: "Testing of Compact Inflatable Wings for Small Autonomous Aircraft". Department of Mechanical and Aerospace Engineering, Oklahoma State University, Stillwater, 29 August 2009.
- [5] Rowe, J.M., Smith S.W., Simpson, A.D., Jacob, J.D. and Scarborough, S., "Development of a Finite Element Model of Warping Inflatable Wings," AIAA No. 2006-1697 AIAA Structures, Structural Dynamics and Materials Conference, 1-4 May 2006, Newport, Rhode Island.
- [6] Zhang Jun-Tao, Hou Zhong-xi, Guo Zheng, and Chen Li-li: "Analysis and Flight Test for Small Inflatable Wing Design", World Academy of Science, Engineering and Technology 69/2012, page 868.

Vibration Damping of Cantilever Beam by Means Piezoelectric Actuator

Salah Mostefa

Mechanics of Structures and Solids Laboratory
Department of Mechanics, Faculty of technology,
Djillali Liabès University of Sidi Bel-Abbès Algeria
mostefa.salah@yahoo.fr

Satla Zouaoui

Mechanics of Structures and Solids Laboratory
Department of Mechanics, Faculty of technology,
Djillali Liabès University of Sidi Bel-Abbès Algeria
satlazouaoui@hotmail.fr

Abstract— The present work is a study of active vibration control of a smart beam. In this regard, piezoelectric patches are using as sensor and actuators. Based on Euler-Bernoulli theory a state space equation is adopt and extend to the case of cantilever beam, moreover, LQR and LQG controller are using. The analysis studies are carried out using Ansys and Matlab.

Keywords—component; formatting; style; styling; insert (key words)

III. INTRODUCTION

Unwanted vibrations can caused a catastrophic breakdown of structures, hence scientist worked toward to provide solutions to prevent this kind of failure. different technique are used to damped vibration we noted passive and active vibration control. Piezoelectric materials are kind of smart structure which have the ability to change behavior under extreme stress, this advantage make piezoelectric material as the most appropriate smart materials for the active and semi-active control of structures such as beams, plates. remarkable research paper dealt with the analytical and numerical analyses of smart structures employing distributed piezoelectric sensors and actuators. [1] developed a finite element model based on the classical laminated plate theory for the active vibration control of a composite plate containing distributed piezoelectric sensors and actuators. [2] developed a finite element model based on third order laminate theory for the active position and vibration control of composite beams with distributed piezoelectric sensors and actuators. [3] presented an analytical solution of composite beams with piezoelectric laminate. [4] developed a three-node beam finite element for the analysis of composite laminated beams with distributed piezoelectric sensor/actuators. in the present paper the active vibration control of isotropic beam is investigated. the Euler-Bernoulli theory is used to provide a state space equation to be able use the LQG and LQR controller. different simulation are presented.

I. EQUATION OF MOTION OF INTELLIGENT BEAM

Consider a beam bonded by with piezoelectric actuators on the top surface and sensors on the bottom surface Based on the Euler Bernoulli theory the beam motion equation can be expressed as

$$E_b I_b \frac{\partial^4 w}{\partial x^4} + \rho_b A_b \frac{\partial^2 w}{\partial t^2} - b \sum_{i=1}^m \frac{\partial^2 M_i^a}{\partial x^2} = 0 \quad (1)$$

Where w is the deflection of the beam are Young's modulus, inertia moment, density, width and cross-sectional area of the beam, respectively; $M_a(t)$ is the force moment induced by actuator i [4], which can be expressed as

$$M_a(t) = C_a V_a(x, t) \quad (2)$$

And

$$C_a = E_a d_{31} h_{an} \quad (3)$$

where d_{31} and E_a are the piezoelectric strain constant and Young's modulus of the actuators, respectively, $V_a(x, t)$ is the voltage applied to actuator i , and h_{an} denotes the distance measured from the neutral surface of the beam to the mid-plane of the actuator.

The voltage distribution of actuator i can be expressed as

$$V_a(x, t) = V_a(t) R(x) \quad (4)$$

in which R is the Heaviside step function that can be expressed as

$$R(x) = H(x - x_{a1}) - H(x - x_{a2}) \quad (5)$$

Where x_{a1} ; x_{a2} are the coordinates of the two ends of actuator i : The general solution of (1) can be expressed as the sum of the normal modes. Hence, the displacement distribution of the beam is represented by

$$w(x, t) = \sum_{i=1}^{\infty} Y_i(x) \phi_i(t) \quad (6)$$

Where $\phi_i(t)$ is the modal displacement vector, $Y_i(x)$ is the mode shape matrix. Substituting (2)– (4) into (1) using the orthogonality properties, taken the case of clamped and using the structural damping yield the following equation:

$$\ddot{\phi}_i(t) + 2\xi_i w_{in} \dot{\phi}_i(t) + w_{in}^2 \phi_i(t) = G_a [Y_i(x_{a2}) - Y_i(x_{a1})] V_a(t) \quad (7)$$

where w_{in} , ξ_i are the natural frequency, the damping ratio and $G_a = b E_a d_{31} h$

the piezoelectric sensors will produce electrical charge while the beam has some external stimulus, the output voltage of the i^{th} piezoelectric sensor can be gained as follows:

$$V^s(t) = \square \sum_{m=1}^{m=2} \sum_{n=1}^{n=2} [Y_i(x_{a2}) - Y_i(x_{a1})] q(t) \quad (8)$$

Where

$$\alpha = \frac{k_{31}^2 h + h_{an}}{g_{31} C_r}$$

In which, g_{31} , k_{31} , C_r are the voltage constant the electromechanical coupling factor, and the Piezoelectric capacitance.

II. LQR OPTIMAL CONTROL

The idea beyond the LQR is to minimize a cost function given as [1]:

$$J = \int_0^\infty (X^T Q X + U^T R U) dt = \min \quad (9)$$

Where the matrices Q and R are weighting matrices. It assumed that the desired state is $\mathbf{x} = \mathbf{0}$, but the initial condition is non-zero, so the matrix Q penalizes the state error in a mean-square sense. Similarly, the matrix R penalizes the control effort, i.e., limits the control signals magnitude.

Design the optimal feedback control force U by the application of classical LQR control method:

$$U = K * x(t) \quad (10)$$

The gain matrix $K = R^{-1} B^T P$ which minimizes J can be found by solving a matrix Riccati equation that given by:

$$PA + A^T P + Q - PBR^{-1}B^T P = 0 \quad (11)$$

III. LQG OPTIMAL CONTROL

In the previous equation it was assumed that all the states were completely observable and there could be directly related to the output and used by the control system. However, that is not always the case and a more realistic approach would consider that only the outputs can be known and measured, hence it will be necessary to estimate the states from a model of the system, usually that estimate is made by a state estimator or observer. Here we use Kalman-Bucy filter.

$$\begin{aligned} \dot{X}(t) &= AX(t) + BU(t) + B_w W(t) \\ Y(t) &= CX(t) + V(t) \end{aligned} \quad (12)$$

$W(t)$ and $V(t)$ are modeled as white noise, featuring Gaussian stochastic processes with zero mean. It is considered that $W(t)$ and $V(t)$ are not correlated. The output vector is the system states, and the output matrix is an identity matrix.

$$W(t) = E[W(t)W^T(t)] = R_f \quad (13)$$

$$V(t) = E[V(t)V^T(t)] = Q_f > 0 \quad (14)$$

E denotes the expectation operator The estimator states \hat{X} would thus be governed by the equation:

$$\dot{\hat{X}}(t) = AX(t) + BU(t) + K_e(t)[CX(t) + V(t) - C\hat{X}(t)] \quad (15)$$

$K_e(t)$ is known as Kalman-Bucy filter given by

$$K_e(t) = P_f C^T V^{-1} \quad (16)$$

IV. LQG OPTIMAL CONTROL

In this section. A clamed beam bonded by piezoelectric actuator on upper surfaces and sensor on the lower surface as shown in Fig.1. The principal material proprieties of the beam and the piezoelectric patches are listed in Tab.1.

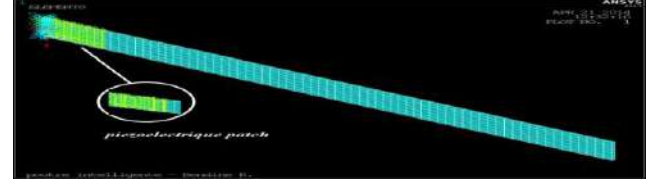


Fig. 1 FEM model of intelligent plate

TABLE I. MATERIAL PROPRIETIES OF SMART BEAM

Proprieties	PZT-5	Aluminum
Elastic modulus E (N/m ²)	6.3 x 10 ¹⁰	70 x 10 ⁹
Poisson's ratio	0.35	0.3
Density ρ (kg/m ³)	7600	2702
Piezoelectric constant d ₃₁ (m/V)	-1.66 x 10 ⁻¹⁰	-
The electromechanical coupling factor k ₃₁	0.34	-
Voltage constant g ₃₁ (Vm/N)	-1.15 x 10 ⁻²	-
Capacitance C(F)	1.05 x 10 ⁻⁷	-

to validate the current method, the natural frequencies of the cantilever beam are compared with those obtained with Ansys and given in Tab.2 . the results are in good agreement and prove the accuracy of the present model. the corresponding mode shape are depicted in fig. 2.

TABLE II. NATURAL FREQUENCIES FOR CANTILEVER BEAM WITH N=2 WITH ANSYS

Modes number	Frequency (ansys)	Frequency (Matlab)
1	8.3347	8.3657
2	51.668	52.43
3	143.69	146.82
4	280.47	287.40
5	463.09	475.10

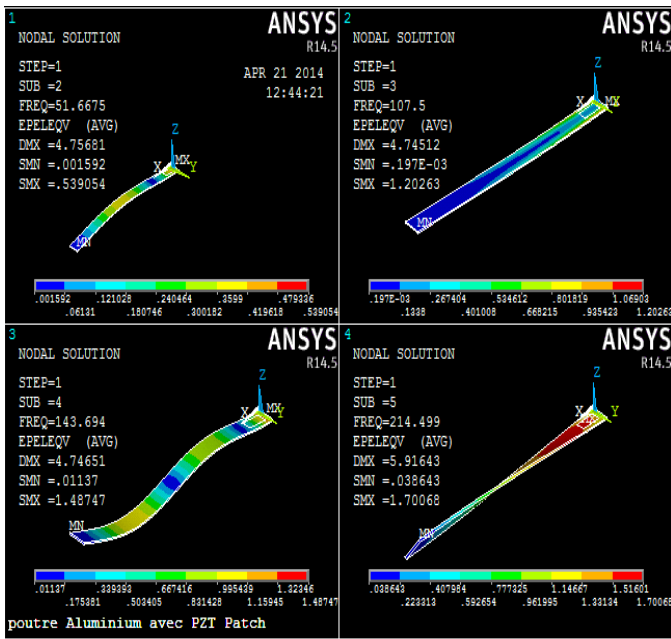


Fig. 2 The modes shape of the beam

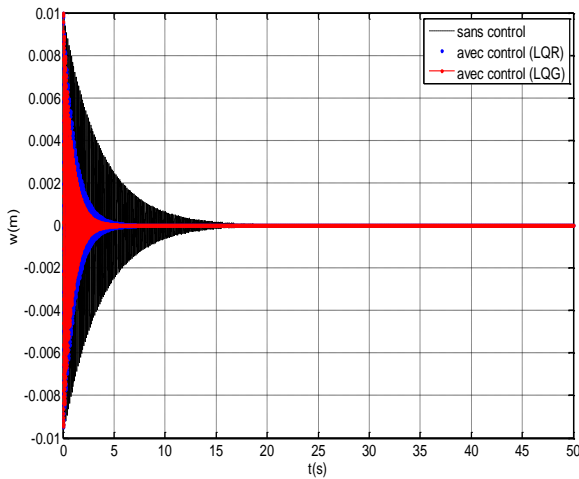


Fig. 3 Vibration of the beam amplitude with and without control

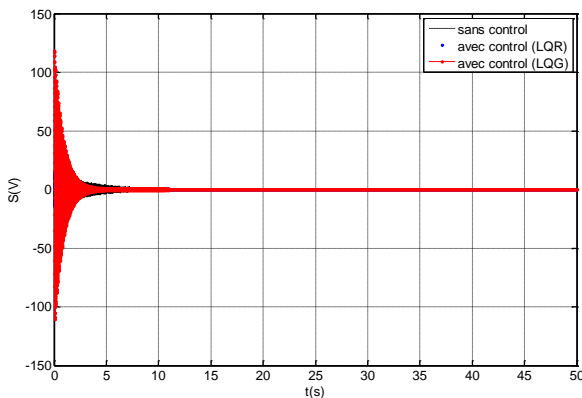


Fig. 4 The output voltage corresponding to the sensor

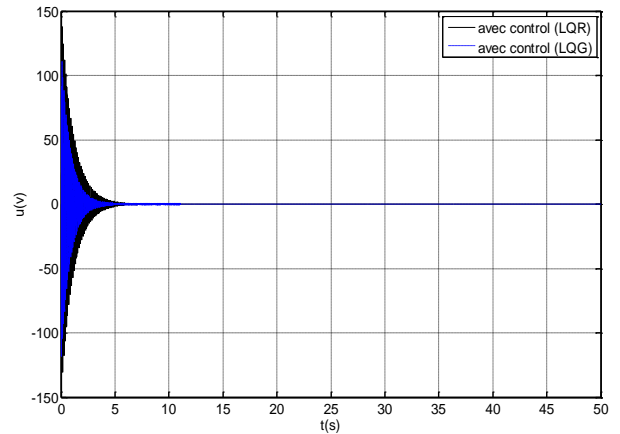


Fig. 5 The input voltage corresponding to actuator

V. CONCLUSION

An extensive study of the active vibration control analysis of cantilever beam using bonded piezoelectric sensor and actuator is presented.

First, the Euler Bernoulli theory have been used to analyze the behavior of the beam ,then an optimal control strategies, linear quadratic regulator (LQR) and linear quadratic Gaussian (LQG) controllers were adopted. The obtained result shows that the stabilization time, around 5 seconds for LQR and 3 seconds for LQG controller and with a maximum voltage of 150 V for LQR and 120 V for LQR. It been clearly seen that LQG presents a better control in bandwidth with a lower control voltage.

REFERENCES

- [1] Lam KY, Peng XQ, Liu GR and Reddy JN (1997), "A Finite-element Model for Piezoelectric Composite Laminates," *Smart Materials and Structures*, 6: 583–91.
- [2] Peng XQ, Lam KY and Liu GR "Active Vibration Control of Composite Beams with Piezoelectric: a Finite Element Model with Third Order Theory," *Journal of Sound and Vibration*, 209(4): 635–650.
- [3] Sun B and Huang D (2000), "Analytical Vibration Suppression Analysis of Composite Beams with Piezoelectric Laminate," *Smart Materials and Structures*, 9: 751–760.
- [4] Beheshti-Aval SB, Lezgy-Nazargah M, Vidal P and Polit (2011), "A Refined Sinus Finite Element Model for the Analysis of Piezoelectric Laminated Beam," *Journal of Intelligent Material Systems and Structures*, 3: 203–219.
- [5] Gergely Takács , Boris Rohal-Likiv, Model Predictive vibration control "Efficient constrained MPC vibration control for lightly damped mechanical structures; *Springer. Aout 26, 2011*

- [6] André Preumont, Vibration control of active structures (2nd Edition), *Kluwer Academic publishers*
- [7] HKaragu"lle, L Malgaca et H F O" ktem, Analysis of active vibration control in smart structures by ANSYS, journal of *smart materials and structures*,13(2004)
- [8] Gergely Takács et Boris Rohal'-Ilkiv, direct closed-loop active vibration control system prototyping in ansys, *noise and vibration : emerging methods*, novembre 2012
- [9] Neda Darivandi, Kirsten Morris et Amir Khajepour, An algorithm for LQ optimal actuator location, *smart materials and structures*, 22 (2013)
- [10] X.Q. He, T.Y. Ng, S. Sivas hanker, et K.M. Liew.Active control of FGM plates with integrated piezoelectric sensors and actuators. *Solids and Structures* 38 (2001) 1641–1655
- [11] Levent Malgaca. Integration of active vibration control methods with finite element models of smart laminated composite structures. *Composite Structures*, 92(7):1651 – 1663, 2010.

Modeling of Drying Performance of the Solar Collector Food Drying System with Artificial Neural Network

Ebru KAVAK AKPINAR
Department of Mechanical Engineering
Firat University
TR-23200 Elazig, Turkey
ebruakpinar@firat.edu.tr

Mehmet DAS
Department of Vocational School
Erzincan University, Ilıc Dursun Yildirim V.S.
TR-24700 Erzincan, Ilıc, Turkey
mdas@erzincan.edu.tr

Abstract— In this study, an air heated solar collector (AHSC) dryer was designed to determine the drying characteristics of the green pepper. In the experiments thinly sliced green pepper samples were used. Collector inlet and outlet air temperatures, drying chamber inlet and outlet air temperatures, ambient temperature, radiation, air velocity and drying rate were considered as parameters affecting the drying feature. The results obtained were presented as a function of drying time. Moisture content (MC), moisture ratio (MR) and drying rate (DR) values obtained from the experiments were modeled with 3-layer artificial neural network (ANN) using Logsig Activation function and Backpropagation learning function. Mean square error (MSE) was used to determine of the statistical validity of the developed model. As a result, drying behavior of green pepper was successfully predicted by ANN for existing drying conditions.

Keywords— Solar Collector, Food Drying, Artificial Neural Networks

I. INTRODUCTION

Solar energy is a clean energy source that does not run out of reserves and does not pollute the environment. Because of its ability to easily convert to heat energy, this energy is widely used in the drying of agricultural products all over the world. The simplest benefit from drying out from solar energy is to spread outdoor agricultural products on the exhibition grounds. Outdoor drying is completed in a long time and the quality of the dried products obtained is low. For this reason, solar energy dryers are needed for quality and quick drying of commercial vegetables and fruits in our country [1].

Drying is the removal of water or other liquids from gases, liquids or solids. The most common use of drying is to evaporate water or volatile substances from solid materials by thermal methods. In drying applications, the heat required

to evaporate the moisture is transferred by convection from the solid surface contacting the article to be dried, radiation, or the substance to be dried by bringing the substance to be dried directly into contact with the hot gases [2].

Various studies have been carried out in the national and international literature in the field of solar energy supported food drying. Durmus and Kurtbas have been dried the apricots in the airy solar collector and vertically positioned tray dryer. They have experimentally examined drying performance. Experiments have shown that drying speed depends on dryer air speed and temperature, collector performance, dried product thickness, and contact surface area [3]. Chen et al. carried out experimental studies on the solar energy assisted food drying system, which was formed from the dryer compartment and the solar air heater. Lemon slices were chosen as an example and dried. It has been observed that the moisture content of the limon (wet) decreases by 75-85% by 7-8% and the heat efficiency of the dryer is 30.86% according to the measurements made during drying [4].

Today, many studies have been done about the modeling of solar energy assisted drying systems with ANN. Koni, Dincer and Turker have been investigated the identification and modeling of the drying process of bread yeast in a fluidized bed. The critical input parameters of this drying process have been determined. In the system identification, they were utilized by the artificial neural network because of the nonlinear nature of the system [5]. Sevik, Aktas and Ozdemir used mushroom dryer with solar energy collector and solar energy heat pump dryer. In the experiments, they dried mushroom at 45 ° C and 55 ° C drying air temperature and 0.9 m / s-1.2 m / s air speeds. The moisture content, removable moisture content and drying rate values obtained from the experiments are modeled by ANN using the Levenberg-Marquardt (LM) backpropagation learning algorithm and the Fermi transfer function [6]. Erenturk examined the drying kinetics of the carrot monolayer for different drying conditions and different sample thicknesses.

They obtained drying curves by using drying data. They have applied four different drying models in the literature to the system in order to express drying kinetics. They compared the models by finding r , r^2 , χ^2 , and SSR values. In addition, they have applied artificial neural network models to predict moisture content and comparisons with selected models [7].

In this study, green pappers was dried in AHSC. It is aimed to model *MC*, *MR* and *DR* with ANN by analyzing drying test results.

II. MATERIALS AND METHOD

A. Experimental Set-Up

Experimental set up mainly consists of an indirect forced convection solar dryer with a solar air collector (1400 mm x 800 mm), a circulation fan and a drying cabinet (Fig. 1). Solar air collector is constructed from stainless steel sheets (thickness, 0.5 mm), outer surface of which is painted with black collector paint. Solar air heater was covered with copper sheet (thickness, 0.4 mm), which was painted with black collector paint. A glass is used as a transparent cover for air heater to prevent top heat losses. Solar heater was oriented southwards under the collector angle of 23.7° (local latitude 38.4°). This angle was fixed by foots. Frame was made of stainless steel sheet.

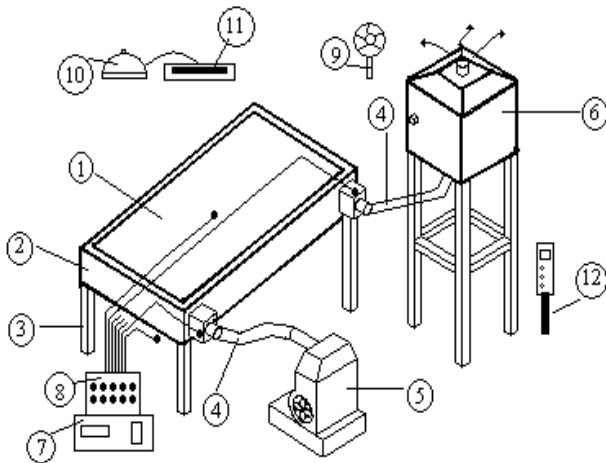


Fig. 1. Experimental set-up

1-Solar collector; 2-Frame; 3-Foot; 4-Connection pipe; 5-Circulation fan; 6-Drying cabinet; 7-Channel selector; 8-Digital thermometer 9-Anemometer; 10- Pyrometer; 11- Digital solar integrator; 12- Hygrometer

Drying cabinet was constructed from wood as a rectangular tunnel (45 cm x 45 cm x 45 cm). Bottom side of the cabinet was a circular tube connected to the same diameter to connect the main collector tube. The connection to this tube was made with bendable spiral aluminium tube of the same diameter. Drying air was exited from circular pipe

at topside of the cabined. One end of the cabinet was manufactured in type of cover, which was used to load or unload the cabinet. One drying tray (40 cm x 40 cm) was placed inside the drying cabinet. A centrifugal fan (0.0833 m³s⁻¹, 0.25 kW, 220 V, 50 Hz, 1380 min⁻¹) connected to drying cabinet provides air (velocity, 0.4 ms⁻¹).

Fresh long green peppers (sweet) obtained from Elazig, were refrigerated. Generally, samples of uniform size were selected. Thickness of pepper was measured as 1.7 ± 0.2 with a micrometer. Solar drying experiments were carried out during the periods of June 2016 in Elazig, Turkey. Test started at 9:30 a.m. and continued till 17:30 p.m. Elazig is locate at $38^\circ 60'N$ and $39^\circ 28'E$ and above 950 m of sea level in the eastern part of Anatolia, Turkey.

In the experiments, weather temperature and relative humidity, inlet and outlet temperatures of air in the solar collector, the temperatures at the various points of drying cabinet, humidity, inlet and outlet temperatures of air in the cabinet, wind speeds, the amount of solar radiation, and mass loss of long green peppers were measured at 30 mins intervals. The flow charts of the thin layer forced drying processes are presented in Fig. 2.

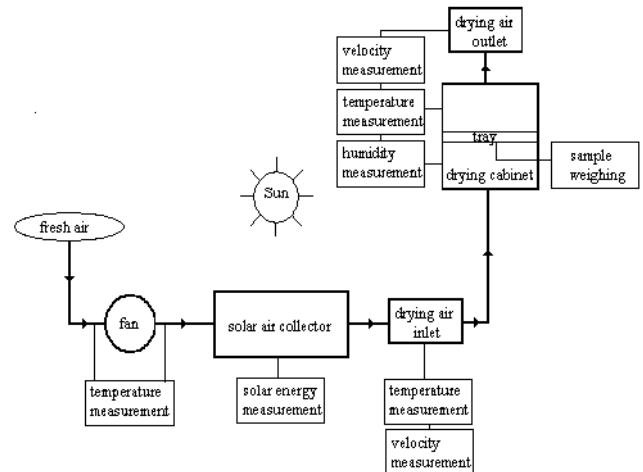


Fig. 2. Flow diagram of thin layer forced solar drying process

In the measurements of temperatures, J type iron-constantan thermocouples were used with a manually controlled 20-channel automatic digital thermometer (ELIMKO, 6400, Turkey), with reading accuracy of $\pm 0.1^\circ C$. A thermo hygrometer (EXTECH, 444731, China) was used to measure relative humidity just above long green peppers, with reading accuracy of $\pm \% 0.1$. The wind speed was measured by a 0-15 m/s range anemometer (LUTRON, AM-4201, Taiwan), with reading accuracy of ± 0.1 m/s. Moisture loss of long green peppers were recorded during drying for determination of drying curves by digital balance (BEL, Mark 3100, Italy) in the measurement range of 0-3100 g and an accuracy of ± 0.01 g. The solar radiation during the

operation period of drying system was measured with a Kipp and Zonen pyrometer in $\pm 0.1 \text{ Wm}^{-2}$ accuracy and its CC12 model digital solar integrator. The initial and final moisture content of long green peppers was determined at 80°C by a Mettler infrared moisture analyzer in $\pm 0.001 \text{ g}$ accuracy.

B. System Analysis

Some general equations used in the drying analysis of the system are given below. For the values of moisture content (MC_{KA}) according to dry basis in green pepper;

$$MC_{KA} = \frac{WW-DW}{DW} \quad (1)$$

for the values of moisture content (MC_{YA}) according to wet basis in green pepper;

$$MC_{KA} = \frac{WW-DW}{WW} \quad (2)$$

equations have been used. In Equations (1) and (2); WW is wet weight and DW is dry weight.

Adjustable moisture ratio (MR) values have been calculated using the following formula.

$$MR = \frac{M-M_e}{M_0-M_e} \quad (3)$$

Drying speed (DR) values have been calculated from the formula below.

$$DR = \frac{M_{t+dt}-M_t}{dt} \quad (4)$$

In Equations (3) and (4); M is moisture, M_e is equilibrium moisture, M_0 is first moisture, M_{t+dt} is moisture content at " $t + dt$ " and M_t is moisture content at " t ".

C. Artificial Neural Networks

Artificial neural networks has emerged as a result of artificial simulated efforts of the human brain's working system. Based on certain values, the ANN links the points in the input field to a particular function in the output field [8]. Artificial neural networks, pattern recognition, estimation, classification, etc. have wide application area. Artificial neural networks learn with examples similar to humans. For this reason, the data set is divided into two parts as training and test cluster [9].

In this study, Levenberg-Marquardt (LM) backpropagation learning algorithm, Logsig activation function and Backpropagation learning function were used in ANN for the moisture content (MC), separable moisture content (MR) and drying rate (DR) values obtained from experiments. Mean squared error (MSE) has been used to compare predicted values to actual values on model

evaluation. MSE values have been calculated using the following formula by ANN.

$$MSE = \frac{1}{n} \sum_{i=1}^n (DATA_{exp,i} - DATA_{ANN,i})^2 \quad (5)$$

In Equations (5); $DATA_{exp,i}$ is experimental data and $DATA_{ANN,i}$ is predicted data.

The time dependent MC , MR , and DR values of the experiments have been calculated from Equations (1), (3) and (4). Solar radiation values were measured with a digital solar integrator. As input data for the network; Time (t), drying air velocity (v), drying air temperature (T), drying air relative moisture (RM) and solar radiation (SR) values were used. As output data; MC , MR , and DR values were used. As a middle layer; Three hidden layers were created and the best solutions were tried to be obtained by changing the number of intermediate layers. The structure of the generated ANN model was given in Fig. 3.

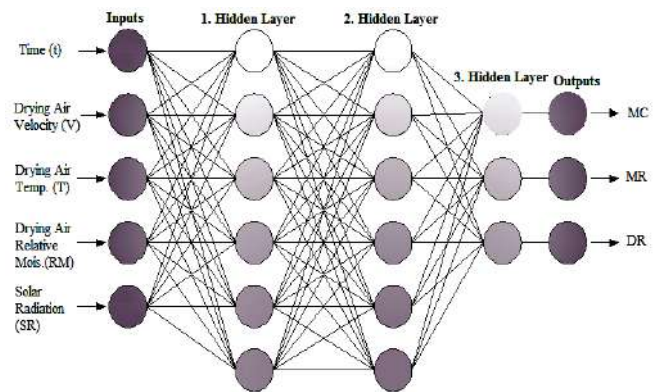


Fig. 3. ANN structure

III. RESULTS AND DISCUSSION

A total of 128 data were used in ANN model. Of these data, 112 were used for training and 16 were used for testing. The ANN structure used for MC , MR , and DR is shown in Table I.

TABLE I. STRUCTURE OF ANN

Structure of ANN used for the estimation of MC, MR, and NR	
Number of Layers	3
Number of Neurons in Layers	6-6-3
Weight Ratings	Random
Activation Function	Logsig
Learning Function	Backpropagation
Learning Ratio	0,97
Mean- Squered Error	1e-06

The network learning process has been successfully completed. The performance of the ANN model developed for *MC*, *MR*, and *DR* is shown in Fig. 4. Since the difference between the predicted values and the experimental values is very small and negligible, it can be seen that there is a harmony between the values.

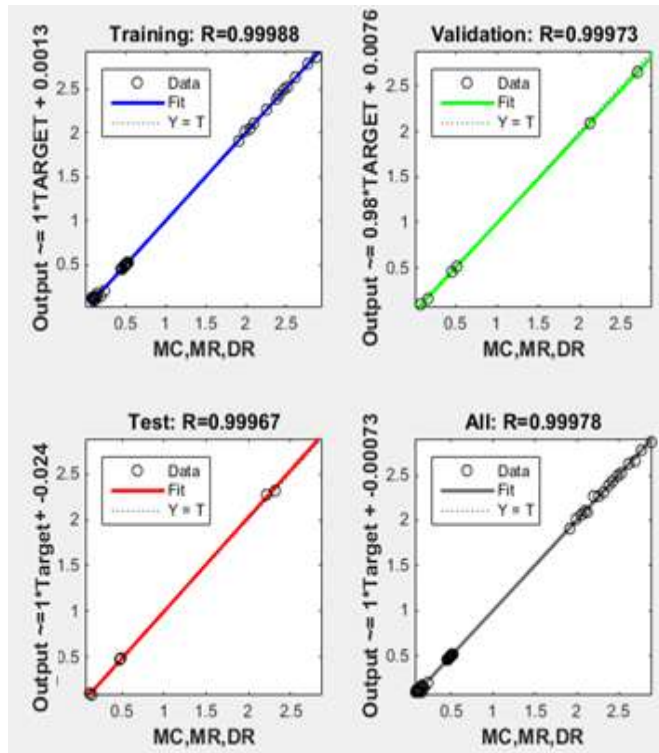


Fig. 4. Regression graph for MC, MR and DR

IV. CONCLUSIONS

In this study, green pepper was dried with AHSC drying system. *MC*, *MR* and *DR* parameters were experimentally calculated for different temperature and air velocity values at 30 minute intervals during green pepper drying. ANN was used for estimation of *MC*, *MR* and *DR* parameters. Estimated values with YSA and actual values obtained after the test are shown in Fig. 5-7. As a result, ANN estimation for *MC*, *MR* and *DR* parameters were successfully performed.

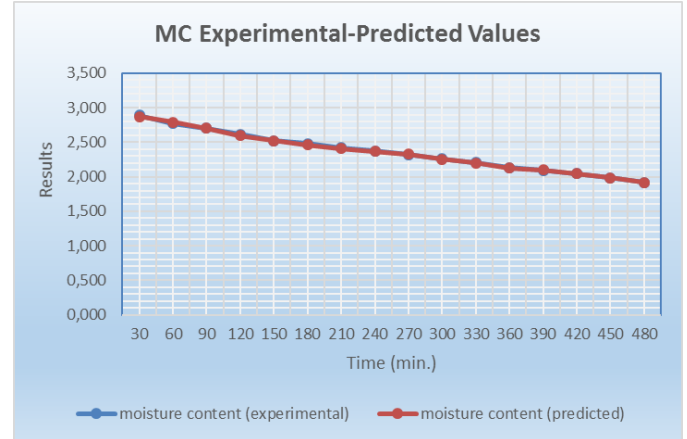


Fig.5. Experimental-predicted moisture content values

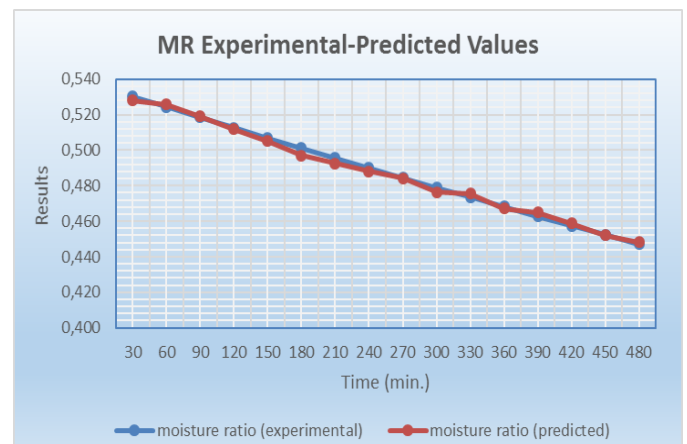


Fig. 6. Experimental-predicted moisture ratio values

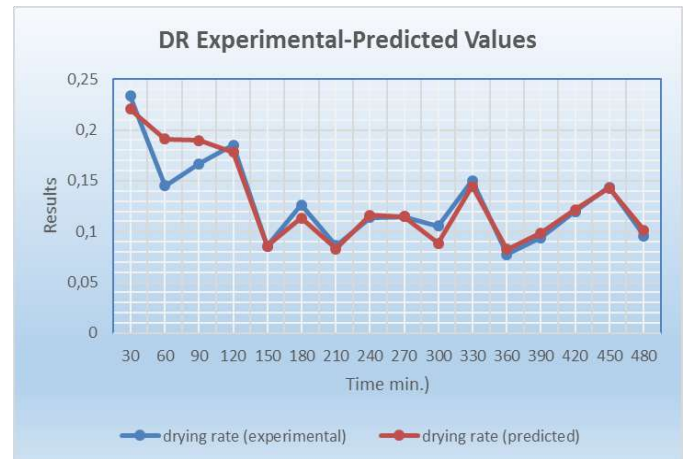


Fig. 7. Experimental-predicted moisture rate values

ACKNOWLEDGEMENT

This study was supported by Firat University Scientific Research Foundation (Project Number 943).

REFERENCES

- [1] S. Tarhan, G. Ergüneş, O. Tekelioğlu, “Tarımsal Ürünler İçin Güneş Enerjili Kurutucuların Tasarım ve İşletme Esasları”, Tesisat Mühendisliği Dergisi Sayı: 99, s.26-32, 2007.
- [2] A. Güngör, N. Ozbalta, “Kurutmanın Temelleri ve Endüstriyel Kurutucular Kurs Notları”, IX. Ulusal Tesisat Mühendisliği Kongresi, 2009.
- [3] A. Durmuş, and I. Kurtbaş, “Yeni Tasarlanan Havalı Kolektör Yardımı İle Elazığ Yöresi Kayısılarının Kurutulması ve Kolektör Verimi”, IV. Mühendislik Mimarlık Sempozyumu, Balıkesir Üniversitesi, September 2002.
- [4] H. Chen, C.E. Hernandez, T. Huang, “A Study of The Drying Effect On Lemon Slices Using A Closed-type Solar Dryer”, Solar Energy, Cilt 78, Sy 97-103, 2005.
- [5] M. Köni, H. Dinçer, M. Türker, “Fermantasyon Ürünlerinin Kurutma Proseslerinin Modellenmesi ve Kontrolü”, Elektrik-Elektronik-Bilgisayar Mühendisliği 11. Ulusal Kongresi; s110, 2006.
- [6] S. Sevik, M. Aktaş, B. Ozdemir, “Modeling of Drying Behaviors of Mushroom in a Solar Assisted Heat Pump Dryer by Using Artificial Neural Network” Journal Of Agricultural Sciences 20 (2014) 187-202, 2013.
- [7] S. Ertürk, K. Ertürk, “Havuç Kuruma Kinetiğinin Tahmininde Regresyon Analizi ve Yapay Sinir Ağlarının Kıyaslanması”. Türkiye 9. Gıda Kongresi; s882, 2006.
- [8] R. Teti, K. Jemielniak, G. O'Donnell, D. Dornfeld, “Advanced monitoring of machining operations”, Cirp Annals-Manufacturing Technology, 59 (2),717-739, 2010.
- [9] T. Findik, Ş. Taşdemir and I. Şahin, “The use of artificial neural network for prediction of grain size of 17-4 pH stainless steel powders”, Sci. Research and Essays, 5, 11, 1274-1283, 2010.

Comparison of Thermal Efficiencies of Fixed and Moving Air-Heated Solar Collectors Modeled by Artificial Neural Network

Mehmet DAS

Department of Vocational School
Erzincan University Ilic Dursun Yildirim V.S.
TR-24700 Erzincan, Ilic, Turkey
mdas@erzincan.edu.tr

Ebru KAVAK AKPINAR

Department of Mechanical Engineering
Firat University
TR-23200 Elazig, Turkey
ebruakpinar@firat.edu.tr

Abstract— In this study, a fixed air heated solar collector (AHSC) and solar tracking AHSC were used. Thermal performance of the collector with moving and fixed have been experimentally investigated. Collector inlet and collector outlet air temperatures, radiation, air outlet velocity, absorbent plate temperature, collector jacket outer surface temperature and transparent cover temperatures were measured. The thermal efficiencies of both collectors were calculated according to the measurements. With the obtained experimental data, the artificial neural network (ANN) module was created and the heat output from the collector and the air temperature were determined for different input parameters. Calculated thermal efficiencies were compared, and moving AHSC was found to work more efficiently. As a result, it was determined that ANN model successfully predicted thermal efficiency and collector output temperature of fixed and moving AHSC.

Keywords— *Solar Tracking System, Solar Collector, Thermal Efficiency*

I. INTRODUCTION

Today, energy demand is increasing due to factors such as population growth, rapid technological developments, economic growth and globalization. In order to be able to respond to increasing energy needs, mankind has begun to focus on alternative energy sources as well as existing energy sources [1].

AHSC is a low-cost simple device that does not have problems such as long life, light, corrosion. A conventional AHSC surrounds a well-insulated enclosure, a scraping plate placed inside the enclosure, and a transparent cover at the top. There is also a fan in the system, depending on whether the airflow is natural or forced. At AHSC the heat transfer coefficient between the damping plate and air is low. For this reason, these collectors can not work at the desired thermal efficiency values [2].

In the literature, solar tracking system studies have been carried out in order to benefit more effectively from solar energy. Iscan designed a solar tracking system circuit that can

follow the sun continuously in two directions throughout the day. He made a working analysis of the system during the day and prepared cost analysis for different powers to be designed [3]. Demirtas designed and manufactured a computer controlled two axis solar tracking system. The vertical and horizontal movement of the system is secured by step motor. It has been used a microcontroller controlled interface to record the obtained data in a computer environment and to control the system with a computer. With the solar tracking system, it produced an average of 16 volts in normal daylight [4]. Seme and Štumberger have developed a new estimation algorithm for solar angles using solar radiation and Differential Evolution on a biaxial solar tracking system [5]. Kırbaş et al. have provided effective use of solar energy in air heated solar collectors using solar tracking mechanism. In their work, two collectors, one fixed and one moving, measured to determine the difference between the output temperatures. In the morning and afternoon they determined that the outlet temperature of the moving type collector is 5-12 ° C higher than the fixed collector [6].

Today, many studies have been done about the modeling of solar energy assisted drying systems with ANN. Altıntaş at all have been examined the efficiency of the solar collector and the output temperature of the collector with with the flat absorber plate and the conical spring absorber plate. They have estimated the values they obtained with ANN and obtained 97% prediction success. [2]. Sevik, Aktas and Ozdemir used mushroom dryer with solar energy collector and solar energy heat pump dryer. In the experiments, they dried mushroom at 45 ° C and 55 ° C drying air temperature and 0.9 m/s -1.2 m/s air speeds. The moisture content, removable moisture content and drying rate values obtained from the experiments are modeled by ANN using the Levenberg-Marquardt (LM) backpropagation learning algorithm and the Fermi transfer function [7]. Erenturk examined the drying kinetics of the carrot monolayer for different drying conditions and different sample thicknesses. They obtained drying curves by using drying data. They have applied four different drying models in the literature to the

system in order to express drying kinetics. They compared the models by finding r , r^2 , χ^2 , and SSR values. In addition, they have applied artificial neural network models to predict moisture content and comparisons with selected models [8].

In this study, AHSC designed with solar tracking ability to increase thermal efficiency was made. The thermal efficiencies of the designed moving AHSC and fixed AHSC were found both experimentally and with the ANN model.

II. MATERIALS AND METHOD

The moving and fixed AHSC's are measuring 800mm x 1400mm and the absorber plates are made of sheet material painted black. One of the most important factors affecting AHSC's performance is the maximum benefit from sunlight. For this, the collector of the rays of the sun must come constantly at 90°. The moving AHSC is designed to track the sun in the east-west and north-south directions with a programmable logic controller (PLC) system for the sun's rays to reach the collar at right angles. Fixed AHSC is fixed to 42° for Elazığ province according to the azimuth angle. The experimental setup is shown in Fig.1.



Fig. 1. Experimental set-up

After the installation of the test apparatus, the system was operated under open air conditions and the necessary measurements were made. The measurement points in the experiment set are given in Fig.2. For this purpose, the temperature was measured from the inlet and outlet, absorber plate and under the cabinet of the collectors. Air speed measurement at the outlet of the collectors. The value of solar radiation is measured by a solar radiation meter. The data recording interval was set to thirty minutes.

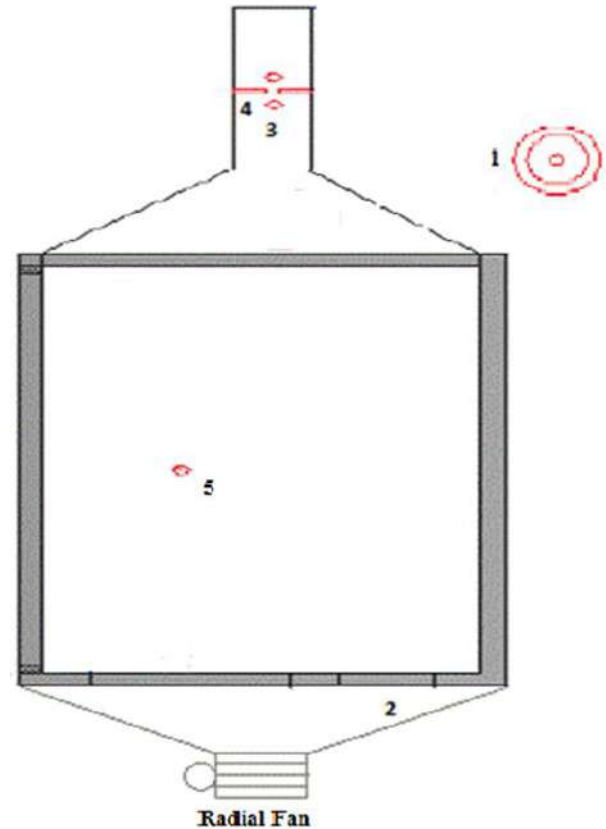


Fig.2 Measuring Points

1. Global radiation value (I)
2. Collector inlet air temperature (T_i)
3. Exit speed of air from the collector (V)
4. Collector output air temperature (T_o)
5. Absorber plate surface temperature (T_p)

values were measured. Tests started at 9:00 a.m. and ended at 17:00 p.m.

A hotwire type anemometer with a sensitivity of $\pm 0,2$ m/s was used for air speed measurement. The air speed was measured by placing an anemometer on the exit air duct. In order to measure the output air temperature, two heat sensors were installed in the output channel and the average of the measurements was taken. The thermal sensors used are sensitive to ± 0.5 °C. A solar radiation meter was used to measure the global amount of radiation. In the experiments, air temperature, air velocity, surface temperature and solar radiation values were measured. With these measurements mass flow rate and thermal efficiency calculations were made.

III. HEAT EFFICIENCY ACCOUNT

The useful energy (Qu) in the solar-powered air collector depends on the inlet and outlet temperatures of the fluid passing through the collector were calculated by Equation (1).

$$Qu = \dot{m} \cdot Cp \cdot (To - Ti) \quad (1)$$

Here, \dot{m} is the mass flux (kg/s) of the air passing through the collector, Cp is the specific heat of the air (J/kgK), Ti and To are the collector inlet and outlet temperatures respectively ($^{\circ}C$).

The mass flux of the air passing through the collector was calculated by Equation (2).

$$\dot{m} = \rho \cdot V \cdot Ak \quad (2)$$

Here, ρ is the density of the air (kg/m³), V is the airflow rate (m/s), and Ak is the output cross-sectional area (m²) of the collector.

Utilizing the first law of thermodynamics, the thermal efficiency of the collector was calculated by Equation (3).

$$\eta = \frac{\dot{m} \cdot Cp \cdot (To - Ti)}{I \cdot AC} \quad (3)$$

Here, η is the heat efficiency, I is the solar radiation coming to the surface of the collector (W/m²), and AC is the surface area of the absorbing plate that is directly hit by solar radiation (m²).

IV. MODELING OF DATA WITH ARTIFICIAL NEURAL NETWORKS

Artificial neural networks, pattern recognition, estimation, classification, etc. have wide application area. Artificial neural networks learn with examples similar to humans. For this reason, the data set is divided into two parts as training and test cluster [10]. Artificial neural networks has emerged as a result of artificial simulated efforts of the human brain's working system. Based on certain values, the ANN links the points in the input field to a particular function in the output field [9].

In the system, artificial neural networks are modeled as five inputs and one output. The collector inlet temperature (Ti) of the air, the absorber surface temperature (Tp), the global radiation (I) value, the air outlet velocity (V) and the collector air outlet temperature (To) were taken as input data. The thermal efficiency (η) is used as the output data. The structure of the generated YSA model is given in Fig 3.

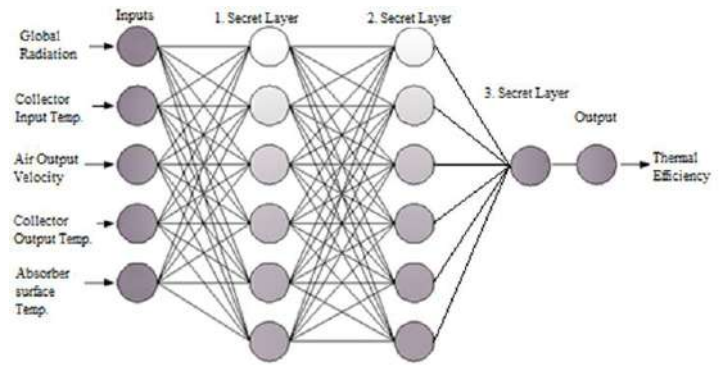


Fig.3 ANN model structure

MATLAB 2014b software was used in the modeling of artificial neural networks. The information cluster contains 192 input and output information. Of these, 168 were used in the training process. 24 were used in the test process. As a learning algorithm, Feed Forward Back Propagation algorithm was used. The ANN structure used for The thermal efficiency (η) is shown in Table I.

TABLE I Structure of ANN

Structure of ANN used for the estimation of The thermal efficiency (η)	
Number of Layers	3
Number of Neurons in Layers	6-6-1
Weight Ratings	Random
Activation Function	Logsig
Learning Function	Backpropagation
Learning Ratio	0,95
Mean- Squared Error	1e-06

The accuracy of the result obtained from the modeling of AHSC with ANN was determined using root mean square error (RMSE). For the training, the coefficient of multiple determinations (R^2) method was used.

$$R^2 = 1 - \left[\frac{\sum_{m=1}^n (\eta_{exp,i} - \eta_{ANN,i})^2}{\sum_{m=1}^n (\eta_{ANN,i})^2} \right] \quad (4)$$

$$RMSE = \sqrt{\frac{\sum_{m=1}^n (\eta_{ANN,i} - \eta_{exp,i})^2}{n}} \quad (5)$$

V. RESULTS AND DISCUSSION

In this study, the thermal performance of the moving AHSC with the fixed AHSC was estimated experimentally and the thermal efficiency was determined by the ANN.

Fig.4 shows the thermal efficiency and predicted thermal efficiency of the fixed AHSC.

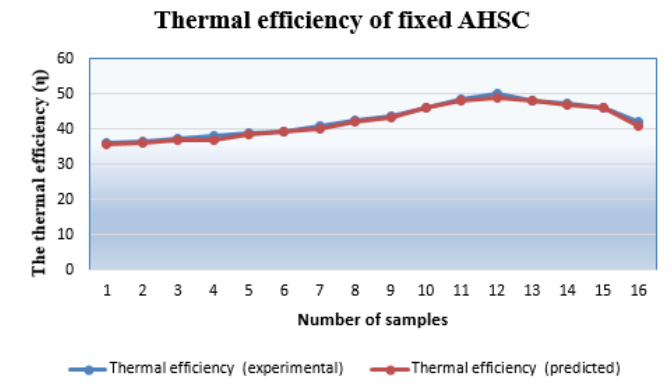


Fig. 4. Thermal efficiency graph of fixed AHSC

Fig.5 shows the thermal efficiency and predicted thermal efficiency values of the moving AHSC.

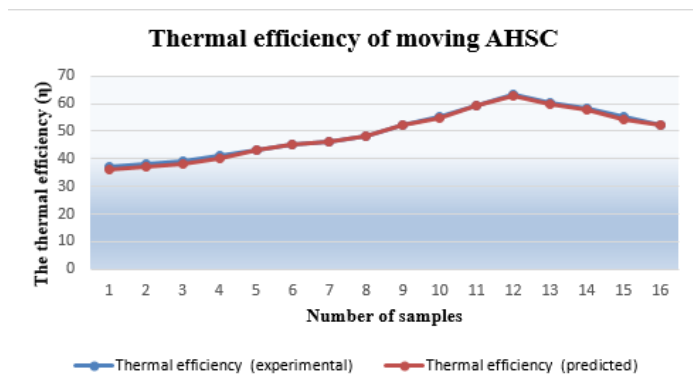


Fig.5. Thermal efficiency graph of moving AHSC

VI. CONCLUSIONS

In this study, the thermal performance of fixed and moving AHSCs was experimentally tested. The heat dissipation of the collectors is calculated by the data obtained from the experiments. It has been seen that the moving AHSC has a higher thermal efficiency than the fixed AHSC.

Different parameters have been tried at training time to improve the predictive ability of Artificial Neural Networks. The structure of artificial neural networks giving the most favorable result was accepted as a training parameter. The predicted thermal efficiency and actually measured thermal efficiency curves of the ANN model generated are similar to each other. It has an accuracy rate of 0.95 according to the R^2 method. The heat efficiency of the moving AHSC has been achieved as a result of its successful prediction with 95% accuracy of ANN.

ACKNOWLEDGEMENT

This work was supported by the Firat University Scientific Research Project Unit. (Project Number 2017-M.F. 16.54)

REFERENCES

- [1] Keçel S., "Türkiye'nin Değişik Bölgelerinde Evsel Elektrik İhtiyacının Güneş Panelleri İle Karşılmasına Yönelik Model Geliştirilmesi", Yüksek Lisans Tezi, Gazi Üniversitesi, Fen Bilimleri Enstitüsü, 2007.
- [2] Altınbaş V., Akgül B.M., Abuşka M., "Yutucu Plaka Üzerine Konik Yayların Yerleştirildiği Güneş Enerjili Hava Kollektörünün Isıl Verim Analizi Ve Yapay Sinir Ağları İle Modellenmesi", Ulusal Tesisat Mühendisliği Kongresi, 2015.
- [3] Demirtaş, M., "Bilgisayar Kontrollü Güneş Takip Sisteminin Tasarımı ve Uygulanması". Politeknik Dergisi, 9: s247-253, 2006.
- [4] İşcan S., "Güneş Takip Sistemi (2-Yönlü)", MKT2012,Proje Tabanlı Mekatronik Eğitim Çalıştayı, 2012.
- [5] Seme, S. and Štumberger, G., "A novel prediction algorithm for solar angles using solar radiation and Differential Evolution for dual-axis sun tracking purposes". Solar Energy, 85: s2757-2770, 2012.
- [6] Kırbaş, İ., Aydoğan, B., Uyumaz, A., " Hava Isıtmalı Güneş Kollektörlerin'de Güneş Takip Mekanizması Kullanımı" Mehmet Akif Erson Üniversitesi Fen Bilimleri Enstitüsü Dergisi, sayı 4: s74-84, 2013.
- [7] Şevik S., Aktaş M., Özdemir B., (2014), "Güneş Destekli Isı Pompalı Bir Kurutucuda Mantarın Kuruma Davranışlarının Yapay Sinir Ağı Kullanılarak Modellenmesi" Journal Of Agricultural Sciences, s187-202.
- [8] Ertürk S., Ertürk K., "Havuç Kuruma Kinetiğinin Tahmininde Regresyon Analizi ve Yapay Sinir Ağlarının Kıyaslanması". Türkiye 9. Gıda Kongresi; s882, 2006.
- [9] Teti, R., Jemielniak, K., O'Donnell, G., Dornfeld, D., "Advanced monitoring of machining operations", Cirp Annals-Manufacturing Technology, 59 (2), s717-739, 2010.
- [10] T. Findik, Ş. Taşdemir and I. Şahin, "The use of artificial neural network for prediction of grain size of 17-4 pH stainless steel powders", Sci. Research and Essays, 5, 11, s1274-1283, 2010.

Prediction of the Thermal Conductivity of Lightweight Building Materials Utilizing Back-Propagation Neural Network Method

Suleyman POLAT

Batman University Engineering Faculty
Department of Geology Engineering
Batman, Turkey
suleyman.polat@batman.edu.tr

Sehmus FİDAN

Batman University Engineering Faculty
Department of Electric-Electronic Engineering
Batman, Turkey
sehmus.fidan@batman.edu.tr

Hasan OKTAY

Batman University Engineering Faculty
Department of Mechanical Engineering
Batman, Turkey
hasan.oktay@batman.edu.tr

Abstract—The growing concern about energy consumption of heating and cooling of buildings has led to a demand for improved thermal performances of building materials. In this study, an experimental investigation is performed to predict the thermal insulation properties of wall and roof structures of which the mechanical properties are known, by using back-propagation artificial neural network (ANNs) method. The produced samples are cement based and have relatively high insulation properties for energy efficient buildings. In this regard, 102 new samples and their compositions are produced and their mechanical and thermal properties are tested in accordance with ASTM and EN standards. Then, comparisons have been made between the determined thermal conductivity of the newly produced structures, which are obtained from experimental method and ANN method that uses mechanical properties as input parameters. From the test results, since the percentage errors in the thermal conductivity values between experimental data and neural network prediction vary from -1.09% to 6.4%, It can be concluded that the prediction of the artificial neural network has proceed in the correct manner.

Keywords— Concrete, thermal conductivity, mechanical properties, back-propagation, energy efficient building

I. INTRODUCTION

Heating ventilating and air conditioning (HVAC) system has been the most important solution for the humanity who can live in spaces having comfort conditions along whole year. The main purpose of the HVAC system is to keep the changing temperature in the comfort zones by heating and cooling air within a space. For this reason, it is necessary to heat the living spaces in winter season by giving sufficient amount of moisture, and to cool the spaces in summer season. Building heating or cooling requirements for the winter and summer seasons constitutes loss or gain through windows, walls, roofs, infiltration and equipment's used. In many

buildings, walls and roofs are responsible for a major fraction of heat loss or gains for the heating or cooling loads due to their large surface area [1]. Since air conditioning systems consume large amount of electricity, especially in hot regions, it is critical to improve the thermal performance of these structures in terms of reducing the energy use. [2] In order to describe the thermal performance of the opaque envelope components, many studies have been conducted to identify the dynamic thermal characteristics of the components which indicate the magnitude of heat loss and gains through building structures under periodic boundary conditions and are influenced by the effective parameters, which can be categorized as environmental parameters (ambient air temperature, solar heat flux, ventilation etc.), design parameters (orientation, solar absorptivity, emissivity etc.) and thermophysical properties (thermal conductivity, specific heat, density, thickness etc.) [3]. Many investigations declared that those characteristics strongly depend on the thermal conductivity of the building's layer materials [4–11]. Besides, the thermal conductivity of a building wall or roof material are strongly affected by microstructure, mineralogical composition, proportion, supplementary materials, moisture content, and porosity, as shown in Fig. 1 [12]. Furthermore, these structures also need to have suitable mechanical properties because they must stand without being damaged from natural causes for many years. Therefore, if these structures having appropriate thermal and mechanical properties are selected, also accurate cooling load calculation is performed, and then suitable HVAC system components can be selected in terms of reducing the energy use. However, it is difficult to determine the ideal thermal conductivity properties of these structures by means of both energy and time efficiency due to the accuracy of test methods and high price of the devices. Hence, this situation leads scientists to search for new solutions. The mathematical models which are

used to describe experiences gathered from data of concrete mixes behaviors are most reliable and accurate as well as recommended methods [13]. These models based on experimental data are generally in regression forms, and called

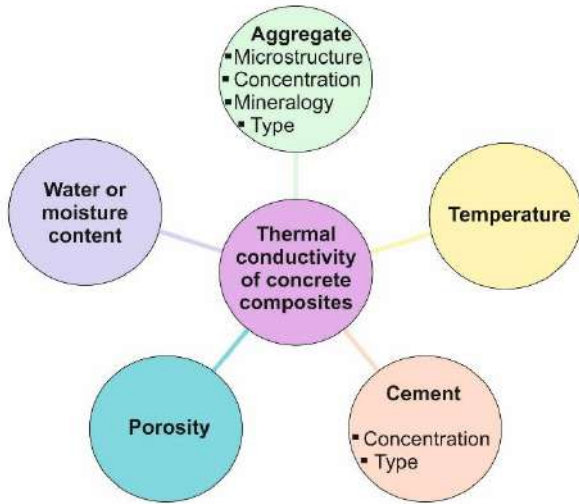


Fig.1. Parameters affecting thermal conductivity of structures

“Free models”[14]. However, because of more assumptions and less accuracy in regression form, regression methods cannot be used when the problem contains many independent variables. Recently many new modeling methods such as artificial neural networks (ANN), expert systems as a free model can complex relation and approximate non-linear due to any parameters and trial and error process by learning real record relationship without any presumptions [15]. Artificial neural networks (ANN) are a family of massively parallel architectures that are producing meaningful solutions to the problems capable of learning and generalization of examples and experiences, even if the input data is incorrect or incomplete. ANN is a powerful tool to solve for some complex engineering problems. The basic strategy for developing a neural network-based model for material behavior is to train a neural network on the results of a series of experiments using that material. If the experimental result contains relevant information on the behavior of the material, the neural network training will contain sufficient information on the behavior of a material to qualify as a model material [16]. This learning of the neural network not only be able to reproduce the experimental results, but would be able to bring the results of other experiments by the generalization ability.

In the literature, the ANN has been used to predict the effect of material behavior, especially on mechanical properties. Marai M. Alshihri et al [15] are used the neural networks (NNs) to predict the compressive strength of light weight concrete (LWC) mixtures after 3, 7, 14, and 28 days of curing. It is concluded that the cascade correlation (CC) neural network model predicated slightly accurate results and learned very quickly as compared to the back propagation (BP)

procedure. Furthermore, Guang and Zong, [17] proposed a method to predict 28-day compressive strength of concrete using multilayer feed-forward neural networks. Dias, [18] presented an artificial neural network model for predicting the strength and slump of ready mixed concrete. Eldin and Senouci, [19] employed a neural network for measuring and predicting of the strength of rubberized concrete. Lai [20] predicted the mechanical properties of concrete by ANNs. Moreover, Gencel et al [21] predicted the thermal conductivity of concrete with vermiculite by using artificial neural networks approaches with 20 datasets. The root mean square error, the mean absolute error, and determination coefficient statistics are used as evaluation criteria of the models, and the experimental results are compared with these models.

Therefore, this research aimed to predict ideal thermal conductivity values of concrete wall or roof structures by using an ANN method so as to reduce the energy consumption of the buildings. The structures were prepared by changing the volume fraction of aggregate materials in the cementitious matrix, which were exposed to the same conditions. The test program was conducted mainly to investigate the effect of pumice (PA), rubber aggregates (RA) and expanded perlite (EPA) on the thermal property of samples by using thermal response method. The findings and results are presented in detail in the following sections.

II. EXPERIMENTAL PROCEDURE

A. Concrete Mixtures, Materials and Test Methods

Several materials were used to obtain different lightweight building elements. The materials were locally available ordinary Portland cement (PC) (CEM I 42.5R), silica fume (SF), fine aggregate, coarse aggregate, RA, PA, EPA and superplasticizer (SP). Concrete mixtures were designed with a constant water–cementitious material (w/c) ratio of 0.48 and total cement content of 350 kg/m³. Normal aggregates were replaced by PA, EPA and RA at different volume fractions vary between 10% and 50%. In total, 102 concrete samples were produced and their mechanical tests which are the compressive strength, bulk density, porosity are performed on air dry samples aged 28 days. The thermal conductivity test was performed on same state with the age of 35 days according to EN 12667. In this study, ISOMET 2104 device (Fig. 2) was used to measure thermal conductivity of concrete samples on the basis of TPS method and the values of the device ranges for the measured parameters are presented in Table 1. In the TPS technique, the source of heat is a hot disc made out of a bifilar spiral, which also serves as a sensor for temperature increase in the samples. In comparison with stationary or steady state methods, the advantage of transient methods is that some of them give a full set of thermophysical properties within a single rapid measurement. All test result measurement values presented in the tables are based on the average values \pm a tolerance limit (less than 4%) in order to cover the range of all properties as measured for different samples of the same category.

B. Construction of Neural Network Model and Parameters

Neural networks have been designed to counterpart the thinking, recognize and problem solving abilities of biological human brain. ANN is a computational model and useful when especially for extremely complex problems. ANN was used in this study to estimate of thermal insulation properties of lightweight building materials. Fig. 3 shows a basic neural model where consist of 4 inputs and a single output. The basic



Fig. 2. The thermal property measurement device used in this study.

structure of ANN is composed of input, hidden, and output layers. The neuron will combine weighted inputs with a threshold value and activation function.

Design procedure of ANN involves two main part: training and validation. In training process, the weights are modified until the model has learnt the problem. Further, in validation phase, the network is tested with new unknown parameters. The back-propagation technique is very common and powerful strategy for the nonlinear functions and thus has inspired many researchers apply ANN to various system.

There are a number of activation functions in use with NN such as step, sigmoid or hyperbolic tangent function. In training process, the error between network prediction and experimental result of concrete samples was calculated. The error was propagated backward through the neural network, and every neuron weights are updated. This was done to ensure that in the next round, the error would be reduced for the same inputs.

For construction of NN, Matlab - Neural Network Toolbox is used to design, train and simulate. In this article, the neural network is designed as three-layer network structure. Every layer in network has 3-5-4 neurons, respectively. Using this program, a neural network model was constructed, trained and tested using the available test data of 102 different concrete mix-designs gathered from experimental setup. The data used in neural network model are arranged in a format of four input parameters that cover the bulk density, porosity, compressive strength, and the percentage lightweight aggregate content (%).

TABLE I. VALUES OF DEVICE RANGE FOR MEASURING PARAMETERS

Measurement	Measurement range	Accuracy
Thermal conductivity coeff.	0.015–6 W/mK	5 % of reading + 0.001 W/mK
Operating temperature	From -20 – +70 °C	1°C

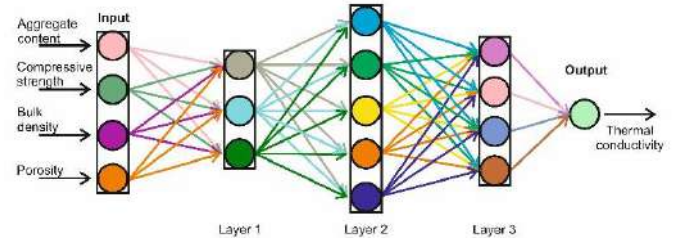


Fig. 3. Basic neural network model

III. RESULT AND DISCUSSION

The results of the experimental tests gathered from the mechanical and thermal properties of PC, NC, EPC and RC, and mixtures prepared, in contrast with the control mixture are shown in Table 2 below.

After experimental setup was performed, an artificial neural network (ANN) method, which is Levenberg-Marquart algorithm is selected for prediction of thermal conductivity of concretes of which the mechanical properties are known. In the training session, validation is stopped after 9 iterations at mean squared error value of 0.019. Fig. 4 presents mean squared error (MSE) performance. In this figure best validation performance occurred at iteration 3 and the neural network at this iteration is returned. After 3 iteration. test set and validation set error have similar properties and no over-fitting occurred.

A linear regression between the network output and the corresponding target is shown in Fig. 5. The output follows the targets well and the correlation coefficient R is 0.96845 for the total response that indicate good matching between the experimental and prediction data.

Table 3 shows a comparison between the predicted thermal conductivity of concrete against experimental data, which emphasizes that it is a good agreement between them. From the

TABLE II. MECHANICAL AND THERMAL PROPERTIES OF PRODUCED CONCRETE SAMPLES^a

Types of concrete	Compressive strength σ_c (MPa)	Bulk density ρ (kg/m ³)	Porosity ϕ (%)	Thermal conductivity λ (W/mK)
NC	51.85	2345.09	8.41	1.96
EPC (10%)	31.21	2139.09	12.86	1.51
EPC (20%)	19.02	1885.52	18.37	1.22
EPC (30%)	10.01	1559.44	23.28	0.70
EPC (40%)	8.15	1376.56	26.12	0.50
EPC (50%)	4.88	1168.63	28.20	0.36
PC (10%)	33.46	2005.34	11.23	1.54
PC (20%)	23.39	1851.02	16.55	1.29
PC (30%)	13.07	1559.95	22.05	0.76
PC (40%)	9.90	1400.72	24.20	0.54
PC (50%)	9.51	1329.97	27.28	0.41
RC (10%)	42.04	2244.30	9.19	1.72
RC (20%)	30.41	2148.07	11.43	1.44
RC (30%)	19.04	2033.93	12.23	1.22
RC (40%)	9.51	1874.62	14.19	0.89
RC (50%)	4.53	1644.98	16.35	0.62

^aThese properties are the average of the five specimens for each test.

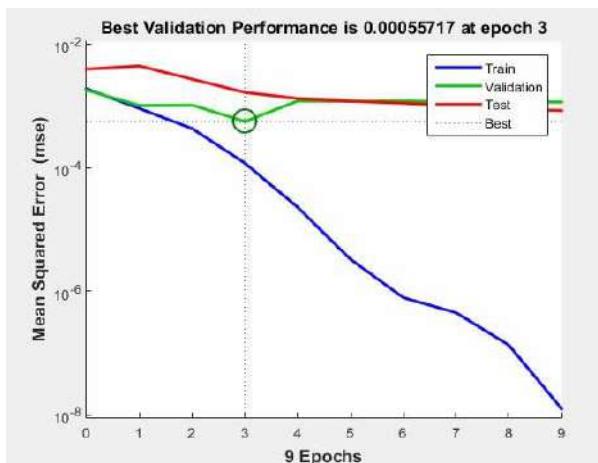


Fig.4-Performance plot for LM algorithm

test results, it is an evident that the error percentage conductivity lies in the range from -1.09% to 6.4% between experimental data and neural network prediction. Therefore, it can be concluded that the prediction of the artificial neural network has proceed in the correct manner.

IV. CONCLUSION

In this study, an experimental investigation is performed to predict the thermal insulation properties of wall and roof

structures of which the mechanical properties are known, by using an artificial neural network (ANNs) method. Then, comparisons have been made between the determined thermal conductivity of the newly produced structures, which are obtained from experimental method and ANN method that uses mechanical properties as input parameters. Initially, the number of neurons in the hidden layer is optimized by trial and error method. Then the neural network 3-5-4 is trained using Levenberg-Marquardt (LM) training algorithm, the value of the mean squared error and the correlation coefficient R were found as 0.019 and 0.99939, respectively. From the test results,

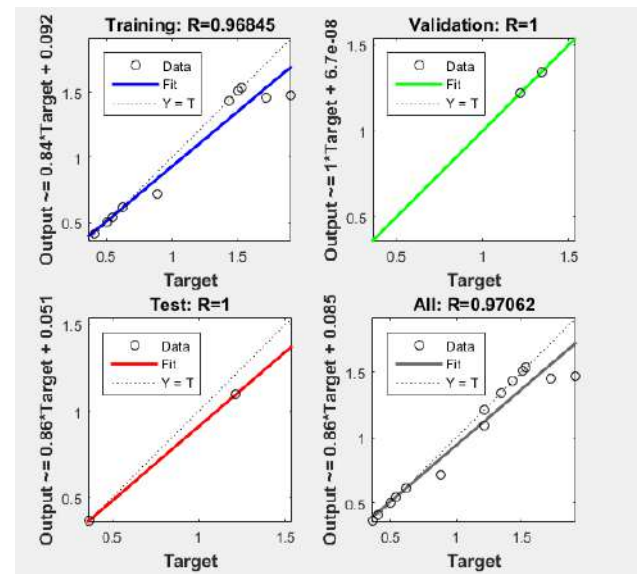


Fig.5-Regression plot for LM algorithm

TABLE III. TEST DATA AND PREDICTED VALUES FROM NEURAL NETWORK

Types of Concrete	Agrega Cont. (%)	Density (kg/m ³)	Compre. Strength (Mpa)	Thermal Conductivity (W/m.K)		
				Exp.	ANN Pred.	Err. (%)
EPC	45	1283.88	6.74	0.50	0.468	6.4
PC	25	1737.80	17.23	1.29	1.276	-1.09
RC	35	1998.06	13.36	1.22	1.268	3.93
EPC	45	1283.88	6.74	0.42	0.4363	3.88
PC	25	1737.80	17.23	0.97	0.9893	1.99
RC	35	1998.06	13.36	1.15	1.1357	-1.24

since the percentage errors in the thermal conductivity values between experimental data and neural network prediction vary from -1.09% to 6.4%.

REFERENCES

- [1] Bansal K, Chowdhury S, Gopal MR. Development of CLTD values for buildings located in Kolkata, India. Appl Therm Eng 2008;28:1127–37.
- [2] Mui KW, Wong LT. Cooling load calculations in subtropical climate. Build Environ 2007;42:2498–504.

- [3] Moosavi L, Mahyuddin N, Ghafar NA, Ismail MA. Thermal performance of atria: An overview of natural ventilation effective designs. *Renew Sustain Energy Rev* 2014;34:654–70.
- [4] Zhang Y, Chen Q, Zhang Y, Wang X, Exploring buildings' secrets: The ideal thermophysical properties of a building's wall for energy conservation. *International J Heat Mass Transf* 2013;65:265–73.
- [5] Asan H. Numerical computation of time lags and decrement factors for different building materials. *Build Environ* 2006;41:615–20.
- [6] Asan H, Sancaktar YS. Effects of Wall's thermophysical properties on time lag and decrement factor. *Energy Build* 1998;28:159–66.
- [7] Jin X, Zhang X, Cao Y, Wang G. Thermal performance evaluation of the wall using heat flux time lag and decrement factor. *Energy Build* 2012;47:369–74.
- [8] Zhang Y, Lin K, Zhang Q, Di H. Ideal thermophysical properties for free-cooling (or heating) buildings with constant thermal physical property material. *Energy Build* 2006;38:1164–70.
- [9] Zhang Y, Dua K, Hec J, Yanga L, Lia Y, Lia S. Impact factors analysis on the thermal performance of hollow block wall. *Energy Build* 2014;75:330–41.
- [10] Kontoleon KJ, Theodosiou ThG, Tsikaloudaki KG. The influence of concrete density and conductivity on walls' thermal inertia parameters under a variety of masonry and insulation placements. *Appl Energy* 2013;112:325–337.
- [11] Barrios G, Huelsz G, Rechtman R, Rojas J. Wall/roof thermal performance differences between air-conditioned and non air-conditioned rooms. *Energy Build* 2011;43:219–23.
- [12] Khan MI. Factors affecting the thermal properties of concrete and applicability of its prediction models. *Build Environ* 2002;37:607–14.
- [13] Pooliyadda SP, Dais WPS. Neural networks for predicting properties of concretewith admixtures. *Constr Build Mater* 2001;15(7):371–9
- [14] Ramezaniyanpour AA, Davapanah A. Concrete properties estimation and mix design optimization based on neural networks, world conference on concrete materials and structures (WCCNS), Kuala Lumpur, Malaysia; 2002.
- [15] Marai M. Alshihri, Ahmed M. Azmy, Mousa S. El-Bisy. Neural networks for predicting compressive strength of structural light weight concrete. *Construction and Building Materials* 2009; 23: 2214 – 2219.
- [16] Masri SF., Chassiakos AG., and Caughey TK., Identification of Nonlinear Dynamic Systems Using Neural Networks, *Journal of Applied Mechanics*; 60: 123-33, 1993
- [17] Guang NH, Zong W.J., Prediction of Compressive Strength of Concrete by Neural Networks, *Journal of Cement and Concrete Research*; 30: 1245-1250, 2000
- [18] Dias W.P.S., Pooliyadda S.P., Neural Networks for Predicting Properties of Concretes with Admixtures, *Journal of Construction and Building Materials*; 15: 371-379, 2001
- [19] Eldin N.N., and Senouci A.B., Measurement and Prediction of the Strength of Rubberized Concrete, *Journal of Cement and Concrete Composites*; 16:287-298., 1994
- [20] Lai S, Serra M., Concrete Strength Prediction by Means of Neural Network, *Journal of Construction and Building Materials*; 11(2): 93-98, 1997
- [21] X O. Gencil , F. Koksai , M. Sahin , M. Y. Durgun , H. E. Hagg Lobland & W. Brostow (2013) Modeling of Thermal Conductivity of Concrete with Vermiculite by Using Artificial Neural Networks Approaches, *Experimental Heat Transfer*, 26:4, 360-383, DOI:10.1080/08916152.2012.669810

Effects of Nanofluids on Heat Transfer and Fluid Flow with Impinging Jet

Mustafa Kilic

Mechanical Engineering Department
Adana Science and Technology
University
Adana, Turkey
mkilic@adanabtu.edu.tr

Mahmut Yavuz

Mechanical Engineering Department
Adana Science and Technology
University
Adana, Turkey
mahmuty90@hotmail.com

İbrahim Halil Yilmaz

Department of Automotive Eng.
Adana Science and Technology
University
Adana, Turkey
iyalmaz@adanabtu.edu.tr

Abstract—Present study is focused on numerical investigation of heat enhancement and fluid flow from a heated surface by using nanofluids and impinging jets. Effects of Reynolds number, different particle diameter and different types of nanofluids (Cu-water, Al_2O_3 -water, TiO_2 -water) on heat transfer and fluid flow were studied numerically. Al_2O_3 -water nanofluid was used as a base coolant. Three impinging jets were used to cool the surface. Low Re k- ϵ turbulent model of PHOENICS CFD code was used for numerical analysis. It is obtained that increasing jet velocities from the first phase to the third phase causes an increase of 51.4% on average Nusselt number (ANN) but increasing jet velocities from the third phase to the fourth phase causes a decrease of 5.6% on ANN. Decreasing particle diameter from $D_p=80\text{nm}$ to 10nm causes an increase of 12.8% on ANN. Using Cu-water nanofluid causes an increase of 9.3%, 8.4%, on ANN with respect to Al_2O_3 -water, TiO_2 -water.

Keywords—heat transfer; nanofluids; particle diameter; Impinging jets

V. INTRODUCTION

Suspension of solid particles which have 1-100 nm size in a base fluid called as nanofluid. Nanoparticles suspended in base fluid can expand thermal capacity of the fluid and also interactions and collisions between nanoparticles cause to increase in turbulence and turbulence intensity of the transition surface. Nanoparticles have 20% of their atoms on the particule surface, making them ready to heat transfer with high heat transfer coefficient. Nanoparticles provide another advantage which called as the particle mobility to nanofluids. Particle mobility causes micro-convection in the liquid due to its nano size and therefore increases heat transfer. Hence, they have a wide range of application in industry as microelectronics medicine and space research.

The jet cooling technique provides an important enhancement in heat transfer. Impinging jet technique can be used to boost up heating, cooling or drying processes on a selected surfaces. Impinging jets technic enhance heat transfer by increasing local heat transfer coefficient between the

impinging fluid and a selected surface. Combination of the liquid jet impingement and the nanofluid technologies provides advantages of both and consequently improves the heat transfer significantly. This improvement means compact size and low weight which reduces the cooling system capital cost.

Many studies on nanofluid or impinging jet, can be found in the literature. Teamah et al. [1] examined the heat transfer and flow structure for a flat plate by numerically and experimentally with different Reynolds numbers ($\text{Re} = 3000\text{--}32000$) and nanofluid volume ratios ($\phi = 0\text{--}10\%$) by using Al_2O_3 nanofluid. It has been observed that as volume fraction of nanoparticles in the fluid are increased, the heat transfer from the surface increases. Heat transfer coefficient can be increased by 62% when compared with the water. Sun et al. [2] searched the effect of a single jet using CuO nanofluid for heat transfer. It has been determined that when the nanofluid is used, a significant increase in heat transfer can be achieved compare with water. When a circular nozzle is used, a higher heat transfer coefficient is obtained compared to a square shaped nozzle, and the highest heat transfer is obtained when the jet angle is 90° . Çakır M.T. [3] experimentally examined the thermal performance of the thermosiphon-type heat pipe which is using nanofluid as a working fluid. The nanofluid contained 2% by volume Al_2O_3 . As a result, significant reduce on thermal resistance is obtained but a complete stabilization at thermal efficiency could not be provided. Manay et al. [4] have compiled recent studies which focusing on using of nanofluids in microchannels. As a result, nanofluids using in microchannels increases heat transfer, but the presence of nanoparticles causes an increase in pressure loss. Chien et al. [5] experimentally observed the application of nanofluid in the flat plate heat pipe. It was acquired that the use of nanofluid achieve 40% reduction in thermal resistance compared to pure water utilization. Kang et al. [6] determined that, when nanofluid which include 10 nm and 35 nm sized Ag nanoparticles is used, thermal resistance diminished by 50% and 80% compared to pure water respectively. Xuan and Li [7]. Prepared nanofluid that include Cu and they investigated heat transfer effect of nanoparticle volume fraction, heat

transfer effect of particle diameter and heat transfer effect of particle geometry. As a result; it has been found that an increase of from 2.5% to 7.5% in the volumetric range causes an increase in the coefficient of thermal conductivity of nanofluid from 1.24 to 1.78. Shang et al. [8] studied the heat transfer characteristics of a closed-loop vibrating heat pipe with Cu-water nanofluid. They obtained that compared with pure water, the heat transfer capacity of the system increased by 83% when nanofluid was used. Umar et al. [9] researched the heat transfer from constant heat flux surface in laminar flow regime for varied volume fraction and Reynolds number. They used Cu-water nanofluid in their analysis. As a result, They observed that as the particle volume ratio increases and the Reynolds number increases, the heat transfer coefficient increases, the highest increase in heat transfer coefficient (61%) occurs at a particle volume ratio of 4% and Reynolds number $Re = 605$. Qu et al. [10] Used Al_2O_3 -water as working nanofluid in their experiment to investigate the thermal performance of a closed-loop vibrating heat pipe. As a result, they observed that the thermal resistance of the system decreased by 32.5% compared to pure water. Naphon et al. [11] investigated the heat transfer between the nanofluids that they built using titanium-ethanol and the closed two-phase thermosiphon. An increase of 10.6% on heat transfer was obtained by using nanoparticles, compared to ethanol using. Kilic et al. [12] examined the cooling of a flat plate by using impinging fluid air jet. It was observed that the mean Nusselt number increases by 49.5% when Reynold numbers is between 4000 and 10000. Lin Z.H. et al. [13] investigated heat transfer in confined fluid jets systematically in their study experimentally. The effects of Reynolds number and jet-target plate spacing on heat transfer were analyzed in their study. They observed that the effect of the change in jet-target plate distance has not significant effect on heat transfer, but the increase in Reynolds number increases heat transfer. In the range of $190 \leq Re \leq 1537$ and $1 \leq H/W \leq 8$ two experimental correlations were determined for the Nusselt number at the starting point and mean Nusselt number.

VI. PRELIMINARY DEFINITIONS

The heat transfer from the surface will take place by convection, conduction and radiation.

$$Q_{convection} = Q_{total} - Q_{conduction} - Q_{radiation} \quad (1)$$

The total amount of heat to be given to the plate is;

$$Q_{total} = \frac{V^2}{R}$$

$$\alpha + \beta = \chi. \quad (1)$$

Where V is the voltage value of the power unit and R is the resistance of the heater. Here, the heat generated by the heater placed under the copper plate will be transmitted to the upper surface of the plate through the copper plate thickness by

conduction, and as a result, the plate surface will be cooled by using nanofluid with impinging jet. Heat transfer by conduction along the plate;

$$Q_{conduction} = \frac{-k_c \cdot A_c \cdot (T_{bottom} - T_{upper})}{L_c} \quad (3)$$

$$\alpha + \beta = \chi. \quad (1)$$

here, k_c is the heat transfer coefficient of the copper plate, A_c is the copper plate surface area, and L_c is the copper plate thickness.

Thermal losses due to radiation;

$$Q_{radiation} = \varepsilon \cdot \sigma \cdot A \cdot F \cdot (T_s^4 - T_{bulk}^4) \quad (4)$$

$$\alpha + \beta = \chi. \quad (1)$$

Where ε is the copper plate emissivity, σ is the Stefan-Boltzmann constant, A is the radiation surface area, T_s is the surface temperature, and T_{bulk} is the mean fluid temperature.

$$T_{bulk} = \frac{T_{in} + T_{out}}{2} \quad (5)$$

It is assumed that heat transfer with radiation is negligible in this study because surface temperature is under $573.15^\circ K$.

Heat transfer from surface with convection;

$$Q_{convection} = h \cdot A \cdot \Delta T \quad (6)$$

$$\alpha + \beta = \chi. \quad (1)$$

Where h is the heat transfer coefficient, A is the convection surface area, ΔT ($\Delta T = T_s - T_{bulk}$) is the difference between the measured surface temperature and the fluid mean temperature.

Nusselt number (Nu) is a dimensionless parameter indicating the ratio of heat transfer with conduction to heat transfer with convection.

$$Nu = \frac{(Q_{convection} \cdot D_h)}{(T_s - T_{jet}) \cdot k_{nf}} \quad (7)$$

$$\alpha + \beta = \chi. \quad (1)$$

Where T_s is the measured surface temperature, D_h is the hydraulic diameter, and k_{nf} is the coefficient of thermal conductivity of the nanofluid. Reynolds number (Re) is used

to determine for forced convection whether the flow is laminar or turbulent. Reynolds number based on turbulent flow;

$$Re = \frac{(\rho_{nf} \cdot V_{jet} \cdot D_h)}{(\mu_{nf})} \quad (8)$$

$$\chi \cdot \quad (1) \quad \alpha + \beta = \quad (1)$$

Where ρ_{nf} is the nanofluid density, V_{jet} is the jet velocity, and μ_{nf} is the nanofluid dynamic viscosity. The density of nanofluids is;

$$\rho_{nf} = (1 - \varphi) \cdot \rho_{bf} + \varphi \cdot \rho_p \quad (9)$$

$$\chi \cdot \quad (1) \quad \alpha + \beta = \quad (1)$$

Where ρ_{bf} is the base fluid (water) density, φ is the volumetric ratio of the nanofluid, and ρ_p is the density of the solid particles in the nanofluid. The volumetric ratio of nanoparticles is;

$$\varphi = \frac{1}{(1/\omega) \cdot (\rho_p - \rho_{bf})} \quad (10)$$

$$\chi \cdot \quad (1) \quad \alpha + \beta = \quad (1)$$

Where ω is the density difference between the fluid and the main fluid (water). The nanofluid specific heat is calculated from;

$$C_{p_{nf}} = \frac{\varphi \cdot (\rho \cdot C_p)_p + (1 - \varphi) \cdot (\rho \cdot C_p)_f}{(\rho_{nf})} \quad (11)$$

Where $C_{p(p)}$ is specific heat of particle, $C_{p(f)}$ is specific heat of base fluid. The effective thermal conductivity of nanofluid is calculated according to Massimo [14];

$$\frac{k_{eff}}{k_f} = 1 + 4.4 Re^{0.4} Pr^{0.66} \left(\frac{T}{T_{fr}} \right)^{10} \left(\frac{k_p}{k_f} \right)^{0.03} \varphi^{0.66} \quad (12)$$

$$\chi \cdot \quad (1) \quad \alpha + \beta = \quad (1)$$

Where Re is the nanoparticle Reynolds number, Pr is the Prandtl number of the base liquid. k_p is the nanoparticle thermal conductivity, φ is the volume fraction of the suspended nanoparticles, T is the nanofluid temperature ($^{\circ}K$),

T_{fr} is the freezing point of the base liquid. The effective dynamic viscosity of nanofluids;

$$\mu_{nf} = \mu_{bf} (1 + 2.5 \varphi + 4.698 \varphi^2) \quad (13)$$

$$\chi \cdot \quad (1) \quad \alpha + \beta = \quad (1)$$

VII. NUMERICAL MODEL

Low Re k- ϵ turbulence model of PHOENICS CFD code was used for this numerical analysis. CFD simulation domain is shown in Fig 1. Mesh structure is shown in Fig.2.

	$U(m/s)$	$V(m/s)$	$W(m/s)$	$T(^{\circ}K)$	k	ϵ
Nanofluid inlet jet 1	U=0	V=0	$W=W_{inlet}$	$T=T_{inlet}$	$(T_1 W_{jet})^2$	$(C_p C_p)^{3/4} \frac{k^{3/2}}{L}$
Nanofluid jet 2	U=0	V=0	$W=W_{inlet}$	$T=T_{inlet}$	$(T_1 W_{jet})^2$	$(C_p C_p)^{3/4} \frac{k^{3/2}}{L}$
Nanofluid jet 3	U=0	V=0	$W=W_{inlet}$	$T=T_{inlet}$	$(T_1 W_{jet})^2$	$(C_p C_p)^{3/4} \frac{k^{3/2}}{L}$
Copper Plate	U=0	V=0	W=0	$q''=q''_{copper}$	k=0	$\frac{\partial \epsilon}{\partial z} = 0$
Outlet	$\frac{\partial U}{\partial x} = 0$	$\frac{\partial V}{\partial x} = 0$	$\frac{\partial W}{\partial x} = 0$	$T=T_{out}$	$\frac{\partial k}{\partial x} = 0$	$\frac{\partial \epsilon}{\partial x} = 0$
Front and Back wall	U=0	V=0	W=0	$\frac{\partial T}{\partial y} = 0$	-	-
Top wall	U=0	V=0	W=0	$\frac{\partial U}{\partial z} = 0$	-	-

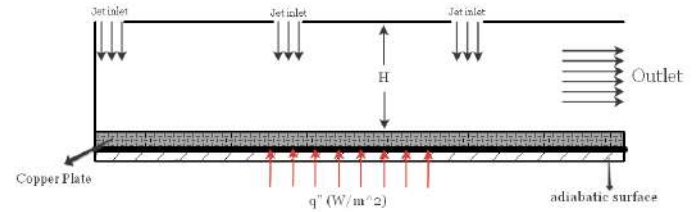


Fig 1. CFD simulation domain

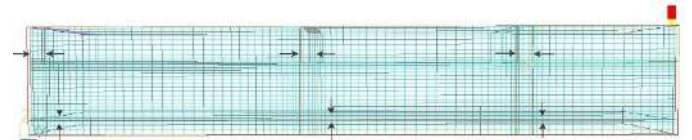


Fig. 2. Mesh structure

The continuity, Reynolds averaged momentum and time averaged energy equations governing 3-dimensional steady, flow of air with constant properties used for turbulent solutions can be written in the Cartesian coordinate system as follows:

Continuity equation:

$$\frac{\partial U_i}{\partial x_i} = 0 \quad (14)$$

Momentum equation:

$$\rho U_i \frac{\partial U_j}{\partial x_i} = -\frac{\partial P}{\partial x_j} + \frac{\partial}{\partial x_i} \left[\mu \left(\frac{\partial U_i}{\partial x_j} + \frac{\partial U_j}{\partial x_i} \right) - \rho \overline{u'_i u'_j} \right] \quad (15)$$

(11)

Energy equation:

$$\rho c_p U_i \frac{\partial T}{\partial x_i} = \frac{\partial}{\partial x_i} \left[k \frac{\partial T}{\partial x_i} - \rho c_p \overline{u'_i T'} \right] \quad (16)$$

All the boundary conditions used in the study are summarized in Table 1. It was used 96x15x34 (48960 elements) meshes for this application. Mesh structure was prepared according to flow conditions. In order to get more precise numerical results we intensified mesh numbers in some region as jet inlet, surface of copper plate. Sweep number was studied between 400 and 2500 and cell number was also studied between 24 and 44. It is observed that numerical geometry was independent from sweep number and cell number when sweep number was 600 and cell number was 96x15x34.

BOUNDARY CONDITIONS

VIII. RESULTS AND DISCUSSIONS

In this section, numerical results were prepared for three parameters.

- Effects of different water flow regime for $R_n/R_1=1-1.33-1.67$ to $1-1.17-1.33$
- Effects of Al_2O_3 -water nanofluid with 25 nm sized particles for different particle diameter on heat transfer ($D_p=10, D_p=25, D_p=40, D_p=80$).
- Effects of different nanofluids on heat transfer (Cu-Water, TiO_2 -Water, Al_2O_3 -Water).

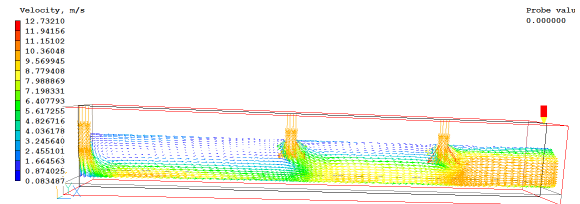
A. Effects of variant Reynolds number

Numerical analysis were conducted for different water flow regime for $R_n/R_1=1-1.33-1.67$ to $1-1.17-1.33$ when particle diameter was $25\mu m$ and inlet temperature $T_{inlet}=20^\circ C$.

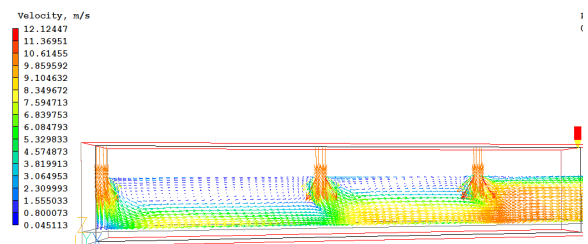
REYNOLDS NUMBERS

	$W_1(m/sn)$	$W_2(m/sn)$	$W_3(m/sn)$	$Re_1(jet-1)$	$Re_2(jet-2)$	$Re_3(jet-3)$	Re_1/Re_1	Re_2/Re_1	Re_3/Re_1
1.phase	6	8	10	21440,42	28587,23	35734,03	1	1,33	1,67
2.phase	8	10	12	28587,23	35734,03	42880,84	1	1,25	1,5
3.phase	10	12	14	35734,03	42880,84	50027,65	1	1,2	1,4
4.phase	12	14	16	42880,84	50027,65	57174,46	1	1,17	1,33

Velocity vectors and Temperature contours for different Reynolds rates are shown in Fig 3 and Fig 4.

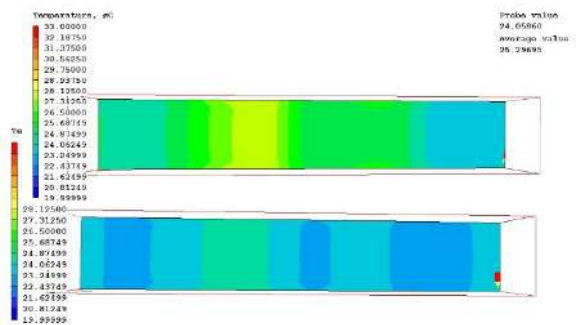


(a)



(b)

Fig 3. Velocity vectors for different Reynolds number (a) $R_n/R_1=1-1.2-1.4$ (b) $R_n/R_1=1-1.17-1.33$



(a)

(b)

Fig 4. Temperature counters for (a) $R_n/R_1=1-1.33-1.67$ (b) $R_n/R_1=1-1.2-1.4$

It can be seen that increasing jet velocities from the first phase to the third phase local surface temperature decreases and local Nusselt number increases. But increasing jet velocities to the fourth phase causes an increase on surface temperature. The reason of this vortexes, which occurs at the bottom of the close side enlarge while velocity on the first jet is increasing. And these vortexes reduce impinging effects and causes an increase on surface temperature. These effects continue at impinging region of second jet but effects of channel flow increases at this region. At the impinging region of the third

jet there is not a significant difference between third and fourth phase because channel flow effects reduces impinging effects at this region by increasing velocities from third to fourth phase. So increasing jet velocities from the first phase to the third phase causes an increase of 51.4% on average Nusselt number but increasing jet velocities from the third phase to the fourth phase causes a decrease of 5.6% on average Nusselt number because of the effects of vortexes and the best velocity profile is the third phase. Local Nusselt number for different jet velocities are shown in Fig 5.

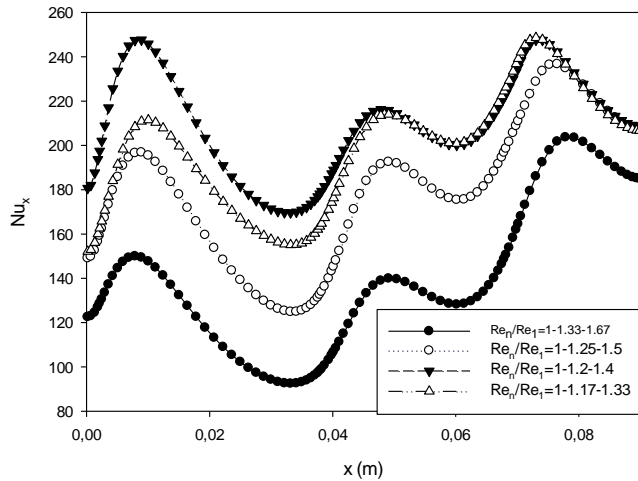


Fig 5. Local Nusselt number for different jet velocities

B. Effects of different nanoparticle diameters

Effect of different particle diameter (10 nm, 25 nm, 40 nm, 80 nm) was analyzed numerically. It was observed that decreasing particle diameter from 80nm to 10nm causes a decrease on a surface temperature. Temperature contours on heated surface and variation of surface temperature for different particle diameter are shown in Fig 6. and Fig 7.

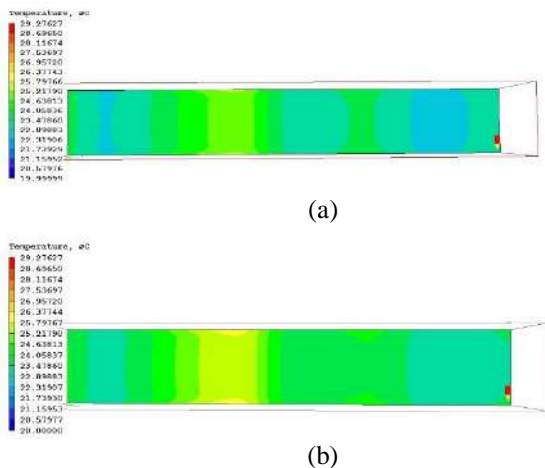


Fig 6. Temperature counters on surface for (a)Dp=10nm and (b)Dp=80nm

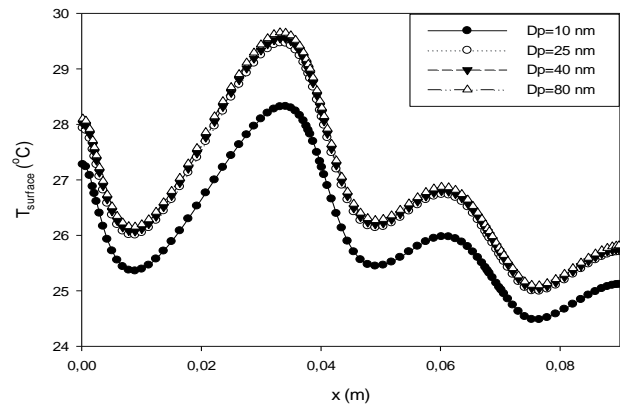


Fig 7. Temperature distribution on surface for different nanoparticles

Average surface temperature increases 1°C between Dp=10nm and 80nm. ANN increases of 10.9% between Dp=10nm and 25nm. But there is not any significant difference on ANN between Dp=25nm and Dp=80nm. So total decrease on average Nusselt number between Dp=10nm and Dp=80nm occurs 12.8%. Variation of local Nusselt number for different particle diameter is shown in Fig 8.

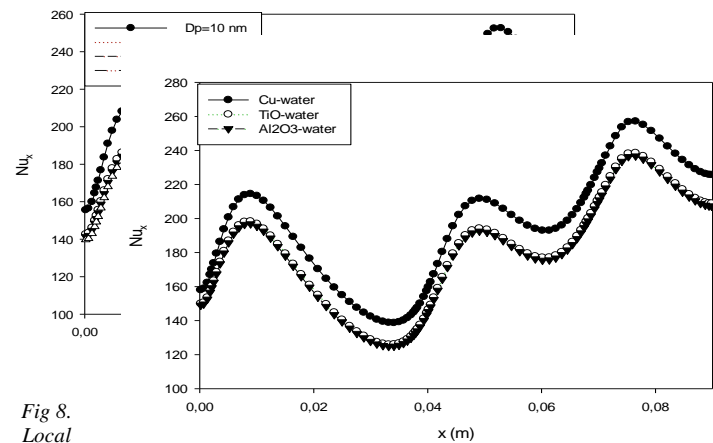


Fig 8.
Local

Nusselt number for different particle diameters

C. Effects of different type of nanofluids

Numerical analysis is conducted for different type of nanofluids (Cu-water, TiO₂-water and Al₂O₃-water) with 25 nm particle size and volume fraction 4%. Calculated properties of nanofluids are shown in Table 2.

THERMO-PHYSICAL PROPERTIES OF NANOFLUIDS AT 293K.

Nanofluid	Density ρ (kg/m ³)	Specific Heat C_p (J/kgK)	Dynamic Viscosity μ (Pa.s)	Kinematic Viscosity ν (m ² /s)	Thermal Conductivity λ (W/mK)	Thermal Expansion Coefficient β (m ² /2)
Al ₂ O ₃ -water	1113,472	3706,840499	0,001099764	0,000000988	0,6635	0,000160745
CuO-water	1218,272	3403,881485	0,001099764	0,000000903	0,6621	0,000159664
TiO-water	1128,272	3655,247586	0,001099764	0,000000975	0,6615	0,000160405
Cu-water	1316,672	3148,451174	0,001099764	0,000000835	0,6684	0,000161244

Temperature difference on surface of heated place is shown

Nomenclature	
C_p	Specific Heat (J/kgK)
ρ	Density (kg/m ³)
ϕ	Nanoparticle volume fraction
μ	Dynamic viscosity (Pa.s)
bf	Base fluid
nf	Nanofluid
p	Particle
Pr	Prandtl Number, $Pr = \frac{C_p \cdot \mu}{k}$
Re	Reynolds number $Re = \frac{(\rho_{nf} \cdot V_{jet} \cdot D_h)}{(\mu_{nf})}$
Nu_x	Local Nusselt number $Nu_x = \frac{(Q_{convection} \cdot D_h)}{(T_s - T_{jet}) \cdot k_{nf}}$
k_{eff}	Effective Thermal Conductivity (W/mK)

in Fig. 9. TiO-water, Al₂O₃-water and Cu-water. It was obtained that using Cu-water causes a decrease of 1°C on average temperature with respect to Al₂O₃ approximately. The maximum temperature difference on local surface temperature between Cu-water and Al₂O₃ is 1.5°C.

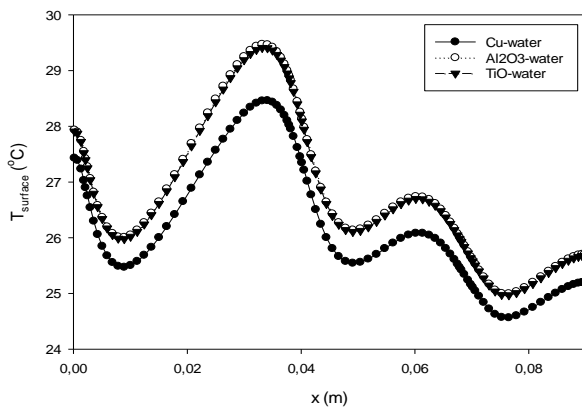


Fig. 9. Temperature distribution on surface for different nanofluids

It was acquired that using Cu-water nanofluid causes an increase of 9.3%, 8.4% on ANN with respect to Al₂O₃-water and TiO-water. It can be seen that using Cu-water nanofluids shows better heat transfer performance. Variation of local Nusselt number for different nanofluids is shown in Fig 10.

Fig 10. Local Nusselt number for different particle diameters

IX. CONCLUSION

Present study is focused on numerical investigation of heat enhancement and fluid flow from a heated surface by using nanofluids and impinging jets. Effects of different Reynolds numbers, particle diameter and different types of nanofluids (Cu-water, TiO-water, Al₂O₃-water) on heat transfer and fluid flow were studied numerically. According to our constraints it is obtained that increasing jet velocities from the first phase to the third phase causes an increase of 51.4% on ANN but increasing jet velocities from the third phase to the fourth phase causes a decrease of 5.6% on ANN. Decreasing volume fraction from Dp=80nm to 10nm causes an increase of 12.8% on ANN. But there is not any significant difference on average Nusselt number between Dp=25nm and Dp=80nm. Using Cu-water nanofluid causes an increase of 9.3%, 8.4%, on average Nusselt number with respect to Al₂O₃-water, TiO-water. Velocity of the third phase, Dp=10 nm and using Cu-water nanofluids shows better heat transfer performance. Research areas for future investigations can be investigation of effect of hybrid nanofluids with different base fluids on heat transfer.

ACKNOWLEDGMENT

The financial support of this study by Scientific Research Project (16103021) of Adana Science and Technology University is gratefully acknowledge.

REFERENCES

- [1] Teamah, M.A., Dawood M.M., Shehata A., "Numerical and experimental investigation of flow structure and behavior of nanofluids flow impingement on horizontal flat plate", Experimental Thermal and Fluid Science, vol 74, 235-246, 2016.
- [2] Sun, B., Qu, Y., Yang, D., "Heat transfer of Single Impinging jet with Cu nanofluids", Applied Thermal Engineering, vol 102, 701-707, 2016.
- [3] Cakir M.T., "Alamına içeren Nanoakışkan kullanarak ısı borularının performanslarının iyileştirilmesi", Journal of The Faculty of Engineering and Architecture of Gazi University, vol 30, 547-556, 2015.
- [4] Manay E., Sahin B., Akyurek E.F., Comakli O. "Mikro kanallarda nanoakışkanların kullanımı", TMMOB MMO Mühendis ve Makina Dergisi, Vol 53, 38-42, 2012.
- [5] Chien, H.T., Tsia C.Y., Chen P.H., Chen P.Y., "Improvement on thermal performance of a disk-shape miniature heat pipe with nanofluid", Proceedings of the fifth International Conference on Electric Packaging Technology, IEEE, 389-391, 2003.
- [6] Kang S.W., Wei, W.C., Tsia S.H., Yang S.H., "Experimental Investigation of silver nano-Fluid on heat pipe thermal

performance", *Applied Thermal Engineering*, vol26, 2377-2382, 2006.

- [7] Xuan Y., Li Q., "Heat transfer enhancement of nanofluids", *Int.Journal of Heat and Fluid Flow*, vol 21, 58-64, 2000.
- [8] Shang F.M., Liu D.Y., Xian H.Z., Yang Y.P., Du X.Z., "Flow and heat transfer characteristics of different forms of nanometer particles in oscillating heat pipe", *Journal of Chemical Industry*, vol 58, 2200-2204, 2007.
- [9] Umer A., Naveed S., Ramzan N., "Experimental Study of laminar forced convection heat transfer of deionized water based copper (I) oxide nanofluids in tube with constant wall heat flux", *Heat Mass Transfer*, vol 52, 2015-225, 2015.
- [10] Qu j., Wu H.Y., Cheng P., "Thermal performance of an oscillating heat pipe with Al₂O₃-water nanofluids", *International Communication Heat and Mass Transfer*, vol37, 111-115, 2010.
- [11] Naphon P., Assdamongkol P., Borirak T., "Experimental investigation of titanium nanofluids on the heat pipe thermal efficiency", *International Communication Heat and Mass Transfer*, vol 35, 1316-1319, 2008.
- [12] Kilic, M., Çalışır, T., Başkaya, Ş, "Experimental and numerical study of heat transfer from a heated flat plate in a rectangular channel with an impinging Jet", *Journal of the Brazilian Society of Mechanical Sciences and Engineering*, vol 48:1-16, 2016.
- [13] Lin, Z.H., Chou, Y.J., Hung, Y.H., "Heat transfer behaviors of a confined slot jet impingement", *Int Jour. of Heat and Mass Transfer*, 49:2760-2780, 1999.
- [14] Corcione M., Empirical correlating equations for predicting the effective thermal conductivity and dynamic viscosity of nanofluids. *Energy Convers. Manag.* 2011;52(1):789-93.

Finite Element Modeling and Analysis of Multilayer Ceramic Coated Femur-Insert Component

Ali Kemal ASLAN
Tunceli Vocational High School
Munzur University
Tunceli, Turkey
akaslan@munzur.edu.tr

Erkan BAHÇE
Department of Mechanical Engineering
Inonu University
Malatya, Turkey
erkan.bahce@inonu.edu.tr

Ender EMİR
Department of Mechanical Engineering
Inonu University
Malatya, Turkey
enderemir44@gmail.com

Caner Cengiz TURAN
Department of Orthopedic Surgery
Hayat Hospital
Malatya, Turkey
ccturan@hotmail.com

Abstract—Surface coating of orthopaedic implants are applied for reduce insert wear and also prevent metal leaching to body fluid which causes allergic diseases. CoCrMo alloys are widely used as femoral component in total knee arthroplasty. In this study, we investigated effect of coating on CoCrMo femoral component articulated insert in terms of wear by finite element modeling. In the analysis, UHMWPE insert was used as insert material and three different femoral materials were used as uncoated CoCrMo alloy, TiN coated CoCrMo alloy and seven layered coated CoCrMo alloy. CAD modeling of insert-femoral component was obtained by using a special 3D scanning system. Assembly of models was performed by using SolidWorks. Assembled model imported to ANSYS16 software and FEM analysis were performed. It is seen that; coating of femoral component has reduced shear stress and deformation of insert.

Keywords—TKA; implants; coating; multilayer; biomaterial, wear

I. INTRODUCTION

Implants used in total knee arthroplasty have a great importance for human health. Thanks to advanced materials and engineering technologies and also advanced surgical techniques, comfortability and lifespan of implants have enhanced. Nevertheless, when the young patients who has knee implants considered, enhancing lifespan of knee implants still an essential research area for researchers.

Wear and metal ionization as a result of corrosion are the main issues of TKA implants [1,2,3]. Materials which are used in knee arthroplasty must have not only biocompatibility but also high corrosion and wear strength [4, 5, 6, 7]. CoCrMo alloys are used widely in femoral component of TKA thanks to good mechanical properties they possess as high elasticity modulus, high tensile strength, high corrosion and wear strength

[8,9]. But on the other hand metal ionization in body fluid causes diseases and also decreases the lifespan of implant as a result of early wear [10]. Therefore early reconstructive surgery are needed [1]. In order to avoid this; biomaterials used in orthopedic implants are coated to prevent metal ionization into human body fluid which causes allergic diseases and also to reduce wear rate of insert [1,11,12].

Application of coating implant surfaces are usually performed as thin ceramic films [13, 14, 15]. Ceramic materials are being preferred in orthopaedia because of their properties as biocompatibility, strength, hardness, wear and corrosion resistance [16]. Ceramics which are widely used in surface coating of implants are alumina (Al_2O_3), zirconia (ZrO_2), zirconia toughened alumina, alumina toughened zirconia, Silicon-nitride (Si_3N_4), TiN, ZrN and hydroxyapatite [17]. Application of ceramic coatings on implant surfaces are usually performed by physical vapour deposition (PVD) or chemical vapour deposition (CVD) processes [18].

There had been a lot of researches about surface coating of implants in the past. Mc Entire et al. have been a comprehensive literature review on ceramics used in orthopaedia and ceramic coatings of orthopaedic materials [17].

Qingliang Wang et al. applied CrN coating on CoCrMo substrate material which is used as implant material. They obtained enhanced hardness on coated surfaces and reduced wear rate of tibial component [19].

B. Alemón et al. have investigated corrosion behavior and metal leaching of CoCrMo substrate that multilayer coated with TiAlVCN/CNx, in simulated body fluid [9]. They observed significant reduces in wear rates and friction coefficients results of tribocorrosion tests. They achieved that multilayer coating has prevent the metal leaching significantly.

C. Balagna et al. coated CoCrMo substrate with Ta because of its properties like biocompatibility, low metal ionisation and high corrosion resistance. They applied three different coating system on substrate material. One coating was with Ta which possesses low carbon content, other coating was with Ta possesses high C content and the last one was metallic Ta. As result of their study they observed that multilayer coating with low C content Ta have high strength values thanks to its multilayered structure [20].

R. Hubler et al. have studied thin surface coating of 316L stainless steel femoral implant with Ti/TiN and Cr/V. Regarding to stoichiometric, microstructure, hardness, wear and corrosion resistance tests they obtained result that TiN coating can be used as protective coating compared to other coatings [13].

Lukasz Łapaja et al. have investigated mechanical properties of 11 retrieved TiN coated femoral heads from patients. According to the results they obtained, coated femoral heads had low wear rate compared to uncoated femoral heads [21].

Peiyun Yi et al. performed multilayered coating of TiAlN on Ti6Al4V alloy via closed field unbalanced magnetron sputter ion plating process. They concluded that multilayer coating has high adhesion strength to substrate material [22].

Sung-Hsiu Huang et al. have performed a study which investigates the mechanical and tribologic properties of multilayer CrN/ZrN coatings which are formed via cathodic arc deposition process. They observed that hardness and tribologic features were significantly affected from bilayer period [23].

Yin-Yu Chang and Chen-Jui Wu have investigated mechanical properties and impact strength of multilayer TiAlN/ZrN coatings. As result of their studies, they obtained that, multilayered coating had higher hardness than one layer ZrN and TiAlN. Furthermore, according to impact strength test results, multilayer coating had the higher impact strength [24].

Mohd. Zakuan Bin Abdullah et al. have performed a study that investigates of metal ionisation from stainless steel substrate material to multilayer ceramic coating. They applied coating on stainless steel substrate material as one layer of Cr, as two layered Cr/CrN, as three layered Cr/CrN/CrCN, five layered Cr/CrN/CrCN/CrN/ZrN and seven layered Cr/CrN/CrCN/CrN/CrCN/CrN/ZrN by PVD process. They obtained as a result of seven days metal release test; except Cr coated material, from uncoated substrate to multilayer coating ion concentration were decreased [25].

With this study, wear analysis of seven layer coated (Zr/CrN/CrCN/CrN/CrCN/CrN/ZrN) [26], one layer TiN coated [26,27] and uncoated CoCrMo [28] femoral components which articulate with UHMWPE insert, has modeled with ANSYS. This study aims to estimate wear behaviour of insert with articulating uncoated femur, seven layered coated femur and TiN coated femur.

II. MATERIALS AND METHOD

A. Materials

Three different femoral components were used for performing analysis. TiN coated, seven layered coated and

TABLE XIII. LAYER SEQUENCE AND THICKNESS OF COATING

Layers	Coating Material	Thickness of Coating (μm)
7th Layer	ZrN	2,5
6th Layer	CrN	0,5
5th Layer	CrCN	0,5
4th Layer	CrN	0,5
3rd Layer	CrCN	0,5
2nd Layer	CrN	0,5
1st Layer	Zr	0,1

TABLE XIV. PROPERTIES OF MATERIALS USED FOR ANALYSIS [29,30]

Material	Young Modulus (GPa)	Poisson's Ratio
CoCrMo	230	0.3
UHMWPE	69	0.29
ZrN	510	0.25
CrN	290	0.22
Zr	88	0.34
CrCN	320	0.25
TiN	590	0,25

uncoated CoCrMo alloy were used as femoral component during analysis. Table 1. shows the materials, their thickness and layer sequence of multilayered coated femoral component. Thickness of TiN coating was set to 5,1 μm . UHMWPE was used for all analysis as insert material. Properties of materials which were used in analysis are given in Table 2.

B. Method

Femur (Size 5, Otimed) and insert components were scanned separately by a 3D Scanner (David-SLS3) system and images were obtained by using its own software. Image of scanning system was given in Fig. 1. Assembly of obtained CAD models were carried out on Solidworks 2016 and imported to Structural Interface of ANSYS software. ANSYS image of modelling was given in Fig. 2. During analyzing material properties were set as given in Table 2. Axial force value was set to 800 N according to ISO14243-1 while performing analysis for three different femoral-insert components.

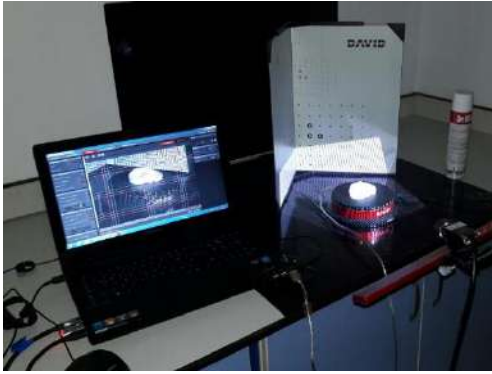


Fig. 17. Image of scanning system

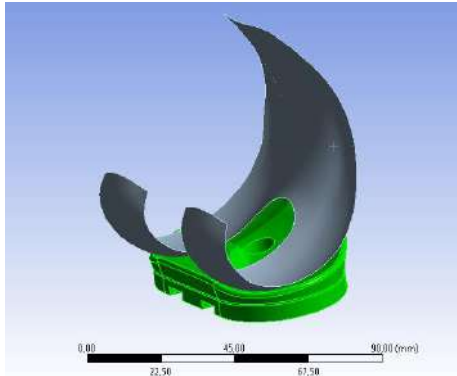


Fig. 18. ANSYS image of assembled model

III. RESULTS AND DISCUSSIONS

A. Contact Pressure

Image of contact pressure analyze of uncoated femur-insert component is given in Fig. 3. Maximum contact pressure was obtained 37,953 MPa for insert that articulate uncoated femur. Fig. 4. shows the contact pressure analysis of TiN coated femur-insert model. Contact pressure value for insert articulated TiN coated femur, was calculated 39,84 MPa. For seven layered coated femoral-insert component this value was 40,451 MPa as can be seen in Fig. 5. According to the results it is thought that coating of CoCrMo alloy femoral head which have same size, will increase the contact pressure between femur-insert interface and therefore wear depth of insert will increase. However, according to the Archard's Wear Law calculation, wear depth calculations showed that obtained increased contact pressure values didn't make big differences in spanlife of insert. Furthermore, it is thought that, forming metal debris will be prevent by reduced metal ionisation from femur to insert thanks to ceramic coating [13].

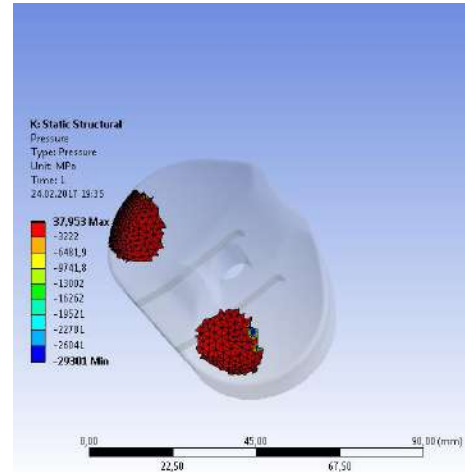


Fig. 19. Pressure Analyze of Insert articulated with uncoated femur

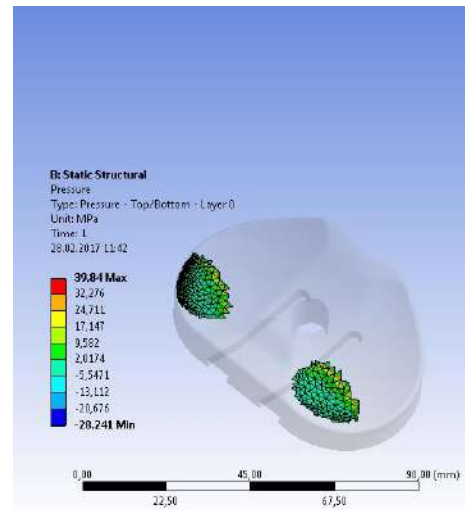


Fig. 20. Pressure Analyze of Insert articulated with TiN coated femur

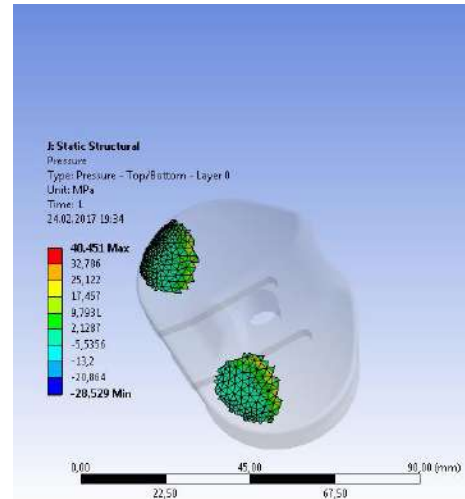


Fig. 21. Pressure Analyze of Insert articulated with seven layered coated femur

B. Von Mises Stress Analysis

Fig. 6. shows the Von Mises Stress Analysis of the models. Maximum equivalent stress for uncoated femur-insert model was obtained 32,246 MPa. While for TiN coated femur-insert

component this value was obtained 32,404 MPa, for seven layered coated femur-insert model it was 31,362 MPa. Von Mises stress analysis shows that coating of femur has decreased the maximum equivalent stress on the insert.

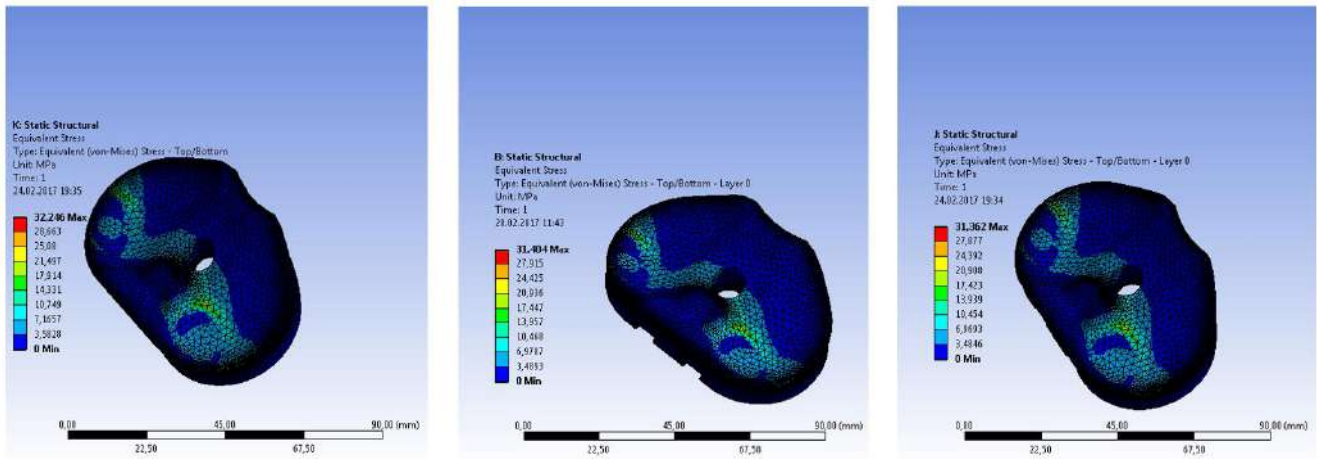


Fig. 22. Von Mises Analysis of a) insert-uncoated femur model b) insert-TiN coated femur c) insert-multilayered coated femur

C. Shear Stress Analysis

Image of shear stress analyze of insert articulated with uncoated femur model is given in Figure 7. Maximum shear stress was measured 10,203 MPa. For TiN coated femur-insert model this value was obtained 9,5513 Mpa. Figure 8. shows the shear stress analyze of insert-TiN coated femur model. As a result of shear stress analyze of insert articulated with seven layered coated femur component, maximum shear stress value was obtained 9,5726 MPa as can be seen in Figure 9. According to the results of shear stress analysis it can be say that coating has a favorable effect on shear stress which occurs on insert.

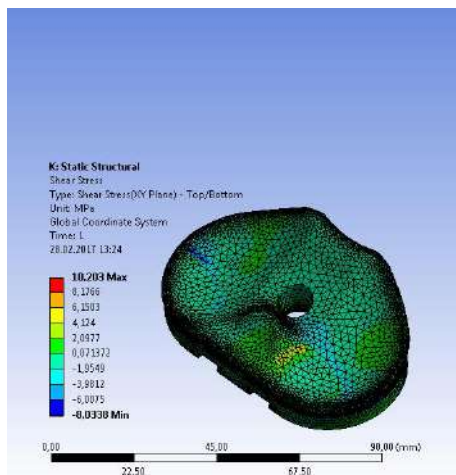


Fig. 23. Shear stress analyze of insert-uncoated femur model

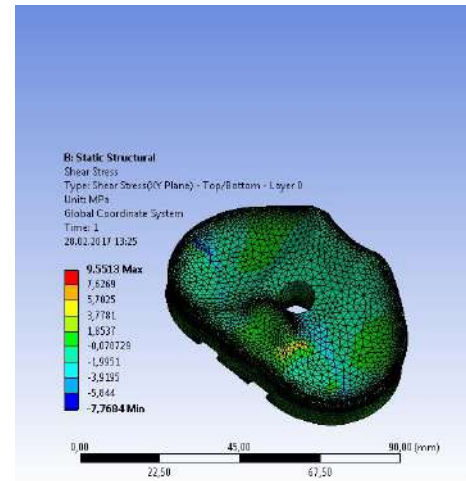


Fig. 24. Shear Stress Analyze of insert-TiN coated femur model

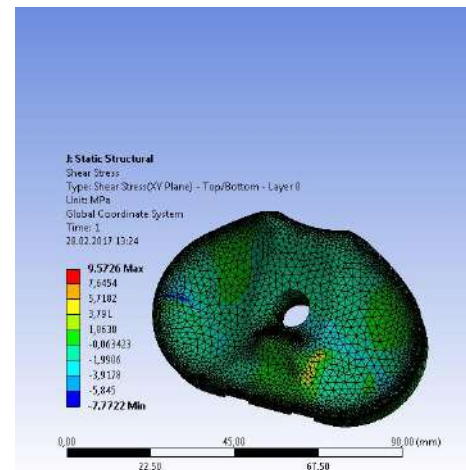


Fig. 25. Shear Stress Analyze of insert-multilayered coated femur model

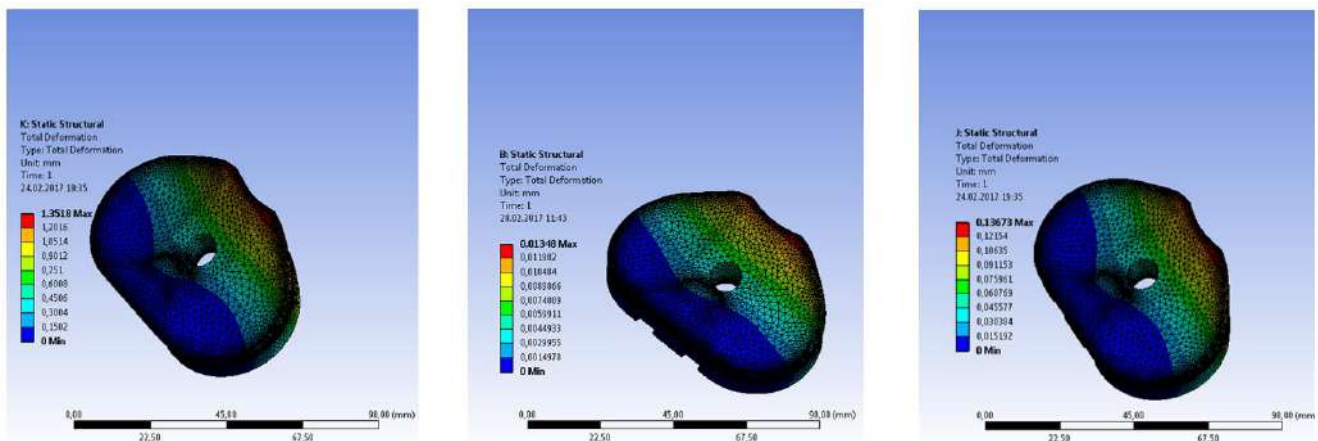


Fig. 26. Deformation analyze of a) insert-uncoated femur model b) insert TiN coated femur c) insert-multilayered coated femur

Fig.10. shows the deformation analysis of all models. Maximum deformation value for uncoated femur-insert model was obtained 1,3518 mm. TiN coated femur-insert model has 0,01348 mm maximum deformation value and multilayered coated femur-insert model has 0,13673 mm maximum deformation. According to these results it can be said that coating has a favorable effect on insert deformation.

IV. CONCLUSIONS

In this study, static analysis of three different femur component articulated with UHMWPE insert performed successfully. It is seen that, coating of femur has increased contact pressure on insert, however when reduced metal ionization considered it was thought that this increase couldn't cause early wear of insert. According to the results of shear stress and deformation analysis, it is thought that, coating of CoCrMo femoral component can be reduce wear rate of UHMWPE.

REFERENCES

- [1] J. Lützner, A. Hartmann, G. Dinnebier, P. Spornraft-Ragaller, C. Hamann, S. Kirschner, "Metal hypersensitivity and metal ion levels in patients with coated or uncoated total knee arthroplasty: a randomised controlled study", *International Orthopaedics (SICOT)*, DOI 10.1007/s00264-013-2010-6
- [2] C. M. Arnholt, DW MacDonald, A.L. Malkani, G.R. Klein, C.M. Rimnac, S.M. Kurtz, "Corrosion Damage and Wear Mechanisms in Long-Term Retrieved CoCr Femoral Components for Total Knee Arthroplasty", *The Journal of Arthroplasty*, DOI:10.1016/j.arth.2016.05.006
- [3] M. Berni, N Lopomo, G. Marchiori, A. Gambardella, M. Boi, M. Bianchi, "Tribological characterization of zirconia coatings deposited on Ti6Al4V components for orthopedic applications", *Materials Science and Engineering C*, Vol. 62, pp 643–655, 2016
- [4] M. Geetha, A.K. Singh, R. Asokamani, A.K. Gogia, "Ti based biomaterials, the ultimate choice for orthopaedic implants – A review", *Progress in Materials Science*, Vol. 54, pp. 397–425, 2009
- [5] Q. Chen, P. Chen, X. Pang, Y. Hu, Y. Zhang, "Adrenomedullin Up-regulates the Expression of Vascular Endothelial Growth Factor in Epithelial Ovarian Carcinoma Cells via JNK/AP-1 Pathway", *Int J Gynecol Cancer*, Vol. 25, pp. 1-6, July 2015
- [6] R. Agarwal, A. J. Garcia, "Biomaterial strategies for engineering implants for enhanced 2 osseointegration and bone repair", *Advanced Drug Delivery Reviews*, Vol. 94, pp. 53-62, November 2015
- [7] Ş.Y.Güven, "Biyoyumluluk ve biyomalzemelerin seçimi", *Suleyman Demirel University Journal of Engineering Sciences and Design*, Vol. 2(3), pp. 303-311, 2014
- [8] N.S. Manam, W.S.W. Harun, D.N.A. Shri, S.A.C. Ghani, T. Kurniawan, M.H. Ismail, M.H.I. Ibrahim, "Study of corrosion in biocompatible metals for implants: A review", *Journal of Alloys and Compounds*, Vol.701, pp. 698-715, 2017
- [9] B. Alemón, M.Flores, W.Ramírez, J.C.Huegel, E.Broitman, "Tribocorrosion behavior and ions release of CoCrMo alloy coated with a TiAlVCN/CNx multilayer in simulated body fluid plus bovine serum albumin", *TribologyInternational*, Vol. 81, pp. 159-168, 2015
- [10] V. Martinez-Nogues, J.M.Nesbitt, R.J.K.Wood, R.B.Cook, "Nano-scale wear characterization of CoCrMo biomedical alloys", *Tribology International*, Vol. 93, pp. 563-572, January 2016
- [11] K. A. Ezzet, J.C. Hermida, C.W. Colwell, D.D. D'Lima, "Oxidized Zirconium Femoral Components Reduce Polyethylene Wear in a Knee Wear Simulator", *Clinical orthopaedics and related research*, Vol. 428, pp. 120-124, 2004
- [12] R. Tsukamoto, S.Chen, T. Asano, M. Ogino, H. Shoji, T. Nakamura, I.C. Clarke, "Improved wear performance with crosslinked UHMWPE and zirconia implants in knee simulation", *Acta Orthopaedica*, Vol. 77 (3), pp. 505-511, 2006
- [13] R. Hübner, A. Cozza, T.L. Marcondes, R.B. Souza, F.F. Fiori, "Wear and corrosion protection of 316-L femoral implants by deposition of thin films", *Surface and Coatings Technology*, Vol. 142-144, pp. 1078-1083, 2001
- [14] P. Bergschmidt, R. Bader, D. Ganzer, C. Hauzeur, C. Lohmann, W. Rütger, "Ceramic Femoral Components in Total Knee Arthroplasty - Two Year Follow-Up Results of an International Prospective Multi-Centre Study", *The Open Orthopaedics Journal*, Vol. 6, pp. 172-178, 2012
- [15] A. Mahapatro, "Bio-functional nano-coatings on metallic biomaterials", *Materials Science and Engineering C*, Vol. 55, pp. 227-251, 2015
- [16] D. G.Poitout, *Biomechanics and bBiomaterials in Orthopedics*, 2nd ed., London, Springer, 2016, pp. 15-16.
- [17] B. J. McEntire, B.S. Bal, M.N.Rahaman, J. Chevalier, G. Pezzotti, "Ceramics and ceramic coatings in orthopaedics", *Journal of the European Ceramic Society*, Vol. 35, pp. 4327-4369, December 2015
- [18] H.J. Griesser, *Thin Film Coatings for Biomaterials and Biomedical Applications*, Woodhead Publishing no:110, 2016

- [19] Q. Wang, L.Zhang, J. Dong, "Effects of Plasma Nitriding on Microstructure and Tribological Properties of CoCrMo Alloy Implant Materials", *Journal of Bionic Engineering*, Vol. 7, pp. 337-344
- [20] C. Balagna, M.G. Faga, S. Spriano, "Tantalum-based multilayer coating on cobalt alloys in total hip and knee replacement", *Materials Science and Engineering C*, Vol. 32, pp. 887-895, February 2012
- [21] Ł. Łapaj, J. Wendland, J. Markuszewski, A. Mroz, T. Wisniewski, "Retrieval analysis of titanium nitride (TiN) coated prosthetic femoral heads articulating with polyethylene", *Journal of the mechanical behaviour of biomedical materials*, Vol. 55, pp. 127-139, 2015
- [22] P. Yi, L. Peng, J. Huang, "Multilayered TiAlN films on Ti6Al4V alloy for biomedical applications by closed field unbalanced magnetron sputter ion plating process", *Materials Science and Engineering C*, Vol. 59, pp. 669-676, October 2016
- [23] S.H.Huang, S.F. Chen, Y.C. Kuo, C.J. Wang, J.W. Lee, Y.C. Chan, "Mechanical and tribological properties evaluation of cathodic arc deposited CrN/ZrN multilayer coatings", *Surface & Coatings Technology*, Vol. 206, pp. 1744-1752, October 2011
- [24] Y.Y. Chang, C.J. Wu, "Mechanical properties and impact resistance of multilayered TiAlN/ZrN coatings", *Surface & Coatings Technology*, Vol. 231, pp. 62-66, March 2012
- [25] M.Z.B. Abdullah, M.A. Ahmad, A.N. Abdullah, M.H. Othman, P. Hussain, A. Zainuddin, "Metal Release of Multilayer Coatings by Physical Vapour Deposition (PVD)", *Procedia Engineering*, Vol. 148, pp. 254-260, 2016
- [26] BrochurePDF, https://www.aesculapimplantsystems.com/assets/base/doc/DOC1021_Re vA-Advanced_Surface_CoatingTechnology_Brochure.pdf
- [27] A.P. Serro, C. Completo, R. Colaço, C.L. da Silva, J.M.S. Cabral, H. Araujo, "A comparative study of titanium nitrides, TiN, TiNbN and TiCN, as coatings for biomedical applications", *Surface&Coatings Technology*, Vol. 203, pp. 3701-3707, June 2009
- [28] P.E. Sinnet-Jones, J.A. Wharton, R.J.K. Wood, "Micro-abrasion-corrosion of a CoCrMo alloy in simulated artificial hip joint environments", *Wear*, Vol. 259, pp. 898-909, May 2005
- [29] B.R. Rawal, A. Yadav, V. Pare, "Life Estimation of knee joint prosthesis by combined effect of fatigue and wear", *Procedia Technology*, Vol. 23, pp. 60-67, 2016
- [30] L. Szparaga, P. Bartosik, A. Gilewicz, J. Ratajski, "Optimization OF multi-module CrN/CrCN coatings", *Arcieve of Metallurgy and Materials*, Vol. 60, pp. 1037-1043, 2015

Design and Analysis of Multilayer Beams which are Used for Motion

Hasan LAFCI

PD Functional Quality
Ford Otosan
Istanbul, Turkey
hlafei@ford.com.tr

Cihan DEMİR

Mechanical Engineering Department
Yıldız Technical University
Istanbul, Turkey
cdemir@yildiz.edu.tr

Abstract- Multilayer beams are widely used in robotic area due to some advantages. To create a special motion in fixed spaces, multilayers are essential for both designers and engineers. This motion can be used for moving a system or another purposes. Nowadays, the soft grip is a new term for robotic and mechanical engineering fields. It uses the same theory of multilayer beams to create a displacement. Unlike conventional multilayers beams, it uses soft material such as silicon, rubber or fabric because of some advantages. In this study, a pneumatic soft gripper have been designed and analysed with engineering softwares. Also a design of experiment (DOE) have been performed to see effect of each factor such as air pressure, material property, geometrical variables etc. Results and graphs of study have been shared at the final stage. According the results of DOE, designers can optimise their systems.

Keywords— Soft grip, Multilayer beam, DOE

I. INTRODUCTION

The development of new types of robots, and materials offers new opportunities for cross-functional researches. This paper focus on a new methodology based on multilayer beam theory. Due to some advantages of bending, science and engineering world have created a new definition, the soft robotic.

With the absence of wheels, electric motors and rigid skeletons, the motions of soft robots are usually inspired from the soft organisms [23]. For the easy fabrication, actuation and control of soft robots, only simple motions of natural species have been used in soft robots, such as caterpillar inspired locomotion [8,9], multi-gait quadruped [10,11], bristle-crawler [12], worm inspired locomotion [13–14], snake inspired locomotion [15], jellyfish inspired swimming [16], etc.

II. THEORY OF MULTILAYER MOTION

A. Relationship Between Multilayer Beams & Soft Robots

Soft robotics is a sub-field of robotics that deals with non rigid robots constructed with soft and deformable materials like silicone, plastic, fabric, rubber, or compliant mechanical parts like springs. Soft robots can actively interact with the environment and can undergo “large” deformations relying on inherent or structural compliance due to their softness and other morphological features.

The multilayer beam bending theory can be explained as follow. A simple cantilever beam can be bend by a concentrated nodal force, pressure or heat. The main question is that can we use this bending for different purposes. This question have been created the soft robotic area.

If we have a beam which has different layers and different stiffness sections, with internal forces like pressure it can be bended. So, this reaction gives a new name the beam. Shown as in figure 2.1 a multilayer beam can work as a robotic gripper to carry objects.

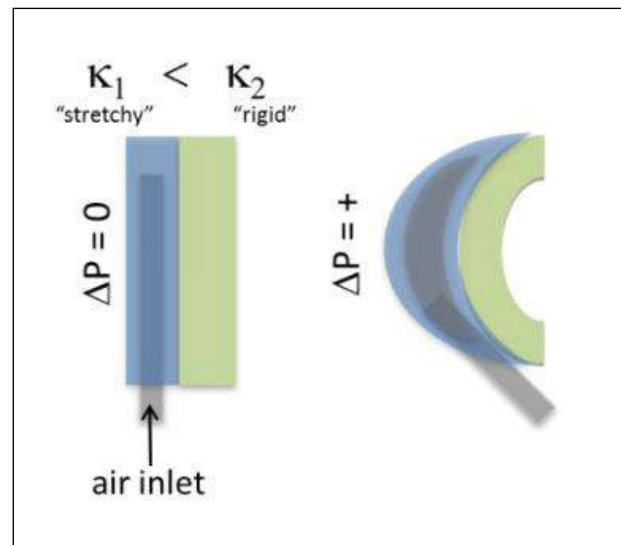


Fig. 2. 1 Two layer beam with one air chamber soft gripper [25]

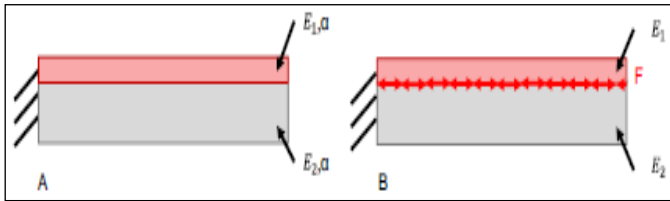


Fig.2.2. Embedded electrical wire can create adequate heat to bend the beam because of thermal expansion [22].

As in practical applications the bending deformation of the beam may be actuated by other methods (e.g. shape memory polymers [4], electroactive polymers [5], dielectric elastomers [6] and pneumatic pressurization [7]),

Shown as in figure 2.3 a muscular thin films also shares the bending theory like multilayer beams. A physical action will create a different reaction in layers not only because of their material properties but also their geometry. For example, if we heat up a multi-layer beam shown as figure 2.2 or like a MTF which is shown in figure 2.3, different axial displacement going to be occurred. Thus, the overall beam going to have a circular shape. Other sources can be used as action like air. In next sections, the effect of pressured air will be discussed widely.

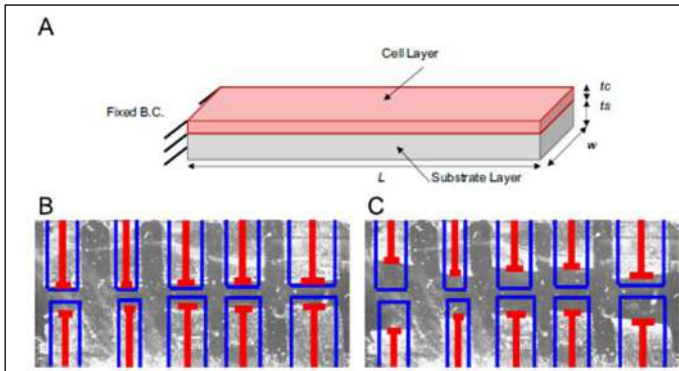


Fig. 2.3. (A) Schema of the MTF cantilevers. A biocompatible cantilever is supported by a fixed boundary condition (B.C.) and a thin cell layer is seeded on the surface. Contraction in the cell layer causes the substrate layer of the MTF to bend upwards. (B) Experimental image of 'Heart-on-a-chip' muscular thin films in their minimum contracted state (diastole). (C) Experimental image of 'Heart-on-a-chip' muscular thin films in their maximum contracted state (systole). In Band C solid blue outlines indicate the original shape of the PDMS film while capped red bars indicate the projection of the thin film during contraction. (For interpretation of the references to color in this figure caption, the reader is referred to the web version of this paper [22].)

B. Pneumatic Pressurization

To bend the system for using bending theory of multilayer beam, pressured air is one of the best method. An inlet line

which comes into between two layer is a force source. High pressure going to push walls from inside to outside to as a reaction. This creates the displacement. The example of pressured air effect can be seen in figure 2.1.

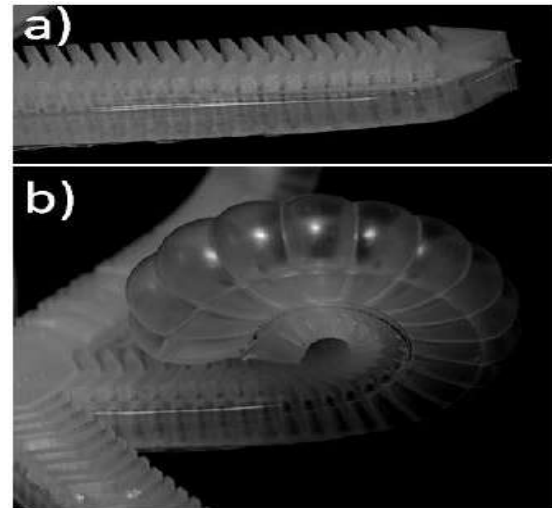


Fig. 2.4 a) A close-up photograph showing a textured surface which has been modified independently of the PneuNets. A set of ridges formed in Ecoflex provided better traction than a flat surface (this texture is more compliant than a solid surface because half of the volume has effectively been removed, and each ridge is pliable and deforms easily). b) A photograph demonstrating an actuated leg on the gripper; the individual chambers that make up the network are visible. The minimum radius of curvature achieved in this design is less than 5 mm [24].

According to design, soft parts can react the pressured air differently. In Figure 2.4 the design shows rotational reaction but there is also creative design which can extent axially. For example, Pneumatically-driven McKibben-type actuators are among the most highly developed soft actuators, and have existed for more than fifty years; they consist of a bladder covered in a shell of braided, strong, inextensible fibers [17].

Another design can provide a crawling motion to system. If the pressure of air changes alternately maximum to zero the beam can move like caterpillar shown as figure 2.5.

As you see, the

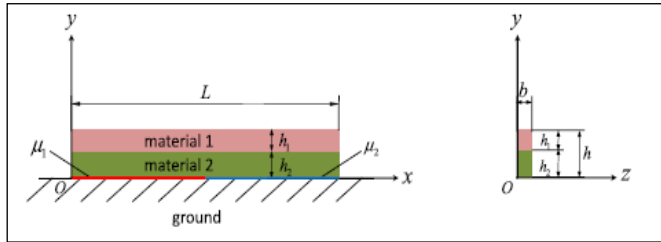


Fig. 2.5 Bilayer beam with different frictional coefficients at the two ends of the contact surface. The cross sections of each layer are rectangular with the same thickness and different heights of h_1 and h_2 [23].

III. SOFT GRIPPER DESIGN

In our modern industry, there are many different robotic parts or systems try to grip object without any damage but the hardness of surfaces of many system causes fundamental material problem. Conventional robotic systems use the rigid material to grip objects. This may create surface cracks or other type damages.

The use of compliant materials allows grippers to manipulate objects such as fruit[20] with varied geometry[21]. The egg example can be seen in figure 3.1. The gripper holds the it gently.

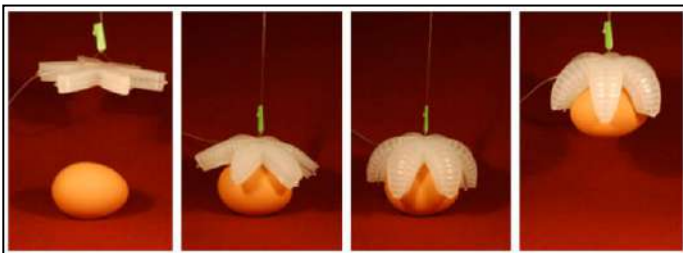


Fig. 3. 1 An egg translated by a soft gripper without any damage in four step.

Figure 3.2 illustrates the 3D model the soft gripper which analyzed in paper. In the egg example the soft gripper has 6 beam. It is clear to say that increasing of beam number going to decrease the contact stress which will be occurred between egg and soft material. In our study, there is only one beam has been designed and analyzed. The results can be optimize or assumed for multi-beam grippers.

CAD data of our soft gripper can be seen in figure 3.2 Cross section of solid model serves some technical trick. Every air chamber connect each other by small links. In next figure (fig. 3.3) these links are occurred.

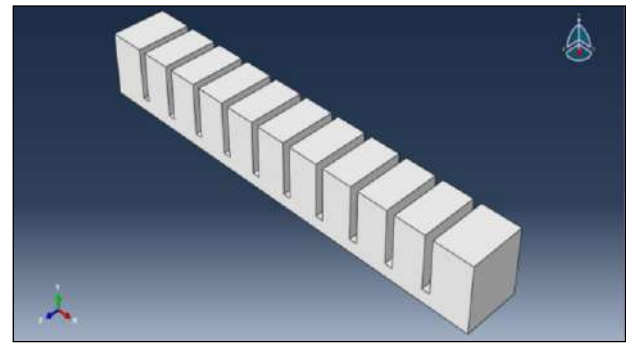


Fig. 3.2 Solid model of Gripper

There are many various factors which plays an important role on soft gripper design. In our study, we have focused on some variables like air pressure, material stiffness, geometrical variables.

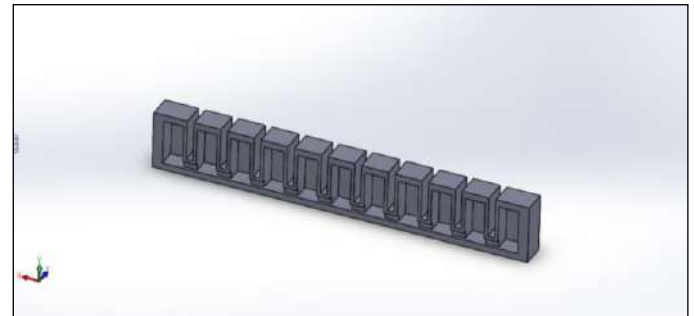


Fig 3. 3 Cross Section of Solid Model. Little tubes let air goes to another chamber. This causes the equal pressure distribution

A. Materials of Soft Robotic Parts

Soft robots are usually fabricated predominantly in elastomeric polymers without hard skeleton. Through appropriate design a simple elastomeric structure can provide a multifunction such as joint [1], bearing [2] and actuation[3], without the complexity of a multicomponent mechanical structure in hard machines.

Silicone rubber is an elastomer (rubber-like material) composed of silicone—itsself a polymer—containing silicon together with carbon, hydrogen, and oxygen. Silicone rubbers are widely used in industry, and there are multiple formulations. Silicone rubbers are often one- or two-part polymers, and may contain fillers to improve properties or reduce cost. Silicone rubber is generally non-reactive, stable, and resistant to extreme environments and temperatures from -55°C to $+300^{\circ}\text{C}$ while still maintaining its useful properties.

B. Geometry Of Gripper

The shape of gripper must designates the purpose of system. There are many different systems in soft robotic area.

According to demands , a system can show a axial or rotational displacement. For example , if someone wants to simulate muscular behaviors, the axial extension type actuators should be used as mentioned previous sections.

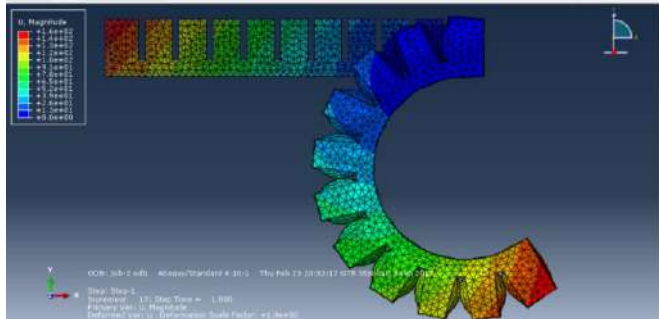


Fig. 3. 4 Three Dimension Analysis Result of Gripper. Touch condition areas can be seen clearly.

In our study , we try to reach and hold an object. Thus, the gripper must show axial and rotational movement at the same time. Thanks to its unique shape this aim can be achieved by our design.

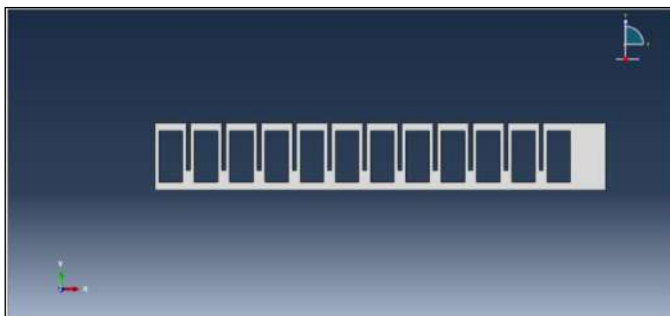


Fig. 3. 5 Two dimension model of gripper

The system work as follows, the air chambers, around top of layer , filled by a pressured air. This force initially extents the gripper axially and rotationally. But the majority of the first stage of movement is extending axially. In first stage, there is only minor rotational displacement . At the same time the walls of chambers close each other as extent from inside to outside due to the pressure. When a chamber wall touch to another, because of frictionless contacts walls slip on each other. This creates a huge rotational torque which can be used to wrap objects.

As you can see ,the design of gripper is the main factor of a gripping strategy which has an important role on behavior of system.

C. Geometry Of Target Object

The target object means that the object which is held by soft gripper in our study. Target objects may have various shapes such as cylindrical, cubic , prismatic etc. One of the advantages of the soft gripper is that they can handle very big range on shapes. Even a cactus can be held by well designed a soft gripper without any damage.

Our analysis have been performed to grip a cylindrical target object with different radius and different center of gravity centers.

IV. ABAQUS CAE

A. Stages of CAE Analysis

Like many other commercial computer added engineering soft wares, Abaqus also needs to be given some specific inputs from user to calculate the finite element method demands such as stress , displacements etc.

Before we start the calculation, we need to set up a few steps as follows.

1) *Create or Import Parts* : There is a embedded CAD module in Abaqus which can be used create 2D,3D or Wire elements. Or import menu can be used import a part which created by another CAD softwares.To decrease work load and use time efficiently, we use the simplified 2D part.

2) *Define Materials* : Two material properties have been created .One of these is hyperelastic material which makes up the gripper. The Neo Hookean method has been chosen for hyperelastic material.Another one is elastic material for target object.

3) *Create Sections* : Both gripper and object section have been created as solid homogenous.

4) *Create Steps* : General ,Static step has been created.

5) *Create Assembly* : Two parts have been imported and arranged in assembly space.

6) *Define Intersections* : There are two intersection in model. One is between gripper and object. Another one is self-intersection which is necessary to see touch condition of walls of air chambers.

7) *Define Boundary Conditions* : One side of gripper has been fixed. For this, encastre boundary condition has been applied.To simulate air the pressure has been applied inside of chamber walls.

8) *Meshing Parts* : To get maximum resolution minimum mesh size has been created

9) *Create A Job* : Jobs allow that a model can be used for different analysis such as static, thermal or explicit. Thus , in abaqus every model requires a job which will has the results according the analysis type

10) *Results* : After completed job running the program creates a output file which can be monitored in visualization menu.

V. DESIGN OF EXPERIMENT ANALYSIS

A. Definiton Of DOE

DOE (design of experiments) helps researchers to investigate the effects of input variables (factors) on an output variable (response) at the same time. These experiments consist of a series of runs, or tests, in which purposeful changes are made to the input variables. Data are collected at each run. You use DOE to identify the process conditions and product components that affect quality, and then determine the factor settings that optimize results.

B. Create Factors

Reaction forces are one of responses of the system. To investigate which factors affect reaction forces, we should investigate main variables. According to a study content, number of factors can be changed. As factors increase, the total time and number of experiments going to rise.

In our study four different factors have been chosen. These are System Pressure (P) , Material Stiffness(K) , Radius of Target Object (R) and Position of Target Object (PTO).

Another criterion of doe method is factor level. It means that variance of factor internally. For example, if the pressure has two different options such as low or high, it means that this factor has two levels. Each factor of study has two levels.

For two levels factor , count of total experiments calculated shown as follows in equation 1. The n means number of factor and two indicates level of factors. In our study, there are four different factors. Thus, we have to run sixteen different cae analysis according to DOE method.

$$\text{Total Experiment Number} = 2^n \quad (1)$$

VI. RESULTS

A. CAE Results

CAE analysis results are shown as below:

Different results have been displayed in various monitoring type . Next graphs going to mention some important output of the analysis and system.

Major output of the system is reaction forces which will be occurred between the target object and soft gripper.

The first image (Figure 6.1) shows the beginning of the analysis. As you can see , there is no any touch condition between the gripper and target object.

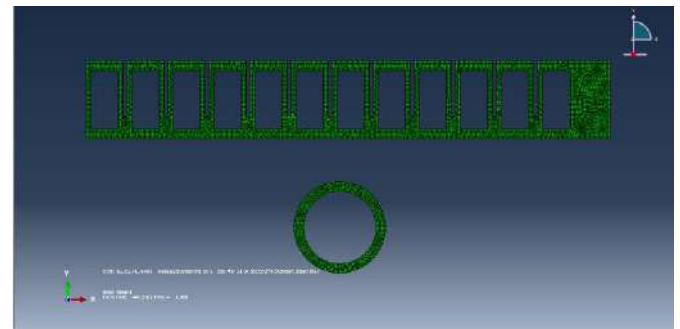


Fig. 6. 1 Meshed Gripper and Target Object

Second image (Figure 6.2) illustrates the stress level which occurred at the end of holding process. High stress areas have occurred mostly at chamber walls. Because of thickness this is not unexpected situation.

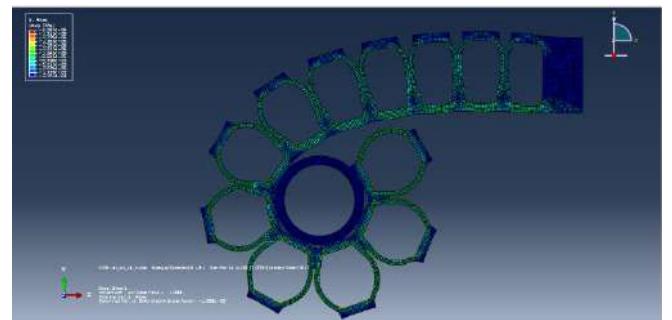


Fig. 6. 2 Stress Areas

The biggest reaction forces have been observed at fixing area of soft gripper. Shown as Figure 6.3 , the reaction forces change at the Y direction.

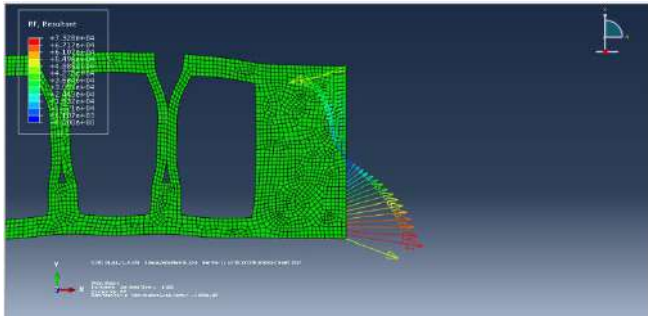


Fig. 6. 3 Changing of Reaction Force Vectors. Maximum reaction force occurred at the bottom

Displacement plot (Figure 6.4) show the total translation magnitude. The gripping process have been completed at this step. More pressure will create self-interaction problems at gripper. So , maximum pressure have been chosen properly and limited.

The aim is achieved. A target object can be wrap by soft gripper which uses pressured air.

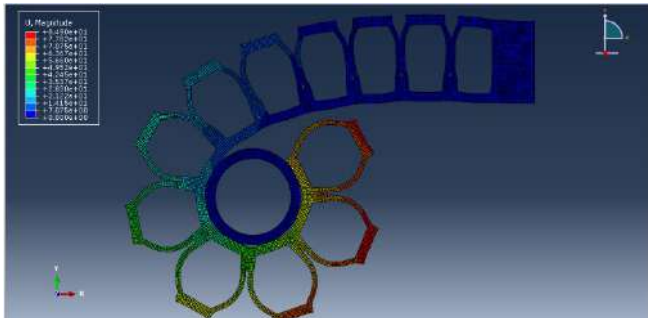


Fig.6. 4 Displacement plot

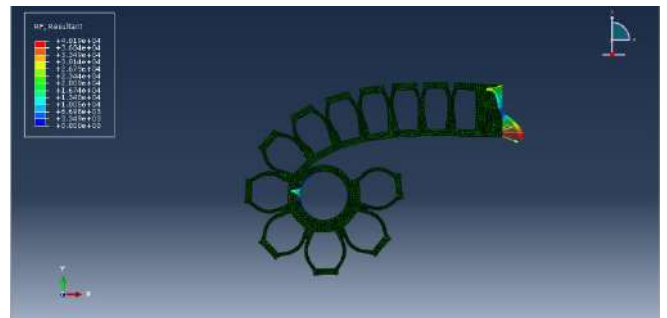
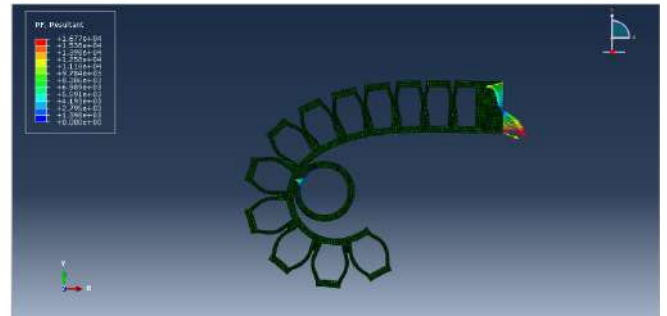
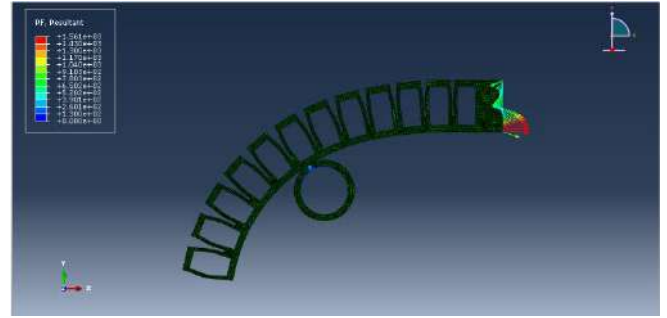
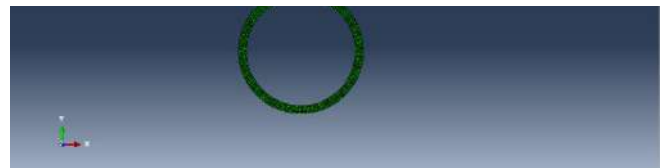
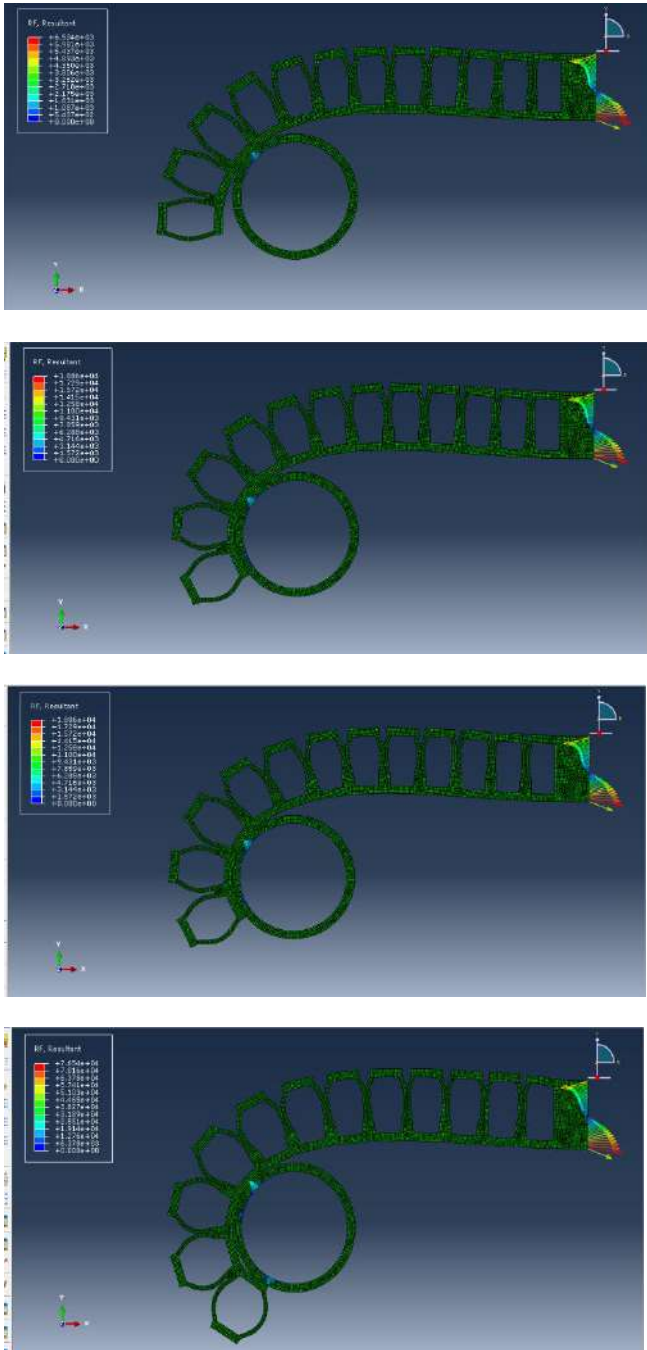


Fig 6.5 : Two different scenarios have been compared to see effect of factors. First scenario, small target radius and big x coordinate of target object gravity center. Second scenario, big target radius and small x coordinate of target object gravity center.





B. DOE Results

Result of CAE analysis have been illustrate in pareto chart , cube plot and main effect plot for reaction forces as shown below.

According to DOE results , it is clear to say that the system pressure has an important role on reaction forces. Second factor is radius of target object. The reaction forces go up while radius is increasing. But the material stiffness of gripper and position of target object show negative behavior. When material stiffness increased , reaction forces decreased.

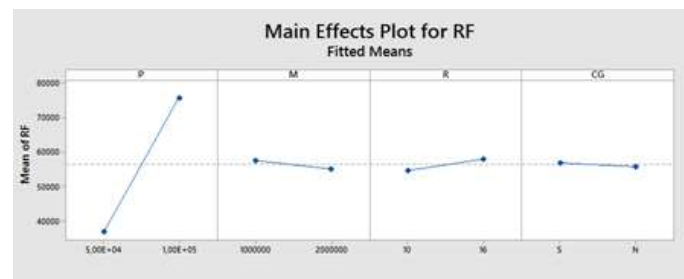
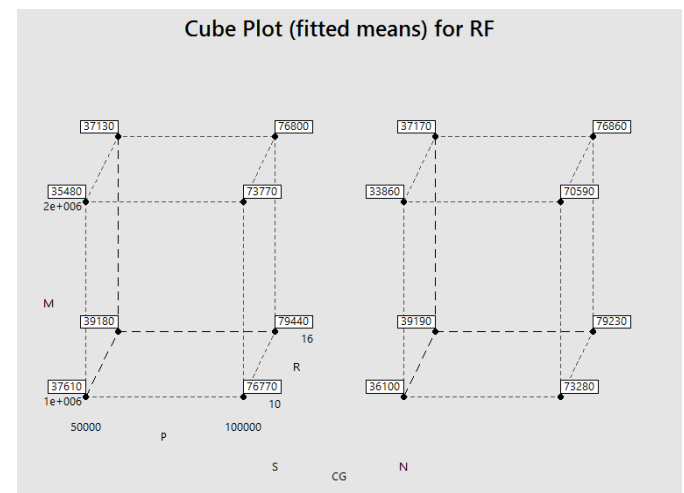
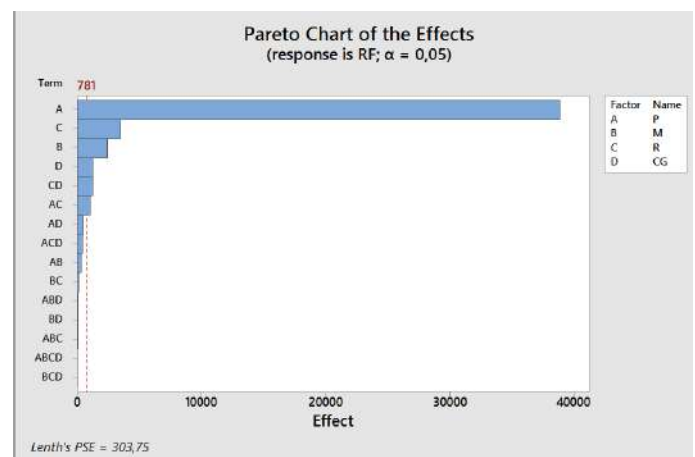


Fig 6. 6 : Result of DOE analysis

VII. CONCLUSION

As a conclusion, the study has reflected the fundamental design rules of a soft grip design. The design basically use the multilayer beam technic but with some modifications. Bended beam has wrapped and held an object as expected and shown as in figures.

CAE and DOE analysis clearly show that there are different factors which play an important role on designing a soft gripper.

For reaction forces, the most important factor is the air pressure according to the results.

As mentioned in the first stages of study, to get maximum mechanical efficiency, factors of soft gripper should be chosen properly. So, the designers and researchers can use this study and its results as a reference.

REFERENCES

- [1] K. Ramesh, R.W. Tock, R.S. Narayan, C.V.G. Vallabhan "Property evaluation of silicone elastomers used in tension – adhesion joints," *J.Mater. Sci. Lett.* 14(1995) 964 – 967 . <http://dx.doi.org/10.1007/Bf02427478>.
- [2] W. Nierzwicki, Z. Majewska, Swelling properties of urethane elastomers and their bearing on microphase separation, *J. Appl. Polym. Sci.* 24 (1979) 1089 – 1099. <http://dx.doi.org/10.1002/app.1979.070240421>.
- [3] B.Li, H.L. Chen, J.H. Qiang, S.L. Hu, Z.C. Zhu, Y.Q. Wang, Effect of mechanical pre-stretch on the stabilization of dielectric elastomer actuation, *J.Phys. D Appl. Phys.* 44(2011) 773 – 780 . <http://dx.doi.org/10.1088/0022-3727/44/15/155301>.
- [4] H. Yuk, D. Kim, H. Lee, S. Jo, J.H. Shin, Shape memory alloy-based small crawling robots inspired by *C. elegans*, *Bioninspir. Biomim.* 6(2011) 1001 – 1004. <http://dx.doi.org/10.1088/1748-3182/6/4/046002>.
- [5] X.D. Wang, G.L. Huang, Wave propagation in electromechanical structures : Induced by surface-bonded piezoelectric actuators, *J. Intell. Mater. Syst. Struct.* 12 (2001) 105 – 115. <http://dx.doi.org/10.1106/Mhd5-062-24eh-8b9t>.
- [6] B. Paul, P. Qibing, Advances in dielectric elastomers for actuators and artificial muscles, *Macromol. Rapid Commun.* 31 (2010) 10 – 36. <https://dx.doi.org/10.1002/marc.200900425>.
- [7] R.V. Martinez, C.R. Fish, X. Chen, G.M. Whitesides, Elastomeric origami: Programmable paper-elastomer composites as pneumatic actuators, *Adv. Funct. Mater.* 22 (2012) 1376 – 1384 . <http://dx.doi.org/10.1002/adfm.201102978>.
- [8] H.T. Lin, G.G. Leisk, B. Trimmer, GoQBot: a caterpillar-inspired soft-bodied rolling robot, *Bioinspir. Biomim.* 6 (2011) 026007. <https://dx.doi.org/10.1088/1748-3182/6/2/026007>.
- [9] B.A. Trimmer, A.E. Takesian, B.M. Sweet, C.B. Rogers, D.C. Hake, D.J. Rogers, Caterpillar locomotion: a new model for soft-bodied climbing and burrowing robots, in: 7th International Symposium on Technology and the Mine Problem: Mine Warfare Association Monterey, CA, 2006, pp. 1–10.
- [10] R.F. Shepherd, F. Ilievski, W. Choi, S.A. Morin, A.A. Stokes, A.D. Mazzeo, et al., Multigait soft robot, *Proc. Natl. Acad. Sci. USA* 108 (2011) 20400–20403. <http://dx.doi.org/10.1073/pnas.1116564108>.
- [11] S.A. Morin, R.F. Shepherd, S.W. Kwok, A.A. Stokes, A. Nemiroski, G.M. Whitesides, Camouflage and display for soft machines, *Science* 337 (2012) 828–832. <http://dx.doi.org/10.1126/science.1222149>.
- [12] G. Noselli, A. Desimone, A robotic crawler exploiting directional frictional interactions: experiments, numerics, and derivation of a reduced model, *Proc. R. Soc. Lond. Ser. A Math. Phys. Eng. Sci.* (2014) 470. <http://dx.doi.org/10.1098/rspa.2014.0333>.
- [13] A. Menciassi, S. Gorini, G. Pemorio, P. Dario, A SMA actuated artificial earthworm, in: *IEEE Int Conf Robot.*, Vol. 4, 2004, pp. 3282–3287. <http://dx.doi.org/10.1109/Robot.2004.1308760>.
- [14] S. Seok, C.D. Onal, R. Wood, D. Rus, S. Kim, Peristaltic locomotion with antagonistic actuators in soft robotics, in: 2010 IEEE International Conference on Robotics and Automation, ICRA, 2010, pp. 1228–1233.
- [15] K.J. Dowling, Limbless locomotion: learning to crawl with a snake robot: NASA, 1996.
- [16] S. Nir, I. Ruchavski, S. Shraga, T. Shteinberg, B. Ben Moshe, A jellyfish-like robot for mimicking jet propulsion, in: 2012 IEEE 27th Convention of Electrical & Electronics Engineers in Israel, IEEEI, 2012, pp. 1–5. <http://dx.doi.org/10.1109/IEEEI.2012.6377056>.
- [17] H. F. Schulte, in *The Application Of External Power In Prosthetics And Orthotics*, National Academy Of Sciences, National Research Council, Washington, DC, 1961.
- [18] K. Suzumori, A. Koga, H. Riyoko, in *Proc. 1994 IEEE Int. Conf. MEMS*, 1994, pp. 136–141.
- [19] K. Suzumori, S. Iikura, H. Tanaka, *IEEE Contr. Syst. Mag.* 1992, 12, 21–27.
- [20] J. Tedford, *Robotica* 1990, 8, 279–283.
- [21] A. S. Brown, *Mech. Eng.* 2009, 131, 22–22.
- [22] Victorai A. Webster, Santiago G. Nieto, Anna Grosberg, Ozan Akkus, Hillel J. Chiel, Roger D. Quinn, Simulating muscular thin films using thermal contraction capabilities in finite element analysis tools, *Journal of the Mechanical Behavior of Biomedical Materials*, Vol 63, Pages 326 – 336. <http://dx.doi.org/10.1016/j.jmbbm.2016.06.027>.
- [23] Z. Yang, L. Zhu, B. Li, S. Sun, Y. Chen, Y. Yan, Y. Liu, X. Chen, Mechanical design and analysis of a crawling locomotion enabled by a laminated beam, *Sciencedirect*, Vol. 8, 2016, Pages 88 – 95 . <http://dx.doi.org/10.1016/j.eml.2016.03.014>.
- [24] Ilievski, Filip, Aaron D. Mazzeo, Robert F. Shepherd, Xin Chen, and George M. Whitesides. 2011. "Soft Robotics for Chemists." *Angewandte Chemie International Edition* 50, no. 8: 1890–1895. <http://nrs.harvard.edu/urn-3:HUL.InstRepos:12967812>.
- [25] <http://softroboticstoolkit.com/book/pneunets-bending-actuator>

Performance Comparison of Circular and Square Cross-Sectioned Helicoidal Heat Exchangers Using Experimental and CFD Analyses

İbrahim Halil YILMAZ

Department of Automotive Engineering
Adana Science and Technology University
Adana, Turkey
iyilmaz@adanabtu.edu.tr

Mustafa KILIÇ

Department of Mechanical Engineering
Adana Science and Technology University
Adana, Turkey
mkilic@adanabtu.edu.tr

Taha Tuna GÖKSU

Department of Mechanical Engineering
University of Muş Alparslan
Muş, Turkey
tt.goksu@alparslan.edu.tr, taha_022@hotmail.com

Mehmet Sait SÖYLEMEZ

Department of Mechanical Engineering
Gaziantep University
Gaziantep, Turkey
sait@gantep.edu.tr

Abstract— The comparison of heat transfer performances of circular and square cross-sectioned helicoidal heat exchangers (HCHEs) for a boiling operation is the subject of this study. An experimental analysis was firstly carried out for the estimation of the heat transfer properties of the circular HCHE. The circular HCHE was modeled numerically using CFD (Computational Fluid Dynamics) tool and its results were validated with the experiments. The testing fluid was selected as thermal oil and the effect of the actual fluid properties instead of constant property approach was established. The flow was considered fully developed turbulent with low Reynolds number based on the fluid inlet temperature ranging from 150–110°C. For the CFD analysis, Ansys Fluent was used with the $k-\omega$ turbulence model closure to evaluate the fluid domain. The results indicated that the square cross-sectioned heat exchanger enhances the heat transfer up to 1.6% relative to the circular one under the given conditions.

Keywords— circular helical coil; square helical coil; heat exchanger; boiling; CFD

I. INTRODUCTION

Curved or helicoidal pipes are widely used in various engineering applications such as power generation, nuclear industry, process plants, heat recovery systems, refrigeration, food industry, etc. [1]. In food industry, the helicoidal pipes are used as a part of heat exchanger which provides to heat foods. Cooking is a type of process applied in these systems which involve boiling realizing at the solid-liquid interface. The energy demand for this process is generally provided by electrical or thermal power. For large applications, thermal energy is used in usual. The thermal energy transfer to the liquid is realized by a heat exchanger which facilitates the exchange of heat between the two fluids separated by a solid wall while keeping them from

mixing with each other. Heat is first transferred from the hot fluid to the wall by convection, through the wall by conduction, and from the wall to the cold fluid again by convection. This is the basic heat transfer mechanism of boiling process to be used for cooking facility.

Heat transfer and flow through a curved tube is comprehensively reviewed by [2–4]. The characteristics of flow, pressure drop and heat transfer have been investigated by many researchers. In most of these studies, constant wall temperature or constant heat flux boundary conditions were applied to evaluate heat transfer coefficient. The constant wall temperature is more suitable for phase changing process in heat exchangers. On the other hand, the constant wall heat flux case is used for heat transfer studies of nuclear fuel elements and electrically heated tubes.

Heat transfer in helical coils has been experimentally investigated by [5] both for laminar and turbulent flow regimes for flow of water under constant wall flux. The curvature ratios of the coils were 0.0096 and 0.0588. The range of Reynolds number (Re) studied was 6000–65,500. Rogers and Mayhew [6] studied heat transfer to fluid flowing inside a helical pipe heated by steam for a range of Re from 10,000 to 100,000. Curvature ratios of the coils used in studies were 0.0926, 0.075 and 0.05. Mori and Nakayama [7,8] investigated forced convective heat transfer in turbulent regime for constant wall temperature and wall heat flux boundary conditions. It was considered two configurations of helical coils with curvature ratio of 0.0535 and 0.025. The effect of torsion on the flow in a helical tube of circular cross-section was experimentally investigated by Yamamoto et al. [9] for a range of Re about 500 to 20,000. Jayakumar et al. [1] analyzed helically coiled heat exchanger considering conjugate heat transfer (fluid-to-fluid) and

Financially supported by the Scientific Research Project Division of GAUN under the contract of MF.11.13.

temperature dependent properties of heat transport media. An experimental study was performed for the estimation of the heat transfer characteristics and compared with the CFD (Computational Fluid Dynamics) results. Jayakumar et al. [10] investigated also the variation of local Nusselt number (Nu) along the length and circumference at the wall of a helical pipe. The effects of pitch circle diameter, tube pitch and pipe diameter on heat transfer were studied. Yilmaz et al. [11] made a thermal model for wheat cooking pot using analytic method and compared the results with the experimental data. Yilmaz and Göksu [12] studied also the numerical heat transfer behavior of the helicoidal heat exchanger (HCHE) used in the cooking pot.

The numerical heat transfer characteristics of circular and square cross-sectioned HCHEs for cooking operation were investigated in this study. An experimental methodology was carried out for the validation of the heat transfer characteristics of the circular HCHE. Obtained satisfactory results were proceeded for comparing the heat transfer performances of both heat exchangers using CFD tool.

II. METHODS

A. Experimental Analysis

An experimental setup was installed for comparing both the results obtained from the numerical and experimental analyses. The setup basically consisted of a temperature controlled electric heater, a cooking pot containing a circular cross-sectioned HCHE (see Table I for the properties), a thermal expansion tank, gear pump and measuring instruments. The heat transfer fluid (HTF) used in the loop was selected as Renolin therm 320. The HTF was circulated by a frequency-controlled gear pump which was used to adjust the flow rate. The effective power capacity of the electric heater was 6000 W which was controlled by a PID controller.

TABLE I. SPECIFICATIONS OF THE CIRCULAR HCHE

Pipe material	304L SS
Inner pipe diameter	0.0157 m
Outer pipe diameter	0.0213 m
Coil pitch	0.085 m
Coil radius	0.175 m
Outer surface area	0.288 m ²

The temperature measurements in the experimental setup were performed by the resistance temperature detectors (Pt100, Class A) connected with two leads. The flowmeter was selected as coriolis type to measure the mass flow rate of the HTF circulating within the loop. During the experimental tests, data on temperature and flow were gathered by the DAQ (Data Acquisition) devices. For this task, highly-accurate voltage and temperature processing DAQ devices were selected and connected to the computer and managed by an interface software program (TracerDAQ Pro) to process data logging. The temperature dependent error of the temperature detectors are designated by the relation $\pm(0.15 + 0.002T)^{\circ}\text{C}$ and calibrated according to the standard of IEC751:1983. The

flowmeter has an accuracy of $\pm 0.1\%$ with a repeatability of less than 0.05%. The temperature processing DAQ contributes additional error except the error of the sensor itself with a typical error of $\pm 0.12^{\circ}\text{C}$ for sensor temperature (between 0°C and 200°C).

B. Numerical Analysis

Figure 1 illustrates the schematic of the circular cross-sectioned HCHE used for the cooking operation, and the square cross-sectioned HCHE for the performance comparison. For performance comparison, only the cross-section of the square HCHE is changed as to be peripherally equal to that of the circular one while keeping all remaining parameters identical.



a) Circular



b) Square

Fig. 1. Geometry of the circular cross-sectioned HCHE

For the numerical simulations, Ansys Fluent v17 software package was used to solve the governing equations (the conservation equations for mass, momentum, and energy) together with the boundary conditions applied. It is considered the flow inside the coil to be steady-state and fully developed turbulent. These considerations are reasonable since the experimental data were taken under steady conditions and the flow is fully developed due to negligible entrance effect compared to the coil length. The boundary conditions used include

- No-slip and no-penetration conditions exist on the coil wall.
- Constant temperature and velocity inlet conditions are used in the tube's inlet.

- The turbulence intensity is assumed to be around 5% at the inlet.

The computational domain was discretized using tetrahedron elements with structured elements in the wall normal directions. The coupling of pressure and velocity was made with the SIMPLE algorithm. Second-order upwind schemes were employed for integrating the governing equations together with the boundary conditions over the computational domain. The y^+ value of about 1 was ensured for all simulations to obtain the high resolution of gradients in the near wall regions. The solution convergence was satisfied when the scaled residuals of continuity, momentum, turbulence kinetic energy, turbulent dissipation rate and energy ceased after about 800 successive iterations. The values of the scaled residuals were in the order of less than 10^{-4} for the continuity equation, less than 10^{-5} for velocity, turbulent kinetic energy and turbulent dissipation rate and less than 10^{-7} for energy. The thermophysical properties of the HTF as a function of temperature were derived from the manufacturer's supplied data as below.

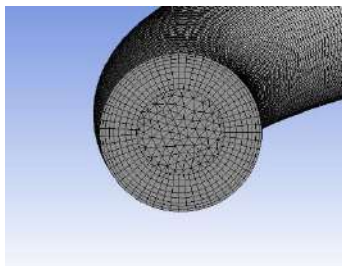
$$\rho = 1058.108 - 0.651T \quad (1)$$

$$c_p = 692.370 + 4.289T \quad (2)$$

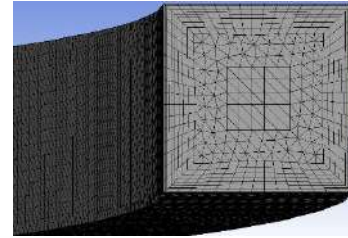
$$k = 0.154 - 7.176E-5T \quad (3)$$

$$\mu = 0.334 - 2.153E-3T + 4.667E-6T^2 - 3.392E-9T^3 \quad (4)$$

Here ρ , c_p and k are valid at the temperature range $273 \text{ K} \leq T < 373 \text{ K}$, μ is valid for $373 \text{ K} \leq T < 473 \text{ K}$. Mesh dependency studies were applied for each run considered in the study. The solution was considered grid independent when the maximum changes in the outlet temperature were less than 1% as the mesh element size was changed. The number of mesh elements with 3685776, 7100622 and 11217391 was applied for the circular cross-sectioned HCHE, respectively. Then 7100622 mesh elements were used in the analyses after mesh refinement. For the square cross-sectioned HCHE, 1336620, 6216296 and 8571340 mesh numbers were applied and 6216296 mesh elements were used after refinement. The mesh structures of the computational domains are illustrated in Figure 2.



a) Circular



b) Square
Fig. 2. Sample mesh for the geometries

III. RESULTS AND DISCUSSION

Table II shows the dataset of boundary conditions resulting from the experimental study of the circular cross-sectioned HCHE and the predicted parameters from the analytical approach given in [12]. These boundary conditions also applied to the square HCHE to analyze the performance variation.

TABLE II. Boundary Conditions

Data set	Flowrate kg/s	Inlet temp. °C	Boiling temp. °C	Surface temp. °C	Convection coeff. W/m ² °C
1	0.0847	150.01	100.02	105.40	2371
2	0.0917	145.03	100.15	105.40	2265
3	0.1000	140.04	100.20	105.31	2152
4	0.1111	135.00	100.03	104.67	1765
5	0.1379	130.06	100.02	104.95	1996
6	0.1380	122.61	100.06	104.47	1597
7	0.1393	115.35	99.90	103.72	1188
8	0.1440	110.00	100.00	103.15	813

Figure 3 shows the results obtained from the experimental and numerical analyses. As it is seen, the results are pretty well suited with each other for the estimation of the outlet temperature. The maximum experimental error is expected to be 0.53°C in temperature measurements due to the accuracy of the temperature detectors. The maximum deviation of the numerical approach from the experimental results is obtained 1.12%.

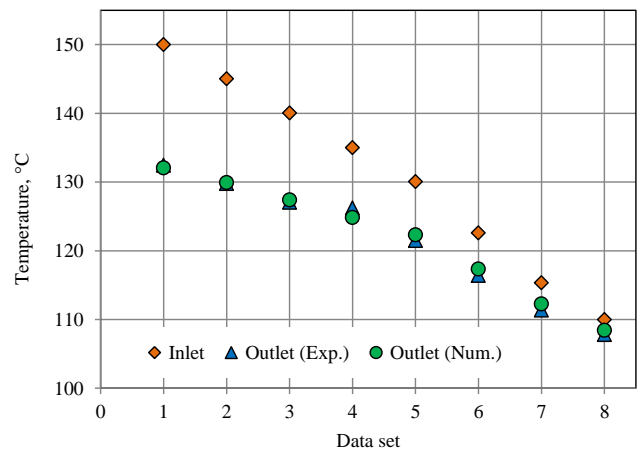


Fig. 3. Comparison of experimental and numerical results

Figure 4 shows the numerical results of both HCHEs obtained under the same conditions. It is clearly seen that the square HCHE enhances the heat transfer at relatively higher inlet temperatures. As the inlet temperature decreases, the outlet temperatures of both HCHEs come close each other due to reduced differential temperature but the square HCHE still shows better performance. Enhancing the heat transfer provides to minimize the size of the HCHE to accomplish the same task with the circular HCHE. This is important for the cooking pot having limited size but needs increased capacity.

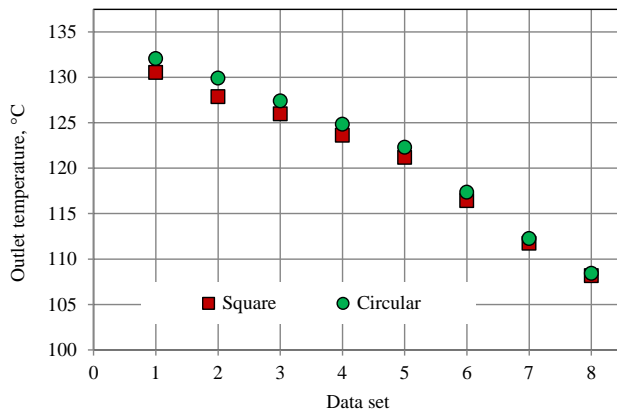


Fig. 4. Effects of cross-section on heat transfer enhancement

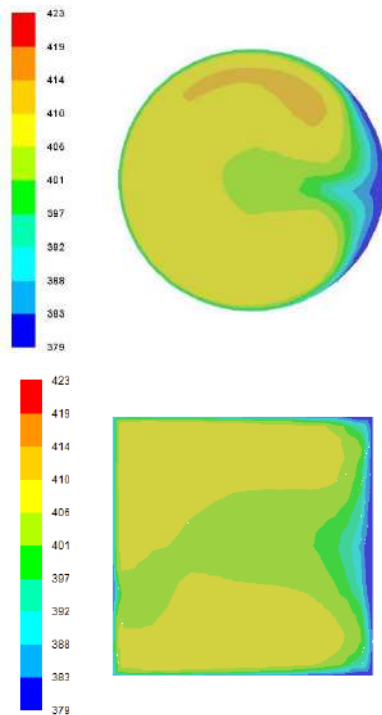


Fig. 5 Temperature contours at the outlet (as Kelvin)

Temperature distributions at the outlet of the HCHEs are shown in Figure 5 for the data set 1. The flow pattern is quite different relative to a straight pipe since the most prominent characteristic of flow in helicoidal pipes is the secondary flow induced by centrifugal force which causes the fluid particles

inner side of the coil to move faster than the outer and thus provides benefit to enhance the heat transfer rate [12].

IV. CONCLUSION

In this study, two different cross-sectioned HCHEs exposed to boiling process were analyzed numerically. Firstly, the circular cross-sectioned HCHE was modeled in Ansys Fluent and the results were validated with the experimental results. The experimental setup was established to measure the primary parameters of the flow in fluid side. The CFD predictions match pretty well with the experimental results with a deviation lower than 1.12% thus this harmony will provide to make various parametric under different conditions. Subsequently, the square cross-sectioned HCHE was modeled to compare its thermal performance to the circular one. The results indicated that the square cross-sectioned heat exchanger enhances the heat transfer up to 1.6% relative to the circular one under the given conditions.

REFERENCES

- [1] Jayakumar, J. S., Mahajani, S. M., Mandal, J. C., Vijayan, P. K., and Bhoi, R. (2008). Experimental and CFD estimation of heat transfer in helically coiled heat exchangers. *Chemical Engineering Research and Design*, 86, 221-232.
- [2] Berger, S. A., Talbot, L., and Yao, L. S. (1983). Flow in curved pipes. *Annual Review of Fluid Mechanics*, 15, 461-512.
- [3] Shah, R. K., and Joshi, S. D. (1987). Convective heat transfer in curved ducts. In S. Kakac, R. K. Shah, and W. Hung (Eds.), *Handbook of single-phase convective heat transfer*. New York: Wiley Interscience.
- [4] Naphon, P., and Wongwises, S. (2006). A review of flow and heat transfer characteristics in curved tubes. *Renewable and Sustainable Energy Reviews*, 10, 463-490.
- [5] Seban, R. A., and McLaughlin, E. F. (1963). Heat transfer in tube coils with laminar and turbulent flow. *International Journal of Heat and Mass Transfer*, 6, 387-495.
- [6] Rogers, G. F. C., and Mayhew, Y. R. (1964). Heat transfer and pressure loss in helically coiled tube with turbulent flow. *International Journal of Heat and Mass Transfer*, 7, 1207-1216.
- [7] Mori, Y., and Nakayama, W. (1967). Study of forced convective heat transfer in curved pipes. *International Journal of Heat and Mass Transfer*, 10, 37-59.
- [8] Mori, Y., and Nakayama, W. (1967). Study of forced convective heat transfer in curved pipes. *International Journal of Heat and Mass Transfer*, 10, 681-695.
- [9] Yamamoto, K., Akita, T., Ikeuchi, H., Kita, Y. (1995). Experimental study of the flow in a helical circular tube. *Fluid Dynamics Research*, 16, 237-249.
- [10] Jayakumar, J. S., Mahajani, S. M., Mandal, J. C., Iyer, K. N. and Vijayan, P. K. (2010). CFD analysis of single-phase flows inside helically coiled tubes. *Computers and Chemical Engineering*, 34, 430-446.
- [11] Yılmaz, İ. H., Hayta, H., Söylemez, M. S., Yumrutaş, R., "Bulgur Potasının termal analizi," ULIBTK'13: 19. Ulusal Isı Bilimi ve Tekniği Kongresi, pp. 746-749, September 2013.
- [12] Yılmaz, İ. H., and Göksu, T. T., "Experimental and CFD analyses of a helicoidal heat exchanger," *International Energy and Engineering Congress*, pp. 638-646, October 2016

Numerical Study Of Square Fin and Thermo Electrics Placed in The Channel

Ali TAŞKIRAN

Department of Mechanical Engineering
Firat University
Elazig, Turkey
ataskiran@firat.edu.tr

İhsan DAĞTEKİN

Department of Mechanical Engineering
Firat University
Elazig, Turkey
idadagtekin@firat.edu.tr

Abstract— In this study, flow and heat transfer were investigated by inserting a square fin into a channel at 5, 10, 15 m/s and 573 K air temperature. A thermoelectric module was placed on the bottom surface of the fin structures. The other surface of the thermoelectric is set to be at 22 °C. The results include parameters such as temperature, Nusselt, Reynolds, current, heat flow for channel flow and thermoelectric using flow and thermal - electric parameters. Numerical results show that the heat transfer coefficient of the square wing is 625 W/m²K and the temperature varies between 476 and 526 K. The results of the temperature, heat flow, current and heat of the thermoelectric placed under the wing structures were found to be 249.09 °C, 9.1852 W/mm², 103.15 mA and 155.58 W, respectively.

Keywords: Channel flow, fin, thermoelectric.

I. INTRODUCTION

In engineering applications, channel flow is frequently encountered. It is used in many places where there are fluid movements such as cooling of electronic devices, heat exchangers, heating and cooling of buildings. Improvement of heat transfer in the duct flow in engineering is a frequently encountered problem that needs to be continuously improved. Especially cooling of electronic devices and turbine blades is important for their performance. One of the methods intensively used to increase heat transfer in today's technology is extended heat transfer surfaces. Finned surfaces, by increasing the surface area and increase the turbulence of the flow of convective heat and mass transfer. The application area of finned surfaces is very diverse. Thermoelectric generators are also used in applications such as heating or cooling various small volumes. Thermoelectric is a fast and quiet machine, one surface is hot and the other surface is cold.

In general, a thermoelectric generator (TEG) consists of a number of semiconductor pairs that are connected electrically in a series and thermally in parallel, and each pair includes a p-type and an n-type element. Although in theory, a single piece of semiconductor material could work, a series connection is used to meet the high voltage potential

requirements. P-type and n-type elements are alternated to assure that the carriers transport in the same direction. [1]

When the literature is surveyed Tsai et al. [2], analyzes were performed on 4 different Reynolds numbers (10000, 20000, 30000 and 40000), 3 different fin sizes (30, 45, 75 mm) and 7 different angle values (45, 60, 75, 90, 105, 120, 135). For the short wing height (30 mm), it was emphasized that increasing the bending angle increased the thermal resistance, the Reynolds number increased from 100 to 100, from 45 to 135, the thermal resistance was changed by 10%, the thermal resistance and the pressure decreased. Karabulut et al. [3], two different types of wing were investigated numerically to increase the heat transfer of the heat exchangers. ANSYS Fluent 3D Navier-Stokes was steady state solution. As a result, for the Re 400, the hot and cold air velocities were set at 0.69 and 1.338 m/s for inlet temperatures of 300 K and 600 K, respectively. Jonsson and Moshfesh [4], have experimentally studied in a channel tunnel, in which the heat sink has 7 different fins (plate, strip and pin fin). They have designed and tested a total of 42 different heat sinks, with a height of 10, 15, 20 for each fin, with a width of 52.8. In the study, they obtained empirical correlations on how heat and hydraulic performances of heat receivers are affected. Re 2000 to 16500, while the fin height / channel height (H / CH) was 1, 0.67, 0.33. Yang et al. studied the effect of heat transfer performance on pin fin heat sinks density in twelve inline and staggered, such as circular, elliptic and square cross-section. Compared to the heat transfer coefficients of the pin fin heat sinks, they found that staggered arrangement were better, while elliptical pin fin had lower pressures [5]. Erturun et al. investigated the power generation performance of the thermoelectric device and the possible effect of the thermomechanical on the different thermoelectric leg geometry. They performed finite element analysis in ANSYS for thermoelectric models with various leg geometries (rectangular prism, trapezoidal prism, cylindrical and octagonal prism) and gradients at different temperatures (100 and 300 °C). For each model, they investigated temperature distribution, power outputs, thermal stresses. As TEG material,

they used bismuth tellurium, bismite tellurium / cobalt lead. The maximum stresses for rectangular and cylindrical legs of 100 °C were 49.9 MPa and 43.3 MPa and 94.2 and 85.7 MPa for the temperature gradient of 300 °C, respectively [6]. In their study of Erturun and Mossi [7], thermomechanical size investigated the effects of different leg structure and power production performance of thermoelectric devices. They have made 4 designs with their original, rotated and coaxial-legs configurations. As a result, in the concentric structure, the maximum temperature decreases by 10% and the conversion efficiency increases by 7%. In the case of rotating, the thermal resistance and the transport efficiency are the smallest between 1.2% and 0.3%, respectively. Rabari et al. in their work, they modeled a two-dimensional TEG system using nanostructured thermoelectric semiconductor material. The p – type nano structured bismuth antimony tellurium (BiSbTe), n – type contains bismuth tellurium (Bi₂Te₃) added 0.1% by volume of silicon carbide [8].

In this study, flow and heat transfer were investigated by inserting a square fin into a channel at 5, 10, 15 m/s and 573 K air temperature. A thermoelectric module was placed on the bottom

surface of the fin structures. Numerical calculations have been investigated in ANSYS 15 with Fluent and Thermal electric module.

II. MATHEMATICAL MODEL AND NUMERICAL METHOD

The schematic diagram of the geometry and the computational domain is shown in Fig. 1. The turbulent three dimensional Navier–Stokes and energy equations are solved numerically (using finite-difference scheme) combined with the continuity equation to simulate the thermal and turbulent flow fields. An eddy viscosity model is used to account for the effects of turbulence. The flow is assumed to be steady, incompressible, and three-dimensional. The buoyancy and radiation heat transfer effects are neglect. In addition, the thermo physical properties of the fluid are assumed to be constant. The three-dimensional governing equations of mass, momentum, turbulent kinetic energy, turbulent energy dissipation rate, and energy in the steady turbulent main flow using the standard k–ε model are as follows [9]:

Continuity equation

$$\frac{\partial \rho u_i}{\partial x_i} = 0 \quad (2.1)$$

Momentum equation

$$\rho u_j \frac{\partial u_i}{\partial x_j} = -\frac{\partial P}{\partial x_i} + \frac{\partial}{\partial x_j} \left[\mu_t \left(\frac{\partial u_i}{\partial x_j} + \frac{\partial u_j}{\partial x_i} \right) \right] \quad (2.2)$$

Energy equation

$$\rho u_j \frac{\partial T}{\partial x_j} = \frac{\partial}{\partial x_j} \left[\left(\frac{\mu_L}{\sigma_L} + \frac{\mu_t}{\sigma_t} \right) \frac{\partial T}{\partial x_j} \right] \quad (2.3)$$

Transport equation for k

$$\rho u_j \frac{\partial k}{\partial x_j} = \frac{\partial}{\partial x_j} \left(\frac{\mu_t}{\sigma_k} \frac{\partial k}{\partial x_j} \right) + \mu_t \left(\frac{\partial u_i}{\partial x_j} + \frac{\partial u_j}{\partial x_i} \right) \frac{\partial u_i}{\partial x_j} - \rho \epsilon \quad (2.4)$$

Transport equation for ε

$$\rho u_j \frac{\partial \epsilon}{\partial x_j} = \frac{\partial}{\partial x_j} \left(\frac{\mu_t}{\sigma_\epsilon} \frac{\partial \epsilon}{\partial x_j} \right) + c_1 \mu_t \frac{\epsilon}{k} \left(\frac{\partial u_i}{\partial x_j} + \frac{\partial u_j}{\partial x_i} \right) \frac{\partial u_i}{\partial x_j} - c_2 \rho \frac{\epsilon^2}{k} \quad (2.5)$$

The empirical constants appear in the above equations are given by the following values [9]:

$$c_1 = 1.44, c_2 = 1.92, c_\mu = 0.09, \sigma_k = 1, \sigma_\epsilon = 1.3, \sigma_t = 0.7$$

Some assumptions in the model solution are;
The flow is solved in three dimensions and turbulence. Newtonian flow, accepted. In the Y-axis direction, the gravitational force -9.81 is used. Steady state of the solution was made. The k-ε turbulence model was made realizable.

III. RESULT AND DISCUSSION

A. Validation and verification

A reference study was taken into account in order to test the accuracy of the results obtained in the

numerical study. In comparison to the study, the emphasis is on the accuracy of the path. The obtained solutions were compared with the results in the reference study. In the first comparison, the comparison between the thermal resistance and the Reynolds number of the square fin in the channel is shown in Fig. 1. Another comparison shows the temperature change of the internal structure of the thermo electrical element shown in Fig. 2. As a result of these comparisons, results that are compatible with the reference works have been obtained. So the result is that the numerical method used is correct.

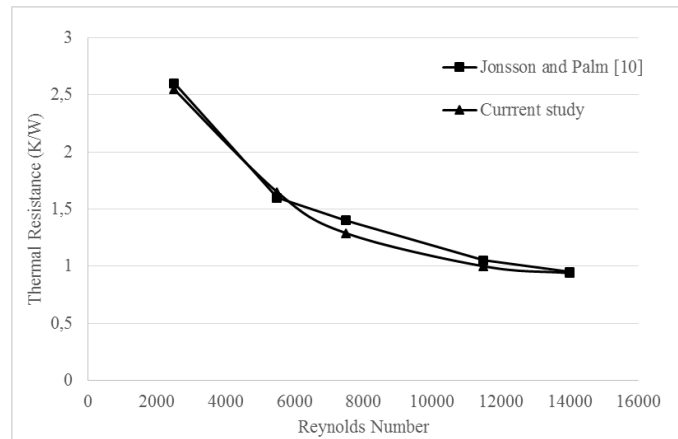


Fig. 1. Literature comparison with current study for channel flow

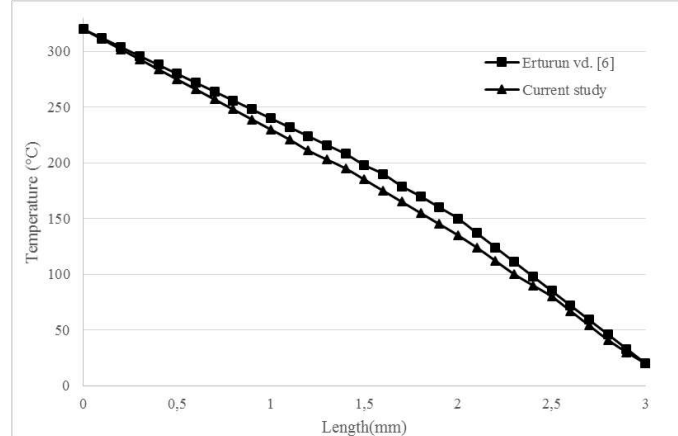


Fig. 2. Literature comparison of the thermoelectric structure with the current study.

B. Module geometries and material properties

The square fin is made of copper material in 40x40x12 mm dimensions and the fin structures are 2x2 mm wide. It is approximately 210 mm from the edge, as it would be in the middle of the channel. It

is shown in Fig. 3 and 4. The geometry is designed with a copper plate with dimensions of 50x50x500 mm and a thickness of 2 mm.

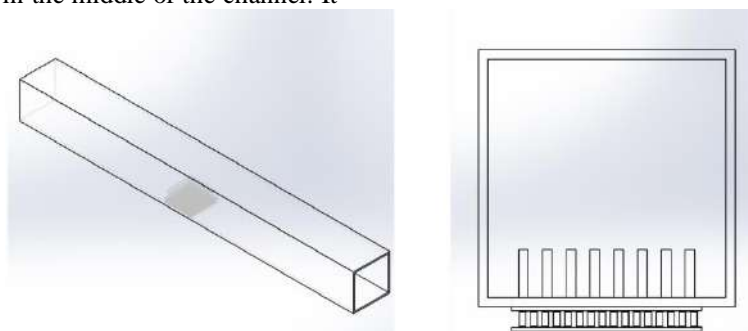


Fig. 3. Geometric features of model

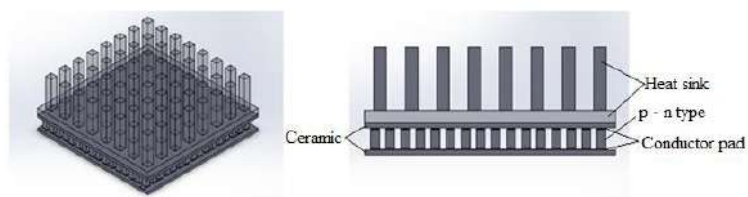


Fig. 4. Schematic representation of the fin and thermoelectrics

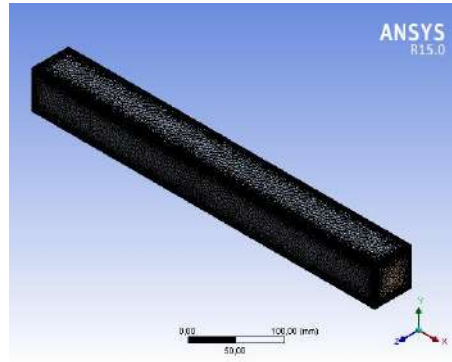


Fig. 5. Mesh structure of model.

Once the geometry and mesh structure has been constructed, it is necessary to enter the boundary conditions required for FLUENT and to describe the fluid properties (Fig. 5 and 6). In this study, the air

to be sent into the channel was considered to have a temperature of 573 K. Channels and fins were made of copper.

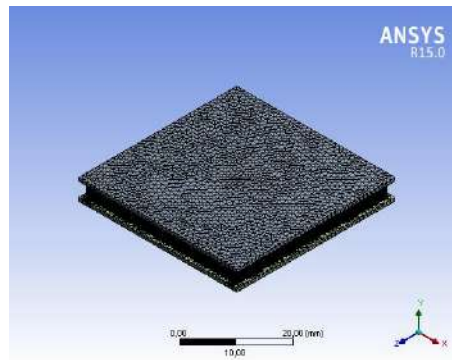
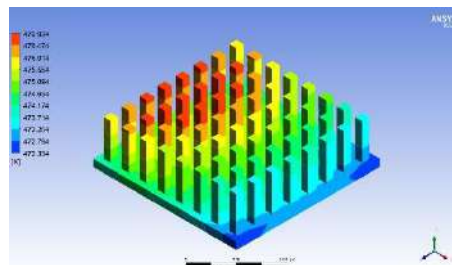


Fig. 6. Thermoelectric mesh structure.

C. Performance comparison of square fin

In this study, air at a temperature of 573 K was sent to a channel at 5, 10 and 15 m/s at different speeds. The square fin structure placed in the channel was modeled and numerically investigated. The temperature distribution for three different velocities of the square fin is shown Fig. 7. The fluid at 573 K temperature sent into the channel decreases with

decreasing speed. The temperature values of the fin are decreasing from the upper parts of the fluid contacting the lower surface. As can be seen, it has a speed of 5 m/s with a minimum temperature of 472 K. As a result, the heat transfer increases as the speed increases.



a)

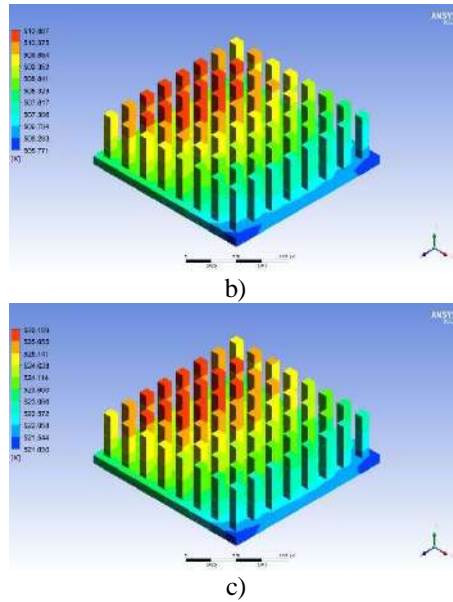


Fig. 7. Temperature distribution for square fin a) $V = 5$ m/s b) $V = 10$ m/s c) $V = 15$ m/s

For a square fin, the temperature variation along the channel, depending on the Reynolds number, is given in Fig. 8. Initially, the temperature of the air at 573 K is reduced to a certain length depending on the number of Reynolds. The temperature is stable between 100 - 200 mm. The cause is the uniformity of the temperature because the flow does not encounter any obstacles until it reaches the region in the channel. A certain temperature rise and drop is found in the fluid channel after it has hit the fin,

which is placed in the channel. After passing the fin, the temperature was held steady, depending on the Reynolds number. Depending on the initial temperature, the curve with the lowest temperature loss $Re = 5247.1$, the highest temperature loss is $Re = 15741.3$. The surprise of the fins is that the greatest increase in temperature is in the square fin. The change in Nusselt number along the canal of Reynolds number for the square fin is given in Fig. 9.

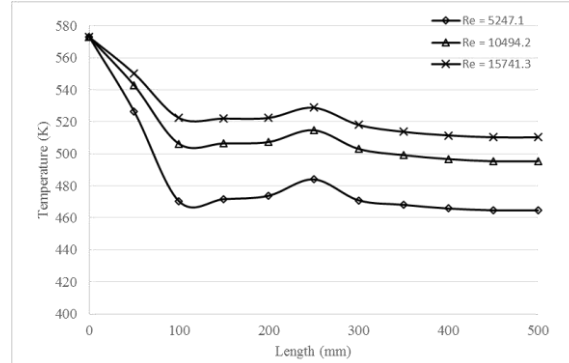


Fig. 8. Variation of temperature across the canal for different Reynolds numbers

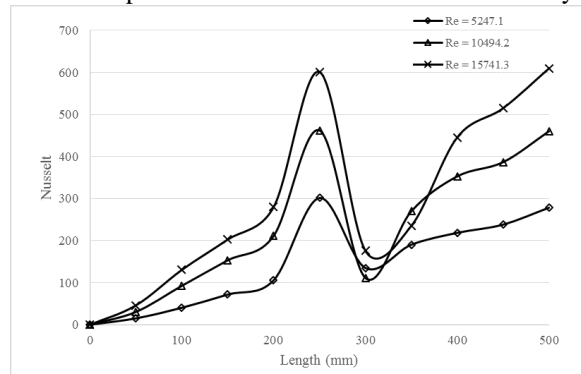


Fig. 9. For different Reynolds numbers, change the local Nusselt numbers along the channel

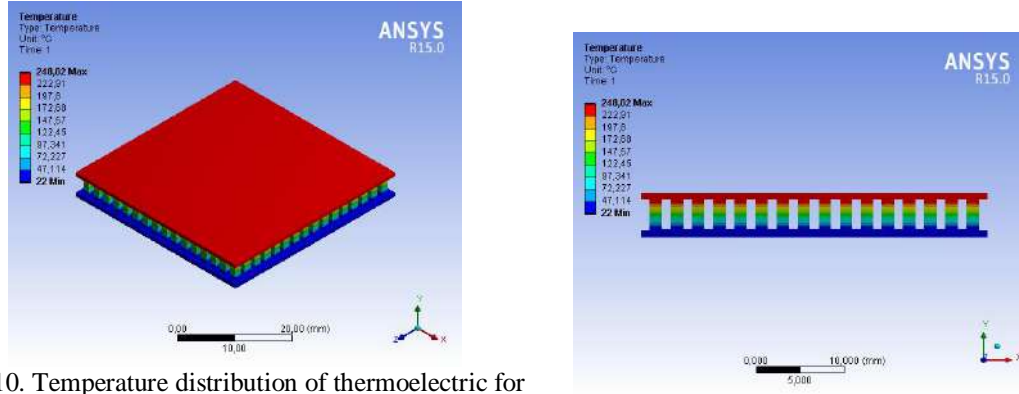


Fig. 10. Temperature distribution of thermoelectric for square fin

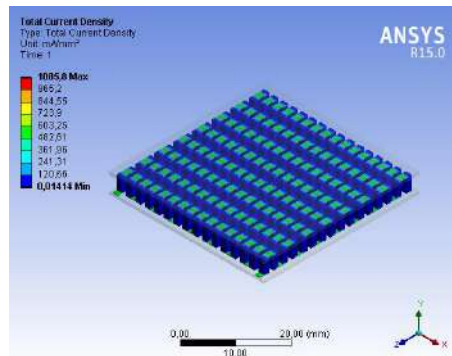


Fig. 11. Current distribution of thermoelectric for square fin

The numerical results of the thermo electrical for square fin in ANSYS thermal - electricity are shown in Table 1. The result for thermoelectricity placed under square fin founded $Re = 15741.3$. Fig. 10 and 11 show the temperature and current distribution for the square fin. The results are presented as a table.

Table 1. Numerical results of thermoelectricity for square and staggered square fin

	Temperature (°C)	Heat Flux (W/mm ²)	Current (mA)	Heat (W)
Square fin (5 m/s)	199.3	7.1718	79.375	121.46
Square fin (10 m/s)	232.76	8.5248	95.35	144.39
Square fin (15 m/s)	248.02	9.1422	102.64	154.85

IV. CONCLUSIONS

Numerical results show that the heat transfer coefficient of the square wing is $625 \text{ W/m}^2\text{K}$ and the temperature varies between 476 and 526 K. The best heat transfer was achieved with 15 m/s, 10 m/s and 5 m/s, respectively. For different speeds for the square fin, the temperature values varied between 476.934 and 526.169 K. When the speeds are compared, the best heat transfer is achieved with 15 m/s, 10 m/s and 5 m/s, respectively. The results of thermoelectric temperature, heat flow, current and heat were found to be 249.09 °C, 9.1852 W/mm², 103.15 mA and 155.58 W respectively.

REFERENCES

- [1] Jang, J.-Y., Tsai, Y.-C. and Wu, C.-W., 2013. A study of 3-D numerical simulation and comparison with experimental results on turbulent flow of venting flue gas using thermoelectric generator modules and plate fin heat sink. *Energy*, 53, 270–281.
- [2] Tsai, G. L., Li, H. Y. and Lin, C. C., 2010. Effect of the angle of inclination of a plate shield on the thermal and hydraulic performance of a plate-fin heat sink. *International Communications in Heat and Mass Transfer*, 37(4), 364–371.
- [3] Karabulut, K., Buyruk, E., Kilin, F., Karabulut, O., Bu, Z. E. T. ve Kelimeler, A., 2013. Farklı geometrilerden oluşan kanatçıklı plakalı ısı değiştiricileri için ısı transferinin üç boyutlu sayısal olarak incelenmesi, 11. Ulusal Tesisat Mühendisliği Kongresi, İzmir, 17-20 Nisan, s. 69–85.
- [4] Jonsson, H. and Moshfegh, B. (2001). Modeling of the thermal and hydraulic performance of plate fin, strip fin, and pin fin heat sinks - Influence of flow bypass. *IEEE Transactions on Components and Packaging Technologies*, 24(2), 142–149.
- [5] Yang, K. S., Chu, W. H., Chen, I. Y. and Wang, C. C., 2007. A comparative study of the airside performance of heat sinks having pin fin configurations. *International Journal of Heat and Mass Transfer*, 50(23–24), 4661–4667.
- [6] Erturun, U., Erermis, K. and Mossi, K., 2014. Effect of various leg geometries on thermo-mechanical and power generation performance of thermoelectric devices. *Applied Thermal Engineering*, 73(1), 126–139.
- [7] Erturun, U. and Mossi, K., 2015. Thermoelectric devices with rotated and coaxial leg configurations: Numerical analysis of performance. *Applied Thermal Engineering*, 85, 304–312.
- [8] Rabari, R., Mahmud, S. and Dutta, A., 2014. Numerical simulation of nanostructured thermoelectric generator considering surface to surrounding convection. *International Communications in Heat and Mass Transfer*, 56, 146–151.
- [9] Yang, Y. T. and Peng, H. S., 2009. Investigation of planted pin fins for heat transfer enhancement in plate fin heat sink. *Microelectronics Reliability*, 49(2), 163–169.
- [10] Jonsson, H. and Moshfegh, B., 2001. Modeling of the thermal and hydraulic performance of plate fin, strip fin, and pin fin heat sinks - Influence of flow bypass. *IEEE Transactions on Components and Packaging Technologies*, 24(2), 142–149.

Fault Estimation on High Voltage Direct Current Transmission Using Hilbert-Huang Transform and Extreme Learning Machines

Fatih Ünal

Energy Systems Engineering
Firat University
Elazığ, Turkey
funal@firat.edu.tr

Sami Ekici

Energy Systems Engineering
Firat University
Elazığ, Turkey
sekici@firat.edu.tr

Abstract—In this study, a novel approach to signal processing namely Hilbert-Huang Transform (HHD) and its application on High Voltage Direct Current (HVDC) are discussed. The virtual ground-phase faults obtained in Matlab environment and fault current and voltage values of each signal recorded simultaneously while the simulation is running. Then, HHD is used to extract feasible features from the instantaneous frequency and magnitude values of each Instant Mode Function (IMF) on Empirical Mode Decomposition (EMD) and Hilbert Spectral Analysis (HSA). Finally, Extreme Learning Machine (ELM) is determined to estimate the fault locations and the performance of the hybrid approach are discussed. Also, It can be seen from results and HHD analysis, this new approach can properly expose the nonlinear and non-stationary elements unlike the traditional methods are inadequate.

Keywords—Hilbert-Huang transform; High Voltage Direct Current transmission; Extreme Learning Machine; fault estimation; empirical mode decomposition.

I. INTRODUCTION

HVDC transmission systems are preferred mostly on the connection of offshore renewable energy sources to the mainland, bulk power transmission through long distance, interconnection systems with different frequencies, power flow, and voltage control of different AC transmission systems, etc. When considering AC transmission, especially bulk power over long distance, HVDC transmission has less overall cost and losses. Also, the major concerns associated with interconnection of two system, like security, reliability, frequency control and so on are no longer become any problem in HVDC systems. Different topologies, multi-terminal applications, fast tripping and robust switching elements of voltage source converters (VSC) increase the application of HVDC systems. Due to its fast controllability, dc transmission has a full control action, and ability to enhance dynamic and transient stability related with ac network and can limit fault current in the dc lines [1]. There are also some obstacles to be overcome in the application of HVDC technology. Some of them are high cost of conversion equipment and converter station [2] the requirement of reactive power supply in converter stations, the complexity of control

action [3]. The widespread of different high voltage and high power switching elements like GTO and IGBT and different Pulse Width Modulation (PWM) techniques accelerated the practical usage of VSC based HVDC systems [4], [5]. Those self-commutating switches can be turned on-off at will. This feature regulates the voltage/current in a VSC properly and controls the power factor as well. Additionally, power reversal in a VSC can be made with both current and voltage at the dc side [6].

HVDC control strategies are mainly focused on protection of the converter stations and protection of the dc transmission line [7]. In this study, we will focus only the dc transmission lines fault techniques and introduce new protection strategies for this purpose. In HVDC systems, the most commonly used fault detection and protection algorithms are differential protection [8], traveling wave protection [9], [10], over current and under voltage derivatives protection [11], impedance measurement, wavelet transform (WT) [12] and short-time Fourier transform (STFT) based signal processing methods and the artificial intelligence applications that have recently attracted attention [13]. Considering protection scheme for point to point HVDC systems, classical main protection and backup protection algorithms do not perform well to detect high impedance faults. In different versions of traveling wave protection and derivative protection, this undesirable situation can be eliminated by using two terminal measurements and fast communication channels. A detailed information of classic HVDC system protections can be found in [14]. Another protection algorithms that mentioned before can be thought as the analysis of high-frequency components or the sampling of fundamental and transient components of fault signals. When a fault occurs on dc line or converter station, non-stationary current and voltage fluctuations continuous until the high-frequency components are damped. By taking advantages of this phenomenon and using different filtering techniques can successfully be exposed the hidden and valuable information in fault signals. In literature surveys, mostly preferred and proposed method be Discrete Wavelet Transform (DWT) and the hybrid approach with traveling wave dispersion to find modulus maximas of traveling voltage and current waves. Also, calculation of signal's energy [15] and

entropy values [16], wavelet coefficients of forward and reverse voltage waves [17], transient current characteristic [18], the measurements of dc line terminals [19], can be thought the different implementation of the wavelet transform. Unlike these, different signal processing methods such as mathematical morphology [20], [21], Stockwell transform (S-transform) [22], [23], HHT [24], [25] are some examples of this area. In this study, as before mentioned, we will mainly focus on HHT and a new machine learning method to locate phase-ground faults in dc line.

II. HILBERT-HUANG TRANSFORM

Data analysis is an essential process in observing the behavior of transient events on power systems and transmission lines. Until now, traditionally the data analysis methods are either Fourier-based or wavelet based for the linear and nonstationary phenomenon are designed. However, considering nonlinear and nonstationary processes, there are very limited options in data analysis methods. At this point, other than the periodicity, constant width Fourier window or wavelet family, the nonlinear and nonstationary processes need different approaches. HHT method proposed by Huang in [26] is an adaptive and time domain based preprocessing tool which consists of two parts as EMD and HSA. The detailed information will mention the following sections.

A. Empirical Mode Decomposition

EMD is an adaptive, direct and intuitive method which is a necessary step to reduce any data set into a collection of IMF. It can be considered as the simple oscillatory modes of significantly different frequencies, one superimposed on the other. At the end of the process, similar to wavelet decomposition levels, each IMF represents not only different frequency levels but also simple oscillatory modes. In HHT method, each IMF must satisfy two conditions. First of all, an IMF must have the same number of extrema, minima, and zero crossings or differ from at most by one. Secondly, at any point, the mean value of the function must be zero. When these conditions are ensured, one can decompose into components any signal through a sifting procedure [27], [28].

For any data set, the local extrema points are identified using a cubic spline envelope. The upper and lower envelopes should encompass all data. When $x(t)$ represents the original signal and its mean values designated as m_1 , the difference between original signal values and mean values is the first proto-IMF component and can be represented as h_1 . This definition is given as in (1).

$$h_1 = x(t) - m_1 \quad (1)$$

Normally, it is expected that h_1 satisfy the definition of IMF but changing a local zero from rectangular coordinate system to curvilinear one may cause new extrema, so the sifting process must be repeated to eliminate background waves and to make the wave profiles more symmetrical. In the each iteration step, the existing proto-IMF h_1 treated as the original signal and in the next iteration process continuous as in (2).

$$h_{11} = h_1 - m_{11} \quad (2)$$

After k times of iterations, expected conditions are satisfied, h_{1k} becomes the first IMF c_1 moreover, mathematically expressed in (3).

$$\begin{aligned} h_{1k} &= h_{1(k-1)} - m_{1k} \\ c_{1k} &= h_{1k} \end{aligned} \quad (3)$$

The first IMF contains high-frequency components and corresponds the detail coefficients in wavelet transform. Obtaining another frequency band components from the original signal, IMF is extracted from the signal and a residue term obtained. The first residue term r_1 moreover, all subsequent terms r_j are shown in (4) and (5), respectively [26], [28].

$$r_1 = x(t) - c_1 \quad (4)$$

$$\begin{aligned} r_2 &= r_1 - c_2 \\ &\vdots \\ r_n &= r_{n-1} - c_n \end{aligned} \quad (5)$$

The decomposition process of the original signal continuous until the residue term becomes a constant or a monotonic function, in other words, a trend. Also, the original signal can be reconstructed by summing up all IMF components and residue term. This expression is given in (6).

$$x(t) = \sum_{j=1}^n c_j + r_n \quad (6)$$

While the sifting process continues for many iterations and makes the amplitude variations of the new constructed waves, some undesirable situations occur on physical properties of the components. Eliminating these side effects and make HHT more compact to implement in different applications, Huang and colleagues proposed two separate stoppage criterions. The first proposed method is similar to Cauchy convergence test but slightly different from the original one. This stoppage criterion mathematical expression is given in (7) [28].

$$SD_k = \frac{\sum_{t=0}^T |h_{k-1}(t) - h_k(t)|^2}{\sum_{t=0}^T h_{k-1}^2(t)} \quad (7)$$

In equation (7), SD_k represents the stoppage criterion and the sifting process repeats if the squared difference of two successive sifting is smaller than the previous determined value. The another stoppage criterion depends on the experiences from the extensive tests and determined between 3 and 8.

B. Hilbert Spectral Analysis

Hilbert spectrum represents the decomposed data in the time-frequency-energy domain and assigns the energy levels of different components correctly. When applying a Hilbert transform to the each IMF components, the instantaneous frequency, and magnitude values are obtained. In contrast to Fourier transform, this IMF functions represents a time-varying function of amplitude and frequency. This time-frequency representation of magnitude is called as a Hilbert spectrum. For any function $x(t)$ of L^p class, its Hilbert transform is given in (8) [29].

$$y(t) = \frac{1}{\pi} P \int_{-\infty}^{+\infty} \frac{x(\tau)}{t-\tau} d\tau \quad (8)$$

Where P represents the Cauchy principal value, τ is the sifting value in time domain and $y(t)$ is Hilbert transform of

$x(t)$. The instantaneous frequency and amplitude values of Hilbert transform of $y(t)$ can be derived from its analytic function as in (9) and (10) respectively.

$$z(t) = x(t) + iy(t) = a(t)e^{i\theta(t)} \quad (9)$$

$$\omega(t) = \frac{d\theta}{dt}, \quad a(t) = \sqrt{x^2 + y^2} \quad (10)$$

Here ω represents instantaneous frequency and a represents the magnitude. When we have both frequency and magnitude values, we can also obtain the energy values in terms of square of the magnitude in time-frequency domain. In HSA, an alternative spectrum expression of the entire data set so called marginal spectrum can measure of the total energy contribution of each IMF. The marginal spectrum is given in (11)

$$h(\omega) = \int_0^T H(\omega, t) dt \quad (11)$$

where $[0, T]$ is the preprocessing domain of IMFs samples is defined temporally.

III. THE SIMULATION STUDY AND FEATURE EXTRACTION BY HHT

The simulation of a monopolar HVDC system is utilized for creating the phase-ground fault data sets. In the simulation, DC line is 300 km length and both rectifier and inverter station uses 12 pulse converter and control systems for inverter and rectifier made up 'Discrete HVDC Controller Block' in Simpowersystems library, in Matlab. The control action of inverter and rectifier uses several parameters like alpha (α) and gamma (γ) control. The alpha (α) value is the firing delay angle ordered by the regulator. Gamma parameter observes the extinction angle for each 6 pulse thyristor bridge. There are also another control system which is called 'Master Control' and generates the current references for both converters and initiates the starting and stopping of the DC power transmission.

At both sides of rectifier and inverter, there are two breakers, 0.5 H reactors, and AC filters. The DC line is a 1000 MW (500 kV, 2 kA) interconnections of two different grid. Rectifier side has a 500 kA, 5000 MVA 60 Hz AC network and inverter side has a 345 kV, 10000 MVA, 50 Hz AC network. The DC transmission line properties are given in Table I.

TABLE I. PROPERTIES OF DC TRANSMISSION LINE IN THE SIMULATION

Transmission Line	Properties
Length	300 km
Class	Distributed parameter
Circuit Structure	Serial RLC
Connection Style	single phase-ground
Smoothing Reactors	0.5 H (2 units)
Primary voltage	0.90 (rectifier side) 0.96 (inverter side)
Sampling Time (s)	50×10^{-6} s
DC line voltage (kV)	500 kV
DC line current (kA)	2 kA
Fault resistance R_d	R_{on} (1 ohm)

Grid frequency	50 / 60 Hz
Multiplication factor	1:100
Per km;	
Resistance	0.015 ohm/km
Inductance	$0.792 \cdot 10^{-3}$ H/km
Capacitance	$14.4 \cdot 10^{-9}$ F/km

A. Steady State and Faulted Conditions of Simulation Study

DC currents (I_dR ve I_dI) and DC voltages (V_dLR ve V_dLI) defined in control blocks are scaled to p.u (1 p.u. current=2 kA, 1 p.u. voltage=500 kV). In steady state condition, the current value of the rectifier (I_{dref}) moreover, the voltage value of the inverter (V_{dref}) pursue a predefined reference value in the system. They set at 0.1 and 0.05 pu, respectively. The current and voltage values of steady-state and faulted state are demonstrated in Fig.1 and Fig.2 respectively.

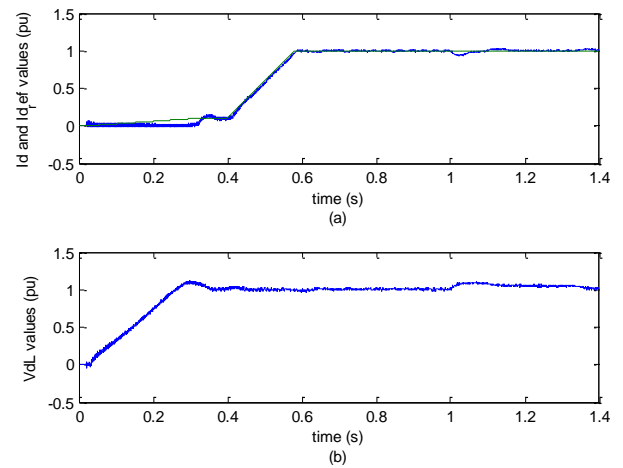


Fig. 1. Steady state conditions of DC line (a) current (b) voltage values, rectifier side

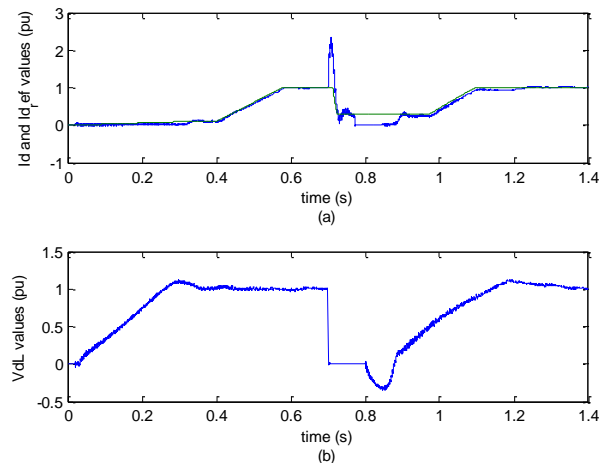


Fig. 2. Phase-ground fault on the 150.km of DC line, (a) fault current, (b) fault voltage, rectifier side

The sample of phase-ground fault occurs at ($t=0.7$ s) and continuous until ($t=0.8$ s). At the beginning of fault application,

current increases to approximately 2.2 pu and DC voltage falls to zero at the rectifier. The Voltage-Dependent Order Limiter (VDOL) and DC protection detect this voltage drop. While current continues to circulate and the voltage falls into negative

region, the protection algorithm is on mode and firing angle is forced to 166 degrees. Then, rectifier operates in inverter mode until the recovery of DC voltage and current is done. The screenshot of the simulation is demonstrated in Fig 3.

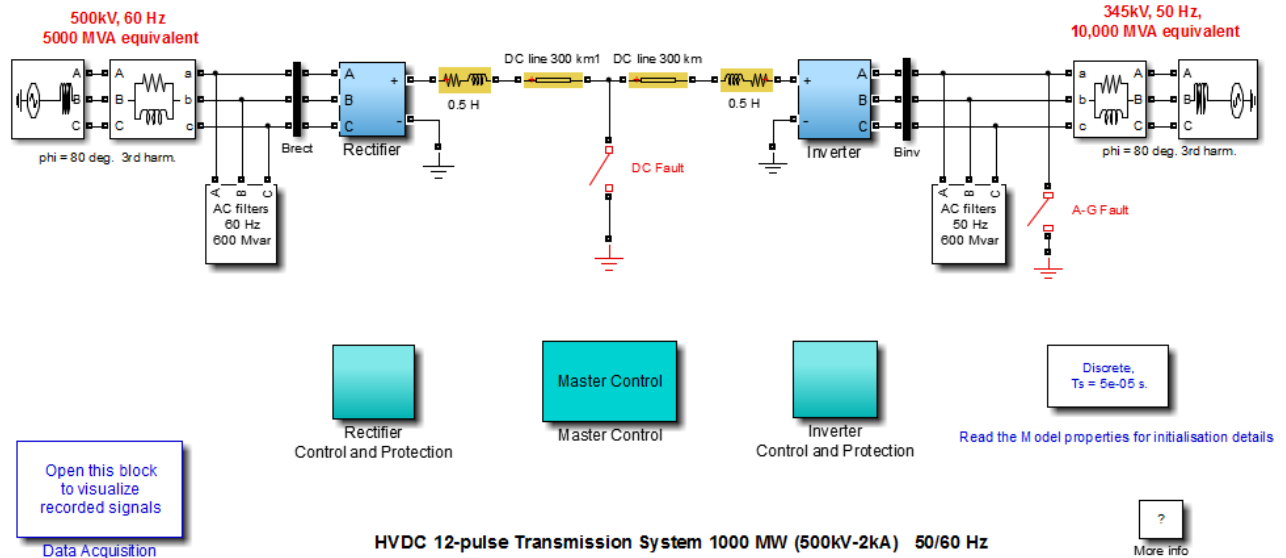


Fig. 3. 12 pulses monopolar HVDC system and equipment in the simulation study

In this study, the fault current and voltage signals recorded between 15.km and 285.km of DC line. Fault resistance and fault duration are kept constant for each km and appeared between [0.7-0.8] seconds after the simulation start.

B. Feature Extraction by Using HHT

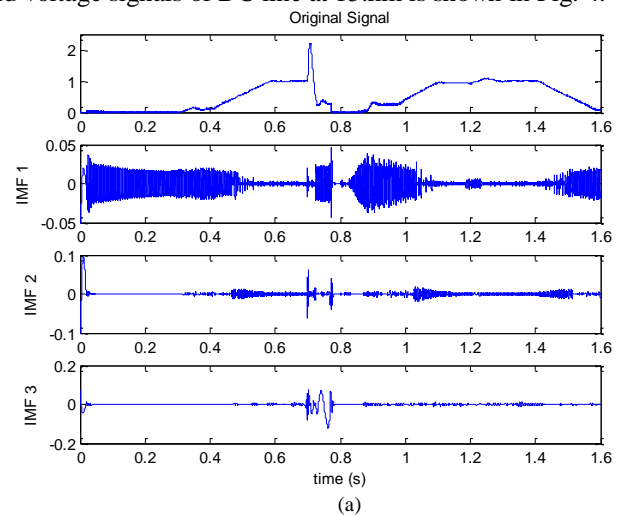
After the recording of the fault signals, HHT is applied to extract instantaneous frequency and magnitude values. Unlike from DWT; it examines the whole data set on the time domain, because of analyzing the IMFs on time domain. In order to obtain each of IMF; the iteration step is adjusted as 10 and it is automatically completed the analysis in the case of the signal became a trend or monotonic function. The sampling period of the HHT is set to 5×10^{-5} s similar to the simulation study. The total duration of the HHT signal analysis is 1.6 seconds.

The numbers of IMF obtained from the HHT are not the same for each fault current and voltage signal. Therefore, while signals are decomposed up to 12 level, the number of IMF to be used during the fault estimation stage has been determined to be the first 3 IMFs that cover all signal data set.

The HHT method, as detailed in Section II, allows being obtained EMDs if certain conditions are met. These are in general; The IMF's average must be zero, the maximum, minimum and zero crossings must be equal or differ from at most by one. These necessary conditions that allows the EMD process can lead some problems as no maximum or

minimum point can exist at the beginning and end of the signal. This undesirable condition, also known as the end effect, causes distortions in waveforms at the beginning and end points of the IMF. Different approaches such as characteristic wave extension, mirroring, data duplication and similarity research are used to eliminate this problem [30].

The first three level of IMF obtained from the fault current, and voltage signals of DC line at 15.km is shown in Fig. 4.



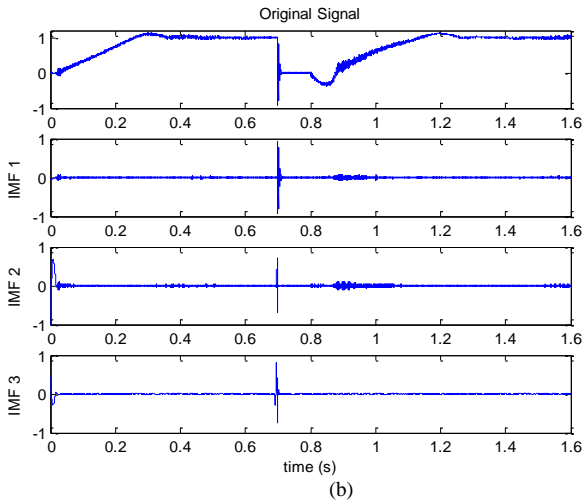


Fig. 4. The first 3 IMF of DC fault signal (a) current (b) voltage at 15.km,rectifier side

The Hilbert energy spectrum obtained from EMD for current and voltage of DC line is shown Fig 5.

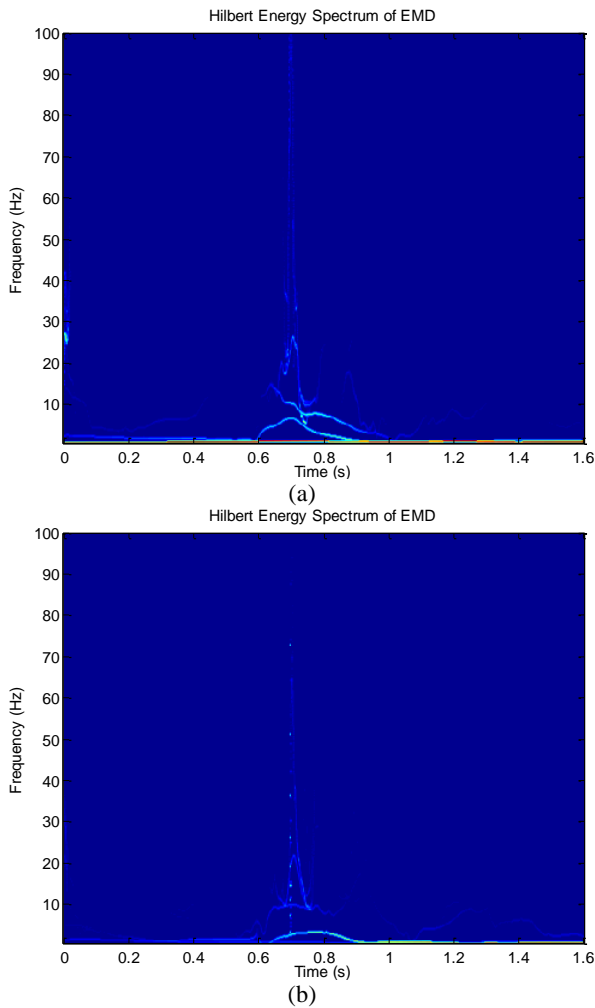


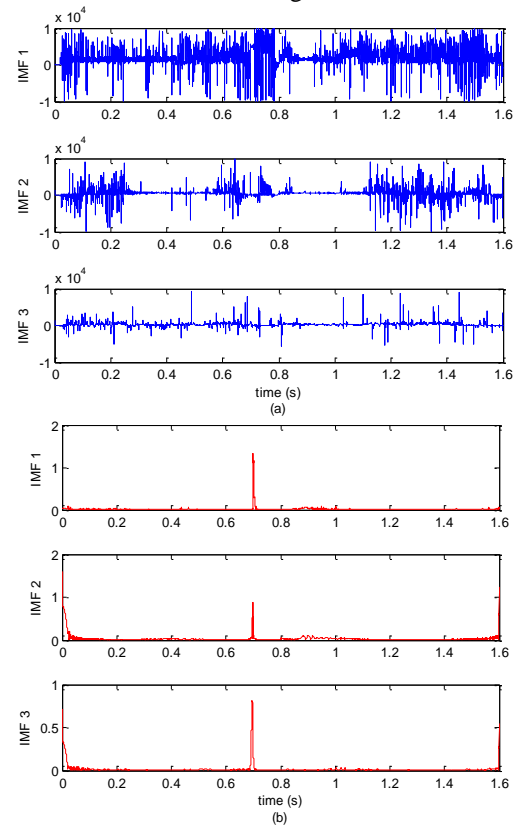
Fig. 5. Hilbert energy spectrum of DC fault signal (a) current (b) voltage

Finally, at the feature extraction process for representing fault signals properly, the average of instantaneous frequency and magnitude and standard deviation of instantaneous frequency and magnitude values have been calculated. This procedure is implemented to the first 3 IMF of both each fault current and voltage signal. So, the feature vector has 24 properties which include both current and voltage values. The property distribution of the first 3 IMFs is mentioned in Table II.

TABLE II. PROPERTY DISTRIBUTION OF THE FIRST 3 IMFS OF FAULT CURRENTS AND VOLTAGES

Parameters	IMF-1	IMF-2	IMF-3
The Average of instantaneous frequency	Feature_1	Feature_2	Feature_3
The Average of instantaneous magnitude	Feature_4	Feature_5	Feature_6
The standard deviation of instantaneous frequency	Feature_7	Feature_8	Feature_9
The standard deviation of instantaneous magnitude	Feature_10	Feature_11	Feature_12

The instantaneous frequency and magnitude values of the first 3 IMF for current and voltage at 15.km of DC line is shown in Fig 6.



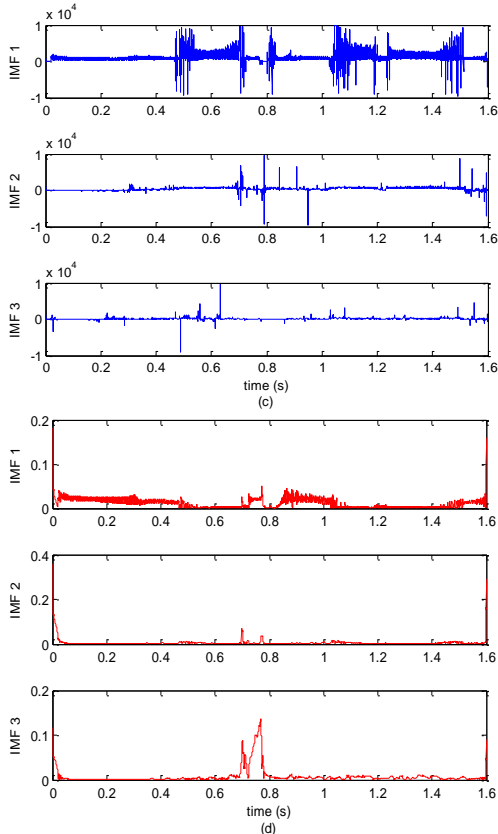


Fig. 6. Instantaneous frequency and magnitude values of voltage (a,b) and current (c,d) signals respectively

IV. PERFORMANCE EVALUATION OF ELM AND FAULT ESTIMATION PROCESS

ELM is a single layer feed forward neural network (SNLF) and proposed firstly by Huang in [31] to overcome some problems such as slow training performances of gradient based algorithms, improper learning steps or easily converge to local minima. Also, the idea of choosing input weights and biases randomly if the activation function is infinitely differentiable, the output of a neuron can be determined numerically. By this approach, a remarkable computational burden can be abolished and still have able to obtain expectable results.

Considering a data set which contains N different sample (x_i, y_i) ; $x_i = [x_{i1}, x_{i2}, x_{i3}, \dots, x_{in}]^T \in \mathbb{R}^n$ moreover, corresponding outputs are $y_i = [y_{i1}, y_{i2}, y_{i3}, \dots, y_{im}]^T \in \mathbb{R}^m$, \tilde{N} represents hidden layer and $g(x)$ activation function, SLFN's can mathematically model as in (12) [32].

$$\sum_{i=1}^{\tilde{N}} \beta_i g_i(x_j) = \sum_{i=1}^{\tilde{N}} \beta_i (w_i x_j + b_i) = o_j \quad j = 1, 2, \dots, N, \quad (12)$$

Where $w_i = [w_{i1}, w_{i2}, w_{i3}, \dots, w_{in}]^T$ is the randomly chosen weight vectors connecting i th hidden layer and input layer, $\beta_i = [\beta_{i1}, \beta_{i2}, \beta_{i3}, \dots, \beta_{im}]^T$ is the weight vectors connecting i th hidden layer and output layer. Also, b_i represents the threshold value of the i th hidden layer.

In the ELM method, mathematical representation of the network in a different manner can be thought as a multiplication of data matrices ($H\beta = T$) [33]. Considering that the output matrix of the hidden layer of the SLFN is H , the weight vector is β and the T matrix expresses the real outputs vectors and can mathematically expressed as shown in (13).

$$H(w_1, \dots, w_{\tilde{N}}, b_1, \dots, b_{\tilde{N}}, x_1, \dots, x_N) = \begin{bmatrix} g(w_1 x_1 + b_1) & \dots & g(w_{\tilde{N}} x_1 + b_{\tilde{N}}) \\ \vdots & \dots & \vdots \\ g(w_1 x_N + b_1) & \dots & g(w_{\tilde{N}} x_N + b_{\tilde{N}}) \end{bmatrix}_{N \times \tilde{N}} \quad (13)$$

$$\beta = \begin{bmatrix} \beta_1^T \\ \vdots \\ \beta_{\tilde{N}}^T \end{bmatrix}_{\tilde{N} \times m} \quad T = \begin{bmatrix} t_1^T \\ \vdots \\ t_N^T \end{bmatrix}_{N \times m}$$

This matrix computation is only possible if the ($H\beta = T$) is a square matrix. However, in most cases, the input vectors are higher than the hidden layer nodes. In ELM method, this equation rearranged by using Moore-Penrose inverse matrix as $\hat{\beta}$. This inverse matrix enables to solve nonsquare matrixes and invertible. The equation of Moore-Penrose transform is given in (14).

$$\hat{\beta} = H^+ T \quad (14)$$

The equation of $\hat{\beta} = H^+ T$ is also one of the least squares solutions of generalized ($H\beta = T$) linear system. The lowest training error can be achieved with this particular solution. The minimum training error criterion is also mathematically expressed in (15).

$$\|H\hat{\beta} - T\| = \|HH^+ T - T\| = \min_{\beta} \|H\beta - T\| \quad (15)$$

In this study, to improve the generalization ability of the standard ELM in which uses a constant such as C is preferred. This approach also is known generalized ELM (RELM) and can improve the performance of ELM. The main difference of ELM and RELM is that training error is reduced simultaneously and the output weights with the regulation parameter is a norm. The mathematical representation of RELM and its Lagrange equivalent is shown in (16) [34].

$$\min_{\beta} C \|e\|_2^2 + \|\beta\|_2^2 \quad (16)$$

$$L(\beta, e, \lambda) = C \|e\|_2^2 + \|\beta\|_2^2 + \lambda^T (y - H\beta - e)$$

where $e = [e_1, e_2, \dots, e_N]^T$ is the training error and λ is the Lagrange multiplier. In RELM, the regulation parameter is set to 1×10^{-6} . The size of the training matrix is $[24 \times 163]$, and the size of the testing and validation matrix is $[24 \times 54]$. The number of hidden layer neuron is defined as ($n=900$). The estimated fault locations and regression value is shown in Fig 7 and Fig 8, respectively.

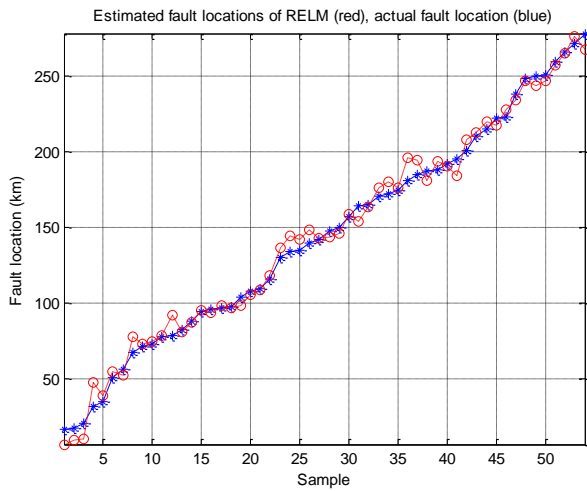


Fig. 7. The estimated fault locations and actual fault locations

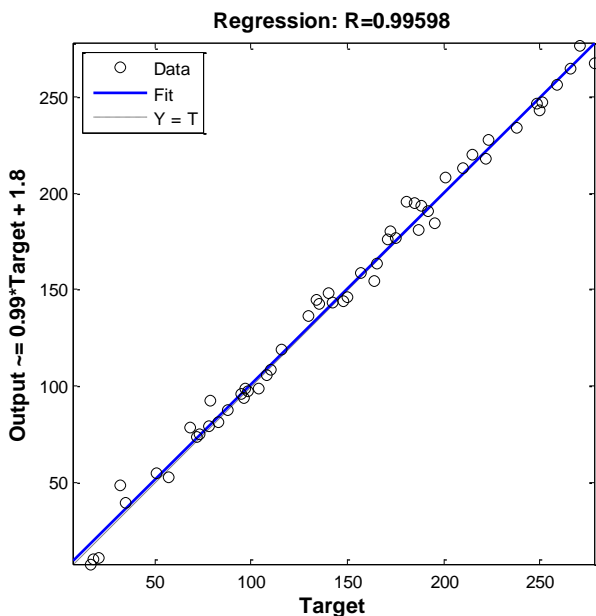


Fig. 8. Regression value of testing process of RELM

In this study, the root mean square error (rmse) calculated as (rmse=6.4858), and total regression value is calculated as (R=0.9987)

CONCLUSION

In this study, a novel signal processing and machine learning method are discussed. The ELM-HHT hybrid protection algorithm as seen from regression value and estimation process can be used for DC phase-ground faults. Also, HHT analysis gives us more information about signal and does not need an extra preprocessing stage.

In the future applications, HHT analysis can be implemented on bipolar and multi-terminal HVDC systems and the performance of proposed algorithm can be investigated by using benchmark tests.

REFERENCES

- [1] Kim, Chan-Ki, V. K. Sood, G.-S. Jang, S.-J. Lim, and S.-J. Lee, *HVDC Transmission: Power Conversion Applications in Power Systems*. Singapore: Wiley-IEEE Press, 2009.
- [2] J. Arrillaga, "High Voltage Direct Current Transmission Lines," in *IET Power and Energy Series*, 2. Edition., vol. 29, London: The Institution of Engineering and Technology, 2011.
- [3] C. M. Franck, "HVDC Circuit Breakers: A Review Identifying Future Research Needs," 2011.
- [4] I. Press, L. Shafer, G. W. Arnold, and D. Jacobson, *Pulsewidth Modulated DC-to-DC Power Conversion*. .
- [5] A. M. Abbas and P. W. Lehn, "PWM Based VSC-HVDC Systems - a Review," pp. 1–9, 2009.
- [6] H. F. Latorre and M. Ghandhari, "Electrical Power and Energy Systems Improvement of power system stability by using a VSC-HVdc q," *Int. J. Electr. Power Energy Syst.*, vol. 33, no. 2, pp. 332–339, 2011.
- [7] L. Wen-li and S. Li-qun, "The Review of High Voltage DC Transmission Lines Fault Location," vol. 3, no. 4, 2014.
- [8] C. Paper, "Differential Equation Based Fault Location Method for HVDC Transmission Line Differential Equation Based Fault Location Method for HVDC Transmission Line," no. JANUARY 2014, 2015.
- [9] L. H. Xie, L. J. Jin, X. L. Wang, S. Member, L. H. Ning, and T. L. Wang, "Improved Protection Method of HVDC Transmission Line Based on the Analysis of Traveling Wave Dispersion," no. Powercon, pp. 20–22, 2014.
- [10] S. Azizi, M. Sanaye-pasand, M. Abedini, and A. Hasani, "A Traveling-Wave-Based Methodology for Wide-Area Fault Location in Multiterminal DC Systems," vol. 29, no. 6, pp. 2552–2560, 2014.
- [11] H. Kunlun, C. Zexiang, and L. Yang, "Study on protective performance of HVDC transmission line protection with different types of line fault," in *DRPT 2011 - 2011 4th International Conference on Electric Utility Deregulation and Restructuring and Power Technologies*, 2011, no. 51077055, pp. 358–361.
- [12] Y. M. Yeap and A. Ukil, "Wavelet based fault analysis in HVDC system," in *IECON 2014 - 40th Annual Conference of the IEEE Industrial Electronics Society*, 2014, pp. 2472–2478.
- [13] M. Ramesh and A. J. Laxmi, "Fault Identification in HVDC using Artificial Intelligence – Recent Trends and Perspective," pp. 1–6, 2012.
- [14] D. Jovcic and K. Ahmed, *High-Voltage Direct-Current Transmission Converters, Systems and DC Grids*. West Sussex: Wiley, 2015.
- [15] J. I. N. Jingxin, "Protection of HVDC Transmission Lines Based on Wavelet Transformation and Analysis of Energy Spectrum," pp. 180–185, 2013.
- [16] S. Wang, T. Bi, S. Member, and K. Jia, "Wavelet Entropy-based Fault Detection Approach for MMC-HVDC Lines," pp. 1–5, 2015.
- [17] P. K. Murthy, J. Amarnath, S. Kamakshiah, and B. P. Singh,

- “Wavelet transform approach for detection and location of faults in HVDC system,” in *IEEE Region 10 Colloquium and 3rd International Conference on Industrial and Information Systems, ICIS 2008*, 2008, pp. 6–11.
- [18] J. Cheng, M. Guan, L. Tang, and H. Huang, “Electrical Power and Energy Systems A fault location criterion for MTDC transmission lines using transient current characteristics,” *Int. J. Electr. POWER ENERGY Syst.*, vol. 61, pp. 647–655, 2014.
- [19] O. M. K. K. Nanayakkara, A. D. Rajapakse, and R. Wachal, “Location of DC line faults in conventional HVDC systems with segments of cables and overhead lines using terminal measurements,” *IEEE Trans. Power Deliv.*, vol. 27, no. 1, pp. 279–288, 2012.
- [20] H. Shu, X. Tian, and Y. Dai, “The Identification of Internal and External Faults for ± 800 kV UHVDC Transmission Line based on Mathematical Morphology,” in *2010 2nd International Workshop on Database Technology and Applications, DBTA2010 - Proceedings*, 2010, pp. 288–292.
- [21] A. Swetha, P. Krishna Murthy, N. Sujatha, and Y. Kiran, “A novel technique for the location of fault on a HVDC transmission line,” *J. Eng. Appl. Sci.*, vol. 6, no. 11, pp. 62–67, 2011.
- [22] P. Srikanth, A. K. Chandel, and K. A. Naik, “HVDC system fault identification using S-transform approach,” in *ICPCES 2010 - International Conference on Power, Control and Embedded Systems*, 2010, no. 2, pp. 2–7.
- [23] W. Li, Zhao, Zou, Guibin, Du, Tao, Yang, “S-transform based pilot protection method for HVDC transmission lines,” in *2015 5th International Conference on Electric Utility Deregulation and Restructuring and Power Technologies (DRPT)*, 2015, pp. 1667–1672.
- [24] F. Kong and B. Zhang, “A novel disturbance identification method based on empirical mode decomposition for HVDC transmission line protection,” no. 2.
- [25] S. Zhang, B. H. Zhang, M. You, and Z. Q. Bo, “Realization of the transient-based boundary protection for HVDC transmission lines based on high frequency energy criteria,” in *2010 International Conference on Power System Technology: Technological Innovations Making Power Grid Smarter, POWERCON2010*, 2010, pp. 1–7.
- [26] N. E. Huang and Z. Wu, “A REVIEW ON HILBERT-HUANG TRANSFORM: METHOD AND ITS APPLICATIONS TO GEOPHYSICAL STUDIES,” *Rev. Geophys.*, vol. 46, no. 2007, pp. 1–23, 2008.
- [27] N. O. A.-O. N.E. Huang, *The Hilbert–Huang Transform in Engineering*. Broken Sound Parkway ,NW,USA: CRC Press,Taylor & Francis Group, 2005.
- [28] N. E. Huang, M.-L. C. Wu, S. R. Long, S. S. P. Shen, W. Qu, P. Gloersen, and K. L. Fan, “A confidence limit for the empirical mode decomposition and Hilbert spectral analysis,” *Proc. R. Soc. A Math. Phys. Eng. Sci.*, vol. 459, no. 2037, pp. 2317–2345, 2003.
- [29] N. Huang, Z. Shen, S. Long, M. Wu, H. SHIH, Q. ZHENG, N. Yen, C. Tung, and H. Liu, “The empirical mode decomposition and the Hilbert spectrum for nonlinear and non-stationary time series analysis,” *Proc. R. Soc. A Math. Phys. Eng. Sci.*, vol. 454, no. 1971, pp. 995, 903, 1998.
- [30] G. Yang, X. Bin Sun, M. X. Zhang, X. L. Li, and X. R. Liu, “Study on ways to restrain end effect of hilbert-huang transform,” *J. Comput.*, vol. 25, no. 3, pp. 22–31, 2014.
- [31] G.-B. Huang, Q. Zhu, C. Siew, G. H. Å, Q. Zhu, C. Siew, G.-B. Huang, Q. Zhu, and C. Siew, “Extreme learning machine: Theory and applications,” *Neurocomputing*, vol. 70, no. 1–3, pp. 489–501, 2006.
- [32] C. S. Guang-bin Huang, Qin-yu Zhu, “Extreme learning machine: A new learning scheme of feedforward neural networks,” in *International Joint Conference on Neural Networks (IJCNN2004)*, 2004, vol. 2, pp. 985–990.
- [33] G.-B. Huang, H. Zhou, X. Ding, and R. Zhang, “Extreme learning machine for regression and multiclass classification,” *IEEE Trans. Syst. man, Cybern. Part B, Cybern.*, vol. 42, no. 2, pp. 513–29, 2012.
- [34] K. Zhang and M. Luo, “Neurocomputing Outlier-robust extreme learning machine for regression problems,” *Neurocomputing*, vol. 151, pp. 1519–1527, 2015.

The Reinforcing Effect Of Nylon 6,6 Nanofibrous Mats On Gfrp Modified With Nanoparticles Subjected To Low Velocity Impact

Vildan ÖZKAN¹, Murat YILDIZ¹, Ahmet YAPICI¹

¹*Mechanical Engineering Department, Iskenderun Technical University, 31200, Hatay.*

This work investigates the low velocity impact resistance of GFR-epoxy laminates interleaved with electrospun nylon 6,6 nano-fibres. The main goal is to investigate the interaction between the nanofibrous mats interleaved into a laminate and their influence on the property of the whole body and in particular their reinforcing effect. Different nanomodified configurations are suggested and tested together with virgin specimens. The multi-walled carbon nanotubes (MWCNTs) and graphene were used as nanoparticles. The prepared solution for electrospinning process contains 16 wt% nylon 6,6. The solvent mixture of formic acid/dichloromethane (2:1 wt/wt ratio) was trusted as an efficient solvent for nylon 6,6 materials. The nylon 6,6 nanofiber layers were studied by SEM. The nanofiber mats were placed between the woven glass fiber materials. Special molds were designed to produce composite materials. The results of the low velocity impact tests show that the interaction between the resin and the nano-fibre is the key feature of the reinforcement mechanism. The relation between the nanofiber layer numbers and the damping ratio was obtained.

Keywords: Electrospinning, Nanofiber, Nylon 6.6, GFRP, MWCNT.

Assessment of Wind Characteristics Using Weibull Distribution in Muğla Sıtkı Koçman University Central Campus

Faruk Şen, Muğla Sıtkı Koçman University
Energy Systems Engineering
Muğla, Turkey
faruksen@mu.edu.tr

Ramazan Özkan, Erciyes University
Wind Engineering and Aerodynamic Research Laboratory,
Department of Energy System Engineering Kayseri, Turkey
ramazanozkan@mu.edu.tr

Serkan Ballı, Muğla Sıtkı Koçman University
Information Systems Engineering
Muğla, Turkey
serkan@mu.edu.tr

Ayşegül Gökdemir, Muğla Sıtkı Koçman University
Energy System Engineering
Muğla, Turkey
aysegulg@mu.edu.tr

Abstract— This study is about analyzing the wind characteristics using Weibull distribution. Weibull is generally used to analysis wind speed data sets in statistical analysis. For this purpose, building-mounted wind measurement masts were established on suitable place in Muğla Sıtkı Koçman University Central Campus in Kötekli. Mean wind speeds were measured hourly at 15 m height. Annual of hourly measured wind data between from July 2015 to June 2016 was analyzed in this study. Weibull parameters were calculated by statistical analysis. Subsequently, considered wind speed distributions were evaluated with The Coefficient of Determinations (R^2) and Root Mean Square Error (RMSE) analysis for determination of Weibull distributions.

Keywords— Wind Speed; Wind Characteristic; Weibull Distribution; Muğla

V. INTRODUCTION

Renewable energy sources are an environmental type of energy compared to fossil fuels that pollute the atmosphere. Wind energy is one of the fastest growing energy sources in the world and in our country among renewable energy sources. At the present time, a lot of studies on the assessment of wind characteristics were investigated.

Ucar and Balo [1] evaluated wind characteristics using the wind speed data collected of the six meteorological stations in Turkey during the period 2000-2006. This study pointed out that the mean annual value of Weibull shape parameter k is between 1.71 and 1.96 while the annual value of scale parameter c is between 6.81 and 9.71 m/s. Yaniktepe et al. [2] investigated the wind energy potential that is a result of the distribution of wind speeds in Osmaniye, which is located east of the Mediterranean Sea in Turkey. Wind data, consisting of wind speed, direction

and flow time at a height of 10 m, were collected by the Turkish State Meteorological service for a period of 44 months, from January 2008 to August 2011. To determine the Weibull parameters, they used a graphical method.

Ozgener [3] determined the wind energy potential of the Celal Bayar University Muradiye Campus. In this study the wind speeds were obtained between 2006 and 2007 using an experimental system. Ozgener predicted that the installation of wind energy system would not be economical due to its low capacity factor of 14.1%. Ozerdem and Turkeli [4] presented the wind characteristics such as wind speed, turbulence intensity and wind direction for Izmir Institute of Technology campus. They concluded that the campus region had a high wind potential to utilize wind turbine systems. Furthermore, they selected the most suitable wind turbines as 600 kW and 1500 kW.

VI. MATERIAL AND METHOD

Information of wind speed distribution is very significant factor for evaluating the wind potential of windy regions [5,6]. In this study, wind characteristics of Muğla Sıtkı Koçman University Central Campus in Muğla were investigated by using Weibull distribution. For this purpose, building-mounted wind measurement masts were established on suitable place in Muğla Sıtkı Koçman University Central Campus in Kötekli. Hourly mean wind speeds were measured at 15 m height. Annual of hourly measured wind data between from July 2015 to June 2016 was analyzed.

A. Site description and Wind data measurement mast

Muğla Sıtkı Koçman University Central Campus is positioned a country known as Menteşe of Muğla province.

Muğla province is located in the south –western Anatolia region. Locations and coordinates of measurement mast in campus are displayed in Fig.1 and Table 1, respectively.



Fig. 1. The location of the wind measurement masts in Campus [7]

Table 1. Geographical coordinates of station used in the study

Station	Latitude	Longitude	Elevation
Campus	37°09'43.1"N	28°22'09.6"E	723 m

The wind speed was measured at 15 meters high by building-mounted wind measurement mast. Measurement mast has direction sensor, anemometer, temperature and pressure sensors. Measured data is transferred to a data collector.

B. Weibull Distribution Method

The wind speed probability density function can be calculated as [8]:

$$f(v) = \frac{k}{c} \times \left(\frac{v}{c}\right)^{k-1} \exp\left(-\left(\frac{v}{c}\right)^k\right), (k > 0, v > 0, c > 1) \quad (1)$$

Where $f(v)$ is the probability of observing wind speed v , c is the Weibull scale parameter and k is the dimensionless Weibull shape parameter. The Weibull parameters k and c , characterize the wind potential of region under study. Mainly, the scale parameter, c , shows how 'windy' a wind location under consideration is, whereas the shape parameter, k , shows how peaked the wind distribution is (i.e if the wind speeds tend to be very close to a certain value, the distribution will have a high k value and is very peaked) [9].

In this study, the shape parameter and the scale parameter are calculated by using statistical analysis.

C. Error Analysis

The errors expressed in terms of the Root Mean Squared Error (RMSE) and coefficients of goodness of fit (R^2) are determined between the observed and calculated wind speed frequencies by using statistical analysis [10]. The Root Mean Squared Error is calculated by:

$$RMSE = \left[\frac{1}{N} \sum_{i=1}^N (y_i - x_i)^2 \right]^{0.5} \quad (2)$$

The coefficients of goodness of fit are calculated by:

$$R^2 = 1 - \frac{\sum_{i=1}^N (y_i - x_i)^2}{\sum_{i=1}^N (y_i - \bar{y})^2} \quad (3)$$

VII. RESULTS AND DISCUSSIONS

The mean monthly values of wind speed variations at a height of 15 m are presented in Fig 2. It indicates that the highest monthly mean wind speed is determined as 2,03 m/s in March 2016 while the lowest mean wind speed 0,87 m/s in December 2015.

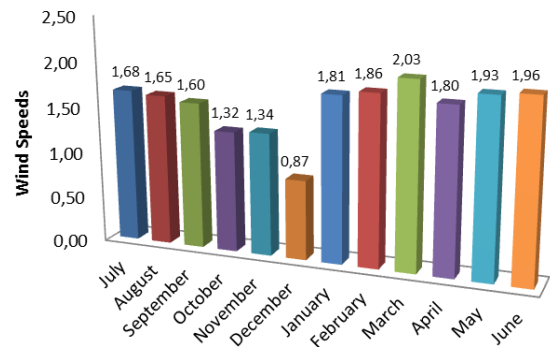


Fig. 2. The mean monthly values of wind speed variations at a height of 15 m

The Weibull parameters calculated for the months measured between July 2015 and June 2016 using the wind data of the wind measurement station are given in Table 2. Accordingly, to this table, Weibull shape parameter k varies between 1.15 and 1.53, while scale parameter c varies between 0.92 and 2.23 m/s

Table 2. Monthly variations of Weibull parameters

	k (shape)	c (scale)
July	1,45	1,86
August	1,48	1,83
September	1,32	1,75
October	1,31	1,42
November	1,21	1,38
December	1,15	0,92
January	1,39	1,83
February	1,30	1,93
March	1,49	2,23
April	1,27	1,94

May	1,50	2,14
June	1,53	2,18

Table 3. Coefficients of determination and root mean square errors (m/s)

	RMSE)	R ² (%)
July	0,0280706	94,7
August	0,0298098	95,9
September	0,0444510	91,9
October	0,035164	96,2
November	0,0316470	97,1
December	0,0412024	97,2
January	0,0554300	86,7
February	0,0397272	91,9
March	0,0449434	87,5
April	0,0456820	89,4
May	0,0386144	91,1
June	0,0357993	92,1
Annual	0,0311973	94,8

It is seen from Table 3 the highest value of RMSE was 0.0554300 m / s, while the lowest value of R² was 86.7%. In addition, annual of RMSE was calculated as 0.0311973 and R² was calculated as 94.8%. When these factors are evaluated, it is expected that the value of R² should be close to 1 when the RMSE value is required to be close to zero in terms of the accuracy of the analyzes. When the chart is examined, it is seen that logical results are obtained. Correlations between observed, Weibull wind speed frequencies in annual are illustrated in Fig. 3.

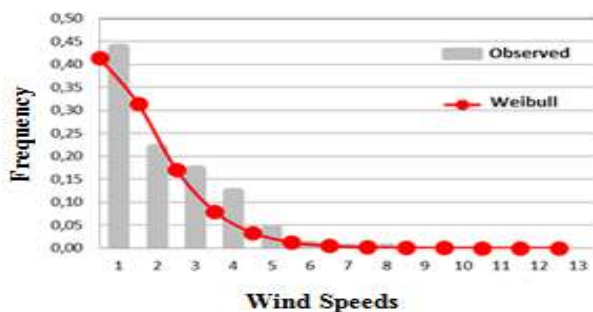


Fig.3. Correlations between observed, Weibull wind speed frequencies in annual

VIII. CONCLUSION

When the error analysis is evaluated, it is seen that the Weibull distribution is highly compatible with the observed wind speeds. Due to the variability of the wind speed, the wind potential may vary from year to year. For this reason, wind measurements should be taken for more than 1 year in order to obtain good results. This study can also be applied to different areas of the campus area to determine the wind map of the campus area.

ACKNOWLEDGMENT

This paper has been granted by the Mugla Sıtkı Kocman University Research Projects Coordination Office. Project Grant Number 15/008 and Title: Bina Montajlı Rüzgâr Ölçüm Sisteminden Elde Edilen Verilerin Analiz Edilmesi.

REFERENCES

- [13] A. Ucar, F. Balo, "Evaluation of wind energy potential and electricity generation at six location in Turkey", *Applied Energy*, 86 (2009), pp. 1864–1872.
- [14] B. Yaniktepe, T. Koroglu, M.M. Savrun, "Investigation of wind characteristics and wind energy potential in Osmaniye, Turkey", *Renewable And Sustainable Energy Reviews*, 21 (2013) pp. 703–711.
- [15] L. Ozgener, "Investigation of wind energy potential of Muradiye in Manisa", *Renewable And Sustainable Energy Reviews*, 14 (2010), pp. 3232–3236.
- [16] B. Ozerdem, H.M. Turkeli, "Wind energy potential estimation and micrositting on Izmir Institute of Technology Campus, Turkey", *Renewable Energy*, 30 (2005), pp. 1623–1633.
- [17] B. Yaniktepe, T. Koroğlu, M.M. Savrun "Investigation of wind characteristics and wind energy potential in Osmaniye, Turkey," *Renewable And Sustainable Energy Reviews*, 21 (2013) pp. 703–711
- [18] M. Gokcek, A. Bayulgen, S. Bekdemir "Investigation of wind characteristics and wind energy potential in Kırklareli, Turkey" *Renewable Energy*, 32 (2007), pp. 1739-1752
- [19] Web-1, Muğla Sıtkı Koçman University, Geographic information systems& UZAL, www.gis.mu.edu.tr/skv1
- [20] T.J. Chang, Y.T. Wu, H.Y. Hsu, C.R. Chu, C.M. Liao, "Assessment of wind characteristics and wind turbine characteristics in Taiwan", *Renewable Energy*, 28 (2003), pp. 851–871.
- [21] A. Keyhani, M. Ghasemi-Varnamkhasti, M. Khanali, R. Abbaszadeh, "An assessment of wind energy potential as a power generation source in the capital of Iran, Tehran" *Energy*, 35 (2010), pp. 188–201.
- [22] M. A. Tavares Lira, E. M. Da Silva, J. M. Brabo Alves And G. V. Oliveira Veras "Estimation Of Wind Resources In The Coast Of Ceará, Brazil, Using The Linear Regression Theory" *Renewable And Sustainable Energy Reviews*, 39 (2014), Pp. 509–529.

Numerical Study on Heat Transfer Enhancement with Fins Between Horizontal Plates

Ilker Goktepli

Department of Mechanical Engineering
Engineering Faculty, Selcuk University
Konya, Turkey
ilker goktepli@selcuk.edu.tr

Ulas Atmaca

Department of Mechanical Engineering
Engineering Faculty, Selcuk University
Konya, Turkey
uatmaca@selcuk.edu.tr

Abstract—Flow separation and reattachment regions significantly affect the heat transfer inside the ducts. Heat transfer is enhanced by using obstacles such as fins, turbulators to provide flow separation in this perspective. The aforementioned method is based on production of secondary flow or fluctuations due to the obstacles and utilized for heat exchangers, solar collectors, cooling parts of appliances etc. In the present study, turbulent flow and heat transfer characteristics is determined in the existence of fins placed between the parallel plates. Symmetrical fins are mounted periodically on the internal walls of the parallel plates. Constant wall temperature is taken as boundary condition to the plates and the fins. At the inlet of the system, the velocity of water is 0.15 m/s. The comparison of finned and unfinned horizontal parallel plates is done in terms of turbulent convective heat transfer at $Re = 6000$. In the numerical study, standard $k-\omega$ turbulence model has been used. As a result of the study, the enhancement in heat transfer due to flow separation has been provided by fins on the internal sides of the parallel plates.

Keywords— CFD; fin; heat transfer; parallel plate; turbulent flow

I. INTRODUCTION

Heat transfer is enhanced by using different techniques. One of these methods is placing of obstacles on the internal sides of the channel. Fundamentally, this method is based on flow separation and reattachment regions which significantly affect the heat transfer inside the devices. Baffles, fins and turbulators have been utilized to provide flow separation which provides the increment of heat transfer. Secondary flow or fluctuations based procedure is preferred for heat exchangers, solar collectors, cooling parts of appliances. In the literature, similar studies for convection heat transfer with fluid flow have been encountered. Kakac (1968) has numerically solved the forced convection heat transfer for air flowing between two parallel plates at $Re = 9370$ and $Re = 17100$. The changes of air velocity and effective diffusion through the cross-section of the channel were considered. Local Nusselt numbers have been obtained via the results of transient runs by assuming that air has fully developed turbulent velocity profile [1]. Kelkar and Patankar (1987) have analyzed the laminar flow and heat transfer in finned passages at $Re = 100$ and $Re = 500$. The fins have been kept at a constant temperature and arranged on parallel plates with staggered distribution. The fins were used for the flow deflection and this

causes the increment of the heat transfer considerably. Heat transfer was increased for fluids with the increment of Prandtl numbers as a result. However, it was found that shorter fins decreased the heat transfer in terms of lower Prandtl numbers [2]. Bejan and Scihubba (1992) have scrutinized the forced convection for the cooling process of parallel plates. The optimum distance between the plates has been determined by considering board length, fluid properties and pressure difference in terms of laminar flow regime in this study. Moreover, maximum total heat transfer has also been given with the dependence on pressure difference, stack thickness and temperature difference [3]. Abe et al. (1994) have recommended a turbulence model to handle the turbulent flows with separation of fluid and heat transfer, which has been developed from low-Reynolds-number $k-\epsilon$ turbulence model. The present model was successful for capturing the separation and reattachment regions of flow in the wake of backward-facing step. The heat transfer coefficient had the maximum value at the reattachment point and eddy viscosity was important for the determination of thermal field in the vicinity of that point [4]. Ooi et al. (2002) have calculated the flow and heat transfer characteristics of blocks periodically placed on the channel wall by conducting Reynolds-averaged simulations. Two and three dimensional v^2-f , Spalart-Allmaras and two-layer $k-\epsilon$ turbulence models were used, but the closest results to the experiments have been obtained with v^2-f model [5]. Bazdidi-Tehrani and Naderi-Abadi (2004) have numerically investigated the laminar fluid flow and heat transfer in the entrance zone of the horizontal channel. Various blockage ratios for $h/H = 0.1, 0.2$ and 0.3 have been considered in case of constant temperature for both sides of the channel at $100 \leq Re \leq 500$. It is declared that local Nusselt numbers increased in the reattachment points owing to separated flow from the ribs. Recirculation zones between the ribs reduced the local Nusselt number so ribs underwhelmed [6]. Korichi and Oufer (2007) have numerically examined heat transfer in rectangular channel including heated obstacles on the internal walls. Two-dimensional and transient analyses for air have been conducted at $Re = 50, 500$ and 1000 corresponding the values of laminar flow regime. As a result, flow characteristics and Nusselt numbers have been determined [7]. Oztog et al. (2009) have considered three blocks with constant surface temperature inside the horizontal channel for the control of fluid flow and heat transfer. In the numerical study, a triangular bar has been

evaluated at two different positions and compared to the case without the bar. As a conclusion, heat transfer has been enhanced by using the bar and the optimum position for the bar has been recommended [8]. Silin et al. (2012) have used the parallel-plate channel with uniformly cooled in the experimental system in which water flowing inside it. The effects of inlet temperature and wall heat flux on the study have been taken into account in the range of $5000 \leq Re \leq 10000$ [9]. Altac and Ugurlubilek (2016) have simulated the unsteady natural convection heat transfer of two- and three-dimensional rectangular enclosures with different slenderness ratios. Various turbulence models have been utilized and compared about aforementioned cases in the range of $10^8 \leq Ra \leq 10^{13}$. As a result of the study, Nusselt numbers have been attained in that range of Rayleigh numbers [10]. Ayli et al. (2016) have studied on steady forced convection regimes of square cross-sectional channel in the range of $1.7 \times 10^8 \leq Re \leq 2.47 \times 10^8$. Rectangular fins have been mounted on the bottom wall and various aspect ratios have been tested both experimentally and numerically and the results have been given as empirical correlation for Nusselt number [11].

In the present study, turbulent flow and heat transfer characteristics have been determined in the existence of obstacles placed between the two-dimensional parallel plates. Symmetrical obstacles have been periodically mounted on the internal walls of the parallel plates. Here, comparison of finned and unfinned horizontal parallel plates has been done in terms of turbulent convective heat transfer at $Re = 6000$.

II. MATERIAL AND METHOD

Transient convection heat transfer with turbulent flow between horizontally placed two parallel plates has been numerically examined by using standard k- ω turbulence model at $Re = 6000$. Reynolds number has been given as $Re = (U_\infty D_H)/\nu$, based on the hydraulic diameter which is $D_H = 2H$. H is the distance between the plates, ν is the kinematic viscosity and U_∞ is the free-stream velocity value.

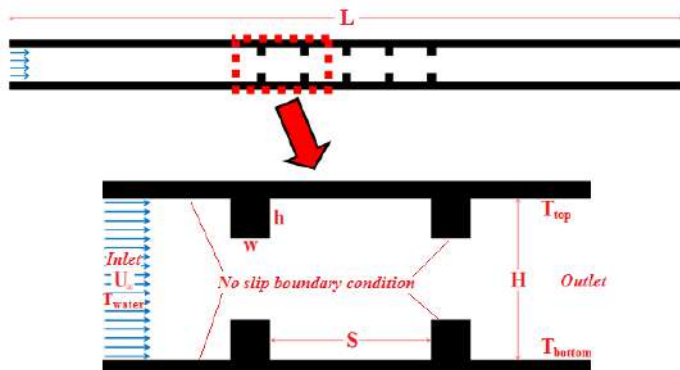


Fig. 27. Schematic of the horizontal parallel plates.

Fig. 1 shows the two-dimensional system with finned plates including all boundary conditions used in the numerical study. Unfinned plates have been considered without the fins on the inside walls. The length of the plate, L , is taken as 1 m and its thickness is taken as zero. The distance between the plates is

expressed as $H = 0.02\text{ m}$. Parallel plates are assumed to be at constant wall temperature of $T_{top} = T_{bottom} = 400\text{ K}$ while water at $T_{water} = 300\text{ K}$ enters to the system with $U_\infty = 0.15\text{ m/s}$. The height of the fin is given by $h = 0.005\text{ m}$ which is equal to its width as $w = 0.0025\text{ m}$. Fin spacing is defined as $S = 0.02\text{ m}$. Moreover, uniform wall temperature of $T = 400\text{ K}$ for the fins has been taken into consideration in case of the finned plates.

Mesh independence analysis has been done for various mesh sizes with respect to dimensionless number which is Nusselt number calculated as $Nu = (h D_H)/k$. At $Re = 6000$, five different numbers of elements have been tested. One of them done via standard k- ω turbulence model has been given as an example in Table 1.

TABLE XV. MESH INDEPENDENCE ANALYSIS AT $Re = 6000$

Number of elements	Mean Nusselt number (Nu)
189885	55.98
322567	54.99
581342	54.86
898803	53.88
1070791	54.12

Nusselt numbers change with the grid sizes. Grid system has been determined with respect to Nusselt number which is given in (1) and (2) as in the empirical correlation expressed by Shah and Bhatti (1987) [12]:

$$Nu_\infty = \frac{(f_m/2)(Re - 1000)Pr}{1 + 12.7(f_m/2)^{1/2}(Pr^{2/3} - 1)} \quad (1)$$

$$f_m = A + \frac{B}{Re^{1/m}} \quad (2)$$

Here, $A = 1.28 \times 10^{-3}$, $B = 0.1143$ and $m = 3.2154$ are the values in (2) which is valid in the range of $4000 \leq Re \leq 10^7$. Prandtl number has been obtained as $Pr = 5.83$ for water [13]. Empirical correlation of Nusselt number has been calculated in respect to empirical correlation in (1) correspondingly applicable for $2300 \leq Re \leq 5 \times 10^6$ and $Pr > 0.5$, respectively. The value for Nusselt number has been evaluated as $Nu_\infty = 44.84$ by using the correlation in (1). For lower grid sizes of flow domain, Nu values are higher and then decrease with increasing numbers of elements. However, the percentage difference is about 0.02% when the number of grid elements ascends from 898803 to 1070791 . Therefore, numerical analyses have been conducted for 898803 grid elements used in the flow domain owing to fewer requirements of computer capacity and computational time.

The governing equations for an incompressible flow form of the continuity equation and the Reynolds-Averaged Navier-Stokes are specified below in the following equations in (3) and (4) [14].

$$\frac{\partial \bar{u}_i}{\partial x_i} = 0 \quad (3)$$

$$\frac{\partial \bar{u}_i}{\partial t} + \frac{\partial \bar{u}_i \bar{u}_j}{\partial x_j} = \frac{1}{\rho} \frac{\partial \bar{p}}{\partial x_i} - \frac{\partial \tau_{ij}}{\partial x_j} + \nu \frac{\partial^2 \bar{u}_i}{\partial x_i \partial x_j} \quad (4)$$

where u_i and u_j are the filtered velocity components along the Cartesian coordinates of x_i and x_j , p is the pressure, ρ is the fluid density and ν is the kinematic viscosity of the fluid [14].

The standard $k-\omega$ model is an empirical model based on model transport equations for the turbulence kinetic energy, k , and the specific dissipation rate, ω , which can also be thought as the ratio of k . As the $k-\omega$ model has been modified over the years, production terms have been added to both the k and ω equations, which have improved the accuracy of the model for predicting free shear flows [14].

$$\frac{\partial}{\partial t}(\rho k) + \frac{\partial}{\partial x_j}(\rho k u_j) = \frac{\partial}{\partial x_j} \left[\left(\mu + \frac{\mu_t}{\sigma_k} \right) \frac{\partial k}{\partial x_j} \right] + G_k - Y_k + S_k \quad (5)$$

$$\frac{\partial}{\partial t}(\rho \omega) + \frac{\partial}{\partial x_j}(\rho \omega u_j) = \frac{\partial}{\partial x_j} \left[\left(\mu + \frac{\mu_t}{\sigma_\omega} \right) \frac{\partial \omega}{\partial x_j} \right] + G_\omega - Y_\omega + S_\omega \quad (6)$$

In these equations (5) and (6), G_k represents the generation of turbulence kinetic energy due to mean velocity gradients. G_ω represents the generation of ω . Γ_k and Γ_ω represent the effective diffusivity of k and ω , respectively. Y_k and Y_ω represent the dissipation of k and ω due to turbulence. All of the above terms are calculated as described below. S_k and S_ω are user-defined source terms [14].

Energy equation is expressed as given in (7) as follows [14]:

$$\frac{\partial}{\partial t}(\rho E) + \nabla \cdot (\bar{\mathbf{v}}(\rho E + p)) = \nabla \cdot \left(k_{eff} \nabla T - \sum_j h_j \bar{\mathbf{J}}_j + \left(\bar{\boldsymbol{\tau}}_{eff} \cdot \bar{\mathbf{v}} \right) \right) + S_h \quad (7)$$

where k_{eff} is the effective conductivity ($k + k_t$, where k_t is the turbulent thermal conductivity, defined according to the turbulence model being used), and $\bar{\mathbf{J}}_j$ is the diffusion flux of species. Energy transfer, E , is due to conduction, species diffusion, and viscous dissipation, respectively. S_h includes the heat of chemical reaction, and any other volumetric heat sources defined.

III. RESULTS AND DISCUSSION

Heat transfer between horizontal parallel plates for turbulent flow has been investigated by using standard $k-\omega$ turbulence model. The results of unfinned plates have also been given for comparison. Fig. 2 indicates the time-averaged results of streamwise velocity components $\langle u \rangle$, cross-stream velocity components $\langle v \rangle$, distributions of temperature $\langle T \rangle$ and pressure $\langle P \rangle$ at the inlet and outlet regions of unfinned and finned plates at $Re = 6000$. Moreover, the aforementioned characteristics have been given in Fig. 3 for the finned region to compare with unfinned one. The dimensions of all images have been normalized with the height between the plates as $L' = L/H$ and $H' = H/H$. The maximum and minimum values are indicated as a legend bar for the contours in each figure and divided with 15 levels.

Time-averaged streamwise velocity components have been given in the range of $-0.01 \text{ m/s} \leq \langle u \rangle \leq 0.15 \text{ m/s}$ for the inlet and the outlet regions of the unfinned and the finned plates in Fig. 2. At the inlet of parallel plates for both the finned and unfinned channel flow, the velocity values are almost identical and the value of inlet velocity is more common.

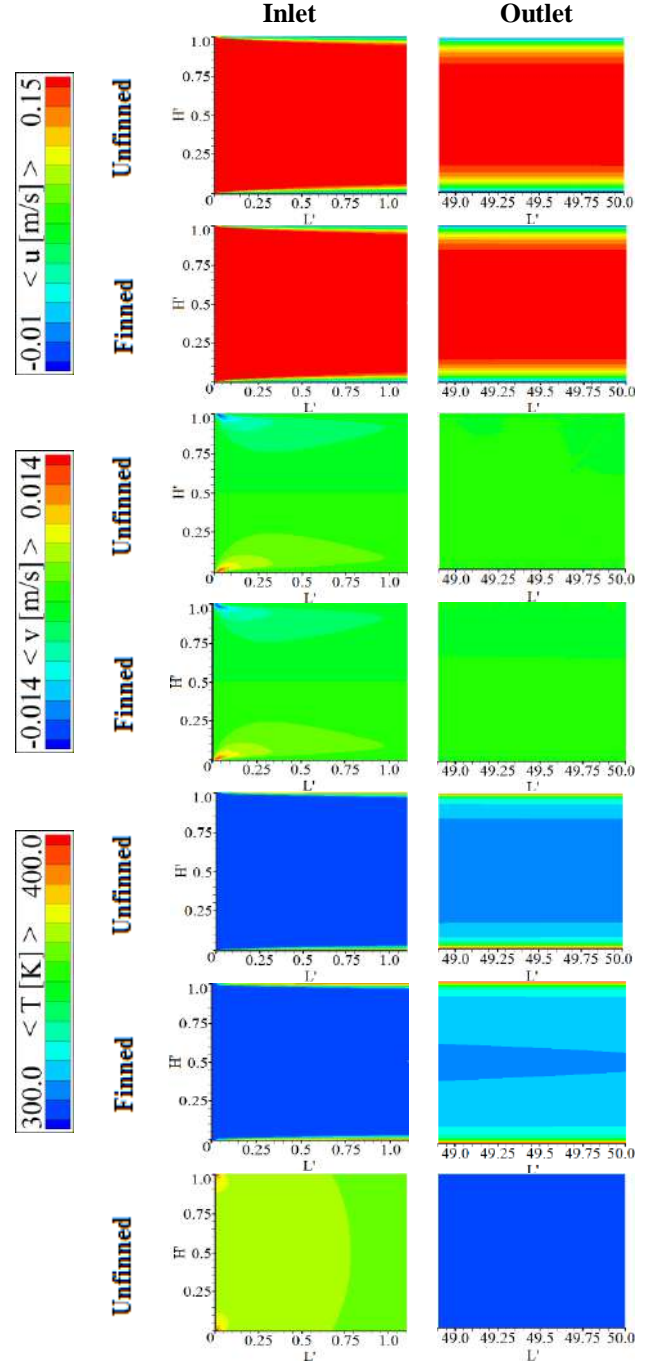
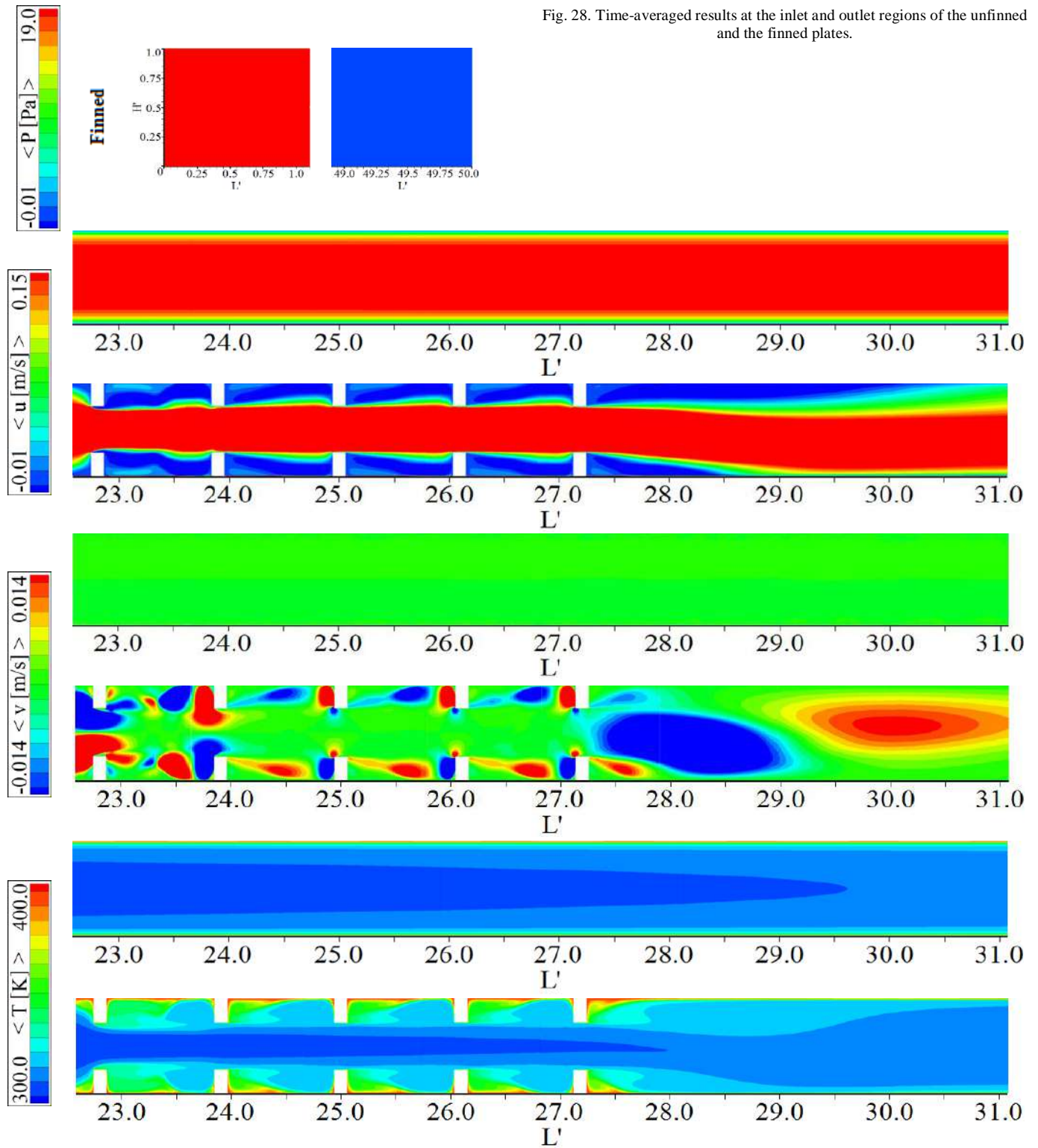


Fig. 28. Time-averaged results at the inlet and outlet regions of the unfinned and the finned plates.



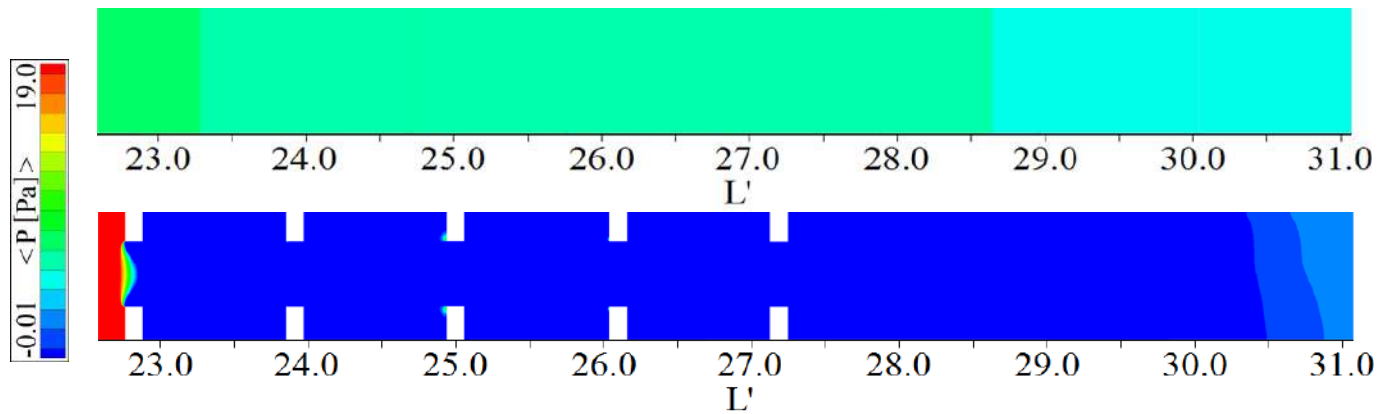


Fig. 29. Comparison of the unfinned and the finned regions in terms of time-averaged results.

The formation of hydrodynamic boundary layer can be seen from the starting point of the plates for both channel types. At the right hand side of the time-averaged streamwise velocity figures, the velocity profile at the exit of the channel is given. It can be seen from the figure that, the distance after the last fin for the finned channel is sufficient for the development of the velocity profile since the hydrodynamic boundary layer of the finned channel gets the same value of unfinned plates. Moreover, streamwise velocity components at the outlet of the parallel plates indicated same characteristics since flow recovery completed long before the outlet region for both unfinned and finned plates. The unfinned and the finned plates have also been investigated for time-averaged cross-stream velocity components for $-0.014 \text{ m/s} \leq \langle v \rangle \leq 0.014 \text{ m/s}$. After the first contact between the fluid and the plates, the symmetrical clusters of cross-stream velocity components have been observed at the inlet. While positive values of cross-stream velocity components are on the bottom side, negative ones are seen on the opposite side. The symmetrical clusters are only effective in the beginning section as $0 \leq L' \leq 1.0$ for both cases. Temperature distributions are shown with $300.0 \text{ K} \leq \langle T \rangle \leq 400.0 \text{ K}$ in terms of the inlet and the outlet regions of the unfinned and the finned plates. At the inlet, the temperature of the fluid is more efficient and its effect lost through the plates as a result of convection heat transfer. At the exit region of the finned plates, the temperature of the fluid is significantly higher than the unfinned ones because of the enhancement effect on heat transfer via the fins. The fins cause the increment of heat transfer surface area between the wall and the fluid; also the fins cause distortion of flow patterns. Secondary flows caused by flow separation increase the temperature of fluid at the exit of the plates. Pressure distributions have been ranged as $-0.01 \text{ Pa} \leq \langle P \rangle \leq 19.0 \text{ Pa}$. For the unfinned plates, mean pressure value is seen at the inlet while maximum pressure value is observed in case of the finned ones with respect to the legend. However, pressure distributions are nearly same for the outlet region. The pressure drop is higher for the finned plates according to the whole pressure loss.

Time-averaged results have been compared for the investigation of the finned region in Fig. 3. At the top of first figure, the streamwise velocity contours $\langle u \rangle$ are given for both the finned and the unfinned plates. As can be seen from the figure, the flow is separated from the first fin at the top and the

bottom surfaces symmetrically and the mean flow is increased owing to the decreasing cross-sectional area. Two circulation zones are occurred between the first and the second fins but only one circulation zone can be seen between the other fins. And also symmetrical circulation zones can be observed at the top side of the plate. The main difference that distorts the symmetry can be seen at the bottom layer after the last fin as the flow reattachment. At the second figure, the cross-stream velocity values $\langle v \rangle$ can be seen. This figure also shows a symmetrical contour of velocity according to the duct axis. The effect of first fin on the fluid flow is much more as can be seen from this figure. After passing through the first fin, the flow recovers at the downstream fins. After the last fin, the flow reattachment region can also be seen with in accordance with the first figure. In the third figure, the temperature distribution is shown. From the whole of the figure, the mean temperature is considerably higher than the unfinned plate for the investigated region. The increment of the heat transfer surface area and secondary flows due to the flow distortion causes the increment of the fluid temperature. Again a symmetric figure is occurred according to the duct axis until the reattachment region after the last fin. In according to the first and the second velocity figures, there is circulation behind the fins; which is coherent with the temperature distribution. The temperature contours between the fins show that the fresh-fluid can enter the cavities much more after the second fin. The point of the flow reattachment after the last fin is coherent with velocity figures. At the exit of temperature profile, the figure gets the values of the unfinned duct since the length after the last fin is adequate for the redevelopment of the thermal boundary layer. The last image of Fig. 3 is related with the pressure distributions along the plate. The difference between the unfinned and the finned plates is significant. As can be seen from the figure, pressure drops suddenly after the first fins and keep its trend until the outlet. In the design of heat transfer equipment, two points should be examined more deeply. First one is the increment of the heat transfer while the second one is the pressure drop.

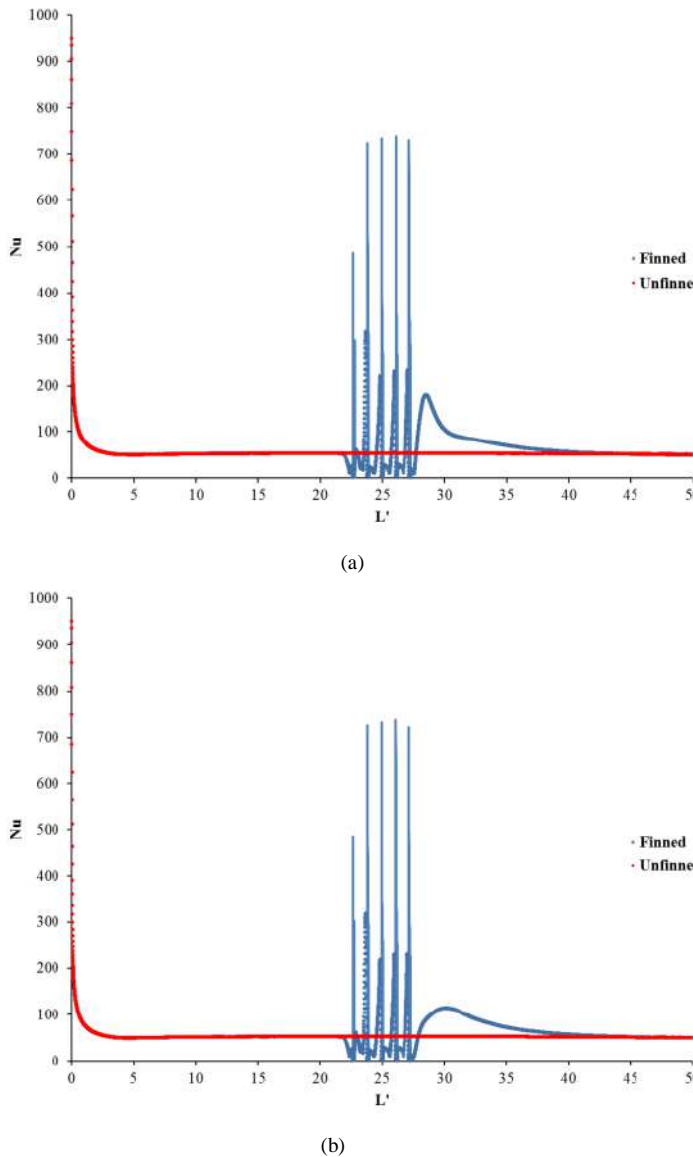


Fig. 30. Comparison of local Nusselt numbers for (a) the bottom plate and (b) the top plate of the unfinned and the finned plates

Fig. 4 indicates the distribution of the local Nusselt numbers at the bottom and the top plates compared with the unfinned ones. As can be seen from both figures, Nusselt numbers values are greater at the second fin compared to the first one on both sides and gradually increase through the fourth one. The value of local Nusselt number is higher after the fifth fin at the bottom plate than the top plate. This result is parallel to the results of Fig. 3. The red line given in Fig. 4 is the local Nusselt number values of the unfinned plates. Nusselt number values are significantly higher than the unfinned plates. After the fifth fin, the flow redevelops and gets the values of the unfinned plates. The local Nusselt number value gets its maximum value at the flow reattachment region for both bottom and top plates. The reattachment point is at about $L' = 28.0$ for the bottom plate and $L' = 30.0$ for the top plate and flow recovery regions are

proportional to these values at both plates. The Nusselt number values gradually decrease before the first fin and get the maximum value at the top of the fin. In the cavities, Nusselt number decreases to the minimum value and increases through the next fin. Nusselt number values draw similar curves after the second one. The circulation in the cavities causes in accordance with the results of Fig. 3.

IV. CONCLUSIONS

The heat transfer and the fluid flow between the horizontal parallel plates for turbulent flow has been investigated by using standard $k-\omega$ turbulence model in terms of the unfinned and the finned plates. The results obtained from the solutions can be outlined as follows:

- 1) The fins placed between the parallel plates affect the heat transfer and fluid flow characteristics significantly when compared to the unfinned plates.
- 2) The fins cause the increment of the velocity and also secondary flow between them.
- 3) The mean temperature of the flow increases significantly compared to the unfinned plates.
- 4) The pressure loss due to the fins has to be considered in the design of heat transfer equipment.
- 5) The turbulent model which is chosen for this problem is adequate to solve this kind of problem.
- 6) The heat transfer values are affected by using fins.

ACKNOWLEDGMENT

The authors would like to acknowledge the funding of Academic Staff Training Program (OYP) for Project No. of 2015-OYP-007.

REFERENCES

- [1] S. Kakac, "Transient forced convection heat transfer in a channel," *Wärme – und Stoffübertragung*, vol. 1(3), pp. 169-176, September 1968.
- [2] K.M. Kelkar and S.V. Patankar, "Numerical prediction of flow and heat transfer in a parallel plate channel with staggered fins," *Journal of Heat Transfer*, vol. 109(1), pp. 25-30, February 1987.
- [3] A. Bejan and E. Sciubba, "The optimal spacing of parallel plates cooled by forced convection," *International Journal of Heat and Mass Transfer*, vol. 35(12), pp. 3259–3264, December 1992.
- [4] K. Abe, T. Kondoh and Y. Nagano, "A new turbulence model for predicting fluid flow and heat transfer in separating and reattaching flows—I. Flow field calculations," *International Journal of Heat and Mass Transfer*, vol. 37(1), pp. 139-151, January 1994.
- [5] A. Ooi, G. Iaccarino, P.A. Durbin and M. Behnia, "Reynolds averaged simulation of flow and heat transfer in ribbed ducts," *International Journal of Heat and Fluid Flow*, vol. 23, pp. 750-757, December 2002.
- [6] F. Bazdidi-Tehrani and M. Naderi-Abadi, "Numerical analysis of laminar heat transfer in entrance region of a horizontal channel with transverse fins," *International Communications in Heat and Mass Transfer*, vol. 31(2), pp. 211-220, March 2004.
- [7] A. Korichi and L. Oufer, "Heat transfer enhancement in oscillatory flow in channel with periodically upper and lower walls mounted obstacles," *International Journal of Heat and Fluid Flow*, vol. 28, pp. 1003-1012, October 2007.
- [8] H.F. Oztop, Y. Varol and D.E. Alnak, "Control of heat transfer and fluid flow using a triangular bar in heated blocks located in a channel,"

International Communications in Heat and Mass Transfer, vol. 36, pp. 878-885, October 2009.

- [9] N. Silin, V.P. Masson and R. Marino, "Heat transfer in a short parallel-plate channel in the transition regime," *Experimental Heat Transfer*, vol. 25(1), pp. 12–29, January 2012.
- [10] Z. Altac and N. Ugurlubilek, "Assessment of turbulence models in natural convection from two- and three-dimensional rectangular enclosures," *International Journal of Thermal Sciences*, vol. 107, pp. 237–246, September 2016.
- [11] E. Ayli, O. Bayer and S. Aradag, "Experimental investigation and CFD analysis of rectangular profile FINS in a square channel for forced convection regimes," *International Journal of Thermal Sciences*, vol. 109, pp. 279-290, November 2016.
- [12] R.K. Shah and M.S. Bhatti, "Assessment of test techniques and correlations for single-phase heat exchangers," In *Proceedings of the 6th NATO Advanced Study Institute on Thermal-Hydraulics and Fundamentals of Two-Phase Flow Heat Exchangers*, Portugal, July 1987.
- [13] F.P. Incropera, D.P. Dewitt, T.L. Bergman and A.S. Lavine, "Fundamentals of Heat and Mass Transfer," John Wiley and Sons, New York, USA, 6th edition, 2002.
- [14] Anonymous, "Fluent 14.0 User Guide," Fluent Inc., 2013.

The Effects of the Ratio of Tool Rotational Speed to The Welding Speed on the Welding Performance for Dissimilar Aluminum Alloys

Şefika KASMAN

Department of Mechanical Engineering

Dokuz Eylül University

Izmir, Turkey

sefika.kasman@deu.edu.tr

Abstract— This study investigates the weldability of EN AW 5083 and EN AW 2024 by friction stir welding. The EN AW 5083 is used in transport applications, including marine and automotive. It is well known that the welding of EN AW 5083 aluminum alloy by the fusion welding techniques is good, but, includes many defects and cause to the loss of some elements. Due to these problems, the strength of the joints decreases when compared to the base material. The other material EN AW 2024 is difficult to weld by the fusion welding technique and mostly used in many aerospace structural applications. Dissimilar welding of EN AW 5083 and EN AW 2024 alloys is difficult by fusion welding techniques. In order to obtain defect free joint weld, the joining of the mentioned materials was performed by friction stir welding which is one of the solid state welding techniques. The ratio of the tool rotational speed to the welding speed was associated with the tool pin shape. All of weld experiments were exposed to the mechanical and microstructural investigations. The results showed that the ratio of the tool rotational speed to the welding speed has an impact on the strength of the weld joint. The tool rotational speed also has an impact on the joint strength irrespective of welding speed. A decrease in tool rotational speed resulted in increased strength of the weld joint.

Keywords—Friction stir welding, tensile properties, dissimilar welding

I. INTRODUCTION

Dissimilar welding of EN AW 5083 and EN AW 2024 alloys is difficult by fusion welding techniques due to the difficulty of the selection of the appropriate filler material and process parameters considering the metals to be welded. In some cases, the solid state welding techniques are considered to be the best alternative. The friction stir welding (FSW) is one of the solid state welding techniques and takes below the melting temperature of subjected material. The FS welding is performed by a tool which consisting of a shoulder and shaped pin. The rotational tool pin and by the effect of heat generated from friction between tool and materials plasticizes materials and with the advance movement of the tool, the

materials on butted surface of the plates are mixed and the joining is finished [1]. The literature related to the dissimilar FS welding of EN AW 5083 and EN AW 2024 alloys is limited. Sundaram et al. [2] have studied weldability of AA2024-T6 and AA5083-H321 by dissimilar friction stir welding. They used five different pin profiles, tool rotational speeds, welding speed and axial forces to determine appropriate welding condition. From the statistical analyze results; they reached a FS welding condition with higher tensile strength and elongation. Apart these, some of researcher studied on AA2XXX and AA5XXX alloys. The Mastanaiah et al. [3] have investigated dissimilar friction stir welds of aluminum alloys AA5083 and AA2219 to attain defect free joints by selecting process parameters. The statistical methods, analysis of variance and response surface methodology were used. Dilip et al. [4] have carried out the dissimilar FSW application to the AA2219 and AA5083. As the process response, weld microstructures, hardness and tensile properties were investigated. Koilraj et al. [5] have performed statistical analyses for dissimilar FSW of AA5083 and AA2219 to predict optimal process parameters (tool rotational speed, welding speed, pin profile and, ratio between tool shoulder diameter and pin diameter. From the literature reviews, it is reached an important knowledge, the pin shape; tool rotational speed and partly welding speed are the most critical factors on the joint performance.

Friction stir welding (FSW) is one of the solid state welding techniques [6] and uses a cylindrical tool consisting of a shoulder and a shaped pin [7]. Both of tool shoulder and pin is responsible from the stirring action and generating heat. The heat for welding is generated from the friction between tool and materials to be welded [7]. Apart this, the tool rotational speed and welding speed determines the heat input per unit area. Higher rotational speed or lower welding speed generates higher heat. Therefore, the tool rotational, welding speed and tool properties are the main factor to achieve defect

free or sound weld joint. A weld joint produced by FSW technique is consisting of three zones for each side of the tool pin. These are nugget zone or stirring zone (NZ), thermo-mechanically affected zone (TMAZ) and heat affected zone (HAZ), respectively. The NZ is highly affected both stirring actions of tool shoulder and pin. By the effect of heat input and stirring action of a pin, the materials to be welded are plastically deformed and then are exposed to dynamically recrystallization, subsequently. Resulting of dynamically recrystallization, the grains at the nugget zone become smaller and equiaxed compared with the other zones [8]. The NZ is affected from the tool rotational speed, welding speed and pin shape. The other zone is TMAZ and this zone is affected by heat and deformation. The difference from the NZ is that the heat is not big enough to complete recrystallization mechanism. The HAZ is affected by heat and the plastic deformation is not issue.

In this study, the main aim is to investigate the effect of the ratio of tool rotational speed to the welding speed (v ratio) on the microstructural alteration and tensile properties. Two different aluminum alloys EN AW 5083 and EN AW 2024 were used and welds were performed according to an experimental layout consisting of two tool pin shapes and v ratios. The relation between the plates material and process conditions were also analyzed.

II. MATERIALS AND METHODS

The materials used for the welding experiments were EN AW 5083-H111 and EN AW 2024-T351 and their chemical compositions and mechanical properties were given in Table 1 and Table 2. For the welding, the EN AW 2024-T351 was placed at the advancing side and the EN AW 5083-H111 was placed at the retracting side of pin. Two types of tools were used for welding applications. The helically threaded pins which were in straight and tapered form are one of the parameters. The tools used in the FSW welding were shown in Fig. 1. The other parameters were tool rotational speed and welding speed. The welding process parameters and their values were listed in Table 3. According to the experimental layout, six different experiments shown in Table 3 were performed. The tool tilt angle was fixed at 2° to the normal of the plate and the tool rotation direction was fixed at the clockwise. A sample for welding experiments was shown in Fig. 2.

TABLE I. THE CHEMICAL COMPOSITION OF ALUMINUM ALLOYS USED IN THE PRESENT STUDY (WT., %)

Alloy /Elements	Cu	Si	Mg	Mn	Zn	Cr	Fe	Al
EN AW5083	0.056	0.093	4.19	0.53	0.09	0.083	0.243	Bal.
EN AW2024	3.91	0.08	1.23	0.52	0.23	0.09	0.14	Bal.

TABLE II. MECHANICAL PROPERTIES OF ALUMINUM ALLOYS

Alloy	UTS (MPa)	ϵ (%)
EN AW 5083 – H111	325	17.6
EN AW2024 – T351	456	22

TABLE III. FSW PROCESS PARAMETERS AND THEIR LEVELS, TOOLS CONFIGURATION

Parameters (unit)	Symbol	Levels		
Tool Rotational Speed (rpm)	TRS	500	630	800
Welding Speed (mm/min)	WS	100	125	-
Tool type	TT	CT	ST	-
Fixed parameters				
Tool tilt angle ($^\circ$)	α	2		
Dwell time (s)	t	20s		

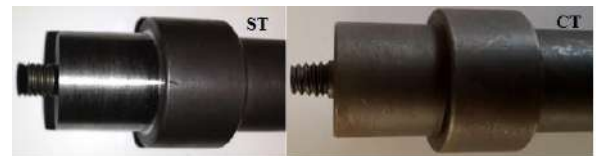


Fig. 1. Tools for FS welding



Fig. 2. A sample for FS welding

III. RESULTS AND DISCUSSION

The main question of this study is the ratio of tool rotational speed to the welding speed (v ratio) has how much effect on the mechanical properties and microstructural alterations. For this purpose, a small experimental group (layout) was conducted and the FS welding experiments were performed according to this layout. Each welding was characterized by the tensile test results and microstructure. The results were evaluated and discussed as below.

A. Mechanical Properties

The mechanical properties were investigated by the ultimate tensile strength (UTS) and percentage of elongation

(ϵ). The results were taken from the tensile tests and listed in Table 4. According to the results for CH shaped pin profile, both of UTS and ϵ increased with the increase of v ratio. The changing in UTS and ϵ is 20% and 68%, respectively. As for the SH shaped pin profile, similar trend shown in the CH shaped pin profile was observed. The changing in between both UTS and ϵ is 14% and 60%, respectively. As clearly seen from the results, the effect of the CH shaped pin profile on tensile properties is higher those of SH shaped pin profile. The literature review showed that the increase in v ratio causes to increase in heat input per unit area. This means that the dynamically recrystallization process after deformation of materials at the nugget zone is realized by the effect of increased heat input. The selection of appropriate pin profile, tool rotational and welding speed is the critical issues because of its effects on the tensile properties. Any defect causes a decrease in ultimate tensile strength and elongation. For the present study, all the FSW joints as shown in Fig. 3 consist defects and therefore, the UTS and ϵ was decreased. The weld joint efficiencies were determined by comparing of UTS for each joint and base material. The results were given in Table 4. As clearly seen that the weld joint efficiency for Exp. 2, Exp. 5 and Exp. 6 is higher compared with the others considering the UTS of EN AW 5083. However, the results compared with the EN AW 2024, the efficiency changes in between 58% to 72%. The reason is the UTS value of base material (EN AW 2024).

In order to compare the v ratios shown in Table 4, an experiment for each tool pin profile was done. In this experiment, the v ratio was kept at 5 by the combination at the TRS of 630 rpm and WS of 125 mm/min. The most important conclusion is that, even if the v ratio is kept at a constant value; the influential mechanism on the UTS and ϵ is the tool rotational speed.

TABLE IV. FSW EXPERIMENTAL LAYOUT (L_9 ORTHOGONAL ARRAY) WITH PERFORMANCE CHARACTERISTICS (UTS, ϵ %)

Exp. No	Process parameters			Process responses		Joint efficiency	Joint efficiency
	TT	TRS	WS	UTS	ϵ	EN AW 2024	EN AW 5083
1	CH	500	100	268.3	3.76	58.8	82.55
2	CH	1000	100	336.2	11.68	73.7	103
3	CH	630	125	291.4	4.05	63.9	89.7
4	SH	500	100	299.4	4.67	65.7	92.1
5	SH	1000	100	348	11.52	76.3	107
6	SH	630	125	329.4	1.02	72.2	101

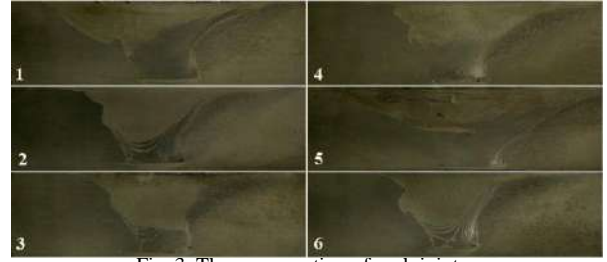


Fig. 3. The cross-section of each joint

B. Microstructural investigations

The macrostructural investigations were done on the entire cross-section of weld joint in order to detect defects and the nugget zone profile. The investigations were presented with the welding condition in the Fig. 3. The most common and existing defects for the weld joints fabricated with FSW are tunnel, voids, cavity, pinhole and wormhole. As mentioned before that the FSW process is performed at the solid phase, therefore the joints do not comprise any defects occurred during the solidification of the materials. The defects shown in fusion welding of dissimilar materials are the mismatch between filler material and welding materials, solidification behavior of materials. As for FSW, the tunnel, void and cavity like defects occurs by the effect of insufficient heat input and lack of material flow. The reason formation of pin hole and wormhole defects is the amount of heat input. The common reason of the defects shown in the FS welded joints is the generated heat. High and low heat input lead to the formation of defects. The generated heat during the FSW process is given in the Eq. 1 [9,10]. Inferences can be made from this equation is that, provided that the tool features keep at constant, the heat input is affected from both tool rotational speed and welding speed. As it can be seen from the Eq. (1), the tool rotational speed and the welding speed are the main factors for determining heat input per unit area. The heat input decreases with increasing in tool movement speed or welding speed.

$$Q = \frac{\alpha \cdot q}{W} = \frac{4}{3} \pi^2 \frac{\alpha \mu P \cdot TRS \cdot R^3}{WS} = \beta \cdot \frac{TRS}{WS} \quad (1)$$

where Q is the heat input per unit length, α is the heat input efficiency, and WS is the welding speed, TRS is the tool rotational speed. For a welding condition, α , μ , P , R and β are the constant values.

A weld joint fabricated by FSW consist of three distinct zones, nugget zone (NZ), thermo-mechanically affected zone (TMAZ) and heat affected zone (HAZ). Materials at the nugget zone are exposed to severe plastic deformation and higher heat input. These two dominant factors cause to recrystallization of materials and finally, the grain size in the NZ become small compared to the grain size in the TMAZ

and HAZ. For an example, a cross-section of weld joint comprising three zones is shown in Fig. 4. The figure is taken from the experiment 6. It is clearly detected that the grain size, the grain orientation and the shape of zones is different from each other. Besides, the grain sizes in a NZ vary depending on the heat input and heat dissipation. Fig. 5 shows the grain sizes in the nugget zones. The intensity of material flow and pin stirring at the tip of pin is higher those of the mid and top of the pin. By the effect of higher stirring and material flow causes decrease in the grain size at the weld joint root. A main point detected in the nugget zone is that the shape of nugget zone is highly affected by the tool rotational speed and welding speed. The tool rotational speed is responsible for the stirring action and the deformation of the grains. An increase in the tool rotational speed is caused to increase in heat input and deformation. It is known that for FS welding of dissimilar materials, the NZ comprises two different materials and the volume of these materials changes depending on the pin shape and the placement of materials. The illustrations in the Fig. 3 explain this approach. Studies performed at the low magnification showed that there are many small and big black lines on microstructure of the weld nugget zone. The mentioned lines can be clearly seen in Fig. 5. In order to detect and understand these lines, the microstructures of Exp. 3 and 5 at higher magnification were given in Fig. 6. The figures show that the small second phase particles are sorted in a zigzag line or small segment. These lines are the defect and called as the small segment [11]. According to the Khodir et al. [11] these defects affect the tensile properties of joints.



Fig. 4. A cross-sectioned joint comprising three zones (Exp. 6)

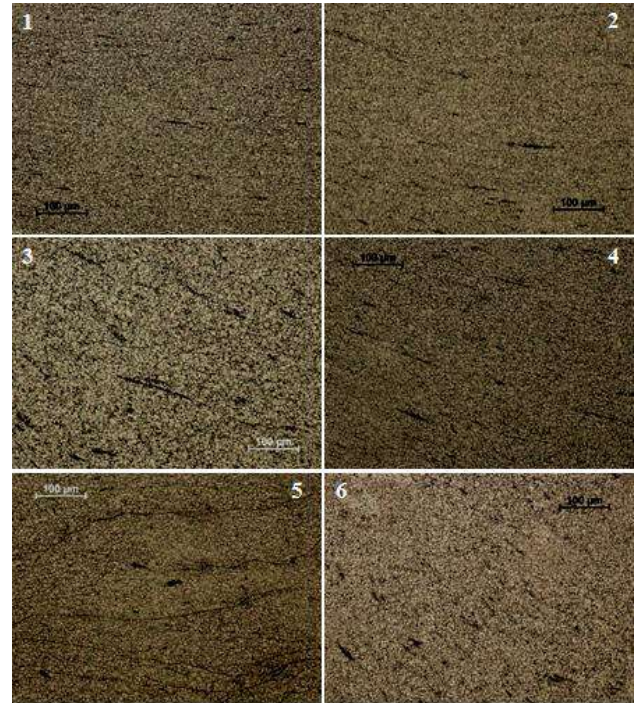


Fig. 5. The nugget zones for each weld joint

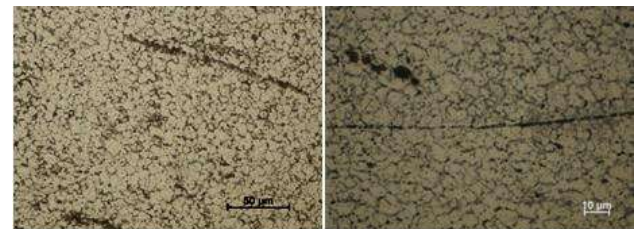


Fig. 6. The clustered second phase particles on the grain borders

IV. CONCLUSION

The dissimilar welding of EN AW2024 and EN AW 5083 was performed by using friction stir welding by employing two different the ratio of tool rotational speed to the welding speed (v ratio) and pin shapes in order to determine the effect of both v ratio and pin shape on the tensile properties. The findings from the FSW experiments were presented as below:

- An increase in v ratio causes to increase in both ultimate tensile strength and percentage of elongation.
- At a constant v ratio (5), the ultimate tensile strength and percentage of elongation increased with increased in tool rotational speed irrespective of v ratio.
- Of the two tool pin shapes used in FSW experiments, conical threaded pin produced higher strength weld joints compared to the other pin shape.

- Of the six weld joints, the weld joint fabricated with the 1000 rpm and 100 mm/min has the highest strength, the measured value is 348.01 MPa.
- All the joins contain many clustered cavity defects.

V. REFERENCES

- [1] Hamilton C., Dymek S. And Blicharski M., "A model of material flow during friction stir welding", *Materials Characterization*, 59, 1206 – 1214, 2008
- [2] Sundaram N.S and Murugan N., "Tensile behavior of dissimilar friction stir welded joints of aluminium alloys", *Materials and Design*, 31, 4184–4193, 2010
- [3] Mastanaiah P., Sharma A. and Reddy G.M., Dissimilar Friction Stir Welds in AA2219-AA5083 Aluminium Alloys: Effect of Process Parameters on Material Inter-Mixing, Defect Formation, and Mechanical Properties, *Trans Indian Inst Met*, DOI 10.1007/s12666-015-0694-6
- [4] Dilip J.J.S., Koilraj M., Sundareswaran V., Ram G.D.J. and Rao S.R.K., "Microstructural characterization of dissimilar friction stir welds between AA2219 and AA5083", *Transactions of The Indian Institute of Metals*, 63(4), 757–764, 2010
- [5] Koilraj M., Sundareswaran V., Vijayan S., Koteswara Rao SR., "Friction stir welding of dissimilar aluminium alloys AA2219 to AA5083 – Optimization of process parameters using Taguchi technique", *Materials and Design*, 42, 1–7, 2012
- [6] Franchim A.S., Fernandez F.F and Travessa D.N., "Microstructural aspects and mechanical properties of friction stir welded AA2024-T3 aluminium alloy sheet", *Materials and Design*, 32, 4684–4688, 2011
- [7] Threadgill P.L., Leonard A.J., Shercliff H.R. and Withers P.J., "Friction stir welding of aluminium alloys", *International Materials Reviews*, 54 (2), 49–93, 2009
- [8] Mishra R.S. and Ma Z.Y., "Friction stir welding and processing", *Materials Science and Engineering R*, 50, 1–78, 2005
- [9] Hao, H.L., Ni, D.R., Huang, H., Wang, D., Xiao, B.L., Nie, Z.R. and Ma, Z.Y. Effect of welding parameters on microstructure and mechanical properties of friction stir welded Al–Mg–Er alloy. *Materials Science & Engineering A*, 559, 889–896, 2013
- [10] Kim Y.G., Fujii H., Tsumura T., Komazaki T. and Nakata K., "Three defect types in friction stir welding of aluminum die casting alloy", *Materials Science and Engineering A*, 415, 250–254, 2006
- [11] Khodir S.A., Shibayanagi T. And Naka M., Microstructure and Mechanical Properties of Friction Stir Welded AA2024-T3 Aluminum Alloy, *Materials Transactions*, 47 (1), 185–193, 2006

Effect of Pin Geometry and Welding Speed to Tool Rotation Speed Ratio on the Welding Performance of AA 7075 Aluminum Alloy

Şefika KASMAN
Department of Mechanical Engineering
Dokuz Eylul University
Izmir, Turkey
sefika.kasman@deu.edu.tr

Fatih KAHRAMAN
Department of Mechanical Engineering
Dokuz Eylul University
Izmir, Turkey
fatih.kahraman@deu.edu.tr

Abstract— In this study, the friction stir welding were performed to investigate the effect of the constant ratio of welding speed to tool rotation speed ratio (WS/TRS) on the weld joint microstructure, hardness and ultimate tensile strength of AA7075 aluminum alloy plates. The welding experiments were carried out using two type pin shape which one is threaded and the other is pentagonal. The joints fabricated by threaded pin were sound and exhibited higher ultimate tensile strength (within the range of 69% - 72%) compared with the base metal. Relatively higher ultimate tensile strengths (UTS) were obtained at the 63/630 ratio for both pin shape and among four weld conditions, the highest strength was obtained at the 63/630 ratio with the pentagonal shaped pin. It is thought that the reason of increase in the strength is the increase in heat input owing to the larger frictional area and excessive deformed grains at the larger area. Shear fracture was investigated for all weld joints and showed that it is located outside the weld area. The fracture surface of the weld joints is almost similar to the base material and characterized by almost uniform small dimples.

Keywords— pin shape, friction stir welding, aluminum alloy

I. INTRODUCTION

Aluminum alloy is the most important material for many industries where weight, thermal and electrical conductivity, resistance to corrosion and energy saving are critical issues. In particular, the automotive, air craft and shipbuilding industries, along with the construction of storage tanks use aluminum alloys in sheet form to produce body parts. The welding is the main process for these industries, and it requires specialized techniques. Depending on the aluminum grade, for some cases and processes, aluminum is either easy or difficult to weld. As is known, the conventional fusion welding (CFW) processes, which is tungsten inert gas (TIG), metal inert gas (MIG) and plasma keyhole arc welding, are performed with inert gas shielding, use filler metal, and require care and skill. Under certain improper conditions, the CFW operation causes many defects in the fusion zone, such

as cracks, porosities, voids and segregations [1-3]. However, solid phase welding techniques are completely different processes, in which, the use of above mentioned instruments for carrying out the welding are not the case [2,3].

Friction stir welding (FSW) is one of the solid – state welding techniques, and it occurs without any melting. The method uses a cylindrical tool which is composed of a shoulder and a geometrically shaped pin. During the FSW operation, three important case occurs; first case is the rotating tool is plunged into the abutted plates, second case is generation of frictional heat is generated and third case is to transfer of generated heat towards to the weld line [4,5]. The most important feature of FSW when compared to CFWs[1] is the metallurgical advantages: very small distortion due to relatively lower heat, finer grain structure and a narrow heat affected zone. Apart from this, the above mentioned defects and the mismatch of filler metal in dissimilar metal welding are not the case in FSW process. A joint fabricated with FSW is divided into three distinct zones; the nugget zone (NZ), the thermo-mechanically affected zone (TMAZ), and the heat affected zone (HAZ) [6]. AA 7XXX series aluminum alloys are mostly used in the automotive and aircraft industries and the alloys in this series are composed from Al-Zn-Mg-Cu which are characterized by its high strength[7-9] and heat treatable and provide good stress-corrosion cracking resistances in sheet products. Despite these advantageous, it is difficult to join this alloy using CFW techniques [9] due to poor solidification microstructure, porosity and the dendritic structure formed in the fusion zone[10-12]. FSW, being a solid phase process, the loss of strength is not the case. Considering this aspect, the FSW technique is the best candidate for joining of difficult to weld alloys.

In many studies related to the joining of AA7075 sheets using the FSW technique, the investigations has concentrated on the effect of pin shape and welding parameters on the mechanical and microstructural properties. In the present study, two types of pin shape (threaded and pentagonal) and a constant welding speed to tool rotational speed (WS/TRS)

ratio (0.1) are associated with the mechanical and microstructural properties. Therefore, the effects of relatively lower or higher tool rotation and lower or higher welding speed on the mechanical and microstructural properties of the joints are investigated.

II. EXPERIMENTAL STUDIES

The FSW butt welds were made on 5mm thick, 100mm wide and 150mm long rolled aluminum alloy grade 7075. The chemical and mechanical properties of AA 7075 are given in Table 1. In order to provide a good overlap between the abutted surfaces, the plate edges were machined. Before welding, each plate was placed on a backing plate and clamped with studs and bolts, as seen in Fig. 1. Welding was performed on the rolled direction of the plates using two different pin, shaped threaded and pentagonal. The nominal diameter of the tool shoulder was 18mm, and the pin lengths were 4.90mm. The tool and pin profiles are shown in Fig. 2, and Table 2 also shows the tool configurations used in the experimental studies. Additionally, all of the FSW experiments were performed at 2° of tilt angle between the tool and the plates. As shown in Table 3, three parameters; pin shape, tool rotational speed (TRS) and welding speed (WS) at different values were selected to perform the welding of AA7075 plates.

The strength of each joint was analyzed with a tensile test. Therefore, tensile samples were cut from the transverse cross section of the weld joint. The dimensions of the tensile samples were taken using the ASTM E8M. The tests were performed at room temperature and at a 2mm/min crosshead speed in a hydraulic tensile machine. For each condition, at least three tests were done, and the average of these was used for the final result for both ultimate tensile strength (UTS) and percentage of elongation (PE). Results of the tests were compared with the base material. The fractured surfaces were characterized using scanning electron microscopy (SEM). The precipitated phase in the fusion zone was determined through energy dispersive spectrometer (EDS) analyses.

The microstructural analyses of joints were performed with the aim of observing the microstructural change as a function of the selected process conditions. With this approach, each cross-sectioned joint was ground and polished. Following these processes, the surfaces were etched with Keller's reagent. A Vicker's microhardness test was employed to determine the hardness distribution on the cross-section of each joint line. The measurements were started at the centerline of the joint and continued throughout the base materials to each side with a spacing of 1mm and applied with a load of 100gr for 10 seconds. In total, fourteen measurements were performed on each side of the joint.

III. RESULTS AND DISCUSSION

The preliminary studies indicated that the pin shape, tool rotational speed and welding speed are the most influential

parameters on the mechanical properties and microstructures of the weld joints fabricated with friction stir

TABLE I. THE CHEMICAL COMPOSITION OF ALUMINUM ALLOYS USED IN THE PRESENT STUDY (WT., %).

Alloy / Elements	Cu	Si	Mg	Mn	Zn	Ti	Cr	Fe	Al
AA 7075	1.45	0.15	2.58	0.06	5.72	0.034	0.2	0.16	Bal.
Mechanical properties of aluminum alloys									
Alloy	UTS (MPa)		Yield Strength (MPa)		ϵ (%)		Hardness (HV _{0.1})		
AA 7075	578		537		12		170		

TABLE II. TOOL CONFIGURATIONS

Tool configurations	Tool type	
	threaded	pentagonal
Tool type (T)	1	2
Pin edge width (l)	6	4
Shoulder diameter (D)	18	18

TABLE III. THE FSW PROCESS PARAMETERS AND THEIR LEVELS

Parameters (unit)	Symbol	Levels	
Tool type	T	1	2
Tool rotational speed (rpm)	TRS	400	630
Welding Speed (mm/min)	WS	40	63
Fixed parameters			
Tool tilt angle (°)	α	2	
Dwell time (s)	t	20	

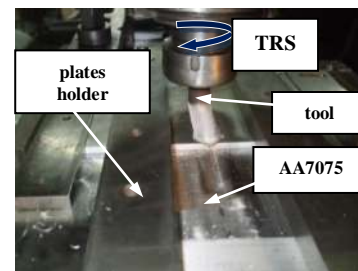


Fig. 1. Friction stir welding components



Fig. 2. Tool and pin figures

A. Macrostructure of Welded Joints

The macrostructure of weld joints, consisting of three distinct zones, HAZ, TMAZ and NZ of each side, is shown in Fig. 3. From the cross-section view of the weld joints, it can clearly be detected that the joints display different images. While the joints in Fig. 3a and 3b are fabricated with the threaded pin, the joints in Fig. 3c and 3d are fabricated with the pentagonal pin. As can be seen in the weld joints, for a constant $WS/TRS(0.1)$ ratio that is obtained at the 40/400 and 63/630, the major conclusion that can be drawn from the macrostructures in Fig. 3a - d is that there is no major changes in macrostructural form with the using of constant WS/TRS ratio. If you need to compare, the NZ form and sizes, and the width of the TMAZ are quite different from each other. When considered in this context, it can be drawn following conclusion from the macro-structure of the weld joints: for the 63/630 of WS/TRS of each group (b and d), the width of the TMAZ is larger than that fabricated by 40/400 of WS/TRS (a and c). Moreover, the weld joints fabricated by the pentagonal pin exhibit a larger NZ size and TMAZ size than those using the threaded pin. Additionally, the shape of the NZ is closer to a basin shape. As is known, the rotation of the tool between two adjacent plates creates turbulence, and the grains around the turbulence are thrown away from the tool. The intensity of this turbulence is determined by the tool rotational speed; the higher the rotational speed, the more intense the turbulence becomes [13]. For the present experimental conditions, *Exp. b* and *d* fabricated at the highest tool rotational speed, and a careful examination of the related macrostructure in Fig.3 shows that the effect of the vortex around the NZ covers a larger area than other conditions (*Exp. a* and *c*). In addition, it can be concluded from the macrostructure that the turbulence intensity is higher in weld joints fabricated by the threaded pin than fabricated by the pentagonal pin. It is considered that there is a relationship between the TMAZ width and turbulence intensity. The shape of the NZ and the width of area in that the grain distributed creates difference in both UTS and PE. Additionally, the generated frictional heat that occurs at interface between tool and plates is the effective factor on the wideness of NZ and TMAZ. It can be drawn second conclusion is that the pentagonal pin is generate more frictional heat per unit joint length than threaded pin due to larger frictional surface. This result overlaps with the NZ profile shown in Fig 3a-c and Fig 3 - d. The common effect of the larger frictional surface and the higher tool rotational speed generates higher heat and causes more deformed grains at the TMAZ due to softened material.

The typical grain structure of base metal is shown in Fig. 4. This grain structure was changed to fine and equiaxed grain structures at the NZ. The reason of this changing is high temperature generated by frictional heat and severe plastic deformation fabricated by tool rotation and movement. These

two factors causes to occurring of dynamic recrystallization and responsible for the grain size. Figure 5 shows microstructures and grain structure of weld nugget zone in the joint fabricated by constant WS/TRS ratio. From the measuring of grain size on microstructure of NZ showed that the grain size at WS/TRS of 63/630 is lower than the WS/TRS of 40/400 for two type pin. The average grain size for NZ was reported at Table 4.

Figure 6 shows microstructures taken from three different region of a weld fabricated with the threaded pin at 63/630 of WS/TRS . The microstructure in Figs. 6a, 6b and 6c was taken from beneath of the shoulder, the middle of the nugget zone, and at the root of the weld joint, respectively. The coarse and elongated grains of base metal transformed into a relatively smaller grains at the beneath of the tool shoulder, middle and root of weld joint. The measurement results were showed that the average grain size at the root of all joint is smaller than compared with the other two regions. The average grain size on the beneath of the tool shoulder is larger than that the root of all joint apart from joint 63/630 of WS/TRS fabricated with the threaded pin. However, the difference is small enough to be neglected. Also, there is a transition area that occurred by the influence of stirring intensity and the amount of generated heat. On the other hand, the defects on the joints are investigated. Microstructural examinations in the Fig. 7 were showed that there are small tunnel like defects in the joint fabricated with pentagonal pin at the condition of 40/400 and 63/630 of WS/TRS . It is thought that the defects were occurred by the effect of higher turbulence, insufficient stirring of the plasticized material and generated fractional heat. The other joints are without defects and sound.

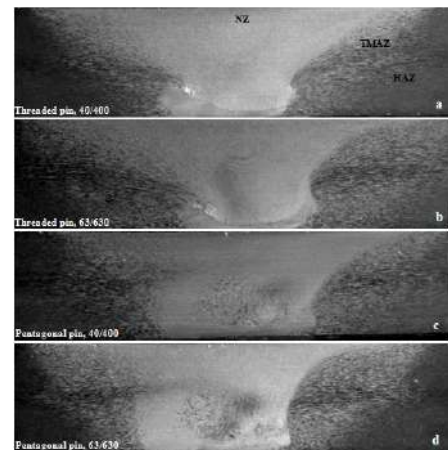


Fig. 3. Macro-structure of nugget zone for each welding and demonstration of TMAZ, HAZ

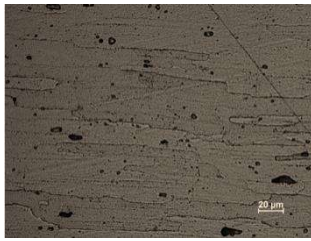


Fig. 4. Microstructure of base metal

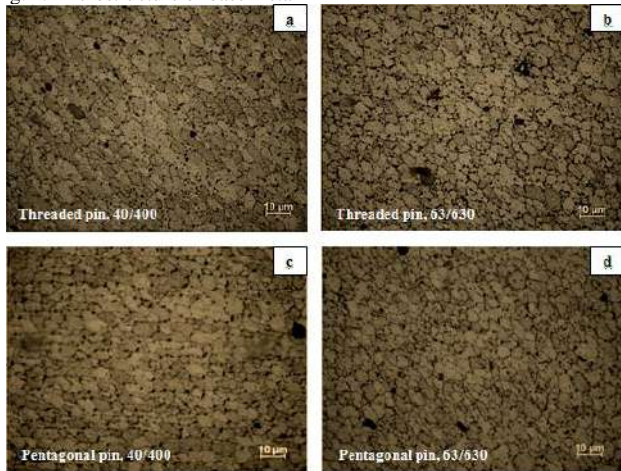


Fig. 5. Microstructure of nugget zone for each welding condition



Fig. 6. The changes in the grain size at the nugget zone (threaded pin, 63/630)

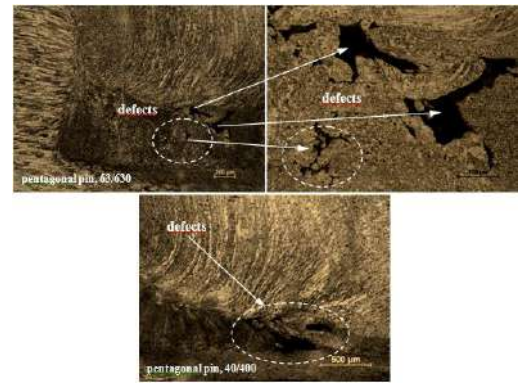


Fig. 7. Defects at the nugget zone (pentagonal pin, 40/400, 63/630)

B. Tensile properties of joints

The results of tensile properties of the joints as a function of pin profile and constant *WS/TRS* ratio composed from different *WS* and *TRS* values for each weld joint were illustrated in Figures 8 and 9. The average UTS results show a noticeable difference for the constant *WS/TRS* ratio range from 40/400 to 63/630. It can be seen from Fig. 8 that the UTS value of each weld joints fabricated at 63/630 of *WS/TRS* ratio are higher than the weld joints fabricated at the 40/400 of *WS/TRS* ratio for two type pin. All results were compared with the base metal strength and showed that the tensile properties of each joint are lower than the base material [15]. The joint efficiency are calculated based on the UTS and reported at Table 4. It was found that the joint efficiency varies between 69% and 75%. The higher joint efficiency was achieved at the weld joint fabricated with the pentagonal pin at the 63/630 of *WS/TRS* ratio. From the results shown in Table 4 can be drawn an obvious conclusion is that the joint strength of 63/630 of *WS/TRS* ratio for each group of weld is closer to the base metal than joint strength of 40/400 of *WS/TRS*. It is considered that the higher UTS can be associated with the intensity of tool rotation and wider *TMAZ* and *NZ*. Furthermore, irrespective of *WS/TRS* ratio, the pentagonal pin generates higher temperature due to the wider frictional surface area. This helps to reduce the stress in the grains around the pin. Hence, the highest UTS are achieved at the joints fabricated with the 63/630 of *WS/TRS*. In all joints, the poor joint was achieved in the first condition of the threaded pin, and its UTS and PE values are 398MPa and 4.22%. Compared to the highest and lowest UTS among the four welding condition, there is a difference of almost 7.65%. However, the difference in the PE is very small and can be considered negligible (as in Fig. 9). The yield strengths (YS) also support this result. The highest YS (335MPa) are obtained for the joint fabricated with the second condition (63/630 of *WS/TRS*) of the pentagonal pin. From Figures 7-9, it can be seen that although the joint fabricated with pentagonal pin at the condition of 63/630 of *WS/TRS* has higher UTS value, it has small defects that cause to decrease in PE value. The similar result was also shown in the joint of 40/400 of *WS/TRS* fabricated with pentagonal pin. It can also be seen from Table 4, the variation in PE is very

small and so that, the joint fabricated with threaded pin at the weld condition of 63/630 of *WS/TRS* as optimal weld condition. This result was also supported by the micrographs.

TABLE IV. WELDING RESPONSES

Group no	Exp. no	Results			
		UTS (MPa)	PE (%)	Joint efficiency (%)	Average grain size (μm)
Group 1	a	398.18	4.22	69	4.55
	b	416	4.62	72	3.57
Group 2	c	405.16	4.45	70	3.68
	d	431.38	4.23	75	3.01

C. Hardness

Hardness measurements were performed on the cross-section of the weld joints and in the middle of the thickness. Results are illustrated in Figure 9. The hardness of AA 7075 – T651 alloy is 175 HV_{0.1}. The highest hardness at the NZ is 166HV_{0.1}, which was measured in the second condition (63/630 of *WS/TRS*) of the pentagonal pin. Minimum hardness was achieved at the HAZ on both sides of all joints and the hardness increases towards to the NZ. The tendency in hardness shows similarity for all joints. In a general approach, a difference can be seen at the hardness of between TMAZ and NZ, but it cannot be said that the tool pin shape and the constant *WS/TRS* creates significant changes in the hardness of the NZ. When the hardness of both the NZ and BM are compared, it can be seen that the hardness of the NZ is lower than the hardness of BM. According to Bahemmat et al. [8], the lower hardness at the NZ compared with the BM is attributed to precipitate dissolution and coarsening. The lowest hardness (103HV_{0.1}) is observed at the HAZ for each joint case. In the HAZ of precipitate hardened aluminum alloy like AA 7075, the hardness shows lowest value when compared the other region [14]. From the HAZ region, there is a steep climb in the hardness towards to the NZ. Comparing the hardness of the HAZ and TMAZ showed that the plastic deformation that is realized on the TMAZ causes the hardness to show an increase. It can be concluded that a considerable difference in the hardness of NZ is achieved irrespective of pin shape and *WS/TRS* ratio. This can be explained by the fact that there is a grain transformation on the NZ owing to the plastic deformation and dynamic recrystallization.

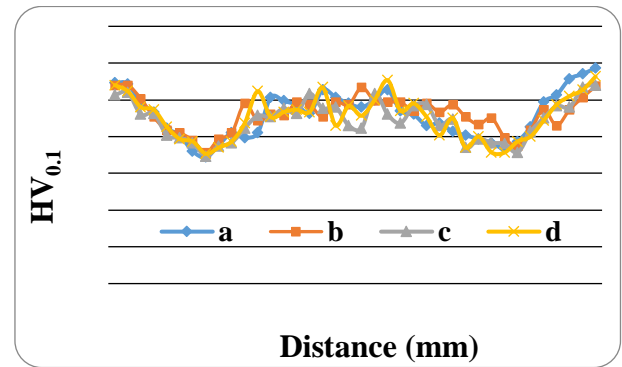


Fig. 8. Hardness distribution between the zones

C. Fracture Observations

The fracture locations are shown in Figs. 11 A and B. It can clearly be seen that all of the joints were fractured outside the weld area and, except for joint “c”, on the advancing side. Defect free joints and defective joint were fractured in the HAZ. Moreover, it is clear that all weld joints show the same shear fracture mode. Both the weld joints fabricated with the threaded pin fractured and the weld joints fabricated with the pentagonal pin fractured at a 45° shear mode. SEM micrographs of the fractured surfaces of the joints and base metal are shown in Fig. 12. The base metal is covered with small dimples which are almost smooth. However, the fractured surface of the weld joints has dimples of varying size. A conclusion that can be drawn from Fig 12 is that the fractured surface of the joints fabricated with the threaded pin has larger dimples and some small voids. It is thought that these voids were formed from the breaking up of second-phase particles inside the dimple. In order to determine the second-phase particles inside the dimple and on the weld area, EDS analyses were performed. Figure 13 shows the particles. Analyzing the particles in Fig. 13A, the results show that the particles are Mg, and Si – rich precipitation. These particles can be Mg₂Si precipitates mostly existing in AA 7075 [8]. The selected particles on the nugget zone are shown in Fig. 13B. The light grey particle referred to as 1 is a Si, Fe, Zn – rich precipitation, and the Cu, Mn and Cr also exist in small amounts when compared to other alloys. However, the dark grey or black particles are composed of a mainly Si, O – rich precipitation, and a small amount of Cu and Zn is also found.

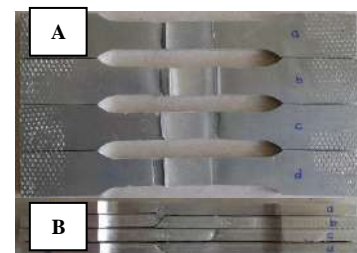


Fig. 19 Fracture location (A) and fracture type (B)

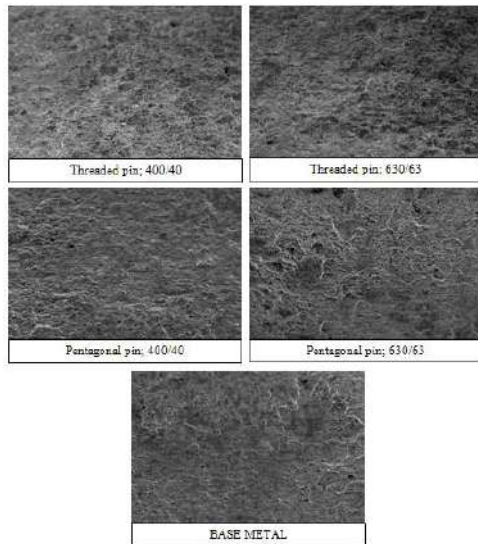


Fig. 10. SEM micrographs of fractured surface for some welding conditions and base metal

percentage of elongation showed a higher value for the second condition in each group. The *WS/TRS* ratio, together with pin geometry, has an effect on the mechanical and microstructural properties. The fracture of each joint is located outside the weld area. A brittle fracture and a 45° shear fracture occurred in all of the joints. The width of the thermo-mechanically affected zone is significantly influenced by the pin geometry and welding parameters value. The highest width was obtained in joints fabricated at a 63/630 ratio and by pentagonal pin geometry. In this condition, the maximum strength (431.38MPa) was achieved. The maximum elongation (4.62%) was achieved at the 63/630 ratio and with a threaded pin geometry. The minimum microhardness values were obtained between the heat affected and nugget zone. The general trend showed that there is not remarkable difference between hardness values.

The values used for tool rotational speed and welding speed were selected based on previous studies. However, the effect of coupled pin geometry with *WS/TRS* ratio was not known. After mechanical and microstructural observations, sound weld and good mechanical properties were achieved. Therefore, this study exhibits original results.

ACKNOWLEDGEMENTS

The present study is fully supported by Dokuz Eylul University under the project no. 2011.KB.FEN.045. The author would like to thank for the financial support.

REFERENCES

- [1] Arora, K.S., Pandey, S., Schaper, M., Kumar, R., 2010, Microstructure Evolution during Friction Stir Welding of Aluminum Alloy AA2219. *J. Mater. Sci. Technol.* 26(8), 747-753.
- [2] DebRoy, T., Bhadeshia, H.K.D.H., 2010. Friction stir welding of dissimilar alloys – a Perspective. *Science and Technology of Welding and Joining* 15 (4) 266–270.
- [3] Rajakumar, S., Balasubramanian, V., 2012. Establishing relationships between mechanical properties of aluminium alloys and optimized friction stir welding process parameters. *Materials and Design* 40, 17–35.
- [4] Gupta, R.K., Das, H., Pal, T.K., 2012, Influence of Processing Parameters on Induced Energy, Mechanical and Corrosion Properties of FSW Butt Joint of 7475 AA. *JMEPEG* 21, 1645–1654.
- [5] Kumar, K., Kailas, S.V., Srivatsan, T.S., 2008, Influence of Tool Geometry in Friction Stir Welding. *Materials and Manufacturing Processes* 23, 188–194.
- [6] Simar, A., Bréchet, Y., Meester, B., Denquin, A., Gallais, C., Pardoën, T., 2012, Integrated modeling of friction stir welding of 6xxx series Al alloys: Process, microstructure and properties. *Progress in Materials Science* 57, 95–183.
- [7] Bahemmat, P., Haghpanahi, M., Givi, M.K.B., Seighalani, K.R., 2012, Study on dissimilar friction stir butt welding of AA7075-O and AA2024-T4 considering the manufacturing limitation. *Int J Adv Manuf Technol* 59, 939–953.
- [8] Bahemmat, P., Besharati, M.K., Haghpanahi, M., Rahbari, A., Salekrostam, R., 2009, Mechanical, micro-, and macrostructural analysis of AA7075-T6 fabricated by friction stir butt welding with

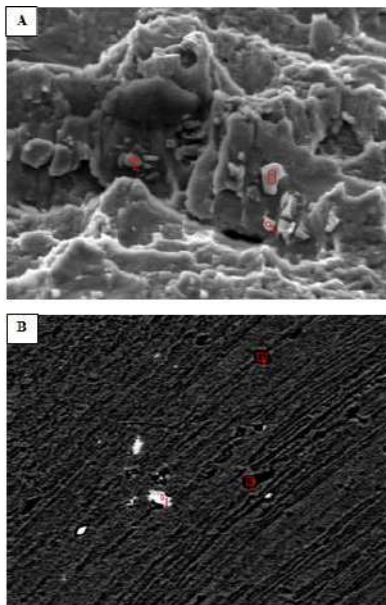


Fig. 11. EDS analysis at particles inside the dimples (A) and particles on the nugget zone (B)

IV. CONCLUSIONS

AA7075 alloy was joined using the friction stir welding technique. The results showed that all of the joints were sound and exhibited a higher ultimate tensile strength compared to the base metal as percentage contribution with a range between 75% - 69%. The ultimate tensile strength and

different rotational speeds and tool pin profiles. Proceedings of the Institution of Mechanical Engineers, Part B: Journal of Engineering Manufacture 224: 419–433.

- [9] Rajakumar, S., Muralidharan, C., Balasubramanian, V., 2011, Influence of friction stir welding process and tool parameters on strength properties of AA7075-T6 aluminium alloy joints. *Materials and Design* 32, 535–549.
- [10] Mishra, R.S., Ma, Z.Y., 2012, Friction stir welding and processing. *Materials Science and Engineering R* 50, 1–78.
- [11] Cavaliere, P., Nobile, R., Panella, F.W., Squillace, A., 2006, Mechanical and microstructural behaviour of 2024–7075 aluminium alloy sheets joined by friction stir welding. *International Journal of Machine Tools & Manufacture* 46, 588–594.
- [12] Rajakumar, S., Muralidharan, C., Balasubramanian, V., 2009, Optimization of the friction-stir-welding process and tool parameters to attain a maximum tensile strength of AA7075–T6 aluminium alloy. *Proc. IMechE Part B: J. Engineering Manufacture* 224, 1175–1191.
- [13] Jayaraman, M., Sivasubramanian, R., Balasubramanian, V., 2009, Effect of Process Parameters on Tensile Strength of Friction Stir Welded Cast LM6 Aluminium Alloy Joints. *J. Mater. Sci. Technol.* 25 (5), 655–664.
- [14] Hafez, H.A.E., 2011, Mechanical Properties and Welding Power of Friction Stirred AA2024-T35 Joints. *Journal of Materials Engineering and Performance* 20, 839–845.
- [15] Liu, H.J., Fujii, H., Maeda, M., Nogi, K., 2003, Tensile properties and fracture locations of friction-stir-welded joints of 2017-T351 aluminum alloy. *Journal of Materials Processing Technology* 142, 692–696.

An experimental Study on Friction Stir Butt Welded AA7075-T651 Alloys and Their Mechanical Properties

Fatih KAHRAMAN
Department of Mechanical Engineering
Dokuz Eylül University
İzmir, Turkey
fatih.karaman@deu.edu.tr

Şefika KASMAN
Department of Mechanical Engineering
Dokuz Eylül University
İzmir, Turkey
sefika.kasman@deu.edu.tr

Abdurrahman AYDIN
Department of Mechanical Engineering
Dokuz Eylül University
İzmir, Turkey
abdurrahmanaydin@yandex.com

Anıl EMİRALİOĞLU
Department of Mechanical Engineering
Dokuz Eylül University
İzmir, Turkey
anilemiralioglu@gmail.com

Waleed YOUSUF
Department of Mechanical and Petroleum Engineering
University of Salford Manchester
Manchester, United Kingdom
w.yousuf@edu.salford.ac.uk

Abstract—Friction stir welding is a new innovative solid state joining method which is a widely used for aluminium alloys that are hard to weld by traditional welding techniques. Friction stir welding is successfully used for aeroplanes, trains, lightweight transport structures and boats. Distortion are importantly lower than in traditional fusion welding techniques in friction stir welding because of the low frictional heat energy input. Traditional joining techniques had number of problems which were all solved by the FSW. Tool geometry and welding speeds are main independent variables which affect the mechanical properties of welding, weld quality and cost. This experimental study, investigates the effect of welding speeds on the FSW joints performance. Welding speed are one of the significant parameter for deciding the performance of the friction stir welded joint. Different butt welded AA7075-T651 plates were manufactured by employing variable rotating speeds and travel speeds. Tensile tests, bending tests, microstructural analysis and macrostructural analysis were applied to specimens taken from welded plates in order to determine the effect of speeds on the mechanical properties of friction stir welded joints.

Keywords—Friction stir welding, mechanical properties, AA7075, aluminum al

I. INTRODUCTION

Friction stir welding (FSW) is a solid state welding method, invented at The Welding Institute (TWI) in 1991 and widely used in dissimilar and similar welding of aluminum alloys. FSW has some mechanical and metallurgical advantages compared to other traditional welding processes [1, 2].

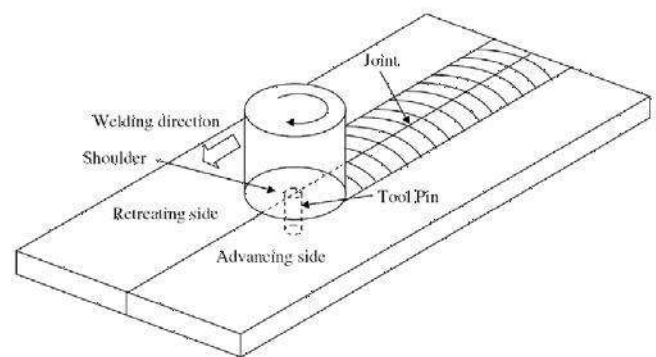


Fig. 1. Schematic diagram of FSW [3,4]

The application of this method is shown schematically in Figure 1. The tool consists of two parts called shoulder and pin. The frictional heat is generated while the tool rotating. The material around the pin is softened because of the frictional heat input between shoulder and base material [2].

During welding, the tool moves along the weld joint [3]. One of the main advantages of FSW is that low distortion occur because of the low heat energy input [3]. The application of friction stir welding is shown in figure 2.

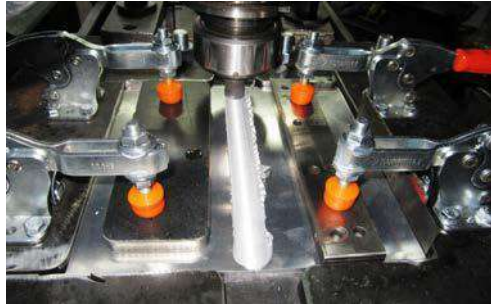


Fig. 4. FSW tool geometry

Chemical composition and mechanical properties of the alloy are given in Table 1 and 2.

Fig. 2. The application of FSW

Three main various zones such as Nugget zone (NZ), thermo-mechanically affected zone (TMAZ) and heat-affected zone (HAZ) are schematically shown in Figure 3.

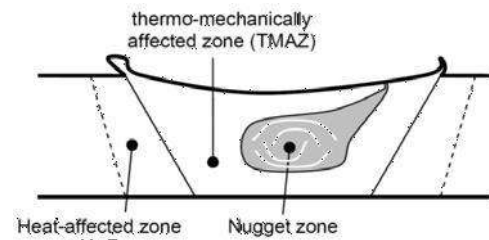


Fig. 3. Schematic presentation of the joint [5]

During welding the Nugget zone is heavily deformed material that roughly corresponds to the location of the pin. The grains within the nugget zone are roughly equiaxed and often an order of magnitude smaller than the grains in the parent material [5].

II. EXPERIMENTAL WORKS

The base material used in the all experimental works were rolled, 5 mm thick sheets of EN AW- 7075 in the state T651 which means they were solution heat treated, stress-relieved by stretching and artificially aged. The aluminum plates were cut in a rectangular shape with 200mm breadth and 100mm width. Single pass friction stir butt welded plates were manufactured by milling machine. The FSW tool was put on a 1° tilt angle and 4.9mm plunge depth. A triangular tool made of DIN 1.7131 steel with 18mm diameter shoulder in this study as shown in Fig. 4. FSW joints fabricated using a tool with 18 mm shoulder diameter.

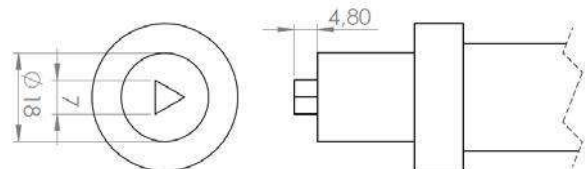


TABLE I. CHEMICAL COMPOSITION OF THE AA7075-T651

Si	Fe	Cu	Mn	Mg	Cr	Zn	Ti	Ni
0,07	0,17	1,57	0,028	2,53	0,19	5,74	0,23	0,058

TABLE II. MECHANICAL PROPERTIES OF THE AA7075-T651

R _m [MPa]	R _{p0,2} [MPa]	A50	Temper
581	512	15	T651

TABLE III. FSW PARAMETERS

Specimen No	Rotating Speed (rpm)	Welding Speed (mm/min)	Tool Direction of Rotating
7075-1	500	50	Clockwise
7075-2	630	63	Clockwise
7075-3	800	80	Clockwise
7075-4	1000	100	Clockwise

Tensile tests and bending tests were used for the mechanical testing of welded joints. The tensile tests and bend tests were carried out using servo-hydraulic controlled Shimadzu testing machine. Specimen dimensions were chosen according to the standard ASTM E8M. The tests were performed at room temperature and at a 2mm/min crosshead speed in machine. The dimension of tensile test specimen and bending test specimen are shown in Figure 5.

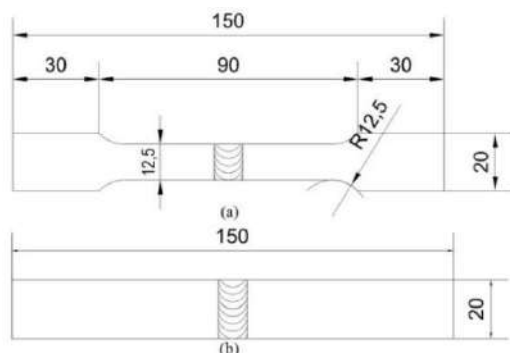


Fig. 5. Tensile test specimen (a), Bending test specimen (b)

Friction stir welded joints were cross-sectioned perpendicular to the welding direction for metallographic inspection. The specimens were polished by diamond suspension and then etched with 190 ml distilled water, 5ml HNO₃, 3 ml HCl, 2 ml HF at room temperature.

A Vickers micro hardness testing machine was used for determining the hardness distribution of the welded joint. The measurements were started at the centerline of the joint and continued throughout the base materials to each side with a spacing of 1mm and applied with a load of 100gr for 10 seconds.

III. RESULTS AND DISCUSSION

In this experimental works, AA 7075 – T651 sheets were successfully joined by FSW techniques. FSW joints have a good welded surface and don't need to post welding cleaning and machining. On the macroscopic scale, the friction stir welding joint revealed a good weld surface is seen Figure 6.



Fig. 6. Friction stir welded joint surface

The specimens were tensile tested and transverse tensile properties such as yield strength (R_{p0,2}), tensile strength (R_m) and percentage of elongation (A50) of the joints were evaluated. To determine the tensile strength of the FSW joints, tensile test specimens were fabricated in accordance with ASTM E8 in the transverse direction perpendicular to the welded line with wire erosion machine as shown in Figure 5.

TABLE IV. TENSILE TEST RESULTS

Specimen No	R _m [MPa]	R _{p0,2} [MPa]	A50
7075-1	328	437	3,9
7075-2	341	457	3,7
7075-3	343	445	3,8
7075-4	359	462	2,5

Bending tests were performed on the welded specimens are shown in figure 7. FSW joint presented allowing for very low bend angles and cracks were observed in the joint.

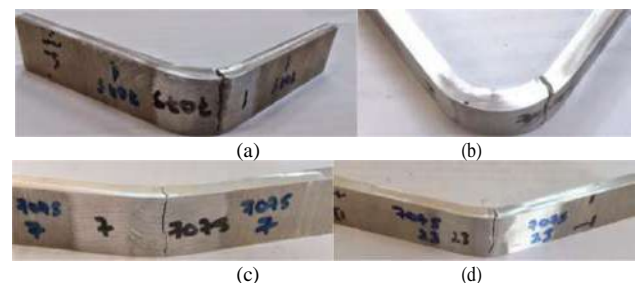


Fig. 7. Results of bending tests; 7075-1(a), 7075-2 (b), 7075-3(c), 7075-4(d)

Typical cross section of the welded joints under different parameters is shown in Figure 8. The size and shape of the

zones formed during welding varies depending on the pin geometry of the tool. Therefore, the stirrer pin profile has an important effect on mechanical properties.

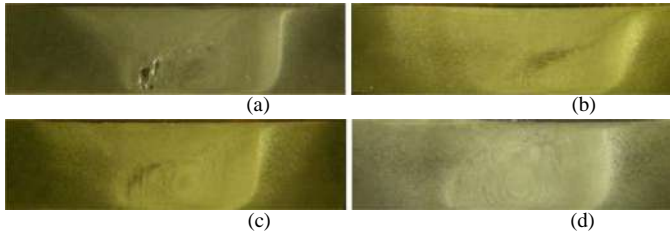


Fig. 8. Macroscopic appearances of the joints; (a) 7075-1, (b) 7075-2, (c) 7075-3, (d) 7075-4

In the sample 7075-1, pinhole defect detected between NZ and TMAZ (see figure 8a and figure 9). Further increase in turbulence of the plasticized metal may be reason of pin hole defect. This specimen gives good results in the tensile test, indicating that these gaps do not form along the weld joint.

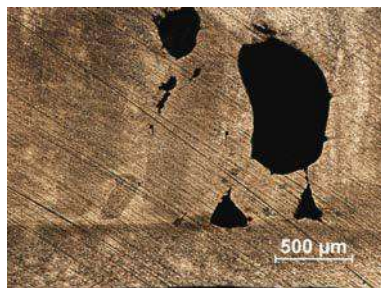


Fig. 9. Pin hole defect in 7075-1

The cross section of the weld joint analyzed using optical microscopy. Weld zone temperature and grain size are interrelated and can be related with the tool rotational speed in friction stir welding process [6]. Weld zone temperature increases with increasing tool rotational speed, if other welding parameters are constant [6].

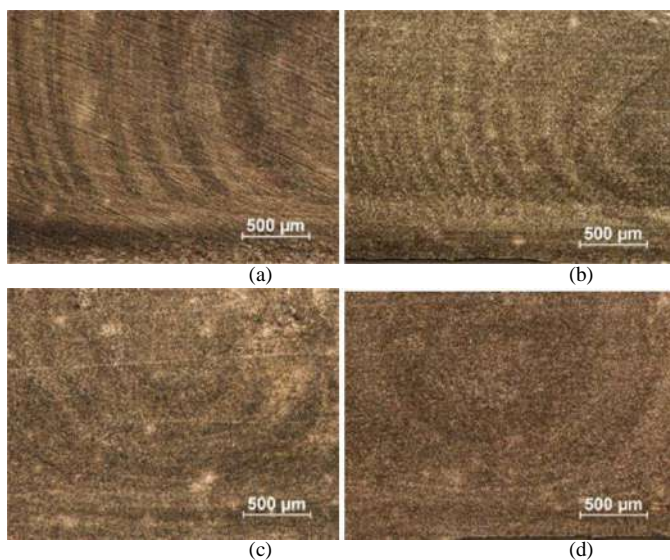


Fig. 10. Microstructures in Nugget zone (NZ); (a) 7075-1, (b) 7075-2, (c) 7075-3, (d) 7075-4

Figure 10 shows microstructures in the nugget zone of the welded joints at different welding speeds. Nugget zone is characterized by a dynamically recrystallized, fine equiaxed grain structure and grain sizes decrease from the top surface to the bottom [7].

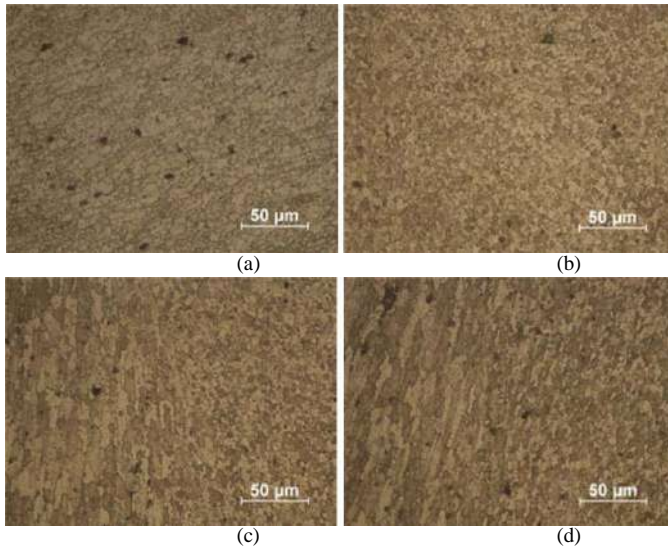


Fig. 11. Microstructures in Nugget zone (NZ); 7075-1(a), 7075-2 (b), 7075-3(c), 7075-4(d)

The heat affected zone (HAZ) is only affected by the welding thermal cycles and no plastic deformation occurs in this zone, therefore the HAZ displays similar grain structures to the base material. The heat affected zone (HAZ) is mechanically unaffected by the welding tool and the grain structure in that region resembles the parent material. The grains are slightly overgrown as a result of the exposure to welding heat.

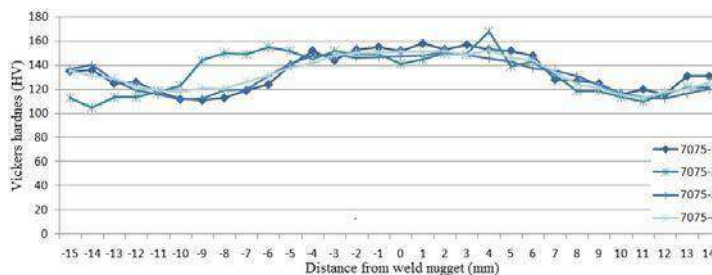


Fig. 12. Microhardness profile of welded joints

Figure 12 shows the micro hardness profile subtracted from the micro hardness values measured along the transverse line of the weld zone. The maximum Vickers

hardness value shows in the base material. The minimum hardness is obtained at the boundary between the TMAZ and HAZ. The hardness value on the nugget zone (joint center) is higher than that of boundary because of the recrystallization and its fine equiaxed grain structure.

IV. CONCLUSION

In this experimental study, the microstructure, the macrostructure, mechanical properties and microhardness of friction stir welded aluminum alloy 7075-T651 were examined precisely with different welding parameters. The present experimental results are concluded below:

- Butt joint of 5mm 7075 aluminum alloy could be successfully made by the FSW process and joint efficiency as high as 79% of base metal could be achieved.
- Clean surface is obtained after FSW process. After the FSW, is not even necessary to clean up the weld zone.
- The maximum tensile strength of FSW joint was achieved with rotational speed of 1000rpm and traverse speed of 100mm/min.
- The microstructure in the nugget zone (NZ) presents the dynamically recrystallized, fine equiaxed grain structure and grain sizes decrease from the top surface to the bottom
- The tensile strength increase with increasing welding speed up.

ACKNOWLEDGMENT

The authors are grateful to the Department of Scientific Research Projects Dokuz Eylül University for the financial support. Project No. 2014.KB.FEN.015.

REFERENCES

- [1] H. J. Aval, S. Serajzadeh, N. A. Sakharova, A. H. Kokabi, A. Loureiro, A study on microstructures and residual stress distributions in dissimilar friction-stir welding of AA5086-AA6061, *J Mater Sci* (2012) 47:5428–5437, DOI 10.1007/s10853-012-6430-2
- [2] I. Dinaharan, N. Murugan, Effect of friction stir welding on microstructure, mechanical and wear properties of AA6061/ZrB2 in situ cast composites, *Materials Science and Engineering A* 543 (2012) 257–266
- [3] D. M. Neto, P. Neto, Numerical modeling of the friction stir welding process: a literature review, Department of Mechanical Engineering (CEMUC) - POLO II, University of Coimbra, 3030-788 Coimbra, Portugal
- [4] R. Nandan, T. DebRoy, H.K.D.H. Bhadeshia, Recent advances in friction-stir welding – Process, weldment structure and properties, *Progress in Materials Science*, 53 (2008), 980–1023
- [5] S. Guerdoux, Numerical Simulation of the Friction Stir Welding Process. Dissertation, Mines ParisTech, 200

- [6] P. Venkateswaran, A.P. Reynolds, Factors affecting the properties of Friction Stir Welds between aluminum and magnesium alloys, *Materials Science and Engineering A* 545 (2012) 26– 37
- [7] W. Xu, J. Liu, G. Luan, C. Dong, Microstructure and mechanical properties of friction stir welded joints in 2219-T6 aluminum alloy, *Materials and Design* 30 (2009) 3460–3467

Experimental and Numerical Buckling Analysis of U-Notched Composite Plates

Experimental&Numerical Study

Kadir TURAN
Dicle University
Department of Mechanical Engineering
Diyarbakır, TÜRKİYE
E-mail: kturan@dicle.edu.tr

Mete Onur KAMAN
Firat University
Department of Mechanical Engineering
Elazığ, TÜRKİYE
E-mail: mkaman@firat.edu.tr

Yeliz PEKBAY
Ege University,
Department of Mechanical Engineering
İzmir, TÜRKİYE
E-mail: yeliz.pekbay@ege.edu.tr

Abstract— In this study, U-notch effect on the critical buckling loads of carbon/epoxy composite plates were investigated with experimentally and numerically. The effects of the different notch depths and fiber reinforced angle were analyzed. The notch depths were changed as 0, 2.5, 5 and 7.5 mm and the notch diameter was constant as 10 mm. The fiber reinforced angles of composite plates were used as $[0^\circ]_4$, $[0/45]_s$ and $[0/90]_s$. In the numerical study, linear buckling analysis was realized in ANSYS finite element software. Obtained experimental results were compared with numerical analysis results which were obtained in ANSYS. The experimental results consistent with numerical results showed that the increasing of the notch depth and fiber orientation angle were lead to decrease of critical buckling loads of composite plates as 11.51% and 66.48%, respectively.

Keywords—U notched, Composite plates, Buckling analysis.

VI. INTRODUCTION

Today, fiber reinforced and laminated composite materials have wide use special areas, like aerospace marine defense industry. To understand the strength and failure mechanisms in the composite materials gains importance to improve their mechanical performances. Composite plates can be subjected to various combine or single loads like bending, buckling or tension/compression. Plates are used often in aircraft and ship bodies and these components are influenced by air and wave that cause buckling on plates. So, buckling analysis is very important, especially for the structural components of aircrafts that were manufactured some pieces from fiber reinforced composites. Recently, the experimental and numerical studies concentrate on this work area with developing numerical analysis programs [1-11].

The central circular notch effect on the buckling behaviors of composite materials was investigated [1-6]. Turan [1] investigated buckling behaviors of adhesively patch repaired composite plates and central circular notched composite plates with experimental and numerical studies. The central circular notched composite plates were repaired with external patch and adhesive. The critical buckling loads of repaired plates were compared with central circular notched composite plates [1]. Solmaz et al. [2] researched the buckling behaviors of central circular notched composite plates with experimental and numerical studies. The numerical study was realized in ANSYS finite element software [2]. Kömür et al. [3] and Ghannadpour et al. [4] investigated buckling behaviors of central circular and elliptical notched composite plates with experimentally and numerically. In these studies, the fiber reinforced angle, layer arrangement, elliptical hole position and notch dimension effect on the critical buckling loads were investigated [3, 4]. Okutan [5] and Okutan et al. [6] researched buckling behaviors of central circular and semicircular edge notched composite plates with experimentally and numerically. Akbulut and Ural [7] analyzed buckling behaviors of corner circular notched composite plates. Akbulut and Sayman [8] researched buckling behaviors of central square hole notched composite plates. Yazıcı et al. [9] and Turan [10] investigated buckling behaviors of U notched composite plates with numerical studies and experimental studies.

In this study, linear buckling behaviors of fiber reinforced and laminated composite plates were analyzed experimentally and numerically. The composite plates were manufactured from unidirectional carbon fiber and epoxy resin matrix as $[0^\circ]_4$,

$[0^\circ/45^\circ]_s$ and $[0^\circ/90^\circ]_s$ lamina sequence configurations. The notch depths were taken as 0, 2.5, 5 and 7.5 mm and the notch diameter was taken as constant value 10 mm. The critical buckling loads were determined from the compression tests. The effect of variations of the notch depth and lamina stacking sequence on critical buckling loads were presented with using graphs. The ANSYS Finite Element Method (FEM) software was used in order to obtain buckling loads, numerically. Finally, compatible compared results for experimental and numerical analyzes were presented in graphs.

VII. EXPERIMENTAL STUDY

In the experimental study, the four layered unidirectional carbon/ epoxy matrix composite plates were used as materials that have $[0^\circ]_4$, $[0^\circ/15^\circ]_s$ and $[0^\circ/45^\circ]_s$ lamina stacking sequences with approximately 1.4 mm thickness. The composite plates were provided from *Izoreel Composite Production Company*. The U-notches were opened to the edge of composite plate with using milling cutter. The geometrical conditions of problem were presented in Figure 1. The width of composite plate was 30

mm and length of plate was 140 mm. Mechanical properties of $[0^\circ]$ laminae were given in Table 1.

TABLE I. THE MECHANICAL PROPERTIES OF CARBON/EPOXY LAMINATED COMPOSITE PLATES [1].

Property	Symbol	Value	Unit
Young module in fiber direction	E_{11}	172891	MPa
Young module in perpendicular to the fiber direction	E_{22}	10796.66	MPa
Poisson ration	ν_{12}	0.32	-
Shear module	G_{12}	3638	MPa

In order to determine the effect of the notch depth on critical buckling load, U-notched composites specimens which have different notch depths as $a=0, 2.5, 5$ and 7.5 mm for a constant notch diameter $d=10$ mm were prepared. Totally, fifteen specimens were used in experiments for fiber orientations $\theta=0, 45$ and 90 in $[0^\circ/\theta^\circ]_s$ lamina stacking sequences and notch dimensions as presented in Figure 1.

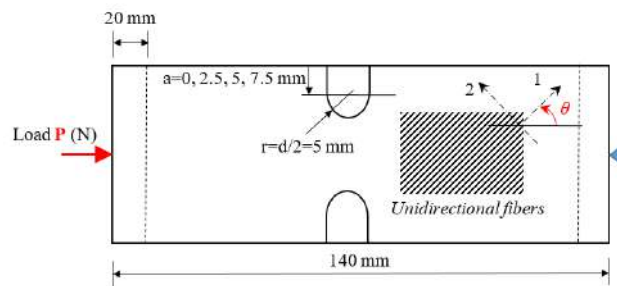


FIGURE 1. THE GEOMETRY OF PROBLEM.

The axial compression tests were realized in 50 kN capacity *Shimadzu* tensile testing machine with 1 mm/min compression speed in Ege University Mechanic Laboratory. The loads were applied to the samples until the buckling was observed. The load and displacement values composites, which were obtained from tensile testing machine and these values, were recorded in the computer. At the end of experiments, the plotted graphs were obtained from these records. The experimental set-up and typical load-displacement behavior of U-notched specimens were presented in Figure 2. Linear behavior zones of load-displacement graphs of U-notched composite plates were used to determine critical buckling loads. The critical buckling load of fiber reinforced and laminated composite plate is the

maximum end of the region that has a linear function as shown in Figure 2. These determine technique was applied to the all compression load-displacement graphs of specimens to obtain critical buckling load [1, 2].

The results of experiments were evaluated at two stages. First of these; the notch depth was changed as 0, 2.5, 5 and 7.5 mm for all θ values. The second of these, the fiber orientation angle was changed as $0^\circ, 45^\circ$ and 90° for symmetric stacking sequence $[0^\circ/\theta^\circ]_s$. In addition, these results were compared with numerical analysis results.

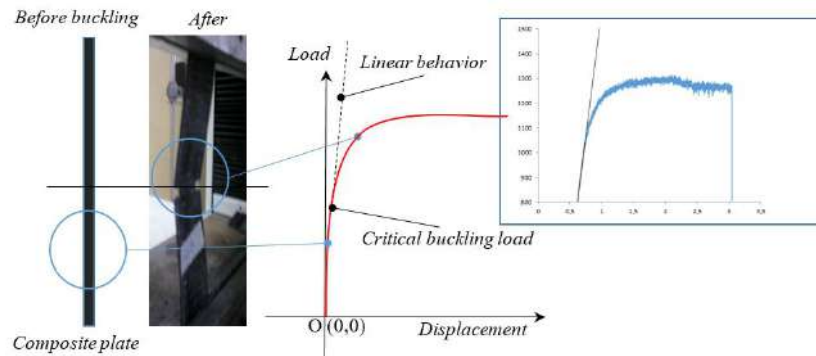


FIGURE 2. OBTAINING CRITICAL BUCKLING LOAD FROM LOAD-DISPLACEMENT GRAPH.

III. NUMERICAL ANALYSIS

In the numerical analysis, *ANSYS* finite element software used in order to obtain critical buckling loads. For all specimens, totally fifteen model was prepared and analyzed. In the modeled of problem *SOLID46* element type was used. The *SOLID46* was used layered composite materials and it had 8-node and three degrees of freedom at each node [11]. Total element and node sizes of numerical models used were linear buckling analyzes are given in Table 2. Typical mesh and boundary conditions of numerical model is present in Figure 3. Linear material properties of orthotropic composite materials in 1-2 planes given Table 1 were used as input in *ANSYS*.

TABLE II. ELEMENT AND NODE SIZES OF NUMERICAL MODELS USED IN LINEAR BUCKLING ANALYSIS.

Notch depth a (mm)	Element size	Node size
0	2000	3273
2.5	2208	3603
5	2208	3603
7.5	2464	4011

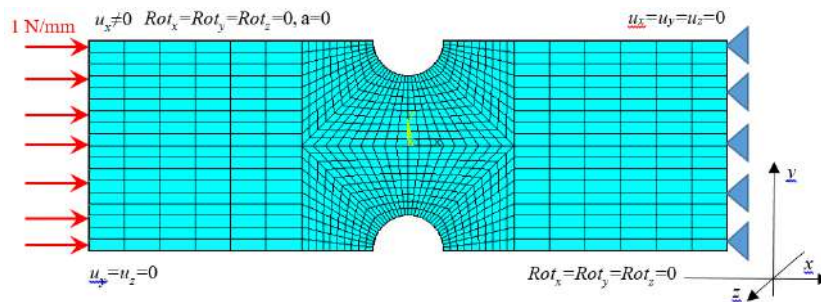


FIGURE 3. FINITE ELEMENT MODEL AND BOUNDARY CONDITION OF LAMNATED UNNOTCHED COMPOSITES (A=0).

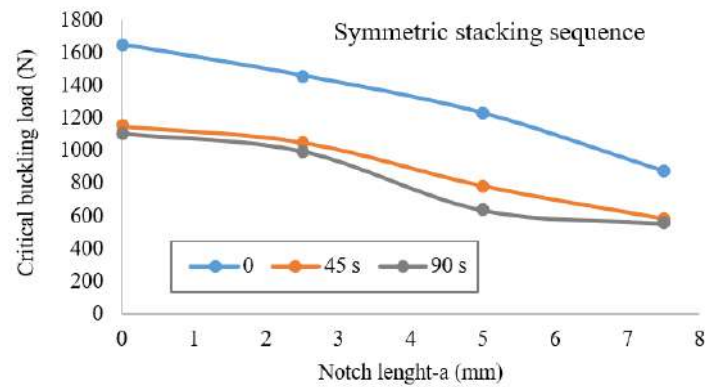


FIGURE 4. VARIATION OF CRITICAL BUCKLING LOAD WITH NOTCH LENGTH FOR DIFFERENT STACKING SEQUENCES

With using procedure, this was explained in Section I. In the experimental study, critical buckling loads were determined, and graphs are obtained. The maximum buckling load was obtained for $[0^\circ]_4$ stacking sequence specimen when a is zero as 1650 N. The minimum critical buckling load was obtained as 250 N for $a=7.5$ mm and $[0^\circ/90^\circ]_s$ lamina sequence configurations. On the other hand, increasing of the fiber orientation angle from 0° to 90° decreased critical buckling load of U-notched carbon/epoxy plates. The buckling loads of all notched specimens and fiber reinforced specimens were compared with $a=0$ having $[0^\circ]_4$ stacking sequence specimen. The calculated decreasing rates according to the $a=0$ were presented for different notch depths in Table 3. It can be seen that the U-notch decreased the buckling loads of composite plates as seen Figure 4. The minimum and maximum percent change ratios of buckling loads for $a=2.5$, 5 and 7.5 mm were calculated as 11.51% and 66.48% rates, respectively.

2.5	11.51	36.36	39.63
5	25.45	52.48	61.57
7.7	46.96	64.46	66.48

The table 3 was showed that the effect of fiber reinforced angle on buckling load was very important parameter. Also, the critical buckling loads decreased with increasing θ . When the fiber orientation angle was increased from 0° to 45° , decreasing rate was obtained approximately in 17.7-28% interval. When the fiber orientation angle was increased from 45° to 90° , the decreasing rate was obtained approximately in 2-9% interval. It can be seen from these results that 0° fiber orientation angle whose axis is identical with compression load is the most strength against the buckling. The increasing of θ effectively is decreased buckling loads up to 45° for all notch depth. Then increasing of θ from 45° up to 90° does not decrease buckling load much as changing of θ from 0° up to 45° . This situation can be explained as compression loading on fiber orientation axis causes to be blocked by fibers. Because fibers have more strength for tensile load than matrix materials.

TABLE III. PERCENT CHANGE RATIOS OF CRITICAL BUCKLING LOADS FOR DIFFERENT NOTCH DEPTHS (%).

Notch depth a (mm)	$[0^\circ]_4$	$[0^\circ/45^\circ]_s$	$[0^\circ/90^\circ]_s$
-------------------------	---------------	------------------------	------------------------

--	--	--	--

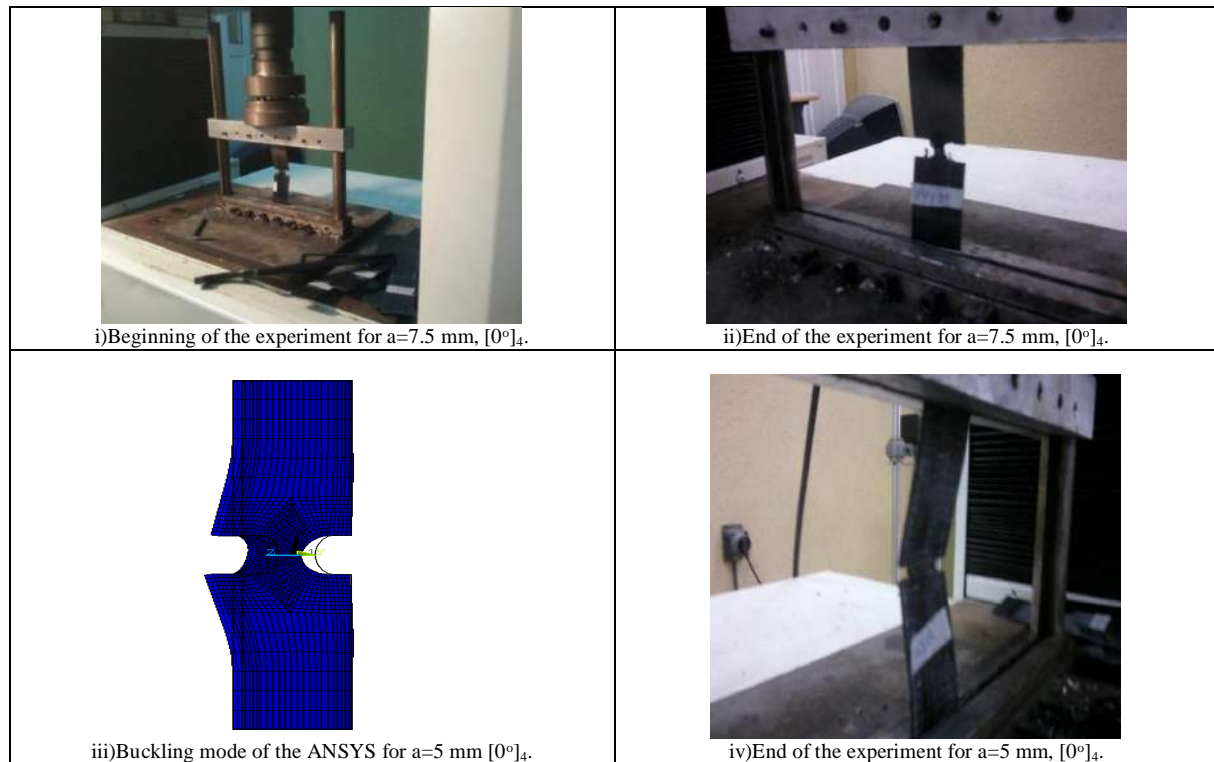


FIGURE 5. EXPERIMENTAL AND NUMERICAL BUCKLING MODES .

In the experimental study, the failure starting and propagating were observed, additionally. The failure mechanisms were showed in Figure 5. Stress concentrations at the tip of notch occur because of the notches. This situation leads to buckling starting at this location. When the ultimate failure was realized, it was expected that the composite plate can cracking and breaking occurred (Figure 5).

Comparative results of experimental and numerical analyzes are presented in Figure 6. It can be seen from these results that experimental and numerical results are very close. As in

experimental results, numerical buckling loads decreased with increasing notch depth and fiber orientation angles. Numerical results are greater than experimental results in some models. However, the opposite is true for some models. The maximum converge ratio was obtained for $[0^\circ/90^\circ]_s$ stacking sequence specimen when $a=2.5$ mm as +14.16%. The minimum converge ratio was obtained as +1.29% for $a=2.5$ mm and $[0^\circ]_4$ lamina sequence configurations.

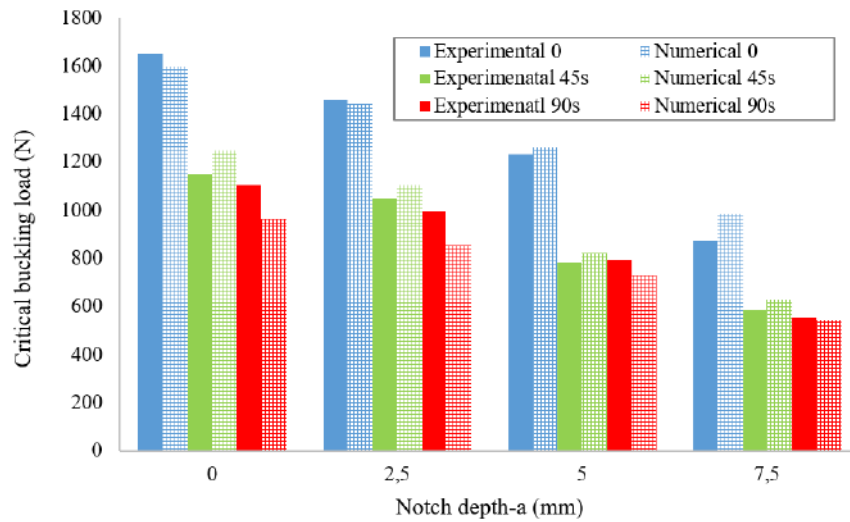


FIGURE 6. EXPERIMENTAL AND NUMERICAL TEST RESULTS FOR DIFFERENT NOTCH DEPTH OF $[0^\circ/\theta^\circ]_s$ COMPOSITES .

IV. CONCLUSIONS

In this study, linear buckling behaviors of carbon fiber reinforced/epoxy composite plates having different U-notch depths as $a=0, 2.5, 5$ and 7.5 mm for a constant notch diameter $d=10$ mm for fiber orientations $\theta = 0^\circ, 45^\circ$ and 90° in $[0^\circ/\theta^\circ]_s$ lamina stacking sequences were analyzed experimentally and numerically. The some of aspects are concluded as follows:

- The critical buckling loads were decreased with increasing notch depth as 11.51% and 66.48.2% rates according to the composite plates having semi-circular notch.
- The critical buckling loads decreased with increasing fiber orientation angle θ . When the fiber orientation angle was increased from 0° to 45° , percent decreasing rate was obtained in 17.7-28% interval. If the fiber orientation angle was increased from 45° to 90° , at this situation percent decreasing rate was obtained in 2-9% interval. In other words, 45° results are close to the 90° results.
- Effect of notch depth on failure and fracture behavior can be expected situation. However, important point of this research can be said that effects of variation of notch depth and fiber orientation angle on buckling loads are close to each other.
- Generally, obtained results shows that the fiber orientation angle effect on the critical buckling load is important parameter and 0° fiber orientation angle have more strength to the buckling. So, if designers use laminated composites having unidirectional carbon fiber applied buckling load, more 0° lamina on load

axis should be chosen in manufacturing process of laminated composite plates.

- Experimental results were obtained in accordance with numerical results in 1.29% and 14.16% interval. It can be said that the finite element method is very accurate and applicable for more complex analyzes of structural components.

V. REFERENCES

- [1] Turan K., Buckling behavior of adhesively patch-repaired composite plates, *Journal of Composite Materials*, Vol. 48, pp: 3253–3261, 2014.
- [2] Solmaz, M.Y., Kaman, M.O., Turan, K., Turgut, A., “Fiber takviye açısının tabakalı kompozit levhaların kritik burkulma yüküne etkisi”, XVI. Ulusal Mekanik Kongresi, 22 – 26 Haziran 2009, KAYSERİ.
- [3] Kömür, M. A., Şen F., Ataş, A., Arslan, N., “Buckling analysis of laminated composite plates with an elliptical/circular cutout using FEM”, *Advances in Engineering Software*, vol.41, pp: 161–164, 2010.
- [4] Ghannadpour, S.A.M., Najafi, A., Mohammadi, B., “On the buckling behavior of cross-ply laminated composite plates due to circular/elliptical cutouts”, *Composite Structures*, vol. 75, pp: 3–6, 2006.
- [5] Okutan, B.O., “Buckling behavior of laminated composite plates”, *Journal of reinforced plastics and composites*, Vol. 26, pp: 1637-1655, 2007.
- [6] Okutan, B.O. Baltaci, A., “Buckling characteristics of symmetrically and antisymmetrically laminated composite plates with central cutout”, *Applied composite materials*, vol. 14, pp:265–276, 2007.
- [7] Akbulut, H., Ural, T., “An investigation on buckling of composite laminated plates with corner circular notches”, *Journal of thermoplastic composite materials*, Vol. 20, pp: 371-387, 2007.
- [8] Akbulut, H., Sayman, O. “An investigation on buckling of laminated plates with central square hole”, *Journal of reinforced plastics and composites*, Vol. 20, pp: 1112-1124, 2001.
- [9] Turan K., “Thermo-aging effect on the buckling behaviors of u-notched composites”, *European Journal of Technic*, Vol 6, pp: 9-15, 2016 .

- [10] Yazıcı, M., Özcan, R., Ülkü, S., Okur, İ. "Buckling of composite plates with u-shaped cutouts", Journal of composite materials, Vol. 37, No. pp: 2179-2195, 2003.
- [11] ANSYS 11.0 (Academic Teaching Introductory), Command References and Gui.

Effect of pH on the Stress Corrosion Cracking of AZ91 Mg Alloys Using Slow Strain Rate Test (SSRT) Method

Recep CATAR / PhD Student
Department of Mechanical Engineering
Bayburt University
Bayburt, TURKEY
recepcatar@yahoo.com

Hikmet ALTUN / Prof. Dr.
Department of Mechanical Engineering
Ataturk University
Erzurum, TURKEY
haltun@atauni.edu.tr

Abstract— The aim of this study is to analyze the effect of pH on the stress corrosion cracking of AZ91 Mg alloys using slow strain rate test (SSRT) method in different media; acidic, basic and neutral NaCl solutions. Slow strain rate test indicated that AZ91 Mg alloys in basic environment were the least susceptible, while the most susceptible to stress corrosion cracking in acidic environment. SEM images showed that intergranular stress corrosion cracking was evident for AZ91 Mg alloys in acidic and basic solution, whereas in neutral environment, transgranular corrosion cracks were observed.

Keywords—AZ91 Mg alloy, stress corrosion cracking, SSRT

VIII. INTRODUCTION

The need of light materials particularly in sectors of automotive, aviation, microelectronics and telecommunication lead engineers to be more creative in choosing materials. Magnesium and its alloys with a quarter density of steel and with two third density of aluminum while its specific strength (strength/weight) is more than both of them, magnesium has properties very good enough to play the role as being a light material.

Magnesium and its alloys have become one of the ideal materials because of being the lightest structural material in order to decrease vehicle weight to the minimum value and in turn to decrease exhaust gas emission to minimum. Moreover magnesium and its alloys have been predicted to be used as orthopedics implants due to being light, bio-solvable and having capability of loading. Although these materials have significant mechanical properties like high specific strength, they have some disadvantages such as bad corrosive features and stress corrosion susceptible that restrict the usage in this area.

The incidence of SCC may increase because of increasingly usage of Mg parts in structural applications compared with the previous non-structural applications. Service conditions are becoming more severe, particularly in the automobile industry,

where cast Mg components are increasingly used in load-bearing applications [1].

Stress corrosion cracking of Mg alloys have been studied by many researchers in the literature. Some common alloys (such as AZ91, AZ31 and AM30) are susceptible to SCC failure even in a mild environment such as distilled water [1]. Mg-Al alloys have been reported to SCC in different media such as air, distilled water and chloride-containing solutions [2]. Miller [3] indicated that SCC occurs in distilled water for AZ91, AM60 and AS41 Mg alloy. Arnon and Aghion [4] found SCC in AZ31 in %0,9 NaCl. It has been reported that AZ91 Mg alloy has TGSCC in 0.5 M MgCl₂ [5].

Environmental effects such as hydrogen, atmosphere, solution composition, electrochemical potential, pH, temperature, coating have been studied to analyze effects of stress corrosion susceptibility of magnesium alloys [1]. There are a few reports on the influence of pH on SCC in the literature and they all agreed that SCC does not occur in chloride-chromate solutions with pH values greater than 12 [6].

This study presents stress corrosion resistance determined by the SSRT test method at different pH values of commonly used AZ91 Mg alloys.

IX. EXPERIMENTS

A. Test Materials

The material used was as-cast AZ91 Mg alloy including (wt.%) 9.231Al, 1.348Zn, 0.286Mn, 0.148Si, 0.012Fe, 0.004Cu and balance Mg. (The composition ratio is not given for the elements below 0.001%.) Untreated 16 mm diameter rod specimens were produced on CNC machines in accordance with ASTM E 8 Test Method standards (Standard Test Methods for Tension Testing of Metallic Materials). The specimen preparation steps are as follows:

1) The surfaces of all samples were polished using 1000, 2000 grit silicon carbide papers,

- 2) All samples were cleaned with distilled water and acetone,
 - 3) Dried in cool air.
- The picture of the produced samples is given in Figure 1.



Fig. 1. Used tensile samples for SSRT test (Unit:mm)

B. Slow Strain Rate Test (SSRT)

In this study, slow strain rate test (SSRT) was applied and the stress corrosion behavior of alloys was investigated. The experiments were carried out in accordance with ASTM G-129 00 standard. Slow deformation in operation was provided by Shimadzu brand universal tensile testing device. The corrosive environment is provided by acidic (pH = 2), basic (pH = 11) and %3.5 NaCl neutral environments with artificial corrosion cell mounted on the tensile testing device. The experimental setup used is shown in Figure 2.

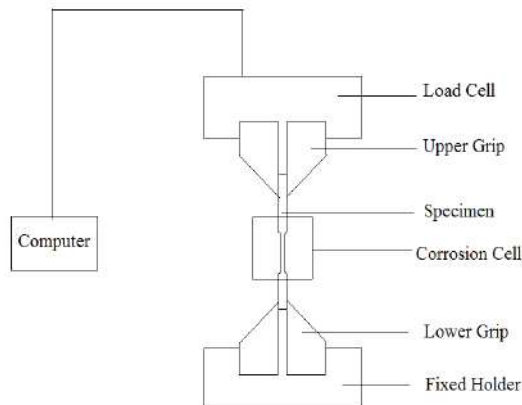


Fig. 2. Schematic picture of SSRT experimental setup

Acidic solution was prepared by adding HCl to 3.5% NaCl solution to decrease the pH value to 2.0, and NaOH was added to 3.5% NaCl solution until pH = 11.0 to obtain a basic solution.

The stress corrosion crack index was calculated by cracking the test specimens in the abovementioned media and at a deformation rate of $6.66 \times 10^{-7} \text{ s}^{-1}$. Stress corrosion crack index can be determined in two ways. Determination of the ratio of the tensile strength value in the corrosive environment to the tensile strength in air in the first sample; And the second is to determine the crack time of the sample in the corrosive environment relative to the crack time of the air sample. Stress corrosion resistance of material with low stress index of crack cracking is low and stress corrosion resistance of material with high index is high.

X. RESULTS

Stress corrosion tests of AZ91 Mg alloy were carried out in acidic, basic and 3.5% NaCl solutions by the slow strain rate test method. Firstly the AZ91 magnesium alloys were subjected to the SSRT test in the air environment, and as a result of the test, the tensile strength was about 146 MPa and the cracking time was about 13 hours. Secondly, the specimens were subjected to the SSRT test in an acidic environment, and as a result of the test, the tensile strength was approximately 77.5 MPa and the cracking time was approximately 6.3 hours. Thirdly, the samples were subjected to the SSRT test in a basic environment and the tensile strength was approximately 106.8 MPa and the cracking time was approximately 7.5 hours. Finally, they were subjected to the SSRT test in neutral 3.5% NaCl and the tensile strength was approximately 89.4 MPa and the cracking time was approximately 6.8 hours. SSRT results are shown in Figure 3.

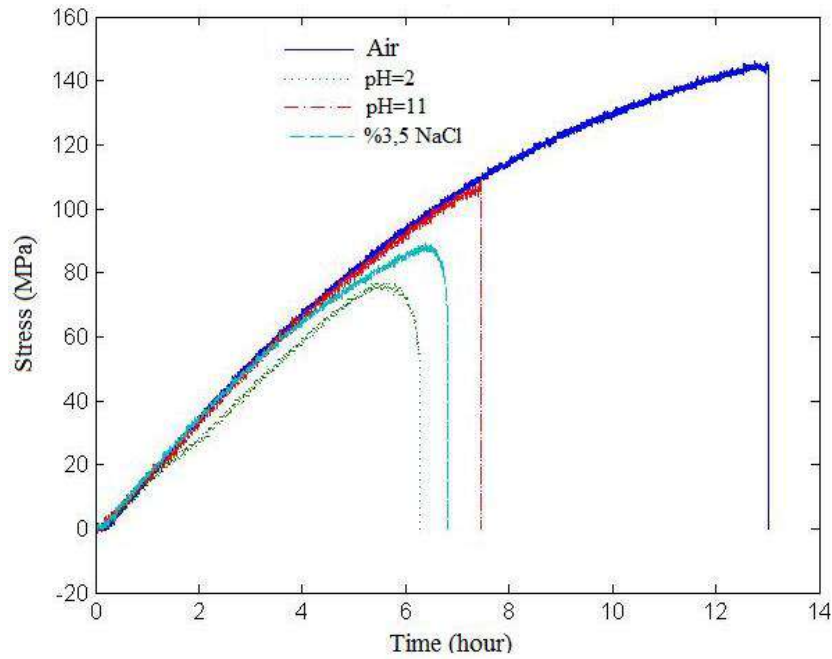
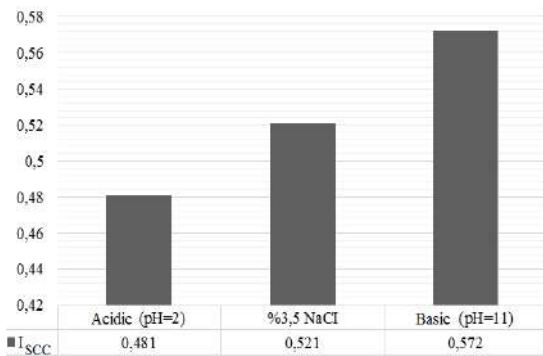


Fig. 3. SSRT test results of AZ91 Mg alloy in air, acidic, basic and 3.5% NaCl solution

Fig.4. I_{SCC} of AZ91 Mg Alloys

TABLE 1. STRESS CORROSION CRACK INDEXES OF AZ91 Mg ALLOY

Atmosphere	Cracking Time (Hour)	I_{SCC}
Air	13,03	-
Acidic (pH=2)	6,27	0,481
%3,5 NaCl	6,80	0,521
Basic (pH=11)	7,46	0,572



Stress corrosion crack indexes of AZ91 magnesium alloys are given in Table 1 and Figure 4. As shown in the diagram, the SSRT test of the AZ91 magnesium alloy in the 3.5% NaCl solution resulted in a stress corrosion crack index (I_{SCC}) of the lowest acidic (pH = 2) and the highest basic (pH = 11). The AZ91 magnesium alloy has been found to be susceptible to stress corrosion crack at three of the working environments (acidic, basic and neutral) and is found to be the acidic medium was the least stress corrosion resistance (or the highest tensile corrosion sensitivity). It can be said that the environment in which the stress corrosion resistance is highest (or at least the tensile corrosion sensitivity) was the basic environment.

The fracture surfaces of AZ91 Mg alloys in acidic, basic and %3,5 NaCl solutions with the slow deformation rate are given Fig. 4. The AZ91 Mg alloy showed inter granular corrosion cracks in acidic and basic media, whereas in neutral environment, trans granular corrosion cracks were observed.

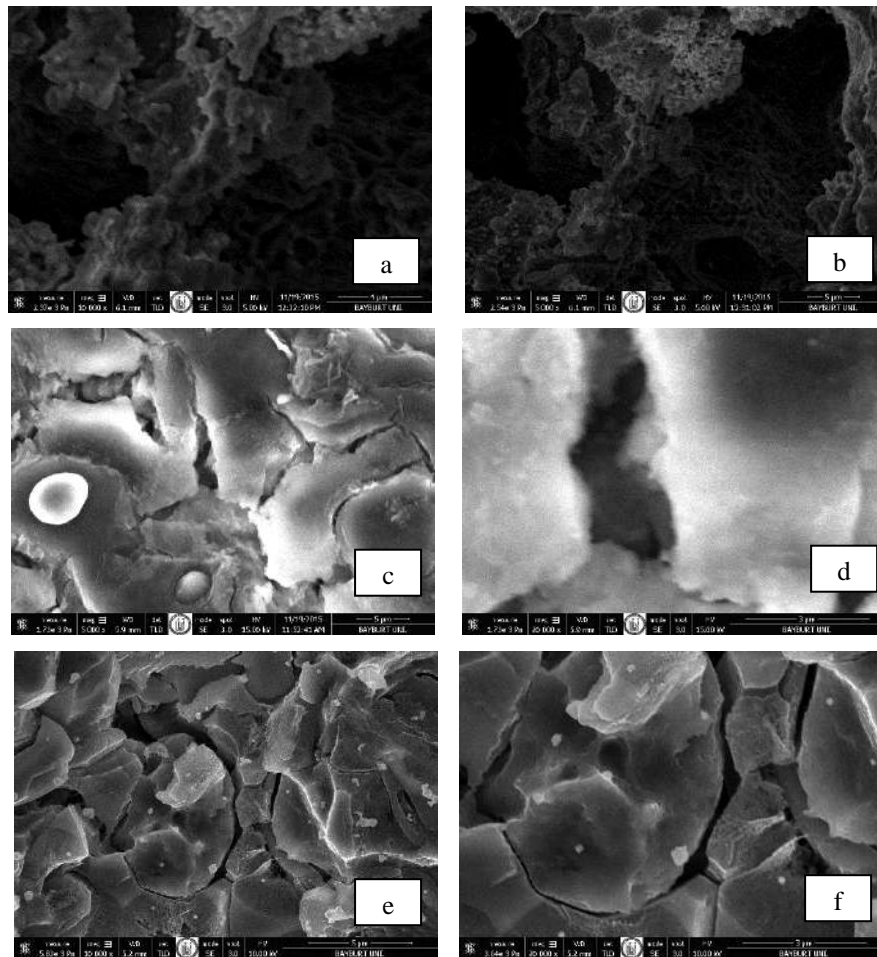


Fig.5. SEM images of AZ91 Mg alloys in solution (a,b) %3,5 NaCl, (c,d) acidic, (e,f) basic

XI. DISCUSSION

In the study conducted, it was found that the stress corrosion resistance of AZ91 magnesium alloys in 3.5% NaCl solution is weak. Especially, as the pH value decreases, tensile corrosion resistance decreases significantly. Depending on the pH value of magnesium alloys, stressed corrosion behavior appears to be a similar effect to corrosion behavior.

[1] and [9] found that the amount of aluminum in the alloy affects corrosion and stress corrosion. (1998): Mg-Al alloys with 2-8% by weight of Al increase the concentration of Al and decrease the amount of corrosion. Low Al contents of about 2-4% Al are caused by α -Mg extensions surrounded by a double-phase $\alpha + \beta$ -eutectic phase at grain boundaries. On the contrary, pure beta bands tend to precipitate along the grain boundaries along the grain boundaries due to the solidification rate in high additions of 6 to 9 wt% Al. If the amount of Al is up to 10%, the Al-rich α phase will cause microsegmentation during solidification and this value will be the appropriate local concentration [9]. [10] β -phase is a very stable and effective cathode in solution. Beta phase, one barrier and the other a galvanic cathode. If the beta phase is present in small quantities in the precipitate between the particles in the alpha matrix, this

acts mainly as a galvanic cathode and accelerates the corrosion of the alpha matrix. If the amount of β phase is large, then β phase can act as an anodic barrier to prevent corrosion of the alloy. The β phase is beginning to appear when Al is more than 2% by weight. As a result, up to 10% of Al content increases corrosion and stress corrosion resistance. For this reason, the stress corrosion resistance of the commonly used AZ91 Mg alloy compared to other AZ31 and AZ61 Mg alloys is likely to be high.

XII. CONCLUSIONS

The effect of pH value on SCC behavior of AZ91 Mg alloys can be summarized as follows.

1. As the pH value decreases, the stress corrosion crack index of AZ91 Mg alloys decreases. This means that stress corrosion susceptibility increases.
2. Studies to improve the stress corrosion resistance of AZ91 magnesium alloys in industrial applications, automotive, defense industry, aerospace, and especially in implant applications in recent years are inadequate, and extensive studies are needed to be done in this regard.

ACKNOWLEDGMENT

This study was supported by BAP of Atatürk University with the project number 2012/434.

REFERENCES

- [1] G.L. Song, "Corrosion of magnesium alloy", Chapter 8, Woodhead Publishing Limited, 2011, pp. 299-354.
- [2] ASM Specialty Handbook, Magnesium and magnesium alloys, ASM International, Metals Park Ohio, 199, pp.211
- [3] Willer M.K., Metaterials research society syposium proceeding, 1988, pp.125-253.
- [4] Arnon A., Aghion E., Stress corrosion cracking of nano/sub-micron E906 magnesium ally, Advanced Engineering Materials, 2008, pp. 742-745.
- [5] Chen J., Ai M., Wang J., Han E., Ke N., Stress corrosion cracking behaviours of AZ91 magnesium alloy in deicer solution using constant load, Material Science and Engineering, 2009, pp. 79-84.
- [6] Atrens A., Winzer N., Dietzel W., Stress corrosion cracking of magnesium alloys, Advanced Engineering materials, 2009, Vol. 13, pp. 11-18
- [7] Annual Book of ASTM Standarts , ASTM G 129-00."Standard Practice for Slow Strain Rate Testing to Evaluate the Susceptibility of Metallic Materials to Environmentally Assisted Cracking", 2013.
- [8] Annual Book of ASTM Standats , ASTM E-8 "Standard Test Methods for Tension Testing of Metallic Materials", 2013.
- [9] Ghali, E., "Corrosion resistance of aluminum and magnesium alloys, understanding, performance, and testing", Jogh Wiley & Sons., USA, 2010.
- [10] Song G., Atrens, A., Wu X., Bo Z., and Zhang B., Corrosion behaviour of AZ21, AZ501 and AZ91 in sodium chloride, Corrosiom Science,

Development Of an Artificial Neural Network That Can Predict Pressure Drop in Pipes With Different Roughness

Ahmet Beyzade DEMİRPOLAT, İsmail Hakkı ŞANLITÜRK, İhsan DAĞTEKİN, Haydar EREN

Mechanical Engineering Department
Firat University
Elazığ, Turkey
ihsanliturk@firat.edu.tr

Abstract—Effect of pressure loss and pressure change in the entrance and fully developed flow region of different pipes which have different roughness have been investigated. Turbulence effects have been accounted for pressure measurements. A neural network have been developed for obtaining pressure drop. Input of the network is pipe material, diameter, flow rate and time. Comparison of the experimental values with the neural network results has been shown graphically. As a result, it was seen that designed neural network predicts pressure drop values accurately.

Keywords— *friction, internal flow, surface roughness, neural networks*

I. INTRODUCTION

The fluid flow in the tubes is commonly utilized in the heating and fluid distribution networks. In such applications, the fluid is often forced to flow in a flow region by a pump. It is necessary to pay special attention to the friction which is directly related to pressure drop and load loss in the pipe flow. At this point, external factors cause the friction to come to the market. One of these external factors is pipe roughness. In this study, an artificial neural network was designed in MATLAB Neural Network program to calculate the pressure drop when the roughness, pipe diameter, pipe material and flow time is entered, using the data obtained by experiments with 5 pipes in different roughness to investigate the effect of pipe roughness on pressure loss.

Numerous studies have been carried out on in-pipe flows. One of the most important of these studies is the relation equation between pressure drop and the flow called Hagen-Poiseuille flow, which developed by G. Hagen (1797-1884) and J. Poiseuille (1799-1869) [1-2].

Cyril F. Colebrook developed the Colebrook equation by combining the available data for smooth and rough piping and for turbulent flows in 1939. Hunter Rouse in 1942 and Lewis F. Moody plotted the relationship between friction factor and Reynolds number two years later, which known as the Moody diagram. The Moody diagram and the Colebrook equation can

only be used with a deviation of fifteen percent due to the size of experimental errors [3-4].

Bhatti and Shah [5] and Kaysa and Crawford [6] have studied the hydrodynamic transit lengths. These studies for finding the pressure loss and friction factor are usually carried out on artificially roughened pipes.

II. EXPERIMENTAL STUDY

The fluid used for performing the experiments was water. Red paint was added in the water for visibility. Five pipes with different roughness were selected for experimental study as iron, PPRC, copper, aluminum and galvanized steel, respectively. The diameters of the pipes were changing from 20,5mm to 27,75mm. The range of the flow rate was changed between 0,92879257m³/s and 0,000247525m³/s. Hydrodynamics transition length and fully developed flow range were taken into account when selecting the pipe lengths. Measurement ports were placed on entering and exit of the pipes. Ports also were placed with narrow spacing for hydrodynamic transition range on those pipes, too.

The flow rate was measured with a hydraulic tank, and static pressure values were recorded by a camera for a time range of 105s. Pressure values then extracted from recorded videos by image-processing technique. The experiments were repeated for 5 different pipes. Fig 1. Show the experimental setup.



Figure 1. Experimental setup

III. NEURAL NETWORKS

A neural network is a powerful tool for problems doesn't have a mathematical model. Since there are assumptions in building a mathematical model, physics of the problem may not be fully represented. A neural network can be built to represent a problem correctly after have trained with experimental data. When building a neural network model, memorization of the problem should be avoided. In this study, a FFBP (Feed Forward Back Propagation) neural network consisted of one input, one hidden, and one output layer was used. The number of input layer cells is 4 as material, diameter, flow rate and time. The output is a single cell as pressure drop. The number of hidden layer cells was determined by inspecting regression results as given below in Table I.

The total of 1575 data points [7] was used in the design of the neural network. %70 of the data was used for training, %15 for validation, and remaining %15 for testing.

As input and output cell numbers are fixed, the neural network was trained and simulated for numerous sizes of the hidden layer. According to results that given in Table I, network size of 4x24x1 was selected and used in this study. Regression and performance results for the selected network has been shown in Fig 2 and 3, respectively.

TABLE I. FFBP NETWORK SIZE AND TRAINING RESULTS

	Network size (Input x Hidden x Output layer)					
	4x12x1	4x16x1	4x18x1	4x20x1	4x24x1	4x28x1
Training	0,8654	0,9945	0,8828	0,8686	0,9949	0,8619
Validation	0,8779	0,9943	0,8553	0,8956	0,9945	0,884
Test	0,8784	0,9949	0,8229	0,8558	0,9946	0,8984
All	0,869	0,9946	0,8705	0,8702	0,9948	0,8706
Best val.	421,123	19,137	51,3	38,069	2,0279	41,947
Epoch	5	127	11	5	434	5

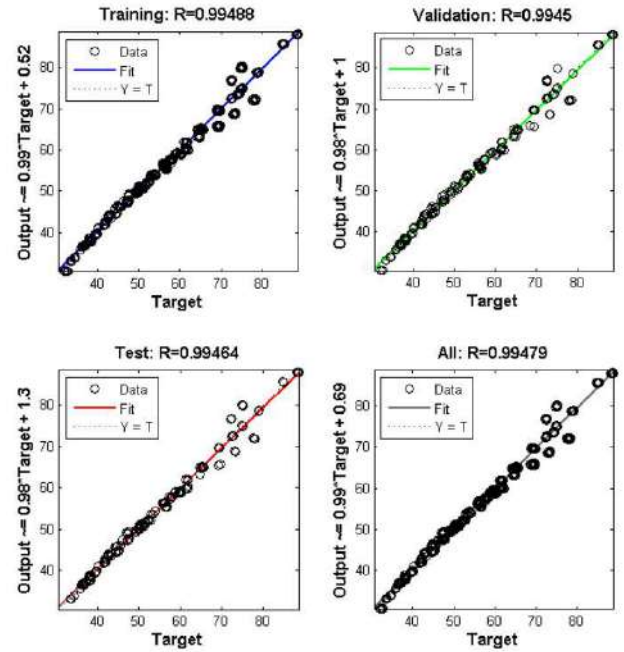


Figure 2. Regression results of the FFBP neural network

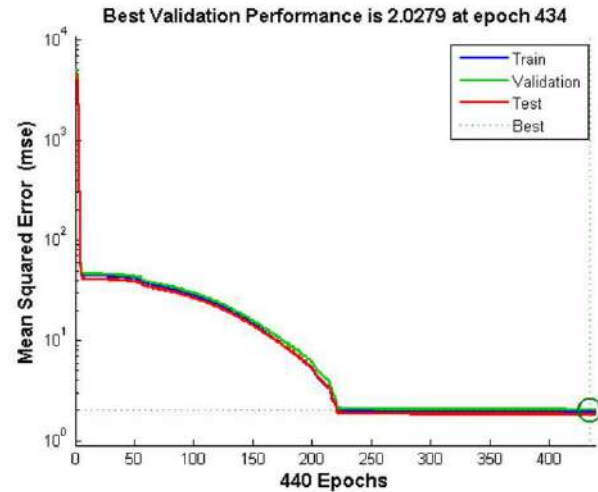


Figure 3. Performance results of the FFBP neural network

IV. RESULTS AND DISCUSSION

The pressure drop corresponding to the change in flow rate, time and pipe material and diameter has been obtained experimentally. The developed neural network has been predicted accurately the pressure drop corresponding to given parameters. This network can be used to determine pressure drop in other pipes.

ACKNOWLEDGMENT

This project is supported by Firat University Scientific Research Projects Department as project no: FUBAP MF.11.18

REFERENCES

- [1] Abraham.J.P.Sparrow. Tong. J.C.K. Bettenhausen. D.W.. 2010. Internal flows which transist from turbulent through intermittent to laminar. International Journal of Thermal Sciences. 49. 256–263
- [2] Çengel.Y. A. JM. Cimbala. Akışkanlar Mekaniği Temelleri ve Uygulamaları. Birinci baskıdan çeviri. İzmir:Güven Kitabevi. 2008.
- [3] White. F. M.. Fluid Mechanics. 5th ed. New York: McGraw-Hill. 2003.
- [4] Colebrook. CF. “Turbulent Flow in Pipes. with Particular Reference to the Transition between the Smooth and Rough Pipe Laws.” Journal of the Institute of Civil Engineers London. 11 (1939). pp. 133–156.
- [5] Moody. L. F.. “Friction Factors for Pipe Flows.” Transactions of the ASME 66 (1944). pp. 671–684.
- [6] Bhatti. M. S. and Shah. R. K.. “Turbulent and Transition Flow Convective Heat Transfer in Ducts.” In Handbook of Single-Phase Convective Heat Transfer. ed. S. Kakaç. R. K. Shah. and W. Aung. NewYork:Wiley Interscience. 1987.
- [7] Demirpolat, A.B., “Farklı pürüzlülüğe sahip borularda giriş ve tam gelişmiş akış bölgesinin deneysel analizi”, Master Thessis, Firat University, Elazığ, 2012.

Investigation of Effect of Coil Spring Turbulators to the Heat Transfer and Pressure Loss in a Concentric Heat Exchanger

Sinan KAPAN

Firat University,
Department of Mechanical Engineering, Elazig Turkey
e-mail: skapan@firat.edu.tr

Ali TASKIRAN

Firat University,
Department of Mechanical Engineering, Elazig Turkey
e-mail: ataskiran@firat.edu.tr

ABSTRACT: The aim of this paper is to investigate the effects of the coiled springs wrapped around a thin rod and located in the entrance of a concentric heat exchanger on heat transfer and pressure drop. The outer surface of the inner tube was maintained at constant temperature (100 C) by continuous contact with saturated water vapor introduced and filled into the annular space between the inner and outer tubes and discharged by a channel, like a teapot. The surface temperatures of the inner pipe, inlet and outlet temperatures of the air and pressure loss through the pipe were measured. The measurements were carried out for the Reynolds number ranged from 6500 to 42000. The only design parameter were considered as the diameter of the springs ($d_1=0.25$ cm, $d_2=1.0$ cm and $d_3=1.5$ cm) which is wrapped to the thin rod. It will be showed and detailed in the following sections. Nusselt number and friction factor were found out based on the measurements. New empirical correlations were found for the results.

Keywords— *turbulator, coiled springs, concentric heat exchanger, pressure drop, heat transfer*

I. INTRODUCTION

The increase of heat transfer in exchangers means saving energy and using energy efficiently. Given the ever-increasing need for energy and the reduction in energy resources, the use of heat transfer is better understood to improve the heat transfer in heat exchangers.

In present study, a coiled spring wrapped around a thin rod inserted in a concentric tube is used to enhance heat transfer. The coiled spring inserted tubes have been used as one of the passive heat transfer enhancement techniques and are the most widely used tubes in several heat transfer applications, for example, heat recovery processes, air conditioning and refrigeration systems, chemical reactors, food and dairy processes. Before introducing the tabulated heat exchanger system in the present study a short blink to the literature will help to understand the effects of the usage of the fins on heat transfer and pressure drop.

Some experimental results for local heat transfer coefficients were presented for a converging channel with rib roughening elements with the cross-section being maintained square from inlet to exit by Abraham and Vedula [1].

Heat transfer and pressure loss in an air to water double pipe heat exchanger were experimentally investigated by Sheikholeslami et al [2].

A circular-ring and perforated circular-ring turbulators were placed in annular pipe. Results indicated that using perforated circular-ring turbulators leads to obtain lower heat transfer enhancement than the circular-ring turbulators. An experimental and numerical work were carried out to study the heat transfer enhancement in a heat exchanger square-duct fitted with oblique horseshoe baffles by Skullong et al [3].

Promvonge [4] studied the increase in heat transfer rate using conical ring with three different diameter ratios and placed with three different arrangements.

El Sayed et al. [5] investigated the effects of height, thickness, inter-fin spaces, number and tip-shroud clearance of fins on the heat transfer, fluid flow and pressure drop.

Naik et al. [6] proposed a design correlation which shows the distribution of optimal rib spacing for a wide range of rib geometries and operational conditions.

Sahin et.al [7] investigated the effects of the longitudinal and lateral separations of consecutively enlarged-contracted arranged fin pairs, widths of the fins, angle of attack, heights of fins and flow velocity on the heat and pressure drop characteristics by using the Taguchi method.

Arulprakasajothi et al [8] aimed to investigate for to circular tube with conical strip inserts as turbulators in a laminar flow condition, using staggered and non-staggered conical strips.

Cakmak and Yildiz [9] performed a study and investigated the influence of the injectors with swirling flow generating on the heat transfer in the concentric heat exchanger.

In present study, the diameter of springs wrapped around thin rod and Reynolds number have been the investigated as parametric values. Heat transfer by means of Nusselt number and pressure drop by means of friction factor are the results of the experimental study.

2. EXPERIMENTAL SETUP

The main structure of the experimental setup was already explained in a previously published paper by Eren et al [10, 11]. Schematic view of the setup is presented in Figure 1. The

air is blown by a fan and its speed is regulated by an inverter. An anemometer was used for measuring the velocity of the air. Pressure differences between the inlet and outlet of the exchanger are measured by an inclined manometer.

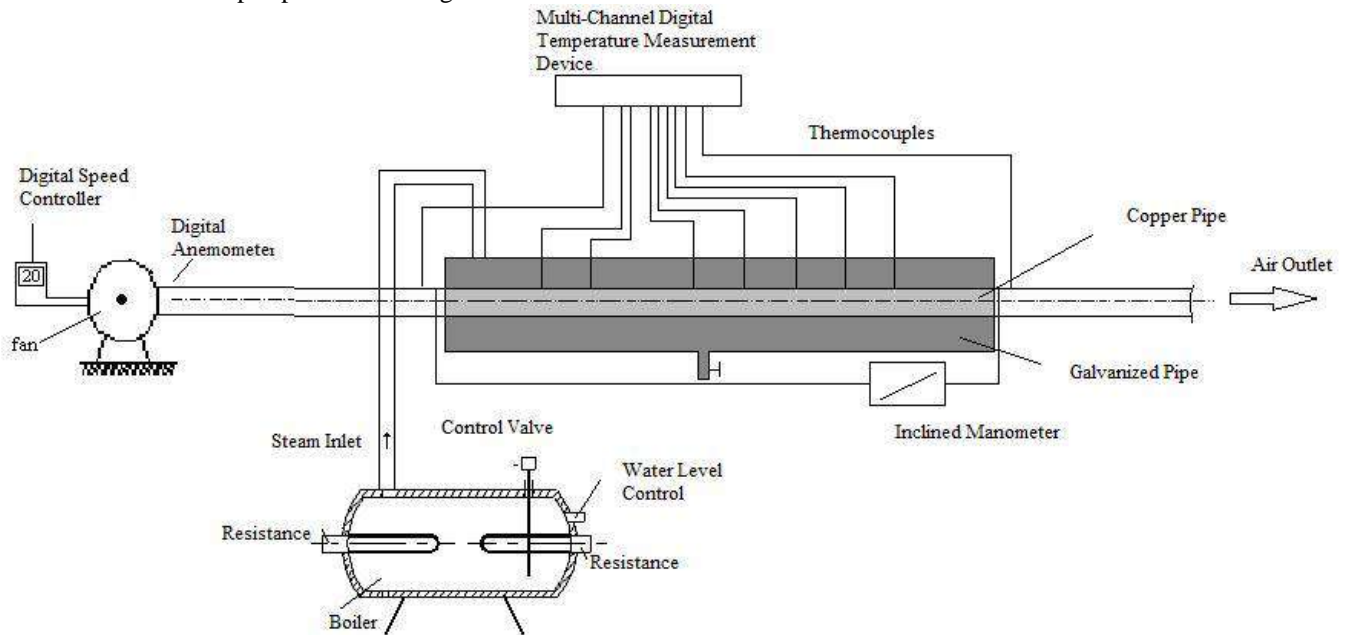


Figure 1 Experimental Setup [10]

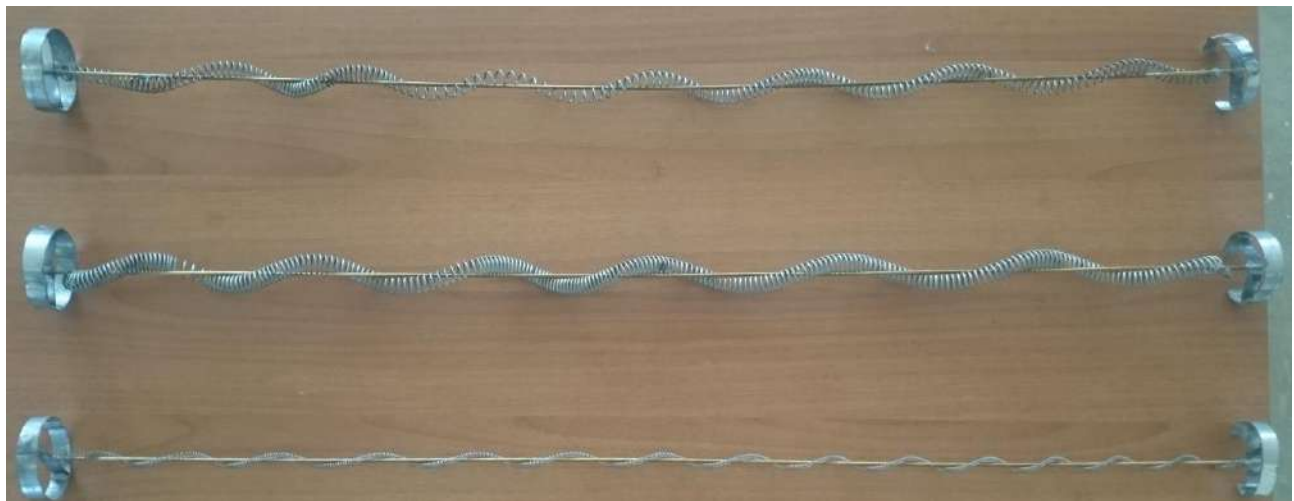


Figure 1 Coil springs wrapped to the thin rod

The heat exchanger is a classical type concentric tube of which outer surface of the inner tube is heated by the condensation of a stream of flowing water vapor. The inner and outer diameters of the inner tube are respectively 65 and 66 mm and the length of the tube is 900 mm. As an outer tube, a 1 mm-thick flat plate with dimensions of 700x1200 mm is rolled to obtain a circular tube with a diameter of 210 mm [10, 11].

The outer surface of the inner tube was kept at a constant temperature (100 C) by continuous contact with saturated water vapor introduced and filled into the annular space

between the inner and outer tube and discharged by a channel. The surface temperatures were measured by T-type thermocouples located every 50 mm distance along the tube length. The mean local wall temperature was determined by means of calculations based on the readings of the thermocouples. The inner and outer temperatures of air were also measured at certain points inside the tube. The pressure loss was maintained by an inclined manometer [10, 11].

3. DATA REDUCTION

All of the experiments are performed under the steady state conditions. Each run takes approximately 30 min. Heat transfer and pressure loss data are parameterized with the Reynolds number which is varied from 6000 to 12000. Re number is found as follows:

$$Re = \frac{VD}{\mu} \quad (1)$$

where V is the velocity of the air at the inlet, μ is kinematic viscosity of the air, D is the inner diameter of inner tube.

The average Nusselt number is found by logarithmic mean temperature difference:

$$LMTD = \frac{T_1 - T_2}{\ln \frac{T_1 - T_m}{T_2 - T_m}}$$

where T_1 is the difference between mean wall temperature and inlet temperature of the air ($T_1 = T_w - T_i$), and T_2 is the difference between mean wall temperature and outlet temperature of the air ($T_2 = T_w - T_o$). The mean wall temperature T_w was determined by means of calculations based on the readings of the thermocouples [10, 11].

The net heat is obtained by subtracting the heat loss from the gained heat occurred because of the water vapor on the surface. The outer surface of the test tube was well insulated and necessary precautions were taken to prevent leakages from the system. Thus, the convection heat transfer to the surrounding is neglected. Also the conductive heat loss through the thickness of copper tube, and radiation between the air and copper surface is neglected. The mentioned neglected heat rates are less than 0.5% of the total heat obtained by heating the surface by water vapor [10, 11].

Net heat is equal to the heat transfer rate occurred by logarithmic mean temperature difference, LMTD:

$$Q = \dot{m} C_p (T_o - T_i) = h A (LMTD)$$

$$h = \frac{Q}{A (T_o - T_i)} \quad (3)$$

where the fluid properties C_p , and k are found based on bulk temperature of the air.

Then average Nusselt number can be calculated as follows:

$$Nu = \frac{h D}{k} \quad (4)$$

The measured pressure loss is used to calculate the friction factor:

$$f = \frac{\Delta P}{L} \frac{D}{\rho V^2} \quad (5)$$

In order to compare the experimental results of the turbulent tube, a smooth tube flow is also tested. In addition, the well-known empirical formula of Dittus-Boelter and Blasius are used for comparisons [12].

$$Nu = 0.023 Re^{0.8} Pr^{0.4} \quad (6)$$

$$f = \frac{0.316}{Re^{0.25}} \quad (Re > 2 \times 10^4) \quad (7)$$

where Prandtl number of the air is considered based on the average of inlet and outlet temperatures.

4. RESULTS AND DISCUSSIONS

The design parameters in this study are the coil spring diameter wrapped on the thin rod (d) and Reynolds number. The effects of mentioned parameters on heat transfer and pressure loss are presented in Figure 3, 4 respectively. For all cases Nu number increases with increasing Re number.

The friction factor decreases with increasing Re number, because friction factor inversely changes to the square of the air velocity.

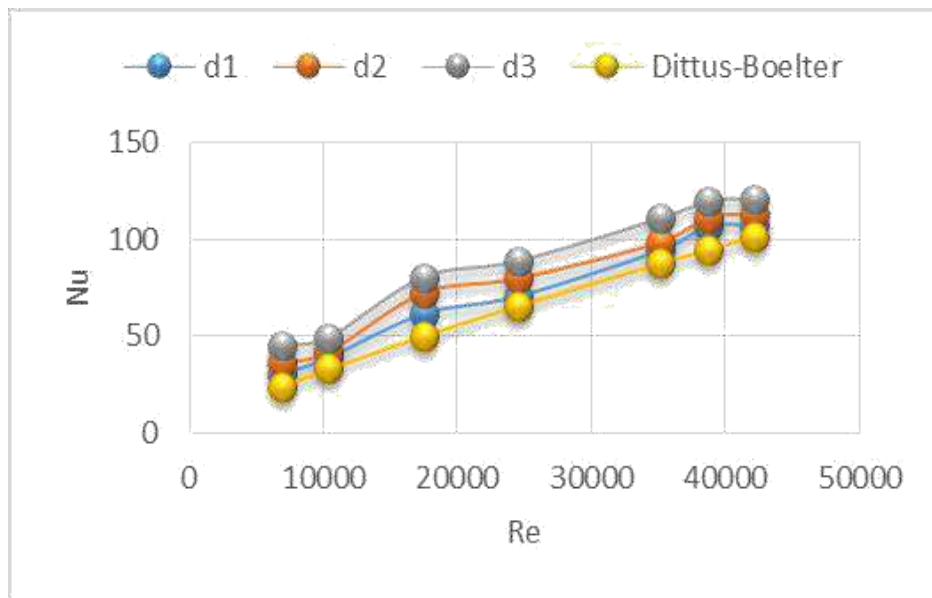


Figure 3 Nu versus Re with respect to hole diameter

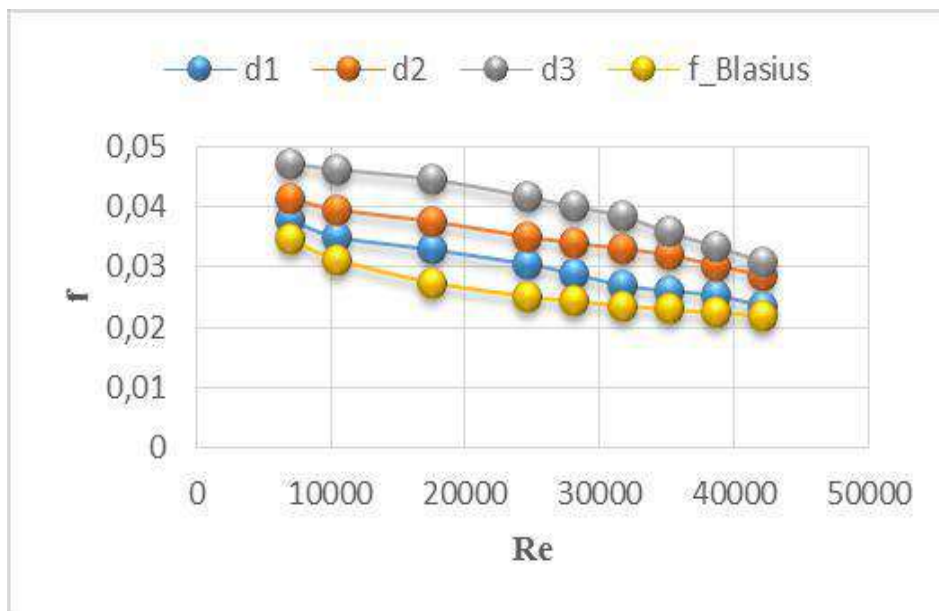


Figure 4 f versus Re with respect to hole diameter

5. CONCLUSIONS

In present study, coil spring turbulators cause some heat transfer enhancement. Major results of the experiments are as follows:

- ☞ Turbulators not only produce more turbulence than the smooth tube but also increase heat transfer area.
- ☞ Highest heat transfer and friction factor are observed for the smallest diameter of the holes on the plates.
- ☞ Highest heat transfer and friction factor are observed for the highest distance between two plates.

- ✓ The location of the hole seems has no great importance on either heat transfer or friction factor.
- ✓ Heat transfer increases with increasing Re , however friction factor decreases with increasing Re .
The recommendation of the authors is to make an optimization analysis for diminishing the pressure loss.

REFERENCES

- [1] [1] Abraham S., and Vedula R.P., Heat transfer and pressure drop measurements in a square cross-section

- converging channel with V and W rib
turbulators,
Experimental Thermal and Fluid Science, Vol. 70,
2016,
pp. 208-219.
- [2] Sheikholeslami M., Gorji-Bandpy M., and Ganji D.D.,
Experimental study on turbulent flow and heat transfer
in an air to water heat exchanger using perforated
circular-ring, *Experimental Thermal and Fluid Science*,
Vol. 70, 2016, pp. 185-195.
- [3] Skullong S., Thianpong, C., Jayranaiwachira N., and
Promvong P., Experimental and numerical heat transfer
investigation in turbulent square-duct flow through oblique
horseshoe baffles, *Chemical Engineering and Processing:
Process Intensification*, Vol. 99, 2016, pp. 58-71.
- [4] Promvong P., Heat transfer behaviours in round tube
with conical ring inserts, *Energy Conversion and
Management*, Vol. 49(1), 2008, pp. 8– 15.
- [5] El-Sayed S.A., Mohamed M.S., Abdel-latif A.M., and
Abouda A.E., Investigation of turbulent heat transfer and
fluid flow in longitudinal rectangular-fin arrays of different
geometries and shrouded fin array, *Experimental Thermal
and Fluid Science*, Vol. 26, 2002, pp.879–900.
- [6] Naik S, Probert S.D., and Bryden I.G., Heat transfer
characteristics of shrouded longitudinal ribs in turbulent
forced convection, *International Journal of Heat and Fluid
Flow*, Vol. 20, 1999, pp. 374–84.
- [7] Sahin B., Yakut K., Kotcioglu I., and Celik C., Optimum
design parameters of a heat exchanger, *Applied Energy*,
Vol. 82, 2005, pp. 90–106.
- [8] Arulprakasajothi M., Elangovan K., Hema Chandra
Reddy K., and Suresh S., Experimental investigation on
heat transfer effect of conical strip inserts in a circular tube
under laminar flow, *Frontiers in Energy* , Article in press,
2015, pp.1-7.
- [9] Cakmak G., and Yıldız C., The influence of the injectors
with swirling flow generating on the heat transfer in the
concentric heat exchanger, *Int. Commun. Heat Mass
Transf.*, Vol. 34, 2007, pp. 728–739.
- [10] Eren H., Celik N., Yildiz S. and Durmus A., Heat
transfer and friction factor of coil springs inserted in the
horizontal concentric tubes, *Transactions of ASME,
Journal of Heat Transfer*, Vol.132(1), 2010, pp.1-11.
- [11] Eren H., Celik N., Yildiz S., and Kurtbas I., Exergy
analysis of coil spring turbulators inserted in the horizontal
concentric tubes, *Transactions of ASME, Journal of Heat
Transfer*, Vol.132(10), 2010, pp.1-10.

Design and Investigation of Impinging Air Jet Oven for Dyed Fabric Drying

Celal Kistak
Firat University
Elazığ, Turkey
ckistak@firat.edu.tr

Oktay Hacıhafizoğlu
Trakya University
Edirne, Turkey
oktayh@trakya.edu.tr

Nevin Çelik
Firat University
Elazığ, Turkey
nevincelik@firat.edu.tr

Abstract— Drying is use to describe a process involving removal of the required amount of humidity from any material. Removal of the humidity in the material is done with different shapes and methods. In the drying technique, the factors such as the nature of the product, its structure, ambient conditions, air quality and speed are effective. In this study, it is aimed to design a impinging jet drying oven due to its ability to provide high heat transfer coefficient, easy to manufacture and low cost. Here; The drying of wet fabric dyed with air jets has been taken into consideration. Thus, the usability of the jet was investigated in textile drying. For this purpose, an adiabatic oven was designed and manufactured. The hot air jet is placed at the opening of the luer with the lid opened from the top of the oven and the drying process which is caused by the hot jet being applied to the fabric placed in the oven is examined.

Keywords— impinging jet, drying, dyed fabric, heat transfer

I. INTRODUCTION

People have often benefited from solar heat in the drying of materials that will meet their needs from the earliest times. This method is often performed on its own in nature and has benefited from solar heat, for example in the drying of various cereals, legumes, fruits and also some textile products. Since the earth is dry with solar heat, it is impossible to get dry everywhere and always by this way. In addition, a variety of methods have been developed for the drying out of many products due to the increasing number of products over time and the fact that many of these products lose their properties while drying under the sun's heat.

Numerous theoretical and experimental investigations have been carried out on drying methods. During drying, the product must be supplied with heat continuously. There are convection drying, heat conduction drying and radiation drying methods according to the heat transfer method in the heat energy dryings.

In the case of convection drying, the intake of the moisture in the product to be dried is ensured by hot and at the same time dry air flow. The temperature of the dry air can be

increased depending on the type of dryer and the speed of passage through the dryer (such as 60-100 C).

In the case of drying by conduction, while the product to be dried remains stationary or moving, heat is transferred to the material from the hot surface it is in contact with during drying.

Impinging air jets (nozzles), due to the high heat and mass transfer occurring in the loading region, single and including multiple, textile, paper and wood drying, cooling of electronic components, the glass sheet tempering, heat treatment, industrial many as cooling the gas turbine blade is often used in practice [1].

In certain regions, large spaced luer arrays are used, where the step between single or luer is large in desired drying processes, while jet arrays are used in large surface drying environments (paper, textile etc. products). The evaporative drying rate axes are increased by hot air jets located in the normal direction of the moving web (paper, plastic, etc.) surface [2].

During the production and rehabilitation process of the textile products, the moisture they get to their structures is removed by drying. drying the textile product by removing moisture on the product shape; Pre-drying by mechanical methods and natural drying on the product without loss of heat, and drying by heat transfer [3].

However, drying the product with heat (main drying) can damage both its structure and its economic value. With this, drying of textile products requires essential drying, and drying steps must be carried out effectively without damaging the product [4].

Avci et al. studied theoretically the jet-drying of thin film strips coated with ink on thin film layers [5]. In another work, they have made an analogy between mass transfer and heat transfer in the drying of ink ribbon [6].

The economic analysis of industrial drying by jet blower drying was done by Etemoğlu and useful information about the applicability of the system was given [7]. Multi jet environments have been created in the practice of impinging jet drying.

II. DESIGN PARAMETERS

The design parameters to be considered in the drying systems in which the impinging air jets are used include:

- nozzle width (diameter)
- nozzle shape
- nozzle height
- air velocity
- air temperature
- distance between nozzles

A. determining the optimum nozzle width or diameter for multi nozzle systems, the designer should consider the fan power, the number of nozzles needed, as well as the effect of the nozzle width (diameter) on heat transfer. Nozzle width affects the average heat transfer coefficient. At a constant fan power, the average heat transfer coefficients increase with decreasing nozzle diameter.

B. Air Velocity (V_E) : The electrical power required by the fans should provide a pressure increase that will compensate for local and friction losses in the system and provide sufficient air velocity to be delivered over the sample to be dried. Heat transfer coefficients are proportional to air jet velocity (V_E). The increase in air velocity requires a significant increase in fan power and also causes an undesirable increase in the noise level of both fans and jets.

C. Air Temperature (T_A) : The air temperature to spray on the sample to be dried is a parameter that will directly affect the heat flow as it will change the difference between air and sample temperatures. At the same time, the energy used to transport the air to the T_A temperature will also affect the total cost [1].

D. Distance between Nozzles X_n : The distance between loops is directly related to the optimum free area (A_f). The free area (A_f) is the ratio of the exit area of the nozzle to the heat transfer surface area and is a basic parameter to be considered.

Figure 1 represents a typical jet flow. Hot air is sprayed from the nozzle to the stagnant area. As the distance from the output point increases, the momentum transfer between the jet and the environment causes the jet free boundary to expand and the constant velocity core to contract. The velocity profile is not constant throughout the jet cross section, the velocity decreases as the distance from the nozzle exit increases. Within the impact

zone, the flow slows down in the upright (Z) direction, accelerates in the cross (R or X) direction, and the zone defined as the "wall jet" occurs [1].

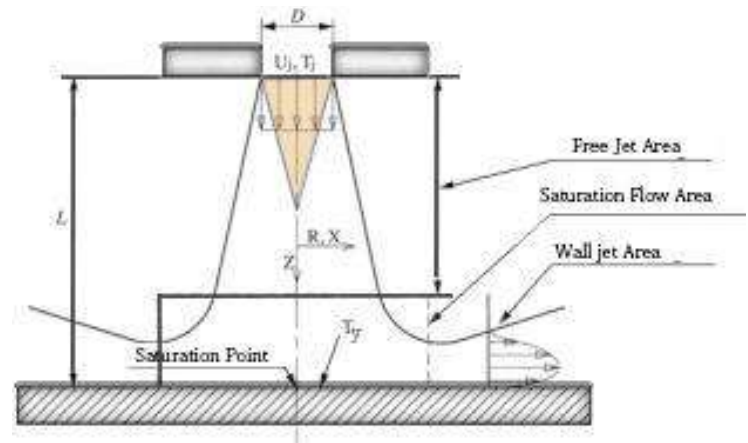


Fig. 1. Impinging jet flow

III. MATERIALS AND METHOD

The aim of this design is to perform temperature determinations of various points on the fabric of the jet drying apparatus, which are influenced by the heater power and the change of nozzle diameter to the drying time.

Xps plates were used as insulation material in the design.



Fig. 2. Insulation material (xps plate)

A wire cage is designed in the oven which is insulated from all the corners in order to hang the fabric to be dried to the size of the design.



Fig. 3. Wire cage used in experiment

The top of the oven is opened and a heater fan is installed to create the jet effect.



Fig. 4. Designed oven for drying

Three different nozzles were used to observe the effect of changing the diameter of the nozzle.



Fig. 5. Nozzles used in experiments

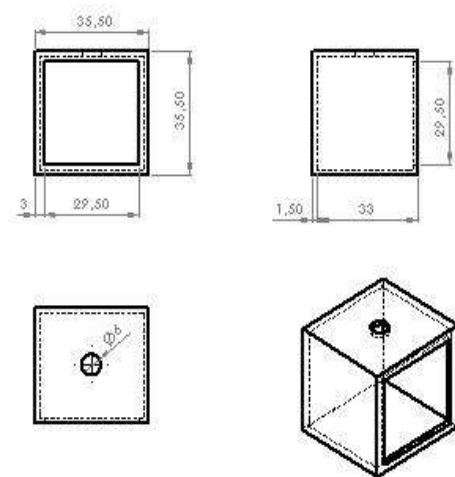


Fig. 6. Dimensions of oven

Mass change measurements during the experiment were made with Radwag PS/600/C/1 precision scale.



Fig. 7. Radwag PS/600/C/1 precision scale

- Before starting the experiments, the test setup connections are checked and then the precision scale and anemometry are checked for known values.
- The two-stage heater fan is operated at the initial air speed. Temperature measurement is performed with the aid of a thermocouple connected to the datalogger.
- Then, after the necessary time has elapsed, the fabric is measured with the precision scale. In order to ensure correctness, each experiment is repeated at least three times and the accuracy of the data is checked.



Fig. 8. Experimental setup

- After entering the first experimental data in to the computer , the parameters such as fan speed and nozzle diameter are changes according to the previously prepared workflow diagram and the experiments are completed.

•

IV. RESULTS AND CONCLUSIONS

During the experiments wet- dry mass, Reynold number , jet velocity, flow rate datas are obtained. The data are given in the following table.

TABLE XVI. DATA FOR 0.0109M³/S FLOW RATE

Flow rate=0.019 m ³ /s				
M _{wet} (gr)	M _{dry} (gr)	T _{amb}	V _{jet} (m/s)	Re
346	340	21,5	5,4	16500
380	358	21,5	10,2	22667
372	334	21,5	18,15	30250

TABLE XVII. DATA FOR 0.013M³/S FLOW RATE

Flow rate =0,013 m ³ /s				
M _{wet} (gr)	M _{dry} (gr)	T _{amb}	V _{jet} (m/s)	Re
347	342	21,5	8	24444
348	325	21,5	15,125	33611
358	320	21,5	26,88	44800

	D 5.5 cm	D 4cm	D 3cm
T ₁ (C°)	48,3	50	60
V ₁ (m/s)	5,40	10,2	18,15
T ₂ (C°)	52	60	73,6
V ₂ (m/s)	8	15,125	26,88
T _∞	21,50	21,50	21,50

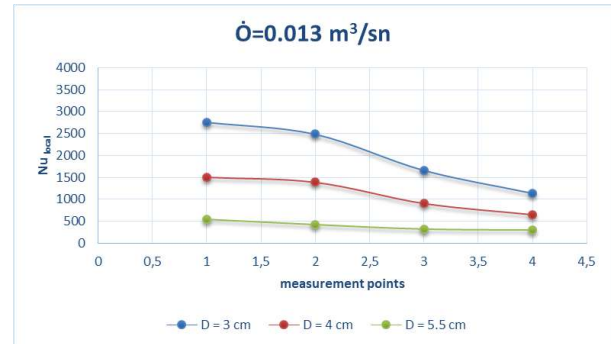


Fig.9. Nu_{local} for 0.013 m³/sn

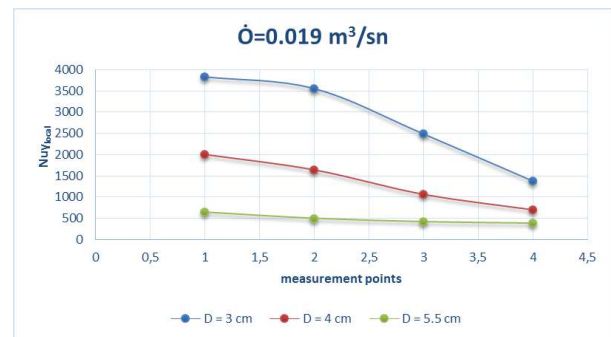


Fig.10. Nu_{local} for 0.019 m³/sn

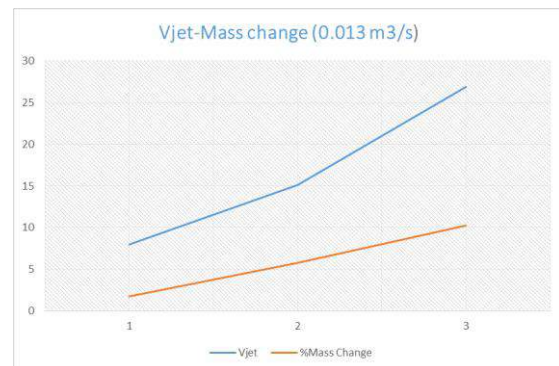


Fig.11 Vjet -% Mass change for 0.013 m³/s

TABLE XVIII. NOZZLE OUTLINE DIAMETER TEMPERATURE DATA

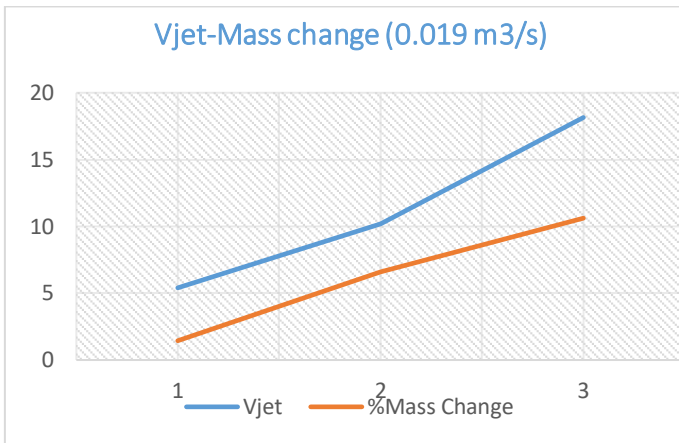


Fig.12. Vjet -% Mass change for 0.019 m³/s

In this study, effects of nozzle diameter, and jet velocity changing on dyed fabric were examined. When the results were analyzed, it is seen that the increase of the jet speed positively affects the drying.

Rapidly reaching high temperatures of drying chamber negatively affected the experiment. In subsequent studies it is planned that more precise testing conditions be achieved by redesigning the heating, cycle rate and drying chamber dimensions.

REFERENCES

- [1] Etemoğlu, A.B., Hava jetli kurutucuların teknik ve ekonomik analizi, Mühendis ve Makina , 38, pp. 24-33, 2003.
- [2] Incropera, F.P. and DeWitt, D.P., Fundamentals of Heat and Mass Transfer, John Wiley and Sons, New York, 886 p., 1996
- [3] Hardisty, H., Can, M., An Experimental Investigation Into the Effect of Changes in the Geometry of a Slot Nozzle on the Heat Transfer Characteristics of an Impinging Air Jet, Proc. Instn. Mech. Eng. Engineering Sciences Division, 197C, pp. 7-15, 1983.
- [4] Polat, S., Huang, B., Mujumdar, A. S., & Douglas, W. J. M. (1989). Numerical flow and heat transfer under impinging jets: a review. Annual Review of Heat Transfer, 2(2).
- [5] Avci, A., Can, M., & Etemoğlu, A. B. (2001). A theoretical approach to the drying process of thin film layers. Applied thermal engineering, 21(4), 465-479.
- [6] Avci, A., & Can, M. (1999). The analysis of the drying process on unsteady forced convection in thin films of ink. Applied Thermal Engineering, 19(6), 641-657.
- [7] Can, M., Etemoğlu, A. B., & Avci, A. (2002). Experimental study of convective heat transfer under arrays of impinging air jets from slots and circular holes. Heat and mass transfer, 38(3), 251-259.

Numerical Investigation of an Exhaust Muffler System

Halil İbrahim YAMAÇ

Firat University
Technology Faculty, Department of Mechatronics Eng.
Elazığ, Turkey
E-mail: halilymc@gmail.com

Okan ÇELİK

Firat University
Technology Faculty, Department of Automotive Eng.
Elazığ, Turkey
E-mail: mr.okancelik@gmail.com

Ömer Faruk CAN

Dicle University, Department of Mechanical Engineering
Diyarbakir, Turkey
E-mail: faruk.can@dicle.edu.tr

Nevin ÇELİK

Firat University, Department of Mechanical Engineering
Elazığ, Turkey
E-mail: nevincelik@firat.edu.tr

Abstract— In this study, exhaust muffler system is simulated to determine the inlet temperature, velocity, pressure with assumed gas properties. Exhaust muffler system is important for engine efficiency about its temperature and back pressure. The noise is caused by gas velocity, so this parameter can be accounted in issue of noise pollution. In this study, commercial software ANSYS-CFX is used and Computational Fluid Dynamics (CFD) analysis is performed. Steady-state analysis is made to receive behavior of the system under assumed conditions.

Keywords-- Exhaust Muffler, CFD analysis, SST Model, CFX

XIII. INTRODUCTION

There are numerous studies about exhaust systems at different types of engines. Numerical studies are made by Computational Fluid Dynamics (CFD) methods by using different software.

Xu et al. is used Solidworks flow simulation to analyze theoretical design of a gasoline engine exhaust pipe. The simulation is made to obtain results that impact of designed exhaust system on engine power, emission and economy [1]. Rajadurai et al. simulate pressure drop CFD analysis for an exhaust muffler. In analysis glass wool is used as porous domain and assembled in muffler. One dimensional (1D) analysis is made via Star CCM+, the results are compared with experimental studies [2]. Mundhe and Deore use Star CCM+ software to analyze perforated muffler in automobile exhaust system. Reducing exhaust gas noise level and noise pollution are the objective of their study [3]. Tutunea et al.

perform CFD analysis on resistance exhaust muffler. Effect of internal flow field on muffler's performance at different designs and constructions is analyzed [4]. Xu and Zhou analyze flow field based on CFD for automotive exhaust system. It is researched that the influence of the distance between sub-muffler and the main muffler on flow field [5]. Tambe et al. analyze semi active exhaust muffler of an internal combustion engine. The exhaust noise generated from engine is reduced by using new construction of system [6]. Puneetha et al. use CFD analysis to study backpressure in single cylinder diesel engine's exhaust muffler. The gas velocity, airflow streamlines and pressure plots, back pressure are results of the study [7]. Tutunea et al. study on aerodynamic performance of the muffler with CFD method. This method is used to explore pressure distribution and pressure loss with modification of structure in the muffler [8]. Yao et al. conducts computational and experimental analysis of reactive muffler with structural optimization. Acoustic insertion loss and pressure loss is a result of aerodynamic CFD analysis. [9]. Pandhare et al. compare two muffler design wit simulation upon gas flow, back pressure, noise by using for ci engine. ANSYS Fluent software is used while simulating CFD analysis [10]. Mishra et al. make experimental and numerical studies on effect of exhaust muffler on back pressure, chamber velocity and temperature. Different muffler structures are analyzed with using different fuels. ANSYS Fluent software is used for numerical analysis [11]. Özkan et al. examine inner design effect on flow and acoustics properties of reactive muffler. Porosity and perforated length are assumed as various parameters to analyze their effects on acoustic properties and pressure drop. ANSYS CFX software is used for CFD analysis [12]. Om Ariara Guhan et al. use ANSYS CFX software to study on

pressure drop and uniformity index of chosen exhaust system. Based on the study, individual system contributions to the total pressure drop and flow uniformity have been analyzed and improvement areas of the existing system for better flow uniformity have been suggested [13]. Durat et al. make CFD and experimental analysis on thermal performance of exhaust system of a spark ignition engine. Three dimensional (3D) CFD analysis are made for whole exhaust pipe. The CFD results of analysis are in good agreement with experimental data [14]. The present work involves CFD study of the exhaust muffler system on gas velocity, pressure drop and temperature. Solid Works software is used for design purpose and system was computationally analyzed by using ANSYS CFX software.

XIV. MUFFLER DESIGN

When sound waves move, they have to suppress air, which creates friction. The more waves back and forth, the more energy they lose and the less noise they generate. The main purpose of the muffler is to cause the sound waves to lose energy and to reach the atmosphere with less energy, that is, less noise pollution. In general, the exhaust silencer includes the front pipe, the inner pipe, the expansion units, the resonance circuit and the tail pipe portions. Figure 1 shows a photograph of the exhaust silencer modeled in the study.

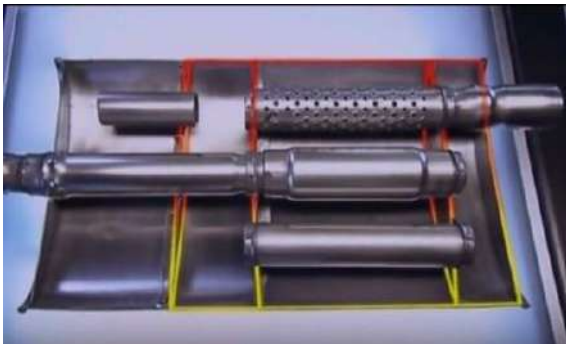


Fig. 1. Exhaust muffler photograph

The design of the exhaust muffler used in the study is drawn by SolidWorks software. Then this model is defined in the ANSYS-CFX to create a mesh structure. SolidWorks model can be seen in Fig. 2.



Fig. 2. Solid model of exhaust muffler

XV. CFD ANALYSIS

Analytical solutions to the Navier-Stokes (N-S) equations can be accepted to exist for only simple flows which are under ideal conditions. Equations are replaced by algebraic approximations to make calculations for complex flows in numerical methods. The calculation is carried out in ANSYS CFX software, which uses CFD method, the movement of the fluid is modeled by the N-S equations, the Reynolds averaged SST turbulence model. Workbench V15.0 CFD numerical codes are used for 3D analysis.

A. CFD Mesh

Mesh structure is generated by CFX tool from CAD model. In the paper; the exhaust muffler as seen in CFD analysis is divided into 1067305 tetrahedral elements and 209694 nodes for mesh generation. Average mesh skewness value is 0.2388. Mesh density in the resonance circuit is higher than in other regions.

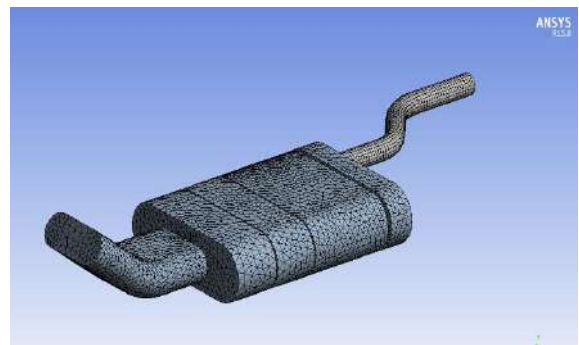


Fig. 3. Mesh structure of geometry

B. CFD Model

N-S Equations are solved by the CFX codes which use finite volume method to discrete N-S Equations. Thermal analysis is chosen to get temperature results of flow. The analysis made is steady state, so the solver neglect the time derivative terms, so Mechanical Energy is $K = \frac{1}{2} U^2$. The

mechanical energy equation is derived by taking the dot product of U with the modified momentum equation: $\nabla(\rho U \otimes U) = -\nabla p + \nabla \cdot \tau + S_M$. Eq. (1) is the modified mechanical energy equation of CFX [15]:

$$\nabla \cdot (\rho U K) = -U \cdot \nabla p + U \cdot (\nabla \cdot \tau) + U \cdot S_M \quad (1)$$

Subtracting this equation from the modified total energy equation: $\nabla \cdot (\rho U h_{tot}) = \nabla \cdot (\lambda \nabla T) + \nabla \cdot (U \cdot \tau) + U \cdot S_M + S_E$ yields the thermal energy equation. Eq. (2) is modified equation from The Thermal Energy Equation of CFX [15]:

$$\nabla \cdot (\rho U h) = \nabla \cdot (\lambda \nabla T) + U \cdot \nabla p + \tau : \nabla U + S_E \quad (2)$$

The term $\nabla \cdot (U \cdot \tau)$ represents the work due to viscous stresses and is called the viscous work term. The term $U \cdot S_M$ represents the work due to external momentum sources and is currently neglected. With further assumptions discussed in a moment, the thermal energy equation is obtained. The term $\tau : \nabla U$ is always positive and is called the viscous dissipation. With further assumptions discussed in a moment, the thermal energy equation is obtained. Equation 3 is modified equation from the Thermal Energy Equation of CFX [15]:

$$\nabla \cdot (\rho U h) = \nabla \cdot (\lambda \nabla T) + \tau : \nabla U + S_E \quad (3)$$

Generally, Reynolds Averaged Navier-Stokes (RANS) equations are the modified average of unsteady N-S equation. Turbulence models base on the RANS equations [15]. While averaging, there is a need of additional terms like *reynolds (turbulent) stresses* in fluid. The analysis is made as steady-state condition, so modified Eq. (4) and (5) is the RANS transport equation [15]:

$$\frac{\partial}{\partial x_j} (\rho U_j) = 0 \quad (4)$$

$$\frac{\partial}{\partial x_j} (\rho U_i U_j) = -\frac{\partial p}{\partial x_i} + \frac{\partial}{\partial x_j} (\tau_{ij} - \overline{u_i u_j}) + S_M \quad (5)$$

Where τ is the molecular stress tensor. The mentioned *reynolds stress* can be expressed in Equation 6 as $\rho \overline{u_i u_j}$ [15]:

$$-\rho \overline{u_i u_j} = \mu_t \left(\frac{\partial U_i}{\partial x_j} + \frac{\partial U_j}{\partial x_i} \right) - \frac{2}{3} \delta_{ij} \left(\rho k + \mu_t \frac{\partial U_k}{\partial x_k} \right) \quad (6)$$

Shear Stress Transport (SST) turbulence model is used for simulation. Highly accurate predictions of the amount of flow and the onset separation under adverse pressure gradients are given by SST model. The transport of the turbulent shear stress is accounted by SST model [15]. The main reason is

that k- ϵ and k- ω models do not account for the transport of the turbulent shear stress. The proper transport behaviour can be obtained by a limiter to formulation of the eddy-viscosity. The relation between kinematic and dynamic viscosity is $\nu_t = \frac{\mu_t}{\rho}$. Equation 7 is the modified equation from the eddy-viscosity of CFX [15]:

$$\nu_t = \frac{\alpha_1}{\max(\alpha_1 \omega, S F_2)} \quad (7)$$

Where F_2 is blending function, ω is turbulent frequency, S is an invariant measure of the strain rate.

k is turbulent kinetic energy: $k = \frac{1}{2} \overline{u_i^2}$ Total enthalpy is given in Equation 8[15]:

$$h_{tot} = h + \frac{1}{2} U_i^2 + k \quad (8)$$

μ_t is turbulent or eddy viscosity. It is decided by The parameters of model. If time derivative is neglected RANS energy equation [15] becomes Equation 9:

$$\frac{\partial}{\partial x_j} \left(\lambda \frac{\partial T}{\partial x_j} - \rho \overline{u_j h} \right) + \frac{\partial}{\partial x_j} [U_i (\tau_{ij} - \rho \overline{u_i u_j})] + S_E \quad (9)$$

C. Boundary Conditions

There are four boundary conditions in the analysis. These are inlet, opening, adiabatic walls between expansion chambers and outside wall of muffler assumed at fixed temperature. In this study, there is no experimental work, so parameters in literature are used for boundary details. Inlet and opening boundary conditions and air flow path can be seen in Figure 4.

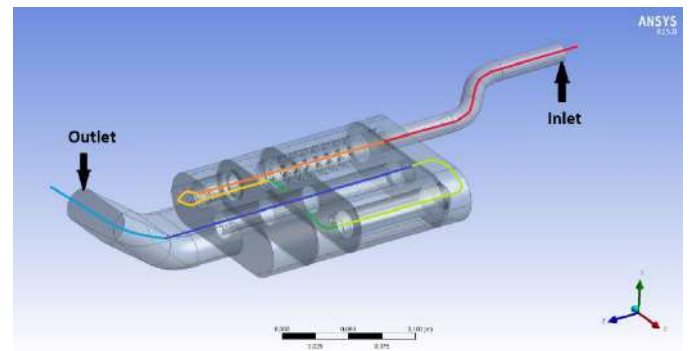


Fig. 4. Boundary conditions of exhaust muffler

D. Properties Of Exhaust Gas

Input conditions in the model are defined in simulations with data obtained from the study of Pandhare et al. Table I shows the inlet properties of exhaust gas [10]. The other

parameters, functions of gas temperature, are calculated from some equations given in study of Durat et al. The parameters are calculated from Equations 10-12 [14].

Table I. Inlet gas properties

Inlet gas properties	
Density	0.696 (kg/m ³)
Enthalpy	503400 (J/kg)
Temperature	500 (K)
Velocity	10.9748 (m/s)
Dynamic Viscosity	2.7e-5 (kg/m.s)

$$\rho = \frac{353}{T_g} \quad (10)$$

$$C_p = 962.097 + 0.1507 T_g \quad (11)$$

$$TC = 8.459 \times 10^{-3} + 5.7 \times 10^{-5} T_g \quad (12)$$

Where T_g is gas temperature, ρ is density, C_p is specific heat, TC is thermal conductivity. Calculated parameters can be seen in Table II.

Table II. Inlet other features

Thermal Conductivity and Specific Heat	
Thermal Conductivity	0.0369 W/mK
Specific Heat	1037.44 J/kgK

XVI.RESULT AND DISCUSSIONS

In this section the attention will be directed to the results of simulation. In Fig. 5-9 the detailed results about the velocity variation is presented. The highest velocity is observed at the inner pipe because of smallest diameter. At this maxima the velocity increases near 2 times of the inlet velocity.

The faster an exhaust pulse moves, the better it can scavenge out all of the spent gasses. So the guiding principle of exhaust pulse scavenging is that a fast moving pulse creates a low pressure area behind it. This low-pressure area acts as a vacuum and draws along the air behind it [11].

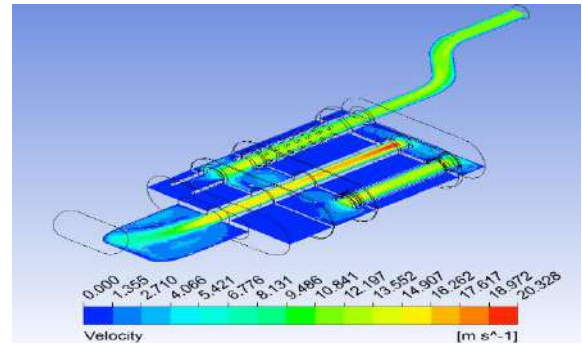


Fig. 5.Velocity contour of whole system

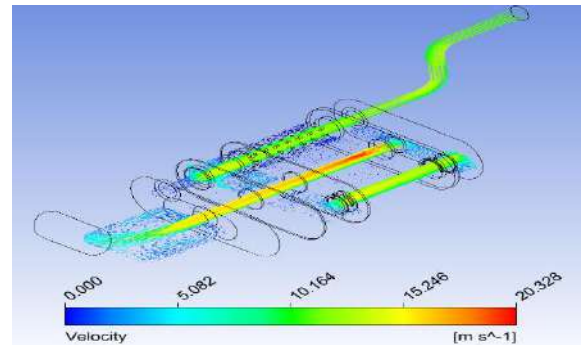


Fig. 6.Velocity vector

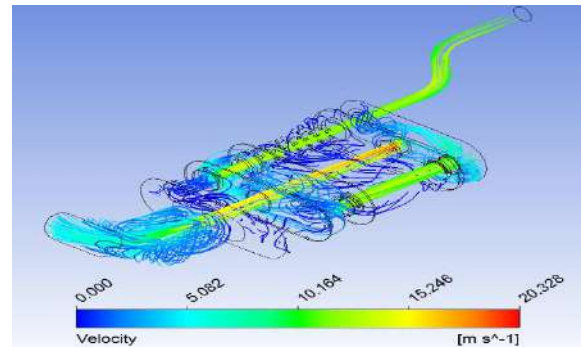
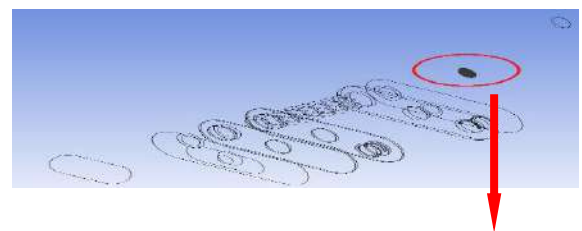


Fig. 7.Velocity streamline

In Fig. 6 and 7 the detailed velocity plots are seen respectively for entrance and exit zones. In the entry zone the velocity is higher at the corrugation way as expected. At the exit zone velocity becomes more uniform and the maxima is observed at the center.



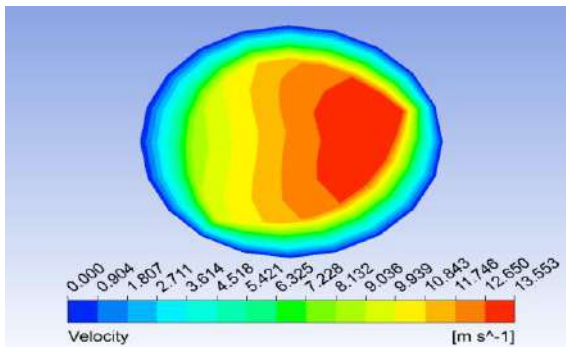


Fig. 8.Velocity contour near to entrance

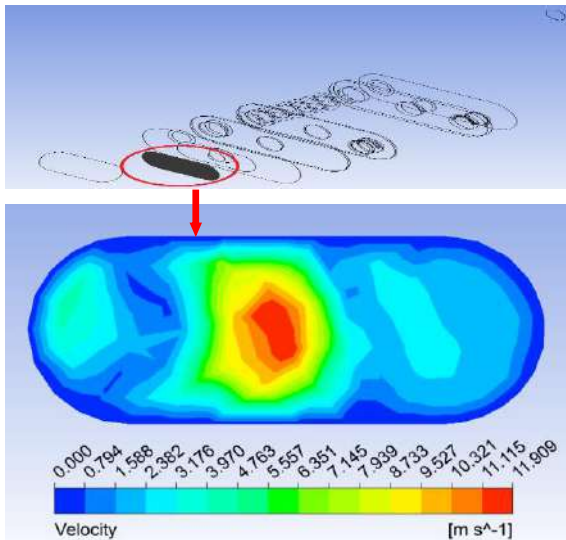


Fig. 9.Velocity contour near to exit

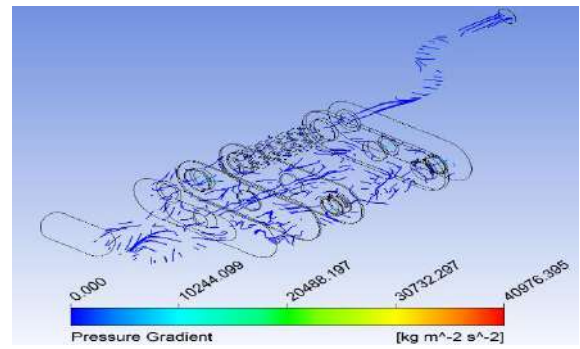


Fig. 11.Pressure gradient streamline

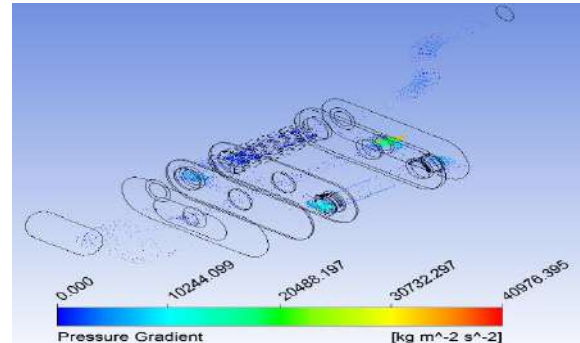


Fig. 12. Pressure gradient vector

Figs. 10-12 represent the simulated pressure values. Evaluating all figures at the same time it will be seen that, the vacuum helps better circulation of exhaust gas. The maximum pressure occurs near to the exit chamber.

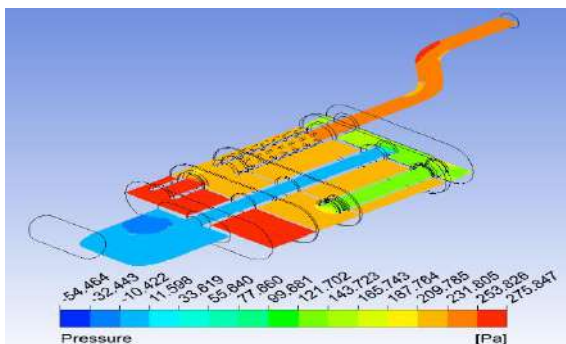


Fig. 10.Pressure contour

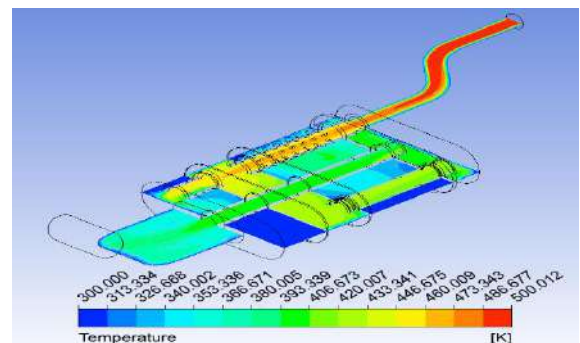


Fig. 13.Temperature contour

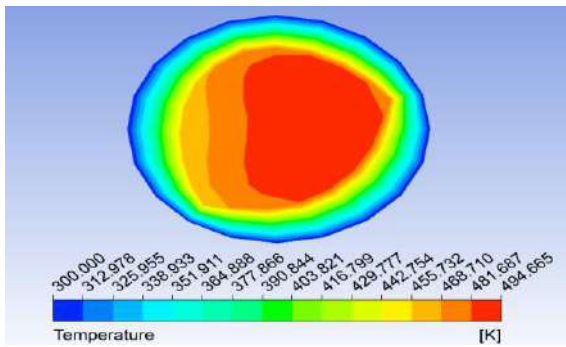


Fig. 14. Temperature contour after entry zone

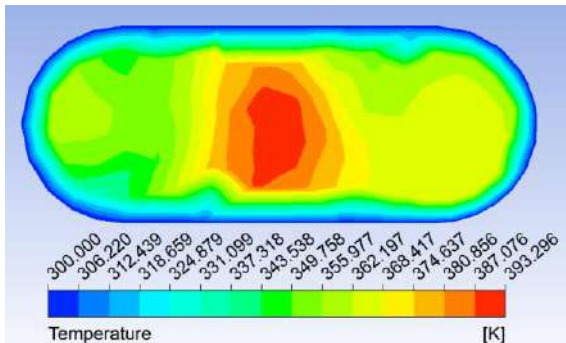


Fig. 15. Temperature contour before out zone

XVII. CONCLUSIONS

CFD simulation of exhaust muffler is done via ANSYS CFX software. The CFD simulation software can be used in numerical analysis. Through aforementioned study, the results as exhaust muffler's pressure field, temperature field and gas velocity are obtained. Numerical analysis gives opportunity for engineers to have information about new designs of exhaust muffler systems before production.

As a future work, exhaust mufflers have different geometrical structures can be modeled and compared with each other. Velocity, pressure and temperature parameters can be assumed as variable for comparison of new designs. Whole exhaust system can be modeled to have information about interaction between engine efficiency and exhaust system.

REFERENCES

- [1] P. Xu, H. Jiang, and X. Zhao, "CFD Analysis of a Gasoline Engine Exhaust Pipe," *Journal of Applied Mechanical Engineering*, vol. 5, no. 2, 2016.
- [2] S. Rajadurai, S. Sukumaran, and P. Madhusudhanan, "CFD Analysis for Flow through Glass Wool as Porous Domain in Exhaust Muffler," *International Journal of Innovative Science, Engineering & Technology*, vol. 1, no. 7, pp. 341–347, 2014.
- [3] V. M. Mundhe and E. R. Deore, "Design and analysis of perforated muffler in Automobile Exhaust System," *International Journal Multidisciplinary research and Development* vol. 2, no.7, pp. 182–187, 2015.
- [4] D. Tutunea, M. X. Calbureanu, and M. Lungu, "The computational fluid dynamics (CFD) study of fluid dynamics performances of a resistance muffler," *Recent Advances in Fluid Mechanics and Heat & Mass Transfer*, pp.31-34.
- [5] J. Xu and S. Zhou, "Analysis of Flow Field for Automotive Exhaust System Based on Computational Fluid Dynamics," *The Open Mechanical Engineering Journal*, vol. 8, pp. 587–593, 2014.
- [6] M. P. Tambe, S. Sanadi, C. Gongale, S. Patil, and S. Nikam, "Analysis of Exhaust System- ' Semi Active Muffler'," *International Journal of Innovative Research in Science, Engineering and Technology*, vol. 5, no. 2, pp. 1366–1376, 2016.
- [7] C. G. Puneetha, H. Manjunath, M.R. Shashidhar , "Backpressure Study in Exhaust Muffler of Single Cylinder Diesel Engine using CFD Analysis," *Altair Technology Conference, India* 2015.
- [8] D. Tutunea, M. X. Calbureanu, and M. Lungu, "The computational fluid dynamics (CFD) study of fluid dynamics performances of a resistance muffler," *International Journal of Mechanics*, vol. 7, no. 4, pp. 401-408, 2013.
- [9] Y. Yao, S. Wei, J. Zhao, S. Chen, Z. Feng, and J. Yue, "Experiment and CFD Analysis of Reactive Muffler," *Research Journal of Applied Science, Engineering and Technology* vol. 6, no. 17, pp. 3282–3288, 2013.
- [10] A. Pandhare, A. Lal, P. Vanarse, N. Jadhav, K. Yemul, "CFD Analysis of Flow through Muffler to Select Optimum Muffler Model for Ci Engine," *IJLTET*, vol. 4, no. 1, pp. 12–19, 2014.
- [11] P. C. Mishra, S. K. Kar, H. Mishra, and A. Gupta, "Modeling for combined effect of muffler geometry modification and blended fuel use on exhaust performance of a four stroke engine: A computational fluid dynamics approach," *Appl. Therm. Eng.*, vol. 108, pp. 1105–1118, 2016.
- [12] Y. Özkan, İ. Özsert, V. Ayhan, and İ. Cesur, "Examination inner design effect on flow and acoustics properties of a reactive muffler," *SAÜ Fen Bil Der*, vol. 20, no. 1, pp. 65-74 , 2016.
- [13] O. Ariara, C. P. Guhan, G. Arthanareeswaren, and K. N. Varadarajan, "CFD Study on Pressure Drop and Uniformity Index of Three Cylinder LCV Exhaust System," *Procedia Eng.*, vol. 127, pp. 1211–1218, 2015.

- [14] M. Durat, Z. Parlak, M. Kapsiz, and A. Parlak, F. Fıçıcı, “CFD and experimental analysis on thermal performance of exhaust system of a spark ignition engine,” *Journal of Thermal Science and Technology*, vol. 33, no. 2, pp. 89–99, 2013.
- [15] ANSYS CFX-Solver Theory Guide.

Effect of Hole Geometry on Buckling Behavior for Steel Plates

Serkan ERDEM

Firat University
Department of Mechanical Engineering
Elazig–TURKEY serdem@firat.edu.tr

Mete Onur KAMAN

*Firat University
Department of Mechanical Engineering
Elazig–TURKEY

Mustafa GUR

Firat University
Department of Mechanical Engineering
Elazig–TURKEY

Gurbet ORCEN

Dicle University
Department of Mechanical Engineering
Diyarbakır–TURKEY

Abstract— In this study, buckling analysis of isotropic steel plates was investigated in two parts, pre-buckling and post-buckling. It was used ANSYS® finite element package program for numerical solutions. Buckling analysis was performed for linear and non-linear condition of steel plates with square and circle holes in various sizes at center. The analytical solution of the plate buckling under pressure force, the results compared with the numerically found critical buckling values, are given graphically.

The values found were found to be compatible with the literature solutions. It has been observed that the maximum critical load values occur in the plates without geometry discontinuity. Parallel to the increase of the hole dimensions on the plates, critical buckling load values decreased and deformations increased.

Keywords— buckling, plates, critical buckling load ling

I. INTRODUCTION

Plates are building elements used in many sectors, especially air craft and ship industry. Buckling analysis of plates is of great importance for such work environments.

Steel was used as an isotropic material and the condition before and after buckling was analyzed for this material. The study by Timoshenko was taken as a reference for the pre-buckling condition [1]. The results of the study are verified using the ANSYS® program. For the post-buckling situation, Hu et al. has been studied [2]. The results analytically found in the study were compared to the results obtained with the ANSYS® program for the same problem. It was determined that the values found were compatible with the literature solutions.

Many researchers have investigated the buckling behavior of plates used as machinery or building elements in designs. Studies on the subject have concentrated on plaques, plates

and plates with various gap and delicate bars. Star, Y.O. And Günay, E., in case of St 37 steel rectangular plates supported by rectangular reinforcement elements, buckling analysis was studied [3]. Güngör, M., analyzed buckling of plates subjected to static loading in single and double direction [4]. The change of plate buckling loads with isotropic material and a rectangular space of different sizes in the middle by Zihni S. has been calculated for different boundary conditions [5]. Hacıoğlu, E. examined thermal spalling of plaques. Critical buckling conditions were investigated for isotropic and anisotropic plates with in-plane displacements inhibited in operation, depending on the uniform temperature change [6]. Cıvlek, Ö. Et al. Two and three-dimensional bending, buckling and free vibration analysis of homogeneous and isotropic rectangular plates by differential quadrature method [7]. Tekin, A. investigated the problem of rectangular thick plaque buckling of delaminated sandwich. The effect of plate material and geometric parameters on critical values has been investigated [8]. Özyigit, P. and Sofiyev, A. have examined the thermal buckling analysis of shallow spherical shells [9]. Bingöl et al. They experimentally and theoretically investigated the buckling behaviors of circular plates made of aluminum and composite materials [10]. Virtual et al. Critical buckling stresses of isotropic and orthotropic rectangular thin plates supported by simple support and transversely supported under shear loading were investigated [11].

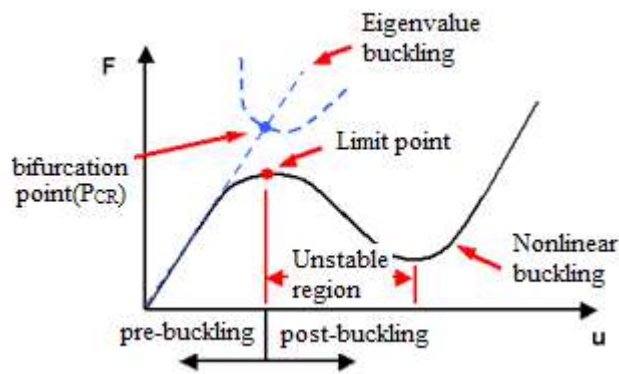
Linear and nonlinear buckling analysis was performed for steel plates with dimensions of 10x10, 20x20 and 30x30 mm² and 200x200x2 mm³ dimensions with holes Ø10, Ø20 and Ø30 mm in diameter at the center of the study. Buckling analysis on isotropic steel plates; Pre-buckling and post-buckling.

II. MATERIALS AND METHODS

As a consequence, the deformation characteristics of many elements subjected to loading vary, and this is called buckling,

in which the deformation mode becomes unstable and the system results in another stable state search. The steady state of the system is explained by the predictability of the behavior of the load effect of that system and the inability of the system to predict how its behavior will be unstable.

The graph obtained from the buckling test is shown in Fig.1. Linear analysis for post-buckling behavior of the system and non-linear analysis for post-buckling behavior is also required. The small displacement theory of the plates in the linear analysis and the large deformation theory of the plates in the nonlinear analysis are used. The difference that separates these two theories is the difference of the deformation equations. In linear analysis, the plate changes in



the non-linear analysis, while the middle plane does not change shape.

A. Linear Analysis (Theory of Small Deformations)

The derivation of the plate differential equation can be started by grouping the loads carried by the thin plates.

These;

- Internal moments and shear forces
- Axial and central shear forces

Such a grouping makes it easier to see and understand the force and moment balances on the differential plate element.

Fig. 9. Buckling test graph [12].

Taking into account the balance of internal moments and shear forces and the balance of axial and central shear forces, the general plate equation (1) used in linear buckling analysis is obtained.

$$\frac{\partial^4 w}{\partial x^4} + 2 \frac{\partial^4 w}{\partial x^2 \partial y^2} + \frac{\partial^4 w}{\partial y^4} = \frac{1}{D} \left(q_z + N_x \frac{\partial^2 w}{\partial x^2} + N_y \frac{\partial^2 w}{\partial y^2} + 2N_{xy} \frac{\partial^2 w}{\partial x \partial y} \right) \quad (1)$$

B. Nonlinear Analysis (Large Deformation Theory)

The Small Deformation Theory of Plates' assumes that there is no deformation in the middle plane of the plate. However, as a consequence, the plaque element bends, and as a result, an elongation occurs in the middle plane. The "Great Deformation Theory of Plates" also accounts for this prolongation of the plaque in the middle plane. This theory was developed by von Karman [14].

$$\frac{\partial^4 w}{\partial x^4} + 2 \frac{\partial^4 w}{\partial x^2 \partial y^2} + \frac{\partial^4 w}{\partial y^4} = \frac{t}{D} \left[q_z + \frac{\partial^2 \phi}{\partial y^2} \frac{\partial^2 w}{\partial x^2} + \frac{\partial^2 \phi}{\partial x^2} \frac{\partial^2 w}{\partial y^2} - 2 \frac{\partial^2 \phi}{\partial x \partial y} \frac{\partial^2 w}{\partial x \partial y} \right] \quad (2)$$

C. Plain Critical Load Account Exposed to Two Side Pressing:

As shown in Fig. (1) is applied to the critical buckling stress, if it is subjected to a uniformly distributed compressive force from two sides of a simple supported rectangular plate of length a, width b;

$$\sigma_{iakr} = \frac{D \pi^2}{t b^2} \left(\frac{mb}{a} + \frac{n^2 a}{mb} \right) \quad (3)$$

equality is found.

The analytical formulation of Timoshenko's critical stress value of a simple supported plate subjected to pressure forces at two ends is given in Equation 3. In the form;

σ_{iakr} : The analytical critical stress value (MPa) for the isotropic material, m is the number of waves along the x-axis, n is the number of waves along the y-axis, a is the plate length, b is the plate width, t plate thickness (mm), D: Bending stiffness.

$$D = \frac{E t^3}{12(1-\nu^2)}$$

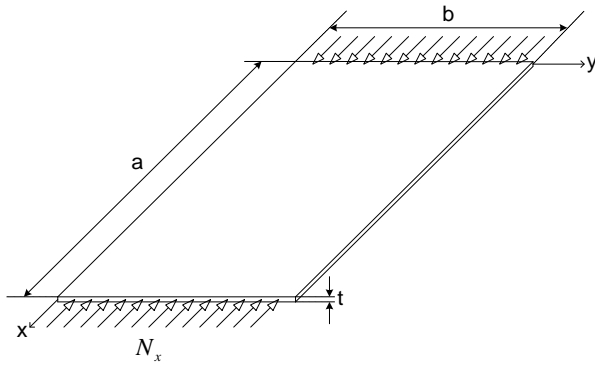


Fig. 10. Plate exposed to pressure force at bothends.

In this study, in order to prove the correctness of the applications made, the solutions of the eigen problem and the nonlinear problem were solved and compared with the studies in the literature. Then, in the plate of dimensions 200x200x2 mm³, circular holes with dimensions of 10x10, 20x20 and 30x30 mm² and Ø10, Ø20 and Ø30 mm were drilled in the middle, and linear and nonlinear buckling analysis was performed for isotropic steel plate.

D. Solving the Eigenvalue Problem for Isotropic Materials

If the desired mode of buckling is specified, the appropriate buckling stress is obtained by writing the appropriate values of m and n, that is, a plurality of critical buckling values can be calculated by changing the buckling characteristics.

The steel plate was selected in dimensions of 200x200x2 mm³. Steel Elasticity Module $E = 210,000$ MPa, Poisson's Ratio $\nu = 0,3$.

In the ANSYS® program, E and ν values for a x b x t dimensions are entered and a simple support boundary condition of four edges is applied as shown in Fig.3. The end element model Shell 181 type contains 400 elements and 441 nodes.

A total of 8 buckling modes were investigated for different values of m and n. The deformations occurring in each plane versus the eight mode values on the plate as a result of buckling are shown in Table 1. The analytically found critical stress results and the results found with the ANSYS® program are given in Table 1 as a comparative example.

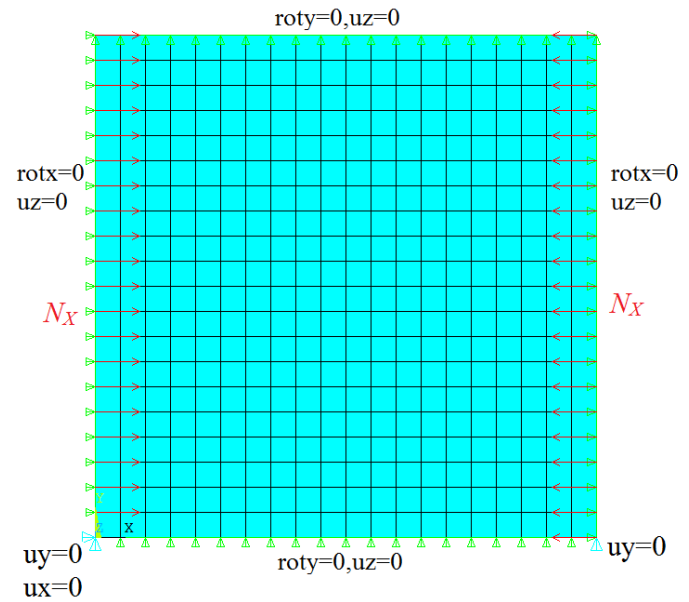


Fig. 11. Finite element model for applied boundary conditions and force.

TABLE XIX. % ERROR RATE BETWEEN σ_{iakr} AND σ_{ANSYS}

$m \times n$	σ_{ANSYS} (N/mm ²)	σ_{iakr} (N/mm ²)	% Relatif hata oranı
1x1	76.225	75.920	0.40
2x1	119.92	118.625	1.08
3x1	217.05	210.889	2.84
2x2	308.585	303.680	1.59
4x1	362.525	342.826	5.43
3x2	364.84	356.402	2.31
1x2	485.685	474.500	2.30
4x2	496.035	474.500	4.34

E. Nonlinear Problem Solution for Isotropic Materials

After the solution of the true problem, the nonlinear problem was solved. The work that Hu et al. [2] conducted analytically for nonlinear problem solving is discussed [2]. The results analytically found in this study were compared with the results obtained with the ANSYS® program for the same problem.

Hu et al. Obtained the results shown in the following graph of a nonlinear analysis of square plates subjected to compressive forces in two directions under simple support boundary conditions.

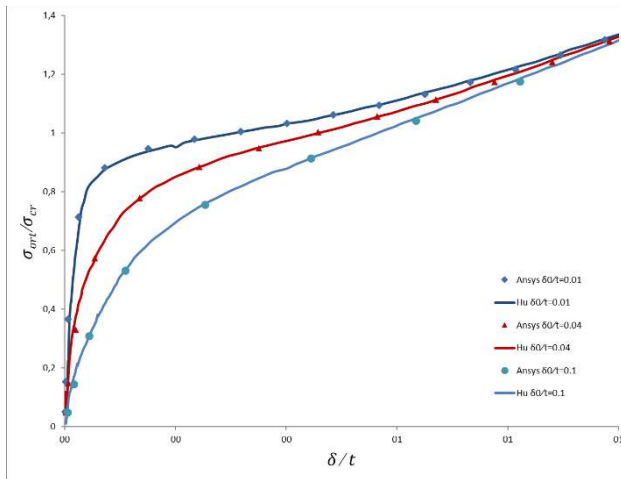


Fig. 12. Change of the ratio $\sigma_{ort} / \sigma_{cr}$ on the isotropic plate with respect to the ratio of δ/t [2].

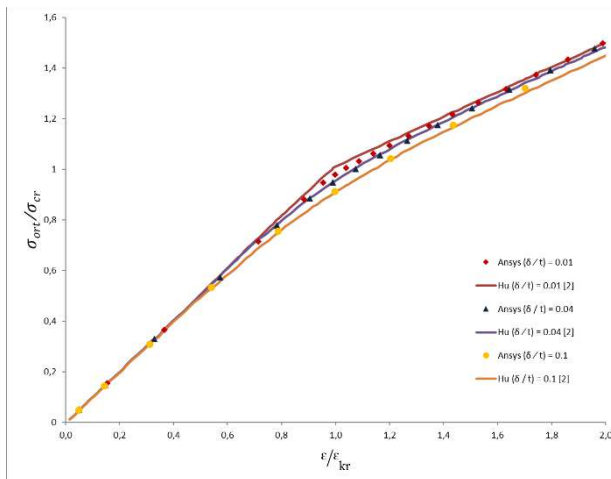


Fig. 13. Change of the ratio $\sigma_{ort} / \sigma_{cr}$ on the isotropic plate with respect to the ratio of $\varepsilon / \varepsilon_{cr}$ [2].

In this study, the analytical results of the nonlinear analysis for square plate with dimensions of 200x200x2 mm³ are compared with the numerical results obtained with the help of the finite element method and Figures 4 and 5 are given.

F. Effect of the hole in the plate center to buckling

The presence of holes in the platens is a notch effect. Linear and nonlinear buckling analyzes on steel plates with square and square holes have examined the effect of hole size and geometry on critical buckling load. Based on the solution for the plate which does not contain discontinuity in the previous section, holes were opened on the plate geometry and re-networked.

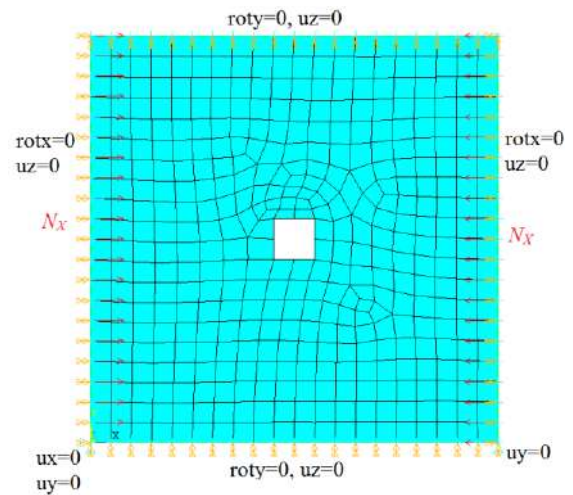


Fig. 14. Finite element model and boundary conditions for square hole plate.

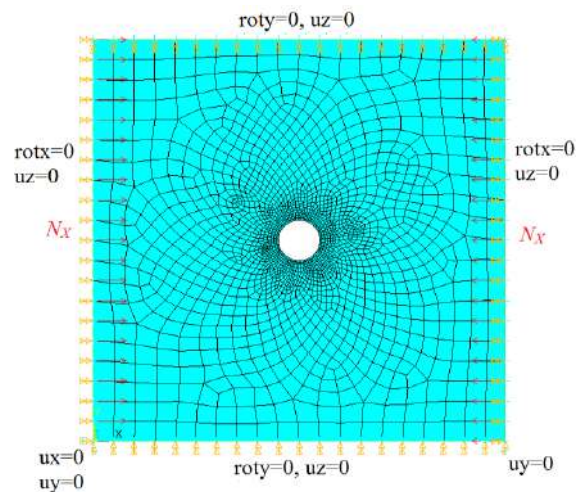


Fig. 15. Finite element model and boundary conditions for circular perforated plate.

The variation of the critical buckling load for the linear analysis with the hole sizes is shown in Fig.8.

Fig. 16. Change in critical buckling load for circular and square hole plates with hole dimensions.

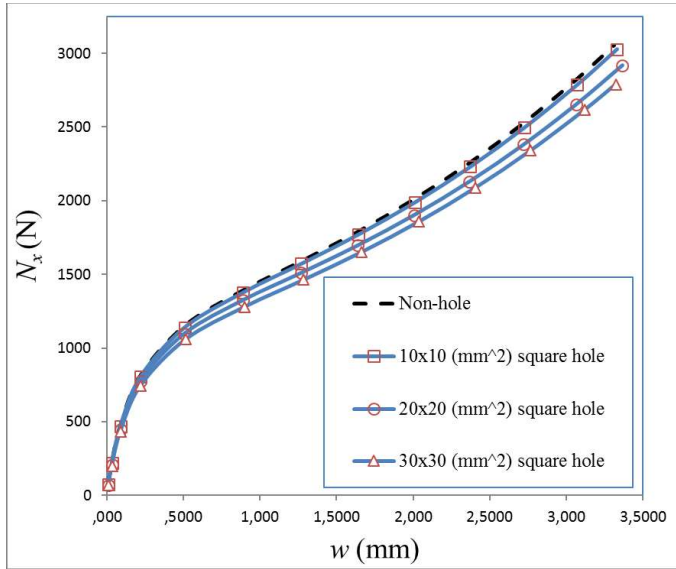


Fig. 17. Load-strain diagram of nonlinear buckling analysis for square hole plate.

In the nonlinear analysis of the same models, the model was subjected to a load at twice the critical buckling load obtained from the linear analysis and the displacement results in the z direction were obtained. The results of the nonlinear buckling analysis obtained for the steel plate are shown in Figure 9 and Figure 10.

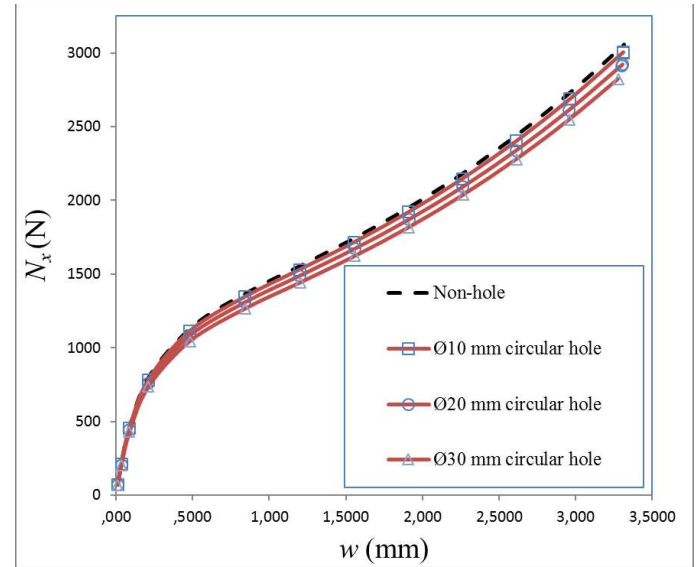
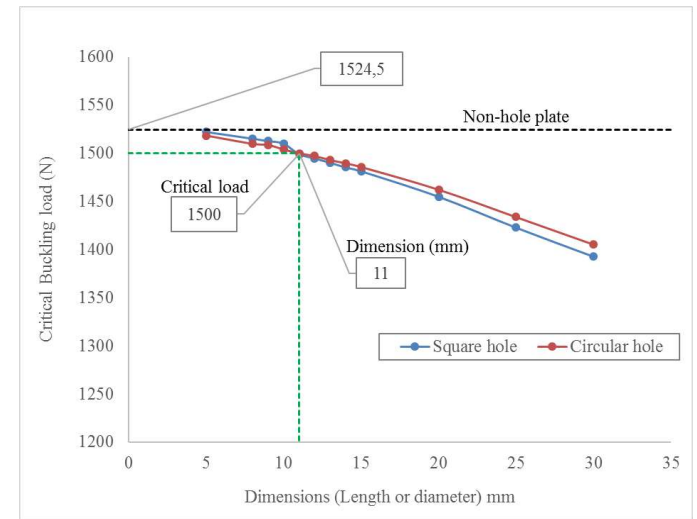


Fig. 18. Dairesel delikli plak için non-lineer burkulma analizi



RESULTS

- Figure 8 shows that the highest critical load value occurs in the plate without holes. Figure 9 and Figure 10 show that as the hole measurements increase, the critical load decreases as the cross-sectional area of the plate decreases and the amount of deformation increases.

- Critical buckling loads for plates with Ø11 mm circular and 11 × 11 mm² square holes were found to be approximately the same values. However, it was seen that the hole geometry in the smaller scale had no effect on the critical buckling load.

- As the hole measurements grew, the critical load decreased as the cross-sectional area of the plate decreased. The buckling critical load values are found to be larger in the

circular hole models than the square hole models, but all of these values are lower than the critical load values obtained for the non-hole geometry.

REFERENCES

- [8] Timoshenko, S. P. And Gere, J. M., 1988. Theory of Elastic Stability, McGraw-Hill, New York, 319-429
- [9] Hu, C. And Eugene, E. And Batdorf, S., 1949. Langley Memorial Aeronautical Laboratory Langley Field, Virginia
- [10] Yıldız, Y.O., Ve Günay, E., “Berkitmeli İzotropik İnce Plakların Sonlu Elemanlar Metodu İle Stabilité Analizi”, Erciyes Üniv. Fen Bilimleri Dergisi, Cilt 23, Sayı 1-2, ISSN 1012-2354, 2007.
- [11] Güngör, M., “İzotropik Plaklarda Mesnet Şartlarının Burkulma Davranışına Etkisi”, Zonguldak Karaelmas Üniversitesi Fen Bilimleri Enstitüsü Yüksek Lisans Tezi, 115 sayfa. 2008,
- Zihni, S., “Çeşitli Sınır Şartlarına Sahip Ortasında Boşluk Bulunan Kirchhoff Plâğının Burkulma Yüğü Bakımından İncelenmesi”, Karadeniz Teknik Üniversitesi, Fen Bilimleri Enstitüsü, Yüksek Lisans

Thermo-mechanical Analysis of a Welded Joint by Using Finite Element Methodology

Okan ÇELİK

Firat University

Department of Automotive Eng. in Technology Fac.

Elazığ, Turkey

E-mail : mr.okancelik@gmail.com

Gizem AYAS

Firat University

Department of Mechanical Eng. in Technology Fac.

Elazığ, Turkey

E-mail: gizemayas4444@gmail.com

Nevin ÇELİK

Firat University, Department of Mechanical Eng.

Elazığ, Turkey

e-mail : nevincelik@firat.edu.tr

Mete O. KAMAN

Firat University, Department of Mechanical Eng.

Elazığ, Turkey

e-mail : mkaman@firat.edu.tr

Abstract— In the present paper, thermal and mechanical behavior of a welded joint is analyzed by using ANSYS commercial software, which works base on finite element method. The transient temperature distribution on the welded plate and the displacement and von Misses stress are the extracted results from the analysis. As the plate material two different steel alloy are used; DP600 and DP1000. The welding material is the St37. The initial temperature is assumed to be 300 K, whilst the temperature of welded zone is 1773 K.

Keywords—thermo-mechanical analysis, couple field analysis

III. INTRODUCTION

As is known a welding joint is a point or edge where two or more pieces of metal or plastic are joined together. Butt, corner, edge, lap and the tee are the five types of welding joints. The welding is not only a mechanical application but also an important thermal problem, since the temperature differences affects the mechanical behavior of the material. In literature there have been many papers including thermo-mechanical analysis. Some of them can be summarized as follow.

Teng et al. [1] performed a numerical analysis to describe the thermomechanical characteristics of the T-joints in fillet welds. The effects of flange thickness, welding penetration depth and restraint condition of welding on the residual stresses and distortions were discussed. Teng et al. [2] also analyzed the thermos-mechanical characteristics of welding sequence in single-pass, multi-pass butt-welded plates and circular patch welds. This was achieved by performing thermal elastoplastic analysis by using commercial software ANSYS. Barsoum and

Lundback [3] modeled 3D welding material and performed some tests. The residual stress predictions showed good agreement with the experimental measurements.

Lindgren [4] used finite element simulation in order to predict temperature fields, residual stresses and deformation due to welding in 2D and 3D geometries. Kong et al. [5] predicted the temperature field and thermally induced residual stress in the hybrid laser–gas metal arc welding process. Zain-ul-abdein et al. [6] investigated the effect of metallurgical phase transformations upon the residual stresses and distortions induced by laser beam welding in a T-joint configuration using the finite element method. Long et al. [7] investigated distortions and residual stresses induced in butt joint of thin plates using metal inert gas welding.

In this study, a butt welded plate is analyzed numerically. The temperature, displacement and stresses after because of the welding joint are obtained. The problem is transient and the total solution time is 2 hours. The initial temperatures are 1773 K and 300 K respectively for welded plate and normal plate. The stress and displacement analyzes are performed base on the elastic material behavior using ANSYS-Structural.

II. PROBLEM DEFINITION

It is considered that an electric arc welding has been applied to the DP plates (DP600 and DP1000) in a single pass. The butt welded joint is simulated two dimensional (Fig. 1).

Fig. 17. Physical view of the problem with the dimensions

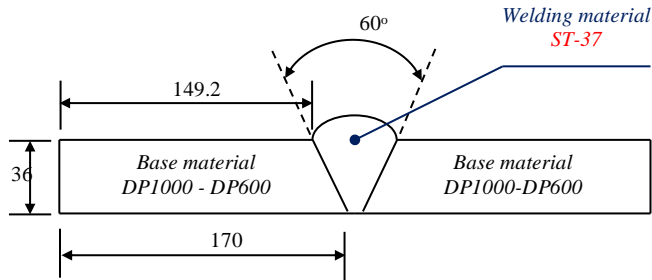


TABLE I. THERMO-MECHANICAL PROPERTIES OF ST-37 [8]

Temperature	Specific heat	Enthalpy	Thermal conductivity	Thermal expansion	Poisson ratio	Elasticity
T (K)	C_p (J kg ⁻¹ K ⁻¹)	H x 10 ⁹ (J kg ⁻¹)	k (W m ⁻¹ K ⁻¹)	α x 10 ⁻⁵ (K ⁻¹)	ν	E x 10 ¹¹ (Pa)
273	450	1	52	1.1	0.276	2.12
473	500	2.32	51.2	1.2	0.287	1.55
673	650	3.82	42.5	1.39	0.305	1.05
873	773.3	4.55	35	1.54	0.31	4.7
973	1090	5	31	1.56	0.313	1.2
2273	735	1.1	31	1.56	0.313	1.2

TABLE II. THERMO-MECHANICAL PROPERTIES OF DP600 BASE ON TEMPERATURE [9]

Specific Heat		Thermal Conductivity		Thermal Expansion		Poisson ratio	Elasticity	Density
T (K)	C_p (J kg ⁻¹ K ⁻¹)	T (K)	k (W m ⁻¹ K ⁻¹)	T (K)	α x 10 ⁻⁵ (K ⁻¹)	ν	E x 10 ¹¹ (Pa)	ρ (kg m ⁻³)
273	520	273	34.6	273	1.2	0.28	2.1	7594
473	550	298	34.8	573	--	0.295	1.9	
673	600	473	35	873	--	0.31	1.2	
873	750	527	35	1073	1.6	0.33	3	
1073	690	1473	25.5	1473	2.5	0.33	3	
1373	520	1573	60	3273	2.5	0.33	3	
1473	610	1673	70					
3273	620	3273	70					

TABLE III. THERMO-MECHANICAL PROPERTIES OF DP1000 BASE ON TEMPERATURE [10]

Specific Heat		Thermal Conductivity		Thermal Expansion	Poisson ratio	Elasticity	Density
T (K)	C_p (J kg ⁻¹ K ⁻¹)	T (K)	k (W m ⁻¹ K ⁻¹)	α x 10 ⁻⁵ (K ⁻¹)	ν	E x 10 ¹¹ (Pa)	ρ (kg m ⁻³)
573	449	573	69.5	1.2	0.28	2.1	7840
673	491	673	66.5				
873	572	873	55.1				
1073	675	1073	44.3				
1273	961	1273	40.5				
1473	607	1473	36.6				
1773	651	1773	36.6				

TABLE IV. CHEMICAL COMPOSITION OF DP600 AND DP1000 [11]

DP600									
C	Si	Mn	Cr	Nb	Ni	Ti	Mo	Al	Fe
0.11	0.182	1.6	0.341	0.0037	0.027	0.002	0.098	0.053	Rest
DP1000									
C	Si	Mn	P	S	Cr	Al	Co	Cu	V
0.123	0.484	1.44	0.01	0.001	0.012	0.043	0.016	0.01	0.007

The thermal and mechanical properties of the welding material depending on the temperature variation is presented in Table 1. Similarly, the thermo-mechanical properties of the base materials DP600 and DP1000 are listed respectively in Table 2 and 3. Finally the chemical composition of the two base materials are exhibited in Table 4.

III. NUMERICAL ANALYSIS

The ANSYS commercial software has a large class of coupled field analysis problems in the multi solver mode. In the presented couple field analysis there are two physics; thermal and structural, and each physics is created as a field with an independent solid model and mesh. Transient heat conduction problem is solved to obtain the temperature variation 2 hours after the welding. As told before, the initial temperature of base material and welding material is respectively 300 K and 1773 K. It is assumed that there is natural convection on the top side of the material having heat transfer coefficient as $13 \text{ Wm}^{-2} \text{ K}$ and bulk temperature as 300 K.

In the thermal model the element type for the 2D simulation is *Quad 4 node 55*, namely *PLANE55*. A mesh accuracy is obtained as the preparation of the simulation, and 0.5% accuracy is obtained at about 19706 elements and 20038 nodes.

In the present analysis, the structural element type is *PLANE182*. The bottom line is assumed to be a fixed support as shown in Fig. 2. Temperature distribution at certain time steps, obtained from the thermal analysis is saved and then used as boundary conditions in the structural analysis. Finally, the mechanical behavior of the welding material is assumed to be elastic.

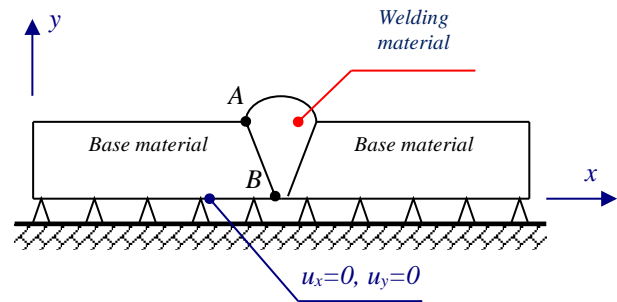
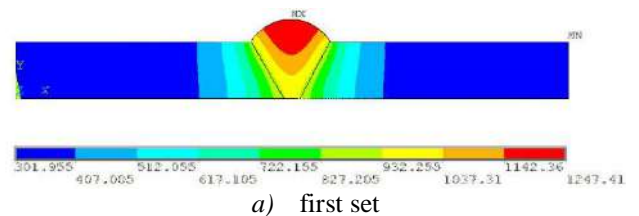


Fig. 2. Boundary conditions for the structural analysis [8]

V. RESULTS AND DISCUSSIONS

The transient temperature distribution on the whole plate, in case of base material is DP600, is given in Fig 3. By checking the temperature contour plots, it can be seen that, the temperature has the minimum value 400 K on the edge sides of the base material at the last set, and 405 K at the welding point, which means the plate is still warmer than the ambient air. Fig 4 presents the temperature contour in the case of using base material DP1000. If the attention is paid to the last time step, it will be seen that the lowest temperature is 402 K at the edges of the base material, 405 K at the welding point. Comparing two base materials it is clear that in the case of using DP1000 the edge of the base material is quite warmer than the case of using DP600. This result can also be seen in the temperature versus time graph in Fig. 5.



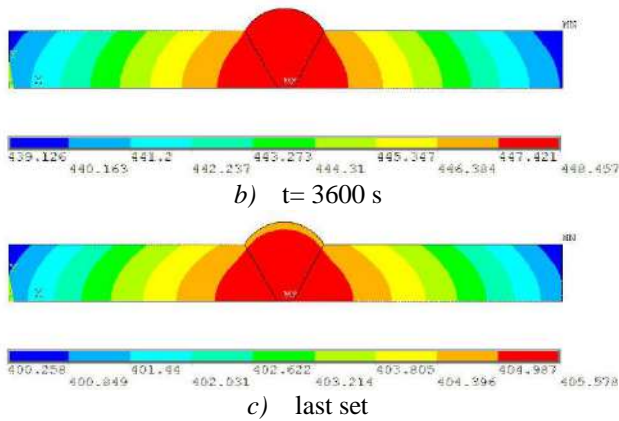


Fig. 3. Temperature distributions on the DP600 plate (K)

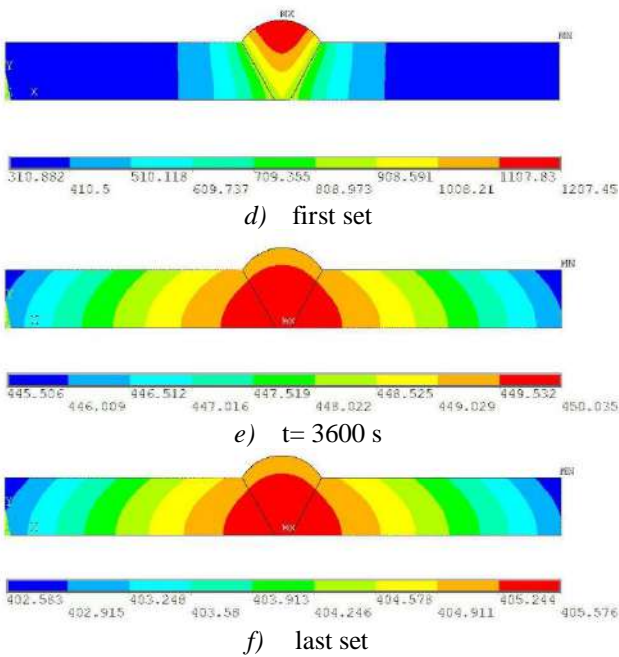


Fig 4. Temperature distributions on the DP1000 plate (K)

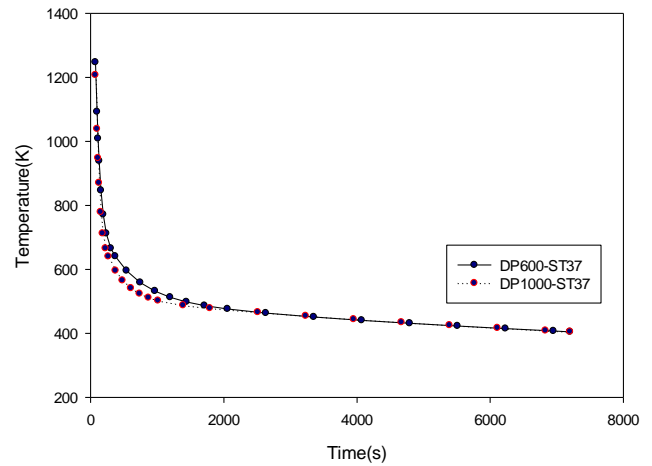


Fig. 5. Temperature versus time variation on a point on the welding joint

Now it is the time to present some structural analysis results and discuss about them. First result is the deformed and un-deformed shape of the plate because of the welding. In Fig 6a and 6b the deformed and un-deformed shapes of the plates respectively for DP600 and DP1000 are presented. Although both figures look like same, the displacement is quite higher for DP600 than that of DP1000.

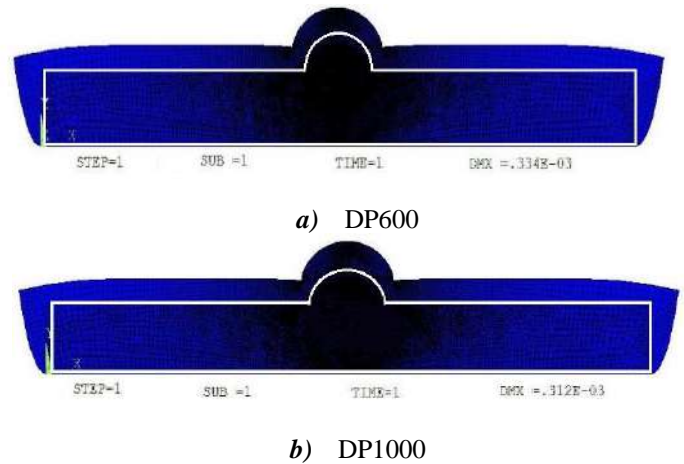


Fig. 6. Deformed and un-deformed cases of the plates

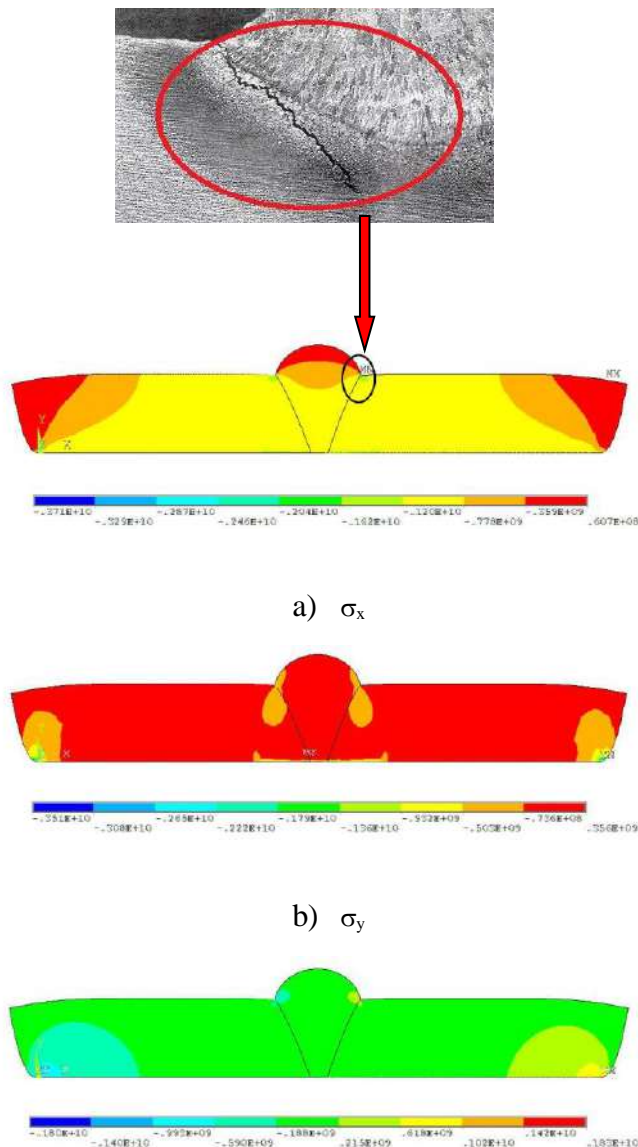
In Fig 7(a-c) and 8(a-c) the stress analysis of the plate is presented. In Fig 7a, the stress along the x-direction, σ_x is shown. It is seen that the maximum stress is observed at the top and edge sides, but seems to be uniform at the rest of area. The σ_x is nearly symmetric at the plate. Absolute maximum values are lower than the absolute minimum values. The interface between the base and welding material

are the points under the risk of fracture because of the high σ_x values seen there.

The stress on especially the welding joint is the probability of the fracture on that point. It is well described with the photo on Fig 7a.

In Fig 7b, the stress along the y-direction is shown. The values for the stress look like same with the σ_y values. But it should be noted that, the min and max values are not same.

If we quickly blink at the Fig 7c, it will be seen that the σ_{xy} namely the shear stress is as important as the σ_x and σ_y because of the values.



c) σ_{xy}

Fig. 7. Structural analysis for DP600

In Fig 8(a-c) the contour plots of the σ_x , σ_y , σ_{xy} are presented. General trend is nearly same to the Fig 7(a-c), that's to say, to the DP600 base material, except for the values. All of the stress values regardless of the type are lower in the case of DP1000 than that of DP600.

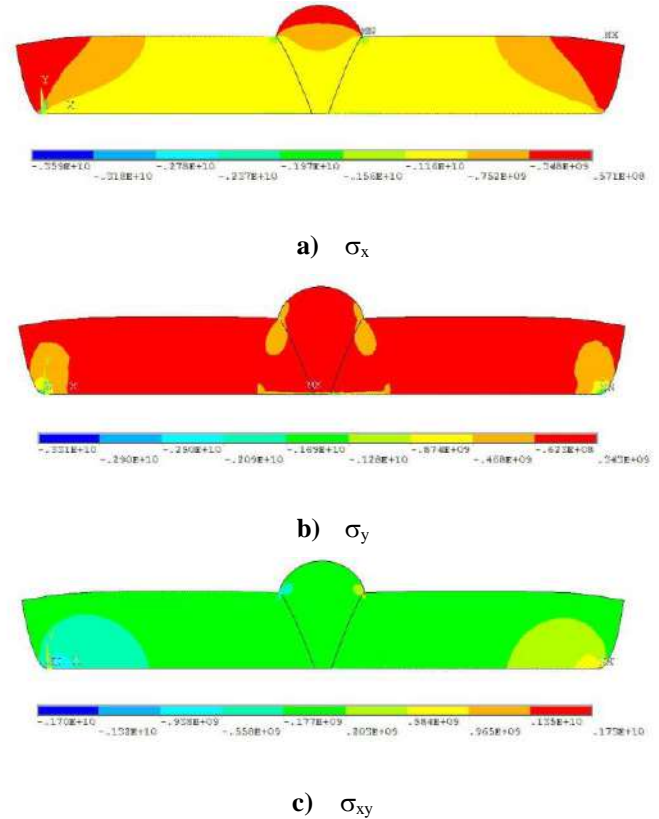
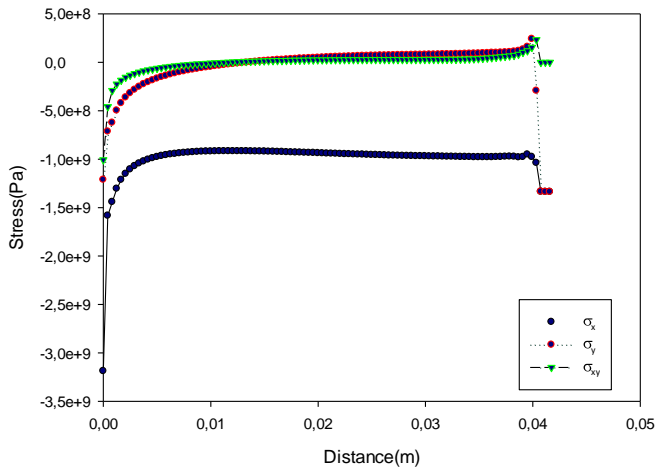


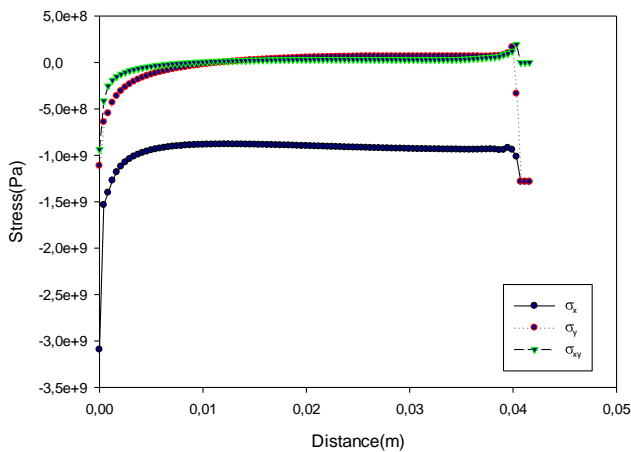
Fig. 8. Structural analysis for DP1000

The three stresses; σ_x , σ_y and σ_{xy} at a selected node on the DP600 and DP1000 base materials are exhibited respectively Fig 9a and Fig 9b. The values of three stresses show that shear stress has nearly the maximum values of all. It can be said that σ_{xy} cannot be neglected anymore.

Final plot (Fig 10) is another comparison of the base materials. It shows the σ_{xx} for two base material. DP1000 seems to have higher values than DP600 does.



a) DP600



b) DP1000

Fig. 9 Comparisons of the stresses

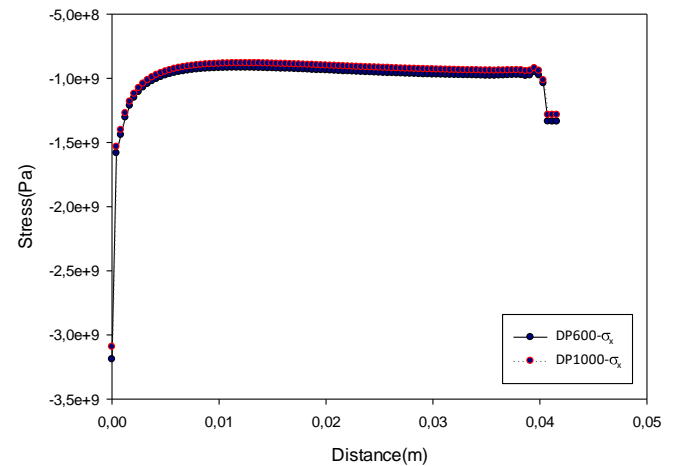


Fig. 10. σ_{xx} for DP1000 and DP600.

VI. CONCLUSIONS

In this study, a two-dimensional couple field analysis of an electric arc welding application including thermal and structural effects is analyzed by using commercial software ANSYS. Transient thermal distribution on ST-37 plate is obtained for all time intervals until it reaches 7200 s. In accordance to this the temperature distribution, deformation and the stresses σ_x , σ_y and σ_{xy} are found. The major conclusions can be listed as follows:

- ✓ The minimum temperature on the plate at the last time step is lower for DP600 than that of DP1000.
- ✓ The three stresses σ_x , σ_y and σ_{xy} are all lower for the case of DP1000, which can be concluded that DP1000 has less probability of fracture than DP600.
- ✓ The displacement is also lower for the base material DP1000.

REFERENCES

- [12] T.L.Teng, C.P.Fung, P.H.Chang, W.C.Yang, "Analysis of residual stress and distortions in T-joint fillet welds", International Journal of Pressure Vessels and Piping, vol.78, pp.523-538, 2001.
- [13] T.L. Teng, P.H. Chang, W.C.Tseng, "Effect of welding sequences on residual stresses", Computers and Structures, pp.273-286, 2002.
- [14] Z. Barsoum, A.Lundbäck, "Simplified FE welding simulation of fillet welds – 3D effects on the formation residual stresses", Engineering Failure Analysis, pp.2281-2289, 2009.
- [15] L.E. Lindgren, "Finite element modelling and simulation of welding, Part2: improved material modelling", Journal of Thermal Stresses, pp.195-231, 2001.
- [16] F. Kong, J. Ma and R. Kovacevic, "Numerical and experimental study of thermally induced residual stress in the hybrid laser-GMA welding process", Journal of Materials Processing Technology, pp. 1102-1111, 2011.

- [17] M. Zain-ul-abdein, D.Nélias, J.F.Jullien, F.,Boitout, L.Dischert, and X. Noe, "Finite element analysis of metallurgical phase transformations in AA 6056-T4 and their effects upon the residual stress and distortion states of a laser welded T-joint", *International Journal of Pressure Vessels and Piping*, pp. 45-56, 2011.
- [18] H. Long , D. Gery, A. Carlier, P.G. Maropoulos, "Prediction of welding distortion in butt joint of thin plates", *Materials and Design* pp. 4126–4135, 2009.
- [19] M.O. Kaman, N. Celik and I. Gokce, "Thermal and residual stress analyses of a welded stainless steel plate," 9th International Conference on Heat Transfer, Fluid Mechanics and Thermodynamics HEFAT12, 17-19 July 2012, Malta.
- [20] T. Gloriant, L. Barrallier and P.Paillard "Evaluation numérique des contraintes résiduelles appliquée à l'acier DP600 soudé par laser de haute puissance, YAG ,Chapter 4, pp.127-176, 2013
- [21] X. Li, L. Wang, L. Yang, J. Wang, and K. Li, "Modeling of temperature field and pool formation during linear laser welding of DP1000 steel", *J. Mater. Process. Tech.*, vol. 214, no. 9, pp. 1844–1851, 2014.
- [22] F. Hayat and B. Demir, "The effect of the weld time on dept intensity factor and strength at rsw junctions of commercial dp600 sheet steel," 5th International Advanced Technologies Symposium, May, 2009.

Investigation of Correlation of Vibration to Burr Height in Drilling Free Form Surfaces

Yusuf Eren ERDOĞDU

Department of Mechanical Engineering
Inonu University
Malatya, TURKEY
eren.erdogdu@inonu.edu.tr

Erkan BAHÇE

Department of Mechanical Engineering
Inonu University
Malatya, TURKEY
erkan.bahce@inonu.edu.tr

Mehmet Emin TAĞLUK

Department of Electrical and Electronics Engineering
Inonu University
Malatya, TURKEY
mehmet.tagluk@inonu.edu.tr

Abstract—In manufacturing industry, particularly which involve free form surfaces, formation of burr on the exit surface is a cost effective problem, and hence its minimization is an important goal in drilling process. The relationship between drilling parameters and burr formation has been investigated in variety of perspectives. It has been mentioned that vibration has a relation to the rate of burr formation. In this study the relation of machine vibration to the burr's height was investigated. Drilling experiments were conducted on a piecework with a free form surface where the drill exit surface was at 15°, 30° and 45° tangential angles. It was observed that average power of longitudinal or thrust vibration signal had an inverse relation to the measured burr's heights, while feed rate had a positive relation when spindle run at 2800 rpm.

Keywords: free form surfaces, vibration, burr formation, drilling

I. INTRODUCTION

In modern manufacturing industry such as medical, aerospace and automotive variety of structures with free form surfaces are widely used. Drilling processes made on such free form surfaces results with some burrs on the exit surface of material. Removal of burr formation in drilling process of free surface materials causes additional operations and costs. Therefore, reduction or totally abolition of burr has become an important objective in drilling process. In order to achieve this, it is necessary to investigate the effects drilling parameters on the formation of burrs and estimate the relationship going between them. It is considered that vibration turned up during drilling also has a relation to the formation of burr. There are some studies in the literature that investigate the relationship of vibration to other drilling parameters and burr formation. Among these studies some examples are:

Roukema and Altintas [1] proposed a 3D dynamic model for drilling contained rigid body motion, torsional-axial and lateral vibrations. Their model allowed virtual testing of various drilling scenarios in time domain and it ensured to predict the hole oversize because of grinding errors on the tool.

Sevim and Genc [2] analyzed the vibration occurred due to cutting forces in drilling with CNC milling machine. They used Al 7075 work piece for their study. They offered low feed rate and high spindle speed to reduce the vibration in drilling Al 7075.

Chang and Bone [3] developed a model to predict exit surface burr height which occurred in vibration assisted drilling (VAD) and conventional drilling of Al 6061-T6 materials. Their model included a hypothesis expressing that only the positive part of the thrust force is responsible for the formation of burrs. They found the suitable vibration frequency for drilling by their approach.

Okamura et al. [4] searched for an interaction between vibration conditions and chip formation, burr formation and drilling temperature on drilled Titanium alloy specimen. They found that in low-frequency vibration, the drilling temperature decreased and exit burr height and burr width reduced.

Adachi et al. [5] by using vibratory drill compared the cutting characteristics of vibratory drilling and conventional drilling. They asserted that the burr size in low frequency vibratory drilling was smaller than burr size occurred in conventional drilling.

Azarhoushang and Akbari [6] studied on ultrasonic assisted drilling and compared it with conventional drilling in terms of cylindricity, circularity, surface roughness and hole

oversize. According to their idea, because of ultrasonic impact action, thrust force reduces and thus plastic deformation decreases, and so smaller chips and burrs occur.

Li et al. [7] studied on vibration drilling of laminated composite materials. They developed a step multi-element varying-parameter vibration drilling model and thus they lowered the exit burr height to 41.55% using this model.

Chang and Bone [8] carried out an experimental study for lowering the size of burr in drilling. They designed a work piece holder which vibrated at ultrasonic levels to set an ultrasonic assisted drilling system. The results obtained with the use of this system revealed that as the vibration frequency became higher than a certain limit, the burr size became small. This technique was said to be more effective than conventional drilling.

Heisel et al. [9] used an ultrasonic assistance in drilling of short holes. They measured the vibration amplitude with and without load by using the change of stimulation power. They reached minimum burr size in case of there was no stimulation but when the power started raise the burr size tended to decrease.

Kadivar et al. [10] drilled Al/SiCp metal matrix composites with ultrasonic assisted drill. In this study, a comparison was made between workpiece vibration system and tool vibration system from burr height, drilling force sand surface roughness of views. When vibration was applied to workpieces, higher thrust force, smaller burrs and smaller surface roughness were achieved compared to conventional drilling.

From the information given above it is understood that there is a relation between vibration and burr formation in drilling process. The purpose of this study is to demonstrate the relationship between vibration and exit burr height at the drilling of free-form surfaces where the drilling forces are much more complex.

II. MATERIAL AND METHOD

For drilling experiments, Al 7075 material, which is also widely used in studies in the literature, was selected. The chemical composition and mechanical and physical properties of Al-7075 alloy are tabulated in Tables 1 and 2[11].

CHEMICAL COMPOSITION OF Al -7075		PHYSICAL AND MECHANICAL PROPERTIES OF Al -7075	
Element	Chemical Composition (wt.%)	Parameters	Values
Al	Balance	Density (g/cm ³)	2.81
Zn	5.1-6.1	Hardness (HB)	60
Mg	2.1-2.9	Ultimate tensile	228

Cu	1.2-2.0	strength (MPa)	
Fe	0.5	Elongation at break (%)	16
Si	0.4	Tensile yield strength (MPa)	103
Mn	0.3		
Ti	0.2		
Cr	0.18-0.28		
Others	0.15		

A curve which contain 15°, 30° and 45° tangential angles, was created using the B-spline theory [12]. A free form surface was designed by means of Solid Works software from the prepared curve. An Al 7075 plate was milled with CNC to obtain a workpiece with a free-form surface.

Since the workpiece has a free-form surface, its thickness varies along curvature of surface. Thus, the channels were opened on the flat surface of the workpiece to provide uniformity between tool feed distances. The channels and holes are shown in fig. 1.

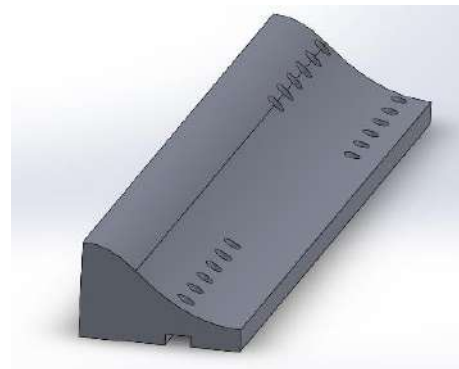


Fig. 1. The workpieces solid model with channels and holes.

The drilling experiments were conducted by HSS drilling tools which have 118° point angle and 7,5 mm diameter. Each tool was used in only one drilling operation. Drilling operations were performed in dry conditions.

Vibration and acoustic emissions were measured by Vibra ZEB VM-7D+ vibration meter during the tests. The vibration sensors built within this device recorded vibrations come up on longitude, transverse, vertical axes. The experimental set up with vibration meter is shown in Fig.2. The signals were recorded at 2048 (sps) sampling frequency.



Fig. 2. The experimental setup.

The images of workpiece were captured by scanning with David s3-3 3D scanning device. Using these 3D data with GOM Inspect software. Burr heights were measured by the method widely used in the literature [13-15]. For each hole, the arithmetic average of the burr height values measured from four points as shown in Fig.3.

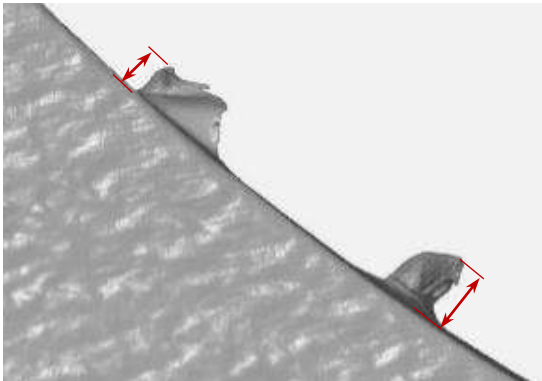


Fig. 3. Shows how burr height was measured.

In order to detect a clear correlation between vibration signal and burr heights the vibration signals filtered by a second order band-pass Butterworth filter with $f_L=40$ and $f_H=53$ Hz. cutoff frequencies. The central frequency of filter was set in such a way that to match with the spindle speed $(2800 \text{ (rpm)}/60 \text{ (sec)}) = 46.6 \text{ Hz}$. In this way the other remaining minor spectral components caused by tangential frictions were excluded. Also the spectra of vibration signals were achieved by using Fourier transform given by

$$S(f) = \int s(t) \exp(-j2\pi ft) dt \quad (1)$$

to analyze the signals in terms of their spectral contents. The obtained filtered vibration signals and signals spectrums are shown in Fig. 4 (a, b and c) for each particular feed rate and tangential angle of exit surface mentioned above. Each panel of the Figure contains longitudinal, transverse and vertical vibration signals which are labeled on the Figure. As can be seen from the Figure for all types of vibration the peaks of signals tend to increase with the increase of feed rate, however it was noticed that the best parameter which could be derived for correlation was the power of longitudinal vibratory signal given by

$$P = \frac{1}{N} \int_1^N \widehat{s(t)}^2 dt \quad (2)$$

where, $\widehat{s(t)}$ is the filtered version of $s(t)$ and N is the number of data points averaged. This correlation may not be a perfectly linear, but seems to be a reasonable one to be used in controlling the drilling system to reduce the burrs' rates.

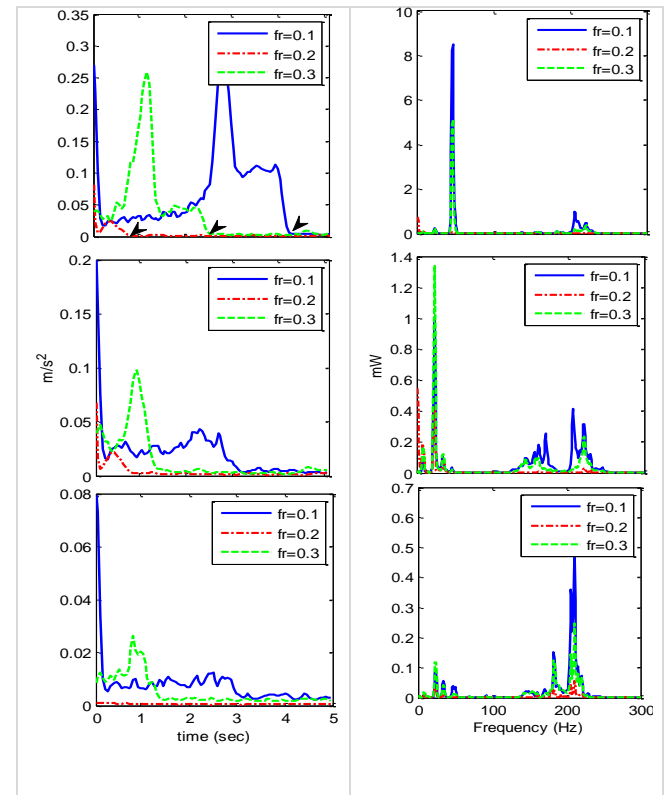


Figure 4. The vibration temporal and spectral signals for 15° exit surface, Longitudinal (upper panel); Transverse (middle panel); vertical (lower panel); Arrows show the exit time of drill from surface.

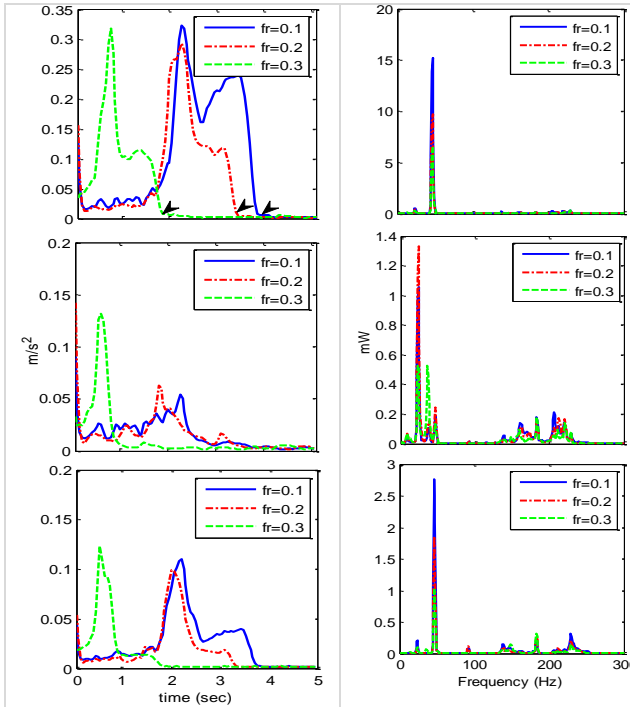


Figure 5. The vibration temporal and spectral signals for 30° exit surface, Longitudinal (upper panel); Transverse (middle panel); vertical (lower panel); Arrows show the exit time of drill from surface.

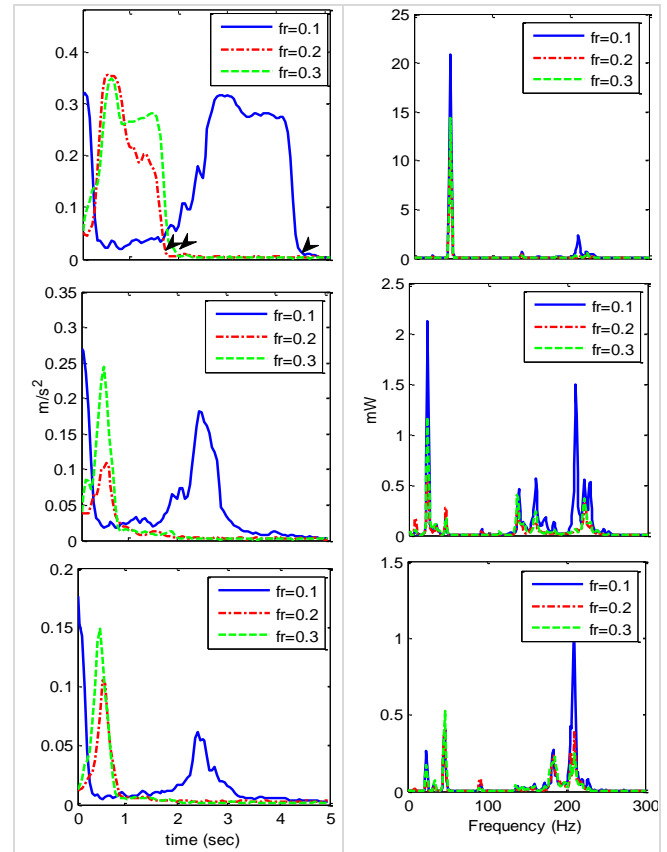


Figure 6. The vibration temporal and spectral signals for 45° exit surface, Longitudinal (upper panel); Transverse (middle panel); vertical (lower panel); Arrows show the exit time of drill from surface.

III. RESULT AND DISCUSSION

A solid model having free form surface shown in Fig 1. was drilled with a tool having 2800 (rpm) spindle speed in such a manner that the exit surfaces were with 15°, 30° and 45° tangential angles. The obtained vibration signals are processed as mentioned in previous section and displayed in Figure 4 (a, b and c). The obtained results in this particular study are tabulated in TABLE III. It is found that the burr heights increase with the increase of feed rate while the longitudinal vibration signal's average power decreases. That is, the signal's power had an inverse relation to the measured burr's heights.

In order to arrive at a significant conclusion in relation to the impact of vibration on the burr's characteristics on uniform exit surfaces a few studies published in literature was analyzed in this perspective. Chang and Bone [3] investigated the impact of vibration on drilling process, and demonstrated that longitudinal vibration assisted drilling performs minimum burr rate compared conventional methods. They have found that burr height reduced to approximately 0.085 microns at 8 KHz thrust vibration. It had also been demonstrated that thrust force considerably reduces with

vibratory drilling [5] and remains almost the same or very slightly reduced levels with the increase of elongation.

In another explanatory study it had been mentioned that ultrasonic vibration in feed direction at 21 KHz could improve the hole quality (10 microns peak) considerably [6]. In that study a quality improvement up to 60% had been achieved. It had been shown that average burr height reduces to 0.4 mm at 20 kHz and 4 microns (pk-pk) vibration amplitude under (3.18mm diameter drill, 4000RPM, 1.90 mm/s feed rate) conditions [8].

Kadivar et al. [10] analyzed the influence of ultrasonic assisted system on finished surface quality in terms of burrs' height values. They had demonstrated the system for tool vibration and workpiece vibration and compared the obtained results. They revealed that workpiece vibration was better, particularly when vibration was applied to workpiece higher thrust force and smaller burr rates were found.

From the above analytical information it can be considered that a vibration (in thrust direction) assisted drilling process resembles to a percussion drill applied on rough surface. Therefore the increase of quality of finished exit surface with VAD system should be quite natural as compared to conventional drilling process.

The proportionality of burr's height to feed rate acquired in this study is in line with the results found in the literature [16,17]. The decrease of burr height with the increase of average power of longitudinal vibration signal can be considered as a good association. This inverse correlation established between average power of longitudinal vibration signal and burr's height can also be linked to the information found in the literature. Here, the power of longitudinal vibration was considered rather than transverse or vertical signals' powers, because of that CAD systems had been developed based on the vibration imposed in thrust direction. With the application of this systems, as discussed above, the drilled exit surface roughness increased with the increase of vibration amplitude up to a certain limit. Our finding is along the lines of this information. The relation of vibration of drilling machine to feed rate for uniform surfaces has somewhat been demonstrated in [2] and the displayed results are similar to ones found in this study. The proportionality of average signal power mentioned here, has not been sufficiently discussed in the literature. Therefore it needs to be considered by other studies which to be conducted in the future.

TABLE III. EXPERIMENTAL PARAMETERS

Hole Number	Exit Surface Angle(°)	Feed Rate (mm/rev)	Average Burr Height (mm)	Mean Power of vibration signal(mW)
1	15	0.1	0.0847	1.20
2	15	0.2	0.2012	0.0044
3	15	0.3	1.3168	1.28
4	30	0.1	0.2943	1.99
5	30	0.2	0.4172	1.55
6	30	0.3	1.4269	1.75

7	45	0.1	0.5115	2.48
8	45	0.2	0.6427	2.27
9	45	0.3	1.5624	3.81

IV. CONCLUSIONS

In this study the relation of machine vibration to the burr's height was experimentally investigated. From the experiments conducted on a free form piecework (at 15°, 30° and 45° tangential angles) an inverse correlation between mean power of longitudinal vibration signal burr's heights as well as a positive relation with feed rate were found out, when spindle speed was 2800 rpm. These findings can be confidently associated to the information found in the literature [6, 8,10]. However the proportionality mentioned here has not been sufficiently discussed in the literature, and therefore remains to be further investigated.

REFERENCES

- [1] J.C. Roukema, and Y. Altintas, "Generalized modeling of drilling vibrations. Part I: Time domain model of drilling kinematics, dynamics and hole formation," *International Journal of Machine Tools and Manufacture* 47.9 (2007): 1455-1473.
- [2] C. Sevim, and O. Genc, "Al-7075 Malzemesinin Freze Tezgâhında Delme İşleminde Farklı Devir ve İlerleme Hızları İçin Oluşan Titreşimlerin İncelenmesi," *International Journal of Scientific & Technology Research*, Volume 4, Issue 04, April 2015.
- [3] S.S.F. Chang, and G. M. Bone, "Burr height model for vibration assisted drilling of aluminum 6061-T6." *Precision Engineering*, 34.3 (2010): 369-375.
- [4] K. Okamura, H. Sasahara, T. Segawa, and M. Tsutsumi, "Low-frequency vibration drilling of titanium alloy," *JSME International Journal Series C Mechanical Systems, Machine Elements and Manufacturing*, 49.1 (2006): 76-82.
- [5] K. Adachi, A. Yoshikawa, and K. Sakurai. "A Study on Burr Low Frequency Vibratory Drilling," *Materials forum*, Vol. 28. 2004.
- [6] B. Azarhoushang, and J. Akbari. "Ultrasonic-assisted drilling of Inconel 738-LC," *International Journal of Machine Tools and Manufacture*, 47.7 (2007): 1027-1033.
- [7] Z. J. Li, M. S. Hong, H. Su, and Y. L. Wei, "Machining accuracy analysis for step multi-element varying-parameter vibration drilling of laminated composite materials," *The International Journal of Advanced Manufacturing Technology*, 21.10-11 (2003): 760-768.
- [8] S.S.F. Chang, and G. M. Bone, "Burr size reduction in drilling by ultrasonic assistance," *Robotics and*

- computer-integrated manufacturing, 21.4 (2005): 442-450.
- [9] U. Heisel, T. Stehle, M. Schaal, and R. Eisseler, "Burr formation in short hole drilling by ultrasonic assistance," *Production Engineering*, 8.1-2 (2014): 1-6.
- [10] M. A. Kadivar, J. Akbari, R. Yousefi, A. Rahi, and M. G. Nick, "Investigating the effects of vibration method on ultrasonic-assisted drilling of Al/SiCp metal matrix composites," *Robotics and Computer-Integrated Manufacturing*, 30.3 (2014): 344-350.
- [11] E. Kilickap, "Modeling and optimization of burr height in drilling of Al-7075 using Taguchi method and response surface methodology," *The International Journal of Advanced Manufacturing Technology*, 49.9-12 (2010): 911-923.
- [12] A. Saxena, B. Sahay, *Computer Aided Engineering Design*, ISBN: 978-1-4020-2555-6, 2005.
- [13] K. Giasin, and S. Ayvar-Soberanis, "An Investigation of burrs, chip formation, hole size, circularity and delamination during drilling operation of GLARE using ANOVA," *Composite Structures*, 159 (2017): 745-760.
- [14] S. Min, J. Kim, and D. A. Dornfeld, "Development of a drilling burr control chart for low alloy steel, AISI 4118," *Journal of materials processing technology*, 113.1 (2001): 4-9.
- [15] V. N. Gaitonde, S. R. Karnik, B. T. Achyutha, and B. Siddeswarappa, "Genetic algorithm-based burr size minimization in drilling of AISI 316L stainless steel," *Journal of materials processing technology*, 197.1 (2008): 225-236.
- [16] L. K. Lauderbaugh. "Analysis of the effects of process parameters on exit burrs in drilling using a combined simulation and experimental approach," *Journal of Materials Processing Technology*, 209.4 (2009): 1909-1919.
- [17] J. Kim, D. A. Dornfeld. "Development of an Analytical Model for Drilling Burr Formation in Ductile Materials," *ASME Trans. J. Engineering Materials and Technology*, 124:192-198, 200

Bending and Torsional Behaviours and Finite Element Analysis of Hollow Circular Glass/Epoxy Composite Shafts at Different Orientation Angles

Hayri YILDIRIM
Dicle University,

Technical Vocational School,
21280 Diyarbakır/Turkey

Haşim PIHTILI
Firat University,
Department of
Mechanical Eng.
23119 Elazığ/Turkey

Şükrü ÇETİNKAYA
Dicle University,
Department of Mechanical Eng.
21280 Diyarbakır/Turkey

Abstract—In this study the mechanic properties and behaviours of the most commonly used in industry and works under various environmental influences hollow circular composite shafts were examined experimentally and numerically. In addition for circular hollow composite shafts glass is used as a fiber material and epoxy resin is preferred as a matrix material. The composite shafts that are in different lengths such as 80mm, 200mm, 250mm and one inner (Dinner=12mm) and outer (Douter=17mm) diameters are used for three point bending test. The composite shafts were manufactured in different orientation angles ($\theta=45^\circ, 60^\circ, 75^\circ, 80^\circ, 88^\circ$) by using filament winding method. The bending behaviour of manufactured circular hollow shafts were tested and repeated for each specimen. As a result of numerical and experimental analyses, it was observed that the bending and torsion behaviours of hollow circular composite shafts vary depending on the orientation angles. Additionally, FEA (finite element analysis) model of the hollow circular glass/epoxy shafts was created and analyzed by using ANSYS workbench. Results of the finite element analysis are compared with values of the bending stress and the modulus rupture in torsion (RT) obtain by experimental tests. The experimental and numerical analysis results were found to be close to each other.

Keywords—Composite shafts, Filament winding, Orientation angle, Three-point bending test, Torsional test

I. INTRODUCTION

In this study, glass/epoxy composite material were used in the three point bending and torsional test. Amounts of bending stress and the modulus rupture in torsion (R_T) of the composite material were examined experimentally and numerically. Moreover, the effects of orientation angle was studied on the bending stress and the modulus rupture in torsion (R_T). And also the novelty of the paper is the first time in that dimensions and load materials are used.

Apart from the fact that shafts, which are used in every field of technology, are among the most important power transfer elements. They are exposed to tensile, compression, bending and torsional stresses due to their operational characteristics. Since shafts transmit power from one machine element to the other, they can be exposed to torsional stress,

which is the most hazardous one of all. Since shafts are exposed to bending due to the elements found on the top of them as well as being exposed to torsion due to rotating, their constructions, designs and calculations are generally made according to combined stresses. However, hollow shafts are usually preferred in the cases in which lightness is required. For this reason, hollow shafts are used in automotive industry and space industries. The following studies were found when a topic-related literature review was made. The variation of the foam solidification rate is another strategy for controlling the micro-and macro-structure. For example, a high cooling rate could decrease the micro-pores and grain sizes in the cell walls that have negative effects because they promote stress concentration and thereby crack initiation. Recently, the potential use of integral-skin foams as stiffening elements inserted in thin-walled tubes (called ex situ FFTs) was evaluated [1]. The deformation mode of ex situ FFTs is a combination between individual components, characterised by failure due to propagation of a main crack visible on the outer surface of the tube, a behaviour that is typical for the individual integral-skin foams. This is a well-known behaviour due to constrained deformation of the foam that does not allow to form a plastic hinge. Therefore, in case of materials with low ductility the failure of the tube is easily reached [2]. Yu et al. Studied the impact behaviour and failure mechanism of sandwich beams and optimized the Gibson model was proposed. Quasi-static three-point bending tests at different temperatures were carried out for sandwich beams with aluminium face sheets and closed-cell aluminium foam core in previous study of ours [3-9]. Qin and Wang derived a new yield condition including the effect of the core strength and studied the finite deflection response of a slender sandwich beam with axial restraints or fully clamped transversely loaded by a flat punch. The effects of the elastic properties of the face sheets and aluminium foam cores on the failure modes are not taken into consideration [10]. As pointed out by Steeves and Fleck, this approach is pertinent to the case of sandwich beams with weak face sheets, and it is inappropriate for the case of strong faces [11]. Mujika et al. for determining in-plane shear properties of unidirectional composite materials, consider a three-point bending test stating that normal and shear stresses change from point to point in the specimen, depending on fibre orientation angle and specimen geometry [12]. El-Hassal and Khashaba studied the fatigue behaviour of unidirectional glass fibre reinforced polyester (GFRP) composites under in-phase

combined torsion/bending loading concluding that torsional fatigue strength was significantly lower than pure bending strength and that the endurance limit of combined torsion/bending fatigue strength was approximately half the fatigue limit of pure bending fatigue strength [13]. Meijer et al. investigate the optimum wind angle, lay-up (stacking sequence), diameter, thickness and other variables for the specific loading conditions in order to obtain the best configuration [14]. Fawaz and Ellyin proposed a multi-axial model for life prediction, based on the modification of a reference fatigue curve to account for the actual load ratio and multi-axial loading condition [15, 16]. Quaresimin et al. reanalysed some of the multi-axial fatigue data available in the literature to verify the accuracy of life prediction by Fawaz and Ellyin method and by a polynomial function criterion [17]. Quaresimin and Carraro studied the biaxial fatigue behaviour of unidirectional composites using tubes made of glass/epoxy plies, with the fibres oriented at 90° with respect to the tube's axis and tested under combined tension-torsion loading [18]. The same authors report an extended study using tubular specimens with three different lay-up ([90n], [0f/90u,3] and [0f/90u,3/0f]) tested under combined tension-torsion loadings showing that the presence of shear stress significantly reduces the life spent for initiation of the transverse crack, for a given value of the transverse stress and the crack nucleation resistance of the [0f/90u,3/0f] tubes is slightly higher than that of the [90u,4] ones [19]. Quaresimin et al. compare the evolution of fatigue damage in laminates with measuring on tubes tested under tension-torsion loading conditions. Using a designed lay-up of the laminates able to introduce a local multi-axial stress state comparable to that present in the tubes subjected to external multi-axial loading these authors showed that the evolution of fatigue damage in multidirectional laminates tested under uniaxial cyclic loading and tubes tested under external multi-axial (tension-torsion) loading was basically the same [20]. Schmidt et al. analysed the damage development in glass fibre winding specimens during biaxial fatigue loading using non-destructive testing methods which reveals that initiation of final failure in the specimens is caused by local fibre waviness [21]. El-Kadi and Ellyin observed that for a given maximum stress in tension-tension loading the fatigue life increases with the increasing of stress ratio [22]. El-Assal and Khashaba studied the fatigue behaviour of unidirectional glass fibre reinforced polyester (GFRP) composites under in-phase combined torsion/bending loading concluding that torsional fatigue strength was significantly lower than pure bending fatigue strength and that the endurance limit of combined torsion/bending fatigue strength was approximately half the fatigue limit of pure bending fatigue strength [23].

II. MATERIALS

In this study, glass ($600 \text{ gr} \times \text{m}^{-2}$) fibers were used as fiber material for hollow circular composite shafts; and epoxy resin was preferred as the matrix material. The fiber volume ratio (V_f) of the glass composite material was determined as 45%. The hollow circular composite shafts manufactured from 80mm, 200mm and 250mm-long glass/epoxy material with inner ($D_{\text{inner}}=12\text{mm}$) and outer ($D_{\text{outer}}=17\text{mm}$) diameter, which consisted of three layers, were subjected to three point bending and torsional tests separately. Composite shaft to have

geometrically different lengths (80mm, 200mm and 250mm in length) were utilized (Fig. 1).



Fig. 1. A test specimens of glass/epoxy

III. MANUFACTURED METHOD

As the manufacturing method in this study was used the most commonly used method in the literature called wet filament winding method (Filament winding machine) (Figure 2). The glass fibers were wound over the rollers in the form of three layers at the orientation angles, $\theta=45^\circ$, 60° , 75° , 80° , and 88° . The manufactured circular hollow composite shafts were designed in given lengths according to ASTM standards and were made available for three point bending and torsional tests in accordance with ASTM standards.



Fig. 2. Filament winding machine

IV. EXPERIMENTAL STUDIES

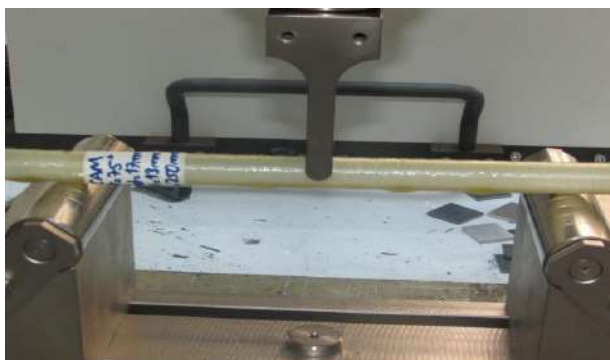
A. Experiment of three point bending

Glass/epoxy hollow circular composite shafts consisting of 3 layers having different lengths (80mm, 200mm and 250mm) and one inner diameter ($D_i=12\text{mm}$) were subjected to three-point bending test (Fig. 3). Three-point bending tests were carried out at room temperature and a test speed of 1 mm x

min-1. According to the ASTM 790-00 standards, maximum tilt values were obtained by applying bending forces to the every center of the shafts for all samples placed between two supports (Fig. 4).



Fig. 3. Test setup for the three point bending test

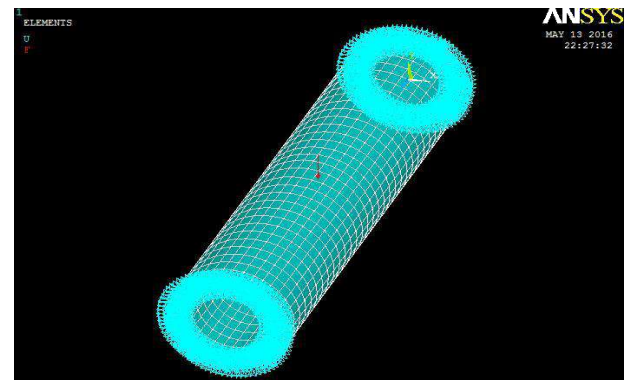


a

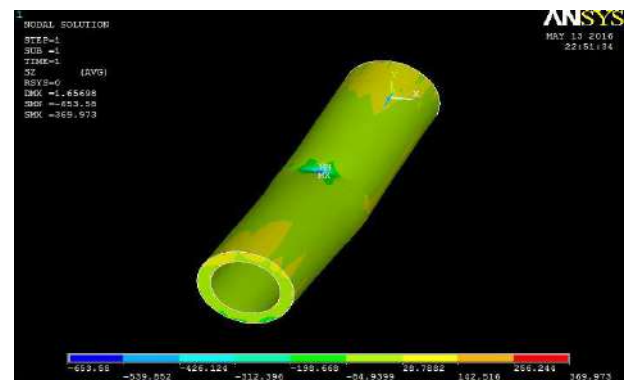


b

Fig. 4. Different lengths of specimens of glass/epoxy subjected to the three point bending test: a) L=250mm, b) L=80mm

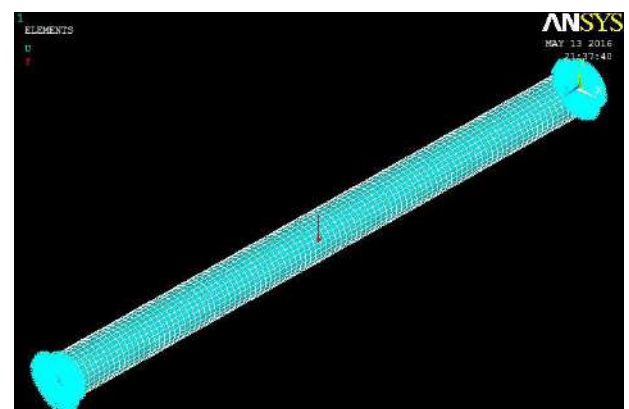


a

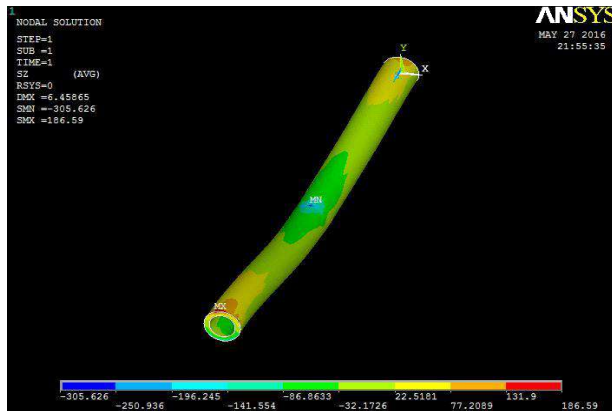


b

Fig.5. Boundary condition of the 80mm long sample of glass/epoxy shafts applied to the three point bending: a) Before ansys, b) After Ansys



a



b

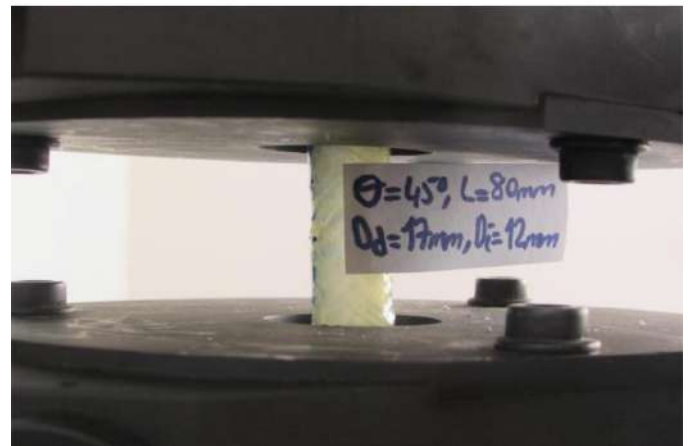


a

Fig. 6. Boundary condition of the 250mm long sample of glass/epoxy shafts applied to the three point bending: a) Before ansys, b) After Ansys

B. Experiment of torsion

The torsion tests were performed at room temperature through the location-type Shimadzu AG-X universal device with 250 kN load cell. The torsion test device operates at the range of 1° - 360° degree/minute (Fig. 7). In this study, the torsion tests were performed at the speed of 20° degree/minute for each sample. In accordance with ASTM standards, all the samples were placed between two jaws in the way that they would be in perpendicular position (Fig. 8). As the result of the fact that the upper jaw remained fixed and the lower jaw turned, a torsion torque was applied on the samples, and then the maximum modulus of rupture in torsion (R_t) was obtained (Fig. 11).

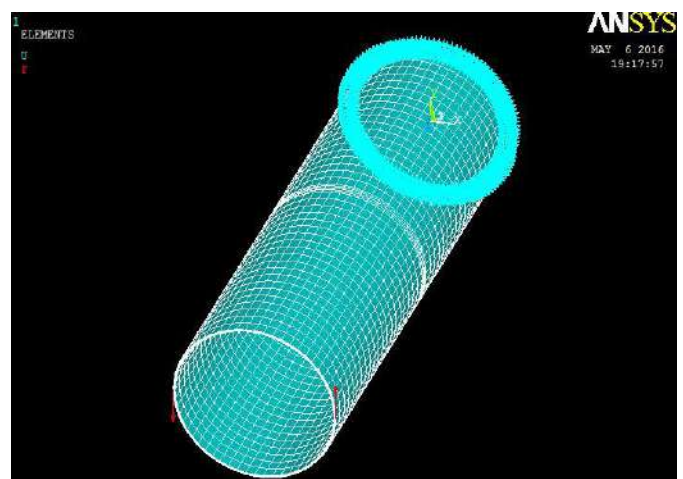


b

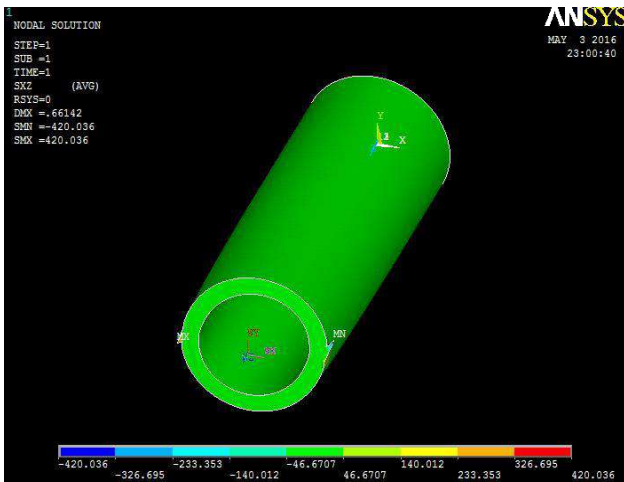
Fig. 8. Different lengths of specimens of glass/epoxy subjected to the torsion test a) $L=250mm$, b) $L=80mm$



Fig. 7. Test setup for the torsion test

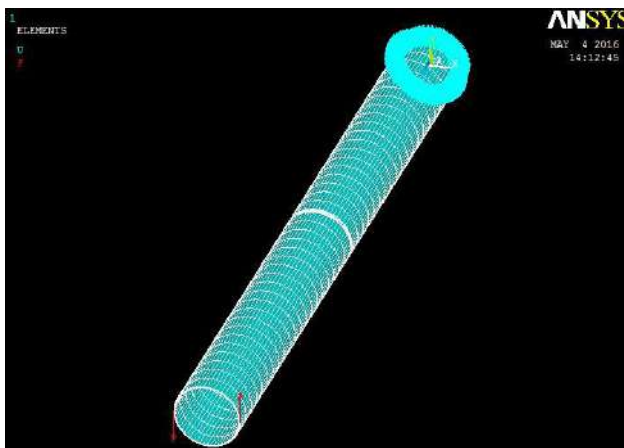


a

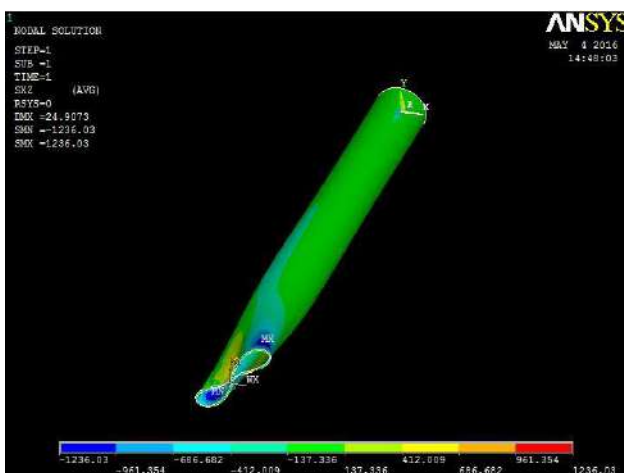


b

Fig. 9. Boundary condition of the 80mm long sample of glass/epoxy shafts applied to the torsion a) Before ansys, b) After Ansys



a

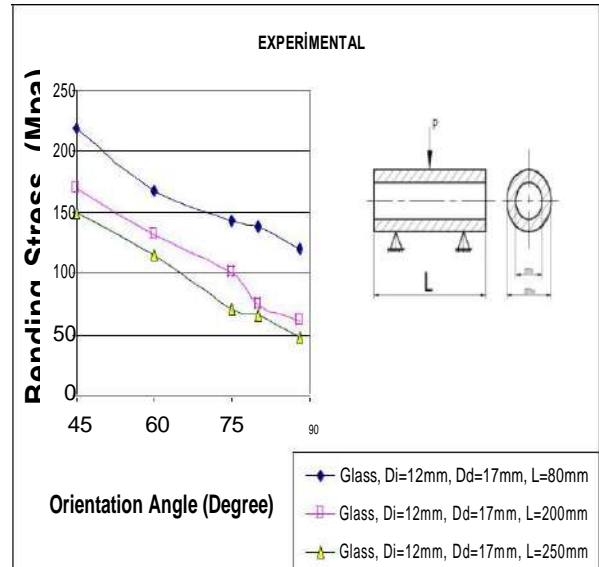


b

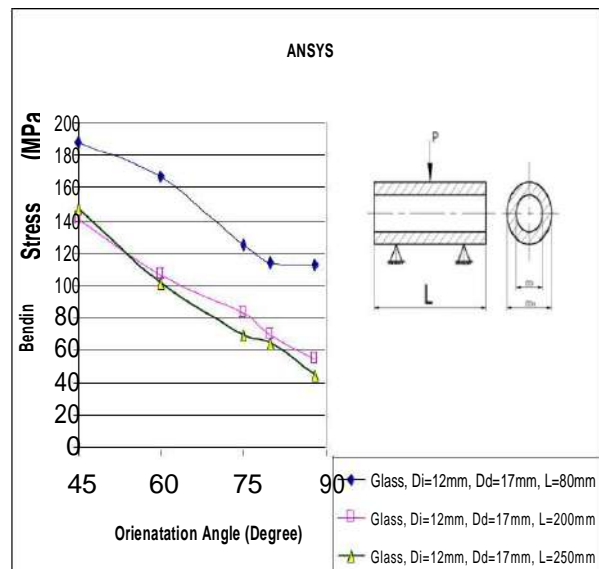
Fig. 10. Boundary condition of the 250mm long sample of glass/epoxy shafts applied to the torsion a) Before ansys, b) After Ansys

RESULT AND DISCUSSION

[11] Effect of orientation angle on bending stress



a



b

Fig. 11. Bending stress- orientation angle and length curve of glass/epoxy for three-point bending stress: a) Experimental, b) Ansys

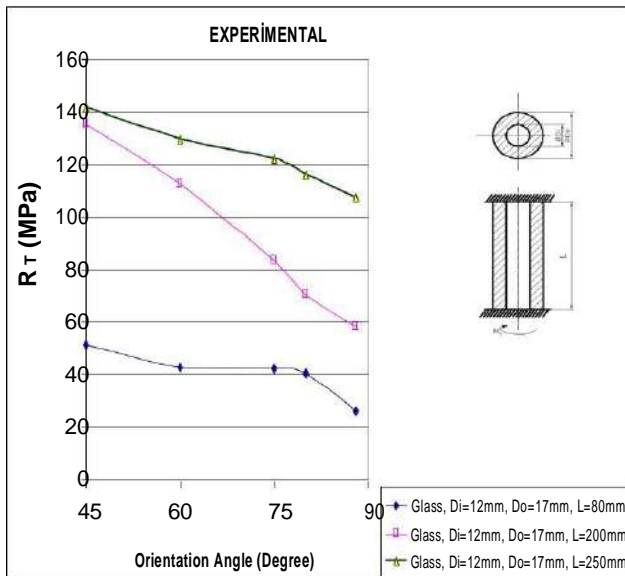
The values of bending stress of glass/epoxy hollow circular composite shafts were analyzed for both experimental and ansys according to the orientation angle,

As displayed in the graphics, it was observed from the both experimental and ansys that the values of bending stresses decrease as the fiber orientation angle is increased (Fig. 11),

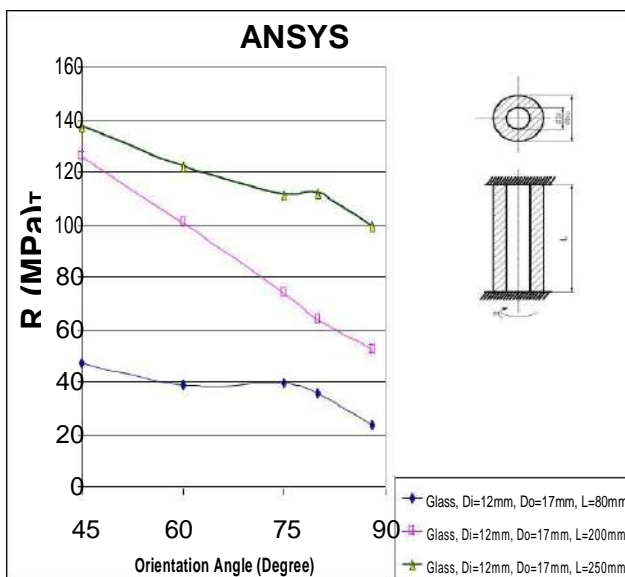
The highest bending stress of three separate hollow circular composite shafts was found to reach a maximum value in both experimental and ansys when the orientation angle is at 45° (Fig. 11),

As will be seen in the graphics; the experimental and numerical analysis results were found to be close to each other (Fig. 11).

□ Effect of orientation angle on modulus of rupture on torsion (R_T)



a



b

Fig. 12. R_T -Orientation Angle and length curve of glass/epoxy for torsion stress; a) Experimental b) Ansys

The values of modulus of rupture in torsion (R_T) of hollow circular glass/epoxy composite shafts were analyzed both experimental and ansys according to the orientation angle. Accordingly;

As will be seen in the graphics; it was observed from both experimental and ansys that as the orientation angle of the fiber increased, the values of the modulus of rupture in torsion of glass/epoxy shafts decreased (Fig. 12).

It was seen that the modulus of rupture in torsion had reached the maximum value in both experimental and ansys when it was at 45° orientation angle (Fig. 12). Separately, since the number of translocations among the fibers will increase once the orientation angle is extended, the values of modulus of rupture in torsion diminishes, as well.

As will be seen in the graphics; the experimental and numerical analysis results were found to be close to each other (Fig. 12)

VI. CONCLUSIONS

In this study, the bending stresses and the modulus rupture in torsion (R_T) of circular hollow shafts manufactured from glass/epoxy composite materials were examined experimentally and numerically at different orientation angles. The circular hollow composite shafts were manufactured by being wound on the rollers at $\theta=45^\circ, 60^\circ, 75^\circ, 80^\circ, 88^\circ$ orientation angles through the use of the filament winding method. Each circular hollow composite shaft that was manufactured was subjected to three point bending and torsion tests. The significant results obtained from the three point bending and torsion tests were mentioned below,

The highest bending stress of hollow circular glass/epoxy composite shafts was found to reach a maximum value in both experimental and ansys when the orientation angle is at 45°,

it was observed that the values of bending stresses in both experimental and ansys decrease as the fiber orientation angle is increased,

It was found that in both experimental and ansys the values of bending of hollow circular composite shafts increase as their wall-thickness increase. This is due to the reduction of the ratio between the inner diameter and the outer diameter. In other words, when the wall-thickness is decreased, it is obvious that the strength will also decrease,

The displacement ratio in the material will also increase as the length of the material increases. Owing to the fact that the deflection is increased as a result of an extension in length, stress ratio will also fall under the same force.

As will be seen in the graphics; it was observed from both experimental and ansys that as the orientation angle of the fiber increased, the values of the modulus of rupture in torsion of glass/epoxy shafts decreased.

It was seen that the modulus of rupture in torsion had[3] reached the maximum value in both experimental and ansys[4] when it was at 45° orientation angle. Separately, since the[5] number of translocations among the fibers will increase once[6] the orientation angle is extended, the values of modulus of[7] rupture in torsion diminishes, as well.

As seen in graphics in both experimental, ansys, three point bending and torsion tests the optimal winding angle was found to be between 45° and 60°,

As will be seen in the graphics in both three point bending and torsion tests; the experimental and numerical analysis results were found to be close to each other.

ACKNOWLEDGMENT

This study was supported by Firat University Scientific Research Coordination Unit (FUBAP) with the project number No: MF 14.03

REFERENCES

- [2] I. Duarte, M. Vesenjak, L. Krstulović-Opara, *Compos Struct*, 2014, 109, 48.
- [3] MH. Shojaeifard, HR. Zarei, R. Talebitooti, M. Mehdikhanlo, *Acta Mech Solida Sinica*, 2012, 25, 616.
- [4] SA. Karamanos, *Int J Solids Struct*, 2002, 39, 2059.
- [5] JL. Yu, X. Wng, ZG. Wei, EH. Wang, *Int J Impact Eng*, 2003, 28, 331.
- [6] JL. Yu, EH. Wang, JR. Li, ZJ. Zheng, *Int J Impact Eng*, 2008, 35, 885.
- [7] ZB. Li, ZJ. Zheng, JL. Yu, CQ. Qian, FY. Lu, *Compos Struct*, 2014, 111, 285.
- [8] QH. Qin, TJ. Wang, *J Appl Mech*, 2012, 79, 041010.
- [9] CA. Steeves, NA. Fleck, Part I: analytical models and minimum weight desig., *Int J Mech Sci*, 2004, 45, 561.
- G. Vargas, F. Mujika, J. *Compos Mater*, 2010, 44, 2487.
- M. El-Assal Ahmed, UA. Khashaba, *Compos Struct*, 2007, 79, 599.
- G. Meijer, F. Ellyin, *Composites: Part A*, 2008, 39, 555.
- L. Parnas, and N. Katirci, *Composite Structures*, 2002, 58, 83.
- M.Z. Kabir, *Composite Structures*, 2000, 49, 247.
- B. Spencer, J. McGee, *Advanced composite material*, Lincon, NE, USA P, 1985, 69–82.
- Fawaz Z, Neale KW. A parametric criterion for biaxial fatigue failure of fibre reinforced composite laminate. *Trans Can Soc Mech Eng* 1990;14(4):93-9.
- Fawaz Z, Ellyin F. Fatigue failure model for fibre-reinforced materials under general loading conditions. *J Compos Mater* 1994;28(15):1432-51.
- Quaresimin M, Susmel L, Talreja R. Fatigue behaviour and life assessment of composite laminates under multiaxial loadings. *Int J Fatigue* 2010;32:2-6
- Quaresimin M, Carraro PA. On the investigation of the biaxial fatigue behaviour of unidirectional composites. *Compos B* 2013;54:200-8
- Quaresimin M, Carraro PA. Damage initiation and evolution in galss/epoxy tubes subjected to combined tension-torsion fatigue loading. *Int J Fatigue* 2014;63:25-35.
- Quaresimin M, Carraro PA, Mikkelsen LP, Lucato N, Vivian L, Bronsted P, Sorensen BF, Varna J, Talreja R. Damage evolution under cyclic multiaxial stress state: a comparative analysis between glass/epoxy laminates and tubes. *Compos B* 2014;61:282-90.
- Schmidt F, Rheinfurth M, Horst P, Busse G. Effects of local fibre waviness on damage mechanisms and fatigue behaviour of biaxially loaded tube specimens. *Compos Sci Technol* 2012;72:1075-82.
- El-Kadi H, Ellyin F. Effect of stress ratio on the fatigue of unidirectional glass fibre/epoxy composite laminates. *Composites* 1994;25(10):917-24
- El-Assal Ahmed M, Khashaba UA. Fatigue analysis of unidirectional GFRP composites under combined bending and torsional loads. *Compos Struct* 2007;79:599-605.

Elasto-plastic stress analysis of V-notched 5754 Al plates

Experimental and numerical approach

Ahmet SAYLIK

Department of Mechanical Engineering
Faculty of Engineering and Architecture
Muş Alparslan University, 49250, Muş, Turkey.
a.saylik@alparslan.edu.tr

Mete Onur KAMAN

Department of Mechanical Engineering
Faculty of Engineering
Firat University, 23119, Elazığ, Turkey.
mkaman@firat.edu.tr

Abstract—In this study, elasto-plastic stress distribution was analyzed V-notched 5754 Aluminum plates by using finite element method, numerically. An experimental study was conducted in order to validate numerical results. Fundamental parameters for notched plates are the notch length and the notch width. With using these parameters, five different notch geometries were prepared. The un-notched and notched specimens were tested under uniform tensile load. Force and displacement graphs of Aluminum plates were obtained at the end of the experiments. Material properties was defined with using un-notched plate test results for input data of the finite element analysis program ANSYS. Firstly, compatible experimental and numerical reaction force-displacement graphs were given then the effect of notch dimensions on the plastic stress distribution was presented with contour graphs.

Keywords—5754 Aluminium; V-notched; elasto-plastic; finite element analysis; stress analysis

I. INTRODUCTION

The materials are damaged in various ways. Much of the damage is caused by structural deformations called fractures. The purpose of the studies related to fracture is to be able to increase the structural strengths of the materials with higher values. Numerical modeling is widely used to investigate the mechanical properties and failure of materials such as isotropic and composites. In order to obtain real stress distribution on structural components in numerical results, it is very important accurately to define behavior material as input data for numerical programs like ANSYS, ABAQUS. Generally, isotropic materials like Steel, Aluminum etc. show elasto-plastic stress-strain behavior under effect of one dimensional stress situation. So, yield stress and non-linear stress-strain behaviors of these type materials must be known. Today, numerical studies concentrate to this research area of elasto-plastic materials with using finite element method.

An experimental and numerical study was conducted to measure the distribution of stresses occurring on the bolt passage region of the bolt-on joints using hybrid composites. According to the analysis of two models developed according to finite element models, hybrid composites have shown that they increase mechanical strength in bolted joints [1]. Models were developed by measuring the responses of braided composites

during elasto-plastic analysis of the matrix during biaxial loading [2]. In order to investigate the mechanical behaviors of the assembled structures in composite layers, numerical models were created and elasto-plastic analyzes were made to produce solutions [3-4]. It was developed numerical models with elasto-plastic analyzes in the detection of damage progression in different axial loading states of reinforced composite [5-6]. Damage determinations were made by performing elasto-plastic analysis of the composite plates prepared with different notched and perforated fiber cores [7]. A new orthotropic elasto-plastic constitutive model has been developed to predict the inelastic response of composite materials under high velocity impact conditions [8]. Nonlinear material response of a sandwich beam with bilinear elasto-plastic constitutive relations for the transverse normal and shear stresses of the core based on the proposed high order sandwich panel theory was improved [9]. A ductile fracture model developed for V-notched structural steels under three-axis tensile loading was developed and analyzed [10]. For elasto-plastic materials, the effect of the material length and crack length on the Q-stress value near the crack tip was investigated under tension [11]. The elasto-plastic damage model was applied to analyze the finite elements of structural joints and the feasibility of the connections in the developed model was verified [12]. Evaluation of notch effects in low cycle fatigue problems generally requires strain calculations. The numerical model was prepared in V-notched form, and the effects of elasto-plastic normal stresses were investigated in predicting the notch behavior during stress. [13]. The fracture behavior under torsion of v-notched round bars made of gray cast iron was investigated. The results showed that Mod III can help evaluate the numerical and theoretical models for fracture of notches in load [14]. Stress-strain comparisons were made during the loading of V-notched Aluminum plates depending on the notch size change. Elasto-plastic analyzes were carried out for tensile behavior in the cracked region in notched plates to develop different numerical models [15-16].

In this study, elasto-plastic stress behavior of V-notched 5754 Aluminum plates is investigated with numerical analysis. Firstly, load-displacement graphs of un-notched Aluminum plates were obtained at the end of tensile tests. Material model of 5754 Aluminum was defined in finite element package program with using stress-strain graph of un-notched plates.

Numerical analyzes were achieved for different notch lengths and depths. Obtained reaction force-displacement results of numerical study were compare with experimental test results. Plastic stress distributions on plate for different V-notch geometries were given with using contour plots.

EXPERIMENTAL STUDY

[12] Preparing V-Notched Specimens

V-notched 5754 Al plates were prepared for the experimental tests with the dimensions of $H=200\text{ mm}$ in length and $W=40\text{ mm}$ in width from the $t=1.94\text{ mm}$ thick as shown in Fig. 1. In Fig. 2, Aluminum plates which have totally five different notch types are shown. Three specimens were prepared from each test. The dimensions of the Aluminum plates used in this study are shown in Table 1.

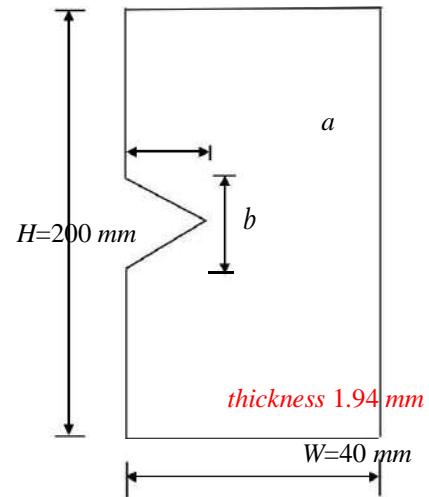


FIGURE. 1. DIMENSIONS OF V-NOTCHED ALUMINUM PLATE.

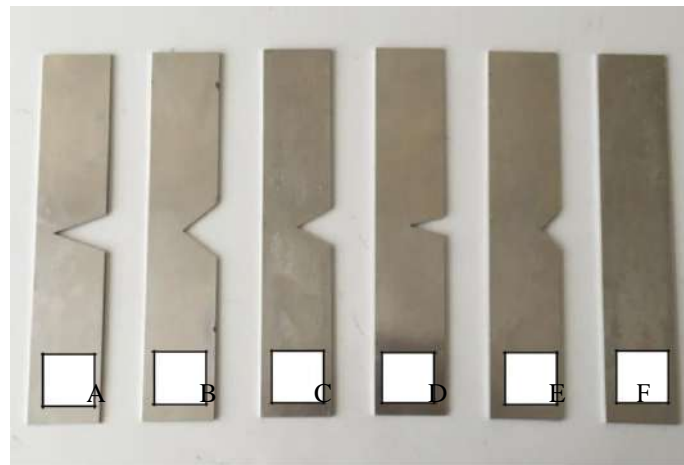


FIGURE. 2. SPECIMEN TYPES PREPARED FOR THE EXPERIMENTS.

TABLE 1. DIMENSIONS OF THE V-NOTCHED SPECIMENS PREPARED FOR EXPERIMENTS.

Specimen Type	$a\text{ (mm)}$	$b\text{ (mm)}$
A Specimen	30	20
B Specimen	20	30
C Specimen	20	20
D Specimen	20	10
E Specimen	10	20

B. Tensile Testing

Three Aluminum specimens of each type notch were prepared. Tensile test was applied to all the specimens. Tensile tests were performed at the speed of 1 mm/min on an Instron 8801 tensile test machine. Tensile tests of Aluminum plates

varying according to notch width and length have been made and finally, the load-displacement values of the plates were recorded and graphics were obtained. To determine the mechanical properties yield stress, Young module etc. of the 5754-Aluminum plate, the un-notched specimens were tested.

C. Experimental observations and results

Graphs were drawn by taking the test results of all Aluminum plate types subjected to tensile test. The stress-strain diagram of the 5754 Aluminum plate without the notch is as shown in Fig. 3. As a result of the tests, the mechanical properties of the 5754-Al plate were determined and are shown in Table 2. The load-displacement graph of un-notched Aluminum plates and notched plates is as shown in Fig. 6. Maximum load values of notched Aluminum plates in Fig. 4, the maximum elastic load values of the plates are shown in Fig. 5, so the effect of the notch size variation is compared.

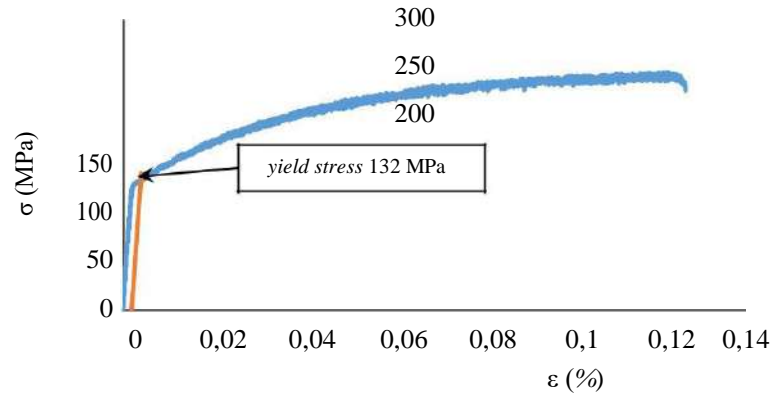


FIGURE. 3. STRESS-STRAIN DIAGRAM OF 5754 ALUMINUM ALLOY PLATE.

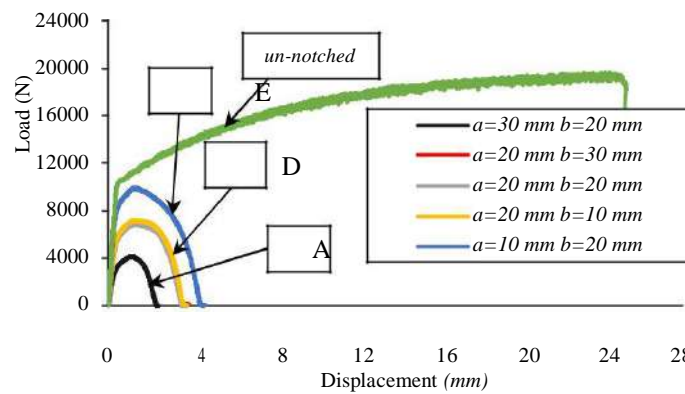


FIGURE. 4. LOAD-DISPLACEMENT GRAPH OF AL ALLOY PLATES FOR DIFFERENT NOTCH LENGTHS.

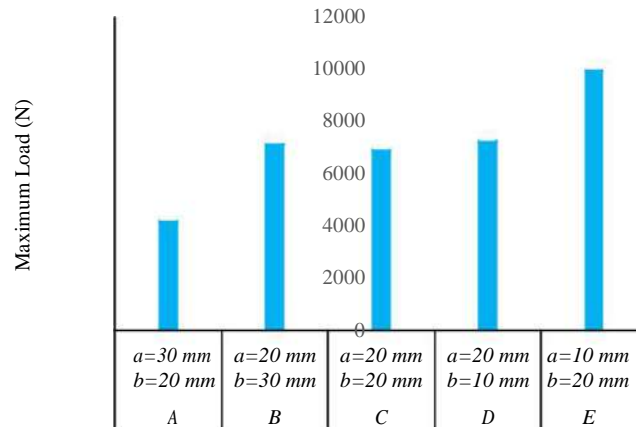


FIGURE. 5. MAXIMUM LOAD VALUES OF V-NOTCHED SPECIMENS FOR TENSILE TEST.

modeling was done in ANSYS. A finite element model was created for the V-notched plate.

III. FINITE ELEMENT ANALYSIS

A. Modeling of V-notched plate

Data obtained from experimental tests were used for elasto-plastic stress analysis of numerical models. In order to analyze the stresses on the plates used in the study, V-notched plate

The mechanical properties of the Aluminum plate shown in Table 2; Young module (E): 69000 MPa, Poisson's ratio (ν): 0.33 and *SOLID186* element type were entered in ANSYS program.

Approximately, 4300 elements and 25000 nodes used in mesh. Solution analyzes were performed in the range of $\Delta L = 1.5 \text{ mm}$ elongation values in horizontal direction ($-x$ axis) and reaction force values of plate were calculated and graphs were prepared.

Elasto-plastic stress analysis was performed for the solution of the prepared model. The finite element mesh model prepared for V-notched plates is shown in Fig 7.

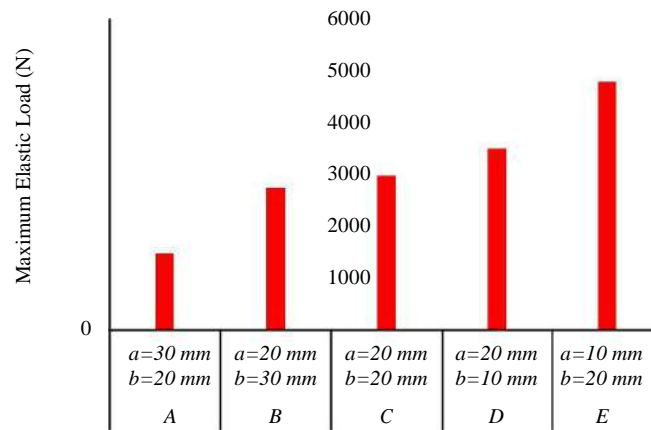


FIGURE 6. MAXIMUM ELASTIC LOAD VALUES OF

V-NOTCHED SPECIMENS FOR TENSILE TEST.

TABLE 2. MECHANICAL PROPERTIES OF THE 5754 ALUMINUM PLATE.

Shear module (G)	25940 MPa
Tensile strength (X_T)	246.72 MPa
Elongation at fracture (ϵ_K)	0.126
Young module (E)	69000 MPa
Poison's ratio (ν)	0.33
Yield stress (σ_Y)	132 MPa

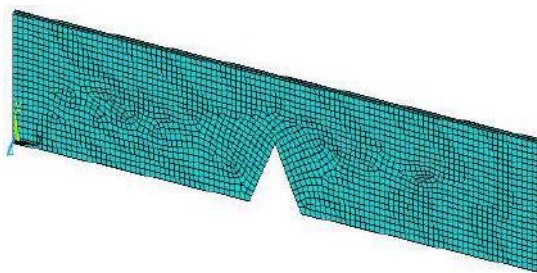


FIGURE 7. MESH MODEL OF V-NOTCHED SPECIMEN FOR C SPECIMEN.

B. Stress Analysis Results

Reaction forces and stress distributions were obtained according to the type of each sample that was created by the model. For example; in the graph shown in Fig. 8, the experimental results of the E specimens and the load-displacement values of the numerical results are compared. It can be seen that results of experiments and numerical analysis are compatible in Fig. 8.

For V-notched Aluminum plate types, stress analysis was performed by choosing constant elongation value ($\Delta L = 0.05 \text{ mm}$). The σ normal stress distributions, on the notch regions of Aluminum sheets are shown in Fig. 9. The stress distribution of all samples is plotted at the same maximum and minimum stress range. It can be said that normal stress increases with increasing notch depth. On the other hand, notch width is a not effective parameter as notch depth on stress distribution.

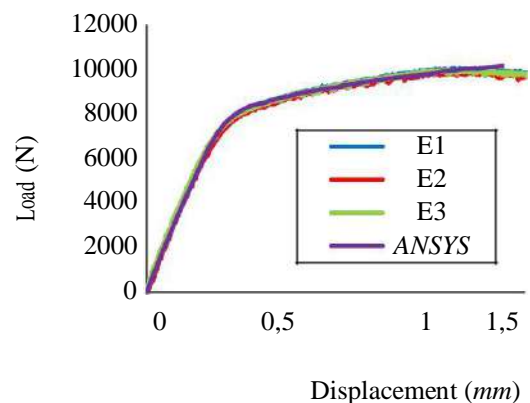


FIGURE 8. COMPARISON OF EXPERIMENTAL AND NUMERICAL RESULTS OF A = 10 MM, B = 20 MM V-NOTCHED SPECIMEN.

Fig. 10 shows variation of plastic stress distribution in loading axis with different elongation values for C specimen ($a = b = 20 \text{ mm}$). Normal stresses increase with increasing elongation values. Maximum stress values are obtained at notch tip. On the other hand, stress concentrations are seen near the notch tip zone. Plate start to the bending situation for a large values of elongation. So, negative stress values are read opposite of notch tip on free plates edges.

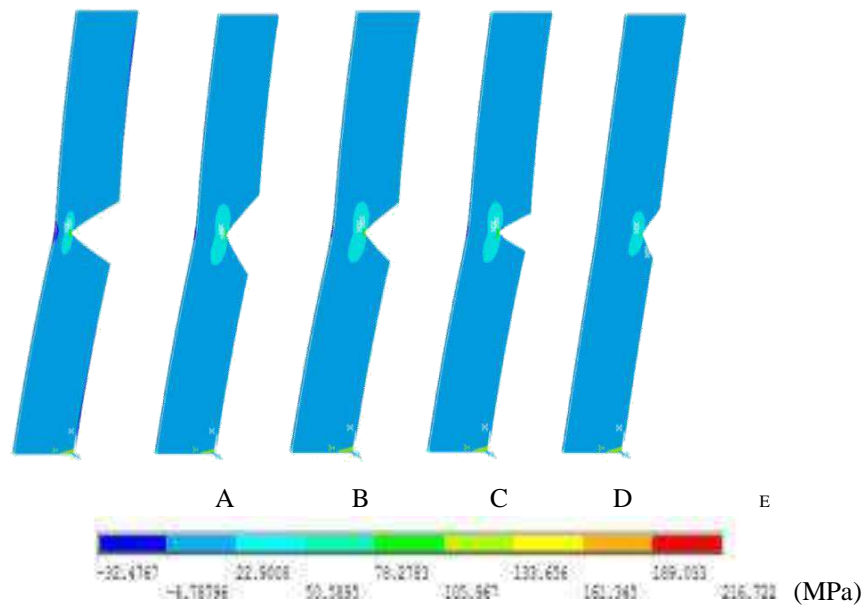


FIGURE 9. STRESS DISTRIBUTION OF V-NOTCHED ALUMINUM PLATES FOR $\Delta L = 0.05$ MM.

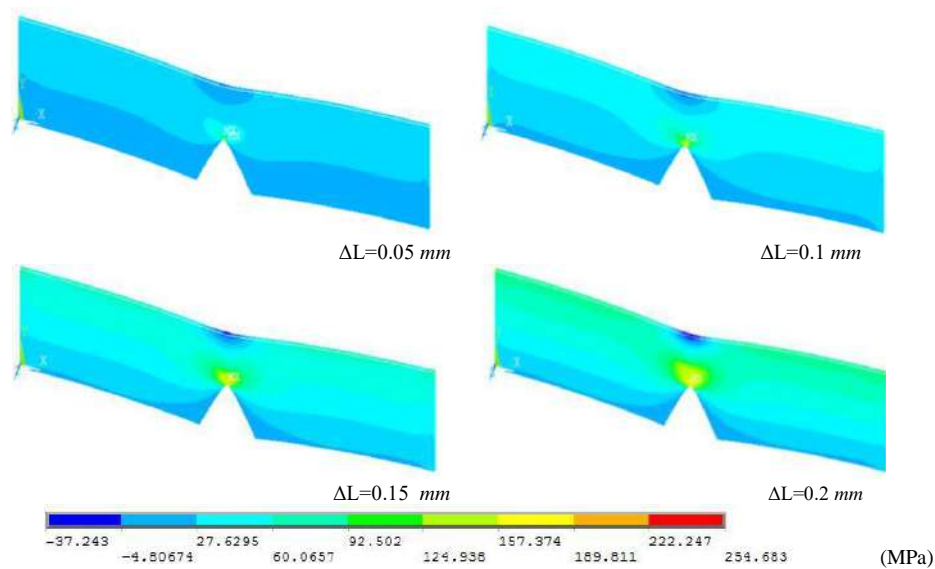


FIGURE 10. VARIATION OF PLASTIC STRESS DISTRIBUTION IN LOADING AXIS WITH DIFFERENT ELONGATION VALUES FOR C SPECIMEN.

IV . CONCLUSIONS

In this study, non-linear stress analysis was performed of Defects like notch and crack etc. on plates are very dangerous for strength. This situation is approved with experiments method and stress analyzes obtained from ANSYS package showed that elongation of un-notched plates is so much bigger than notched plates. The results of the study can be summarized as follows:

- When the behavior of the Aluminum plates under the tensile load is evaluated, the notch width is constant; It has been observed that as the notch length of the plate decreases, the values of maximum load, maximum elastic load and elongation amounts increase very clearly.

- When the behavior of the Aluminum plates under the tensile load is evaluated, the notch length is fixed; It has been observed that as the notch width of the plate decreases, the values of maximum load, maximum elastic load and elongation amounts increase at the small ratios.
- It has been observed that the load values change more significantly in the evaluations made due to the reduction of the notch depth, opposite to the notch width. So, it can be said that V-notch depth is more important parameter than V-notch width for tensile loading in plates.
- In order to obtain numerical results of sample types; yield values were obtained from the stress-strain diagram of the Aluminum material obtained from the experimental results for un-notched plate. This data was analyzed by elasto-plastic stress analysis in ANSYS.
- V-notched Aluminum plate models were calculated by performing elasto-plastic analysis for the reaction forces versus the determined elongation amount of ΔL . As shown in Figures, experimental and numerical results are found to be very close to each other in all plate models.
- When the stress analysis of V-notched Aluminum plates is examined; It is seen that the greatest stresses on the plate concentrate on the tip of the notch.
- Plate models in which the same notch width is constant and the notch neck variation is numerically solved. It has been observed that the C sample ($a = 20 \text{ mm}$ $b = 20 \text{ mm}$) has the greatest σ_x normal stress value.
- Designers of structural components should decide and define their design considering notch depth and effect of non-linear stress behavior should be investigated for ductile materials analysis due to compatible experimental and numerical results.

ACKNOWLEDGMENT

The authors would like to thanks to the Department of Mechanical Engineering, Faculty of Engineering, Dicle University for assistance in performing tensile tests of Aluminum plates used in the works.

REFERENCES

- [1] P.P.Comanho, A.Fink, A. Obst, S.Pimenta, "Hybrid titanium-CFRPlaminatesforhigh-performance boltedjoints", Composites:Part A 40 ,2009, pp.1826-1837.
- [2] N.V. De Carvalho, S.T.Pinho, P.Robinson, "Numerical modelling of woven composites: Biaxial loading", Composites:Part A 43,2012, pp.1326-1337.
- [3]A.Riccio , R. Ricchiuto, F. Di Caprio, A. Sellitto, A. Raimondo, "Numerical investigation of constitutive material models on bonded joints in scarf repaired composite laminates", Engineering Fracture Mechanics, 2017.
- [4]Jing-Fen Chen and Evgeny V. Morozov, "A consistency elasto-viscoplastic damage model for progressive failure analysis of composite laminates subjected to various strain rate loadings", Composite Structures 148, 2016, pp. 224-235.
- [5]R. Higuchi, T.Okabe, T. Nagashima, Numerical simulation of progressive damage and failure in composite laminates using XFEM/CZM coupled approach", Composites:Part A 95, 2017, pp.197-207.
- [6]A.Dean, J.Reinoso, S. Sahraee, R.Rolfes, "An invariant-based anisotropic material model for short fiber-reinforced thermoplastics: Coupled thermo-plastic formulation", Composites:Part A 90, 2016,pp.186-199.
- [7]L.Wu, L. Noels, L.Adam, L. Doghri, "An implicit-gradient-enhanced incremental-secant mean-field homogenization scheme for elasto-plastic composites with damage", International Journal of Solids and Structures 50, 2013, pp.3843-3860.
- [8]C. Hoffarth , S. D. Rajan , R. K. Goldberg , D. Revilock , K.S. Carney , P. Dubois , G. Blankenhorn, "Implementation and validation of a three-dimensional plasticity-based deformation model for orthotropic composites", Composites:Part A 91,2016, 336-350.
- [9]S.J. Selami, M. Sadighi , M. Shakeri, "Improved high order analysis of sandwich beams by considering a bilinear elasto-plastic behavior of core: An analytical and experimental investigation", International Journal of Mechanical Sciences, vol. 93, 2015, pp. 270-289.
- [10] L. Kang, H. Ge, X. Fang, " An improved ductile fracture model for structural steels considering effect of high stress triaxiality", Construction and Building Metaterials, vol. 115, 2016, pp. 634-650.
- [11] M. Graba," The influence of material properties and crack length on the Q -stress value near the crack tip for elastic-plastic materials for single edge notch plate in tension", Archives of Civil and Mechanical Engineering, vol. 11, 2011, pp. 2.
- [12] P. Jousset and M. Rachik, "Implementation, identification andvalidationofan elasto-plastic damage model for the finite element simulation of structural bonded joints", Internatinal Journal of Adhesion & Adhesives", vol. 50, 2014, 107-118.
- [13] M.A. Meggiolaro, J.T.P. Castro, R.C.O. Goes, "Elastoplastic nominal stress effects in the estimation of the notch-tip behavior in tension", Theoretical and Applied Fracture Mechanics, vol.84, 2016, pp. 86-92.
- [14] F.Berto, D.A.Centon, M.Elices, "Fracture behavior under torsion of notched round bars made of gray cast iron", Theoretical and Applied Fracture Mechanics, vol.84, 2016, pp. 157-165.
- [15] P.Gallo, F. Berto, G.Gilinka, "V-notched components under non-localized creeping condition: numerical evaluation of stresses and strains", Structural Integrity Procedia 2, 2016, pp. 809-816.
- [16] A.R. Torabi and M. Keshavarzian, "Evaluation of the load-carrying capacity of notched ductile plates under mixed mode loading", Theoretical and Applied Fracture Mechanics, vol. 85, 2016, pp. 375-386.

A Numerical Study of Heat Transfer and Fluid Flow in a Wavy Duct with Rectangular Blocks Mounted Upper Wall

Gülten GÜLDEMİR

Firat University
Engineering Faculty, Mech. Eng. Dept.
Elazığ, Turkey
gguldemir@gmail.com

İhsan DAĞTEKİN

Firat University
Engineering Faculty, Mech. Eng. Dept.
Elazığ, Turkey
idadtekin@firat.edu.tr

Mehmet DURANAY

Firat University
Engineering Faculty, Mech. Eng. Dept.
mduranay@firat.edu.tr

Abstract— In this study, laminar flow and heat transfer in a duct mounted rectangular blocks (electronic components) to the duct upper surface and sinusoidal undulating bottom wall are numerically investigated. Two simulated electronic components are subjected to a uniform heat flux of 250 W/m². The lower and upper surface of the duct is insulated. As the working fluid Air is used (Pr = 0.71). Computations are conducted for different Reynolds numbers (Re = 500, 1000, 1500, 2000, 2500). The steady state, incompressible, two-dimensional and laminar flow were considered cases. The wavelengths and wave amplitude of sinusoidal surface of the duct are varied from 0.02 to 0.08 during the analysis. Obtained results have been presented as local Nusselt numbers and shear stress.

Keywords— Laminar flow, Sinusoidal Surface, Friction factor, Electronic Components (Blocks)

• INTRODUCTION

System temperature is crucial for efficient and safe operation of the systems. The heat generated for system security must be removed from the system. At present, many researchers are working on the development of more efficient cooling system not to exceed a certain value of temperature of electronic components [1]. Because of inadequacy of forced and natural convection mechanisms for heat transfer to outside (operating temperature must be below 70°C), usage of microchannel cooling system which has high ratio of heat transfer area to volume has gained high importance. These systems include many microchannel in different geometry of the structure. For an optimum design, the flow and heat

transfer characteristics of the channel (heat transfer coefficient, friction factor, hydraulic diameter, number of channels, etc.) need to be known.

Nomenclature

μ	: Dynamic viscosity (Pa.s)
a	: Amplitude (m)
h	: Heat transfer coefficient (W/m ² K)
h	: Block height (m)
H	: Channel height (m)
k	: Thermal conductivity (W/m.K)
L	: Channel length (m)
Nu_{mean}	: Mean Nusselt number
Nu_x	: Local Nusselt number
p	: Wavelength (m)
ϕ	: Viscose loss function
T_o	: Flow inlet temperature (K)
U_o	: Inlet velocity (m/s)
u, v, y	: Velocity components in x, y and z directions respectively (m/s)
w	: Block width (m)
x, y, z	: Dimensionless Cartesian coordinates
ν	: Kinematic viscosity (m ² /s)
ρ	: Fluid density (kg/m ³)
τ	: Surface shear stress $\tau = \mu \frac{du}{dy}$ (N/m ²)

In this study, the effect of sinusoidal surface on the cooling of electronic components in a rectangular channel has been investigated. Firstly, the effect of the fluid surfaces at different Reynolds numbers of components in a rectangular channel has been examined. The local and mean Nusselt numbers have been obtained. Secondly, components bottom surface have been changed as sinusoidal surface and analysed with different amplitude and Nusselt number value on the components surface for the period. The ratio between these two results (Numean-u/Numean-s) is calculated. In addition to this, surface shear stress on the block surface over undulated surface have been presented.

[13] LITERATURE

In today, many electrical and electronical items that contain electronic circuit structure have been widely used in the global world. When electronic circuits expose to electrical current,

Electrical current on electronic circuits causes heat rising and power loss of the system ($P = I^2R$). The amount of power loss must be same with the amount of power that was previously specified in catalogues. Once the system exceeds the specified amount, they can not work safely and efficiently. In the electronic circuits temperature rise is uncontrollable so, cooling method for such systems is emerged. There are lots of previous studies about cooling of the system in the literature. Furthermore, new researches on cooling for the electrical circuit continue to increase day by day.

Mohammed et al. [2] numerically studied of the effect of using nanofluids on heat transfer and fluid flow characteristics in rectangular shaped microchannel heat sink (MCHS) for wave amplitude range of $125 \mu\text{m}$ - $500 \mu\text{m}$. In microchannel heat sink (MCHS), water flow and heat transfer have been simulated and the results compared with straight microchannel. As a result of simulation, the performance of MCHS has been recorded better than straight microchannel in the same section. Furthermore, increasing the amplitude of the microchannel led to increase both friction factor and shear stress.

Wang and Chen [3] researched the rates of heat transfer for Newtonian fluid (laminar, incompressible, steady and 2D) through symmetrical undulating wall using a simple coordinate transformation method. The impacts of the wavy geometry, Prandtl number and Reynolds number on the skin-friction and Nusselt number have been analysed in detail. The results present that increasing Reynold number and the amplitude-wavelength ratio caused to increase the amplitudes of the Nusselt number and the skin-friction coefficient.

Guzmán et al. [4] examined the enhancement characteristics of heat transfer in asymmetric wavy wall channels using the spectral element method on simulations of the mass, momentum and energy equations. The heat transfer characteristics, transition scenarios and flow bifurcation were determined by increasing the Reynolds numbers for three geometrical structures. With this study, notable heat transfer enhancements were captured during the appropriate

transitional Reynolds number range for asymmetric wavy channel.

Sui et al.[5] studied laminar liquid-water flow and heat transfer using numerical simulation for three-dimensional wavy microchannels with rectangular cross section. The simulation results figure out that when liquid coolant flows through the wavy microchannels, secondary flow (Dean Vortices) may be generated during the liquid coolant flowing through the wavy microchannels. Furthermore, quantity and the vortices location can change on the flow direction, leading to chaotic advection, which may greatly effect and increase the convective fluid mixing. Therefore, the wavy microchannel shows much better heat transfer performance that of straight microchannel at the same cross section. It was observed that the pressure drop of the present wavy microchannels may be much smaller than the heat transfer enhancement. Moreover, the relative wavy amplitude of the microchannels on the flow direction can be changed for different useful aims.

Szumbariski et al. [6] theoretically and numerically analysed the issue of mixing enhancement a viscous incompressible flow in a channel with wavy walls. The obtained results were compared and the first experimental results were verified with the same rectangular cross-section flow channel.

□ PHYSICAL GEOMETRY AND SOLUTION METHOD

A. Physical Properties and Geometry

This study has been conducted with ANSYS software. The differential equation problems have been solved by algebraic equations. Then, velocity and temperature distribution have been determined in the solution area. The geometry of the problem was displayed in the subsequent Figure 1. Upper and bottom surfaces of the channels were insulated. In order to obtain flow and heat transfer characteristics of the problem, continuity, momentum and energy equations have been utilized with the boundary conditions. In the research, air and its thermal properties at temperature of 25°C were used as the fluid. The vertical component of the fluid velocity has been assumed to be zero.

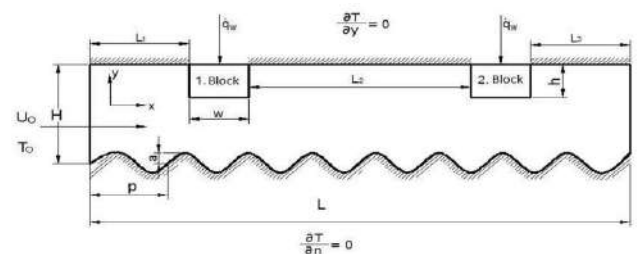


Fig. 1. Physical geometry and parameters

Some parameters used in the model geometry are given below.

$$\begin{aligned} Y &= a \sin(\pi x/p) & w &= 2/3H & H &= 0.06 \text{ m} \\ L_2 &= 0.20 \text{ m} & L_3 &= 0.18 \text{ m} & L &= 0.64 \text{ m} \\ h &= 1/3H & L_1 &= 0.18 \text{ m} \end{aligned}$$

The continuity, momentum and energy equations and boundary conditions for the problem can be written as:

Continuity equation:

$$\frac{\partial u}{\partial x} + \frac{\partial v}{\partial y} + \frac{\partial w}{\partial z} = 0 \quad (1)$$

X-Momentum equation:

$$\rho \left(\frac{\partial u}{\partial t} + u \frac{\partial u}{\partial x} + v \frac{\partial u}{\partial y} + w \frac{\partial u}{\partial z} \right) = -\frac{\partial P'}{\partial x} + \mu \left(\frac{\partial^2 u}{\partial x^2} + \frac{\partial^2 u}{\partial y^2} + \frac{\partial^2 u}{\partial z^2} \right) \quad [10]$$

Y-Momentum equation:

$$\rho \left(\frac{\partial v}{\partial t} + u \frac{\partial v}{\partial x} + v \frac{\partial v}{\partial y} + w \frac{\partial v}{\partial z} \right) = -\frac{\partial P'}{\partial y} + \mu \left(\frac{\partial^2 v}{\partial x^2} + \frac{\partial^2 v}{\partial y^2} + \frac{\partial^2 v}{\partial z^2} \right)$$

Energy equation:

$$\rho c_p \left(u \frac{\partial T}{\partial x} + v \frac{\partial T}{\partial y} + w \frac{\partial T}{\partial z} \right) = k \left(\frac{\partial^2 T}{\partial x^2} + \frac{\partial^2 T}{\partial y^2} + \frac{\partial^2 T}{\partial z^2} \right)$$

Boundary conditions:

Channel inlet: $u = U_0$, $v = 0$ and $T = T_0$

Channel upper and bottom surfaces: $u = v = 0$

Heat flux on the block surfaces: $q = 250 \text{ W/m}^2$

Nondimensional numbers: $Nu_x = h_x/k$, $Re = U_0 H/\nu$

B. Benchmark for Validation

Mabarki et al. [14] numerically analysed the laminar flow and heat transfer regimes using forced convection in a rectangular horizontal channel. In order to simulate electronic components three blocks have been mounted to the bottom wall of the channel. Each block is 0.25 cm height (h), 2 cm width (w). The 2-D horizontal plane channel is 1 cm height (H) and 20 cm length (L). The fluid temperature and heat flux generated by each block have been taken 20°C and 1000 W/m², respectively. The upper and bottom walls have been assumed as adiabatic. The working fluid has entered to the channel with uniform velocity and temperature. A rectangular cross section bar has been mounted to the upper wall to increase heat transfer rate and control the fluid flow.

As a result of the research, the best enhancement of heat transfer was observed by a rectangular control element attached to the upper wall of the channel. The study proves that the control element significantly effects to increase heat dissipation and causes to reduce the temperature of the blocks simulated the electronic components. For Reynolds number of 547, maximum local Nusselt numbers have been obtained on 1st block upper left corner and 2nd block top corner, $Nu_x = 23$ and $Nu_x = 16$, respectively.

In order to verify this research, same conditions, materials and parameters, which were used in Mabarki's study [14], have been selected and solved for the defined problem. At the end of the calculation, simulation results proved that outputs were nearly same when compare Mabarki's research [14]. For instance, in this study, maximum local Nusselt numbers of 1st and 2nd blocks have been recorded as $Nu_x = 24$ and $Nu_x =$

10.5, respectively. Figure 3.2 presented the some results of current study and Mabarki's study for validation.

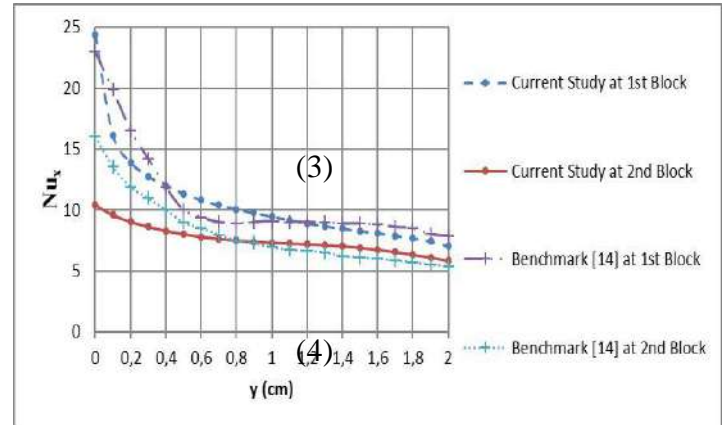


Fig. 2. Comparison of Nu_x values for both blocks ($Re = 547$)

IV. RESULTS AND DISCUSSION

A. Analysis of Local Nusselt Numbers on Undulated Channel

In the following figures, variation of Nu_x numbers have been defined at a channel with undulated surface and heated blocks surfaces. These expressions, characterized heat transfer from blocks to fluid, have been obtained temperature distribution results in solution of Navier-Stokes and energy equations. According to the results, the maximum local Nu_x number has been observed at the left bottom corner of the 1st block. The Nu number values have decreased through flow direction of the bottom surface and continued to reduce at the right surface of the block. Furthermore, the effect of Nu numbers on the bottom surfaces of the blocks are higher than that of the side surfaces of the blocks. This is because enhancement of the heat transfers from block surface to fluid results from deterioration and rupture of the boundary layer [1]. The same fluctuations are observed on the 2nd block as well.

Fig. 1. shows heat transfer variations in the channel with referencing amplitude and wavelength of undulated surface, the maximum local Nusselt number (Nu_x) for Reynolds of 2500 has been observed at 1. Block of undulating channel

during the values of $a = 0.02$ (m) and $p = 0.08$. At the rates of $a = 0.005$ and $p = 0.02, 0.04$ and 0.08 , decrease of local Nusselt number (N_{ux}) has been obtained during constant amplitude and high wavelength for all Reynolds number values ($Re = 500, 1000, 1500, 2000, 2500$) used in the analysis. The Reynolds number rates increases, also increasing the N_{ux} numbers. Namely, heat transfer enhances.

Moreover, in Fig. 2. the maximum N_{ux} number has been observed at the conditions as $a = 0.01$ and $p = 0.02, 0.04$ and 0.08 for Reynolds of 2500 and $p = 0.04$ values. Like the previous case, as the Reynolds number increases the N_{ux} numbers are also increasing.

As a result of the evaluations, enhancement of Nusselt numbers has been determined for the constant wavelength and high amplitude. On the other hand, the decreasing of mean Nusselt numbers has been recorded for constant amplitude and double the wavelength.

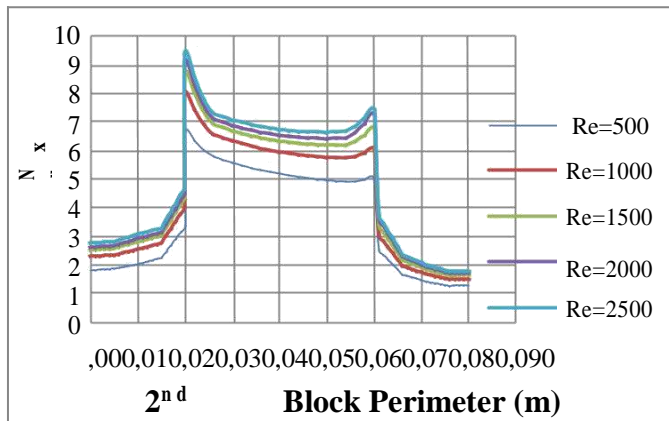


Fig. 3. Change of N_{ux} number with respect to Re number on the 2. Block ($a = 0.005, p = 0.08$)

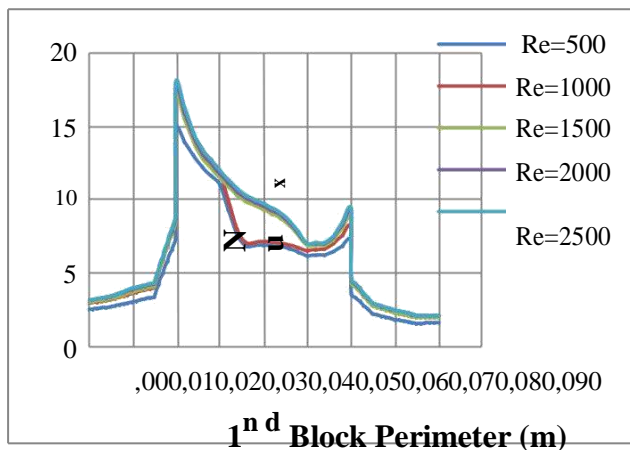


Fig. 4. Change of N_{ux} number with respect to different Re numbers on the 1. Block ($a = 0.02, p = 0.02$)

B. The Ratio of mean Nusselt Numbers on the Undulated Channel to Straight Channel (Nu_{mean-u}/Nu_{mean-s})

Fig. 5 shows the ratio of mean Nusselt numbers on the sinusoidal undulating channel to straight channel (Nu_{mean-u}/Nu_{mean-s}) for various Reynolds numbers. The maximum value in these rates has been noted on second block left surface with Reynolds of 500. Furthermore, the maximum recorded mean Nusselt number can be listed as second block right surface, first block right surface, second block bottom surface, first block left surface and first block bottom surfaces, respectively. Graphic changes indicate the same results that prove such ratio decreases with the increasing of Reynolds number.

In comparison the previous amplitude and wavelength values, different structure occurred as expected with amplitude of $a = 0.02$ and wavelength of $p = 0.04$. At the first block right surface, a parabolic graph change has been observed with the $Re = 500, 1000$ and 1500 . The maximum value takes place with the Reynolds of 1000.

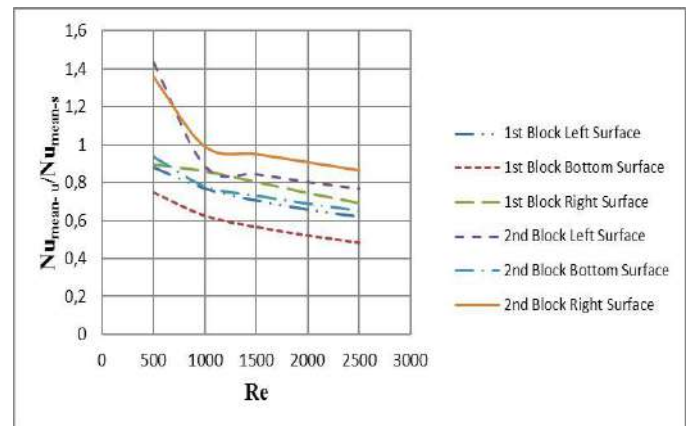


Fig. 5. The ratio of mean Nu numbers on the undulated channel to straight channel (Nu_{mean-u}/Nu_{mean-s}) for different Re numbers ($a = 0.005, p = 0.02$)

Fig. 6 indicates the change of surface shear stress along the block mounted upper wall surface. As it seen as Re number increases surface shear stress is increasing especially on top surface of the blocks.

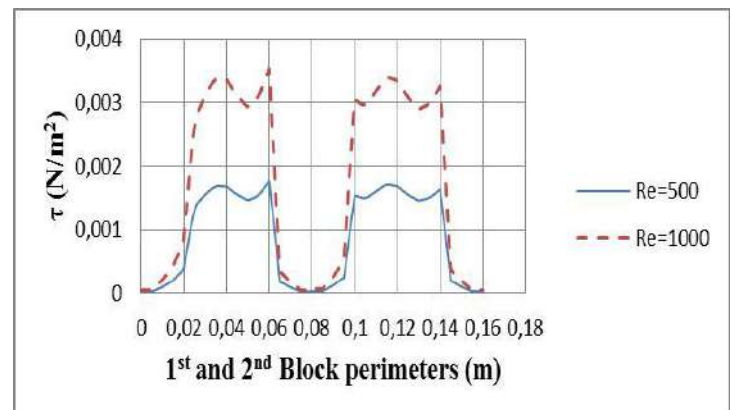


Fig. 6. Changes of surface shear stress values on block surfaces for different Re numbers ($a = 0.02, p = 0.02$)

RESULTS AND DISCUSSION

In this study, laminar flow and heat transfer in a duct mounted two blocks (as electronic components) to the duct upper surface and sinusoidal undulating bottom channel have been analysed numerically. With this study, some obtained important results are summarized as follows:

The maximum Nu number values have been occurred on undulated channel with amplitude of $a = 0.002$, wavelength of $p = 0.008$ and Reynolds of 2500.

Obtained results prove that the as Reynolds number increases local Nux and mean Numean numbers are increasing. That means that the heat removing from electronic components are enhanced.

Another investigation has been performed on Nusselt numbers with different undulated surface periods and amplitude values. As amplitude is fixed with increasing of wavelength local Nusselt numbers, Nux, are decreasing. That is, the heat transfer are decreasing.

Furthermore, as wavelength is fixed with increasing of amplitude local Nusselt numbers, Nux, are increasing. That is, the heat transfer enhances.

REFERENCES

- [1] Demircan, T., 2012. İçerisinde Isıtıcı Bloklar Bulunan Bir Kanalda, Osilasyonlu Akışın ve Isı Transferinin Sayısal ve Deneysel Olarak İncelenmesi, Doktora Tezi, Gazi Üniversitesi Fen Bilimleri Enstitüsü, Ankara.
- [2] Mohammed, H.A., Gunnasegaran, P. and Shuaib, N.H., 2010. Heat Transfer in Rectangular Microchannels Heat Sink using Nanofluids, International Communications in Heat and Mass Transfer, 37 (10), 1496-1503.
- [3] Wang, C. C. and Chen, C. K., 2002. Forced Convection in A Wavy-Wall Channel", International Journal of Heat and Mass Transfer, 45, 2587–2595.
- [4] Guzmán, A. M., Cárdenas, M., Urzuá, F. A. and Araya, P. E., 2009. Heat Transfer Enhancement by Flow Bifurcations in Asymmetric Wavy Wall Channels, 52 (15-16), 3778–3789.
- [5] Sui, Y., Teo, C.J., Lee, P.S., Chew, Y.T. and Shu, C., 2010. Fluid Flow and Heat Transfer in Wavy Microchannels, International Journal of Heat and Mass Transfer, 53 (13), 2760-2772.
- [6] Szumbarski J., Blonski, S. and Kowalewski, T.A., 2008. Flow Destabilization and Chaotic Mixing in The Channel with Transversely Corrugated Walls, XXII International Congress of Theoretical and Applied Mechanics, CD-ROM proceedings ISBN 978-0-9805142-1-6, Adelaide, Australia, August 25-29.
- [7] Ramgadia, A.G. and Saha, A.K., 2012. Fully Developed Flow and Heat Transfer Characteristics in A Wavy Passage: Effect of Amplitude of Waviness and Reynolds Number, International Journal of Heat and Mass Transfer, 55 (9), 2494-2509.
- [8] Wang, G. and Vanka, S.P., 1995. Convective Heat Transfer in Periodic Wavy Passages, International Journal of Heat and Mass Transfer, 38 (17), 3219-3230.
- [9] Rush, T.A., Newell, T.A. and Jacobi, A.M., 1999. An Experimental Study of Flow and Heat Transfer in Sinusoidal Wavy Passages, International Journal of Heat and Mass Transfer, 42 (9), 1541-1553.
- [10] Niceno, B. and Nobile, E., 2001. Numerical Analysis of Fluid Flow and Heat Transfer in Periodic Wavy Channels, International Journal of Heat and Fluid Flow, 22, 156-167.
- [11] Russ G. and Beer, H., 1997. Heat Transfer and Flow Field in A Pipe with Sinusoidal Wavy Surface-I. Numerical Investigation, International Journal of Heat and Mass Transfer, 40 (5), 1061-1070.
- [12] Etemoğlu, A. B., İşman, M. K., Pulat, E. ve Can, M., 2004. Tek Yongalı Elektronik Cihazların Laminar ve Türbülanslı Akışta Soğutulmalarının Analizi, Mühendis ve Makina - Cilt: 45 Sayı: 535.
- [13] Young, T. J. and Vafai, K., 1998. Convective Cooling of A Heated Obstacle in A Channel, International Journal of Heat and Mass Transfer, 41, 3131-3148.
- [14] Mebarki, G., Rahal, S. and Hamza, A., 2013. Heat Transfer Enhancement by Flow Control in a Rectangular Horizontal Channel, International Journal of Materials Mechanics and Manufacturing, Vol. 1, No.

Investigation of Patch Geometry Effects for Patch Bonding Repair in Laminated Composite Materials

Şükrü ÇETİNKAYA

Dicle University, Mechanical Engineering Department, 21280 Diyarbakır/Turkey

Haşim PIHTILI

Fırat University, Mechanical Engineering Department, 23119 Elazığ/Turkey

Hayri YILDIRIM

Dicle University, Diyarbakır Technical Science Vocational School, 21280 Diyarbakır/Turkey

Abstract— For this study, woven glass and carbon fibres reinforced composite materials have been produced with eight laminates. For experimental study, specimens with 10 mm internal hole were prepared. Then, these specimens have been repaired by using adhesive and composite patches. For repair of the damaged specimens different patch parameters were used. Necessary curing temperature and pressure were applied to the specimens in laboratory conditions. By performing the unidirectional tensile test, the ultimate failure loads of these repaired specimens were indicated. By comparing these ultimate failure loads of repaired specimens, the effects of patch parameters on the ultimate failure strength are investigated. These repair parameters are patch thickness, patch bonding length and patch geometry.

Keywords— Laminate Composite Materials, bonded repair, patch, adhesive, failure strength

I. INTRODUCTION

By performing technological improvements, applications of composite materials have been increased both commercial and military aircraft structures applications in recent years. Because, these type materials have excellent properties. Due to high cost of these materials, maintenance of them, have been important. In industry, for composite materials, repair of spare parts have been preferred than replacement of spare parts. Sometimes, replacements of the damaged spare parts are costly and unnecessary. More structures with defects or local damages can be repaired successfully with composite patch bonding by using adhesive.

In industry, various repair techniques have been successfully applied. Among them, adhesively bonded structural repair has gained more favour than mechanically fastened structural repair for the reason that fiber reinforced composites are essentially bonded in nature. Therefore, in recent years, considerable experimental and numerical studies have been conducted to investigate the influence of different repair parameters on the stress distributions, ultimate strength and stress intensity factor of the bonded repaired structures [1].

A number of authors [1-9,11] have studied the analysis of failure mechanism of the bonded patch repair in laminated composite materials. Wisnom M.R. [10] has reviewed the size effects in the testing of fibre-composite materials. Predictive fracture model for composite bonded joints has been proposed by Goyal V.K. and et al. [12]. Principles and practices of adhesive bonded structural joints and repairs have studied by Davis M. [13]. Little research has been carried out to analyse the ultimate failure load of repaired structures with various repair parameters [15].

In aircraft applications, less weight is the important criteria for the maintenance of the parts. For such repair applications in laminated composite materials, external bonded patch repair technique has been more preferable than using mechanical fastened repair. Because, using mechanical fasteners increase the weight and the stress concentration factor of the repaired structures. Also, in external patch bonding repair, the optimum quantity of repair materials must be used in order to protect weight increment of the repaired structure. These main repair materials are adhesives and composite patches. The adhesives and patches should have been used in minimum quantity in repairs without decrease the load carrying capacity of the structures. Also, in adhesively bonded repairs, the stresses that occur in bonded joints are more uniform than that of pinned joints. These stress representations for various connections are illustrated in Fig. 1.

In this study, various experimental specimens have produced with different repair parameters. Then, by performing unidirectional tensile testing to these prepared specimens, the ultimate failure loads of them were indicated. By analysing these failure loads of the specimens, the effects of repair parameters have been specified.

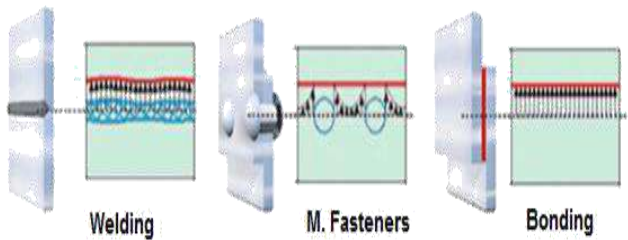


Fig. 1. Presentation of stress concentration effects for various joint techniques [15].

II. EXPERIMENTAL

The current work investigated the performance of the external bonded patch repairs under tensile loading by indicating the ultimate failure loads of repaired laminated composite structures. For this study, eight plies laminated woven glass and carbon fibers reinforced parent plates were used. By using these parent plates, experimental specimens were prepared. 10 mm holes were drilled in the center of the parent plates to simulate the damages in the structures. Then, these damaged specimens were repaired by using adhesive and composite patches with different parameters in necessary curing temperatures and laboratory conditions. The repaired experimental specimens were shown in Fig. 2 and their geometrical parameters were shown Fig. 3. The materials that used for parent plate specimens, adhesives and patches in repair were listed in Table 1. During the tests, specimens were subjected to longitudinal tensile loads on tensile testing machine in order to indicate the failure loads of repaired structures.



Fig. 2. Presentation of repaired experimental specimens [15].

Table 1. Materials that were used in repair of laminated composite materials

Bonding type	Parent Materials	Adhesive	Patch Material
Wet layout	Woven carbon fibres	Hysol EA9396	0020989
	Woven glass fibres	Hysol EA9396	0021438-09
Prepreg	Woven carbon fibres	C992275 ADH FILM	C992268-14
	Woven glass fibres	C991957-37 ADH FILM	C992270

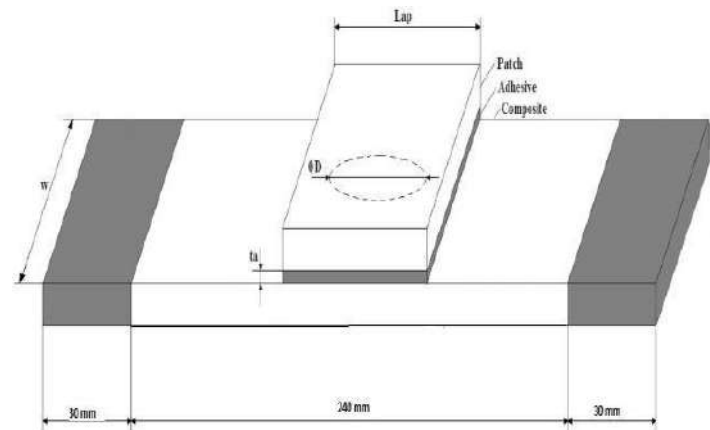


Fig 3. Geometric presentation of repaired experimental specimens [15]

III. RESULT AND DISCUSSION

[14] Effect of Patch Thickness

The effect of the patch thickness to the ultimate failure loads of repaired structure was indicated in Fig. 4. The ultimate failure loads of the structures repaired with prepreg bonding technique were increased by increasing the patch thickness (increase the ply number). But, for the structure that repaired with W.L. bonding technique, the failure loads have increased gradually to the patch thickness of the 3 plies values and after that, the peeling effect has occurred in repaired structure than, the failure load decrease dramatically. Increase the bonded patch thickness after a certain value (3 plies) in repair of the laminate composite materials does not improve the ultimate failure load. Increase the patch thickness further in repair of air craft structures may cause the weight stability effect. This is the main drawback in repairs of such applications.

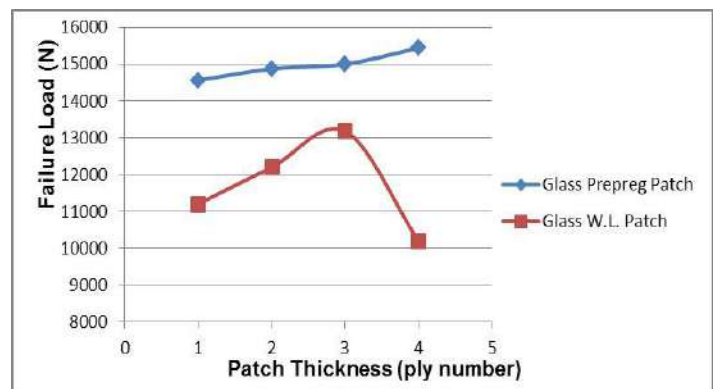


Fig. 4. Effect of patch thickness to the failure load of repaired structures with glass prepreg and wet layout patches [15].

B. Effect of Bonding Length

In external bonded patch repairs, if the patch overlap length or bond length too short, the entire adhesive layer is under high shear stress. In the case of longer bond length, most of the load is carried at the ends of the bonded overlap which is the reason for why too large patches fails to enhance the expected ultimate strength [14]. Effect of bonding length of

the patch to failure loads in repaired structures has presented in Fig. 5. The failure loads of structures repaired with glass prepreg patch bonding were increased gradually by increasing the bonding length in repair. In that repair with glass W.L. patch bonding; the failure loads were increased to the bonding length of 40 mm gradually, than decrease dramatically to the 5850 N value due to peeling effect that presented in W.L. applications. In bonded patch repair, for both W.L. and prepreg techniques, 40 mm value of bonding length, was seen as the optimum value.

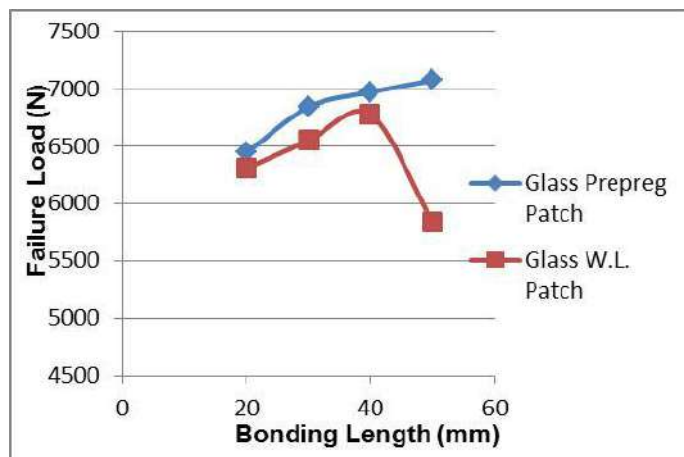


Fig. 5. Presentation of the effect of bonding length to the failure load of W/D=2 glass repaired structures with glass prepreg and wet layout patches [15].

C. Effect of Patch Shape

In order to specify the effect of patch shapes to the external patch repair, square and circular shape of patches were used. These repairs were performed both with W.L. and prepreg techniques. By performing uniaxial tensile test, the failure loads of specimens were indicated. These failure loads were shown in Figure 6.

As seen in Figure 6, in repair of woven glass fiber reinforced laminated composite materials patch shape had no significant effect in the failure loads of the specimens. But, in repair of woven carbon fiber reinforced laminated composite materials, the shape of patch had significant effect to the ultimate failure loads. In repair of these materials, for prepreg technique, using the circular patch shape had increased the ultimate failure loads of specimens. But, for W.L. techniques, using the square patch shape had increased the ultimate failure loads

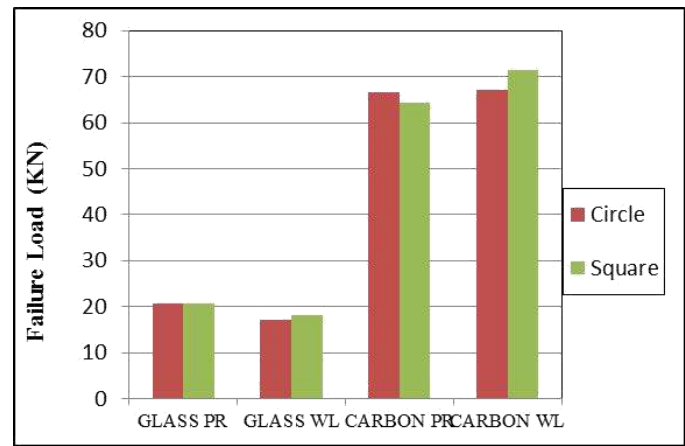


Fig. 6. Presentation of the patch shape effect to the failure load of W/D=5 glass repaired structures with glass prepreg patch and wet layout patch [15].

IV. CONCLUSIONS

In the present study, experimental study is carried out to investigate patches parameters effects on the ultimate failure load of adhesively bonded repaired structures, and the following conclusions can be drawn from this study.

1. The ultimate failure loads of the structures repaired with prepreg bonding technique were increased by increasing the patch thickness. But, for the structure that repaired with W.L. bonding technique, the failure loads have increased gradually to the patch thickness of the 3 plies values and after that, the peeling effect has occurred easily and this decrease the failure loads of repaired structures.
2. In bonded patch repair, for both W.L. and prepreg techniques, 40 mm value of bonding length, was obtained as the optimum value.
3. In repair of woven glass fiber reinforced laminated composite materials, patch shape had no significant effect in the failure loads. But, in repair of woven carbon fiber reinforced materials, using the circular patch shape had increased the failure loads for prepreg technique. But, for W.L. technique, using the square patch shape had increased the ultimate failure loads.
4. Ultimate failure loads of repaired structures can be increased by choosing the optimum repair parameters, such as patch thickness and bonding length.

ACKNOWLEDGMENT

This research was supported by the Firat University Scientific Research Projects Coordination Committee by the project number of FÜBAP 2053. The authors thanks for their support.

REFERENCES

- [1] Liu X., Wang G., "Progressive failure analysis of bonded composite repairs", *Composite Structures*, Vol. 81, pp.331-340, 2007.
- [2] Papanikos P., Tserpes K.I., Pantelakis Sp., "Initiation and progression of composite patch debonding in adhesively repaired cracked metallic sheets", *Composite Structures*, Vol. 81, pp. 303-311, 2007.
- [3] Xiaoquan C., Baig Y., Renwei H., Yujian G., Jikui Z., "Study of tensile failure mechanisms in scarf repaired CFRP laminates", *International Journal of Adhesion & Adhesives*, Vol. 41, pp. 177-185, 2013.
- [4] Breitzman T.D., Larve E.V., Cook B.M., Schoeppner G.A., Lipton R.P., "Optimization of a composite scarf repair patch under tensile loading", *Composites: Part A*, Vol. 40, pp. 1921-1930, 2009.
- [5] Tse P.C., Lau K.J., Wong W.H., "Stress and failure analysis of woven composite plates with adhesive patch-reinforced circular hole", *Composites: Part B*, Vol. 33, pp. 57-65, 2002.
- [6] Jones R., Chiu W.K. and Smith R., "Airworthiness of Composite Repairs: Failure Mechanisms" *Engineering Failure Analysis*, Vol. 2, pp.117-128, 1995.
- [7] Cheng P., Gong X. J. , Hearn D., Aivazzadeh S., "Tensile behaviour of patch-repaired CFRP laminates", *Composite Structures*, Vol. 93, pp.582-589, 2011.
- [8] Her S. C., "Stress analysis of adhesively-bonded lap joints", *Composite Structures*, Vol. 47, pp. 673-678, 1999.
- [9] Campilho R.D.S.G., Moura M.F.S.F., Domingues J.J.M.S., "Numerical prediction on the tensile residual strength of repaired CFRP under different geometric changes", *International Journal of Adhesion & Adhesives*, Vol. 29, pp.195-205, 2009.
- [10] Wisnom M. R., "Size effects in the testing of fibre-composite materials", *Composites Science and Technology*, Vol. 59, pp. 1937-1957, 1999.
- [11] Madani K., Touzain S., Feaugas X., Cohendouz S., Ratwani M., "Experimental and numerical study of repair techniques for panels with geometrical discontinuities", *Computational Materials Science*, Vol. 48, pp. 83-93, 2010.
- [12] Goyal V.K., Johnson E.R., Goyal V.K., "Predictive strength-fracture model for composite bonded joints" *Composite Structures*, Vol. 82, pp.434-446, 2008.
- [13] Davis M., Bond D., "Principles and practices of adhesive bonded structural joints and repairs", *International Journal of Adhesion & Adhesives*, Vol.19, pp. 91-105, 1999.
- [14] Adhesives, Vol.19, pp. 91-105, 1999.
- [15] Caminero M.A., Pavlopoulou S., Lopez-Pedrosa M., Nicolaisson B.G., Pinna C., Soutis C., "Analysis of adhesively bonded repairs in composites: Damage detection and prognosis" *Composite Structures*, Vol. 95, pp. 500-517, 2013.
- [16] Çetinkaya Ş., "Investigation of circular damage repairing by using adhesive in laminate composite materials experimentally", *Firat University, Phd. Thesis*, 2017



CIVIL ENGINEERING

ORAL SUBMISSIONS



Deformation Measurements and Analysis with Robust Methods: A Case Study, Deriner Dam

Berkant Konakoğlu/Research Assistant
(Research Assistant): Department of Geomatics
KTU Engineering Faculty
Trabzon, Turkey
bkonakoglu@ktu.edu.tr

Ertan Gökalp/Prof. Dr.
(Prof. Dr.): Department of Geomatics
KTU Engineering Faculty
Trabzon, Turkey
ertan@ktu.edu.tr

Abstract—Dams, one of the country's most natural and cheapest way to product energy, are built for energy production, agricultural activities and flood protection. Dams with high construction costs are subject to deformation due to some physical factors. Therefore, dams should be kept safe to prevent possible dam accidents, loss of life and property. Engineering structures (such as dams) should be monitored periodically by geodetic and non-geodetic techniques. Deriner dam is Turkey's highest double-curved concrete arch dam. In this study, we monitored deformation with GPS measurements. For this purpose, two period static GPS measurements were performed on the reference and object networks in the study. Afterwards, GPS measurements are adjusted separately with respect to free adjustment method and then deformation analysis were carried out by using the adjusted coordinates and their cofactor vectors. Iterative Weighted Similarity Transformation (IWST) and Least Absolute Sum (LAS) methods were used as deformation methods to detect the displacement of the reference and object points.

Keywords—concrete; arc dam; deformation; analysis; IWST; LAS; GPS

I. INTRODUCTION

The dams are one of the most important engineering structures used for water supply, flood protection and agricultural activities. Besides, it is the most natural and cheapest way of energy production for a country. Dams constructed with high cost expenditures are subjected to deformation due to various loading factors such as water level, air, water temperature and rock deformability. Controlling these dams has become compulsory in order to prevent disasters. In the literature, many deformation monitoring based studies have been reported [1]-[8]. Reference [1] investigated the surface movements of Alibey dam by means of geodetic and geotechnical methods. Geodetic displacement measurements were analysed using the Karlsruhe method. Also, Finite Element Method (FEM) was used to determine the behaviour of the dam. The results of geodetic measurements were compared with those of the FEM analyses. Reference [2] examined the long-term settlement behaviour of the Mornos dam in Greece. The result of geodetic monitoring analysis and that of the the Finite

Element Back analysis were compared. The findings showed a very good agreement between the measured and computed displacements. Reference [3] utilized the Global Positioning System (GPS) technique for monitoring horizontal movements in the Altinkaya dam. A deformation network consisting of 6 reference points and 11 object points along the dam crest were observed for 4 periods. Geodetic displacement measurements were analysed using the IWST and LAS methods to determine the points stability. Reference [4] investigated the magnitude and the direction of radial deformations of the Atatürk dam by means of conventional and GPS techniques. No significant correlation was detected between the radial movements on embankment and reservoir water level. Reference [5] investigated the relationship between displacement and reservoir water levels of the Koyna dam in India. The correlation between the movements and reservoir water level was investigated. Reference [6] evaluated the horizontal movements of the Ermenek dam based on periodic conventional geodetic measurement campaigns during the first filling of the reservoir. The coordinates of the GPS measurements are WGS-84 coordinate system. The points of the coordinates need to be converted from Cartesian to the local topocentric coordinate system in order to see the real directions of the the displacements. Geodetic measurements were compared with those of the FEM. [3]. The aim of this work is to evaluate the horizontal movements of the Deriner dam with GPS measurements. Deformation analyses were performed with the Iterative Weighted Similarity Transformation (IWST) and the Least Absolute Sum (LAS) methods. Finally, the results of these two methods have been compared.

II. ROBUST METHODS

Robust methods are used when there is no previous information about the movement of the points within the network [9]. In this study, the IWST and LAS methods are used to estimate the movements of a monitoring network. The IWST, proposed by [10], is a robust method. According to [11], the Danish, LAS and Huber methods are some of the frequently used robust methods. The IWST and LAS methods are based on

S-transformation [10]-[12]. Both methods are applied as follows;

Adjusted coordinates of the points x_1, x_2 and their cofactor matrix Q_{x1}, Q_{x2} are calculated with two separate free adjustments. The displacement values (d) and cofactor matrix of d Q_d are calculates as;

$$d = x_2 - x_1 \quad (1)$$

$$Q_d = Q_{x1} + Q_{x2} \quad (2)$$

Then displacement values (d) are calculated as (3);

$$\begin{aligned} d^{(k+1)} &= [I - H(H^T W^{(k)} H)^{-1} H^T W^{(k)}] d^{(k)} \\ &= S^{(k)} d^{(k)} \end{aligned} \quad (3)$$

d = displacement vector

k = number of iterations

I = identity matrix

W = weight matrix

S = S-transformations matrix

H matrix for the 3D networks is written as;

$$H = \begin{bmatrix} e & 0 & 0 & 0 & -z_0 & -y_0 & x_0 \\ 0 & e & 0 & -z_0 & 0 & x_0 & y_0 \\ 0 & 0 & e & y_0 & -x_0 & 0 & z_0 \end{bmatrix}_{3m \times 7} \quad (4)$$

where, $e^T = (1, \dots, \dots, 1)$ x_0, y_0 and z_0 are the coordinates of points P_i , which are reduced to the centre of the network (5).

$$\begin{aligned} X_0^i &= X_i - \frac{1}{m} \sum_{i=1}^m x_{i0}, \\ Y_0^i &= Y_i - \frac{1}{m} \sum_{i=1}^m y_{i0}, \\ Z_0^i &= Z_i - \frac{1}{m} \sum_{i=1}^m z_{i0} \end{aligned} \quad (5)$$

Above, z_0^i, y_0^i and x_0^i the i^{th} elements of z^0, y^0 and x^0 respectively, and z_i, y_i and x_i are approximate coordinates of point P_i and m is the number of the points in the network [13]-[15]. The main difference between the IWST and LAS method is in forming the weight matrix. In the first transformation ($k = 1$) the weight matrix is taken as identity ($W^{(k)} = I$) for

all common points, then in the ($k+1$) transformation the weight matrix is defined as;

For the IWST method,

$$W^{(k)} = \text{diag}\{1/|d^{(k)}|\} \quad (6)$$

For the LAS method,

$$W^{(k)} = \text{diag}\left\{\frac{1}{\sqrt{(dx_i^{(k)})^2 + (dy_i^{(k)})^2}}\right\} \quad (7)$$

In equation (6), d is the displacement vector. However, in equation (7), dx_i and dy_i refer to the displacement components in x and y axis respectively. The iterative procedure continues until the differences between displacements of all common points ($d^{(k+1)} - d^{(k)}$) are smaller than a tolerance value ϵ (i.e. 0.0001 m.). In the final iteration cofactor matrix is calculated as;

$$Q_d^{(k+1)} = S^{(k)} Q_d (S^{(k)})^T \quad (8)$$

The IWST method minimizes the total sum of absolute values of the displacement components,

$$\left(\sum |d_i| \Rightarrow \text{minumum}\right) \quad (9)$$

while the LAS method minimizes the sum of the lengths of the displacement,

$$\left(\sum \sqrt{(dx_i^{(k)})^2 + (dy_i^{(k)})^2} \Rightarrow \text{minumum}\right) \quad (10)$$

Equation (11) can be used in order to determine unstable reference and object points in the deformation network with a single point test as shown below [14];

$$T_i = \frac{(d_i^{(k+1)})^T (Q_{di}^{(k+1)})^{-1} d_i^{(k+1)}}{u_d \hat{\sigma}_0^2} \sim F(\alpha, u_d, df) \quad (11)$$

d_i = displacement vector of point i

Q_{di} = cofactor matrix of point i

u_d = dimension of the confidence region (1, 2 or 3)

$\hat{\sigma}_0^2 = \frac{df_i \hat{\sigma}_i^2 + df_j \hat{\sigma}_j^2}{df_i + df_j}$ = pooled variance factor

$\hat{\sigma}_i^2, \hat{\sigma}_j^2$ = a posteriori variance factors of epoch i and j

df_i, df_j = degrees of freedom of epoch i and j

α = significance level

If the test is passed, the point is assumed to be stable, otherwise, it is considered unstable.

III. APPLICATION

The Deriner dam, a double-curvature concrete arch dam, is located on the Çoruh River at Artvin province in the north-eastern part of Turkey. It is the highest dam with a body height of 249 meters in Turkey. The underground powerhouse near the dam includes four units, with an overall capacity of 670 MW. Also, the powerhouse annually generates 2.118 GWh of electricity. The picture of the dam and technical specifications are given in Figure 1 and in Table 1, respectively.

TABLE I. TECHNICAL CHARACTERISTICS OF THE DERINER DAM

Type	Double-curvature concrete arch
Dam crest elevation	397.00 m
Length of dam crest	720.00 m
Height of crest	249.00 m
Total reservoir area	26.40 km ²
Total reservoir volume	1969 hm ³
Electric production capacity	2.117,75 Gwh per year

In order to determine the possible horizontal movements on the crest, 14 reference and 7 objects points were used (Figure 2).



Fig. 1. Deriner Dam



Fig 2. Distrubition of Reference and Object Points in Deriner Dam

The deformation measurements of Deriner dam involved two measurement campaigns. The first campaign was carried out in May 2016 and the second one in September 2016. During the GPS measurements, Topcon Hiper Pro and Topcon GR-5 dual-frequencies receivers were used. The observation period was selected as 2 hours and 1.5 hours for reference and object points, respectively. The sampling rate was chosen as 10 seconds and the satellite elevation mask was selected at 15°. The baselines were processed with the Topcon Tools v.8.2.3 software. MATLAB script was used for network adjustment and deformation analysis. The significance level for deformation detection was specified as 0.05. The adjusted coordinates (WGS-84) and cofactor matrix were obtained from a free network adjustment. Deformation analysis was made with respect to the first period measurement. The two dimensional deformation analysis was made. All WGS-84 coordinates (X, Y, Z) and cofactor matrices were transformed to the local coordinate system (E, N, U). The displacement values (d) were computed by the IWST and LAS methods are shown in Tables 2 and 3. These tables also depicts whether or not the points are stable. Water levels were 389.33 m in the first period and 377.22 m in the second period. The reduction of water level in between the two periods is 12.11 m.

TABLE II. STABLE AND UNSTABLE POINTS DETERMINED BY IWST

Between 1-2 periods				
IWST				
		dN	dE	
		cm	cm	
Object Points	1139	-0.19	0.18	stable
	1133	0.91	-0.59	unstable
	1127	1.17	-1.15	unstable
	1121	1.09	-1.93	unstable
	1115	0.52	-2.01	unstable
	1109	-0.45	-0.82	unstable
	1103	-0.25	-0.16	stable
Reference Points	105	-0.37	0.53	unstable
	108	0.02	0.24	unstable
	109	-0.09	0.32	unstable
	112	-0.01	-0.12	stable
	118	0.00	0.14	unstable
	101	0.00	-0.03	stable
	102	0.56	0.16	unstable
	104	-0.16	0.47	unstable
	107	-0.13	0	stable
	111	-0.14	0.06	stable
	113	0.01	0.23	stable
	114	0.08	-0.27	stable
	116	0.02	-0.13	stable
	117	-0.14	0.24	unstable

TABLE III. STABLE AND UNSTABLE POINTS DETERMINED BY LAS

Between 1-2 periods				
LAS				
		dN	dE	
		cm	cm	
Object Points	1139	-0.17	0.17	stable
	1133	0.93	-0.61	unstable
	1127	1.19	-1.16	unstable
	1121	1.11	-1.93	unstable
	1115	0.53	-2.00	unstable
	1109	-0.43	-0.82	unstable
	1103	-0.24	-0.17	stable
Reference Points	105	-0.35	0.52	unstable
	108	0.04	0.23	unstable
	109	-0.07	0.31	unstable
	112	0.00	-0.13	stable
	118	0.02	0.14	stable
	101	0.03	-0.02	stable
	102	0.59	0.17	unstable
	104	-0.13	0.47	unstable
	107	-0.11	0.00	stable
	111	-0.13	0.06	stable
	113	0.04	0.23	stable
	114	0.12	-0.26	stable
	116	0.05	-0.13	unstable
	117	-0.12	0.24	unstable

IV. CONCLUSION

Since we have no prior information about the movement of the points within the network, the IWST and LAS methods were used in this study. The IWST and LAS were used to perform 2D deformation analyses. It can be concluded from the results of the analysis that the displacements are dependent on the water level on the reservoir. The maximum horizontal displacement was experienced in the middle of the dam's crest. These results will also be examined with new measurements to be conducted in further periods. Also, precise differential levelling of levelling line along the dam crest will be performed.

ACKNOWLEDGMENT

The authors would like to thank the Turkish General Directorate of State Hydrologic Works (DSI), the 26th Regional Directorate Artvin. This research was supported by the Scientific Research and Projects Unit (5482, 5252) of Karadeniz Technical University.

REFERENCES

- [1] G. Guler, H. Kilic, G. Hosbas, K. Ozaydin, "Evaluation of the movements of the dam embankments by means of geodetic and geotechnical methods," *Journal of surveying engineering*, vol. 132(1), pp. 31-39, 2006.
- [2] V. Gikas and M. Sakellariou, "Settlement analysis of the Mornos earth dam (Greece): Evidence from numerical modeling and geodetic monitoring," *Engineering Structures*, vol. 30(11), pp. 3074-3081, 2008.
- [3] L. Taşçi, "Dam deformation measurements with GPS," *Geodezija kartografija*, vol. 34(4), pp. 116-121, 2008.
- [4] Y. Kalkan, "Geodetic deformation monitoring of Atatürk Dam in Turkey," *Arabian Journal of Geosciences*, vol. 7(1), pp. 397-405, 2014.

- [5] N. Radhakrishnan, "Application of GPS in structural deformation monitoring A case on Koyna dam," *Journal of Geomatics*, vol. 8(1), pp. 48-54, 2014.
- [6] C. O. Yigit, S. Alcay, and A. Ceylan, "Displacement response of a concrete arch dam to seasonal temperature fluctuations and reservoir level rise during the first filling period: evidence from geodetic data," *Geomatics, Natural Hazards and Risk*, vol. 7(4), pp. 1489-1505, 2016.
- [7] J. O. Ehiorobo and R. Irughe-Ehigiator, "Monitoring for horizontal movement in an earth dam using differential GPS," *Journal of Emerging Trends in Engineering and Applied Sciences*, vol. 2(6), pp. 908-913, 2011.
- [8] S. I. Pytharouli and S. C. Stiros, "Ladon dam (Greece) deformation and reservoir level fluctuations: evidence for a causative relationship from the spectral analysis of a geodetic monitoring record," *Engineering Structures*, vol. 27(3), pp. 361-370, 2005.
- [9] R. Singh and H. Setan, "Comparison of different datum definitions in detection of deformation of a geodetic monitoring networks," in Presented at Research Seminar on Construction, Materials and Environmental Technology, Universiti Teknologi Malaysia, Johor, Bahru, 1999.
- [10] Y. Q. Chen, "Analysis of Deformation Surveys - A Generalized Method," Technical Report No. 94, Department of Surveying Engineering, University of New Brunswick, Fredericton, N.B., 1983.
- [11] W.F. Caspary and H. Borutta, "Robust estimation in deformation models," *Survey Review*, vol. 29(223), pp. 29-45, 1987.
- [12] Y. Q. Chen, A. Chrzanowski and J.M. Secord, "A strategy for the analysis of the stability of reference points in deformation surveys," *CISM JOURNAL ACSGC*, 44(2), pp. 141-149, 1990.
- [13] S. Kuang, "Geodetic network analysis and optimal design: concepts and applications," Ann Arbor Press Inc, 1996.
- [14] H. Setan and R. Singh, "Deformation analysis of a geodetic monitoring network," *GEOMATICA-OTTAWA*, vol. 55(3), pp. 333-346, 2001.
- [15] L. Taşçi, "Analysis of dam deformation measurements with the robust and non-robust methods," *Scientific Research and Essays*, vol. 5(14), pp. 1770-1779, 2010.

Multy Variable Grey Method For Multy Point Deformation Analysis

Levent TAŞÇI
Fırat University Engineering Faculty
Elazığ TURKEY
e- mail: ltasci23@gmail.com

Erkan KÖSE
Nuh Naci Yazgan University Engineering Faculty
Industrial Engineering Department Kayseri TURKEY
E-MAIL: erkankose93@gmail.com

Abstract-Grey theory is one of the methods used to study uncertainty. The uncertain systems characterized by small sample and poor information are the study object of grey system theory. Multivariable grey prediction models are part of grey forecasting system. They are presented if there are mutual relations among the factors in the system. They believe that all the influencing factors are not independent of each other and should be regarded as a whole. In multivariable grey forecasting models, the future value of a variable is tried to be forecasted considering the other influential factors in the system. In this study, deformation consisting on the crest of a Dam is aimed to determine by using multivariable grey prediction models.

Keywords—Deformation, Grey method, Deformation predict

I. Introduction

The evaluation of measurements and geodetic deformation measurements covers a significant portion of the engineering measurements. The monitoring of the movements of big engineering structures begins during the construction of the building and continues throughout life. The evaluation of the data and the interpretation phase of the results is the last and most important part of the deformation study. There are damages that can't be compensated by a wrong decision. As a result, it is necessary to be very careful and the results must be absolutely reliable. A large number of measures are needed to be able to give decisions about the behavior of constructions and to interpret the results. But, being able to make more accurate decisions with less data is very important in every circumstance.

The main strength of grey prediction is that it only requires short-term, current and limited data. Grey systems theory was first proposed by Deng [1]. Grey theory is one of the methods used to study uncertainty. The uncertain system characterized by small sample and poor information are the study object of grey system theories. The grey system puts each stochastic variable as a grey quantity that changes within

a given range. It does differ from statistical analysis method to deal with the grey quantity. It deals directly with the original data and searches the intrinsic regularity of the data [2].

II. Multy variable Grey Forecast model

Multivariable grey prediction models are part of grey forecasting system. They are presented if there are mutual relations among the factors in the system. They believe that all the influencing factors are not independent of each other and should be regarded as a whole. In multivariable grey forecasting models, the future value of a variable is tried to be forecasted considering the other influential factors in the system. Because of high accuracy and easy application procedures, multivariable grey models have been applied to many areas in the literature [3-9].

MGM(1,N) model is set up by using Accumulating Generation Operator (AGO). The primitive data are subjected to the AGO to smooth the randomness of the data and to weaken the tendency of variation [10]. Assume that $X^{(0)} = \{x^{(0)}(1), x^{(0)}(2), \dots, x^{(0)}(m)\}$ is an original, non-negative data series taken in consecutive order and at equal time intervals, then $X^{(1)} = \{x^{(1)}(1), x^{(1)}(2), \dots, x^{(1)}(m)\}$ is called 1-AGO where

$$x^{(1)}(k) = \sum_{j=1}^k x^{(0)}(j), \quad k = 1, 2, \dots, m. \text{ Suppose that the}$$

number of variable is represented by n and the number of observation period by m , MGM(1,N) procedure is described in the following parts [10]. The first-order ordinary differential equation for the MGM(1, N) can be written as follows:

$$\begin{aligned}\frac{dx_1^{(1)}}{dt} &= a_{11}x_1^{(1)} + a_{12}x_2^{(1)} + \dots + a_{1m}x_m^{(1)} + b_1 \\ \frac{dx_2^{(1)}}{dt} &= a_{21}x_1^{(1)} + a_{22}x_2^{(1)} + \dots + a_{2m}x_m^{(1)} + b_2 \\ &\dots\dots\dots \\ \frac{dx_n^{(1)}}{dt} &= a_{n1}x_1^{(1)} + a_{n2}x_2^{(1)} + \dots + a_{nm}x_m^{(1)} + b_n\end{aligned}\quad (1)$$

marked as:

$$\frac{dX^{(1)}}{dt} = AX^{(1)} + B \quad (2)$$

The estimate value is obtained by using the least square method:

$$H = (L^T L)^{-1} L^T Y \quad (3)$$

where

$$L = \begin{bmatrix} \bar{x}_1^{(1)}(2) & \bar{x}_2^{(1)}(2) & \dots & \bar{x}_n^{(1)}(2) & 1 \\ \bar{x}_1^{(1)}(3) & \bar{x}_2^{(1)}(3) & \dots & \bar{x}_n^{(1)}(3) & 1 \\ \dots\dots\dots \\ \bar{x}_1^{(1)}(m) & \bar{x}_2^{(1)}(m) & \dots & \bar{x}_n^{(1)}(m) & 1 \end{bmatrix}$$

$$Y = \begin{bmatrix} x_1^{(0)}(2) & x_2^{(0)}(2) & \dots & x_n^{(0)}(2) \\ x_1^{(0)}(3) & x_2^{(0)}(3) & \dots & x_n^{(0)}(3) \\ \dots\dots\dots \\ x_1^{(0)}(m) & x_2^{(0)}(m) & \dots & x_n^{(0)}(m) \end{bmatrix}$$

and $\bar{x}_i^{(1)}(k) = \frac{1}{2}(x_i^{(1)}(k) + x_i^{(1)}(k-1))$. The estimated value \hat{A} and \hat{B} can be obtained from H:

$$\hat{A} = \begin{bmatrix} \hat{a}_{11} & \hat{a}_{21} & \dots & \hat{a}_{n1} \\ \hat{a}_{12} & \hat{a}_{22} & \dots & \hat{a}_{n2} \\ \dots\dots\dots \\ \hat{a}_{1m} & \hat{a}_{2m} & \dots & \hat{a}_{nm} \end{bmatrix}, \quad \hat{B} = \begin{bmatrix} \hat{b}_1 \\ \hat{b}_2 \\ \dots \\ \hat{b}_n \end{bmatrix} \quad (4)$$

Then accumulated predicted values can be calculated by using Equation (4).

$$\hat{X}^{(1)}(k) = e^{\hat{A}(k-1)}(\hat{X}^{(1)}(1) + \hat{A}^{(-1)}\hat{B}) - \hat{A}^{(-1)}\hat{B} \quad (5)$$

where

$$e^{\hat{A}(k-1)} = I + \sum_{i=1}^{\infty} \frac{\hat{A}^i}{i!} (k-1)^i \quad (6)$$

After the inverse first-order accumulated generation operation (1-AGO), we obtain the sequence as $\hat{X}^{(0)}(k) = \hat{X}^{(1)}(k) - \hat{X}^{(1)}(k-1)$. The average fitting precision of the model is

$$\sigma^2 = \frac{\sum_{i=1}^n V_i^T V_i}{nm} \quad (7)$$

where

$$v_i k = x_i^{(0)}(k) - \hat{x}_i^{(0)}(k), V_i = (v_i(1), v_i(2), \dots, v_i(m))^T \quad (8)$$

III. Application

Multivariable Grey Prediction Model which is very efficient methodology in the situation of the limited number of the data has been used to predict deformation in a dam. In this study 11 periods' real measurement values has been used to predict deformations depending on the water level for object points 11, 12 and 13 which are located in the middle of the rockfill dam crest. The first 6 periods' measurements have been used to establish multivariable grey prediction model, and the last six periods' measurement are used to test the accuracy of the proposed method. The original and predicted values are shown in Table 1. The outcomes also presented in Figure 1-3.

The 7th column in the Table 1 shows predicted values for object point 11 depending on the water level. 8th and 9th columns show the predicted values when we apply grey prediction procedure for two object points at the same time. The last three columns show the results if we apply prediction procedure for all object points in this study.

Table 1. Original and Predicted Values

Years	Period	Heights of Point AS11 (m.)	Heights of Point AS12 (m.)	Heights of Point AS13 (m.)	Dam Lake Water Level (m.)	Multy Variable					
						MGM(1,2)	MGM(1,3)		MGM(1,4)		
						AS11	AS11	AS12	AS11	AS12	AS13
						Predicted value	Predicted value	Predicted value	Predicted value	Predicted value	Predicted value
13.01.1975	1.Period	851.659	851.727	851.796	803.960	851.660	851.659	851.727	851.659	851.727	851.796
21.03.1975	2.Period	851.653	851.721	851.791	805.290	851.620	851.555	851.623	851.6049	851.673	851.7416
24.06.1976	3.Period	851.540	851.605	851.662	842.090	851.564	851.391	851.456	851.475	851.539	851.597
01.06.1977	4.Period	851.506	851.568	851.623	836.210	851.532	851.299	851.361	851.413	851.475	851.531
24.03.1978	5.Period	851.493	851.554	851.610	828.040	851.411	851.231	851.292	851.379	851.441	851.496
20.11.1979	6.Period	851.502	851.563	851.618	828.500	851.501	851.173	851.234	851.356	851.417	851.472
30.07.1980	Predicted.1	851.448	851.508	851.563	841.400	851.471	851.115	851.176	851.335	851.396	851.451
04.03.1982	Predicted.2	851.398	851.456	851.514	834.290	851.441	851.057	851.118	851.315	851.377	851.432
17.05.1982	Predicted.3	851.402	851.496	851.514	844.350	851.411	850.995	851.056	851.295	851.357	851.412
15.11.1984	Predicted.4	851.369	851.420	851.479	831.830	851.381	850.941	851.002	851.276	851.338	851.392
14.05.1985	Predicted.5	851.361	851.419	851.475	835.210	851.350	850.881	850.942	851.256	851.319	851.373

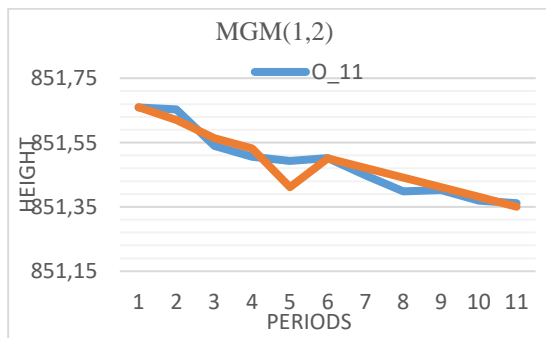


Figure 1. Multivariable Grey Model (1, 2)

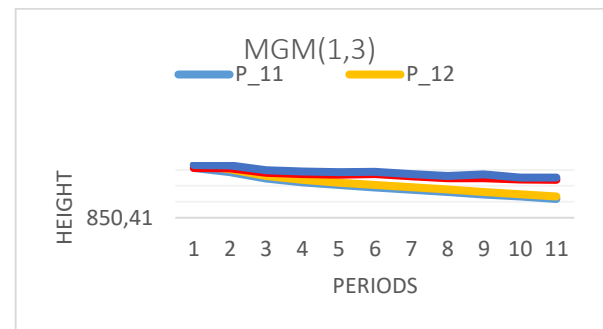


Figure 2. Multivariable Grey Model (1, 3)

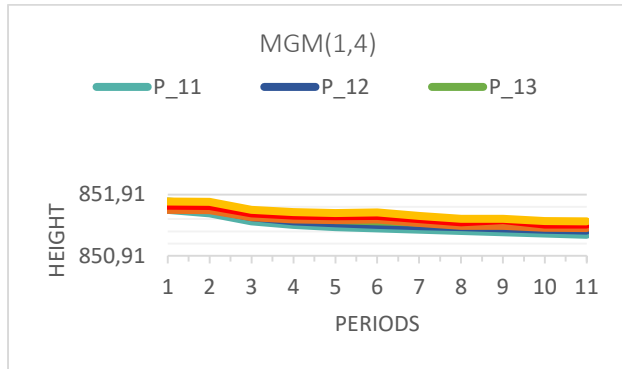


Figure 3. Multivariable Grey Model (1, 4)

IV. Results

The Grey System Theory provides a solution to the problem even in the case of very limited number of data. The Multi Variable Grey Prediction Model can be used to predict deformation not only for one point but also for many points at the same time. In this study deformation level of the three different object points in a dam crest has been tried to be forecasted depending on the water level by multi variable grey model. Results show that there are great consistency between grey prediction values and real values. Based on the outcomes it is possible to conclude that grey prediction model is a very reliable prediction model in limited data circumstances.

References

- [1] Deng, J.L. Control problems of grey systems. *Systems and Control Letters*, 1982, 1(5): 211–215.
- [2] Huang, Y.P. and C.C. Huang, C.C. The integration and application of fuzzy and grey modeling methods. *Fuzzy Sets and Systems*, 1996, 78(1): 107–119.
- [3] T. Tien. The indirect measurement of tensile strength of material by the grey prediction model GMC(1,n). *Measurement Science and Technology*, 2005, 16(6): 1322–1328.
- [4] Wu, W.Y. and Chen, S.P. A prediction method using the grey model GMC(1,n) combined with the grey relational analysis a case study on internet access population forecast. *Applied Mathematics and Computation*, 2005, 169(1): 198–217.
- [5] Hsu, L. Forecasting the output of integrated circuit industry using genetic algorithm based multivariable grey optimization models. *Expert Systems with Applications*, 2009, 36(4): 7898–7903.
- [6] Hsu, L. and Wang, C. Forecasting integrated circuit output using multivariate grey model and grey relational analysis. *Expert Systems with Applications*, 2009, 36(2): 1403–1409.

[7] Luo, Y.X., Wu, X., Li, M. and Cai, A.H. Grey dynamic model GM(1,N) for the relationship of cost and variability. *Kybernetes*, 2009, 38(3): 435–440.

[8] Tien, T.L. A research on the grey prediction model GM(1,n). *Applied Mathematics and Computation*, 2012, 218(9): 4903–4916.

[9] Niu, W., Zhai, Z., Wang, G., Cheng, J. and Guo, Y. Adaptive multivariable grey prediction model. *Journal of Information Computer Science*, 2011, 8(10): 1801–1808.

[10] Hui, H., Li, F., and Shi, Y. An Optimal Multi-Variable Grey Model for Logistics Demand Forecast. *International Journal of Innovative Computing, Information and Control*, 2013, 9(7): 2907–2918.

Integration of Thematic Information to UAV-Based Point Clouds for Ground Filtering

Volkan Yilmaz

Geomatics Department
Karadeniz Technical University
Trabzon, Turkey

Cigdem Serifoglu Yilmaz

Geomatics Department
Karadeniz Technical University
Trabzon, Turkey

Oguz Gungor

Geomatics Department
Karadeniz Technical University
Trabzon, Turkey

Abstract— Advancing technology enables the extraction of accurate spatial information relating to the features on the ground. Owing to low-altitude flights, stereo aerial photos taken from digital cameras mounted on unmanned aerial vehicles (UAV) make it possible to generate point clouds as dense as LiDAR (Light Detection and Ranging) point clouds. Contrary to stereo aerial photogrammetry, LiDAR technology is capable of providing multiple returns. This is because laser beams are able to penetrate through the vegetation and reach the ground surface to record the spatial information of the ground point to which the laser beam has reached. This, of course, makes it easier to classify the points belong to the bare earth surface and to the above-ground objects, which is the main reason that most of the ground filtering algorithms focus on filtering LiDAR point clouds. However, LiDAR technology is still costly, especially for large-scaled areas. Apart from enabling the generation of dense point clouds, UAV photogrammetry is also cost-efficient with easy-deployable UAVs. Hence, it may be reasonable to use UAV-based point clouds for ground filtering in the absence of LiDAR data. However, ground filtering algorithms developed for LiDAR point clouds are more likely to be unsuccessful in filtering UAV-based point clouds, which encourages the analysts to seek for alternative approaches to filter UAV-based point clouds. This study uses a simple methodology to filter UAV-based point clouds. This methodology filters a UAV-based point cloud with an image classification-based approach. Thematic image produced with the Support Vector Machine (SVM) classifier is overlaid with the point cloud to determine the points corresponding to the above-ground objects. Determined points are then discarded to retrieve ground points. It can be concluded from the evaluation results that the used methodology filtered the UAV-based point cloud with a type I error of 2%, a type II error of 20% and a total error of 10%.

Keywords— *point cloud; image classification; ground filtering; unmanned aerial vehicle; aerial photogrammetry*

I. INTRODUCTION

Ground filtering, which is the removal of the points belong to above-ground objects to retrieve only the ground points, is essential for most photogrammetric projects. Retrieved ground points are interpolated to generate the Digital Terrain Model (DTM). Ground filtering is a challenging process [1]. Land

topography, and complexities and heights of the above-ground objects are just some of the factors making the ground filtering process challenging. Various ground filtering algorithms have been reported in the literature. These algorithms can be categorized as slope-based [2], segmentation-based [3], morphology-based [4-7] and interpolation-based [8,9] algorithms.

The ground filtering algorithm proposed in [4] separates the ground and non-ground points by comparing the slopes between each point and its neighbors. If the maximum slope is found to be greater than a predefined threshold, then the candidate point is said to be a non-ground point and removed. The slope-based filtering approach was enhanced in [5] by means of a two-step procedure. The first step approximated a rough DTM by using local minima. In the second step, the ground and non-ground points are classified based on a threshold. Reference [10] proposed a TIN (Triangulated Irregular Network)-based approach to remove the non-ground points. This approach uses some seed points to be used for the formation of a sparse TIN. This TIN is then densified iteratively until there is no unclassified points. Reference [11] introduced a multi-directional ground filtering approach that uses the pattern variability along different directions. Reference [12] utilized progressive densification and segmentation techniques to filter LiDAR data. References [13] and [14] conducted a morphology-based procedure that benefits from a variable-size structure element. Reference [15] used an object-based filtering approach that forms the objects with a segmentation algorithm implemented based on a grid index. Repetitive interpolation was utilized in [16] to filter a laser scanner data of a forested area. References [17] and [18] used a 3D active contour to separate the ground and non-ground points. Reference [19] introduced a filtering approach that performs a one-dimensional labelling in two opposite directions. An image classification-based filtering methodology was introduced in [20]. This methodology overlaps a point cloud with a thematic map to detect the points corresponding to the non-ground class. Detected non-ground points are then removed to retrieve ground points.

This study uses the ground filtering methodology proposed in [20] to remove the non-ground points. Further information about this methodology is given in Section II.

II. MATERIAL AND METHODS

A. Study Area

The study area was chosen in Karadeniz Technical University campus, in the city of Trabzon. The city is situated on the north-east of Turkey. A wide variety of different structured above-ground objects exist in the campus, which enables a comprehensive investigation of the success of the used methodology. Elevation ranges from 31 m to 71 m in the study area. The study area is shown in Figure 1.

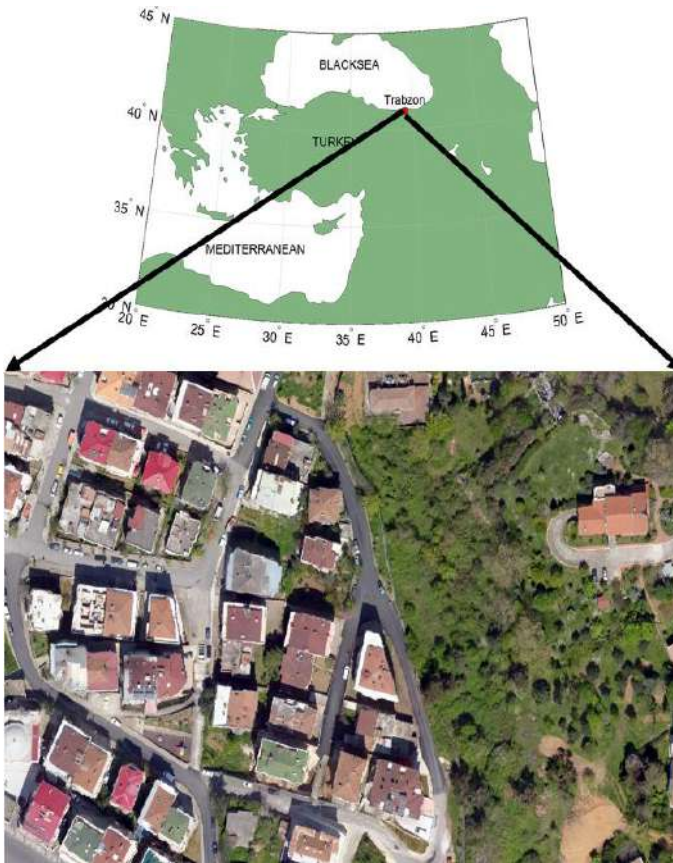


Fig. 1. Study area.

B. Methodology

As a first step, 12 ground control points (GCP) were established in the entire campus. Plenty of attention was paid to distribute the points evenly over the campus. 3D positions of the GCPs were then measured with the RTK GPS technique. Afterwards, 256 aerial photos (3648 x 2736 resolution) of the entire campus were captured with the RICOH GR DIGITAL IV digital camera mounted on the Gatewing X100 UAV. The aerial photos were taken along nine paths from an altitude of 185 m. After the flight, captured aerial photos were processed in the Agisoft Photoscan Professional software and the point

cloud and orthophoto of the study area were generated. The density of the produced point cloud was 0.1 point/m², whereas the spatial resolution of the orthophoto was 15 cm. Since the density of the point cloud was not enough to separate the ground and non-ground points, the point cloud was densified and a point cloud with a density of 17.1 point/m² was generated. The point cloud and orthophoto were then cropped with respect to the boundary of the study area in order to test the performance of the used methodology. The orthophoto image was classified with Support Vector Machines (SVM) classification algorithm. The reason for using this classifier was that it has been proven to be very successful in classifying the images [20]. The thematic image included six classes as building, soil, shadow, grass, road and tree. Building and tree classes were merged to form non-ground class, whereas the other ones were merged to form the ground class. Densified point cloud was then overlaid with the thematic image and the points corresponding to the non-ground class were identified and removed. As a final step, the DTM of the study area was interpolated from the ground points by means of the Bi-linear interpolation technique.

III. RESULTS AND DISCUSSION

The produced DSM (Digital Surface Model) and DTM are shown in Figures 2 and 3, respectively. Visual investigations showed that the used methodology was, in general, successful in separating the ground and non-ground points. In addition to visual evaluation, quantitative measurements would also be of help to test the performance of the used ground filtering methodology.

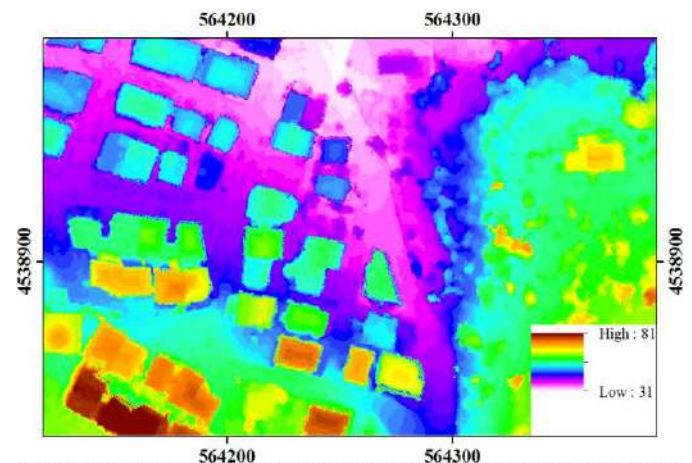


Fig. 2. Produced DSM.

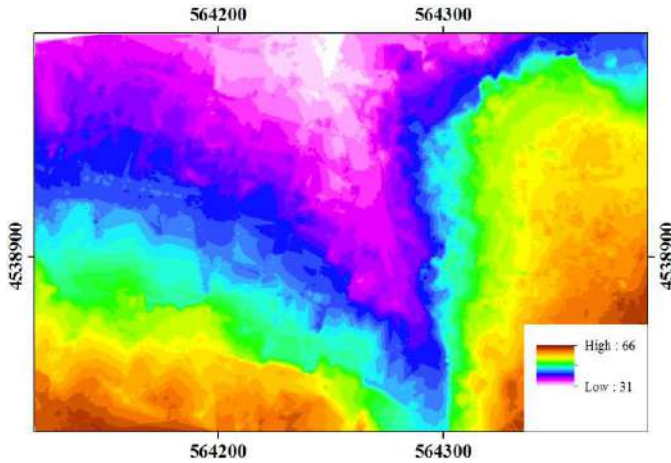


Fig. 3. Produced DTM.

Two types of errors arise out of ground filtering process, namely the omission and commission errors [21]. The Type I error (omission error) is the classification of ground points as non-ground, whereas the Type II error (commission error) is the classification of non-ground points as ground [1,21,22]. Evaluation of all points in a point cloud is not practical. Hence, these error metrics are computed by using randomly selected test points [20]. The Type I, Type II and Total error metrics are calculated as [22];

$$\text{Type I error} = o / G \quad (1)$$

$$\text{Type II error} = c / NG \quad (2)$$

$$\text{Total error} = o + c / G + NG \quad (3)$$

where, o , c , G and NG stand for the omission error, commission error, total number of ground points and total number of non-ground points, respectively.

In the study, the number of required test points were calculated with the multinomial distribution approach used in [23]. In cases where there is no information about the area of each class, which is the case in this study, this approach estimates the number of required test points as;

$$n = B / 4b^2 \quad (4)$$

where, $B = \alpha / k$, α is the confidence interval, k is the total number of classes and b is the desired accuracy [20,24]. In the study, the confidence interval was chosen as 95%. Since there are two classes (ground and non-ground) in thematic image, B was computed as 0.025 ($\alpha / k = 0.05 / 2$). It can be seen from the χ^2 table that the corresponding value for 0.025 is 5.02 at one degree freedom. Hence, n was computed as 502 ($5.02 / 4 (0.05^2)$). As can be seen, a minimum of 502 test points were needed to investigate the ground filtering result accurately.

Hence, 665 test points were randomly selected from the point cloud to use for calculation of the metrics. These test points were then overlaid with the orthophoto to evaluate each of them with the aid of the very high-resolution orthophoto. Visual observation of the test points revealed that 288 of the test points were selected for above-ground objects, while the others for the ground. Table 1 shows the calculated metric results.

TABLE 1. CALCULATED METRIC RESULTS

Omission E.	Commission E.	Type I E.	Type II E.	Total E.
9	58	0.02	0.20	0.10

As seen in Table 1, 9 ground points were classified as non-ground; whereas 58 non-ground points were classified as ground. The Type I, Type II and Total errors were calculated as 2%, 20% and 10%, respectively.

IV. CONCLUSIONS

Metric results indicated that the methodology used in this study is capable of keeping ground points successfully. However, in some parts of the study area, it misclassified the non-ground points. In general, 90% of all test points were classified successfully. The advantage of this methodology is that it does not use any morphological operations and require any thresholds. The success of this methodology depends heavily on the performance of the used classification algorithm. Hence, advance classification algorithms such as the SVM, Artificial Neural Network (ANN), Random Forest, Rotation Forest etc. tend to increase the performance of this methodology. In addition, precise selection of training pixels is necessary to perform an accurate classification, which makes high-resolution images more advantageous when using this methodology.

ACKNOWLEDGMENT

The aerial photos used in this study were acquired by the UAV owned by the Geomatics Department of Karadeniz Technical University.

REFERENCES

- [1] C. Serifoglu Yilmaz, and O. Gungor, "Comparison of the performances of ground filtering algorithms and DTM generation from a UAV-based point cloud," *Geocarto International*, pp. 1-16, 2016.
- [2] C.K. Wand, and Y.H. Tseng, "DEM generation from airborne LiDAR data by an adaptive dual-directional slope filter," *ISPRS Symposium – 100 Years ISPRS*, Vienna, Austria, vol. XXXVIII 7B, pp. 628-632, July 5-7, 2010.
- [3] D. Tóvári, and N. Pfeifer, "Segmentation based robust interpolation-a new approach to laser data filtering," *International Archives of Photogrammetry, Remote Sensing and Spatial Information Sciences*, vol. 36(3/19), pp. 79-84, 2005.
- [4] G. Vosselman, "Slope based filtering of laser altimetry data," *International Archives of Photogrammetry and Remote Sensing*, vol. 33(B3/2), pp. 935-942, 2000.

- [5] M. Roggero, "Airborne laser scanning-clustering in raw data," *International Archives of Photogrammetry Remote Sensing and Spatial Information Sciences*, vol. 34(3/W4), pp. 227-232, 2001.
- [6] G. Sithole, "Filtering of laser altimetry data using a slope adaptive filter," *International Archives of Photogrammetry Remote Sensing and Spatial Information Sciences*, vol. 34(3/W4), 203-210, 2001.
- [7] K. Kim, and J. Shan, "Adaptive morphological filtering for DEM generation," *IEEE International Geoscience and Remote Sensing Symposium (IGARSS)*, pp. 2539-2542, 2011.
- [8] K. Kraus, and N. Pfeifer, "Determination of terrain models in wooded areas with airborne laser scanner data," *ISPRS Journal of Photogrammetry and Remote Sensing*, vol. 53, pp. 193-203, 1998.
- [9] J.S. Evans, and A.T. Hudak, "A multiscale curvature algorithm for classifying discrete return LiDAR in forested environments," *IEEE Transactions on Geoscience and Remote Sensing*, vol. 45, pp. 1029-1038, 2007.
- [10] P. Axelsson, "DEM generation from laser scanner data using adaptive TIN models," *International Archives of Photogrammetry and Remote Sensing*, vol. 33.B4/1, pp. 111-118, 2000.
- [11] X. Meng, L. Wang, J.L. Silván-Cárdenas, and N. Currit, "A multi-directional ground filtering algorithm for airborne LIDAR," *ISPRS Journal of Photogrammetry and Remote Sensing*, vol. 64, pp. 117-124, 2009.
- [12] J.L. Pérez-García, J. Delgado, J. Cardenal, C. Colomo, and M.A. Ureña, "Progressive densification and region growing methods for LIDAR data classification," *International Archives of the Photogrammetry, Remote Sensing and Spatial Information Sciences*, vol. 39(B3), pp. 155-160, 2012.
- [13] P. Lohmann, A. Koch, and M. Schaeffer, "Approaches to the filtering of laser scanner data," *International Archives of Photogrammetry and Remote Sensing*, vol. 33(B3/1), pp. 540-547, 2000.
- [14] K. Zhang, S.C. Chen, D. Whitman, M.L. Shyu, J. Yan, and C. Zhang, "A progressive morphological filter for removing nonground measurements from airborne LIDAR data," *IEEE Transactions on Geoscience and Remote Sensing*, vol. 41, pp. 872-882, 2003.
- [15] M. Yan, T. Blaschke, Y. Liu, and L. Wu, "An object-based analysis filtering algorithm for airborne laser scanning," *International Journal of Remote Sensing*, vol. 33, pp. 7099-7116, 2012.
- [16] A. Kobler, N. Pfeifer, P. Ogrinc, L. Todorovski, K. Oštir, and S. Džeroski, "Repetitive interpolation: A robust algorithm for DTM generation from Aerial Laser Scanner Data in forested terrain," *Remote Sensing of Environment*, vol. 108, pp. 9-23, 2007.
- [17] M. Elmqvist, E. Jungert, F. Lantz, A. Persson, and U. Soderman, "Terrain modelling and analysis using laser scanner data," *International Archives of Photogrammetry Remote Sensing and Spatial Information Sciences*, vol. 34(3/W4), pp. 219-226, 2001.
- [18] M. Elmqvist, "Ground surface estimation from airborne laser scanner data using active shape models," *International Archives of Photogrammetry Remote Sensing and Spatial Information Sciences*, vol. 34(3/A), pp. 114-118, 2002.
- [19] J. Shan, and S. Aparajithan, "Urban DEM generation from raw lidar data," *Photogrammetric Engineering and Remote Sensing*, vol. 71, pp. 217-226, 2005.
- [20] V. Yilmaz, B. Konakoglu, C. Serifoglu, O. Gungor, and E. Gokalp, "Image classification-based ground filtering of point clouds extracted from UAV-based aerial photos," *Geocarto International*, pp. 1-11, 2016.
- [21] G. Sithole, and G. Vosselman, "Experimental comparison of filter algorithms for bare-Earth extraction from airborne laser scanning point clouds," *ISPRS Journal of Photogrammetry and Remote Sensing*, vol. 59, pp. 85-101, 2004.
- [22] A.L. Montealegre, M.T. Lamelas, and J. de la Riva, "A comparison of open-source LiDAR filtering algorithms in a mediterranean forest environment," *IEEE Journal of Selected Topics in Applied Earth Observations and Remote Sensing*, vol. 8, pp. 4072-4085, 2015.
- [23] R.G. Congalton, and K. Green, *Assessing the accuracy of remotely sensed data: principles and practices*, Boca Raton, FL: Lewis, 1999.
- [24] Ö. Akar, and O. Güngör, "Integrating multiple texture methods and NDVI to the Random Forest classification algorithm to detect tea and hazelnut plantation areas in northeast Turkey," *International Journal of Remote Sensing*, vol. 36, pp. 442-464, 2015.

Making Maps with Inexpensive Drones

Levent TAŞÇI
Firat University
Engineering Faculty Geomatic Department
Elazığ, TURKEY
e-mail: ltasci@firat.edu.tr

Abstract— *The maps can also be made with inexpensive Unmanned Aerial Vehicle (UAV). The UAVs carry lightweight cameras that can capture good quality images. These cameras on the UAVs can be set to take pictures at regular intervals. Also, thanks to the lightweight GPS units mounted on the UAVs 3-D positions of the UAVs can be recorded when taking each picture. There are plenty of drones with varying prices. In this study, Orthophoto map of Firat University Campus area is produced with the pictures captured with the digital camera mounted on the DJI Phantom3 professional Unmanned Aerial Vehicles. To increase the geometric accuracy of the produced orthophoto map, 7 control points are established and their positions are measured with the RTK GPS method.*

Keywords—Unmanned Aerial Vehicle; Drones; Image Processing; GPS

I. INTRODUCTION

Unmanned aerial vehicles (UAV) are among the common and frequently used tools in mapping activities in recent years. The hints that these tools, which have developed at a high rate of use and technology, will cause a great change especially in the cartography sector and its activities are already seen in studies. Unmanned aerial vehicles can be described as vehicles that operate without a pilot, with the ability to automatically or semi-automatically fly continuously without regard to aerodynamic flight principles [1]. The advantages of these unmanned vehicles can be listed as;

- Affordable prices,
- Quick collection of topographical data,
- Offers orthophoto maps if desired,
- Offers very high-resolution images,
- Makes repetitive measurements possible,
- Autonomous flights with improved navigation software,
- Does not require very talented and very knowledgeable users to use UAVs and process images taken,
- Offers horizontal accuracies generally around 3 - 10 cm.

II. UNMANNED AERIAL VEHICLE (UAV)

Generally known as "Drone" which means male bee in English. The technical meaning is unmanned aerial vehicle or remotely controlled aircraft technology, or shortly called UAV or UAV (Unmanned Aerial Vehicle). The term used to describe UAV in Turkish is taken directly from English equivalent unmanned aerial vehicle remotely controlled from the ground [3-5]. Though they are inexpensive, small and portable, UAVs can carry lightweight digital cameras that can take very good quality images. These cameras can be set to shoot pictures at regular intervals. Their storage areas can be increased via cheap memory cards. UAVs are also equipped with lightweight and portable GPS units.

III. THE PRODUCTION STEPS OF TOPOGRAPHIC MAPS WITH UAVs

The steps in the production of Topographical Maps with UAV is given below. For more detailed information, should be viewed to 6, 7 and 8 resources.

A. Flight Planning

Either for autonomous or manual flight, flight plans should be made carefully before each flight. In any case, project area needs to be analyzed thoroughly before the flight. There can be energy transmission lines, large trees, sensitive/banned zones or other possible dangers in the flight zone. As a result, it would be useful to examine the existing satellite images before flight.

B. Flight Route Planning

Determination of the flight path is an important part of the unmanned aerial mapping process. In this process, proprietary software of drone manufacturers is used. Software with open source code such as Mission Planner, Map Pilot and PIX4D are the most commonly used software. The contents of these software are very similar.

C. Image Overlays

Before flight, forward and side overlap ratios should be determined. The image processing programs should be

designed so that the images overlap sufficiently from the front and side. There is no a universal rule for image overlay and it varies according to topography and flight altitude. While some researchers suggest 80% forward and 70% side overlaps, others suggest 80% forward and 80% side overlapping images. Pix4D software suggests at least 75% forward and 60% side overlapping photos on its web page.

D. Image Quality-Oriented Flight Planning

To get the best image quality, the flight height, the size and the number of pixels of the sensor, the type of the sensor (CCD or CMOS), the focal length of the lens in the camera, the shutter speed, the light condition, the ISO sensitivity and other camera settings are very important.

E. Height

Height is another important criterion to be considered before flight since it directly affects flight security and legal constrains. Although high altitude images have lower spatial resolution, they cover wider areas with fewer images.

F. Viewing Angles

The most used viewing angles are vertical (nadir) and oblique (off nadir). Nadir-viewing photographs are taken at the top of the field where the camera will exactly look down. This perspective is used in the traditional mapping as common. If the angle is oblique, information about the topography of the earth is collected from the photographs taken with an off-nadir angle.

G. GPS and Coordinate Transformation

Coordinate transformation is a necessary process if the maps obtained by unmanned aerial vehicles will have an Earth-based coordinate system. To perform coordinate transformation between image and Earth-based coordinate system, a few points with known coordinates on both systems must be used. These points are called ground control points. Some unmanned aerial vehicles use RTK (Real Time Kinematic) GPS, which eliminates ground control point need in the field.

H. Ground Control Points

The software needs approximately 5 ground control points to perform georeferencing process. More control points will lead to a more accurate results. Ground control points must be evenly distributed over the ground for more accurate results.

J. 3-D Modeling

To produce 3-D map of the project area requires hundreds of overlapping images. UAV photogrammetry software

creates 3D maps by analyzing these overlapping images with the following steps:

1. Image matching and aligning process by finding common points on overlapping images
2. Improving the calibration parameters by finding the camera's position for each image
3. Sparse point cloud creation. This sparse cloud may be sufficient to create a coarse 3-D model that does not require precise coordinates.
4. Creating a dense point cloud cluster.
5. Obtaining a 3-D "mesh" polygon model representing the surface of the object area.
6. Placing texture taken from the original picture on the model and depth and volume rendering.

IV. APPLICATION


Campus area of Firat University, Faculty of Engineering has been selected for the project area (Figure 1). The selected area covers approximately 0.481 km² =481 Acres. Study area has a uniform slope in a North-South direction. There are no obstacles to threaten and obstruct flight safety within the study area. The terrain is covered with buildings, trees and vegetation.



Fig 1. Working area

The DJI Phantom3 Professional Quadcopter, which is purchased with the financial support of FUBAP was used to create the maps. The technical specifications of this Quadcopter are given in the Table 1.

Table 1. Technical specifications of Quadcopter

	
Weight including battery and propeller	1280 gr.
Maximum rise rate	5m/sn
Maximum Descending velocity	3m/sn
Maximum velocity	16m/sn
Operating temperature	0- 40°
GPS mode	GPS/GLONASS
Maximum flight time	23 minute
Sensor	1/2.3" CMOS Effective pixel: 12.4 M (total pixel: 12.76 M)
Maximum image size	4000*3000 (12 Mp)
Lens	FOV 94° 20 mm (35 mm format equivalent) f/2.8, fokus at ∞
Image saving format	JPG, DNG

In order to georeference the Orthophoto map, 7 control points were evenly distributed over the campus area and their positions were measured using RTK GPS method. The distribution of the control points used for georeferencing is shown in Fig 2.



Fig 2. The distribution of the control points

For flight planning, Map Pilot software, developed by Drones Map Easy software for DJI, was used. Flight planning for the study area is given below (Fig 3.).

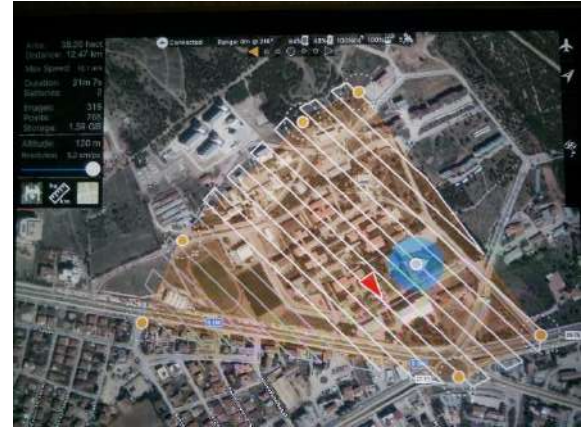


Fig 3. Flight planning for the study area

According to this plan, the flight will take place over an area of 0.481 km². The maximum flight height is 120 m. and at this altitude 321 pictures will be taken using 2 batteries. Quadcopter will make an autonomous flight according to the pre-determined flight plan.

V. PROCESSING IMAGE DATA OBTAINED FROM UNMANNED AIR VEHICLES

321 images were evaluated with Agisoft Photoscan data processing software. Figure 4 demonstrates how images are overlapped during flight, and the Figure 4 indicates very good forward and side overlaps. This implies that no problems will be encountered in 3-D models obtained from these overlaps. As a result of the evaluation of the images with software, Digital Surface Model (DSM), Orthophoto images and the desired frequency of point cloud data of the study area were obtained.

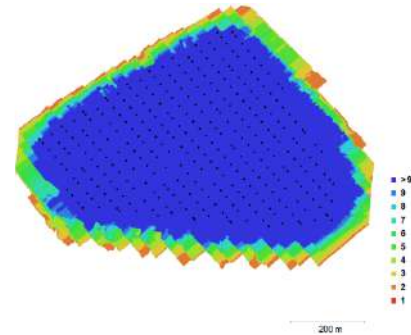


Fig 4. Images overlap

Once the photos have been aligned, the program creates a sparse point cloud containing the parameters of the camera. Point cloud created in the study is shown in Figure 5.

If ground control points are used, the positions of these points in the ground coordinate system must be entered in the software. In this phase: Camera positions, orientation of the pictures and the production of the 3-dimensional point cloud is performed. 3D point cloud and ground control points produced by software are seen in Figure 5.



Fig 5. 3D point cloud and ground control points produced by software

The software obtains a 3-dimensional "mesh" polygon model representing the object surface from the dense cloud cluster (Fig 6).



Fig 6. 3-dimensional "mesh" polygon model

The last step is to place the texture from the original images onto this model (Figure 7-9). This process gives depth and volume to model.



Fig 7. Texture 1



Fig 8. Texture 2

The digital elevation model is a model that gives the height information of a geographical region. The digital elevation model (DEM) of the study area is given Fig 10. The resolution of this model is 9.76 cm / pixel and the point density is 105 points / m²

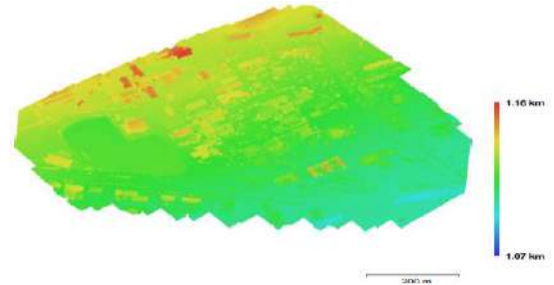


Fig 10. The digital elevation model

VI. RESULTS

This study showed that it is possible to produce 3 dimensional map with high position accuracy with the help of the photographs obtained from UAV 's which are not produced for photogrammetric purpose. In this study, the technical specifications of the purchased UAV were used in its original form untouched. The DJI Phantom3 model uses fish-eye lens. Although we do not recommend a fish-eye lens for photogrammetric purposes, the results we obtained are quite reasonable. The studies done with UAV in the literature have obtained values very close to the point position accuracy obtained in this study. As a result of the analysis, the image resolution for the work area of 0.481 km² is 4.88 cm / pixel. This obtained resolution is equivalent to the work done in the literature. Quadcopter was flown in the project area with autonomous flight mode. Although it does not require much pilot experience for such flights, there are many drawbacks. Used UAV does not recognize any obstacles (for example, electrical wires, etc.) automatically and this may lead to danger of falling. So, the land structure for autonomous flight should be analyzed very well before flight. The duration of flights should also be planned by considering the number of sparse batteries you have. In the used system, it is impossible to start from the same place for another flight. When determining the flight height, the optimum height should be determined by considering the legal height limit. With this study, it is seen that the results obtained by using the photogrammetric techniques can serve to needs of different disciplines.

REFERENCES

- [1] [1] Akgül, M., Yurtseven, H., Demir, M., Akay, A.E., Gülci, S., Öztürk, T., 2016. İnsansız hava araçları ile yüksek hassasiyette sayısal yükseklik modeli üretimi ve ormancılıkta kullanım olanakları. Journal of the Faculty of Forestry Istanbul University 66(1): 104-118. DOI: 10.17099/jffiu.23976.
- [2] [2] Avdan,U., Şenkal, E., Çömert,R., Tuncer, S., İnsansız Hava Aracı İle Oluşturulan Verilerin Doğruluk Analizi, V. Uzaktan Algılama ve Coğrafi Bilgi Sistemleri Sempozyumu (UZAL-CBS 2014), 14-17 Ekim 2014, İstanbul.
- [3] [3] Yakar, M., Toprak, A.S., Ulvi, A., Uysal,M., Konya Beyşehir Bezariye Hanının (Bedesten) İha İle Fotogrametrik Teknik Kullanılarak Üç Boyutlu Modellenmesi, 15. Türkiye Harita Bilimsel ve Teknik Kurultayı, 25 28 Mart 2015, Ankara.
- [4] [4] Drone Nedir, Ne İşe Yarar? <http://yeyete.com/drone-nedir/> Ziyaret tarihi:15.11.2016.
- [5] [5] Wikipedi, İnsansız Hava Aracı, https://tr.wikipedia.org/wiki/%C4%B0nsans%C4%B1z_hava_arac%C4%B1, Ziyaret tarihi:15.11.2016.
- [6] [6] Kakaes, K., Greenwood,F., Lippincott, M., Dosemagen, S., Meier, P., Wich, S., Drones And Aerial Observation: New Technologies For Property Rights, Human Rights, And Global Development A Primer, July 2015.
- [7] [7] Abt Associates, Field Operations Manual for Unmanned Aerial Vehicle (UAV) Survey In the VBS/RM Process, 4 July 2016.
- [8] [8] Remondino, F., Barazzetti, L., Nex,F., Scaioni, M., Sarazzi,D., UAV Photogrammetry For Mapping And 3D Modeling-Current Status And Future PerspectivesInternational Archives of the Photogrammetry, Remote Sensing and Spatial Information Sciences, Volume XXXVIII-1/C22, ISPRS Zurich Workshop,14-16 September 2011.

Ground Filtering of a UAV-based Point cloud with the Cloth Simulation Filtering Algorithm

Cigdem Serifoglu Yilmaz

Geomatics Department
Karadeniz Technical University
Trabzon, Turkey

Volkan Yilmaz

Geomatics Department
Karadeniz Technical University
Trabzon, Turkey

Oguz Gungor

Geomatics Department
Karadeniz Technical University
Trabzon, Turkey

Abstract— Digital Terrain Model (DTM) generation is one of the leading applications in photogrammetry. A DTM is generated by the interpolation of ground points retrieved by ground filtering, which is the removal of the points belong to above-ground objects from point cloud. In the literature, a wide variety of ground filtering approaches have been reported for ground filtering. Complexity of topography makes ground filtering process more challenging, which forces the researchers to developed filtering approaches that require a number of parameters. This, of course, leads the users to try different parameters until they find the optimum filtering result, which is very time consuming in most cases. This study uses the Cloth Simulation Filtering (CSF) algorithm, a recently introduced ground filtering algorithm developed to filter LiDAR (Light Detection and Ranging) data, to filter a point cloud extracted from the aerial photos taken from an unmanned aerial vehicle (UAV). The biggest advantage of the CSF algorithm is that, compared to previously developed ground filtering algorithms, it utilizes less parameters. The results showed that the CSF algorithm committed a type I error of 12.7%, a type II error of 16.7% and a total error of 14.8%.

Keywords— *point cloud; cloth simulation filtering; ground filtering; unmanned aerial vehicle; aerial photogrammetry*

I. INTRODUCTION

DTMs are used in many applications such as mapping, mining engineering, remote sensing, land planning, geology and geomorphology [1,2]. Since a DTM is generated by the interpolation of the points belong to the bare earth surface, there is a need to separate the ground points and points belong to above-ground objects, which is called 'ground filtering'. Ground filtering can be a hard challenge in areas with complex surface variability [3]. A wide variety of ground filtering algorithms have been proposed so far. The users who are willing to perform ground filtering generally try a large number of filtering algorithms until they find the optimum filtering result.

Reference [3] categorized the ground filtering algorithms as morphological filters, segmentation- and cluster-based filters, TIN (Triangulated Irregular Network)-based filters, contour-

based filters, interpolation-based filters and directional scanning filters.

Reference [4] introduced a slope-based filtering approach in which ground filtering is implemented by comparing slopes between a point and its neighbors. Reference [5] used a dual rank filter to remove non-ground points. Reference [6] removed non-ground LiDAR measurements with a progressive morphological filter. This approach filters a point cloud by means of a gradually increasing window and elevation difference thresholds. In this algorithm, slope of the processing area is assumed to be constant, which may lead to poor ground extraction results [7]. To cope with this problem, [8] defined some adjustable parameters to better describe the topography. Reference [9] proposed a morphological filtering algorithm based on multi-gradient analysis. This algorithm first organizes the point clouds by an index mesh. Afterwards, a morphological method is used to compute the multi-gradient of each point. Finally, to remove the above-ground objects, the algorithm iteratively performs an enhanced opening operation constrained by multi-gradient. Reference [10] introduced a TIN (Triangulated Irregular Network)-based filtering algorithm in which seed points are used to generate a sparse TIN, which is then densified until all points are classified as ground and non-ground. This algorithm uses two important parameters; one is the distance between a candidate point and TIN facet, and the other one is the angle between the TIN facet and the line connecting the closest vertex of the facet and candidate point [7]. Reference [11] proposed another surface-based filtering algorithm based on a weighted linear least-squares interpolation. Reference [12] introduced a filtering algorithm in which a hierarchical approach is used together with a weighing function to detect the raster elements containing data relating to above-ground objects. In [13], ground and non-ground points were separated by performing one-dimensional labelling in two opposite directions, both along the scan line profile. Reference [14] used a two-step procedure to remove the non-ground points. The first step includes the initialization of the region growing from ground seeds. In the second step, neighbor points are gradually added based on three mathematical measurements [3].

This study uses the CSF algorithm, a recently introduced ground filtering algorithm, to filter a UAV-based point cloud. Further information about the CSF algorithm can be found in Section II.

II. MATERIAL AND METHODS

A. Study Area

The study area, which is shown in Figure 1, is a small part of the Karadeniz Technical University (KTU) campus in the city of Trabzon, located on the northeastern part of Turkey. As seen in the figure, various above-ground objects (building, tree, mosque etc.) exist in the study area. Elevation ranges from 69 m to 111 m in the study area, whose size is 146 m x 203 m.

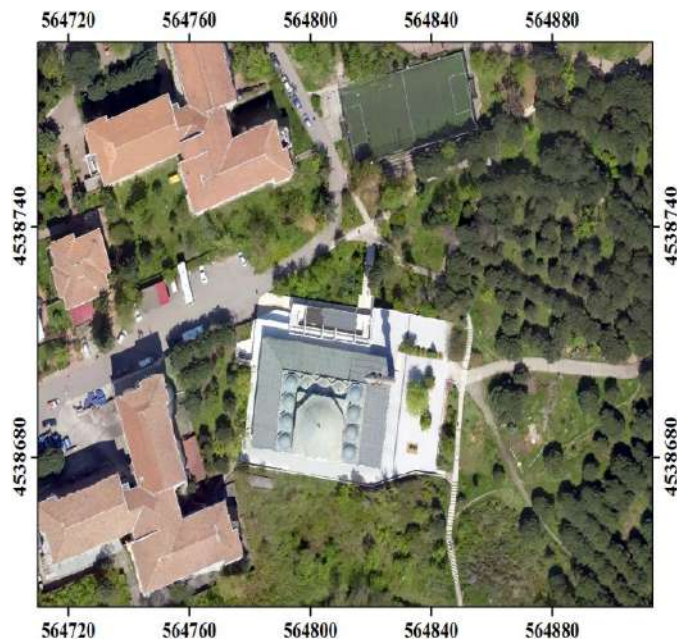


Fig. 1. Study area.

B. Methodology

Before the flight, 12 ground control points (GCP) were established in the KTU campus. 3D positions of the GCPs were then measured by means of the RTK GPS technique. Next, the flight was planned, and the flight altitude and total number of flight lines were decided. Afterwards, the flight was conducted with the Gatewing X100 UAV and 256 aerial photos were taken during the flight. The aerial photos were taken by the RICOH GR DIGITAL IV digital camera mounted on the UAV. The flight was conducted from an altitude of 185 m along nine flight lines. After the flight, captured aerial photos were processed by using the Agisoft Photoscan Professional software. A point cloud with a density of 15.2 point/m² was extracted with the software. A 10-cm orthophoto and a 15-cm Digital Surface Model (DSM) were also generated with the same software. The point cloud was then cropped with respect to the boundary of the study area in order to test the performance of the CSF algorithm.

The CSF algorithm, introduced in [7], simulates a simple physical process. Imagine a piece of cloth is placed above a terrain. In this case, the cloth drops because of gravity. If the cloth is soft enough, DSM would be the final shape of the cloth. However, if the terrain is turned upside down and the cloth is specified with rigidity, DTM would be the final shape of the cloth. The CSF algorithm simulates this process [7].

The fundamental implementation steps of the CSF algorithm are as follows [7];

- The outliers are removed with a third-party software.
- The point cloud is inverted.
- The number of particles are determined with respect to the user defined grid resolution.
- All points and grid particles are projected to a horizontal plane. In this plane, a nearest point (CP – corresponding point) is found for each cloth particle.
- The height value of the CP is specified by an intersection height value (IHV), which shows the lowest possible position of each particle.
- The current height value (CHV) of a particle is compared with the IHV in each iteration. A particle is moved back to the position of the IHV and made ‘unmovable’ if the CHV is equal or lower than the IHV.
- Simulation continues until the maximum height variation of all particles is small enough or the maximum iteration number defined by the user is exceeded.
- The cloud-to-cloud distance between the point cloud and grid particles is calculated.
- A point is classified as ground if its distance to the simulated particles is smaller than a threshold, otherwise it is classified as non-ground.

The CSF algorithm uses four user-defined parameters as grid resolution, which is the horizontal distance between two neighboring particles; class threshold, which is a threshold to classify the points as ground and non-ground based on the distances between the original point cloud and the simulated terrain; iterations, which is the maximum iteration times; and time step, which controls the displacement of particles from gravity.

In this study, the CSF algorithm was implemented in MATLAB environment. First, default parameter values given in [7] were tried for three terrain types (flat terrain, steep terrain, and high and steep slopes). Visual observations revealed that the default parameter values did not give satisfactory filtering results. After only a few trials, optimum parameters were found as 0.6, 500, 1 and 0.65 for grid resolution, iterations, class threshold and time step, respectively. Terrain type was also selected as gentle slope. The CSF algorithm removed 235,756 of 449,627 points. The ground points were then interpolated by the bi-linear

interpolation technique to generate the 15-cm DTM of the study area.

III. RESULTS AND DISCUSSION

The produced DSM and DTM are shown in Figures 2 and 3, respectively. It can be seen from Figure 3 that the CSF algorithm performed well in most parts of the study area. However, there can be seen some filtering errors at the boundaries of objects.

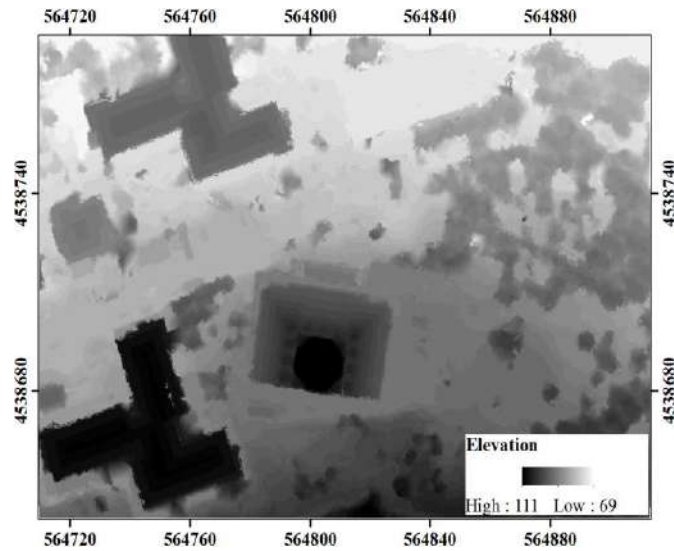


Fig. 2. Produced 15-cm DSM.

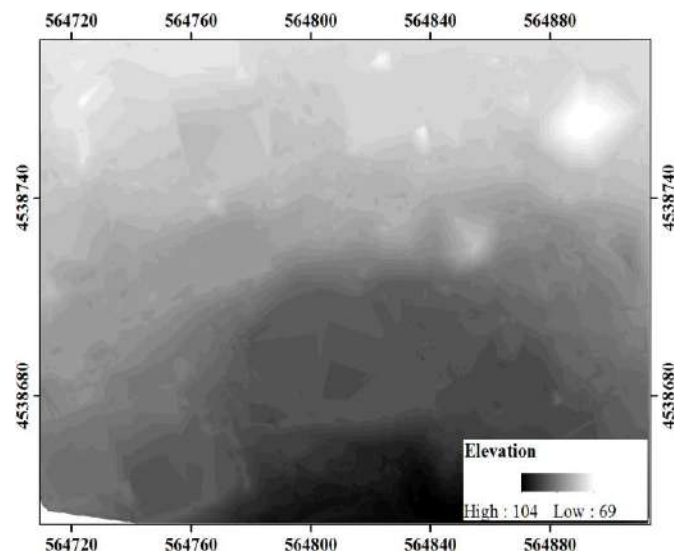


Fig. 3. Produced 15-cm DTM.

Since visual evaluation depends on the perspective of the analyst, quantitative evaluations may better reveal the performance of the filtering algorithm. Reference [15] stated that there may be two types of errors in ground filtering process; omission error, which is related to the misclassification of ground points; and commission error,

which is the misclassification of non-ground points [15-17]. The Type I, Type II and Total error metrics are calculated as [16];

$$\text{Type I error} = o / G \quad (1)$$

$$\text{Type II error} = c / NG \quad (2)$$

$$\text{Total error} = (o + c) / (G + NG) \quad (3)$$

where, c , o , NG and G are the commission error, omission error, total number of non-ground points and total number of ground points, respectively.

In the study, the Type I, Type II and Total errors were calculated by using 600 test points, which were randomly selected from the point cloud. Actual classes of these test points were specified by overlapping them with the 10-cm orthophoto. Investigation of the test points showed that 283 of them were belong to the ground class and 317 of them belong to the non-ground class. The CSF algorithm misclassified 36 of the 283 ground points, which resulted in a Type I error of 12.7%. These misclassified points generally situate in the vicinity of the above-ground objects. The algorithm did not manage to remove 53 of 317 non-ground points, which shows that the algorithm committed a Type II error of 16.7%. In the study area, there are different interlocking trees with different heights. Commission errors generally occurred in these regions. The Total error was found to be 14.8%, which can be considered quite good for a ground filtering algorithm.

IV. CONCLUSIONS

This study aimed at investigating the UAV-based point cloud filtering capability of the CSF algorithm, which was originally developed to filter raw LiDAR data. It can be inferred from the results that the CSF algorithm is quite successful in filtering point clouds. Since the algorithm does not use complex parameters, it does not take too much time to search for suitable parameters for this algorithm. In addition, the CSF algorithm performs in a short span of time, which is very advantageous compared to other algorithms in the literature. Future studies will focus on comparing the performance of this algorithm with those of other successful filtering algorithms in terrains with higher surface variability.

ACKNOWLEDGMENT

The aerial photos used in this study were acquired by the UAV owned by the Geomatics Department of Karadeniz Technical University.

REFERENCES

- [1] K. Kraus, and N. Pfeifer, "Determination of terrain models in wooded areas with airborne laser scanner data," *ISPRS Journal of Photogrammetry and remote Sensing*, vol. 53, pp. 193-203, 1998.
- [2] N.V. Iurist, V.E. Oniga, and F. Statescu, "Comparative study on digital terrain models created based on als data and pleiades images," *Journal of Geodesy and Cadastre RevCAD*, vol. 19, pp. 127-134, 2015.
- [3] X. Meng, N. Currit, and K. Zhao, "Ground filtering algorithms for airborne LiDAR data: A review of critical issues," *Remote Sensing*, vol. 2, pp. 833-860, 2010.
- [4] G. Vosselman, "Slope based filtering of laser altimetry data," *International Archives of Photogrammetry and Remote Sensing*, vol. 33(B3/2), pp. 935-942, 2000.
- [5] P. Lohmann, A. Koch, and M. Schaeffer, "Approaches to the filtering of laser scanner data," *International Archives of Photogrammetry and Remote Sensing*, vol. 33(B3/1; PART: 3), pp. 540-547, 2000.
- [6] K. Zhang, S.C. Chen, D. Whitman, M.L. Shyu, J. Yan, and C. Zhang, "A progressive morphological filter for removing nonground measurements from airborne LIDAR data," *IEEE Transactions on Geoscience and Remote Sensing*, vol. 41, pp. 872-882, 2003.
- [7] W. Zhang, J. Qi, P. Wan, H. Wang, D. Xie, X. Wang, and G. Yan, "An easy-to-use airborne lidar data filtering method based on cloth simulation," *Remote Sensing*, vol. 8, pp. 1-22, 2016.
- [8] Q. Chen, P. Gong, D. Baldocchi, and G. Xie, "Filtering airborne laser scanning data with morphological methods," *Photogrammetric Engineering & Remote Sensing*, vol. 73, pp. 175-185, 2007.
- [9] Y. Li, "Filtering airborne LiDAR data by an improved morphological method based on multi-gradient analysis," *International Archives of the Photogrammetry, Remote Sensing and Spatial Information Sciences*, vol. 40, pp. 191-194, 2013.
- [10] P. Axelsson, "DEM generation from laser scanner data using adaptive TIN models," *International Archives of Photogrammetry and Remote Sensing*, vol. 33.B4/1, pp. 111-118, 2000.
- [11] K. Kraus, and N. Pfeifer, "Determination of terrain models in wooded areas with airborne laser scanner data," *ISPRS Journal of Photogrammetry and remote Sensing*, vol. 53, pp. 193-203, 1998.
- [12] R. Wack, and A. Wimmer, "Digital terrain models from airborne laser scanner data - A grid based approach," *International Archives of Photogrammetry, Remote Sensing and Spatial Information Sciences*, vol. 34(3/B), pp. 293-296, 2002.
- [13] J. Shan, and S. Aparajithan, "Urban DEM generation from raw lidar data," *Photogrammetric Engineering and Remote Sensing*, vol. 71, pp. 217-226, 2005.
- [14] D. Tóvári, and N. Pfeifer, "Segmentation based robust interpolation-a new approach to laser data filtering," *International Archives of Photogrammetry, Remote Sensing and Spatial Information Sciences*, vol. 36(3/19), pp. 79-84, 2005.
- [15] G. Sithole, and G. Vosselman, "Experimental comparison of filter algorithms for bare-Earth extraction from airborne laser scanning point clouds," *ISPRS Journal of Photogrammetry and Remote Sensing*, vol. 59, pp. 85-101, 2004.
- [16] A.L. Montealegre, M.T. Lamelas, and J. de la Riva, "A comparison of open-source LiDAR filtering algorithms in a mediterranean forest environment," *IEEE Journal of Selected Topics in Applied Earth Observations and Remote Sensing*, vol. 8, pp. 4072-4085, 2015.
- [17] C. Serifoglu Yilmaz, and O. Gungor, "Comparison of the performances of ground filtering algorithms and DTM generation from a UAV-based point cloud," *Geocarto International*, pp. 1-16, 2016.

A numerical modeling on shotcrete strength and excavation depth in tunneling

Mustafa KANIK

Firat University
Faculty of Engineering, Geological Engineering Department
Elazig, Turkey
mkanik@firat.edu.tr

Zulfu GÜROCAK

Firat University
Faculty of Engineering, Geological Engineering Department
Elazig, Turkey
zgurocak@firat.edu.tr

Abstract— In tunneling, one of the effective parameters on cost is the type of support systems to be used during tunnel excavation. The most important factor in determining the support type depends on the geological and geotechnical characteristics of the rock mass to be excavated. Until today, many empirical rock mass classifications were proposed to determine the type of support such as Rock Mass Rating (RMR), Rock Mass Quality (Q) and Rock Mass Index (RMI). In these classifications, the engineering properties of discontinuities and the rock material are used as input parameters, and the support elements should be used is determined. Today, the most common support elements used are shotcrete and rock bolts. These two support elements are used either alone or together according to the rock mass class. However, the support systems of empirical rock mass classification are inadequate in some cases or may lead to excessive use of support. Another important issue is the technical properties of the support elements such as the strength of shotcrete, the diameter and strength of rock bolt. These technical properties are not defined in the empirical rock mass classification systems and engineers use supports with different technical characteristics in practice. In addition, the effect of the overburden is another important issue that is not explained in empirical rock mass classification. Although revision of the support elements is inevitable in case of the increase in tension due to overburden, actually, support systems with the same technical properties are preferred for different excavation depths in practice.

The aim of this study is to determine the change in the strength of the shotcrete with the increase in depth of the excavation for the same rock mass class. For this aim, numerical modeling was developed by using Finite Element Method (FEM), in order to determine the relationship between the strength of the shotcrete and excavation depth. For the modeling, a tunnel of 10 m wide, 7 m height, single tube, modified horseshoe shaped, was modeled with the Phase² software, using weak, fair and good rock classes obtained from RMR₈₉ system. Very poor and very good rock masses of RMR₈₉ system were not included in this study, due to the main support element type is I-Beam for the very poor rock and spot bolting for the very good rock. In the first stage, shotcrete strength was assumed as 30 MPa and analyses were started to carry out from 10 m depth. The support elements of the poor rock mass provide stability up to 190 m, and the shotcrete elements were yielded after 190 m. Fair rock mass's shotcrete elements were started to yield from 280 m and the yielding depth of the shotcrete for the good rock mass was 530 m. These obtained data showed, the increase in the strength of the shotcrete is necessary for the poor, fair and good rock masses. In the second stage, shotcrete strength was increased to 40 MPa and the numerical analyses developed again. The results of the analysis showed that the shotcrete elements started to yield at 270 m in the weak rock mass, 430 m in the fair rock mass, and 630 m in the good rock mass. In this study, for the support system of the RMR₈₉ to be applicable, the shotcrete strength should be increased with the increase in the overburden was revealed.

Keywords—*Empirical rock mass classification; support system; shotcrete strength; excavation depth; numerical modeling*

Determination of friction angles between soil and steel - FRP piles

H. Suha Aksoy
Firat Univ. Eng. Faculty
Civil Eng. Dept.
Elazig / TURKEY
saksoy@firat.edu.tr

Mesut Gör
Firat Univ. Eng. Faculty
Civil Eng. Dept.
Elazig / TURKEY
mgör@firat.edu.tr

Esen İnal
Firat Univ. Eng. Faculty
Civil Eng. Dept.
Elazig / TURKEY
inal.esen@gmail.com

Abstract— Forces of friction between structure and soil are taken into account in the design of geotechnical engineering constructions such as piles, retaining walls, sheet piles and diaphragm walls. Although many studies were carried out about the soil-structure interaction in recent years. However, in pile design, frictional forces are still calculated by using the empirical formulas proposed in the first half of the 20th century. Throughout history, wood was often used as friction piles. Steel piles are used extensively in practice. Nowadays, in harsh environmental conditions fiber-reinforced polymer (FRP) piles come into use in numerous cases. As is known, the effect of pile point tip resistance on the bearing capacity is ignored particularly in loose sands and the bearing capacity is fully taken equal to the skin friction. Hence, it is understood that correct determination of skin friction angle is very important in engineering calculations. In this study, various ratios of low plasticity clays (CL) were added to the sandy soil and compacted to standard Proctor density. Thus, soils with various internal friction angles were obtained. By performing interface shear tests (IST), skin friction angles of these soils with steel (st37) and FRP were determined. Based on the data obtained from the test results, a chart was proposed, which engineers can use in pile design. By means of this chart, the skin friction angles of the soils, of which only the internal friction angles are known, with steel and FRP materials can be determined easily.

Keywords— skin friction; design chart; pile materials; direct shear test

I. INTRODUCTION

Skin friction angle between soil and pile materials emerges as an important component in the designs made by geotechnical engineers. Frictional forces between structure and soil are taken into consideration in the design of civil engineering constructions such as retaining walls, sheet piles, diaphragm walls and piles. As is known, the effect of pile point tip resistance on the bearing capacity is ignored particularly in loose sand soils and the bearing capacity is fully taken equal to the skin friction. Hence, it is understood that correct determination of skin friction angle is very important in geotechnical design.

Many geotechnical engineers consider the skin friction angle (δ) as equal to $2/3$ of the internal friction angle (ϕ) of soil

in their designs [1]. However, it is known that δ can change in the event of frictions between the same soil and different materials. Even today, skin friction angles (δ) between soil and pile materials are not exactly known and design engineers use approximate values. δ values used in designs are of essential in the determination of pile number, diameter and length. A low δ value leads making non-economic designs and increases project costs substantially. On the other hand, a high δ value causes to safety problems.

Wood was used as a driven pile material up to the first half of the 20th century. However, the use of wood declined almost non-existing in today due to increasing costs. Nowadays, steel is commonly used as the driven pile material. Plastic composite materials have also been started to be used in recent years as alternative to steel. Today, FRP (fiber-reinforced polymer) material is ever-increasingly used due to the reasons such as being economic, having high tensile and compressive strengths and its resistance to harsh environmental conditions.

Potyondy (1961) conducted interface shear tests (IST) on the soils prepared in four sand/clay ratios and determined the skin friction angles of wood, steel and concrete materials. When examine the IST results, it is seen that the critical value for the cohesion is the situation where sand/clay ratio is 1. The cohesion rises quickly in all values over this ratio [2]. Uesugi and Kishida (1986) determined the friction between mild steel and dry sand by using IST. They found that the type and mean grain diameter of sand (D_{50}) had significant effects on friction angle [3]. There are many studies where the frictions between geosynthetics and sands were analyzed thorough IST [4, 5, 6, 7]. When articles in the literature are examined, it is generally seen that the frictions of clean sands (without fine-grained soils) and pile material surfaces were determined [6, 8, 9, 10]. However, clean sands are hardly seen in nature. Therefore, mixing various ratios of sand and clay soils will allow more realistic results to be obtained in the in laboratory of the soils encountered in the field [11].

Clayey sand soils containing various ratios (0%, 20%, 30%, 40% and 45%) of clay were used in laboratory tests. The produced soils have different internal friction angles, skin friction angles between the soils and pile materials (steel and FRP) were obtained. As a result of the laboratory studies, a

chart was proposed, which shows the relationship between the internal and skin friction angles. By means of this chart, the skin friction angles between soil and pile materials can be obtained based only on the internal friction angles of soils.

II. MATERIAL AND METHOD

The index properties of the sand and low plasticity clay (CL) soil used in the tests were determined and given in Table 1. Black basalt originated river sand (specific gravity 2.77) used in the tests. The sieve analyses, Atterberg limits tests and specific gravity tests were conducted according to standards [12, 13, 14]. Sieve analysis of sand and clay soils can be seen in Figure 1.

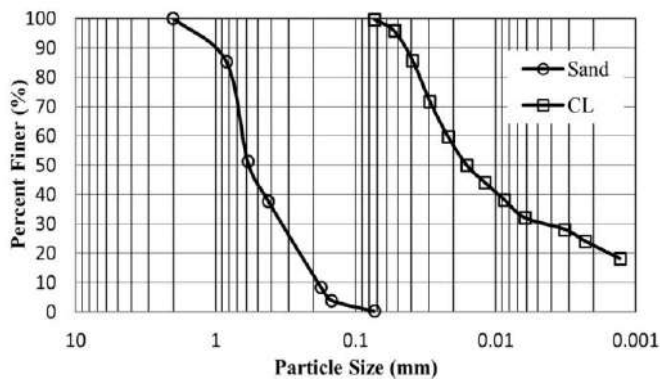


Fig. 1. Grain size distribution of soils

CL at the ratios of 0%, 20%, 30%, 40% and 45% in weight were mixed in the sand and optimum water contents (w_{opt}) were determined by performing standard Proctor tests on these mixtures [15]. w_{opt} values and soil classifications according to Unified Soil Classification System (USCS) are shown for each mixture in Table 2. The mechanical properties of the steel and FRP materials used in the tests are shown in Table 3.

TABLE I. INDEX PROPERTIES OF SOILS

	Sand	CL
D_{30} (mm)	0.33	0.0045
D_{50} (mm)	0.57	0.016
Liquid Limit, W_L (%)	-	30
Plastic Limit, W_P (%)	-	15
Specific Gravity, γ_s	2.77	2.68

TABLE II. MIXING RATIOS AND OPTIMUM MOISTURE CONTENT

Mixture	Clay (%)	Sand (%)	Soil Group (USCS)	w_{opt} (%)
m_0	0	100	SP	6.0
m_{20}	20	80	SC	9.0
m_{30}	30	70	SC	10.0
m_{40}	40	60	SC	11.5
m_{45}	45	55	SC	13.0

TABLE III. PROPERTIES OF PILE MATERIALS

	Steel (st37)	FRP (50% glass)
Compression strength (Mpa)	240	200
Tensile strength (Mpa)	360	240
Tensile Elasticity Modulus (Gpa)	210	23
Density (gr/cm ³)	7.85	1.8

The direct shear test (DST) was performed to obtain the internal friction angles (ϕ) of the soil mixtures [16]. Interface shear tests (IST) were conducted in order to determine the skin friction angles (δ) between the produced soil samples and steel, FRP [17]. Test setups can be seen in Figure. 2. and Figure 3. DST and IST tests were performed at a rate of 0.5 mm/min horizontal displacement. Samples prepared at the standard Proctor density and optimum water content were used in DST and IST tests and the results obtained from the tests can be seen in Table 4.

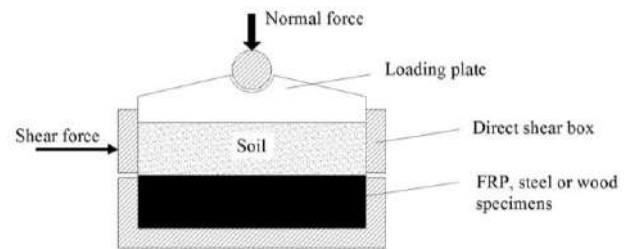


Fig. 2. Sketch of interface shear test setup

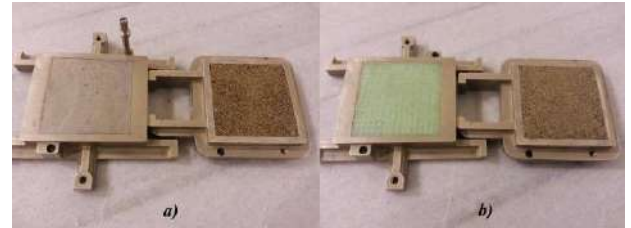


Fig. 3. Interface shear test setup; a) IST (steel soil) b) IST (FRP-soil)

TABLE IV. DIRECT SHEAR TEST (DST) AND INTERFACE SHEAR TEST (IST) RESULTS

Mixture	Internal friction angle of soil, ϕ (°)	Skin friction angle, δ (°)	
		Steel	FRP
m_0	43.0	26.5	34.5
m_{20}	39.5	31.5	37.0
m_{30}	41.5	29.2	36.0
m_{40}	35.0	27.0	32.0
m_{45}	28.0	18.0	22.7

Even today, in most projects, skin friction angle is calculated by using $\delta=2\phi/3$ equation. But every material have different skin friction angle with soils [11]. Especially for FRP this equation gives significantly lower δ values than test results. For example, for $\phi=35^\circ$ it is calculated that $\delta=23.3^\circ$. This δ value obtained from IST tests for FRP as 32.0° .

Therefore, as skin friction angle assumed lower values causes increase in number, diameter and depth of piles. Consequently non-economical designs can be made by using this equation.

III. SKIN FRICTION CHART

The results determined from the tests and then analyzed. A skin friction chart was proposed to be used in pile design (Figure 4.). Thanks to this chart, geotechnical engineers will be able to obtain the skin friction angles between the soil and pile materials based on the internal friction angle of soil in the field.

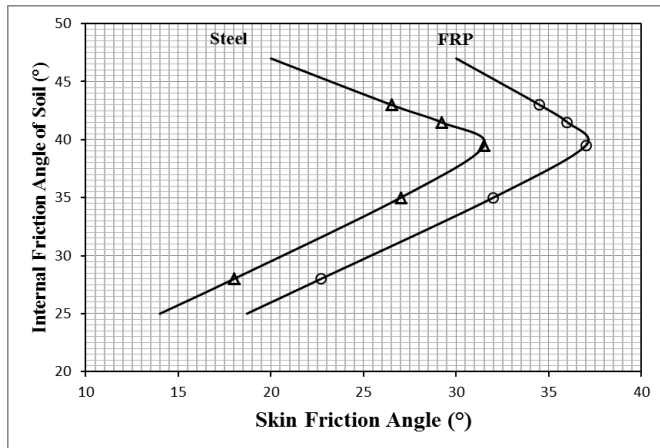


Fig. 4. Skin friction chart for steel and FRP

IV. LITERATURE REVIEW WITH CASES

The results determined through the chart and the studies conducted in the past are shown in Table 5. When the table is examined, it is seen that the δ values obtained through the proposed chart and the values determined in the study performed by Potyondy (1961) show nearly 100% similarity for steel [2]. When results of the chart and the study of Pando et al. (2002) are compared, it is seen that the δ values obtained for FRP material show approximately 90% of similarity [18]. When the results of the chart are compared with the study of Sakr et al. (2005), the δ values show 91% similarity for steel and 94% for FRP material [8]. And when the results of the chart and the studies of Tiwari et al. (2010) and Tiwari and Al-Adhahd (2014) are compared, it is seen that δ values show approximately 90% similarity for steel [10, 19].

Consequently, when δ values obtained from the chart and the studies conducted in the past are compared, these values show similarity more than 90%. The small differences around 10% are considered to arise from types of pile materials (steel hardness and FRP types) used in the tests and the use of dry sand in most studies.

TABLE V. COMPARISON BETWEEN CHART AND OTHER STUDIES

Soil (ϕ) (°)	Potyondy (1961), δ (°)	Pando et al. (2002), δ (°)	Sakr et al. (2005), δ (°)	Tiwari et al. (2010), δ (°)	Tiwari and Al- Adhahd (2014), δ (°)	Similarities between Literature and Skin Friction Chart (%)	
						Steel	FRP
31.0	-	-	-	24.4	-	21.7	89
31.4	-	-	-	-	26.1	22.4	86
33.1	-	-	-	27.6	-	24.6	89
33.3	-	-	-	28.5	-	24.9	87
33.4	-	-	-	-	27.4	25.1	92
34.7	-	29.2	-	-	-	26.6	93
37.0	-	-	26.6	-	-	29.1	91
40.0	31.5	-	-	-	-	31.2	99
43.4	-	29.5	-	-	-	25.8	87
44.5	24.2	-	-	-	-	24.3	100

V. CONCLUSIONS

The use of different pile materials, significantly changes the angle of skin friction (δ). Diameter, length and number of piles are considerably affected from these changes.

- IST were performed on the interfaces between soils and pile materials (steel and FRP). The skin friction angles between these materials and various soils were determined.
- In laboratory studies, soils with internal friction angles ranging between 28° and 43° were used.
- When the results determined from the tests and then analyzed, a chart is proposed which allows acquiring the angle of skin friction to take place between soil, the internal friction angle of which is known, and various pile materials.
- Many articles are found in the literature and then these studies were compared with the chart proposed and it was observed conformity over 90% in the δ values determined.

Nowadays, design engineers use equations that accept δ values equal for all pile materials ($\delta=2\phi/3$). This approach prevents make more realistic designs. True skin friction angles (δ) can be determined by means of the proposed chart. Thus, more economic designs can be made by selecting reasonable pile diameter, length and number.

When the internal friction angles (ϕ) of sand-clay mixture soils are examined, it can be seen that ϕ value decreases as the clay percentage increases. However, a slight increase occurred in ϕ in any cases where the clay content is around 30%. These slight increases in the internal friction angles of sand-clay mixtures with the increase of the clay content were observed by Dafalla (2013) and Bayoğlu (1995) as well [20, 21].

REFERENCES

- [1] Terzaghi, K. & Peck, R.B. (1948). Soil Mechanics in Engineering Practice. John Wiley and Sons, N. York.
- [2] Potyondy, J., G. (1961). Skin friction between various soils and construction materials. *Geotechnique*, 11(4): 339-353.
- [3] Uesugi, M., Kishida, H. (1986). Influential factors of friction between steel and dry sands. *Soils and Foundations*, 26(2): 33-46.
- [4] O'Rourke, T., Druschel, S., and Netravali, A. (1990). Shear strength characteristics of sand-polymer interfaces *J. Geotech. Geoenviron. Eng.*, 116(3): 451-469.
- [5] Izgin, M. and Wasti, Y. (1998). Geomembrane-sand interface frictional properties as determined by inclined board and shear box tests. *Geotextiles and Geomembranes*, 16(3): 207-219.
- [6] Frost, J. and Han, J. (1999). Behavior of interfaces between fiber-reinforced polymers and sands. *J. Geotech. Geoenviron. Eng.*, 125(8): 633-640.
- [7] Palmeira, E. M. (2009). Soil-geosynthetic interaction: modelling and analysis. *Geotextiles and Geomembranes*, 27(5): 368-390.
- [8] Sakr, M., El Naggat, M., and Nehdi, M. (2005). Interface characteristics and laboratory constructability tests of novel fiber-reinforced polymer/concrete piles. *J. Compos. Constr.*, 9(3): 274-283.
- [9] Gireesha, N. T., and Muthukkumaran, K. (2011). Study on soil structure interface strength property. *International Journal of Earth Sciences and Engineering*, 4(6) SPL: 89-93.
- [10] Tiwari, B. and Al-Adhahd, A. R. (2014). Influence of relative density on static soil-structure frictional resistance of dry and saturated sand. *Geotechnical and Geological Engineering*, 32(2): 411-427.
- [11] Aksoy, H. S., Gör, M. and İnal E. (2016). A new design chart for estimating friction angle between soil and pile materials. *Geomechanics and Engineering*, 10(3): 315-324.
- [12] ASTM D422-63(2007)e2 (2007). ASTM International, Standard test method for particle-size analysis of soils, West Conshohocken, PA.
- [13] ASTM D4318-10e1 (2010). ASTM International, Standard test methods for liquid limit, plastic limit, and plasticity index of soils, West Conshohocken, PA.
- [14] ASTM D854-14 (2014). ASTM International, Standard test methods for specific gravity of soil solids by water pycnometer, West Conshohocken, PA.
- [15] ASTM D698-12e1 (2012). ASTM International, Standard test methods for laboratory compaction characteristics of soil using standard effort (12 400 ft-lbf/ft³ (600 kN-m/m³)), West Conshohocken, PA.
- [16] ASTM D3080 / D3080M-11 (2011). ASTM International, Standard test method for direct shear test of soils under consolidated drained conditions, West Conshohocken, PA.
- [17] ASTM D5321 / D5321M-14 (2014). ASTM International, Standard test method for determining the shear strength of soil-geosynthetic and geosynthetic-geosynthetic interfaces by direct shear, West Conshohocken, PA.
- [18] Pando, M., Filz, G., Dove, J. and Hoppe, E. (2002). Interface shear tests on frp composite piles. *Deep Found.*, 1486-1500.
- [19] Tiwari, B., Ajmera, B., and Kaya, G. (2010). Shear strength reduction at soil structure interface. *GeoFlorida 2010*: 1747-1756.
- [20] Dafalla, M. A. (2013). Effects of clay and moisture content on direct shear tests for clay-sand mixtures. *Advances in Materials Science and Engineering*, 2013, Article ID 562726: 1-8.
- [21] Bayoğlu, E. (1995). Shear strength and compressibility behavior of sand - clay mixtures. M.Sc. Thesis, Middle East Technical University, Ankara, Turkey.

Usability of Nakayasu Synthetic Unit Hydrograph Method on Turkey's Small Scale Basins

Mahsum AYDIN

Yuzuncu Yil University, Engineering Faculty, Civil Eng.
Department, Van, TURKEY
maydin@yyu.edu.tr

Tamer BAGATUR

Dicle University, Engineering Faculty, Civil Eng.
Department, Diyarbakir, TURKEY
tbagatur@dicle.edu.tr

Abstract

In this study, it is aimed to examine the usability of Nakayasu Synthetic Unit Hydrograph (NSUH) method for small scale basins in Turkey. For this purpose, observed average unit hydrograph (OAUH) data of seven small scale basins located in Turkey were used. It has been understood that there are large differences between the unit hydrograph parameters calculated with the help of the NSUH method and the parameters of the observed average unit hydrographs (OAUH) and that the equations given by the NSUH method cannot be used in Turkey's basins. The equations given by NSUH method has been modified to make it suitable for Turkey's basins with the help of regression analysis using OAUH parameters. The difference between the parameters calculated by the help of the modified new equations and the parameters of OAUHs was found to be quite small. For testing the performance of MNSUH equations, the unit hydrograph parameters are calculated by using Mockus method. When the calculated values are examined, it is thought that the equations given by NSUH method can be used by modifying on Turkey's small scale basins.

Keywords: Nakayasu; Synthetic Unit Hydrograph; Watershed; Turkey's Basins

I. INTRODUCTION

When calculating and designing water structures, it is necessary to determine the flood discharge of the regions where they are located. It is known that there are many methods for calculation of flood discharge, but unit hydrograph methods give more realistic results [1]. The unit hydrograph (UH) method can only apply to the watershed where rainfall and stream flow data measured [2]. But always measured data may not be available. In this situation the flood discharge can be calculated using synthetic unit hydrograph methods. There are already several synthetic unit hydrograph (SUH) methods. Among these methods Snyder, Mockus and DSI methods are the most widely used SUH methods in Turkey [3, 4]. One of these SUH methods is NSUH method. NSUH method is developed by Dr. Nakayasu in 1940's for estimating flood discharge of small urban watersheds of Japan [5]. Although this method is widely used in Far Eastern countries it is not used in Turkey and European countries [6].

The aim of this study is to examine usability of NSUH method in Turkey's small-scale basins. For this purpose, seven small-scale basin OAUH data were used.

Firstly, calculations were made by using the equations given by NSUH method. When the calculated UH parameters and OAUH parameters are compared, it has been concluded that the equations given by the NSUH method are not suitable for using in Turkey's small-scale basins.

For this reason, it would be appropriate to use the equations given by NSUH method by modifying, using OAUH data.

The Snyder's SUH method should be applied on the basins which are bigger than 1000 km², DSI SUH method can be applied on drainage area up to 1000 km², since the unit hydrograph used in this method is obtained according to the 2-hour heavy rainfall, the rising time in the unit hydrograph (T_p) should not be less than 2 hours. Otherwise DSI SUH Method does not give healthy results. The Mockus SUH method is used in precipitation areas with a collection time (T_c) of less than 30 hours [15]. Therefore, for testing the effectivity of MNSUH method, the unit hydrograph parameters are calculated by using MNSUH and Mockus method and the results are compared.

II. MATERIAL

In this study, for modifying Nakayasu SUH equations Turkey's 7 small-scale basins were selected. The OAUH datas belong to these basins are taken from KHGM Soil and Water Resources Research Final Reports.

Selected sub-basins are show in Table 1.

TABLE I. SELECTED SUB-BASINS AND LOCATIONS

Name of Sub-Basins	Location of Sub-Basins
Izmir-Menemen-Ulucak	Number 5 Gediz Basin
Konya-Seydisehir-Glabbera	Number 16 Konya Basin
Mersin-Tarsus-Topçu	Number 17 East Mediterranean Basin
Konya-Beysehir-Karabalçık	Number 16 Konya Basin
Adiyaman-Kahta-Harabe	Number 21 Euphrates Basin
Yozgat-Sorgun-Ikikara	Number 15 Kizilirmak Basin
Ankara-Haymana-Catalkaya	Number 12 Sakarya Basin

The OAUH parameters of selected sub-basins shown in Table 1 are taken from KHGM Soil and Water Resources Investigation Result Reports [3, 7, 8, 9, 10, 11, 12].

The selected sub-basins' area (A), length (L) values and observed average unit hydrographs' (OAUH) peak discharge (Q_p), reaction times (t_r), peak time (T_p), unit hydrograph base

time (T_b) and the time of the peak discharge reducing %30 ($T_{0.3}$) values are given in Table 2.

The selected sub-basins geographic locations are shown in Figure 1.

TABLE II. THE CHARACTERISTICS OF SMALL SCALE BASINS AND OBSERVED AVERAGE UNIT HYDROGRAPHS

	Sub-Basins	A (km ²)	L (km)	Q_p (m ³ /s mm)	t_r (h)	T_p (h)	T_b (h)	$T_{0.3}$ (h)
1	Izmir-Menemen-Ulucak	0.34	1.30	0.068	0.69	1.19	5.39	1.04
2	Konya-Seydisehir-Glabbera	1.20	2.00	0.293	1.00	1.29	4.64	0.75
3	Mersin-Tarsus-Topçu	1.69	2.00	0.435	1.00	1.27	5.09	0.69
4	Konya-Beysehir-Karabalçık	10.60	5.00	1.284	1.00	1.75	8.89	1.77
5	Adiyaman-Kahta-Harabe	11.66	6.00	1.599	1.00	1.88	7.65	1.46
6	Yozgat-Sorgun-Ikikara	13.00	5.00	1.525	1.00	1.75	6.66	1.84
7	Ankara-Haymana-Catalkaya	18.70	7.50	2.579	1.00	2.00	7.67	1.42

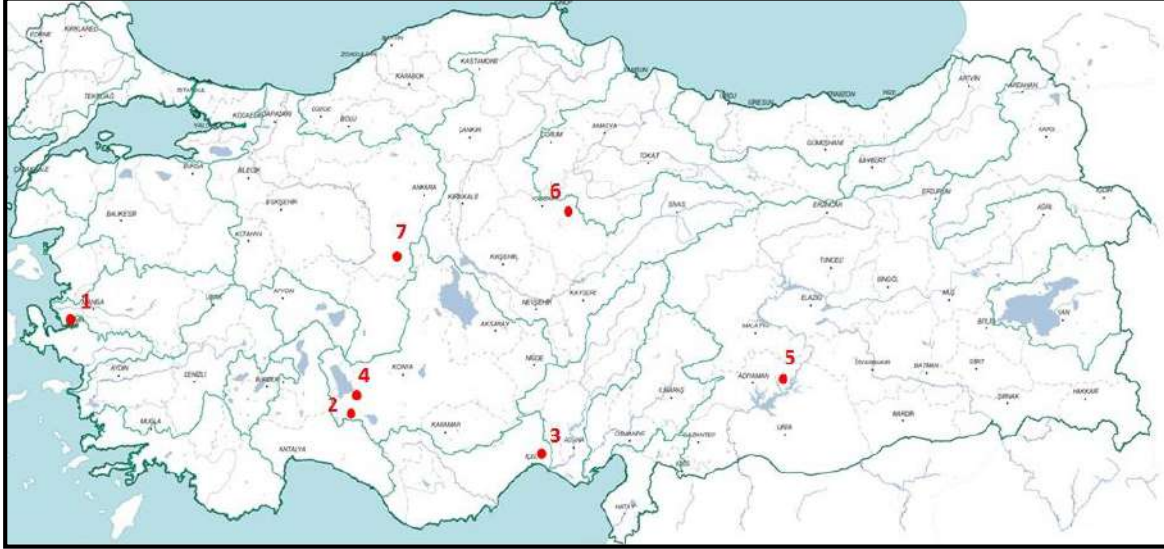


Figure 1. The geographic locations of selected sub-basins

1-Izmir-Menemen-Ulucak 2-Konya-Seydisehir-Glabbera 3- Mersin-Tarsus-Topcu 4-Konya-Beysehir-Karabalcik 5-Adiyaman-Kahta-Harabe 6-Yozgat-Sorgun-Ikikara 7-Ankara-Haymana-Catalkaya

III. NAKAYASU SUH METHOD

In this study, the NSUH method used for detecting UH parameters such as peak flow, lag time, peak time and base time. The equations given by NSUH method for calculation of these parameters are as follows.

For calculating peak time (T_p) Eq. (1) is used. The peak time is given as a function of lag time (t_g) and effective rainfall duration (t_r) :

$$T_p = t_g + 0.8 t_r \quad (1)$$

The lag time (t_g) is calculated for two different cases. The first case when river length (L) is less than 15 km the lag time (t_g) is calculated by Eq.2:

$$t_g = 0.21 L^{0.7} \quad (2)$$

The second case is when the river length is more than 15 km the lag time (t_g) is calculated by Eq.3:

$$t_g = 0.4 + 0.058 L \quad (3)$$

One of the important parameters of NSUH method is $T_{0.3}$. This means that the time required for reducing the peak discharge up to %30 and this parameter is calculated by Eq.4:

$$T_{0.3} = \alpha t_g \quad (4)$$

In Eq.4, α value is a coefficient of basin characteristics and this coefficient is given as follows [13, 14]:

For common sloped basins: $\alpha=2$

For low sloped basins: $\alpha=1.5$

For high sloped basins $\alpha=3$

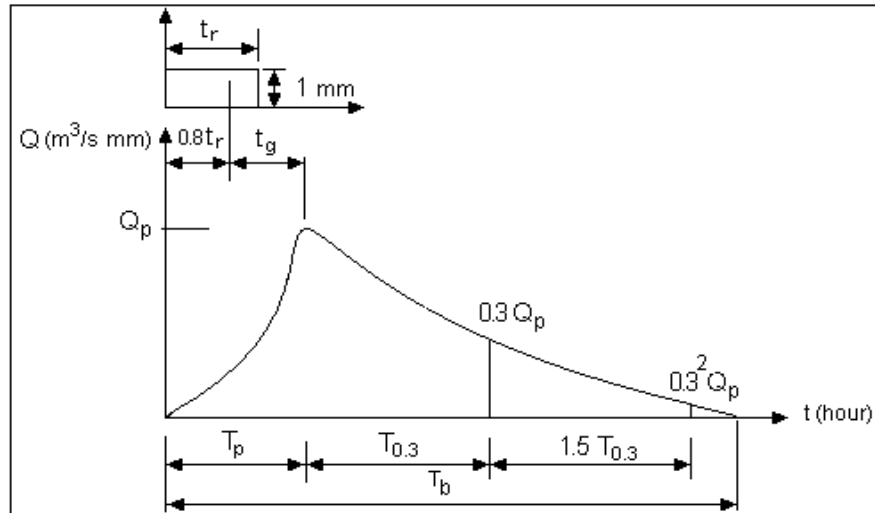


Fig 2. Nakayasu SUH parameters

In NSUH method peak discharge (Q_p) is calculated by Eq.5, the peak discharge (Q_p) is given as a function of watershed area (A), rainfall coefficient (C), the unit rainfall (R_0), peak time (T_p), the time required for the reduction peak discharge rate up to 30% ($T_{0.3}$). The Eq.5 is as following:

$$Q_p = \frac{C \cdot A \cdot R_0}{3.6(0.3T_p + T_{0.3})} \quad (5)$$

A unit hydrograph shape consists rising and decreasing limbs. In NSUH method rising limb curve discharge (Q_a) is calculated by Eq. (6):

$$Q_a = Q_p \left(\frac{t}{T_p} \right)^{2.4} \quad (6)$$

The decreasing limb curve discharge (Q_d) is calculated by using given equations for separately three regions. The given equations are as follows:

$$Q_d > 0.3Q_p \rightarrow Q_d = Q_p \cdot 0.3^{\frac{t-T_p}{T_{0.3}}} \quad (7)$$

$$0.3Q_p > Q_d > 0.3^2Q_p \rightarrow Q_d = Q_p \cdot 0.3^{\frac{t-T_p+0.5T_{0.3}}{1.5T_{0.3}}} \quad (8)$$

$$Q_d < 0.3^2Q_p \rightarrow Q_d = Q_p \cdot 0.3^{\frac{t-T_p+1.5T_{0.3}}{2T_{0.3}}} \quad (9)$$

IV. APPLICATION OF NSUH

In order to analyze the usability of NSUH method, seven small scale sub-basins observed unit hydrographs are tested in application. The UH parameters have been calculated by using NSUH method's equations. These calculated parameters given in Table 3. The comparison of the NSUH and OAUH is depicted in Figure 3 to Figure 9. The difference and error ratios between observed UH parameters and parameters calculated by NSUH are given in Table 4.

TABLE III. THE UH PARAMETERS CALCULATED BY NSUH METHOD

Basins		Parameters Calculated by NSUH Method					
		t_g (h)	T_p (h)	Q_p (m³/s mm)	α	$T_{0.3}$ (h)	T_b (h)
1	Izmir-Menemen-Ulucak	0.252	0.804	0.152	1.5	0.379	3.4
2	Konya-Seydisehir-Glabbera	0.341	1.141	0.390	1.5	0.512	5.4
3	Mersin-Tarsus-Topcu	0.341	1.141	0.550	1.5	0.512	5.8
4	Konya-Beysehir-Karabalcik	0.648	1.448	1.702	2.0	1.296	15.6
5	Adiyaman-Kahta-Harabe	0.736	1.536	2.070	1.5	1.104	13.9
6	Yozgat-Sorgun-Ikikara	0.648	1.448	2.087	2.0	1.296	16.0
7	Ankara-Haymana-Catalkaya	0.861	1.661	2.904	1.5	1.291	16.9

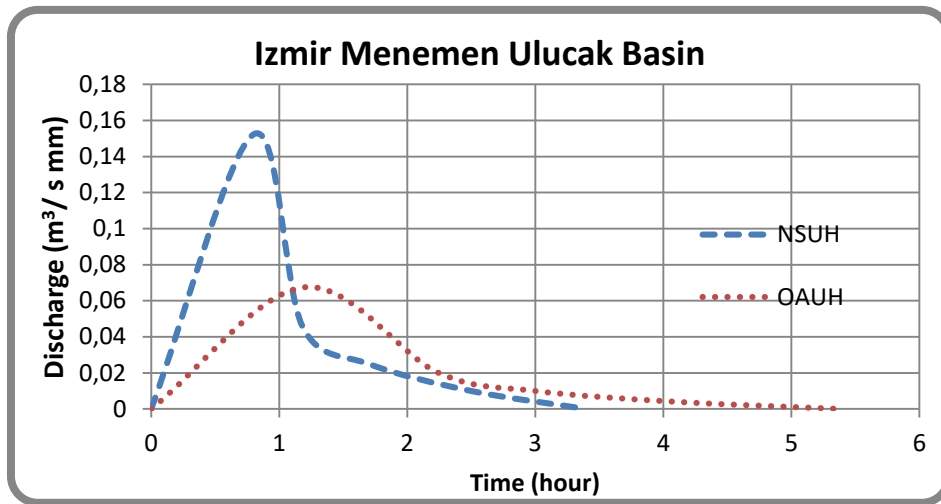


Figure 3. Observed and computed unit hydrograph of Izmir Menemen Ulucak Basin

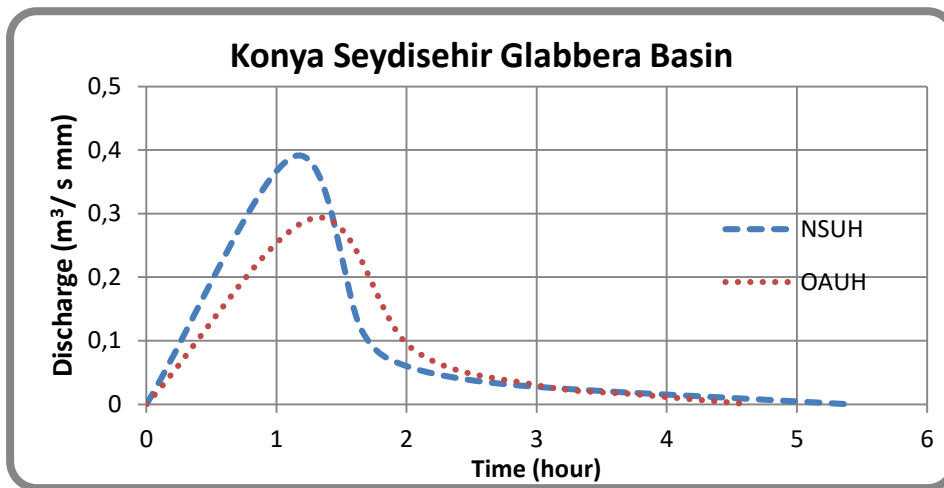


Figure 4. Observed and computed unit hydrograph of Konya Seydisehir Glabbera Basin

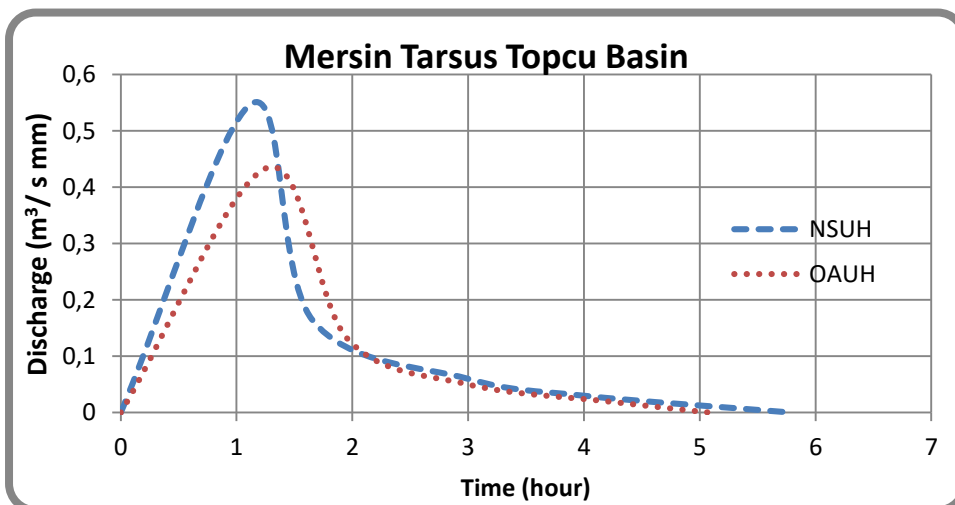


Figure 5. Observed and computed unit hydrograph of Mersin Tarsus Topcu Basin

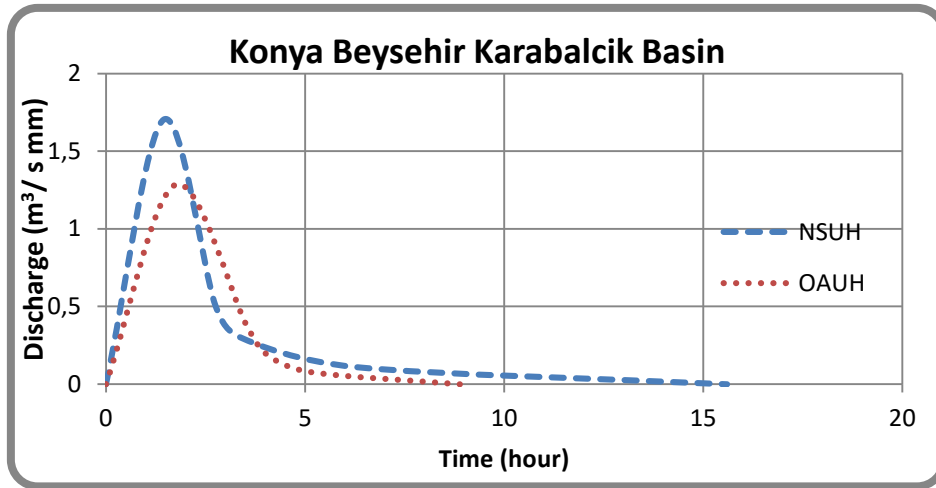


Figure 6. Observed and computed unit hydrograph of Konya Beysehir Karabalcik Basin

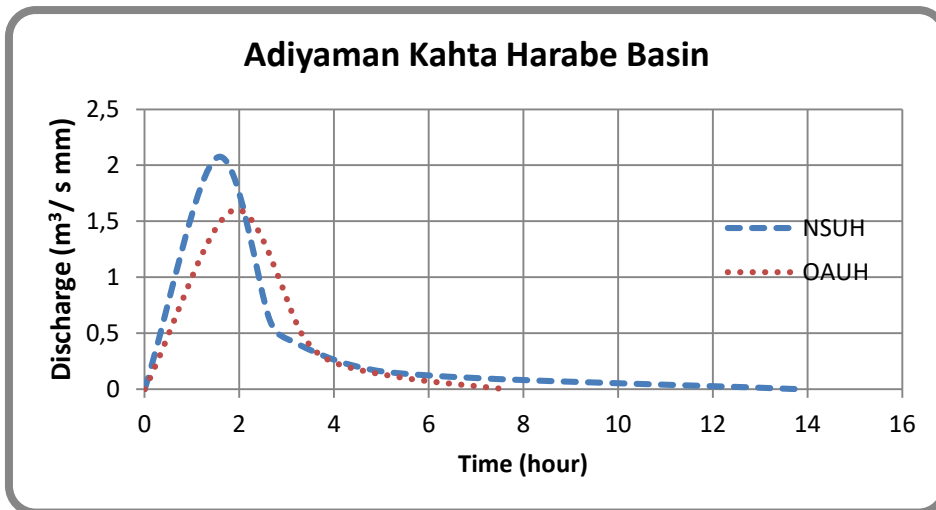


Figure 7. Observed and computed unit hydrograph of Adiyaman Kahta Harabe Basin

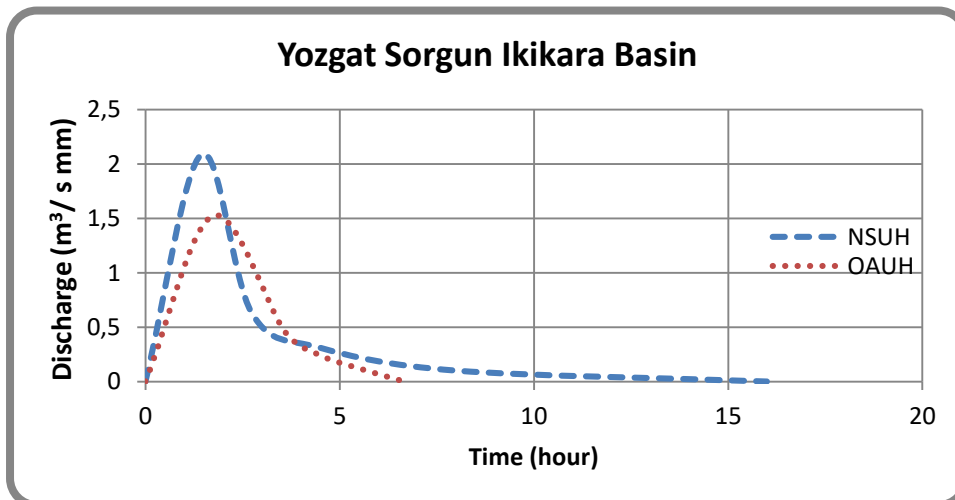


Figure 8. Observed and computed unit hydrograph of Yozgat Sorgun Ikikara Basin

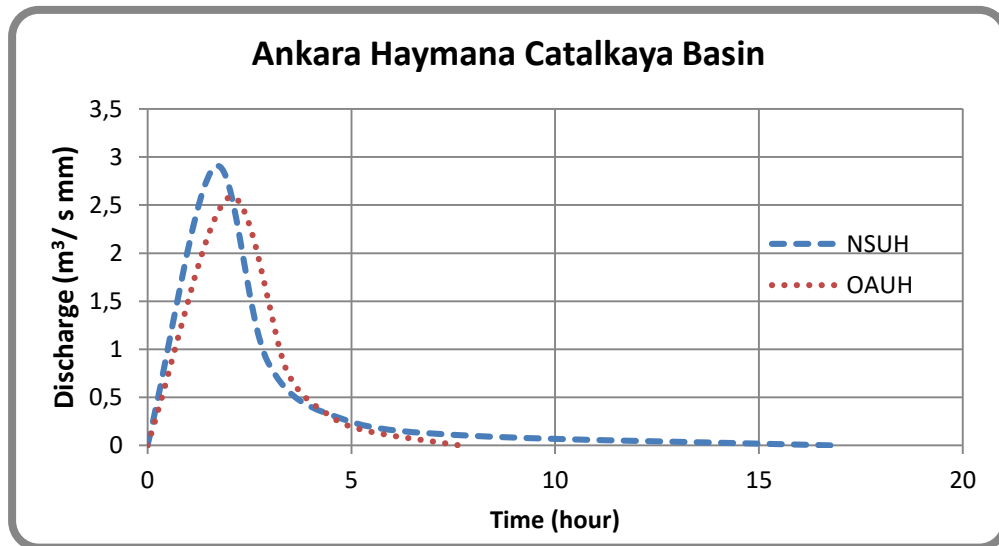


Figure 9. Observed and computed unit hydrograph of Ankara Haymana Catalkaya Basin

TABLE IV. COMPARISON OF THE PARAMETERS OF OAUH AND PARAMETERS CALCULATED BY NSUH

Parameters		Basins						
		1	2	3	4	5	6	7
		Ulucak	Glabbera	Topcu	Karabalcik	Harabe	Ikikara	Catalkaya
Q_p	OAUH	0.068	0.293	0.435	1.284	1.599	1.525	2.579
	NSUH	0.152	0.390	0.550	1.702	2.070	2.087	2.904
	Dif.	0.084	0.097	0.115	0.418	0.471	0.562	0.325
	Err.%	123.529	33.106	26.437	32.555	29.456	36.852	12.602
T_p	OAUH	1.190	1.290	1.270	1.750	1.880	1.750	2.000
	NSUH	0.804	1.141	1.141	1.448	1.536	1.448	1.661
	Dif.	0.386	0.149	0.129	0.302	0.344	0.302	0.339
	Err.%	32.437	11.550	10.157	17.257	18.298	17.257	16.950
t_g	OAUH	0.638	0.490	0.470	0.950	1.080	0.950	1.200
	NSUH	0.252	0.341	0.341	0.648	0.736	0.648	0.861
	Dif.	0.386	0.149	0.129	0.302	0.344	0.302	0.339
	Err.%	60.502	30.408	27.447	31.789	31.852	31.789	28.250
α	OAUH	1.630	1.531	1.468	1.863	1.352	1.937	1.183
	NSUH	1.500	1.500	1.500	2.000	1.500	2.000	1.500
	Dif.	0.130	0.031	0.032	0.137	0.148	0.063	0.317
	Err.%	7.975	2.025	2.180	7.354	10.947	3.252	26.796
$T_{0.3}$	OAUH	1.040	0.750	0.690	1.770	1.460	1.840	1.420
	NSUH	0.379	0.512	0.512	1.296	1.104	1.296	1.291
	Dif.	0.661	0.238	0.178	0.474	0.356	0.544	0.129
	Err.%	63.558	31.733	25.797	26.780	24.384	29.565	9.085
T_b	OAUH	5.390	4.640	5.090	8.890	7.650	6.660	7.670
	NSUH	3.400	5.400	5.800	15.600	13.900	16.000	16.900
	Dif.	1.990	0.760	0.710	6.710	6.250	9.340	9.230
	Err.%	36.920	16.379	13.949	75.478	81.699	140.240	120.339
Q_p = Peak discharge, T_p =Peak time, t_g =Lag time, α =Basin coefficient, $T_{0.3}$ = The time required for reducing the peak discharge up to %30, T_b = UH base time								

V. MODIFICATION OF NSUH EQUATIONS

While making modification it is aimed to re-determine the coefficients of equations given by NSUH method by regression analysis.

By using OAUH's of basins, the equations given by Nakayasu were modified for Turkey's small scale basins. The developed new equations are given as following:

Modified Nakayasu equation for t_g is:

$$t_g = 0.388 L^{0.552} \quad (10)$$

The coefficient of basin α is necessary for calculating $T_{0.3}$, but for calculating α no equation is proposed in Nakayasu method. For this reason, it is difficult to determine the α coefficient. To make the method easier to implement, a new α equation has been developed. The developed new equation is given as following:

$$\alpha = -1.933 T_p + 12.279 t_g - 1.485 L + 0.090 A \quad (11)$$

The Q_p equation is determined as follows by using T_p and $T_{0.3}$ values which are calculated by modified equalities.

Modified Nakayasu Equation for Q_p is:

$$Q_p = \frac{(0.9953 A R_0)}{(3.6 (0.3 T_p + T_{0.3}))} \quad (12)$$

In Nakayasu method no formula is proposed for the calculation of UH base time (T_b) value. The T_b value is calculated by using decreasing limb equations. The time value at the point where the decreasing limb curve discharge is zero, at the same time equal to T_b value. For this reason, determining the T_b value is quite difficult and this causes the T_b to be calculated incorrectly. The equation developed for the calculation of T_b value is given as follows:

$$T_b = 2.2 \left(\frac{T_{0.3} + T_p}{t_r} \right)^{1.01} \quad (13)$$

According to new equations, the UH parameters have been calculated. The calculated new values according to modified Nakayasu synthetic unit hydrograph method (MNSUH) for seven basins are shown in Table 5. Also, the comparison of MNSUH and observed values is given in Table 6.

TABLE V. THE UH PARAMETERS CALCULATED BY MNSUH METHOD

Basins		Parameters calculated by Modified Nakayasu SUH Method					
		t_g (h)	T_p (h)	Q_p (m ³ /s mm)	α	$T_{0.3}$ (h)	T_b (h)
1	Izmir-Menemen-Ulucak	0.449	1.001	0.089	1.674	0.751	5.639
2	Konya-Seydischir-Glabbera	0.569	1.369	0.265	1.479	0.842	4.904
3	Mersin-Tarsus-Topcu	0.569	1.369	0.366	1.523	0.867	4.960
4	Konya-Beysehir-Karabalcik	0.944	1.744	1.350	1.745	1.647	7.557
5	Adiyaman-Kahta-Harabe	1.044	1.844	1.609	1.389	1.451	7.340
6	Yozgat-Sorgun-Ikikara	0.944	1.744	1.514	1.960	1.850	8.014
7	Ankara-Haymana-Catalkaya	1.181	1.981	2.556	1.209	1.428	7.600

TABLE VI. COMPARISON OF THE PARAMETERS OF OAUH AND PARAMETERS CALCULATED BY MNSUH METHOD

Parameters		Basins						
		1	2	3	4	5	6	7
		Ulucak	Glabbera	Topcu	Karabalcik	Harabe	Ikikara	Catalkaya
Q_p	OAUH	0.068	0.293	0.435	1.284	1.599	1.525	2.579
	MNSUH	0.089	0.265	0.366	1.350	1.609	1.514	2.556
	Dif.	0.021	0.028	0.069	0.066	0.010	0.011	0.023
	Err.%	30.882	9.556	15.862	5.140	0.625	0.721	0.892
T_p	OAUH	1.190	1.290	1.270	1.750	1.880	1.750	2.000
	MNSUH	1.001	1.369	1.369	1.744	1.844	1.744	1.981
	Dif.	0.189	0.079	0.099	0.006	0.036	0.006	0.019
	Err.%	15.882	6.124	7.795	0.343	1.915	0.343	0.950
t_g	OAUH	0.638	0.490	0.470	0.950	1.080	0.950	1.200
	MNSUH	0.449	0.569	0.569	0.944	1.044	0.944	1.181
	Dif.	0.189	0.079	0.099	0.006	0.036	0.006	0.019
	Err.%	29.624	16.122	21.064	0.632	3.333	0.632	1.583
α	OAUH	1.630	1.531	1.468	1.863	1.352	1.937	1.183
	MNSUH	1.674	1.479	1.523	1.745	1.389	1.960	1.209
	Dif.	0.044	0.052	0.055	0.118	0.037	0.023	0.026
	Err.%	2.699	3.396	3.747	6.334	2.737	1.187	2.151
$T_{0.3}$	OAUH	1.040	0.750	0.690	1.770	1.460	1.840	1.420
	MNSUH	0.751	0.842	0.867	1.647	1.451	1.850	1.428
	Dif.	0.289	0.092	0.177	0.123	0.009	0.010	0.008
	Err.%	27.788	12.267	25.652	6.949	0.616	0.543	0.563
T_b	OAUH	5.390	4.640	5.090	8.890	7.650	6.660	7.670
	MNSUH	5.639	4.904	4.960	7.557	7.340	8.014	7.600
	Dif.	0.249	0.264	0.130	1.333	0.310	1.354	0.070
	Err.%	4.620	5.690	2.554	14.994	4.052	20.330	0.913
		Q_p = Peak discharge, T_p =Peak time, t_g =Lag time, α =Basin coefficient, $T_{0.3}$ = The time required for reducing the peak discharge up to %30, T_b = UH base time						

VI. MOCKUS SUH METHOD

The Mockus method, in terms of its practically calculation and the ease of drawing triangular hydrograph is preferred. The Mockus method is applied for drainage areas of up to 30 hours of concentration, if the drainage area has bigger than 30 hours of concentration time, the drainage area is divided into sub-areas and hydrographs to be drawn for each are superposed according to the lag time [16]. According to the Mockus method calculating some unit hydrograph parameters by using following equations.

$$T_c = 0.00032 \frac{L^{0.77}}{S^{0.385}} \quad (14)$$

$$t_p = 0.6T_c \quad (15)$$

$$T_p = \sqrt{T_c + 0.6T_c} \quad (16)$$

$$t_r = 1.67T_p \quad (17)$$

$$T_s = T_p + t_r \quad (18)$$

$$Q_p = \frac{K.A.h_a}{T_p} \quad (19)$$

Here, T_p is the peak time of unit hydrograph, T_c is the concentration time, t_p is the lag time, t_r is the decreasing time, T_s is the base time, K is a coefficient and it is accepted to be 0.208 and h_a basin surface flow height [16, 17].

The calculating UH parameters by using Mockus equations is given in the Table 7, the difference and the error ratio between observed and calculated value are given in Table 8 and the root mean square error (RMSE) of NSUH and MNSUH and Mockus method are given in Table 9.

The comparison of the MNSUH, NSUH, Mockus and OAUH is indicated in Figures 10 to 16.

TABLE VII. THE UH PARAMETERS CALCULATED BY MOCKUS SUH METHOD

Basins		Parameters calculated by Mockus SUH Method				
		t_p (h)	T_p (h)	Q_p (m^3/s mm)	T_c (h)	T_s (h)
1	Izmir-Menemen-Ulucak	0.255	0.908	0.078	0.426	2.424
2	Konya-Seydisehir-Glabbera	0.955	2.217	0.113	1.592	5.919
3	Mersin-Tarsus-Topcu	0.281	0.965	0.364	0.468	2.578
4	Konya-Beysehir-Karabalcik	0.544	1.496	1.474	0.906	3.994
5	Adiyaman-Kahta-Harabe	0.677	1.739	1.394	1.128	4.644
6	Yozgat-Sorgun-Ikikara	0.519	1.449	1.866	0.865	3.868
7	Ankara-Haymana-Catalkaya	0.582	1.567	2.482	0.970	4.184

TABLE VIII. COMPARISON OF THE PARAMETERS OF OAUH AND PARAMETERS CALCULATED BY MOCKUS SUH METHOD

Parameters		Basins						
		1	2	3	4	5	6	7
		Ulucak	Glabbera	Topcu	Karabalcik	Harabe	Ikikara	Catalkaya
Q_p	OAUH	0.068	0.293	0.435	1.284	1.599	1.525	2.579
	Mockus	0.078	0.113	0.364	1.474	1.394	1.866	2.482
	Dif.	0.010	0.180	0.071	0.190	0.205	0.341	0.097
	Err.%	14.705	61.433	16.322	14.798	12.821	22.361	3.761
T_p	OAUH	1.190	1.290	1.270	1.750	1.880	1.750	2.000
	Mockus	0.908	2.217	0.965	1.496	1.739	1.449	1.567
	Dif.	0.282	0.927	0.305	0.254	0.141	0.301	0.433
	Err.%	23.697	41.813	31.606	14.514	7.500	17.200	27.632
t_g	OAUH	0.638	0.490	0.470	0.950	1.080	0.950	1.200
	Mockus	0.255	0.955	0.281	0.544	0.677	0.519	0.582
	Dif.	0.383	0.465	0.189	0.406	0.403	0.431	0.618
	Err.%	60.031	94.898	40.213	42.737	37.315	45.368	51.500
T_s	OAUH	5.390	4.640	5.090	8.890	7.650	6.660	7.670
	Mockus	2.424	5.919	2.578	3.994	4.644	3.868	4.184
	Dif.	2.966	1.279	2.512	4.896	3.006	2.792	3.486
	Err.%	55.028	27.565	49.352	55.073	39.294	41.922	83.317
	Q_p = Peak discharge, T_p =Peak time, t_p =Lag time T_s = UH base time							

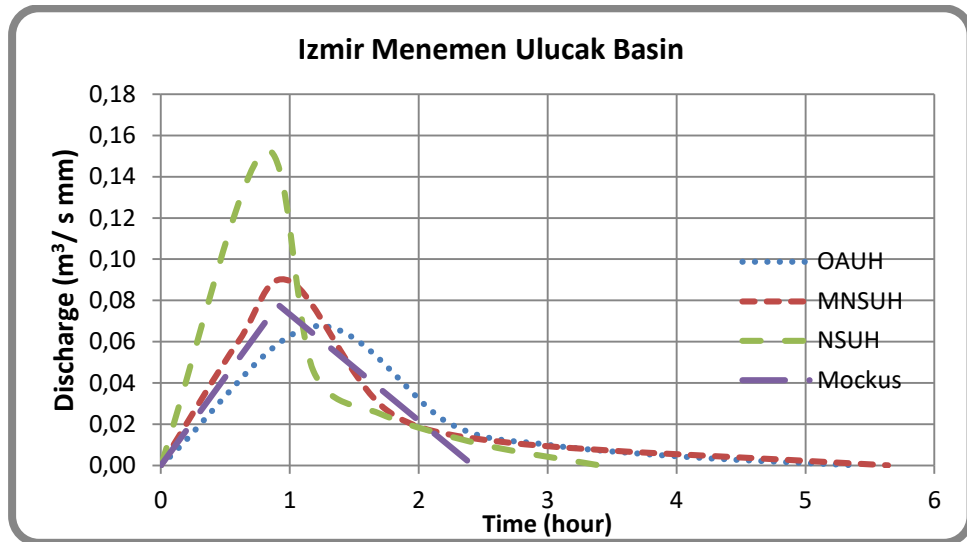


Figure 10. Comparison of MNSUH, NSUH and OAUH of Ankara Izmir Menemen Ulucak Basin

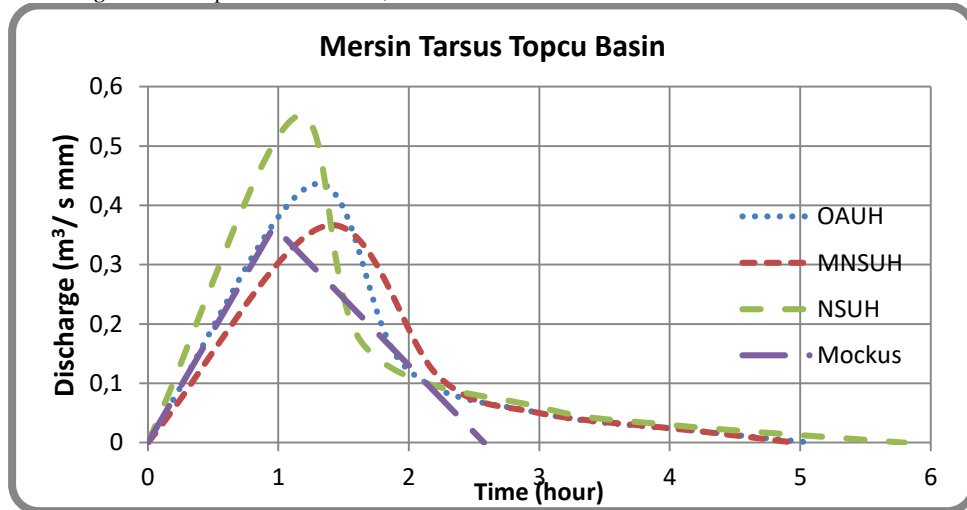


Figure 11. Comparison of MNSUH, NSUH and OAUH of Ankara Mersin Tarsus Topcu Basin

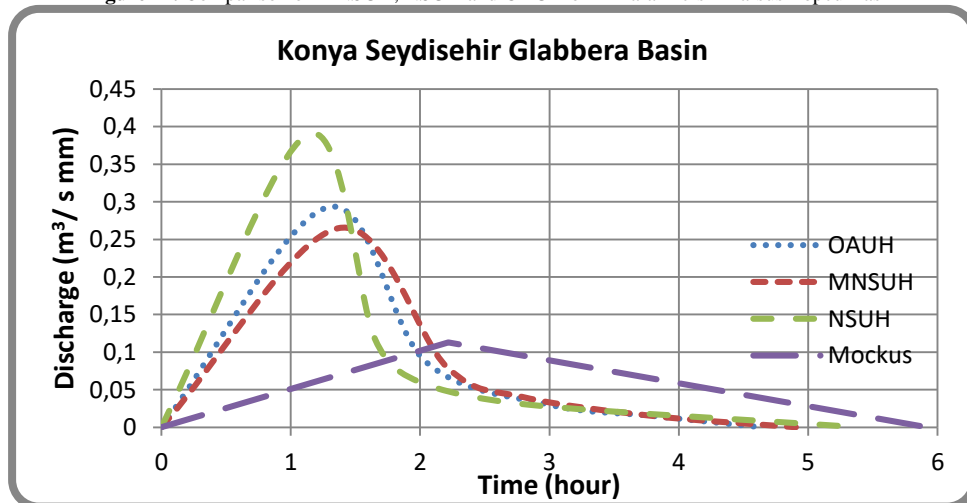


Figure 12. Comparison of MNSUH, NSUH and OAUH of Ankara Konya Seydisehir Glabbera Basin

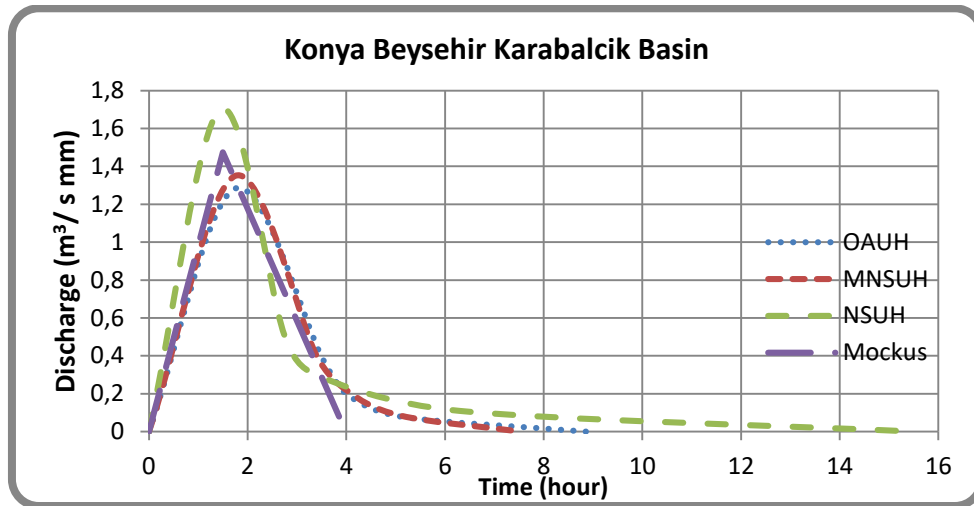


Figure 13. Comparison of MNSUH, NSUH and OAUH of Konya Beysehir Karabalcik Basin

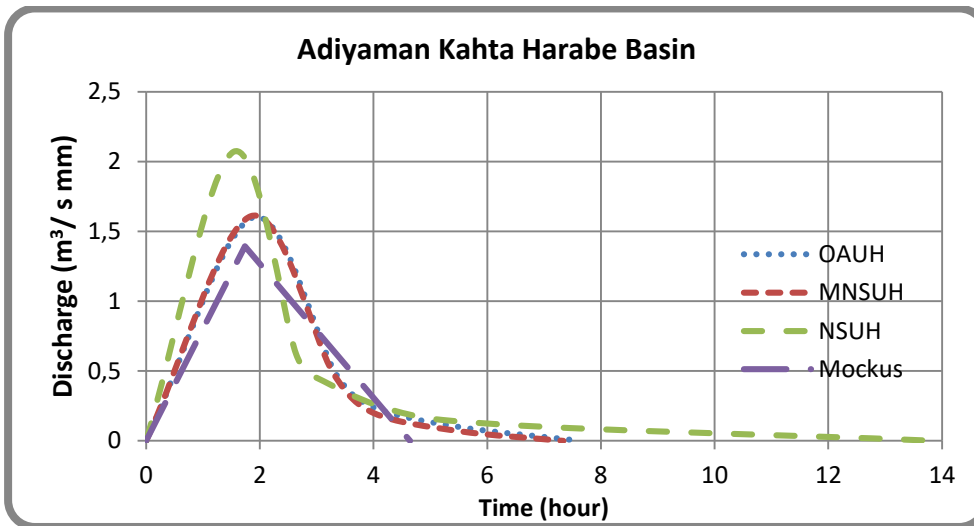


Figure 14. Comparison of MNSUH, NSUH and OAUH of Adiyaman Kahta Harabe Basin

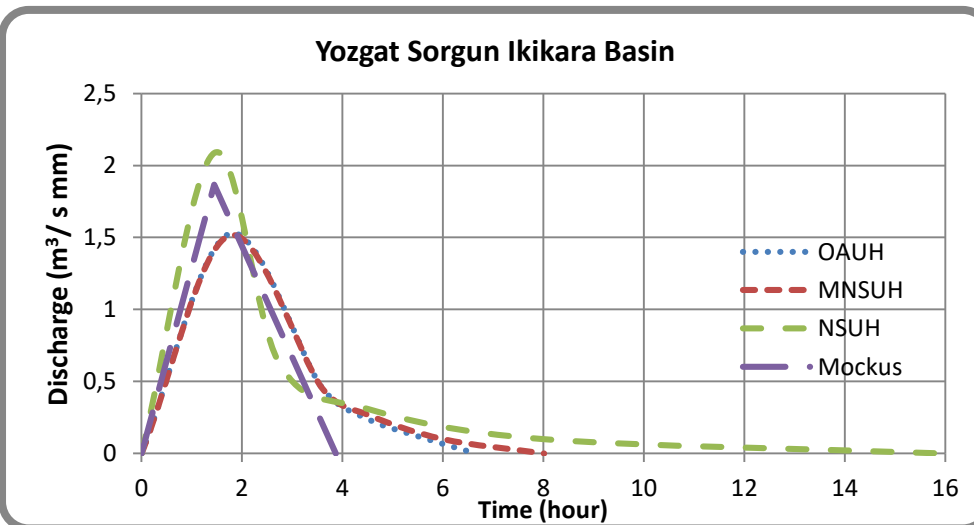


Figure 15. Comparison of MNSUH, NSUH and OAUH of Yozgat Sorgun Ikikara Basin

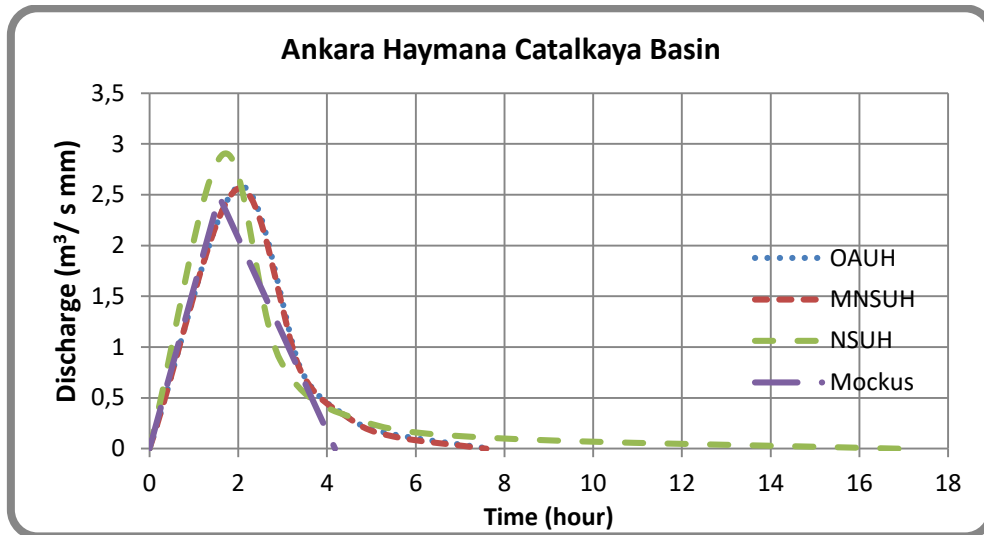


Figure 16. Comparison of MNSUH, NSUH and OAUH of Yozgat Sorgun Ikikara Basin

TABLE IX. THE RMSE RATIO OF NSUH, MOCKUS AND MNSUH METHOD

SUH Methods	RMSE values of NSUH and MNSUH method (m ³ /s mm)						
	1	2	3	4	5	6	7
	Ulucak	Glabbera	Topcu	Karabalcik	Harabe	Ikikara	Catalkaya
NSUH	0.0376	0.0425	0.0531	0.2047	0.2440	0.2664	0.2391
Mockus	0.0127	0.0929	0.0618	0.1690	0.1369	0.2869	0.3142
MNSUH	0.0135	0.0191	0.0444	0.0367	0.0297	0.2116	0.0187

VII. CONCLUSION

In this study, Turkey's seven small scale basins have been selected. The OAUH parameters of these basins calculated by NSUH method. When the results were examined, it is seen that the error ratios between calculated and observed parameters are high. For this reason, the equations given by Nakayasu method were modified by regression analysis using OAUH data. The determined new equations have been used for calculating the UH parameters.

When the entire outcome was analyzed, it shows that parameters that belong to the unit hydrograph such as Q_p , T_p , T_g , $T_{0.3}$, T_b ; were calculated with a very low error ratio by the modified Nakayasu method. Additionally, when the RMSE value of all methods were analyzed it is seen that the UH shape is perfectly simulated by using MNSUH method.

Additionally, the MNSUH method has no restriction on application, whereas, DSI and Mockus methods have some restriction on the application. DSI method is not applicable on the rising time (T_p) less than 2-hour drainage area and Mockus

method is not applicable on the drainage area which have more than 30 hours of concentration time.

Consequently, it was seen that the modified equations are more effective in calculating the UH parameters and simulating UH's shape. For this reason, the MNSUH method gives appropriate results for Turkey's small scale basins.

It should be considered that; the modified equations can only be used for calculating in similar characteristic basin's UH parameters.

References

- [1] O. Sonmez, M. Ozturk, and E. Dogan, "İstanbul derelerinin taskin debilerinin tahmini," *Sakarya University Science Journal*, vol. 16, no. 2, pp. 130-135, 2012.
- [2] V.T Chow, D.R. Maidment and L.W. Mays, *Applied Hydrology*. McGraw-Hill, New York, 1988.
- [3] A. Istanbuluoglu, F. Konukcu, and I. Kocaman, "Precise determination of Turkish spillway sizes from synthetic unit hydrographs to prevent flood damage," *ACTA Agriculturae Scandinavica Section B. Soil and Plant Science*, vol. 54, no.3, pp. 1-8, 2004.
- [4] N. Usul and B. Tezcan, "Determining synthetic unit hydrographs and parameters for four Turkish basins," *Journal of Soil and Water Conservation*, vol. 50, no. 2, pp. 170-173, 1995.
- [5] S. Jung and J. Moon, "The comparison existing synthetic unit hydrograph method in Korea," *Journal of Korea Water Resources Association*, vol. 34, no. 6, pp. 659-672, 2001.
- [6] M. Aydin and T. Bagatur, "Nakayasu sentetik birim hidrograf metodunun Türkiye havzalarında kullanılabilirliğinin incelenmesi: Goksu Nehri Havzasi ornegi," *Dicle University Journal of Engineering*, vol. 7, no.3, pp. 377-386, 2016.
- [7] K. Kuskuvran and M. Canbolat, *Icel Tarsus Topcu Havzasi Yagis ve Akim Karakteristikleri (Ara Raporu 1985-1999)*. KHGM Toprak ve Su Kaynaklari Arastirma Sonuc Raporu, APK Dairesi Baskanligi Yayinlari, Yayin No. 117, Ankara, 2001.
- [8] A. Istanbuluoglu, F. Konukcu and I. Kocaman, "Determination of the project parameters for the small earth reservoirs to be built in the sub-basins of thrace region," *International Symposium on Water for Development Worldwide*, General Directorate of State Hydraulic Works (DSI), pp. 24-35, September 2005.
- [9] I. Oguz, M. Balcin, *Yozgat Sorgun Ikikara Havzasi Yagis ve Akim Karakteristikleri (Ara Raporu 1990-1999)*. KHGM Toprak ve Su Kaynaklari Arastirma Sonuc Raporu, APK Dairesi Baskanligi Yayinlari, Yayin No. 117, Ankara, 2001.
- [10] S. Kaya, *Adiyaman Kahta Harabe Deresi Havzasi Yagis ve Akim Karakteristikleri (Ara Raporu 1985-1999)*. KHGM Toprak ve Su Kaynaklari Arastirma Sonuc Raporu, APK Dairesi Baskanligi Yayinlari, Yayin No. 117, Ankara, 2001.
- [11] İ. Tekeli, H.G. Babayigit, *Ankara Haymana Catalkaya Deresi Havzasi Yagis ve Akim Karakteristikleri (Ara Raporu 1994-1999)*. KHGM Toprak ve Su Kaynaklari Arastirma Sonuc Raporu, APK Dairesi Baskanligi Yayinlari, Yayin No. 117, Ankara, 2001.
- [12] M. Demiryurek, İ.E. Tongarlak and M. Okur, *Seydisehir Tarasci Glabbera Deresi Havzasi Yagis ve Akim Karakteristikleri (Ara Raporu 1985-1999)*. KHGM Toprak ve Su Kaynaklari Arastirma Sonuc Raporu, APK Dairesi Baskanligi Yayinlari, Yayin No. 117, Ankara, 2001.
- [13] A.B. Safarina, H.T. Salim, I.K. Hadihardaja and M.B.K. Syahril, "Clusterization of synthetic unit hydrograph methods based on watershed characteristics," *International Journal of Civil & Environmental Engineering*, vol. 11, no. 6, pp. 76-85, 2011.
- [14] C.D. Soemarto, *Engineering Hydrology*. Usaha Nasional, Surabaya, Indonesia, 1987.
- [15] DSI, *Muhendislik Hidrolojisi Hizmetleri Teknik Sartnamesi*, Internet Adres:http://www.dsi.gov.tr/docs/proje-teknik/C5%9Fartnameler/m%C3%BChendislik-hidrolojisi-hizmetleri-teknik-%C5%9Fartnamesi_r00_20061110.pdf?sfvrsn=2, Date of Access: 30.03.2017
- [16] Y. Yuksel, H. Agaccioglu, A. Cosar, Y. Celikoglu, S. Güner, "Halic Islah Projesinde Kagithane ve Alibeykoy Derelerinin Etkisinin Incelenmesi", *TMMOB IMO II. Ulusal Kentsel Altyapi Sempozyumu*, pp. 239-252, Adana, 1999.
- [17] E. Gocmen, "Edirne Ili Alt-Havzalarda Taskin Debisi ve Su Verimi Hesaplamalari Icin Ampirik Yontemlerin Etkinliklerinin Belirlenmesi", *Master Thesis*, Trakya University Institute of Science, 2006.

CFD Analysis of Ilisu Dam Sluice Outlet

M. Cihan AYDIN¹

Department of Civil Engineering
Bitlis Eren University
Bitlis, TURKEY

Ali Emre ULU²

Department of Civil Engineering
Bitlis Eren University
Bitlis, TURKEY

Çimen KARADUMAN³

Department of Civil Engineering
Bitlis Eren University,
Bitlis, TURKEY

Abstract—Ilisu Dam is one important energy projects in Turkey. After it is completed, it is expected that it will contribute to the country economy approximately \$300 million annually. One of the most remarkable engineering designs of the dam is the conversion of diversion tunnels of 12 m in diameter and about 1 km in length into sluice outlet structure. In this study, the CFD simulation of Ilisu Dam sluice outlet were performed with 1/40 scale. The obtained CFD results were compared with physical model observations conducted by the State Water Works (SWW). A good agreement was achieved between both results, and some useful results of CFD were presented for design of the outlet.

Keywords—Ilisu Dam; Sluice Outlet; CFD.

I. INTRODUCTION

Sluice outlet is a hydraulic structure which is designed to completely discharge the dam when necessary, to reduce the spillway capacity and to release the water to be left to the downstream of the river. The sluice outlet can be of different shapes and lengths depending on the needs or shapes of the dams. An important consideration when designing the sluice way is to prevent cavitation damage. In order to avoid this problem engineers may choose different solutions in the sluice outlet design. Experimental studies are conducted to observe how the cavitation phenomenon will actually have an effect. However, these experiments may be time consuming, costly and require a lot of attention. Instead, using the developed computational fluid dynamics (CFD) is now a more functional and reliable method that has been tested many times. There are many studies exist in the literature that was performed using the CFD. Some of those studies can be seen as follows:

Reference [1] establishes a 3D CFD model of The Dalles Dam forebay. The aim of the model is to investigate the effects of clogging resulting from the accumulation of debris in the 12.3 m section above the turbine intake. The model includes approximately 0.80 million cells consisted from 22 power plant units, two fish turbine units, station services unit and a forebay

bathymetry. The CFD model has quite well simulated the velocity distributions observed in a physical model. Numerical simulations indicated that blocked garbage pits would change velocity distributions around the powerhouse to a significant extent [1]. Reference [2] defines the flow properties at a large opening to improve the discharge calculation for submerged channel gates. To do so, the technical note investigated the upstream and downstream flow characteristics of the channel inlet gates experimentally and numerically by means of a fluid method using average Navier-Stokes two-dimensional simulations by Reynolds [2]. Reference [3] develops a dynamic numerical model to investigate a laboratory experiment. Through analysis and modeling of the observed data, the river water quality and quantity (WQQ) operations under the water channel regulation were examined and the interaction between the WQQ and the regulatory capacity downstream of a water channel was investigated [3]. Reference [4] developed a numerical model to simulate the flow of probable maximum flow (PMF) on a system consisting of an existing service spillway and a new auxiliary spillway. In the study, approach channel geometries consisted from different combinations were simulated. The article demonstrates the successful implementation of a CFD model in the design process of an auxiliary spillway and encourages the hydraulic engineers and CFD modelers for designing the hydraulic structures [4]. Reference [5] investigated CFD model used applications to reveal its limitations and to make some assumptions. At the end, article noted that CFD numerical models are a good way to recognize the hydraulic conditions [5].

A technical report modified a previously computed fluid dynamics model, and it was used to characterize tailrace hydraulic and sluice outlet exit conditions for low total river and low level spillway flows [6]. Reference [7] investigated the preliminary test results obtained from a large scale Deriner Dam of tunnel spillway model are presented. A number of test models have also been carried out for the original and final

project cases. In the article it was seen that the original designed ventilator did not work effectively from the values obtained according to the original project status. For this reason, it became necessary to change the original progeny in terms of location and geometry of the aerator [7].

From the current literature, it can be said that CFD models are valuable, useful and reliable tools for the hydraulic structures. As one can understand that there is limited study about the CFD models of the sluice outlet. This study investigates the working principle of sluice outlet of Ilisu Dam by using CFD model.

II. ILISU DAM AND HPP

Ilisu Dam and Hydroelectric Power Plant (HPP) is one of most important energy project with 1200 MW installed capacity in Turkey. After completed, the total produced energy will be 3833 GWh/year, and it is expected to bring about \$300 million incomes to the economy annually. This energy corresponds to 10% of the hydroelectric energy to be produced in Turkey. The general project characteristics of Ilisu Dam and its sluice outlet structures were given in Table 1 [8], [9].

DT2 derivation tunnel of Ilisu Dam was converted to the outlet structure. DT1 derivation tunnel parallel to DT2 tunnel also were designed as an aeration tunnel for air supply purpose. Two tunnels were connected by a horseshoe cross-section air gallery. The detail of outlet structures converted from DT2 derivation tunnel were showed in the Fig. 2

TABLE 1. ILISU DAM AND HPP PROJECT CHARACTERISTICS

Type of Dam	Embankment, concrete-face rock-fill
Purpose	HP, flood control and irrigation
Status	Under construction
Location	Dargeçit County, between Mardin and Şırnak
River	Dicle River
Construction cost	1.7 billion \$
Height from thalweg	135 m
Length	1.820 m
Dam volume	43,800,000 m ³
Installed capacity	1,200 MW
Average annual energy production	6 x 200 MW Francis-type
Hydraulic head	122.6 m
Annual generation	3,833 GWh
Derivation slope	0.1%
Derivation structures	DT1+DT2+DT3 derivation tunnels
Sluice outlet	DT2 derivation tunnel
Diameter of sluice outlet	12 m
Length of the outlet	1016.1 m
Type of control valve	Sluice valve
Number of control valve	2
Dimensions of control valve	2.65x4.00 m
Spillway type	Service overflow, controlled-chute
Spillway capacity	18,000 m ³ /s

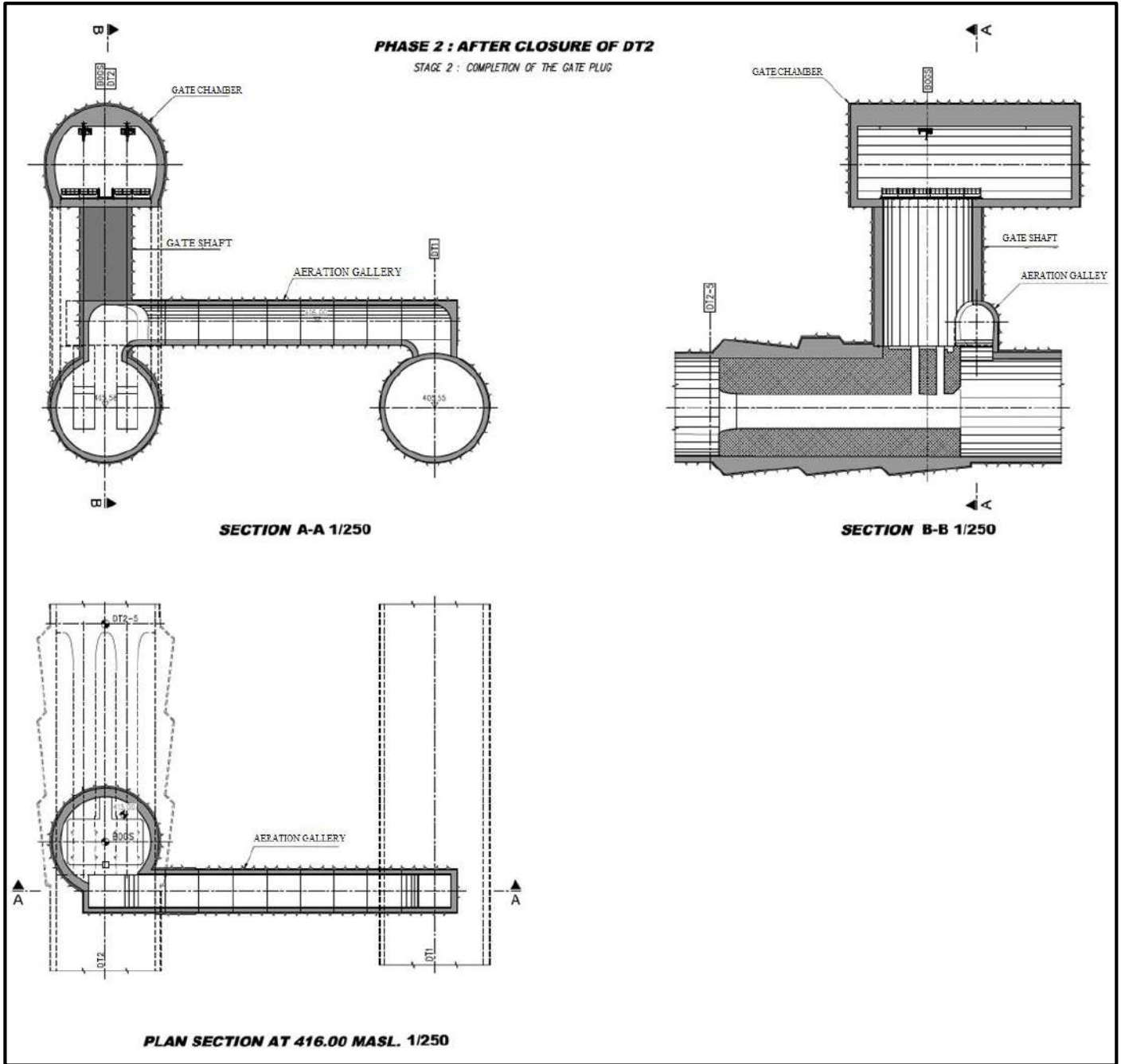


Fig. 1. Details of the sluice outlet converted from DT2 derivation tunnel of Ilisu Dam [8].

III. METHOD

In this study, a three-dimensional (3D) numerical simulation using FLOW-3D software was applied to Ilisu Dam sluice outlet to determine the two-phase (air-water) flow properties. FLOW-3D is a general purpose CFD program which is especially effective free surface flows for one and two phase flows. The program solves the mass continuity and the Navier-Stokes equations as the momentum equation for each element to estimate properties of fluid motions. These equations can be

given as follows respectively for Cartesian coordinate system [10].

$$V_F \frac{\partial p}{\partial x} + \frac{\partial}{\partial x}(\rho u A_x) + \frac{\partial}{\partial y}(\rho v A_y) + \frac{\partial}{\partial z}(\rho w A_z) = R_D + R_S \quad (1)$$

where, V_F is volume fraction, ρ is the density of fluid; R_D is a turbulent diffusion term; R_S is a mass source; A_x , A_y , and A_z are the fractional areas in the x , y and z ; u , v and w are velocity

components. The Navier-Stokes are used to describe three-dimensional fluid dynamics.

$$\begin{aligned} \frac{\partial u}{\partial t} + \frac{1}{V_F} \left[u A_x \frac{\partial u}{\partial x} + v A_y \frac{\partial u}{\partial y} + w A_z \frac{\partial u}{\partial z} \right] &= -\frac{1}{\rho} \frac{\partial p}{\partial x} + G_x + f_x - \frac{R_S}{\rho V_F} (u - u_w - \delta u_s) \\ \frac{\partial v}{\partial t} + \frac{1}{V_F} \left[u A_x \frac{\partial v}{\partial x} + v A_y \frac{\partial v}{\partial y} + w A_z \frac{\partial v}{\partial z} \right] &= -\frac{1}{\rho} \frac{\partial p}{\partial y} + G_y + f_y - \frac{R_S}{\rho V_F} (v - v_w - \delta v_s) \\ \frac{\partial w}{\partial t} + \frac{1}{V_F} \left[u A_x \frac{\partial w}{\partial x} + v A_y \frac{\partial w}{\partial y} + w A_z \frac{\partial w}{\partial z} \right] &= -\frac{1}{\rho} \frac{\partial p}{\partial z} + G_z + f_z - \frac{R_S}{\rho V_F} (w - w_w - \delta w_s) \end{aligned} \quad (2)$$

where; G_x, G_y, G_z are body acceleration components, f_x, f_y, f_z are viscous accelerations components, u_w, v_w, w_w are the components of velocity source; u_s, v_s, w_s are the velocity components at the surface.

A. Physical Model

The experimental studies on the revised design of the sluice outlet structure and aeration tunnel were conducted by State Hydraulic Works in Turkey. In the first design of the Ilisu Dam sluice outlet, the transport tunnels to the sluice outlet vane chamber were planned as ventilation galley providing air flow. However, in the tests and analyzes conducted, it was understood that the air in the narrowing sections would reach a speed as high as 100 m/s and eventually air explosions and operational problems would occur. For this reason, one of the two sluice outlet (DT1) was planned as an air gallery with a diameter of 12 m and a length of about 1000 m, and the air for the DT2 sluice outlet was provided by an air gallery with a horseshoe section here. Different alternatives of this system have been experimentally investigated by DSI with 1/40 model and solution proposal has been introduced. The experimental setup of the outlet and aeration tunnels performed by DSI was showed in Fig. 2.

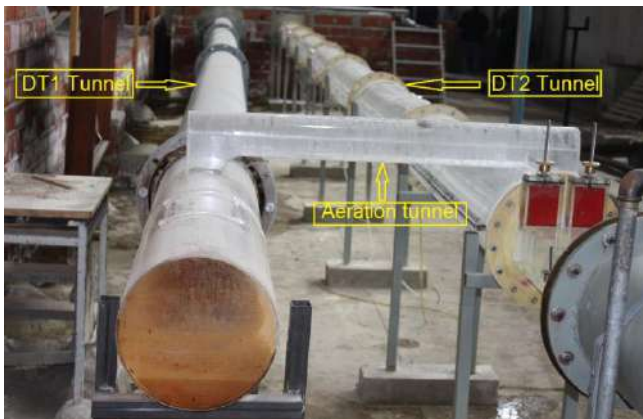


Fig. 2. Experimental setup of the outlet and aerations tunnels (DSI, 2010)

B. Numerical Model

The 3D numerical model was given in the Fig. 3. Numerical model was divided into 3,900,000 structured 3D hexahedral elements. The simulation duration is approximately 7 hours with two real core xenon processor and 8 GB ram. Two phases model with *renormalized group (RNG)* turbulence model were used in the numerical solution. Numerical model with 12 m diameter of DT1 and DT2 tunnels were scaled by 1/40 scale similar to the experimental model. The dimension of the rectangular sluice section is 2.65x4.00m. The height and width of the horseshoe air tunnel are 4.5 m and 4.20 m respectively.

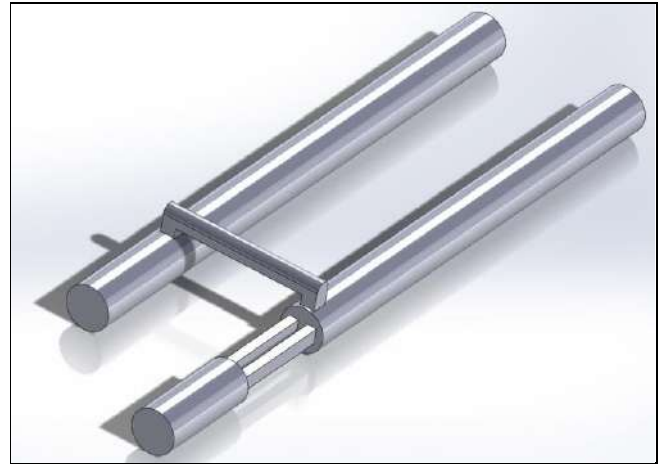


Fig. 3. Geometry of 3D numerical model

The CFD analysis were performed for 24.75 m of the hydraulic head and 430 m³/s of water outlet discharge with laboratory model dimensions (1/40 scale). The solution convergence was achieved in 5.0 second. The solution convergence curves and water velocity of the sluice flow were illustrated in Fig. 4. As seen at the convergence curves in Fig. 5, the air flow rate in the aeration tunnel is almost steady while approaching to 0.012 m³/s and velocity of 1.2 m/s. This corresponds 121.43 m³/s and 7.58 m/s of prototype values. The air entrainment discharges and average air velocity were observed by DSI as 118.76 m³/s and 7.35 m/s experimentally [8]. The air entrainment rates ($\beta=Q_a/Q_w$) are calculated as 0.303

of experiment, and 0.309 of CFD. The relative percent error between experimental and numerical (CFD) results is approximately 2%. These comparisons were given in Table 2.

TABLE 2. COMPARISON OF EXPERIMENTAL AND CFD RESULTS

	Hydraulic Head, H_t (m)	Water discharge, Q_w (m^3/s)	Air entrainment discharge, Q_a (m^3/s)	Average Air Velocity, V_a	Air entrainment coefficient ($\beta=Q_a/Q_w$)
Experiments	24.75	392	118.76	7.35	0.303
CFD	24.75	392	121.43	7.58	0.309
Error (%)			2.2	3.0	2.0

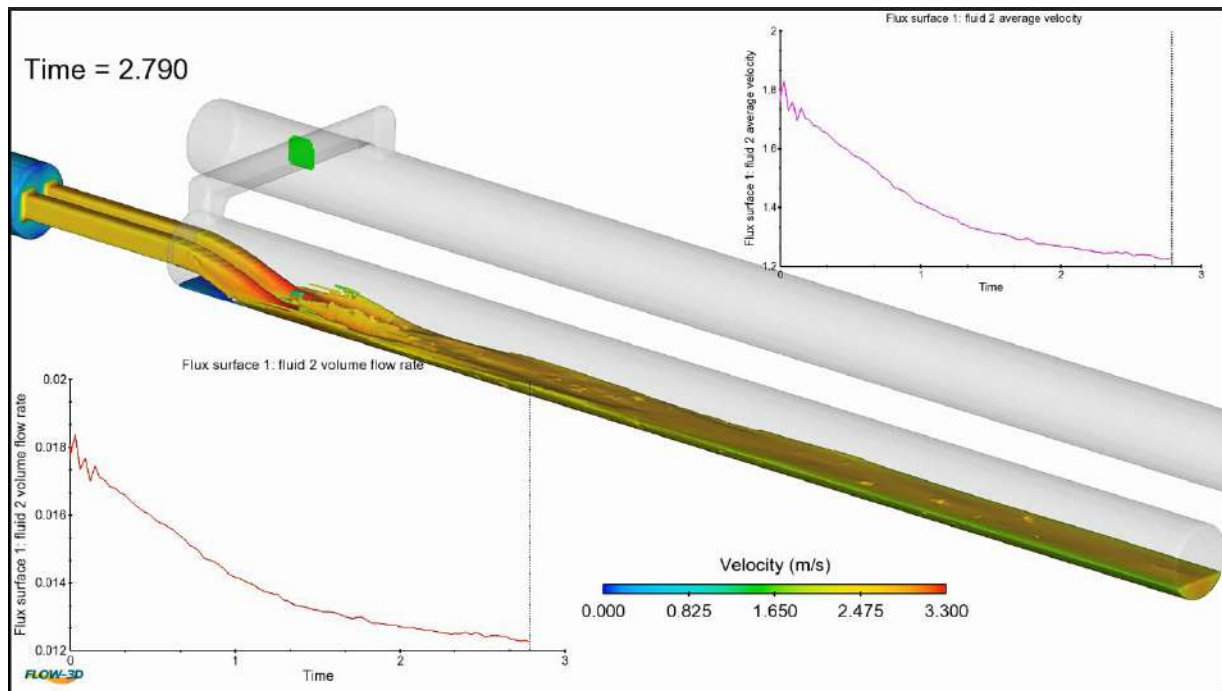


Fig. 4. Solution of the numerical model with convergence curves.

The maximum velocity of water flow was observed in jet near to impact region at the downstream of sluice gate. The streamlines of the water flow are shown in the Fig. 5. This figure also indicates same the maximum water velocity position.

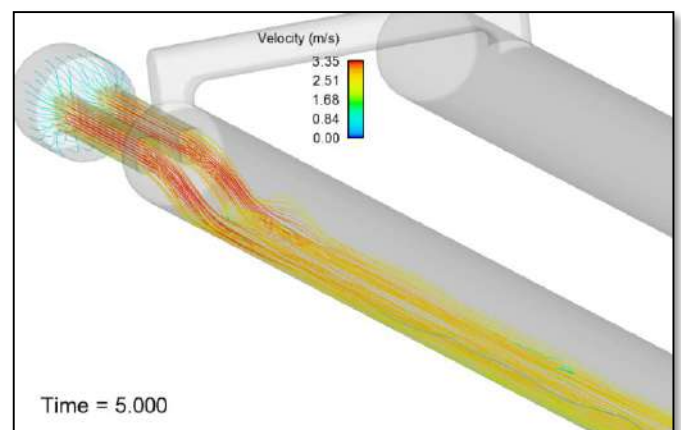


Fig. 5. Streamlines of the water flow in the sluice outlet

Fig. 6 shows the streamlines of air flow (on the left) and velocity contours at the middle section of aeration tunnel (on the right). It is observed in these figures that the air velocity on the section is irregular and the maximum velocity occurs at the top of the section while the velocity at a lower part of the section was almost zero. The maximum air velocities in the DT2 tunnel were observed near to water surface probably owing to slip velocities between air and water flow.

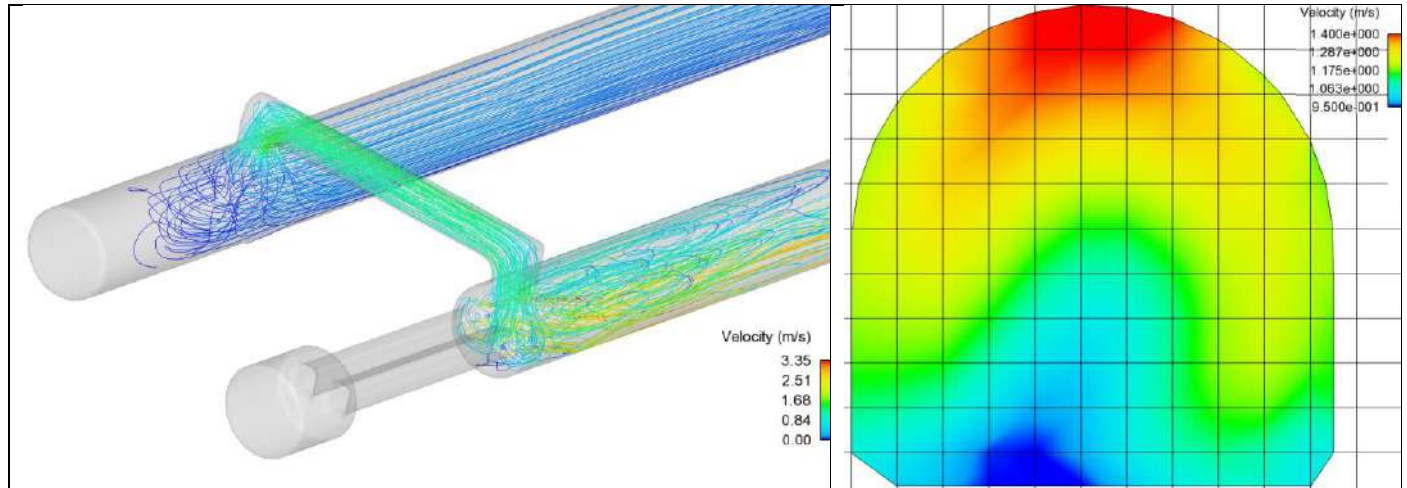


Fig. 6. Streamlines of air flow (on the left), and the velocity distribution at the cross-section of the aeration tunnel (on the right).

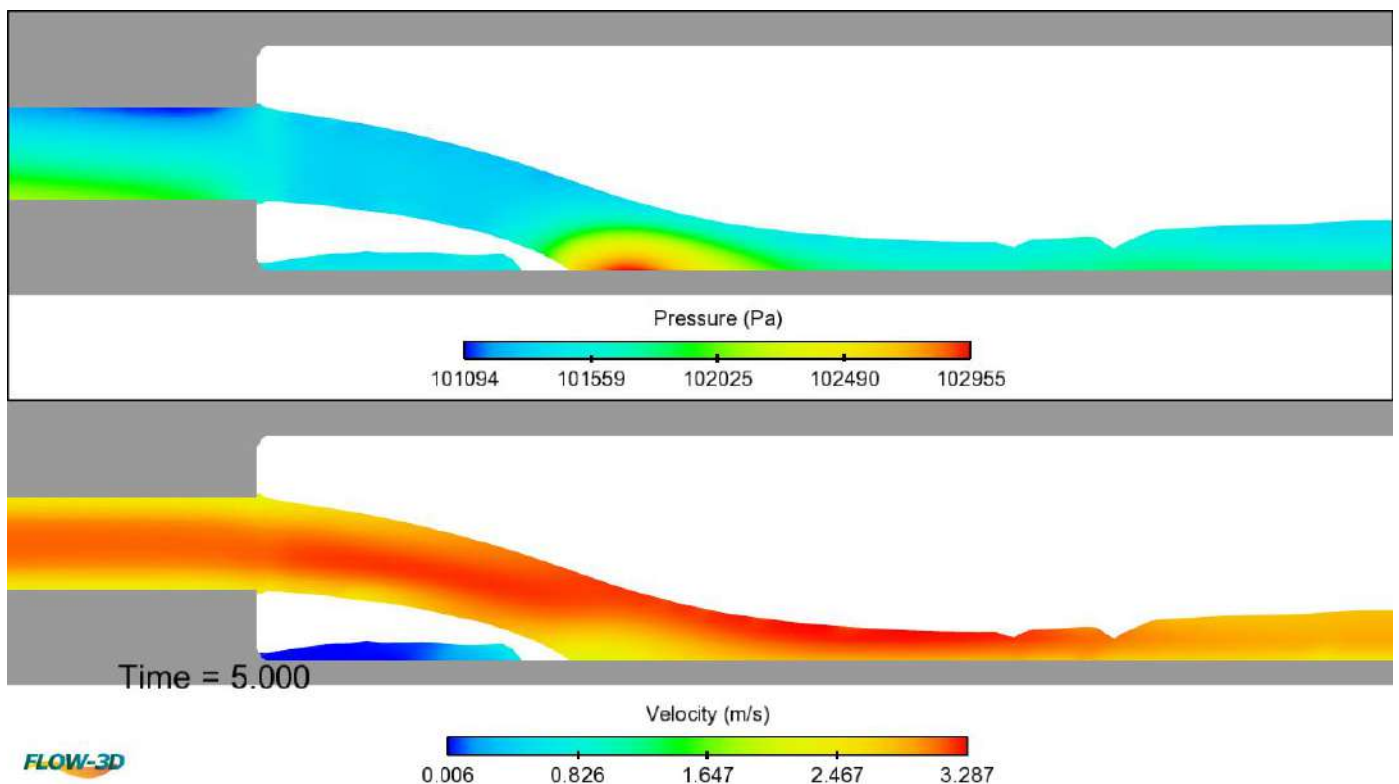


Fig. 7. Pressure and velocity contours of water flow jet downstream of sluice gate.

IV. CONCLUSIONS

In this study, Ilisu Dam's sluice outlet, which have 12 m diameter, was analyzed by using CFD simulation technic, and was discussed. The results of CFD analysis were compared to the experimental tests with 1/40 scale performed by DSI, and a good agreement was achieved in terms of air entrainment by air supply tunnel. The CFD results are reasonably compatible with the experimental observations with the percent errors from 2.00 to 3.00%. The experimental study is more expensive and required more effort than CFD analyses. Bu still, the CFD models need to be calibrated with some experimental data. The calibrated numerical models may be more useful and easier to determine hydraulic characteristics than experimental studies. The results encouraged the further researches for detailing the design of the Ilisu Dam outlet and the other similar projects.

ACKNOWLEDGEMENT

We thanks to Firat University Department of Civil Engineering, the State Water Works (SWW) and IOG Engineering for their valuable contribution.

REFERENCES

- [1] L.A. Khan, E.A. Wicklein, M. Rashid, L.L. Ebner, and N.A. Richards, "Case study of an application of a computational fluid dynamics model to the forebay of the Dalles Dam, Oregon", *Journal of Hydraulic Engineering*, 2008, 134(5), 509-519.
- [2] L. Cassan, and G. Belaud, "Experimental and numerical investigation of flow under sluice gates" *Journal of Hydraulic Engineering*, 2011, 138(4), 367-373.
- [3] Y. Zhang, J. Xia, Q. Shao, and X. Zhang, "Experimental and simulation studies on the impact of sluice regulation on water quantity and quality processes" *Journal of Hydrologic Engineering*, 2011, 17(4), 467-477.
- [4] S. Li, S. Cain, M. Wosnik, C. Miller, H. Kocahan and R. Wyckoff, "Numerical modeling of probable maximum flood flowing through a system of spillways", *Journal of hydraulic engineering*, 2010, 137(1), 66-74.
- [5] L.L. Ebner, "Practical Use of Computational Fluid Dynamic Models as a Design Tool-Limitations and Assumptions" In *Critical Transitions in Water and Environmental Resources Management*, 2004, pp. 1-10.
- [6] C.L. Rakowski, M.C. Richmond, J.A. Serkowski, and W.A. Perkins, "Computational Fluid Dynamics Modeling of the Bonneville Project: Tailrace Spill Patterns for Low Flows and Corner Collector Smolt Egress (No. PNNL-20056)", Pacific Northwest National Laboratory, 2010, (PNNL), Richland, WA (US).
- [7] M.A. Kökpınar, H. Ç. Çelik, "Deriner Barajı Tüneli Dolusavak Havalandırıcıları Büyük Ölçekli Hidrolik Model Çalışmaları", 2002.
- [8] DSI, "İlisu Barajı ve HES Projesi Dipsavak Tüneli Ek Hidrolik Çalışmaları (M-398)", Fiziksel Model Deney Raporu, DSI TAKK Dairesi Başkanlığı Hidrolik Model Laboratuvarı Şube Müdürlüğü. Ankara. Rapor No: Hİ-1022, 2013, 119 s.
- [9] Wikipedia, Ilisu Dam.
https://en.wikipedia.org/wiki/Il%C4%B1su_Dam, Accessed date: 26 Feb. 2017.
- [10] FLOW-3D, User Manual, Theory Guide, 2016.

The Non-linear Dynamic Analysis for Andiraz Dam by Using Euler Liquid-Structure Interaction

Seçkin AYDIN¹

Department of Dams and Hydroelectric Power Plant
The General Directorate of State Hydraulic Works
Ankara, TURKEY

Mehmet Cihan AYDIN²

Department of Civil Engineering
Bitlis Eren University
Bitlis, TURKEY

Ercan IŞIK³

Department of Civil Engineering
Bitlis Eren University
Bitlis, TURKEY

Aydın BÜYÜKSARAÇ⁴

Department of Civil Engineering
Bitlis Eren University
Bitlis, TURKEY

Abstract— In this study, the roller compacted concrete dams were summarized and two-dimensional nonlinear dynamic analyses of Andiraz Dam which its building is planned in the border of Kastamonu were done with the use of 3 Safety-Based Earthquake (2475-years repetition) and the nonlinear analyses were done with the use of Drucker-Parager elasto-plastic material model. The results for Vertical and Principal Contraction Stress - Duration in the critical points which were considered on the stem of dam were gotten, the dam's stability after the earthquake was evaluated in consideration of the damage areas which were obtained.

Keywords—Roller Compacted Concrete (RCC), Dam, Nonlinear dynamic analysis

I. INTRODUCTION

The great majority of The Roller Compacted Concrete (RCC) dams are built after they are designed in the type of gravity dam. The arch dams are built by RCC and also, there aren't efficient experience savings and common implementations on their motions. In the simplest description, the gravity dam is a mass structure which is offending against the sliding and rollover with its gravity that they will occur as a result of all external loads' effect , which has mostly got right triangle section. The Roller Compacted Concrete (RCC) gravity dam is closely resemble to the concrete gravity dam which is done with the classical concrete casting. The classical concrete gravity dam has got a overcosting structure with the properties which are required in the concrete and the concrete's materials (the requirement for washing aggregate etc.) and with the aspect of building technique. An important saving were gotten in the construction of the Roller Compacted Concrete (RCC) with the similar use of the building machinery and a concrete material which is equivalent with the classical concrete properties in RCC dams was obtained as it was in the

construction of rock-fill or earth-fill dams for the manufacturing, transport, sprawl and compacting zero-slump concrete with roller as a different concrete material. It became possible to build a concrete dam in a short time and with a low cost with this concrete material which provides opportunity for the rollers and other building machinery to get about without sinking. In this case, The Roller Compacted Concrete (RCC) dams got in a race with earth-fill and rock-fill dams and other dam type in terms of the cost.

The analyses in the duration-description field are defined as the mostly effective method to review the dynamic motions of structures which are exposed to the place motion because the equations of motion are analysed by being taken directly as integral in the small time step [1]. The dam's earthquake motion can be calculated in the calculation method during all of the earthquake records that the balance of motion is provided in each of time steps so the temporal change of the stress and deformations can be followed. The dam's dynamic motion can be reviewed in a more realistic way as the foundation rock, reservoir water, main dam and the mutual interaction with each other are modelled in the aforementioned.

An important advantage of the analyses in the duration-description field is that it gives opportunity to the full controlling the performance criteria of Operating-based Earthquake (OBE) and Maximum Design Earthquake (MDE) in the sense of the solution of the linear and non-linear systems. The method provides the valid and reliable results for the cases that the concrete stresses remain within the elastic limits, and also, it is recommended for all of dam designs by the international specifications [1,2]. in the purpose that the dam's motions on the linear limits and the damages that would occur are foreseen.

The vertical construction joints are included in both of the casting concrete and the roller compacted concrete dams and also, the horizontal casting joints which are lower than the tensile and shear strength stem concrete occur during the manufacturing of stem. It is possible to be fractures depending on the repetitive folding on the vertical joints, the horizontal casting joints, the tensile on the corners that concrete-rock contact or stress concentration occurs during the low-level place motion [1]. In this sense, the great majority of deformations will occur on these fractures, and the occurrence of fractures will be prevented as the tensile stresses decrease in the other areas of the dam stem. Thus, it should be expected that there would be a few of main fracture surfaces on the concrete dams in the case of a great earthquake [3].

Two or three dimensional, static or dynamic, elastic or ultra elastic analyses are done on the estimation of RCC Dams' earthquake performance. The potential damage areas are found with the areas of stress concentration as a result of analyses. The reliability of section is determined as the effect of damage areas on the dam stability following the earthquake is examined in the ultra elastic analyses in consideration with the stress limits in the elastic analyses.

The investigations which are required after an earthquake are summarized with the analyses of an earthquake at Figure 1. The critical points are investigated with the linear elastic stress analyses which will be done for OBE, MDE and EED. The section of dams which their criteria aren't provided can be extended or the higher-strength concrete or grout can be used in the areas that they are found as inefficient. The reliability of dam stem would be investigated with the ultra elastic non-linear analyses for the sections that their stress criteria aren't provided as a result of the linear elastic analyses but the ultra elastic motion would be limited. Generally, the ultra elastic analyses which are done in the duration- description field are very hard and complex analyses. These structure models should be used after it is assured that the concrete fracture motion is modelled in these models definitely in a correct way.

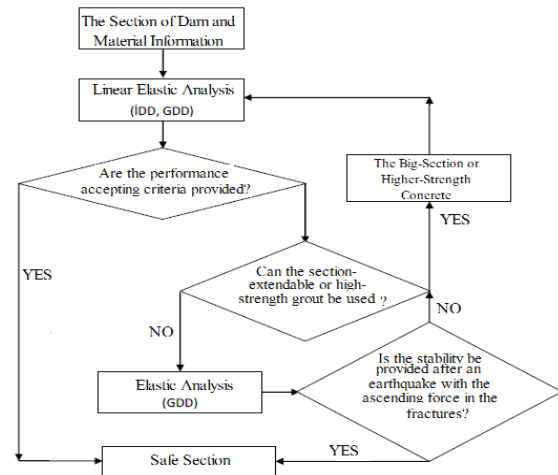


Fig. 1. The flowchart for earthquake investigations

It is necessary to consider the static and dynamic loads in the analyses of earthquake. The results of static and dynamic analyses are directly collected in the linear elastic analyses. The loads are reflected to the models in the ultra elastic analyses according to their occurrence orders. The dynamic loads which affect on the dams, the inertia forces of dams' stem and the hydrodynamic loads arising from the reservoir and tailwater in the source and downstream are the dynamic effects that the reservoir base and if it is available, the filling material would create them. The static loads are the weight of dam, hydrostatic pressure, silt loads which occur on the base of dam and the ascending forces. Hydrostatic and hydrodynamic loads should be considered for the different cases as the minimum and maximum water levels of dams' water level are considered.

In this study, two-dimensional linear elastic dynamic analyses of Andiraz Dam which its construction is planned within the border of Kastamonu were done with the use of 3 MDE Earthquake acceleration records and 3 EED records. It was provided to obtain the total ultra elastic motion duration - the demand capacity rate curves on the same points as the results of vertical and principal tensile stress -duration were obtained on the aforementioned critical points which were considered on the dam's stem.

II. DATA, MATERIAL PARAMETERS AND DYNAMIC LOADS BELONGING TO DAM

II.a. Geometry and Model

The project's area which consists of Andiraz Dam's stem place and the lake area which is within the border of Kastamonu and which will be done on Soganli Small Stream is seen at Figure 2.



Fig. 2. The project's area

Andiraz Dam has got 142 m height at the maximum section, it has got the roller compacted concrete (RCC) filling type, and it has got 10 m crest width. The dam which its geometry at the maximum section is given at Figure 3 was designed as the source's surface was given as vertical and the river mouth's side slope was given as 1D/1Y. Maximum water level takes place lower than 1,3 m crests. The crest depression on the dam's stem, the change in acceleration and the change great principal stress

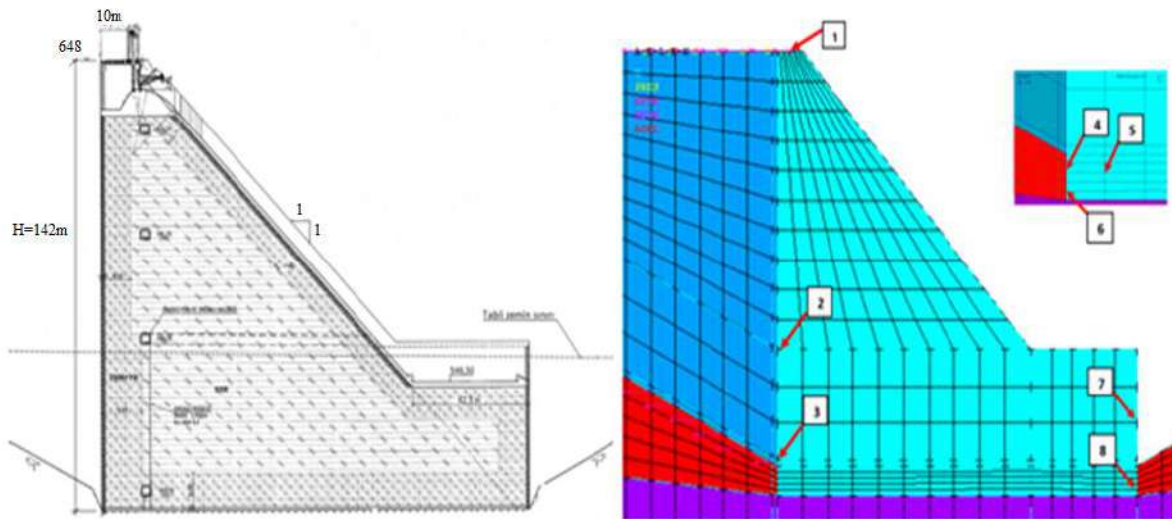


Fig. 3. Max. stem cross section and the points which are examined in the model

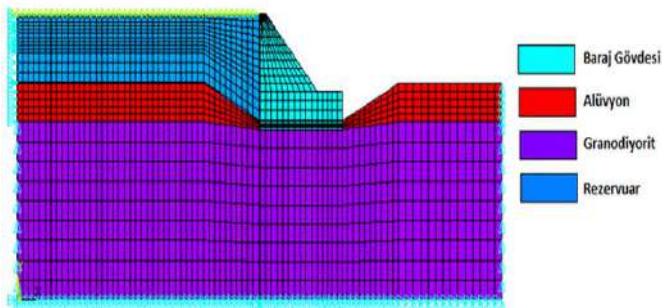


Fig. 4. Dam- foundation - reservoir finite element model

changes in 7 points with points were obtained and the cumulative-aggregation duration -demand capacity curves were obtained.

The model which is done in order that the dam's earthquake motion could be reviewed by the method of finite elements is shown at Figure 4. The model was divided into 1876 elements and the model's right and left sides were chosen as the river mouth at three floors of the dam height at the direction of source and at two floors of the height at the direction of base in order to decrease the effect of limit conditions on the system's dynamic motion. As the reservoir was included to the model as three floors of height at the direction of river mouth, Sommerfeld limit condition wasn't implemented at the end of reservoir. The effect of alluvion layer nearly at 40 m depth on the basement of reservoir to reflect the wave of earthquake was included into the model with the proper parameters. The element of Alluvion was used in the model which was done with the use of ANSYS program, PLANE 42 was used for the base and the dam's stem, FLUID 29 was used for the reservoir

II.b. Material Parameters and Damping

The elasticity module was determined as $E_r = 5.5$ GPa for Granodiorite base rock with the help of the geological evaluations and the laboratory experiments and the base rock was modelled as a linear elastic material. The speed of shear wave at the base rock is nearly 950 m/s, it includes in the B class rock or rocklike ground class bu NEHRP and in A class rock or rocklike ground class bu Eurocode-8. The elasticity module was taken as $E_r = 0.12$ GPa for alluvion nearly at 40 m thickness which is available at the stream bed.

It was seen as efficient in the pre-analyses that RCC target compressive strength is 20 MPa. The target tensile strength which is at the vertical direction on the horizontal joints and which is at the principal direction on the stem concrete was determined in a way which was given at the equations 1,2,3,4 by the criteria of USACE (2000) [4] in consideration that the padstone which will prevent the occurrence of cold joint between the layers in the necessary places will be implemented.

RCC tensile strength for OBE earthquake is

$$\sigma_{tv} = 0.05 \sigma_c = 1.00 \text{ MPa}, \sigma_{tv\text{-dynamic}} = 1.35 \sigma_{tv} = 1.35 \text{ MPa} \quad (1)$$

$$\sigma_{tp} = 0.09 \sigma_c = 1.80 \text{ MPa}, \sigma_{tp\text{-dynamic}} = 1.35 \sigma_{tp} = 2.43 \text{ MPa} \quad (2)$$

RCC tensile strength for MDE and EED earthquakes is

$$\sigma_{tv} = 0.05 \sigma_c = 1.00 \text{ MPa}, \sigma_{tv\text{-dynamic}} = 2.00 \sigma_{tv} = 2.00 \text{ MPa} \quad (3)$$

$$\sigma_{tp} = 0.09 \sigma_c = 1.80 \text{ MPa}, \sigma_{tp\text{-dynamic}} = 2.00 \sigma_{tp} = 3.60 \text{ MPa} \quad (4)$$

σ_{tv} ve $\sigma_{tv\text{-dynamic}}$ shows respectively the statical and dynamic tensile strength at the vertical direction; σ_{tp} ve $\sigma_{tp\text{-dinamik}}$ shows respectively the statical and dynamic tensile strength at the principal direction, on the above statements. The material parameters which were used for the statical and dynamic analyses of Andiraz Dam are seen at Table 1. It was provided that the ground doesn't create an inertia effect as the ground was modelled in a massless form in the finite element model. The rental rate wasn't gotten in order to neglect the radiation effects at the base. Drucker-Prager material model was used for the dam's stem in the non-linear analyses. The non-linear motion of the material occurs as the fracture of concrete in the tensile and as the plasticisation in the pressure in this model. Drucker-Prager approach is a material model that these effects would be considered [5]. This approach was obtained from the generalisation of von mises criterion in a way to include the effects of hydrostatical stress. The flowing surface of Drucker-Prager approach which was stated depending on C cohesion and ϕ angle of internal friction has got a vertical cone form and was presented at Figure 5. This graphical representation shows that the material's motions are different at the tensile and pressure. Their magnitude which is seen at Figure 10 reflects the principal stress. The plastic form changing occurs with the change in the volume for Drucker-Prager approach.

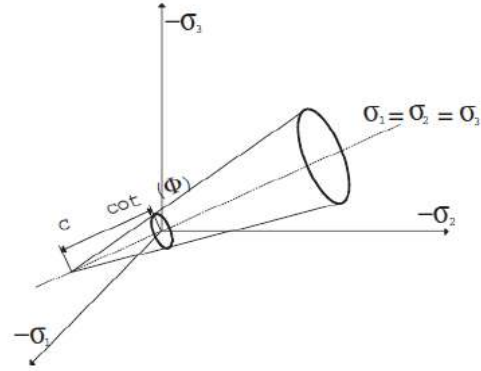


Fig. 5. The flow surface in the principal stress space of Drucker-Prager approach

In the document of USAGE-EP-1110-2-12 which grounds on Fenves and Chopra's studies (1985) [6], it was stated that the finite element which is solved with the help of massless base would be calculated in consideration with the effect of rental rate's three factors (structure-ground-reservoir) which will be used in the concrete dam analyses.

$$\xi = \frac{1}{R_r R_f^3} \xi_1 + \xi_f + \xi_b \quad (5)$$

In this formula, the structural rental rate of the dam which was modified with R coefficient (the rate of soft-base dam period on the rigid-base dam period, the rate of reservoir-filled dam period on the reservoir-free dam period) states the additional rental rate which will be added to the the system's rental rate due to the reservoir while the dam is empty and it states the additional rental rate which will be added to the the system's rental rate due to the base. Chopra and Fenves (1985) [6] thinks that the rock and concrete elasticity rate at 0.26 (for 20 MPa concrete) was determined as the coefficients 1.29 and 1.55 at 100% reservoir level in consideration with alluvion at the basement of reservoir. It was taken as the recommended value at the document of USACE-EP-1110-2-12 and the values were obtained as 3.2% and 15% with the use of the tables that Chopra and Fenves (1995) [6] gave them. The rental rate for all of the system was obtained as 19% as these values were written in their places on the equation. The mode that 90% participation was gotten with the first vibration mode was gotten with the system model analysis and Rayleigh coefficients were calculated as $\alpha = 1,096$ and $\beta = 0,033$ in a way to give 19% rental rate with the use of angular frequencies. System modal analysis was performed to obtain the mode with 90% participation by the first natural vibration mode, and Rayleigh coefficients $\alpha = 1,096$ and $\beta = 0,033$ were calculated to give 19% damping using $\omega_1 = 5,526 \text{ rad/s}$ and $\omega_2 = 6,03 \text{ rad/s}$ angular frequencies.

TABLE I. MATERIAL PARAMETERS

Name of Parameters	The Dam's Stem Concrete	Granodionite	Alluvion	Reservoir
Statcal Elasticity Module (Es) (GPa)	21.2	5.5	0.12	2.02
Poisson Rate	0.02	0.2	0,3	-
Mass Density kg/m3	2400	2609,5	1835	1000
Cohession (MPa)	1	100	0	-
Angle of Internal Friction(°)	45	42	32	-
Compressive Strength (MPa)	20	-	-	-
Vertical Tensile Strength (MPa)	1	-	-	-
Dynamic Vertical Tensile Strength (MPa)	2	-	-	-
Principal Tensile Strength (MPa)	1.8	-	-	-
Dynamic Principal Tensile Strength (MPa)	3.6	-	-	-
Dynamic Elasticity Module (GPa)	26.5	-	-	-
Reservoir Sediment Reflection Coefficient	-	-	-	0.8
Sonic Wave Speed (m/s)	-	-	-	1440

III. EULER FORMULATION FOR THE LIQUID STRUCTURE INTERACTION

The structure's motion is stated as the change of location and the motion of liquid is stated as the pressure in the analysis of liquid-structure system with the Euler approach. Two dimensional motion of lineer compressible, non-viscose liquid without rotation can be given under the small-amplitude changes with the wave equation,

$$P_{,xx} + P_{,yy} = \frac{1}{C^2} P_{,tt} \quad (6)$$

x,y,z states the cartesian coordinations, t states time, C states the pressure wave speed in liquid and P_{,ii} states two-time partial derivative by i variable of hydrodynamic pressure. The hydrodynamic pressures which occur in the liquid system as a result of any effects are obtained with the resolution of (6) equation under the proper limit conditions. The limit conditions should determined for the liquid system on the liquid-structure interface, the liquid basement, the liquid surface and the back surface (the condition of wave propagation) that the finite element net is gone of. The liquid system's limit conditions are collectively given at the following:

- 1- On the liquid-structure (dam-reservoir) inter-surface,

$$P_{,n} = -\rho_w \ddot{U}_n \quad (7)$$

- 2- On the liquid (reservoir) surface,

P=0 (If there isn't surface waves on the liquid free surface) (8)

$$P_{,n} = -\frac{P_{,tt}}{g} \quad (\text{If there is surface waves on the liquid free surface}) \quad (9)$$

- 3- On the liquid basement (on the basement of reservoir),

$$P_{,n} = -\rho_w \ddot{U}_{ng} \quad (\text{If the reservoir basement is rigid}) \quad (10)$$

$$P_{,n} = -\rho_w \ddot{U}_{ng} - qP_{,t} \quad (11)$$

- 4- For Sommerfeld wave propagation on the liquid's (reservoir's) back surface,

$$P_{,n} = -\frac{P_{,t}}{C} \quad (12)$$

They are defined as the above ones [7, 8]. As the New magnitudes which are seen at the equation 7~12; n states the liquid's surface external normal, the pressure's derivative in the direction of surface normal, the structure accelerations in the normal direction on the liquid-structure inter-surface, the mass density of liquid, g states the acceleration of gravity, the ground acceleration in the direction of liquid basement external normal, the pressure's one-time derivative to time and q states the reservoir basement rental rate coefficient. As the condition of one-dimensional wave propagation is used in the reservoir basement, q rental coefficient can be given with the equation [9];

$$q = \frac{(1-\alpha)}{C(1+\alpha)} \quad (13)$$

α coefficient shows the rate of wave reflecting from the reservoir basement to the the coming wave.

Hydrodynamic pressures would be obtained as the equation (6) which represents the motion of liquid environment is resolved under the limit conditions whih are given with te equations (7,9,11-12). If the finite element approach is used for the aforementioned liquid equations, the finite element motion equations belonging to the liquid system can be written on the form of matrix as the following;

$$[M_f^p]\{\ddot{P}\} + [C_f^p]\{\dot{P}\} + [K_f^p]\{P\} = -\rho_w[R]^T\{\ddot{U}_{sf}\} + \{F_{fg}\}$$

This shows the liquid mass matrix which includes the effect of surface waves, the liquid rental rate matrix which includes the rental rate which occurs due to the reservoir basement wave absorption effect with the propagation limit condition, the liquid rigidity matrix. It is a matrix related to the liquid-structure interface; it is used to determine the liquid load vector from the accelerations which occur from the structure

environment and the structure vital point additional forces from the pressures which occur in the liquid environment. It shows the structure accelerations on the liquid-structure inter-surface, the liquid load vector which occurs from the ground accelerations on the liquid basement, the hydrodynamic pressure vector and the one-two-time partial derivatives by this vector's time on this equation.

The finite element equations belonging to the dynamic motion of structure environment can be given with the following formula;

$$[M_s]\{\ddot{U}_s\} + [C_s]\{\dot{U}_s\} + [K_s]\{U_s\} = \{F_s\} + \{F_{sf}\} \quad (15)$$

It represents the mass, damping ratio and matrix belonging to the structure environment (dam+base) respectively; and their magnitudes represents the vectors for the acceleration, speed and change of location belonging to the structure environment. The structure's external vector states the additional external load vector which comes to the structure from the hydrodynamic pressures which occur in the liquid environment. The vector can be written as the following;

$$\{F_{sf}\} = [R]^T \{P\} \quad (16)$$

Thus, the common motion equations belonging to the liquid-structure system can be obtained with the combination of (9) and (10) equations as the following;

$$\begin{bmatrix} [M_s] & [0] \\ [M_{fs}] & [M_f^P] \end{bmatrix} \begin{Bmatrix} \{\ddot{U}_s\} \\ \ddot{P} \end{Bmatrix} + \begin{bmatrix} [C_s] & [0] \\ [0] & [C_f^P] \end{bmatrix} \begin{Bmatrix} \{\dot{U}_s\} \\ \dot{P} \end{Bmatrix} + \begin{bmatrix} [K_s] & [K_{sf}] \\ [0] & [K_f^P] \end{bmatrix} \begin{Bmatrix} \{U_s\} \\ \{P\} \end{Bmatrix} = \begin{Bmatrix} \{F_s\} \\ \{F_{fg}\} \end{Bmatrix}$$

Here, it is;

$$[M_{fs}] = \rho_w [R]; [K_{sf}] = -[R]^T \quad (18)$$

IV. DYNAMIC LOADS

EED value was given as 0,636 g at Andiraz Dam's Seismic Hazard Analysis Report. Three acceleration records which were recorded on the Class B rock and rocklike formulations in order to use in the dynamic analyses and these records were scaled with the use of target spectrum specific to the area which was given at the seismic risk analysis report in a way to be EED=0,636g which its safety evaluation earthquake is 2% possibility of exceedance in 50 years (2475-years repetition) the acceleration records of Coalinga earthquake were used for EED-1 record which has got 2% possibility of exceedance in 50 years, Pallsprings earthquake's records were used for EED-2 record and Morgan Hill earthquake's records were used for EED-3 record. 1/3 of the horizontal acceleration record was implemented to the model as the vertical acceleration record in the analyses. The scaled acceleration records are seen at Figure 5.

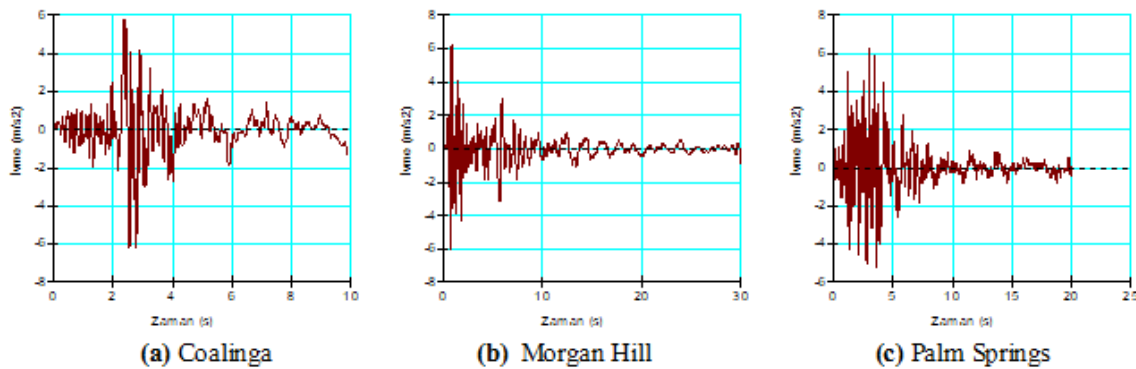


Fig. 5. The safety-based earthquake accelerograms which are scaled with the target spectrum specific to the area

V. RESULTS OF THE ANALYSIS AND RECOMMENDATIONS

VI.

V.I. The Determination of Structural Performance

The structural performance of concrete weight dams is determined with the linear analysis especially in the time-

description field. The deformations and stresses are calculated in consideration with the various compounds' elastic properties with the linear analyses. The possible damage levels which correspond to the dam's structural performance are determined, using the data. The damage terms which are used for the dam's performance are related to the fracture of concrete which is used

in the dam, the opening of joints and if it is available, the flowing in the equipment [10].

In normal conditions, the linear analyses are efficient for the structure systems which are sized by the design earthquake, which have got a smooth geometry, rigidity and mass distribution. The linear analyses which are done by the elastic methods may not be efficient in the big structure systems such as the drawbridge, towers and concrete dams which it is difficult for these properties to be together. Thus, the deformations, stresses and performance curves from the structural performance parameters which are obtained with the linear analyses to determine the real motions of the kind of structure systems provide to determine the structure's damage level. Namely, it was tried to be determined on what the scale the structure systems' linear analyses are efficient by the damage levels which are gotten from the performance curve.

The demand-capacity rate (TKO) which is seen at Figure 7; it is defined as the rate of the tensile stresses which are obtained at a point which is reviewed on the concrete dam as a result of the linear analysis to the dam concrete's strength stresses. The non-elastic cumulative time is defined as the cumulative total of each time step which exceeds the capacity of concrete tensile stress.

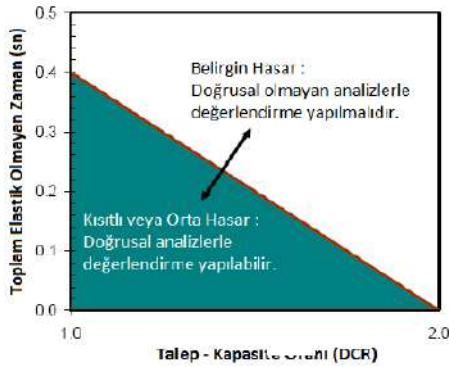


Fig. 7. The linear elastic analysis evaluation diagram [10]

It is considered that the dam motion remains within the elastic area and isn't damaged for the cases that TKO is smaller than 1. It states that the area under the curve on the performance curve which was obtained by the case that TKO is 1 and 2 is efficient for the linear analysis to determine the structure's motion, the area above the curve isn't efficient for the linear analysis and it is necessary to make the non-linear analyses to determine correct fracture sizes which occurs on the concrete stem (USACE 2003). The followings manners which are examined on the linear-elastic calculations which are done for Andiraz dam;

V.II. The Analyses for Earthquakes

As a result of Linear Elastic dynamic analyses which were done for 3 EED records on Andiraz Dam, it was observed that there was a capacity exceedance on 3 numbered point and this point's bottom levels in a way that it is expected on the heel of dam's source. This case was observed much more in Pall Springsearthquake especially as it is relatively. The performance curves came down to the certain damage section for 3 and 4 numbered points at Figure 9 (a). While 6 numbered point which was reviewed at the heel of source came down to the linear area for Coalinga earthquake, it includes in the certain damage area for Pall Springsearthquake. This case can be explained as the duration of Coalinga earthquake was the shorter one respectively. The performance curves which were obtained as a result of the linear analyses show that the non-linear analysis should be done to determine the damage much more correctly, at Figure 9. Thus, the nonlinear- analyses were done with the use of Drucker-Parager Elastic Plastic material model with the material parameters at Table 1. Some results of those analyses are seen at Figure 10-11-12 and 13.

The changes of principle tensile strength respectively in the earthquakes of Coalinga, Pall Springs and Morgan Hill during the earthquake at 6 numbered critical point, the principle stress during the maximum effect and the vertical stress distribution are seen at figures of 10-11-12 (a), (b), (c). The damage areas which occurred on the dam's stem at the end of the earthquake respectively in the earthquakes of Coalinga, Pall Springs and Morgan Hill are seen at the figures 13 (a), (b), (c). While there wasn't seen any permanent damage on the dam's stem at the end of Coalinga earthquake, there were the damaged areas on the dam's source's heel at 3 m thickness and 28 m depth in the earthquake of Pall Springs, at 5 m thickness and 21.3 m depth in the earthquake of Morgan Hill.

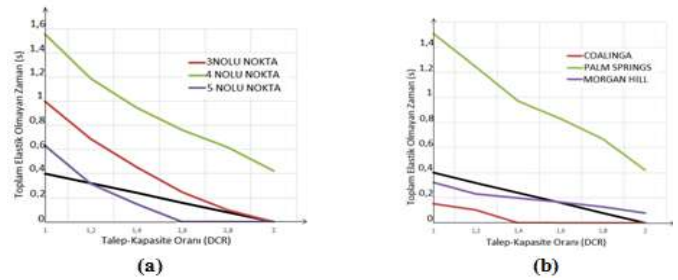


Fig. 9. (a) 3-4 and 5 no. points' performance curves under Palm Springs Earthquake (b) The Performance curves under SBE's for 6 no. point

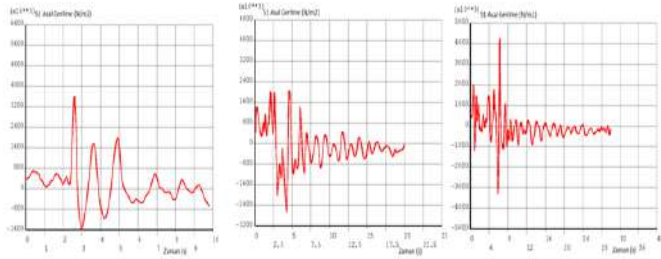


Fig. 10. S1 principal stress changes during the earthquake at 6 no.point under the earthquakes of (a)Coalinga, (b) Palm Springs, (c) Morgan Hill

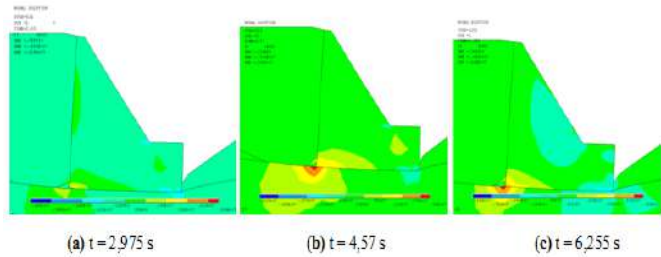


Fig. 11. S1 principal stress distributions on the critical areas under the earthquakes of (a)Coalinga, (b) Palm Springs, (c) Morgan Hill

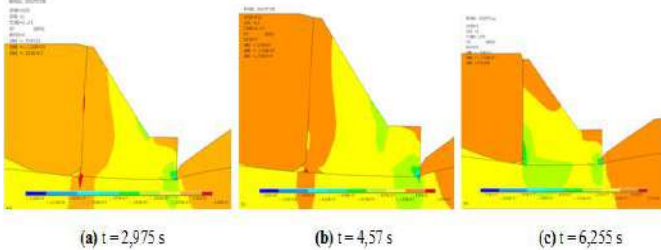


Fig. 12. The vertical stress distributions in the critical areas under the earthquakes of (a)Coalinga, (b) Palm Springs, (c) Morgan Hill

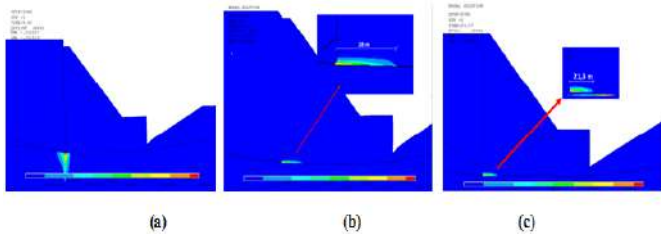


Fig. 13. Plastic Damage Distribution at the end of earthquakes; (a)Coalinga, (b) Palm Springs, (c) Morgan Hill

It is seen that 20 MPa target strength which were foreseen with the use of the classical stress analysis methods at the beginning of project studies were property at the end of the analyses. A set of damages were considered to be possible as a design philosophy in EED earthquakes which have got 2% possibility of exceedance in 50 years (2475-years repetition) which were used in this study and the dam's statical reliability after an earthquake was evaluated. Andiraz dam's statical reliability after an earthquake was evaluated in consideration with the damages which occur on the heel of dam's source and it was seen that Andiraz Dam will overcome the seismic loads to be possible with the damages which would be acceptable without getting out of its precision.

REFERENCES

- [1] USACE (2007). Earthquake Design and Evaluation of Concrete Hydraulic Structures, EM-1110-2-6053.
- [2] FEMA (2005). Federal Guidelines for Dam Safety, Earthquake Analysis and Design of Dams.
- [3] Wieland, M. (2008). Analysis aspects of dams subjected to strong ground shaking. International Water Power and Dam Construction, March 2008, 28-31.
- [4] USACE. (2000). Roller Compacted Concrete, EM-1110-2-2006.
- [5] Bangash, M. Y. H., (1989). Concrete and concrete structures: numerical modelling and applications", Middlesex Polytechnic Faculty of Engineering, London, Elsevier Applied Science.
- [6] Fenves, G. ve Chopra, A. K. (1985) Simplified analysis for earthquake resistant design of concrete gravity dams. Report No. UCB/EERC-85/10, Earthquake Engineering Research Center, University of California, Berkeley.
- [7] Humar, J., Roufaiel, M., (1983), Finite element analysis of reservoir vibration, Journal of Engineering Mechanics, ASCE, 109(1), 215-230.
- [8] Yang, R., Tsai, C. S., Lee, G. C., (1996), Procedure for Time-domain Seismic Analyses of Concrete Dams, Journal of Engineering Mechanics, ASCE, 122(2), 116-122.
- [9] Hall, J. F., Chopra, A. K., (1982), Two-dimensional dynamic analysis of concrete gravity and embankment dams including hydrodynamic effects, Earthquake Engineering and Structural Dynamics, 10(2), 305-332.
- [10] USACE. (2003). Time History Dynamic Analyses of Concrete Hydraulic Structures, EM-1110-2-6051.

Completion of missing data in rivers flow measurement (Case study Seydisuyu Basin)

Recep Bakış

Civil Engineering Department
Anadolu University
Eskişehir, Turkey
rbakis@anadolu.edu.tr

Yıldırım Bayazıt

Civil Engineering Department
Bilecik Şeyh Edebali University
Bilecik, Turkey
yildirim.bayazit@bilecik.edu.tr

Murat Mahmut Dağhan

Graduate Student
Civil Engineering Department
Bilecik Şeyh Edebali University
Bilecik, Turkey
mmdaghan@gmail.com

Dost Mohammad Ahmady

Graduate Student
Civil Engineering Department
Anadolu University
Eskişehir, Turkey
dostahmady@gmail.com

Abstract—For planning of water resources based on the demands through the basin, water potential of the basin is required to be analyzed carefully. For an accurate and reliable analysis, complete meteorological and flow data must be obtained which covers a long period of previous years. Because, especially missing flow monitoring data used at the planning stage of water structures have been reported to induce serious hazards at the operating stage. In this paper, completion of data deficient (missing data) obtained from the flow gauging stations (FGS) was performed using regression analyses related to the correlation method. Seydisuyu basin has been selected as the study area. In order to fill data deficient (missing data), linear and non-linear regression equations have been used to identify the missing values without affecting the statistical structure of the original (long) data sets. It is examined by comparison of the original and filling data with flow duration curve. In this way, it has been investigated how statistically it is true. The magnitude of missing part of the data, however, is one of the most important points to be considered in filling the missing values. Especially in case of large amount of missing values, regression method resulted in large deviation when compared with original data. Therefore, instead of using a single method, different methods should be practiced and compared if possible, for completion of missing values. Comparison of the results from different methods would lead the best missing data filling method.

Keywords—Missing flow data; Flow duration curve; Regression analysis; Seydisuyu Basin

I. INTRODUCTION

Meteorological and hydrological data such as evaporation, precipitation, snow, temperature and flow have always been required towards water resources management and planning on the basis of watershed management and researches. Completeness and continuity of these data are extremely important. Except that, meteorological (precipitation, temperature, evaporation, snow, etc.) and hydrological (flow

measurement) data, obtained from different institutions might be deficient belonging to the previous years due to various reasons. Data deficient might come out for a variety of reasons (climatic challenges, transportation challenges, measuring device issues, ...etc.).Comprise of gaps in flow data due to inconvenient climatic conditions creates some serious problems in terms of effectively planning, design and operation of water resources [1,2]. When the literature is analyzed, generally, in flow data, we are met %5-%10, or even %25 of data deficient [3-5]. Due to the mentioned reasons above, there are considerably deficient, specially in hydrological data in our country, Turkey [5]. In hydrology, data deficient can cause some key issues, specially in hydrologic modeling, and design studies in terms of water resources management. There are numerous methods used for completion of deficient data. Among all, the most popular and commonly used ones are interpolation, regression analysis, time-series analysis, artificial neural nets, and hydrologic models [6-10].

Completion of data deficient (missing) might also be practiced using algorithms found in different statistic programs (EM-Expectation Maximization), and using posterior probabilities of the data [11-12].

In addition, data deficient of meteorological and flow measurements having similar watershed characteristics, can also be complemented using different empiric equations such as (M. Turc, Langbein and Coutagne methods) [13,14]. However, besides practicality of the empiric approaches like M. Turc method, we can encounter with important deviations in region adaptation including data deficient of flow, used in the parameters of the method, and the impossibility to obtaining an accurate flow data has been stated correspondingly in the literature [14]. In addition to these methods, using the observed data from an existing stream gaging station, the flow of any

unknown point in the watershed can be estimated applying area ratio method, that is commonly used in literatures. Although different methods are used in completion of flow data deficient, correlation between the data has to be taken into consideration as well. Thereby, possibility of comparison among multiple stations will be provided rather than a single station.

Within this study, flow data belonging to General Directorate of State Hydraulic Works, and General Directorate of Electric Power Resources Survey and Development Administration, has been investigated in Seydisuyu basin, that is a sub-basin of Sakarya river. The high percentage of data deficient, is the main reason for choosing this study area. Accurate completion of the data deficient and usage of the complemented/filled data has become significant in planning water structures.

For this purpose, Seydisuyu basin has been investigated as part of scientific research projects. Totally there are 6 stream gaging stations existing in Seydisuyu basin and its sub-streams. 5 of them are run by General Directorate of State Hydraulic Works and the remaining one is run by General Directorate of Electric Power Resources Survey and Development Administration. Unmeasured months on these stations were determined using regression analysis and flow relationships between the gauges. Also mathematical relationships between these stream gaging stations were found out in this study. Using these mathematical relationships, data deficient in each flow gauging station belonging to unmeasured years, were calculated separately. Accuracy of filling data deficient were compared by evaluation of the original data set.

II. DATA AND METHOD

The research area is Seydisuyu basin, which is a sub-basin of the Sakarya River. Seydisuyu basin is in the Central Anatolian Region, between $38^{\circ}.85'-39^{\circ}.36'$ north latitudes and $30^{\circ}.16'-31^{\circ}.07'$ east longitudes. Water of the basin is discharged into the Sakarya River by Seydisuyu River. Seydisuyu basin is surrounded by Sakarya-Sarisu, Porsuk-Sarisungur, Porsuk-Kalabak in the east, by Buyuk Menderes, Gediz and Porsuk-Sarisungur in the southwest, and by Sakarya-Bardakci and Akarcay basins in the south-east. As the hydrologic basin border, a great part of the basin is in the provincial borders of Eskisehir, and the remaining parts are in the provincial borders of Afyon and Kutahya. Seyitgazi, Mahmudiye districts of Eskisehir province, Kirka town, and 51 other villages are located in the basin. Seydisuyu basin covers an area of 1816.1 km^2 , corresponds to 13% surface area of Eskisehir approximately. Geographical position of the basin in Turkey is given in Figure 1.

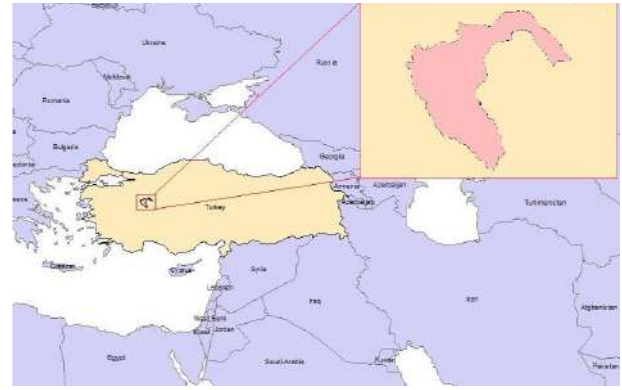


Fig. 1. Location of study area

The 53 years of long-term monthly data for the periods 1952-2005 were provided from 3. Regional Directorate of State Hydraulic Works. 5 of the stream gaging stations are belonging to General Directorate of State Hydraulic Works and the remaining one is belonging to General Directorate of Electric Power Resources Survey and Development Administration. Location of the stations in the basin, their coordinates, their precipitation area, the data as obtained and belonging which water year is given in Table 1.

Table 1. Flow gauging stations (FGS) in the study area

FGS No	Province	Coordinate	Elevation (m)	Drainage Area (km^2)	Year
DSİ-12183	Eskişehir	39.3809 E	2032	94.85	1986-2005
		30.5274 N			
DSİ -12184	Eskişehir	39.3575 E	1857	406	1986-2005
		30.5731 N			
DSİ-12185	Eskişehir	39.3453 E	1742	218.23	1986-2005
		30.5053 N			
DSİ-12192	Eskişehir	38.7268 E	1005	712	1988-2005
		31.0477 N			
DSİ-12194	Eskişehir	39.2472 E	1045	517	1990-2005
		30.5868 N			
EİE-1223	Eskişehir	39.5686 E	895	1636.3	1953-1997
		30.9267 N			

Scarcely, missing of monthly records in the basin belonging to some operated flow gauging stations were indicated as by virtue of climatic challenges and so couldn't have been recorded. Investigations were done extensively with regard to existing condition of raw data, provided from General Directorate of State Hydraulic Works. For this purpose, a database per Microsoft Excel program was constituted.

Data provided from General Directorate of State Hydraulic Works were analyzed. Also the deficient part, based upon the missing dates were determined and drawn graphically in Figure 2. Data belonging to each inspected flow gauging station were

investigated statistically. Regression analysis were applied to examine the relations among the gauges. Microsoft Excel program was practiced on, to determine correlation coefficients which are interpreting the mathematical relationships among the stations and statistical evaluations.

A. Completion of Flow Data Deficient (Missing Data) in the Research Area

Locations of flow gauging stations, used in the research area were given in Figure 2.

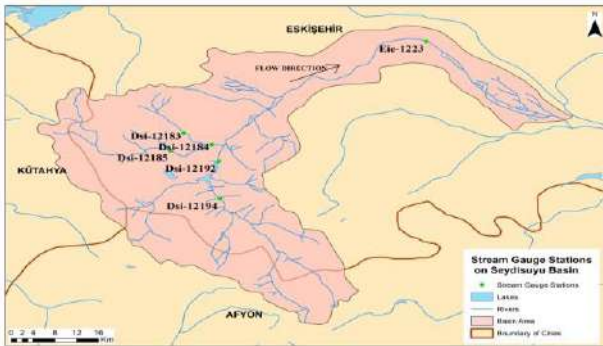


Fig. 2. Flow Gauging Stations (FGS) in the study area

Provided time-related status of monthly flow data for the periods 1952-2005 is given in Figure 3.

When the flow gauging stations are analyzed, considerable deficient could be noticed in the data provided from General Directorate of State Hydraulic Works.

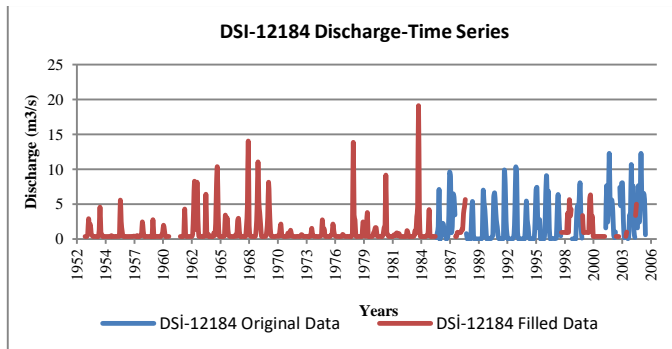


Fig. 3. Time-related status of provided dailyflow measured data results

As it is noticed in Figure 3. , flow gauging data are missing in some specific dates. By investigating whether there is a mathematical relationship between these stations or not, group of stations compatible with each other and could be used for completion of data deficient (missing data), were determined. Data analysis modulus were benefited in Microsoft Excel 2010, to determine these groups and to investigate the mathematical relationships between these stations.

Regression-correlation analysis is performed to determine whether there are relations between two or more variables or not,

and determine the direction and strength of these relations, if exist.

Approximation of the coefficients found as the result of the correlation to 1, shows the higher accuracy of the analysis, and is an indicator of pretty strong hydrologic relation between the stations.

Correlation coefficient is calculated from the equation given as follows.

$$r_x = \frac{\sum_{i=1}^n (x_i - \bar{x})(y_i - \bar{y})}{\sqrt{\sum_{i=1}^n (x_i - \bar{x})^2 \sum_{i=1}^n (y_i - \bar{y})^2}} \quad (1)$$

Here; r_{xy} , shows the correlation coefficients related to 2 flow gauging stations, x_i and y_i show flow data measured in the same period, belonging to investigated flow gauging stations, and ... show the average flow values, belonging to flow gauging stations.

Correlations between flow gauging stations is given in Table 2. While the values of correlation coefficients are investigated, the highest relation (correlation coefficients with greater absolute values $|r|$) between two stations are shown with bold colors.

In the calculations towards correlation matrix, data missing of two flow stations belonging to the same date, were shown with dash lines. For estimation of correlation, as shown in Equation 1. , the investigated flow gauging station data must have been recorded at the same date. For this reason, some parts in the correlation matrix, were remained blank or empty.

Table 2. Correlations between flow gauging stations

	dsi-12183	dsi-12185	dsi-12194	eie-1223	dsi-12184	dsi-12192
dsi-12183	1					
dsi-12185	0,452886	1				
dsi-12194	0,52006	0,729207	1			
eie-1223	0,476829	0,417583	0,458892	1		
dsi-12184	0,319158	0,086062	0,249459	0,349014	1	
dsi-12192	-0,06292	-0,34911	-0,17548	-0,08732	0,353843	1

After determination of the stations that have got strong relations with each other (higher absolute R^2 values), linear and non-linear regression analysis were performed/practiced, to present the mathematical statement of relations between these stations. According to data obtained from correlation matrix diagram, relations between flow gauging stations were examined whether it possess a linear or a non-linear structure.

In the analysis, to determine whether there is a linear relation between two stations or not, linear regression was applied. In addition, exponential relation and regression analysis of natural logarithms taken, were practiced on each station separately. To specify the best and proper representations of obtained mathematical relations between station data at the end of performed regression analysis, regression coefficient, r^2 values were calculated. In the calculation of regression coefficient,

$$r^2 = \frac{\sum_{i=1}^n (y_i - \bar{y})^2 - \sum_{i=1}^n (y_i - \hat{y})^2}{\sum_{i=1}^n (y_i - \bar{y})^2} \quad (2)$$

Here; y_i , \hat{y} , \bar{y} , represent recorded flow data, produced flow values with mathematical model, average values of recorded flow data, respectively. Within this study, mathematical relations with the highest r^2 values were taken in consideration (Figure 4). Along the entire time-scale, it is impossible to find both possessing the optimal relation and flow gauging data relevant period of time, by all means. In this case for the deficient time periods, another gauging data containing and possessing second best mathematical data relation, have been used.

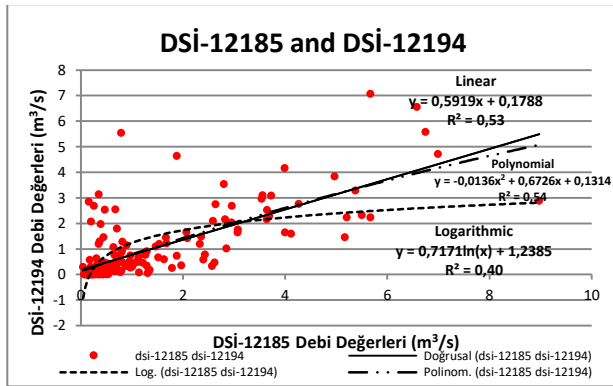


Fig. 4. Investigation of relations between stations (DSI-12185 and DSI-12194) and selection of mathematical equations

It is determined optimal mathematical relations located in the basin (study area), for completion of data deficient (missing data) in flow gauging stations.

If the recorded flow data between the years of 1952-2005, belonging to 6 FGS found in Seydisuyu basin, it is specified that there is no data found or recorded at all FGSs in 1961 water year. In this case, completion of data deficient (missing data) at all 6 FGSs in 1961 have been impossible due to nonexistence of recorded data at any of FGSs. Because there is no existing data to reveal a relation between FGSs. For this reason, long-term average flow values were used to complement/fill values of 1961 water year mentioned above. Monthly long-term seasonal average flow values, were estimated according to average values of stations in consideration of each month. For example, the flow values of January 1961, were calculated by averaging January month's value of long-term annual data for the periods 1952-2005 (accepted as flow value of January in 1961). In this manner using long-term average monthly flow values, data deficient of monthly flow values belonging to 1961, were complemented/filled.

B. Accuracy Analysis of Complement/Filled Data

After completion of original monthly flow data in FGSs, continuity curves of original data recorded in FGSs and complemented/filled data deficient, were drawn and compared for the purpose to check and determine whether there has been a difference cause over the characteristics of hydrologic structure in terms of statistics or not.

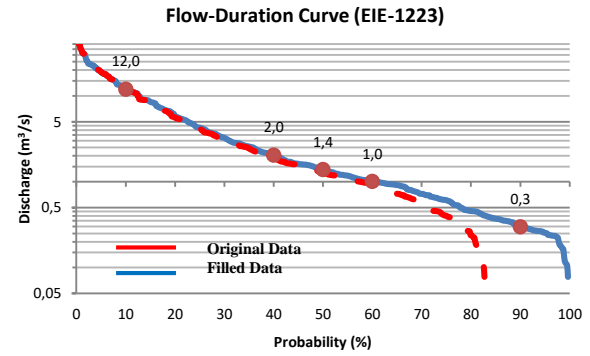


Fig. 5. Comparison of continuity curves drawn from original flow data of gauge noie-2620, and complemented/filled flow gauge values

Originated flow continuity curves were noticed in Figure 5, using complemented/filled flow values and original recorded data of station no. EİE-1223. As it is noticed in the figure, any important changes have not occurred, in terms of hydrologic characteristics. Thereby, actualized data deficient prediction, meaningfulness of data completion process in terms of statistics and suitability of statistical structure dataset by filling gap process, could be noticed clearly in the figure.

III. RESULT AND DISCUSSION

Within this research, flow gauging data found Seydisuyu basin were investigated. Monthly missing data of the flow gauging stations were estimated/complemented by applying and using correlation method between stations. Correlation method has been widely used and has given satisfactory results in completion/filling of flow gauging data deficient, in the cases if there are few numbers of data deficient. After data deficient completion/filling process, nonoccurrence of any important changes in terms of hydrologic characteristics were noticed. Thus, actualized data deficient prediction, meaningfulness of data completion/filling process in terms of statistics and suitability of statistical structure dataset by filling gap process, were noticed in the method.

However, some inconsequence could occur in completion of data deficient, due to having limited numbers of data and nonproduction of sufficient correlation with other gauging stations. This inconsistency could be noticed easily, by drawing continuity curve.

If we investigate continuity curve of station that have weak correlation after completion of data, considerable effects are clearly noticed on hydrologic characteristics. This is because of insufficiency in number of observations and consisted weak correlation with other stations

As a consequence, to prevent from such type of problems and obtain a satisfactory result in completion of data deficient, it is required to practice, apply and compare various methods.

ACKNOWLEDGMENT

This study has been supported within the context of project no. 1609F626 accepted by Commission of Scientific Research Projects of Anadolu University. In addition, we would like to thank General Directorate of State Hydraulic Works (DSI) for their support.

REFERENCES

- [1] Dursun Ö.F. and Karabatak M., “Fırat Havzasındaki eksik akım verilerinin korelasyon ve yapay sinir ağları metotları ile tahmin edilmesi”, *e-Journal of New World Sciences Academy* 4(1), 30-40 pp., 2009.
- [2] Hipel K.W. and McLeod A.I., “Time Series Modelling of Water Resources and Environmental Systems”, Elsevier, Amsterdam, 1994.
- [3] Elshorbagy, A.A. Panu, U.S., Simonovic, S.P. “Group-based estimation of missing hydrological data: I. Approach and general methodology”, *Hydrological Sciences-Journal-des Sciences Hydrologiques*, 45(6):849-866., 2000.
- [4] Panu, U. S., Khalil, M. & Elshorbagy, A., “Streamflow Data Infilling Techniques Based on Concepts of Groups and Neural Networks”, Chapter 12 in: *Artificial Neural Networks in Hydrology* (ed. by R. S. Govindaraju & R. Rao), 235-258. Kluwer, Dordrecht, The Netherlands., 2000.
- [5] Bakış R. and Göncü S., “Akarsu Debi Ölçümlerinde Eksik Verilerin Tamamlanması: Zap Suyu Havzası Örneği”, *Anadolu Üniversitesi Bilim ve Teknoloji Dergisi A-Uygulamalı Bilimler ve Mühendislik*, Cilt:16, Sayı:1, 63-79 pp., 2015.
- [6] Göktaş B., “Sakarya Seydisuyu Su Toplama Havzası” Eskişehir, 1991.
- [7] Dastorani M.T, Moghadamnia A., Piri J. and Rico-Ramirez M., “Application of ANN ANFIS models for reconstructing missing flow data”, DOI 10.1007/s10661-009-1012-8, *Environ. Monit. Assess.* 166(1-4):421-434., 2010.
- [8] Smits A., Baggelaar P.K. “Estimating Missing Values In The Time Series”, *Rhine Water Works*, Netherland, 2010.
- [9] Gümüş V. and Kavrut E. “Zamanti Nehri- Ergenusağı İstasyonu Eksik Aylık Akım Verilerinin Tahmini”, *Gazi Üniversitesi Fen Bilimleri Dergisi Part:C, Tasarım Ve Teknoloji*, 1(2):81-91., 2013.
- [10] Keskin, M.E. and Taylan, D. “Artificial Models for interbasin flow prediction in southern Turkey”, *J. Hydrologic Eng.* 14(7):752-758., 2009.
- [11] Anonymous, “SPSS Missing Values™ 17 Users Guide”, SPSS Inc., Chicago, IL, USA., 15., 2009.
- [12] Bal, C. and Özdamar, K., “Eksik gözlem sorununun türetilmiş veri setleri yardımıyla çözülmesi”, *Osmangazi Üniversitesi Tıp Fakültesi Dergisi* 26(2):67-76., 2004.
- [13] Gündoğdu K. S., Demir A. O. and Akkaya Aslan, Ş. T. “Göletlerin Bazı Hidrolojik Analizlerinin Coğrafi Bilgi Sistemi (CBS) Ortamında Yapılma Olanakları”, *I. Ulusal Sulama Kongresi*, 8-11 Kasım, 247-253, Antalya., 2001.
- [14] Vanlı M., “Göletlerde Su Temini Çalışmaları”, T.C. Bayındırlık ve İskan Bakanlığı Devlet Su İşleri Genel Müdürlüğü, Hidrometri ve Taşkın Hidrolojisi Semineri, 3-4 Eylül, İstanbul, 1990.

Investigation of Live-Bed Scour at Labyrinth Side Weirs

Mustafa Tunc

Firat University

Faculty of Engineering, Department of Civil Engineering
Elazig, Turkey
mtunc@firat.edu.tr

M. Emin Emiroglu

Firat University

Faculty of Engineering, Department of Civil Engineering
Elazig, Turkey
memin.emiroglu@gmail.com

Abstract — Side weirs, also known as lateral weirs, and overflow dams are free overflow regulation and diversion devices commonly encountered in hydraulic engineering. The lateral loss of water is reducing the sediment transport capacity in the main-channel and the formation of a local sediment deposit in the downstream of weir. The head over the side weir rises and the side overflow discharge as well. The design discharge to be diverted over the weir is increased by this flow-sediment transport interaction. Although there were no studies that scrutinized the scouring depth and geometry that occurs around the labyrinth side weirs in channels with movable bed, there are limited number of studies that examined the scouring geometry around the classical side weir. In the present study, local scour depths formed in the periphery of triangular labyrinth side weir mounted in a live-bed rectangular cross-section straight channel were experimentally investigated under steady state flow and free overflow from the side weir conditions. To provide for live-bed conditions, the sediment was added to bed material in the experiments. A series of experiments were conducted for live-bed scouring conditions (for flow intensity greater than one) to determine the maximum scour depths that occur around the triangular labyrinth side weir with different flow depths, different main channel discharges, different volumetric amounts of sediment feed, different crest heights, different Froude numbers, different flow intensities and using uniform bed material. In the experiments, the dimensions of the scours and sediment deposits that occur upstream and downstream of the weir exhibited a periodic change (increase and decrease). The maximum depth of scour occurred at the downstream end of the triangular labyrinth side weir frequently.

Keywords — *triangular labyrinth side weir; flow intensity; local scour; live-bed scour; sediment transport*

I. INTRODUCTION

A structure, located in a stream bed or built later, could change certain properties of the flow. If these changes in flow could be predicted beforehand, the structure would be designed in a sounder manner, or necessary precautions against the problems that are caused by these changes would be taken. Otherwise, this case leads to damages in the structure or to the failure in fulfilling its function. The scouring observed in the intake structure, scouring formed in the downstream of the spillway, and the scouring occurring in the abutment wall and

midfoot of the bridges and the scouring observed in the downstream of the baffle structures are of major problems encountered in hydraulic engineering.

The decrease in velocity and shear stress due to the lateral over flow causes the realization of a reverse current via creating a stagnation region in the downstream of the side weir. Scouring is formed between the main channel axis in the downstream region of the side weir and the outer bank, as a result of the changes in the shear stress.

Although there were no studies that scrutinized the scouring depth and geometry that occurs around the labyrinth side weirs in live-bed channels, there are limited number of studies that examined the scouring geometry around the classical side weir. Rosier et al. (2011) conducted an experimental research on the geometrical behavior of bed forms in a classical side weir region placed in a rectangular channel [1]. Paris et al. (2012) researched the applicability of De Marchi hypothesis on the determination of discharge capacity of side weirs under subcritical flow regime and live-bed conditions. This study presents experiments demonstrating the relationship between bed morphology and overflow discharge. The experiments were conducted in a main channel with small dimensions (0.30 m x 5 m x 0.30 m) and within a small discharge range (2-12 L/s). Studies reported that De-Marchi approach could be used in live-bed channels [2]. Onen and Agaccioglu (2013) conducted an experimental research examining clear-water scouring and live-bed scouring conditions in rectangular cross-section side weirs with $L = 0.25, 0.40$ and 0.50 m weir opening and $p = 0.07, 0.12$ and 0.17 m crest height from the sand bed in a live-bed 180° curved channel, considering subcritical flow regime and overfall conditions [3].

Since there are limited number of studies in the literature on the change in bottom topography and the scouring problem, which both occur around the labyrinth side weir that are placed in the streams, a complete theoretical basis on this subject was not constituted. Therefore, it is considered that it would be useful to examine the scouring problem, especially in our country that is rich in rivers. The aim of the present study is; to investigate the maximum scouring depth and the bottom geometry in the labyrinth side weirs, under the live-bed scouring conditions.

II. HYDRAULICS OF SIDE WEIR FLOW

The most important function of the side weir is to discharge the excessive water, when the optimum capacity, determined by taking into account the requirement and economy, is exceeded. Side weirs are used in numerous engineering applications. As the water level in the reservoir reaches a level that could damage the dam, side weirs are used to discharge the water (Fig. 1). Although they are built next to the reservoir due to the flow conditions in the reservoir, these weirs act as normal weirs. This condition should be taken into consideration while conducting the hydraulic design.



Fig. 1. Walshaw Dean Reservoir [4]

Figure 2 presents the side weir plan and section. It is stated that; y_1 = flow depth at the upstream end of the side weir at the centerline of the main channel (m), y_2 = flow depth at the downstream end of the side weir at the centerline of the main channel (m), y = flow depth at any point in the main channel (m), Q_1 = main channel discharge (m^3/s), Q_2 = main channel discharge after the side weir (m^3/s), Q_w = total flow over side weir (m^3/s), V_1 = mean approach flow velocity at the upstream of the side weir in the main channel (m/s), V_2 = mean approach flow velocity at the downstream of the side weir in the main channel (m/s), V_s = mean approach flow velocity of the side weir in the collection channel (m/s), B = main channel width (m), L = around a triangular labyrinth side weir of width (m), Ψ = angle of deflection ($^\circ$), p = weir crest height (m), x = longitudinal coordinate (m).

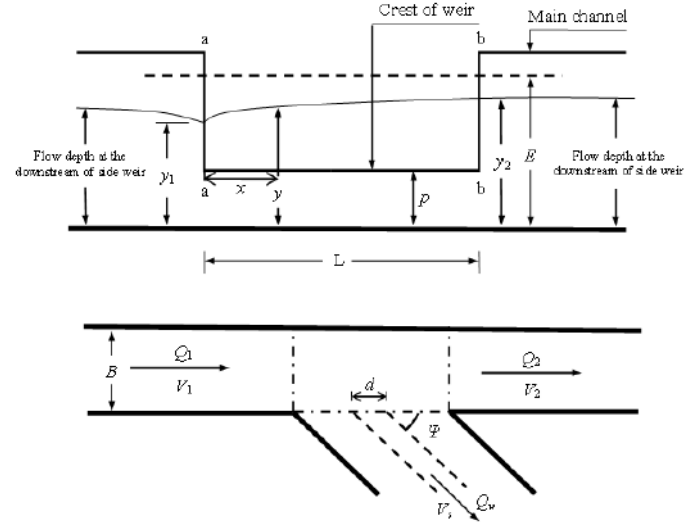


Fig. 2. Plan and section of the side weir flow [5]

III. LABYRINTH WEIRS

Increasing the flow rate that could overflow in a particular lake level or transmitting a constant flow rate by a smaller crest water load is aimed via the labyrinth spillways, through increasing the effective length of the spillway crest. These weirs could be considered as an alternative, which are advantageous in conditions where the space in the upstream is restricted for the reservoir water level that would especially be created by the flood discharge or in conditions where the spillway width is limited due to topography. Labyrinth weirs could be constructed in trapezoidal, triangular, and circular-shaped (Fig. 3). Most preferred type is the trapezoidal-shaped type. Equation (1) is used to find the rate of flow, that pass over the labyrinth weir. Total crest length should be considered instead of the distance "L" in Eq. (1) [6].

$$Q = 1.83.(L-0.2h).h^{3/2} \quad (1)$$

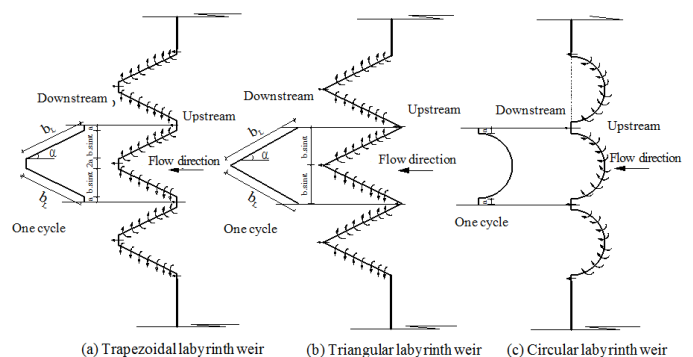


Fig. 3. Labyrinth weirs [7]

IV. THE DETERIORATION OF EQUILIBRIUM IN SEDIMENT TRANSPORTATION

In the case that the amount of solid material transported in an alluvial stream changes locally, changes such as sediment deposit in the bed and scouring could occur. As the amount transported increases scouring is observed, and when decreases, sediment deposit is observed.

The construction of a hydraulic structure such as a weir might cause changes in the stream bed. Such changes in the bed of the stream are observed either as sediment deposit in some parts or as scouring in others, depending on the amount of material that comes from the upstream, on the amount of material that is transported and on the amount of material that is over flown (Fig. 4). Both the sediment deposit and the scouring phenomena continue until they obtain a stable cross-sectional shape. Sediment deposit starts primarily with the sediment deposit of coarse particles, with their departure from the bed the velocity increases and the suspension discharge increases due to the decrease of the mean diameter of the material transported in suspension. Thus, due to the increase in the transported material, equilibrium condition is approximated. On the other hand, as the material coming from the upstream is smaller than the discharge transport capacity, the coarse particles remain in the bed since initially the fine particles in the bed would be scoured. In addition, occurrence of ripples in the bed would as well cause the decrease of the discharge transport capacity. Thereby, either in case of scouring or in sediment deposit, several secondary degree factors accelerate the achievement of the equilibrium condition [8].



Fig. 4. Sediment deposit and scouring observed in the present study

In a bed with cohesionless loose-material, the movement starts when the bed conditions reach a critical value required for movement. The particles that depart the bed due to the bed movement are washed away along the bed by depositing.

Bed shapes encountered in the rivers are as follows:

- a. Ripples
- b. Dunes

- c. Plane bed
- d. Antidunes

The order of the bed shapes provided above is made according to the change depending on the velocity of the flow. In other words, sand ripples occur with lower velocity flows, and as the velocity increases the bed has the shapes of ripple, dune, plane bed and antidune, respectively. Various shapes that the bed could take are given in Fig. 5 [9].

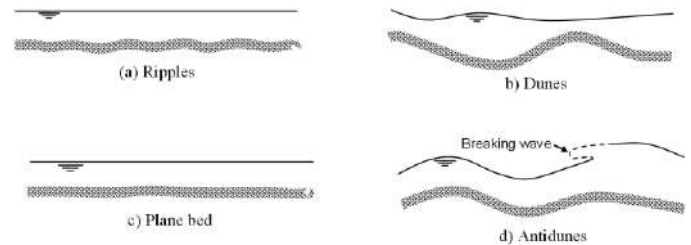


Fig. 5. Bed forms developed in alluvial channels [9]

Ripple and dune formations observed in this study are presented in Fig. 6.



Fig. 6. Ripple and dune formations observed in this study

V. EXPERIMENTAL STUDY

This study was conducted at the Firat University Hydraulics Laboratory using the experimental setup depicted in Figure 7. The experimental setup was 18.20×0.50 m and the side wall of the main channel was made of glass. The slope of the main channel bottom was approximately 0.1%. The collection channel was 0.50 m wide and 0.70 m high. The main channel and collection channel were separated by a steel wall. The section of the collection channel where the side weirs would be installed was built in a circular form with a diameter of 1.30 m to provide free nappe overflow from the labyrinth side weir (Fig. 7).

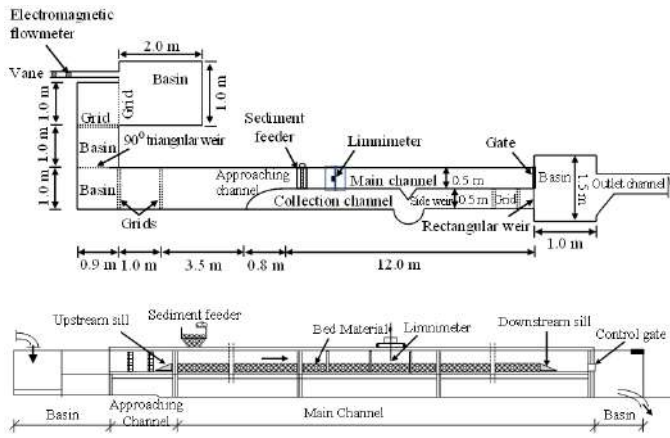


Fig. 7. Experimental setup plan and longitudinal cross-section: Plan view (a), Longitudinal section (b).

The experiments are conducted in a linear channel with a rectangular cross-section; for a side weir opening of $L = 0.25$ meters, and for triangular labyrinth side weirs, with crest height of $p = 0.07, 0.12$ and 0.16 meters from the sand bed and with an apex angle of $\theta = 90^\circ$. The experiments were carried out under steady flow conditions, and in the case of bed scouring ($V_1/V_c > 1$) for free over flowing condition. The experiments were conducted at a discharge of $50 - 90$ L/s. The flow depth (y_1) was measured at the channel axis at the upstream end of the side weir. The water depth at the main channel axis upstream of the side weir was used as the side weir upstream water depth. Novak and Cabelka (1981) suggested a minimum upstream water depth of 30 mm [10]. Thus, in this study a minimum upstream water depth of 30 mm was used to prevent surface tension affects.

Two sills of 20 centimeters height are placed at the upstream and downstream ends of the main channel, as seen in Figure 8. Quartz sand was placed between the upstream and downstream sills on the main channel. For this sand laid on the channel bed, following values are determined, $d_{50} = 1.16$ millimeters and $\gamma_s = 26$ kN/m³. The parts before the upstream sill and after the downstream sill are made up of sheet metal with an approximate slope angle of 15° , reaching the channel bed. Thus, the provided sand base was protected against deterioration. In order to ensure stable flow conditions (i.e. to provide time-invariant flow conditions), hollow bricks are placed at the upstream part of the channel and in front of the specific points at the end of the collecting channel. The aim is to ensure taking accurate measurements over the weir.

This experimental study was carried out for the labyrinth side weirs placed in the middle part of a linear channel. The bed material was laid 4 meters forth and 4 meters backwards from the center of the side weir, covering 8 meters of the channel. Experiment system application assembly is shown in Fig. 8.

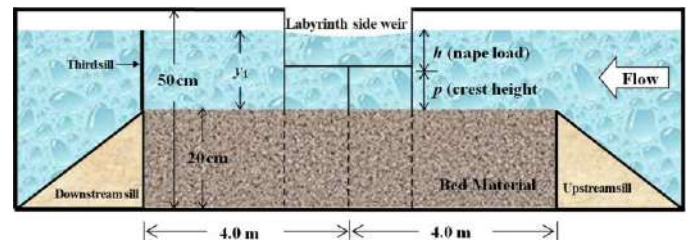


Fig. 8. Experiment system application assembly

Prior to each experiment, the sand was mixed and compacted and the bed was leveled. After the channel bed is compressed and flattened, water was supplied slowly to the channel by turning on the valve very little. As the water slowly flowed over the sand by rising slowly from the ramp in front of the sill of the upstream end of the channel, a thirdsill is placed 20 centimeters above the sill on side of the downstream (i.e., as it should be 40 centimeters high from the channel bed). In such way, deformation the flat shape of the sand in the bed is prevented. Then, it was waited until the depth of water in the next section of the downstream sill of the main channel reached the same water depth in the main channel. After all water level along the channel became even, the requirement flow was attained and the experiment was commenced by slowly removing the thirdsill that prevented the deformation of the shape of the sand in the bed, on the sill at the downstream part. By keeping the flow rate constant, flow height in the channel (y_1) was adjusted to the required level via the radial caps at the end of the channel.

Once the experiment is completed, the valve was slowly turned off, and the thirdsill was placed back on the downstream sill of the channel in order to preserve the topography that was formed on the bed, and thus the discharge of the water from the channel was provided. Consequent to all these processes, maximum scouring depth that occurred at the side weir area was measured via a digital limnimeter. In addition, for the bed topography, bed level measurements were taken at the side weir area at 268 points with particular intervals through the aid of the digital limnimeter. Figure 9 presents the points, at which the bed topography measurements were taken.

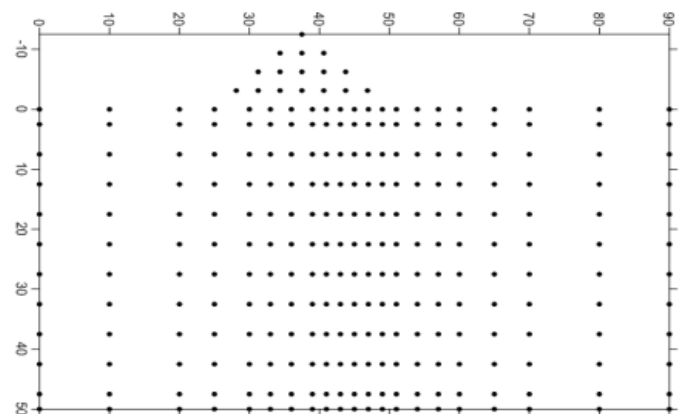


Fig. 9. The demonstration of the points of topography measurements at the labyrinth side weirs that were tested: $L = 0.25$ m

Initially pilot experiments were conducted in order to determine the bed load flow for various flow conditions. In case of a moving bed ($V_1/V_c > 1$), since bed ripples occur in a short time, and the bed is constantly in a movement, solid material transportation occurs at a high level, and the amount of the overflow material increases constantly due to the increase in the flow rate (V_1/V_c). Thus, in order to provide the moving bed condition, constant supply of solid material was provided in the channel via the portable machine, which is designed in the Hydraulics Laboratory of the Firat University's Civil Engineering Department, seen in Fig. 10. The velocity of the volumetric amount of sediment feed ($Q_{s,up}$) was adjusted by taking into consideration the " V_1/V_c " values through this machine.



Fig. 10. Portative machine that provide solid material supply to the channel

Side weir properties and flow conditions in this study are presented in Table 1.

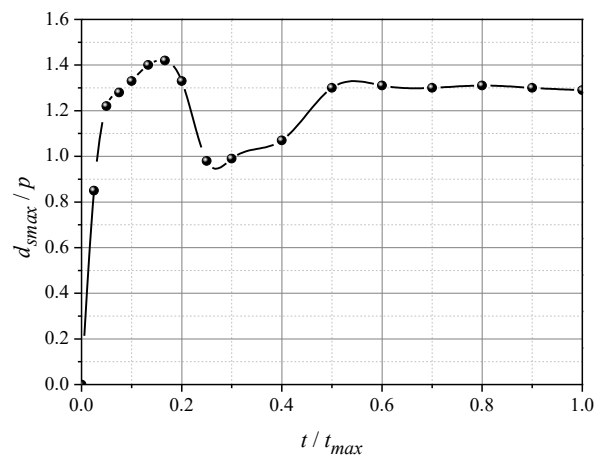
Table 1. Side weirs and flow conditions tested in the experiments

Experiment No	p (m)	L (m)	Q_1 (L/s)	y_1 (m)	$Q_{s,up}$ (m ³ /s)	V_1/V_c (-)	F_1 (-)
1	0.07	0.25	50	0.12	0.00075	1.94	0.77
2	0.12	0.25	55	0.16	0.00019	1.52	0.55
3	0.16	0.25	90	0.19	0.20	2.06	0.69

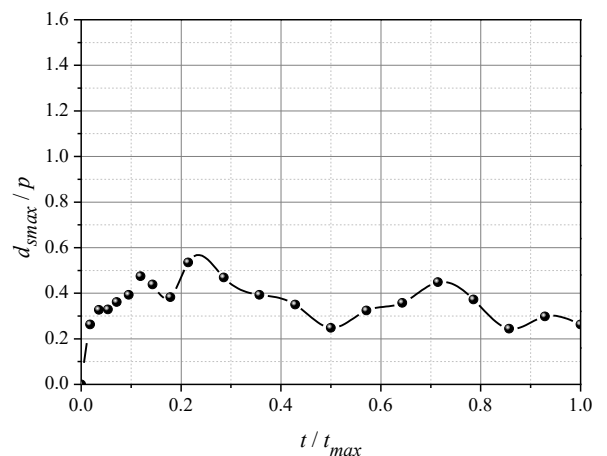
VI. EVALUATION OF THE EXPERIMENT RESULTS

In this section, non-dimensional maximum scouring depth's (d_{smax}/p) change in non-dimensional time (t/t_{max}) was investigated in case of moving bed scouring, for side weirs with $L = 0.25$ meters opening and $p = 0.07, 0.12, 0.16$ meters crest height, and is presented in Figure 11(a-c). For moving bed scouring, " V_1 ", which is the velocity value in the main channel, is selected greater than the " V_c " value, which is the initial velocity of the movement in the bed. The experiments were carried out in the range between $V_1/V_c = 1.0-3.0$ and each experiment were carefully elaborated to be sustained for 1080 minutes. Figure 4 presents the areas in which maximum scouring depths were observed. The experiments pointed out that the duration required to obtain the maximum scouring depth during equilibrium for moving bed scouring is

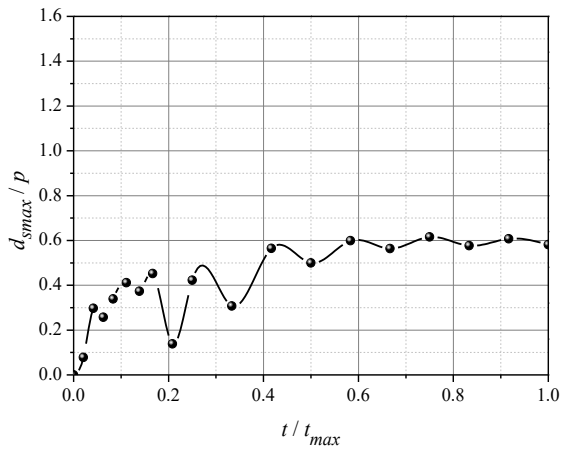
approximately 480 minutes. For larger " V_1/V_c " values, this duration was around maximum 900 minutes. After this duration, maximum scouring depths were observed to exhibit amplitudes close to the equilibrium scouring depths (Fig. 11). On the other hand, for the same " V_1/V_c " values in side weirs with larger crest heights, scouring depth at the time of equilibrium was observed to be smaller, and the equilibrium time was attained in a shorter duration. Scouring depth-duration graphics for each experiment is presented in Figs. 11 (a-c) and the flow characteristics are presented in Table 1. The tendency of the experiment results is parallel to the change of scouring depth as a function of time graphics in the studies of Tsujimoto and Mizukami (1985) and Yanmaz and Altinbilek (1991), [11 and 12].



a) No.1 experiment



b) No.2 experiment

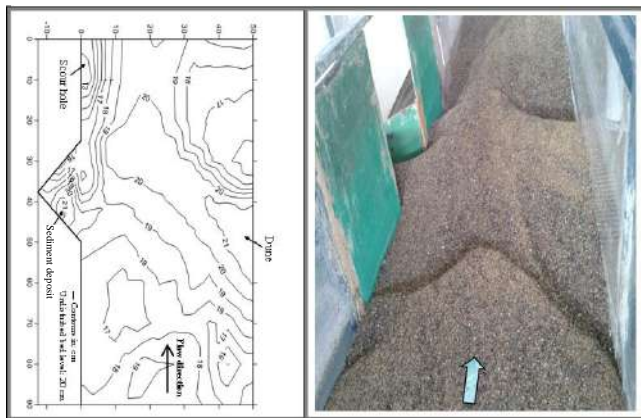


c) No.3 experiment

Fig. 11. Time-dependent change of the scouring depth for $L=0.25$ m in the maximum scouring area: $p=0.07$ m (a), $p=0.12$ m (b), $p=0.16$ m (c)

Bathymetric contour lines of the bed occurrence as a result of the experiment for $L = 0.25$ meters and $p = 0.07, 0.12$ and 0.16 meters and the related images are presented in Figs. 12 (a-c).

In Figure 12 (a), it is possible to observe that the topography at the interior edge of the channel did not change significantly. Scours and peaks were observed in the labyrinth triangular side weir area placed at the exterior edge. Scouring depth at equilibrium time occurred at a certain distance from the weir area.



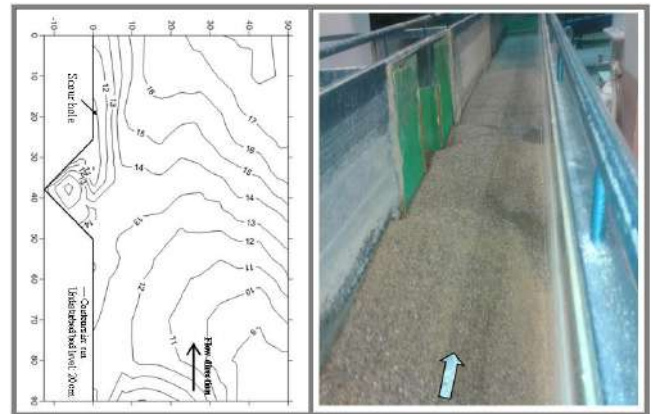
a) No.1 experiment

Scouring depth at equilibrium time in Figure 12(b) was formed in an elliptical shape from the center of the downstream of the weir to the downstream end. At the upstream overflow part, a small peak formation was observed. Due to the increasing crest height and decreasing flow rate (V_1/V_c), less material was transported to the collection channel.



b) No.2 experiment

In Figure 12(c), it was observed that the topography at the interior edge of the channel did not alter significantly and small-dimensioned sand ripples were formed. However, at the exterior edge of the channel, it was observed that scours and peaks were formed. Scouring depth was formed with an elliptical shape at the weir's downstream end. Bed ripple formation is observed. Maximum scouring formation is observed at the downstream overflowing part. Due to the large crest height and lower side weir length of the side weir used for this experiment, little amount of material was overflowed.



c) No.3 experiment

Fig. 12. Bed bathymetry and related images for $L=0.25$ m: $p=0.07$ m (a), $p=0.12$ m (b), $p=0.16$ m (c)

VII. CONCLUSIONS

Along a linear, rectangular cross-section channel with a moving bed, in constant flow and free overflowing conditions; following results are obtained from this study, which scrutinized the topographical changes that occur around the side weir and at the main channel bed and the scouring depths at the non-dimensional equilibrium time, in conditions of moving bed scouring in labyrinth side weirs with $L = 0.25$ meters length and $p = 0.07, 0.12$ and 0.16 meters crest height from the sand bed.

- In this experimental study ($V_1/V_c = 1.0 - 3.0$), it was observed that scouring depth became evident after a short duration from the initiation of the experiment and this duration shortened due to the increase of the flowrate.
- For the flow rate $V_1/V_c = 1.52$ value, while usually ripple formation was observed in the bed, mostly dune formations were observed at 1.94 and 2.06 values.
- The transformation of the channel bed from ripple form to dune form, scatterings were observed in the scouring depths due to the changing bed roughness.
- While the duration to reach the maximum value of the scouring pit decreased due to the increase of the side weir crest height, the duration for obtaining the maximum value in larger " V_1/V_c " values increased.
- The place of the scouring pit formation was determined as around the side weir and close to the downstream end. As the " V_1/V_c " value increased, it was observed that the place of the scouring pit was shifted from the downstream end of the side weir to the downstream.
- With the larger values of flow rate (V_1/V_c), scouring depth at the non-dimensional equilibrium time (d_{se}/p) also reached larger values.
- Larger scouring depths were obtained in side weirs with large crest heights.
- When the flow conditions were considerably same, bed scouring started earlier as the side weir crest height decreased, and bed scouring started later as the side weir crest height increased.
- It was determined that scouring shape that occurred in the bed was directly related to the flow rate (V_1/V_c) and non-dimensional side weir crest height (y_1/p) in the rectangular cross-section linear channel, under moving bed flow conditions.
- While the side weir height is 0.07 meters, the shape of the scouring in the bed is formed with circular cross-sections due to the vortex occurrence, and when the side weir crest height increases to 0.12 and 0.16 meters, the scouring was observed to have an elliptical shape.
- It was determined that the scouring depth at non-dimensional equilibrium time (d_{se}/p) changed directly with the increase in flow rate (V_1/V_c) and after a certain period it presented an amplitude around the peak values.

REFERENCES

- [1] Rosier, B., Boillat, J. L., and Schleiss, A. J. (2011). "Influence of lateral water withdrawal on bed form geometry in a channel." *Journal of Hydraulic Engineering*, 10.1061/(ASCE)HY.1943-7900.0000472, 1668-1675.
- [2] Paris, E., Solari, L., and Bechi, G. (2012). "Applicability of the De Marchi hypothesis for side weir flow in the case of movable beds." *Journal of Hydraulic Engineering*, 10.1061/(ASCE)HY.1943-7900.0000566, 653-656.
- [3] Onen, F., and Agaccioglu, H. (2013). "Live bed scour at a side-weir intersection located on an alluvial channel." *Irrigation and Drainage*, 62(4), 488-500.
- [4] Tunc, M., and Emiroglu, M. E. (2014). "Effect on bed topography of labyrinth side weirs located in movable bed rivers." *With International Participation 4th National Symposium and Exposition on Dam Safety*, 759-770 (in Turkish).
- [5] Emiroglu, M. E., Kaya, N., and Agaccioglu, H. (2010). "Discharge capacity of labyrinth side weir located on a straight channel." *J. Irrig. and Drain. Eng.*, 10.1061/(ASCE)IR.1943-4774.0000112, 37-46.
- [6] USBR., 2001. Water measurement manual, 3rd Edition, Water Resources Research Laboratory, Bureau of Reclamation, U. S. Department of the Interior.
- [7] Emiroglu, M. E., Kaya, N. ve Dogan, Y. (2010). Effect on discharge coefficient of crest shape at weirs, *DSİ Technical Bulletin*, 108, 57-70 (in Turkish).
- [8] Tunc, M. (2014). An investigation of the hydrodynamics of flow at the labyrinth side weirs in the movable bed rivers, *Firat University, Graduate School of Science* (in Turkish).
- [9] Bayazit, M., and Avci I. (2010). Flow in streams and sediment transport, *Istanbul Technical University, Civil Engineering Faculty Press*, Istanbul (in Turkish).
- [10] Novak P. and Cabelka J. (1981). Models in Hydraulic Engineering, *Pitman Publishing Limited*, London.
- [11] Tsujimoto, T. and Mizukami T. (1985). Effect of migration to local scour around a bridge pier, *Memoirs, Faculty of Technology, Kazanawa University*, 19(1): 23-34.
- [12] Yanmaz, A. M., and Altinbilek, H. D. (1991). "Study of time – dependent local scour around bridge piers." *Journal of Hydraulic Engineering*, 10.1061/(ASCE)0733-9429(1991)117:10(1247) 1247-1267.

Investigation of Architectural Design Failures in Earthquake Resistant Design of Buildings based on Turkish Earthquake Code (TEC)

Tuğba İnan

Department of Architecture
Ömer Halisdemir University
Niğde, Turkey
tugbainan85@gmail.com

Ebru Şahin Mercimek

Department of Architecture
Aksaray University
Aksaray, Turkey
mim-sahin@hotmail.com

Kutluğ Savaşır

Department of Architecture
Dokuz Eylül University
İzmir, Turkey
kutlug.savasir@deu.edu.tr

Abstract— Turkey is situated in a seismically active region and exposes to earthquakes at frequent intervals, which cause considerable loss of life and property. Designing earthquake resistant buildings is considerably significant in terms of the durability of buildings against to the earthquake loads. This statement supports the general objective of the study that earthquake resistant design of buildings is a vital need for Turkey. Earthquake is a common and significant research field ranging from social sciences to technical sciences. However, the structural problems are generally seen as an engineering problem even though they can be eliminated through the architectural design phase. This study mainly aims to gain an understanding of the earthquake design issues in the architectural design phase in terms of structural irregularities and after perceiving the problem, develop solutions to the earthquake resistance problems in buildings. The failures which are commonly observed in the reinforced concrete (RC) buildings after earthquakes and the solution suggestions to these problems will contribute to the consciousness in the earthquake resistant architectural design. In this study, structural irregularities, which has a serious effect on earthquake behavior of buildings, have been investigated in detail based on Turkish Earthquake Code 2007. These structural irregularities are examined with the examples of damaged buildings after the Marmara earthquake in 1999 and Van earthquake in 2011. The problems causing structural irregularities are evaluated in detail with their solutions. The detected effective factors or commonly encountered problems on the earthquake performance of buildings are architectural form, configuration of structural elements, aspect ratio, floor openings, projections in plan, cantilevers, differences in the rigidity between floors both in plan and vertical direction, short columns and pounding effect.

Keywords—*earthquake; earthquake resistant design; reinforced concrete buildings; structural irregularities; earthquake architecture*

I. INTRODUCTION

Turkey, with more than 90 percent of its territory located in highly seismic regions. It is an earthquake prone country that has been struck by various devastating earthquakes throughout history. During last century, 22 earthquakes took place with magnitudes greater than 7 with the last Van earthquake in 2011

($M=7.2$). These earthquakes resulted in thousands of deaths and destroying or heavily damaging 500,000 buildings [1]. Therefore, earthquake resistant building design is considerably significant.

If the earthquake effects on existing buildings from the past destructive earthquakes are considered, it can be clearly seen that failures on buildings start at the beginning of the architectural design phase. Therefore, there is a strong relationship between the architectural design of buildings and their earthquake safety. “Earthquake resistant architectural principles are not the provisions that could be inserted by the structural engineer after the completion of architectural design. They should be applied to the project during the architectural design phase” [2]. Architectural Design error cannot be corrected by a mathematical calculation. Therefore, architectural design decisions play an active role in the earthquake behaviour of buildings.

In Turkey, the mainstream construction system is reinforced concrete (RC). Most of the buildings were severely damaged or collapsed after earthquakes (Erzincan earthquake in 1939 and 1992, Marmara earthquake in 1999, Van earthquake in 2011, etc.). These severely damages or collapses are related to many factors such as architectural form, configuration of structural elements, storey number, floor openings, projections in plan, cantilevers, differences in the rigidity between floors both in plan and vertical direction, short columns and pounding effect, etc.

Municipality of Düzce conducted a damage survey in buildings after 1999 Marmara Earthquakes to investigate the relation between storey number of buildings and damage levels. These results are illustrated in Figure 1. It is pointed out that building vulnerability increases remarkably with the increase in the storey number. The percentages of damage levels are given for each storey number separately. Buildings, especially having four or five storeys appear to be more vulnerable than the others [3].

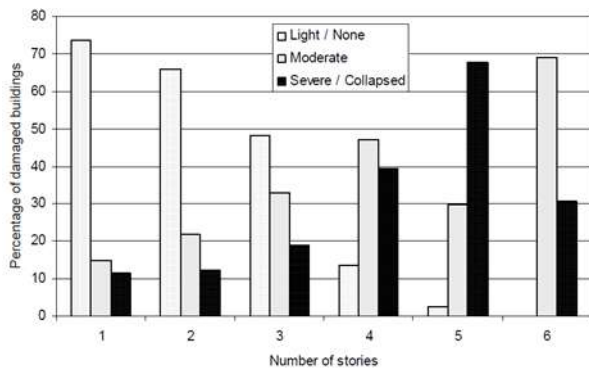


Figure 1. Building damage levels with the number of storeys after 1999 earthquakes in Düzce [3]

After the Marmara Earthquake in 1999, an investigation was made on ten heavily damaged or destroyed buildings [4]. These buildings have been investigated in terms of their structural irregularity mechanism. It is observed that they are all multi-storey R/C skeleton buildings which are commonly used for commercial or dwelling purposes. Based on Bakar's study [4], the structural irregularities on these ten investigated buildings is presented in Table 1. The table draws attention to the torsional irregularity(A1) and soft storey irregularity (B2) and nonparallel axes (A4) which are explained in Turkish earthquake code 2007 (TEC-2007) [5].

Table 1. Structural irregularities on chosen ten buildings after the Marmara Earthquake

	Reviewed Project Number	Existant	Nonexistant
A1	10	-	10
A4	10	2	8
B2	10	-	10

The structural irregularities are described in the Turkish Earthquake Code, 2007(TEC, 2007) [5]. However, in practice it is very significant and required to gain an understanding of the problems in projects at least in terms of structural irregularity, and then manage to solve the problems using problem-oriented solutions. Earthquake is a common and significant research field ranging from social sciences to technical sciences. However, the structural problems caused by an earthquake are generally seen as an engineering problem even though they can be eliminated through the design phase. Safety precautions should have a significant position in architectural design. The safety of a building is strongly related to its architectural design and its structural system [6]. For this reason, architects should have an awareness of the problems about structural irregularities in terms of both problems in plan and structural configuration in order to achieve the reasonable and logical solutions. This study aims to explore architectural problems in earthquake resistant design and then their interaction with structural configuration to emphasize the

architectural failures. Commonly encountered structural irregularities are examined with the examples of damaged buildings after the Marmara earthquake in 1999 and Van earthquake in 2011. The problems causing structural irregularities are examined in detail with their solutions from literature.

II. SEISMICITY OF TURKEY

The Earth that we are living on has witnessed lots of disasters such as earthquakes, floods, storms, and avalanche. Earthquake is a major problem for all human being because of killing thousands each year. The great part of the World is under the threat of earthquakes [7]. Its specific time, location, and magnitude cannot be estimated before it has happened. Based on the long-term seismic records in the World, it is expected that one very strong earthquake will occur each year. Estimated numbers of earthquakes per year are listed depending on their magnitudes below in Table 2.

Table 2. Estimated earthquake frequency in the World [8]

Group	Magnitude	Annual Average Number
Very Strong	$M > 8.0$	1
Strong	$7.0 < M < 8.0$	17
Medium	$5.0 < M < 7.0$	1453
Small	$3.0 < M < 5.0$	143000
Micro	$1.0 < M < 3.0$	1300000
Ultra Micro	$M < 1.0$	

There are three prominent earthquake belts in the world. These are Pacific earthquake belt, mid-Atlantic belt, and the third one is Alp Himalayan earthquake belt which affects the seismicity of Turkey. Nearly 17 % of the world's major earthquakes occur at Alp Himalayan earthquake belt [9]. The 17 August 1999 Kocaeli earthquake with a magnitude 7.4 and the 12 August 1999 Düzce earthquake with a magnitude 7.1 Düzce can be given as the most striking examples occurred on Alp Himalayan earthquake belt. Turkey is a tectonically active country that lies on the Anatolian Peninsula on the Alp Himalayan earthquake belt. Turkey has surrounded three main faults. These are North Anatolian Fault (NAF), East Anatolian Fault and West Anatolian Host Graben system.

Turkey is separated on five earthquake zones according to their risk conditions, of which the 1st and 2nd earthquake zones are the most hazardous ones due to the existence of the high magnitude earthquakes in the past. Seismic Hazard map of Turkey is given in Figure 2. 1st earthquake zone is red coloured regions and 2nd earthquake zone is orange coloured. According to the seismic zone map of Turkey, approximately 96 % of its land is located on considerably risky earthquake zones and 80 % of its population is imposed upon to the large scale earthquakes.

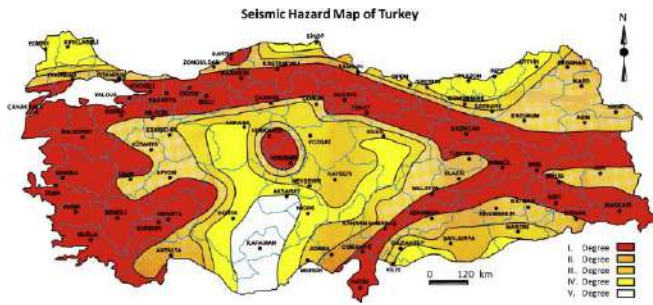


Figure 2. Seismic Hazard Map of Turkey [10]

III. STRUCTURAL IRREGULARITIES

Irregular buildings are defined in the Turkish earthquake code (TEC-2007) as buildings whose design and construction should be avoided because of their unfavorable seismic behavior. Structural irregularities begin in the initial part of the architectural design phase. There are many factors causing structural irregularity and affects adversely earthquake performance of buildings. These are irregular design in plan and vertical direction, discontinuity in mass and rigidity distribution, configuration of structural elements on nonparallel axis, height differences between floors, short columns, pounding effects, etc. [11]. Accordingly, TEC-2007 divides structural irregularities into two main groups: irregularities in plan and irregularities in the vertical direction. Irregularities in plan consist of three different types of structural irregularities, which are torsional irregularity denoted as A1, floor discontinuities denoted as A2 and projections in plan denoted as A3. Irregularities in the vertical direction comprise three types of structural irregularities, which are weak storey denoted as B1, soft storey denoted as B2 and discontinuity of structural elements denoted as B3. These irregularities are explained in Table 3 and Table 4.

Table 3. Irregularities in Plan [5]

A- IRREGULARITIES IN PLAN	
A-1 Torsional Irregularity:	
The case where Torsional Irregularity Factor η_{bi} which is defined for any of the two orthogonal earthquake directions as the ratio of the maximum storey drift at any storey to the average storey drift at the same storey in the same direction, is greater than 1.2 $[\eta_{bi} = (\Delta_i)_{\max} / (\Delta_i)_{\text{ort}} > 1.2]$	
A-2 Floor Discontinuities:	
In any floor; I - The case where the total area of the openings including those of stairs and elevator shafts exceeds 1/3 of the gross floor area, II - The cases where local floor openings make it difficult the safe transfer of seismic loads to vertical structural elements, III - The cases of abrupt reductions in the in-plane stiffness and strength of floors.	
A-3 Projections in Plan:	
The cases where projections beyond the re-entrant corners in both of the two principal directions in plan exceed the total plan dimensions of the building in the respective directions by more than 20%.	

Table 4. Irregularities in Vertical Direction [5]

B- IRREGULARITIES IN VERTICAL	
B1 – Interstorey Strength Irregularity (Weak Storey) :	
In reinforced concrete buildings, the case where in each of the orthogonal earthquake directions, Strength Irregularity Factor η_{ci} , which is defined as the ratio of the effective shear area of any storey to the effective shear area of the storey immediately above, is less than 0.80. $[\eta_{ci} = (\Sigma Ae)_i / (\Sigma Ae)_{i+1} < 0.80]$	
Definition of effective shear area in any storey :	
B2 – Interstorey Stiffness Irregularity (Soft Storey) :	
The case where in each of the two orthogonal earthquake directions, Stiffness Irregularity Factor η_{ki} , which is defined as the ratio of the average storey drift at any storey to the average storey drift at the storey immediately above or below, is greater than 2.0. $\eta_{ki} = (\Delta_i / h_i)_{\text{ort}} / (\Delta_{i+1} / h_{i+1})_{\text{ort}} > 2.0$ or $\eta_{ki} = (\Delta_i / h_i)_{\text{ort}} / (\Delta_{i-1} / h_{i-1})_{\text{ort}} > 2.0]$	
B3 - Discontinuity of Vertical Structural Elements :	
The cases where vertical structural elements (columns or structural walls) are removed at some stories and supported by beams or gusseted columns underneath, or the structural walls of upper stories are supported by columns or beams underneath.	

A. Torsional Irregularity

Various seismic codes define torsional irregularity as a significant irregularity, because of its devastating effects on buildings. The main factors causing torsional irregularity are the architectural form of the building and rigidity distribution in the plan geometry. Earthquake loads act on gravity centre of the structure (G). However, the rigidity centre of the structure (R) responds to these loads (Figure 3). If the eccentricity between these two centres is great, a torsional moment will occur around the centre of rigidity. Therefore, the structure begins to rotate around the rigidity axis [12]. The distance between the center of gravity and the centre of rigidity should be kept as minimum as possible [13].

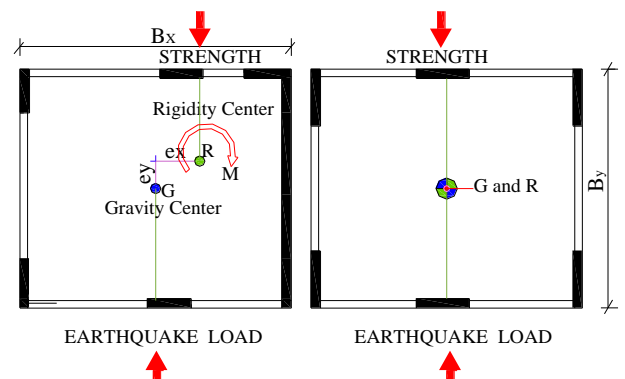


Figure 3. Working mechanism of Gravity and Rigidity centre

The design of a building is the geometrical arrangement of all the architecture, structure and contents. It should include both appropriate form and the structural distribution. This should be considered in the early design phase by architects. The most appropriate form in terms of earthquake loads is circle and square due to their symmetric and simple plan geometry. Besides, the rectangular form is a suitable alternative solution owing to its simplicity and symmetry provided that the lengths of both short and long edges are close to each other [13]. These simple forms react the same inertia forces under earthquake loads coming from in every direction. Structures which have asymmetric and complex plan geometry such as L, H, T, U, Y, +, have little energy absorbing capacity due to the torsional effects and stress concentrations at notch points on reentrant corners [12-13]. Apart from the simplicity of the plan geometry, irregular rigidity distribution in plan cause torsional irregularity. It can create torsional irregularity despite the regular plan geometry [12-13]. For instance, if shear walls or rigid core are located on one side of the building, flexible and rigid parts occur in the structure. In Figure 4, a heavily damaged building due to the torsional irregularity from 1999 Marmara Earthquake is presented.



Figure 4. A heavily damaged building from 1999 Marmara Earthquake

To prevent the torsional irregularity, complex forms separated into simple forms by using seismic separation joints. The distance between gravity and the rigidity center should be minimized. Symmetry both in the building form and rigidity distribution should be provided. In the complex plan geometries such as L and T types, acute angle reentrant corners should be Strengthened at notch points by vertical structural elements or reentrant corners should be softened.

B. Floor Discontinuities

Some cases such as big holes in the slabs, the existence of the openings adjacent to the vertical structural members, abrupt reduction in the slabs or improper local floor holes prevent the regular distribution of the earthquake loads to the vertical

structural members [12-13]. This type of irregularity also causes torsional irregularity via creating flexible and rigid parts in the building. The reinforcement around the corners and edges of the openings may contribute to the continuity in floors [12]. The rigidity of the columns and beams around the openings should be increased or shear walls should be placed around the openings to balance the rigidity between floors [12]. Openings on the floors should be positioned symmetrically in the plan geometry. Floor openings should be separated by dilatation joints and slabs should be made void-free.

C. Projections in Plan

The projection ratio has significant role on earthquake behaviour of structures. This irregularity which is called projections in plan is the cases where projections beyond the reentrant corners in both of the two principal directions in plan exceed the total plan dimensions of the building in the respective directions by more than 20 % (TEC, 2007). It is illustrated on the Figure 5.

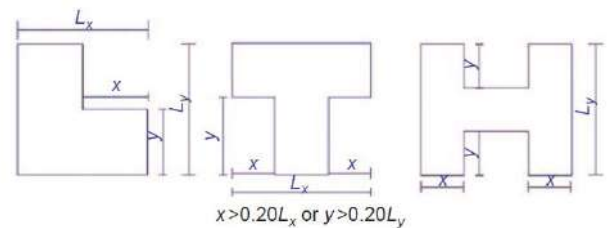


Figure 5. Projections in plan

The buildings which have large projections are seriously damaged from earthquakes [12]. Because, the building wings make different movements on different directions under earthquake loads and stress concentration occurs at the notch points of the building. Therefore, critical shear forces and moments occur in the reentrant corners where the projections connect. There are two alternative solutions to prevent this type of irregularity. The first is to divide building blocks into simple parts by seismic joints (Figure 6). The second is to tie the building wings strongly with a linkage element to reduce torsion[14] (1)



Figure 6. Separating building blocks by seismic joints

D. Soft and Weak Storeys

Weak storey irregularity is a kind of vertical configuration issue in which there is a major reduction in strength of the storey when it is compared with above storey [12]. It can be observed at any storey of a building. However, it frequently occurs at the first storey due to the considerable loads accumulation at the first storey of the building. It is due to the differences in stiffness or flexibility between storeys. All stories of the building should be designed nearly equal in terms of strength or stiffness in order to distribute the earthquake forces homogeneously among stories. However, architectural design issues in a building limit that type of planning. For instance, the ground floors are generally used as shops while the upper stories are used for housing in residential buildings in Turkey. The storey heights are different between the ground floor and above. Thereby, shops are designed as to have large window openings and vertical structural elements inside the shops are removed which is coming from upper floors because of the need to create large areas. Open ground storey such as shops, meeting rooms, banking halls creates remarkable damages in buildings under earthquake loads. Because, while a great storey drift occurs in the ground floor, the upper floors move like a diaphragm. High stress concentration occurs along the connection line between the ground and first floor that leads to distortion or collapse in buildings.

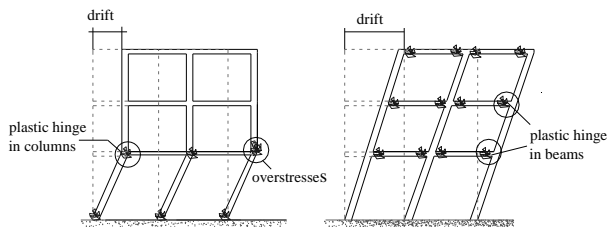


Figure 7. The soft first storey failure mechanism

There are many factors leading to the weak and soft storey irregularity. For instance, buildings with vertical setbacks are one of them. A setback can be defined as an abrupt and major change of strength and stiffness. For that reason, it prepares both soft and weak storey irregularity on the ground floor. It can be visualized like a building having vertical reentrant corners. The building having vertical setbacks suffers from damages in the line of the setback or notch point due to the great stress concentration. The vertical setbacks in the building start making different displacement due to the different natural period of vibration between the typical storey and the storey with setbacks [15]. Their earthquake behaviour is quite complex to predict. Projections which are designed in order to animate the facades of a building cause considerable damage due to the earthquake forces. All storeys should have the same plan geometry [15]. Even though setback exists in a single building block, it can also occur in adjacent buildings having different heights due to the deficiency in the amount of seismic separation joint or having no seismic separation joint.

Cantilevers are another factor that lead to weak and soft storeys. In Turkey, approximately 70 or 80 % of buildings have

constructed with cantilevers [16]. The building shown below in Figure 8 subjected to great earthquake damage due to the insufficient cross sections of columns at ground floor. There are stiffness differences between floors especially related to the heavy closed cantilever and weak columns at the ground floor. For this reason, the columns broke at the ground floor level on connection points and collapsed. The cross sections of the columns should be increased and shear walls should be added on the ground floor. Binders should be increased along the column height, especially on across to the connection points.



Figure 8. Damage due to the heavy cantilevers [Photo by Kutlu Darılmaz]

There are various alternative solutions to reduce or eliminate the negative effects of the weak and soft storey irregularities. Some of them are presented in Figure 9. The cross sections of the columns can be increased on the ground floor or additional columns or shear walls may be added. Open ground floors may be supported additional walls. Bracing elements can be added to the ground floor which contribute to the vertical structural elements for load transfer. Joints should be left between columns and walls.

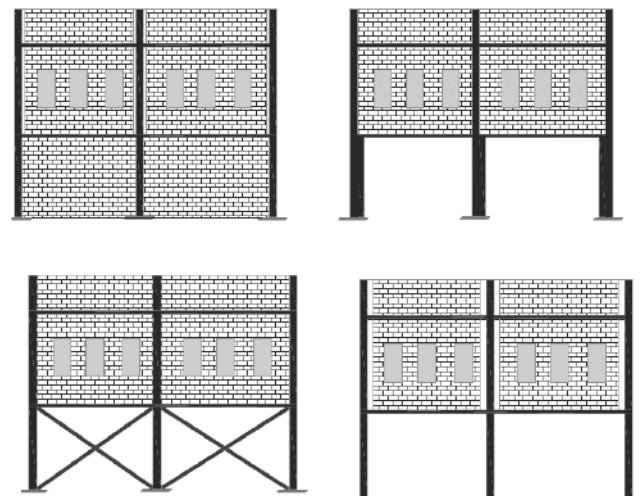


Figure 9. Solutions for Weak and Soft storey

E. Discontinuity of Vertical Structural Elements

This irregularity is described as the case where vertical structural elements are positioned improperly. Some vertical configurations of structural elements are prohibited in Turkish Earthquake Code (TEC-2007) illustrated in Figure 10. Gusseted columns or the columns which rest on cantilever beams are prohibited. A damaged gusseted building is given in Figure 11. In no case the shear walls should be allowed to rest under the columns and In no case the shear walls should be allowed to rest on the beams. In the case where a column rest on a beam supported with columns at both ends, all internal forces consisting vertical loads and seismic loads from the earthquake direction shall be increased by 50 % at all sections of the all beams and the columns which are adjacent to the beam.

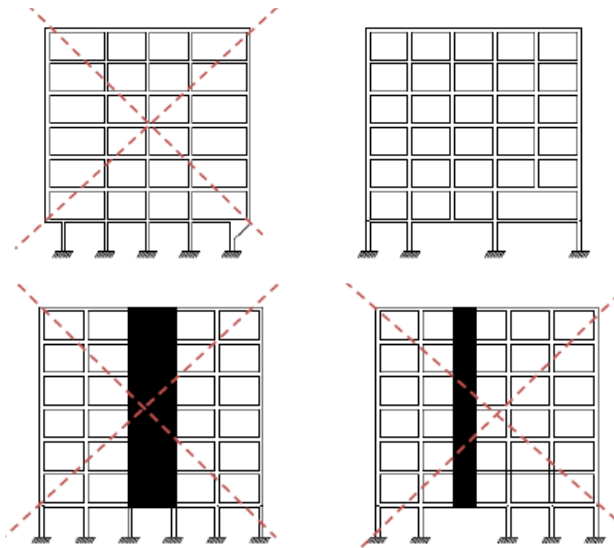


Figure 10. Discontinuity of Vertical Structural Elements



Figure 11. Gusseted column damage [Photo by Elif Çiftçi]

F. Short Column Effect

When a building has both long and short columns in the same storey, the columns expose to different shear forces due to their height differences. The lateral loads firstly come to the long and flexible columns, and then go towards to the short column and accumulate in there. Due to the excessive accumulation of the seismic energy, shear cracks occurs at both ends of the columns. The long and short column having the same cross section show the same displacement under earthquake loads. However, the short columns are more stiff or rigid as it compared with the long column and expose greater earthquake forces than short columns [17]. Mezzanine floors, Mechanical floors, Hillside sides, Graded foundation, Adjacent columns to the openings, Stair landing cause short columns. The damage in these short columns is often in the form of X-shaped cracking that occurs due to shear failures. heavy non-structural walls must be isolated from the columns to prevent the formation of the short column. To prevent short column due to the stair landing, sliding support should be placed between the steps on the intermediate landing (Figure 12).



Figure 12. Sliding support problem



Figure 13. X cracking due to the short column

G. Other irregularities

In a structure, it is desired that beams should begin deforming before columns. Failure in a column can affect the stability of the overall building. However, beams deformation partly affects the building. For that reason, beams need to be made ductile rather than the columns. Sufficient ductility is ensured in the structural members where the damage is estimated to happen under earthquake loads. Plastic hinging at both ends of the columns may initiate a storey displacement or even leading to the overall collapse of the building [6]. The beams should have weakest links instead of columns to prevent plastic hinging in columns. This condition can be provided by correctly sizing the structural members and using sufficient amount of steel in them. In Figure 14, the building is collapsed due to the strong beam-weak column irregularity.



Figure 14. Damage due to the hollow-tile floor slab [Photo by Elif Çiftçi]

Pounding is a damage type in two buildings or different parts of the same building under earthquake loads. It causes hitting the buildings one another. It commonly occurs due to the insufficient seismic gap or no gap between two adjacent buildings. If the size of the seismic gap is insufficient based on the expected storey drifts, pounding between adjacent structures may occur. In Figure 15, the buildings damaged from pounding effect are given.



Figure 15. Pounding effect [Archive of the Istanbul Metropolitan Municipality]

IV. CONCLUSIONS

Architecture is a profession which exists to solve the shelter problems of humanity in a way that is in harmony with nature and the force of nature. The interaction of architectural form and structural configuration has become a serious issue in the building industry because of the poor seismic performance of reinforced concrete buildings in Turkey. Producing earthquake safety environment is one of the duties of architectural design. For that reason, this study aims to explore architectural problems in earthquake resistant design to underline and understand architectural faults, and then its interaction with structural configuration to develop basic knowledge and perspective. In this study, the structural irregularities are investigated comprehensively with solutions suggested in literature and Turkish earthquake code, and then the effective factors on earthquake performance of structures are explored. The detected effective factors or commonly encountered problems on the earthquake performance of buildings are architectural form, configuration of structural elements, aspect ratio, floor openings, projections in plan, cantilevers, differences in the rigidity between floors both in plan and vertical direction, short columns and pounding effect. If the factors causing structural irregularities are investigated, it is observed that many of them can be prevented with the decisions in the early stage of architectural design. Architects are primary responsible from the overall picture observed after earthquakes due to the being the designer of the buildings. It is important to underline that ERD should not be seen just as an engineering calculation issue. Nevertheless, there is still hope for earthquake resistant structures through an understanding of the problems and problem-oriented solutions.

REFERENCES

- [1] I.H. Çağatay, "Experimental evaluation of buildings damaged in recent earthquakes in Turkey", *Engineering Failure Analysis*, Vol. 12 No. 3, pp. 440-542, 2005.
- [2] E. Erman, *Deprem bilgisi ve deprem güvenli mimari tasarım* [Earthquake Information and Earthquake Safety Architectural Design], ODTU Press, Ankara, 2002.
- [3] H. Sucuoğlu and T. Yılmaz, *Düzce, Turkey: A City Hit by Two Major Earthquakes in 1999 within Three Months*. Turkey, Ankara: Earthquake Engineering Research Center, 2000.
- [4] V. Bakar, 17 Ağustos 1999 depreminde ağır hasar gören binaların ortak özellikleri [Common faults of the buildings heavily damaged during the 17 August 1999 earthquake]. *Ankara TMMOB Chamber of civil engineers bulletin*, vol.8, pp. 28-32, 2003.
- [5] *Turkish Earthquake Code (TEC) (2007)*.
- [6] N. Bayülke, *Depreme Dayanıklı Betonarme ve Yığma Yapı Tasarımı* [Earthquake Resistant Reinforced Concrete and Masonry Building Design], Civil Engineering Press, Izmir, 2001.
- [7] E. Karaesmen, *Öncesiyle Sonrasıyla Deprem* [Before and After Earthquake], Atılım Üniversitesi yayınları, İstanbul, 2002.
- [8] United State Geological Survey [USGS]. (2010a). Frequency of earthquake occurrence. Retrieved from <http://earthquake.usgs.gov/earthquakes/eqarchives/year/eqstats.php>.

- [9] Z. Celep, and N. Kumbasar, Deprem Mühendisliğine Giriş, ve Depreme Dayanıklı Yapı Tasarımı [Introduction to Earthquake Engineering and Earthquake Resistant Building Design], Beta Press, Istanbul, 2004.
- [10] Republic of Turkey, Prime Ministry Disaster and Emergency management Presidency, AFAD, 1996.
- [11] S. Tezcan, Depreme Dayanıklı Tasarım için Bir Mimarın Seyir Defteri [An Architect's Log Book for Earthquake Resistant Design], Türk Deprem Vakfı, Istanbul, 1998.
- [12] C. Arnold and R. Reitherman, Building Configuration and Seismic Design, John Wiley & Sons, New York, NY, 2002.
- [13] T. Inan, and K. Korkmaz, "Evaluation of structural irregularities based on architectural design considerations in Turkey", Struct, Survey, 29(4), 303-319, 2011.
- [14] F. Naeim, The Seismic Design Handbook, Van Nostrand Reinhold, New York, NY, 2001.
- [15] J. Ambrose and D. Vergun, Seismic design of buildings, USA, New York: Wiley & Sons Inc, 1985.
- [16] M., Doğan, E. Ünlüoğlu and H. Özbaşaran, "Earthquake failures of cantilever projections buildings", Engineering Failure Analysis, 1458-1465, 2007.
- [17] D.B.N. Murthy, Disaster Management: Text and Case Studies, Deep Publications, New Delhi, IN, 2007.

Assessment of Earthquake Behavior of Reinforced Concrete Buildings with Slab Discontinuity

Sibel Sağlıyan¹

Firat University, vocational school of higher education,
Construction Department,
Elazığ, Turkey
ssagliyan@firat.edu.tr

Burak Yön²

Munzur University Engineering, Faculty, Civil Engineering
Department,
Tunceli, Turkey
burakyon@gmail.com

Abstract— The most important principle of the earthquake-resistant design of reinforced concrete structures is that the structural elements must carry both vertical loads and horizontal loads as a whole. For this reason, it is required that the structural elements carry their own weight with sufficient safety and the loads arose from external forces must be transferred safely to the load carrying vertical elements. However, discontinuity of the slabs disturbs the integrity of the structures and causes problems in transferring earthquake loads to the structural elements. In this study, the effect of slab discontinuity in plan on seismic behaviors of multi - storey reinforced concrete structures was investigated by using incremental linear dynamic analysis method. To investigate this irregularity situation, one regular and three irregular multi-storey reinforced concrete building models were selected. Dynamic envelopes of the structures were obtained from the analysis results and compared with each other. Thus, it was observed that the irregular structures subjected to more shear force than the regular structure.

Keywords—reinforced concrete building, slab discontinuity, incremental linear dynamic analysis

I. INTRODUCTION

The earthquake effect is a natural catastrophe that has caused massive devastation on people and the environment. But the main reason of the losses in the earthquakes is that the structures not provided the desired earthquake behavior. While designing the building systems, it is aimed that the buildings resist the earthquake forces at least must be provide life safety level. To provide this performance level, the structure has symmetrical and regular load carrying system. Regular structures; both in practice and in dimensioning, provide simple the calculation and forces are calculated accurately. For this reason, regular construction is the most practical choice for a good design.

Lateral forces are transmitted to the vertical load carrying elements by slabs. It is assumed that the slab behaviors as a rigid diaphragm during the design of structure. But the large openings in the slab invalids rigid diaphragm assumption [1-4]. So, Turkish Seismic Code (TSC-2007) [5] requires some requirements about this irregularity. These requirements are shown in Fig.1. According to code, In any floor

a) The case where the total area of the openings including those of stairs and elevator shafts exceeds 1/3 of the gross floor area,

b) The case where local floor openings which make the safe transfer of seismic loads difficult to vertical structural elements,

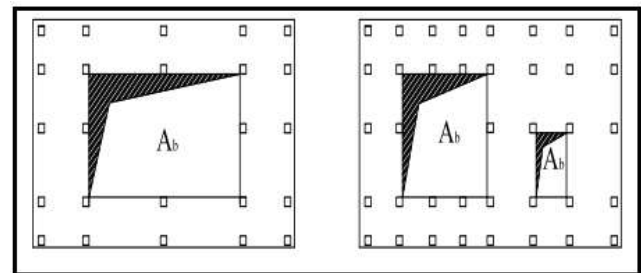
c) The cases of abrupt reductions in the in-plane stiffness and strength of floors.

$$A_b = A_{b1} + A_{b2}$$

$$\frac{A_b}{A} > \frac{1}{3}$$

where

A_b shows sum of the openings and A shows gross floor area, respectively.



a)

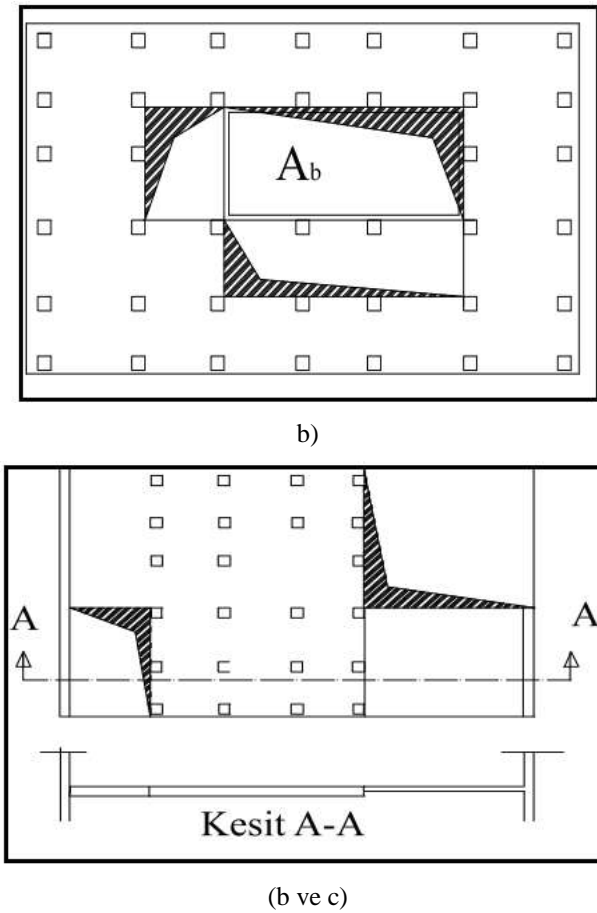


Fig. 1. Slab discontinuity situations defined in TSC

To investigate this irregularity situation, one regular and three irregular multi-storey reinforced concrete building models were selected. Incremental linear dynamic analyses were performed and dynamic envelopes of the structures were obtained from the analysis results. In dynamic analysis, elastic diaphragm assumption was made.

II. NUMERICAL STUDY

A. Selected Building Models

For dynamic analyses three 3D irregular and a regular building models were selected. These models have five stories and height of stories are 3.50 m. The dimensions for columns were selected as 50x50 cm, and dimensions for beams were selected as 30x60 cm. Slab thickness was selected as 13 cm. It was assumed that, the building importance coefficient is 1.0 and, concrete class is C25 and reinforcement steel class is S420. Selected models and rates of slab openings are illustrated in Figs.2-5. In this models, first and end bays are 500 cm and the middle bays are 450 cm in x direction. For y direction first and end bays are 600 cm, the other bays are 500 cm. The dynamic analyses are performed by SAP2000 structural analysis program [6]

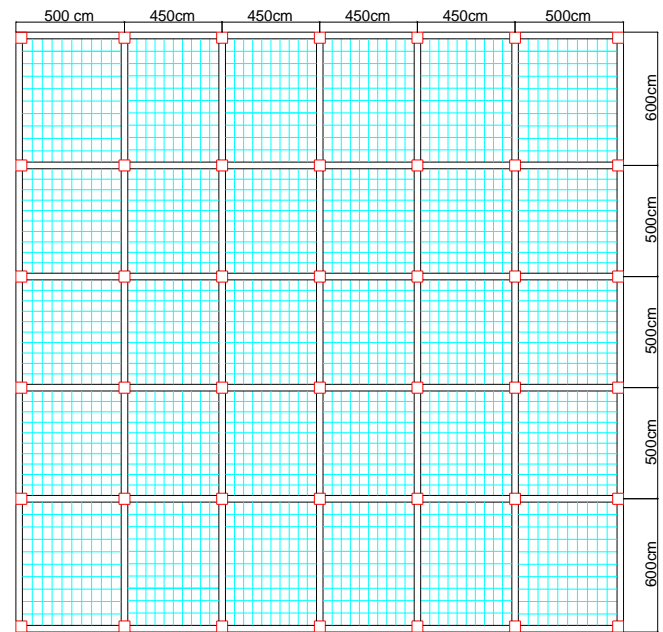


Fig. 2. Regular model

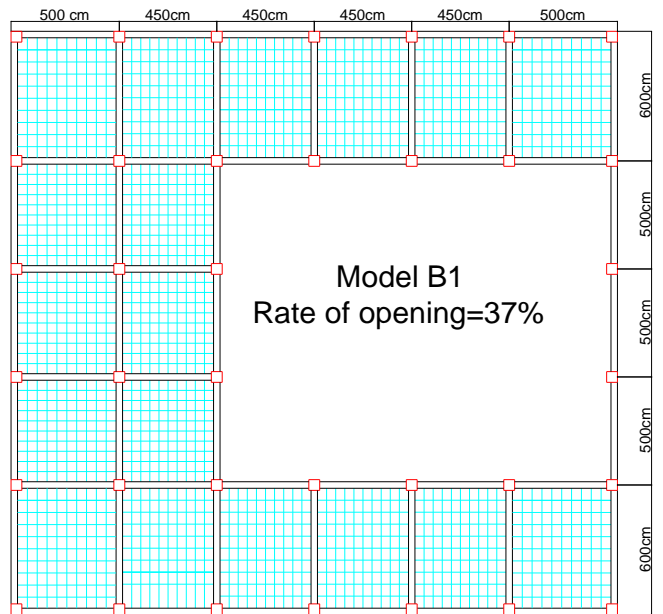


Fig. 3. B1 irregular model

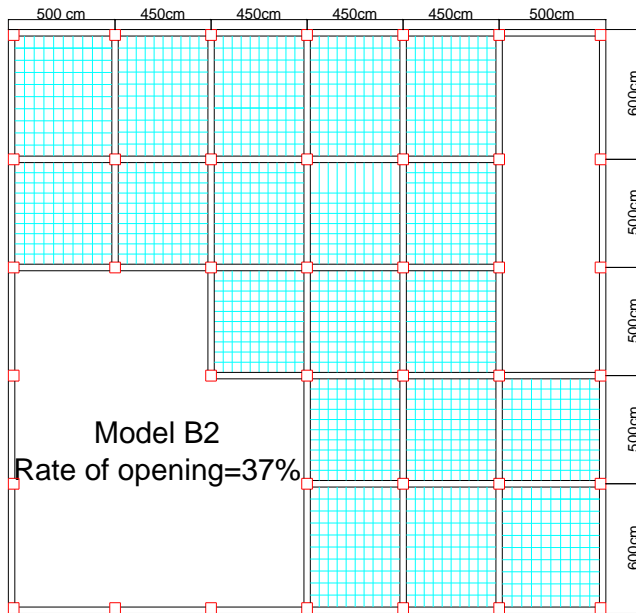


Fig. 4. B2 irregular model

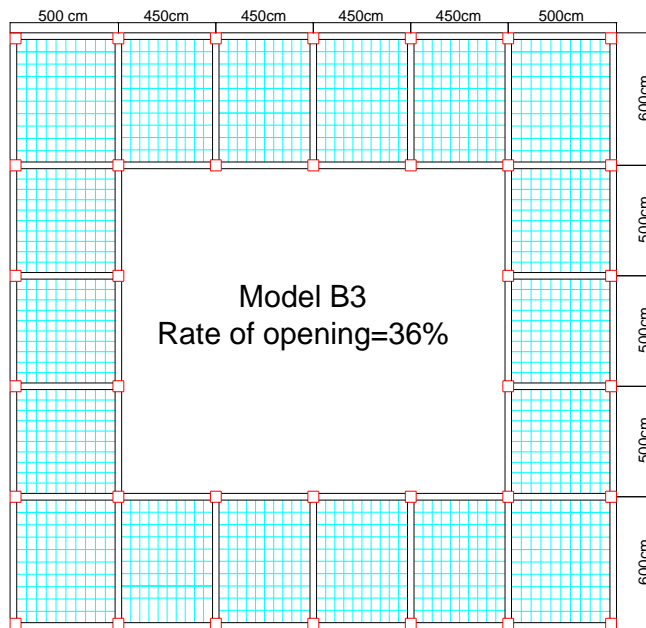


Fig. 5. B3 irregular model

B. Earthquake Parameters and Local Site Conditions

Table 1 shows selected earthquake accelerations properties used in dynamic analysis. The seismic records have been selected from the PEER Strong Motion Database [7] and scaled in order to be compatible with the design spectrum according to seismic zones and local site conditions in TSC. Soil classes (from Z1 to Z4) are characterized in term of periods T_A and T_B . The design spectra are given according to local site classes in Fig. 6.

TABLE 1. SELECTED EARTHQUAKE ACCELERATION RECORDS FOR DYNAMIC ANALYSIS

Earthquakes	Station	Direction	Date	Magnitude	PGA (g)
Kocaeli	Sakarya	North-South	August 17,1999	7.4	0.376
Loma Prieta	Corralitos	East-West	October 18, 1989	6.9	0.644
Imperial Valley	El Centro Array	East-West	May 19,1940	7.0	0.313

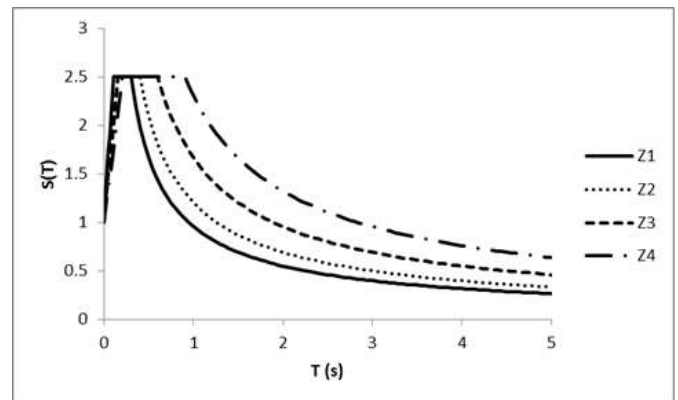
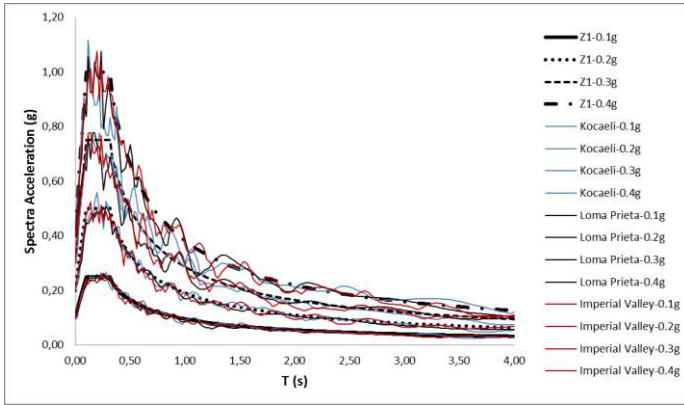
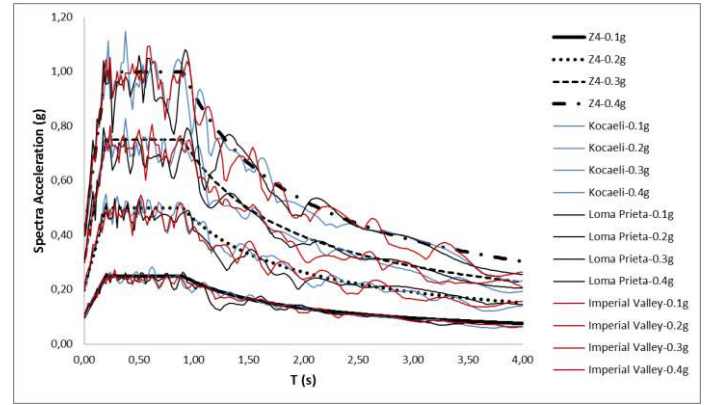


Fig. 6. Recommended elastic response spectra for ground types Z1 to Z4 (for 5% damping)

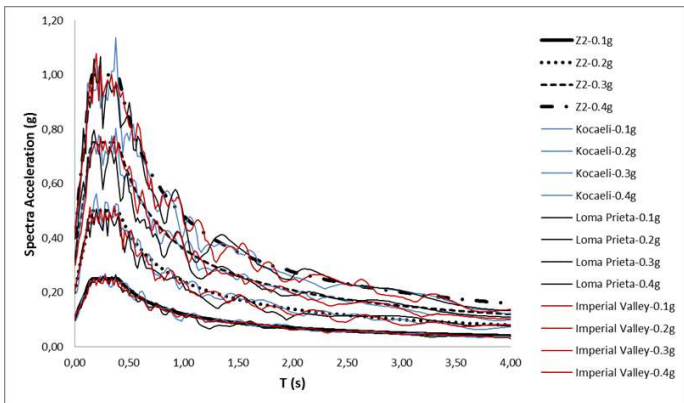
Selected earthquake records were scaled in frequency content in order to be compatible with the target design spectrum of four effective ground accelerations and different soil classes (Fig. 7a-d). The records were scaled using SeismoArtif and SeismoSignal programs.



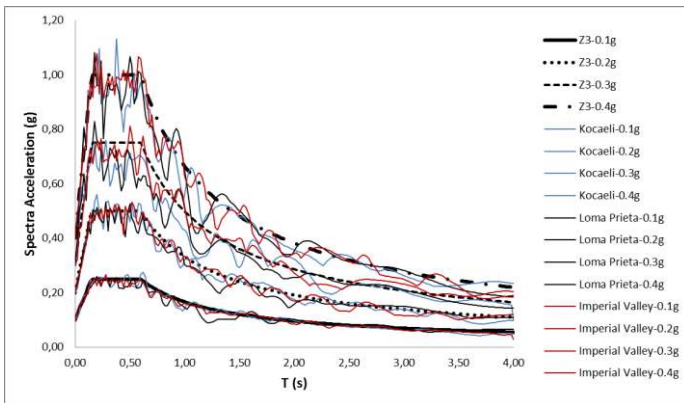
a) Response spectra of the earthquake acceleration records scaled according to the elastic design spectrum for Z1 soil class and effective ground accelerations



d) Response spectra of the earthquake acceleration records scaled according to the elastic design spectrum for Z4 soil class and effective ground accelerations



b) Response spectra of the earthquake acceleration records scaled according to the elastic design spectrum for Z2 soil class and effective ground accelerations



c) Response spectra of the earthquake acceleration records scaled according to the elastic design spectrum for Z3 soil class and effective ground accelerations

Fig. 7. Response spectra of the earthquake acceleration records scaled according to the elastic design spectrum for four soil classes and effective ground accelerations defined in TSC.

III. ANALYSES RESULTS

Maximum responses of the incremental dynamic time history analyses are given in Figs. 8-10 for the x direction and Figs. 11-13 for the y direction. Dynamic envelopes are obtained according to these responses. Each irregular models are compared with regular building. According to these figures, the correlation coefficient values, are exceed 0.90 for x direction. Also, it is seen that dynamic envelopes of each irregular building models exceed the dynamic envelope of regular building. This situation is a evidence of the irregularity causes more shear forces.

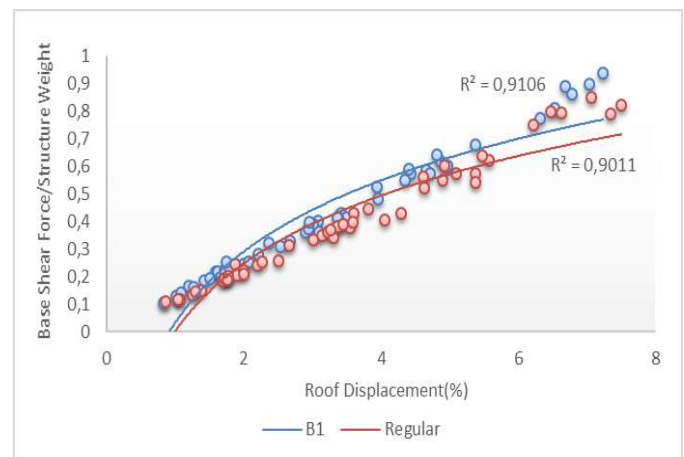


Fig. 8. Comparison of dynamic envelopes of B1 irregular model and Regular model for x direction

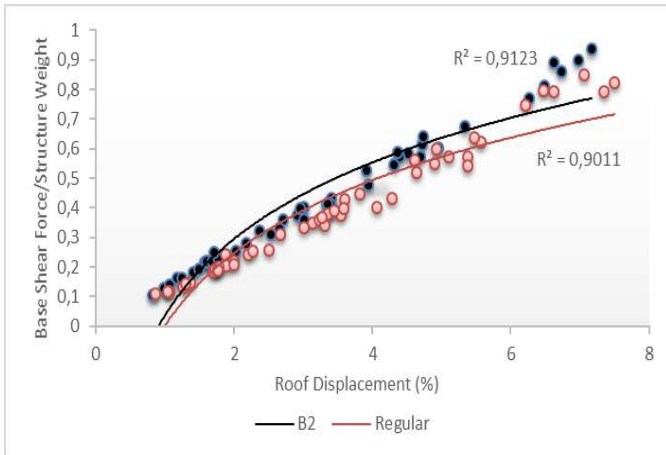


Fig. 9. Comparison of dynamic envelopes of B2 irregular model and Regular model for x direction

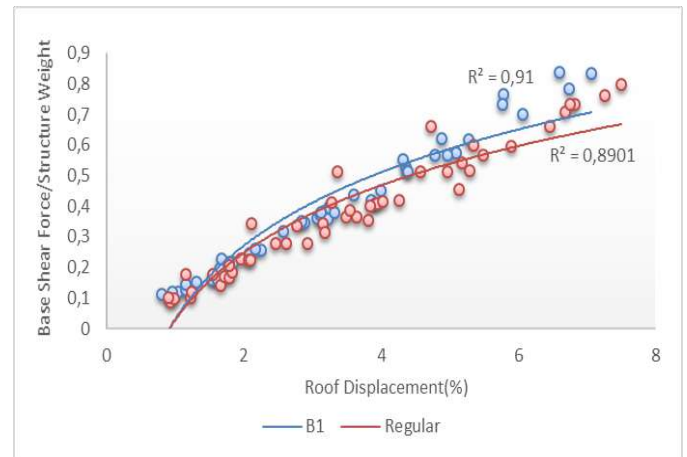


Fig. 11 Comparison of dynamic envelopes of B1 irregular model and Regular model for y direction

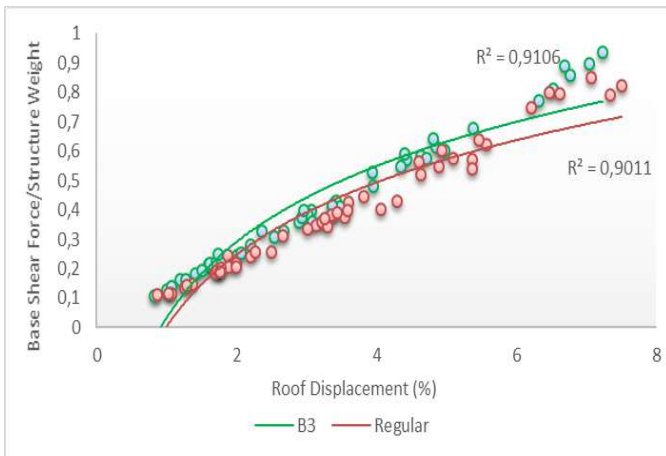


Fig. 10. Comparison of dynamic envelopes of B3 irregular model and Regular model for x direction

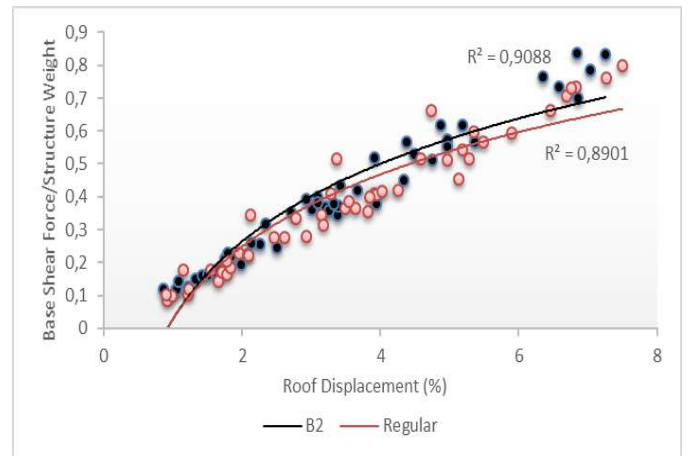


Fig. 12 Comparison of dynamic envelopes of B2 irregular model and Regular model for y direction

According to Figs.11-13, the correlation coefficient values are approximately 0.90 for regular building and for the other coefficient exceed the 0.90 for y direction. Seismic actions obtained from the scaled earthquakes follow the same trend and shape to that of the dynamic envelopes, similar to that in the x direction.

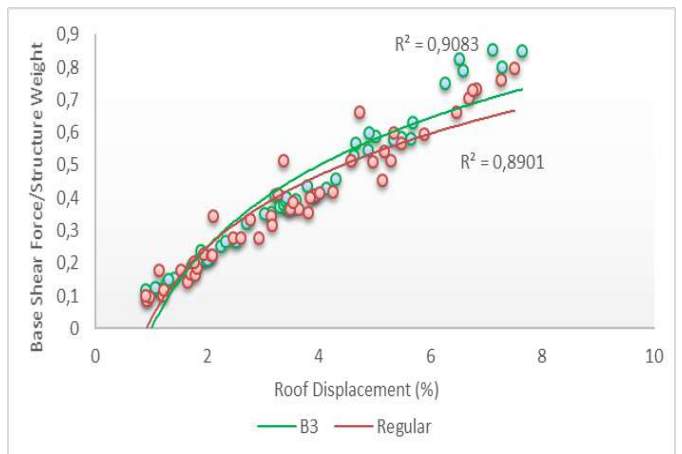


Fig. 13 Comparison of dynamic envelopes of B3 irregular model and Regular model for y direction

IV. CONCLUSIONS

In this paper, the effect of slab discontinuity in plan on seismic behaviors of multi-storey reinforced concrete structures was investigated by using incremental dynamic analysis method. To investigate this irregularity situation, one regular and three irregular multi-storey reinforced concrete building models were selected. Dynamic envelopes of the structures were obtained from the analysis results.

According to analysis results, dynamic envelopes obtained from each irregular building models exceed the dynamic envelope of regular building for x and y directions. This situation shows that this type of irregularity causes more shear forces. So, it is should be abstain from the application of this irregularity.

REFERENCES

- [1] C. Özmen and A.İ. Ünay “Commonly Encountered Seismic Design Faults due to the Architectural Design of Residential Buildings in Turkey”. *Building and Environment*, (42), 1406–1416, 2007.
- [2] Z. Ç. Ulucan and B. Yön, “Nonlinear Earthquake Response of A2 Slab Discontinuity Irregularity Structures Using Rigid and Elastic Diaphragm Assumptions”, *Science and Engineering Journal of Firat University*, 20 (2), 315–323, 2008 (in Turkish).
- [3] B. Yön, M. E. Öncü, and Z. Ç. Ulucan. “Investigation of Effect of Slab Opening Location to the Shear Stress”. *Journal of Pamukkale University Engineering Science*, 16(1), 45-51, 2010 (in Turkish).
- [4] Z. Celep, ve Kumbasar, N. *Introduction to Earthquake Engineering and earthquake resistant structural design*, 2004 pp. 700. Beta Distribution, İstanbul.(in Turkish).
- [5] Turkish Sesimic Code, 2007, Ankara-Turkey.
- [6] SAP 2000 V9.0.1. (2004), *Integrated Finite Element Analysis and Design of Structures*, Computer and Structures Inc. Berkeley, California.
- [7] Pacific Earthquake Engineering Research Center Strong Motion Database
- [8] SeismoArtif v2.1: A computer program for generating artificial earthquake accelerograms matched to a specific target response spectrum. Available at: www.seismosoft.com [July 19, 2013]
- [9] SeismoSignal v5.1 - A computer program for the processing of strong-motion data. Available at: www.seismosoft.com [July 19, 2013]

Optimal design of multiple tuned mass dampers based on Den Hartog's method

Volkan Kahya

Department of Civil Engineering
Karadeniz Technical University
Trabzon, Turkey
volkan@ktu.edu.tr

Onur Araz

Department of Civil Engineering
Gümüşhane University
Gümüşhane, Turkey
onuraraz29@hotmail.com

Abstract—This paper presents a new and simple approach to design multiple tuned mass dampers (MTMDs) based on the calibration formulas proposed by Den Hartog for the stiffness and damping of a single TMD. Keeping the mass of all TMD units to be constant and identical, TMD properties are recalibrated based on the natural frequencies of the system on which the number of TMDs is one less than the current system. This is a sequential procedure, where it does not require to do iterations for each step, instead it requires to start from the case with a single TMD, and then move up in numbers one TMD at a time until the desired number is reached. Accuracy and efficiency of the proposed method is shown by numerical examples.

Keywords—Multiple tuned mass dampers; Vibration control; Optimal design

I. INTRODUCTION

To control excessive vibrations of tall buildings, bridges and other civil engineering structures due to environmental loads such as earthquake, wind and traffic loads has been attracted to the interest of many researchers. Research efforts on vibration control of structures have resulted in developing various control devices. Among them, tuned mass dampers (TMDs) consisting of a mass, a spring and a viscous damper is one of the simplest, reliable and low cost control devices.

In 1909, a TMD, which consists of a mass and a spring, was first introduced by Frahm [1]. It has a narrow operation region, and its performance reduces significantly when the exciting frequency varies. Many efforts have been, then, made to obtain optimum parameters of TMDs. Den Hartog [2] proposed a closed form solution to minimize the dynamic response of undamped single degree of freedom (SDOF) system under harmonic loads. Randall et al. [3] proposed numerical optimization procedures for determination of optimum TMD parameters. Fujino and Abe [4] presented a perturbation technique to derive formulas for optimal TMD parameters. Asami et al. [5] gave a series solution for the H_∞ optimization and an exact solution for the H_2 optimization. Ghosh and Basu [6] presented a closed-form expression for optimal tuning ratio of TMDs based on the fixed-point theory of Den Hartog. Brown and Singh [7] proposed a mini-max procedure to design a TMD in the presence of uncertainties in

forcing frequency. Anh and Nguyen [8] carried out an approximate analytical solution for optimal tuning ratio of TMDs by using the equivalent linearization method.

All studies mentioned above are concerned with tuning TMD to a dominant frequency of the main system. However, single TMD is very sensitive to any change in the frequency of TMD and/or the main system. Errors in identifying the main system frequency or in manufacturing TMD lead to the detuning effect. To overcome the detuning due to a frequency deviation, Xu and Igusa [9] proposed to use multiple tuned mass dampers (MTMDs) instead of classic single TMD. They indicated that the use of MTMDs with distributed natural frequencies in a frequency bandwidth can be more effective than a single TMD with the same total mass. This kind of TMD system has also been studied by many researchers [10-15]. The main difference in these studies is the optimization methods and criteria adopted.

Although different techniques exist to obtain optimal tuning parameters, they are not simple as much as Den Hartog's approach. The most useful aspect of Den Hartog's approach is to give simpler, closed form formulas for optimal parameters of classic TMD. The purpose of this paper is to develop a simple design procedure for optimal MTMD devices based on Den Hartog's method.

II. THEORETICAL FORMULATION

A. Governing equations

Consider a single-degree-of-freedom (SDOF) structure with MTMD shown in Fig. 1. The natural frequencies of TMD units are tuned to a frequency range vicinity to the natural frequency of the main structure. Note that total DOFs of the coupled system is $n + 1$ where n is the number of TMD units. The equation of motion for the main structure with MTMD under harmonic excitation is

$$m_s \ddot{x}_s + c_s \dot{x}_s + k_s x_s + \sum_{j=1}^n c_j (\dot{x}_s - \dot{x}_j) + k_j (x_s - x_j) = P e^{i\omega t} \quad (1)$$

and the vertical motion of the j th TMD is

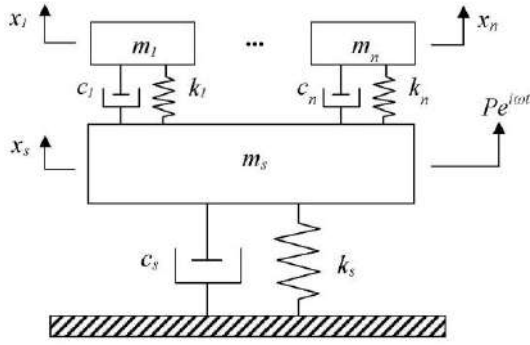


Fig. 1. Main structure – MTMD coupled system

$$m_j \ddot{x}_j + c_j (\dot{x}_j - \dot{x}_s) + k_j (x_j - x_s) = 0 \quad j = 1, 2, \dots, n \quad (2)$$

where over dot denotes differentiation with respect to time t , and m_s , c_s and k_s are the mass, damping coefficient and stiffness of the main structure, respectively, m_j , c_j and k_j are the mass, damping coefficient and stiffness of j th TMD, respectively. x_s and x_j indicate the vertical displacement of the main structure and j th TMD, respectively.

Combining (1) and (2), the equations of motion can be given in the following matrix form:

$$\mathbf{M}\ddot{\mathbf{X}} + \mathbf{C}\dot{\mathbf{X}} + \mathbf{K}\mathbf{X} = \mathbf{F} \quad (3)$$

where \mathbf{M} , \mathbf{C} , \mathbf{K} are the mass, damping and stiffness matrices, $\ddot{\mathbf{X}}$, $\dot{\mathbf{X}}$ and \mathbf{X} are the acceleration, velocity and displacement vectors, respectively. \mathbf{F} is the external force vector. They can be defined as:

$$\mathbf{M} = \text{diag}(m_s \quad m_1 \quad m_2 \quad \dots \quad m_n) \quad (4)$$

$$\mathbf{C} = \begin{bmatrix} c_s + \sum_{j=1}^n c_j & -c_1 & -c_2 & \dots & -c_n \\ -c_1 & c_1 & 0 & \dots & 0 \\ -c_2 & 0 & c_2 & \dots & 0 \\ \vdots & \vdots & \vdots & \ddots & \vdots \\ -c_n & 0 & 0 & \dots & c_n \end{bmatrix} \quad (5)$$

$$\mathbf{K} = \begin{bmatrix} k_s + \sum_{j=1}^n k_j & -k_1 & -k_2 & \dots & -k_n \\ -k_1 & k_1 & 0 & \dots & 0 \\ -k_2 & 0 & k_2 & \dots & 0 \\ \vdots & \vdots & \vdots & \ddots & \vdots \\ -k_n & 0 & 0 & \dots & k_n \end{bmatrix} \quad (6)$$

$$\mathbf{X} = \{x_s \quad x_1 \quad x_2 \quad \dots \quad x_n\}^T, \quad \mathbf{F} = e^{i\omega t} \{P \quad 0 \quad 0 \quad \dots \quad 0\}^T \quad (7)$$

The normalized displacement amplitude or dynamic magnification factor (DMF) for the main structure under harmonic excitation is [12]:

$$\text{DMF} = \frac{x_1}{x_{st}} = \sqrt{\frac{1}{\text{Re}(z_1)^2 + \text{Im}(z_1)^2}} \quad (8)$$

where

$$\begin{aligned} \text{Re}(z_1) &= 1 - \beta^2 - \beta^2 \sum_{j=1}^n \mu_j \frac{\frac{\beta_j^2}{\beta^2} - 1 + 4\xi_j^2}{\left(\frac{\beta_j}{\beta} - \frac{\beta}{\beta_j}\right)^2 + 4\xi_j^2}, \\ \text{Im}(z_1) &= 2\beta\xi_s + \beta^2 \sum_{j=1}^n \mu_j \frac{2\beta\xi_j}{\left(\frac{\beta_j}{\beta} - \frac{\beta}{\beta_j}\right)^2 + 4\xi_j^2} \end{aligned} \quad (9)$$

where $x_{st} = P / k_s$ is the static displacement of the structure, $\beta = \omega / \omega_s$ is the frequency ratio between the external force and the structure, ξ_s is the damping ratio of the structure, $\mu_j = m_j / m_s$ is the mass ratio, $\beta_j = \omega_j / \omega_s$ is the frequency ratio, and $\xi_j = c_j / 2m_j\omega_j$ is the damping ratio of j th TMD

B. Den Hartog's approach

Tuning parameters for a single TMD are given in this section. Here, we assume that the system given in Fig.1 for $n = 1$ which represents a single TMD. DMF for the main system is

$$\text{DMF} = \frac{x_1}{x_{st}} = \sqrt{\frac{P}{Q}} \quad (10)$$

where

$$\begin{aligned} P &= 4\xi_s^2 \beta^2 + (\beta^2 - \beta_1^2)^2, \\ Q &= 4\xi_s^2 \beta^2 (\beta^2 - 1 + \mu\beta^2)^2 \\ &\quad + [\mu\beta_1^2 \beta^2 - (\beta^2 - 1)(\beta^2 - \beta_1^2)]^2 \end{aligned} \quad (11)$$

with

$$\beta_1 = \frac{\omega_1}{\omega_s}, \quad \beta = \frac{\omega}{\omega_s}, \quad \mu = \frac{m_1}{m_s} \quad (12)$$

Den Hartog [2] gave the followings for the optimal tuning ratio f_{opt} and the optimal damping ratio ξ_{opt} :

$$f_{opt} = \frac{1}{1 + \mu}, \quad \xi_{opt} = \sqrt{\frac{3\mu}{8(1 + \mu)}} \quad (13)$$

C. Proposed design method

It can be obviously seen in Table 1 that the natural frequency of the main structure without TMD is split into two independent modes, when TMD-1 ($n=1$) is attached to it. Therefore, if a MTMD is installed on the main structure, the natural frequency of the main structure without TMD will be split into $n+1$ independent modes. In the approach presented here, MTMD properties are re-calibrated based on the natural frequencies of the system on which the number of TMDs is one less than the current system. This is a sequential procedure, where it does not require to do iterations for each step, instead it requires to start the procedure from the case with a single TMD, and then move up in numbers one TMD at a time until the desired number is reached. For example, the natural frequency of a single TMD attached on the main structure is tuned to that of the structure without TMD. If two parallel TMDs ($n=2$) are attached to the main structure, each TMD is tuned to those of the main system with single TMD ($n=1$). Therefore, we can write the following expressions for the optimal tuning parameters of TMDs:

$$\begin{aligned} \mu &= \frac{\sum_{j=1}^n m_{j,n}}{m_s}, \quad \mu_j = \mu_T = \frac{\mu}{n}, \quad \omega_{j,n} = \frac{\bar{\omega}_{j,n-1}}{1 + \mu_T}, \\ \xi_{j,n} &= \xi_T = \sqrt{\frac{3\mu_T}{8(1 + \mu_T)}}, \quad \beta_{j,n} = \frac{\omega_{j,n}}{\bar{\omega}_{1,0}}, \\ \omega_T &= \sum_{j=1}^n \frac{\omega_{j,n}}{n}, \quad f_T = \frac{\omega_T}{\bar{\omega}_{1,0}}, \quad \Delta_n = \frac{\omega_{n,n} - \omega_{1,n}}{\omega_T} \end{aligned} \quad (14)$$

where m_s is the mass of the main structure, μ is the mass ratio between MTMD and the structure, $\bar{\omega}_{1,0}$ is the natural frequency of the main structure without TMD, $\omega_{j,n}$ is the natural frequency of the j th TMD in MTMD, $\beta_{j,n}$ is the

frequency ratio of the j th TMD, ω_T is the average frequency of MTMD, f_T is the average frequency ratio of MTMD, and Δ_n is the non-dimensional frequency bandwidth of MTMD. In general, $\bar{\omega}_{j,n-1}$ denotes the j th natural frequency of the main structure carrying $(n-1)$ TMD units. In the proposed approach, MTMD system is designed with identical mass ratio (μ_T), i.e., $m_{1,n} = m_{2,n} = \dots = m_{n,n}$, and the stiffness of each TMD unit is adjusted based on $\omega_{j,n} = \sqrt{k_{j,n} / m_{j,n}}$. However, we assume the damping ratio ξ_T units to be constant for all TMDs.

TABLE I. NATURAL FREQUENCIES (RAD/S) OF A SDOF SYSTEM WITH TMD- n

Mode	$n=0$	$n=1$	$n=2$	$n=3$
1	10.000	9.2261	8.9246	8.7487
2	-	10.6263	9.8769	9.5252
3	-	-	10.9031	10.2106
4	-	-	-	11.0721

III. RESULTS

Some illustrative results are presented and discussed. The effectiveness of MTMDs with $n=5$ and 11 designed by the proposed method is compared with that of the optimum TMD-1. Robustness analysis is also performed to understand how the performance of the proposed MTMD and the classical TMD is affected by the changes in the tuning frequency of TMD units. The main system is assumed to be undamped.

Fig. 2 gives the maximum displacement amplitudes of the undamped main system with TMDs in case of the error in the tuning frequency ratio. The abscissa shows the error in the estimated tuning frequencies of TMDs, and the ordinate is the normalized maximum amplitude (DMF) calculated by (8) for $0.5 \leq \beta \leq 1.5$. It can be clearly seen that the robustness of the proposed MTMD system is better than that of TMD-1, which agrees with the literature. As seen, we still have more smooth curves for MTMD devices, especially for greater mass ratio, despite increasing amount of the frequency detuning. That is, MTMD devices are less sensitive to the frequency detuning compared to the classical TMDs. This figure also indicates that the effectiveness of TMD-1 rapidly decreases for lower mass ratio when the error in tuning frequency increases. Finally, increasing the total number of TMD units increases the robustness. However, as reported in the literature, there is almost no difference between the curves for the maximum amplitudes for $n > 7$ as seen in the figure.

Optimal tuning parameters of TMD-5 and TMD-11 obtained by the proposed design method are shown in Table 2, and compared to those of [18]. As seen, the present method gives slightly greater damping ratios, and slightly smaller frequency ratios than those of [18] for MTMDs considered. The frequency bandwidth obtained from the present study significantly larger than that of [18].

Figs. 3 and 4 show comparison of the maximum displacement amplitudes of the primary structure with optimal TMD-5 and TMD-11 devices in case of the frequency

detuning. Here, undamped and damped ($\xi_s = 2\%$) main systems are considered. In the figures, TMD-5* and TMD-11* represent TMD devices designed by [18]. As can be seen from the figures, the effectiveness of TMD-5* and TMD-11* are better than that of MTMDs designed by the present method when the frequency detuning is rather small. However, the effectiveness of TMD-5* and TMD-11* rapidly decrease as the tuning error increases. When the error greater than $\pm 5\%$, their performance in reducing vibration is worst compared to MTMDs proposed in this study. Figs. 3 and 4 also indicate robustness of the proposed MTMDs are better than that of [18].

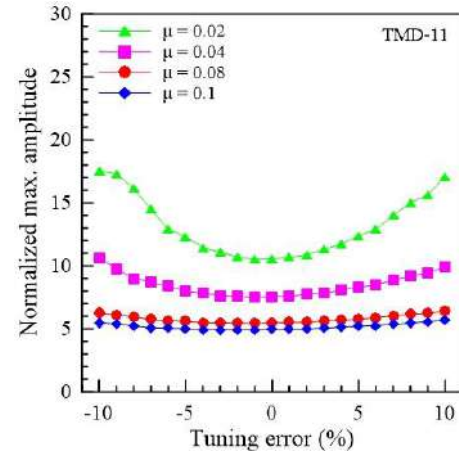
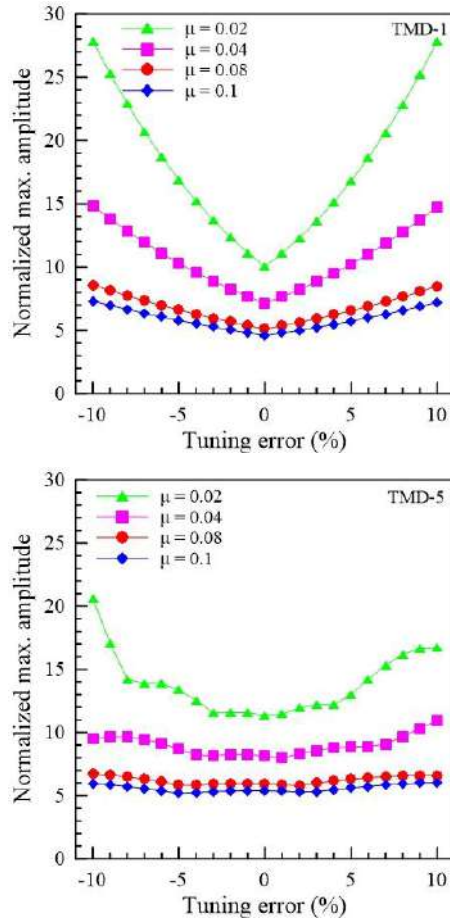


Fig. 2. Normalized maximum displacement amplitude vs. tuning error for undamped main system with different TMDs

TABLE II. OPTIMAL TUNING PARAMETERS OF TMD-5 AND TMD-11 WITH THE PROPOSED DESIGN METHOD

n	μ	ξ_T (%)		f_T		Δ_n	
		Present	[18]	Present	[18]	Present	[18]
5	0.01	2.74	2.39	0.9926	0.9957	0.1833	0.1113
	0.05	6.09	5.30	0.9614	0.9789	0.4106	0.2404
11	0.01	1.85	1.70	0.9923	0.9968	0.2334	0.1353
	0.05	4.12	3.67	0.9626	0.9847	0.5254	0.2956

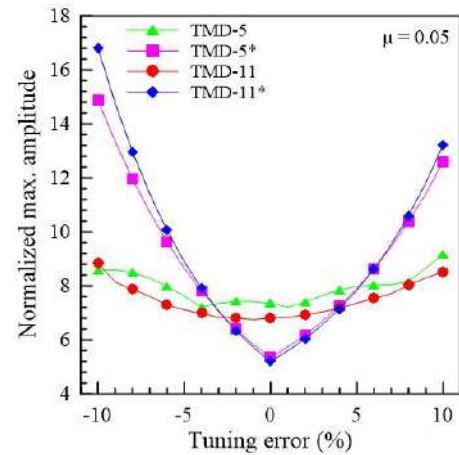


Fig. 3. Normalized maximum displacement amplitude vs. tuning error for undamped main system with different MTMDs

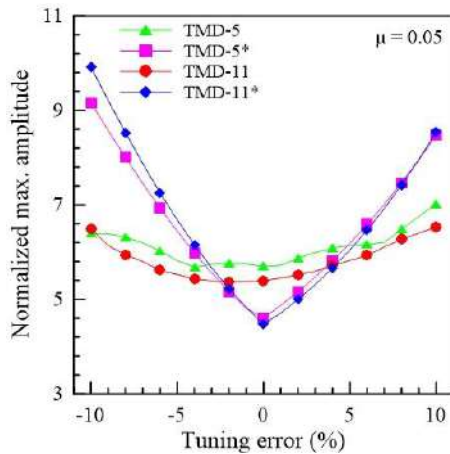


Fig. 4. Normalized maximum displacement amplitude vs. tuning error for damped main system with different MTMDs

IV. CONCLUSIONS

In this paper, a new approach to design MTMD devices with the basis of Den Hartog's optimal criterion is presented. We demonstrated that significantly increased robustness can be obtained when the proposed MTMD is attached to the main system. We have the following conclusions from the study:

- The numerical studies proved that the proposed MTMD is quite effective for suppressing the maximum amplitudes of the main system under external excitation.
- Although the proposed MTMD has the same control effectiveness as the classical single TMD (TMD-1) tuned by Den Hartog's criteria without frequency detuning, it is more robust to the natural frequency changes in TMD units than TMD-1.
- By using the optimization methods, it is extremely difficult to get the optimum parameters of MTMD system theoretically. Thus, the tuned frequency ratio and the damping ratio of TMD units can easily be obtained with through the explicit formulas derived in this study.
- It is interesting to note that the maximum displacement amplitudes of the proposed MTMD is almost

insensitive to $\pm 10\%$ changes in the tuning frequency of TMD units with higher mass ratio.

REFERENCES

- [1] H. Frahm, Device for damped vibration of bodies, U.S. Patent no. 989958, 30 October 1909.
- [2] JP. Den Hartog, Mechanical Vibrations, New York: McGraw-Hill, 1956.
- [3] SE. Randall, DM. Halsted, DL. Taylor, "Optimum vibration absorbers for linear damped systems", ASME Journal of Mechanical Design, vol. 103, pp. 908-913, 1981.
- [4] Y. Fujino, M. Abe, "Design formulas for tuned mass dampers based on a perturbation technique", Earthquake Engineering and Structural Dynamics, vol. 22, pp. 833-854, 1993.
- [5] T. Asami, O. Nishihara, AM. Baz., "Analytical solutions to H_∞ and H_2 optimization of dynamic vibration absorbers attached to damped linear systems", Journal of Vibration and Acoustics, vol. 124, pp. 284-295, 2002.
- [6] A. Ghosh, B. Basu, "A closed-form optimal tuning criterion for TMD in damped structures", Structural Control and Health Monitoring, vol. 14, pp. 681-692, 2007.
- [7] B. Brown, T. Singh, T., "Minimax design of vibration absorbers for linear damped systems", Journal of Sound and Vibration, vol. 330, pp. 2437-2448, 2011.
- [8] ND. Anh, NX. Nguyen, "Extension of equivalent linearization method to design of TMD for linear damped systems", Structural Control and Health Monitoring, vol. 19, pp. 565-573, 2012.
- [9] K. Xu, T. Igusa, "Dynamic characteristics of multiple substructures with closely spaced frequencies", Earthquake Engineering and Structural Dynamics, vol. 21, pp. 1059-1070, 1992.
- [10] C. Li, Y. Liu, "Optimum multiple tuned mass dampers for structures under the ground acceleration based on the uniform distribution of system parameters", Earthquake Engineering and Structural Dynamics, vol. 32, pp. 671-690, 2003.
- [11] N. Hoang, P. Warnitchai, "Design of multiple tuned mass dampers by using a numerical optimizer", Earthquake Engineering and Structural Dynamics, vol. 34, pp. 125-144, 2005.
- [12] HN. Li, XL. Ni, "Optimization of non-uniformly distributed multiple tuned mass damper", Journal of Sound and Vibration, vol. 308, pp. 80-97, 2007.
- [13] E. Dehghan-Niri, SM. Zahrai, A. Mohtat, "Effectiveness-robustness objectives in MTMD system design: an evolutionary optimal design methodology", Structural Control and Health Monitoring, vol. 17, pp. 218-236, 2012.
- [14] TP. Bandivadekar, RS. Jangid, "Mass distribution of multiple tuned mass dampers for vibration control of structures", International Journal of Civil and Structural Engineering, vol. 3, pp. 70-84, 2012.
- [15] JP. Bandivadekar, RS. Jangid, "Optimization of multiple tuned mass dampers for vibration control of system under external excitation", Journal of Vibration and Control, vol. 19, pp. 1854-1871, 2012.

Free vibration of cracked cantilever beams: Analytical and experimental modelling

Volkan Kahya

Department of Civil Engineering
Karadeniz Technical University
Trabzon, Turkey
volkan@ktu.edu.tr

Sebahat Karaca

Department of Civil Engineering
Karadeniz Technical University
Trabzon, Turkey
krc-91@hotmail.com

Abstract—This study presents free vibration of cantilever beams with multiple cracks. The problem is solved analytically by the transfer matrix method (TMM), and is validated experimentally by the operational modal analysis (OMA). Six damage scenarios are considered to study crack effect on the natural frequencies and corresponding mode shapes. Graphs and tables for numerical results are given and discussed. Results show that crack occurrence in a beam significantly changes its dynamic behavior.

Keywords—Crack; Beam; Free vibration; Transfer matrix method; Experimental model

I. INTRODUCTION

Engineering structures are exposed to different types of environmental loads such as earthquakes, wind and traffic loads etc. Over time, stresses and strains due to these loadings lead to reduce in lifetime of the structure, and may cause damages (cracks), which is a serious threat to performance of structure. Early detection of any structural damage is important to prevent structural failures that causes human casualties and financial costs. Thus, an accurate and comprehensive study on structures including cracks are necessary.

Beams are structural elements in which cracks are commonly observed. Therefore, they have been frequently studied by researchers with through different analytical, numerical and experimental techniques. Dimarogonas [1] presented a comprehensive review of various methods in studying structural members with cracks.

Dimarogonas and Paipetis [2] proposed the local flexibility concept to model an open edge crack in a beam, which can be derived from the stress intensity factors in the theory of fracture mechanics. The cracked section in a beam can be replaced by massless rotational springs representing the local flexibility of the crack. Studies on vibrations of cracked beams using the local flexibility concept have generally focused on two main aspects: The first is to estimate the effects of cracks on the eigenparameters of beams as a direct problem, and the second is to detect the location and size of the crack from the measured information as an inverse problem. Direct analysis of beam vibrations in the presence of cracks is, however, required for solution of the inverse problem.

Methods in studying free vibration of beams with cracks are, in general, divided into two main groups: continuous and discrete methods. In continuous methods, the beam is divided into several sub-beams connected by massless springs. Differential equations are, then, solved for each sub-beam individually with considering the boundary and continuity conditions. As a continuous method, the transfer matrix method is an efficient tool for free vibration of cracked beams, and have been widely preferred [3-8]. Viola et al. [9] derived the explicit dynamic stiffness matrix of a cracked axially loaded beam under coupled bending-torsion with considering the effects of the rotatory inertia and the shear deformation. Among discrete methods, the finite element method [10-12] and the discrete element method [13] can be mentioned.

Experimental measurements including ambient and forced vibration tests have also been used to extract the dynamic characteristics of cracked beams during operational conditions as well as to verify their analytical and/or numerical models [14-16]. Experimental measurements can also be used to identify cracks in a beam in inverse problems.

As can be seen in the literature summarized above, there are many studies on cracked beam vibrations using different analytical/numerical and experimental methods. However, the studies on extracting dynamic characteristics of cracked beams by operational modal analysis (OMA), and validating the experimental results with analytical solution are limited. This study presents free vibration analysis of cantilever beams with multiple cracks. The problem is solved analytically by the transfer matrix method (TMM), and is validated experimentally by the operational modal analysis (OMA). The cantilever beam is assumed to obey Bernoulli-Euler theory. Six damage scenarios are considered to study crack effect on the natural frequencies and corresponding mode shapes. Comparative graphs and tables for numerical results are given and discussed.

II. THEORETICAL FORMULATION

A. Analytical model

Consider a cantilever beam with N cracks along its length, and has a rectangular cross-section of width b and height h shown in Fig. 1. The beam is assumed to be connected by

massless rotational springs at cracked section as shown in Fig. 2. Equation of motion for each segment of the beam is given by

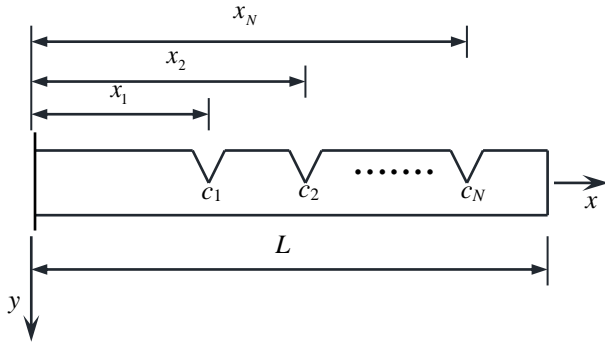


Fig. 1. A cantilever beam with multiple cracks.

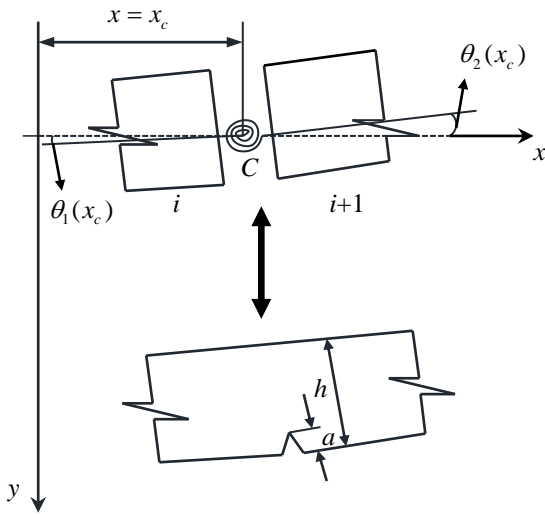


Fig. 2. Cracked section represented by massless rotational spring.

$$EI \frac{\partial^4 Y_i(x, t)}{\partial x^4} + \rho A \frac{\partial^2 Y_i(x, t)}{\partial t^2} = 0 \quad (i = 1, 2, \dots, N+1) \quad (1)$$

where $Y_i(x, t)$ is the deflection function, EI is the flexural rigidity, ρ is the mass density, $A = bh$ is the cross-sectional area of the beam. Introducing

$$\bar{x} = x / L \quad (2)$$

into (1) yields

$$\frac{EI}{L^4} \frac{\partial^4 y_i(\bar{x}, t)}{\partial \bar{x}^4} + \rho A \frac{\partial^2 y_i(\bar{x}, t)}{\partial t^2} = 0 \quad (i = 1, 2, \dots, N+1) \quad (3)$$

where $Y(x, t) \equiv y(\bar{x}, t)$.

Assuming the solution of (3) as

$$y_i(\bar{x}, t) = X_i(\bar{x}) e^{i\omega t} \quad (i = 1, 2, \dots, N+1) \quad (4)$$

where $X_i(\bar{x})$ denotes the modal shape function, and ω is the natural frequency of the beam, and substituting it into (3) gives the following:

$$\frac{d^4 X_i}{d\bar{x}^4} - \beta^4 X_i = 0 \quad (i = 1, 2, \dots, N+1) \quad (5)$$

where

$$\beta^4 = \frac{\rho A L^4}{EI} \omega^2 \quad (6)$$

Solution of (5) is

$$X_i(\bar{x}) = A_i \sin \beta \bar{x} + B_i \cos \beta \bar{x} + C_i \sinh \beta \bar{x} + D_i \cosh \beta \bar{x} \quad (i = 1, 2, \dots, N+1) \quad (7)$$

where A_i , B_i , C_i and D_i are constants to be determined from the boundary and continuity conditions given by

$$y(0, t) = y'(0, t) = -EI y''(1, t) = -EI y'''(1, t) = 0 \quad (8)$$

$$\begin{aligned} y_i(\bar{x}_i, t) &= y_{i+1}(\bar{x}_i, t) \\ y'_i(\bar{x}_i) &= y'_{i+1}(\bar{x}_i) - (h/L) f(d_i) y''_{i+1}(\bar{x}_i) \\ y''_i(\bar{x}_i, t) &= y''_{i+1}(\bar{x}_i, t) \\ y'''_i(\bar{x}_i) &= y'''_{i+1}(\bar{x}_i) \end{aligned} \quad (9)$$

where $f(d_i)$ is a dimensionless function, which is given by single-sided open cracks as

$$f(d_i) = 2[d_i / (1 - d_i)]^2 (5.93 - 19.69 d_i + 37.14 d_i^2 - 35.64 d_i^3 + 13.12 d_i^4) \quad (10)$$

where $d_i = a_i / h$ is dimensionless crack depth.

Substituting (4) into (9), we have the following:

$$\mathbf{P}_i \mathbf{a}_i = \mathbf{Q}_i \mathbf{a}_{i+1} \quad (i = 1, 2, \dots, N) \quad (11)$$

where $\mathbf{a}_i = \{A_i \ B_i \ C_i \ D_i\}^T$ and

$$\mathbf{P}_i = \begin{bmatrix} \sin \beta \bar{x}_i & \cos \beta \bar{x}_i & \sinh \beta \bar{x}_i & \cosh \beta \bar{x}_i \\ \cos \beta \bar{x}_i & -\sin \beta \bar{x}_i & \cosh \beta \bar{x}_i & \sinh \beta \bar{x}_i \\ -\sin \beta \bar{x}_i & -\cos \beta \bar{x}_i & \sinh \beta \bar{x}_i & \cosh \beta \bar{x}_i \\ -\cos \beta \bar{x}_i & \sin \beta \bar{x}_i & \cosh \beta \bar{x}_i & \sinh \beta \bar{x}_i \end{bmatrix} \quad (12)$$

$$\mathbf{Q}_i = \mathbf{P}_i + \mathbf{S}_i \quad (13)$$

where

$$\mathbf{S}_i = \chi \begin{bmatrix} 0 & 0 & 0 & 0 \\ -\sin \beta \bar{x}_i & -\cos \beta \bar{x}_i & \sinh \beta \bar{x}_i & \cosh \beta \bar{x}_i \\ 0 & 0 & 0 & 0 \\ 0 & 0 & 0 & 0 \end{bmatrix} \quad (14)$$

where $\chi = -\beta(h/L)f(a_i)$. From (11), we have

$$\mathbf{a}_{i+1} = \mathbf{Q}_i^{-1} \mathbf{P}_i \mathbf{a}_i \quad (i = 1, 2, \dots, N) \quad (15)$$

Considering (15), the following relation between the constants of $(N+1)$ th and those of first segment can be written:

$$\mathbf{a}_{N+1} = \mathbf{Q}_N^{-1} \mathbf{P}_N \mathbf{Q}_{N-1}^{-1} \mathbf{P}_{N-1} \dots \mathbf{Q}_1^{-1} \mathbf{P}_1 \mathbf{a}_1 = \mathbf{T} \mathbf{a}_1 \quad (16)$$

where \mathbf{T} is the transfer matrix.

Using the first two conditions of (8) into (7) gives $D_1 = -B_1$ and $C_1 = -A_1$. Substituting the latter two of (8) into (7) gives

$$\mathbf{W} \mathbf{a}_{N+1} = \mathbf{0} \quad (17)$$

where

$$\mathbf{W} = \begin{bmatrix} -\sin \beta & -\cos \beta & \sinh \beta & \cosh \beta \\ -\cos \beta & \sin \beta & \cosh \beta & \sinh \beta \end{bmatrix} \quad (18)$$

Substituting (16) into (17) gives

$$\mathbf{Z} \mathbf{a}_1 = \mathbf{0} \quad (19)$$

where $\mathbf{Z} = \mathbf{W} \mathbf{T}$. Re-calling $D_1 = -B_1$ and $C_1 = -A_1$ and rearranging equation (19), we have

$$\begin{bmatrix} Z_{11} - Z_{13} & Z_{12} - Z_{14} \\ Z_{21} - Z_{23} & Z_{22} - Z_{24} \end{bmatrix} \begin{bmatrix} A_1 \\ B_1 \end{bmatrix} = \begin{bmatrix} 0 \\ 0 \end{bmatrix} \quad (20)$$

Equation (20) has real roots different from zero when the determinant of its coefficient matrix is zero. Thus,

$$\det \begin{bmatrix} Z_{11} - Z_{13} & Z_{12} - Z_{14} \\ Z_{21} - Z_{23} & Z_{22} - Z_{24} \end{bmatrix} = 0 \quad (21)$$

which gives a characteristic equation as $f(m, \bar{x}_i, d_i) = 0$ depending on natural frequencies, crack size and location. Using the roots β_n ($n = 1, 2, \dots$) of the characteristic equation into (6), the natural frequencies of beam can be obtained from

$$\omega_n = \frac{\beta_n^2}{L^2} \sqrt{\frac{EI}{\rho A}} \quad (22)$$

For modal shape functions, constants \mathbf{a}_i for each segment can, then, be obtained from (20) for $i = 1$ and (15) for $i = 2, 3, \dots$

B. Experimental model

Three steel cantilever beams are constructed for laboratory tests. A typical representation of the model is shown in Fig. 3. The beam has uniform rectangular cross-section along its length. In experimental measurements, B&K3560 data acquisition system with 17 channels, B&K8340-type uni-axial accelerometers and uni-axial signal cables are used as test equipment. Six sensitive accelerometers are located on the laboratory model to extract natural frequencies and corresponding mode shapes of the beam shown in Fig. 4.

Measurements are performed during 10 minutes for all cases (damaged and undamaged) considered. Frequency range, FFT analyzers and Multi-buffer are selected to be 0-800Hz, 800 lines and 100 averages, 50 size and 500m update, respectively. The signals from the accelerometers are recorded on the computer with applying FFT process in PULSE [17] software. This transformed data is, then, filtered by the weight functions in OMA [18] software. Modal parameters are obtained by Enhanced Frequency Domain Decomposition (EFDD) method in frequency domain which gives the spectral density functions of the signals in each channel. Natural frequencies and modal damping ratios are, then, determined using the spectral density functions.

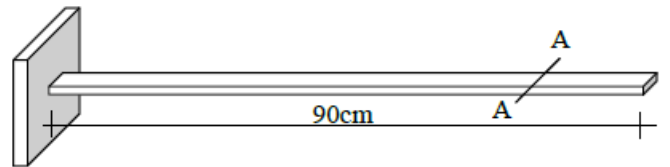


Fig. 3. Dimensions of the steel cantilever beam considered.

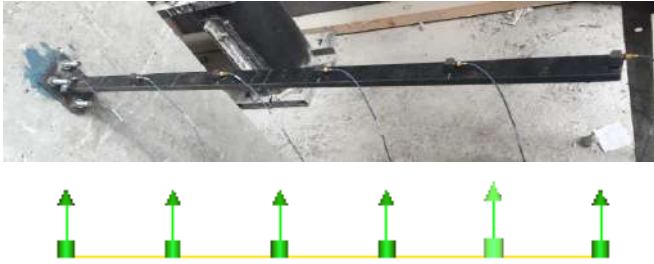


Fig. 4. Laboratory model and accelerometer locations.

TABLE I. DAMAGE SCENARIOS CONSIDERED.

Scenario	Crack location (mm)			Crack depth (mm)		
	x_1	x_2	x_3	a_1	a_2	a_3
Damage-1	90	-	-	3	-	-
Damage-2	90	270	-	3	3	-
Damage-3	90	270	450	3	3	3
Damage-4	90	270	450	6	3	3
Damage-5	90	270	450	6	6	3
Damage-6	90	270	450	6	6	6

TABLE II. FIRST SIX NATURAL FREQUENCIES (Hz) CALCULATED FROM TMM.

Mode	Natural frequencies (Hz)						
	Intact	Damage-1	Damage-2	Damage-3	Damage-4	Damage-5	Damage-6
1	10.25	10.10	10.04	10.03	9.18	8.87	8.77
2	64.24	63.88	63.73	63.16	61.27	60.47	57.07
3	179.83	179.64	178.07	178.02	177.11	168.58	168.58
4	352.42	352.42	351.17	347.91	347.91	342.20	323.51
5	582.60	581.61	580.83	580.75	575.82	571.73	571.73
6	870.24	866.22	857.95	849.86	830.07	796.00	767.36

TABLE III. FIRST SIX NATURAL FREQUENCIES (Hz) MEASURED BY OMA

Mode	Natural frequencies (Hz)						
	Intact	Damage-1	Damage-2	Damage-3	Damage-4	Damage-5	Damage-6
1	9.92	9.77	9.69	9.75	8.93	8.68	8.59
2	62.53	62.26	61.98	61.56	59.96	59.34	57.54
3	175.30	175.21	173.40	173.70	172.80	167.20	166.90
4	342.10	341.80	340.90	338.60	338.30	334.80	325.30
5	562.00	560.60	559.10	560.00	552.10	548.20	547.50
6	856.70	850.30	844.40	828.60	808.60	776.70	763.50

TABLE IV. CHANGE IN NATURAL FREQUENCIES (%) WITH INCREASING DAMAGE SEVERITY.

Case	Change in natural frequencies (%)					
	f_1	f_2	f_3	f_4	f_5	f_6
Intact vs. Damage-1	1.48	0.55	0.10	0.00	0.17	0.46
Damage-1 vs. Damage-2	0.59	0.24	0.87	0.35	0.13	0.95
Damage-2 vs. Damage-3	0.11	0.89	0.03	0.93	0.01	0.94
Damage-3 vs. Damage-4	8.44	2.98	0.51	0.00	0.85	2.33
Damage-4 vs. Damage-5	3.35	1.30	4.82	1.64	0.71	4.11
Damage-5 vs. Damage-6	1.14	5.63	0.00	5.46	0.00	3.59

III. RESULTS

Comparisons between the calculated and measured values are given. Material properties are $E = 206\text{GPa}$ and $\rho = 7800\text{kg/m}^3$. Free vibration analyses are performed for six damage scenarios in Table 1. Analytical results are obtained through a computer code written in MATLAB environment.

Tables 2-4 show the first six natural frequencies of the cantilever beam for all cases considered. As can be seen, the natural frequencies decrease with increasing the damage severity. This is more notable when the crack depth increases, i.e., between Damage-3 and Damage-4 cases. Results obtained from TMM and OMA slightly differ. This may be from several reasons such that: (a) fixed support condition at left-end cannot be provided exactly in laboratory environment, and (b) the beam cross-section, thus the flexural rigidity, cannot be uniform along the beam length. The modal updating, which is already out of the scope of this study, is therefore required. Fig. 5 shows the spectral density functions obtained from OMA. In there, the peak points which are selected manually show natural frequencies of the beam.

Modal Assurance Criterion (MAC) is used to establish the correlation between the measured and the calculated results, which is defined by

$$\text{MAC}(X_a, X_e) = \frac{|X_a^T X_e|^2}{(X_a^T X_a)(X_e^T X_e)} \quad (23)$$

where X_a and X_e denote analytical and experimental mode shapes. MAC values are greater than 90% means the mode shapes are good correlated [19]. Figs. 6 and 7 show MAC values between analytical and experimental mode shapes for undamaged and Damage-6 cases, respectively. As seen, the correlation between the calculated and measured mode shapes are very good, which verifies the laboratory measurements performed.

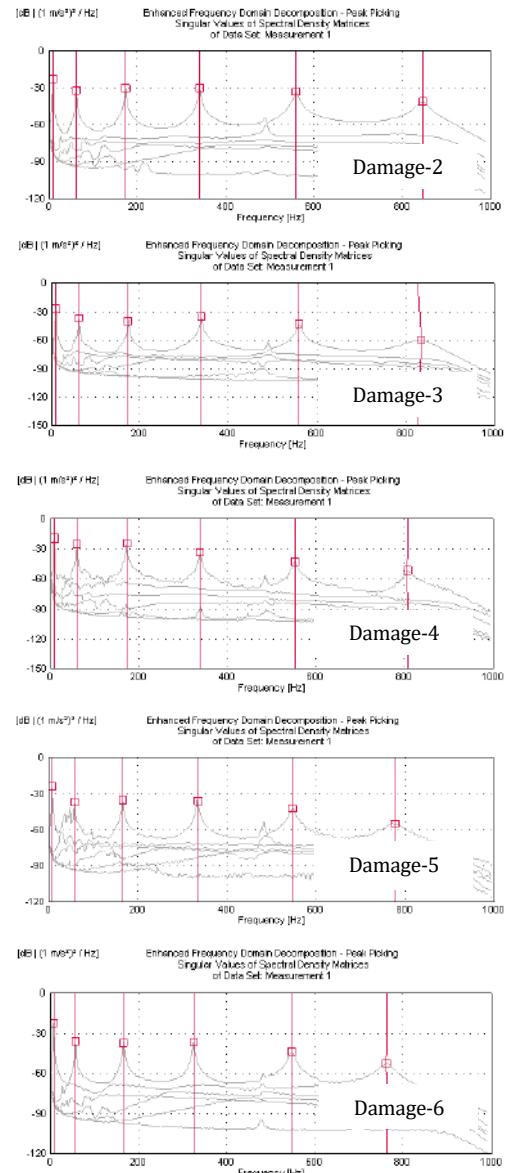


Fig. 5. Singular values of spectral density matrices.

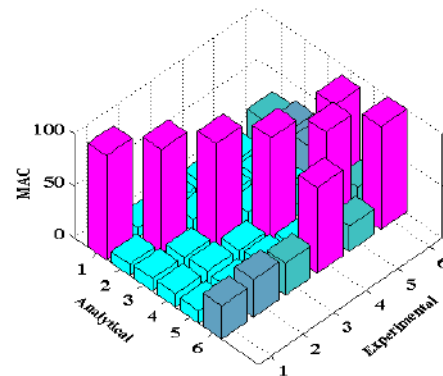
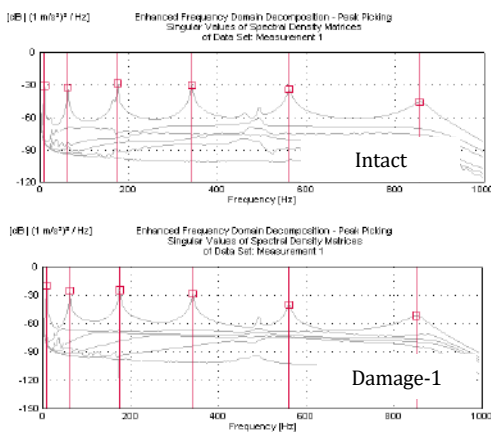


Fig. 6. MAC values between analytical and experimental mode shapes for undamaged case.

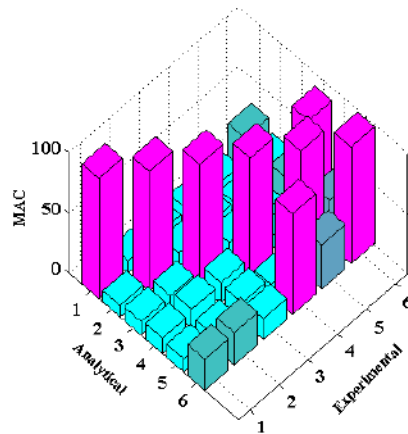


Fig. 7. MAC values between analytical and experimental mode shapes for Damage-6 case.

IV. CONCLUSION

Free vibration of cracked cantilever beams is considered by analytical and experimental methods. Results are in good agreement. The followings can be drawn from the study:

- Natural frequencies are strongly affected by crack presence in the beam.
- Crack depth is more effective on the natural frequencies compared to the number of cracks.
- Operational modal analysis is very suitable for experimental analyses of cracked beams. For more accurate results, modal updating should be recommended.
- Transfer matrix method gives the frequency equation to solve the inverse problem for damage detection. However, the solution is required more symbolic computation and thus computing time when the number of cracks increases.

REFERENCES

- [1] Dimarogonas, A.D., "Vibration of cracked structures: a state of the art review", *Engineering Fracture Mechanics*, vol. 55(5), pp. 831-857, 1996.
- [2] Dimarogonas, A.D. and Paipetis, S.A., *Analytical Methods in Rotor Dynamics*, Applied Science Publisher, London, 1983.
- [3] Shifrin, E.I. and Ruotolo, R., "Natural frequencies of a beam with an arbitrary number of cracks", *Journal of Sound and Vibration*, vol. 222(3), pp. 409-423, 1999.
- [4] Lin, H.P., Chang, S.C. and Wu, J.D., "Beam vibrations with an arbitrary number of cracks", *Journal of Sound and Vibration*, vol. 258(5), pp. 987-999, 2002.
- [5] Zheng, D.Y. and Fan, S.C., "Vibration and stability of cracked hollow-sectional beams", *Journal of Sound and Vibration*, vol. 267, pp. 933-954, 2003.
- [6] Lin, H.P., "Direct and inverse methods on free vibration analysis of simply supported beams with a crack", *Engineering Structures*, vol. 26, pp. 427-436, 2004.
- [7] Loya, J.A., Rubio, L. and Fernández-Sáez, J., "Natural frequencies for bending vibrations of Timoshenko cracked beams", *Journal of Sound and Vibration*, vol. 290, pp. 640-653, 2006.
- [8] Attar, M., "A transfer matrix method for free vibration analysis and crack identification of stepped beams with multiple edge cracks and different boundary conditions", *International Journal of Mechanical Sciences*, vol. 57, pp. 19-33, 2012.
- [9] Viola, E., Ricci, P. and Aliabadi, M.H., "Free vibration analysis of axially loaded cracked Timoshenko beam structures using the dynamic stiffness method", *Journal of Sound and Vibration*, vol. 304, pp. 124-153, 2007.
- [10] Ruotolo, R. and Surace, C., "Natural frequencies of a bar with multiple cracks", *Journal of Sound and Vibration*, vol. 272, pp. 301-316, 2004.
- [11] Lee, J., "Identification of multiple cracks in a beam using natural frequencies", *Journal of Sound and Vibration*, vol. 320, pp. 482-490, 2009.
- [12] Nandakumar, P. and Shankar, K., "Multiple crack damage detection of structures using the two-crack transfer matrix", *Structural Health Monitoring*, vol. 13(5), pp. 548-561, 2014.
- [13] Neves, A.C., Simões, F.M.F. and Pinto da Costa, A., "Vibrations of cracked beams: Discrete mass and stiffness models", *Computers and Structures*, vol. 168, pp. 68-77, 2016.
- [14] Sinha, J.K., Friswell, M.I. and Edwards, S., "Simplified models for the location of cracks in beam structure using measured vibration data", *Journal of Sound and Vibration*, vol. 251, pp. 13-38, 2002.
- [15] Patil, D.P. and Maiti, S.K., "Experimental verification of a method of detection of multiple cracks in beams based on frequency measurements", *Journal of Sound and Vibration*, vol. 281, pp. 439-451, 2005.
- [16] Nandakumar, P. and Shankar, K., "Structural crack damage detection using transfer matrix and state vector", *Measurement*, vol. 68, pp. 310-327, 2015.
- [17] PULSE Analyzers and Solutions, Release 11.2. Bruel and Kjaer, Sound and Vibration Measurement A/S, Denmark, 2006.
- [18] OMA Operational Modal Analysis, Release 4.0. Structural Vibration Solution A/S, Denmark, 2006.
- [19] Ewins, D.J., *Modal Testing: Theory and Practice*, John Wiley & Sons, Inc, New York, 1995.

Free vibration and buckling analysis of functionally graded beams by finite element method

Volkan Kahya

Department of Civil Engineering
Karadeniz Technical University
Trabzon, Turkey
volkan@ktu.edu.tr

Muhittin Turan

Department of Civil Engineering
Karadeniz Technical University
Trabzon, Turkey
m.turan@ktu.edu.tr

Abstract—A finite element model based on the first-order shear deformation theory for free vibration and buckling of functionally graded beams is presented. The present element has five nodes and ten degrees-of-freedom. Material properties vary continuously through the beam thickness according to the power-law form. Governing equations are derived with employing Lagrange's equations. Natural frequencies and buckling loads are calculated numerically for different end conditions, power-law indices, and span-to-depth ratios. Accuracy of the present element is demonstrated.

Keywords—Functionally graded materials; Finite element method; Free vibration; Buckling; First-order shear deformation theory

I. INTRODUCTION

Functionally graded materials (FGMs) are special composites formed of two or more constituents with a continuous spatial variation. They are usually made of a mixture of ceramics and metals, and can thus resist high-temperature environments while keeping their strength. Therefore, they have been preferred in different applications in aerospace, marine, mechanical, and civil engineering. Increasing demand to FGMs necessitates to well understand the mechanical behavior of such structures.

Compared to functionally graded plates and shells, research on functionally graded beams (FGBs) are relatively less. Bending, buckling and vibration problems of FGBs were solved by different analytical and numerical methods based on various beam theories. Among analytical works, we can mention the followings: Aydogdu and Taskin [1] investigated free vibration of simply-supported FGB based on classical, parabolic and exponential shear deformation theories. Sina et al. [2] developed a novel beam theory different from the classical first-order shear deformation theory to analyze free vibration of FGBs. They assumed the lateral normal stress of the beam is zero. Thai and Vo [3] studied bending and free vibration of FGBs based on various higher-order shear deformation theories. They considered higher-order variation of transverse shear strain through the depth of the beam with

satisfying stress-free boundary conditions. Nguyen et al. [4] developed the first-order shear deformation theory for statics and free vibration of axially loaded FGBs with rectangular cross-section. They derived the improved transverse shear stiffness from the in-plane stress and equilibrium equation, and thus the shear correction factor was obtained analytically. In the foregoing works, researchers used Navier's method to solve governing equations. With the aid of the method of Lagrange multipliers, Şimşek [5] studied free vibration of FGBs considering different higher-order beam theories. A higher-order theory with the assumption of hyperbolic distribution of transverse shear stress was proposed by Nguyen et al. [6] for vibration and buckling analyses of FG sandwich beams. Li and Batra [7] derived analytical relations between the critical buckling load of a FGM Timoshenko beam and that of the corresponding homogenous Bernoulli-Euler beam subject to axial compressive load.

Finite element method (FEM) is one of the mostly used numerical method in analyses of structures. Some authors developed different finite element models based on various beam theories in analyzing FGBs. Chakraborty et al. [8] proposed a beam element based on the first-order shear deformation theory to study the thermoelastic behavior of FGBs. They considered the static, free vibration and wave propagation problems to highlight the difference of FGM beam with pure metal or pure ceramic beams. Based on the classical beam theory, Alshorbagy et al. [9] developed a two-noded, six degrees-of-freedom finite element to investigate free vibration of FGBs. Their element can consider the material graduation in both axial and transversal direction. Kapuria et al. [10] presented a finite element model based on a third-order zig-zag theory for dynamic analysis of layered FGBs. They also gave some experimental results for validation of their proposed theory. Vo et al. [11] developed a finite element model for vibration and buckling of FG sandwich beams based on a refined shear deformation theory. In the formulation, they considered the bending and shear components of transverse displacement as C^1 -continuous whereas the axial displacement is C^0 -continuous. Most recently, Vo et al. [12,13] presented a two-noded C^1 -

continuous beam element with six degrees-of-freedom per node for static, buckling and vibration analyses of FG sandwich beams based on a quasi-3D theory. They considered both shear deformation and thickness stretching effect in the analyses.

This study aims to develop an accurate and simpler finite element model based on the first-order shear deformation theory for vibration and buckling of FGBs. Material properties within the beam vary continuously through the thickness according to the power-law form. The beam element proposed here has five nodes and ten degrees-of-freedom. Governing equations of motion are derived by using Lagrange's equations. Accuracy of the element is validated through comparisons with the results available for buckling loads and natural frequencies of FGBs with different end conditions, power-law indices, and span-to-depth ratios.

II. THEORY AND FORMULATION

A. Material properties

Fig. 1 shows an isotropic, nonhomogeneous elastic beam with length L and rectangular cross-section of $b \times h$. The beam is loaded by an axial compressive force N at its ends. The beam is assumed to be composed of a mixture of two constituents such as ceramic and metal, which are located at its top and bottom surfaces, respectively. Material behavior obeys Hooke's law. The gravity is not considered. Material properties vary continuously through-the-thickness according to the power-law rule given by

$$P(z) = (P_c - P_m) \left(\frac{z}{h} + \frac{1}{2} \right)^k + P_m \quad (1)$$

where k is the non-negative power-law exponent, P_m and P_c are the corresponding material properties of the metal and ceramic constituents, e.g., Young's modulus E , Poisson's ratio ν , and mass density ρ , respectively.

B. Finite element model

Fig. 2 shows a five-noded beam finite element with four equally spaced nodes and a node at the middle. It has ten degrees-of-freedom including three axial, four transversal and three rotational displacements which are measured at neutral axis of the beam. The nodal displacement vector can thus be given as:

$$\mathbf{u} = \{u_1 \ u_2 \ u_3 \ w_1 \ w_2 \ w_3 \ w_4 \ \phi_1 \ \phi_2 \ \phi_3\}^T \quad (2)$$

where u , w and ϕ are the axial and the transverse displacements, and the total bending rotation of the cross-sections at any point on the neutral axis, respectively. Note that ϕ is assumed to be geometrically unrelated to the slope $\partial w / \partial x$ to account for the shear deformation.

According to the first-order shear deformation theory, the displacement field can be given by

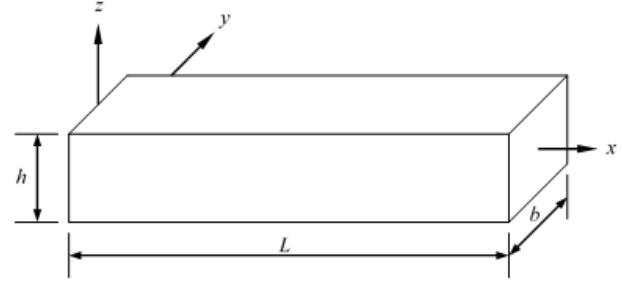


Fig. 1. Geometry and coordinate system of a functionally graded beam

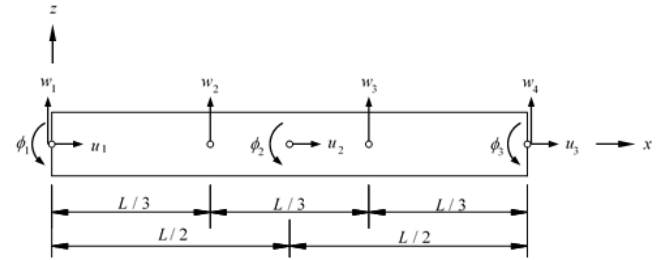


Fig. 2. Ten degrees-of-freedom beam element

$$\begin{aligned} U(x, z, t) &= u(x, t) - z\phi(x, t), \\ W(x, z, t) &= w(x, t) \end{aligned} \quad (3)$$

where t denotes time. The strain-displacement relations are given by

$$\begin{aligned} \varepsilon_{xx} &= \frac{\partial U}{\partial x} = \frac{\partial u}{\partial x} - z \frac{\partial \phi}{\partial x} = u_{,x} - z\phi_{,x}, \\ \gamma_{xz} &= \frac{\partial U}{\partial z} + \frac{\partial W}{\partial x} = \frac{\partial w}{\partial x} - \phi = w_{,x} - \phi \end{aligned} \quad (4)$$

where ε_{xx} and γ_{xz} are the normal and shear strains, respectively. $(\cdot)_{,x}$ denotes the derivative with respect to x . Since the material behavior obeys Hooke's law, the constitutive relations can be written as

$$\sigma_{xx} = E(z)\varepsilon_{xx}, \quad \tau_{xz} = KG(z)\gamma_{xz} \quad (5)$$

where σ_{xx} and τ_{xz} are the normal and shear stresses, respectively. K is the shear correction factor, $E(z)$ is the Young modulus, and $G(z) = E(z) / [2(1 + \nu(z))]$ is the shear modulus.

The strain energy of the beam can be given by

$$U = \frac{1}{2} \int_0^L \int_A (\sigma_{xx}\varepsilon_{xx} + \tau_{xz}\gamma_{xz}) dA dx \quad (6)$$

where A is the cross-sectional area of the beam. Substituting (4) and (5) into (6) yields

$$U = \frac{1}{2} \int_0^L \{ A_0 (u_{,x})^2 - 2A_1 u_{,x} \phi_{,x} + A_2 (\phi_{,x})^2 + B_0 [(w_{,x})^2 - 2w_{,x} \phi + (\phi)^2] \} dx \quad (7)$$

where the stiffness coefficients are defined as

$$[A_0, A_1, A_2] = \int_A E(z) [1, z, z^2] dA, \quad B_0 = \int_A KG(z) dA \quad (8)$$

The work done by the axial compressive force N can be expressed as

$$V = \frac{1}{2} \int_0^L N (w_{,x})^2 dx \quad (9)$$

The kinetic energy is obtained by

$$T = \frac{1}{2} \int_0^L \int_A \rho(z) (\dot{U}^2 + \dot{W}^2) dA dx \quad (10)$$

where dot denotes the derivative with respect to time. Taking the derivative with respect to time in (3), and substituting the result into (10) gives

$$T = \frac{1}{2} \int_0^L [I_0 (\dot{u})^2 - 2I_1 \dot{u} \dot{\phi} + I_2 (\dot{\phi})^2 + I_0 (\dot{w})^2] dx \quad (11)$$

where the inertia coefficients are

$$[I_0, I_1, I_2] = \int_A \rho(z) [1, z, z^2] dA \quad (12)$$

Assume the solutions to $u(x, t)$, $w(x, t)$ and $\phi(x, t)$ as

$$u(x, t) = \sum_{i=1}^3 \varphi_i(x) u_i(t), \quad w(x, t) = \sum_{i=1}^4 \psi_i(x) w_i(t), \quad \phi(x, t) = \sum_{i=1}^3 \theta_i(x) \phi_i(t) \quad (13)$$

where $\varphi_i(x)$, $\psi_i(x)$ and $\theta_i(x)$ are the shape functions, and $u_i(t)$, $w_i(t)$ and $\phi_i(t)$ are the generalized nodal displacements. Since the axial displacement of a point not on the neutral axis is a linear function of both u and ϕ , the degree of polynomials for $\varphi_i(x)$ and $\theta_i(x)$ must be the same order. In addition, since the shear strain is a linear function of both the rotation $\phi_i(t)$ and the slope $\partial w / \partial x$, the degree of

polynomial for $\psi_i(x)$ must be one order higher than that for $\varphi_i(x)$ and $\theta_i(x)$ to ensure compatibility. A cubic polynomial for $\psi_i(x)$ and quadratic polynomials for $\varphi_i(x)$ and $\theta_i(x)$ are selected for consistency, which are obtained by the Lagrange interpolation formula (see Appendix A).

The governing equations of motion can be obtained by Lagrange's equations. Letting

$$L = T - (U + V) \quad (14)$$

which is the Langragian functional, Lagrange's equations are defined by

$$\frac{d}{dt} \left(\frac{\partial L}{\partial \dot{q}_i} \right) - \frac{\partial L}{\partial q_i} = 0 \quad (15)$$

in which q_i denote the generalized coordinates corresponding to unknowns u_i , w_i and ϕ_i . Substituting (7), (9) and (11) into (14) with considering (13) leads to

$$\mathbf{m} \ddot{\mathbf{u}} + (\mathbf{k} - N\mathbf{g}) \mathbf{u} = \mathbf{0} \quad (16)$$

where the element mass (\mathbf{m}), stiffness (\mathbf{k}), and geometric stiffness (\mathbf{g}) matrices are defined as

$$\mathbf{m} = \begin{bmatrix} \mathbf{m}^{11} & \mathbf{0} & \mathbf{m}^{13} \\ \mathbf{0} & \mathbf{m}^{22} & \mathbf{0} \\ \mathbf{m}^{13} & \mathbf{0} & \mathbf{m}^{33} \end{bmatrix}, \quad \mathbf{k} = \begin{bmatrix} \mathbf{k}^{11} & \mathbf{0} & \mathbf{k}^{13} \\ \mathbf{0} & \mathbf{k}^{22} & \mathbf{k}^{23} \\ \mathbf{k}^{13} & \mathbf{k}^{23T} & \mathbf{k}^{33} \end{bmatrix}, \quad (17)$$

$$\mathbf{g} = \begin{bmatrix} \mathbf{0} & \mathbf{0} & \mathbf{0} \\ \mathbf{0} & \mathbf{g}^{22} & \mathbf{0} \\ \mathbf{0} & \mathbf{0} & \mathbf{0} \end{bmatrix}$$

C. Free vibration and buckling problem

For the beam with length of L , matrix equation of motion can be written as

$$\mathbf{M} \ddot{\mathbf{U}} + (\mathbf{K} - N\mathbf{G}) \mathbf{U} = \mathbf{0} \quad (18)$$

where \mathbf{M} , \mathbf{K} and \mathbf{G} are the global mass, stiffness and geometric stiffness matrices, respectively. \mathbf{U} is the vector of unknowns. For free vibration of the beam without axial loading, ignoring \mathbf{G} matrix and assuming $\mathbf{U} = \mathbf{U}_0 e^{i\omega t}$ in (18), we have the following eigen-value problem:

$$(\mathbf{K} - \omega^2 \mathbf{M}) \mathbf{U}_0 = \mathbf{0} \quad (19)$$

where ω denote the natural frequencies of the beam. For buckling analysis, ignoring \mathbf{M} matrix and assuming $\mathbf{U} = \mathbf{U}_0 e^{\lambda x}$, the stability equation becomes

$$(\mathbf{K} - \lambda \mathbf{G})\mathbf{U}_0 = \mathbf{0} \quad (20)$$

where $\lambda = N_{cr}$ are the buckling loads. The natural frequencies and buckling loads of the beam can be obtained by non-trivial solutions of (19) and (20).

III. RESULTS AND DISCUSSION

Some numerical examples are given and discussed for validation of the present element. A FG beam composed of aluminum (Al) as metal and alumina (Al_2O_3) as ceramic is considered for which $E_m = 70\text{GPa}$, $\rho_m = 2702\text{kg/m}^3$, $\nu_m = 0.3$, $E_c = 380\text{GPa}$, $\rho_c = 3960\text{kg/m}^3$, and $\nu_c = 0.3$ [5]. Boundary conditions for the beam are assumed to be clamped-clamped (C-C), simply supported (S-S) and clamped-free (C-F). The shear correction factor is $K = 5/6$ for the first-order shear deformation theory. Natural frequencies and critical buckling loads are given in the following normalized form:

$$\bar{\omega}_n = \frac{\omega_n L^2}{h} \sqrt{\frac{\rho_m}{E_m}}, \quad \bar{N}_{cr} = N_{cr} \frac{12L^2}{E_m h^3} \quad (21)$$

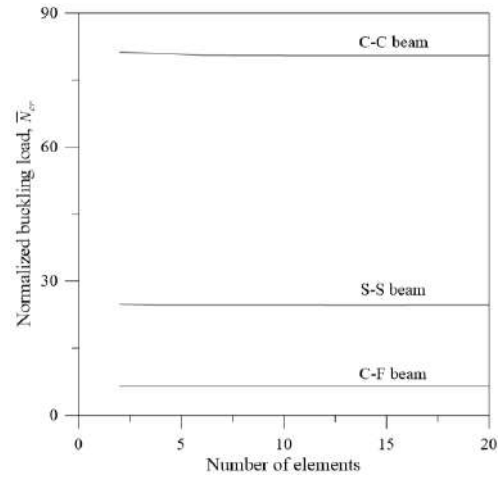
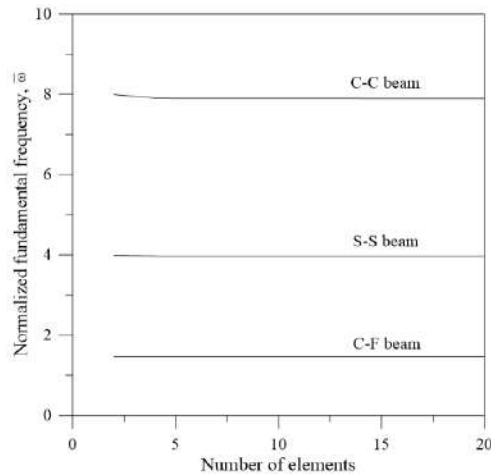


Fig. 3. Convergence of the present element for FGBs with different boundary conditions ($L/h = 5$, $k = 1$)

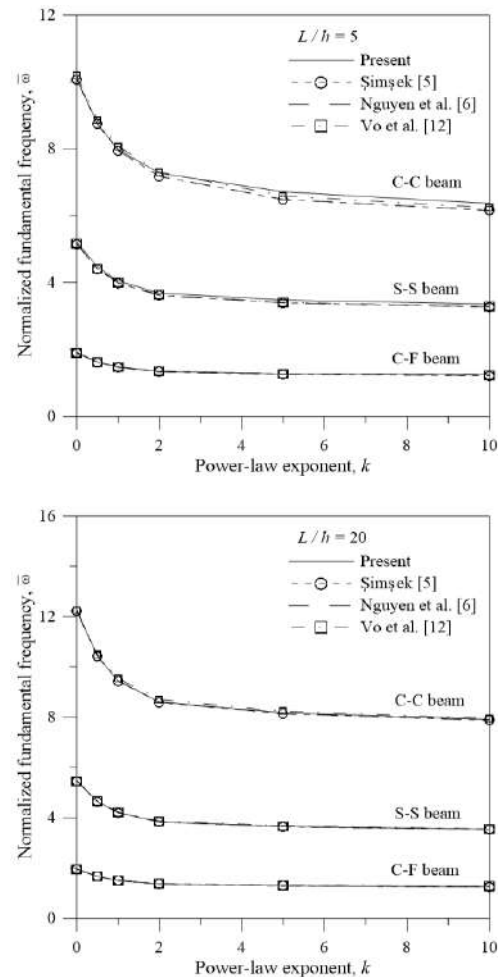


Fig. 4. Variation of the normalized fundamental frequency of FGBs with the power-law exponent

Convergence study is first carried out for the present element. Fig. 3 shows the normalized fundamental frequencies

and critical buckling loads of FGBs with different end conditions for $L/h = 5$ and $k = 1$. As seen in the figure, the present element rapidly converges when the number of elements increase. Twelve elements seem to be enough for the desired accuracy in numerical calculations.

Variation of the normalized fundamental frequencies and critical buckling loads of FGBs with the power-law exponent are given by Figs. 4 and 5, respectively. In these figures, the fundamental frequencies and buckling loads obtained from the present model are compared to the results of different higher-order beam theories such as parabolic shear deformation theory [5], higher-order shear deformation theory with a hyperbolic distribution of shear stress [6], Reddy-Bickford beam theory [11] and a quasi-3D theory including thickness stretching effect [12]. Note that Refs. [5] and [6] gave analytical solution while the others gave finite element solution. As can be seen, the fundamental frequencies and buckling loads computed by the present element agree well with the reference solutions for all beams considered. Although the present element is based on simpler beam theory compared to other theories considered, we have quite satisfactory results for the fundamental frequencies and the buckling loads. This result furtherly validates our element's accuracy in calculation of natural frequencies and critical buckling loads of FGBs. Greater frequencies and buckling loads are obtained for C-C beams than the others. As can also be seen, the power-law exponent has significant effect on both the fundamental frequencies and buckling loads, both of that decrease when the power-law exponent increases.

Fig. 6 gives variation of the normalized fundamental frequencies and critical buckling loads of FGBs with the slenderness (L/h) for $k = 1$. Here, $\nu_m = \nu_c = 0.3$ is considered. Logarithmic (base 10) scale is used for the abscissa, i.e., L/h values, in graphical representation. As seen, the fundamental frequencies and the buckling loads increase with increasing the slenderness. This result agrees with the literature. C-C beams seem more sensitive to change in the slenderness compared to the others.

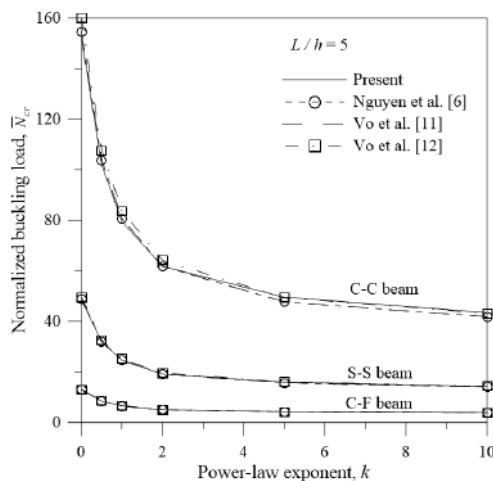


Fig. 5. Variation of the normalized buckling load of FGBs with the power-law exponent

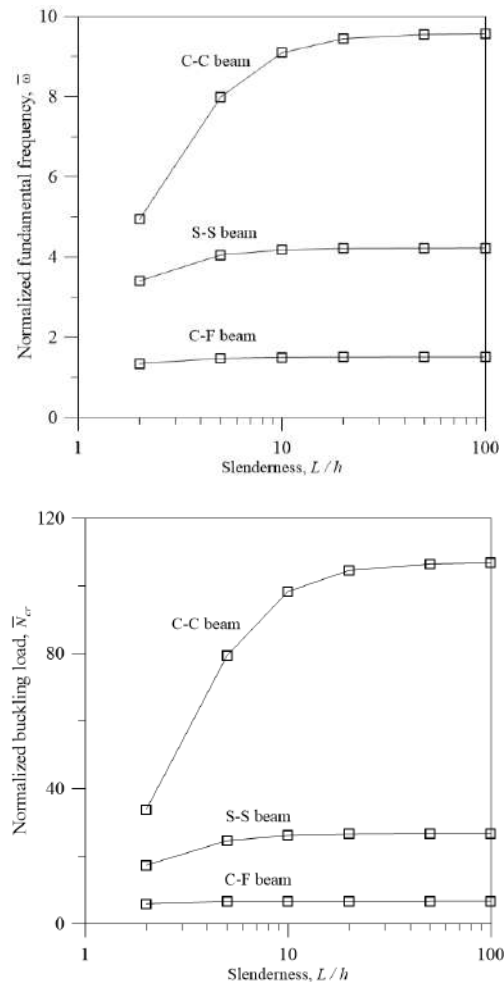


Fig. 6. Variation of the normalized fundamental frequency and critical buckling load of FGBs with the power-law exponent ($k = 1$)

IV. CONCLUSION

A five-noded, ten degrees-of-freedom finite element based on the first-order shear deformation theory is presented for free vibration and buckling analyses of FGBs. Element matrices are derived with the aid of Lagrange's equations. Some numerical results are given for the aim of verification. According to the results of this study, the present model can accurately predict the natural frequencies and the critical buckling loads of FGBs with different end conditions. Accuracy and performance of the present model in computation is well enough.

REFERENCES

- [1] M. Aydogdu, and V. Taskin, "Free vibration analysis of functionally graded beams with simply supported edges," *Mater Design*, vol. 28(5), pp. 1651-1656, 2007.
- [2] S.A. Sina, H.M. Navazi, and H. Haddadpour, "An analytical method for free vibration analysis of functionally graded beams," *Mater Design*, vol. 30(3), pp. 741-747, 2009.
- [3] H.T. Thai, and T.P. Vo, "Bending and free vibration of functionally graded beams using various higher-order shear deformation beam theories," *Int J Mech Sci*, vol. 62(1), pp. 57-66, 2012.
- [4] T.K. Nguyen, T.P. Vo, and H.T. Thai, "Static and free vibration of axially loaded functionally graded beams based on the first-order shear deformation theory," *Compos Part B-Eng*, vol. 55, pp. 147-157, 2013.
- [5] M. Simsek, "Fundamental frequency analysis of functionally graded beams by using different higher-order beam theories," *Nucl Eng Des*, vol. 240(4), pp. 697-705, 2010.
- [6] T.K. Nguyen, T.T.P. Nguyen, T.P. Vo, and H.T. Thai, "Vibration and buckling analysis of functionally graded sandwich beams by a new higher-order shear deformation theory," *Compos Part B-Eng*, vol. 76, pp. 273-285, 2015.
- [7] S.R. Li, and R.C. Batra, "Relations between buckling loads of functionally graded Timoshenko and homogeneous Euler-Bernoulli beams," *Compos Struct*, vol. 95, pp. 5-9, 2013.
- [8] A. Chakraborty, S. Gopalakrishnan, and J.N. Reddy, "A new beam finite element for the analysis of functionally graded materials," *Int J Mech Sci*, vol. 45(3), pp. 519-539, 2003.
- [9] A.E. Alshorbagy, M.A. Eltaher, and F.F. Mahmoud, "Free vibration characteristics of a functionally graded beam by finite element method," *Appl Math Model*, vol. 35(1), pp. 412-425, 2011.
- [10] S. Kapuria, M. Bhattacharyya, and A.N. Kumar, "Bending and free vibration response of layered functionally graded beams: A theoretical model and its experimental validation," *Compos Struct*, vol. 82(3), pp. 390-402, 2008.
- [11] T.P. Vo, H.T. Thai, T.K. Nguyen, A. Maheri, and J. Lee, "Finite element model for vibration and buckling of functionally graded sandwich beams based on a refined shear deformation theory," *Eng Struct*, vol. 64, pp. 12-22, 2014.
- [12] T.P. Vo, H.T. Thai, T.K. Nguyen, F. Inam, and J.H. Lee, "A quasi-3D theory for vibration and buckling of functionally graded sandwich beams," *Compos Struct*, vol. 119, pp. 1-12, 2015.
- [13] T.P. Vo, H.T. Thai, T.K. Nguyen, F. Inam, and J. Lee, "Static behaviour of functionally graded sandwich beams using a quasi-3D theory," *Compos Part B-Eng*, vol. 68, pp. 59-74, 2015.

Continuous and Discontinuous Contact Problem of a Functionally Graded Layer Under Gravity

Gökhan Adıyaman

Civil Engineering Department
Karadeniz Technical University
Trabzon, Turkey
gadiyaman@ktu.edu.tr

Erdal Öner

Civil Engineering Department
Bayburt University
Bayburt, Turkey
eoner@bayburt.edu.tr

Ahmet Birinci

Civil Engineering Department
Karadeniz Technical University
Trabzon, Turkey
birinci@ktu.edu.tr

Abstract—In this study, frictionless contact problem for a functionally graded (FG) layer under gravity is considered. The top of the FG layer is subjected to normal tractions over a finite segment and rested on a rigid foundation. The graded layer is modeled as a non-homogenous medium with a constant Poisson's ratio and exponentially varying shear modules and density. The problem is considered for two cases namely continuous and discontinuous contact. For continuous contact, the problem is solved analytically using plane elasticity and integral transform techniques. The critical load that causes first separation and contact pressures are investigated for various material properties and loadings. The problem is reduced to a singular integral equation using plane elasticity and integral transform techniques in case of discontinuous contact. Obtained singular integral equation is solved numerically using Gauss-Jacobi integration formulation and an iterative scheme is employed to obtain the correct separation distance. The separation distance and contact pressures between the FG layer and the foundation are analyzed for various material properties and loading. The results are shown in tables and figures. It is seen that decreasing stiffness and density at the top of the layer results in an increment both critical load in case of continuous contact and separation distance in case of discontinuous contact.

Keywords—Continuous contact; discontinuous contact; functionally graded layer; Gauss-Jacobi

I. INTRODUCTION

Problems, in which body forces neglected the layer bends and the contact area between the layer and the subspace, will diminish to a finite size independent of the magnitude of the applied load. However, particularly in large scale structures and layered media, in practice clearly this may not be the case, that is, in such problems the contact area is expected to depend on the applied load and furthermore away from the loading region the layer will remain in contact with the subspace because of gravity [1].

An examination of the related literature shows that studies involving layers or coatings with body forces have consisted of homogeneous materials [1-3] whereas studies involving FG layers or coating [4-6] have neglected body forces. Therefore, this study aims to solve the continuous and discontinuous contact problem of an FG layer resting on a rigid foundation by taking the body force the body force of the FG layer into account. Further, the calculations are made under the assumption that the FG layer is isotropic and the shear modulus and mass density exponentially vary along the direction of the layer's thickness.

II. FORMULATION OF THE PROBLEM

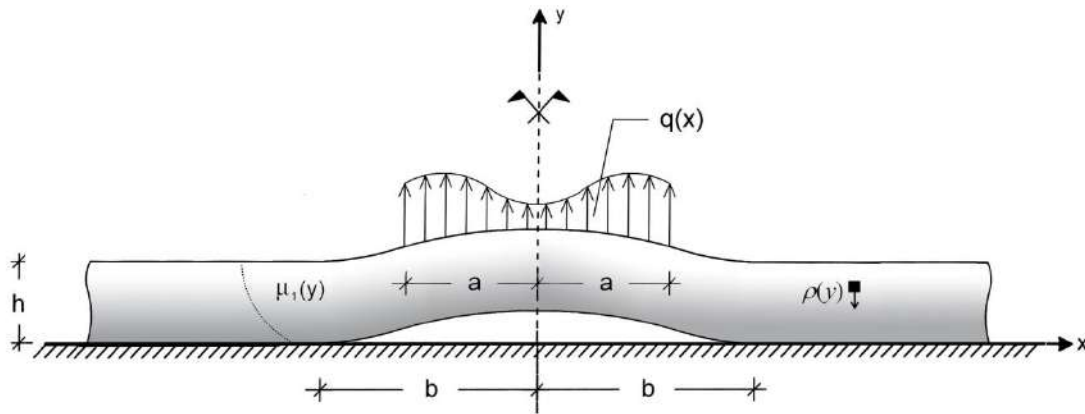
As shown in Fig. 1, a symmetric plane strain problem that consists of an infinitely long functionally graded (FG) layer of thickness h resting on a rigid foundation is considered. Poisson's ratio is taken as constant, the shear modulus and the density depend on the y -coordinate only as follows:

$$\mu(y) = \mu_0 \exp(\beta y), \quad \rho(y) = \rho_0 \exp(\alpha y), \quad 0 \leq y \leq h, \quad (1a,b)$$

where μ_0 and ρ_0 are the shear modules and the density of the graded layer at $y=0$, β and α are the non-homogeneity parameter controlling the variation of the shear modules and the density in the graded layer, respectively.

The top of the layer is subjected to a distributed load $q(x)$ over the segment $|x| \leq a$. It is assumed that the contact surfaces are frictionless and is to be the plane of symmetry with respect to external loads as well as geometry, for simplicity. Clearly, it is sufficient to consider one half (i.e. $x \geq 0$) of the medium only.

B. Discontinuous Contact



a separation
ation in the
id assuming
 $x < b$, the

Fig. 1. Geometry and loading of the contact problem

A. Continuous Contact

If the load is sufficiently small, then the contact between the FG layer and the rigid foundation becomes continuous and the boundary conditions can be as follows.

$$\sigma_y(x, h) = q(x)H(a - |x|), \quad \tau_{xy}(x, h) = 0, \quad (2a, b)$$

$$v(x, 0) = 0, \quad \tau_{xy}(x, 0) = 0, \quad 0 \leq x < \infty \quad (2c, d)$$

The problem is solved analytically using plane elasticity and integral transform techniques and following equations can be obtained.

$$\frac{1}{\lambda_{cr}} = \frac{\alpha h}{\exp(\alpha h) - 1} \frac{2 \exp(-\beta h)}{\pi(a/h)} * \int_0^\infty \frac{1}{\xi \Delta F} \sum_1^4 [F_{j1} S_1 \exp(n_j y)] \sin \xi a \cos \xi x d\xi \quad (3)$$

where, S_1 is a known function, F_{j1} ($j = 1, \dots, 4$) are obtained functions applying boundary conditions, λ_{cr} is the critical load that causes to first separation and defined as:

$$\lambda_{cr} = \frac{P_{cr}}{\rho_0 g h^2} \quad (4)$$

in which, P_{cr} is the critical resultant force of the distributed load that causes to first separation, g is gravitational acceleration, and h is the height of the layer. The separation of the FG layer occurs at $x = 0$ symmetry axis and the critical load, λ_{cr} , that cause to first separation can be found equating Eq. (4) to zero at $y = 0$.

$$\sigma_y(x, h) = q(x)H(a - |x|), \quad \tau_{xy}(x, h) = 0, \quad (5a, b)$$

$$\frac{\partial v(x, 0)}{\partial x} = f(x), \quad \tau_{xy}(x, 0) = 0, \quad 0 \leq x < \infty, \quad (5c, d)$$

$$\sigma_y(x, 0) = 0 \quad -b < x < b \quad (5e)$$

in which, v is the vertical displacement and $f(x)$ is the derivative of v with respect to x . Single-valuedness for vertical displacement requires that satisfies the following condition.

$$\int_{-b}^b f(x) dx = 0 \quad (6)$$

The problem is reduced to a singular integral equation using plane elasticity and integral transform techniques given as follows.

$$\frac{1}{\pi} \int_{-1}^1 \phi(s) \left[\frac{1}{t-x} + \frac{b}{h} k_1 \right] ds + \frac{1}{a/h \exp(\beta h)} \frac{\lambda}{\pi} k_2 - \frac{\exp(\alpha h) - 1}{\alpha h} = 0 \quad (7)$$

III. NUMERICAL SOLUTION OF THE PROBLEM

Using following dimensionless quantities, the numerical solution of the continuous and discontinuous contact problem can be simplified.

$$t = sb, \quad dt = bds, \quad x = rb, \quad (8a-c)$$

$$w = \xi h, \quad dw = h d\xi, \quad (8d,e)$$

$$\phi(s) = \frac{4\mu_0}{(\kappa+1)} f(t) \quad (8f)$$

Expressions for critical load factor (3), singular integral equation (7) and single-valuedness condition (6) become:

$$\frac{1}{\lambda_{cr}} = \frac{\alpha h}{\exp(\alpha h) - 1} \frac{2 \exp(-\beta h)}{\pi(a/h)} *$$

$$\int_0^\infty \frac{1}{w \Delta F} \sum_1^4 [F_{j1} S_1 \exp(n_j y)] \sin\left(w \frac{a}{h}\right) \cos\left(w \frac{x}{d}\right) dw \quad (9)$$

$$\frac{1}{\pi} \int_{-1}^1 \phi(s) \left[\frac{1}{t-x} + \frac{b}{h} k_1 \right] ds + \frac{1}{a/h \exp(\beta h)} \frac{\lambda}{\pi} k_2 - \frac{\exp(\alpha h) - 1}{\alpha h} = 0 \quad (10)$$

$$\frac{b}{h} \int_{-1}^1 \phi(s) ds = 0 \quad (11)$$

Since $f(t)$ or $\phi(s)$ is an odd function, i.e. $f(t) = -f(t)$, (11) is automatically satisfied. In addition, one may notice that because of the smooth contact at the point $s = -1$ and $s = 1$, the function $\phi(s)$ equals zero at the both ends. Hence, the index of the integral equation is -1 and the solution may be sought as described by Erdogan and Gupta [7] using appropriate Gauss-Jacobi integration formulas.

IV. RESULTS

The height of the graded layer is taken as 1 whereas the Poison's ratio of the graded layer is taken as 0,25. Note that all quantities are normalized.

As it is seen from Eq. (1a), the top of the layer becomes stiffer if non-homogeneity parameter β increases or vice versa. Similarly, it can be observed from Eq. (1b), the top of the layer becomes heavier if non-homogeneity parameter α increases. In addition, the layer can be assumed as homogenous for non-homogeneity parameters $\beta = 0.001$ and $\alpha = 0.001$.

Table 1 shows the comparison of λ_{cr} in case of continuous contact and b/h in case of discontinuous contact between the values reported in [1] and obtained in this study for homogenous layer, i.e. $\beta = 0.001$ and $\alpha = 0.001$. It can be

seen that values of b/h and λ_{cr} in this study are approximately the same value given by Civelek and Erdogan [1].

TABLE 1. THE COMPARISON OF λ_{cr} IN CASE OF CONTINUOUS CONTACT AND b/h IN CASE OF DISCONTINUOUS CASE ($a/h = 0.01$).

	λ_{cr}	b/h		
		$\lambda = 1.2$	$\lambda = 2.0$	$\lambda = 4.0$
Civ.and Erd. [1]	1.088	0.28	0.96	2.35
This study	1.088625	0.287155	0.970928	2.387936

Table 2 shows the variation of critical load factor λ_{cr} for various non-homogeneity parameters β and α . It is seen from this table that λ_{cr} increases for increasing α if others are fixed β . Similarly, increasing β results in an increase at load factor λ_{cr} .

TABLE 2. THE COMPARISON OF λ_{cr} IN CASE OF CONTINUOUS CONTACT AND b/h IN CASE OF DISCONTINUOUS CASE ($a/h = 0.01$).

	$\alpha = -1.0$	$\alpha = -0.5$	$\alpha = 0.001$	$\alpha = 1.00$
$\beta = -1.0$	0.660946	0.822824	1.046125	1.796639
$\beta = -0.5$	0.672888	0.837691	1.065026	1.829100
$\beta = 0.001$	0.687798	0.856253	1.088625	1.869630
$\beta = 0.5$	0.705887	0.878772	1.117255	1.918800
$\beta = 1.0$	0.727571	0.905767	1.151576	1.977743

The effect of load factor λ and non-homogeneity parameter α on contact pressure in case of continuous contact are shown in Figs. 2 and 3, respectively. It can be seen from these figures that the lowest pressure occurs on the symmetry axis and pressure becomes zero for critical load factor. In addition, the effect of the loading decreases moving away from the symmetry axis and goes to a definite value that corresponds to the weight of the layer and changes with mass density, i.e. ρ_0 and α .

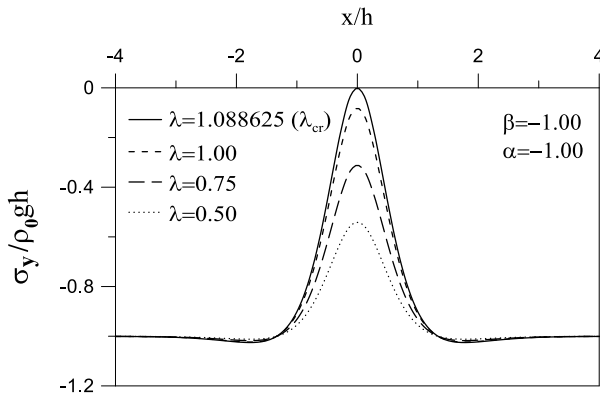


Fig. 2. The effect of λ on contact pressure in case of continuous contact ($a/h = 0.01$, $\kappa = 2.0$)

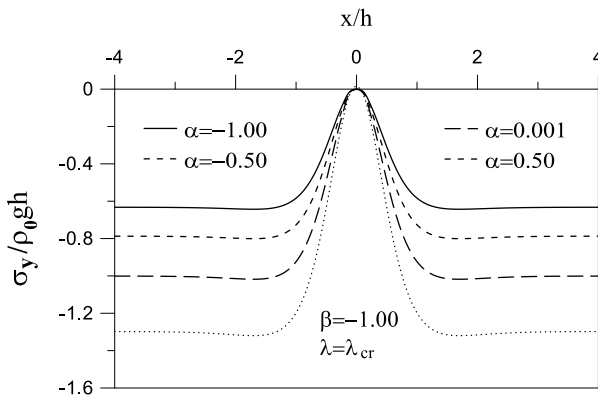


Fig. 3. The effect of α on contact pressure for $\lambda = \lambda_{cr}$ in case of continuous contact ($a/h = 0.01$, $\kappa = 2.0$)

Table 5 shows the variation of half contact distance b/h between the FG layer and the rigid foundation for various non-homogeneity parameters β and α in case of discontinuous contact for a constant load factor, λ . It can be seen from the table, b/h decreases with increasing β for a fixed value of α . Similarly, increasing α results in a reduction of half separation distance.

TABLE 3. THE VARIATION OF b/h FOR THE VARIOUS NON-HOMOGENEITY PARAMETER β AND α IN CASE OF DISCONTINUOUS CONTACT ($a/h = 0.01$, $\lambda = 4$).

	$\alpha = -1.0$	$\alpha = -0.5$	$\alpha = 0.001$	$\alpha = 1.0$
$\beta = -1.0$	4.751669	3.308814	2.436338	1.208481
$\beta = -0.5$	4.238259	3.226682	2.406783	1.195486
$\beta = 0.001$	4.115861	3.186628	2.387936	1.182186
$\beta = 0.5$	4.042882	3.156730	2.371358	1.167690
$\beta = 1.0$	3.985572	3.129293	2.354350	1.151203

The effect of load factor λ and α on contact pressure in case of discontinuous contact are shown in Figs. 4 and 5, respectively. Similar to continuous contact case, the effect of the loading decreases moving away from the symmetry axis and goes to a definite value that shows the weight of the layer and changes with mass density, i.e. ρ_0 and α . It can be seen from these figures that the biggest pressure occurs near the end of the separation. Moreover, they increase for increasing α and λ .

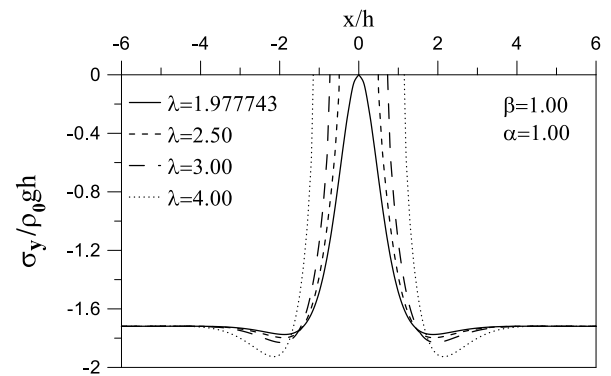


Fig. 4. The effect of λ on contact pressures in case of discontinuous contact ($a/h = 0.01$, $\kappa = 2.0$)

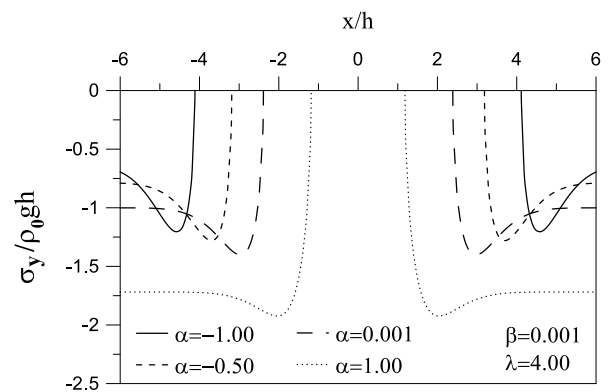


Fig. 5. The effect of α on contact pressure in case of discontinuous contact ($a/h = 0.01$, $\kappa = 2.0$)

V. CONCLUSIONS

In this paper, the continuous and discontinuous contact problem of FG layer resting on a rigid foundation is considered. The top of the FG layer is subjected to normal tractions over a finite segment. The calculations are made under the assumption that the FG layer is isotropic and the shear modulus and mass density exponentially vary along the direction of the layer's thickness.

For continuous contact, the problem is solved analytically using plane elasticity and integral transform techniques. The critical load that causes first separation and contact pressures are investigated for various material properties. It is seen that the critical load increased with increasing non-homogeneity parameter α . In addition, the lowest pressure occurs on the symmetry axis.

For discontinuous contact, the problem is reduced to a singular integral equation using plane elasticity and integral transform techniques. Obtained singular integral equation is solved numerically using Gauss-Jacobi integration formulation. The effect of the non-homogeneity parameters α and loading on the separation distance b/h and on the contact pressure are investigated using a parametric study. It is seen that, the separation distance decreases with increasing non-homogeneity parameter α . In addition, the biggest pressure occurs near the end of the separation and increase for increasing α and λ .

It was also seen that, the effect of the loading decreases moving away from the symmetry axis. The contact pressure goes to a definite value that corresponds to the weight of the layer and changes with mass density, *i.e.* ρ_0 and α .

REFERENCES

- [1] M. B. Civelek, and F. Erdogan, "Frictionless Contact Problem for an Elastic Layer under Gravity," *J Appl Mech-T Asme*, Vol. 42(1), pp. 136-140, 1975.
- [2] A. Birinci, and R. Erdol, "A frictionless contact problem for two elastic layers supported by a Winkler foundation," *Struct Eng Mech*, Vol. 15(3), pp. 331-344, Mar 2003.
- [3] E. Oner, and A. Birinci, "Continuous Contact Problem for Two Elastic Layers Resting on an Elastic Half-Infinite Plane," *J Mech Mater Struct*, Vol. 9(1), pp. 105-119, Jan 2014.
- [4] S. El-Borgi, R. Abdelmoula, and L. Keer, "A receding contact plane problem between a functionally graded layer and a homogeneous substrate," *Int J Solids Struct*, Vol. 43(3-4), pp. 658-674, Feb 2006.
- [5] J. Yang, and L. L. Ke, "Two-dimensional contact problem for a coating-graded layer-substrate structure under a rigid cylindrical punch," *Int J Mech Sci*, Vol. 50(6), pp. 985-994, Jun 2008.
- [6] M. Turan, G. Adiyaman, V. Kahya, and A. Birinci, "Axisymmetric analysis of a functionally graded layer resting on elastic substrate," *Struct Eng Mech*, Vol. 58(3), pp. 423-442, May 10 2016.
- [7] F. Erdogan, and G. D. Gupta, "Numerical Solution of Singular Integral-Equations," *Q Appl Math*, Vol. 29(4), pp. 525-&, 1972.

Optimum design of plane steel frame including corrosion effect using harmony search algorithm

Musa Artar/ Asist. Prof.
Department of Civil Engineering
Bayburt University, Bayburt 69000, Turkey
martar@bayburt.edu.tr

Recep Çatar/ Phd.Student
Department of Mechanical Engineering
Bayburt University, Bayburt 69000, Turkey
repeccatar@yahoo.com

Ayşe T. Daloğlu/ Prof. Dr.
Department of Civil Engineering
Karadeniz Technical University, Trabzon 61000, Turkey
aysed@ktu.edu.tr

Abstract—Optimum design of plane steel frame are studied including corrosion effect on steel cross-sections by using harmony search algorithm. The stress constraints according to AISC-LRFD specifications (American Institute of Steel Construction- Load and Resistance Factor Design), geometric size (column-column and column-beam) constraints, top displacement and inter story drift constraints are applied to the steel frame optimization. Optimum sections are carried out from a profile list including 128 W profiles taken from AISC. A program was developed in MATLAB programming to interact with SAP2000-OAPI (Open Application Programming Interface). Harmony search algorithm method is selected in the design optimization. Optimum designs of a five-story frame carried out for two different cases with/without corrosion effect in industrial site. The results show that corrosion effect plays an important role in the minimum weight of optimum designs.

Keywords—Optimum design, harmony search algorithm, corrosion effect, plane steel frame

I. INTRODUCTION

Minimum weight design of steel frames according to required specifications is very significant subject for structural engineering. In this study, optimum design of plane steel frames are researched for two different cases namely with and without corrosion effect on steel cross sections in industrial site. Stochastic algorithm methods such as genetic algorithm, harmony search algorithm, particle swarm optimization, ant colony algorithm, artificial bee algorithm, bat inspired algorithm, teaching learning optimization methods exist in literature. In this study a basic stochastic technique, Harmony Search Algorithm, is selected for optimum solutions. This

algorithm mimics musical harmony processes. Analyses in the method are conducted by harmony matrix (HM). Values in harmony matrix are updated by harmony memory consideration rate (HMCR) and pitch adjustment ratio (PAR). This algorithm method has been widely studied by many researchers in recent years. A basic study of a new structural optimization based on harmony search algorithm was carried out in 2004 [1]. Optimum design of geometrically non-linear steel frames with semi-rigid connections using a harmony search algorithm was studied in 2009 [2]. Optimum design of steel sway frames to BS5950 using harmony search algorithm was researched in 2009 [3]. Harmony search algorithm was used for minimum cost design of steel frames with semi-rigid connections and column bases in 2010[4]. Optimization of trusses under uncertainties with harmony search was carried out in 2011 [5]. Optimum design of geometrically nonlinear steel frames with semi-rigid connections using improved harmony search method was studied in 2011 [6]. Optimum design of steel space frames under earthquake effect using harmony search was researched in 2016 [7]. Harmony search method was used for optimum design of steel space frames including soil-structure interaction in 2016 [8]. This method was also used in a comparative study on optimum design of multi-element truss structures in 2016 [9].

This study presents optimum designs of a five story plane steel frame in industrial site. Optimum designs of the steel frame are performed for two different cases with and without corrosion effect. A program was developed in MATLAB programming to interact with SAP2000-OAPI to get optimum solutions for both cases. The results obtained from analyses

show that corrosion effect in industrial site increases minimum structural weight and plays very crucial role in optimum designs.

II. THE FORMULATION OF OPTIMUM DESIGN

The discrete optimum design for minimum weight of plane steel frame is determined as below,

$$\min W = \sum_{k=1}^{ng} A_k \sum_{i=1}^{nk} \rho_i L_i \quad (1)$$

where W is the weight of the frame, A_k is cross-sectional area of group k , ρ_i and L_i are density and length of member i , ng is total number of groups, nk is the total number of members in group k .

The objective function $\varphi(x)$ is calculated as below,

$$\varphi(x) = W(x) \left(1 + P \sum_{i=1}^m c_i \right) \quad (2)$$

where P is a penalty constant, $\varphi(x)$ is objective function, c_i is constraint violations. The constraint violations are calculated as follows;

$$g_i(x) > 0 \rightarrow c_i = g_i(x) \quad (3)$$

$$g_i(x) \leq 0 \rightarrow c_i = 0 \quad (4)$$

The stress constraints for the frame are incorporated as specified in AISC-LRFD [12], geometric size (column-column and column-beam) maximum lateral displacement and inter-storey drift constraints are calculated as below,

$$\begin{aligned} \text{for } \frac{P_u}{\phi P_n} \geq 0.2 \\ g_{il}(x) = \left(\frac{P_u}{\phi P_n} \right)_{il} + \frac{8}{9} \left(\frac{M_{ux}}{\phi_b M_{nx}} \right)_{il} - 1.0 \leq 0 \quad \begin{matrix} i = 1, \dots, nm \\ l = 1, \dots, nl \end{matrix} \end{aligned} \quad (5)$$

$$\begin{aligned} \text{for } \frac{P_u}{\phi P_n} < 0.2 \\ g_{il}(x) = \left(\frac{P_u}{2\phi P_n} \right)_{il} + \left(\frac{M_{ux}}{\phi_b M_{nx}} \right)_{il} - 1.0 \leq 0 \quad \begin{matrix} i = 1, \dots, nm \\ l = 1, \dots, nl \end{matrix} \end{aligned} \quad (6)$$

where nm is the total number of members, nl is the total number of loading conditions, P_u is the required axial strength, P_n is the nominal strength, M_{ux} is the required flexural strength about major axis, M_{uy} is the required flexural strength about minor axis, M_{nx} is the nominal flexural strength about major axis, M_{ny} is the nominal flexural strength about minor axis, ϕ

is resistance factor for compression (0.85) and for tension (0.90), ϕ_b is resistance factor for flexure (0.90).

Column-to-column geometric constraints are determined as below,

$$g_n(x) = \frac{D_{un}}{D_{ln}} - 1 \leq 0 \quad n = 2, \dots, ns \quad (7)$$

where D_{un} is the depth of upper floor column, D_{ln} is the depth of lower floor column.

The beam-to-column geometric constraints are defined as below,

$$g_{bb,i}(x) = \frac{b_{fbk,i}}{b_{fck,i}} - 1 \leq 0 \quad i = 1, \dots, n_{bf} \quad (8)$$

where n_{bf} is number of joints where beams are connected to the flange of column, $b_{fbk,i}$ and $b_{fck,i}$ are flange widths of the beam and column, respectively.

Displacement constraints are calculated as below,

$$g_{jl}(x) = \frac{\delta_{jl}}{\delta_{ju}} - 1 \leq 0 \quad \begin{matrix} j = 1, \dots, m \\ l = 1, \dots, nl \end{matrix} \quad (9)$$

where δ_{jl} is the displacement of j^{th} degree of freedom under load case l , δ_{ju} is the upper bound, m is the number of restricted displacements, nl is the total number of loading cases.

Inter-storey drift constraints are calculated as below,

$$g_{jil}(x) = \frac{\Delta_{jil}}{\Delta_{ju}} - 1 \leq 0 \quad \begin{matrix} j = 1, \dots, ns \\ i = 1, \dots, nsc \\ l = 1, \dots, nl \end{matrix} \quad (10)$$

where Δ_{jil} is the inter-storey drift of i^{th} column in the j^{th} storey under load case l , Δ_{ju} is the limit value, ns is the number of storey, nsc is the number of columns in a storey.

Corrosion tests are available in the literature for a period of two years on structural steel in industrial site [13]. The results of this literature study [13] are used in optimum design of plane steel frame including corrosion effect. Corrosion effects on steel cross section surface are presented in Fig. 1.

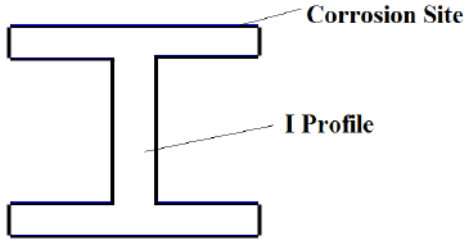


Fig. 1. Corrosion effect on a steel profile surface

The well-known bilogarithmic equation for the effect of atmospheric corrosion in an industrial site is as follows,

$$C = At^B \quad (11)$$

where C is the weight loss in terms of thickness (μm), t is the exposure time (months) and A, B are constants [13].

III. HARMONY SEARCH ALGORITHM METHOD

Harmony Search Algorithm, a basic stochastic algorithm method, is developed by some procedures which mimics musical harmony processes. Analyses in optimization are conducted harmony memory matrix (HM) and each row in this matrix represents a structural model. Harmony memory matrix is defined as

$$H = \begin{bmatrix} x_1^1 & x_2^1 & \dots & x_{n-1}^1 & x_n^1 \\ x_1^2 & x_2^2 & \dots & x_{n-1}^2 & x_n^2 \\ \dots & \dots & \dots & \dots & \dots \\ x_1^{HMS-1} & x_2^{HMS-1} & \dots & x_{n-1}^{HMS-1} & x_n^{HMS-1} \\ x_1^{HMS} & x_2^{HMS} & \dots & x_{n-1}^{HMS} & x_n^{HMS} \end{bmatrix} \quad (12)$$

Harmony Memory Size (HMS) in here expresses a specified number of solutions. Harmony memory consideration rate (HMCR) and pitch adjustment ratio (PAR) are two important operators to get a stronger harmony memory matrix for better solutions. They are defined as below,

$$\begin{cases} x_i^{nh} \in \{x_i^1, x_i^2, \dots, x_i^{HMS}\} \text{ with probability of } HMCR \\ x_i^{nh} \in X_{st} \text{ with probability of } (1 - HMCR) \end{cases} \quad (13)$$

$$\begin{cases} \text{Yes, with probability of } PAR \\ \text{No, with probability of } 1 - PAR \end{cases} \quad (14)$$

Detailed information about the process and the steps of harmony search algorithm can be found from the studies of [1-4]. In this study, a computer program is developed in

MATLAB [10] to interact with SAP2000 OAPI [11]. A flowchart of Harmony Search Algorithms is shown in Fig.1.

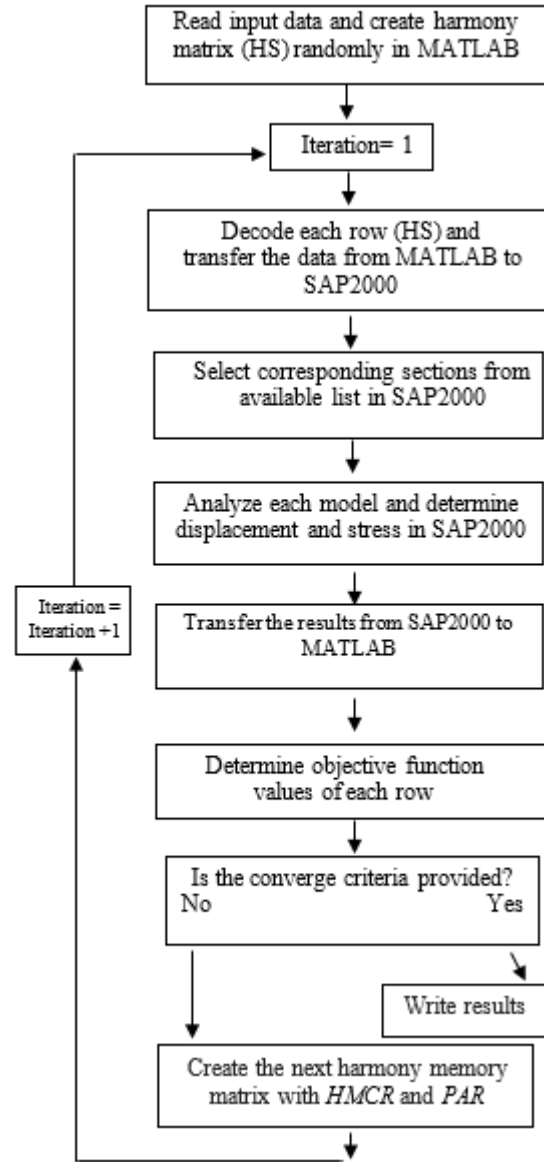


Fig. 2. Flowchart for the optimum design procedure of plane steel frame

IV. DESIGN EXAMPLE: 25-MEMBER PLANE STEEL FRAME

Figure 3 presents a five story steel plane frame structure consisting of 25 elements. All members are collected in 9 groups as given in Table 1. The figure also shows loading information. The top displacement as being the maximum lateral displacement and inter story drifts are restricted 4.375 cm and 0.875 cm (height/400), respectively. Optimum cross sections are selected from a specified list including 128 W

taken from AISC. The material properties are $E=200$ GPa, $f_y=250$ MPa and $\rho=7.85$ ton/m³. Optimum solutions for both cases are also given Table 1. Moreover, their design histories are shown Fig.3.

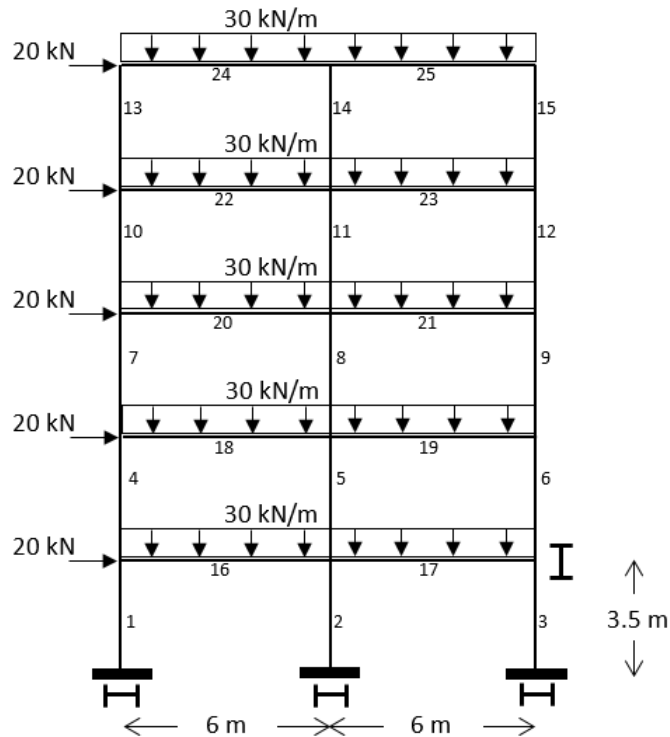


TABLE 1. Optimum Solutions

Group No	Member No	Case 1 without corrosion effect	Case 2 with corrosion effect
1	1,3	W24X55	W24X68
2	2	W16X50	W21X57
3	4,6,7,9	W16X40	W24X55
4	5,8	W16X45	W14X38
5	10,12,13,15	W12X26	W14X26
6	11,14	W16X31	W14X30
7	16,17	W16X36	W12X26
8	18,19,20,21	W14X34	W14X34
9	22,23,24,25	W16X26	W14X26
Weight (kN)		56.91	59.14
Top displacement (cm)		3.27	3.41
Max. inter story drift (cm)		0.86	0.86

Fig. 3. 25-member plane steel frame

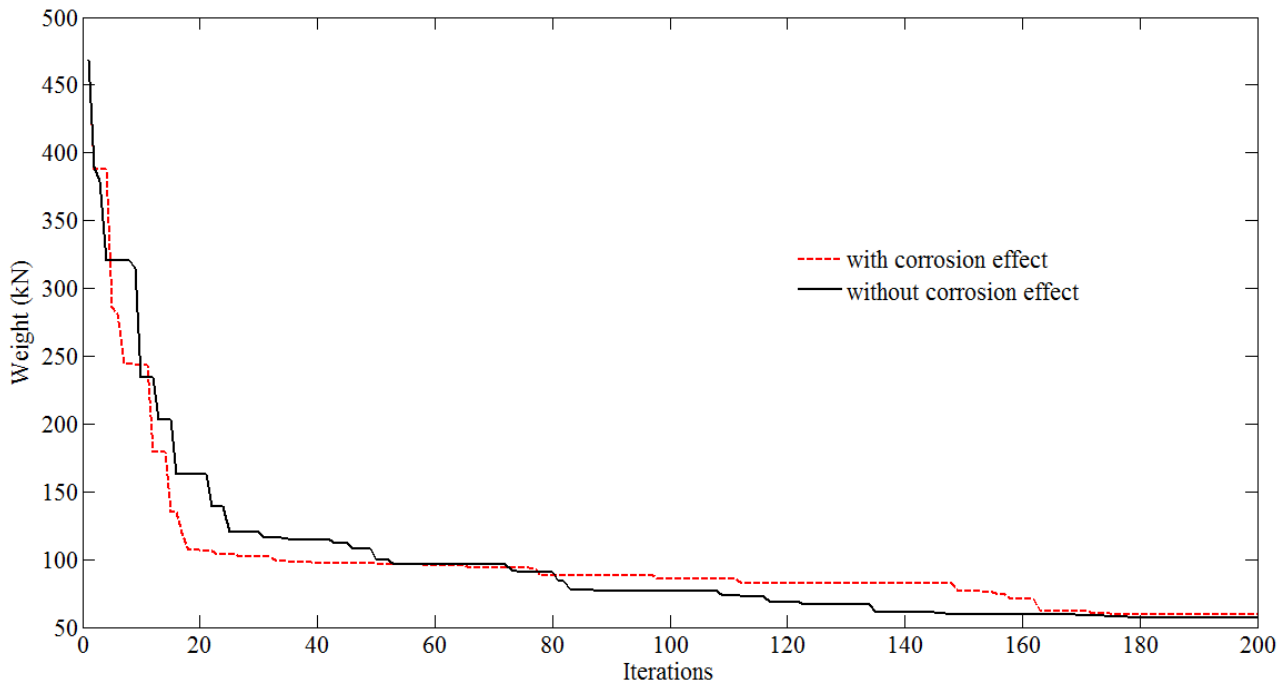


Fig. 3. The design histories of both solutions

Table 1 shows that the minimum weight of 25-member plane steel frame for the case of without corrosion effect is 56.91 kN. On the other hand, this minimum value for the case with corrosion effect is 59.14 kN. Therefore, it indicates that corrosion effect in industrial site increases the minimum structural weight by about 3.92%. Table 1 also shows that the maximum inter story drift values for both cases are very close to limit value of 0.875 cm. This results expresses that inter story drift constraints play very active role in the optimizations process.

V. CONCLUSIONS

This study presents optimum designs of plane steel frame consisting of 25 members in industrial site for two different cases with and without corrosion effect. The stress constraints according to AISC-LRFD, geometric size (column-column and column-beam), maximum lateral displacement and inter-story drift constraints are considered on the optimum design of plane steel frame. A program is coded in MATLAB programming incorporated with SAP2000-OAPI to carry out optimum solutions. Although, the minimum weight for the case without corrosion effect is 56.91 kN, the weight for the case with corrosion effect becomes 59.14 kN. In other words, the minimum steel weight increases by about 3.92% if necessary precaution against corrosion is not taken on the surface of steel profile. The analysis results also show that inter story drift constraints are very important determinants in the optimum designs.

References

- [1] K.S. Lee and Z.W. Geem, "A new structural optimization method based on the harmony search algorithm", *Comput. Struct.*, vol.82, pp. 781-798, 2004.
- [2] S.O. Degertekin, M.S. Hayalioglu and H. Gorgun, "Optimum design of geometrically non-linear steel frames with semi-rigid connections using a harmony search algorithm", *Steel Compos. Struct., Int. J.*, vol. 9, pp. 535-555, 2009.
- [3] M.P. Saka, "Optimum design of steel sway frames to BS5950 using harmony search algorithm" *J. Constr. Steel Res.*, vol. 65, pp. 36-43. 2009.
- [4] S.O. Degertekin and M.S. Hayalioglu, "Harmony search algorithm for minimum cost design of steel frames with semi-rigid connections and column bases", *Struct. Multidisc. Optim.*, vol. 42, pp. 755-768, 2010.
- [5] V. Togan, A.T. Daloglu and H. Karadeniz, "Optimization of trusses under uncertainties with harmony search", *Struct. Eng. Mech.*, vol. 37, pp. 543-560, 2011.
- [6] S.O. Degertekin, M.S. Hayalioglu and H. Gorgun, "Optimum design of geometrically nonlinear steel frames with semi-rigid connections using improved harmony search method", *Journal of Engineering, Dicle University, Department of Engineering*, vol. 2, pp. 45-56, 2011.
- [7] M. Artar, "Optimum design of steel space frames under earthquake effect using harmony search", *Struct. Eng. Mech.*, vol. 58, pp. 597-612, 2016.
- [8] A.T. Daloglu, M. Artar, K. Özgan and A.İ. Karakas, "Optimum design of steel space frames including soil-structure interaction", *Struct. Multidisc. Optim.*, vol. 54, pp. 117-131, 2016.
- [9] M. Artar, "A comparative study on optimum design of multi-element truss structures", *Steel Compos. Struct.*, vol. 22, pp. 521-535, 2016.
- [10] MATLAB, *The Language of Technical Computing*, The Mathworks Inc., Natick, MA, USA, 2009.
- [11] SAP2000, *Integrated Finite Elements Analysis and Design of Structures*, Computers and Structures, Inc, Berkeley, CA, 2008.
- [12] AISC-LRFD, *Manual of steel construction: Load and resistance factor design*; American Institute of Steel Construction, Chicago, IL, USA, 2001.
- [13] Y. Ma, Y. Li and F. Wang, "Corrosion of low carbon steel in atmospheric environments of different chloride content", *Corrosion Science*, vol. 51, pp. 997-1006, 2009.

Evolutionary Optimization of Continuous Structures Under Impact Load

Sedat SAVAS

Firat Univ. Eng. Faculty
Civil Eng. Dept.
Elazig/TURKEY
ssavas@firat.edu.tr

Abstract— In this study, the evolutionary topological design of two and three dimensional structural systems under impact load. Impact effect was performed with a macro program prepared in the ANSYS LS-DYNA package program. Materials used in construction systems were considered homogeneous and von-mises stresses were taken into account. These stresses have been used as constrains. The purpose of the program is to gradually remove elements from a structural element under a certain impact load and to optimize the construction by controlling the extreme maximum stress increments that the element will bring to the structure and making a homogeneous stress distribution.

Keywords— *impact load; optimisation; evolutionary; ls-dyna; shape optimisation*

I. INTRODUCTION

Mankind observed the nature around him and was influenced by him and guided him. Instinctively, energy has been found in behaviors that make economic use and maximize comfort. Finding and using rollers and levers is a testament to the desire to maximize people's mechanical efficiency. Thus, simply developing and using a system is not enough. As time goes by, creating the best and most suitable systems has become the main purpose. In the optimization process, it is tried to get the best results (the lightest, the cheapest, the most efficient, the fastest, etc.) according to the current constraints of a job done.[1,2,3]

II. EVALUATION OF EVOLUTIONAL STRUCTURE OPTIMIZATION (ESO) METHOD

A. ESO method

In recent years, many structural optimization methods have been developed. Analytical and numerical methods are generally used as optimization methods. But the analytical methods are left to numerical methods due to the fact that the structures are becoming ever more complex systems and because of the financial reflection of the increase in accounting time [4,5]. The numerical method can also be called the programming method and this method is a branch of the numerical mathematics field. Generally it is made up of iterative operations.[6]

The topological design of continuous structures is an important part of structural optimization. It is possible to obtain a more economical design with topological optimization and new optimization methods are used for this. These come at the beginning of evolutionary optimization methods[7].

In recent years, many algorithms have been developed for evolutionary optimization. The basic principle of these algorithms is adaptation to external conditions. Evolutionary structural optimization (ESO) has been developed as an example of these methods [8]. With this method, there is an answer to the questions such as how the objects will be shaped or the best possible structural performance of an object. The ESO method has also been shown to be able to solve size, shape and topology optimization problems.

To avoid inefficiency in structural optimization, a full-strength design concept has been developed. At full strain design phase, each component is exposed to a maximum or minimum permissible limit value. When the stresses of all the structural components are about the same, the final structure becomes fully stretched and a fully stressed design is achieved [theoretical approaches]. Equally stressed state in the literature is also called full stress. Often optimization algorithms consist of loops aimed at redesigning to achieve a full-stretch state.

B. Basic Concepts of ESO Method

1. Operating sequence

The ESO method presented in this study uses a finite element analysis package program (ANSYS LS-DYNA) as the calculation technique. At the end of each analysis, the computer determines the FEA results and then applies simple ESO rules to remove the ineffective material.

The ESO method is an application of topology optimization and it is based on a process that involves briefly describing the inefficient material in a more economical way by gradually removing it from the structure [ESO]. The ESO method is conceptually simple and easy to implement when compared with other optimization methods [9,10]. This is why there are no complicated mathematical operations and

equations. It consists of systematically removing ineffective elements and making the system fully stressed.

2. Basic Concepts of ESO Method

In general engineering design analysis, the minimum weight or volume is used as the objective function. Differences can be seen in the constraints. For the purpose of use of the structure, as a limit depending on the environmental conditions and the economic conditions; Stiffness, thickness, frequency etc. can be used. Design variables also vary according to the algorithm or material to be used, but mostly variables such as number of elements, element thickness, and element volume are used [11,12].

In the conventional ESO method, von Mises stresses are used as extraction criterion (i.e., constraints). However, it has been found appropriate to use principal stresses as substitution criterion for von Mises stresses when the system is available in both tension and pressure elements [13]. For this reason, principal stresses have been used as limitations in obtaining optimum structures in our works.

Primarily, each element has principal stresses σ_{11} and σ_{22} . The extraction criterion is applied according to the zones where the pressure or tensile stresses dominate the structure. In areas where pressure stress is dominant, the elements subjected to tensile stress ($\sigma_{22} \leq 0.0$ and $|\sigma_{22}| \gg |\sigma_{11}|$) are removed. In contrast, in areas where tensile stress is effective, pressure stressed elements are removed ($\sigma_{11} \geq 0.0$ and $|\sigma_{11}| \gg |\sigma_{22}|$). We use this element extraction algorithm to create the kernel of the ESO method.

The above operation continues in each cycle until the effect of the multiplication event begins and ends. The time period for this event is divided into certain intervals. In our work, this interval is 50 pieces. These tensile values are compared in each range, and the largest tensile stresses and minimum stresses are determined in the structure. In each range, these stress values are compared and the largest tensile stresses and minimum stresses are determined in the structure.

The algorithm described above can be expressed mathematically. Such an expression is shown in equations (3.5) and (3.6), where pulling or compressive stress is dominant.

$$|\sigma_{11}^e| \leq FF_i \times |\sigma_{11, \max}|, \sigma_{22}^e \leq 0.0 \quad (3.5)$$

Equation (1) is used as the criterion that pressure stress is dominant and tensile stressed elements are to be removed.

$$|\sigma_{22}^e| \leq FF_i \times |\sigma_{22, \max}|, \sigma_{11}^e \geq 0.0 \quad (3.6)$$

In these equations, $|\sigma_{11, \max}|$ and $|\sigma_{22, \max}|$ the absolute maximum stresses of the elements, and FF_i represents the subtraction rate which will result in fewer elements subtracted at each iteration. The steady state, that is to say the end of the iterations, the cycle of the element analysis and the removal of the element are continued until it comes to the condition that no element is removed. But in the present iteration, the evolutionary ratio (EF) becomes active when there are no more elements to be removed, and the EF constant number is added to the subtraction rate FF_i .

$$FF_{i+1} = FF_i + EF, \quad i = 0, 1, 2, 3, \dots \quad (3.7)$$

The new finite element analysis cycles are created with this increased removal rate and the removal process continues until the new steady state is reached.

III. OPTIMIZATION APPLICATIONS WITH ESO METHOD

A. Example of steel sphere drop on Michell beam

As the ESO application, the michell beam example shown in Figure 3.1 which is frequently used in structural optimization problems is used. The structure width L is an anchored joint with height H , fixed on the left. It has been found that the optimum height $H = 2L$ is obtained by calculations made from analytical paths.

In order to obtain such a structure using the evolutionary structure optimization method, the model shown in figure 3.2 is used. Taking into consideration that the model has a predictable final design size, our initial model has been chosen to be a rectangular shape larger than $2L \times L$ dimensions.

The design area in Figure 3.2 is divided into four-node dotted plane stress elements of 50×150 equally dimensioned Beam thickness is chosen as 1mm. Young's modulus $E = 100$ GPa and Poisson's ratio $\nu = 0.3$.

A steel sphere is dropped at a rate of 5 m / sec to the junction of the elements in the beam center. The shapes obtained after the impact are given below.

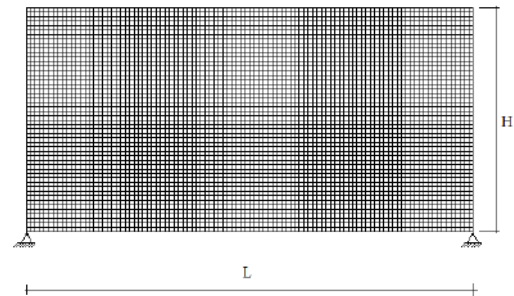


Fig 3.1 Michell beam

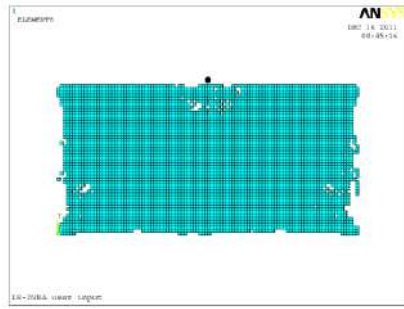


Fig 3.2. Beam geometry at 50. iteration

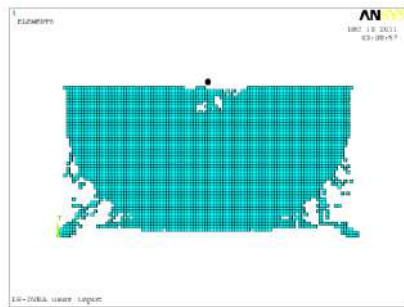


Fig 3.3 Beam geometry at 150. iteration

B. Example of a 20x20 cube falling under the influence of gravity

In this example, a cube made of concrete was dropped onto a 1.5 m dense steel plate. The gravitational acceleration is 9.81 m/s^2 . Cube element density is 2.5 t/m^3 . As a result of this fall effect, the new geometries connected to the iteration that is happening in the system are given below.

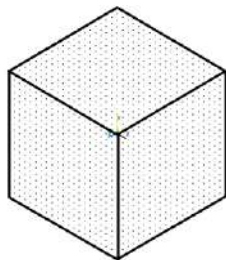


Fig. 3.4. 20x20 cm cube element

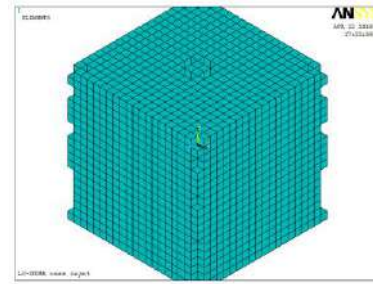


Fig 3.5.a. Cube element geometry at 50. iteration

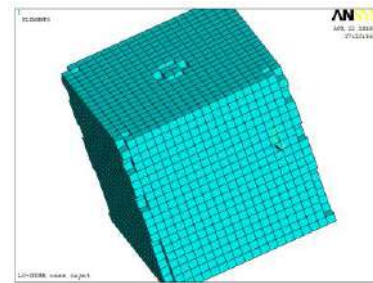


Fig 3.5.b. Cube element geometry at 50. iteration

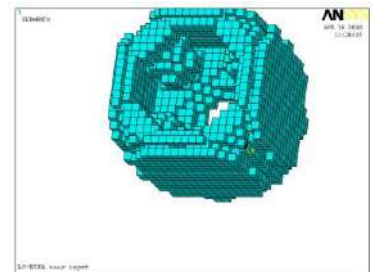


Fig 3.6.a. Cube element geometry at 200. iteration

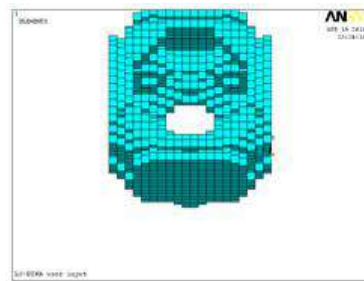


Fig 3.6.b. Cube element geometry 200. iteration

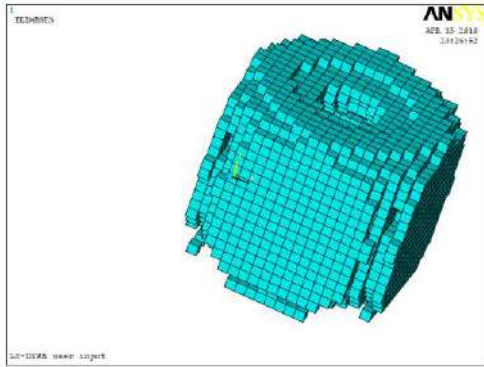


Fig 3.6.c. Cube element geometry at 200. iteration

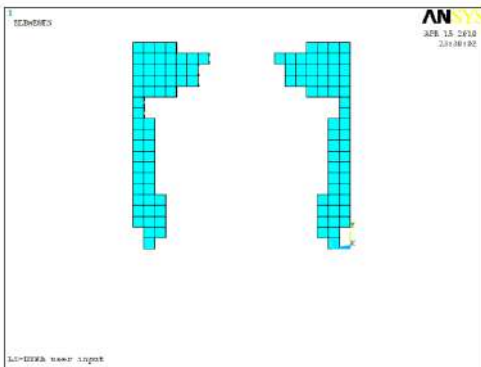


Fig 3.6.d. Cube element cross section at 200. iteration

SUMMARY AND CONCLUSION

Evolutionary method optimization of a structure under impact load is performed for the first time in literature reviews. Due to the length of the solution and the theory of evolution, it is disadvantageous to use too many end elements. However, due to the necessity of solution accuracy, the number of elements is not reduced and indirectly the reduction of the solution time is not possible. The system is forced to fully stretch by the Eso method. The figures after the calculation are given in detail in this study. As can be seen from the second sample we gave, when the cube element was forced to fully stressed, there was a more than half reduction in volume. The result of the calculation is the result of the shape, The same impact effect occurs with a smaller volume.

REFERENCES

- [1] M. Osaki, C.C. Swan, "Topology and Geometry Optimization of Trusses", Recent Advances in Optimal Structural Design, Ed. S.A. Burns, 5, 97-124, ASCE, 2002.
- [2] W.M. Jenkins, "Towards Structural Optimization Via Genetic Algorithm", Computers and Structures, 40, 1321-1327, 1991.
- [3] B.H.V. Topping, A. I. Khan, J.P. Leite, "Topological Design of Truss Structures Using Simulated Annealing", Structural Engineering Review, 8, 301-314, 1996.
- [4] Y.M. Xie, G.P. Steven, "Evolutionary Structural Optimization", Springer-Verlag, Berlin, 1997.
- [5] C. Mattheck, "Design in Nature: Learning from Trees", Springer-Verlag, Berlin, 1997.
- [6] F. Walther, C. Mattheck, "Local Stiffening and Sustaining of Shell Structures by SKO and CAO" Proceedings of International Conference on Structural Optimisation, Zaragoza, Spain, edited by C. A. Brebbia and S. Hernandez, 181-188, Computational Mechanics, Southampton, U.K., 1993.
- [7] M. E. Hinton, J Sieng, "Fully Stresses Topological Design of Structures Using an Evolutionary Approach", Engineering computations, 12, 229-244, 1995.
- [8] E. Hinton, J Sieng, B. Hassani, "Fully Integrated Design Optimization for Engineering Structures with Benchmarking", Advances in Structural Engineering Optimization, Ed. B H V Topping, Civil-comp press, Edinburgh, 1-21, 1996.
- [9] Y. M. Xie, G. P. Steven "Optimal Design of Multiple Load Case Structures Using an Evolutionary Procedure", Internal report, FEARC-9205, Finite Element Analysis Research Center, University of Sydney, Sydney, Australia, 1992.
- [10] Y. M. Xie, G. P. Steven, "A Simple Evolutionary Procedure for Structural Optimization", Computers and Structures, 49, 885-896, 1993.
- [11] Y. M. Xie, G. P. Steven, "Optimal Design of Multiple Load Case Structures Using an Evolutionary Procedure", Engineering Computations, 11, 295-302, 1994.
- [12] V. Young, O. M. Querin, G. P. Steven, Y. M. Xie, "3D and Multiple Load Case Bidirectional Evolutionary Structural Optimization", Structural Optimization, 18, 183-192, 1999.
- [13] S. Savas, M. Ulker, M. P. Saka, "Evolutionary Topological Design of Two Dimensional Solid Structures", Civil and Structural Engineering Computing, Ed. B H V Topping, Civil-comp press, Stirling Scotland, 132, 2003.

Transient Analysis of In-Plane Loaded Elastic Stepped Circular Arches

Ahmad Reshad NOORI

*Department of Civil Engineering
Cukurova University
Adana, Turkey
a.reshadnoori@yahoo.com*

Timuçin Alp ASLAN

*Department of Civil Engineering
Cukurova University
Adana, Turkey
taslan@cu.edu.tr*

Beytullah TEMEL

*Department of Civil Engineering
Cukurova University
Adana, Turkey
btemel@cu.edu.tr*

Abstract - This study aims to investigate the transient response of homogeneous, isotropic and elastic stepped circular arches under various in-plane dynamic loads in the Laplace domain. The effect of shear deformation is taken into consideration. The governing equations are first obtained in the time domain. Laplace transform is then applied and the obtained canonical form of the first order ordinary differential equations has been solved by the Complementary Functions Method (CFM) in the transformed domain. The fifth-order Runge–Kutta (RK5) method has been applied for the numerical solution of the obtained differential equations. The solutions obtained are transformed to the time domain by an appropriate inverse numerical Laplace transform method. A computer program is coded in Fortran for the forced vibration of the considered structures. Verification and exactness of the written program is performed by comparing the results of the present methods and results of ANSYS which is a commercial finite element program. It is emerged that present method is highly accurate and efficient compared to conventional step by step integration methods.

Keywords— *Two-Point Boundary Value Problems; Complementary Functions Method (CFM); Inverse Laplace Transforms; Stepped Circular Arches.*

I. INTRODUCTION

Extensive practical applications of arches in many engineering fields have attracted considerable attention of researchers in determining the static and dynamic behavior of those crucial engineering structures. Several investigators

studied the forced vibrations of in-plane loaded circular arches with uniform cross-sections but there are few studies addressed to dynamic response of arches with stepped cross-section.

The static behavior of isotropic elastic in-plane rods is investigated by Haktanır [1] with stiffness matrix method based on the CFM and fourth-order Runge–Kutta numerical method. Bayhan [2] studied the static behavior of planar frames with members of circular axes with the aid of both transfer and stiffness matrix methods. The CFM is used for the bending analysis of circular planar systems, helicoidal stair cases axisymmetric shell structures, and cylindrical vault structures under static loadings by Bozkurt [3]. Yildirim, İnce and Kiral [4] investigated the static response of compound planar frames with members of linear and circular axes by stiffness matrix method. The stiffness matrixes and force vectors of the frame members with circular axes, under planar loads and perpendicular loads to plane, were calculated by transfer matrix method. The dynamic behavior of isotropic, anisotropic, elastic and viscoelastic cylindrical helical rods under time dependent loads is investigated by Çalım [5] in the Laplace domain. The obtained solutions transformed to the time domain by using a proper inverse Laplace transform method. Kırac [6] examined the dynamic behavior of composite straight rods subjected to time dependent loads in the Laplace domain theoretically. The free vibration was considered as a special case of forced vibration. In the formulations, the effect of the rotary inertia, axial and shear deformations were taken into account. The

ordinary differential equations obtained in canonical form in the Laplace domain were solved numerically by the CFM to calculate the dynamic stiffness matrix. Aktan [7] studied the free vibration of in-plane circular beams. The Timoshenko beam theory was used and the effect of the rotary inertia was considered. Çoban [8] investigated the dynamic analysis of curved beams using mixed finite element method with Gâteaux derivative. Akkurt [9] investigated the dynamic behavior of straight and circular rods resting on elastic foundation in the Laplace domain. Karaca [10] studied the static and dynamic analysis of circular Timoshenko rods which are loaded in-plane and out-of-plane. The longitudinal vibrations of elastic bars were investigated using the Gâteaux differential method and the mixed finite element method by Ecer [11]. Manolis and Beskos [12] and Beskos and Narayanan [13] analyzed the dynamic responses of a straight beam. Huang, Teng and Leissa, [14] investigated the dynamic response of circular arches with dynamic stiffness method and the Laplace transform. Huang, Tseng and Lin [15] combines the dynamic stiffness method with the Laplace transformation to obtain the transient responses of an arch with variable curvature while the dynamic stiffness matrix and equivalent nodal force vector for an arch with variable curvature is formulated based on a series solution. Temel, Aslan and Noori [16] investigated the forced vibration of isotropic-elastic planar curved rods in Laplace domain with the CFM. The dynamic and static analysis of in-plane and out of plane loaded curved structural elements is examined by Aslan [17] in Laplace Domain, while RK5 algorithm is used for the solution of differential equations based on the CFM.

Tüfekci and Özdemirci [18] investigated the free in-plane vibration of stepped circular arches. The effects of axial extension, transverse shear deformation and rotatory inertia are included in the governing equations. The solution was obtained exactly by using the initial value method.

When the cross-section of the arch is considered to be stepped, the literature regarding to the forced vibration of circular arches is rare. However, to the best of authors' knowledge the transient analysis of elastic stepped circular arches using the unified approach of Laplace transform and the CFM has not been reported yet. In present research, the forced vibration of in-plane stepped circular arches has been analyzed under various types of dynamic loads by Laplace transform method and the CFM for the first time. The CFM is a numerical solution method which transforms a two point boundary value problem to a system of initial value problems. For the solution of initial value problems RK5 is applied in this research. The application of Laplace Transform, with respect to time, to partial differential equations, converts them to ordinary differential equations in the transformed domain. Thus the numerical solution of partial differential equations in the Laplace domain can be done easily. To transform the obtained solutions in the Laplace domain to the time domain an efficient inverse Laplace transform method has been used. The results of the present method are compared with those solutions obtained by ANSYS, the finite element program which analyses the dynamic response of structures by conventional step by step

integration method. The comparison of the results demonstrate the accuracy and exactness of the present study.

II. GOVERNING EQUATIONS

The time and location depended partial differential equations of in-plane loaded stepped circular arches under dynamic loads are given as follows:

$$\frac{\partial U_t}{\partial \phi} = U_n + r \frac{T_t}{EA(\phi)} \quad (1)$$

$$\frac{\partial U_n}{\partial \phi} = -U_t + r\Omega_b + r \frac{T_n \alpha_n}{GA(\phi)} \quad (2)$$

$$\frac{\partial \Omega_b}{\partial \phi} = r \frac{M_b}{EI_b(\phi)} \quad (3)$$

$$\frac{\partial T_t}{\partial \phi} = r\rho A(\phi) \frac{\partial^2 U_t}{\partial t^2} + T_n - rp_t \quad (4)$$

$$\frac{\partial T_n}{\partial \phi} = r\rho A(\phi) \frac{\partial^2 U_n}{\partial t^2} - T_t - rp_n \quad (5)$$

$$\frac{\partial M_b}{\partial \phi} = r\rho I_b(\phi) \frac{\partial^2 \Omega_b}{\partial t^2} - rT_n - rm_b \quad (6)$$

$$A(\phi) = \pi h(\phi)^2 \quad (7)$$

$$I_b(\phi) = \frac{\pi h(\phi)^4}{4} \quad (8)$$

Here, E , ρ , $h(\phi)$, $A(\phi)$, $I_b(\phi)$, α_n and r indicate the modulus of elasticity, mass density, radius of the cross-section, cross-section area, the moment of inertia, shear correction factor and radius of curvature respectively.

The unknown column matrix, $\{Y(\phi, t)\}$, for the forced vibration of in-plane loaded stepped circular arches is given as:

$$\{Y(\phi, t)\} = \{U_t, U_n, \Omega_b, T_t, T_n, M_b\}^T \quad (9)$$

The Laplace transform of a time-dependent function $f(t)$ is the function " $\bar{F}(s)$ ".

$$L[f(t)] = \bar{F}(s) = \int_0^{\infty} f(t) e^{-st} dt \quad (10)$$

where s is the Laplace variable also known as operator variable in the Laplace domain. The Laplace transform of first and second derivatives with respect to time are as follows:

$$L\left[\dot{f}(t)\right] = s\bar{F}(s) - f(0) \quad (11)$$

$$L\left[\ddot{f}(t)\right] = s^2\bar{F}(s) - sf(0) - \dot{f}(0) \quad (12)$$

Applying the Laplace transform to equations (1-6), converts these partial differential equations to variable-coefficient ordinary differential equations. Thereby, the governing ordinary differential equations of the dynamic behavior of in-plane loaded stepped circular arches can be obtained in the Laplace domain as follows:

$$\frac{d\bar{U}_t}{d\phi} = \bar{U}_n + r \frac{\bar{T}_t}{EA(\phi)} \quad (13)$$

$$\frac{d\bar{U}_n}{d\phi} = -\bar{U}_t + r\bar{\Omega}_b + r \frac{\bar{T}_n\alpha_n}{GA(\phi)} \quad (14)$$

$$\frac{d\bar{\Omega}_b}{d\phi} = r \frac{\bar{M}_b}{EI_b(\phi)} \quad (15)$$

$$\frac{d\bar{T}_t}{d\phi} = rs^2\rho A(\phi)\bar{U}_t + \bar{T}_n - r\bar{p}_t \quad (16)$$

$$\frac{d\bar{T}_n}{d\phi} = rs^2\rho A(\phi)\bar{U}_n - \bar{T}_t - r\bar{p}_n \quad (17)$$

$$\frac{d\bar{M}_b}{d\phi} = rs^2\rho I_b(\phi)\bar{\Omega}_b - r\bar{T}_n - r\bar{m}_b \quad (18)$$

Where the terms shown by (\bullet) indicates the Laplace transform of the quantities.

$$\begin{aligned} L\left[\rho A(\phi) \frac{\partial^2 U_t}{\partial t^2}\right] &= \rho A(\phi) \left[s^2 \bar{U}_t - s U_t(\phi, 0) - \frac{\partial U_t(\phi, 0)}{\partial t} \right] \\ L\left[\rho A(\phi) \frac{\partial^2 U_n}{\partial t^2}\right] &= \rho A(\phi) \left[s^2 \bar{U}_n - s U_n(\phi, 0) - \frac{\partial U_n(\phi, 0)}{\partial t} \right] \\ L\left[\rho I_b(\phi) \frac{\partial^2 \Omega_b}{\partial t^2}\right] &= \rho I_b(\phi) \left[s^2 \bar{\Omega}_b - s \Omega_b(\phi, 0) - \frac{\partial \Omega_b(\phi, 0)}{\partial t} \right] \end{aligned} \quad (19)$$

The second and third terms on the right-hand side of the equation (19) are the initial conditions given for $t=0$; in present study those terms are assumed to be zero.

III. COMPLEMENTARY FUNCTIONS METHOD

The matrix notation of the ordinary differential equations (13-18) obtained in the Laplace domain is given below:

$$\{\bar{Y}(\phi, s)\} = \{\bar{U}_t(\phi, s), \bar{U}_n(\phi, s), \bar{\Omega}_b(\phi, s), \bar{T}_t(\phi, s), \bar{T}_n(\phi, s), \bar{M}_b(\phi, s)\}^T \quad (21)$$

$$\frac{d\{\bar{Y}(\phi, s)\}}{d\phi} = [\bar{A}(\phi, s)]\{\bar{Y}(\phi, s)\} + \{\bar{F}(\phi, s)\} \quad (20)$$

Here ϕ is independent variable and s is the Laplace transform parameter. The state vector for in-plane stepped circular arches is given by equation (21).

The CFM is based on the principle of the solution of equation (20) with the help of the initial conditions. This method is basically the reduction of two-point boundary value problems to initial-value problems. The general solution of Eq. (20), is given by

$$\{Y(\phi, s)\} = \sum_{m=1}^n C_m [\bar{U}^{(m)}(\phi, s)] + \{\bar{V}(\phi, s)\} \quad (22)$$

Where $[\bar{U}^{(m)}(\phi, s)]$ is the complementary solution such that its m^{th} component is equal to 1, whereas all the others are zero. $\{\bar{V}(\phi, s)\}$ is the inhomogeneous solution with all zero initial conditions, the integration constants C_m will be determined from the boundary conditions at both ends.

The results, obtained in the Laplace domain, are transformed to the time domain with the help of modified Durbin's numerical inverse Laplace transform method given by Durbin [19] and Temel, Çalim and Tütüncü, [20].

IV. NUMERICAL EXAMPLES AND DISCUSSIONS

A fixed-ended isotropic stepped circular arch, shown in figure 1.a, is now considered under a point dynamic load applied to its midpoint. Material properties density, $\rho=7850 \times 10^{-6}$ kgf/cm³, Poisson's ratio, $\nu = 0.3$, and modulus of elasticity, $E=2.1 \times 10^6$ kgf/cm². Three types of time depended point loads, shown in figure 1.b, with the amplitude $p_0 = 1$ kgf are implemented to the arch. The radius of the cross section of the arch ($h(\phi)$) is considered to be;

$$h(\phi) = \begin{cases} 0.5 & , \quad -\frac{\pi}{6} < \phi < \frac{\pi}{6} \\ 1.0 & , \quad \frac{\pi}{6} \leq \phi \leq \frac{\pi}{4} \\ 1.0 & , \quad -\frac{\pi}{4} \leq \phi \leq -\frac{\pi}{6} \end{cases}$$

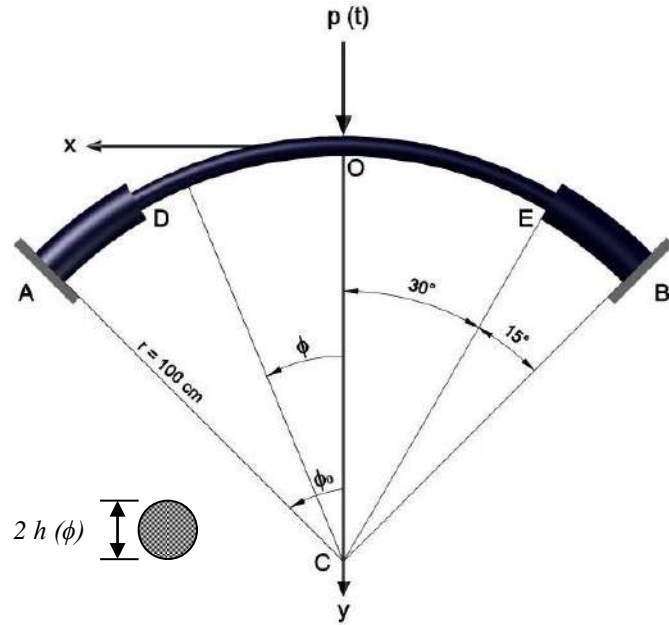
Here the flexural rigidity and cross section of arch is;

$$EI_b(\phi) = E \frac{\pi h(\phi)^4}{4}; \quad A(\phi) = \pi h(\phi)^2$$

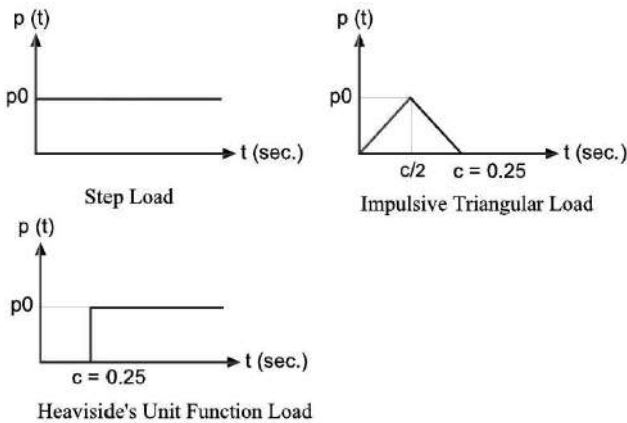
The boundary conditions of fixed-end and symmetric point are given as follows:

$$\phi = 0 \rightarrow \begin{cases} U_t = 0 \\ \Omega_b = 0 \\ T_n = -p/2 \end{cases} \quad \phi = \phi_0 \rightarrow \begin{cases} U_t = 0 \\ U_n = 0 \\ \Omega_b = 0 \end{cases}$$

The equations (13-18) given in canonical form are solved numerically in the Laplace domain by the CFM. The results are compared with those obtained from ANSYS. Comparisons are shown in the graphics. In this problem the effect of shear deformation is taken into account.



(a)



(b)

Figure 1: (a) Fixed –ended circular stepped arch; (b) Dynamic loads.

The geometric properties of the arch are as follows:

Shear correction factor $\alpha_n = 1.11$, radius of curvature of the circular arch $r = 100$ cm and $\phi_0 = \pi/4$.

$$h = 0.5\text{cm} \rightarrow \begin{cases} A = 0.7854\text{cm}^2 \\ I_b = 0.0491\text{cm}^4 \end{cases}$$

$$h = 1.0\text{cm} \rightarrow \begin{cases} A = 3.1416\text{cm}^2 \\ I_b = 0.7854\text{cm}^4 \end{cases}$$

Laplace transforms of the step load, sinusoidal load and the Heaviside's unit function load are available in closed-form. The vertical U_n displacement and M_b bending moment of the midpoint of the arch under a point step load obtained by present method is presented in Figs. 2 - 3 respectively.

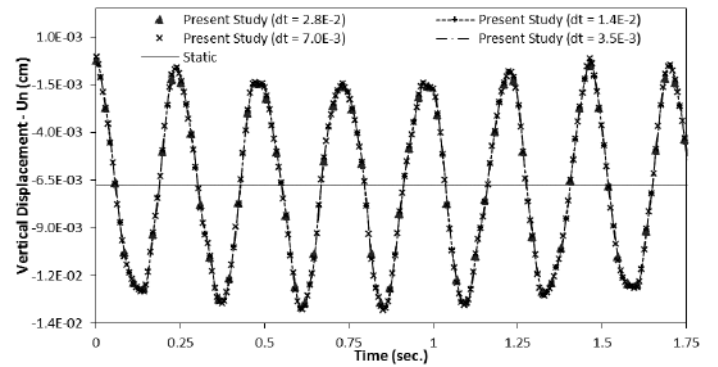


Figure 2: U_n Vertical displacement of the midpoint of the arch versus time under a point step load.

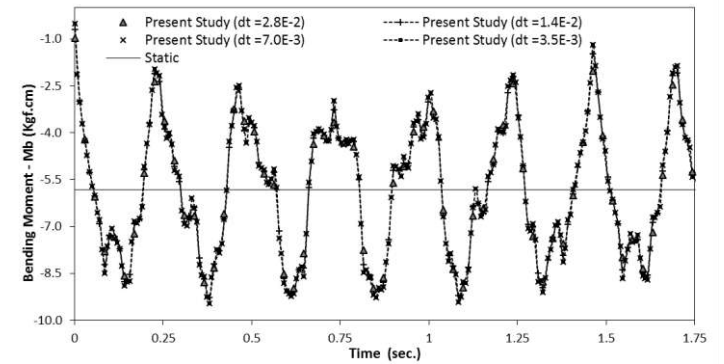


Figure 3: M_b Moment of bending versus time at the arch midpoint under a point step load.

The M_b bending moment results obtained by the present study at the fixed-end of the arch subjected to a point step load is presented in Fig. 4.

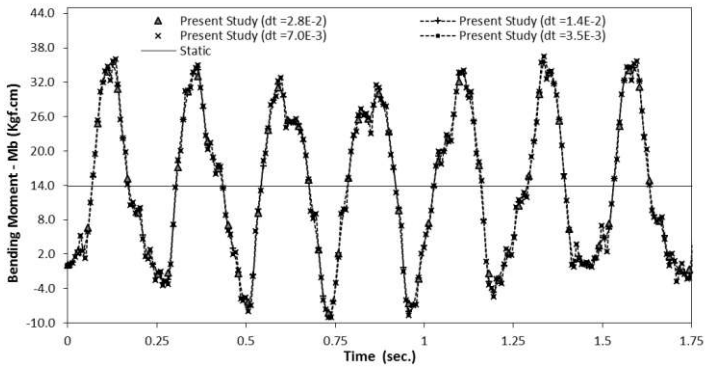


Figure 4: M_b Moment of bending versus time at the arch fixed-end under a point step load.

A uniaxial element with tension, compression and bending capabilities is used to analyze the circular arch problem in ANSYS. Time varying results of the vertical U_n displacement and M_b bending moment of the symmetric point and M_b bending moment under a point step load at the fixed support are given in Figs. 5 – 7.

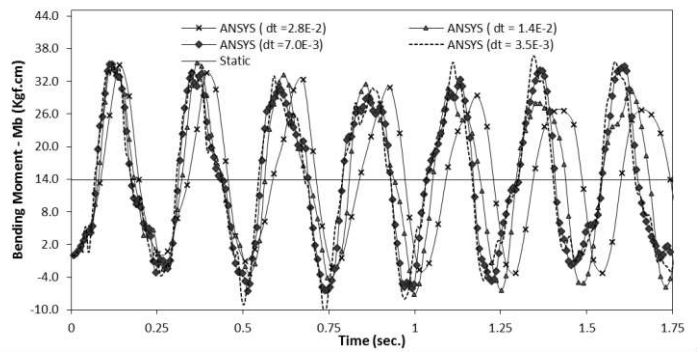


Figure 7: M_b Moment of bending versus time at the arch fixed-end under a point step load.

The problem has been solved for various time increments as transform parameters ($dt=2.8E-2$ sec., $N = 64$), ($dt=1.4E-2$ sec., $N = 128$), ($dt=7.0E-3$ sec., $N = 256$) and ($dt=3.5E-3$ sec., $N = 512$). It is apparent that results obtained for a coarse time increment along with fewer Laplace transform parameters overlap the results obtained with finer increments and higher parameters. This indicates the efficiency and exactness of the present method.

As it is obvious in the figures above the accuracy of the results of conventional numerical time integration methods depends on the appropriate selection of the optimum time increment. Thus a small time increment is needed to acquire efficient results.

The comparison of present study and conventional step by step time integration methods for various time increments and stepped cross section given in Figs. 8 – 10 show the U_n vertical displacement, M_b bending moment at the midpoint and bending moment at the fixed supported end of the arch for a step load respectively.

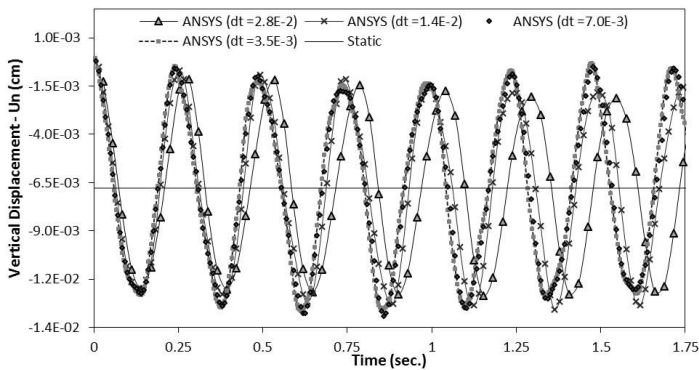


Figure 5: U_n Vertical displacement of the midpoint of the arch versus time under a point step load.

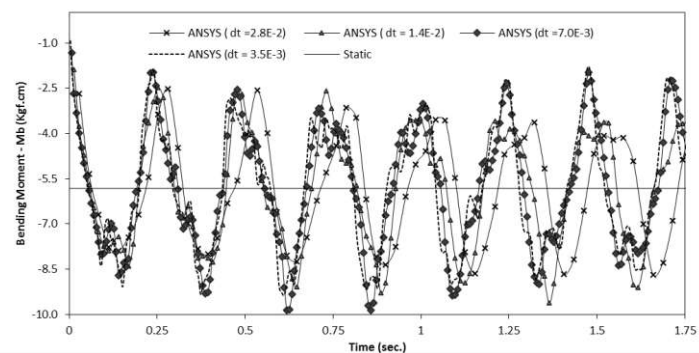


Figure 6: M_b Moment of bending versus time at the arch midpoint under a point step load.

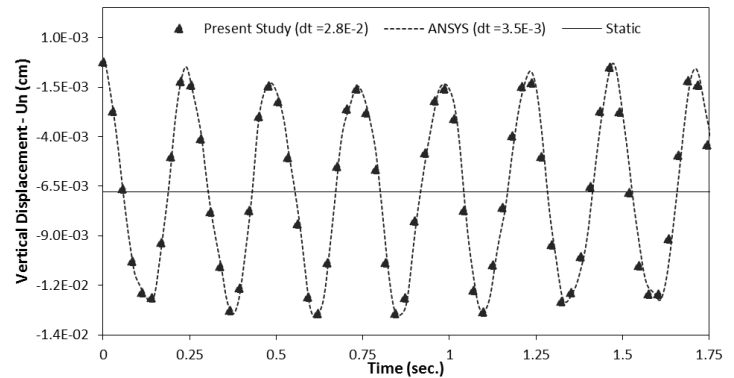


Figure 8: Comparison of U_n vertical displacement versus time at the arch midpoint for step load.

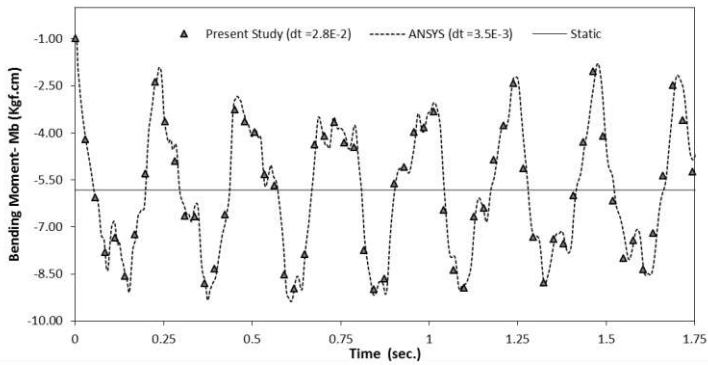


Figure 9: Comparison of M_b Moment of bending versus time at the arch midpoint for step load.

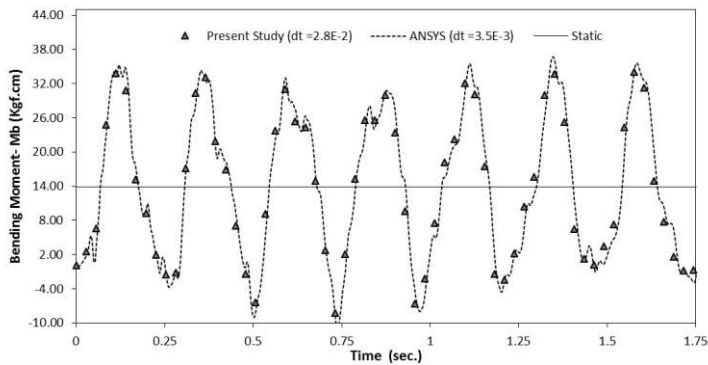


Figure 10: Comparison of M_b Moment of bending versus time at the arch fixed-end under a point step load.

It can be seen that time increments of $3.5E-3$ sec. and finer had to be considered for consistent results in ANSYS. An exact match is obtained by using a coarse time increment of $2.8E-2$ sec. in the present method as opposed to much finer increment of $3.5E-3$ sec. in Newmark method.

To examine the dynamic response of this structure under different time depended loads the impulsive triangular dynamic point load is implemented to the stepped circular arch. Solutions are obtained in the similar manner as step load and comparisons are given in Figs. 11 - 13.

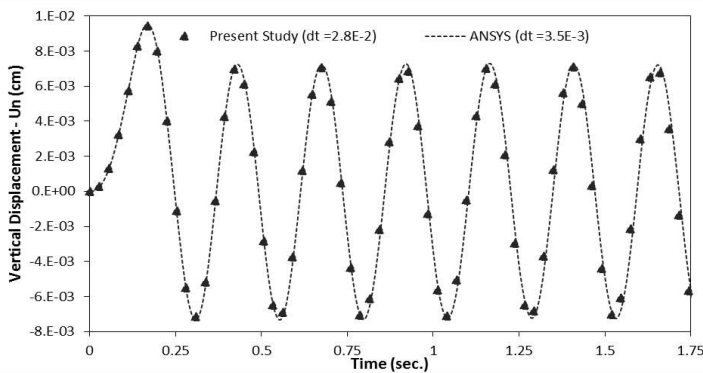


Figure 11: Comparison of U_n vertical displacement versus time at the arch midpoint under point impulsive triangular load.

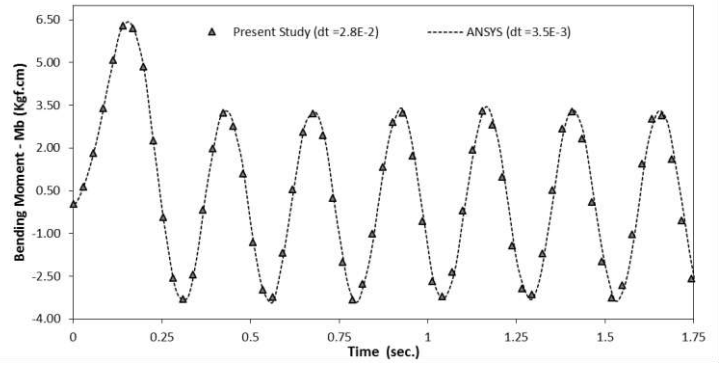


Figure 12: Comparison of M_b Moment of bending versus time at the arch midpoint under point impulsive triangular load.

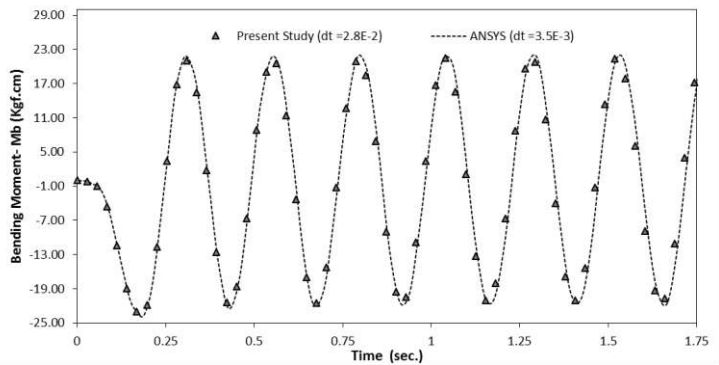


Figure 13: Comparison of M_b Moment of bending versus time at the arch fixed-end under point impulsive triangular load.

Given figures include the results obtained by present method and ANSYS. The comparison show that an exact match is obtained by using a coarse time increment of $2.8E-2$ sec. in the present method as opposed to much finer increment of $3.5E-3$ sec. in ANSYS.

The behavior of isotropic stepped circular arch is examined under Heaviside's unit function step point load by proposed method. The results are given in Figs. 14 - 16.

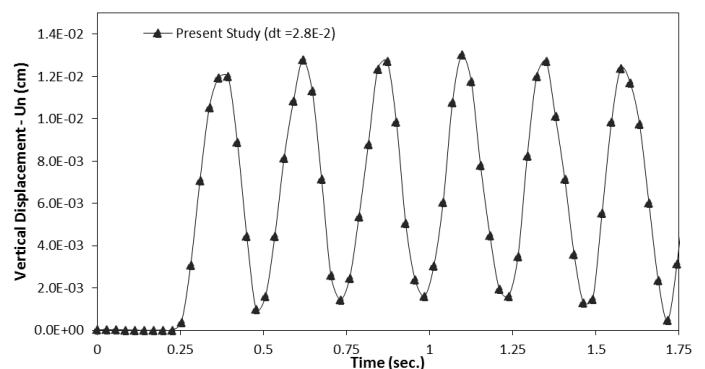


Figure 14: U_n vertical displacement versus time at the arch midpoint under point Heaviside's function step load.

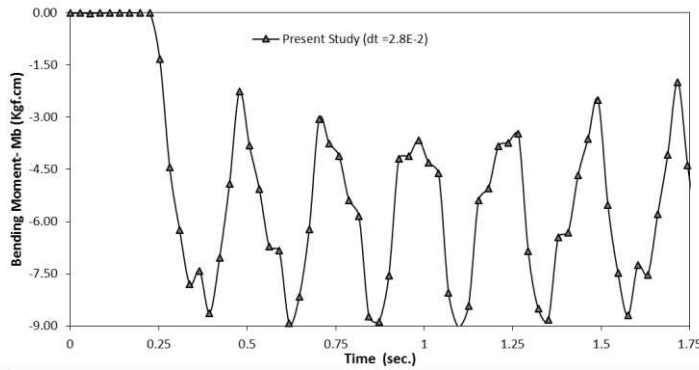


Figure 15: M_b Moment of bending versus time at the arch midpoint under point Heaviside's function step load.

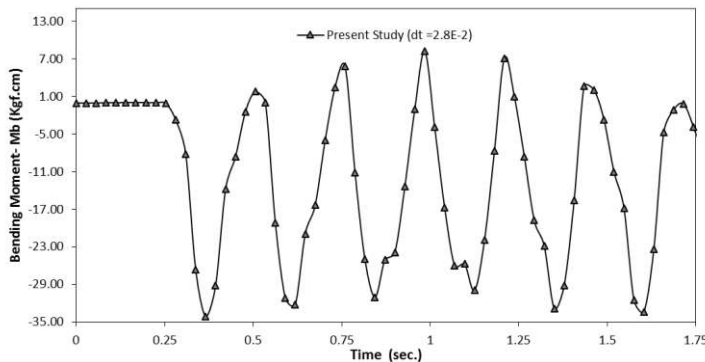


Figure 16: M_b Moment of bending versus time at the arch fixed-end under point Heaviside's function step load.

V. CONCLUSION

In this paper, the transient analysis of stepped circular arches made up of linear elastic materials is investigated under various types of time depended loads. The dynamic behavior of such structures is examined by the unified method of Laplace transform and the CFM as the effect of shear deformation and is considered. RK5 algorithm is used for the numerical solution of the initial value problems. The governing equations of the related problem are first obtained in the time domain. Laplace transform is then applied and the set of simultaneous linear algebraic equations are solved by the CFM in the Laplace domain for a set of Laplace parameters. The solutions obtained are transformed to the time domain using an efficient inverse numerical Laplace transform method. For the suggested model, a computer program is coded in Fortran. Results of the presented method are compared with those obtained from ANSYS.

The accuracy of the results of conventional step by step time integration method depends on the appropriate selection of the optimum time steps. By using the presented method, highly accurate results can be obtained, even with a coarse time steps. It is manifest that combination of Laplace transform and the CFM is far more efficient than the conventional step-by-

step time integration methods. Laplace transformation gives a time-independent boundary-value problem in spatial coordinate which is then solved by the CFM. The numerical examples has proved that the suggested procedure is highly accurate and efficient compared to various other numerical methods available in the literature and it can be easily applied to the stepped circular arches.

Acknowledgment

The authors thank the Scientific Research Projects Directorate of Cukurova University for supporting the present study (FBA-2016-6007).

REFERENCES

- [1] V. Haktanir, "Investigation of the static, dynamic and buckling behavior of cylindrical helical rods by transfer matrix method," PhD. Thesis, University of Cukurova, Adana, 1990.
- [2] S. Bayhan, "Analysis of planner curved rods by stiffness matrix and transfer matrix method," MSc. Thesis, University of Cukurova, Adana, 1993 (In Turkish).
- [3] [M. Bozkurt, "The Analysis of cylindrical vaults, circular and helicoidal structural systems by the complementary functions method-Mathematica applications," MSc. Thesis, University of Cukurova, Adana, 1995 (In Turkish).
- [4] V. Yildirim, N. İnce and , E. Kiral, "Static analysis of compound planar frames with members of linear and circular axes by stiffness matrix method," J. of Engineering and Environmental Sciences, pp.137-148, 1997.
- [5] F.F. Çalim, "Dynamic analysis of viscoelastic, anisotropic curved spatial rod systems," PhD. Thesis, University of Cukurova, Adana, 2003 (In Turkish).
- [6] M. Kiraç, "Dynamic analysis of straight composite rods," MSc. Thesis, University of Mustafa Kemal, Hatay, 2007 (In Turkish).
- [7] H. Aktan, "In-Plane dynamic analysis of circular beams," MSc. Thesis, Istanbul Technical University, Istanbul, 2008 (In Turkish).
- [8] M. Çoban, "Out-Of-plane dynamic analysis of curved beams using mixed finite element method," MSc. Thesis, Istanbul Technical University, Istanbul, 2008 (In Turkish).
- [9] F.G. Akkurt, "Dynamic analysis of straight and circular rods on elastic foundation," MSc. Thesis, University of Mustafa Kemal, Hatay, 2011 (In Turkish).
- [10] N. Karaca, "Static and dynamic analysis of planar rods by the transfer and stiffness matrix methods," MSc. Thesis, University of Mustafa Kemal, Hatay, 2014 (In Turkish).
- [11] S. Ecer, "Longitudinal vibration analysis of straight bars using mixed finite element method," MSc. Thesis, Istanbul Technical University, Istanbul, 2015 (In Turkish).
- [12] G. D. Manolis, and D. E. Beskos, "Dynamic response of framed underground structures," Comp. and Struct., vol. 15(5), pp. 521-531, 1982.
- [13] D. E. Beskos, and G. V. Narayanan, "Dynamic response of frameworks by numerical Laplace transform," Comp. Method in Appl. Mech. and Eng., vol. 37(3), pp. 289-307, 1983.

-
- [14] C. S. Huang, C. S. Teng, and A. W. Leissa, "An accurate solution for the in-plane transient response of a circular arch," *J. Sound and Vibration*, vol. 196(5), pp. 595-609, 1996.
- [15] C.S. Huang, Y.P. Tseng, and C.J. Lin, "In-plane transient responses of arch with variable curvature using dynamic stiffness method," *J. Eng. Mech.*, vol. 124, pp.826-835, 1998.
- [16] B. Temel, T.A. Aslan, and A.R. Noori, "An efficient dynamic analysis of planar arches," 1st International Mediterranean Science and Engineering Congress, pp.3046-3053, 2016.
- [17] T.A. Aslan, "A Study on an efficient numerical analysis of the curved structural elements," University of Cukurova, Adana, 2016 (In Turkish).
- [18] E. Tüfekci, Ö. Özdemirci, "Exact solution of free in-plane vibration of a stepped circular arch," *J. Sound and Vibration*, vol. 295, pp. 725-738, 2006.
- [19] F. Durbin, "Numerical inversion of laplace transforms: an efficient improvement to Dubner and Abate's method," *Comput. J.*, vol. 17, pp.371 – 376, 1974.
- [20] B. Temel, F.F. Çalim, and N. Tütüncü, "Quasi-static and dynamic response of viscoelastic helical rods," *J. Sounds Vib.*, vol. 271, pp.921 – 935, 2004.
- [21] ANSYS Swanson Analysis System, Inc., 201 Johnson Road, Houston, PA15342-1300,USA.

Effect of Incoherency Models on Isolated and Nonisolated Highway Bridge

Muhammet YURDAKUL

Civil Engineering
Bayburt University
Bayburt, Turkey
myurdakul@bayburt.edu.tr

Şevket ATEŞ

Civil Engineering
Karadeniz Technical University
Trabzon, Turkey
sates@ktu.edu.tr

Abstract—In this study, stochastic analysis of isolated and nonisolated highway bridges under spatially varying ground motion are examined. Spatially varying earthquake ground motion model includes incoherency, wave passage and site response effect. Incoherency effect is taken into account in the scope of this study. Site response effect is not taken account in the analyses. Soil, supported bridge, is assumed to be homogeneous and soft. Two different incoherency models are used analysis to represent incoherency effects. These are Harichandran and Vanmarcke, and Uscinski incoherency models. Triple Concave Friction Pendulum (TCFP) bearing system is used as a frictional pendulum system. Utilization of this isolation system is more effective than other frictional pendulum and conventional isolator systems against severe earthquake. The means of the maximum responses of displacement and internal forces of bridge deck are investigated. These responses are consisted by quasi-static, dynamic and total of internal forces and displacements. The results of these stochastic analyses are also compared with the results of under uniform ground motion. Analysis results revealed that using TCFP bearing on Highway Bridge reduces means of maximum values of total axial force, shear force and bending moment of deck by 85%, 81% and 86%, respectively. Generally, the results from stochastic analysis demonstrated that using Harichandran and Vanmarcke incoherency model is more effective than Uscinski incoherency model and using uniform ground motion at isolated and nonisolated bridges.

Keywords—spatially varying earthquake ground motion; seismic isolation; triple friction pendulum bearing; incoherency effect; highway bridge

I. INTRODUCTION

Highway Bridge is an important transportation network. This type of structures should be protected against effect of severe earthquake. This detrimental effect can be decreased if the fundamental period of structure is lengthened or energy dissipating of bridge is increased. Hence, different types of seismic isolation systems are used to protect structure against detrimental effects of severe earthquake.

Some researchers study to indicate that TCFP bearing system is more effective than other sliding systems on severe earthquake [1-3]. Dynamic response analysis of long span isolated and nonisolated bridges subjected to spatially varying

ground motions were investigated by [4]. [5] performed a study of spatially varying ground motions on stochastic response of isolated bridge with friction pendulum bearing systems. [6] compared stochastic response of isolated and nonisolated cable-stayed bridge with double concave friction pendulum (DCFP) bearing subjected to spatially varying ground motion. [7] performed an analysis of multiple support seismic response of Bosphorous Bridge for various random vibration methods.

While stochastic responses of bridges isolated with different sliding systems have been investigated, TCFP bearing system is not taken into account so far. Aim of this paper is comparing incoherency models at isolated and nonisolated with TCFP bearing under spatially varying ground motion.

II. MATERIAL AND METHOD

TCFP bearing system is to be effective in severe earthquake ground motion. These system used as an isolation device installed between deck and pier in this study. To determine parameters of TCFP bearing, a sample design proposed by [8] is used. Properties of TCFP bearing are given in Table1. Stochastic analyses of isolated and nonisolated bridge are performed under spatially varying ground motion by taking into account only the incoherence effect. The incoherency effect results from reflections and refractions of seismic waves through to the soil during their propagation. Incoherency effect is examined by considering the Harichandran and Vanmarcke and Uscinski models. Also, in the case of uniform ground motion is used for compare results of incoherency models. The soil which is under all supports is homogeneous and soft soil.

Harichandran and Vanmarcke model proposed by [9] is defined as

$$\gamma_{lm}(\omega) = A \exp \left[-\frac{2d_{lm}}{\alpha\theta(\omega)}(1-A+\alpha A) \right] + (1-A) \exp \left[-\frac{2d_{lm}}{\theta(\omega)}(1-A+\alpha A) \right] \quad (1)$$

Where, d_{lm} is the distance between support points l and m . Also, $\theta(\omega)$ is defined as

$$\theta(\omega) = k \left[1 + \left(\frac{\omega}{2\pi f_0} \right)^b \right]^{-\frac{1}{2}} \quad (2)$$

Where A , α , k , f_0 ve b are 0.636, 0.0186, 31200, 1.51 Hz. and 2.95 respectively proposed by [10]. Second incoherency model, Uscinski, is proposed by [11] and defined as

$$|\gamma_{lm}(\omega)|^k = \exp \left[\left(\frac{\alpha d_{lm} \omega}{v_s} \right)^2 \right] \quad (3)$$

Where α and v_s are dimensionless inconsistency parameter and shear wave velocity, respectively. In this study, value of α/v_s is taken as 2×10^{-4} [12-13].

Incoherency effect decreases with increasing frequency and distance between supports. Incoherency effect is equal to one for all frequency and distance between support at case of uniform ground motion [14].

TABLE I. PROPERTIES OF TCFP IN ALL CASES

Properties	$W_1=9094$ kN	$W_2=12122$ kN	Combined system
$R_{eff1} = R_{eff4}$ (mm)	3759	3759	3759
$R_{eff2} = R_{eff3}$ (mm)	1403	1403	1403
$d_1^* = d_4^*$ (mm)	566	566	566
$d_2^* = d_3^*$ (mm)	58	58	58
$\mu_1 = \mu_4$ lower bound	0.058	0.041	0.048
$\mu_2 = \mu_3$ lower bound	0.037	0.010	0.021
μ lower bound	0.050	0.030	0.038
$\mu_1 = \mu_4$ upper bound	0.096	0.069	0.081
$\mu_2 = \mu_3$ upper bound	0.061	0.016	0.035
μ upper bound	0.083	0.049	0.064

III. NUMERICAL EXAMPLE

In order to investigate the stochastic response of isolated bridge with TCFP bearing and nonisolated highway bridge, two dimensional analytical model used by [14] is selected as a numerical model (Fig.1).

Stochastic analyses of isolated and nonisolated bridges are examined for spatially varying ground motion by taking only incoherency effect. Soil supported bridge assumed to be homogeneous and soft soil. For these purpose two different incoherency models are used for analysis to represent incoherency effects. These are Harichandran and Vanmarcke and Uscinski incoherency models. Also, analysis results of bridge under uniform ground motion is showed to comparison results of incoherency effects. The

analyses are carried out computer code SVEM [15] that is the modified to include a TCFP bearing system's behavior. The first 15 modes and %5 damping ratio are selected for analyses. The periods obtained from analyses for isolated with TCFP bearing and nonisolated bridges are given in Table II.

The analyses results show that using TCFP bearing may length period of the highway bridge. Means of maximum values of quasi-static, dynamic and total axial forces of the deck of the isolated and nonisolated bridges are compared in Fig. 2.

Mean of maximum quasi-static, dynamic and total axial forces of the deck of the isolated and nonisolated bridges are calculated for Harichandran and Vanmarcke, Uscinski incoherency models and uniform ground motion are compared in Fig. 2. Using TCFP bearing decreases values

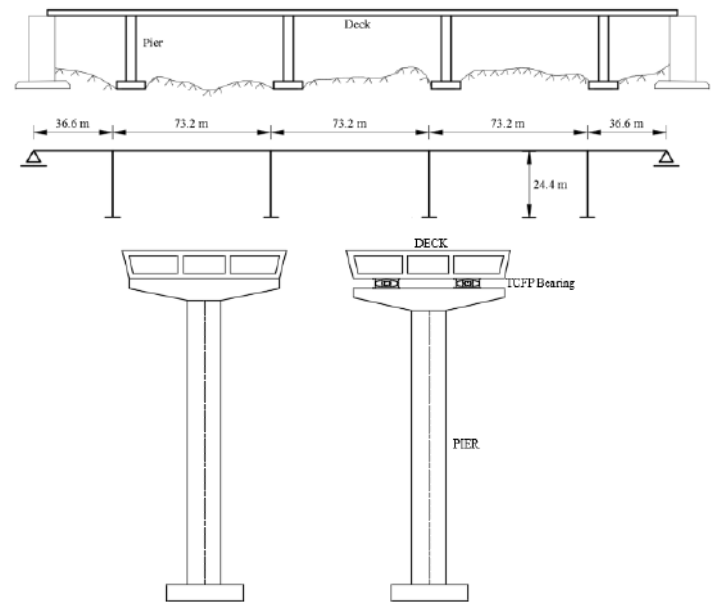


Fig. 1. Selected Highway Bridge and its model

TABLE II. THE PERIODS OF ISOLATED AND NONISOLATED BRIDGE

Mode	Period (s)	
	Isolated	nonisolated
1	3.6607	1.1929
2	1.0310	0.8144
3	0.7700	0.6844
4	0.5964	0.5784
5	0.3028	0.2739
6	0.2799	0.262
7	0.2419	0.2354
8	0.2123	0.2136
9	0.2003	0.205
10	0.1718	0.1698
11	0.1378	0.1357
12	0.1297	0.1301
13	0.1239	0.1258
14	0.0866	0.0862
15	0.0585	0.0583

of maximum of quasi-static, dynamic and total normal forces of bridge deck by 82%, 65% and 85%, respectively. While the values of quasi-static and total axial forces increase the middle of the bridge length, these forces decreases towards abutment. While Harichandran and Vanmarcke incoherency model is the most effective for quasi-static and total axial forces, it is least effective for dynamic axial force both seismic isolated and nonisolated bridges.

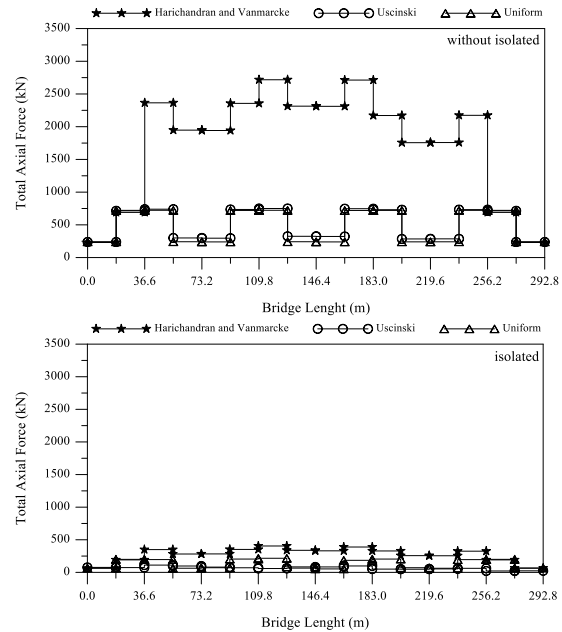
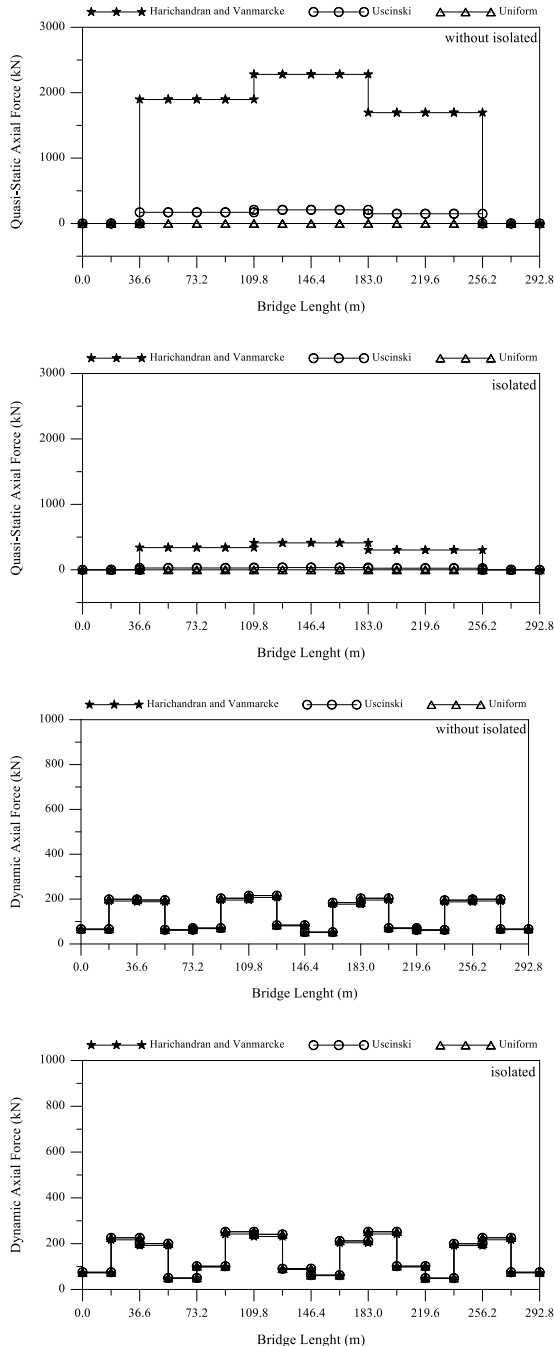


Fig. 2. Mean of maximum axial forces of the deck isolated and nonisolated

Mean of maximum quasi-static, dynamic and total shear forces of the deck of the isolated and nonisolated bridges are calculated for Harichandran and Vanmarcke, Uscinski incoherency models and uniform ground motion are compared in Fig. 3. Using TCFP bearing decreases values of maximum of quasi-static, dynamic and total shear forces of bridge deck by 93%, 68% and 81%, respectively. Harichandran and Vanmarcke incoherency model is more effective than Uscinski model and uniform ground motion for quasi-static and total shear forces at nonisolated bridge. The values obtain from the stochastic analyses considering Harichandran and Vanmarcke and Uscinski models and uniform ground motion are nearly same for dynamic shear forces.

Means of maximum quasi-static, dynamic and total bending moment of the deck of the isolated and nonisolated bridges are calculated for Harichandran and Vanmarcke, Uscinski incoherency models and uniform ground motion are compared in Fig. 4. Using TCFP bearing decreases values of maximum of quasi-static, dynamic and total bending moment of bridge deck by 92%, 74% and 86%, respectively. While Harichandran and Vanmarcke incoherency model is the most effective for quasi-static and total bending moment, case of uniform ground motion is more effective than considering Harichandran and Vanmarcke and Uscinski incoherency models for dynamic bending moment both seismic isolated and nonisolated bridges.

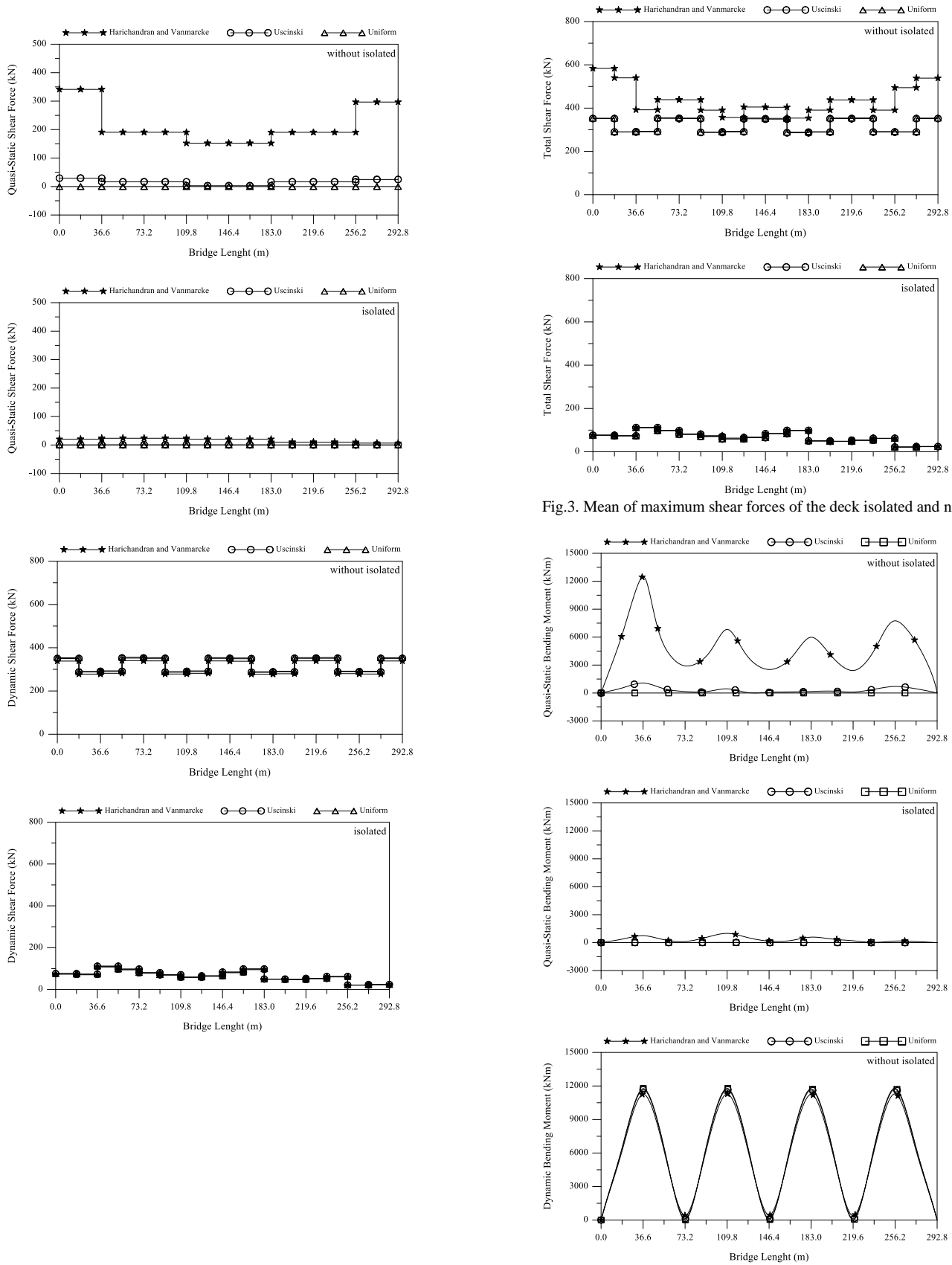
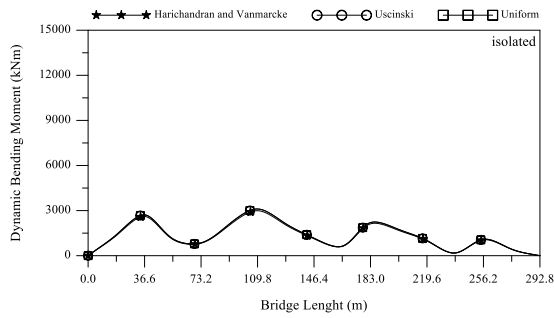


Fig.3. Mean of maximum shear forces of the deck isolated and nonisolated



Means of maximum quasi-static, dynamic and total displacements of the deck of the isolated and nonisolated bridges are calculated for Harichandran and Vanmarcke, Uscinski incoherency models and uniform ground motion are compared in Fig. 5. Using TCFP bearing increases values of maximum of quasi-static, dynamic and total shear forces of bridge deck by 27%, 150% and 37%, respectively. The displacements of bridge deck obtained from stochastic analysis for situation of uniform ground motion are nearly similar to these obtained for Uscinski incoherency model in all graphics. The displacements of deck obtained from stochastic analyses for Harichandran and Vanmarcke are 4.2% smaller than those from analysis for Uscinski incoherency model and situation of using uniform ground motion.

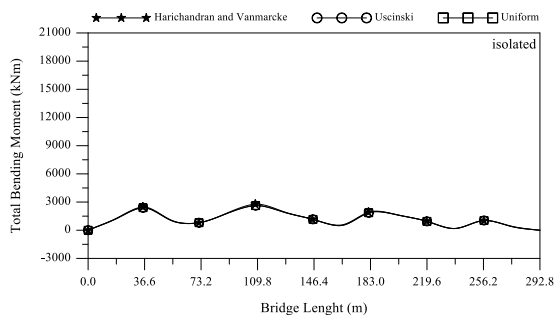
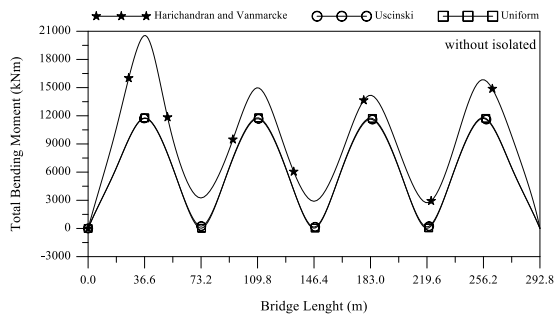
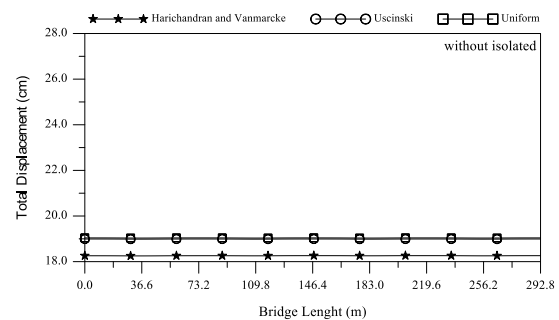
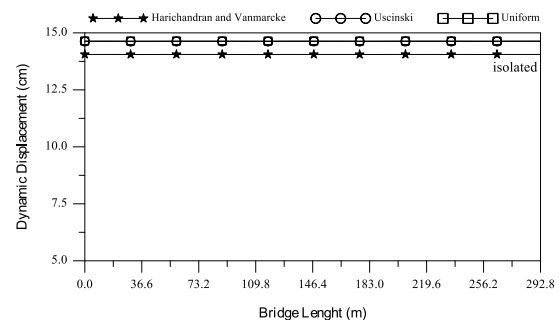
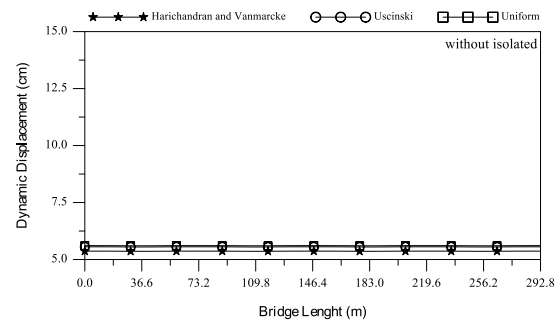
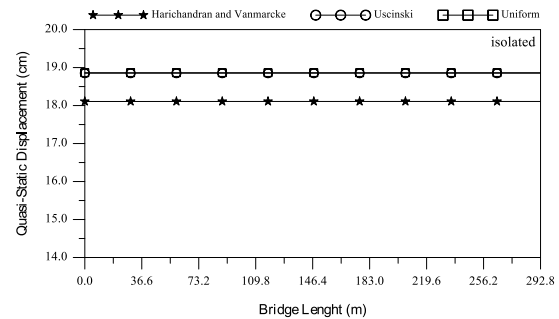
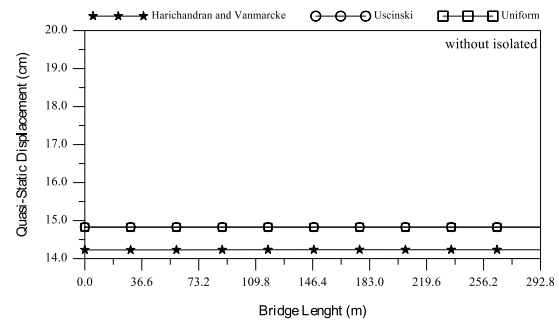


Fig.4. Mean of maximum bending moment of the deck isolated and nonisolated



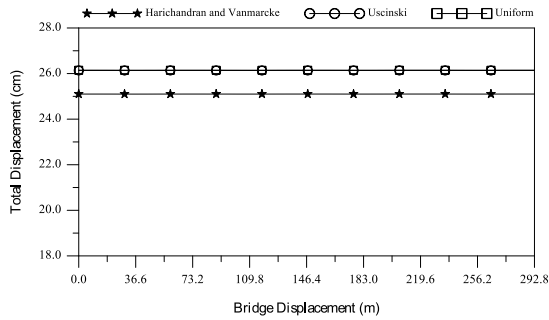


Fig.5. Mean of maximum horizontal displacement of the deck isolated and nonisolated

CONCLUSION

This study outlines an investigation of the stochastic response of an isolated with TCFP bearing and nonisolated highway bridge. Only the incoherency effect is taken into account in the spatially varying ground motion. Site response effect is not taken account in the analyses. Soil, supported bridge, is assumed to be homogeneous and soft. The stochastic analyses are performed for isolated and nonisolated bridge, separately. In the stochastic analysis, Harichandran and Vanmarcke, and Uscinski incoherency models are taken into account, separately. Also, uniform ground motion which has infinite velocity is used for comparing results. The conclusions drawn from this paper can be written as:

- The value of the periods of the bridge significantly lengths when TCFP bearing system is used.
- The results from stochastic analyses indicated that TCFP bearing decreases element forces of highway bridge deck by 65% to 93%.
- While Harichandran and Vanmarcke incoherency model is the most effective for quasi-static and total axial forces, it is least effective for dynamic axial force both seismic isolated and nonisolated bridges.
- Harichandran and Vanmarcke incoherency model is more effective than Uscinski model and using uniform ground motion for total shear forces on nonisolated bridge. Using difference incoherency models may not influence responses of shear forces of the isolated bridge.
- Harichandran and Vanmarcke incoherency model is more effective than Uscinski model and using uniform ground motion for total bending moment on nonisolated bridge. Using difference incoherency models may not influence responses of bending moment of the isolated bridge.
- Considering to incoherency effect may not influence displacement of bridge deck under spatially varying

ground motion in both seismically isolated and nonisolated highway bridge.

REFERENCES

- [1] Tajammolian, H., Khoshnoudian, F., Talaei, S., and Loghman, V., "The effects of peak ground velocity of near-field ground motions on the seismic responses of base-isolated structures mounted on friction bearings", *Earthquakes and Structures*, vol. 7, pp. 1259-1281, 2014.
- [2] Loghman, V. and Khoshnoudian, F., "Comparison of seismic behavior of long period sdof systems mounted on friction isolators under near-field earthquakes", *Smart Structures and Systems*, vol. 16, pp. 701-723, 2015.
- [3] Fallahian, M., Khoshnoudian, F., and Loghman, V., "Torsionally seismic behavior of triple concave friction pendulum bearing", *Advances in Structural Engineering*, vol. 18, pp. 2151-2166, 2015.
- [4] Harichandran, R.S., and Wang, W., "Response of one-and two-span beams to spatially varying seismic excitation", Report to the National Science Foundation MSU-ENGR-88-002. Michigan (MI): Department of Civil and Environmental Engineering, College of Engineering, Michigan State University, 1988.
- [5] Ates, S., Bayraktar, A., and Dumanoglu, A. A., "The effect of spatially varying earthquake ground motions on the stochastic response of bridges isolated with friction pendulum systems", *Soil Dynamics and Earthquake Engineering*, vol. 26, pp. 31-44, 2006.
- [6] Ates, S., Soyul, K., Dumanoglu, A. A., and Bayraktar, A., "Earthquake response of isolated cable-stayed bridges under spatially varying ground motions", *Structural Engineering and Mechanics*, vol. 31, pp. 639-662, 2009.
- [7] Adanur, S., Altunışık, A. C., Soyul, K., Bayraktar, A., and Dumanoglu, A. A., "Multiple-support seismic response of Bosphorus Suspension Bridge for various random vibration methods", *Case Studies in Structural Engineering*, vol. 5, pp. 54-67, 2016.
- [8] Constantinou, M.C., Kalpakidis, I., Filiatrault A. and Ecker Lay, R.A., "Lrfd-Based analysis and design procedures for bridge", February 28, Technical Rapor, 2011.
- [9] Harichandran, R.S. ve Vanmarcke, E.H., "Stochastic variation of earthquake ground motion in space and time", *Journal of Engineering Mechanics*, vol. 112, pp. 154-174, 1986.
- [10] Harichandran, R.S., Hawwari A. ve Sweidan B.N., "Response of long-span bridges to spatially varying ground motion", *Journal of Structural Engineering*, vol. 122, 5, pp. 476-484, 1996.
- [11] Uscinski, B. J., "The Elements of wave Propagation in Random Media", Mc Graw-Hill, New York, 1977.
- [12] Luco, J.E. ve Wong, H.L., "Response of a rigid foundation to a spatially random ground motion", *Earthquake Engineering and Structural Dynamics*, vol. 14, pp. 891-908, 1986.
- [13] Luco, J.E. ve Mita, A., "Response of circular foundation to spatially random ground motion", *Journal of Engineering Mechanics*, vol. 113, pp. 1-16, 1987.
- [14] Ateş, Ş., "Sürtünmeli sarkaç sistemi ile izolasyonlu karayolu köprülerinin değişerek yayılan yer hareketi için stokastik analizi", Doktora Tezi, Karadeniz Teknik Üniversitesi, Fen Bilimleri Enstitüsü, Trabzon, 2004.
- [15] Dumanoglu, A.A. and Soyul, K., "SVEM: a stochastic structural analysis program for spatially varying earthquake ground motions", Turkish Earthquake Foundation, TDV/KT 023-76, 2002.

Frictionless Contact Problem for a Graded Layer-Half Plane Structure under a Rigid Punch

Erdal ÖNER

Department of Civil Engineering
Bayburt University
Bayburt, TURKEY
eoner@bayburt.edu.tr

Gökhan ADIYAMAN

Department of Civil Engineering
Karadeniz Technical University
Trabzon, TURKEY
gadiyaman@ktu.edu.tr

Ahmet BİRİNCİ

Department of Civil Engineering
Karadeniz Technical University
Trabzon, TURKEY
birinci@ktu.edu.

Abstract—The objective of this study is to solve a smooth continuous contact problem between a functionally graded layer and a homogeneous half-plane. The problem is considered under the assumption of plane strain. The half-plane is homogeneous, while the functionally graded layer is inhomogeneous with its shear modulus and mass density changing arbitrarily along the thickness direction. The functionally graded layer is indented by a rigid cylindrical punch subjected to a concentrated normal force. Since the contact between the two bodies is assumed to be frictionless, then only compressive normal tractions can be transmitted in the contact area. By using the Fourier integral transform and the boundary conditions, the problem is reduced to a singular integral equation in which the contact half-width and the contact pressure under rigid punch are unknown. The integral equation is solved numerically by making use of appropriate Gauss-Chebyshev integration formula. The presented numerical results illustrate the influences of the inhomogeneity parameters, load ratio and punch radius on the contact pressure distribution under rigid punch, initial separation load and initial separation distance between functionally graded layer and homogeneous half-plane.

Keywords—contact pressure; functionally graded layer; initial separation load; initial separation distance.

I. INTRODUCTION

The concept of functionally graded materials (FGMs) was proposed in 1984 by Japanese material scientists to prepare thermal barrier materials [1]. Then, FGMs were used in electromagnetic engineering, aerospace and many other fields. Since many of potential applications of functionally graded materials (FGMs) involve contact problems, studies to apply the FGM concept to contact mechanics have attracted the attention in the recent years. Some of these studies are summarized below:

Guler and Erdogan [2–4] applied the singular integrate equation method to solve the two-dimensional contact problem of functionally graded coatings. The sliding contact problem of a graded coating using piecewise linear model for different indenter geometries was examined by [5–7]. Two-dimensional frictionless contact problem of a coating structure consisting of a surface coating, a functionally graded layer and a substrate

under a rigid cylindrical punch was studied by [8]. The problem of a functionally graded coated half-space indented by an axisymmetric smooth rigid punch was investigated by [9]. The thermoelastic frictional contact of functionally graded materials with arbitrarily varying thermoelastic properties was examined by [10]. A theoretical analysis of two-dimensional frictionless sliding contact over orthotropic piezoelectric materials indented by a rigid sliding punch was carried out by [11]. The contact problem for a functionally graded layer supported by a Winkler foundation was solved by [12]. A semi-analytical algorithm for the determination of the contact half width and surface pressure which results from both adhesive and non-adhesive contact problems involving functionally graded materials was presented by [13]. A frictional receding contact plane problem between a functionally graded layer and a homogeneous substrate was solved by [14]. Double receding contact plane problem between a functionally graded layer and an elastic layer was studied by [15]. Frictional receding contact analysis of a layer on a half-plane subjected to semi-infinite surface pressure was examined by [16]. The analytical and finite element solution of plane contact problem of a rigid cylindrical punch sliding over a functionally graded orthotropic medium was investigated by [17].

In this study, the frictionless contact problem for a functionally graded layer resting on a homogeneous half-plane is considered using linear elasticity theory. The problem is reduced to a Cauchy-type singular integral equation in which the unknowns are contact half-width and contact pressure using Fourier integral transforms. The numerical results for the contact pressure distribution under punch, initial separation load and initial separation distance between functionally graded layer and homogeneous half-plane are calculated for various values of the material inhomogeneity parameters, load ratio and punch radius.

II. PROBLEM DESCRIPTION AND FORMULATION

Consider the plane strain problem as shown in Fig. 1. Medium 2 is a homogeneous half-plane and medium 1 is the functionally graded layer with a thickness h . The functionally graded layer and homogeneous half-plane occupy, respectively,

the domains $-h \leq y \leq 0$ and $y \leq -h$. A normally concentrated force P acts on the rigid punch. The shear modulus of the functionally graded layer and homogeneous half-plane are given by $\mu_1(y)$ and μ_2 , respectively. Poisson's ratio ν is taken constant in both the functionally graded layer and the homogeneous half-plane. Where applicable, the germane quantities are reckoned per unit length in the z -direction.

The shear modulus and mass density of the functionally graded layer vary in the thickness direction, i.e. in y -direction. This variation is presented by two exponential functions in the following form:

$$\mu_1(y) = \mu_0 e^{\beta y}, \quad (1)$$

$$\rho_1(y) = \rho_0 e^{\gamma y}, \quad (2)$$

where μ_0 and ρ_0 are the shear modulus and mass density at the top surface of the functionally graded layer, respectively. β and γ are arbitrary non-zero constants characterizing the material inhomogeneity.

For functionally graded layer, the general expressions of the stress and displacement fields can be obtained as [18]

$$\sigma_{1y} = \frac{2\mu_0 e^{\beta y}}{\pi(\kappa_1 - 1)} \int_0^\infty \sum_{j=1}^4 A_j C_j e^{n_j y} \cos(\xi x) d\xi, \quad (3)$$

$$\tau_{1xy} = \frac{2\mu_0 e^{\beta y}}{\pi} \int_0^\infty \sum_{j=1}^4 A_j D_j e^{n_j y} \sin(\xi x) d\xi, \quad (4)$$

$$v_1(x, y) = \frac{2}{\pi} \int_0^\infty \sum_{j=1}^4 A_j m_j e^{n_j y} \cos(\xi x) d\xi, \quad (5)$$

where

$$m_j = \frac{(3\beta + 2n_j - \beta\kappa_1)[n_j(\beta + n_j)(\kappa_1 + 1) - \xi^2(\kappa_1 + 3)]}{\xi[4\xi^2 - \beta^2(\kappa_1 - 3)(\kappa_1 + 1)]}, \quad (6)$$

$$n_1 = -\frac{1}{2} \left(\beta + \sqrt{4\xi^2 + \beta^2 - 4\xi\beta i \sqrt{\frac{3-\kappa_1}{\kappa_1+1}}} \right), \quad (7)$$

$$n_2 = -\frac{1}{2} \left(\beta - \sqrt{4\xi^2 + \beta^2 - 4\xi\beta i \sqrt{\frac{3-\kappa_1}{\kappa_1+1}}} \right), \quad (8)$$

$$n_3 = -\frac{1}{2} \left(\beta + \sqrt{4\xi^2 + \beta^2 + 4\xi\beta i \sqrt{\frac{3-\kappa_1}{\kappa_1+1}}} \right), \quad (9)$$

$$n_4 = -\frac{1}{2} \left(\beta - \sqrt{4\xi^2 + \beta^2 + 4\xi\beta i \sqrt{\frac{3-\kappa_1}{\kappa_1+1}}} \right), \quad (10)$$

$$C_j = [(\kappa_1 + 1)m_j n_j + \xi(3 - \kappa_1)], \quad (11)$$

$$D_j = [n_j - \xi m_j]. \quad (12)$$

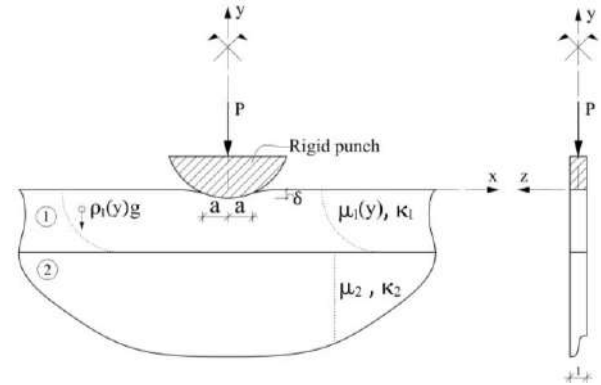


Fig. 1. Geometry and loading condition of the problem

For homogeneous half-plane, the general expressions of the stress and displacement fields can be obtained as [19]

$$v_2(x, y) = \frac{2}{\pi} \int_0^\infty \left[-B_1 + \left(\frac{\kappa_2}{\xi} - y \right) B_2 \right] e^{\xi y} \cos(\xi x) d\xi \quad (13)$$

$$\frac{1}{2\mu_2} \sigma_{2y}(x, y) = \frac{2}{\pi} \int_0^\infty \left[-\xi(B_1 + B_2 y) + \left(\frac{1 + \kappa_2}{2} \right) B_2 \right] e^{\xi y} \cos(\xi x) d\xi \quad (14)$$

$$\frac{1}{2\mu_2} \tau_{2xy}(x, y) = \frac{2}{\pi} \int_0^\infty \left[\xi(B_1 + B_2 y) + \left(\frac{1 - \kappa_2}{2} \right) B_2 \right] e^{\xi y} \sin(\xi x) d\xi \quad (15)$$

Boundary conditions relating to continuous contact case of the problem can be written as

$$\tau_{1xy}(x, 0) = 0, \quad (0 \leq x < \infty), \quad (16)$$

$$\sigma_{1y}(x, 0) = \begin{cases} -P(x) & (0 \leq x < a) \\ 0 & (a \leq x < \infty) \end{cases}, \quad (17)$$

$$\tau_{1xy}(x, -h) = 0, \quad (0 \leq x < \infty), \quad (18)$$

$$\tau_{2xy}(x, -h) = 0, \quad (0 \leq x < \infty), \quad (19)$$

$$\sigma_{1y}(x, -h) = \sigma_{2y}(x, -h), \quad (0 \leq x < \infty), \quad (20)$$

$$\frac{\partial}{\partial x} [v_1(x, -h) - v_2(x, -h)] = 0, \quad (0 \leq x < \infty), \quad (21)$$

$$\frac{\partial}{\partial x} [v_1(x, 0)] = f(x), \quad (0 \leq x < a), \quad (22)$$

where subscripts 1 and 2 indicate related to functionally graded layer and homogeneous half-plane, respectively. a and $p(x)$ are the contact half-width of the rigid punch and the unknown contact pressure under rigid punch. $f(x)$ is the derivative of the profile of the rigid punch; one may write

$$f(x) = \frac{x}{R}, \quad (23)$$

where R is the punch radius.

By making use of the boundary conditions (16-21), unknown constants A_j ($j=1, \dots, 4$) and B_i ($i=1, 2$) can be obtained in terms of the unknown function $p(x)$. By substituting the values of these constants into (22), after some routine manipulations and using symmetry condition $p(x)=p(-x)$, one may obtain the following singular integral equation:

$$\int_{-a}^a \left[\frac{1}{t-x} + k_1(x, t) \right] p(t) dt = -\frac{4\pi\mu_0}{1+\kappa_1} \frac{x}{R}, \quad (24)$$

where

$$k_1(x, t) = \int_0^\infty \left(\frac{4}{1+\kappa_1} Z(\xi) - 1 \right) \sin \xi(t-x) d\xi, \quad (25)$$

$$Z(\xi) = \sum_{j=1}^4 (-\xi A_j m_j). \quad (26)$$

For a complete solution of the problem an additional condition is needed. The contact pressure $p(x)$ must satisfy

$$\int_{-a}^a p(t) dt = P, \quad (27)$$

where P is the resultant compressive force.

In order to calculate initial separation load and distance between functionally graded layer and homogeneous half-plane, the contact pressure $\sigma_{1y}(x, -h)$ needs to be evaluated. In the case including the body force of the FG layer, $\sigma_{1y}(x, y)$ can be obtained as [20]

$$\sigma_{1y}(x, y) = \left[\frac{2\mu_0 e^{\beta y}}{\pi(\kappa_1 - 1)} \int_0^\infty \sum_{j=1}^4 A_j C_j e^{\beta_j y} \cos(\xi x) d\xi \right] + \left(\frac{e^{\gamma y} - 1}{\gamma} \rho_0 g \right), \quad (28)$$

where g is acceleration of gravity.

Substituting the values of A_j ($j=1, \dots, 4$) into (28), after some manipulations, the contact pressure $\sigma_{1y}(x, -h)$ can be obtained as

$$\sigma_{1yg}(x, -h) = \frac{\rho_0 g (e^{-\gamma h} - 1)}{\gamma} + \frac{1}{\pi h} \int_{-a}^a k_2(x, t) p(t) dt, \quad (29)$$

in which $k_2(x, t)$ is given by [20]. To simplify the numerical analysis, the following dimensionless quantities are defined:

$$x = aw, \quad t = a\eta, \quad (30)$$

$$g(\eta) = \frac{p(a\eta)}{(P/h)}, \quad \lambda = \frac{P}{\rho_0 g h^2},$$

Using these quantities, (24), (27) and (29) can be written as

$$\int_{-1}^1 \left[\frac{1}{\eta - w} + \frac{a}{h} k_1(w, \eta) \right] g(\eta) d\eta = -\frac{4}{1+\kappa_1} \frac{\mu_0}{(P/h)} \frac{(a/h)}{(R/h)} w, \quad (31)$$

$$\frac{a}{h} \int_{-1}^1 g(\eta) d\eta = 1, \quad (32)$$

$$\frac{\sigma_{1y}(x, -h)}{P/h} = \frac{(e^{-\gamma h} - 1)}{\gamma h} \frac{1}{\lambda} + \frac{1}{\pi h} \int_{-1}^1 k_2(x, a\eta) g(\eta) d\eta. \quad (33)$$

The contact pressures are zero at the edges of the contact because of the smooth contact at the end points. Thus (31) has an index -1 [21]. Its solution may be expressed as

$$g(\eta) = G(\eta)(1-\eta^2)^{1/2}, \quad (-1 \leq \eta \leq 1). \quad (34)$$

Using appropriate Gauss-Chebyshev integration formula, (31-32) are replaced by

$$\sum_{i=1}^N \Gamma_i \left[\frac{1}{\eta_i - w_j} + \frac{a}{h} k_1(w_j, \eta_i) \right] G(\eta_i) = -\frac{4}{1+\kappa_1} \frac{\mu_0}{(P/h)} \frac{(a/h)}{(R/h)} w_j, \quad (j=1, \dots, N+1), \quad (35)$$

$$\frac{a}{h} \sum_{i=1}^N \Gamma_i G(\eta_i) = \frac{1}{\pi}, \quad (36)$$

where

$$\Gamma_i = \frac{1 - \eta_i^2}{N + 1}, \quad (i = 1, \dots, N), \quad (37)$$

$$\eta_i = \cos\left(\frac{i\pi}{N + 1}\right), \quad (i = 1, \dots, N), \quad (38)$$

$$w_j = \cos\left(\frac{2j - 1}{N + 1} \frac{\pi}{2}\right), \quad (j = 1, \dots, N + 1). \quad (39)$$

In (35) the additional equation is equivalent to consistency condition of the integral equation. It may be shown that the $(N/2 + 1)$ -th equation in (35) is automatically satisfied. Thus, (35) and (36) provide $N + 1$ algebraic equations to determine $N + 1$ unknowns, which are $G(\eta_i)$, $(i = 1, \dots, N)$, and the contact half-width (a). The system of equations is linear for $G(\eta_i)$, but nonlinear in terms of the variable (a). Therefore, an iteration scheme had to be used to obtain this unknown. In this iterative procedure, firstly N equations $[j = 1, \dots, (N/2), (N/2 + 2), \dots, (N + 1)]$ are chosen from (35). After predicting value for (a), $G(\eta_i)$ ($i = 1, \dots, N$) are calculated using previously determined N equations. If the chosen (a) and obtained $G(\eta_i)$ values ensure (36), the solution would have been found. Otherwise, $G(\eta_i)$ values are recalculated after predicting new (a) value.

To determine the initial separation load and the initial separation distance between the functionally graded layer and the homogeneous half-plane, (33) needs to be equalized to zero. Using this equation, the initial separation load and the initial separation distance can be determined together.

III. RESULTS AND DISCUSSION

This section presents the numerical results generated by using analytical procedures whose details are provided in Section II. We take into consideration four cases of functionally graded layer, a stiffer layer with $\beta h < 0$, a softer layer with $\beta h > 0$, the heavier layer with $\gamma h < 0$, the lighter layer with $\gamma h > 0$ from the top surface of the functionally graded layer to that of the bottom surface.

Fig. 2 illustrates the effect of the punch radius R/h on the normalized contact pressure under rigid punch. From this figure, it can be concluded that increasing the value of punch radius results in a reduction of the peak value of contact pressure. The effect of the load ratio $\mu_0/(P/h)$ on the normalized contact pressure under rigid punch is shown in Fig. 3. The results of Fig. 3 reveal the fact that for increasing values of the load ratio, the peak value of the contact pressure increases. Fig.

4 depicts effect of the inhomogeneity parameter (βh) on the normalized contact pressure under rigid punch. It is seen that as the inhomogeneity parameter (βh) increases in the positive sense, i.e. as the rigidity of the layer decreases from top to bottom, the peak value of the normalized contact pressure decreases. It can also be seen from this figure, negative values of the inhomogeneity parameter (βh) increases in absolute value, i.e. as the rigidity of the layer increases from top to bottom, the peak value of the normalized contact pressure increases.

Fig. 5 shows the normalized contact pressure distribution between functionally graded layer and homogeneous half-plane for various values of punch radius. It is clearly evident from this figure that as punch radius increases, the initial separation load and distance between functionally graded layer and homogeneous half-plane increase. The normalized contact pressure distribution between functionally graded layer and homogeneous half-plane for various values of load ratio is given in Fig. 6. Examination of Fig. 6 indicates that, the initial separation load and distance between functionally graded layer and homogeneous half-plane decreases for increasing values of load ratio. The normalized contact pressure distributions between functionally graded layer and homogeneous half-plane for various values of inhomogeneity parameter (βh) is presented in Fig. 7. As can be seen in the figure, the inhomogeneity parameter (βh) increases in the positive sense, i.e. as the rigidity of the layer decreases from top to bottom, the initial separation load decreases and the initial separation distance increases. Besides, the opposite effect can be obtained when negative values of the inhomogeneity parameter (βh) increases in absolute value. Fig. 8 shows the normalized contact pressure distribution between functionally graded layer and homogeneous half-plane for various values of inhomogeneity parameter (γh). It is observed that as the inhomogeneity parameter (γh) increases in the positive sense, i.e. as the functionally graded layer becomes lighter, the initial separation load between functionally graded layer and homogeneous half-plane decreases. Besides, the initial separation distance between functionally graded layer and homogeneous half-plane is not affected by the change in the inhomogeneity parameter (γh).

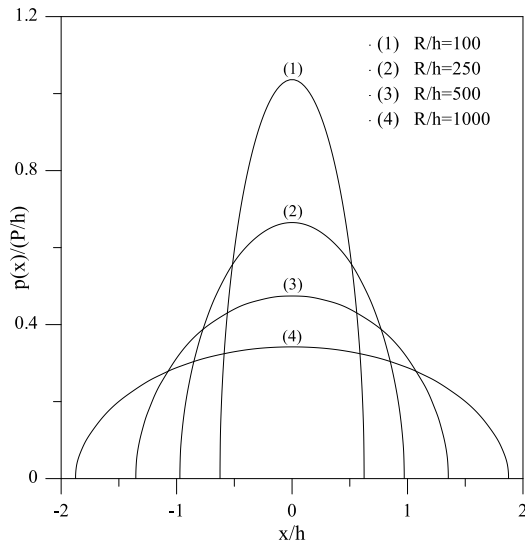


Fig. 2. Effect of the punch radius R/h on the normalized contact pressure under rigid punch ($\kappa_1=\kappa_2=2$, $\mu_0/(P/h)=100$, $\beta h=-0.6931$, $\mu_0=1$, $h=1$, $\mu_h/\mu_2=1$)

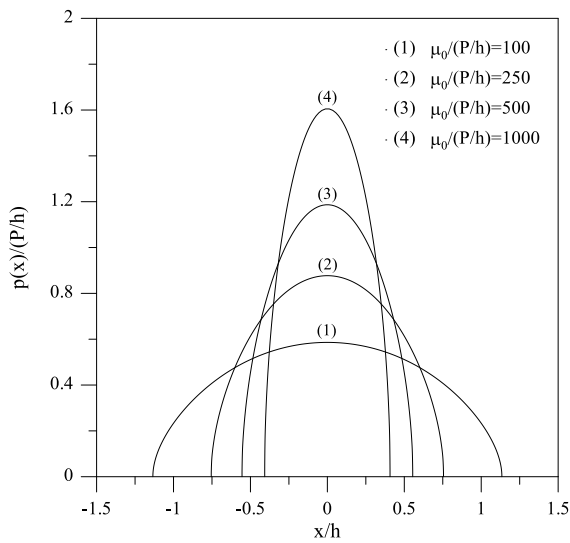


Fig. 3. Effect of the load ratio $\mu_0/(P/h)$ on the normalized contact pressure under rigid punch ($\kappa_1=\kappa_2=2$, $R/h=500$, $\beta h=-1.3863$, $\mu_0=1$, $h=1$, $\mu_h/\mu_2=1$)

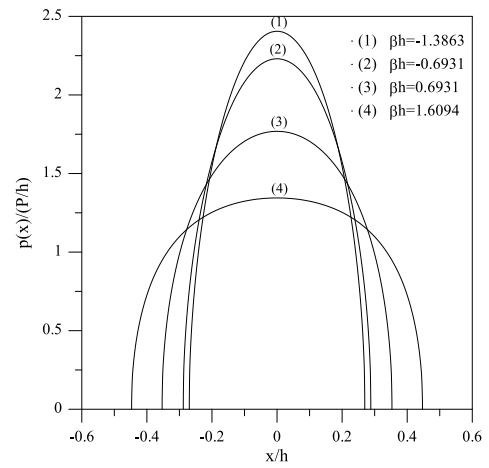


Fig. 4. Effect of the inhomogeneity parameter βh on the normalized contact pressure under rigid punch ($\kappa_1=\kappa_2=2$, $R/h=100$, $\mu_0/(P/h)=500$, $\mu_0=1$, $h=1$, $\mu_h/\mu_2=1$)

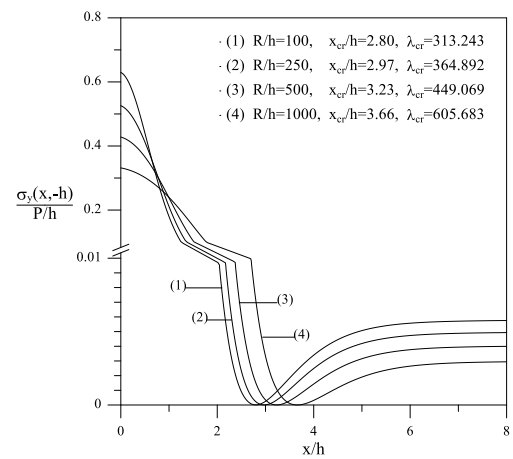


Fig. 5. Normalized contact pressure distribution between functionally graded layer and homogeneous half-plane for various values of punch radius R/h ($\kappa_1=\kappa_2=2$, $\mu_0/(P/h)=100$, $\gamma h=-1.0986$, $\beta h=-0.6931$, $\mu_0=1$, $h=1$, $\mu_h/\mu_2=1$)

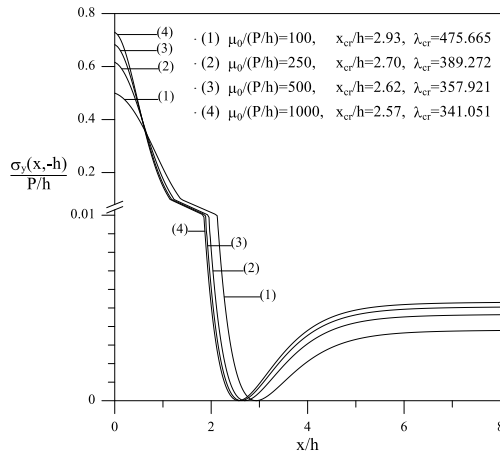


Fig. 6. Normalized contact pressure distribution between functionally graded layer and homogeneous half-plane for various values of load ratio $\mu_0/(P/h)$ ($\kappa_1=\kappa_2=2$, $R/h=500$, $\gamma h=-1.0986$, $\beta h=-1.3863$, $\mu_0=1$, $h=1$, $\mu_h/\mu_2=1$)

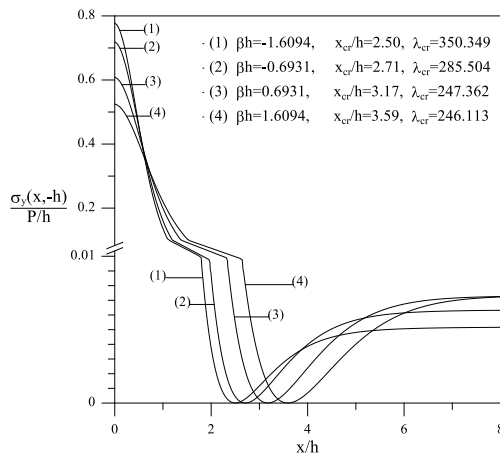


Fig. 7. Normalized contact pressure distribution between functionally graded layer and homogeneous half-plane for various values of inhomogeneity parameter βh ($\kappa_1=\kappa_2=2$, $R/h=100$, $\mu_0/(P/h)=500$, $\gamma h=-1.0986$, $\mu_0=1$, $h=1$, $\mu_h/\mu_2=1$)

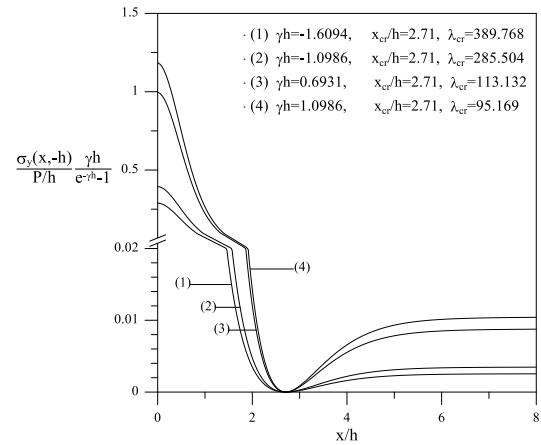


Fig. 8. Normalized contact pressure distribution between functionally graded layer and homogeneous half-plane for various values of inhomogeneity parameter γh ($\kappa_1=\kappa_2=2$, $R/h=100$, $\mu_0/(P/h)=500$, $\beta h=-0.6931$, $\mu_0=1$, $h=1$, $\mu_h/\mu_2=1$)

IV. CONCLUSION

The conclusions drawn from this study can be written as:

- As the punch radius increases, the peak value of contact pressure under punch decreases, the initial separation load and distance between functionally graded layer and homogeneous half-plane increase.
- As the load ratio increases, the peak value of contact pressure under punch increases, the initial separation load and distance between functionally graded layer and homogeneous half-plane decrease.
- As the functionally graded layer becomes stiffer, the peak value of contact pressure under punch increases, the initial separation load increases and the initial separation distance decreases.
- As the functionally graded layer becomes softer, the peak value of contact pressure under punch decreases, the initial separation load decreases and the initial separation distance increases.
- As the functionally graded layer becomes heavier, the initial separation load increases
- As the functionally graded layer becomes lighter, the initial separation load decreases.
- The initial separation distance is not affected by the fact that the functional graded layer is heavier or lighter.

REFERENCES

- [1] M. Koizumi, "FGM activities in Japan," *Compos Part B-Eng*, vol. 28, pp. 1-4, 1997.
- [2] M.A. Guler, and F. Erdogan, "Contact mechanics of graded coatings," *Int J Solids Struct*, vol. 41, pp. 3865-3889, 2004.
- [3] M.A. Guler, and F. Erdogan, "Contact mechanics of two deformable elastic solids with graded coatings," *Mech Mater*, vol. 38, pp. 633-647, 2006.
- [4] M.A. Guler, and F. Erdogan, "The frictional sliding contact problems of rigid parabolic and cylindrical stamps on graded coatings," *Int J Mech Sci*, vol. 49, pp. 161-182, 2007.
- [5] L.-L. Ke, and Y.-S. Wang, "Two-dimensional contact mechanics of functionally graded materials with arbitrary spatial variations of material properties," *Int J Solids Struct*, vol. 43, pp. 5779-5798, 2006.
- [6] L.-L. Ke, and Y.-S. Wang, "Two-dimensional sliding frictional contact of functionally graded materials," *Eur J Mech A-Solid*, vol. 26, pp. 171-188, 2007.
- [7] L.-L. Ke, and Y.-S. Wang, "Fretting Contact of Two Dissimilar Elastic Bodies with Functionally Graded Coatings," *Mech Adv Mater Struc*, vol. 17, pp. 433-447, 2010.
- [8] J. Yang, and L.-L. Ke, "Two-dimensional contact problem for a coating-graded layer-substrate structure under a rigid cylindrical punch," *Int J Mech Sci*, vol. 50, pp. 985-994, 2008.
- [9] T.-J. Liu, and Y.-S. Wang, "Axisymmetric frictionless contact problem of a functionally graded coating with exponentially varying modulus," *Acta Mech*, vol. 199, pp. 151-165, 2008.
- [10] J. Liu, L.-L. Ke, Y.-S. Wang, J. Yang, and F. Alam, "Thermoelastic frictional contact of functionally graded materials with arbitrarily varying properties," *Int J Mech Sci*, vol. 63, pp. 86-98, 2012.
- [11] Y.T. Zhou, and K.Y. Lee, "Exact solutions of a new, 2D frictionless contact model for orthotropic piezoelectric materials indented by a rigid sliding punch," *Philos Mag*, vol. 92, pp. 1937-1965, 2012.
- [12] İ. Çömez, "Contact problem of a functionally graded layer resting on a Winkler foundation," *Acta Mech*, vol. 224, pp. 2833-2843, 2013.
- [13] S.J. Chidlow, W.W.F. Chong, and M. Teodorescu, "On the two-dimensional solution of both adhesive and non-adhesive contact problems involving functionally graded materials," *Eur J Mech A-Solid*, vol. 39, pp. 86-103, 2013.
- [14] S. El-Borgi, S. Usman, and M.A. Güler, "A frictional receding contact plane problem between a functionally graded layer and a homogeneous substrate," *Int J Solids Struct*, vol. 51, pp. 4462-4476, 2014.
- [15] J. Yan, and X. Li, "Double receding contact plane problem between a functionally graded layer and an elastic layer," *Eur J Mech A-Solid*, vol. 53, pp. 143-150, 2015.
- [16] K.S. Parel, and D.A. Hills, "Frictional receding contact analysis of a layer on a half-plane subjected to semi-infinite surface pressure," *Int J Mech Sci*, vol. 108-109, pp. 137-143, 2016.
- [17] M.A. Güler, A. Kucuksucu, K.B. Yilmaz, and B. Yildirim, "On the analytical and finite element solution of plane contact problem of a rigid cylindrical punch sliding over a functionally graded orthotropic medium," *Int J Mech Sci*, vol. 120, pp. 12-29, 2017.
- [18] G. Adıyaman, A. Birinci, E. Öner, and M. Yaylacı, "A receding contact problem between a functionally graded layer and two homogeneous quarter planes," *Acta Mech*, vol. 227, pp. 1753-1766, 2016.
- [19] A.O. Çakiroğlu, and F.L. Çakiroğlu, "Continuous and discontinuous contact problems for strips on an elastic semi-infinite plane," *Int J Eng Sci*, vol. 29, pp. 99-111, 1991.
- [20] E. Öner, G. Adıyaman, and A. Birinci, "Continuous contact problem of a functionally graded layer resting on an elastic half-plane," *Arch Mech*, vol. 69, pp. 53-73, 2016.
- [21] F. Erdogan, and G.D. Gupta, "On the numerical solutions of singular integral equations," *Q Appl Math*, vol. 29, pp. 525-534, 1972.

Adopted Material Properties of Historical Masonry Structures for Finite Element Models: Mosques and Bridges

Onur Onat

Civil Engineering Department
Munzur University
Tunceli
onuronat@munzur.edu.tr

Burak Yön

Civil Engineering Department
Munzur University
Tunceli
burakyon@gmail.com

Abstract—This paper aims to present adopted material properties of masonry elements to historical mosque and bridge structures. The importance of this study is to adopt correct material properties with reliable reference according to material types and structure types.

Keywords—material properties; historical structures; historical mosques; historical bridges

I. INTRODUCTION

Historical structures are the most important part of civilization where constructed. Therefore, these cultural heritages of the urban population should be protected through centuries against external extreme loads. Conservation of cultural heritages are commonly considered as suitable restoration. However, with developing numeric analysis tools, it is possible to estimate global behavior of a historical structures available and after restoration situation under severe loads like earthquake. Structural characteristics of a historical monument mostly depend on the availability of local construction materials during construction era [1]. Moreover, it is difficult to determine the engineering properties of materials adopted to the historical structures due to the lack of experimental data and forbidden destructive test by authorities [2]. For this reason, indirect methods are developed to evaluate historical structures to reveal information related to available conditions. These indirect assessment methods are based on visual inspection, geometrical and crack pattern survey, surface decay mapping, radar, geoelectric and ultrasonic testing. Listed indirect methods are not convenient for the assessment of historical masonry structure alone. In addition, these methods cannot be substituted by destructive testing [3]. These are necessary to understand the damages and their causes and carry out a first interpretation of the phenomena [4].

During the analytical modelling, defining incorrect or uncertain material properties causes unavoidable wrong results. For a typical masonry heritage, the most difficult step is defining input parameter to quantify the material properties of masonry and mortar assembly. When developing a (FE)

models, especially for historic masonry structure, it is possible to define imprecise input parameters that can result in unrealistic models and erroneous solutions [5]. Indefinite references or insufficient material data force researcher to use wide range of data with lower boundary and upper boundary [6]. The aim of using upper and lower boundary material data is to adapt randomly selected engineering property due to insufficient material data for modelled structure. The reliability of the selected material properties depends mostly on model calibration of the FE model. Basic philosophy of model calibration is to compare dynamic identification test result of investigated structure with FE model of the same structure on the base of natural vibration period and frequencies. The success of model calibration depends not only on selecting the correct comparative quantitative but also in updating the correct quantitative. Thus, if the extreme use of the FE model is to assess damage in historical structures, the engineering properties must be adapted well to represent linearity and nonlinearities. Model calibration includes engineering judgment and self-intuition about selecting calibration parameters. Moreover, the unforeseen dependencies or correlations of parameters possibly arise among the calibrated inputs. If these dependencies or correlations are strong, this will raise the problem of the calibration of one parameter compensating for imprecision in another [5]. Besides, purchasing accelerometer always not possible due to extreme cost of test set up and non-destructive application. For listed reason above, it is very important to define certain and robust material properties for investigated historical structures.

This study presents 14 different study composed of mosques and bridges.

II. STRUCTURE TYPES

A. Mosques

Mosques are one of the most prominent religious structures in the history. Nearly all dominated sultans let to construct mosque to shown power. Many of the available mosques are still in use. For this reason, response of their behavior against

external loads needs to be assessed. Koçak and Köksal (2010) investigated seismic behavior of Little Hagia Sophia with FE modelling. Adopted material properties were suited with destructive and non-destructive methods [7] and addressed to Aköz and Yüzer (1995) [8]. Teomete and Aktaş (2010) implemented destructive tests on historical masonry and brick elements of an historical Urla Kamanlı mosque in İzmir Turkey [9]. Demir and İlki (2014) studied on material properties and characterization of single layer and multi-layer Küfeki stone in other words limestone which is commonly used to construct mosques [10]. Demir and İlki (2014) characterized the multi layered Küfeki stone in other words limestone according to sample dimensions 40x30 cm, 40x26 cm and 40x20 cm respectively [10]. Altunışık et al. (2015) assessed the performance of Kaya Çelebi Mosque in Turkey. For this purpose, dynamic modal analysis and seismic spectral analysis were performed on model [11]. Material properties were adopted by Altunışık et al. (2015) addressed to Can et al. (2012) [12], Dal-Cin and Russo (2014) [2014] and Saloustros (2015) [14]. Cakir et al. (2015) modelled and analyzed Erzurum Lala Pasha Mosque. For this purpose, firstly material characterization was implemented and then FE model was prepared. Compressive strength and tensile strength of materials were obtained from experimental characterization. However, elasticity modulus and density adapted from literature [15]. Nohutcu et al. (2015) studied Hafsa Sultan Mosque in Turkey. In their study, ultrasonic pulse velocity was used to obtain mechanical properties of granite and stone. Homogenization approach was used to determine mechanical properties of FE model [16]. Nohutcu et al. (2015) obtained mechanical properties by using ultrasonic pulse velocity test and then these values evaluated as bigger to adapt complete model of masonry elements [16]. Güllü and Karabekmez (2016) investigated seismic behavior of 125 years old Gaziantep Kurtuluş mosque. Material properties were adopted from literature [17]. Elasticity modulus, poisson ratio and compressive strength values were obtained from predicting with genetic algorithm by Baykasoğlu et al. (2008) [18]. Tensile strength value is adopted like $1/f_c$. İlerisoy and Soyuk (2012) studied on Şehzade Mehmet mosque to assess seismic performance [19]. Adopted material properties was addressed to similar studies by Kaya et al. (1998) [20]. Addressed reference contains a numeric study related to Süleymaniye mosque. Altunışık et al. (2016) studied on seismic safety of Kaya Çelebi mosque [21]. Material properties were adopted from Can et al. (2012) [12], Dan Cin and Russo (2014) [13] and Saloustros et al. (2015) [14]. Mangia et al. (2016) assessed seismic performance of Eltihatun Mosque located in Tunceli province. Adopted material properties obtained from literature on the base of medium hard masonry elements [22]. These properties can be seen in Table 1. There are eight mosques and experimental studies related to mosque. Material properties of these investigated mosques can be seen in Table 1.

TABLE I. ADOPTED MATERIAL PROPERTIES TO MOSQUES

Author(s)	Age and Material Properties				
	Age	Density (kg/m ³)	Young's Modulus (MPa)	Compressive Strength (MPa)	Tensile Strength (MPa)
Koçak and Köksal (2010)	536	NA	10000	10	1
Teomete and Aktaş (2010)	14 th century	1700	2700	4.25	0.425
Demir and İlki (2014)	15 th century	2050	2615	7.91	1.6
Altunışık et al. (2015)	1660	2000	1600	0.3	NA
Cakir et al. (2015)	1562	1900	350	17.49	2.69
Nohutcu et al. (2015)	16 th century	2200	1500 (1210)	7.42	0.74
Güllü and Karabekmez (2016)	1892	2500	25000	40	4
İlerisoy and Soyuk (2012)	1548	2190 (Arch), 2000 (Dome)	8500 (Arch), 3000 (Dome)	NA	NA
Altunışık et al (2016)	1663	2400	1200	NA	NA
Mangia et al. (2016)	1252	2200	1500	3	0.15

The numbers in bracked demonstrates calibrated parameters

B. Bridges

There are many historical bridges either restored or non-restored in our country. A few of these bridges were studied by researchers. Hacıfendioglu et al. (2015) assessed seismic behavior of masonry arch Kurt bridge in Turkey against blast induced ground motion [23]. Material properties of bridge adopted from Sevim et al. (2011) [24]. Güllü and Jaf (2016) modelled a historical arch bridge with two different boundary condition approach. One of them is soil structure interaction and other of them is with fixed base boundary condition [25]. Material properties were adopted from similar study by Ural and Doğangün (2007) [2]. However, Ural and Doğangün estimated material properties on the base of their experiences for the same arch bridge. Altunışık et al. (2015) modelled a historical arch bridge called as Göderni bridge. Adopted material properties were obtained from laboratory test results. Sayın (2016) performed nonlinear dynamic analysis on a historical masonry arch bridge called as Nadir bridge [27]. The source of adopted material parameters is unknown. Sevim et al. (2011) presented earthquake response of historical masonry arch bridge [24]. Adopted material properties were referenced to similar studies by Frunzio et al. (2001) [28], Tokar and Unay (2001) [29] and Brencich and Sabia (2008) [30].

TABLE 2 ADOPTED MATERIAL PROPERTIES TO BRIDGES

Author(s)	Age and Material Properties				
	Age	Density (kg/m ³)	Young's Modulus (MPa)	Compressive Strength (MPa)	Tensile Strength (MPa)
Hacıfendioglu et al. (2015)	13th century	2140.7	3000	NA	NA
Güllü and Jaf (2016)	18th century	2354, 2353, 1961	3000, 2500, 1000	NA (Arch), NA (Spandrel), NA (Parapet)	NA
Altunışık et al. (2015)	19th century	2000	5000 (Arch), 3000 (Abutment)	NA	NA
Sayın (2016)	1569	2300, 2200	2500 (Arch), 2000 (Spandrel)	NA	0.5, 0.4
Sevim et al. (2011)	19th century	1600, 1400	3000 (Arch), 2500 (Side Wall)	NA	NA

III. STATISTICAL ANALYSIS

This section contains statistical evaluation and correlation of Young's modulus and compressive strength of historical masonry material. The most common and used masonry materials are limestone and brick. Statistical evaluations are performed on these materials to easily obtain missing parameters with a known parameter.

A. Limestone

Limestone is of the most used material among historical masonry structures. Even if material properties are more abundant while compared with other materials, abrasion factor and environmental interference change the material properties of this material based on local conditions.

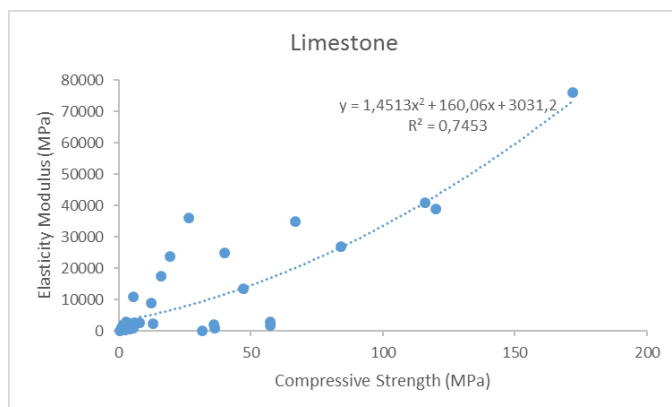


Figure 1. Young's modulus versus compressive strength of Limestone

As seen from the Figure 1, correlation between the Young's modulus and compressive strength is polynomial. This correlation can be defined with an equation indicated in the figure above. The confidence percent is 74.53%. This equation is proposed to determine unknown parameter with known one.

B. Brick

Brick is one another abundant material after stone masonry. One of the most important property of brick is more consistent than stone masonry. Because, while plotting the data and fitting the best curve to this material type, none of the data was ignored.

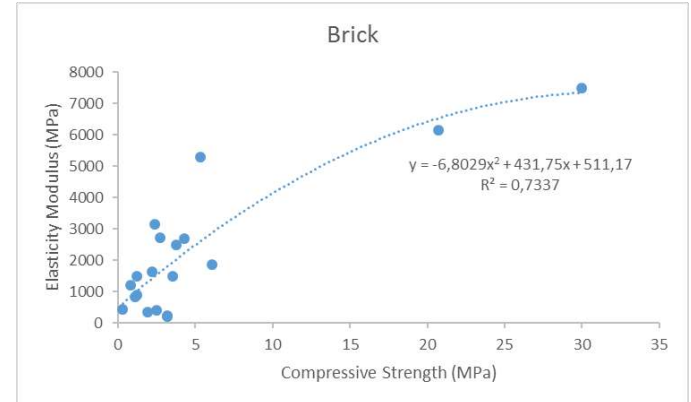


Figure 2. Young's modulus versus compressive strength of brick

The best fitted curve between the Young's modulus and compressive strength is polynomial as seen in Figure 2. Confidence percent is 73.37%.

IV. DISCUSSION

After the FE modelling procedure, one of the most important key point is to define correct parameter of historical heritage. Many researchers are missing a few important parameters like poison ratio, compressive strength or tensile strength. However, each parameter has own importance. Ural and Doğangün (2007) [2] investigated changing mechanical properties of infill and arch material parameters on the seismic performance of historical masonry arch bridge. However, Ural and Doğangün adopted material properties on the base of their experiences and considered intervention of material by external natural events. Güllü and Jaf (2016) [25] modelled a historical masonry arch bridge with soil structure interaction (SSI) and without SSI and then addressed Ural and Doğangün related to material properties of Mataracı bridge located at Trabzon. But, Ural and Doğangün performed sensitivity analysis on the base of masonry arch and infill material properties. Moreover, Ural and Doğangün considered natural intervention on mechanical properties of material [2]. Güllü and Karabekmez (2016) obtained material properties of investigated mosque by prediction with genetic algorithm on the base of in-situ testing [17]. Mangia et al. (2016) obtained material properties from literature referenced to medium strong masonry elements. Indeed, this assumption does not reflect actual behavior of the historical mosque [22]. Sayın (2016) implemented a numeric study on a historical Nadir bridge to assess seismic performance of the bridge [27]. However, adopted material properties has not been addressed to any reference. In addition, the used material type is not clearly presented in the study. This unknown information decrease reliability of the study. One

another example is randomly selected material properties on the base of self-experience like Ramos et al. (2010) performed model calibration on historical masonry tower before starting structural analysis [31]. However, randomly 1000 MPa elasticity modulus was selected for FE model of the historical tower. This random selection was implemented on the base of self-experience and high confidence of dynamic identification. However, due to high instrumentation cost, dynamic identification is always not possible for researcher.

V. CONCLUSION

The purpose of this paper is to present material properties of historical structures. Mosques and bridges were considered for this study. Moreover, this study limited with national historical structures. Recently, there are numerous study revealed by investigators that seek for performance evaluation of historical structures. However, reliability of these investigations depends completely on the adopted material properties of the investigated structure. External intervention is nearly impossible on historical monuments in order not to disturb available property of value. For this purpose, reliable references are required especially for numeric model of the investigated monument. Correct material properties that adapted to numeric model is indispensable to implement risk assessment of any type of historical structure. This study collected all material properties of investigated historical structures either with destructive or non-destructive testing evaluation. Moreover, this study includes experimental tests to determine engineering properties of the historical element or structure. This paper has contributions to the literature on the base of listed aspects;

1. Before performing a numerical assessment of a historical structure, precise material properties should be adopted to the structure with the same material and the structural type.

2. In an investigated structure, material properties of all element type cannot be the same properties. Vault, arch and wall element of the same model may contain different material properties even if these element type composed of the same material.

3. Adopted material properties can be calculated by different approaches like homogenization. This calculated property reflects overall behavior of brick and mortar unit. While calculating these parameters, selected material properties of the unit and mortar should be selected on the base of individual characterized elements.

4. Adopted material properties should simulate structural intervention and restoration well.

REFERENCES

- [1] Dogangun, A., Sezen, H. "Seismic vulnerability and preservation of historical masonry monumental structures". *Earthquake and Structures*, 2012, 3(1), 83-95.
- [2] Ural A, Dogangun A, "Arch bridges in East Blacksea Region of Turkey and effects of infill materials on a sample bridge". In: Lourenco PB, Oliveira DV, Portela A (eds) ARCH'07-5th international conference on arch bridges, proceedings of the 5th international conference on arch bridges, 12-14 September, Madeira, 2007, pp 543-550.
- [3] Wenzel, F., Kahle, M.. Indirect methods of investigation for evaluating historic masonry. 1993, IABSE reports, Zurich
- [4] Binda, L., Tiraboschi, C. Flat-Jack Test: A slightly destructive technique for the diagnosis of brick and stone masonry structures. *International Journal for Restoration of Buildings and Monuments*, 1999, 5(5), 449-472.
- [5] Atamturktur, S., Laman, J. A. "Finite element model correlation and calibration of historic masonry monuments: review." *The Structural Design of Tall and Special Buildings*, 2012, 21(2), 96-113.
- [6] Atamturktur, S., Bornn, L., Hemez, F. "Vibration characteristics of vaulted masonry monuments undergoing differential support settlement". 2011, *Engineering Structures*, 33(9), 2472-2484.
- [7] Koçak, A., Köksal, T. "An example for determining the cause of damage in historical buildings: Little hagia sophia (Church of St. Sergius and Bacchus)-İstanbul, Turkey. 2010, *Engineering Failure Analysis*, 17(4), 926-937.
- [8] Akoz, F., Yüzer, N. "Investigation of Material Properties of Kucuk Ayasofya Mosque-Sts Sergius and Bacchus of Istanbul". 1995, *WIT Transactions on The Built Environment*, 16.
- [9] Teomete, E., Aktaş, E. "Structural analyses and assessment of historical Kamanlı Mosque in Izmir", Turkey. *Journal of performance of constructed facilities*, (2010), 24(4), 353-364.
- [10] Demir, C., Ilki, A. "Characterization of the materials used in the multi-leaf masonry walls of monumental structures in Istanbul, Turkey." *Construction and Building Materials*, 2014, 64, 398-413.
- [11] Altunisik, A. C., Kanbur, B., Genc, A. F. "The effect of arch geometry on the structural behavior of masonry bridges". *Smart Structures and Systems*, 2015, 16(6), 1069-1089.
- [12] Can, H., Kubin, J., Unay, A. I. "Seismic behavior of historical masonry buildings with irregular geometry". *Journal of the Faculty of Engineering and Architecture of Gazi University*, 2012, 27(3), 679-686.
- [13] Dal Cin, A., Russo, S. "Influence of the annex on seismic behavior of historic churches". *Engineering Failure Analysis*, 2014, 45, 300-313.
- [14] Saloustros, S., Pelà, L., Roca, P., and Portal, J. "Numerical analysis of structural damage in the church of the Poblet Monastery". *Engineering Failure Analysis*, 2015, 48, 41-61.
- [15] Cakir, F., Seker, B. S., Durmus, A., Dogangun, A., Uysal, H. "Seismic assessment of a historical masonry mosque by experimental tests and finite element analyses". *KSCE Journal of Civil Engineering*, 2015, 19(1), 158-164.
- [16] Nohutcu, H., Demir, A., Ercan, E., Hokelekli, E., Altintas, G. "Investigation of a historic masonry structure by numerical and operational modal analyses". *The Structural Design of Tall and Special Buildings*, 2015, 24(13), 821-834.
- [17] Güllü, H., Jaf, H. S. "Full 3D nonlinear time history analysis of dynamic soil-structure interaction for a historical masonry arch bridge". *Environmental Earth Sciences*, 2016, 75(21), 1421.
- [18] Baykasoğlu, A., Güllü, H., Çanakçı, H., & Özbakır, L. "Prediction of compressive and tensile strength of limestone via genetic programming". *Expert Systems with Applications*, 2008, 35(1), 111-123.
- [19] İlerisoy, Z. Y., Soyluk, A. "Impact of shallow earthquakes on the Sehzade Mehmet Mosque". *Gravevinar*, 2012, 64(9), 735-740.
- [20] Kaya, S. M., Aydinoglu, M. N., Erdik, M., Yuzugullu, O. "Determination of Dynamic Characteristics of Suleymaniye Mosque by Analytical and Experimental Methods". *Compatible Materials for the Protection of European Cultural Heritage*. Istanbul, 1998, 56-68.

- [21] Altunisik, A. C., Bayraktar, A., Genc, A. F. "A study on seismic behaviour of masonry mosques after restoration". *Earthquakes and Structures*, 2016, 10(6), 1331-1346.
- [22] Mangia, L., Ghisassi, B., Sayin, E., Onat, O., Lourenço, P. B., "Pushover Analysis of Historical Elti Hatun Mosque", 12th International Congress on Advances in Civil Engineering, 2016, Boğaziçi University, Istanbul
- [23] Hacıfendioglu, K., Banerjee, S., Soyluk, K., Alpaslan, E. "Stochastic dynamic analysis of a historical masonry bridge under surface blast-induced multi-point ground motion". *Stochastic Environmental Research and Risk Assessment*, 2015, 29(5), 1275-1286.
- [24] Sevim, B., Bayraktar, A., Altunisik, A. C., Atamtürkür, S., Birinci, F. "Finite element model calibration effects on the earthquake response of masonry arch bridges". *Finite Elements in Analysis and Design*, 2011, 47(7), 621-634.
- [25] Güllü, H., Jaf, H. S. "Full 3D nonlinear time history analysis of dynamic soil-structure interaction for a historical masonry arch bridge". *Environmental Earth Sciences*, 2016, 75(21), 1421.
- [26] Altunisik, A. C., Kanbur, B., Genc, A. F. "The effect of arch geometry on the structural behavior of masonry bridges". *Smart Structures and Systems*, 2015, 16(6), 1069-1089.
- [27] Sayin, E. "Nonlinear seismic response of a masonry arch bridge". *Earthquakes and Structures*, 2016, 10(2), 483-494.
- [28] Frunzio, G., Monaco, M., Gesualdo, A. "3D FEM analysis of a roman arch bridge". *Historical constructions*, 2001, 591-598.
- [29] Toker, S., Ünay, A. I. "Mathematical modeling and finite element analysis of masonry arch bridges". *Gazi University Journal of Science*, 2004, 17(2), 129-139.
- [30] Brencich, A., Sabia, D. "Experimental identification of a multi-span masonry bridge: The Tanaro Bridge". *Construction and Building Materials*, 2008, 22(10), 2087-2099.
- [31] Ramos, L. F., Marques, L., Lourenço, P. B., De Roeck, G., Campos-Costa, A., Roque, J. "Monitoring historical masonry structures with operational modal analysis: two case studies". *Mechanical Systems and Signal Processing*, 2010, 24(5), 1291-1305.

The Effect of Centric Steel Braced Frames with High Ductility Level on the Performance of Steel Structures

¹Mustafa ÜLKER, ²Ercan IŞIK, ³Mehmet ÜLKER

¹Technical Sciences VHS, Bitlis Eren University, Bitlis, Turkey

²Bitlis Eren University, Engineering Faculty, Civil Engineering Department, Bitlis, Turkey

³Firat University, Engineering Faculty, Civil Engineering Department, Elazig, Turkey

Email: ¹ mulker444@gmail.com, ² eisik@beu.edu.tr, ³ mulker@firat.edu.tr

Abstract--The basic functions expected from any structure are generally sufficient rigidity, ductility and stiffness. In this study, the effect of steel ducts with high ductility level on the performance of steel structures was investigated. For this purpose, calculations were made using five different types of central steel curtains for steel flues of any hospital building. Period, frequency, modal addition rates, displacement and rotation values are calculated and compared for each different central steel screen. The aim of the study is to be informed about the central steel slabs with high ductility level and to have information about which of the most suitable central steel slabs will be chosen.

Keywords--Ductility; High Ductility; Steel Structures; performance; Steel Cross Braced Frame

I. INTRODUCTION

Rigidity, ductility and strength must be sufficient to ensure that the earthquake loads are transmitted continuously and safely to the foundation of the earthquake loads as well as in each of the elements constituting the earthquake loads at the same time [1]. Adequate rigidity, strength and ductility are at the top of the principles considered in the design of earthquake-affected structures. In the regulation of the structural bearing system, the material strength, the ductility and

stiffness concepts in the elements are important parameters. These parameters need to be built into the structure.

Generally, ductile conveying systems are the foreground in the depressive structure design. However, it is emphasized that the selection of the regular carrier system in the horizontal and vertical sections and the encouragement to be shown in the junctions of the elements.

Ductility is defined as the extent of displacement of a section, of an element or of a carrier system, without significant change in external load, beyond the elastic limit, and the system ductility rate is proportional to the linear shape changes of the total shape changes in the displacement order. The result of the system ductility ratio taking large values ensures that the structure can change its nonlinear shape sufficiently before migration.

Central crossed structures are very popular for medium height structures. Design and production are simple and the required horizontal stiffness and strength can be obtained with low cost. The horizontal stiffness of the central steel cross curtains is provided by vertically positioned cage beams. This lattice behavior is obtained by crossing the column and the beams [2], [3], [4].

In this study, calculations were made in the case of using five different centric steel braced frames for a steel chimney belonging to a structure designed as a hospital building. The results were compared and recommendations were made.

II. METHODOLOGY

Structural engineering is the science and art of designing and making, with elegance and economy, buildings, bridges, frameworks and other similar structures so that they can safely resist the forces to which they may be subjected. The main purpose of structural design is to produce suitable structure. We must consider not only the initial cost, but also the cost of maintenance, damage and

failure. Thus, the optimum design of a structure requires a general view on the total process.

The design of steel seismic resistant structures took a dramatic turn after the last Californian and Japanese events. The heavy damage observed as a result of these earthquakes was never before recorded in the history of building design. These events gave rise to a general effort all over the world to improve the seismic resistance of steel structures. A comprehensive program started to evaluate both the design specifications and detail

rules. In this perspective, clear attention has been paid to the evaluation of local ductility erosion at the level of sections [2].

A ductility is a measure of the ability of a section, an element, or a carrier system to deform beyond the elastic limit, without significant change in external load. The numerical definition of the system ductility ratio is the ratio of the total shape change to the linear shape change during the displacement.

The two most important features of steel are energy absorption capacity under ductility and repeated inelastic loading. In terms of behavior against depression, horizontal load carrier systems of steel buildings are separated into two classes in terms of ductility level [1].

In Turkish Seismic Code, DBYBHY-2007, based on their behaviour against seismic events, the lateral load bearing systems of the steel constructions are classified in two sections based on their ductility.

a. *Systems with High Ductility*

b. *Systems with Low Ductility*

Based on this, the classifications are further divided to

- *Frames with High Ductility,*
- *Shears with Steel Cross Beam Bars with High Ductility,*
- *Shears with Outer Steel Cross Beam Bars with High Ductility,*
- *Frames with Standard Ductility” and*
- *Shears with Steel Cross Beam Bars with Standard Ductility,*

to form a list with five different titles with descriptions in seismic activity regulations.

In this study, centric steel braced frames with high ductility level are shown in Figure 1. The lateral load carrying capacity of these systems is large, along with their bending strength. Obviously, these shear wall systems can be interpreted as earthquake walls in a reinforced concrete structure.

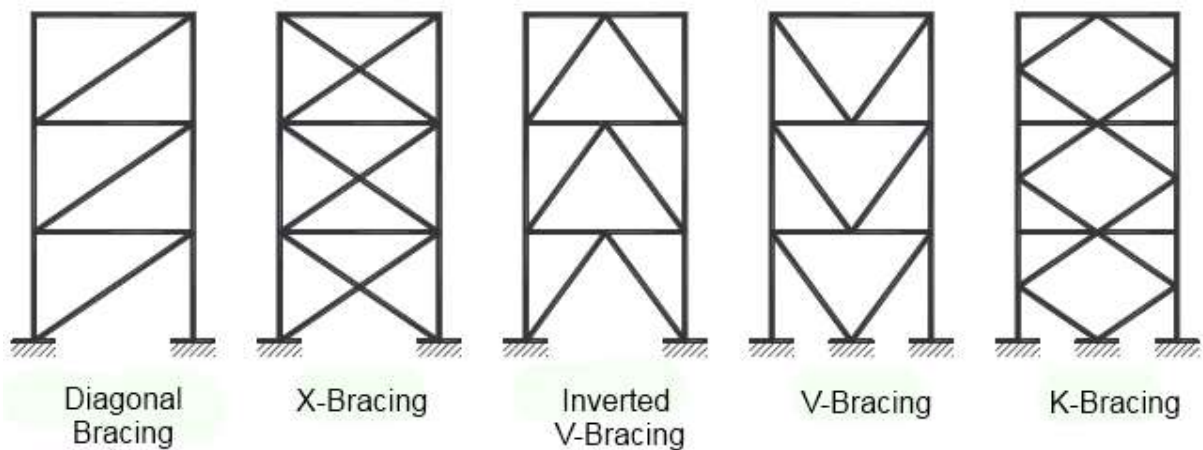


Fig. 1. Centric Steel Braced Frames with High Ductility

III. NUMERICAL APPLICATIONS

As a numerical application, a steel chimney of hospital structure was analyzed. In the project, the steel chimney was transferred to the rectangular truss system. The steel chimney has an area of 3,125 m² and a span of 2.5 m. The building height is 12 m. 150 * 150 * 5 mm was used for the structural system columns and 60 * 60 * 4 mm box

profiles were used for the beams and bracing members (Figure 2).

Fe37 steel was used as material. In Fe37 steel $\sigma_{saf} = 14.1 \text{ kN/cm}^2$, $\sigma_{yield} = 24 \text{ kN/cm}^2$, $\sigma_{weld} = 11 \text{ kN/cm}^2$ were taken.

In calculations, truss span $L = 2,50 \text{ m}$, truss space $L' = 1,25 \text{ m}$ and number of truss were two. The wind load is taken as $q = 0.8 \text{ kN/m}^2$ from TS498 Specification [5].

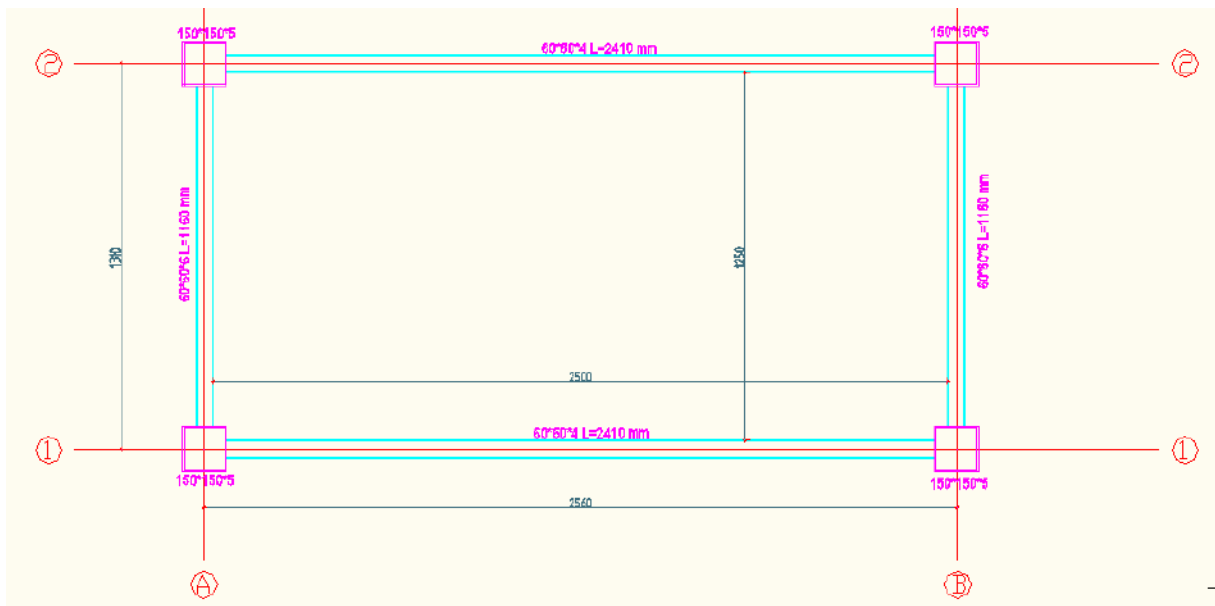


Fig. 2. Steel Chimney Plan

The steel chimney was modeled and analyzed in the SAP2000 package program [6]. It is modeled as a 12-storey structure while modeling a 12 m high chimney system. Five different centric

steel braced frames were used in this study. Centric steel braced frame types considered in the study are taken from the SAP2000 program and shown in Figure 3.

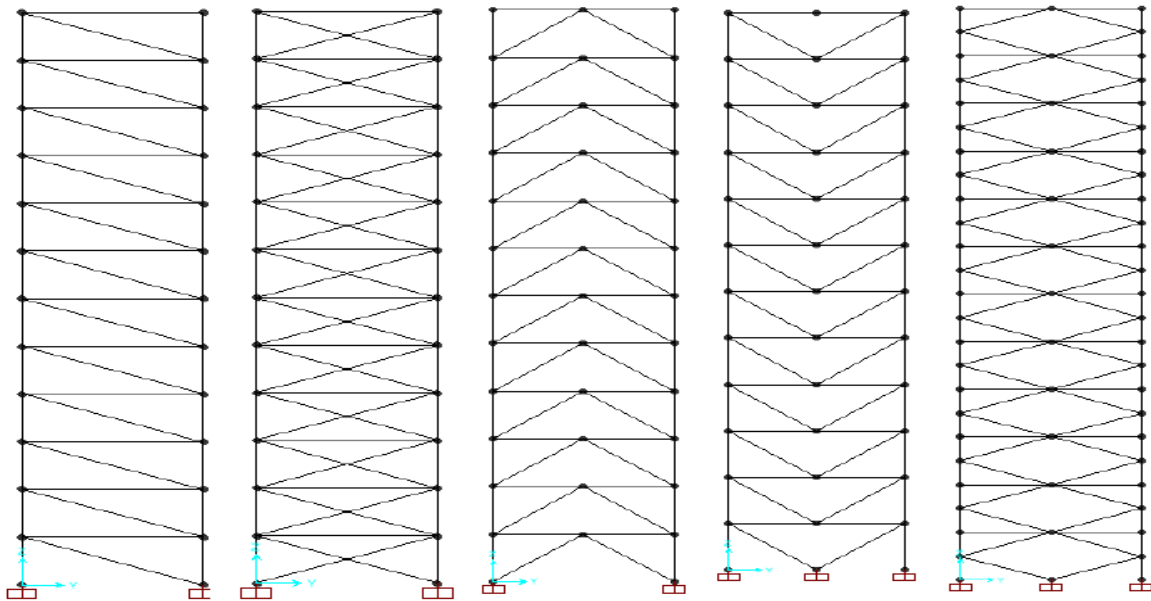


Fig. 3. SAP2000 model of Centric Steel Braced Frames

In the dynamic analysis of the chimney system, the seismic parameters and function values shown in Figure 4 are entered. Period, frequency

and eigenvalues are calculated for each braced type with these values.

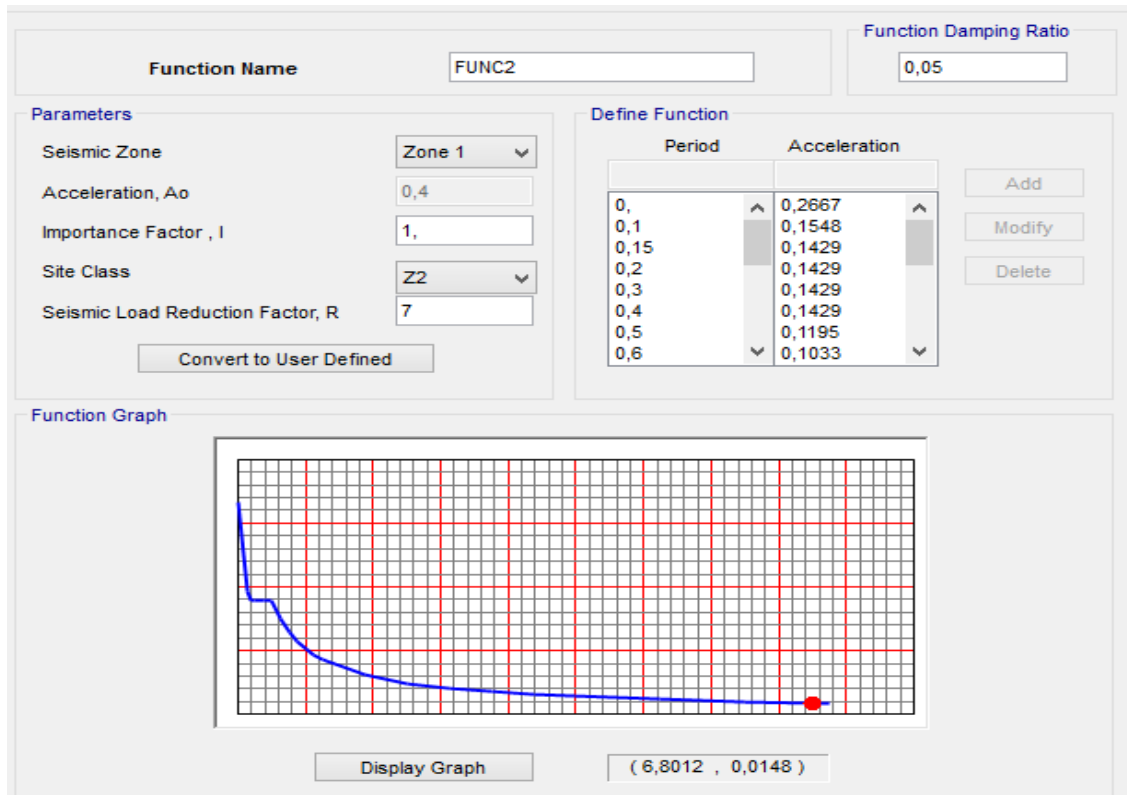


Fig. 4. Seismic parameters in SAP2000 program

The displacements and rotations calculated in the SAP2000 program for the five different steel

braced frames given in Figure 3 above are presented in Table 1.

TABLE 1. Displacements and rotations of centric steel braced frames

FRAME TYPE	Displacements [mm]			Rotations [rad]		
	U _x	U _y	U _z	R _x	R _y	R _z
Diagonal Bracing	10,40	-0,10	-0,70	0,00000	0,00095	-0,00013
X-Bracing	8,90	0,27	-0,70	0,00000	0,00090	-0,00010
Inverted V-Bracing	8,20	0,00	-0,50	0,00000	0,00082	0,00000
V-Bracing	10,70	0,00	-0,70	0,00000	0,00100	0,00000
K-Bracing	8,90	0,00	0,60	0,00000	0,00090	0,00000

As shown in Table 1, the maximum lateral displacement is calculated as $U_x = 10.7$ mm at the top of the steel chimney. In the specifications, displacement is generally given as $U_x \leq \Delta_{\max} =$

$H/300$ limit. From here, if the constraint is checked, $U_x = 10.7 \text{ mm} \leq \Delta_{\max} = 12000/300 = 40 \text{ mm}$ will be seen.

IV. RESULTS

In this study, the effect of five frames with high ductility level centric steel braced frames were investigated. Horizontal displacement values occurring in the building under lateral loads (earthquake and wind loads) are given in Table 1. The limitation given by the specifications is provided with confidence. That is, the frame with high ductility level centric steel braced frames is provided with a rigidity of about four times.

Nearly the same performance was achieved with five types of centric steel braced frames applied to lateral displacements.

With the classic Moment-resisting frames, larger lateral displacements are obtained and displacement limits can not be achieved.

Finally, it is concluded that the systems providing the best limitations for earthquake performance and specifications are high ductility level centric steel braced frames.

REFERENCES

- [1] DBYBHY-2007 (2009), Turkish Earthquake codes, Specification for structures to be built in disaster areas, Ankara, Turkey.
- [2] ANSI/AISC 341-10 (2010), Seismic Provisions for Structural Steel Buildings, American Institute of Steel Construction, Chicago, Illinois, USA.
- [3] Denavit, M. D., Hajjar, J. F., Perea, T. and Leon, R. T. (2016). "Seismic performance factors for moment frames with steel-concrete composite columns and steel beams", *Earthquake Engineering and Structural Dynamics*, **45**(10), 1685-1703.
- [4] Montuori, R., Nastri, E. and Piluso, V. (2015), "Seismic response of EB-frames with inverted Y-scheme: TPMC versus eurocode provisions", *Earthquakes and Structures*, **8**(5), 1191-1214.
- [5] TS-498 (1997), Design Loads for Buildings, Turkish Standards Institution, Ankara, Turkey.
- [6] SAP2000 (2015) Integrated Finite Elements Analysis and Design of Structures, Computers and Structures, Inc, Berkeley, CA.

Finite element solution of the contact problem*

Pembe Merve Karabulut 1nd Affiliation (*Author*)

Civil Engineering Department
Karadeniz Technical University
Trabzon, Turkey
pembemerve.karabulut@ktu.edu.tr

Murat Yaylaci 2nd Affiliation (*Author*)

Civil Engineering Department
Recep Tayyip Erdogan University
Rize, Turkey
murat.yaylaci@erdogan.edu.tr

Ahmet Birinci 3rd Affiliation (*Author*)

Civil Engineering Department
Karadeniz Technical University
Trabzon, Turkey
birinci@ktu.edu.tr

Abstract—In this paper, continuous and discontinuous contact problems for layers loaded by symmetrical distributed loads whose lengths are $2a$ on an elastic semi-infinite plane is solved using finite element method. The elastic layer also subjected to uniform vertical body force because of effect of the gravity. Thickness in z direction is taken to be unit. It is assumed that the contact surfaces are frictionless, only normal tractions can be transmitted through the contact areas. The contact along the interface between elastic layer and half plane is continuous if the value of load factor is less than a critical value. In continuous and discontinuous contact cases, the stress distribution on the contact interface are plotted for different dimensionless quantities. The finite element method of the problem is constituted using ANSYS software and analysis of the problem is carried out. Finally, the results obtained from the finite element solution are verified by comparison with the analytical results. (*Abstract*)

Keywords—mechanic, continuous contact, discontinuous contact, elasticity, half plane, finite element analysis.

I. INTRODUCTION

Since contact problems have possible application to a variety of structures of practical interest such as foundation grillages, pavements in roads and runways, railway ballasts and other structures consisting of layered media, there has been an increasing attention on the contact problems. There is large body of literature concerned with contact problems both analytically [1-9] and numerically [10-15].

Except for these papers, El-Borgi et al. investigated a receding contact problem between a functionally graded layer and a homogeneous substrate and they studied the effect of the material nonhomogeneity parameter and the thickness of the graded layer on the contact pressure and on the contact lengths. Kahya et al. studied a receding contact problem for an anisotropic elastic medium consisting of a layer and a half plane and they obtained contact stresses and contact lengths for

different fibre orientations. A double receding contact axisymmetric problem between a functionally graded layer and a homogeneous half plane is solved Rhimi et al.. Effects of surface tension on axisymmetric Hertzian contact problem and they obtained helpful results to characterize and measure the mechanical features of soft materials or biomaterials through micro-indentation. El-Borgi et al. considered a frictional receding contact problem between a functionally graded layer and a homogeneous semi-infinite plane and they analyzed the effect of friction coefficient and nonhomogeneity factor on the contact pressure distribution and contact lengths. Gun and Gao presented a quadratic boundary element formulation for continuously nonhomogeneous, isotropic and linear elastic functionally graded material contact problems with friction. Yan and Li analyzed double receding contact problem between functionally graded layer and elastic layer. Li et al. are presented fundamental contact solutions of a magneto-electro-elastic half space indented by a smooth and rigid half infinite punch. Comez studied moving contact problem for a rigid cylindrical punch and a functionally graded layer and he obtained an effect of relative moving velocity for contact problem of functionally graded layer.

In this paper, continuous and discontinuous contact problem for infinite layer on an elastic semi-infinite plane is solved using FEM. The load which will occur by initial separation and the bigger values than this load, the stress distribution on the contact surfaces are plotted for different dimensionless quantities. Finally, the results obtained from FEM are verified by comparison the analytical results.

II. DEFINITION OF THE PROBLEM

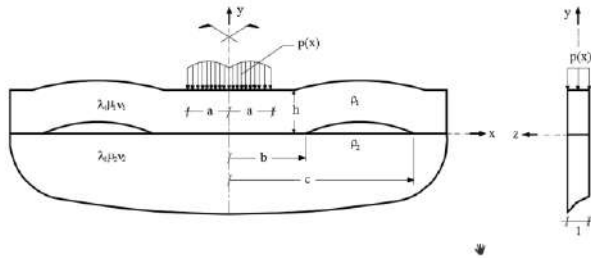


Fig. 1. Geometry and loading of the contact problem

In this paper continuous and discontinuous contact problems for layers on an elastic semi-infinite plane is solved using finite element method. Layers are loaded by symmetrical distributed loads whose lengths are $2a$ and thickness in z direction is taken to be unit. It is assumed that the contact surfaces along the interfaces is frictionless, only normal tractions can be transmitted through the contact surfaces, body forces of elastic layer is taken into account and body force of semi-infinite plane is neglected.

As shown in Fig. 1, consider the symmetric plane strain problem consist of an infinitely long homogeneous layer of thickness h in smooth contact with semi-infinite plane. μ_1 , ν_1 and ρ_1 are the shear modulus, poisson ratios and density of a layer respectively. Similarly μ_2 , ν_2 and ρ_2 are the shear modulus, poisson ratios and density of a half space respectively.

III. THE FINITE ELEMENT SOLUTION

The finite element method is a numerical method for solving problems of engineering and mathematical physics. In this method, problem divides into simpler parts that are called finite elements and the model transform into large system of equations. With recent developments in computer technology and package programs for FEM solution of large system of equations is fulfilled.

In this study, the finite element analysis is performed by ANSYS software program. The geometrical model is created with the standart tools in ANSYS software. Because of the problem exhibits symmetry in geometry, material proportions and loading, only half of the problem is modeled. The geometry and the applied load are shown symmetrically in Fig. 2. The layer and semi-infinite plane are considered as linear elastic and isotropic. In the analysis, geometric properties are taken as $L = 12m$ (length of the layer in x direction), $h_1 = 1m$ (thickness of the layer in y direction). Other parameters are choosen such that $p_0/\rho gh$, μ_1/μ_2 , κ_1/κ_2 . Are compatible with analytical values.

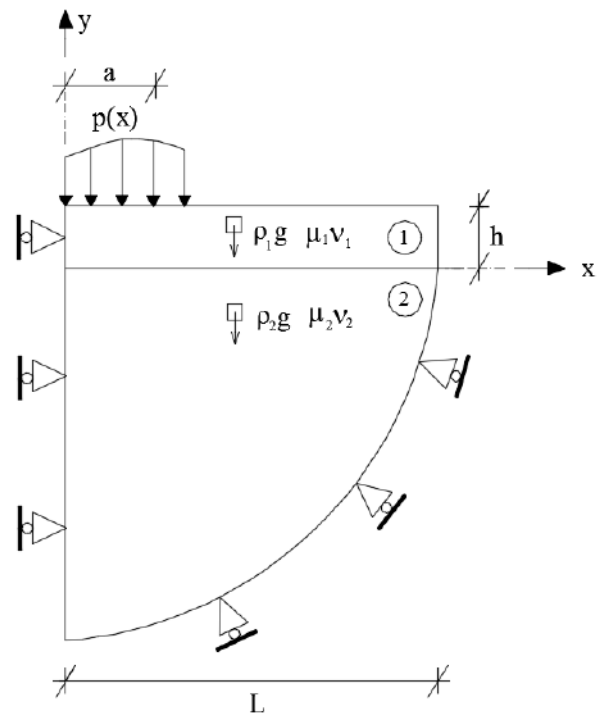


Fig. 2. Schematic model of the contact problem (symmetric finite element model)

PLANE183 element is used for the modeling elastic layer and semi-infinite plane. PLANE183 element consist of eighth nodes having two degrees of freedom: translations in the nodal x and y directions. Frictionless surface-to-surface 2D contact elements are used to model the interaction between the contact surfaces: CONTA172 and TARGE169. CONTA172 is used to represent contact. Target surfaces is defined by TARGE169 for the associated contact elements CONTA172. Several numerical solution methods have been proposed to solve the variational equation of elastic contact problem, including penalty method, augmented Lagrangian method, Lagrange multiplier method method and augmented Lagrangian multiplier method. These methods incorporated to general finite element analysis (FEA) technology, are applied to solve the contact problem that involves complex geometry shapes. In the penalty method, the accuracy of the solution depends on the choice the penalty parameter. Too small a penalty parameter may cause unacceptable error in the solution. Also the penalty method suffers from ill-conditioning as the penalty parameter becomes large. The augmented Lagrangian method is an iterative series of penalty methods. The contact tractions (pressure and frictional stresses) are augmented during equilibrium iterations so that the final penetration is smaller than the allowable tolerance. Compared to penalty method, the augmented

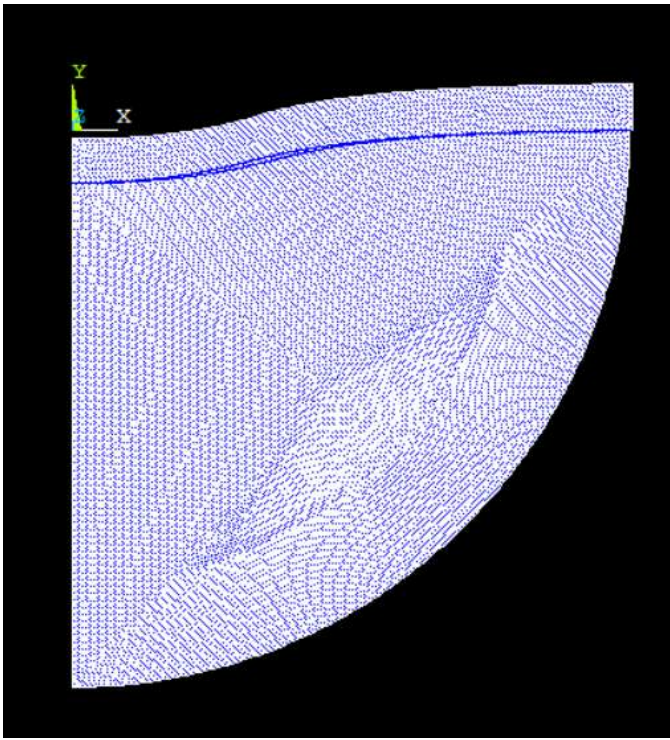


Fig. 3. Deformed shape after finite element analysis.

Lagrangian method usually leads to better conditioning and is less sensitive to the magnitude to contact stiffness. The Lagrange multiplier method introduces new unknowns for each constraint. Therefore, it always increases the dimension of the system equations to be solved. For large scale problems where the contact surface consist of a large number of nodes, the number of unknowns introduced by the Lagrange multiplier method is also large. This increases the CPU time to solve the problem. For the augmented Lagrangian multiplier method, both penalty parameters and Lagrangian multipliers are applied, and penetration is admissible but controlled by allowable tolerance [28]. In this study, Augmented Lagrangian method is used as the contact algorithm. And the deformed shape after analysis is shown in Fig. 3

IV. CONCLUSIONS

In this paper, continuous and discontinuous contact problem for infinite layer and semi-infinite plane is solved by using finite element method and results obtained from finite element method are verified by comparing with analytical results in literature. Note that all quantaties are dimentionless.

Fig. 4-5 shows contact stress distributions for the continuous contact cases. It can be seen that the initial separation point x_{cr} seems to increase as a/h increases.

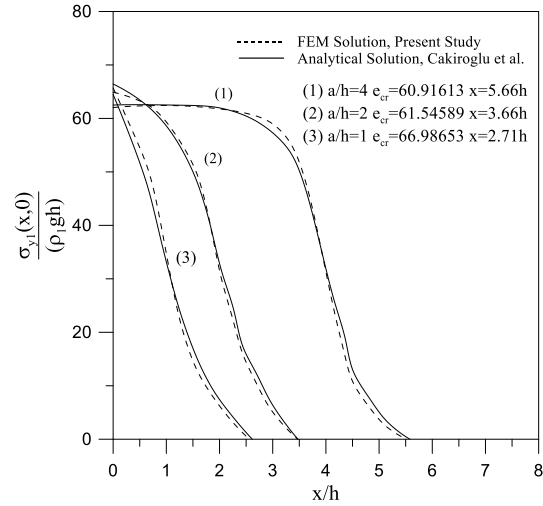


Fig. 4. Contact stress distributions for the cases of continuous ($e=e_{cr}$) for the first loading condition. ($\mu_1/\mu_2 = 1/3$, $e_{cr} = p_0/(\rho_0 gh)$)

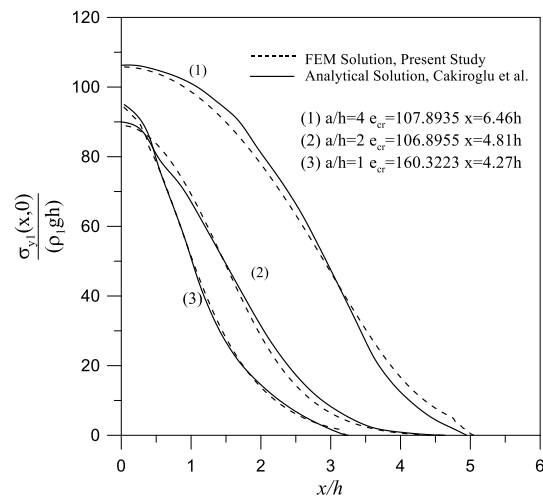


Fig. 5. Contact stress distributions for the cases of continuous ($e=e_{cr}$) for the second loading condition. ($\mu_1/\mu_2 = 3$, $e_{cr} = p_0/(\rho_0 gh)$)

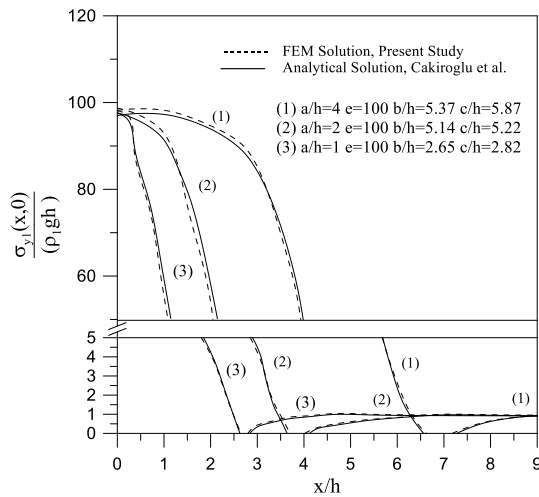


Fig. 6. Contact stress distributions for the cases of discontinuous ($e > e_{cr}$) for the first loading condition. ($\mu_1/\mu_2 = 1/3$, $e_{cr} = p_0/(\rho gh)$)

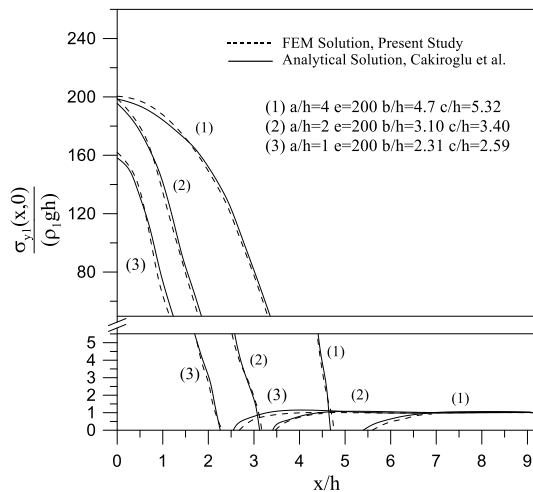


Fig. 7. Contact stress distributions for the cases of discontinuous ($e > e_{cr}$) for the first loading condition. ($\mu_1/\mu_2 = 1/3$, $e_{cr} = p_0/(\rho gh)$)

The variation of the normalized contact stress $\sigma_y(x,0)/(\rho gh)$ between the infinite layer and semi-infinite plane is shown Fig. 5-6. As it can be seen in graphics, there are three regions in the discontinuous contact between the layer and semi-

infinite plane. These are the continuous contact region, separation zone, and the discontinuous contact region where the effect of the external load (P) decreases and disappears infinitely. If the a/h increases, initial separation point occurs a longer distance from the origin and separation zone decreases for similar material proportions.

Finally, based of the comprasion of numerical values obtained from finite element solution and analytical solution in literature [11], difference between finite element solution and analytical solution in literature is in a acceptable range.

REFERENCES

- [1] S. K. Chan and I. S. Tuba, "A finite element method for contact problems of solid bodies - part I: theory and validation," *International Journal of Mechanical Sciences*, vol. 13(7), pp. 615-625, July 1971.
- [2] L. M. Keer, J. Dundurs and K. C. Tsai, "Problems involving a receding contact between a layer and a half space," *Journal of Applied Mechanics*, vol. 39(4), pp. 1115-1120, December 1972.
- [3] F. Erdogan and G. D. Gupta, "Numerical solution of singular integral equations," *Quarterly of Applied Mathematics*, vol. 29(4), pp. 525-&, 1972.
- [4] M. Ratwani and F. Erdogan, "On the plane contact problem for a frictionless elastic layer," *International Journal of Solids and Structures*, vol. 9(8), pp. 921-936, August 1973.
- [5] A. Francavilla and O. C. Zienkiewicz, "A note on numerical of elastic contact problems," *Inetenational Journal for Numerical Methods in Engineering*, vol. 9(4), pp. 913-924, January 1975.
- [6] G. G. Adams D. B. Bogy, "The plane symmetric contact problem for dissimilar elastic semi-infinite strips of different widths," *Journal of Applied Mechanics-ASME*, vol. 44(4), pp. 604-610, December 1977.
- [7] M. B. Civelek, F. Erdogan and A.O. Cakiroglu, "Interface separation for an elastic layer loaded by a rigid stamp," *International Journal of Engineering Science*, vol. 16(9), pp. 669-679, 1978.
- [8] M. R. Gecit, "Axisymmetric contact problem for a semi-infinite cylinder and a half space," *International Journal of Engineering Science*, vol. 24(8), pp. 1245-1256, 1986.
- [9] M. A. Abdou, "Integral equation and contact problem for a system of impressing stamps," *Applied Mathematics and Computation*, vol. 106(2-3), pp. 141-148, December 1999.
- [10] A. Francavilla and O. C. Zienkiewicz, "A note on numerical computation of elastic contact problems," *International Journal for Numerical Methods in Engineering*, vol. 9(4), pp. 913-924, 1975.
- [11] A. O. Cakiroglu and F.L. Cakiroglu, "Continuous and discontinuous contact problems for strips on an elastic semi-infinite plane," *International Journal of Engineering Science*, vol. 29, pp. 93-111, 1991.
- [12] H. -S. Jing and M. -L. Liao, "An improved finite element scheme for elastic contact problems with friction," *Mathematical and Computer Modeling*, vol. 15, pp. 143-154, 1990.
- [13] J. A. Gorrido, A. Foces and F. Paris, "BEM applied to receding contact problems with friction," *Mathematical and Computer Modeling*, vol. 15, pp. 143-154, 1991.
- [14] J. A. Gorrido, A. Foces and F. Paris, "BEM applied to receding contact problems with frictions," *Mathematical and Computer Modeling*, vol. 15(3-5), pp. 143-153, 1991.
- [15] J. A. Gorrido, A. Lorenzana, "Receding contact problem involving large displacements using the BEM," *Engineering Analysis with Boundary Elements*, vol. 21(4), pp. 295-303, June 1998.
- [16] S. El-Borgi, R. Abdelmaula and L. Keer, "A receding contact plane problem between a functionally graded layer and a homogeneous substrate," *International Journal of Solids and Structures*, vol. 43(3-4), pp. 658-674, February 2006.
- [17] V. Kahya, T. S. Ozsahin, A. Birinci and R. Erdol, "A receding contact problem for an anisotropic elastic medium consisting of a layer and a

- half plane,” *International Journal of Solids and Structures*, vol. 44(17), pp. 5695-5710, August 2007.
- [18] M. Rhimi, S. El-Borgi and N. Lajnef, “A double receding contact axisymmetric problem between a functionally graded layer and a homogeneous substrate,” *Mechanics of Materials*, vol. 43(12), pp. 787-798, December 2011.
- [19] J. M. Long and G. F. Wang, “Effects of surface tension on axisymmetric Hertzian contact problem,” *Mechanics of Materials*, vol. 56, pp. 65-70, January 2013.
- [20] H. Gun and X. W. Gao, “Analysis of frictional contact problems for functionally graded materials using BEM,” *Engineering Analysis with Boundary Elements*, vol. 38, pp. 1-7, January 2014.
- [21] X. -Y. Li, R. -F. Zheng and W. -Q. Chen, “Fundamental solutions to contact problems of a magneto-electro-elastic half space intended by a semi-infinite punch,” *International Journal of Solids and Structures*, vol. 51(1), pp. 164-178, January 2014.
- [22] S. El-Borgi, S. Usman and M. A. Guler, “A frictional receding contact plane problem between a functionally graded layer and a homogeneous substrate,” *International Journal of Solids and Structures*, vol. 51(25-26), pp. 4462-4476, December 2014.
- [23] G. Adiyaman, M. Yaylaci and A. Birinci, “Analytical and finite element solution of a receding contact problem,” *Structural Engineering and Mechanics*, vol. 54, pp. 69-85, 2015.
- [24] E. Oner, M. Yaylaci, and A. Birinci, “Analytical solution of a contact problem and comparison with the results from FEM,” *Structural Engineering and Mechanics*, vol. 54, pp. 607-622, 2015.
- [25] A. Birinci, G. Adiyaman, M. Yaylaci and E. Oner, “Analysis of continuous and discontinuous cases of a contact problem using analytical method and FEM,” *Latin American Journal of Engineering Science*, vol. 12, pp. 1771-1789, February 2015.
- [26] J. Yan and X. Li, “Double receding contact plane problem between a functionally graded layer and an elastic layer,” *European Journal of Mechanics A-Solids*, vol. 53, pp. 143-150, September 2015.
- [27] I. Comez, “Contact problem for a functionally graded layer intended by a moving punch,” *International Journal of Mechanical Sciences*, vol. 100, pp. 339-344, September 2015.
- [28] X. Liao and G. G. Wang, “Non-linear dimensional variation analysis for sheet metal assemblies by contact modeling,” *Finite Elements in Analysis and Design*, vol. 44, pp. 34-44, December 2015.

MS EXCEL Macro Applications of Finite Difference and Integration Method for Simply Supported Rectangular Plates Under Sinusoidal Load

Sedat SAVAŞ

Firat Univ. Eng. Faculty
Civil Eng. Dept.
Elazig/TURKEY
ssavas@firat.edu.tr

Abstract— In this study, an elastic plate under sinusoidal loading was compared with the finite differences and integration methods. This question type, which is one of the common examples in the literature, is available with various methods. In this study, Microsoft Excel excel macro program, VBA, has written program codes for both finite element method and integration method. The difference between the results of these programs and the CPU time is calculated.

Keywords— *Finite Difference Method; Integration Method; Elastic Plate ; microsoft Exell Macro*

I. INTRODUCTION

Numerous calculations have been made up to now on the solution of elastic plates. These studies were carried out by varying the dimensions of the elastic plaques from time to time and changing the loading conditions applied on the bases, changing the boundary conditions at the bases. In this study, four edges under sinusoidal loading resolve a simple supported elastic plate problem [1]. These solutions were compared with manual solutions and also within themselves.

In this analysis, VBA programming language in Microsoft Excel is used. The reason for choosing this applet is that it is easy to access and is easy to implement by every engineer. In addition, the ability to read data from the file and write data to the file is easier, as well as the wide selection of graphics. However, the CPU time is not the performance seen in other programming languages .

II. SINUSOIDAL LOAD UNDER ELASTIC PLATE

A. System geometry and loading condition

In the coordinate system given 2.1, the rectangular plate with long side a, short side b is simply supported. We assumed that the sinusoidal load distributed over surface of rectangular plate is given by the expression

$$q = q_0 \sin\left(\frac{\pi x}{a}\right) \cos\left(\frac{\pi y}{a}\right) \quad (1)$$

in which q_0 represents the intensity of the load at the center of the plate.

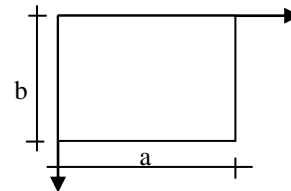


Fig 2.1. Rectangular plate

III. INTEGRATION METHOD

Generally, numerical approximation methods require reaching in several steps of solving by dividing time or space region into specific intervals, or in most cases require successive iteration solutions [2,3,4]. Numerical methods developed for this reason. They have various advantages or disadvantages in terms of the computational needs they require, the time spent on the solution or the CPU (Central Processing Unit) time, the stability of the equations, the number of node points used, the preprocessing for problem solving, and most importantly the time spent on this solution.

In this method, Elastic curve equation for (1) equation loading condition ;

$$\frac{\partial^4 w}{\partial x^4} + 2 \frac{\partial^4 w}{\partial x^2 \partial y^2} + \frac{\partial^4 w}{\partial y^4} = \frac{q}{D} \quad (2)$$

The differential equation (2) for the deflection surface in this case becomes;

$$\frac{\partial^4 w}{\partial x^4} + 2 \frac{\partial^4 w}{\partial x^2 \partial y^2} + \frac{\partial^4 w}{\partial y^4} = \frac{q_0}{D} \sin\left(\frac{\pi x}{a}\right) \cos\left(\frac{\pi y}{a}\right) \quad (3)$$

in which the quantity D, taking the place of the quantity EI in the case of beams, is called the flexural rigidity of the plate. The boundary conditions for simply supported edges are

$$w=0 \quad M_x=0 \quad \text{for } x=0 \text{ and } x=a$$

$$w=0 \quad M_y=0 \quad \text{for } y=0 \text{ and } y=b$$

we can represent the boundary conditions in the following form:

$$w=0 \quad \frac{\partial^2 w}{\partial x^2} = 0 \quad \text{for } x=0 \text{ and } x=a$$

$$w=0 \quad \frac{\partial^2 w}{\partial y^2} = 0 \quad \text{for } y=0 \text{ and } y=b$$

All boundary conditions are satisfied if we take for deflections the expression;

$$w = C \sin\left(\frac{\pi x}{a}\right) \cos\left(\frac{\pi y}{a}\right) \quad (4)$$

in which the constant C must be chosen so as to satisfy Eq. (3). Substituting expression (4) into Eq. (3), we find

$$\pi^4 \left[\frac{1}{a^2} + \frac{1}{b^2} \right]^2 C = \frac{q_0}{D} \quad (5)$$

and we conclude that the deflection surface satisfying Eq. (3) and boundary conditions is

$$w = \frac{q_0}{\pi^4 \left[\frac{1}{a^2} + \frac{1}{b^2} \right]^2 D} \sin\left(\frac{\pi x}{a}\right) \cos\left(\frac{\pi y}{a}\right) \quad (6)$$

In the light of these equations, we have applied this equation to find the displacements along the entire plate surface with the aid of the program we have done in excel macro.

Step of program:

- 1- Once plates surface is defined.
- 2- The plate lengths are divided into equal parts
- 3- Cyclic increments are made in the x and y directions

- 4- These values are placed in the equation
- 5- Program is stopped

IV. FINITE DIFFERENCE METHOD

Boundary value problems do not have many definite and closed solutions. Approximate solutions are available for this. Approximate methods are divided into characters. Some agrees with the provision of boundary conditions, but requires that the differential equation be precisely met. In the second group of methods, there is approximation in the presence of the differential equation, even if the boundary conditions are precise. The finite difference method is a method that can be applied to almost every other form entering this second group[].

It is possible to approximate the derivative of a function $y = f(x)$ at a certain set of discrete points, using known values. Similarly, approximate partial derivative formulas can be given for multivariable functions of type $z = f(x, y)$. Considering the definition of derivative, advanced difference approach, backward difference approach and central difference approach are emphasized.

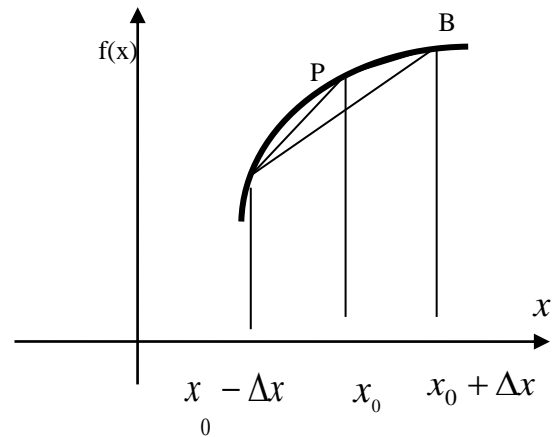


Fig. 2.2. The derivation of $f'(x)$ at point P using forward and backward and central differences

Advanced difference formula:

$$f'(x_0) = \frac{f(x_0 + \Delta x) - f(x_0)}{\Delta x} \quad (7)$$

Back difference formula:

$$f'(x_0) = \frac{f(x_0) - f(x_0 - \Delta x)}{\Delta x} \quad (8)$$

Central difference formula:

$$f'(x_0) = \frac{f(x_0 + \Delta x) - f(x_0 - \Delta x)}{2\Delta x} \quad (9)$$

The theory of elasticity is a branch of the theoretical physics, and the strain and shape changes that occur in elastic bodies under the influence of the objective external loads are calculated precisely by moving from a certain set of differential equations. In this case, the vehicle used for the solution is the differential equation theory[3].

The principal equation of plane elasticity theory;

$$\Delta(\sigma_x + \sigma_y) = \Delta\Delta F = \frac{\partial^4 F}{\partial x^4} + 2 \frac{\partial^4 F}{\partial y^2 \partial x^2} + \frac{\partial^4 F}{\partial y^4} = 0 \quad (10)$$

From the boundary conditions:

$$F_s = M(s) \text{ and } \left(\frac{dF}{dn} \right) = -Q_t(s) \quad (11)$$

Here;

F_s : Stress function,

$M(s)$: Static moment,

Q_t : It is the trace of the boundary value forces on the tangent.

The way to solve the problem of boundary value:

- Equation (11) calculates the values of the den function at the boundary precisely,
- The coefficients of the finite difference are calculated
- We extend the function to the outside of the region to be calculated,
- Divide the calculated shape into the desired number of node points to form the finite difference equations,
- Since the gauss-elimination method is used, conversion of the results to square matrix
- By solving these results into a matrix format.

V. SUMMARY AND CONCLISION

In this study, an elastic plate finite difference method and a generalized computer program were used to obtain the elastic plate deflection graph for a complex loading situation of the geometry. The results were compared and the solutions were made. In the comparison made, 0.01 percent error was observed between the integration method and the final difference method. Displacement graphics have topped. The reason is that The number of segment is excessive. But the solution time is ten times more in the finite difference method.

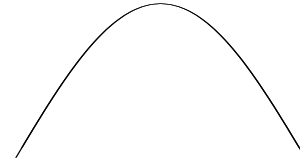


Fig. 5.1. Exaggerated displacement curve in the long side

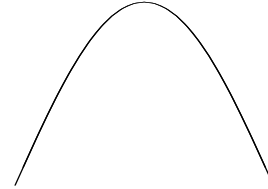


Fig. 5.2. Exaggerated displacement curve in the short side

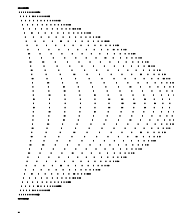


Fig. 5.3 Plate displacement view

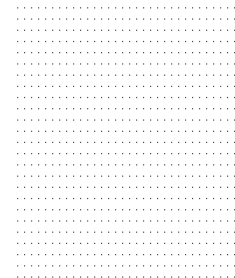


Fig. 5.4 Plate top view

REFERENCES

- [1] M. İnan, "Düzlemde Elastisite Teorisi" ,Matbaa Teknisyenleri Basımevi,bölüm 4,1976
- [2] C. F. Gerald and P. O. Wheatley, "Applied Numerical Analysis," by Addison Wesley Longman, Inc. (1997)
- [3] S. Tameroğlu "Elastisite Teorisi" İTÜ Matbaası, 1991
- [4] Ö. Cıvlek, M. Ülker "Polinomal Diferansiyel Quadrature(PDQ) ve Sonlu Farklar (SF) Metod Çifti ile Elastik Zemin Oturan Dikdörtgen Plakların Geometrik Bakımdan Lineer Olmayan Analizi"*İMO Teknik Dergi, (2006) 3739 -3760, Yazı 246

Determining dynamic characteristics of reinforced concrete minarets and updating of their finite element models using environmental vibration data

Musa YETKİN

Firat University
Department of Civil Engineering
Elazig, Turkey
E-mail : musayetkin@firat.edu.tr

Hakan ERKEK

Osmaniye Korkut Ata University
Department of Civil Engineering
Osmaniye, Turkey
E-mail : hakanerkek@osmaniye.edu.tr

Yusuf CALAYIR

Firat University
Department of Civil Engineering
Elazig, Turkey
E-mail : ycalayir@firat.edu.tr

Abstract— Structures are exposed to various dynamic effects such as earthquake, wind and traffic load. It need to be taken various measures for surviving the structures under dynamic loads. Taking the appropriate measures depends on the well-known of dynamic behavior of existing structures. This behavior of the structure can be known through analytical or experimental methods. In the analytical methods, many acceptance is made in finite element modeling of the structure and it is considered that the created model represents its existing case. However, it is rather difficult to fully represent of the existing structure with the accepted assumptions. In experimental methods, the dynamic characteristics of the structure (natural frequencies, mode shapes and damping ratios) are determined for the present case. Using these dynamic characteristics, the existing analytical model of the structure can be updated and the evaluation of the structure according to this new model can be made more realistic. In this study, analytical and experimental analyses of the minaret of Firat University Engineering Campus Mosque were carried out. The finite element model has been updated depending on the dynamic characteristics obtained from the experimental analysis.

Keywords— Dynamic characteristics; Reinforced concrete minaret; Analytical model; Environmental vibration data; updating of finite element model.

I. INTRODUCTION

As depending on the fast progress of the technology, the produced electronic devices enable easy observation of the behaviors of living things and also enable observation of the behaviors of the structures [1]. The analysis of the acceleration signals obtained with the help of accelerometers gives some

information about the structure. By comparing the results obtained for different situations, it can be determined whether there is any change in the behavior of the structure. Experimental Modal Analysis method is widely used for this purpose [2]. The basis of experimental modal analysis studies, which have application scope in many engineering disciplines, is based on the 1940s. At early times, non-practical approaches was mostly used since transformers measuring dynamic forces were simple. In the 1960s, the modern era of experimental modal analysis began as depending on the development of digital computers and Fast Fourier Transforms [3].

Structures are exposed to various dynamic effects such as earthquake, wind and traffic load. It need to be taken various measures for surviving the structures under dynamic loads. Taking the appropriate measures depends on the well-known of dynamic behavior of existing structures. While the dynamic characteristics of the structures (natural frequencies, mode shapes and damping ratios) are used to determine its dynamic behavior with using the mode superposition method, it also helps to control the accuracy of the analytical model. These characteristics cannot be at the expected values due to cracking, fatigue, collapse of support in the structures and/or workmanship faults during construction [4]. Therefore, it is considered that using of the dynamic characteristics obtained from analytical methods in determining dynamic response of the structures can be given incorrect results. Since experimental methods are applied on the current state of the structures, dynamic characteristics obtained by these methods reflect the current situation. Updating of analytical models of structures

with respect to results of experimental methods will lead to more realistic results [5-7].

There are many studies on determining the dynamic characteristics of structures based on experimental measurements [8-14]. In these studies, the dynamic characteristics of many structures such as minaret, tower, mosque, church, etc., which are constructed as reinforced concrete/masonry, are determined.

II. EXPERIMENTAL METHOD

Vibration is the behavior of structures under initial conditions or under applied external loads. Basically, there are two types of vibration, free and forced vibration [7,15]. Free vibration occurs under the initial conditions of the structure and ends with the effect of damping after a while. In this type of vibration, the fundamental frequency is the smallest frequency and usually the most effective frequency of the structure. If an external load is applied to the structure, the name of this vibration is the forced vibration. As long as the structure is exposed to external load, vibration of the structure continues [16]. The experimental method to be used varies depending on whether vibration is known or not. If the numerical values of vibration applied to the structure are known, Conventional Modal Analysis (CMA) method, if the numerical values of the vibration are unknown and the structure vibrates under of environmental effects, Operational Modal Analysis (OMA) method is used. OMA method are not needed expensive devices when compared to CMA method at large volume structures for artificial excitation [5,17].

OROS-OR36 Multichannel Noise and Vibration Analyzer is used in the experimental measurements based on the OMA method (Figure 1).



Fig. 1. OROS-OR36 Multichannel Noise and Vibration Analyzer

III. NUMERICAL APPLICATION

In this study, theoretical and experimental analyses of the minaret of Firat University Engineering Campus Mosque (Figure 2) were carried out. This minaret had built as reinforced concrete.

A. Theoretical Analysis

The analytical model of the selected reinforced concrete minaret was created with shell elements by using SAP2000 finite element package program. In the initial analytical model, the modulus of elasticity of the concrete was taken as $11 \cdot 10^3$ MPa (Figure 3). The values of first three frequencies obtained

from the modal analysis using the initial analytical model are 2.30, 2.45 and 8.77, respectively.



Fig. 2. Minaret of Firat University Engineering Campus Mosque

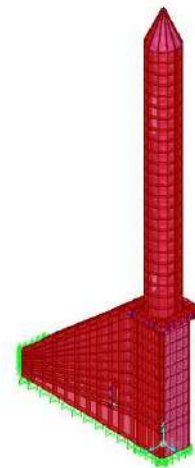


Fig. 3. Finite element model of Minaret

B. Experimental Analysis

1) *Creating Experimental Model:* OMA method were used in the experimental measurements of the structure. Measurements were taken with the accelerometers attached to 4 different points of the structure. The measurement points on each floor are selected as points having the same coordinates in the "x" and "y" directions. 8 accelerometers were totally used for the measurement without reference as two accelerometers each of which are placed in x and y directions for each point (Figure 4).

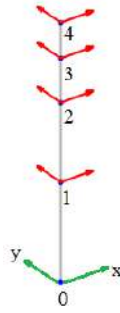


Fig. 4. The accelerometer system for measurement without reference

2) *Experimental Measurement and Updating Analytical Model*: After the preliminary tests of structure carried out, (finite element model solutions and in-situ wide frequency range measurements), the measurement frequency range, time and other parameters were determined. The Modal Indication Function was created by processing raw signals obtained from measurements. With the help of this function, first three frequencies were selected and values of that are 2.15, 2.32 and 9.56 Hz, respectively. Mode shapes with related these frequencies were given in Figure 5-6.

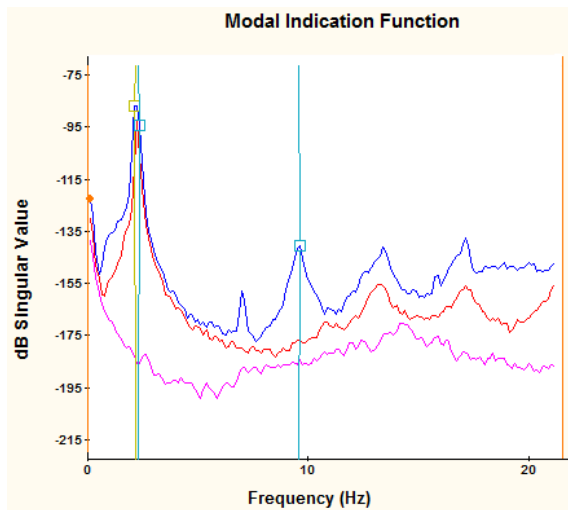


Fig. 5. Selected frequencies from modal indication function

The compatibility of analytical and experimental modes was controlled by a criterion called Modal Assurance Criteria (MAC). This criterion [16] is defined by the (1) equation.

$$MAC(\psi_a, \psi_d) = \frac{|\psi_a^T \psi_d|^2}{(\psi_a^T \psi_a)(\psi_d^T \psi_d)} \quad (1)$$

where ψ_a and ψ_d refer to analytical and experimental mode shape, respectively. If the analytical and experimental mode shapes are entirely the same, the MAC value must be 1, otherwise this value must be less than 1.

In comparison of the initial analytical model solutions and experimental results (Table I), the frequency and MAC values

were seen to be compatible for both method. It was also given experimental damping ratios in Table I. It is thought that differences between analytical and experimental frequencies can be minimized if the initial model of the structure is updated. The minaret mass is considerably known. There is more uncertainty in stiffness. Factors affecting the stiffness can be expressed as concrete elasticity and boundary conditions. Here, elasticity module of concrete was updated as 10×10^3 MPa. Modal analysis of the updated analytical model was performed and, the first three frequencies and mode shapes were presented in Table II and Figure 7, respectively. Now, the frequency and MAC values of first two modes for the updated analytical model are closer to the results of the experimental method.

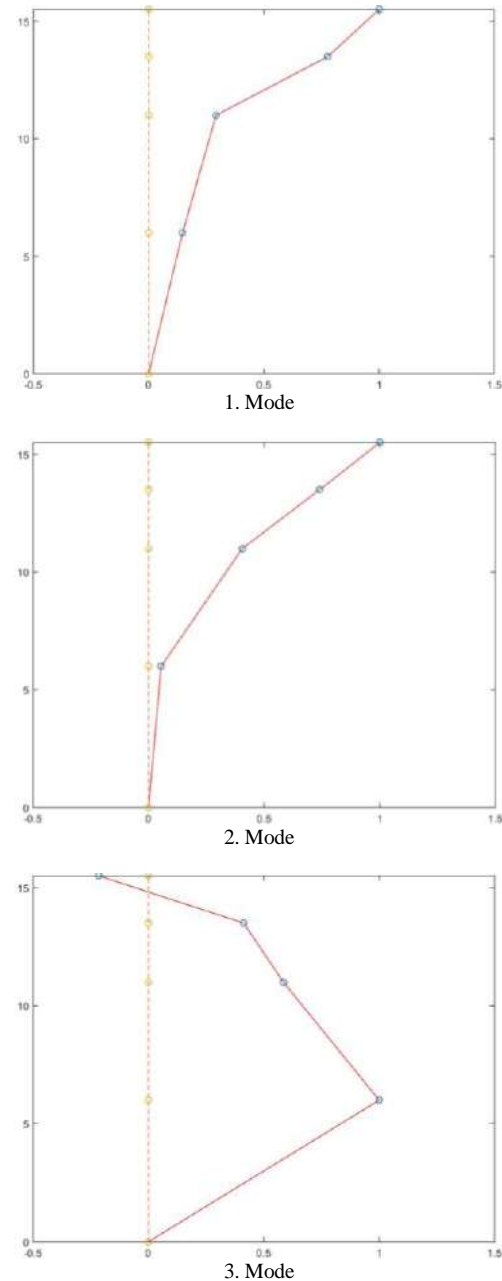


Fig. 6. Mode shapes for selected frequencies

TABLE I. COMPARISON OF INITIAL ANALYTICAL MODEL SOLUTIONS AND EXPERIMENTAL RESULTS

Mode Number	Analytical Frequencies (Hz)	Experimental Frequencies (Hz)	Experimental Damping Ratios (%)	MAC (%)
1	2.30	2.15	4.09	96.281
2	2.45	2.32	3.29	91.841
3	8.77	9.56	2.89	90.419

TABLE II. COMPARISON OF UPDATED ANALYTICAL MODEL SOLUTIONS AND EXPERIMENTAL RESULTS

Mode Number	Updated Analytical Frequencies (Hz)	Experimental Frequencies (Hz)	MAC (%)
1	2.24	2.15	96.366
2	2.34	2.32	95.898
3	8.58	9.56	90.397

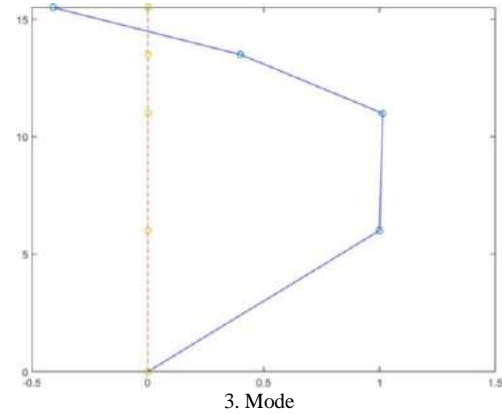
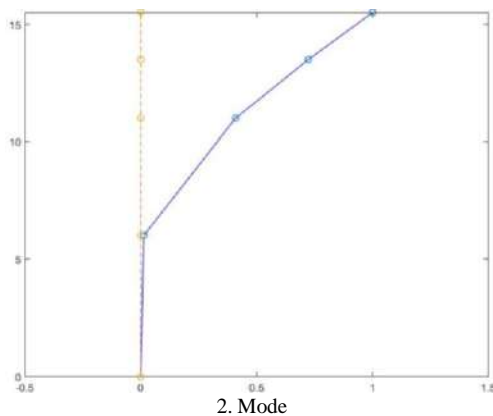
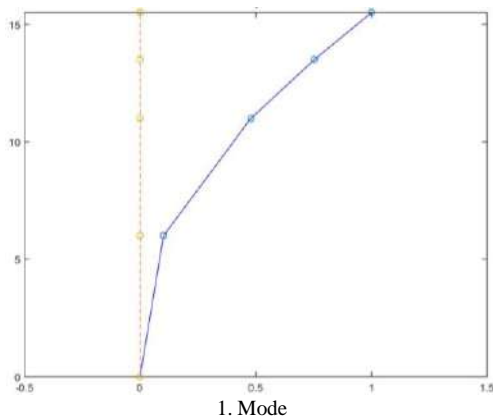


Fig. 7. The first three modes obtained using updated analytical model

IV. RESULTS

In this study, dynamic characteristics of a reinforced concrete minaret were determined by using Operational Modal Analysis (OMA) method and the analytical model of this minaret was updated. The analytical model solution was obtained by using SAP2000 finite element package program. Modal analysis of the analytical model was performed to find the dynamic characteristics and the first three frequencies were obtained at the range of 2.30-8.77 Hz.

The OROS-OR36 Multichannel Noise and Vibration Analyzer was used for experimental measurements. In these measurements, the first three frequencies are in the range of 2.15-9.56 Hz and the damping ratios related to these frequencies are in the range of 2.89-4.09%.

In comparison of the initial analytical model solutions and experimental results, the frequency and MAC values were seen to be compatible for both method. Differences between analytical and experimental frequencies can be minimized if the initial model of the structure is updated. The minaret mass is considerably known. There is more uncertainty in stiffness. Factors affecting the stiffness can be expressed as concrete elasticity and boundary conditions. Here, elasticity module of concrete was updated. The first three frequencies of the modal solutions of the updated model were obtained in the range of 2.24-8.58Hz. For the frequency and MAC values of first two modes, modal solution of the updated analytical model are closer to the results of the experimental method.

It has also been shown in this study that the dynamic characteristics of structures can be obtained using experimental methods and the analytical models can be updated according to the results of the experimental methods.

REFERENCES

- [1] C., Rainieri, and G., Fabbrocino, "Operational modal analysis for the characterization of heritage structures," *Geofizika*, 28.1: 109-126, 2011.
- [2] T., Türker, "Çevresel Titreşim Verileri Kullanılarak Yapıların Hasar Durumlarının Tespiti Ve Değerlendirilmesi," Doctoral Thesis, Karadeniz Technical University, Institute of Science and Technology, Trabzon, 2011.
- [3] A., Şahin, "Yapıların DeneySEL ve Operasyonel Modal Analizleri İçin Sayısal Sinyal İşleme, Dinamik Karakteristik Belirleme ve Sonlu Eleman Model İyileştirme Yazılımları: SignalCAD - ModalCAD - FemUP," Doctoral Thesis, Karadeniz Technical University, Institute of Science and Technology, Trabzon, 2009.
- [4] F.N., Turan, "Dengeli Konsol Betonarme Köprülerin Dinamik Karakteristiklerinin Çevresel Titreşim Verileri Kullanılarak Belirlenmesi," Master's Thesis, Karadeniz Technical University, Institute of Science and Technology, Trabzon, 2012.
- [5] M., Yetkin, "Betonarme Yapıların Çevresel Titreşim Verileri Kullanılarak Dinamik Davranışının İncelenmesi," Master's Thesis, Firat University, Institute of Science and Technology, Elazığ, 2016.
- [6] A., Bayraktar, A.C., Altunışık, B., Sevim, T., Türker, and F., Birinci, "Tarihi Yapıların Deprem Güvenliklerinin Tahribatsız DeneySEL Yöntemlerle Belirlenmesi," *İMO İstanbul*, cilt.98, ss.10-20, 2010.
- [7] M., Yetkin, Y., Calayır, and H., Erkek, "Çevresel Titreşim Verileri Kullanılarak Yapıların Dinamik Karakteristiklerinin Belirlenmesi Ve Sonlu Eleman Modellerinin Güncelleştirilmesi," *International Symposium on Natural Hazards and Hazard Management (Uluslararası Doğal Afetler ve Afet Yönetimi Sempozyumu - DAAYS'16)*, s. 133-138, Karabük Üniversitesi, Karabük, 2-4 Mart, 2016.
- [8] A., Bayraktar, B., Sevim, A.C., Altunışık, and T., Türker, "Tarihi Yığılma Minarelerin Deprem Güvenliklerinin Operasyonel Modal Analiz Yöntemiyle Belirlenmesi," *Tarihi Eserlerin Güçlendirilmesi ve Geleceğe Güvenle Devredilmesi Sempozyumu 1*, pp.415-428, Ankara, Türkiye, 2007.
- [9] A., D'Ambrisi, V., Mariani, and M., Mezzi, "Seismic assessment of a historical masonry tower with nonlinear static and dynamic analyses tuned on ambient vibration tests," *Engineering Structures*, 36, pp. 210-219, 2012.
- [10] G., Bartoli, M., Betti, and S., Giordano, "In Situ Static and Dynamic Investigations on the Torre Grossa Masonry Tower", *Engineering Structures*, 52, pp. 718-733, 2013.
- [11] İ., Çalık, B., Demirtaş, A., Bayraktar, and T., Türker, "Yığılma Taş Minarelerin Analitik Ve DeneySEL Yöntemlerle Güvenliğinin Belirlenmesi: Trabzon Muhittin Camii Minaresi Örneği," *Vakıflar Dergisi*, cilt.38, ss.121-139, 2012.
- [12] S., Choi, Park, C.H., Hyun, M.S., Kim, and K.R., Choi, "Modal Parameter Identification Of A Containment Using Ambient Vibration Measurements," *Nuclear Engineering and Design*, 240, pp.453-460, 2010.
- [13] C., Ventura, B., Laverick, R., Brincker, and P., Andersen, "Comparison of Dynamic Characteristics of Two Instrumented Tall Buildings," In *Proceedings of IMAC-21: A Conference on Structural Dynamics*, February 3-6, (pp. 236-242), The Hyatt Orlando, Kissimmee, Florida, 2003.
- [14] A.D., Vivo, C., Brutti, and J.L., Leofanti, "Modal shape identification of large structure exposed to wind excitation by operational modal analysis technique," *Mechanical Systems and Signal Processing*, (39), pp. 195-206, 2013.
- [15] A.R.P., Heerah, "Field Investigation of Fundamental Frequency of Bridges Using Ambient Vibration Measurements," Master of Engineering, McGill University Montreal, Canada, 2009.
- [16] D.J., Ewins, "Modal Testing: Theory and Practice," John Wiley & Sons, New York, 1995.
- [17] P., Mendes, M.A., Baptista, L., Agostinho, S., Lagomarsino, and J.P., Costav, "Structural and dynamic analysis of N. Sra. do Carmo church," *Proceedings EURO-DYN2005, Structural Dynamics*, 311-318, Lagos Portugal, 2005.

Linear Elastic Analyses of Masonry Walls

Erkut Sayın

Department of Civil Engineering,
Faculty of Engineering, Firat Universitii
Elazığ, Turkey
erkutsayin@gmail.com

Yusuf Calayır

Department of Civil Engineering,
Faculty of Engineering, Firat Universitii
Elazığ, Turkey
ycalayir@firat.edu.tr

Abstract — Masonry structures are commonly used in many countries. Load bearing masonry walls are the most important structural element in the masonry structures. In this study, a computer program was written in MATLAB for linear elastic analyses of masonry walls. In addition, a mesh program which meshes the wall as two dimensional model was written in MATLAB. These models were constituted with macro modeling approach. Three different load cases were applied to two dimensional masonry model with opening. The obtained results from the linear elastic analysis were compared with ANSYS software results.

Keywords —masonry walls; linear elastic behaviour; finite element method

I. INTRODUCTION

Masonry is the oldest building material that still finds wide use in today's building industries [1]. Masonry structures are the construction systems where walls, comprised of mortar and masonry units such as briquette, brick, stone and adobe, are used as load bearing system. Undoubtedly, the most important structural element for masonry structures is the load bearing walls. These structures are commonly used in many countries all over the world. The most important characteristic of masonry construction is its simplicity. Laying pieces of stone, bricks or blocks on top of each other, either with or without cohesion via mortar, is a simple, though adequate, technique that has been successfully used ever since remote ages [2]. Half of the existing building stock is consist of masonry structures in Turkey [3]. The vast majority of these structures are located in the rural areas and neighborhoods around the city.

Masonry structures prefer over other structural systems because the relevant materials can be easily obtained and their construction and workmanship are easier. For this reason, the ratio of masonry structures increase to 82% in rural regions [4]. Masonry structures can be divided into three groups as confined, unreinforced and reinforced masonry structures. These structures are commonly constructed as to be unreinforced masonry in Turkey. These structures are constructed with traditional techniques using locally available materials. Nearly no engineering services are used in these buildings.

II. MODELING OF MASONRY

Masonry is a material which exhibits distinct directional properties due to the mortar joints which act as planes of weakness. In general, the approach towards the numerical representation of masonry can focus on the micro-modeling of the individual components, unit (brick, block, etc.) and mortar, or the macro-modeling of masonry as a composite [5]. Depending on the level of accuracy and the simplicity desired, it is possible to use one of the modeling strategies. Three different strategies which called detailed micro modeling, simplified micro modeling and macro modeling are used for modeling the masonry structure. One modeling strategy cannot be preferred over the other because different application fields exist for micro- and macro-models.

In the detailed micro-modelling, the material specifications of the masonry units and the mortar, i.e., the modulus of elasticity, density and Poisson ratio are evaluated separately.

The masonry units are widened by as much as half of the mortar layer in the simplified micro-modelling. Thus, the mortar layer is neglected, and the masonry units are separated from each other with interface lines.

Macro-modelling is an equivalent material model that assumes the construction elements to be a composite without any exception among stone, brick and mortar. These modeling strategies are given in Figure 1.

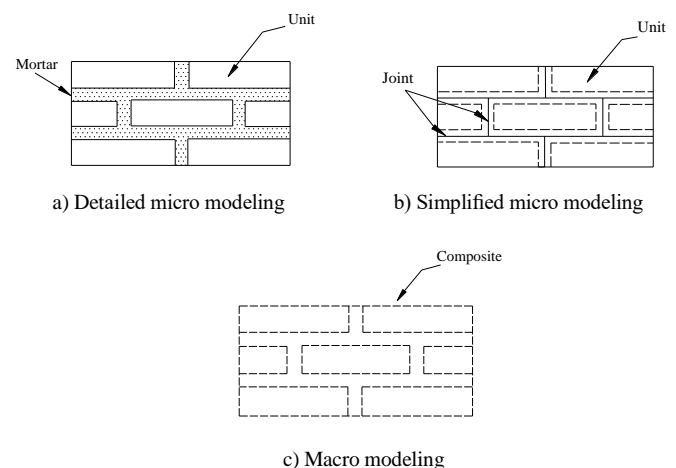
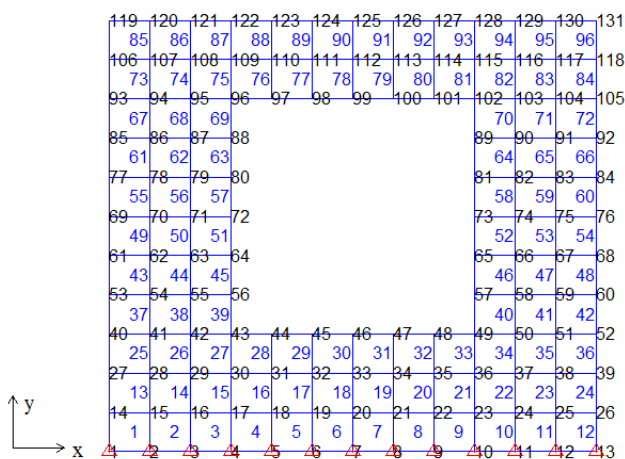


Fig. 1. Modeling strategies of masonry structures (Lourenço, 1996)

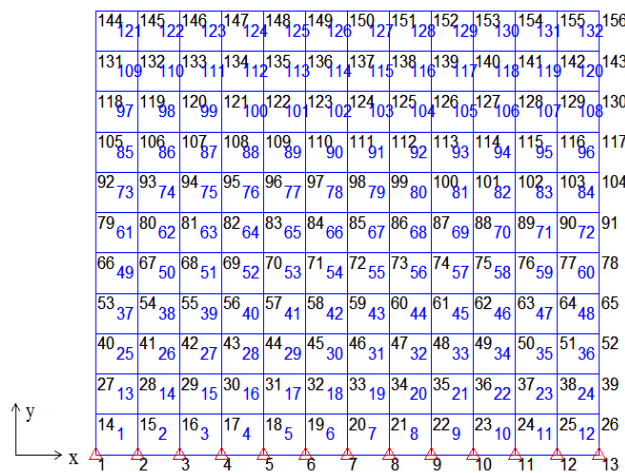
III. LINEAR ELASTIC ANALYSES

In this study, linear elastic analyses of a masonry wall was performed. For this purpose, a program that can perform linear analyses of masonry walls was written in MATLAB. The program was named as masonry-lin. Also, a mesh program was written in MATLAB that can draw the wall with and without opening and prepare the necessary information as input file for the masonry-lin [6]. The mesh program is modelled the masonry wall as two dimensional by means of the macro modelling approach. Node coordinates, element and node numbers, element connectivity, restrained nodes and material properties are prepared with the mesh program as the input file for the masonry-lin.

Finite element mesh of the wall with and without opening created by the mesh program is presented in Figure 2. In this figure, black and blue numbers on the wall show node points and element numbers, respectively.



a) with opening



b) without opening

Fig. 2. Finite element mesh of the masonry wall

The masonry-lin. uses this input file and starts the analysis. It calculates displacement, stress and strain values of the node points. In finite element implementation, finite element model

of the masonry wall is constructed using quadrilateral elements, with four nodal points and two degrees of freedom on each nodal point. Element stiffness matrixes were found using 2x2 Gauss integration rule. The flow diagram of the masonry-lin. is presented in Fig. 3.

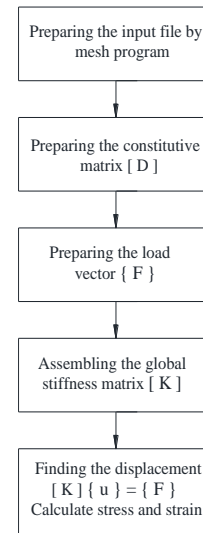


Fig. 3. Flow diagram of the masonry-lin.

Three different load cases were applied to two dimensional masonry model with opening. The base nodes of the wall were fixed in x and y directions at all load cases. For first and second load case, single load is applied at horizontal and vertical direction, respectively. For third load case, these two single loads are applied together to the masonry wall model. Value of the single load is considered as 50 kN. The modulus of elasticity, mass per volume and Poisson's ratio for the masonry unit is considered as 5×10^3 Mpa, 1.2 t/m^3 , and 0.20, respectively. The dimension of the masonry wall used in the analysis is shown in Figure 4.

For first load case, the single load was applied in the x direction at nodal point 119. For second load case, the single load was acted in the negative y direction at nodal point 125. For third load case, these two single loads were applied at the same nodes and at the same directions (Fig. 5).

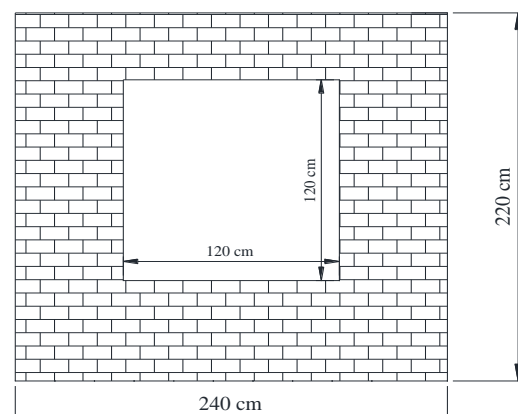


Fig. 4. Dimension of the masonry wall

Deformed and undeformed shape of the masonry wall for three different load cases obtained the masonry-lin. is shown in Figure 5. In this figure, solid blue and dashed green lines show the undeformed and deformed shape of the masonry wall.

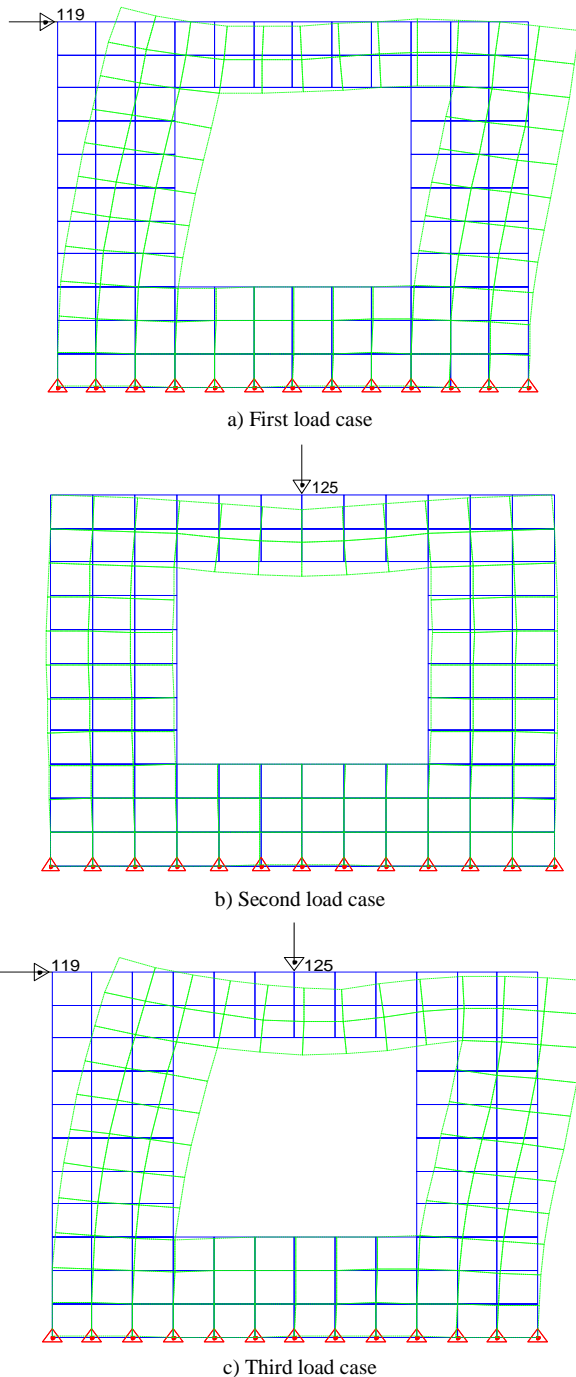


Fig. 5 Undeformed and deformed shape of the masonry wall with different load cases

Displacement values of the node point 131 obtained from the masonry-lin. and ANSYS software under first, second and third load cases is presented in Table 1.

Also, the masonry-lin. can calculate the maximum and minimum principal stress of the node points. Maximum and minimum principal stress values of the node point 117 under first, second and third load cases is presented in Table 2.

Table 1. Displacement values of the node point 131

Load cases	Masonry-lin.		ANSYS	
	x (mm) direction	y (mm) direction	x (mm) direction	y (mm) direction
First load case	1.285	-0.277	1.285	-0.277
Second load case	-0.0542	-0.0104	-0.0542	-0.0104
Third load case	1.233	-0.282	1.233	-0.282

Table 2. Maximum and minimum principal stress of the node point 117

Load cases	Masonry-lin.		ANSYS	
	max. principal stress (kPa)	min. principal stress (kPa)	max. principal stress (kPa)	min. principal stress (kPa)
First load case	144.24	-141.06	144.24	-141.06
Second load case	84.45	-94.17	84.45	-94.17
Third load case	227.60	-232.95	227.60	-232.95

IV. CONCLUSIONS

In this study, a computer program was written in MATLAB to perform linear elastic analyses of masonry walls. Furthermore, a mesh program which meshes the wall as two dimensional was written in MATLAB. These masonry walls were constituted with macro modeling approach. Three different load cases were applied to these walls. Accuracy of the results obtained from the masonry-lin. were compared with ANSYS software results.

REFERENCES

- [1] Lourenco, P.B. (1996). Computational strategies for masonry structures, Delft University of Technology, Netherlands.
- [2] Lourenco, P.B. (1998). "Experimental and numerical issues in the modelling of the mechanical behaviour of masonry", Structural Analysis of Historical Constructions II, Barcelona.
- [3] Building Census, (2000). State Institute of Statistics Prime Ministry Republic of Turkey, Ankara, Turkey.
- [4] Erdik, M. and Aydinoglu, N. (2003). "Earthquake vulnerability of buildings in Turkey", Third International Symposium on Integrated Disaster Risk Management, Kyoto, 3-5 July 2003, Japan.
- [5] Rots, J.G. (1991). "Numerical simulation of cracking in structural masonry." Heron, 36(2) , 49-63.
- [6] Sayin, E. (2009). Nonlinear static and dynamic analysis of masonry structures, Firat University, Graduate School of Natural and Applied Sciences, (in Turkish).
- [7] ANSYS. (2015). Finite Element Software. Houston, TX, USA: Swanson Analysis System. Inc.
- [8] MATLAB. (2014). The MathWorks, Inc.

Geochemical Features and Study of the Usability as an Industrial Raw Material of the Euphrates River Bank Sediments Between Palu and Keban Dam Lake

Aynur IRMAK

Firat University, Faculty of Engineering,
Department of Geological Engineering, Elazığ,
23119

Leyla KALENDER

Firat University, Faculty of Engineering,
Department of Geological Engineering, Elazığ,
23119

Mehmet YILMAZ

Firat University, Faculty of Engineering,
Department of Civil Engineering, Elazığ, 23119

Özge ERDOĞAN YAMAÇ

Firat University, Faculty of Engineering,
Department of Civil Engineering, Elazığ, 23119

Abstract— Chemical composition of the Fırat River bank sediments which are located between Palu and Keban Dam Lake show that the Fırat River's sediments can be named as sub-litharenite and felspar litharenite. Pb isotope composition ratios of the studied sediment samples show that the natural weathering of the local lithologic units is to be more effective on the river sediment chemistry than anthropogenic effects. Average of $^{206}\text{Pb}/^{207}\text{Pb}=1,205$ ratio of the river sediments shows that the sediments are mostly between natural lead values which come from the mafic volcano-sedimentary rocks. The units have characterization of Plio-Quaternary Palu Formation, Upper Miocene Çaybağı Formation, and Upper Cretaceous Elazığ Magmatic rocks. Physico-mechanic experiments show that the sediments of the Fırat River have 2.6 gr /cm^3 specific weight and sediments' content of optimum bitumen is 4.6 % and their kind of combination's stability value is 2300 kg.

The sample sediment (P39) has taken from the east side of the East Anatolian Fault Zone, and has different chemical features from the other samples. The sample sites from P39 to P50 have physical-mechanical features of clay size fraction due to the superficial water circulation within fault zone, and increase on the sedimentation of clay minerals because of abundance of suspension matter within the river water. According to the all results, the whole sediment samples which have taken from the sample site from P1 to P39 (East Anatolian Fault Zone) are suitable for aggregate and asphalt as construction industry raw materials in terms of stability and fluxing.

Keywords— *The Fırat River Sedimentary; Chemical and physico-mechanic experiments; Industrial raw material*

A RESEARCH ON RHEOLOGICAL PROPERTIES OF BITUMEN MODIFIED BY MOLASSES-BASED FLY ASH COMPOUND

Şeyma ÖZTÜRK

Civil Engineer

Ankara, Turkey

seymaozturk88@gmail.com

Deniz ARSLAN

Civil Engineer

Selcuk University Faculty of Engineering, Konya, TURKEY

M. Kürşat ÇUBUK

Civil Engineer

Gazi University Faculty of Engineering, Ankara, TURKEY

Metin GÜRÜ

Civil Engineer

Gazi University Faculty of Engineering, Ankara, TURKEY

Abstract— A new additive material composed of sugar beet molasses and fly ash was synthesized in laboratory conditions. It was called as molasses-based fly ash compound (MFAC) and used to modify the base bitumen of 50/70 penetration grade with different concentrations from 1% (w/w) to 8% (w/w). The effects of MFAC on the rheological properties of the base bitumen were investigated through penetration, softening point, dynamic shear rheometer (DSR) and bending beam rheometer (BBR) tests. The short and long term ageing of the bitumen samples for DSR and BBR applications were performed with rolling thin film oven test (RTFOT) and Pressure aging vessel (PAV). Also, Marshall tests were carried out in order to determine the effects of the additive on bituminous mixture properties. According to the BBR test results, MFAC was found to improve the creep stiffness (S) of the base bitumen by 14 % indicating the better performance of the modified bitumen at low temperatures.

Keywords—Modified bitumen; Sugar beet molasses; Fly Ash; BBR Test method; DSR Test method; Marshall Stability

I. INTRODUCTION

Pavement types are generally flexible, rigid and composite feature on road haulage. Flexible pavements are the most preferred pavement versions nowadays. They are exposed to the deterioration due to environment, climate and traffic. These deformations are rutting, fatigue, stripping and low temperature crackings. Studies on the modification made by using additives are very important to bituminous mixtures behave as expected [1]. Bitumen may show different performances depend on conditions during the production-service and rheological properties, even though they have the same physical characteristics. The bitumen stress-strain relationship is

dependent on the amount and the duration of application of the load because of the rheological material [2]. Aging is very important due to the bitumen becoming brittle. Separation of volatile components from bitumen, mixing-laying processes and wide aggregate surface area cause oxidation of aging. Hardening of bitumen that occur during mixing and laying is provided on the laboratory conditions by RTFOT. Performance and behavior of bituminous mixtures are related to loading time and temperatures. In consideration of these factors, DSR method is applied to samples. The studies show that additive materials improves the resistance against distortion. $G^*/\sin\delta$, the rutting parameter, can be successfully improved by the styrene-butadiene-styrene (SBS) modification [3,4,5]. Additionally, SBS has a positive impact on mechanical properties of the bituminous mixtures [6,7,8]. Ethylene vinyl acetate (EVA) increases the penetration index of bitumen and Marshall stability of bituminous mixtures [4,9]. Rubber is used to improve adhesion properties and viscoelastic characteristics of bitumen [10,11]. Low density polyethylene (LDPE) increases in softening point and a decreased in ductility data, so it developed rutting resistance of bitumen [12]. Phenol-formaldehyde is increased Marshall stability, softening point, viscosity, though heat sensitivity, penetration, surface energy, stripping are decreased [13]. Polyethylene terephthalate (PET) modification enhance low temperature performance and fatigue resistance of bitumen and the Marshall stability, stripping resistance of bituminous mixtures [14]. Organomontmorillonite is a kind of clay. It was stated that Organomontmorillonite affected the rheological behavior and aging properties of bitumen [17]. The purpose of the study is to investigate the modification of the bitumen and bituminous mixtures with molasses-based fly ash compound (MFAC).

Fly ash is puzzolanic material. It can be extensively used construction industry. Fly ash is usually gray in colour and may become darker according to the amount of unburned carbon. Fly ash which is round consists of very fine particles[15]. Sugar beet molasses are an organic waste material which includes approximately 50% sugar. Sugar beet molasses use in fertilizer industry, in ethanol production, in animal food, etc. It approximately consists of 25% water. Sugar beet molasses and fly ash hasn't been used as a bitumen modifier before when they are together. The additive material was called molasses-based fly ash compound (MFAC) which was obtained in the laboratory condition using fly ash and sugar beet molasses. Various tests were performed on laboratory as penetration, softening point, dynamic shear rheometer (DSR) and bending beam rheometer (BBR) test, rolling thin film oven test (RTFOT) and Pressure aging vessel (PAV).

II. MATERIALS AND METHODOLOGY

A. Bitumen

50/70 penetration grade bitumen was obtained from General Directorate of Highways in this study. The basic properties of the base bitumen of 50/70 penetration were summarized in **Hata! Başvuru kaynağı bulunamadı..**

Table 1. Basic Properties of the Base Bitumen

Penetration, 25 °C, 100 g, 5 s, 0,1 mm	61.8	ASTM D5
Softening Point (°C)	54.6	ASTM D36
Flash Point (°C)	271	BS EN 22592
Specific Gravity, 25 °C, (g/cm ³)	1.028	ASTM D70
Viscosity, 140 °C(Pa.s)	0.212	ASTM D4402
130 °C(Pa.s)	0.336	ASTM D4402

B. Aggregate

Basalt aggregate was supplied from Islamdag quarry of Ordu/Turkey. The specific gravity of each aggregate portion was given in Table 2. Aggregate gradation used and local gradation limits were shown in Figure 1 to prepare Marshall samples. The average value of type II is used for wearing courses in Turkey.

Table 2. Specific Gravity of Each Basalt Aggregate Portion

Aggregate Portion	Specific Gravity
Coarse aggregate, bulk	2.551
Apparent	2.633
Fine aggregate, bulk	2.691
Apparent	2.712
Filler, bulk	-
Apparent	2.598

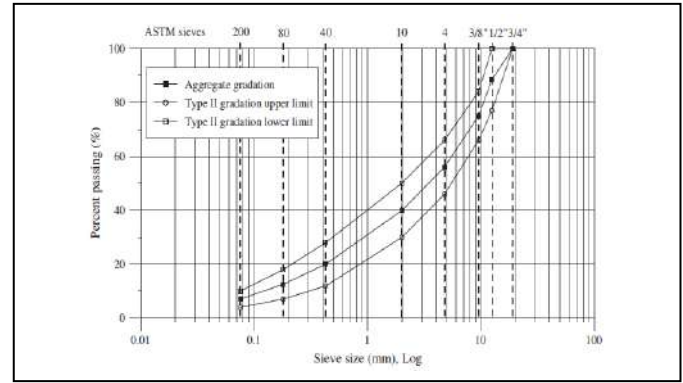


Figure 1 Aggregate gradation and specification limits

C. Preparation of MFAC and Modified Bitumen

Fly ash, molasses and caustic were used and a new material was developed in laboratory condition. A heater and reactor equipped were used in this synthesise study of the MFAC(Figure 2). Additive materials were mixed in the heater by a magnetic stirrer at 100°C.

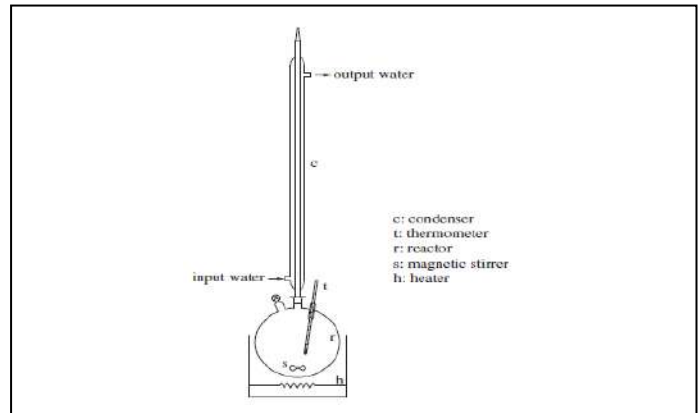


Figure 2 Equipment of MFAC synthesizing

Features of using molasses and fly ash were shown in Table 3 and

Table 4. The molasses used in the modification of the base bitumen were supplied from sugar refinery in Ankara, Turkey.

Table 3. Features of using molasses

Property	Value
Density	1g/cm ³
Physical state	Semifluid
Saccharose	48%
Invert sugar	1.6%
Inorganic oxides	25.3%
H2O	25.1%

Table 4. Chemical Properties

Features	Standard limits
$\text{SiO}_2 + \text{Al}_2\text{O}_3 + \text{Fe}_2\text{O}_3$	Min. 70%
MgO	Max. 5%
SO	Max. fr 5%
Moisture	Max. 3%
Loss on ignition	Max. 10%

Different concentration of MFAC was added to the base asphalt between 1% and 8% by weight of the base bitumen. The synthesis process was carried out at 120°C during 20 minutes mixed in oil bath.

III. RESULT AND DISCUSSION

Penetration and softening point tests are ones of the parameters used to relate any bitumen. The impacts of the MFAC on the softening test and penetration of the original bitumen are pointed out in Figure 3. Penetration values generally increase and softening points decrease. Because these parameters are related converseley to each other.

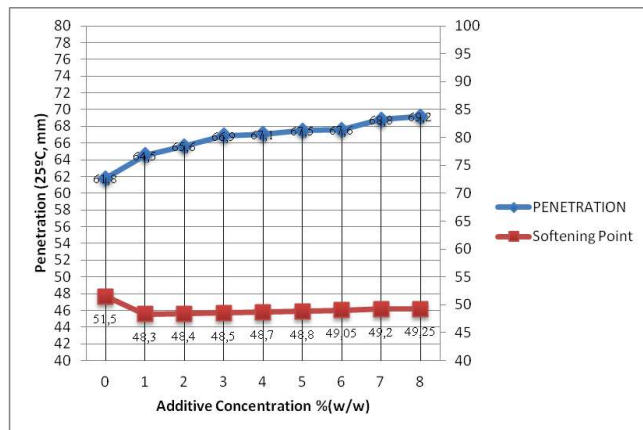


Figure 3. Penetration and softening point test results

Marshall Stability test method is one of the most important test methods base and modified bitumens. 5% value is the optimum content of base bitumen aggregate combinations. These test results are pointed to Table 5. According to the results Marshall stability value only increased on 2% (w/w) additive concentration. Specification limit values are $3 < V_a < 5$. V_{air} of 0% concentration value has slightly exceeded these limit values, but sample has provided V_{air} limits to work with MFAC.

Table 5. Marshall Stability Test Results

%	Stability(kg)	Specific gravity	V_a %	VMA%	V_f %
0	1010	2.283	5.06	14.8	65.9
2	1041	2.294	4.61	14.41	68
3	967	2.302	4.25	14.1	69.8
5	916	2.288	4.86	14.64	66.8
8	910	2.288	4.83	14.62	66.9

DSR tests are performed to determine high temperature properties of bitumen. DSR test were conducted at 64°C and 70 °C to unaged and RTFO aged binders. They are shown that Figure 4 and Figure 5. Complex shear modulus(G^*) and phase angle(δ) were determined and were calculated $G^* \sin \delta$ at different temperatures after PAV. $G^* \sin \delta$ and additive concentration graphics were in Figure 6. $G^* \sin \delta$ parameter is minimum 1.00 kPa on base bitumen because of rutting to decrease minimum. In the other words, $G^* \sin \delta$ parameter should be higher than 1 kPa for unaged specimen. $G^* \sin \delta$ should't be lower 2.2kPa for aged specimen after RTFO test. Specification limit values are delivered at 64 °C temperature in Figure 4.

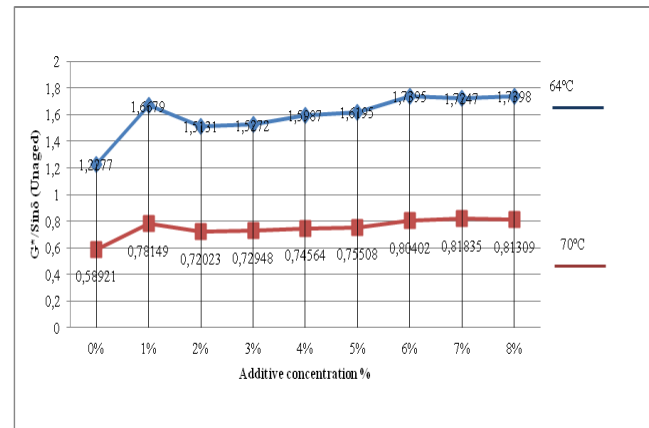


Figure 4. $G^* \sin \delta$ Results Before RTFO

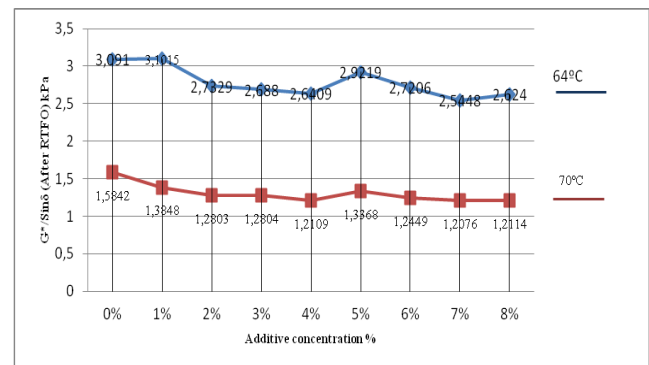


Figure 5. After RTFO $G^*/\sin\delta$ results

$G^*\sin\delta$ value represents fatigue parameter in Figure 6. The fatigue crack according to superpave specifications shouldn't exceed to 5000kPa.

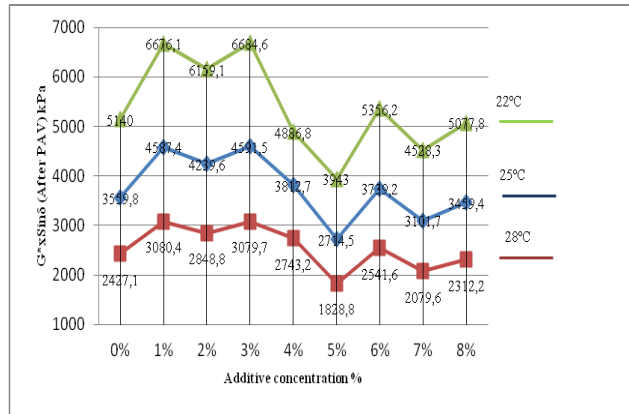


Figure 6. After PAV $G^*\sin\delta$

Creep stiffness(S) and creep ratio(m) are determined through BBR test. These test results at (-12) °C and(-18) °C are indicated in Table 6.

Table 6. BBR Results

	Creep stiffness, S(Mpa) (-12) °C	Creep rate, m (-12) °C	S/m (-12)°C	Creep stiffness, S(Mpa) (-18) °C	Creep rate, m (-18) °C	S/m (-18)°C
0%	222	0.323	687.30	507	0.229	2213.97
1%	210	0.330	636.36	501	0.259	1934.36
2%	191	0.339	563.42	414	0.277	1494.58
3%	202	0.337	599.40	444	0.264	1681.81
4%	190	0.345	550.72	395	0.271	1457.56
5%	207	0.334	619.76	463	0.263	1760.45
6%	197	0.333	591.59	447	0.272	1643.38
7%	209	0.324	645.06	446	0.267	1670.41
8%	206	0.342	602.33	458	0.264	1734.84

Creep stiffness(S) of measured at the BBR test according to Superpave specification is limited at a maximum of 300 MPa. Creep rate (m) have to be higher than 0.3. Creep stiffness(S) and creep rate(m) are suitable accordance with limits in Table 6. S and m parameters point to resist low temperature cracking. Smaller "S" and larger "m" is better of resisting to low temperature cracking[16]. The most increase

rate of m and the maximum reduction rate in S is 4% concentration value at (-12) °C. The increase in Marshall stability was at a 2% concentration. S and m rate of change at 2% are almost similar to 4% result at (-12) °C. These situation supports the increase in Marshall stability. 2% is more economical than 4% concentration. If S/m parameter is smaller than other results, cold weather performance is better than another concentration.

IV. CONCLUSION

Synthesized materials, namely MFAC, were used to modify base bitumen. In this study, 50/70 penetration of bitumen was used to modify process. Penetration and softening point tests are inverse of each other. If lower softening point and higher penetration is test results, $G^*/\sin\delta$ parameters of unaged specimen increase in DSR. Original and short term ageing parameters show that rutting.

According to the BBR test results, MFAC was found to improve the creep stiffness (S) of the base bitumen by 14 % indicating the better performance of the modified bitumen at low temperatures. As a result, using MFAC modified bitumen in cold and rainy regions, in heavy motor and peak- hour traffic highways will supply increase for highway pavement performance.

ACKNOWLEDGMENT

General Directorate of Highways and Gazi University are thankfully acknowledgment for the laboratory facilities.

REFERENCES

- [1] Çubuk M.,Çubuk M.K. , Gürü M., "The effect of polytetrafluoroethylene on the rheological properties of bitumen", J. Fac. Eng. Arch. Gazi Univ., Vol 26, No 3, 623-630, 2011.
- [2] Arslan D., improvement of performance properties of flexible pavements by synthetic metal and polyboron additives, Ph.D. Thesis, Gazi University Institute of Science and Technology, Ankara 2010.
- [3] Airey, G. D."Rheological properties of styrene butadiene styrene polymer modified road bitumens." Fuel, 82(14), 1709–1719,2003.
- [4] Bulatovic, V. O., Rek, V., and Markovic, K. J. "Effect of polymer modifiers on the properties of bitumen." J. Elastomers Plast., 46(5),448–469,2014.
- [5] Galooyak, S. S., Dabir, B., Nazarbeygi, A. E., and Moeini, A. "Rheological properties and storage stability of bitumen/SBS/montmorillonite composites." Constr. Build. Mater., 24(3), 300–307,2010.
- [6] Al-Hadidy, A. I., and Tan, Y. "Mechanistic analysis of ST and SBS-modified flexible pavements." Constr. Build. Mater., 23(8),2941–2950,2009.
- [7] Karakaş, A. S., Sayin, B., and Kuloğlu, N. "The changes in the mechanical properties of neat and SBS-modified HMA pavements due

- to traffic loads and environmental effects over a one-year period.” *Constr. Build. Mater.*, 71, 406–415, 2014.
- [8] Singh, M., Kumar, P., and Maurya, M. R. “Strength characteristics of SBS modified asphalt mixes with various aggregates.” *Constr. Build. Mater.*, 41, 815–823, 2013.
- [9] Haddadi, S., Ghorbel, E., and Laradi, N. “Effects of the manufacturing process on the performances of the bituminous binders modified with EVA.” *Constr. Build. Mater.*, 22(6), 1212–1219, 2008.
- [10] Navarro, F. J., Partal, P., Martinez-Boza, F., Valencia, C., and Gallegos, C. “Rheological characteristics of ground tire rubber-modified bitumens.” *Chem. Eng. J.*, 89(1–3), 53–61, 2002.
- [11] Aksoy, A., Şamlıoğlu, K., Tayfur, S., and Ozen, H. “Effects of various additives on the moisture damage sensitivity of asphalt mixtures.” *Constr. Build. Mater.*, 19(1), 11–18, 2005.
- [12] Jun, L., Yuxia, Z., and Yuzhen, Z. “The research of GMA-g-LDPE modified Qinhuangdao bitumen.” *Constr. Build. Mater.*, 22(6), 1067–1073, 2008.
- [13] Çubuk, M., Gürü, M., Çubuk, M. K., and Arslan, D. “Rheological properties and performance evaluation of phenol formaldehyde modified bitumen.” *J. Mater. Civ. Eng.*, 10.1061/(ASCE)MT.1943-5533.0000889, 04014015, 2014.
- [14] Gürü, M., Çubuk, M. K., Arslan, D., Farzanian, S. A., and Bilici, İ. “An approach to the usage of polyethylene terephthalate (PET) waste as roadway pavement material.” *J. Hazard. Mater.*, 279, 302–310, 2014.
- [15] Aruntaş H., “The potential of fly ash usage in construction sector”, *J. Fac. Eng. Arc. Gazi Univ.*, Vol 21, No1, 193-203, 2006.
- [16] Arslan D., Gürü M., Çubuk M.K., “Improvement of Bitumen and Bituminous Mixtures Performance Properties with Organic Based Zincphosphate Compound”, *J. Fac. Eng. Arch. Gazi Univ*, Volt 28, No 3, 577-586, 2013.
- [17] Liu, G., Wu, S., Ven, M. V. D., Yu, J., and Molenaar, A. “Influence of sodium and organo-montmorillonites on the properties of bitumen.” *Appl. Clay Sci.*, 49(1–2), 69–73, 2010.

Determination of the Resistance of Hot Mix Asphalt Samples Prepared Under Different Conditions Against Wheel Tracking

¹Taner ALATAŞ, ²Mehmet YILMAZ, ³Baha Vural KÖK

^{1,2,3} Firat University, Engineering Faculty, Civil Engineering Department, Elazığ, Turkey.

Email: ¹ talatas@firat.edu.tr ² mehmetyilmaz@firat.edu.tr ³ bvural@firat.edu.tr

Abstract--The present study aimed to examine the resistance of pure hot mixes and those prepared with 4% of three different polymers two types of SBS (styrene-butadiene-styrene) and one type of EVA (ethylene-vinyl-acetate) against permanent deformation. Samples were prepared with application of vibration so that they would have 4% void ratio using a roller compactor and without this application. The effect of vibration application during sample preparation on the wheel track formation was also assessed in the current study. Wheel track tests demonstrated that use of additives increased the resistance of hot mixes against wheel track formation. It was also determined that the most effective additive was EVA. Furthermore, it was determined that application of vibration during sample preparation increased the resistance of specimens against permanent deformation.

Keywords-- Wheel Tracking;

I. INTRODUCTION

Two basic components of bituminous hot mixes (BHM) are aggregate and bitumen and aggregates used in BHMs consist 90-95% of the total BHM weight. 1.6 billion tons of bituminous hot mix is produced every year worldwide. For this purpose, approximately 1.5 billion tons of aggregate is used. Environmental damages caused by highway construction are those resulting from construction activities (CO₂ emissions, use of nature lands, change in current conditions and ecological balance, change in natural structure) and the damages caused by the material utilized for construction (destruction of natural lands, technological equipment causing chemical pollution, noise and vibration) [1].

One of the most encountered deformations observed with bituminous hot mixes, permanent deformations occur as a result of two basic conditions. The first occurs due to the inappropriate construction of the base course or the asphalt base course. In the second condition, while there is no deformation in lower layers, the permanent deformation (wheel tracks) form on the wearing course [2].

Wheel track formation is frequently observed on pavement courses in hot temperatures and on roads where heavy vehicle traffic is present. Deformations cause expensive rehabilitations or reconstruction, as well as new material needs, resulting in harming the environment again.

To improve the features of BHMs, postponing expensive rehabilitation and reconstructions, additive substances are utilized. Polymers used as the most common additive substances used in modification of bituminous binders are grouped in four categories of plastomers, elastomers, fibers and pavements. To improve the features of bitumen, selected polymer should form a new bond in bitumen, chemically reacting with bitumen. Obtaining a high performance polymer modified bitumen is dependent on the better distribution of the polymer in bitumen and the chemical structure of the bitumen [3]. Most frequently used bitumen additives are styrene-butadiene-styrene (SBS) from the elastomer group and ethylene-vinyl-acetate (EVA) from the plastomer group [4]. Several studies demonstrated that resistance against ageing [5], permanent deformation [6], low temperature fractures [7], and moisture damage [8] increased by the use of SBS modified bitumen. EVA especially increases resistance against permanent deformation [9], [10].

It is possible to adjust the polybutadiene structure of SBS block copolymers using a special catalyzer. Thus, it is possible to obtain an SBS with the same molecular weight, but with a shorter polymer chain. This means low viscosity, and a better and more homogenous mixture with bitumen [11], [12].

It is of utmost significance to prepare bituminous hot mixes in laboratory environment reflecting the field conditions, for the accuracy of the design and accurate determination of the material that would be applied in the field. In the present study, bituminous hot mix samples containing pure bitumen and bitumen modified by three different additives (two types of SBS and one type of EVA) were prepared using roller compactor. The mixes were compacted with and without vibration to create the same void ratio. Afterwards, wheel track tests were conducted on these mixes. Thus, the effect of mix preparation method on permanent deformation performance of the mixes was assessed.

II. MATERIAL AND METHODOLOGY

Limestone type aggregate procured from Karayazı region in Elazığ province in Turkey was used in the study. Properties of the aggregate is presented in Table 1 and the gradation selected according to Superpave method is given in Figure 1. Triangular signs depict control points, closed field shows forbidden zone, and square signs show utilized gradation points in Figure 1.

PG 58-35 bitumen procured from TÜPRAŞ refinery was used as the main binder in the present study. Two different types of SBS produced by Shell Corporation (Kraton D 1101 and Kraton MD 243) and EVA produced by Arkema Corporation (Evatane® 2805) were used as additives. A four-bladed mixing head was used in

preparing modified bitumen. Pure bitumen and additives were mixed in a special mixer for 60 minutes at 180°C temperature and 1000 rpm.

To evaluate the effect of these additives on the performance of bituminous hot mixes, all additives were used at a rate of 4% (Table 2). Dynamic shear rheometer (DSR) and beam bending rheometer (BBR) test results for pure and with 4% SBS D1101 (MB_{SBS-D}), SBS MD243 (MB_{SBS-M}), and Evatane® 2805 (MB_{EVA}) bitumen are presented in Table 3. It was determined that the performance levels for MB_{SBS-D} and MB_{SBS-M} modified bitumen were similar (PG 70-34), and the low temperature value for MB_{EVA} modified bitumen was one level higher (PG 70-28).

TABLE 1. PHYSICAL PROPERTIES OF AGGREGATE

Properties	Standard	Limit	Coarse	Fine	Filler
Abrasion loss (%) (Los Angeles)	ASTM D 131	Max 30	27.8	-	-
Abrasion loss (%) (Micro Deval)	ASTM D 6928	Max 15	13.6	-	-
Frost action (%) (with Na ₂ SO ₄)	ASTM C 88	Max 10	5.8	-	-
Specific gravity (g/cm ³)	ASTM C127		2.544	2.571	2.675

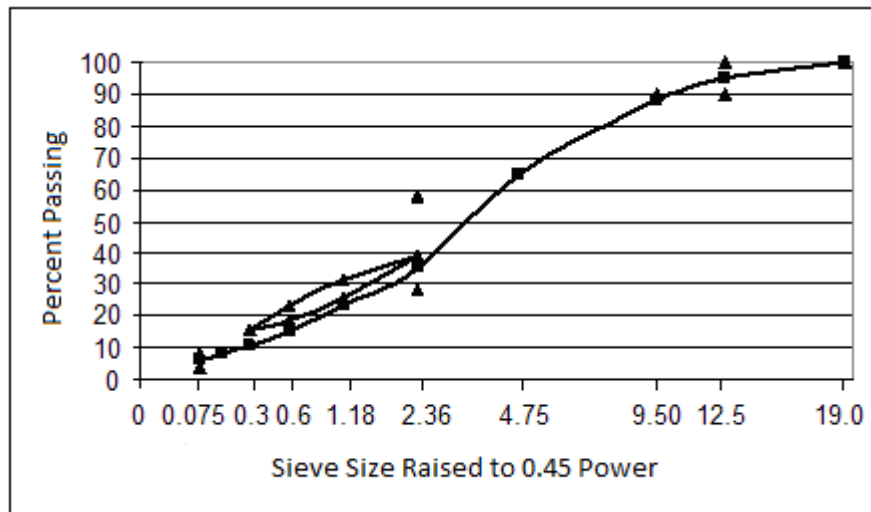


Fig. 1. Used aggregate gradation.

TABLE 2. ABBREVIATIONS USED FOR MODIFIED BITUMEN

Additive type and ratio	%4 SBS-D1101	%4 SBS-MD243	%4 EVA
Denomination	MB _{SBS-D}	MB _{SBS-M}	MB _{EVA}

TABLE 3. DSR AND BBR TEST RESULTS OF BINDERS

DSR test results				
Temperature (°C)	G*/sinδ (Pa) (Specification limit min. 1000 Pa)			
	PG 58-34	MB _{SBS-D}	MB _{SBS-M}	MB _{EVA}
58	1258	4890	4204	4534
70	-	1326	1183	1512
Temperature (°C)	G*/sin δ (Pa) RTFOT residue (Specification limit min. 2200 Pa)			
	PG 58-34	MB _{SBS-D}	MB _{SBS-M}	MB _{EVA}
58	7862	-	-	-
70	-	5599	5171	6862
Temperature (°C)	G*.sin δ (Pa*10 ⁶) PAV residue (Specification limit max. 5*10 ⁶ Pa)			
	PG 58-34	MB _{SBS-D}	MB _{SBS-M}	MB _{EVA}
16	1.83	-	-	-
22	-	1.69	1.52	-
25	-	-	-	1.34
BBR test results				
Temperature (°C)	m-value (Specification limit min. 0.300)			
	PG 58-34	MB _{SBS-D}	MB _{SBS-M}	MB _{EVA}
-18	-	-	-	0.306
-24	0.309	0.314	0.325	0.277
-30	0.266	0.221	0.291	-
Temperature (°C)	Creep stiffness (Mpa) (Specification limit max. 300 MPa)			
	PG 58-34	MB _{SBS-D}	MB _{SBS-M}	MB _{EVA}
-18	-	-	-	131.3
-24	108.3	144.7	98.5	160.6
-30	140.9	242.6	121.9	-
Performance Grade (PG)				
	58-34	70-34	70-34	70-28

Rotational viscometer tests were conducted on unaged pure and modified bitumen under 135°C and 185°C temperatures to determine the workability of the binders and aggregate mixing and compacting temperatures. For workability, the viscosity values for the binders should be below 3 Pa.s (3000 cP) at 135°C [13]. Furthermore, it is required that the viscosity value of bituminous binders during mixing with aggregate should be 170 ± 20 cP, and during compacting it should be 280 ± 30 cP [14]. Utilizing the viscosity-temperature graphs plotted in the study, aggregate mixing and compacting temperature for each binder was identified. Results of viscosity tests are displayed in Table 4.

Data presented in Table 4 shows that all binders met the workability criterion. Furthermore, using additives increased viscosity values and mixing and compacting temperatures rose as a result. Modification indices were obtained by division of viscosity values of modified bitumen by viscosity value of pure binder. As could be seen in Table 4, the highest modification index value was

obtained with MB_{EVA} modified bitumen at both 135°C and 165°C temperatures. This situation indicates that more energy would be required in the plant during mixing with aggregate with EVA use.

During preparation of bituminous hot mixes, aggregate and bitumen were heated to mixing temperature and mixed using a special mixer. Non-compacted samples were placed in trays 21-22 kg per square meter and aged for a short period of time for 4 hours in an incubator at 135°C. Then, the mixtures were heated to mixing temperatures and compacted using a 1.25° angle gyratory compactor for 100 revolutions. The design was determined based on the volumetric properties of bitumen content mixtures. It was determined that design bitumen content increased with modified bitumen use. Volumetric properties of mixtures in design bitumen content and Superpave specification criteria are presented in Table 5. It was confirmed that all mixtures met Superpave specification criteria.

TABLE 4. ROTATIONAL VISCOSITY TEST RESULTS

Properties	Standard	PG 58-34	MB _{SBS-D}	MB _{SBS-M}	MB _{EVA}
Viscosity (cP, 135°C)	ASTM D4402	275.0	1125.0	825.0	1250.0
Viscosity (cP, 165°C)	ASTM D4402	112.5	350.0	262.5	375.0
Mixing temperature range (°C)	-	151-158	171-173	169-171	171-173
Compaction temperature range (°C)	-	129-140	167-169	163-166	167-169
Modification index (135°C)	-	-	4.09	3.00	4.54
Modification index (165°C)	-	-	3.11	2.33	3.33

TABLE 5. VOLUMETRIC PROPERTIES OF MIXTURES

Mixture properties	Specification limits	Binder type			
		PG 58-34	MB _{SBS-D}	MB _{SBS-M}	MB _{EVA}
Design binder content (%)	—	4.88	5.27	5.35	5.07
Air Voids (Va, %)	4.0	4.04	4.09	4.09	3.99
Voids in mineral aggregate (VMA, %)	min. 14.0	14.61	15.39	15.50	14.86
Voids filled with bitumen (VFA, %)	65–75	72.37	73.42	73.63	73.13
Dust ratio (DP)	0.8–1.6	1.07	0.98	0.97	1.02

III. WHEEL TRACK TESTS

Wheel track formation on pavement layer was examined in the study. The tests were conducted based on EN 12697-22 standard B procedure to examine the wheel track resistance of samples that contained pure PG 58-34, 4% SBS-D, SBS-M and EVA modified binders. Since maximum aggregate grain diameter was 19 mm according to the standard, sample height was selected as 6.0 cm. Initially 30.5 * 30.5 * 6 cm plate samples were compacted using rolling compactor so that they would have 4% air void ratio. Some samples were compacted with application of vibration, and the others were compacted without. Required BHM amount for plate samples was determined using the following equation:

$$M = 10^{-6} * L * l * e * \rho_m * ((100 - v) / 100) \quad (1)$$

where M is sample weight (kg), L is inner length of the mold (mm), l is the inner width of the mold (mm), e is the final height of the sample (mm), ρ_m is the maximum density of the bituminous mixture (kg/m³), and v is the void ratio of the sample (%).

In wheel track experiment the samples were tested at 60°C temperature. The device took 27 deformation

measurements, out of which one was taken from the center of the sample, and 13 were taken from the left of the center and right of the center. At the end of 10,000 wheel revolutions, wheel track depths were determined using the average of these 27 values. For each mixture sample, two samples were tested and average of the values were taken. According to EN 12697-22 standard, the test is terminated either after 10,000 load repetitions or when 20 mm wheel track depth is formed. In mixtures containing pure binder, 20 mm wheel track depth was obtained after 2,940 load repetitions and the test was ended. The tests conducted with modified bitumen were terminated after 10,000 load repetitions. The relationship between wheel track depth and number of load repetitions in mixtures prepared with vibration is presented in Figure 2, while relationship between wheel track depth and number of load repetitions in mixtures prepared without vibration is displayed in Figure 3. The load that caused 20 mm deformation in mixtures prepared with pure binder is displayed with a dashed line.

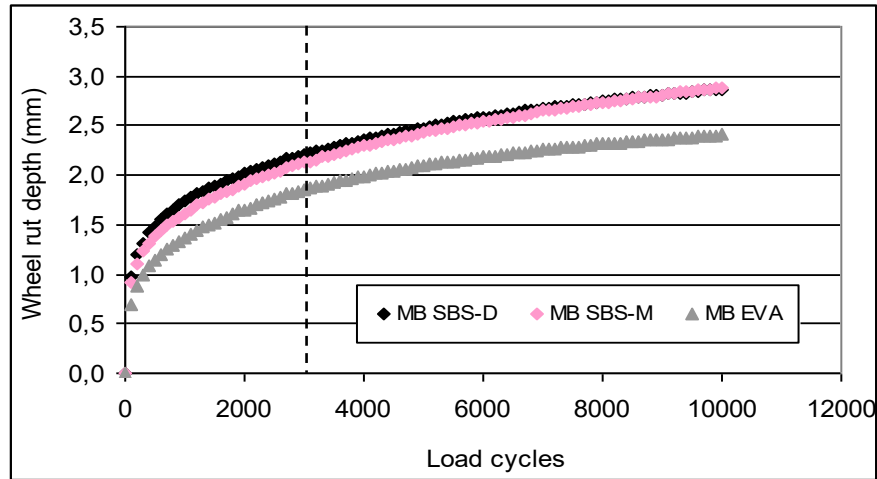


Fig. 2. The wheel track depth-number of load repetition relationship in mixtures prepared with vibration.

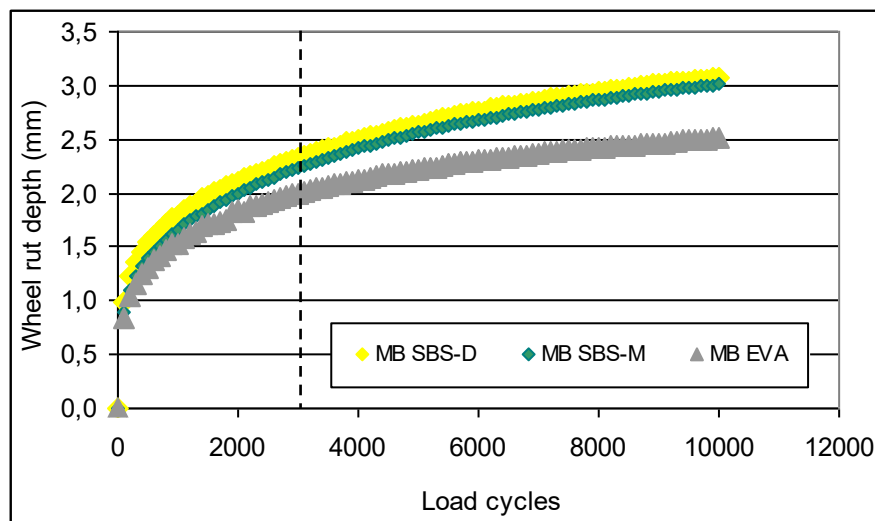


Fig. 3. The wheel track depth-number of load repetition relationship in mixtures prepared without vibration.

It was determined that wheel track values for mixtures prepared with MB_{SBS-D} and MB_{SBS-M} were close to each other as displayed in Figures 2 and 3. Comparison of mixtures prepared with modified bitumen showed that the lowest wheel track value was obtained with the mixture prepared with MB_{EVA}, and the highest wheel track value was obtained with the mixture prepared with MB_{SBS-D}. Deformation values for 5,000 and 10,000 load repetitions are presented in Table 6.

As could be observed in Table 6, wheel track depths for 5,000 and 10,000 load repetitions in mixtures prepared without vibration and using EVA modified bitumen were 18.5% and 22.7% lower than the mixture prepared using SBS-D modified bitumen, respectively. Furthermore, wheel track depths for 5,000 and 10,000 load repetitions in mixtures prepared using EVA modified bitumen were 15.3% and 20.3% lower than the mixture prepared without vibration using SBS-D modified bitumen, respectively.

As could be observed in Table 6, wheel track depths for 5,000 and 10,000 load repetitions in mixtures prepared with vibration and using EVA modified bitumen were 18.1% and 19.1% lower than the mixture prepared using SBS-D modified bitumen, respectively. Furthermore, wheel track depths for 5,000 and 10,000 load repetitions in mixtures prepared with vibration and using EVA modified bitumen were 15.7% and 19.9% lower than the mixture prepared using SBS-M modified bitumen, respectively.

As a result of vibration application, wheel track formation in mixes prepared using SBS-D modified bitumen decreased 5.7% after 5,000 load repetitions and 6.8% after 10,000 load repetitions. As a result of vibration application, wheel track formation in mixes prepared with SBS-M modified bitumen decreased 5.1% after 5,000 load repetitions and 4.3% after 10,000 load repetitions.

TABLE 6. WHEEL TRACK VALUES FOR MIXTURES UNDER DIFFERENT LOAD REPETITIONS

Mixtures prepared without vibration				
Deformation (mm)	Mixture type (according to used binder)			
	PG 58-34	MB _{SBS-D}	MB _{SBS-M}	MB _{EVA}
@5000 load cycles	-	2.63	2.56	2.22
@10000 load cycles	-	3.08	3.02	2.51
Mixtures prepared with vibration				
Deformation (mm)	Mixture type (according to used binder)			
	PG 58-34	MB _{SBS-D}	MB _{SBS-M}	MB _{EVA}
@5000 load cycles	-	2.48	2.43	2.10
@10000 load cycles	-	2.87	2.89	2.41

As a result of vibration application, wheel track formation in mixes prepared using EVA modified bitumen decreased 5.4% after 5,000 load repetitions and 4.0% after 10,000 load repetitions.

Overall consideration of mixes showed that vibration application decreased wheel track formation. This finding demonstrated that, although the mixes had the same volume, the mix compacted better as a result of implementation of vibration. As a result of comparison of additive types, values obtained after 10,000 load repetitions showed that the mix affected by vibration the most was the one prepared with SBS-D and the mix affected by vibration the least was the one prepared with EVA based on permanent deformation. It was observed that compacting especially the SBS-D modified bitumen using vibration was more significant for wheel track formation.

IV. RESULTS

In the present study, initially the effect of three different bitumen additives (SBS-D, SBS-M and EVA) on the resistance of bituminous hot mixes against wheel track formation was examined. Later on, the effect of vibration application on the preparation of wheel track samples was attempted to be identified. Additive ratio was kept constant at 4% for all additives. Thus, the convenient comparison of all additive types was aimed. In the field, vibrating rollers are used to compact bituminous hot mixes. A roller compactor with vibration capabilities was used to obtain compatible samples with the field conditions. Samples were prepared using modified bitumen both by using and not using vibration. Wheel track tests were conducted on these samples to assess the effects of vibration.

It was determined that performance levels for modified bitumen that contained SBS-D and SBS-M equal to 4% of bitumen weight were PG 70-34, and the performance level of those that contained EVA were PG 70-28. It was identified that design bitumen content of the

mixes prepared with SBS-D, SBS-M and EVA modified bitumen were 5.27%, 5.35%, and 5.07%, respectively.

Wheel track samples that contained pure and modified bitumen with 4% void ratio consistent with the field applications were prepared with roller press. Samples were prepared both using vibration and without using vibration. It was determined that mixes prepared with EVA modified bitumen had the lowest wheel track depth for both vibration applied and not vibration applied mixes. Furthermore, it was identified that wheel track values for mixes prepared with SBS-D and SBS-M modified bitumen were similar. It was also determined that vibration applied mixes displayed lower wheel track formation when compared to mixes that were not applied vibration.

It was determined that vibration was more effective especially in mixes prepared with SBS-D modified bitumen. It was considered that this condition was due to better compacting of the mixes as a result of vibration. To determine the compatibility of vibrated and non-vibrated samples with the field conditions, it would be beneficial to compare the test results for samples obtained from the field with the test results for the samples prepared at the laboratory in the future.

ACKNOWLEDGEMENTS

The support for this work was provided by FUBAP (Firat University Scientific Research Projects Unit) with project number MF.11.30, which we gratefully acknowledge.

REFERENCES

- [1] A. M. Nicuta, "Life Cycle Assessment Study for New and Recycled Asphalt Pavements", Bulletin of the Polytechnic Institute of Iasi, Vol. 61, Issue 2, pp. 81-91, 2011.
- [2] S.F. Said, H. Hakim, E. Oscarsson and M. Hjort, "Prediction of Flow Rutting in Asphalt Concrete Layers", International Journal of Pavement Engineering, Vol. 12, Issue 6, pp. 519-532, 2011.
- [3] U. Isacsson and X. Lu, "Testing and Appraisal of Polymer Modified Road Bitumens", State of the Art, Materials and Structures, Vol. 28, pp. 139-159, 1995.
- [4] B. Sengoz and G. Isikyakar, "Evaluation of the Properties and Microstructure of SBS and EVA Polymer Modified Bitumen", Construction and Building Materials, Vol. 22, Issue 9, pp. 1897-1905, 2008.
- [5] M. S. Cortizo, D. O. Larsen, H. Bianchetto and J. L. Alessandrini, "Effect of the Thermal Degradation of SBS Copolymers During the Ageing of Modified Asphalts", Polymer Degradation Stability, Vol. 86, Issue 2, pp. 275-282, 2004.
- [6] S. Tayfur, H. Ozen and A. Aksoy, "Investigation of Rutting Performance of Asphalt Mixtures Containing Polymer Modifiers", Construction and Building Materials, Vol. 21, pp. 328-337, 2007.
- [7] U. Isacsson and H.Y. Zeng, "Relationships Between Bitumen Chemistry and Low Temperature Behavior of Asphalt", Construction and Building Materials, Vol. 11, Issue 2, pp. 83-91, 1997.
- [8] S. Shuler and I. Douglas, "Improving Durability of Open-Graded Friction Courses", Transportation Research Record, Vol. 1259, pp. 35-41, 1990.
- [9] G. Airey, "Rheological Evaluation of Ethylene Vinyl Acetate Polymer Modified Bitumens", Construction and Building Materials, Vol. 16, pp. 473-487, 2002.
- [10] A. Topal, "Evaluation of the Properties and Microstructure of Plastomeric Polymer Modified Bitumens", Fuel Processing Technology, Vol. 91, pp. 45-51, 2010.
- [11] W. Vonk, E. J. Scholten and J. Korenstra, "Novel Class of SBS Polymers for Enhanced Effectiveness in Bitumen Modification", Australian Asphalt Paving Association Thirteenth International Flexible Pavements Conference, Queensland, Australia, 2010.
- [12] E. J. Scholten, W. Vonk and J. Korenstra, "Towards Green Pavements with Novel Class of SBS Polymers for Enhanced Effectiveness in Bitumen and Pavement Performance", International Journal of Pavement Research Technology Vol. 3, Issue 4, pp. 216-222, 2010.
- [13] R. B. McGennis, S. Shuler and H. U. Bahai, "Background of Superpave Asphalt Binder Test Methods", Report No. FHWA-SA-94-069, 1994.
- [14] J. P. Zaniewski and M.E. Pumphrey, "Evaluation of Performance Graded Asphalt Binder Equipment and Testing Protocol", Asphalt Technology Program, 2004.

Surface Strain Response of Asphalt Pavement on Steel Bridge Deck Based on Static Loading Tests

J. T. Wu

College of civil engineering
Tongji University
Shanghai, P. R. China
wujinting0215@163.com

F. Ye

Key Laboratory of Road and Traffic Engineering of the
Ministry of Education, Tongji University
Shanghai, P. R. China
yefen@tongji.edu.cn

Abstract—In order to evaluate the bearing capacity of pavement system on steel bridge deck and the rationality of pavement structure design, and accumulate empirical data for the theoretical design of pavement system, a static loading test was carried out on the Zhoupu Pond Bridge with the asphalt pavement of double-layer SMA (Stone Matrix Asphalt), under 3 groups 51 loading conditions, and the surface strains were tested, as well as the temperature. According to the test results, it is concluded that: for the transverse surface strain corresponding to the in-between position of two diaphragms, it was almost not affected by the traffic loading outside the diaphragms; when the loading began to cross the adjacent diaphragm, the transverse surface strain began to change, and the measuring point was under lateral pressure; when the loading just acted on the measuring point or was located within the range of 0.2m, the transverse strain reached the maximum value and the point was objected to tension strain; when the loading was far away, the measuring point was compressed. For the longitudinal strain corresponding to the diaphragm, it was not affected when the loading was out of the range of 0.4m away the diaphragm; when the loading just acted on the diaphragm, the longitudinal strain reached a maximum. The transverse and longitudinal strain values corresponding to the web were greater than those of corresponding to the U-rib edge, and the former was 10 times and 5 times that of the latter, respectively.

Keywords—asphalt pavement on steel bridge deck; surface strain; static loading test; transverse strain; longitudinal strain

I. INTRODUCTION

The asphalt pavement on steel bridge deck with large flexibility is in more complicated and challenging stress condition than the ordinary asphalt pavement, that is because that apparent stress or strain concentrations appear in the ribs and across beam joint under heavy vehicle loads [1]. Besides, the factors, such as the high temperature, waterproof and interlayer binding, aggravate the deformation of asphalt pavement on the steel bridge deck, different from the general asphalt concrete pavement.

Due to the complexity and variability of materials' composition and nature, the impact randomness of environment and load factors, and the quality instability of non-factory construction, it is very difficult for the purely mechanical method to learn the real response of actual pavement structure. Moreover, although the long-term performance observation

could systematically summarize the performance development in the entire life cycle, it is really a long process which costs lots of manpower, material and financial resources as well as analysis difficulty with many influencing factors. As a result, information monitoring in asphalt pavement on testing bridges with intelligent sensors gradually becomes a hot issue [2].

Researches on the testing bridge about the pavement on steel bridge deck started relatively early abroad. Hameau and Esslinger obtained the strains of pavement and steel deck through a two-span continuous compound beam test [3]. In England, a similar test section as same as the Severn Bridge was built in a heavy traffic artery in 1963, and after 10 years observation, TRRL (Transport and Road Research Laboratory) concluded that the guss-asphalt (GA) was suitable for the environment there. In 1976, Japan Longpu steel bridge test was conducted and the pavement composed of GA as the lower layer and the modified dense-graded asphalt mixture as the upper layer was thought to be the best. In order to choose the pavement system for the Esplanade Bridge in Sweden in 1993, eight pavements were paved on the test bridge of BD1337 and then observation and investigation were done in the following four years [4]. In China, the test research of asphalt pavement on steel bridge deck began from the Humen Bridge. And then, relevant units built indoor ring or straight models of orthotropic steel bridge deck, and through accelerated loading tests compared the performance of different pavement structures, mainly relates to the relevant research work of literatures [5]~[12]. The research group of Runyang Yangtze River Highway Bridge used strain gauges to measure the strains before and after the pavement construction [4, 13]. Wu et al. conducted a loading test on a steel bridge to measure the strains at different asphalt layers [14].

In order to measure the surface strains of asphalt pavement on the steel bridge deck, a loading test was conducted on a typical steel bridge, and FBG (Fiber Bragg Grating) strain sensors and temperature sensors were laid to monitor the whole real-time mechanical performance. This paper summarized the development and change rules for dimensional static strains on the top surface of asphalt pavement on the steel bridge deck.

Authors appreciate the support of the Postdoctoral Science Foundation of China (Grant No. 2016M591709)

II. TEST OVERVIEW

A. Pavement Structure

Zhoupu Pond Bridge is a steel-box girder bridge with a single span, a part of Lin Hai highway (A20~A30). Its length is 35km, with eight lanes in two-way. The total design thickness of asphalt pavement on the steel bridge deck is 10cm, and the structure is shown in Table I. The performance of materials and structures all meet the specification requirements (JTJ 052-2000, JTG E42-2005 and JTG E40-2007).

TABLE I. ASPHALT PAVEMENT STRUCTURE

Structure Layer	Paving Material
Upper layer	5cm SMA-13 (modified by high viscosity asphalt)
Tack coat	Modified emulsified asphalt (0.4kg/m ² ~0.6kg/m ²)
Lower layer	5cm SMA-13 (modified by high viscosity asphalt)
Waterproof adhesive layer	Reactive waterproof adhesive layer
	Covered by 3mm~5mm diabase gravel (covering rate of 50%~60%)
	1mm epoxy asphalt binder layer
Steel deck	Surface treatment with epoxy zinc-rich paint

B. Strain Measurement

The stress pattern of asphalt pavement on steel bridge deck is different from general asphalt concrete pavement, that is, under vehicle loads, negative bending moment exists in the pavement surface of the top of rib (such as box girder), and then the maximum tensile stress or strain appears on the surface of the pavement layer.

In the case of static force, the vehicle load is the most harmful to the pavement system on bridge deck. According to previous studies, the general failure mode of bridge deck pavement system is "from top to bottom", because the existence of stiffened rib structure leads to excessive tensile strain on the top surface of the pavement. For structural damage analysis of pavement system on steel deck (such as fatigue cracking, low-temperature cracking and so on) and functional damage (such as rutting, shoving, passing and bulging etc.), it is more effective to learn under the most unfavorable conditions. Under static loads, in order to analyze the most unfavorable longitudinal and transverse load positions, it is necessary to consider the geometric characteristic of stiffened rib and orthotropic steel deck, and the relative location effect of the vehicle load and transverse stiffener on the pavement.

In this paper, two transverse and two longitudinal strain sensors are arranged on the surface of asphalt pavement, which are used to test the transverse and longitudinal strain values of the pavement structure under different loading conditions. Layout scheme of the strain sensors is shown in Fig. 1. Transverse and longitudinal sensors are arranged on the asphalt

surface corresponding to the bridge structure of in-between position of two diaphragms and the intermediate diaphragm, respectively; besides, a group of transverse and longitudinal sensors is placed corresponding to the U-rib edge, another group corresponding to the web.

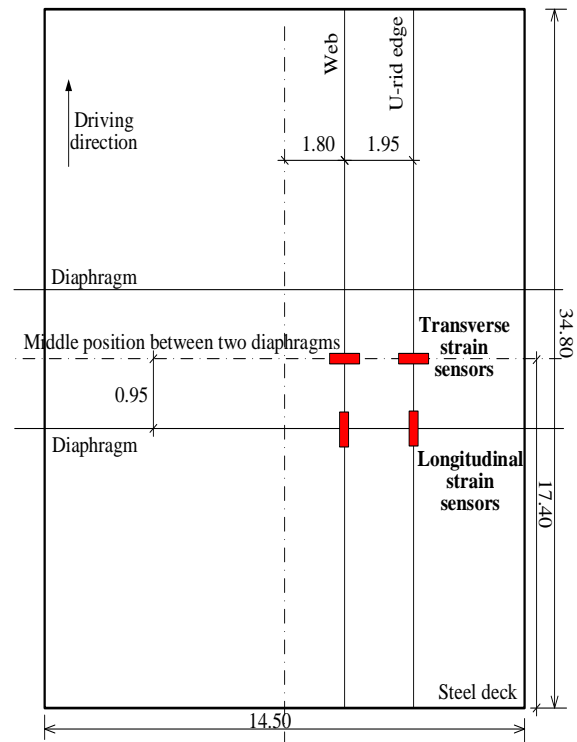


Fig. 1. Layout scheme of strain sensors (unit: m)

The strain sensors are lamellar FBG ones, named by QSS100B, with the measuring range of $\pm 1500\mu\epsilon$. The strain collection system is FBG8600. The strain of FBG sensor expressed by ϵ can be determined through the following Equation (1).

$$\epsilon = \frac{(\Delta\lambda - \alpha_T \Delta T)}{\alpha_\epsilon} \quad (1)$$

Where, $\Delta\lambda$ is the change of central wavelength, α_ϵ is the sensitivity coefficient, α_T is the temperature correction coefficient calibrated with structure, ΔT is the change relative to calibration temperature (20°C).

C. Temperature Measurement

Because of the asphalt, asphalt concrete and so on are temperature sensitive materials, whose deformations are greatly affected by temperature. Therefore, in order to accurately describe and analyze strains on the asphalt pavement, it needs simultaneous temperature acquisition in the strain measuring process. Furthermore, in order to analyze the temperature field on the steel bridge, and to make the temperature compensation for the corresponding strain value, the temperature test is required. Temperature sensors are arranged on the pavement surface, under the upper layer, under the lower layer, and on the upper and lower surfaces of steel

deck. Besides, another temperature sensors hung on the handrail to collect the air temperature at the same time. Due to the space limitations, this paper just analyzes the pavement surface temperature and air temperature which are closely related to the surface strains in the following sections. Customized Pt100 sensors are selected to measure temperature, with the measuring range of $-200^{\circ}\text{C} \sim 650^{\circ}\text{C}$, and the accuracy is 0.01°C .

D. Loading Parameters

The vehicle parameters in the loading test are shown in Table II.

TABLE II. VEHICLE PARAMETERS IN THE LOADING TEST

Parameter	Weight /kg		Area per Wheel / cm^2	Pressure /MPa	Distance /m	
	Left	Right			Between front-rear axles	Wheel clearance of rear-axle
Front-axle	1,450	1,455	22×16.5	0.40	4.70	1.75
Rear-axle	5,470	4,850	22×16.5	0.70		

The static loading test is divided into three groups of 51 conditions, and each group includes 17 conditions expressed by the imaginary lines in Fig. 2 (Group 1 taken for the example). The first group: the right tire center of the front-axle is located on the longitudinal loading line of the U-rib edge, and the distance from left tire center of the front-axle to the strain sensors corresponding to the web surface is 30cm; the second group: the centers of left and right tires of rear-axle are coincided with the web and U-rib edge, respectively; the third group: the left tire center of the front-axle is coincided with the longitudinal loading line corresponding to the web, and the right tire center of the front-axle keeps the distance of 30cm away from the surface strain sensors corresponding to the U-rib edge. In every loading condition, the loading vehicle flames out and remains stationary for 5min at least.

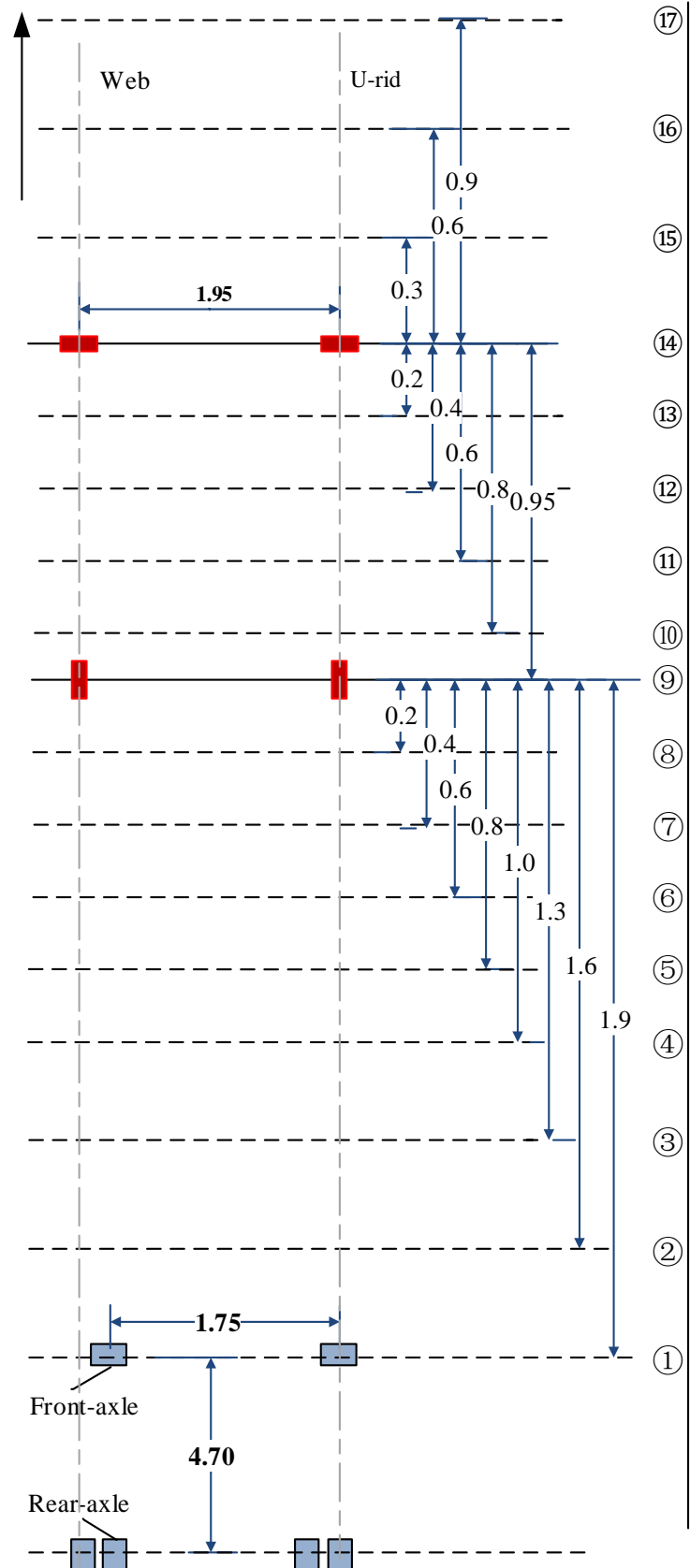


Fig. 2. Static loading conditions (Group 1, unit: m)

III. RESULT ANALYSIS

A. Temperature Test Results

The air temperature and the pavement surface temperature during 12:00~13:00 reach the maximum values of 30.5°C and 40.7°C, respectively, and the both at 2:50 reached the lowest values of -20.8°C. So, the pavement surface bears 10°C higher than the air temperature, which is an ordeal for the high-temperature performance of asphalt pavement. In the temperature-rise period, from 7:00 to 13:00, the pavement surface temperature is higher than air temperature. In the temperature-decrease period, that is, from 14:30 to the next day at 7:00, pavement surface temperature is higher than air temperature, too. Temperature rate curves show that the rising and decreasing rate of pavement surface temperature is slightly larger than that of air temperature. The former is about 1.5 times of the latter.

B. Strain Test Results

The strain test results are shown in Fig. 3. According to the test results under different static loading conditions, it is concluded that:

- For the transverse surface strain corresponding to the in-between position of two diaphragms, it was almost not affected by the traffic loading outside the diaphragms; when the loading began to cross the diaphragm, the transverse surface strain began to change, and the measuring point was under lateral pressure; when the loading just acted on the measuring point or was located within the range of 0.2m, the transverse strain reached the maximum value and the point was objected to tension strain; when the loading was far away, the measuring point was compressed.
- For the longitudinal strain corresponding to the diaphragm, it was not affected when the loading was out of the range of 0.4m away the diaphragm; when the loading just acted on the diaphragm, the longitudinal strain reached a maximum.
- The transverse and longitudinal strain values corresponding to the web were greater than those of corresponding to the U-rib edge, and the former was 10 times and 5 times that of the latter, respectively.

REFERENCES

- [1] Z. J. Dong, L. P. Cao, Y. Q. Tan and S. G. Wu, "Analysis of the dynamic response of three directional strains in asphalt pavement under moving vehicle loads", China Civil Engineering Journal, vol. 42, 2009, pp. 133~139.
- [2] W. Huang, "Theory and method of deck paving design for long-span bridge", Beijing: China Building Industry Press, 2006.
- [3] W. Hameau and M. Esslinger, "Die Stahlfahrbahn berechnung und konstruktion", Maschinenfabrik- Augsburg-Nuernberg. Forschungsheft, vol. 7, 1957, pp. 305.
- [4] S. D. Wu, "The collection of Runyang Yangtze River Bridge construction", Beijing: China Communications Press, 2006.
- [5] P. Fang and B. Wu, "Static loading test and finite element analysis of steel bridge deck and pavement", East China Highway, vol. 4, 2000, pp. 38~42.
- [6] B. Wu and P. Fang, "Finite element analysis and circular model design of steel deck pavement", Highway, vol. 1, 2001, pp. 24~27.
- [7] L.W. Tong and Z. Y Shen, "Fatigue assessment of orthotropic steel bridge decks", China Civil Engineering Journal, vol. 33, 2000, pp. 16~21.
- [8] Z. C. Huang, "Study on the mechanical behavior and structure optimization of steel box Girder deck pavement". Xi'an: Chang An University, 2010.
- [9] G. P. Shen and X. Q. CAO, "Experimental study on pavement fatigue of orthotropic steel deck plate", Journal of Shanghai Tiedao University, vol. 3, 1996, pp. 100~108.
- [10] S. Q. Yang, "The accelerated testing study on the steel bridge deck Pavement", Xi'an: Chang An University, 2010.
- [11] C. M. Li and Y. Z. Li, "Study on variation of strain in the surfacing of asphalt mixture on the steel bridge deck", Journal of Highway and Transportation Research and Development, vol. 17, 2000. pp. 1~4.
- [12] L. G. Shao, Q. S. Zhang, Y. Z. Li and J. Wu. "Dynamic strain test and analysis of steel deck asphalt pavement layer on straight track test model", Highway, vol. 1, 2001, pp. 63~66.
- [13] G. W. Hu, "Mechanical analysis and structural optimum design for deck paving of long-span steel bridge", Nanjing: Southeast University, 2005.
- [14] J. T. Wu, F. Ye, H. R. Wu, and X. Y. Jia, "Strain dynamic response of asphalt pavement on steel bridge with field loading test", Journal of Tongji University (Natural Science), vol. 42, 2014, pp. 413~420.

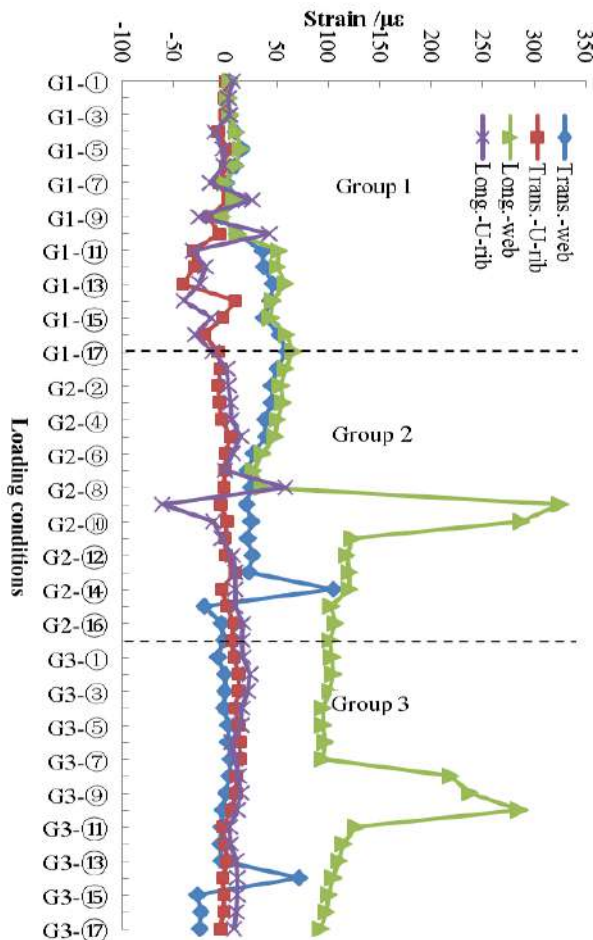


Fig. 3. Strain results in loading conditions

Investigation of the Properties of Warm Mix Asphalt Involving Organic Additive

Ali Topal^a, Baha Vural Kök^b, Derya Kaya^{*a}, Burak Şengöz^a, Peyman Dokandari^a, Mehmet Yılmaz^b

^a Department of Civil Engineering, Dokuz Eylül University, Izmir, Turkey

^b Department of Civil Engineering, Fırat University, Elazığ, Turkey

*d.kaya@deu.edu.tr

Abstract— Demand for sustainable pavements increases day by day in asphalt paving industry. Warm Mix Asphalt (WMA) technology has begun to be an interesting topic for researchers owing to sustainability and environmental issues. Within the scope of this study, the effect of an organic WMA additive was evaluated in terms of mixture characteristics and performance. The fundamental and rheological properties of bitumen samples involving organic WMA additive were determined by conventional bitumen tests and dynamic shear rheometer (DSR). Mixtures modified with organic WMA additives were produced according to Marshall mix design method and the optimum bitumen content of the samples were determined. Following the determination of optimum bitumen content, the effect of the organic WMA additive was investigated in terms of indirect tensile stiffness modulus, fatigue and creep behaviour. Hamburg wheel tracking device was also applied to evaluate the permanent deformation characteristics of WMA mixtures in comparison to Hot Mix Asphalt (HMA) mixtures. The results appraised the effect of the organic WMA additive on rheological and performance characteristics of bituminous mixtures.

Keywords— Warm Mix Asphalt, Organic additive, Mixture characteristics, Dynamic shear rheometer, fatigue behaviour, Hamburg wheel tracking device

INTRODUCTION

Most of the field pavement practices around the world consist of conventional hot mix asphalt (HMA). For the last decade, implementing of warm mix asphalt (WMA) technologies has gained popularity in Europe and in some other countries as well as in the USA. The goal of WMA technologies is to obtain required strength and durability which is equivalent to or even better than HMA pavements [1]. The use of WMA technologies offers many benefits to asphalt industries. Many studies have common sight about the various advantages of the utilization of WMA technologies. These advantages are all originated from the major feature of WMA additives which is reducing the viscosity of the bitumen [2]. This reduction results in increasing workability and ease of use, ecological benefits due to less emissions and reduction in costs due to less energy use. In terms of workability, the reduced viscosity helps the aggregates to be coated more easily [3, 4]. When discussing about environmental benefits, there are serious worries about the greenhouse gases emissions in HMA pavement applications. Due to lower application temperatures of WMA mixes, the emission of carbon dioxide (CO₂) and other so called greenhouse gases are lowered in comparison with HMA mixes [5]. Besides, the evaporation of less heavy components of

bitumen occurs less than conventional applications. This causes less odours in asphalt plants, therefore provides more pleasant working conditions. Builders comments also indicate that the fumes are rather less in WMA production in comparison with HMA production [6]. The fuel consumption of WMA technologies is rather less than conventional HMA mixtures. Energy consumption for WMA production has been reported as 60–80% of HMA production [4]. Some studies have also reported the range of 20–35% of savings in burner fuel with use of WMA technologies [5]. In asphalt industry, a common way of achieving lower application temperatures in order to produce WMA is the utilization of WMA additives. All of the current WMA additives facilitate lowering of production temperature by either lowering the viscosity and/or expanding the volume of the bitumen at a given temperature [7, 8]. There are many kinds of WMA additives, these additives are categorized as chemical, zeolite or organic additive etc. Organic WMA additives those are the most common as aforementioned, WMA additives used to improve workability by reducing the viscosity of bitumen [9]. By lowering the viscosity, asphalt can be produced at lower temperatures compared to conventional HMA. Organic WMA additives are reported as resistance improvers against permanent deformation by composing crystallized structures after cooling [10].

In this research, WMA mixture has been prepared with an optimum rate of organic WMA additive that is based on the recommendation of manufacturers. The mechanical performances of the samples were evaluated by Marshall stability test. Following, WMA samples involving organic WMA additive; indirect tensile stiffness modulus (ITSM) and fatigue behaviour of WMA were analyzed and compared with control specimens (HMA). Hamburg wheel tracking device was also used to determine the rutting performance of WMA mixture.

EXPERIMENTALS

Materials

In this study, 50/70 penetration grade base bitumen provided from Aliğa/Izmir petroleum refinery was used. In order to characterize the properties of the base bitumen, conventional tests such as: penetration test, softening point test, Rolling Thin Film Oven Test (RTFOT) and etc. were conducted. These tests were performed in conformity with the relevant standards. Results are presented in Table 1.

TABLE 1. PROPERTIES OF BASE BITUMEN

Test	Specifications	Results	Limits
Penetration (25 °C; 0.1 mm)	ASTM D5/D5M-13 TS EN 1426	55	50-70
Softening point (°C)	ASTM D36/D36M-12 TS EN 1427	49	46-54
Viscosity at (135 °C)-Pa.s	ASTM D4402/D4402M-13	412.5	-
Viscosity at (165 °C)-Pa.s	ASTM D1754/D1754M-09 TS EN 12607-2	-	-
Change of mass (%)	-	0.04	0.5(maks.)
Retained penetration after RTFO (%)	ASTM D5/D5M-13 TS EN 1426	25	-
Softening point rise after RTFO (°C)	ASTM D36/D36M-12 TS EN 1427	54	48 (min)
Specific gravity	ASTM D70-09e1 TS EN 15326	1.03	-
Flash point (°C))	ASTM D92-12b TS 123 EN 22592	260	230 (min)

The aggregates used in this study consist of a mix of basalt and limestone aggregates provided from Dere Madencilik Inc. quarry located in Belkahve/Izmir. The mix gradation of basalt and limestone was intentionally chosen to provide desired performance in conformity with Turkish specifications concerning the Type 1 wearing course. Basalt plays the role of strengthening constituent as coarse aggregate while limestone participates in the fine aggregate framework. Table 2 presents the final gradation chosen for basalt–limestone aggregate mixture. The properties of the aggregate were investigated by several tests such as specific gravity, Los Angeles abrasion resistance, sodium sulphate soundness, fine aggregate angularity and flat and elongated particles. Test results conducted on both aggregate types are presented in Table 3.

TABLE 2. GRADATION FOR BASALT–LIMESTONE AGGREGATE MIXTURE

Test	19 – 12,5 mm Basalt	12,5 – 5 mm Basalt	5 – 0 mm Limestone	Combine d Grad. (%)	Spec. Limits
Mix.(%)	15	45	40		
(3/4) "	100	100	100	100	100
(1/2) "	35.7	100	100	90.5	83-100
(3/8) "	2.5	89	100	80.5	70-90
No.4	0.4	16	100	47.3	40-55
No.10	0.3	1.2	81	33	25-38
No.40	0.2	0.7	33	13.5	10-20
No.80	0.15	0.4	22	9	6-15
No.200	0.10	0.2	13	5.3	4-10

TABLE 3. THE PROPERTIES OF BOTH BASALT AND LIMESTONE

Test	Specifications	Results		Spec. Limits
		Limestone	Basalt	
Specific Gravity (Coarse Agg.)	ASTM C127-12			
Bulk		2.686	2.666	-
SSD		2.701	2.810	-
Apparent		2.727	2.706	-
Specific Gravity (Fine Agg.)	ASTM C128-12			
Bulk		2.687	2.652	-
SSD		2.703	2.770	-
Apparent		2.732	2.688	-
Specific Gravity (Filler)		2.725	2.731	-
Los Angeles Abrasion (%)	ASTM C131-06 TS EN 1097-2	24.4	14.2	maks. 45 maks. 27
Flat and Elongated Particles (%)	ASTM D4791-10 TS EN 933-3	7.5	5.5	maks 10 maks. 25
Sodium Sulphate Soundness (%)	ASTM C88-13			maks. 10-20
Fine Aggregate Angularity	ASTM C1252-06	47.85	58.1	min. 40

Sasobit® is an organic WMA additive which is product of Sasol Wax Inc. It is a long-chain aliphatic polymethylene hydrocarbon produced from the Fischer-Tropsch (FT) chemical process with a melting temperature of 120°C. The longer chains help keep the wax in solution, which reduces bitumen viscosity at typical asphalt production and compaction temperatures. Based on the literature, dosages for organic additive ranged from 1.0% to 4.0% by weight of the bitumen [11–13]. In this research, the organic additive content was chosen as 3.0% based on the past research [14]. Organic additive added to the virgin bitumen at 120°C and mixed by using the high shear mixer for 10 minutes.

TEST METHODS

Conventional bitumen tests

The base bitumen and the bitumen sample containing organic additive were subjected to the following conventional bitumen tests; penetration, ring and ball softening point, thin film oven test (TFOT), penetration and softening point after TFOT as well as the storage stability test determined by the difference in softening point test results taken from the top and bottom of the tube (ASTM D5-06 2006; ASTM D36-95 2000; ASTM D 1754-97 2002) [15–17]. In addition, the temperature susceptibility of the bitumen samples has been calculated in terms of penetration index (PI) using the results obtained from penetration and softening point tests [18].

The viscosity defined as resistance of a fluid to flow is significant since it affects the workability of the bitumen [19]. Brookfield viscometer was employed to inspect the mixing and compaction temperatures of the mixtures in according to ASTM

D4402-06 [20]. The test was performed at 135°C and 165°C and the temperatures corresponding to bitumen viscosities 170±20 mPa.s and 280±30 mPa.s were chosen as mixing and compaction temperatures respectively.

Mechanical Properties

The effect of organic WMA additive on the mechanical properties of WMA has been determined by Marshall mix design method (ASTM D3549) in terms of stability, flow and air void content as well as by indirect tensile stiffness modulus test and indirect tensile fatigue test [21-24]. The tests were conducted on WMA samples at recommended contents and on HMA as control samples. Asphalt concrete specimens were prepared with a compaction effort of 75 blows simulating heavy traffic loading conditions. The ITSM test is a non-destructive test that is used to evaluate the relative quality of materials and study the effect of temperature and loading rate. The ITSM Sm in MPa is defined as below [23];

$$Sm = F(R + 0.27)/LH \quad (1)$$

Where F is the peak value of the applied vertical load (repeated load, N), H is the mean amplitude of the horizontal deformation (mm) obtained from five applications of the load pulse, L is the mean thickness of the test specimen (mm), and R is the Poisson's ratio (assumed as 0.35). The test was performed by way of a universal testing machine (UTM) in deformation-controlled mode. The magnitude of the applied force was adjusted by the system during the first five conditioning pulses such that the specified target peak transient diametral deformation was obtained. An appropriate value was chosen to ensure that sufficiently high signal amplitudes were obtained from the transducers which would produce consistent and accurate results. Accordingly, this value was selected as 5 mm for this test. The rise time, which is measured from the origination of load pulse and denotes the duration of the applied load rising from zero to the maximum value, was set at 124 ms. The load pulse application was adjusted to 3.0 s. ITSM tests were conducted at three different temperatures (20 °C, 25 °C and 30 °C).

The indirect tensile fatigue test is one of the constant stress test that characterizes the fatigue behaviour of the mixture [25]. In this study, the fatigue test was performed in a controlled stress mode based on BS DD AFB standard [24]. The UTM was also used for this purpose. The loading frame was housed in an environmental chamber to control temperature during the test. The desired load level, load rate and load duration were controlled by a computer. The deformation of the specimen was monitored through linear variable-differential transducers (LVDTs). The LVDTs were clamped vertically onto the diametrical side of the specimen. A repeated dynamic compressive load at 350 kPa was applied to specimens at 20°C, 25°C and 30°C test temperatures, across the vertical cross-section along the depth of the specimen using two loading strips 12.5 mm in width. Finally, the resulting total deformation corresponding to the applied force was measured.

Rheological Properties

The DSR test was performed on WMA samples by using a Bohlin Gemini II DSR rheometer to evaluate their rheological characterization. The test was performed under controlled stress loading conditions using low (0.01 Hz) and high (10 Hz) frequency sweeps at temperature between 30 °C and 80 °C (for every 10 °C). The stress amplitude for all the tests was confined within the linear visco-elastic response of the bitumen.

Rutting test

The loss of pavement serviceability is a common result from rutting which is defined as the formation of the longitudinal depressions under the wheel paths caused by the progressive movement of materials under traffic loading in the asphalt pavement layers [26]. The Hamburg wheel tracking device is designed to evaluate the rutting characteristics of bituminous mixtures by dint of aggregate structure, bitumen properties, moisture susceptibility and adhesion between bitumen and aggregates. The test is carefully contemplated to simulate bearing capacity of pavement under actual wheel tracks.

The working principle is to roll a steel wheel with a specified diameter over a bituminous mixture specimen with a standard thickness for a specified number of wheel passes. The test measures the depth of rut after the specified number of passes is reached. Various organizations may define their own specifications with different testing conditions such as specimen dimensions, wheel diameter, rolling length, applied load and temperature. Within this context, there are many devices designed to carry out the task under various conditions.

The test device used within the scope of this study, was an electronically powered device which rolls a steel wheel (capable of using rubber wheel) with a diameter of 203 mm and width of 50 mm over a well compacted specimen with dimensions of 430×280×50 mm. The device is capable of making about 50 passes in minute over the specimen's surface by rolling length of 230 mm. The applied load was chosen as 710 N by default as per EN 12697-22 standard test method [27]. Prior to compaction of the specimens, HMA and WMA mixtures were carefully mixed at their pre-defined mixing temperatures using a mixer capable of mixing adequate amount of materials at desired temperature. The Hamburg wheel tracking device comes with a roller compactor in order to compact mixtures within standard molds to fit in wheel tracking device frames. The roller compactor also makes it convenient to prepare specimens with desired thickness (50 mm) with specified air voids (4%). The amount of loose mix to reach the desired compacted bulk specific gravity corresponding to 4% air voids considering mold dimensions was calculated and poured into compaction molds. After cooling the specimens at room temperature, the specimens were subjected to 30.000 passes of wheel tracks. In this study, two specimens of HMA and WMA were prepared and tested for right and left wheels. The rut depth was measured and recorded for right and left wheels simultaneously by an electronic system at every 5.000 passes while the test was running.

RESULTS AND DISCUSSIONS

Conventional test results

The conventional properties of the bitumen prepared with organic additive are presented in Table 4. As depicted in Table 4, the addition of the organic WMA additive decreased the penetration values and increases the softening point values.

As seen in Table 4, WMA sample exhibits higher penetration index values (which is an indicator of reduced temperature susceptibility) compared to base bitumen. Asphalt mixtures containing bitumen with higher PI are more resistant to low temperature cracking as well as permanent deformation [28]. Storage stability test indicate that, the bitumen samples with WMA additive is much more storage stable compared to HMA.

As depicted in Table 4, the additive reduce the viscosity of bitumen which indicates that, WMA additives increase the workability and make relatively reductions for mixing and compaction temperatures. The viscosity of results related to WMA additive 135°C and 165°C are drawn at semi logarithmic figure and the temperature corresponds to compaction and mixing range is also summarized in Table 5. Based on the Table 5, it can be seen that, the addition of organic WMA additive reduced the mixing and compaction temperature between 10-15°C.

TABLE 4. CONVENTIONAL PROPERTIES OF BASE AND ORGANIC WMA MODIFIED BITUMEN

Test	Base bitumen	Bitumen including Organic WMA Additive
Penetration (0.1mm)	55	37
Softening point (°C))	49.1	69.3
Viscosity at (135 °C) (mPa.s)	412.5	287.5
Viscosity at (165 °C)- (mPa.s)	137.5	75.0
Loss of mass (%)	0.04	0.07
Retained penetration (after TFOT (%))	75	87
Softening point rise after (afterTFOT (°C)	5.0	4.0
Pen. In	-1.20	1.95
Storage Stability	0	1.6

TABLE 5. MIXING AND COMPACTION TEMPERATURES

Additive Content (%)	Mixing Temperature Range(°C)	Compaction Temperature (°C)
0	156-163	143-149
3	144-149	134-138

Results of Mechanical Properties

In this study, the optimum bitumen content related to HMA mixture as well as WMA mixture containing organic WMA additive were determined by the Marshall mix design method,

retrieved directly as the bitumen content corresponding to 4% air voids on content–air voids graphic based on second degree polynomial trend lines. The optimum bitumen content for HMA mixture and WMA mixture containing organic WMA additive were determined as 4.76%, and 4.25% respectively. The ITSM values at 20°C, 25°C and 30°C temperatures for HMA and WMA mixtures containing organic WMA additive are shown in Fig. 1. As depicted in Fig. 1, the ITSM values of WMA are higher than HMA mixtures at all tested temperatures. The ITSM values of HMA mixtures and WMA mixtures containing Organic WMA additive have significantly decreased by increase in temperature.

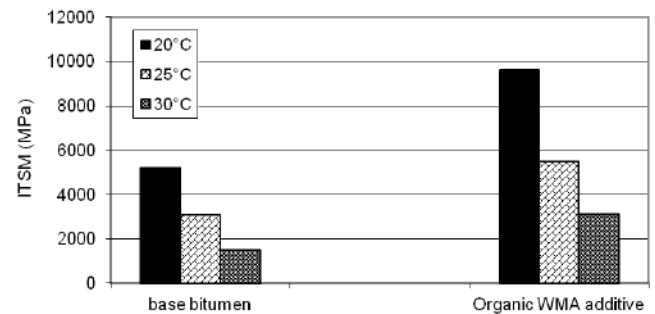


Figure 1. ITSM values of HMA WMA mixtures including organic WMA additive

The variation of load cycle numbers by temperature change is given in semi-logarithmic graphs in Fig. 2. As presented in Fig. 3, the load cycle numbers which caused the specimens to be cracked declined considerably as the temperature increased.

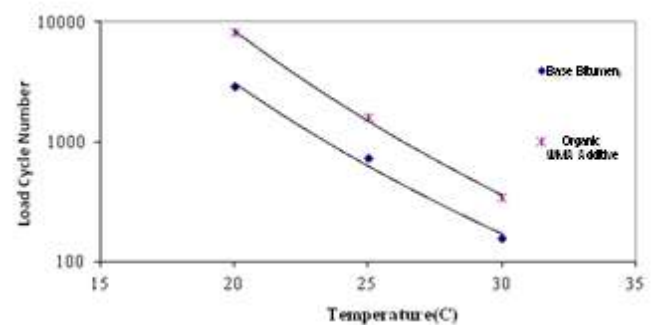


Figure 2. Variation of load cycle numbers by temperature change

The deformation of the specimens was monitored through linear variable–differential transducers (LVDTs) during the indirect tensile fatigue test. The graphs for the load cycle number corresponding permanent deformation are given in Fig. 3 for HMA and WMA mixtures at 20°C temperature. As shown in Fig. 3, HMA and WMA mixtures were cracked at approximate values of 4.3 mm, 4 mm deformation strains respectively. The specimens prepared with organic WMA additive could withstand higher load cycles and have cracked at lower deformation strains.

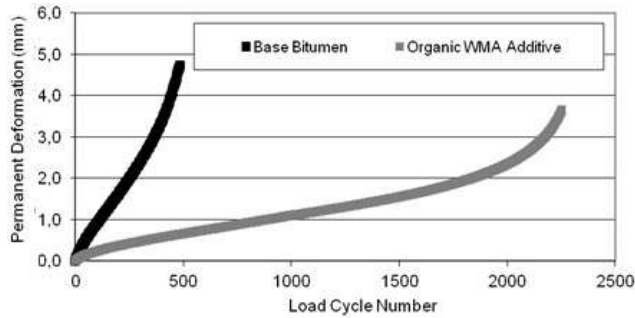


Figure 3. Permanent deformations corresponding load cycle numbers

Results of Rheological Properties

The variation of complex modulus (G^*) of the base bitumen and the bitumen samples involving variable content of organic WMA additive at low (0.01 Hz) and high frequency level (10 Hz) and at six different temperatures are presented in Figs. 4a and 4b. As depicted in Figs. 4a-4b complex modulus increases by the decrease of temperature. An increment in G^* indicates higher elastic part, thus an improved elastic behaviour. Besides, G^* increases with increase in frequency. This is due to the rheological behaviour of the bitumen samples since bitumen under shorter loading times (high frequency level) exhibit elastic behaviour. G^* values of the samples involving organic WMA additive are greater than G^* of base bitumen for all temperatures and frequencies as seen in Figs. 4a and 4b.

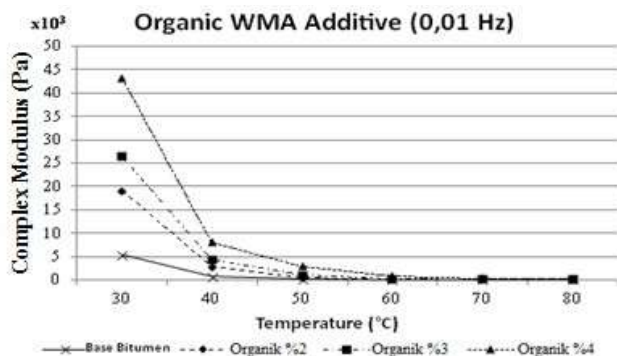


Figure 4a. Complex Modulus of organic WMA additive at 0.01 Hz.

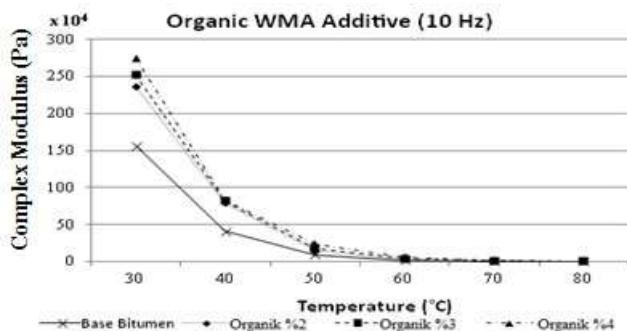


Figure 4b. Complex Modulus of organic WMA additive at 10 Hz.

Rutting Test Results

The Hamburg wheel tracking test was performed in accordance with EN 12697-22 standard [27]. The rut depths at 50°C are presented in Figure 5. Results are given as percent values indicating the ratio of actual rut depth over the total thickness of tested specimen (50 mm). The real rut depths (mm) are obtainable by halving the percent values. The rut depths at 50°C of HMA and WMA mixtures involving organic WMA additive were determined at each 5.000 passes initiating at 5.000 and ending at 30.000.

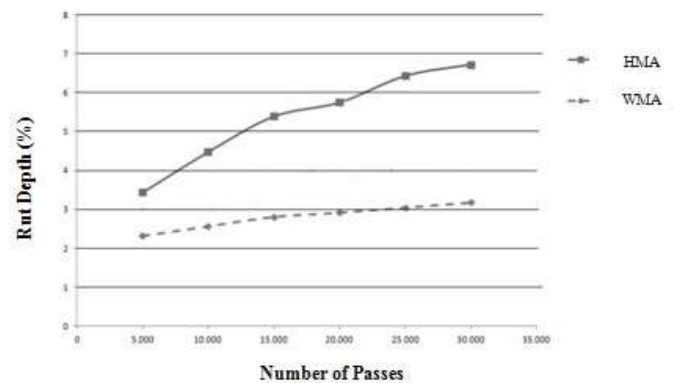


Figure 5. The rut depth % values corresponding number of passes for HMA and WMA mixtures including Organic WMA Additive

As expected the rut depth values typically increased with increase in the number of passes. Based on each number of passes, WMA mixture involving organic additive performed better than HMA mixture in terms of rut depth.

CONCLUSIONS AND RECOMMENDATIONS

Lowering mixing and compaction temperatures and consequently the reduction of energy costs as well as emissions are the dominant advantages of utilization of WMA technologies. The utilization of organic WMA additive helps in the reduction of viscosity values which in turn reduces the mixing and compaction temperatures.

The results obtained from Marshall design demonstrated that the optimum bitumen content decreases by WMA additive. This reduction can be described as an advantage of using organic WMA additive in terms of initial cost.

ITSM values regarding HMA mixture and WMA mixture showed that the utilization of organic WMA additive increases the stiffness of mixtures. The ITSM values of all mixtures tested within the scope of this study significantly decreased by increase in temperature. As well as PI values of bitumen containing organic additive exhibited that the use of WMA additive potentially improves the temperature susceptibility.

When evaluating the load cycle numbers which caused the specimens to be cracked, WMA additive improves the repetitive loading strength of bituminous mixtures. The load

cycle numbers of all mixtures significantly decrease by increase in temperature. Taking into consideration the deformation strains, WMA mixture exhibits better performance under constant loading cycles. The utilization of organic WMA additive improves the ability of asphalt pavements against permanent deformation and increases the rigidity of bituminous mixtures. The formation of crack in lower deformation levels as a result of repetitive loading is an indicator for brittle susceptibility level of a specimen.

Detailed investigation performed by DSR test at low and high frequency level and at different temperatures indicated that, the complex modulus value increases with increase in frequency and decreasing temperature. Increment in G^* is attributed to improved elastic behaviour of the sample.

In the light of findings from rutting test, it is possible to consider that the organic WMA additive improves resistance to rutting characteristics of bituminous mixtures. Organic WMA additive has structural modification effects on bituminous mixtures.

Acknowledgements

This research was sponsored by the Scientific and Technological Research Council of TURKEY (TUBITAK) under the project number 110M567 for which the authors are greatly indebted. The findings and evaluations of the results of this study are not the official view of TUBITAK.

REFERENCES

- [1] D. Newcomb, "An introduction to warm-mix asphalt," National Asphalt Pavement Association, 2006.
- [2] GC. Hurley, and BD. Prowell, "Evaluation of potential process for use in warm mix asphalt", J Assoc Asphalt Paving Technol., vol. 75, pp. 41–90, 2006
- [3] O. Kristjansdottir, ST. Muench, L. Michael, and G. Burke, "Assessing potential for warmmix asphalt technology adoption", Transport Res Rec., vol. 2040, pp. 91–9, 2007.
- [4] MC. Rubio, G. Martinez, L. Baena, and F. Moreno, "Warm mix asphalt: an overview", J Cleaner Prod., vol. 24, pp. 76–84, 2012.
- [5] J. D'Angelo, E. Harm, J. Bartoszek, G. Baumgardner, M. Corrigan, J. Cowser, et al. "Warm-mix asphalt European practice", American Trade Initiatives, 2008.
- [6] JM. Croteau, and B. Tessier, "Warm mix asphalt paving technologies: a road builder's perspective" The 2008 Annual Conference of the Transportation Association of Canada, 2008.
- [7] JW. Button, C. Estakhri, A. Wimsatt, "A synthesis of warm-mix Asphalt" Texas Transportation Institute, The Texas A&M University, 2007.
- [8] GC. Hurley, and BD. Prowell, "Evaluation of Sasobit for use in warm mix asphalt", National Center for Asphalt Technology, 2005.
- [9] A. Jamshidi, M. O. Hamzah, Z. You, "Performance of Warm Mix Asphalt containing Sasobit®: State-of-the-art." Construction and Building Materials, vol. 38, pp. 530–553, 2013.
- [10] M. Zaumanis, "Warm mix asphalt investigation." M.Sc. Thesis, Technical University of Denmark, Kgs.Lyngby, 2010.
- [11] J. D'Angelo, E. Harm, J. Bartoszek, G. Baumgardner, M. Corrigan, J. Cowser, T. Harman, M. Jamshidi, , W. Jones, D. Newcomb, B. Prowell, R. Sines, and B. Yeaton, "Warm-mix asphalt: European practice." American Trade Initiatives, 2008.
- [12] A. J. Austerman, W. S. Mogawer, R. Bonaquist, "Evaluating the effects of warm mix asphalt technology additive dosages on the workability and durability of asphalt mixtures containing recycled asphalt pavement." Transportation Research Board 88th Annual Meeting, 2009.
- [13] K. Kanitpong, K. Nam, W. Martono, and H. Bahia, "Evaluation of a warm mix asphalt additive." Construction Materials. Vol. 161(1), pp. 1-8. 2008.
- [14] K. O'Sullivan, and P. Wall, "The effect of warm mix asphalt additives on recycled asphalt pavement." Worcester Polytechnic Institute, 2009.
- [15] ASTM D5-06 "Standard test method for penetration of bituminous materials." American Society for Testing and Materials; West Conshohocken, PA, 2006.
- [16] ASTM D36-95 "Test method for softening point of bitumen (ring-and-ball apparatus)." American Society for Testing and Materials; West Conshohocken, PA, 2000.
- [17] ASTM D 1754-97 "Standard test method for effects of heat and air on asphaltic materials (thin-film oven test)." American Society for Testing and Materials; West Conshohocken, PA, 2002.
- [18] J. Read, and D. Whiteoak, "The Shell bitumen handbook." Thomas Telford Publishing, London. 2003.
- [19] L. P. Specht, O. Khatchatourian, L. A.T. Brito, J. A. P. Ceratti, "Modelling of asphalt-rubber rotational viscosity by statistical analysis and neural networks." Materials Research. Vol. 10(1), pp. 69-74, 2007.
- [20] ASTM D4402-06 "Standard test method for viscosity determination of asphalt at elevated temperatures using a rotational viscometer." American Society for Testing and Materials; West Conshohocken, PA, 2002.
- [21] ASTM D3549-11. Standard test method for thickness or height of compacted bituminous paving mixture specimens. West Conshohocken (PA), USA: American Society for Testing and Materials; 2011.

- [22] ASTM D6931-12. Standard test method for indirect tensile (IDT) strength of bituminous mixtures. West Conshohocken (PA), USA: American Society for Testing and Materials; 2012.
- [23] BS DD 213. Method for determination of the indirect tensile stiffness modulus of bituminous mixtures. Draft for development, London: British Standards Institution; 1993.
- [24] Bs DDABF. Method for determination of the fatigue characteristics of bituminous mixtures using indirect tensile fatigue. Draft for development. London: British Standards Institution; 1997.
- [25] FM. Nejad, E. Aflaki, and MA. Mohammadi, "Fatigue behavior of SMA and HMA mixtures", *Constr Build Mater.*, vol. 24, pp. 1158-1165, 2010.
- [26] F.M. Nejad, A. Azarhoosh, G.H. Hamed., H. Roshani, "Rutting performance prediction of warm mix asphalt containing reclaimed asphalt pavements", *Road Materials and Pavement Design*, vol. 15(1), pp. 207-219, 2014.
- [27] EN 12697-22. Bituminous mixtures - Test methods for hot mix asphalt - Part 22: Wheel tracking, 2003.
- [28] B. Sengoz, G. Isikyakar, "Analysis of styrene-butadiene-styrene polymer modified bitumen using fluorescent microscopy and conventional test methods", *Journal of Hazardous Materials*, vol. 150, pp. 424-432, 2008.

Daily Temperature Change in Concrete Pavements, Albedo effect and Stress Analysis by 3D Finite Element Method

Muhammet Vefa Akpınar¹
Civil Engineering
Karadeniz Technical University
Trabzon, Turkey

Mehmet Tevfik Seferoğlu²
Civil Engineering
Karadeniz Technical University
Trabzon, Turkey
mtseferoglu@gmail.com

Ayşegül Güneş Seferoğlu³
Civil Engineering
Gümüşhane University
Gümüşhane, Turkey

Sedat Sevin⁴
Civil Engineering
Gümüşhane University
Gümüşhane, Turkey

Muhammet Çelik⁵
Civil Engineering
Provincial Directorate of Disaster and Emergency, AFAD
Trabzon, Turkey

Abstract— One of the most common reasons for deterioration in concrete pavements are thermal strains which occurs due to daily temperature changes. Additional strains occur due to thermal differences between bottom and top layers of concrete covers.

Even if thermal related cracks do not cause fundamental structural problems in its initial development stage, these cracks could increase due to freeze and thaw of the rigid pavement. Consequently, the drained water in the base layers cause deteriorations in base ground and other layers.

The most common used concrete pavement class in Turkey and around the world C30 class concrete was poured in accelerated pavement test laboratory facility in 1/1 scale ratio conditions and thermal measures were daily taken from the edge and middle of the 5 m by 4.5 m and 150 mm thick concrete plate section. Thermal variations through the 150 mm thickness were measured every 50 mm depth by the thermocouples in summer and winter.

In recent years, an Albedo device, which is an innovative method for determining the amount of reflection of sunlight coming to the surface of the pavement, is used. Reflections from the surface of concrete slabs were recorded with the Albedo device while temperature measurements were taken in this study. In this study, it was investigated how the temperature which occurs on the surface of a concrete pavement of C30 standard progressed along the thickness. Finally, thermal data were entered in ANSYS finite element models and afterwards strains were computed.

Keywords- Thermal stresses, ANSYS, Daily temperature, Thermal cracks, Albedo

I. INTRODUCTION

Concrete pavements are used as an alternative to asphalt pavement, especially in roads exposed to heavy vehicle traffic. This type of coating is suitable for use even in the case where the subgrade layer is weak due to its advantages such as high strength, long life, less maintenance and repair.

Concrete pavements are exposed to formations such as expansion and shrinkage due to seasonal temperature cycling and daily temperature changes. These physical changes cause a number of problems in concrete pavements. Concrete pavements can be constructed using reinforcement and/or joints so that they can be used smoothly with expansion and contraction problems during service life.

While the concrete surface expands in hot weather and shrinks in cold weather. The difference in temperature between the bottom and the top surface of the concrete coatings causes thermal stresses in the concrete. As the plate thickness increases, the temperature difference between the surfaces increases.

Although the temperature distribution in concrete pavements depends on the weather conditions, the impact angle of the sun's rays on the pavement surface can also affect the temperature distribution. The amount of reflection from the pavement surface of the sun's rays can be determined with the Albedo device. At this point, the temperature distribution obtained during the pavement thickness and the sun rays reflected from the surface can be found.

Considering the literature studies, it has been found that there are significant stresses in concrete roads due to thermal stresses. These stresses have been found in the literature with modeling of land studies or end-elements. It is seen that the nonlinearity of the temperature distribution along the depth in the concrete coatings is more stressed than the linearity.

A. Temperature Effect in Concrete Pavements

Experimental and numerical studies are widely used to determine the temperature distribution in concrete slabs. Measurements must be taken in the field conditions in order to remove the temperature profile of the concrete pavement. The temperature distribution along the pavement thickness is measured and recorded and displayed by thermocouples placed at different depths [1, 2, 3]. This data is accurate for short-circuited readings, but can lead to significant errors due to zero point deviations for long-run thermocouple readings. At the same time, these data can lead to misleading results because in situ observations cannot cover areas with special conditions that are affected by heat transfer between the pavement and the environment [1, 2, 4].

It would be useful to compare the measurements taken from the field with analytical solutions or computer models. After the measurement results are clarified, the extra internal stresses introduced into the concrete pavement are investigated. The temperature distribution that occurs in concrete pavement creates internal stresses that will result in increased curl and shrinkage of the pavement. It is accepted that the temperature distribution during the design and analysis of concrete pavement is linear across the layer thickness. However, when field measurements are taken, it can be seen that there is a nonlinear distribution.

In a study by Huang in 1993, it was determined that the temperature difference between the lower and upper surface of the pavement reached a maximum of 0.5-0.6 °C/mm during the day, and reached up to half of this value at nights [5]. Zhang et al. found that the linear temperature distribution in the pavement produced excessive tensile stresses and observed that the nonlinear distribution caused an increase of about 75% compared to the linear one by forming the maximum tensile stress [6]. Tensile stresses can occur as flexural and shrinkage stresses in concrete slabs. These curling and shrinkage stresses cause damage in rigid pavement. Since the shrink-covered concrete forms significant stresses at early ages, the capillary cracks formed along the pavement after turning on the road are transformed into continuous cracks [7].

B. Relationship Between Surface Temperature and Albedo

Albedo, or solar reflectance, is the ratio of reflected solar radiation to the total amount that falls on that surface, known as incident solar radiation. Albedo values range from 0, for perfect absorbers, to 1, for perfect reflectors. In pavement structures,

the topmost surface is the only layer which affects albedo. Therefore, pavement type selection should also include a consideration of albedo where heat generation is a concern. If concrete and especially asphalt surfaces coated with 'cool material', its surface temperature and heat absorption can be reduced. Therefore the use of high albedo urban surfaces is an inexpensive measure that can reduce summertime temperatures [8].

The term of solar reflectance is the ability of a material to reflect solar energy from its surface back into the atmosphere. Some previous studies related to cool materials, Pearlmutter et al. showed that light-colored walls would reflect more short-wave radiation and generate a slightly higher heat gain for pedestrians based on a pedestrian-centered conceptual model [9]. Brender and Lindsey conducted experiments in Las Vegas and observed hotter interior temperatures (5°C at maximum) in the conduit over a white roof as compared to dark-colored roofs [10]. And results of experiments by Li implied that the temperature of the building Wall would be heated up by the reflected energy from the pavement surface, which could be at maximum ≈ 2 to 5°C higher around noon [11].

Subsequently, the increased temperature makes air conditioning units work harder, accelerates the heat aging of the membrane, damages surrounding building components, and causes heat discomfort for pedestrians. This effect causes potential problems for the high density urban areas where building components are in close proximity to each other [11]. For example, increasing the albedo from 0.15 to 0.5 would substantially impact the comfort of people standing on the more reflective pavement, increasing the temperature they feel by 3 to 6°C [12]. Taha et al. measured the albedo and surface temperatures of various materials used in urban surfaces and found that white elastomeric coatings that have an albedo of over 0.72, were 45 °C cooler than black coatings with an albedo of 0.08 [13].

Various studies have been performed to understand better the thermal performance of paving materials. Berg and Quinn reported that in mid-summer, white painted roads with an albedo close to 0.55 have almost the same temperature with the ambient environment, while unpainted roads with albedo close to 0.15 were approximately 11 °C warmer than the air [14]. Asaeda et al. have reported the experimental results of a study where the impact of various pavement materials used commonly in urban environments were tested during the summer period. They found that the surface temperature, heat storage and its subsequent emission to the atmosphere were significantly higher for asphalt than for concrete and bare soil [15].

C. Methods of Analyzing Stresses Due to Temperature Distribution

Wastergaard first demonstrated that heat exchange in concrete produces stress [16]. The assumption of a linearly distributed temperature distribution over its pavement depth is widely accepted in the prediction of curvature stresses in concrete pavement subjected to curling [17]. The idea that Wastergaard's thermal stresses along the concrete slab has been reduced to the final dimensions by Bradbury and that the thermal stress to be formed when the temperatures of the lower and upper surfaces of the slab are known is precisely defined [18]. Subsequent work has shown that the exposed edge surfaces of the concrete pavements have a nonlinear temperature distribution, rather than a linear, since they can be easily affected by the heat flow in the upper surface.

Channakesava et al. made a nonlinear static analysis of concrete pavements in 1993. He used a spring element to place the ground layer under the concrete cover which he designed as a three-dimensional solid element. Analyzes were carried out under thermal load and wheel load to observe fractures caused by nonlinearity in concrete. After determining that the joints are close to each other, the bond has been replaced by a dowel bar [19]. Zaman et al. developed an algorithm using the finite element method to determine the dynamic responses in rigid airport pavement exposed to shrinkage caused by temperature change and traffic overhead. The concrete plate is defined as a thin plate element and is placed on a viscoelastic base layer which is uniformly formed by spring elements. He studied the effect of joint spacing and temperature distribution on the basis of his work [20].

II. MATERIAL AND METHOD

A. Experimental Study

Within the scope of this study, 5 different concrete plates were utilized. Three of these plates are 150 mm thick and two of them are 200 mm thick. It is separated by grouting between plates and its dimensions are 4.5x5 meters. The compressive strengths of the plates are 25, 30 and 35 MPa. We used a 150 mm high plate with a compressive strength of 30 MPa.

Temperature measurements were taken using a K-type thermocouple at 50 mm intervals along the depth of the selected concrete plate from the edge of the joint and from the center of the plate near the joint (Fig.1.).

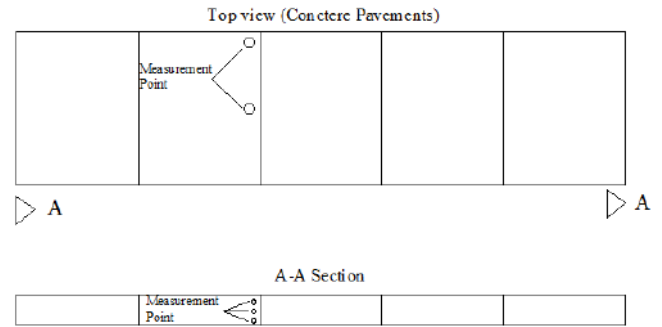


Fig.1. Settlement of concrete pavements

The temperature of the concrete pavement was set separately in May and January. Temperature measurements taken separately from the edge and center of the plates were recorded at intervals of 15 minutes (Fig.2). At the same time the air temperature is recorded and the measurements are confirmed to be correct.

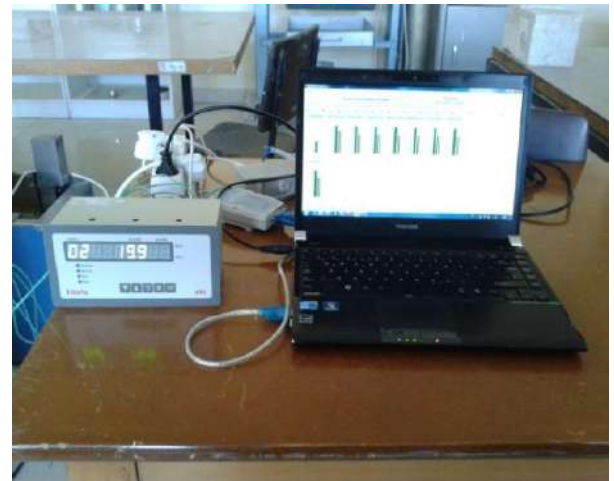


Fig.2. Datalogger settlement

In the course of the study, Albedo was placed and reflections were recorded as the sunlight hits the cover (Fig.3). The effect of the temperature of the pavement surface of the sunlight was recorded. According to the data of the General Directorate of Meteorology between 1950 and 2015, the maximum sunshine duration of Trabzon province was determined as May-June and the minimum sunshine duration was determined as December and January [21]. The time of study is set according to this calendar.



Fig.3. Albedo device

B. Finite Element Model

This part of the work is concerned with the process of preparing and analyzing the finite element model. ANSYS 14.5 Workbench interface is used when finite element modeling is done [22]. Boundary conditions and geometric modeling steps constitute a significant part of the finite element operation. Analyses made to determine the thermal stresses occurring in concrete pavements are the basis of the study.

Finite element modeling includes steps such as geometry creation, material model preparation, mesh and boundary conditions. The geometry of the model is based on the measurements of the concrete plate in the laboratory environment. For concrete plate material properties, "Concrete" element was selected and concrete elasticity modulus, density, poisson ratio, thermal expansion coefficient and thermal conductivity coefficient values were entered as in Table 1. After the concrete slab was formed, mesh analysis was carried out to separate it into finite elements, and then 'fine mesh' was made after the most appropriate mesh sizes were determined.

TABLE 1. PROPERTIES OF CONCRETE ENTERED IN ANSYS

Modulus of elasticity of concrete, MPa	32000
Poisson ratio	0.2
Thermal expansion coefficient, C^{-1}	1.3×10^{-5}
Density, kg/m^3	2300
Thermal conductivity coefficient, W/mK	0.72

III. RESULT AND DISCUSSION

A. Temperature Measurements

The temperatures of the concrete pavements are measured via thermocouples placed along the depth. Measurements were taken in May and January. The temperature distribution on the cover could be watched in both summer and winter seasons. The data taken from the edge region and center of the pavement are shown in Figures 4-11.

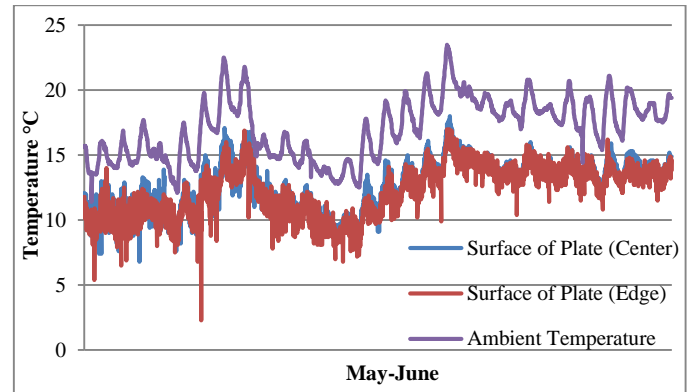


Fig.4. Temperature distribution on surface in May

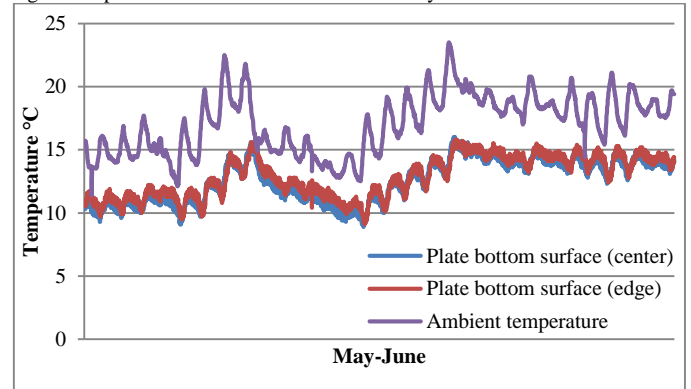


Fig.5. Temperature distribution on bottom in May

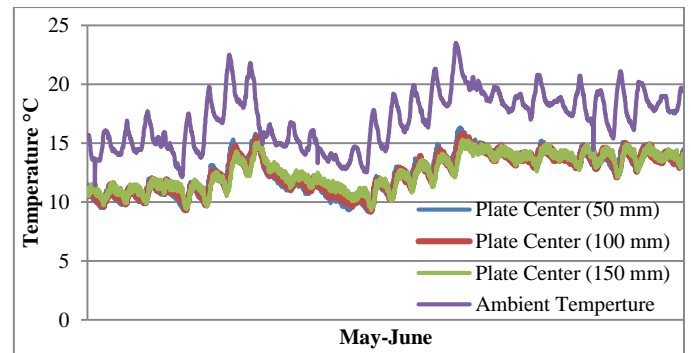


Fig.6. Temperature distribution along the thickness of the plate center in May

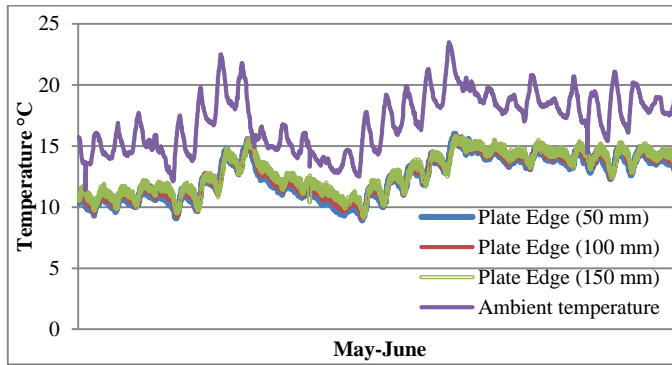


Fig.7. Temperature distribution along the thickness of the plate edge in May

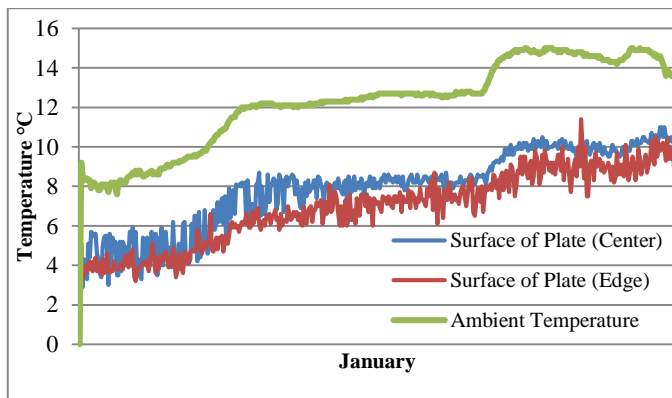


Fig.8. Temperature distribution on surface in January

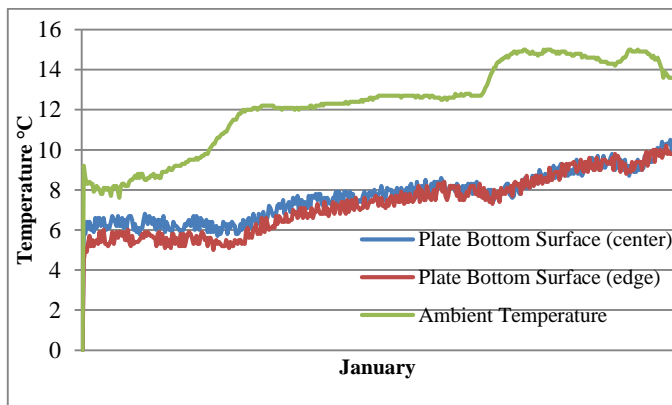


Fig.9. Temperature distribution on bottom in January

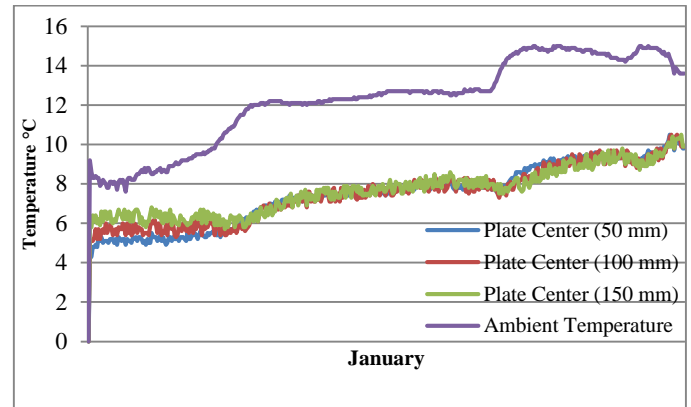


Fig.10. Temperature distribution along the thickness of the plate center in January

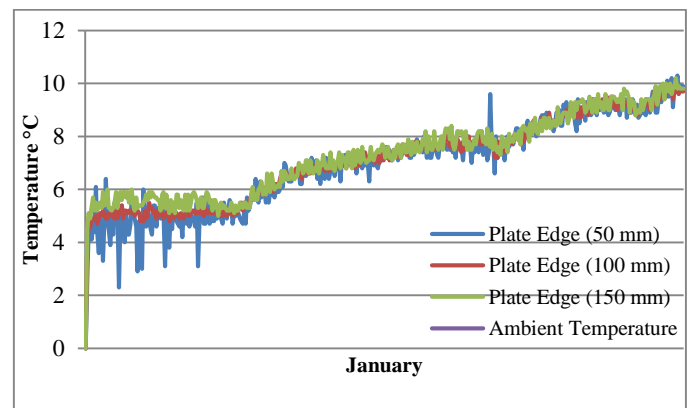


Fig.11. Temperature distribution along the thickness of the plate edge in January

It is known from the literature that surface expansion occurs when the temperature of the coating surface is higher than the temperature of the bottom. The expansion occurring in the concrete pavements causes elongation in the joints. The amounts of elongation were not determined experimentally but tried to be determined with the models created by the finite elements method.

Because the thickness of the coating is 150 mm, which is a thin value, the temperatures in the pavement are close to each other. But in some days the temperature differences between the pavement surface and the bottom have increased. When the Fig 4 and 8 are examined, it is seen that the temperatures formed on the pavement surface are very close to the ambient temperature. It was observed that the temperatures at the center of plate surface provided this condition, while the temperature changes at the edge region were more shifting. This is because there is more air flow at the edge of the pavement.

This is not evident during the pavement depth. On the contrary, the temperatures taken along the thickness of the plate center and the plate edge are close to each other. It is seen that

the difference between the ambient temperature and the lower surface of the pavement increases.

B. Albedo Measurements

Albedo is the ratio of the amount of sunlight reflected from the pavement surface to the amount of sunlight coming from the pavement surface. The daily albedo values of the pavements are calculated in this way.

The average of all values was calculated as 0.24, with a minimum of 0.18 and a maximum of 0.36 for the albedo values during the 30-day May-June period on the concrete pavement (Table 2).

TABLE 2. ALBEDO VALUES DURING THE 30-DAY MAY-JUNE PERIOD

Day	Albedo	Day	Albedo	Day	Albedo
1.	0.18	11.	0.21	21.	0.18
2.	0.20	12.	0.20	22.	0.20
3.	0.20	13.	0.22	23.	0.20
4.	0.25	14.	0.21	24.	0.25
5.	0.25	15.	0.20	25.	0.25
6.	0.23	16.	0.32	26.	0.23
7.	0.23	17.	0.34	27.	0.36
8.	0.22	18.	0.32	28.	0.22
9.	0.23	19.	0.21	29.	0.23
10.	0.22	20.	0.22	30.	0.22

Albedo measurements vary depending on the amount of incoming and reflected sunlight. As can be seen in Figure 12, the albedo values are very close to each other in May, when the number of sunny days is high, while the albedo value decreased by about 10% in January when the number of sunny days is low.

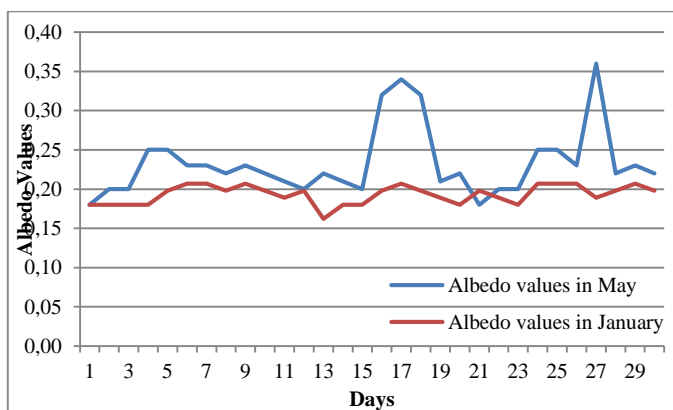


Fig.12. Albedo values in May and January

C. ANSYS Analysis

The temperature data obtained in the laboratory environment were analyzed and the temperature differences on the upper and lower surfaces of the concrete pavement were examined within 30 days. The days when the temperature difference was maximum were determined and the temperature differences formed during those days were applied to the concrete pavement. The reason why the process performed in this step is the highest temperature difference occurring on the upper and lower surfaces of the coating is that it causes the maximum curling stress.

Total displacement amounts in concrete plates were determined and the elongation amounts in the "x" and "y" directions were determined (Figure 13). As a result of the analyzes, it is seen that the maximum amount of displacement is 0.48 mm. In addition, it was observed that the maximum tensile stresses were determined as the regions where the tensile strength of concrete was not exceeded. The sample temperature distribution in the coatings is as shown in figure 14.

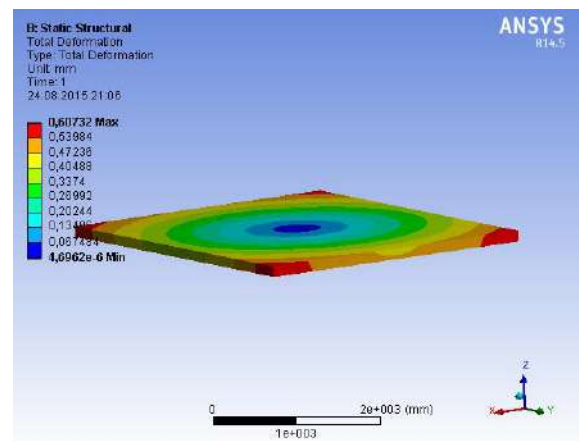


Fig.13. Thermal stresses in concrete plate

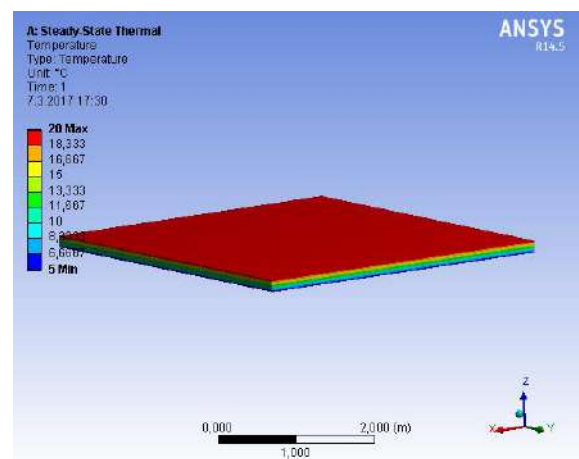


Fig.14. Temperature distribution along pavement thickness

IV. CONCLUSION

In this study, it was investigated how the temperature which occurs on the surface of a concrete pavement of C30 standard progressed along the thickness. Furthermore, the reflections from the surface of concrete slabs were recorded with the Albedo device while temperature measurements were taken, experimentally. Finally, thermal data were entered in ANSYS finite element models and afterwards strains were computed. The conclusion drawn from the results obtained in this study are as follows:

- It was observed that the temperatures at the center of plate surface provided this condition, while the temperature changes at the edge region were more shifting. This is because there is more air flow at the edge of the pavement.
- Especially when the temperature measurements taken in the summer months are examined, it is seen that the ambient temperature is closer to the pavement temperatures. But in winter this difference has increased considerably.
- The albedo values are very close to each other in May, when the number of sunny days is high, while the albedo value decreased by about 10% in January when the number of sunny days is low.
- According to AASHTO standards, the width of expansion joints in concrete casings is recommended as 20 mm and more. This situation leads to the problem of Hydro pumping and presents very negative conditions in terms of driving comfort. It has been shown that a gap of 1-2 mm is sufficient at joints where 20 mm joint opening is excessively large in these working conditions.
- The results obtained without this work can be compared later by adapting to thicker concrete slabs. In addition, the amount of expansion in joints will be measured experimentally.

REFERENCES

- [1] Richardson, JM, Armaghani, JM. Stress caused by temperature gradient in Portland cement concrete pavement. Transportation Research Record: Journal of the Transportation Research Board, 1987, 1121:7-13.
- [2] Yu H., Khazanovich L., Darter M., Ardani A. Analysis of Concrete Pavement Responses to Temperature and Wheel Loads Measured from Instrumented Slabs, Transportation Research Record: Journal of the Transportation Research Board, 1999, 1639(-1):94-101.
- [3] Jeong J-H., Zollinger D., Development of Test Methodology and Model for Evaluation of Curing Effectiveness in Concrete Pavement Construction, Transportation Research Record: Journal of the Transportation Research Board, 2003, 1861(-1):17-25.
- [4] Mohamed A., Hansen W., Effect of Nonlinear Temperature Gradient on Curling Stress in Concrete Pavements, Transportation Research Record: Journal of the Transportation Research Board, 1997, 1568:65-71.
- [5] Huang, Y. H., *Pavement Analysis and Design*, Prentice Hall, Inc., New Jersey, 1993.
- [6] Zhang, J., T. W. Fwa, K. H. Tan, and X. P. Shi. Model for Nonlinear Thermal Effect on Pavement Warping Stresses, *Journal of Transportation Engineering*, ASCE, Vol. 129, No. 6, November-December 2003, pp. 695-702.
- [7] Hiller, JE, Roesler, JR., Simplified nonlinear temperature curling analysis for jointed concrete pavement. *Journal of Transportation Engineering*, 2010.131(8):654-663.
- [8] ACPA, *Concrete Pavement Research & Technology*. Retrieved from Albedo: A Measure of Pavement Surface Reflectance, June 2002.
- [9] Pearlmuter, D., Berliner, P., Shaviv, E., Physical modeling of pedestrian energy exchange within the urban canopy. *Build. Environ.*, 2006, 41(6):783-795. doi:10.1016/j.buildenv.2005.03.017
- [10] Brender, D., Lindsey, T., Effect of rooftop exposure in direct sunlight on conduit ambient temperatures. *IEEE Transactions on Industry Applications*, 2008, 44(6):1872-1878. doi:10.1109/TIA.2008.2006301
- [11] Li, H., Evaluation of Cool Pavement Strategies for Heat Island Mitigation. PhD dissertation, Univ. of California, Davis, 2012.
- [12] Lynn, BH., Carlson, TN., Rosenzweig, C., Goldberg, R., Druyan, L., Cox J, Gaffin, S., Parshall, L., Civerolo, K. A Modification to the NOAA LSM to Simulate Heat Mitigation Strategies in the New York City Metropolitan Area. *J. Appl. Meteor. Climatol*, 2009, 48(2):199-216. doi:10.1175/2008JAMC1774.1
- [13] Taha, H., Sailor, D., Akbari, H., High Albedo Materials for Reducing Cooling Energy Use. Lawrence Berkley Laboratory Report 31721, UC-350, Berkley CA, 1992.
- [14] Berg, R., Quinn, W., Use of light colored surface to reduce seasonal thaw penetration beneath embankments on permafrost.
- [15] Asaeda, T., Ca, V.T., Wake, A., 1996. Heat storage of pavement and its effect on the lower atmosphere. *Atmospheric Environment* 30 (3), 1978, 413-427.
- [16] Westergaard, H. M. Analysis of Stressed in Concrete Pavements due to Variations of Temperature. Proc., *Highway Research Board*, Vol. 6, National Research Council, Washington, D.C., 1926, pp. 201-217.
- [17] Papagiannakis AT, Masad EA. Pavement design and materials. Hoboken, NJ: John Wiley & Sons, 2007.
- [18] Bradbury, RD., Reinforced concrete pavement. Washington D.C.: Wire Reinforcement Institute, 1938.
- [19] Channakeshava, C., F. Barzegar, and G. Z. Voyiadjis. Nonlinear FE Analysis of Concrete Pavements with Doweled Joints, *Journal of Transportation Engineering*, ASCE, Vol. 119, No. 5, September/October 1993, pp. 763-781.
- [20] Zaman, M. M., A. M. R. Taheri, and V. Klianna. Dynamics of Concrete Pavement to Temperature Induced Curling, 72nd Annual Meeting of *Transportation Research Board*, Washington, D.C., 1993.
- [21] MGM, <https://www.mgm.gov.tr/veridegerlendirme/il-ve-ilceler-istatistik.aspx?m=TRABZON>
- [22] Swanson Analysis System, ANSYS, Pennsylvania, USA, 2015.

Comparison of the Cost, Construction and Benefit of the Innovative Steel Barriers and Embankment Walls in Trabzon

Muhammet Çelik¹

Civil Engineering

Provincial Directorate of Disaster and Emergency, AFAD

Trabzon, Turkey

m.celik53@gmail.com

Mehmet Tevfik Seferoğlu³

Civil Engineering

Karadeniz Technical University

Trabzon, Turkey

Ayşegül Güneş Seferoğlu²

Civil Engineering

Gümüşhane University

Gümüşhane, Turkey

Muhammet Vefa Akpınar⁴

Civil Engineering

Karadeniz Technical University

Trabzon, Turkey

Abstract—In this study; the special problems of the Eastern Black Sea region related to rock fall are examined and solution proposals are presented. The subjects to be considered during the construction stages of the projects to be applied in the field and the methods and materials used during the manufacturing have been examined through the sample projects. The study also includes information about the innovative steel barriers of neighborhood of Güney in Maçka District which have been tendered and completed in the same period, and the tender and acceptance stages of compacted soil reinforced embankment walls of neighborhood of Yesilyurt in Araklı are presented.

The study includes information on how approximate costs are initially calculated and the rates of bidding. Later, the difficulties encountered during the manufacturing process will be examined. According to these difficulties, the experience gained about the selection of the type of production, preparation before and after manufacture, extra costs, etc. will be shared. Finally, at the end of the manufacturing, unit length costs, energy capacities and other aspects will be examined and a general comparison will be made. As a result of the studies, it has been found that the domestic product (Reinforced Soil Embankments) saves 3 times cheaper than compared to the innovative steel barriers. Furthermore, the steel barriers have at least 5-10 times less energy absorption capabilities than the embankment walls. However, according to the conditions of the region, it is necessary to find suitable land type for the construction of the embankment wall or to take precautions with extra costs.

Keywords—Rockfall, Steel barriers, Domestic products, Embankment walls, Gabions

I. INTRODUCTION

In our country, many settlement centers, dams and transport networks are experiencing rockfall events. In particular, the Eastern Black Sea region is one of the places where this situation is most experienced. The settlements in which the rock falls have been made up of generic villages and neighborhoods, some of them being provincial and district centers. In case the rockfall is dangerous and frequent, the disaster exposed area announcement is made pursuant to the Law no. 7269 on the aids to be made with the measures to be taken in the event of a disaster. Accordingly, the region was declared a disaster exposure, housing and urban development is prevented. However, there are no obstacles to the creation and operation of the transportation network. This situation threatens the safety of life and goods, especially sustainability in highways. Falling rock masses disrupt the road superstructure and lead to long-term closing of the traffic.

There are many methods to solve the problem in rocky areas. In particular, there are studies to ensure the stability of rocks, with or without bullion steel grid nets and / or ropes, or to ensure that with steel barriers, which are energy absorption features. Both of these methods are of foreign origin and in particular almost all of the energy mitigation steel barriers are imported. The most important reason for this is that imported products are patented and experimental works are carried out abroad. The reason for doing this work is to provide domestic alternative energy absorbers (especially embankment walls) as an alternative to imported products, aiming to ensure the residential safety and sustainability of road traffic. In this study; special problems of the zone related to rockfall have been examined and suggestions for solutions have been mentioned. Particularly focused on alternative methods for the protection of local roads and houses in the area exposed to rockfall. The issues to be

considered during the construction of the projects to be applied in the field and the methods and materials used during manufacturing have been examined through the sample projects [1].

Slope currents and rock fall events are common in our country's highway transportation line. For this reason, rock improvement projects have become one of the frequently used methods in our country day by day. There are a number of considerations that must be taken into account during the project. First of all, the probability of falling rocks should be assessed under regional conditions and the physical characteristics of the rocks likely to fall should be well defined. These definitions should be supported with information gained from experience so that they can be made nearest to the truth. Rockfall; can be defined as rocks separated from the main rock due to physical or chemical reasons or risk of separation, rolling down the road edge through the slope or the palms of the ground with factors contributing to the initial movement of the rock such as soil structure, humidity, precipitation regime, vegetation cover, sudden temperature changes, volcanic mobility and seismicity [2]. The most important reason for rock falls is cracks on the rocks. The likelihood of falling rocks varies with different types of cracks. Rock falls occur in the form of superficial rash or fall of block rocks, caused by deep instabilities along the slope [3]. Types of instability give information about the dimensions of the rocks. Dimensions are used to calculate rock weights and help determine the type of measure to be selected. Furthermore, the speed, energy and jump heights that the moving rocks have during motion must be known during the projecting phase. Keeping rocks that are likely to fall in place using various technical methods, stopping without any danger in case of a fall, or ensuring that they fall controlled and safely, form different types of rock reclamation projects. Rock rehabilitation studies in Turkey are being implemented by many public institutions and organizations, especially DSİ, General Directorate of Highways, AFAD. Generally, we can gather applied methods under four headings.

A. Surface Coating with Steel Nets (Wire Net)

This method is used in rubble, debris flowed slopes and areas where instabilities do not form large blocks. In particular, rocks which act on large area but do not have excess mass are kept in place by surface coating method. In case of falling rocks on steep slopes, if they gained energy or speed of the rock cannot be prevented by other methods, the surface coating method should be preferred and the rocks should be stopped before moving. In this method, rocks are allowed to flow in certain sizes from slopes wrapped with steel mesh as figure 1. In the areas where this method is applied, nets should be examined periodically. Since the fatigue effect of the so-called Debris on the steel web of the broken rock materials will cause the net to break, the material that accumulates in the net must be cleaned. Steel nets are reinforced with steel ropes and bolts. The steel net tensile strength capacity, which is important for steel network



calculations, is that it can carry three loads. These loads are: the load of the steel net and the ropes, the load of the breakage rocks and the snow load.

Fig. 1. Rockfall Mitigation with nets at Maçka made by Trabzon AFAD

B. Gabions (Embankment walls)

If the rocks that are likely to fall have a very high value of energy or speed to gain during the movement, construction of earthed walls should be preferred. A well-designed earthed structure can reach very high energy absorption capacities thanks to the on-site soil. Moreover, the distortions and deformations caused by the impact of the rocks affect the earthed walls less than other methods. Also, this method is quite advantageous in terms of cost compared to other methods. However, it is difficult to be preferred due to the effects of implementation difficulties, location and material selection. It works as a retaining wall with the material placed inside [4, 5].

C. Cleaning and Stacking

In some of the areas where rock rehabilitation works are carried out, rocks are divided into small pieces due to physical reasons. Since some slopes do not have much slope gradient, rather than covering with steel mesh, which is more costly, rocks are being rehabilitated by clearing the rocks along the slope and stacking them at appropriate locations. The medium sized rocks randomly scattered in the ground can be crushed by hand crushers to get rid of the burden and can be stacked in location.

D. Energy Breaker Barrier/Embankments Systems

It is not always possible to apply surface coating systems and stabilization methods with technical, topographical, practical or economic reasons in large scale and difficult terrain (land) conditions. In such situations, Energy Breaker Barrier or embankments Systems, which will be placed on the slope surfaces in the proper direction and position as the most effective and efficient solution against the rock falls, are at the forefront. The primary role of these barrier or embankment systems is to absorb the energies of large rock blocks that will fall from the hillside or slope surfaces and stop the rockfall. The capture nets in barrier systems are made up of materials with specific height,

length and energy absorption capacity. In these barriers with energy absorption effect, steel nets, which have an absorption characteristic, are stretched between the steel posts made of various angles. There are some difference between steel barrier and embankments given at Table 1. The following three main points should be taken into account when designing this system:

- The energy that the rock will gain during the fall
- Speeds at which the rock will gain during the fall (Max. 30 m/sec)
- Bounce movements that the rock can make during the fall

According to these three main criteria, dimensional drawings and cross sections prepared previously are examined and barrier placement is made at the most suitable location. The location where the barrier is placed directly affects the barrier dimensions (height and width). Since this affects cost, it is very important to select the location where the barrier will be placed [6].

TABLE I. COMPARISON BETWEEN EMBANKMENTS AND BARRIERS [7]

Feature	Reinforced soil embankment	Rockfall barrier
Energy absorption capacity	Much more than 5000 kJ	Up to 5000 kJ in the current market
Resistance to multiple impacts	Yes	Variable depending on barrier type
Downslope deformation after impact	Negligible	Not negligible
Ability to intercept high speed impacts	Can withstand impact velocities up to 50 m/sec	Tested up to 25 – 30 m/sec
Maintenance required for low-energy impact	Negligible to none	Variable depending on impact, barrier type, and barrier manufacturer
Installation tolerances (geometric) of the structure	There are no specific geometric requirements	Barrier must be installed within specific geometric requirements
Required slope topography for installation	Suitable for slopes with medium to low gradient	Can be installed on any type of slope
Cost of installation of the structure	Cost efficient for energies greater than approx. 3000 kJ	Cost efficient for energies below approximately 4000 kJ
Environmental compliance	Potential LEED compliance and blending with landscape by vegetating embankment facing	Structure is likely transparent to a distant observer

II. THE PROBLEMS ENCOUNTERED WHEN DESIGNING ROCKS IN THE REGION

Deep valley: The topography of the region consists of deep valleys. The rocks with the risk of falling are located near settlements but on rough terrain that is difficult to access. For this reason, during the project work, these rugged terrains create various difficulties in terms of transportation. In addition, alternative measures should be taken in advance by considering that a rock part that is accidentally fell while working in these areas will cause loss of life and property in the settlements or transportation located below.

Vegetation: There are dense vegetation in the Black Sea Region. This makes it difficult to project and conduct rehabilitation works. As seen figure 2, rocks that are in danger of falling do not appear due to dense vegetation, which makes mapping and projecting works difficult. Because the accuracy of the project is directly proportional to the mapping detail, also mapping cannot be done due to the systems that are flown to the developed technology in the region, so traditional methods should be applied carefully. In addition, it is difficult to work by preserving the trees in the forest during construction. This should be taken into account during the projecting phase.



Fig. 2. Dense vegetation cause not appear rocks.

Climate: Continuous rainfall in the zone creates various difficulties during the projecting and construction works. This situation both prolongs the manufacturing process and requires extra precautions. For example, during the rock rehabilitation work on a dry creek bed in Şalpazarı Çetrik neighborhood, due to heavy rainfall the water of the river has high flow rate information has become necessary to add to the project [8].

Site selection : The lack of flat areas in the region affects the project and construction of rehabilitation work. Since expropriation is not carried out, applications are usually carried out in treasury land, forest area or pasture. This makes it difficult to select the most suitable location for manufacturing. While the project is being carried out in limited flat land belonging to the citizen, there is also a problem of persuasion of the citizen. Figure 3 shows us treasury land, that made by villagers. This area is the only part of area suitable for cultivation



Fig. 3. Trabzon Çaykara, some villagers make stone wall with difficult conditions for farming.

Slope cleaning: Rocky areas with high risk of falling before manufacturing are very common in the Black Sea Region as well as in the general areas where rock breeding works are to be carried out. These slopes need to be pre-cleaned or fixed as they may fall during manufacturing and may cause accidents. During the projecting phase these rocks must be identified and added to the metric figure 4. Some rocks rest against the buildings. The precautions to be taken during the cleaning of these rocks, which are rested and dangerous to the houses, must be considered during the projecting phase.



Fig. 4. Before making preventive structure, pre-cleaning and fixed

III. RESULTS AND DISCUSSION

In this report will compare two protective structure made by Trabzon Provincial Directorate of Disaster and Emergency Directorate. One of structure made at Maçka disaster (Steel barrier) and the other made at Araklı disaster (Soil compacted reinforced wall).

A. Pre-tender Works

The two neighborhoods where the rock rehabilitation work was done were declared as the area affected by the disaster and details given in the Table 2 . 19 residences in Maçka and 24 residence in Araklı were determined to be affected. In addition, hazelnut gardens, fruit trees, stables, poultry houses, outbuildings and various public buildings (roads, electricity / telephone / water lines, schools, health clinic, etc.) are also included in the areas exposed to the disaster. When these structures are taken into account, as shown in Table 2, the total estimated cost of the site where the rock is to be emerged [8]. Rock treatment is planned in three neighborhoods at the same time in Maçka district. In this study, manufacturing in the Güney Neighborhood will be examined. In the project prepared for the rehabilitation of the affected area in the Güney Neighborhood, it was decided to construct a rock barrier with a height of 80 m and a capacity of 500 Kjoules and a height of 2 m. At Yeşilyurt Neighborhood in Araklı District, it was decided to construct a earthed barrier with a length of 3 m a length of 212 m and a capacity of at least 7500 Kjoule in accordance with the type of production. Approximate costs of manufacturing and contract costs are given in Table-2. According to this table, it is seen that the cost of transporting the citizens living in the affected areas to another region is considerably high. However instead of this, making rock fall protection structures works yield 15-20 times more profitable. According to this information, it has been observed that the embankment wall is 3 times more profitable than the steel barriers, although it can

be absorbed by at least 15 times more energy, 1.5 times higher and 2.65 times longer.

TABLE II. ARAKLI-MAÇKA PRETETIVE STRUCTURE COMPARISON

B. Projecting

The rock improvement project work consists of three phases.

The first is detailed dimensional drawing studies and preparation of critical sections, the second is the preparation of rock-related geotechnical data that can be fall down, and finally the determination of precautions. These steps were followed in two studies conducted in the province of Trabzon. After mapping, Trabzon Provincial Directorate of Disaster and Emergency Directorate made the necessary inspections in the field, and in consequence of these examinations, the cross sections of the routes are desired, where the rocks have fallen before and the elevation has occurred rapidly. Various details about the rock that can be fallen have been prepared, and the largest rock sizes that can be fallen according to the crack type are estimated. Finally, the highest energy, bounce heights and speeds were determined using statistical programs related to rock treatment on the computer. With program outputs, best routes (Economic and safety) were chosen. The dimensions of the measures to be used and the energy capacities have been chosen to remain in the safe zone.

C. Manufacturing Practices and Challenges

The production started after the delivery of the place to the company that took the tender. The manufacturing stages were checked and accepted by the Disaster Emergency Directorate.

Situations during manufacturing:

- Due to the fact that the Steel Barriers are of foreign origin, it took a certain period of time for the material to come to Turkey and to leave warehouses. This disadvantage has not been found on the embankment wall. Moreover, it is obvious that the same problems will be experienced again when a possible project is going to increase in steel barriers. Grounding barriers are completely domestic production barriers. It is also produced at about 3 times less cost than steel barriers.
- The steel barriers need to be anchored in a sound manner. The stability of anchors is directly related to the work of energy dampers. The anchor, which is located at 2 anchorage bases made in Maçka, has prevented the dampers from working due to the excessive load coming from the place. Embankment walls do not need base courses.
- The ground floor of the embankment walls is quite wide. It has almost one-to-one dimensions with its length. The

height of the embankment wall made in Araklı as the figure 5 is 3 meters and the width is 3.5 meters. In addition to this broadness, it is also necessary to have a specific area for the accumulation of rocks falling on the part facing the

Location/ Number of House	Height and length (m)	Energy absorption capacity (KJoule)	Approx. cost of rock treatment (TL)	Contract cost of rock treatment (TL)	Estimated cost of transfers of citizens (TL)	Profit. Ratio (times)
Maçka/19 Steel Bar.	2 - 80	500	250.612,80	141.190,30	2.175.000,00	15,404
Yeşilyurt/24 Rein. Soil. Embankm.	3-240	Min. 7500	157.411,01	156.880,00	3.000.000,00	19,122

source rock. In other words, it is necessary to place at least 6 meters of a tilting structure at a height of about 3 meters. This distance can go up to 7-8 meters to run the excavator. In regions where flat land, such as the Black Sea region, is rarely found, especially in areas where there is hardly any reclamation, construction of a soil barrier create problems or is made on fill.



Fig. 5. Compacted soil and reinforced embankment wall at Araklı Yeşilyurt

- Araklı Yeşilyurt project was planned to create a flat area 7 meters wide before slope. Approximately 1.5 to 2 meters of this area is filling. The embankment wall was required to straighten 8 meters of the slope by pulling in 1 meter to avoid putting it directly on the end of this dolman. In the future, it has been decided that reinforced concrete retaining walls should be added to the project under filling, in order to make the soil flow and filling pavement more comfortable during operation.
- In embankment walls, the material used must be small. More energy damping and different seating durability can be achieved. However, the soil-clay material in the nearby environment is filled with small stones. For this reason, it was subjected to screening process. The sieve was not used at the desired level due to the precipitation of the area and the fact that this work corresponds to the autumn winter months. Precipitation has prevented the removal of material.

- Embankment walls need to be compacted well. The 3 meter high wall was built on the 4 layers. Each layer is 75 cm and subjected to a compression process at every 25 cm. However, especially in the areas close to the tools used for compaction cannot enter the compression is not exactly wanted.
- Embankment walls consist of galvanized steel hexagonal wire and erosion cover. A triangular shaped frame is used to mount the walls at the desired angle.
- Steel barriers are stretched with ropes. This causes some loss in size as seen figure 6. This loss should be taken into account during the projecting phase.
- Steel barriers work by energy damping of parts called disparator during rockfall. After a rockfall has occurred, it may be necessary to change the disaster according to the damage level. For this reason, quality control is required. Moreover, since disparators are patented products abroad, they cannot be imitated without permission and thus constitute foreign dependence. Because embankment walls have a lot of energy capacities, they usually need to be cleaned for a certain period of time as they accumulate material behind them.
- Because the embankment walls are greening, they can be harmonious with nature. Climate and vegetation cover our region in a short time without using this method. The



citizens planted hazelnut trees in the highest elevations. Steel barriers take up less space in nature, but they cannot fully conform to nature.

Fig. 6. Lose of height steel barriers

- Because the ground walls are 240 meters long, it is divided into 3 for the citizen's animals to go to the grassland. In order to make such a production in steel barriers extra material is needed, so it is necessary to inform the foreign origin factory in advance.

IV. CONCLUSIONS

Grounding walls are native, fast-reachable, environmentally compatible barriers that do not have the burden of increasing work. They are about 3 times cheaper than steel barriers. However, there are at least 10 times more energy damping capacities. The main disadvantage of grounding walls is that they must have a flat surface of at least 6-7 meters in width. The steel barriers can be manufactured only by foundation without any leveling work. Grounding walls should be preferred in order to prevent the growth of the current open due to domestic production. However, if the ruggedness and physical conditions of the manufacturing area are not available, steel barrier alternatives should also be considered.

REFERENCES

- [1] Peckover, F. L. and Kerr, W. G. Treatment and maintenance of rock slopes on transportation routes, Canadian Geotechnical Journal, 14 (4), 487-507, 1977.
- [2] Talobre, J., Kaya Mekanîğin ve İnşaat İşlerinde Tatbikatı, Mars Matbası, Ankara, 1970.
- [3] Heyelan ve Kaya Düşmesi Temel Kılavuzu, AFAD Başkanlık, Ankara, 2015.
- [4] Oggeri C., Peila D., Ronco C., Numerical analysis of embankments behaviour done with reinforced soil – Preliminary report – contract of research between DITAG Politecnico di Torino and Maccaferri SPA (in Italian), 2008.
- [5] Peila, D., Oggeri, C., and Castiglia, C.: Ground reinforced embankments for rockfall protection: design and evaluation of full scale tests, Landslides Investigations and Mitigation, 4 (3), 255-265, 2007.
- [6] Jacquemoud, J.: Swiss guideline for the design of rockfall protection galleries: background, safety concept and case histories, in: Proceedings of the Joint Japan-Swiss Scientific Seminar on Impact load by rockfall and design of protection structures, Kanazawa, Japan, 4-7 October 1999, 95-102, 1999.
- [7] Brunet, G., Protection From High Energy Rockfall Impacts Using Terramesh Embankments: Desing and Experiences, 60th Highway Geology Symposium, September, 2009.
- [8] Çelik, M., Seferoğlu, M.T., Seferoğlu, A.G., Akpınar, M.V., "Rehabilitation Methods, Challenges, Cost Benefit Analysis of Disaster Area Exposed due to Rockfalls in Trabzon Province" Doğal Afet ve Afet Yönetimi Sempozyumu (DAAYS'16), Karabük, Türkiye, 2-4 Mart 2016.

Thermal Stress Analysis of Concrete Pavement under Different Albedo Values

Muhammet Vefa Akpınar¹
Civil Engineering
Karadeniz Technical University
Trabzon, Turkey

Mehmet Tevfik Seferoğlu³
Civil Engineering
Karadeniz Technical University
Trabzon, Turkey

Sedat Sevinç²
Civil Engineering
Gümüşhane University
Gümüşhane, Turkey
sedat_sevin17@hotmail.com

Ayşegül Güneş Seferoğlu⁴
Civil Engineering
Gümüşhane University
Gümüşhane, Turkey

Abstract---Daily changing temperature causes significant thermal stress and deformations in concrete pavement. These stresses are important parameters included durability of pavement and are significantly depended on thermal difference (i.e. difference in temperature between upper and lower surface plane) and surface temperature of pavement. The surface temperature of the pavements has a great influence on the temperature profiles, displacements and thermal stress. When increase the albedo value, the surface temperatures of the concrete pavements reduce. For this reason, the surface temperature can be reduced and the thermal stress can be reduced by increasing the albedo value of the pavements.

Keywords- concrete pavement; thermal stress; albedo; displacement

I. INTRODUCTION

The pavement surface temperature is critical to the pavement deterioration [1-4]. High daily temperature amplitude developed in a rigid pavement causes structural defects such as warping and curling [2, 5-7]. Curling stresses result from linear thermal difference in the whole thickness of slab. It is assumed that temperature remains constant in the normal middle plane of pavement whereas temperature at the top of slab is different from its bottom. These two major components of thermal stresses are combined by algebraic addition to obtain the overall stress in the slab due to temperature variations [8].

Traditionally, deformation behavior of a concrete slab due to temperature differential along its depth is referred to as curling. Many researchers have made an effort to evaluate the temperature gradient (or termed temperature differential between the top and bottom of a slab) during daily times and the corresponding motions of curling in actual concrete slabs [9, 10]. Several former studies [11-13] have shown that temperature gradients along the slab depth are typically nonlinear, with greater daily temperature fluctuations at the

top surface than at the bottom. If the temperature and moisture gradients are nonlinear, the slab tends to deform in accordance with its compensation plane (or a sectional average plane) as each concrete element along the depth should meet the linear continuity condition [13]. Balbo and Severi [14] have documented the influence of weather conditions on daily and seasonal variations in temperature through the slab depths in a hot and wet tropical climate in Brazil. It was found that the night-time temperature differentials were not as extreme as the daytime differentials.

Especially in hot summer months, the surface temperature of concrete covers can reach 50-55 °C. As a result, the positive temperature difference (ΔT_+) varies from 15 to 20 °C for pavements with a thickness of 20 cm, and this difference in temperature can cause cracks due to thermal stress [15]. In order to prevent overheating of the coating surfaces, it has become especially popular to coat the surface of the coatings with materials having high solar albedo for the last 20 years. Thus, "cool pavements" with low surface temperature were obtained. Albedo is a technical name to describe the fraction of incident reflected sunlight. Albedo, also known as solar reflectance, is the percentage of the solar radiation reflected by a surface with respect to the total incident solar radiation falling on the surface [16]. Boriboonsomsin and Reza, 2007 have observed the use of cool paving materials or 'cool pavements' has been identified as one strategy that can help to decrease pavement surface temperature. One method of creating a cool pavement is to increase the solar reflectance or *albedo* of its surface. This can be achieved by many existing paving technologies.

Surface albedo plays an important role in the thermal-energy behavior of pavements and other ground surfaces and their resultant impact on humans and the environment. Bretz *et al.* [17] showed therefore that significant energy saving and increased comfort levels of urban areas can be reached through solar-reflective and high-albedo materials,

by estimating the achievable increases in albedo for different surfaces.

In this study, the change of thermal expansion is observed by modeling with finite element method (FEM) and compared with 3 different formulas widely used in the literature. While these models are being built, the maximum of the previously measured surface temperature measurements is used. As a result of the analyzes, the surface temperature measurements of the albedo high values of the coatings, the layer temperature distributions, the horizontal displacement amount and the thermal stresses were lower than the measurements and analyzes in the conventional concrete coating. Similarly, stress values calculated with 3 different formulas give consistent results when compared to FEM. The results show that the application of a concrete road design with low surface temperature can reduce thermal stresses and deformations by increasing the coverage albedo value.

II. CLIMATE CONDITIONS OF THE REGION

In order to better understand the effect of the Albedo effect on the surface temperature and the temperature distribution, it was decided to carry out the measurement in July, taking into consideration the average daily sunshine periods and the monthly maximum temperature values of the region from 1950 to 2015 belonging to the General Directorate of Meteorology. This is mainly due to the highest sunshine duration in July, and it is estimated that the albedo values and effect will be observed more efficiently and that the surface temperature will rise to the maximum level since the daily temperature value in the same month is 37 °C and the second highest month in the year. As shown in Fig. 1, the daily sunshine duration has reached its maximum annual value in 10 hours and July.

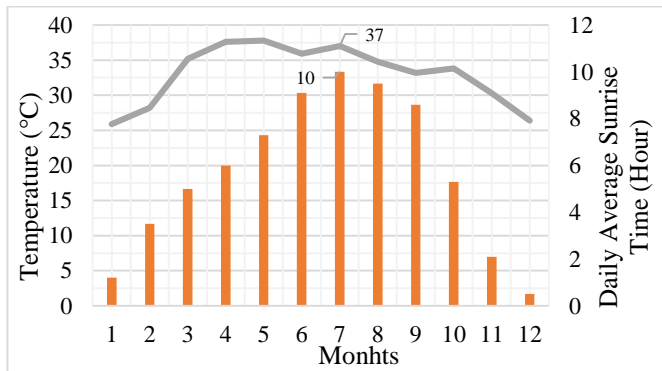


Fig.1. Values of Trabzon the monthly maximum temperature and the average daily sunlight hours [18].

III. CREATION OF 3D MODELS

A. Determination of Surface Temperature

The temperature values taken from the concrete roadways in the campus area of the KTU campus were measured for 10 days of albedo in August and a maximum of 48.1 °C (A1 concrete pavement, albedo value 0.18) at 15:00 on day 7 as a result of surface temperature measurements, was measured as 38.3 °C (A2 painted with high-reflected materials, albedo value 0.29) (Fig. 2).

This study was performed with a single-headed pyranometer in the form of albedo measurements in accordance with ASTM E1918. The CMA6 parameter provides solar reflectance (W/m^2) of the surfaces 50 cm above the area to be measured, as specified in the standard.

These temperature values are entered as the surface temperature in the created 3D models. Thus, in summer, the natural temperature of the concrete surfaces will be subjected to 3D modeling and performance analysis of the road pavement under field conditions.

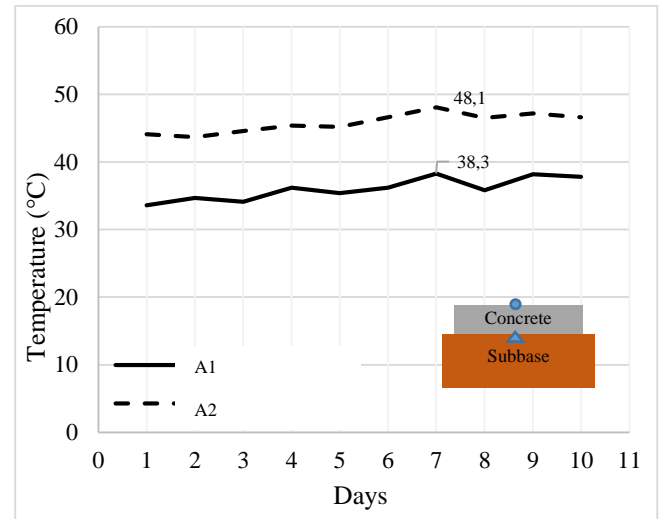


Fig.2. Daily surface temperature values (A1: Concrete pavement, A2: Painted-Concrete pavement)

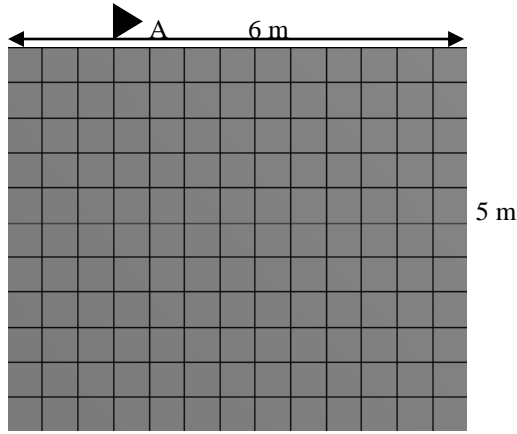
B. Design of Layers

The concrete plate is designed to sit on a foundation layer geometrically as shown in Fig. 3 with the ANSYS 3D finite element analysis program. Analysis of 3D models was done as ANSYS-Linear. CONCRETE plate The CONCRETE element in the ANSYS material library is selected and the pre-set values in it are used. For the basal plate, SOLID element design is done according to the parameters in Table 1 in linear-elastic form. $f = 1.5$ between the foundation layer and the concrete plate is defined as the friction coefficient. The subbase values used in the study are

taken from the literature. No experimental work has been done for this.

TABLE 1. PARAMETERS OF LAYERS

	Thickness (m)	Modulus of layer (MPa)	Poisson ratio	Coef. of thermal expansion ($1/^\circ\text{C}$)	Thermal conductivity ($\text{W/m}^\circ\text{C}$)	Density (kg/m^3)
Concrete	0.2	30000	0.2	1.0E-05	2.5	2400
Subbase	0.5	2900	0.3	7.0E-06	0.05	2100



(a)



(b)
Fig.3. 3D model top view (a) and A-A sectional view (b)

IV. THERMAL ANALYSIS OF PLATES

A. Determination of Temperature Profile

The solutions for both surface temperatures were linearized according to the basic heat conduction equation in Equation (1). Finally, the base temperature of the substrate with a surface temperature of 48.1°C decreased to a minimum of 29.69°C (Fig. 4). For this layer, $\Delta T1 = 18.41^\circ\text{C}$ was obtained. The same solution was obtained at a temperature of 26.88°C for the second surface with a surface temperature of 38.3°C and $\Delta T2 = 11.42^\circ\text{C}$. With a temperature difference of about 10°C between the two surfaces, $\Delta T2$ is 38% lower.

$$\rho C \frac{\partial T}{\partial t} = k \left(\frac{\partial^2 T}{\partial x^2} + \frac{\partial^2 T}{\partial y^2} + \frac{\partial^2 T}{\partial z^2} \right) \quad (1)$$

Where:

T: Surface Temperature ($^\circ\text{C}$)

t: Time (second)

ρ : Density (kg/m^3)

C: Specific heat ($\text{J/kg } ^\circ\text{C}$)

k: Thermal conductivity ($\text{W/m } ^\circ\text{C}$)

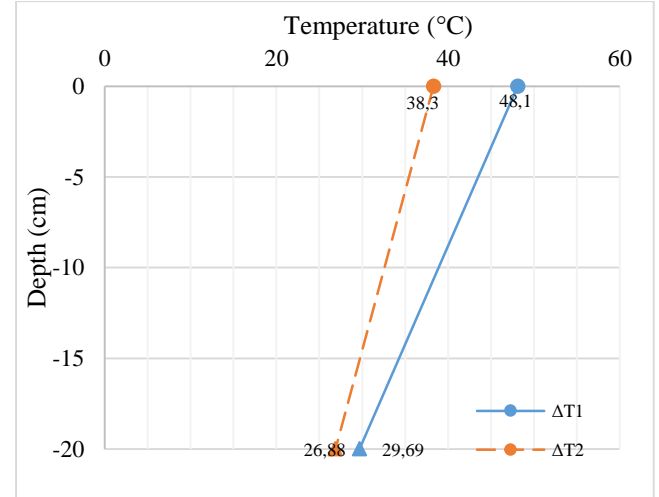


Fig.4. Temperature profiles

B. Analysis of Thermal Stress-Displacement

Firstly, the maximum displacement amounts of concrete plates for $\Delta T1$ and $\Delta T2$ were analyzed Fig. 5. The linear relationship between the bed temperature distribution and the displacement amount is shown in Fig. 6. The maximum horizontal displacement at $\Delta T1$ was 1.4 mm, while at $\Delta T2$ it decreased by about 42% to 0.8 mm.

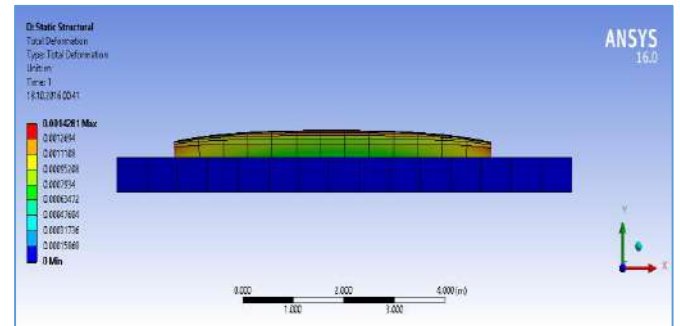


Fig.5. Plate displacement cross-section (for $\Delta T1$)

For the mathematical solution of the displacement calculation; $\Delta L = L \alpha t (\Delta T)$ (2)

Where:

L= Plate size (m) (where 6 m in x direction is used)
 α_c = Concrete thermal expansion coefficient (1/°C)
 ΔT = Temperature profil (°C)

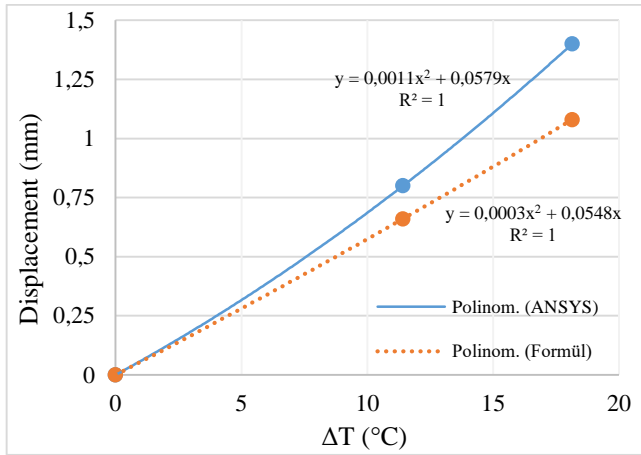


Fig.6. Relationship between plate temperature distribution and displacement (for 6 m direction)

Secondly, the thermal stresses between the two layers are investigated depending on the ΔT temperature difference

The thermal stress is calculated as:

$$\{\sigma\} = [D](\{\epsilon\} + \{\epsilon_t\}) \quad (3)$$

Where;

$\{\sigma\}$ = Stress vector
 $[D]$ = Elastic matrices
 $\{\epsilon\}$ =Total strain vector; $\{\epsilon\} = \Delta T \{\alpha\}$
 $\{\alpha\}$ = Thermal stress vector

Because the analysis represents tensile stress, "Max. Principal Stress" is considered. 4.51 MPa and 2.61 MPa for ΔT_1 and 2.81 MPa and 1.68 MPa for ΔT_2 , respectively, were obtained with the maximum and minimum principal stress sequences. Similar to the displacement change, the maximum tensile stress of ΔT_2 , which has a low surface temperature, is also 35% lower in the case of tensile elongation. Piotr notes that ΔT values for concrete slabs with a layer thickness of 20-25 cm exceeded 20 °C and that thermal stresses reached critical levels in the concrete they were using in studies conducted in 2014 [8] and IRC 2002 [15]. In this study, the tensile strength of the CONCRETE element in the ANSYS material library is 5 MPa. In the present analysis, the maximum tensile stress is 4.51 MPa,

and the tensile stresses do not cause cracking in concrete casings. However, the use of lower strength concrete can lead to cracks due to thermal expansion if the temperature difference $\Delta T \geq 20$ °C is increased to high values.

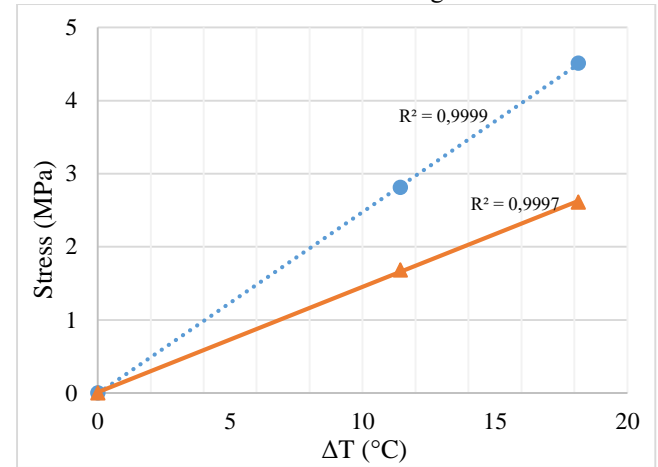


Fig.7. Relationship between plate temperature distribution and stress

Max and Min prime stresses are analyzed as shown in Fig. 7 The tensile strengths of the concrete road are compared with the finite element thermal stresses calculated by using 3 different formulas in the literature.

1. Westergaard, 1927 [2];

In 1927, Westergaard conducted the first extensive research to find the thermal expansion of concrete slabs. In this study, we have obtained the following formula as the temperature distribution will be linear in the layer.

$$\Sigma_x = \Sigma_y = \sigma_0 = \frac{E \alpha T}{(1-\mu)} \quad (4)$$

Where;

E= Elasticity modulus
 α = Thermal expansion coefficient
T= Linear average temperature ($\Delta T/2$)
 μ = Poisson ratio

Westergaard's formula is arranged in the following manner for a finite plate of length L, so that the maximum prime stress (σ) at the center of the plate is assumed.

$$\Sigma = \sigma_0 \left[1 - \frac{2(\sin \lambda \cosh \lambda + \cos \lambda \sinh \lambda)}{\sin 2\lambda + \cos 2\lambda} \right]; \quad (5)$$

$$\lambda = L/(l\sqrt{8}); \quad l = \sqrt[4]{\frac{Eh^3}{12(1-\mu^2)k}} \quad (6)$$

2. Bradbury, 1938 [20];

Bradbury calculated the thermal stress formula Winkler calculated the elastic plate in contact with the basic conditions, depending on the boundary condition coefficient, as follows.

$$\Sigma = \frac{CE\alpha\Delta t}{2} \text{ (Plate edge tensions), (7)}$$

$$\sigma = \frac{E\alpha\Delta t}{2} \left(\frac{C_x + \mu C_y}{1 - \mu^2} \right) \text{ (Internal stresses) (8)}$$

C, C_x, C_y : Boundary condition coefficient (Takes values according to plate dimensions)

3. Iwama, 1963[19];

As a result of the research I have conducted, I have calculated 30% of the internal stresses in the concrete plate of 20-25 cm thickness. Thus, we found that the daily nonlinear thermal stress distribution accounts for 70% of the total total stress. This formula, found by Iwama, has been used in the design of concrete roads in Japan for 40 years.

$$\Sigma = 0.7 \frac{E\alpha\Delta T}{(1 - \mu)} \quad (9)$$

The results obtained from the calculated calculations are given in Table 2.

TABLE 2. THEMAL STRESS VALUES OF ALL ANALYSIS

	$\Delta T1$				$\Delta T2$			
	ANSYS	(Westergaard, 1927)	(Bradbury, 1937)	(Iwama, 1964)	ANSYS	(Westergaard, 1927)	(Bradbury, 1937)	(Iwama, 1964)
Thermal Stress (MPa)	4.51	4.01	3.97	2.80	2.61	2.06	1.92	1.44

C. Relationship between Thermal Stress and ΔT

The difference between the thermal stresses in the thermal stress analyzes and in the calculations obtained by the three different formulas seems to be seen in Fig.8. As can be seen, analyzes made with the ANSYS program have obtained thermal stresses greater than the other 3 calculation methods for $\Delta T1$ and $\Delta T2$ temperature differences. Especially the tensile strengths obtained with the Westergard and Bradbury formulas are almost the same.

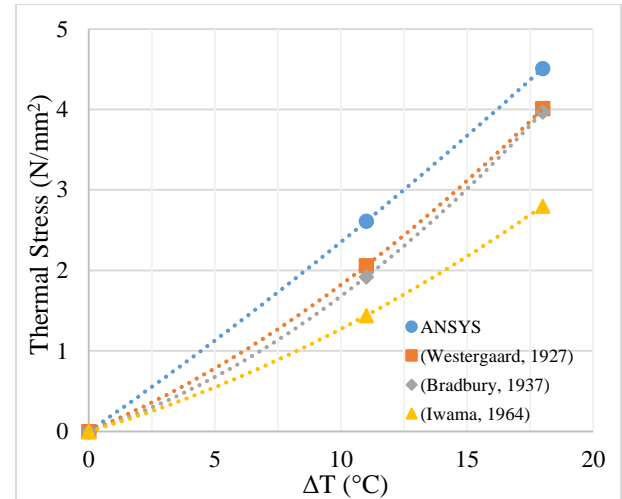


Fig.8. Relationship between plate temperature distribution and stress

V. CONCLUSION

In this study, the sheet temperature distribution (ΔT) of the different surface reflectance properties of concrete slabs with the same properties and accordingly the variation of thermal stresses under daily temperature variation were investigated. The main purpose of the work is to keep the thermal stresses at a level that will not crack and to reveal the plate temperature difference (ΔT) that will provide it. The following results were obtained from the study;

- As the surface reflectivity of concrete coatings increases (Albedo), the surface temperature decreases and accordingly the layer temperature difference decreases. Thus, an increase of approximately 0.1 of albedo has reduced the surface temperature by almost 10 °C. Similarly, Albedo's 0.1 increase increased the sheet temperature distribution (ΔT) by about 7 °C.
- In the displacement analyzes performed on the plates, the maximum horizontal displacement at $\Delta T1$ was 1.4 mm, while at $\Delta T2$ it decreased by about 42% to 0.8 mm. According to the results obtained, as the albedo increases, it is seen that the horizontal displacement is reduced.
- As the layer temperature increased in the analyzes performed, the tensions obtained for both ANSYS and 3 different formulations tended to increase parabolically. The analysis with ANSYS showed an increase of 63% from $\Delta T1$ to $\Delta T2$, while the thermal stress increased from 2.61 MPa to 4.51 MPa by 72%. The difference between such temperature increase and stress increase is clearly visible.

- Obtained results clearly show that as the albedo value of the coatings increases, the layer temperature distribution, the maximum amount of displacement, the layer temperature distribution and the thermal stresses decrease, especially the surface temperature. Thus, due to the daily temperature difference, the curling-warping effect of the concrete coatings can be removed and the cracks in the coating can be removed.

REFERENCES

- [1] H.M. Westergaard, Stresses in concrete pavements computed by theoretical analysis, *Public Roads* 7 (1926) pp.25-35.
- [2] H.M. Westergaard, Analysis of stresses in concrete due to variations of temperature, in: *Proceedings of the 6th Annual Meeting Highway Research Board*, vol. 6, National Research Council, 1927, pp. 201-215.
- [3] E.J. Yoder, M.W. Witczak, *Principles of Pavement Design*, second ed., John Wiley & Son, Inc., New York, USA, 1975.
- [4] L.W. Teller, E.C. Sutherland, The structure design of concrete pavements, part 2: observed effects of variations in temperature and moisture on the size, shape, and stress resistance of concrete pavement slabs, *Public Roads* 16 (1935) 169-197.
- [5] B. Choubane, M. Tia, Analysis and verification of thermal-gradient effects on concrete pavement, *J. Transp. Eng.* 121 (1995) 75-81.
- [6] A.R. Mohamed, W. Hansen, Effect of Nonlinear Temperature Gradient on Curling Stress in Concrete Pavements, *Transportation Research Record* 1568, TRB, Washington D.C., USA, 1997.
- [7] J. Zhang, T.W. Fwa, K.H. Tan, X.P. Shi, Model for nonlinear thermal effect on pavement Warping stresses, *J. Transp. Eng. ASCE* 129 (2003) 695-702.
- [8] Piotr M., Thermal stress analysis of jointed plane in concrete pavements., 2014, 1359-4311.
- [9] Jeong JH, Zollinger DG. Environmental effects on the behavior of jointed plain concrete pavements. *ASCE J Transport Eng* 2005;131(2):140-8.
- [10] Sidiq ZQ, Hossain M, Meggers D. Temperature and curling measurements on concrete pavement. In: *Proceedings of the 2005 mid-continent transportation research symposium*, Ames, Iowa; 2005.
- [11] Mohamed AR, Hansen W. Effect of nonlinear temperature gradient on curling stress in concrete pavements. *Transport Res Rec* 1997;1568:65-71.
- [12] Yu HT, Khazanovich L, Darter MI, Ardani A. Analysis of concrete pavement responses to temperature and wheel loads measured from instrumented slabs. *Transport Res Rec* 1998;1639: 94-101.
- [13] Ghali A, Favre R, Elbadry M. *Concrete structures: stresses and deformations*. 3rd ed. London: E&FN Spon; 2002.
- [14] J.T. Balbo, D.S. Pereira, A. Severi, Behavior and performance of UTW on thin asphalt pavement, in: *Proceedings of the 7th International Conference on Concrete Pavements*; International Society for Concrete Pavements, Orlando, USA, 2001, pp. 825-838.
- [15] The Indian Roads Congress, *Guidelines for the design of plain jointed rigid pavements for highways*, 2002.
- [16] American Concrete Pavement Association, "Albedo: A Measure of Pavement Surface Reflectance", *R&T Update: Concrete Pavement Research & Technology*, June 2002 www.pavement.com/Downloads/RT/RT3.05.pdf
- [17] Bretz, S.; Akbari, H.; Rosenfeld, A. Practical issues for using solar reflective materials to mitigate urban heat islands. *Atmos. Environ.* 1998, 32, 95-101.
- [18] MGM, <https://www.mgm.gov.tr/veridegerlendirme/il-ve-ilceler-istatistik.aspx?m=TRABZON>
- [19] Iwama, S. *Experimental Studies on the Structural Design of Concrete Pavement*. Tokyo, Japan Society of Civil Engineers, 1963.
- [20] Bradbury, R. D. *Reinforced Concrete Pavements*. Wire Reinforcement Institute, Washington, D.C., 1938.

Effects of the Combined Use of Styrene-Butadiene-Styrene and Gilsonite in Bitumen Modification on The Stiffness and Thermal Sensitivity of Bitumens

Özge ERDOĞAN YAMAÇ

Firat University
Faculty of Engineering, Department of Civil Engineering
Elazığ, Turkey
E-mail : ozgeerdogan@firat.edu.tr

Mehmet YILMAZ

Firat University
Faculty of Engineering, Department of Civil Engineering
Elazığ, Turkey
E-mail : mehmetyilmaz@firat.edu.tr

Baha Vural KÖK

Firat University
Faculty of Engineering, Department of Civil Engineering
Elazığ, Turkey
E-mail : bvural@firat.edu.tr

Abstract—In the present study, the effects of styrene-butadiene-styrene (SBS) and American gilsonite (AG) on the stiffness and thermal sensitivity of bituminous binders were investigated in bitumen modification. Şanlıurfa province was chosen as the application field. It was determined that 18% AG and 5% SBS additives should be used separately to obtain the adequate binder for Şanlıurfa province. It was also determined that 13% AG with 2% SBS, 10% AG with 3% SBS and 6% AG with 4% SBS were required to obtain binders with the same performance level. Penetration, softening point and rotational viscometer tests were conducted on neat and modified bitumen to determine the consistency of binders. Furthermore, thermal sensitivities of binders were determined from penetration index and penetration viscosity number values. It was determined that all additives increased the consistency of the binders, the most effective additive type and ratio was 18% AG on penetration values, and all additives had similar effects on the softening point and viscosity values. In addition, it was determined that the temperature susceptibility was reduced with additive use and the most effective contribution came from 5% SBS.

Keywords—Bitumen; styrene-butadiene-styrene; American gilsonite; consistency; temperature susceptibility.

I. INTRODUCTION

Bitumen obtained by distillation from crude oil is produced from the residues of this process. Bituminous binders are a complex mixture of organic particles containing aliphatic, aromatic and naphthenic hydrocarbons and could be divided into two basic groups, namely maltenes and asphaltenes [1]. The asphaltenes are dispersed in the maltene phase with a continuous phase and the structure that forms the bitumen structure includes saturates (S), aromatics (A), resins (R) and asphaltenes (AS). The complexity, aromaticity and molecular weight of the fractions are ranked as follows: $S < A < R < AS$ [2, 3].

The bitumen exhibits binding properties that binds aggregates due to their cohesive properties in road applications. The bituminous binder also prevents the aggregate particles

from falling apart under traffic loads, improves the driving comfort with the smooth surfaces they create, increases mixture stability with its cohesion, and provides impermeability by filling the voids in the mixture. Bituminous binders have a great effect on mixture performance, even though they are used at a low rate of 5 to 7% by weight in hot mix asphalts [4].

Various additives (modifiers) have been used to improve the properties of binders for a long time, thereby increasing the service life of the pavement by preserving its performance for a longer period of time. The additives used for this purpose vary depending usage. To increase the resistance of bitumens and bituminous hot mixes to heat and traffic loads, generally additive materials of polymer origin are added. Mostly Styrene-Butadiene-Styrene (SBS) Block Copolymers are used in these additives. Several previous studies determined that SBS improves the fracture resistance at low temperatures, and the generation of rutting and fatigue resistance at high temperatures [5-9].

Gilsonite is a solid hydrocarbon mineral available in nature with a potential to improve physical and chemical properties of bitumen [10]. Gilsonite can rapidly dissolve in bitumen since it is a kind of natural asphalt binder [11]. Gilsonite offers different advantages over other modifiers such as easy mixing and compatibility with asphalt mixtures [12]. Economically significant Gilsonite mineral is found in the United States and Iran.

When Gilsonite is added to the bitumen, the penetration of the bitumen decreases, its viscosity increases and as a result, a harder modified bitumen is obtained. Mixtures prepared with Gilsonite modified bitumens have higher stability, lower permanent deformation and temperature susceptibility, as well as higher resistance to stripping caused by water when compared to mixtures prepared with unmodified bitumen [13-16].

Several previous studies reported that storage stability of SBS modified bitumen is low, even though the rheological properties of SBS modified bitumen are superior to that of the neat binder [17, 18]. Furthermore, SBS is also a more expensive additive compared to Gilsonite. Using SBS and Gilsonite together in bitumen mixture instead of using only SBS-modified bitumen, so that the resulting performance would be the same, provides economic benefits [19]. The combined use of the two additives has been common during recent years and aimed to remove the negative aspects of the additives and to increase the rheological properties of the bituminous binders, and thus, increasing the performance of the BHM in different aspects [20-23].

In the present study, the effect of the combined use of SBS and AG in bitumen modification on consistency and temperature susceptibility of the bituminous binders were examined. For this purpose, penetration, softening point and rotational viscometer experiments were conducted with neat and five different modified bitumen samples. Furthermore, using penetration and softening point values, penetration index value, which is the indicator of temperature susceptibility, is determined. Thus, the effect of two different additives on the consistency and thermal sensitivity of the bituminous binders was determined.

II. MATERIAL AND METHOD

The binder design was conducted with the Superpave method in the study. Şanlıurfa, the warmest province in Turkey, was selected as the application field. The information on the highest temperature values for 7 consecutive days and the coldest day during the last 21 years was obtained from Regional Meteorology Directorate and it was assumed that the design traffic estimate was 3-30 million standard axle load equivalent and there was low-speed traffic (<50 km / Hour). It was determined that the binder class that should be used in the design criteria determined for Şanlıurfa was PG 76-10.

In the present study, Styrene-Butadiene-Styrene (SBS) Block Copolymer produced by Shell Bitumen Company and American Gilsonite (AG) obtained from American Gilsonite Company were used as additives to B 160/220 grade bitumen that was procured from TÜPRAŞ refinery in Turkey. The mix was obtained by mixing the neat bitumen and additive material for 60 minutes with 1000 rpm. mixer at a temperature of 180 °C (Figure 1). In previous studies, it was determined that when 5% SBS (MB_{5S}), 18% American Gilsonite (MB_{18G}), 2% SBS + 13% AG (MB_{2S+13G}), 3% SBS + 10% AG (MB_{3S+10G}), and 4% SBS + 6% AG (MB_{4S+6G}) were used, the performance level (PG 76-16) was suitable for Şanlıurfa province and the test results for these mixtures were similar. For this reason, 5 different additive ratios determined in the previous study were used.



Fig. 1. Modified bitumen mixer and mixing apparatus

A. Penetration Test (EN 1426)

The penetration test was conducted to determine the stiffness or consistency of the bituminous binder. Penetration is the amount of vertical penetration by a standard needle at a given temperature under a given load, and over a period of time (Figure 2). The unit of penetration is 0.01 cm. In the penetration test, a load of 100 g was applied to the bituminous binder sample at 25°C for 5 seconds.

In the penetration test, the bituminous binder sample is taken according to EN 58 standard and transferred to the sample container after heating. The samples are allowed to cool for 60-90 minutes at a temperature of 5-30°C. The sample containers are then placed in a constant temperature water bath in the transfer chamber for 1-1.5 hours.



Fig. 2. Penetration test apparatus

The transfer container that contains the sample container is placed on the penetration device plate. The needle loaded with the desired weight is adjusted to have contact with the sample surface. At least 3 tests should be conducted using points that are not closer to each other and the side of the container for more than 1 cm. The arithmetic mean of accepted measurements is rounded to the nearest whole number, which is taken as the penetration value.

B. Softening Point Test (EN 1427)

The softening point test aims to measure the resistance of bituminous binders to high temperatures. Softening point is the temperature at the moment when the softened material touches the base as a result of heating the bituminous material in the standard ring at a certain speed, which was placed in a water bath, with a ball on it. The test setup is shown in Figure 3.

Before the experiment, the bitumen sample is heated and poured into the standard ring up to the top of the ring and cooled for 1 hour. The bitumen overflowing the ring is cut off using a heated spatula.

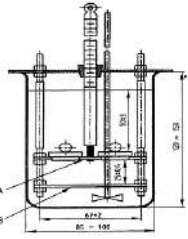


Fig. 3. Softening point test apparatus

Pure water at a temperature of 5°C is placed in the beaker and the ring that contains the sample is submerged into the water. Then the ball is placed in the beaker filled with water. The temperature of the water bath is kept constant at 5°C for 15 minutes. The ball is then placed in the middle of the sample in the ring using a pair of suitable tongs. The water is heated at a rate of 5°C per minute. The temperature read from the thermometer is recorded as the softening point when the softening material touches the base of the bath as a result of the increase in temperature.

C. Rotational Viscosimeter (RV) Test (ASTM D 4402)

The Rotational Viscosimeter (RV) test is conducted to determine the viscosity properties of the bituminous binders at high temperatures. The high temperature viscosity values of binders are identified to determine whether the binders are sufficiently fluid during pumping and mixing procedures. In the experiment, viscosity values are obtained by measuring the resistance of a shaft rotating at 20 rpm within the binder (Figure 4). In the RV test conducted with the original binders, it is best when the viscosity at 135°C does not exceed 3 Pa.s (3000 cP) [24, 25].

Approximately 30 gr. sample is taken and it is heated in a drying oven with a temperature of less than 150°C. Approximately 11 gr. of this material is placed in the sample compartment, and the sample compartment is placed in a temperature-controlled container with a constant temperature. After the sample is kept at a constant temperature for 15 minutes, the test is conducted. After almost equal viscosity values are obtained, three readings are conducted, and the viscosity of the binder is accepted as the average of these three measurements.

Viscosity values are used to determine the mixing and compaction temperatures of hot mix asphalts (HMAs). For this purpose, the RV test is carried out at 135°C and 165°C temperatures. A temperature-viscosity graph is plotted and the viscosity values are marked on the graph and these values are connected by a straight line. The viscosity values of the bituminous binder of 0.170 ± 0.20 Pa.s and a compaction value of 0.280 ± 0.30 Pa.s are desired when mixing HMAs [24]. The

temperature values corresponding to these viscosity values are accepted as the mixing and compaction temperatures.

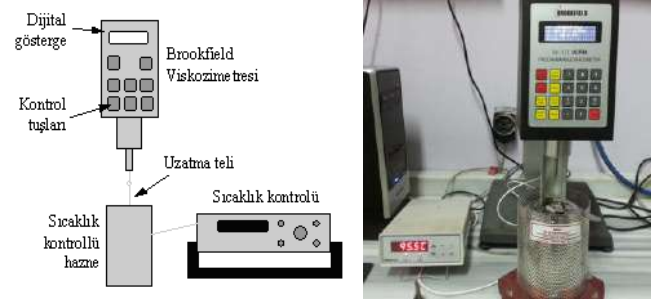


Fig. 4. Brookfield Viscosimeter

D. Temperature Susceptibility of Bituminous Binders

1) Penetration Index Method

Penetration Index (PI) is used to determine the temperature susceptibility of bituminous binders. The Penetration Index is determined with the standard penetration and softening point test results (Formulas 1, 2). P25 in the formula depicts the penetration value of the bitumen at 25°C and TYN indicates the softening point. The PI values decrease as the temperature susceptibility of bitumen binders increases. If the Penetration Index is less than -2, the bitumen is very sensitive to heat, whereas when it is greater than +2, it indicates that the bitumen is less sensitive to heat [26].

$$A = \frac{\log 800 - \log P_{25}}{T_{YN} - 25} \quad (1)$$

$$PI = \frac{20 - 500A}{1 + 50A} \quad (2)$$

2) Penetration Viscosity Number Method

Penetration-Viscosity Number (PVN), also called Pen-Vis Number, is an empirical correlation between asphalt cement factors and low temperature pavement cracking experiences. Asphalt cement factors considered in the original correlation are penetrations at 25°C, viscosity at 135°C and equation is proposed for selecting asphalt cements to prevent low temperature cracking of asphalt concrete pavements. The PVN method is used to quantify temperature susceptibility of an asphalt cement and estimate its ability to prevent low-temperature cracking. Lower values of PVN indicate higher temperature susceptibility, and asphalt mixtures containing binders with lower temperature susceptibility should be more resistant to cracking. The PVN number of a paving asphalt can be calculated precisely from the equations as follows [27];

$$PVN = -1.5 \frac{4.258 - 0.7967 \log P_{25} - \log V}{0.795 - 0.1858 \log P_{25}} \quad (3)$$

In the formula, P_{25} indicates the bitumen penetration at 25°C and V indicates the viscosity value at 135°C.

III. EXPERIMENTAL STUDY

In the present study, neat and modified binders were subjected to penetration, softening point and rotational viscometer tests to determine their consistency. Furthermore, the penetration index values, which indicate the temperature susceptibility of the bituminous binders, are determined using softening point and penetration values.

A. Penetration Test Results

The results obtained from the penetration tests applied to binders are presented in Figure 5.

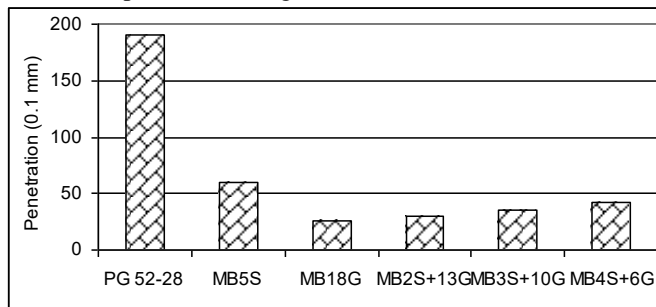


Fig. 5. Penetration test results

Figure 5 demonstrates that penetration values decreased with the use of additives. It was determined that the use of 18% AG and 5% SBS were the least effective methods for decreasing the penetration value when compared to the neat bitumen. The penetration values increased as the SBS content increased when dual additives were used. The penetration values of the modified bitumen that contained 5% SBS, 18% AG, 2% SBS + 13% AG, 3% SBS + 10% AG and 4% SBS + 6% AG were 3.14, 7.50, 6.32, 5.34 and 4.56 times lower than neat binder, respectively.

B. Softening Point Test Results

The results obtained in the softening point tests applied to the binders are presented in Figure 6. Figure 6 demonstrates that the softening point values increased with the use of additives. This indicated that all utilized additives would increase the high temperature resistance of the bituminous binders. When the impact of the additives on the softening point values is considered, it was found that all the additives had similar effects on the softening point and increased the softening point values by about 45% when compared to the neat binder.

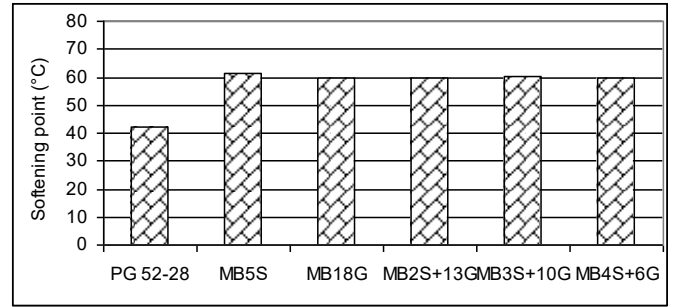


Fig. 6. Softening point test results

C. Specific Gravity of Bituminous Binders

Specific gravity values of neat and modified bitumen are determined based on the EN 15326 standard. The results obtained in specific gravity tests are presented in Figure 7.

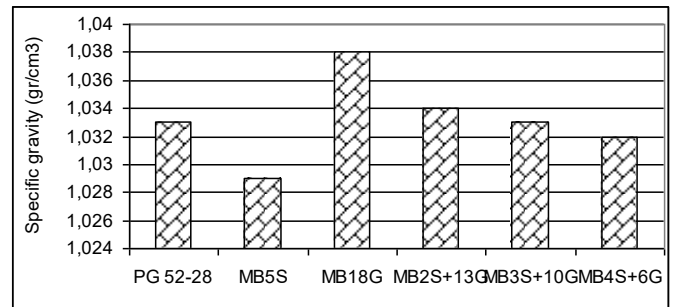


Fig. 7. Specific gravity values of neat and modified binders

As can be seen in the figure above, the specific gravity values of bituminous binders were between the specification limits 1.0-1.1. When the changes in specific gravity with the use of additives were examined, it was observed that the specific gravity of binders increased with the use of American Gilsonite, whereas the specific gravity values decreased with the use of SBS. With the combined use of AG and SBS, specific gravity values increased regularly when compared to the use of 5% SBS, but decreased regularly when compared to 18% AG use.

D. Penetration Index Values

The Penetration Index values for neat and modified bituminous binders determined using formulas (1) and (2) are given in Figure 8.

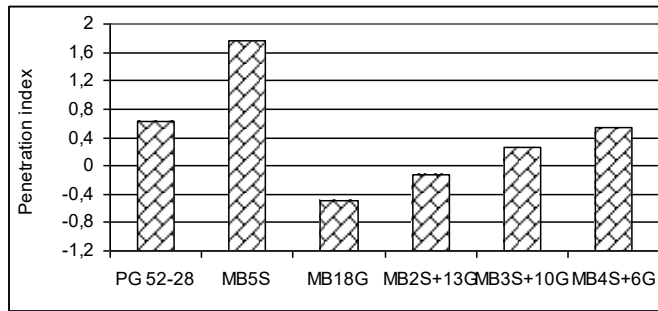


Fig. 8. Variation in binder penetration index values with additive use

The Penetration Index results that demonstrate the temperature susceptibility of bituminous binders showed that the PI value increased as the SBS ratio in modified binders increased (Figure 8). Since the temperature susceptibility of bituminous binders decrease as the PI value increased, it could be argued that the use of SBS decreased the temperature susceptibility of bituminous binders. It was determined that as AG content in modified bitumen increases, the PI values decreases and thus, the temperature susceptibility increases. When SBS and AG are used together in the modified bitumen, it was determined that AG had a negative effect on the temperature susceptibility, and that this problem was eliminated by using SBS in conjunction with AG.

E. Penetration Viscosity Number Values

The Penetration Viscosity Index values for the neat and modified bituminous binders determined using the formula (3) are given in Figure 9.

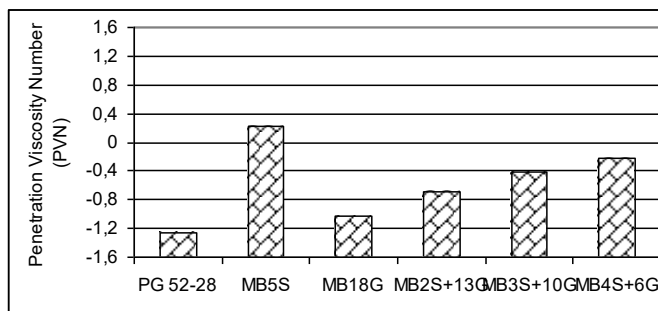


Fig. 9. Variations in binder penetration viscosity number values with additive use

When the penetration viscosity number results that reflect the susceptibility of bituminous binders to low temperatures were evaluated, it was determined that the use of AG had a negative effect on temperature susceptibility in PVN values,

similar to the PI values, when compared to that of the SBS. It was also determined that SBS can be used to avoid the negative impact of AG on temperature susceptibility. It was determined that the temperature susceptibility decreased with the use of SBS instead of AG in dual modified bitumen (Figure 9).

F. Rotational Viscometer Test Results

Neat and modified binders were subjected to rotational viscometer tests at 135°C and 165°C temperatures. In the experiment, 20 rpm speed was used. Modification index values were obtained from the ratio of the viscosity value of the modified binder to the viscosity value of the neat binder ($\eta_{\text{modified}} / \eta_{\text{neat}}$). The viscosity results obtained from the tests are presented in Figure 10. The viscosity and modification index values obtained at high temperatures (135°C and 165°C) demonstrated that SBS increases the stiffness of the binders and reduces the workability at high temperatures.

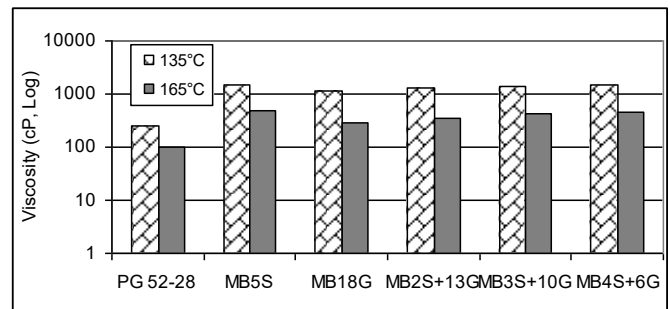


Fig. 10. Variations in binder viscosity values with temperature and additive use

Figure 10 demonstrates that the viscosity values of all binders met the Superpave specification limit maximum value of 3000 cP at a temperature of 135°C. With additive use, the viscosity values increased at all temperatures. It was determined that the viscosity values of 5% SBS modified binders were the highest and the bituminous viscosity values with 18% AG were the lowest, despite their similar performance levels. It was determined that as the SBS content in the modified bitumen increased, the viscosity values increased at both temperatures.

The modification index ($\eta_{\text{modified}} / \eta_{\text{neat}}$) values determined by the ratio of the viscosity value of the modified bitumen to the viscosity value of the neat binder are given in Figure 11. When the modification index values were examined, it was determined that the additive that maximizes the viscosity value at all temperatures was SBS and the least contributing additive was AG. It was determined that the viscosity values of SBS and AG were higher than those of the sole use of AG and the viscosity values increased regularly as the SBS ratio in the mixture increased.

When the bituminous binders are mixed with the aggregates at the plant and the hot mix asphalts are compacted in the field, they must possess adequate workability. It is desirable that the bituminous binder has a viscosity value of

0.170 ± 0.20 Pa.s for compaction and 0.280 ± 0.30 Pa.s for the mixing [24]. In the plotted temperature-viscosity graphs, the viscosity values were marked and these values were joined with a straight line. The temperature values that correspond to these viscosity values are accepted as the mixing and compaction temperatures. As an example, the viscosity-temperature graph that shows the mixing and compaction temperature ranges for the modifier binder that contains 18% AG is presented in Figure 12.

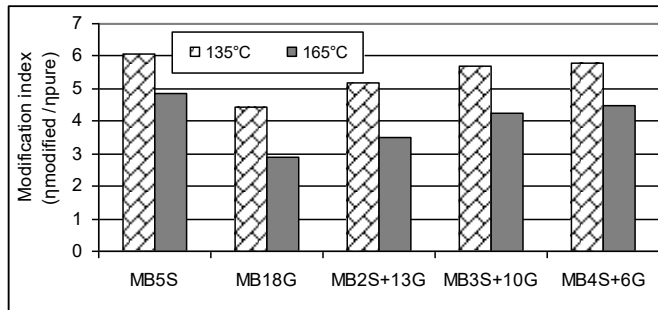


Fig. 11. Variations in binder modification indexes with temperature and additive use

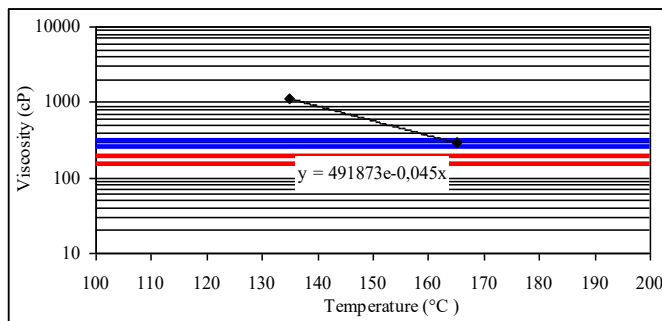


Fig. 12. Viscosity-temperature chart for the modified binder including 18% AG

The variation in the mixing and compaction temperatures with the type of additive is presented in Figure 13.

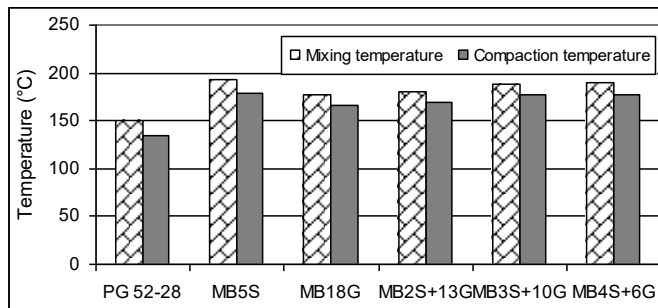


Fig. 13. Mixing and compaction temperatures of binders

As shown in Figure 13, higher mixing and compaction temperatures were required with the use of additives. This demonstrates that although higher binder performance is achieved with additive use, higher temperatures will be required during mixing it with the aggregate and compaction of the HMA, thus requiring more energy during the preparation at the plant. When the effects of the additive types and combined use of additives were evaluated, it was determined that the highest mixing and compaction temperatures were found with 5% SBS modified bitumen and the lowest values were found with 18% AG modified bitumen. As the SBS content in the modified bitumen increased, higher mixing and compaction temperatures were needed.

IV. RESULTS

In the study, consistency and specific gravities of neat and 5 different modified bitumen were determined and their temperature susceptibility was evaluated with two different methods. Initially, 18% AG and 5% SBS were used as additives separately, then 2% SBS and 13% AG, 3% SBS and 10% AG, and 6% AG and 4% SBS were used in conjunction to obtain bituminous binders with the same performance level.

- Penetration tests demonstrated that all additives increased the stiffness significantly. It was determined that the most effective additive was 18% AG and the least effective additive was 5% SBS.
- Softening point tests demonstrated that all additives increased the high temperature resistance of the bituminous binders significantly, and all modified bitumen had similar softening point values.
- It was determined that the specific gravity values of AG modified bitumen were higher since both the usage ratio and density of AG was higher than those of SBS as demonstrated in specific gravity tests.
- Penetration index values demonstrated that 5% SBS modified bitumen had the lowest thermal sensitivity and 18% AG modified had the highest. This negative aspect of AG modified binders was reduced with the addition of SBS.
- Penetration viscosity number values were consistent with PI values. With the use of AG additive, the low temperature susceptibility of bituminous binders have increased, and the use of SBS has reduced the low temperature susceptibility.
- It was determined that additive use increased binder stiffness values as observed in viscosity values. Consequently, the mixing and compaction temperatures increased with the modification values. The most effective additive on viscosity values was 5% SBS modification.

ACKNOWLEDGMENT

This study was conducted within the scope of the Scientific and Technological Research Council of Turkey (TUBITAK) project no. MAG-214M669. The authors would like to thank TUBITAK for their support.

REFERENCES

- [1] T.W. Kennedy, R.J. Cominsky, "Hypotheses and models employed in the SHRP asphalt research program," SHRP-A/WP-90-008, Strategic Highway Research Program, Washington, 1990.
- [2] P. Claudy, J.M. Letoffe, G.N. King, B. Brule, J.P. Planche, "Caracterisation des bitumes routiers par analyse calorimetrique differentielle," Bull Liaison Lab Ponts Chaussees, issue 165, pp. 85-92, 1990.
- [3] M. Garcia-Morales, P. Partal, F.J. Navarro, F.J. Martinez-Boza, C. Gallegos, "Process rheokinetics and microstructure of recycled EVA/LDPE-modified bitumen," Rheol Acta., vol. 45, pp. 513-524, 2006.
- [4] A. Tunç, Esnek Kaplama Malzemeleri El Kitabı. Asil Yayın Dağıtım, 352 s., 2004.
- [5] X. Lu, U. Isacsson, "Laboratory study on the low temperature physical hardening of conventional and polymer modified bitumens", Constr. Build. Mater., vol. 14, pp. 79-88, 2000.
- [6] F.J. Navarro, P. Partal, F. Martinez-Boza, C. Valencia, C. Gallegos, "Rheological characteristics of ground tire rubber-modified bitumens," Chem. Eng. J., vol. 89, pp. 53-61, 2002.
- [7] G.D. Airey, "Rheological properties of styrene butadiene styrene polymer modified road bitumens," Fuel, vol. 82(14), pp. 1709-1719, 2002.
- [8] H. Aglan, A. Othman, L. Figueroa, R. Rollings, "Effect of styrene-butadiene-styrene block copolymer on fatigue crack propagation behavior of asphalt concrete mixtures," Transp. Res. Rec., vol. 1417, pp. 178-186, 1993.
- [9] M.J. Khattak, G.Y. Baladi, "Engineering properties of polymer-modified asphalt mixtures," Transp. Res. Rec., vol. 1638, pp. 12-22, 1998.
- [10] H. Hamidi, Stiffness Modulus and Permanent Deformation Characteristics of Asphalt Mix Containing Gilsonite, PhD Thesis, Bandung Technology Institute, India, 1998.
- [11] J. Liu, P. Li, "Experimental study on gilsonite-modified asphalt," Proceeding of the 2008 Airfield and Highway Pavement Specialty Conference, Washington, pp. 222-228, 2008.
- [12] URL-1, <http://www.asiagilsonite.com/?page=gilsonite> Asia Gilsonite. 27 Ocak 2017.
- [13] E. Yalçın, Filler Olarak Kireç Kullanımının Modifiye Bitümlerle Hazırlanan Karışımların Performansına Etkisinin İncelenmesi, Yüksek Lisans Tezi, Fırat Üniversitesi, Fen Bilimleri Enstitüsü, Elazığ, 2014.
- [14] M.E. Çeloğlu, Farklı Doğal Asfaltların Bitüm ve Bitümlü Sıcak Karışımların Özelliklerine Etkileri, Yüksek Lisans Tezi, Fırat Üniversitesi, Fen Bilimleri Enstitüsü, Elazığ, 2014.
- [15] I. Widyatmoko, R. Elliott, "Characteristics of elastomeric and plastomeric binders in contact with natural asphalts," Construction and Building Materials, vol. 22, pp. 239-249, 2008.
- [16] R. Babagoli, M. Hasaninia, N.M. Namazi, "Laboratory evaluation of the effect of gilsonite on the performance of stone matrix asphalt mixture," Road Materials and Pavement Design, vol. 16(4), pp. 889-906, 2015.
- [17] G. Wen, Y. Zhang, Y. Zhang, K. Sun, Y. Fan, "Rheological characterization of storage-stable SBS-modified asphalts," Polymer Testing, vol. 21, pp. 295-302, 2002.
- [18] D. Sun, W. Lu, "Investigation and improvement of storage stability of sbs modified asphalt," Petroleum Science and Technology, vol. 21(5-6), pp. 901-910, 2003.
- [19] N. Davis, C.E. Tooman, "New laboratory tests evaluate the effectiveness of gilsonite resin as a borehole stabilizer," SPE Drilling Engineering, vol. 4(1), pp. 47-56, 1989.
- [20] B.V. Kök, M. Yılmaz, M. Akpolat, "Evaluation of the conventional and rheological properties of SBS + Sasobit modified binder," Construction and Building Materials, vol. 63, pp. 174-179, 2014.
- [21] I.A. Carcer, R.M. Masegosa, M.T. Vinas, C. Salom, M.G. Prolongo, V. Contreras, F. Barcelo, A. Paez, "Storage stability of SBS/Sulfur modified bitumens at high temperature: Influence of bitumen composition and structure," Construction and Building Materials, vol. 52, pp. 245-52, 2014.
- [22] T.F. Pamplona, B.C. Amoni, A.E.V. Alencar, A.P.D. Lima, N.M. Ricardo, J.B. Soares, S.A. Soares, "Asphalt binders modified by SBS and SBS/Nanoclays: Effect on rheological properties," Journal of the Brazilian Chemical Society, vol. 23(4), pp. 639-647, 2012.
- [23] Y. Peng, R. Ruiibo, W. Lizhi, Z. Xiaoning, "Characteristic behavior of asphalt with SBS and PE," Sustainable Construction Materials, pp. 421-429, 2012.
- [24] J.P. Zaniwski, M.E. Pumphrey, "Evaluation of performance graded asphalt binder equipment and testing protocol," Asphalt Technology Program, pp. 107, 2004.
- [25] R.B. McGennis, S. Shuler, H.U. Bahia, "Background of Superpave asphalt binder test methods", No. FHWA-SA-94-069, pp. 104, 1994.
- [26] P. Ullidtz, Pavement Analysis. Elsevier, Amsterdam, pp 318. 1987.
- [27] N.W. McLeod, "Asphalt cements: pen-vis number and its application to moduli of stiffness," Journal of Testing and Evaluation, vol. 4(4), pp. 275-282, July 1976.

The Mechanical and Physical Properties of Unfired Earth Bricks Stabilized with Gypsum and Elazığ Ferrochrome Slag

İbrahim TÜRKMEN
Department of Civil Engineering
İnönü University
Malatya, Turkey
ibrahim.turkmen@inonu.edu.tr

Enes EKİNCİ
Department of Civil Engineering
İnönü University
Malatya, Turkey
enes.ekinci@inonu.edu.tr

Fatih KANTARCI
Department of Civil Engineering
İnönü University
Malatya, Turkey
fatih.kantarci@inonu.edu.tr

Abstract-During the last few years, an increasing interest has been appeared for earth as a building material. Earth-based materials have been studied because of energy efficient and ecologically sustainable. The chromite deposits, 10% of the world reserves, are processed in Elazığ Ferrochrome Factory in Eastern of Turkey. Elazığ Ferrochrome slag (EFS) as a by-product of the factory is produced roughly 50.000 tons in a year. The disposal, removal and storage of this by-product is a serious problem. Therefore, the evaluation of this waste material in building applications is very important. The aim of this work is to investigate effects of gypsum and EFS additives on mechanical and physical properties of unfired earth brick (UEB) materials in order to assess their potential advantages in building applications. The earth material was characterized by laboratory tests. The four different UEB samples were produced by using different compositions of earth, gypsum, EFS and straw fibers. Compressive strength, water absorption coefficient, drying shrinkage and ultrasonic pulse velocity (UPV) of the prepared UEB samples were determined. The experimental findings have showed that the usage of gypsum and EFS in stabilizing process of UEBs was advantaged.

Keywords: *Elazığ ferrochrome slag, unfired earth brick, compressive strength, water absorption*

I. INTRODUCTION

The demand to reduce CO₂ emissions and to find more sustainable construction materials constitutes nowadays are a major economic and ecological challenge. Earthen construction can lead to reduce environmental problems. Actually, raw earth is one of the most widely used building materials in human history. It is estimated that nearly a third

of the world's population lives in some type of earthen houses. It is one of the oldest building materials used in many different ways around the world for centuries. Approximately 50% of the population of developing countries, the majority of rural populations, and at least 20% of urban populations live in earthen constructions [1]. During the last few years, an increasing attention has been appeared for earth as a sustainable material, therefore has been investigated in the engineering laboratories around the world in the purpose of the certification of earth building materials. The reason for this interest is that it presents several advantages that allow it to be a current response to energy and climate issues. In fact, raw earth is an abundant natural and recyclable resource. It is low embodied energy building material, compared to fired clay bricks and concrete. It reduces the amount of energy required for construction as well as transportation needs [2, 3].

Zami and Lee [4] summarized advantages of unfired earth brick (UEB) as follows: i) earth construction is economically beneficial, ii) it requires simple tools and less skilled labour, iii) it encourages self-help construction, iv) suitable for very strong and secured, v) it saves energy, vi) it balances and improves indoor air humidity and temperature which ensures thermal comfort, vii) earth is very good in fire resistance, viii) earth construction is regarded as a local job creation opportunity, ix) earth construction is environmentally sustainable, x) easy to design and high aesthetical value, xi) earth building provides noise control, xii) earth construction promotes local culture and heritage,

xiii) earth is readily available in large quantities in most regions.

The deterioration of porous building materials is mainly due to the interactions between their structures and water. Depending on the material characteristics, physical state of water (liquid or vapor) and environmental conditions, the quantity of water absorption and sorption mechanisms may be different [5]. In particular, the absorption of humidity from air, the capillary rise, the rain penetration, and water condensation phenomenon can lead to the formation of superficial moisture [6]. In brick production, there are two types of moisture content required for molding. The first one is the shrinkage water (initial water) which helps molding process. It exists in the brick body among the particles. The shrinkage water is also necessary for clay plasticity. The second one is the porosity water (or interstitial water) [7]. Drying shrinkage of the bricks was primarily governed by the plasticity index and cement content. Water-loss also contributes to the shrink of the clay fraction. For low clay mineral content (index plasticity below 20%), drying shrinkage showed steady increase with the increase of clay content, but for plasticity index beyond 25% – 30% drying shrinkage increased rapidly as the clay content also increased [8]. The compressive strength is a mechanical property used in brick specifications, which has assumed great importance for two reasons. Firstly, with a higher compressive strength, other properties like flexure, resistance to abrasion, etc., also improve. Secondly, while other properties are relatively difficult to evaluate, the compressive strength is easy to determine [9]. In some countries such as Papua New Guinea clayey soils are stabilized with native materials, e.g. volcanic ash, finely ground natural lime, cement and their combinations [10].

There is a need to improve the durability, production, and workability of earthen construction technology. Throughout its history as a building material, earth has been stabilized with different additives. Istanbul Technical University recovered gypsum used as a stabilizer from historical buildings in Eastern Turkey. Ongoing research since 1978 [11] proves that this combination of earth and gypsum called Alker (an abbreviated form of the Turkish words for gypsum and adobe, meaning gypsum-stabilized adobe) has improved physical properties. There are Alker buildings constructed and inhabited since 1983. Construction of Alker Building, 1995, can be seen in Fig. 1a and Urfa Pilot Building 1999 on Fig. 1b. [12]. Except for these pilot studies, there are also new buildings constructed with gypsum-stabilized earth bricks in Malatya (Fig. 1c).

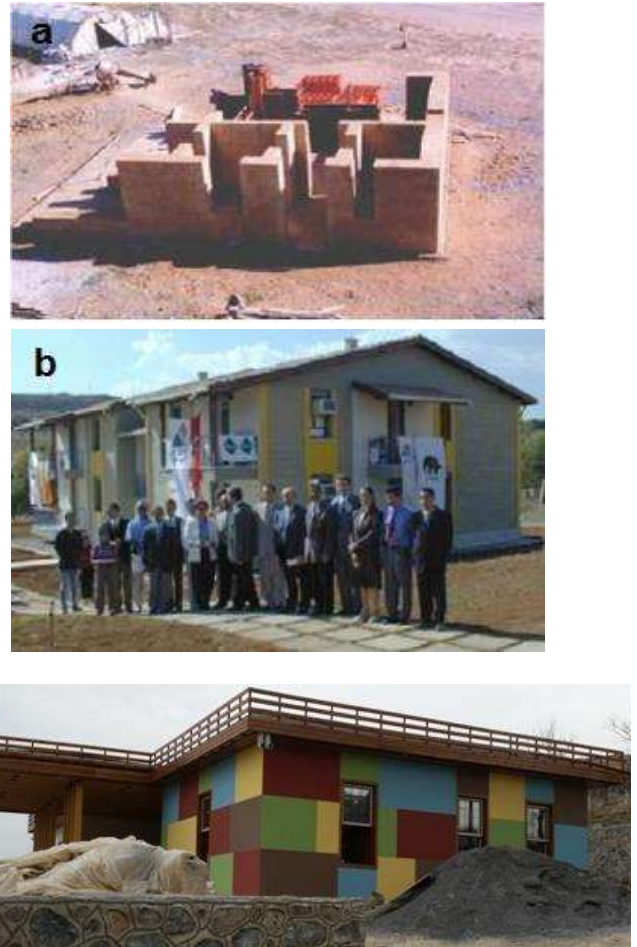


Fig. 1. a) Construction of Alker Building, b) Urfa Pilot Building, c) Building constructed in Malatya

The chromite deposits, 10% of the world chromite reserves located within the boundaries of Maden town-Alacakaya village of Elazığ, are processed in Elazığ Ferrochrome Factory. Apart from the main product, many by-products are produced in this factory. One of these by-products is Elazığ Ferrochrome slag (EFS). The amount of slag generation is roughly 330 kg per ton of ferrochrome produced, and the annual production of EFS exceeds 50.000 tons. The disposal, removal and storage of by-products is a big problem. When considering accumulated amount of EFS so far and accumulate in the future, it is important to discover potential use of this by-product in UEB materials. The aim of this study is to examine effects of gypsum and EFS additives on mechanical and physical properties of UEB materials in order to assess their potential usage in building applications. Compressive strength, water absorption coefficient, drying shrinkage and ultrasonic pulse velocity (UPV) of UEB samples were tested.

II. MATERIALS AND METHODS

A. Materials

The four different materials were used, i.e. cohesive soil, gypsum, EFS and straw fibers. Cohesive soil used in this study was obtained from Malatya in Eastern of Turkey. EFS was obtained from Elazığ Ferrochrome Factory in Eastern of Turkey. EFS was ground to less than 45 μm particle size in order to increase the reactivity. Locally available gypsum and straw fibers were used. The average straw length was approximately 2 cm. The fibers were selected because of their positive impact on drying shrinkage of earth building materials. The drinking water at a temperature of 20 ± 2 °C was used. The composition of the cohesive soil texture was as 18% clay, 23% silt, 54% sand and 5% gravel.

B. Sample preparation

Initially, oversized gravel were removed from the natural soil. The cohesive soil was put in an oven to obtain dry weight at 105°C for 24h. Presence of organic matters in a raw material is inconvenient and undesirable, because organic compounds significantly reduce the strength and binding properties of building materials. The content of organic matter in the soil was determined in accordance with TS EN 1744-1 [13] and at the end of experiment, resulting color demonstrated that no organic matter was found.

Particle size distribution was determined using a wet sieving and a sedimentation test, according to standard [14]. The grain size distribution of soil used in this study is given in Fig. 2. The chemical composition of the soil was determined by X-Ray Fluorescence (XRF) technique. The chemical composition of soil and EFS are presented in Table 1. The Atterberg limits were determined as WL = 54.7% (liquid limit), WP = 34.3% (plastic limit) and IP = 20.4% (plasticity index).

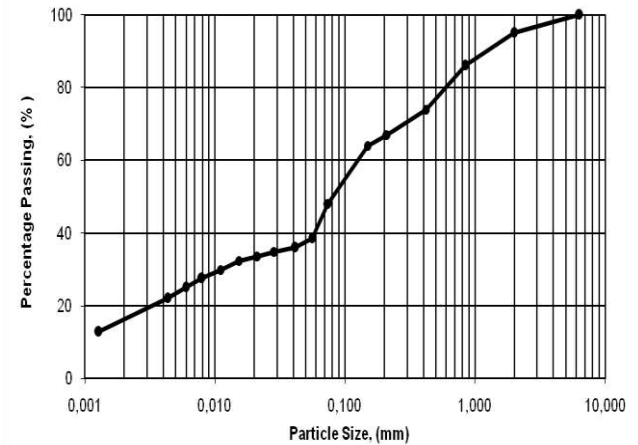


Fig. 2. Grain size distribution of soil

Table 1. The chemical composition of the materials, (% wt)

Component, (%)	Soil	EFS
SiO ₂	58.56	33.80
Al ₂ O ₃	15.12	25.48
Fe ₂ O ₃	4.72	0.61
CaO	3.10	1.10
MgO	2.50	35.88
Cr ₂ O ₃	0.02	2.12
TiO ₂	0.78	-
Na ₂ O	1.30	-
K ₂ O	3.10	-
LOI	10.65	1.01



Fig. 3. a) Mixing process, b) Compressive strength test, c) UPV test

The four different UEB samples were produced by using different compositions of earth, gypsum, EFS and straw fibers. Mixture proportion of UEB samples is given in Table 2. Water content is one of the most important factors affecting mechanical and physical properties of UEB materials. Optimum water/solid ratio was determined as 0.30, experimentally. The amounts of materials were calculated as dry weights. Then, the specified amounts of raw materials of cohesive soil, gypsum, EFS, straw fibers and water were poured into mechanical mixer (Fig. 3a). The mixture was stirred until a homogeneous mixture was obtained. Finally, the freshly mixed brick mortar was taken from the mixer, fed into specimen moulds and vibrated until to obtain full compaction.

Table 2. Mixture proportion of UEB samples

Sample code	Description of UEB samples
R (Reference)	Soil with 1 mass per cent straw fibers
G10*	Soil with 10 mass per cent gypsum and 1 mass per cent straw fibers
S10	Soil with 10 mass per cent EFS and 1 mass per cent straw fibers
G5S5*	Soil with 5 mass per cent gypsum, 5 mass per cent EFS and 1 mass per cent straw fibers

*Due to the early setting time of gypsum, deformation and crack risk to the structure during the drying period was prevented by adding 1-2% lime.

C. Testing apparatus and procedure

Sample production and testing of compression strength of mortars are stated in EN 1015-11 standard [15]. 7 and 28-day compressive strengths of UEB samples were determined in accordance with this standard (Fig. 3b). Compressive strength specimens are prisms with the dimensions of 160 x 40 x 40 mm. The UPV tests were conducted in accordance with ASTM C 597-97 [16] (Fig. 3c). 2004-Relationship between ultrasonic velocity. Shrinkage is the physical phenomenon, which occurs during drying process, due to the evaporation of moisture content in the brick. The drying shrinkage (S_d) was calculated according to testing method ASTM C326-09 [17] and defined in Eq. (1). Drying length (L) and initial length (L_0) were used in the calculation.

$$S_d = \frac{L_0 - L}{L_0} \times 100 \quad (1)$$

The determining method for the water absorption characteristics were conducted in accordance with BS EN 772-11 [18]. After drying to constant mass, a face of UEB samples was immersed in water for a specific

period of time and the increase in mass was determined. The minimum immersion period is usually one hour, as specified in BS EN 771-4 [19]. The coefficient of water absorption of masonry materials is normally stated at 10, 30, 60 and 90 minutes [20]. Water absorption coefficient of UEB samples was calculated by using the following Eq. (2) [18].

$$C_w = \frac{M_w - M_d}{A \sqrt{t}} \quad (2)$$

Where,

C_w: Water absorption coefficient (kg/m²min^{0.5}),

M_w: Wet mass (kg), M_d: Dry mass (kg),

A: Surface area (cm²) and t: Time (min)

III. RESULT AND DISCUSSION

A. Compressive strength

The 7 and 28-day compressive strengths of UEB samples are given in Fig. 4 and Table 3. As can be easily seen in Fig. 4, maximum compressive strength was obtained from G10 samples containing 10 mass per cent gypsum. Although the highest compressive strength was obtained in samples containing only gypsum, a dramatic difference was not observed between samples with or without EFS. Addition of 10 mass per cent EFS brought about slightly reduce in compressive strength, but the usage of gypsum and EFS together increased compressive strength. The overall results showed that the gypsum stabiliser led to higher compressive strength values compared to EFS stabiliser. The results also showed that the compressive strength increased progressively from 7 days to 28 days curing period. When compared to other samples, increase in compressive strength from 7 to 28 days of S10 is higher. The reason of this behaviour may be due to the puzzolanic effect of EFS.

The influence of stabilizers was studied by Hossain et al. [21]. The compressive strength in this case varies between 0.39 and 3.10 MPa. Isik and Tulbentci [12] stated that compressive strength of gypsum-stabilized earth brick ranges from 2 to 4 MPa. In this study, compressive strength of gypsum-stabilized UEB samples is higher than mentioned these values. Furthermore, compressive strength of reference samples in this study is higher than values obtained from previous studies [10, 22, 23].

Table 3. Compressive Strength and UPV values of UEB samples

Sample Code	Compressive Strength, (MPa)		UPV, (m/s)	
	7 day	28 day	7 day	28 day
R (Reference)	4.14	4.24	1086	1116
G10	4.51	4.58	1228	1251
S10	3.39	3.84	987	1051
G5S5	3.86	4.1	1167	1193

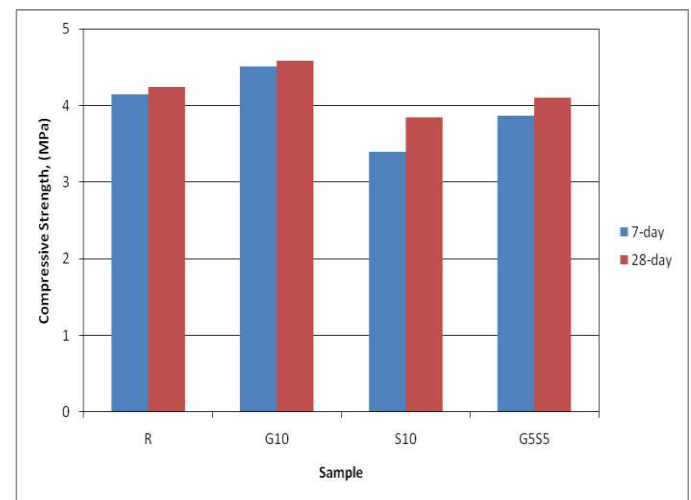


Fig. 4. Compressive strength of UEB samples

B. Capillary Water Absorption Coefficient

The presence of water is one of the main decay factors in buildings. Capillary water absorption curve of UEB samples was obtained as a function of the root of time. Fig 5 shows the results of the average mass variation per contact area in the capillary absorption process for UEB. The capillary water absorption coefficients were calculated according to BS EN 772-11 [18], and obtained coefficient values are shown in Fig. 6 and Table 4. The maximum water absorption coefficient value was obtained from S10 sample which has minimum compressive strength. The minimum capillary water absorption coefficient value was obtained from G10 sample which exhibits the best behaviour in compressive strength. Likewise, Isik and Tulbentci [12] stated that gypsum addition improves the water resistance, workability, and mechanical properties of UEBs. It is also

stated that basic principle of the stabilization is to prevent water attacks to obtain a durable material [24].

From the experimental data, it was observed that there was an inverse relationship between the compressive strength and the capillary water absorption coefficient. Also, this observation was supported by the coefficient values of the R and G5S5 samples. Oti et al. [25] stated that the amount of water absorption of unfired clay masonry bricks depends on compressive strength. The overall capillary water absorption coefficient values for all stabilised mixtures were within the acceptable limits for stabilized UEB. The curve of water absorption, by capillary action, as a first step of absorption (short-time faster) is directly proportional to the square root of time just as it would be expected [26].

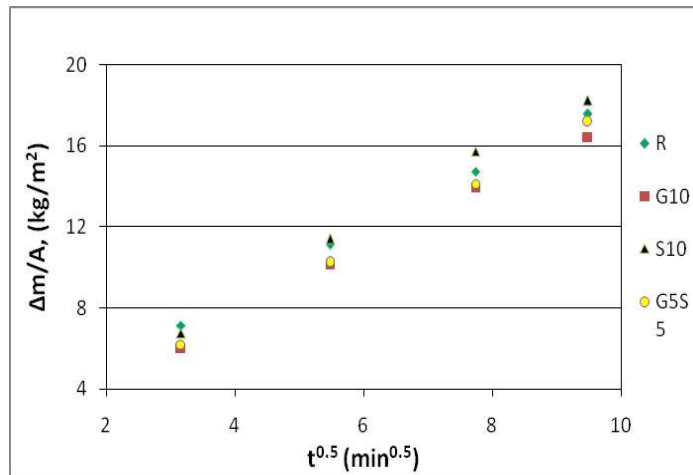


Fig. 5. Capillary water absorption curve of samples, as a function of the root of time

Table 4. Capillary Water Absorption Coefficient of samples, ($\text{kg}/\text{m}^2\text{min}^{0.5}$)

Time, (min)	R (Reference)	G10	S10	G5S5
10	2.25	1.96	2.13	1.96
30	2.03	1.9	2.08	1.87
60	1.9	1.81	2.03	1.82
90	1.85	1.69	1.92	1.81

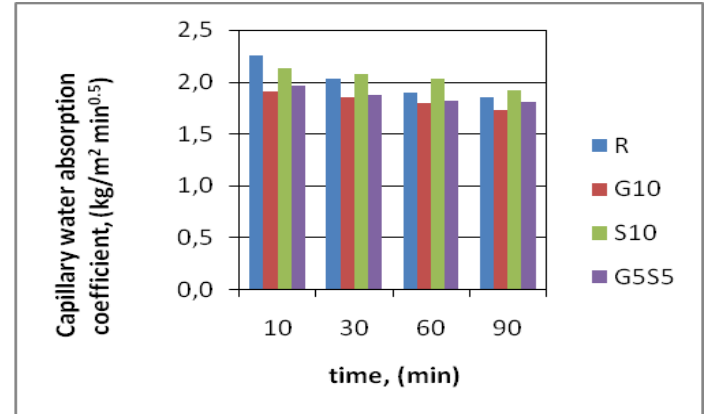


Fig. 6. Capillary Water Absorption Coefficient of samples

C. Drying shrinkage

In the drying experiments, drying shrinkage behavior of UEB samples produced with different additives was investigated. For all UEB samples, shrinkage measurements were performed up to 30 days. Drying shrinkage values of UEB samples are shown in Fig. 7. At the end of 30th day, while minimum drying shrinkage value was obtained from G10 sample with 4.12%, maximum drying shrinkage value was obtained from reference sample with 7.57%. As can be observed in Fig. 7, drying shrinkage values of G10 samples are approximately half of reference ones. The reason of this significant decrease in drying shrinkage can be explained by addition of gypsum and lime. Similarly, Pekmezci et al. [27] stated that the low shrinkage values and crack free adobe can be attributed to a rigid skeleton formed by a hardening of gypsum and lime in the structure. Calcite crystals and binding gels formed as a result of the pozzolanic reaction also result in lower shrinkage of gypsum and lime adobe samples. Finally, the secondary structure, which prevents deformations from stresses caused by shrinkage, may be an effective parameter in reducing shrinkage values [27].

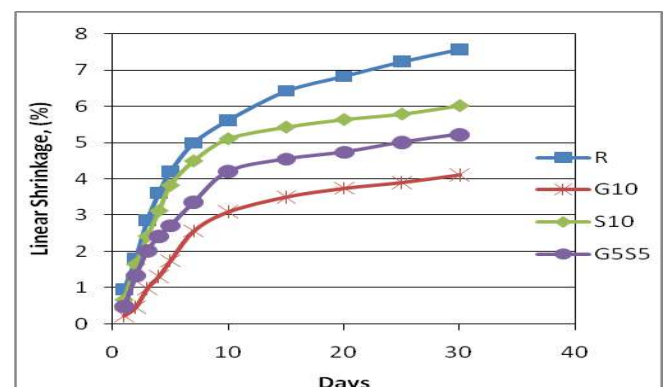


Fig. 7. Drying shrinkage of UEB samples

When compared to reference samples, the addition of EFS contributed to decrease in shrinkage values of UEB samples. Moreover, the addition of both gypsum and EFS led to further decrease in drying shrinkage of UEB samples. It is stated that the drying shrinkage depends on the characteristics of clay such as the mineralogical nature and the particle size. If the material shrinks more than 8%, drying process may cause problems in the bricks such as cracking and internal fractures [7, 28, 29]. In the light of this information, overall drying shrinkage values obtained in this experimental study are within acceptable limits.

D. Ultrasonic Pulse Velocity (UPV)

UPV values of UEB samples are displayed in Fig. 8 and Table 3. As can be seen in Fig. 8, UPV values are ranging from 1086 to 1428 m/s and 1123 to 1451 m/s for 7 and 28-days samples, respectively. Maximum UPV values were obtained from G10 samples which have highest compressive strength. On the other hand, minimum UPV values were obtained from reference samples. It was observed that there was a slight increase in UPV values 7 to 28 days. When the increases are evaluated, the highest increase in UPV was obtained from S10 samples 7 to 28 days. This increase may be due to pozzolanic reactions of EFS. Likewise, Galan-Marín et al. [30] investigated influence of utilising natural polymers as a form of soil stabilization. UPV and mechanical strength tests were conducted. Obtained UPV results ranged from 1075 to 1818 m/s in accordance with compressive strength.

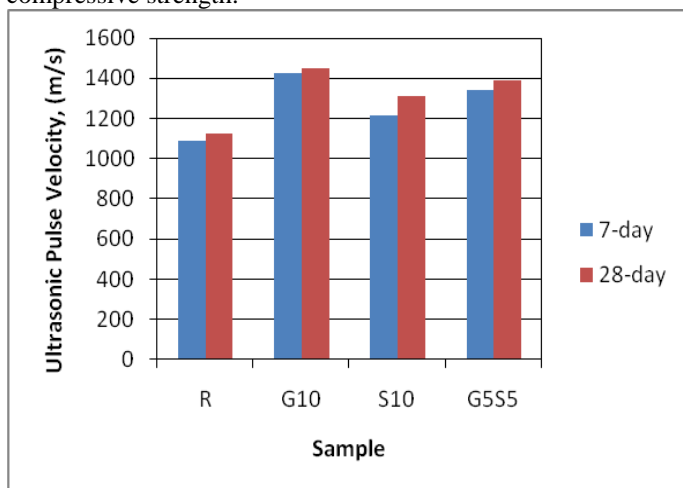


Fig. 8. UPV values of UEB samples

IV. CONCLUSION

In this article, it was investigated the effect of gypsum and EFS additives on mechanical and physical properties of UEB materials for a potential usage in building applications. The results of the obtained experimental findings are as follows:

1. Gypsum stabiliser indicated the higher compressive strength values compared to EFS stabiliser. However, there was not a significant decrease in compressive strength by using EFS additives.
2. Compressive strength increased progressively from 7 days to 28 days curing period. When compared to other samples, increase in compressive strength from 7 to 28 days of S10 is higher. The reason of this difference may be associated with the pozzolanic effect of EFS.
3. It was determined that there is an inverse relationship between the compressive strength and the capillary water absorption coefficient.
4. From the capillary water absorption experiments, it was seen that there was an obvious decrease in water absorption coefficient with increasing time.
5. The use of gypsum and lime together led to a significant decrease in shrinkage values compared to other samples. Similarly, the addition of EFS contributed to decrease in shrinkage values.
6. Maximum UPV values were obtained from G10 samples which has highest compressive strength.

As a result of this experimental study, it was shown that EFS (a by-product) can be used in stabilising of UEBs because usage of EFS in stabilising of UEBs improved overall properties except for compressive strength. Additionally, it will be beneficial to investigate effect of different mineral additives and mixture proportions on mechanical and physical properties of UEBs.

REFERENCES

- [1] H. Houben, H. Guillaud, Earth Construction, Intermediate Technology Publications, London, 1994.
- [2] J.C. Morel, A. Mesbah, M. Oggero, P. Walker, Building houses with local materials: means to drastically reduce the environmental impact of construction, Building and Environment 36 (2001) 1119–1126.
- [3] F.E. Fgaier, Z. Lafhaj, E. Antczak, C. Chapiseau, Dynamic thermal performance of three types of unfired earth bricks, Applied Thermal Engineering, 93 (2016) 377–383.
- [4] M.S. Zami, A. Lee, Stabilised or unstabilised earth construction for contemporary urban housing, in: Proceedings of International Conference on Responsive Manufacturing-Green Manufacturing (ICRM) Symposium 2010, Ningbo, China.
- [5] A. Pasculli, N. Sciarra, A numerical one-dimensional modeling of water transport through a porous material under saturated and unsaturated condition: parametric

- studies, *Memorie della Societa Geologica Italiana*, 56 (2001) 367-374.
- [6] T. Ashour, A. Korjenic, S. Korjenic, Equilibrium moisture content of earth bricks biocomposites stabilized with cement and gypsum, *Cement Concrete Composites* 59 (2015) 18-25.
- [7] E. Mancuhan, S. Özen, P. Sayan, S. Titiz-Sargut, Experimental investigation of green brick shrinkage behavior with Bigot's curves, *Drying Technology* 34:13 (2016) 1535-1545.
- [8] F.V. Riza, I.A. Rahman, A.M.A. Zaidi, A Brief Review of Compressed Stabilized Earth Brick (CSEB), in: *Proceedings of International Conference on Science and Social Research (CSSR) Symposium 2010*, Kuala Lumpur, Malaysia.
- [9] O. Azeez, O. Ogundare, T.E. Oshodin, O.A. Olasupo, B.A. Olunlade, Evaluation of the Compressive Strength of Hybrid Clay Bricks, *Journal of Minerals Materials Characterization Engineering* 10:7 (2011) 609-615.
- [10] P. Zak, T. Ashour, A. Korjenic, S. Korjenic, W. Wu, The influence of natural reinforcement fibers, gypsum and cement on compressive strength of earth bricks materials, *Construction and Building Materials* 106 (2016) 179-188.
- [11] R. Kafescioglu, N. Toydemir, B. Ozuekren, E. Gurdal, Stabilizing earth with gypsum as a construction material, *The Scientific And Technological Research Council Of Turkey (TUBITAK) MAG505*, (1980) Istanbul.
- [12] B. Isik, T. Tulbentci, Sustainable housing in island conditions using Alker-gypsum-stabilized earth: A case study from northern Cyprus, *Building and Environment* 43 (2008) 1426-1432.
- [13] TS EN 1744-1. Tests for chemical properties of aggregates- Part 1: Chemical analysis
- [14] XP CEN ISO/TS 17892-4. Geotechnical investigation and testing-laboratory testing of soil-Part 4: determination of particle size distribution.
- [15] EN 1015-11. Methods of Test for Mortar for Masonry – Part 11: Determination of Flexural and Compressive Strength of Hardened Mortar.
- [16] ASTM C 597-97. Standard Test Method for Pulse Velocity through Concrete, *Annual Book of ASTM Standards*.
- [17] ASTM C326-09. Standard Test Method for Drying and Firing Shrinkages of Ceramic White-ware Clays, *Annual Book of ASTM Standards*.
- [18] BS EN 772-11. Methods of test for masonry units. Determination of water absorption of aggregate concrete, autoclaved aerated concrete, manufactured stone and natural stone masonry units due to capillary action and the initial rate of water absorption of clay masonry units.
- [19] BS EN 771-4. Specification for masonry units. Autoclaved aerated concrete masonry units.
- [20] C. Gorse, D. Johnston, M. Pritchard, *A Dictionary of Construction, Surveying, and Civil Engineering*, Oxford, 2012.
- [21] K.M.A. Hossain, M. Lachemi, S. Easa, Stabilized soils for construction applications incorporating natural resources of Papua new Guinea resources, *Resources, Conservation and Recycling* 51 (2007) 711-731.
- [22] M.C. Jiménez Delgado, I. Cañas Guerrero, Earth building in Spain, *Construction and Building Materials* 20 (2006) 679-690.
- [23] J.C. Morel, A. Pkla, P. Walker, Compressive strength testing of compressed earth blocks, *Construction and Building Materials* 1 (2007) 303-309.
- [24] A.J. Fopossi1, R.N. Mutuku, F. Ngapgue, Effects Of Stabilizers On Water Absorption Of Compressed Earth Blocks Made From Mangu Soil, *International Journal of Engineering Sciences & Emerging Technologies* 7:1 (2014) 490-495.
- [25] J.E. Oti, J.M. Kinuthia, J. Bai, Engineering properties of unfired clay masonry bricks, *Engineering Geology* 107 (2009) 130-139.
- [26] A. S. Guimarães, V. P. de Freitas J.M.P.Q. Delgado, T. Rego, The Interface Effect in the Water Absorption in Ceramic Brick, *Energy Procedia* 78 (2015) 1395 – 1400.
- [27] B.Y. Pekmezci, R. Kafescioglu, E. Agahzadeh, Improved Performance Of Earth Structures By Lime And Gypsum Addition, *Journal of the Faculty of Architecture* 29:2 (2012) 205-221.
- [28] M. Kornmann, *Clay Bricks and Rooftiles, Manufacturing and Properties*; Lasim: Paris, (2007) 308.
- [29] L. Ajam, M.B. Ouzezdou, H.S. Felfoul, R.E. Mensi, Characterization of the Tunisian phosphogypsum and its valorization in clay bricks, *Construction and Building Materials* 23 (2009) 3240-3247.
- [30] C. Galán-Marín, C. Rivera-Gómez, F. Bradley, *Ultrasonic, Molecular and Mechanical Testing Diagnostics in Natural Fibre Reinforced, Polymer-Stabilized Earth Blocks*, 2013.
- [31] C.S. Shon, D. Saylak, D.G. Zollinger, Potential use of stockpiled circulating fluidized bed combustion ashes in manufacturing compressed earth bricks, *Construction and Building Materials* 23 (2009) 2062-2071.

Determination of fracture parameters of effective crack model by wedge-splitting test

A. Tevfik Bildik

Firat Univ., Engng. Faculty, Civil Engng. Dept.
Elazig/TURKEY

Ragip Ince

Firat Univ., Engng. Faculty, Civil Engng. Dept.
Elazig/TURKEY

Abstract—Although the cracked beams have been widely utilized in fracture mechanics of concrete, there have been some advantages of the cubical/cylindrical specimens such as compactness and lightness. In the present work, the wedge-split-tension tests on cubical specimens with different cement contents and water/cement ratios were initially performed for the effective crack model. Finally, some relationships based on regression between the fracture parameters and the strength properties of concrete were derived. The results of the split-tension cube tests look viable and very promising.

Keywords—concrete; effective crack model; wedge-splitting test

I. INTRODUCTION

Fracture mechanics applications of cement-based materials were initiated by Kaplan [1]. However, in 1970s, experimental investigations on concrete fracture revealed that Linear Elastic Fracture Mechanics (LEFM) has been no longer valid for cementitious materials such as rock and concrete [2]. Because of the existence of a relatively large process zone in front of and around the tip of the main notches and this inelastic zone is ignored by LEFM, it is inapplicable for concrete. Therefore, several deterministic fracture-mechanics approaches have been developed to describe fracture-dominated failure of concrete structures [3-8].

These models can be categorized as cohesive crack models [3, 4] and effective crack models [5-8]. LEFM uses a single fracture parameter such as the critical strain energy release rate, but these models need at least two experimentally determined fracture parameters to estimate failure of concrete/reinforced concrete structures.

The cracked beam tests have been widely utilized, because they were used in the first LEFM standard test for metals in order to estimate fracture parameters of quasi-brittle materials. Nevertheless, there are some important advantages of cubical/cylindrical specimens as follows [9-13]:

- 1) They are compact and lighter than notched beams. Therefore they are useful for investigating the size effect.
- 2) They can be easily cast at the construction site by using the same molds as for strength tests.
- 3) The self-weight of the specimens can be neglected in the computing of fracture parameters, contrary to cracked beams.

The tests on the cylinder and cube samples in fracture mechanics of concrete can be classified as split-tension tests and wedge-splitting tests. The wedge-splitting tests have been performed on the cylinder/cube specimens with an edge crack. The wedge-splitting tests are also useful for the effective crack models although they were initially developed for the cohesive crack fracture models [9].

In the present work, the wedge-splitting tests (WST) on cube specimens with different cement contents and water/cement ratios were initially performed for the effective crack fracture model (ECM). Finally, some relationships based on regression between the strength properties and the fracture parameters of concrete were determined.

II. EFFECTIVE CRACK MODEL (ECM)

The effective notch length a_e in the effective crack model for the fracture of cementitious materials recommended by Nallathambi and Karihaloo [6] is computed from the secant stiffness of the real concrete body at the maximum load. The main idea behind this approach may be emphasized with Figure 1, in which the load and deflection curve of the cracked three-point beam up to maximum load is indicated. When the secant stiffness of the real body is equal to tangent stiffness of the body, of which the notch length is a_e , the fracture toughness achieves its critical value K_{Ic}^e . Consequently, according to the effective crack model, the fracture of cement-based materials is defined by two-parameter: the critical fracture toughness K_{Ic}^e and the effective notch length a_e .

Though the effective notch length is computed from the load and displacement curves by trial and error approach in practice, it can also be calculated by the following regression formula:

$$\frac{a_e}{d} = \gamma_1 \left(\frac{\sigma_u}{E_c} \right)^{\gamma_2} \left(\frac{a_0}{d} \right)^{\gamma_3} \left(1 + \frac{d_{max}}{d} \right)^{\gamma_4} \quad (1)$$

in which a_0 is the initial notch length, d is the specimen depth, d_{max} is the maximum aggregate size, the nominal strength $\sigma_u = 6M_u / (bd^2)$, M_u is the maximum moment and $\gamma_1 = 0.088$, $\gamma_2 = -0.208$, $\gamma_3 = 0.451$ and $\gamma_4 = 1.653$. When elasticity modulus

of cement-based materials E_c is estimated from the separate experiments, these constants are $\gamma_1 = 0.198$, $\gamma_2 = -0.131$, $\gamma_3 = 0.394$ and $\gamma_4 = 0.600$ [14]. Nevertheless, elasticity modulus of cementitious materials in Eq. (1) may be determined according to the following expression [15]:

$$E_c = 4730 \sqrt{f'_c} \quad (2)$$

where f'_c is the cylindrical strength for concrete. E_c and f'_c in Eq. (2) are in [MPa]. The critical fracture toughness K_{Ic}^e according to the effective crack model may be determined from Eq. (3):

$$K_{Ic}^e = \sigma_u \sqrt{a_e} Y(\alpha_e = a_e/d) \quad (3)$$

in which α is the relative notch length (a/d) and $Y(\alpha)$ is the function of geometry for computing the fracture toughness of the notched three-point beam and may be obtained from any fracture mechanics handbook [16].

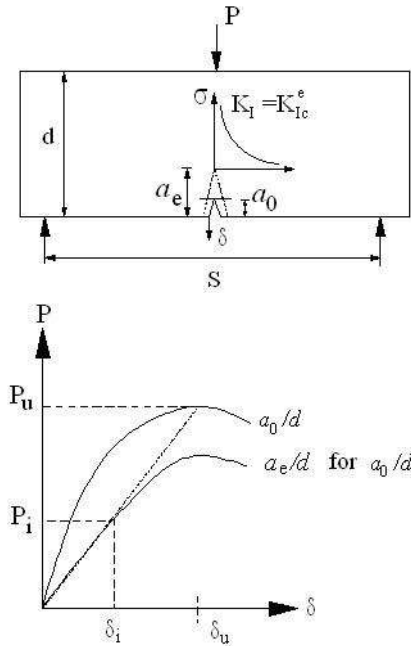


Fig. 1. Determination of fracture parameters of concrete according to ECM

III. WEDGE-SPLITTING TEST

Although notched-beam specimens have been widely used in concrete fracture mechanics, compact tension (CT) and wedge-splitting (WS) specimens have some advantages over beams, such as compactness and lightness (Fig. 2). CT specimens were initially used by Wittmann et al. [10] to determine the fracture energy and evaluate the strain-softening behavior of cement-based materials. Brühwiler and Wittmann [9] proposed a popular wedge-splitting test, which has been used in recent years in concrete fracture testing with test specimens.

A WS specimen can be considered a compact form of the three-point bending beam, as shown in Fig. 2b. WS specimens with grooves were developed for use as CT specimens, as shown in Fig. 2c. WS and CT testing can be conducted on both cylindrical and cubical specimens. The use of cylindrical test specimens, which may be obtained from existing concrete/reinforced concrete structures by coring, offers the great advantage of estimating the fracture properties of existing structures based on fracture mechanics. In WS testing, the load is applied to the specimen by means of a wedge and a loading device with roller bearings, as illustrated in Fig. 2d. The horizontal load P_H acts on the rollers because of the vertical load (P_V) on the wedge, as shown in Fig. 2e. Friction forces also occur between the rollers and the wedge. However, the friction forces can be ignored when the wedge angle $\theta=15^\circ$. The horizontal load can be calculated as follows:

$$P_H = \frac{P_V}{2 \tan \theta} \quad (4)$$

For CT and WS test samples, the fracture toughness can be computed as follows:

$$K_I = \frac{P_H}{bd} \sqrt{d} Y(\alpha) \quad (5)$$

where the dimensionless function $Y(\alpha)$ is given by the following equation [16]:

$$Y(\alpha) = \frac{(2 + \alpha)(0.886 + 4.64\alpha - 13.32\alpha^2 + 14.72\alpha^3 - 5.6\alpha^4)}{(1 - \alpha)^{3/2}} \quad (6)$$

The accuracy of Eq. (6) is $\pm 0.5\%$ for $\alpha > 0.2$.

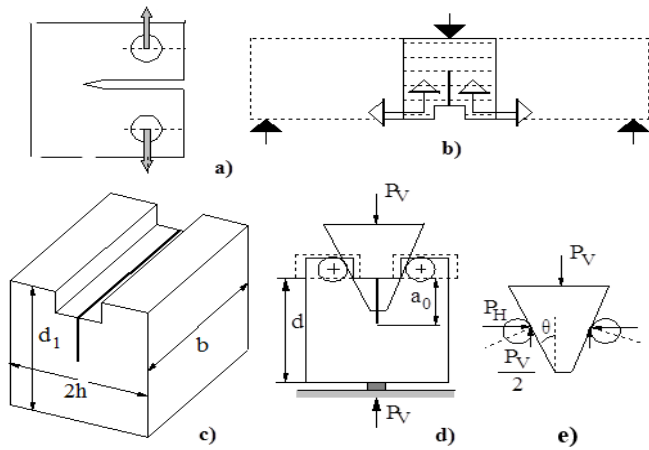


Fig. 2. Wedge-splitting test

a) Standard CT specimen b) WS specimen as "compact" three-point bending specimen [9] c) Specimen configuration d) Loading e) Wedge forces

IV. EXPERIMENTAL STUDIES

Cubical wedge-splitting (WS) specimens with 150 mm were used in this study (Figure 2). The maximum aggregate diameter of 16mm was used. The cement contents varied from 250 kg/m³ to 490 kg/m³ whereas the water-cement ratios (w/c) varied from 0.44 to 0.81. The batches were designed for two slump values=6±1 and 12±2 cm. Eight series specimens (48 cube specimens), namely A, B, C, D, E, F, G and H, were tested concerning the above variables in different combinations. The test specimens in each batches were cast from the same mix of concrete. The cracks were precast in all test samples. The test specimens in all series were of the same size, but they had different notch lengths for each specimen geometry. Table 1 summarizes the cement content, the initial crack length, a_0 , the concrete compressive strength, f'_c , and the ultimate vertical load, P_V , of the test specimens.

Three identical cube specimens with 150 mm were also cast from each mix of concrete in order to estimate the compressive strength of concrete. All test specimens and identical test cubes were removed from the mold after 1 day and then were cured at 20 °C in water until testing at 28-day. The compression tests and the split-tension tests were made by using a digital compression machine with a capacity of 100 kN. Typically, approximately 3 min (± 30 sec) elapsed before the peak load capacity for each test specimen was reached. Identical cubes were tested at an age similar to the other specimens.

V. ANALYSIS OF TEST RESULTS

In this study, WS specimens were analyzed according to ECM. For this, equations 1-6 were utilized. The nominal strength in Eq. (1) may be computed for WS specimens according to the principles of the classical strength of materials as follows:

$$\sigma_u = \frac{P_H}{bd} + \frac{6P_H d/2}{bd^2} = \frac{4P_H}{bd} \quad (7)$$

The computed fracture parameters of concrete based on ECM: the effective fracture toughness and the relative effective notch length values were also given in the last two columns in table 2. It is well known that there is a very strong correlation between f'_c and water-cement ratio. f'_c decreases with increasing w/c. The following formula by Abrams may utilized to stabilize the effects of the factors related to curing conditions, concrete age and cement properties, which directly influence the internal structure of cement-based materials:

$$f_c = \frac{K_1}{K_2^{w/c}} \quad (8)$$

where K_1 and K_2 are the empirical constant and the constants which depends on the cement properties, respectively [17]. These constants may be computed as $K_1=A$ and $K_2=e^{-C}$ from the regression based on exponential function performed on $Y=AX+C$ with $Y=f'_c$, $X=w/c$. Fig. 3 shows the two relationships $K_{Ic}^e - f'_c$ and $K_{Ic}^e - w/c$. The two empirical formulas were derived in this figure. The results indicate that K_{Ic}^e increases with increasing f'_c while K_{Ic}^e decreases with increasing w/c.

Tests have revealed that fracture parameters of cement-based materials are generally influenced by the four material parameters; namely compressive strength, aggregate type, maximum aggregate diameter and water/cement ratio (w/c) [11-13, 18-20]. It is noted that fracture parameters of concrete can also be affected by other material parameters such as cement type, aggregate/sand ratio, curing conditions and porosity etc. Therefore, these empirical formulas are approximate and they should only be utilized for preliminary design and for the bodies of low fracture sensitivity although their correlation coefficients are very high $r>0.900$.

TABLE 1. Experimental results and analysis results

Series-Slump	Cement kg/m ³	w/c	f'_c MPa	a_0 mm	P_v kN	K_{Ic}^e MPa \sqrt{m}	a_e/d
A-12	250	0.81	19.24	50	2.59	0.883	0.523
				50	2.71	0.914	0.520
				80	1.23	0.843	0.695
				80	1.21	0.836	0.696
				95	0.71	0.948	0.799
B-6	250	0.76	22.45	50	2.78	0.949	0.524
				50	2.93	0.988	0.520
				80	1.42	0.944	0.689
				80	1.36	0.922	0.692
				95	0.89	1.056	0.783
C-12	330	0.58	35.56	50	3.37	1.160	0.527
				50	3.65	1.234	0.521
				80	1.68	1.149	0.694
				80	1.68	1.149	0.694
				95	1.01	1.299	0.794
D-6	325	0.56	36.97	50	3.45	1.186	0.526
				50	3.35	1.159	0.528
				80	1.72	1.174	0.694
				80	1.71	1.171	0.694
				95	0.97	1.311	0.800
E-12	410	0.54	44.07	50	3.71	1.280	0.527
				50	3.71	1.280	0.527
				80	1.78	1.247	0.699
				80	1.63	1.193	0.707
				95	0.96	1.412	0.811
F-6	400	0.53	46.63	50	3.60	1.258	0.531
				50	3.64	1.269	0.531
				80	1.82	1.279	0.699
				80	1.83	1.282	0.699
				95	1.00	1.454	0.809
G-12	490	0.45	51.35	50	3.99	1.378	0.528
				50	4.18	1.428	0.524
				80	1.86	1.324	0.702
				80	1.78	1.295	0.706
				95	1.03	1.523	0.811
H-6	480	0.44	54.07	50	3.87	1.353	0.531
				50	4.11	1.418	0.527
				80	1.79	1.316	0.708
				80	1.93	1.366	0.701
				95	1.06	1.563	0.811
				95	0.95	1.550	0.823

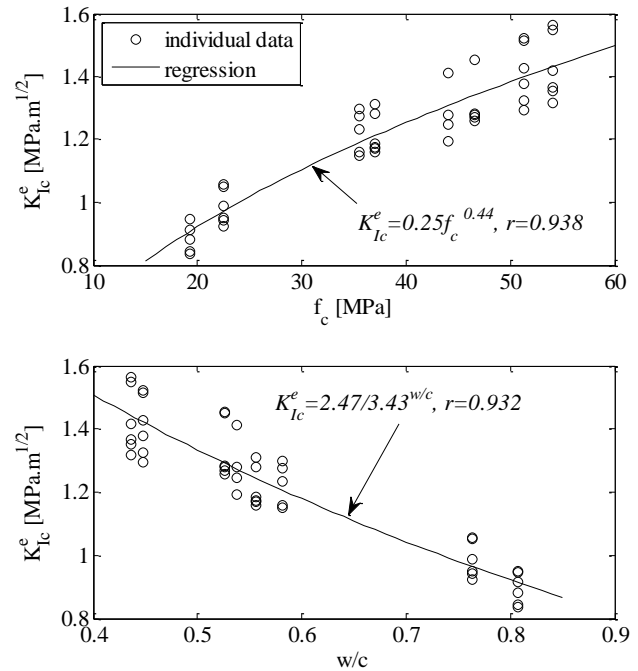


Fig. 3. Variation of K_{Ic}^e with f'_c and w/c

VI. CONCLUSIONS

In recent years, splitting specimens such as compact-tension, wedge-splitting and cylindrical/cubical splitting tension test specimens have been commonly preferred over beams for use in concrete fracture testing. Wedge-splitting test results were used for the first time in this study to determine the fracture parameters of cement-based materials via the effective crack model. The following conclusions should be drawn from the results of this study:

- 1) Notched compact tension specimens and beams have been used with the effective crack model. The results of this study indicate that the effective crack model can be successfully applied to wedge-splitting specimens.
- 2) Many structural laboratories do not have sophisticated testing equipment such as closed-loop testing systems and displacement-controlled testing machines. The effective crack model offers the great advantage of requiring measurement of only the maximum load applied to specimens to determine the values of the fracture parameters of concrete.
- 3) The fracture parameters of cementitious materials required for the effective crack model were investigated in this study. Nevertheless, the results obtained may easily be transformed to other fracture models, such as the size effect fracture model, the two-parameter model and the double-K model by the related LEFM formulas.

REFERENCES

- [1] M.F. Kaplan, "Crack propagation and the fracture of concrete", *ACI J.*, 58(11), 1961, pp. 591-610.
- [2] C.E. Kesler, D.J. Naus, and L.L. Lott, "Fracture mechanics-its applicability to concrete", *The Soc. of Mater. Sci.*, 4, 1972, pp. 113-124.
- [3] A. Hillerborg, M. Modeer and P.E. Petersson, "Analysis of crack formation and crack growth in concrete by means of fracture mechanics and finite elements", *Cem. Conc. Res.*, 6, 1976, pp. 773-782.
- [4] Z.P. Bazant and B.H. Oh, "Crack band theory for fracture concrete", *Mater. and Struct. (RILEM)*, 16(93), 1983, pp. 155-157.
- [5] Y.S. Jenq and S.P. Shah, "Two-parameter fracture model for concrete", *ASCE J. Engng. Mech.*, 111(10), 1985, pp. 1227-1241.
- [6] P. Nallathambi and B.L. Karihaloo, "Determination of the Specimen Size Independent Fracture Toughness of Plain Concrete", *Mag. Conc. Res.*, 38(135), 1986, pp. 67-76.
- [7] Z.P. Bazant and M.T. Kazemi, "Determination of fracture energy, process zone length, and brittleness number from size effect with application to rock and concrete", *Int. J. Fract.*, 44(2), 1990, pp. 111-131.
- [8] S. Xu and H.W. Reinhardt, "Determination of double-K criterion for crack propagation in quasi-brittle fracture, Part II: Analytical evaluating and practical measuring methods for three-point bending notched beams", *Int. J. of Fract.*, 98, 1999, pp. 151-177.
- [9] E. Brühwiler and F.H. Wittmann, "The wedge splitting test, a method of performing stable fracture tests", *Engng. Fract. Mech.*, 35, 1990, pp. 117-126.
- [10] F.H. Wittmann, K. Rokugo, E. Brühwiler, H. Mihashi and P. Simonin, "Fracture energy and strain softening of concrete as determined by means of compact tension specimens", *Mater. and Struct.*, 21, 1988, pp. 21-32.
- [11] R. Ince, "Determination of concrete fracture parameters based on two-parameter and size effect models using split-tension cubes", *Engng. Fract. Mech.*, 77, 2010, pp. 2233-2250.
- [12] R. Ince, "Determination of concrete fracture parameters based on peak-load method with diagonal split-tension cubes", *Engng. Fract. Mech.*, 82, 2012, pp. 100-114.
- [13] R. Ince, "Determination of the fracture parameters of the Double-K model using weight functions of split-tension specimens", *Engng. Fract. Mech.*, 96, 2012, pp. 416-432.
- [14] B.L. Karihaloo and P. Nallathambi, "An improved effective crack model for the determination of fracture toughness of concrete", *Cem. Conc. Res.*, 19, 1989, pp. 603-610.
- [15] ACI-318, "Building code requirements for structural concrete and commentary", Farmington Hills, Michigan, 2002.
- [16] H. Tada, P.C. Paris and G.R. Irwin, "The stress analysis of cracks handbook", ASME Press, 2000.
- [17] A. M. Neville AM, "Properties of concrete. Fourth Edition", Longman, London, 1995.
- [18] Z. P. Bazant and E. Becq-Giraudon, "Statistical prediction of fracture parameters of concrete and implications for choice of testing standard", *Cem. Conc. Res.* 32, 2002, pp. 529-556.
- [19] R. Ince, "Prediction of fracture parameters of concrete by artificial neural networks", *Engng. Fract. Mech.*, 71, 2004, pp. 2143-2159.
- [20] R. Ince, "Artificial neural network-based analysis of effective crack model in concrete fracture", *Fatigue. Fract. Engng. Mater. Struct.*, 33(9), 2010, pp. 595-606.

Influence of Elevated Temperatures on the Strength Properties of Lightweight Concrete Masonry Units Prepared With Pumice Aggregates

Lütfullah GÜNDÜZ

Department of Civil Engineering
İzmir Katip Çelebi University
İzmir, Turkey
lutfullah.gunduz@ikc.edu.tr

Şevket Onur KALKAN

Department of Civil Engineering
İzmir Katip Çelebi University
İzmir, Turkey
sevketonur.kalkan@ikc.edu.tr

Abstract—In this study, the lightweight concrete masonry units with pumice aggregates were analyzed to determine the compressive strengths and porosities at elevated temperatures ranging from 20 to 350°C. In order to produce the lightweight concrete mixtures for production of masonry wall units, the pumice aggregates were supplied from Nevşehir region in Turkey and they were crushed and screened into two grain sizes of 0-4mm (as fine pumice aggregate) and 4-8mm (as coarse pumice aggregate). To analyse the effects of elevated temperature on the strength properties of lightweight concrete masonry units, the range of different pumice aggregate/cement (A/C) ratios of 3.11, 3.17, 3.22 and 3.28 by weight and constant cement content of 210 kg/m³ were used to make up the pumice aggregate lightweight concrete (PALWC) mixture testing samples with the slump of 3 mm. To accomplish this purpose, cubic concrete specimens of 150x150x150mm were prepared. Also PALWC masonry units with 4 different mixture batches were cast into a mould with vibro-compacting, de-moulded immediately and transferred to a storage area for curing up to 360 days in normal air condition. PALWC masonry units were produced suitable according to BS 1881 and EN 771-3 specifications. The web and shell thickness of the unit were designed as 20 mm. Totally 21 cellular space with 14 mm in width were placed in the block design and the block dimensions are 190 mm in height, 390 mm in length and 190 in width as mostly used block dimensions in Turkey. After their production the block specimens were analysed at different elevated temperatures for 28 and 90 days. All measurements have been carried out after cooling of the material.

The experimental research findings showed that PALWC masonry units have the strength change comparable to normal weight concrete masonry units at different elevated temperatures. The experimental analyses showed that initial strength of the masonry samples reduced up to 100°C at 28 days of curing, whereas the reduction was continued up to 150°C at 90 days of curing. Beyond these temperatures, strength of the masonry samples all gradually increased. Although the initial strength value at 20°C for 90 days of curing was higher compared to the value of 28 days curing, strength of the masonry samples at 350°C for 28 days of curing was higher than that of 90 days curing. Porosity of the masonry samples were also affected by the temperature changes. Consequently, it seems to be that for

the high temperatures, age of the concrete influence the initial strength reduction.

Keywords—pumice; lightweight masonry; temperature dependency; compressive strength; porosity

I. INTRODUCTION

The success of designing lightweight aggregated building elements for a required fire endurance depends on how accurately certain properties of the component materials are known in the 0 to 1200°C temperature range. Lightweight concrete masonry unit is among the most commonly used building materials and deserves priority in a program intended to develop the knowledge of the behavior of building materials at elevated temperatures. Some research results and discussions are available in literature on some thermal and mechanical properties of hydrated Portland cement and lightweight concretes. However, there is very limited information for lightweight concrete masonry units at elevated temperatures. When considering building in fire occurrence and processes, the behavior of the lightweight concrete units at elevated temperatures is an issue that should be examined in detail. In addition, the role of porous aggregate type and its production utilization rate by the temperature effect are another important issue to understand the structural and mechanical changes in concrete masonry units.

Pumice displays as an ideal aggregate for its light and insulate character caused by the porous structure. It is used in lightweight building elements, prefabricate building components, roofing, lightweight mortar and plaster production, as roof and floor isolation filler and in lightweight concrete production in building trade. Accept all of these; its usage in these areas is well known as wide spread. The lightweight concrete; derived from appropriate pumice aggregate that is produced with appropriate granulometric components can be used in different production forms according to their strength values in industrial areas. The lightweight concrete can be produced in bearing, semi-load bearing and non-load bearing forms.

Temperature is a key variable affecting the curing of cement-based materials because it influences both the early hydration kinetics and the properties of the hardened cement paste or concrete. Although concrete initially gains strength more rapidly when cured at elevated temperatures, the final strength is lower and the permeability is higher. Elevated temperatures also reduce the tendency for irreversible creep and shrinkage [1]. Most of these effects have been related to the increased rate of silicate polymerization at elevated temperatures [2, 3, 4], which densifies and stiffens the C-S-H as it forms.

The behavior of concrete subjected to high temperatures is a result of many factors [5, 6]; such as heating rate, peak temperatures, dehydration of C-S-H gel, phase transformations, and thermal incompatibility between aggregates and cement paste. On the other hand, quality control of concrete, by means of non-destructive methods, in structures subjected to fire or not so high temperature exposure conditions, is not particularly easy to be carried out. The correlation already exists usually refers to the hydration age of 28 days [7]. Many investigations have been carried out on the residual mechanical properties of normal weight concrete with using lightweight aggregates subjected to elevated temperatures, but limited data on the deterioration of durability of masonry units produced by pumice lightweight aggregate concrete are available in the past researches. Limited conclusions only, therefore, have been drawn for lightweight concrete masonry units, where damage is not only due to a combination of chemical and mechanical changes to the constituents of concrete, but is greatly influenced by factors such as the properties of lightweight concrete itself, fines aggregate ratio of the mixture, and the curing conditions.

Neville [8] has reported that after exposure to 600°C heat affects much more less strength loss in lightweight concrete compared to normal weight concrete. No more experimental study has been experienced in literature related to strength properties of pumice derived lightweight concrete after heat exposure. Usually, there is literature data about high strength concretes derived from different aggregate species. In these studies, the mechanical properties of concrete exposed to 200 °C and higher have been evaluated. Altun [9] has performed a study which evaluates the mechanical changes under heat effect of the low cement ratio aggregate derived concrete. Xu et. all. [10] has examined the effects of the concrete under high heat derived from fly ash. Mahdy et. all. [11] evaluated the effect of high temperatures on the weight and strength of high strength concrete. Cülfik and Özturan [12] have also evaluated the effect of high temperatures on the mechanical properties of high strength mortar. In all of these experimental studies, the heat effect on concrete and mortar which is derived from different aggregate and addition agent species was evaluated and different results have been achieved. For example; Cülfik and Özturan [12], pointed out that the graphite dust addition to concrete mixture has increased the high temperature resistance. Xu et. all. [10] observed that generally strength is declined as the temperature inclines. But controversially they reported strength incremental at 250°C derives. This strength increase is

probably related to strengthening of cement paste caused by drying.

The scope of this work is to provide experimental data on the residual compressive strength properties of lightweight concrete masonry units subject to curing conditions at different elevated temperatures. These properties are very important for the safe design of lightweight aggregate concrete masonry units and in the repair of masonry structures.

II. EXPERIMENTAL STUDY

A. Purpose of Assessment

The purpose of this research is to examine the influence of elevated temperatures on the strength properties of new generation design lightweight concrete masonry units prepared with special reference to Nevşehir pumice aggregates. The research basically was focused to evaluate the effects of elevated temperatures on strength – porosity relationship for the masonry units for non-load bearing conditions. No admixtures or additions apart from pumice fine and coarse aggregates, powder calcite, cement and water were used in the mixtures.

B. Materials Used in the Research

In order to analyse the lightweight concrete masonry units, general block dimensions mostly used in Turkey was used as a model block with 190 mm in height, 390 mm in length and 190 mm in width throughout the experimental work. The web and shell thickness of the unit were designed as 20 mm. Totally 21 cellular space with 14 mm in width were placed in the block design. The model of masonry unit is represented in Fig. 1.

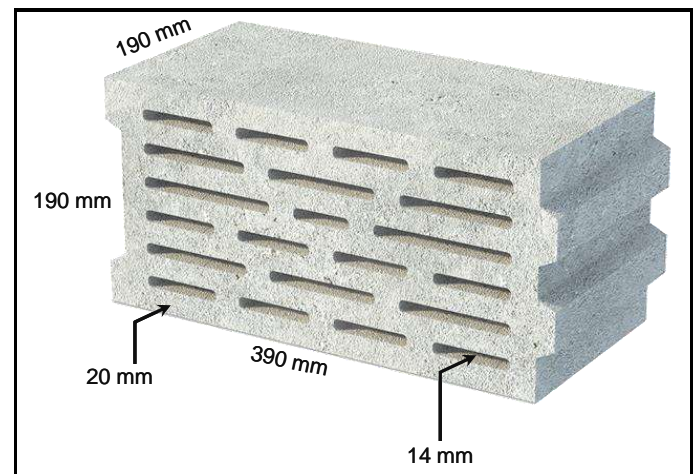


Fig. 1. The model of masonry unit.

The pumice aggregate samples were taken from the quarry in Nevşehir region, Turkey. The pumice aggregate samples were first crushed by a primer crusher and then they were screened into two different sizes of 0-4 mm as fine pumice aggregate (FPA) and 4-8 mm as coarse pumice aggregate (CPA) to produce pumice aggregate lightweight concrete (PALWC) with different mixture proportions. These size fractions are commercially used in pumice aggregate masonry block productions in Turkey [13]. The physical properties of pumice aggregate are given in Table 1. Pumice is not a trade name but a type of glassy volcanic rock originating from lava of strictly determined chemical composition. The chemical contents of the pumice aggregates are given in Table 2. Pumice is a well known lightweight concrete aggregate, although its use has mainly been restricted to dry mixes such as for block making and masonry use. There are both advantages and drawbacks connected with the material as an aggregate [14, 15, 16]. Dry bulk density and water absorption of the pumice aggregate samples, as received from the quarry, were determined as 920 ± 30 kg/m³ and $28 \pm 5\%$, respectively. The compressive strength of the pumice aggregate is about to 15.7 ± 1.5 MPa in accordance with DIN 1604.

TABLE I. PHYSICAL PROPERTIES OF THE PUMICE AGGREGATE

Properties	FPA	CPA
Colour	Light Grey	Light Grey
MOHS Hardness	5 - 5.5	5 - 5.5
pH	5	5
Specific Gravity, gr/cm ³	2.24	2.24
Dry Bulk Density, kg/m ³	875	690
Water Absorption, %	29	34
Detrimental Material Analysis	Inert	Inert
Sulphur Analysis, %	0.29	0.31
Structural Spoiling,	846	828
Melting Point, °C	1210	1210

TABLE II. CHEMICAL COMPOSITION OF CEMENT AND PUMICE AGGREGATES

Chemical Content	OPC (%)	FPA or CPA (%)	PCF (%)
SiO ₂	20.65	70.50	0.05
Al ₂ O ₃	5.60	13.00	0.10
Fe ₂ O ₃	4.13	1.20	0.04
CaO	61.87	1.35	55.20
Na ₂ O	0.14	3.75	0.03
K ₂ O	0.83	4.55	0.02
MgO	2.60	0.20	0.55
LOI	1.39	5.25	-
Bogue composition			
C ₃ S	41.67	-	-
C ₂ S	29.07	-	-
C ₃ A	8.77	-	-
C ₄ AF	11.39	-	-

Ordinary Portland Cement (OPC) conforming to ASTM C 150 Type 1 (42.5 N/mm²) was used for this study. The chemical composition of the cement is given in Table 2. The Bogue compound composition of the cement was calculated according to ASTM C 150 [17] and is also given Table 2. The cement was tested for its mineral content and the loss on ignition using the X-ray Fluorescence (XRF) analysis. The average particle size distribution was determined by laser particle analyzer. The specific gravity of cement was determined according to the British Standard (BS 1377:Part 2) using the small pycnometer method. The fineness of the cement was determined by conducting the Blaine surface area test according to ASTM C 204-94a and given in Table 3. The mechanical and physical properties of the cement used in this research are given in Table 3.

TABLE III. MECHANICAL AND PHYSICAL PROPERTIES OF THE CEMENT

Specific gravity (g/cm ³)	3.12
Blaine specific surface (cm ² /g)	3254
Initial setting time (min)	146
Final setting time (min)	198
Volume expansion (mm/m)	2.87
Compressive strength (MPa)	
2 days	14.8
7 days	27.4
14 days	35.3
28 days	43.4

The calcite used in the composition of mixture combinations was also a commercial product in Turkey. The calcite used in this experimental program was a white powder form obtained by grinding from calcite minerals. The calcite material was as a powder calcite filler (PCF) material in mixture combinations. Its maximum particle size was 750 µm and its bulk dry density value was also 1240 kg/m³. The chemical composition of PCF is given in Table 2.

Mixing water was general drinking water liquid.

C. Mixture and Manufacturing of Samples

The test specimens for the whole experimental program made from the lightweight concrete mixture compositions are given in Table 4.

TABLE IV. MIX DESIGN OF LIGHTWEIGHT CONCRETES

Mixture	OPC (kg/m ³)	FPA (kg/m ³)	CPA (kg/m ³)	PCF (kg/m ³)	Water (kg/m ³)	Aggregate/Cement Ratio	Fines Ratio by weight (%)	W/C
M1	210	147	343	164	147	3.11	30	0.70
M2	210	200	300	164	147	3.17	40	0.70
M3	210	256	256	164	147	3.22	50	0.70
M4	210	315	210	164	147	3.28	60	0.70

In order to analyze the effects of low elevated temperatures on the compressive strength of pumice aggregate lightweight concrete masonry units, four mixture batches (M1, M2, M3 and M4) were cast in different fine and coarse pumice aggregate ratios as 30%, 40%, 50% and 60% by weight of the total pumice aggregate amount, respectively. Each mixture batch consists of the constant cement content of 210 kg/m³. The water/cement (W/C) ratio of all mixture batches was used as constant in value of 0.70, too. The pumice aggregates were soaked in water for 30 minutes prior to mixing so as to allow them to absorb the water which they would have absorbed in the mixing phase. Therefore the water used during mixing was only the reaction water. It has shown that to give the best results as to resistance and workability characteristics.

BS 1881: Part 125 [18] was used for mixing and sampling the fresh concrete in laboratory and BS 1881: Part 114 [19] was used for measuring the density of hardened concrete. According to the preliminary trial batch results, the fines content for optimum plastic properties in the concrete was determined. After completing the trial experiments, the final mixture compositions for the concrete work were determined. Cube samples of 150x150x150 mm were used for the preliminary trials in testing the mixture strengths and the effectiveness of fines content. For each mixture, twelve samples were cast. After casting the samples, they were cured in a special condition as illustrated in [20]. The concrete specimens were first covered with polyethylene foil which restrained the leakage of excessive water from the surface bed of the test bodies. Then, approximately 10 h after the manufacturing ended, the samples, including the forms, were covered the polyethylene foil.

A cellular hollow block form suitable with the specifications of BS 6073: Part 1 [21] standard was used for preparation of PALWC masonry samples. The ratio of solid area and solid volume of the block form are the same values of 68.7% due to being open sub-section of the block. The web and shell thickness of the block are 20 mm and the block dimensions are 190 mm in height, 390 mm in length and 190 mm in width. For each mixture, 24 block samples were cast and compacted on a vibration machine. Block samples were then air cured in laboratory conditions up to 28 days and there after until the time of testing. After curing, the samples were analyzed in air dry condition for compressive strength testing in accordance with BS 6073: Part 1 [21].

D. Heat Treatment of Specimens and Test of Strength and Porosity Properties

Heat treatment of the concrete samples was carried out as similar testing schedule stated in [20]. The cube and the masonry samples of PALWC were analyzed at the age of 7, 14, 28, 90, 120, 150, 200 and 360 days with 20°C curing condition, respectively. However, the masonry samples were only tested at elevated temperatures at the age of 28 and 90 days, respectively. They were exposed to stabilize the heating 1oC per minute. The specimens then remain at the chosen elevated temperatures approximately 180 minute and after that they were cooled down in a controlled way to the room temperature during 24 h. Actually this duration of exposure at elevated temperatures was determined with the experiments of specific heat capacity of PALWC samples in laboratory trials during this research. It was observed that the concrete samples are heated uniformly and the required stable temperature is reached within the whole testing sample volume with sufficient accuracy. A similar characteristic phenomenon was also stated by [20]. Testing activities have been followed on unsealed concrete samples which were continuously heated up to temperatures 20, 80, 100, 150, 180, 200, 250, 300 and 350°C.

After curing at elevated temperatures, the samples as fully cooled condition were tested for compressive strength in accordance with BS 1881: P116. Determination of porosity is, in fact a quite complex problem. Pore structure of concrete consists of several types of pores: gel micropores (of characteristic sizes 0.5-10 nm), capillary mesopores (10-5000 nm) and macropores [20]. Although the influence of the gel pore distribution (via overall porosity of concrete) may be neglected in S(P) relationship, to measure the remaining pore system through mercury porosimetry means that the maximal pressure has to be sufficient to cause intrusion of Hg into the smallest capillary pores; otherwise rather apparent porosity is determined [22]. In our case, porosity of hardened cement paste of lightweight concrete was determined using the Vacuum Saturation Apparatus. Basic measurement aspects of the apparatus were defined by Cabrera and Lynsdale [23, 24]. Porosity measurements were conducted on slices of 68 mm diameter cores that were drilled out of the centre of a 150 mm cube samples. The slices were dried at 105± 5°C until constant weight had been achieved and were then placed in a desiccator under vacuum for at least 4 h, where after the desiccator was filled with de-aired, distilled water. This is the reason why it was impossible to determine porosity exactly at room

temperature. This means that corresponding to the case without heat pretreatment of the sample [20]. The porosity of the tested samples is the sum of the entrained air voids and the voids within the paste.

III. RESULTS AND DISCUSSION

As a first trial work, the change of strength for PALWC masonry unit samples at 20°C curing condition (representing the room temperature) was examined depending on the curing age. The tests for this trial were conducted up to 360 days after casting the masonry unit samples. Fresh and hardened average densities of PALWC mixture and the compressive strength of the masonry samples at 28 days and 90 days curing are given in Table 5. The strength characteristics of PALWC masonry samples in relation to the curing time at 20°C room temperature were presented in Fig. 2.

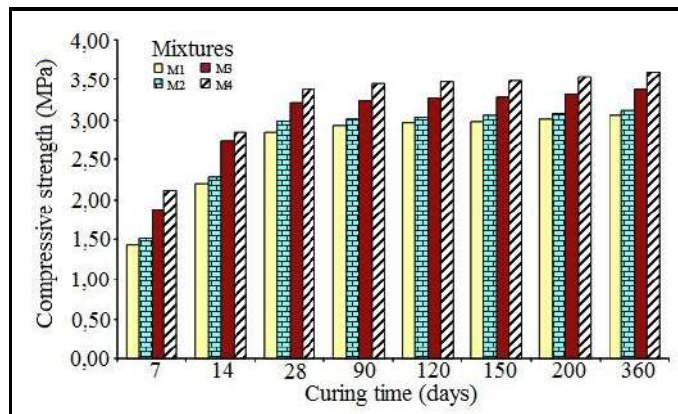


Fig. 2. Effect of curing time on compressive strength of PALWC cube samples.

It was experienced from the trial results as expected that the strength of all the mixtures increased with curing time. The effects of fines ratio of the mixture on the strength development were further studied in beginning of this research. In generally, it is assumed that fines ratio of the concrete increases the compressive strength.

According to compressive strength results of the trial mixtures, the last hydration duration was estimated as 90 days of curing for the concretes because strength of the concrete remained acceptably stable over 90 days of curing time. Therefore, it was decided that the research work to analyze the effects of elevated temperatures on the compressive strength of the concretes was followed at 28 days and 90 days curing time. Dependence of compressive strength on heating temperature is presented in Figs. 3 to 6 for 30%, 40%, 50% and 60% fines ratios for PALWC masonry unit samples, respectively.

TABLE V. TEST RESULTS OF PALWC MASONRY UNIT SAMPLES.

	Fresh Density of Concrete (kg/m ³)	Dry Density of Hardened Concrete (kg/m ³)	Compressive strength of masonry samples after 28 days (MPa)	Compressive strength of masonry samples after 90 days (MPa)	Oven Dry unit weight of masonry samples (kg)
M1	1212	1049	2.84	2.92	10.15
M2	1226	1062	2.98	3.01	10.28
M3	1240	1077	3.21	3.24	10.42
M4	1255	1092	3.37	3.45	10.56

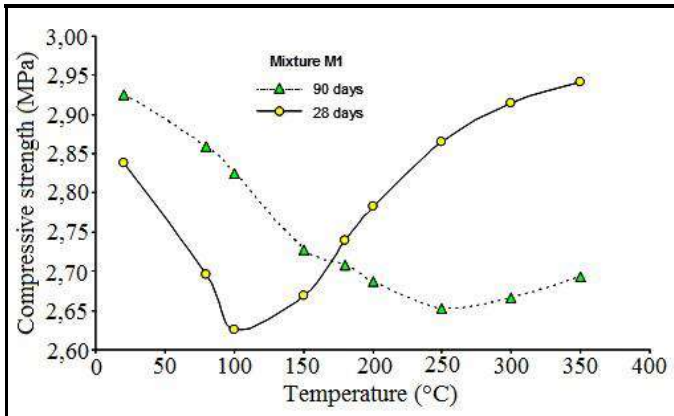


Fig. 3. Effect of temperature on compressive strength of PALWC masonry unit (30% fines ratio).

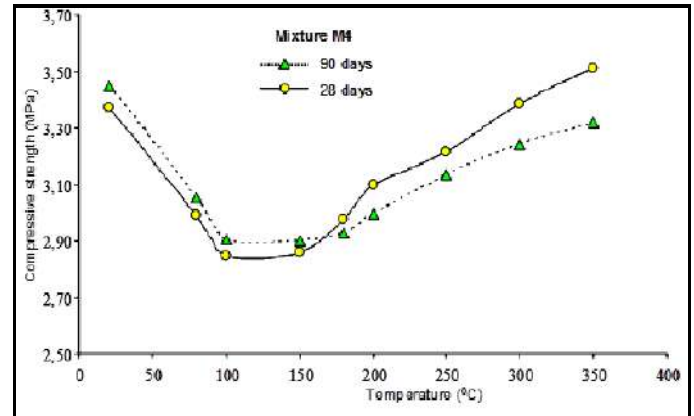


Fig. 6. Effect of temperature on compressive strength of PALWC masonry unit (60% fines ratio).

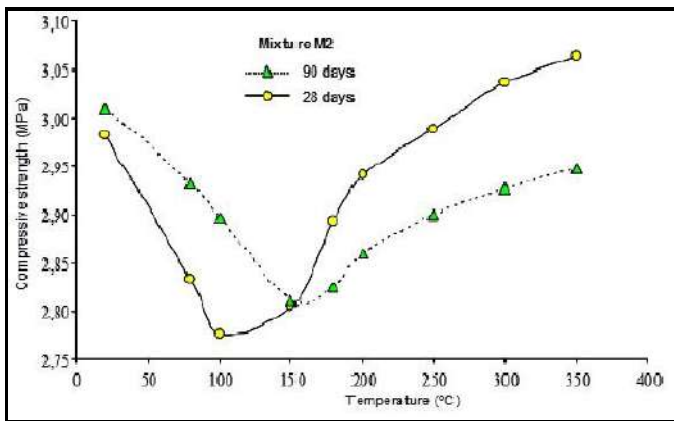


Fig. 4. Effect of temperature on compressive strength of PALWC masonry unit (40% fines ratio).

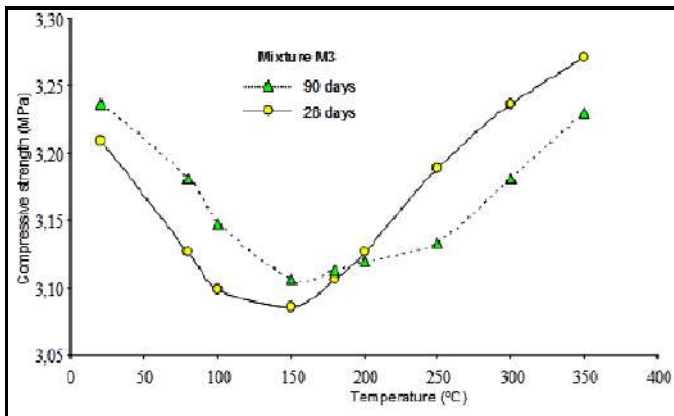


Fig. 5. Effect of temperature on compressive strength of PALWC masonry unit (50% fines ratio).

The research showed that there is a reduction in the tendency to strength up to 100°C and an increase in the tendency to strength after 100°C elevated temperatures at 28 days of curing. However, this strength tendency was different at 90 days of curing. The strength tends to decrease up to 150°C and tends to increase after 150°C elevated temperatures at 90 days of curing for PALWC masonry units. These temperature values were accepted in this study as “turning point of strength for elevated temperature” depending on the cure time. The strength value of 28 days curing time at 20°C temperature for PALWC masonry units was evaluated as initial strength of the tested masonry units throughout the research. Effect of elevated temperature on the strength was also variable with the fines ratio of masonry mixture combinations. Increase of fines ratio relatively defers the strength change based on progressive elevated temperatures.

Furthermore, the ratio of strength value after cooling of the masonry sample and its original value before heat pretreatment is generally referred to be “residual strength ratio” [20]. In this research, the residual compressive strength after heating at different temperatures T was expressed as a ratio f_T/f_{20} , where f_T is the strength after heating at $T^\circ\text{C}$ and f_{20} is the initial strength of concrete at 20°C [7, 25]. The strength ratio f_T/f_{20} as a function of PALWC masonry samples versus temperature T is represented in Figs. 7 and 8 for the mixtures.

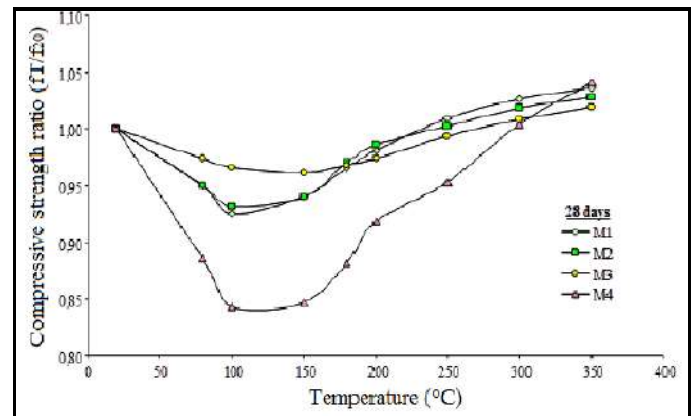


Fig. 7. Residual compressive strength of PALWC masonry unit (at 28 days).

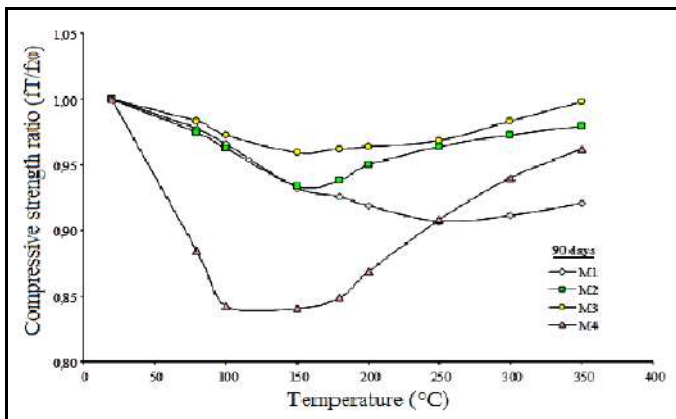


Fig. 8. Residual compressive strength of PALWC masonry unit (at 90 days).

The initial strength was acutely varied depending on the fines ratio and curing time. PALWC masonry samples with 30% fines ratio had a reduction in strength of 7.40% at 28 days curing up to 100°C and of 3.42% at 90 days curing up to 150°C, while the respective reduction for the masonry samples with 40% fines ratio was 6.71% and 3.65% at 28 days and 90 days curing times, respectively. The change of initial strength of the masonry samples for 50% and 60% fines ratio was a convergent value comparing both these two concrete mixtures: 3.43% and 15.7% at 28 days and 2.78% and 15.6% at 90 days curing times, respectively. It can be stated that another important factor influencing the initial strength loss up to turning points of strength for elevated temperature was the curing time. As evaluating the above mentioned strength values; the change of initial strength was lower at 90 days of curing than at 28 days of curing. These results are very similar to those published by Vodak et. al. [20].

Several physical phenomena occurred in the temperature range between 100°C and 350°C. At these temperatures interval, it was observed that all masonry samples begin again to gain the strength beyond the turning point of strength for elevated temperature. These strength gains were ranged from 11.8%, 10.10%, 5.48% and 23.60% with 30% to 60% fines ratio at 28 days curing, respectively. Similar strength increasing trend was also depicted at 90 days curing. Therefore, it was observed that increasing the fines ratio of the concrete mixture become evident the strength changes. Upper limit of the strength change in the masonries was ranged from 23.6% to 14.5% at 28 and 90 days curing for 60% fines ratio mixtures, respectively. However, increasing age of the concrete showed not the same condition as dictated with 28 days of curing. The initial strength was only slightly altered depending on low fines ratio. The research showed that the change of initial strength of the concrete increased at 28 days of curing time with the increase of fine pumice aggregate and it decreased at 90 days of curing. Therefore, up to 350°C, the best performance was accepted by 40% fines ratio to concrete at 28 days of curing.

Changes of porosity with temperature of heating are depicted in Figs. 9 and 12 for 30%, 40%, 50% and 60% fines ratios for PALWC masonry unit samples, respectively. Every point of all these curves corresponds to the statistically averaged value obtained from 5 to 8 measurements.

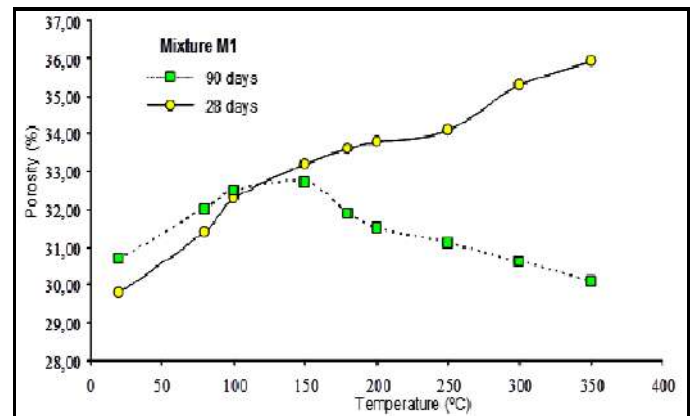


Fig. 9. Effect of temperature on porosity of PALWC masonry unit (30% fines ratio).

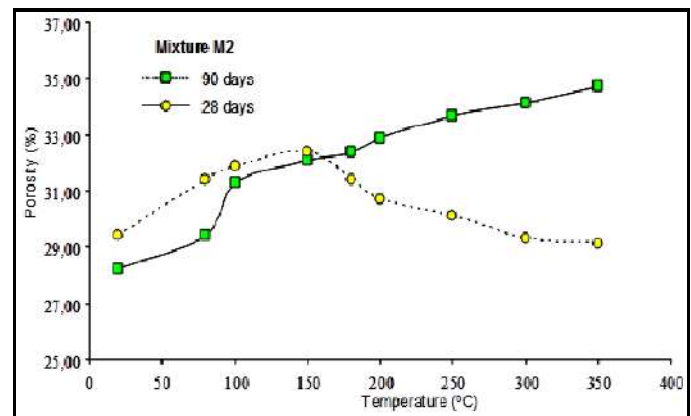


Fig. 10. Effect of temperature on porosity of PALWC masonry unit (40% fines ratio).

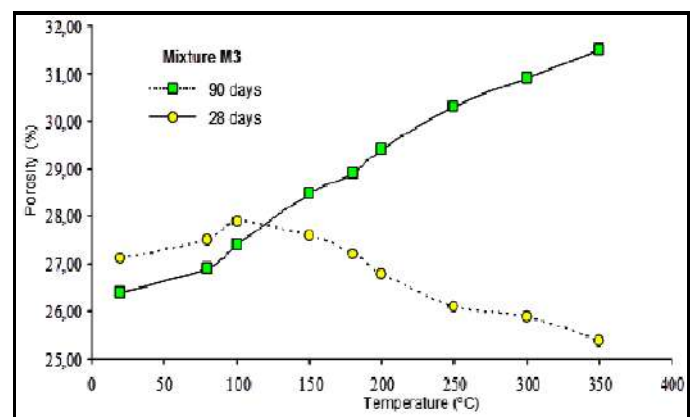


Fig. 11. Effect of temperature on porosity of PALWC masonry unit (50% fines ratio).

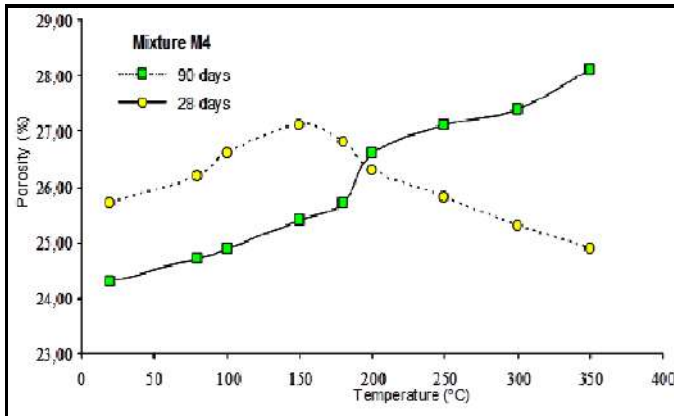


Fig. 12. Effect of temperature on porosity of PALWC masonry unit (60% fines ratio).

The lightweight aggregate concrete includes capillary water, physically absorbed water and interlayer and chemically bound water in C-S-H and Ca(OH)_2 . During heating the cement paste dried and water was free to be driven out. The strength reduction was evaluated as due to the stresses generated at the interface between the aggregate and hardened cement paste on heating. Mahdy et. al. [26] also stated the similar conclusions that the difference between the thermal expansion for the cement paste and aggregate can result in microcracking and disruption of the cement-aggregate bond with consequent reduction strength. Kaplan et. al. [27] investigated the changes of concrete structural properties at elevated temperatures. They demonstrated that changes in physical properties of unsealed specimens exposed to low temperatures of 70, 100 and 150°C were greater than those sealed specimens exposed to higher temperatures of 250 and 400°C. They also found that changes in concrete properties were mainly related to loss of water from the cement gel and the capillary pores in cement paste.

The water in the form of steam is eliminated most intensively and affects the surrounding phases of cement paste. Mainly due to the flow resistance and high temperature, steam creates a high pressure in the paste [7]. An increase of hydration products in concrete leads to the increase of its strength [28]. This effect originates probably from by larger mobility of water molecules in gaseous phase (as compared with their mobility in liquids) for temperatures ranging from 100 to 300°C [20]. In consequence, so-called steam curing or internal autoclaving causes similar behavior of concrete as certain curing treatments and it appears in the cement paste. This process results an additional hydration of anhydrous cement grains.

During hydration, a system of capillary pores is formed in the cement paste. The radii of these pores are smaller than the pores of pumice aggregates. Due to hydration and drying, a humidity gradient develops as soon as relative humidity decreases [29]. The capillary forces of the cement paste are high enough to absorb the water from the lightweight aggregate grain and transport it to the dryer cement paste where a reaction with the anhydrous cement takes place, forming Ca(OH)_2 .

After reaction of Ca(OH)_2 new hydration products of types calcium silicate hydrate (C-S-H) are built [30]. They grow in the pores of the cement paste, in available space and into the microcracks thus causing them to get smaller. The capillary suction, which is the inverse to the square of the pore radius, increases as the radius becomes smaller and thus enabling the pores to continue to absorb water from the lightweight aggregate. This continues until all the water from the lightweight aggregate has been transported to the cement paste [29]. This is actually a time dependent transport of at the begin water and in the end vapour with higher rate in the early age of concrete and lower at later age. The research showed that hydration process for PALWC mixtures dominantly increased especially at the age of 28 days curing due to intensifying hydration with elevated temperatures between 100 and 350°C. This process was continued with relatively large volume of unhydrated cement. Due to water evaporation beyond 100°C the gradient increased and the higher strength values were obtained at 28 days of curing. However, although the initial strength values were higher at 90 days of curing than at 28 days curing time, strength values of the masonry units beyond 100°C elevated temperatures were all lower at 90 days of curing due to practically terminating the hydration process. In this respect as a hypothesis stated by [20], the major role is played by microcracking. This effect is illustrated by experimental study in Fig. 13 as the changes of pores size distribution. Additional very low hydration is caused mostly by water molecules of relatively high kinetic energies released at temperatures above 250°C. Similar act was also declared by [20]. This event leads to increasing of the strength and decreasing of porosity.

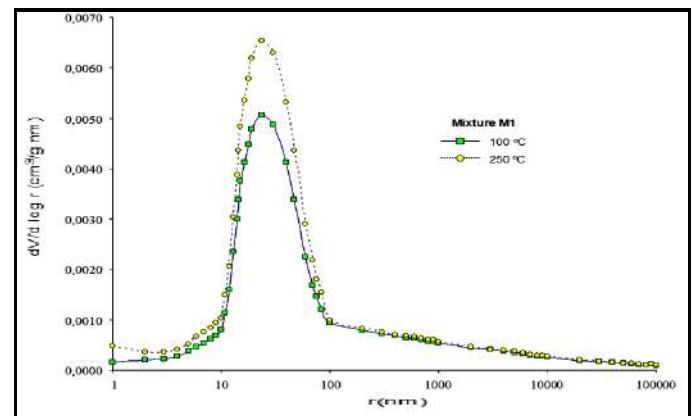


Fig. 13. Effect of temperature on pore size distribution of PALWC concrete at 90 days curing.

In experiments on the compressive strength evaluation, it was also observed that pumice aggregate lightweight concretes with improved strength, enhanced degree of hydration, and reduced autogenous shrinkage could be obtained by addition of fine saturated pumice aggregates up to 40% fines ratio in the mixture.

Actually, it should be emphasized that this research work was carried out for one particular concrete mixture with using constant w/c ratio of 0.7 and cement dosage of 210 kg/m³. This

study is still an ongoing work with the different w/c ratios and cement dosages. Furthermore, the type of lightweight aggregate and the characteristic of pumice aggregates are also investigated in these experimental studies to determine their effects on the compressive strength of masonry concrete mixtures at elevated temperature curing.

REFERENCES

- [1] J.J. Thomas, D. Rothstein, H.M. Jennings, B.J. Christensen, Effect of hydration temperature on the solubility behavior of Ca-, S-, Al-, and Si-bearing solid phases in Portland cement pastes, *Cement and Concrete Research* 33 (2003) 2037-2047.
- [2] A. Bentur, R.L. Berger, J.H. Kung, N.B. Milestone, J.F. Young, Structural properties of calcium silicate pastes: Part II Effect of curing temperature, *J. Am. Ceram. Soc.* 62 (1979) 362-366.
- [3] J. Hirljac, Z.Q. Wu, J.F. Young, Silicate polymerization during the hydration of alite, *Cement and Concrete Research* 13 (1983) 877-886.
- [4] S.U. Al-Dulaijan, G. Parry-Jones, A.H.J. Al-Tayyib, A.I. Al-Mana ²⁹Si magic-angle-spinning nuclear magnetic resonance study of hydrated cement paste and mortar, *J. Am. Ceram. Soc.* 73 (1990) 736-739.
- [5] J. Piasta, Z. Sawicz, L. Rudzinski, Changes in structure of hardened cement paste due to high temperature. *Mater Construct* 1984;17100:291-6.
- [6] Y.N. Chan, G.F. Peng, M. Anson, Residual strength and pore structure of high strength concrete and normal strength concrete after exposure to high temperatures, *Cement and Concrete Composites* 1999;21:23-7.
- [7] A. Savva, P. Manita, K.K. Sideris, Influence of elevated temperatures on the mechanical properties of blended cement concretes prepared with limestone and siliceous aggregates, *Cement & Concrete Composites* 27 (2005), 239-248.
- [8] Neville, A., M., 1997. *Properties of Concrete*, Fourth Edition
- [9] Altun, İ. A., 2001. Effect of temperature on the mechanical properties of self-flowing low cement refractory concrete. *Cement and Concrete Research*. 31 (8), 1233-1237.
- [10] Xu, Y., Wong, Y. L., Poon, C. S., Anson, M., 2001. Impact of temperature on PFA concrete. *Cement and Concrete Research*. 31 (7), 1065-1073.
- [11] Mahdy, M., Speare, P. R. S., Abdel-Reheem, A. H., 2002. Effect of transient high temperature on heavyweight, high strength concrete. 15th ASCE Engineering Mechanics Conference. Columbia University, New York.
- [12] Cülfik, M. S., Özturan T., 2002. Effect of elevated temperatures on the residual mechanical properties of high-performance mortar. *Cement and Concrete Research*, 32 (5), 809-816.
- [13] L. Gündüz. A technical report on lightweight aggregate masonry block manufacturing in Turkey, Suleyman Demirel University, Isparta, Turkey, 2005, pp 1-110.
- [14] H.Ásgeirsson. Létsteypur ur vikri (Lightweight pumice concrete), IBRI, 1984.
- [15] S. Thorarinnsson, Hekla, Almenna bókafélagið, Reykjavík, 1979.
- [16] O. Berge, Lätt isolerande konstruktionsbeton med isländsk pimpsten som ballast, Västra Frölunda, nov.1983.
- [17] ASTM C 150 Standard specification for Portland cement, in: *Annual Book of ASTM Standards*, Vol.04.01, American Society for Testing and Materials (ASTM) Philadelphia, 1993.
- [18] BS 1881: Part 125, Testing concrete. Methods for mixing and sampling fresh concrete in the laboratory, 1986, UK.
- [19] BS 1881: Part 114, Testing concrete. Methods for determination of density of hardened concrete, 1983, UK.
- [20] F. Vodak, K. Trtik, O. Kapickova, S. Hoskova, P. Demo, The effect of temperature on strength – porosity relationship for concrete, *Construction and Building Materials* 18 (2004), 529-534.
- [21] BS 6073: Part 1, Precast concrete masonry units. Specification for precast concrete masonry units, 1981, UK.
- [22] Diamond S. Mercury porosimetry; an inappropriate method for the measurement of pore size distribution in cement-based materials. *Cement and Concrete Research*, 2000; 30; 1517 – 25.
- [23] J.G. Cabrera, C.J. Lynsdale, A new gas permeameter for measuring the permeability of mortar and concrete, *Mag. Concr. Res.* 40 (144) (1988) 177 ± 182.
- [24] B.A. Gaafar, The effect of environmental curing conditions on the gas and water permeability of concrete, PhD Thesis, Dept. Civil Eng. University Leeds, UK, 1995.
- [25] Bazant ZP, Kaplan MF, *Concrete at high temperatures*. Essex:Longman, 1996.
- [26] M. Mahdy, P.R.S. Speare and A.H. Abdel-Reheem, Effect of transient high temperature on heavy weight, high strength concrete, 15th ASCE Engineering Mechanics Conf. June 2-5, 2002, Columbia University, New York, NY.
- [27] M. F. Kaplan, F.J. Roux, Variations in the properties of concrete at elevated temperatures, *Transactions of the 6th international conference on Structural Mechanics in Reactor Technology*, Palais des Congres, vol. E. H1/2, North-Holland Publishing, Amsterdam, Oxford, 1981.
- [28] J. Jambor, Porosity, pore structure and strength of cementitious composites (in Slovak), *Staveb cas* 1985;33:743-64.
- [29] G.C. Hoff, The use of lightweight fines for the internal curing of concrete, August 2002, A Technical Report, Hoff Consulting LLC, Clinton, Mississippi, pp24.
- [30] S.Weber, Curing of high strength concrete using lightweight aggregates, *Bauberatung Zement Stuttgarti Loenberg*, 1997, pp377-391.

Strength, Sorptivity and Porosity of Self-Compacting Mortar Containing High-Calcium Fly Ash and Silica Fume

Mehmet KARATAŞ
Firat University
Civil Engineering Department
Elazığ, Turkey
mkaratas@firat.edu.tr

Ahmet BENLİ
Bingol University
Civil Engineering Department
Bingol, Turkey
abenli@bingol.edu.tr

Abstract—The aim of this study is to investigate the mechanical properties and durability of self-compacting mortars (SCMs) produced from high-calcium fly ash (HCFA) and silica fume (SF) as mineral additives. In this scope, 12 series of SCMs including control mixture were prepared that consist of binary mixes of silica fume (SF) by the ratios of %6, %10 and %14, and HCFA with the ratios of %10, %20 and %30. In ternary mixes, provided that mineral additive ratio doesn't exceed %30 of cement, %10 of HCFA with 6% , %10, % 14 of SF and %20 of HCFA with %6 , %10 of SF were produced by weight of cement. A total of 48 specimens of 40x40x160 mm were produced and cured at the age 28 day for compressive and tensile strength tests and 36 specimens of 50 mm cube specimens were prepared and cured at 28 days for water absorption, sorptivity, porosity and density tests. Flexural tensile strength and compressive strength of 40x40x160 mm specimens were measured at the curing age of 28 days. All of the SCMs mixes examined provide satisfactory fresh self-compacting properties, In addition, the FA series performed better with workability properties when compared to the SF series. Ternary mixes of FA10SF10 and FA10SF14 have the lowest relative slump values as compared to control and other binary and ternary mixes of SCMs. In both binary and ternary mixes of SCMs, as FA content increases, relative slump values also increases. In other words, less amount of SP was needed to ensure the same slump diameter while increasing the amount of FA. This can be explained as existing lower internal friction of FA which has relatively smooth surface and spherical shape replacing cement which has angular particles. the relative funnel speed values that are between 0.9-1.4 as suggested by EFNARC (2002) The relative funnel speed of binary mixes of FA10 and FA20 is higher than all binary and ternary mixes and almost the same as the control mix. It can be concluded that the workability of binary mixes of FA is better than the other mixes of SCMs except FA30. The compressive strength of binary mixes of FA reduces as the content of FA increases up to 30% which has the lowest value in all SCMs. FA10 and SF6 performed well in the binary mixes of SCMs. The slow pozzolanic reaction and the dilution effect of FA caused the decrease in compressive strength of the FA blended of SCMs. Binary mixes of SF and ternary mixes of SCMS containing 10% of FA generally have higher compressive strength than binary mixes of FA and ternary mixes of high replacement content of FA. When FA and SF content increased, the sorptivity coefficient values of SCMs with FA increased while the sorptivity coefficient of SCMs with SF decreased. It is well known that the compressive strength of mortar/concrete is affected by porosity. The sorptivity coefficient values of the mortars with SF were lower than that of all mortars except for SF5 while the mixtures with SF10 had lowest sorptivity coefficient in all SCMs due to filler effect of SF as well as pozzolanic activity. The results also indicated that binary and ternary mixes of SCMs having high sorptivity values generally exhibits low compressive strength as the sorptivity results are compared to compressive strength of samples cured in water at the age of 28 d.

Keywords— *Self-compacting mortar; Silica fume; Fly ash; Durability; Fresh properties; Mechanical properties*

Strength, Sorptivity and Porosity of Self-Compacting Mortar Containing Ground Pumice Powder

Ahmet BENLİ
Bingol University
Civil Engineering Department
Bingol, Turkey
abenli@bingol.edu.tr

Mehmet KARATAŞ
Firat University
Civil Engineering Department
Elazığ, Turkey
mkaratas@firat.edu.tr

Abstract— The aim of this study is to investigate the mechanical properties and durability of self-compacting mortars (SCMs) produced from ground pumice powder (GPP) as a mineral additive. In this scope, 8 series of SCMs including control mixture were prepared that consist of 5%, 10%, 15%, 20%, 25%, 30% and 35% of ground pumice powder by weight of cement. A total of 72 specimens of 40x40x160 mm were produced and cured at the age of 3, 28 and 90-day for compressive and tensile strength tests and 24 specimens of 50 mm cube specimens were prepared and cured in water at 28 days for water absorption, sorptivity, porosity and density tests. Flexural tensile strength and compressive strength of 40x40x160 mm specimens were measured at the curing age of 7, 28 and 90-day. Mini V-funnel flow time and mini slump flow diameter tests were also conducted to assess rheological properties. The results indicated that SCMs containing 20% of GPP have the highest slump value as 5.1 which are in the range of limits recommended by EFNARC committee. This slump value is slightly higher than control mixtures. SCMs incorporating 5, 10 and 35% of GPP have relative slump of 4.8. It can be concluded that slump values increases up to 20% of GPP the decreases as the content of GPP goes to 35%. The results of relative funnel speed showed that 20% of GPP had the lowest relative funnel speed time as 1.17 (1/s) in all SCMs mixes including control mixtures. Relative funnel speed time of all SCMs mixtures including control mix is in the range of EFNARC limits which is 0.9-1.4.10%. SCMs with 10% of GPP have the highest relative funnel speed value. The value of relative funnel speed reduced to 20% of GPP and then increased to 35% of GPP. The strength properties of GPP revealed better results. The compressive and flexural tensile strength of GPP increased up to 15% of GPP replacement and then decreased to the lowest strength value for 35% of GPP for all SCMs and control specimens. The compressive strength values are in the range of 34.84-84.87 MPa. The highest value belongs to 15% of GPP at the curing age of 90 days. The lowest value belongs to 35%GPP at the curing age of 3 days. The flexural tensile strength behaves similar to the compressive strength. The range of tensile strength varies between 5.04-10.54 MPa, mortars having 15% of GPP 15 gained the highest strength at the age of 90 days, mortars having 35% of GPP gained the lowest strength. Both total water absorption and porosity decreases parabolically up to about 15% of GPP replacement then total water absorption and porosity increases as GPP replacement increases up to 35%. Sorptivity coefficients decrease as the GPP replacement changes from 5% to %10. When GPP content ratios are between 15% and 25 %, the sorptivity coefficient values of SCMs have the highest as compared to other mixes. This sorptivity coefficient nearly the same as the control mix with the value of $3.5 \times 10^{-3} \text{ cm/s}^{0.5}$. GPP30 mixture possesses the lowest value as $2.81 \times 10^{-3} \text{ cm/s}^{0.5}$.

Keywords— *Self-compacting mortar; Ground pumice powder; Durability; Fresh properties; Mechanical properties.*

Camber Calculation of Prestressed Concrete Girder After Detensioning

Barbaros ATMACA

Department of Civil Engineering
Karadeniz Technical University
Trabzon, TURKEY
atmaca@ktu.edu.tr

Şevket ATEŞ

Department of Civil Engineering
Karadeniz Technical University
Trabzon, TURKEY
sates@ktu.edu.tr

Abstract— In this study, it is aimed to determine the camber of prestressed concrete girder after detensioning. At the time of strand release, detensioning, prestressed concrete girders are under the dead and prestressing loads effect. At this stage, camber of prestressed girder is summation of the upward deflection due to the prestressing force and the downward deflection due to dead loads. For the calculation of these deflections, it is generally considered that prestressed concrete girder behaves linear-elastic. In this paper, differences between camber calculations with the linear-elastic beam and elastic-stability theories are presented. Two prestressed concrete girders with the same number of prestressing cable but different configuration are chosen as examples. Girders have 100 cm height and 24.8 m effective span length. 3D finite element models (FEM) of the girders are developed by SAP2000 software, and the deflections of girder are obtained from linear and nonlinear-static analyses. Only geometric nonlinearity is taken into account for nonlinear-static analyses. The results of the linear-elastic beam and elastic-stability theories are compared with FEM results and each other. It is seen that the camber calculation by elastic-stability theory gives acceptable results than the linear-elastic beam theory while strand releasing.

Keywords— *camber, deflection, detensioning, finite element model, linear and non-linear static analyses, elastic-stability, prestressed concrete.*

I. INTRODUCTION

Prestressed concrete girder bridge construction consists of some stages. At these stages, girders are under the effect of different material properties, prestress losses, and load conditions. For all these reasons, deflection behavior of girder at any stage is different from each other. Generally the deflection of prestressed concrete is classified into two groups: short-term and long-term. Short-term deflection refers to the immediate deflection after detensioning, while the long-term deflection occurs over a long period of time largely due to losses of prestress, shrinkage and creep of the materials. In order to better predict long-term camber of girder, it is important to be able to better predict the camber at release [1]. The uncertainty of the predicted camber in precast, prestressed girders can lead to problems during construction. Predicting of camber accurately is difficult because the camber depends on

many random variables, some of which are interdependent and change over time. Some of the most important variables are the compressive strength and Young's modulus of concrete, amounts of creep and shrinkage, thermal gradients within the girder, and the time-dependent variations in prestressing force [2].

Numerous theoretical as well as experimental investigations on structural behavior and load-deflection behavior of prestressed concrete structures have been carried out over the last decades. [3] found considerable variations between the predicted and actual cambers of eight identical American Association of State Highway and Transportation Officials Type IV girders. [4] presented a model for the calculation of both short and long-term deformations in reinforced, prestressed, and composite concrete beams with generalized end conditions subjected to bending about any transverse axis. [5] conducted to develop improved methods of predicting camber in prestressed concrete girders. They used adjustment factor for Young's modulus to minimize the predicted error on the camber immediately after release. [6] presented several factors related to girder production that have a significant impact on the prediction of camber and examined the accuracy of the current NCDOT method for predicting the prestress losses and camber for prestressed concrete girders as compared to field measurements. [1] carried out an experimental research to determine both short-term and long-term deflections of prestressed girders. [2] investigated factors related to prestressed concrete girder production that could affect the camber, and recommended the camber prediction methods. [7] presented the development of a finite element model for the geometric and material nonlinear analysis of bonded prestressed concrete continuous beams.

The main objective of this research is to investigate the differences between calculation of camber after detensioning with linear-elastic beam and elastic-stability theories and effect of cable configuration on camber. For this purpose two prestressed concrete girders with 100 cm height, 24.8 m effective span length and different cable configuration are selected as an application. The 3D FEM of the girders are developed by SAP2000 software [8]. Nonlinear and linear-static analyses are performed under dead and prestressing loads to obtain deflection of the selected girders. Only geometric

nonlinearity is taken into account. The results of the linear-elastic beam and elastic-stability theories are compared with FEM results and each other.

II. CAMBER CALCULATIONS

During the manufacturing process of prestressed concrete girders, prestressing force is transferred from strands to concrete by bond at their interface. Due to existence of the eccentrically located tendons, the girders tend to deflect upwards also called camber. Camber of prestressed girder at detensioning is a summation of the upward deflection due to the prestressing force and the downward deflection due to the dead loads. The magnitude of camber depends on the self-weight of the girder, the amount of strand and prestressing force. The schematic form of deflection of prestressed girder after detensioning is shown Fig. 1.

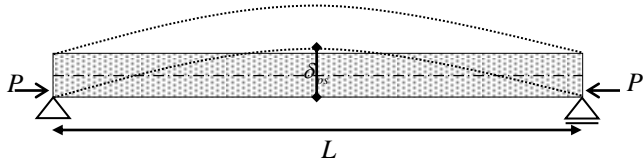


Fig. 1. Deflection of prestressed girder after detensioning

In this study, deflection of girder is calculated with the linear-elastic beam and elastic-stability theories. According to the linear-elastic beam theory, the equilibrium equation is formulated for undeformed state of girder, in which secondary moment is neglected. However the elastic-stability beam theory is formulated the equilibrium equation for deformed state of girder. According to the linear-elastic beam theory, mid-span downward deflection of prestressed concrete girder under the effect of self-weight is determined by:

$$\delta_{sw} = \left(\frac{5 \times q_{beam} \times L^4}{384 E_{ci} I_{girder}} \right) \quad (1)$$

where L is the length of girder, q_{beam} is the linearly distributed dead load over the length of girder, E_{ci} is the Young's modulus of concrete and I_{girder} is the moment of inertia.

The upward deflection of prestressed concrete girders at mid-span due to prestressing force is determined by:

$$\delta_{ps} = - \frac{P_{re} \times e \times L^2}{8 E_{ci} I_{girder}} \quad (2)$$

where e and P_{re} are the eccentricity of strand and the total prestress force at release, respectively.

The downward deflection due to dead loads can be calculated with linear-elastic beam theory because the secondary moment does not occur with deformation of girder. However, under the effect of prestressing force the direction of force and displacement are perpendicular to each other, so the

effects of secondary moment due to prestressing force must be taken into consideration. In this case, the elastic-stability theory formulated the equations of equilibrium in the deformed state should be used. According to the elastic-stability theory it is assumed that the girder is initially straight and materials obey Hooke's law [9].

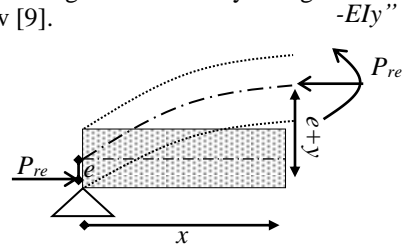


Fig. 2 Eccentrically loaded girder

A simple supported girder exposed eccentricity load cut at a distance x from the pinned support is shown in Fig. 2. This partial section of the girder must be equilibrium. Thus we have

$$EIy'' + P_{re}(e + y) = 0 \quad (3)$$

where EIy'' is the internal resisting moment. By solving Eq. (3), the upward deflection due to prestressing force at the mid-span according to the elastic-stability theory can be obtained as

$$\delta_{ps} = e \left(\frac{1}{\cos \left(\frac{L}{2} \sqrt{\frac{P_{re}}{E_{ci} I_{girder}}} \right)} - 1 \right) \quad (4)$$

III. PRESTRESSED CONCRETE GIRDER MODELS

In this paper, simply supported prestressed I-girder with 100 cm height and 24.8 m effective span length is selected as an application. A typical appearance and the dimensions of cross section are seen in Fig. 3. The ultimate strength of concrete (f_c) is taken as 45 MPa. The low-relaxation Grade 270 prestressing strand (characteristic tensile strength f_u of 1860 MPa) 15 mm (0.6 in.) in diameter is selected as a strand type. Strands layout along the girder length is assumed as linear. The distance between strands (5 cm) given by the American Association of State Highway and Transportation Officials' AASHTO LRFD Bridge Design Specifications [10] is used. To determine the Young's modulus of concrete, there are many models and expressions. These models and expressions predict the Young's modulus of concrete based on the concrete strength and, possibly, other parameters ([11], [12], [13] etc). [1] determined that the Pauw equation most closely predicted the Young's modulus in comparison with the other models at detensioning. The expression for the Young's modulus of concrete according to Pauw equation is given as:

$$E_{ci} = 0.043 K_1 \gamma_c^{1.5} \sqrt{f'_c} \quad (5)$$

where γ_c is the unit weight of concrete at time of test, in kg/m^3 , f_c is the concrete compressive strength at time of test, in MPa and K_I is the correction factor for source of aggregate to be taken as 1.0 unless determined by physical test. The other material properties considered in the numerical analysis are given in Table 2.

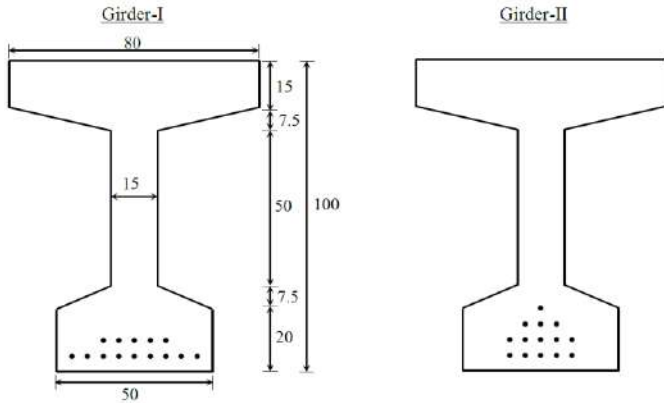


Fig. 3. Cross-section of the investigated girders

Table 2. Material properties.

Material	Young's Modulus (MPa)	Poisson's Ratio	Density (kg/m^3)
Concrete	33914	0.2	2400
Strand	197000	0.3	0

Efficient design of prestress concrete bridges demands an accurate prediction of prestress losses. The prestress losses are defined as the loss of tensile stress in the prestress steel due elastic shortening, creep, shrinkage and relaxation. During the transfer operation of prestress, the girder tends to reduce in length, which is called elastic shortening. The prestress loss due to elastic shortening is

$$\Delta f_{pES} = \frac{E_p}{E_{ci}} f_{cgp} \quad (6)$$

where, E_p is the Young's modulus of prestressing steel, f_{cgp} is the sum of concrete stresses at the center of gravity of prestressing tendons due to the prestressing force at transfer.

Strand relaxation that occurs between the time of strand pull and release is another effect that leads to prestress loss. However, this effect is rather small (i.e., prestress losses on the order of approximately 1%) and is neglected by MnDOT and by the precasters [1].

IV. FINITE ELEMENT MODELING

Nonlinear-static and linear-static analyses of the girders are performed with SAP2000 in order to obtain the deflections of the girders. In nonlinear-static analysis, only geometric nonlinearity is taken into account. Three-dimensional FEM of girder is given in Fig. 4. The girder model consists of 10 frame elements and 14 tendons. The girder and strands are represented by frame and tendon, respectively. As a boundary condition, the left and right hand supports are selected as pinned and roller, respectively.

Self-weight of girder is calculated from the finite element software directly. Prestressing force is calculated as 181 kN when the prestressing losses are taken into account. This force is simultaneously applied to all strands at both sides. During the strand release time-dependent factors such as creep and shrinkage are not taken into consideration.

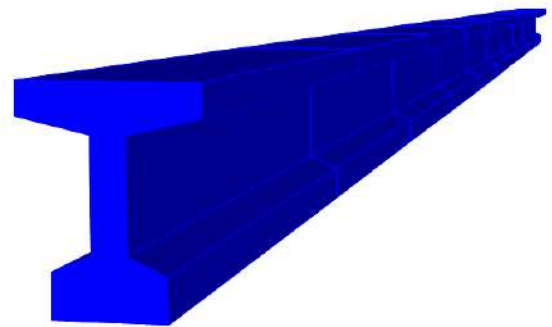


Fig. 5. Finite element model of the girder

V. NUMERICAL RESULTS

The maximum deflections occur due to the self-weight, prestressing force and total of these forces obtained from analytical methods and FEM are shown in Table 2. The downward deflection obtained from FEM and beam theories are equal each other. It is clearly seen that calculation of downward deflection due to the self-weight of girder is not affected from the geometric nonlinearity.

According to the linear-static and nonlinear-static analyses, the maximum upward deflection is obtained from Girder-I and Girder-II 6.24cm - 6.99cm and 5.82cm - 6.52cm, respectively. The upward deflection of girder obtained from the nonlinear-static analysis, in which P-Delta displacement is considered is greater than that of the linear-static analysis. Total net upward deflection of prestressed girder is a summation of the upward deflection due to the prestressing force and the downward deflection due to the self-weight of girder. According to the linear-static and nonlinear-static analyses, the maximum camber is obtained from Girder-I and Girder-II 3.54cm - 4.23 cm and 3.06cm - 3.76 cm respectively.

Method	Deflection		
	Self-weight of girder (cm)	Prestressing force (cm)	Total net camber (cm)
GIRDER-I	Linear-elastic beam theory	-2.73	6.24
	Elastic-stability theory	-2.73	6.99
	SAP2000(Linear-static)	-2.76	6.24
	SAP2000(Nonlinear-static)	-2.76	6.99
GIRDER-II	Linear-elastic beam theory	-2.73	5.82
	Elastic-stability theory	-2.73	6.52
	SAP2000(Linear-static)	-2.76	5.82
	SAP2000(Nonlinear-static)	-2.76	6.52

VI. CONCLUSION

The aim of this paper is to investigate the calculation differences of short-term deflection of prestressed concrete girder after detensioning with the linear-elastic beam and elastic-stability theories. According to the linear-elastic beam theory, the equilibrium equation is formulated for undeformed state of girder, but in elastic-stability theory, the equilibrium equation is formulated for deformed state of girder so secondary moment is taken account. Simply supported prestressed I-girder with 1.0 m height and 24.8 m effective span length is selected as an application. FEM of girders are developed by SAP2000 software, and the nonlinear and linear-static analyses are performed under dead and prestressing load. In nonlinear-static analysis, only geometric nonlinearity is taken into account. The prediction of girders' short-term deflection with linear-elastic beam and elastic-stability theories is compared with each other and the result of FEM. The main conclusions drawn from this analytical study are:

- The downward deflection of the girders obtained from the linear and nonlinear analyses of FEM and beam theories are equal to each other. It is clearly seen that the calculation of downward deflection due to dead load is not affected from geometric nonlinearity because the deflection of girder is in the same direction with the load, thus secondary moment does not occur.
- The downward deflection due to the self-weight of girder can be accurately calculated with the linear-elastic beam theory.
- The upward deflection of girders obtained from the nonlinear-static analysis, in which P-Delta displacement criterion is taken into account is greater than the linear-static analysis of FEM. Also, the result of elastic-stability theory is greater than the linear-elastic beam theory. It is seen that, as the strands are released and the girder begins to camber up, the secondary moment occurs due to prestressing force.
- The maximum upward deflection obtained from the linear-elastic beam theory and linear-static analysis of FEM is pretty close to each other. Also, the nonlinear-static analysis of FEM has almost same results with the elastic-stability theory.

REFERENCES

- [1] French, C.E, "Validation of prestressed concrete I-beam deflection and camber estimates," Final report no. MN/RC 2012-16, Department of Civil Engineering University of Minnesota, 2012.
- [2] Storm, T. K., Rizkalla, S.H. and Zia, P. Z, "Effects of production practices on camber of prestressed concrete bridge girders," PCI Journal, 96-111, 2013.
- [3] Kelly, D., Bradbury T., and Breen J., "Time-dependent deflections of pretensioned beams," ACI Materials Journal, 98(2), 159-167, 1987.
- [4] Rodriguez-Gutierrez, J.A. and Aristizabal-Ochoa, J.D., "Short- and long-term deflections in reinforced, prestressed, and composite concrete beams", Journal of Structural Engineering, 133(4), 495-506, 2007.
- [5] Rosa, A. M., Stanton, J. F. and Eberhard, M.O., "Improving predictions for camber in precast, prestressed concrete bridge girders", Report no. WA-RD 669.1, Washington State Department of Transportation, 2007.
- [6] Rizkalla, S., Zia, P. and Storm, T., "Predicting camber, deflection, and prestress losses in prestressed concrete members", Report no. FHWA/NC/2010-051, North Carolina Department of Transportation, 2010.
- [7] Lou, T., Lopes, S.M.R. and Lopes, A. V. "Numerical modelling of nonlinear behaviour of prestressed concrete continuous beams", Computers and Concrete, 15(3), 391-410, 2015.
- [8] Computers and Structures Inc., SAP2000: Static and dynamic finite element analysis of structures, Berkeley, CA, USA; 2016.
- [9] Chajes, A., Principles of Structural Stability Theory, Department of Civil Engineering University of Massachusetts, Prentice-Hall, Inc., Englewood Cliffs, New Jersey, USA, 1974.
- [10] AASHTO., LRFD bridge design specifications, 6th Ed., Washington, D.C., 2012.
- [11] Carrasquillo, R.L., Nilson, A.H. and Slate, F.O., "Properties of high strength concrete subject to short-term loads", ACI Journal, 87(3), 171-178, 1981.
- [12] Comité Euro-International du Béton (CEB) and the Fédération International de la Précontrainte (FIP) (1990). CEB-FIP Model Code 1990, Final Draft.
- [13] Gardner, N.J. and Lockman, M.J. "Design provisions for drying shrinkage and creep of normal-strength concrete", ACI Materials Journal, 98(2), 159-167, 2001.

Papercrete, lightweight environmental friendly building material utilizing paper waste as ingredient

Zahid Ali

Consultant, Structures, Building Materials & Green Buildings

zee9_786@yahoo.com

Abstract: According to a recent study of resource consumption and waste generation of the financial sector, sixty percent (60%) of the waste produced in company head offices was paper waste, including printing and writing paper, newspapers and magazines and cardboard. Statistics say most GCC countries rank in the top ten (10) worldwide in terms of waste production, Saudi Arabia producing 60% of the waste in the region, followed by the UAE (20%) and the others Kuwait, Qatar, Oman and Bahrain. Recycling is of immense importance in today's world as it reduces the amount of garbage thrown in landfills thereby reducing the negative impact on the environment. Papercrete was originated way back in 1928 but could not find its way in the market, until recently rediscovered in 1983. A name for it is yet to be settled, as some call it fibrous cement and others call it papercrete, the later used by the author in this paper. Papercrete is composed of soaked paper waste, old magazines, newspaper, etc and cement or soaked paper waste, sand and cement. Generally, 60% soaked paper waste, 30% sand and 10% cement. Blocks can be made for low cost housing or for lightweight insulation tiles / blocks for roof insulation or it can be poured into wall forms as well. Papercrete is an environmental friendly material as it utilizes paper waste, lessen the burden on resources, resource efficient and has good insulating value thereby can be used for energy efficiency. The paper deliberates about its properties, utility and benefits.

INTRODUCTION

Recently tremendous interest has been developed in the development of sustainable building materials ranging from bamboo, mud straw to cob. Relatively newcomer to the green materials arena is papercrete or fibrous concrete. Papercrete can be used as a building material being lighter in weight and having high insulating properties. Papercrete was originally patented back in 1928, but it was too cheap and simple to be profitably marketed at that time. It has been independently rediscovered by several experimenters, beginning in 1983. It's so new that people haven't even settled on a name for it yet. Some calls it fibrous cement while others call it Papercrete, the name used by the author. The unlikely marriage of re-pulped paper and portland cement has produced a material with some intriguing characteristics.

Papercrete can be used in many of the same applications as concrete, but is lighter in weight and has a high insulating value, as with many new green materials, papercrete is being researched and tested, (Michael Cockram, 2002) [1].

An important aspect in case of resource efficiency, in sustainable development, is to look for products with identifiable recycle content and papercrete can fulfill this very effectively by recycling paper waste.

PAPER WASTE

In the period from 1983 to 1996, consumption of paper and cardboard had increased by 46 per cent, corresponding to 3.5 per cent per year in EU countries. In absolute figures the increase is from 41 million to 64 million tonnes. It is reasonable to assume that consumption is equivalent to waste generation (Christian Fischer, 1998) [2].

According to Regional Report / Saudi Arabia published in Clean Middle East Issue 2011, the municipal waste landfill in Riyadh received more than 3.5 million tons of different kinds of waste during the first six months this year. Disposed commercial and domestic waste reached 1.4 million tons while other waste including construction debris reached 2.1 million tons. It is a given fact that a rise in GDP registers a rise in consumer spending which gives rise to more waste. It is the same with industrialization and urban growth which increases levels of pollution and waste. Saudi Arabia's annual garbage production has reached 12 million tons, with each citizen producing an average of 1.4 kilograms of waste per day, making the kingdom look for more effective and advanced recycling and waste management solutions, (Clean Middle East, Issue# 6, Vol:2, 2011) [3].

In UAE, "The general trend shows an increase in the amount of waste generated annually," says Naji Alradhi, Head of Waste Treatment Section,

Environment Department of Dubai Municipality. Dubai generates about 31,000 tons of waste every day. The total waste collected in 2005 was 11.3 million tons, an increase of 71.2 per cent over the 6.6 million tons of waste generated in 2003 (Libini Joy, 2006) [4].

According to a recent report by the Arab Foundation for Environment and Development (AFED), the Arab world produces approximately 250,000 tons of solid waste every day, most of it dumped untreated in make shift landfills, if it is collected at all. Skyrocketing income levels in areas such as UAE has resulted in increased consumer spending which has had a direct effect on waste levels. The per capita production of solid waste in Arab cities such as Kuwait, Riyadh and Abu Dhabi is over 1.5 Kg per day, placing them among the highest waste producers in the world, (Jane Meikle, Gulf Times Qatar, 2009) [5].

The mounting levels of waste produced in Dubai are sounding alarm bells for officials. Hussain Lootah highlighted that in year 2000, up to 3000 tons of waste was heading straight to landfills daily, and by year 2008 this had grown to 11000 ton every day making the yearly growth rate of waste 20 per cent, Gulf News, 2009 [6].

In 2010, about 6.5 million tons of waste was generated in Singapore, and each person generated around 1,280 kg of waste in a year. The recycling rate in Singapore for 2010 is 58% and has been increasing steadily over the years. The government has set a target of 60% recycling rate by 2012 in the Singapore Green Plan 2012, and 70% recycling rate by 2030 in the Sustainable Singapore Blueprint.

42% of Singapore's waste is still disposed of, with 40% going to the waste-to-energy plants for incineration and energy recovery, and 2% of non-incinerable waste such as construction and demolition waste, used slag and treated sludge, going to the Semakau Landfill for land filling.

According to % Composition of Waste Generated, the top 5 waste types make up 74% of the total waste generated in Singapore, which are either disposed of at the waste-to-energy plants and landfill, or recycled locally and exported: Paper/Cardboard (21%), Ferrous Metal (18%), Construction Debris (14%), Plastics (11%), Food Waste (10%). According to % Composition of Waste Disposed, the top 3 waste types make up 66% of the total waste disposed in Singapore: Paper/Cardboard (23%), Plastics (24%) and Food Waste (19%). According to % Composition of Waste Recycled, the top 3 waste types make up 74% of the total waste recycled in Singapore: Paper /Cardboard (20%), Ferrous Metal (30%), Construction Debris (24%).

More efforts are needed to reduce the amount of paper, plastics and food waste disposed and to increase their recycling rates. Half of the paper and cardboard waste generated still ends up being burned at the waste-to-energy plants, (Zero waste Singapore, Singapore 2010 Waste Statistics, May 3, 2011 by Eugene) [7].

Major constituents of the municipal solid waste (MSW) are organic, whereas recyclable materials constitute almost 1/3 of total MSW in big cities. Paper/board constitutes 12% and 14.2% of solid waste in Izmir Greater Municipality and Istanbul Greater Municipality [8].

EYES ON SUSTAINABLE DEVELOPMENT

The widely used definition of sustainable development, coined by Brundtland in its report, is "Sustainable development is development which meets the needs of the present without compromising the ability of future generation to meet their own needs." (World Commission on Environment and Development, Harlem Brundtland, 1987) [9]. This report was quite significant as it helped in triggering a wide range of actions such as UN Earth Summits (Rio de Janeiro 1992 and Johannesburg 2002), International Climate Change Convention and World "Agenda 21" programs. Sustainable Construction is the application of sustainable development to the construction industry. Resource Efficiency is one of the important factors of sustainable development. Besides various other means, resource efficiency can be accomplished by using Products with identifiable recycled content. Buildings can play a key role in combating climate change, the U.N. Environment Program said in a report issued in Oslo during a conference on ways to promote economic growth without damaging the environment (Alister Doyle, 2007) [10].

In Turkey, more than half of the waste generated could be reused and recycled, and transformed from a problem into an asset. However, it is a well known fact that the rates of recycling are very low, although there are no hard data in this area. Since a sound waste management infrastructure is not established in Turkey, each and every year, millions of tons of natural resources, the employment opportunity for thousands of people, a wealth of millions of dollars are wasted and the revival capacity of environment is rapidly exhausted [11].

Thus, we need to keep our eyes open in order to keep in mind sustainable and resource efficiency for reusing and recycling our waste product into materials beneficial for building industry and energy conservation.

PAPERCRETE

Papercrete is the product having a distinct identifiable recycled content. Papercrete is composed of water soaked paper waste, old magazines, newspaper, etc and cement or water soaked paper waste, sand and cement. Blocks can be made for low cost housing or for lightweight building partitions or it can be poured into wall forms as well. Papercrete is an environmental friendly material as it utilizes paper waste, lessen the burden on resources thereby providing resource efficiency. A small amount of lime can also be added for getting the benefits of lime like smoother finish and for avoiding damage by wet/dry cycles, incase any.

Some have combined sand and fly ash as well and termed the recipe for the material, as "papercrete" or "fibercrete," with a combination of wastepaper, water, Portland cement, sand and fly ash, which is captured through giant smoke stack filters and reported that the material is environmentally friendly and can cut heating and cooling costs by as much as 70 percent and construction costs by one-third, Chris Casacchia, 2006 [12].

Presently, Blocks of sizes 75 mm x 150 mm x 300 mm some solid and some with a 25 mm hole at the center were made as per the first category of soaked paper waste and cement. The two ratios of 90% soaked paper waste: 10% cement and 80% soaked paper waste: 20% cement were tried. Samples of 100 x 100 x 100 mm size were also made. Block and samples sizes are shown in Figure-1 and Figure-2 respectively.

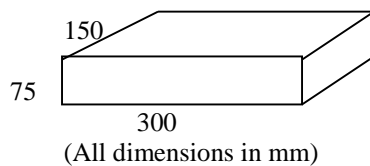


Fig.1 - FIRST CATEGORY SAMPLE SIZE

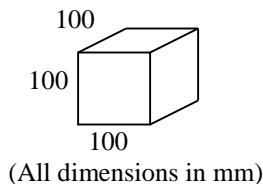


Fig.2 - SECOND CATEGORY SAMPLE SIZE

Density

The density of the first category of ratio 90% soaked paper waste and 10% cement recorded as 299 Kg / cubic meter (18.68 lbs / cubic foot) or 300 Kg / cubic meter (19 lbs / cubic foot). The density or weight of

the second category of ratio 80% soaked paper waste and 20% cement recorded as 580 Kg / cubic meter (36.2 lbs / cubic foot) or 581 Kg / cubic meter (36.3 lbs / cubic foot) as shown in Table-1.

TABLE 1 – DENSITY RANGE OF SAMPLES

Type	Size (mm)	Volume (cu m)	Weight (kg)	Density
1st	75x125x300	0.002812	843	300 kg / cu m
	80x125x270	0.002808	840	299 kg / cu m
2nd	100x100x100	0.001000	580	580 kg / cu m
	80x95x95	0.000722	419	581 kg / cu m

R-Value

R-Value is a measure of a material's resistance to heat flow. The R-Value of papercrete is reported to be between 2.0 and 3.0 per inch and mostly ranges between 2.5 and 3.0 per inch. Papercrete is lightweight and has a high insulation value estimated around R 2.8 per inch. (Gordon Solberg, 2002) [13]. Thus, it qualifies to be a very good insulation wise building materials in very hot climatic regions. Thus, the papercrete roofing tiles can greatly help in reducing the energy cost consumed in air conditioning.

Compressive Strength

Several sample of 100mm cubes of the two categories of ratios that is soaked paper waste : cement that is 90% : 10% and 80% : 20% were tested under compression. It was observed that Papercrete has very low compressive strength (160-320 psi), but fails by slow compression rather than in a brittle manner (quite different from cement concrete cube compression failure). The failure under compression is not in a brittle fashion like in case of cement concrete but it rather converges to pressed form. The samples under compression test are shown in Figures 3 & 4.



Fig.3 - PAPERCRETE CUBE IN PLACE FOR COMPRESSION TEST



Fig.4 – PAPERCRETE CUBE AFTER COMPRESSION FAILURE

Fire Resistance

The papercrete 100x100x100 mm block was held in an open flame for three minutes but it did not catch fire as shown in Figure-5. The only visible change was that it got blackened which can be seen in Figure-6. This is not to say that papercrete will never burn. Any material will burn or melt or disintegrate if enough heat is applied but the test was carried out to dispel the impression that because of the higher content of paper it might catch fire.



Fig.5 – Cube Sample Held in Flame



Fig.6 – Sample after removing from flame

LIGHTWEIGHT CONCRETE COMPARISON

"We believe that ultra-lightweight concrete is one of the most fundamental bulk materials of the future." From the book "A Pattern Language" by Christopher Alexander & Associates, Oxford Press, 1977, page 958 [14].

The majority of regular concrete produced is in the density range of 150 pounds per cubic foot (pcf). The last decade has seen great strides in the realm of dense concrete and fantastic compressive strengths (up to 20,000 psi) which mix designers have achieved. Yet regular concrete has some drawbacks. It is heavy, hard to work with, and after it sets, one cannot cut or nail into it without some difficulty or use of special tools. Some complaints about it include the perception that it is cold and damp. Still, it is a remarkable building material - fluid, strong, relatively cheap, and it is available in almost every part of the world.

Lightweight concrete begins in the density range of less than 120 pound per cubic foot. It has traditionally been made using such aggregates as expanded shale, clay, vermiculite, pumice among others. Each has their peculiarities in handling, especially the volcanic aggregates which need careful moisture monitoring and are difficult to pump. Decreasing the weight and density produces significant changes which improves many properties of concrete, both in placement and application. Although this has been accomplished primarily through the use of lightweight aggregates, since 1928 various preformed foams have been added to mixes, further reducing weight. Lightweight concrete mostly ranges between 300-1600 Kg / cubic meter (19-100 lbs / cubic foot). Comparing papercrete densities of 300 Kg / cubic meter (19 lbs / cubic foot) to 582 Kg / cubic meter (36 lbs / cubic foot) with above mentioned lightweight concrete ranges of 300 to 1600 Kg / cubic meter (19 to 100 lbs / cubic foot), we can easily say that papercrete falls in a reasonable good category of lightweight concrete as shown in Figure-7.



Fig. 7 – Papercrete Comparison with Lightweight Concrete

DISCUSSION

Waste paper is defined as used newspapers, magazines, journals, books and cartons. In general, such waste represents up to 33% of total waste in countries which could negatively impact the environment, if not properly handled. The potential harm of waste paper briefly listed as:

- Waste paper normally ends up in garbage disposal dumping sites in quantities that exceed the capacity of the landfill site for such waste.
- Waste paper would be dumped along with the other types of waste materials. As a result of the excessive humidity conditions, mosquitoes and other insects multiply at very high rates.
- Burning the waste materials causes pollution to the atmosphere, environment and nearby localities.

Utilizing and recycling waste paper serves to eliminate above harmful effects and results in the following benefits:

- Disposing of waste materials in an economical, scientific way.
- Preservation of the environment
- Raising environmental awareness and healthy practices of the public.

As a reference the Author would like to quote an example from Brazil. Due to environmental, social and economic reasons, the recycling of solid waste is an expanding activity in Brazil. According to the Business Commitment to Recycling (CEMPRE), compared to other countries, the Country presents high levels of recycling, and has potential to develop even more in this area, (Recycling, Bracelpa) [15].

Besides being its renewable source, paper is among the products that have the largest recycling rates in Brazil. In total, 43.7% of all papers used in the country in 2008 were sent to recycling post-consumption, according to Ciclossoft Research from

the Business Commitment to Recycling (CEMPRE). Besides, a large quantity of wastepaper is used in the manufacture of other products – such as roofing tiles – whose volume is not included in statistics. Additionally, the recovery of material after its consumption helps decrease the volume of debris dumped in the already filled-to-capacity sanitary landfills, (Paper Recycling) [16].

Thus, instead of overburdening landfill site with waste paper, it seems to be a better and efficient way of utilizing paper waste in making papercrete which in turn will result in resource efficiency and will be a step towards sustainable development. Papercrete with its good insulating quality can be utilized in energy efficiency there by saving our precious energy resources and further having an additional effect / achievement towards sustainable development. We need to develop a thought process in order to save our precious resources and use the material and energy resources efficiently.

CONCLUSIONS

- Instead of burning and dumping in landfills, Papercrete is an effective and environmental friendly way of taking care of the paper waste material.
- Papercrete can become an important means of resource efficiency as it recycles paper waste into a useful building material. Resource efficiency in turn leads to sustainable development.
- Papercrete can effectively be used in low cost houses in masonry walls in the form of blocks or by pouring into wall formwork.
- In multistoried buildings structural weights could also be reduced by having papercrete partition walls.
- Papercrete can be used in roof insulation resulting in reducing energy cost that is contributing to energy efficiency and in turn the environment.

REFERENCES

- [1] Cockram, Michael , 2002. "Building with Papercrete". *Architecture Week, Building Department*, Page B2.1, December.
- [2] Fischer, Christian, 1998. "Future waste amounts in the EU". *European Topic Centre /W-DK* (Reference: Ren Viden 6/98).
- [3] Clean Middle East, 2011. "Positive outlook for Saudi Recycling Industry". Issue# 6 Volume 2.
- [4] Joy, Libini, 2006. "Reduce, reuse and recycle". *Gulfnews Supplements Earth Watch*, Nov 06.
- [5] Meikle, Jane, 2009. "Cities in the Middle East are drowning in waste". *Gulf Times, Doha, Qatar*, Nov 02.
- [6] Lootah, Hussain, 2009. "20% annual growth in domestic waste". *Gulf News (UAE)*, May 27.
- [7] Eugene, 2011. "Singapore 2010 Waste Statistics". Zero waste Singapore, May 3.
- [8] E. Metin, A. Erozturk, C. Neyim, "Solid waste management practices and review of recovery and recycling operations in Turkey", *Waste Management* 23 (2003) 425–432, Science Direct, www.sciencedirect.com
- [9] Brundtland, H., 1987. "World Commission on Environment and Development, Our Common Future". Oxford University Press, New York.
- [10] Doyle, Alister, 2007. "UNEP Says Greener Buildings Could Slow Global Warming", *Environmental News Network*, March 29.
- [11] Dr. H. Ömer KÖSE, Principal Auditor Sait AYAZ, Principal Auditor Burak KÖROĞLU, Auditor Translated by: Seher ÖZER, *Waste Management in Turkey, performance audit report no. 5181/1 dated 12.3.2007*, www.sayistay.gov.tr
- [12] Casacchia, Chirs, 2006. "Paper-cement recipe cuts construction costs, energy bills". *The Business Journal of Phoenix*, June 2.
- [13] Solberg, Gordon, 2002. "Building With Papercrete and Paper Adobe: A Revolutionary New Way to Build Own Home for Next to Nothing".
- [14] Christopher Alexander & Associates, 1997. *The Book "A Pattern Language"*. Oxford Press, page 958.
- [15] Brazilian Pulp and Paper Association. "Recycling". *Bracelpa*, www.bracelpa.org.br
- [16] Brazilian Pulp and Paper Association. "Paper Recycling". *Bracelpa*. www.bracelpa.org.br

Feasibility analysis of NDT methods using to estimate the concrete strength as part of urban regeneration

Kursat Esat ALYAMAC
Firat University, Faculty of Engineering
School of Civil Engineering
Elazig, TURKEY
kealyamac@firat.edu.tr

Merve ACIKGENC ULAS
Firat University, Faculty of Architecture
School of Architecture
Elazig, TURKEY
merveacikgenc@firat.edu.tr

Yavuzhan TAS
Ministry of Transport
8th Regional Directorate of Highways
Elazig, TURKEY
yavuzhantas@gmail.com

Ehsan Ghafari
Purdue University, Faculty of Engineering
School of Civil Engineering
West Lafayette, USA
eghafari@purdue.edu

Abstract— Most of the countries are placed in a seismic zone which has high activity and has extremely experienced large-scale losses due to several destructive earthquakes such as Turkey. Therefore, governments are seriously trying to produce the projects that will significantly reduce the earthquake effects in order not to experience this kind of potential disasters. The most important part of these projects is urban regeneration. Within the context of urban regeneration activities, renewal of the buildings which have low earthquake-resistant is targeted. While the earthquake resistance level of a building is decided, one of the important steps is the determination of the strength of the building materials. There are many standard NDT methods that will be able to be used to determine the compressive strength. However, it is necessary to choose the appropriate methods in order to quickly and reliably estimate the strength properties of the materials. The purpose of this study is to determine the optimum NDT method for the urban regeneration. So, feasibility analysis was carried out for the standard NDT methods, and the performance of these methods was evaluated based on the cost and the accuracy. The result is the requirement new NDT method which is the practical and efficient for the large-scale projects such as urban regeneration.

Keywords—*NDT; compressive strength; urban regeneration; in-place test; earthquake*

I. INTRODUCTION

The most popular performance measure which is used by design engineers to estimate the actual strength of concrete is the compressive strength, which is usually measured by breaking cylindrical or cubic specimens in a compression-testing machine. The compressive strength results can be used for the quality control, the formwork stripping times, the curing times, the fault diagnosis on the existing reinforced concrete/masonry structures, the research works, and the in-place strength of concrete/mortar. Specifically, it is critical to estimate the in-place compressive strength of concrete, mortar

and rock to establish the safety of the concrete and the masonry buildings. Because most of the countries in the world are frequently exposed to the destructive earthquakes. After these earthquakes and tragedies, millions of buildings were severely damaged or collapsed [1-7]. To figure out this problem, the governments have been trying to renew the buildings using urban regeneration/transformation policy or post-earthquake rehabilitation and reconstruction before the earthquakes [8, 9] and, for instance, Turkey is one of these countries. Urban regeneration was regulated with the Law: “The Regeneration of the Areas under Disaster Risk (Law No: 6306)” in Turkey in May 2012. Decreasing the risk before the disasters, which are especially earthquakes, is aimed at this law [10]. Minimizing the risk before the earthquakes mean that hundreds of thousands of existing buildings, which have low earthquake resistance or insufficient resistance, should be renewed. First of all, earthquake resistance of these buildings, namely safety, must be determined. The in-situ strength of concrete, mortar and rock is an important part to establish the safety of the buildings [11].

Urban regeneration projects where the buildings have been rebuilt, include not only a building, but also at least dozens of buildings. Although the earthquake resistance of these buildings which are usually reinforced concrete or masonry buildings are estimated to be weak or inadequate, this problem still legally needs to be proven. For this reason, it is necessary to estimate the in-place compressive strength of the concrete in the buildings. Standard NDT methods and drilling core method are usually used together to estimate the strength properties of the concrete. However, since the number of buildings is very high, the cost of determining the strength of the concrete is greatly increasing. In addition, a considerable amount of time is lost. It is critical to determine the concrete strength quick and reliable so that urban regeneration projects continue economically and rapidly.

Many standard NDT methods, such as UPV, rebound hammer, and penetration tests, are presently used to estimate the strength of the concrete. In this paper, the most preferred standard NDT methods are evaluated in terms of cost, reliability and practicality, and a feasibility analysis is carried out considering carefully requirements and expectations. The purpose of this study by the feasibility analysis is to provide the possibility of comparing the NDT methods for the researchers and engineers. So, they will be able to determine the most effective method for their projects at the earliest convenience. Consequently, a practical graphic-based method is proposed to choose the NDT methods to be used in urban regeneration projects.

II. NDT METHODS

There are many NDT techniques used to determine the concrete strength. The most known of these can be listed as follows:

- Rebound Number (Schmidt Hammer Test) [12, 13]
- Ultrasonic Pulse Velocity [12, 14]
- Penetration Resistance (Probe and Pin Tests) [12, 15]
- Pullout Test [12, 16]
- Break-off Number [12, 17]
- Maturity Method [12, 18]
- Cast-in-place Cylinders [12, 19]
- PNT-G Test [20]
- Drilling Resistance [21]
- Nail Penetration [22]
- Twist-off Test [23]

For the feasibility analysis, the NDT methods just used in the standard, current, and for existing buildings have been taken into consideration, and their characteristics have been clearly presented.

A. Rebound Number Test

The rebound number test is technically a test for surface hardness, and it approximately provides for establishing relationship between the rebound hammer number and the compressive strength of concrete. The Rebound Hammer has been around since the late 1940s and today is a commonly utilized method for estimating the in-place compressive strength of the concrete. Basic operation of the rebound hammer test is illustrated in Fig. 1. Schmidt Hammer is usually used for this test [24].

The tests can be carried out in horizontal, vertically upward, downward or any intermediate angled positions. The rebound hammer is simple to use, and a large number of readings may be obtained in a relatively minimum amount of time. This method is non-destructive and characteristically more economical than other NDT methods. However, with

these advantages come disadvantages related to technical limitations on accuracy, and the need for exact calibration and correlation with cores for assessment of an existing structure [25]. The surface texture, moisture content, and carbonation significantly affect the rebound (R) number of the tests.

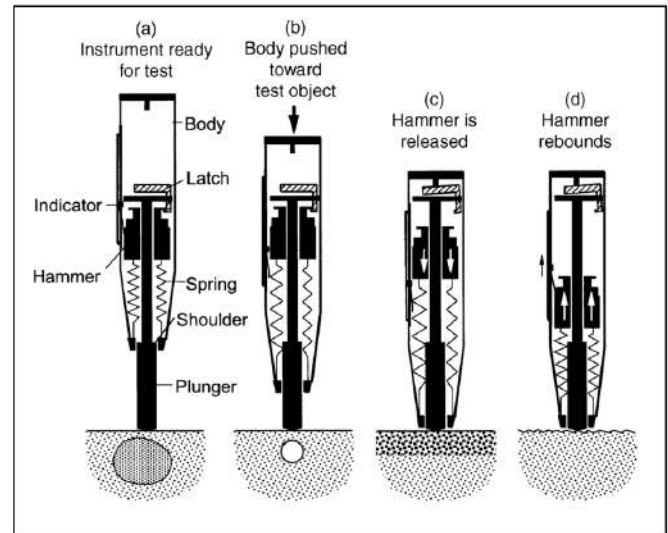


Fig. 1. Operation of the rebound hammer as schematic [12].

The advantages and limitations of the RH test should be recognized and figured on if the rebound hammer will be used for a large-scale project about existing buildings.

B. Ultrasonic Pulse Velocity (UPV) Test

Pulses of the waves are produced by an acoustical transducer that is kept in contact with one surface of the concrete under evaluation. After traversing through the concrete, the pulses are gotten and altered into electrical energy by a second transducer placed a distance L from the transmitting transducer. The transit time T is directly measured electronically. The pulse velocity V is calculated by dividing L by T . The operational principle of modern testing equipment is illustrated in Fig. 2 [14].

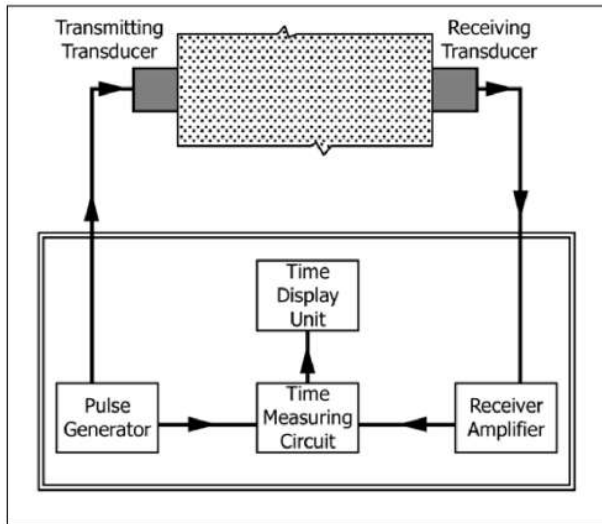


Fig. 2. Schematic diagram of the pulse velocity test [14].

UPV can be utilized for the following properties [26]:

- Estimation of the relationship between the strength and the pulse velocity.
- Estimation of uniformity of the concrete.
- Assessment of alters obtaining with time in the common properties of the concrete.

There are three possible configurations where the transducers can be settled as illustrated in Fig. 3. These are direct transmission (Fig. 3a), semidirect transmission (Fig. 3b), and indirect (surface) transmission (Fig. 3c). Indirect transmission should be used when only one face of the concrete is available. These configurations provide significant advantages for estimation of the in-place strength of the concrete [25].

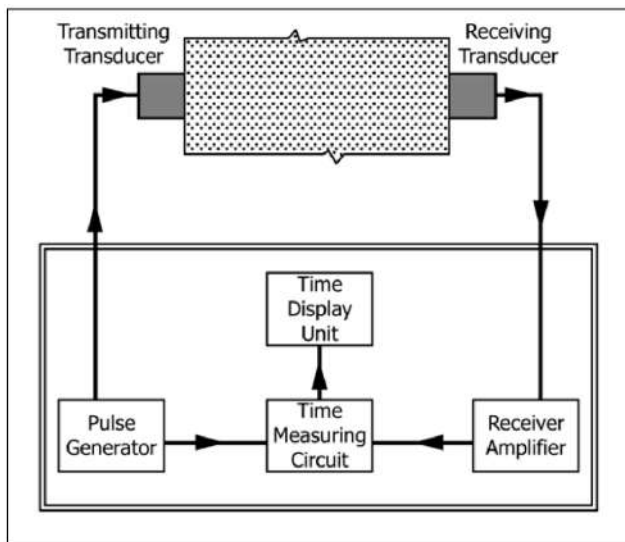


Fig. 3. Configuration of the UPV test application [25].

UPV method adequately provides the examination of relationship between the compressive strength and the pulse velocity of the sample, but the test results of UPV are affected by moisture content, properties of aggregates, cracks, voids. The usability of UPV test is much more limited to predict the compressive strength of concrete, mainly owing to steel reinforcement bars in concrete because the pulse velocity through steel is about 40% greater than through concrete. These limitations should be considered before preferred the UPV method [27, 28].

C. Pin Penetration Test

Nasser and Al-Manaseer described an NDT in which a new production hammer that forces a steel pin into the concrete is used to estimate the when it is safe to remove the concrete forms [29]. The apparatus occurs a spring-loaded hammer which may follow a pin of 3.56mm diameter and 30.5mm length with the tip machined [15].

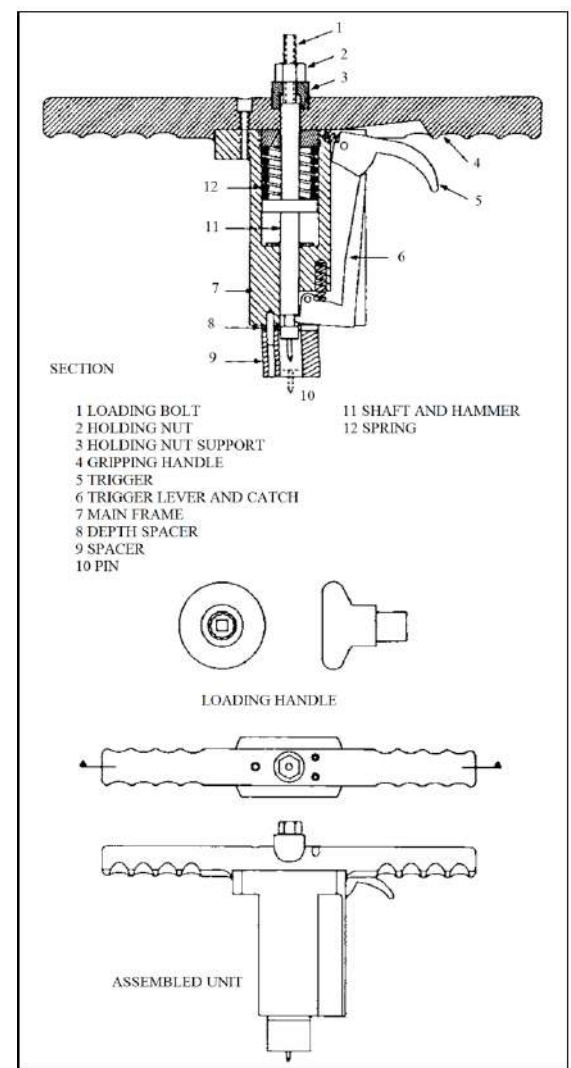


Fig. 4. Configuration of the UPV test application [29].

The spring is forced by pressing the hammer against the surface of the concrete, and is released by a trigger causing the pin and the attached shaft and hammer to strike the surface of the concrete with an energy of about 108 Nm. After cleaning, the hole depth generated is measured with a dial gauge device [28]. There is an acceptable correlation between the pin penetration and the compressive strength of the concrete. Pin penetration (depth of the blind hole in the concrete element) test which requires less energy than the Windsor probe test. The pin test, although easy in concept, has technical disadvantages. The pin penetrates only a small depth into the concrete, and thus, the results can be seriously infected by the properties of the concrete at the surface.

D. Windsor Probe Test

The probe-penetration technique requires the use of a specially designed gun to run the steel probe into the concrete [15]. (This test system is commonly known as the Windsor Probe Test, as seen in Fig. 5).



Fig. 5. Windsor Probe Test equipments.

The Windsor probe test, like the rebound hammer test, is a hardness tester, and its inventors maintain that the penetration of the probe shows the exact compressive strength in a localized area is not certainly true [30]. Nevertheless, the probe penetration does refer to the some property of the concrete, so it has been possible to improve empirical correlations between the compressive strength and the probe penetration [25]. Schematically, failure of the concrete during Windsor probe penetration test is illustrated in Fig 6.

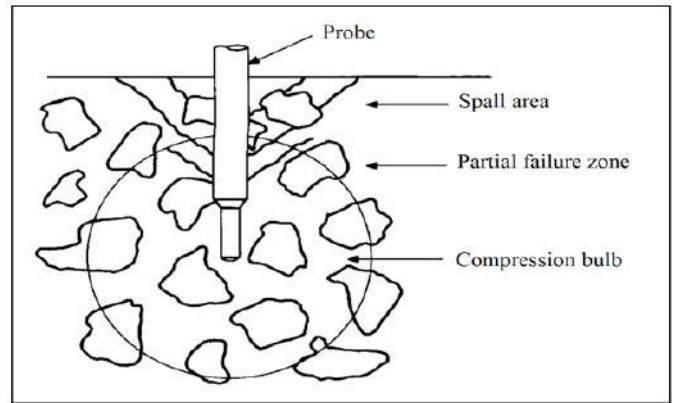


Fig. 6. Failure of the concrete during Windsor test schematically [28].

The advantages of the Windsor probe test are [25, 28, 31]:

- The test is adequately fast, and the result is obtained immediately provided an appropriate curve with good correlation is ready for use.
- The correlation with the concrete compressive strength is changed by a relatively small number of variables.
- Application is only required to one surface.

The limitations of the Windsor probe test are [25, 28, 31]:

- The test damages an about 8 mm blind hole in the sample in which the probe penetrated and, in elder concrete, this zone around the point of the penetration is usually broken.
- The least distance from a test location to any edges of the concrete sample or between two tests location is of the order of 150 mm to 200 mm.
- The distance from reinforcement can also be affected the depth of the penetration, especially if the distance is less than about 100 mm.
- The least thickness of the sample, that can be tested, is about three times the estimated depth of steel probe penetration.
- The costs of the operations are really high.

Although the PR method has some advantages, it is particularly sensitive to characteristics of aggregate and minimum member thickness, which can be tested. The advantages and limitations of the Windsor probe test should be recognized and taken into account if this test will be utilized for the existing buildings.

III. URBAN REGENERATION AND THE IN-PLACE TEST

Turkey connects the tectonic plates that are including the Eurasian, Arabian, and African and the Anatolian plates [32] and Turkey has a high seismic activity because of its location. Many destructive earthquake occurred in the past two decades in Turkey and the social and economic damages were really

huge [33]. So, Turkey is really important model to evaluate for the urban regeneration.

The Turkish earthquake knowledge and data regarding urban projects are seriously little and limited. In urban areas, risks related not only community services and infrastructure but also housing [34]. Erzincan earthquake which occurred in 1992 supplied valuable data to understand the dangerous of the building stock which has not been enough earthquake resistance. However, unfortunately, this experience was not enough to protect from the disasters which were occurred in Kocaeli (1999), Bingol (2003), Van (2011) et al [7].

Critical amount of Turkey's building stock does not comply with either the design codes, standards, and specifications that were efficient at the time of their built, or the ever more stringent modern design code applied today. It is not practicable to perform reliable estimates of seismic losses due to aforementioned complexities. However, researches based on the scenario earthquakes possible to Istanbul harshly predict 30.000 – 40.000 heavily damaged structures and eleven billion in direct losses due to damage to buildings [33]. The building stock which has low earthquake resistance is a very serious problem threatening many countries like Turkey. To solve this problem, governments are trying to produce efficient urban generation projects.

Urban regeneration is a first step in the rebuilding of a part of the cities, and that it has been designed as a governments-assisted urban regeneration strategy. The origin of the conversation of urban regeneration within the Turkish planning literature was an extension of government programs that were formed by efforts to secure a place in the 1980s world order [35]. Disaster risk resulted from the destructive earthquakes has become the main theme of the urban regeneration in Turkey, especially, in the last decade, and has soon become the primary reason for the application of urban regeneration projects with the Law on the 6306, "Regeneration of Areas under the Risk of Disasters", which was accepted on 16.05.12. This has added to the "legality" of urban regeneration projects that will be implemented all over the country with a quick and public model of rebuilding [36].

One of the most important parts of the existing urban regeneration projects is to determine earthquake risk levels of the buildings. When the risk levels of the buildings are determined, one of the basic steps is estimation of the compressive strength of the concrete. Determination of the strength of the concrete by just using the core drilling method is expensive, difficult and time-consuming. Therefore, as far as possible, the destructive methods should be used as minimum and NDT methods usually should be used. Even so, it is not easy to select the most suitable one/more from many NDT methods. Accordingly, in this study, a feasibility analysis was carried out for NDT methods in line with the urban regeneration requirements.

For the urban regeneration projects, estimation of the in-place strength of the concrete is the topic of discussion. Because, as all NDT is unsuitable for determination of the in-

place concrete strength, and also any NDT may not be suitable for urban generation projects.

Since the 1900s, there has been an ongoing investigation of the in-place strength of the concrete [37]. Although there are many in-place test methods, very few of them are standard [38, 39]. The standard methods have many advantages such as comparability with the previous works, experience, and easy reachability to the test equipment.

IV. FEASIBILITY ANALYSIS OF THE NDT METHODS

Feasibility analyses are originally formed by social scientist. In this study, the feasibility studies made is one of the first examples of its kind, and these methods will hopefully be more commonly performed in the future researches. A feasibility analysis estimates and observes an economic opportunity based on certain theory and estimations that have been put forward in the process of starting a new project [40]. Feasibility analyses aim to decide whether a business opportunity is possible, practical, and workable [41]. A number of the factors are considered and assessed in a feasibility analysis to calculate the most effective results.

Within the framework of urban regeneration projects, to determine the in-place strength of the concrete, priority expectations from the NDT methods are listed below:

- Economy (cost of the operation)
- Time (minimum labor and test time)
- Accuracy (more than 90%, if possible)

The critical issue for the project is that the cost of the operation should be more economical than the cost of the test equipment. The approximate cost of the operations and test equipment are presented in Table 1.

TABLE I. COST INFORMATION FOR THE NDTs

NDT Methods	Operation Cost (\$)	Equipment Cost (\$)
Rebound Hammer	Only labor	\$300.00
UPV	Only labor	\$4000.00
Pin Penetration	\$10/each	\$5000.00
Windsor Probe	\$18/each	\$5500.00

In order to be able to apply the tests in Table 1, there must be no plaster or coating on the surfaces of the concrete elements. If it is present, it has to be removed from the concrete surface. So, it is assumed that the labor that is for removing the coating will be in equal amounts, \$100, for all the tests.

At least three tests should be performed to determine the compressive strength of the concrete. These three tests are accepted as a set. In order to compare NDT methods, a certain number of test must be taken into account in feasibility analysis. Windsor probe test is taken as reference to determine this numerical value. This value is the test number that makes

the cost of the operation equal to the cost of the equipment. The number of the tests = $5500 / 18 \cong 305$.

Two parameters were used for feasibility analysis. The first is based on cost; the second is based on the benefit. The parameters of the analysis are explained in Table II.

TABLE II. PARAMETERS OF THE FEASIBILITY ANALYSIS

NDT Methods	CO/CE ^a	T ^b	A ^c	T/A ^d
Rebound Hammer	0.3	3	3	1
UPV	> 0.1	2	2	1
Pin Penetration	0.63	3	2	1
Windsor Probe	1	3	1	3

^a. CO/CE=(Cost of operation + labor) / cost of the equipment

^b. T: Application Time (0–15 min: 3, 16–60 min: 2, more than 60 min: 3)

^c. A: Accuracy (Excellent: 1, Good: 2, Approximate: 3)

^d. T/A: Time/Accuracy

The rate of CO/CE is developed to consider the cost effect on the choosing of the NDT. The rate of T/A is developed to consider the technical benefit on the selecting of the NDT.

Graphic based feasibility analysis is illustrated in Fig. 7. If it is desired to determine as fast, practical and approximate whether an NDT method is suitable for an urban regeneration project, first, the numerical values of the parameters of this method, CO/CE and T/A, are calculated. And then, these parameters are marked on the graphics, finally; the feasibility region is determined by Fig 7. The RED, YELLOW and GREEN Zones mean the unfeasible, acceptable and feasible NDT methods, respectively.

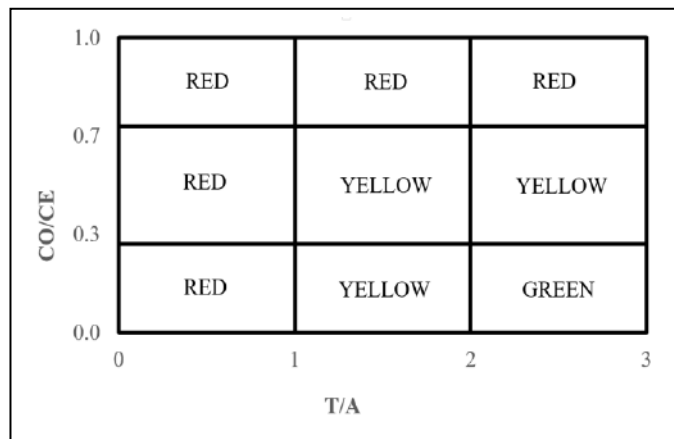


Fig. 7. Graphic of the feasibility analysis.

V. DISCUSSION AND RESULTS

Graphic based feasibility analysis is performed for the standard NDT methods, and result of the feasibility analysis are given in Table III.

TABLE III. FEASIBILITY RESULT OF THE NDT METHOD

NDT Methods	Feasibility Zone
Rebound Hammer	YELLOW
UPV	YELLOW
Pin Penetration	YELLOW
Windsor Probe	RED

Rebound hammer, UPV, pin penetration, and Windsor probe tests are in the yellow and red zones, respectively. Existing methods are not feasible but acceptable methods to utilize for the urban regeneration projects. Because these methods, which are in the yellow zone are neither economical nor sufficiently useful. The Windsor probe test is unfeasible because of the cost of the operation. This method is reliable and practical. However, cost of the operation of Windsor Probe test is so high. It is evident how large the economic loss will be, if it is assumed that the test will be used for tens of thousands of buildings in urban regeneration projects.

The proposed method in the current paper is a preliminary and practical method. This feasibility analysis can be used in non-standard NDT methods. However, accuracy must be carefully determined. The most important thing is that these analysis are done by experienced engineers. Because, if every numerical result passes from the engineer's filter, it gains significant value.

VI. CONCLUSION

Urban regeneration has become a strategy to avoid the earthquake damages in many countries like Turkey. Because the target is building stock, the strength of the concrete, which is the most-used material to produce the buildings needs to be determined. A feasibility analysis was carried out for the methods of determining the in-place concrete strength in this study. Following are some of the important conclusions.

- The number of drilled core specimens should be reduced as much as possible while the concrete strength is determined as the number of buildings in urban regeneration projects is too high. Even if it is possible, reliable results should be tried to be obtained without using destructive methods. It can be economically and quickly carried out.
- The efficiency of an NDT method by the help of the graphic based feasibility method can be evaluated with cost, time and accuracy limiters.
- None of the existing methods are in the green zone when the feasibility analysis performed. This

conclusion implies that a new feasible NDT method is required.

- Windsor probe test has high accuracy but not economic. So, it can be used for the specific works.
- None of the existing NDT methods can be applied to surface that has coating. Before the NDT is applied, the coating/plaster must be removed. Therefore, a new NDT is required to test the concrete elements without removing the coating, especially for the urban regeneration projects.

REFERENCES

1. Bikce, M. and T.B. Celik, "Failure analysis of newly constructed RC buildings designed according to 2007 Turkish Seismic Code during the October 23, 2011 Van earthquake," *Eng Fail Anal*, 2016. 64: p. 67-84.
2. Dogangun, A., "Performance of reinforced concrete buildings during the May 1, 2003 Bingol Earthquake in Turkey," *Eng Struct*, 2004. 26(6): p. 841-856.
3. Norio, O., et al., "The 2011 Eastern Japan Great Earthquake Disaster: Overview and Comments," *Int J Disaster R Sci*, 2011. 2(1): p. 34-42.
4. Saatcioglu, M., A. Ghobarah, and I. Nistor, "Performance of structures in Indonesia during the December 2004 great Sumatra earthquake and Indian Ocean tsunami," *Earthq Spectra*, 2006. 22: p. S295-S319.
5. Sezen, H., et al., "Performance of reinforced concrete buildings during the August 17, 1999 Kocaeli, Turkey earthquake, and seismic design and construction practise in Turkey," *Eng Struct*, 2003. 25(1): p. 103-114.
6. Zhao, B., F. Taucer, and T. Rossetto, "Field investigation on the performance of building structures during the 12 May 2008 Wenchuan earthquake in China," *Eng Struct*, 2009. 31(8): p. 1707-1723.
7. Yon, B., et al., "Lessons learned from recent destructive Van, Turkey earthquakes," *Earthquakes and Structures*, 2015. 9(2): p. 431-453.
8. Karaman, O., "Urban Renewal in Istanbul: Reconfigured Spaces, Robotic Lives," *Int J Urban Regional*, 2013. 37(2): p. 715-733.
9. Anthony, O.-S., "Post-Disaster Housing Reconstruction and Social Inequality: A Challenge to Policy and Practice," *Disasters*, 1990. 14(1): p. 7-19.
10. Gunay, Z., T.K. Koramaz, and A.S. Ozuekren, "From Squatter Upgrading to Large-scale Renewal Programmes: Housing Renewal in Turkey," in *Renewing Europe's Housing*, R. Turkington and C. Watson, Editors. 2015, Thu University of Chicago Press. p. 215-243.
11. Alyamac, K., "Earthquake Resistance and Future Planning of the Existing Building Stock in Elazig/TURKEY," in *The International Congress on Elazig from the Past to the Present*. 2014, Prime Ministry of Turkish Republic, Ataturk Culture Language and History Higher Institution, Ataturk Research Center. p. 583-600.
12. ACI_2281r_03, "In-Place Methods to Estimate Concrete Strength." 2003, American Concrete Institute: Farmington Hills. p. 44.
13. ASTM C805/C805M-13a, "Standard Test Method for Rebound Number of Hardened Concrete." 2014, ASTM International: West Conshohocken. p. 4.
14. ASTM C597-09, "Standard Test Method for Pulse Velocity Through Concrete." 2010, ASTM International: West Conshohocken. p. 4.
15. ASTM C803/C803M-03, "Standard Test Method for Penetration Resistance of Hardened Concrete." 2010: West Conshohocken. p. 4.
16. ASTM C900-15, "Standard Test Method for Pullout Strength of Hardened Concrete." 2015: West Conshohocken. p. 10.
17. ASTM C1150-96, "Standard Test Method for The Break-Off Number of Concrete." 1996: West Conshohocken. p. 4.
18. ASTM C1074-11, "Standard Practice for Estimating Concrete Strength by the Maturity Method." 2011: West Conshohocken. p. 10.
19. ASTM C873/C873M-15, "Standard Test Method for Compressive Strength of Concrete Cylinders Cast in Place in Cylindrical Molds." 2016: West Conshohocken. p. 4.
20. Gucci, N. and R. Barsotti, "A non-destructive technique for the determination of mortar load capacity in situ," *Mater Struct*, 1995. 28(5): p. 276-283.
21. Rodrigues, J.D., A.F. Pinto, and D.R. da Costa, "Tracing of decay profiles and evaluation of stone treatments by means of microdrilling techniques," *J Cult Herit*, 2002. 3(2): p. 117-125.
22. Selcuk, L., et al., "A Nondestructive Testing Technique: Nail Penetration Test," *ACI Struct J*, 2012. 109(2): p. 245-252.
23. Naderi, M., "New twist-off method for the evaluation of in-situ strength of concrete," *J Test Eval*, 2007. 35(6): p. 602-608.
24. Kolek, J., "An appreciation of the Schmidt rebound hammer," *Magazine of Concrete Research*, 1958. 10(28): p. 27-36.

25. Malhotra, V.M. and N.J. Carino, "Handbook on Nondestructive Testing of Concrete. 2004: CRC Press.
26. Panzera, T.H., et al., "Advances in Composite Materials–Analysis of Natural and Man-Made Materials, chapter 17," in *Ultrasonic Pulse Velocity Evaluation of Cementitious Materials*. 2011, InTech.
27. Yaman, I.O., et al., "Ultrasonic pulse velocity in concrete using direct and indirect transmission," *ACI Materials Journal*, 2001. 98(6): p. 450.
28. Hellier, C.J., "Handbook of Nondestructive Evaluation. 2003: The McGraw-Hill Companies, Inc.
29. Nasser, K. and A. Al-Manaseer, "New non-destructive test," *Concrete International*, 1987. 9(1): p. 41-44.
30. Malhotra, V., "Evaluation of the Windsor probe test for estimating compressive strength of concrete," *Matériaux et Construction*, 1974. 7(1): p. 3-15.
31. Bin Ibrahim, A., et al., "Guidebook on non-destructive testing of concrete structures," *International Atomic Energy*, 2002.
32. Bommer, J., et al., "Development of an earthquake loss model for Turkish catastrophe insurance," *Journal of Seismology*, 2002. 6(3): p. 431-446.
33. Gunes, O., "Turkey's grand challenge: Disaster-proof building inventory within 20 years," *Case Studies in Construction Materials*, 2015. 2: p. 18-34.
34. Erdik, M., "Developing a comprehensive earthquake disaster masterplan for Istanbul," in *Issues in Urban Earthquake Risk*. 1994, Springer. p. 125-166.
35. Güzey, Ö., "Urban regeneration and increased competitive power: Ankara in an era of globalization," *Cities*, 2009. 26(1): p. 27-37.
36. Güzey, Ö., "The last round in restructuring the city: Urban regeneration becomes a state policy of disaster prevention in Turkey," *Cities*, 2016. 50: p. 40-53.
37. Jones, R., "The non-destructive testing of concrete*," *Magazine of Concrete Research*, 1949. 1(2): p. 67-78.
38. McCann, D. and M. Forde, "Review of NDT methods in the assessment of concrete and masonry structures," *NDT&E Int*, 2001. 34(2): p. 71-84.
39. Uomoto, T., "Non-destructive testing in civil engineering 2000. 2000: Elsevier.
40. Blocher, E.J., "Teaching cost management: A strategic emphasis," *Issues in Accounting Education*, 2009. 24(1): p. 1-12.
41. Hassan, A. and S. Jones, "Non-destructive testing of ultra high performance fibre reinforced concrete (UHPFRC): A feasibility study for using ultrasonic and resonant frequency testing techniques," *Construction and Building Materials*, 2012. 35: p. 361-367.

Masonry structures in Turkey: codes, seismic performance and future strategies

Kursat Esat ALYAMAC

Firat University, Faculty of Engineering
School of Civil Engineering
Elazig, TURKEY
kealyamac@firat.edu.tr

Zulfu Cinar ULUCAN

Firat University, Faculty of Engineering
School of Civil Engineering
Elazig, TURKEY
zculucan@firat.edu.tr

Humeyra SAHIN

Firat University, Faculty of Engineering
School of Civil Engineering
Elazig, TURKEY
hsahin@firat.edu.tr

Ali Sayil ERDOGAN

Bingol University, Faculty of Engineering and Architecture
School of Civil Engineering
Bingol, TURKEY
aserdogan@bingol.edu.tr

Abstract— Turkey is one of the countries, which is on the risky earthquake zone. Turkey has been exposed to destructive earthquakes many times and has experienced significant losses. The reason of these huge losses is the building stock which has not earthquake-resistant. Although a significant part of the existing building stock constitutes masonry structures, the number of masonry structures in newly constructed structures is steadily decreasing. In this study, the seismic codes and the performances of the masonry structures after the earthquakes have been widely examined. The reason for this review is to be able to decide the future strategy of masonry structures. As a result, the importance of necessary has not been given to the design of the masonry structures in Turkey. If the masonry building technology were supported enough, it would be realized that to construct the masonry buildings is easier and more economical than reinforced concrete buildings, which have earthquake-resistant. It is greatly desired that this study will create a new perception of the design of the masonry buildings in Turkey.

Keywords—masonry buildings; earthquake; performance; seismic codes; Turkey

I. INTRODUCTION

Masonry means a well-proven building material owning superior properties in terms of appearance, durability and cost in comparison with options [1]. Even so, the characteristic of the masonry in a building depends on the materials used, and therefore, all the masonry materials must adjust to certain minimum rules and standards. The fundamental elements of the masonry are brick, blocked stone, and mortar [2].

In Turkey, the existing building stock is usually consisted of the masonry and the reinforced concrete buildings [3]. However, considering the new buildings, the rate of the masonry buildings is decreasing gradually. New-generation buildings are being constructed as reinforced concrete both in the cities and in the rural areas. Even if new structures build as

masonry buildings, many of these buildings have so little engineering experience [4]. This situation may lead to prolonged problems in the future. The degree of these problems often arises after destructive earthquakes.

Turkey, after many destructive earthquakes, has experienced significant losses. In particular, the earthquakes of Erzincan [5], Marmara [6], Bingol [7], Elazig [8], and Van [9] have not been erased from the memories. After these earthquakes, and the damages some strategies are developed to reduce the losses. Unfortunately, the strategies commonly are based on the reinforced concrete structures. Although the masonry buildings are so important, but they are sometimes overlooked, and this overlooked detail causes significant problems.

If the new-generation structure strategy is planned by considering with masonry buildings, great economic advantages will be achieved [10]. The main reason for economic losses is due to the buildings in the rural areas. Required construction quality cannot be achieved for the structures built in the rural areas due to many reasons. Some of these reasons can be described as follows:

- Ready-mixed concrete plants are far from the rural areas
- Difficulties in finding the masters for the construction
- Difficulty of on-site concrete producing

For these reasons, the performance of the buildings can be low under seismic loading, so, the service life of these buildings is under the expectations. In addition, the structures are more suitable to be built in-place. The masonry buildings are more economical and the safe when considering their service life, since they have the less number of the floor and the floor area.

The purpose of this study is to draw attention to the importance of the masonry buildings. The increase in the

number of high-quality buildings will contribute to the economy of the country and the safety of its citizens in natural disasters like earthquakes. The strategy of this paper certainly does not mean that the earthquake resistance of reinforced concrete structures is weak. Every structure that is planned and built according to the seismic codes and the standards is robust. However, the main topic to be emphasized in this study is that the structure system must be selected by taking into account the conditions. In Turkey, the masonry buildings seem more suitable for rural areas, which are far from the cities and counties. As a result, it is very important, first, to develop a design code only for the masonry buildings, then to use masonry structural system in rural areas, for the life safety and the national economy.

II. MASONRY MATERIALS AND CONSTRUCTION SYSTEMS

Masonry building is one of the oldest forms of structure known to humanity. The name masonry refers comprehensively to brick, tile, stone, and concrete-block. In this section, masonry materials, units, types and design of the masonry construction systems are presented.

A. Masonry Units

The most popular buildings materials are brick and stone. Using brick has major advantages like has serial production, easy operation, economic, etc. Several popular uses of units in the masonry buildings are given as follows [11]:

- Valve vaults and manholes
- Backing for stones and bricks
- Curtain walls, party walls and firewalls
- Plasters and coatings
- Load-bearing walls (exterior and interior)

B. Masonry Materials

Bricks are made of calcium silicate or fired clay. Every country almost has its own standards for bricks. The compressive strength, frost resistance, absorption, dimensional changes, sulfate attack, and fire resistance tests are performed for the bricks. More than 90% of the masonry structures in Turkey are built with bricks [12].

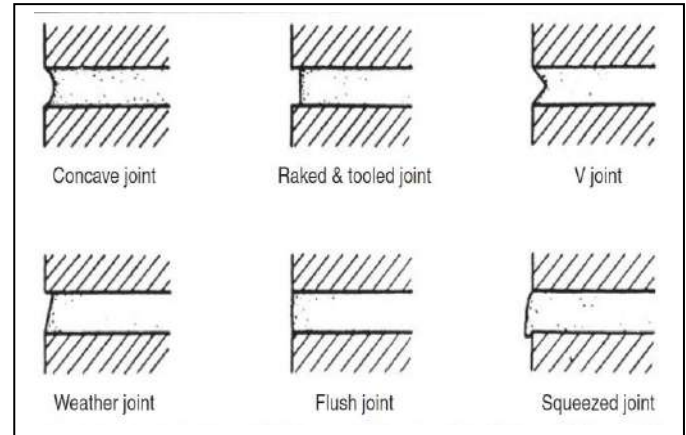
Mortar is the mixture of the lime and/or cement, aggregates and water. Occasionally, mineral or chemical admixture are added to mortar to improve its fresh/hardened properties [13].

C. Mortar Joints

Mortar joints have a significant role in the bond designs and quality of a wall [14]. Thickness of the mortar joints are greater than the 3 mm for traditional mortar. Mortar joints can be finished as specified, when the surfaces of the masonry walls are not to be coated. Several types of the masonry joints are illustrated in Fig. 1.

D. Masonry Construction System

Masonry buildings, which mainly occur structural elements,



walls and floors, are box-type constructional systems [15]. The steel ties or reinforced-concrete floor levels to connect the walls. During earthquakes, floors should behave as a rigid horizontal diaphragm.

Fig. 1. Masonry joints of uncoated walls [16].

Although there are many different masonries, these can be collected in three general groups.

- Unreinforced/plain masonry (Fig. 2)
- Confined masonry (Fig. 3)
- Reinforced masonry (Fig. 4)

Plain masonry is obtained by just using the brick/stone/block and the mortar. It has basic design and is non-ductile structural materials.

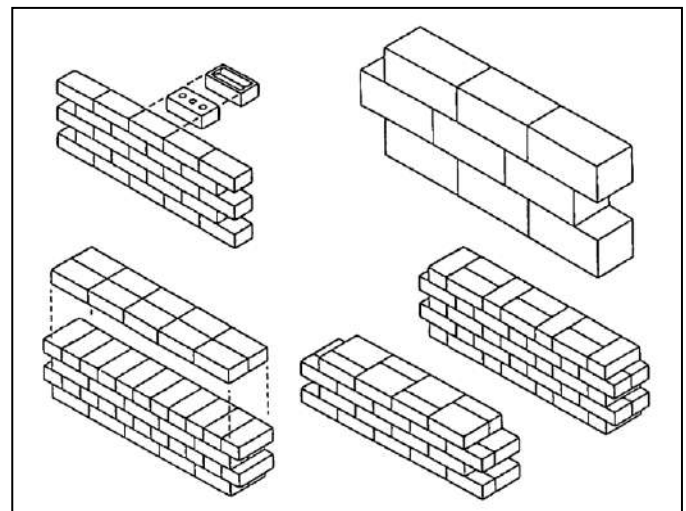
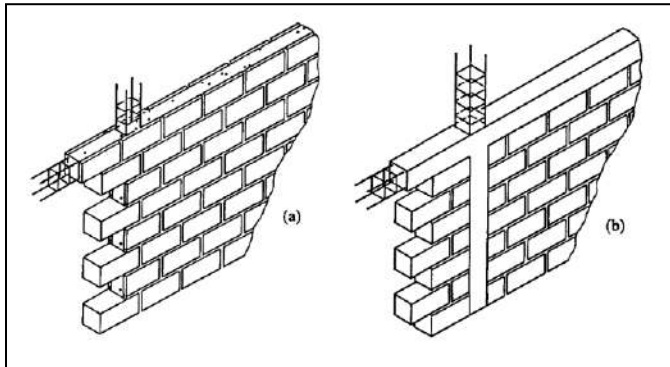


Fig. 2. Plain masonry walls [17].

If masonry structural walls are confined with reinforced concrete on all four sides, this constructional system called as confined masonry. The confined masonry is not design to resist

seismic and the vertical loads. Their purpose of the construction mainly supports the floors.

The steel rebar or mesh is inserted in the mortar or placed in the holes and filled with grout is a construction system that



named as reinforced masonry. The resistance and the energy absorption capacity of the masonry buildings under seismic loads can be improved by using reinforced masonry system.

Fig. 3. Confined masonry walls [17].

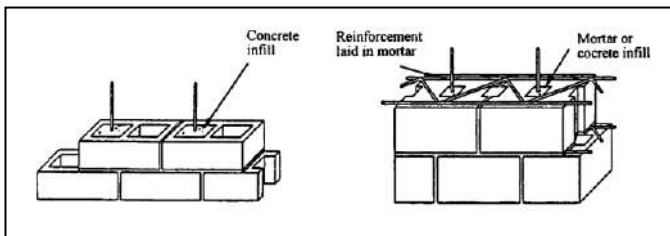


Fig. 4. Reinforced masonry walls [17].

III. SEISMIC CODES AND STANDARDS IN TURKEY

When the natural disasters are mentioned in Turkey, the first earthquakes come to mind [18]. Since the earthquakes greatly affect the structures, the design codes have been constantly renewed so that robust structures can be built [19]. Seismic design codes [20], which were established from past to today are listed as follows:

- 1940 - Temporary building regulation in earthquake zones [21].
- 1944 - Temporary building regulation in earthquake zones [22].
- 1949 - Turkish building regulation in earthquake zones [23].
- 1953 - Regulation for structures in disaster areas [24].
- 1962 - Regulation for structures in disaster areas [25].
- 1968 - Regulation for structures in disaster areas [26].
- 1975 - Regulation for structures in disaster areas [27].
- 1998 - Regulation for structures in disaster areas [28].

- 2007 - Regulation for structures in earthquake areas [29].

In the first regulation published in 1940, a design method for the masonry buildings was not contained. In this regulation, constructive rules were given for the masonry buildings according to seismic zones (Zone I and II). Minimum limits for the structural elements such as height and number of the floors, wall lengths and thickness were determined.

There were no significant updates in the regulations established in 1944. However, in the regulation published in 1949, the number of rules related to masonry structures is increasing, and the content becomes more comprehensive. In particular, there were important explanations about the beams which were placed on the structural walls.

In the 1953 disaster regulation, significant developments were noteworthy. The structures were classified, and the rules are effectively separated for each structure. The rules of the masonry structures were given for different sections such as foundation, walls and flooring.

In the 1962 disaster regulation, dynamic analysis was applied the first time to the structure design. In the disaster regulations of 1968, 1975, 1998 and 2007, important developments were made in the sections related to reinforced concrete structures; however, the masonry buildings did not have the same development.

In the current regulation, there are only rules about the plain masonry structure. The design rules of confined and reinforced masonry buildings should be in the earthquake regulation. For this reason, efficient strategies have not been able to develop for the masonry buildings which are earthquake-resistant [30].

IV. SEISMIC PERFORMANCE OF THE MASONRY BUILDINGS

Seismic performance of the plain, confined, and reinforced masonry buildings are evaluated in many research, especially, after the destructive earthquakes [31, 32]. The seismic performance of the masonry buildings can be clearly explained by macro-seismic scales, also named intensity scales, as seen in Fig. 5. The macro-seismic scale has five damage grade to determine the damage class of the plain masonry buildings. These grades are explained as follows [33, 34]:

- Grade 1: There is no structural damage for the walls. It can be seen hair-line cracks in few walls and small damages for plasters.
- Grade 2: The buildings have slight structural damage. There are bigger cracks in the wall and moderate damage for plasters/
- Grade 3: There are substantial heavy damages. The cracks are large and extensive and placed in most walls. The roof and non-structural elements has significant damage.

- Grade 4: The building has very heavy damage. All the elements, structural and non-structural have very heavy damage. There are serious failure of floors, roof and the walls. It is no longer possible for the building to be restored and reused.
- Grade 5: The building is partially or completely collapsed. Destruction and very heavy structural damage.

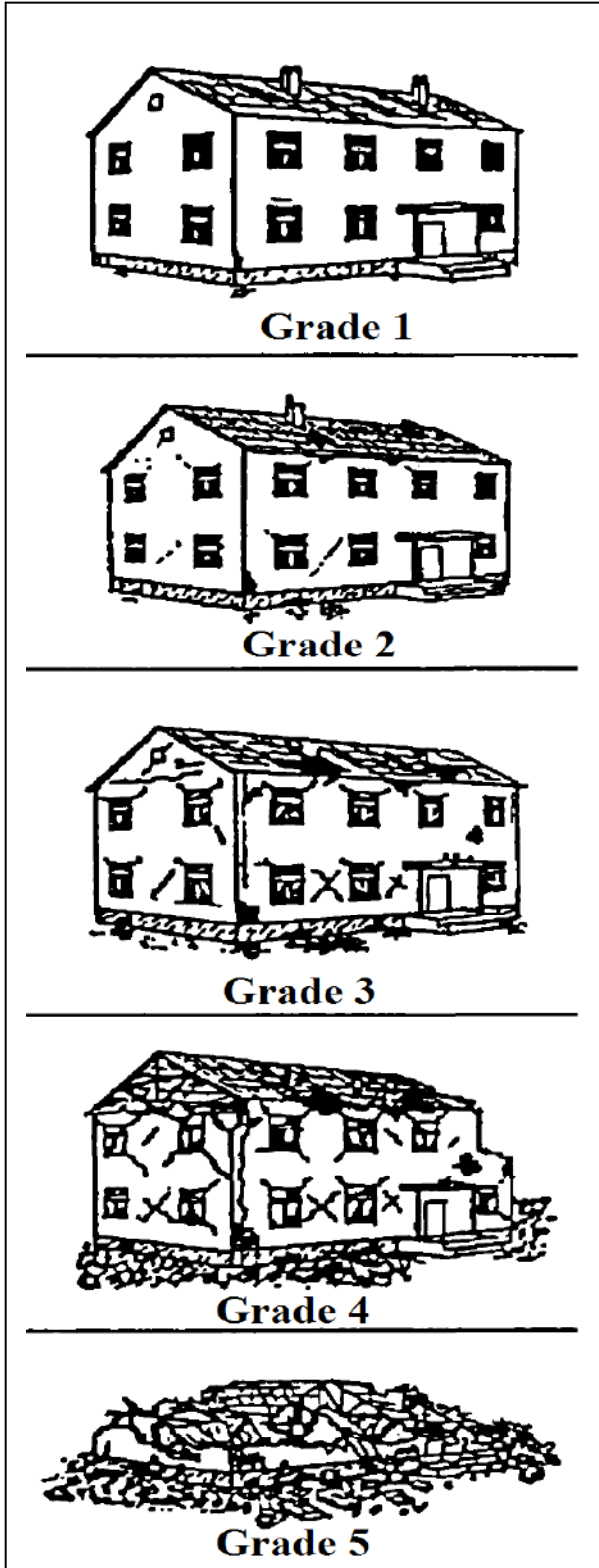


Fig. 5. Damage classification of the masonry buildings [33].

While the damage levels of the buildings are determined after the earthquakes, the important consequences relevant to the masonry buildings are noteworthy. There are many types of masonry structures, in addition, the most commonly used types of these structures have stone and brick walls. Today, all of the masonry buildings are almost built by using bricks.

If the investigations on the buildings after the destructive earthquakes in Turkey and elsewhere are considered, there is general satisfaction from the seismic behavior of the masonry buildings. Many researchers have stated that in their papers. However, the seismic behaviors of unreinforced, and reinforced masonry buildings are different from each other.

The weakest point of the masonry structures is the non-ductile behavior. The reinforced masonry structures have the high ductility. Especially, old-adobe, field-stone and simple-stone masonry structures do not have the earthquake resistant (Fig. 6 and 7).



Fig. 6. Adobe masonry structure.



Fig. 7. Regular stone masonry structures.

The reasons of the damages of the heavy damaged structures are very critical [35]. With the analyzing of these data, urban and rural structural strategy can be determine. The

reasons of the destructions of the heavy damaged structures are very critical. With the analyzing of these data, urban and rural structure strategies can be obviously determined.

V. DISCUSSION AND THE FUTURE STRATEGIES

When the current seismic zone map of Turkey checks carefully, more than 90% of the Turkish population lives in the high risky zone (Fig. 8). Turkey needs a comprehensive strategic plan for housing. If these strategic plans cannot be made or are not made sufficiently sensitive, unfortunately, Turkey will continue to loss own citizens and physical resources [36].

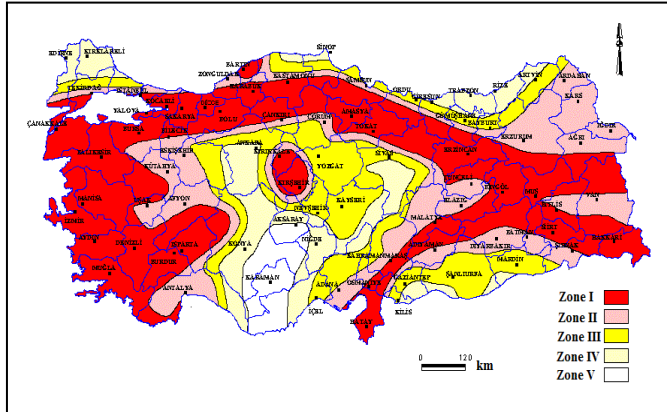


Fig. 8. Current seismic zone map of Turkey.

Planning the housing strategy in Turkey separately for the city and rural areas will provide many benefits. There are two important objectives for the housing process. The first one is life safety during the earthquakes, and the second one is economy. The budget spent for the elimination of losses after the earthquakes in Turkey brings a great burden to the nation's economy. For this reason, the housing strategy is critical [37].

After 1970's there have been huge increases for the building stock. An important part of the building stock is reinforced concrete structures. The majority of the buildings especially in the cities are reinforced concrete. It is interesting to note that the majority of the structures built in rural areas during recent years are reinforced concrete structures.

Unfortunately, after the Marmara earthquakes of 1999, authorities started to work on construction control system. The implementation of the construction control system throughout Turkey is quite new. The problems with the building audit already are continuing [38].

Project, manufacturing, inspection, regulations, rules are inseparable parts of construction. The combining of all of them reveals the strategy of construction. When the 2007 earthquake regulations are examined, the dominance of reinforced concrete structures attracts attention. The reinforced concrete structures absolutely have many advantages. However, it should not be forgotten that they have many disadvantages.

To build earthquake-resistant reinforced concrete structures in rural areas is really difficult due to problems related to

placing of the steel rebar, insufficiency of the building audit, and workers faults. Building earthquake-resistant reinforced concrete structures in rural areas is really difficult due to problems related to placing of the steel rebar, insufficiency of the building audit, and workers faults. Structures have been damaged even during small-scale earthquakes in the past and even if lives were not lost, there were big economic damages.

In the current seismic design code of Turkey, the section related to the masonry buildings is very short. However, today, the masonry structures built as confined, and reinforced masonry buildings. So, it is possible to obtain the earthquake-resistant structures. Economic losses can be reduced by these structures.

Technological masonry structures can be constructed faster and more securely. The potential of the brick production in Turkey supports this advantage [39].

For the development of the new generation of masonry structures in rural areas, firstly, only a regulation of the masonry structure should be published as it is in many countries. This regulation must be prepared by considering the conditions of Turkey. With the new regulation, the sector will gain momentum.

In addition, in the civil engineering departments, and architecture faculties, the masonry structure system should be taught in more detail. In the meantime, the next generation will provide a well development of the building stock.

VI. CONCLUSION

The aim of this study is to summarize the steps of the strategy plan that to take in order to benefit from the advantages of confined and reinforced masonry building technology and to draw attention to its importance. Following are some of the important conclusions.

- For the safe building stock in Turkey, the strategy of the masonry structure needs to be updated. It is the first step of this innovation to publish a new seismic regulation only for masonry structures. Regulation for masonry buildings is a necessity.
- The rules for unreinforced, confined, and the reinforced masonry buildings must be included in the new regulation.
- Economic and robust structures in rural areas will provide significant contributions to the nation's economy.
- The designing and building of both confined masonry and reinforced masonry structures should be encouraged. Seminars and conferences can be organized for importance of the masonry structures.
- In the civil engineering departments, the masonry structures should be introduced in a comprehensive manner. The syllabuses should be updated about the masonry structures which are earthquake-resistant.

REFERENCES

1. Hendry, A.W., B.P. Sinha, and S. Davies, "Design of masonry structures. 2003: CRC Press.
2. Hendry, E.A., "Masonry walls: materials and construction," Construction and Building materials, 2001. 15(8): p. 323-330.
3. Gulkan, P., M. Aschheim, and R. Spence, "Housing Report Reinforced Concrete Frame Buildings with Masonry Infills," World Housing Encyclopedia, Report, 2002. 64.
4. Inel, M., H.B. Ozmen, and H. Bilgin, "Re-evaluation of building damage during recent earthquakes in Turkey," Engineering Structures, 2008. 30(2): p. 412-427.
5. Sucuoğlu, H. and A. Erberik, "Performance Evaluation of A Three-Storey Unreinforced Masonry Building During The 1992 Erzincan Earthquake," Earthquake engineering & structural dynamics, 1997. 26(3): p. 319-336.
6. Sezen, H., et al., "Performance of reinforced concrete buildings during the August 17, 1999 Kocaeli, Turkey earthquake, and seismic design and construction practise in Turkey," Eng Struct, 2003. 25(1): p. 103-114.
7. Dogangun, A., "Performance of reinforced concrete buildings during the May 1, 2003 Bingöl Earthquake in Turkey," Eng Struct, 2004. 26(6): p. 841-856.
8. Alyamaç, K.E., et al., "Observations on Damages at Buildings in the Rural Area due to the Basyurt-Karakocan (Elazığ) Earthquake," Turkish Journal of Science & Technology, 2011. 6(2): p. 117-128.
9. Yon, B., et al., "Lessons learned from recent destructive Van, Turkey earthquakes," Earthquakes and Structures, 2015. 9(2): p. 431-453.
10. Bibbee, A., et al., "Economic Effects of the 1999 Turkish Earthquakes," 2000.
11. Schneider, R.R. and W.L. Dickey, "Reinforced masonry design. 1994: Pearson College Division.
12. Allen, G., "Hydraulic lime mortar for stone, brick and block Masonry: a best practice guide. 2015: Routledge.
13. London, M., "Masonry: How to care for old and historic brick and stone. 1988: Preservation Press.
14. Hamid, A.A. and R.G. Drysdale, "Concrete masonry under combined shear and compression along the mortar joints," in Journal Proceedings. 1980.
15. Rai, D.C., "Structural use of unreinforced masonry," IITK-GSDMA EQ, 2005. 12: p. 19.
16. Narendra, T. and T. Narendra, "Design of Reinforced Masonry Structures." 2010, McGraw-Hill.
17. Tomazevic, M., "Earthquake-resistant design of masonry buildings. Vol. 1. 1999: World Scientific.
18. Korkmaz, K.A., "Earthquake disaster risk assessment and evaluation for Turkey," environmental Geology, 2009. 57(2): p. 307-320.
19. Ilki, A. and Z. Celep, "Earthquakes, existing buildings and seismic design codes in Turkey," Arabian Journal for Science and Engineering, 2012. 37(2): p. 365-380.
20. Alyamaç, K.E. and A.S. Erdoğan, "Geçmişten Günümüze Afet Yönetmelikleri ve Uygulamada Karşılaşılan Tasarım Hataları," Deprem Sempozyumu, 2005: p. 23-25.
21. Works, M.o.P., "Zelzele Mıntıkları Muvakkat Yapı Talimatnamesi (Temporary building regulation in earthquake zones)." 1940.
22. Works, M.o.P., "Zelzele Mıntıkları Muvakkat Yapı Talimatnamesi (Temporary building regulation in earthquake zones)." 1944.
23. Works, M.o.P., "Türkiye Yersarsıntısı Bölgeleri Yapı Yönetmeliği (Turkish building regulation in earthquake zones)." 1949.
24. Works, M.o.P., "Yersarsıntısı Bölgelerinde Yapılacak Yapılar Hakkında Yönetmelik (Regulation for structures in disaster areas)." 1953.
25. Housing, M.o.P.W.a., "Afet Bölgelerinde Yapılacak Yapılar Hakkında Yönetmelik (ABYYHY) (Regulation for structures in disaster areas)." 1962.
26. Housing, M.o.P.W.a., "Afet Bölgelerinde Yapılacak Yapılar Hakkında Yönetmelik (ABYYHY) (Regulation for structures in disaster areas)." 1968.
27. Housing, M.o.P.W.a., "Afet Bölgelerinde Yapılacak Yapılar Hakkında Yönetmelik (ABYYHY) (Regulation for structures in disaster areas)." 1975.
28. Housing, M.o.P.W.a., "Afet Bölgelerinde Yapılacak Yapılar Hakkında Yönetmelik (ABYYHY) (Regulation for structures in disaster areas)." 1998.
29. Housing, M.o.P.W.a., "Deprem Bölgelerinde Yapılacak Yapılar Hakkında Yönetmelik (ABYYHY) (Regulation for structures in earthquake areas)." 2007.
30. Büyükgökmen, D., "Donatılı Yığma Yapı Tasarımı." 2015, Fen Bilimleri Enstitüsü.
31. Alyamac, K.E., "Yığma Yapıların Deprem Güvenliğinin Belirlenmesinde Kullanılacak Faktörler," in Yapısal Onarım ve Güçlendirme Sempozyumu (YOGS). 2007: Pamukkale, Denizli.
32. Alyamac, K.E., "Yığma Yapıların Yaklaşık Deprem Dayanımlarının Belirlenmesinde Yeni Bir Yöntem Önerisi: Trafik Lambaları Metodu (Tlm) (Proposal For A New Method To Determine The Approximate Earthquake Resistance Of Masonry Structures: Traffic Lights Method)," in Seventh National Conference on Earthquake Engineering. 2011, İnşaat Mühendisleri Odası: İstanbul, Turkey.
33. Commission, E.S., "European Macroseismic Scale 1998," Luxembourg, Joseph Beffort, Helfent-Bertrange, 1998.
34. Musson, R.M., G. Grünthal, and M. Stucchi, "The comparison of macroseismic intensity scales," Journal of Seismology, 2010. 14(2): p. 413-428.
35. Penna, A., et al., "Performance of masonry buildings during the Emilia 2012 earthquake," Bulletin of earthquake engineering, 2014. 12(5): p. 2255-2273.
36. Alyamac, K., "Earthquake Resistance and Future Planning of the Existing Building Stock in Elazığ/TURKEY," in The International Congress on Elazığ from the Past to the Present. 2014, Prime Ministry of Turkish Republic, Atatürk Culture Language and History Higher Institution, Atatürk Research Center. p. 583-600.
37. Lewis, J., "Housing construction in earthquake-prone places: Perspectives, priorities and projections for development," Australian Journal of Emergency Management, The, 2003. 18(2): p. 35.
38. Sakallı, F., "Yapı denetim sisteminde yaşanan sorunlar, 4708 sayılı Yapı Denetim Hakkında Kanun'daki eksiklikler ve çözüm önerileri." 2008, Fen Bilimleri Enstitüsü.
39. Toker, S., A.E. Akan, and S.A. Selçuk, "Depreme dayanıklı tasarım için Türkiye'de yığma yapıların yeniden canlandırılması/Revival of masonry buildings in turkey for earthquake resistant design," Erciyes Üniversitesi Fen Bilimleri Enstitüsü Dergisi, 2016. 26(1).

Investigation of Soft Stories in Buildings with Hollow Block Slab

Ozan INCE

Firat University, Faculty of Engineering
School of Civil Engineering
Elazig, TURKEY
ozann.ince@gmail.com

Humeyra SAHIN

Firat University, Faculty of Engineering
School of Civil Engineering
Elazig, TURKEY
hsahin@firat.edu.tr

Kursat Esat ALYAMAC

Firat University, Faculty of Engineering
School of Civil Engineering
Elazig, TURKEY
kealyamac@firat.edu.tr

Zulfu Cinar ULUCAN

Firat University, Faculty of Engineering
School of Civil Engineering
Elazig, TURKEY
zculucan@firat.edu.tr

Abstract— Hollow block slab is a floor slab system that consists of a thin slab and joists. There are nonstructural materials between joists. Because of advantages of ribbed slabs in architectural areas, the using of this type slabs have become more common. Hollow block slab usually consists of wide and shallow beams. Because of low beam height in this system, its lateral stiffness is less than beam floor systems. Because hollow block slab has low lateral stiffness, there is a risk under lateral loads in buildings that tend to be soft-story. Therefore, in building with hollow block slab should be detailed investigated regarding soft story. For this reason, in this study buildings with stores of 5, 8 and 11, which constructed with hollow block slab were numerically investigated for different ground story height. According to analysis, lateral drift ratios was acquired for each story. As ground story height increased, the lateral drift ratios of buildings with hollow block slab were increased nearly between 33% and 50%. The high values of drift ratios in ground story increase soft-story risk. This situation has a negative effect on building performance under lateral loads. For improving this negative effect shear walls that restrict lateral drift ratios under lateral loads added to the system and analysis was repeated. Because shear walls have decreased drift ratios of buildings nearly between 40% and 60%, the performance of the building is improved under lateral loads. According to results of analysis, in the high seismic zone, it is agreed on that building with hollow block slab should be designed as a wall-frame system.

Keywords— *hollow block slab; soft story; lateral drift ratio; reinforced concrete building*

I. INTRODUCTION

Hollow block slab is a floor slab system that consists of a thin slab and joists. There are nonstructural materials between joists. Hollow block slab provides important advantages such as effective using of story height and interior design in buildings for architects. Furthermore, hollow block slab that has a flat

slab ceiling reduce formwork and construction time. Because of these advantages, the using of this type slabs have become more common.

Hollow block slab usually consists of wide and shallow beams for providing a flat slab ceiling. The height of hollow block slab is determined compatible with nonstructural materials (styrofoam, briquette, tile) that use between joists. In Turkey, the thickness of the hollow block slab is usually 300 mm or 320 mm [1]. Because of low beam height in this system, its lateral stiffness is less than beam floor systems. Because hollow block slab has low lateral stiffness and more clear height of columns, lateral drift ratio in this system may be more under lateral loads, and this system may show weak performance under earthquake load.

In Turkey, the ground story of buildings that is existed two sides of main streets is used as commercial areas. For this reason, the height of this story is more than other stories and infill walls that are existed in upper stories between frames partly or completely remove in ground story. Recent years, in this building, hollow block slab have become more common for using story height effectively and for providing a flat slab ceiling [2]. This situation reduces the drift stiffness of buildings especially ground story and increase the risk of soft-story effect. This situation has a risk for buildings in Turkey where has earthquake zones. In Turkey, the soft-story effect is one of the main reason of damage sustained by reinforced concrete buildings during earthquakes [3, 4].

In this study, soft-story in building with hollow block slab was numerically investigated for different ground story height. For numerically study, 5, 8, 11 stories buildings that are used commonly in Turkey were investigated. Structure analysis software SAP2000 and IdeCAD was used for analysis [5, 6].

According to analysis, lateral drift ratios was obtained for each story. It is shown that as ground story height increased, the lateral drift ratios of buildings have reached limits that have negative effects on building performance under earthquake load. For restricting lateral drift ratios and improving building performance under earthquake load, shear walls added to the system and analysis was repeated. It is shown that because shear walls restrict lateral drift ratios of ground story, the earthquake performance of the building is improved.

II. THE EARTHQUAKE PERFORMANCE OF BUILDING WITH HOLLOW BLOCK SLAB

Over three decades, because of advantages of hollow block slab have been commonly used in Middle East countries including Turkey [7]. Because there is not enough experimental and numerical study that investigate the performance of hollow block slab under lateral loads, the performance of this system under earthquake loads doesn't know as much as beam floor systems. Because there is not enough experimental study that investigates the performance of hollow block slab under earthquake loads, most country's earthquake codes prevent using this system in seismic regions or allow with some requirement about dimensions or spacing of reinforcement using this system in seismic regions [8, 9].



Fig 1. A building with hollow block slab

Hollow block slab (Fig.1.) usually consists of wide and shallow beams. Because of low beam height in this system, its lateral stiffness is low. Because hollow block slab has low drift stiffness, this system may have more lateral drift ratio under lateral loads. In the building, more lateral drift ratios may cause more second order theory. This situation has a negative effect on building performance under earthquake loads. For example, in 23 October 2011 Van-Erciş earthquake, it is shown that damage to infill walls in building with hollow block slab are

more than beam floor system. The reason for this is that hollow block slab that has shallow beam can't restrict the rotation at the end of the column at enough level under lateral loads, and big lateral drift ratios happen in building [13].



Fig 2. A damaged building with hollow block slab after Van earthquake (2011)

In hollow block slab, weak performance because of low lateral stiffness has been considered and restricted by Turkey Earthquake Code (TEC). TEC-1997 and TEC-2007 allow using of hollow block slab in high seismic zones only if structural elements (column, beam and beam-column joints) are designed ductile. If the structural elements are not ductile, shear walls have to be used in the system [11, 12]. TEC-1975 allows using this system in a seismic zone with a requirement which shear walls must be used in this system [10]. But, in existing buildings with hollow block slab, TEC requirements are neglected, and buildings with largely weak performance under earthquake loads have been built. The most important proof of this situation is that these type buildings were heavily damaged in Bingöl Earthquake (2003) and Van Earthquake (2011) [3, 2]. Fig 2. shows a damaged building with hollow block slab after Van earthquake (2011).

III. SOFT-STORY EFFECT

In Turkey, the ground story of buildings that exist two sides of main streets is used as commercial areas. For this reason, the height of this story is more than other stories. Furthermore, infill walls that exist in the upper story between frames partly or completely remove in ground story. In this situation, in the ground story that has big earthquake loads, lateral stiffness of building is decreased, and because of lateral drift ratio, the building experiences degradation of strength. Furthermore, recent years, in these buildings, hollow block slab have become more common for using story height effectively and for providing a flat slab ceiling [2]. Authors think that in these type buildings, the using of hollow block slab reduces the performance of building under earthquake loads. After Van-Earthquake (2011), observations in field influence this opinion. Designing of the ground story with more height than upper story and removing of infill walls of the ground story have

negative effects on reinforced concrete (RC) building performance under earthquake load. Because infill walls restrict lateral drift ratios of the building, infill walls increase the load carrying capacity of the building. For example, a research analyzes performance, under Lorca earthquake, of RC buildings with one-way slabs with wide beams. For buildings, three wall densities are considered: no walls, low wall density, and high wall density. Results show that infill walls increase the lateral stiffness of buildings and decrease lateral drift ratios of buildings under earthquake loads [14]. Especially, because infill walls that exist in the upper story between frames partly or completely remove in ground story, ground story have more lateral drift ratio than the upper story. Past studies show that if infill walls of the ground story are removed, the lateral load carrying capacities of building reduce 30% and the lateral drift ratios of building increase 10% [15]. Although TEC-2007 in the design of reinforced concrete building considers the weight of infill walls, it neglects the effect of infill walls on frame system [12]. The real performances of the buildings cannot be calculated due to this negligence. For this reason, they think that design of these type buildings should be detailedly investigated. Authors are planning a long-term study that considers the effect of infill walls on the building.

IV. NUMERICAL STUDY

In this study, soft-story in buildings with hollow block slab was numerically investigated for different ground story height. For numerical analysis 5, 8 and 11 stories square plan of buildings was investigated. Fig 3. show the typical square plan of buildings. According to common using heights of the first floor was determined for 3.0 m, 3.5 m, 4.0 m, 4.5 m. Except for height of ground story, all heights of stories are 3.0m.

In hollow block slab, the dimension of joists was chosen as 15/32 cm and the dimension of the slab as 7 cm. The nonstructural material was chosen as styrofoam. For providing a flat slab ceiling, heights of all beams of frames was chosen as 32 cm, and for providing enough stiffness, wide of all beams was chosen as 60 cm. Material properties were chosen 25 MPa for concrete compressive strength and 420 MPa yield strength for steel.

Buildings were designed minimum requirement accordance with TEC-2007 and TS-500 (*Turkish Building Code*) [12, 16]. Buildings were designed for first earthquake zone and Z3 soil class. Dimensions of the column in a building stayed unchanged so that only effect of changing of ground story height is investigated. Table 1. presents the dimension of columns and beams.

For linear analysis of design buildings, structure analysis software SAP2000 and IdeCAD was used for analysis. According to analysis, lateral drift ratios was obtained for each story. Two different software, in these sensitive systems, were considered for investigating accuracy rating of software. According to analysis, lateral drift ratios were acquired for each story. For the different height of the ground floor, changing of obtained lateral drift ratios have been presented in tables and graphics. The lateral drift ratios that were obtained from

structure analysis software IdeCAD have been presented in graphics (Fig 4-9). The lateral drift ratios that were obtained from structure analysis software SAP2000 have been presented in tables (show in Table II). The limited number of paper influences this presentation.

According to analyses result in a frame system, as ground story height increased, the lateral drift ratios became more. For designing safety building against to earthquake, TEC-2007 state that the lateral drift ratios can't exceed 2% [12]. But it is shown that as the number of stories increased, the lateral drift ratios have approached limits and the lateral drift ratios of 11 stories building have reached 2%. This increment increases the risk of soft-story.

TABLE I. DIMENSIONS OF COLUMNS AND BEAMS			
	Dimensions of Columns		Dimensions of Beams
	Inside	Outside	
5 stories	45/45	45/45	60/32
8 stories	50/50	45/45	60/32
11 stories	55/55	50/50	60/32

For reducing the lateral drift ratios, in the horizontal and vertical direction in systems, as much as 1% of the area plan, shear walls added to system and analysis was repeated. At both direction, four shear walls that have 30/210 dimension symmetrically added to the system. It is shown that shear walls have considerably reduced the lateral drift ratios and have reduced negative effects from the increment of ground story height. It is shown that in the frame-wall system, lateral drift ratios have reached maximum 1.4%.

V. CONCLUSION

In this study, the performance of hollow block slabs under earthquake loads was investigated regarding lateral drift ratios. The effect of the height of ground story that is designed with more height than an upper story on lateral drift ratios was numerically investigated.

In Turkey, the height of ground story is more than upper story, the effect of this situation on lateral drift ratios was numerically investigated. For numerically study, lateral drift ratios of 5, 8, 11 story RC buildings was obtained for different ground story height. According to analyses;

- For frame structures, it is shown that when the height of ground story reached from 3.0 m to 4.5 m, lateral drift ratios of ground story increased nearly 50%.
- As the number of stories increased, the lateral drift ratios approach upper limit 2% which is recommended by TEC-2007. For 11 stories buildings, drift ratios that are obtained from using structure software SAP2000 reached this limit.

The effect of infill walls was not considered for this study. In case infill walls which are usually used for design are removed

in ground story, it is thought that the increasing in lateral drift ratios will exceed the limit 2% value. Because TEC-2007 don't consider the effect of infill walls on the frame in design, the risk of soft-story is high in these type buildings. For preventing the risk of soft-story, shear walls should be added the systems. It is shown that shear walls reduce the lateral drift ratios of 5 stories buildings on average 65%, 8 stories buildings on average 55%, 11 stories buildings on average 45%. In the wall-frame system, lateral drift ratios reached maximum 1.4%.

Because hollow block slab has low lateral stiffness, it shows weak performance under earthquake loads. This type slabs in the high seismic zone should be carefully designed as a wall-frame system. Furthermore, lateral drift ratios in hollow block slab should be investigated with the effect of infill walls on the building.

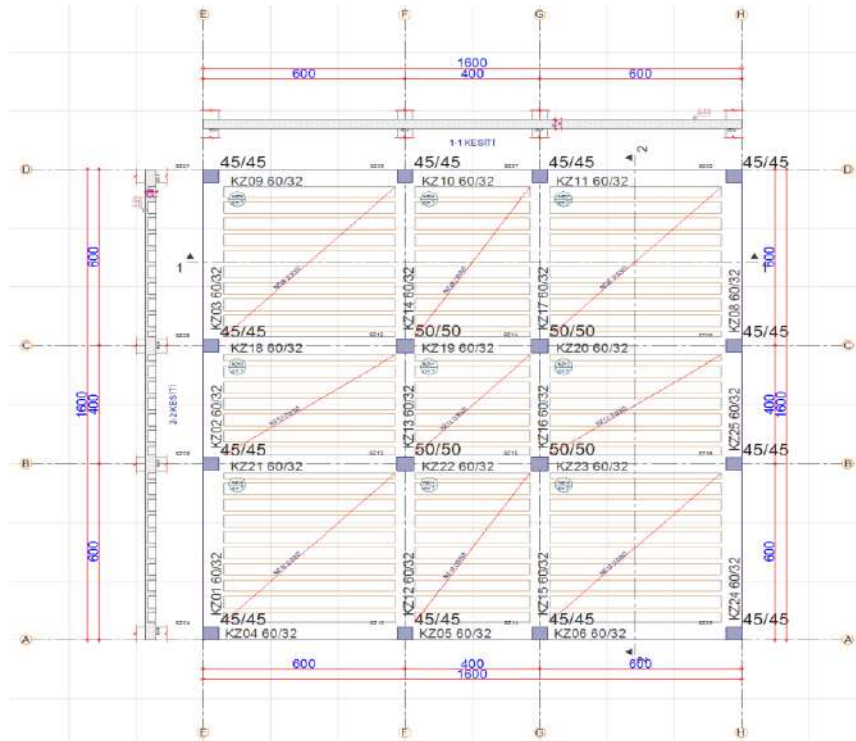


Fig 3. Square Plan of a Building

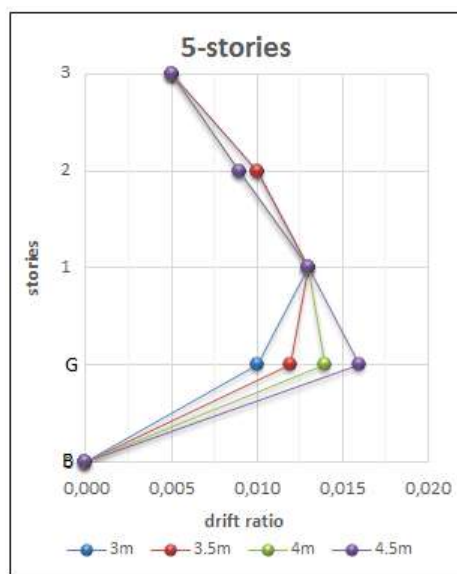


Fig 4. Frame structure with story of 5

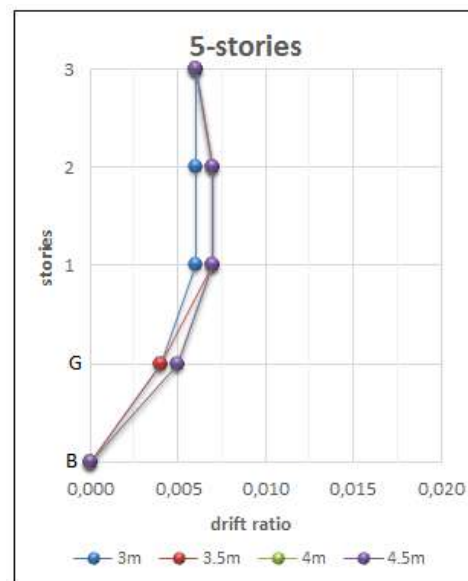


Fig 5. Frame-wall structure with story of 5

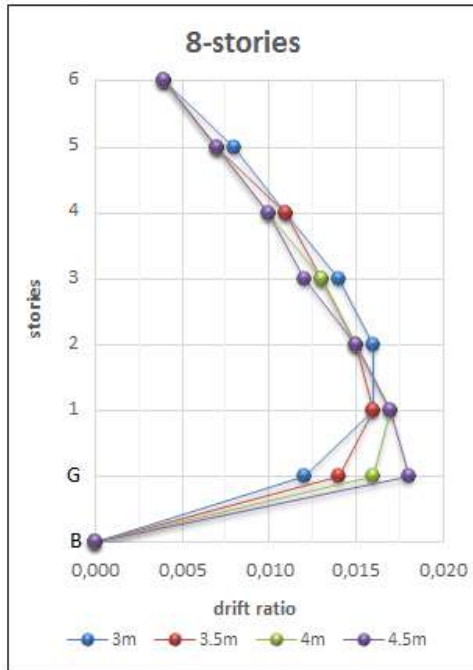


Fig 6. Frame structure with story of 8

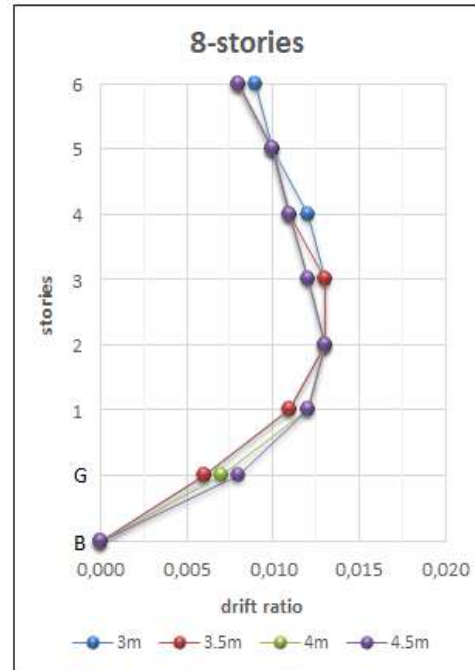


Fig 7. Frame-wall structure with story of 8

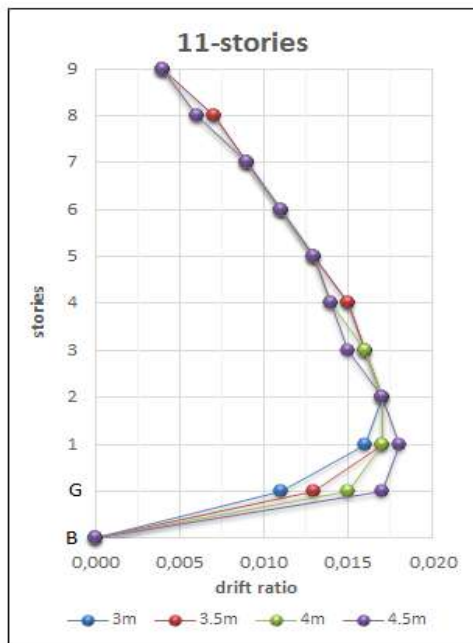


Fig 8. Frame structure with story of 11

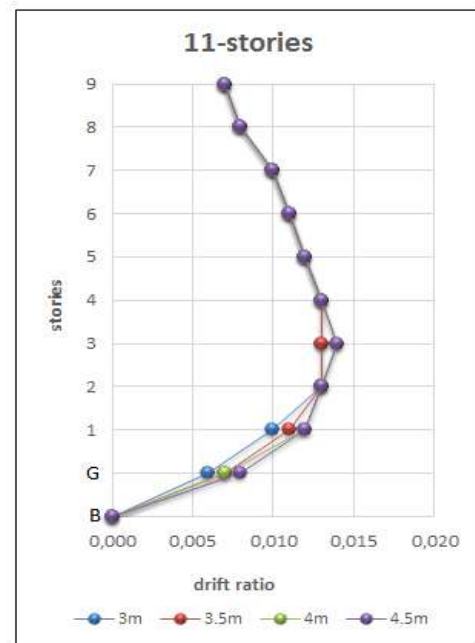


Fig 9. Frame-wall structure with story of 11

TABLE II. LATERAL DRIFT RATIOS OF BUILDINGS FROM SAP2000

5 Stories Frame Structure					
Ground Story h(m)	B	Z	1	2	3
3	0.000	0.010	0.014	0.010	0.006
3.5	0.000	0.012	0.014	0.010	0.005
4	0.000	0.014	0.014	0.009	0.005
4.5	0.000	0.016	0.013	0.009	0.005
5 Stories Frame-Wall Structure					
Ground Story h(m)	B	Z	1	2	3
3	0.000	0.003	0.005	0.005	0.005
3.5	0.000	0.003	0.005	0.006	0.005
4	0.000	0.004	0.006	0.006	0.005
4.5	0.000	0.004	0.006	0.006	0.006

8 Stories Frame Structure								
Ground Story h(m)	B	Z	1	2	3	4	5	6
3	0.000	0.012	0.017	0.016	0.014	0.011	0.007	0.004
3.5	0.000	0.014	0.017	0.016	0.013	0.011	0.007	0.004
4	0.000	0.016	0.017	0.015	0.013	0.010	0.007	0.004
4.5	0.000	0.018	0.018	0.015	0.013	0.010	0.007	0.004
8 Stories Frame-Wall Structure								
Ground Story h(m)	B	Z	1	2	3	4	5	6
3	0.000	0.005	0.009	0.01	0.01	0.009	0.008	0.007
3.5	0.000	0.005	0.009	0.01	0.01	0.009	0.008	0.007
4	0.000	0.006	0.01	0.011	0.01	0.009	0.008	0.007
4.5	0.000	0.006	0.01	0.011	0.01	0.009	0.008	0.007

11 Stories Frame Structure											
Ground Story h(m)	B	Z	1	2	3	4	5	6	7	8	9
3	0.000	0.012	0.019	0.02	0.018	0.017	0.015	0.012	0.01	0.007	0.004
3.5	0.000	0.014	0.019	0.02	0.018	0.017	0.014	0.012	0.01	0.007	0.004
4	0.000	0.016	0.02	0.02	0.018	0.016	0.014	0.012	0.009	0.007	0.004
4.5	0.000	0.018	0.021	0.019	0.018	0.016	0.014	0.012	0.009	0.006	0.004
11 Stories Frame-Wall Structure											
Ground Story h(m)	B	Z	1	2	3	4	5	6	7	8	9
3	0.000	0.006	0.01	0.012	0.013	0.013	0.012	0.011	0.009	0.008	0.006
3.5	0.000	0.006	0.011	0.013	0.013	0.013	0.012	0.011	0.009	0.008	0.006
4	0.000	0.007	0.011	0.013	0.013	0.013	0.012	0.01	0.009	0.007	0.006
4.5	0.000	0.007	0.012	0.013	0.013	0.013	0.012	0.011	0.009	0.008	0.006

REFERENCES

1. Sezen H, Elwood KJ, Whittaker AS, Mosalam KM, Wallace JW, Stanton JF, "Structural Engineering Reconnaissance of the August 17, 1999 Kocaeli (Izmit), Turkey Earthquake", PEER 2000/09, Technical Report, Berkeley, CA., Pacific Earthquake Engineering Research Center, University of California, CA December 2000. <http://nisee.berkeley.edu/turkey>.
2. ODTÜ, "23 Ekim 2011 M_w 7.2 Van Depremi Sismik ve Yapısal Hasarlara İlişkin Saha Gözlemleri", METU/EERC 2011-04, Kasım 2011, Ankara
3. Dogangun, A., "Performance of reinforced concrete buildings during the May 1, 2003 Bingol Earthquake in Turkey," Eng Struct, 2004. 26(6): p. 841-856.
4. Ozturk M., "Field Reconnaissance of the October 23, 2011, Van, Turkey, Earthquake: Lessons from Structural Damages", J. Perform. Constr. Facil., 2015, 29(5): 04014125.
5. SAP 2000 [Computer software]. Berkeley, CA, Computers and Structures.
6. İdeCAD Analiz Programı, <http://idecad.com.tr/>
7. Benavent-Climent, A., X. Cahis, J.M. Vico, "Interior wide beam-column connections in existing RC frames subjected to lateral earthquake loading". Bulletin of Earthquake Engineering, 2010, 8(2): p. 401-420.
8. Fadwa, I., vd., "Reinforced concrete wide and conventional beam-column connections subjected to lateral load", Engineering Structures, 2014, 76: p. 34-48.
9. Gentry, T.R., "Reinforced concrete wide beam-column connections under earthquake-type loading", 1992, University of Michigan.
10. Turkish Earthquake Code (TEC). (1975). "Specifications for structures to be built in disaster areas." Ministry of Public Works and Settlement, General Directorate of Disaster Affairs, Earthquake Research Dept., Ankara, Turkey.
11. Turkish Earthquake Code (TEC). (1997). "Specifications for structures to be built in disaster areas." Ministry of Public Works and Settlement, General Directorate of Disaster Affairs, Earthquake Research Dept., Ankara, Turkey.
12. Turkish Earthquake Code (TEC). (2007). "Specifications for structures to be built in disaster areas." Ministry of Public Works and Settlement, General Directorate of Disaster Affairs, Earthquake Research Dept., Ankara, Turkey.
13. ODTÜ, "9 Kasım 2011 M_w 5.6 Van-Edremit Depremi Sismik ve Yapısal Hasara İlişkin Gözlemler", METU-EERC / İMO 2012, Ankara.
14. D. Domínguez, F. López-Almansa, A. Benavent-Climent, "Would RC wide-beam buildings in Spain have survived Lorca earthquake (11-05-2011)?" Engineering Structures 2016 (108), p.134-154
15. Arslan, M. H., and Korkmaz, H. H., "What is to be learned from damage and failure of reinforced concrete structures during recent earthquakes in Turkey." Eng. Fail. Anal., 2007, 14(1), p. 1-22.
16. TSE-TS-500.: Requirements for design and construction of reinforced concrete structures. Turkish Standards Institution, Ankara (2000) (in Turkish)

Wind-Catchers in Iranian Traditional Architecture as a Sustainable Solutions for Building Ventilation

Saeideh Farnian

Department of Architecture
Karadeniz Technical
University Trabzon, Turkey
s.farnian@gmail.com

Abstract— Sustainability which is one of the most crucial issues in many scientific field has gained a particular significance within recent decades due to the increasing awareness on restriction of irreplaceable energies and risk of energy crisis. A considerable number of studies also are done in field of architecture on designing more energy-efficient and sustainable buildings.

Taking a look at traditional architecture also opens up new windows and gives new perspectives towards sustainability. Environmental and natural conditions have significant role in construction of the region's interrelated cultural, economic, and social infrastructures. Studying the valuable achievements of traditional architecture, not only provides us with precious information about our ancestor's genius on coping with their environmental difficulties and facilitating comfortable living places but also can be inspiring for contemporary architects to design more sustainable works.

In this research, values of sustainable design is handled regarding Iranian traditional and vernacular architecture focusing on one of the most significant elements of Iranian traditional architecture which is called Badgir in Persian.

Wind catcher (Badgir) is a significant element of Iranian traditional architecture which has been used as a natural ventilation element in the buildings throughout centuries and valuable examples of them still exist in diverse Iranian cities located in desert plateau. This architectural element plays a great role in cooling and moderating interior spaces of the buildings located in the central and southern parts of Iran with hot and arid climate.

This study aims to introduce the wind catchers and how their system works since conventional and the modern versions of wind-catchers can be incorporated appropriately into the designs of modern buildings in the hot-arid regions of Iran and other areas of the world with similar climate, to provide summer thermal convenience with less use of non-renewable energy.

Keywords— *Wind-catcher; Sustainability.*

I. INTRODUCTION

A wide range of studies have demonstrated that the issues related to sustainability can influence all aspects of human life. Sustainability principles which encompass a great number of fields aim to improve quality of life for human parallel to

preserving natural and environmental resources and guarantee their durability for coming generations [1].

Hřebík et al. [2] define sustainable development as a better quality of life for everybody, now and for the next generations and it is type of development which meets the requirements of the present without compromising the ability of future generations to satisfy their own needs.

Various tasks are defined in order to achieve a sustainable development some of which comprise attaining a balance between preserving the existing cultural heritage, attracting new investments and supporting existing living and working communities and conserving and improving the natural built environment [3].

These studies raise questions among the policy makers and scholars as well as designers about the effectiveness of sustainable approaches to human activities including architecture. Most studies tend to focus on the issue from view of energy consumption both in terms of energy-efficient modern designs and investigating the roots of sustainability ideology through past but there is still lack of conclusive studies on how the sustainable architecture methods and techniques particularly those employed in traditional architecture can be appropriately used in order to achieve the desired level of sustainability.

Iran is a rather vast country extended from Caspian Sea to Persian Gulf. Therefore, it owns different sorts of climatic conditions in each part of the country. Since central and southern part of Iran is located in hot and arid climate with vast desert regions, Iranian traditional architecture has developed rich vernacular solutions for human comfort in response to difficult climatic conditions of the region. Studying valuable elements and technics of traditional architecture not only provides us with valuable information about our ancestors genius on handling their environmental difficulties and facilitating convenient living places but also can be inspiring for contemporary architects to design more sustainable works. Moreover, gaining such a knowledge on traditional architecture can be guiding in deciding for appropriate usage of technology in a sustainable way [4].

The buildings in Iranian desert regions are constructed according to experiences and knowledge being accumulated by paying attention to climatic and geographic features of the region throughout long centuries and this factor has made them

valuable and worth-studying. Due to lack of any modern heating and cooling equipment in ancient times the architects were obliged to rely on usage of natural energies and utilizing local and climatic potentials of the region to provide interior space with ideal condition and convenience [5].

Wind-catchers (Badgir) can be dealt from diverse perspectives and there are a vast range of subjects about them which worth to be investigated but this study is confined to handle the subject by abstractly expressing what wind-catchers are and how their mechanism work in shade of their relation with sustainability principles. The results taken by studies of this research can enlighten architects to design more sustainable and energy efficient buildings by employing natural potentials.

II. THE STRUCTURAL AND FUNCTIONAL SYSTEM OF WIND - CATCHERS

As a ventilation structure wind catchers were very crucial in cooling interior of the buildings in Iranian traditional architecture. The wind-catcher operates according to the condition of the wind and sun radiation in the region. In ancient times this part of building functioned like the present modern air conditioning system. Wind-catcher is like a chimney whose end is in the underground and the top is set over a specific height on roof and they were majorly built at entrance of the house over underground water reservoirs or ponds built inside house. Dry and warm wind passes over a cool pond which in some cases is equipped with a fountain and gets cooler and gains moisture through evaporation. The system of a wind catcher is schematically demonstrated in Fig. 1.

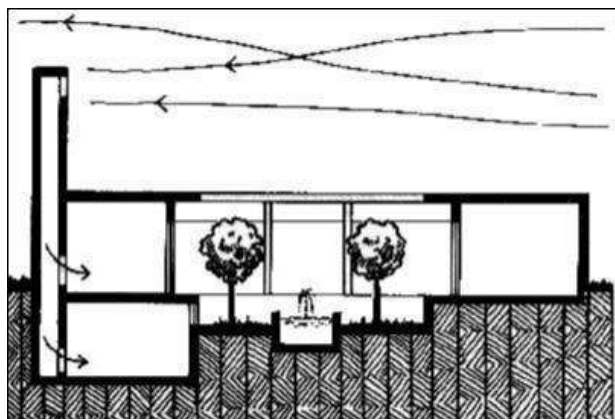


Fig. 1. Schematic model for the function of wind-catchers

The material of wind catchers is very crucial because of high fluctuation of temperature between day and night in hot and arid climate. They are majorly made by mud-bricks.

Two different types of wind-catchers can be seen in two different parts of Iran. The first type is in the hot and humid area in south (such as Lenghe Port) and the second type in hot and dry area of central plateau (such as Yazd city).

The function of both type is the same while some details of their physical form may vary according to climatic conditions and wind orientation of the region (Fig. 2). Since the function of wind-catcher is to get desired wind and transfer it to internal

space, its dimensions acts as a canal through which the air passes and the ratio of length to height and width to length has particular importance in functionality of it [6].

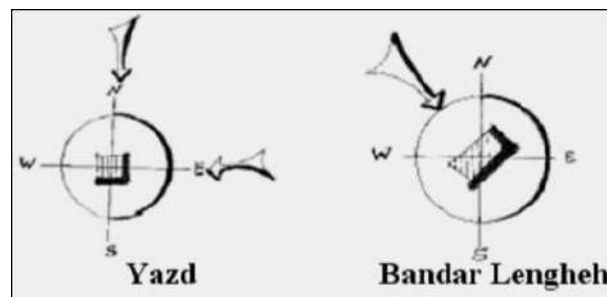


Fig. 2. Comparing location of wind catchers according to wind direction in Yazd city and Bandar Lenghe [6].

The height of wind catchers are different in each city since the speed and orientation of wind is different in each city. The top of wind-catchers are open and the interior of the shaft is majorly divided to one, two, four, six or eight diagonal partitions in a way that from whichever direction wind blows down, in the opposite direction wind is sucked out. This process ventilates the air within the building [7].

III. FUNCTION OF WIND CATCHERS DURING DAY AND NIGHT

During the day, since the sun rays hit on the southern elevation of the wind catcher, the air in the southern part gets hot. Accordingly its density decreases and the hot air goes up. This air taken above through the inner air of the porch is compensated and in fact it makes a kind of proportional vacuum inside the porch and takes the cool air of the inner court into itself. Therefore, the existing air in the northern opening of wind catcher is pulled down as well (Fig. 3).

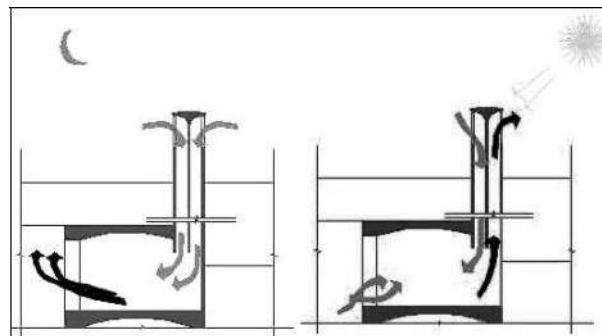


Fig. 3. Comparing the function of wind-catcher during the day and night [6].

During the night due to excessive temperature difference between day and night in desert regions, there is a sudden decrease in outside temperature and the cold air which is more dense moves down from wind catcher shaft. This cool air absorbs the heat being trapped within building materials and becomes warm and then goes up. This circle continues until the temperature of the walls and outside become equal.

This is how the system of a wind-catcher is similar to a modern water cooler. When wind enters a wind-catcher, it is channeled to pass above a water pool. After being exposed to water and evaporation process due to absorbing the heat

brought by hot winds of desert, the cool breeze is directed to the summer rooms through small windows [8].

IV. SORTS OF WIND-CATCHERS

Wind-catchers are classified according to their number of partitions which affect their external form. The simplest of them are one-sided wind catchers (Fig. 4). In this type in order to be protected from storms and heavy winds, wind-catchers are built in the direction of the most agreeable wind and are closed off in all other directions [9].

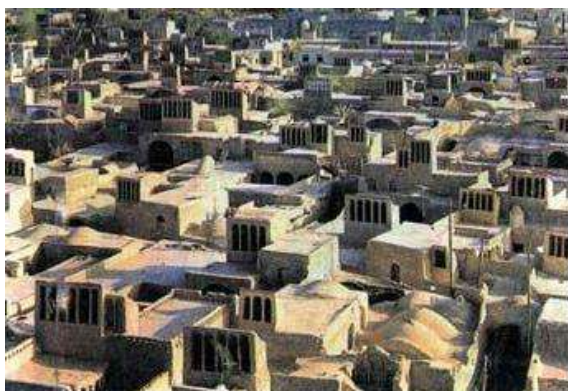


Fig. 4. One-sided wind catchers in Yazd whose entrances are built toward agreeable wind.

As the number of division partitions increases the system of wind-catchers get more complicated (Fig. 5).



Fig. 5. The plans of different sorts of wind-catchers [9].

In those with more than one partition the interior part of wind-catchers shaft usually is divided by brick, wood or plaster partitions to direct the wind to a particular direction.

In Yazd and some other central regions of Iran, multi-directional (eight and sometimes even circular) wind-catchers can be observed. The reason of designing such a sort is that due to extremely hot days in most months of year, these multi-sided wind-catchers can draw agreeable and pleasant winds from almost any direction and channel it into the building to ventilate hot air inside.

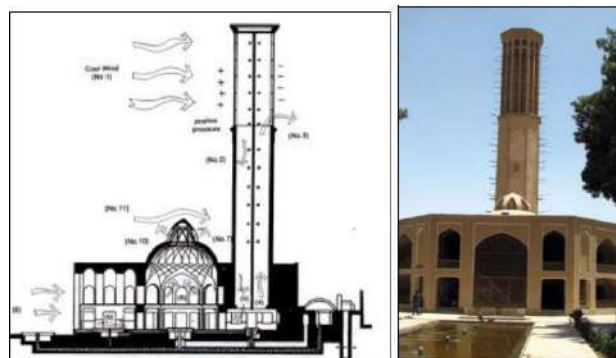


Fig. 6. A section and a picture from Dolatabad Garden, Yazd City [5].

As it can be observed in Fig. 6, this sort of multi-sided wind-catcher performs as the wind hits an obstacle. Since the density of the cool air is more than warm air, on the side of the wind direction where the cool wind is caught by the top of the shaft, a positive pressure becomes generated in this direction while a negative pressure caused by warm air from interior space with less density exist on the other side. Therefore the cool wind is drawn into interior of building and the warm air circulating inside is piped out simultaneously. As mentioned above the wind coming from outside gets moisturized by superficial evaporation of water within a pool and provides building interior with a pleasing air condition [10].

V. CONCLUSION

The wind-catcher which can be counted as one of the masterpieces of Iranian traditional architecture has been used since early times. The results information given in this investigation and other similar studies can have many advantages for us and future generations. Firstly, elaborately studying the application system and construction technics of such a valuable architectural element can help us to better preserve them. Secondly, despite of existing technological facilities of today due to economic and environmental outcomes of using non-renewable energy in ventilation of buildings, wind catchers with their original form and function still can get used particularly as an option particularly in rural areas and the places which has access problem to technological products. Lastly, studying wind-catchers as well as other traditional architecture element can be inspiring for contemporary architects to design more sustainable works.

REFERENCES

- [1] V. Shoarian Sattari and M. Moosavi, "An Analysis to Implications of Sustainability in Physical Structure of Abyaneh Village," *J. Basic Appl. Sci. Res.*, vol. 3(2), pp. 494-499, 2013.
- [2] Š. Hřebík, V. Třebický and T. Gremlica, "Manual for planning and evaluation of sustainable development at the regional level," EnviConsult, Ltd., Office of the Government of the Czech Republic, Prague, 2006.
- [3] M. Jancic, "'Prefaces", European Rural Heritage Observation Guide" CEMAT, 2003.
- [4] S. Farnian, "Sustainable and Functional Architecture in Rural Areas: Case studies of Abyaneh and Masouleh in Iran," *J. Basic. Appl. Sci. Res.*, vol. 6(10), pp. 23-30, 2016.

-
- [5] B. Ahmadkhani Maleki , "Improve ventilation by wind tower (badgir) modified in iranian hot and arid region" *Int. J. Tech. Phys. Prob. Eng. (IJTPE)*, vol. 5, no. 17 , pp. 124-129, 2013.
- [6] A. Azami , "Badgir in traditional Iranian architecture" in *International Conference "Passive and Low Energy Cooling for the Built Environment"*, Santorini, Greece, Santorini, Greece, 2005.
- [7] M. Mahmoudi and S. Mofidi, "Analysis on Typology and Architecture of Wind-Catcher and Finding the Best Type" *Honarhaye Ziba J.*, vol. Vol. 36, no. 8, pp. 22-30, 2008.
- [8] M. Bahadori, "An improved design of wind towers for natural ventilation and passive cooling" *Sol. Energy*, vol. 35, no. 2, pp. 30-41, 2005.
- [9] M. Mahmoudi , , "Wind tower as a natural cooling system in Iranian architecture" in *Passive and Low Energy Cooling in Buildings Conference*,, Greece, 2005.
- [10] B. Ahmadkhani Maleki, , "Traditional sustainable solutions in Iranian desert architecture to solve the energy problem" *Int. J. Tech. Phys. Probl. Eng. (IJTPE)*, vol. 3, issue 6, pp. 84-91, 2011.

The design of self-compacting lightweight smart concrete and investigation of some properties

Nusret BOZKURT

Engineering Architecture Department
Bitlis Eren University
Bitlis, Turkey
nbozkurt@beu.edu.tr

M. Tansu BAYDAŞ

Engineering Architecture Department
Bitlis Eren University
Bitlis, Turkey
tansu.baydas@gmail.com

Abstract—This paper reports an experimental study results on the design of Self-Compacting Lightweight Smart Concrete (SCLWSC) and investigation of some properties produced with acidic pumice. In this study, CEM I 42.5 type N cement and fly ash were used as a binder and powder materials obtaining from Elazığ and Sivas respectively. 6 type SCLWSCs were designed together with carbon based micro steel fibre and micro carbon fibre in different percentages. Acidic volcanic pumice and river sand were used as aggregates. Slump-flow, L-box and V-funnel tests were conducted out to obtain self-compacting concrete properties. Compressive strength, flexural tensile strength and ultrasonic pulse velocity (UPV) tests were applied after 7, 14 and 28 days water curing. Moreover, electrical conductivity tests were performed to identify smart properties on designed concretes for the situations under the flexural tensile load and without any load at 28 day.

Keywords— *Fibre reinforcement; lightweight concrete; self-compacting concrete; smart concrete.*

I. INTRODUCTION

Conventional concrete is composed of aggregate, water and cement and is widely used because of its strength, durability and economy. Because the concrete produced with the advancing technology is produced according to the characteristics of the building elements, it is called special concrete [1]. Heavy concrete, lightweight concrete, self-compacting concrete and fibre reinforced concrete can be given as examples of novel concrete. Every single special or novel concrete is produced for a special purpose. In this study, lightweight, self-compacting and smart concretes have been described firstly because these concretes are constitute the main frame of this work idea.

A. Lightweight Concrete

It is possible to produce concrete by reducing dead-load, earthquake and vertical loads to minimum level by using lightweight aggregate such as pumice, tuff, expanded perlite etc. Lightweight concrete or construction material similar with lightweight concrete was used primarily in a temples in Rome in the year 100 BC with pumice aggregates. In our country, it is seen first in the Hagia Sophia. It was also used in the British Museum in England (1950) as a non-load bearing block. It was used in England after World War II. The first foamed

lightweight concrete was produced in 1950 as a Swedish block. Because natural aggregate source are not sufficient, lightweight concrete is more preferred in Europe [2].

B. Self-Compacting Concrete

Self-compacting concrete (SCC) is invented by the development of effective chemical materials which are influenced by the progressive concrete technology [3]. This special type of construction material is a concrete that does not require any vibration and it can be placed with its own weight without any segregation its constituents [4]. Most commonly it is used that the vibrator-machine can not apply in to the construction elements for concrete pouring. Self-compacting concrete was first developed in 1988 to form a permanent reinforced concrete structure in Japan. The first paper on SCC was presented in 1989 by Ozawa in the East Asian and Pacific Structural Engineering Conference. This declaration by Ozawa was presented at the Canmet & Aci International Conference in Istanbul in 1992, accelerating the announcement of the SCC to the world. This statement has become widespread development of SCC. [3]. Standard test methods for self-compacting concrete design have been developed. The main fresh concrete design tests are slump-flow, L-box and V-funnel test. In the slump-flow test, the spread diameter of the fresh concrete with its own weight gives information about the filling and spreading ability in the moulds. The V-funnel test describes flow-ability of concrete by recording the elapsed time with concrete's own weight. In the L-box test, it is possible to see the concrete's ability to pass between from the re-bars, as well as the ability to fill and flow into the moulds.

C. Smart Concrete

Concrete is simply described as a composite material but has a weak resistance against flexural tensile stresses. Because of these stresses, smart concrete has emerged to prevent all damages that may occur in the concrete [1]. Smart concrete is divided into two classes, externally and internally smart concrete. Such concrete is called externally smart concrete if it is provided in the concrete or on its surface by intelligence by embedding or mounting detectors, exciters and chemicals. It is not necessary to bury the probes in concrete in order to be smart concrete from the outside. By applying silver paint to the

probes, the concrete can be intelligent and traceable [5]. The inner concrete is obtained by adding a very small amount of conductive carbon fiber to the mixture. The carbon concrete, known as the intelligent concrete, was developed and tested by Chung, a professor at SUNY (State University of New York)-Buffalo [1].

The carbon fiber added to the concrete increases the electrical conductivity and gives the ability to follow the concrete. The method of electrical resistance is a method that can determine the damages that may occur in the concrete without damaging it [6]. The electrical conductivity in the carbon fiber-reinforced concrete shows a direct correlation with the volume of the fiber [7]. This fiber increases the bending strength of the concrete and increases the resistivity when exposed to the draw [8]. In this study, the electrical current permeability of concrete designed with pumice stone aggregate and fiber reinforcement, which is prevalent in Bitlis province, was investigated and intelligent lightweight concrete design that settled spontaneously was realized. The technical advantages of the intelligent concrete have been determined by examining the changes in the electrical current permeability of the specimens subjected to tensile stress with this designed concrete.

II. MATERIALS AND METHODS

A. Materials

Portland cement described from the TS EN 197-1 [9] and known as CEM I 42.5 N type was used as a binder material. The cement was provided from Elazığ Çimento Plant in the amount to be used in the experiments and kept under the laboratory conditions that would not deteriorate its chemical structure. The fly ash used in the concrete mix was provided in Sivas-Kangal. Some features of cement and fly ash were given in Table 2.1.

Table 2.1 Chemical properties of fly ash and cement

Content	Fly Ash	Cement
SiO ₂	38.35	21.15
Al ₂ O ₃	16.68	5.65
Fe ₂ O ₃	5.11	3.32
CaO	27.62	62.98
MgO	1.61	2.76
SO ₃	4.43	1.8
Na ₂ O	0.62	-
Other	5.55	-
Spec.Grav. (gr/cm ³)	2.26	3.1
Loss in ign.	0.79	1.79
f _{ce} (MPa)	18.2 (with Cem.)	51.7
Blane (cm ² /gr)	1345	3749

For the purpose of designing lightweight concrete, volcanic pumice aggregate belonging to Bitlis region was used. The aggregate diameter was 16 mm maximum and some physical properties of volcanic pumice aggregates were given in Table 2.2. The sand used as fine aggregate in the mixtures was obtained from Bitlis-Ahlat region. Physical properties related to sand were given in Table 2.3.

Table 2.2 Physical properties of pumice aggregate

Coarse Aggregate Group	Water Absorption Rate (%)	Dry Unit Weight (kg/m ³)	Specific Gravity (kg/m ³)
4-8 mm	38.9	381.7	0.88
8-16 mm	51.8	295.5	0.69

Table 2.3 Physical Properties of Sand

Water Absorption Rate	3.72
Specific Gravity (kg/m ³)	2.22

Sika Hi-Tech Viscocrete-28, a third-generation hyperplasticizer supplied by Sika Construction Chemicals Inc., was used as a chemical additive. The properties of this material is given in Table 2.4.

Table 2.4 Properties of chemical additives

Appearance	Color: Light brown liquid
Ph value	5-9
Chemical structure	Modified polycarboxylate based polymer
Density (kg/l, in 20°C)	1.045-1.085
Freezing point (°C)	-6
Water soluble chlorine (%)	Not more than 0.1%, chloride free

The fibres were added to 0.5% of the cement volume. Carbon fibre taken as a fabric was cut into 6 mm and used in concrete mix. The reason for using this size is that the carbon-based metal fibre and the carbon fibre should be of equal length. The length of the carbon-based metal fibre was 6 mm length. The properties of the fibres were given in Table 2.5.

Table 2.5 Properties of fibers used

	Carbon Fibre	Carbon Based Steel Fibre
Specific Grav. (gr/cm ³)	1.82	7.17
Length (mm)	6	6
Equivalent dia. (mm)	15±3µm	0.15
Length / Diameter	-	40
Tensile Str. (MPa)	4950	2000
Geometry	fibrillated	Straight

B. Method

In this study, the design and properties of SCLWSC with acidic volcanic pumice belonging to Bitlis region were investigated. In particular, the relevant literature, information and documents and resources have been examined. Materials to be used in the study were then investigated. Main materials to be used in the laboratory work; Cement, aggregate, chemical and mineralogical additives had been provided for optimum supply and shortest time. After all these preliminary studies were made, necessary systems and devices were created and experimental studies were done in laboratory conditions according to the standards. Firstly, mixture calculations were made in accordance with the experimental purpose and trial mixtures were prepared based on EFNARC and Turkish Standards [10-14].

In the slump-flow test, the prepared mixture is filled into the funnel. Then the funnel is raised upright in 30 seconds. Fresh concrete is expected to fully spread. The widest span is measured and recorded. This recorded spread was assessed according to the standards. According to EFNARC, the standard limitations of the slump-flow test is given in Table 2.6

Table 2.6 Slump-flow limitation [14]

Class	Propagation Diameter (mm)
SF1	550-650
SF2	660-750
SF3	760-850

The prepared fresh mixture is filled in the V-Funnel and the lid is opened after 10 seconds from the time the top of V-Funnel is cleaned. This elapsed time is recorded by the chronometer. This recorded time is evaluated again according to the standards. According to EFNARC, the limitations of the V-Funnel test is given in Table 2.7.

Table 2.7 V-Funnel test limitations [14]

CLASS	T ₅₀₀ , s	V-Funnel Flow Time
VS1/ VF1	≤ 2	≤ 8
VS1/ VF2	> 2	9-25

In the L-box test, the concrete is poured from the container into the filling hopper of the L-box and allowed to stand for (60 ± 10) sn. Then, the gate is raised so that the concrete flows into the horizontal section of the L-box. When fresh concrete movement has ceased, the vertical distance is measured, at the end of the horizontal section of the L-box, between the top of the fresh concrete and the top of the horizontal section of the L-box at three positions equally spaced across the width of the L-box. The standards limitations on L-box according to EFNARC are given in Table 2.8.

Table 2.8 L-Box Standards according to EFNARC [14]

CLASS	PASSING ABILITY
PA1	≥ 0.80 with 2 rebars
PA2	≥ 0.80 with 3 rebars

After the design process on fresh concrete mixtures, hardened concrete samples were prepared and tested at the ages of 7, 14 and 28-days. Firstly, ultrasonic pulse velocity test was made with the device called Pundit at the same curing ages. The device is calibrated before starting the experiment. The two probes on the device are fixed with jell so that they can come into full contact with the sample. The probes stuck to the samples must be in the same line. In the experiment, three different measurements are made in one sample to minimize the error rate.

In the electrical current permeability test, an alternating current is applied to the samples completing the curing time using the signal generator and multi-meter. Inside the beam sample, two 4x6 cm plate probes are fixed and current is applied. Electrical current permeability test was applied two different way in this study after 28 curing day. Firstly, this alternating current is given at different frequencies (5-1000000 Hz.). Reading the current value in the sample takes 15 seconds and the read value is recorded. In the second application, alternating current is given at constant frequency (25000 Hz.) but increasing the flexural tensile load.

In the flexural tensile strength test, the beam samples (75x75x300 mm) were placed in the device according to the procedures specified in TS EN 12390-5 [15] after completing the curing time mentioned above. For the samples completing 28 curing day, the probes for the plate alternating current in the sample are connected. Once the device is installed, in the same frequency, electrical current and flexural tensile load are recorded. As for the compressive strength test, it was conducted out according to TS EN 12390-3 standard [16].

III. MIXTURE DESIGN AND FRESH PROPERTIES

In the concrete mixtures design, firstly cement, sand as fine aggregate, acidic volcanic pumice as coarse aggregate and mineral admixture were added, then water and chemical additives were added. As for the concrete mixtures including fibres, the same mixture was prepared and the fibres were added by taking care to homogeneously disperse with different percentages and combinations. The reason for paying attention to homogeneity was that the fibres exhibit different electrical behaviour according to the amorphous or crystalline structure [17]. The mix proportions of designed concretes were given in Table 3.1.

Table 3.1 Concrete mix proportions for 1000 dm³

Concrete Type	CTRL	S	S1C1	S2C2	S3C3	C
Water (kg)	160	160	160	160	160	160
Cement (kg)	400	400	400	400	400	400
Fly Ash (kg)	150	150	150	150	150	150
Sand (kg)	989.37	989.37	989.37	989.37	989.37	989.37
4-8 mm Pumice (kg)	46.5	46.5	46.5	46.5	46.5	46.5
8-16 mm Pumice (kg)	55.75	55.75	55.75	55.75	55.75	55.75
Chemical Add. (%)	2.25	2.25	2.25	2.25	2.25	2.25
Carbon Based Metal Fibre (gr)	-	110	82.5	55	27.5	-
Carbon Fibre (gr)	-	-	7.5	15	22.5	30

Fresh properties of designed concrete mixes were determined by applying the SCC fresh state test methods mentioned above (ps. in section II) and obtained results were presented in Table 3.2. Obtained fresh concrete test results are very similar because the only variable is fibre inclusion. The fibre inclusion in concrete design takes so small place (0.5% of cement) in the concrete matrix. For this reason, fresh properties of all designed concretes gave the similar results. This results are suitable for SCC requirements and it can be said that all designed concretes could be called self-compacting-lightweight-concretes.

Table 3.2 Fresh Concrete Test Results

Concrete Mix.	Slump-Flow Diameter (mm)	Slump-Flow Time, T ₅₀₀ (sn)	V-Funnel (sn)	L-box (H2/H1)
CTRL	800	1.97	11.25	0.93
S	790	2.05	7.70	0.95
S1C1	790	2.01	8.25	0.96
S2C2	795	1.95	7.55	0.92
S3C3	795	2.10	10.25	0.95
C	805	2.05	9.05	0.95

After the determining mixture design and fresh properties, SCLWSCs were prepared for hardened state test based on Table 3.1. Prepared SCLWSC samples were removed after waiting for a day in the mould. Then, the samples were allowed to stand for 3-4 hours in laboratory conditions and then left in the pool for water curing at the ages of 7, 14, 28 days in accordance with TS EN 12390-2 [18]. The samples that completed the curing period were removed from the curing-pool and was dried for two days in 50°C so that electrical current measurement stability. The dried samples were stored for 3-4 hours under laboratory conditions. For each sample,

ultrasonic sound permeability test and electrical measurements were performed for varying frequencies. Based on the strength properties of the samples and the differences of changing electric resistance, the electric resistance was monolithically decreased after 14 and 28 days while increased after 7 days tests [19]. Thus, the effect of curing time of concrete was examined.

IV. RESULT AND DISCUSSION

The flexural tensile strength, compressive strength and UPV test results of the prepared concrete samples are presented in Figure 1-3. The electric current values in the different frequency values of these samples are shown in Fig. 4. The current values of each sample under flexural tensile load are also shown in Figure 5-10. When the strength characteristics are presented in Fig. 1-2 and the UPV test results are presented in Fig. 3, it is understood that each concrete gives close results. The main reason why these results are close to each other is that only the fibre inclusion differs in the concrete mix. The fiber materials used do not make a great difference in strength due to the use of a very low percentage of the concrete volume. The flexural tensile strength results of designed SCLWSCs changed between 5.7 MPa and 7.4 MPa after 28 curing day while compressive strength test results varied from 42.1 MPa to 48.6 MPa after 28-day. Figure 1-2 show that concrete specimens using steel carbon based micro-fibres relatively exhibit higher strength properties when examined more carefully. UPV test results also confirm the strength test results (ps Figure 3). When Figure 4, in which the current values are presented under different frequencies, it is seen that the current value increases with increasing frequency value and with increasing amount of carbon fiber. In this figure, it is seen that the worst results are obtained from the control series and interestingly from the carbon based steel fibre including dense percentage in the mix. When Figure 5-10 in which the current values were presented under the flexural tensile loads, if the applied load increased, then the current values increased. The specimens subjected to the test show a sudden decrease in the current value at the time of cracking and breakage. However, in the control concrete where no fibre is used in the mixture, the current value decreases with the increase of the load. This general result suggests that the fracture can be detected by adding carbon based steel and carbon fibres to the concrete structure at certain ratios. The uncommon and interesting result between the Figure 5-10 is presented in Figure 8 and 10. These two figures include the very similar electric current values under the similar flexural tensile loads. S2C2 concrete presented in Figure 8 has 50% of carbon based steel fibre and 50% of carbon fibre while C concrete include 100% carbon fibre. This result is remarkable in terms of economy and smart properties.

V CONCLUDING REMARKS

The SCLWSCs were designed successfully in the frame of SCC criteria. There was no significant change in compressive strength and UPV test results with addition of carbon and steel carbon fibre to concrete. In the flexural tensile strengths, higher strength values were obtained in concrete using carbon based steel fibre. Produced SCLWSCs gave 48.6 MPa (S2C2) compressive strength while flexural tensile strength value obtained 7.4 MPa in the highest range. The current values were increased with increasing frequency without loading on the samples. It has been observed that there is a steady decrease in the current value at the moment when the fracture occurs, while the constant frequency under flexural load has an increase in the current in the fibre-concretes with the increase of the load. On the other hand, the current value of the control concrete under the increasing load was observed to decrease. These results show that carbon based steel fibre and carbon fibre can be used to provide concrete sensing capability. This capability could be called smartness or intelligence property of concrete.

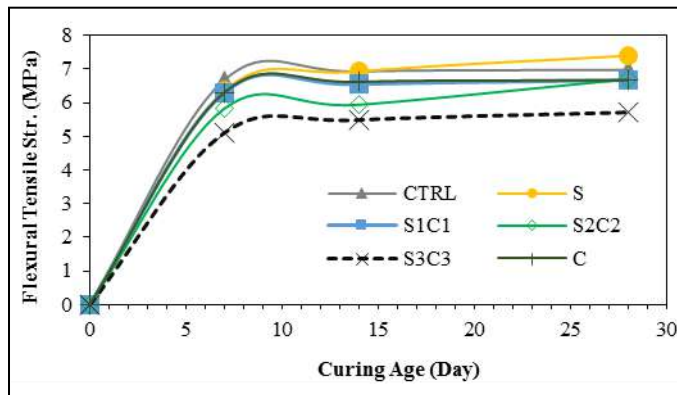


Figure 1. Flexural tensile strength test results.

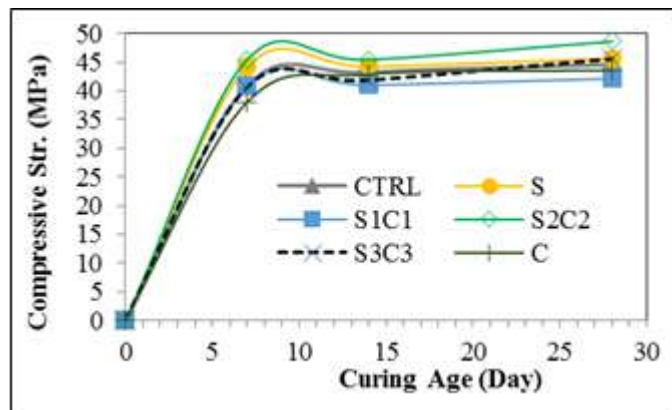


Figure 2. Compressive strength test results

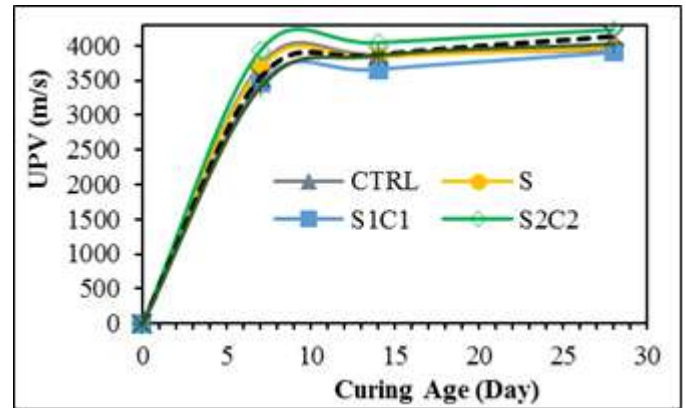


Figure 3. UPV test results

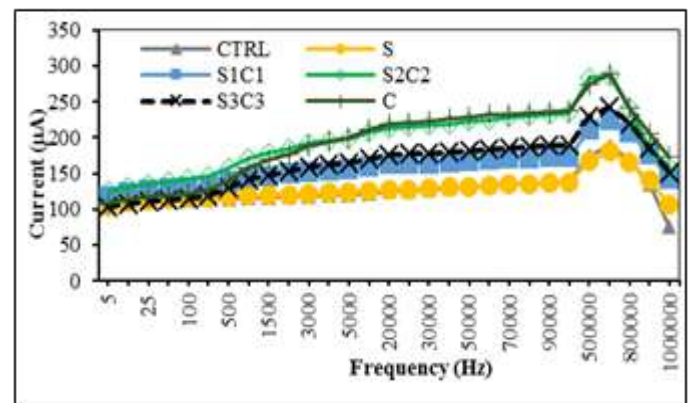
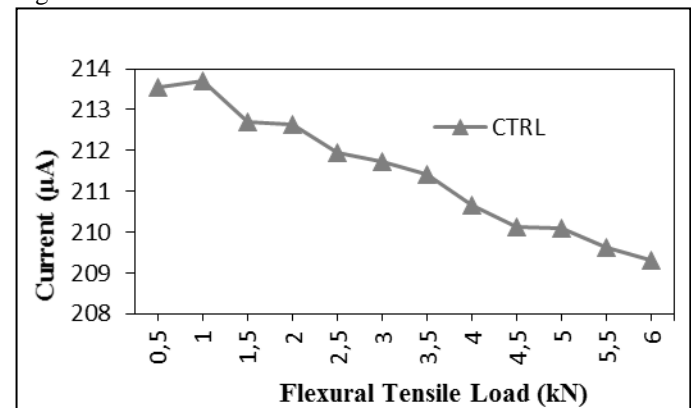


Figure 4. Current values under different frequencies

Figure 5. Current values under flexural tensile loads for CTRL



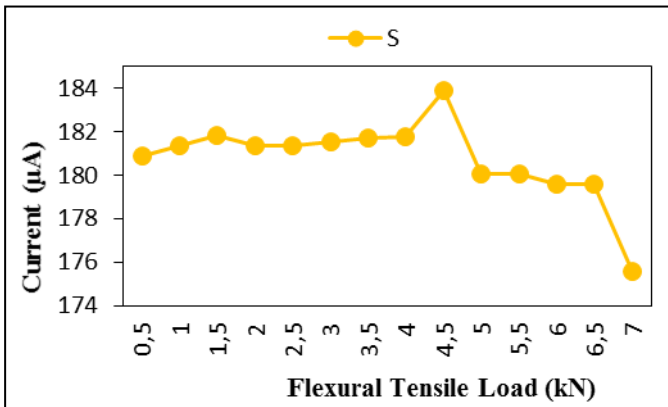


Figure 6. Current values under flexural tensile loads for S

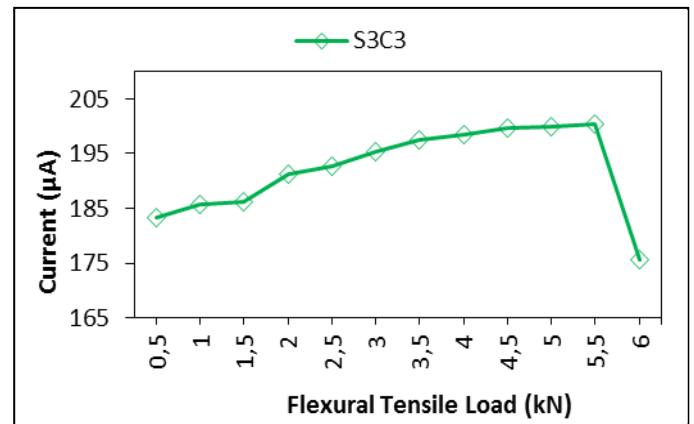


Figure 9. Current values under flexural tensile loads for S3C3

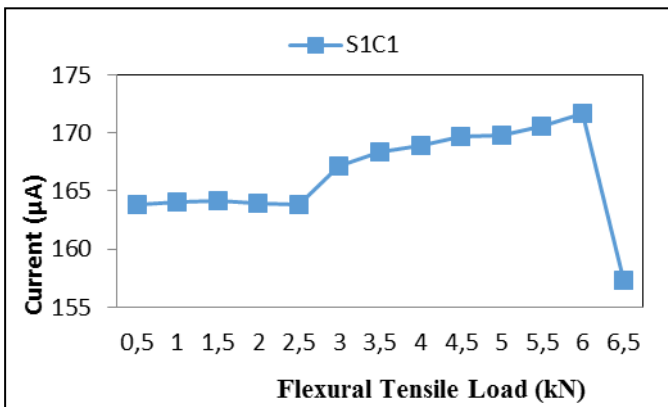


Figure 7. Current values under different frequencies for S1C1

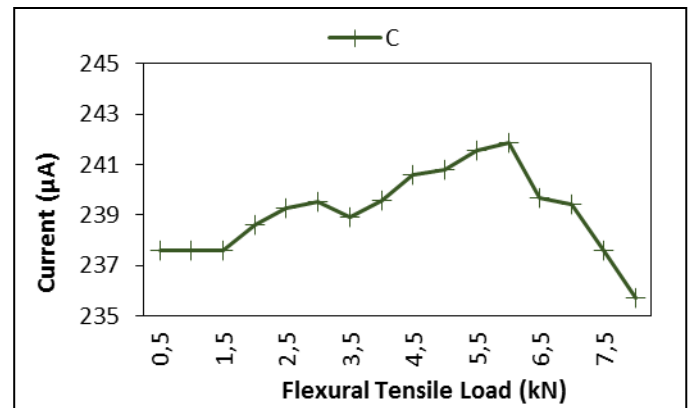


Figure 10. Current values under flexural tensile loads for C

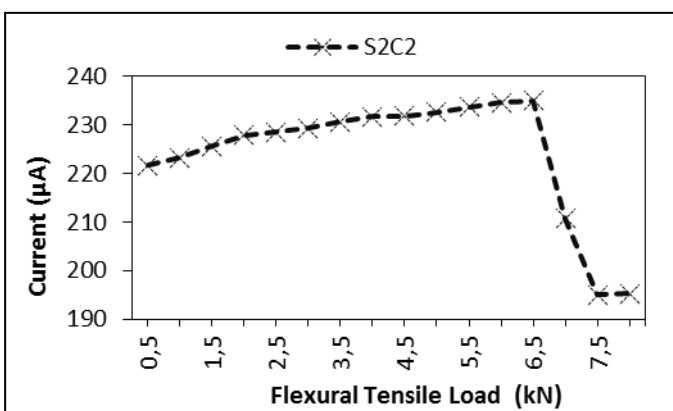


Figure 8. Current values under different frequencies for S2C2

References

- [1] B. Demirel, "The investigation of stress and temperature behaviours of the smart lightweight concrete", Turkey, 2006.
- [2] www.atacanannue.com/2014/06/hafif-betonlari.html
- [3] B. Felekoğlu, B. Baradan "The mechanical properties of self compacting concretes", London.
- [4] A. R. Sağlam, N. Parlak, Ü.A. Doğan, and M.H. Özkul, "Self compacting concrete and compatibility of cement and admixture", Turkey.
- [5] P.P. Chen, D.D.L. Chung "Carbon fiber reinforced concrete as an electrical contact material for smart structures", Smart Mater. Struct., pp. 181-188, 1993.
- [6] F. Xuli, D.D.L. Chung "contact electrical resistivity between cement and carbon fiber: its decrease with increasing bond strength and its increase during fiber pull-out," Cement and Concrete Research. USA, Vol. 25, No. 7, pp. 1391-1396. 1995
- [7] N. Banthia, S. Djeridane, and M. Pigeon, "Electrical resistivity of carbon and steel micro-fiber reinforced cements," Cement and Concrete Research. London, vol. 22, pp. 804-814, 1992.
- [8] S. Wen, D.D.L. Chung, "Effect of carbon fiber grade on the electrical behavior of carbon fiber reinforced cement," Composite Materials Research Laboratory, 2000
- [9] TS EN 197-1 Cement – Part 1: Composition, specification and conformity criteria for common cements, Turkish Standart Institution, Ankara, 2012.
- [10] D-M. Bontea, D.D.L. Chung, and G.C. Lee, "Damage in carbon fiber-reinforced concrete, monitored by electrical resistance measurement," Composite Materials Research, 1997.
- [11] TS EN 12350-8 Testing fresh concrete - Part 8: Self-compacting concrete- Slump-flow test, Turkish Standart Institution, Ankara, 2011.
- [12] TS EN 12350-9 Testing fresh concrete - Part 8: Self-compacting concrete - V funnel test, Turkish Standart Institution, Ankara, 2011.
- [13] TS EN 12350-10 Testing fresh concrete - Part 10: Self-compacting concrete - L box test, Turkish Standart Institution, Ankara, 2011.
- [14] EFNARC, The European Guidelines for Self Compacting Concrete-Specification, The European Federation of Specialist Construction Chemistry and Concrete Systems, 2005, p.68.
- [15] TS EN 12390-5 Testing hardened concrete - Part 5: Flexural strength of test specimens, Turkish Standart Institution, Ankara, 2010.
- [16] TS EN 12390-3 Testing hardened concrete - Part 3: Compressive strength of test specimens, Turkish Standart Institution, Ankara, 2010.
- [17] S. Wen, D.D.L. Chung, "Uniaxial tension in carbon fiber reinforced cement, sensed by electrical resistivity measurement in longitudinal and transverse direction," Composite Materials Research, 2000.
- [18] TS EN 12390-2 Testing hardened concrete - Part 2: Making and curing specimens for strength tests, Turkish Standart Institution, Ankara, 2010.
- [19] P.-W. Chen, D.D.L. Chung, "Concrete reinforced with up to 0.2 vol% of short carbon fibres," USA, 1992.

Analysis of Composite Steel I-Girder Bridges

¹Fatma ÜLKER, ²Ragıp İNCE

¹DSİ General Directorate, Ministry of Forestry and Water Management, Ankara, Turkey

²Firat University, Engineering Faculty, Civil Engineering Department, Elazığ, Turkey

Email: ¹ fulker@dsi.gov.tr, ² rince@firat.edu.tr

Abstract--In this study, the analysis and design of composite steel I beamed straight bridges were performed by Line-Girder method in SAP2000 package program. Bridge analysis with Line-Girder is done with influence lines classically. The classic Line-Girder bridge analysis is quite complex. Here, based on AASHTO HL-93 truck for bridge analysis, a practical and precise solution method based on Line-Girder is given in SAP2000 program. In practice, a two-span composite I-girder steel bridge is solved. Composite steel I-Girder bridge analysis results are compared for Line-Girder and influence line solutions.

Keywords—Bridge; AASHTO; Steel beams: Line-Girder; Bridge design

I. INTRODUCTION

Steel Girder Bridges are structurally the simplest and the most commonly used on short and medium span bridges. Steel I-section is the simplest and most effective solid section for resisting bending and shear [1], [2].

In this study straight composite steel-concrete plate girder bridges are investigated by the Line-girder method and influence lines. A design example of the two span continuous composite plate girder bridge is given to illustrate the design procedure. ASTM A 709 (Grade 50) structural steel is used for this bridge structure [3].

Concrete with 28-day compressive strength $f_c' = 4.5$ ksi is used in concrete deck slab construction.

The line girder analysis method uses load distribution factors to isolate a single girder from the rest of the superstructure system and evaluates that girder individually. The load distribution factors can be simply determined by some approximate formulae for both straight bridges [4].

II. DESIGN EXAMPLE – TWO-SPAN CONTINUOUS COMPOSITE PLATE GIRDER BRIDGE

A two-span continuous composite I-girder bridge has two equal spans of 165 ft and a 42 ft deck width. The concrete slab is 9.5 inch thick. A typical 2.75 inch haunch was used in the section properties. The elevation and Bridge Cross Section are shown in Figure 1 [4].

Concrete barriers weighing 640 plf and an asphalt wearing surface weighing 60 psf have also been applied as a composite dead load. HL-93 loading was used per AASHTO, including dynamic load allowance [2], [4], [5].

Steel girder I section dimensions for positive and negative flexure regions are given in Figure 2. Steel girder bridges are modeled as beam elements (See Figure 3). Flexural stiffness of composite section is assumed over the entire bridge length even though the negative moment regions may be designed as non-composite for the section capacity. Moment zero points (contraflexure points) of girder bridges are taken as 0.8 times of beam space (i.e. 0.8×165 ft = 132 ft).

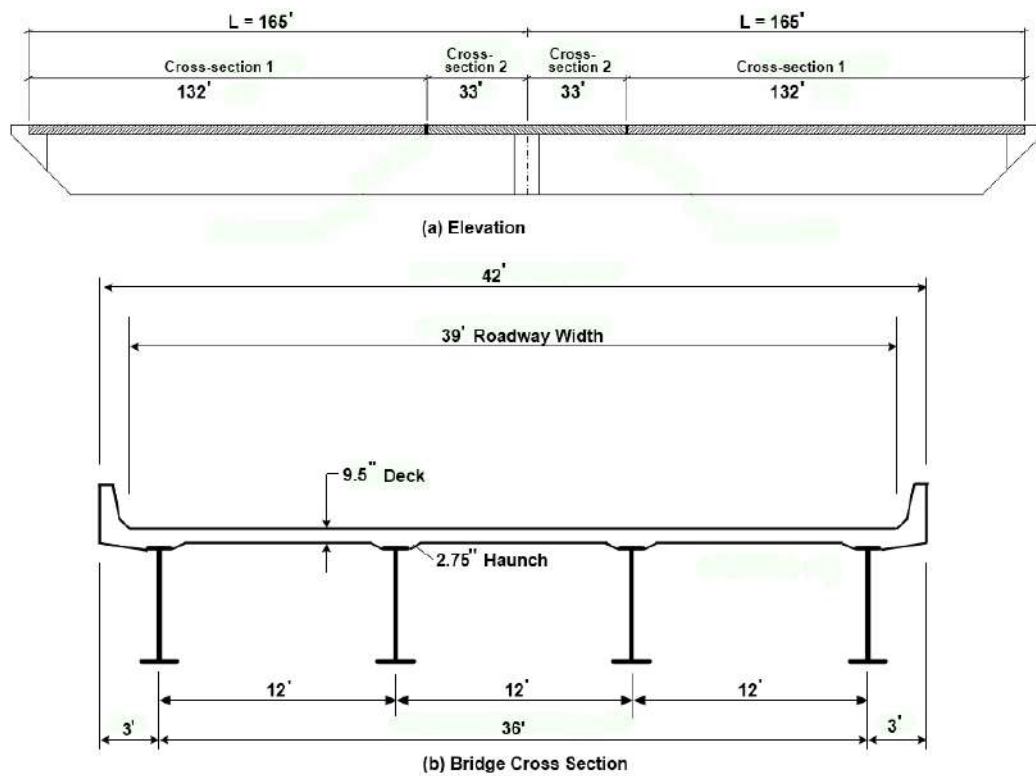


Fig. 1. Two-span Continuous Steel Plate Girder Bridge

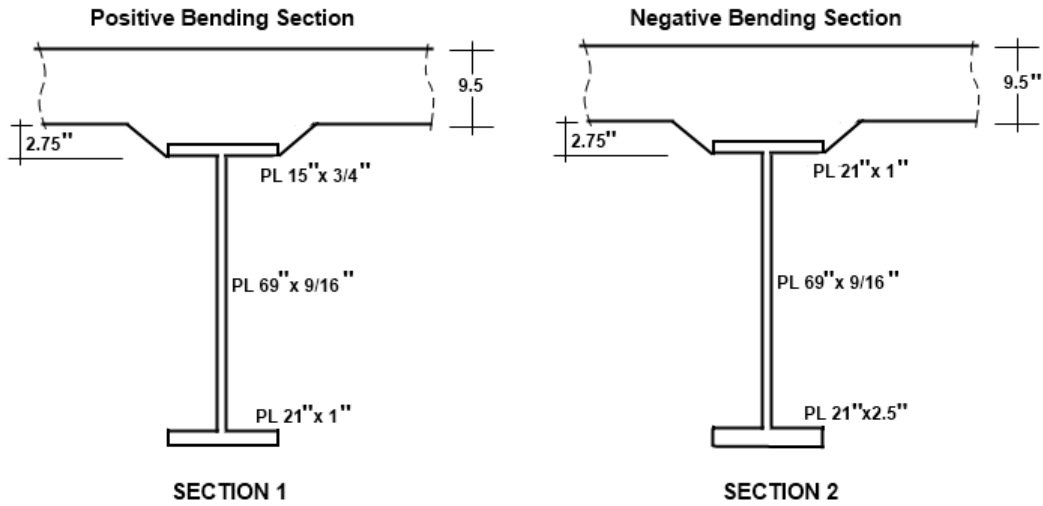


Fig. 2. Steel girder I section dimensions for positive and negative flexure regions

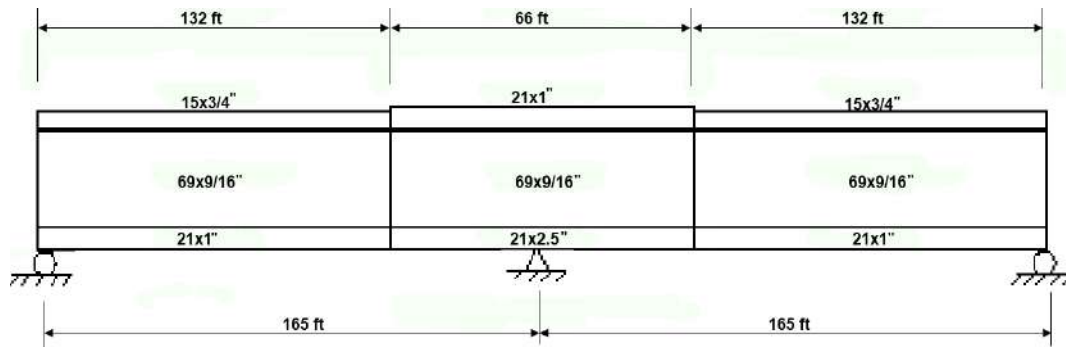


Fig. 3. Two-span girder elevation

A. Bridge Load Calculations

1) Dead Load Calculations

DC dead loads (structural components) include; Steel girder self weight (DC1), Concrete deck self weight (DC1), Haunch self weight (DC1), Barrier walls (DC2).

DW dead loads (structural attachments) include; Wearing surface (DW).

Dead Load Calculations for SECTION1, SECTION 2, DECK, HAUNCH and BARRIER walls are given as follows [4], [5]:

Steel girder self-weight DC1:

$$W_{\text{SECTION},1} = 278.1 \text{ lb/ft}$$

$$W_{\text{SECTION},2} = 439.5 \text{ lb/ft}$$

Deck self-weight DC1:

$$W_{\text{DECK}} = 1425 \text{ lb/ft}$$

Haunch self-weight DC1:

$$W_{\text{HAUNCH}} = 52.5 \text{ lb/ft}$$

Barrier walls DC2:

$$W_{\text{Barrier}} = 320 \text{ lb/ft}$$

Wearing surface DW:

$$W_{\text{Wsr}} = 585 \text{ lb/ft}$$

This calculations are carried out for a per girder.

The following Dead Load results were obtained from the FE analysis (shown Table 1): The maximum positive live-load moments occur at stations 58.7' and 271.3', The maximum negative live-load moments occur over the center support at station 165.0'

TABLE 1. DEAD LOAD RESULTS

	Max (+) Moment [k-ft]			Max (-) Moment [k-ft]	
	Ref(4)	This study		Ref(4)	This study
DC1-Steel	475	476,79		-1189	-1186,18
DC1-Deck	2415	2421,18		-5708	-5689,36
DC1-Haunch	89	89,2		-210	-209,61
DC1-Total	2979	2987,17		-7107	-7085,16
DC2	553	543,7		-1251	-1277,61
DW	1011	994		-2286	-2335,65

The DC1-Total moments calculated as M3-3 in SAP2000 [6] are shown in Figure 4. In this

study, almost 100% results were obtained with SAP2000 Line-girder method.

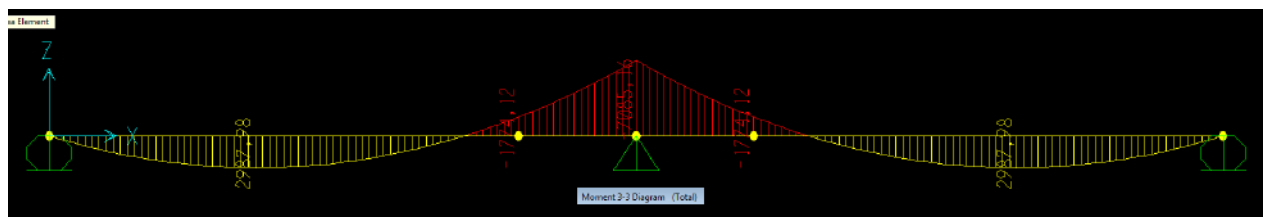


Fig. 4. DC1-Total moments

2) Live Load Calculations

The following design vehicular live load cases described in AASHTO-LRFD are considered [4], [5]:

- TANDEM+LANE load:** The design tandem consists of two 25^{kip} axles spaced 4.0ft apart. The lane loading consists of a 0.64^{kif} uniform load on all spans of the bridge. (HL-93M in SAP2000)
- TRUCK+LANE load:** The effect of one design truck with variable axle spacing combined with the effect of the 0.64^{kif} lane loading. (HL-93K in SAP)
- TRUCK-TRAIN Negative Moment Loading:** 90% of the effect of a truck-train combined with 90% of the effect of the lane loading. The truck train consists of two design

trucks spaced a minimum of 50ft between the lead axle of one truck and the rear axle of the other truck. The distance between the two 32^{kip} axles should be taken as 14ft for each truck. The points of contraflexure were taken as the field splices at 132ft and 198ft from the left end of the bridge. (HL-93S in SAP)

All live load calculations were performed in SAP 2000 using a Line-Girder analysis. The nominal moment data from SAP2000 was then input into Table 2. An Impact Factor of 1.33 was applied to the truck and tandem loads within SAP2000.

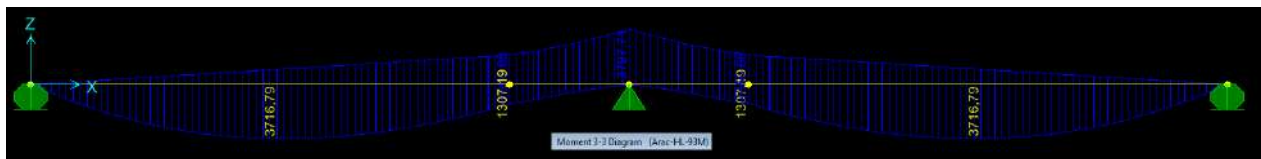
The maximum positive live-load moments occur at stations 73.3ft and 256.7ft, The maximum negative live-load moments occur over the center support at station 165.0ft.

TABLE 2. LIVE LOAD RESULTS

	Max (+) Moment [k-ft]		Max (-) Moment [k-ft]	
	Ref(4)	This study	Ref(4)	This study
HL-93M	3725	3716.79	-3737	-3797.71
HL-93K	4396	4395.55	-4261	-4323.09
HL-93S	N/A		-5317	-4789.14

The Live load (HL-93 vehicle) moments calculated as M3-3 in SAP2000 are shown in Figure 5. In this study, under the load of HL-93M and HL-93-K, almost 100% results were obtained

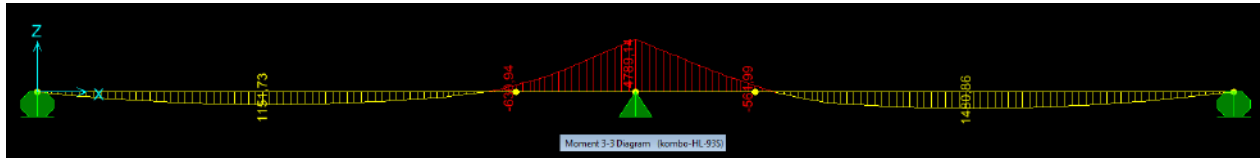
with SAP2000 Line-girder method. For TRUCK-TRAIN Negative Moment loading (i.e. HL-93S), the approach is 90% as shown in Table 2.



a) HL-93M Vehicle



b) HL-93K Vehicle



c) HL-93S Vehicle

Fig. 5. HL-93 Vehicle Moments

B. Influence Line Analysis

This two-span bridge is also analyzed by the influence lines and the moments of the moving load (HL-93 vehicle) are calculated. The influence lines are obtained by defining a general vehicle in SAP2000 and applying unit loading.

HL-93M, HL-93K and HL-93S moving loads were also taken as vehicle loading in the

analysis with influence lines. Moving load moments are determined by multiplying the influence line ordinates by vehicle loads and impact factor. The results are given in Table 3.

Using the influence lines, the moment value of 5343.60 k-ft was calculated, especially for the negative moment on the internal support (HL-93S Vehicle). This value is exactly the same as that calculated in Reference [4].

TABLE 3. LINE-GIRDER AND INFLUENCE LINE MOMENTS

	Max (+) Moment [k-ft]			Max (-) Moment [k-ft]		
	Ref(4)	This Study		Ref(4)	This Study	
		Line-Girder	Influence Line		Line-Girder	Influence Line
HL-93M	3725	3716.78	3613.83	-3737	-3797.71	3716
HL-93K	4396	4395.55	4266.10	-4261	4323.09	4229.60
HL-93S	N/A			-5317	4789.13	5343.60

III. RESULTS

In this study, it was shown that Straight Composite Steel I-Girder bridges can be solved by Line-Girder method. The finite element method is used for the solution in SAP2000 by Line-girder method. The results obtained here are acceptable. Again, more precise results were obtained with the influence line in the SAP2000 program.

From all these calculations, the following result has been achieved: By deriving from the influence line analysis, the moments obtained with the SAP2000 program can be reliably used for bridge analysis and design.

Highway Structures Design Handbook, Published by AISI in cooperation with HDR Engineering, Inc. [6] SAP 2000-V14.2-V15.1-V18.0, *Structural Analysis Program*, Computers and Structures Inc.

REFERENCES

- [1] *Bridge Engineering Handbook*, Wai-Faf Chen and Lian Duan, CRC Press, 1999.
- [2] ASTM, American Society for Testing and Materials, West Conshohocken, 2009, PA.
- [3] AASHTO 2010, *AASHTO LRFD Bridge Construction Specifications*, Third Edition with Interims, American Association of State Highway and Transportation Officials, Washington.
- [4] *AASHTO LRFD Bridge Design Specifications*, The University of Cincinnati, James A. S. and Richard A. M., 4th Ed., July 2007.
- [5] *Four LRFD Design Examples of Steel Highway Bridges*, Vol. II, Chapter 1A

Derivation of Damage Probability Matrices For Hinge Connected Precast Industrial Buildings

Mehmet Palanci
Department of Civil Engineering
İstanbul Arel University
İstanbul, Turkey
mehmetpalanci@arel.edu.tr

Sevket Murat Senel and Ali Kalkan
Department of Civil Engineering
Pamukkale University
Denizli, Turkey
smsenel@pau.edu.tr and akalkan@pau.edu.tr

Abstract— Seismic risk determination of precast buildings is a key subject in mitigation of economic losses in the future seismic events as these buildings play important role on the economic growth and one of the primary sources of workmanship in Turkey. For this reason, seismic risk of precast industrial buildings under potential destructive earthquakes should be determined. From this perspective, one story hinge connected buildings which constitutes a great part of industrial building stock of Turkey were selected and seismic capacity of these buildings were determined by the current Turkish Earthquake Code. Seismic demand of buildings were obtained by performing nonlinear time history analyses using more than 300 real ground motion records. Earthquake records were selected to represent low, moderate and high intensity levels in terms of their peak ground velocity (PGV) and selected earthquake records were then divided into numerous groups according to their intensity levels. Then, damage probability of precast buildings was calculated by different probabilistic methods based on comparison of performance levels and seismic demands for each earthquake intensity group and performance levels. Three different methods were used to calculate damage probability of buildings and each method has different aspects in calculating the probabilities of structural damages. By this way, damage probabilities and consequently the Damage Probability Matrices (DPM) were derived for each earthquake and performance levels. Results obtained from DPM of precast buildings have indicated that damage probabilities can highly be affected from the calculation method used.

Keywords—Precast Buildings; damage probability matrices; nonlinear time history analysis

I. INTRODUCTION

In last decade, various moderate to large scale earthquakes occurred in Turkey. Important part of precast industrial buildings suffered from excessive damages in Adana-Ceyhan and Marmara earthquakes [1-2] occurred in 1999. Although some studies were performed on the reasons and causalities of damages in precast buildings [3-5], damage-earthquake intensity relations and collection of damage evaluation data of these buildings were not conducted at effected sites or regions. However, destructive earthquakes occurred in the past caused

adverse effects on economic growth of the country. Occurrence of damage probabilities and their relation with ground motion indices might be very helpful to make risk assessment of precast buildings in the future seismic events. For this reason, derivation of damage probability matrices for precast industrial buildings will be important step in understanding of damage-earthquake relations and may be helpful in reducing economic losses of seismic events in the future.

Determination of knowledge between ground motion indices and structural damages very appropriate to the probabilistic methods and they are commonly used to determine such relations. Although fragility or vulnerability curves are available to describe damages of building with earthquake damage indices [6-8] the other probabilistic method is damage probability matrices (DPMs). Damage probability matrices are actually determined by collecting damage data [9] from the region affected by earthquakes. Compared to fragility curves, damage probability matrices define the discrete probabilities of reaching damage state at specified or various ground motion levels and DPMs are empirical as they are mainly based on expert-opinions. This method is also the basis of ATC-13 [10]. DPMs can also be used for the estimation of earthquake insurance rates [11-13]. In this regard, it can be said that derivation of DPMs has a critical importance in determining seismic risk of precast buildings and mitigation of economic losses.

For this purpose, 98 real hinge connected precast industrial buildings located in Denizli Organized Industrial Zone (DOIZ) were used and damage probability matrices (DPM) of considered precast buildings were derived by using three different methods which have different aspects in calculating the damage probabilities. Results obtained from DPM of precast buildings have indicated that damage probabilities can considerably be affected from the calculation method used.

II. CAPACITY DETERMINATION IN HINGE CONNECTED PRECAST BUILDINGS

Precast industrial buildings, constitutes majority of lightweight industrial facilities [14] in Turkey and most of

them are constructed as one story [15]. For this reason, one story hinge jointed precast building are considered in this study. As a consequence this connection type, precast columns behave like cantilever components, so strength and displacement response of members can directly be used for the determination of capacity curve. For this purpose, moment-curvature analyses of precast columns were performed. During the analyses, ultimate displacement capacity of columns was described in terms of strain limits of confined concrete and tensile longitudinal reinforcement considering the TEC-2007 [16] (see (1)). In the equation, ε_{ccu} and ε_{su} define the strain value of confined concrete and tensile reinforcement. Minimum curvature value is attained that corresponds to these strain limits.

$$\phi_u = \phi_{\min}[(\varepsilon_{ccu} = 0.04 + 0.014(\rho_s/\rho_{sm}) \leq 0.018); (\varepsilon_{su} = 0.06)] \quad (1)$$

The intermediate damage levels, on the other hand, were determined by using 10% and 75% of plastic deformation capacity of the RC sections. Finally, base shear capacity (V_i) of the buildings were calculated by summing of individual strength capacity of precast columns (v_{ui}). Furthermore, performance limits of were determined by taking minimum of individual columns deformation responses for considered damage limit as shown in Fig. 1.

III. ESTIMATION OF SEISMIC DEMAND

In order to determine relation with damage and ground motion parameters, seismic demand should also be calculated for considered buildings. For this aim, nonlinear time history analysis was performed and real earthquake records were used for seismic demand estimation. During the selection of ground motion records Peak Ground Velocity (PGV) was selected as reference seismic damage quantity and records were chosen to represent low, medium and high intensity earthquake sizes. More than three hundred ground motion records were used and some of these records (72 of 364 records) were scaled to fulfill the need of high intensity earthquake sizes, but maximum scale was not taken higher than 1.54. Selected records were divided into twelve PGV groups with increments of 5cm/s. Some salient attributes of PGV groups are given in Table I. It can be seen from the table that number records of individual groups are almost identical as it was aimed to reduce bias between the

TABLE I. FEATURES OF EARTHQUAKE RECORDS USED IN TIME HISTORY ANALYSIS

Intensity Level	PGV Group No	Number of Records	Average PGV of the group (cm/s)	Standard Deviation (cm/s)
I	1	29	21.69	1.21
	2	31	27.31	1.5
	3	34	32.05	1.48
	4	30	37.35	1.49
II	5	30	41.77	1.28
	6	30	47.15	1.54
	7	30	52.16	1.47
	8	30	57.18	1.32
III	9	30	62.07	1.14
	10	30	67.52	0.97
	11	30	72.55	0.75
	12	30	77.31	1.09

results. Minimum and maximum value of PGV was 20cm/s and 80cm/s respectively. These PGV intensity levels were proposed to make rapid assessment in reinforced concrete structures in Turkey by Sucuoglu and Yazgan [17]. Sucuoglu and Yazgan used three intensity zones having PGV increments of 20 cm/s.

IV. DERIVATION OF DAMAGE PROBABILITY MATRICES

Whitman [9] was first time used to determine damage probability of prototype buildings by using damage observations from site investigation reports. Even though, DPM are based on empirical damage observations of experts, three different damage probability matrix calculation methods based on the analytical nonlinear dynamic analysis of precast buildings is presented in this study,. Before the description of calculation methods, some information about typical DPM is given. In Table II, damage states (DS), central damage ratios (CDR) of each damage state and damage probabilities $Pr_k(DS, I)$ for each ground motion size for k type of buildings can be seen as common components of DPM.

TABLE II. TYPICAL TABULAR FORM OF DPM

Damage State	Central Damage Ratio (CDR)	Seismic Damage Quantity (e.g. MMI)			
		V	VI	VII	VIII
No Damage	0	$Pr_k(DS, I)$			
Slight Damage	5				
Moderate Damage	30				
Extensive Damage	70				
Collapse	100				

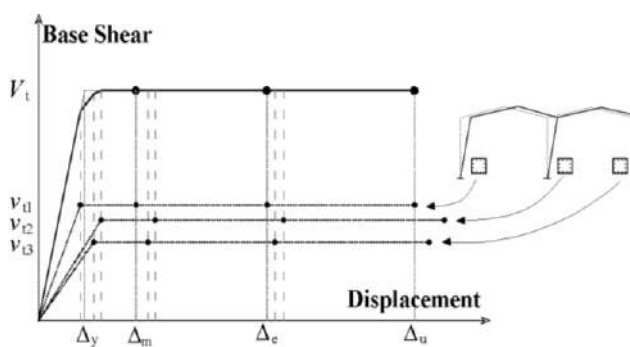


Fig. 1. Typical representation of capacity curve construction

It should be stated that CDR values have important contribution on calculation of MDR curves. In this study, CDR values given in Table II, proposed by Gurpinar et al. [18], is used for calculation of MDR curves.

Although table gives detailed information about the probabilities of each damage state (DS), yet does not indicate the probability of damage to structure at specific earthquake size. In order to determine such quantity, Mean Damage ratio (MDR), sum of product of damage state probabilities and central damage ratios (CDR), should be calculated (see (2)). By this way, DPMs of different buildings or calculation methods can be compared easily by using MDR curves as also used in this study. In further sections, DPM calculation methods are expressed.

$$MDR(I) = \sum_{DS} Pr(DS, I) \times CDR(DS) \quad (2)$$

A. Method-1

This method is based on the empirical calculation method as shown in equation (3). In the equation, $N(DS, I)$ and $N(I)$ express the number of k -type buildings in damage state DS and total number of k type buildings under earthquake intensity I .

$$Pr_k(DS, I) = N(DS, I)/N(I) \quad (3)$$

This equation can also be used for analytical dynamic time history analysis results as the total number of buildings and damage state of buildings for each earthquake size after dynamic analysis can be determined. However, each earthquake size has more than one record, for instance 30 ground motion records, so selection of appropriate DS becomes essential. In this case, it can be assumed that the worst damage state can be the crucial on seismic behavior.

TABLE III. APPLICATION OF METHOD-1 TO SAMPLE BUILDING

PGV Group No		1	2	3	...	10	11	12
Cumulative number of damage occurrence numbers								
DS	NoDamage	25	15	13	...	2	1	0
	$> \Delta_y$	4	16	21	...	28	29	30
	$> \Delta_{MN}$	0	4	13	...	28	28	28
	$> \Delta_{GV}$	0	0	0	...	5	7	12
	$> \Delta_{G\check{C}}$	0	0	0	...	0	0	4
Damage Occurances according to Method-1								
DS	NoDamage	0	0	0	...	0	0	0
	Slight	1	0	0	...	0	0	0
	Moderate	0	1	1	...	0	0	0
	Extensive	0	0	0	...	1	1	0

PGV Group No	1	2	3	...	10	11	12
Collapse	0	0	0	...	0	0	1

By this way, the most unfavorable condition can be considered by using two digits system like 0 and 1. As the cumulative damage states of building can be determined for each building and PGV group, then undesired damage state can apparently be seen and digit of 1 can be marked to related DS and PGV groups and rest of other DS can be marked as "0" in the table. Aforementioned process is clearly shown in Table III for sample building which exists in the inventory. If such calculation is applied to rest of building in the inventory then empirical DPM based on analytical calculation results can be obtained for considered building type.

B. Method-2

In Method-1, the worst damage states are considered, but in this method all possible damage states are considered. By this way, possibility of any damage case on the damage probabilities of buildings is taken into account.

In this method, firstly cumulative damage state occurrence numbers are found by comparison of performance limits. These values are shown in Table III for sample building in the inventory. Later, damage state occurrence numbers are determined by extracting the adjacent damage levels and this step is illustrated in Table IV for same building. If the pre-described methodology is applied to the rest of precast buildings in the inventory, occurrence numbers of each damage state for each earthquake size can be calculated. As in method-1, damage probabilities can be calculated for each PGV bin by proportion of occurrence number of damage state and sum of all possible damages.

C. Method-3

Damage probability matrices are used to specify the discrete probabilities of reaching damage state at specified or various ground motion levels. Fragility curves, on the other hand, describe the reaching or exceeding of damage state probabilities, for various ground motion sizes. In this case, occurrence damage probabilities can be obtained by subtracting the adjacent curves. It should be reminded that, fragility curves are continues functions, but DPMs are discrete, so damage probabilities should be calculated for considered earthquake size. This procedure is also illustrated in Fig. 2. In this study, each earthquake size is described in Table I in terms of average PGV value of each PGV bin.

TABLE IV. APPLICATION OF METHOD-2 TO SAMPLE BUILDING

PGV Group No		1	2	3	...	10	11	12
Occurrence number of damage states								
DS	NoDamage	25	15	13	...	2	1	0
	Slight	4	12	7	...	0	1	2
	Moderate	0	4	13	...	13	15	14
	Extensive	0	0	0	...	5	7	8
	Collapse	0	0	0	...	0	0	4

and hence the MDR curves of the buildings. For this reason, selection of ground motion records has also important effect on damage probabilities of buildings. In this study, effect of ground motion selection on the damage probabilities is not taken into consideration. So, sensitivity of MDR curve determined from Method-1 is not investigated. Nevertheless, independent from the ground motion records used, it is possible to admit that Method-1 can be used represent the worst condition for the building type considered.

In fig. 3, MDR curves of Method-2 and Method-3 is also

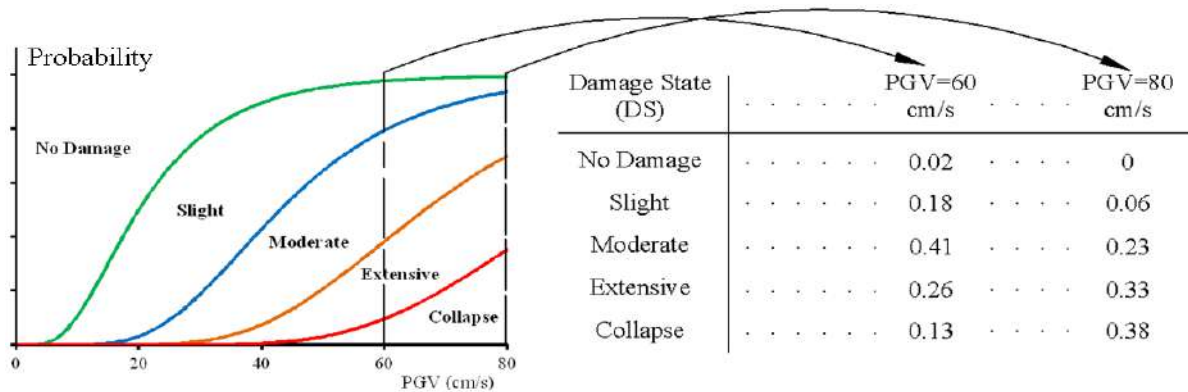


Fig. 2. Transformation of probabilities from fragility curves to Damage Probability Matrices for Method-3

In order to determine DPMs of inventory buildings in this study, average fragility curves provided by Palanci [11] for inventory buildings are used. Considering the similar circumstances, Palanci and Senel [19] also determined the DPMs of one-story inventory buildings.

V. COMPARISON OF DAMAGE PROBABILITY MATRICES

It can be said that all presented methods is established on different probabilistic views. For this reason, it is possible to determine different damage probabilities for precast industrial buildings. As mentioned earlier, DPMs are used to represent discrete probabilities of damage states in terms of different earthquake intensity levels. To represent the damage probability of related building type to distinct earthquake levels MDR values are used. By this way, damage curves can be drawn and compared.

In fig 3, MDR curves of all presented methods are drawn according to PGV level. Ordinate values of the graph are determined by using (2). It can be seen from the figure that MDR curve of Method-1 is very different from the Method-2 and Method-3. It can be understood from the MDR curve of Method-1 that this method may be used to represent for upper level of damage probabilities. Since Method-1 uses the worst damage case for buildings, it probable to determine higher damage probabilities compared to other methods. As empirical DPM curves are determined from the damage observations after destructive earthquakes, these curves or damage probabilities maybe also be determined higher for non-code conformed buildings. Except from the quality of the buildings, the use of ground motion records may also affect the DPMs

drawn. From the figure, it can be implied that both methods gives almost similar damage probabilities. Note that Method-2 uses the all possible damage cases in calculation of damage probabilities for this reason each damage case have contribution on damage probabilities of buildings. In method-3 damage probabilities are calculated by subtracting the damage probabilities of adjacent damage probabilities. This situation indicates that both methods may likely be similar in estimating the damage probabilities as they almost use identical probabilistic view. The difference is that Method-2 directly uses the damage occurrence numbers and then calculates the probabilities by taking the ratio of occurrence number for each damage case and all occurrence numbers for considered earthquake size.

Finally, it can be said that all obtained damage probabilities are the consequences of use of probabilistic view. The difference between the results also is the indicator of uncertainties caused by lack of knowledge, use of different probabilistic view, in selection of ground motion records and etc. In this case, if the obtained results were combined with

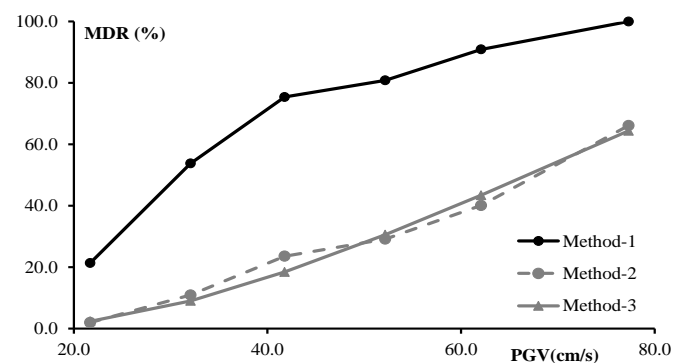


Fig. 3. Comparison of MDR curves of all presented methods

appropriate approach, an important finding could be drawn about the damage probabilities of the precast buildings.

In the scope of this study, all presented methods are combined by summing of all damage probabilities multiplied by constant coefficients. Mathematical expression of this statement is given in (4). According to (4), 50% of Method-1 and 25% of Method-1 and Method-2 is used. This situation shows that weight of Method-2 and Method-3 is taken equal. Coefficients were taken equal owing to damage probability similarities of these methods. Actually, equation can be considered as the weight of Method-1 and weight of Method-2 and Method-3 are equal since the damage probabilities of Method-2 and Method-3 is very similar.

$$\sum_{DS} \Pr(DS, I) = \sum_{DS} [0.5\Pr(DS, I)_{M-1} + 0.25(\Pr(DS, I)_{M-2} + \Pr(DS, I)_{M-3})] \quad (4)$$

In fig. 4, MDR curves of individual methods and their combination determined according equation (4) is plotted. In the figure, MDR curve determined from (4) is described as "Combination". It can be seen from the figure that, MDR curve of combined curve is range between the presented methods. It is expected that all methods presented herein can be used to represent the upper and lower damage probabilities limits of buildings and they naturally involves uncertainties. Combined MDR curve of presented methods, on the other hand, clearly emphasizes the importance of evaluating the different approaches together. In addition, this situation stresses that with appropriate approach, combination of different views of probabilistic calculations may be beneficial for risk assessment not only for precast industrial building but also any of interested building type.

VI. SUMMARY AND CONCLUSIONS

In this study, 98 existing one-story precast industrial buildings are used for determination of Damage Probability Matrices (DPMs). Determination of damage probabilities were performed by using nonlinear time history analysis of precast buildings. Dynamic analyses were performed by real ground motion records selected according to ground motion parameter of PGV. Selected records were divided to several groups to represent low, medium and high intensity earthquake levels.

Three different probabilistic calculation methods, called Method-1, Method-2 and Method-3, are presented in the scope of this study. Each method is based on the distinct probabilistic view so different damage probabilities were calculated from the presented methods. Observations have shown that Method-1 represents the highest damage probabilities for considered building type as the method uses the worst damage state for each earthquake intensity level. It was determined that outcomes of Method-2 and Method-3 are almost similar. Investigations on the reasons of this situation have implied that both methods uses almost similar views, but not completely identical. Method-2 is based on the damage state occurrence

numbers and occurrence numbers are determined from the subscription of adjacent damage levels. Different from the method-2, Method-3 concerns about the direct use of damage probabilities determined from fragility curves of precast buildings. However, it is worth to remind that fragility curves are continuous functions and they are mostly constructed by using probability distributions like lognormal distribution. As fragility functions are derived by fitting the best curve for probabilities of damage states, it may be difficult to construct best fitting curve to real damage probabilities of damage states in every circumstances. As the Method-2 is based on direct use of damage probabilities, the difference between these methods can also be observed. Furthermore, similarities in damage probabilities of method-2 and method-3 also highlights that constructed fragility curves for existing buildings are quite well as there is a good relation between the damage probabilities of these methods.

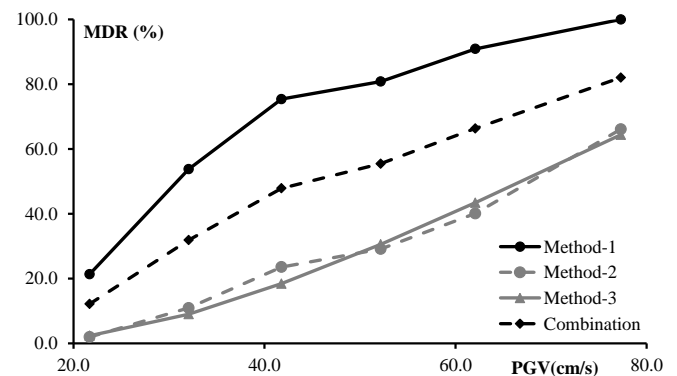


Fig. 4. Comparison of MDR curves of all presented methods and their combination

Consequently, it is noted that presented methods can be used to represent the upper and lower damage probabilities for precast industrial buildings. Considering the uncertainties involved in calculation methods, in selection of records, outcomes of all presented methods are combined. Results clearly stress the importance of using different probabilistic calculation methods to make risk assessment for structures.

ACKNOWLEDGMENT

The authors acknowledge support provided by Scientific and Technical Research Council of Turkey (TUBITAK) under Project No: 110M255. The authors wish to express their gratitude to directorate of DOIZ) for providing design projects of precast buildings. Ground motion records used in this study are downloaded from the PEER web site. The authors also acknowledge the PEER for providing the processed data..

REFERENCES

- [1] H. Atakoy, "The August 17th earthquake and the prefabricated structures built by the members of the prefabric union." *Concrete Prefabrication*, 2000, 52–53(3), 5–14.
- [2] U. Ersoy, G. Ozcebe, T. Tankut, "Observed precast building damages in 1999 Marmara and Duzce Earthquakes" *Proceedings of 10th prefabrication symposium*, 2000, Istanbul, Turkey.
- [3] M. Posada, S.L. Wood, "Seismic performance of precast industrial buildings in Turkey", *Proceedings of the 7th U.S. national conference on earthquake engineering*, 2002, Boston, US.
- [4] S. S. Tezcan and, H. K. Colakoglu, "Weak points of the TEC-98 precast building code provisions." *Proceedings of 5th National Conf. Earthq. Eng.*, 2003, Istanbul Technical University Press, Istanbul, Turkey, 149–158.
- [5] M. Zorbozan, G. Barka and, F. Sarifakioglu, "Observed precast building damages in Ceyhan Earthquake, reasons and solutions." *Concret. Prefabr.*, 1998, 12(48), 12–16.
- [6] M. Palanci, S.M. Senel, A. Kalkan, Assessment of one story existing precast industrial buildings in Turkey based on fragility curves. *Bulletin of Earthquake Engineering*, 2017, 15(1): 271–289.
- [7] A.D. Baltzopoulou, A.K. Eleftheriadou and A.I. Karabinis, "Seismic Vulnerability and Risk Assessment of the Building Stock of Attica (Greece) and Correlation to the Actual Repair Cost", *Proceedings of the 15th World Conference on Earthquake Engineering*, 2012, Lisbon, Portugal.
- [8] A.K. Eleftheriadou, A.D. Baltzopoulou, and A.I. Karabinis, "Seismic Risk Assessment of Buildings in the Extended Urban Region of Athens and Comparison with the Repair Cost", *Open Journal of Civil Engineering*, 2014, 3:115-134.
- [9] R.V. Whitman, "Seismic Design Decision Analysis, Report No. 8: Damage Probability Matrices for Prototype Buildings, R73-57", Massachusetts Institute of Technology, Cambridge, 1973.
- [10] Applied Technology Council, *Earthquake Damage Evaluation Data for California*. ATC-13, Applied Technology Council, Redwood City, CA, 1985.
- [11] M. Palanci, "Estimation of earthquake insurance rates by using probabilistic methods in existing industrial precast buildings." PhD Thesis, Pamukkale University, 2014.
- [12] A. Deniz, "Estimation Of Earthquake Insurance Premium Rates Based On Stochastic Methods", M.Sc. Thesis, Civil Engineering Department, Middle East Technical University, 2006.
- [13] M.S. Yucemen, C. Yilmaz, M. Erdik, "Probabilistic Assessment of Earthquake Insurance Rates for Important Structures: Application to Gumusova Gerede Motorway", *Structural Safety*, 2008, 30(5): 420–435.
- [14] E. Karaesmen, "Prefabrication in Turkey: Facts and figures", Dept. of Civil Engineering, Middle East Technical Univ., Ankara, Turkey, 2001.
- [15] S.M. Senel and M. Palanci, "Structural aspects and seismic performance of 1-story precast buildings in Turkey". *J Perform Constr Facil*, 2013, 27(4):437–449.
- [16] Turkish Earthquake Code (TEC), "Specifications for structures to be built in seismic areas." TEC-2007, Ministry of Public Works and Settlement, Ankara, Turkey, 2007.
- [17] H. Sucuoglu, U. Yazgan, "Simple survey procedures for seismic risk assessment in urban building stocks". In: Wasti ST, Ozcebe G (eds) *Seismic assessment and rehabilitation of existing buildings*. NATO Science Series IV Kluwer, Netherlands, 2003, pp 97–118.
- [18] A. Gurpinar, M. Abali, M.S. Yucemen, Y. Yesilcay, "Feasibility of mandatory earthquake insurance in Turkey. *Earthquake Engineering Research Center*", Report No. 78-05, Middle East Technical University, 1978.
- [19] M. Palanci and S.M. Senel, "Determination Of Seismic Risk In Precast Industrial Buildings By Different Damage Probability Approaches", *Proceedings of Eighth National Conference on Earthquake Engineering*, 2015, Istanbul, Turkey.

Hardened State Properties of Modified Concrete Produced with Demolish Waste, Steel and Plastic Fiber

Selim Cemalgil

Civil Engineering Department
Munzur University, Aktuluk Campus
Tunceli, Turkey
selimcemalgil@hotmail.com

Onur Onat

Civil Engineering Department
Munzur University, Aktuluk Campus
Tunceli, Turkey
onuronat@munzur.edu.tr

Serkan Etli

Civil Engineering Department
Munzur University, Aktuluk Campus
Tunceli, Turkey
serkanetli@munzur.edu.tr

Abstract—This paper presents hardened state properties of concrete produced with demolish waste as control concrete and concrete produced with steel and plastic fiber chips. Two sets concrete production were implemented and results were compared in terms of compressive strength, split tensile strength, ultrasonic pulse velocity and Schmidt hammer test.

Keywords—concrete; demolish waste; steel fiber; plastic fiber; mechanical properties

I. INTRODUCTION

Concrete is known as artificial rock. This artificial material composed of many ingredients. Last two decades' waste or any other natural or artificial materials are started to be added to concrete to evaluate fresh and hardened state properties. For this purpose, many researchers implemented experimental campaign. Liu et al. [1] investigate that the effect of the recycled aggregate on concrete failure mechanism. In this study, Elasticity modulus and strength parameters of recycled concrete under both compressive force and tensile loading were experimentally studied to present failure mechanism. Results show that the old mortar has more predominant influence on both the strength and the Elasticity modulus of recycled concrete. Padmini [2], Xiao and Du [3] produce concrete and tested the Young's modulus and strength of the concrete as a former step by using it to make recycled concrete. Presented experiments demonstrated that for a known w/c ratio, the recycled concrete containing basic concrete with superior properties has a higher compressive strength and a higher Elasticity modulus. A similar experimental study was made by Etxeberria et al. [4]. In their experimental program they used recycled coarse aggregates obtained by crushed concrete. Concrete mix were designed and produced with 0%, 25%, 50%

and 100% of recycled coarse aggregates, respectively. The mix design calculations were made to reach the similar compressive strength class for the all usage level of recycled coarse aggregate. The level of the standard deviation of the compressive strength achieved up to 50% for concrete made with 100% of recycled concrete aggregate. The standard deviation change is derived from the recycled aggregate qualification distribution in the mix. The water absorption capacity is another important parameter. Recycled aggregate has a great amount of absorption capacity. For this reason, water content of recycled aggregate must be known prior to the utilization in concrete production to control properties of fresh and hardened concrete. Some of the investigators propose to limit recycled aggregate ratio at 30% level to maintain the ordinary requirements of 5% of absorption capacity of aggregates for structural concrete [5,6]. Compressive strength of the concrete made with 100% recycled coarse aggregate is smaller when the usage of lower level w/c ratio respect to the conventional aggregate produced with the same w/c content. Furthermore, the w/c ratio is utilized at the same level to produce the conventional and recycled concrete, the conventional concrete has the biggest compressive strength [7]. Cement produced 100% of recycled aggregate in concrete to achieve the same workability and compression strength as ordinary concrete is higher amount against the cement content of traditional concrete [8]. Sagoe-Crentsil et al. [9] made an investigation for the fresh and hardened properties of concrete made with commercially produced coarse recycled concrete aggregate and natural fine sand. The test results of these samples compared with the characteristics of fresh and hardened recycled aggregate concrete and natural aggregate concrete mixtures. The abrasion loss of recycled aggregate concrete made with ordinary portland cement is about 12%

higher than compared to normal concrete, while the corresponding drying shrinkage was about 25% higher at 1 year. Lotfi et al. [9] investigated that the compressive strength and related mathematical curvature like the stress-strain curve (SSC) of recycled aggregate concrete (RAC) made with changing replacement ratio of recycled coarse aggregate (RCA). For the testing of concrete samples uniaxial compression loading is applied. Recycled concrete made with fully recycled aggregate has a reduction in modulus of elasticity about 45% while the peak strain is 20% higher than the normal concrete. Previous studies shown that [10] the stress-strain relationship for recycled aggregate concrete is very close to the shape of normal concrete. When a structures made of recycled aggregate desired to design, theory of plasticity can be use like structures made of normal concrete. Stress-strain curves of concretes with different RCA replacement percentages shows similar inclination. When the level of the replacement is increased, the curvature of the curve is developed gradually. While the replacement level is increased with the coarse aggregate, the values of compressive strength, toughness, plastic energy capacity and elastic energy, and the elastic modulus decrease. Some of the experimental investigation offers some empirical model that can be used directly in design [11,12,13]. Rahal [14] made an experimental study for the difference of the tension and compressive strength with the changes of age. The mixes of concrete with target compressive cube strength ranging from 20 to 50MPa were cast using normal or recycled coarse aggregates. The indirect shear strength of recycled aggregate concrete was nearly the 90% of those of natural aggregate concrete with the same mix proportions. The modulus of elasticity of RAC was very closely that of normal aggregate concrete (NAC). With 100% replacement of coarse aggregates with recycled aggregates decrease the compressive strength between 9% to 45%. The change of the modulus of elasticity is reduced 15% for the lower water-cement ratio but with the higher water-cement ratio this level come to 45% [15-17]. Koper [18] produce RCA was obtained by crushing laboratory concrete having a wide range of water/cement (w/c) ratio (from 0.35 to 0.7); it allowed to obtain the concrete having compressive strength from 30 to 60 MPa. According to the experimental results, the water absorption of the best quality RCA approaches 5% and the mineral dust content in aggregates, obtained from concrete debris crushing, must be in the range of 0.3 – 1%. The quality of the RAC is directly related with the aggregate obtained from the primary concrete recycling. The replacement level of coarse and fine natural aggregates by RCA higher than 50% or above significantly reduced the compressive strength while 50% of air-dried RCA contamination of was optimal for producing the RAC up to 60 MPa [19-21]. Nováková and Mikulica [22] used precast demolished member as a RCA in concrete mix. Investigation based on the replacement of natural aggregates with the RCA produced from precast production defected elements which are carted off and recycled with other demolition waste. Results from testing of RAC proved that the replacement of raw aggregates by RCA up to 20% has no negative influence on physico-mechanical properties of concrete. The main reason of the strength loss is the weak interfacial transition zone (ITZ). It can be improved this connection face between old mortar and new mortar with the

usage of fly ash, nano-silica or other fine materials. The positive changes of carbonation depth in case of RC with 20% of replacement of (natural aggregate) NA by RCA [23-26]. ITZ mechanical strength is strongly influenced by the coarse aggregate types and their surface and shape. Concrete made with crushed aggregates provides higher values of the fracture energy than for concrete made with spherical ones. Due to their smoother surface and therefore weaker anchorage, pebble aggregates present areas dislodged from the matrix, leading to concretes with them have lower fracture energy than those with crushed rock [37-29]. Guo et al. [30] produced rubber crumb and steel fiber reinforced recycled aggregate concrete (RSRAC). A series of concrete mixes were prepared with Ordinary Portland Cement (OPC), recycled concrete coarse aggregates (RCA) or natural coarse aggregates (NCA), 1% steel fibre (by volume) and rubber particles with different fine aggregate (sand) replacement ratios. The investigators examine the compressive properties, including compressive strength, Young's modulus (stiffness), stress-strain curves and energy absorption capacity (toughness) of the different concrete mixes subjected to elevated temperatures. The results showed that both the compressive strength and stiffness of concrete mixes decreased after exposure to elevated temperature, with higher replacement of fine aggregate by rubber leading to lower compressive strength and stiffness magnitude. Nevertheless, rubber crumbs significantly enhanced the energy absorption capacity and explosive spalling resistance. Evangelista and Brito [31] experimentally investigated that the use of fine recycled concrete aggregates to partially or partially replace natural fine aggregates (sand) in the production of structural concrete. Compressive strength, split tensile strength, modulus of elasticity and abrasion resistance test were made on the produced RAC. From these results, the use of fine recycled concrete aggregates does not much more influential on the mechanical properties of concrete, for replacement ratios up to 30%. All these research also have clearly promoted the promising use of RCA in construction. To date, RAC has been successfully applied in pavements and building structures in China, as shown by Li et al. [32].

In this study, two sets of concrete production were implemented. These two sets composed of concrete with waste demolish as control concrete and concrete with steel and plastic fiber. Hardened state properties were studied in terms of compressive strength, split tensile strength, ultrasonic pulse velocity test and Schmidt Hammer test.

II. EXPERIMENTAL DESCRIPTION

A. Design of Experiments

This experimental campaign was carried out with two sets of experiments. Control concrete specimens were produced as conventional concrete. Target strength is determined 25 MPa for control concrete. Modified set of concrete composed of ternary ingredient like demolish waste, steel fiber and polypropylene fiber. Dimensions of the waste demolish aggregate used in concrete is between 8 mm and 16 mm diameter. These demolish waste is used 40 % of total aggregate. Maximum aggregate diameter is determined 16 mm for this study. Steel and polypropylene fibers were used in the

concrete mix for second set of production. Control concrete properties and amounts were tabulated in Table 1. Used steel fiber chips can be seen in Figure 1 and Polypropylene fiber can be seen in Figure 2.

TABLE I. AMONTH OF MATERIAL FOR 1000 DM³ CONTROL CONCRETE

Water (lt)	Cement (kg)	0 – 4 mm	4 – 8 mm	8 – 16 mm
195	367.92	881.85	348.53	487.96



Figure 1. 12 mm length steel fiber chips



Figure 2. Polyproplene fiber

Waste demolish was replaced with aggregate to produce second set of specimen 40% of 8 – 16 mm aggregate. Amount and dimensions of steel fiber and polypropylene fiber were tabulated in Table 2.

TABLE II. AMONTH AND PROPERTIES OF STEEL AND POLYPROPYLENE FIBER

Fiber	L/D Ratio	Length	Amount
Steel	0.55	NA	55 kg/m ³
Polypropylene	NA	12 mm	90 gr/m ³

III. RESULTS AND DISCUSSION

Results of these experimental study divided into three sub title in terms of axial compressive and split tensile test results, Ultrasonic pulse velocity and Schmidt hammer test results.

A. Axial Compressive and Split Tensile Test Results

Axial compressive test results of produced concrete specimens were evaluated and reported in this section. Compressive strength and split tensile strength test results were tabulated in Table 3 and Table 4.

TABLE III. 7 DAYS COMPRESSIVE AND SPLIT TENSILE STRENGTH TEST RESULTS FOR CONTROL CONCRETE

Number	Unit Weight (Kg/m ³)	Compressive Strength (MPa)	Unit Weight (Kg/m ³)	Split Tensile Strength (MPa)
1	2319	15.66	2310	3.43
2	2316	16.02	2319	3.12
3	2224	15.52	2303	3.11
Avg.	2286	15.73	2311	3.22

TABLE IV. 28 DAYS COMPRESSIVE AND SPLIT TENSILE STRENGTH TEST RESULTS FOR CONTROL CONCRETE

Number	Unit Weight (Kg/m ³)	Compressive Strength (MPa)	Unit Weight (Kg/m ³)	Split Tensile Strength (MPa)
1	2291	48.06	2278	9.62
2	2342	45.23	2325	9.49
3	2360	46.63	2355	10.06
Avg.	2331	46.64	2319	9.72

After substituting demolish waste with aggregate, adding steel and polypropylene fiber results of compressive strength and split tensile strength test results were obtained as indicated in Table 5 and Table 6 below.

TABLE V. 7 DAYS COMPRESSIVE AND SPLIT TENSILE STRENGTH TEST RESULTS FOR MODIFIED CONCRETE

Number	Unit Weight (Kg/m ³)	Compressive Strength (MPa)	Unit Weight (Kg/m ³)	Split Tensile Strength (MPa)
1	2366	21.28	2376	5.85
2	2359	22.65	2371	5.78
3	2372	22.18	2364	6.04
Avg.	2366	22.04	2370	5.89

TABLE VI. 28 DAYS COMPRESSIVE AND SPLIT TENSILE STRENGTH TEST RESULTS FOR MODIFIED CONCRETE

Number	Unit Weight (Kg/m ³)	Compressive Strength (MPa)	Unit Weight (Kg/m ³)	Split Tensile Strength (MPa)
1	2389	30.42	2380	8.81
2	2388	30.92	2351	9.92
3	2396	31.57	2364	9.47
Avg.	2391	30.97	2365	9.4

TABLE IX. 7 DAYS ULTRASONIC VELOCITY TEST RESULTS FOR MODIFIED CONCRETE

Number	Unit Weight (Kg/m ³)	Pulse Velocity (m/s)	Pulse Duration (μ)
1	2291	3978	27.9
2	2342	3978	27.9
3	2360	4051	27.3
Avg.	2331	4002	27.7

As indicated from test results externally added ternary group of materials developed early age compressive and split tensile strength of conventional concrete. 7 days compressive strength test results increased from 15.73 MPa to 22.04 MPa. However, 28 days test results decreased from 46.64 MPa to 30.97 MPa. Split tensile strength test results increased with adding ternary compounds to concrete from 3.22 MPa to 5.89 MPa for 7 days. Moreover, these ternary material additions resulted very slight decrease for 28 days split tensile strength. These slight decreases occurred from 9.72 MPa to 9.4 MPa.

TABLE X. 28 DAYS ULTRASONIC VELOCITY TEST RESULTS FOR MODIFIED CONCRETE

Number	Unit Weight (Kg/m ³)	Pulse Velocity (m/s)	Pulse Duration (μ)
1	2389	3908	28.04
2	2388	3864	28.50
3	2396	3964	28.00
Avg.	2391	3922	28.20

B. Ultrasonic Pulse Velocity Test Results

Ultrasonic pulse velocity test results of concrete specimens were tabulated in Table 7 and Table 8 for control concrete, Table 9 and Table 10 for modified concrete.

TABLE VII. 7 DAYS ULTRASONIC VELOCITY TEST RESULTS FOR CONTROL CONCRETE

Number	Unit Weight (Kg/m ³)	Pulse Velocity (m/s)	Pulse Duration (μ)
1	2319	3908	28.4
2	2316	3922	28.3
3	2224	3978	27.7
Avg.	2286	3936	28.1

Ultrasonic pulse velocity test results proved that added ternary materials filled porous volumes. There is only 5.7% increase in pulse velocity time and there is a 4.8% decrease in ultrasonic pulse velocity at 7-day age while compared with control and modified concrete specimens. There is a 2% decrease in ultrasonic pulse velocity and naturally 1.7% increase in pulse velocity time while compared control and modified concrete specimens.

C. Schmidt Hammer Test Results

Schmidt hammer test results obtained from all specimen with ten reading. These results were tabulated in Table 11 below. Table 11 shows average of ten readings.

TABLE VIII. 28 DAYS ULTRASONIC VELOCITY TEST RESULTS FOR CONTROL CONCRETE

Number	Unit Weight (Kg/m ³)	Pulse Velocity (m/s)	Pulse Duration (μ)
1	2366	3675	30.5
2	2359	3788	29.4
3	2372	3775	29.3
Avg.	2366	3746	29.7

TABLE XI. SCHMIDT HAMMER TEST RESULTS

Avg. Reading of Specimens	Control 7 Days (MPa)	Control 28 Days (MPa)	Modified 7 Days (MPa)	Modified 28 Days (MPa)
1	24.1	30.7	24.2	28.2
2	23.4	32.1	21.5	29.2
3	21.4	32.7	23.1	28.2
Avg.	22.97	31.83	22.93	28.53

As seen from Table 11, test results show that there is no change of 7 days Schmidt hammer test results with control and modified concrete test results. However, there is a certain decrease in 28 days' hammer test results of modified concrete while compared with control concrete.

IV. CONCLUSION

In this study, hardened properties of two different set of concrete specimens were evaluated in terms of compressive strength, split tensile strength, ultrasonic pulse velocity and Schmidt hammer. First set of concrete was produced with conventional concrete without external additive material usable in concrete. Second set of concrete was produced with demolish waste, steel and plastic fiber. Demolish waste substituted with 40% of 8 – 16 mm aggregate. Compressive strength results proved that mentioned external materials developed early age mechanical properties of modified concrete. However, these materials decreased long term mechanical properties of concrete. Split tensile strength property was increased with adding demolish waste, steel and polypropylene fiber. There is a 40% increase in compressive strength test results for 7-day age, but 34% decrease in compressive strength test results for 28-day age. Ternary materials for modified concrete developed 83% split tensile strength for 7-day age. However, the same materials resulted in 3.4% decrease in split tensile strength test results for 28-day age. Ultrasonic pulse velocity decreased with adding ternary materials and velocity time was increased for 7-day age and 28-day age specimens. Schmidt hammer test results are nearly the same for both set of specimens at early age. There is only 10% decrease in 28-day age specimens.

REFERENCES

- [1] Liu, Q., Xiao, J., Sun, Z., "Experimental study on the failure mechanism of recycled concrete". *Cement and Concrete Research*, 2011, 41(10), 1050-1057.
- [2] A.K. Padmini, "Influence of parent concrete on the properties of recycled aggregate concrete", *Constr. Build. Mater.* 23, 2009, 829–836.
- [3] Jianzhuang Xiao, J. Du, Complete stress–strain curve of concrete with different recycled coarse aggregates under uniaxial compression, *J. Build. Mater.* 11 (2008) 111–115 (in Chinese).
- [4] Etxeberria, M., Vázquez, E., Marí, A., Barra, M. "Influence of amount of recycled coarse aggregates and production process on properties of recycled aggregate concrete." *Cement and concrete research*, 2007, 37(5), pp. 735-742.
- [5] EHE, Instrucción del hormigón Estructural (Spanish Concrete Structural Code), Ministerio de Fomento, Madrid, Spain, 1999.
- [6] M. Kikuchi, T. Mukai, H. Koizumi, "Properties of concrete products containing recycled aggregate, Demolition and Reuse of Concrete and Masonry: Reuse of Demolition Waste", Chapman and Hall, London, 1988, pp. 595–604.
- [7] M. Tavakoli, P. Soroushian, Strengths of recycled aggregate concrete made using field-demolished concrete as aggregate, *ACI Materials Journal* 93 (2), 1996, 182–190.
- [8] T.C. Hansen, Recycled aggregate and recycled aggregate concrete, Second State-of-the-art Report developments 1945–1985, Materials and structures, vol. 111, RILEM, 1986.
- [9] Etxeberria, M., Vázquez, E., Marí, A., & Barra, M. (2007). Influence of amount of recycled coarse aggregates and production process on properties of recycled aggregate concrete. *Cement and concrete research*, 37(5), 735-742.
- [10] A. Herinhsen, B. Jensen, Styrkeegenskaber for beton med genanvendelses materialer, Internal report, 1989, only available in Danish.
- [11] N.K. Bairagi, R. Kishore, Behavior of concrete with different proportions of natural and recycled aggregates, *Resour. Conserv. Recycl.* 9 (3) (1993) 109– 126.
- [12] I.B. Topcu, Using waste concrete as aggregate, *Cem. Concr. Res.* 25 (7) (1995) 1385–1390.
- [13] M. Rqhl, G. Atkinson, The influence of recycled aggregate concrete on the stress–strain relation of concrete, *Darmstadt Concrete*, vol. 14, 1999, TU Darmstadt, Germany (only available in German).
- [14] Rahal, K. (2007). Mechanical properties of concrete with recycled coarse aggregate. *Building and environment*, 42(1), 407-415.
- [15] Yamato T, Emoto Y, Soeda M. Mechanical properties, drying shrinkage and resistance to freezing and thawing of concrete using recycled aggregate. *ACI Special Publication SP 179-7*. Farmington Hills, MI, USA: American Concrete Institute; 1998. p. 105–121.
- [16] Frondistou-Yannas S. Waste concrete as aggregate for new concrete. *ACI Journal, Proceedings* 1977;74(8):373–6.
- [17] Ravindraraj RS, Tam TC. Properties of concrete made with crushed concrete as coarse aggregate. *Magazine of Concrete Research* 1985;37:3.
- [18] Koper, A., Koper, W., & Koper, M. (2017). Influence of Raw Concrete Material Quality on Selected Properties of Recycled Concrete Aggregates. *Procedia Engineering*, 172, 536-543.
- [19] Poon, C.S., Kou, S.C., Lam, L., 2002. Use of recycled aggregates in molded concrete bricks and blocks. *Constr. Build. Mater.* 16 (5), 281-289.
- [20] Poon, C.S., Shui, Z.H., Lam, Z.H., Kou, S.C., 2004a. Influence of moisture states of natural and recycled aggregates on the slump and compressive strength of concrete. *Cem. Concr. Res.* 34 (1), 31-36.
- [21] Poon, C.S., Shui, Z.H., Lam, L., 2004b. Compressive behavior of fibre reinforced high performance concrete subjected to elevated temperatures. *Cem. Concr. Res.* 34 (12), 2215-2222.
- [22] Nováková, I., & Mikulica, K. (2016). Properties of Concrete with Partial Replacement of Natural Aggregate by Recycled Concrete Aggregates from Precast Production. *Procedia Engineering*, 151, 360-367.
- [23] D. Kong, T. Lei, J. Zheng, Ch. Ma, J. Jiang, J. Jiang, Effect and mechanism of surface-coating pozzalanic materials around aggregate on properties and ITZ microstructure of recycled aggregate concrete, *Constr. Build. Mater.* 24 (2010) 701–708.
- [24] S.C. Kou, C.S. Poon, Enhancing the durability properties of concrete prepared with coarse recycled aggregate, *Constr. Build. Mater.* 35 (2012) 69–76.
- [25] H. Zhang, Y. Zhao, T. Meng, S.P. Shah, The modification effects of a nano-silica slurry on microstructure, strength, and strain development of recycled aggregate concrete applied in an enlarged structural test, *Constr. Build. Mater.* 95 (2015) 721–735.
- [26] S.M. Levy, P. Helene, "Durability of recycled aggregates concrete: a safe way to sustainable development", *Cement Concrete Res.* 34, 2004, 1975–1980.
- [27] T. Sadowski, G. Golewski, "Effect of aggregate kind and graining on modelling of plain concrete under compression", *Comput. Mater. Sci.* 43, 2008, 119–126.
- [28] T. Özturan, C. Çeçen, "Effect of coarse aggregate type on mechanical properties of concretes with different strengths", *Cem. Concr. Res.* 27 1997, 165–170.
- [29] C.G. Rocco, M. Elices, "Effect of aggregate shape on the mechanical properties of a simple concrete", *Eng. Fract. Mech.* 76, 2009, 286–298.
- [30] GUO, Yong-chang, et al. Compressive behaviour of concrete structures incorporating recycled concrete aggregates, rubber crumb and reinforced with steel fibre, subjected to elevated temperatures. *Journal of Cleaner Production*, 2014, 72: 193-203.
- [31] Evangelista, L., & De Brito, J. "Mechanical behaviour of concrete made with fine recycled concrete aggregates. *Cement and concrete composites*, 2007, 29(5), 397-401.
- [32] Li, L.J., Chen, Z.Z., Xie, W.F., Liu, F., "Experimental study of recycled rubber filled high strength concrete. *Mag. Concr. Res.* 2009, 61 (7), 549-556.

The Comparision Of Moyas* Dormitory Buildings Types Projects With Moyas* Accomodation Building Standards And The Evaluation Of Their Availability

Hasan POLAT

Firat University, Architecture Faculty, Elazığ
23119

Ebru DOĞAN

Bingol University, Architecture Faculty, Bingol
12000

Abstract— Housing right is one of the basic rights that is guaranteed by the constitution and accorded to individuals by the executive power of the state. Executive branch tries to realize this according to the principles of equality and justice.

Housing is one of the major problems for university students in our country. They cope with this problem by staying at private and state dormitories, apart-hotels, and rented flats or by staying with relatives. Socio-economic status of the student, housing and building capacity of the city a student lives in play a role in choosing the form of housing. The authority to plan and build the housing buildings and facilities to meet the students' need of sheltering belongs to the Ministry of Youth and Sport. To this end, the Ministry developed standards and launch projects to meet the need for dormitory buildings throughout the country fast and economically. These standards that are established by taking into consideration building cost, management, function, aesthetic and efficiency levels of housing are very important in terms of spatial comfort of the users.

In this study, the availability level is evaluated by comparing the Ministry regulations for preparing projects and the typical project for building dormitories for 500 people that is currently applied by the Ministry.

Keywords— *Dormitory Building Design, Project Standards*

References

1. 1982 Anayasası , Gençliğin korunması, MADDE 58
2. Gençlik ve Spor Bakanlığının Teşkilat ve Görevleri Hakkında KHK, 3/6/2011, No : 638, 8/6/2011 Tarihli Resmi Gazete, Ankara
3. Filiz Z., Çemrek F., An Examination of the Accommodation Problem of University Students Through Multiple Correspondence Analysis, Zeynep, Journal of Social Sciences, Eskişehir Osmangazi University, 8(2).
4. Yükseköğrenim Kredi ve Yurtlar Kurumu Genel Müdürlüğü Genel ve Teknik Şartlar, T.C. Gençlik ve Spor Bakanlığı, 2015, Ankara.

An Investigation of Modular Construction Buildings In terms of Flexibility

Ebru DOĞAN

Bingol University, Architecture Faculty, Bingol
12000

Hasan POLAT

Firat University, Architecture Faculty, Elazığ
23119

İlkay MERT

Mimar Sinan University, Architecture Faculty,
Istanbul 34427

Abstract— In the buildings, the conventional building systems offer limited opportunities in order to provide the requirements of user demands. The new construction technologies along with the development in technology occur producing flexible and adaptable solutions have tried to provide the requirements. Modular constructions include more flexible opportunities than the conventional building systems.

After industrialization experienced the population growth, intensive urbanization, intensive housing demand and developments in technologies have led to emergence the construction with low cost and craftsmanship, little time and produce higher quality building. In a rapidly developing and changing society, different space requirements occur depending on the building owners and users. The flexible and adaptable spaces gain important to respond the requirements.

Today, the developments in technology offer flexible spaces created with easy disassembled, assembled, maintained and repaired construction systems and components. The construction provide the flexibility to remove or renovation whole building.

In this context, modular construction systems are highly effective system to build flexible structure in order to respond the requirements with mobile building construction and building components. In this study, modular construction systems are examined in terms of flexibility and adaptability with case studies.

Keywords— *Modular Construction, Flexibility, Adaptability.*

References

- [1] Gibb, Alistair G. F. 1999. Offsite Fabrication: Prefabrication, Pre-assembly and Modularization. Scotland, UK: Whittles Publishing.
- [2] Haas, Carl T., James T. O'Connor, Richard L. Tucker, Jason A. Eickmann, and Walter R. Fagerland. 2000. Prefabrication and Preassembly Trends and Effects on the Construction Workforce. Austin, Texas: Center for Construction Industry Studies.
- [3] Hartley, Andrew, and Alex Blagden. 2007. Current Practices and Future Potential in Modern Methods of Construction. Banbury, UK: Wrap.
- [4] Smith, Elizabeth A. T. 2007. *Case Study Houses: 1945-1966: The California Impetus*. Hong Kong: TASCHEN GmbH.
- [5] Dini, Massimo. 1984. *Renzo Piano, Projects and Buildings, 1964-1983*. Translated by Richard Sadleir. Milan, Italy: Rizzoli International Publications, Inc.

-
- [6] McQuaid, Matilda. 2003. *Shigeru Ban*. New York: Phaidon Press, Inc.
- [7] Safdie, Mosche. 1970. *Beyond Habitat*. Edited by John Kettle. Montreal, Quebec: Tundra Books of Montreal.
- [8] MBI Modular Building Institute, Charlottesville, USA. Source: <http://www.mbinet.org/About/Defined.aspx>. Last viewed on 20 January 2006.
- [9] Van Gassel, Frans, (2006) *Modular Construction*. ARKO In print.
- [10] Permanent Modular Construction 2011: Annual Report. 2011. The Modular Building Institute.
- [11] Relocatable Buildings: 2011 Annual Report. 2011. The Modular Building Institute.
- [12] Lu, Na. 2007. Investigation of the Designers' and General Contractors' Perceptions of Offsite Construction Techniques in the United States Construction Industry, Department of Career and Technology Education, Clemson University, Clemson, GA.
- [13] Cowee, N. P., & Schwehr, P. (2012). *The Typology Of Adaptability In Building Construction*. Berlin, Germany.
- [14] Barwick, Timi, and Jennifer McGarey. 2001. Annandale Regional Planning Study. In Report of the Middle School/High School Committee. Annandale, VA.
- [15] MKThink. 2004. *Modular Learning Environments: Beyond the 'Classroom in a Can'*.
- [16] Schoenborn, M, Joseph., 2012. *A Case Study Approach To Identifying The Constraints And Barriers To Design Innovation For Modular Construction*. Thesis Submitted To The Faculty Of The Virginia Polytechnic Institute And State University In Partial Fulfillment Of The Requirements For The Degree Of Master Of Science In Architecture. Virgini. America.

OTHER ENGINEERINGS

ORAL SUBMISSIONS



A Metasurface Polarization Converter Designed by Two Metallic Patches Placed in the Cross Corner of a Rectangular Loop

Olca Altıntaş, Oguzhan Akgöl, Emin Unal, Muharrem Karaaslan

Department of Electrical and Electronics Engineering
Iskenderun Technical University
Iskenderun, Hatay, 31200, Turkey.

Murat Aksoy

Department of Electrical and Electronics Engineering
Cukurova University
Saricam, Adana, 01330, Turkey

Abstract—We present a Metasurface (MS) polarization converter to transform linearly polarized signals into circularly polarized signals. The unit cell of the proposed structure consists of two metallic patches placed in the cross corners of a rectangular loop. Polarization conversion quality referred to axial ratio is kept below 3 dB. The axial ratio is obtained numerically and experimentally by the division of cross-polar and co-polar responses of the antennas. Quite good axial ratio bandwidth, 260 MHz, is achieved experimentally which supports the simulation results. The proposed MS structure can be fabricated and configured easily for any desired frequency range due to its simple design. It can be used efficiently in many applications such as weather radar, airport surveillance radar and satellite communications.

Keywords—axial ratio; axial ratio bandwidth; metasurface; polarization conversion

I. INTRODUCTION

Metamaterials (MTMs) are artificial materials having unusual electromagnetic properties which cannot be found in nature. First theoretical study about double negative material (DNG) was carried out by Veselago in 1968 [1]. In the late 20th century, Pendry et al. produced materials which have negative value of dielectric permittivity [2] in 1996 and magnetic permeability [3] in 1999. In 2000, Smith et al. realized the first DNG material which consists of a split ring and wires providing negative permittivity and negative permeability, simultaneously [4]. In recent years, many researchers study MTMs and its application areas and this attention gradually increases [5]-[7].

Metasurfaces (MSs) are the two dimensional equivalent of MTMs. MSs take up less volume and they can be less

lossy structures comparing to the three dimensional MTMs [9]. There are many potential application areas concerning MS structures such as controllable smart surfaces [10], wave guide structures [11] and absorbers [12]. In addition to these topics, MSs are also configured as polarization converter structures. Many radar and satellite systems need circularly polarized signals rather than linearly polarized ones, because circular polarization keeps signal constant at bad weather conditions.

In this study, we present a polarization converter MS structure to transform linearly polarized signal into circularly polarized one, numerically and experimentally. In order to show the conversion feature, the axial ratio (AR) of the proposed MS is calculated by dividing cross and co-pol responses. In the design, metallic patches placed in cross corners of rectangular loops are provide phase difference to obtain circular polarization. The proposed MS has two dip points which provide perfect polarization conversion activity at 2.85 GHz and 3.10 GHz. It has also 260 MHz of axial ratio bandwidth (ARBW) at two separate frequency ranges. The polarization converter can be efficiently used in S-band applications such as weather radar, airport surveillance radar, and satellite communications and so on.

Furthermore, in antenna industry, you must design two separate antennas if you need both linear and circular polarization. It is not only costly and time consuming but it also requires more physical space which is extremely important in the sector. Physical space for the antenna integration is generally limited meaning that the engineers mostly faced up the problem shrinking the antenna to fit the limited space on the radio transmitter or receiver structures. Therefore, there are many studies and researches concerning about the miniaturization of antennas. This problem can be overcome by

using the proposed structure, having an antenna which is capable of radiating both linearly and circularly polarized waves will be possible. In other words, designing a linear polarized antenna will be enough to work with in any application requiring both linearly and circularly polarized signals. In addition, the structure only contains a single layer which makes it possible for us to integrate the structure on any traditional radomes of antennas. Thus, no extra space will be used and radiation in a desired polarization can be achieved by a simple radome change which can be considered another advantage of the proposed model. Using multilayer structures may give good results in polarization conversion but it will most probably ruin the radiation pattern as well as the gain and directivity.

II. DESIGNING OF THE METASURFACE POLARIZATION CONVERTER

The unit cell of the proposed MS polarization converter consists of two metallic patches placed in crossed corners of a rectangular loop. The construction of MS structure is arranged by 16 unit cell in 4X4 layout. Rogers RT 5870 is used in the structure substrate with a thickness, loss tangent and relative permittivity of 1.575 mm, 0.012 and 2.33, respectively as shown in Fig. 1(a). The unit cell of the periodic structure is shown in Fig. 1(b) with a strip line whose thickness is $w = 0.48$ mm while the width and length are $x = 14.68$ mm $y = 14.90$ mm, respectively connecting the metallic patches. Dimensions of each metallic patches are $R_x = 4.90$ mm, $R_y = 4.64$ mm.

The goal of the study is to obtain circularly polarized signals from linearly polarized signals that can be investigated by the axial ratio (AR) which can be simply written in dB as;

$$AR(dB) = Mag(20 \log(AR(\omega))) \quad (1)$$

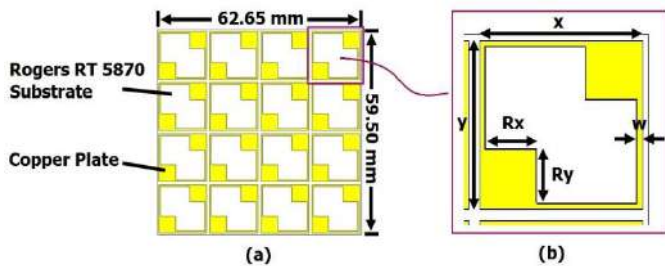


Figure 1.(a) Linear to circular polarization converter MS (b) unit cell dimensions of MS

AR is;

$$AR(\omega) = \frac{T(\omega)_{cross-polar}}{T(\omega)_{co-polar}} \quad (2)$$

III. NUMERICAL AND EXPERIMENTAL STUDY

Numerical study of the proposed MS structure is realized by CST Microwave Studio which is a commercial simulation software and 3D full wave electromagnetic solver based on finite integration technique. Periodic boundary conditions and floquet port mode are chosen for this study. To obtain efficient circular polarization, AR is kept below 3 dB. The proposed MS has two dip points at 2.95 GHz and 3.15 GHz which give perfect polarization activity in the simulation results of AR as shown in Fig. 2(b). About 300 MHz of ARBW is also obtained between the frequencies of 2.92 GHz and 3.22 GHz.

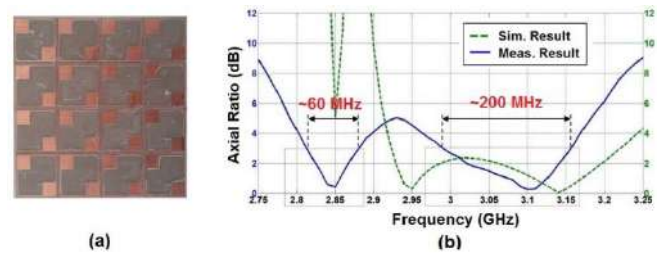


Figure 2.(a) Fabricated MS sample (b) simulated and measured AR results of proposed structure

Experimental study is achieved by Rohde & Schwarz ZVL6 vector network analyzer (VNA) with two linearly polarized microwave horn antennas. Fabrication of MS is realized by using LPKF E33 Protomat as shown in Fig. 2(a).

To obtain transmission values ($T(\omega)$), VNA is calibrated by using free space measurement. Both co-pol and cr-pol responses should be measured in order to obtain AR for the working frequencies. To measure co-polar response, the MS is placed between two horn antennas whose E-fields are in the same direction and for cross-polar response measurement, one of the horn antennas is simply rotated by 90° and the scattering parameters for the transmission (S_{21}) is measured and recorded. Finally, AR is calculated by the division of these two responses as in Eq. (2). There are two frequency bands below 3 dB which is optional to choose operating frequency range of MS as shown in Fig. 2(b). First band is between 2.82 GHz and 2.88 GHz with a ARBW of 60 MHz. The second one is occurred between at 2.98 GHz and 3.16 GHz with a ARBW of 200 MHz. Since we have dual working frequency band, the proposed MS polarization rotator can be used with dual band antennas, either. Another dip points are also obtained at 2.85 GHz and 3.10 GHz for the proposed structure.

Although there is a small mismatch between numerical and experimental results as shown in Fig. 2(b), AR dip points and ARBW of these results are almost at the same level and agree well with each other. The deficiencies are originated by not having ideal measurement conditions in the laboratory and the manufacturing defects of MS sample.

IV. CONCLUSION

A metasurface polarization converter which transforms linearly polarized signals into circularly polarized one is realized in this study. Simulated and measured results are compared to each other and it shows that the results are in a good agreement. AR is kept below 3 dB for polarization conversion quality. The perfect polarization conversion activities are obtained at frequencies of 2.83 GHz and 3.10 GHz and the ARBW of 260 MHz is also obtained at two frequency bands when the measured results are considered. Since circularly polarized signals are not affected by the weather conditions, the proposed MS can be used effectively in S-band radar and satellite systems. In addition, this design can be used on the existing linearly polarized antennas without using any extra space on the enclosures on which antennas are mounted. Furthermore, the proposed MS structure can be easily fabricated, integrated and reconfigured for any desired frequency range.

REFERENCES

- [1] V.G. Veselago, "The electrodynamics of substances with simultaneously negative values of ϵ and μ ," *Sov. Phys. Usp.*, vol. 10, no. 4, p. 509–514, 1968.
- [2] J.B. Pendry, W.J. Stewart and I. Youngs, "Extremely low frequency plasmons in metallic mesostructures," *Physical Review Letters*, vol. 76, p. 4773–4776, 1996.
- [3] J.B. Pendry, A.J. Holden, D.J. Robbins and W.J. Stewart, "Magnetism from conductors and enhanced nonlinear phenomena," *IEEE Transactions on Microwave Theory and Techniques*, vol. 47, p. 2075–2084, 1999.
- [4] D.R. Smith, W.J. Padilla, D.C. Vier, S.C. Nemat-Nasser and S. Schultz, "Composite medium with simultaneously negative permeability and permittivity," *Physical Review Letters*, vol. 84, p. 4184–4187, 2000.
- [5] M. Karaaslan and M. Bakir, "Chiral metamaterial based multifunctional absorber and sensor applications," *Progress In Electromagnetics Research*, vol. 149, p. 55–67, 2014.
- [6] F. Dincer, M. Karaaslan, S. Colak, E. Tetik, O. Akgol, O. Altintas, C. Sabah, "Multi-band polarization independent cylindrical metamaterial absorber and sensor application", *Modern Physics Letter B*, vol. 30, p. 1650095, 2016.
- [7] H.L. Zhu, S.W. Cheung, K.L. Chung and T.I. Yuk, "Linear-to-circular polarization conversion using metasurface," *IEEE Transactions on Antennas and Propagation*, vol. 61, no. 9, p. 4615–4623, 2013.
- [8] C.L. Holloway, E.F., Kuester, J.A. Gordon, J.F. O'hara, J. Booth and D.R. Smith, "An overview of the theory and applications of metasurfaces: The two-dimensional equivalents of metamaterials," *IEEE Antennas Propag. Mag.*, vol. 54, No. 2, p. 10–35, 2012.
- [9] C.L. Holloway, M.A. Mohamed, E. F. Kuester and A. Dienstfrey, "Reflection and transmission properties of a metafilm: with an application to a controllable surface composed of resonant particles," *IEEE Trans. Electromag. Compat.*, vol. 47, no. 4, p. 853–865, 2005.
- [10] S. Sajuyigbe, M. Ross, P. Geren, S.A. Cummer, M. H. Tanielian and D.R. Smith, "Wide angle impedance matching metamaterials for waveguide-fed phased-array antenna," *IET Microwaves, Antennas, and Propagation*, vol. 4, no. 8, pp. 1063–1072, 2010.
- [11] Y. Kotsuka, K. Murano, M. Amano and S. Sugiyama, "Novel right-handed metamaterial based on the concept of 'autonomous control system of living cells,' and its absorber applications," *IEEE Trans. Electromag. Compat.*, vol. 52, no. 3, p. 556–565, 2010.

Microfluidic Chemical Sensor Applications by Using a Metamaterial Based Sensor

Olca Altıntaş, Oguzhan Akgöl, Emin Unal, Muharrem Karaaslan

Department of Electrical and Electronics Engineering
Iskenderun Technical University
Iskenderun, Hatay, 31200, Turkey.

Murat Aksoy

Department of Electrical and Electronics Engineering
Cukurova University
Saricam, Adana, 01330, Turkey

Abstract—A metamaterial based sensor is designed and demonstrated numerically and experimentally for the detection of microfluids. The structure consisting of a single circular split ring resonator (CSRR) has a simple geometry and can be adjusted to any desired frequency depending on the material to be characterized. In this study, two different chemical liquid sensor applications have been investigated. First, a liquid sensor application which can successfully achieve the alcohol content of the ethanol water mixture. Second, application of chemical liquid sensor to distinguish branded and unbranded diesel samples from each other are designed. The results show that the proposed structure is especially applicable to liquid sensor applications in biochemistry.

Keywords—metamaterial; biochemical sensor; liquid sensor; microwave

I. INTRODUCTION

Sensor applications have always attracted the attention of many scientists. In this work, a novel sensor technology recently interested by many scientists is being investigated. This technology is based on metamaterials (MTM) exhibiting unusual electromagnetic behaviors. Using these extraordinary materials, it is possible to achieve negative permeability and permittivity at the same time. MTMs [1]-[3] have great potential and wide application prospects in perfect absorber [4], perfect lenses [5], invisible cloaks [6], chirality [7], and super definition [8] and so on.

Recently, many MTM-based sensor structures have been investigated in microwave frequencies. Characterization and applications of various sensing devices such as liquid sensing based on a discrete ring resonator was performed by Withayachumnankul et al [9]-[10]. The operating principle of such microfluidic sensing devices depends on the interaction

between the samples placed in the sensing layer and the electric field provided by the microstrip lines. A chiral MTM sensor structure has been designed by Karaaslan et al [11] to determine the properties of samples with chiral properties. Various MTM-based strain sensor applications have been implemented by Melik et al [12] to detect mechanical deformation in microwave frequencies.

In this work, we proposed a metamaterial sensor with the ability to detect ethanol-alcohol mixed liquid detection and branded-unbranded diesel fuels in microwave frequency regime theoretically and experimentally. The proposed structure has a simple circular split ring resonator (CSRR) topology coupled with a microstrip transmission line to investigate the transmitted signal. First, the operating frequency of the structure was investigated numerically and experimentally, assuming that the sensor layer was empty. To perform the liquid sensing application, the dielectric constant and dielectric loss values of the ethanol-water mixture and the diesel samples were measured using the dielectric probe kit at the operating frequency band. The sensing ability of the proposed structure according to the obtained dielectric properties of the fluids was analyzed numerically and experimentally with a simulation program and a vector network analyzer.

II. NUMERICAL AND EXPERIMENTAL DESIGN

The proposed sensor structure is designed and fabricated as a circular split ring resonator (CSRR). A microstrip transmission line, which forms the magnetic coupling effect with the CSRR, is integrated on the structure to observe the shifts in resonance frequency as shown in Fig. 1 (d). The back side of the structure is covered with a metallic plate, which is set as the ground plane. A radial gap was created in the CSRR

to measure the sensitivity of the samples by monitoring the shifts in resonance frequency, which is an important parameter for the sensor applications. Typical dimensions of the CSRR and microstrip line obtained from parametric studies are given in Table 1.

Table 1. Typical dimensions of the proposed structure

r1	r2	sr1	sr2	rg	rd
7.0 mm	5.0 mm	4.35 mm	3.85 mm	2.0 mm	7.30 mm

Numerical studies were carried out with electromagnetic simulator software based on finite integration technique. As shown in Fig. 1 (c), two separate connection points are integrated at both ends of the microstrip transmission line to monitor the transmission coefficient S_{12} . Electromagnetic properties of the ethanol water mixtures and diesel samples were measured with the Agilent 85070E dielectric probe kit and these mixtures and diesel samples are defined as new materials according to the values measured in the simulation program.

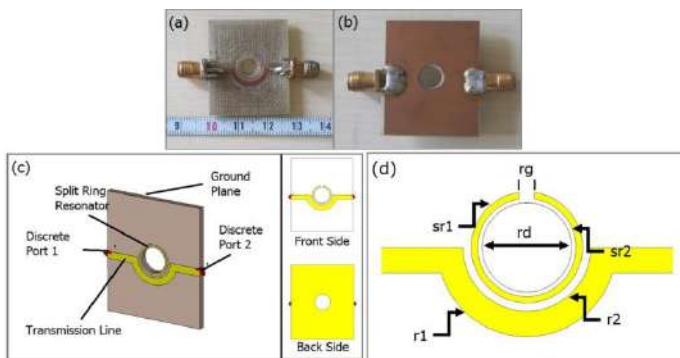


Figure 1. (a) The front side of the proposed structure, (b) the back side of the proposed structure, (c) The simulation model of the sensor structure, and (d) the geometrical dimensions of the proposed structure.

The metamaterial-based sensor structure was fabricated by the LPKF E33 Protomat PCB prototyping machine as shown in Fig. 1 (a) and (b). The dielectric substrate used in simulation and production is FR4 with a thickness of 1.6 mm, relative permittivity of $\epsilon_r = 4.3$ and loss tangent of $\tan \delta = 0.02$. The metal plates on the dielectric substrate is copper with a thickness of 35 μm and an electrical conductivity of $\sigma = 5.80001 \times 10^7 \text{ S/m}$. In addition, 50 Ω connectors are soldered on both sides of the transmission lines.

Experimental study of the sensor was performed with the PNA-L Agilent vector network analyzer (VNA) with operating frequency up to 43.5 GHz. The experimental setup is shown in Fig. 2. Before connecting the sensor structure for measurement, the VNA was calibrated using the appropriate calibration kit.



Figure 2. The experimental setup

The structure was then connected to the VNA and measured without the sample to be measured in the sensing layer. The corresponding simulation and test results for the sensor structure without any sample placed in the sensing layer are shown in Fig. 3. It is observed that the proposed sensor structure has a resonance frequency of about 4 GHz. There was a slight difference between the measurement and simulation results, due to calibration errors and manufacturing errors.

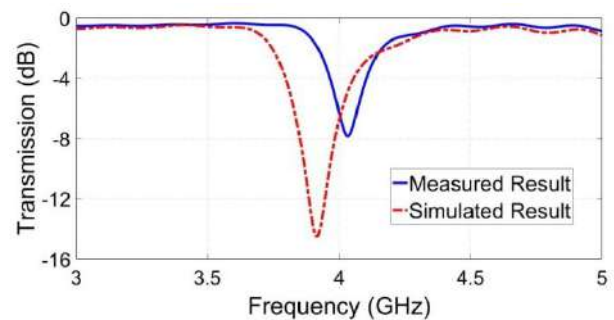


Figure 3. Simulation and experimental results of the transmission coefficient

III. ETHANOL-WATER MIXTURE SENSING APPLICATION

An ethanol water mixture was used for liquid detection application. The dielectric constant and dielectric loss factor values of the mixtures were determined with Agilent 85070E dielectric probe kit based on the percentage of ethanol in the mixture. After the dielectric probe kit was calibrated, the ethanol ratio of the mixture was increased by 20% each time, and the measurements are carried out at the operating frequency of 4.1 GHz. Table 2 shows the dielectric properties of the alcohol content in purified water measured at 4.1 GHz by means of a dielectric probe connected to the network analyzer. The dielectric properties given in Table 2 are those obtained at 4.1 GHz.

Table 2. Dielectric and loss tangent values of the ethanol-water mixture at 4.1 GHz

Ethanol Content (%)	ϵ'	ϵ''	Loss Tan.	Sim. Res. Freq. (GHz)
0	78,64	11,34	0,144	3,897
20	69,42	11,03	0,159	3,911
40	52,85	10,03	0,190	3,924
50	45,03	9,27	0,206	3,930
60	37,66	8,16	0,217	3,943
80	25,35	6,99	0,276	3,987
100	8,96	5,22	0,583	4,057

In this section, the application of liquid sensor for specific ethanol and water mixture ratios of the CSSR sensor structure has been investigated. The observed transmission coefficient values are obtained numerically and experimentally as shown in Fig. 4. Examining the simulation results given in Fig. 4 (a), the resonance frequency is found to be at about 3.897 GHz for pure water content. When the percentage of ethanol in the mixture increases by 20%, the resonance frequency shifts to the right to new value of 3.911 GHz. As the amount of ethanol content in the mixture increases, the shift in the resonance frequency of the proposed sensor appears to be approximately linear as shown in the simulation results in Fig. 4(a). Such linear variation is also observed in the experimental results as seen in Fig. 4 (b). The experimental results have the resonance frequencies obtained for 0%, 20%, 40%, 50%, 60%, 80% and 100% of the ethanol content of the mixture at 4.024 GHz, 4.029 GHz, 4.033 GHz, 4.035 GHz, 4.038 GHz, 4.043 GHz, and 4.0, respectively. Numerical and experimental results demonstrate that the proposed CSSR based sensor structure has the potential to be used as a liquid sensor.

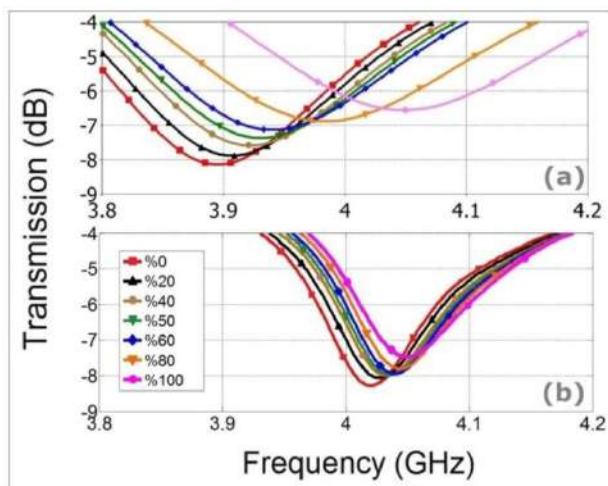


Figure 4.(a) simulation and (b) test results for the liquid sensor with respect to ethanol content

IV. BRANDED AND UNBRANDED DIESEL SENSING APPLICATION

In this section, an experimental study was conducted to distinguish branded and unbranded diesel fuels. First, the dielectric properties of the diesel samples were determined with the Agilent 85070E dielectric probe kit as shown in Table 3. Although the values are close to each other, the sensor structure of the proposed sensor has different capacitive effects on the sensor layer.

Table 3. Dielectric and loss tangent values of branded and unbranded diesel samples at 4.1 GHz

	ϵ'	ϵ''	Loss Tan.	Meas. Res. Freq. (GHz)
Branded Diesel	2.642	0.584	0.221	4.082
Unbranded Diesel	2.689	0.614	0.228	4.091

The experimentally obtained resonance frequencies for branded and unbranded diesel samples are shown in Fig. 5. It has been observed that the branded and unbranded diesel samples placed in the sensor layer shift the resonance frequency of the CSRR. The resonance frequency was obtained at 4.082 GHz for the branded diesel sample and 4.091 GHz for the unbranded diesel sample. A difference of about 9 MHz has occurred between the resonance frequencies of the two samples. When the results are examined, it is understood that the proposed sensor structure has the ability to separate two samples from each other.

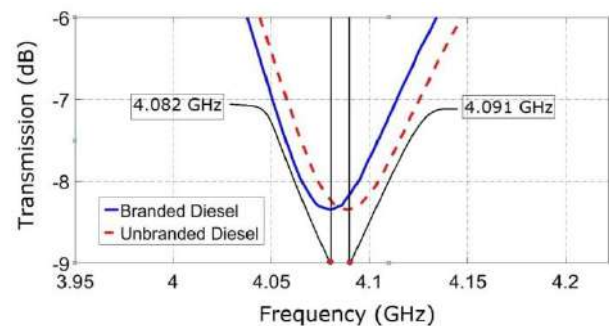


Figure 5. Experimental results for branded and unbranded diesel samples

V. CONCLUSION

A CSRR type sensor structure with a metamaterial base exhibiting chemical liquid sensor characteristics has been analyzed both numerically and experimentally at microwave frequencies. In the study, first, the dielectric properties of the ethanol water mixture and diesel samples were determined. The samples are then tested both experimentally and numerically. When the findings are examined, it is understood that the proposed sensor structure works well as a chemical liquid sensor.

REFERENCES

- [1] D. R. Smith and N. Kroll, "Negative Refractive Index in Left-Handed Materials," *Phys. Rev. Lett.*, vol. 85(14), pp. 2933-2936, 2000.
- [2] R. A. Shelby, D. R. Smith and S. Schultz, "Experimental Verification of a Negative Index of Refraction," *Science*, vol. 292(5514), pp. 77-79, 2001.
- [3] D. R. Smith, J. B. Pendry and M. C. K. Wiltshire, "Metamaterials and Negative Refractive Index," *Science*, vol. 305(5685), pp. 788-792, 2004.
- [4] F. Dincer, M. Karaaslan, E. Unal, O. Akgol and C. Sabah "Multi-Band Metamaterial Absorber: Design, Experiment and Physical Interpretation" *ACES Journal*, vol. 29(3), pp. 197-202, 2014.
- [5] N. Fang and X. Zhang, "Imaging properties of a metamaterial superlens," *Applied Physics Letters*, vol. 82, pp. 161, 2016.
- [6] S. Maci, "A Cloaking Metamaterial Based on an Inhomogeneous Linear Field Transformation," *IEEE Antennas and Wireless Propagation Letters*, vol. 58(4), pp. 1136-1143, 2010.
- [7] F. Dincer, M. Karaaslan, O. Akgol, E. Unal and C. Sabah "Asymmetric transmission of linearly polarized electromagnetic waves using chiral metamaterials with constant chirality over a certain frequency band," *Modern Physics Letters B*, vol. 28 (32), pp. 1450250, 2014.
- [8] J. Helsing, R. C. McPhedran and G. W. Milton "Spectral super-resolution in metamaterial composites," *New Journal of Physics*, vol. 13, pp. 115005, 2011.
- [9] W. Withayachumnankul, K. Jaruwongrunsee, C. Fumeaux and D. Abbott, "Metamaterial-Inspired Multichannel Thin-Film Sensor," *IEEE Sensors Journal*, vol. 12(5), pp. 1455-1458, 2012.
- [10] W. Withayachumnankul, K. Jaruwongrunsee, A. Tuantranont, C. Fumeaux and D. Abbott "Metamaterial-based microfluidic sensor for dielectric characterization," *Sensors and Actuators A*, vol. 189, pp. 233-237, 2013.
- [11] M. Karaaslan and M. Bakir, "Chiral metamaterial based multifunctional sensor applications," *Progress In Electromagnetics Research*, vol. 149, pp. 55-67, 2014.
- [12] R. Melik, E. Unal, N. K. Perkgoz, C. Puttlitz, and H. V. Demir, "Metamaterial-based wireless strain sensors," *Applied Physics Letters*, vol. 95, pp. 011106, 2009.

Investigation of Information Security Awareness Review

Abdülkadir BİLEN

Elazığ İl Emniyet Müdürlüğü
abdulkadir.bilen82@gmail.com

Ahmet Bedri ÖZER

Firat University, Engineering Faculty
Elazığ, Turkey
bedriozer@firat.edu.tr

Abstract— As information security is one of the economic and national security problems, its importance has increased tremendously. It is very important in the military and intelligence fields of the countries. The components threat information security have entered the agenda not only in national governments but also in international communities. With evolving technology, all national and international community systems have searched new ways for security.

Keywords— Information Security, Cyber Attack, Information Security Awareness

I. INTRODUCTION

In recent years, with the use of the internet and developing technology, the importance given to information security, which has become one of the most important economic and national security problems of the countries, has increased greatly. Information security is of great importance especially in the military and intelligence fields of countries. Day by day, the intractable and complicated cyber threats have entered the agenda of not only national states but also international communities.

The unlimited progress of cyber attacks threatens many areas from international trade to personal banking. Our electronic devices, which become indispensable parts of our everyday life, are vulnerable to the Internet at any moment and can lead to serious problems against cyber attacks by computer hackers or even worse terrorist organizations. For example, a rogue hacker could penetrate into the operating system of a vehicle that is in the intelligent transport system and steer the flow in traffic, leading to huge problems that can not be predicted. Smart cities, energy stations, reliable sub-structures, etc. Increasing the usage areas and remote control of the oven, fridge computer and other devices in our house which can be connected by means of remote connection is a very serious security risk. Recently, the threats of artificial intelligence in

the world of science have been discussed, and many writers and screenwriters believe that intelligent robots and people produced by humans will fight in the future [1]. Cambridge University scientist Stephen Hawking, famous physicist, "artificial intelligence can bring the end of humanity" was found in the description [2]. Scientific and technological studies towards an autonomous system, which can be defined as the Cyber-Physical System (SFS) of today, are continuing rapidly [3]. Again, some systems used in our government institutions are also important for cyber security. It is also possible that an aggressor who seizes the remote controlled Mobile Electronic System Integration (MOBESE) system used in our security units will prevent detection of the offense leading to the incident and misguide it. Nowadays, the Internet, which has become one of the most used communication tools by people, has become a means of communication in many social events. This is an indication of how quickly information spreads on the Internet. For example, if you have 50 friends, this problem is solved in a few seconds by a social media group that is created together with each other.

Many people no longer wait in bank tails and do all banking work in the office or at the place where they live at home. Nowadays, many criminals are infiltrated into the computer system by finding exploits on the internet. Imagine that when a hacker who has leaked into your system runs an action defined as a crime in the world and your country's law from your computer, you may now be exposed to situations you do not want to be suspected or arrested. This is only a question that you can live individually and it is inevitable that everybody who uses the computer system absolutely must secure the information. Now, when an international crisis arises between countries, it is possible to start a cyber war immediately. The existence of this cause has also made it a requirement for countries to take themselves to the next level in combating cyber warfare.

Given that cyber attacks are taking place very quickly on the Internet, the prospect of designing very strong cyber security systems against attack will emerge. Various work has been done in this area. In the work done by Akyildiz [4], it is

determined how to infiltrate systems that have not been tested for safety by applying a network application. Afterwards, the importance of leakage tests has been emphasized, contributing to the awareness of the cyber security. Risk analysis methods have been determined by Aktaş [5] and four selected risk analysis methods have been tested and applied on a model. The proposed approach aims to increase confidence in risk analysis and management. In the work done by Mongol [6], it is emphasized why information security is important for companies, information about the company exposed to cyber attack and how important information protection is. A study by Durmuş [7] conducted a web-based survey on information security and examined the awareness of five different groups and highlighted the shortcomings of security measures in the

network structures of government employees and raised awareness among participants.

Today, these types of attacks, which are transformed into cyber warfare, have to make their own cyber security and have organizations that will respond quickly to this attack [8]. Countries have also been emphasized to work in coordination with institutions in this sector in order to ensure information security and to increase various penal sanctions within the country [9]. We need to identify the security level and risks in each system we use for information security and develop various security methods by analyzing these risks.

II. CONCLUSION

If information security is not emphasized, people or corporations can cause very important assets to be handed over to malicious people. Therefore, everyone should act sensitively to protect their knowledge and increase the continuity of their awareness.

- In the future, the following measures may be taken to enhance information security in the future:

- Institutions should provide information security training.

- Public institutions should conduct awareness raising activities.

- Countries should make more precise and clear laws by increasing the security of information security. .

- Security counseling and technical assistance units should be established in each unit.

- The awareness of individuals and institutions should be increased by conducting lectures on information security in universities.

- Ensure that basic information security training is as free as possible.

- Trainings on information security standards and policies should be given and the use of both institutions and employees should be ensured.

REFERENCES

[1] Convertino S., Demattei L., Knierim T., "Flying and Fighting in Cyberspace", Air War College Maxwell Paper, No. 40, July 2007.

[2] http://www.bbc.com/turkce/haberler/2014/12/141202_hawking_yapay_zeka (Erişim: 11 Aralık 2015).

[3] U.S. Department of Defense, "Unmanned Systems Integrated Roadmap FY2013-2038", U.S. DoD, 2013.

[4] Akyıldız M.A., "Siber Güvenlik Açısından Sızma Testlerinin Uygulamalar İle Değerlendirmesi", S.D. Üniversitesi. Yüksek Lisans Tezi 2013.

[5] Aktaş F. Ö., "Bilgi Güvenliği Risk Yönetiminde En Uygun ve Objektif Yöntemin Belirlenmesi", Gebze İleri Teknoloji Üniversitesi, Yüksek Lisans Tezi, 2009.

[6] Moğol Ş.H., "Importance Of Information Security Awareness", Yıldırım Beyazıt Üniversitesi, Yüksek Lisans Tezi, 2016

[7] Durmuş A., "The Observation Of Information Security Awareness In Turkey", Çankaya Üniversitesi, Yüksek Lisans Tezi, 2014

[8] Bıçakçı S., "NATO'un Gelişen Tehdit Algısı: 21. Yüzyılda Siber Güvenlik", Uluslararası İlişkiler Akademik Dergisi, Cilt 10, Sayı 40(Kış 2014), S101-130.

[9] Gökçe K.G., Şahinaslan E., Dinçel S., "Mobil Yaşamda Siber Güvenlik", 7. Uluslararası Bilgi Güvenliği ve Kriptoloji Konferansı, 17-18.10.2014

The Effect of Using Carbon Fiber and Carbon Dust in Automotive Brake Pads

İbrahim MUTLU

Afyon Kocatepe University, Technology Faculty
Afyon, Turkey
ibrahimmutlu@aku.edu.tr

Muhammet Hüseyin GÜZEL

Konya Selçuk University, Technical Sciences Vocational
School
Konya, Turkey
Mguzel@selcuk.edu.tr

Muhammed ARSLAN

Afyon Kocatepe University, Çay Vocational High School,
Afyon, Turkey
arslanmuhammed10@gmail.com/muarslan@aku.edu.tr

Abdullah Malak

Afyon Vocational and Technical Anatolian High School,
Motor Vehicle Technology,
Afyon, Turkey
abdullah.malak@hotmail.com

Abstract— In this study, the effect of using carbon fiber and carbon powder to the characteristic of wear and friction in automotive brake pads was investigated. Five different mixtures of brake pads were produced. The produced samples were tested in Friction Assessment and Screening Test (FAST) machine in order to determine the characteristic of wear and friction. Also, the microstructure of the friction surface of the samples were scrutinized by Scanning Electron Microscope (SEM). The sample in which %15 of carbon fiber is used showed more stable tribologic and mechanical properties than the other samples. So, it can be advised to use in automotive friction materials.

Keywords— Carbon fiber, wear, friction, brake pad

I. INTRODUCTION

In vehicle brake systems, kinetic energy in wheels is converted into heat energy via friction. The heat energy which occurs during severe braking conditions and cannot be got rid of the system, causes an overheating in the system. This is an undesired situation. Disc brake systems which are more advantageous than the drum brake systems in terms of cooling, are used commonly at present (Handa and Kato, 1996; Hee and Filip, 2005; Bijwe, 1997).

Braking system consist of a lot of parts such as master cylinders, wheels cylinders, tandem cylinders and a control system that is pneumatic or hydraulic system. Brake pads are of importance in each wheel for braking systems (Abhik et. al, 2014). In order that braking will have highly efficient, the wear level between disc and pad surface should be minimum and, a high and stable friction coefficient should be formed (Ertan and Yavuz, 2006). It should be known that there are many parameters which should be considered such as lower wear rate, stable coefficient of friction at different working speed, temperature, pressure and environmental condition in

order to develop a brake pad having better properties (Abhik et. al, 2014). The most important parameter is the composition and microstructure of the brake pad material. In the studies made on the brake materials, generally it is aimed to get the desired specifications by changing the composition. At the same time production method and production parameters should be evaluated together with composition. Because the pads which were produced with the same composition and different production method may show different performances (Ertan and Yavuz, 2006). There are several expectations from brake pads; they always should show constant friction coefficient, have a high friction coefficient and not be broken at high temperature (Ikpambese et. al, 2016). The production practices continue for friction materials which are not harmful for human health and show high tribological performance with low cost. In the production process of the pads materials which are high wear resistant and stable friction coefficient at high temperatures are used as basic bulk material. These materials are ceramic, metallic, polimeric and non-asbestos organic materials (Bijwe, 1997; Pauntenbach et. al, 2003).

Carbon fibers are materials which have micro graphite structure and are not used alone. They are generally used as reinforcing materials in the production of resin, ceramic and metal matrix composite materials. Due to high tensile and compressive strength, high hardness, low coefficient of expansion and self-lubricating properties, carbon fibers can be used for break pads. In the experiments, It was seen that which the carbon fiber ratios in the lining composition increased, the friction coefficient and wear values between the lining and the disc increased (Guan et. al, 2004).

In this study, In order to examine wear and friction characteristics of brake pads produced with carbon fiber having 30 mm of lenght and carbon powder, five samples were prepared different ratios and, wear and friction tests were conducted. As the mass ratio of the carbon fiber in the

composition increases, the mass ratio of the powder carbon is reduced. Using FAST test device, Tribological properties of brake pads samples were obtained. Frictional surfaces were investigated by SEM for microstructure characterization of brake pads samples. As a result of experiments, it was found that % 15 ratio of carbon fiber had positive effects on wear and friction characteristics (Malak, 2014).

II. MATERIAL and METHOD

The mass ratio was used to determine the composition of the brake pads samples. In order to examine the friction and wear behaviors of carbon fiber in the five selected composites, The total ratio of carbon fiber and powder carbon mixture was kept constant at 45%. The ratio of other materials was also kept constant at 55%, thus ensuring a clearer interpretation of the results. Three samples were produced from each sample and averages of the test results was taken into account by testing each samples by FAST.

Table 1. The Ingredients (Formulation) of Samples (WT.%)

Sample Code	3005	3010	3015	3020	3025
Carbon Fiber (30mm)	5	10	15	20	25
Carbon Powder	40	35	30	25	20
Steel Fiber	10	10	10	10	10
Cu Particles	5	5	5	5	5
Al ₂ O ₃	3	3	3	3	3
Rice Husk Dust	2,5	2,5	2,5	2,5	2,5
Graphite	7	7	7	7	7
Cashew	7,5	7,5	7,5	7,5	7,5
Phenolic Resin	20	20	20	20	20
TOTAL	100	100	100	100	100

The materials shown in Table 1 were prepared at the specified ratios and mixed for 20 minutes in a high-speed mixer to ensure homogeneity of the mixture. The homogenized mixture was cold pressed for 1 minute at pressure of 9.81 MPa for preforming. Hot pressing at 180 °C with a pressure of 14.71 MPa was then carried out for one minute per mm. The produced samples were tested by FAST test device in Figure 1.

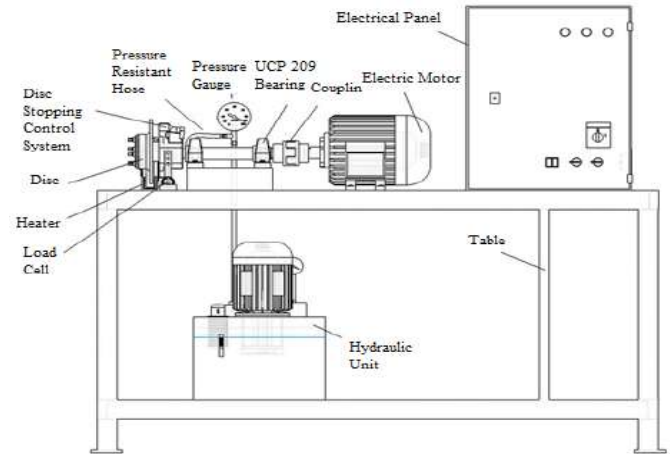


Fig. 1. FAST test setup (Timur, 2007)

Before and after the test, the thickness measurements and weights of the samples were measured. Before the experiments, conditioning process was applied for overlap of %95 of friction surface at 0,7 MPa for 15 minutes.. After the conditioning process, the samples whose surfaces were cleaned and cooled were tested at pressure of 0,551 MPa for 90 minutes in order for friction performance tests. Datas obtained at each second were recorded on the computer.

In order for friction performance, friction coefficient-temperature-time graphs were generated with the datas obtained from experiments for every samples.

III. RESULTS

CHARACTER OF FRICTION SURFACE

SEM images were taken from the wearing surfaces to make microstructure studies on the friction surfaces. All samples showed both of abrasive and adhesive wearing. Abrasive wearing was detected at dark areas, and adhesive wearing was detected at light gray and white areas in the following pictures. When the image of five different samples is generally examined, it can be said that the components in the pads are homogeneous. Also it can be said that carbon fiber has an active role in friction and increases the amount of wearing by breaking off the surface in the friction surface areas.

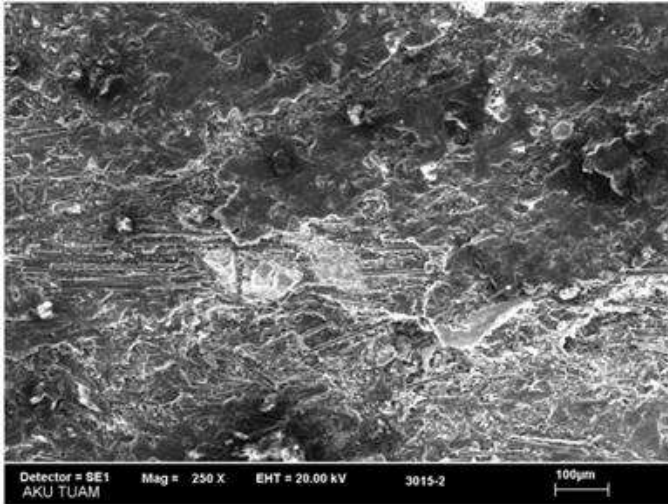


Fig. 2. SEM image of sample with number 3005

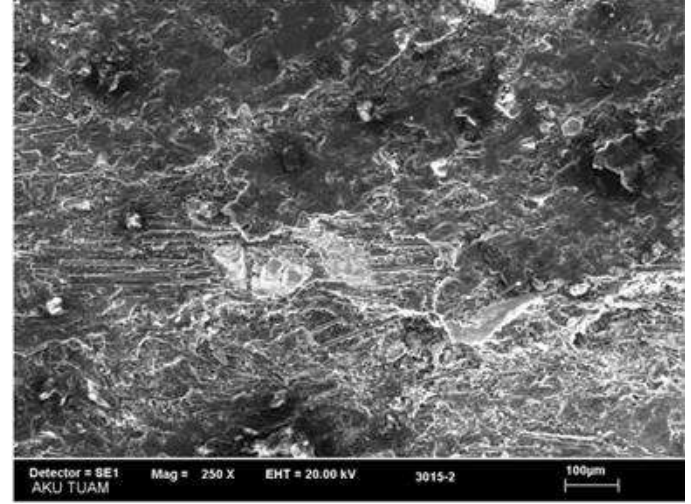


Fig. 4. SEM image of sample with number 3015

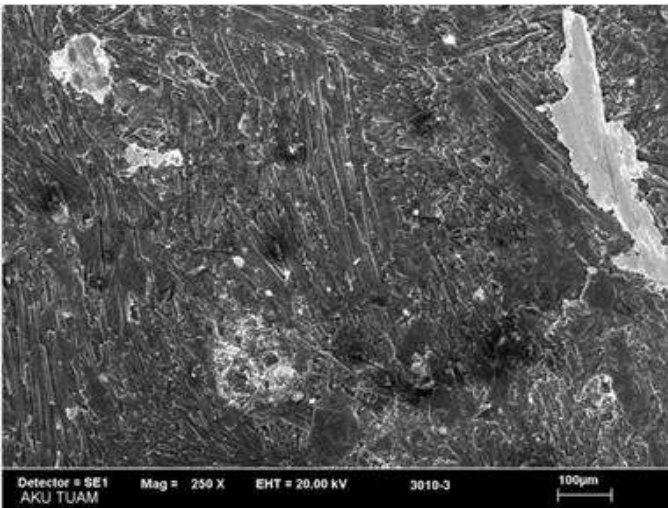


Fig. 3. SEM image of sample with number 3010

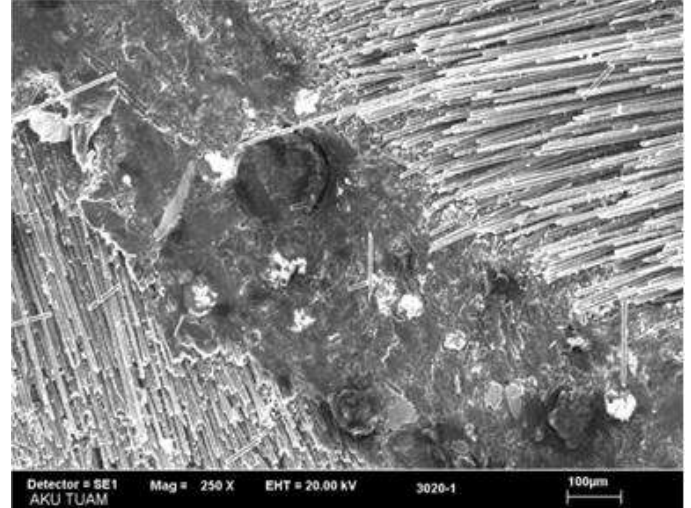


Fig. 5. SEM image of sample with number 3020

When Figure 2 is examined, it can be seen that splits on the surface accumulates on the friction surface and continues to rub on the surface due to wear. In Figure 3, it can be said that the carbon fibers play an active role in friction and so increase the friction coefficient as well as the wearing amount.

The microstructure of the wear surface of the sample with number 3015 was given in Figure 4. It is seen that both the adhesive and the abrasive wear are carried out in the picture and all the components in the pads homogeneously affect to friction. This homogeneity plays an important role for reducing the specific wearing with increasing of the friction coefficient. In the Figure 5 and 6, It is estimated that specific wearing increases as carbon fibers can not be as homogenous as other samples and so the carbon fibers on the pad surface can be separated more easily in the pad.

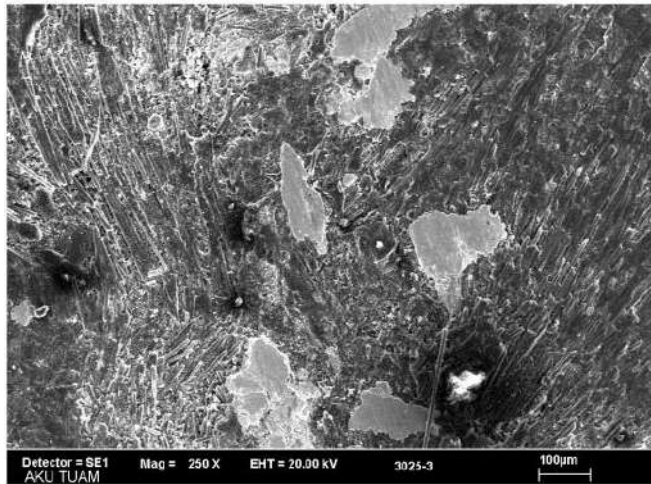


Fig. 6. SEM image of sample with number 3025

FRICTION PERFORMANCE

The temperature-friction coefficient-time graph generated by the datas from experiments is shown in Figure 7. The graph was generated by taking the 5 minute averages of the values recorded for each second. Interface temperature increases with friction between the brake pad and the brake disk. With effect of this temperature, tribological properties of pad changes. In the Ostermeyer's study, it is defined that friction coefficient decreases with interface temperature (Ostermeyer, 2003).

When Figure 7 is examined, there is a steady decreasing change which is bumpy. The roughnesses on the surfaces of pad and disk combine, adhere and then separate. When this process continues as a continuous loop, there is a steady increase and decrease tendency in the friction coefficient (Boz and Kurt, 2005; Stachowiak and Batchelor, 2006). It is seen that the friction coefficient and temperature are different according to the brake pad composition.

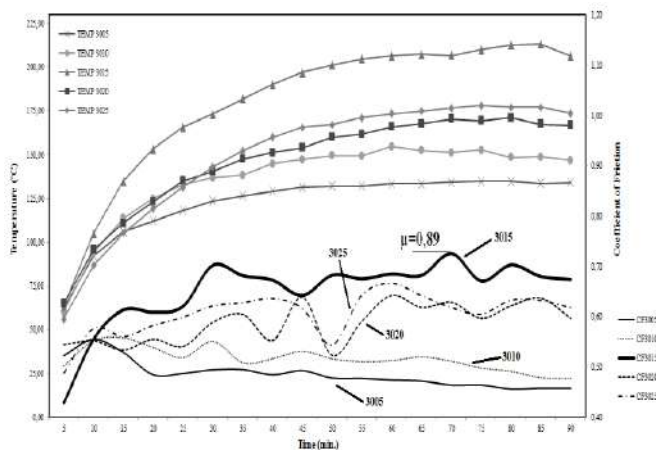


Fig. 7. Temperature-Friction Coefficient-Time graph

The mean friction coefficient of $\mu = 0.65$ of the 3015 code sample is the highest coefficient of friction value. $\mu = 0.65$ which is average friction coefficient of sample with number 3015 was the highest friction coefficient. The lowest average friction coefficient was $\mu=0.49$ which belongs sample with number 3005. The average friction coefficient of sample with number 3010 was obtained as $\mu=0.52$. The average friction coefficient of sample with number 3020 and 3025 were lower than sample with number 3015, but higher than the others. The average friction coefficient of sample with number 3020 and 3025 were $\mu=0.58$ and $\mu=0.61$, respectively.

It is expected from pad materials that friction coefficient is high and stable. The sample with number 3005 and 3010 have the most stable structure with respect to friction coefficient. However, the frictional coefficient of these two samples is lower than the others. The sample with number 3020 and 3025 have unstable friction coefficient having high standart deviation. The friction coefficient of sample with number 3015 is high as well as generally stable. In this case, it can be recommended as the most suitable material.

Since the change in the friction coefficient directly affects the temperature, it is seen that the temperature graph is also parallel to the friction coefficient graph. The temperature in the samples which have high friction coefficient is higher. In addition, While the temperature increases, the friction coefficient decreases in general as phenolic resin deteriorated, that is, it lost its binding property (Anderson et. al, 1992). As a result of the friction test, the maximum temperature was measured as 218 °C for sample with 3015. The maximum average temperature is 180 °C which belongs sample with number 3015. The lowest average temperature is 122 °C which belongs sample with number 3005 having the lowest carbon fiber ratio.

The density of the samples was determined with Archimedes method. As the carbon fiber ratio in the composition increased, it was determined that the sample density generally decreased. After the friction test, the hardness values of the friction surfaces of the samples were determined with Brinell hardness measurement method. The surface roughness of the samples was also measured. As the carbon fiber ratio in the composition increased, the hardness and surface roughness of sample increased. Since 3 samples are produced from each sample, the values obtained from experiments are the average of the values of these three samples. The average values obtained are given in Table 2.

Table 2. Average density-hardness-roughness

Sample Code	Average Density (g/cm ³)	Average Surface Roughness (μm)	Average Brinell Hardness Number (HB)
3005	1,939	2,62	11,9
3010	1,874	3,04	16,1
3015	1,783	3,99	16,7
3020	1,783	4,53	13,8
3025	1,795	4,79	17,3

Average specific wear values were calculated using average friction coefficients, mean densities and average mass loss. As the friction coefficient increased, the specific wear value increased in general. Although the friction coefficient of sample with number 3015 was higher than the others, the specific wear value of sample with number 3015 was lower.

Table 3. Mean specific wear-friction coefficient-mass loss

Sample Code	Average Specific Wear (g/mm ²)*10 ⁻⁶	Average Mass Lose (g)	Average Temperature (°C)	Average Coefficient of Friction	Standart Deviation of Coefficient of Friction
3005	1,578	0,336	122,47	0,49	0,0600
3010	1,859	0,406	135,98	0,52	0,0574
3015	1,374	0,357	179,73	0,65	0,0989
3020	1,913	0,451	145,83	0,58	0,0695
3025	1,919	0,471	149,45	0,61	0,0778

IV. CONCLUSION

The friction coefficient value increased up to the additive ratio of 15%, but the friction coefficient value decreased above this ratio for 30 mm of the carbon fiber lenght. The highest friction coefficient was obtained as $\mu=0,65$ from sample with number 3015 reinforced %15 carbon fiber. The lowest friction coefficient was obtained as $\mu=0,49$ from sample with number 3005 reinforced %5 carbon fiber. Also, since the high friction coefficient will increase the temperature at friction areas, the samples having high friction coefficient have high interface temperature. While the maximum average temperature is 180 °C which belongs sample with number 3015, the lowest average temperature is 122 °C which belongs sample with number 3005.

It was found that while the carbon fiber ratio of samples increased, the density of samples decreased; the hardness and surface roughness increased. The minimum average density was 1,795 g/cm³ which belongs sample with number 3025, the maximum average density was 1,939 which

belongs sample with number 3005. Also, the maximum average hardness and surface roughness were 4,79 μm and 17,3 HB; the minimum average hardness and surface roughness were 2,62 μm and 11,9 HB, respectively.

The specific wear is a parameter which depends on density, friction coefficient and mass loss. As a disadvantage, with increasing of the friction coefficient, the specific wear increased. The minimum average specific wear was 1,578 g/mm²*10⁻⁶ which belongs sample with number 3005; the maximum average specific wear was 1,919 g/mm²*10⁻⁶ which belongs sample with number 3025.

Due to mentioned effects of carbon fiber on the brake pads, it can be used as a reinforcing material to brake pads in the automotive sector and the sample with number 3015 was the most suitable sample in all samples.

REFERENCES

- [1] Abhik, R., Umasankar, V. and Xavier, M.A. 2014 "Evaluation of Properties for Al-SiC Reinforced Metal Matrix Composite for Brake Pads", Procedia Engineering, vol. 97, pp. 941-950.
- [2] Anderson, E.A. 1992 "Friction, Lubrication, and Wear Technology", ASM Handbook. ASM International, vol. 18, pp. 569-577.
- [3] Bijwe, J. 1997 "Composites As A Friction Material: Recent Developments In Non-Asbestos Fiber Reinforced Friction Materials-A Review", Polymer Composites, vol. 18, pp. 378-396.
- [4] Boz, M. and Kurt, A. 2005 "Wear Behaviour of Organic Asbestos Based and Bronze Based Powder Metal Brake Lining", Materials and Design, vol. 25, pp. 343-347.
- [5] Ertan, R. and Yavuz, N. 2006 "Polimer Matriksli Fren Balata Malzemelerinin Kompozisyon ve Üretim Parametreleri Açısından Değerlendirilmesi", Mühendis ve Makine, vol. 47, pp. 24-30.
- [6] Guan, Q.F., Li, G.Y., Wang, H.Y. and An, J. 2004 "Friction-Wear Characteristics of Carbon Fiber Reinforced Friction Material", Journal of Material Science, vol. 39, pp. 641-643.
- [7] Handa, Y. and Kato, T. 1996 "Effects of Cu Powder, BaSO₄ and Cashew Dust on the Wear and Friction Characteristics of Automotive Brake Pads", Tribology Transactions, vol. 39, pp. 346-353.
- [8] Hee, K.W. and Filip, P. 2005 "Performance of Ceramic Enhanced Phenolic Matrix Brake Lining Materials for Automotive Brake Linings", Wear, vol. 259, pp. 1088-1096.
- [9] Ikpambese, K.K. Gundu, D.T. and Tuleun, L.T. 2016 "Evaluation of palm kernel fibers (PKFs) for production of asbestos-free automotive brake pads", Journal of King Saud University - Engineering Sciences, vol. 28, pp. 110-118.
- [10] Malak, A. 2003 "Investigate of Long-Dimension-Carbon Fiber Usage In Brake Linings", Afyonkarahisar, Afyon Kocatepe University.
- [11] Ostermeyer, G.P. 2003 "On The Dynamics of The Friction Coefficient", Wear, vol. 254, pp. 852-858.
- [12] Pauntenbach, D.J., Richter, R.O., Finley, B.L. and Sheehan, P.J. 2003 "An evaluation of the historical exposures of mechanics to asbestos in brake dust", Applied Occupational and Environmental Hygiene, vol. 18, pp. 786-804.
- [13] Stachowiak, W.G. and Batchelor, A.W. 2006 "Engineering Tribology", Butterworth-Heinemann.
- [14] Timur, M. 2007 "Otomotivde Kullanılan Sürtünme Malzemelerinin Sürtünme Katsayısını Tespit Eden Test Cihazı Tasarımı ve İmalatı", Afyonkarahisar, Afyon Kocatepe University.

Determination of Self-incompatibility mechanisms in Prunus Species by Modern Techniques

Zehra Tuğba MURATHAN
Ardahan University, Faculty of Engineering
Food Engineering Department
Ardahan/Turkey
e-mail:ztugbaabaci@hotmail.com

Abstract—*Prunus* genus have over 400-430 species but only 98 species are of commercially importance. All the stone fruits are included in this group. Many important *Prunus* species have homomorphic gametophytic self-incompatibility (SI) mechanism, controlled by a simple multi-allelic *S* locus, which denies its own pollen. The incompatibility status is unknown in *Prunus* species causes significant economic losses in breeding programs. Identification of the incompatibility status can be detected by conventional and modern breeding methods. The modern breeding methods are fast, safe and saving on time. In this study, we analyzed so far makes SI studies by modern techniques in *Prunus* species. SI have been identified in 20 different *Prunus* species. It was determined 66 alleles in *P.armeniaca*, 54 alleles in *P. dulcis*, 51 alleles in *P.speciosa*, 41 alleles in *P.salicina*, 38 alleles in *P.avium*, 36 alleles in *P.cerasus*, 36 alleles in *P.mume*, 24 alleles in *P.spinosa*, 22 alleles in *P.virgiana*, 20 alleles in *P.africana*, 15 alleles in *P.cerasifera*, 14 alleles in *P. pseudocerasus*, 9 alleles in *P.humulis*, 9 alleles in *P.domestica*, 8 alleles in *P.davidiana*, 4 alleles in *P.japonica*, 2 alleles in *P.webbi*, 2 alleles in *P.yedoensis*, 1 alleles in *P.subhirtella* and 1 alleles in *P.tangutica*.

Keywords—*Prunus*, Incompatibility, *S* allele, Modern techniques

Eco-friendly plant Moringa oleifera

Zehra Tuğba MURATHAN
Ardahan University, Faculty of Engineering
Food Engineering Department
Ardahan/Turkey
e-mail:ztugbaabaci@hotmail.com

Abstract— *Moringaceae family has 14 species and Moringa oleifera is one of the species of this family. The plant has wide climatical adaptability and it can be grown many tropic and sub-tropic regions of the world. In this study, the benefits of Moringa were described. Moringa oleifera is one of the World's most useful trees, as almost every part of the tree can be used for food, medication and industrial purposes. Moringa is uses biomass, human food, animal food, , blue dye, foliar nutrient, antimicrobial agent, gum, honey and sugar cane juice-clarifier, medicine, tannin for tanning hides. Moringa has been used as a traditional medicine around the world, for anemia, skin infections, blackheads, anxiety, bronchitis, catarrh, chest congestion, asthma, blood impurities, cholera, glandular, swelling, headaches, conjunctivitis, cough, diarrhea, eye and ear infections, fever, abnormal blood pressure, hysteria, pain in joints, pimples, psoriasis, respiratory disorders, scurvy, semen deficiency, sore throat, sprain, tuberculosis, for intestinal worms, lactation ,diabetes and pregnancy. It is also an environmentally friendly due to the use of plants as a fertilizer, biogas, biopesticide, domestic cleaning agent, erosion preventive effect. The seeds of Moringa oleifera contains some coagulant matters and it is used in water purification.*

Keywords— *Moringa, Ecology, Benefits, Fertilizer, Purification*

COMPUTER ENGINEERING

ORAL SUBMISSIONS



Moving Object Removal from Video Sequences

Şafak ALTAY AÇAR

Department of Mechatronics Engineering
Faculty of Technology, Karabük University
Karabük, Turkey
safakaltay@karabuk.edu.tr

Şafak BAYIR

Department of Computer Engineering
Faculty of Engineering, Karabük University
Karabük, Turkey
safakbayir@karabuk.edu.tr

Abstract—This study focuses on moving object removal from video sequence. Firstly, all frames are extracted from video sequence. Then, an object is determined in the first frame and the determined object is detected and removed from all frames one by one. Empty region which is occurred after removing process, is restored by utilizing an inpainting algorithm. A software and an interface are designed for these processes. Synthetic and real video sequences are used to test and evaluate the developed method.

Keywords—*inpainting; object removal*

I. INTRODUCTION

In recent years, image and video processing have become more important because of developing technology and increasing usage of social media. Sometimes users are obliged to edit their photo or video due to undesired object, damaged region, noise etc. and these problems can be solved by image and video processing methods such as object removal, inpainting and texture synthesis.

When the relevant literature is taken into consideration, it is seen that many academic studies are made on object removal from video sequence and video completion. Zarif et al. [1] propose an approach to remove static object from video scene by utilizing local similarity and 3D hole filling. They state that proposed method has a faster processing and high quality. Bhatewara et al. [2] propose an inpainting system to remove undesired object from a video. They compare their method with other methods and show results visually. A video text removal method is presented by Mosleh and Bouguila [3] which uses stroke width transform and unsupervised clustering. They evaluate their method utilizing by different algorithms and they compare their method with other methods by computing mean square error. Herling and Broll [4] present a pixel based image and video inpainting study. They show visual results of comparisons with other methods and time performances. Yoo et al. [5] propose an approach to complete video using mosaicking, local motion computation and block matching. They show experimental results visually. A fast video completion study is presented by Afifi et al. [6]. Developed method which is based on patch synthesis and image registration is evaluated by human visual observation. Ebdelli et al. [7] present a novel video inpainting method which has a few steps such as spatial inpainting and global energy minimization. They state that proposed approach provides high quality inpainting results.

Zarif et al. [8] propose a video completion method based on gray level co-occurrence matrix. They show results visually and comparison of the execution time between the proposed method and other methods. A method is presented by Yang et al. [9] which detects and removes caption from video. They use colour edge detector and a method based on Criminisi algorithm. They show experimental results as correct rate, false detecting rate and missing rate. Jia [10] proposes a video inpainting algorithm based on texture synthesis. They show peak signal to noise ratio value of test results. Almatrafi and Sasi [11] present an object addition and removal study. The method can be used for image and video. Results are shown visually.

This paper presents a moving object removal method. After all frames are extracted from video sequence, an object is determined in the first frame. The determined object is detected and removed from all frames one by one. Empty region which is occurred after removing process is restored by utilizing an inpainting algorithm. We use the same shape of neighbourhood and searching method described in [12] for this process. Since we do not have an example texture patch, we searched appropriate pixel colour value within the empty region's surrounding.

II. MOVING OBJECT REMOVAL

Process of moving object removal consists of some sub-processes. Firstly, all frames are extracted from video sequence and they are registered as an image. Then an object is determined in the first frame manually. Determined object is removed from first frame and an inpainting algorithm is applied to fill occurred empty region. After processes related to first frame are finished, object is searched around previous location of object in the second frame so that if the object is moving, it is detected easily. After detection, removing and inpainting are carried out again. These processes are applied for all frames one by one.

Search and detection processes are shown in Fig. 1. Red square denotes search region (100x100 pixels). Sum of Absolute Difference (SAD) is used to find best matched region. Computing SAD is realized by summing absolute differences of R-G-B values. The region which has the lowest SAD, is accepted as detected moving object which is determined in first frame.

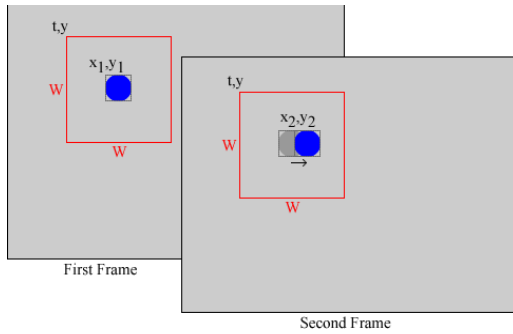


Fig. 1. Search and detection processes

Used inpainting algorithm is shown in Fig. 2. Shape of neighbourhood and searching method described in [12] are used. Red square denotes search region. Yellow squares denote pixels which are compared. White squares denote empty pixels which are occurred after removing object.

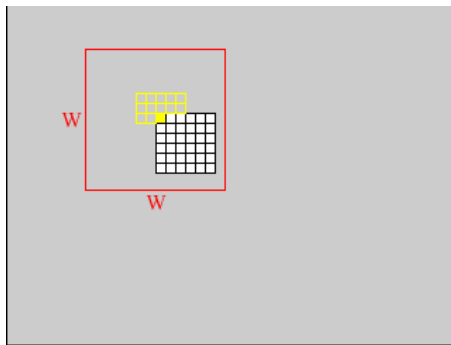


Fig. 2. Inpainting algorithm

The value of each empty pixel is determined by comparing its neighbours with all pixels in the search region. Its neighbours are shifted on searching region like a block. SAD is used to compare the difference of colour values. Computing SAD is realized by summing absolute differences of R-G-B values. The pixel which has the lowest SAD, is determined as best matched pixel. SAD which is applied in this algorithm, is given in (1).

$$SAD = \sum_{i=1}^{12} \alpha_i + \theta_i + \beta_i \quad (1)$$

α , θ and β denote absolute differences of R-G-B values between empty pixel's neighbours and pixels of search region. Algorithm is applied from left to right and top to bottom. Search region's height and width are accepted as 100x100 pixels.

III. EXPERIMENTAL RESULTS

We evaluate proposed method by using two real and three synthetic videos. Sample results of real videos are shown in Fig. 3 and Fig.4. Videos are obtained from [13]. They are explained and used in [14]. A person crossing the road is marked to remove in the first video. A static object is marked to remove in the second video but camera moves.



(a)



(b)



(c)



(d)

Fig. 3. Results of the first real video a) marked person b) result of the first frame c) result of the second frame d) result of the third frame.



(a)



(b)



(c)



(d)

Fig.4. Results of the second real video a) marked object b) result of the first frame c) result of the second frame d) result of the third frame.

We use three texture images from Described Texture Dataset [15] which is explained and used in [16] to make synthetic videos. These textures are used for video's background and a synthetic moving ball whose diameter is 20 pixels is added on these textures so that synthetic videos are created. Moving ball is marked to be removed in these videos. Mean absolute errors (MAE) are calculated for each red, green and blue colour values to evaluate synthetic videos. First four frames of each video are used for this process. Tables I and II report two kind of evaluations. In the first one, one pixel shifting is applied in inpainting process. In the second one, two pixels shifting is applied. In Tables, v1-f1 means first video's first frame and v1-f2 means first video's second frame.

TABLE I. EVALUATION OF SYNTHETIC VIDEOS

(One pixel shifting)			
Frame	MAE (Red)	MAE (Green)	MAE (Blue)
v1-f1	24.27	23.07	25.73
v1-f2	7.53	6.43	5.95
v1-f3	27.18	27.39	29.75
v1-f4	6.80	6.31	5.57
v2-f1	28.03	30.76	33.53
v2-f2	30.92	37.77	44.52
v2-f3	33.98	47.66	63.78
v2-f4	31.13	34.58	39.22
v3-f1	37.63	42.12	40.45
v3-f2	33.43	31.64	34.22
v3-f3	25.93	33.97	33.60
v3-f4	20.66	21.01	19.63

TABLE II. EVALUATION OF SYNTHETIC VIDEOS

(Two pixels shifting)			
Frame	MAE (Red)	MAE (Green)	MAE (Blue)
v1-f1	40.86	58.60	51.17
v1-f2	7.95	7.01	6.36
v1-f3	29.06	27.74	30.87
v1-f4	6.16	5.57	5.28
v2-f1	31.16	34.59	37.97
v2-f2	33.11	39.54	45.47
v2-f3	35.41	48.47	66.21
v2-f4	30.33	35.20	41.87
v3-f1	33.43	40.02	40.28
v3-f2	29.42	28.51	29.85
v3-f3	24.63	29.98	30.02
v3-f4	20.27	19.85	20.16

Average errors of red, green and blue values are computed as 25.62, 28.56 and 31.33 respectively for the first evaluation. Average errors of red, green and blue values are computed as 26.82, 31.26 and 33.79 respectively for the second evaluation. Otherwise algorithm which uses two pixels shifting is three times faster than the one pixel shifting.

According to experimental results, assessments occur as follows;

- If the object which is determined to be removed is big or video's background is complicated, worse results are obtained for real videos.

- Computed averages errors of evaluations are not very different from each other but algorithm which uses two pixels shifting is three times faster than the one pixel shifting.

IV. CONCLUSION

Moving object removal is achieved by using a moving object detection algorithm and an inpainting algorithm. Proposed method is evaluated by utilizing real and synthetic videos. Results of real videos are shown visually. Otherwise, results of synthetic videos are evaluated by computing mean absolute errors. Occurred assessments according to results are explained. In the future we will add some processes to improve our method in terms of process duration and performance.

REFERENCES

- [1] S. Zarif, I. Faye, and D. Rohaya, "Static object removal from video scene using local similarity," IEEE 9th International Colloquium on Signal Processing and Its Applications, pp. 54-57, March 2013, Kuala Lumpur, Malaysia.
- [2] N. Bhatewara, P. Kumar, and A. Agrawal, "Intelligent video inpainting system for texture reconstruction," 4th International Conference on Computer and Communication Technology, pp. 60-65, 2013.
- [3] A. Mosleh and N. Bouguila, "Automatic inpainting scheme for video text detection and removal," IEEE Transactions on Image Processing, vol. 22, no. 11, pp. 4460-4472, November 2013.
- [4] J. Herling and W. Broll, "High-quality real-time video inpainting with pixmix," IEEE Transactions on Visualization and Computer Graphics, vol. 20, no. 6, pp. 866-879, June 2014.
- [5] S. Yoo, A. K. Katsaggelos, G. Jo, E. Chae, H. Cheong, S. Jeon, M. Kim, J. Paik, and C. Park, "Video completion using block matching for video stabilization," 18th IEEE International Symposium on Consumer Electronics, June 2014.
- [6] M. Afifi, K. F. Hussain, H. M. Ibrahim, and N. M. Omar, "Fast video completion using patch-based synthesis and image registration," International Symposium on Intelligent Signal Processing and Communication Systems, pp. 200-204, December 2014.
- [7] M. Ebdelli, O. L. Meur, and C. Guillemot, "Video inpainting with short-term windows: application to object removal and error concealment," IEEE Transactions on Image Processing, vol. 24, no. 10, pp. 3034-3047, October 2015.
- [8] S. Zarif, I. Faye, and D. Rohaya, "Video completion method for static object removal based on GLCM," IEEE 11th International Colloquium on Signal Processing and Its Applications, pp. 57-62, March 2015, Kuala Lumpur, Malaysia.
- [9] S. Yang, J. Xue, and Y. Zong, "Caption detection and removal from video images with complicated background using intelligent inpainting scheme," 12th World Congress on Intelligent Control and Automation, pp. 611-616, June 2016, Guilin, China.
- [10] C. Jia, "Video inpainting algorithm based on texture synthesis," International Conference on Smart Grid and Electrical Automation, pp. 201-204, August 2016.
- [11] B. Almatrafi and S. Sasi, "Object addition, removal and video authenticity testing," International Conference on Electrical, Electronics, and Optimization Techniques, pp. 814-820, March 2016.
- [12] L. Y. Wei and M. Levoy, "Fast texture synthesis using tree-structured vector quantization," SIGGRAPH, 2000.
- [13] ChangeDetection.net (2017, January), Retrieved from <http://changedetection.net/>.
- [14] Y. Wang, P. M. Jodoin, F. Porikli, J. Konrad, Y. Benezeth, and P. Ishwar, "CDnet 2014: an expanded change detection benchmark dataset," IEEE Workshop on Change Detection, pp. 387-394, 2014.
- [15] Describable Textures Dataset (2017, January), Retrieved from <https://www.robots.ox.ac.uk/~vgg/data/dtd/>.
- [16] M. Cimpoi, S. Maji, I. Kokkinos, S. Mohamed, and A. Vedaldi, "Describing textures in the wild," IEEE Conference on Computer Vision and Pattern Recognition, 2014.

Genetic Algorithm Based Floor Planning System

Hamide Ozlem Dalgic, Erkan Bostanci, Mehmet Serdar Guzel
SAAT Laboratory, Computer Engineering Department
Ankara University, Golbasi Campus,
Ankara, Turkey
ddalgicozlemm@gmail.com, {ebostanci, mguzel}@ankara.edu.tr

Abstract—Genetic Algorithms are widely used in many different optimization problems including layout design. The layout of the shelves play an important role in the total sales metrics for superstores since this affects the customers' shopping behaviour. This paper employed a genetic algorithm based approach to design shelf layout of superstores. The layout design problem was tackled by using a novel chromosome representation which takes many different parameters to prevent dead-ends and improve shelf visibility into consideration. Results show that the approach can produce reasonably good layout designs in very short amounts of time.

Keywords—market shelves layout, genetic algorithm, DEAP (evolutionary algorithm framework), python,

I. INTRODUCTION

Genetic Algorithm (GA) is one type of evolutionary algorithms which uses the evolutionary principles found in nature to find the optimal solution of problems [1-2]. Genetic Algorithms work according to probability rules and aim to find an answer for the existing problem and this answer is optimised over generations.

Although the design process for market shelves (Figure 1) seems to be easy, it is an important factor in the revenue and cost. For example, in a market design, a customer should be able to see all products on the shelves. The market shelves should not occlude each other. Another important factor includes the placement of entrance and exit doors. Customers should be able to navigate easily between shelves until they reach the exit door after entering through the entrance door.



Figure 1. A market shelf layout example

This paper describes the implementation of GA to the Floor Planning System. We describe our approach to designing a chromosome structure and fitness function to yield the optimal layout of the shelves. The result is a 2D map describing the shelf organization.

The rest of the paper is structured as follows: Section II describes the previous studies found in the literature which is followed by a brief explanation of the library used for the evolutionary system, namely Evolutionary Algorithm Framework (DEAP), in Section III. Section IV is dedicated to the description of the chromosome design and other implementation issues. Experimental results are described in Section V. Finally, the paper is concluded and future directions are outlined in Section VI.

II. BACKGROUND

Arrangement problems have a very important place when real life problems are considered. Since these problems are difficult to solve, heuristic algorithms such as genetic algorithm are used to produce near optimal results instead of traditional optimization algorithms.

In 2010, facility's layout plan was generated on Two Dimensional Shape Allocation with Genetic Algorithm [3]. Therein, the important point was shapes allocation with minimum space requirement on a 2D surface. Their results showed that the genetic algorithm gives optimal results in two dimensional shape fitting problems [3-4]. Our approach differs from this study in that we mainly focus on navigable corridors for customer walk instead of obtain the minimum space between shapes.

As a similar study, Rojas and Torres [5] designed a system using genetic algorithm to solving bank offices' layouts problem. They represented their problem solution in a chromosome that has five parts. First four parts of the chromosome represent the flanks of the office and fifth part contains the numbers of the departments located in the back part of office.

Maze generation problems are also quite related to floor planning problems [6-7], especially for computer games. Such

as automated maze generation for Ms. Pac-Man using Genetic Algorithms. In that study, a genetic algorithm was designed optimal mazes by specifying fitness function to create different mazes which can allow the game to be finished by the player [8]. The navigable corridor issue tackled here is very similar to the one in [8].

III. DEAP (EVOLUTIONARY ALGORITHM FRAMEWORK)

DEAP is an evolutionary computation algorithm developed by François-Michel De Rainville, Félix-Antoine Fortin and Marc-André Gardner in 2009 with the help of the Python program language [9]. Rapid prototyping allows users to quickly apply their own algorithms instead of limiting them [10]. Therefore, it is fairly easy to implement. The DEAP core consists of two basic structures; creator and toolbox. The Creator module allows generation of genes and populations from data structures such as list, set, dictionary. Toolbox is a structure that contains evolutionary algorithm operators.

IV. GENETIC ALGORITHM

Genetic Algorithms provide heuristic solutions to complex and difficult problems. GA based on natural biological evolution rules [11-13]. The fundamental principle of the GA is the survival of the fittest as it is in nature. Through the evolutionary process, each generation comes out to have superior features than their parents. To produce a fitter generation in time, the chances of reproduction of failed individuals are reduced. This is provided by several genetic algorithm operators. The most commonly used and important one is crossover operation in which an exchange of sections of the parents' chromosomes is performed.

Yet another GA operation is mutation. Only crossover on chromosomes can be insufficient for variation. Mutation operation ensures that a random modification of the chromosome. Selection of new individuals are made by a fitness function which constitutes the basis of an individual's quality. This function is defined in a problem specific fashion. It assigns a value to all individuals in a population. Selection operation is performed according to these fitness values assigned by fitness function. Outline of a GA can be described with the steps below:

- Creating initial random population.
- Calculating fitness of the each individuals in the population.
- Selection best fit from current population and generate offspring.
- Crossover and mutation operations to provide variety.
- Evaluating fitness of each offspring.
- Replacing failed individuals with newly generated ones.
- Repeating from step two until termination condition reached.

A. Chromosomal Representation

A solution to our market layout problem is created using blocks to represent market shelves. These blocks are represented in a chromosome which are divided four parts. The first part of the chromosome represents a block's direction; true for vertical blocks and false for horizontal blocks. The second and third parts of the chromosome represents position of block. The last one represents length of the block.

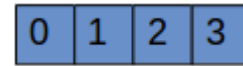


Figure 2. Block representation

```
isVertical = block[0]
xValue = block[1]
yValue = block[2]
blockLength = block[3]
```

An example chromosome may have the values (1,6,7,3) for a block with the following properties: This block was created vertical and 3 units lengths at (6,7) coordinates. This notation made it easier to implement the genetic algorithm and reach the solution.

B. Initial Population

Initial population is created with certain number of blocks that formed randomly. Each individual is represented by a 10x10 2-dimensional array with 10 blocks. For subsequent graphical display made easy, blocks were represented by 1 and corridors were represented by 0 in the array.

```
population [Individual([[0, 0, 0, 0, 0, 0, 0, 0, 0, 0],
                        [0, 0, 0, 0, 0, 0, 0, 0, 0, 0],
                        [0, 0, 0, 0, 0, 0, 0, 0, 0, 0],
                        [0, 0, 0, 0, 1, 1, 0, 0, 0, 0],
                        [0, 0, 0, 0, 1, 1, 0, 1, 0, 0],
                        [0, 0, 0, 0, 1, 1, 0, 1, 0, 0],
                        [0, 0, 1, 1, 0, 1, 0, 1, 0, 0],
                        [0, 0, 0, 0, 0, 0, 0, 0, 0, 0],
                        [0, 0, 0, 0, 0, 0, 0, 0, 0, 0],
                        [0, 0, 0, 0, 0, 0, 0, 0, 0, 0]])]
```

Figure 3. Map made out from blocks

C. Fitness Function

Fitness function is defined as a function which determined how good the individuals are as a solution. It assigns a value to each individual in the population considering their suitability for the solution. In GA Based Floor Planning System fitness values are assigned conforming to following purposes; floor design should let go around between all shelves and reaching all products to customers. That navigation control is provided by A* algorithm using a similar approach in [8]. Another criteria

for quality of the block is whether blocks are spread homogeneously on the floor and total number of blocks.

According to these constraints, we define the following,

$$r = \begin{cases} 0.05n, n \geq 5 \\ 0.05/n, otherwise \end{cases}$$

$$a = \begin{cases} +0.05, s \\ -0.5, otherwise \end{cases}$$

$$f = b/5.0$$

where

- b = total block count (1's in an individual)
- s = A* algorithm result that the map can complete process
- b = number of neighbours for a block
- r = neighbour count based fitness value
- a = A* algorithm based fitness value
- f = block count based fitness value

$$Fitness = f + a + r$$

D. Crossover

The crossover operator is used to create new solutions from existing solutions. This operator exchanges the genes information between individuals and puts together different parts of good solutions for create better solutions [14].

In this problem, crossover operator was applied to blocks instead of individuals. Selected blocks of population individuals were crossed to ensure variety as in Figure 4.

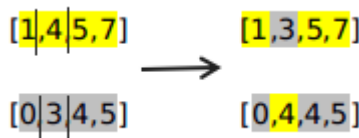


Figure 4. Two point crossover

DEAP's two point crossover method was used for floor planning system. In addition to this there are 2 more crossing methods including one point crossover and uniform crossover methods. In the first stage, a population of 100 individuals were generated. Then this number was increased and the effect of the number of population on the solutions was examined.

E. Selection

Selection process determines which individuals are chosen for reproduction. Main principle of the selection is gathering a group of high quality individuals have a higher chance of becoming parents in a mating pool. There are three major types of selection in Genetic Algorithm approach: tournament selection, rank-based selection and roulette wheel selection [15]. In this study, roulette wheel selection was employed.

The probability of selecting an individual in the roulette wheel method is the ratio of the fitness value of that individual to the total fitness values of all individuals as depicted in Figure 5.

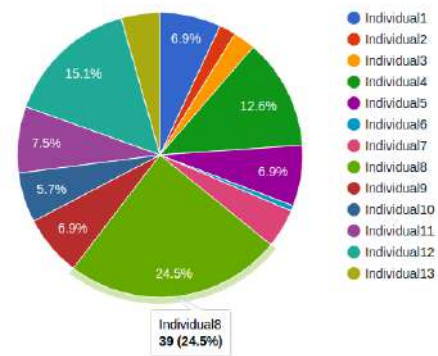


Figure 5. Roulette selection for five candidates with different fitness values.

V. VISUAL INTERFACE GENERATION

Interface allows easy monitoring the improvements of generations. The python library graphics.py was used to create the interface. Graphics.py is a simple and easy object oriented graphics library written by John Zelle. The library is not a part of standard Python distribution so it must be imported. 500x500 pixels rectangle is created for the floor planning system using graphics.py.

10x10 empty grid is generated in this rectangle. In each individual which is result of crossover 1 values are replaced with a simple 2D box. A map can be directly visualised in this way as shown in Figures 6 and 7.

0	0	0	0	0	0	0	0	0	0
0	0	0	1	0	0	0	0	0	0
0	1	0	1	0	0	0	0	0	0
0	1	0	1	0	0	0	0	0	0
0	1	0	0	0	0	0	0	0	0
0	1	0	0	0	0	0	0	0	0
0	0	0	0	1	1	1	0	0	0
0	0	0	0	0	0	0	1	1	0
0	0	0	0	0	0	0	0	0	0

Figure 6. Blocks represented by 1s and 0s

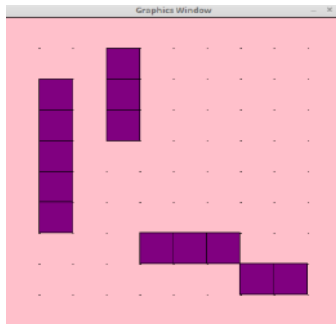


Figure 7. Graphical representation of blocks in Figure 6

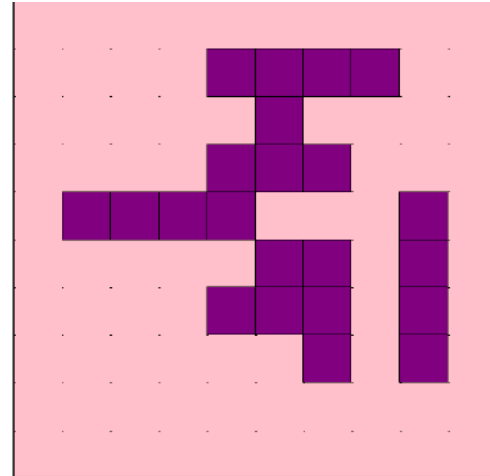


Figure 9. First generation resulting from GA

VI. EXPERIMENTAL RESULTS

The result of the study, individuals close to the expected solution are obtained. Low quality individuals are eliminated from the population. It is obtained that fitness values for next generations increased or remained stable in time.

Figure 8 shows how the fitness values change over time for 100 generations.

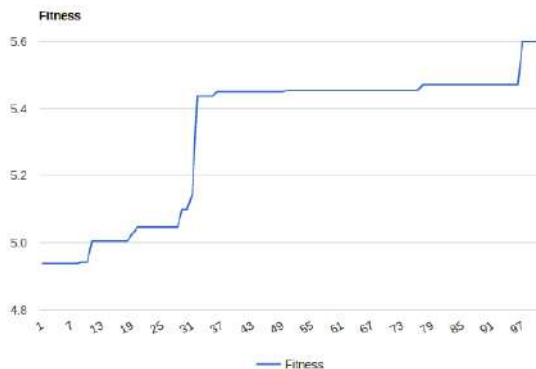


Figure 8. Fitness values alteration of individuals in time

Initial solutions are not ideal since they have many overlapping parts, see Figures 9. Note that these initial layouts are clustered together and hard to navigate.

The algorithm produces better layout designs over time. The evolutionary process eliminates the solutions where navigation is impossible and many overlapping parts exist. Further, the algorithm tries to make the best use of the whole floor by spreading the shelves across the whole surface as shown in the intermediate generation of Figure 11.

Figure 12 and 13 depict the final solutions, two best are shown here. These solutions definitely have navigable corridors where all shelves can be accessed. In addition, the use of the floor is more efficient than the initial solutions.

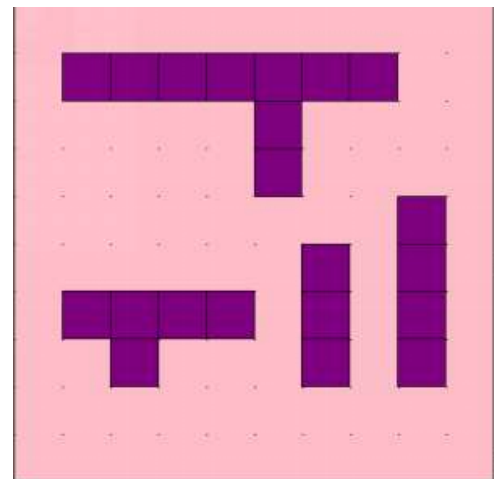


Figure 11. 50 th generation resulting from GA

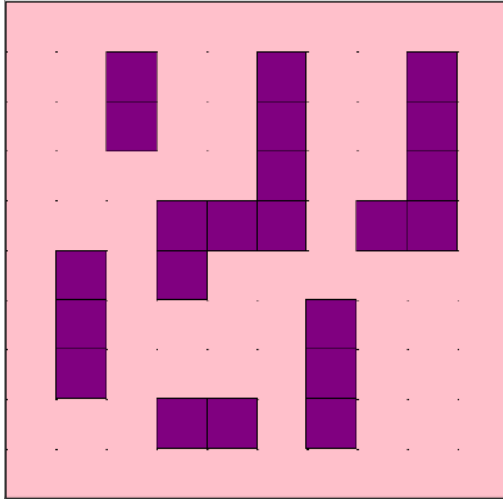


Figure 12. 100 th generation resulting from GA

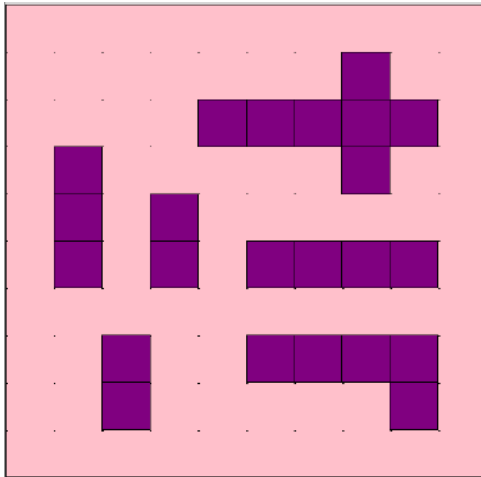


Figure 13. 100 th generation resulting from GA

VII. CONCLUSION

The genetic Algorithm solution has become an effective algorithm that can be used to achieve fast and easy solution of many difficult and complex problems. This paper provided a solution to the design of market layouts. The ability of the genetic algorithm to obtain more than one optimum solution, possibilities to work with many parameters has also played a significant role in its acceptance. It is observed that the performance of the GA result changes according to given parameters and probability values. Results show that this approach was successful in generating good designs in an automated fashion.

In future work, fitness function will be improved to create better market layout. A way to achieve this is to integrate the shopping basket analysis along with this approach so that the market layout is in an agreement with users' shopping behaviour [16-17].

REFERENCES

- [1] Sivanandam, Deepa "Introduction to Genetic Algorithm", Springer, 2008
- [2] J. H. Holland. "Outline for a logical theory of adaptive systems". Journal of the Association for Computing Machinery, 3, 1962, pp. 297- 314.
- [3] Özşahin, Metin, and Mustafa Oral. "Genetik Algoritma ile İki Boyutlu Şekil Yerleştirme." (2010).
- [4] Ahmad, A. R., Basir A. O., Hassanein K. and Imam M. H.(2004), Improved Placement Algorithm for Layout Optimization, The 2nd International Industrial Engineering Conference (IIEC2004), December 19-21, 2004, Riyadh, Saudi Arabia.
- [5] Rojas, G. S., and J. F. Torres. "Genetic Algorithms For Designing Bank Offices Layouts." Prosiding Third International Conference on Production Research–Americas' Region, 2006.
- [6] Gordon, V. Scott, and Zach Matley. "Evolving sparse direction maps for maze pathfinding." Evolutionary Computation, 2004. CEC2004. Congress on. Vol. 1. IEEE, 2004.
- [7] Choubey, Nitin S. "A-Mazer with Genetic Algorithm." *International Journal of Computer Applications* 58.17 (2012).
- [8] Aykut Burak Safak, Erkan Bostanci and Ali Emre Soylucicek, Automated Maze Generation for Ms. Pac-Man Using Genetic Algorithms, International Journal of Machine Learning and Computing, Vol. 6, No. 4, August 2016
- [9] Fortin, Félix-Antoine, et al. "DEAP: Evolutionary algorithms made easy." *Journal of Machine Learning Research* 13.Jul (2012): 2171-2175.
- [10] Rainville, De, et al. "Deap: A python framework for evolutionary algorithms." *Proceedings of the 14th annual conference companion on Genetic and evolutionary computation*. ACM, 2012.
- [11] Whitley, Darrell. "A genetic algorithm tutorial." *Statistics and computing* 4.2 (1994): 65-85.
- [12] Harik, Georges R., Fernando G. Lobo, and David E. Goldberg. "The compact genetic algorithm." *IEEE transactions on evolutionary computation* 3.4 (1999): 287-297.
- [13] Mitchell, Melanie. *An introduction to genetic algorithms*. MIT press, 1998.
- [14] Chan, K. C., and H. Tansri. "A study of genetic crossover operations on the facilities layout problem." *Computers & Industrial Engineering* 26.3 (1994): 537-550.
- [15] Noraini, Mohd Razali, and John Geraghty. "Genetic algorithm performance with different selection strategies in solving TSP." (2011).
- [16] Raorane, A. A., R. V. Kulkarni, and B. D. Jitkar. "Association rule-extracting knowledge using market basket analysis." *Research Journal of Recent Sciences* ISSN 2277 (2012): 2502.
- [17] Van Nierop, Erjen, Dennis Fok, and Philip Hans Franses. "Interaction between shelf layout and marketing effectiveness and its impact on optimizing shelf arrangements." *Marketing Science* 27.6 (2008): 1065-1082.

A Comparison of Nonstationary Fuzzy Logic for Cyber-Physical Systems

Hasan YETİŞ

Firat University, Engineering Faculty
Elazığ, Turkey
h.yetis@firat.edu.tr

Mehmet KARAKÖSE

Firat University, Engineering Faculty
Elazığ, Turkey
mkarakose@firat.edu.tr

Abstract—The popularity of cyber-physical systems, which has a wide application area from military to medicine, is increasing day by day. It is practice and common to implement control algorithms such as fuzzy logic in the cyber layer in these systems where the cyber and physical layers are separate. Reliability and consistency are very important for cyber-physical systems, which is often used in large and critical jobs. Uncertainties, which is hard to be modelled, are the greatest threat to the consistency of a system. Type 2 fuzzy logic is a method developed to deal with uncertainties in fuzzy systems. However, computational complexity has prevented the widespread use of this method and has led to the emergence of non-stationary fuzzy logic. In this study, in order to see the appropriateness of using non-stationary fuzzy logic in cyber physical systems, where consistency and reliability are important, various effects on the system have been investigated. Different membership functions are represented by non-stationary fuzzy logic and comparative results are given.

Keywords—cyber-physical system; fuzzy systems; non-stationary fuzzy; uncertainty.

I. INTRODUCTION

Cyber-physical systems (CPS) are the systems whose physical elements -such as sensor, actuator, etc.- and cyber elements -such as algorithms- are not in the same place [1]. The integration and communication of these distinct layers are actualized thanks to communication technologies. Fig. 1 represents a basic diagram for CPS structure.

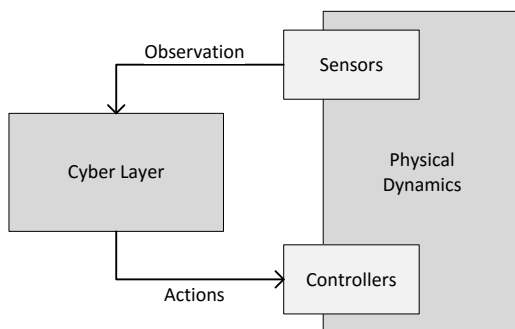


Fig. 1. Basic cyber-physical system structure.

In a cyber-physical system, data obtained by sensors are transported to cyber layer to be processed. As a result of the necessary operations which are actualized in cyber layer, it is calculated how the machines must move. The commands, which tell how the machines must behave, are transported to actuators in physical layer. At the end of the process, the machines know how to act and the systems work within this loop basically. As you can see from the basic principles of CPS working mechanism, the correctness of the system is directly related to the accuracy of the data obtained and transmitted. Uncertainty, which may have occurred unexpected times, is the major factor that affects the consistency of the system. In order to implement a robust CPS, uncertainties should be handled [2].

Fuzzy logic is used many times for solution of many different problems since it was introduced by Zadeh in 1965 [3]. In order to overcome the shortage of fuzzy sets in expressing uncertainties, the type 2 fuzzy logic was introduced by him after 10 years. Although the type 2 fuzzy sets make able to handle uncertainty, it is not common in real because of its complex computation requirements. The complexity of interval type 2 sets is reasonable for implementation in real problems, but such systems are not appropriate to represent variation in time [4]. Thus, non-stationary fuzzy sets are emerged to handle uncertainties with low computational efforts [5].

CPS has a wide application area from agriculture to medicine [6-8]. Lee et al. represented a CPS architecture for Industry 4.0 based manufacturing, which is new production trend of era [6]. Rad et al. established a system for monitoring potato crop with the help of CPS. The data obtained by sensors at field can be observed by user and farmer can make decisions based on other farmers' experiences according to that study [7]. Another study using CPS architecture is done in medicine by Pahlavan et al. They used micro cameras for taking pictures by endoscopy. The captured images sent to a computer by wireless technologies and the images are used to construct 3D map of human internal organs [8]. There are also studies about uncertainties and CPS under uncertainties in literature [9-11].

On the other hand, studies are done about fuzzy systems and handling uncertainties in fuzzy systems [12-16]. In this study, we investigated the effect of change in non-stationary fuzzy inputs to systems for being used in CPS. Different combines of non-stationary and type-1 inputs are given to system. Furthermore, randomly and uniformly created non-stationary sets are used and comparative results are given.

II. FUZZY SYSTEMS

A. Type-1 Fuzzy Systems

Fuzzy systems are emerged from the need of emulating human decision mechanism. Fuzzy sets, the sets used in fuzzy systems, is different from classical set theory. For further information about fuzzy sets, readers are advised to read fuzzy sets [A]. This paper will continue with the general steps of fuzzy systems. A type-1 fuzzy system consist of fuzzification, inference, and defuzzification steps. A block diagram of these steps are given by fig. 2.

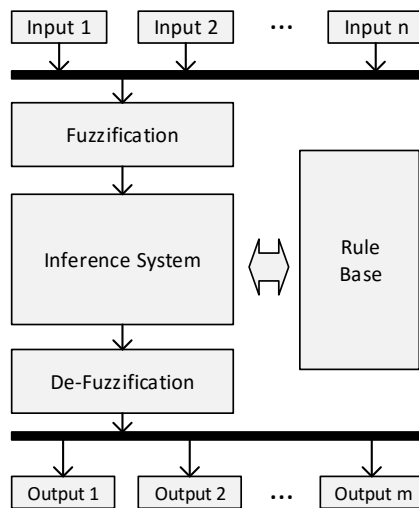


Fig. 2. Type-1 fuzzy system block diagram [17].

As seen in fig. 2, crisp inputs are given to fuzzy systems and crisp outputs are obtained. In fuzzification step, the crisp inputs are fuzzified by the help of membership functions. Most used membership functions in fuzzy systems are triangular, trapezoid, sigmoid, and gaussian functions [18].

After the fuzzification step, inference system come into work by the help of rule base. Rule base is the collection of if-else statements which are detected by experts. The result of cartesian product of the linguistic expressions in the separate entries which are obtained as the result of the fuzzification phase is determined according to this rule base. After that, the results are calculated according to inference mechanism. One of the most used inference mechanism in the literature is min-max method. Defuzzification is the step that makes crisp the variables again which are fuzzified. After output membership functions are limited by the inference results, a method, which

is called defuzzification method, is employed to obtain crisp output values. Center of area, center of gravity, first of maximum, last of maximum, indexed center of gravity, mean of maxima, and middle of maximum are some of the most used defuzzification methods [19].

B. Type-2 Fuzzy Systems

Type-2 fuzzy systems, which is introduced 10 years later from its first version by Zadeh, are developed to handle to uncertainties. Type-1 fuzzy sets are not able to represent uncertainties by single membership function. In order to handle them, in type-2 fuzzy systems there are two membership function which are upper and lower membership function. In type-2 systems, unlike type-1 systems, there is type reducer step before de-fuzzification step. A block diagram belongs to type-2 systems are given by fig. 3.

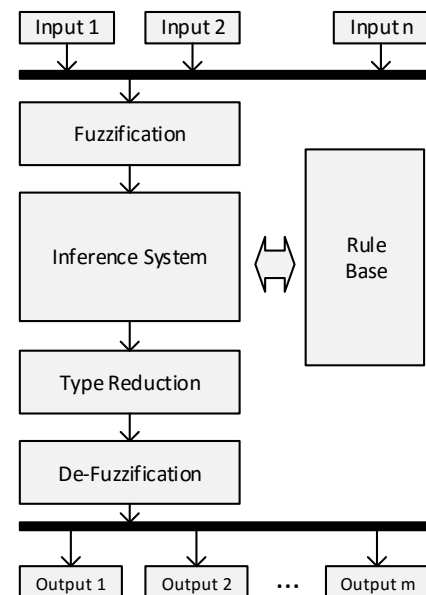


Fig. 3. Type-2 fuzzy system block diagram [17].

Because there are two membership function for each linguistic variable in type-2 fuzzy system, membership degrees cannot be specified by single value. Instead of this, a function which is called secondary membership function is used to express memberships.

The secondary is a constant function. Such systems which has constant secondary membership functions are called interval type-2 systems. Because of its complex computational requirements, interval type-2 systems are more preferable than general type-2 systems. But there still was a need for a new method due to the lack of representation of change over time.

C. Non-stationary Fuzzy Systems

Non-stationary fuzzy systems have emerged to eliminate the disadvantages of type-1 and type-2 systems. It represents

the change in time by low computational burden. In non-stationary systems, sub-type-1 systems are used to model type-2 fuzzy systems. A block diagram that shows the mechanism of non-stationary fuzzy system is shown by fig. 4.

As seen by fig. 4, type-2 system is represented by collection of sub-type-1 systems. Each sub-system is calculated and at the end of the processes, final de-fuzzification operation is applied to obtain single value for each output.

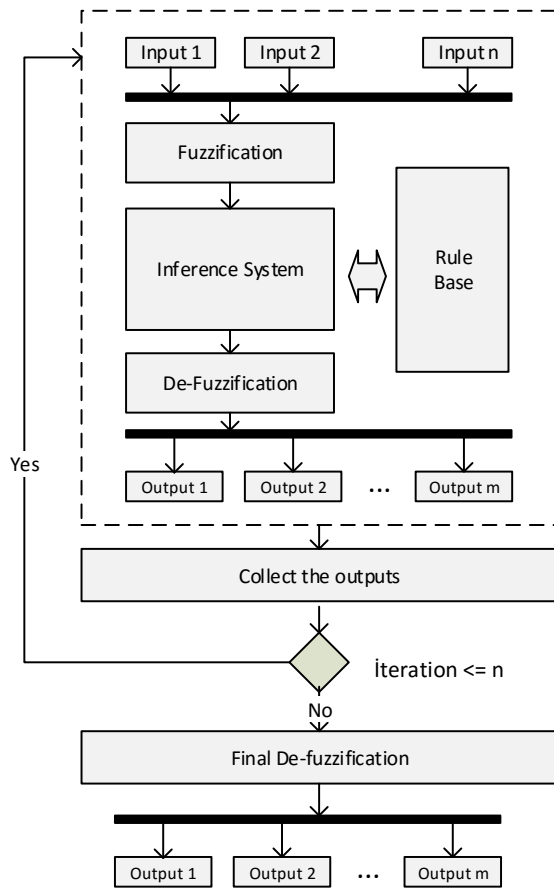


Fig. 4. Non-stationary fuzzy system block diagram [17].

III. COMPARATIVE RESULTS

In this study, in order to demonstrate the effect of non-stationary inputs a comparative study is done. A study that makes non-stationary the inputs for XOR operation done by Garibaldi before [4]. We aimed to take this one step further and see the consequences for different variations of entries in practice. XOR operation consist of two inputs and one output. The three functions have the same formula and there are two linguistic variables for each one. The linguistic variables and triangular type-1 membership function for the problem is given by fig. 5.

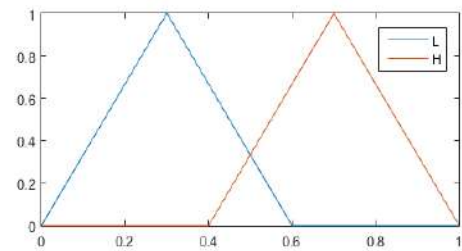


Fig. 5. Triangular membership functions for type-1 [4].

The general formula for triangular functions are given by (1). The a,b,c parameters are 0, 0.3, 0.6 respectively for linguistic variable 'low'; and 0.4, 0.7, 1 respectively for linguistic variable 'high'.

$$\max(\min\left(\frac{x-a}{b-a}, \frac{c-x}{c-b}\right), 0) \quad (1)$$

The truth table and fuzzy input values for this problem, which consist the rules, is given by table 1. While the values written in brackets in table 1 is fuzzy input values; 0 means low (L), 1 means high (H). A sample linguistic rule of the system is such that 'if input 1 is L and input 2 is L then output is L' for case 1.

TABLE I. XOR TRUTH TABLE AND INPUT VALUES

	Input 1	Input 2	Output
Case 1	0 (0.25)	0 (0.25)	0
Case 2	0 (0.25)	0 (0.75)	1
Case 3	1 (0.75)	0 (0.25)	1
Case 4	1 (0.75)	0 (0.75)	0

For comparison, 4 different scenarios have been implemented. The scenarios are given by table 2. The inputs for type-1 is like given in fig 5. Uniform and normal perturbation are employed to make the inputs non-stationary respectively. Non-stationary inputs are given by fig. 6 and fig. 7. While the amplitude remains constant, changes are made in the center within 0.1 (± 0.05) tolerance.

TABLE II. SCENARIOS TO BE USED IN COMPARATION

	Input 1	Input 2	Output
S1	type-1	type-1	type-1
S2	type-1	non-stationary	type-1
S3	non-stationary	non-stationary	type-1
S4	non-stationary	non-stationary	non-stationary

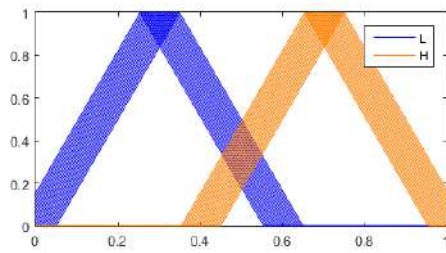


Fig. 6. Uniformly 20-times repeated non-stationary sets

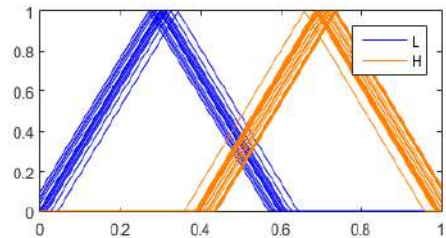


Fig. 7. Randomly 20-times repeated non-stationary sets

TABLE III. TEST INPUTS AND OUTPUTS FOR EACH SCENARIO WITH UNIFORMLY CREATED NON-STATIONARY

Input1	Input2	S1	S2	S3	S4
0.25	0.75	0.7	0.7	0.7	0.7
0.32	0.72	0.7	0.7	0.7	0.7
0.69	0.81	0.3	0.3	0.3	0.3
0.27	0.79	0.7	0.7	0.7	0.7
0.45	0.6	0.591	0.567	0.567	0.571
0.55	0.67	0.409	0.433	0.433	0.429
0.44	0.60	0.611	0.582	0.582	0.586
0.47	0.53	0.554	0.527	0.539	0.542
0.3	0.57	0.632	0.632	0.597	0.601
0.44	0.27	0.389	0.418	0.418	0.41

TABLE IV. TEST INPUTS AND OUTPUTS FOR EACH SCENARIO WITH RANDOMLY CREATED NON-STATIONARY

Input1	Input2	S1	S2	S3	S4
0.25	0.75	0.7	0.7	0.7	0.696
0.32	0.72	0.7	0.7	0.7	0.695
0.69	0.81	0.3	0.3	0.3	0.294
0.27	0.79	0.7	0.7	0.7	0.695
0.45	0.6	0.591	0.547	0.547	0.557
0.55	0.67	0.409	0.418	0.418	0.413
0.44	0.60	0.611	0.561	0.561	0.571
0.47	0.53	0.554	0.513	0.522	0.527
0.3	0.57	0.632	0.632	0.613	0.619
0.44	0.27	0.389	0.439	0.439	0.423

IV. CONCLUSIONS

Different combinations of type-1 and non-stationary fuzzy sets for XOR operation used to compare the results. The results with uniformly created non-stationary and randomly (normal) created non-stationary are given by table 3 and table 4. When we look the results, we can see that there is no difference or a few difference between scenarios when the inputs near to peak values (0.3 for low, 0.7 for high). But when the inputs near the middle value (0.5), the outputs for each case differs from each other. The results indicate that non-stationary makes the results softer. Thus, changes due to uncertainties don't affect the results too much as type-1 systems. And they can be used for CPS, when the effect of uncertainties must be declined.

ACKNOWLEDGMENT

This work was supported by Scientific Research Projects Coordination Unit of Firat University. Project number: MF.17.09.

REFERENCES

- [1] H. Yetis, M. Baygin, M. Karkose, "An investigation for benefits of cyber-physical systems in higher education courses," 15th International Conference on Information Technology Based Higher Education and Training, İstanbul, pp. 1-5, September 2016.
- [2] M. Zhang, B. Selic, S. Ali, T. Yue, O. Okariz, and R. Norgren, "Understanding Uncertainty in Cyber-Physical Systems: A Conceptual Model," European Conference on Modelling Foundations and Applications, pp. 247-264, June 2016.
- [3] L. Zadeh, "Fuzzy Sets," Information and Control, vol. 8, pp. 338-353.
- [4] J. M. Garibaldi, M. Jaroszewski, and S. Musikuwan, "Nonstationary Fuzzy Sets," IEEE Transactions on Fuzzy Systems, vol. 16, no. 4, pp. 1072-1086, August 2008.
- [5] J. M. Garibaldi, S. Musikuwan, and T. Ozen, "The Association between Non-Stationary and Interval Type-2 Fuzzy Sets: A Case Study," IEEE International Conference on Fuzzy Systems, May 2005.
- [6] J. Lee, B. Bagheri, and H.A. Kao, "A Cyber-Physical Systems architecture for Industry 4.0-based manufacturing systems," Manufacturing Letters, vol. 3, pp. 18-23, January 2015.
- [7] C. R. Rad, O. Hancu, I. A. Takacs, and G. Olteanu, "Smart Monitoring of Potato Crop: A Cyber-Physical System Architecture Model in the Field of Precision Agriculture," Agriculture and Agricultural Science Procedia, vol. 6, pp. 73-79, 2015.
- [8] K. Pahlavan, Y. Geng, D. R. Cave, G. Bao, L. Mi, E. Agu, A. Karellas, K. Sayrafian, and V. Taraokh, "A Novel Cyber Physical System for 3-D Imaging of the Small Intestine in Vivo," IEEE Access, vol. 3, pp. 2730-2742, December 2015.
- [9] S. Ali, and T. Yue, "U-Test: Evolving, Modelling and Testing Realistic Uncertain Behaviours of Cyber-Physical Systems," IEEE 8th International Conference on Software Testing, Verification and Validation (ICST), April 2015.
- [10] S. Bi, M. Zawodniok, "PDF-based tuning of stochastic optimal controller design for cyber-physical systems with uncertain delay dynamics," IET Cyber-Physical Systems: Theory & Applications, pp. 1-9, January 2017.
- [11] F. Hua, Y. Lua, A. V. Vasilakos, Q. Haoc, R. Maa, Y. Patila, T. Zhanga, J. Lua, X. Lia, and N. N. Xiong, "Robust Cyber-Physical Systems: Concept, models, and implementation," Future Generation Computer Systems, vol. 56, pp. 449-475, March 2016.

- [12] M. Karakose, "Fuzzy logic approach for analysis and simulation of human motion," National Conference on Electrical, Electronics and Computer Engineering (ELECO), December 2010.
- [13] P. A. Herman, G. Prasad, T. M. McGinnity, "Designing an Interval Type-2 Fuzzy Logic System for Handling Uncertainty Effects in Brain-Computer Interface Classification of Motor Imagery Induced EEG Patterns," IEEE Transactions on Fuzzy Systems, vol. 25, no. 1, pp. 29-42, February 2017.
- [14] M. Karakose, "Sine-square embedded fuzzy sets," IEEE International Conference on Systems Man and Cybernetics (SMC), 2010.
- [15] C. H. Wu, R. K. Chiu, and S. A. Wang, "A cloud-based fuzzy expert system for the risk assessment of chronic kidney diseases," International Journal of Business and Systems Research, vol. 9, pp. 315-333, 2015.
- [16] T. S. Wu, M. Karkoub, W. S. Yu, C. T. Chen, M. G. Her, and K. W. Wu, "Anti-sway tracking control of tower cranes with delayed uncertainty using a robust adaptive fuzzy control," Fuzzy Sets and Systems, vol. 290, pp. 118-137, May 2016.
- [17] M. Karakose, "Bulanık integral tabanlı rastgele belirsizlik içeren bulanık sistemler," Otomatik Kontrol Ulusal Toplantısı (TOK), pp. 541-546, September 2010.
- [18] S. Saha, S. Bhattacharya, and A. Konar, "Comparison between type-1 fuzzy membership functions for sign language applications," International Conference on Microelectronics, Computing and Communications (MicroCom), July 2016.
- [19] A. Talon, and C. Curt, "Selection of appropriate defuzzification methods: Application to the assessment of dam performance," Expert Systems with Applications, vol. 70, pp. 160-174, March 2016.

Information Extraction by Mobile Monitoring of Water Quality Measurements at Buildings for Smart Cities

Büşra AKARSU, Mehmet KARAKÖSE, Koray Şener PARLAK, Alişan SARIMADEN, Erhan AKIN
Firat University, Engineering Faculty

Elazığ, Turkey

busra.akarsu@hotmail.com, mkarakose@firat.edu.tr, ksparlak@firat.edu.tr, alisansarimaden@medelelektronik.com,
eakin@firat.edu.tr

Abstract—The determination of the needs of a city and the fulfillment of these needs in a short time are important for the development of the city. Many examples of smart cities have been created in the world in line with this purpose. The issues of how the city's residents can live more comfortably and how the city can develop are involved in countries' effort to transform their cities into smart cities. Many smart city models have been proposed so far. Water is the sub-heading of smart city wheel smart environment key of Boyd Cohen and people pillar in the smart city model proposed by IBM. This is due to the fact that water has had a crucial place for people's lives. The fact that water becomes poor quality while being distributed to people living in the city is one of the factors that threaten human health. It is possible to determine which pipes are unhealthy by comparing the water resources and the quality of running water in houses. In this article, it is aimed to help to take necessary precautions by continuously controlling water pipes. In the designed architecture, this process is performed by comparing the knowledge of the city's water source and the quality of the water received from the buildings.

Keywords—IoT, control of water pipes, city water quality check, mash-up, water quality sensor

I. INTRODUCTION

Nowadays, many scientists and entrepreneurs are developing various smart city applications for the solution of the problems faced by the people in city life and for people to live more comfortably. These applications are performed under many names such as smart city, digital city and intelligent city [1]. However, a precise definition has not yet been made in smart city studies carried out. Because there is not a model that will comply with every city [1]. The reason for this situation is the fact that each city has different problems and priorities. The

objectives to develop each city are different since they have different development levels, geographical structure, demographic structure and sources of income. However, some problems such as water are important for all cities. While the emerging problems are of top priority as the large cities of India have been continuously immigrated [2] one of these problems is clean water, the primary problems for Dubai are mobility, energy, water, open data, education and continuous learning, health, entrepreneurship, business incubation, and international exposure [3].

Problems need to be identified correctly for the solution of the problems. This situation causes Information and Communication Technology (ICT) to become an indispensable part of smart city. However, there has not been a precise definition of the role of ICT and technology type in the studies that have been carried out until today [4]. In [4], it was determined that ICTs such as web portal, NFC and RFID used in smart city studies that have been carried out until today have been used intensively.

Mash-up service means creating a new service by bringing together the services that are independent of each other [5]. While designing smart city, techniques such as mash-ups, widgets and portals are used to collect and access data from the real world [4].

The Internet of Things and Big Data systems have emerged in order for city to be more efficient and able to respond to problems more easily [6]. The Internet of Things provides data collection via software by connecting daily objects to the network [7].

There are various models developed in smart city design. In [8], the features of smart city are gathered under six headings. These are Smart Economy, Smart Environment, Smart Governance, Smart Living, Smart Mobility and Smart People. All of these features are defined by a series of factors. Each factor is defined by a series of indicators.

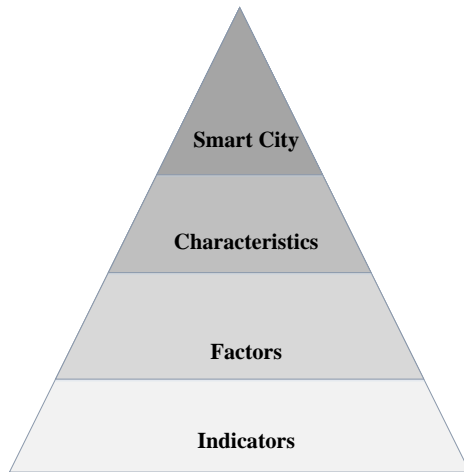


Figure 1.R. Giffinger Smart City Model Structure

Boyd Cohen defined a model that he called as smart cities wheel [9]. In the model, six key features were defined as smart people, smart economy, smart Environment, Smart Governance, Smart Living and Smart Mobility. Each feature has its own subcomponents. Since each city has different needs, the primary criteria of each city should be defined and the city should follow its own initial principles [10]. However, a series of indicators are assigned to each sub-component of each of the wheel in order to measure the sub-components of the wheel by considering that it does not have enough depth to add value to city planning [11].

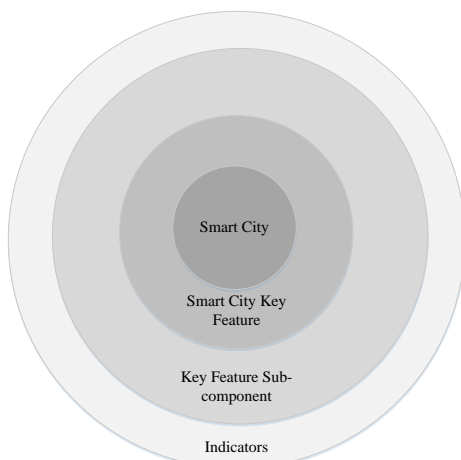


Figure 2. Smart City Wheel Model Structure

Etzkowitz et al. defined the triple helix model, and this model has been used by many people in the smart city concept [12]. Triple helix model proposed the cooperation of academy, government and industry [13]. This cooperation positively affects the economic performance [13]. Effendi et al. developed the penta helix model based on the Triple helix model. In this model, media components were added to media support for the community and all stakeholders, for training

and interaction for ensuring digital adaptation to the triple helix model [12].

IBM defined three pillars in the model it defined [10]. They consist of the subheadings of people; education, health-care and social programs, infrastructure: energy, water and transportation and planning, planning and management: city governance, public safety, urban planning and managing natural resources and buildings [10].

The studies carried out should contribute to the development of environment, human, quality of life and so on and should be sustainable and secure for a city to be defined as a smart city [10][14]. Environment, people and quality of life are factors that affect each other. Water is one of the most important factors that will affect people's health. This shows us that the water source and the pipes used in the transmission of water should be quality.

In the article, the quality of the pipes can be consistently controlled by comparing the data of quality of water received from the water source with the quality of the water used by the residents of the city.

II. PROPOSED WORK

It is necessary to determine the problems of a city and to resolve these problems in a short time to make that city a smart city. But each city has its own dimension, social life, economy and demographic structure, therefore each city has its own priority problems. For instance, while the median age of people living in Vienna is 49.15 [14], it is 27 in Dubai [15]. The fact that the intensity of people that can be considered in the elderly group in Vienna is higher makes the precautions to be taken to make this group more comfortable even more important than the precautions to be taken by Dubai for themselves. However, the age alone does not show what the measures to be taken are. Because each person's needs are different. But there are also problems that will affect all people. One of these is water.

The fact that one of the most important sources in human life is water makes the problem of whether the cities' water supply networks are suitable for healthy water transmission a current issue. In this article, it is possible to determine whether the water in the regions is suitable for human life by using the data received from the sensors and controlling the water quality in order to solve this problem.

A. Receiving Data

The quality of the water resources of each city and the data obtained from the houses provide us information about the suitability of the method used for water transmission. Continuous control of a city's water pipes is almost impossible and difficult process. However, it is possible to reach the data on how healthy the pipes are by measuring the water quality of the city by means of the Internet of things. The Internet of things provides us with an access to information obtained from the objects through micro-

controllers and appropriate protocols [17]. The features of water such as conductivity, Ph value and TDS value can be obtained depending on the sensor used. Pipe systems consist of main and secondary pipes. As it is presented in Figure 3, all buildings are connected to each other by pipelines starting from the main source. This also allows us to control in order.

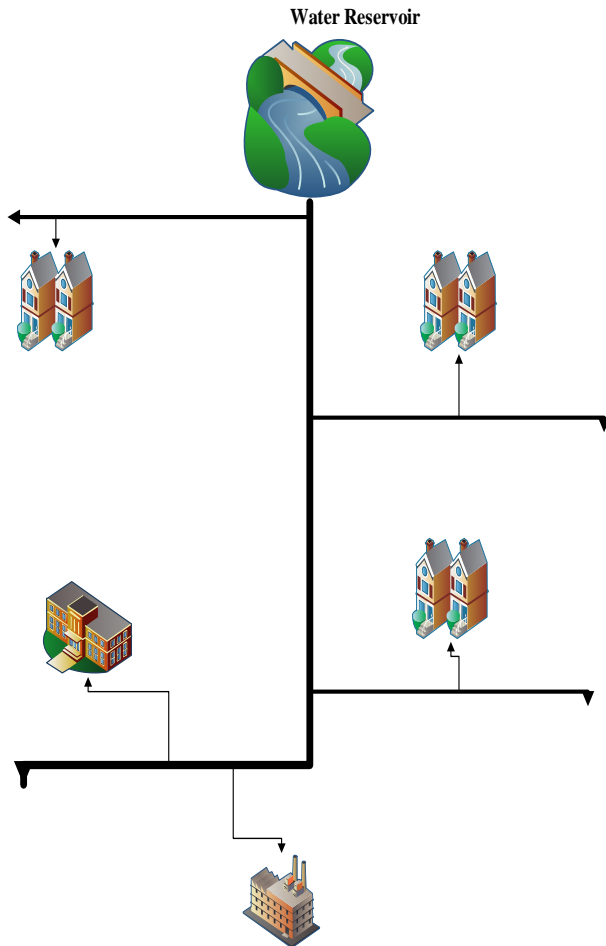


Figure 3. Water Network Sample

It is necessary to acquire the water quality data to be received from the whole buildings in the city and water sources for the assessment of water pipes in the city. The unhealthy conditions in water transmission reduce the water quality no matter how quality the water resource is. Therefore, data can be obtained by the sensors that measure the quality of water to be placed in each house and water resource. As it is shown in figure 3, Municipal office can reach the data obtained from the sensors by means of the Internet of things. It is possible to determine which water pipes are unhealthy by comparing these data obtained.

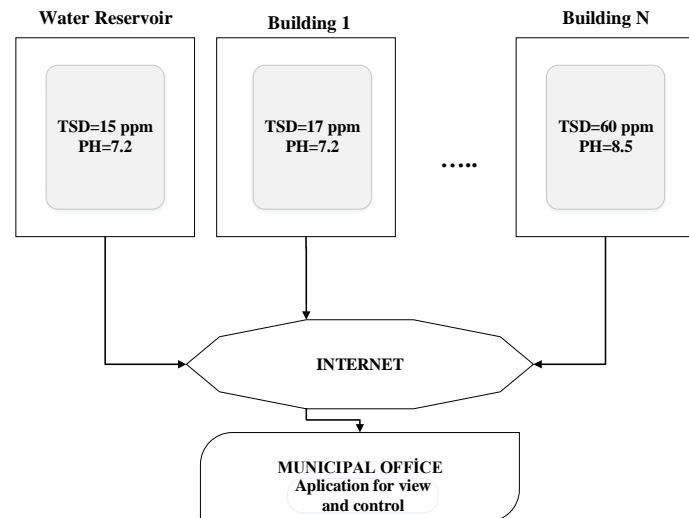


Figure 4. The architecture of the system that controls water quality with IoT

B. Evaluation of Data

When the data are obtained from the sensors with the information of the region where they are located, they will help us to obtain data about which regions provide higher quality transmission, in which regions the water delivery pipes are unhealthy and should be replaced. In addition, the changes in water quality information that are continuously received will help us to take precautions before the pipes reach at a level that will harm human health.

Table 1. SAMPLES OF INFORMATION FROM SENSORS

Adress	Information from Sensors		
	TSD	PH	...
Water reservoir	15	7.2	.
S1-B1	15	7.2	.
S1-B2	15	7.3	.
.	.	.	.
.	.	.	.
.	.	.	.
S99-B60	120	8.2	.

Only TSD and PH values are illustrated in the table above. However, all negative effects of the pipes on health can be controlled by the sensors. If the address process is performed in accordance with the mains supply, unhealthy pipes can be detected with the help of changing values.

While determining which pipe should be repaired, whether the pipes are healthy or not is firstly determined by comparing the data obtained from the buildings near the source. Then, the unhealthy pipe is determined by going away from the resource and continuing to control. The data about the location and water quality received from the whole buildings in the city and the water resource are compared, and the quality of the pipes providing the transmission between them can be measured.

There is no need to check the subsequent data if an unhealthy pipe is detected by controlling in a certain order. Because the water that passes over that pipe becomes poor quality. This will save us from performing unnecessary operations. If the data are obtained in order from water resource to the last point of the pipeline according to the city's own structure before receiving them collectively, it will be possible to prevent the system from slowing down with intensive data while determining the unhealthy pipe.

Mash-up further performs the merging of data and information obtained from more than one sources [18]. For the proposed study, it will be more convenient to determine which pipe is damaged according to the data obtained if the building locations and pipeline are shown on a city map.

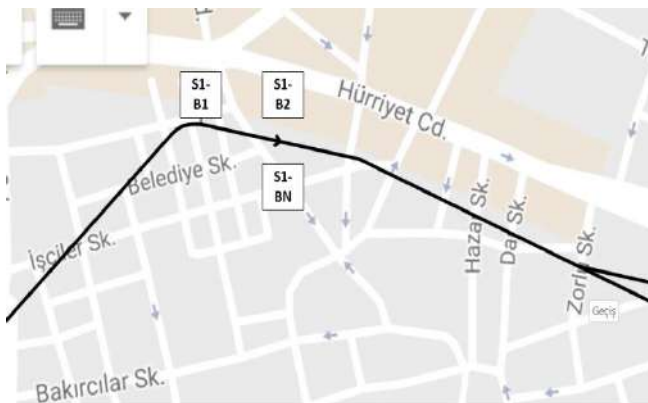


Figure 4. Mash-up Exemple for Recommended system

III. CONCLUSION

Water is one of the most important sources for human life. The fact that water is one of the subheadings of IBM smart city model and smart city wheel model from among smart city models, indicates how essential the water is for human life. Therefore, the health of the citizens should be protected by constantly controlling the quality of the water distributed to the city.

In the proposed study, it is determined whether the transmission pipes are suitable for human life by comparing the data of water source and water quality received from all houses of the city. These data reach the sensor data obtained by means of internet of things, and thus we have the opportunity to make comparisons. Thus, this smart city application is ensured to have both applicable and sustainable features. More than one water-related data can also be obtained depending on the sensor to be used.

It is possible to have a more convenient access to the data about which pipe is unhealthy by showing the locations of houses and pipes on a city map by Mash-up.

REFERENCES

- [1] Alamsyah, Nurwahyu, Tony Dwi Susanto, and Tzu-Chuan Chou. "A comparison study of smart city in Taipei and Surabaya." *ICT For Smart Society (ICISS)*, 2016 International Conference on. IEEE, 2016.
- [2] Madakam, Somayya, and R. Ramaswamy. "100 New smart cities (India's smart vision)." *Information Technology: Towards New Smart World (NSITNSW)*, 2015 5th National Symposium on. IEEE, 2015.
- [3] <https://www.siemens.com/customer-magazine/en/home/cities/smart-dubai.html>
- [4] El Hendy, Mahmoud, Sami Miniaoui, and Hussein Fakhry. "Towards strategic information & communication technology (ICT) framework for smart cities decision-makers." *2015 2nd Asia-Pacific World Congress on Computer Science and Engineering (APWC on CSE)*. IEEE, 2015.
- [5] Kim, Taeyoung, et al. "Design of an effective framework for mash-up service development." *2016 International Conference on Information Networking (ICOIN)*. IEEE, 2016.
- [6] Mohanty, Saraju P., Uma Choppali, and Elias Kougianos. "Everything you wanted to know about smart cities: The Internet of things is the backbone." *IEEE Consumer Electronics Magazine* 5.3 (2016): 60-70.
- [7] Sarin, Gaurav. "Developing Smart Cities Using Internet of Things: An Empirical Study." Available at SSRN 2780756 (2016).
- [8] Giffinger, R., Fertner, C., Kramar, H., Meijers, E., Smart cities: Ranking of European medium-sized cities, Vienna University of Technology, 2007.
- [9] Cohen, Boyd. "What Exactly is a Smart City". *Fastcoexist.com*. Retrieved 2012.
- [10] Arroub, Ayoub, et al. "A literature review on Smart Cities: Paradigms, opportunities and open problems." *Wireless Networks and Mobile Communications (WINCOM)*, 2016 International Conference on. IEEE, 2016.
- [11] Cohen, Boyd. "The Smartest Cities In The World 2015: Methodology". *Fastcoexist.com*. Retrieved 2015.
- [12] Effendi, Dudy, et al. "Smart city Nusantara development through the application of Penta Helix model (A practical study to develop smart city based on local wisdom)." *ICT For Smart Society (ICISS)*, 2016 International Conference on. IEEE, 2016.
- [13] CHEN, Fei-yu; WU, Chong; YANG, Wei-ning. Research on triple helix of university-industry-government relations: Empirical evidence from China. In: *2014 International Conference on Management Science & Engineering 21th Annual Conference Proceedings*. IEEE, 2014. p. 213-220.
- [14] Giovannella, Carlo, et al. "Villard-de-Lans: A Case Study for Participatory People-Centered Smart City Learning Design." *2013 IEEE 13th International Conference on Advanced Learning Technologies*. IEEE, 2013.
- [15] Vienna Demographics (<https://www.househunt.com/OH/Vienna/Real-Estate/>)
- [16] Demographics of Dubai (https://en.wikipedia.org/wiki/Demographics_of_Dubai#cite_note-2)
- [17] Zanella, Andrea, et al. "Internet of things for smart cities." *IEEE Internet of Things journal* 1.1 (2014): 22-32.
- [18] Mattila, Anna-Liisa, et al. "Mashing up software issue management, development, and usage data." *Rapid Continuous Software Engineering (RCoSE)*, 2015 IEEE/ACM 2nd International Workshop on. IEEE, 2015.

Use of a Convolutional Neural Networks Method in Image Classification

Vedat TÜMEN
Munzur University,
Tunceli Vocational School
Tunceli, Turkey
vtumen@munzur.edu.tr

Ömer Faruk SÖYLEMEZ
Dicle University Engineering Faculty
Diyarbakır, Turkey
osoylemez@dicle.edu.tr

Burhan ERGEN
Firat University Engineering Faculty
Elazığ, Turkey
bergen@firat.edu.tr

Abstract—with the vast increase in utilization of multimedia and communication technologies, the presence of digital records has increased tremendously. Every day people share something on the internet, in their e-mail boxes or in photo-video archives. It is evident that one needs to spend a lot of time searching this data to reach meaningful and necessary conclusions. Various methods are proposed to minimize this time necessity to be spent on. In recent days, image analysis has been performed by using different methods in combination with content based image retrieval which is a method that is mostly worked on. In this study, a portion of a public image database ‘imagenet’ has been used to classify images within it via convolutional neural networks which is one of the most popular deep learning methods.

Key Words: Content Based Image Retrival, Deep Learning, Convolution Neural Networks

I. INTRODUCTION

Image processing has become a very important topic nowadays because of rapid development in computer technologies. By employing image processing techniques, one can evaluate data at hand with lighting speeds and it would cost less time with lower error rates and simply easier. Machine learning technology facilitates our lives with a wide range of applications. Offering most relevant content with Internet searches, offering products according to our interests during online shopping, tagging images automatically on social media and speech recognition and voice control of mobile devices are just some examples of what machine learning offering to us. Moreover it is also employed in such areas like object detection and recognition, natural language processing, medical applications, autonomous cars and so on. Most of these said technologies are based on deep learning techniques and the number of never techs employing it is also growing [1].

Image processing is a field that manipulates, obtains inferences or defines patterns from still or moving images. It is utilized on many fields of science and its applications are increasing day by day.

It is desired to access and process data that are formed on digital platforms. As for today, these data are growing in such an exceptional way that handling, transmitting and accessing it demands some dedicated algorithms and workforce. Therefore,

content based image retrieving systems are assisting to solve this phenomenon in many areas [2].

II. CONTENT BASEING IMAGE RETRIVER

Accessing to images and classifying them have become important topics in today's access and retrieval systems. Therefore, need for Content Based Image Retrieval (CBIR) systems arose that will successfully match same or similar patterns on many problem domains [3]. Figure 1 depicts a usual subroutine to form a content based image retrieving system.

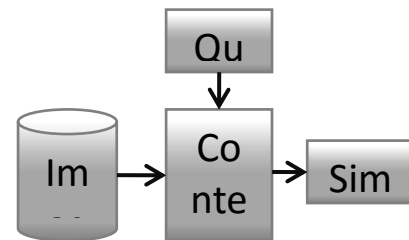


Fig 1. Block scheme for a content based image retrieving system

A system based on content based image access and classification mainly consists of the following three main elements.

A. Feature Extraction

In feature extraction stage, methods like pixel relation or post-conversion pixel relation are applied on both query images and the database. Feature extraction from textures that are found in nature is the most important step of the CBIR process [4]. The most important step for feature extraction is to create a model for every texture in feature space by using statistical data that distinguishes every texture from each other. When examined from a different point of view, textures that are found in nature rarely possess same scale, orientation, pose and contrast so therefore we can imply that it is crucial to find independent features for textures.

Many conversion methods have been developed to detect independent features such as scale, orientation and exposure.

SIFT [5], RIFT [6], GLOH [7] and SURF [8] provide successful performances in various fields. But a major deficit with overuse of these techniques is that vast increase in number of features and those yielding confusion. For instance in case of SIFT, when it yields successful results regarding independent features on scale and orientation, feature vector length could be in range of 1000's. Working with large feature vectors is accompanied by high memory and computational overhead requirements. With the help of feature extraction, color, texture and shape attributes of visual objects are transferred to the system and their visual contents are indexed [9].

B. Training

Feature training of a class is realized by using the common features of the images formed in the specified class. In this training phase, the acquired features of the images are trained on their own, and the common class inferences of the images are made according to the obtained values.

C. Testing

In the comparison phase, which is the last stage of image access, the resulting class features are compared to the database. As a result, it is determined which class does image belongs or similar images belonging to the specified class are acquired. All the images in the database are processed through the same way and the classification performance is obtained.

This process, which is applied to the query image and all the images in the database in the same way, is the most basic step to ensure a successful comparison. A number of features of the images in the database are extracted and saved into the system. Various transformations are made on this data. Although the number of selected features for image classification seems to be a success in image recognition, the increase in the number of features used during classification will lead to mixed and undesirable results in terms of both calculation complexity and similarity between classes. With respect to that, it is important to select the most appropriate and distinguishing basic attributes of the relevant class.

D. SIFT Algorithm

Scale Invariant Feature Transform (SIFT) is an algorithm that identifies and defines regional features that are unvarying for a picture like illumination, rotation and scaling. Image processing with the SIFT method consists of 3 steps [10]. These are:

Step 1: In this stage, the scale is used to determine the extreme value points in the space

$$L(x, y, \sigma) = G(x, y, \sigma) * I(x, y) \quad (1)$$

Here '*' symbol denotes convolution operator, $G(x, y, \sigma)$ denotes variable scaled Gaussian function, $I(x, y)$ denotes original image, (x, y) denotes processed images pixel coordinates and σ denotes scaling factor. Gaussian convolution equation is;

$$G(x, y, \sigma) = \frac{1}{2\pi\sigma^2} e^{-(x^2+y^2)/2\sigma^2} \quad (2)$$

Difference-of-Gaussian (DoG) defined as $D(x, y, \sigma)$ find scale-space endpoints with equations x.

$$\begin{aligned} D(x, y, \sigma) &= (G(x, y, k\sigma) - G(x, y, \sigma) * I(x, y)) \\ &= L(x, y, k\sigma) - L(x, y, \sigma) \end{aligned} \quad (3)$$

Here $k=1,2,3,\dots$ is used to present different scale space. The local minimum or local maximums of $D(x, y, \sigma)$ are calculated by matching each pixel with the neighborhood of the specified number in the upper and lower scales.

Step 2: Unwanted points that reside on the edges of the images that have weak description or low contrast are eliminated.

$$z = \frac{-\partial^2 D^{-1}}{\partial x^2} \frac{\partial D}{\partial x} \quad (4)$$

The 2×2 Hessian matrix is prepared by using spatial variants of 'z' belonging to a small area around the extremes. By looking at the relative proportions of the features at Hessian matrix, candidate edges and similar regions with low contrast are eliminated.

$$H = \begin{bmatrix} D_{xx} & D_{xy} \\ D_{yx} & D_{yy} \end{bmatrix} \quad (5)$$

The elimination criterion for a badly-defined long edge can be formed as follows:

$$\frac{Tr(H)^2}{Det(H)} < \frac{(r+1)^2}{r}, r = \frac{\alpha}{\beta} \quad (6)$$

Here α is big sized, β is small sized Eigen value. If this equation turns true than key points are eliminated.

Step 3: It aims to assign an orientation to the correct lock points according to local visual properties. In other words, it is desired that the lock points do not change according to their rotation movements. This orientation approach consists of four steps:

- Keypoint scaling is used to select the L-smoothed Gaussian method and the gradient size is calculated
-

$$m(x, y) = \sqrt{(L(x+1, y) - L(x-1, y))^2 + (L(x, y+1) - L(x, y-1))^2} \quad (7)$$

$$\theta(x, y) = \tan^{-1} \left[\frac{(L(x, y+1) - L(x, y-1))}{(L(x+1, y) - L(x-1, y))} \right] \quad (8)$$

- A trend histogram is formed from the gradient orientations of the sample points
- The highest peak value in the histogram is located.
- Corresponding orientations and local peaks up to 80% of this peak are assigned to the key points.

In the final step, descriptive vectors are calculated for the feature points. From a 16×16 region around the feature point,

for every 4×4 clusters 8 partitioned histograms are obtained. The value in each partition in the histogram is a component of the $4 \times 4 \times 8 = 128$ dimensional descriptor vector. The effect of the change on illumination is removed by resizing the 128 dimensional vector into unit length.

III. DEEP LEARNING

Deep learning is the training process of multi-layered feed-forward neural networks. This name is given because of having a hidden layer for learning. Deep learning is used by data scientists working in the academic and private sectors in a variety of applications, including image classification, image segmentation, video analysis and classification, voice recognition and processing and natural language processing. Deep learning occurs with the use of multi-level deep neural networks. It is often used to create systems that can extract information from large quantities of untagged training data by employing feature extraction techniques.

Deep learning architecture comes in many layers and hidden variables. The most commonly used algorithms are Deep Artificial Neural Networks, Automatic Encoders and Restricted Boltzmann Machines which is a derivative of Boltzmann Machines [11]. Convolution method is used together with this concept for separating data into classes or clusters. This method is also employed in this study.

A. Convolutional Neural Networks(CNN)

Convolutional Neural Networks (CNN), developed by YannLeCun in 1988, is a special type of multilayer neural networks. Although they have different architectures, like other neural networks, they are trained with a version of the feed forward algorithm [12]. CNN is designed to recognize direct visual patterns from pixel images with minimal preprocessing. They are very successful against over variable patterns and simple geometric transformations. It is also the most well-known and widely used network structure in all deep learning algorithms. CNN includes feature duplication and summarization layers thus offering different feature extraction approaches from other algorithms. CNN basically consists of 4 layers. These are convolution layer, Activation function layer (ReLU), Pooling and Normalization layers.

1) *Convolutional Layers*: The convolution layer performs a series of mathematical operations for each sub-region to produce a single value in the output feature map. The convolutional layers are then subjected to a ReLU activation function at the output to bring some non-linearity.

2) *Rectified Linear Unit Function(ReLU) Layers*: It is accomplished by following a linear filter with a non-linear activation function applied to each component of a feature map (i.e., pointwise). Such simple functions are called Rectified Linear Units (ReLU). There are many activation functions. List of activation functions and their mathematical interpretations are given below.

Maximum activation function;

$$y_{ijk} = \max\{0, x_{ijk}\}, \quad (9)$$

Sigmoid activation function;

$$y_{ijk} = 1/(1 + e^{-x}) \quad (10)$$

Tangential activation function;

$$y_{ijk} = 2\sigma(2x) - 1 \quad (11)$$

is shown as. In this study, the maximum activation function was selected for the ReLU layer.

3) *Pooling*: It combines the feature values near each pixel value by applying an appropriate operator. The most commonly used pooling methods are max-pooling and mean-pooling methods. Max-pooling takes the highest pixel value of a group of pixels while Mean-pooling calculates the average of them. Pooling layer, gradually reduces spatial size of representation, reduce the number of parameters and amount of computation in a network and thus controlling the over fitting. It is a common practice to place a pooling layer between convolutional layers in CNN architectures.

4) *Normalization*: Normalizes the vector of feature channels in each spatial location in the input map. It is calculated as shown in the following equation.

$$y_{ijk'} = \frac{x_{ijk}}{\left(k + \sum_{k \in G(k')} x_{ijk}^2\right)^{\beta}} \quad (12)$$

Here $G(k) = [k - [p/2], k + [p/2]] \cap 1, 2, \dots, k$ is a group of consecutive feature channels in the input map. In normalization, the adjustment of the image is performed with altering of 4 parameters. After the normalization phase, images are on their final forms and all features are obtained. By using these features, it is possible to perform many image processing operations such as classification, segmentation, edge extraction, object recognition, face recognition, background extraction and the so on.

IV. EXPERIMENTS

The system was tested on the network created with the images obtained from the Image-net project [13] and its performance was evaluated. We transferred learning for our selected dataset with respect to acquired network. Our database consists of actual images in the form of aircrafts and cars was presented as input to the prepared system and the classification achievements of these image classes were evaluated. A total of 350 car images and 1037 aircraft images were used in the study.

A. Convolution Neural Network Structure Used

The CNN model that occurs in the convolution, ReLU, Pooling, Normalization layers is shown in Fig 2.

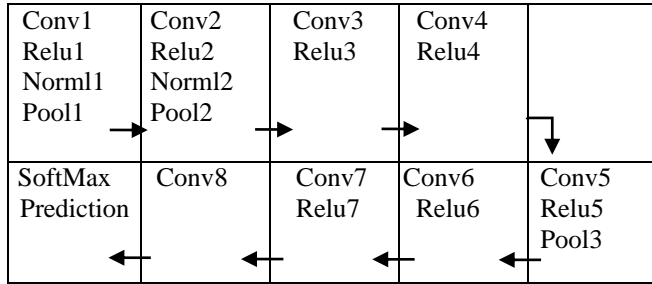


Fig 2. CNN model used

As shown in Fig. 2, the network consists of 21 layers and consists of 8 layers of convolutions, 7 layers of ReLU, 3 layers of pooling, 2 layers of normalization and finally a layer of Softmax. When these layers come together, a CNN model is created and the test operation was performed on this model.

B. Method

Imagenet's [13] publicly accessible web - based images and dataset models were tested separately and their performance was examined. The obtained image database has been pre-processed before hand.

Images are forwarded through layers according to the proposed CNN. Input images that are fed into the first stage of the CNN were resized to 224x224x3 dimensions in order to conduct a proper evaluation. We tried to obtain the features for different image categories by passing them through the CNN model. Then we matched these features to previously prepared dataset in order to reveal a class information. As a result of these operations, correct classification rate of the image class information was tried to be determined.

C. Database

The actual images that contain images of aircraft and cars are transformed into a dataset. We need to point out that entire database is formed of different types of aircraft and car images. For cars, we can tell that there are sports cars, panel vans, racing cars, jeeps and etc. For airplanes, there are passenger aircraft, private aircraft and jets. Figure 3 shows images from both categories. These images are obtained from the web address of imagenet.



Fig 3. Real image in the car and airplane category.

D. Implementation Results

In this study, a total of 350 images for cars are passed through the CNN model, then the resulting pattern is tested on the image-net dataset and the category information of the image is obtained. Table 1 below shows the statistical values for each car type

TABLE 1. CLASSIFICATION RESULTS OF IMAGES IN CAR TYPE

Car Type	Number of vehicle	Average similarity	Maximum similarity
Sports car	227	0,6200	0,9786
Race car	75	0,5686	0,9781
Open car	33	0,4967	0,8461
Taxi	8	0,4052	0,4821
Others (wrong)	40	0,3653	0,3659

When Table 1 is examined, the images in the car type are tried to be classified under 5 categories. The examples in this class are categorized as sports cars, racing cars, open cars, taxis and other vehicles. When the achievements in this category are considered, the highest performance rate is found in the category of sports cars. The maximum similarity rate was 0.9786 for sports cars and 0.9781 for race cars. The number of vehicles determined according to the category are 227 sports cars, 75 race cars, 33 open cars, 8 taxis from 350 images. 40 of the images tested in this dataset were incorrectly classified. The average similarity of 0.3654 was found to be very unstable during the test phase. In Table 2, statistical information is shown when the cars are separated as automobiles and others.

TABLE 2. CLASSIFIED ACHIEVEMENTS OF THE CAR TYPE

Car Type	Number of vehicle	Average similarity	Maximum similarity	Achievement ratio
Automobile	310	0,6549	0,9786	0,8857
Others(False)	40	0,3653	0,3655	0,1142
Total	350	0,6218	0,9786	1,00

The classification performance is 0.8857, and the error rate is 0.1142, which can be considered as a high performance.

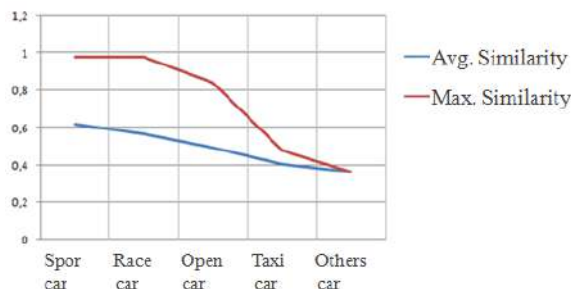


Fig. 4. Performance ratios of car-type images

Figure 4 shows the maximum and average performance ratios of the car types. It has been determined that the lowest values are the mean and maximum similarities of misclassified images. Figure 5 shows a sample image that is incorrectly classified.



Fig 5. Example of misclassified image

In the second phase of this study, the image containing 1037 real aircraft objects was passed through the CNN model, and then the obtained pattern was tested on the dataset that we used before and tried to reach the category information of the images. Table 3 shows the statistical values of real images in the aircraft type.

TABLE 3. AIRPLANE CLASSIFICATION PERFORMANCE

Plane Type	Number of vehicle	Average similarity	Maximum similarity	Achievement ratio
Airplane	892	0.7567	0.9996	0,8602
Others(False)	145	0.4513	0.935	0,1398
Total	1037	0.7570	0.9996	1,00

When Table 3 is examined, it is classified under 2 categories in images of aircraft type. They are categorized as airplanes and others as misclassified. When we look at the performances achieved in this category, we obtained a performance ratio of 0.8602 in the category of airplanes. This rate was found to be very high in some airplanes (which is often close to this value) is 0.9996. When looking at the number of airplanes detected, 892 of the 1037 airplanes were identified as passenger airplanes, while the 145 images seemed to be misclassified, including the different types of airplanes (54 of them were described as warplanes). The error rate was limited to 0.138.

V. CONCLUSION AND FUTURE WORK

In this study, randomly selected images that have RGB channels are classified with the help of Convolutional Neural Networks. This study is classified according to the CNN method on the commonly used images. The correct classification performance ratio of the data in the airplane group is 0.8602 and the classification performance ratio for the cars is 0.8857. In the next studies, different CNN methods will be developed to try to develop and implement success on different images and videos.

VI. REFERENCES

- [1] LeCun, Y., Bengio, Y., & Hinton, G. 2015. Deep Learning. Nature, 521(7553), 436-444.
- [2] Ayan, M. The design and application of content based image retrieval system based on color and texture features by using genetic algorithm, Master Thesis, Gazi University, Ankara, 2016.

- [3] Shereena V.B and Julie M. David, Content based image retrieval: classification using neural Networks, The International Journal of Multimedia & Its Applications (IJMA) Vol.6, No.5, October 2014
- [4] Park, W.-B., Ryu, E.-J., Song, Y.-J. ve Ahn, J.H. 2005. Visual feature extraction under wavelet domain for image retrieval. Key Engineering Materials, 277-279
- [5] Lowe, D., Object recognition from local scale-invariant features". Proc. of the International Conference on Computer Vision, Corfu Sept. 1999
- [6] Lazebnik, S., Schmid, C., and Ponce, J., 2005 A sparse texture representation using local affine regions. IEEE Transactions on Pattern Analysis and Machine Intelligence, 27(8):1265–1278.
- [7] Mikolajczyk K. and Schmid C. 2004, Scale & Affine Invariant Interest Point Detectors, International Journal of Computer Vision 60(1), 63–86
- [8] Herbert Bay, Andreas Ess, Tinne Tuytelaars, Gool, L. V. 2008, Speeded-Up Robust Features (SURF), Computer Vision and Image Understanding 110, 346–359
- [9] LeCun, Y., Bengio, Y., & Hinton, G. 2015. Deep Learning. Nature, 521(7553), 436-444.
- [9] Nagaraja S. and Prabhakar C.J., Low-level features for image retrieval based on extraction of directional binary patterns and its oriented gradients histogram, Computer Applications: International Journal (CAIJ), Vol.2, No.1, February 2015
- [10] Oral M., Gençal M. C., SIFT Yöntemini Kullanarak Madeni Para Tanıma, Elektrik-Elektronik ve Bilgisayar Sempozyumu, EEB 2016.
- [11] Gehring J, Miao, Y, Metze F., Extracting deep bottleneck features using stacked auto-encoders, Acoustics, Speech and Signal Processing (ICASSP), 2013 IEEE International Conference on May 2013.
- [12] Phung S. L., Bouzerdoum A., Gender Classification Using a New Pyramidal Neural Network, International Conference on Neural Information Processing pp 207-216 ICONIP 2006
- [13] <http://www.image-net.org/> Access date: 02.02.2017.

Performance Analysis of Stochastic Fractal Search Algorithm for Global Optimization within Uni-modal and Multi-modal Benchmark Functions

Feyza Altunbey Ozbay
Department of Software Engineering
Firat University
Elazig, Turkey
faltunbey@firat.edu.tr

Bilal Alatas
Department of Software Engineering
Firat University
Elazig, Turkey
balatas@firat.edu.tr

Abstract—Computational intelligence methods are algorithms that utilize a simple approach as a solution technique of search and optimization problems and are recently getting strong and becoming more popular due to their advantages. Computational intelligence optimization algorithms have been proposed and used to find well-enough solutions at a reasonable computation time when the classical algorithms are not applicable or do not provide good solutions to these problems due to the unmanageable search space in many different fields such as management science, engineering, computer, etc. Many existing algorithms are nature-inspired, which work by simulating or modeling different natural processes. Due to the philosophy of continually searching the best and absence of the most efficient computational intelligence algorithm for all types of problems, novel algorithms or new variants of current algorithms are being proposed. Stochastic Fractal Search Algorithm (SFSA) is the one of four mathematics inspired global optimization algorithm inspired by the natural phenomenon of growth using a mathematic concept called the fractal. This paper explains the operators of SFSA used in optimization and search problems and represents the comparative results obtained from other mathematics based computational intelligence algorithm, namely Sine-Cosine Algorithm for different benchmark functions for the first time. Although no optimization has been implemented for its parameters and no variants have been proposed, obtained results from the experiments are promising. SFSA seems a simple and efficient global optimization algorithm that may efficiently be used in many complex search and optimization problems. Its variants with optimized parameters may be proposed for more efficient solutions in future works.

Keywords—Computational Intelligence; Global Optimization; Stochastic Fractal Search Algorithm

I. INTRODUCTION

There are many challenging problems in industry and science which can be formulated as optimization problems. Nowadays, many companies have faced problems in need of optimization. Computational intelligence search and optimization algorithms

are the methods that utilize a simple approach as a solution technique of search and optimization problems and are recently getting strong and becoming more popular. They provide general solution strategies that can be applied to the problem in case of concurrent different decision variables, objective functions, and constraints and they do not depend on the solution space type, the number of decision variables, and the number of constraints [1, 2]. Furthermore, they do not require very well defined mathematical models that are hard to organize for system modeling and objective function. Their computation power is also good and they do not require excessive computation time. Their transformations and adaptations are easy. They give efficacious solutions to the high-scale combinatorial and non-linear problems. These algorithms do not require the assumptions that are hard to be approved to adapt a solution algorithm to a given problem as done in classical algorithm. They do not require the alteration on the interested problem as done in the classical algorithms. They are adaptable in order to solve different types of search and optimization problems. Due to these advantages, these algorithms are densely being used in many different fields such as management science, engineering, computer, etc. General purposed computational intelligence algorithms are generally classified in different groups like biological based, social based, music based, sports based, water based, plant based, chemistry based, physics based, and math based. There are also hybrid methods formed with these methods [1].

Although there are many effective and successful methods that have been introduced to the literature, it is an important task for the science that there should be always effort to improve and search for the best. Also, there have not been any algorithm that can solve all types of problems effectively, often new algorithms are introduced and also improved versions of the introduced ones are proposed in order to improve their effectiveness. Especially in recent years, researchers have introduced such new computational intelligence methods to the literature and

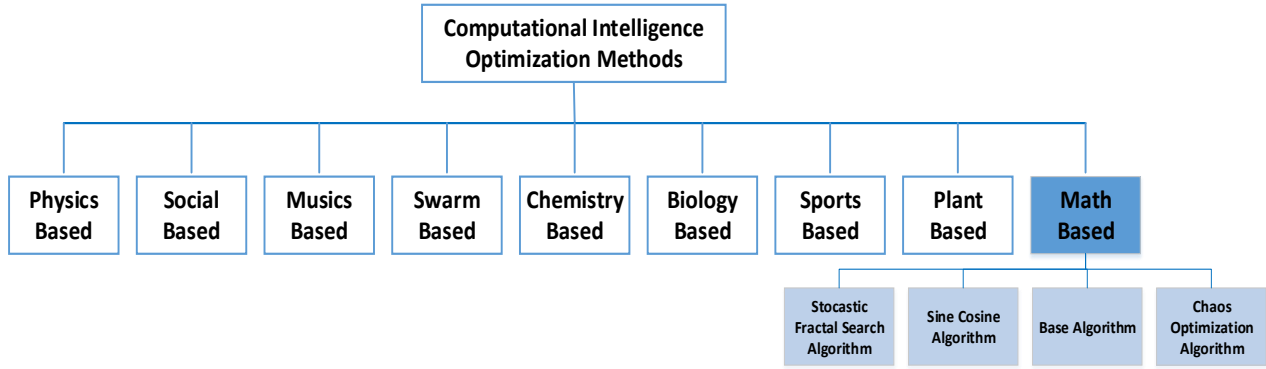


Figure 1. Classification of artificial intelligence optimization methods.

performed successful applications [3]. Due to the philosophy of continually searching the best and absence of the most efficient computational intelligence algorithm for all types of problems, novel algorithms or new variants of current algorithms are being proposed [1-4]. These algorithms can be classified in nine different main categories, as shown in Figure 1. There are also hybrid version of these methods. There are only four algorithms which are based on mathematics. They are, Sine Cosine Algorithm (SCA) [5], Base Algorithm (BA) [6], Chaos optimization algorithms [7], and Stochastic Fractal Search Algorithm (SFSA) [8]. The term Matheuristic is also used for optimization algorithms made by the interoperation of mathematical programming techniques and (meta) heuristics [9].

In this paper, the operators of SFSA has been introduced and the comparative results obtained from other mathematics based Sine Cosine algorithm for different benchmark functions have been presented. Section 2 SFSA has been explained. Section 3 describes the works about SFSA. Section 4 defines the benchmark functions used for comparisons. Section 5 presents the experimental results and finally Section 6 concludes the paper along with future research directions.

II. STOCHASTIC FRACTAL SEARCH ALGORITHM

A fractal is a mathematical set that exhibits a repeating self-similar pattern displayed at every scale. Random fractals can be generated by modifying the iteration process via stochastic rules such as Levy flight, Gaussian walks, percolation clusters, self-avoiding walks, fractal landscapes, trajectories of Brownian motion and the Brownian tree. SFSA is a new global search algorithm based on random fractals. This algorithm has been proposed overcome the shortcomings of basic fractal search. All procedures in SFSA can be divided into two processes called Diffusing and Updating processes. In the first process, each particle diffuses around its current position using Gaussian Walks and Levy Flight to increase the chance of finding the global minimum and it can be considered as exploitation phase of the SFSA. In the latter process, SFSA uses some random methods as updating

processes based on the positions of other selected candidates in the group to explore the problem space efficiently and this can be considered as exploration phase of SFSA [8]. After initializing a set of points uniformly distributed within the search range, the Diffusion process is started to generate new particles using one of the two Gaussian Walks as shown in (1) and (2).

$$GW_1 = \text{Gaussian}(\mu_{BP}, \sigma) + (\varepsilon \times BP - \varepsilon' \times P_i) \quad (1)$$

$$GW_2 = \text{Gaussian}(\mu_p, \sigma) \quad (2)$$

ε and ε' are two uniform random numbers within the [0, 1] interval, BP is the position of best point while P_i is the position of the i th candidate. The two means μ_{BP} and μ_p are equal to BP and P_i . Standard deviation σ is computed as shown in (3) t is the generation number.

$$\sigma = \left| \frac{\log t}{t} \times (P_i - BP) \right| \quad (3)$$

Update process consists of two procedures. The first one uses (4) to update the j th index of each point while second procedure uses (5) to update the point.

$$P'_i(j) = P_r(j) - \varepsilon \times (P_t(j) - P_i(j)) \quad (4)$$

$$P'_i = \begin{cases} P_i - \varepsilon \times (P_t - BP), & \varepsilon \leq 0,5 \\ P_i + \varepsilon \times (P_t - P_r), & \varepsilon > 0,5 \end{cases} \quad (5)$$

P'_i is the new point, P_r and P_t are two different random values selected from the candidates; BP is the best point and ε is a random number within the [0, 1] interval [8]. Flowchart of SFSA has been depicted in Figure 2.

III. WORKS ABOUT SFSA

After introducing the SFSA, it has been used in many different fields and new variants have been proposed. In [10] query optimization problem in large distributed databases has been solved with SFSA. SFSA has been proposed for optimization of planer frame to minimize its weight subjected to the

strength and displacement requirements and effective results have been reported against other methods [11]. Solution of multi objective economic and emission dispatch problem has been solved by SFSA in [12] and competitive results have been obtained. In [13], a penalty guided SFSA has been adapted for solving reliability allocation, redundancy allocation, and reliability–redundancy allocation problems and superiority of the method compared to others from literature has been reported. In [14], SFSA has been proposed for Power system tracking state estimation under sudden load changes and improved results compared to genetic algorithm and particle swarm optimization have been reported. Chaos has been embedded to SFSA in [15] to improve SFSA in terms of convergence speed and fitness accuracy.

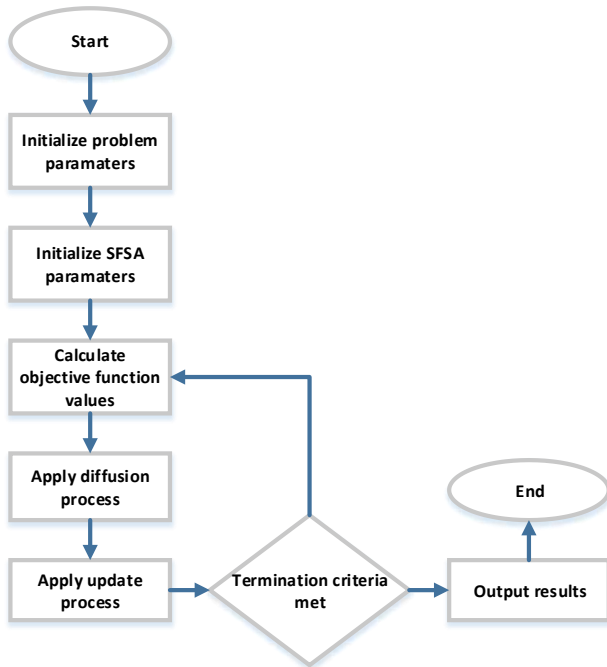


Figure 2. Flowchart of SFSA.

SFSA has been hybridized with differential algorithm in [16]. In [17], chaotic SFSA has been used parametric modelling of a twin rotor system and superior results have been obtained. In [18], authors have introduced a novel hybridization between differential evolution and update processes of the SFSA and statistically superior performance over most of the tested benchmarks, especially hybrid and composition test functions compared to the other contestant algorithms have been reported. In [19], a hybrid SFSA and pattern search based cascade PI-PD controller has been proposed for automatic generation control of thermal, hydro and gas power unit based power systems in presence of plug in electric vehicles and competitive result have been obtained.

IV. BENCHMARK FUNCTIONS

Benchmark test functions are used to evaluate and compare the characteristics of optimization algorithms in terms of

convergence, precision, robustness, and general performance as a rule. The nature, complexity and other properties of these benchmark functions can be easily obtained from their definitions. The difficulty levels of most benchmark functions are adjustable by setting their parameters [20].

A. Chung Reynolds Function

Chung Reynolds Function is a continuous, unimodal and scalable function with less complexity and it can be used to evaluate the converging behaviors of search and optimization algorithms [21]. It is represented by (6).

$$f_1(x) = (\sum_{i=1}^n x_i^2)^2 \quad (6)$$

subject to $-100 \leq x_i \leq 100$. The global minimum is located at $x^* = f_1(0, \dots, 0)$ and $f_1(x^*) = 0$. Graph of this function with two dimensions has been shown in Figure 3.

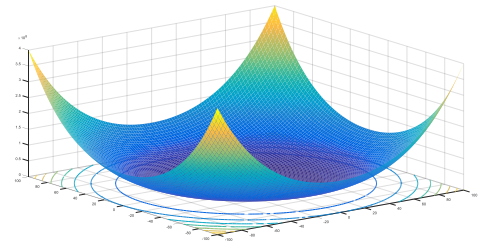


Figure 3. Chung Reynolds function with two dimensions intervals of which are $[-100, 100]$.

B. Griewank Function

Griewank function has many widespread local minima regularly distributed [22]. It is a continuous, multimodal, scalable, convex, and quadratic test function and it can be used to test the global search ability of algorithms in avoiding premature convergence. It is represented by (7).

$$f_2(x) = 1 + \frac{1}{4000} \sum_{i=1}^n x_i^2 - \prod_{i=1}^n \cos\left(\frac{x_i}{\sqrt{i}}\right) \quad (7)$$

where the bounds are $-600 \leq x_i \leq 600$. The global minimum is at $x^* = (0, 0, \dots, 0)$ and $f_2(x^*) = 0$. The terms of the summation produce a parabola, while the local optima are above parabola level. Figure 4 shows its graphs with two dimensions. The dimensions of the search range increase on the basis of the product, which results in the decrease of the local minimums. The more the search range increases, the flatter the function becomes [23].

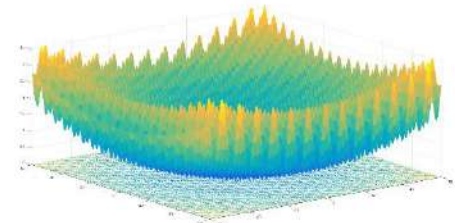


Figure 4. Griewank function with two dimensions intervals of which are $[-60, 60]$.

C. Rastrigin Function

Rastrigin function is example of non-linear highly multimodal function. This function contains millions of local optima in the interval of consideration. It has several local minima [24]. It is represented by (8):

$$f_3(x) = \sum_{i=1}^p (x_i^2 - 10 \cos(2\pi x_i) + 10) \quad (8)$$

subject to $-5,12 \leq x_i \leq 5,12$. The global minimum is located at $x^* = f_3(0, \dots, 0)$ and $f_3(x^*) = 0$. Graph of this function with two dimensions has been shown in Figure 5.

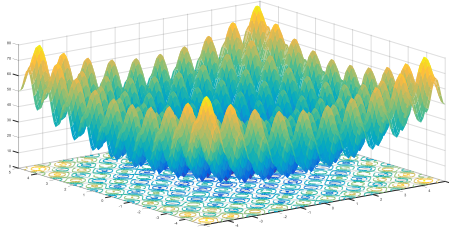


Figure 5. Rastrigin function with two dimensions intervals of which are $[-5, 5]$.

V. EXPERIMENTAL RESULTS

In the first experiment, the performance of SFSA has been tested with one of the other math inspired computational intelligence optimization algorithms, namely Sine Cosine Algorithm (SCA) in Chung Reynolds function with 30 dimensions. Initial population size of all algorithms is selected as 50 and maximum iteration number for termination criteria is determined as 100.

Parameter values for SFSA such as maximum diffusion and walk and parameter values for SCA are listed in Table 1.

Table 1. Parameter values for SFSA

	SFSA		SCA
Parameter	Maximum Diffusion	Walk	a
Value	2	1	2

All of the algorithms have been run for 30 times and objective function values obtained from Chung Reynolds function have been demonstrated in Table 2.

Wilcoxon rank-sum tests have also been performed for these experiment results. Table 3 reports the obtained test results from Chung Reynolds function using two math inspired SFSA and SCA. This is used to test the null hypothesis that the means of two populations (obtained from SFSA and SCA) are equal with 95% confidence. With a two-tail test (inequality), if $t \text{ Stat} < -t \text{ Critical two-tail}$, $(-3,338449603 < -2,045229642)$ we reject the null hypothesis. It can be seen that the observed difference between the sample means is convincing enough to say that success of SFSA is significantly better than that of SCA in this unimodal function.

Table 2. Obtained results from SFSA and SCA in Chung Reynolds Function

Exp #	SFSA	SCA	Exp #	SFSA	SCA
1	2,9800205127 89075e-178	22731345,07 24	16	1,801574515 072202e-181	886108,2616
2	6,8907901793 66117e-169	628563,0115	17	3,611162284 705918e-176	2188037,219 9
3	2,9962718285 06034e-199	3818807,611 8	18	1,068058373 932954e-174	288245,4912
4	3,4680223013 56144e-162	16676879,09 25	19	3,445936137 135308e-187	20470786,37 29
5	6,5497841074 84379e-168	122327542,7 451	20	4,045289530 290438e-166	12861718,25 31
6	7,5035984133 15204e-172	18809049,92 82	21	1,885660801 481966e-177	286107,4546
7	2,7003849325 15142e-179	26164211,69 25	22	1,995984711 067662e-166	1122458,486 6
8	7,5895908165 88856e-193	4781161,754	23	4,938360983 090467e-176	334122,7663
9	4,6219879803 41730e-176	1067185,248 7	24	9,499035447 700210e-177	5202320,377 2
10	1,6877498094 23972e-172	1794740,311 7	25	1,107362952 337784e-179	31383681,14 94
11	3,5181691094 99576e-182	8842760,706 8	26	1,517602293 836084e-169	38196719,40 43
12	1,6057802516 77047e-192	6335750,533 5	27	5,663767782 713541e-180	33028835,74 25
13	4,8267381281 71555e-187	2229820,382 5	28	1,539962658 198887e-167	3735535,319 7
14	3,8264790967 71805e-188	204296,5614	29	1,839035487 460783e-193	23212570,00 03
15	6,2342022146 01058e-178	94038030,46 41	30	1,737210785 472667e-170	463887,3278

Table 3. Wilcoxon Rank-Sum Test results obtained from SFSA and SCA for Chung Reynolds Function

	SFSA	SCA
Mean	1,1562E-163	16803709,29
Variance	0	7,6005E+14
Observations	30	30
Hypothesized Mean Difference	0	
Df	29	
t Stat	-3,338449603	
P(T<=t) one-tail	0,001161985	
t Critical one-tail	1,699127027	
P(T<=t) two-tail	0,00232397	
t Critical two-tail	2,045229642	

In the second experiment, the performance of SFSA has been tested with SCA in multimodal Griewank function with 30 dimensions. Initial population size of all algorithms is selected as 50 and maximum iteration number for termination criteria is determined as 100.

All of the algorithms have been run for 30 times and objective function values obtained from multimodal Griewank function have been demonstrated in Table 4. Wilcoxon rank-sum tests have also been performed for these experiment results. Table 5 reports the obtained test results from Griewank function using SFSA and SCA. $t \text{ Stat} < -t \text{ Critical two-tail}$ $(-16,76937873 < -2,045229642)$ and thus the sample means is convincing enough to say that success of SFSA is significantly better than that of SCA in this multimodal function.

Table 4. Obtained results from SFSA and SCA in Griewank Function

Exp.#	SFSA	SCA	Exp.#	SFSA	SCA
1	0	0,62392	16	0	0,74331
2	0	0,46791	17	0	0,61844
3	0	0,54574	18	0	0,5039
4	0	0,7016	19	0	0,4587
5	0	0,89902	20	0	0,48672
6	0	0,48839	21	0	0,81169
7	0	0,79333	22	0	0,18556
8	0	0,71586	23	0	0,90589
9	0	0,44904	24	0	0,93044
10	0	0,75563	25	0	0,55762
11	0	0,49643	26	0	0,96318
12	0	0,71747	27	0	0,43772
13	0	0,71633	28	0	0,33106
14	0	0,71378	29	0	0,24668
15	0	0,53313	30	0	0,90523

Table 5. Wilcoxon Rank-Sum Test results obtained from SFSA and SCA for Griewank Function

	SFSA	SCA
Mean	0	0,623457
Variance	0	0,041467
Observations	30	30
Hypothesized Mean Difference	0	
Df	29	
t Stat	-16,76937873	
P(T<=t) one-tail	9,15307E-17	
t Critical one-tail	1,699127027	
P(T<=t) two-tail	1,83061E-16	
t Critical two-tail	2,045229642	

In the third experiment, the performance of SFSA has been tested with SCA in multimodal Rastrigin function with 30 dimensions. Initial population size of all algorithms is selected as 50 and maximum iteration number for termination criteria is determined as 100.

All of the algorithms have been run for 30 times and objective function values obtained from multimodal Rastrigin function have been demonstrated in Table 6. Wilcoxon rank-sum tests have also been performed for these experiment results. Table 7 reports the obtained test results from Rastrigin function using SFSA and SCA. $t \text{ Stat} < -t \text{ Critical two-tail}$ ($-16,39482536 < -2,045229642$) and thus the sample means is convincing enough to say that success of SFSA is significantly better than that of SCA in this multimodal function.

Table 6. Obtained results from SFSA and SCA in Rastrigin Function

Exp.#	SFSA	SCA	Exp.#	SFSA	SCA
1	0	148,525	16	0	164,9357
2	0	124,687	17	0	148,1981
3	0	200,825	18	0	164,7712
4	0	136,1159	19	0	66,7611
5	0	101,5	20	0	195,1869
6	0	157,9761	21	0	118,4515
7	0	151,5547	22	0	121,057
8	0	141,4146	23	0	174,6472
9	0	162,5559	24	0	83,2774
10	0	152,3562	25	0	33,6834
11	0	136,204	26	0	179,669
12	0	144,4903	27	0	137,0395
13	0	193,9397	28	0	55,8917
14	0	202,5062	29	0	103,291
15	0	147,7367	30	0	36,6648

Table 7. Wilcoxon Rank-Sum Test results obtained from SFSA and SCA for Rastrigin Function

	SFSA	SCA
Mean	0	136,1971
Variance	0	2070,348
Observations	30	30
Hypothesized Mean Difference	0	
Df	29	
t Stat	-16,39482536	
P(T<=t) one-tail	1,65877E-16	
t Critical one-tail	1,699127027	
P(T<=t) two-tail	3,31753E-16	
t Critical two-tail	2,045229642	

VI. CONCLUSIONS

Due to the many advantages of natural phenomena inspired computational intelligence algorithms, they are efficiently used for solving different highly complex problems providing working solutions in time, especially with dynamic problem definitions, fluctuations in constraints, incomplete or imperfect information, and limited computation capacity. Some researchers study to incrementally improve the algorithm by proposing the new versions while others explore the application of these algorithms in a novel context. Due to the philosophy of continually searching the best and absence of the most efficient artificial intelligence algorithm for all types of problems, recently novel algorithms are also being proposed. SFSA is a relatively one of the most recent mathematics based computational intelligence algorithm and inspired by the natural phenomenon of growth using a mathematic concept called the fractal.

In this paper, the main steps of SFSA are introduced and its comparative performance within the unimodal and multimodal benchmark functions which are as complex as

engineering search and optimization problems has been presented. The performance of SFSA has been tested with other mathematics based computational intelligence optimization algorithm, Sine-Cosine Algorithm (SCA), within benchmark functions. From the experimental results, it can be concluded that SFSA has better performance than SCA in unimodal and multi-modal benchmark functions. More efficient multi-objective, distributed, and parallel versions of SFSA may be proposed for future works.

REFERENCES

- [1] Altunbey, F., Alatas, B., 2015 "Review of Social-Based Artificial Intelligence Optimization Algorithms for Social Network Analysis", *International Journal of Pure and Applied Sciences*, vol. 1, pp. 33-52.
- [2] Altunbey Ozbay, F., Alatas, B., 2016 "Review of Computational Intelligence Method Inspired from Behavior of Water", *Afyon Kocatepe University Journal of Science and Engineering*, vol. 16, pp. 137-147.
- [3] Altunbey Ozbay, F., Alatas, B., 2016 "Müzik Tabanlı Hesapsal Zeka Algoritmalarının İncelenmesi", 1st International Conference on Engineering Technology and Applied Sciences, pp. 663-669.
- [4] Akyol, S., Alatas, B., 2016 "Efficiency Evaluation of Crow Search Algorithm in Benchmark Functions for Optimization", 2nd International Conference on Engineering and Natural Sciences, pp. 939-943.
- [5] Mirjalili, S., 2016 "SCA: a sine cosine algorithm for solving optimization problems", *Knowledge-Based Systems*, vol. 96, pp. 120-133.
- [6] Salem, SA., 2012 "BOA: A novel optimization algorithm", *International Conference on Engineering and Technology (ICET)*, pp. 1-5.
- [7] Yang, D., Li, G., Cheng, G., 2007 "On the efficiency of chaos optimization algorithms for global optimization", *Chaos, Solitons & Fractals*, vol. 34, pp. 1366-1375.
- [8] Salimi, H., 2015 "Stochastic fractal search: a powerful metaheuristic algorithm", *Knowledge-Based Systems*, vol. 75, pp. 1-18.
- [9] Caserta, M., Voß, S., 2009 "Metaheuristics: hybridizing metaheuristics and mathematical programming", *Metaheuristics: Intelligent Problem Solving*, Springer, Berlin, pp. 1-38, 2009.
- [10] Sohal, M., Singh, A., Virk, RS., 2015 "A Framework for Optimizing Distributed Database Queries Based on Stochastic Fractal Search", *Int J Comput Sci Mob Comput*, vol. 4, pp. 544-551.
- [11] Bhensdadia, VH., 2015 "Investigation of Size Optimization of Frame Structure Using Grey Wolf Optimizer (Gwo) and Stochastic Fractal Search (Sfs) Algorithms Doctoral Dissertation", Department Of Mechanical Engineering School Of Engineering, Rk University, 2015.
- [12] Dubey, HM., Pandit, M., Panigrahi, BK., Tyagi, T., 2015 "Multi-objective Power Dispatch Using Stochastic Fractal Search Algorithm and TOPSIS", *International Conference on Swarm, Evolutionary, and Memetic Computing*, Springer International Publishing, pp. 154-166.
- [13] Mellal, MA., Zio, E., 2016 "A penalty guided stochastic fractal search approach for system reliability optimization", *Reliability Engineering & System Safety*, vol. 152, pp. 213-227.
- [14] Mosbah, H., El-Hawary, M., 2016 "Power system tracking state estimation based on stochastic fractal search technique under sudden load changing conditions", *Electrical and Computer Engineering (CCECE)*, 2016 IEEE Canadian Conference, pp. 1-6.
- [15] Rahman, TA., Tokhi, MO., 2016 "Enhanced stochastic fractal search algorithm with chaos", In 7th IEEE Control and System Graduate Research Colloquium (ICSGRC), pp. 22-27, 2016.
- [16] Awad, NH., Ali, MZ., Suganthan, PN., Jaser, E., 2016 "Differential evolution with stochastic fractal search algorithm for global numerical optimization", In IEEE Congress on Evolutionary Computation (CEC), pp. 3154-3161.
- [17] Rahman, TA., 2016 "Parametric modelling of twin rotor system using chaotic fractal search algorithm", In 7th IEEE Control and System Graduate Research Colloquium (ICSGRC), pp. 34-39, 2016.
- [18] Awad, NH., Ali, MZ., Suganthan, PN., Jaser, E., 2016 "A decremental stochastic fractal differential evolution for global numerical optimization", *Information Sciences*, vol. 372, pp. 470-491.
- [19] Padhy, S., Panda, S., 2017 "A hybrid stochastic fractal search and pattern search technique based cascade PI-PD controller for automatic generation control of multi-source power systems in presence of plug in electric vehicles", *CAAI Transactions on Intelligence Technology*, 2017.
- [20] Alatas, B., Akin, E., Ozer, AB., 2009 "Chaos Embedded Particle Swarm Optimization Algorithms", *Chaos, Solitons & Fractals*, vol. 40, pp. 1715-1734.
- [21] Chung, CJ., Reynolds, RG., 1998 "CAEP: An Evolution-Based Tool for Real-Valued Function Optimization Using Cultural Algorithms", *International Journal on Artificial Intelligence Tool*, vol. 7, pp. 239-291.
- [22] (January 2017) GEATbx: Examples of Objective Functions. Available: <http://www.pg.gda.pl/~mkwies/dyd/geadocu/fcnfun8.html>
- [23] Fister Jr, I., Mlakar, U., Yang, XS., Fister, I., 2016 "Parameterless Bat Algorithm and its Performance Study", *Nature-Inspired Computation in Engineering*, Springer International Publishing, pp. 267-276.
- [24] Digalakis, JG., Margaritis, KG., 2002 "An experimental study of benchmarking functions for genetic algorithms", *International Journal of Computer Mathematics*, vol. 79, 403-416. *System Sciences*, 7, 417-422, www.nat-hazards-earth-syst-sci.net.

Evaporation Rate Based Water Cycle Algorithm for Engineering Design Optimization

Feyza Altunbey Ozbay

Department of Software Engineering
Firat University
Elazig, Turkey
faltunbey@firat.edu.tr

Bilal Alatas

Department of Software Engineering
Firat University
Elazig, Turkey
balatas@firat.edu.tr

Abstract—In recent years, many nature-inspired metaheuristic optimization algorithms have been proposed and applied to solving constrained optimization and engineering design problems. The aim of developing metaheuristic methods are to provide robust and efficacious solution strategies for high-scale combinatorial and non-linear problems and to solve problems faster. Water Cycle Algorithm is a new optimization method which is inspired from nature and based on the observation of water cycle process and how rivers and streams flow to the sea in the real world. The Evaporation Rate based Water Cycle Algorithm is the new concept of Water Cycle Algorithm. Evaporation rate for different rivers and streams offer improvement in search. To verify the performance of the ER-WCA, two classical engineering design optimization problems are solved and results are compared with those available in the literature. It has been observed that the optimization method can effectively be used for solution of constrained engineering design optimization problems.

Keywords—Metaheuristics; Performance; Evaporation Rate based Water Cycle Algorithm

I. INTRODUCTION

Optimization plays an important role in many real-world problems such as engineering, economics, management, and medicine. Many real life and engineering problems are commonly quite difficult to solve and search space of these problem increases exponentially with problem size. In addition, real world problems contain complex objective function and different decision variables under constraints. Providing of suitable solution for these problems in rational time has been received considerable attention among engineers and researchers. Therefore, during the last decades, many new optimization methods have been proposed to solve various problems in real world.

Optimization methods are classified into two general categories: mathematical programming and metaheuristic methods. Different mathematical programming methods such as linear programming, homogeneous linear programming, integer programming, dynamic programming, and nonlinear

programming have been developed to solve various optimization problems. These methods use gradient information to generate the solution space that convergence to a global optimum solution. However, mathematical programming methods are insufficient to solve the complexity of real world structural design problems. Metaheuristic optimization methods have been proposed as an alternative to mathematical programming methods to obtain the global optimum solution of these problems. These methods have gained a lot of popularity in recent years because of their ability to solve complex, multimodal, high dimensional and nonlinear search and optimization problems. Most of these methods usually mimic some natural or social phenomenon, such as physic, social, music, swarm, chemistry, biology, sports, and math. Therefore, metaheuristic optimization methods can be evaluated in nine different main groups as shown in Figure 1.

Various physic based metaheuristic methods have been presented in literature. The most popular methods are Gravitational Search Algorithm, Electromagnetism-Like Algorithm, Big Bang-Big Crunch Algorithm, Ions Motion Optimization, Artificial Physics Algorithm, Magnetic Optimization Algorithm, Water Drops Algorithm, River Formation Dynamics Algorithm, Water Cycle Algorithm, Water Flow Algorithm, Water Flow-like Algorithm, Water Wave Optimization, Circular Water Wave Algorithm, Artificial Showering Algorithm [1, 2]. The last eight method is inspired by the natural behavior of water. Evaporation Rate based Water Cycle Algorithm (ER-WCA) is one of the physic based metaheuristic optimization method and modified version of Water Cycle Algorithm (WCA).

In this paper, ER-WCA has been introduced and the comparative performance results obtained by other metaheuristic methods for engineering design problems have been presented. Section 2 presents a brief overview of ER-WCA. In section 3, engineering design problems used for comparisons have been defined. Section 4 presents

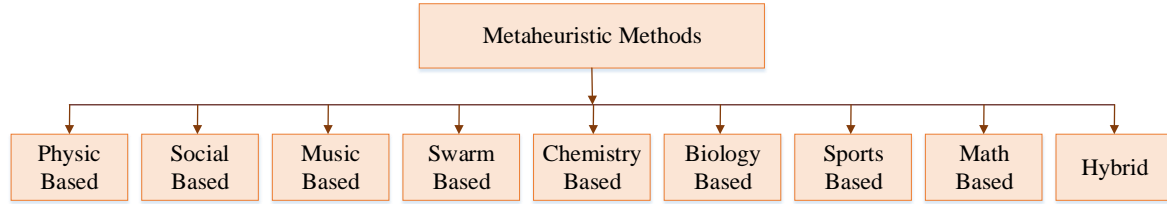


Figure 1. Metaheuristic Methods

experimental results. Finally, conclusions are given in Section 5.

II. EVAPORATION RATE BASED WATER CYCLE ALGORITHM

Evaporation Rate based Water Cycle Algorithm (ER-WCA) is modified version of Water Cycle Algorithm (WCA) [3]. The basic idea of WCA is inspired from nature and based on water cycle process [4]. WCA observes the flow of rivers and streams to the sea. ER-WCA have been proposed by applying new modifications to the WCA [5]. These modifications are listed as:

(a) Evaporation process has been used for exploitation capability of WCA. Evaporation rate for rivers and streams is proposed in ER-WCA.

(b) In the ER-WCA, variable evaporation rate (ER) is used to set the evaporation of the water as shown in (1).

$$ER = \frac{Sum(NS_n)}{(N_{sr}-1)} \times rand, \quad n = 2, \dots, N_{sr} \quad (1)$$

NS_n is the number of streams and N_{sr} is the total of number of rivers.

(c) Streams are forced to be searched in sea coast by ER-WCA using the concepts of variance as shown in (2) if the evaporation condition is satisfied.

$$X_{Stream}^{New} = X_{Sea} + \sqrt{\mu} \times randn(1, N) \quad (2)$$

μ is used for area being searched around the sea.

(d) In the ER-WCA, the occurrence of evaporation considerably reduces during the repetition process.

The pseudo code of ER-WCA is given in Figure 2.

III. ENGINEERING DESIGN OPTIMIZATION PROBLEMS

The first stage of engineering design problem is to form a mathematical model. The mathematical model can be expressed as (3).

$$\begin{cases} \text{Minimize } f(X) \\ \text{Subject to } g_i(X) \leq 0 \quad i = 1, 2, \dots, m \\ h_j(X) \quad j = 1, 2, \dots, n \\ X_L \leq X \leq X_U \end{cases} \quad (3)$$

Where $f(X)$ is called objective function of engineering design problem, $g_i(X)$ inequality constraint and m is the number of inequality constraint. $h_j(X)$ is known as constraint function and n is number of function $h_j(X)$. $X = (x_1, x_2, \dots, x_k)$ is design variables and X_L, X_U are variable upper and lower boundary respectively.

A. Welded Beam Design Optimization Problem

The structure of welded beam shown in Figure 3, was introduced by Rao [6], is a standard constrained engineering problem that has been used as benchmark problem. The objective of the problem is to design a welded beam that has minimum cost subject to constraints on shear stress (τ), bending stress in the beam (σ), buckling load on the bar P_c , and deflection of the beam (δ), and side constraints. The design variables are the thickness of the weld $h(x_1)$, length of the welded joint $l(x_2)$, the width of the beam $t(x_3)$ and thickness of the beam $b(x_4)$. The decision vector is $X = (h, l, t, b) = (x_1, x_2, x_3, x_4)$. The mathematical formulation of the problem is defined in Table 1.

Step 1. Choose the initial parameters: N_{sr} , d_{max} , N_{pop} and maximum number of iteration.
Step 2. Generate random initial population and form the initial streams, rivers and sea.
Step 3. Calculate cost value for each stream.
Step 4. Determine the intensity of flow for rivers and sea.
Step 5. Streams flow to the rivers and sea.
Step 6. Exchange positions of rivers/sea with a stream which gives the best solution.
Step 7. Rivers flow to the sea.
Step 8. Exchange positions of river with the sea.
Step 9. Calculate the evaporation rate.
Step 10. Check the evaporation condition among rivers and streams and calculate the new positions of rivers and streams.
Step 11. Check the evaporation condition between sea and rivers /streams and calculate the new positions of rivers and streams.
Step 12. Reduce the d_{max} .
Step 13. Check the stopping condition. If the stopping criteria is satisfied, the algorithm will be stopped, otherwise return to Step 5.

Figure 2. Pseudo code of ER-WCA

B. Tension/Compression Spring Design Optimization Problem

Tension/compression spring design optimization problem was introduced by Arora [7]. The aim of this problem is to minimize the weight of a tension/compression spring subject to constraints on minimum deflection (g_1), shear stress (g_2), surge frequency (g_3) and limits on outside diameter (g_4). This problem has three continuous variables defined as: the wire diameter $d(x_1)$, the mean coil diameter $D(x_2)$ and the number of active coils $N(x_3)$. The problem is shown in Figure 4.

The mathematical formulation of the problem is defined in Table 2.

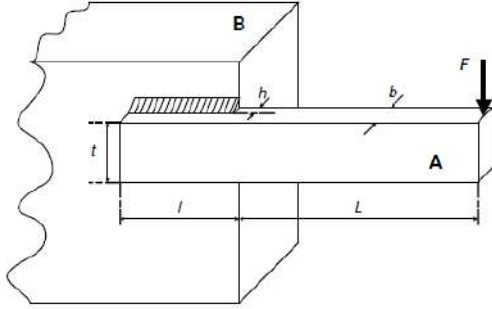


Figure 3. Welded beam design optimization problem

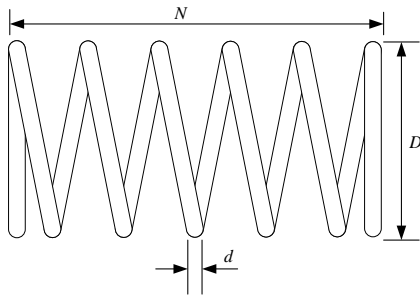


Figure 4. Tension/compression spring design optimization problem

Table 1. Welded Beam Optimization Problem

Problem: Welded beam design optimization problem	
Minimize:	$f(X) = 1.10471x_1^2x_2 + 0.04811x_3x_4(14 + x_2)$
Subject to:	$g_1(X) = \tau(X) - \tau_{max} \leq 0$
	$g_2(X) = \sigma(X) - \sigma_{max} \leq 0$
	$g_3(X) = x_1 - x_4 \leq 0$
	$g_4(X) = 0.125 - x_1 \leq 0$
	$g_5(X) = \delta(X) - 0.25 \leq 0$
	$g_6(X) = P - P_c(X) \leq 0$
	$g_7(X) = 0.10471x_1^2 + 0.04811x_3x_4(14 + x_2) - 5 \leq 0$
Where:	$\tau(X) = \sqrt{\tau_1^2 + 2\tau_1\tau_2(x_2/2R + \tau_2^2)}$
	$\tau_1 = P/\sqrt{2}x_1x_2$
	$\tau_2 = MR/J$
	$M = P(L + \frac{x_3}{2}); J(X) = 2\left\{\frac{x_1x_2}{\sqrt{2}}\left[\frac{x_2^2}{12} + (\frac{x_1+x_3}{2})^2\right]\right\}$
	$R = x_2^2/4 + ((x_1 + x_3)/2)^2$
	$\sigma(X) = 6PL/x_4x_3^2$
	$\delta(X) = 4PL^3/Ex_3^3x_4$
	$P_c(X) = (4.013\sqrt{EGx_3^2x_4^6/36/L^2})(1 - x_3/2L\sqrt{E/4G})$
	$G = 12 \times 10^6[psi], E = 30 \times 10^6[psi], P = 6000[lb]$
	$L = 14[in], \sigma_{max} = 30000[psi], \tau_{max} = 13600[psi]$
	$\delta_{max} = 0.25[in]$
	With boundary conditions: $0.1 \leq x_1 \leq 2; 0.1 \leq x_2 \leq 10; 0.1 \leq x_3 \leq 10; 0.1 \leq x_4 \leq 2$

Table 2. Tension/Compression Spring Design Optimization Problem

Problem: Tension/compression spring design optimization problem	
Minimize:	$f(X) = (x_3 + 2)x_2x_1^2$
Subject to:	$g_1(X) = 1 - \frac{x_2^3x_3}{71785x_1^4} \leq 0$
	$g_2(X) = -\frac{4x_2^2 - x_1x_2}{12466(x_2x_1^2 - x_1^4)} + \frac{1}{5108x_1^2} - 1 \leq 0$
	$g_3(X) = 1 - \frac{140.45x_1}{x_2^2x_3} \leq 0$
	$g_4(X) = \frac{x_1 + x_2}{1.5} - 1 \leq 0$
With boundary conditions: $0.05 \leq x_1 \leq 2; 0.25 \leq x_2 \leq 1.3; 2 \leq x_3 \leq 15$	

IV. EXPERIMENTAL RESULTS

In this section, the ER-WCA is evaluated against the previous robust methods by using two well-studied problems: welded beam design problem and tension/compression spring design problem. To evaluate the performance of ER-WCA for optimizing the two constrained problems, the same constraint handling have been used. For each problem, population size of all methods is selected as 50 and maximum iteration number for termination criteria is determined as 1000. The results of the compared methods for these two problems are taken from related studies in the literature.

Until now, a variety of optimization methods have been applied to solve the welded beam design problem by other researchers [7-18]. Table 3 summarizes the best results obtained by ER-WCA and other different methods. The convergence curve of ER-WCA for welded beam design optimization problem is given in Figure 5.

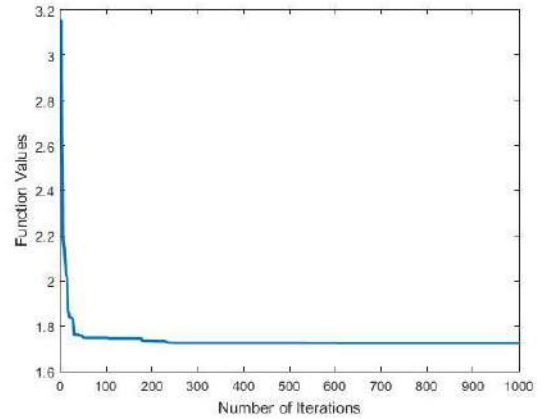


Figure 5. Convergence curve of ER-WCA for welded beam design optimization problem

From the Table 3, illustrates that ER_WCA is more optimal than that of references [8-18].

In the literature, different approaches proposed to tackle the tension/compression spring design optimization problem. The comparison of the best results obtained by ER-WCA and other methods are reported in Table 4. The convergence curve of ER-WCA for tension/compression spring design optimization problem is shown in Figure 6.

Table 3. Comparison of the best solution for Welded Beam Problem found by different methods

Method	Design Variables				Cost $f(X)$
	$h(x_1)$	$l(x_2)$	$t(x_3)$	$b(x_4)$	
Coello [8]	0.208800	3.420500	8.997500	0.210000	1.748309
He and Wang [9]	0.202369	3.544214	9.048210	0.205723	1.728024
Dimopoulos [10]	0.2015	3.5620	9.041398	0.205706	1.731186
Coello and Montes [11]	0.205986	3.471328	9.020224	0.206480	1.728226
Montes and Coello [12]	0.199742	3.612060	9.037500	0.206082	1.73730
Hedar and Fukushima [13]	0.205644 261	3.472578	9.036623	0.205729	1.725002
Hu et al. [14]	0.20573	3.47049	9.03662	0.20573	1.724850
Kaveh and Talatahari [15]	0.205700	3.471131	9.036683	0.205731	1.724918
Mirjalili et al. [16]	0.205463	3.473193	9.044502	0.205695	1.72645
Mirjalili et al. [17]	0.205676	3.478377	9.03681	0.205778	1.72624
Present study	0.205729	3.470472	9.036663	0.205729	1.724857

Table 4. Comparison of the best solutions for Tension/Compression Spring Design Optimization Problem found by different methods

Method	Design Variables			Cost $f(X)$
	$d(x_1)$	$D(x_2)$	$N(x_3)$	
Belegundu [18]	0.05	0.315900	14.25000	0.012833
Montes and Coello [12]	0.051643	0.355360	11.397926	0.012698
Omran and Salman [19]	0.051683	0.356589	11.2964717	0.012665
Ray and Saini [20]	0.050417	0.321532	13.979915	0.013060
Coello and Montes [11]	0.051989	0.363965	10.890522	0.012681
Arora [7]	0.053396	0.399180	9.185400	0.012730
He and Wang [9]	0.051728	0.357644	11.244543	0.012674
Coello [8]	0.051480	0.351661	11.632201	0.012704
Raj et al. [21]	0.053862	0.411283	8.684379	0.012748
Akay and Karaboga [22]	0.051749	0.358179	11.203763	0.012665
Mahdavi et al. [23]	0.051154	0.349871	12.076432	0.0126706
Mirjalili et al. [17]	0.05169	0.356737	11.28885	0.012666
Present Study	0.051521	0.352691	11.528973	0.012665

From Table 4, it has been observed that the ER_WCA performs much better in comparison to the algorithms.

V. CONCLUSIONS

Due to the simplicity, flexibility and inexpensive computational cost of the metaheuristic optimization methods, they are efficiently used to solve constrained optimization and engineering design problems. Many metaheuristic optimization methods mimic natural phenomena. ER-WCA is physics based metaheuristic

optimization method inspired by nature. In this paper, ER-WCA has been briefly introduced and its performance has been tested with other available methods in the literature for welded beam and tension/compression spring design optimization problems. The comparison results with other optimization methods demonstrate that the ER-WCA proves to be effective and efficient for locating the global solution or finding a near-global solution to each problem tested. This powerful metaheuristic optimization method may be extended to study multi-objective optimization application.

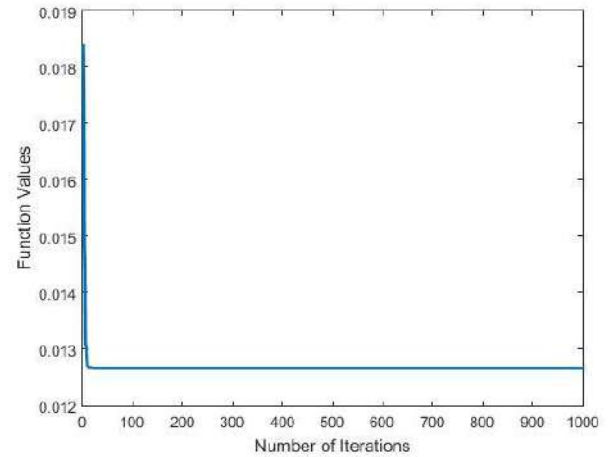


Figure 6. Convergence curve of ER-WCA for Tension/Compression Spring Design Optimization Problem

REFERENCES

- [1] Altunbey, F., Alatas, B., 2015 "Review of Social-Based Artificial Intelligence Optimization Algorithms for Social Network Analysis", International Journal of Pure and Applied Sciences, vol. 1, pp. 33-52.
- [2] Can, U., Alatas, B., 2015 "Physics Based Metaheuristic Algorithms for Global Optimization", American Journal of Information Science and Computer Engineering, vol. 1, pp. 94-106.
- [3] Sadollah, A., Eskandar, H., Bahreinejad, A., Kim, J. H., 2015 "Water cycle algorithm with evaporation rate for solving constrained and unconstrained optimization problems", Applied Soft Computing, vol. 30, pp. 58-71.
- [4] Altunbey Ozbay, F., Alatas, B., 2016 "Review of Computational Intelligence Method Inspired from Behavior of Water", Afyon Kocatepe Üniversitesi Fen ve Mühendislik Bilimleri Dergisi, vol. 16, pp. 137-147.
- [5] Eskandar, H., Sadollah, A., Bahreinejad, A., Hamdi, M., 2012 "Water cycle algorithm – A novel metaheuristic optimization method for solving constrained engineering optimization problems", Computers and Structures, vol. 110, pp. 151-166.
- [6] Rao, S. S., 1996 Engineering optimization theory and practice, third, John Wiley & Sons, Chichester.
- [7] Arora, J., "Introduction to optimum design", Academic Press, New York.
- [8] Coello, CAC., 2000 "Use of a self-adaptive penalty approach for engineering optimization problems", Computer in Industry, vol. 41, pp. 113-127, 2000.
- [9] He, Q., Wang, L., 2007 "An effective co-evolutionary particle swarm optimization for constrained engineering design problems", Engineering Applications of Artificial Intelligence, vol. 20, pp. 89-99.

- [10] Dimopolus, GG., 2007 "Mixed-variable engineering optimization based on evolutionary and social metaphors", Computer methods in applied mechanics and engineering, vol. 196, pp. 803-817, 2007.
- [11] Coello, CAC., Montes, EM., 2002 "Constraint-handling in genetic algorithms through the use of dominance-based tournament selection", Advanced Engineering Informatics vol. 16, pp. 193-203.
- [12] Mezura-Montes, E., Coello, CAC., 2008 "An empirical study about the usefulness of evolution strategies to solve constrained optimization problems", International Journal of General Systems, vol. 37, pp. 443-473.
- [13] Hedar, AR., Fukushima, M., 2006 "Derivative-free filter simulated annealing method for constrained continuous global optimization", Journal of Global Optimization, vol. 35, pp. 521-549, 2006.
- [14] Hu, X., Eberhart, RC., Shi, Y., 2003 "Engineering optimization with particle swarm", IEEE Swarm Intelligence Symposium, pp. 53-57.
- [15] Kaveh, A., Talatahari, S., 2010 "An improved ant colony optimization for constrained engineering design problems", Engineering Computations, vol. 27, pp. 155-182, 2010.
- [16] Mirjalili, S., Mirjalili, SM., Hatamlou, A., 2016 "Multi-verse optimizer: a nature-inspired algorithm for global optimization", Neural Computing and Applications, vol. 27, pp. 495-513.
- [17] Mirjalili, S., Mirjalili, SM., Lewis, A., 2014 "Grey wolf optimizer", Advances in Engineering Software, vol. 69, pp. 46-61, 2014.
- [18] Belegundu, AD., Arora, JS., 1985 "A study of mathematical programming methods for structural optimization Part I: Theory" International Journal for Numerical Methods in Engineering, vol. 21, pp. 1583-1599, 1985.
- [19] Omran, MG., Salman, A., 2009 "Constrained optimization using CODEQ", Chaos, Solitons & Fractals, vol. 42, pp. 662-668, 2009.
- [20] Ray, T., Saini, P., 2001 "Engineering design optimization using a swarm with an intelligent information sharing among individuals", Engineering Optimization, vol. 33, pp. 735-748.
- [21] Raj, KH., Sharma, R., 2005 "An evolutionary computational technique for constrained optimization in engineering design", IE (I)-J-MC, vol. 86, pp. 121-128, 2005.
- [22] Karaboga, D., Akay, B., 2009 "A comparative study of artificial bee colony algorithm", Applied mathematics and computation, vol. 214, pp. 108-132, 2009.
- [23] Mahdavi, M., Fesanghary, M., Damangir, E., 2007 "An improved harmony search algorithm for solving optimization problems", Applied mathematics and computation, vol. 188, pp. 1567-1579, 2007.

Mobile Device, Computer, Internet And Social Media Use In Turkey

Rojan Gümüş

Dicle University, Diyarbakır Vocational School,
Dep. Of Computer Technologies, Diyarbakır, Turkey
gumusrojan@gmail.com

Yasin Sönmez

Dicle University, Diyarbakır Vocational School,
Dep. Of Computer Technologies, Diyarbakır, Turkey
yasin.sonmez@dicle.edu.tr

Abstract—Development in technology and transition to information society brought a lot of innovations. Mass media keeps up with change most. By the help of widespread use of internet, provision of wide band internet services mass media take part in every aspect of life using a lot of internet based programs. These platforms are free from place and time owing to 20 million mobile phones used since 1994. These mobile devices have advanced features to execute many features as computers. Thanks to these features they are able to carry, send, receive and store data. Therefore mobile devices are spreading in individually and institutionally usage. Nowadays by the help of mobile devices easy access and variety of contents is possible. Users are choosing contents considering downloading time, mobile application template, user friendly design, security of sending and receiving data, code to text ratios and out of page redirect. Usage of internet is spreading in all over the world and Turkey. Owing to its young generation Turkey is becoming one of the leader countries in the world on behalf of internet usage.

This study aims to analyze mobile device, computer, internet and social media use and habits in Turkey. A survey was conducted by habitants living in İstanbul. In the study demographics such as age, gender and education of participants analyzed. Also frequency of internet using, reasons of internet using such as social media, entertainment, information gaining, news, travelling, shopping, communication, internet using device such as mobile device or computer were investigated. Relationships between computer, internet, mobile device, and social media use and demographics were analyzed. Additionally reasons of internet usage were predicted for participants. According to results of our study young and educated people uses internet more. Additionally most of responders use internet by mobile devices. They used internet for communication, information and social media most.

Keywords—Mobile device, computer, internet, social media, usage

I. INTRODUCTION

Development in technology and transition to information society brought a lot of innovations. Mass media keeps up with change most. By the help of widespread use of internet, provision of wide band internet services mass media take part in every aspect of life using a lot of internet based programs. These platforms are free from place and time owing to 20 million mobile phones used since 1994. These mobile devices have advanced features to execute many features as

computers. Thanks to these features they are able to carry, send, receive and store data[1]. Therefore mobile devices are spreading in individually and institutionally usage. Nowadays by the help of mobile devices easy access and variety of contents is possible. Users are choosing contents considering downloading time, mobile application template, user friendly design, security of sending and receiving data, code to text ratios and out of page redirect[2].

Internet use is recognized as an essential part of modern life. Owing to web-based technologies and increases of internet Access, internet use has increased dramatically across the world reaching the number of global users more than 3 billion in 2015[3].

However, online activities are extremely diverse, ranging from sending emails to gambling to selling products. The diversity of uses is related to the interactive nature of the internet as a medium where users – audiences – make active decisions about how to engage with the breadth of possible uses of the internet[4,5].

It is clear that the mobile internet will play a key role in bringing the next billion users online. Mobile internet has already leap-frogged fixed access in many countries because of limitations in the coverage of the fixed network, and the availability of mobile internet access significantly outpaces adoption today. The mobile internet is therefore central to realising the internet society vision that ‘The Internet is for everyone’.

Further benefits of the mobile internet are arising from new innovative services based on mobile access to the internet, using all the features embedded into the smart devices, and accessed through apps. These services enable social inclusion, interaction with government, and commerce, among other applications. These innovations are already driving a further evolution of the internet that has been in a state of constant change since its founding.

Laptop and tablet ownership also went up, and no doubt contributed to the increase in internet users. But smartphones are the most commonly owned internet access device as of last year.

We highlight a few key statistics and trends regarding internet users:

- 3 billion Internet users were likely by May 2015.

- Mobile Internet penetration is forecast to reach 71% by 2019.
- Usage per device is forecast to more than triple by 2019.
- 192 countries have active 3G mobile networks, which cover almost 50% of the global population.
- Smartphone sales are the majority of mobile handsets sold worldwide; tablet sales will soon exceed total PC sales.
- While there are at least five mobile platforms, Android has an 84% share of smartphones, and 72% of tablets.
- There are well over 1 million apps available, which have been downloaded more than 100 billion times.
- Time spent using apps exceeds time spent on mobile browsers, and in the US, at least, exceeds time spent on desktop and mobile browsers combined[3].

Usage of internet is spreading in all over the world and Turkey. Owing to its young generation Turkey is becoming one of the the leader countries in the world on behalf of internet usage.

The share of the population in Turkey ages 16 to 74 who use the internet has nearly doubled since 2008, from 32.2% to 58.3% in 2016, according to an August 2016 report by the Turkish Statistical Institute. While there are stil more male internet users than female, the growth from 2008 to this year is nearly identical across the genders.

While the percentage of the population that used the internet grown incrementally every year, the largest leap, for both genders and thus in total as well, came from 2015 to 2016.

In 2015, about 61% of the male population of Turkey were internet users; this year, that figure is nearly 68%. Women, meanwhile, jumped from 42% to 49% [6].

This study aims to analyze mobile device, computer, internet and social media use and habits in Turkey. A survey was conducted by habitants living in İstanbul. In the study demographics such as age, gender and education of participants analyzed. Also frequency of reasons of internet using such as social media, entertainment, information, news, travelling, shopping, communication and, internet using device such as mobile device or computer were analyzed.

II. METHOD

In this study, the results of the survey conducted by 442 participants living in İstanbul were analyzed. Questions about demographics, and internet usage habits were asked to responders. Data were analyzed by SPSS 21 package program.

III. RESULTS AND DISCUSSIONS

Demographics and internet usage habits of 442 participants were investigated and results were shown on Table 1.

Of 442 participants 55.7% were male and 44.3% were female. Most of the participants were between 20-30 (31.4%), 31-40 (27.6%) and 41-50 (24.7%). The majority of the participants had university degree (51.4%). A serious number of responders reported that they used internet everyday (44.1%) and more than three hours a day (40.9%). Most of the responders (67.6%) declared that they used mobile devices while using internet. Nearly 32% of participants reported that they used computers additionally. Most of participants were using internet for communication, information, social media and shopping.

Statistical analysis were conducted in order to find relationships between demographics and frequency of internet usage of participants. All results can be followed from Table 2.

It can be seen from Table 2 that there is a non significant relationship between gender and internet usage but it is obvious that young people utilizes internet more ($\chi^2=32,836$, $p<0,05$). Education plays an important role on internet usage, participants who are more educated utilize internet more ($\chi^2=49,356$, $p<0,01$).

Table1. Demographics and internet usage habits of participants

	N	(%)
Gender		
Female	196	44.3
Male	246	55.7
Age		
20-30	139	31.4
31-40	122	27.6
41-50	109	24.7
51-60	51	11.5
65+	21	4.8
Education		
High school	41	10.2
Vocational High School	71	16.1
University	227	51.4
Master	79	17.9
Phd	20	4.5
Frequency of Internet using		
Rarely	3	0.7
A few times a month	14	3.2
A few times a week	49	11.1
Every day	195	44.1
More than 3 hours a day	181	40.9
Internet using device		
Only mobile phone/tablet	299	67.6
Both mobile device and computer	143	32.4
Reason for internet usage		
Communication	121	27.37
Information	97	21.94
Social media	77	17.42
Shopping	66	14.93
News	34	7.69
Travelling	27	6.10
Other	20	4.52
Total	442	100

Table 2. Relations between demographic variables and internet usage frequency

	Internet usage frequency	
	χ^2	p
Gender	5,79	0,326
Age	32,836	0,035*
Education	49,356	0,003**

*p<0,05, **p<0,01

IV. CONCLUSION

In our study results of a survey conducted by 442 people living in İstanbul, Turkey and using internet actively are analyzed. We analyzed mobile device and internet usage habits in Turkey. It is found that young people and educated ones are using internet more frequently. This is in agreement with some studies [7,8,9] which found similar results as ours. In the study demographics such as age, gender and education of participants analyzed. As social media became a very important part of our lives most of the participants are using internet for social media. On the other hand internet is used for communication firstly for many responders. Most of our responders were young, so it is not surprising that accessing internet by mobile devices is more widespread among them.

REFERENCES

- [1] Vaala, S. E., Bleakle A. Monitoring, mediating, and modeling: Parental influence on adolescent computer and Internet use in the United States. *Journal of Children and Media* 9.1 (2015): 40-57.
- [2] Joiner, R, et al. "Comparing first and second generation digital natives' Internet use, Internet anxiety, and Internet identification." *Cyberpsychology, Behavior, and Social Networking* 16.7 (2013): 549-552.
- [3] Internet Society, Global Internet Report 2015, Available from: http://www.internetsociety.org/globalinternetreport/2015/assets/download/IS_web.pdf
- [4] Jelenchick, L. A., Skyler T. H., Megan A. M.. "Problematic internet use and social networking site use among Dutch adolescents." *International journal of adolescent medicine and health* 28.1 (2016): 119-121.
- [5] Ruggiero, T. E. (2000). Uses and gratifications theory in the 21st century. *Mass Communication and Society*, 3.1, 3-37.
- [6] Internet Usage Up in Turkey, Thanks in Part to Smartphones, Available from: <https://www.emarketer.com/Article/Internet-Usage-Up-Turkey-Thanks-Part-Smartphones/1014458>
- [7] Jiang, Qiaolei. "Internet addiction among young people in China: Internet connectedness, online gaming, and academic performance decrement." *Internet Research* 24.1 (2014): 2-20.
- [8] Zhong, Zhi-Jin. "Civic engagement among educated Chinese youth: The role of SNS (Social Networking Services), bonding and bridging social capital." *Computers & Education* 75 (2014): 263-273.
- [9] Akhtar, N. "Relationship between internet addiction and academic performance among university undergraduates." *Educational Research and Reviews* 8.19 (2013): 1793.

Evaluation of Technical Qualities Of Hospital Websites In Istanbul, Turkey

Rojan Gümüş

Dicle University, Diyarbakır Vocational School,
Dep. Of Computer Technologies, Diyarbakır, Turkey
gumusrojan@gmail.com

Yasin Sönmez

Dicle University, Diyarbakır Vocational School,
Dep. Of Computer Technologies, Diyarbakır, Turkey
yasin.sonmez@dicle.edu.tr

Abstract—In this study technical quality of 100 hospitals in Istanbul, Turkey were analyzed by a tool developed by writers. SSL (Secure Sockets Layer), downloading time, google page score, browser compatibility of the websites were analyzed. Also having mobile application template is a very important issue for webpages. Broken links on the web page is also another factor that always downgrades the quality of the website. The code to text ratio of a page is used by search engines and spiders to calculate the relevancy of a web page. Having a higher code to text ratio than your competitors gives you a good start for on-site optimization (seo chat). Meta elements are tags used in HTML and XHTML documents to provide structured meta data about web page, which can be used by search engines to help categorize the page correctly. Well-written meta tags can help make the page rank higher in search results. These features were analyzed by scoring each website.

In order to analyze technical features of hospital web pages we used some different methods. We utilized a web tool named R10.net-Webmaster Tools (r10net, www). It is a website to test technical quality of websites. Among these tools SSL Checker was used to check SSL certificates. To assess the sites' broken links we used Broken Link Checker. We used Website Speed Test to measure the loading time and Google speed scores. To evaluate the code to text ratio we used Website Code to Text Ratio Checker. For browser compatibility we used Responsive Design Checker. To determine meta tags information we used Website meta tag Xtractor. The evaluation process was conducted between 2.2.2017 and 7.2.2017. The time of evaluation was between 11:46 Am and 13:46 Am.

Keywords—Website, hospital, quality, technical, Istanbul

I. INTRODUCTION

An electronic commerce marketing channel is fully mediated by information technology, stripping away much of a product's physical informational cues, and creating information asymmetries (i.e., limited information). These asymmetries may impede consumers' ability to effectively assess certain types of products, thus creating challenges for online sellers [1,2].

To succeed in the highly competitive e-commerce environment, it is vital to understand the impact of website quality in enhancing customer conversion and retention. Although numerous contingent website attributes have been identified in the extant website quality studies, there is no unified framework to classify these attributes and no

comparison done between customer conversion and retention according to the different website quality attributes and their varying impact [3,4].

The rapid growth in use of the Internet and World Wide Web for acquiring health information has received a great deal of attention in recent years. In that time, the Web has been variously described as a harbinger of empowerment and as a threat to the wellbeing of patients.

Website credibility is one factor that consumers use to make judgments about the quality and utility of information posted on a site. As such, website credibility has the potential to influence consumer [decision-making](#) and health behaviors [5,6]

Usability is all about the practical considerations of what goes into good website design, such as speed, user-friendliness, security, technical details like sitemaps, etc. A lot of these details aren't visually apparent; you don't see a website's security when you type in its URL. Nonetheless, usability is a make-or-break issue for websites that work. If a visitor can't find what he or she is looking for because of poor navigation, he or she will usually leave. If pages take too long to load, both search engines and visitors will notice. So to see how usable your site is, ask yourself the following:

- How long does it take my pages to load, and will visitors get bored waiting? How easy is it to find information?
- Is there a search button for visitors?
- Do all the links work?
- Does the site work in different browsers? (Internet Explorer, Safari, Firefox, Chrome, etc.)
- Does my site work on mobile devices?
- If I'm asking for personal details or use a commerce option, is customer information secure? Have I communicated this to my readers? [7]

In this study websites of 100 hospitals in Istanbul were investigated according to their technical features. As it is very important for patients to access information about hospitals, websites have a crucial role for individuals. Also a technically strong website serves better and leads more people to prefer the hospital.

II. METHOD

In our study a cross sectional study was conducted analysing 100 private hospitals' websites. In İstanbul, among 172 private hospitals 135 have active web sites. We gave scores to websites objectively, by measuring some features. All scores were scaled according to frequencies of criteria and evaluated by a computer engineer and professional in the area of health management. Data were analyzed using descriptive and analytical statistics. The study data were collected by using a checklist.

For technologic evaluation of websites 8 subcategories were defined. For Presence of SSL certificate, Browser Compability and Mobile Application two scores were defined (Presence=1, Absence=0). On the other hand for broken links criterion it was opposite (Presence=0, Absence=1). As downloading time was mesured in seconds, metric of seconds were turned into scores, 1 for slowest, 2 for normal and 3 for fastest website respectively. Alsolikert scale was used in order to evaluate scores for google page scores and code to text ratio and meta tags information. By

the help of the checklist we could therefore calculate a score for each website and % of response defined as the percentage of items found over the total number of items. We calculated a mean website evaluation score for each dimension and calculated a mean website evaluation score for each of the four dimensions of the checklist to identify the strengthness and weakness of hospitals' online services.

III. RESULTS AND DISCUSSIONS

Scores of 100 hospital websites were analyzed and results were shown in Table 1.

The average % of response for Technical features was moderate (58,5%). Among Technical features, % of response of downloading time scores were highest (89%) and the second was browser compatibility (65%). It was found that only 54,40 % of them provided high google page score, while near 44% of them had mobile application. Only 56% of webpages don't have broken links. Regarding meta tag information criteria scores seemed to be lowest (39%).

Table1. Scores of 100 Hospitals' websites according to Technical features

Technical features	Score	%	Total Score	% of response
SSL Certificate				
Presence	1	59	59/100	59,0
Absence	0	41		
Downloading Time(in seconds)				
1,33- 2 sec	1	9	9	3,00
0,67- 1,32 sec	2	3	6	2,00
0-0,66 sec	3	88	264	88,00
Total		100	279/300	93,00
Google page score				
0-20	1	9	9	1,80
21-40	2	40	80	16,00
41-60	3	21	63	12,60
61-80	4	30	120	24,00
81-100	5	0	0	0
Total	100	100	272/500	54,40
Browser compatibility				
Presence	1	65	65/100	65,0
Absence	0	35		

Mobile application template				
Presence	1	43	43/100	43,0
Absence	0	57		
Absence of Broken Links				
Absence	1	56	56/100	56,0
Presence	0	44		
The code to text ratio (%)				
0-%3,2	1	5	5	1,00
3,21-6,4	2	36	72	14,40
6,41-9,6	3	32	96	19,20
9,61-12,8	4	22	92	18,40
12,81-16	5	5	25	5,0
Total			290/500	58,0
Meta tag information				
0	25	25	0	0
1	28	28	28	5,60
2	10	10	20	4,00
3	13	13	39	7,80
4	12	12	48	9,60
5	12	12	60	12,00
Total			195/500	39,00
Average % of response				58,5

REFERENCES

IV. CONCLUSION

Many health systems' websites have begun to include tools and information for both patients and visitors designed to make navigating complex health encounters more "user-friendly"; provide information about conditions, treatment, and follow-up; and create a positive organizational image [8,9]. If hospital websites are going to play an important role in delivering care information, it is likely that these sites will play a role in forming patients' expectations against which they will form service satisfaction judgments. To the extent that discharge instructions and other postcare information are made available through hospitals' websites, they may play a direct role in the care experience and influence patients' satisfaction assessments. [10].

We evaluated total scores of websites of hospitals in İstanbul and found that average score of them was moderate. As it is very important for consumers to access technically strong websites, patients also demand qualified service while accessing websites of hospitals. Hospital websites in İstanbul should be strength more.

- [1] Wells, J D , Joseph S. Valacich, and Traci J. Hess. "What signal are you sending? How website quality influences perceptions of product quality and purchase intentions." *MIS quarterly* (2011): 373-396.
- [2] Rainie, L. *Internet, broadband, and cell phone statistics*. Washington, DC: Pew Internet & American Life Project.(2010)
- [3] Kuan, H, et al. Comparing the effects of website quality on customer initial purchase and continued purchase at e-commerce websites . *Behaviour & Information Technology* 27.1 (2008): 3-16.
- [4] Jones, S., et al. *Generations online in 2009*. Washington, DC: Pew Internet &
- [5] American Life Project, 2009–2004 (2009).
- [6] Rains, S, et al. Health information-seeking and perceptions of website credibility: Examining Web use orientation, message characteristics and structural features of websites. *Computers in Human Behavior* 25.2 (2009): 544-553.
- [7] Loges, W, et al. Exploring the digital divide. *Communication Research*,28.5(2001):

Performance Comparisons of Chicken Swarm Algorithm with Swarm Inspired Metaheuristic Algorithms in Unconstrained Benchmark Functions

Elif Varol

Department of Software Engineering, Firat University
Elazig, Turkey
evarol@firat.edu.tr

Bilal Alatas

Department of Software Engineering, Firat University
Elazig, Turkey
balatas@firat.edu.tr

Abstract— Metaheuristic algorithms are very popular due to their many advantages and are used in many fields for search and optimization. Swarm intelligence is one of the most popular branch of metaheuristic algorithms and is developed by observing the movements of live swarms such as bird, fish, cat, and bee. In this paper, the performances of the newest swarm intelligence based search and optimization algorithms, namely; Chicken Swarm Optimization, Crow Search Algorithm, and Krill Herd Algorithm, have been compared in unimodal and multimodal unconstrained problems for the first time to the best of our knowledge. From the simulation results Chicken Swarm Optimization has shown better performances than other swarm based algorithm within both unimodal and multimodal test functions. Chicken Swarm Optimization is relatively new swarm intelligence based algorithm and it can be efficiently designed for different types of problems by proposing new versions and adjusting its parameters.

Keywords— Chicken Swarm Optimization, Metaheuristic Algorithms, Benchmark Functions

I. INTRODUCTION

Metaheuristic optimization algorithms are algorithms that produce solutions that are close to optimum in the acceptable time for large-scale optimization problems. They are recently getting strong and increasingly increasing its popularity. They are used extensively in various fields such as management, computer, engineering due to advantages such as not having difficult mathematical models to set up, good calculation powers, and requiring no change on the interested problems like classical algorithms and new versions are proposed. Recently, the herd-based optimization algorithms, developed inspired by the herd-like behavior of the living, have begun to become popular in the solution of many complex problems that can take a long time to solve, even if the mathematical model cannot be created or created [1].

General purposed metaheuristic optimization algorithms are evaluated in eight different groups including biology-based, physics-based, swarm-based, social-based, music-based, chemistry-based, sports based, and mathematics based. Genetic Algorithm, Differential Evolution Algorithm, and Ant Colony

Algorithm are biology based; Water Cycle Algorithm, Electromagnetism Algorithm, Artificial Physics Optimization Algorithm are physics based; Tabu Search Algorithm, Imperialist Competitive Algorithm, Social Emotional Optimization Algorithm, Teaching-Learning Based Optimization Algorithm, Brain Storm Optimization Algorithm, Social Based Algorithm, Parliamentary Optimization Algorithm are social based; Artificial Chemical Reaction Optimization Algorithm is chemistry based; Harmony Search Algorithm is musical based; League Championship Algorithm is sports based algorithms and models. Although there are many effective and successful methods that have been introduced to the literature, there have not been any algorithm that can solve all types of problems effectively. New algorithms are introduced and suggestions are given in order to improve the effectiveness of existing versions. Especially in recent years, researchers have introduced such new metaheuristic methods to the literature and performed successful applications [2].

There are many metaheuristic optimization methods that are based on swarm intelligence. Swarm intelligence based optimization algorithms have been developed by observing the movements of live swarms such as bird, fish, cat, and bee. Some of the search and optimization algorithms based on swarm intelligence can be listed as: Particle Swarm Optimization (PSO), Ant Colony Algorithm, Artificial Bee Colony, Bird Swarm Algorithm, Swallow Swarm Algorithm, Chicken Swarm Optimization (CSO), Crow Search Algorithm (CSA) [3], Krill Herd Algorithm (KHA) [4]. CSO, CSA, and KHA are some of the newest swarm based metaheuristic algorithm. CSO aims to simulate the intelligent behavior of the chickens to find the solution of search and optimization problems.

In this paper, the operators of CSO have been introduced and the comparative results obtained from other novel metaheuristic algorithms (CSA, KHA) for different benchmark functions have been presented. In Section 2, CSO has been explained. Section 3 defines the benchmark functions used for comparisons. Section 4 presents the experimental results and finally Section 5 concludes the paper along with future research directions.

II. CHICKEN SWARM OPTIMIZATION

Chicken Swarm Optimization (CSO), an optimization algorithm based on swarm intelligence, was proposed by Meng et al. in 2014 [5]. It mimics the hierarchal order in the chicken swarm and the behaviors of the chicken swarm. CSO can efficiently extract the chickens swarm intelligence to optimize problems. The chicken swarm can be divided into several groups, each of which consists of one rooster and many hens and chicks. CSO consists of 4 rules.

- (1) There are several groups of chickens. Each group comprises a dominant rooster, a couple of hens and chicks.
- (2) Chicken swarm are divided into various groups and suitability values are used to identify the identity of the chickens (rooster, hens, chicks). Each of the chickens with the best fitness value behaves like a head cock in a group. Chickens with the worst fitness values would be determined as chicks. The rest would be hens. The hens randomly choose which group to live in. Mother-child relationships are also randomly established between hens and chicks.
- (3) Hierarchical order, dominance relationship, and mother-child relationship in a group remain unchanged. These situations only update every several time steps.
- (4) Chickens are watching their group mate rooster to search for food, when they can prevent ones from eating their own food. It is assumed that chickens have stolen randomly the food previously found by others. The chicks search for food around their mother (hen) and the dominant individuals have considered advantage in competition for food [5].

Chicken Swarm Optimization. Framework of the CSO

```

Initialize a population of  $N$  chickens and define the related parameters;
Evaluate the  $N$  chickens' fitness values,  $t=0$ ;
While ( $t < \text{Max\_Generation}$ )
    If ( $t \% G = 0$ )
        Rank the chickens' fitness values and establish a hierarchal order in the swarm;
        Divide the swarm into different groups, and determine the relationship between the
        chicks and mother hens in a group; End If
    For  $i = 1 : N$ 
        If  $i == \text{rooster}$  Update its solution/location; End If
        If  $i == \text{hen}$  Update its solution/location; End If
        If  $i == \text{chick}$  Update its solution/location ; End If
    Evaluate the new solution;
    If the new solution is better than its previous one, update it;
End For
End While

```

III. BENCHMARK FUNCTIONS

Well-defined benchmark functions based on mathematical functions can be used to measure and test the performance of optimization methods. The nature, complexity, and other characteristics of these benchmark functions can easily be derived from their definitions and have the nature and complexity of most engineering problems. The selected benchmark functions and its properties have been demonstrated in Table I. Sphere function and Chung Reynolds function are unimodal with less complexity and they can be used to evaluate the converging behaviors of algorithms [6, 7]. Ackley function and Griewank function are multi-modal functions with many

local optima and they can be used to test the global search ability of the algorithms in avoiding premature convergence [8, 9]. Their graphs with two dimensions have been shown in Figure 1, Figure2, Figure3, and Figure4.

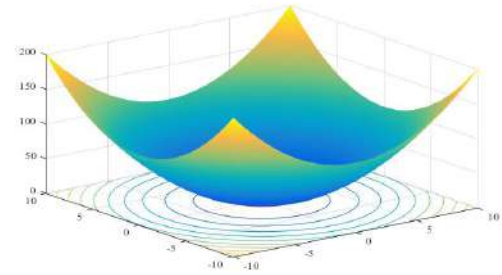


Fig 1. Sphere function with two variables

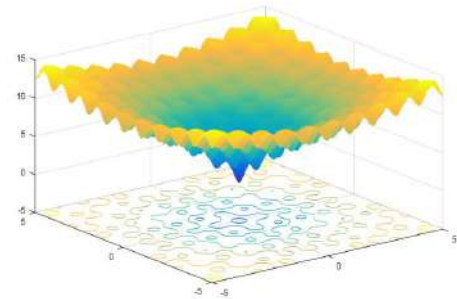


Fig 2. Ackley function with two variables

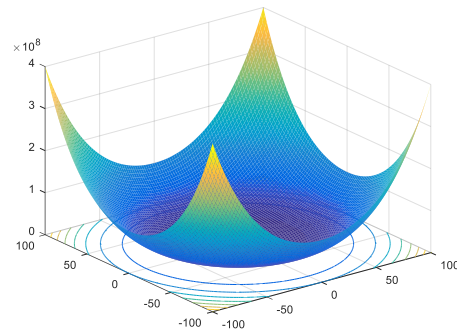


Fig 3. Chung Reynolds function with two variables

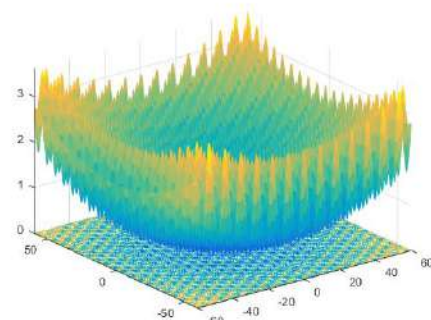


Fig 4. Griewank function with two variable

TABLE V. BENCHMARK FUNCTIONS

Function No	Function Name	Definition	Interval	Dimension	Global Minimum
F ₁	Sphere	$f_1(x) = \sum_{i=1}^d x_i^2$	$-5.12 \leq x_i \leq 5.12$	30	0
F ₂	Ackley	$f_2(x) = a \exp \left(-b \sqrt{\frac{1}{d} \sum_{i=1}^d x_i^2} \right) - \exp \left(\frac{1}{d} \sum_{i=1}^d \cos(cx_i) \right) + a + \exp(1)$	$-50 \leq x_i \leq 50$	30	0
F ₃	Chung Reynolds	$f_3(x) = \left(\sum_{i=1}^d (x_i^2) \right)^2$	$-100 \leq x_i \leq 100$	30	0
F ₄	Griewank	$f_4(x) = \frac{1}{4000} \sum_{i=1}^d (x_i)^2 - \prod_{i=1}^d \cos \left(\frac{x_i}{\sqrt{i}} \right) + 1$	$-600 \leq x_i \leq 600$	30	0

IV. EXPERIMENTAL RESULTS

The obtained results from CSO for Sphere function have been compared with those obtained from other newest swarm based algorithms named CSA and KHA. Simulation has been run 30 times with different numbers of initial population size (10, 30, 50, and 100) for all of the algorithms. Dimension is 30 and the maximum iteration number is 1000 for all of the algorithms. The results have been shown in Table II. From these reported results, CSO has better performance than other used swarm based algorithm.

The obtained results from CSO for Ackley function have been compared with those obtained from other newest swarm inspired metaheuristic methods named, CSA and KHA. All of the algorithms have been run 30 times with different numbers of initial population size (10, 30, 50 and 100). Dimension is selected as 30 and the maximum iteration number is selected as 1000 for all of the algorithms. The results have been shown in Table III. According to the results of this experiment, CSO has better performance than other used swarm based algorithm.

The obtained results from CSO for Chung Reynolds function have been compared with those obtained from CSA

and KHA. Algorithms have been run 30 times with different numbers of initial population size (10, 30, 50, and 100). Dimension is 30 and the maximum iteration number is 1000 for all of the algorithms.

The results have been shown in Table IV. According to the results of this experiment, CSO has better performance than other selected swarm based algorithm.

The obtained results from CSO for Griewank function have been compared with those obtained from other newest swarm inspired metaheuristic methods named, CSA and KHA. All of the algorithms have been run 30 times with different numbers of initial population size (10, 30, 50, and 100). Dimension is selected as 30 and the maximum iteration number is selected as 1000 for all of the algorithms.

The results have been shown in Table V. According to the results of this experiment, CSO has better performance than other used swarm based algorithms.

TABLE VI. OBTAINED RESULTS FOR SPHERE FUNCTION FROM CSO, CSA, AND KHA WITH POPULATION SIZE 10, 30, 50, AND 100

Initial population size	10			30			50			100		
	CSO	CSA	KHA	CSO	CSA	KHA	CSO	CSA	KHA	CSO	CSA	KHA
Mean	1.46E-37	0.00950	1.050e-004	7.72957E-55	0.00024	2.49e-007	3.91592E-49	4.00E-05	1.1539e-007	2.0071E-54	3.02E-06	1.655e-008
Best	1.31E-47	0.00184	1.58378e-007	3.02389E-43	7.873E-05	1.462e-008	3.92415E-57	1.69E-05	1.1086e-009	2.47284E-59	9.47E-07	3.20e-010
Worst	3.06E-36	0.03341	0.0028	1.80846E-44	0.00078	2.04e-006	9.67945E-48	1.04E-04	6.6398e-007	2.42315E-53	6.83E-06	1.098e-007

TABLE VII. OBTAINED RESULTS FOR ACKLEY FUNCTION FROM CSO, CSA, AND KHA WITH POPULATION SIZE 10, 30, 50, AND 100

Initial population size	10			30			50			100		
	CSO	CSA	KHA	CSO	CSA	KHA	CSO	CSA	KHA	CSO	CSA	KHA
Mean	0.680190729	6.093735	1.09496	6.4541E-15	3.989244	0.03855	6.57252E-15	3.48773	0.054877	5.50671E-15	2.673442	2.3525e-007
Best	4.44089E-15	3.421174	3.8894e-004	4.44089E-15	2.677627	5.7023e-007	4.44089E-15	1.350876	6.0554e-008	4.44089E-15	0.932467	1.74318e-009
Worst	20.40572187	9.171448	4.4234	7.99361E-15	5.534855	1.156223	1.5099E-14	5.952686	1.64622	7.99361E-15	4.211573	3.34543e-006

TABLE VIII. OBTAINED RESULTS FOR CHUNG REYNOLDS FUNCTION FROM CSO, CSA, AND KHA WITH POPULATION SIZE 10, 30, 50, AND 100

Initial population size	10			30			50			100		
	CSO	CSA	KHA	CSO	CSA	KHA	CSO	CSA	KHA	CSO	CSA	KHA
Mean	1.85709E-61	7.958515	8.57832	1.71851E-81	0.01564	0.02620	1.27695E-88	0.00025	0.021108	5.76084E-96	1.55E-06	0.014912
Best	1.94092E-90	1.094479	0.03158	3.94381E-97	0.00098	0.01638	7.5804E-108	9.46718E-06	0.01274	2.2564E-115	1.85E-07	0.00726
Worst	5.57097E-60	30.91199	20.00803	3.53303E-80	0.07988	0.038907	3.8277E-87	0.001106	0.03305	1.20104E-94	9.81E-06	0.02098

TABLE IX. OBTAINED RESULTS FOR GRIEWANK FUNCTION FROM CSO, CSA, AND KHA WITH POPULATION SIZE 10, 30, 50, AND 100

Initial population size	10			30			50			100		
	CSO	CSA	KHA	CSO	CSA	KHA	CSO	CSA	KHA	CSO	CSA	KHA
Mean	0.023663	1.003562	0.2188461	0.012765	0.310247	0.1387886	3.70067E-14	0.100045	0.1162738	0	0.030674	0.102058
Best	0	0.84116403	0.0597388	0	0.157124	0.03035584	0	0.056576	0.0409914	0	0.010692	0.026879
Worst	0.4078	1.07897596	0.3731231	0.1467	0.44507	0.32472798	1.11E-12	0.166959	0.2224144	0	0.0857	0.18661

V. CONCLUSIONS

Metaheuristic methods are very popular and efficiently used in many complex real world search and optimization problems. Due to the philosophy of continually searching the best and absence of the most efficient metaheuristic method for all types of problems, novel algorithms or new versions of current algorithms are being proposed. Chicken Swarm Optimization (CSO) is one of the newest swarm intelligence based metaheuristic algorithm and aims to simulate the intelligent behavior of the chickens to find the solution of search and optimization problems. In this paper, the performances of the newest swarm intelligence based search and optimization algorithms, namely; Chicken Swarm Optimization, Crow Search Algorithm, and Krill Herd Algorithm, have been compared in unimodal and multimodal unconstrained problems for the first time to the best of our knowledge. From the experimental results CSO has shown better performances than other swarm based algorithms within both unimodal and multimodal test functions. CSO is relatively new swarm intelligence based algorithm and it can be efficiently designed for different types of problems by proposing new versions and adjusting its parameters efficiently and dynamically.

In general, it is expected that the algorithm will be used effectively in many problems in the future because CSO provides good results in both unimodal and multimodal benchmark functions. Since CSO is still new, single and

multidimensional chaotic maps, orthogonal arrays and uniform population can be used for initializing the algorithm to improve the performance. In addition, multi-objective, distributed, and parallel versions of the algorithm can be proposed and effectively used in different search and optimization problems.

REFERENCES

- [1] G.A.E.A. Said, A. M. Mahmoud, E. M. El-Horbaty, "A comparative study of meta-heuristic algorithms for solving quadratic assignment problem". *IJACSA* 5, 1- 6, 2014
- [2] M. Canayaz, "Çırcır Böceği Algoritması: Yeni Bir Metasezgisel Yaklaşım ve Uygulamaları", Doktora Tezi, 2015.
- [3] A. Askarzadeh, "A Novel Metaheuristic Method for Solving Constrained Engineering Optimization Problems: Crow Search Algorithm", *Computers & Structures*, vol. 169, pp. 1-12, 2016.
- [4] A. H. Gandomi, A. H. Alavi, "Krill herd: A new bio-inspired optimization algorithm", *Elsevier Communications in Nonlinear Science and Numerical Simulation*, Volume 17, Issue 12, pp 4831-4845, 2012
- [5] X. Meng, Y. Liu, X. Gao, H. Zhnag, "A New Bio-inspired Algorithm: Chicken Swarm Optimization", *Advanced in Swarm Intelligence*, 5th International Conference, ICSI 2014, pp 86-94
- [6] (January 2017) GEATbx: Examples of Objective Functions. Available: <http://www.pg.gda.pl/~mkwies/dyd/geadocu/fcnfun1.html>
- [7] <http://al-roomi.org/benchmarks/unconstrained/n-dimensions/165-chung-reynolds-function>
- [8] (January 2017) GEATbx: Examples of Objective Functions. Available: <http://www.pg.gda.pl/~mkwies/dyd/geadocu/fcnfun10.html>
- [9] (January 2017) GEATbx: Examples of Objective Functions. Available: <http://www.pg.gda.pl/~mkwies/dyd/geadocu/fcnfun8.html>

An Image Processing based Object Counting Approach for Machine Vision Application

Mehmet BAYGIN¹, Mehmet KARAKOSE²

Computer Engineering Department

¹Ardahan University, 75000

Ardahan, Turkey

mehmetbaygin@ardahan.edu.tr, mkarakose@firat.edu.tr

Alisan SARIMADEN³, Erhan AKIN²

Computer Engineering Department

²Firat University, 23119

Elazig, Turkey

medel@medelektronik.com, eakin@firat.edu.tr

Abstract—Machine vision applications are low cost and high precision measurement systems which are frequently used in production lines. With these systems that provide contactless control and measurement, production facilities are able to reach high production numbers without errors. Machine vision operations such as product counting, error control, dimension measurement can be performed through a camera. In this paper, a machine vision application is proposed, which can perform object-independent product counting. The proposed approach is based on Otsu thresholding and Hough transformation and performs automatic counting independently of product type and color. Basically one camera is used in the system. Through this camera, an image of the products passing through a conveyor is taken and various image processing algorithms are applied to these images. In this approach using images obtained from a real experimental setup, a real-time machine vision application was installed. As a result of the experimental studies performed, it has been determined that the proposed approach gives fast, accurate and reliable results.

Keywords—otsu threshold; hough circle; object counting; image processing.

I. INTRODUCTION

Production lines have become very easily controllable and auditable with machine vision applications [1, 2]. With these systems measurement operations can be carried out without the need for an expert control. These measurements are made in a completely non-contact manner, and defective products are sorted out as they pass through the conveyor [3]. Very fast machine vision systems allow for many measurements in a short period of time. This increases the instantaneous production capacity of production facilities. It is critical that machine vision based applications are able to work with near perfect precision [4, 5]. The products to be delivered to the end user must be complete, exact and identical, and are the most important criteria in these applications [6].

A conveyor is basically a system in which products are passed over and faulty products are sorted out on this band. An image of the products through a camera integrated in this system is taken and the faulty products are determined [7]. The general structure of these systems is shown in Fig. 1.

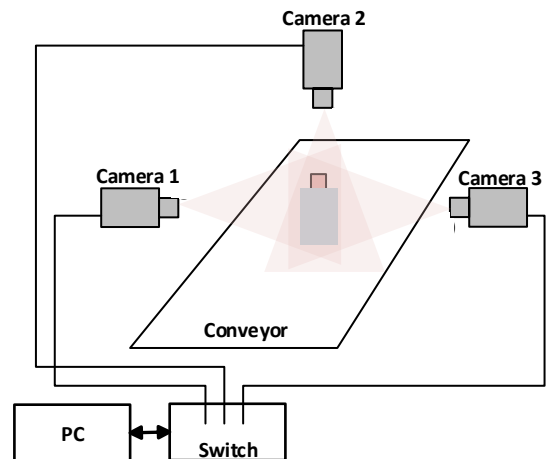


Fig. 8. General structure of machine vision systems [7]

Object counting is a frequently encountered problem in many machine vision applications [8]. Especially in production systems operating at high speed, it is very difficult to perform measurement without using computer vision. Object counting is a frequently encountered problem in many machine vision applications. Especially in production systems operating at high speed, it is very difficult to perform measurement without using computer vision. As a result, the use of machine vision systems becomes essential. In one of these studies using high speed cameras, products passing through the conveyor were recorded via a camera capable of recording 60 fps. In this study, basement background extraction was performed and moving objects were detected. Then, it is checked whether the objects in a specified area pass or not, and the counting process is performed. A block diagram summarizing this proposed approach is as shown in Fig. 2 [9].

Image processing based computer vision applications use many different areas. In one of the works carried out for this purpose, image processing is used for diagnosing the fault. In the proposed method, pantograph catenary images taken from the railway are used. Images were thresholded using the otsu method. The obtained results were combined with the time series and particle swarm optimization to detect faults. The flow diagram of the proposed method is given in Fig. 3. [10].

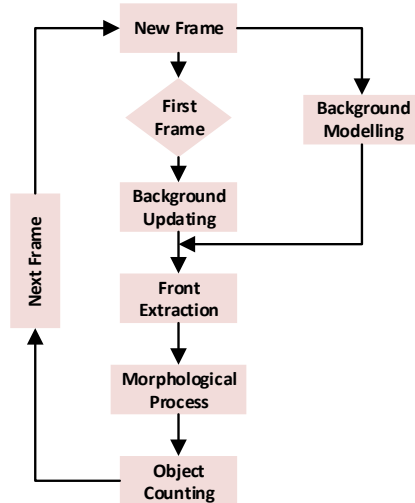


Fig. 9. A proposed approach in the literature [9]

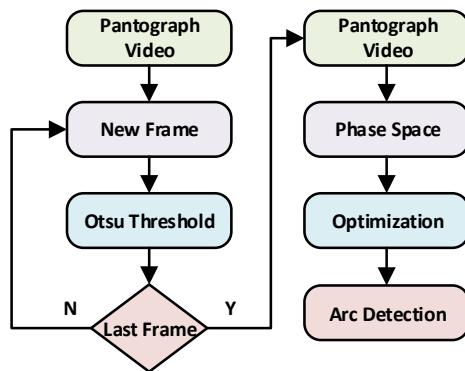


Fig. 10. A proposed approach in the literature [10]

In a study related to the subject, an application was developed to detect biscuit cracks for quality control. In the study, the characteristics of the cracks were determined using Hough transformation, Canny filter and Laplace edge extraction [11]. In another study, object counting was performed. In this application, which is performed for counting the objects which are overlaid, the boundaries of the objects are determined and the counting process is performed with classical geometric operations [12]. Khlule and dig. [13] performs the counting of the objects contained within the tablets. The proposed approach includes the steps of input image, preprocessing, segmentation and counting. The automatic counting method proposed in this study is tested on two applications and high performance is achieved.

In this study, an automatic object counting method based on grassy thresholding has been developed. Images of products passing through a moving conveyor were taken through a camera and pre-processed. Later, Otsu and Hough methods were applied to these images, and the detection and counting of the products was performed. Eggs and soda bottles were used in the tests and high precision counting process was performed.

II. PROPOSED METHOD

The object counting process that is frequently encountered in machine vision applications are used in many areas. Detection of objects on conveyors running at high speed and counting with high precision is a very important issue. The counting of the objects in the egg and soda bottle packets performed with the proposed approach in this study. The proposed approach works independently of the object type in real time. Sample images of the objects used in the study are shown in Fig. 4.

The study mainly involves the monitoring, detection and counting of the products passing through the conveyor by means of a camera. For this purpose, Otsu thresholding and Hough transformations were used. The images used in the study were obtained from a system that operates in real time. A camera that monitors the conveyor from above is integrated into the system and the images of the products are taken instantaneously. The steps of the machine vision based automated product counting approach proposed in this study are presented in Fig. 5.

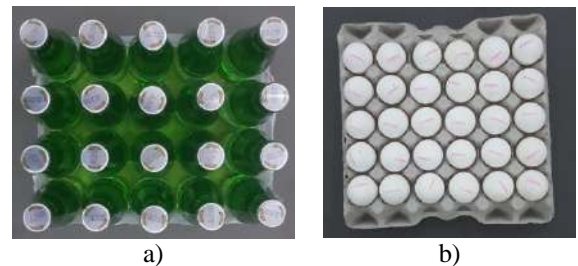


Fig. 11. Sample images a) Soda bottle pack b) Egg packet

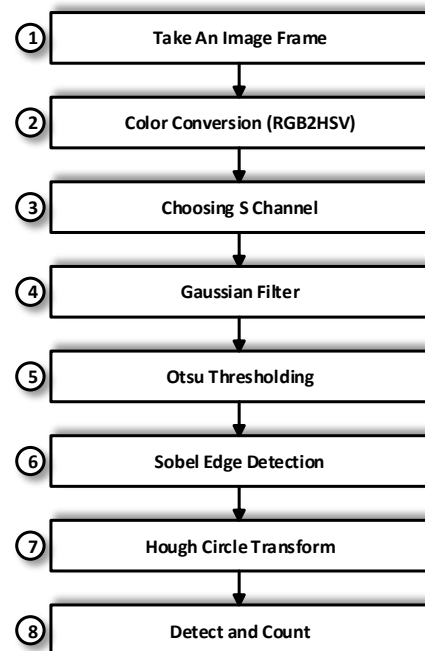


Fig. 12. A block diagram of proposed method

The proposed approach first takes an image of the object through the camera. The image in RGB color format is converted into HSV color space. The aim of this transformation is to be able to obtain the details of the image more clearly, independent of the light conditions [14]. Only the saturation (S) channel is used in the system after this conversion. The conversion from RGB color space to HSV color space and the calculation of S channel are given in Equation 1.

$$\begin{aligned} MAX &= \max\{R, G, B\} \\ MIN &= \min\{R, G, B\} \\ S &= \begin{cases} 0, & \text{if } MAX = 0 \\ 1 - \frac{MIN}{MAX}, & \text{else} \end{cases} \end{aligned} \quad (1)$$

After reducing the image to single channel, this image is subjected to a Gaussian filter. The general mathematical expression of this filter used to eliminate the noises on the image is presented in Equation 2.

$$G(r) = \frac{1}{(2\pi\sigma^2)^{w/2}} e^{-r^2/(2\sigma^2)} \quad (2)$$

The threshold values in the image can be determined adaptively by the Otsu threshold method. Techniques using this process in the literature generally work according to the two-level Otsu method [15]. Three-level Otsu method was developed and used in this study. With this approach, adaptive 3 different threshold levels are determined and the image applied by gauss filter is divided into 4 color ranges. In this process the aim is to reveal all the details in the image. In the other step of the proposed approach, edge detection of the thresholded image is performed. Sobel edge detection method is used in this process. The reason why this method is preferred is that it is very easy to apply. Basically, two convolution matrices, called G_x and G_y , are the process of navigating through the image data [16, 17]. These convolution matrices are given in Equation 3.

$$G_x = \begin{bmatrix} -1 & 0 & 1 \\ -2 & 0 & 2 \\ -1 & 0 & 1 \end{bmatrix}, \quad G_y = \begin{bmatrix} 1 & 2 & 1 \\ 0 & 0 & 0 \\ -1 & -2 & -1 \end{bmatrix} \quad (3)$$

Hough transformation is used in the last step of the proposed method. This method basically works with the ratios of the geometric shapes of the edges [18, 19]. With this method applied to the image removed the edges, geometric objects in the image can be detected. A pseudo code fragment shows the flow of this method are given in Fig. 6.

The Hough transformation marks the geometric shapes identified as the working principle and finds the center of these shapes [20, 21]. In this sense, there is no need for a process such as determining the boundaries of objects again. In this case, the algorithm does not perform any extra processing and contributes to the algorithm in terms of time.

```

For each pixel (x,y)
  For each radius r=10 to r=60
    For each theta t=0 to 360
      a=x - r * cos(t * PI/180);
      b=y - r * sin(t * PI/180);
      A[a, b, r] + = 1;
    end
  end
end

```

Fig. 13. A pseudo code for Hough circle transform

III. EXPERIMENTAL RESULTS

The data obtained in this study was obtained from a real-time working system. For this purpose, a camera has been installed which continuously monitors the conveyor. This camera has a capacity of 60 frames per second. Imagery from the camera is instantly transferred to a computer via the Ethernet port. On the computer side of the system, an automatic object counting algorithm developed within the scope of the study is carried out. A block diagram summarizing the experimental setup presented is shown in Fig. 7. Detailed features such as resolution, frame rate of the camera used in the study are given in Table 1.

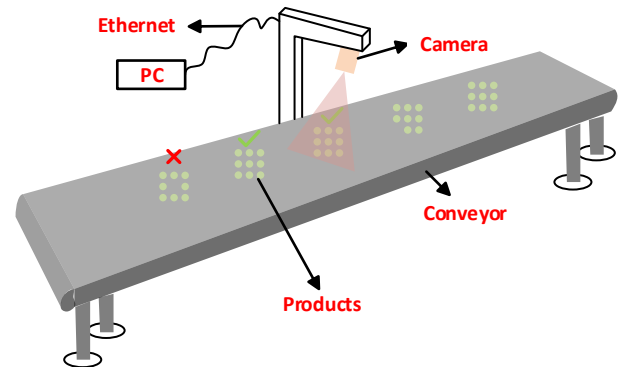


Fig. 14. A pseudo code for Hough circle transform

TABLE I. CAMERA FEATURES USED STUDY

Camera Features	
Feature	Values
Resolution	1280x720 px
Frame Rate	59 fps
Shutter Type	Global
Sensor Type	CCD
Interface	GigE
Pixel Bit Depth	12 bit
Mono/Color	Color

In this study, the test procedures were performed for two different product groups. These products are egg and soda bottles respectively. The same procedure was applied to both test groups and successful results were obtained. The sample image processing results obtained by applying the proposed approach on egg packages are given in Fig. 8.

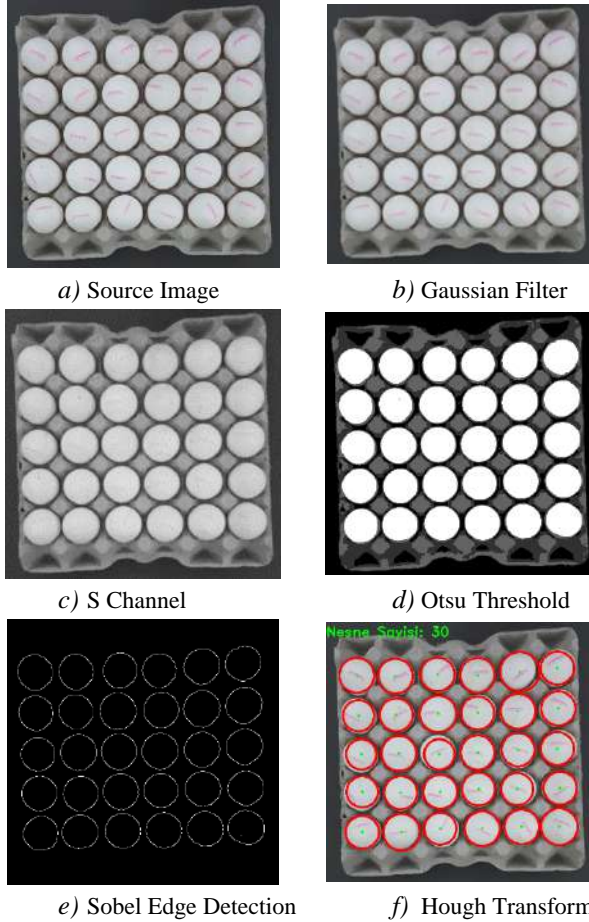


Fig. 15. The proposed automatic object counting method

As can be seen from Fig. 8, the method basically consists of 8 steps. In this frame, the egg packages were tested under different conditions. The sample results from these tests are shown in Fig. 9.

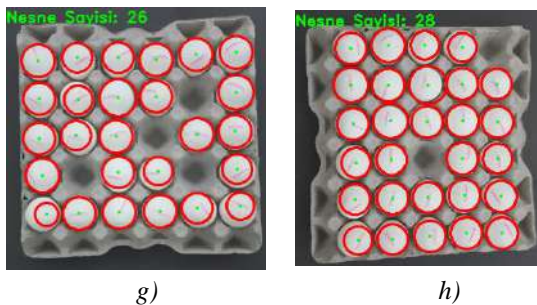


Fig. 16. The example test results for egg packets

As mentioned at the beginning of the section, the studies was carried out for two different product groups. One of these products is soda bottle packages. All of the steps of the image processing application are implemented in these images and good results are obtained. The results of the image processing algorithm performed for this product group are presented in Fig. 10.

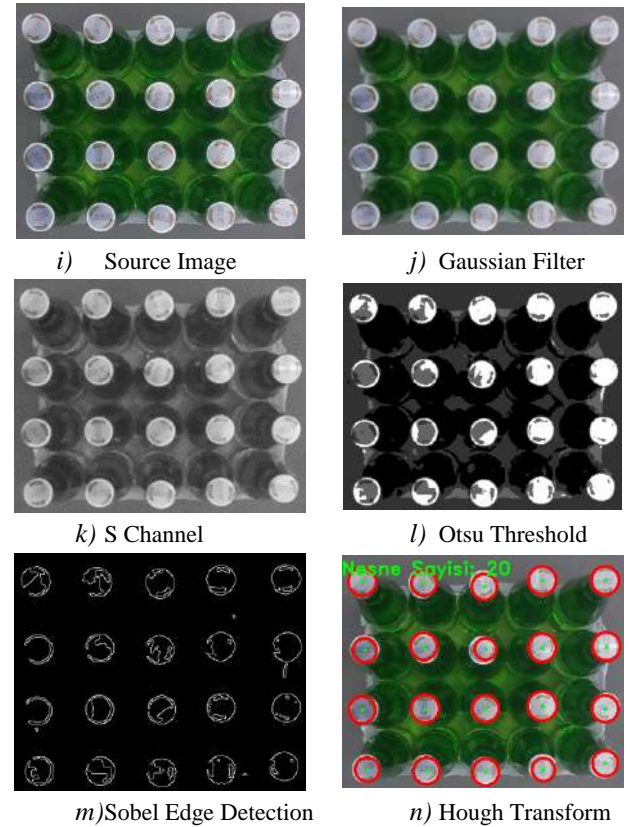


Fig. 17. Steps of the proposed approach

All the steps of the proposed approach are tested in this product group and very good results are obtained. As in the case of egg packages, test procedures were performed in different conditions within these products and the results of these tests are given in Fig. 11.

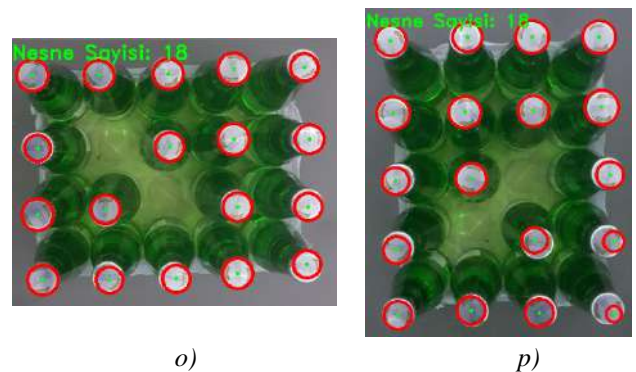


Fig. 18. The example test results for soda bottle packets

IV. CONCLUSIONS

Today, machine vision applications are actively used almost entirely in production systems. Especially contactless measurement is preferred because of its ability to provide high speed and precise measurement. Machine vision based systems have the some advantages such as low installation and maintenance costs as well as excellent production capacity of these systems.

In this paper, object counting, which is a frequently encountered problem in machine vision, has been performed. When the studies done in the literature are examined, it is seen that the applications carried out are directed to a specific product group. With the proposed approach, we have come from the top of this situation and have been able to count different product groups with a single algorithm. For this purpose, Otsu thresholding and Hough transformation methods are used. The images were taken in real time from a conveyor and tested with the machine vision application suggested in the study. When compared with the current studies in the literature, the proposed approach has shown that the method can measure accurately, quickly and with high accuracy.

ACKNOWLEDGMENT

This study has been supported by The Scientific and Technological Research Council of Turkey (SANTEZ Programme) under Research Project No: 0743.STZ.2014 (TUBITAK Grant No:112D021).

REFERENCES

- [1] P. H. Perera, W. S. K. Fernando, H. M. S. P. B. Herath, G. M. R. I. Godaliyadda, M. P. B. Ekanayake, and J. V. Wijayakulasooriya, "A generic object counting algorithm under partial occlusion conditions," 8th IEEE International Conference on Industrial and Information Systems (ICIIS), Sri Lanka, 2013, pp. 554-559.
- [2] P. Thammasorn, S. Boonchu, and A. Kawewong, "Real-time method for counting unseen stacked objects in mobile," 20th IEEE International Conference on Image Processing (ICIP), Melbourne, Australia, 2013, pp. 4103-4107.
- [3] M. S. Raman, and M. Sukanya, "A novel labelling algorithm for object counting," Third International Conference on Computing Communication & Networking Technologies (ICCCNT), Coimbatore, India, 2012.
- [4] J. Ni, Z. Khan, S. Wang, K. Wang, and S. K. Haider, "Automatic detection and counting of circular shaped overlapped objects using circular hough transform and contour detection," 12th World Congress on Intelligent Control and Automation (WCICA), Guilin, China, 2016, pp. 2902-2906.
- [5] S. Rahman, and R. Islam, "Counting objects in an image by marker controlled watershed segmentation and thresholding," IEEE 3rd International Advance Computing Conference (IACC), Ghaziabad, India, 2013, pp. 1251-1256.
- [6] S. Subramanian, and L. V. Bhadrinarayana, "A Memory Efficient Algorithm for Real Time Object Counting," IEEE International Advance Computing Conference (IACC), Patiala, India, 2009, pp. 245-248.
- [7] M. Baygin, and M. Karakose, "A new image stitching approach for resolution enhancement in camera arrays," 9th International Conference on Electrical and Electronics Engineering (ELECO), Bursa, Turkey, 2015, pp. 1186-1190.
- [8] P. S. Khude, and S. S. Pawar, "Object detection, tracking and counting using enhanced BMA on static background videos," IEEE International Conference on Computational Intelligence and Computing Research (ICCIC), Tamilnadu, India, 2013.
- [9] M. Karakose, M. Baygin, I. Aydin, A. Sarimaden, and E. Akin, "Endüstriyel Sistemlerde Arkaplan Çıkarımı Tabanlı Hareketli Nesne Tespiti ve Sayılması için Yeni Bir Yaklaşım," Muş Alparslan Üniversitesi Fen Bilimleri Dergisi, 2016, vol. 4, no. 2, pp. 373-381.
- [10] O. Yaman, M. Karakose, and E. Akin, "PSO Based Diagnosis Approach for Surface and Components Faults in Railways," International Journal of Computer Science and Software Engineering (IJCSE), 2016, vol. 5, no. 5, pp. 89-96.
- [11] S. Nashat, A. Abdullah, and M. Z. Abdullah, "Machine vision for crack inspection of biscuits featuring pyramid detection scheme," Journal of Food Engineering, 2014, vol. 120, pp. 233-247.
- [12] S. Bera, "Partially occluded object detection and counting," Third International Conference on Computer, Communication, Control and Information Technology (C3IT), Hooghly, India, 2015.
- [13] A. A. Khule, M. S. Nagmode, and R. D. Komati, "Automated object counting for visual inspection applications," International Conference on Information Processing (ICIP), Quebec City, Canada, 2015, pp. 801-806.
- [14] M. Karakose, and M. Baygin, "Image processing based analysis of moving shadow effects for reconfiguration in pv arrays," IEEE International Energy Conference (ENERGYCON), Dubrovnik, Croatia, 2014, pp. 683-687.
- [15] D. AlSaeed, A. Bouridane, and A. El-Zaart, "A novel fast Otsu digital image segmentation method," International Arab Journal of Information Technology, 2016, vol. 13, no. 4, pp. 344-427.
- [16] O. R. Vincent, and O. Folorunso, "A descriptive algorithm for sobel image edge detection," In Proceedings of Informing Science & IT Education Conference (InSITE), 2009, vol. 40, pp. 97-107.
- [17] G. T. Shrivakshan, and C. Chandrasekar, "A comparison of various edge detection techniques used in image processing," IJCSI International Journal of Computer Science Issues, 2012, vol. 9, no. 5, pp. 272-276.
- [18] O. Yaman, M. Karakose, I. Aydin, and E. Akin, "Detection of pantograph geometric model based on fuzzy logic and image processing," 22nd Signal Processing and Communications Applications Conference (SIU), Trabzon, Turkey, 2014, pp. 686-689.
- [19] A. Herout, M. Dubska, and J. Havel, "Review of hough transform for line detection," In Real-Time Detection of Lines and Grids, 2013, Springer London, pp. 3-16.
- [20] Y. J. Cha, K. You, and W. Choi, "Vision-based detection of loosened bolts using the Hough transform and support vector machines," Automation in Construction, 2016, vol. 71, pp. 181-188.
- [21] L. Baker, S. Mills, T. Langlotz, and C. Rathbone, "Power line detection using Hough transform and line tracing techniques," IEEE International Conference on In Image and Vision Computing (IVCNZ), New Zealand, 2016, pp. 1-6.

Performance Analysis of Social Spider Optimization within Unconstrained Problems

Cem Baydogan

Department of Software Engineering
Firat University
Elazig, Turkey
cembaydogan@gmail.com

Bilal Alatas

Department of Software Engineering
Firat University
Elazig, Turkey
balatas@firat.edu.tr

Abstract— Swarm intelligence is a study area that investigates the behavior of insects or other animals herd with a collective manner of intelligence. In this study, the performance of an algorithm called Social Spider Optimization (SSO) proposed for herd intelligence has been investigated. The SSO algorithm is based on the simulation of the behavior of spiders in collaboration. The SSO algorithm performance, stability, and sensitivity are compared with Ant Lion Optimization (ALO) and Moth Flame Optimization (MFO). The success of the algorithm is examined using Uni-Modal (UM) and Multi-Modal (MM) benchmark functions. The results are presented in tables and graphs. It is predicted that the SSO algorithm will make a lot of attention in the literature.

Keywords—Optimization, Heuristic Algorithms, Swarm Intelligence, Benchmark Test Functions, Social Spider Algorithm (SSO), Ant Lion Optimization (ALO), Moth Flame Optimization (MFO)

I. INTRODUCTION

The intelligent behavior of many animal or insect groups such as ant colonies, fish flocks, bees, and termite flocks, has shown to be of interest to researchers. The collective behavior of insects or animals is known as herd behavior. This artificial intelligence is called the herd of swarms, dealing with the collective behavior of the elderly through complex and interactional interactions among them. Bonabeau described herd intelligence as "inspired by the collective behavior of other animal communities and social insect colonies when attempting to design any algorithms or to design a common problem solving device." [1]. Herd intelligence has many advantages such as scalability, fault tolerance, adaptation, speed, modularity, autonomy and parallelism [2].

The key components of herd intelligence are self-organization and the workforce. In a self-organizing system, each of the closed units responds to local stimuli individually and acts together to perform the global task by separating the workforce from the central control. Thus, the entire system is in harmony with internal and external changes. Various herd algorithms have been developed by mimicking the behavior of groups of insects or animals in nature and by establishing deterministic rules or random combinations.

Although Particle Swarm Optimization (PSO) and Artificial Bee Colony (ABC) are the most popular algorithms for solving complex optimization problems, these algorithms have serious

exploits such as early convergence and difficulty over local minimum points [3]. The reason for changing individual positions is related to the operators. Thus, during the evolution of such algorithms, the position of each agent for the next iteration is updated (in the case of PSO) or updated for other randomly selected individuals (in the case of ABC), showing an appeal to the position of the best particle as yet. As the algorithm evolves, such behavior causes the entire population to concentrate around the best particle or move away uncontrollably [4].

Interesting and exotic collective behaviors of social insects have attracted the attention of researchers for years. Social spiders are an example of social insect representation. The spider maintains social spiders with a complex set of collaborative behavior of members of the family. Most spiders are aggressive towards other members of their family, while social spiders tend to create long-lived communities, often referred to as colonies, to live in groups [5]. Each member of the social spider column performs various tasks according to their gender, such as hunting, mating, network design and social interaction. Here the network is an important part of the column. Because the network is used as a common living space for all individuals, it is also used as a communication channel between individuals. Moreover, important information is transmitted by small vibrations over the network [6].

In this study, SSO algorithm which is a new algorithm based on intelligence is examined in detail. The SSO algorithm is based on the cooperation and behavior of social spiders. In this algorithm, it is seen that the colony's biological laws are based on the cooperation and interaction of the individuals with each other. The algorithm considers two different search agents (spiders): females and males. Depending on the sex, the simulation based on the different cooperation of each individual within a column is expressed by a series of evolutionary operators. The most important difference between the proposed approach and the algorithm based on current herd intelligence is that each individual model is modeled considering the gender.

The results of The SSO algorithm is compared with two different heuristic algorithms (ALO, MFO) under equal conditions. The results of this test, carried out with unimodal and multimodal quality testing functions, are reported in detail via tables and graphs.

II. SOCIAL SPIDER OPTIMIZATION ALGORITHM

A. Biological Structure of SSO Algorithm

The social insect community is a complex system of business associations that is self-organizing within a set of constraints. Within collaborative groups, behaviors such as allowing task privatization among group members, advocating resources and using the environment have been observed [7]. As an integrated unit, the social insect colony function undertakes the task of building the enormous structure of the global program at the same time as having the ability to operate in a distributed fashion. In social insects, it is necessary to recognize that global borders are a result of the internal interaction between the members [8].

The grading and display of the social behavior of several species of spiders has been documented [9]. The behavior of spiders can be generalized in two forms, alone and social spiders [10]. This classification is based on the level of cooperation they exhibit [11]. On the one hand, spiders alone maintain and build their networks by contacting other individuals of similar species, while on the other side, social spiders form columns that remain together on the social network with spatial relationships to other group members [12].

B. Mathematical Model and SSO Algorithm

The Social Spider Optimization Algorithm proposed by Cuevas is based on the behavior of social spiders [13]. The search field is considered a common network and the position of a spider represents the optimal solution. An interesting feature of social spiders is the female-oriented population. The number of male spiders reaches almost 30% of total colony members. Female spiders are randomly selected N_f at 65-90% of all population (N). For this reason, N_f is calculated as shown in Equation 1:

$$N_f = [(0.9 - rand \times 0.25) \times N] \quad (1)$$

Here $rand$ is a random number between 0 and 1. The number of male spiders N_m is in Equation 2 as follows:

$$N_m = N - N_f \quad (2)$$

Each spider takes a weight based on the fitness value of its solution. This weight value is calculated in Equation 3:

$$w_i = \frac{fitness_i - worst}{best - worst} \quad (3)$$

Here $fitness_i$ is calculated by evaluating the positions of all the spiders ($i = 1, 2, 3, \dots, N$). $worst$ and $best$ values were found as the best and worst values, respectively, by scanning the entire population.

The common network (search field) is used as a mechanism for communicating information between colony members. The information is encoded as small vibrations and depends on the distance between the weights and the spider that produces them. This relationship is shown in Equation 4:

$$V_{ij} = w_j \times e^{-d_{ij}^2} \quad (4)$$

Here d_{ij} is the distance of the euclidean between i and j spiders. Three special relationships can be considered:

- Vibration $Vibc_i$ is calculated according to Equation 5 and the individual perceived by the i individual as a result of the information transmitted by c has two important features. Compared to the nearest i member, it has a higher weight ($w_c > w_i$). This situation is shown in Figure 1. (a).

$$Vibc_i = w_c \times e^{-d_{ic}^2} \quad (5)$$

- Vibration $Vibb_i$ is calculated according to Equation 6 and the property of the individual perceived by the i individual as a result of the information transmitted by b is that the entire population (N) has the best fitness value. This situation is shown in Figure 1. (b).

$$Vibb_i = w_b \times e^{-d_{ib}^2} \quad (6)$$

- Vibration $Vibf_i$ is calculated according to Equation 7 and is the closest female individual to the individual i who is perceived by the i individual as a result of the information transmitted by f . This situation is shown in Figure 1. (c).

$$Vibf_i = w_f \times e^{-d_{if}^2} \quad (7)$$

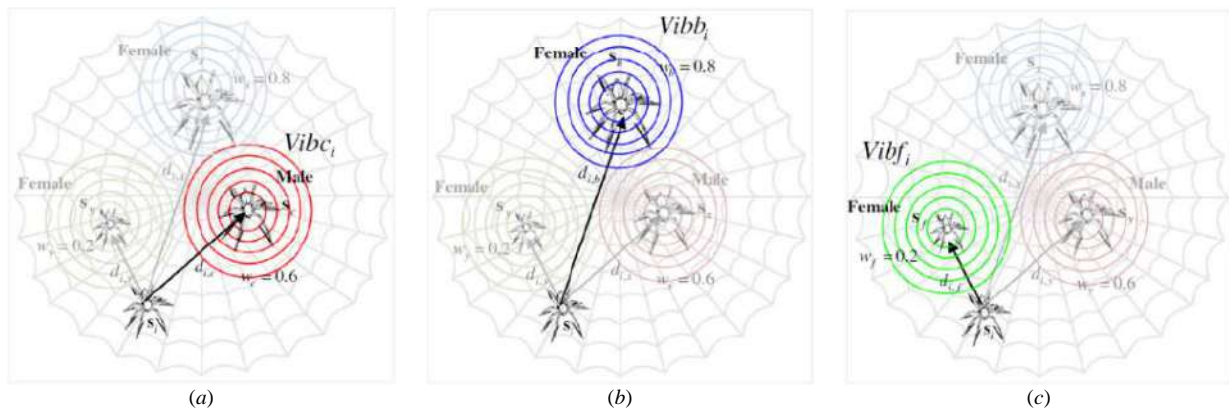


Fig. 1. The formation of $Vibc_i$ vibration (a), the formation of $Vibb_i$ vibration (b) and the formation of $Vibf_i$ vibration (c) [14].

Social spiders perform cooperative interaction on other colony members depending on sex. A new operator is described in Equation 8 to simulate the common behavior of female spiders. The pull-in-thrust motion is developed on the other spiders according to their vibrations spread over the common network:

$$f_i^{t+1} = \begin{cases} f_i^{(t)} + \alpha V_{i,c}(s_c - f_i) + \beta V_{i,b}(s_b - f_i^{(t)}) + \\ + \gamma \left(\sigma - \frac{1}{2} \right) & \text{if } r_m < PF; \\ f_i^{(t)} - \alpha V_{i,c}(s_c - f_i^{(t)}) - \beta V_{i,b}(s_b - f_i^{(t)}) + \\ + \gamma \left(\sigma - \frac{1}{2} \right) & \text{if } r_m \geq PF, \end{cases} \quad (8)$$

Here r_m , α , β , γ and σ the numbers are uniform random numbers between 0 and 1. f_i^{t+1} is expressed as a standard for the position of $t+1$ female spider at step i . s_c indicates an instantaneous parameter of the PF and s_b represent the highest weight and best member of the entire population, respectively.

The male spider population is divided into two classes: dominant and non-dominant. The dominant class has a better suitability value than the spider dominant, and these spiders are attracted to the common network center by the nearest female spider. On the other hand, non-dominant male spiders tend to concentrate male population in center C as a strategy to exploit the resources wasted by dominant men. This situation is shown in Equation 9:

$$m_i^{(t+1)} = \begin{cases} m_i^{(t)} + \alpha V_{i,f}(s_f - m_i^{(t)}) + \gamma \left(\sigma - \frac{1}{2} \right) & \text{if } w_{N_f+i} > w_{N_f+c}; \\ m_i^{(t)} + \alpha \left(\frac{\sum_{h=1}^{N_m} m_h w_{N_f+h}}{\sum_{h=1}^{N_m} w_{N_f+h}} \right) & \text{if } w_{N_f+i} \leq w_{N_f+c} \end{cases} \quad (9)$$

Here, s_f represents the female spider that is the closest to the i . male spider. At the time of step $t+1$, m_i^{t+1} shows the position of i . male spider.

Mating is done by dominant male and female members in the social spider column. When r is taken as a radius (calculate according to Equation 10), if the dominant male spider finds a female member in r , it mates and forms a new young.

$$r = \frac{\sum_{j=1}^n p_j^{high} - p_j^{low}}{2n} \quad (10)$$

Here, n (the number of variables to be optimized) is the size of the problem, p_j^{high} and p_j^{low} are the standard for upper and lower bounds, respectively. After the new spider has formed, it is compared to the best spider of the colony. If the new spider is better, the bad spider is replaced by a new one.

III. EXPERIMENTS AND RESULTS

There are many benchmark test functions to measure the success of the algorithms. The selected benchmark functions and their characteristics are shown in Table 1.

TABLE I. BENCHMARK FUNCTIONS

Functions	Lower and Upper Limits	Min	D	Type	Equation
f_1 -Sphere	[-5.12, 5.12]	0	30	UM	$\sum_{i=1}^n x_i^2$
f_2 -Rosenbrock	[-30, 30]	0	30	UM	$\sum_{i=1}^{n-1} [100(x_{i+1} - x_i) + (x_i - 1)^2]$
f_3 -Powell	[-4, 5]	0	24	UM	$\sum_{i=1}^{n/4} \left[(x_{4i-3} + 10x_{4i-2})^2 + 5(x_{4i-1} - x_{4i})^2 \right] + (x_{4i-2} - 2x_{4i-1})^4 + 10(x_{4i-3} - x_{4i})^4$
f_4 -Rastrigin	[-5.12, 5.12]	0	30	MM	$\sum_{i=1}^n [x_i - 10 \cos(2\pi x_i) + 10]$
f_5 -Ackley	[-32, 32]	0	30	MM	$-20 \exp \left(-0.2 \sqrt{\frac{1}{n} \sum_{i=1}^n x_i} \right) - \exp \left(\frac{1}{n} \sum_{i=1}^n \cos(2\pi x_i) \right) + 20 + e$
f_6 -Griewank	[-600, 600]	0	30	MM	$\frac{1}{4000} \sum_{i=1}^n x_i^2 - \prod_{i=1}^n \cos \left(\frac{x_i}{\sqrt{i}} \right) + 1$

In this study, the biological structure and mathematical model of the SSO algorithm are investigated. The SSO algorithm were compared with ALO and MFO under equal conditions as the benchmark test functions.

ALO, MFO, and SSO algorithms for each function specified in Table 1 were run 30 times. Table 2 presents the best, worst, average, median, and standard deviation of the three algorithms as a result of this experiment. The superiority of SSO can be seen from this table.

TABLE II. COMPARISON OF ALGORITHMS

Functions	Algorithms	The Best Value	The Worst Value	Mean	Median	Standard Deviation
f_1	ALO	2.13E-009	1.07E-007	3.20E-008	1.98E-008	2.73E-008
	MFO	2.66E-008	5.24E+001	6.99E+000	5.54E-007	1.52E+001
	SSA	1.41E-003	1.06E-002	5.51E-003	5.26E-003	2.08E-003
f_2	ALO	1.92E+001	1.47E+003	2.86E+002	9.34E+001	4.19E+002
	MFO	1.02E+000	8.00E+007	2.68E+006	2.02E+002	1.46E+007
	SSA	2.95E+002	9.63E+002	5.09E+002	4.75E+002	1.49E+002
f_3	ALO	7.60E-002	2.17E+000	7.43E-001	6.26E-001	4.78E-001
	MFO	8.75E-003	3.74E+003	6.40E+002	1.47E+002	1.01E+003
	SSA	1.43E+000	8.47E+000	4.03E+000	3.81E+000	1.85E+000
f_4	ALO	2.68E+001	1.38E+002	8.27E+001	7.86E+001	2.82E+001
	MFO	7.86E+001	2.46E+002	1.54E+002	1.55E+002	4.29E+001
	SSA	3.52E+001	5.78E+001	4.66E+001	4.89E+001	6.30E+000
f_5	ALO	6.67E-004	4.46E+000	1.97E+000	2.01E+000	8.76E-001
	MFO	1.09E-002	1.99E+001	1.44E+001	1.90E+001	7.86E+000
	SSA	3.11E-001	1.15E+000	7.43E-001	7.17E-001	2.03E-001
f_6	ALO	2.27E-004	4.71E-002	1.33E-002	8.42E-003	1.36E-002
	MFO	1.01E-004	1.80E+002	2.11E+001	2.34E-002	4.56E+001
	SSA	7.41E-001	1.03E+000	9.73E-001	1.00E+000	7.27E-002

The performance of the SSO algorithm has been investigated using the unimodal and multimodal benchmark testing function.

The convergence graphs for the average fitness values of the algorithms run 30 times for each function are shown in Figure 2.

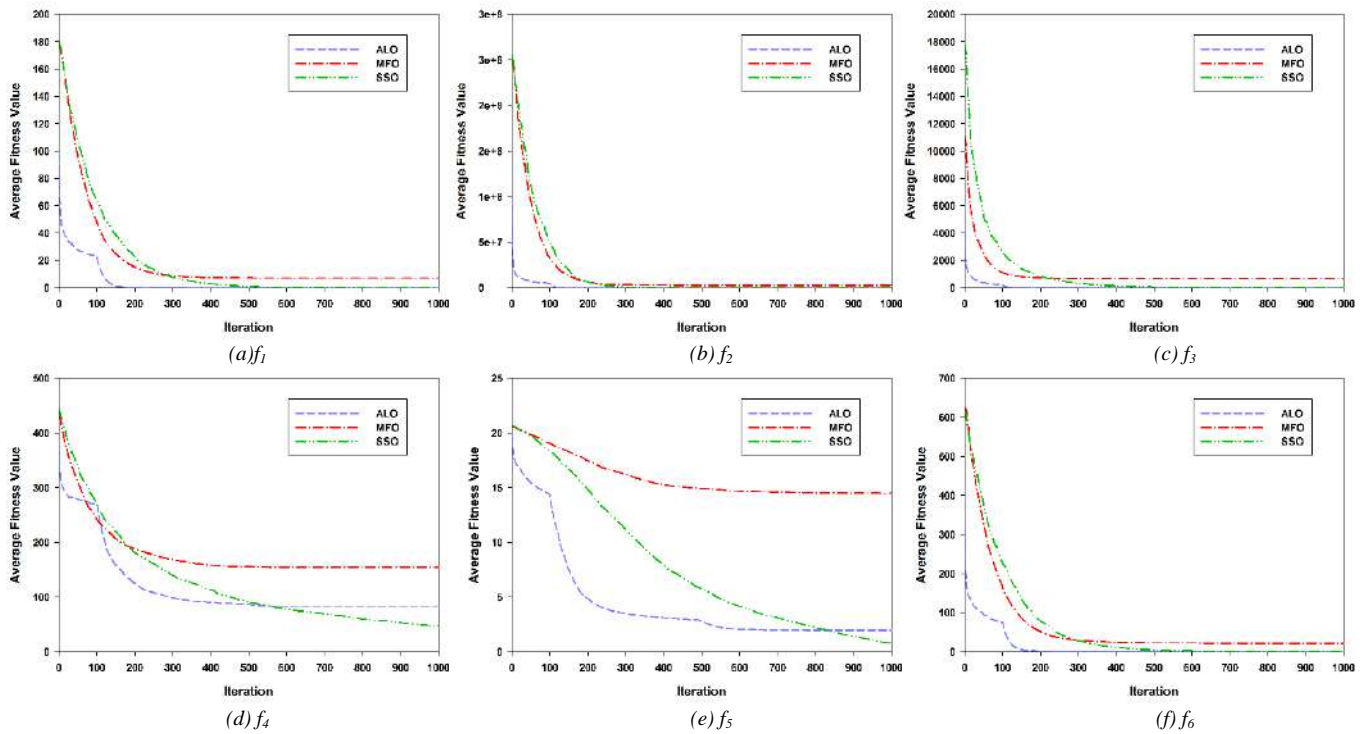


Fig. 2. Convergence graphs of average fitness values for benchmark functions(f_1 , f_2 , f_3 , f_4 , f_5 , f_6).

As shown in Figure 2. (a), (b), (c), the convergence speed of the SSO algorithm for UM functions is slightly slower than that of other algorithms. However, as shown in Figure 2. (d), (e), (f), the convergence speed of the SSO algorithm for MM functions is higher than that of other algorithms.

IV. RESULTS

The performance, stability, and sensitivity of the SSO algorithm are compared with different optimization algorithms (ALO, MFO) using the six different benchmark test function. The results show that the covariance of the SSO algorithm is lower than that of the ALO algorithm. However, we can say that it is equivalent to the MFO algorithm. The convergence speed of the SSO algorithm is much better than the MFO algorithm.

The most important conclusion to be drawn from this study is that the more remarkable results can be obtained if the parameter values are set well for all algorithms.

REFERENCES

- [1] Bonabeau, E., Dorigo, M., & Theraulaz, G. (1999). *Swarm intelligence: From natural to artificial systems*. New York, NY, USA: Oxford University Press, Inc..
- [2] Kassabalidis, I., El-Sharkawi, M. A., Marks, R. J., Arabshahi, P., & Gray, A. A. (2001). *Swarm intelligence for routing in communication networks*. Global Telecommunications Conference, GLOBECOM '01 (Vol. 6, pp. 3613–3617). IEEE.
- [3] Wang, Y., Li, B., Weise, T., Wang, J., Yuan, B., & Tian, Q. (2011). Self-adaptive learning based particle swarm optimization. *Information Sciences*, 181(20), 4515–4538.
- [4] Wang, H., Sun, H., Li, C., Rahnamayan, S., & Jeng-shyang, P. (2013). Diversity enhanced particle swarm optimization with neighborhood. *Information sciences*, 223, 119–135.
- [5] Gordon, D. (2003). The organization of work in social insect colonies. *Complexity*, 8(1), 43–46.
- [6] Yip, C., & Eric, K. S. (2008). Cooperative capture of large prey solves scaling challenge faced by spider societies. *Proceedings of the National Academy of Sciences of the United States of America*, 105(33), 11818–11822.
- [7] Hölldobler, B., & Wilson, E. O. (1994). *Journey to the ants: A story of scientific exploration*. ISBN 0-674-48525-4.
- [8] Hölldobler, B., & Wilson, E. O. (1990). *The ants*. 0-674-04075-9. Harvard University Press.
- [9] Lubin, T. B. (2007). The evolution of sociality in spiders. In H. J. Brockmann (Ed.), *Advances in the study of behavior* (Vol. 37, pp. 83–145).
- [10] Aviles, L. (1986). Sex-ratio bias and possible group selection in the social spider *Anelosimus eximius*. *The American Naturalist*, 128(1), 1–12.
- [11] Burgess, J. W. (1982). Social spacing strategies in spiders. In P. N. Rovner (Ed.), *Spider communication: Mechanisms and ecological significance* (pp. 317–351). Princeton, NJ: Princeton University Press.
- [12] Maxence, S. (2010). Social organization of the colonial spider *Leucauge* sp. in the Neotropics: Vertical stratification within colonies. *The Journal of Arachnology*, 38, 446–451.
- [13] E. Cuevas, M. Cienfuegos, D. Zaldívar, and M. Pérez-Cisneros, “A swarm optimization Algorithm inspired in the behavior of the social-spider,” *Expert Systems with Applications*, vol. 40, no. 16, pp. 6374–6384, 2013.
- [14] Erik Cuevas, Miguel Cienfuegos, Daniel Zaldívar, Marco Pérez-Cisneros “A swarm optimization algorithm inspired in the behavior of the social-spider” 2013.

Reducing Error Rate in Mathematical Modeling to Determine Surface Roughness at CNC Milling Using Social Spider Algorithm

Cem Baydogan

Department of Software Engineering
Firat University
Elazig, Turkey
cembaydogan@gmail.com

Bilal Alatas

Department of Software Engineering
Firat University
Elazig, Turkey
balatas@firat.edu.tr

Abstract— In this study, Social Spider Optimization Algorithm (SSO) which is a metaheuristic algorithm is used to reduce the error rate in determining the surface roughness (Ra) which is one of the most important conditions in the processing process. The correct setting of the cutting parameters is very important to obtain better surface roughness. Using the Multiple Regression Method, the SSO algorithm was used to determine the correlation of the initial parameters to each other. Using the Multiple Regression Method, the mean percent deviation of the test set was 9.8% while it was 9.1% by adjusting the initial parameters with the SSO algorithm. With the improvement of this statistical model by the SSO algorithm, the accuracy of 90.1% of the test data sets has been increased to about 91%. Two different sets of data were used randomly for the test set. The greatest feature of the SSO algorithm used in this study is the simulation of the co-existing biological lives of the spiders.

Keywords— Optimization, Heuristic Algorithms, Swarm Intelligence, Social Spider Algorithm (SSO), Surface Roughness

I. INTRODUCTION

Most of the optimization problems in the literature assume that the parameters, constraints or variables affecting the system are fixed during the solution of the problem. However, in real life applications, the situation is different. In real life conditions, the parameters, variables or constraints to be used in the solution of the problem may vary with time or probable reasons, and a new problem arises when the problem has not been solved yet. These problems are called optimization problems in the literature. The goal here is to find the best solution or the best solution to be found under changing conditions instead of finding the best solution.

Movement of associations occurs through mutual communication of the individuals in the herd. These movements are exhibited in nature by some animals such as fish, birds and ants. The dual relations between individuals can be expressed in the simplest way by three rules: the approach of the individual to the other individuals at a certain distance, as close as possible, and the departure to prevent their collision [1].

Until today, metaheuristic methods are often used to solve different types of problems in different subjects. It can be defined as a problem optimization problem involving the finding of unknown parameter values so as not to violate certain constraints. In optimization problems, the initial step is to set the set of parameters called decision variables.

There are many optimization algorithms in the literature. Particle Swarm Optimization (PSO), an intuitive optimization algorithm, is population based and developed by Dr. Eberhart and Dr. Kennedy [2]. Krill Swarm Algorithm, metaheuristic algorithm has gained a lot in the near term based on the literature in order to solve real life problems. The algorithm performance continuously-variable-number in the literature have been used in non-linear optimization problems [3]. The Artificial Bee Colony (ABC), examines the cooperative behavioral technique of bee colonies [4]. Bacterial Foraging Optimization Algorithm (BFO), bacteria social aggregator behavior (metacognitive) [5], Firefly (FF), is firefly beetles mating behavior [6] and Cuckoo Optimization Algorithm (COA), is based on the basic social behavior, such as life style of the cuckoo [7].

In this study, biological and mathematical structure of SSO algorithm is examined. In order to improve the method used for CNC milling, it is aimed to benefit from the strong structure of SSO algorithm. As a result of studies on two different test data, it is desired to reduce the error rate. Correct setting of the initial parameters increases the accuracy of the existing problem.

II. SOCIAL SPIDER OPTIMIZATION ALGORITHM

As a social insect, spiders perform collaborative interactions with other colony members [8]. These collaborative behaviors depend on the sex of the spider. Because vibrations are tied to the distance and weight of the members that trigger them, strong vibrations are produced by both the big spiders and the nearest neighbors [9]. This is illustrated in Figure 1.

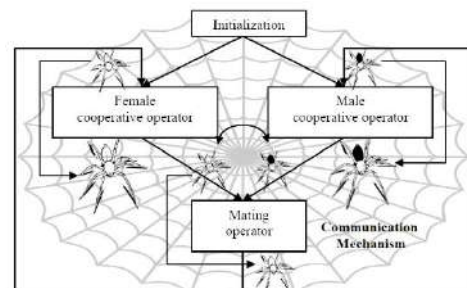


Fig 1. Schematic representation of the SSO algorithm data-flow

The bigger the spider is, the better the well thought colonial member. The ultimate decision of interaction or hate on a designated member is influenced by several factors such as the other random event and curiosity reproduction period in the room, which is taken according to the internal state of the network [10].

Mating is not only the survival of the colonies, but also an important process allowing the exchange of information between members. Mating in the social spider colonies is carried out by dominant men and female members. In this case, if the dominant male spider has one or more female members located within a certain area, the pups mate with all the teeth to produce [11, 12]. The evolutionary operators and structure of the SSO algorithm are as shown in Figure 2.

Algorithm 1 SOCIAL SPIDER ALGORITHM

```

1: Assign values to the parameters of SSA.
2: Create the population of spiders pop and assign memory for them.
3: Initialize vtar for each spider.
4: while stopping criteria not met do
5:   for each spider s in pop do
6:     Evaluate the fitness value of s.
7:     Generate a vibration at the position of s.
8:   end for
9:   for each spider s in pop do
10:    Calculate the intensity of the vibrations V
        generated by other spiders.
11:    Select the strongest vibration vbest from V.
12:    if The intensity of vbest is larger than vtar then
13:      Store vbest as vtar.
14:    end if
15:    Perform a random walk towards vtar.
16:    Generate a random number r from [0,1).
17:    if r < pj then

```

```

18:      Assign a random position to s.
19:    end if
20:    Attenuate the intensity of vtar.
21:  end for
22: end while
23: Output the best solution found.

```

Fig 2. SSO algorithm pseudo code

Colony levels are produced as a result of internal interaction, despite the complexity existing among all colony members in global co-operation [13]. Such internal interactions include the simple behavioral sequence followed by each spider in the colony. Behavioral rules are divided into two classes as social interaction (cooperative behavior) and mating [14].

A social spider colony consists of two main components. These are members and commercial networks. Members divide into two different categories, men and females. The most interesting feature of social spiders is that they have a predominantly female based population. Some studies show that the number of male spiders barely reaches 30 percent of total colonies [15]. Depending on their sex, each member in the colony displays different activities such as building and maintaining commercial networks for social communication and development [16]. Interaction between members is both direct and indirect [17]. Direct interaction implies the exchange of fluids, such as reproduction, or the interaction of the bodies. Indirect interaction is used as the middle of the commercial network communication, so information transmission is important [18]. All steps of the SSO algorithm are shown in the flow chart in Figure 3.

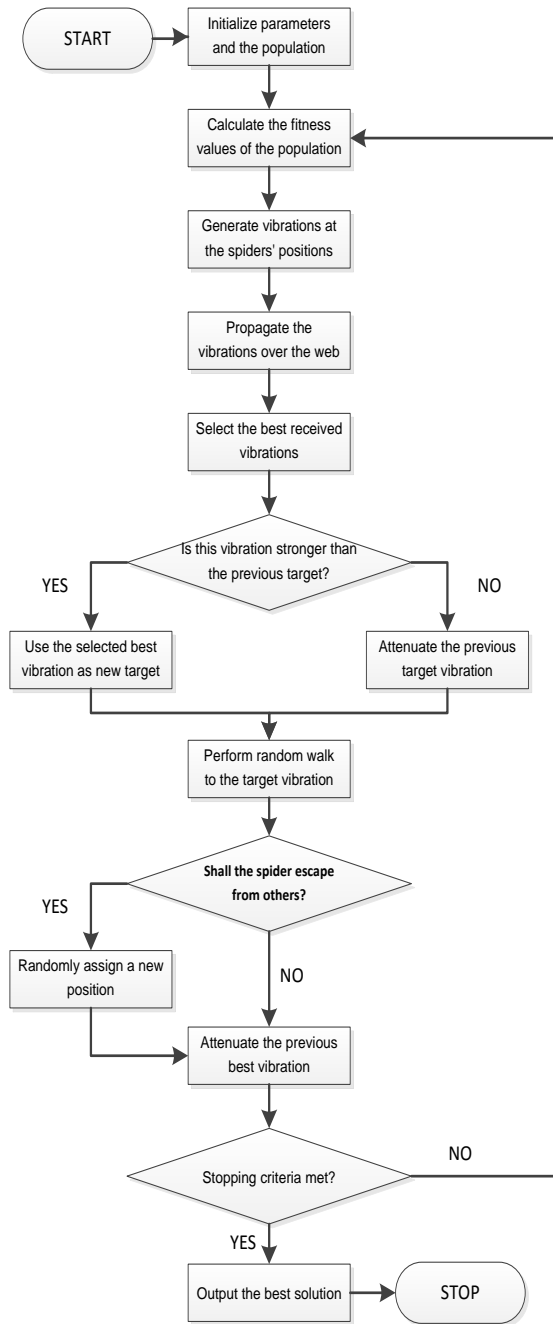


Fig 3. The flow chart of the SSO algorithm

III. METHODOLOGY

In this study by Rashid on 84 samples, the samples are divided into two random data sets [19]. There are 60 examples in the part 1 data set (Table II) and 24 examples (Table I) in the part 2 data set to test the flexibility of the SSO algorithm. All examples consist of four elements: spindle speed, feed rate, cutting depth and measured surface roughness (R_a). A regression model was constructed using the three-way interaction Equation 1:

$$Y_i = \alpha_i + \beta_1 X_{1i} + \beta_2 X_{2i} + \beta_3 X_{3i} + \beta_4 X_{1i} X_{2i} + \beta_5 X_{1i} X_{3i} + \beta_6 X_{2i} X_{3i} + \beta_7 X_{1i} X_{2i} X_{3i} \quad (1)$$

Where Y_i : Surface roughness (R_a), X_{1i} : Spindle speed (S), X_{2i} : Feed rate (F), X_{3i} : Depth of cut (D). Values α and β are constants set by the SSO algorithm.

TABLE I. PART 1 DATASET

N	Spindle Speed X_1 (rpm)	Feed Rate, X_2 (mm/min)	Depth of Cut, X_3 (mm)	Actual R_a
1	1500	152	0.76	1.224
2	1500	152	1.27	1.301
3	1000	229	0.25	2.037
4	1000	229	0.76	2.088
5	1500	229	1.27	1.478
6	750	305	0.25	3.217
7	1250	305	0.76	2.215
8	1500	305	0.76	1.783
9	1500	305	1.27	2.088
10	750	380	0.25	2.975
11	1250	380	0.25	2.392
12	1250	380	0.76	2.138
13	1500	380	0.76	1.808
14	750	457	0.76	3.434
15	1000	457	0.76	2.85
16	1000	457	1.27	2.134
17	1500	457	0.76	1.91
18	750	515	0.25	4.221
19	1000	515	1.27	3.214
20	1500	515	0.76	2.291
21	750	588	0.25	4.45
22	750	588	1.27	3.452
23	1000	588	1.27	3.307
24	1250	588	1.27	2.773

The percent deviation (Equation 2) and the mean percentage deviation (Equation 3) are used to evaluate the correctness of the multiple regression prediction model produced by the SSO:

$$\phi_i = \frac{|R\hat{\alpha}_i - R\alpha_i|}{R\hat{\alpha}_i} \times 100\% \quad (2)$$

Where ϕ_i : percentage deviation, $R\hat{\alpha}_i$: actual R_a , $R\alpha_i$: the estimated R_a generated by SSO.

$$\bar{\phi}_i = \frac{\sum_{i=1}^m \phi_i}{m} \quad (3)$$

Where $\bar{\phi}_i$: average percentage deviation, m : number of samples.

TABLE II. PART 2 DATASET

No	Spindle Speed X_1	Feed Rate, X_2	Depth of Cut, X_3	Actual R_a
----	---------------------	------------------	---------------------	--------------

	(rpm)	(mm/min)	(mm)	
1	750	152	0.25	1.351
2	750	152	0.76	1.300
3	750	152	1.27	1.629
4	1000	152	0.25	1.173
5	1000	152	0.76	1.681
6	1000	152	1.27	1.275
7	1250	152	0.25	1.276
8	1250	152	0.76	1.301
9	1250	152	1.27	1.603
10	1500	152	0.25	1.128
11	750	229	0.25	2.469
12	750	229	0.76	2.212
13	750	229	1.27	2.113
14	1000	229	1.27	2.291
15	1250	229	0.25	1.707
16	1250	229	0.76	1.757
17	1250	229	1.27	2.037
18	1500	229	0.25	1.503
19	1500	229	0.76	1.554
20	750	305	0.76	2.291
21	750	305	1.27	2.088
22	1000	305	0.25	3.002
23	1000	305	0.76	1.833
24	1000	305	1.27	2.037
25	1250	305	0.25	2.265
26	1250	305	1.27	1.859
27	1500	305	0.25	1.935
28	750	380	0.76	2.799
29	750	380	1.27	2.342
30	1000	380	0.25	2.265
31	1000	380	0.76	2.443
32	1000	380	1.27	2.367
33	1250	380	1.27	2.137
34	1500	380	0.25	2.392
35	1500	380	1.27	2.215
36	750	457	0.25	4.339
37	750	457	1.27	2.773
38	1000	457	0.25	3.205
39	1250	457	0.25	2.621
40	1250	457	0.76	2.037
41	1250	457	1.27	2.113
42	1500	457	0.25	2.723
43	1500	457	1.27	2.342
44	750	515	0.76	3.84
45	750	515	1.27	3.61
46	1000	515	0.25	3.485
47	1000	515	0.76	3.383
48	1250	515	0.25	2.875
49	1250	515	0.76	2.24
50	1250	515	1.27	2.367
51	1500	515	0.25	2.697
52	1500	515	1.27	2.57
53	750	588	0.76	4.018
54	1000	588	0.25	3.84
55	1000	588	0.76	3.586
56	1250	588	0.25	3.637
57	1250	588	0.76	2.469
58	1500	588	0.25	2.723
59	1500	588	0.76	2.316
60	1500	588	1.27	2.469

IV. EXPERIMENTS AND RESULTS

In this study, firstly, the general structure of the SSO algorithm is examined. The proposed model for the determination of the surface roughness in the CNC milling process is reinforced by the SSO algorithm. The error rates in the measurements made using Perthometer S2 are 9.8% for part 1 data set (Table I). With the model created by SSO, this ratio has been reduced to about 9.1%. In addition, the accuracy of measurement by the Perthometer S2 for the part 2 data set (Table II) is 90.1%. With the help of the SSO algorithm, this value has been increased to about 91%. The SSO algorithm was run 30 times for each data set and these results were obtained.

V. RESULTS

There are many studies in the literature for solving the linear equations of the SSO algorithm. As a result of this study, it is seen that there are no undesirable situations such as early convergence and local minimum in SSO algorithm. It can be said that the SSO algorithm is suited for solving engineering problems.

REFERENCES

- [1] Can, F. C., Şen, H., (2014). Sürü Simülasyon Programı Geliştirilmesi ve Performansının İncelenmesi, ASYU'2014: Akıllı Sistemlerde yenilikler ve Uygulamaları, 163-166.
- [2] Kennedy, J., & Eberhart, R. (1995). Particle swarm optimization. In Proceedings of the 1995 IEEE international conference on neural networks (Vol. 4, pp. 1942–1948).
- [3] Hossein, A., & Hossein-Alavi, A. (2012). Krill herd: A new bio-inspired optimization algorithm. Communications in Nonlinear Science and Numerical Simulation, 17, 4831–4845.
- [4] Karaboga, D. (2005). An idea based on honey bee swarm for numerical optimization. Technical report-TR06. Engineering Faculty, Computer Engineering Department, Erciyes University.
- [5] Passino, K. M. (2002). Biomimicry of bacterial foraging for distributed optimization and control. IEEE Control Systems Magazine, 22(3), 52–67.
- [6] Yang, X. S. (2010). Engineering optimization: An introduction with metaheuristic applications. John Wiley & Sons.
- [7] Rajabioun, R. (2011). Cuckoo optimization algorithm. Applied Soft Computing, 11, 5508–5518.
- [8] Hölldobler, B., & Wilson, E. O. (1994). Journey to the ants: A story of scientific exploration. ISBN 0-674-48525-4.
- [9] Hölldobler, B., & Wilson, E. O. (1990). The ants. 0-674-04075-9. Harvard University Press.
- [10] Maxence, S. (2010). Social organization of the colonial spider Leucauge sp. in the Neotropics: Vertical stratification within colonies. The Journal of Arachnology, 38, 446–451.
- [11] James J.Q. “A Social Spider Algorithm for Global Optimization” Technical Report No. TR-2003-004, Dept. of Electrical & Electronic Engineering, The University of Hong Kong, Oct 2013.
- [12] L. A. M. Pereira, D. Rodrigues, P. B. Ribeiro, J. P. Papa “Social-Spider Optimization-Based Artificial Neural Networks Training And Its Applications For Parkinson’s Disease Identification” 2014.
- [13] Gove, R., Hayworth, M., Chhetri, M., & Rueppell, O. (2009). Division of labour and social insect colony performance in relation to task and mating number under two alternative response threshold models. Insectes Sociaux, 56(3), 19–331.
- [14] Ann, L., & Rypstra, R. S. (1991). Prey size, prey perishability and group foraging in a social spider. Oecologia, 86(1), 25–30.
- [15] Aviles, L. (1986). Sex-ratio bias and possible group selection in the social spider Anelosimus eximius. The American Naturalist, 128(1), 1–12.
- [16] Yip, C., & Eric, K. S. (2008). Cooperative capture of large prey solves scaling challenge faced by spider societies. Proceedings of the National

Academy of Sciences of the United States of America, 105(33), 11818–11822.

- [17] Rayor, E. C. (2011). Do social spiders cooperate in predator defense and foraging without a web? *Behavioral Ecology & Sociobiology*, 65(10), 1935–1945.
- [18] Maxence, S. (2010). Social organization of the colonial spider *Leucauge* sp. in the Neotropics: Vertical stratification within colonies. *The Journal of Arachnology*, 38, 446–451.
- [19] D. Ab. Rashid M.F.F., Gan S.Y., and Muhammad N.Y., Mathematical Modeling to Predict Surface Roughness in CNC Milling, *International Journal of Mechanical, Aerospace, Industrial, Mechatronic and Manufacturing Engineering* Vol:3, No:5, (2009)

BRAIN TUMOR DETECTION BASED ON IMAGE PROCESSING AND STATISTICS

Zehra KARHAN, Durmuş Özkan ŞAHİN, Erdal KILIÇ
Department of Computer Engineering
Ondokuz Mayıs University
Samsun, Turkey
zehra.karhan, durmus.sahin, erdal.kilic@bil.omu.edu.tr

Abstract— *Magnetic resonance (MR) imaging technique is used to assess the accuracy of evaluation of brain tumors during diagnosis. In the stage of diagnosis of brain tumors, identify the tumor region and determine its properties together with its areas and bounds are important. This diagnosis is usually made manually by people (radiologists-doctors). In this study, a technique has been proposed based on image processing and statistical, it can be used at the stage of diagnosis, it can detect that the tumor is benign or malign and detected objectively and classified high percentage of accuracy. Thus, tumor detection can be performed quickly and in a short time as the patient has fulfilled the requirements. In this tumor diagnosis with image processing and statistical basis, for the feature extraction, we first used segmentation and then Gray-Level Co-occurrence Matrices (GLCM) method. Stage of Classification; K-Nearest Neighbor, Naive Bayes (NB), Support Vector Machine (SVM) using linear kernel and Maximum Likelihood Estimation (MLE) algorithms are used. To enhance the image before the feature extraction, the image is passed through the filter and is utilized from morphological operations and segmentation to distinguish the region of interest. As a result, the experimental results show that MLE classifier is more successfully than other classification methods for BRATS (Brain Tumor Image Segmentation) 2015-dataset with a 75% correct classification rate.*

Keywords— *Brain Tumor Detection, K- Nearest Neighbor, Naive Bayes, Support Vector Machine, Maximum Likelihood Estimation*

Examination of Data Erasure Tools and Methods

Erhan AKBAL

Dept. of Digital Forensics Engineering
University of Firat
Elazig, Turkey
erhanakbal@firat.edu.tr

Sengul DOGAN

Dep. of Digital Forensics Engineering
University of Firat
Elazig, Turkey
sdogan@firat.edu.tr

Abstract—Data storage devices are areas that people and institutions use to store data. The erasing of critical information without proper methods creates significant security vulnerabilities in the information security. The simple erasing of the data that is not needed for storage is incomplete in terms of digital forensics. Many software and hardware tools allow the recovery of erasing data. Safe and permanent erasing of unwanted data is important for forensic information. Many hardware and software tools have been produced for this purpose. These tools use certain defined standard methods. In order to reliably erasing data, it is necessary to use accepted data erasure methods in the field of digital forensics. In this study, software and hardware tools used to erasure secure data are shown. The differences of the methods used and performance of erasure process are evaluated

Keywords— *erasure methods; data recovery ; forensics; information security*

I. INTRODUCTION

The rapid development of information technologies has led to an increase in the amount of data. People, institutions, countries keep all operations and data in the digital environment in storage media [1]. The significance of the stored data varies depending on the field used. Unauthorized acquisition, use or publication of high-severity data can cause losses such as reputation, time, money in terms of people and institutions. For this reason, data must be stored in secure tools and erased in a method that cannot be recovered. If the data is not permanently deleted, it is possible to recover with various software and hardware tools. The safety of the data has to be ensured with the storage of the data in digital media [2]. At the same time, regulations are in place to ensure the safety of critical data in the legislation of countries. If the data are not being used, it is necessary to safely erase them from storage devices. Data on disks using the ATA, SCSI technology via commands, software tools and various hardware can be erased. Files stored on discs can be deleted one by one or all of them with various techniques [3]. Software solutions are implemented by writing data over and over with algorithms that work to prevent residual data in the physical or logical areas of the drive. The entire disk can be cleaned using ATA and SCSI commands. Many of the methods used in this area have been developed to erase magnetic disk unit. The storage of data in Solid State Disk (SSD) technology is not like the storage methods in magnetic disks. While magnetic discs write via the read / write head on data platter, the

SSD determines the area in the disc where the controller writes, the controller in the SSD disk determines the area to write [3,4].

There are different methods to make the disc unusable or permanent erasure of data. In this study, the erasure methods proposed in the literature are examined and the erasure principles are presented. At the same time, differences in methods and erasure processes are evaluated.

II. SOFTWARE OF DATA ERASURE METHODS

Many methods for data erasure have been developed [5-7]. The erasure of the data in a storage device is performed according to the rules in the methods developed using hardware or software tools. DoD 5220.22M, developed by US Department of Defense and NCSC-TG, US Air Force AFSSI-5020, US Army AR 380-19, US Navy NAVSO P-5239-26, RCMP TSST OPS-II, Canada CSECITSG-06, UK HMG IS5, ISM 6.2. 92, NZSIT 402, German VSITR, Russian GOST P50739-95, Gutmann, Schneir, Pfizner methods are recommended for safe data erasure [6-8].

A. *Us DoD 5220.22-M and NCSC-TG-025*

Us DoD 5220.22-M and NCSC-TG-025 were developed by the US Department of Defense and the national security agency. The methods are software based. Other data is written on the data in the storage units to perform erasure. Thus, recovery of deleted data from the device by file recovery methods are prevented. Data is mostly not available in hardware data recovery methods. The Us DoD 5220.22-M and NCSC-TG-025 methods operate in 3 stages and performs similar process. At the first stage, "0" is written to the whole disc and verified. "1" is written to the device to and the write is verified in the second step. At the last stage, random characters are written and the writing process is verified. Thus, the deleted data from the disk becomes unrecoverable [9].

B. *AFSSI-5020*

AFSSI-5020 is a method developed by US Air Force. The AFSSI-5020 method is similar to the methods of Us DoD 5220.22 and NCSC-TG-025. However, the number written to the device, sorting and verification procedures are different from the other two methods. This method works in 3 stages. In this method, "0", "1" and random characters are written and then verification is performed [10].

C. AR 380-19

AR 380-19 is an erasure method developed by Us Army. This method is realized in 3 stages. In the first step, random characters are written. In the second step, the selected special character is written. In the last stage, more than one selected character is written and verified. Thus, the disk is safely erased in 3 steps. Verification is only done in the last stage [10].

D. NAVSO P-5239-26

NAVSO P-5239-26 is a wiping method developed by Us Navy. This method works similarly to the AR380-19 erasure method. There are differences only in the array of the erasing steps. There are differences only in the locations of the erasure steps. In the method, a special character such as 0 or 1 is written in the first step. In the second stage, the complement of the selected character in the first stage is written. In the last stage, the random character is written and the writing is verified. The NAVSO P-5239-26 method is one of the standard methods used by many data erasure programs [10].

E. RCMP TSSIT OPS-II

RCMP TSSIT OPS-II is a method by Royal Canadian Mounted Police Technical Security standard. In this method the erasure process is defined in 7 steps. It writes 0,1,0,1,0,1 respectively and verifies by writing random character at last stage [11].

F. CSEC ITSG-06

It is an erasure method developed by Communications Security Establishment of Canada. The CSEC ITSG-06 method operates in three stages. In the first step, binary 1 or 0 is written. In the second stage, the complement of the selected character in the first step is written. For example, if 1 is selected in the first step, 0 is selected in the second step. At the end, the random character is written and the write is verified [12].

G. HMG IS5

There are two types of HMG-IS5 methods as Baseline and Enhanced. Baseline works in two steps, enhanced three steps. Baseline writes binary 0 in the first step. In the second stage, it writes random characters and verifies the writing. Enhanced writes binary 0 value in the first stage and 1 value in the second stage. At the last stage, he writes random characters and verifies the writing [13].

H. ISM 6.2.92

ISM 6.2.92 is a standard published by the Australian Government Information Security Manual. The ISM 6.2.92 method works in one step. Random characters are written and verified. In the method, when the disk capacity is below 15GB, it requires writing 3 times to each piece of information on the storage device [10].

I. NZSIT 402

It is a method developed by the New Zealand Government Communications Security Bureau. It contains the same steps as the ISM 6.2.92 method. The NZSIT 402 method is single-stage. In the method, Random characters are written and verified. This ensures permanent erasure of the data [12].

J. VSITR

The VSITR method is used as the German standard. It works in 7 stages. In the method, each data field on the device are written "0" and "1" in three rows. At the end, random characters are written. Verification is not performed in this method [12,14].

K. GOST R 50739-95

GOST R 50739-95 is the Russian standard. This method writes zero to sectors in the first instance. Random characters are written in the second step. Verification is not performed [15].

L. Gutmann Method

The Gutmann method is a method proposed by Peter Gutmann. A 35-stage write process is defined to prevent recovery of data on the storage device. All of the steps include separate processing steps. According to other methods, the slowest method is the Gutmann method. Gutmann method is known as the safest method in terms of data recovery. The character patterns suggested for this algorithm are shown in Table 1 [1].

TABLE X. GUTMANN METHOD PATTERN

Pass No	Pattern	Pass No	Pattern
1	Random	18	10001000 10001000 10001000
2	Random	19	10011001 10011001 10011001
3	Random	20	10101010 10101010 10101010
4	Random	21	10111011 10111011 10111011
5	01010101 01010101 01010101	22	11001100 11001100 11001100
6	10101010 10101010 10101010	23	11011101 11011101 11011101
7	10010010 01001001 00100100	24	11101110 11101110 11101110
8	01001001 00100100 10010010	25	11111111 11111111 11111111
9	00100100 10010010 01001001	26	10010010 01001001 00100100
10	00000000 00000000 00000000	27	01001001 00100100 10010010
11	00010001 00010001 00010001	28	00100100 10010010 01001001
12	00100010 00100010 00100010	29	01101101 10110110 11011011
13	00110011 00110011 00110011	30	10110110 11011011 01101101
14	01000100 01000100 01000100	31	11011011 01101101 10110110
15	01010101 01010101 01010101	32	Random
16	01100110 01100110 01100110	33	Random
17	01110111 01110111 01110111	34	Random
		35	Random

M. Bruce Schneier Method

It is an erasure method proposed by Bruce Schneier. The method works in 7 stages. In the first stage, "binary 1", in the second stage "binary 0", in the next 5 steps a random character sequence is written. Verification is not performed in the method [16].

N. Pfizner Method

Pfzner method is developed by Roy Pfzner. It works in 33 stages. Random characters are written in all steps. It is similar to the Gutmann method. Verification is not done [12].

The erasure methods used in Table 2 are shown comparatively.

TABLE XI. COMPARISON OF ERASURE METHODS

No	Methods	Erasure Steps	Verify
1	Us DoD 5220.22-M	3 Pass 0x00, 0x01, Random	3 (per pass)
2	NCSC-TG-025	3 Pass 0x00, 0x01, Random	3 (per pass)
3	AFSSI-5020	3 Pass 0x00, 0x01, Random	1 (last pass)
4	AR 380-19	3 Pass Random, 0x00 or 0x01, 0x01 or 0x00	1 (last pass)
5	NAVSO P-5239-26	3 Pass Random, 0x00 or 0x01, 0x01 or 0x00	1 (last pass)
6	RCMP TSSIT OPS-II	7 Pass, 0x00, 0x01, 0x00, 0x01, 0x00, 0x01, Random	1 (last pass)
7	CSEC ITSG-06	3 Pass, 0x00 or 0x01, 0x01 or 0x00, Random	1 (last pass)
8	HMG IS5	3 Pass, 0x00, 0xFF, Random	1 (last pass)
9	ISM 6.2.92	1 Pass, Random	1
10	NZSIT 402	1 Pass, Random	1
11	VSITR	7 Pass, 0x00, 0x01, 0x00, 0x01, 0x00, 0x01, Random	No
12	GOST R 50739-95	2 Pass, 0x00, Random	No
13	Guttman Method	35 Pass, Specified Random	No
14	Bruce Schneier Method	7 Pass, 0x00, 0x01, 0x00, 0x01, 0x00, 0x01, Random	No
15	Pfzner Method	33 Pass, Random	No
16	Write zero		No
17	Random Data		No

O. Software Tools for Secure Erasure

There are many software programs used for deleting secure data. The software uses the deletion methods mentioned in the previous section. The used software and supported erasure methods are shown in Table III [9-16].

TABLE XII. SOFTWARE TOOLS COMPARE

	1	2	3	4	5	6	7	8	9	10	11	12	13	14	15	16	17
CBL Data Shredder	+										+		+	+			
Disk Wipe	+							+				+	+			+	+
Secure Eraser	+										+		+				+
Macrorit Data Wiper	+															+	+
Eraser	+		+	+		+		+			+		+	+			+
PrivaZer	+		+	+												+	
PC Shredder	+												+				+
BitKiller	+												+			+	+
Puran Wipe Disk	+															+	+
File Secure Free				+									+				+
Free EASIS Data Eraser	+										+		+		+	+	+
WipeDisk	+												+			+	+
Super File Shredder	+												+			+	+
Hard Drive Eraser	+			+									+			+	
CCleaner	+												+	+		+	
Hardwipe	+										+	+	+	+	+	+	+
Freeraser	+												+			+	
DBAN (Darik's Boot and Nuke)	+					+							+			+	+

III. HARDWARE METHODS FOR SECURE ERASURE

A. Degausser Usage

Degauss devices aim to destroy data by removing or reducing the magnetic field effect in all devices that store data magnetically, such as hard drives. The Degauss device neutralizes the data on the magnetic disks with strong magnetic field. This method is the most guaranteed method to permanently erase the data in the disk. Degauss devices provide a controlled magnetic field measured by Gauss and Oersteds (Oe) units. The OE shows how hard a magnetic storage device can be wiped. In other words, OE is a mathematical term that indicates the magnetic field strength and density. The Gauss value is a mathematical value that indicates the intensity of the magnetic field generated by a degauss device. In general, the gauss value on a degauss device should be at least twice the Oe of the magnetic storage device to be erased. Degauss devices are available in many different brands and models. However, the erasure method works the same in all products. It is known as

the most guaranteed method to permanently erasure data [1,13,17].

B. Physical Destroy

Physically destroying a storage device is the only option to ensure that the data is not accessible. Physically destroying a storage device is the most important option to ensure that no data is available.

Several methods have been described by the National Institute of Standards and Technology for physically destroying hard drives such as disintegrate, pulverize, incinerate, melt [18].

IV. CONCLUSION

In this study, methods for permanently erasing data that do not require in digital storage device are shown. For this purpose, various software and hardware methods are used. In the study, tools used for permanent erasing and methods supported by these tools are presented. Hardware tools are more successful than software destruction methods for erasing data. The most effective method of guaranteeing permanent deletion of the data on a storage device is physical destruction. For this reason, the use of physical erasure methods is the safest solution for organizations with very critical data.

REFERENCES

- [20] P. Gutmann, "Secure deletion of data from magnetic and solid-state memory." Proceedings of the Sixth USENIX Security Symposium, San Jose, CA. Vol. 14. 1996, p. 77-89.
- [21] G. F. Hughes, T. Coughlin, and D. M. Commins. "Disposal of disk and tape data by secure sanitization." IEEE Security & Privacy 7.4 (2009).
- [1] Police, Royal Canadian Mounted. "G2-003." Hard Drive Secure Information Removal and Destruction Guidelines (2003). RCMP.
- [2] B. Schneier, Applied cryptography: protocols, algorithms, and source code in C. John Wiley & Sons, 2007. Schneir.
- [3] J. Reardon, D. Basin, and S. Capkun. "Sok: Secure data deletion." Security and Privacy (SP), 2013 IEEE Symposium on. IEEE, 2013.
- [4] G. Hughes, and T. Coughlin. "Tutorial on disk drive data sanitization." cmrr. ucsd. edu/people/Hughes/DataSanitizationTutorial. pdf (2006).
- [5] Z. Peterson, R. C. Burns, et al. "Secure Deletion for a Versioning File System." FAST. Vol. 5. No. 2005. 2005.
- [6] B. Lee, K. Son, et al. "Secure Data Deletion for USB Flash Memory." J. Inf. Sci. Eng. 27.3 (2011): 933-952.
- [7] U. S. Defense Security Services. Clearing and Sanitization Matrix, June 2007.
- [8] O. Tsur. "Enabling data security with COTS solid-state flash disks." Non-Volatile Memory Technology Symposium, 2004. IEEE, 2004.
- [9] Royal Canadian Mounted Police. G2-003, Hard Drive Secure Information Removal and Destruction Guidelines, October 2003.
- [10] T. Martin, and A. Jones. "An evaluation of data erasing tools." (2011).
- [11] MYC. Wei, LM, Grupp, et al. "Reliably Erasing Data from Flash-Based Solid State Drives." FAST. Vol. 11. 2011.
- [12] AS. Poonia, "Data Wiping and Anti Forensic Techniques." Compusoft 3.12 (2014): 1374.
- [13] BV. Avdeev, AV Berdyshev, et al. "The Problem of Reliable Destruction of Information on Electronic Media." Telecommunications and Radio Engineering 70.5 (2011).
- [14] D. Leong, V. Bahl, et al. "Secure data sanitization for archaic storage devices." Global Science and Technology Journal 1 (2013): 41-52.
- [15] SB. Geller, "Erasing myths about magnetic media." Datamation 22.3 (1976): 65-70.
- [16] YJ. Kim, YJ. Won, and RK Kim. "SOAR: Storage Reliability Analyzer." Journal of KIISE: Computer Systems and Theory 35.6 (2008): 248-262.

Software Modeling of Remote Controlled Beehive Design

Alisan Balta
Department of
Ecoinformatics,
Firat University,
Elazig, Turkey
alisanblt@gmail.com

Sengul Dogan
Department of Digital
Forensic Engineering,
Firat University, Elazig,
Turkey
sdogan@firat.edu.tr

Gonca Ozmen Koca
Department of
Mechatronics Engineering,
Firat University, Elazig,
Turkey
gozmen@firat.edu.tr

Erhan Akbal
Department of Digital
Forensic Engineering,
Firat University, Elazig,
Turkey
erhanakbal@firat.edu.tr

Abstract - Nowadays, beekeeping is at the forefront of agricultural activities, which are widely performed in the world. Beekeeping activities are also widespread in Turkey due to the favorable ecological and climatic characteristics. However, due the development of technology and the reduction of beekeeping activities because of environmental and climatic characteristics all over the world, it has become an important field of study in scientific activities. In this study, a software model for a remote controlled beehive design is presented. In order to solve the communication distance between hives and beekeepers, a software architecture has been studied on the platform where the system can be managed remotely

Keywords— beekeeping; beehive design; software modeling; ecoinformatics

A Comparison Study of Rail Fault Detection Methods in the Literature

Canan Tastimur, Mehmet Karakose, Erhan Akın
Firat University, Engineering Faculty
Elazığ, Turkey
{ctastimur, mkarakose, eakin}@firat.edu.tr

Abstract—Rails are one of the most important components of railway transportation. It is needed that the rails can be observed at regular interval in order to ensure the safety of railway transportation, prevent the disruption of transportation, and avoid accidents. To be inspected of rail surface by using manual techniques, both damage the rail surface and lead to disruption of railway transport.

Rail profile analysis methods that utilize contactless image processing techniques are available in the literature in order to avoid these problems. This paper presents a comparison of rail defect detection methods that are available in the literature. These methods in the literature have been compared in terms of feasibility, performance, accuracy, elapsed time, and image processing techniques used. The advantages and disadvantages of these methods relative to each other are examined in this article.

Keywords—Rail defects; image processing techniques; defect detection; rail surface analysis

I. INTRODUCTION

Railway transportation is considered as one of the safest transportation types all over the world. The railroad transportation is spreading rapidly. As railway transportation has become widespread throughout the world, the importance given to the maintenance and safety of railways has also increased. Railways are composed of several components. The most important component is rail. Train accidents happened every year in the world due to heavy task. And the train accidents resulted in serious destruction of property and injury or death of passengers and crew members [1]. Many of the railway transport accidents happen because of driver's tiredness, bad weather conditions, and defective rail components, etc. To prevent these accidents, importance is attached to the detection of faulty regions in the tracks, and other rail components.

Safety of railroad transportation can be enhanced by utilizing intelligent systems that provide additional information about the exact location of the train, its speed and upcoming obstacles. The rails face more and more risk of damage with the increase of speed [2]. Therefore, the rails should be closely inspected for internal and surface faults. Rail profile analysis using manual methods both damages the

rail surface and temporarily disrupts railway access. For this reason, rail profile analysis for railway transportation has been done using contactless image processing techniques. Methods, which detect the rail failures by means of contactless image processing techniques, are available in the literature. Sambo et al. [3] presented a novel algorithm that detect rail surface rolling contact fatigue (RCF) damage and automatic incorporation in a crack growth model recommended an important contribution to the development of modern techniques for non-destructive rail inspection.

Mao et al. [4] developed a sensor fault detection scheme for rail vehicle passive suspension systems, using a fault detection observer, in the presence of uncertain track regularity and vehicle noises that are modeled as external disturbances and stochastic process signals. Faghih-Roohi et al. [5] proposed a deep convolutional neural network solution to the analysis of image data for the detection of rail surface defects. They compared the results of different network architectures characterized by different sizes and activation functions. Hu et al. [6] detected uneven brightness and noise, the heavy rail surface defects, according to the characteristics of heavy rail surface defects, based on the mathematical morphology of multi-scale and dual-structure elements. Compared with the traditional edge detection operators, the results show that their method owns strong anti-noise performance, can detect the small defect edge accurately under noise.

Shen et al. [7] investigated the feature extraction of the turnout defects based on the bogie acceleration measurements. They established the normal turnout model and faulty turnout model based on SIMPACK and then analyzed the acceleration signal in time- frequency domain. The results showed that the power spectral density (PSD) and all the frequency-domain features are useful for detecting the poor fit defect of the switch point. Vijaykumar and Sangamithirai [8] developed a method that detect the surface defect on railheads. The proposed method used Binary Image Based Rail Extraction (BIBRE) algorithm to extract the rails from the background. The extracted rails were enhanced to achieve uniform background with the help of direct enhancement method. The enhanced rail image used Gabor filters to identify the defects from the rails. Thresholding was done based on the energy of the defects.

Yaman et al. [9], took images from two cameras placed at different angles on the established experimental structure. The images were preprocessed using the Otsu method. Then, rail surfaces are detected using Canny edge extraction and Hough transformation algorithms. The rail surfaces detected in the images taken from the two cameras are combined to detect failures on the track surface. The accuracy of the proposed method is enhanced by images taken from two different cameras. Block diagram of this study is given in Fig. 1. Tastimur et al. [10] offered Morphological feature extraction based image processing algorithm in order to determine the breakdowns of rails. The rail was determined through applying the image processing methods and Hough transform to the received images of rail. Headcheck breakage, apletic and undulation of defects was determined by proposed method. Faulty regions was determined through extracting features of regions in images by applying Morphological operations to detected rail images. Jie et al. [11] represented present a new vision based inspection technique for detecting special Rolling Contact Fatigue (RCF) defects that particularly occur on rail head surface. Wei et al. [12] proposed a rail defect detection method based on vibration acceleration signals. Molodova et al. [13] developed a method that the focuses on the early detection of short surface defects called squats and uses axle box acceleration (ABA) measurements.

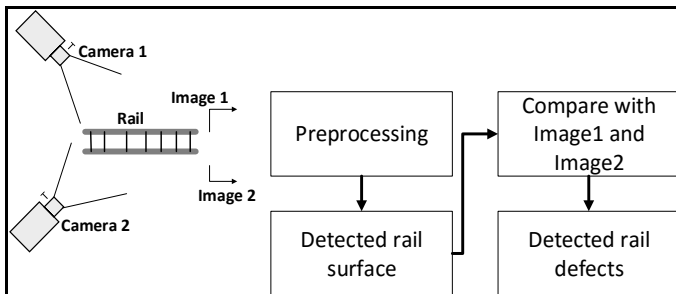


Figure 1. Block diagram of rail failure detection in the literature [9].

In this paper, we have compared several methods that exist in the literature to each other. It is examined rail fault detection algorithms, the performance of these algorithms, and the advantages and disadvantages of these algorithms in relation to each other. Moreover, these algorithms have been compared in terms of feasibility. Comparative tables are presented in the following sections.

II. RAIL SURFACE DEFECTS

Failures that have occurred in the rails can be expressed as wear, scour, breakage, undulation, headcheck, and oxidation [14]. Horizontal and vertical abrasions occur on the surface where the rails are exposed to the wheel. If the amount of wear on the rails is greater than 33 degrees, railings will be changed or curbing will be done because of climbing. Rail erosion occurs in horizontal curves, in scissors tongues and in scissors tongue. Raw abrasions are divided into vertical and lateral

wear. Vertical wear are erosion in the form of spreading and crushing, which occurs in the rail mushroom of curves, in the corners of the scissors and on the rail heads in the seals. Lateral abrasion occurs on the inner cheeks and scissors tongues of the outer rail under the influence of centrifugal force in the curves [15].

Headcheck defect is found around the gauge corner of outer rail and this fault ascending inclines to happen when cracks reach 30 mm in surface length [16]. The undulation failure can be expressed that different collapses happen in the rail surface [14]. The scour fault that can happen in the rail is one or several places of the rail due to the spinning of the locomotive. It should be exchanged rails exceeding the amount scour [14]. Rail oxidation is that crusting, decay, rust and small holes occur in the rail by effecting humidity, soil and water [14].



Figure 2. An example of the rail fracture [17].



Figure 3. An example of headcheck failure that occur in the rail [16].



Figure 4. An example of undulation defect that occur in the rail [14].



Figure 5. An example of scour defect that can happen in the rail [16].



Figure 6. An example of wear defect that can happen in the rail [18].



Figure 7. An example of oxidation defect that can happen in the rail [19].

III. THE RAIL DEFECT DETECTION METHODS

Many methods that detect rail surface defects exist in the literature. These methods employ contactless image processing techniques. So that the rail surface is not damaged. Besides, possible accidents are prevented by early detection of many rail failures. Rail fault detection methods that are frequently used in the literature are presented below.

A. Rail Damage Detection using Neural Networks

An onboard measurement system is done for measuring the rail robot's excursions from the rails midlines and the rail-robot's heights above the rail [1]. In this method, to deal with the nonlinearity of the measurement models, the coupling between the outputs, and the noise contamination, a neural network method is proposed for building high precision measurement models [1]. In addition to different measurement models for different types of rail tracks are also built based on the proposed neural network module. Signal processing and neural network module of the method used in [1] appear in Fig. 8.

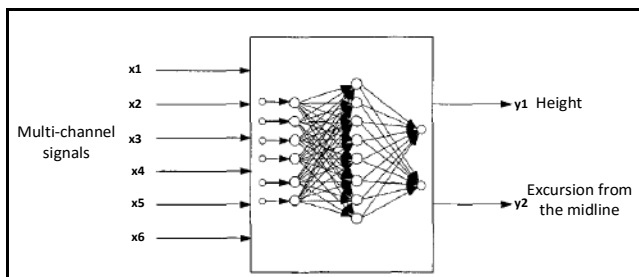


Figure 8. Signal processing and neural network module in [1].

B. Rail Fault Detection based on the Morphology of Multi-scale and Dual-Structure Elements

Heavy rail surface defects are detected based on the mathematical morphology of multi-scale and dual-structure elements according to the characteristics of heavy rail surface defects, uneven brightness and noise in [6]. When this method is compared with the traditional edge detection operators, the results show that this method owns strong anti-noise performance, can detect the small defect edge accurately under noise. Using the morphology of multi-scale and dual-structure elements, defects such as scratches, rolled-in scale, and uneven rolling on the rails are detected [6].

C. Rail Defect Detection using Gabor filters

In the [8], Binary Image Based Rail Extraction (BIBRE) algorithm is used to extract the rails from the background. The extracted rails are enhanced to achieve uniform background with the help of direct enhancement method [8]. The direct enhancement method enhance the image by enhancing the brightness difference between objects and their backgrounds [8]. The enhanced rail image uses Gabor filters to identify the defects from the rails. The Gabor filters maximizes the energy difference between defect and defect less surface. Thresholding is done based on the energy of the defects. From the thresholded image the defects are identified and a message box is generated when there is a presence of defects [8]. The faulty rail image taken as input and the faulty region detected are shown in Fig. 9 [8].

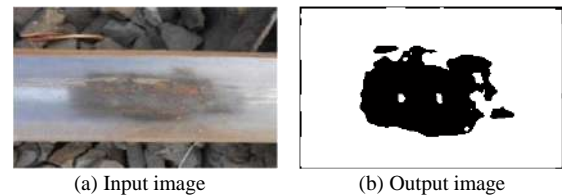


Figure 9. The faulty rail image and detected defects [17].

D. Rail defect detection with images taken from two cameras

In the [9], the images are taken from two cameras, which of them are placed at different angles on the experimental setup. The preprocessing stage is made by applying OTSU method to obtained images [9]. The rail surface is determined by using Canny edge detection and Hough transform. Faults occurred on the rail surface are detected by combining images taken from two cameras [9]. The accuracy of the proposed method was increased by using the images taken from two different cameras [9].

E. Detection of Surface Defects Using Wavelets

The signature tunes identified from numerical simulations are validated by field measurements in [13]. These signature tunes are employed in automatic detection algorithm for squats [13]. For the investigated Dutch tracks, the power spectrum in the frequencies between 1060-1160Hz and around 300Hz indicate existence of a squat and also provide information of whether a squat is light, moderate or severe. The detection algorithm in [13] is based on scale averaged

wavelet power. The averaging of the wavelet spectrum is performed at frequency bands related to squats [13]. The thresholds for detection of squats on Dutch track are obtained empirically [13].

F. Detection of Rail Faults using Morphological Feature Extraction

An algorithm using Morphological feature extraction based image processing is offered in order to determine the breakdowns of rails in [10]. The rail is determined through applying the image processing methods and Hough transform to the received images of rail [10]. Head check breakage, apletic and undulation of defects are determined by method in [10]. Faulty regions is determined through extracting features of regions in images by applying Morphological

operations to detected rail images [10]. In [10], all steps of the offered method is applied to the images of rail under different direction and lighting.

IV. COMPARISON STUDY OF THE RAIL DEFECT DETECTION METHODS IN THE LITERATURE

Studies in [1], [6], [8], [9], [10], and [13] have been compared in several respects. These respects are algorithm's accuracy rate and operation time, feasibility, techniques used in fault detection, detectable failures, hardware resource requirement, used software development environments, and images used in the algorithm. The advantages and disadvantages of these algorithms relative to each other are given in the following table.

Table 1. A comparison of these methods in literature

Study in the literature	Techniques used in fault detection	Detectable failures	Hardware resource requirement	Used software development environments	Feasibility	Algorithm's performance criteria
[1]	Neural Networks Proximity Sensors Levenburg-Marquart algorithm Signal Processing	Detect nonlinearity of the measurement models (defects)	Hardware are required (Proximity Sensors)	-	High	High accuracy rate
[6]	Mathematical morphology of multi-scale Dual-structure elements Edge detection algorithms	Scratch defect Backfin defect Uneven rolling Rolled-in scale	Hardware are required (CCD Camera)	-	Medium	Strong anti-noise performance Peak signal to noise ratio is 24.5 dB
[8]	Binary Image Based Rail Extractio	Scour defect	Hardware are required	Matlab	High	Accuracy rate 89.9%

	<p>n (BIBRE) algorithm</p> <p>Gabor filters</p> <p>Threshol ding</p> <p>Texture analysis</p>		(Digital camera of 12 megapi xels)			
[9]	<p>Otsu method</p> <p>Canny edge detection</p> <p>Hough transform</p> <p>Gauss Filter</p>	Wear defect	<p>Hardw are require d</p> <p>(Specia l light sources and laser camera)</p>	Matlab	High	<p>84.3 millisec ond elapsed time</p> <p>Standar d deviatio n 1.5</p> <p>The approximate speed of the system for 1 frame is 12fps</p>
[10]	<p>Morphol ogical feature extraction</p> <p>Hough transform</p> <p>Edge detection</p> <p>Laplacian filter</p> <p>Gradient computin g</p>	<p>Headche ck defects</p> <p>Breakage defects</p> <p>Apletilic defects</p> <p>Undulati on defect</p>	No hardwa re require	Matlab	Medi um	<p>0.6 sec.</p> <p>Accura cy rate 85.3%</p>
[13]	Axle box accelerati on (ABA) measure ments	Squats defect	No hardwa re require d	-	Medi um	<p>Accura cy rate</p> <p>78% for light squats</p>

	Wavelet power spectrum					100% for severe squats
	Low-pass filtering					

The algorithms in the literature are superior and weak to each other. It is suitable for on-line rail damage detection and measurement applications in [1]. Moreover different measurement models for different types of rail tracks are also built based on the in [1] neural network module. To deal with the nonlinearity of the measurement models, the coupling between the outputs and the noise contamination, a neural network method is proposed for building high precision measurement models in [1].

When studies in [9] and [10] are compared, study in [9] is superior to study in [10] in terms of elapsed time. Study in [10] is superior to study in [9] in terms of the type of failure detected. When studies in [6] and [13] are compared, study in [6] is superior to study in [13] in terms of the type of failure detected and study in [6] is weak according to study in [13] in terms of the hardware required. The number of failures detected among comparative methods is at most [10]. Superiority of method in [6] over other methods is that this method owns strong anti-noise performance. While the advantage of algorithm in [8] among other tasks is that the enhanced image has uniform background and defects highlighted from the illuminated background, the advantage of algorithm in [9] among other tasks is that failures on the track surface can be clearly identified by combining images taken from two cameras. The implementation in [13] has been checked with the real-life tests in the Netherlands.

ACKNOWLEDGMENT

This work has been supported by TÜBİTAK (The Scientific and Technological Research Council of Turkey). Project Number: 114E202

REFERENCES

- [1] Z.G. Hou, and M. M. Gupta, "A rail damage detection and measurement system using neural networks.", 2004 IEEE International Conference on. IEEE, Computational Intelligence for Measurement Systems and Applications, 2004. CIMSAA, 2004.
- [2] Q. Li, and S. Ren, "A visual detection system for rail surface defects.", IEEE Transactions on Systems, Man, and Cybernetics, Part C (Applications and Reviews) Vol. 42.6, pp. 1531-1542, 2012.
- [3] B. Sambo, A. Bevan, and C. Pislariu, "A novel application of image processing for the detection of rail surface RCF damage and incorporation in a crack growth model.", The International Conference on Railway Engineering (ICRE) 2016, pp.1-9, doi. 10.1049/cp.2016.0521, 2016.
- [4] Z. Mao, Y. Zhan, G. Tao, B. Jiang, and X.G. Yan, "Sensor Fault Detection for Rail Vehicle Suspension Systems with Disturbances and Stochastic Noises", IEEE Transactions on Vehicular Technology, Vol. PP, Issue 99, pp. 1-1, doi: 10.1109/TVT.2016.2628054, 2016.

- [5] S. Faghieh-Roohi, S. Hajizadeh, A. Núñez, R. Babuska, B. D. Schutter, "Deep Convolutional Neural Networks for Detection of Rail Surface Defects", 2016 International Joint Conference on Neural Networks (IJCNN), pp. 2584-2589, doi: 10.1109/IJCNN.2016.7727522, 2016.
- [6] G. Hu, L. Xiong, and J. Tang, "Heavy rail surface defects detection based on the morphology of multi-scale and dual-structure elements.", Chinese Automation Congress (CAC), 2015. IEEE, pp. 2126 - 2129, DOI: 10.1109/CAC.2015.7382856, 2015.
- [7] S. Li, X. Wei, and L. Jia, "Surface defects detection of railway turnouts.", Control Conference (CCC), 2015 34th Chinese. IEEE, pp. 6285 - 6290, DOI: 10.1109/ChiCC.2015.7260626, 2015.
- [8] V. R. Vijaykumar and S. Sangamithirai, "Rail Defect Detection using Gabor filters with Texture Analysis", 2015 3rd International Conference on Signal Processing, Communication and Networking (ICSCN), pp. 1 - 6, DOI: 10.1109/ICSCN.2015.7219838, 2015.
- [9] O. Yaman, M. Karaköse, E. Akin, and İ. Aydın, "Image Processing Based Fault Detection Approach for Rail Surface", 2015 23rd Signal Processing and Communications Applications Conference (SIU), pp. 1118 - 1121, DOI: 10.1109/SIU.2015.7130031, 2015.
- [10] C. Taştımur, E. Akin, M. Karaköse, and İ. Aydın, "Detection of rail faults using morphological feature extraction based image processing", 2015 23rd Signal Processing and Communications Applications Conference (SIU), pp. 1244 - 1247, DOI: 10.1109/SIU.2015.7130063, 2015.
- [11] L. Jie, L. Siwei, L. Qingyong, Z. Hanqing, and R. Shengwei, "Real-time Rail Head Surface Defect Detection: a Geometrical Approach", 2009 IEEE International Symposium on Industrial Electronics, pp. 769 - 774, DOI: 10.1109/ISIE.2009.5214088, 2009.
- [12] Q. Wei, X. Zhang, Y. Wang, N. Feng, and Y. Shen, "Rail defect detection based on vibration acceleration signals", Instrumentation and Measurement Technology Conference (I2MTC), 2013 IEEE International. IEEE, pp. 1194 - 1199, DOI: 10.1109/I2MTC.2013.6555602, 2013.
- [13] M. Molodova, Z. Li, A. Núñez and R. Dollevoet, "Monitoring the Railway Infrastructure: Detection of Surface Defects Using Wavelets", Proceedings of the 16th International IEEE Annual Conference on Intelligent Transportation Systems (ITSC 2013), The Hague, The Netherlands, October 6-9, 2013.
- [14] Y. Santur, M. Karaköse and E. Akin, "Random Forest Based Diagnosis Approach for Rail Fault Inspection in Railways", in The 9th International Conference on Electrical and Electronics Engineering (ELECO 2015), pp. 714-719, Bursa, Turkey, 26-28 November, 2015.
- [15] C. Taştımur, M. Karaköse, E. Akin, and İ. Aydın, "Rail defect detection with real time image processing technique", 2016 IEEE 14th International Conference on Industrial Informatics (INDIN), pp. 411 - 415, DOI: 10.1109/INDIN.2016.7819194, 2016.
- [16] R.P.B.J. Dollevoet, Design of an Anti Head Check profile based on stress relief, University of Twente, 2010.
- [17] Rail System Net, (2015), "Derailment". [Online]. Available: <http://www.railsystem.net/derailment/>
- [18] MPRNews, (December, 2015), "MN rail inspector's quest: Find the flaws, stop a future accident". [Online]. Available: <https://www.mprnews.org/story/2015/12/28/minnesota-rail-inspector>
- [19] Chapter My Chicago, (2014), "The Oxidation Rail". [Online]. Available: <http://www.capturemychicago.com/users/stackstack6>

Different Approaches for Language Identification

Ahmet Anil MÜNGEN

Department of Computer Engineering,
University of Firat,
Elazığ, Turkey
amungen@gmail.com

Mehmet KAYA

Department of Computer Engineering,
University of Firat,
Elazığ, Turkey
kaya@firat.edu.tr

Abstract— As a result of increasing internet usage, people who use over 100 different language creating resources and data on internet. In that situation, language identification is a very crucial problem on the Web also is a very important part of Natural Language Processing. This paper presents different approaches for language identification from beginning of the story to today. Also, we compare these different approaches in terms of implementation of a platform, accuracy, speed and complexity. We review over 10 methods and some of them are short words or common words, bi-graph and tri-graph models, letter combinations, n-grams, two-and three-letter clusters, multi-stream language identification methods. That is obviously come up that Artificial neural networks is the most successful method for language identification and machine learning. We give detailed comparison and their results.

Keywords— *language identification; agglutinating; Artificial neural networks*

I. INTRODUCTION

In the web, language identification and as a continuation translation have more and more important because of increasing internet usage rate. Also everyday documents which are written over 100 language uploading and accessing from other users via the Internet. Actually, language identification is a more complex problem as classification and recommendation. There is a lot of approach for language identification over years.

First of all, expert claim that language identification of written language is different than language identification for speech language. We are focus on writing language.

Language identification is not a new topic so there is a lot of different approach and method. There is the different type of document for Language Identification. One of them is monolingual document. In that type document, only one language are used for preparing document. However a big part of the academic article also document have preparing as multiple languages (multilingual). Working on monolingual document generally more easily than Multilanguage. The main differences from them is mono document requires only one language knowledge however Multilanguage are knowledge of several languages [1]. Also there are some other general problems for Language Identification[2].

Document length: Unfortunately, working on small data for Language Identification is a very problematic situation. That is why, vocabulary diversity is used for Language Identification in almost all methods. For example, micro blog websites like twitter limits users to write below 140 characters [3, 4, 5].

Noisy text: noisy in data is the one of the popular problem in data science for all areas like signal processing. Also text is a data and noises like abbreviation, short forms of words and tags are problems [4, 5]. Filtering these text is challenging. Also except of other areas, character encoding is one of main problem in texts [6].

Multilanguage Document: Sometimes documents are written in more than one language. In that time, approach have to successfully split different language regions [1].

Common words and phrase: Language occur repeating some words. Some words are used more frequently than others. Also some words can be used in different two language. Dedection common words and phrase, and removing them from methods is a very important.

Related and similar languages. Some languages root are same there for word diversity and dialects of these languages are closely similiary. Also lexical and grammatical features of these language is similar. Identification language between similar language is a crucial problem.

There have been many approaches for language identification. Generally short words or common words, bi-graph and tri-graph models, letter combinations, n-grams, two-and three-letter clusters, multi-stream language identification methods have been used for this task [7][8][9][10][11][12]. [13][14][15][16][17][18]. These approach generally based on characteristic letter and linguistic information also some approach using n-gram models, decision trees and Hidden Markov Models. Language Identification approaches can be categorize as feature-based models, support vector machines and similarity based classification [19].

Artificial neural networks (ANN) are using and applied for many different application in a variety areas due learning capability, generalizing and fast real-time computation features. Also, language identification is a appropriate task for for Artificial neural networks. In this paper, we make summary general approach for language detection and identify the language of a document based on neural networks.

The article is organized as follows: In Section 2, related works has been described. In Section 3, Artificial neural networks (ANN) is expressed. Section 4. The work as then concluded in the last section.

II. RELATED WORKS

A. Physical Quality of Geomaterials

Language Identification considered as a combining of Natural Language Processing and text classification. Both classification and NLP training set like predefined labels usually are used W. B. Cavnar and J. M. Trenkle [10] proposed N-gram based method for text classification also this method is used in many works for LI [20, 4, 21, 22, 23, 24]. N gram mainly is N-character longer string and N-grams of different lengths. In generally, N gram methods training set for all language to create language profile System measure similary of the input model to pre defined languages due to training set and selects the most similar language. A lot of N-Gram based approach are used for LI. Bashir Ahmed and friend [20] used ad-hoc cumulative N-grams in 2-grams to 7-grams to identification language in 12 languages. According to their paper, speed of their approach is more good than Naïve Bayes method

Erik Tromp and friends [4] propose a graph-based N-gram approach to identification language for medium and small texts. Almost all other approaches give importance to word occurrence. However this approach give importance both word occurrence and words order. Tromp apply their method on Twitter messages which are written in six languages detect language with very good accurate than the other N-gram based approaches. Ali Selamat and friend proposed An improved N-grams approach which are original N-grams approach and improved N-Gram Approach are combined [21]. They use distance measurement based feature from the original N-grams also Boolean matching approach from the improved N-grams methods. Yew Choong Chew and friends [22] improved N-gram algorithm for Language Identification for Asian languages based on non-Latin script. The performance of the algorithm was accuracy rate of 94.04% and can be used for 182 languages from Asia, Africa, America, Europe and Oceania. Except for these there are some unpopular works for identification of Indian languages [3,6,23,25].

Abdelmalek Amine and friends [26] have developed an algorithm which combine k-means and artificial ant class algorithm for especially using in multilingual document. They used N-Grams and/also similart text in completely unsupervised manner. Rafael DueireLins and friends [27], using closed word clases like Articles, Interjections,

Numerals and Prepositions for recognition strategy in English, French Portuguese and Spanish. Bruno Martins and friends [28] works on heuristics and a new similarity measure with N-gram to identify language. Marcos Zampieri [24] published article which proposed bag-of-words approach for language detection using Multinomial Naïve Bayes (MNB). MarcoLui and friend [1] using a generative mixture model which is similar with supervised topic modeling for multilingual documents

Kheireddine Abainia and friends [5] focus on filtering noisy text and they propose hybrid approach to removing noisy short texts. They combine term-based and character-based methods for filtering in noisy texts.

In general, four approaches exist:

The linguistic approach: Character based language detection is simply and basic method for language identification [29,30,34]. However these type of methods are pretty unsuccessful than others because of several problems [31]. For example "ü" and "ı" characters are contained from Turkish and Polish.

In the lexical approach all word compare to target words in lexical analyse for dedecting language. Also there is a lot of problem in this method. Almost all language lexicon is not complate (missing some words) also spelling mistakes or typing error break this method. For example, OCR which reproduce from scanning document, text results is very low with this method.

The grammatical approach: language has a grammatical rules like using prepositions, conjunctions but only %50 of grammatical rules regularly using correctly [32]. This approach is really faster but it have several problems like the texts should be segmented into words also have to removed stop words [33].

The statistical and probabilistic approach: N-Grams approach are contained by this category. Usually they focus on frequency or probability of occurrence and calculate the probability that a text which based on text classification [35,36,37,38] Actually, n-grams-based approach seems to be a widespread solution.

III. ARTIFICIAL NEURAL NETWORKS (ANN)

Artificial neural networks actually based on human biology and brain activity. Computer scientist try to simulate this biological approach to algorithm. Artificial neural networks gather information and easily understand and detect patterns and interactions between data and learn from data. There are many different type of Artificial neural networks for different application [39].

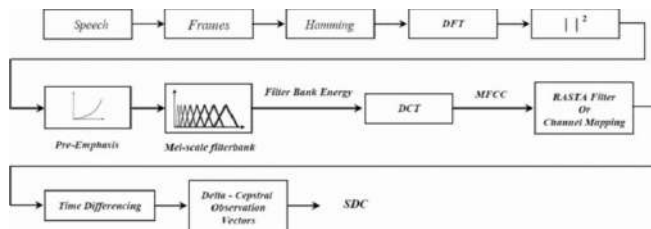


Figure 1. General Path for ANN [40]

Multilayered perceptron neural networks (MLPNNs) one of the simplest and fundamental model in Artificial neural networks. As a result of this, MLPNN is the most popular neural network model [39].

As shown in Figure 1, there is three types of layers which are contain by MLPNNs. First layer is an input layer which processing elements in the input layer when read something like input signals. In the hidden layer, input signals and derived signals weighting with the connections. This function has similarity with threshold function and tangent hyperbolic function.

In Artificial neural networks training is needed so approaches try to optimize the weights with decreasing sum of squared error (E) between the desired and actual values of outputs. Each weight consist of neighborhood and other connection also they are easily adjusted by adding an change with adding or reducing connection Therefore, training take several iteration until a satisfactorily small value of mistake.

At last but not least according to Google lab papers, google Translation API and Language Identifical API use Artificial neural networks and Google has Language Identifical with Artificial neural networks patents.

IV. CONCLUSION

The free dumping of municipal waste were carried on the slopes of landfill bottom layer of slag-fly ash, such as compacted fine-grained parts-upper geotextile and disturbed samples of bottom layer were taken. The experiments were conducted on compacted layer. The grain size distribution curves of the samples showed fine grains unit weight over 80% which limited consistency of coarse was less.

By the cutting box test effective cohesion (c) the effective shear strength and friction angle (ϕ°) of bottom layer and soils were determined.

Water content in the ground, the ratio of clay and fly ash affected significantly. As the evaluated according to the percentage of clay and fly ash in the samples showed cohesive or low cohesive property. The saturated unit weight is given in Table 2. Fixed level permeability test instrument is used to determine the permeability of the ground. Degree of permeability of the soil was determined by evaluating the test results (Table 3). As examined in Table 3, S2, S3 and S4 floors were permeable ground. Proctor tests showed the slag-fly ash effect on compaction,

V. CONCLUSION

The bond between the grains at geolayer and the compaction was critical in strength. The weathering of rocks in the study area is weakening quickly change the height and tilt angle of the slopes to erosion and slope. Dissociation seen in geolayer materials in the study area also offers a negative contribution to permeability problems. The compression strength could be easily tested by indentation on the landfill as shown in Figure 2. The durability of the landfill bottom layer was tested easily on the chart of fly ash and slag mixture content as given in the Table 2.

As a result of the geotechnical analysis performed in the study area should be considered in the future danger of very large stacks and site reclamation methods are suitable to be determined. In addition, the working area of the project due to be opened to urban use contraceptive methods studied and developed instability poses a special importance.

REFERENCES

- [1] Marco Lui, Jey Han Lau and Timothy Baldwin, (2014), "Automatic Detection and Language Identification of Multilingual Documents", Transactions of the Association for Computational Linguistics, pp. 27–40.
- [2] Jauhainen, T., Lindén, K., & Jauhainen, H. (2016). HeLI, a Word-Based Backoff Method for Language Identification. VarDial 3, 153.
- [3] Kavi Narayana Murthy and G. Bharadwaja Kumar, (2006), "Language Identification from Small Text Samples", Journal of Quantitative Linguistics, 2006, Volume 13, Number 1, pp. 57 – 80.
- [4] Tromp, E. & Pechenizkiy, M. (2011), "Graph-Based N-gram Language Identification on Short Texts", In Proceedings of the Twentieth Belgian Dutch Conference on Machine Learning (Benelearn 2011), pp. 27-34.
- [5] Kheireddine Abainia, Siham Ouamour, Halim Sayoud, (2014), "Robust Language Identification of Noisy Texts - Proposal of Hybrid Approaches", 11th International Workshop on Text-based Information Retrieval (TIR) 2014, Munich, Germany, September 2014.
- [6] Kosuru Pavan, Niket Tandon, Vasudeva Varma, (2010), "Addressing Challenges in Automatic Language Identification of Romanized Text", Proceedings of ICON-2010: 8th International Conference on Natural Language Processing, Macmillan Publishers, India
- [7] R.D. Lins, P. Gonçalves, "Automatic Language Identification of Written Texts", Proceedings of SAC-2004 the 2004 ACM symposium on Applied computing, pp. 1128-1133, 2004.
- [8] H. Takci, I. Sogukpinar, "Letter Based Text Scoring Method for Language Identification" in Lecture Notes in Computer Science, Berlin:Springer, pp. 283-290, 2004.
- [9] H. Takci, I. Sogukpinar, "Centroid Based Text Scoring Method for Language Identification" in Lecture Notes in Computer Science, Berlin:Springer, pp. 640-648, 2004.
- [10] W.B. Cavnar, J.M. Trenkle, "N-Gram-Based Text Categorization", Proceedings of SDAIR-94 3rd Annual Symposium on Document Analysis and Information Retrieval, pp. 161-175, 1994.
- [11] L.F. Lamel, J.L. Gauvain, "Language Identification using Phone-based Acoustic Likelihoods", Proceedings of the IEEE International Conference on Acoustics Speech and Signal Processing [ICASSP 94], vol. 1, pp. 1/293-1/296, 1994.
- [12] S. Parandekar, K. Kirchhoff, "Multi-stream Language Identification using Data-driven Dependency Selection", Proceedings of the IEEE

- International Conference on Acoustics Speech and Signal Processing. (ICASSP 03), vol. 1, pp. 128-I-31, 6-10 April 2003.
- [13] A.A. Reyes, T. Seino, S. Nakagawa, "Three Language Identification Methods based on HMMs", ICSLP, pp. 1895-1898, 1994.
- [14] P. Newman, "Foreign Language Identification: First Step in the Translation Process", Proceedings of the 28th Annual Conference of the American Translators Association, pp. 509-516, 1987.
- [15] T. Dunning, "Statistical Identification of Language", Technical report mcs 94-273, 1994.
- [16] J. Hayes, "Language Recognition using Two-and Three-Letter Clusters", Technical Report, 1993.
- [17] J. Hakkinen, J. Tian, "N-gram and Decision Tree-based Language Identification for Written Words", Proceeding of IEEE Workshop on Automatic Speech Recognition and Understanding, 2001.
- [18] G. Churcher, J. Hayes, S. Johnson, C. Souter, "Bigraph and Trigraph Models for Language Identification and Character Recognition", Proceedings of 1994 AISB Workshop on Computational Linguistics for Speech and Handwriting Recognition, 1994.
- [19] B. Hughes, T. Baldwin, S. Bird, J. Nicholson, A. MacKinlay, "Reconsidering Language Identification for Written Language Resources", Proceedings of the 5th International Conference on Language Resources and Evaluation (LREC 2006), 2006.
- [20] Bashir Ahmed, Sung-Hyuk Cha, and Charles Tappert, (2004), "Language Identification from Text Using N-gram Based Cumulative Frequency Addition", Proceedings of Student/Faculty Research Day, CSIS, Pace University, May 7th, 2004.
- [21] Selamat, Ali, (2011), "Improved N-grams Approach for Web Page Language Identification", Transactions on Computational Collective Intelligence V, Lecture Notes in Computer Science, Volume 6910, 2011, pp. 1-26.
- [22] Yew C. Chew, YoshikiMikami, Robin L. Nagano, (2011), "Language Identification of Web Pages Based on Improved N-gram Algorithm", International Journal of Computer Science Issues, Vol. 8, Issue 3, No. 1, May 2011, pp. 47-58.
- [23] Deepamala. N, Ramakanth Kumar. P, (2012), "Language Identification of Kannada Language using N-Gram", International Journal of Computer Applications, 6(4), pp. 24-28, May 2012.
- [24] Zampieri, M., (2013), "Using bag-of-words to distinguish similar languages: How efficient are they?" IEEE 14th International Symposium on Computational Intelligence and Informatics (CINTI), 2013, pp. 37-41, 19-21 Nov. 2013.
- [25] Sreejith C, Indu M, Dr. Reghu Raj P C, (2013), "N-gram based Algorithm for distinguishing between Hindi and Sanskrit texts", Proceedings of the Fourth IEEE International Conference on Computing, Communication and Networking Technologies, July 4 - 6, 2013.
- [26] Abdelmalek Amine, ZakariaElberrichi, Michel Simonet, (2010), "Automatic Language Identification: An Alternative Unsupervised Approach Using a New Hybrid Algorithm", IJCSA 7(1), 2010, pp. 94-107.
- [27] Rafael DueireLins, Paulo Gonçalves Jr., (2004), "Automatic Language Identification of Written Texts", ACM Symposium on Applied Computing, March 14-17, 2004, Nicosia, Cyprus.
- [28] Bruno Martins and Mário J. Silva, (2005), "Language Identification in Web Pages", SAC'05 March 13-17, 2005, Santa Fe, New Mexico, USA
- [29] S. Mustonen, "Multiple Discriminant Analysis in Linguistic Problems", Statistical Methods in Linguistics, vol. 147, pp. 195-197, 1965.
- [30] C. Souter, C. Churcher, G. Hayes, J. Hughes, J. Johnson, "Natural Language Identification Using Corpus-Based Models", Hermes Journal of Linguistics, vol. 13, 1994.
- [31] T. Dunning, "Statistical Identification of Languages. rapport MCCS" in Computing Research Laboratory, Las Cruces, New Mexico, pp. 94-273, 1994.
- [32] E. Giguet, "Méthode pour l'analyse automatique de structures formelles sur documents multilingues", 1998.
- [33] M. Sahami, "Using Machine Learning to Improve Information Access", 1999.
- [34] Gadri, Said, Abdelouahab Moussaoui, and Linda Belabdelouahab-Fernini. "Language identification: A new fast algorithm to identify the language of a text in a multilingual corpus." Multimedia Computing and Systems (ICMCS), 2014 International Conference on. IEEE, 2014.
- [35] R.M. Milne, R.A. O'Keefe, A. Trotmana, "A study in language identification" in ADCS December 05-06 2012, Dunedin, New Zealand, 2012.
- [36] M. Zampieri, B.G. Gebre, "Automatic identification of language varieties: the case of portuguese", Proceedings of KONVENS 2012 (Main track: poster presentations), September 20, 2012.
- [37] M. Sahami, "Using Machine Learning to Improve Information Access", 1999.
- [38] W.M. Geiger, J. Rauch, K. Hornik, "Text categorization in R: A Reduced N-grams Approach" in , Berlin Heidelberg:Springer-Verlag, 2012.
- [39] I. Biskri, S. Delisle, "les n-grammes de caractères pour l'aide à l'extraction de connaissance dans des bases de données textuelles multilingues", TALN 2001 Tours 2-5 juillet 2001.
- [40] Shadmand, Ali, and Khalil Monfaredi. "Language Detection with GMM Optimization Using Neural Networks." Computational Science and Optimization (CSO), 2010 Third International Joint Conference on. Vol. 1. IEEE, 2010

Performance Measurement for Distributed Systems using OPNET Principles

Subhi R. M. Zeebaree[†], Bishar Rasheed Ibrahim[‡], Mehmet Kaya^{*}

[†] Computers and Communications Engineering, Nawroz University, Duhok, Iraq

[‡] Bardarash Technical Institute-IT, Duhok Polytechnic University, Duhok, Iraq

^{*} Department of Computer Engineering, Firat University, Elazığ, Turkey
kaya@firat.edu.tr

Abstract— This paper presents a comparative study of two designs and analysis: Two Tier Architecture (2TA) and Three Tier Architecture (3TA). By using Optimized Network Engineering Tool (OPNET) modeler network-efficiency is done evaluation. OPNET, a professional simulation tool, is relied on to check the system with many clients from networks for both 2TA and 3TA. The outcomes demonstrate that 3TA is more capable than 2TA in term of data assessment is done utilizing OPNET modeler, which gives a convenient and easy-to-utilize platform for simulating extensive criterion networks. So, it will give more achievement when extended with many clients from networks with eight or sixteen clients. The models are utilized to study how the performance of the network is influenced by the different design decisions that are made to upgrade the system. This paper likewise examines ways in which the OPNET modules have been produced so that students could learn computer network concepts, and not exactly how to use OPNET software.

Keywords— Network Network ,OPNET,Three Tier Architecture (3TA)

I. INTRODUCTION

Network simulators have developed in development since them introductory showed as performance, establishment and expectation apparatuses. Simulators are usually utilized as network management apparatuses, for which packet level analysis is not generally employed. In spite of this, more studies are needed to build up rules for researchers so that they may choose and customize simulator to suite fine-grained packet level analysis [1, 2]. The breach of credibility that studies based on simulation devices need to handle which is one motivation behind this paper. The simplicity and facility that simulators give in assessing “radical” changes in a network environment cannot be ignored. There are impressive number of simulation tools in the market that have main characteristics such as exactness, speed, ease of use, and monetary expense. It concentrates on the accuracy of the simulation in comparison to a real network for packet level investigation. OPNET (Optimized Network Engineering Tools) is a comprehensive programming environment for demonstrating, simulating, and analyzing the performance of communications networks (define the Internet). Recent

articles [7] have described how it has been utilized as a part of education and research. Features of OPNET include object-oriented editors that mirror the structure of genuine networks, and support for most network type and technologies. OPNET has become the business standard tool for designing networks and assessing network performance under different test conditions. Thus, students will profit from introduction of this product. Configuring network models with OPNET requires many steps, and this can be overpowered for new users. Then student performs investigations on the essential model. The following stride involves adjustments of the fundamental network model and investigations of the modified networks. Along these lines the students can focus on learning computer network concepts, and gradually be acquainted to learning the stage on how to build network models with it. We introduce the modeling approach to another issue of assessing the execution of measure for distributed network systems. Our objective is to build up a simulation environment that would empower such an assessment. So, this is an introductory project. OPNET simulators have developed in development since they initially appeared as execution, administration and expectation tools. Simulators are normally utilized as network administration tools for which packet level investigation is not commonly employed. However, more studies are needed to build up rules for researchers so that they may select and customize a simulator to suit fine-grained parcel level analysis [1, 2].

The paper is organized as follows. Section II gives an overview of the developed model and presents its key components and functionalities. In Section III, simulation setup is introduced and the outcomes obtained with the OPNET modeler are discussed. In Section IV, the paper is concluded with few remarks on future work.

II. RESEARCH METHODOLOGY

Each electronic system needs both of software and hardware parts. It is preferred to have two different types of computers. The servers-side computers must be more powerful than clients-side ones (but if the client hosts are powerful too, it is not a problem). So, it is important to describe all software and applications utilized for designing

the proposed system. Also, required hardware features for the proposed system must be depicted. The system is implemented utilizing hosts with various features in order to give more practical applications and to be more close to the genuine situation. OPNET modeling and simulation flow diagram is shown in Fig. 1.

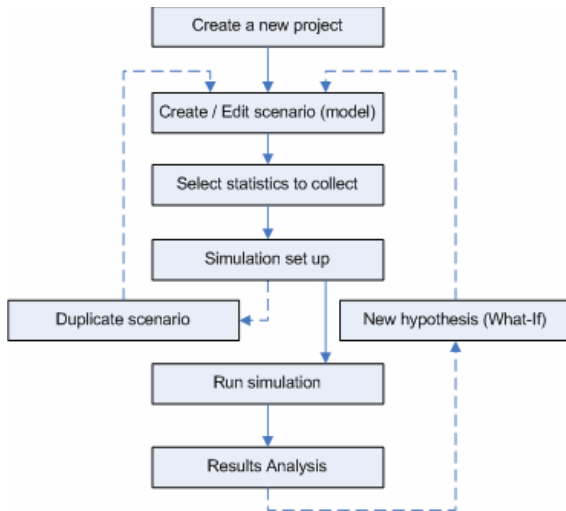


Fig. 1. OPNET modeling and simulation

A. Required Software for Windows-7

- Operating System: Windows-7
- Applications: OPNET Modeler
- Web Browser: HTTP server and Database server

Web communication environment consists of following elements:

1. Servers: Continually running programs that serve information to the web.
2. Clients: Web browsers that allow users to access the web.
3. Protocols: Database and hypertext transfer protocol (http)
4. Networks: Connected devices to a local area network and a wide area network with the form of Internet.

B. Architectures Diagram

Some of the modern design models of the software application [5] are illustrated in Fig. 2. and Fig. 3.

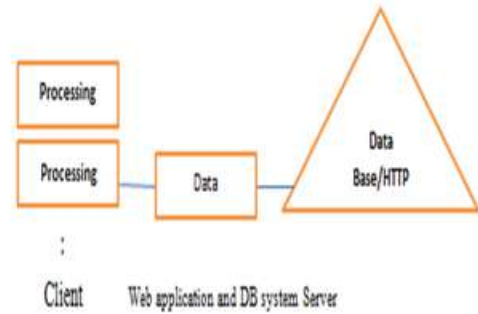


Fig. 2. Two tier architecture

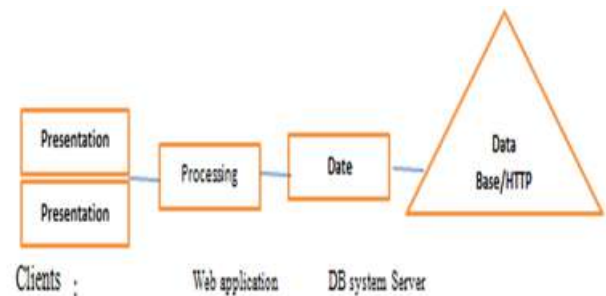


Fig. 3. Three tier architecture

Each of structures shown in Figs. 2 and 3 has its specific features. In the structure of Fig. 2., there is one server-host used for both of web-applications and database system, while the structure of in Fig. 3. includes two hosts for the servers-side, which one of them is specified for the web-application and the other for database system. Splitting the servers-side provides more security to the system. The focused point of this proposed system is to determine the performance of different organizations of network. The performance measures include Total-Network-Delay (TND), Server Delay (SD) and Server-Load (SL).

C. Evaluation Parameters

The evaluation parameters utilized in performance network are as follows:

- **Load:** It represents all control packets sent by the nodes in the network for finding and keeping up the server during the emulation. Loading capacity can be utilized to compare the scalability and efficiency as well as the ability to configure network congestion in various networks. Server protocols with extensive loading capacity have more probability of packet collision and delay.
- **Average delay:** This parameter refers average lag time of the packet going from the source node to the goal node. It consists of the buffer delay in the server finding

process, the transmission delay in the MAC layer and the transmission time.

III. RESULTS AND DISCUSSIONS

There are two main parts of the assessment. Firstly, the similar scenarios are applied for 2TA. Then, scenario is applied for 3TA. Both of scenarios utilize eight and sixteen clients and Windows 7. The consumed-time and the data flow for the general network and the server(s) are resolved.

Results obtained from evaluation-scenarios using OPNET tool are as follows.

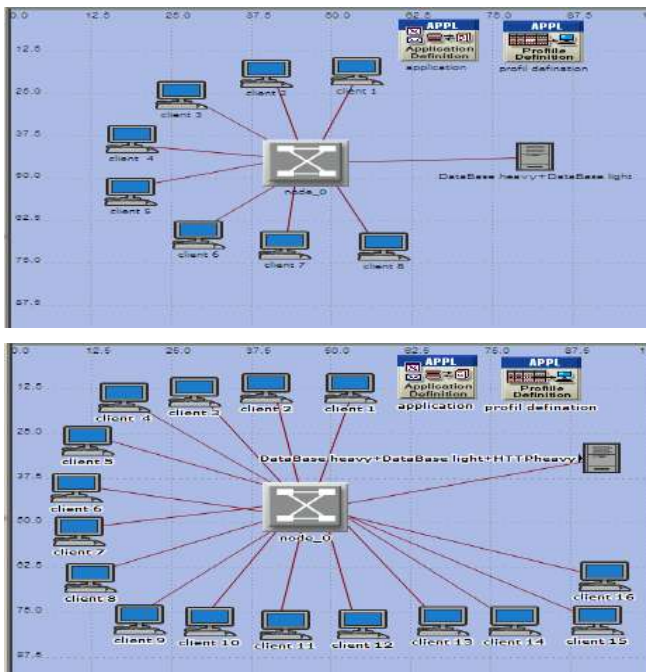


Fig. 4. Two tier architecture (A) utilizing 8 clients. (B) Utilizing 16 clients

TND, SD and SL are considered here that are related to the system performance measurements. From Table I, Fig. 5 and Fig. 6, it is clear that general delay of the network is more than that of the server-host (which are typical and expected outcomes). In general, server load can be noticed obviously because both of web application program and database system are put in one server-host (for 2TA).

TABLE XIII. TOTAL-NETWORK-DELAY AND SERVER-LOAD FOR 2TA

No. of Clients	Total Network Delay (sec.)	Server Delay (sec.)	Server Load (Bits/sec.)
8	0.0038	0.0048	1800000
16	0.0038	0.0048	3000000

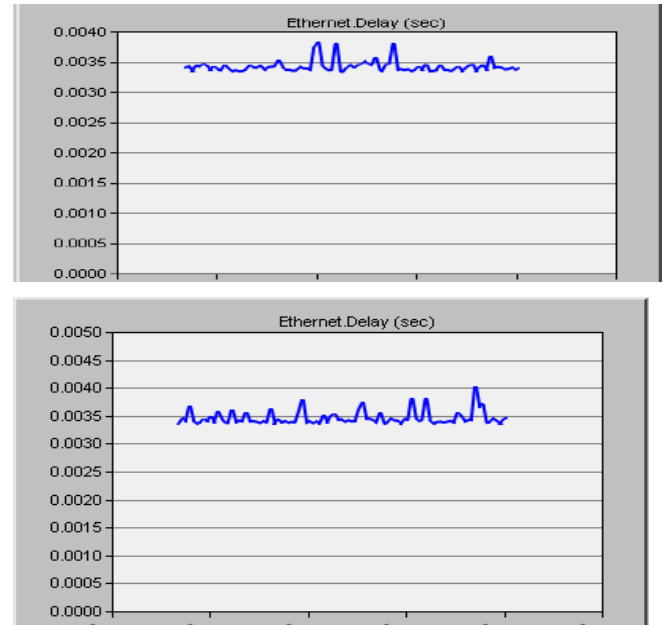


Fig. 5. Total-Network-Delay comparison of the two evaluation-scenarios for (A 8 clients, B 16 clients) 2TA

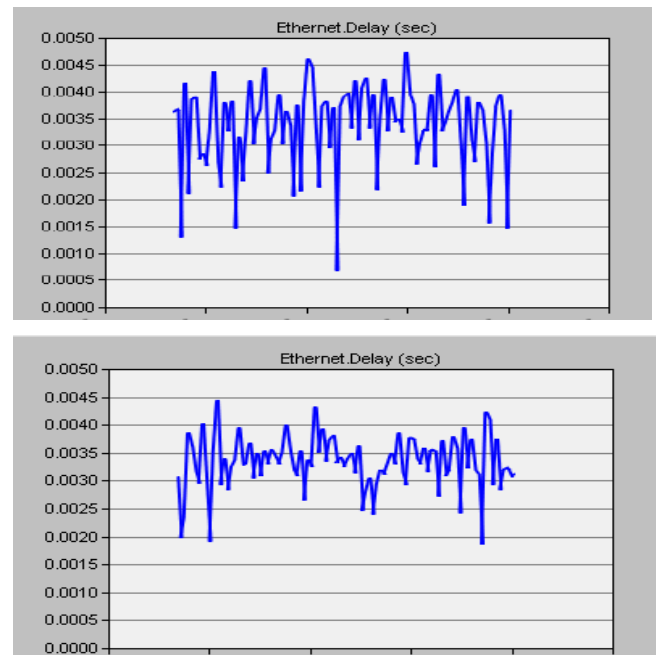


Fig. 6. HTTP-Server-Delay comparison of the two evaluation - scenarios for (A 8 clients B 16 clients) 3TA

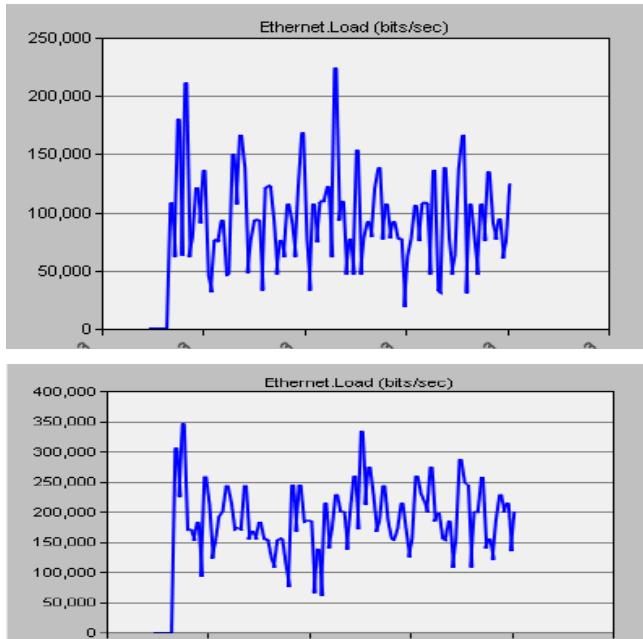
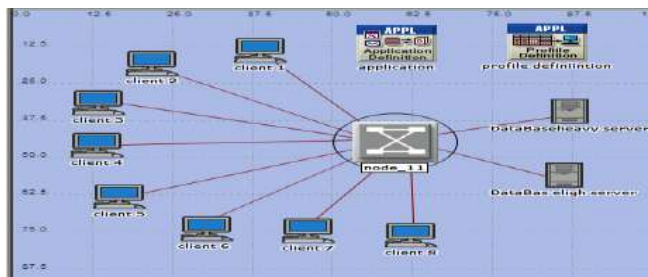
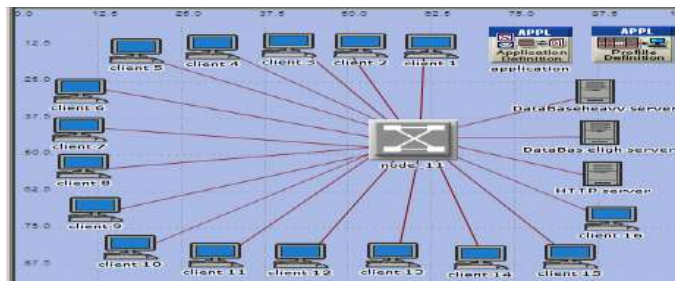


Fig. 7. Server-Load comparison of the two evaluation-scenarios for (A 8 clients, B 16 clients) 2TA



(A)

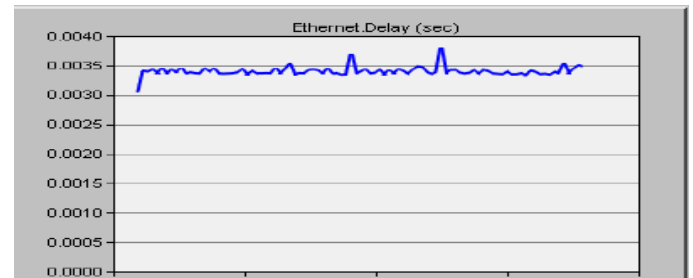


(B)

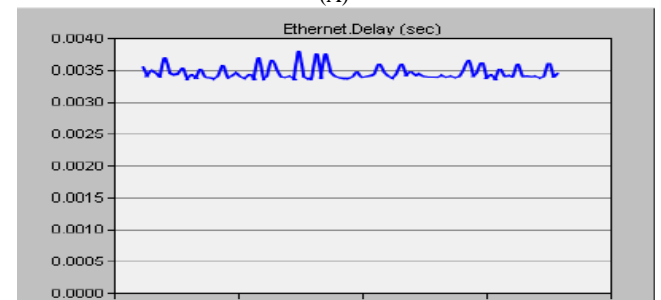
Fig. 8. Three tier architecture (A) utilizing 8 clients. (B) Utilizing 16 clients

TABLE XIV. TOTAL-NETWORK-DELAY AND SERVER-LOAD FOR (A 8 CLIENTS B 16 CLIENTS) 3TA

No. Of Clients	Total Network Delay (sec.)	Server Delay (sec.)	Server Load (Bits/sec.)
8	0.0038	0.0048	100000
16	0.0039	0.0049	200000

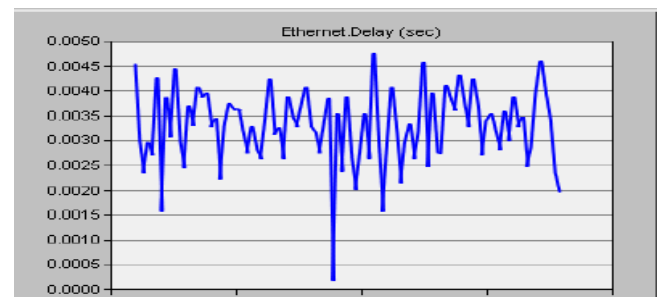


(A)

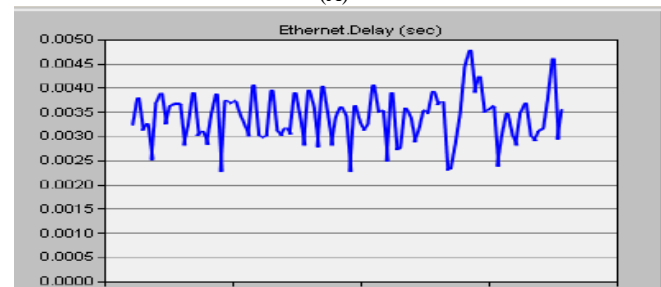


(B)

Fig. 9. Total-Network-Delay comparison of the two evaluation (A 8 clients B 16 clients) -scenarios for 3TA



(A)



(B)

Fig. 10. HTTP-Server-Delay comparison of the Two evaluation-scenarios for (A 8 clients B 16clients) 3TA

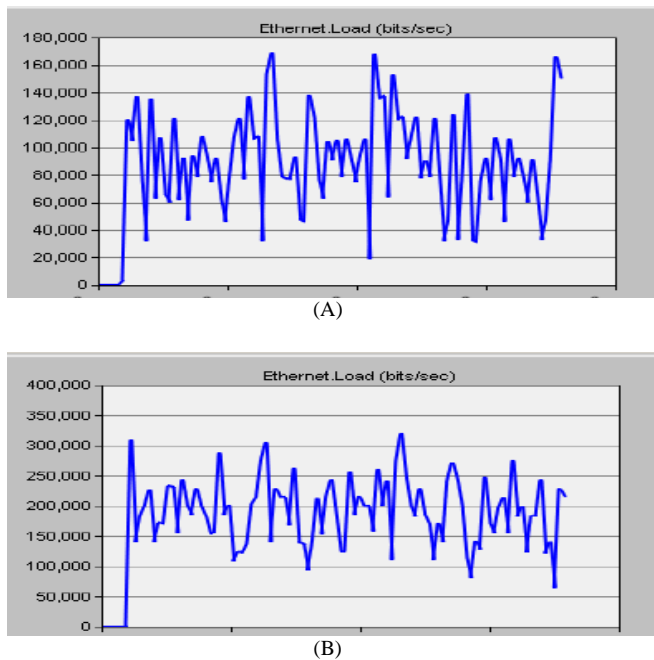


Fig. 11. HTTP-Server-Load comparison of the two evaluation-scenarios for (A 8 clients B 16 clients) 3TA

Fig. 7 outlines the impact of increasing number of clients on the amount of server load in term of (bit/sec). Subsequently, there is an instant proportion between number of client and server load. Fig. 8 represents the assessment-scenarios for 3TA utilizing eight and sixteen clients and OPNET tool. Table II represents Total-Network-Delay (TND), Server Delay (SD) and Server-Load (SL). Figs. 9, 10 and 11 represent TND, SD and SL comparisons of the two evaluation-scenarios for 3TA using OPNET tool. It can be appeared from Table II that the TND is greater with respect to those values of 2TA because of adding an extra server. Likewise, the SD values are less than those of 2TA because just http-server is considered (i.e. the delay of server that contains only the web application program). The http-server load will have higher load than that of 2TA because of the extra server in 3TA. The impact of these outcomes is outlined obviously in the plotted curves in Figs. 9, 10 and 11 that are extracted from Table II. Fig. 9 shows the impact of average values of TND for 3TA, and the differences can be taken note. Fig. 10 represents the average values of http-server-delay utilizing 8 and 16 clients. It is clear that there are no large differences among these values because just this server will face all received packets and the impact of communication between this server and database server can be ignored. The impact of increasing number of clients on the http-server is depicted in Fig. 11. This relation is instant proportion with increasing server load.

The overall evaluation of the proposed system shows that the 3TA is perfectly reliable with optimum results for both mentioned techniques. This section deals with two main parts.

The first part deals with the comparison related to both architectures of the proposed system (2TA and 3TA) whereas the second part deals with the evaluation of the obtained results compared with those of previous works.

IV. CONCLUSION AND FURTHER WORK

In this paper, the problem and motivation for modeling design/analysis networks was discussed and proposed an OPNET model for assessing measure in distributed network. System how effectively in the lessening of important factors, e.g. process-devoured -time, overhead-effort, expended -cost, reducing the issues of conjunction traffic, and even decreasing the side effects of environment causes depending on the obtained got from this system that demonstrated by evaluator programming called OPNET tools. The performance of the system utilizing 3TA was more precise than that of 2TA. As a result of utilizing two servers in 3TA, high security is provided by part both of application-server and DB-server. Adding to that, utilizing OPNET simulator as an expert assessment and designing tool and a vital performance assessment tool demonstrated the proficiency of 3TA than that of 2TA. Depending on the proposed system that has been designed, implemented and assessed. Also, thus, this office can be connected together to build an office. Designing and implementing human resources administration system is related to the administration part. Applying the details proposed by this system about extra services for example: operation rooms.

REFERENCES

- [1] [1] R. Currier. Test-drive your network designs. Network World, May 1999.
- [2] [2] J. Heidemann and K. Mills. Expanding confidence in network simulations. IEEE Network Magazine, 15(5): 58-63, 2001.
- [3] [3] Lazar R., Y. Huang, and A. Rizvi, "Strategic IT Alignment in Swedish Public Healthcare System " M.D. Lytras et al. (Eds.): WSKS 2008, LNAI 5288, pp. 105– 113, Springer-Verlag Berlin Heidelberg 2008, pp.105-113, 2008.
- [4] [4] Computer Networks A system Approach, Larry L.Peterson and Bruce S.Davie, April 2003.
- [5] [5] Faraj K., "Design and Implementation of an Automated ERecruitment System", PhD thesis, Sulamani University, 2009.
- [6] [6] Daniel Minoli by John Wiley & Sons, IP MULTICAST WITH APPLICATIONS TO IPTV AND MOBILE DVB-H, 2008.
- [7] [7] Telecommunications and Internet converged Services and Protocols for Advanced Networking (TISPAN); Service Layer Requirements to integrate NGN Services and IPTV Doc. Nb. TS 181 016 Ver. 3.3.1Ref. RTS/TISPAN-01059-NGN-R3,ITU-T,2009.
- [8] [8] OPNET Users' Manual, OPNET Architecture, OV.415, <http://forums.opnet.com>.
- [9] [9] M. Masuda and J. Ichimura. Evaluation of simulation accuracy and network planning case study, OPNETwebsitewhitepaper.
- [10] [10] K. Salah, A. Alkhoraidly, " An OPNET-based simulation approach for deploying VoIP", International Journal of Network Management archive, May 2006, Volume 16 Issue 3.

- [11] [11] Huijie Li, Xiaokang Lin, “An OPNET-based 3-tier network simulation architecture” Communications and Information Technology.
- [12] [12] Mohorko, J.; Fras, M., “Modeling methods in OPNET simulations of Tactical Command and Control Information Systems”, Systems, Signals and Image Processing, 2007 and 6th EURASIP Conference focused on Speech and Image Processing, Multimedia Communications and Services, 14th International Workshop on date: 27-30 June 2007, pp 446 – 449.
- [13] [13] Chow, Jocelyn, “Development of channel models for simulation of wireless systems in OPNET”, Transactions of the Society for Computer Simulation. Vol. 16, no. 3, pp. 86-92. Sept. 1999.
- [14] [14] Harding, C.; Griffiths, A., “An Interface between MATLAB and OPNET to Allow Simulation of WNCS with MANETs”, Networking, Sensing and Control, IEEE International Conference, 15-17 April 2007 ,pp 711 – 716.
- [15] [15] http://www.opnet.com/solutions/network_rd/modeler.html

SSVEP Tabanlı Beyin Bilgisayar Arayüzü İçin Görsel Uyarıların Sınıflandırılması

Classification of Visual Stimuli for SSVEP-Based Brain Computer Interface

Harun ÇİĞ

Harran University, Engineering Faculty
Şanlıurfa, Turkey
haruncig@harran.edu.tr

Davut HANBAY

İnönü University, Engineering Faculty
Malatya, Turkey
davut.hanbay@inonu.edu.tr

Özetçe— Güç spektrum yoğunluğu analizi (GSYA) ve Hilbert Dönüşümü (HD), Beyin-Bilgisayar Arabirimi (BBA) uygulaması için SteadyStateVisuallyEvokedPotentials (SSVEP) tanımayla başarıyla uygulanmıştır. Bu çalışmada SSVEP sınıflandırma işleminde yön ve uyaran frekansı tespiti için veri seti üzerinde aynı yön ve uyaran frekansına göre sinyal kümeleme işlemi yapılmıştır. Bu sinyaller 4-18 Hz arası bant geçiren filtreden geçirilip, HD uygulanmıştır. Daha sonra GSYA işlemi uygulanarak YSA ile sınıflandırma işlemi yapılmış ve ortalama %90 üzeri başarı elde edilmiştir. Önerilen GSYA-HD yönteminin üstünlüğü, gerçek zamanlı bir SSVEP tabanlı BBA'nın sınıflandırma konusunda geliştirilmesinin umut verici olduğunu göstermektedir.

Anahtar Kelimeler—Hilbert Dönüşümü; EEG; SSVEP; Yapay Sinir Ağları; Sınıflandırma

Abstract—PowerSpectralDensity Analysis (PSDA) andHilbertTransform (HT) has beensuccessfullyappliedto SSVEP recognitionforbrain-computerinterface (BCI) application. Inthisstudy, signalswereclassifiedwhichthesamedirectionandstimulus in the data set fortodeterminedirectionandstimulus of the signals in SSVEP classification. Thesesignalswereprocessedbythebandpassfilters at 4-18 Hz then HD processwereapplied. AfterthenpowerspectrumdensityanalysiswereappliedandclassifiedbyNeural Network. Evaluatedaveragesuccess rate is over 90 %. Thesuperiority of theproposed PSDA- HT method is promisingforthedevelopment of a real-time SSVEP-based BCI. **Keywords**—Hilbert Transform; EEG; SteadyStateVisuallyEvokedPotentials; Neural Network; Classification.

Keywords—Hilbert Transform; EEG; Steady State Visually Evoked Potentials; Neural Network; Classification.

I. GİRİŞ

İnsan beyni yaklaşık 100 milyar nöron hücrelerinden oluşan bir ağıdır. Farklı olaylar, farklı duyguları oluşturan farklı nöral bağlantılar oluşturur. Hangi nöronun uyarıldığına bağlı olarak bazıbelirli bağlantılar çok daha güçlü ve etkin olurken, diğerleri daha zayıf olabilir.

EEG sinyallerinin temelde genlik, frekans ve bazen faz yapısına dayalı olarak ortaya konan avantajları dikkate alınarak karakteristik özellikleri çıkarılır. EEG sinyallerinden öznitelikleri çıkarmak için çeşitli yöntemler geliştirilmiştir. Geliştirilen yöntemler arasında Zaman-Frekans (T-F) tabanlı olanların daha başarılı olduğu tespit edilmiştir. T-F tabanlı yöntemler, durağan olmayan sinyalleri zaman frekans alanı üzerindeki 2 boyutlu bir görüntüye dönüştürerek sinyallerin olası tüm özelliklerini açığa çıkarır [1].

EEG sinyalleri, T-F alanında gösterilen bu görüntülerden istatistiksel veya dokusal bazı genel ve yerel özellikler çıkarılarak bu amaç için tasarlanmış herhangi bir sınıflandırıcı aracılığıyla sınıflandırılır [1]. SSVEP, denek belli frekansta titreşen bir uyarıya dikkat ettiğinde titreşim frekansı ile aynı frekansta Oksipital bölgede kafa derisi üzerindeki harmoniklerinde ortaya çıkan periyodik bir beyin aktivitesidir [2].

Beynin nöral aktivitelerinin frekans tepki fonksiyonunu test etmek için SSVEP kullanılabilir. Ancak oküler motor bozuklukları veya ciddi nöromüsküler problemleri olan hastalar için SSVEP tabanlı BBA kullanılamayabilir [3].

Göz retinası belirli bir frekansta bir uyarıcı tarafından uyarıldığında, beyin; katları veya harmonikleri ile aynı frekansta bir elektriksel aktivite üretir [3]. Bu uyaran küçük genlikte sabit bir Görsel Uyarılmış Potansiyel (VEP) üretir. SSVEP' ler kullanıcının bakış yönüne de bağlıdır ve dolayısıyla kas kontrolünü gerektirir. Bu tür potansiyelleri üretmek için, kullanıcı belli bir frekansta salınım yapan titreşen bir uyarıcıya bakar [4].

Regan'a göre sabit yoğunluklu farklı frekanstaki titreşim bir uyarı, düşük (5-12 Hz), orta (12-25 Hz) ve yüksek (25-50 Hz) frekanstaki veya daha da yüksek frekans bantları ayrı ayrı sinyallerle SSVEP'leri tetikleyebilir [5]. BBA'lar son yıllarda SSVEP ile tasarlanmıştır. Olaya bağlı potansiyel veya sensorimotor ritim EEG ile kaydedilmiştir [6]. Görsel uyarılmış potansiyellerin saptanmasındaki iyileştirmeler GSYA olarak bilinen Fourier güç spektrumu ile çok boyutlu analiz edilerek önemli gelişmeler kaydedilmiştir [7], [8].

Doğrusal ve durağan olmayan bir sinyalden zaman-frekans bilgisi çıkarmak için Ampirik Kip Ayırıştırması (AKA) ve HD, sinyal analiz metodu olarak, Huang ve arkadaşları tarafından uygulamaya koyulmuştur [9]. Bu metod FastFourierTransform'undan (FFT) sonra önemli bir gelişme olarak görülmüştür. 2007'den beri, simüle edilmiş uyarı sinyallerinin (şablonlar) kullanılması SSVEP'lerin tanımlanmasında etkili olmuştur ve standart öznelik çıkarma, eşik değeri ya da karar ağaçları kullanımına göre daha yüksek performans elde edilmiştir [10].

2014'te Zhang ve arkadaşları Multivariate Synchronization Index (MSI) adlı yeni bir yöntem geliştirdi [7]. MSI, uyarı frekansını tanımak için bir potansiyel indeks olarak karışık sinyaller ve referans sinyaller arasındaki mevcut senkronizasyonu tahmin eden bir tekniktir. SSVEP tabanlı BBA, FFT ile GSYA kullanılıp SSVEP'i tanıyarak, öznenin kaydedilen EEG sinyallerinin bilgisayar komutlarına dönüştürülmesi için geliştirilmiştir. Sıradan bir SSVEP-BBA'da, kullanıcılara farklı frekanslarda yanıp sönen birkaç uyarı sunulmakta ve denekten bakış yönünü ve dikkatini uyarana vermesi istenmektedir. Bu tür SSVEP-BBA'lar genelde "bağımlı" olarak adlandırılır. Çünkü kas aktivitelerinden sayılan göz hareketlerinin farklı yönlerde değiştirilmesi istenmektedir [11]. Bununla birlikte "bağımsız" SSVEP-BBA'lar da vardır. Bunlar başın nöromusküler kontrolü veya göz hareketlerini yerine getiremeyen kişilerin dikkatleri tarafından kontrol edilir. Bu dikkatin gizli şekilde oluştuğu anlamına gelir. Bu tür SSVEP-BBA'lar da genelde "bağımsız" olarak adlandırılır.

Denek dikkatinin belirgin renklerde iki nokta kümesinden birine gizli kaydırılmasında SSVEP genlik ve faz tepkisinin modülasyon etkileri, Zhang ve arkadaşları tarafından araştırılmıştır [11]. Görsel dikkat yoğunlukla göz hareketleri aracılığıyla kontrol edilir ve dikkat edilen nesneler genellikle nettir, belirsiz değildir.

II. MATERYAL VE METOTLAR

BBA kullanıcının beyin sinyalleriyle bilgisayar arasında doğrudan iletişim sağladığı bir arayüzdür. Kas hareketine dayalı olmayarak alternatif iletişim kanalı üreten bir teknolojidir. BBA ile kaydedilen beyin sinyalleri belirli ön işleme tabi tutularak bazı özellikler çıkarılır. Bu özellikler ile sinyal reel komutlara dönüştürülür. Geleneksel EEG sinyal analizi filtreleme, özellik çıkarma ve sınıflandırma olmak üzere üç aşamadan oluşur. Bu çalışmada SSVEP tabanlı EEG sinyal veri seti uyarı frekans ve bakış yönüne göre

ayrıştırılıp, 4-18 Hz. arası bant geçiren filtreden geçirilerek HD uygulanmıştır. Son olarak GSYA işlemi uygulanıp, sadece prefrontal ve oksipital bölgelerinde olan AF3, AF4, O1 ve O2 kanallarından alınan sinyaller kullanılarak YSA ile sınıflandırma işlemi yapılmıştır.

A. STFT Spektrogram

STFT spektrogramı normalize edilmiş ve STFT katsayılarının karesi alınmış olarak tanımlanır. Matematiksel olmayan bir tanıma göre, STFT katsayıları, sinyali küçük parçalara bölmek için zaman domeninde kayan bir pencere kullanarak elde edilebilir ve daha sonra frekansları belirlemek için her bir parça Fourier dönüşümü ile analiz edilir [12]. Böylece zamanla değişen bir spektrum elde edilebilir. Matematiksel görünümde, STFT şu şekilde tanımlanabilir:

$$X(n, \omega) = \sum_{m=-\infty}^{\infty} x[m]w[n-m]e^{-j\omega m} \quad (1)$$

denklemde $x[m][n-m]$, $x[m]$ giriş sinyalinin n zamanındaki kısa süreli bir parçasıdır. Ayrıca ayrık STFT;

$$X(n, k) = X(n, \omega) \Big|_{\omega = \frac{2\pi}{N}k} \quad (2)$$

olarak tanımlanan denklemde, N , ayrık zamandaki örnek sayısını gösterir. Bu nedenle, logaritmik ölçekte spektrogram;

$$S(n, k) = \log |X(n, k)|^2 \text{ olarak tanımlanır.}$$

B. Hilbert Dönüşümü

Hilbert dönüşümü, FFT'nin aksine, durağan olmayan ve doğrusal olmayan zaman serilerinin analiz edilmesi için çok uygundur.

HD'nin kullanılması ile, analitik düzlemdeki sinyalin faz farkı ve potansiyel anomalinin kompleks gradyanları arasındaki dönüşümü hesaplanır.

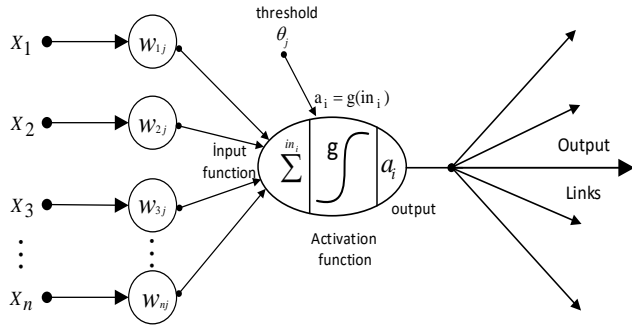
$$H(u(t)) = \lim_{\epsilon \rightarrow 0} \frac{1}{\pi} \int_{|s-t| > \epsilon} \frac{u(s)}{t-s} ds \quad (3) [13].$$

C. Yapay Sinir Ağları

Birçok nöron içeren, fiziksel olarak insan beyninden ilham alınan ve ondan karakterize edilen yapay sinir ağları (YSA) modeli ve ilişkili nöron bağlantılarının da gösterildiği tipik bir mimari Şekil 1'de gösterilmiştir. Bu nöronlar genelde ağ oluşumunda kullanılırlar. Ayrıca, her bağlantı ağırlık denen sayısal bir değer ile ilişkilendirilir. Her ağırlık, ağda transfer edilen ve sinyal ile çarpılan belirli bir değere sahiptir [14].

Nöronun çıktısı, aktivasyon fonksiyonuyla belirlenir. Literatürde doğrusal, tanjant sigmoid gibi birçok aktivasyon fonksiyonu kullanılır [15]. YSA'ların genelleme kabiliyeti

vardır; Bu nedenle eğitilen ağı bilinmeyen bir girdi uygulandığında uygun bir çıktı üretebilirler.



Şekil 1 YSA Model Yapısı

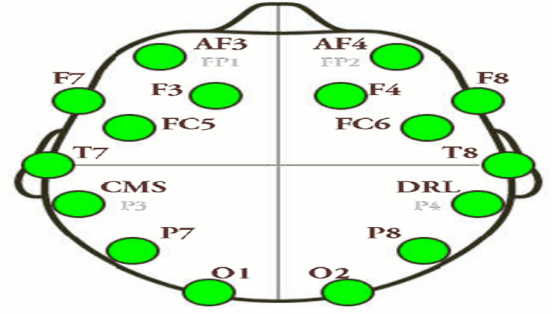
$$y(t+1) = a \left(\sum_{j=1}^n w_{ij} x_j(t) - \theta_i \right) \quad \text{ve}$$

$$f_i \triangleq net_i = \sum_{j=1}^n w_{ij} x_j - \theta_i \quad (4)$$

Burada $x = (xX1, xX2, \dots, xXn)$ nöronun n giriş parametrelerini, W_i , X_i girişi için ağırlıkları, θ bias değeri, $a(i)$ aktivasyon fonksiyonunu temsil eder. YSA'lar; veri madenciliği, iletişim, doğrusal olmayan sistemlerin modellenmesi, tıbbi uygulamalar ve paralel işleme yetenekleri nedeniyle desen eşleştirmeleri için kullanılmışlardır [16].

D. Veri Seti

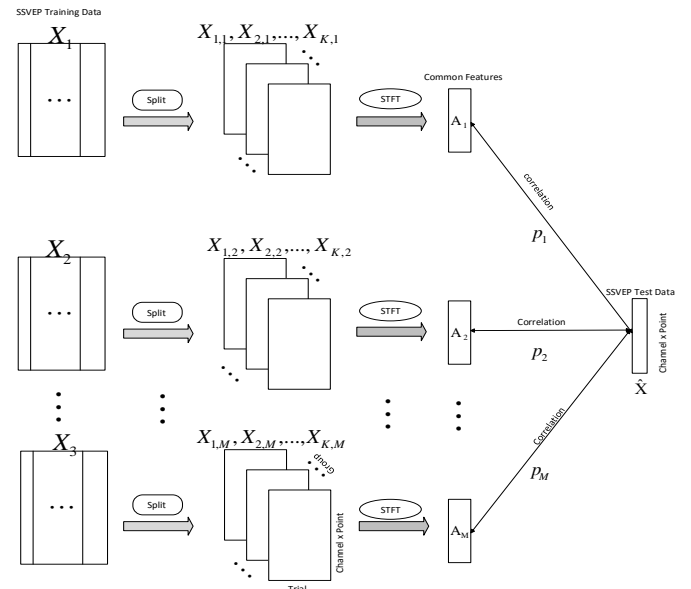
Bu çalışmada SSVEP tabanlı EEG veri seti kullanılmıştır. Bu veri seti MAMEM tarafından sağlanmıştır. Bu veri birçok araştırmacı tarafından sınıflandırma, oyun ve robot kontrolü gibi çeşitli amaçlarla kullanılmıştır. Bu çalışmaya araştırma ve teknoloji merkezi (CERTH) mevcut çalışanlarından 11 gönüllü katılmıştır. Yaşları 25 ila 39 arasında ve 8'i erkek, 3'ü kadın olup bilinen herhangi bir nöro-kas veya zihinsel rahatsızlığı olmayan deneklerdir. Deney uyarıcıları aynı anda beş farklı (6.66, 7.50, 8.57, 10.00 ve 12.00 Hz) frekansta titreşen beş mor kutudan oluşmuştur [17]. Yüksek kaliteli EEG verileri Emotiv Epoc ile 14 kablosuz kanalı (USB bağlantısı üzerinden) ve 128 Hz'lik bir örnekleme oranı kullanılarak kaydedilmiştir. Elektrotların, 10-20 uluslararası Sisteme karşılık gelen topoğrafik gösterimi Şekil 2'de gösterilmektedir.



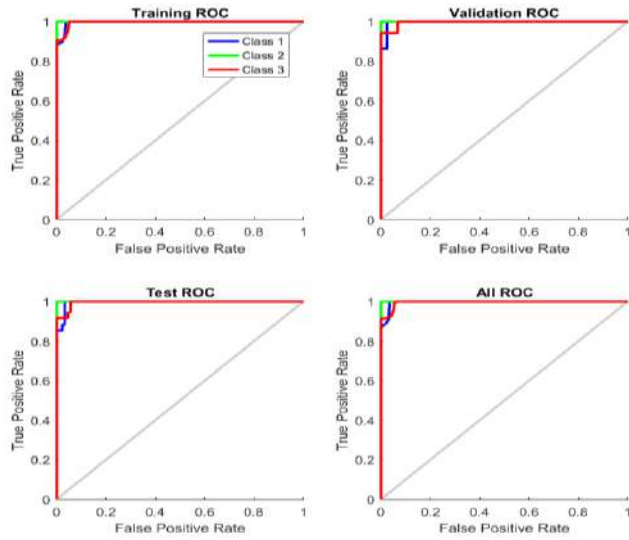
Şekil 2 10-20 Uluslararası Elektrot topoğrafik gösterimi

III. EEG SİNYAL ANALİZİ VE SONUÇ

Bu çalışmada veri seti içerisinde yön ve uyarın frekansına göre kümeleme yapılmıştır. Şekil 3' de gösterildiği gibi $X_1 - X_m$ Emotiv Epoc+ cihazından MAMEM tarafından alınan sinyallerdir. Bu sinyaller ayrıştırılarak aynı frekans ve yönde uyarın sinyaller beş sınıf oluşturacak şekilde bir araya getirilmiştir. Sinyal kümesi haline getirilen bu sinyallere 4-18 Hz bant geçiren filtre uygulandı, Hilbert dönüşümü hesaplanmıştır ve STFT' si alınmıştır. Daha sonra her sınıfın ayrı ayrı entropi, ortalama ve standart sapma değeri alınarak öz nitelikleri elde edilmiştir. Bu öz nitelikler ile SSVEP tabanlı farklı frekanslardaki (6,66, 8,57, 12 Hz) görsel uyarınlar ve sol, sağ ve yukarı olmak üzere farklı yöndeki göz hareketinden oluşturulan 3 küme YSA ile sınıflandırıldı ve ortalama % 90 üzeri başarı oranı elde edilmiştir. Şekil 4 de ise bu sınıflandırma sonucunun ROC eğrisi gösterilmektedir



Şekil 3 SSVEP tabanlı EEG sinyal işleme



Şekil. 4 YSA Sınıflandırma ROC grafiği

IV. TEŞEKKÜR

Bu çalışma İnönü Üniversitesi Bilimsel Araştırma Projeleri Koordinasyon Birimi Tarafından Desteklenmiştir. Proje numarası: 2016 -29 dur.

REFERANSLAR

- [1] A. Şengür, Y. Guo, and Y. Akbulut, "Time-frequency texture descriptors of EEG signals for efficient detection of epileptic seizure," *Brain Informatics*, vol. 3, no. 2, pp. 101–108, 2016.
- [2] G. R. Müller-Putz, R. Scherer, C. Brauneis, and G. Pfurtscheller, "Steady-state visual evoked potential (SSVEP)-based communication: impact of harmonic frequency components," *J. Neural Eng.*, vol. 2, no. 4, pp. 123–130, 2005.
- [3] R. M. G. Tello, S. M. T. Müller, M. A. Hasan, A. Ferreira, S. Krishnan, and T. F. Bastos, "Biomedical Signal Processing and Control An independent-BCI based on SSVEP using Figure-Ground Perception," *Biomed. Signal Process. Control*, vol. 26, pp. 69–79, 2016.
- [4] He B, Gao S, Yuan H, Wolpaw JR. Brain-computer interfaces. In: He B, editor. *Neural engineering*. Boston, MA: Springer; 2013. pp. 87–151.
- [5] D. Zhu, J. Bieger, G. Garcia Molina, and R. M. Aarts, "A Survey of Stimulation Methods Used in SSVEP-Based BCIs," *Comput. Intell. Neurosci.*, vol. 2010, pp. 1–12, 2010.
- [6] X. Chen, Y. Wang, S. Gao, T.-P. Jung, and X. Gao, "Filter bank canonical correlation analysis for implementing a high-speed SSVEP-based brain-computer interface," *J. Neural Eng.*, vol. 12, no. 4, p. 46008, 2015.
- [7] Y. Zhang, P. Xu, K. Cheng, and D. Yao, "Multivariate synchronization index for frequency recognition of SSVEP-based brain – computer interface," *J. Neurosci. Methods*, vol. 221, pp. 32–40, 2014.
- [8] Z. Lin, C. Zhang, W. Wu, and X. Gao, "Frequency Recognition Based on Canonical Correlation Analysis for SSVEP-Based BCIs," *IEEE Trans. Biomed. Eng.*, vol. 53, no. 12, pp. 2610–2614, 2006.
- [9] Z. N. Han and J. X. Gao, "Gear Local Fault Diagnosis with Empirical Mode Decomposition and Hilbert Huang Transformation," *AMR*, vol. 199–200, pp. 899–904, 2011.
- [10] R. M. G. Tello, S. M. T. Muller, T. Bastos-Filho, and A. Ferreira, "A comparison of techniques and technologies for SSVEP classification," 5th ISSNIP-IEEE Biosignals and Biorobotics Conference (2014): Biosignals and Robotics for Better and Safer Living (BRC). Institute of Electrical and Electronics Engineers (IEEE), 2014.
- [11] D. Zhang, X. Gao, S. Gao, A. K. Engel, and A. Maye, "An independent brain-computer interface based on covert shifts of non-spatial visual attention," 2009 Annual International Conference of the IEEE Engineering in Medicine and Biology Society. Institute of Electrical and Electronics Engineers (IEEE), 2009.
- [12] "9 Analysis of Sequences: Power Spectra and Periodograms," *Data Analysis for Scientists and Engineers*. Walter de Gruyter GmbH, 2016.
- [13] "Hilbert transform: Mathematical theory and applications to signal processing," 2015.
- [14] S. M. J. Pappu and S. N. Gummedi, "Artificial neural network and regression coupled genetic algorithm to optimize parameters for enhanced xylitol production by *Debaryomyces nepalensis* in bioreactor," *Biochem. Eng. J.*, vol. 120, pp. 136–145, 2017.
- [15] Ş. SAĞIROĞLU, N. ALASULU, M. C. ÇOLAK, M. A. ATICI, and C. ÇOLAK, "Radial Basis Function Neural Network and Logistic Regression Analysis For Prognostic Classification of Coronary Artery Disease Koroner Arter Hastalığının Sınıflandırılmasında Radial Basis Fonksiyonu Sinir," *Ankara Üniversitesi Tıp Fakültesi Mecmuası*, vol. 60. Ankara Üniversitesi, pp. 97–102, 2014.
- [16] S. Palaniappan and T. Pushparaj, "A Novel Prediction on Breast Cancer from the Basis of Association rules and Neural Network," *Comput. Sci. Inf. Technol.*, vol. 2, no. April, pp. 269–277, 2013.
- [17] İnternet 1: <http://www.mamem.eu/01/03/2017>.

An ANFIS Model for Geometry Optimization of Single Wall Carbon Nanotubes

Mehmet ACI

Department of Computer
Engineering
Mersin University
Mersin, TURKEY
maci@mersin.edu.tr

Çiğdem ACI*

Department of Computer
Engineering
Mersin University
Mersin, TURKEY
caci@mersin.edu.tr

* Corresponding Author

Mutlu AVCI

Department of Biomedical
Engineering
Çukurova University
Adana, TURKEY
mavci@cu.edu.tr

Abstract—Geometry optimization of Carbon Nanotubes (CNTs) is a very time-consuming process, even in the simulation environment, due to Density Functional Theory (DFT) calculations. The main aim of this research is to reduce DFT calculation time using an Adaptive Network-Based Fuzzy Inference Systems (ANFIS) based model for atomic coordinates from days to minutes. The dataset was created with the combination of the atomic coordinates of carbon atoms and chiral vectors using CASTEP software. The accuracy of the proposed models is evaluated with Mean Square Error (MSE), Mean Absolute Error (MAE), Standard Error of the Estimate (SEE) and Correlation Coefficient (R) metrics. The dataset is studied separately with and without using 10-fold cross-validation. The ANFIS prediction model yielded lower MSE and MAE results than previous study which uses only artificial neural network based prediction models.

Keywords—Neuro-fuzzy applications; Carbon Nanotube; Prediction.

1. INTRODUCTION

Nowadays, semiconductor technology is directed to carbon and carbon-derived structures which are IVA group of semiconducting elements and this situation makes simulations of structures to be synthesized important. For these simulations, the methods of preterm delivery (ab initio) are being implemented with each passing day. There is a need for alternative approaches that will facilitate operations in the face of complex computations of these methods.

Density functional theory (DFT) calculates atomic coordinates faster than other mathematical approaches and reaches more accurate results and therefore it is the most successful method. Nevertheless, the elapsed calculation time measured in this study using BIOVIA Materials Studio CASTEP [1] for high number of atoms is quite long [1]. Due to calculation capability limits of workstation computers, calculations may even take several days. Thus, to reduce the calculation time, researchers need to buy and use more

powerful but expensive workstations and parallel computer grids. In literature, many researchers remark this calculation time problem in their studies. General view of the researchers who studied on geometry optimization using DFT can be summarized as “DFT calculations are time consuming” [2–5].

This research has the motivation that is the calculation time reducing from days to minutes for atomic coordinates. Also, it is clear that the calculation time cannot be reduced up to this level using the current mathematical methods. In this work, the problem is investigated in another perspective. An accurate and fast prediction of the atomic coordinates is done instead of calculation. In some researches predicted atomic coordinates may be enough in accuracy. In that cases the proposed approach with direct result outcomes may be the fastest solution. The prediction mechanism to reach faster results with limited accuracy may be obtained by using neuro-fuzzy methods.

In this study, the main aimed objective is developing a prediction model using Adaptive Network-Based Fuzzy Inference Systems (ANFIS) to estimate the atomic coordinates of Carbon Nanotubes (CNTs). Two distinct datasets named as input dataset and output dataset are prepared to be used in prediction models. The 5 parameters of input dataset are initial atomic coordinates (u , v and w) and chiral vector (n and m). On the other hand, the 3 parameters of output dataset are calculated atomic coordinates (u' , v' and w'). CASTEP software is used for three processes: the CNTs simulation, the geometry optimization calculation and the creation of output file for each chiral vector including the initial and calculated atomic coordinates. Mean Squared Normalized Error (MSE), Mean Absolute Error (MAE), Standard Error of Estimation (SEE) and Multiple Correlation Coefficient (R) are determined to evaluate the performance of prediction models.

The organization of the study is presented as follows: This section covers short reviews of CNTs, Ab Initio Method, and DFT. In Section 2, summaries of the researches performed on this topic are given briefly as past works. In Section 3, the materials used in this study and ANFIS, specifically the ANFIS toolbox in MATLAB are explained. The results of

fuzzy/neural approach used in atomic coordinate prediction is discussed in Section 4. In last, Section 5 contains concluding remarks.

A. A. Single-Wall Carbon Nanotubes (SWCNTs)

Fullerenes[6], graphene[7] and CNTs [8] are very constant sp^2 carbon bonded materials at nanometer size and their discoveries motivated to make investigations in this field. Graphene and CNTs have many common physical properties which are derived from graphene. Carbon atoms of graphene are densely arranged in a regular sp^2 -bonded atomic-scale honeycomb (hexagonal) pattern. For other sp^2 carbon bonded materials (allotropes) like fullerenes and CNTs, this pattern is a basic structure. The theoretical difference of CNT is being a cylinder fabricated of rolled up graphene sheet. It has two types according to wall types. Single-wall carbon nanotubes (SWCNTs) were reported in 1993 [9] and have only one wall. Iijima[10] were first discovered multi-wall carbon nanotubes (MWCNTs) in 1991 and these nanotubes have more than one wall (Fig.1)[11].

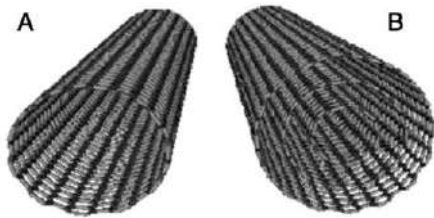


Fig. 1. Schematic structure of SWCNT (A) and MWCNT (B)[11]

The diameter of a SWCNT differ from 0.4 to 3 nm and its length is generally of the micrometer range. Usually they come together to form bundles (ropes). They organized hexagonally in a bundle structure and form a crystal-like construction [8]

SWCNTs can exist in three forms named as armchair, chiral, and zigzag according to wrapping to a cylinder way (Fig.2). Chiral vector is a pair of indices (n, m) that directly effects electrical properties of nanotubes and characterizes the structure of SWCNTs. The integers, n and m , determine the number of unit vectors along two directions in the honeycomb crystal lattice of graphene. According to the general opinions, the nanotubes are called as zigzag nanotubes when $m=0$. If $n=m$, then they are called as armchair nanotubes and for all other states they are named as chiral[11].

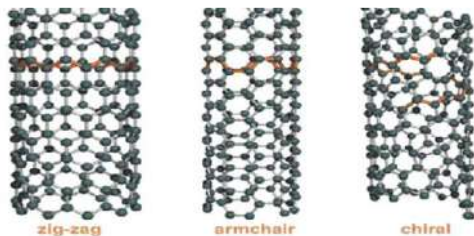


Fig. 2. Models of three atomically perfect SWCNT structures[11]

The tube diameter d [4, 5] and the direction of rolling a graphene sheet are determined by the chiral vector $C_h = na_1 + ma_2 \equiv (n, m)$, where a_1 and a_2 are the base cell vectors of graphite (Fig. 3). Thus, the carbon tube diameter (Eq. 1) can be calculated by

$$d = \frac{a\sqrt{m^2 + mn + n^2}}{\pi} \quad (1)$$

where a is the lattice constant in the graphite sheet [11].



Fig. 3. The chiral vector C [11]

A nanotube is classified as 'metallic' or highly conducting nanotubes if $n - m$ is a multiple of 3, otherwise it is a semimetallic or semiconductor. However, an armchair formed nanotube is always classified as metallic.

B. B. Ab Initio Method, Density Functional Theory and CASTEP

The atomistic viewpoint becomes a very critical issue for both scientists and engineers after the materials behavior at nanoscale are dominated by the effects of single atoms. Nevertheless, to achieve the straightforward manipulation of the nanostructure is rather complex and for this reason it is difficult to measure the experimental results of mechanical properties at nanoscale. So, to investigate the mechanical properties of nanostructures, the importance of computer modeling becomes more important every day for new technologies development. The interaction between atoms is considered dynamically and statically with dynamic and static models, respectively. Ab initio and tight-binding methods, and classical molecular dynamics simulations are three types of the dynamic methods[12].

Ab initio method needs a wave function description for the electrons because it treats separately the electronic and ionic degrees of freedom. The ab initio is an expensive and time-consuming method and for this reason some approximations like the DFT are incorporated instead of many-body interacting wave functions. DFT is based on the fact that the ground-state electronic energy is a unique function of the electronic density [12].

Hohenberg and Kohn [13] and Kohn and Sham [14] developed a simple method, DFT, that describes the effects of exchange and correlation in an electron gas. The total energy, that contains exchange and correlation, of an electron gas is a unique functional of the electron density and this fact proved by [13]. The ground-state energy of the system is the minimum value of the total-energy functional. The exact

single-particle ground-state density is this minimum value which is obtained from the density. It is showed that an exactly equivalent set of self-consistent one-electron equations is used instead of the many-electron problem by [14].

The ground state energy is given in Eq. 2

$$E = \sum_i \epsilon_j - \frac{1}{2} \int \frac{n(r)n(r')}{|r-r'|} dr dr' - \int v_{xc}(r)n(r)dr + E_{xc}[n(r)] \quad (2)$$

where E_{xc} is the exchange correlation energy, V_{xc} is the exchange correlation potential energy, $n(r)$ is the electron density and the ϵ_j and n are the self-consistent quantities [15].

The CASTEP software [16] is used to perform electronic structure calculations as a first principles quantum mechanical code. A wide range of materials like surfaces, crystalline solids, liquids, molecules and amorphous materials can be simulated with CASTEP within the density functional formalism [17].

Depending on the finite speed and memory of the used computer, CASTEP can calculate the properties of any material that formed from an assembly of nuclei and electrons. This is an ambitious approach that aims to rely on quantum mechanics instead of to use experimental (empirical) data [17].

CASTEP has numerous capabilities and it is a fully featured first principles code. The total energy derived from many other quantities is the basic quantity aiming to calculate any physical property of the system from first principles.

2. RELATED WORK

In recent years many researchers studied on CNTs to obtain perfect CNTs and widen their application areas. Some of the studies are focused on geometry optimizations of the CNTs. Also many of the researchers that study on CNT calculations, incorporate artificial intelligence methods into their works. Nowadays, this incorporation trend has been increasing.

DFT calculations in CASTEP were used by many researchers for CNT studies. Bauschlicher and Ricca [2] utilized from DFT and the second-order Møller-Plesset approaches to study the interaction of NH₃ with graphite and a (9,0) CNT. They used CASTEP for DFT calculations and denoted that the optimization calculations are very time consuming even running in parallel. Hong-Xia et al. [18] achieved the structure of heterojunctions made up of an (8, 0) CNT and an (8, 0) boron nitride nanotube, and an (8, 0) CNT and an (8, 0) silicon carbide nanotube through geometry optimization implemented in the CASTEP with two distinct studies. They designed a two-probe system of the heterojunction and calculated its transport properties with a method combining nonequilibrium Green's function with DFT. They limited the bias range -3.0 to 3.0 V to avoid from the time consuming calculations. A numerical study of conjoined structures of graphene nanoribbons and CNTs

were performed by [4]. They performed all calculations in CASTEP. As the calculations were time consuming, they were made for relatively small super-cells, including several hundreds of atoms. Mao and Zhong [19] investigated the geometries and electronic properties of junctions constructed from armchair and zigzag CNT insertion graphene matrix using first-principles DFT calculations. The study was implemented in the CASTEP and based on the first-principles plane-wave pseudopotential DFT. Because of the larger number of atoms in the supercell and expensiveness of the calculation time, more K points along the tube axis are considered in the calculation of the band structure instead of the structural optimization.

There are many studies can be seen in the literature working on CNTs that use ANFIS. A new methodology is presented by Al-Khedher et al. [20] to investigate the correlation between indentation resistance of MWCNT turfs, Raman spectra and the geometrical properties of the turf structure. They used adaptive neuro-fuzzy phenomenological modeling for the study. Ahadian and Kawazoe [21] proposed an ANFIS for modeling of water flow in CNTs. An input-output mapping based on both human knowledge in the form of fuzzy if-then rules and stipulated input-output data pairs can be constructed by the presented ANFIS approach. They obtained good performance with the designed ANFIS. A set of novel models employing field effect transistor structures using graphene has been proposed and the current-voltage characteristics of graphene have been employed to model the sensing mechanism by Akbari et al [22]. For the current-voltage characteristic, another model is provided using an ANFIS. The study showed that the proposed model and the experimental data exhibit satisfactory agreement with each other and Escherichia coli bacteria can detected by this biosensor with high levels of sensitivity. Alibabaiy et al. [23] applied ANFIS for modeling and simulation of CNT metal-oxide-semiconductor field-effect transistors. They mentioned that the computational time is reduced with ANFIS model while the accuracy of physics-based model like nonequilibrium Green's function formalism is kept. In last, they imported the proposed ANFIS model into HSPICE software as a sub-circuit and the results showed that the ANFIS model is suitable to be incorporated into Spice-like tools for nanoscale circuits simulation. A network is trained by Savari et al. [24] to simulate pressure drop and convective heat transfer coefficient in a circular tube with a constant heat flux. They obtained experimental data in the presence of non-covalently and covalently functionalized MWCNT-based water nanofluids. They modeled the experimental results by the ANFIS method and investigated the proposed method of ANFIS modeling in terms of validity. Lastly, they proposed a valid ANFIS method for MWCNT-based water nanofluids in a circular tube with constant heat flux. The hardness of copper/carbon nanotube nanocomposite is predicted by Sahraei et al. using Two different proposed fuzzy inference systems (FISs) [25]. A predictive framework is simulated for

current case study with engaging of two different machine learning algorithms. The requirements for fast adaption of the consequent parts of FIS are provided by the classic least square optimization method. In the second method, the rudiments of neural computing through layering the FIS and back-propagation optimization algorithm is used. The results showed that the knowledge required to predict the hardness of copper/CNT nanocomposite can be extracted using the adopted fuzzy systems. The buckling instability of perfect and defective CNTs is predicted using an ANFIS by Fakhrebadi et al[26]. Firstly, they obtained the results for some cases using structural mechanics and due to the uneven trends of the results, they are fed into an to predict the buckling loads of the unmodeled CNTs. Some special cases are used to validate the capability of the predictive tool and the accuracy of the predicted results.

Although there are many studies summarized above regarding the use of ANFIS in CNT field, there is no study about calculation of atomic coordinates. Only, Aci and Avci[27] developed four artificial neural network (ANN) models that predicts atomic coordinate of CNTs. They obtained very satisfied results and showed that instead of mathematical calculations, ANN models can be successfully used to predict atomic coordinates of CNTs.

3. MATERIAL AND METHOD

C. A. Dataset

In this study, the used dataset is generated using CNT geometry optimization with CASTEP. Geometry optimizations of the simulated CNTs are calculated and saved in distinct files using CASTEP. The initial coordinates of carbon atoms are randomly generated. SWCNTs are built by user after selecting chiral vectors as shown in Fig. 4. Different chiral vectors, except zigzag and armchair, are selected for every CNT simulation. Also, carbon and 1.42 Å (default value) is selected as atom type and bond length, respectively. Then, as shown in Fig. 5, the CNT is simulated by CASTEP. The calculation interface of CASTEP depicted in Fig. 6 and the default parameters are used for the calculations.

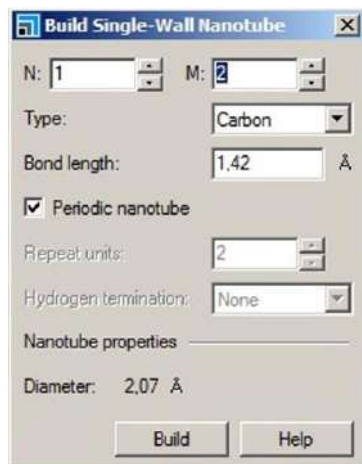


Fig. 4. Single-wall nanotube building in CASTEP[1]

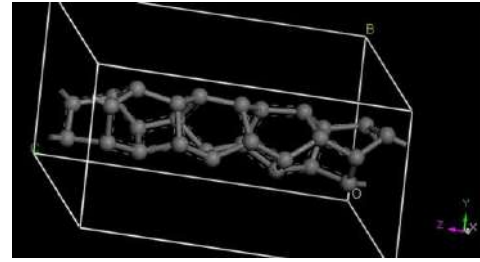


Fig. 5. Simulated CNT in CASTEP[1]

The `elec_energy_tol` (electrical energy tolerance) parameter represents the change in the total energy from one iteration to the next remains below some tolerance value per atom for a few self-consistent field steps to finalize the computation. The calculation level of inputs and outputs are also determined with this parameter. The default value of the parameter is usually suitable and it is 1×10^{-5} eV per atom [1].



Fig. 6. Calculation interface of CASTEP[1]

All calculated data for each CNT simulation are saved in many files that are created after the calculation step. For creation of the input and the output datasets, SWNT.castep file is used as output file.

All calculations were run on a workstation that has a 2.0 Ghz power on 4 cored 2 processors and a RAM of 8 GB, using all cores under Linux operating system. The calculation time according to these calculations are approximately varies from 10 minutes to 5 days as given in Table 1 in seconds. These calculation times will take weeks and months for higher atom numbers.

The input dataset attributes, initial atomic coordinates (u, v and w) and chiral vector (n and m), are obtained from the output files. Also the output dataset attributes, calculated atomic coordinates (u', v' and w'), are extracted from same files. The dataset consists of 10,721 data samples and it is firstly divided into training, validating and testing data randomly. Their distribution is selected as 70–15–15% for training, validating and testing sets, respectively. Then, the accuracy is determined using cross-validation techniques that compared the actual and the estimated values. The datasets

are evaluated by means of tenfold cross-validation. The average error of estimates is predicted by cross validation using the dataset with one individual removed. 90 and 10% of the data are split as training and test data for cross-validated datasets, respectively. The evaluation of the generated prediction models are done whether using tenfold cross-validation or without using cross-validation. In Table 2, descriptive statistics summary (minimum, maximum, mean and standard deviation values) of the dataset is given.

Table 1. The elapsed calculation time of CNT simulations

ID of CNT	Number of Atoms	Calculation Time (Seconds)
1	28	1050.14
2	52	1256.40
3	76	2254.18
4	84	2816.61
5	56	834.04
6	148	18496.07
7	124	33280.80
8	156	9604.28
9	196	59998.78
10	244	19389.07
11	172	64102.59
12	104	7207.22
13	84	6842.67
14	152	7715.19

15	364	78421.39
16	228	13513.07
17	268	27799.53
18	316	35982.11
19	372	94767.02
20	436	266027.27
21	508	233190.94
22	292	27792.55
23	168	13292.91
24	388	106542.26
25	112	6838.91
26	516	201214.72
27	296	34136.32
28	364	103759.38
29	412	95275.60
30	156	9558.96
31	532	427956.63
32	228	27392.57
33	444	159893.39
34	248	74997.74
35	312	40999.97
36	140	10014.92
37	392	83173.05
38	588	397369.36
39	344	89653.65
40	252	26127.05
41	208	23123.48
42	168	11826.42

Table 2. Descriptive statistics for the dataset

	Inputs					Outputs		
	u	v	w	m	n	u'	v'	w'
Minimum	0.0451	0.0451	0	2	1	0.0385	0.0389	0
Maximum	0.9548	0.9548	0.9999	12	6	0.9614	0.9610	0.9996
Mean	0.5000	0.5000	0.4994	8.2252	0.3378	0.5000	0.4999	0.4993
Standard Deviation	0.2900	0.2900	0.2900	2.1400	1.6800	0.2909	0.2910	0.2884

D. B.Adaptive Network-Based Fuzzy Inference Systems (ANFIS)

Jang and Sun [28], [29] first developed the adaptive network-based fuzzy inference systems (ANFIS) to take advantage of the best attributes from neural networks and fuzzy systems. ANFIS is a FIS that uses neural network algorithms to adapt itself in order to achieve better results. As an advantage of ANFIS against neural networks is accepting linguistic information and adapting itself using numerical data [30].

Any FIS structure includes a fuzzification interface, a rule base, and a database for the membership functions definitions used in the rules. Also, a fuzzy reasoning method to perform the inference procedure, and a de-fuzzification interface are the other parts of the structure. Neural network training techniques are used by an ANFIS for adjusting the membership functions. The rule base is usually in the form of fuzzy if-then rules [30].

A Sugeno-type [31] FIS is used by MATLAB's implementation of ANFIS. An adaptive neural network technique is used to train the Sugeno-type FIS parameters.

Inputs are mapped through input membership functions and associated parameters by ANFIS. Then through output membership functions and associated parameters to outputs, can be used to interpret the input/output map. The parameters associated with the membership functions change through the learning process. A gradient vector facilitates the computation of these parameters. A measure of how well the FIS is modeling the input/output data for a given set of parameters is provided by this gradient vector. When the gradient vector is obtained, any of several optimization routines can be applied in order to adjust the parameters to reduce some error measure. The sum of the squared difference between actual and desired outputs usually defines this error measure. Either back propagation or a combination of least squares estimation and backpropagation for membership function parameter estimation is used by ANFIS [32].

A matrix of the training data forms the input training data and the last column is the target output data. Test input data is used also in the same way. While the fuzzy toolbox provides many membership function types, Generalized bell-shaped membership function (gbellmf), Gaussian curve

membership function (gaussmf) and Pi-Shaped Membership Function (pimf) (Fig. 7) performed the best for the prediction of atomic coordinates. The block diagram of one FIS that is used in the u' coordinate estimation is illustrated in Fig. 8.

After the five inputs enter the ANFIS then they processed for the u' coordinate prediction. Similar FIS models are also designed for prediction of v' and w' coordinates

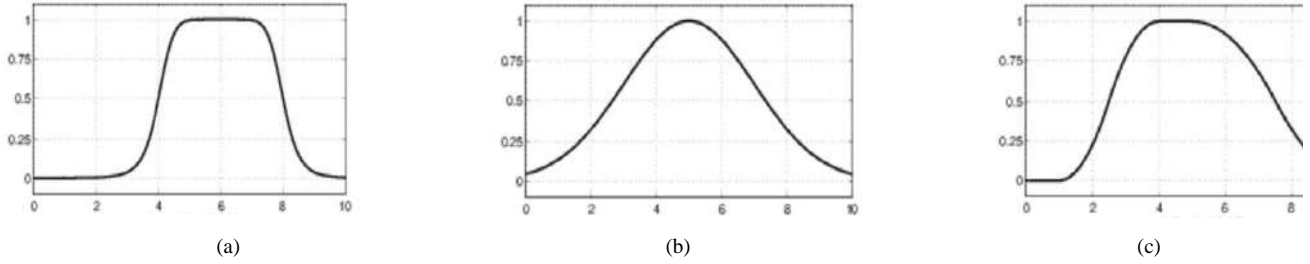


Fig.7. Membership Functions: (a) gbellmf (b) gaussmf (c) pimf

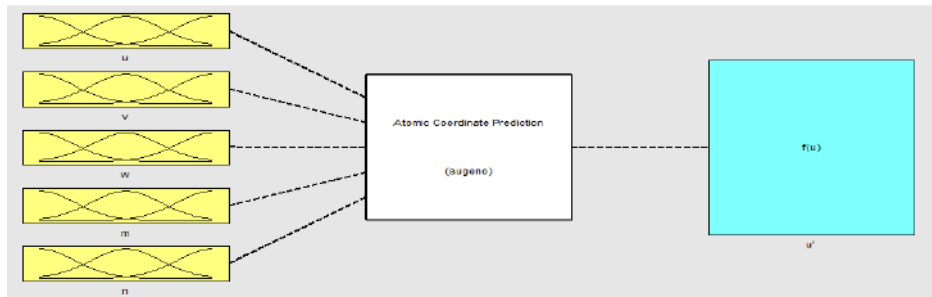


Fig. 8. FIS of u' coordinate prediction

4. RESULTS AND DISCUSSION

E. A. Performance Measures

Four performance measures are evaluated for the prediction model. Correlation between target and predicted values are measured by R and the average of the squares of the errors are measured by MSE . The closeness of the predictions to the target values is measured by MAE and the standard error of the estimates of the prediction models are calculated by SEE . In Eqs. 3, 4, 5 and 6, the mathematical equations of the used performance measures are given as

$$R = \sqrt{1 - \frac{\sum_{i=1}^n (O_i - P_i)^2}{\sum_{i=1}^n (O_i - O_m)^2}} \quad (3)$$

$$MSE = \frac{1}{n} [\sum_{i=1}^n (O_i - P_i)^2] \quad (4)$$

$$MAE = \frac{1}{n} \sum_{i=1}^n |O_i - P_i| \quad (5)$$

$$SEE = \sqrt{1 - \frac{\sum_{i=1}^n (O_i - P_i)^2}{n}} \quad (6)$$

where O_i and P_i is the observed and predicted values, respectively, O_m is the average of the observed values and n

is the number of data points used for testing. MATLAB (R2015b 64 bit) [32] was utilized for designing proposed models and obtaining performance measures.

F. B. Performance results of the ANFIS Model

Before the ANFIS model is developed, the input and output data is normalized and presented on a scale from 0–1. After that, noisy data is removed by using exhaustive search method [33]. *gbellmf* has been used for prediction of u' and v' coordinates whereas *pimf* has been used for w' coordinate prediction with the non-cross-validated dataset. When 10-fold cross-validation is considered, the best results were obtained from *pimf* for u' and w' coordinates and *gaussmf* for v' coordinate.

The observed and predicted coordinates for the test set plotted in Fig.9. the following points can be made, based on the performance results of u' , v' and w' coordinates prediction using the ANFIS prediction model with the non-cross-validated dataset (Table 3):

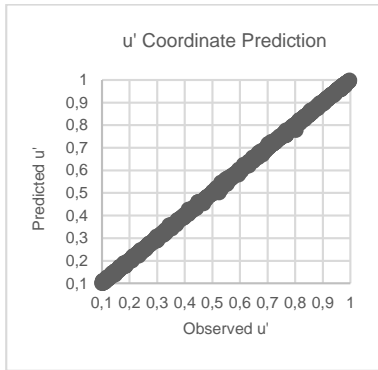
- The best result is obtained from w' coordinate prediction (MSE=4.962E-08, MAE=1.534E-04, SEE=2.228E-04, R=1.000E+00).
- All of the performance results are very similar for u' and v' coordinates prediction.

- As is clearly seen from Fig. 9, the observed and predicted values of three coordinates very close to each other.

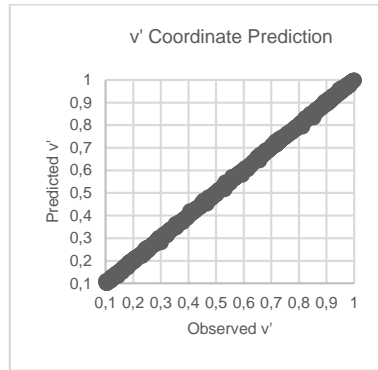
Table 3. Performance results of u' , v' and w' coordinates prediction using anfis model with the non-cross-validated dataset

Coordinates	Performance Metrics			
	MSE	MAE	SEE	R
u'	1.077E-05	2.224E-03	3.282E-03	9.999E-01

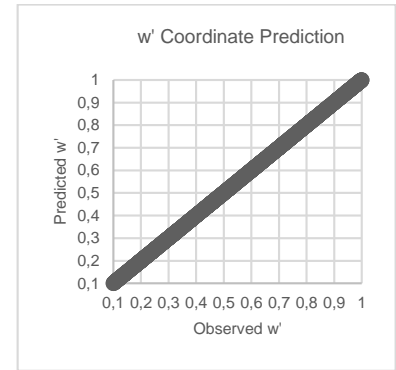
v'	1.101E-05	2.294E-03	3.318E-03	9.999E-01
w'	4.962E-08	1.534E-04	2.228E-04	1.000E+00
Average of three coordinates	7.277E-06	1.557E-03	2.274E-03	9.999E-01



(a)



(b)



(c)

Fig. 9. Plots of observed versus predicted values of u' coordinate (a), v' coordinate (b) and w' coordinate (c).

Tables 4, 5 and 6 show the MSE, MAE, SEE and R results of the ANFIS prediction model by means of 10-fold cross-validation for u' , v' and w' coordinates respectively. The summary of the detailed 10-fold cross-validation results are given in Table 7. The following comments can be made based on the results:

- As is seen from the tables, the performance of w' coordinate prediction is better than u' and v' coordinates prediction in terms of MSE, MAE and SEE metrics. For R metric, the values of w' coordinate prediction are better or approximately equal to the performance of other coordinates.
- The results of u' coordinate prediction showed the second best results and the worst results are taken from v' coordinate prediction
- The best MSE (4.386E-08) is achieved with w' coordinate prediction at second fold.
- Very close performance results were obtained for u' and v' coordinates prediction in terms of SEE and R.

Table 4. Performance results of u' coordinate prediction by means of 10-fold cross-validation

Fold Number	Performance Metrics			
	MSE	MAE	SEE	R
1	1.087E-06	2.287E-04	3.297E-04	9.999E-01

2	1.210E-06	2.363E-04	3.479E-04	9.999E-01
3	1.120E-06	2.250E-04	3.347E-04	9.999E-01
4	1.136E-06	2.208E-04	3.371E-04	9.999E-01
5	1.176E-06	2.405E-04	3.429E-04	9.999E-01
6	1.220E-06	2.306E-04	3.493E-04	9.999E-01
7	1.062E-06	2.207E-04	3.259E-04	1.000E+00
8	1.167E-06	2.367E-04	3.416E-04	9.999E-01
9	9.026E-07	2.103E-04	3.004E-04	1.000E+00
10	1.057E-06	2.252E-04	3.252E-04	1.000E+00
Average	1.114E-06	2.275E-04	3.334E-04	9.999E-01

Table 5. Performance results of v' coordinate prediction by means of 10-fold cross-validation

Fold Number	Performance Metrics			
	MSE	MAE	SEE	R
1	1.078E-05	2.272E-03	3.283E-03	9.999E-01
2	1.066E-05	2.256E-03	3.265E-03	1.000E+00
3	1.209E-05	2.368E-03	3.477E-03	9.999E-01
4	1.153E-05	2.295E-03	3.396E-03	9.999E-01
5	1.213E-05	2.373E-03	3.483E-03	9.999E-01
6	1.103E-05	2.217E-03	3.321E-03	9.999E-01
7	1.109E-05	2.221E-03	3.330E-03	9.999E-01
8	1.067E-05	2.208E-03	3.266E-03	9.999E-01
9	1.234E-05	2.317E-03	3.513E-03	9.999E-01
10	1.076E-05	2.256E-03	3.280E-03	9.999E-01
Average	1.131E-05	2.278E-03	3.361E-03	9.999E-01

Table 6. Performance results of w' coordinate prediction by means of 10-fold cross-validation

Fold Number	Performance Metrics			
	MSE	MAE	SEE	R
1	4.395E-08	1.468E-05	2.096E-04	1.000E+00
2	4.386E-08	1.486E-05	2.094E-04	1.000E+00
3	5.079E-08	1.511E-05	2.254E-04	1.000E+00
4	4.605E-08	1.455E-05	2.146E-04	1.000E+00
5	4.768E-08	1.445E-05	2.184E-04	1.000E+00
6	5.748E-08	1.541E-05	2.398E-04	1.000E+00
7	4.756E-08	1.482E-05	2.181E-04	1.000E+00
8	4.423E-08	1.480E-05	2.103E-04	1.000E+00

9	4.841E-08	1.447E-05	2.200E-04	1.000E+00
10	5.446E-08	1.526E-05	2.334E-04	1.000E+00
Average	4.845E-08	1.484E-05	2.199E-04	1.000E+00

The most important results are summarized in Table 7. When the average values of 10-fold cross-validation results are compared with the results in Aci and Avci[27] study, ANFIS prediction model performed better than classical ANN-based prediction models.

Table 7. Overall comparison of the average performance results by means of 10-fold cross-validation

Coordinates	Performance Metrics			
	MSE	MAE	SEE	R
u'	1.114E-06	2.275E-04	3.334E-03	9.999E-01
v'	1.131E-05	2.278E-03	3.361E-03	9.999E-01
w'	4.845E-08	1.484E-05	2.199E-04	1.000E+00
Average of three coordinates	4.157E-06	8.401E-04	2.305E-03	9.999E-01

5. CONCLUSIONS

In this work, an ANFIS based prediction model is proposed to predict the atomic coordinates of CNTs. A dataset is created to carry out the prediction model using CASTEP. The dataset of 10,721 data samples contain atomic coordinates (u, v and w) and the chiral vector (n and m) as totally five inputs and three final atomic coordinates (u', v' and w') as outputs. The dataset is organized into two types for evaluation strategy: cross validated dataset and non-cross validated dataset. Training of the prediction models is done by 90% of the cross validated dataset. The rest of the dataset usually serves as an independent test set by which the generalization performance of the prediction models. The dataset is randomly split to three, in which there are 70-15-15% training, validating and testing sets, respectively for the non-cross validated dataset. MSE, MAE, SEE and R values have been calculated for the developed model for performance evaluation.

The proposed prediction model performed good level of success when we look at all results with a general view. The first aim of this study is to use predicted atomic coordinates instead of simulated ones. This aim is reached by i) obtaining very low MSE, MAE and SEE values; ii) getting very high R

values when the average values are considered for the cross validated dataset. The second aim is to achieve better results than the previous study that used ANN[27]. This aim is also reached by getting lower MSE and MAE values than the previous study. It has been understood that the ANFIS-based prediction model performs better than ANN-based models in atomic coordinate estimation.

REFERENCES

- [1] BIOVIA Materials Studio, "CASTEP." [Online]. Available: <http://www.castep.org/>. [Accessed: 19-Jan-2017].
- [2] C. W. Bauschlicher and A. Ricca, "Binding of NH₃ to graphite and to a (9,0) carbon nanotube," *Phys. Rev. B*, vol. 70, no. 11, p. 115409, Sep. 2004.
- [3] W. Geng, H. Liu, and X. Yao, "Enhanced photocatalytic properties of titania-graphene nanocomposites: a density functional theory study," *Phys. Chem. Chem. Phys.*, vol. 15, no. 16, p. 6025, 2013.
- [4] V. Krasnenko, V. Boltrushko, M. Klopov, and V. Hizhnyakov, "Conjoined structures of carbon nanotubes and graphene nanoribbons," *Phys. Scr.*, vol. 89, no. 4, p. 44008, Apr. 2014.
- [5] Y. Tao et al., "Tunable hydrogen separation in porous graphene membrane: first-principle and molecular dynamic simulation," *ACS Appl. Mater. Interfaces*, vol. 6, no. 11, pp. 8048–8058, Jun. 2014.
- [6] H. Kim et al., "Direct observation of localized defect states in semiconductor nanotube junctions," *Phys. Rev. Lett.*, vol. 90, no. 21, p. 216107, May 2003.
- [7] M. Ouyang, J.-L. Huang, C. L. Cheung, and C. M. Lieber, "Atomically resolved single-walled carbon nanotube intramolecular junctions," *Science* (80-.), vol. 291, no. 5501, pp. 97–100, 2001.
- [8] L. Chico, V. H. Crespi, L. X. Benedict, S. G. Louie, and M. L. Cohen, "Pure carbon nanoscale devices: nanotube heterojunctions," *Phys. Rev. Lett.*, vol. 76, no. 6, pp. 971–974, Feb. 1996.
- [9] S. Iijima and T. Ichihashi, "Single-shell carbon nanotubes of 1-nm diameter," *Nature*, vol. 363, no. 6430, pp. 603–605, Jun. 1993.
- [10] S. Iijima, "Helical microtubules of graphitic carbon," *Nature*, vol. 354, pp. 56–58, 1991.
- [11] A. Eatemadi et al., "Carbon nanotubes: properties, synthesis, purification, and medical applications," *Nanoscale Res. Lett.*, vol. 9, no. 1, pp. 393–405, 2014.
- [12] K. I. Tserpes and N. Silvestre, *Modeling of Carbon Nanotubes, Graphene and Their Composites*. London: Springer, 2014.
- [13] P. Hohenberg and W. Kohn, "Inhomogeneous electron gas," *Phys. Rev.*, vol. 136, no. 3B, pp. B864–B871, Nov. 1964.
- [14] W. Kohn and L. J. Sham, "Self-consistent equations including exchange and correlation effects," *Phys. Rev.*, vol. 140, no. 4A, pp. A1133–A1138, Nov. 1965.
- [15] W. Kohn, A. D. Becke, and R. G. Parr, "Density functional theory of electronic structure," *J. Phys. Chem.*, vol. 100, no. 31, pp. 12974–12980, Jan. 1996.
- [16] M. D. Segall et al., "First-principles simulation: ideas, illustrations and the CASTEP code," *J. Phys. Condens. Matter*, vol. 14, no. 11, pp. 2717–2744, Mar. 2002.
- [17] S. J. Clark et al., "First principles methods using CASTEP," *Zeitschrift für Krist. - Cryst. Mater.*, vol. 220, no. 5/6, pp. 567–570, Jan. 2005.
- [18] L. Hong-Xia, Z. He-Ming, S. Jiu-Xu, and Z. Zhi-Yong, "Electronic transport properties of an (8, 0) carbon/boron nitride nanotube heterojunction," *Chinese Phys. B*, vol. 19, no. 3, p. 37104, Mar. 2010.
- [19] Y. Mao and J. Zhong, "The computational design of junctions by carbon nanotube insertion into a graphene matrix," *New J. Phys.*, vol. 11, no. 9, p. 93002, Sep. 2009.
- [20] M. Al-Khedher, C. Pezeshki, J. McHale, and F. Knorr, "Adaptive neuro-fuzzy modeling of mechanical behavior for vertically aligned carbon nanotube turfs," *J. Mater. Sci. Technol.*, vol. 27, no. 4, pp. 301–308, Apr. 2011.
- [21] S. Ahadian and Y. Kawazoe, "An artificial intelligence approach for modeling and prediction of water diffusion inside a carbon nanotube," *Nanoscale Res. Lett.*, vol. 4, no. 9, pp. 1054–1058, Sep. 2009.
- [22] E. Akbari, Z. Buntat, E. Shahraki, A. Zeinalinezhad, and M. Nilashi, "ANFIS modeling for bacteria detection based on GNR biosensor," *J. Chem. Technol. Biotechnol.*, vol. 91, no. 6, pp. 1728–1736, Jun. 2016.
- [23] M. Alibabai, H. Alikhani, and H. Sahoolizadeh, "Carbon nanotube field-effect transistors (CNTFET) modeling by neuro-fuzzy networks," *Banaras Hindu Univ. J.*, vol. 3, no. 1, pp. 93–102, 2014.
- [24] M. Savari et al., "Hydrodynamic and thermal performance prediction of functionalized MWNT-based water nanofluids under the laminar flow regime using the adaptive neuro-fuzzy inference system," *Numer. Heat Transf. Part A Appl.*, vol. 70, no. 1, pp. 103–116, Jul. 2016.
- [25] A. A. Sahraei, A. Fathi, A. Mozaffari, M. K. Besharati Givi, and M. H. Pashaei, "Predicting the hardness of carbon nanotube reinforced copper matrix nanocomposites using two adaptive fuzzy inference system identifiers," *Proc. Inst. Mech. Eng. Part E J. Process Mech. Eng.*, vol. 229, no. 3, pp. 192–203, Aug. 2015.
- [26] M. M. S. Fakhraei, N. Khani, S. Pedrammehr, and M. M. Mashhadi, "Prediction of buckling instability of perfect and defective carbon nanotubes," *J. Comput. Theor. Nanosci.*, vol. 11, no. 11, pp. 2356–2369, Nov. 2014.
- [27] M. Acı and M. Avcı, "Artificial neural network approach for atomic coordinate prediction of carbon nanotubes," *Appl. Phys. A*, vol. 122, no. 7, p. 631, Jul. 2016.
- [28] J.-S. R. Jang, "ANFIS: adaptive-network-based fuzzy inference system," *IEEE Trans. Syst. Man. Cybern.*, vol. 23, no. 3, pp. 665–685, 1993.
- [29] J.-S. R. Jang and C.-T. Sun, *Neuro-Fuzzy and Soft Computing: A Computational Approach to Learning and Machine Intelligence*, 1st ed. New Jersey: Prentice Hal, 1997.
- [30] H. Danker-McDermot, "A fuzzy/neural approach to cost prediction with small data sets," *University of New Orleans*, 2004.
- [31] T. Takagi and M. Sugeno, "Fuzzy identification of systems and its applications to modeling and control," *IEEE Trans. Syst. Man. Cybern.*, vol. SMC-15, no. 1, pp. 116–132, Jan. 1985.
- [32] Mathworks, "MATLAB." [Online]. Available: <http://www.mathworks.com/products/matlab/>.
- [33] C. Lin and S. Wang, "Training algorithms for fuzzy support vector machines with noisy data," 2004.

Deception Detection From Speech Signals

Sami Ekici

Firat University,
Technology Faculty,
Elazig, Turkey
sekici@firat.edu.tr

Turgut Kavaz

Firat University,
Technology Faculty,
Elazig, Turkey
sekici@firat.edu.tr

Yaman Akbulut

Firat University,
Department of Informatics,
Elazig, Turkey
yamanakbulut@firat.edu.tr

Abdulkadir Sengur

Firat University,
Technology Faculty,
Elazig, Turkey
ksengur@gmail.com

Abstract—In this study, an effective method is presented to detect deception by using only verbal features of the human voice. The data set benefitted in this study contains different real-world video clips. After extracting speech signals from the video clips, the Hamming Windowing method is applied to each signal. Discrete Wavelet Transform is used to obtain time-frequency features of the speech signals. Each speech is labeled as truthful (1) or deceptive (0). A 5-level signal decomposition with Daubechies-4 mother wavelet is employed for the feature extraction stage. To reduce the size of the feature set, some statistical parameters such as standard deviation, energy, entropy, kurtosis and skewness of the decomposed signals are obtained. After obtaining the feature set, finally, the Extreme Learning Machine, a fast and effective classifier, is applied to the feature set to classify the truthful and deceptive speeches. The various simulations clearly show us; the proposed method has higher performance than the previous studies performed in the literature.

Keywords—deception detection; feature extraction; discrete wavelet transform; extreme learning machine.

I. INTRODUCTION

Deception is a well-known term that involves acting in such a way leading another person to believe something that is not true. Deception is a very common occurrence in daily life. Concealing or misrepresenting the truth are sometimes a big problem especially for the judgment, intelligence services, police departments, call centers, customer services, banking etc. To cope with this problem, deception detection has an increasing amount of attention recently. While some researchers use only verbal techniques to detect deception [1], some other researchers use nonverbal features by investigating some physical and emotional actions of peoples [2]. On the other hand, another group of researchers uses both verbal and nonverbal features [3]. Previous attempts on detecting lies are performed by using trained experts [1]. But the performance of these methods is very poor. In fact, deception detection is a very

difficult task and humans can detect deception in the range of 45-65% [2], [3]. Another drawback of these approaches is that they require a large amount of time and effort for the analysis

[1]. Peoples usually intend to identify deception with non-verbal cues and give less attention to the verbal cues [4]. It was reported that audible and verbal clues are better than the visual and emotional clues [5]. However, some researchers show that thermal imaging is a good indicator to detect deceit by observing blood flow to human face [6], [7]. Actually, liars have some feelings of anxiety, fear, shame or anger much more than truth tellers [6]. These feelings may give important clues to the experts directly or indirectly by using different sensor data [8], [9]. In addition, some researchers tried to identify deception from the writing by using syntactic stylometry and obtain 91.2% accuracy [10].

Recently, computer based deception detection methods have attracted much more attention than the others mentioned above. Because of their capability of analyzing big and complex datasets which include non-linear relationship, the machine learning algorithms such as artificial neural networks (ANN), support vector machines (SVM), extreme learning machines (ELM), etc., may give better results of deception detection than the conventional methods. The main problem to establish an automatic deception detection algorithm is to give distinctive features of speech signals to the classifiers as inputs. To cope with this problem an efficient speech processing algorithm is required.

In this study, a new and effective deception detection method is presented. The proposed approach detects deceptive and truthful speeches with higher accuracy rate than previous studies performed in the literature. A dataset which is called "Real Life Trial Data" and contains 61 deceptive and 60 truth trial video clips is used in the study [4] [5]. Because of the fact that we will use only speech signal, we extract speeches from the clips. After applying Hamming Windowing method to the speech signals, discrete wavelet transform (DWT) is employed to obtain time-frequency information from each signal. Then,

some statistical parameters such as energy, entropy, kurtosis, skewness and standard deviation are used to build a feature dataset. Finally, ELM is employed to classify deceptive and truthful voices. After a lot of trials, the results obtained show us the proposed method can achieve the task of automatic deception detection with an accuracy above 95%.

II. DECEPTION DETECTION

We use machine learning approaches to assess the performance of extracted features from the real life dataset which includes truthful and deceptive speeches. As mentioned above, these speeches extracted from video clips.

The most commonly used machine learning methods are artificial neural networks, support vector machines, extreme learning machines and decision trees. We perform detection of deception by using extreme learning machines (ELM) classification algorithm. The simulations were implemented by using the Matlab software. The feature matrix obtained in the classification process has a great significance. In the feature extraction stage, DWT is employed. The proposed algorithm for deception detection is depicted in Fig.1.

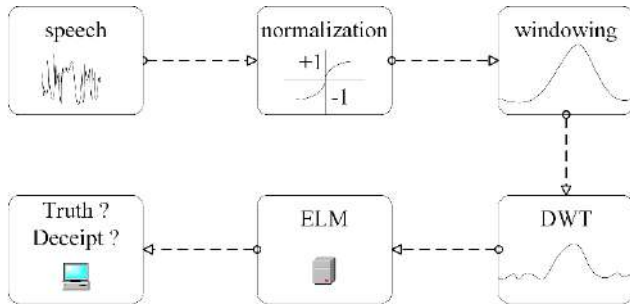


Fig. 1. Proposed method for deception detection.

A. Feature Extraction

The speech data are primarily windowed. The most commonly used windows are the Hamming, Hann and Blackman functions [6]. These functions help to emphasize the middle parts of the signal parts. On this count, parts that do not work in the extraction of the attribute are discarded. Windowing is very important at the output of the attribute. It is then transformed by wavelet transform. Then the mean, standard deviation, skewness, kurtosis, energy and entropy are calculated. The attribute matrix is obtained from the obtained values. In the next sections, the mathematical definitions of these methods are presented briefly. The obtained results will be given in Section III.

B. Hamming Window

One of the most primary filter type used in digital signal processing (DSP) is finite impulse response (FIR) filter. FIR filters are restricted to discrete-time implementations. A simple way to obtain a FIR filter is called as “windowing method” and start with an ideal desired function as [6],

$$H_d(e^{j\omega}) = \sum_{n=-\infty}^{\infty} h_d[n]e^{-j\omega n} \quad (1)$$

where $h_d[n]$ is the corresponding impulse response sequence and can be stated as,

$$h_d[n] = \frac{1}{2\pi} \int_{-\pi}^{\pi} H_d(e^{j\omega}) e^{j\omega n} d\omega. \quad (2)$$

To obtain a casual FIR filter by using $h_d[n]$ a new system $h[n]$ with impulse response can be defined as,

$$h[n] = \begin{cases} h_d[n], & 0 \leq n \leq M, \\ 0 & \text{otherwise.} \end{cases} \quad (3)$$

We can represent $h[n]$ the product of desired impulse response and a fined duration window as,

$$h[n] = h_d[n]w[n] \quad (4)$$

where $w[n]$ is the window function. Then, the Hamming window can be defined by the equation given below as,

$$w[n] = \begin{cases} 0.54 - 0.46 \cos(2\pi n/M), & 0 \leq n \leq M, \\ 0 & \text{otherwise.} \end{cases} \quad (5)$$

C. Wavelet Transform

The WT is a mathematical technique which is used for a lot of signal processing application [7]. WT is more powerful than conventional methods such as Fourier transform in the processing of the non-stationary signals because of the capability of analyzing waveforms in both time and frequency domain. The band of wavelet analysis is adjusted so that both low frequency and high-frequency components are windowed by different scale factors [8]. The continuous wavelet transform (CWT) of the $f(t)$ function can be defined as [7], [8];

$$CWT_{\psi} f(a,b) = \int_{-\infty}^{\infty} f(t) \psi_{a,b}(t) dt \quad (6)$$

where, ψ is mother wavelet [8] and written as,

$$\psi_{a,b}(t) = |a|^{-1/2} \psi\left(\frac{t-b}{a}\right) \quad (7)$$

In the discrete time domain, the continuous mother wavelet can be dilated and translated discretely by selecting $a = a_0^m$ and $b = nb_0 a_0^m$, where a_0 and b_0 are fixed constants with $a_0 > 1$, $b_0 > 0$, $m, n \in \mathbb{Z}$. Then ψ re-defined as;

$$\psi_{m,n}(t) = a_0^{-m/2} \psi\left(\frac{t - nb_0 a_0^m}{a_0^m}\right) \quad (8)$$

Then, discrete wavelet transform (DWT) is written for any function $f(t)$ as,

$$DWT_{\psi} f(m, n) = \int_{-\infty}^{\infty} f(t) \psi_{m,n}(t) dt \quad (9)$$

D. Multiresolution Analysis (MRA)

MRA is the representation of wavelets and scaling functions at different resolution levels to decompose and reconstruct the investigated signal. In MRA there are two filters which are the low pass (LPF) and high pass (HPF) in each decomposition level.

The original signal can be divided a series of orthogonal high-frequency and low-frequency spaces by using a set of orthogonal scaling function $\varphi(t)$ and mother wavelet $\psi(t)$ [8]. By this way, MRA gives the time-frequency picture of the decomposed signal $f(t)$ at different frequency levels. The original signal $f(t)$ is decomposed as:

$$f(t) = \sum_k c_j(k) \varphi_{jk}(t) + \sum_{j=1}^k \sum_k d_j(k) \psi_{jk}(t) \quad (10)$$

In this equation, j shows the wavelet decomposition level whereas c_j and d_j are the weighted sequences of the space projection of $f(t)$ respectively [9]. Two-level decomposition of the original signal is shown in Fig.2.

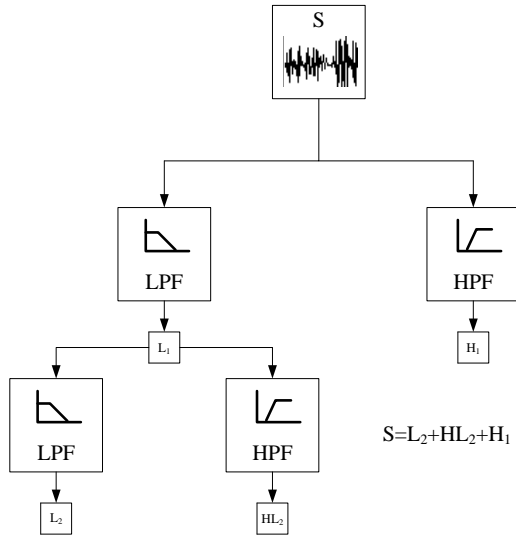


Fig. 2. Filter bank representation of the DWT dilation.

E. Extreme Learning Machines

Extreme learning machines (ELM) is a single hidden layer feed-forward neural network which is proposed by Huang at al., [10]. The ELM is a very fast training method and has a simple nature in which the input weights and biases are randomly initialized and then the weights between the hidden layer and output layer are optimized [10]–[12]. As a new and simple method, ELM can surpass the other time-consuming algorithms such as the conventional back propagation algorithms [13].

ELM with L hidden nodes and activation function $g(x)$ can be expressed mathematically for a given data set containing N training samples $\{(x_i, y_i)\}_{i=1}^N$, where input $x_i \in \mathbb{R}^n$ and corresponding desired output $y_i \in \mathbb{R}$, as;

$$\sum_{i=1}^L \beta_i g(w_i x_j + b_i) = y_j \quad j = 1, 2, 3, \dots, N \quad (11)$$

where $w_i = [w_{i1}, w_{i2}, \dots, w_{in}]^T$ is the randomly chosen input weight vector connecting the i th hidden neuron and the input neurons, b_i is the randomly chosen bias of the i th hidden node, and β_i is the weights between the hidden layer and output layer.

$$H\beta = y \quad (12)$$

$$H = \begin{bmatrix} g(w_1 x_1 + b_1) & \dots & g(w_L x_1 + b_L) \\ \vdots & \ddots & \vdots \\ g(w_1 x_N + b_1) & \dots & g(w_L x_N + b_L) \end{bmatrix} \quad (13)$$

$$\beta = [\beta_1, \beta_2, \dots, \beta_L]^T \text{ and } y = [y_1, y_2, \dots, y_L]^T.$$

The main purpose of ELM method is to find optimum β values [10], [13]. However, in most cases, H is a non-square matrix. So, Eq.(12) may not be solved by taking the inverse of H directly. One solution of this equation is to find the optimal least squares solution of $\hat{\beta}$ by minimizing the associated loss function, i.e., $\min \|y - H\beta\|_2^2$.

$$\hat{\beta} = H^\dagger \quad (14)$$

where H^\dagger is the Moore–Penrose generalized inverse of the hidden layer output matrix ELM with L hidden nodes and activation function H [11]. Since the number of training samples is usually greater than the number of hidden nodes i.e., $N > L$, Eq. (12) can be rewritten as

$$\hat{\beta} = (H^T H)^{-1} H^T y \quad (15)$$

III. EXPERIMENTAL RESULTS

A. Dataset

In this paper, we used the dataset called "Real Life Trial Data" [4]. This dataset was created by Rada Mihalcea, Verónica Pérez-Rosas and friends. This dataset was created from court records where deceptive and truth statements can be observed and verified very easily. These records are in the form of video. The defendant or witness in the video should be clearly

identified. Audio quality is enough for hear the voices and understand what the person is saying. When the videos are labeled, the accused and witness statements are taken into account. Police views are also taken into account. It is precisely determined by these three factors that the statement is true or false. The final dataset consists of 121 videos including 61 deceptive and 60 truthful trial clips.

The average length of the videos in the dataset is 28.0 seconds. The average video length is 27.7 seconds for the deceptive clips and 28.3 seconds for the truthful clips. The data consist of 21 unique female and 35 unique male speakers, with their ages approximately ranging between 16 and 60 years. Video files were converted into audio files. The frequency value is 16000 Hz, the bit rate value is 128 kbps and the mono channel is specified. The final set of transcriptions consists of 8,055 words, with an average of 66 words per transcript [4].

B. Application of the Proposed Method

Firstly, all speech signals were normalized between -1 and 1 interval. Then, the Hamming windowing method was applied to each normalized signals as a FIR filter. The length of Hamming window was selected as 15 msec. The original speech and windowed signals for both truth and deceptive examples are shown in Fig.3 and 4 respectively.

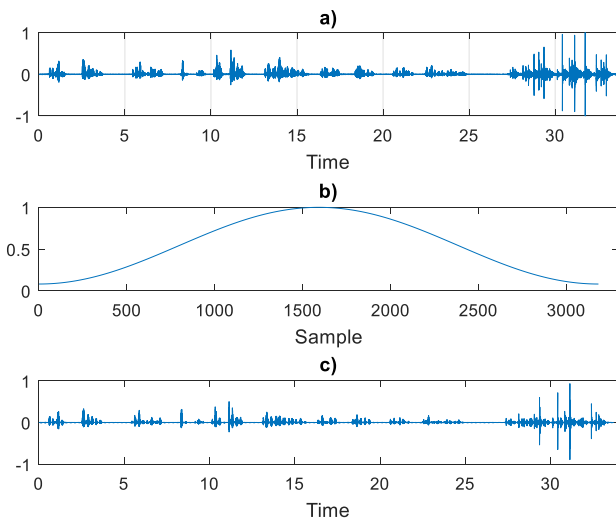


Fig.3. The original and windowed signals of a truth speech a) original signal, b) Hamming window, c) windowed signal.

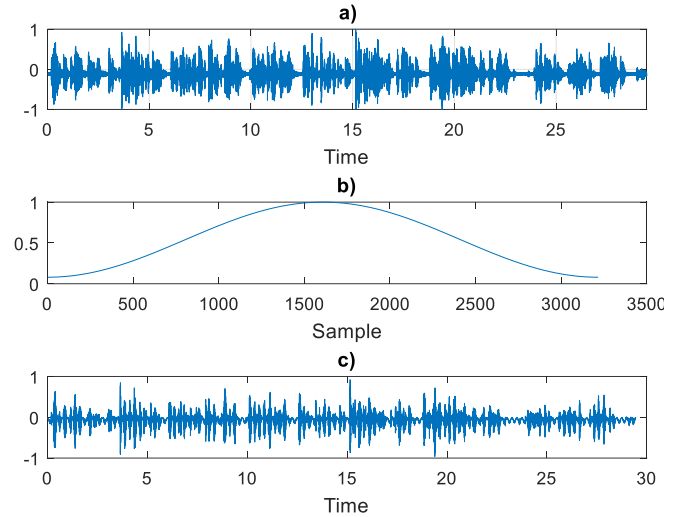


Fig.4. The original and windowed signals of a deceptive speech a) original signal, b) Hamming window, c) windowed signal.

In the next step, DWT was used to extract the distinctive features of the speeches. 5-level decomposition with Doubechies-4 mother wavelet (dB4) was used in the MRA. 5-level DWT decomposition for a deceptive speech signal is shown in Fig. 5. As it is obvious that there a lot of data for in each speech signal, we must find a way to represent these signals as a short way without losing important features. For this purpose, we calculated 5 statistical parameters as energy, entropy, kurtosis, skewness and standard deviation of the decomposed signals to obtain final feature dataset. Then final dataset was divided two groups randomly to be used in training and testing of ELM.

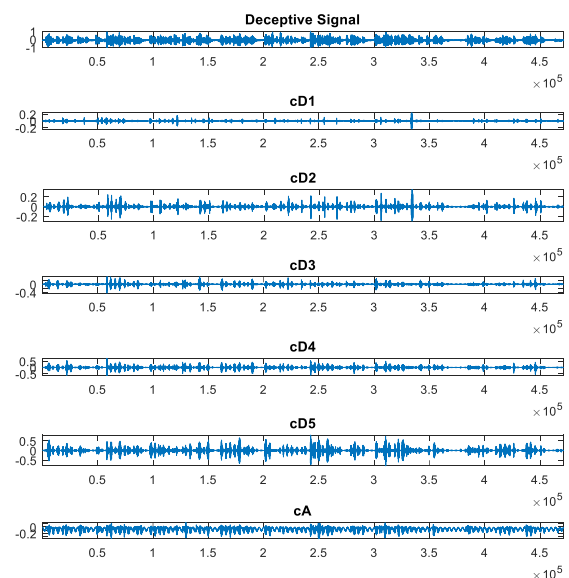


Fig.5. Wavelet coefficients for deceptive signal

Where cD_i represents i th detail coefficients whereas cA represents the approximation coefficients. It has to be noticed that first detail coefficient (cD_1) has the highest frequency and

cA has the lowest frequency according to multi-resolution analysis as mentioned above. Fig. 6 shows the ELM results without windowing. 80 percent of Dataset was used for training and 20 percent for testing. Number of neurons selected 100.

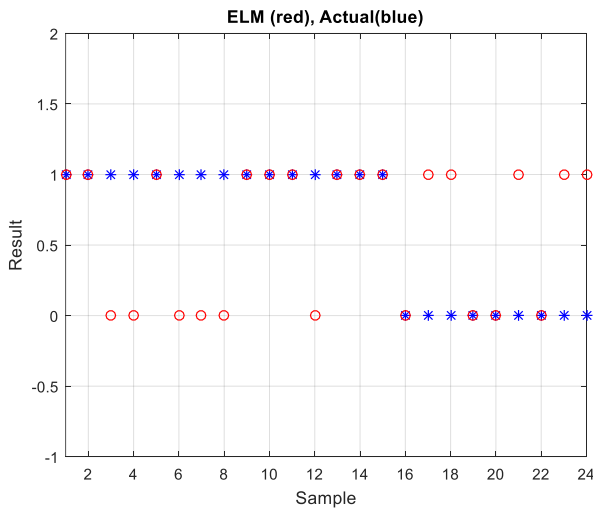


Fig. 6. ELM results without windowing

As can be seen from the Fig.6, the classification results are not satisfactory. Only 13 of 24 speeches were classified with the correct class label (0-deceptive, 1-truthful).

Fig. 7 shows the ELM results with windowing. 90 percent of Dataset was used for training and 10 percent for testing. Number of neurons selected 50. In this simulation, ELM classified all testing samples correctly. This result is the achievement of the windowing process before the DWT decomposition.

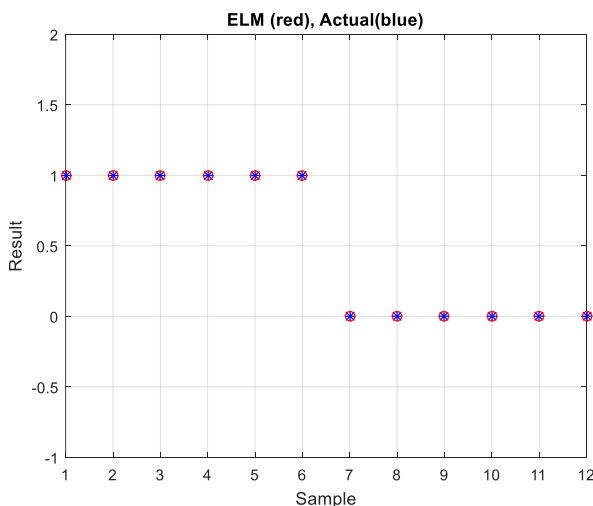


Fig. 7. ELM results with windowing.

In Fig.8., the results of ELM with 100 neurons are depicted. 80 percent of the data is used for training whereas 20 percent is used for testing of ELM. As shown from the figure, only two

examples belonging to the truth speeches are misclassified as deceptive.

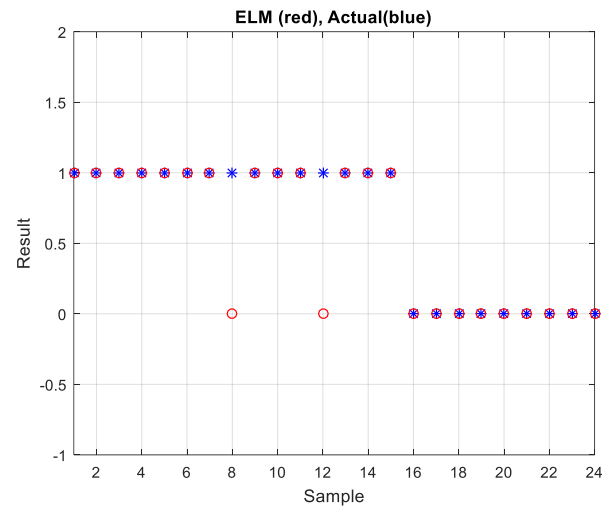


Fig. 8. ELM results with decreased training data.

IV. CONCLUSION

A machine learning based algorithm is proposed to discriminate truthful and deceptive human speeches. The speech dataset used in this study was extracted from video clips. After normalization stage, Hamming windowing method was applied to each signal. Discrete wavelet transform was employed to obtain distinctive features from the speech signals. To reduce the size of feature space, some statistical parameters such as signal energy, entropy, kurtosis, skewness and standard deviation were obtained. Finally, ELM was employed for the classification task. The feature dataset was divided randomly to validate the performance of the proposed method. Therefore, we obtain 91,66% performance ratio when 24 speech examples were tested. Our method achieved 100% accuracy when 10-percent of the dataset was tested. We also examined the effect of windowing process. The obtained results show that the performance of ELM classifier decreases to 54,16% in this case.

As mentioned above, the feature dataset obtained in this study was divided as randomly to investigate the robustness of the proposed method. In the next studies, we will study both on the preparation of dataset for training stage and also on selecting more effective features from the feature space.

ACKNOWLEDGMENT

We are grateful to Rada Mihalcea, Verónica Pérez-Rosas and their friends for sharing us the data collection used in this study.

REFERENCES

- [1] [1] F. Enos, "Detecting deception in speech," Dissertation Abstracts International, B: Sciences and Engineering, vol. 70, no. 2, p. 1119, 2009.
- [2] [2] M. J. Farah, J. B. Hutchinson, E. a Phelps, and A. D. Wagner, "Functional MRI-based lie detection: scientific and societal challenges," Nature Publishing Group, vol. 15, no. 2, pp. 123–131, 2014.

- [3] [3] G. An, "Literature review for Deception detection," Doctoral dissertation, The City University of New York, 2015.
- [4] [4] V. Pérez-rosas, "Deception Detection using Real-life Trial Data," pp. 59–66, 2015.
- [5] [5] V. Pérez-Rosas, M. Abouelenien, R. Mihalcea, Y. Xiao, C. Linton, and M. Burzo, "Verbal and Nonverbal Clues for Real-life Deception Detection," *Proceedings of the 2015 Conference on Empirical Methods in Natural Language Processing*, no. September, pp. 2336–2346, 2015.
- [6] [6] A. V. Oppenheim, "Discrete-Time Signal Processing," *Electronics and Power*, vol. 23, no. 2. p. 157, 1977.
- [7] [7] M. J. Gómez, C. Castejón, and J. C. García-Prada, "Review of recent advances in the application of the wavelet transform to diagnose cracked rotors," *Algorithms*, vol. 9, no. 1, 2016.
- [8] [8] I. Daubechies, "Ten Lectures of Wavelets," *CBMS-NSF Regional Conference Series in Applied Mathematics*, 1992.
- [9] [9] S. Ekici, "A pattern recognition system for blind object identification," in *A PPattern Recognition System for Power Disturbance Identification*, 2008, pp. 95–100.
- [10] [10] G. Huang, "Introduction to Extreme Learning Machines," *Hands-on Workshop on Machine Learning for BioMedical Informatics 2006*, 2006.
- [11] [11] G.-B. Huang, H. Zhou, X. Ding, and R. Zhang, "Extreme learning machine for regression and multiclass classification.," *IEEE transactions on systems, man, and cybernetics. Part B, Cybernetics : a publication of the IEEE Systems, Man, and Cybernetics Society*, vol. 42, no. 2, pp. 513–29, 2012.
- [12] [12] G.-B. Huang, Q.-Y. Zhu, and C.-K. Siew, "Extreme learning machine: a new learning scheme of feedforward neural networks," *Proceedings of IEEE International Joint Conference on Neural Networks*, vol. 2, pp. 985–990, 2004.
- [13] [13] S. Ekici, "Electric Load Forecasting Using Regularized Extreme Learning Machines," *International Journal of Industrial Electronics and Electrical Engineering*, no. 6, pp. 119–122, 2016.

Forecasting of Daily Passenger Numbers at Bus Stops With Artificial Neural Networks

Emrah AYDEMİR
Ahi Evran University,
Kırşehir, Turkey
emrah.aydemir@firat.edu.tr

Sevinç GÜLSEÇEN
İstanbul University
İstanbul, Turkey,
sevincg@yahoo.com

Abstract—Compared to the population increase in the metropolitan areas, the demand for in-city transportation is rising and the quality expected from the service is increasing. Knowing the demand for each station and route in the public transportation service will provide a great advantage for strategy setting and infrastructure building for the relevant institutions and companies. In this study, using artificial neural networks, estimates of daily passenger numbers for two regions of Istanbul, both Anatolian and European, have been evaluated and the error rates of the predictions obtained have been evaluated. For this, passenger information on each dutiable vehicle has obtained from İETT (Istanbul Electricity Tramway and Tunnel Enterprises) as station name, date-time, line name and number of persons, and weather report and temperature information have been also obtained from the General Directorate of Meteorology. In addition, holidays, elections and official holiday data have been collected. All these data have been combined in a single database. Transformations were converted to numbers and normalization was applied so that each value is expressed at equal importance. As a result, an artificial neural network model with 14 inputs and one output was obtained. In the hidden layer, it is aimed to reach the lowest average absolute error by performing tests with different numbers of nerves. These results reached the lowest error with the number of 9 on the third layer of the third layer 17, on the second layer 14 of the three layer model. The number of people in the group were gathered in 11 groups and the lowest absolute error of 1.0301 was reached for the results of four stations, while the highest mean absolute error of 1.5877 was reached. Thus, estimates with 90.64% accuracy were obtained.

Keywords— Forecasting, Public Transportation, İETT, Istanbul, Artificial Neural Networks

Examination of Eye Tracking Technology in Terms of Usage

Mehmet Emin UĞUR

Dumlupınar University

Department of Electrical and Electronics Eng. Master Std.

Kutahya, Turkey

me.ugur@hotmail.com

Assist. Prof. Dr. Durmuş ÖZDEMİR

Dumlupınar University

Department of Computer Engineering

Kutahya, Turkey

durmus.ozdemir@dpu.edu.tr

Abstract— Eye tracking method is one of the important products of science which aims to facilitate human life. In this research, it is aimed to determine the existing situation by examining the working principles of eye tracking systems from daily using practices and literature. In this study, it was aimed to evaluate the findings obtained by investigating eye tracking technologies. Advantages and disadvantages of the systems which was used for this purpose was evaluated. It's intended to given suggestions and future directions in terms of eye tracking systems.

Keywords— eye tracking, eye movement, technology, innovation

I. INTRODUCTION

Human development is based on finding out what is happening in the environment, identifying problems and finding solutions. Thanks to this development, many obstacles that have made life difficult in the past have been removed and progress has been made. In the simplest terms, eye tracking is the measurement of eye activity. Eye tracking method is one of the important products of science which aims to facilitate human life[1]. There are studies showing that eye tracking systems can be used as an input element in control software as well as in psychological and neurological inferences by following changes related to eye movements. In this study, the studies performed with eye tracking systems and the findings obtained from these studies were evaluated. After the evaluation, the deficiencies and needs in the field related to the work to be done regarding eye tracking systems have been determined. In the scope of the study, Integration of disabled people, identification of psychological and neurological problems, individual recognition in commercial activities, ergonomics design, game development, integration of military systems [2].

II. EYE TRACKING SYSTEMS

In this section, firstly the human vision system is discussed, then the development of eye tracking systems and the study structure of eye tracking devices are examined.

A. Human Vision System

The ease of access to the developments and devices in the eye tracking system has also increased the number of studies on eye tracking technology [3]. The eye, which consists of optical components such as retina, cornea, eye baby, and eye lens, is one of the most important sensory organs of human life that communicate with the outside world, and 80% of human perception is realized with eyes[4].

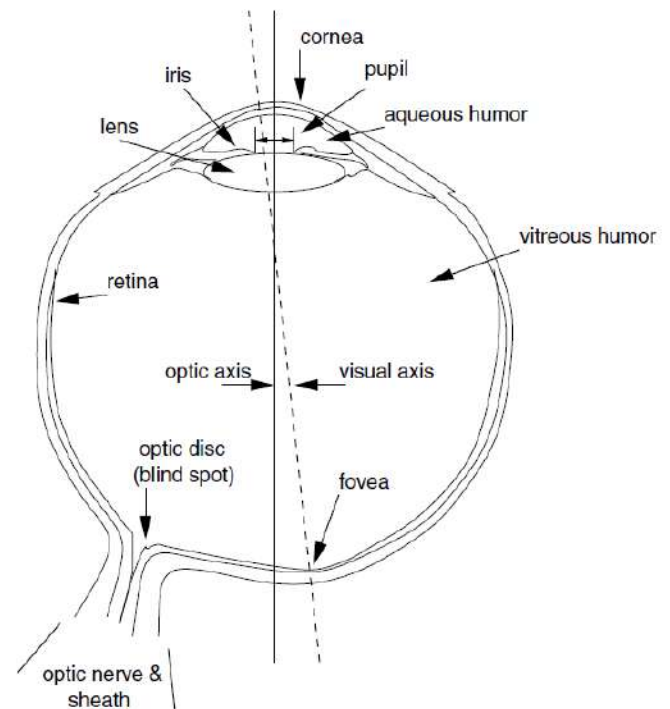


Fig. 1. Structure Of The Eye

The rays reflected from the objects at the visual angle reach the cornea layer first. An important part of the light-breaking ability of the eye occurs in the cornea layer and the incoming rays are transmitted to the eye baby. The rays that are refracted by the eye lens focus on the retina layer through the vitreous at the back of the eye sphere. Turns the light into

electrical signals on a 127 million light-sensitive retina layer. Electrical signals reach the eyes of the vision with the aid of the optic nerve that is formed by the convergence of the nerve endings. The image that reaches to the vision center of the brain as an electrical stimulus is detected and assessed in the vision center. In order to be able to realize as clearly as possible, it should fall on the yellow spot. The fovea, located on the yellow stain, allows only 2% of the field of view to be seen and allows humans to communicate with the outside world in this small proportion[4]. All the eye and head movements that people make in order to communicate with the outside world are the movements they make to cross the foveal center with the area to focus on. All the movements and the general structure of the eye that people perceive for visual perception are called Human Visual System.

B. Development of Eye Tracking Systems

The first studies on the examination of eye movements took place in the early 1900's[5]. In 1901, the first serious work on this field was examined by Cline and Dodge and the motion of the eye in the horizontal direction with the corneal reflection falling on the photographic film[6].

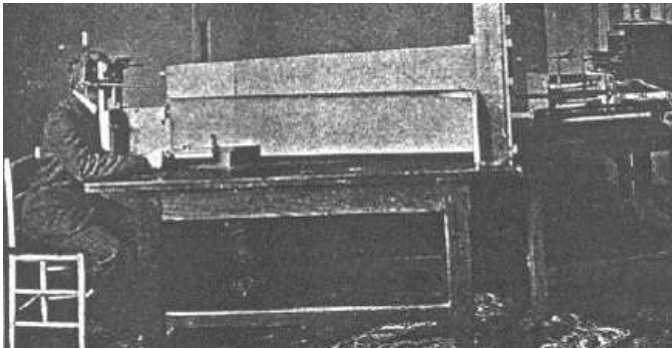


Fig. 2. In 1901, First Study With Eye Tracking

In 1905, Judd, McAllister and Steel made a study of a cismin placed in the eye and the horizontal and vertical movements of the eye were recorded [7]. During the 1930's, eye movements were examined at the time of reading and the effects of reading speed and eye movements of formal factors such as type, character size and page order were investigated [8]. Towards the mid-1900's, research was conducted on the eye movements of the pilots and it was attempted to have knowledge of how Kokpitte used flight equipment and equipment during aircraft landing and launch[9].

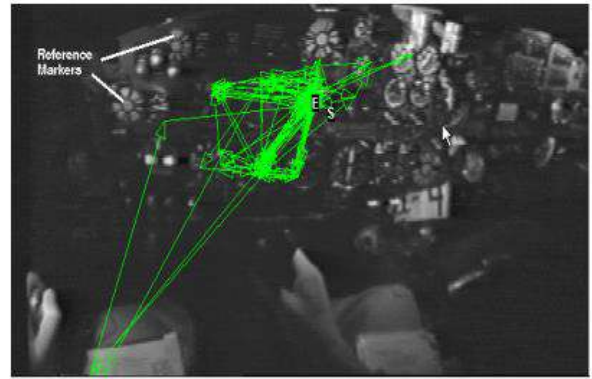


Fig. 3. First Usability Studies For Cockpit Staff

Developed by Hartridge and Thompson in 1948, fixes the problems caused by eye tracker and head movements[10].

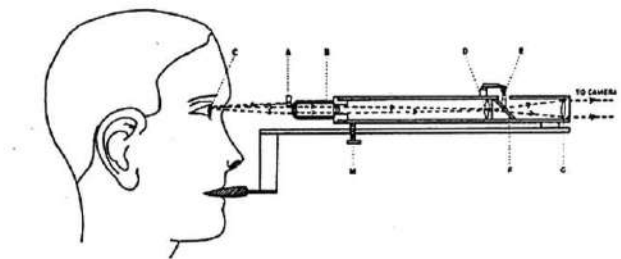


Fig. 4. Hartridge and Thomson's Eye Tracker in 1948

When it came to 1970's, it was understood that the eye tracking technique could be used in psychology and studies were carried out to investigate the relationship of eye movements with perceptual and conceptual events. As analyzes in this context took too long, developments in psychology have progressed more slowly than in other areas of work. The alignment of eye and head movements must be known so that tracking and recording of eye movements can be performed automatically. In this context, Honeywell and EG & G companies, which are close to the point of research and development activities with American Air and Naval Forces, have developed systems that eliminate user restrictions and do not have physical contact with the user. This makes data collection and analysis tasks easier.

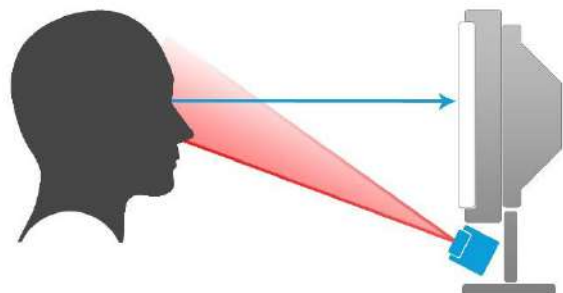


Fig. 5. Honeywell and EG&G's Eye Tracking Model

With the widespread adoption of home computers in the 1980s, the work towards interactive use of eye tracking technology has also gained momentum. The most concrete example of the use of eye movements as an input element in a computer is a computerized writing system based on eye movements developed by Stephen Hawking in 1997 with Intel's support (In Fig.6). With this system, Hawking can transform the words that it wants to express by using eye movements on the screen and through ACAT software developed by Intel[11]. Eye tracking systems nowadays provide convenience for many usability studies. Researchers in availability studies are looking for ways to make more use of this technology, especially as applications such as the internet, social media, video conferencing become more commonplace.



Fig. 6. Stephen Hawking's Eye Tracker

As a result of the literature review, eye tracking systems are classified as follows.

- Electronic Based
 - Electrooculogram (EOG)
- Mechanical Base
 - Scleral Coil
 - Mirror Reflector
- Optical/Video Based
 - Single point
 - Limbus
 - Pupil
 - Two point
 - Corneal
 - Pupil

The most used method is to place skin electrodes around the eyes and measure the potential differences in eye. This technique has wide range but poor accuracy. It was better for relative than absolute eye movements. Mainly used in neurological diagnosis.

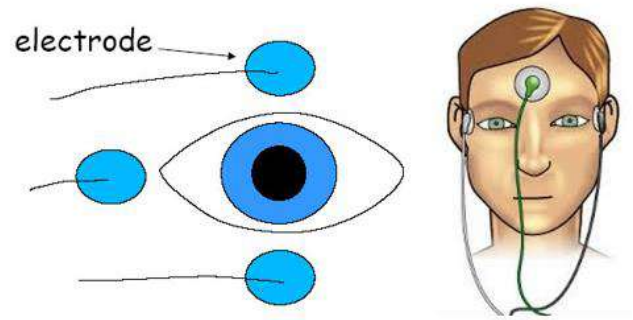


Fig. 7. Electrooculogram (EOG)

The Mechanical Based eye tracking system was on contact lenses with mirror planes. It was reflecting IR-Light. It can be used with coil system. It has a magnetic field. This technique was very accurate. But it was uncomfortable for users who are not used to wear lenses. This can be usable only for laboratory studies.

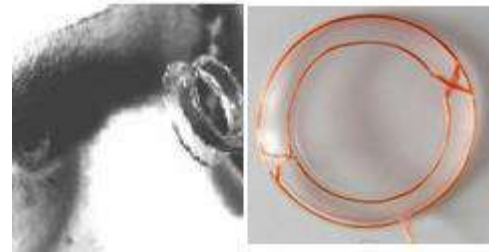


Fig. 8.Coil Technique

Video based Pupil/Corneal Reflection is the most used eye tracking method. When looking at the camera, the reflection on the cornea layer appears near the center of the pupil. When the eye moves upward in relation to the reflection in the central corneal layer, the pupil reflection vector also forms upward.

C. Eye Tracking Device Working Principle

Pupil Center Corneal Reflection (PCCR) is an eye-tracking method that has become popular in recent years for usability and human-computer interaction studies and enables us to measure eye gaze. [12][13].In this method, infrared rays are sent from an LED in the infrared camera to the target. Most of the rays return from the retina layer, so strong reflections come into play. As a result of the rays transmitted from the LED, the eye baby is displayed as a bright and clear circle. The cornea reflection of the pupil is seen as a small glare.

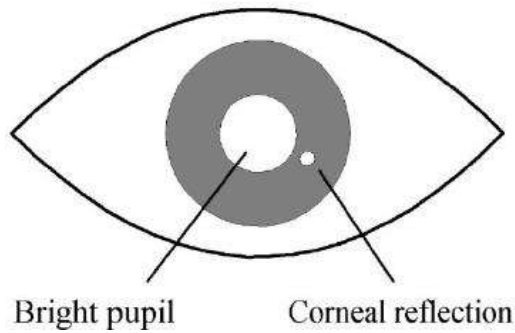


Fig.9. Corneal Reflection With Pupil [14]

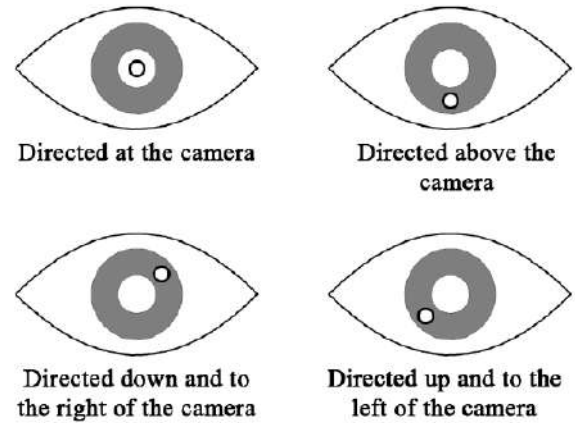


Fig. 11. Corneal Reflection Positions[14]

The working principle of this method is that the reflection from the cornea layer to the center of the pupil is directly related to the vector giving the eye-gaze direction, so the direction of looking at the eye is determined. This vector is known as the pupil reflection vector (In Fig.8).

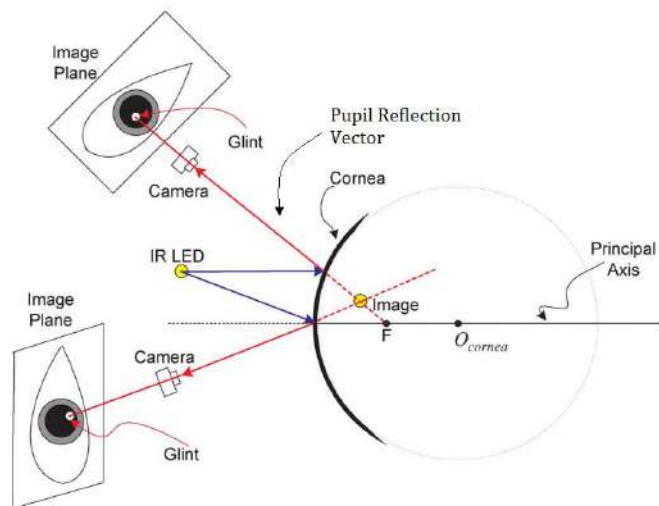


Fig.10. Pupil Centre Corneal Reflection[15]

When looking at the camera, the reflection on the cornea layer appears near the center of the eye baby. When the eye is moved upwards, the eye moves upward in relation to the reflection in the central corneal layer, and the pupil reflection vector also forms upward. Depending on the movements in the right, left, and downward directions, the pupil reflectance vector changes. When looking directly at the camera, the image of the pupil is formed at the middle point of the reflection on the cornea layer, and the pupil reflection vector is reset. The PCCR method is developed on this logic, giving precise and highly reliable results[12].

III. SCOPE OF APPLICATION

- A. Collective Integration with Interactive Applications of Disadvantaged Individuals
 - Communication via computer in patients with ALS (amyotrophic lateral sclerosis)
 - Communication with autism patients through head-to-head and eye tracking computer,
 - For computer-mediated communication in cerebral palsy patients (Spastic cerebral palsy, Athetoid cerebral palsy etc.),
 - Communication via computer in traumatic brain injuries,
 - Rett syndrome is an eye for communicating with patients through the computer,
 - For stroke patients to participate in social life through an eye computer,
 - For communicating by partial paralysis and spinal cord paralysis via computer,
 - Heavy rheumatism is used to communicate with patients through the computer.
- B. Detection of Psychological and Neurological Problems
 - For communicating via computer in children with neurological developmental distress,
- C. Developing Individuals Recognition and Marketing Policies in Commercial Activities
- D. Ergonomics Design
- E. Increasing Game Development and Interaction
- F. Simulator Applications

IV. CONCLUSION

There are many methods for tracking a person's eye movements. Systems based on tight-fitting contact lenses can provide accurate tracking but are awkward and potentially dangerous to the subject. Corneal and limbus eye trackers can measure very small eye movements, but their absolute accuracy is poor. We can choose different methods according to application area. Looking at the eye tracking systems, it is seen that the systems that are worn by the user (monitoring with special lenses attached to the eye, monitoring with the aid of EOG). Although these are not suitable for Human Computer Interaction, optical monitoring systems are used for personal use and presented to the user. It has been observed that the eye was monitored by the help of the infrared rays sent to the user or with the help of the camera. These systems are more suitable for HCI. It is seen that the eye-tracking systems developed for users are usually based on usability tests. Eye tracking systems appear to be used in the literature, especially for gaming applications, web site usability studies, marketing policies in commercial activities, Training and Simulators and for ALS, or stroke patients. This study also formed the basis of our study in distance education class control and participation rate determination using eye tracking technology.

REFERENCES

- [1] Mengsen Huang, "Eye-Tracking Technology In Human-Computer Interaction", University Of Birmingham, Pp 3,2012
- [2] <http://www.economist.com/news/technology-quarterly/21567195-computer-interfaces-ability-determine-location-persons-gaze> [Last Accessed Feb.20,2017]
- [3] Duchowski, A. T., "Eye Tracking Methodology: Theory And Practice",in Springer Verlag, 2003
- [4] <http://hyperphysics.phy-astr.gsu.edu/hbase/hframe.html> [Last Accessed Feb.20, 2017]
- [5] R.J.K. Jacob and K.S. Karn, "Eye Tracking in Human-Computer Interaction And Usability Research: Ready To Deliver The Promises (Section Commentary)", in The Mind's Eye: Cognitive And Applied Aspects Of EyeMovement Research, Amsterdam: Elsevier Science, pp. 573-605, 2003
- [6] Dodge and Cline, "The Angle Velocity Of Eye Movements", in PsychologicalReview, No. 8, pp. 145-157, 1901
- [7] Judd, C.H., Mcallister, C.N. and Steel, W.M., "General Introduction To A Series Of Studies Of Eye Movements By Means Of Kinetoscopic Photographs",in Psychological Review, Monograph Supplements, No.7, pp. 1-16, 1905
- [8] Miles A. Tinker, "Bases For Effective Reading", in University Of MinnesotaPress, 1965
- [9] Fitts, P. M., Jones, R. E. and Milton, J. L., "Eye Movements Of Aircraft PilotsDuring Instrument-Landing Approaches", in Aeronautical EngineeringReview, Vol. 9, Pp. 24-29, 1950
- [10] Hartridge, H. and Thompson, L.C., "Methods of Investigating EyeMovements", in British Journal Of Ophthalmology. 32:581-591, 1948
- [11] <http://www.hawking.org.uk/the-computer.html>, [Last Accessed Mar.03,2017]
- [12] Duchowski and Vertegaal, "Eye-Based Interaction in Graphical Systems:Theory And Practice", in SIGGRAPH 2000 Course Notes #5. ACMSIGGRAPH, 2000
- [13] Redline, C. D., and Lankford, C. P., "Eye-Movement Analysis: A New Tool For Evaluating The Design Of Visually Administered Instruments (Paper And Web)", in Proceedings of the Section on Survey Research Methods of theAmerican Statistical Association, 2001
- [14] Ismail EL HADDIOUI, Mohamed KHALDI, Learner Behaviour Analysis through Eye Tracking, International Journal of Computer Science Research and Application 2012, Vol. 02, Issue. 02, pp. 11-18
- [15] Zhiwei Zhu and Qiang Ji, Novel Eye Gaze Tracking Techniques Under Natural Head Movement, IEEE Transactions On Biomedical Engineering, Vol. 54, No. 12, 2007).

Performance Comparisons of Sports Inspired Metaheuristic Algorithms on Global Optimization

Elif Varol

Department of Software Engineering, Firat University
Elazig, Turkey
evarol@firat.edu.tr

Bilal Alatas

Department of Software Engineering, Firat University
Elazig, Turkey
balatas@firat.edu.tr

Abstract—Studies on sports in recent years have shown that processes, concepts, rules, and events in various sports can be considered and modelled as novel efficient search and optimization methods with extremely effective exploration capabilities in many cases, which are able to outperform existing classical and computational intelligence based optimization methods within different types of search spaces. These novel and interesting sports based algorithms have shown to be more effective and robust than alternative approaches in a large number of applications. In this work, performance comparisons of sports based optimization algorithms, namely League Championship Algorithm (LCA) and Soccer League Competition Algorithm (SLCA) have been demonstrated within benchmark function for the first time. These algorithms are relatively interesting and novel and many efficient versions of them may be proposed for many different complex search and optimization problems.

Keywords—League Championship Algorithm, Soccer League Competition, Optimization, Benchmark Functions

I.

INTRODUCTION

Optimization is the process of searching for the optimal solution. Analytical, enumeration, and heuristic methods can be used for optimization task. Heuristic refers to experience-based techniques for problem-solving and learning. Heuristics are problem-dependent and designed only for the solution of a specific problem. A metaheuristic is a higher level heuristic that may provide a sufficiently good solution to any optimization problem [1]. General purposed metaheuristic methods can be categorized according to ten different inspiration fields such as biology, physics, swarm, sociology, music, chemistry, sports, plant, water, and mathematics. Furthermore, there are hybrid methods which are combination of these [2]. Categorization is depicted in Figure 1.

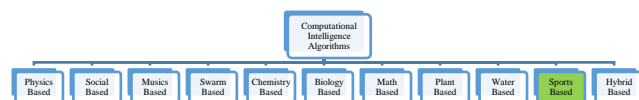


Fig. 1 Computational intelligence search and optimization methods

Processes, concepts, rules, and events in various sports, especially in football, have also been considered and modelled as novel efficient search and optimization methods with extremely effective exploration capabilities in many cases. League championship algorithm and soccer league competition algorithm are sports based computational intelligence algorithms.

In this work, performance comparisons of sports based optimization algorithms, namely League Championship Algorithm (LCA) [3] and Soccer League Competition Algorithm (SLCA) [4] have been demonstrated within benchmark function for the first time.

II. SPORT INSPIRED METAHEURISTICS

Processes, concepts, rules, and events in sports, modeled as computational intelligence algorithms, are able to produce completely new and effective search and optimization procedures, with extremely effective exploration capabilities in many cases, which are able to outperform existing classical and metaheuristic based optimization approaches. This section describes all of the existing computational intelligence algorithms based on sports.

A. League Championship Algorithm (LCA)

LCA is one of the interesting sports inspired population based algorithm for global optimization which tries to imitate a championship situation where artificial football clubs participate in an artificial league for a number of weeks [3, 5].

Each team (individual) in the league (population) represents a feasible candidate solution for the interested problem. These teams compete in an artificial league for several weeks (iterations). Based on the league schedule at each week, teams play in pairs and the outcome is determined in terms of win or loss based on each team playing strength (corresponding to the fitness value) resultant from a particular team formation (solution). In the recovery period, keeping track of the previous week events, each team devises the required changes in its formation to set up a new formation (a new solution is generated) for the next week contest and the championship goes on for a number of seasons (stopping

criterion). Table I shows same meaning terms of both evolution and sports terminologies.

LCA is the firstly proposed sports based computational intelligence algorithm and works with a population of candidate solutions. Hence, in the initialization step a league (population) of L (the league size) teams (solutions) is generated and their playing strengths (fitness values) are computed. Each team is composed of n players corresponding to the number of decision variables of the related problem. In this step, the teams' best formations take the initialization values. Then, competition step is started. Based on the league schedule, the artificial teams compete in pairs for $S \times (L - 1)$ weeks where S is the number of seasons and a week is noted as t . After each competition or game between team i and team j , based on the playing strength of each team, the outcome is given in terms of win or loss.

TABLE XV. METAPHORS

Sports Terminology	LCA
1 League	Population
2 Week	Iteration
3 Team I	i -th member in the population
4 Formation	Solution
5 Playing strength	Fitness value
6 Number of seasons	Maximum iterations

LCA performs the SWOT (Strength, Weakness, Opportunity, and Threats) analysis for the variation operators. In the recovery step, each team elaborate a new formation taking into account the team's current best formation and previous week events. In LCA, the selection is performed with a greedy approach. It replaces the current best formation with a more productive team formation with a better playing strength. In other words, if the new formation is the fittest one, hereafter consider the new formation as the team's current best formation. The algorithm stops after the termination criterion is met and the team who has the best fitness value (playing strength in LCA) wins the championship [3, 5]. Flowchart of LCA is shown in Figure 2.

B. Soccer League Competition

Soccer League Competition Algorithm (SLCA) inspired by professional soccer league is based on the competitions among teams and internal competitions among players of each team [4]. Team's power depends on the power of its players. Players within a team compete with each other to attract the head coach's attention by improving their performance which leads to a growth in the quality and power of their team. In each team, there is a key player, called Star Player (SP), which has the best performance among other players in the team. Furthermore there is a unique most powerful player in each league and is called the Super Star Player (SSP).

After every match, players in winner and loser teams of each match adopt different strategies for improving their

future performance. These strategies have been performed by four operators in SLCA.

Imitation Operator: When a team wins a match, fix players try to imitate the team's SP, and the SSP of the league. They aim to experience a promotion to the SP or, optimistically, occupy the place of SSP in the league. Solution vectors relating to the fixed players in the winner team move toward the best solution of the own team and the best solution vector of the league for this purpose.

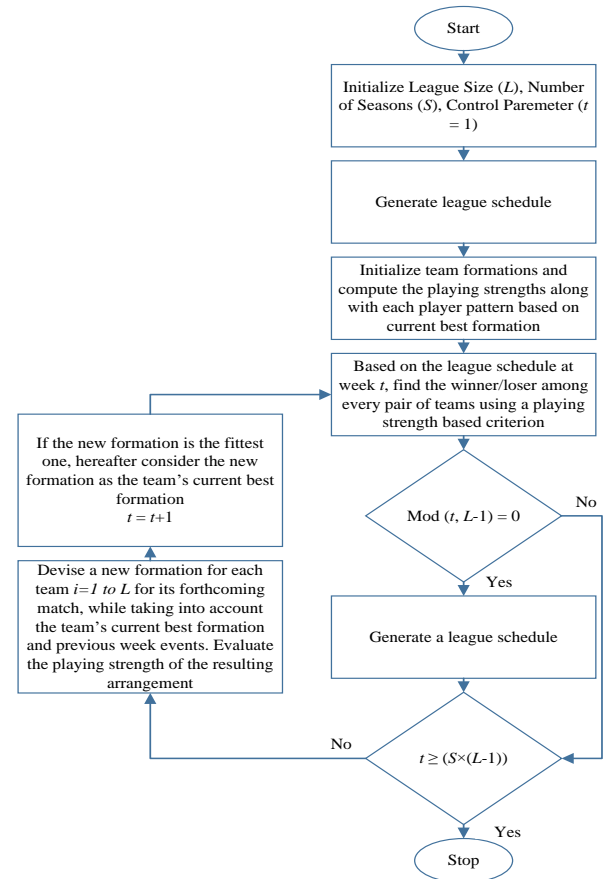


Fig. 2 Flowchart of LCA

Provocation Operator: Winner's substitutes try to have a performance approximately equal to the average level of fixed players in the team. In other words, higher provocation for advancement gives them more chance of being a fixed player in the future.

Mutation Operator: Loser teams seek for ways of improving their performance for reaching better results in future matches. For this reason, fixed players of these teams have to revise their playing style. To perform this operation, the positions of some players are randomly changed for creating diversification in solutions.

Substitution Operator: Head coach usually considers new combinations of substitutes in order to stop the failures in the future. Similarly, a random-based approach is applied to reflect the head coach impact in SLCA. To do this, a pair of new substitute vectors is being tested. If a suitable solution is obtained, this effective pair is entered to the team [4].

Flowchart of SLCA is depicted in Figure 3.

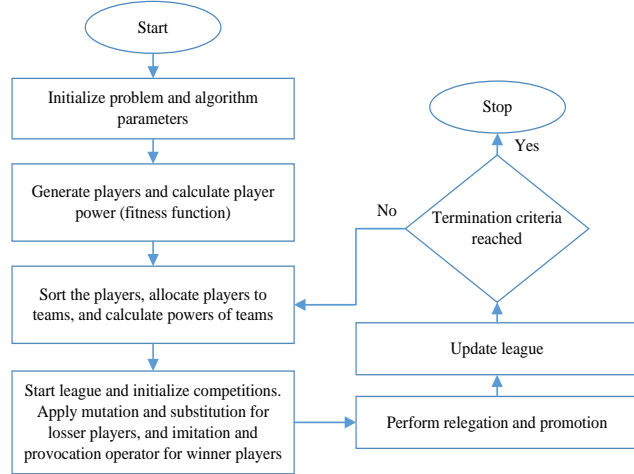


Fig. 3 Flowchart of SLCA

III. BENCHMARK FUNCTIONS

Benchmark test functions are used to evaluate and compare the characteristics of optimization algorithms in terms of convergence, precision, robustness, and general performance as a rule. The nature, complexity and other properties of these benchmark functions can be easily obtained from their definitions. The difficulty levels of most benchmark functions are adjustable by setting their parameters [6]. The selected benchmark functions and its properties have been demonstrated in Table II. The dimensions for all functions have been determined as 30. Sphere function is unimodal with less complexity and it can be used to evaluate the converging behaviors of algorithms [7]. Schwefel function is multi-modal function with many local optima and it can be used to test the global search ability of the algorithms in avoiding premature convergence [8].

Their graphs with two dimensions have been shown in Figure 4 and Figure 5.

IV. EXPERIMENTAL RESULTS

Obtained results for Sphere function from LCA and SLCA have been demonstrated in Table III and Table IV. Both algorithms have been run 10 times with different numbers of starting search points (10, 20, 30, 50, and 100). During each run, the maximum number of function evaluations is 10^5 . The maximum number of algorithm iterations is equal to the result of dividing the maximum number of function evaluations to the number of starting search points. Mutation rate and mutation probability for SLCA have been selected as 0.2 and

0.1 respectively. Numbers of main players and reserve players are equal to the dimension of the problem for SLCA. Retreat coefficient, approach coefficient, and P_c for LCA have been selected as 0.5, 0.1, and 0.7 respectively. It can be seen that when the maximum number of iteration is fixed, with low population size, performance of LCA is better than that of SLCA. Increasing the number of initial search point results in poor performance of the LCA whereas results in better performance of the SLCA.

TABLE XVI. BENCHMARK FUNCTIONS

Function Name	Definition	Interval
Sphere	$\sum_{i=1}^D x_i^2$	$-100 \leq x_i \leq 100$
Schwefel	$f_2(x) = n \times 418.9829 + \sum_{i=1}^n -x_i \sin(\sqrt{x_i})$	$-500 \leq x_i \leq 500$

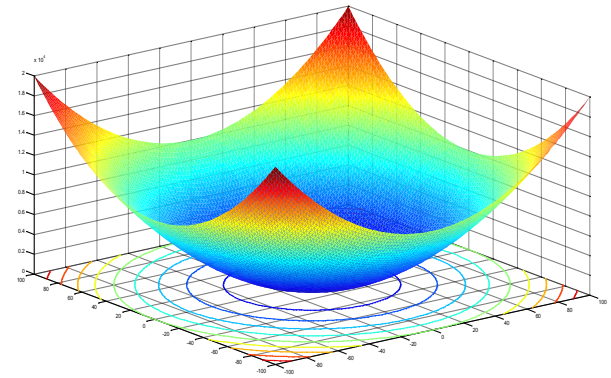


Fig. 4. Sphere function with two variables

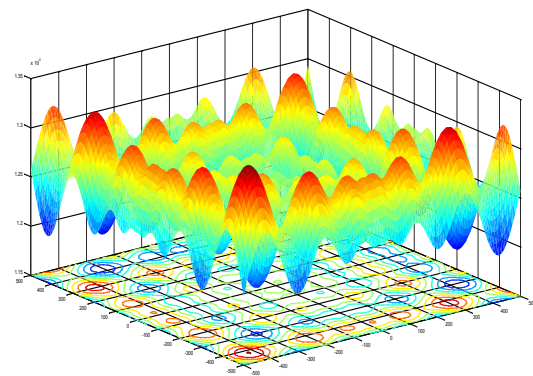


Fig. 5. Schwefel function with two variables

TABLE XVII. OBTAINED RESULTS FOR SPHERE FUNCTION FROM LCA AND SLCA WITH POPULATION SIZE 10 AND 20

Initial population size	10		20	
	LCA	SLCA	LCA	SLCA

Mean	1.07703E-90	4.39880E-55	7.89105E-44	3.79020E-30
Best	3.03661E-92	2.46520E-55	1.42103E-44	9.83814E-31
Worst	2.56096E-90	1.0905E-54	1.86844E-43	8.45996E-30

TABLE XVIII. OBTAINED RESULTS FOR SPHERE FUNCTION FROM LCA AND SLCA WITH POPULATION SIZE 30, 50, AND 100

Initial population size	30		50		100	
	<i>LCA</i>	<i>SLCA</i>	<i>LCA</i>	<i>SLCA</i>	<i>LCA</i>	<i>SLCA</i>
Mean	5.69552E-28	5.52190E-24	4.47706E-15	5.32600E-19	1.36133E-05	1.83953E-38
Best	2.59198E-28	1.20850E-24	1.65469E-15	2.11033E-20	7.07496E-06	6.27750E-39
Worst	1.84634E-27	8.26620E-23	8.65256E-15	6.72970E-17	2.09039E-05	3.30390E-36

Obtained results for Schwefel function from LCA and SLCA have been reported in Table V and Table VI. Both algorithms have been run 10 times with different numbers of starting search points (10, 20, 30, 50, and 100). During each run, the maximum number of function evaluations is 10^5 . The same parameter values of the algorithms have been used for this function. From these tables, it can be concluded that performance of LCA is better than that of SLCA in multi-modal Schwefel function.

TABLE XIX. OBTAINED RESULTS FOR SCHWEFEL FUNCTION FROM LCA AND SLCA WITH POPULATION SIZE 10 AND 20

Initial population size	10		20	
	<i>LCA</i>	<i>SLCA</i>	<i>LCA</i>	<i>SLCA</i>
Mean	71.0633826	6679.5	0.000382	5989.06066
Best	0.000381827	3750.2	0.000382	3800.26351
Worst	355.3153857	6891.6	0.000382	6326.36354

TABLE XX. OBTAINED RESULTS FOR SCHWEFEL FUNCTION FROM LCA AND SLCA WITH POPULATION SIZE 30, 50, AND 100

Initial population size	30		50		100	
	<i>LCA</i>	<i>SLCA</i>	<i>LCA</i>	<i>SLCA</i>	<i>LCA</i>	<i>SLCA</i>
Mean	0.00038	4389.23256	0.00502	2849.36250	270.40560	2262.02263
Best	0.00038	3659.68682	0.00090	1989.56550	97.718792	1625.26623
Worst	0.00038	7102.22000	0.02992	4189.36561	396.48090	2352.02220

V. CONCLUSIONS

Processes, concepts, rules, and events in various sports, especially in football, have been considered and modelled as novel efficient search and optimization methods with extremely effective exploration capabilities in many cases. League championship algorithm and soccer league

competition algorithm are sports based computational intelligence algorithms. In this paper, their global optimization performances have been compared within unimodal and multimodal unconstrained benchmark functions. When the maximum number of iteration is fixed, with low population size, performance of LCA is better than that of SLCA on unimodal function. Increasing the number of initial search point results in poor performance of the LCA whereas results in better performance of the SLCA. Besides, performance of LCA is better than that of SLCA in multi-modal function.

These algorithms are very new computational methods and they can be improved in many ways. They can be combined with heuristic methods or other global optimization algorithm and their hybrid versions may be proposed for efficient results for different search and optimization problems. More validation studies should be performed to discover the capabilities of these algorithms in dealing with the search and optimization problems. On the other hand; design, development, and implementation of novel algorithms is an important task under the philosophy of improvement in the scientific field and always searching better. There are positive challenges in terms of their efficiency and best possible use of these algorithms. This paper may lead to many future contributions in exciting and emerging area of engineering problems.

REFERENCES

- [1] Du, Ke-Lin, and M. N. S. Swamy. Search and Optimization by Metaheuristics. Springer, 2016.
- [2] Sinem Akyol, Bilal ALATAŞ, Efficiency Evaluation of Crow Search Algorithm in Benchmark Functions for Optimization, ICENS2016, Bosna, 2016
- [3] Kashan, Ali Husseinazadeh. "League championship algorithm: a new algorithm for numerical function optimization." Soft Computing and Pattern Recognition, 2009. SOCPAR'09. International Conference of. IEEE, 2009.
- [4] Moosavian, Naser, and Babak Kasaei Roodsari. "Soccer league competition algorithm: A novel meta-heuristic algorithm for optimal design of water distribution networks." Swarm and Evolutionary Computation 17 (2014): 14-24.
- [5] Kashan, Ali Husseinazadeh. "League Championship Algorithm (LCA): An algorithm for global optimization inspired by sport championships." Applied Soft Computing 16 (2014): 171-200.
- [6] Sinem Akyol, Bilal ALATAŞ, Chaotically Initiated Flower Pollination Algorithm for Search and Optimization Problems, ICENS2016, Bosna, 2016.
- [7] (January 2017) GEATbx: Examples of Objective Functions. Available: <http://www.pg.gda.pl/~mkwies/dyd/geadocu/fcnfun1.html>
- [8] (January 2017) GEATbx: Examples of Objective Functions. Available: <http://www.pg.gda.pl/~mkwies/dyd/geadocu/fcnfun7.html>

Wireless And Impreadable Wireless Sensor Networks

Ünal Sınır

Computer Engineering Department
Istanbul SabahattinZaim University
Istanbul,Turkey
ist.unal@gmail.com

Farzad Kiani

Computer Engineering Department
Istanbul SabahattinZaim University
Istanbul,Turkey
farzad.kiyani@gmail.com

Amir Seyyedabbasi

Computer Engineering Department
Istanbul SabahattinZaim University
Istanbul,Turkey
amir.seyyedabbasi@std.izu.edu.tr

Abstract— Computer systems and personal health applications. There is a primary research area that makes a difference in wireless sensor network (WSN) technologies to improve the quality of life. The current development of WBAN and IWBAN systems provides advantages and disadvantages and a snapshot for future work. The role of WBAN technology in the maintenance and quality care of WBAN technology is described in the article because of the increasing population density of the elderly, which is increasing day by day, without needing sickness or diseases that cause chronic illnesses. The article is an example of the latest technologies related to designs such as reliability, scalability, energy efficiency and security, as well as an analysis of the diversity and disadvantages of these systems.

Keywords—Wireless Sensor Networks, Wearable Sensors, Health.

I. INTRODUCTION

Wireless Sensor Network technology has the potential to change the quality of life through work done in areas such as health, entertainment, travel, industry, care-requiring patients and emergency management.

The combination of wireless sensors and sensor networks with computing and artificial intelligence research have built a cross-disciplinary concept of ambient intelligence in order to overcome the challenges we face in everyday life[1]. One of the main challenges facing the World in recent years has been the increase in the elderly population in developed countries. According to the Population Reference Bureau [2], over the next 20 years, the 65-and over population in the developed countries will become almost 20% of the total population. Hence the need to provide quality care and service in these countries for a rapidly growing population of elderly people, while reducing the healthcare costs is an important issue for governments and health service providers in such countries.

It is a vehicle that uses wearable and implantable body sensor networking systems to accomplish these goals without interfering with the day-to-day activities of people.

Body sensor network systems can help people by providing healthcare services such as medical monitoring,

memory enhancement, control of home appliances, medical data access, and communication in emergency situations [3, 4]. Monitoring people with wearable technologies and body sensor networks that can be placed on the body. Immediate delivery of emergency situations in risky patients to central systems will increase early detection of diseases. It can be used not only for elderly people and chronic patients but also for babysitting services.

Researchers in various interdisciplinary fields such as computing, engineering, and medicine fields are working together in order to ensure that the broad vision of wearable and implantable body sensor networks (WIBSNs) for smart healthcare, as illustrated in Figure 1, can be fulfilled.

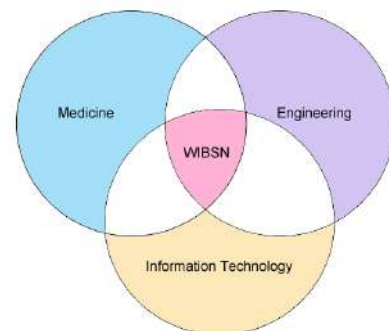


Figure 1 WIBSN

The importance of integrating wireless telecommunication technologies such as 3G, Wi-Fi Mesh and WiMAX with health technologies has been addressed by some researchers. For this purpose, Alzheimer's disease, such as people with cognitive disorders are considered for continuous monitoring of people. While some applications focus on posture detection and location tracking, some use biological and environmental sensors to identify patients' "health status."

In addition, significant research is being conducted on the development of wearable technology or small wireless sensor devices implanted in the human body. The range of wearable and implantable biomedical devices will significantly

increase in recent years, thanks to improvements in micro-electro-mechanical systems (MEMS) technology, wireless communications, and digital electronics. These studies will lead to the development of sensor nodes that include sensing, data processing and communication components of low-cost, low-power, low-cost sensors. The lower power consumption, as well as the lower cost of components, will make the products more affordable and increase their usability, and will also provide energy efficiency.

The connections with leads and cables used in most current monitoring devices present obvious drawbacks in that they restrict the mobility of patients and, in addition, they may cause skin irritations or infections, and therefore contribute to deterioration of health conditions. Sensor networks thus represent a significant improvement compared to conventional sensors [6]. Despite the fact that a wireless connection is not a requirement for physiological parameter monitoring with implanted sensors, the issue mentioned above is one of the main motivations for this trend to use wireless technology in modern biomedical implanted systems [7]. Examples of physiological data collection platforms with wireless connectivity include a wide range of biomedical applications. Coosemans et al. [8], for example, have described a system for continuous wireless intracavitary pressure monitoring of the bladder, while other authors have assembled neural prosthetic devices [9-10].

Tang et al. have described their vision [11] of a future when one device will be able to build a WSN with a large number of nodes, both inside and outside the human body that may be either predefined or random, according to the application. This vision can only be applied through the use of common communication protocols for wireless sensor networks. The standardized hardware and software architectures can support compatible devices, which are expected to significantly affect the next generation of healthcare systems. Some of these devices can then be incorporated into the wireless body area network (WBAN), providing new opportunities for technology to monitor health status [12].

This article investigates wearable wireless sensor networks (WWBAN) and body-deployable body sensor network (IWBAN) systems that provide more comprehensive monitoring of patients more sterily, providing alternative contextual information and warning mechanisms for possible anomalies. In addition, this article highlights the latest trends in the future of intelligent applications for monitoring patients, the advantages of sensor networks and body-area network technology.

II. RELATED WORKS

Many implementations of body area networks used for body sensor communication have recently been reported in the literature [13-16]. Many of these studies are mainly

focused on MAC protocols. The system in Figure 2 uses an architecture that provides point-to-point communication of data from multiple sensors on the body to the main node. Transmission docks are synchronized using signaling signals transmitted within predetermined periods.

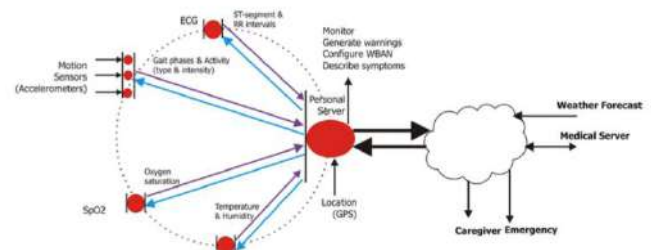


Figure 2 Data stream in an integrated WWBAN [13]

The mechanisms reported in Figure 3 include adaptation of the standard IEEE 802.15.4 / ZigBee-based MAC to the body.

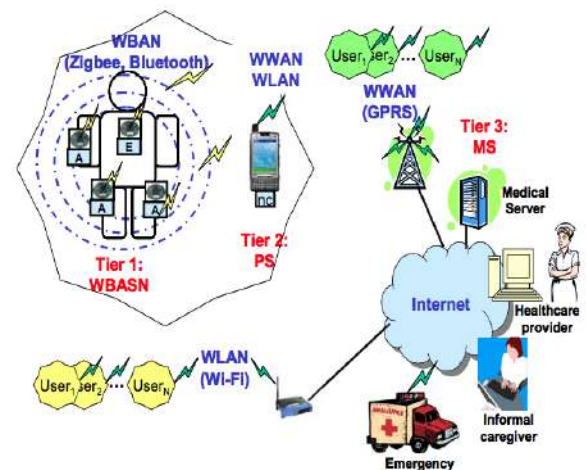


Figure 3 The Structure of the Zigbee Based Mac Protocol

The work reported in [15,16] investigated on-body MAC-routing cross-layer issues via distributed transmission coordination in the presence of specific routing structures. In [15], the authors presented an energy-efficient slotted MAC in the presence of a Wireless Autonomous Spanning tree Protocol (WASP) that is used for on-body packet routing.

The protocol in [16] adopts a similar tree-based cross-layer approach, but is designed specifically for reducing packet delivery delays over an on-body spanning tree. Another advantage of this protocol is that the WASP, which is used for packet routing, also performs body movement through reconstruction and maintenance.

Knowledge-based strategies are generally designed to deliver single copy packages. In order to be able to make efficient referral decisions, it is necessary to use information about dynamics. In hybrid systems, when a packet arrives at another node, the routing rule must determine whether a copy

of the packet or packet has been transferred to that node. In this case, the energy consumption of the nodes should not be ignored.

The above mentioned implementations are applied to networks that extend to the local area wide area. The objective of the work described in [14] is to apply the key DTN routing concepts, as identified above, in an ultra-short-range body area environment. The challenge is to develop mechanisms for capturing the locality of on-body node movements caused by human postural mobility.

BASNs have carried out a variety of interesting applications in the fields of health, sports and entertainment where human centered perception is possible. The authors identified the heart rhythm, detected irregularities, and identified emergencies in technology that would notify the staff. These studies are not too far from the research labs, but they show the promises of the important field WBANs.

III. WIRELESS SENSOR NETWORKS

A. History and Overview

Most of the devices we use on a daily basis, from wristwatches to PDAs, mobile phones to cars, are controlled by embedded systems. Today, with the advantages of technological developments, more than 99% of manufactured microprocessors are used in embedded systems. The concept of ambient intelligence reflects the vision that technology will not only develop but be embedded, invisible, and fully hidden in our natural surroundings, but present whenever we need it, enabled by simple and easy interactions [21,22].

Wireless sensor networks [23,24] are usually considered one of the technological foundations of ambient intelligence. Agile, low-cost, ultra-low power networks can capture a significant amount of information from the surrounding environment. Sensor networks can be seen as the sensory system of the intelligent environment of the human body. Sensor networks can share data collected from the built-in sensors with neighboring nodes or data collection stations.

Current sensor network applications in ambient intelligence range from the environmental monitoring of ecosystems and industrial processes for tracking assets and people to the maintenance of buildings, etc. [25]. In these applications, each application domain has different requirements and constraints depending on the nature of the problem. In this article, we will focus on a specific model of practice, such as the monitoring of people based on human body implacable sensors, to come up with the use of wireless sensor networks in healthcare and to overcome new challenges. There are important reasons for this choice. Human watching is a very important issue for everyone. It introduces new challenges, such as unobtrusive, safe and low energy consumption requirements. Finally, the media in

which AR-GE activities are most active is one of the areas of intelligence application.

The design, implementation, and deployment of WSNs requires input from a wide range of disciplines such as medicine, engineering, and computing, as mentioned earlier in the paper, in addition to consideration of the numerous application-specific constraints. In the last five years, significant progress has been made in the development of WSNs, and some WSN-based commercial products have already appeared on the market. We refer readers interested in studies on software and network architectures to any of the many excellent surveys that have recently been published on these topics [26, 27].

A sensor network consists of a large number of sensor nodes, which are deployed either inside the phenomenon to be monitored or very close to it. Sensor networks represent a significant improvement over traditional sensor networks, which are deployed in the following two ways [28]:

- If the sensors are far from the scene to be monitored, large sensors must be used that use some complicated methods to distinguish targets from environmental noise.
- Only a variety of sensors can be used to perform detection. The locations of the sensors and network topology must be carefully designed. The data related to the event are sent to the central nodes where the time series, the calculations are made and the data are combined.

B. Wireless Sensor and Ad Hoc Networks

Wireless Ad Hoc Networks, creation techniques, can be used for wireless sensor network applications. Many protocols and algorithms have been proposed for traditional Wireless Ad Hoc Networks. However, the unique features and application requirements of the proposed protocol and algorithms are not appropriate for sensor networks. In this subsection, we briefly compare sensors and ad hoc networks to highlight the important role of wireless sensor networks in monitoring the human body. To explain this point, the differences between sensor networks and ad hoc networks can be summarized as follows:

- **Number of Sensor Nodes:** The number of sensor nodes in a sensor network can be much larger than nodes in a temporary network.
- **Activity:** Sensor nodes may be positioned intensively.
- **Fault:** Sensor nodes are prone to failure.
- **Network Topology:** The topology of a sensor network changes frequently. If a network sensor fails, new topologies and data transmission paths may need to be selected.
- **Communication Capability:** Sensor nodes often use broadcast communication paradigm. Most ad

hoc networks are based on point-to-point communication.

- **Computation:** Sensor nodes are limited by their power, computation capacity and memory.

C. WSN Applications

In wireless network systems; the integration of sensors embedded microcontrollers and radio interfaces into a single chip has ensured a new generation of wireless sensor networks for many applications. The features described in the previous section provide a wide range of applications for sensor networks. Wireless sensor networks can be used for military applications, habitat monitoring, machine health monitoring and guidance, traffic pattern monitoring and navigation, plant monitoring in agriculture [29], and infrastructure monitoring. One of the most exciting applications is health monitoring [30, 31]. This article focuses on health practices and body sensor networks that are predominantly wearable and can be placed in the body. A number of physiological sensors that monitor vital signs, environmental sensors, and a location sensor can be integrated into a wearable wireless body area network (WBAN) [32]. In addition, the concept of micro-sensing and wireless connectivity of network nodes promises many new application areas. The practices are classified into military, environmental, health, home and other commercial areas. It is possible to spread this classification to a wider range. However, since the focus was on the body sensor nets, the fan was narrowed. You can refer to reference [33] for other application areas.

1) Military Applications

The rapid deployment of sensor networks, self-organization and fault tolerance features make wireless sensor networks a very promising detection technique for military command, control, communications, computing, intelligence, surveillance, discovery and targeting systems. Some of the military applications of sensor networks follow friendly forces, equipment and ammunition. Nuclear, biological and chemical attack detection has recently been seen as critical attack methods.

2) Environmental Applications

Another important area of wireless sensor networks is the environmental applications that follow the movements of intelligent houses, birds, small animals and insects; To monitor environmental conditions affecting plants and animals; irrigation; Applications are being made for large scale soil monitoring, precision agriculture, flood detection, meteorological or geophysical surveys.

3) Home Applications

Home automation: as technology evolves, intelligent sensor nodes and actuators can be incorporated into devices such as vacuum cleaners, microwave ovens and refrigerators. The sensor nodes in the device have reached the point where they can communicate with each other via the Internet or

satellite and the external network. This not only makes life easier for people but also economically saves energy.

4) Health Applications

Some of the health applications of sensor networks involve providing interfaces for the disabled, integrated patient monitoring, diagnostics, drug administration in hospitals, tele monitoring of human physiological data, and tracking and monitoring doctors and/or patients inside a hospital [34-36].

Observation of Human Physiological Data: Physiological data collected by sensor networks can be stored for a long time so that they can be used later in medical research. In addition, sensors are used to monitor the behavior of older people. As an example, a health smart home was designed by the Faculty of Medicine in Grenoble-France to check the feasibility of such systems [38].

a) Monitoring of Physicians and Patients at the Hospital:

Each patient can be monitored by means of a small sensor node connected to them. A sensor node in a patient can sense heart rate while another can detect blood pressure. In Turkey, there are studies on systems to follow patients in intensive care units and to intervene in emergency situations by doctors. Doctors can also carry a sensor knot that allows other doctors to find them at the hospital, as well as a sensor node where the physician can monitor fatigue, concentration data.

b) Drug Monitoring in Hospitals:

With the sensors placed on the medicine or medicine boxes, information about which medicine will be given to the patient can be easily reached. In this way, wrong drug delivery or contamination will be prevented. Thus, patients will have sensor nodes that indicate allergies and need drug treatment. Computerized systems as described in [35] have shown that they can help minimize the side effects of drugs.

IV. WIRELESS BODY AREA NETWORKS (WBANS)

The WSNs used in the current system are expanding for medical applications and causing the technology to turn into body sensor networks (BSNs). Among biosensors, other health parameters used in the human body, electrocardiograms, electromyographies, body temperature and blood pressure, electro-dermal activity may be measured. For example, an accelerometer can be used to sense the calibration rate, movement, or muscle activity.

Thanks to mobile devices such as mobile phones and popular MP3 players; in 2001, Zimmerman [38] studied how such electronic devices operate at or near the human body. This increases the usability of the technology as it allows people to be transparent to these systems.

Medical environments in which the conditions of many patients are constantly monitored in a real-time environment are the targets of WBANs. Wireless monitoring of the physiological signals of a large number of patients is one of the existing requirements for the establishment of a complete WSN in health systems. The main goal of WBANs is to provide biofeedback data, the ability to continuously monitor health parameters such as body/intra-body temperature, heartbeat rate, arterial blood pressure, in an unobtrusive and efficient way [39].

A typical WSN system that senses and transmits signals from a human body:

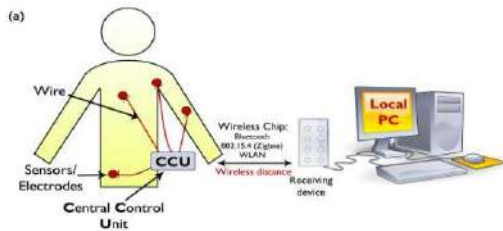


Figure 4 Health sensor network available application

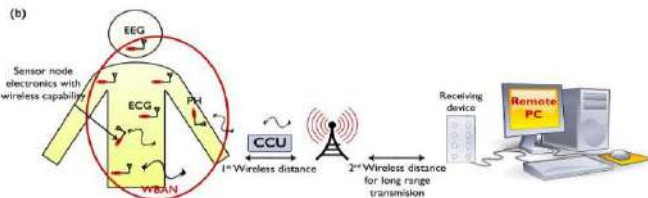


Figure 5 Future implementation of health sensor targeted by wireless body network

Such sensor networks may vary from point to point or point to point depending on the application. While the distributed detection of an athlete's posture [40] would need point-to-point data sharing across various on-body sensors, applications such as monitoring vital signs as shown in Figure 5, will require all body mounted and/or implanted sensors [41,42] to route data multipoint-to-point to a sink node, which in turn can relay the information wirelessly to an out-of-body server.

The wireless body-area network consists of a series of miniature sensors, lightweight, low-power sensing devices, management electronics and wireless receiver receivers. For these components, which are indispensable and the most important part of the system, the power source must be small size, lightweight, environment friendly and long lasting.

A. Requirements for Wireless Medical Sensors in WBAN

Wireless medical sensors should satisfy the following main requirements such as wearability, reliability, security, and interoperability [43]:

1) Wearability

Wireless medical sensors must be lightweight and small to be monitored in a healthy way. Size and weight of sensors are mainly determined by the size and weight of batteries [44, 45]. However, the capacity of a battery is directly proportional to its size. This is seen as a disadvantage to developers. We can expect that the further development of the integrated circuits and the miniature technology of the pillars will help the user to improve the level of comfort.

2) Reliable Communication

Secure communication in WBANs is of great importance for medical applications. For example, instead of sending raw data from sensors, we can extract the attribute on the sensor and only transmit information about an event. In addition to reducing high demands on communication channels, reduced communication requirements save on total energy expenditure and thus extend battery life. However, calculations on the sensor can increase the energy consumption of the sensor even though the system reduces the complex energy consumption. The choice between communication and computing will provide the best system design for the application area.

3) Security

The security problems of the WBAN based telemedicine system arise at all three levels. At the lowest level, wireless sensor networks must meet the confidentiality requirements provided by law for all medical devices and ensure data integrity. A relatively small number of nodes in a typical WBAN and communications areas are able to accomplish these tasks, although keystrokes, authentication, and data integrity are difficult tasks in limited sources of medical sensors.

4) Interoperability

Wireless medical sensors should ensure that users can easily set up a robust WWBAN, depending on the health of the users. Standards governing the interaction of wireless medical sensors help vendors compete and eventually lead to more accessible systems.

B. Wearable Wireless Networks (WWBAN)

WSN technology has the potential to offer a wide range of benefits for patients, medical personnel and the community through continuous monitoring in an environment, early detection of abnormal conditions, and exploration of all collected information through data mining. This subdivision shows how the architecture and mechanics of the WWBANs can be used to provide a basic infrastructure that provides continuous, everyday health monitoring that is as invisible as one of the main points of this article. This sub-section also

describes some important application problems. Finally, we present some applications of wearable sensors, such as smart t-shirt (intelligent life) and bio potential acquisition system application.

WWBANs are an important part of a multi-stage or multi-layer system, as shown in Fig. The architecture incorporates the first stage of the wireless sensor integrated into the WWBANs, including the wireless node count, while the sensor node detects, processes and processes one or more physiological signals.

In the first stage, sensors are installed for different purposes. These sensors can be used to differentiate the user's situation and estimate the activity level.

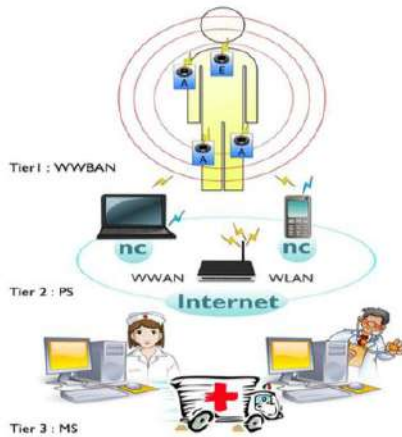


Figure 6 WWBAN Architecture

In the second stage, there is a personal server application running on a mobile phone or a home personal computer that will be used to transfer data from the data collected by the sensor to the remote user. The personal server is responsible for a variety of goals that provide an interface for wireless medical sensors, users and the medical server. The WWBAN interface includes network configuration and management features. With this interface, it is possible to activate the different features provided by the system.

1) Wearable Intelligent T-Shirt Application

A number of wearable physiological monitoring systems have been developed to monitor the health status of the individual wearer or the elderly [17, 46-47]. A wearable physiological monitoring system called „Smart Vest“ to monitor various physiological parameters such as electrocardiograms, photo plethysmographs, heart rate, blood pressure, body temperature and galvanic skin response has been developed [48]. Figure 7 shows the general architecture of wearable systems for health and activity monitoring anywhere in a t-shirt with integrated wireless sensor nodes, a base station and a server personal computer for remote monitoring.



Figure 7 A wearable smart shirt system architecture

2) Wearable Biopotential Picking System Application

Experts explain that more than 98,000 people die in hospital each year because of medical errors in the US alone. Diagnostic and treatment errors associated with the conditions and disadvantages of systems that enable people to make mistakes are mentioned. In addition to this problem, the costs of existing health systems are also increasing significantly. Patients are connected to volume and network independent devices for monitoring bio potential signals. These devices cause the inconvenience to increase in cost due to the necessity of lowering mobility as well as being performed in a hospital environment.

Figure 8 shows a typical configuration using a readout circuit to extract signals from the human body using bio potential electrodes.

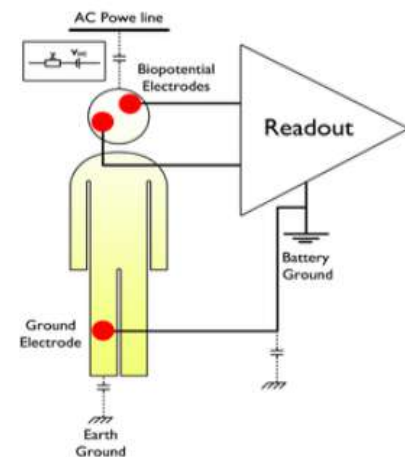


Figure 8 Biopotential reading cycle

3) Implantable Wireless Networks (IWBAN)

Conditions need to be determined without the need for patient intervention and the physiological status of the patient. Implantable biosensors are an important class of biosensors based on their ability to continuously measure metabolite levels, without the need for patient intervention and regardless of the patient's physiological state (sleep, rest, etc.) [49].

Thanks to the advanced technology of Microsystems technology over the past decade, the range of implantable biomedical devices has increased dramatically over the next decade. IWBANs are more attractive than WWBAN for many advantages. WWBANs have some disadvantages: they limit the mobility of patients; In addition, they can cause skin infections, thus contributing to poor health conditions. This problem is considered as one of the main motivations for the trend in modern biomedical implanted systems to use wireless technology [18].

There are a large number of researches which deal with implantable body sensor networks such as [65, 69, and 20]. One of the prominent applications of implantable sensor networks in healthcare is that IWBAN can help blind people [19] to improve their vision. Patients with non-visual impairment can see at a reasonable level using retinal prosthesis implants implanted in the human eye, as shown in Fig 9.

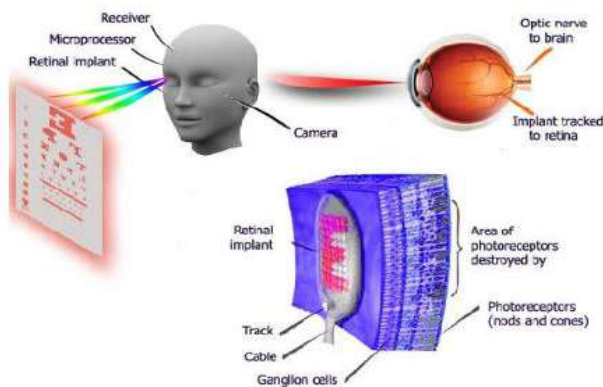


Figure 9 Implanted artificial retina

V. RESULTS

With this rapid progress in technology, wireless sensor networks and body sensor networks will begin to be used in our lives in the coming years. Wireless sensor nodes are predicted to revolutionize health care in one or more vital signs, medical care records that are transmitted almost instantaneously over the Internet. Technology that will play an important role in facilitating the lives of people with disabilities in the pre-diagnosis and treatment processes of many diseases is also a clear feature that cost management will also be effective. Despite the concentration of research efforts on various technical and economic issues, there are still many technical barriers to decide whether WBAN is

suitable, flexible, reliable, and safe and energy efficient for medical applications.

In developed applications, energy consumption, desired parameters, density in network traffic and a differentiation due to calculations are going to be reduced to maximum levels in technological and application methods in the following processes.

Each technology has its advantages and disadvantages depending on its usage area. Each of the WSN, WBANS, IWBAN and WWBAN technologies mentioned in our paper has different uses. While WWBAN provides an advantage of being used for parameters that must be measured by contact with the human body, it also has the disadvantage of causing allergic or skin irritations. In the course of application development, it may sometimes be necessary to take advantage of the advantages and disadvantages of the technology used. In such trade-off situations, staying in the choice of application for stable and efficient operation leads to different quests.

VI. REFERENCES

- [1]. Cook, D.J.; Augusto, J.C.; Jakkula, V.R. Ambient intelligence: Technologies, applications, and opportunities. *Pervasive Mob. Comput.* 2009, 5, 277-298. Kinsella, K.; Phillips, D.R. Global aging: The challenge of success. *Pop. Bull.* 2005, 60, 1-42.
- [2]. Stanford, V. Using pervasive computing to deliver elder care. *IEEE Pervasive Comput.* 2002,1, 10-13.
- [3]. Mcfadden, T.; Indulska, J. Context-aware environments for independent living. In *Proceedings of the 3rd National Conference of Emerging Researchers in Ageing*, Brisbane, Australia, December 2004; pp. 1-6.
- [4]. Leonov, V.; Fiorini, P.; Sedky, S.; Torfs, T.; van Hoof, C. Thermoelectric MEMS generators as a power supply for a body area network. In *Proceedings of the 13th International Conference on Solid-State Sensors, Actuators and Microsystems*, Seoul, Korea, 5-9 June 2005; pp. 291-294.
- [5]. Intanagonwiwat, C.; Govindan, R.; Estrin, D. Directed diffusion: A scalable and robust communication paradigm for sensor networks. In *Proceedings of the ACM MobiCom'00*, Boston, MA, USA, August 2000; pp. 56-67.
- [6]. Mohseni, P.; Najafi, K. A 1.48-mw low-phase-noise analog frequency modulator for wireless biotelemetry. *IEEE Trans. Biomed. Eng.* 2005, 52, 938-943.
- [7]. Coosemans, J.; Puers, R. An autonomous bladder pressure monitoring system. *Sens. Actuat. A* 2005, 123-124, 155-161.
- [8]. Troyk, P.; Schwan, M. Closed-loop class E transcutaneous power and data link for microimplants. *IEEE Trans. Biomed. Eng.* 1992, 39, 589-599.
- [9]. Neihart, N.; Harrison, R. Micropower circuits for bidirectional wireless telemetry in neural recording applications. *IEEE Trans. Biomed. Eng.* 2005, 52, 1950-1959.
- [10]. Tang, Q.; Tummala, N.; Gupta, S.; Schwiebert, L. Communication scheduling to minimize thermal effects of implanted biosensor networks in homogeneous tissue. *IEEE*

- Trans. Biomed. Eng. 2005, 52, 1285-1294.
- [11]. Jovanov, E.; Milenkovic, A.; Otto, C.; de Groen, P. A wireless body area network of intelligent motion sensors for computer assisted physical rehabilitation. *J. Neuroeng. Rehabil.* 2005, 1, 2-6.
 - [12]. Otto, C.; Milenkovic, A.; Sanders, C.; Jovanov, E. System architecture of a wireless body area sensor network for ubiquitous health monitoring. *JMM* 2006, 1, 307-326.
 - [13]. Quwaider, M.; Biswas, S. DTN routing in body sensor networks with dynamic postural partitioning. *Ad Hoc Netw.* 2010, 8, 824-841.
 - [14]. Braem, B.; Latre, B.; Moerman, I.; Blondia, C.; Demeester, P. The wireless autonomous spanning \square tree protocol for multihop wireless body area networks. In *Proceedings of the 3rd Annual International Conference on Mobile and Ubiquitous Systems—Workshops*, San Jose, CA, USA, July 2006; pp. 1-8.
 - [15]. Latre, B.; Braem, B.; Moerman, I.; Blondia, C.; Reusens, E.; Joseph, W.; Demeester, P. A low-delay protocol for multihop wireless body area networks. In *Proceedings of the 4th Annual International Conference on Mobile and Ubiquitous Systems: Networking and Services*, Philadelphia, PA, USA, 6–10 August 2007; pp. 1-8.
 - [16]. Anliker, U.; Ward, J.A.; Lukowicz, P.; Troster, G.; Dolveck, F.; Baer, M.; Keita, F.; Schenker, E.; Catarsi, F.; Coluccini, L.; Belardinelli, A.; Shklarski, D.; Alon, M.; Hirt, E.; Schmid, R.; Vuskovic, M. AMON: A wearable multi parameters medical monitoring and alert system. *IEEE Trans. Inf. Technol. Biomed.* 2004, 8, 1-11.
 - [17]. Mohseni, P.; Najafi, K. A 1.48-mw low-phase-noise analog frequency modulator for wireless biotelemetry. *IEEE Trans. Biomed. Eng.* 2005, 52, 938-943.
 - [18]. Khan, P.; Hussain, M.A.; Kwak, K.S. Medical applications of wireless body area networks. *JDCTA* 2009, 3, 185-193.
 - [19]. Aziz, O.; Lo, B.; King, R.; Darzi, A.; Yang, G.Z. Pervasive body sensor network: An approach to monitoring the postoperative surgical patient. In *Proceedings of International Workshop on Wearable and Implantable Body Sensor Networks (BSN 2006)*, Cambridge, MA, USA, 2006; pp. 13-18.
 - [20]. Ambient Intelligence: Impact on Embedded System Design; Basten, T., Geilen, M., De Groot, H., Eds.; Springer: Berlin, Germany, 2003; pp. 51-67.
 - [21]. AmbientIntelligence; Weber, W., Rabaey, J.M., Aarts, E., Eds.; Springer: Berlin, Germany, 2005; pp. 499-508.
 - [22]. Culler, D.; Estrin, D.; Srivastava, M. Overview of sensor networks. *IEEE Comput.* 2005, 37, 41-49.
 - [23]. Zhao, F.; Guibas, L. *Wireless Sensor Networks: An Information Processing Approach*; Morgan Kaufmann: Los Altos, CA, USA, 2004; pp. 240-245.
 - [24]. Romer, K.; Mattern, F. The design space of wireless sensor networks. *IEEE Wirel. Commun.* 2004, 6, 11-54.
 - [25]. Stankovic, J.A.; Abdelzaher, T.E.; Lu, C.; Sha, L.; Hou, J.C. Real-time communication and coordination in embedded sensor networks. *Proc. IEEE* 2003, 91, 1002-1022.
 - [26]. Akyildiz, I.F.; Su, W.; Sankarasubramaniam, Y.; Cayirci, E. Wireless sensor networks: A survey. *Comput. Netw.* 2002, 38, 393-422.
 - [27]. Intanagonwiwat, C.; Govindan, R.; Estrin, D. Directed diffusion: A scalable and robust communication paradigm for sensor networks. In *Proceedings of the ACM Mobi-Com'00*, Boston, MA, USA, August 2000; pp. 56-67.
 - [28]. Szewczyk, R.; Osterweil, E.; Polastre, J.; Hamilton, M.; Mainwaring, A.; Estrin, D. Habitat monitoring with sensor networks. *Commun. ACM* 2004, 6, 34-40.
 - [29]. Burrell, J.; Brooke, T.; Beckwith, R. Vineyard computing: Sensor networks in agricultural production. *IEEE Pervasive Comput.* 2004, 1, 38-45.
 - [30]. Jovanov, E.; Price, J.; Raskovic, D.; Kavi, K.; Martin, T.; Adhami, R. Wireless personal area networks in telemedical environment. In *Proceedings of the Third International Conference on Information technology in Biomedicine (ITAB-ITIS2000)*, Arlington, VA, USA, November 2000; pp. 22-27.
 - [31]. Jovanov, E.; Lords, A.; Raskovic, D.; Cox, P.; Adhami, R.; Andrasik, F. Stress monitoring using a distributed wireless intelligent sensor system. *IEEE Eng. Med. Biol. Mag.* 2003, 22, 49-55.
 - [32]. Jovanov, E.; Milenkovic, A.; Otto, C.; de Groen, P.C. A wireless body area network of intelligent motion sensors for computer assisted physical rehabilitation. *JNER* 2005, 1, 2-6.
 - [33]. Akyildiz, I.F.; Su, W.; Sankarasubramaniam, Y.; Cayirci, E. Wireless sensor networks: A survey.
 - [34]. Benhaddou, D.; Balakrishnan, M.; Yuan, X. Remote healthcare monitoring system architecture using sensor networks. In *Proceedings of IEEE Region 5 Conference*, Kansas City, MO, USA, April 2008; pp. 1-6.
 - [35]. Noury, N.; Herve, T.; Rialle, V.; Virone, G.; Mercier, E.; Morey, G.; Moro, A.; Porcheron, T. Monitoring behavior in home using a smart fall sensor. In *Proceedings of IEEE-EMBS Special Topic Conference on Microtechnologies in Medicine and Biology*, Lyon, France, 12–14 October 2000; pp. 607-610.
 - [36]. Sinha, A.; Chandrakasan, A. Dynamic power management in wireless sensor networks. *IEEE Des. Test Comput.* 2001, 18, 62-74.
 - [37]. Zimmerman, T.G. Personal Area networks: Near-field intrabody communication. *IBM Syst. J.* 1996, 35, 609-617.
 - [38]. Joel, J.P.C.R.; Pereira, O.E.; Neves, P.C.S. Biofeedback data visualization for body sensor networks. *J. Netw. Comput. Appl.* 2011, 34, 151-158.
 - [39]. Quwaider, M.; Biswas, S. Body posture identification using hidden Markov model with a wearable sensor network. In *Proceedings of the ICST 3rd International Conference on Body Area Networks*, Tempe, AZ, USA, March 2008; pp. 1-8.
 - [40]. Quwaider, M.; Biswas, S. Body posture identification using hidden Markov model with a wearable sensor network. In *Proceedings of the ICST 3rd International Conference on Body Area Networks*, Tempe, AZ, USA, March 2008; pp. 1-8.
 - [41]. Quwaider, M.; Biswas, S. Physical context detection using multimodal sensing using wearable wireless networks. *J. Commun. Softw. Syst.* 2008, 4, 191-202.
 - [42]. Aleksandar, M.; Chris, O.; Emil, J. Wireless sensor networks for personal health monitoring: Issues and an implementation. *Comput. Commun.* 2006, 29, 2521-2533.
 - [43]. Anastasi, G.; Conti, M.; Di Francesco, M.; Passarella, A. Energy conservation in wireless sensor networks: A Survey. *Ad Hoc*

- Netw. 2009, 7, 537-568.
- [44]. Li, P.; Wen, Y.; Liu, P.; Li, X.; Jia, C. A magnetoelectric energy harvester and management circuit for wireless sensor network. *Sens. Actuat. A* 2010, 157, 100-106.
- [45]. Pandian, P.S.; Safeer, K.P.; Gupta, P.; Shakunthala, D.T.; Sundershesu, B.S.; Padaki, V.C. Wireless sensor network for wearable physiological monitoring. *J. Netw.* 2008, 3, 21-28.
- [46]. Gopalsamy, C.; Park, S.; Rajamanickam, R.; Jayaraman, S. The wearable motherboard TM: The first generation of adaptive and responsive textile structures (ARTS) for medical applications. *Virtual Reality* 2005, 4, 152-168.
- [47]. Pandian, P.S.; Mohanavelu, K.; Safeer, K.P.; Kotresh, T.M.; Shakunthala, D.T.; Gopal, P.; Padaki, V.C. Smart vest: Wearable multi-parameter remote physiological monitoring system. *Med. Eng. Phys.* 2007, 30, 466-477.
- [48]. Shults, M.C.; Rhodes, R.K.; Updike S.J.; Gilligan, B.J.; Reining, W.N. A telemetryinstrumentation system for monitoring multiple subcutaneously implanted glucose sensors. *IEEE Trans. Biomed. Eng.* 1994, 41, 937-942.

A Time-Limited Park Violation Detection Approach Using Size Based Image Feature Extraction

Turan Göktuğ Altundoğan
Computer Engineering Department
Firat University
Elazığ, Turkey
goktugaltundogan@gmail.com

Mehmet Karaköse
Computer Engineering Department
Firat University
Elazığ, Turkey
mkarakose@firat.edu.tr

Abstract— Nowadays, with the increase of vehicle densities, violations in parked or partially parked areas become an important problem. Recently, sensors, communication or image processing based solutions have been developed especially for such problems with the increase of smart city applications. In this study, a real time and high performance image processing based approach is proposed for the problem mentioned. In the developed algorithm, first of all, the area where the parking violation is to be detected is used for background subtraction, and then the vehicles are detected by a size based feature extraction. In particular, the performance of the approach developed in terms of high accuracy and real-time interoperability criteria has been confirmed by experimental evidence. Considering the results obtained, it is seen that the proposed method works with high performance in different scenarios and different working conditions.

Keywords—Park violation; Image processing; Real time; Feature extraction.

I. INTRODUCTION

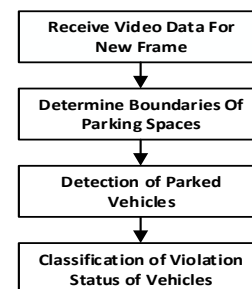
Nowadays, especially smart city and campus applications are entering into our lives, solutions of certain problems are provided with digital methods in city, campus and routes. Smart city applications provides solutions to problems in the cities which they are applied, like energy, security, health, traffic.

In the study, an algorithm was developed to provide control of some rules that were introduced to cities in order to make efficient use of parking spaces that are problematic in traffic. Parking spaces and parking problems are described as a major traffic weakness, especially on crowded routes. There are many studies in the literature that mention the importance of parking problem [1-3].

In one of these studies, the researcher examined the accumulation of the park in the city of Rajshahi metropolitan city of Bangladesh, where the park problem was quite experienced. As a result of the obtained data, the main recommendation for the solution of the parking problem in the city is that the vehicle owners are charged according to the parking times of the vehicles [1]. As can be seen here, efficient

use of the park time on routes with parking problems is an important issue for solving parking problems.

In another study, the impact of parking violations in St. Petersburg on St Petersburg's overall traffic problem was emphasized [2]. Yet another study emphasized that the intense demand for short-term parking in the major cities of India is a major problem and that appropriate parking policies should be developed to solve this problem [3]. All these examples in the literature emphasize the importance of parking problem in urban traffic patterns. Since the implementation of smart city applications in cities, some smart city applications have begun to be implemented in Turkey to solve the problem of parking. The Park Violation Detection System which is conducted it's R&D works by IMM and using in some areas in Istanbul can be shown as an example this [4]. The solution proposed in this study is a real-time video-based algorithm that determines parking time for routes and parking lots where the parking time is restricted or the parking time is charged, and whether the parking lot is in violation. There have been many studies in the literature on video-based parking infringement, availability of parking space and parking density [5-14]. Some studies in the literature have concentrated on the detection of video-based parking intensity on the route, but there is no question of finding a time violation in these studies [5-7]. In other some literature studies, the focus is on the proposal of a solution that determines the available parking spaces. There is no control over any park time violations in these studies too [8-11]. In another study, location based violations of vehicles were detected. In the mentioned study, it is not possible to determine time-based violations of vehicles while parked [12].



Identify applicable sponsor/s here. If no sponsors, delete this text box (sponsors).

Figure 1. Block diagram of the a parking lot violation detection algorithm in literature

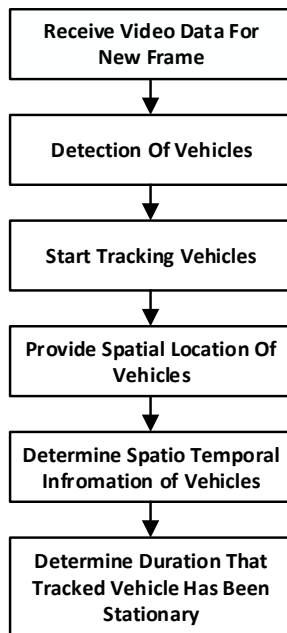


Figure 2. Block diagram of a parking time violation detection algorithm in literature

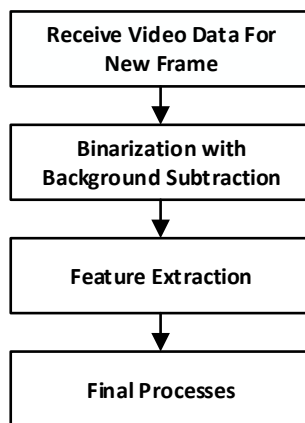


Figure 3. The general diagram of similar studies in literature.

In one of the studies done in the literature, time violation for video based short duration parks was detected [13]. The block diagram of the work is shown in Figure 2. When the studies in the literature are examined, the algorithmic steps applied to solve the problems interested are as in Figure 3.

The main difference that distinguishes this study from other studies in the literature is that the feature extraction step applied for vehicle identification is based on the size. Feature extraction, made for object detection in image processing

based solution proposals, are very diverse. For example, learning-based feature extractions have a high cost in terms of algorithmic complexity, although they are highly productive in terms of the results. The reason of the using size based approach in the feature extraction in this study is having a low cost of algorithmic complexity although its efficiency is enough for the object detection.

II. THE PROPOSED METHOD

In this study, an algorithm was developed to perform video-based detection of vehicles parking time and possible time violations. The developed algorithm has been tested on video taken on parkable routes and it has been observed to produce efficient results.

The algorithm first accepts the frame of area which no vehicles aren't on it as an background then make the coming image frames a subtraction which it depends the background frame. Subsequently, a feature extraction based on size is performed on the binary image obtained as a result of background subtraction, and the vehicles on the image are detected. After the extraction of the feature and the detection of the vehicles, it is determined whether the vehicles are parked and the parking time is determined with the help of the image frame value processed per second. If the obtained parking time exceeds the threshold of violation, the algorithm shows this situation on the image with the outputs it produces. The block diagram of the developed algorithm is shown in Figure 4.

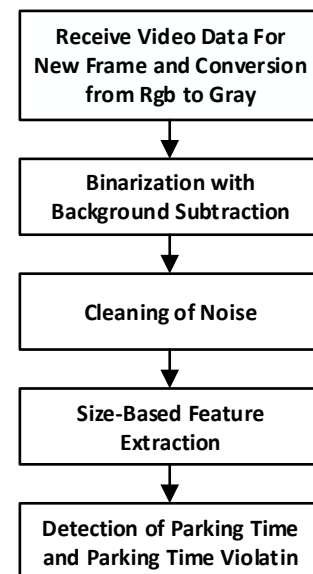


Figure 4. Block diagram of the algorithm which developed in this study.

Receiving Video Data For New Frame and Conversion from RGB to Gray

The first step of the algorithm is to take the video frame to process and convert the RGB color space to the gray color space. The main reason for this transformation is that image processing algorithms vary considerably with respect to the color space of the ease of implementation of the operations. However, in RGB images, each pixel occupies 24 bits in the memory source. But on a gray scale, each pixel of a view occupies only 8 bits. This causes the operations on the gray scale images to have a lower complexity cost than the operations on the RGB scale images. For the conversion from RGB color space to gray color space, the representation of the mathematical operation applied on each pixel is as follows.

Binarization with Background Subtraction

In the second step, the algorithm assumes that a previously introduced reference frame is a background and performs background subtraction. This reference image, presented as a background image, is on the gray scale and is a took image of a moment when no vehicles is found on the area . As a result of background subtraction, a binary image is obtained as output. It is very important that the remaining operations are performed on binary images. As it is known, computers and computer science perform their operations with binary-based methods. The binary system in computer science, uses the opposition of true-false for the logical operations , uses the opposition of the 1-0 for the math operations and it uses the opposition of black-white for the image operations. The mathematical representation of the background subtraction is as follows.

Cleaning of Noise

The algorithm has been tested on many different videos, especially for the vehicle detection step. However, on the video of the final test of all the features of the algorithm, some noises have been detected due to environmental factors after background subtraction. The feature extraction of the algorithm is size-based as mentioned before. The presence of noises exceeding the threshold field size, which provides feature extraction during testing of the algorithm, adversely affects the accuracy of the algorithm negatively. For this reason, a Canny edge detection filter and an median filter are applied on the binary image before the feature extraction step. In this way, more efficient display of the neighborhoods of the white pixels on the binary image is achieved and the neighborhood of the white pixels of noise quality is prevented.

Size-Based Feature Extraction

The biggest difference of algorithm from other algorithms performing the same task in the literature is that feature extraction is based on size. For the feature extraction, detection of the objects expressing the contour on the binary image subjected to the noise reduction process is performed first. After the detection of the objects which is expressing contour, algorithm calculates areas of these object in square pixel. Then a field threshold value check is performed intuitively. The last step of the feature extraction is to compare

the threshold field value with a threshold value of the aspect ratio value of the past objects. Objects that provide this criterion are considered vehicles. The block diagram of the feature extraction step is as shown in Figure 5.

Detection of Parking Time and Parking Time Violation

The last step of the algorithm is to determine the parking times of the vehicles detected as a result of the feature extraction and to check whether there is a violation of the detected vehicle. The fps value of the source video was used to determine the parking time of the vehicles. First, if each frame of the video is treated like a coordinate plane, this plane is divided into 100 equal areas. For each of these divided areas, a logic variable is defined that expresses true and false couple whether or not the fields have vehicles on it. However, for each field, a variable is defined that acts as a kind of counter that keeps detection of vehicle in how many frames . The determination of whether or not the vehicle is on the area is carried out according to the coordinates of the center of gravity of the objects detected as vehicles. The algorithmic steps for detecting the parking time and detecting the parking time violation are shown in Figure6.

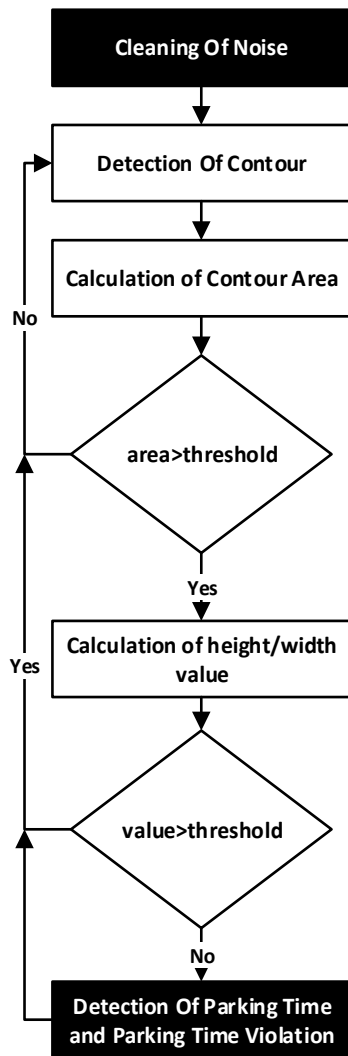


Figure 5. Block diagram of the size based feature extraction in the algorithm which studied in this paper

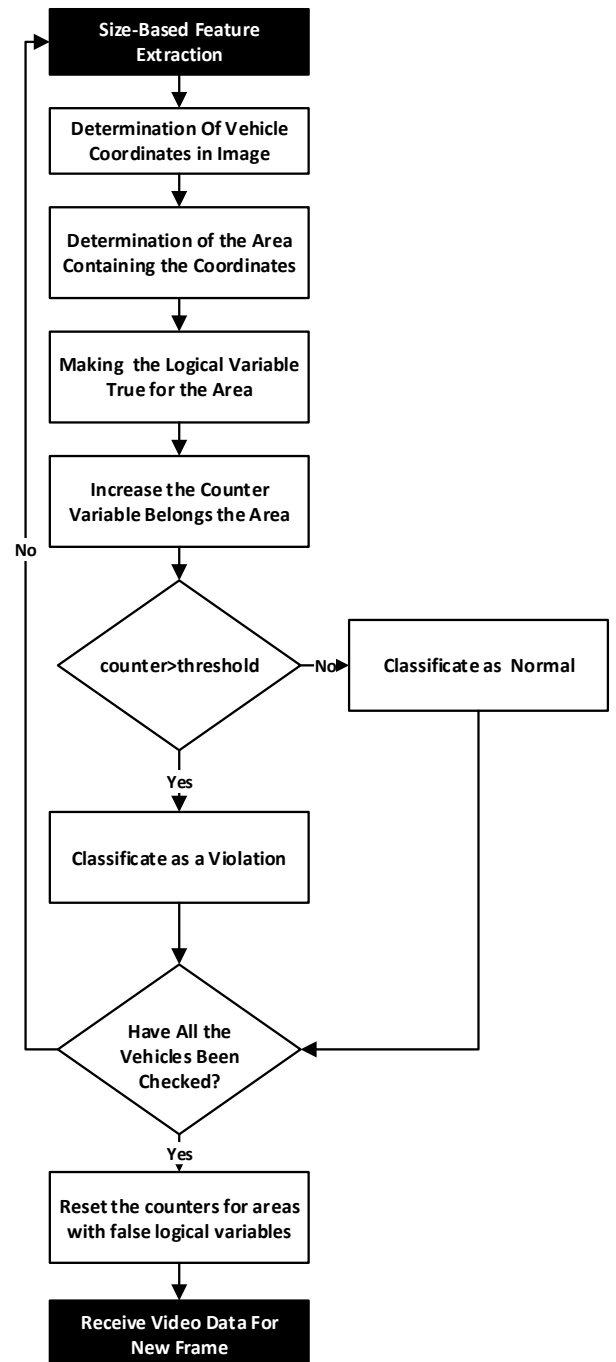


Figure 6. Block diagram of the parking violation detection step in algorithm which studied in this paper

III. EXPERIMENTAL RESULTS

The developed algorithm was tested on the images of the cameras belonging to a private property parking lot. The test of the algorithm was performed in two separate steps. The first one was completed by updating some of the threshold control

values that were given intuitively according to the result of the feature extraction tests and the results of these tests. The square pixels in different positions on the image of the vehicles detected in images for different scenarios are shown in Figure 7. As a result of the obtained data, the lowest measured field value for all scenarios and instruments was found to be 1892 pixels square. The threshold field value was set at 1500 pixels square so that vehicles with smaller footprints could be detected. However, height / width ratio was used as a second factor in extracting features of vehicles. The height / width ratio was set to 0.1 in an intuitive manner. The second test step was on the verdict of whether the identified vehicles were in breach according to the threshold of the violation given. In tests based on different violation threshold times, the algorithm obtained correct results according to the given threshold. (Vehicle: The vehicles which detected in video; Region: Regions where areas of vehicles detected on the square are measured)

TABLE XXI.

	Vehicle1	Vehicle2	Vehicle3
Region1	6703px2	4892px2	6002px2
Region2	6167px2	4652px2	5838px2
Region3	6923px2	5215px2	6336px2
Region4	6321px2	4702px2	4927px2
Region5	3121px2	2005px2	2102px2
Region6	2336px2	1892px2	2009px2

The developed algorithm gives different image output in different steps. First of these outputs shows the background frame in the gray scale. The mentioned output is shown in Figure 8. As another output, the algorithm yields the resulting binary image of the background subtraction. The output is shown in Figure 9. After the background subtraction, the canny filter and the median filter are removed for noise removal. The image is shown in Figure 10. After this step, there is an output which it includes the detected vehicles. In this output, if a detected vehicle is in a violation, vehicle is shown in the output, framed by a red rectangle. If the vehicle is not in a violation, it is shown in the output, framed by a green rectangle. The output which is before the parking time violation, is shown in Figure 11. The output which is after the parking time violation, is shown in Figure 12. All output shown belongs to the same scenario, and the algorithm for the park time violation threshold is 20 seconds.

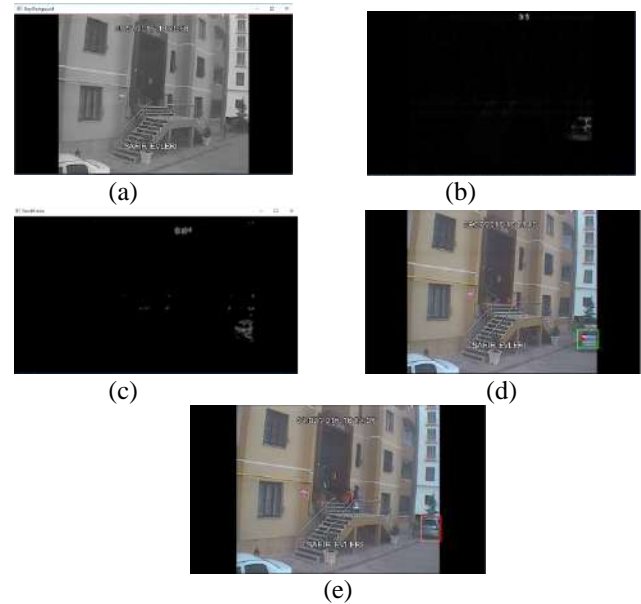


Figure 7. Outputs of different steps in the algorithm which studied in this paper

IV. CONCLUSIONS

In this study, a solution to the inefficient use of parking times was developed, and an algorithm was developed to detect parking violations for areas where parking periods are restricted or charged and to check for any violations. Since the widespread use of smart city applications, solutions based on digital methods such as image processing have been increasing in the literature to solve the problems related to traffic. The algorithm developed in this study can be enriched by some methods to produce a free parking proposal output, which can be forwarded to vehicle drivers with some intelligent communication technologies. Of course, the main difference that distinguishes this study from other studies in the literature is the feature extraction based on the dimension for vehicle detection. There are many types of parking violations that can be detected by digital means other than time-based parking violations. Therefore, it is also possible to perform location based parking violation detection using the same feature extraction.

ACKNOWLEDGMENT

This study has been supported by Firat University Scientific Research Project Support Center under Research Project No: MF.16.49.

REFERENCES

- [9] S.M.Z Tanzim , M.M. Miah Study Of Parking Accumulation in Major On-Street Parking Spots In Rajshahi City, Bangladesh, Journal Of Construction And Building Materials Engineering, Volume2 Issue 1, pp. 1-15, 2016
- [10] Antonina Ushakova, Development of underground space as transportation problem solution in St. Petersburg, Procedia Engineering vol. 165, pp. 166-174 · December 2016.

- [11] Sanjay M Dave, Nandan H Dawda, Prashant J Parmar, Gaurang J Joshi, Parking demand assessment and response to paid parking policy for the CBD area of Vadodara city , Urban Mobility India Research Symposium ,pp.1-15,2016.
- [12] Available,<http://isbak.istanbul/akilli-ulasim-sistemleri/elektronik-denetleme-sistemi/park-ihlal-tespit-sistemi-2/>
- [13] Orhan Bulan , Robert P Loce, Wencheng Wu , Edgar Andres Bernal , Video Based Real Time On Street Parking Occupancy Detection System, Journal Of Electric Imaging ,pp. 1-15, October 2013.
- [14] Robert P Loce, Video Based System And Method For Parking Occupancy Detection , Patent Application Publication, pp. 1-13, 2017.
- [15] Guiseppo Amato, Fabio Carrera, Fabrizio Falchi, , Car parking occupancy detection using smart camera networks and Deep Learning , Conference Paper, pp. 1212-1217, June 2016.
- [16] Elena Marmol Soley, Xavier Sevillano Quick Spot: A Video Analytics Solution for On Street Vacant Parking Spot Detection, Multimedia Tools and Applications, pp. 1-35, July 2016.
- [17] Marc Tschentscher , Marcel Neuhasen, Video Based Parking Space Detection, Conference Paper,pp. 1-6, January 2012
- [18] Ivan Aleksii, Tomislav Caklovic, Zejiko Hocenski, Managing And Monitoring Of Parking Lot By A Video Camera, ,Available, <https://www.researchgate.net/publication/267220668>, .pp 1-4
- [19] Imen Masmoudi, Ali Wali , Anis Jamousi , Adel M. Alimi Vision Based System For Vacant Parking Lot Detection : VPLD, Conference Paper, pp. 1-8, January 2014
- [20] Robert P Loce , Edgar Andres Bernal, Orhan Bulan , Video Based Method For Detecting Parking Boundary Violations , Patent Application ,pp. 1-18, Publication 2017
- [21] Robert P Loce, Edgar Andres Bernal, Video Based Detector and Notifier For Short Term Parking Violation Enforcement , Patent Application Publication, pp. 1-7, 2017
- [22] Md Mostafa Kamal Sarker, Cai Weihua ,Moon Kyou Song , Detection And Recognition Of Illegally Parked Vehicle based on Adaptive Gaussian Mixture Model and Seed Fill Algorithm , Journal Of Information and Communication Convergence Engineering, pp. 197-204 September 2015

A User Friendly Test Program for Random Number Generator

Erdoğan Avaroğlu

Mersin University, Engineering
Faculty

Mersin, Türkiye

eavaroglu@gmail.com

Ahmet Bedri Özer

Fırat University, Engineering
Faculty

Elazığ, Türkiye

bozer@firat.edu.tr

Mustafa Türk

Fırat University, Engineering
Faculty

Elazığ, Türkiye

mturk@firat.edu.tr

Abstract -- Test packages such as Crypt-X, Diehard, FIPS 140 and NIST have been developed in order to check statistical properties of random numbers generated by random number generators. However, users are required to have sufficient programming knowledge so as to apply these test packages. Besides, users are to attain required programs and compilers in order to run released test codes. These situations sometimes can be quite complicated for many users; thus, randomness tests cannot be implemented. To eliminate the complexity drawback of these tests, a user friendly program of NIST test package, which can be run on Windows operating system and does not require any compiler or package, was developed in C# language. The program is exhibited in a web environment that all users are able to access.

Keywords -- Random number, Random number generation, NIST statistical test

1. INTRODUCTION

Randomness is basically being unpredictable. In other words, it means unpredictability in cryptography and being unrelated in terms of samples in statistics [1, 2]. Random numbers are defined for a certain range; they have equal probability of generation and they are statistically independent numbers. Random numbers are commonly used in simulation, sampling, numeric analysis, decision making, entertainment, computer programming and cryptography fields. Random numbers should satisfy several properties such as they are to be unpredictable; they are not to be periodic; they should have good statistical properties and uniformity [3].

Various random number generators were developed to obtain random numbers; namely, pseudo-random number generators (PRNGs), true random number generators (TRNGs) and hybrid random number generators (HRNGs). Pseudo-random number generators start with a seed value and are subject to an algorithm to generate long random number streams. True random number generators use real physical phenomenon as a noise source and generate random numbers. Hybrid random

number generators use the random number from TRNG as a seed value in PRNG and generate random numbers by combining two systems [4].

Various test packages such as FIPS140, Knuth, Ent, NIST, Diehard and Crypt-X have been developed to check randomness of random number streams from random number generators. Generally, FIPS140 and NIST tests were preferred to check random number streams. Many users preferred FIPS140 test packages especially because it is easy to use and implement. On the other hand, a lot of users have not chosen to utilize NIST test, which is a more acceptable standard and able to check long random number streams, due to difficult implementation despite published codes of this test. The reason for this situation is that users were required to have sufficient level of programming knowledge in order to understand and run the codes. Besides, even executable programs of randomness tests need additional packages during the run. Many users are not able to utilize randomness tests due to mentioned reasons.

In this study, a program of tests which can operate in Windows environment were developed in C# programming language by examination of NIST test documents in order to eliminate complexity of tests. The minimum requirement of the program is .Net framework to operate in Windows environment, and .Net framework is already installed in Windows XP and upper Windows versions. Therefore, users do not have to install any additional package for the developed program. The program was designed to have a user friendly interface. Linear Congruential Method, a common PRNG in literature, was benefited to demonstrate usage of the developed program. Statistical tests of the random number stream from LCG were carried out by NIST tests in the program.

Random number generation methods were mentioned in Section 2. LCG was addressed to show generation of random bit sequence. In Section 3, NIST statistical test packages were mentioned. In Section 4, the developed NIST software was

explained and test results of the number stream by LCG were given. Conclusion was given in Section 5.

II. RANDOM NUMBER GENERATION METHODS

Random numbers are produced by random number generators. Random number generators are systems or devices which generate unpredictable, uncorrelated, aperiodic and statistically independent number streams. They are critical in modelling of complex phenomenon, sampling, numeric analysis and decision making. Generated numbers should not have high storage requirements, and they should not take long time to reach a desired level of true randomness. Numbers generated in this way can be sufficiently "random" for an application, while they can be insufficient for some applications [5].

Random number generators are classified in three groups as pseudo-random number generators, true random number generators and hybrid random number generators.

PRNG uses seed value from some entropy sources as a random input and it generates bit sequences which computationally cannot be differentiated from bits sequences generated by TRNG. The output value of these generators cannot reach the input seed value since these generators are deterministic. Besides, sequences may start repeating themselves after a certain time period. Thus, these systems have periodicity. Storage amount required by the system must be great in order to design an aperiodic system. However, it also slows down the system. The security of system in PRNGs depends on unpredictability of seed value and complexity of functions used in system. In addition, parameters used in functions should be carefully selected. Linear feedback shift register, middle-square method and linear congruential generator (LCG) are some commonly known algorithms used in PRNG [3, 6-8].

TRNGs define the entropy source (seed) as nondeterministic natural physical phenomenon and use it to generate random numbers. Generally, it includes conversion of analog noise into digital signal. The randomness and properties of random numbers generated by TRNGs are dependent on the randomness

of the physical phenomenon. Being slow, expensive and dependent on hardware are disadvantages of TRNGs. However, TRNGs have been used in many applications due to being unpredictable, aperiodic and providing good statistical features [4, 6-8].

The hybrid random number generator is a system where TRNG and PRNG work together in a way that random number generated by TRNG is used as seed value in PRNG.

In this study, LCG, one of the methods used in PRNG, was used to generate bit sequence. The equation of LCG can be seen in (1). LCG is defined to be a recursive relation to generate integer sequence such as X_1, X_2, \dots between 0 and $m-1$ [9].

$$X_{n+1} = (aX_n + c) \bmod m \quad (1)$$

$$R_n = X_n / m \quad n=1,2,\dots \quad (2)$$

X : random numbers generated in $(0, m-1)$

a : Multiplier

c : Increment

m : Mod

R : random numbers generated in $(0,1)$

$X_0=100$ as seed value, $a=65535$, $c=0$ and $m=2^{31}$ in LCG. LCG which is designed in FPGA environment is shown in Figure 1. To design LCG in FPGA environment, ready modules are used which is performed by Altera. These modules are respectively *Lmp_constant*, *Lmp_mult* and *div* module. These modules are respectively fulfill fixed number of impressions, multiplication and mode making process. First *Lmp_constant* modules with constant a , x_0 and m values are defined in circuit. MUX is used to allow the introduction of the system in the next iteration, the value x_n which is produced from output in the system. Multiplication with *Lmp_mult* module is realized. With *div* module mod taking, with *div2* division process have been fulfilled. Generated $S(n)$ values were subject to expression in (3) and a sequence of 1000000 bits composed of 0 and 1 was obtained.

$$S(n) = \begin{cases} 0 & R_n < 0.5 \\ 1 & R_n \geq 0.5 \end{cases} \quad (3)$$

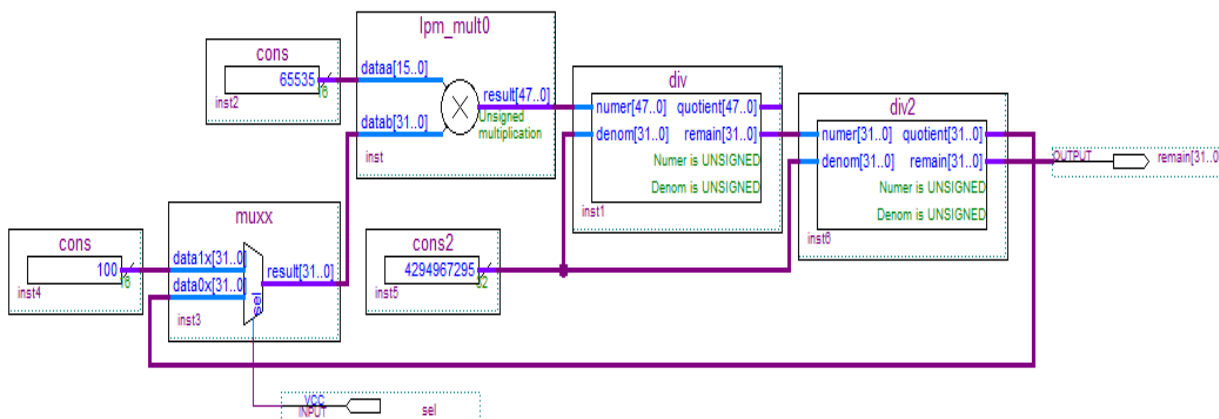


Figure 1. Implementation of LCG on FPGA

III. NIST STATISTICAL TESTS

NIST tests are based on hypothesis testing as other tests [10]. Hypothesis tests are a kind of procedure deciding whether claims about population features are logical. In other words, NIST test was developed to measure randomness of long binary bit sequences generated by random number generators.

A statistical test is formulized to check validity of a particular null hypothesis (H_0). The null hypothesis is that the tested sequence is random. Apart from the null hypothesis, the alternative hypothesis claims that the sequence is not random. As shown in Table 1, every applied test results in a decision or result that the null hypothesis is accepted or rejected.

Table 1. General results of hypothesis testing

Real Situation	Result	
	H_0 is accepted	H_a is accepted
Data is random (H_0 is correct)	No error	Type I error
Data is not random (H_a is correct)	Type II error	No error

If data is really random, the result will very soon be clear that the null hypothesis is rejected (It is accepted that data is not random). This result is known as type I error. If data is not random in fact, the acceptance of the null hypothesis is named as type II error (It is accepted that data is random). Results which accept H_0 when data is really random are correct. Similarly, results which reject H_0 when data is not random are correct.

The probability of making type I error is expressed as α . This is also significance level of the test. The null hypothesis is rejected when p value is lower than α value. The probability of making type II error is expressed as β . When sequence is in fact not random, the test will show that sequence is random with β probability. Test statistics are used to find p value which is more like a summary of proof force against the null hypothesis. Each p value for tests is the probability of a perfect random number generator which can generate sequence with lower randomness than the tested sequence, and each p value gives the kind of being nonrandom. If p value is obtained to be 1 for a test, it means that the sequence has perfect randomness. If p value is 0, then it is understood that the sequence is not completely random. A significance level (α) might be chosen for tests. If p value $\geq \alpha$, then the null hypothesis is accepted; for instance, the sequence is random. If p value $< \alpha$, the null hypothesis is rejected. The value of α is selected to be 0.01 in NIST tests.

Evaluation procedure for a single binary sequence was shown step by step in Table 2.

Table 2. Evaluation procedure for a single binary sequence step by step process [19].

Process	Comments
1. State your null hypothesis.	Assume that the binary sequence is random.
2. Compute a sequence test statistic.	Testing is carried out at the bit level.
3. Compute the P-value.	$P\text{-value} \in [0, 1]$.
4. Compare the P-value to α .	Fix α , where $\alpha \in (0.001, 0.01]$. Success is declared whenever $P\text{-value} \geq \alpha$; otherwise, failure is declared.

NIST test is a statistical test package containing 16 tests. These tests focus on nonrandom structures in a sequence. The order of usage of 16 tests is optional. However, it is suggested that frequency test is to be initially applied. If frequency test has failure, it is highly probable that other tests will also fail [10]. Explanation of NIST Statistical Test Suite is given in Table 3.

Table 3. Nist statistical test suite explanation

NIST Statistical Test Suite	
Test	Defect Detected
Frequency	It examines 1 and 0 balance in bit sequence.
Frequency Test within a Block	It is based on observation of number of 1 in m-bit block.
Runs Test	It is related with total number of runs in bit sequence.
Test for the Longest Run of Ones in a Block	It examines lengths of 0 and 1 blocks in sequence. It focuses on the longest group of 1 in m-bit blocks.
Binary Matrix Rank	A matrix is formed by using blocks in constant length so that each block defines a line. Linear dependency between blocks is examined by calculating rank of matrix.
Discrete Fourier Transform	Discrete Fourier Transformation of the current bit sequence is performed and its periodicity is examined.
Non-overlapping Template Matching	It examines whether m-bit block repeats in sequence. If it repeats, new m-bit blocks are formed from the block that is repeated.
Overlapping Template Matching	It examines whether m-bit block repeats in the sequence. If it repeats, the block is shifted by 1 bit and new block is formed.
Maurer's Universal Statistical	It examines how much the sequence can be compressed without loss of data.
Linear Complexity	It examines the complexity of the bit sequence by checking feedback register.
Serial Test	It examines number repetitions of 2m m-bit repeating blocks.
Approximate Entropy Test	It compares the frequency of two repeating blocks in consecutive lengths (m and m+1) with the expected frequency of a random sequence.
Cumulative Sums Test	This test is based on research of random walk maximal excursions which are defined to be cumulative sum of adjusted (-1, +1) digits in the sequence. The aim of the test is to determine whether cumulative sum of partial subsequences in the tested sequence is too large or too small compared to the expected value of a random sequence. This

	cumulative sum can be regarded as random walk.
Random excursions	This test focuses on number of K-visits cycles in cumulative sum of random walk
Random excursions variants	In this test, number of visits done to a special state is measured in cumulative sum random walk. The aim of the test is to observe deviations in the expected number of visits to special states in a random walk.

IV.THE DEVELOPED SOFTWARE

NIST test package was used to statistical properties of bit sequences generated by random number generators. The program was developed in C# language and has been used in several studies [11,12]. No additional package is required to run the program. It is enough for users to run the setup file in order to install the program. The Interface design of the program is shown in Figure 2. Bit sequence generated by LCG was tested by this program. Test results are given below.

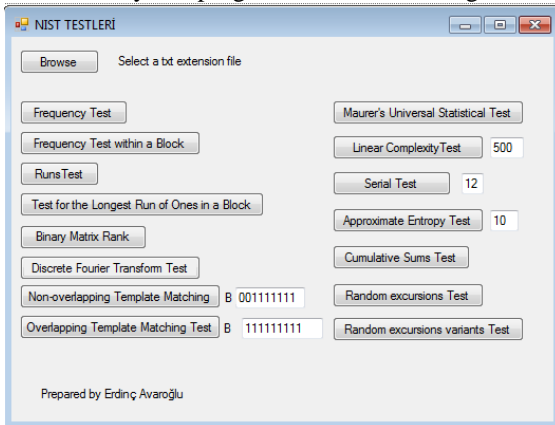


Figure 2. The Screen output of NIST program

The generated bit sequence should be inserted into a text file as shown in Figure 3. Bit sequence should be inserted in a way that each line should have 1 character (in one-column matrix format) and there should not be any space between instances. By using “file select” menu on the software, selection of the file to be tested is done. The length of bit sequence is automatically set by the program itself. After the file selection, test procedure is performed by using other menus. Test results were given in Table 4. According to given results, random number sequences must pass all the tests which are subjected to NIST test. Otherwise the test will be considered unsuccessful.

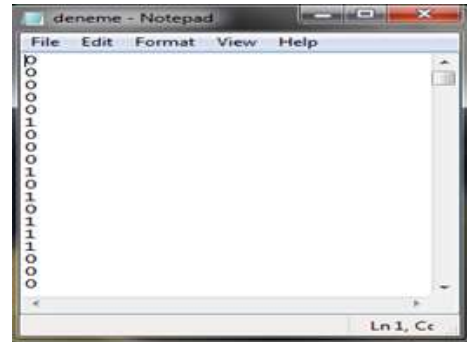


Figure 3. Content of the selected file

Table 4. Test results from LCG

Test Name	P value		Result
Frequency (Monobit) Test	0.524		Passed
Frequency Test within a Block	0.816		Passed
Runs Test	0.238		Passed
Test for the Longest Run of Ones in a Block	0.093		Passed
Binary Matrix Rank Test	0.495		Passed
Discrete Fourier Transform Test	--		Unpassed
Non-overlapping Template Matching Test	0.358		Passed
Overlapping Template Matching Test	0.250		Passed
Maurer's Universal Statistical Test	0.404		Passed
Linear Complexity Test	0.676		Passed
Serial Test	0.830		Passed
	0.894		
Approximate Entropy Test	0.547		Passed
Cumulative Sums Test	0.857		Passed
Random excursions	-4	0.376	Passed
	-3	0.011	
	-2	0.660	
	-1	0.404	
	1	0.513	
	2	0.641	
	3	0.354	
	4	0.561	
Random variants	-9	0.139	Passed
	-8	0.182	
	-7	0.196	
	-6	0.146	
	-5	0.112	
	-4	0.155	
	-3	0.209	
	-2	0.320	
	-1	0.244	
	1	0.138	
	2	0.062	
	3	0.029	
	4	0.105	
	5	0.327	
	6	0.411	
	7	0.432	
	8	0.432	
	9	0.213	

V.CONCLUSION

Random number streams obtained from LCG were subject to NIST tests and the program successfully operated. The most important feature of the developed software is that the program does not require any additional package installation, has a user friendly interface and can be used comfortably by an average computer user to test generated random bit equences. The setup file of the program can be downloaded at

http://web.firat.edu.tr/cemuh/download/MTURK/nisttes_tenglish.rar..

In the next stage, the program will be able to run at web environment so that downloading can be eliminated.

REFERENCES

- [1] Rukhin, A. , Soto, J., Nechvatal, J., Smid, M., and Banks. D., 2001, A statistical test suite for random and pseudorandom number generators for statistical applications, *NIST Special Publication in Computer Security*
[2] Park, Y., and Lee, 2013, Y.Group-ID based RFID Mutual Authentication ,Advances in Electrical and Computer Engineering, volume 13, number 4

- [3] Deng and Lin, "Random Number Generation for the New Century", *The American Statistician*, May 2000; 54
[4] Koç. C.K., 2009 "Cryptographic Engineering", *Springer*
[5] Alatas, B., Akin, E., and Ozer, AB., 2007, Kaotik Haritalı Parçacık Sürü Optimizasyon Algoritmaları, *XII. Elektrik Elektronik Bilgisayar Biyomedikal Mühendisliği Ulusal Kongresi*, Eskişehir Osmangazi Üniversitesi
[6] Akram., R.N.,2012, "Pseudorandom Number Generation in Smart Cards: An Implementation, Performance and Randomness Analysis", *New Technologies, Mobility and Security (NTMS)*, 2012 5th International Conference on, 1-7
[7] Kohlbrenner, P. and Gaj. K., 2004, "An embedded true random number generator for FPGAs", *FPGA '04 Proceedings of the 2004 ACM/SIGDA 12th international symposium on Field programmable gate arrays*, 71-78
[8] Sobotka, J., and Zeman, V., 2011, "Design of the true random numbers generator", *Elektrorevue*, 2(3):1-6
[9] <http://lamar.colostate.edu/~grad511/lcg.pdf>
[10] <http://csrc.nist.gov/groups/ST/toolkit/rng/documents/nissc-paper.pdf>
[11] Tuncer, T., Avaroğlu, E. , Türk, M., Özer.,AB., 2014, Implementation of Non-periodic Sampling True Random Number Generator on FPGA, *Journal of Microelectronics Electronic Components and Materials*, Vol 4, issue 4
[12] Avaroğlu, E., Tuncer, T., Türk, M., Özer.,AB.,A New Method For Hybrid Pseudo Random Number Generator, *Journal of Microelectronics, Electronic Components and Materials*, Vol 4, issue 4 (2014)

H Function Implementation On True Random Number Generators

Erdoğan Avaroğlu
Mersin University- Engineering Faculty
Mersin, Türkiye
eavaroglu@mersin.edu.tr

Hatice Kübra KOÇ
Mersin University
Mersin, Türkiye
h.kubrakoc01@gmail.com

Abstract-The numbers generated must be unpredictable, reproduced and show good statistical properties in order to security of cryptographic systems. Random bit streams with these properties are generated using true random number generators. However, bit streams obtained from TRNG are correlated due to environmental factors. In order to solve these kind of problems, post processing algorithms are applied to the generated bit streams. For this purpose, post processing algorithms are examined and NIST test results of the bit streams passed from the Post processing are given.

Keywords- Random number generator, post processing, H function, statistical test

I. INTRODUCTION

Random Numbers are numbers produced by statistically random selection of a part of a clusters or elements of an array. Random numbers are needed in fields such as sampling, simulation, numerical analysis, entertainment and cryptology. Random numbers are especially required for cryptographic applications. Because the security of cryptographic systems depends on the fact that the resulting random bit streams must be unpredictable, reproduced and show good statistical properties. Various random number generators (RSUs) are designed to generate random numbers. These random number generators are classified as True Random Number Generators (TRNG) and Pseudo Random Number Generators (PRNG) [1].

The Pseudo Random Number Generators start from a seed value and algorithmically generate random numbers. The advantage of PRNG is that it generates a very large number of random numbers in a short period of time, is cheap and does not require hardware. However, Despite these advantages of SRSUs, If the seed value is known and the functions used are not complicated enough, It is disadvantageous that the numbers generated can be estimated. True random number generators generate random numbers using real physical processes that can not be controlled and can not be predicted as entropy source. While The disadvantage of the TRNGs is that they are slow, costly, and hardware-dependent, the advantage of the TRNG is that the random bit streams generated are essential for

cryptographic applications, providing unpredictable, reproduced and show good statistical properties. Because of these advantages, it has been used in many applications in cryptology [4]. The properties and randomness of the random numbers generated by TRNG depends on the quality of the entropy source. However, because entropy resources used in TRNG are affected by environmental changes, bit streams generated Show statistical weakness. In order to overcome these weaknesses, the generated bit stream was subjected to post processing. However, the post processing leads to a decrease in the bit rate, while eliminating the correlation between bit streams [1–3].

In this study, the post processing for corelation of bit streams generated from GRSUs was investigated. Von Neumann, XOR and H functions are explained. The ring oscillators were used as the entropy source, and the NIST test suite was used to test the randomness of the generated streams.

TRNG and post processing are discussed in Chapter 2. In Chapter 3, the ring oscillator used as an entropy source is mentioned. The NIST test results were given the bit stream produced after the post processing in Chapter 4. Chapter 5 gives the results.

II. TRUE RANDOM NUMBER GENERATOR

TRNG uses non-deterministic natural physical phenomena as a source of entropy. The general design of TRNG is shown in Figure 1. TRNG converts the analog noise signal into a digital noise signal by sampling. Random numbers generated from TRNG showed weak statistical properties due to environmental factors. The signals generated for the purpose of this weakness have been passed through the post processing [1].

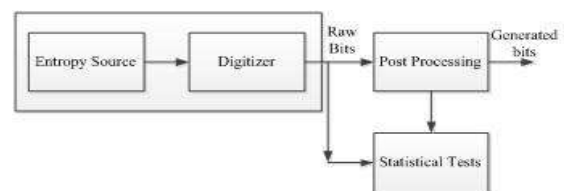


Figure 1. The general design of TRNG [5]

The basic block structure of TRNG is described below.

A. Noise (Entropy) Source

There are noise sources in various types used in TRNG. The entropy source for TRNG is the source of physical randomness. There are many noise sources used in TRNG:

- * Electrical noise: thermal noise, flicker noise and jitter noise are used.
- * Quantum mechanical properties of photons
- * Human-induced interactions: mouse and keyboard movements

B. Sampling

In this section, conversion of analog noise signal to digital noise signal is performed. Sampling is called the Harvesting Mechanism. Usually D-type flip flops are used as samplers.

C. Post Processing

In order to increase the randomness of random numbers generated as a result of the sampling, post processing algorithms are applied. Entropy distributions of random bit stream applied to post processing have a regular distribution. Von Neumann, XOR and H function final operations, which are the most frequently used post processing, are described below.

XOR: XOR Verification is a simple linear function. It is applied on n bits ($n = 2$) blocks to produce an output bit. While eliminating the correlation on the output bit, it also caused the output bit efficiency to decrease by $1/n$ times. The advantage of this verification is the possibility of providing simplicity and constant output bit rate [4].

Von Neumann: It is the oldest and simplest post processing method. He's been out of his bit streams irregularities. As shown in Table 1, Von neumann produces uniformly distributed 0 and 1 bits. This validation is to bring entropy closer to ideal value 1. The bit rate is reduced by $1/4$ of the input bit rate [5].

Table 1. Von Neumann [4]

Input Bit Pairs	Von neumann output
00	discard
01	0
10	1
11	discard

H-Function: The h function is a type of post-processing that achieves more successful results than the XOR finishing. Randomly generated numbers are processed in groups of 16 bits, with a base of 2. the first 8 bits of Each 16 bit is subjected to XOR with shifted left by 1 bit of the first 8 bits. With the result obtained from this operation,

the last 8 bits are XORed. As a result of these operations, 8 bit output is produced [6].

In the example given in Table 2, the bit stream generated for the post processing taken 16 bits with a_0, a_1, \dots, a_{15} . The first 8 bits of 16 bits are a_1 , the last 8 bits are 2 bits as a_2 . In the a_{i-1} cell, a bit shift operation of the first eight bits is performed. H function is shown in Equation 1

$$H(A1,A2)=XOR(XOR(A1,rotateleft(A1,1)),A2) \quad (1)$$

In Figure 2., the function of H function is given.

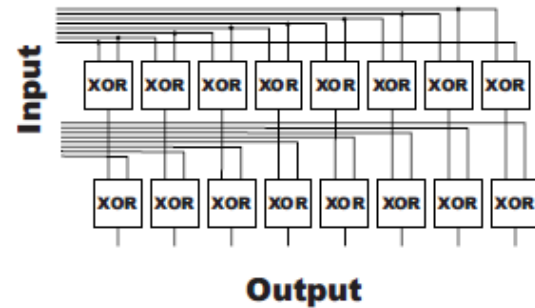


Figure 2. H Function [6]

In Table 3, as indicated in Table 2, the bits that are divided into 8 bits and shifted 1 bit to the left are taken separately and XOR operation is applied. In Table 4, the results of the bit streams with H function are given. When the results are examined, it is seen that the bit rate of the H function is reduced by $1/2$.

Table 2 process in the input bit stream

Entered random bits (16 bit)	A1	A1 rotate left 1 bit (A1-1)	A2
110100101011 1000	110100 1 0	1010010 1	101110 0 0
111011011100 0010	111011 0 1	1101101 1	110000 1 0
110001011001 0010	110001 0 1	1000101 1	100100 1 0

Table 3. XOR Process

(A1) XOR (A1-1)	((A1) XOR (A1-1)) XOR A2
01110111	11001111
00110110	11110100
01001110	11010100

Table 4. Output of H function

Entered random bits (16 bit)	Output of H function
1101001010111000	10111000
1110110111000010	11000010
1100010110010010	10010010

III. RING OSCILLATOR

One of the methods used as a source of randomness in TRNG systems is RO. The clock signals obtained from the RO shows deviations from the correct positions. This variability is called jitter. The jitter signal period generated by the RO is equal to $2 \times N \times \tau_p$. Where N is the number of inverters used and τ_p is the propagation delay of the used inverter elements. Often jitter is an undesirable feature in a system. However, because the jitter is random, the use of jitter in TRNG is ideal. Besides, jitter produced by ring oscillator is not good quality [7]. Post processing is used in TRNG systems for this shortcoming. Figure 3 shows a ring oscillator design implemented in FPGA environment.

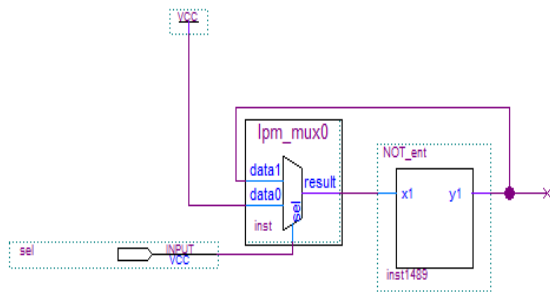


Figure 3. Ring Oscillator

A bit stream was achieved using the Sunar HO design, which was performed [7] and the overall design shown in Figure 4.

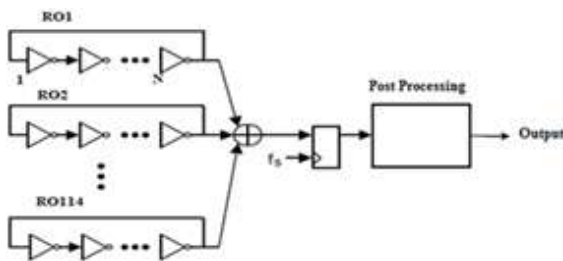


FIGURE 4. SUNAR RO

IV. STATISTICAL TEST RESULT AFTER POST PROCESSING

Bit arrays produced using Sunar HO in Chapter 3 may show weakness due to environmental factors such as

temperature, pressure. In order to overcome these weaknesses, Von Neumann, XOR and H function are applied. These post processings are performed using the program used in Figure 5. Whether the resulting bit streams are random is determined by applying the NIST 800-22 test suite.

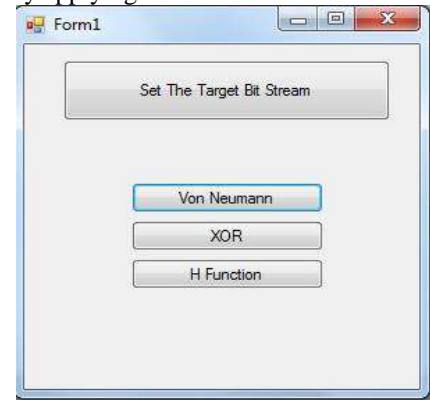


Figure 5. Post Processing Software

NIST test results are given in Table 5.

Table 5. NIST Test Result

	PureBit Stream	XOR	Vonneuman n	H Function	Result
Frequency	-	-	0,859	0,698	Passed
Frequency Test within a Block	-	-	0,487	0,288	Passed
Runs	-	-	0,020	0,348	Passed
Test for the Longest Run of Ones in a Block	-	0,521	0,850	0,285	Passed
Binary Matrix Rank	0,06	0,718	0,177	0,065	Passed
Discrete Fourier Transform	-	0,774	0,215	0,880	Passed
Non-overlapping Template Matching	0,370	0,574	0,832	0,188	Passed
Overlappig Template Matching	0,022	0,360	0,744	0,523	Passed
Maurer'sUniversal Statistical	-	0,762	0,358	0,952	Passed
Linear Complexity	0,271	0,950	0,543	0,715	Passed
Serail	-	0,148	0,237	0,946	Passed
	0,661	0,785	0,910	0,987	

Approximate Entropy	-	-	0,287	0,373	Passed
Cumulative Sums	-	-	0,132	0,589	Passed

V. CONCLUSION

In this work, we present the results of applying the post processing to a stream obtained from the real random number generator and the results of this application. For this purpose, Von Neumann, XOR and H function post processings, which we have implemented in our software, have been applied to bit streams produced using HO. Even though the pure bit streams pass the tests, quality bit streams required for cryptographic security will be obtained after the post processing. It is also seen to be an important step in the post processing of TRNG. In future studies, it is aimed to present software to other users in web environment by making software in other finishing algorithms.

REFERENCES

- [1] Koç, Ç. K., 2009, "About Cryptographic Engineering," in *Cryptographic Engineering*, Ç. K. Koç, Ed. Springer US, 1–4.
- [2] Avaroğlu, E., Tuncer, T., Özer, A. B., and Türk, M., 2014, "A New Method for Hybrid Pseudo Random Number Generator," *J. Microelectron. Electron. Compon. Mater.*, vol. 44, no. 4, 303–311.
- [3] Rukhin, A., *et al.*, "A statistical test suite for random and pseudo random number generators for cryptographic applications." National Institute of Standards and Technology.
- [4] Davies, R. B., 2002, "Exclusive OR (XOR) and hardware random number generators."
- [5] Avaroğlu, E., and Türk, M., 2013, "Son işlemin Gerçek Rasgele Sayı Üreteçleri Üzerindeki Etkisinin İncelenmesi," presented at the 6. Uluslararası Bilgi Güvenliği ve Kriptoloji Konferansı, 290–294.
- [6] Dichtl, M., 2007, "Bad and Good Ways of Post-processing Biased Physical Random Numbers," in *Fast Software Encryption*, 137–152.
- [7] Avaroğlu, E., Tuncer, T., Özer, A. B., Ergen, B., and Türk, M., 2015, "A novel chaos-based post-processing for TRNG," *Nonlinear Dyn.*, pp. 1–11, Feb. 2015.

METALURGICAL AND MATERIALS ENGINEERING

ORAL SUBMISSIONS



Effect of Magnesium Additive Element on the Hydrogen Storage Characteristics of La-Ni Based Alloys

Alanur BİNAL AYBAR, Mustafa ANIK

Eskisehir Osmangazi University,
Department of Metallurgical and Materials Engineering
Eskisehir, Turkey
abinal@ogu.edu.tr, manik@ogu.edu.tr

Abstract—In this study A_2B_7 type La-Ni based alloys were synthesized directly from sintered mixture in the molten $CaCl_2$ electrolyte by the electro-deoxidation method at 750°C . The effect of Mg additive element for La on hydrogen storage characteristics of electro-deoxidized $(La_{1-x}Mg_x)_2(Ni_{0.8}Co_{0.2})_7$ ($x = 0, 0.125, 0.25$) alloys have been studied. Mg substitution for La changed the sintered structure. Sintering (at 1200°C for 3 h) caused the hygroscopic La_2O_3 to disappear and the non-hygroscopic $LaNiO_3$ and $Mg_{0.4}Ni_{0.6}O$ to form depending on the substitution element content. The X-ray diffraction analyses revealed electro-deoxidized materials have multi-phase structure. The X-ray diffraction peaks indicated $LaNi_5$, La_2Ni_7 , and $La_{1.5}Mg_{0.5}Ni_7$ phases were the main phases present in the synthesized alloys. $(La_{1-x}Mg_x)_2(Ni_{0.8}Co_{0.2})_7$ ($x = 0, 0.125, 0.25$) alloys had promising discharge capacities changed between 331 mAh g^{-1} and 356 mAh g^{-1} . The results obtained in this study showed that the electro-deoxidation technique is very promising in the synthesizing of the high performance hydrogen storage alloy.

Keywords—electro-deoxidation; hydrogen storage; A_2B_7 structure type; La-Mg-Ni system

I. INTRODUCTION

Partial substitution of alloy elements by other transition metals was used to improve the electrochemical hydrogen storage properties of La-Ni alloys [1]. La-Mg-Ni based hydrogen storage alloys, attracted great attention as a negative electrode material for nickel/metal hydride batteries, [2,3]. Among different types of La-Mg-Ni based alloys, A_2B_7 -type alloys are believed to have superior overall electrochemical properties [4]. La-Mg-Ni-based hydrogen storage alloys are typically prepared by melting [5-7]. Generally, after this processes products need annealing for several time to get structural homogeneity [8,9]. Clearly the production route is long and the cost is high [10].

Many hydrogen storage alloys have been directly synthesized by electro-deoxidation technique from their oxides in molten salt [11-20]. Reported studies have showed that the energy consumption of the FFC Cambridge process is generally lower and operation is simpler than many existing technologies [21-23].

In this work electro-deoxidation method was used to prepare A_2B_7 type La-Mg-Ni-Co hydrogen storage alloys. Effect of Mg additive element on the electrochemical hydrogen storage characteristics of La-Ni based alloy was determined.

II. MATERIAL AND METHOD

Commercially available La_2O_3 , NiO, MgO and CoO powders were obtained from Alfa Aesar. Required amounts of the oxide powders were mixed homogeneously in anhydrous ethanol includes 3% (by weight) polyethylene glycol (PEG) with a planetary ball mil. The powder was then dried overnight at room temperature. Dried powder was cold pressed into pellets of 10 mm in diameter, under a pressure of $1.5 \text{ tonne cm}^{-2}$. The oxide mixture pellet of $La_2O_3+NiO+CoO+MgO$ was then sintered at 1200°C for 3 h.

100 gr $CaCl_2$ was mixed with 1 gr CaO and placed into graphite crucible. Before electro-deoxidation process $CaCl_2$ -CaO powder mixture was dried under Ar gas. Drying was carried out by slow heating to 150°C and holding at 150°C for 15 h and then slow heating to 300°C and holding at 300°C for 15 h and then finally slow heating to the target temperature of 750°C for the electro-deoxidation experiments.

In order to fully remove the water and the possible redoxactive impurities, pre-electrolysis were carried out at 2.5 V and 750°C for 4 h. During the pre-electrolysis graphite crucible was used as anode and another graphite rod was used

as cathode. The electro-deoxidation was conducted at 3.2 V for various times at 750°C. The potential control was carried out by the programmable direct current source.

After the electro-deoxidation experiments the pellet electrodes were removed from the molten melt. The solidified salt on the pellet was washed out by tap water. After slight surface grinding the pellets were kept in 1 M HCl for few minutes. Finally the deoxidized pellet samples were dried at 100°C for 24 h under vacuum.

The deoxidized pellet samples were ground into fine powder (alloy powder). Working electrodes were prepared by mixing 0.1 g alloy powder with 0.3 g nickel powder and then cold pressing into pellets of 10 mm in diameter, under a pressure of 10 tonne cm⁻². The working electrode was wrapped by Ni mesh and a Ni lead wire was attached to Ni mesh by spot-welding to prepare a hydrogen storage alloy electrode (negative electrode). Hg/HgO reference electrode was used in 6 M KOH solution. Tests were performed with GAMRY Model Reference 3000 potentiostat/galvanostat unit. The charge current density was 100 mA g⁻¹ and the charging was carried out down to the severe gassing potential. The charging was followed by a 10 min rest before the discharging. The discharge current density was 25 mA g⁻¹ and the discharge cut-off potential was -0.5 V_{Hg/HgO}.

The phase structure of the synthesized alloy powders (well mixed to get homogeneity) was examined by the X-ray diffractometer (Bruker axs D8) using Cu K α radiation. The powder morphologies were observed by ZEISS SUPRATM 50 VP Scanning Electron Microscope (SEM).

III. RESULTS AND DISCUSSIONS

A. The Molten Salt Electrolysis

The XRD patterns of the sintered samples prepared to obtain (La_{1-x}Mg_x)₂(Ni_{0.8}Co_{0.2})₇ (x = 0, 0.125, 0.25) alloys are provided in Fig. 1.

Partial substitution of La by Mg changes the sintered structure. NiO and LaNiO₃ are present in all samples. In addition to these oxides Mg_{0.4}Ni_{0.6}O are present in Mg including alloys. Instead of hygroscopic La₂O₃, the formation nonhygroscopic LaNiO₃ and Mg_{0.4}Ni_{0.6}O during sintering makes possible synthesizing of A₂B₇ type alloys by electro-deoxidation technique in molten CaCl₂ salt.

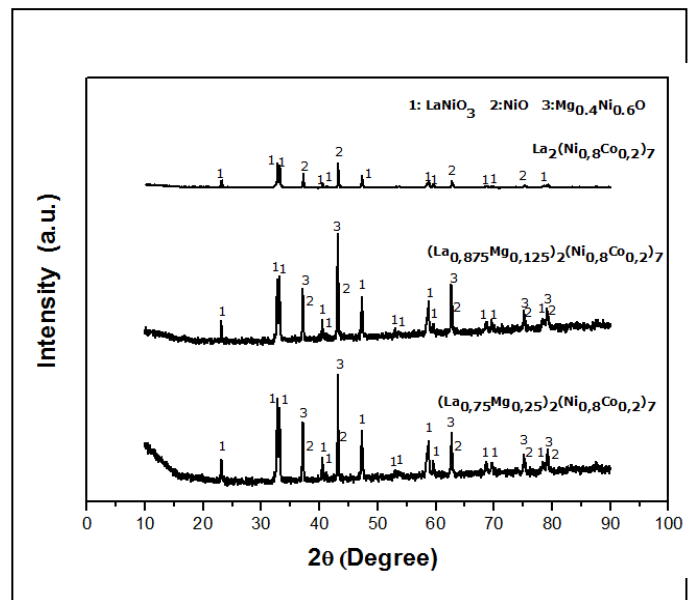


Fig.1 XRD patterns of the sintered samples prepared to obtain La₂(Ni_{0.8}Co_{0.2})₇, (La_{0.875}Mg_{0.125})₂(Ni_{0.8}Co_{0.2})₇ and (La_{0.75}Mg_{0.25})₂(Ni_{0.8}Co_{0.2})₇ alloys

The XRD patterns of the 20 h electro-deoxidized (La_{1-x}Mg_x)₂(Ni_{0.8}Co_{0.2})₇ (x = 0, 0.125, 0.25) alloys are also presented in Fig. 2. LaNi₅ phase can be seen in all compositions in this work. At (La_{1-x}Mg_x)₂(Ni_{0.8}Co_{0.2})₇ (x = 0) alloy; after 20h electrolysis LaNi₅ and La₂Ni₇ form as the electro-deoxidation product.

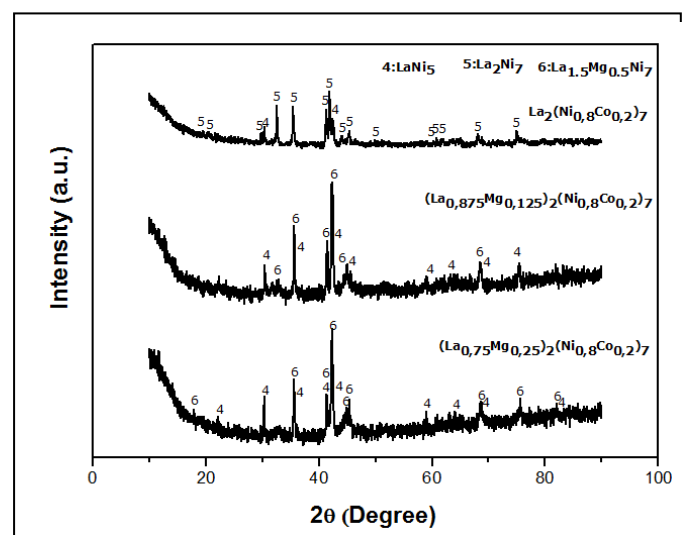


Fig.2 XRD patterns of the 20h electro-deoxidized samples prepared to obtain La₂(Ni_{0.8}Co_{0.2})₇, (La_{0.875}Mg_{0.125})₂(Ni_{0.8}Co_{0.2})₇ and (La_{0.75}Mg_{0.25})₂(Ni_{0.8}Co_{0.2})₇ alloys

When Mg substitutes is added in (La_{1-x}Mg_x)₂(Ni_{0.8}Co_{0.2})₇ (x = 0.125, 0.25) alloys, after 20h

electrolysis LaNi_5 and $\text{La}_{1.5}\text{Mg}_{0.5}\text{Ni}_7$ form as the electro-deoxidation product. This shows that during the electrolysis the sintered structure is completely deoxidized. The X-ray diffraction analyses revealed electro-deoxidized material has multi-phase structure. Depend on the production method this phases can be changed in literature [1,5,24].

Scanning electron micrographs of the as-sintered oxide powder and 20 h electro-deoxidized powder of $(\text{La}_{0.875}\text{Mg}_{0.125})_2(\text{Ni}_{0.8}\text{Co}_{0.2})_7$ alloy are provided in Fig. 3a and 3b, respectively. Since the morphologies of other compositions are very similar to those of ones in Fig. 3a-b, they are not provided. As-sintered powder has typical fine oxide powder appearance in Fig. 3a. At the end of 20 h electrodeoxidation process, however, the large crystalline metallic powder morphology develops as in Fig. 3b. The porous structure of the developed alloy is also apparent in Fig. 3b.

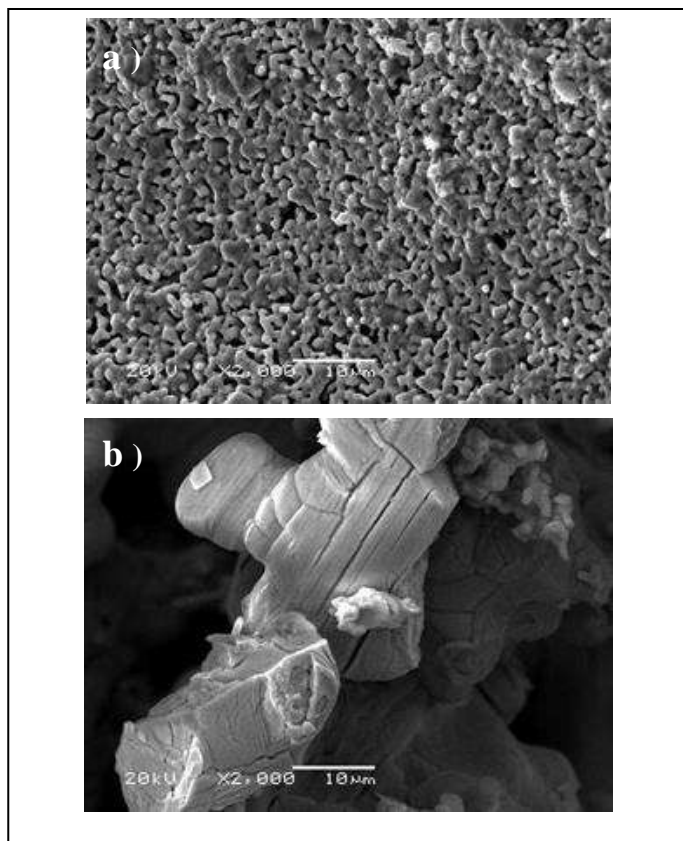


Fig.3 Powder morphologies of $(\text{La}_{0.875}\text{Mg}_{0.125})_2(\text{Ni}_{0.8}\text{Co}_{0.2})_7$ alloy after (a) sintering and (b) electro-deoxidation for 20 h.

B. The Hydrogen Storage Characteristics of the Synthesized Alloys

Fig. 4. shows charge/discharge curves of 20h electro-deoxidized $(\text{La}_{1-x}\text{Mg}_x)_2(\text{Ni}_{0.8}\text{Co}_{0.2})_7$ ($x = 0, 0.125, 0.25$) alloy electrodes for 15 charge/discharge cycles.

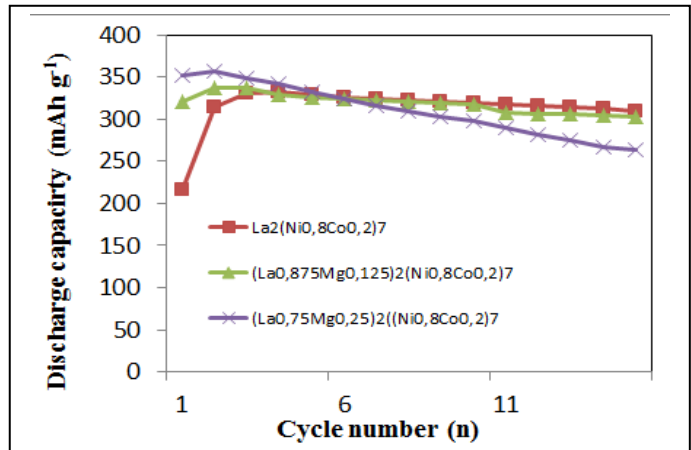


Fig.4 Discharge capacities of 20h electro-deoxidized $(\text{La}_{1-x}\text{Mg}_x)_2(\text{Ni}_{0.8}\text{Co}_{0.2})_7$ ($x = 0, 0.125, 0.25$) alloys depending on the charge/discharge cycle.

It can be seen that all the synthesized alloys can be activated in few cycles to reach their maximum discharge capacities and as x increases, the maximum discharge capacity gradually increases. The maximum discharge capacities of $\text{La}_2(\text{Ni}_{0.8}\text{Co}_{0.2})_7$, $(\text{La}_{0.875}\text{Mg}_{0.125})_2(\text{Ni}_{0.8}\text{Co}_{0.2})_7$, and $(\text{La}_{0.75}\text{Mg}_{0.25})_2(\text{Ni}_{0.8}\text{Co}_{0.2})_7$ alloys are 331 mA h g^{-1} , 337 mA h g^{-1} and 356 mA h g^{-1} , respectively. The reported discharge capacity for $\text{La}_{1.5}\text{Mg}_{0.5}\text{Ni}_7$ alloy synthesized by the induction melting method changes between $309.5 \text{ mA h g}^{-1}$ and $358.2 \text{ mA h g}^{-1}$ [5,24].

IV. CONCLUSION

$(\text{La}_{1-x}\text{Mg}_x)_2(\text{Ni}_{0.8}\text{Co}_{0.2})_7$ ($x = 0, 0.125, 0.25$) alloys were synthesized directly from sintered oxide mixture by the molten salt electro-deoxidation method at 750°C , and the effect of Mg substitution for La on the electrochemical properties of the alloys has been investigated. The following conclusions may be derived:

- Sintering converted the hygroscopic La_2O_3 as a result of the reaction with NiO totally into the non-hygroscopic LaNiO_3 and $\text{Mg}_{0.4}\text{Ni}_{0.6}\text{O}$.
- Mg substitution for La in La-Ni alloys can enhance electrochemical hydrogen storage characteristics of $\text{La}_2(\text{Ni}_{0.8}\text{Co}_{0.2})_7$.

- The discharge capacity of $(\text{La}_{0.75}\text{Mg}_{0.25})_2(\text{Ni}_{0.8}\text{Co}_{0.2})_7$ alloy was higher than these of both $\text{La}_2(\text{Ni}_{0.8}\text{Co}_{0.2})_7$, $(\text{La}_{0.875}\text{Mg}_{0.125})_2(\text{Ni}_{0.8}\text{Co}_{0.2})_7$ alloys.
- Electro-deoxidation is an effective method of synthesizing La-Ni based alloys for hydrogen storage materials.

ACKNOWLEDGMENTS

Financial assistance from The Scientific and Technological Research Council of Turkey is gratefully acknowledged (Project No: MAG 113M139).

REFERENCES

- [1] M. Balcerzak, M. Nowak, M. Jurczyk, "Hydrogenation and electrochemical studies of La-Mg-Ni alloys," *Int. J. Hydrogen Energy*, In press, 2016.
- [2] J. Liu, S. Han, Y. Li, X. Zhao, S. Yang, and Y. Zhao, "Cooperative Effects of Sm and Mg on Electrochemical Performance of La-Mg-Ni-based Alloys with A2B7- and A5B19-type Super-Stacking Structure," *Int. J. Hydrogen Energy*, vol.40, pp. 116-1127, Jan. 2015.
- [3] H. Hayakawa, E. Akiba, M. Gotoh, and T. Kohno, "Crystal Structures of La-Mg-Ni_x (x = 3-4) System Hydrogen Storage Alloys," *Mater. Trans.*, vol. 46, pp. 1393- 1401, Jun. 2005.
- [4] J. Liu, S. Han, D. Han, Y. Li, S. Yang, L. Zhang, and Y. Zhao, "Enhanced Cycling Stability and High Rate Dischargeability of (La,Mg)₂Ni₇-type Hydrogen Storage Alloys with (La,Mg)₅Ni₁₉ Minor Phase" *J. Power Sources*, vol. 287, pp. 237-246, Aug. 2015.
- [5] Zhang FL, Luo YC, Chen YP, Yan RX, Chen JH, "La-Mg-Ni ternary hydrogen storage alloys with Ce₂Ni₇-type and Gd₂Co₇-type structure as negative electrodes for Ni/Mh batteries," *J. Alloys Compd.* 2007; 430: 302-7
- [6] Denys R, Riabov B, Yartys VA, Delaplane RG, Sato M, "Hydrogen storage properties and structure of $\text{La}_{1-x}\text{Mg}_x(\text{Ni}_{1-y}\text{Mn}_y)_3$ intermetallics and their hydrides," *J. Alloys Compd.* 2007; 446-447: 166-172.
- [7] Chu HL, Qiu SJ, Sun LX, Zhang Y, Xua F, Jiang T, Li WX, Zhu M, Hu WY, "The improved electrochemical properties of novel La-Mg-Ni-based hydrogen storage composites," *Electrochim. Acta* 2007; 52: 6700-6.
- [8] Zhang F, Luo Y, Wang D, Yan R, Kang L, Chen J, "Structure and electrochemical properties of $\text{La}_{2-x}\text{Mg}_x\text{Ni}_{7.0}$ (x = 0.3-0.6) hydrogen storage alloys," *J. Alloys Compd.* 2007; 439: 181-8.
- [9] Mohandas KS, Fray DJ, "FFC Cambridge process and removal of oxygen from metal-oxygen systems by molten salt electrolysis: an overview," *Trans. Indian Inst. Met.* 2004; 57:579-592.
- [10] L. Dai, S. Wang, Y. Li, L. Wang, G. SHAO, "Direct electrochemical preparation of CeCo₅ alloy from mixed oxides," *Trans. Nonferrous Met. Soc. China*, vol. 22, pp. 2007-2013, May. 2012.
- [11] W. Chen, S. Wang, J. Ge, S. Jiao, and H. Zhu, "Electrochemical Synthesis of Nb₅Si₃ Intermetallic Compound From Molten Calcium Chloride Salt," *Intermetallics*, vol. 25, pp. 66-69, June, 2012.
- [12] Zhao B, Wang L, Dai L, Cui G, Zhoua H, Kumarb RV, "Direct electrolytic preparation of /nickel hydrogen storage alloy powder in molten salt," *J. Alloys Compd.* 2009; 468: 379-385.
- [13] Qiu G, Wang D, Jin X, Chen GZ, "A direct electrochemical route from oxide precursors to the terbium-nickel intermetallic compound TbNi₅," *Electrochim. Acta* 2006; 51: 5785-5793.
- [14] Dai L, Wang S, Li YH, Wang L, Shao GJ, "Direct electrochemical preparation of CeCo₅ alloy from mixed oxides," *Trans. Nonferrous Met. Soc. China* 2012;22: 2007_2013.
- [15] Zhu Y, Wang D, Ma M, Hu X, Jin X, Chen GZ, "More affordable electrolytic LaNi₅-type hydrogen storage powders," *Chem. Commun.*, 2007,24: 2515-7
- [16] Anik M, Hatirnaz N B, Aybar A B, "Molten salt synthesis of $\text{La}(\text{Ni}_{1-x}\text{Co}_x)_5$ (x = 0,0.1,0.2,0.3) type hydrogen storage alloys," *Int. J. Hydrogen Energy* 2016; 41: 361 -8.
- [17] Anik M, Aybar A B, Küçükdeveci N, Erken H, Baksan B, Gaşan H, Hatirnaz N B, Lökçü E, "Synthesis of La_2Ni_7 hydrogen storage alloy by the electro-deoxidation technique," *Int. J. Hydrogen Energy* 2015; 40: 22 48- 54
- [18] Anik M, Aybar A B, Hatirnaz N B, Özdemir D, "Synthesis of $\text{La}_2(\text{Ni}_{1-x}\text{Co}_x)_7$ (x = 0.05, 0.1, 0.2) hydrogen storage alloys by the electro-deoxidation technique," *J. Electrochem. Soc.* 2015; 162: A1080-4.
- [19] Anik M, Baksan B, Orbay T Ö, Küçükdeveci N, Aybar A B, Özden R C, Gaşan H, Koç N, "Hydrogen storage characteristics of Ti_2Ni alloy synthesized by the electro-deoxidation technique," *Intermetallics* 2014; 46: 51-5.
- [20] Dai L, Wang S, Wang L, Yu Y, Shao G-J, "Preparation of ZrMn_2 hydrogen storage alloy by electro-deoxidation in molten calcium chloride," *Trans. Nonferrous Met. Soc. China* 2014; 24: 2883-9.
- [21] G.Z. Chen, "Forming metal powders by electrolysis," *Advances in Powder Metallurgy*, Chang I., and Zhao Y. (Eds) Woodhead Publishing Limited, pp. 19-41, 2013.
- [22] S.J. Oosthuizen, "In search of low cost titanium: the Fray Farthing Chen (FFC) Cambridge process," *SAIMM Journal*, vol.111, pp. 199-202, Oct. 2010.
- [23] B. Zhao, L. Wang, L. Dai, G. Cui, H. Zhou, R.V. Kumar "Direct electrolytic preparation of cerium/nickel hydrogen storage alloy powder in molten salt" *Journal of Alloys and Compounds* vol.209, pp. 379-385, May. 2009.
- [24] L. Gal, V.Charbonnier, J. Zhang, L. Goubault, P. Bernard, M. Latroche, "Optimization of the La substitution by Mg in the La_2Ni_7 hydride-forming system for use as negative electrode in Ni-MH battery" *Int. J. Hydrogen Energy*, vol.40, pp. 17017-17020, Jun. 2015.

The Influence of Silica Fume on Fly Ash Added Brick Properties

Gülfem BİNAL^a, Ertuğrul ERDOĞMUŞ^b

^aDepartment of Metallurgical and Materials Engineering

^bDepartment of Environmental Engineering

Bartın University

Bartın, TURKEY

gbinal@bartin.edu.tr, eerdogmus@ bartin.edu.tr

Abstract—In this study, the effects of silica fume addition to 15 wt. % fly ash (Seyitömer thermal power plant fly ash) containing brick properties were investigated. Silica fume is a by-product of producing silicon metal or ferrosilicon alloys in smelters using electric arc furnaces. Different brick mixtures which were containing clay – silica fume - 15 wt.% fly ash were prepared according to Table 1 and Figure 1. Prepared brick samples were sintered in a laboratory kiln at 950 °C firing temperature.

Table 1. Brick mixtures

Recipe Code	Fly Ash (wt. %)	Silica Fume (wt. %)	Brick Clay (wt. %)
S1	15	5	80
S2	15	10	75
S3	15	15	70
S4	15	20	65

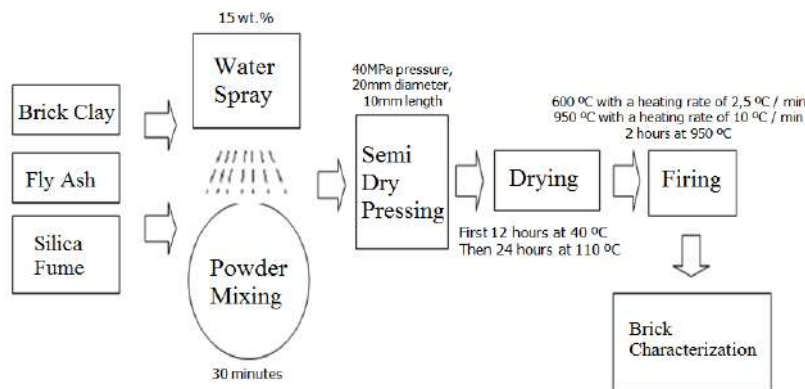


Fig 1. Flow Chart of Production Process

Physical and mechanical properties of the samples were determined. It has been seen that the addition of silica fume increases the water absorption and porosity values (Fig 2) and decreases the compressive strength values (Fig 3). The amount of SiO₂ is increasing in the bricks to which silica fume is added in an increasing amount. The decrease in the clay content reduces the amount of the flux in the brick mixtures. Because of this the sintering temperature rises and the amount of liquid phase formed decreases. The pores cannot be closed when the amount of liquid phase is low. Depending on the increasing amount of pores the water absorption values increases and strength values decreases. Increasing of the porosity of the bricks helps to improve their thermal insulating properties.

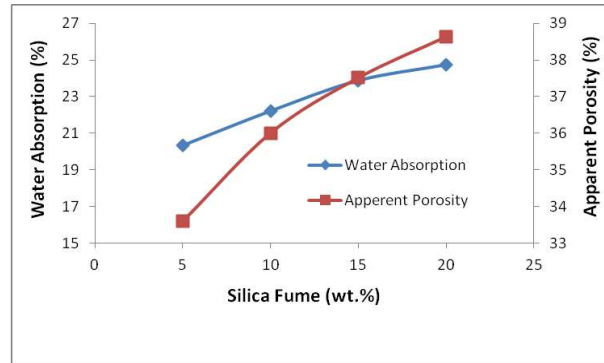


Fig 2. Variation in water absorption and apperent porosity values in relation to silica fume content.

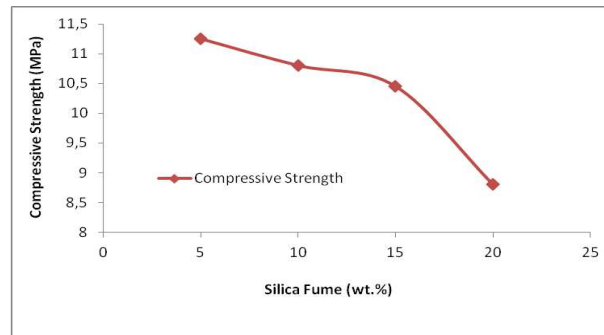


Fig 3. Variation in compressive strength values in relation to silica fume content.

SEM analysis of resultant products was also investigated. As a result of this study, it has been shown that appropriately qualified bricks can be produced with using 15 wt.% fly ash and different amounts of silica fume. The use of waste such as fly ash and silica fume in the production of bricks will prevent environmental pollution and contribute to the economy of the country.

Keywords—silica fume; fly ash; brick

The Effect of Encapsulation Time on the Encapsulation Carbon of Boron Powder with CVD Method

Haluk Koralay*,
Department of Physics, Faculty of Science,
Gazi University, Ankara, Turkey

A. Tolga Tasci,
Department of Physics, Faculty of Science,
Kastamonu University, Kastamonu, Turkey

Naki Kaya,
Vocational School, Opticianry Programme,
İstanbul Arel University, İstanbul, Turkey

Özgür Öztürk,
Department of Physics, Faculty of Science,
Kastamonu University, Kastamonu, Turkey

Şükrü Çavdar,
Department of Physics, Faculty of Science,
Gazi University, Ankara, Turkey

Burhanettin Çiçek,
Chemical Engineering Department,
Ankara University, Ankara, Turkey

Nihat Tuğluoğlu,
Department of Energy Systems Engineering, Faculty of Engineering,
Giresun University, Giresun, Turkey

email: hkoralay@gmail.com

Abstract— Since 1991, the discovery of carbon nanotubes has opened new fields of study for many scientific disciplines, especially in materials science, chemistry and physics. Very good electrical, magnetic and mechanical properties of carbon nanotubes are involved in the use of carbon nanotubes on a wide scale. Despite the existence of multiple carbon nanotube production methods, each has its own advantages and disadvantages. Besides providing impurity in the production of carbon nanotubes, studies are being made on how to obtain carbon nano structures that can be produced fast in the desired geometries by cheap routes. Advanced equipment is needed to make carbon nanotubes in desired geometries. In many synthetic methods, there is still no controlled synthesis associated with the diameters and lengths of the tubes. Arc discharge method, laser melting method and chemical vapor deposition method are some of the methods of producing carbon nanotubes. The Chemical Vapor Deposition (CVD) method from these methods is often used due to some advantages. Some of the advantages are cheap cost, easy to obtain, homogeneity, adjustment of experiment parameters.

After the discovery of nanotube production by the CVD method, factors that affect the productivity on this method has begun to be investigated. Some factors that effect CVD process are the length of the test period, type of hydrocarbon source, the chemical properties of the material to be encapsulated, the test temperature, the type of inert used gas.

In this study, we determined the factors such as temperature, material impurity and hydrocarbon slipperly and experiment period and we carried out the 30 - minutes periodic increments and examined the results. In this study, at 700 °C, boron powder in 95-97 % purity by using acetylene gas as the hydrocarbon source carbon were encapsulated by the CVD method , during 30, 60 and 90 min. By using SEM and elemental analysis method it was searched to find whether carbon nanotubes were occurred or not and percentage of carbon structures' in whole structure was investigated.

In the experiment that was carried out 30 and 60 minutes, a few carbon nanotubes structures appeared and in the experiment that was carried out 90 minutes, carbon structures were significant clear in the SEM images (Fig 1). As a result of elemental analysis It was determined that in the carbon encapsulated process lasted for 90 min. carbon phase's percentage was % 14.70, in the carbon encapsulated process lasted for 60 min carbon phase's percentage was % 7.79 and in the carbon encapsulated process lasted for 30 min carbon phase's percentage was % 5.98.

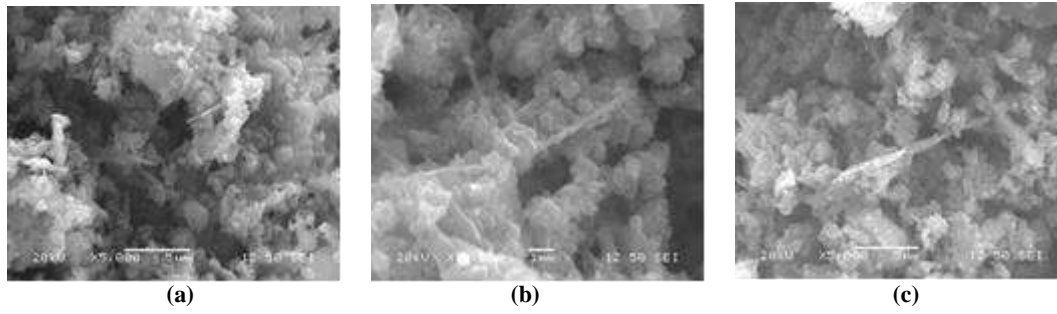


Figure 1. Respectively, SEM images of encapsulated carbon boron at 700 °C during a) 30, b) 60 and c) 90 min

Keywords—CVD, SEM, MgB_2

*This study is supported by the Scientific and Technological Research Council of Turkey (TUBITAK) reference number (115F237)

The Investigation of Structural Features of $\text{Bi}_{(1.8-x)}\text{Pb}_{0.2}\text{Ga}_x\text{Sr}_2\text{CaCu}_2\text{O}_y$ Glass Ceramic Superconductivity

Şükrü Çavdar*, Department of Physics, Faculty of Science,
Gazi University, Ankara, Turkey

aki Kaya, Vocational School, Opticianry Programme,
İstanbul Arel University, İstanbul, Turkey

Nihat Tuğluoğlu, Department of Energy Systems Engineering, Faculty of Engineering,
Giresun University, Giresun, Turkey

Özgür Öztürk, Department of Physics, Faculty of Science,
Kastamonu University, Kastamonu, Turkey

Haluk Koralay, Department of Physics, Faculty of Science,
Gazi University, Ankara, Turkey

Selçuk İzmirli, Department of Physics, Faculty of Science,
Gazi University, Ankara, Turkey

email: sukru.cavdar@gmail.com

Abstract— Glass ceramics are preferred in many applications due to their advantages such as hardness, high temperature, abrasion resistance and electrical conductivity. Glass ceramics are materials with fine crystal structure. Due to these properties they have good surface smoothness. Good surface smoothness allows glass ceramics to be used as an electronic base. Glass ceramic bases are frequently used in thin and thick film technology. The first study on the BSCCO (Bi-Sr-Ca-Cu-O) system using the glass ceramic method was carried out by Komatsu. et al. Studies related to the BSCCO glass system have been carried out by different working groups for many years. The thermal, mechanical, electrical and magnetic properties of the system were investigated by making various contributions to the BSCCO system.

In this study, the effect of Bi-Ga partial displacement on materials $\text{Bi}_{(1.8-x)}\text{Pb}_{0.2}\text{Ga}_x\text{Sr}_2\text{CaCu}_2\text{O}_y$ (Bi-2212) glass-ceramic superconductor was investigated. This study consists of sample preparation, casting, sintering and analyses-procedures. In sample preparation stage, on the condition of different rates of ($x=0.025, 0.1, 0.3, 0.8$), 4 samples were prepared and prepared powder samples were mixed in automatic mixer. Then, melt solution was obtained after we got sample powders in furnace within room temperature and keep it waited in a furnace at 1150°C . Then we withdrew the melted materials from furnace and we got glass material by leaving it in shock cooling at the end. Obtained glass materials were sintered in Oxygen atmosphere within 845°C for 120 hours. The magnetic susceptibility of sintered materials was measured and surface morphology was analysed by scanning electron microscope (SEM).

It can be seen the growth of crystal structure based on increase of Ga rate. Besides, amorphous structures were also occurred in $x=0.1$ sample. The more the value of x increased, the less features of superconductive materials owned (Fig. 1).

At the result of susceptibility measurement, it was determined that the increase of Ga rate leads to the decrease of critical temperature value. In this situation, we can come to the conclusion that it can be seen the deformation of crystal structure; decrease of amorphous structure, and the superconductivity properties can be affected negatively. Moreover, the increase of the value of ΔT with direct proportion through partial displacement demonstrates the increase of impurity in previously formed structure (Fig. 2).

Keywords—Bi-2212, Glass Ceramic, Superconductivity

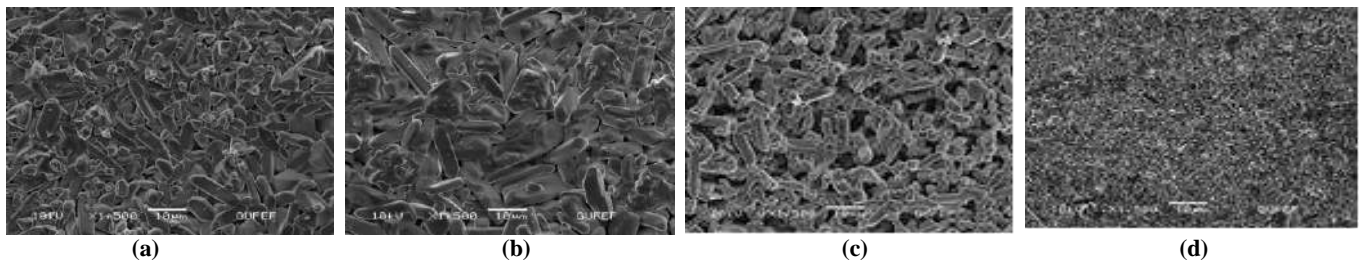


Figure 1. a) $x=0.025$ b) $x=0.1$ c) $x=0.3$ d) $x=0.8$ surface photographs of samples with partial displacements

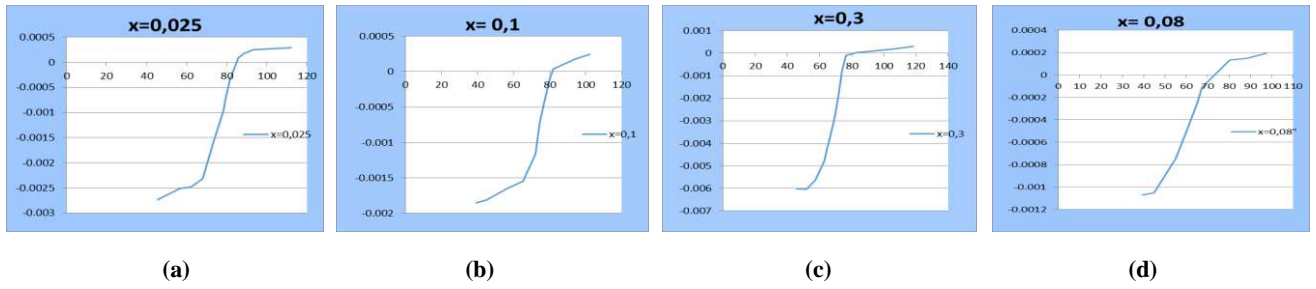


Figure 2. a) $x=0,025$ b) $x=0,1$ c) $x=0,3$ d) $x=0,08$ Susceptibility of samples with partial displacements

This study is supported by the Scientific and Technological Research Council of Turkey (TUBITAK) reference number (115F237)

Preparation of Carbon Nanotube Decorated Fiber Reinforced Polymeric Composite Structures by Using Microwave Energy

Selcuk Poyraz

Department of Textile Engineering, Corlu Faculty of Engineering, Namik Kemal University
Corlu/Tekirdag, Turkey
spoyraz@nku.edu.tr

Abstract—Through a facile, simple, yet efficient, affordable and ultrafast (30 s) microwave (MW) energy heating process, hierarchical composites made up of carbon fibers (CFs) decorated with multi-walled carbon nanotube (MWCNT) forest were produced at ambient conditions in one-step. Morphological features of the as-produced composites were characterized in details by using scanning and transmission electron microscopy (SEM, TEM) and the elemental analysis (EDX) techniques. Both the composite material characterization results and the versatile and easily controllable nature of the above mentioned process strongly support its promising success for the fabrication of such hierarchical composites that could be effectively used for the next generation advanced engineering applications.

Keywords—microwave energy; carbon nanotube; carbon fiber; hierarchical polymeric composite

I. INTRODUCTION

Not only because of its excellent mechanical strength but also its thermal and electrical conductivity, light weight and high processability, CF and its products have been extensively utilized as a building material in various advanced engineering systems such as aerospace ships, communication satellites, planes, hybrid vehicles, wind turbine blades, sports equipment, prosthetic limbs and so on [1]. As an expected result of its unique fibrous structure, CF usually serves as a reinforcing component to enhance the multi-scale properties of the above mentioned bulk composite materials made up of both thermoset and thermoplastic polymers, metals and concrete, as well [2]. A great deal of research effort has been devoted to enhance the reinforcing performance of CFs, in order to; (i) reduce or even eliminate the problems that are often caused by phase separation and also shearing upon excessive and repeating stress, and (ii) to achieve strong, light-weight, durable and high performance composite materials that can be used for a wide variety of real-life engineering applications [3-5]. In recent years, CNT growth on CF surface has been proposed as a promising solution in order to address the

needs and tackle the challenges in the above mentioned matters, since a nanostructured, 3D CNT forest surrounding the CF surface can both provide sufficient number of anchoring points and can significantly increase the effective specific surface area to reach a better adhesion performance between CFs and the bulk material matrix [6-8]. Moreover, with the addition of distinct mechanical, thermal, and electrical features of the CNTs into the structure, enhanced transverse and shear resistance can also be expected from the as-produced CNT/CF hierarchical composites, as a result of the intense interfacial interactions that exist between the as-grown CNT forest and CFs.

In general, the CNT forest is grown on the CFs' surface by following either a bottom-up method such as chemical vapor deposition (CVD) or a top-down method such as lithography [9, 10]. Although these methods can provide highly precise and uniform products, they usually suffer from their complex production process and from their need of harsh process conditions, i.e. high vacuum, high temperature, high pressure and hazardous chemicals' use. Additionally, these methods' overall fabrication processes are not easily scalable and are very time consuming, as well. Thus, the as-obtained sample amounts are usually limited and this restricts the common uses of such methods for the applications at industrial level. In order to eliminate these obstacles and to realize a practical application for the CNT/CF composites preparation, in this study, a well-established MW energy-assisted fabrication technique, which can rapidly grow a homogenous MWCNT forest decoration on CFs surface, is proposed [11]. The as-prepared CNT/CF composites from this method offer promising and wide range application potential for various advanced engineering and scientific fields including fiber reinforced composites' preparation for wind energy harvesting, super-capacitance, microelectronics, telecommunication, transportation, sports equipment and medical applications.

II. METHOD

A. Materials Used

Plain weave CF fabric, acetone (JT Baker), toluene (JT Baker) and ferrocene (AlfaAesar) were all used as purchased without further purification, unless otherwise specified.

B. Pre-treatment and Preparation of CF Mesh Samples

Prior to the MW energy-assisted rapid CNT forest growth process, several 1"×1" CF fabric samples were continuously heated in a conventional kitchen MW oven (Panasonic Inverter) at full power (1250 W) for 60 s, in order to; (i) remove the protective thin sizing layer, and (ii) to reveal as much reactive sites as possible on CFs' surface for the following process steps (Figure 1). Next, 0.2 M ferrocene solution was prepared by dissolving 0.11 moles of ferrocene in 550 mL of toluene, for the homogenous deposition of the carbon and catalyst source precursor chemical on the as-treated CF samples. After that, CF fabrics were individually soaked into this solution for 10 min under continuous gentle shaking. Eventually, all the samples were drip dried on a nylon string before the ultrafast MW heating process (Figure 2).

C. MW Energy-assisted Ultrafast CNT Forest Growth Process on CFs

The as-prepared CF fabric sample was tightened vertically between a pair of glass rods on a handmade PVC stand, and then it was placed on the glass MW tray. Here, the evenly deposited thin ferrocene layer was clearly observed on the CF fabric with an orange tint. The glass tray was then placed into the MW oven chamber. The CF fabric on the PVC stand was irradiated at the maximum power level, while intensive reactions were observed inside, as indicated by the sparking flames and dense chemical vapor emission. After getting heated by MWs for 30 s, the CF fabric sample with the as-grown CNT forest decoration on its surface was taken out and then gently rinsed with acetone to remove any impurities and unreacted chemicals (Figure 3).

D. Characterization of the As-prepared Composite Material

Morphological and elemental analyses of the as-obtained composite materials were done by using a JEOL JSM-7000F scanning electron microscope (SEM) equipped with an energy dispersive X-ray (EDX) detector. An EMS 550X auto sputter coating device was also utilized for surface Au

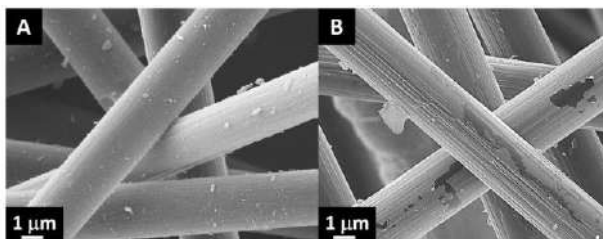


Fig. 1. Scanning electron microscopy (SEM) images of CFs; **A.** before and **B.** after MW pre-treatment.

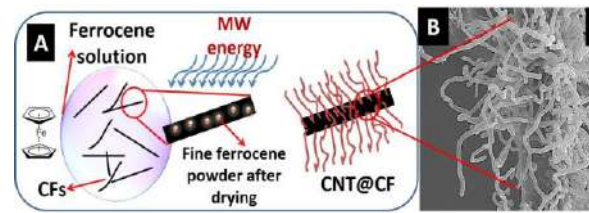


Fig. 2. **A.** Schematic representation of the MW energy-assisted ultrafast CNT forest growth process on CFs, **B.** SEM image of a single CF covered by CNT forest on its surface.

sputter coating of composite samples, which were readily prepared on carbon tape mounted sample holders, prior to their analysis. The in-depth morphological property analysis of the as-prepared composites was performed on a JEOL 2100F transmission electron microscope (TEM), operated at 200 kV. Here, CF strands from the as-treated fabric sample were carefully removed and dispersed in ethyl alcohol by ultrasonication for 10 min. in order to separate the as-grown CNTs from the CFs. Next, droplets (~5μL) from the supernatant surface were collected with a pipette and then transferred onto a carbon coated copper Formvar grid and left to get dried at ambient conditions before TEM testing.

III. RESULTS AND DISCUSSIONS

After the MW heating process, a dense CNT forest layer was intensively grown on the CF fabric surface and covered almost the entire fiber surface with a radially aligned and entangled assembly look, which is clearly exhibited in the SEM images shown in Figures 4A and 4B. At higher magnifications, the nano/micro interface between CNTs and CF can be clearly observed, as the dense CNT forest was grown perpendicularly from the CF surface (Figure 4C).

The CNT forest's coverage on the CF fabric surface was high, since the growth was observed to span along the full fiber axis length. Both long-winding and short-rigid CNT types were grown in this forest, indicating the heterogeneous nature of the catalytic growth process induced by MWs [11].

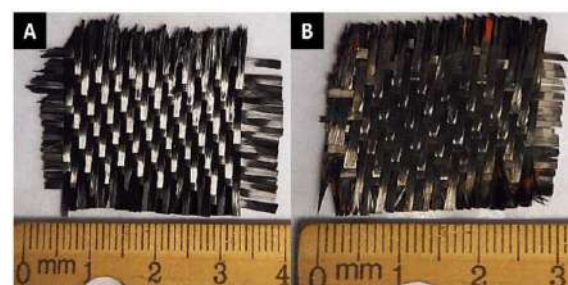


Fig. 3. Digital images of a CF fabric sample; **A.** before and **B.** after the MW energy-assisted ultrafast CNT forest growth process.

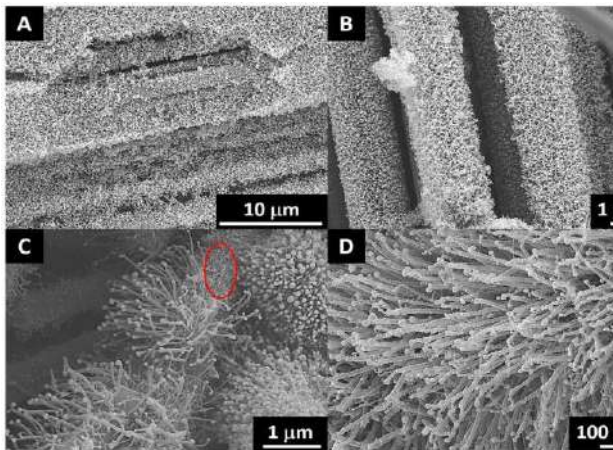


Fig. 4. SEM images of; **A.-B.** Hierarchically structured CNT/CF composites, **C.** CFs covered by the as-grown CNT forest on their surfaces, **D.** zoomed-in view of the marked area in Figure 4C.

Morphological property details of the as-obtained CNTs were also investigated, and their average diameter was calculated to be ~ 50 nm while their length could extend up to couple of microns (Figure 4D). The high aspect ratio of these CNTs thus provide an ultra-high surface area, which enables enhanced interfacial interactions and enable multi-scale functions for the composite, through the formation of new interfaces.

In good agreement with the relevant previous literature results [12-14], the tip-growth mechanism was also effective on the current CNT forest's growth on CF fabric samples. The characteristic matchstick-like morphology, which is composed of hollow and multi-walled stem with oxidized iron nanoparticle (NP) tip, of the as-grown CNTs in this forest (Figure 4D) clearly indicates the effective tip-growth mechanism, as well.

After proving the as-proposed MW-energy based ultrafast CNT growth technique's success on generating CNT/CF hierarchical composites via SEM characterization, the in-depth morphological and elemental features of these

structures were further characterized by both TEM microscopy and EDX analysis. Collected results from these analyses are shown in Figure 5. The TEM image in Figure 5A provides more detailed information about the as-grown CNTs by showing their hollow stems that encapsulate catalyst iron NPs. This morphological structure was obtained during the tip-growth process, whose working mechanism would be explained along the following paragraphs. As it also can be seen from the TEM image in Figure 5C, a single ~ 25 nm \times 5 nm iron catalyst NP was encapsulated within the as-grown MWCNTs' wall, which was made up of ultrathin graphene layers. The EDX analysis results of both the as-grown MWCNTs and the encapsulated catalyst iron NPs are shown in Figures 5B and 5D. These diffractograms provide more evidence for the presence of the as-grown MWCNTs and iron NPs that are made up of C and Fe elements, respectively. Also, there are two sharp peaks with Cu indicators in these diffractograms, both of which were caused by the copper grid used for the TEM imaging process as the sample holder.

It is thus revealed that the MW-energy assisted ultrafast heating technique was successful on generating CNT/CF nano-micro hierarchical composite structures with high yield and density and within a short period of time. It is strongly believed that the ultrafast CNT growth mechanism on the CF fabric sample surface majorly depends on the high reaction temperature between ferrocene particles and CFs upon MW irradiation. That is to say, as soon as absorbing the MW energy; (i) highly conducting CF fabric sample started sparking and arcing, (ii) then its surface temperature was rapidly increased above 1000 °C, and (iii) this caused a large amount of heat release within a few seconds. As a result, the fine ferrocene particles on the sample fabric surface got decomposed into its iron and cyclopentadienyl ligands through an instant chain reaction, in gas form. At this point, the iron NPs served as catalysts while the cyclopentadienyl groups were realigned and served as the carbon source for the formation of MWCNTs, respectively [11-14]. After all, the dense CNT forest was grown on the CF fabric surface through this liquid-solid-vapor transition mechanism.

IV. CONCLUSION

Hierarchical CNT/CF composites with aligned nano-micro interfacial structure were fabricated within seconds by applying MW irradiation. Homogenously grown CNT forest was obtained on the CF fabric surface with high yield, high aspect ratio, and high coverage density. The as-produced hierarchically structured CNT/CF composites offer promising potential for widespread advanced applications including medical applications, supercapacitors, transportation, microelectronics and so on. The as-proposed highly efficient and cost-effective MW energy-assisted fabrication technique also secures the industrial scale production of relevant next generation composites, as well.

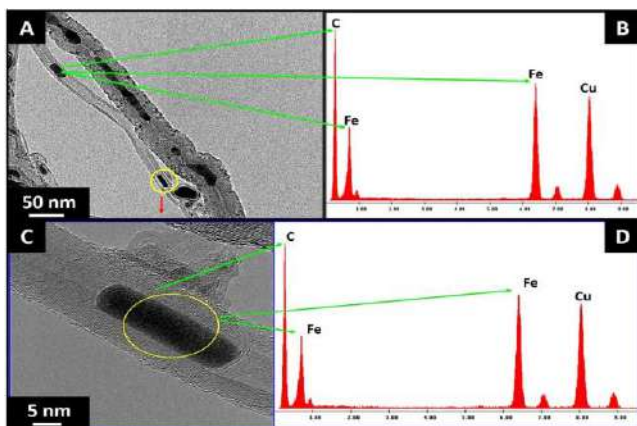


Fig. 5. **A.** TEM image of the catalyst iron NPs encapsulated within the as-grown MWCNTs, **B.** the EDX diffractogram of the catalyst iron NP and the as-grown MWCNT, **C.** HR-TEM image of the marked area in Figure 5A, and **D.** the EDX diffractogram of the marked area in Figure 5C.

REFERENCES

- [1] S. Chand, "Carbon fibers for composites," *J. Mater. Sci.*, vol. 35(6), pp. 1303-1313, 2000.
- [2] E. Thostenson, Z. Ren, T. Chou, "Advances in the science and technology of carbon nanotubes and their composites: a review," *Compos. Sci. Technol.*, vol. 61(13), pp. 1899-1912, 2001.
- [3] M. Delamar, G. Desarmot, O. Fagebaume, R. Hitmi, J. Pinson, J. M. Saveant, "Modification of carbon fiber surfaces by electrochemical reduction of aryl diazonium salts: Application to carbon epoxy composites," *Carbon*, vol. 35(6), pp. 801-807, 1997.
- [4] B. Xu, X. Wang, Y. Lu, "Surface modification of polyacrylonitrile-based carbon fiber and its interaction with imide," *Appl. Surf. Sci.*, vol. 253(5), pp. 2695-2701, 2006.
- [5] H. Yuan, C. Wang, S. Zhang, X. Lin, "Effect of surface modification on carbon fiber and its reinforced phenolic matrix composite," *Appl. Surf. Sci.*, vol. 259, pp. 288-293, 2012.
- [6] E. T. Thostenson, W. Z. Li, D. Z. Wang, Z. F. Ren, T. W. Chou, "Carbon nanotube/carbon fiber hybrid multiscale composites," *J. Appl. Phys.*, vol. 91(9), pp. 6034-6037, 2002.
- [7] R. Samsur, V. K. Rangari, S. Jeelani, L. Zhang, Z. Y. Cheng, "Fabrication of carbon nanotubes grown woven carbon fiber/epoxy composites and their electrical and mechanical properties," *J. Appl. Phys.*, vol. 113(21), pp. 214903-214908, 2013.
- [8] B. Yu, Z. Jiang, X. Z. Tang, C. Y. Yue, J. Yang, "Enhanced interphase between epoxy matrix and carbon fiber with carbon nanotube-modified silane coating," *Compos. Sci. Technol.*, vol. 99, pp. 131-140, 2014.
- [9] Z. G. Zhao, L. J. Ci, H. M. Cheng, J. B. Bai, "The growth of multi-walled carbon nanotubes with different morphologies on carbon fibers," *Carbon*, vol. 43, pp. 651-673, 2005.
- [10] H. Chen, A. Roy, J. B. Baek, L. Zhu, J. Qu, L. Dai, "Controlled growth and modification of vertically-aligned carbon nanotubes for multifunctional applications," *Mater. Sci. Eng., R*, vol. 70, pp. 63-91, 2010.
- [11] Z. Liu, J. Wang, V. Kushvaha, S. Poyraz, H. Tippur, S. Park, M. Kim, Y. Liu, J. Bar, H. Chen, X. Zhang, "Poptyube approach for ultrafast nanotube growth," *Chem. Commun.*, vol. 47, pp. 9912-9914, 2011.
- [12] S. Poyraz, Z. Liu, Y. Liu, X. Zhang, "Devulcanization of scrap ground tire rubber and successive carbon nanotube growth by microwave irradiation," *Curr. Org. Chem.*, vol. 17, pp. 2243-2248, 2013.
- [13] H. Xie, S. Poyraz, M. Thu, Y. Liu, E. Y. Snyder, J. W. Smith, X. Zhang, "Microwave-assisted fabrication of carbon nanotubes decorated polymeric nano-medical platforms for simultaneous drug delivery and magnetic resonance imaging," *Rsc Adv.*, vol. 4, pp. 5649-5662, 2014.
- [14] S. Poyraz, L. Zhang, A. Schroder, X. Zhang, "Ultrafast microwave welding/reinforcing approach at the interface of thermoplastic materials," *ACS Appl. Mater. Interfaces*, vol. 7, pp. 22469-22477, 2015.

Synthesis of Thermochromic VO₂ Thin Films for Use in Smart Glass Systems

Eren Doğan, Muhammed, Berkay Güven, Miray Çelikkilek Ersundu, Ali Erçin Ersundu
 Department of Metallurgical and Materials Engineering
 Yildiz Technical University
 Istanbul, Turkey
 ersundu@yildiz.edu.tr

Abstract—Most of energy consumed in the world has been lost from the exterior of the building and more than half of this energy is lost from the windows. For this reason, smart glass systems are being developed to save energy in buildings. Vanadium dioxide (VO₂) thin films demonstrate thermochromic property by changing their optical properties with temperature. Therefore, there has been a lot of research on VO₂-based thin films for their use in smart glass systems. VO₂ exhibits thermochromic behavior with a reversible semiconductor-metal phase transition when it undergoes a structural transformation from monoclinic to tetragonal at around 68°C by having higher infrared reflectance above this critical temperature. Although this critical temperature is fairly high for outdoor applications, VO₂ is still the most suitable candidate for smart window applications. In this study, sol-gel based thermochromic thin films were synthesized on soda-lime glass substrates by dip-coating method using vanadium oxy acetylacetonate (VO(acac)₃) as a starting material. Doping metallic elements to VO₂ has the ability to decrease the critical thermochromic temperature. Hence, in this study VO₂ was doped using tungsten chloride (WCl₆). W-doped VO₂ thin films having different compositions (0.5, 1, 3, 5 molar ratio %) were annealed under N₂ atmosphere at 550°C for 30 minutes. VO₂ thin films were characterized by XRD analysis using thin film attachment. The morphology of thin films were observed using SEM. The transmittance value differences at room temperature and 100 °C were determined using UV-VIS spectrometer having custom made in-situ temperature attachment.

Keywords— vanadium oxy acetylacetonate; thermochromic thin films; sol-gel; W-doping; smart glass systems

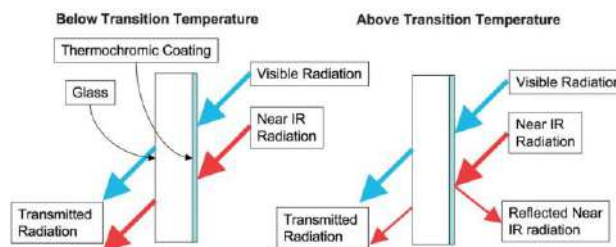


Fig. 1. Schematic presentation of thermochromic behavior [1].



Fig. 2. A skyscraper with smart windows

[1] M.E.A. Warnick, and R. Binions, "Advances in thermochromic vanadium dioxide films," J. Mater. Chem. A, vol. 2, pp. 3275-3292, February 2014.

A study on thermal behavior of volcanic particle filled high-density polyethylene

Onur ÇOBAN¹

Faculty of Aeronautics and Astronautics,
Kocaeli University,
Kocaeli, Turkey
onur.coban@kocaeli.edu.tr

Togayhan KUTLUK³

Department of Chemical Engineering
Kocaeli University,
Kocaeli, Turkey
togayhan.kutluk@kocaeli.edu.tr

Mustafa Özgür BORA²

Faculty of Aeronautics and Astronautics,
Kocaeli University,
Kocaeli, Turkey
ozgur.bora@kocaeli.edu.tr

Abstract- Melting behavior and coefficient of thermal expansion (CTE) of volcanic particle (VP) filled high-density polyethylene (HDPE) composites were reported. Melt mixing followed by injection molding was used to manufacture VP/HDPE composites. Melting behavior of HDPE and its composites were investigated by differential scanning calorimetry (DSC). Melting enthalpy values of the composite samples were found to be varied with VP incorporation. Otherwise, the incorporation of VP into the HDPE did not have a significant effect on the melting temperature values of the HDPE composites. CTE analysis was performed between 25 to 100°C by a dilatometer. CTE of the composites display substantial reduction with the increasing of VP content in HDPE, while with increasing temperature CTE increases linearly. Additionally CTE reductions illustrated an increase in dimensional stability of HDPE as VP added to it.

Keywords- HDPE; thermal; volcanic particle; filler

I. INTRODUCTION

High-density polyethylene (HDPE) is among the most widely used polyolefin polymers because of its moderate strength, low cost, excellent process ability and high chemical resistance [1-2]. However, with the insufficient thermal properties, HDPE is usually compounded with various fillers such as; CaCO₃, silica, clays, mica, talc, graphite, bentonite etc., because compounding fillers with thermoplastic materials in order to introduce a desired property is a conventional practice and useful method [3-6]. Inorganic particle reinforced polymer composites have the advantages of the polymeric properties together with the characteristics of homogeneously dispersed inorganic particles [7]. This inorganic particle filled polymer composites with the enhanced mechanical, thermal and electrical properties could be consumed in various industries such as; automobile, medical, packaging and electrical etc., [8-10]. Volcanic particles (VP) created during volcanic eruptions are readily accessible and can be economically mined with very low cost and limited negative environmental impact. Turkey and Italy are the leading

producers of VP, followed by Greece, Iran, Chile, Syria, and the United States [11].

VPs are known as mesoporous material, which usually has high specific surface area, significant porosity and an appropriate pore structure. Due to these properties the use of VPs as an alternative filler material in polymers can lead to both, a global cost reduction of final product with enhanced properties and a possibility for countries to use their natural VP resources. There are some research engineers at Hyundai and Kia which have used a ground VP in a polypropylene and rubber composite to reduce costs and achieve a cloth-like appearance [12]. So, it was thought that by filling such material with thermoplastics, useful composite materials can be produced that have improved thermal properties when compared to thermoplastics containing conventional fillers. It has been found that there is no study in the literature about the effect of VP addition on the thermal properties of HDPE. For this reason for the first time in literature, in this study thermal behavior of VP/HDPE composites were investigated by differential scanning calorimetry (DSC) and coefficient of thermal expansion (CTE) measurements.

II. MATERIALS AND METHODS

A. Materials

The polymer used in this study was high-density polyethylene (HDPE) Marlex® HHM 50100. It has a density of 0.951g/cm³ and a melt flow index of 0.35g/10 min (2.16kg at 190°C). A black masterbatch M117605 with carbon content of 40% was used for HDPE. VP with density of 2.82g/cm³ and size of “<25µm” were taken from Kula/Turkey. SEM and energy dispersive spectrometer analyzes were shown in Fig. 1.

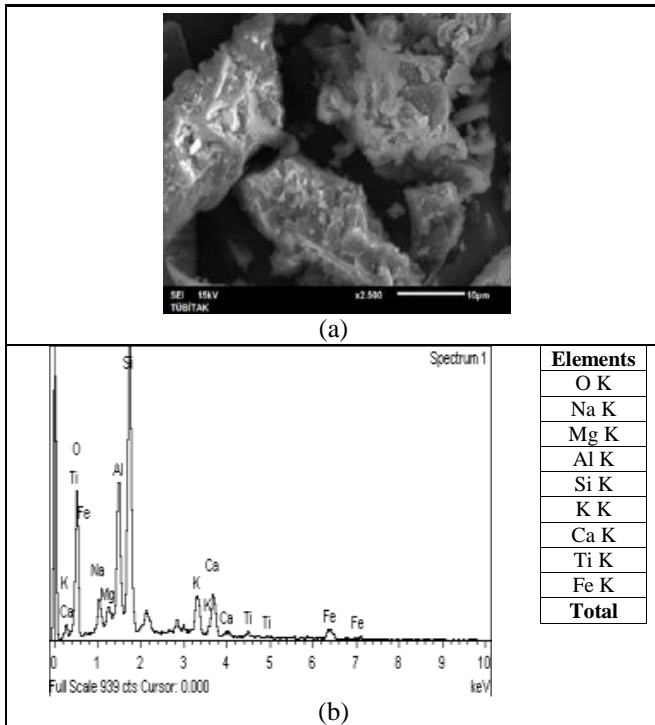


Figure 1. SEM image (a) and spectrometer analysis (b) of VPs

As seen in Fig. 1-a, VPs have high specific surface area with indented view. According to spectrometer analysis in Fig. 1-b, VPs were estimated as rhyolite due to silica (SiO_2) rich composition.

B. Sample preparation

HDPE composites were prepared by melt compounding and injection molding processes. DSM micro-compounder (conical co-rotating twin-screw extruder) (DSM Xplore, Gleen, The Netherlands) was used for compounding HDPE and VP filler material with various contents such as 0, 6, 12, 18 and 24 wt.%. At the completion of mixing, the melt compound was extruded into the heated barrel of a DSM injection molding machine (DSM Xplore, Gleen, The Netherlands), which used a plunger driven by compressed air to inject the melt into a standard dog-bone tensile specimen mold held at 40°C with an injection pressure of 8 bar. Micro-compounding and injection molding parameters were given in Table 1.

C. Differential scanning calorimetry (DSC)

Melting behavior analysis was carried out by a differential scanning calorimetry (Mettler Toledo DSC1). DSC samples were prepared by shaving approximately 10mg from the injection molded tensile specimens and then were sealed in aluminum pans. Heat scanning was performed from -50 °C to 240°C under nitrogen atmosphere (nitrogen purge with a flux of 50 ml/min) with the heating rate of 10°C/min.

Table 1. Micro compounding and injection molding process parameters

Process Machines	Process Parameters	Unit	Level
Microcompounder	Barrel temperature	(°C)	210
Microcompounder	Compounding round	(rpm)	50
Microcompounder	Compounding time	(min)	4
Injection Molding	Mold temperature	(°C)	40
Injection Molding	Injection pressure	(bar)	8
Injection Molding	Holding pressure	(bar)	8
Injection Molding	Holding time	(s)	5

According to obtained thermograms average values of five repetitions for melting temperatures (T_m) and melting enthalpies (ΔH_m) were determined and discussed. The apparent enthalpy of melting per gram of HDPE in the VP added composites was calculated by Equation (1):

$$\Delta H_{HDPE} = \Delta H_C / W_{HDPE} \quad (1)$$

Where, W_{HDPE} is the mass fraction of HDPE in composites and ΔH_C is the apparent enthalpy of melting of VP added HDPE composites.

D. Coefficient of thermal expansion (CTE) measurement

In order to predict dimensional stability of HDPE and its composites dilatometry test was performed between 25°C and 100°C at a heating rate of 5°C/min by the dilatometry machine of Netzsch DIL 402C. At least three samples for each material were tested and the results are presented as an average for tested samples.

III. RESULTS

A. Melting behavior of VP/HDPE composites

Fig. 2 illustrates DSC results of HDPE and its VP added composites. DSC thermogram of HDPE in Fig. 2-a showed that melting state was started at 50°C and then was ended at 150°C. In this melting state, 155.3 J/g melting enthalpy value was achieved to melt the entire polymer. Melting temperature and melting enthalpy variation according to VP content was illustrated in Fig. 2-b. It is clear that melting temperature values did not changed significantly with VP addition, therefore it can be said that melting temperature is dominantly depends on polymer matrix of HDPE instead of VP filler. A better comparison can be obtained by using the enthalpy of melting per gram of HDPE in the composite sample was calculated according to the Equation (1). As it is seen, melting enthalpy value was significantly increased to 170 J/g with 6 wt.% VP content, however further incorporation of VP decreased this value from 170 to 155 J/g. It is important that, the melting enthalpy values did not decreased below the value of neat HDPE up to 24 wt.% VP content.

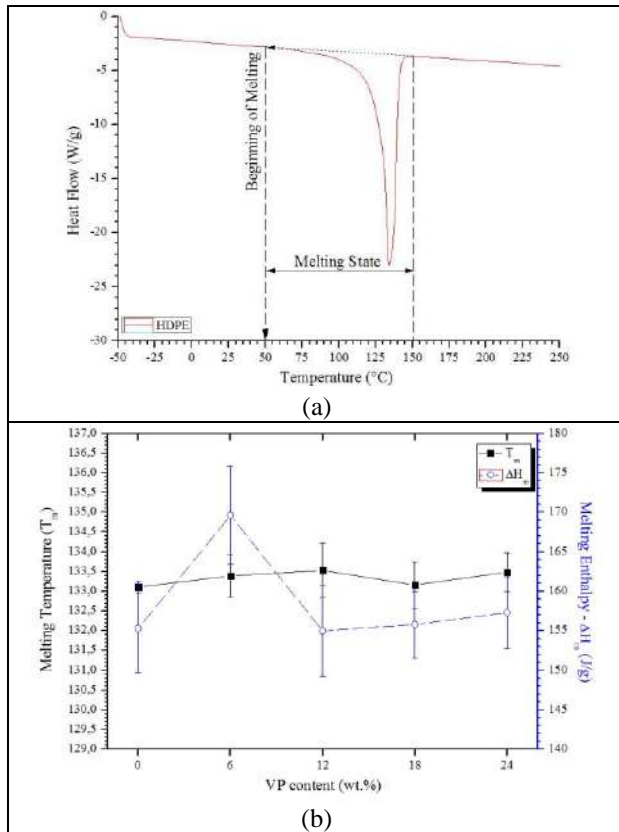


Figure 2. DSC results, a: thermogram of HDPE; b: melting properties as a function of VP content

This phenomenon is believed to be the result of a good agreement between nucleating and retarding effects of VP on the host polymer HDPE during the crystallization [13-14]. This result also showed that crystallinity was firstly increased with low content of VPs, which exhibited a strong nucleating effect and acted as heterogeneous nucleating sites at the VP-HDPE interfaces [13]. In addition to this, if the VP content increased to a high content, the filler particles in the matrix hindered the movement of macromolecular chains. Therefore the crystallinity was reduced. However, it is still could not be decreased under the degree of neat HDPE

B. CTE of the VP/HDPE composites

CTE results of VP/HDPE composites were determined as a function of temperature and VP content as shown in Fig. 3. It is clear that CTE of all composite samples was linearly increased with the temperature up to 50°C. This result can be explained by the onset of melting phenomenon similarly reported by P. Ghosh in Ref. [15]. However, CTE values began to decrease as a function of temperature after melting was started. In addition to this, for all compositions CTEs were steadily decreased with VP incorporation entirely at all temperature levels. As is expected, the HDPE composites with increasing VP contents showed consistently lower CTE

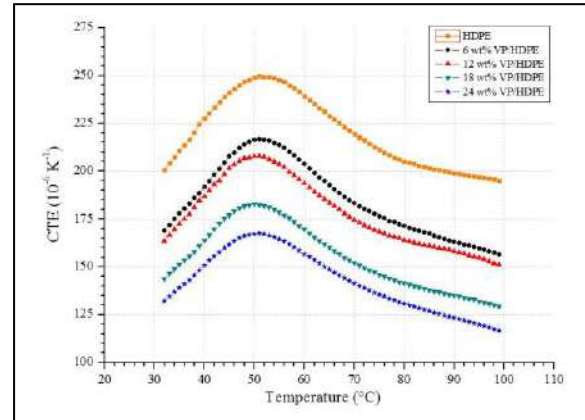


Fig. 3. CTE versus temperature for HDPE and its VP added composites

values than the composites with lower VP contents. This reduction depends on the difference between the CTE of the polymer matrix HDPE and the filler VPs. Similar to the literature reports, this reduction can be attributed to lower CTE of VPs, respect to HDPE matrix [16-17]. Additionally the reduction of CTE was also contributed to the strong interfacial adhesion between the HDPE matrix and VP filler particles [16].

IV. CONCLUSION

In order to investigate the role of VPs in the thermal behavior of HDPE composites, series of HDPE composites with different VP contents were prepared. DSC and CTE results were obtained experimentally and discussed in detail. As a result following inferences were done:

- DSC results suggest that VP particles played a heterogeneous nucleation role with relatively low content in the HDPE matrix, resulting in enhancing the crystallization capability.
- After 6 wt% VP content, crystallization capability was decreased with further VP incorporation, however it is still almost equal to the value of HDPE.
- CTE of VP/HDPE composites was increased linearly up to onset melting temperature and then was decreased as a function of temperature.
- VP incorporation has decreased the CTE values due to the difference between the CTE of HDPE and VP.
- Reduction of CTE was also showed that a strong interfacial adhesion was achieved between the HDPE matrix and VP filler particles.

REFERENCES

- [1] A. Zehtabeyazdi, S. M. Zebarjad, S. A. Sajjadi, J. Abolfazli Esfahani, "On the sensitivity of dimensional stability of high density polyethylene on heating rate", *eXPRESS Polymer Letters* Vol.1, No.2, 92-97, DOI: 10.3144/expresspolymlett.2007.16, 2007.

- [2] D.W. Chae, K. J. Kim, B. C. Kim, "Effects of silicalite-1 nanoparticles on rheological and physical properties of HDPE", *Polymer* 47, 3609–3615, doi:10.1016/j.polymer.2006.03.053, 2006.
- [3] H.Kim, J. Biswas, S. Choe, "Effects of stearic acid coating on zeolite in LDPE, LLDPE, and HDPE composites", *Polymer* 47, 3981–3992, doi:10.1016/j.polymer.2006.03.068, 2006.
- [4] Y. Wang, J. Shi, L. Han, and F. Xiang, "Crystallization and mechanical properties of T-ZnOw/HDPE composites," *Materials Science and Engineering A*, vol. 501, no. 1-2, pp. 220–228, 2009.
- [5] S. M. Zebarjad, S. A. Sajjadi, Tahani, M., and Lazzeri, A. A study on thermal behaviour of HDPE/CaCO₃ nanocomposites, *Journal of Achievements in Materials and Manufacturing Engineering* 1-2, 173-176, 2006.
- [6] S. Changzhi, Z. Wenyuan, C. Shigang, Studies on the comprehensive performance of graphite and additives filled high density polyethylene composites. *J Appl Polym Sci* ;107:4000–4, 2008.
- [7] J. Jung, J. Kim, Y. R. Uhm, J.K. Jeon, S. Lee, H. Min Lee, C. K. Rhee, "Preparations and thermal properties of micro- and nano-BN dispersed HDPE composites", *Thermochimica Acta* 499 8–14, doi:10.1016/j.tca.2009.10.013, 2010.
- [8] M. Alexandre, P. Dubois, "Polymer-layered silicate nanocomposites: preparation, properties and uses of a new class of materials", *Materials Science and Engineering*, 28, 1-63, 2000.
- [9] E. Chan, S. N. Leung, M. O. Khan, H. Naguib, F. Dawson, V. Adinkrah, L. L. Hayward, "Fabrication and characterization of ceramic-filled Thermoplastics composites with enhanced multifunctional properties", *Journal of Thermoplastic Composite Materials*, Vol. 27(4) 541–557, DOI: 10.1177/0892705712452746, 2014.
- [10] L.C. Sima, S.R. Ramanan, H. Ismail, K.N. Seetharamu, T.J. Goh, "Thermal characterization of Al₂O₃ and ZnO reinforced silicone rubber as thermal pads for heat dissipation purposes", *Thermochimica Acta* 430, 155–165, doi:10.1016/j.tca.2004.12.024, 2005.
- [11] R.C. Crangle, *Pumice and Pumicite*, US Geological Survey, Mineral Commodity Summary 2010.
- [12] <https://www.plasticstoday.com/content/volcanic-ash-coconut-fiber-debut-plastic-automotive-applications/74411408416565>, visit date, 21.02.2017
- [13] X. Jiang, L. T. Drzal, "Properties of Injection Molded High Density Polyethylene Nanocomposites Filled with Exfoliated Graphene Nanoplatelets", Michigan State University, Composite Materials and Structures Center, Department of Chemical Engineering and Materials Science, East Lansing, Michigan, USA, www.intechopen.com, Some Critical Issues for Injection Molding, issue 11.
- [14] E. Di Maio S. Iannace, L. Sorrentino, L. Nicolais, "Isothermal crystallization in PCL/clay nanocomposites investigated with thermal and rheometric methods", *Polymer* 45, pp. (8893–8900), 0032-3861, doi:10.1016/j.polymer.2004.10.037, 2004.
- [15] P. Ghosh, *Polymer Science and Technology – Plastics, Rubbers, Blends and Composites*, 2nd ed., Tata McGraw Hill, New Delhi, 2002.
- [16] T.K. Dey, M. Tripathi, "Thermal properties of silicon powder filled high-density polyethylene composites", *Thermochimica Acta* 502, 35–42, doi:10.1016/j.tca.2010.02.002, 2010.
- [17] S. Sahebian, S.M. Zebarjad, J. Vahdati Khaki, S.A. Sajjadi, "The effect of nano-sized calcium carbonate on thermodynamic parameters of HDPE", *Journal of Materials Processing Technology*, 209 1310–1317, doi:10.1016/j.jmatprotec.2008.03.066, 2009.

Scratch Deformation Characteristics of Calcium Carbonate Filled High Density Polyethylene Composites

Mustafa Özgür BORA

Faculty of Aeronautics and Astronautics,
Kocaeli University
KOCAELI
ozgur.bora@kocaeli.edu.tr

Togayhan KUTLUK

Department of Chemical Engineering
Kocaeli University
KOCAELI
togayhan.kutluk@kocaeli.edu.tr

Onur ÇOBAN

Faculty of Aeronautics and Astronautics,
Kocaeli University
KOCAELI
onur.coban@kocaeli.edu.tr

Eyüp AKAGÜNDÜZ

Materials Institute
TUBİTAK-Material Institute
KOCAELI
eyup.akagunduz@tubitak.gov.tr

Abstract— This article presents research on the influence of calcium carbonate (CaCO_3) particle contents on the scratch behavior of high density polyethylene (HDPE). Melt compounding was carried out using a twin-screw micro compounder and injection molding with various CaCO_3 particle contents such as 0, 6, 12, 18 and 24 wt.%. Scratch testing was performed using the testing apparatus and methodology outlined in ASTM D7027–05 at scratch velocities of 30 mm/min using a radius of 50 μm stainless steel ball bearing scratch tip. Coefficient of friction values and scratch hardness of various CaCO_3 particle filled HDPE composites were determined. Results showed that coefficient of friction values increased nearly 16% for 24 wt.% CaCO_3 particle filled composites compared to neat HDPE. After scratch tests, optical microscope analysis was done for determining the variation of scratch damage mechanisms because of CaCO_3 particle filling content.

Keywords— Scratch Behavior, Calcium Carbonate, Coefficient of Friction, Optical Microscope

I. INTRODUCTION

Polyethylene is a largely used thermoplastic because of its physical and mechanical properties, good workability and low cost. However, the polyethylene has low deformation and melting temperature that restrict its use [1]. There are various types of polyethylene (molecular weight (MW), molecular weight distribution (MWD), density, percentage crystallinity, and degree of long chain and short chain branching) having the same basic repeating unit with different properties and applications [2]. High density polyethylene (HDPE) which is used in this study is a thermoplastic made from petroleum and thipfy the largest portion of polyethylene manufactured. HDPE is more rigid and harder than low density polyethylene

(LDPE) [3]. Polymers have been using instead of metallic materials for friction wear parts for many years. However, unmodified polymer could not please the demands a rising from situations where an integration of good properties such as mechanical and tribological is essential [4]. One of the potential alternative processes to reduce HDPE wear rate is improving the tribological properties of HDPE by reinforcement methods. Inorganic particles such as molybdenum disulphide (MoS_2), alumina (Al_2O_3), titanium dioxide (TiO_2) and silicate (SiO_2) were commonly added in polymers to increase wear resistance, some of which have been reported in the literatures for HDPE [5-7]. Pettarin et al.[5] assessed the effect of the addition of commercial MoS_2 on the tribological behavior of high molecular weight high density polyethylene (HMW-HDPE). The results showed that the incorporation of MoS_2 to HMW-HDPE improves its sliding and abrasive wear performance with a content of MoS_2 for minimum wear rate around 10 wt.%. Taşdemir and Yerleşen [6] studied the mechanical, morphological and tribological properties of high density polyethylene based composites filled with glass spheres (hollow) and HDPE/glass sphere (filled with alumina and silicate) particles. From results, HDPE filled with a high level content of fillers showed higher wear rate than pure HDPE under dry sliding wear test. Abbas and Muslim [7] investigated the mechanical properties (hardness and wear) and physical properties (thermal conductivity and water absorption) for HDPE/ Al_2O_3 , HDPE/ TiO_2 composites and HDPE/ Al_2O_3 / TiO_2 hybrid composites with different weight percentages of fillers prepared by hot pressing method. Wear results showed that the wear rate of composites decrease with the increasing the weight percentages of fillers, hybrid composites have less wear rate compared to other composites.

The scratch test is a very old experimental procedure used to study the surface mechanical properties and the tribological performances of materials. Scratch testing is applied to polymers for about 10 years because polymers are more often used to increase the scratch and wear resistance in many applications, in particular, in petroleum and gases industries as a pipe coating [8]. Scratch performance of polymeric materials is dependent on the scratch stress field associated with the indenter geometry and properties of the polymeric material [9]. Additional factors such as percent crystallinity, lubricant, filler, and additives also influence the scratch performance of thermoplastic olefins [9]. Despite the enhancement in other mechanical properties such as tensile or flexural properties, inorganic particle fillers may improve the coefficient of friction and scratch hardness of thermoplastic polymers; hence, deeper investigations into the scratch response of CaCO₃ filled HDPE based composites seem to be necessary. However, little information is available on the detailed correlations between the effect of CaCO₃ filler incorporation and scratch hardness of HDPE. Surampadi et al. [10] studied the determining role of scratch indenter radius on surface deformation of high density polyethylene and CaCO₃ reinforced composite. They compared the scratch indenter's type (Loop, Needle, Hoffman) with the scratch hardness of CaCO₃ filled HDPE. However, there is not any information about the coefficient of friction values or the effect of CaCO₃ content. In the current study, the scratch tests were conducted on CaCO₃ filled HDPE composites with different contents (0, 6, 12, 18 and 24 wt.%) of CaCO₃ in order to determine the scratch properties such as scratch hardness and coefficient of friction. The scratch damage mechanisms and scratch widths were also observed and determined with optical microscope.

II. MATERIALS AND METHODS

A. Materials

The polymer used in this study was high-density polyethylene (HDPE) Marlex® HHM 5202BN. It has a density of 0.951 g/cm³ and a melt flow index of 0.35 g/10 min (2.16 kg at 190°C). Compound filler used MD9765, a masterbatch containing 78% micro calcium carbonate (CaCO₃) was supplied from Maskom Masterbatch &Compound Technologies Co, Turkey. It was prepared as granulate form and it has a carrier resin of polyethylene for the micro CaCO₃. It should be noted that surface of CaCO₃ is not treated. A black masterbatch M117605 with carbon content of 40% was used for HDPE.

B. Sample Preparation

Table 1. Micro compounding and injection molding process parameters

Process	Process Parameters	Unit	Level
Microcompounder	Barrel temperature	(°C)	210
Microcompounder	Compounding round	(rpm)	50
Microcompounder	Compounding time	(min)	4
Injection Molding	Mold temperature	(°C)	40
Injection Molding	Injection pressure	(bar)	8
Injection Molding	Holding pressure	(bar)	8
Injection Molding	Holding time	(s)	5

HDPE composites were prepared by melt compounding and injection molding processes. Micro-compounding and injection molding parameters were given in Table 1. DSM micro-compounder (conical co-rotating twin-screw extruder) (DSM Xplore, Gleen, The Netherlands) twin-was used for compounding HDPE and CaCO₃ filler materials with various contents such as 0, 6, 12, 18 and 24 wt. %. At the completion of mixing, the melt compound was extruded into the heated barrel of a DSM injection molding machine (DSM Xplore, Gleen, The Netherlands), which used a plunger driven by compressed air to inject the melt into a standard dog-bone tensile specimen mold held at 40 °C with an injection pressure of 8 bar.

C. Scratch Tests

“CSM Micro Scratch Tester” was used for the evaluation of the scratch behavior of various CaCO₃ particle filled HDPE composite samples. Rockwell S-218 with a spherical diamond notch was used for tests (50 µm radius). The indenter was held on a pivoted beam so that it could be positioned orthogonally to the flat sample. The sample surface was positioned so that it is parallel to the indenter motion by a specific, automatically, controlled process. The unit was controlled by a computer, which also controls the various test parameters. By using dead weights, normal load was applied to the samples which are fixed on a leveling mount attached to a displacement stage. For eliminating surface roughness and skin thickness effects, a preload of 0.03 N was applied by the indenter. By using a load of 15 N at a velocity of 30 mm/min through a length of 10 mm, a scratch damage occurred on the surface. Three independent repetitions for each sample tests were carried out and average was used for evaluation. The scratch behavior of CaCO₃/HDPE composites was evaluated by using coefficient of friction and scratch hardness.

D. Observations of Scratch Damage Mechanisms

For determining the general damage mechanisms, the scratched surface of each CaCO₃/HDPE composite sample was inspected using an optical microscope (Nikon L150). In addition, for stating the variation on scratch hardness values of HDPE due to CaCO₃ particle contents, scratch widths were also determined by using optical microscope.

III. RESULTS AND DISCUSSIONS

The typical curves of coefficient of friction values of various CaCO₃ particle filled HDPE composites versus scratch length were shown in Fig. 1. The scratch resistance of a material indicates its ability to withstand mechanically induced surface damage when the material interacts and comes in contact with another material of higher hardness. In indentation, the direction of applied force is normal to the surface, whereas in scratch deformation, sequential accumulation and release of tangential force makes the deformation behavior non-uniform [11]. Also, in a scratch deformation process, a significant amount of plastic deformation occurs and the indenter is only supported in the front or leading part, while the material behind the indenter partly supports the indenter in the rear half [11].

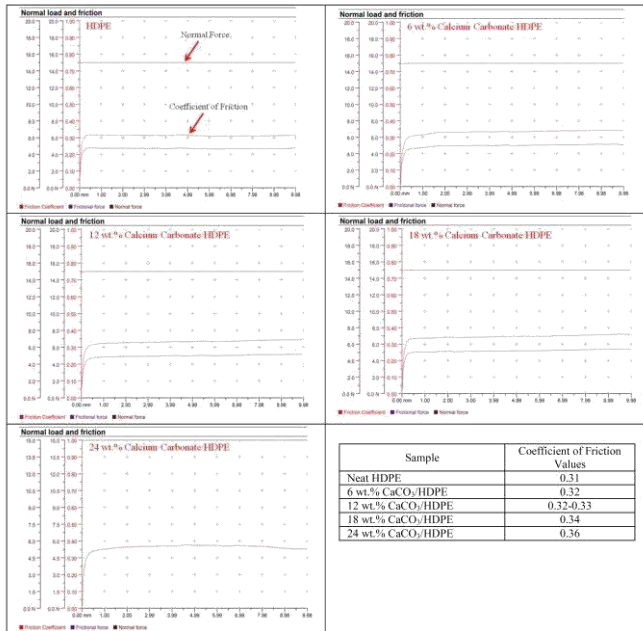


Figure 1. The variation of coefficient of friction values of CaCO₃/HDPE composites

The coefficient of friction is defined as the ratio of the tangential force to the normal force [12]. The coefficient of friction changes from 0 to nearly 0.30 continuously at the beginning of scratching, which is corresponding to the loading stage [12]. Then it keeps invariant at 0.3-0.36 due to CaCO₃ particle content for about 10 mm scratch length during the steady scratching process. An abrupt change takes on subsequently after the steady state because of the detachment of the indenter tip during the unloading stage when the scratching completed. The average values of the steady stage were taken as the effective frictional coefficient [12]. The coefficient of friction values are in steady variation to increasing with CaCO₃ particle contents. The scratch resistance of CaCO₃/HDPE composites increased due to the CaCO₃ particle contents with 24 wt.%. Maximum coefficient of friction value was determined with 24 wt.% CaCO₃ particle content as 0.36. As compared to neat HDPE, coefficient of friction value was increased nearly % 16 with 24 wt.% CaCO₃ content. The increment of the coefficient of friction values implies the potential increase of abrasive wear resistance to hard counterparts.

Scratch paths of various CaCO₃ filled HDPE composites were illustrated in Fig.2. It was easily recognized that scratch widths of each sample were nearly same along the scratch paths. Beside this, the scratch widths of the samples were decreased with the CaCO₃ content. At 24 wt.% CaCO₃ content, the scratch width was 85.75 μm. On the other hand, the scratch width value of neat HDPE was 98.8 μm. Because of rigid CaCO₃ particles, the scratch indenter did not penetrate the sample surface easily. The CaCO₃ particle made the composite sample harder than neat HDPE.

To characterize scratch resistance of CaCO₃/HDPE composite samples, scratch hardness can also be used. Scratch hardness, which is also a measure of the scratch resistance, was calculated using [13]:

$$H = x \cdot (4.F/\pi.w^2) \quad (1)$$

Where H is the scratch hardness in N/mm², F_N is the scratch load in N, and $\pi w^2/4$ is the projected load-supporting area, in mm², w is the residual scratch width. Thus, the scratch hardness was given by: where x is a parameter that assumes a value of 1 for purely elastic contact and 2 when the contact is plastic. Other types of material behavior involving visco-elastic and visco-plastic contacts will have a value for the parameter x between 1 and 2 [13]. In the present study, x was assumed to be 1. It may be noted that Equation (1) involving scratch width is sensitive to the nature of the material. There is a direct relationship between the scratch width and scratch hardness. Materials with higher scratch hardness were expected to exhibit higher scratch resistance to scratch damage. Table 2 presents the calculated scratch hardness of CaCO₃/HDPE composite samples. Average scratch width of each sample was measured from optical microscopic photographs as also given in Table 2. From Table 2, it was determined that scratch hardness values were improved due to CaCO₃ content. It was thought that because of adding hard particles to soft polymer matrix (HDPE), the surface of the material behaved as a rigid material. By this way, the scratch hardness value of 24 wt.% CaCO₃/HDPE composite sample was increased with 32.75% as compared to neat HDPE.

IV. CONCLUSION

The scratch behavior of CaCO₃/HDPE composites was investigated. The variations of coefficient of friction, scratch widths and scratch hardness were determined and listed below individually;

- The coefficient of friction values were improved from 0.31 to 0.36 with rigid CaCO₃ incorporation. Due to hard CaCO₃ particles, the surface of the composite material showed resistance to scratch indenter.

Table 2. Average widths and scratch hardness of CaCO₃/HDPE composites

Composite Sample	Average widths (μm)	Scratch hardness (N/mm ²)
Neat HDPE	98.8	1956.53
6 wt.% CaCO ₃ /HDPE	96.25	2061.58
12 wt.% CaCO ₃ /HDPE	92.50	2232.12
18 wt.% CaCO ₃ /HDPE	88.60	2432.95
24 wt.% CaCO ₃ /HDPE	85.75	2597.37

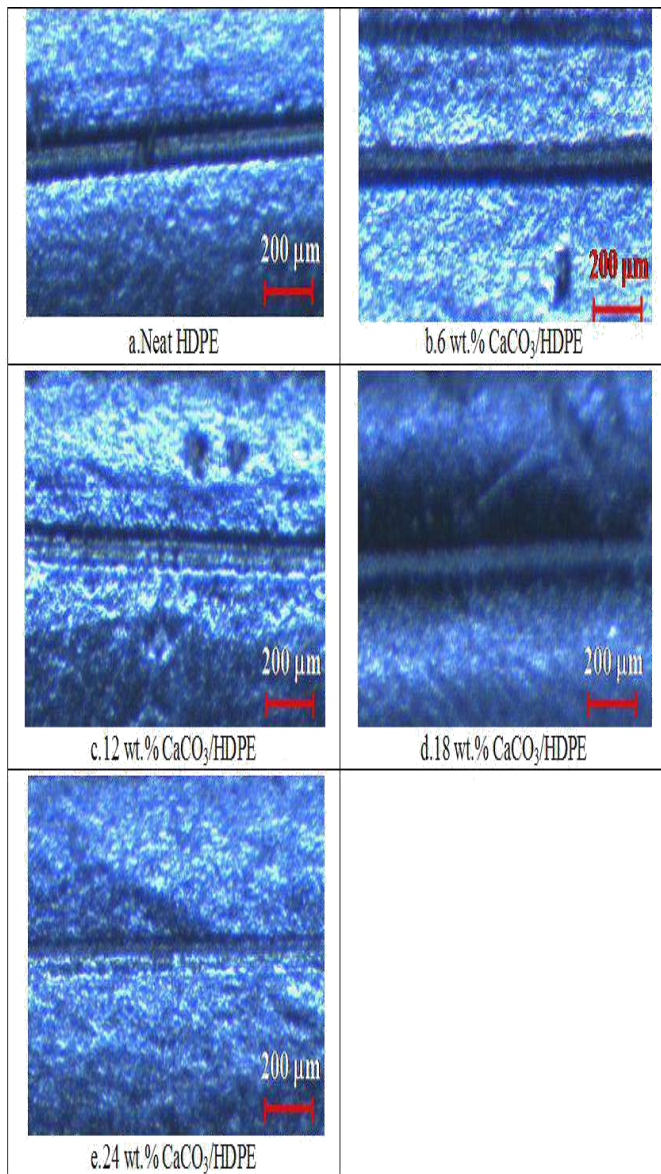


Figure 2. Scratch paths of $\text{CaCO}_3/\text{HDPE}$ composites

- Scratch widths were decreased with higher CaCO_3 contents. By this way, scratch hardness of the composite material was significantly increased. Maximum scratch hardness value was found as 2597.37 N/mm^2 for 24 wt.% $\text{CaCO}_3/\text{HDPE}$. As similar to coefficient of friction results, the main effect on the scratch hardness values of $\text{CaCO}_3/\text{HDPE}$ composite samples was the hard particles of CaCO_3 . Because of these rigid particles in the matrix, the indenter could not penetrate the material surface easily.

REFERENCES

- [1] A.J. Peacock, "The chemistry of polyethylene", J. Macromol. Sci. Part C Polym. Rev. DOI:10.1081/MC-100107860, 2001.

- [2] S. Hosoda, "Degree of branch inclusion into the lamellar crystal for various ethylene/[alpha]-olefin copolymers", Polymer, vol. 31, pp. 1999-2005, 1990.
- [3] V. R. Gowariker, N. V. Viswanathan, and J. Sreedhar, "Individual Polymers" in Polymer Science, 1 st Ed. Reprint, New Delhi, India: New Age International Ltd., pp 217, 2005.
- [4] X. W Huang, and N. Tian, "Friction and wear properties of NBR/PVC composites", Journal of Applied Polymer Science, 2565-2570, 2007.
- [5] V. Pettarin, M. J. Churrua, D. Felhos, J. Karger-Kocsis, and P. M. Frontini, "Changes in tribological performance of high molecular weight high density polyethylene induced by the addition of molybdenum disulphide particles", Wear 269, 31-45, 2010.
- [6] M. Taşdemir, and U. Yerleşen, "Study on the Friction and Wear Behaviors of Modified HDPE/Glass Spheres Composites", Revista Română De Materiale / Romanian Journal Of Materials, 45 (1), 59 – 66, 2015.
- [7] A. A. Abbas, and Z. R. Muslim, "Physical and Mechanical Properties of Hybrid Materials , As Biomaterials" , LAP LAMBERT Academic Publishing, ISBN-13: 978-3-659-94318-8, 2016.
- [8] N. Guermazi, K. Elleuch, H.F. Ayedi, H. Zahouani, and Ph. Kapsa, "Susceptibility to scratch damage of high density polyethylene coating", Materials Science and Engineering A 492, 400-406, 2008.
- [9] A. Dasari, R. D. K. Misra, and J. Rohrmann, "Scratch Deformation Characteristics of Micrometric Wollastonite-Reinforced Ethylene-Propylene Copolymer Composites", Polymer Engineering and Science, Vol. 44, No. 9, 1738-1748, 2004.
- [10] N.L. Surampadi, T.C. Pesacreta, and R.D.K. Misra, "The determining role of scratch indenter radius on surface deformation of high density polyethylene and calcium carbonate-reinforced composite", Materials Science and Engineering A 456, 218-229, 2007.
- [11] R. Hadal, A. Dasari, J. Rohrmann, R.D.K. Misra, "Susceptibility to scratch surface damage of wollastonite- and talc-containing polypropylene micrometric composites", Materials Science and Engineering A 380, 326-339, 2004.
- [12] Z.Z. Wang, P. Gu, and Z. Zhang, "Indentation and scratch behavior of nano- SiO_2 /polycarbonate composite coating at the micro/nano-scale", Wear 269, 21-25, 2010.
- [13] Mustafa Özgür Bora, Sinan Fidan, Onur Çoban, and Zafer Yücel, "Scratch Behavior of Glass Fiber Reinforced Polyester Matrix Composite After Solid Particle Erosion", Polymer Composites, 36, 1958-1966, 2015.

Microstructure of Heat treated Wood Material

A.Dilek DOGU

Istanbul University, Faculty of Forestry, Department of
Forest Biology and Wood Protection Technology, Istanbul,
TURKEY

F.Digdem TUNCER

Istanbul University, Faculty of Forestry, Department of
Forest Biology and Wood Protection Technology, Istanbul,
TURKEY

Davut BAKIR

Istanbul University, Faculty of Forestry, Department of
Forest Biology and Wood Protection Technology, Istanbul,
TURKEY

Corresponding author: davut.bakir@istanbul.edu.tr

Suleyman KORKUT

Duzce University, Faculty of Forestry, Department of Wood
Mechanics and Technology, Duzce, TURKEY

Zeki CANDAN

Istanbul University, Faculty of Forestry, Department of Wood
Mechanics and Technology, Istanbul, TURKEY

Abstract— *The heat treatment is mainly applied to improve the dimensional stability and durability of wood material. It is known that the heat treatment affects the anatomical structure of wood but these effects depend on the wood species and process conditions that are used. Therefore, in recent years, there has been great interest to determine the changes in the anatomical structure of wood species by using the different wood modification methods. In this study, the effects of heat treatment method on the anatomical structure of *Fraxinus* spp. (ash wood) wood were studied. The materials were obtained from a local sawmill in Duzce, Turkey and different temperatures (120 °C, 150 °C and 180 °C) and durations (2h, 6h and 10 h) were applied. Changes in the microstructure of the wood samples were detected by using a light microscope. Wood samples were kept under vacuum in the presence of alcohol, glycerin, and water at room temperature to be softened for sectioning process. The samples were cut into thin sections by using a sliding microtome. Those microscopic sections were then stained with safranin and fast-green- for to obtain good contrast between lignified cell walls (red color) and cellulose (green color). A microscopic slide of ash wood was taken from the Xylarium of Faculty of Forestry, Istanbul University (ISTUFw) served as control, which was already stained with safranin. All the microscopic evaluations were realized only visually on cross, radial and tangential sections. The results showed that the defects in microstructure of wood samples increased with increasing heat treatment temperature and time. The defects in microstructure of wood samples were mostly occurred in the early wood part of the growth rings, the largest damages were observed in the fibers and vessels depend on the increase of heat treatment temperature and time.*

Keywords— Wood microstructure, ash, defects, heat treatment, light microscopy

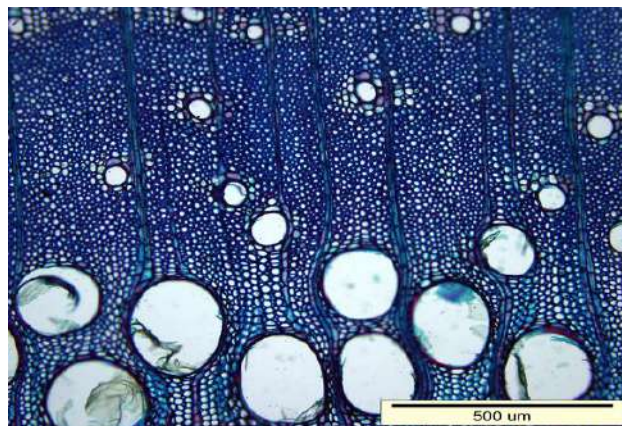


Figure 1. No visible distortion in the vessel and fiber cell walls at 120 °C / 2 h (cross sections).

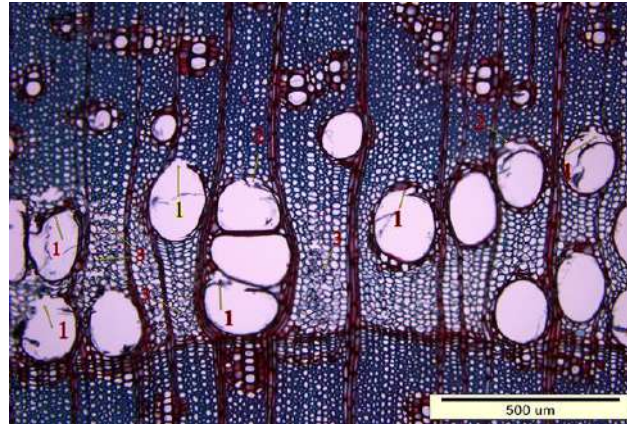


Figure 2. Ruptures in the vessel cell walls (arrow 1), the low degree defects in the walls of axial parenchyma cells (arrow 2) and severe damage (arrow 3) in the fiber cell walls at the earlywood region of *Fraxinus* spp. at 180 °C / 10 h (cross sections).

Synthesis of Cobalt Based Composite Thin Film on Copper Collector for Energy Storage Devices

Abdulcabbar Yavuz

Department of Metallurgical and Materials Engineering
Gaziantep University, Sehitkamil, 27310,
Gaziantep, Turkey
ayavuz@gantep.edu.tr

Metin Bedir

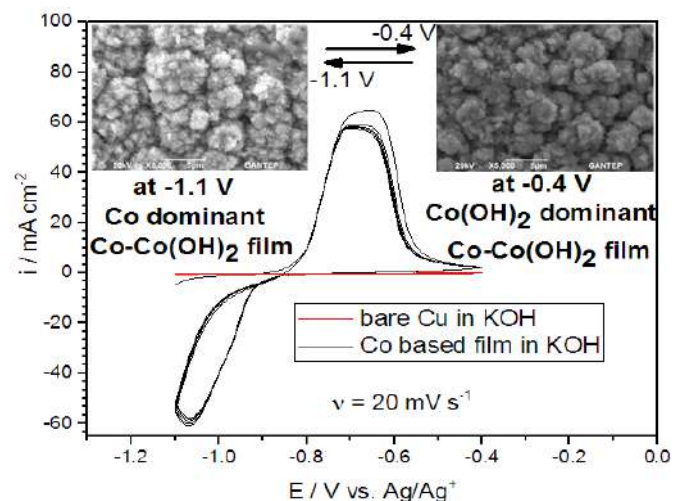
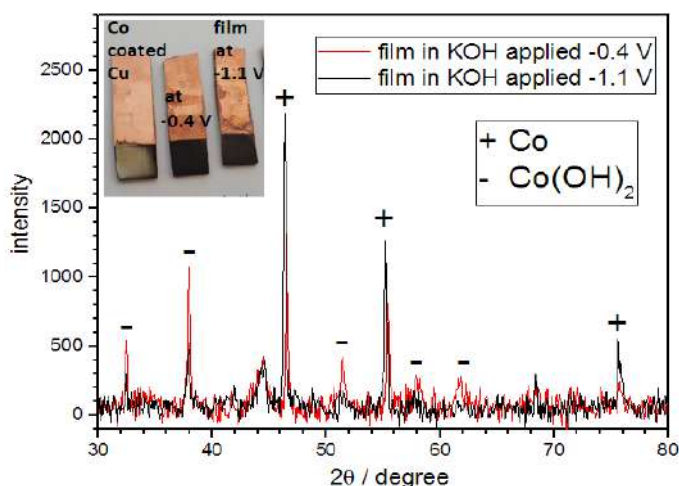
Department of Engineering Physics
Gaziantep University, Sehitkamil, 27310,
Gaziantep, Turkey
bedir@gantep.edu.tr

M. Yakup Hacıbrahimoglu

Department of Metallurgical and Materials Engineering
Gaziantep University, Sehitkamil, 27310,
Gaziantep, Turkey
yakup@gantep.edu.tr

Abstract— A Co-Co(OH)₂ modified electrode was formed on a copper current collector in ambient conditions. The composite film of Co-Co(OH)₂ illustrates anodic characteristic for energy storage devices. Cobalt was firstly deposited potentiostatically on copper substrate from pyrophosphate electrolyte and then this modified electrode was potentiodynamically treated OH⁻ included solution for the purpose of Co(OH)₂ formation. Co-Co(OH)₂ modified film however was obtained. This film was dominated by Co(OH)₂ at positive potential (anodic side of voltammetry) and the film is dominated by Co at negative side (-1.1 V) in OH⁻ included electrolyte. OH⁻ ions diffuses into the Co-Co(OH)₂ film during oxidation and these ions diffuses out of the film during reduction. As OH⁻ ions do not react with copper substrate, the Co-Co(OH)₂ electrode deposited on copper current collector is a promising anode material for energy storage devices. Specific capacitance of cobalt based modified electrode depends on film thickness. The redox reaction between the modified electrode and OH⁻ electrolyte has diffusion controlled mechanism meaning that film has a fast charge and discharge property. Capacity values are generally constant up to first 250 scans until the film is evolved. Capacity retention of the film is 84% (after 450 cycles). A specific capacitance of the Co-Co(OH)₂ composite electrode in 6 M KOH at a scan rate of 5 mV s⁻¹ is 549 F g⁻¹. 73% of capacitance is reached when the scan rate is increased from 5 mV s⁻¹ to 100 mV s⁻¹.

Keywords— energy storage; composite modified electrode; alkaline treatment; copper current collector; anode material.



Metals and Alloys Deposition on Aluminium Based Substrate from an Ionic Liquid

Abdulcabbar Yavuz

Department of Metallurgical and Materials Engineering
Gaziantep University, Sehitkamil, 27310,
Gaziantep, Turkey
ayavuz@gantep.edu.tr

M. Yakup Hacıbrahimoglu

Department of Metallurgical and Materials Engineering
Gaziantep University, Sehitkamil, 27310,
Gaziantep, Turkey
yakup@gantep.edu.tr

Metin Bedir

Department of Engineering Physics
Gaziantep University, Sehitkamil, 27310,
Gaziantep, Turkey
bedir@gantep.edu.tr

Abstract— The methods for coating a metal on an aluminium or aluminium based alloy substrate are limited. In this research a novel method is studied to obtain a metal and an alloy coated aluminium substrate. A type of ionic liquid called Ethaline (formed from choline chloride + ethylene glycol in a 1:2 molar ratio) composed of only ions is used as a deposition electrolyte. The strategy of this process was firstly to remove Al_2O_3 layer naturally formed on aluminium surface (about 20 nm) and then reduce a metal or an alloy on bare aluminium surface which does not have Al_2O_3 layer anymore. When bare aluminium or aluminium alloy is in contact with atmosphere or an aqueous solution, Al_2O_3 thin layer immediately formed on aluminium surface. To avoid aluminium from atmosphere, removing Al_2O_3 layer from bare aluminium and deposition a new metal on bare aluminium should be carried out within the same electrolyte (an in-situ technique) and this electrolyte has to be water free. To electrodeposit a metal or an alloy on aluminium alloy substrate, an anodic voltage (greater than +1.5) is applied potentiostatically for removing Al_2O_3 layer in Ethaline. After this process, the extreme cathodic potential (less than -1.5 V) is applied for the formation of a required metal or alloy on newly prepared aluminium alloy whose Al_2O_3 this layer has been removed. In this study; Cu, Ni, Mn, Zn and some of their alloy combinations were deposited on aluminium surface. These metals and their alloys were selected as models. This technique could be however applied for other metals and alloys.

Keywords— alloy, aluminium, ionic liquid, electrodeposition, thin film .

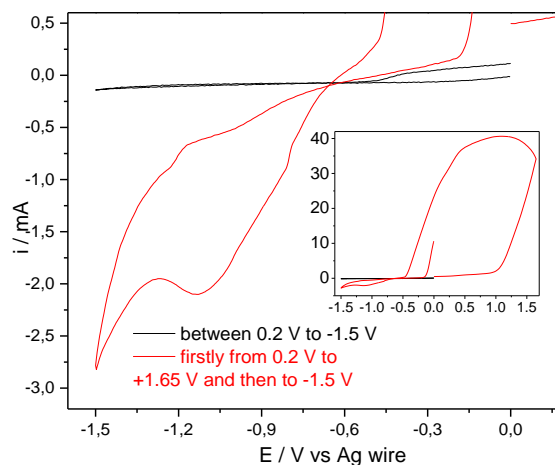


Figure 1 : Cyclic voltammogram data of Al alloy working electrode in Zn containing electrolyte (0.1 M ZnSO_4 in Ethaline) at a sweep rate of 20 mV s^{-1} . a) potential window directly from 0 V to -1.5 V (black line) compared with the potential window starting from 0 V and going to the positive direction (+1.65 V) and then going to the negative direction (-1.5 V) (red line). The inset is whole cycle. The experiment was conducted at 50°C .

Growth and passivation study of zinc based alloys electrodeposited from pyrophosphate medium

Metin Bedir

Department of Engineering Physics
Gaziantep University, Sehitkamil, 27310,
Gaziantep, Turkey
bedir@gantep.edu.tr

M. Yakup Hacıbrahimoğlu

Department of Metallurgical and Materials Engineering
Gaziantep University, Sehitkamil, 27310,
Gaziantep, Turkey
yakup@gantep.edu.tr

Abdulcabbar Yavuz

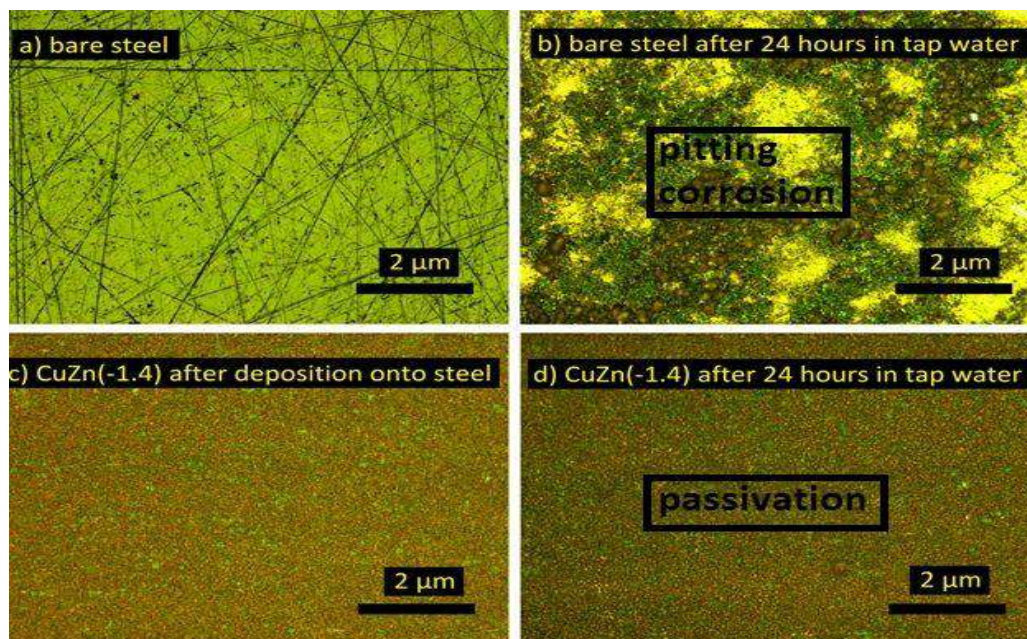
Department of Metallurgical and Materials Engineering
Gaziantep University, Sehitkamil, 27310,
Gaziantep, Turkey
ayavuz@gantep.edu.tr

Zihni Öztürk

Department of Engineering Physics
Gaziantep University, Sehitkamil, 27310,
Gaziantep, Turkey
ozturkz@gantep.edu.tr

Abstract— Zinc based alloys (Co-Zn, Mn-Zn, Ni-Zn, Cu-Zn and Bi-Zn) were electrodeposited from pyrophosphate medium on Pt electrode in order to examine their corrosion behaviors. Apart from Ni-Zn, the passivation behavior of all these alloys was investigated. Among all zinc based alloys studied in this research, one of passivable zinc based alloys (Cu-Zn) was deposited and their growth and corrosion behavior was explored in detail. Carbon steel working electrode was used to elucidate precise electron transfer mechanism during deposition and stripping of pure Cu, pure Zn and brass. Brass films were prepared by potentiodynamical and potentiostatical techniques. Growth potential affects the morphology and structure of crystals. Brass coatings are more porous than its pure components. Monocrystalline structure of (111) Cu-Zn alloys were obtained by changing deposition potential. Zinc contents in brass increased upon a decrease in applied voltage. However, growth potential and ratio of zinc in brass do not affect the passivation behavior of resulting alloys. The coatings obtained by applying different growth potential were immersed into tap water for 24 hours to compare its corrosion behaviors with carbon steel having pitting formation.

Keywords— Passivation; Deposition; Brass; Pyrophosphate; Carbon Steel.



Surface Design of Gun Barrel of Infantry Troops' Rifle

Esra Akkuş

Dept. of Metallurgy and Materials
Engineering Marmara University, Faculty of
Engineering Istanbul, Turkey
esraakkus94@hotmail.com

Burcu Nilgün Çetiner

Dept. of Metallurgy and Materials
Engineering Marmara University, Faculty of
Engineering Istanbul, Turkey
nilgun.cetiner@marmara.edu.tr

Ecem Turhan

Dept. of Metallurgy and Materials
Engineering Marmara University, Faculty of
Engineering Istanbul, Turkey
ecmtrhn94@gmail.com

İsmail Topçu

Dept. of Metallurgy and Materials
Engineering Marmara University, Faculty of
Engineering Istanbul, Turkey
itopcu@marmara.edu.tr

M. Ufuk Şahin

Dept. of Metallurgy and Materials
Engineering Marmara University, Faculty of
Engineering Istanbul, Turkey
m.ufuk.sahin@gmail.com

Arif Nihat Güllüoğlu

Dept. of Metallurgy and Materials
Engineering Marmara University, Faculty of
Engineering Istanbul, Turkey
gulluoglu@marmara.edu.tr

Özgür Çınar

Dept. of Metallurgy and Materials
Engineering Marmara University, Faculty of
Engineering Istanbul, Turkey
ozgur.cinar@marmara.edu.tr

Abstract — *In the defense industry, metal coatings are not only applied for decorative but also protective purposes. The smooth surface with high service life is expected, too. Electroless nickel-PTFE plating with perfect corrosion resistance, adequate abrasion resistance and hardness also shows interesting tribological properties such as low friction and non-stick properties, at the mean time low roughness. Thus, this coating application is appropriate for the surface design of gun barrel of infantry troops' rifle compared to conventional manganese phosphate bath coating which does not offer a coating layer as homogeneous as electroless nickel-PTFE plating's. In this project, the application of this composite coating was made possible by successive implementation of electroless nickel plating and PTFE coating one after another. The two different grades of steel – AISI 4140 and 5140 Steels, respectively- were selected in order to compare the alteration of their mechanical properties after process application. The specimens were carefully cut by an abrasive cutter, one of the each specimen groups was reserved for metallographic examination before the procedure, the other specimens' surfaces were treated; afterward each specimen was mounted, subsequently ground and polished. The abrasion resistance of the specimens were tested for 24 h. The microstructure was observed by optical microscope before and after treatment. The microhardness and the surface roughness of each specimen were measured before and after each process. The coating thickness of each layer -electroless nickel and PTFE- on the samples were monitored by scanning electron microscope, the elemental analysis for each layer on the surface of the steels was conducted by EDS. The differences on the mechanical properties depending on the type of the steel used in procedure were studied.*

Keywords — *Electroless nickel plating, PTFE coating, AISI 4140 and 5140 steels, defense industry.*

Design of Glass Shaping Molds

Esra Akkuş

Dept. of Metallurgy and Materials Engineering
Marmara University, Faculty of Engineering
Istanbul, Turkey
esraakkus94@hotmail.com

Hande Gümüşlü

Dept. of Metallurgy and Materials Engineering
Marmara University, Faculty of Engineering
Istanbul, Turkey
handegumuslu@gmail.com

Merve Altınay

Dept. of Metallurgy and Materials Engineering
Marmara University, Faculty of Engineering
Istanbul, Turkey
altinaymerve93@gmail.com

Sibel Daşcı

Dept. of Metallurgy and Materials Engineering
Marmara University, Faculty of Engineering
Istanbul, Turkey
sibeldasci@gmail.com

Nazan Özgöz

Dept. of Metallurgy and Materials Engineering
Marmara University, Faculty of Engineering
Istanbul, Turkey
ozgoznazan@hotmail.com

Özgür Çınar

Dept. of Metallurgy and Materials Engineering
Marmara University, Faculty of Engineering
Istanbul, Turkey
ozgur.cinar@marmara.edu.tr

Burcu Nilgün Çetiner

Dept. of Metallurgy and Materials Engineering
Marmara University, Faculty of Engineering
Istanbul, Turkey
nilgun.cetiner@marmara.edu.tr

Arif Nihat Güllüoğlu

Dept. of Metallurgy and Materials Engineering
Marmara University, Faculty of Engineering
Istanbul, Turkey
gulluoglu@marmara.edu.tr

Abstract — *Boronizing is a thermochemical surface treatment in which boron atoms are diffused into the surface of a workpiece to form borides with the base material. This method is used in surface finishing and that can be efficient in terms of the surface quality of material. The surfaces that boronizing is applied on have increased hardness, increased abrasion resistance, high temperature insulation, low friction coefficient, the property of holding lower surface, corrosion resistance against acids, increased fatigue life and expansion coefficient proper for iron. When applied to the appropriate materials, boronizing provides wear and abrasion resistance comparable to sintered carbides. Cast irons used in glass production are the cheapest and the most easily formed materials in the mold materials that provide the expected properties. Cast iron molds' surfaces are damaged in the case of continuous contact of glass drop and these molds cannot be used after the harm of this damage. Heat differences that are composed by high temperatures and rapid cooling create thermal stress on the material of molds. Additionally the oxidation that occurs in high temperatures break the property of mold surfaces so this affects surface quality negatively and decrease the lifetime of the molds. There is a significant difference between the hardness value obtained from the layer of composed boron and the hardness value obtained from other surface finishing methods (nitriding, carburizing etc.). Hardness of the surface obtained from boronizing is 1800-2100 HV in steels, 3000 HV in titanium whereas it is between 600-1100 HV when other methods used. Current project includes the design of boronizing process that is applied to metal molds used in glass shaping in a well timed and cost effective way. One grade of cast iron -GG35- and one grade of steel - AISI 1035- respectively- were selected in order to compare the alteration of their mechanical properties after pack boronizing. The specimens were carefully cut by an abrasive cutter, one of the each specimen groups was reserved for metallographic examination before the procedure, the other specimens' surfaces were treated; afterward each specimen was mounted, subsequently ground and polished. The microstructure was observed by optical microscope before and after boronizing. The microhardness and the surface roughness of each specimen was measured before and after treatment. The abrasion resistance of the specimens were tested for 24 h. The coating thickness and diffusion of boron into deeper of the samples were monitored by scanning electron microscope, the elemental analysis for boron on the surface of the steels was conducted by EDS. The differences on the mechanical properties depending on the type of the steel used in procedure were studied.*

Keywords – Pack boronizing, AISI 1035 steel, GG 35 cast iron, glass mold design.

Characterization of Borided Ternary Fe-8Ni-Cr Alloys with Different Cr Content

Yucel Gencer

Department of Material Science and Engineering
Gebze Technical University
Gebze, Kocaeli, Turkey
gencer@gtu.edu.tr

Mehmet Tarakci

Department of Material Science and Engineering
Gebze Technical University
Gebze, Kocaeli, Turkey
mtarakci@gtu.edu.tr

Naim Burak Mackan

Department of Material Science and Engineering
Gebze Technical University
Gebze, Kocaeli, Turkey
burackmackan@hotmail.com

Abstract—The harsh conditions such as highly corrosive environment and elevated temperatures decrease the performance of the materials. To gain high performance at those conditions, improving the surface properties of the metallic materials instead of changing their bulk properties is a more economical and time saving process. Boriding is one of the thermochemical processes to enhance the surface properties of the steels and it guarantees high performance in extreme conditions. Boriding process provides high surface hardness, wear resistance and corrosion resistance for steels. Although the effects of alloying elements on the boronizing of steel are recognized, the individual influences of alloying additions on the boronizing mechanism of steel are not totally clear yet although some enlightening studies were reported recently. It was reported that the morphology, growth, phase composition, microhardness and thickness of the boride layer were affected by the alloying elements in the steels. To overcome the complex effect that arose due to the other alloying elements in steels, some systematical studies were carried out to reveal the specific effect of some alloying elements by boriding the binary alloys of Fe-M (M = Cr, Ti, Ni, V, Mn, Si, Mo, Cu, W, Co). Although, there are some studies on individual effect of Cr and Ni, the effect of addition of Cr along with Ni elements on boride layer properties is lacking in the literature. So, rod shaped Fe-8Ni, Fe-8Ni-1Cr and Fe-8Ni-16Cr alloys were prepared under controlled atmosphere by induction melting. The samples were pack boronized in Ekabor-II powder at 1000°C for 3 hours. The borided samples were characterized using OM, SEM, SEM-EDS, XRD and microhardness tester. The boride layer having saw-tooth morphology flattened with the increase of Cr content in the substrate. The formation of the FeB and Fe₂B phases was verified. The thickness of the boride layer decreased with amount of Cr and the thicknesses were found as 160 µm, 91 µm and 36 µm for Fe-8Ni, Fe-8Ni-1Cr and Fe-8Ni-16Cr, respectively. The transition region increased with increasing Cr contents in the Fe-8Ni-Cr ternary alloys. The presence of Cr and Ni in the main boride layer was verified by SEM-EDS analysis.

Keywords— Boronizing, Iron Boride, Fe-Ni-Cr alloys, steel coating

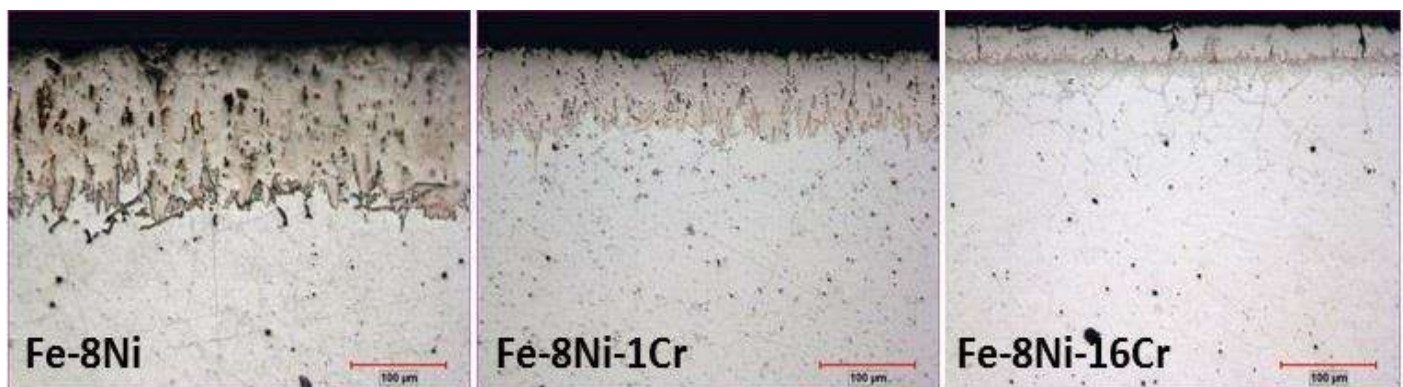


Fig.1. OM micrographs of borided Fe-8Ni, Fe-8Ni-1Cr, Fe-8Ni-16Cr Alloys.

The Effect of Process Current Density on the Properties of the Coatings Layer on Zirconium

Yucel Gencer

Department of Material Science and Engineering
Gebze Technical University
Gebze, Kocaeli, Turkey
gencer@gtu.edu.tr

Sezgin Cengiz

Department of Material Science and Engineering
Gebze Technical University
Gebze, Kocaeli, Turkey
scengiz@gtu.edu.tr

Abstract— Zirconium and its alloys are good alternative for biomedical and dental applications due to their high corrosion resistance and biocompatibility. However, dental and medical application of Zr based materials are limited because of their poor bioactivity. The bioactivity properties of zirconium based materials are improved by surface modification methods such as plasma electrolytic oxidation method (PEO) which is also called microarc oxidation (MAO). The technique is an effective, eco-friendly, economic and easy. The PEO method is a multi-controlled process and current, voltage, duty cycle, time, chemical composition of the substrate and the composition of the electrolyte are effective on the structure and composition of the coating. In this study, the effect of process current densities on the microstructure, phase content of the coating synthesized on pure Zr by PEO was examined. The PEO process was carried out using a homemade PEO unit with pulsed DC power supply in the Ca-P containing electrolytic solution for different the current density of 0.5-4 A/cm². The coating layers were characterized by using X-ray Diffractometry (XRD), Scanning Electron Microscopy (SEM) and Energy Dispersive Spectroscopy (EDS). The thickness of the coatings was increased by the process current and the thickness values were approximately 8 µm and 60 µm for 0.5 A/cm² and 4 A/cm², respectively. The XRD data revealed that, all the samples were formed at different process current densities contained m-ZrO₂ (monoclinic zirconia) and Ca_{0.134}Zr_{0.86}O_{1.86} (calcium zirconium oxide) phases. The new phase namely HA (Hydroxyapatite) was formed at 4 A/cm². The surface roughness values of the coatings were increased with current values and the surface roughness was 0.8 µm and 9.0 µm for 0.5 A/cm² and 4 A/cm², respectively. The amount of the Ca and P elements increased, while the amount of the Zr and O elements on the surface of the coatings decreased with increasing current density according to the SEM-EDS results.

Keywords— Plasma Electrolytic Oxidation, Microarc Oxidation, Zirconium, Zirconium oxide, Current density

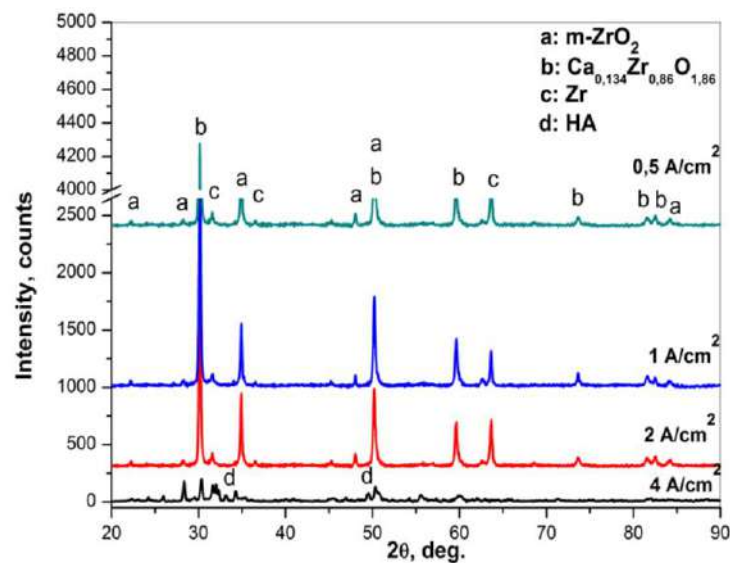


Fig. 1. XRD patterns of the coatings for different current density.

Table 1. Quantitative SEM-EDS elemental analysis results of the coatings for different current density.

Samples	0,5 A/cm ²	1 A/cm ²	2 A/cm ²	4 A/cm ²
Element	% At.	% At.	% At.	% At.
O	70,28	65,42	67,67	61,63
P	1,05	2,26	3,69	7,06
Zr	56,18	56,08	16,04	23,25
Ca	9,35	10,41	12,61	21,73

REFERENCES

- [1] S. Cengiz, A. Uzunoglu, L. Stanciu, M. Tarakci, Y. Gencer, "Direct fabrication of crystalline hydroxyapatite coating on zirconium by single-step plasma electrolytic oxidation process," *Surf. Coat. Technol.*, Vol. 242, 132-140, 2015.
- [2] S. Cengiz, A. Yunus, M. Tarakci, L. Stanciu, Y. Gencer, "Microarc oxidation discharge types and bio properties of the coating synthesized on zirconium," *Mat. Sci. Eng C-*, Vol. 77, 374-383, 2017.
- [3] M. Sandhyarani, T. Prasadrao, N. Rameshbabu, "Role of electrolyte composition on structural, morphological and in-vitro biological properties of plasma electrolytic oxidation films formed on zirconium," *Appl. Surf. Sci.*, Vol. 317, 198-209, 2014.
- [4] Y. Han, Y. Y. Yan, C. G. Lu, Y. M. Zhang, K. W. Xu, "Bioactivity and osteoblast response of the micro-arc oxidized zirconia films," *J. Biomed. Mater. Res. A.*, Vol. 88a, 117-127, 2009.

High Temperature Oxidation of NiAlCr and NiAlCr-Mg Alloys

Mehmet Tarakci*

Materials Science and Engineering Department
Gebze Technical University
Kocaeli, Turkey
mtarakci@gtu.edu.tr

Yunus Azakli

Materials Science and Engineering Department
Gebze Technical University
Kocaeli, Turkey
yazakli@gtu.edu.tr

Abstract— High temperature oxidation resistance is crucial for the alloys used in the jet engines and power plants. Especially, Ni-based superalloys are one of the candidates, which can meet the demands such as creep and corrosion resistance. In this study, NiAlCr and NiAlCr-Mg alloys were produced by induction melting under controlled atmosphere. The alloys were annealed for 96 h at 1050°C. The cyclic oxidation tests were conducted at 1027°C under airflow of 90 l/h. The oxidation products were analyzed by microbalance, X-Ray Diffractometer, Scanning Electron Microscope and Energy Dispersive Spectrometer. After conducting the first cycle oxide product formed on Mg free M0-A alloy was mostly composed of Al_2O_3 . Even after first cycle this alloy, extensive spallation of the oxide scales was observed. As the regions close to the alloy surface grow poor in Al with the lapse of time, a continuous layer of Al_2O_3 did not form. Instead, thermodynamically more stable $NiCr_2O_4$ phase formed as small crystals on the outermost surface of the oxide scale due to the oxidation of Ni and Cr elements simultaneously. With the addition of 2.5 at. % Mg to the alloy (M2-A) almost no spallation was observed. Addition of Mg inhibited the oxidation of Cr and Ni elements thus formation of distinct or complex oxide layers of these elements were hindered. The formation of continuous $MgAl_2O_4$ and MgO layers was observed first time on Ni-based alloys during high temperature exposure.

Keywords— High temperature oxidation, NiAlCr, NiAlCrMg, Ni based alloys, corrosion

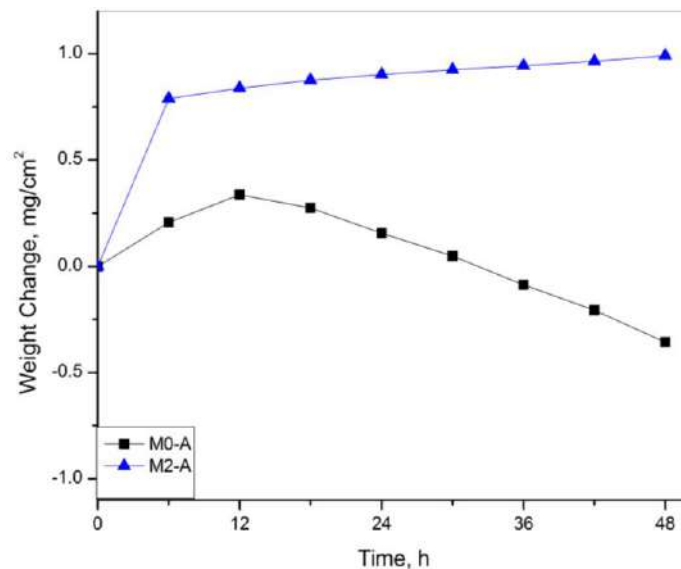


Fig. 1. Mass changes of M0-A and M2-A alloys during high temperature oxidation.

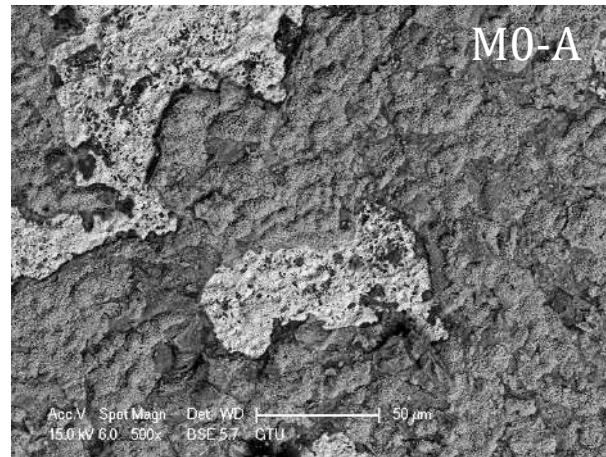


Fig. 2. Surface SEM image of M0-A alloy after 48 h of oxidation.

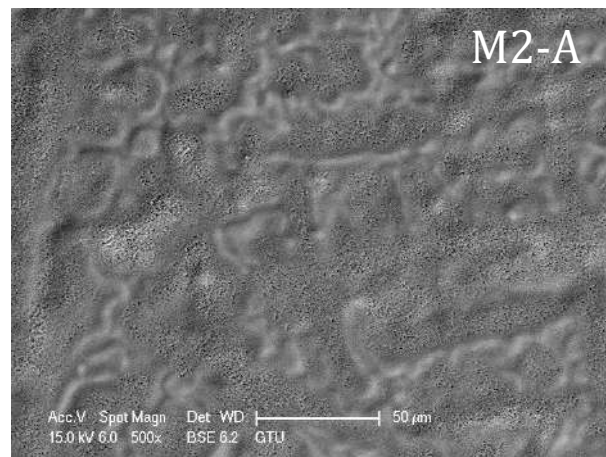


Fig. 3. Surface SEM image of M2-A alloy after 48 h of oxidation

Surface Design of Aluminium and Zinc Extrusion Dies

Ahmet Batuhan Yılmaz

Dept. of Metallurgy and Materials Engineering
Marmara University, Faculty of Engineering
Istanbul, Turkey
ahmetbatuhanyilmaz@gmail.com

Burcu Nilgün Çetiner

Dept. of Metallurgy and Materials
Engineering Marmara University, Faculty of
Engineering Istanbul, Turkey
nilgun.cetiner@marmara.edu.tr

Fahri Kemal Patır

Dept. of Metallurgy and Materials Engineering
Marmara University, Faculty of Engineering
Istanbul, Turkey
fahrikemalpatir@gmail.com

Özgür Çınar

Dept. of Metallurgy and Materials
Engineering Marmara University, Faculty of
Engineering Istanbul, Turkey
ozgur.cinar@marmara.edu.tr

Asel Damla Şimşek

Dept. of Metallurgy and Materials Engineering
Marmara University, Faculty of Engineering
Istanbul, Turkey
aselsimsek93@gmail.com

Ayhan Mergen

Dept. of Metallurgy and Materials
Engineering Marmara University, Faculty of
Engineering Istanbul, Turkey
ayhan.mergen@marmara.edu.tr

Arif Nihat Güllüoğlu

Dept. of Metallurgy and Materials Engineering
Marmara University, Faculty of Engineering
Istanbul, Turkey
gulluoglu@marmara.edu.tr

Abstract—Extrusion method is one of the most important of aluminium shaping methods. With the help of new techniques developed, extrusion parameters and consequently the quality of product has been improved. Necessary attention should be given for fabrication of extrusion dies since they give the final shape on semi-finished products. In this study, the thermal spray coating application using an oxy-acetylene thermal spray torch which delivers very precise anti-wear protective coatings. Alloy powders containing nickel, boron, silicon, cobalt and chrome were sprayed onto the part to be coated and were fused simultaneously using a welding torch. Bonding with the base metal by diffusion ensured that it did not reach its melting point. The dense coating was not affected by dilution and retained all its designed properties. AISI 1040 steel was selected in order to improve its surface properties and to show the alteration.

The specimens were carefully cut by an abrasive cutter, one of the each specimen groups was reserved for metallographic examination before the procedure, the other specimens' surfaces were treated; afterward each specimen was mounted, subsequently ground and polished. The abrasion resistance of the specimens were tested for 24h. The microstructure was observed by optical microscope before and after treatment. The microhardness and the surface roughness of each specimen were measured before and after each process. The coating thickness on the samples were monitored by scanning electron microscope, the elemental analysis for each layer on the surface of the steels was conducted by EDS. The differences on the mechanical properties depending on the coating composition used in the procedure were studied.

Keywords— Thermal spray coating, spray and fused coating, AISI 1040, aluminium and extrusion dies.

Obtaining Homogeneous Distributed BNp in Si₃N₄ Matrix Synthesised by CRN Process

*Fatih ÇALIŞKAN

Dept. of Metallurgical and Materials Engineering
Sakarya University, Faculty of Technology
Turkey

[*fcaliskan@sakarya.edu.tr](mailto:fcaliskan@sakarya.edu.tr)

Turgay TEHÇİ

Dept. of Metallurgical and Materials Engineering
Sakarya University, Faculty of Technology
Turkey

turgaytehci@hotmail.com

Adem DEMİR

Dept. of Metallurgical and Materials Engineering
Sakarya University, Faculty of Technology
Turkey

ademir@sakarya.edu.tr

Zafer TATLI

Dept. of Metallurgical and Materials Engineering
Sakarya University, Faculty of Technology
Turkey

ztatli@sakarya.edu.tr

ABSTRACT

Carbothermal reduction and nitridation (CRN) is preferred because of taking place the reaction at a single stage and enabling the production of non-oxide ceramics. In this study, fabrication of silicon nitride and boron carbide composite material containing fine boron carbide particles distributed via the chemical reaction in the result silicon nitride matrix were achieved during the CRN combined with mechanical milling process. XRD analysis gave phase formation, alpha Si₃N₄ has dominant and characteristic peaks together B₄C peaks. The EDS mapping results showed that combination the mechanical milling and the carbothermic synthesising supported more homogeneous distribution of reinforcement particle (B₄C) in the Si₃N₄ matrix compared with conventional mixing methods.

Keywords: Silicon nitride, Boron carbide, Non-oxide ceramics, Silicon dioxide

I. INTRODUCTION

In the last two decades considerable effort has been made to develop and to modify mechanical properties of silicon nitride (Si₃N₄) ceramics. Si₃N₄ ceramics have relatively high fracture toughness, resistance to corrosion, resistance to wear, resistance to elevated temperatures. One of the most important properties of Si₃N₄ is the improved fracture toughness which is strongly related with the presence of highly enhanced aspect ratio of β-Si₃N₄ in the microstructure of silicon nitride ceramics [1-4]. Monolithic ceramics with highly anisotropic rod-like β-Si₃N₄ particles have potential as a low cost

alternative to fiber-reinforced ceramic matrix composites because they possess exceptional fracture resistance, yet they do not contain costly fibers [5].

Several Si₃N₄-based ceramic matrix composites (CMCs) have been tested for this purpose. Ceramic reinforcements (SiC, TiC, TiN, BN), in particulate or whisker forms, have been added in order to yield self-lubricating tribolayers by selective oxidation of these compounds, or simply to increase the fracture toughness of the ceramic body [7-8]. Hexagonal boron nitride (BN) ceramic is a well-known in-situ lubricating material because of the formation mechanism of oxide or hydrated layers on its surface. [9-11]. Thus, BN ceramics have a beneficial effect on the tribological performance of Si₃N₄-BN composites and BN has a significant contribution on the reducing the wear coefficient one order of magnitude to $K \approx 10^{-6} \text{ mm}^3 \text{ N}^{-1} \text{ m}^{-1}$, as to the Si₃N₄ matrix. [8]. BN starts to oxidise at 300°C, hindering the lubricating role of this dispersoid. At 400 °C, the wear coefficient rises to a catastrophic value of $K > 10^{-4} \text{ mm}^3 \text{ N}^{-1} \text{ m}^{-1}$ [12]. This oxidation effect was suppressed with adding carbon black having high chemical activity and working under Ar controlled atmosphere. Therefore, BN particles were preserved from exothermic oxidation reaction releasing energy.

This work focused on investigation of a new process for the homogeneously distributed Si₃N₄-BN composite powder. The produced ceramic composite powder aims to be used in fabrication of machinable ceramic materials. The key factor for

all process was $\text{SiO}_2 \rightarrow \text{Si}_3\text{N}_4$ conversion and its parameters such as stoichiometric ratio. It was a puzzler how to influence the contribution of boron nitride to the conversion.

II. EXPERIMENTAL

SiO_2 as silicon source, carbon black as reducing agent and BN powders as additive were used as starting materials. Silicon nitride and hexagonal boron nitride ceramic composite powders were produced at a relatively low temperature by using the carbothermal reduction and nitridation process. The nitridation rate was determined by X-ray diffraction (XRD). As well as the weight changes before and after nitridation were discussed in detailed. Scanning electron microscopy was used to reveal morphologies and distribution of the converted Si_3N_4 grains and as-received BN grains. There batches were used to determine optimum parameters and variables of the process, 0/100, 15/85, 30/70 (in wt. %) BN/ Si_3N_4 compositions, respectively. All batches were subjected to mechanical activation process. The powder mix was heated and hold at $>1400^\circ\text{C}$ for 4h.

III. RESULTS AND DISCUSSION

The efficiency of CRN process was evaluated in terms of weight loss in Table 1. The weight change results showed that is directly related to the amount of BN. This is because BN suppressed the conversion and the CRN reaction became more unstable. It can be due to missing unreacted reactants before completing the reaction.

TABLE 1. THE CHANGE OF EFFICIENCY FOR THE CRN PROCESS WITH BN RATIO

Composition (wt.%)	Before carbon burning (wt.%)	After carbon burning (wt.%)
15 BN	48,67	14,29
30 BN	33,00	30,77

XRD ANALYSIS

Conversion reactions was carried out under nitrogen gas flowing. After the conversion, the excess carbon was burn out at 900°C for 2h. The XRD result of the remain powder was given in Fig. 1. The synthesis of Si_3N_4 from silica plus carbon mixtures by CRN was considered to proceed as follows:

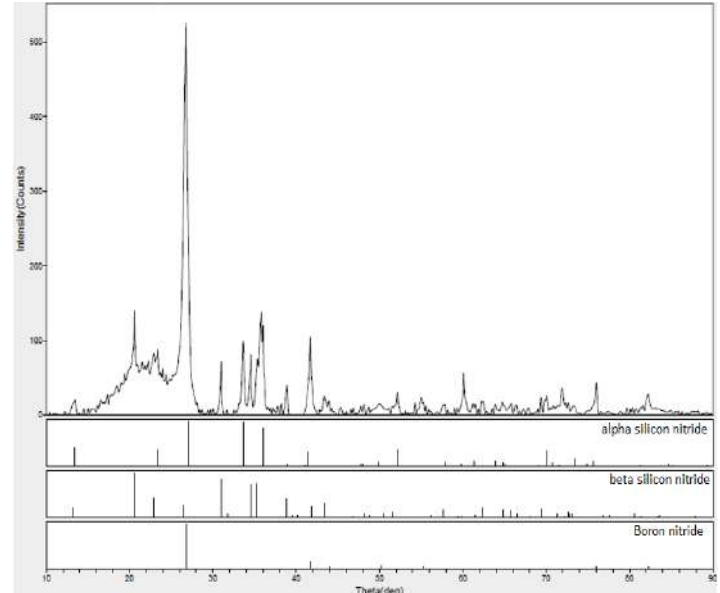
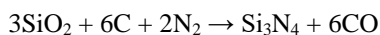


Fig 1. XRD analysis for $\text{Si}_3\text{N}_4/\text{BN}$ -85/15 (wt.%) at 1450 for 4h.

In Fig. 1, XRD peaks are belong to alpha and beta phases for silicon nitride. While α peaks are minor, β peaks are dominant in the yield powder which was converted at 1450 for 4h. One of the first sign of the addition of boron nitride into the starting material after the conversion was to increase the amorphous phase as seen in Fig 2. When BN ratio in the starting composition increase, the conversion kinetics partly supported formation of the metastable alpha silicon nitride instead of the formation of stable beta silicon nitride.

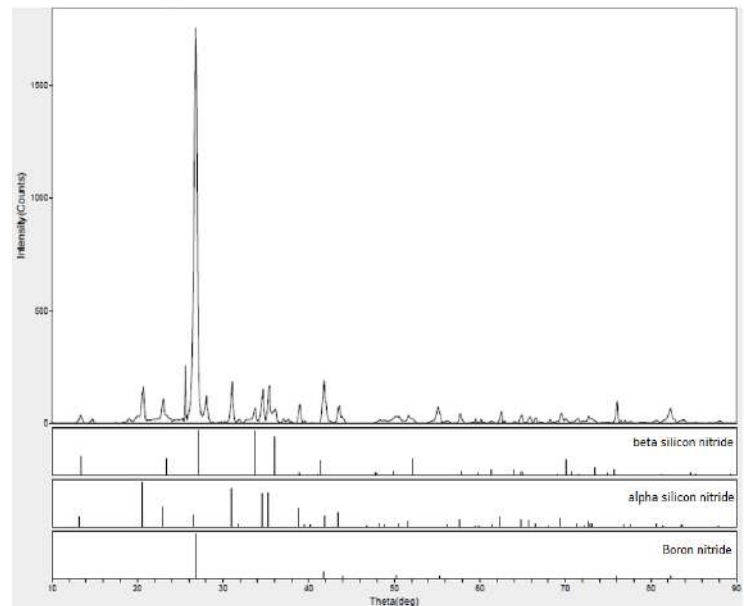


Fig 2. XRD analysis for $\text{Si}_3\text{N}_4/\text{BN}$ -70/30 (wt.%) at 1450 for 4h.

As shown in Fig 3, the phase analysis by X-ray diffraction (XRD) indicated that the BN addition could deteriorate the conversion to silicon nitride ceramic. The nitridation ratio of silicon slightly decreased with increasing the amount of BN.

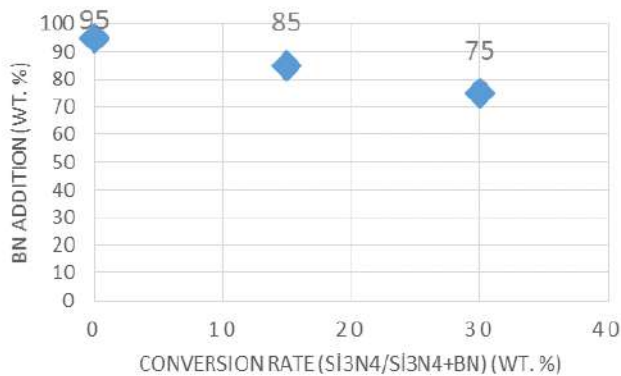


Figure 3. The change of amount of the nitrided silicon with changing BN ratio

SCANNING ELECTRON MICROSCOPY AND EDAX ANALYSIS OF THE NITRIDED POWDERS

As can be seen in Fig. 4, highly rod-like silicon nitride grains are clear and these grains can be accepted as coarse which means grain with high aspect ratio. This grain is subjected to beta phase Si₃N₄ and is to give the improved fracture toughness. Hexagonal boron nitride particles are homogeneously distributed and uniformly covered all silicon nitride grain surfaces. This shows to reach the success that means more affected distribution and minimum interface mismatches between the silicon nitride matrix and the boron nitride particles. BN particles are very fine.

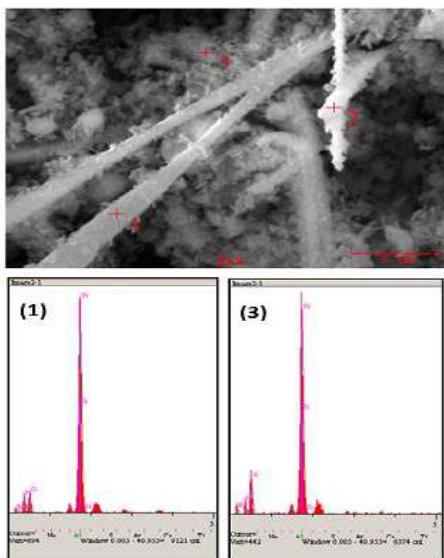


Figure 4. SEM micrograph and EDAX elemental analysis of the CRN yield at 1450°C for 4h

Elemental dispersive spectroscopy revealed that “1” and “2” points consist of Si, N and O elements. Si and N are main component of the Si₃N₄ compound but O element. This can cause from surface silica and it is well-known that is all but impossible to escape Si-N-Si-O bonding reaction in presence oxygen. “3” point consists Si, N, O, B and N elements. B and N stem from hexagonal boron nitride particles.

IV. CONCLUSION

The nitridation process of silicon powder was successfully carried out. Highly rod-like silicon nitride grains were obtained at 1450°C for 4h as optimum. Both XRD and SEM analyses revealed the nitridation conversion and morphologies of consisting silicon nitride grains and presence of the stable BN particles. More homogeneous BN distribution around the silicon nitride grains, which is one of the main object, was significantly achieved after reduction and nitridation reactions. The authors propose that the synthesized composite powders can be used to produce the ceramic composites having good machinability and dry sliding features.

REFERENCES

- [1] L. A. Genova, V. A. Izhevskiy, J. C. Bressiani, Effect of processing variables on synthesis of β -Si₃N₄ particles, Journal of the European Ceramic Society 28 (2008) 295–301.
- [2] Lange, F. F., Fracture toughness of Si₃N₄ as a function of the initial β -contents. J. Am. Ceram. Soc., 1979, 62, 428–430.
- [3] Hoffmann, M. J. and Petzow, G., Tailored microstructures of silicon nitride ceramics. Pure Appl. Chem., 1994, 66, 1807–1814.
- [4] Sajgalik, P., Dusza, J. and Hoffmann, M. J., Relationship between microstructure, toughening mechanisms, and fracture toughness of reinforced silicon nitride ceramics. J. Am. Ceram. Soc., 1995, 78, 2619–2624.
- [5] D. Kovar, B. H. King, R. W. Trice And J. W. Halloran, J. Amer. Ceram. Soc. 80(10) (1997) 2471.
- [6] S. Y. Lienard, D. Kovar, R. J. Moon, K. J. Bowman, J. W. Halloran, Texture development in Si₃N₄/BN fibrous monolithic ceramics, Journal of Materials Science 35 (2000) 3365 – 3371.
- [7] A. Skopp, M. Woydt, Ceramic–ceramic composite materials with improved friction and wear properties, Tribol. Int. 25 (1) (1992) 61–70.
- [8] M. Woydt, Ceramic–ceramic composites for dry sliding in closed tribosystems, Am. Ceram. Soc. Bull. 72 (1) (1993) 66–67.
- [9] A. Gangopadhyay, S. Jahanmir, M.B. Peterson, Self-lubricating ceramic matrix composites, in: S. Jahanmir (Ed.), Friction and Wear of Ceramics, Marcel Dekker, New York, 1997, pp. 163–197.
- [10] T. Saito, T. Hosoe, F. Honda, Chemical wear of sintered Si₃N₄, hBN and Si₃N₄-hBN composites by water lubrication, Wear 247 (2001) 223–230.
- [11] J. M. Carrapichano, J. R. Gomes, R. F. Silva, Tribological behaviour of Si₃N₄-BN ceramic materials for dry sliding applications, Wear 253 (2002) 1070–1076.
- [12] A. Skopp, M. Woydt, K.H. Habig, Tribological behavior of silicon nitride materials under unlubricated sliding between 22°C and 1000 °C, Wear 181–183 (1995) 571–580.

The Design of New Type Mixer for More Efficient Powder Mixing

Fatih ÇALIŞKAN

¹Sakarya University, Faculty of Technology, Dept.
Metallurgical and Materials, Sakarya/TURKEY

Zafer TATLI

¹Sakarya University, Faculty of Technology, Dept.
Metallurgical and Materials, Sakarya/TURKEY

Yunus Emre ANTİKA

¹Sakarya University, Faculty of Technology, Dept.
Metallurgical and Materials, Sakarya/TURKEY

Harun GÜNGÖRDÜ

¹Sakarya University, Faculty of Technology, Dept.
Metallurgical and Materials, Sakarya/TURKEY

²Eksan Mechanism Industry and Trade Inc., Hendek,
Sakarya, TURKEY

Adem DEMİR

¹Sakarya University, Faculty of Technology, Dept.
Metallurgical and Materials, Sakarya/TURKEY

Abstract— In this work, Powder mixing techniques for metal, ceramic and intermetallic powder mainly influence mechanical and microstructural properties. Mixer type affects size reinforcement particles and distribution of reinforcing phase in matrix material. The present study aims to design and to manufacture a new powder milling and mixer without conventional mechanisms. The machine was designed and assembled according to crankpiston principle. This system worked at high cycle/min rates, and circular rotation on horizontal axis. The work aims more efficiency and more homogeneous mixing system.

Keywords: mixer design, powder metallurgy, homogeneous distribution

I. INTRODUCTION

Rapid developments in the field of technology make it necessary to use new materials with superior properties compared to conventional materials. New materials have been produced under the name of "Composite Materials" which have superior qualities than other materials [1, 2, 3].

The composite material is a material formed by a mixture or combination of two or more micro- or macro-components separated by their shapes and chemical compositions and essentially insoluble in each other [4].

Composite materials are formed by combining different materials as shown in Figure 1 [5].

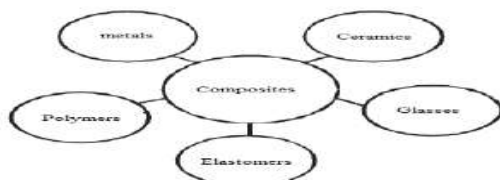


Fig. 1. Matrix Materials [6].

The use of different matrix and reinforcement materials has led to the development of different techniques in the production of MMCs. One of these techniques is powder metallurgy [7].

The purpose of powder metallurgy is to produce powders of metal and metallic alloys by mechanical and physico-chemical methods and to produce in various shaped parts from the powders via pressure and temperature without melting [8].

II. PRODUCTION OF METAL POWDER

The techniques used in the manufacture of metal powders determine many properties of powders. Depending on the method of production of morphology of the powder, it can be very different from the spherical to the complicated shapes. The surface condition of the powder varies according to the production method [9].

As well as being a metal powder production technique, grinding, which is also used to break the powder produced by other techniques, is made in the most ball mills. In this method of producing fine particles, the basic principle is to bring a high energy crushing between the material to be ground and a hard object.

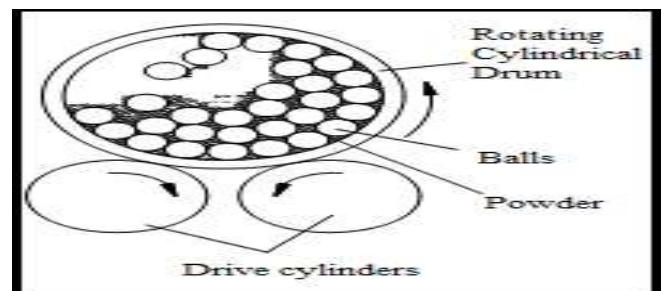


Fig. 2. Ball Milling

The metal powder to be grinded in coarse sizes is placed in a container together hard and abrasive balls. The coarse-grained material is divided into very small fresh particles by the effect of impact by rotating or vibrating together with large diameter, hard and abrasion-resistant balls in the grinder vessel (Figure 2).

For a homogenous mixture, the volume of the balls to be placed in the container and the amount of material to be ground is very important parameter. Approximately half of the volume of the vessel and the amount of material to be ground must be approximately 25% of the vessel volume. Iron alloys, iron - chromium, iron - silicon etc. materials can mechanically be ground in ball mills [10].

III. TYPES OF GRINDERS USED

A. Planetary type grinder

Another milling system to make mechanically alloying (MA) is the "planetary" milling equipment (Figure 4). A couple of hundred grams of powder can be grinded in this shot. These mills are called as "planetary" because their chambers act like planets. They are placed on a rotating support disc and take their movement around their axis from a special mechanism [10].



Fig. 4. Planetary type ball mill

B. Atritor type grinder

The atomiser consists of a vertical cylinder with a series of mixers. Powder is deformed with the help of shaft arms and balls, and fractures and cold welds occur in these powders. Crushing of the balls with the container wall, between each other and the agitator shaft cause reduction in the powder size and form a homogeneous microstructure [10].

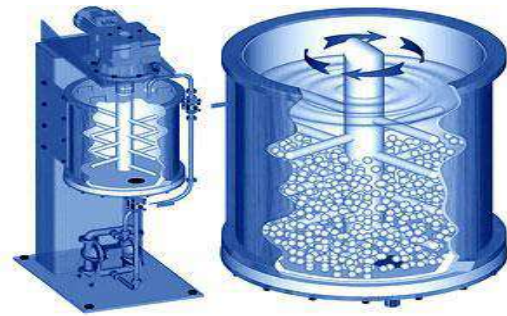


Fig. 5. Atritor type (vertical) ball mill [10].

IV. MECHANICAL GRINDING

At the basis of the size reduction process with mechanical grinders, crushings between the sample, the grinding medium and the sample are based on the final energy application. Figure 6 shows the grinder and the processes in it [12].

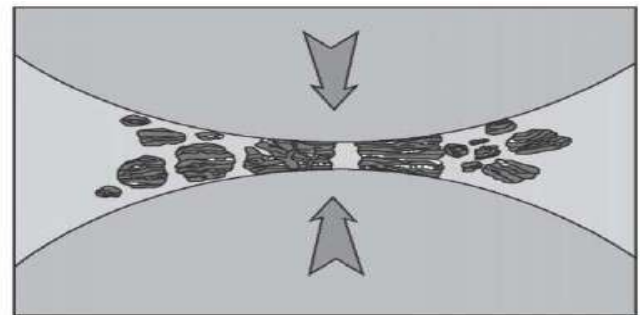


Fig. 6. Minimization of particles by mechanical grinding [13, 14].

The model in Figure 6 shows the crushing model and, as can be seen in Fig 6, the particles remain between the two colliding balls. The grinding media contains dense powder clouds, balls and powder particles. The first phase of re-arrangement and stacking of powders between the balls. Fine and irregular particles form with minimal deformation and fracture and slip from one particle to another. In the second phase of the cracking, particles are subjected to elastic and plastic deformation. At this stage, cold welding is observed in metallic systems. In the third stage, particles are broken by further deformation or fragmentation [15, 12].

In this work, a new method has been designed and produced outside of the existing mixing methods. The powders were mixed at high speed per minute on the horizontal axis with crankshaft working principle. In the previous methods, the limited number of materials encountered were disadvantages such as mixing, stacking, cold welding, as well as speeds of up to 800-1000 d / d, reaching 1000-3000 d / d.

This work aims to design a new type mixing system. The authors think that the system performs with high energy and relatively efficiency. All affected parameters were considered during the design of the high energy mixer.

V. EXPERIMENTAL

Materials and Method

Catia V5R20 and Solidworks programs to draw and to design were used in manufacturing the new grinding system. Crankshaft, connecting rod, slide bar and pins are fabricated from 4140 steel.

VI. RESULTS AND DISCUSSION

Designing and Manufacturing of The Mixer

The speed required for the system was provided using an inverter device that helps to set the frequency of the motor.

The PLC touch panel was used to make the inverter more simple and practical. The desired speeds can be easily adjusted on this screen.

The linear mixer relies on the ability to mix different powder materials with each other in a tube with the help of the balls used in existing systems. The tube is moved back and forth in the linear axis at high speeds. The agitator provides the necessary action for this operation by means of the crank-rod mechanism.

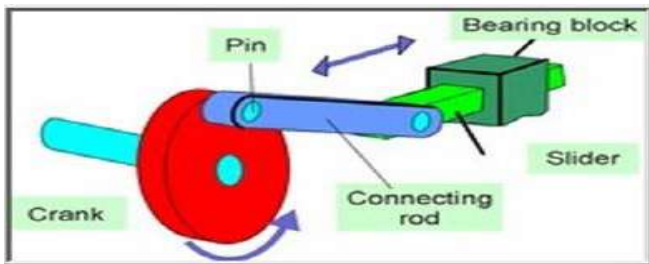


Fig. 7. Schematic demonstration of the new desing mixer

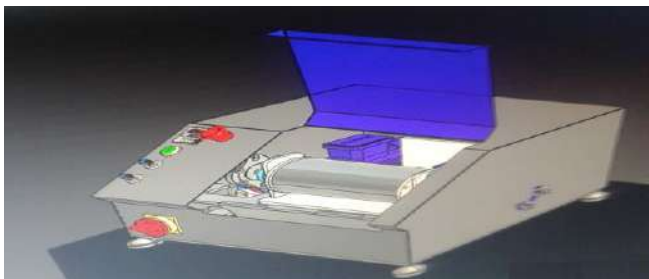


Fig. 8. The desinged machine

The crankshaft rotates the circular motion of the motor connected to the shaft to a linear motion by means of the crank, connecting rod. The tube placed on the sliding bar moves by adjusting with the help of the control panel at the desired speed between 0 and 3000d / d. In this respect, powder materials in the tube act by the propulsion force provided by the linear motion. Powder deposits that may form in the powder material during the movement and adverse conditions such as cold welding are lifted by the help of the balls in the tube. The absence of a mixer miller outside the

balls allows the movement of the powders to be only with the acceleration generated from the instantaneous velocity within the tube, allowing the parts to undergo less deformation and without excessive thermal rubbing. It has powder mixing capacity up to maximum 5kg.

VII. CONCLUSION

In previous methods, the disadvantages such as small amount of material mixing, batch forming, cold welding and thermal heat increase have been solved. In addition to these disadvantages, maximum speeds of 800-1000d/d have been reached, reaching speeds of 1000-3000d/d. This new type mixing and milling system was designed and manufactured with new style driving system.

VIII. REFERENCES

- [1] Çıtak, R., 1998, "Metalik Ba-Al Başlangıç tozlarının Düşük Sıcaklıklarda Oksidasyonu ile Al Matrisli Kompozit Üretimi", Doktora Tezi, Gazi Üniversitesi Fen Bilimleri Enstitüsü, Ankara, 2-26.
- [2] Sur, G., 2002, "Alüminyum Esaslı Kompozitlerin Üretimi ve İşlenebilirliğinin İncelenmesi", Yüksek Lisans Tezi, Gazi Üniversitesi Fen Bilimleri Enstitüsü, Ankara, 3-42.
- [3] Acılar, M., 2002, "Al/SiC Kompozitlerin Vakum infiltrasyon Yöntemi ile Üretimi ve Asınma Davranışlarının Araştırılması", Doktora Tezi, Gazi Üniversitesi Fen Bilimleri Enstitüsü, Ankara, 44-62.
- [4] Smith, W.F., 2012, Malzeme Bilimi ve Mühendisliği, Çeviri Kınkoğlu, N.G., Literatür
- Yayınılık, İstanbul,
- [5] Varol T., 2012, AA2024 Matrisli B4C Parçacık Takviyeli Metal Matrisli Kompozitlerin Toz Metalurjisi Yöntemiyle Üretimi Ve Özelliklerinin İncelenmesi, Yüksek Lisans Tezi, Karadeniz Teknik Üniversitesi Fen Bilimleri Enstitüsü, Trabzon, 3-6.
- [6] Nazik C., Tarakçıoğlu N., 2013, "Alüminyum Matrisli B4C Parçacık Takviyeli Kompozitlerin Toz Metalurjisi Yöntemiyle Üretimi ve Mekanik Özelliklerinin İncelenmesi", Yüksek Lisans Tezi, Selçuk Üniversitesi Fen Bilimleri Enstitüsü, Konya, 13-14.
- [7] Eker, A.A., 2008, Metal Matrisli Kompozit Malzemeler ve Üretim Yöntemleri, Yıldız Teknik Üniversitesi,
- http://www.yarbis.yildiz.edu.tr/web/userCourseMaterials/akdogan_81544a85d0e6510467de73b57b89f0fe.pdf
- [8] Şahin, Y., 2006, Kompozit Malzemelere Giriş, Ankara, 113-131.
- [9] Ünal, R., 2007, Toz Üretim
- http://rahmiunal.net/toz/tozuretimi/powder_product.html.
- [10] Suryanarayana, C., 2001, "Mechanical alloying and milling", Progress in Materials Science, 46: 1-184.
- [11] Retsch Cryomill
- [12] Claudio, L. D. C., Brian, S. M., Nanoparticles from Mechanical Attrition, Synthesis, Functionalization and Surface Treatment of Nanoparticles, M.I. Barton, editor, American Scientific Publishers, 2002.
- [13] Suryanarayana, C., Mechanical Alloying and Milling, ISBN 9780824741037 - CAT# DK1314, September 2004.
- [14] Dictionary of nanotechnology (Nanodictionary), http://www.nanodic.com/nanofabrication/Mechanical_alloying.htm, Erişim 1 Mayıs 2015.
- [15] Yazıcı, E., Ultrasonik sprej piroliz tekniğiyle küresel gümüş nano-parçacıklarının üretimi, İ.T.Ü. Fen bilimleri Enstitüsü yüksek lisans tezi, 2009.

Synthesis and Characterization of Photoluminescent $\text{Ho}_{1.90}\text{Eu}_{0.10}\text{Sn}_2\text{O}_7$ Material

Erkul KARACAOGLU

Department of Metallurgy and Materials
Karamanoglu Mehmetbey University
Karaman, TURKEY
ekaracaoglu@kmu.edu.tr

Esra ÖZTÜRK

Department of Metallurgy and Materials
Karamanoglu Mehmetbey University
Karaman, TURKEY

Abstract— $\text{A}_2^{3+}\text{B}_2^{4+}\text{O}_7$ pyrochlores, in which A sites are generally occupied by rare earth ions, are more common than those of formula $\text{A}_2^{2+}\text{B}_2^{5+}\text{O}_7$. Partial substitution at A and B cationic sites as well as oxygen sites is possible. Vacancies in the crystal lattice at A and oxygen sites are possible to a certain extent. The possibilities of selecting A and B cations or introducing lattice defects in these solids gives rise to a wide variety of chemical and physical properties [1]. Among the pyrochlores, the lanthanide stannates $\text{Ln}_2\text{Sn}_2\text{O}_7$ (Ln= rare-earths) with the cubic structure $\text{Fd}\bar{3}\text{m}$ have emerged as important functional materials due to their catalytic activity, defect structures and high thermal stability. They act as potential panacea for the material research fields, such as metal–semiconductor transitions, magnetic frustration/spin ices, colossal magnetoresistance, luminescence and superconductivity [2]. They also have a number of attractive features for designing catalysts, sensors, dielectrics, fast ion conductors, superconductors, ferromagnet, nuclear waste encapsulation, and thermal barrier coatings and high temperature stability. Rare earth stannate pyrochlores exhibit good catalytic activity and high thermal stability, which make them promising when used as a catalytic promoter in the electrode for electrochemical decomposition of NO_x [3].

In this research, the rare-earth stannate pyrochlore was synthesized by high temperature solid state reaction method under open atmosphere. The phase formation process was investigated by thermal analysis (DTA/TG) until 1600°C . The X-ray diffraction (XRD) analysis resulted as the cubic phase structure with lattice parameters $a=b=c=10.374 \text{ \AA}$ and $\alpha=\beta=\gamma=90^\circ$. The photoluminescence (PL) analysis including excitation, emission and decay time were determined by a PL spectrometer under room temperature. The excitation wavelength at 296 nm of sample was based on ligand-to- Eu^{3+} charge-transfer transitions (LMCT). The emissions at 622 nm and 711 nm concerning the typical $^5\text{D}_0 \rightarrow ^7\text{F}_2$ and $^5\text{D}_0 \rightarrow ^7\text{F}_4$ transitions of the Eu^{3+} -ions, respectively (Figure 1) [4].

Keywords— Rare-earth stannate pyrochlore; Eu^{3+} ; solid-state reaction; photoluminescence.

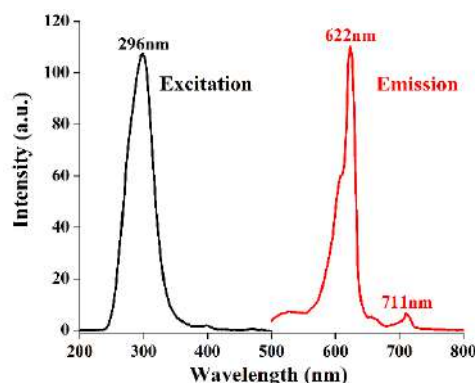


Figure 1. The PL spectra of $\text{Ho}_{1.90}\text{Eu}_{0.10}\text{Sn}_2\text{O}_7$ pyrochlore.

ACKNOWLEDGMENT

The authors would like to thank TUBITAK (The Scientific and Technological Research Council of Turkey) for the support to the project numbered 114Z438.

REFERENCES

- [1] R. Trujillano, M. Douma, El H. Chtoun, V. Rives, "Crystallographic Study by X-ray Rietveld Analysis of New Synthetic Pyrochlores $[\text{Eu}_{2-x}\text{M}_x][\text{Sn}_{2-x}\text{M}_x]\text{O}_{7-3x/2}$ (M = Mg or Zn)", revista de la sociedad española de mineralogía, 11, 187-188, 2009.
- [2] W. Wang, S. Liang, J. Bi, J. C. Yu, P. K. Wong, L. Wu, "Lanthanide stannate pyrochlores $\text{Ln}_2\text{Sn}_2\text{O}_7$ (Ln = Nd, Sm, Eu, Gd, Er, Yb) nanocrystals: Synthesis, characterization, and photocatalytic properties", Mat. Res. Bull., 56, 86–91, 2014.
- [3] J. Feng, B. Xiao, Z. X. Qu, R. Zhou, W. Pan, "Mechanical properties of rare earth stannate pyrochlores", Appl. Phys. Lett., 99, 201909, 2011.
- [4] F. Zhang, Y. Wang, Y. Tao, "VUV spectroscopic properties of $\text{Ba}_2\text{Gd}_2\text{Si}_4\text{O}_{13}:\text{Re}^{3+}$ ($\text{Re}^{3+} = \text{Ce}^{3+}, \text{Tb}^{3+}, \text{Dy}^{3+}, \text{Eu}^{3+}, \text{Sm}^{3+}$)", Mat. Res. Bull., 48, 1952–1956, 2013.

Characterization and Calcination of a Turkish Manganese Ore

Saeid POURNADERI

Department of Metallurgical and Materials Engineering,
Karadeniz Technical University,
Trabzon, Turkey
s.pournaderi@gmail.com

Yavuz A. TOPKAYA, Naci SEVİNÇ

Department of Metallurgical and Materials Engineering,
Middle East Technical University,
Ankara, Turkey

Abstract— A Turkish manganese ore was characterized and its calcination behavior was studied. The ore contained 40.43% manganese and 6.67% iron. The XRD analysis of the Run-of-Mine ore revealed that it was composed mainly of pyrosulite, calcite, goethite, quartz. The ore also contained minor amounts of clay minerals. Thermal analysis of the sample recorded five endothermic peaks at different temperatures ranging from 100 to 900°C. In order to determine the transformations during the course of heating, ore samples were calcined at specified temperatures according to the thermal analysis of the ore. Mineralogical changes were traced by the use of XRD. The main reactions during the calcination were decomposition of goethite at 300-400°C, dehydroxylation of clay minerals at 400-500°C, decomposition of MnO₂ to Mn₂O₃ at 600-700°C, decomposition of calcite at 700-900°C and decomposition of Mn₂O₃ to Mn₃O₄ above 1000°C.

Keywords— Manganese ore; Characterization; Calcination

I. INTRODUCTION

Manganese is one of the most important additives in the iron and steel industry. It acts as both sulfide former and deoxidant. In addition, it improves hardenability, workability, wear resistance and mechanical properties of the iron alloys [1]. Manganese is generally added to the molten alloy in the form of ferromanganese and silicomanganese. About 85% of the produced manganese is used in steelmaking as ferromanganese [2]. Ferromanganese has conventionally been smelted in blast furnaces. Nevertheless, the blast furnaces have been replaced by electric arc furnaces over time (Fig. 1) mainly due to the lower average production cost per ton of the product.

Although not very large, there are lots of manganese reserve in Turkey distributed throughout the country [4] and some researches have been conducted on the production of ferromanganese from these ores [5]. In spite of the fact that some of the reserves are large enough to commercially be considered, ferromanganese is not smelted in Turkey thanks to the expensive electrical energy which increases the

production cost and discourages investment. A cost-effective alternative way for the electric arc furnace process may be the Rotary Kiln-Electric Furnace (RKEF) process through which the ore is dried, calcined and prereduced in a rotary kiln [4]. The hot calcine from the rotary kiln can be directly charged into the arc furnace. The objective is to carry out a part of the energy-intensive smelting process by the low cost hydrocarbon fuels in the rotary kiln thereby decreasing the electrical energy consumption in the arc furnace. In addition, the calcination and prereduction of the ore in the rotary kiln eliminate volatile matters and substantial portion of oxygen in the ore which in turn provides an enriched charge to the arc furnace.

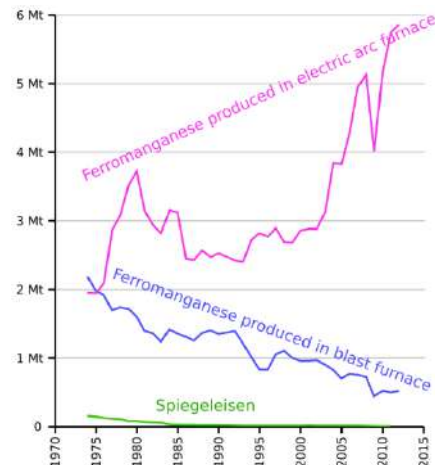


Fig. 1. Evolution of global manganese production, by processes [2].

A successful application of the RKEF process for the treatment of manganese ores requires a comprehensive study of the ore behavior upon heating. However, there are only a limited number of researches [7, 8, 9] addressing the chemical and mineralogical changes of the ore during heating. Manganese ores show significant variations in chemistry and mineralogy and this intensifies the need for further investigations on thermal decomposition of these ores. This

article reports the results of a laboratory-scale research on the calcination behavior of a Turkish manganese ore.

II. EXPERIMENTAL PROCEDURE

A. Ore Preparation

Ten kilograms of a representative run-of-mine (ROM) ore was received. The ore was further crushed to -1 mm and divided into batches of about 50 g which were used in the experiments. One batch was finely ground which was used for characterization of the ROM ore.

B. Characterization of the Ore

The finely ground ore was analyzed for its Mn and Fe content by ICP. Mineralogical analysis of the ore was achieved by XRD. Differential thermal analysis (DTA) and thermogravimetric analysis (TGA) were carried out to study the thermal behavior of the ore. Twenty milligrams of the ground ore was heated from ambient temperature to 1000°C at a rate of 10°C/min- in air.

C. Calcination of the Ore

A muffle furnace was used for the calcination experiments. The ore was dried overnight before calcination. Forty five grams of -1 mm dried ore was charged into an alumina crucible and heated in air to constant weight at predetermined temperatures. The calcined samples were analyzed by XRD to determine the mineralogical changes during the calcination.

III. RESULTS AND DISCUSSION

A. Chemical Analysis

Manganese and iron concentrations of the ore are given in Table 1.

Table 1. Manganese and iron concentrations in the ROM ore.

Mn ⁺⁴	Mn ⁺²	Mn (Total)	Fe
37.77	2.66	40.43	6.67

B. XRD Analysis

The XRD pattern of the ROM ore is shown in Fig. 2. The ore was mainly composed of pyrosulite (MnO₂) and calcite (CaCO₃). Goethite and quartz were also present in minor quantities. In addition, small amounts of clay minerals, identified by a weak peak at 2θ about 9, were present in the ore.

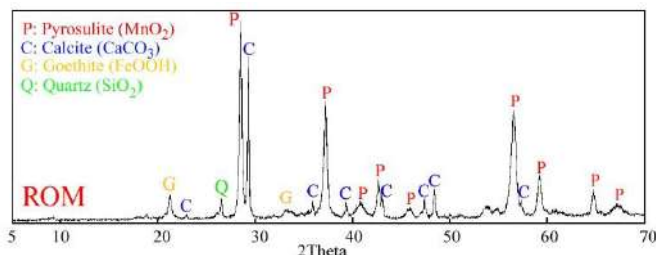


Fig. 2. The XRD pattern of the ROM ore.

C. Thermal Analysis

DTA and TGA curves of the ore are shown in Fig. 3. Three weak endothermic peaks at about 100, 350 and 450°C together with three intense peaks between 600 and 800°C were recorded. Sample weight decreased mildly up to 600°C but decreased significantly between 600 and 800°C. Sample weight remained almost unchanged up to 950°C and again began to decrease at higher temperatures. The low-temperature endothermic peaks at about 100°C was related to the evaporation of free water. It was difficult to discuss about the nature of the other effects using only the current diagram. For this reason, calcination experiments were conducted at different temperatures and XRD was used to identify any possible reactions or transformations taking place during the course of heating.

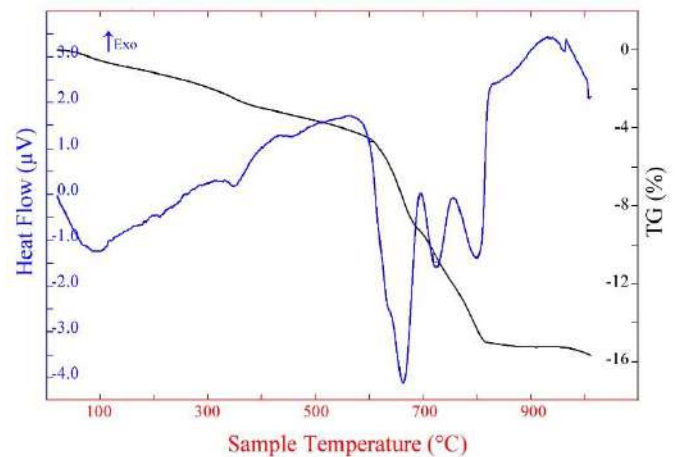


Fig. 3. DTA/TGA results of the ROM ore.

D. Calcination Experiments

Fig. 4 illustrates how the sample weight changed during calcination at different temperatures. Only about 1.8% of the sample weight lost at 300°C. Heating of the sample at 500°C increased the final weight loss to about 3.5% and, at the same time, decreased the calcination time by about 15 min-.

Comparing the XRD pattern of the sample calcined at 300°C (Fig. 5) and that of the ROM ore in Fig. 1, it was concluded that the main fraction of the goethite dehydroxylated at this temperature. The remainder dehydroxylated when the sample heated at 400°C as the characteristic peaks of goethite completely disappeared at this temperature. The reaction can be written as below:



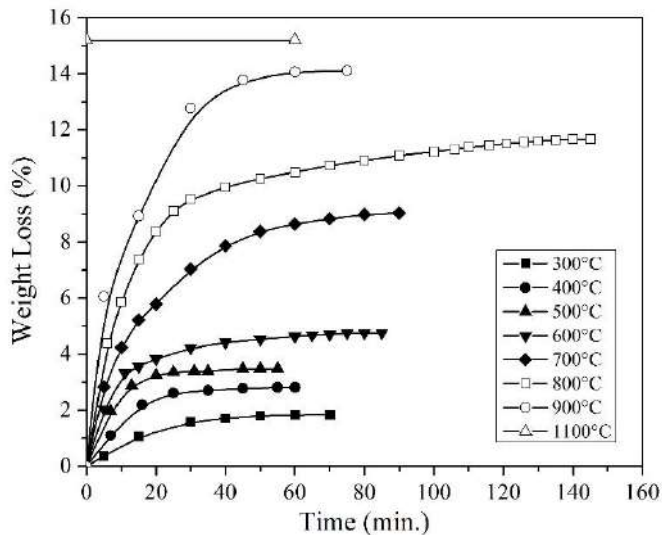


Fig. 4. Weight loss at various temperatures as a function of time.

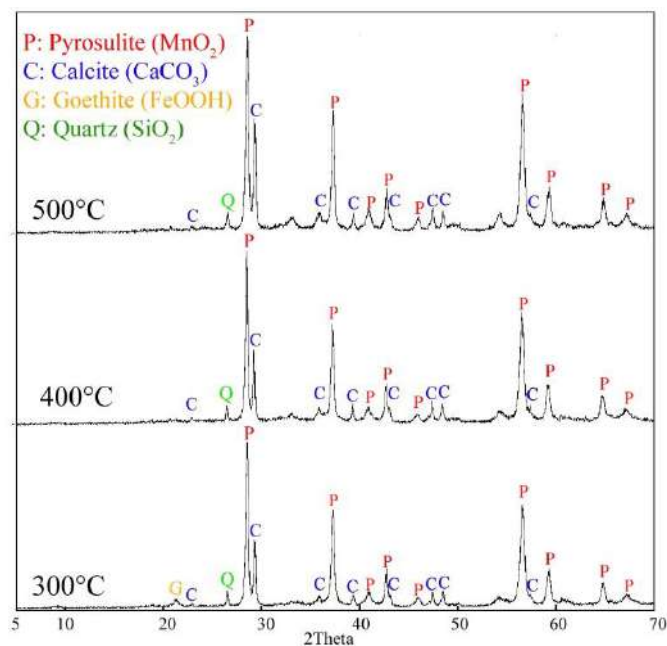


Fig. 5. The XRD pattern of the samples calcined at 300, 400 and 500°C.

Although no change was detected between 400 and 500°C from XRD (Fig. 5), the weight of the sample continued to decrease in between. This weight loss may be attributed to the dehydroxylation of clay minerals which were present in minor quantities in the ore. Accordingly, the endothermic peaks at 350 and 450°C in DTA result (see Fig. 3) can be related to the dehydroxylation of goethite and clay minerals, respectively.

When the ore heated to 600°C, the final weight loss increased to about 4.8% while the calcination time also increased to more than 80 min. The increased time at 600°C implied that at least one new reaction began between 500 and

600°C. Calcination of the ore at 700°C resulted in a considerable increase in the weight loss. It was almost doubled when temperature increased from 600 to 700°C. This results are in agreement with the thermal analysis of the ore (see Fig. 3) according to which an endothermic reaction initiates just below 600°C and reached its maximum at about 675°C. This endothermic peak accompanied with a sharp decrease in the weight of the sample.

The XRD pattern of the samples calcined at 600 and 700°C are given in Fig. 6. This figure also includes the XRD pattern of the sample calcined at 500°C for comparison. A careful examination of these patterns revealed that the characteristic peaks of pyrosulite weakened as temperature rose and only a very small peak remained when it reached 700°C. At this temperature a new phase, bixbyite (Mn_2O_3), came to existence. Therefore, the strong peak at about 675°C and associated large weight loss in DTA results (see Fig. 3) were related to the transformation of MnO_2 to Mn_2O_3 based on the reaction below:

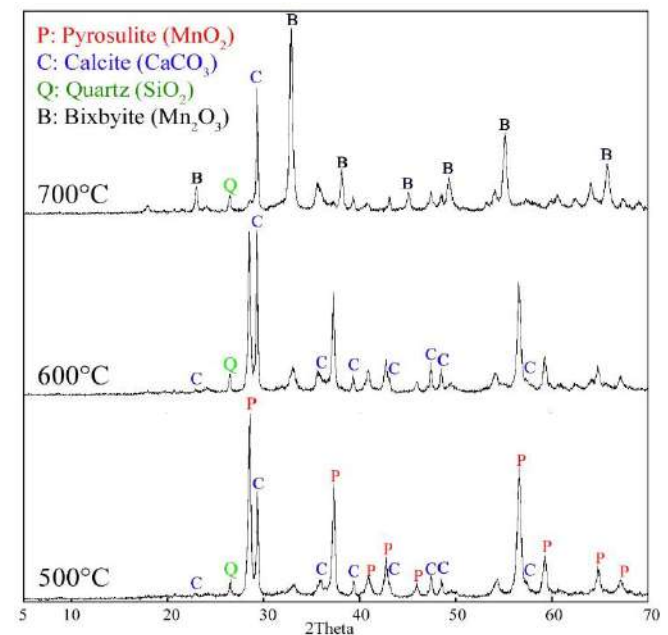


Fig. 6. The XRD pattern of the samples calcined at 500, 600 and 700°C.

The sample continued to lose weight at higher temperatures and the final weight loss reached about 11.7% at 800°C and 14.1% at 900°C. The longer calcination time at 800°C was indicative of a new reaction at this temperature. Examination of the XRD patterns of the samples calcined at 700, 800 and 900°C (Fig. 7) indicated that calcite decomposed above 700°C. Calcite decomposes to give CaO and CO_2 according to the reaction below:



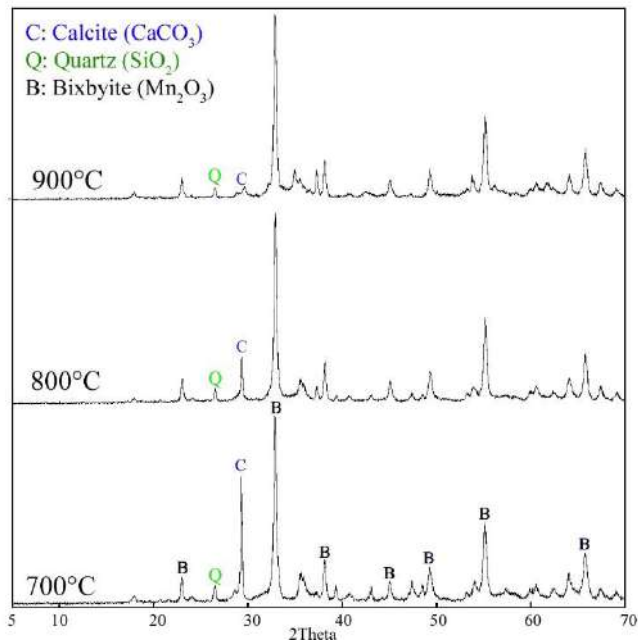


Fig. 7. The XRD pattern of the samples calcined at 700, 800 and 900°C.

Although no other transformation could be detected from the XRD analysis, there were two endothermic peaks at about 720 and 800°C in the DTA results. One possible explanation may be that the decomposition of calcite was achieved via a two-step process.

The thermal analysis (see Fig. 3) showed that the weight of the sample remained almost unchanged above 850°C, but again began to decrease when temperature exceeded 950°C. Another sample was calcined at 1100°C for 60 minutes. Weight of the sample was recorded at the end of the experiment. The weight loss at this temperature was obtained to be 15.2%. The XRD analysis of this sample (Fig. 8) revealed that Mn_2O_3 transforms into Mn_3O_4 according to the reaction below:

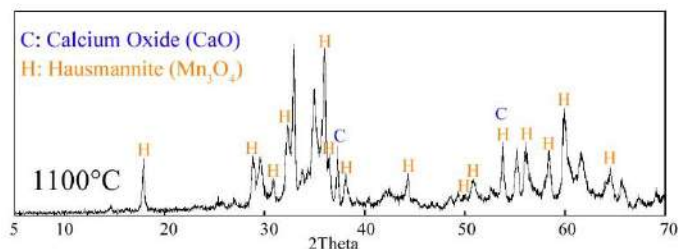


Fig. 8. The XRD pattern of the sample calcined at 1100°C.

IV. CONCLUSION

Calcination behavior of a Turkish manganese ore was studied. The calcination process included dehydroxylation of hydroxide minerals and decomposition of carbonate and oxide minerals all of which are highly endothermic reactions. In the electric arc furnace process, the ore is directly charged into the furnace and calcination reactions, therefore, take place at the expense of expensive electrical energy. The rotary kiln-electric furnace (RKEF) process, which uses low cost hydrocarbon fuels, can be an alternative for the electric arc furnace process. Reduction behavior of the ore is not included in this article. However, in the rotary kiln, reduction reactions also take place because of its reducing atmosphere. Reduction reactions can even be encouraged by the addition of coal to the rotary kiln. This can additionally reduce the energy consumption in the electric arc furnace.

REFERENCES

- [1] G. Krauss, Steels: processing, structure, and performance, United States of America: ASM International, 2005.
- [2] D.B. Wellbeloved, P.M. Craven, J.W. Waudby, "Manganese and Manganese Alloys", Ullmann's Encyclopedia of Industrial Chemistry.
- [3] Wikipedia, The Free Encyclopedia, [Online]. Available: <https://en.wikipedia.org/wiki/Ferromanganese>. [Accessed 25 02 2017].
- [4] G. Ateşok, "Türkiye çamganez yataklarının değerlendirilmesi ve konunun ülkemiz açısından önemi," [Online]. Available: http://www.maden.org.tr/resimler/ekler/40ac9371ec2671a_ek.pdf. [Accessed 25 02 2017].
- [5] İ. S. Çardaklı, N. Sevinç and T. Öztürk, "Production of high carbon ferromanganese from a manganese ore located in Erzincan," *Turkish J. Eng. Env. Sci.*, vol. 35, pp. 31-38, 2011.
- [6] T. Ogura, K. Kuwayama, A. Ono and Y. Yamada, "Production of Fe-Ni by the rotary kiln-electric furnace process at Hyuga Smelter," *Inter. J. Miner. Proc.*, vol. 19, no. 1-4, pp. 189-198, 1987.
- [7] M. Pereira, M. Lima and R. Lima, "Calcination and characterisation studies of a Brazilian manganese ore tailing," *Int. J. Miner. Process.*, vol. 131, pp. 26-30, 2014.
- [8] B. Sorensen, S. Gaal, E. Ringdalen, M. Tangstad, R. Kononov and O. Ostrovski, "Phase compositions of manganese ores and their change in the process of calcination," *Int. J. Miner. Process.*, vol. 94, pp. 101-110, 2010.
- [9] A. Geveci, H. Keçeli, Y. A. Topkaya and N. Sevinç, "Calcination of the Turkish manganese ore from Denizli-Tavas region" *Fizykochemiczne Problemy Mineralurgii*, vol. 32, pp. 203-2013, 1998.

Dissolution Behaviour of Base Metals in Ionic Liquid during Recovery of Valuable Metals from Anode Slime

Mehmet Ali TOPÇU

Department of Metallurgical and Materials Engineering
Karamanoglu Mehmetbey University
Karaman, Turkey

Aydın RÜŞEN

Department of Metallurgical and Materials Engineering
Karamanoglu Mehmetbey University
Karaman, Turkey

Abstract— In recent years, ionic liquids are frequently used to recover valuable metals from ores and secondary sources by hydrometallurgical method. However, besides precious metals, the dissolution of undesirable metals is a major problem in terms of cleaning the pregnant solution. Copper anode slime is an industrial waste which has economic value due to the presence of precious metals such as copper, gold, silver and platinum group metals. In this paper, the dissolution behaviour of base metals (Pb, Sn, Zn, Ni, Ba and Sb) in 1-ethyl-3-methylimidazolium hydrogen sulphate ($\text{Emim}[\text{HSO}_4]$, $\geq 95\%$) ionic liquid during the precious metal recovery from anode slime was investigated for different experimental conditions. The chemical analysis of anode slime indicated that it was consisted of 23.32% Cu, 20.51% Sn, 15.40% Pb, 5.87% Ba, 0.55% Sb, 0.13% Zn, 0.013% Fe, 2204.2 ppm Ag, and 21.9 ppm Au. According to mineralogical characterization, it was mainly composed of PbSO_4 , SnO_2 and Cu_2O . After several trials, the experimental results showed that Pb, Sn, Zn, Ni and Sb had low dissolution rate in ionic liquid. On the contrary, Ba dissolution rate increased with increasing ionic liquid concentration and temperature. According to the results, low dissolution rates of base metals make attractive this new leaching agent to recover precious metals from copper anode slime.

Keywords—Anode Slime; Leaching, Ionic Liquid, Dissolution

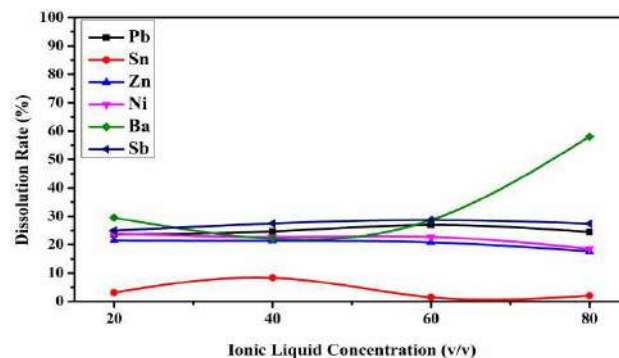


Figure 1. Dissolution behaviour of base metals with ionic liquid concentration

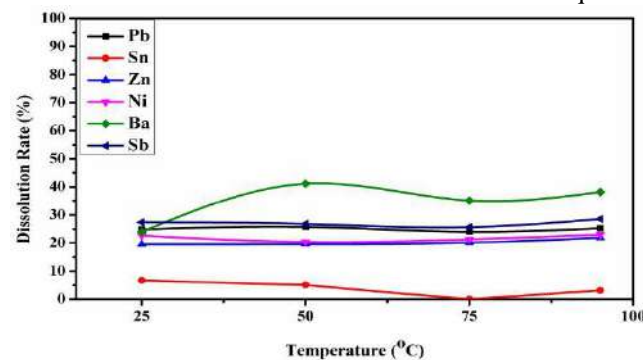


Figure 2. Dissolution behaviour of base metals with temperature

ACKNOWLEDGMENT

This work was supported by Karamanoğlu Mehmetbey University Scientific Research Council (BAP) with project no KMU-BAP-04-YL-16.

REFERENCES

- [1] Wang, S., Cui, W., Zhang, G., Zhang, L., & Peng, J. (2017). Ultra fast ultrasound-assisted decopperization from copper anode slime. *Ultrasonics Sonochemistry*, 36, 20-26.
- [2] Sethurajan, M., Huguenot, D., Jain, R., Lens, P. N., Horn, H. A., Figueiredo, L. H., & Van Hullebusch, E. D. (2017). Leaching and selective zinc recovery from acidic leachates of zinc metallurgical leach residues. *Journal of hazardous materials*, 324, 71-82.
- [3] Tian, Q., Xin, Y., Wang, H., & Guo, X. (2017). Potential-controlled selective recovery of manganese and cobalt from cobalt slag leaching solution. *Hydrometallurgy*, 169, 201-206.

CHEMICAL ENGINEERING

ORAL SUBMISSIONS



Adsorption of Basic Blue 3 Dye Molecules from Aqueous Media By Sulfuric Acid-Activated Montmorillonite Mineral

Şeyda TAŞAR

Department of Chemical Engineering
Firat University
Elazig, Turkey
sydtasar@firat.edu.tr

Fatih KAYA

Department of Chemical Engineering
Firat University
Elazig, Turkey
fatihkaya@firat.edu.tr

Ahmet ÖZER

Department of Chemical Engineering
Firat University
Elazig, Turkey
aozer@firat.edu.tr

Abstract— In this study, sulfuric acid-activated montmorillonite mineral (SAM) was used as an adsorbent for the removal of Basic Blue 3 (BB3) from aqueous media. The natural montmorillonite mineral (NM) was activated by treating with a 6 M H_2SO_4 solution for 4 hours at 395 K. After sulfuric acid treatment the SAM samples were characterized using a BET surface analyzer and FTIR spectroscopy. The adsorption kinetics and equilibrium of BB3 from aqueous media on SAM were investigated in a batch system at various conditions, i.e., contact times (0-120 min), initial pH values (2-8), temperatures (298-318 K), and initial dye concentrations (100-350 mg/l).

The experimental results indicated that the optimum values of temperature, initial pH, initial BB3 concentration of aqueous media, and contact time were 298 K, 6 ± 0.02 , 350 ppm, and 60 min, respectively. The maximum adsorption capacity was determined to be 277 mg/g at the optimum conditions. Langmuir and Freundlich isotherm models were used to describe the equilibrium data mathematically. The isotherm constants were calculated at different temperatures. It was observed that the adsorption of BB3 onto SAM was described better by the Freundlich isotherm. Pseudo first-order and second-order kinetic model constants were calculated for the adsorption kinetics. The pseudo second-order model was the best-fitting model for the adsorption kinetics of BB3 on SAM. The thermodynamic parameters of adsorption, which were calculated using thermodynamic equations, indicated that the removal process was spontaneous at all values of temperatures and the exothermic nature of adsorption. The results of the study showed that, compared with commercial adsorbents, SAM could be used as a low-cost and suitable adsorbent for the adsorption of BB3 from aqueous media.

Keywords: Adsorption, basic blue 3, sulfuric acid-activated montmorillonite mineral (SAM), thermodynamic and kinetic parameters

I. INTRODUCTION

The textile industry is one of the fastest-growing major industries in Turkey. The wastewaters released from this industry contain high amounts of dyes and pigments, which generally have been synthesized and contain complex aromatic molecules. They contain a lot of double bonds and various functional groups [1]. Therefore these dyes and pigments are

not biologically decomposed due to their stable structures, so they accumulate easily in natural bodies of water [2]. When these wastewaters are discharged into aquatic media, serious environmental problems may be occurred such as impairment of the aesthetic nature, the reduction of the degree of penetration of light and decrease in the solubility of gases. [3]. Such effluents can also cause cancer, skin irritation, allergic dermatitis and mutations [2-4]. For that reason the removal of pigments and dyes from wastewater is very important for the protection of the ecosystem and the health of people who may use or be exposed to that waste waters. Many treatment techniques can be used for the removal of these pollutants from wastewater before they are discharged to aquatic media. These techniques include adsorption [5-11], membrane processes [12], oxidation processes [13], ion exchange [7,8], reverse osmosis [14], electrocoagulation [2], and coagulation [15]. Unlike other remediation techniques, the adsorption process is considered to be one of the most attractive treatment options because of its simplicity, ease of use, and high efficiency [16-18]. It is known that the cost, sustainable resource, accessibility and adsorptive capacity of the adsorbent are very significant parameters that affect the efficiency, effectiveness, and costs of the process.

The aim of this research was to investigate the adsorption kinetics and thermodynamic characteristics of Basic Blue 3 (BB3) on sulfuric acid-activated montmorillonite mineral (SAM). To do this, the SAM samples were firstly characterized with BET and FTIR techniques. Then, the effects of the adsorption parameters on the efficiency and rate of adsorption of BB3 on the SAM samples were investigated in a batch system. The thermodynamic and kinetic parameters were calculated using appropriate models.

II. MATERIAL AND METHODS

A. Preparation and characterization of adsorbent

The natural montmorillonite mineral was provided by a local industry in Elazig, Turkey. The mineral was dried at 105 °C in an oven and then divided into fractions based on the particle

sizes. The fraction between 50 and 100 mesh was activated using 6 M H₂SO₄ solution at 97 °C for 6 hr. After the activation process, the sulphuric-activated montmorillonite mineral (SAM) was washed with water until the sulphate ions were completely removed. The SAM samples were stored in desiccators for subsequent use in the study.

The SAM samples were characterized using BET Surface Area Analyzer (ASAP 2020, Micromeritics Inc., USA) and FTIR spectrometer (ATI Unicam Mattson 1000). The pH of zero point of charge (pH_{zpc}) of the activated montmorillonite mineral was measured by using the pH drift methods [19, 20]. FTIR spectra were recorded using an FTIR spectrometer by averaging 16 scans. IR absorbance data were obtained for the range of wave numbers from 400 to 4000 cm⁻¹. BET surface area of SAM samples analysis was determined by the adsorption of N₂ at 77 K.

B. Experimental Procedure

The stock solution of Basic Blue 3 (BB3) was prepared from 25 % dye content, Sigma Aldrich in a concentration of 1000 mg/L. All working solutions were prepared by diluting stock solution of BB3 using distilled water. During the experimental studies, (especially in studies in which the effects of pH were investigated), the pH values of the solutions were adjusted using 0.1 M solutions of NaOH and HCl.

The experiments were performed in 14 parallel erlenmeyer flasks using a thermostatic water bath and a mechanical shaker at an agitation speed of 180 rpm. The contents of all of the erlenmeyer flasks were prepared in the same conditions. Each experiment was conducted by mixing 50 ml of the BB3 solution with a certain amount of SAM in 100-ml erlenmeyer flasks. The adsorption of BB3 on SAM were carried out by investigated the affects of various parameters such as temperature of solution (298-318 K), initial pH (2-8), contact time (5-120 min) and initial concentration of BB3 (100-350 ppm). At the end of the desired contact time, each flask was removed from the water bath and the SAM was separated from the aqueous phase by centrifugation at 5000 rpm for three minute. The residual concentration of BB3 in the filtrate was analyzed by a UV-vis spectrophotometer. The experiments were performed in duplicate, and the average results were reported. The adsorption efficiency and the adsorption capacity of the SAM, q_e (mg/g), which is expressed as the quantity of BB3 adsorbed by using the SAM, were calculated using Eqs. (1) and (2), respectively.

$$\text{Adsorption efficiency}(\%) = \frac{C_o - C_e}{C_o} \times 100 \quad (1)$$

$$q_e = \frac{v \times (C_o - C_e)}{m}, \quad (2)$$

In that equations, m (g) is the mass of the SAM, v (L) is the volume of the BB3 solution, q_e (mg/g) is the adsorption capacity of SAM, C_o (mg/L) is the initial concentration of BB3 molecules in solution, and C_e (mg/L) is the final (equilibrium) concentration of BB3 molecules in solution.

III. RESULT AND DISCUSSION

The average pore diameter and single-point BET surface area were determined by the nitrogen adsorption method as 21.2 Å and 113.3 m²/g for the sulfuric acid activated montmorillonit mineral (SAM). Same quantities for the natural montmorillonite mineral (NM), were obtained as 65.4 Å and 73.6 m²/g.

Fourier transform infrared (FTIR) spectroscopy was used to identify the functional groups on the surface of montmorillonite mineral before and after activation, and the significant peaks are given in Table 1. Researchers have reported similar peaks for other clay minerals in the literature [21, 22].

It is well known that the point of zero charge (pH_{zpc}), which is indicative of the types of surface active centers and the adsorption mobility of surface, is an important factor in adsorption processes [23]. Fig.1, which was drawn using the drift method, shows that the value of pH_{zpc} was 5.1. The experimental results indicated that, when the pH of the BB3 solution was less than 5.1, the surface of the SAM was positively charged and could attract anions from the solution. When the pH of the solution was greater than 5.1, the surface of the SAM was negatively charged and attracted cations.

Table 1. FTIR spectrum of the SAM and NM

Frequency (cm ⁻¹)		Assignment
After activation SAM	Before activation NM	
3435	3403	OH stretching of inner hydroxyl groups
-	2930	Aliphatic C-H stretching
1639	1633	OH deformation of water
-	1516	C=C stretching vibrations of aromatic ring
1415	1420	Aromatic methyl (-CH ₃) group vibrations
-	1262	C-H bending
1074	1043	Si-O stretching
1013	-	In-plane Si-O stretching
794	-	Si-O
690	690	Si-O perpendicular
525	530	Al-O-Si deformation
469	469	Si-O-Si deformation
433	-	Si-O deformation

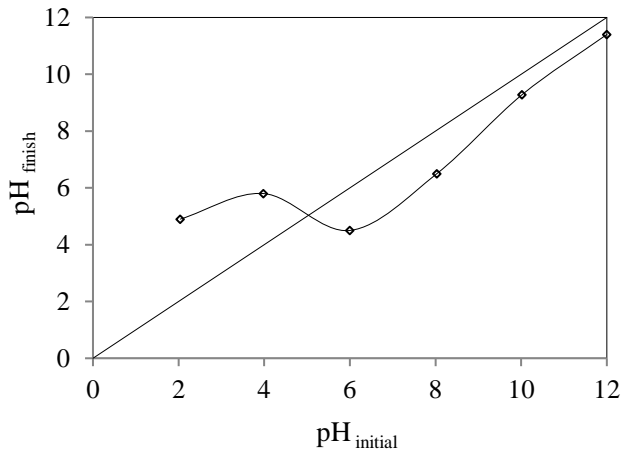


Figure 1. Zeta potential of SAM.

Effect of the initial pH of the solution and the contact time:

Figure 2 shows the relationship between contact time and the adsorption capacity of the SAM for different initial pH values. The figure indicates that the adsorption of the BB3 molecules was relatively higher in the first 30 min. After that period the adsorption efficiency declined because the active sites on the surface area available for adsorption was decreased. Also, the high adsorption efficiency during the initial stage have been due to the higher driving force's producing faster transfer of BB3 molecules to the surface of the SAM. In addition, the adsorption capacity of the SAM increased with contact time and reached its maximum value in the range of 85-99 mg/g for different initial pH values after approximately 60 min. After this time, the adsorption capacity remained almost constant, for that reason contact time of 60 min was considered the equilibrium time for BB3 adsorption.

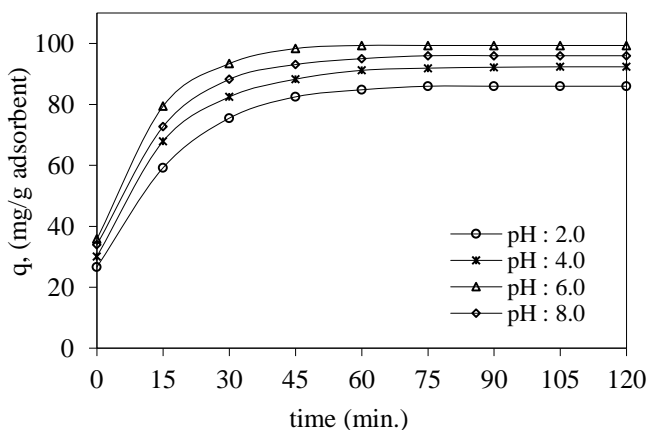


Figure 2. Effect of contact time on adsorption capacity of SAM (initial BB3 con. 100 ppm; contact time: 120 min; SAM con: 2 g/L; temperature: 298 K)

It can be seen that the initial pH of the BB3 solution was a significant parameter (Figure 3), The adsorption capacity of BB3 molecules increased linearly up to a maximum value of

about 99 mg/g as the pH of the solution was increased up to 6.0. After that point the adsorption capacity decreased.

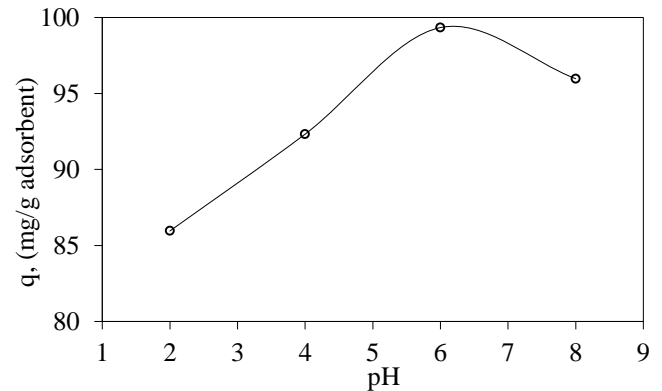


Figure 3. Effect of initial pH on adsorption capacity of SAM (initial BB3 con. 100 ppm; contact time: 120 min; SAM con: 2 g/L; temperature: 298 K)

These results indicated that the initial pH of the BB3 solution affected the surface charges of the SAM, the concentration of the counter ions on the functional groups of the SAM and the degree of ionization/dissociation of the SAM during adsorption [24-26]. These results are consistent with the pH_{zpc} value of the SAM samples ($pH_{zpc} = 5.1$). Similar results have been reported in the literature [27].

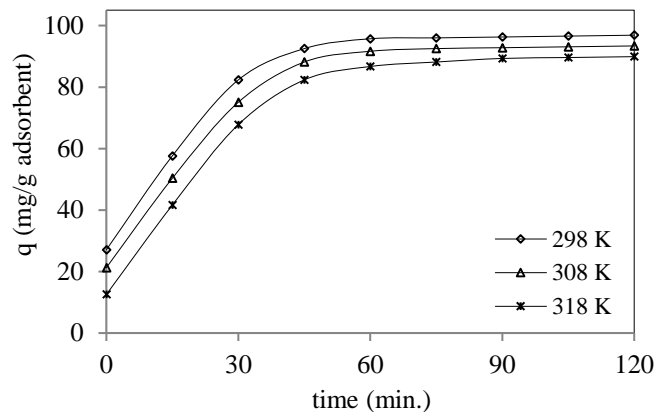


Figure 4. Effect of temperature on adsorption capacity of SAM (initial BB3 con. 100 ppm; contact time: 120 min; SAM con: 2 g/L; pH: 6±0.02)

The kinetic analysis of the adsorption: The effect of the temperature on the adsorption of BB3 molecules by SAM in is shown in Fig.4. It was observed that the adsorptive capacity of the SAM was increased as the temperature decreased from 318 K to 298 K. The equilibrium adsorption capacity of the SAM was determined to be about 97 and 89 mg BB3/g at 298 and 318 K, respectively. The increase in the removal of BB3 with decrease in temperature of solution showed that the adsorption process was exothermic.

Adsorption processes are time dependent; therefore, while designing the reactor for this process, the relationship between the adsorption rate and the contact time should be known. This relationship can be demonstrated by kinetic model equations. For that reason, the adsorption data were analyzed with pseudo first-order and pseudo second-order kinetic models. The pseudo first-order kinetic model of Lagergren is given as [28]:

$$\frac{dq_t}{dt} = k_1(q_e - q_t) \quad (3)$$

By integrating of Eq (3) for the boundary conditions from $t = 0$ to $t = t$, the following equation is obtain.

$$\ln(q_e - q_t) = \ln q_e - k_1 t \quad (4)$$

The pseudo second-order model is given by Eq. (5) [29]:

$$\frac{dq_t}{dt} = k_2(q_e - q_t)^2 \quad (5)$$

The linearized integrated form of Eq. (5) is given by Eq. (6):

$$\frac{t}{q_t} = \frac{1}{k_2 q_e^2} + \frac{t}{q_e} \quad (6)$$

Where t (min) is the contact time; q_e (mg/g) and q_t (mg/g) are the amounts of BB3 on the surface of the SAM at equilibrium and at any contact time, respectively; and k_2 (g/mg min) and k_1 (min⁻¹) are the pseudo second-order and the pseudo first-order rate constants, respectively.

The values of the adsorption rate constant (k_1) can be obtained from the plot of $\ln(q_e - q_t)$ against t (Fig. 5). The rate parameters, k_2 and q_e , can be obtained from the plot of (t/q_t) versus t (Fig. 6).

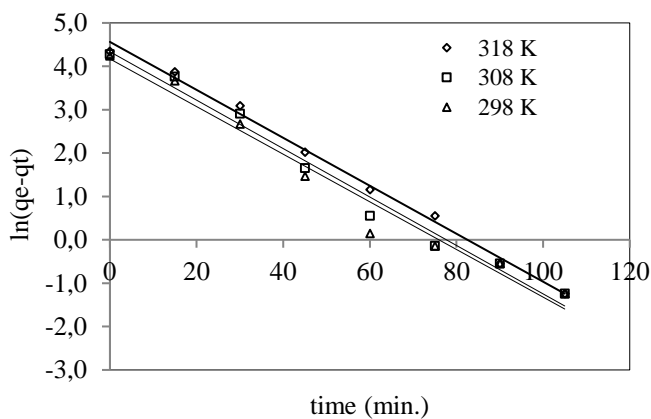


Figure 5. Pseudo first-order kinetic plots for the removal of BB3 molecules

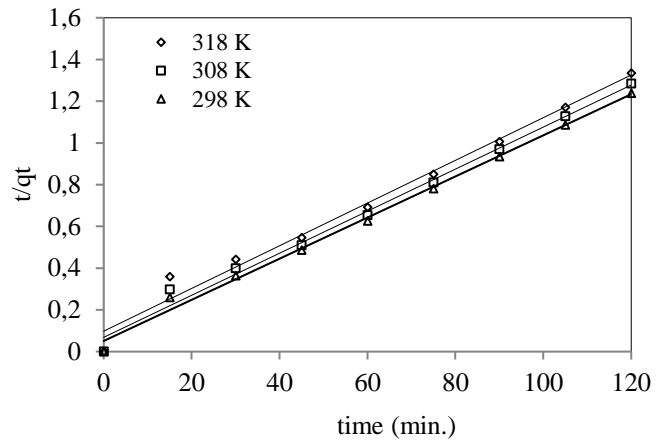


Figure 6. Pseudo second-order kinetic plots for the removal of BB3 molecules

Table 2. Kinetic parameters for the removal of BB3 by SAM

Temperature (K)	q_e (mg/g)	Pseudo-first-order kinetic model		
		R^2	$k_1 \times 10^3$ (min ⁻¹)	q_{ec1} (mg/g)
298	99.3	0.97	54.9	64.71
308	93.4	0.98	55.8	76.71
318	89.8	0.99	55.3	95.85
Temperature (K)	q_e (mg/g)	Pseudo-second-order kinetic model		
		R^2	$k_2 \times 10^3$ (g/mg min)	q_{ec2} (mg/g)
298	99.3	0.99	1.1	101.0
308	93.4	0.99	1.5	99.00
318	89.8	0.98	1.9	98.04

The values of k_1 , q_{ec1} , k_2 , q_{ec2} , and the correlation coefficient (R^2) are given in Table 2. The correlation coefficient (R^2) and the difference between the calculated adsorption capacity (q_{ec}) and the experimental adsorption capacity (q_e) indicate that the pseudo second-order kinetic model simulated the kinetic data better than the pseudo first-order kinetic model.

Thus, the rate constants (k_2) of the pseudo second-order model in the Arrhenius equation (Eq. 7) were used to calculate the activation energy of the adsorption process of BB3 molecules by the SAM.

$$\ln k_2 = \ln A - \frac{E_a}{RT} \quad (7)$$

Where A (g/mg min) is the Arrhenius constant; E_a (J/mol) is the activation energy; T (K) is the temperature of the solution; and R (8.314 J/mol K) is the ideal gas constant.

To calculate the activation energy (E_a) for the adsorption process, $\ln k_2$ was plotted versus $1/T$. The activation energy value (E_a) was calculated as about 19 kJ/mol, and this value indicated that physical adsorption is a dominate mechanisms on the removal process. On the other hand, it was observed that the values of q_{ec2} increased and the values of k_2 decreased with decrease in temperature. These results indicated that the

adsorption of BB3 by the SAM occurred more rapidly at higher temperatures.

The thermodynamic analysis of adsorption: The experimental data showed that the adsorptive capacity of the SAM was a function of the initial concentration of BB3 molecules in the aqueous solution. It was observed that the the adsorption capacity of BB3 increased from 130 to 180 mg/g at the range of initial concentrations values between 100 to 350 mg/L because the initial BB3 concentration provides an important driving force to overcome all mass transfer resistance. Similar results have been reported by Özer et al. [30]. An slight decrease in the BB3 adsorption using SAM was associated with an increase in temperature from 298 to 318 K, thereby suggesting that the adsorption process is thermodynamically stable. When the temperature of the solution decreased from 318 to 298 K, the value of the maximum adsorption capacity increased from approximately 89.8 to 99.3 mg/g for 100 ppm. and 210 to 280 mg/g for 350 ppm. These results show that these adsorption reactions were exothermic and appeared to have a favorable adsorption at a lower temperature. They stated that the decrease in adsorption with increasing temperature is a result of poor interaction between the dye and adsorbent as the interaction forces of hydrogen bonds and Van der Waals are not strong. Similar results have been reported by Vimoneses et al. [31] and Toor et al. [32].

The equilibrium adsorption isotherm is fundamentally important in the design of an adsorption system. In this research, the Langmuir [33] and Freundlich [34] models were used to explain the experimental data.

The Langmuir isotherm is given by Eq. (8):

$$\frac{C_e}{(x/m)} = \frac{1}{q_{\max} K} + \frac{C_e}{q_{\max}} \quad (8)$$

Where C_e (mg/L) is the equilibrium concentration of BB3, q_{\max} (mg/g) is the maximum adsorptive capacity of the SAM, K

(L/mg) is the Langmuir constant, and $(\frac{x}{m} = q_e)$ (mg/g) is the

adsorptive capacity of the SAM at equilibrium.

The Freundlich isotherm is given by Eq. (9):

$$x/m = K_f C_e^{1/n} \quad (9)$$

Equation (9) can be written in linear form as:

$$\ln(x/m) = \ln K_f + \frac{1}{n} \ln C_e \quad (10)$$

Where n is the adsorption intensity, and K_f (mg/g) is the adsorptive capacity.

The adsorption data were analyzed with the Freundlich and Langmuir sorption models. Figs. 7 and 8 show the Langmuir and Freundlich isotherm plots, respectively. The correlation coefficients (R^2) and the isotherm constants are given in Table 3.

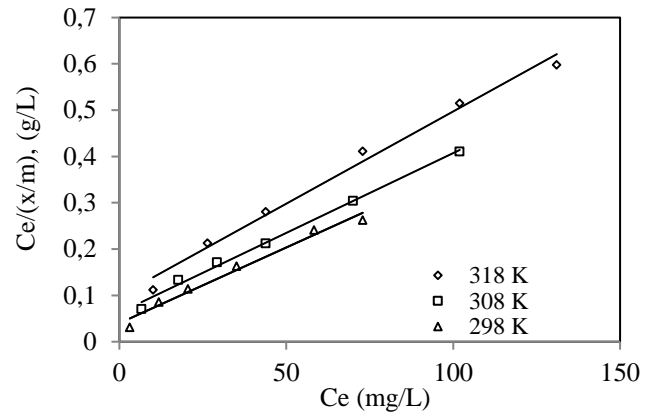


Figure 7. Langmuir isotherm

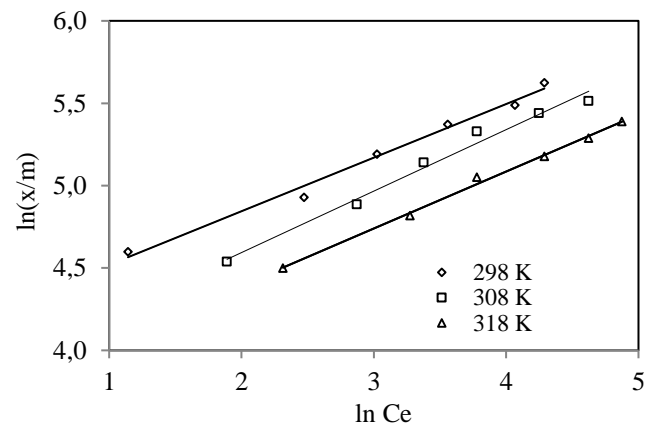


Figure 8. Freundlich isotherm

Table 3. Langmuir and Freundlich isotherm constants for the removal of BB3 molecules

Temperature K	Langmuir Constants		
	q_{\max} (mg/g)	K (L/mg)	R^2
298	303.0	0.081	0.979
308	294.1	0.054	0.985
318	250.0	0.040	0.989

Temperature K	Freundlich Constants		
	K_f (mg/g)(L/mg) ⁿ	n	R^2
298	64.53	3.00	0.991
308	46.86	2.68	0.984
318	40.56	2.89	0.996

It was found that the Freundlich isotherm represented the equilibrium adsorption of BB3 by the SAM better than the Langmuir isotherm. The relationship between temperature and the adsorption equilibrium constant, called van't Hoff equation, is given as:

$$\frac{d(\ln K)}{dT} = \frac{\Delta H^\circ}{RT^2} \quad (11)$$

An integrated form of the van't Hoff equation is presented in Eq. (12):

$$-\ln K = \frac{\Delta H^\circ}{R} \left(\frac{1}{T} \right) + C \quad (12)$$

Eq. (13) is obtained when the constant is replaced by $(-\Delta S^\circ/R)$:

$$\ln K = \frac{\Delta S^\circ}{R} - \frac{\Delta H^\circ}{R} \left(\frac{1}{T} \right) \quad (13)$$

If $\Delta G^\circ = -RT \ln K$ is combined with Eq. (13) the following equation is obtained:

$$\Delta G^\circ = \Delta H^\circ - T \Delta S^\circ \quad (14)$$

Where ΔG° , ΔH° , and ΔS° are changes in free energy, enthalpy, and entropy, respectively; K is the adsorption equilibrium constant; T is absolute temperature; and R is the universal gas constant (8.314 J/mol K). The intercept and the slope of the plots of $\ln K$ versus $1/T$ were used to determine the values of ΔS° and ΔH° .

The thermodynamic parameters were calculated for the process. The change in entropy (ΔS°) and enthalpy (ΔH°) were determined to be 21.86 J/mol K and -27.78 kJ/mol, respectively. The change of free energy (ΔG°) was calculated as -21.27, -21.05, -20.80 kJ/mol for 298, 308 and 318 K, respectively by using Eq.(14). The positive value of ΔS° indicates the affinity of the SAM for BB3. Negative values of ΔH° and ΔG° reflect the feasibility and the exothermic nature of the spontaneous adsorption process. The negative values of ΔH° , which revealed that the adsorption is likely to be dominated by physical processes in nature involving weak forces of attraction [35-36].

IV. DISCUSSION

The sulfuric acid-activated montmorillonite mineral (SAM) was prepared by natural montmorillonite mineral (NM), and it was used for the removal of BB3 from an aqueous solution in a batch system. The thermodynamic and kinetic parameters were calculated using appropriate models.

- The experimental results indicated that the adsorption of the BB3 depended on the initial pH of the solution, the initial concentration of the adsorbate, the temperature, and the contact time. The optimum values of temperature, initial pH, initial BB3 concentration of aqueous media, and contact time were 298 K, 6 ± 0.02 , 350 ppm, and 60 min, respectively. The maximum adsorption capacity was determined to be 277 mg/g at the optimum conditions.
- It was observed that the adsorption of BB3 onto SAM was described better by the Freundlich isotherm. The pseudo second-order model was the best-fitting model for the adsorption kinetics of BB3 on SAM.
- The experimental results indicated that SAM can be used as an effective, low-cost, and eco-friendly alternative adsorbent for the adsorption of BB3 molecules from aquatic systems. Additional studies should be conducted to

investigate the feasibility of using the SAM as an adsorbent for other molecules of dyes and toxic heavy metals.

REFERENCES

- [1]. RM Gong, M Li, C Yang, YZ Sun, Chen J. Removal of cationic dyes from aqueous solution by adsorption on peanut hull. *J Hazard Mater* 121, 247-250, 2005.
- [2]. M Chhabra, S Mishra, T R Sreekrishnan, Combination of chemical and enzymatic treatment for efficient decolorization/degradation of textile effluent: High operational stability of the continuous process, *Biochemical Engineering Journal*, 93, 17-24, 2015.
- [3]. V Dulman, SM. Cucu-Man, Sorption of some textile dyes by beech wood sawdust. *J Hazard Mater* 162, 1457-1464, 2009.
- [4]. Annadurai G, LY Ling, Lee J.F. Adsorption of reactive dye from an aqueous solution by chitosan: isotherm, kinetic and thermodynamic analysis. *Journal of Hazardous Materials* 152, 337-346 2008.
- [5]. N.M. Mahmoodi, R. Salehi, M. Arami, H. Bahrami, Dye removal from colored textile wastewater using chitosan in binary systems, *Desalination* 267, 64-72 2011.
- [6]. V. Selen, D. Özer, Reactive Blue 19 Boyarmaddesinin Sulu Çözeltilerden Uzaklaştırılması, *Fırat Univ. Journal of Science* 24(2), 63-75. 2012.
- [7]. V. Selen, Ö.Güler, D.Özer, E.Evin, Synthesized Multi-Walled Carbon Nanotubes As A Potential Adsorbent for the Removal of Methylene Blue Dye: Kinetics, Isotherms, and Thermodynamics, *Desalination and Water Treatment*, 578, 826-883, 2016.
- [8]. A. Dilek, Utilization of activated carbon produced from fruit juice industry solid waste for the adsorption of Yellow 18 from aqueous solutions, *Bioresource Technology* 168,259-266. 2014.
- [9]. W.H. Zou, K. Li, H.J. Bai, X.L. Shi, R.P. Han, Enhanced cationic dyes removal from aqueous solution by oxalic acid modified rice husk, *J. Chem. Eng. Data* 56, 1882-1891, 2011.
- [10]. J.Y. Song, W.H. Zou, Y.Y. Bian, F.Y. Su, R.P. Han, Adsorption characteristics of methylene blue by peanut husk in batch and column modes, *Desalination* 265, 2011.
- [11]. TH Kim, C Park, S. Kim Water recycling from desalination and purification process of reactive dye manufacturing industry by combined membrane filtration. *J Clean Prod* 13, 779-786, 2005.
- [12]. Turgay O, Ersoz G, Atalay S, Forss J, Welandar U. The treatment of azo dyes found in textile industry wastewater by anaerobic biological method and chemical oxidation. *Sep Purif Technol* 79: 26-33, 2011.
- [13]. SK Nataraj, KM Hosamani, TM. Aminabhavi Nanofiltration and reverse osmosis thin film composite membrane module for the removal of dye and salts from the simulated mixtures. *Desalination* 249: 12-17, 2009.
- [14]. SS Moghaddam, MRA Moghaddam, M. Arami Coagulation/flocculation process for dye removal using sludge from water treatment plant: Optimization through response surface methodology. *J Hazard Mater* 175, 651-657, 2010.
- [15]. T. Bohli, a. Ouederni, N. Fiol, I. Villaescusa, Uptake of Cd²⁺ and Ni²⁺ Metal Ions from Aqueous solutions By Activated Carbons Derived from Waste Olive Stones, *Int. J. Chem. Eng. Appl.* 3 232-236, 2012.
- [16]. F. Rozada, M. Otero, a. Morán, a. I. Garcia, Adsorption of heavy metals onto sewage sludge-derived materials, *Bioresour. Technol.* 99 6332-6338. 2008.
- [17]. Y. Ma, N. Gao, W. Chu, C. Li, Removal of phenol by powdered activated carbon adsorption, *Front. Environ. Sci. Eng.* 7, 158-165, 2013.
- [18]. S Banerjee, MC Chattopadhyaya, Adsorption characteristics for the removal of toxic dye, tartrazine from aqueous solutions by a low cost agricultural by-product, *Arabian Journal of Chemistry*, Available online 15 June 2013, In Press.
- [19]. G Vijayakumar, R Tamilarasan, Dharmendirakumar, Adsorption,

- Kinetic, Equilibrium and thermodynamic studies on the removal of basic dye Rhodamine-B from aqueous solution by the use of natural adsorbent perlite, *J. Mater. Environ. Sci.* 3(1), 157-170, 2012.
- [20]. J. Madejova, P. Komadel. Baseline Studies Of The Clay Minerals Society Source Clays: Infrared Methods[J]. *Clays And Clay Minerals*, 49, 410-432, 2001.
- [21]. H M Liu, P Yuan, Z H Qin, D Liu, D Y Tan, J X Zhu, H P He. Thermal Degradation Of Organic Matter In The Interlayer Clay-Organic Complex: A TG-FTIR Study On A Montmorillonite/12-Aminolauric Acid System[J]. *Applied Clay Science*, 80-81, 398-406, 2013.
- [22]. B. K. Suyamboo R, Srikrishnapuram Biosorption of crystal violet onto *Cyperus rotundus* in batch system: kinetic and equilibrium modeling, *Desalination and water treatment*, 52, 3535-3546. 2014.
- [23]. J. W., Lee, S. P., Choi, R., Thiruvengatachari, W. G. Shim, and H. Moon, Evaluation of the performance of adsorption and coagulation processes for the maximum removal of reactive dyes. *Dyes Pigments*, 69, 196-203 2006.
- [24]. Y J, Yao B, He F F, Xu X F. Chen Equilibrium and kinetic studies of methyl orange adsorption on multiwalled carbon nanotubes[J]. *Chemical Engineering Journal*, 170, 82-89, 2011.
- [25]. P F, Wang M H, Cao C, Wang Y H, Ao J, Hou J. Qian Kinetics and thermodynamics of adsorption of methylene blue by a magnetic graphene-carbon nanotube composite[J]. *Applied Surface Science*, 290, 116-124. 2014.
- [26]. A, Ozer G, Akkaya M. Turabik Biosorption of Acid Blue 290 (AB 290) and Acid Blue 324 (AB 324) dyes on *Spirogyra rhizopus*[J]. *Journal of Hazardous Materials*, 135, 355-364, 2006.
- [27]. K, Vijayaraghavan YS. Yun Bacterial biosorbents and biosorption *Biotechnol Adv* 26, 266–291, 2008.
- [28]. S. Lagergren, *Kungliga Svenska Vetenskapsakademiens: Handlingar*, 24, 1–39, 1898.
- [29]. Y.S. Ho, G. McKay, Pseudo-second order model for sorption processes, *Process Biochem.* 34, 451-465, 1999.
- [30]. D. Özer, G. Dursun, , A. Özer, Methylene blue adsorption from aqueous solution by dehydrated peanut hull *Journal of Hazardous Materials*, 144, 1–2, 171–179, 2007.
- [31]. V. Vimonses, S. Lei, B. Jin, C.W.K. Chow, C. Saint Kinetic study and equilibrium isotherm analysis of Congo red adsorption by clay materials, *Chem. Eng. J.*, 148, 354–364, 2009.
- [32]. M. Toor, B. Jin Adsorption characteristics, isotherm, kinetics, and diffusion of modified natural bentonite for removing diazo dye *Chemical Engineering Journal*, 187, 79–88, 2012.
- [33]. Langmuir, The constitution and fundamental properties of solids and liquids, *J. Am. Chem. Soc.* 38, 11 2221–2295, 1916.
- [34]. H.M.F. Freundlich, Über die adsorption in lösungen, *Z. Phys. Chem.* 57A 385–470, 1906.
- [35]. Y. Yu, Y.Y. Zhuang, Z.H. Wang, Adsorption of water-soluble dye onto functionalized resin, *J. Colloid Interf. Sci.* 242, 288–293, 2001.
- [36]. S. Chatterjee, S. Chatterjee, B.P. Chatterjee, A.K. Guha, Adsorptive removal of congo red, a carcinogenic textile dye by chitosan hydrobeads: Binding mechanism, equilibrium and kinetics, *Colloids Surf. A: Physicochem. Eng. Aspects* 299, 146–152, 2007.

Thermal and mechanical properties of cement-EPS-marble powder composites

Ayse Bicer

Department of Chemical Engineering, Firat University,
Elazığ, Turkey
e-mail: abicer@firat.edu.tr

Filiz Kar

Department of Chemical Engineering, Firat University
Elazığ, Turkey
e-mail: fkar@firat.edu.tr

Abstract—This work was undertaken to produce a new construction materials which could have insulation and mechanical strength properties by using two different wasted materials. The waste expanded polystyrene (EPS) and marble powder were used as the aggregate in order to produce a new concrete material. After waste EPS is collected as packaging material, it is mixed with the cement of percentages; 20%, 40%, 60% and 80%. Marble powder is added to each of this cement at 0.0%, 0.5%, 1% and 1.5% of the weight of the mixture. 16 different samples were produced. At the end of 28 days of drying period, the samples were subjected to a number of tests so that their physical characteristics could be identified. As a result of these test, it was concluded that EPS ratio of the samples increased, their density, thermal conductivity, the compression and tensile strength decreased, while porosity increased. It was recommended that; using EPS aggregated and marble powder added concrete, (i) the waste EPS and marble powder can be evaluated as construction material, (ii) building heating and cooling energy will be saved.

Key words; *Waste expanded polystyrene, marble powder, light concretes, insulation material*

1. INTRODUCTION

Today expanded polystyrene can be used as insulation material in buildings; it is also widely used in packaging industry. As an important waste material in terms of environmental pollution, this material has to be recycled and re-economized. Revaluation of waste EPS as construction material is important both in terms of its contribution to economy and as a solution to environmental solution problem. Several studies have been made on the usage of EPS as construction material. A considerable portion of these studies are related to the use of aggregate in concrete. Some of these studies are summarized below.

Babu et al [1], examined the mechanical features of light concretes produced by using fly ash along with expanded polystyrene along with regular aggregate. Miled et al. [2], studied the impact of the change in the amount and dimensions of EPS found on aggregated concrete samples on the pressure resistance of the concrete. Bourvard et al [3], worked on the physical features of high-performance concretes consisting of

expanded polystyrene balls. Chen [4] studied on the characteristics of the light concrete which consists of polystyrene foam reinforced with steel fibre. Babu et al [5], investigated the mechanical behaviours of the concretes which were mixed with silica fume at different rates in order to increase the resistance of low-intensity concrete consisting of

EPS. Demirboga and Kan [6], displayed the changes in thermal conductivity, density and average drying contraction values of the concrete in the samples they produced by using 25, 30 and 100% EPS as aggregate in concrete. Rossignolo and Agnesini [7], studied the technical properties of concretes created with light aggregate mixtures of styrene-butadiene rubber (SBR) modified with two types of light aggregates. Kaya and Kar [8] investigated the physical characteristics of light concrete and gypsum coatings with waste EPS aggregates. Kaya and Kar [9] tested thermal and mechanical properties of the light weight concretes with EPS and tragacanth resin. Sariisik and Sariisik [10] determined the thermal conductivity value of concrete mixtures with cement, pumice and EPS. Khedari et al. [11] investigated a new lightweight construction material, composed of cement, sand and fiber of waste coconut.

In this paper, the mechanical features of samples produced by granulating the EPS particles which are liberated as waste material in packaging industry using certain amounts of cement and marble powder have been examined.

II. EXPERIMENTAL STUDY

A. Materials

Expanded Polystyrene Foam (EPS) is a foam-like- closed-pored thermoplastic material, typically in white colour, obtained from polymerization of styrene monomer (Figure 1). EPS products were acquired by bulking and amalgamation of polystyrene particles. "Pentane" gas was used for particle bulking and foam acquiring. Pentane is an organic component and after it ensures formation of many small particles within particles, it is exchanged by air in a very short time during and after the production. With the liberation of pentane, inert air is trapped in the abounding (3-6 billion in 1 m³ EPS depending on density) number of small pored cells. 98 percent of the material is air and the rest is polystyrene [8]. EPS is a close-pored material. Due to its very low level of water absorption, its features do not change even if it directly contacts with water. As it does not dissolve and disintegrate in water, the pore walls are water-proof.



Fig 1. Polystyrene and expanded polystyrene [8].

Marble Powder (MP) are obtained from Marble manufacturing facility in Elazig.

CEM IV/B(P)32.5 R pozzolanic cement were used to EPS and marble powder as a binder. Chemical components of cement are given in Table 1.

The prepared blends were mixed with sufficient amount of water and poured into the pre-assembled molds. The molds that were formed had the dimensions of 100x100x100 mm for mechanical tests and the dimensions of 20x60x150 mm for thermal tests (Figure 2)



Fig 2. Rectangular and cubical blocks samples

B. Thermal and mechanical Test

The thermal conductivities of specimens were detected by *Isomet 2104* unit, which makes measurements by using the hot wire method according to *DIN 51046*. Its range and sensitivity were 0.02-6.00 W/mK respectively and its precision was $\pm 5\%$ [9]. Each sample block was measured three times at three locations to show the average of nine values. The temperature was between 22°C and 25°C during measurement.

Compressive strength tests on the samples were undertaken according to the *ASTM C 109-80* standard. The tensile strength values calculated according to the *TS 500* standard by Eq. 1 [13].

$$f_{ctk} = 0.35\sqrt{f_{ck}} \quad (1)$$

Here;

f_{ck} : Compressive strength (MPa)

f_{ctk} : Tensile strength (MPa)

Elasticity module is mostly calculated by theoretical methods [12]. Elasticity module values are calculated according to the *TS 500* standard by Eq. (2) [13]:

$$E = 3.25 \cdot (f_{ck})^{1/2} + 14 \quad (2)$$

In this equation, E is the elasticity module (GPa), and f_{ck} is the characteristic compressive strength (MPa).

The water absorption test aimed to analyze the maximum water uptake amount. This characteristic is significant to designate whether the material is appropriate for use against freezing risks. The critical moisture amount is 30% of the total dry volume and the material does not deform when frozen below this amount. The tests were performed by complying with BS 812, Part 2 standard and keeping the samples in water.

$$\text{Water absorption} = \left\{ \frac{W_d - W_k}{W_k} \right\} \cdot 100 \quad (3)$$

In the equation, W_k is the dry weight of sample and W_d is the wet weight of sample.

The purpose of drying ratio test is to search the respiration abilities of the samples. After being left in water contained for 48 hours the samples were taken from the water, wiped with a wet piece of cloth and left to natural drying at 22°C room temperature. The drying ratio values are calculated by Eq. (4). Drying occurs through evaporation from the surface of the material; here it is about the movement of water from the depth of the material through capillary canals, meaning that moisture is expelled from the body through steam permeability resistance and drying occurs.

$$\text{Drying ratio} = \left\{ \frac{W_d - W_k}{W_d} \right\} \cdot 100 \quad (4)$$

III. RESULTS AND DISCUSSIONS

When Figure 3 is examined, it can be seen that density values of the samples decrease as EPS ratio increases. This reduction is directly related to the density of EPS. But density of the samples increase marble powder ratio decreases.

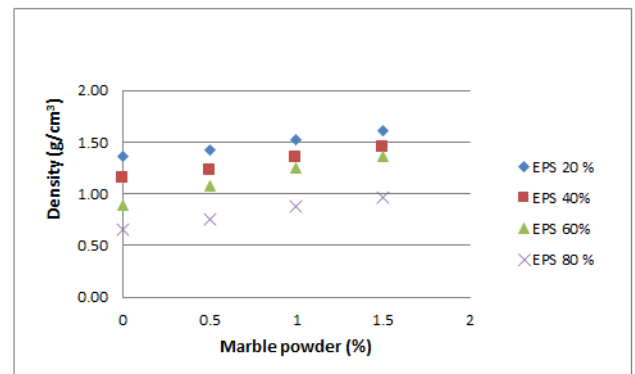


Figure 3. Density ratio of samples versus EPS and MP percentages

Considering Figure 4, it is clear that thermal conductivity drops as EPS ratio climbs. Thermal conductivity depending on EPS ratios, 20% and 80%, decreased by 81.79 %. In the case of

0% and 1.5% ratios of marble powder in the mixture the thermal conductivity increased as 28.16-17.94%.

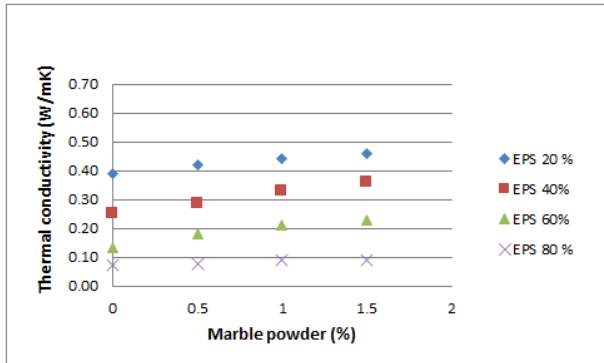


Figure 4. Thermal conductivity variation according to EPS and MP

The Figures 5, 6, 7 shows that compressive strength, tensile strength and elasticity module values increases from 0 to 60% EPS and marble powder 1% ratios. But their values decreases after from the rate of the 1% marble powder. Because, cement and marble powder aggregate (1%) are creating a good mix

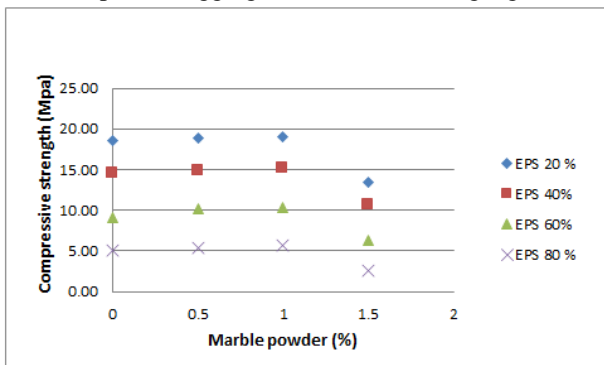


Figure 5. Compressive strength EPS and marble MP percentage relation in the specimens

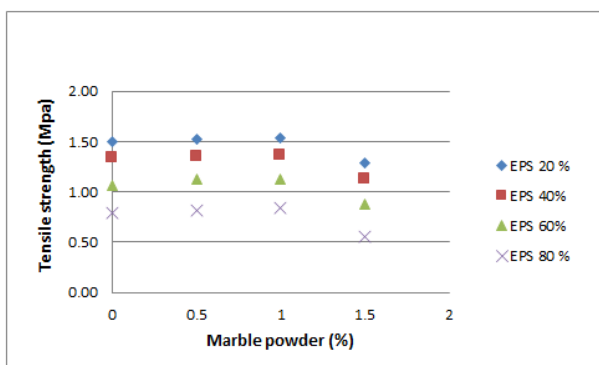


Figure 6. Tensile strength EPS and MP percentage relation in the specimens

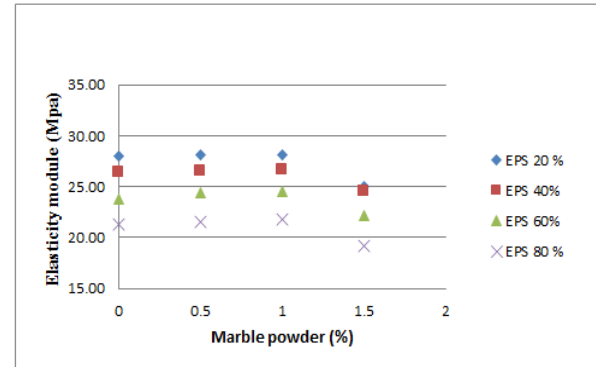


Figure 7. Variation of drying ratio of samples versus EPS and MP percentages

Almost all of the samples with resin added cement binders remained below 30%, which is the critical level for water absorption (Fig. 8). Therefore these materials can be used without the risk of freezing under 0°C temperature in places which is in contact with water.

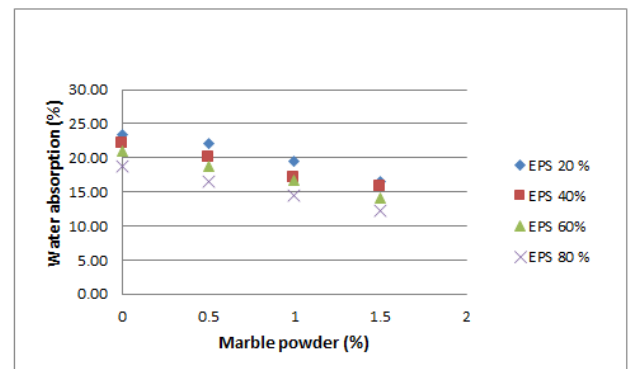


Figure 8. Variation of water absorption ratio of samples versus EPS and MP percentages

Considering Figure 9, it is clear that the sample drying ratios diminish as the EPS particle addition ratio grows. The moisture contained in the material moves towards the surface by means of capillary channels. This indicates the material's respiration ability.

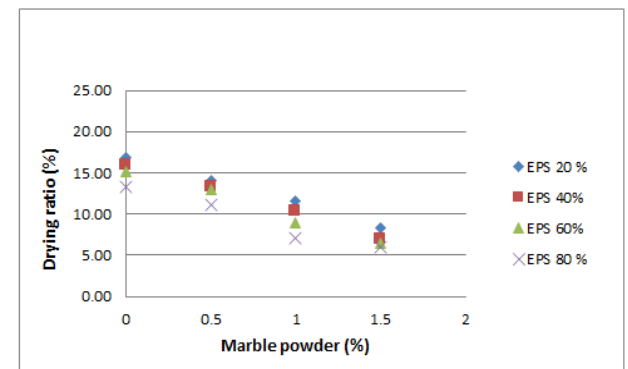


Figure 9. Variation of drying ratio of samples versus EPS and MP percentages

IV. CONCLUSION

This study was conducted to illustrate whether the use of waste EPS and marble powder in concrete was possible in place of natural aggregate materials.

Low-density concrete with EPS and marble powder aggregate can be used in panel walls, floorings and floor deck concretes as well as construction applications such as concrete briquettes, whereas blocks of plaster with the same additives can be used as insulation coating.

These materials should not be used as columns and beams components in buildings due to low compressive, tensile strength and elasticity module values of the samples.

Nevertheless, these concretes with low density are designated as flooring, ceiling and wall concrete.

The rate of water absorption of samples is less than 30%. From this result, it is concluded that these materials can be used as concrete and external plaster or inner plaster material that subjected to water

In conclusion, the concrete material containing EPS and marble powder can be used as building material and simultaneously solve the environmental pollution problem by recycling waste EPS and marble powder.

Table 1. Chemical composition of cement used

Component	SiO ₂	CaO	Al ₂ O ₃	Fe ₂ O ₃	MgO	SO ₃	Cl	Fire loss	Not available
(%)	23.51	58.51	6.15	4.00	2.27	2.37	0.10	2.04	0.72

Table 2. Details of the cement-EPS-marble powder mixes

Samples	Volumetric ratio (%)		Weight (g)		Total weight (g)	Marble powder (%)	Marble powder (g)	(W)/(C+E+M)
	EPS	cement	EPS	cement				
Sample 1	80	20	20.4	450	470.4	0.0	-	0.5
Sample 2	60	40	15.6	900	915.6		-	
Sample 3	40	60	10.4	1350	1360.4		-	
Sample 4	20	80	5.2	1800	1805.2		-	
Sample 5	80	20	20.4	450	470.4	0.5	23.53	0.5
Sample 6	60	40	15.6	900	915.6		45.78	
Sample 7	40	60	10.4	1350	1360.4		68.02	
Sample 8	20	80	5.2	1800	1805.2		90.26	
Sample 9	80	20	20.4	450	470.4	1	47.0	0.5
Sample 10	60	40	15.6	900	915.6		91.5	
Sample 11	40	60	10.4	1350	1360.4		136	
Sample 12	20	80	5.2	1800	1805.2		180.52	
Sample 13	80	20	20.4	450	470.4	1.5	70.5	0.5
Sample 14	60	40	15.6	900	915.6		137	
Sample 15	40	60	10.4	1350	1360.4		204	
Sample 16	20	80	5.2	1800	1805.2		270	

W:Water, C:cement, E:EPS, M:marble powder

Table 3. Thermal and mechanical properties of samples

Sample no	Density (g/cm ³)	Thermal conductivity (W/mK)	Compressive strength (MPa)	Tensile strength (MPa)	Elasticity module (GPa)	Water absorption (%)	Drying ratio (%)
1	1.36	0.071	18.50	1.50	27.98	23.41	16.83
2	1.15	0.135	14.58	1.34	26.41	22.06	14.10
3	0.89	0.250	9.15	1.06	23.83	19.55	11.66
4	0.65	0.390	5.12	0.79	21.35	16.6	8.32
5	1.42	0.083	18.94	1.52	28.14	22.05	16.00
6	1.22	0.184	14.89	1.35	26.54	20.10	13.25
7	1.08	0.290	10.18	1.12	24.37	17.11	10.42
8	0.75	0.424	5.38	0.81	21.54	15.85	7.00
9	1.52	0.094	19.04	1.53	28.18	20.90	15.10
10	1.35	0.213	15.15	1.36	26.64	8.80	12.96
11	1.25	0.333	10.36	1.13	24.46	16.74	8.90
12	0.88	0.441	5.70	0.84	21.75	14.17	6.50
13	1.61	0.101	13.48	1.29	25.93	18.75	13.28
14	1.45	0.232	10.60	1.13	24.58	16.45	11.05
15	1.36	0.360	6.27	0.88	22.14	14.56	7.10
16	0.96	0.462	2.58	0.56	19.22	12.28	6.02

REFERENCES

- [1] D. S. Babu, K. G. Babu, T.H. Wee, "Properties of lightweight expanded polystyrene aggregate concretes containing fly ash", *Cement and Concrete Research*, 35, 1218–1223, 2005.
- [2] K. Miled, K. Sab, R. Le Roy, "Particle size effect on EPS lightweight concrete compressive strength: Experimental investigation and modeling", *Mechanics of Materials*, 39, 222-240, 2007.
- [3] D. Bouvard, J. M. Chaix, R. Dendievel, A. Fazekas, J. M. Létang, G. Peix, D. Quenard, "Characterization and simulation of microstructure and properties of EPS lightweight concrete", *Cement and Concrete Research*, 37, 1666-1673, 2007.
- [4] B. Chen, J. Liu, "Properties of lightweight expanded polystyrene concrete reinforced with steel fiber", *Cement and Concrete Research*, 34, 1259–1263, 2004.
- [5] K. G. Babu and D. S. Babu, "Behavior of lightweight expanded polystyrene concrete containing silica fume", *Cement and Concrete Res.*, 33, 755-762, 2003.
- [6] R. Demirboga, A. K. Kan, "Thermal conductivity and shrinkage properties of modified waste polystyrene aggregate concretes", *Construction and Building Materials*, 35, 730–734, 2012.
- [7] Y. A. Rossignolo, M. V. C. Agnesini, "Mechanical properties of polymer modified lightweight aggregate concrete", *Cement and Concrete Research*, 32, 329-334, 2002.
- [8] A. Kaya, F. Kar, "Thermal and mechanical properties of concretes with Styropor", *Journal of Applied Mathematics and Physics*, 2-6, 310-315, 2014.
- [9] A. Kaya, F. Kar, "Properties of concrete containing waste expanded polystyrene and natural resin". *Construction and Building Materials*, 105: 572-578, 2016.
- [10] A. Saiisik, G. Sariisik, "New production process for insulation blocks composed of EPS and lightweight concrete containing pumice aggregate", *Mater. Struct.* 45(9), 1345-1357, 2002.
- [11] J. Khedari, B. Suttisonk, N. Pratinthong, J. Hirunlabh, "New lightweight composite construction materials with low thermal conductivity". *Cement and Concrete Composites*, 23: 65-70, 2001.
- [12] H. Z. Cui, T. Y. Lo, S. A Memon, F. Xing, X. Shi. "Analytical model for compressive strength, elastic modulus and peak strain of structural lightweight aggregate concrete". *Construction and Building Materials*, 36: 1036-1043, 2012.
- [13] TS 500, (2000), *Turkish Standard*, Ankara.

The Production of Vegetable Oil-Based Polyols and Modelling of Rheological Properties

Ercan Aydoğmuş, Müge Gür, Fethi Kamışlı
Firat University, Engineering Faculty
Elazığ, Turkey

ercanaydogmus@firat.edu.tr, gurmuge2301@gmail.com

Abstract— In this study, some vegetable-oil based polyols were produced from the different vegetables oils with the catalysts. The produced polyols compared with commercial polyols in terms of rheological properties such as viscosity, temperature, shear stress, shear rate. The rheological properties of the polyols were modelling with general equations based on experimental data. Canola, cotton, linseed, corn, hazelnut and soybean oils were used in the production of polyols. The polyol production was accomplished by oxygen bonding to the structure followed by hydroxyl bonding by breaking the double bonds in the oil. These steps were, respectively, the steps of epoxidation, hydroxylation and purification. In this study, variations of viscosities of soybean oil, cottonseed oil, corn oil, hazelnut oil, canola oil, linseed oil-based polyols and commercial polyols were determined a function of temperature. It is known that the viscosity of the fluid decreases as temperature increases. The tested polyols showed Newtonian and non-Newtonian fluids behavior at certain temperature range. According to the experimental data; the linear and non-linear regression were made to determine coefficients of regression in the model equations.

Keywords— *Vegetable oil; Polyols; rheological properties; modelling*

I. INTRODUCTION

Compared to petroleum-based polyols in polyurethane production from vegetable oil polyol produced with a smaller amount of isocyanate used. The polyurethane produced with the polyol produced from vegetable oil decreased compression resistance [8].

Wood powder was added as filler to the polyurethane derived from castor oil-based polyol. The polyurethane of the swelling time was compared with commercial polyols, and castor oil-based polyols. Effective thermal conductivity compared to commercial polyurethane material of the castor oil-based polyurethane material has been found to be lower. Increasing the filler has negative impact on the effective heat transfer coefficient. Density of polyurethane material was found to be between 36 and 39 kg/m³. TGA value of the thermal stability of the castor oil-based polyurethane material was found to be more commercially polyol product [12].

The goal of this study is to determine the rheological properties of different oil-based polyols and choose the best model complying with experimental data and the viscosity to each waste vegetable oil based-polyols are measured at different temperatures (25, 30, 35, 40, 45 and 50 °C) by using a rotary viscometer (Brookfield DV-II). Samples were sheared with several different rotational speeds at an increasing order. One of the most important parameters required in the design of technological processes in polyurethane industries is the viscosity of raw materials. Data obtained for apparent viscosity and rotational speed were used to describe the flow behavior by the model equations both in the forward and backward - measurement.

The polyols are produced from the waste vegetable oils in three consecutive steps which are epoxidation, hydroxylation and purification. The temperature of the system is kept under the control using a thermostat. When it is reached to the desired reaction temperature, the peroxides are added into the vegetable oils in acidic medium by the aid of dropping funnel in the certain time.

After the reaction is completed, the mixture is taken into separatory funnel and after for a while the mixture separates in two phases with the upper phase of the epoxidized vegetable oil. After the epoxidation step, neutralization with water and the hydroxylation starts. Especially hydroxylation with alcoholysis is frequently preferred in the production of polyols. The purification process is being carried with rotary evaporator to get rid of impurities such as water, heptane and etc. The polyols produced from the vegetable oil are being used in the production of polyurethane by checking the number of hydroxyl. The structures of the hydroxyl compounds were investigated with the FTIR spectrometer. The polyurethane was produced from the different vegetable oil-based polyols and commercial polyols. The characteristic properties of the polyurethane such as thermal conductivity, the structures of porosity, density were determined. The polyurethane produced from the different vegetable oils is compared one another in terms of thermal properties.

II. MATERIAL, METHODS AND MODELLING

In this study, a system consisting of a three necked balloon joe, thermometer, water bath, magnetic stirrer, condenser and funnel was used for the epoxidation reaction, which is the first step of obtaining polyols from vegetable oils used as raw materials. A three-necked balloon was used in the atmospheric pressure with a magnetic stirrer to heat the water bath to 325 – 330 K. A condenser system was attached to the ball of three necks and a thermometer is placed with the help of plugs. The refined oil was placed in the amount determined in a three-necked balloon with the aid of a funnel. Acetic acid, sulfuric acid and heptane were added with the necessary optimizations. Hydrogen peroxide was added dropwise to the system after reaching a temperature of 325 K, and the epoxidation step was carried out in 4 hours. After the reaction was complete, the epoxy-oil is separated off with the separating funnel. Since the epoxy-oil was acidic, the pH value was raised by washing with pure water. Neutralization was also achieved using a basic ion exchange resin. In the experimental system, the hydroxylation was carried out by adding the certain amounts of methanol, water and acetic acid to the three necked balloon. The mixture was heated to the boiling temperature of the methanol while it was stirred. When the boiling temperature was reached, epoxy-oil was added to the three necked balloon. Hydroxylation proceeded for about 2 hours. Neutralization was performed again after this step. In the last step, impurities such as water, methanol, heptane were removed by using vacuum evaporator. The hydroxyl value of the obtained polyol was determined according to ASTM D 4274 D method.

The viscosities of the polyols produced from different the vegetable oils were measured by using a rotary viscometer (Brookfield DV-II) at different temperatures (25, 30, 35, 40, 45 and 50 °C). Samples were sheared with several different rotational speeds (2.5, 5, 10, 20, 30 and 50 rpm) at an increasing order. Data obtained for apparent viscosity and rotational speed were used to describe the flow behavior by the model equations. Brookfield rotational viscometer (Model DV-II, Brookfield Engineering Laboratories) equipped with spindle 21 was used to measure viscosities of produced and commercial polyols. Enough samples nearly 8 mL in the beaker were used to immerse the groove on the spindle with guard leg. Temperature was kept constant at a desired value using thermostatically controlled electrical system. Shear rate ($\dot{\gamma}$) and shear stress (τ) were read from viscometer directly. Shear stress and shear rate can also be calculated by using Eq. (1), (2) and (3).

$$\dot{\gamma} = \beta \cdot N \quad (1)$$

$$\tau = \mu \cdot \dot{\gamma} \quad (2)$$

$$\tau = \kappa \cdot (\mu)^{\delta} \quad (3)$$

Where; N is rotational speed (rpm), τ is shear stress (Pa), μ is the apparent viscosity (mPa. s), κ is the consistency coefficient

(mPa.s), δ is flow behavior index and β is coefficient (dimensionless).

The viscosity of a blend as a function of temperature can be calculated using one of the equations given below. Here all the equations given below are used to determine how the viscosity depends on temperature. In order to choose the best model for each blend, R^2 is calculated for each model.

$$\mu_{\text{linear}} = a \cdot T + b \quad (4)$$

$$\mu_{\text{exponential}} = c \cdot \exp(d \cdot T) \quad (5)$$

$$\mu_{\text{power}} = e \cdot T^f \quad (6)$$

$$\mu_{\text{logarithmic}} = g \cdot \ln(T) + h \quad (7)$$

$$\mu_{\text{polynomial}} = i \cdot T^2 + j \cdot T + k \quad (8)$$

$$\mu_{\text{new}} = \exp(-T) + m \cdot T + n \quad (9)$$

A. Figures and Tables

CORRELATION COEFFICIENTS FOR LINEAR MODEL

Polyols	a	b	R ²
Soybean	-9.6579	3058.5	0.9702
Cotton	-7.9912	2508.7	0.9855
Corn	-1.9308	643.23	0.9588
Hazelnut	-5.8209	1793.2	0.9567
Canola	-2.1367	707.18	0.9296
Linseed	-4.4974	1355.3	0.9929

CORRELATION COEFFICIENTS FOR EXPONENTIAL MODEL

Polyols	c	d	R ²
Soybean	2.10 ⁶	-0.109	0.7668
Cotton	5.10 ¹⁶	-0.113	0.7897
Corn	2.10 ¹⁰	-0.065	0.8920
Hazelnut	4.10 ¹⁸	-0.131	0.7809
Canola	1.10 ⁹	-0.056	0.9653
Linseed	5.10 ³⁷	-0.283	0.9066

CORRELATION COEFFICIENTS FOR POWER MODEL

Polyols	e	f	R ²
Soybean	6.10 ⁸²	-32.56	0.7542
Cotton	7.10 ⁸⁵	-33.85	0.7809
Corn	4.10 ⁵¹	-20.11	0.8773
Hazelnut	1.10 ⁹⁷	-38.55	0.7717
Canola	2.10 ⁴⁴	-17.19	0.9593
Linseed	4.10 ²⁰⁸	-83.91	0.9044

CORRELATION COEFFICIENTS FOR LOGARITHMIC MODEL

Polyols	g	h	R ²
Soybean	-2906	16736	0.9667
Cotton	-2400	13798	0.9830
Corn	-601.1	3492.4	0.9600
Hazelnut	-1721	9862.8	0.9524
Canola	-663.2	3848.3	0.9404
Linseed	-1335	7619.5	0.9935

CORRELATION COEFFICIENTS FOR POLYNOMIAL MODEL

Polyols	i	j	k	R ²
Soybean	-0.095	47.629	-5576.5	0.979
Cotton	-0.105	55.433	7025.3	0.995
Corn	0.006	-5.377	1179.4	0.961

Hazelnut	-0.144	79.46	-10842	0.987
Canola	0.039	-26.51	4465.6	0.994
Linseed	0.132	-82.93	12991	0.998

CORRELATION COEFFICIENTS FOR NEW MODEL

Polyols	m	n	R ²
Soybean	-9.65795	3058.480	0.9996
Cotton	-7.97888	2505.030	0.9997
Corn	-1.93083	643.2298	0.9998
Hazelnut	-5.82090	1793.152	0.9998
Canola	-2.13662	707.1342	0.9997
Linseed	-4.49741	1355.300	1.0000

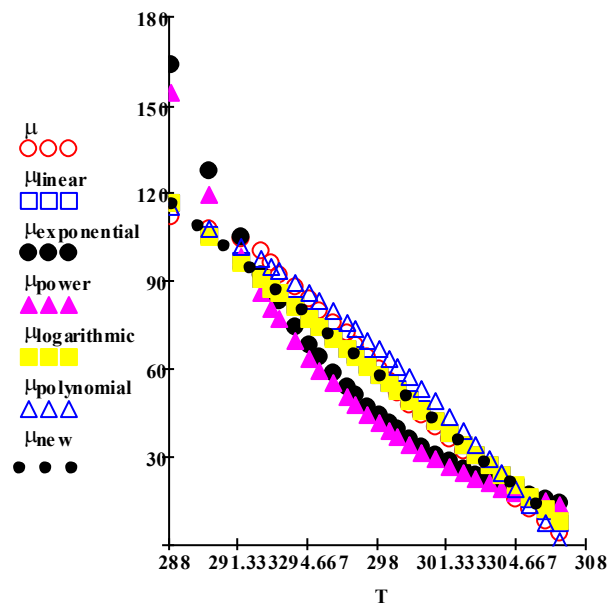


Figure 1. The effect of temperature on viscosity, hazelnut oil-based polyols, comparison with model equations

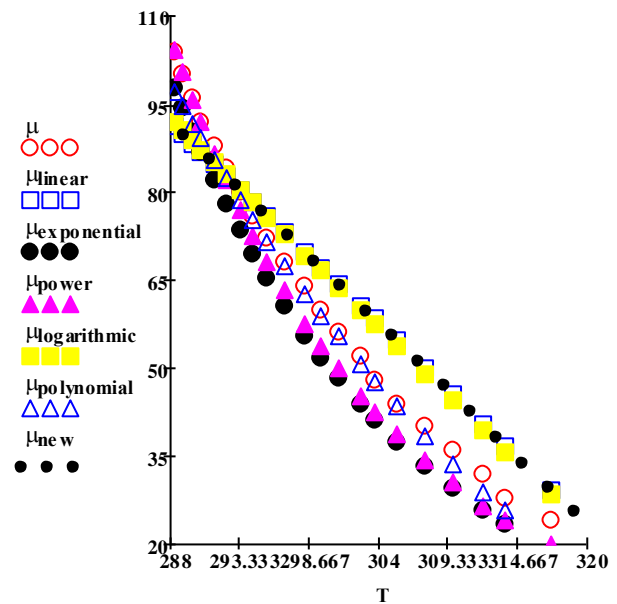


Figure 2. The effect of temperature on viscosity, canola oil-based polyols, comparison with model equations.

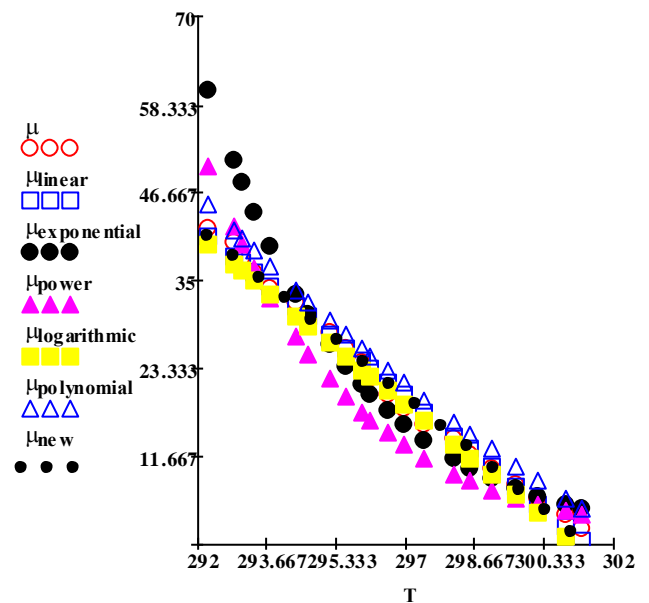


Figure 3. The effect of temperature on viscosity, linseed oil-based polyols, comparison with model equations.

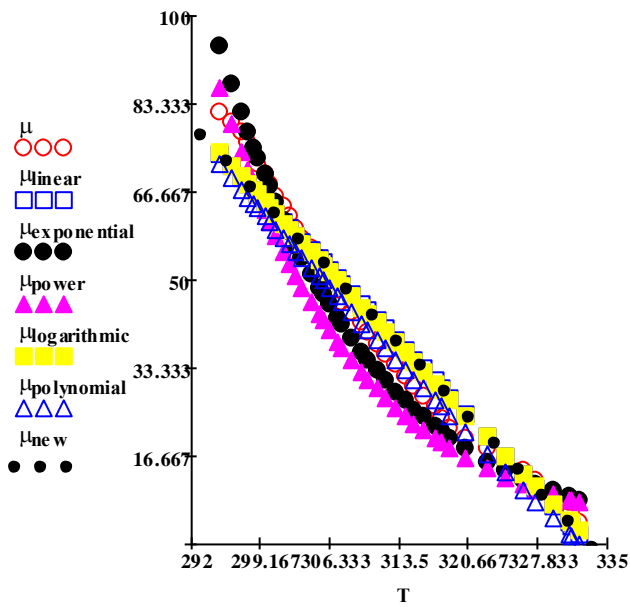


Figure 4. The effect of temperature on viscosity, corn oil-based polyols, comparison with model equations.

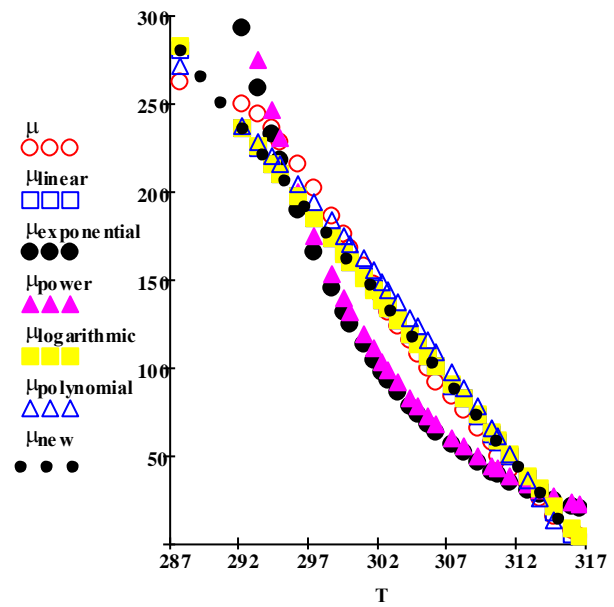


Figure 6. The effect of temperature on viscosity, soybean oil-based polyols, comparison with model equations.

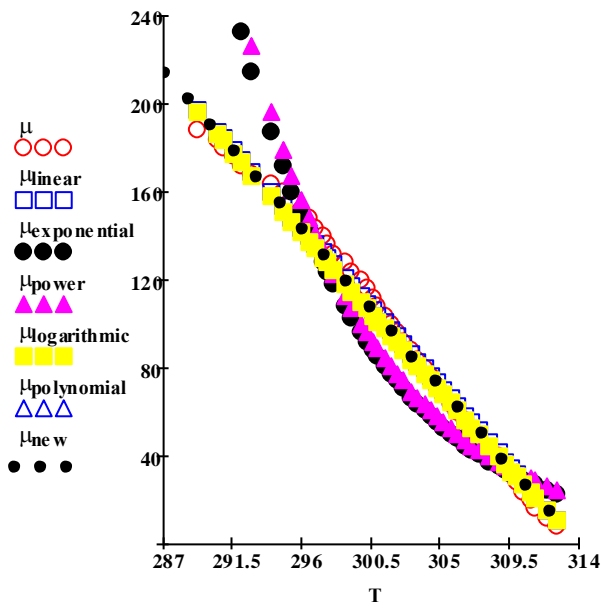


Figure 5. The effect of temperature on viscosity, cottonseed oil-based polyols, comparison with model equations.

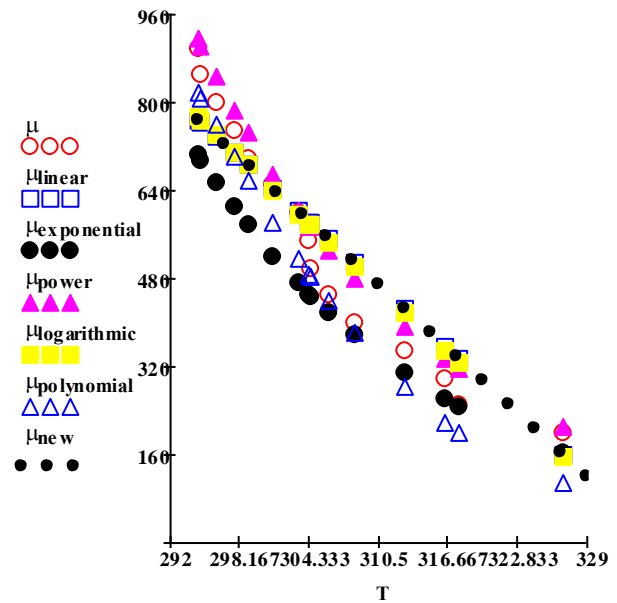


Figure 7. The effect of temperature on viscosity, commercial polyols, comparison with model equations.

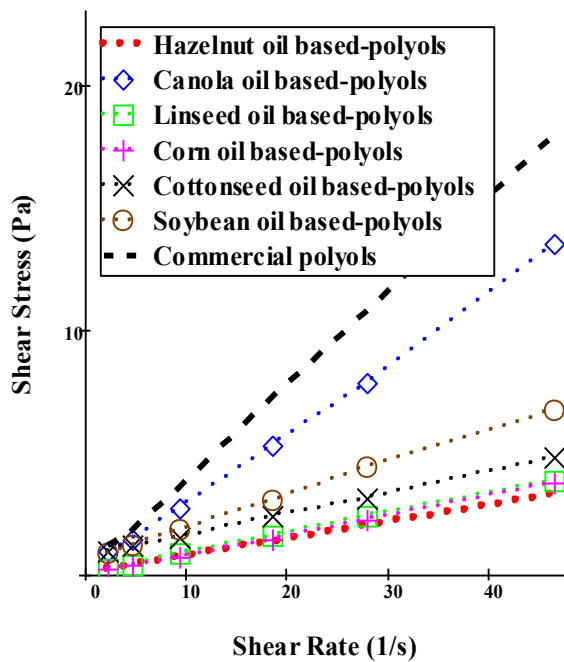


Figure 8. Shear stress vs shear rate for different vegetable oil-based polyols

III. RESULTS AND DISCUSSION

In this study, the temperature dependence of the viscosity of the vegetable oil-based polyols; model equations compared with experimental data. In Figures: 1, 2, 3, 4, 5, 6 and 7; the variation of apparent viscosities of polyols as a function of temperature were compared model equations with experimental results. Operating temperatures of the assay were measured by raising temperature stepwise in a water bath. The viscosities of vegetable oil-based polyols were measured by different rotational speeds at an increasing order. According to the experimental results regression coefficients of model equations (4), (5), (6), (7), (8) and (9) were determined.

In this study, variations of viscosities of soybean oil, cottonseed oil, corn oil, hazelnut oil, canola oil, linseed oil-based polyols and commercial polyols were determined a function of temperature. As expected that the viscosity of the fluid decreases as temperature increases. The tested polyols showed Newtonian and non-Newtonian fluids behavior at certain temperature range. Heating may rupture molecular entanglement and bonds may stabilize the molecular structure and reduce the effect of molecular volume in the vegetable oil-based polyols. As temperature increases, thermal energy of molecules increase and molecular distance develops due to reduction of intermolecular forces, hence viscosity of the fluid decreases.

As can be seen in Figures (1), (2), (3), (4), (5), (6) and (7) the viscosities of all types polyols irrespective of their production sources decrease substantially with increasing temperature. Heating may rupture molecular entanglement and bonds may stabilize the molecular structure and reduce the effect molecular volume in the polyols. In other words, as temperature increases, thermal energy of molecules increases and molecular distance develop due to reduction of intermolecular force and hence viscosity of fluid decreases. When thermal energy of molecules increases, molecular entanglement aligns easily and molecular structure stabilizes quickly since the molecules with high thermal energy move over one another easily.

As can be seen in Figure 8 the highest viscosity belongs to the commercial polyols while the lowest viscosity belongs to the polyol obtained from the raw hazelnut oil. The viscosities of polyols from high to low can be put in order as $\mu_{\text{commercial}} > \mu_{\text{canola}} > \mu_{\text{soybean}} > \mu_{\text{cottonseed}} > \mu_{\text{linseed}} > \mu_{\text{corn}} > \mu_{\text{hazelnut}}$, here $\mu_{\text{commercial}}$, μ_{canola} , μ_{soybean} , $\mu_{\text{cottonseed}}$, μ_{linseed} , μ_{corn} and μ_{hazelnut} denote the viscosities of commercial polyol and polyols obtained from raw canola oil, soybean oil, cottonseed oil, linseed oil, corn oil and raw hazelnut oil, respectively. Furthermore, it can be seen that all types of polyols show almost Newtonian behavior.

The regression coefficients and correlation coefficients of each model equation for each polyol obtained from different vegetable oils are given Tables 1, 2, 3, 4 and 5. As can be figured out from comparison of Tables, high values of R-squared were obtained for polynomial model irrespective of polyols obtained sources. Moreover, the developed new model has the highest values for R-squared.

In addition, density of vegetable oil based-polyols was measured to be 880 and 910 kg/m³.

The petroleum-based polyols and vegetable-based polyols have different hydroxyl numbers. The hydroxyl numbers of vegetable-based polyols were optimized by varying temperature, reaction time and catalyst.

The temperature dependent-apparent viscosity of vegetable oil-based polyols; model equations and experimental data were compared with one another.

The operating temperature of the assay was measured by raising temperature stepwise in a water bath. According to the experimental data; the linear and non-linear regression were made to determine coefficients of regression in the model equations.

REFERENCES

- [1] Andersson A., Lundmark S., Magnusson A. and Maurer F. H. J., "Vibration and Acoustic Damping of Flexible Polyurethane Foams Modified with a Hyper branched Polymer," *Journal of Cellular Plastics*, vol. 01, pp. 01-21, 2009.
- [2] Armenta J. L. R., Heinze T. and Martinez A. M. M., "New Polyurethane Foams Modified with Cellulose Derivatives," *European Polymer Journal*, vol. 40, pp. 2803-2812, 2004.
- [3] Bashirzadeh R. and Gharehbaghi A., "An investigation on reactivity, mechanical and fire properties of PU flexible foam," *Journal of Cellular Plastics*, vol. 01, pp. 01-30, 2009.
- [4] Bian X. C., Tang J. H. and Li Z. M., "Flame retardancy of whisker silicon oxide/rigid polyurethane foam composites with expandable graphite," *Journal of Applied Polymer Science*, vol. 110, pp. 3871-3879, 2008.
- [5] Bian X. C., Tang J.H. and Li Z. M., "Flame retardancy of hollow glass microsphere/rigid polyurethane foams in the presence of expandable graphite," *Journal of Applied Polymer Science*, vol. 110, pp. 3871-3879, 2008.
- [6] Han D. S., Park I. B., Kimi M. H., Noh B. J., Kim W. S. and Lee J. M., "The effects of glass fiber reinforcement on the mechanical behavior of polyurethane foam," *Journal of Mechanical Science and Technology*, vol. 24, pp. 263-266, 2010.
- [7] Indennitate L., Cannoletta D., Lionetto F., Greco A. and Maffezzoli A., "Nanofilled polyols for viscoelastic polyurethane foams," *Society of Chemical Industry*, vol. 59, pp. 486-491, 2009.
- [8] Lubguban A. A., Tu Y. C., Lozada Z. R., Hsieh F. H. and Suppes G. J., "Noncatalytic polymerization of ethylene glycol and epoxy molecules for rigid polyurethane foam applications," *Journal of Applied Polymer Science*, vol. 112, pp. 2185-2194, 2009.
- [9] Meng X. Y., Ye L., Zhang X. G., Tang P. M., Tang J. H., Ji X., and Li Z. M., "Effects of expandable graphite and ammonium polyphosphate on the flame-retardant and mechanical properties of rigid polyurethane foams," *Journal of Applied Polymer Science*, vol. 114, pp. 853-863, 2009.
- [10] Mello D., Pezzin S. H. and Amico S. C., "The effect of post-consumer pet particles on the performance of flexible polyurethane foams", *Polymer Testing*, vol. 28, pp. 702-708, 2009.
- [11] Michel F. S., Chazeau L. and Cavaillé J. Y., "Mechanical properties of high density polyurethane foams: II effect of the filler size," *Composites Science and Technology*, vol. 66, pp. 2709-2718, 2006.
- [12] Mosiewicki M. A., Dell'Arciprete G. A., Aranguren M. I. and Marcovich N. E., "Polyurethane foams obtained from castor oil-based polyol and filled with wood flour," *Journal of Composite Materials*, vol. 01, pp. 1-16, 2009.
- [13] Nikje M. M. A. and Tehrani Z. M., "Thermal and mechanical properties of polyurethane rigid foam/modified nanosilica composite," *Polymer Engineering and Science*, vol. 50, pp. 468-473, 2010.
- [14] Nikje M. M. A. and Tehrani Z. M., "Polyurethane rigid foams reinforced by doubly modified nanosilica," *Journal of Cellular Plastics*, vol. 01, pp. 01-14, 2010.
- [15] Racz I., Andersen E., Aranguren M. I. and Marcovich N. E., "Wood floor-recycled polyol based polyurethane lightweight composites," *Journal of Composite Materials*, vol. 43, pp. 2871-2884, 2009.

Modelling Rheological Properties of some Molasses–Sesame Paste Blends

Ercan Aydoğmuş, Fethi Kamışlı
Firat University, Engineering Faculty
Elazığ, Turkey

ercanaydogmus@firat.edu.tr, fkamisli@firat.edu.tr

Abstract— In this study viscosities of some ratios of the molasses - sesame paste blends such as ratios of date, mulberry and grape with sesame paste blends at the different volume ratios (10, 20, 30, 40 and 50 %) were measured at different temperatures (25, 30, 35, 40, 45 and 50 °C) by using a rotary viscometer (Brookfield DV-II) since one of the most important parameters required in the design of technological processes in food industries.

Rheological properties of some molasses obtained for apparent viscosities and rotational speeds were used to describe the flow behavior of those blends

This study was to determine the rheological properties and develop models for some ratios of the sesame paste; mulberry, grape and date molasses blends at the different volume ratios and the viscosity of each blends was measured at different temperatures using a rotary viscometer. The viscosity of each blends as a function of the shear rate, those samples were sheared with several different rotational speeds at an increasing order.

In this study, the rheological properties of some molasses, sesame paste and their blends were investigated.

Keywords— Molasses, Sesame Paste, Rheology, Modelling

I. INTRODUCTION

Sesame paste is a pure product of sesame, without adding or removing any of its constituents. It has considerable antioxidant activity due to the major components of sesame oil. The antioxidants, sesamin and sesamol, are effective chemicals to suppress the formation of free radicals thus act as anti-carcinogenic substances. Moreover, sesame oil can resist oxidative deterioration and rancidity due to these antioxidants [1].

They determined the rheological and sensory properties of grape molasses-sesame paste blends as functions of concentrations of 2 %, 4 % and 6 % at 30, 40, 50, 60, 65 and 75 °C. They used the power law model to determine the relationship between the apparent viscosity and the shear rate. They concluded that all blends exhibited pseudo-plastic behavior. The molasses content and temperature influenced the flow behavior and consistency index values. They observed that the addition of molasses improved the emulsion stability of the blends. Temperature sensitivity of the consistency index was assessed by applying an Arrhenius-type equation [2]. They worked on the sesame paste-molasses blends by determining rheological properties of the blends at different

sesame paste concentrations (20 – 32 %) and temperatures (35 – 65 °C) by using a rotational viscometer. Sesame paste-molasses blends were found to exhibit non-Newtonian, shear thinning behavior at all temperatures and sesame paste concentrations. They concluded that the power-law model was successfully applied to the data for apparent viscosity versus strain rate. They determined that the flow behavior index, n varied in the range of 0.7 – 0.85 and the consistency coefficient, K was in the range of 282 – 2547 cP. Both parameters were significantly affected by temperature [3].

They investigated on the rheological behaviors of molasses samples (mulberry, grape, rosehip and carob molasses). Viscosity was measured at 5, 10, 15, 20 and 30 °C using a rotational viscometer in the shear rate range of 0–93 s⁻¹. They used the empirical power-law model to describe the rheological behaviors of molasses samples. In their work molasses samples were found to exhibit non-Newtonian behaviors. Arrhenius type equation was used to determine the effect of temperature on viscosities of molasses samples and thus E_a values of molasses samples were calculated. They observed that the activation energies varied from 18.509 to 74.658 kJ/mol depending on the solid contents (39.44, 60.48, 67.08, 69.68, 71.98, 74.22, 75.4 and 75.46 °Brix) [10].

II. EXPERIMENTAL STUDIES

Brookfield rotational viscometer (Model DV-II) equipped with different spindles were used to measure a viscosity as a function of shear rate. Enough samples were used to immerse the groove on the spindle with guard leg. The flow behaviors of several different blends were determined at 25, 30, 35, 40, 45 and 50 °C as forward measurement (speed increasing) and also as backward measurement (speed decreasing). Temperature was maintained at a certain constant value using thermostatically controlled electrical system.

Brookfield rotational viscometer used in the experimental work is available in our laboratory and °Brix level of each molasses was determined by using the refractometer.

III. MODELLING RHEOLOGICAL PROPERTIES

Brookfield rotational viscometer equipped with spindle 28 was used to determine viscosity of a blend as a function of shear rate. Enough samples nearly 12 mL in the beaker were used

to immerse the groove on the spindle with guard leg. Temperature was kept constant at a certain value using thermostatically controlled electrical system. The used rotational viscometer allow shear rate ($\dot{\gamma}$) and shear stress (τ) to be read directly from viscometer. Shear stress and shear rate can also be calculated by using Eq. (1), (2) and (3).

$$\dot{\gamma} = \beta \cdot N \quad (1)$$

$$\tau = \mu \cdot \dot{\gamma} \quad (2)$$

$$\tau = \kappa \cdot (\mu)^\delta \quad (3)$$

Where; N is rotational speed (rpm), τ is shear stress (Pa), μ is the apparent viscosity (mPa. s), κ is the consistency coefficient (mPa.s), δ is flow behavior index and β is coefficient (dimensionless).

The viscosity of a blend as a function of temperature can be calculated using one of the equations given below. Here all the equations given below are used to determine how the viscosity depends on temperature. In order to choose the best model for each blend, R^2 is calculated for each model.

$$\mu_{lin} = a T + b \quad (4)$$

$$\mu_{exp} = a \exp(b T) \quad (5)$$

$$\mu_{pow} = a T^b \quad (6)$$

$$\mu_{ln} = a \ln T + b \quad (7)$$

$$\mu_{pol} = a T^2 + b T + c \quad (8)$$

Equations have a lot of constants such as x , y and z .

IV. RESULTS AND DISCUSSION

A. Figures and Tables

TABLE I. CORRELATION COEFFICIENTS FOR MULBERRY MOLASSES

Shear Rate: 2,80/s Models	Constants			
	a	b	c	R^2
Linear (lin)	-182,0	59636	-	0,9147
Exponential (exp)	$3 \cdot 10^{11}$	-0,060	-	0,9926
Power (pow)	$6 \cdot 10^{49}$	-18,60	-	0,9936
Logarithmic (ln)	-56668	328275	-	0,9207
Polynomial (pol)	7,0714	-4573,4	740879	0,9883

Table I shows that values of constants in Eq. (4) – Eq. (8) and R^2 . As can be seen in Table I the power model for mulberry molasses has the highest value for R^2 ; therefore, it can be said that the best model for mulberry molasses is the power model if the value of R^2 is taken to be as an indicator of the most suitable model. The lowest value belongs to linear model and it can be said the worst model is the linear model due to the same reason.

The values of constants in Eq. (4) – Eq. (8) and R^2 for date are given in Table II. As can be seen in Table II the polynomial model has the highest value of R^2 and as explained earlier, it

can be said that the best model for variation of the viscosity of date with temperature is the polynomial model and the worst model is the linear model if a value of R^2 is taken to be as an indicator of the most suitable model.

TABLE II. CORRELATION COEFFICIENTS FOR DATE MOLASSES

Shear Rate: 2,80/s Models	Constants			
	a	b	c	R^2
Linear (lin)	-60,571	19757	-	0,8771
Exponential (exp)	$3 \cdot 10^{11}$	-0,064	-	0,9803
Power (pow)	$3 \cdot 10^{52}$	-19,86	-	0,9834
Logarithmic (ln)	-18877	109262	-	0,8845
Polynomial (pol)	3,0	-1923,6	308769	0,9919

TABLE III. CORRELATION COEFFICIENTS FOR GRAPE MOLASSES

Shear Rate: 2,80/s Models	Constants			
	a	b	c	R^2
Linear (lin)	-34,286	11096	-	0,8643
Exponential (exp)	$1 \cdot 10^{13}$	-0,079	-	0,9608
Power (pow)	$4 \cdot 10^{63}$	-24,49	-	0,9638
Logarithmic (ln)	-10685	61760	-	0,8717
Polynomial (pol)	1,7143	-1098,9	176245	0,9796

TABLE IV. CORRELATION COEFFICIENTS FOR SESAME PASTE

Shear Rate: 2,80/s Models	Constants			
	a	b	c	R^2
Linear (lin)	-23,714	8538,3	-	0,9155
Exponential (exp)	516,850	-0,020	-	0,9445
Power (pow)	$2 \cdot 10^{18}$	-6,115	-	0,9495
Logarithmic (ln)	-7385	43547	-	0,9218
Polynomial (pol)	0,9643	-622,54	101435	0,9962

Table III shows the values of constants for grape molasses in Eq. (4) – Eq. (8) and R^2 . As seen in the Table polynomial model for the changes of viscosity of grape molasses as a function of temperature is the best model since the highest value of R^2 belongs to this model and it can be said that the worse model is linear model due to the same reason.

The values of constants in Eq. (4) – Eq. (8) and R^2 for sesame paste are given in Table IV. The values for R^2 indicate that the best model for viscosity of sesame as a function of temperature is polynomial model if a value of R^2 is taken to be an indicator of the most suitable model.

Fig. 1 illustrates variations of viscosity of mulberry molasses as a function of shear rate at various values of temperature. As can be seen in the figure viscosity of mulberry molasses decreases with increasing shear rate at all values of temperature tested. As expected that the viscosity of mulberry molasses decreases with increasing temperature. As can be seen in the figure an increase in the temperature results in substantial decrease in the viscosity of mulberry molasses. Heating may rupture molecular entanglement and bonds may stabilize the molecular structure and reduce the effect of molecular volume in mulberry molasses. As temperature increases, thermal energy of molecules increase and molecular distance develops due to reduction of intermolecular forces, hence viscosity of the fluid

decreases. A decrease in viscosity with increasing shear rate indicates that the mulberry molasses exhibits pseudo plastic behavior at the all considered values of temperature. The decrease in viscosity as the shear rate is increase is related to the increased alignment of constituent molecules of the tested system [11]. The pseudo plastic behavior at low values of temperature (298 K) is more pronounced than that at high value of temperature (323 K).

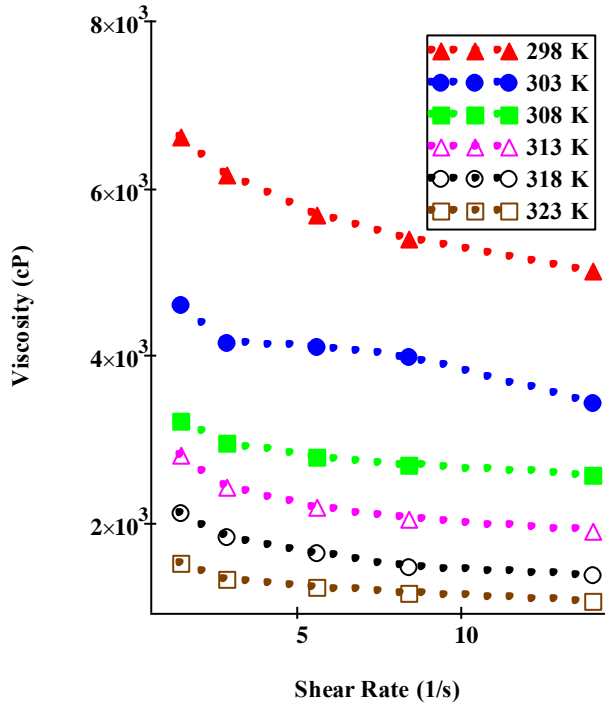


Figure 1. Variation of viscosity of mulberry molasses as a function of shear rate at various values of temperature

The variations of viscosity of date molasses as a function of shear rate are illustrated in Fig. 2 for various values of temperature. As can be seen in the figure the viscosity of date molasses decreases with increasing temperature as expected. As can be also seen in the figure the viscosity of date molasses decreases with increasing shear rate at the all considered values of temperature. At high temperature ($T > 308$ K) the variation of viscosity with shear rate for date molasses is almost negligible. As expected, the effect of shear rate at low temperature is more pronounced than that at high temperature. As seen in the figure it can be said that date molasses shows pseudo plastic behavior at all values of temperature tested.

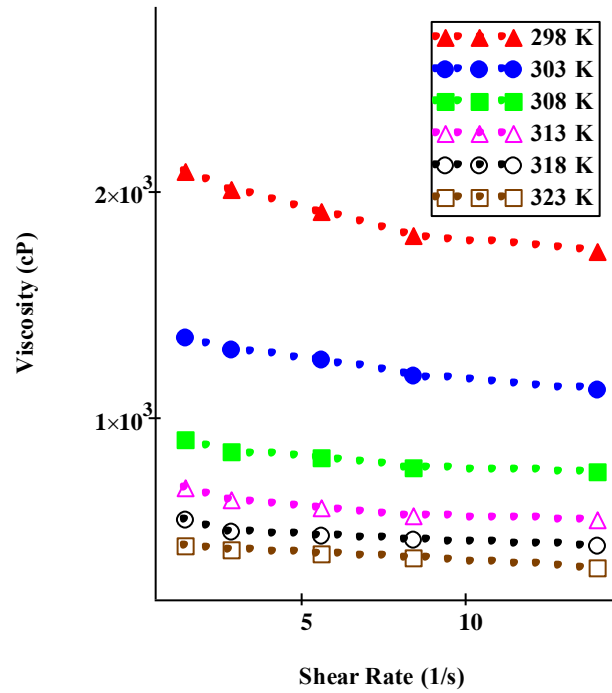


Figure 2. Changes of viscosity of date molasses as a function of shear rate at various values of temperatures

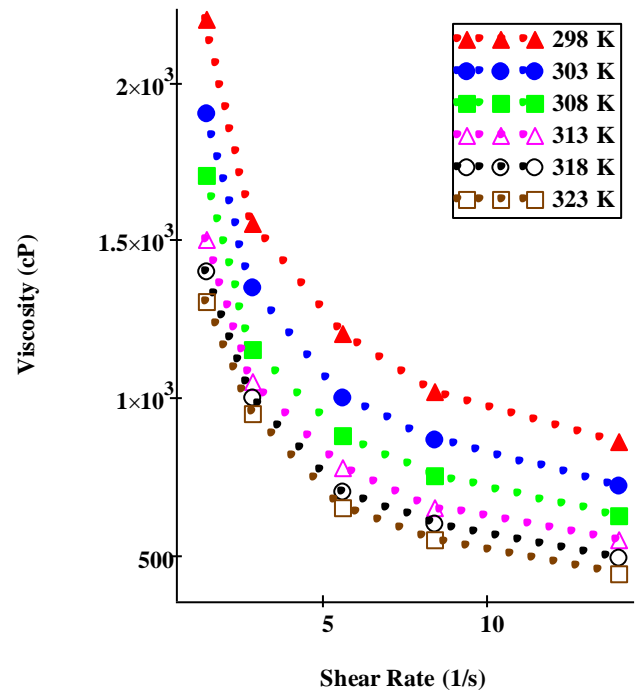


Figure 3. Variations of viscosity of sesame paste as a function of shear rate at various values of temperatures

Fig. 3 shows that variation in viscosity of sesame paste as a function of shear rate at various values of temperature tested. As can be seen in the figure the effect of shear rate on viscosity of sesame paste is very pronounced at all considered values of temperature and the viscosity decreases with increasing shear rate as evidenced in Fig. 3. As explained earlier a decrease in viscosity as shear rate is increased is related to the increase alignment of constituent molecules of the sesame consisting of oil and protein. A decrease in viscosity with increasing shear rate indicates the sesame paste exhibits pseudo plastic behavior at all temperature tested. It can be also seen in the figure the viscosity of sesame paste is very sensitive toward temperature and decreases with increasing temperature. The thermal energy of molecules increases and molecular distances develop because of reduction of intermolecular forces when temperature increases; therefore, the viscosity of fluid decreases.

Fig. 4 illustrates variations in viscosity of the blend consisting of sesame paste (80%) and mulberry molasses (20%) as a function of shear rate at the different values of temperature. As can be seen in the figure the viscosity of the blend decreases with increasing shear rate. As mentioned previously the alignment of constituent of molecules can be increased as shear rate is increased, which causes a decrease in viscosity of a fluid tested.

Even a high shear rate itself can cause an increase in temperature, in turn heating may rupture molecular entanglement and bonds may stabilize the molecular structure and reduce the effective molecular volume in protein and sugars resulting in a decrease in viscosity. As seen in the figure the viscosity of blend decreases with increasing temperature all values of shear rate tested in the present work. The viscosity of a fluid decreases with increasing temperature since, as expected, the thermal energy of molecules increases with increasing temperature and thus, molecular distances develop due to reduction of intermolecular force. At low values of temperature (298 K, 303 K), the effect of shear rate on viscosity is more pronounced than that at high values of temperature.

An entanglement of chain is progressively aligned with shear rate, an alignment that responds nearly instantaneously to changes in the imposed shear; therefore, viscosity of a fluid decreases with increasing shear rate. When alignment is completed at high shear rate, the apparent viscosity of a fluid become constant as evidenced in the figures given above. In other words, when a shear thinning fluid is disturbed by shear rate, the fluid structure deforms to align molecular entanglement while some of molecules break down as shear rate is increased.

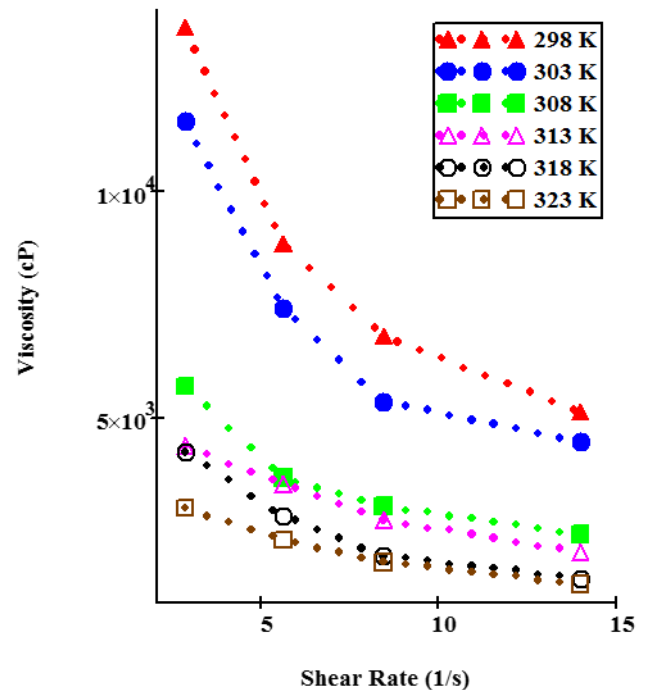


Figure 4. Changes in viscosity of the blend consisting of sesame paste (80%) and mulberry molasses (20%) as a function of shear rate at the different values of temperature.

V. CONCLUSION

Mulberry molasses, date molasses, grape molasses, sesame paste and the blend consisting of sesame paste (80 %) and mulberry molasses (20 %) were examined to determine their viscosities as functions of temperature and shear rate. In this context different equations were used to determine the relationship between temperature and viscosities of considered fluids. Furthermore, viscosities of those materials were measured as a function of shear rate at various values of temperature. It was found that all fluids tested in the present study exhibited pseudo plastic behavior. It can be concluded that temperature and shear rate are very effective parameter on viscosities of the considered fluids.

REFERENCES

- [1] Abu-Jdayil B., Al-Malah K. and Asoud H., "Rheological characterization of milled sesame (Tahin)," *Food Hydrocolloids*, vol. 16, pp. 55-61, 2002.
- [2] Alpaslan M. and Hayta M., "Rheological and sensory properties of pekmez (grape molasses)/tahin (sesame paste) blends," *J. Food Sci.*, vol. 54, pp. 89-93, 2002.
- [3] Arslan E., Yener M. E. and Esin A., "Rheological characterization of tahin/pekmez (sesame paste/concentrated grape juice) blends," *J. Food Sci.*, vol. 69, pp. 167-172, 2005.
- [4] Marcotte M., Taherian Hoshahili A. R. and HRamaswamy H. S., "Rheological properties of selected hydrocolloids as a function of concentration and temperature," *Food Res. Intl.*, vol. 34, pp. 695-703, 2001.

- [5] Maskan M. and Göğü F., "Effect of sugar on the rheological properties of sunflower oil-water emulsions," *J. Food Eng.*, vol. 43, pp. 173-177, 2000.
- [6] Mohamed M. A. and Ahmed A. A., "Libyan date syrup (Rub-AL-Tamr)," *J. Food Sci.*, vol. 46, pp. 1162-1166, 1981.
- [7] Rao M. A. and Anantheswaran R. C., "Rheology of fluids in food processing," *Food Technol.*, vol. 36, pp. 116-126, 1982.
- [8] Rezzoug M. Z., Bouvier J. M., Allaf K. and Patras C., "Effect of principal ingredients on the rheological behavior of biscuit and on quality of biscuits," *J. Food Eng.*, vol. 35, pp. 23-42, 1998.
- [9] Suzuki K, Maeda T., Matsuoka K. and Kubota K., "Effects of constituent concentration on rheological properties of corn oil-in-water emulsions," *J. Food Sci.*, vol. 56, pp. 796-798, 1991.
- [10] Yoğurtcu H. and Kamışlı F., "Determination of rheological properties of some pekmez samples in Turkey," *J. Food Sci.*, vol. 77, pp. 1064-1068, 2016.
- [11] Rha C., "Theories and principle of viscosity," in C. Rha (Ed.), *Theory, determination and control of physical properties of food material* (pp. 7-24), Dordrecht, The Netherlands: Reidel, 1975.

Graphene Nanoplatelet/MIL-101 Nanoadsorbents for Removal of Antibiotics

Şahika Sena BAYAZIT
Beykent University, İstanbul TURKEY
sahikasena@gmail.com

Abstract— Antibiotics in wastewater cause very serious problems. The antibiotic resistant bacterias increase and epidemic diseases can occur. So the water treatment is very important. Adsorption is a mostly used method for water treatment. Last decade, advanced adsorbents have been synthesized for this purpose. Different kinds of graphenes and metal organic frameworks take attention of researchers. In this study, graphene nanoplatelet and MIL-101 were used. Graphene nanoplatelet has high specific surface area and porosity. Also, MIL-101 has high specific surface area and porosity. The hydrothermal method was used for the preparation of graphene nanoplatelet/MIL-101 nanocomposite. And suitable purification methods were applied to the composite. XRD, TEM, SEM, BET surface area and FTIR analysis were used for the characterization of the composite. Ciprofloxacin antibiotic was chosen for the adsorption studies. Because ciprofloxacin is one of the most used antibiotic in worldwide. Adsorption variables were investigated for ciprofloxacin, in this study. And the results of bare MIL-101 and composite was compared. Composite gained higher adsorption capacity to bare MIL-101. When 1 mg of adsorbent was used for adsorption of 20 mg/L of ciprofloxacin solution, the adsorption capacity of MIL-101 was found as 15.81 mg/g but the composite was 61.56 mg/g.

Keywords— Graphene nanoplatelet, metal organic frameworks, composites, adsorption

Modeling of solid-liquid extraction of total phenolics from *Capsicum annuum* L.

Bilgesu Sahin, Sibel Yigitarslan
Suleyman Demirel University, Engineering Faculty
Isparta, Turkey
yildizsibel@sdu.edu.tr

Abstract— In this paper, the extraction kinetics of gallic acid equivalent of polyphenols from *Capsicum annuum* was investigated. Ethanol was used as a solvent for extraction at different temperatures and the extraction medium was set at mixed and unmixed conditions to observe the changes in the kinetics. Two different strategies were applied for modeling. In the first one, four different models; namely Peleg, Mass Transfer, Logarithmic, and Page's Models were used for mathematically describing the physicochemical behavior of the extraction. The yields of extraction ranged from 1.39-3.27 mg/g depending on the extraction conditions. Mass transfer was found the best model representing the experimental data. Molecular and effective diffusivities were calculated. In the second strategy, extraction was modeled with the aid of response surface methodology. Extraction yield surface showed a linear relation with temperature, time, and solid-to-liquid ratio. The optimum conditions of extraction were 70°C, 90 minutes and 1/50 g/ml, and 3.29 mg/g gallic acid equivalent of total phenolics were extracted at those conditions. The model equations of this process could contribute to optimize the industrial extraction process and design of drug-delivery systems.

Keywords— extraction; modeling; polyphenols; gallic acid; response surface methodology

I. INTRODUCTION

In recent years, several researchers have been focused on polyphenols of vegetables, fruits and herbs due to their contribution to human health. Phenolic compounds are capable of scavenging free radicals [1, 2], and are known as antioxidants [3]. Gallic acid, quercetin, kaempferol and catechin are well known phenolics [4-6], and they have been used especially in cancer treatments [7, 8]. One of the herbs containing gallic acid is *Capsicum annuum* L. (red pepper) from Solanaceae family. It contains calcium, phosphorus, sodium, iron, B₁, B₃, C vitamins, lipids, carbohydrates, proteins, fibers and organic compounds producing its characteristic color [9]. Researchers had been analyzed its phenolic content by HPLC analysis in detail [10, 11]. The amount and the type of phenolic components in a plant material depend on not only genotype, maturation and growth conditions of the plant [12-14], but also the type and conditions of extraction.

The studies on extraction of phenolics from *Capsicum annuum* focused on application of different type of solvents including pure methanol [15], methanol-water mixture [12, 16], pure ethanol [13, 14]. In those papers, since they paid attention to the types of flavonoids in a plant, they analyzed the extracts after hydrolyzing them. When extraction temperature was increased up to 65°C, the increase in the extraction yield was observed because of the increase in stability of phenolics due to non-enzymatic reactions [15].

All of the literature deals with the types of flavonoids in the plant, and there is scarce data on modeling of the extraction process of them. Mathematical modeling of the extraction is a useful engineering tool which facilitates the understanding, optimization, design and control of the processes with minimal time and energy consumption. There are two types in modeling of a process; namely mathematical models and Response Surface Methodology. Several equations have been proposed in the literature for mathematical modeling [17-20] and it seems that the best model differs due to the plant material and the extraction conditions. Response surface method is a combination of statistical and mathematical techniques used for analyzing several independent variables and also interactive effects among the variables on the response [21]. This method has been used in several different optimizations including adsorption, extraction, fermentation etc. in an efficient manner [22-26]. The advantages of the method are reduced number of experimental runs, cost and time [27, 9]. In addition, the final equation found by this method can adaptable to any situation faced in the industry. There is not any research aiming to combine them in a special extraction case for comparison.

This study aimed to obtain a model equation for extraction of phenolics from *Calendula officinalis* by applying two procedures for optimization. Peleg's, Page's, mass transfer and logarithmic models were applied in mathematical modelling. The molecular and convective diffusion coefficients were determined. In addition, response surfaces were constructed and the influences of temperature, solid-to-liquid ratio, and time on extraction yields were analyzed.

II. METHOD

A. Materia

In the experiments of classical extraction, *Capsicum annuum L.* was purchased from the herbalist has capable of growing this plant itself. Ethanol, Folin-Ciocalteu, and sodium carbonate were at analytical grade, and bought from Sigma-Aldrich.

B. Solvent Extraction

Ethanolic extraction was realized batch-wise in a 250 mL Erlenmeyer flask. Extraction temperature, solid-to-liquid ratio, and mixing rate were chosen as the parameters of single- and multiple-parameter experimental designs. At the end of the specified extraction conditions the content of the flask was filtered through 110 mm filters (FilterLab) and filtered samples were used for total flavonoid analysis.

C. Determination of Total Phenolics

The concentrations of the total polyphenols in the extracts filtered were determined using the Folin-Ciocalteu method. In the analysis 0.4 ml of the extract was mixed with 5.1 ml of distilled water and 0.5 ml of Folin ciocalteu reagent. 1.5 ml of sodium carbonate solution (20% by weight) was added into the medium immediately and after mixing they kept in dark during two hours at room temperature. The color resulted from the colorimetric reaction between gallic acid in the sample and the Folin reagent was analyzed by UV-vis spectrophotometer (Perkin-Elmer) at 765 nm. The gallic acid equivalents (GAE) of total phenolics were calculated from the calibration curve (Absorbance = 0.01532 x Concentration (μg/ml); $R^2=0.9989$) and the results were expressed as mg GAE/g dry herb.

D. Extraction Kinetics

Since the extraction curves (concentration of phenolics vs. time) have similar shape with the sorption curves, all of the extraction processes could be described with a non-exponential equation of Peleg [17]:

$$c_t = c_0 + \frac{1}{K_1 + K_2 t} \quad (1)$$

where c_t is the concentration of phenolics at time t (mg GAE/g), c_0 is the initial concentration of phenolics at time $t=0$ (i.e. $c_0=0$ in all experiments), t is the extraction time, K_1 is Peleg's rate constant (min.g/mg GAE), and K_2 is Peleg's capacity constant (g/mg GAE). In that equation, K_1 relates to the extraction rate (B_0) at the very beginning of the extraction ($t=t_0$):

$$B_0 = \frac{1}{K_1} \quad (\text{mg GAE/g}) \quad (2)$$

and K_2 relates equilibrium concentration (c_{eq}) at $t \rightarrow \infty$:

$$c_{eq} = \frac{1}{K_2} \quad (\text{mg GAE/g}) \quad (3)$$

Page's Model

Another model used for the mathematical modeling of the extraction proposed by Page as follows [19]:

$$c_t = \exp(-kt^n) \quad (4)$$

Logarithmic Model

In mathematical modeling of extraction processes, Logarithmic model can also be used as follows:

$$c_t = a \text{Log}t + b \quad (5)$$

where a and b are the logarithmic model constants.

Mass Transfer Model

Extraction occurs through two steps; Firstly, the solvent penetrates into the solid to dissolve the extractable material, and then the extractable material diffuses from inside the solid to the bulk liquid. The rate determining step of the overall process is the diffusion [28]. The rate of this step under unsteady-state conditions is defined by Fick's second law as:

$$\frac{\partial c}{\partial t} = D \frac{\partial^2 c}{\partial x^2} \quad (6)$$

where, c is the concentration of the solute (mg/g), t is time (min), D is the diffusion coefficient (m^2/min), and x is the distance of diffusion. This equation is valid when very dilute solution is used in the extraction and the diffusivity is assumed to be constant [29]. If the shapes of the solid particles are assumed to as perfect spheres having the same properties and also if the perfect mixing of the solid-liquid medium occurs, the time of mass transfer at infinity, the general solution of this equation becomes:

$$\text{Ln} \left(\frac{c_\infty}{c_\infty - c} \right) = 0.498 + \frac{9.87Dt}{R^2} \quad (7)$$

where, c is the concentration of the extracted material in the solution at time t (mg/g), c_∞ is the concentration of the extracted material at time $t=\infty$, and R is the characteristic distance (m); i.e. for spheres it is equal to the radius. This equation can be rewritten as:

$$\text{Ln} \left(\frac{c_{eq}}{c_{eq} - c} \right) = a + K_{obs}t \quad (8)$$

Since c_∞ is considered as equilibrium concentration, a is a constant (0.498), and

$$K_{obs} = \frac{9.87D}{R^2} \quad (9)$$

In this research, Equation 8 was used to fit the experimental data and to obtain a, K_{obs} and diffusion coefficient values.

Validity of Model Prediction

The consistency between the predicted and experimental data evaluated by using the coefficient of determination (r^2), which is defined as:

$$r^2 = 1 - \frac{\sum_{i=1}^n (y_i - y_{model})^2}{\sum_{i=1}^n (y_i - y_{mean})^2} \quad (10)$$

where, n is the number of samples, y_i is the actual experimental data of the i th sample, y_{model} is the model-fitting data of the i th sample, and y_{mean} is the mean value of all experimental data. A high r^2 value indicates high consistency between the fitted and experimental data.

E. Response Surface Methodology

In designing the experiments, firstly, the potential design factors of extractions, namely extraction temperature, solid-to-liquid ratio, time and mixing rate were studied to determine the most effective three parameters on the extraction yield by single-parameter procedure. It was found that mixing rate was not as effective as the other parameters (data not shown). Then, Box-Behnken design (BBD) was constructed for analysis of multi-parameter effects. The highest levels of respective parameters producing the highest yield were chosen as the center point values (coded as “0” in Table 1) of the optimization of the extraction, while the least and the highest values were used as minimum and maximum points (coded as “-1” and “+1” in Table 1), respectively. The chosen independent variables were coded according to (1).

Table 1. levels and codes of experimental parameters used in Box-Behnken design

Parameter	-1	0	+1
x_1 : Temperature ($^{\circ}\text{C}$)	30	50	70
x_2 : Time (min)	30	60	90
x_3 : Solid/liquid (g/mL)	1/30	1/40	1/50

$$x_i = \frac{x_i - x_0}{\Delta x} \quad (11)$$

where x_i is the dimensionless coded value of i th independent variable, x_0 is the value of x_i at the center point, and Δx is the step change value. The behavior of the system is explained by the following second-order polynomial model:

$$Y = \beta_0 + \sum_{i=1}^k \beta_i x_i + \sum_{i=1}^k \beta_{ii} x_i^2 + \sum_{i=1}^{k-1} \sum_{j=2}^k \beta_{ij} x_i x_j + \varepsilon \quad (12)$$

where Y is the predicted response, x_i, x_j, \dots, x_k are input variables, which affect the response Y , $x_i^2, x_j^2, \dots, x_k^2$ are the square effects, β_0 is the intercept term, $x_i x_j, x_j x_k$ and $x_i x_k$ are the interaction effects, β_i ($i = 1, 2, \dots, k$) is the linear effect, β_{ii} ($i = 1, 2, \dots, k$) is the squared effect, β_{ij} ($i = 1, 2, \dots, k$) is the interaction effect, and ε is the random error [30-31].

The Design-Expert 9.0 (Stat-Ease Inc., Minneapolis, MN, USA) software was used for regression and graphical analysis of the experimental data to fit the equations developed. Design of fifteen experiments consisting of three replicates at the central point was fitted into a polynomial model. The optimum values of the selected variables were obtained by solving the regression equation in which desired values of the process responses were set as the optimization criteria.

III. RESULTS AND DISCUSSIONS

The aim of the present study was to determine the mathematical equation fitting to the experimental results of batch extraction yields. Two different optimization methods were applied to reach this aim by plotting the values of gallic acid equivalent of total phenolics extracted versus time for different extraction conditions.

In the first approach, four different mathematical relations defining the physicochemical behavior of extraction were chosen; i.e., Peleg's, Mass transfer, Logarithmic, and Page's equations. The models were statistically analyzed and compared with their respective determination of coefficient (r^2) value. The constants of respective models and their r^2 values were summarized in Table 2.

As it can be seen from Table 2, Peleg's model was not as successful as other methods applied. Mass transfer model produced the highest value of determination of coefficient and the a-values were close to its exact value of 0.498. Although, values of determination of coefficient in mass transfer, logarithmic and Page's models were all acceptable, it seemed that logarithmic model caused more reliable results than the others because it produced nearly the same values for regression coefficients under different extraction conditions. In the literature, different models were found as the best model on the kinetic analysis of extraction depending on the different plants and extractable materials [19,32-34]. It is impossible to compare the kinetic results of this research with the one in the literature that focused on the extraction of total phenolics from *Capsicum annuum* since there is not any research focusing on it.

Table 2. model parameters of extraction kinetics

PELEG'S MODEL			
	K ₁	K ₂	r ²
70°C-molecular	3.0392	0.3048	0.8414
70°C-convective	1.1899	0.326	0.7463
MASS TRANSFER MODEL			
	K _{obs}	A	r ²
70°C-molecular	0.0361	0.4247	0.9804
70°C-convective	0.0370	0.5534	0.9187
LOGARITHMIC MODEL			
	A	b	r ²
70°C-molecular	1.2769	0.5614	0.9662
70°C-convective	1.1163	1.0375	0.9146
PAGE'S MODEL			
	K	n	r ²
70°C-molecular	0.2338	0.3723	0.9704
70°C-convective	0.4461	0.2227	0.9723

In the detailed analyses of the models, results were employed by plotting the calculated values of concentrations for each model and their respective experimental values (Figures 1-8) vs. time. As it was expected from its lower r² value, high discrepancies between concentrations estimated by Peleg's equation and experimental data were observed in both molecular (unmixed extraction medium; Figure 1) and convective extractions (mixed extraction medium; Figure 2). Comparing the other three models, the excellent fitness between the experimental data obtained under unmixed extraction medium conditions at 70°C and estimated concentrations of phenolics were obtained by mass transfer model (Figure 3). Either in logarithmic or Page's model equations caused less (especially in logarithmic model; Figures 5 and 6) or higher estimated values under all conditions (Figures 7 and 8). Figures clearly showed that, extraction yield increases rapidly at the beginning of extraction due to high driving force (concentration difference between solid and solvent), and that this increase getting lesser as the time passes due to decrease in driving force. In each case, extraction is reached equilibrium at the end. This behavior is explained by the mass transfer model appropriately. From Equation 9, the molecular and convective diffusion coefficients were calculated as $2.67 \cdot 10^{-10} \text{ m}^2/\text{s}$ and $2.73 \cdot 10^{-10} \text{ m}^2/\text{s}$ by using the average diameter of the particle size of 0.27 mm, respectively. According to the results, a 2.2% increase of diffusion coefficient with mixing was observed. This result was in accordance with the single-parameter effect

analysis in which mixing rate was found less effective than the other parameters on extraction yield. In addition, the yields were determined as 3.11 mg GAE/g and 3.27 mg/GAE for molecular and convective extractions, respectively. As a result, the increase in diffusion coefficient yielded nearly 5% increases in extraction.

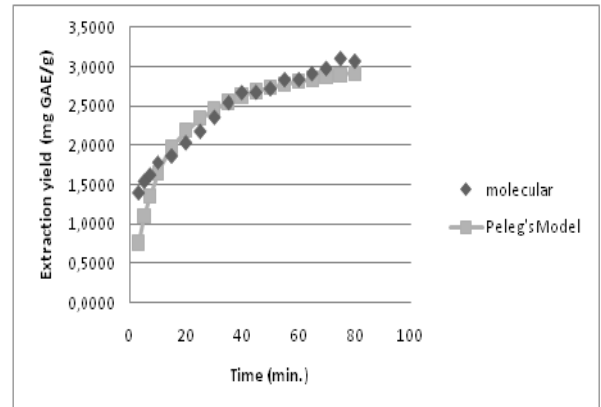


Fig. 1. The experimental data obtained at 70°C under unmixed extraction medium fitted to Peleg's Model

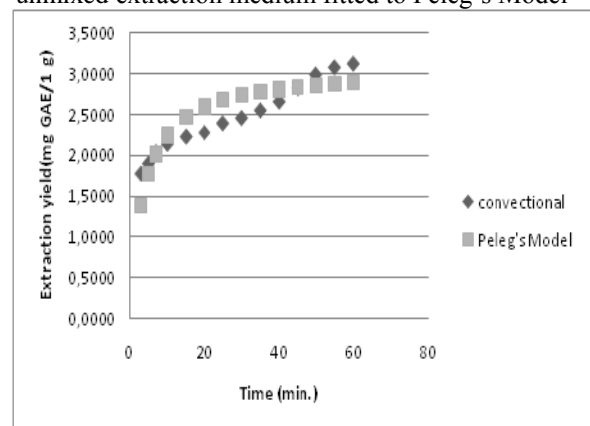


Fig. 2. The experimental data obtained at 70°C under mixed extraction medium fitted to Peleg's Model

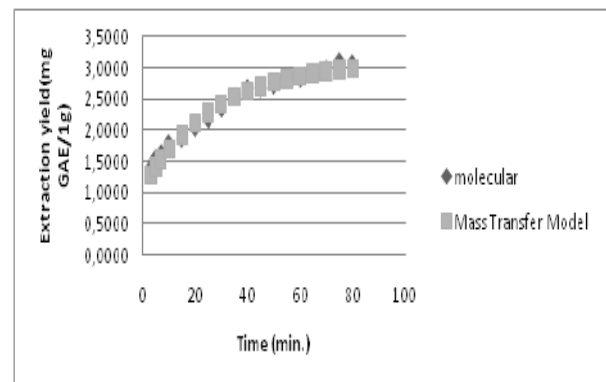


Fig. 3. The experimental data obtained at 70°C under unmixed extraction medium fitted to Mass Transfer Model

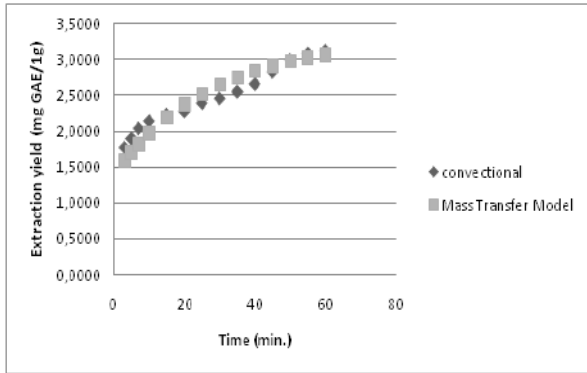


Figure 4. The experimental data obtained at 70°C under mixed extraction medium fitted to Mass Transfer Model

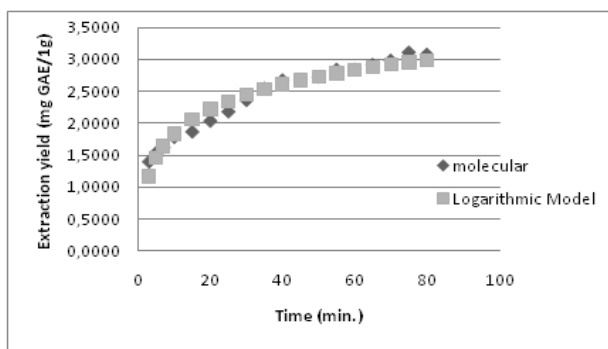


Figure 5. The experimental data obtained at 70°C under unmixed extraction medium fitted to Logarithmic Model

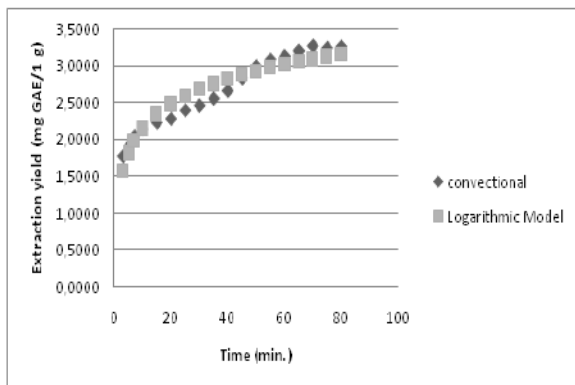


Figure 6. The experimental data obtained at 70°C under mixed extraction medium fitted to Logarithmic Model

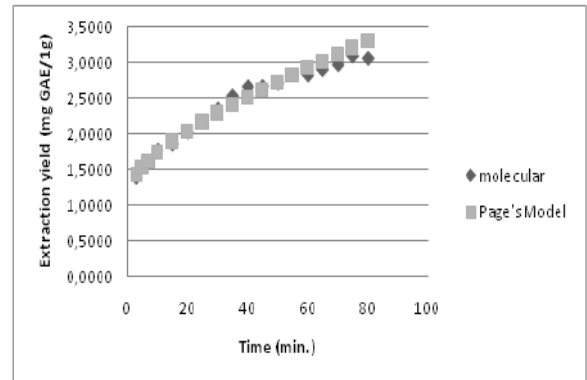


Figure 7. The experimental data obtained at 70°C under unmixed extraction medium fitted to Page's Model

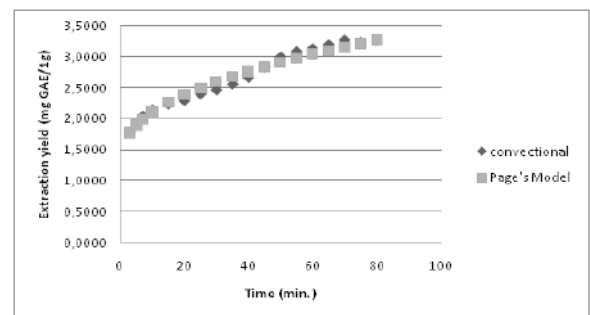


Figure 8. The experimental data obtained at 70°C under mixed extraction medium fitted to Page's Model

In the second procedure of optimization of extraction, three-parameter three-level Box-Behnken design applied within response surface methodology. In the study, the calculated values of gallic acid equivalents of phenolics (Table 3) at respective conditions were entered into the Design-Expert 9.0 software. In the experiments the yield of extraction ranged from 1.45 to 3.30 mg GAE/g depending on the extraction conditions. The standard deviation of experimental results at the center points was 2.2%. All of the suggested functions were investigated by applying statistical analysis of the program, and the linear model was found to be the best function (Table 4) representing the extraction surface of the total polyphenols from *Capsicum annuum*. In this decision, the highest regression coefficient ($R^2=0.9834$), and the highest fitness in between the experimental data (actual) and their respective calculated values of the function (predicted) were considered (Figure 9). The symmetrical relationship between them (Figure 9) approved the applicability of the function chosen.

Generally, second order polynomials found the most appropriate functions when response surface methodology was applied to the systems [28-29]. This observation results from the interrelation of parameters on the process response.

In this study, the interactive effects between parameters were so low that the linear relations were found as enough for presentation of the extraction surface. This was approved by the statistical analysis of software function in which showing the model as “significant”, and lack of fit as “insignificant” (Table 4). The larger the F value and the smaller the p value, the higher the effect of the parameter on the extraction of the flavonoids of this plant. So, the dominant parameter was determined as temperature, whereas the least effective parameter was solid-to-liquid ratio. This result showed that at the extraction conditions, liquid had capable of dissolving all of the phenolic compounds in the solid.

At this point, three-dimensional response surfaces were constructed in this study by using software. The interactive effects of the parameters were shown in Figures 10-12. In those, red regions shows the highest amount of total flavonoids extracted, yellow and blue parts represent the lower and much lower extraction yields than those. As it can be seen from figures, extraction temperature must be in the coded range of [0.5;1] for the highest flavonoid extraction.

Table 3. experimental design and yields of extraction

No	x ₁	x ₂	x ₃	Gallik Asit Miktarı (mg/100g)
1	-1	-1	0	145,175
2	1	-1	0	291,206
3	-1	1	0	166,080
4	1	1	0	330,475
5	-1	0	-1	150,299
6	1	0	-1	289,531
7	-1	0	1	167,194
8	1	0	1	304,941
9	0	-1	-1	209,034
10	0	1	-1	241,636
11	0	-1	1	215,123
12	0	1	1	254,214
13	0	0	0	248,468
14	0	0	0	238,997
15	0	0	0	242,102

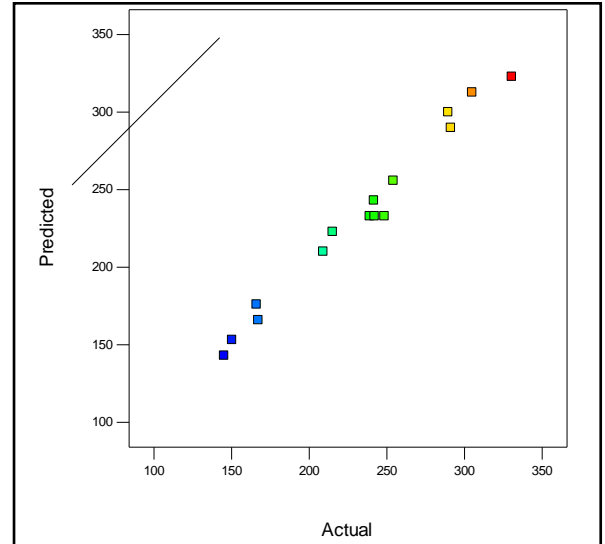


Fig. 9. Experimental results and estimated values of linear function of response surface model

Table 4. anova table

9	Sum of Squares	d f	Mean Square	F Value	p-value Prob > F
Model	45629,32	3	15209,77	217,39	< 0,0001
A-Temperature	43130,87	1	43130,87	616,45	< 0,0001
B-Time	2173,68	1	2173,68	31,07	0,0002
C-Solid/liquid	324,77	1	324,77	4,64	0,0542
Residual	769,63	11	69,97		
Lack of Fit	723,01	9	80,33	3,45	0,2451
Pure Error	46,62	2	23,31		
Core Total	46398,95	14			

Model: Significant; Lack of fit: Not significant; R-Squared: 0.9834;
Adjusted R-Squared: 0.9789; Predicted R-Squared: 0.9722

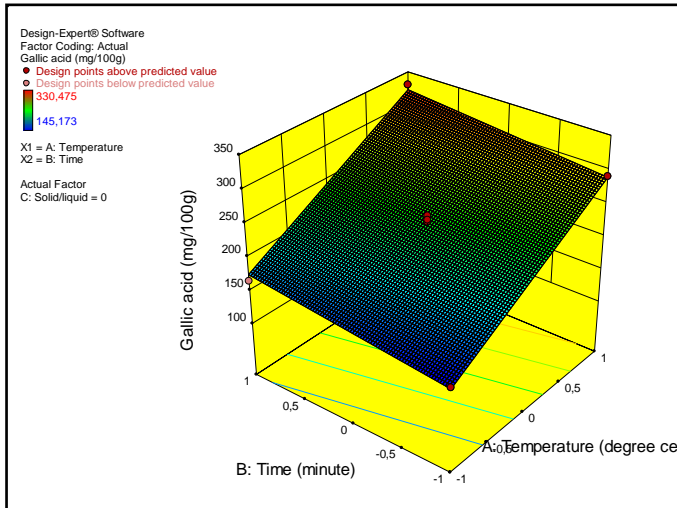


Fig. 10. Three-dimensional response surface of extraction yield depending on time and temperature

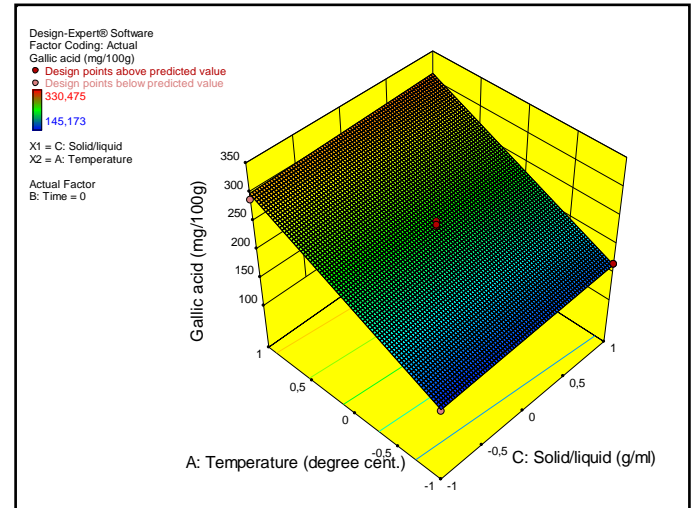


Fig. 12. Three-dimensional response surface of extraction yield depending on temperature and solid/liquid ratio

As a result, the empirical relation explaining the response surface was found as:

$$\begin{aligned} \text{Gallic acid (mg/100g)} &= +232,96487 + (73,42587) \cdot \text{temperature} + (16,48363) \cdot \text{time} \\ &+ (6,37150) \cdot (\text{solid/liquid}) \end{aligned} \quad (13)$$

Finally, the required extraction conditions were analyzed by using this equation and numerical analysis section of the software. In the analysis, restrictions of the parameters were selected as “in range” (has a meaning that they are in the experimental range), and the response criterion was determined as “max”. As a result of the multi-parameter optimization, the optimum conditions producing the highest yield (5.29 mg GAE/g) were determined as 70°C, 90 minutes, 1/50 g/mL.

V. CONCLUSION

This research investigated the extraction of gallic acid equivalents of total phenolics of red pepper. At the experimental conditions of the study, the yield and kinetics of solid-liquid extraction were influenced especially by temperature. The extracted total phenolics were in the range of 1.39-3.27 mg GAE/g. Mass transfer model found as the most suitable model for the extraction kinetics of phenolics from red pepper. Temperature increased the diffusion coefficients. The results of this work could contribute in the optimization of extraction of total phenolics from *Capsicum annuum* and in the design of drug-delivery systems including them in where the same value of diffusion coefficient may be more “natural” to the human body cells.

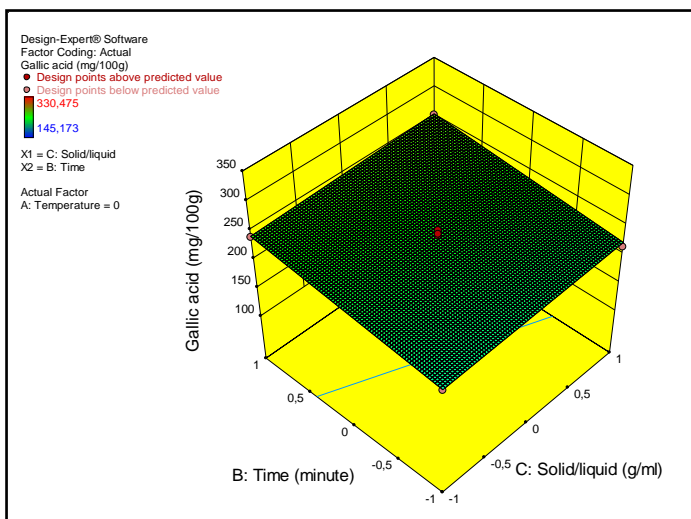


Fig. 11. Three-dimensional response surface of extraction yield depending on time and solid/liquid ratio

REFERENCES

- [1] X. Deng, H. Song, Y. Zhou, G. Yuan and F. Zheng, "Effects of quercetin on the proliferation of breast cancer cells and expression of survivin in vitro," *Exp. Ther. Merd.*, 6(5):1155-1158, 2013.
- [2] Z. Liu, D. Li, L. Yu and F. Niu, "Gallic acid as a cancer-selective agent induces apoptosis in pancreatic cancer cells," *Chemotherapy*, 58(3):185-98, 2012.
- [3] J. P. Cornard and J. C. Merlin Jacobs, "Spectroscopic and structural study of complexes of quercetin with Al(III), *Journal of Inorganic Biochemistry*, 92, 19-27, 2002.
- [4] J. W. Higdon and B. Frei, "Tea catechins and polyphenols: health effects, metabolism and antioxidant functions," *Crit. Rev. Food Sci. Nutr.*, 43(1), 89-143, 2003.
- [5] L. Pavun, P. Durdevic, M. Jelkic-stankov, D. Dikanovic, A. Ciric and S. Uskokovic-Markovic, "Spectrofluorimetric determination of quercetin in pharmaceutical dosage forms," *Macedonian Journal of Chemistry and Chemical Engineering*; Vol.33, 209-215, 2014.
- [6] H.H. Ho, C.S. Chang, W.C. Ho, S.Y. Liao, C. H. Wue and C. J. Wanga, "Anti-metastasis effects of gallic acid on gastric cancer cells involves inhibition of NF-kB activity and downregulation of PI3 K/AKT/small GTPase signals," *Food Chem. Toxicol.*, 48, 2508-2516, 2010.
- [7] G.R. Cleonice, C. D. Borges, R. C. Zambiasi, M. R. Nunes, E. V. Benvenutti, S. R. da Luz, R. F. D'avila and J. K. Rutz, "Microencapsulation of gallic acid in chitosan, β -cyclodextrin and xanthan", *Industrial Crops and Products*, 46(2013)138-146, 2013.
- [8] V.R. Punithavathi, P.S.M. Price, R. Kumar and J. Selvakumari, "Antihyperglycaemic antilipid peroxidative and antioxidant effects of gallic acid on streptozotonic induced diabetic Wistar rats. *Eur. J. Pharmacol.* 650, 465-471, 2011.
- [9] A. Akgül, "Baharat bilimi ve teknolojisi," *Gıda teknolojisi derneği yayınları*, No:15, 106-115, 1993.
- [10] M. Materska and I. Perucka, "Antioxidant activity of the main phenolic compounds isolated from hot pepper fruit (*Capsicum annuum* L.); *J. Agric. Food Chem.* 53(5), 1750-1756, 2005.
- [11] A. Marin, F. Ferreres, F. A. Tomas- Barberan and M. I. Gil, "Characterization and quantitation of antioxidant constituents of sweet paper (*Capsicum annuum* L.); *Journal of Agricultural and Food Chemistry*, 10.1021/f0497915, July 2004.
- [12] Y. Lee, L. R. Howard and B. Villalon, "Flavonoids and antioxidant activity of fresh pepper (*Capsicum annuum*) cultivars; *Journal of Food Science*, Volume, 60; 473-476, 1995.
- [13] N. Deepa, C. Kaur, B. George, B. Singh and H. C. Kapoor, "Swiss society of food science and technology," Published by Elsevier Ltd. All rights reserved, 121-129, 2005.
- [14] W-R. Kim, E.O. Kim, K. Kang, S. Oidowsambuu, S. H. Jung, B.S. Kim, C. W. Nho and B-H. Um, "Antioxidant activity of phenolics in leaves of three red peper (*Capsicum annuum*) cultivars," *J. Agric. Food Chem.*, 62, 850-859, 2014. Sons, New York
- [15] N.Y. Shotorbani, R. Jamei and R. Heidari, "Antioxidant activities of two sweet pepper *Capsicum annuum* L. varieties phenolic extracts and effects of thermal treatment," *Avicenna Journal of Phytomedicine*, Vol-3; No.1; winter 2013; 25-34, 2012.
- [16] A.L. Medina-Juarez, D. M. A. Molina-Quijada, C. L. D. Toro-Sanchez, G. A. Gonzalez-Aguilar and N. Gamez-Meza, "Antioxidant activity of peppers (*Capsicum annuum* L.) extracts and characterization of their phenolic constituents," *Interciencia*, Vol 37, 588-593, Aug. 2012.
- [17] M. Peleg, "An empirical model for the description of moisture sorption curves," *Journal of Food Science*, 53, 1216-1219, 1988.
- [18] J. Cranck, "The mathematics of diffusion," Claredon Press, Oxford, 1975.
- [19] S. Jokic, D. Velic, M. Bilic, A. Bucic-Kojic, M. Planinic and S. Tomas, "Modelling the process of solid-liquid extraction of total polyphenols from soybeans," *Czech Journal of Food Science*, 28(3), 206-212, 2010.
- [20] D. F. Othmer and W. A. Jaatinen, "Extraction of soybeans," *Industrial and Engineering Chemistry Research*, 51, 543-546, 1959.
- [21] D. M. Amirah, R. Prasad and M.R. Khan, "Comprarison of extraction techniques on extraction of gallic acid from stem bark of *Jatropha curcas*, *Journal of Applied Sciences*, 12(11): 1106-1111, 2012.
- [22] H. Turkyilmaz, T. Kartal and S. Yildiz Yigitarslan, "Optimization of lead adsorption of mordenite by response surface methodology: characterization and modification," *Journal of Environmental Health Science and Engineering*, Volum 12 (1): paper no 1, 2014.
- [23] M. Dashtianeh, A. Vatanara, S. Fatemi and F. Sefidkon, "Optimization of supercritical extraction of *Pimpinella affinis ledeb.* using response surface methodology," *Journal of CO₂ Utilization*, Volume 3-4; 1-6, 2013.
- [24] L. Levin, V. L. Papinutti, "Optimization of lignocellulolytic enzyme production by the white-rod fungus *Trametes trogii* in solid-state fermentation using response surface methodology," *Biochemical Engineering Journal*, Vol 39, No.1, pp. 207-214, 2008.
- [25] C. Zhao, W. Ying-long, X. Xiao-jie and L. Jie and L. Qiang, "Optimization of schizothorax prenanti tchang protein enzymatic hydrolysis technology by response surface methodology," *Science and Technology of Food Industry*, Volume 2, pages; 045, 2012.
- [26] L. Sun, S. Wan, Z. Yu and L. Wang, "Optimization and modeling of preparation conditions of TiO₂ nanoparticles coated on hollow glass microspheres using response surface methodology," *Separation and Purification Technology*, Volume: 125, pages: 156-162, 2014.
- [27] C. Pal, S. Bindu, S. Dey, A. Alam, M. Goyal, M. S. Iqbal, P. Maity, S. S. Adhikari and U. Bandyopadhyay, "Gallic acid prevents nonsteroidal anti-inflammatory drug-induced gastroathy in rat by blocking oxidative streaa and apoptpsis," *Free Radical Biol. Med.*, 49, 258-267, 2010.
- [28] Y. C. Cheung, K. C. Siu and J. Y. Wu, "Kinetic models for ultrasound-assisted extraction of water-soluble components and polysaccharides from medicinal fungi," *Food and Bioprocess Technology*, 6, 2659-2665, 2012.
- [29] J. E. Cocae and G. Mazza, "Mass transfer process during extraction of phenolic comounds from milled berries," *Journal of Food Engineering*, 59, 379-389, 2003.
- [30] Y. Zhao, Y. Hou and G. Tang et al., "Optimization of ultrasonic extraction of phenolic compounds from *Epimedium brevicornum* Maxim using response surface methodology and evaluation of its antioxidant activities in vitro," *Journal of Analytical Methods in Chemistry*, Vol. 2014, Article ID 864654, 7 pages, 2014.
- [31] Z. Sun, R. Su, J. Qiao, Z. Zhao and X. Wang, "Flavonoids extraction from *Taraxacum officinale* (Dandelion): Optimization using response surface methodology and antioxidant activity," *journal of Chemistry*, vol.2014, Article ID 956278, 7 pages, 2014.
- [32] M. M. Poojary and P. Passamonti, "Extraction of lycopene from tomato processing waste: Kinetics and modeling," *Food Chemistry*, 173, 943-950, 2015.
- [33] M. S. Guerrero, J. S. Torres and M. J. Nunez, "Extraction of polyphenols from white distilled grape pomace: Optimization and modeling," *Bioresource Technology*, 99, 1311-1318, 2008.
- [34] A. Bucic-Kojic, M. Planinic, T. Srecko, M. Bilic and D. Velic, "Study of solid-liquid extraction kinetics of total polyohenols from grape seeds," *Journal of Food Engineering*, 81, 236-242, 2007.

Sensitive non-enzymatic glucose sensor based on bimetallic metals

Hilal Çelik Kazıcı

Yüzüncü Yıl University, Faculty of Engineering
Department of Chemical Engineering
Van, Turkey
hcelik@eng.ankara.edu.tr

Fırat Salman

Yüzüncü Yıl University, Faculty of Engineering
Department of Chemical Engineering
Van, Turkey
frtsalman.che@gmail.com

Müge Yayla

Yüzüncü Yıl University, Faculty of Engineering
Department of Chemical Engineering
Van, Turkey
myayla.23@gmail.com

Hilal Demir Kıvrak

Yüzüncü Yıl University, Faculty of Engineering
Department of Chemical Engineering
Van, Turkey
hilalkivrak@gmail.com

Abstract— In this study, a new non-enzymatic glucose sensor was developed based on Pd-Au nanoparticles were synthesized by using carbon support material. Synthesized nanoparticles were characterized and carried out glucose measurement by cyclic voltammetry method. The linear calibration graphs were obtained in the concentration range of 0.05-6.55 mM glucose.

Keywords— Glucose; Pd; Au; Nanocatalyst

I. INTRODUCTION

Glucose; it is a monosaccharide with 6 carbons which can be found in single chain or ring structure and high polar structure, easily broken off in water (1). Also is one of the most important carbohydrates for living organisms. For example, the concentration of glucose in a healthy person's blood should be 4.4-6.6 mM (2). The high level of glucose in the bloodstream leads to diabetes, which is a common disease nowadays (3).

At present, quantitative determination of glucose in the bloodstream is still one of the active research topics, and has received wide interest in determining the amount of glucose. Spectroscopic (4) and electrochemical (5) methods are used. The simplicity of electrochemical methods is very advantageous for the determination of glucose. Nanotechnology; today is an important discipline in science and technology (6). Nanomaterials have been interesting molecules in sensor applications due to some features such as small size, large surface area. In addition, nanoparticles are effective markers that increase signaling in the electrochemical determination of analytes. Conductivity properties of metal nanoparticles allow the design of material structures with controlled electrochemical functions (7). For example, gold nanoparticles (AuNp) are among the other metal nanoparticles are the most frequently used nanoparticles (8). In this study, a novel electrochemical sensor was developed that is glucose-sensitive and enzyme-free. The most serious problem of enzymatic sensors; It is easily affected by factors such as pH, temperature, substrate

concentration, and the disappearance of enzyme activity. In addition, enzymes have high cost.

II. EXPERIMENTAL PROCEDURE

Voltammetric measurements were carried out using CHI 660E Electrochemical Analysers with a three electrodes system consisted of a working electrode (bare GCE, Nafion/GCE, Pd-Au-NNGCE), a platinum wire counter electrode and an Ag/AgCl (sat.KCl) reference electrode, respectively. Cyclic voltammetry (CV), Chrono Amperometric (CA) were used throughout the electroanalytical studies. The pH measurements were made with Autolab analyzer meter pH. Magnetic stirrer model was Isolab.

GCE was activated by polishing with different grade of Al_2O_3 slurry (0.05-3 micron) on a synthetic cloth then rinsing with pure water and then ultrasonicated for 3 minutes in ethanol/ultrapure water (1:1 v/v) mixture. GCE was also electrochemically cleaned by keeping 10 minutes at constant potential at 1.0 V. For the electrode preparation, 5 mg of catalyst was dispersed in 1 mL of Aldrich 5% Nafion solution to obtain the catalyst ink. Then 5 μL of the ink was spread on the surface of the glassy carbon electrode. The electrode was dried at room temperature to remove the solvent.

Carbon supported PdAuNPs catalysts were prepared by polyol method. To investigate the effect of addition to glucose the carbon supported PdAuNPs catalysts were prepared at different Pd:Au (90:10, 80:20, 70:30, 50:50) atomic ratios. Then, the non-enzymatic glucose sensing activities of these catalysts were measured by electrochemical techniques.

III. CHARACTERIZATION

SEM images can effectively prove the morphological surface characterization of the modified electrodes. In the current study, the surface chemistry and morphologies of electrodes prepared using chemical reduction procedures were characterized by scanning electron microscopy, energy

dispersive X-ray spectroscopy (EDX) and X-ray photoelectron spectroscopy.

Scanning electron microscopy (SEM) and energy dispersive X-ray (EDX) measurements were carried out using a FEI QUANTA 250 FEG scanning electron microscope. X-ray diffraction (XRD) patterns were recorded by means of Rigaku RadB-DMAX II with an area detector that used a Cu K α source ($\lambda = 1.54056 \text{ \AA}$). Samples were obtained by depositing carbon-supported nanoparticles on a glass slide and then drying overnight under vacuum.

IV. RESULTS AND DISCUSSION

A. X-Ray Diffraction (XRD) characterization of the Pd-Au/C catalysts

Surface crystallographic information of Pd/C and Pd-Au/C catalysts were obtained from the XRD measurements. The diffraction patterns show that the structure can be indexed using Pd face centred-cubic (fcc) lattice, with (111), (200), (220) crystal planes. The diffraction peaks in the Pd-Au/C the catalysts are slowly shifting to higher heights. 2θ values refers to the formation of an alloy between Pd and Au relative to corresponding peaks in the Pd / C catalyst. (Figure 1).

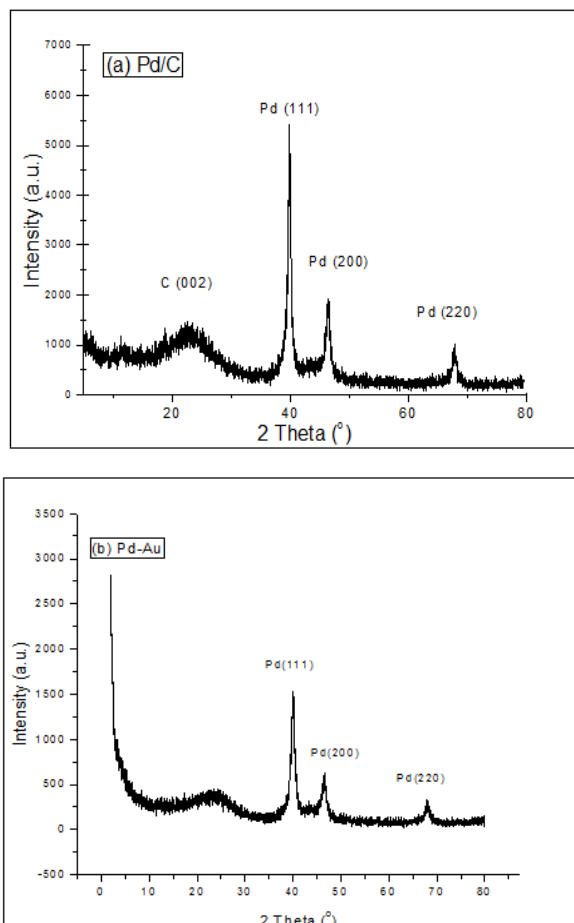


Figure 1. XRD patterns of (a) Pd/C, (b) Pd-Au/C catalysts.

B. SEM-EDX Measurements

SEM images of Pd-Au/C electrodes have presented in Figure 2a. and the EDX spectrum for Pd-Au/C is expressed at the same time 2b. For the Pd-Au/C catalyst, EDX analysis exhibited the presence of Pd and Au. With respect to EDX results, Pd-Au/C catalyst have 72.25: 27.75 Pd/Au atomic ratio, good agreement with the stoichiometric ratio 70:30 used in the preparation procedure.

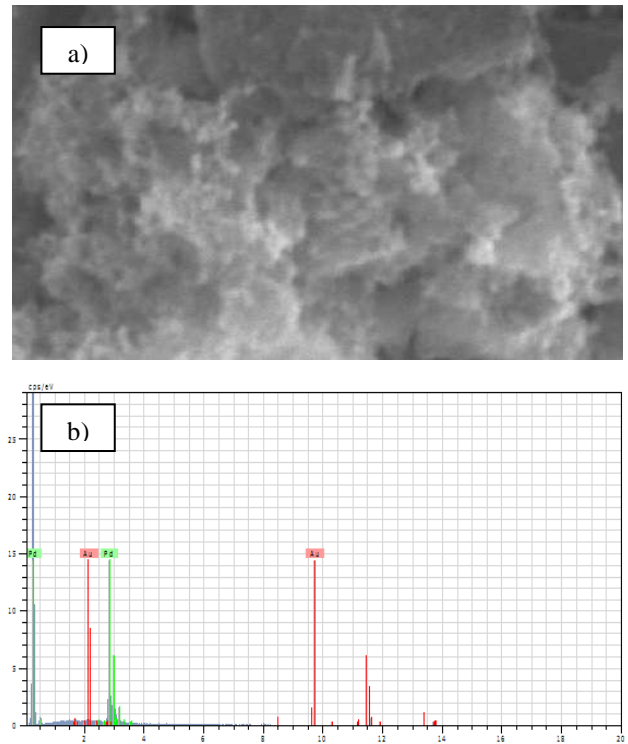


Figure 2. a) SEM images of Pd-Au/C and b) EDX spectra of Pd-Au/C catalysts.

C. Electrochemical characterization of Glucose over the Pd-Au/C

The voltammetric behavior of glucose at various atomic ratio (Pd₉₀:Au₁₀, Pd₈₀:Au₂₀, Pd₇₀:Au₃₀, Pd₅₀:Au₅₀) was investigated at 0.1 M phosphate buffer solution with a scan rate of 100 mV s⁻¹.

Firstly, glucose measurements were performed in the 6.55 mM concentration for the Pd₉₀:Au₁₀, Pd₈₀:Au₂₀, Pd₇₀:Au₃₀, Pd₅₀:Au₅₀ catalysts (Figure 3).

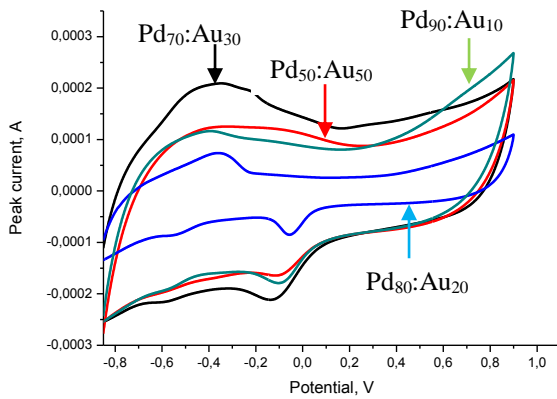


Figure 3. CV of the 4 synthesized catalysts with the highest current density in 0.1 M phosphate tested at a scanning rate of 100 mVs⁻¹.

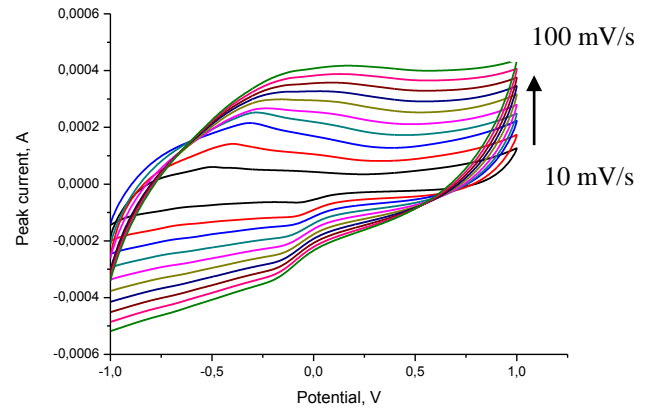


Figure 5. Cyclic voltammograms at various scan rates 10, 20, 30, 40, 50, 60, 70, 80, 90, 100 mV s⁻¹

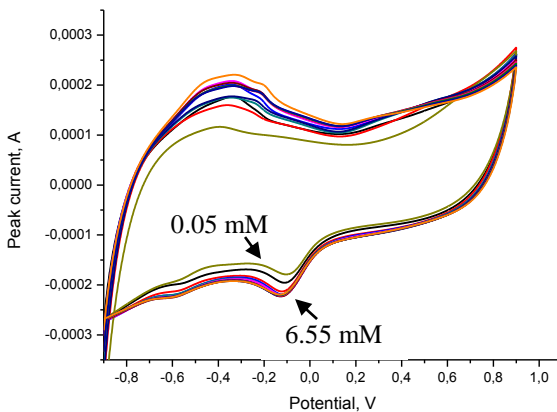


Figure 4. Effect of concentration of glucose in 0.1 M phosphate tested at a scanning rate of 100 mVs⁻¹.

The best current value was obtained at 6.55 mM. Scan rate experiments were carried out for 6.55 mM glucose concentration and atomic ratio Pd₇₀:Au₃₀. Under these conditions, the reaction mechanism is clarified with the scan rate studies. (Figure 5)

Cyclic voltammogram of Pd-AuNPs/C in 0.1 M PBS electrolyte shows one oxidation potential at -0.5 V and one reduction peak potential at -0.1 V. In addition to, observed peak potential shifted more positive potential by increasing scan rate (Figure. 5). This phenomenon could be attributed to irreversible electrode process.

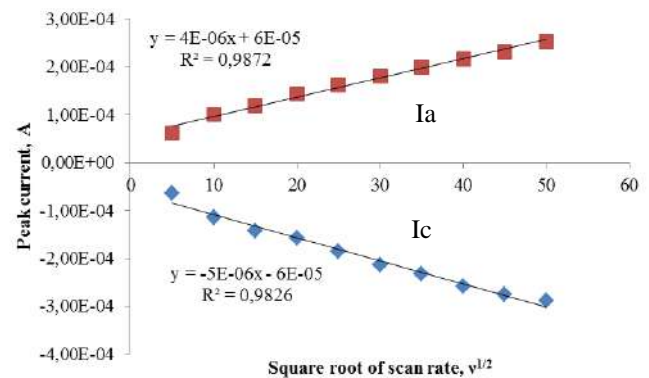


Figure 6. The plot of the peak current (Ip) against the square root scan rates (v^{1/2})

The peak current increased with the square root of the scan rates (Figure 6). This result showed that Pd-AuNPs/C catalyst was controlled by diffusion of electrode surface.

V. CONCLUSION

The aim of this work was advisable a new non-enzymatic glucose sensor based on activated carbon, which was prepared in polyol method. Especially, experimental results showed that Pd-Au/NPs were able to catalyze the electro-reduction of glucose by modified electrode with Nafion solution and displayed a good catalytic activity to glucose.

REFERENCES

- [1] A. Olsan, Glucose and glucose containing syrups, Ullmann's Encyclopedia of Industrial Chemistry, VCH Publishers, New York. 12: 457-475, 1991.
- [2] Y. Li, X. Liu, H. Yuan and D. Xiao, "Glucose biosensor based on the roomtemperature phosphorescence of TiO₂/SiO₂ nanocomposite," Biosensors and Bioelectronics, vol.24, 2009, pp. 3706-3710
- [3] F.N. Comba, M.D. Rubianes, P. Herrasti and G.A. Rivas, "Glucose biosensing at carbon paste electrodes containing iron nanoparticles," Sensors and Actuators B., vol. 149, 2010, pp. 306-309.
- [4] L. Cao, J. Ye, L. Tong, B. Tang, "A New Route to the Considerable Enhancement of Glucose Oxidase (GOx) Activity: The Simple Assembly of a Complex from CdTe Quantum Dots and GOx, and Its Glucose Sensing," Chem. Eur. J. vol. 14, 2008, pp. 9633-9640.
- [5] M. Gerard, A. Chaubey, B.D. Molhotra, "Application of conducting polymers to biosensors," Biosens. Bioelectron. vol.17, 2002, pp. 345-359.
- [6] H. Bouwmeester, S. Dekkers, M.Y. Noordam, W.I. Hagens, A.S. Bulder, S.W.P. Wijnhoven, H.J.P. Marvin, A.J.A.M Sips, "Review of health safety aspects of nanotechnologies in food production," Regulatory Toxicology and Pharmacology, vol. 53, 2009, pp.52-62.
- [7] A. Merkoçi, "Nanobiomaterials in electroanalysis", Electroanal., vol. 19, 2007, pp. 739-731.
- [8] S. Guo, E. Wang, "Synthesis and electrochemical applications of gold nanoparticles," Anal. Chim. Acta, vol. 598, 2007, pp. 181-192.

Drinking Water And Acid And Base Production From Rivers, Lake, And Sea Waters With A Three-Compartment Membrane Electrodialysis Cell

Jülide Erkmen

Sinan Yapıcı

Erbil Kavcı

Chemical Engineering Department, Engineering Faculty,
Kafkas University,
Kars, Turkey

İnönü University,
Malatya Turkey

Kafkas University, Kars,
Turkey

jerkmen@hotmail.com, jerkemen@kafkas.edu.tr

Abstract -The increasing need for water in the world brought along the need to improve the processes of drinking water production from waste waters, sea, and lake waters. Bipolar membrane processes recently joined the ion exchange membrane processes as among the most effective separation processes. Three-compartment electrolysis comprises three separate membranes: anion exchange and cation exchange membranes, and a special membrane called a bipolar membrane. In these three separate ion exchange membranes and the compartments separated by these membranes, the cationic components of water are separated by the cation exchange membrane and transferred to the base compartment. The anionic components of water are separated by the anion exchange membrane and transferred to the acid compartment, and the water is simultaneously separated and cleansed of both its anionic and cationic components. This system enables simultaneous production of drinking water and of acids and bases.

In our previous study, we determined that this type of electrodialysis costs less than usual electrodialysis techniques. In regions, such as Turkey where seas have low salinity, and lakes and rivers contain heavy metals at low levels, it is easy to obtain drinking water using this method. Moreover, previous studies obtained very valuable acids at diluted concentrations, including HF and HBr.

Key Words: Three-Compartment Membrane Electrodialysis, Drinking Water, Acid and Base

SYNTHESIS AND CHARACTERIZATION OF ZEOLITE ZSM-5 AND ITS DERIVATIVES

Vildan ÖZKAN

Iskenderun Technical
University, Department of
Petroleum and Natural Gas
Engineering, 31200 Hatay,
vildanaybek@gmail.com

Zeki AYDIN

Mustafa Kemal University,
Department of Chemistry,
31024, Hatay.

Abdullah ÖZKAN

Iskenderun Technical
University, Department of
Petroleum and Natural Gas
Engineering, 31200 Hatay.

Şana SUNGUR

Mustafa Kemal University,
Department of Chemistry,
31024, Hatay.

Abstract—*In this study, ZSM catalysts were synthesized and the effects of synthesized zeolite in catalytic cracking were investigated. ZSM types were synthesized by varying synthesis time, synthesis method and calcination temperatures. The composition of the synthesis was kept constant and then compared with ultrasonic method and hydrothermal method.*

Two different ZSM derivative was synthesized with changing the synthesis method. Beta zeolite is obtained as a result of the synthesis with low temperature in 20 minutes with using of ultrasonic method. On the other hand, ZSM-5 zeolite is achieved at the end of the synthesis with high temperature in 72 hours with using of hidrothermal method.

The X-Ray Powder Diffraction (XRD) patterns and Scanning Electron Microscopy (SEM) images of ZSM-5 zeolites showed that the crystal structure and phase purity of ZSM-5 increased with increase in synthesis time and not affected by the calcination temperature. Otherwise, the crystal structure and phase purity of beta zeolite increased with increase in calcination temperature.

To determine the catalytic performances of the products, the catalytic cracking processes were performed. First of all, thermal cracking was realized without catalyst for comparison with the others. Then, catalytic cracking was carried out with CaO, Al₂O₃, SiO₂, natural zeolite, ZSM-5 and beta zeolite.

Comparing the results, the catalytic efficiency of the synthesized products were higher than the others. Yield of over 70 % was obtained with synthesized ZSM-5 and zeolite beta.

Keywords—*Synthesis of Zeolite, ZSM-5, Zeolite Beta, Catalytic Cracking, The Catalyst.*

Dielectric Properties of Cu⁺²-Doped 6,7-Dihydroxy-3-(3-chlorophenyl)coumarin Compound

Kenan KORAN

Department of food technology, Karakoçan Vocational
School, University of Firat,
Elazığ, Turkey
kkoran@firat.edu.tr

Fatih BİRYAN

Department of Chemistry, Faculty of Science, University of
Firat,
Elazığ, Turkey,

Abstract— Coumarin derivatives are an important group of compounds of synthetic and natural organic chemistry. The compounds with carbonyl group in the α -position of the benzopyrane ring are called coumarin (2H-1-benzopyrane-2-one). Coumarin analogues possess different physical properties [1]. In this study, 6,7-dihydroxy-3-(3-chlorophenyl)coumarin (CFHC) was obtained according to method in the literature [2]. We aimed to investigate the dielectric constant, dielectric loss and ac conductivity of CFHC at different mole ratios of Cu⁺² metal ions as a function of frequency.

Dielectric measurements for CFHC were carried out by means of an impedance analyzer as a function of frequency. Dielectric properties of samples prepared in a plate form were measured at room temperature over the frequency from 100 Hz to 20 kHz and given as compared with each other [3].

The dielectric measurements were realized by adding the increasing amounts of Cu²⁺ to a solution of CFHC, and remarkable decrease was detected.

Keywords— dielectric properties, Cu+2-doped, coumarin

References

- [1] Margar, S.N., Sekar, N. 2016. Red and near-infrared emitting bis-coumarin analogues based on curcumin framework-synthesis and photophysical studies, Journal of Photochemistry and Photobiology A: Chemistry, 327, 58-70.
- [2] Elmas, S.N.K., Ozen, F., Koran, K., Yilmaz, I., Gorgulu, A.O., Erdemir, S. 2017. Coumarin Based Highly Selective "off-on-off" Type Novel Fluorescent Sensor for Cu²⁺ and S²⁻ in Aqueous Solution, Journal of Fluorescence, 27, 463-471.
- [3] Koran, K., Biryhan, F., Özen, F., Demirelli K., Görgülü, A.O. 2016. Eu+3-doped chalcone substituted cyclotriphosphazenes: Synthesis, thermal and dielectric properties, Inorganica Chimica Acta, 450, 162-169.

A Holistic Analysis of Biogas Energy and Its Potential

Berrin KURŞUN
Marmara University Faculty of Engineering,
Istanbul, Turkey
berrin.kursun@marmara.edu.tr

Abstract— Lots of the heavy metals and their salts are widely used in the industrial applications. As a result of their widespread use, heavy metal pollution in waters is an important environmental problem encountered at industrial areas. Heavy metals are extremely toxic and their adverse effects can last for a long time in nature. Therefore, the wastewater containing heavy metals must be treated with an effective treatment method such as chemical precipitation, ion exchange, membrane processes and adsorption before the discharging [1]. Among these methods, adsorption is recognized as a promising method owing to the properties of high adsorption capacity, easy operation, low-cost and eco-friendly nature.

Usages of the low-cost adsorbents such as agricultural wastes and residuals, metallurgical slags, fly ashes and different minerals have been used or tested for heavy metal removal from the wastewaters recently [2-6]. Agricultural wastes or residues have become the subject of considerable interest due to their low cost, abundant and readily available. Starting from this information, in this study; effects of some parameters such as pH, adsorbent dosage, contact time, particle size, initial Pb(II) concentration and temperature on Pb(II) removal from aqueous solutions by agro-based adsorbent prepared from grape stalk were investigated. The data was analyzed with first and second-order kinetics models and Langmuir and Freundlich adsorption isotherms. It was found that the adsorption kinetics followed the second-order rate law and adsorption fitted to the Langmuir isotherm. The Pb(II) maximum adsorption capacity of the grape stalk was calculated to be 32.8947 mg/g at 25°C.

Keywords— Biogas, environmentally friendly energy options, climate change

A SERS-Based Biosensor Design for Botulinum Toxin Detection

Elvan EKMEN

Faculty of Engineering
Department of Chemical Engineering
Yuzuncu Yil University
Van, Turkey
elvan1988efe@gmail.com

Adem ZENGİN

Faculty of Engineering
Department of Chemical Engineering
Yuzuncu Yil University
Van, Turkey
ademzengin@yyu.edu.tr

Abstract— *Biological weapon agents that manifest themselves by affecting human metabolism can spread in the form of outbreaks, leading to the death of hundreds, thousands or even millions of people in the world. However, some people think that the construction of such weapons is even chilling, these weapons are stockpiled in high quantities in some countries. Especially, yet bioterror agents are highly resistant to a variety of condition and can lead to serious diseases, when exposed to even the lowest dosages. With the decoding of the gene map, the production of more efficient microbiological weapons, which can be obtained at a lower cost instead of the present technological weapons, has gained importance. Today, bio-terrorism, whose impact limits are not yet known, uses toxins, which have many biological activities such as bacteria, viruses and sports. For this reason, there will also be a need for biosensors that will allow early identification of diseases that can be caused by toxins of this type which are potentially usable as weapons in future generations. Thanks to nanobiotechnology, which has developed in parallel with nanotechnology, many biochips can be designed with different techniques today. One of these techniques is polymeric brush-based biochips prepared on macroscopic surfaces (gold, glass, silicon, etc.) and exhibiting biological activity after appropriate functionalization at the nanoscale.*

In the present study, a novel hybrid biosensor composed of polymer brush coated magnetic nanoparticles and gold nanoparticle was prepared for detection of Botulinum toxin which is the most important bio-terror agent. Surface compositions and other characteristic features of the prepared polymer brushes was investigated by X-Ray Photoelectron Spectroscopy (XPS), Grazing Angle Fourier Transform Infrared Spectroscopy (FTIR). The characterization of the prepared nanoparticles was carried out by UV Spectrophotometry and Transmission Electron Microscope (TEM). The feasibility of the prepared hybrid systems as a SERS-based sensor was investigated by determining the limits of detection with various real samples (milk, product, juice, etc.).

Keywords— *Magnetic nanoparticle, polymer brush, Botulinum toxin, SERS*

Adsorption Effects of Clay, Treated With Acid at Different Concentrations

Tülay ARASAN

Department of Chemical Engineering
Munzur University
Tunceli, Turkey
tulayarasan@munzur.edu.tr

Çiğdem SARICI ÖZDEMİR

Department of Chemical Engineering
Inonu University
Malatya, TURKEY
cigdem.ozdemir@inonu.edu.tr

Abstract— The purpose of this study examining changes imposed by heat effects in adsorption capacity, structures of clay that used as natural adsorbent. The clay samples were synthesized by subjecting clay with acid at different concentration at 200 °C. Adsorption studies are done with obtained clay samples and adsorption capacities of them are found. The structure and surface properties of clay were examined by FTIR, XRD, SEM, TGA- DTA, Boehm titration, and adsorption of methylene blue and iodine.

In this study, a clay sample from Battalgazi / Malatya region selected as the material and after sample is broken with the aid of suitable breaker and grinding clay minerals were obtained under 200 by sieving with the help of molecular sieves. After the clay sample dried in the oven at 105 °C for 24 hours. Then effect of temperature examined with acid, H_3PO_4 in different concentrations (0.5N, 1N, 2N) was mixed with clay 1:3 ratio for 2 hours at 100 °C and 1 hour the product was processed in the furnace ash at 500 °C. Adsorption from aqueous solutions of copper is done with these samples. For this 500 ppm $CuSO_4 \cdot 5H_2O$ stock solution was prepared. 0,1 gram sample was stirred with solutions whom concentrations are 100, 200, 300, 400, 500 ppm 1 hour at 25 °C. Then quantity of Cu was recorded by measuring the filtrate obtained [1,2]. The structure and surface properties of obtained clays were examined by SEM, FT-IR, XRD, Boehm titration, and adsorption of methylene blue and iodine. One of the most widely used methods for the quantitative determination of the organic structural functionality of carbonaceous materials is the Boehm titration. With NaOH, Na_2CO_3 , $NaHCO_3$ compounds, various surface functional groups can be distinguished from each other. The carboxylic groups in the structure can be quantitatively determined by $NaHCO_3$ interaction, lactic groups Na_2CO_3 interaction and phenolic groups NaOH interaction [3,4]. The pH values were also found to be in the acidic zone. Another process with temperature was investigated using different concentrations of H_3PO_4 with SEM. Different constructions can be seen in which the amount of concentration can form within the structure. When the concentration is taken as 2N, a sedimented porous environment emerges from the whole SEM image. FTIR analysis of materials has an important place in terms of structure of a molecule, molecular bonds and functional groups. Decrease in the strength of the carbonates and OH groups in the structure resulting from the chemical treatment with phosphoric acid occurs. This change is supported by the decrease in the number of phenolic groups in the Boehm titration.

Adsorption from aqueous solutions of copper is done with each sample. Then amount of Cu was calculated and was observed that adsorption compliance with Freundlich isotherm. It has been found that the adsorption capacity increased with increasing concentration.

Keywords— clay; adsorption; characterization

Effects of Temperature on Clay Treated With Base

Tülay ARASAN

Department of Chemical Engineering
Munzur University
Tunceli, Turkey
tulayarasan@munzur.edu.tr

Çiğdem SARICI ÖZDEMİR

Department of Chemical Engineering
Inonu University
Malatya, TURKEY
cigdem.ozdemir@inonu.edu.tr

Abstract— Clay and clay minerals, has been one of the common workspace art, in many disciplines. Today, clays plasticity, moisture retention and strength besides organic or displacement with iodine all kinds of inorganic, high adsorption and other technological properties such as catalytic activity are used as industrial raw materials in the area of more than 100. Regarding the use of clay areas; from ceramics and cement production; paper, petrochemical and construction industries; vegetable oil, beer, wine and fruit juices of the bleached; radioactive waste and waste water to be cleaned; medicine, soap, detergent, diaphragm, electrodes, catalyst, rubber and plastic production can be listed a wide range of area [1, 2]. Adsorption properties of clay are due to wide surface area, surface functional groups and microporosity. Clay allowing them to use for different purposes in different areas, they have the common presence of clay minerals in nature are superior chemical and physical properties [3]. The purpose of this study examining changes imposed by heat effects in structures of clay that used as natural adsorbent. The clay samples were synthesized by subjecting clay with base at the same concentration, different temperature.

In this study, a clay sample from Battalgazi / Malatya region selected as the material and after sample is broken with the aid of suitable breaker and grinding clay minerals were obtained under 200 by sieving with the help of molecular sieves. After; the clay sample dried in the oven at 105 °C for 24 hours. Then NaOH particles added onto clay sample directly at 300 °C; 400 °C; 500 °C; 600 °C; 700°C [4, 5]. The structure and surface properties of obtained clays were examined by SEM, FT-IR, XRD, Boehm titration, and adsorption of methylene blue and iodine. The results of boehm titration shows that the presence of phenolic groups has little effect. According to SEM results, it is seen that the porosity distribution in the structure differs with the changing temperature. In XRD runs; as a result of the heat treatment with NaOH, a decrease in crystallinity is observed with increasing temperature. SEM images support this situation.

Keywords— clay; structure ; characterization;

Decolorization of Jakofix Yellow Dye Solutions by Electrocoagulation

Zürriye Gündüz

Balıkesir University, Engineering Faculty

Balıkesir, Turkey

zyilmaz@balikesir.edu.tr

Abstract— The textile industry is regarded as a significant threat to groundwater resources due to both the large water demands and the production of effluent, containing significant concentrations of dyes, surfactants, suspended solids and organic matter. Between 1% and 15% of dye is lost during the dyeing process and is released into the wastewater with toxicity to microorganisms and humans. Most dyes are resistant to biodegradation due to their design requirements to withstand both oxidizing and reducing conditions, washing and light exposure. A pretreatment for removing toxic dyes and decolorization is therefore necessary before biological degradation processes can be employed. Much attention has been paid to methodologies for the removal of dyes from colored effluents; electrochemical oxidation, adsorption and coagulation, nanofiltration and reverse osmosis, enzymatic decolorization and ozone oxidation, some of which have been applied by industry.

In this study, treatment of synthetic wastewater containing Jakofix Yellow dye by electrocoagulation (EC) has been investigated in a batch process reactor with iron electrode. Effects of process parameters such as operating time (5, 10, 15, 20, 25, 30, 35, 40 and 45 minutes) and current for EC process are investigated on dye removal efficiency. After the electrocoagulation process, all samples are measured for pH, concentration, temperature and conductivity. Concentration determination is studied with spectrophotometric method at $\lambda=420$ nm wavenumber. The study revealed that at a neutral pH there was a colour removal efficiency of almost 100% with minimum electricity consumption. These performance characteristics indicate that the EC may be more promising in terms of practical application, as a cost-effective treatment for textile dye removals.

Keywords— *electrocoagulation; jakofix yellow dye; decolorization; removal efficiency*

Synthesis and Characterization of Iron Nanoparticles Using *Eriobotrya japonica* Leaves Aqueous Extract for Effective Adsorption of Cr(VI)

Emel Simal ÖNAL, Tolga YATKIN, Tural ASLANOV, Memduha ERGÜT, Ayla ÖZER

Mersin University, Faculty of Engineering, Department of Chemical Engineering
Mersin, Turkey

memduha.ergut@gmail.com, ayozer@mersin.edu.tr

Abstract— In this study, Fe nanoparticles (FeNPs) were synthesized via a green method using loquat (*Eriobotrya japonica*) leaves aqueous extract as a renewable reducing agent. The synthesized FeNPs were characterized by DLS, XRD, FTIR, and SEM/EDX analysis and they were used as a sorbent for Cr(VI) removal from aqueous solutions. Batch adsorption experiments were carried out to investigate the optimum adsorption parameters such as the solution pH, temperature, initial Cr(VI) ion concentration and adsorbent concentration. The optimum adsorption conditions were determined as pH 3.0, temperature 45°C, initial Cr(VI) concentration 100 mg/L and adsorbent concentration 1 g/L. The biosynthesized FeNPs showed the high removal levels higher than 90% for Cr (VI) adsorption at a wide range of initial metal ion concentrations (50 - 500 mg/L) at optimum temperature. The experimental equilibrium data were modelled with Langmuir and Freundlich isotherm models and it was found that, experimental equilibrium data could be well described by Langmuir isotherm model. The maximum monolayer coverage capacity of FeNPs for Cr (VI) adsorption found to be 312.5 mg/g. The pseudo-first order and the pseudo-second order kinetic models were applied to the experimental adsorption data and it was concluded that the data were defined the best agreement with the pseudo-second order kinetic model. Weber Morris model was used to investigate the effect of mass transfer on the adsorption of Cr (VI) onto FeNPs, it was observed that both the film (boundary layer) and intra-particle diffusion affected the studied adsorption process. The thermodynamic studies suggested that Cr (VI) adsorption onto FeNPs was endothermic, non-spontaneous and the positive ΔS value indicated increased disorder at the solid-solution interface during the adsorption.

Keywords—adsorption; Cr(VI) removal; *Eriobotrya japonica*; iron nanoparticles.

I.

INTRODUCTION

Water pollution is one of the most important burning environmental issue among the various kinds of environmental pollution since water resources are contaminated by a variety of organic, inorganic and biological pollutants owing to day to day utilization and potential applications of water at domestic, industrial and agricultural areas all over the world [1, 2]. The

heavy metals (arsenic, zinc, copper, nickel, mercury, cadmium, lead and chromium, etc.) are the best known non-biodegradable water pollutants which are extremely toxic and dangerous for ecosystem, agriculture and human health [3].

The chromium ions exist in industrial wastewaters both trivalent and hexavalent forms. Cr(VI) ion exists in different forms in solutions as $\text{Cr}_2\text{O}_7^{2-}$, HCrO_4^- or CrO_4^{2-} depending on the pH and the Cr(VI) concentration. Otherwise, Cr (III) ion is relatively less toxic than Cr(VI) ion. The Cr(III) species in aqueous solutions present in the forms of Cr^{3+} , $\text{Cr}(\text{OH})^{2+}$, $\text{Cr}(\text{OH})_2^+$, $\text{Cr}(\text{OH})_3$, or $\text{Cr}(\text{OH})_4^-$ depending on the solution pH [4, 5]

Cr (VI) is widely used in paints and pigments, chrome chemicals, leather tanning, electroplating industries, cement and photography industries that lead to producing great quantities of effluents containing the toxic Cr (VI) metal ions [6]. Moreover, Cr(VI) is classified as the top 16 th hazardous substance by the Agency for Toxic Diseases Registry (ATSDR) due to its carcinogenic properties and toxicity degree [4]. It is quite harmful for the living organisms due to it has potential to pass through cell membranes and reduces to reactive intermediates. These reactive intermediates can attack DNA, proteins, and membrane lipids and cause damage to the cellular functions [7]. The acceptable discharge level for hexavalent chromium ion in industrial wastewaters is reported as 0.1 mg/L by United States Environmental Protection Agency (US EPA) and the permitted Cr(VI) ion limit in drinking water is 50 $\mu\text{g/L}$ according to the World Health Organization (WHO) data [4, 5]. Therefore, in order to reduce Cr(VI) ion to the standard level, effective, eco-friendly and economic treatment methods should be improved.

There are commonly used treatment methods for discharging chromium ions from wastewaters such as adsorption, biosorption, coagulation, chemical precipitation, reverse osmosis, ion exchange, extraction and membrane filtration techniques. Among them, adsorption offers good opportunity for the removal of chromium ion from the wastewaters because of its low cost, simple operation, capability of trace level pollutant removal and high efficiency [4, 6].

Recently, the usage of metal/metal oxide nanoparticles such as; Fe^0 , Fe_3O_4 , TiO_2 , ZnO and their composites as a sorbent, has attracted great attention in the treatment of various heavy metals like chromium. The advantage of these functional nanomaterials is high adsorption capacity that is associated with their large specific surface area and high reactivity in the adsorption processes [3].

Biosynthetic approaches are quite popular for synthesis of metal nanoparticles using microorganisms, enzyme and plant extracts; due to their predominant advantages compared to traditional chemical synthesis methods include toxic and expensive compounds such as NaBH_4 as reducing agent. Among biosynthetic procedures, the exploitation of plant extracts has a privileged position for nanoparticle preparing since plant leaves are inexpensive, natural, environmentally friendly, harmless, readily available and suitable for scale-up steps. Loquat (*Eriobotrya japonica*) is an Asian yellow fruit belonging to the Rosaceae family and its leaves are used widely for medicinal purpose against cough and asthma diseases in Turkey [8, 9]. Loquat leaves are very rich in terms of phenols, flavonoids, triterpene acids and polysaccharides and these special compounds act as a bioreduction agent for metallic ions. To the best of our knowledge, loquat leaves extract was used for synthesis of silver and gold nanoparticles [10, 11], but; this is the first study reported in literature about using of loquat leaves aqueous extract for the green synthesis of FeNPs. However biosynthesized zero-valent iron nanoparticles [12]; crystalline and amorphous Fe and Al-oxides such as; hematite [$\alpha\text{-Fe}_2\text{O}_3$], goethite [$\alpha\text{-FeOOH}$], alumina [$\alpha\text{-Al}_2\text{O}_3$] [4, 13] and composite materials include iron minerals such as; Fe_3O_4 magnetite graphene oxide encapsulated in calcium alginate beads [7], Fe-modified activated carbon [14] were reported as effective adsorbents for removal of Cr(VI) ions.

The aim of the present study was to synthesize of FeNPs using *Eriobotrya japonica* leaves aqueous extract as a reducing or capping agent and to investigate the Cr(VI) adsorption efficiency. For this purpose, a systematic characterization studies of the synthesized FeNPs were carried out by DLS, XRD, FTIR, and SEM/EDX analysis methods and then, the adsorbent properties of FeNPs for Cr(VI) ions and the adsorption mechanism for the studied adsorption process were investigated in a batch system.

II. EXPERIMENTAL PROCEDURE

A. Materials

All the chemicals used in experiments were of analytical grade and was used without further purification. $\text{FeSO}_4 \cdot 7\text{H}_2\text{O}$ to be used in synthesis of FeNPs and 1,5-diphenylcarbazide were supplied from Carlo Erba and acetone (> 99.5%) and HCl (37%) were provided from Sigma-Aldrich. A stock solution of 1000 mg/L of Cr(VI) was prepared by dissolving appropriate amount of $\text{K}_2\text{Cr}_2\text{O}_7$ (Carlo Erba) in 1000 mL distilled water. The solution with desired Cr(VI) concentration was prepared

by appropriate dilutions from stock Cr(VI) solution. The pHs of the solutions were adjusted with 0.1 N hydrochloric acid and 0.1 N sodium hydroxide.

B. Biosynthesis of FeNPs

Loquat (*Eriobotrya japonica*) leaves were collected from loquat trees grown in Mersin, Turkey. Aqueous extract of *E. japonica* leaves was prepared by heating the certain amount of air-dried leaves as it's concentration will be 60 g/L, at 100°C , 500 ml of distilled water for 1 h. Subsequently, the filtered aqueous extract was added to 0.1 mol/L $\text{FeSO}_4 \cdot 7\text{H}_2\text{O}$ solution in 1:1 volume ratio and the final mixture was kept under vigorous stirring for 3 h [15]. The immediate changing of the colour of the solution from clear to intense black indicated the formation of FeNPs. The formed nanoparticles were separated by evaporating water from solution on a hot plate and then collected nanoparticles, washed several times with deionized water and dried in an oven at 120°C overnight.

C. Characterization of FeNPs

The mean hydrodynamic particle size and size distribution of the green synthesized FeNPs was measured by dynamic light scattering (DLS) analysis with the Malvern Zetasizer. The functional groups of FeNPs before and after adsorption, were determined by Fourier transform infrared spectrometer (FT-IR) in the range of $4000\text{--}400\text{ cm}^{-1}$. Crystal structure was observed by XRD analysis, using nickel-filtered Cu K α radiation in a Philips XPert MPD apparatus operated at 40 kV and 30 mA, in the 2θ range of $10^\circ\text{--}80^\circ$. The morphology of the FeNPs was analyzed by Zeiss/Supra 55 SEM analysis and elemental identification and quantitative compositional information of the adsorbent was determined by Zeiss/Supra 55 energy dispersive X-ray analyzer (EDX) pre- and post adsorption. The pH at point of zero charge (pH_{PZC}) of prepared FeNPs was obtained by measuring ζ (zeta) potential at different ranges of pH (2.5 – 12) with Zeta-Sizer (Malvern Zetasizer Nano ZS model). The pH values of the FeNPs suspensions were adjusted from 2.5 to 12 by adding 0.1 M HCl and/or 0.1 M NaOH solutions as required.

D. Batch adsorption studies

The adsorption experiments were carried out in 250 mL Erlenmeyer flasks containing 100 mL of Cr (VI) adsorption solution. 0.1 g of FeNPs, except for adsorbent concentration experiments, was contacted with 100 mL of Cr (VI) solution at known initial Cr (VI) concentration and initial pH in an Erlenmeyer flask and then the flasks were agitated at a constant temperature and shaking rate for 480 min, which is more than ample time for adsorption equilibrium. Samples were taken before mixing the FeNPs and metal bearing solution and at pre-determined time intervals for the unadsorbed metal ion concentration in the solution. Samples were centrifuged at 3500 rpm for 5 min and the supernatant liquid was analysed.

The unadsorbed Cr (VI) concentration was analyzed in a spectrophotometer (Cheibos UV-vis model) according to

1151

green synthesized FeNPs indicated that the material was completely amorphous structure (figure not shown).

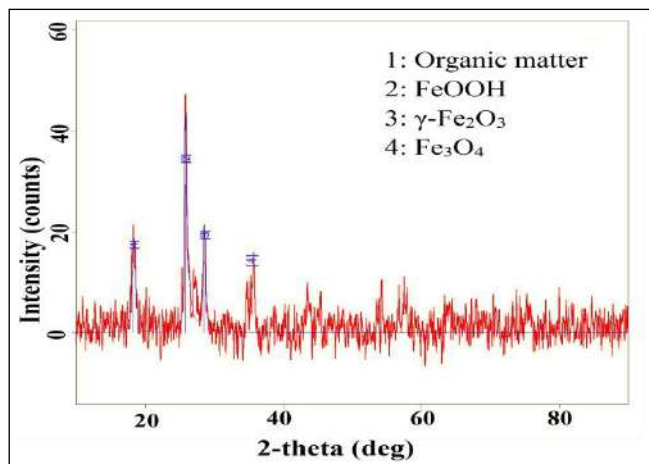


Fig.3. XRD pattern of FeNPs

The differences in the XRD patterns of FeNPs between before and after adsorption may be due to change the crystallinity and phase of the FeNPs during the chemisorption of Cr(VI).

FTIR study of crude extract and FeNPs before and adsorption was carried out to investigate the functional groups responsible for adsorption. The absorption bands were observed in all the samples, as presented in Fig. 4, Fig. 5 (a) and Fig.5 (b), respectively. The FT-IR spectrum of loquat leaves extract (Fig.4), the broad band at 3270.9 cm^{-1} may correspond to the surface O-H group related to the phenolic compounds. The 2928 and 2187 cm^{-1} bands are because of the C-H stretching vibration of the $-\text{CH}_2$ and CH_3 functional groups [12, 19]. The band at 1720 cm^{-1} is identified as carbonyl groups from dimerized saturated aliphatic acids [20], 1595.36 cm^{-1} and 1378.12 cm^{-1} are attributed to C=O, C-O and O-H groups and the presence of C-O stretching in carboxyl groups, respectively. The broad band in 1243 cm^{-1} corresponds to the C-O-C or C=O stretching vibration and 1036 cm^{-1} band may be assigned to C-O-C and O-H absorption [20]. The bands observed at 889.03 , 763.93 and 599.63 cm^{-1} are correspond to phenol groups and bending vibrations of aromatics, carboxylic acids and amides [12]. These peaks demonstrate the presence of phenolics could be probably responsible for the bioreduction of Fe^{2+} ions and formation of FeNPs.

According to the FT-IR spectrum of synthesized FeNPs (Fig. 5(a)), the bands at 3236.66 , 2155 cm^{-1} are attributed to O-H group related to the phenolic compounds and C-H stretching vibration of $-\text{CH}_2$ and CH_3 functional groups, the band at 1605 cm^{-1} corresponds to C=O, and the band at 1077 cm^{-1} due to C-O stretching [21]. Moreover, adsorption bands at 596 cm^{-1} and 458.88 cm^{-1} refer to Fe-O stretches of Fe_3O_4 and Fe_2O_3 [22], confirming the formation Fe NPs. After Cr(VI) adsorption, as seen from Fig. 5 (b) the FT-IR spectrum, a slight

change was observed in the peaks due to chemisorption of Cr(VI) ions. Based on the FT-IR results, the

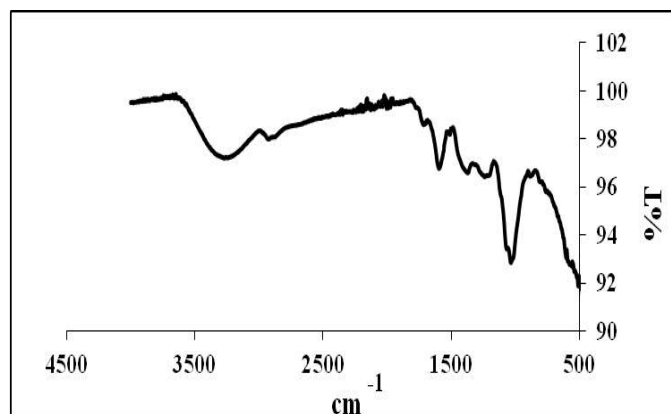


Fig.4. FT-IR spectrum of loquat (*Eriobotrya japonica*) leaves aqueous extract

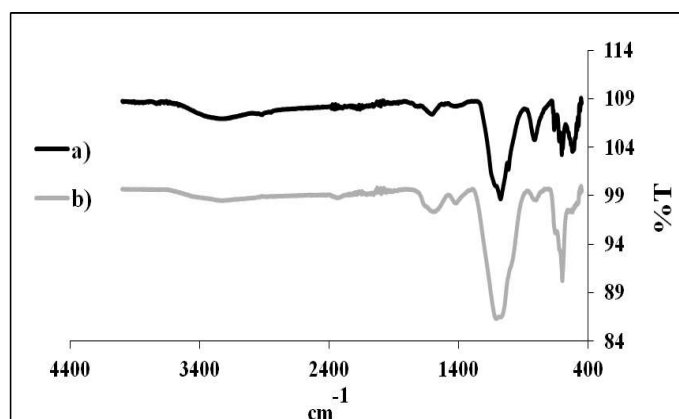


Fig 5. FT-IR spectrum of FeNPs a) before adsorption b) after adsorption

adsorption mechanism of the Cr(VI) ions onto FeNPs is due to the chemical interaction between $-\text{OH}$ and $-\text{C}=\text{O}$ functional groups on the FeNPs surface and Cr(VI) ions in the solution [2].

B. Effect of Environmental Conditions on the Cr(VI) Adsorption onto FeNPs

The solution pH is an important factor on the adsorption capacity due to its impact on the ionic forms of chromium in solutions and the surface properties of the adsorbent [7]. The effect of initial pH on the adsorption of Cr(VI) ions onto FeNPs was presented in Fig. 6.

According to Fig. 6, Cr(VI) removal by green synthesized FeNPs was a pH dependent adsorption system. The maximum equilibrium uptake value was found to be 99.28 mg/g at pH 3.0 and then started to gradually decrease while pH value increases up to 8.0. Cr(VI) ion exists in solution as $\text{Cr}_2\text{O}_7^{2-}$, HCrO_4^- or CrO_4^{2-} and their solubilities are strongly depend on the solution pH and the Cr(VI) concentration.

The logarithmic concentration diagram for the species distribution of Cr(VI) in an aqueous system was shown in

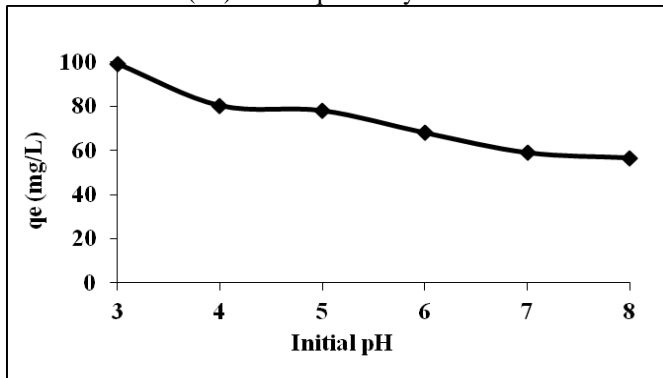


Fig. 6. The effect of initial pH (initial Cr(VI) concentration 100 mg/L, adsorbent concentration 1 g/L, temperature 25°C).

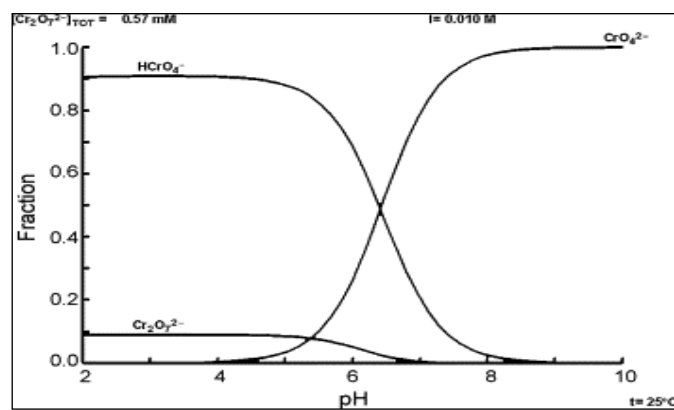


Fig. 7. The concentration diagram for Cr(VI) species depends of pH.

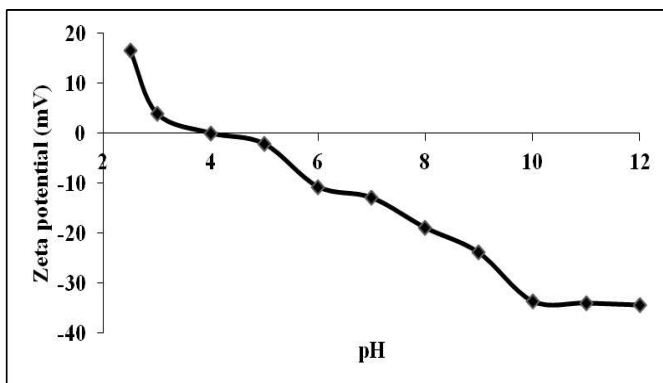
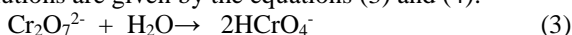


Fig. 8. The isoelectric point of the prepared FeNPs.

Fig. 7. [4]. According to this diagram, HCrO_4^- is dominant form of Cr(VI) at acidic medium in the range of pH 2.0 – 4.0; CrO_4^{2-} is the predominant form in an neutral and basic medium pH 7.0, [4, 7, 23]. HCrO_4^- ions occur as a result of the hydrolysis of dichromate ions and an increase in pH would ease of the formation of $\text{Cr}_2\text{O}_7^{2-}$ from HCrO_4^- [24].

The formation of different species of Cr(VI) in aqueous solutions are given by the equations (3) and (4):



In this study, the active form of Cr(VI) was chosen as HCrO_4^- because of obtaining high removal in acidic medium.

The attitude of the maximum adsorption capacity at pH 3, can be explained by isoelectric point of adsorbent. The isoelectric point of FeNPs (pH_{pzc}) was determined as 4.0 by the zeta (ζ) potential measurement was given in Fig.8.

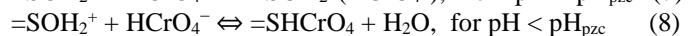
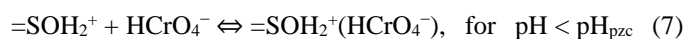
The surface of adsorbent was charged positively at the lower pH values than isoelectric point of adsorbent and adsorption capacity increased due to strong electrostatic attraction between positively charged adsorbent surface and negatively charged HCrO_4^- ions. Conversely, at the higher pH values than isoelectric point of adsorbent, the number of negatively charged sites increases and the number of positively charged sites decreases, so; Cr(VI) adsorption capacity was decreased due to the electrostatic repulsion between surface and HCrO_4^- ions.

Metal ion adsorption onto hydrous solids such as metal oxides is a complex reaction between surface sites and adsorbent. The developed surface sites for a hydrated adsorbent are formulated in equations (5) and (6):



There S represents the FeNPs surface sites, S-OH_2^+ , S-OH and S-O^- refer to protonated, neutral and deprotonated surface hydroxyl functional groups, respectively. In this work, at pH value below pH_{pzc} , the positively charged adsorbent surface (S-OH_2^+) accelerates the uptake the anionic HCrO_4^- , adsorption whereupon the coulombic interaction forces can easily occurred [24].

Therefore, two possible reactions would be suggested as given below in equations (7) and (8), about adsorption mechanism depending on interaction between HCrO_4^- ions and the surface sites of adsorbent at pH value below pH_{pzc} [4].



where $=\text{SOH}_2^+(\text{HCrO}_4^-)$ and $=\text{SHCrO}_4$ are the bonding complexes.

The initial metal ion concentration is an important factor on the adsorption capacity in terms of providing higher driving force to overcome mass transfer resistances of the metal ions between the aqueous and solid phases. The effect of initial Cr(VI) concentration on adsorption was depicted in Fig.9. As can be seen from Fig.9, the adsorption capacities increased linearly ($q_e = 0.9453 \cdot C_o$, $R^2 = 0.997$) with the initial Cr(VI) concentration at optimum temperature 45°C, initial pH 3.0, 1.0 g/L adsorbent concentration and 480 min equilibrium time.

The adsorbent concentration effect on the percentage of adsorption and equilibrium uptake was presented in Fig. 10.

According to Fig. 10, the equilibrium uptakes of FeNPs for Cr(VI) ion concentrations decreased with increasing the

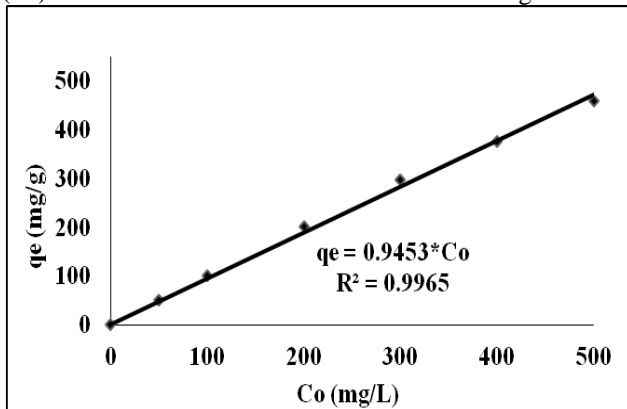


Fig. 9. The effect of initial Cr(VI) concentration (temperature 45°C, initial pH 3, adsorbent concentration 1 g/L)

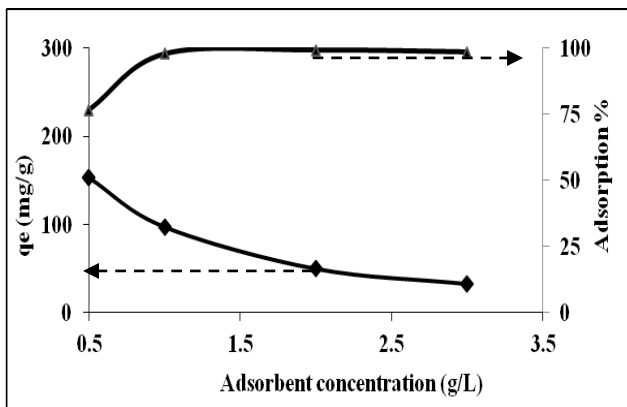


Fig. 10. The effect of adsorbent concentration (temperature 45°C initial pH 3, contact time 90 min, initial Cr(VI) concentration 100 mg/L)

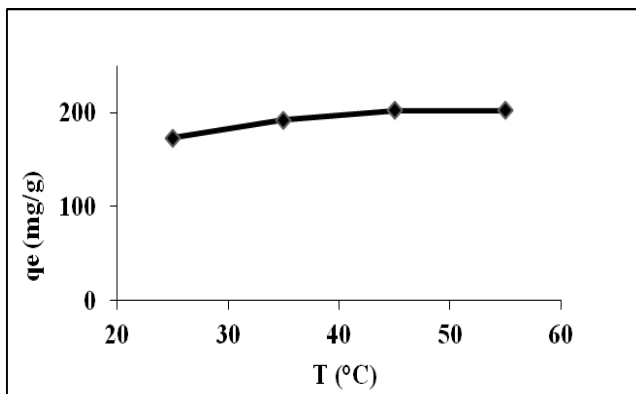


Fig.11. The effect of temperature (initial pH 3, initial Cr(VI) concentration 200 mg/L, adsorbent concentration 1 g/L)

adsorbent concentration from 0.5 g/L to 3 g/L, but; it was seen that the adsorption percentage increased up to 1.0 g/L of adsorbent concentration, and then slightly remained constant with further increase in adsorbent concentration. The decrease in uptake values with increasing adsorbent concentration may be arise from the interaction between adsorbent particles such

as aggregation, resulted from high adsorbent concentration. The agglomeration of the adsorbent particles would lead to decrease in active surface area of the adsorbent and an increase in diffusional path length, hence the lower adsorption capacities were observed at high adsorbent concentrations. As a result, the optimum adsorbent concentration was selected as 1.0 g/L for Cr (VI) ion adsorption onto FeNPs.

The effect of temperature on adsorption was investigated in the range of 25 – 55°C temperature values and results was presented in Fig. 11. According to Fig. 11, it was seen that high adsorption capacity was obtained with increase in temperature from 25°C to 45°C and then, moderately remained constant at 55°C. Therefore, the optimum temperature value for Cr(VI) ion adsorption was determined as 45°C. Based on the results, high operation temperature indicated that, the studied adsorption process was endothermic nature.

The thermodynamic parameters such as, Gibb's free energy change (ΔG), enthalpy change (ΔH) and entropy change (ΔS) which were calculated from Van't Hoff equation were supported the results of temperature effect. The equilibrium constant (K_c) values for the Cr(VI) adsorption on FeNPs were calculated from the $K_c = C_{Ae}/C_e$ equation [1]; where C_{Ae} and C_e are the adsorbed metal ion concentration (mg/L) and the unadsorbed metal ion concentration at equilibrium (mg/L), respectively. When the adsorbent concentration is 1.0 g/L, C_{Ae} is equal to q_e at studied temperature. ΔH and entropy change ΔS were calculated from the slope and intercept of the Van't Hoff's $[\ln K_c = (\Delta S/R) - (\Delta H/R)1/T]$ plot of $\ln K_c$ versus $1/T$ [25]. In this study, the linear form of Van't Hoff equation for the adsorption of Cr(VI) onto FeNPs was found as $\ln K_c = -8041*1/T + 23.03$ with the regression coefficient 0.999 (data not shown) and the thermodynamic parameters were calculated and were presented in Table II.

According to Table II, the positive enthalpy change indicated the endothermic nature of the studied adsorption process and also, this result confirmed the results of temperature effect for Cr(VI) ion onto FeNPs.

TABLE II. Thermodynamic parameters of adsorption system.

Metal ion	Thermodynamic parameters				
	T (K)	Kc	ΔH (kJ/mol)	ΔS (kJ/mol.K)	ΔG (kJ/mol)
Cr (VI)	298	0.01905	66.853	0.1915	9.813
	308	0.04703			7.828
	318	0.10389			5.986

The calculated ΔG [$\Delta G = -RT \ln K_c$] values had positive indicating that adsorption of Cr(VI) on FeNPs was non-spontaneous. The positive value of ΔS suggested that randomness of the adsorbed Cr(VI) species at the solid-solution interface during adsorption [5]. Moreover, the

calculated ΔH values higher than 42 kJ/mol indicated the process results from chemisorption of the Cr(VI) ions onto FeNPs [26].

C. Equilibrium, Kinetic and Mass Transfer Modelling

The Langmuir and Freundlich isotherm models are commonly used to describe the adsorption data so, get idea about the interactions of adsorbed materials with the adsorbent [27]. The Langmuir isotherm model suggests a monolayer adsorption occurring on a homogeneous surface comes from finite number of similar active sites and Freundlich isotherm model is valid for adsorption take place heterogeneous surface [26]. The well-known linearized forms of Langmuir and Freundlich isotherm models were given in equations 9 and 10:

$$\text{Langmuir: } 1/q_e = 1/Q^\circ b(1/C_e) + 1/Q^\circ \quad (9)$$

$$\text{Freundlich: } \ln q_e = \ln K_F + (1/n) \ln C_e \quad (10)$$

The linear forms of Langmuir and Freundlich isotherm models were applied to experimental equilibrium data at different temperatures and the isotherm constants calculated from the isotherm equations and regression coefficients were summarized in Table III. Also, the experimental and predicted isotherms for Cr(VI) adsorption at 45°C and initial pH 3 were given in Fig. 12. As seen from Table III and Fig.12, Langmuir isotherm model was better agreement with experimental equilibrium data.

T (K)	Langmuir isotherm model			Freundlich isotherm model		
	Q°	b	R^2	K_F	$1/n$	R^2
298	161.29	0.2059	0.998	52.07	0.2147	0.878
308	166.66	0.2255	0.997	52.35	0.2234	0.917
318	312.50	0.3950	0.998	85.115	0.3194	0.917
328	277.78	0.1791	0.998	59.08	0.3315	0.929

TABLE III. The isotherm model constants and regression coefficients
 Q° (mg/g), b (L/mg), K_F [(mg/g)/(L/mg)^{1/n}]

Adsorbent	pH	Langmuir isotherm model		References
		Q° (mg/g)	b (l/mg)	
Multiwalled carbon nanotubes	4.28	1.177	0.526	[28]
Commercial hematite [α -Fe ₂ O ₃]	8	2.299	0.388	[4]
Commercial activated carbon-Fe	2.0 – 3.0	1.68	1.21	[29]
Olive oil factory wastes	2.0	18.69	0.0554	[5]
Hydrous titanium (IV) oxide (CHTO)	1.5	27.11	0.2766	[30]
The activated carbon from rubber wood	2.0	65.78	0.2443	[25]
Graphene hybridized Fe ₃ O ₄ nanoparticles	–	78.5	0.0006	[27]
L. speciosa bark embedded magnetic iron oxide nanoparticles	2.05	434.78	11.499	[1]
FeNPs synthesized with aqueous <i>E. japonica</i> leaves extract	3.0	312.50	0.3950	This study

TABLE IV. Comparison of results obtained in this study for the adsorption of Cr(VI) with those of other adsorbents

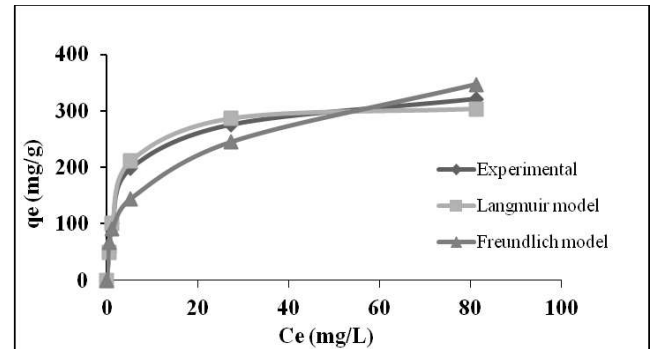


Fig.12. The comparison of the experimental and predicted isotherms for Cr (VI) adsorption (temperature 45°C, initial pH 3).

This result demonstrated that, the adsorption occurred at specific homogeneous sites within the adsorbent forming monolayer coverage of Cr (VI) at the surface of FeNPs.

The maximum monolayer coverage capacity of adsorbent was determined as 312.5 mg/g at 45°C which is the optimum temperature. As seen from Table III, the maximum monolayer coverage capacity values of FeNPs for Cr(VI) were increased by increasing temperature may be due to the endothermic nature of the studied adsorption process. The adsorption capacity of the green synthesized FeNPs in this study for the removal of Cr (VI) have been compared with those of other adsorbents reported in literature and their adsorption capacities have been presented in Table IV. According to Table IV, FeNPs in this study, has a good adsorption capacity in comparison with most of the other adsorbents.

However, the exactly comparison of adsorption capacity of sorbents is actually difficult due to the differences of optimum experimental conditions and physicochemical properties of adsorbents such as functional groups and specific surface areas.

The adsorption kinetics were elucidated by correlating the adsorption kinetic data of the Cr(VI) onto FeNPs using the linear forms of the pseudo-first-order [$\log(q_e - q_t) = \log(q_e) - k_1 t / 2.303$] and the pseudo-second order [$(1/(q_e - q_t)) = (1/q_e^2 k_2) + (t/q_e)$] kinetic models [31]. For the adsorption of Cr(VI) onto FeNPs, the parameters of the pseudo first-order and pseudo second-order kinetic models with regression coefficients were presented in Table V. From Table V, the adsorption kinetic of Cr (VI) onto FeNPs was better described by the pseudo second-order kinetic model due to consistency of the experimental and calculated q_e values and high regression coefficients than pseudo first-order model at all initial Cr(VI) concentrations. Based on the assumptions of the pseudo-second-order model, the chemisorption was the rate determining step in the adsorption of Cr(VI) on FeNPs.

In order to evaluate the boundary layer and intra-particle diffusion mechanism between Cr(VI) ions and FeNPs, Weber-Morris model [$q_e = K_i \cdot t^{0.5} + I$] was used and model parameters and regression coefficients were summarized at Table V.

TABLE V. Kinetic and intra-particle mass transfer model parameters.

Co (mg/L)	qe, exp (mg/g)	Pseudo-first-order			Pseudo-second-order			Weber-Morris Model		
		$k_1(\text{min}^{-1})$	$q_{e,cal1}$ (mg/g)	R^2	k_2 (g/mg.min)	$q_{e,cal2}$ (mg/g)	R^2	K_i (mg/g.min ^{0.5})	I	R^2
50	49.761	0.004145	5.2372	0.431	0.00904	50.237	0.999	0.3708	44.837	0.995
100	100.95	0.01174	19.7424	0.723	0.00378	101.19	0.999	4.1859	70.642	0.995
200	202.38	0.00460	119.922	0.748	0.000535	199.27	0.994	5.2275	84.077	0.991
300	297.85	0.00460	224.026	0.637	0.000879	302.62	0.996	5.8675	107.30	0.998
400	376.19	0.003915	361.826	0.799	0.001181	401.90	0.997	5.9466	107.34	0.992
500	458.809	0.003685	445.041	0.830	0.000629	496.94	0.991	7.8679	108.88	0.996

In Weber-Morris equation; I is the intercept related to the boundary layer effect and K_i is the intraparticle diffusion rate constant which can be evaluated from the slope of the linear plots of qt versus $t^{0.5}$. If Weber-Morris plot of qt versus $t^{0.5}$ is linear and pass through the origin, the intraparticle diffusion is the sole rate determining step but, when the plots in the figure are multi linear with three distinct regions, in that case there are three different kinetic mechanisms. The initial region corresponds to the external surface uptake, the second stage relates the gradual uptake indicating intraparticle diffusion as the rate limiting step and final plateau region represents equilibrium uptake [32]. Based on the results, it was observed a multilinear plot (figure not shown) indicated that both intraparticle and film diffusion were effective on the adsorption of Cr(VI) on FeNPs. Moreover, according to Table V; it was seen that the internal (K_i) and external diffusion constants (I) gradually increased with increasing initial Cr(VI) concentration.

IV. CONCLUSIONS

In summary, iron nanoparticles were biosynthesized by using a green reducing agent, loquat leaves aqueous extract and prepared FeNPs were tested as a adsorbent for Cr(VI) ions under our experimental conditions. The conclusions of this study can be summarize:

- The characterization studies confirmed the synthesis of FeNPs successfully. The synthesized FeNPs have irregular spherical morphology as well as they are relatively agglomerated. The XRD spectrum showed the diffraction peaks belong to mainly iron hydroxide and iron oxyhydroxide. According to FT-IR spectrums, the peaks refer to Fe-O stretches of Fe₃O₄ and Fe₂O₃.
- The optimum adsorption conditions were determined to be initial pH 3.0, temperature 45°C, initial Cr(VI) concentration 100 mg/L and adsorbent concentration 1.0 g/L.
- The adsorption equilibrium data best fitted to the Langmuir isotherm model. The monolayer coverage capacity calculated from Langmuir isotherm model was found to be 312.5 mg/g.

- The thermodynamic parameters; ΔG , ΔH , and ΔS were calculated as positive and results indicated that the studied adsorption process was endothermic and non-spontaneous.
- The adsorption kinetic data followed the pseudo-second-order kinetic model and both intraparticle and film diffusion were effective on the adsorption process.
- Based on the results, the biosynthesis method could be suggested for preparing iron nanoparticles in terms of ecofriendly, cost-effective and easy-to-handle synthesis process with large-scale, owing to abundance of loquat or other plant leaves.
- Consequently, green synthesized FeNPs can be a good candidate for Cr(VI) removal owing to their high adsorption capacity.

V. NOMENCLATURE

- b : A constant related to the affinity of the binding sites (L/mg)
 C_e : Unadsorbed Cr(VI) metal ion concentration at equilibrium (mg/L)
 C_o : Initial Cr(VI) metal ion concentration (mg/L)
 K_F : Freundlich constant indicating adsorption capacity ((mg/g)/(L/mg)^{1/n})
 K_i : Intraparticle diffusion rate constant (mg/g.min^{0.5})
 k_1 : Pseudo first order kinetic rate constant (1/min)
 k_2 : Pseudo second order kinetic rate constant (g/mg.min)
 q_e : Adsorbed amount per unit mass of adsorbent (mg/g)
 $q_{e,cal1}$: Calculated adsorbed amount per unit mass of adsorbent from pseudo first order kinetic model (mg/g)
 $q_{e,cal2}$: Calculated adsorbed amount per unit mass of adsorbent from pseudo second order kinetic model (mg/g)
 $q_{e,exp}$: Experimental adsorbed amount per unit mass of adsorbent (mg/g)
 q_t : Adsorbed amount per unit mass of adsorbent at any time (mg/g)
 Q_o : Maximum monolayer coverage capacity of adsorbent (mg/g)
 $1/n$: Freundlich constant indicating adsorption intensity

REFERENCES

- [1] S. Srivastava, S.B. Agrawal, and M.K. Mondal. "Synthesis, characterization and application of Lagerstroemia speciosa embedded magnetic nanoparticle for Cr (VI) adsorption from aqueous solution," *J. Environ. Sci.*, in press, September 2016.
- [2] L. P. Lingamdinne, J. R. Koduru, Y. L. Choi, Y. Y. Chang, and J. K. Yang, "Studies on removal of Pb (II) and Cr (III) using graphene oxide based inverse spinel nickel ferrite nano-composite as sorbent," *Hydrometallurgy*, vol. 165, pp. 64-72, October 2016.
- [3] S. Abhalaxmi, and S. K. Sahoo, "Magnetic nanoparticles: a novel platform for cancer theranostics." *Drug Discovery Today*, vol. 19(4), pp. 474-481, April 2014.
- [4] O. Ajouyed, C. Hurel, M. Ammari, L.B. Allal, and N. Marmier, "Sorption of Cr (VI) onto natural iron and aluminum (oxy) hydroxides: effects of pH, ionic strength and initial concentration," *J. Hazard. Mater.*, vol. 174(1), pp. 616-622, September 2010.
- [5] E. Malkoc, Y. Nuhoglu, and M. Dundar, "Adsorption of chromium (VI) on pomace—an olive oil industry waste: batch and column studies," *J. Hazard. Mater.*, vol. 138(1), pp. 142-151, November 2006.
- [6] S. S. Baral, S. N. Das, and P. Rath, "Hexavalent chromium removal from aqueous solution by adsorption on treated sawdust," *Biochem. Eng. J.*, vol. 31(3), pp. 216-222, October 2006.
- [7] H.C. Vu, A.D. Dwivedi, T.T. Le, S.H. Seo, E.J. Kim, Y.S. Chang, "Magnetite graphene oxide encapsulated in alginate beads for enhanced adsorption of Cr (VI) and As (V) from aqueous solutions: Role of crosslinking metal cations in pH control," *Chem. Eng. J.*, vol. 307, pp. 220-229, January 2017.
- [8] S. Uysal, A. Cvetanović, G. Zengin, S. Đurović, and A. Aktumsek, "Optimization of the extraction process of antioxidants from loquat leaves using response surface methodology," *J. Food Process. Preserv.* January 2017.
- [9] Y. Hong, B. Lin, H. Cao, Y. Gao, and S. Lin, "Analysis of major triterpene acids and total polysaccharides in the leaves of 11 species of Eriobotrya," *In BIO Web of Conferences, EDP Sciences*, vol. 8, pp. 03012, 2017.
- [10] A.M. Awwad, N.M. Salem, and A.O. Abdeen, "Biosynthesis of silver nanoparticles using Loquat leaf extract and its antibacterial activity," *Adv Mat Lett.*, vol. 4(5), pp. 338-342, January 2013.
- [11] A. Sharma, N. Dhiman, B.P. Singh, and A.K. Gathania, "Green synthesis of gold nanoparticles using extracts of Artocarpus Lakoocha fruit and its leaves, and Eriobotrya Japonica leaves," *Mater. Res. Express*, vol. 1(2), pp. 025042, June 2014.
- [12] M. Fazlzadeh, K. Rahmani, A. Zarei, H. Abdoallahzadeh, F. Nasiri, and R. A Khosravi, "novel green synthesis of zero valent iron nanoparticles (NZVI) using three plant extracts and their efficient application for removal of Cr (VI) from aqueous solutions," *Adv. Powder Technol.*, vol. 28 (1), pp. 122-130, January 2017.
- [13] S. Kuo, and R. Bembenek. "Sorption and desorption of chromate by wood shavings impregnated with iron or aluminum oxide." *Bioresour. Technol.*, vol. 99 (13), pp. 5617-562, September 2008.
- [14] W. Liu, J. Zhang, C. Zhang, Y. Wang, and Y. Li, "Adsorptive removal of Cr (VI) by Fe-modified activated carbon prepared from Trapa natans husk," *Chem. Eng. J.*, vol. 162 (2), pp. 677-684, August 2010.
- [15] T. Shahwan, S. A. Sirriah, M. Nairat, E. Boyaci, A. E. Eroğlu, T. B. Scott, and K.R. Hallam, "Green synthesis of iron nanoparticles and their application as a Fenton-like catalyst for the degradation of aqueous cationic and anionic dyes," *Chem. Eng. J.*, vol. 172(1), pp. 258-266, August 2011.
- [16] APHA, Standard Methods for the Examination of Water and Wastewater, 16th (ed.), American Public Health Association, Washington, 1981.
- [17] A. Heller, M.S. Fleys, J. Chen, G.P. van der Laan, M.H. Rausch, A.P. Fröba, "Thermal and Mutual Diffusivity of Binary Mixtures of n-Dodecane and n-Tetracontane with Carbon Monoxide, Hydrogen, and Water from Dynamic Light Scattering (DLS)," *J. Chem. Eng. Data*, vol. 61(3), pp. 1333-1340, February 2016.
- [18] Y. Kuang, Q. Wang, Z. Chen, M. Megharaj, R. Naidu, "Heterogeneous Fenton-like oxidation of monochlorobenzene using green synthesis of iron nanoparticles," *J. Colloid Interface Sci.*, vol. 410, pp. 67-73, November 2013.
- [19] A. M. Awwad, and N.M. Salem, "Kinetics and thermodynamics of Cd (II) biosorption onto loquat (Eriobotrya japonica) leaves," *J. Saudi Chem. Soc.* (2014), vol. 18(5), pp. 486-493, November 2014.
- [20] T. Wang, X. Jin, Z. Chen, M. Megharaj, and R. Naidu, "Green synthesis of Fe nanoparticles using eucalyptus leaf extracts for treatment of eutrophic wastewater," *Sci. Total Environ.*, vol. 466, pp. 210-213, January 2014.
- [21] R. K. Gautam, V. Rawat, S. Banerjee, M.A. Sanroman, S. Soni, S.K. Singh, and M.C. Chattopadhyaya, "Synthesis of bimetallic Fe–Zn nanoparticles and its application towards adsorptive removal of carcinogenic dye malachite green and Congo red in water," *J. Mol. Liq.*, vol. 212, pp. 227-236, December 2015.
- [22] M. Iram, C. Guo, Y. Guan, A. Ishfaq, and H. Liu, "Adsorption and magnetic removal of neutral red dye from aqueous solution using Fe₃O₄ hollow nanospheres," *J. Hazard. Mater.*, (2010), vol. 181(1), pp. 1039-1050, September 2010.
- [23] F. Hussain, S. Guo, and G. Zhang. "Preparation and characterization of bifunctional Ti–Fe kaolinite composite for Cr (VI) removal." *J. Colloid Interface Sci.* vol. 442, pp. 30-38, March 2015.
- [24] C. H. Weng, Y. C. Sharma, and S. H. Chu, "Adsorption of Cr (VI) from aqueous solutions by spent activated clay," *J. Hazard. Mater.*, vol. 155(1), pp. 65-75, June 2008.
- [25] T. Karthikeyan, S. Rajgopal, and L.R.Miranda. "Chromium (VI) adsorption from aqueous solution by Hevea Brasilensis sawdust activated carbon." *J. Hazard. Mater.*, vol. 124 (1), pp. 192-199, September 2005.
- [26] N.C. Olivares, M.C. Díaz-Nava, and M. Solache-Ríos, "Enhanced decolorization of dyes by an iron modified clay and thermodynamic parameters," *Water Sci. Technol.*, vol. 73(8), pp. 2007-2016, April 2016.
- [27] H. Gao, S. Lv, J. Dou, M. Kong, D. Dai, C. Si, and G. Liu, "The efficient adsorption removal of Cr (vi) by using Fe₃O₄ nanoparticles hybridized with carbonaceous materials," *RSC Advances*, vol. 5(74), pp. 60033-60040, July 2015.
- [28] J. Hu, C. Chen, X. Zhu, and X. Wang, "Removal of chromium from aqueous solution by using oxidized multiwalled carbon nanotubes," *J. Hazard. Mater.*, vol. 162(2), pp. 1542-1550, March 2009.
- [29] P. Maneechakr, and S. Karnjanakom, "Adsorption behaviour of Fe (II) and Cr (VI) on activated carbon: Surface chemistry, isotherm, kinetic and thermodynamic studies," *J. Chem. Thermodyn.*, vol. 106, pp. 104-112, March 2017.
- [30] S. Debnath, and U. C. Ghosh, "Kinetics, isotherm and thermodynamics for Cr (III) and Cr (VI) adsorption from aqueous solutions by crystalline hydrous titanium oxide," *J. Chem. Thermodyn.*, vol. 40(1), pp. 67-77, January 2008.
- [31] Y. Yan, Q. An, Z. Xiao, W. Zheng, and S. Zhai, "Flexible core-shell/bead-like alginate@ PEI with exceptional adsorption capacity, recycling performance toward batch and column sorption of Cr (VI)," *Chem. Eng. J.*, vol. 313, pp. 475-486, April 2017.
- [32] S. R., Popuri, Y., Vijaya, V. M., Boddu, & K. Abburi, "Adsorptive removal of copper and nickel ions from water using chitosan coated PVC beads," *Bioresour. Technol.*, vol. 100(1), pp. 194-199, January 2009.

Synthesis and Characterization of Alginate/ Fe_3O_4 Nanoparticles for Methylene Blue Adsorption

Ceylan Uzun, Nuran Efeyik, Deniz Uzunoğlu, and Ayla Özer

Mersin University, Department of Chemical Engineering, Mersin, Turkey

ceylanuzun34@gmail.com, nuraneefeyik@gmail.com, denizuzunoglu4@gmail.com, and ayozzer4@gmail.com

Abstract— In this study, alginate/ Fe_3O_4 nanoparticles (Alg/ Fe_3O_4 NPs) were synthesized by a fast and facile reduction (partial reduction of Fe^{3+} with sodium sulfite)-precipitation method (precipitation with ammonia) at room temperature. The characterization of Alg/ Fe_3O_4 NPs was performed by FT-IR, SEM, EDX, and XRD analysis methods. The adsorbent and catalysis properties of Alg/ Fe_3O_4 NPs for methylene blue dye were investigated in a batch system. The studies to determine effects of environmental conditions on the adsorption of methylene blue dye on Alg/ Fe_3O_4 NPs were done and the optimum experimental conditions were determined as follows: initial pH of 8.0, initial dye concentration of 300 mg/L, temperature of 308 K, and adsorbent concentration of 0.5 g/L. The adsorption equilibrium data of methylene blue on Alg/ Fe_3O_4 NPs fitted well to Langmuir isotherm model with the maximum monolayer coverage capacity of 393.39 mg/g. The studied adsorption process followed the pseudo second order kinetic model, and both intraparticle and film diffusion were effective on the adsorption system. Thermodynamic parameters such as Gibb's energy (ΔG) change, activation energy (E_a), enthalpy change (ΔH), and entropy change (ΔS) indicated that the adsorption was spontaneous, exothermic, physical, and decreasing in randomness of adsorbed species. The effect of H_2O_2 on catalytic degradation with Alg/ Fe_3O_4 NPs of methylene blue dye in the Fenton-like system was also investigated and the optimum H_2O_2 concentration was determined to be 5.0 % with 99 % of the degradation efficiency at the end of 40 minute.

Keywords—adsorption, alginate, degradation, Fe_3O_4 nanoparticles, Methylene blue

I. INTRODUCTION

Fe_3O_4 nanoparticles have been widely evaluated in many application areas like separation processes, biotechnology, sensors, optoelectronics, catalysts, medical diagnosis [1]. Especially due to the substantial properties of Fe_3O_4 nanoparticles like the advantages of strong catalytic activity, long-term stability, low toxicity, biocompatibility, and environment-friendly, they can be thought as ideal nanomaterials for the removal of various pollutants, including phenol species (2,4-dichlorophenol, p-nitrophenol), aniline, heavy metal, and dye pollutants. However, the aggregation of the nanoparticles is a significant problem causing decrease in the effective surface area of nanoparticles and thus reducing their removal capacities. The aggregation of nanoparticles could be overcome by the combine of the nanoparticles with organic, inorganic, and biological substances, such as

polyacrylic acid, activated carbon, multiwalled carbon nanotube, mesocellular carbon foam, thiol, cetyltrimethylammonium bromide, zeolite, poly(3,4-ethylenedioxythiophene), alginate, chitosan, gum, hydroxyapatite, yeast, and so on [2]. It is wanted that the substances must have high stability, environmental-friendliness, cost-efficiency, wide resource. Among these substances; natural polymers like alginate, chitosan, etc. are promising alternatives for the combining of the nanoparticles due to their low price, wide sources, and environmental friendliness [3]. In our study, sodium alginate, consisted of guluronic (G) and mannuronic (M) acid residues (linear copolymer of (1–4) linked β -D-mannuronic acid and α -L-guluronic acid units), was selected as the substance for combining of Fe_3O_4 nanoparticles. In the literature, there are some combination methods of Fe_3O_4 nanoparticles with the substances like co-precipitation, oxidation–precipitation, forced hydrolysis, and so on. However; since these methods generally required either the emulsifying agents, or protective gas, and high-temperature, the reduction–precipitation method with the advantages of being fast and simple, non-use of a protective/reactive gas and surfactant has been developed [4]. In this study, alginate/ Fe_3O_4 nanoparticles (Alg/ Fe_3O_4 NPs) were synthesized by the reduction–precipitation method and characterized by FT-IR, SEM, EDX, and XRD analysis. The adsorbent and catalysis properties of Alg/ Fe_3O_4 NPs for methylene blue dye were investigated in a batch system.

II. MATERIALS AND METHODS

A. Synthesis and Characterization of Alg/ Fe_3O_4 NPs

The synthesis of alginate/ Fe_3O_4 nanoparticles (Alg/ Fe_3O_4 NPs) was carried out via a reduction–precipitation process. Unlike the other synthesis methods; in this method, Fe^{3+} is partially reduced before the formation of Fe_3O_4 nanoparticles, that providing to prevent the aggregation. Firstly, 0.13 mole/L FeCl_3 and 20 mg/mL alginate solutions were separately prepared by solving the appropriate amounts of FeCl_3 and alginate in 1.0 % (v/v) solution of HCl, and then 35 mL of 0.13 mole/L FeCl_3 was added to 25 mL of 20 mg/mL alginate solution, the colloidal solution was in yellow color and it was stirred magnetically for 1 h. After that, 15 mL of 0.1 mole/L Na_2SO_3 solution in pure water was put into as-prepared

colloidal solution, and the color of the final solution changed from yellow to red immediately. As soon as the color altered from red to yellow again, 10 mL of 25 % (v/v) ammonia solution was added quickly to the final solution under vigorous stirring at room temperature and the black precipitates of Alg/Fe₃O₄ NPs occurred in a short time. In order to stabilization of Alg/Fe₃O₄ NPs, 2.5 mL of 1.0 % (w/v) starch solution was added to the black suspension and it was stirred magnetically at 60 °C for 3.0 h. Lastly, the resulting precipitates of Alg/Fe₃O₄ NPs were separated with centrifuge at 4000 rev/min for 5.0 min, washed with pure water, and then dried in an oven at 80 °C for 24 h. Alg/Fe₃O₄ NPs in closed vessels were stored in a refrigerator at +4 °C for the further studies [4]. The characterization studies of Alg/Fe₃O₄ NPs were performed by Fourier Transform Infrared Spectrometer (FT-IR- Perkin Elmer, Shelton), Scanning Electron Microscope (SEM- Zeiss/Supra 55, Germany), Energy Dispersive X-ray Spectroscopy (EDX- Zeiss/Supra 55, Germany), and X-ray Diffractometer (XRD- Philips XPert, Netherlands).

B. Adsorption Experiments

The experiments of Methylene Blue (MB; C₁₆H₁₈ClN₃S; M_w=319.852) adsorption onto Alg/Fe₃O₄ NPs were conducted in a single stage batch adsorption process. Firstly; a required amount of Alg/Fe₃O₄ NPs (0.1 g except for adsorbent concentration experiments) was put into 100 mL of the aqueous solution of MB at a known initial pH and initial dye concentration in conical flask, and then it was agitated in a water bath for a required period of adsorption to attain adsorption equilibrium. The samples were taken at predetermined time intervals and they were centrifuged at 3000 rev/min for 3.0 min to be separated from the adsorbent. The residual dye concentration in the supernatant was analyzed at 665 nm by UV-vis spectrophotometer (Chebios Optimum-One, Italy). Experiments were replicated for different initial pH, initial dye concentration, temperature, and adsorbent concentration values.

C. Degradation Experiments

The degradation studies were carried out as follows briefly; 0.1 g of Alg/Fe₃O₄ NPs were blended with 100 mL and 100 mg/L of MB solution at initial pH of 3.0 in conical flasks, and then the degradation was initiated by rapid adding of 10 mL H₂O₂ for different concentrations (1.0, 3.0, 5.0, and 10 %, v/v) to the reaction solution while they were being agitated in a water bath at 298 K. At given time intervals, 3.0 mL aliquots of MB solution were sampled, and immediately separated with centrifuge at 4000 rev/min for 30 second. After that, UV-vis spectrum scanning of the supernatant was done.

III. RESULTS AND DISCUSSION

Alg/Fe₃O₄ NPs were synthesized by the reduction-precipitation method and the predicted steps in this method were exhibited in Fig. 1. Accordingly, Fe³⁺ ions were firstly

chelated with COONa and OH groups of alginate, that providing homogenous dispersion of Fe³⁺ ions and thus prevention of agglomeration of the nanoparticles, and then they partially reduced to Fe²⁺ ions with the addition of Na₂SO₃ solution. Lastly, Alg/Fe₃O₄ NPs were formed in around 5.0 min with the aid of ammonia solution. Consequently, Alg/Fe₃O₄ NPs could be synthesized by a simple and fast method at mild conditions.

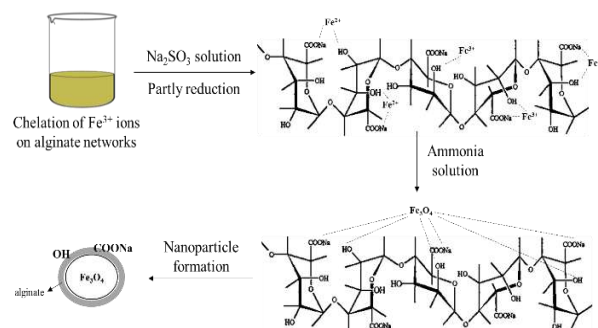


Fig. 1. The predicted steps of the reduction-precipitation process

The morphology of Alg/Fe₃O₄ NPs was characterized by SEM analysis and its image was presented in Fig. 2. It was observed from Fig. 2 that Alg/Fe₃O₄ NPs had porous and mostly spherical-like structures in nanoscale, and their growth were irregular. Also, the presence of the elements in Alg/Fe₃O₄ NPs such as basically iron, oxygen, carbon, sodium along with chlorine and sulfur in trace amounts was determined by EDX analysis. The elements of iron, oxygen, carbon, sodium arose from Fe₃O₄ and sodium alginate (Fe, Na, C, and O) structure while the others (S and Cl) were residual.

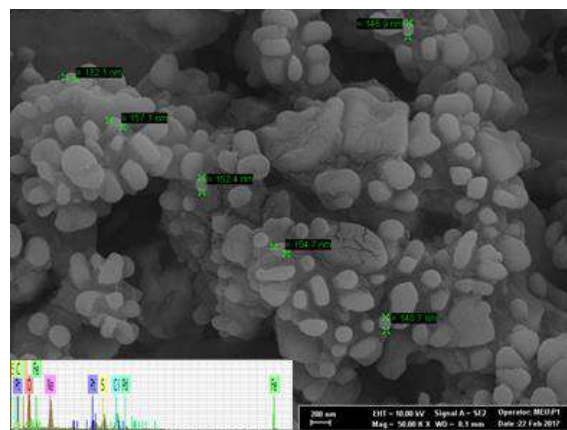


Fig. 2. SEM image with EDX spectrum of Alg/Fe₃O₄ NPs

FT-IR spectrums of alginate (Alg) and Alg/Fe₃O₄ NPs were recorded in order to determine the functional groups of Alg/Fe₃O₄ NPs and they were presented in Fig. 3. The broad peak placed at around 3200 cm⁻¹ was attributed to hydrogen bonded O-H stretching. The carbonyl group of Alg was into carboxylate anion form (O-C-O asymmetric stretching at 1600

cm^{-1}). The band at 1406 cm^{-1} was assigned to C–OH deformation vibration with contribution of O–C–O symmetric stretching vibration of carboxylate group. The weak bands at 1085 cm^{-1} and more intense at 1028 cm^{-1} represented C–O and C–C stretching vibrations of pyranose ring, respectively [5]. The strong peak at 615 cm^{-1} was attributed to Fe–O, confirming the presence of Fe_3O_4 NPs in Alg chains [6]. Moreover, the formation of new peaks at $3200\text{--}3000\text{ cm}^{-1}$ and the shifts of $1600, 1406, 1085,$ and 1028 cm^{-1} to $1594, 1404, 1102,$ and 1038 cm^{-1} , respectively showed that the carbonyl and hydroxyl groups of Alg were involved in complexation with Fe^{3+} ions [4].

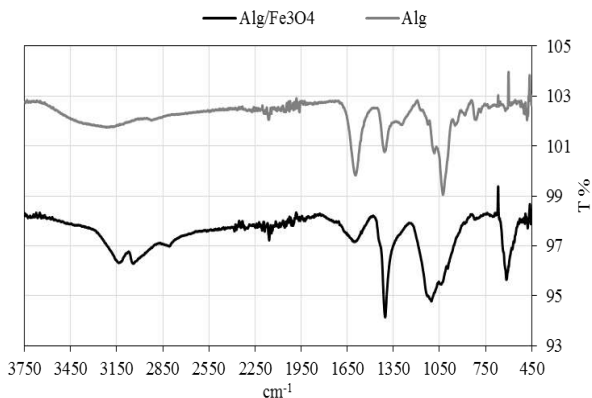


Fig. 3. FT-IR spectrums of Alg/ Fe_3O_4 NPs and alginate

The crystal structure of Alg/ Fe_3O_4 NPs was determined by using XRD analysis method. The XRD pattern (Fig. 4) showed six characteristic diffraction peaks ($2\theta = 29.94, 35.54, 45.48, 53.50, 57.20,$ and 62.72°), corresponding to (220), (311), (400), (422), (511), and (440) crystal planes of inverse cubic spinel structure of Fe_3O_4 . It revealed that the crystal phase of Fe_3O_4 nanoparticles did not alter during the binding process [7].

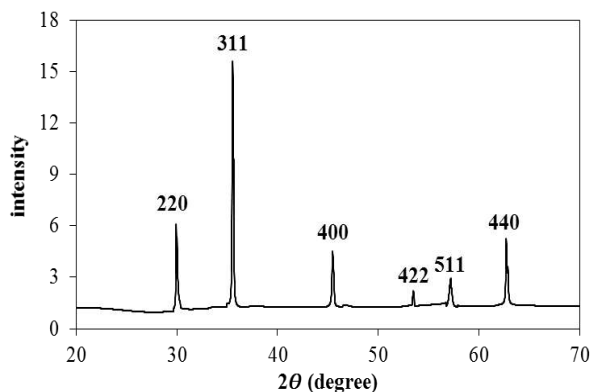


Fig. 4. XRD pattern of Alg/ Fe_3O_4 NPs

The pH value of aqueous solution is a crucial factor affecting the adsorption processes. The plot of the adsorbed amounts at equilibrium (q_{eq}) versus initial pH values was presented in Fig. 5.a. It was indicated that high adsorption

capacities were obtained at the studied initial pH range. High adsorption capacities in the studied pH range can be explained with the point of zero charge (pH_{pzc}) of the adsorbent. In this study, the pH_{pzc} of the synthesized Alg/ Fe_3O_4 NPs was determined to be 5.7 by using experimental method in the previous work [8]. Mainly, the surface charge of adsorbent is positive at pH values lower than pH_{pzc} , zero at $\text{pH}=\text{pH}_{\text{pzc}}$, and negative at pH values higher than pH_{pzc} . At $\text{pH} > \text{pH}_{\text{pzc}}$, the surface of Alg/ Fe_3O_4 NPs were negatively charged which enhanced their interaction with MB cations through electrostatic force of attraction.

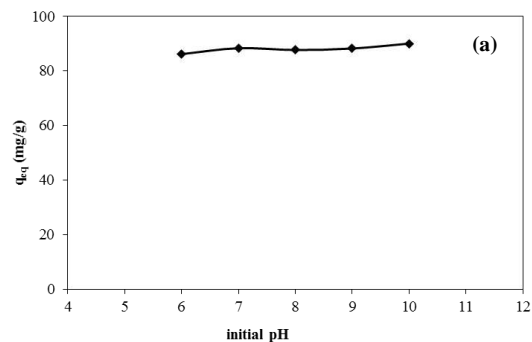


Fig. 5. a. Effect of initial pH ($T=298\text{ K}, C_0=100\text{ mg/L}, X_0=1.0\text{ g/L}$)

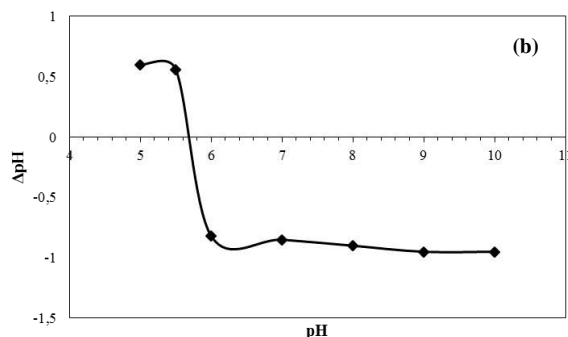


Fig. 5. b. Point of zero charge of Alg/ Fe_3O_4 NPs

The experiments in order to evaluate the influence of initial dye concentration on the adsorption were conducted at initial pH of 8.0, temperature of 308 K , and adsorbent concentration of 1.0 g/L in the initial dye concentration range of $25\text{--}500\text{ mg/L}$ and results were presented in Fig. 6. Fig. 6 indicated that q_{eq} values increased from 23.84 to 289.70 mg/g while the adsorption percentages decreased from 94.51 to 55.52% , as the experimental initial dye concentration increased from 25 to 504 mg/L . Also, the adsorption of MB onto Alg/ Fe_3O_4 NPs showed a saturation trend while the adsorption percentages diminished sharply at high initial dye concentrations since the adsorbent suggested a finite number of surface binding sites for dye cations. Hence, the optimum initial dye concentration was observed as 300 mg/L .

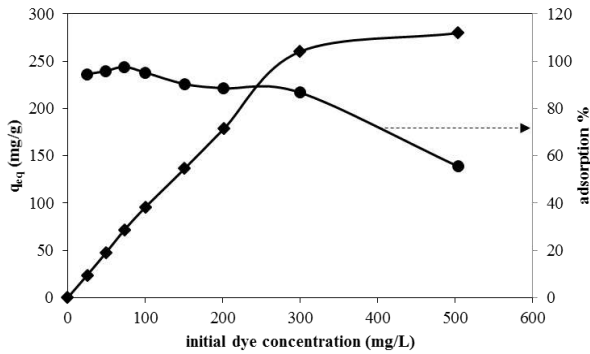


Fig. 6. Effect of initial dye concentration (initial pH=8.0, T=308 K, X₀=1.0 g/L)

The transfer of an adsorbate from the liquid phase to the solid phase takes place in the adsorption processes. In order to get information about this transfer mechanism, which is very crucial efficiency of the process, the kinetic and mass transfer models could be evaluated. For this purpose, the pseudo first order (PFOM) [$\log(q_{eq}-q_t)=\log(q_{eq})-(k_1 \cdot t/2.303)$] and the pseudo second order (PSOM) [$(t/q_t)=(1/(q_{eq}^2 \cdot k_2))+(t/q_{eq})$] order (PSOM) kinetic models along with Weber-Morris intraparticle diffusion model ($q_t=K_i \cdot t^{0.5}+C$) were tested for different initial dye concentrations at initial pH of 8.0, temperature of 308 K, and adsorbent concentration of 1.0 g/L.

The calculated rate constants and regression coefficients from the kinetic model plots ($\log(q_{eq}-q_t)$ vs. t for PFOM and t/q_t vs. t for PSOM; figures not shown) were summarized in Table I. The consistency between the experimental $q_{e,eq}$ values and the calculated $q_{cal,eq}$ values from the kinetic model plots was also presented in Fig. 7. The regression coefficients for the linear plots of PSOM were higher than PFOM and also the calculated $q_{eq,cal}$ values from PSOM showed an excellent agreement ($R^2 \approx 1$) with the experimental $q_{eq,exp}$ values, thus suggesting that the kinetics of the studied adsorption system could be described by the pseudo second order kinetic model.

TABLE V. THE ADSORPTION RATE CONSTANTS OF PFOM AND PSOM AT DIFFERENT INITIAL DYE CONCENTRATIONS (INITIAL PH=8.0, T=308 K, X₀=1.0 G/L)

C ₀ (mg/L)	k ₁ (1/min)	R ₂	k ₂ (g/mg.min)	R ₂
25	0.00806	0.7739	0.005879	0.9953
50	0.01635	0.7411	0.003311	0.9983
75	0.01251	0.8878	0.002416	0.9991
100	0.01474	0.8693	0.002081	0.9990
150	0.02027	0.9402	0.002961	0.9999
200	0.01474	0.8737	0.001780	0.9997
300	0.01313	0.7854	0.000704	0.9987
500	0.01612	0.9402	0.000781	0.9996

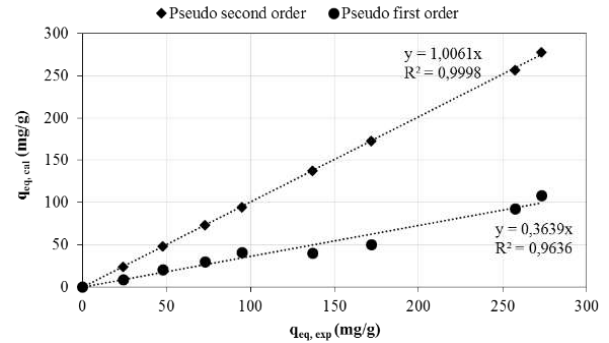


Fig. 7. The plots of the experimental adsorbed amount at equilibrium ($q_{eq,exp}$) vs. the calculated adsorbed amount at equilibrium from the kinetic models ($q_{eq,cal}$)

The adsorbate transport from the liquid phase to the surface of the adsorbent particles occurs in several steps, e.g. external diffusion, intraparticle diffusion, surface diffusion, and adsorption, or a combination of more than one step. Weber-Morris intraparticle diffusion model ($q_t=K_i \cdot t^{0.5}+C$) was applied to the experimental data for different initial dye concentrations in order to determine which steps were effective in the adsorption system. The slope and intercept value of the plot of q_t vs. $t^{0.5}$ give intraparticle diffusion rate constant (K_i) and C value attributed to external diffusion, respectively; K_i and C values along with regression coefficients were displayed in Table II. It showed that K_i and C values increased with increase in initial dye concentration. According to Weber-Morris intraparticle diffusion model, if the only intra-particle diffusion is effective in the adsorption process, then the plot of q_t vs. $t^{0.5}$ gives a linear line with intercept C equal to zero. However, if the plot of q_t vs. $t^{0.5}$ is multilinear, then adsorption is governed by more than one mechanism [9]. The plots of Weber-Morris model in Fig. 8 had three linear parts with different slopes, which indicated that the more than one mechanism took place in the process. The initial portion corresponded to the external diffusion, the second portion described the adsorption stage where intraparticle diffusion was effective on the process, and the third portion indicated the final equilibrium stage. Therefore, it was concluded that both external and intraparticle diffusion were effective on MB adsorption by Alg/Fe₃O₄ NPs.

TABLE VI. WEBER-MORRIS INTRAPARTICLE DIFFUSION MODEL PARAMETERS AT DIFFERENT INITIAL DYE CONCENTRATIONS (INITIAL PH=8.0, T=308 K, X₀=1.0 G/L)

C ₀ (mg/L)	K _i (mg/g.min ^{0.5})	C	R ₂
25	1.49	12.64	0.9903
75	9.36	18.14	0.9870
150	9.90	71.74	0.9938
500	11.81	160.78	0.9841

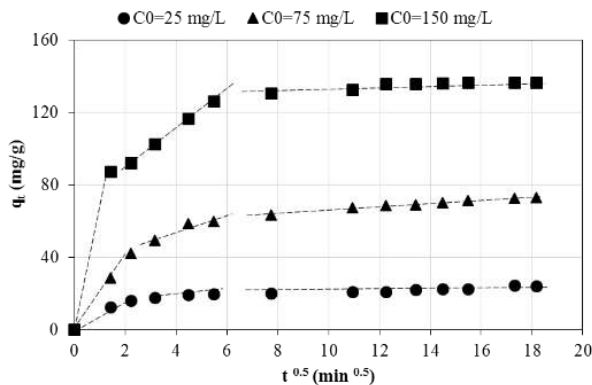


Fig. 8. The plots of Weber-Morris intraparticle diffusion model (initial pH=8.0, T=308 K, X₀=1.0 g/L)

The variation of the equilibrium uptake amounts (q_{eq}) with temperature values (298-328 K) was displayed in Fig. 9. It was observed that the adsorption capacity of Alg/Fe₃O₄ NPs for MB adsorption increased up to 308 K, and thereafter it was negatively affected by further increase in temperature. So, the optimum temperature was determined as 308 K for MB adsorption onto Alg/Fe₃O₄ NPs.

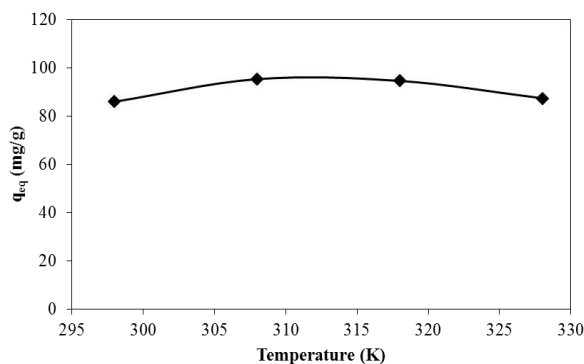


Fig. 9. Effect of temperature (initial pH=8.0, C₀=100 mg/L, X₀=1.0 g/L)

The effect of temperature on the studied adsorption process was also evaluated with thermodynamic studies by calculating the activation energy (E_a), entropy change (ΔS), enthalpy change (ΔH), and Gibbs energy change (ΔG). The activation energy could be determined by Arrhenius equation (Eq. 1) whereas Van't Hoff equation (Eq. 2) is used for the other thermodynamic parameters (Table III). These parameters were calculated by using following equations:

$$\ln(k_2) = \ln(k_0) - E_a/RT \quad (1)$$

$$\ln(K_c) = (\Delta S/R) - (\Delta H/RT) \quad (2)$$

$$\Delta G = -RT \ln(K_c) \quad (3)$$

where k_0 is the Arrhenius factor, k_2 is the pseudo second order rate constant (i.e. model that best described the adsorption kinetics), R is the gas constant (8.3145 J/mole.K), and K_c is the equilibrium constant at temperature T .

The values of ΔH and ΔS were calculated from the slope and intercept of the linear plot of $\ln(K_c = C_{ad,eq}/C_{eq})$ vs $1/T$, respectively, according to Eq. 2. The activation energy of MB adsorption on Alg/Fe₃O₄ NPs was determined from the slope of the linear plot of $\ln(k_2)$ vs $1/T$ by using Eq. 1. For the observation of the adsorption type, e.g. physisorption or chemisorption, the values of ΔH and E_a could be analyzed; accordingly, the ΔH value of physisorption system is lower than 84 kJ/mole whereas ΔH value of the chemisorption system is in the range of 84–420 kJ/mole [10]. Also, the activation energy of physisorption usually lies from 5 to 40 kJ/mole due to weak forces while higher activation energies offer chemisorption and its activation energy is usually in the range of 40–800 kJ/mole [11]. Hence it was concluded that the studied removal process proceeded through the physisorption with respect to the values of ΔH and E_a . Also, this result confirmed with FT-IR and XRD analysis that it was not observed any difference between before and after adsorption for FT-IR spectrum and XRD pattern of Alg/Fe₃O₄ NPs (figure not shown), which was indicating the physical adsorption in nature. Besides, the negative values of ΔS , ΔH , and ΔG showed that the adsorption system was decreasing in randomness of adsorbed species, exothermic, and spontaneous, respectively.

TABLE VII. THERMODYNAMIC PARAMETERS (INITIAL PH=8.0, T=308 K, C₀=100 MG/L, X₀=1.0 G/L)

T (K)	ΔG (J/mole)	ΔS (J/mole.K)	ΔH (kJ/mole)	E_a (kJ/mole)
308	-7651.43	-96.31	-37.33	-29.79
318	-6740.36			
328	-5723.01			

The linear forms of Langmuir [$(1/q_{eq}) = (1/(Q_{max} \cdot b \cdot C_{eq})) + (1/Q_{max})$] and Freundlich [$\ln(q_{eq}) = \ln(K_F) + (1/n) \cdot \ln(C_{eq})$] isotherm models, the most frequently used adsorption isotherm models, were applied to the experimental equilibrium data at different temperature values and the calculated isotherm model parameters along with regression coefficients (R^2) were displayed in Table IV. It revealed that the experimental equilibrium data fitted well to Langmuir model due to the higher R^2 values rather than Freundlich model. Langmuir model suggested that the studied adsorption process was monolayer in nature meaning that only one MB cation adsorbed onto adsorbent surface and no further adsorption could take place at that site. Moreover, as it was expected from the results of temperature effect (Fig. 9) that Q_{max} values were close to each other and the maximum value of Q_{max} =393.39 mg/g was obtained at 308 K.

TABLE VIII. THE CONSTANTS OF THE ADSORPTION ISOTHERM MODELS ALONG WITH THE RELATED REGRESSION COEFFICIENTS (INITIAL PH=8.0, C₀=100 MG/L, X₀=1.0 G/L)

T	Langmuir isotherm model			Freundlich isotherm model		
	Q_{max}	b	R^2	K_F	$1/n$	R^2
298	376.3643	0.02119	0.9958	16.32	0.6286	0.9879
308	393.3910	0.03829	0.9998	17.21	0.7550	0.9826

318	388.3495	0.03299	0.9934	18.86	0.6823	0.9899
328	380.3728	0.03038	0.9972	19.49	0.6505	0.9877

[T: K, Q_{max} : mg/g, b: L/mg, K_F : mg/g(L/mg)^{1/n}]

The comparison of Q_{max} values of various types of Fe_3O_4 nanoparticles for various dye molecules in the literature was shown in Table V. Accordingly, Alg/ Fe_3O_4 NPs used in this study had a relatively high adsorption capacity. The studies in the recent years shown that Fe_3O_4 nanoparticles have been supported with various substances in order to improve of the adsorption capacities.

TABLE IX. THE COMPARISON OF Q_{max} VALUES OF VARIOUS TYPES OF Fe_3O_4 NANOPARTICLES

Adsorbent	Dye	Q_{max} (mg/g)	Reference
Fe_3O_4 magnetic nanoparticles modified with sodium dodecyl sulfate	Safranin O	769.23	12
Fe_3O_4 nanoparticles loaded onto wheat straw	Basic Blue 9	627.10	13
Alginate/ Fe_3O_4 nanoparticles	Methylene Blue	393.39	This study
Humic acid (HA) modifying Fe_3O_4 nanoparticles	Rhodamine B	161.80	14
Fe_3O_4 nanoparticle produced with rice husk ash	Acid Red 114	111.00	15
Fe_3O_4 nanoparticles modified by polypyrrole	Reactive Red 195	99.00	16
Humic acid-coated Fe_3O_4 nanoparticles	Methylene Blue	93.08	17
Fe_3O_4 nanoparticles	New Coccine	35.50	18
Polyaniline/ Fe_3O_4 nanocomposite	Titan Yellow	34.00	19
Fe_3O_4 -loaded coffee waste hydrochar	Acid Red 17	16.30	20

The effect of adsorbent concentration on MB adsorption onto Alg/ Fe_3O_4 NPs was presented in Fig. 10 for initial pH of 8.0, initial dye concentration of 100 mg/L, and temperature of 298 K in the adsorbent concentration range of 0.5-3.0 g/L. As can be seen from Fig. 10, as increasing adsorbent concentration, the adsorption capacities decreased sharply while the adsorption percentages remained nearly constant. The reduction in adsorption capacities may be due to particle aggregation at higher than 0.5 g/L adsorbent concentration, that causing decrease in effective surface area of the adsorbent and an increase in diffusional path length. Therefore, the optimum adsorbent concentration was determined as 0.5 g/L.

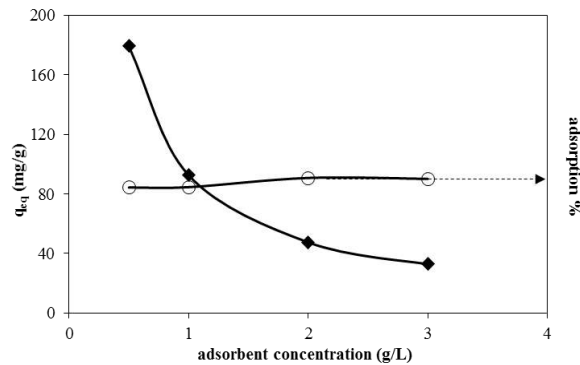


Fig. 10. Effect of adsorbent concentration (initial pH=8.0, T=298 K, C_0 =100 mg/L)

The various iron oxide materials, such as magnetite (Fe_3O_4), hematite (α - Fe_2O_3), goethite (α - $FeOOH$), Fe^0/Fe_2O_3 , and Fe^0/Fe_3O_4 can be utilized as heterogeneous catalysts to activate H_2O_2 by generating hydroxyl radicals, which can degrade organic pollutants to H_2O , CO_2 , and inorganic salts. Hence, the effect of the presence of H_2O_2 on the degradation of MB in the Fenton-like process was also investigated in this study. In the Fenton-like process, it is known that the optimum pH is generally obtained as 3.0 for organic pollutant degradation [21]; so, the experiments of MB degradation in the presence of H_2O_2 were conducted at initial pH of 3.0, initial dye concentration of 100 mg/L, temperature of 298 K in the H_2O_2 concentration range of 1.0-10 %, and Fig. 11 exhibited the degradation of MB for different H_2O_2 concentrations. Accordingly, the degradation increased with an increase in H_2O_2 concentration. However, when H_2O_2 concentration was greater than 5.0 %, the degradation was not improved with further increase in H_2O_2 concentration. So, the optimum H_2O_2 concentration was observed as 5.0 % for MB degradation with 99 % decolorization efficiency. This case could be explained as follows; more H_2O_2 concentration at the beginning of the Fenton process provides more producing of hydroxyl radicals, that increasing the degradation efficiency. However, the excess of H_2O_2 concentration leads to scavenging effect for more hydroxyl radicals by generating perhydroxyl radicals, having lower oxidation capabilities, and eventually the degradation efficiency decreases at higher than optimum H_2O_2 concentration. Hence, the maximum degradation efficiency could be only attained when the concentration of H_2O_2 is optimal [22].

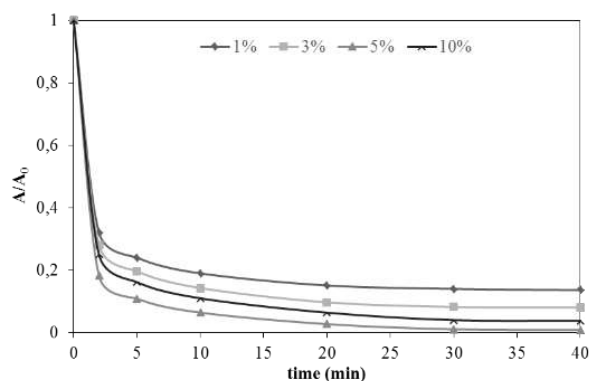


Fig. 11. Effect of H_2O_2 concentration (initial pH=3.0, $T=298\text{ K}$, $C_0=100\text{ mg/L}$, $X_0=1.0\text{ g/L}$)

Besides, the recorded UV-vis spectra during the Fenton-like degradation process was presented in Fig. 12. It showed that the solution of MB exhibited bands at 290, 610, and 665 nm that decreased rapidly and disappeared after 40 min, without the appearance of new absorption bands. Consequently, the complete degradation for decolorization of MB was achieved at the end of 40 min and the color of the MB solution altered from blue to colorless.

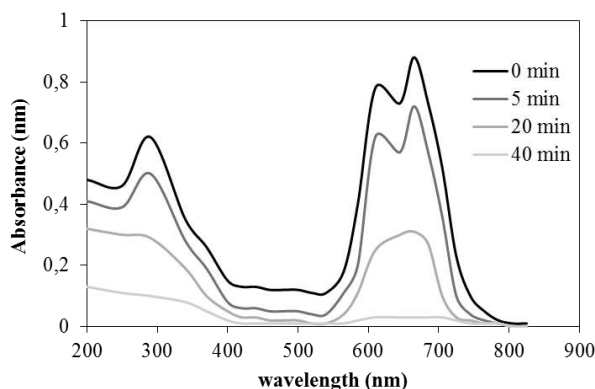


Fig. 12. UV-vis spectra of MB solution in the presence of 5.0 % H_2O_2 (initial pH=3.0, $T=298\text{ K}$, $C_0=100\text{ mg/L}$, $X_0=1.0\text{ g/L}$)

IV. CONCLUSION

In the present work, Alg/ Fe_3O_4 NPs were synthesized by using a simple and fast reduction-precipitation method and the synthesized Alg/ Fe_3O_4 NPs were characterized by FT-IR, XRD, SEM, and EDX analysis. The stretching and vibrations of O–H, O–C–O, C–O, C–C, and Fe–O were determined by FT-IR analysis. XRD analysis showed that Alg/ Fe_3O_4 NPs presented the characteristic pattern of cubic spinel structure of Fe_3O_4 . The porous structure and spherical-like structures in nanoscale of Alg/ Fe_3O_4 NPs were observed by SEM analysis. EDX analysis indicated that Alg/ Fe_3O_4 NPs had the elements of iron, oxygen, carbon, sodium, chlorine, and sulfur. Also, Alg/ Fe_3O_4 NPs were evaluated as potential adsorbents for removal of Methylene Blue from aqueous solutions in a single stage batch mode. The

adsorption studies were performed as a function of initial pH, initial dye concentration, temperature, and adsorbent concentration. The optimum conditions were obtained as follows: initial pH of 8.0, initial dye concentration of 300 mg/L, temperature of 308 K, and adsorbent concentration of 0.5 g/L. The pseudo second order kinetic model fitted quite well to the adsorption kinetic data, and both intraparticle and film diffusion were effective on the studied adsorption process. Thermodynamic parameters indicated that the adsorption was spontaneous ($\Delta G < 0$), exothermic ($\Delta H < 0$), physical ($E_a < 40\text{ kJ/mole}$), and decreasing in randomness of adsorbed species ($\Delta S < 0$). Moreover, the degradation of MB in the presence of H_2O_2 was also investigated; and it was found that the MB degradation efficiency of 99 % was achieved in 40 min. It was concluded that high removal capacities for MB with Alg/ Fe_3O_4 NPs could be achieved by both adsorption and degradation processes. Besides, Langmuir isotherm model was found as the best-described isotherm model for the adsorption equilibrium and the maximum monolayer capacity of 393.39 mg/g indicated the sufficient adsorption capability of Alg/ Fe_3O_4 NPs with respect to the other types of Fe_3O_4 nanoparticles in the literature.

REFERENCES

- [1] Y.C. Chang and D.H. Chen, "Preparation and adsorption properties of monodisperse chitosan-bound Fe_3O_4 magnetic nanoparticles for removal of Cu (II) ions," *J. Colloid. Interface Sci.*, vol. 283(2), pp. 446-451, March 2005.
- [2] W. Li, D. Wan, G. Wang, K. Chen, Q. Hu, and L. Lu, "Heterogeneous Fenton degradation of Orange II by immobilization of Fe_3O_4 nanoparticles onto Al-Fe pillared bentonite," *Korean J. Chem. Eng.*, vol. 33(5), pp. 1557-1564, May 2016.
- [3] X. Zhang, P. Zhang, Z. Wu, L. Zhang, G. Zeng, and C. Zhou, "Adsorption of methylene blue onto humic acid-coated Fe_3O_4 nanoparticles," *Colloids Surf. A Physicochem. Eng. Asp.*, vol. 435, pp. 85-90, October 2013.
- [4] C. Cao, L. Xiao, C. Chen, X. Shi, Q. Cao, and L. Gao, "In situ preparation of magnetic Fe_3O_4 /chitosan nanoparticles via a novel reduction-precipitation method and their application in adsorption of reactive azo dye," *Powder Technol.*, vol. 260, pp. 90-97, July 2014.
- [5] S. El Atouani, F. Bentiss, A. Reani, R. Zrid, Z. Belattmania, L. Pereira, L., and B. Sabour, "The invasive brown seaweed *Sargassum muticum* as new resource for alginate in Morocco: Spectroscopic and rheological characterization," *Phycological Res.*, vol. 64(3), pp. 185-193, July 2016.
- [6] A. Konwar, A. Gogoi, and D. Chowdhury, "Magnetic alginate- Fe_3O_4 hydrogel fiber capable of ciprofloxacin hydrochloride adsorption/separation in aqueous solution," *RSC Advances*, vol. 5(99), pp. 81573-81582, August 2015.
- [7] S.Y. Shaw, Y.J. Chen, J.J. Ou, and L. Ho, "Preparation and characterization of *Pseudomonas putida* esterase immobilized on magnetic nanoparticles," *Enzyme Microb. Tech.*, vol. 39(5), pp. 1089-1095, September 2006.
- [8] D. Uzunoğlu and A. Özer, "Adsorption of Acid Blue 121 dye on fish (*Dicentrarchus labrax*) scales, the extracted from fish scales and commercial hydroxyapatite: equilibrium, kinetic, thermodynamic, and characterization studies," *Desalin. Water Treat.*, vol. 57(30), pp. 14109-14131, July 2015.
- [9] L. Gonsalves, S.P. Marinov, G. Gryglewicz, R. Carleer, J. Yperman, "Preparation, characterization and application of polystyrene based activated carbons for Ni (II) removal from aqueous solution," *Fuel Process. Technol.*, vol. 149, pp. 75-85 August 2016.
- [10] E. Alver, and A.U. Metin, "Anionic dye removal from aqueous solutions using modified zeolite: Adsorption kinetics and isotherm studies," *Chem. Eng. J.*, vol. 200, pp. 59-67, August 2012.

- [11] A.A. El-Bindary, A.Z. El-Sonbati, A.A. Al-Sarawy, K.S. Mohamed, and M.A. Farid, "Adsorption and thermodynamic studies of hazardous azocoumarin dye from an aqueous solution onto low cost rice straw based carbons," *J. Mol. Liq.*, vol. 199, pp. 71-78, November 2014.
- [12] S. Shariati, M. Faraji, Y. Yamini, and A.A. Rajabi, " Fe_3O_4 magnetic nanoparticles modified with sodium dodecyl sulfate for removal of safranin O dye from aqueous solutions," *Desalination*, vol. 270(1), pp. 160-165 April 2011.
- [13] A. Ebrahimian Pirbazari, E. Saberikhah, N. Gholami Ahmad Gorabi, " Fe_3O_4 nanoparticles loaded onto wheat straw: an efficient adsorbent for Basic Blue 9 adsorption from aqueous solution," *Desalin. Water. Treat.*, vol. 57(9), pp. 4110-4121, December 2014.
- [14] L. Peng, P. Qin, M. Lei, Q. Zeng, H. Song, J. Yang, and J. Gu, "Modifying Fe_3O_4 nanoparticles with humic acid for removal of Rhodamine B in water," *J. Hazard. Mater.*, vol. 209, pp. 193-198 March 2012.
- [15] G. Kaykioglu, and E. Gunes, "Comparison of Acid Red 114 dye adsorption by Fe_3O_4 and Fe_3O_4 impregnated rice husk ash," *J Nanomater.*, July 2016.
- [16] M. Shanehsaz, S.M.R. Shoja, T. Poursaberi, S. Rouhani, and Y. Ghorbani, "Removal of Reactive Red195 Synthetic Textile Dye using Polypyrrole-coated Magnetic Nanoparticles as an Efficient Adsorbent," *JACR*, vol. 10(2), pp. 85-96, March 2016.
- [17] X. Zhang, P. Zhang, Z. Wu, L. Zhang, G. Zeng, and C. Zhou, "Adsorption of methylene blue onto humic acid-coated Fe_3O_4 nanoparticles," *Colloids Surf. A Physicochem. Eng. Asp.*, vol. 435, pp. 85-90, October 2013.
- [18] M.A. Salem, I.A. Salem, M.G. Hanfy, and A.B. Zaki, "Removal of Titan Yellow Dye From Aqueous Solution by Polyaniline/ Fe_3O_4 Nanocomposite," *Eur. Chem. Bull.*, vol. 5(3), pp. 113-118, 2016.
- [19] C.H. Weng, Y.T. Lin, C.L. Yeh, and Y.C. Sharma, "Magnetic Fe_3O_4 nanoparticles for adsorptive removal of acid dye (new coccine) from aqueous solutions," *Water Sci. Technol.*, vol. 62(4), pp. 844-851 August 2010.
- [20] A. Khataee, B. Kayan, D. Kalderis, A. Karimi, S. Akay, and M. Konsolakis, "Ultrasound-assisted removal of Acid Red 17 using nanosized Fe_3O_4 -loaded coffee waste hydrochar," *Ultrason. Sonochem.*, vol. 35, pp. 72-80, March 2017.
- [21] L. Zhou, Y. Shao, J. Liu, Z. Ye, H. Zhang, J. Ma, Y. Li, "Preparation and characterization of magnetic porous carbon microspheres for removal of methylene blue by a heterogeneous Fenton reaction," *ACS Appl. Mater. Inter.*, vol. 6(10), pp. 7275-7285, April 2014.
- [22] B. Yang, Z. Tian, L. Zhang, Y. Guo, and S. Yan, "Enhanced heterogeneous Fenton degradation of methylene blue by nanoscale zero valent iron (nZVI) assembled on magnetic Fe_3O_4 /reduced graphene oxide," *J. Water Process Eng.*, vol. 5, pp. 101-111, April 2015.

Investigation of Diffusion and Adsorption of Acetone in Building Materials by Dynamic Method

Şakir Yılmaz

Department of Chemical Engineering
Yüzüncü Yıl University
Elazığ, Turkey
sakiryilmaz@yyu.edu.tr

Cevdet Akosman

Department of Chemical Engineering
Firat University
Elazığ, Turkey
cakosman@firat.edu.tr

Abstract- Volatile Organic Compounds (VOCs) are one of the main sources of the indoor air contaminants. VOCs including acetone, toluene and methanol in building materials such as adhesives, sealants, paints, solvents, stains, carpets, vinyl flooring, wallboard and engineered woods can act to indoor air quality due to their toxic effect. For this reason, these compounds emitted by building materials are considered as a rising problem for productiveness, comfortable and healthy life. On the other hand, gypsum plasters or boards are widely used to cover the interior walls or ceilings of the residential buildings because of their properties as aesthetics, easily workable, low density, and insulating behavior. One of the most properties of gypsum plasters is a highly porous material. The diffusion and adsorption of many compounds including moisture and low molecule weight vapors found in indoor environment can cause through this property. The effective diffusivity of the compounds is a key parameter to understand the transport and/or adsorption phenomena in porous media. This study aimed to investigate the diffusion and adsorption behavior of acetone, onto various gypsum plasters (perlite plaster, thermal isolation plate plaster and machine plaster) in the one-sided single pellet at different temperature and isobaric conditions.

The experimental setup includes (1) Carrier gas tube, (2) Rotameter, (3) Sample inlet, (4) Diffusion/adsorption pellet cell, (5) Soap bubble meter, (6) TCD detector, (7) Oven, (8) GC, and (9) Recorder. The experimental runs were performed under isobaric conditions were carried out at flow rates ranging from 50-175 ml/min and at different temperatures ranging from 25 to 60 °C. The pulses of the diffusing and adsorbing tracers were injected into the carrier gas stream by using a syringe, in order to flow past the upper face of the pellet. The response peaks obtained by GC were analyzed by the moment technique. The calculation of adsorption parameters and diffusion coefficient were obtained through the moments computed by using experimental data. The results showed that the adsorption of acetone on all gypsum plasters used was found to be reversible. The results indicated that the adsorption degree of acetone on the thermal insulation plaster was the lowest value. The acetone adsorption decreased with increasing temperature while the effective diffusivities of acetone increased with increasing temperature in the gypsum plasters. Moreover, the studies revealed that the adsorption process was physical adsorption process and exothermic. The study concluded that a considerable amount of VOC (acetone) was physically adsorbed onto the building material used in this study. In addition, the diffusion of VOC likely occurs in the building materials. Moreover, the reasons such as testing of different volatile organic compounds from acetone, moisture effect on VOC diffusion and adsorption in gypsum plaster samples and binary or multi-component diffusion and adsorption can be recommended for further investigation.

Keywords— adsorption, effective diffusivities, acetone, gypsum plaster, dynamic method

Investigation of the Effect of Ammonium Persulfate Concentration on Electrochemical Polymerization of Catechol

Osman Cem Altıncı

Faculty of Engineering, Chemical Engineering Dept.,
Osmaniye Korkut Ata University,
Osmaniye, Turkey
cemaltinci@osmaniye.edu.tr

Bahadır K. Körbahti*

Faculty of Engineering, Chemical Engineering Dept.,
Mersin University,
Mersin, Turkey
korbahti@mersin.edu.tr

*Corresponding Author

Abstract— The effect of ammonium persulfate (APS) concentration on electrochemical polymerization of catechol was investigated between 2-10 g/L at 6 g/L catechol concentration and 40°C reaction temperature in 120 min reaction time. Graphite working electrode, Ag/AgCl reference electrode and platinum auxiliary electrode were used in a batch electrochemical cell. Increasing APS concentration increased the catechol removal, amount of polymer obtained and the reaction selectivity. In the study, catechol removal, amount of polymer obtained and reaction selectivity were obtained between 65.2-77.6%, 4.8-117.7 mg, and 1.3-37.6%, respectively.

Keywords— catechol; electrochemical polymerization; wastewater treatment

I. INTRODUCTION

Catechol is a phenolic compound that can be found in various industrial wastewater (Zhang *et al.*, 2010) and must be treated due to its high toxicity and hazardous properties for humans and aquatic environment. The treatment methods include adsorption, solvent extraction, and advanced oxidation methods (Zhang *et al.*, 2010; Hou *et al.*, 2015; Aktaş and Tanyolaç, 2003; Liu *et al.*, 2017; Singh and Balomajumder, 2016; Kujawski *et al.*, 2004; Yang *et al.*, 2006).

In electrochemical polymerization, monomer dissolves in supporting electrolyte solution and a potential applies to working electrode for the formation of a radical cation. Polymer films and conductive polymers can produce by electrochemical polymerization (Bao *et al.*, 2010).

The aim of this study is to investigate the effect of ammonium persulfate (APS) concentration on the removal of catechol from aqueous solutions using electrochemical polymerization.

II. METHOD

The polymerization reaction was conducted in a batch electrochemical cell that consists graphite working electrode, Ag/AgCl reference electrode and platinum auxiliary electrode using VoltaLab 40 potentiostat. The volume of the electrochemical

reactor was 100 mL. Reaction medium was mixed with a magnetic stirrer at 400 rpm. Reaction temperature was controlled with circulating water recycled from a temperature controlled water bath using a peristaltic pump.

III. RESULTS AND DISCUSSIONS

The effect of ammonium persulfate (APS) concentration was investigated between 2-10 g/L at 6 g/L catechol concentration and 40°C reaction temperature in 120 min reaction time in a batch reactor. The increasing APS concentration increased the catechol removal, the amount of polymer obtained and the reaction selectivity as outlined in Table 1.

When the APS concentration was increased from 2 g/L to 10 g/L, the catechol removal increased from 65.2% to 77.6% while the reaction temperature and initial catechol concentration were held constant. Reaction selectivity increased from 1.3% to 37.6% that indicates the decrease of the amount of reaction by-products. Increasing APS concentration increased the polymer mass and as a result catechol removal was increased.

Table 1. Effect of initial APS concentration on electrochemical polymerization catechol.

APS (g/L)	Catechol removal (%)	Polymer (mg)	Reaction selectivity (%)
2	65.2	4.8	1.3
6	66.0	51.1	17.1
10	77.6	117.7	37.6

The FTIR spectrum and SEM images of the catechol polymer can be seen in Figures 1 and 2.

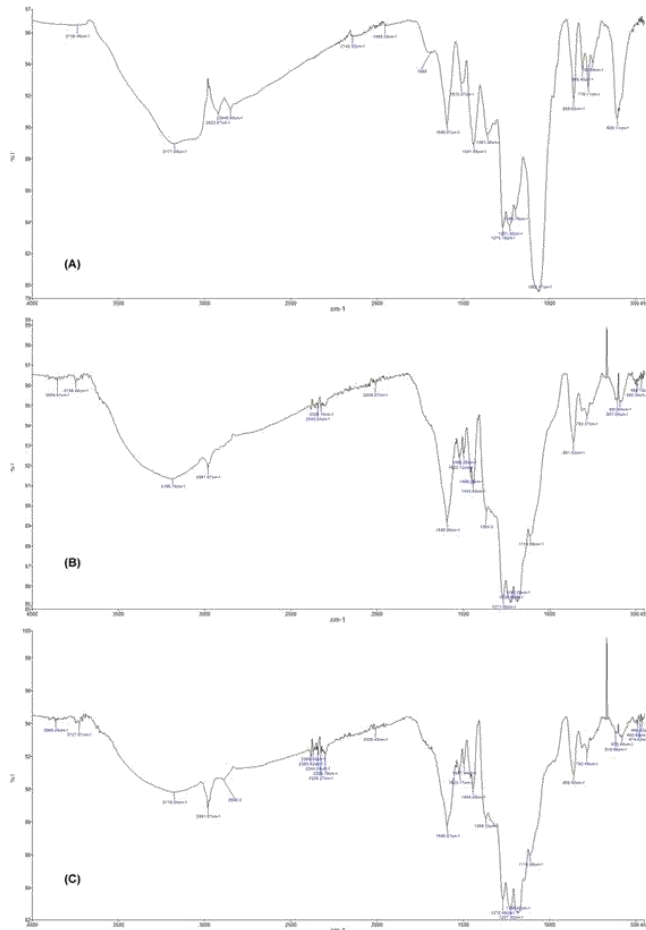


Figure 1. FTIR spectrum of catechol polymer. (A) APS=2 g/L, (B) APS=6 g/L, (C) APS=10 g/L.

In Figure 1, increasing APS concentration increased the OH stretching at 3700 cm^{-1} and the broad band at 3200 cm^{-1} was extended. A new peak was observed at 700 cm^{-1} with the increase of APS concentration and the peak at 1690 cm^{-1} was disappeared with increasing APS concentration to 10 g/L .

Aktaş and Tanyolaç (2003) produced catechol by oxidative polymerization using laccase enzyme. They reported 3370 cm^{-1} broad band phenolic -OH bond, aromatic $\text{C}=\text{C}$ bond peaks at 1400 cm^{-1} and 1600 cm^{-1} , C-O-C bond peaks at 1260 cm^{-1} and 1050 cm^{-1} , and $=\text{C-H}$ bond peaks at 810 cm^{-1} and 920 cm^{-1} . The obtained homogenous polymeric structures are seen in Figure 2B and 2C. The increase in the APS concentration showed positive effect on the formation of polymer chains whereas the aggregated polymeric structure can be seen in Figure 2A.

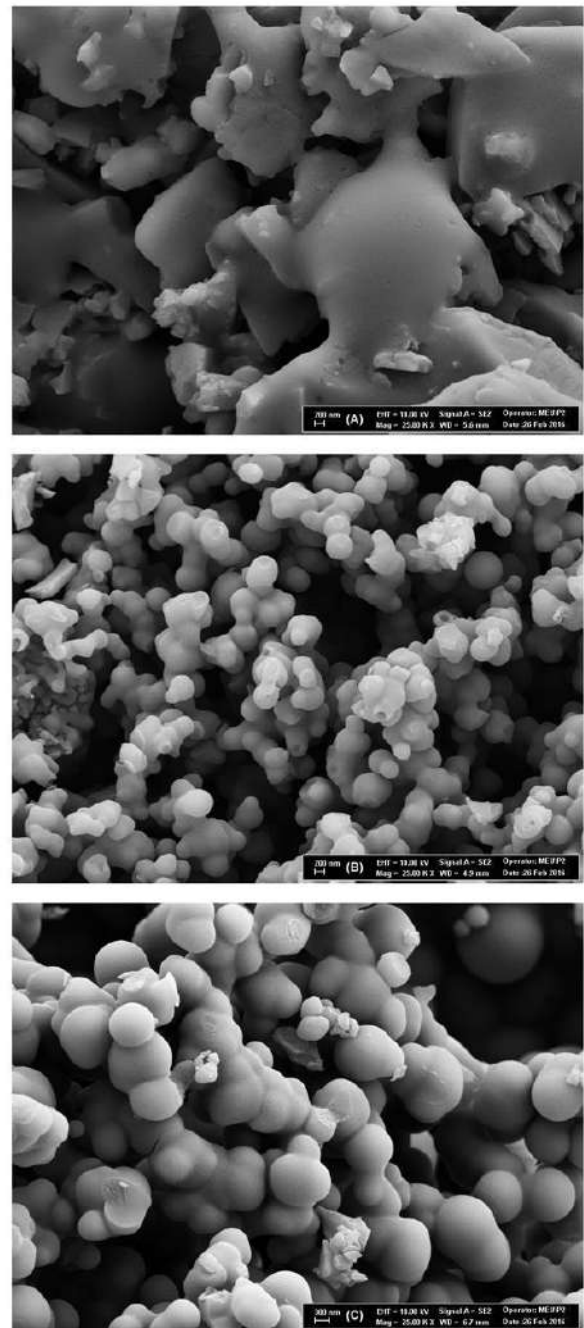


Figure 2. SEM images of catechol polymer (X25000). (A) APS=2 g/L, (B) APS=6 g/L, (C) APS=10 g/L.

IV. CONCLUSION

The effect of ammonium persulfate (APS) concentration on electrochemical polymerization of catechol in aqueous solutions was investigated in this study. The increasing APS concentration increased the catechol removal, the amount of polymer obtained and the reaction selectivity. In the study, catechol removal, amount of polymer obtained and reaction selectivity were obtained between 65.2-77.6%, 4.8-117.7 mg, and 1.3-37.6%, respectively. The results of this study indicated that ammonium persulfate (APS) could be used as an effective initiator for the electrochemical polymerization of catechol.

ACKNOWLEDGMENT

This project was supported by Mersin University Scientific Research Projects Center (MEÜ BAP) with Grant No. 2015-TP2-1039.

REFERENCES

- [1] Aktaş, N., Tanyolaç, A., 2003, "Reaction conditions for laccase catalyzed polymerization of catechol", *Bioresource Technology*, 87, 209-214.
- [2] Bao, L., Xiong, R., Wei, G., 2010, "Electrochemical polymerization of phenol on 304 stainless steel anodes and subsequent coating structure analysis", *Electrochimica Acta*, 55, 4030-4038.
- [3] Hou, C.H., Huang, S.C., Chou, P.H., Den, W., 2015, "Removal of bisphenol A from aqueous solutions by electrochemical polymerization on a carbon aerogel electrode", *Journal of the Taiwan Institute of Chemical Engineers*, 51, 103-108.
- [4] Kujawski, W., Warszawski, A., Ratajczak, W., Porebski, T., Capała, W., Ostrowska, I., 2004, "Application of pervaporation and adsorption to the phenol removal from wastewater", *Separation and Purification Technology*, 40, 123-132.
- [5] Liu, X., Yin, H., Lin, A., Guo, Z., 2017, "Effective removal of phenol by using activated carbon supported iron prepared under microwave irradiation as a reusable heterogeneous Fenton-like catalyst", *Journal of Environmental Chemical Engineering*, 5, 870-876.
- [6] Singh, N., Balomajumder, C., 2016, "Simultaneous removal of phenol and cyanide from aqueous solution by adsorption onto surface modified activated carbon prepared from coconut shell", *Journal of Water Process Engineering*, 9, 233-245.
- [7] Yang, C., Qian, Y., Zhang, L., Feng, J., 2006, "Solvent extraction process development and on-site trial-plant for phenol removal from industrial coal-gasification wastewater", *Chemical Engineering Journal*, 117, 179-185.
- [8] Zhang, Y., Li, Q., Zhai, J., 2010, "Removal of phenols from the aqueous solutions based on their electrochemical polymerization on the polyaniline electrode", *Electrochimica Acta*, 55, 7219-7224.

Photocatalytic Degradation of Reactive Red 195 in Aqueous Solution by UV/ZnO Process

Veyis SELEN

Department of Bioengineering

Firat University

Elazig, TURKEY

vselen@firat.edu.tr

Gülbeyi DURSUN

Department of Chemical Engineering

Firat University

Elazig, TURKEY

gdursun@firat.edu.tr

Abstract— In the world, many countries produce chemical materials such as dyes, hydrocarbons, phenolic compounds, rubber, plastics and pesticides. Dyes are one of the highest toxic, carcinogenic, hazardous and bulk produced compounds discharged into rivers, lakes and coastal areas, which are not degradable in its case [1]. Since the textile dye industry consumes large quantities of clean water and produces large volume of waste water from different steps in processing operations including dyeing, printing, pre-treatment and so on, environmental purification of dye has increasingly become a global concern calling for considerable attention. In recent decade, many researchers and strategists wanted to remove these pollutants by using traditional methods such as physical, biological and chemical and also advanced oxidation process (AOP) for degradation or a least to remove from the medium [2-4]. However, the traditional methods are often costly and can cause secondary pollution thus limiting large-scale using. Therefore, innovation efforts for creating a cost-effective and green solution have been passion for everyone in earth which provide us fresh water supply in an economic manner. That is why more efficient and economic methods such as AOP and the others need to be developed [5].

In this study, the photocatalytic degradation of C.I. Reactive Red (RR195) was studied using UV-C radiation in the presence of ZnO semiconductor (0.0-5.0 g/L; Figure 1.) as a function of initial dye concentration of RR195 (150-550 mg/L), air feed rate (0.0-1.0 L/min; Figure 2.) and temperature (283-323 K). It was found that the photodegradation efficiency was affected by the amount of ZnO, initial dye concentration, air feed rate and temperature of the solution. The color removal rate is faster in low initial dye concentration and also increased with increasing ZnO dosage, air feed rate and temperature increase.

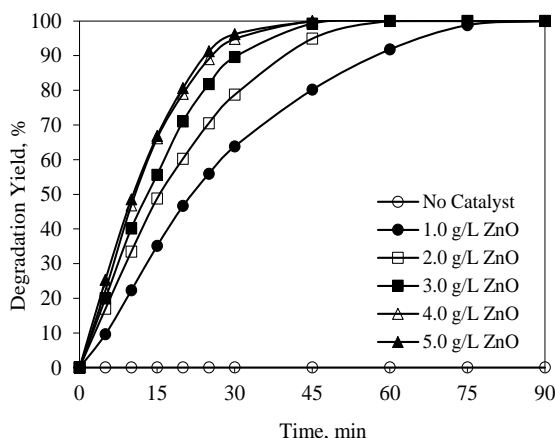


Figure 1. Effect of ZnO amount (Conditions: 250 mg/L RR195; 0.5 L/min aeration rate; pH_{in} = 5.6 (natural pH of dye solution); 293 K reaction temperature; 1000 rpm mixing rate).

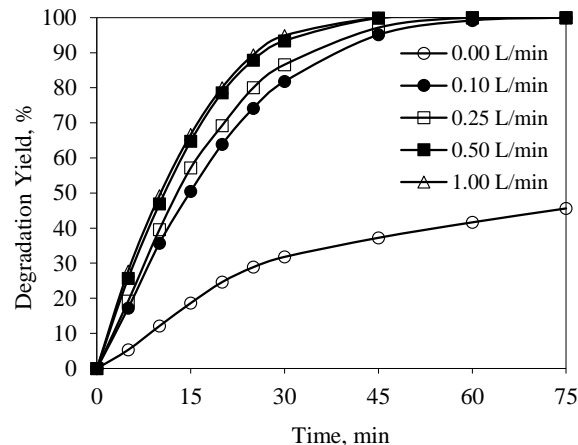


Figure 2. Effects of Aeration Rate (Conditions: 250 mg/L RR195; 4.0 g/L ZnO; pH_{in} = 5.6 (natural pH of dye solution); 293 K reaction temperature; 1000 rpm mixing rate).

The degradation of RR195 increase with the increasing ZnO, air feed rate and temperature but decrease with initial RR195 concentration. The efficiency values of photocatalytic degradation process of the RR195 dye at 30 minutes reaction time were 100, 94.8, 79.1, 57.3 and 46.2 % for the initial dye concentration values of 150, 250, 350, 450 and 550 mg/L respectively, at the conditions of 4.0 g/L ZnO; 0.5 L/min aeration rate; pH_{in} = 5.6 (natural pH of RR195 solution); 293 K reaction temperature; 1000 rpm mixing rate.

A comparison of the maximum photocatalytic activity of ZnO with other catalysts is shown in Table 1.

Table 1. Comparison of photocatalytic degradation of dyes using various photocatalysts.

Photocatalyst	Dye	Deg., %	Reference
Ti-SBA-15	Methylene Blue	80.0	[6]
N-TiO ₂	Rhodamine B	33.0	[7]
TiO ₂ (P25)	Rhodamine B	67.0	[7]
TiO ₂ thin films	Reactive Blue 19	87.0	[8]
TiO ₂ thin films	Reactive Yellow 17	93.0	[8]
TiO ₂ (P25)	Rhodamine 6G	84.4	[9]
ZnO	Reactive Red 195	99.9	This study

Keywords—component; Photocatalytic Degradation, Ractive Red 195, UV-C, ZnO.

REFERENCES

- M.S. Lucas, P.B. Tavares, J.A. Peres, J.L. Faria, M. Rocha, C. Pereira, C. Freire, "Photocatalytic degradation of Reactive Black 5 with TiO₂-coated magnetic nanoparticles," *Catalyst Today*, vol. 209, pp. 116-121, 2013.
- V.K. Gupta, R. Jain, S. Agarwal, A. Nayak, M. Shrivastava, "Photodegradation of hazardous dye quinoline yellow catalyzed by TiO₂," *Journal of Colloid and Interface Science*, vol. 366, pp. 135-140, 2012.
- V. Selen, O. Guler, D. Ozer, E. Evin, "Synthesized multi-walled carbon nanotubes as a potential adsorbent for the removal of methylene blue dye: kinetics, isotherms, and thermodynamics," *Desalination and Water Treatment*, vol. 57, pp. 8826-8838, 2016.
- D. Ozer, G. Dursun, A. Ozer, "Methylene blue adsorption from aqueous solution by dehydrated peanut hull," *Journal of Hazardous Materials*, vol. 144, pp. 171-179, 2007.
- T.S. Jiang, L. Zhang, M.R. Ji, Q. Zhao, X.Q. Fu, H.B. Yin, "Carbon nanotubes/TiO₂ nanotubes composite photocatalysts for efficient degradation of methyl orange dye," *Particuology*, vol. 11, pp. 737-742, 2013.
- S.K. Das, M.K. Bhunia, A. Bhaumik, "Highly ordered Ti-SBA-15: efficient H₂ adsorbent and photocatalyst for eco-toxic dye degradation," *Journal of Solid State Chemistry*, vol. 183, pp. 1326-1333, 2010.
- A. Charanpahari, S.S. Umare, R. Sasikala, "Visible light active N doped GeO₂ for the photodegradation of both anionic and cationic dyes," *Catalysis Communications*, vol. 40, pp. 9-12, 2013.
- N. Fagnern, R. Leotphayakkarat, C. Chawengkijwanich, M.P. Gleeson, N. Koonsaeng, S. Sanguanruang, "Effect of titanium-tetraisopropoxide concentration on the photocatalytic efficiency of nanocrystalline thin films TiO₂ used for the photodegradation of textile dyes," *Journal of Physics and Chemistry of Solids*, vol. 73, pp. 1483-1486, 2012.
- T.K. Ghorai, N. Biswas, "Photodegradation of rhodamine 6G in aqueous solution via SrCrO₄ and TiO₂ nano-sphere mixed oxides," *Journal of Materials Research and Technology*, vol. 2, pp. 10-17, 2013.

Investigation of the Chemical Exergy of Torrefied lignocellulosic fuels using Artificial Neural Networks

Ugur ÖZVEREN

Chemical Engineering Department
Marmara University
Istanbul, Turkey
ugur.ozveren@marmara.edu.tr

Ömer Faruk DİLMAÇ

Chemical Engineering Department
Çankırı Karatekin University
Çankırı, Turkey
omerfarukdl@yahoo.com

Mehmet Selçuk MERT

Energy Systems Engineering Department
Yalova University
Yalova, Turkey
msmert@yalova.edu.tr

Fatma KARACA ALBAYRAK

Chemical Engineering Department
Marmara University
Istanbul, Turkey
fatma.karaca@marmara.edu.tr

Abstract— Torrefaction is a type of thermo-chemical pretreatment process to enhance energy density of lignocellulosic fuels. For a torrefaction process, a key challenge is to develop efficient thermal conversion technologies for torrefied fuels which can compete with fossil fuels. The calculation of chemical exergy is an essential step for designing efficient thermal conversion systems. However, there is a few correlation to predict the chemical exergy of solid fuels has been published so far. This study deals with a new method to characterize the chemical exergy of different kinds of torrefied lignocellulosic fuels by using Bayesian trained artificial neural network (ANN). The proposed model based on proximate analysis and higher heating values of torrefied fuels. Use of the artificial neural network method is encouraged to reduce variance in model results. The results indicate that the proposed model offers a high degree of correlation ($R^2=0.9999$) and its robustness and capability to compute the chemical exergy of any torrefied lignocellulosic fuels from its proximate analysis and heating value.

Keywords: Lignocellulosic fuels, chemical exergy, proximate analysis, neural networks.

I. INTRODUCTION

Environmental and economic concerns of fuel supply have been motivating the torrefied fuel for thermal conversion systems. Torrefaction is a thermochemical process in which raw biomass is heated under atmospheric pressure, at a temperature range of 200–300 °C, in the absence of oxygen or under low oxygen concentrations[1]. An efficient technology for torrefaction process which can produce torrefied fuel to substitute fossil fuels is a key challenge. Exergy analysis is commonly accepted as the most natural way to evaluate the performance of different processes and calculation of chemical exergy is the first step of exergy evolution [2] However, there is a few correlation to predict the chemical exergy of solid fuels have been published so far. These correlations are based on

ultimate analysis of fuels. However, the ultimate analysis requires very expensive equipment and highly trained analysts. The proximate analysis on the other hand only requires standard laboratory equipment and can be run by any competent scientist or engineer [3].

Artificial neural network is an effective alternative of linear and nonlinear correlations in that they can represent highly complex and nonlinear processes. Furthermore, they are quite flexible and robust against input noise and, once developed and their coefficients determined, they can provide a rapid response for a new input [4].

In this study, a new artificial neural network model was developed to evaluate the chemical exergy of torrefied biomass fuel, which is based on higher heating value and torrefied fuel content obtained by proximate analysis.

II. MATERIAL AND METHODS

A. Sample

The data of 116 torrefied biomass samples with their proximate and ultimate analysis were taken from the study of Daya Ram Nhuchhen [5], who acquired the data from previous studies in this field [6-16]. In order to develop a predictive model, the dataset used in this study was divided into two parts: the first part for training the model and the second for assessing the estimation capability of the obtained neural network architecture (called the “testing set”). All 116 torrefied biomass samples as well as a split of the samples into a training set with 97 samples and a testing set with 19 samples were randomly selected by using the MATLAB software. Description of torrefied biomass samples was given Table 1.

TABLE I. TORREFIED BIOMASS SAMPLES [5]

	Minimum (%)	Maximum (%)
Oxygen (% DAF*)	7.23	44.35
Nitrogen (%DAF)	0.00	2.65
Hydrogen (%DAF)	3.24	7.50
Carbon (%DAF)	49.25	88.50
Total sulfur (%DAF)	0.00	0.26
VM (%DAF)	15.71	87.37
FC (%DAF)	12.67	84.29
HHV (MJ/kg)	16.63	33.30

*DAF = Dry Ash free VM: Volatile Matter HHV: Higher Heating Value

In order to validate the artificial neural network model, untorrefied biomass samples from the study of Chun-Yang Yin[17] also were tested to measure the extensity of the proposed exergy model in this study. Description of biomass samples used in this study for 23 samples was given Table 2.

TABLE II. BIOMASS SAMPLES

	Minimum (%)	Maximum (%)
Oxygen (% DAF*)	33.02	48.99
Nitrogen (%DAF)	0.30	5.49
Hydrogen (%DAF)	4.49	7.34
Carbon (%DAF)	42.26	56.73
Total sulfur (%DAF)	0.02	0.85
VM (%DAF)	71.38	87.16
FC (%DAF)	12.84	28.57
HHV (MJ/kg)	15.09	21.95

*DAF = Dry Ash free VM: Volatile Matter HHV: Higher Heating Value

B. Artificial Neural Networks

An ANN is a massively parallel-distributed information processing system that simulates the functions of neurons using artificial neurons inspired from the studies of the brain and the nervous system[18]. An artificial neuron is the fundamental processing element of ANN and can be implemented in many different ways. The general architecture of an artificial neuron is shown in Fig. 1 [18, 19].

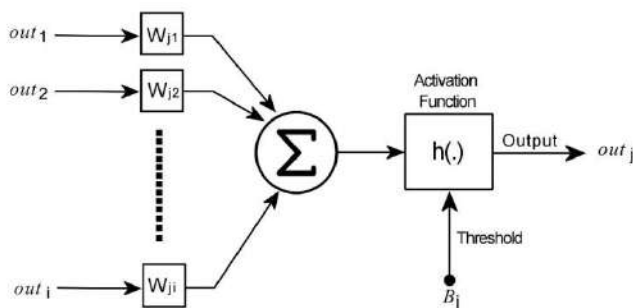


Fig. 1. Architecture of an artificial neuron

In this figure, input from the output (out_i) of the preceding layer neuron is multiplied by its weight value (W_{ji}). Then,

results of these multiplications are summed with bias value (B_j). The initial weights and biases are usually assigned randomly. The output of a neuron, which is in Fig. 1, can be described by Eq. (1).

$$out_j = h(\sum_{i=1}^N (W_{ji}X_i + B_j)), \quad (1)$$

where h is the activation (transfer) function. The activation function can be found in different forms, either linear or non-linear. In this work, logarithmic sigmoid, $h(x)$, function was used as an activation function which defines as:

$$h(x) = 1/(1+\exp(-2*x)) \quad (2)$$

Bayesian methods are the ideal methods for solving learning problems of neural network [20], which can automatically select the regularization parameters and integrate the properties of high convergence speed of traditional BP and prior information of Bayesian statistics [21]. The Bayesian Regularization method changes the error performance function by attaching a standard deviation of the weights and the thresholds [22] and can be expressed by [23]:

$$F = \beta E_D + \alpha E_w \quad (3)$$

where α and β are the regularization parameters.

Using (Eqn. 3) to minimize the performance error, enables the network to possess less weights and thresholds. This is equivalent to reducing the size of the network in such a way that it can respond smoothly, thus reducing overfitting [23].

C. ANN Model

The exergy value of a solid fuel is related to higher heating values and proximate analysis. Therefore, the correlation between the exergy values of torrefied fuels and their proximate analysis with higher heating values has been examined to develop an artificial neural network model. There are several classes of neural network architectures, classified according to a number of layers, neurons, and their interconnections. In this paper, we adopt a single-output three layered BP neural network with Bayesian regularization to predict the dry ash free based chemical exergy (e_{DAF}^{CH}) of the torrefied fuels. Fig. 2 presents the neural network structure of proposed model.

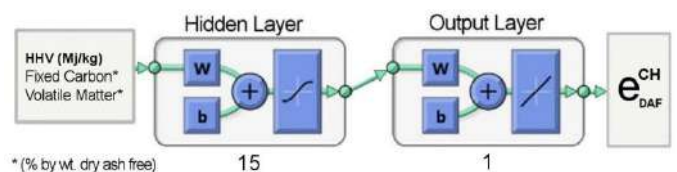


Fig.2. ANN Model

D. Validation of the correlations

In this study, Coefficient of determination (R^2) is employed to assess correlations for the chemical exergy of torrefied biomass, which is computed as follows:

$$R^2 = \left(\frac{\sum_{i=1}^n (x_i - \bar{x})(y_i - \bar{y})}{\sqrt{\sum_{i=1}^n (x_i - \bar{x})^2} \sqrt{\sum_{i=1}^n (y_i - \bar{y})^2}} \right)^2 \quad (4)$$

Where y and x denote the estimated and calculated values, respectively. \bar{y} is the predicted average while, \bar{x} is the calculated average value. R^2 is used as a universal parameter to measure the accuracy of any model. A higher R^2 value means a better estimation and fitting.

III. RESULTS AND DISCUSSIONS

In order to use an artificial neural network model, one needs first to train the proposed model with training dataset. Fig.3 showed the quality of fit between the chemical exergy values and predicted chemical exergy values of torrefied fuels.

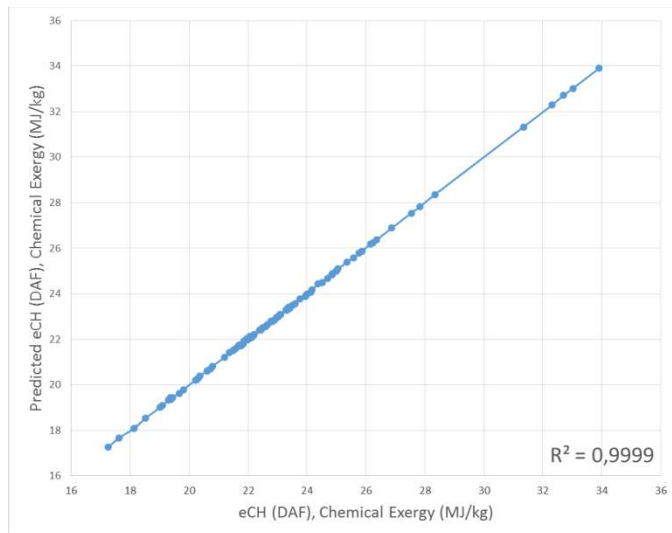


Fig.3. Training dataset

The artificial neural network model was tested for reliability using the testing dataset (Fig. 4).

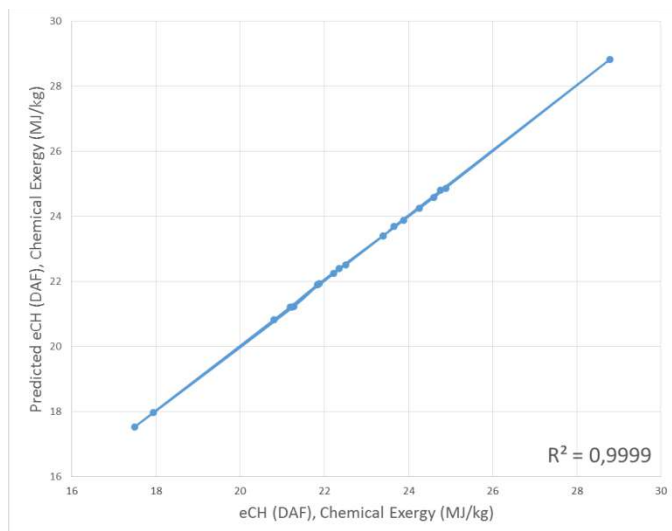


Fig. 4. Test dataset

In this study, a high degree of correlation ($R^2 = 0.9999$) between actual and predicted chemical exergy was observed, as shown in Fig. 4, for test datasets of the torrefied lignocellulosic fuels. It can thus be apprehensible that the ANN model used in this study possesses chemical exergy prediction of good torrefied biomass accuracies and generalization performance.

To ensure the capability and predictive ability of the model, biomass fuel dataset also were used for the robustness of the proposed model. Fig. 5 shows the parity plots of the chemical exergy values and the corresponding ones estimated by the model in this study.

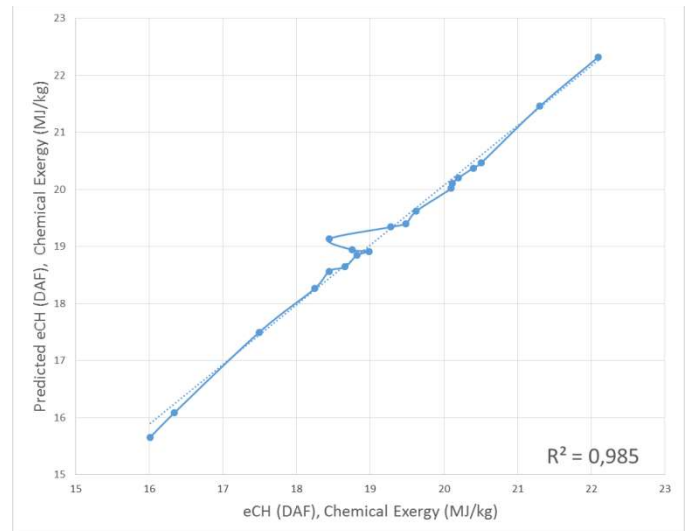


Fig. 5. Biomass Samples

IV. CONCLUSIONS

A model for chemical exergy prediction of lignocellulosic fuels was developed using artificial neural networks. The high R^2 values and the good fit in testing dataset lead to the conclusion that the artificial neural network model provides accurate predictions of the chemical exergy for a variety of torrefied lignocellulosic fuels. The major advantage of this model is its capability to compute chemical exergy of any torrefied fuels simply from its proximate analysis instead of ultimate analysis. Thereby provides a useful tool for exergy analysis of thermal conversion processes.

REFERENCES

- [1] P. Rousset, C. Aguiar, N. Labbe, and J. M. Commandre, "Enhancing the combustible properties of bamboo by torrefaction," *Bioresour Technol*, vol. 102, pp. 8225-8231, Sep 2011.
- [2] G. H. Song, L. H. Shen, and J. Xiao, "Estimating Specific Chemical Exergy of Biomass from Basic Analysis Data," *Industrial & Engineering Chemistry Research*, vol. 50, pp. 9758-9766, Aug 17 2011.
- [3] J. Parikh, S. A. Channiwala, and G. K. Ghosal, "A correlation for calculating HHV from proximate analysis of solid fuels," *Fuel*, vol. 84, pp. 487-494, Mar 2005.

- [4] I. Estiati, F. B. Freire, J. T. Freire, R. Aguado, and M. Olazar, "Fitting performance of artificial neural networks and empirical correlations to estimate higher heating values of biomass," *Fuel*, vol. 180, pp. 377-383, Sep 15 2016.
- [5] D. R. Nhuchhen, "Prediction of carbon, hydrogen, and oxygen compositions of raw and torrefied biomass using proximate analysis," *Fuel*, vol. 180, pp. 348-356, Sep 15 2016.
- [6] R. H. H. Ibrahim, L. I. Darvell, J. M. Jones, and A. Williams, "Physicochemical characterisation of torrefied biomass," *Journal of Analytical and Applied Pyrolysis*, vol. 103, pp. 21-30, Sep 2013.
- [7] J. G. Pohlmann, E. Osorio, A. C. F. Vilela, M. A. Diez, and A. G. Borrego, "Integrating physicochemical information to follow the transformations of biomass upon torrefaction and low-temperature carbonization," *Fuel*, vol. 131, pp. 17-27, Sep 1 2014.
- [8] M. Pala, I. C. Kantarli, H. B. Buyukisik, and J. Yanik, "Hydrothermal carbonization and torrefaction of grape pomace: A comparative evaluation," *Bioresource Technology*, vol. 161, pp. 255-262, Jun 2014.
- [9] D. Eseltine, S. S. Thanapal, K. Annamalai, and D. Ranjan, "Torrefaction of woody biomass (Juniper and Mesquite) using inert and non-inert gases," *Fuel*, vol. 113, pp. 379-388, Nov 2013.
- [10] J. Wannapeera and N. Worasuwanarak, "Upgrading of woody biomass by torrefaction under pressure," *Journal of Analytical and Applied Pyrolysis*, vol. 96, pp. 173-180, Jul 2012.
- [11] T. G. Bridgeman, J. M. Jones, A. Williams, and D. J. Waldron, "An investigation of the grindability of two torrefied energy crops," *Fuel*, vol. 89, pp. 3911-3918, Dec 2010.
- [12] B. Arias, C. Pevida, J. Feroso, M. G. Plaza, F. Rubiera, and J. J. Pis, "Influence of torrefaction on the grindability and reactivity of woody biomass," *Fuel Processing Technology*, vol. 89, pp. 169-175, Feb 2008.
- [13] J. Wannapeera, B. Fungtammasan, and N. Worasuwanarak, "Effects of temperature and holding time during torrefaction on the pyrolysis behaviors of woody biomass," *Journal of Analytical and Applied Pyrolysis*, vol. 92, pp. 99-105, Sep 2011.
- [14] S. D. Soponpongpiat N, Sae-Ueng U., "Higher heating value prediction of torrefaction char produced from non-woody biomass," *Front Energy*, vol. 9, pp. 461-471, 2015.
- [15] M. Strandberg, I. Olofsson, L. Pommer, S. Wiklund-Lindstrom, K. Aberg, and A. Nordin, "Effects of temperature and residence time on continuous torrefaction of spruce wood," *Fuel Processing Technology*, vol. 134, pp. 387-398, Jun 2015.
- [16] D. Y. Chen, J. B. Zhou, Q. S. Zhang, X. F. Zhu, and Q. Lu, "Upgrading of Rice Husk by Torrefaction and its Influence on the Fuel Properties," *Bioresources*, vol. 9, pp. 5893-5905, Nov 2014.
- [17] C. Y. Yin, "Prediction of higher heating values of biomass from proximate and ultimate analyses," *Fuel*, vol. 90, pp. 1128-1132, Mar 2011.
- [18] U. Ozveren, "An artificial intelligence approach to predict a lower heating value of municipal solid waste," *Energy Sources Part a-Recovery Utilization and Environmental Effects*, vol. 38, pp. 2906-2913, 2016.
- [19] L. V. Fausett, *Fundamentals of neural networks : architectures, algorithms, and applications*. Englewood Cliffs, NJ: Prentice-Hall, 1994.
- [20] B. G. Heydecker and J. Wu, "Identification of sites for road accident remedial work by Bayesian statistical methods: an example of uncertain inference," *Advances in Engineering Software*, vol. 32, pp. 859-869, Oct-Nov 2001.
- [21] Z. Sun, Y. Chen, X. Y. Li, X. L. Qin, and H. Y. Wang, "A Bayesian regularized artificial neural network for adaptive optics forecasting," *Optics Communications*, vol. 382, pp. 519-527, Jan 1 2017.
- [22] X. Li and D. S. Wang, "A Sensor Registration Method Using Improved Bayesian Regularization Algorithm," *International Joint Conference on Computational Sciences and Optimization, Vol 2, Proceedings*, pp. 195-199, 2009.
- [23] R. V. A. Monteiro, G. C. Guimaraes, F. A. M. Moura, M. R. M. C. Albertini, and M. K. Albertini, "Estimating photovoltaic power generation: Performance analysis of artificial neural networks, Support Vector Machine and Kalman filter," *Electric Power Systems Research*, vol. 143, pp. 643-656, Feb 2017.

Comparison of the properties of chitosan hydrogel and cryogel

Seda CEYLAN

Bioengineering Department, Adana Science and Technology University, Adana, Turkey

Didem DEMİR, Nimet BÖLGEN KARAGÜLLE

Chemical Engineering Department, Mersin University

Mersin, Turkey

nimetbolgen@yahoo.com

Abstract— *The architecture of scaffolds is important for tissue engineering applications. Because, scaffolds should have high porosity with interconnected pore structure to ensure cellular penetration and adequate diffusion of nutrients.*

In this study, chitosan was used to produce scaffolds in the form of hydrogel and cryogel. Hydrogels are mainly prepared by crosslinking polymerization of monomers at room temperature. On the other hand, the cryogelation technique is based on the crosslinking of polymers at sub zero temperatures. The aim of this study was to investigate the effect of system temperature on the final properties of the scaffold. Chitosan based scaffolds with a fixed polymer concentration of %1 (w/v) were prepared by adding the polymers in %6 (v/v) acetic acid solution. Three different temperatures (+25 °C, 0 °C and -25 °C) have been used to prepare scaffolds; chemical and physical structure of the scaffolds were analysed by FTIR and SEM; swelling and degradation profiles were followed. The results suggest that system temperature has significant effects on the characteristics of the chitosan gels.

Keywords— *Cryogel, Hydrogel, Scaffolds, Chitosan*

Estimating the Chemical Exergy of Coal Using Nonlinear Model

Ugur ÖZVEREN
Chemical Engineering Department
Marmara University
Istanbul, Turkey
ugur.ozveren@marmara.edu.tr

Fatma KARACA ALBAYRAK
Chemical Engineering Department
Marmara University
Istanbul, Turkey
fatma.karaca@marmara.edu.tr

Abstract—Chemical exergy is an influential parameter in the assessment of any fuel value as an indicator of the stored energy. Therefore, the determination of chemical exergy is the initial step in an application of any power plant. In this study, a model was developed to evaluate the chemical exergy of coal which was based on higher heating value and proximate analysis. The statistical validation shows that the proposed model in this study is reliable and accurate.

Keywords— Coal, chemical exergy, proximate analysis, nonlinear regression.

I. INTRODUCTION

Coal is a crucial energy source because of its low procurement costs attributed to a significant amount of recoverable reserves and stable supply [1].

The chemical exergy of coal is an important property in designing, operating and optimizing coal-based thermal processes. The exergy value can be utilized as a tool for the assessment of energy quantity as well as quality in thermolysis process using operational data at different conditions. There exist thermodynamics models based on the known homogeneous organic substances. Coal has unknown structure and chemical composition. Therefore, coal exergy value cannot be calculated directly [2].

Rant is one of the first researchers proposed the correlation of a semi-empirical formula to predict the exergy content of solid fuels [3, 4]. Szargut and Styrylska [5] improved Rant's equation and showed the ratio of exergy correlations depends significantly on the chemical composition of fuels. The correlation was commonly used for evaluation of chemical exergy of solid fuels in previous works. However, the states of some organic compounds had been mistaken in Szargut's source data, and the correlations do not involve the effect of sulfur on solid fuels [2]. Shieh and Fan [6] proposed a correlation to estimate the specific chemical exergy of a structurally complicate fuels. Stepanov modified Shieh and Fan model and applied the entropy model developed by Ikumi et al [7]. Bilgen and Kaygusuz [8] improved Stepanov's correlation for the estimation of the chemical exergy of coals by using the entropy model from the study of Eisermann et al [9].

In this study, we developed a new exergy correlation based on proximate analysis and higher heating value. The study aims to provide a simple model for the calculation of chemical exergy of coal.

II. METHOD

A. Sample

The coal data for this work is acquired from the study of Chelgani et. al [10]. A training set of 708 coal samples and a testing set of 177 coal samples were randomly selected by using the MATLAB software. The training dataset was employed for generation of the coal exergy model. Description of coal samples from the study was given in Table I [10].

Table 1. Coal samples [10]

	Minimum (%)	Maximum (%)
Oxygen (% DAF*)	0.43	14.74
Hydrogen (%DAF)	3.56	6.79
Carbon (%DAF)	72.28	88.6
Total sulfur (%DAF)	0.35	14.54
VM (%DAF)	27.72	54.95
HHV (MJ/kg)	26.43	36.92

*DAF = Dry Ash free VM: Volatile Matter HHV: Higher Heating Value

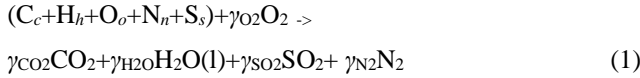
To choose the best suitable correlations, Turkish Lignites [11] also were tested to measure the accuracy of the proposed coal exergy model in this study. Description of Turkish Lignites data used in this study for 13 samples was given Table II.

Table 2. Turkish Lignites [11]

	Minimum (%)	Maximum (%)
Oxygen (% DAF*)	12.80	45.80
Hydrogen (%DAF)	4.20	7.30
Carbon (%DAF)	45.30	76.90
Total sulfur (%DAF)	0.10	7.20
VM (%DAF)	47.59	71.23
HHV (MJ/kg)	8.20	23.00

B. Chemical Exergy of Coal

Through a complete combustion at the reference state, the basis of 1 kg of DAF coal entering the control volume reacts with oxygen to produce carbon dioxide, water, nitrogen, and sulfur dioxide; that is,



where c, h, o, n, and s, each in kmol/kg (DAF), balancing the reaction equation, we have

$$\gamma_{CO_2} = c, \quad (2)$$

$$\gamma_{H_2O} = (1/2)h, \quad (3)$$

$$\gamma_{SO_2} = s, \quad (4)$$

$$\gamma_{N_2} = (1/2)n, \quad (5)$$

$$\gamma_{O_2} = c + (1/4)h + s - (1/2)o \quad (6)$$

For this case, chemical exergy equation takes the form [12]:

$$e_{DAF}^{CH} = (HHV)_{DAF} - T_0 [s_{DAF} + \gamma_{O_2} \bar{s}_{O_2} - \gamma_{CO_2} \bar{s}_{CO_2} - \gamma_{H_2O} \bar{s}_{H_2O} - \gamma_{SO_2} \bar{s}_{SO_2} - \gamma_{N_2} \bar{s}_{N_2}] + [\gamma_{CO_2} e_{CO_2}^{CH} + \gamma_{H_2O} e_{H_2O}^{CH} + \gamma_{SO_2} e_{SO_2}^{CH} + \gamma_{N_2} e_{N_2}^{CH} - \gamma_{O_2} e_{O_2}^{CH}] \quad (7)$$

The data of standard molar chemical exergy and absolute entropy of various pure substances at $T_0 = 298.15$ K and $p_0 = 1$ atm are presented in Table III [12].

Table 3. Standard molar chemical exergy and absolute entropy of pure substances [12]

Substances	$s^0/\text{kJ kmol}^{-1} \text{K}^{-1}$	$e^{\text{ch}}/\text{kJ kmol}^{-1}$
O ₂ (g)	205.15	3951
CO ₂ (g)	213.79	14176
SO ₂ (g)	284.09	301939
N ₂ (g)	191.61	639
H ₂ O (l)	69.95	45
H ₂ O (g)	188.82	8636

The absolute entropy for the dry and ash free coal can be estimated, in kJ/kgK, as follows [9]:

$$s_{DAF} = c[37.1653 - 31.4767 \exp(-0.564682 \frac{h}{c+n}) + 20.1145 \frac{o}{c+n} + 54.3111 \frac{n}{c+n} + 44.6712 \frac{s}{c+n}] \quad (8)$$

C. Validation of the correlations

In this study, three statistical parameters are employed to assess correlations for the chemical exergy of coal, which are computed as follows:

$$R^2 = \left(\frac{\sum_i^n (x_{cal,i} - \bar{x}_{cal})(x_{est,i} - \bar{x}_{est})}{\sqrt{\sum_i^n (x_{cal,i} - \bar{x}_{cal})^2} \sqrt{\sum_i^n (x_{est,i} - \bar{x}_{est})^2}} \right)^2 \quad (9)$$

$$\text{Average bias error (ABE)} = \frac{1}{n} \sum_{i=1}^n \frac{x_{est,i} - x_{cal,i}}{x_{cal,i}} \cdot 100 \quad (10)$$

$$\eta: \text{Relative Error} = \frac{|x_{est} - x_{cal}|}{x_{cal}} \quad (11)$$

where x_{est} and x_{cal} denote the estimated and calculated values, respectively. \bar{x}_{cal} is the calculated average value, while \bar{x}_{est} is the estimated average value. Statistical parameters are used as a universal parameter to measure the accuracy of the coal exergy model. A higher R^2 and lower ABE with η value means a better estimation and fitting.

III. RESULTS AND DISCUSSIONS

A. Predictive Model

The exergy value of a solid fuel is related to higher heating values and proximate analysis. Therefore, the correlation between the standard exergy values of coals and their proximate analyses with higher heating values has been examined to develop a new model. The correlation of the exergy values of coal can be represented as:

$$e_{DAF}^{CH} = \gamma_1 x_{HHV} + \gamma_2 x_{FC} + \gamma_3 x_{VM} \quad (12)$$

Where the coefficients from γ_1 to γ_3 denote the regression coefficients corresponding to the higher heating value (MJ/kg) and dry ash free components of coal proximate analyses: Fixed carbon and volatile matter, respectively. The model equation was solved in MATLAB using the fitlm function for the optimization of the values of the model coefficients. The fitted model was found as follows:

$$e_{DAF}^{CH} = 0.957420HHV + 0.034952FC + 0.010809VM \quad (13)$$

The specific chemical exergy of coal can be calculated by using the developed model (Eq. 14), in MJ/kg, as follows [12]:

$$e^{CH} = 0.791e_{DAF}^{CH} + \frac{0.1112}{18.015} e_{H_2O(l)}^{CH} \quad (14)$$

B. Validation of Proposed Model

To develop a generalized and unified exergy model, the training dataset was only utilized for the training of the nonlinear model. Fig.1 showed the quality of fit between the specific coal exergy values and predicted specific coal exergy values.

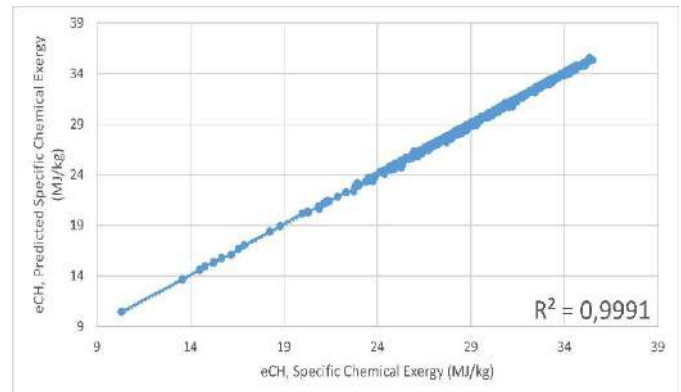


Fig.1. Training dataset

A high degree of correlation ($R^2 = 0.9991$) between actual and predicted coal exergy values was observed, as shown in Fig.1, for training datasets. The average bias error from estimating the training dataset for coal samples was only 0.29%.

To confirm the reliability of the proposed model, the testing datasets containing all 177 samples selected by using the MATLAB software were examined.

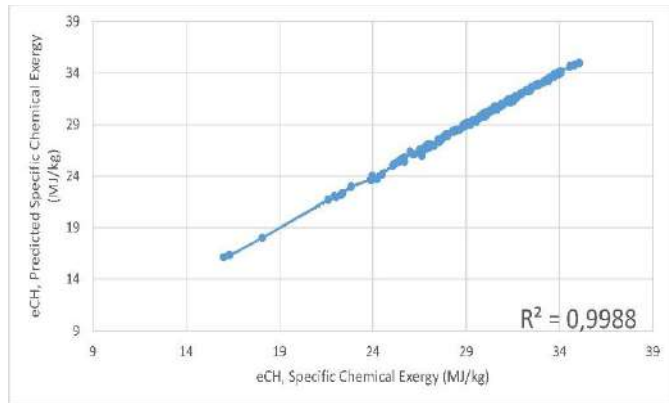


Fig. 2. Testing dataset

As shown in Fig. 2, the coefficient of determination (R^2) value was calculated as 0.9988. The average bias error from estimating the testing dataset for U.S. coals is only 0.32%. The results show that the equation provides a simple way to obtain a good prediction for the specific exergy values.

To ensure the robustness of the proposed correlation for calculating the exergy of any coal sample, Turkish Lignite datasets containing all 13 samples also were used for the predictive ability of the produced model. Fig. 3 shows the parity plots of the specific exergy values for Turkish Lignites and the corresponding ones predicted by the model in this study.

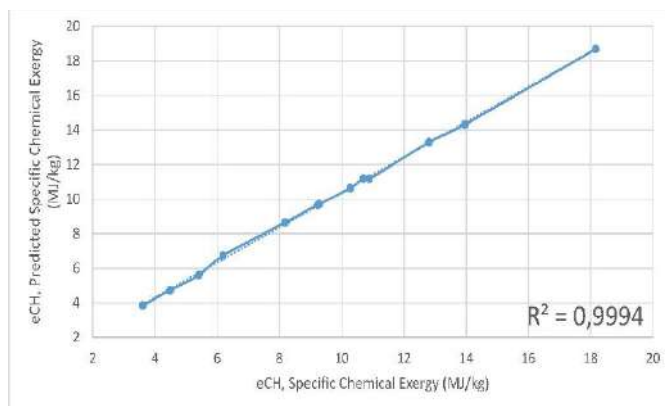


Fig. 3. Turkish Lignite dataset

Turkish Lignites is considered to be of poor quality because of its high ash and moisture content. The correlation coefficient

(R^2) for Turkish Lignites in Fig. 3 is 0.9994. Table IV shows the relative errors for Turkish Lignites between predicted specific chemical exergy versus calculated values.

Table 4. Comparison of specific chemical exergies of turkish lignites

e^{CH} (MJ/Kg)	Predicted e^{CH} (MJ/Kg)	η
10.2731	10.6354	0.0353
9.2240	9.6658	0.0479
12.8007	13.2940	0.0385
10.8916	11.1699	0.0256
9.2772	9.7054	0.0462
18.1617	18.6896	0.0291
8.1748	8.6461	0.0577
5.4063	5.5973	0.0353
6.1808	6.7235	0.0878
3.6039	3.8435	0.0665
4.4808	4.7250	0.0545
10.6934	11.1915	0.0466
13.9583	14.3215	0.0260

* η : Relative Error

The model is very sensitive to fixed carbon and volatile matter content with higher heating value. According to Table 4, it can thus be apprehensible that the model used in this study possesses excellent chemical exergy prediction accuracies and generalization performance.

IV. CONCLUSIONS

Some correlations are currently available to calculate chemical exergy of coal. Typical drawbacks of these equations are the determination of elemental analyses. The key merit of the proposed model in this study is an easy and robust method to predict the specific chemical exergy, when sophisticated measurement for ultimate analysis is not available. Furthermore, this approach can be easily applied via simple calculation.

REFERENCES

- [1] M. Muto, K. Yuasa, and R. Kurose, "Numerical simulation of ignition in pulverized coal combustion with detailed chemical reaction mechanism," *Fuel*, vol. 190, pp. 136-144, Feb 15, 2017.
- [2] F. C. Eboh, P. Ahlstrom, and T. Richards, "Estimating the specific chemical exergy of municipal solid waste," *Energy Science & Engineering*, vol. 4, pp. 217-231, May 2016.
- [3] Z. Rant, "Towards the estimation of specific exergy of fuels," *Allg Wärmetechn*, vol. 10, pp. 172-176, 1961.
- [4] V. S. Stepanov, "Chemical-Energies and Energies of Fuels," *Energy*, vol. 20, pp. 235-242, Mar 1995.
- [5] J. S. Szargut, T., "Approximate evaluation of the exergy of fuels," *Brennstoff Waerme Kraft*, vol. 16, pp. 589-596, 1964.
- [6] J. H. Shieh and L. T. Fan, "Estimation of Energy (Enthalpy) and Exergy (Availability) Contents in Structurally Complicated Materials," *Energy Sources*, vol. 6, pp. 1-45, 1982.
- [7] S. Ikumi, C. D. Luo, and C. Y. Wen, "A Method of Estimating Entropies of Coals and Coal Liquids," *Canadian Journal of Chemical Engineering*, vol. 60, pp. 551-555, 1982.
- [8] S. Bilgen and K. Kaygusuz, "The calculation of the chemical exergies of coal-based fuels by using the higher heating values," *Applied Energy*, vol. 85, pp. 776-785, Aug 2008.

- [9] W. Eisermann, P. Johnson, and W. L. Conger, "Estimating Thermodynamic Properties of Coal, Char, Tar and Ash," *Fuel Processing Technology*, vol. 3, pp. 39-53, 1980.
- [10] S. C. Chelgani, S. Mesroghli, and J. C. Hower, "Simultaneous prediction of coal rank parameters based on ultimate analysis using regression and artificial neural network," *International Journal of Coal Geology*, vol. 83, pp. 31-34, Jul 1 2010.
- [11] H. Haykiri-Acma, S. Yaman, S. Kucukbayrak, and M. H. Morcali, "Does blending the ashes of chestnut shell and lignite create synergistic interaction on ash fusion temperatures?," *Fuel Processing Technology*, vol. 140, pp. 165-171, Dec 2015.
- [12] A. Bejan, G. Tsatsaronis, and M. J. Moran, *Thermal design and optimization*. New York: Wiley, 1996.

Optimization with Response Surface Methodology of Green Synthesis Conditions of Silver Nanoparticles as an Antibacterial Agent

Semra Arslantürk, Deniz Uzunoğlu, Ayla Özer
Mersin University, Department of Chemical Engineering,
Mersin, Turkey
semra_008@hotmail.com, denizuzunoglu4@gmail.com,
ayozer4@gmail.com

Esma Eser, H. İbrahim Ekiz
Mersin University, Department of Food Engineering,
Mersin, Turkey
esmaeser@mersin.edu.tr, hiekiz@gmail.com

Abstract— In the present work, the synthesis of silver nanoparticles (AgNPs) through a green synthesis method using avocado (*Persea americana*) leaf as a biological reductant and capping agent. The synthesized AgNPs were characterized by zetasizer, FTIR, UV-vis spectrophotometer, XRD, and SEM. Also, response surface methodology was used to understand and optimize the effect of the experimental parameters on the green synthesis of AgNPs. Three experimental parameters were chosen as independent variables: temperature, AgNO₃ concentration and aqueous leaf extract volume. A quadratic model was established as a functional relationship between three independent variables and the effective hydrodynamic diameter (nm) of AgNPs. The results of model fitting and statistical analysis demonstrated that only AgNO₃ concentration was statistically significant parameter. The optimum conditions for minimum effective hydrodynamic diameter (nm) of AgNPs (32.74 nm) were temperature of 25 °C, AgNO₃ concentration of 0.001 M, and aqueous leaf extract volume of 50 mL. Moreover, the antibacterial activities of AgNPs for *S. typhimurium*, *E. coli* O157:H7, *S. aureus*, and *L. monocytogenes* were tested and it was found that AgNPs had stronger inhibitory effects on growth of *L. monocytogenes* than the other bacteria.

Keywords—antibacterial activity, avocado leaf, optimization, response surface methodology, silver nanoparticles

I. INTRODUCTION

Silver nanoparticles (AgNPs) are amongst the crucial metallic nanomaterials that have become the focus of much investigation interest due to their unique optical, electrical, and biological properties which makes them to be used in various application areas such as catalysis, water treatment, electronics, biomedical, agriculture, food industry (packaging), accessories, animal husbandry, cosmetics, military, and textile industry. Besides, AgNPs are of significant interest in the area of especially biological systems, living organisms, and medicine because they are regarded safe and nontoxic inorganic antibacterial agents, which have been described as

“oligodynamic” due to its ability to exhibit bactericidal effect at even low concentrations [1]. There are various synthesis methods of metallic nanomaterials that include physical, chemical, and biological routes like sonochemical reduction,

microwave assisted process, hydrothermal synthesis, electrochemical method, reverse micelles/microemulsion method, green synthesis, and chemical reduction [2]. Among these methods, physical and chemical processes generally require to use of expensive and hazardous chemicals as well as high energy (high pressure and/or temperature). However, in the green synthesis method, environmental-friendly and biocompatible reagents are used in order to minimize the toxicity of the resulting nanomaterials and the environmental impact of the byproducts [3]. The basis of the green synthesis method is the reduction from the metal salt with the aid of the biological agents such as plant, algae, bacteria, and fungi. It is generally preferred to use plants, renewable sources, as reducing and capping agents for the nanoparticle synthesis because the green synthesis method using plants eliminates process of cell culturing and also it is a simple, efficient and low cost route [1]. Besides, the investigation of the effects of experimental conditions on the nanoparticle synthesis have become very important research area in order to understand and interpret the synthesis mechanisms. For this purpose, the optimization analysis could be evaluated by the traditional and statistical techniques. The optimization by the traditional ‘one-factor-at-a-time’ technique, where a single factor is varied while others are kept constant, requires a considerable amount of work and time; hence, an alternative statistical optimization techniques like response surface methodology (RSM) have been developed. The conventional optimization technique do not take into account the possible interaction of various

independent factors while RSM can be used to evaluate the relationship between a set of controllable experimental factors and observed results with limited number of experiments [4].

The aim of the present work is to synthesize of AgNPs by a fast, simple (one-step), environmental-friendly, and low-cost route using avocado (*Persea americana*) leaf, which acts as both reducing and stabilizing agent. Also, the effect of experimental conditions on the green synthesis of AgNPs was investigated with response surface methodology (RSM), the most widely used statistical technique for process optimization. Moreover, the antibacterial activity of AgNPs was tested against common foodborne pathogens such as *S. typhimurium*, *E. coli* O157:H7, *S. aureus*, and *L. monocytogenes*.

II. MATERIALS AND METHODS

A. Green Synthesis and Characterization of AgNPs

Extraction from avocado (*Persea americana*) leaves: The aqueous leaf extract, as a biological reducing and capping agent, was prepared for the green synthesis of AgNPs. For this purpose; 10 g of the purified and dried avocado (*Persea americana*) leaves were boiled in 500 mL of distilled water at 100 °C for 5.0 h. After cooling at room temperature, the brown aqueous leaf extract was filtered using by Whatman no. 1 filter paper and then it was stored in a refrigerator at +4 °C.

Synthesis and Characterization of AgNPs: The required volume of the aqueous leaf extract was added to 100 mL of AgNO₃ at the required concentration in the conical flasks. Then, they were shaken in an agitation vessel at constant temperature for 1 h. They were allowed to stand at the reaction temperature for 1.0 day to be accomplished the synthesis. After that, the resulting mixture was centrifuged at 4000 rev/min for 10 min and the precipitated AgNPs were washed with distilled water. They were dried at 110 °C in an oven for 24 h, and were stored at +4 °C in the refrigerator [5]. The characterization studies of AgNPs were performed by zetasizer (Malvern, UK) using Dynamic Light Scattering (DLS) technique, Fourier Transform Infrared Spectrometer (FTIR- Perkin Elmer, Shelton), X-ray Diffractometer (XRD- Philips XPert, Netherlands), and Scanning Electron Microscope (SEM- Zeiss/Supra 55, Germany).

B. Experimental Design and Optimization using Response Surface Methodology

The face centered central composite design (CCD) with free Minitab 17 software (Minitab Inc.) for the response surface methodology (RSM) was employed to optimize the experimental conditions such as temperature, AgNO₃ concentration, and aqueous leaf extract volume for green synthesis of AgNPs. The ranges and levels of the independent variables for the experimental design strategy were presented in Table I while the experimental design along with the responses for the effect of three independent variables in 20 sets of experiments was shown in Table II.

THE RANGES AND LEVELS OF THE INDEPENDENT VARIABLES

Symbol	Independent variable	Coded levels		
		Low (–1)	Center (0)	High (+1)
A	Temperature (°C)	25	45	65
B	AgNO ₃ concentration (M)	0.0010	0.0505	0.1000
C	Aqueous leaf extract volume (mL)	10	30	50

In the optimization process, the responses can be simply related to chosen factors by linear or quadratic models. A quadratic model, which also includes the linear model, is given as [6];

$$Y = b_0 + b_1A + b_2B + b_3C + b_{11}A^2 + b_{22}B^2 + b_{33}C^2 + b_{12}AB + b_{13}AC + b_{23}BC \quad (1)$$

where Y represents the response of the effective hydrodynamic diameter (nm) of AgNPs, where b₀ is intercept term, b₁, b₂, and b₃ are linear coefficients, b₁₁, b₂₂, and b₃₃ are quadratic coefficients, b₁₂, b₁₃, and b₂₃ are interactive coefficients, and the independent variables are coded A, B, and C. The interaction between the independent variables and the responses was tested by using ANOVA and the effect of the variables was also evaluated with response surface graphs.

THE EXPERIMENTAL DESIGN WITH THE OBTAINED RESPONSES

Run order	Independent variables			Response Y
	A	B	C	
1	25	0.1000	10	127.56
2	65	0.0010	50	44.00
3	45	0.0010	30	48.00
4	65	0.0505	30	66.18
5	25	0.0010	10	43.41
6	25	0.0505	30	55.00
7	65	0.0010	10	46.75
8	45	0.0505	30	60.82
9	45	0.0505	10	73.69
10	65	0.1000	10	140.00
11	25	0.0010	50	35.27
12	45	0.0505	30	61.00
13	45	0.0505	50	52.00
14	45	0.0505	30	61.51
15	65	0.1000	50	132.00
16	45	0.0505	30	62.77
17	45	0.0505	30	63.91
18	45	0.1000	30	96.10
19	25	0.1000	50	74.40
20	45	0.0505	30	61.68

C. Antibacterial Activity of AgNPs

Bacteria selection: In this study, *Escherichia coli* (O157:H7), *Listeria monocytogenes*, *Staphylococcus aureus* and *Salmonella typhimurium* bacteria species were selected for determining of antibacterial activities of AgNPs because they are common foodborne pathogens. Also they are used here as representative gram positive (*Listeria monocytogenes*, *Staphylococcus aureus*) and gram negative (*Escherichia coli* (O157:H7), *Salmonella typhimurium*) pathogens.

Culture and Inoculum Preparation: *Escherichia coli* (O157:H7), *Listeria monocytogenes*, *Staphylococcus aureus* and *Salmonella typhimurium* cultures were obtained from the Microbiology Laboratory of Food Engineering Department of Mersin University. The bacterial cultures were grown on TSA slants and kept at 4°C. Isolated colonies obtained from the TSA slants were inoculated into TSB medium. The broth culture was incubated at 37°C for 24 h. The optical density of the culture was adjusted between 0.08 to 0.1 at 625 nm to obtain inoculum size of 1×10^7 colony-forming unit (CFU)/mL.

Antibacterial Activity: Antimicrobial susceptibility was tested by the agar disk diffusion method on Mueller Hinton Agar. Surface of agar plate was inoculated by spreading of the test microorganism over entire surface. Then, antimicrobial discs with the diameter of 6 mm were treated with AgNPs solution and the excess solution was removed from discs. The Petri dishes are incubated at 37°C for 24 h. The test compound diffuses into the agar and inhibits the growth of the test microorganism. The diameters of inhibition growth zones are measured with a digital caliper.

III. RESULTS AND DISCUSSION

Optimization of Experimental Conditions of Green Synthesis of AgNPs

The effects of experimental conditions such as temperature, AgNO₃ concentration, and aqueous leaf extract volume on green synthesis of AgNPs were investigated by using RSM according to CCD. The experimental results were evaluated and the empirical relationship between the independent variables and the effective hydrodynamic diameter (nm) of AgNPs (Y) was given in Eq. 2:

$$Y = 78.6 - 0.79 A + 25 B - 1.475 C + 0.0046 A^2 + 5434 B^2 + 0.0103 C^2 + 7.32 AB + 0.01580 AC - 6.35 BC \quad (2)$$

The statistical significance of the quadratic model equation was evaluated by F-test for analysis of variance (ANOVA) and the results of ANOVA were presented in Table III. As can be seen from Table III, the model F-value of 31.36 and P-value<0.0001 indicated that the model was statistically significant. Besides, the independent variable B, AgNO₃ concentration, was the only significant term (P-value<0.0001) for the quadratic model. The R² of 0.9658 was in conceivable agreement with the R²_{adj} of 0.9350. Adequate precision measures the signal (response) to noise (deviation) ratio, and a ratio greater than 4 is required. The ratio of 7.7034 implied an adequate signal and the quadratic model can be used to navigate the design space [6]. Consequently, this quadratic model could be used for the purpose of predicting future responses successfully for the green synthesis of AgNPs.

ANOVA RESULTS OF THE QUADRATIC MODEL

Source	Degree of freedom	Sum of squares	Mean squares	F-value	P-value	Remarks
Model	9	16749.4	1861.0	31.36	<0.0001	Significant

Linear	3	14183.8	4727.9	79.67	<0.0001	Significant
A	1	870.3	870.3	14.67	0.003	
B	1	12434.8	12434.8	209.54	<0.0001	Significant
C	1	878.7	878.7	14.81	0.003	
Square	3	1510.2	503.4	8.48	0.004	
AA	1	9.5	9.5	0.16	0.698	
BB	1	487.5	487.5	8.22	0.017	
CC	1	46.4	46.4	0.78	0.397	
2-way interaction	3	1055.4	351.8	5.93	0.014	
AB	1	420.1	420.1	7.08	0.024	
AC	1	319.4	319.4	5.38	0.043	
BC	1	315.9	315.9	5.32	0.044	
Error	10	593.4	59.3			
Lack of fit	5	586.5	117.3	84.26	<0.0001	Significant
Pure error	5	7.0	1.4			
Total	19	17342.8				

R²=0.9658; R²_{adj}=0.9350; Adequate precision=7.7034

The plot of the standardized residuals vs predicted effective hydrodynamic diameter (nm) of AgNPs was presented in Fig. 1. As can be seen from Fig. 1, it exhibited nearly a funnel-shaped pattern because the variance of the response depended on the mean level of Y, thus suggesting no need for transformation of the response variable [6].

Fig. 2 showed that the points of data were close to a straight line (R²=0.9658), which indicated a good correlation between the predicted and experimental responses. Also, it could be concluded that the chosen quadratic model was acceptable for the experimental data of the green synthesis of AgNPs [7].

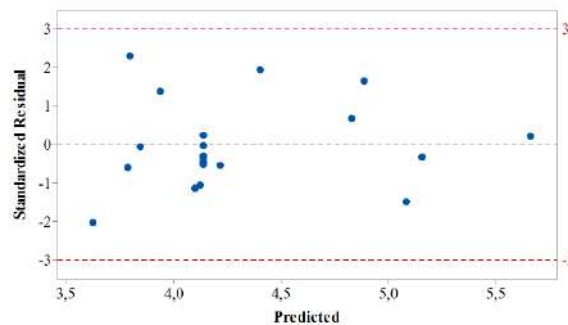


Fig. 1. The standardized residual vs predicted effective hydrodynamic diameter (nm) of AgNPs plot

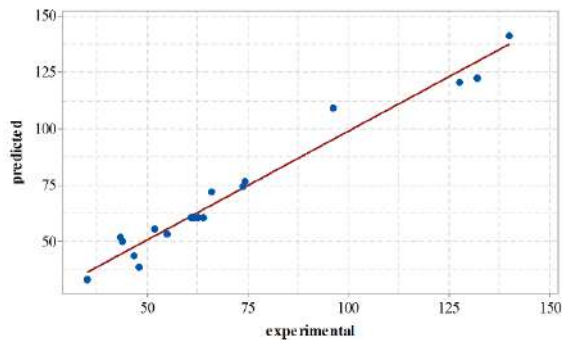


Fig. 2. The experimental and predicted plot for the green synthesis of AgNPs

The optimum effective hydrodynamic diameter (nm) of AgNPs was predicted as 32.7370 nm at temperature (A) of 25 °C, AgNO₃ concentration (B) of 0.001 M, and aqueous leaf extract volume (C) of 50 mL from the quadratic model. In order to investigate the interaction among the variables, 3D response surfaces were plotted on the basis of the model equation (Fig. 3. a-c). According to Fig. 3; as expected from ANOVA, only AgNO₃ concentration (B) significantly affected the effective hydrodynamic diameter of AgNPs. As B increased, the effective hydrodynamic diameter increased resulting from the substantially agglomeration of the AgNPs at high AgNO₃ concentrations. Also, temperature and aqueous leaf extract volume were not significant model parameters but it could be said that the effective hydrodynamic diameter slightly increased with increase in temperature while it decreased with increase in aqueous leaf extract volume. This could be explained as follows; the increase in the temperature raised the kinetic energy of the AgNPs, thereby resulting the collision frequency between the nanoparticles and this led to the increase in agglomeration [8]. Also, at high volumes of aqueous leaf extract, the biomolecules in the leaf extract acted as reducing agents and capped the nanoparticles protecting them from aggregation [9].

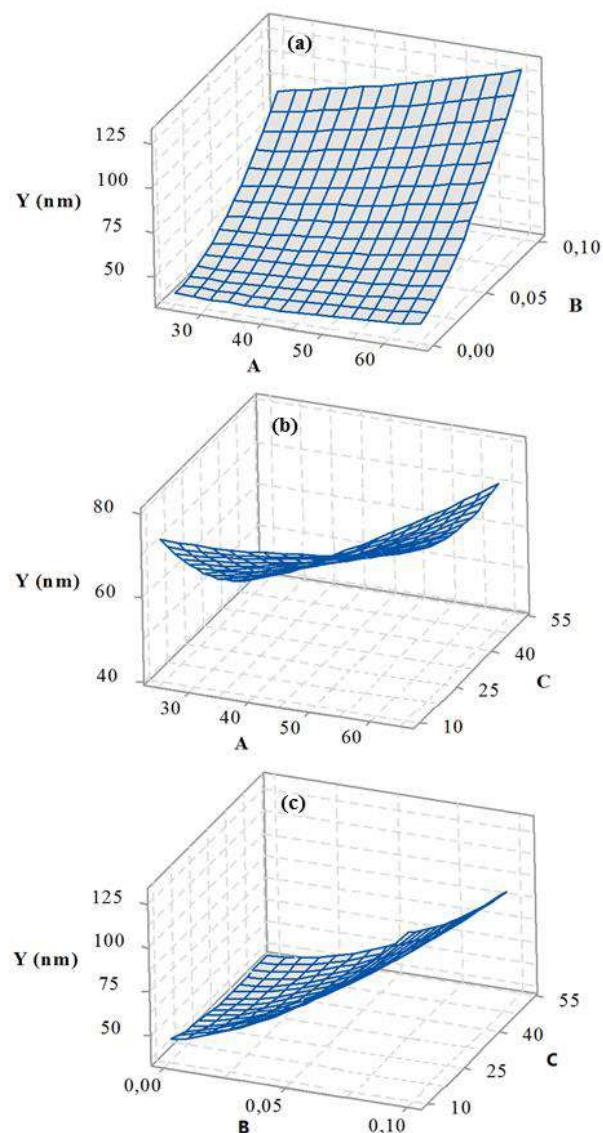


Fig. 3. Response surface plots of the model showing the effective hydrodynamic diameter (nm) of AgNPs as a function (in coded levels) of: a. temperature and AgNO₃ concentration, b. temperature and aqueous leaf extract volume, c. AgNO₃ concentration and aqueous leaf extract volume

Characterization of AgNPs

The formation of AgNPs was firstly noted by visual observation of the color of AgNO₃-aqueous leaf extract solution and then the UV-vis spectra of the solutions were performed against pure water with 1 mm optical path length quartz cuvette. Fig. 4 presented that the color of the solution altered from light brown to dark brown by the time of synthesis progress indicating silver nanoparticle formation due to the surface plasmon resonance (λ_{SPR} , nm) phenomenon. Also, as shown in Fig. 4, a characteristic and well-defined λ_{SPR} value for AgNPs was recorded at nearly 430 nm whereas AgNO₃ solution (for control) did not exhibit any characteristic peak.

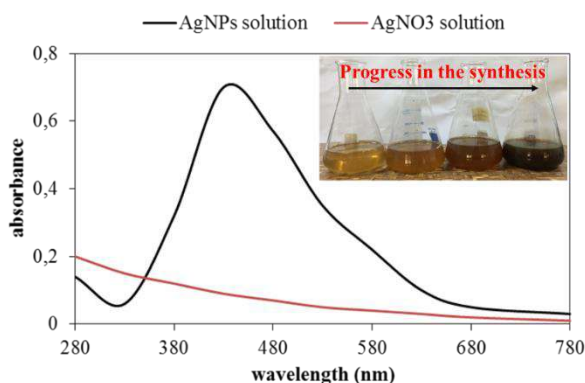


Fig. 4. UV-vis spectra of AgNPs and AgNO₃ solutions along with the color change upon formation of silver nanoparticles

Besides, the values of λ_{SPR} were recorded for the run orders of 5 (A=25 °C, B=0.001 M, and C=10 mL), 7 (A=65 °C, B=0.001 M, and C=10 mL), 11 (A=25 °C, B=0.001 M, and C=50 mL), 15 (A=65 °C, B=0.1 M, and C=50 mL), and 19 (A=25 °C, B=0.1 M, and C=50 mL) and it was presented in Fig. 5.

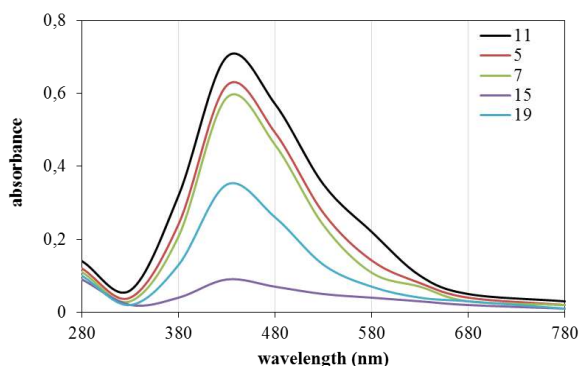


Fig. 5. UV-vis spectra of AgNPs solution at different experimental conditions

As seen from Fig. 5, λ_{SPR} values were also observed at around 430 nm, which was the characteristic peak of AgNPs. Mainly, the sharp and narrow peak shows the stable and smaller formation of nanoparticles in the homogeneous distribution [9]. Hence, it can be seen from Fig. 5 that the maximum λ_{SPR} value, indicating the formation of smallest nanoparticles, was detected for the run order of 11, the optimum synthesis conditions. Consequently, the decrease in λ_{SPR} with increase in temperature and AgNO₃ concentration, and with decrease in aqueous leaf extract volume could be attributed to the decrease in the diameters of AgNPs. These observations confirmed the ANOVA results.

In the green synthesis method, +1 valent silver ion in AgNO₃ structure is reduced to zero valent silver, silver nanoparticles (AgNPs), with the aid of the various compounds in the aqueous leaf extract such as proteins, amino acids, organic acids, vitamins, flavonoids, alkaloids, polyphenols,

terpenoids, and polysaccharides. In order to determine the functional groups of AgNPs, FT-IR analysis was performed and it was presented in Fig. 6. O–H group in polyphenols or proteins/enzymes or polysaccharide (3400 cm⁻¹), =C–H alkenes (2980 cm⁻¹), –COOH carbonyl group (1630 cm⁻¹), –C–H alkane (1387 cm⁻¹), C–N stretch aliphatic amines (1091 cm⁻¹), C–N amines (1005 cm⁻¹), C–C bending (660 cm⁻¹) peaks were observed from FT-IR spectra of AgNPs. These FTIR peaks confirmed that the aforementioned compounds in the aqueous leaf extract played important roles in the reduction of Ag¹⁺ (AgNO₃) into Ag⁰ (AgNPs) [10, 11].

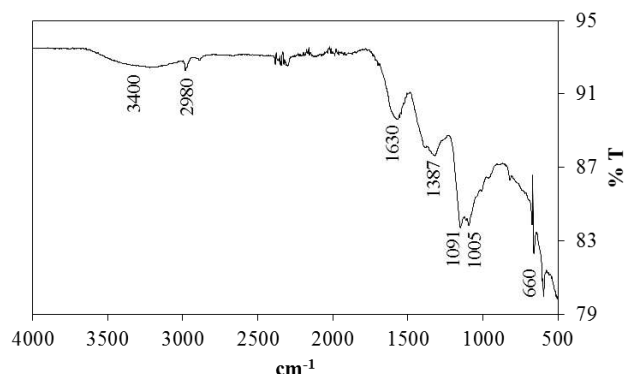


Fig. 6. FT-IR spectra of AgNPs

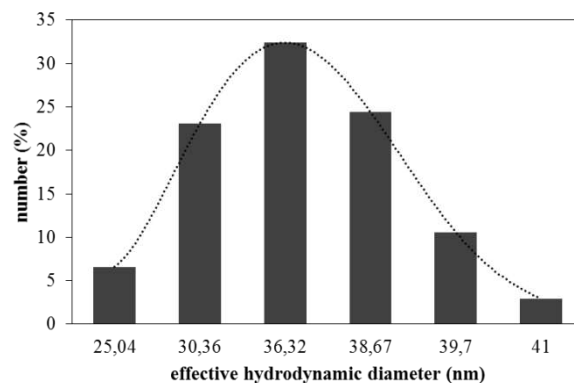


Fig. 7. The distribution of effective hydrodynamic diameters of AgNPs

At the optimum synthesis conditions (A=25 °C, B=0.001 M, and C=50 mL), the distribution of effective hydrodynamic diameters of AgNPs was measured by DLS technique and the results were represented in Fig. 7. The mean diameter of AgNPs was determined as 35.27 nm with low polydispersity index (PDI) of 0.377. The morphology of AgNPs was evaluated by SEM analysis for the optimum synthesis conditions (A=25 °C, B=0.001 M, and C=50 mL). As seen from Fig. 8., the nearly spherical-like nanoparticles were synthesized successfully and also it could be said that the mean diameter of AgNPs in SEM image was smaller than that observed with DLS technique. In DLS technique, the hydrodynamic diameters of materials dispersed in solvents are measured, that resulting in the bigger structures [12].

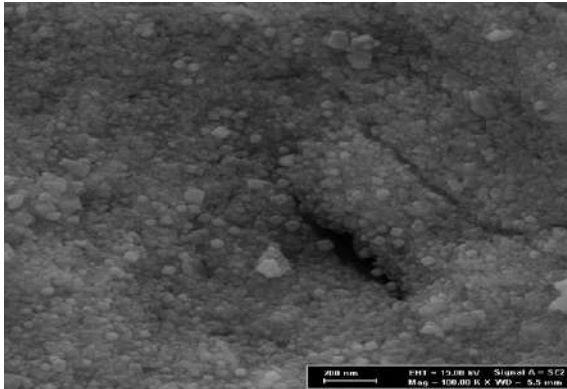


Fig. 8. SEM image of AgNPs

In order to investigate the crystal phase of AgNPs, XRD analysis was performed in 2θ value ranging from 30° to 90° for the optimum synthesis conditions ($A=25^\circ\text{C}$, $B=0.001\text{ M}$, and $C=50\text{ mL}$). XRD pattern of AgNPs (Fig. 9) exhibited peaks at 2θ angles of 38.10 , 44.28 , 64.41 , and 77.36° which corresponded to the $[1\ 1\ 1]$, $[2\ 0\ 0]$, $[2\ 2\ 0]$, and $[3\ 1\ 1]$, crystal planes of a cubic lattice structure of AgNPs. The unassigned peaks stemmed from the crystallization of bio-organic phase (as obtained in FT-IR spectra) on the surface of the silver nanoparticles due to the aqueous leaf extract [9].

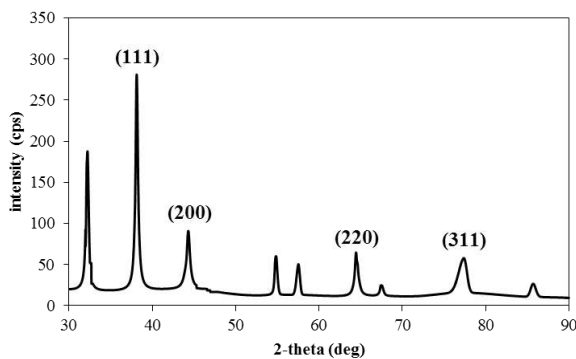


Fig. 9. XRD pattern of AgNPs

Antibacterial Activity of AgNPs

The synthesized AgNPs at the optimum experimental conditions were effective against all selected bacteria, *S. typhimurium*, *E. coli* O157:H7, *S. aureus*, and *L. monocytogenes*, and the inhibition zone diameters of test compound for these bacteria were given in Table IV and Fig. 10. The results indicated that AgNPs had stronger inhibitory effected on growth of *L. monocytogenes* than the other bacteria. These results suggested that AgNPs could be successfully used as effective antimicrobial agents in food packaging to control the growth of pathogenic bacteria.

THE INHIBITION ZONE DIAMETERS

Bacteria	Inhibition zone diameter (mm)
<i>S. typhimurium</i>	10.00 ± 0.87
<i>E. coli</i> O157:H7	10.55 ± 0.68
<i>S. aureus</i>	10.72 ± 0.63
<i>L. monocytogenes</i>	12.26 ± 0.23

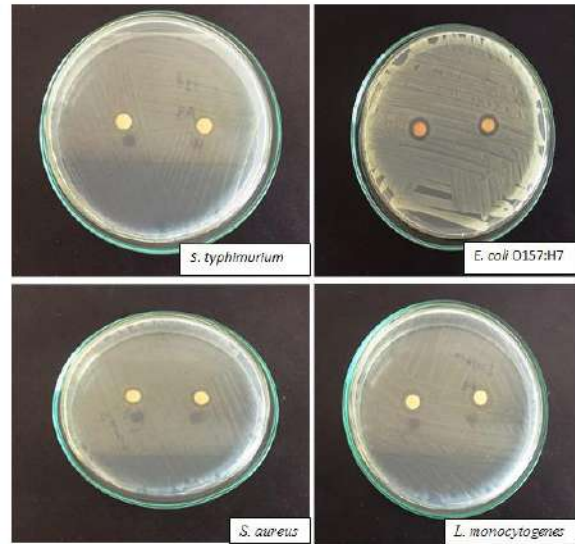


Fig. 10. Antibacterial activity of AgNPs

IV. CONCLUSION

In this work, an ecological method for synthesizing silver nanoparticles (AgNPs) was established by using avocado (*Persea americana*) leaf as a biological reductant and capping agent. The characterization studies of AgNPs were conducted by zetasizer (with DLS technique), FTIR, UV-vis spectrophotometer, XRD, and SEM. The size distribution obtained by DLS showed that the synthesized AgNPs had a relatively narrow size distribution (25–41 nm) and the mean effective hydrodynamic diameter of AgNPs was obtained as 35.27 nm. According to UV-vis spectra; AgNPs had characteristic surface plasmon resonance band at around 430 nm and it was a narrow and sharp band, which indicating the formation of homogeneous, stable, and small nanoparticles. XRD pattern exhibited the characteristic peaks of cubic lattice structure of AgNPs. The nearly spherical-like nanoparticles was found by SEM analysis. Moreover, response surface methodology (RSM) was practicable to optimize the effective hydrodynamic diameter (nm) of AgNPs for the green synthesis method. According to RSM, AgNO_3 concentration significantly influenced the size of AgNPs. Also, it was observed from response surface plots that the effective hydrodynamic diameter slightly decreased with decrease in temperature while it decreased with increase in aqueous leaf extract volume. The smallest particle size was obtained at the optimum synthesis conditions of temperature 25°C , AgNO_3 concentration 0.001 M, and aqueous leaf extract volume 50 mL. Besides, the

antibacterial activity of AgNPs was investigated and it was found that AgNPs synthesized at the optimum conditions were effective against *S. typhimurium*, *E. coli* O157:H7, *S. aureus*, and *L. monocytogenes*.

REFERENCES

- [1] A. Mehmood, G. Murtaza, T.M. Bhatti, M. Raffi, R. Kausar, "Antibacterial efficacy of silver nanoparticles synthesized by a green method using bark extract of *Melia azedarach* L.," *J. Pharm. Innov.*, vol. 9(3), pp. 238-245, September 2014.
- [2] A. Umer S. Naveed, N. Ramzan M.S. Rafique, "Selection of a suitable method for the synthesis of copper nanoparticles," *Nano. Vol.* 7(05), pp. 1230005, October 2012.
- [3] A. Ahmad, Y. Wei, F. Syed, K. Tahir, A.U. Rehman, A. Khan, Q. Yuan, "The effects of bacteria-nanoparticles interface on the antibacterial activity of green synthesized silver nanoparticles," *Microb. Pathog.*, vol. 102, pp. 133-142, January 2017.
- [4] L. Sun, S. Wan, Z. Yu, and L. Wang, "Optimization and modeling of preparation conditions of TiO₂ nanoparticles coated on hollow glass microspheres using response surface methodology," *Sep. Purif. Technol.*, vol. 125, pp. 156-162, April 2014.
- [5] A.M. Awwad, N.M. Salem, A.O. Abdeen, "Green synthesis of silver nanoparticles using carob leaf extract and its antibacterial activity," *IJIC*, vol. 4(1), pp. 1-6, December 2013.
- [6] A. Özer, G. Gürbüz, A. Çalimli, B.K. Körbahti, "Biosorption of copper (II) ions on *Enteromorpha prolifera*: application of response surface methodology (RSM)," *Chem. Eng. J.*, vol. 146(3), pp. 377-387, February 2009.
- [7] A. Fakhri, "Investigation of mercury (II) adsorption from aqueous solution onto copper oxide nanoparticles: optimization using response surface methodology," *Process Saf. Environ.*, vol. 93, pp. 1-8, January 2015.
- [8] A. Gade, S. Gaikwad, N. Duran, and M. Rai, "Green synthesis of silver nanoparticles by *Phoma glomerata*," *Micron.*, vol. 59, pp. 52-59, April 2014.
- [9] M.M. Khalil, E.H. Ismail, K.Z. El-Baghdady, and D. Mohamed, "Green synthesis of silver nanoparticles using olive leaf extract and its antibacterial activity," *Arab. J. Chem.*, vol. 7(6), pp. 1131-1139, December 2014.
- [10] T. Kathiraven, A. Sundaramanickam, N. Shanmugam, and T. Balasubramanian, "Green synthesis of silver nanoparticles using marine algae *Caulerpa racemosa* and their antibacterial activity against some human pathogens," *Appl. Nanosci.*, vol. 5(4), pp. 499-504, April 2015.
- [11] U. Muthukumaran M. Govindarajan M. Rajeswary S.L. Hoti, "Synthesis and characterization of silver nanoparticles using *Gmelina asiatica* leaf extract against filariasis, dengue, and malaria vector mosquitoes," *Parasitol. Res.*, vol. 114(5), pp. 1817-1827, May 2015.
- [12] Q. Zhong, and M. Jin, "Zein nanoparticles produced by liquid-liquid dispersion," *Food Hydrocoll.*, vol. 23(8), pp. 2380-2387, December 2009.

Occupational Health Risk Analysis and Assessment in Cement Production Processes

Vedat Karahan

Department of Chemical Engineering
Firat University
Elazığ, Turkey
vdtkrhn@gmail.com

Cevdet Akosman

Department of Chemical Engineering
Firat University
Elazığ, Turkey
cakosman@firat.edu.tr

Abstract- The workers in a cement factory are exposed to many occupational hazards which contribute to work injuries, dies and allergic problems to cement components. Cement can cause ill health in workers through skin and eye contact or inhalation. The risk of injuries and occupational health problems for cement factory workers depends on the duration and level of exposure and individual sensitivity. Because of inevitable work-related diseases and accidents, occupational safety regulations are compulsive to prevent such risks through recognition, evaluation and control of the hazards in an ideal world. Safety management not only saves lives but also is a profit maker for the countries. Diverse studies for assessing the risks in cement plants have been previously investigated in various studies. This study aimed to identify risks and to assess the health risks may occur during cement production.

The case study is carried out in Elazığ-Altınova Cement Plant to determine safety risk scores by carrying out risk analysis within plant site according to the occupational health and safety risk managements in the cement production processes. The methodology used to determine occupational health risks scores in the Cement Plant is the 5x5 L type risk matrix. The plant site visit program covers the sections of raw material processing, storage and transportation, raw material milling, clinker production and cement milling. Data collection and assessment included listing of all possible risks, determination of likelihood and severity of the risks and calculation of risk scores by using these values. After determining the risks for the workers, the safety risk tables were prepared and the possible risks were classified as high, moderate and low risk degrees with respect to occupational and safety risk management system. The results showed that there were 413 risks in the Cement Plant. It was observed that the risk scores were cumulated between 20 and 6 risk scores, and there are no risks both at 25 risk score and under 6 risk score for the entire cement plant. It was also observed that among these risks, 76 of them were high risks (18,4 %), 333 of them moderate risks (80,6 %), and 4 of them were low risk (1 %). As a result of risk assessment, 128 risk scores of the total risk scores (31,0 %) are determined in the raw material milling section and these risks are encountered as the most dangerous risks. On the other hand, the highest risk score of 20 (only 1) was also seen in raw material milling section. The study concluded that the most dangerous risks which were determined in the raw material milling. On the other hand, the highest risk scores were also obtained in the raw material milling section. It was also observed that the crusher, raw material and cement mills and rotary kiln are the most dust, noise and vibration producing units. The study recommended that (1) work needed to improve occupational health and safety performance for workers, (2) periodic checkup needed for workers for early detection of occupational hazards, (3) periodic educational training are needed for all workers in cement factory about the occupational hazards, (3) emphasizing on the importance and usefulness of personal protective equipment are needed.

Keywords— cement Process, occupational health and safety, risk definition, risk analysis, risk assessment

Green Synthesis of Copper Oxide Nanoparticles (CuONPs) by Using *Myrtus Communis* Leaves Extract: Telon Blue AGLF Adsorption

Müjde HOCAOĞLU and Ayla ÖZER

Department of Chemical Engineering
Mersin University, Faculty of Engineering
33343, Yenişehir, Mersin, Turkey

E-mail address: hocaoglumujde@gmail.com and ayozer@mersin.edu.tr

Abstract— In this study, the green synthesis of copper oxide nanoparticles (CuONPs) was achieved by using *Myrtus communis* leaves extract as reducing agent. The biosynthesized CuONPs were characterized by various physicochemical characterization techniques such as X-Ray Diffraction (XRD), UV-Vis Spectroscopy, Scanning Electron Microscopy (SEM), Fourier Transform Infrared Spectroscopy (FT-IR) and Energy Dispersive X-Ray Spectroscopy (EDX). Thereafter, the biosynthesized CuONPs were used as an adsorbent for batch adsorption of Telon Blue AGLF (TB AGLF) dye. The optimum adsorption conditions were determined to be initial pH 7.0–8.0, temperature 25 °C and adsorbent dose 1.0 g/L. The adsorption equilibrium was described well by the Langmuir isotherm model with maximum adsorption capacity of 3225.8 mg/g at 25 °C. The intraparticle diffusion and the pseudo-second order kinetic models were applied to the experimental data in order to describe the removal mechanism of TB AGLF by CuONPs. The pseudo-second order kinetic model described very well the adsorption kinetics of TB AGLF dye.

Keywords— Adsorption, biosynthesis, *Myrtus communis*, copper oxide nanoparticles, isotherm.

I. INTRODUCTION

The use of nanotechnology in environmental applications for wastewater treatment has attracted considerable attention in recent years. Nanomaterials in water treatment have revealed enormous performances that might be based on their unique characteristics such as large surface area to volume ratio, smaller particle sizes, presence of a large numbers of active sites, and a high capacity for regeneration [1,2]. The improving of influential green chemistry methods for synthesis of metal nanoparticles has become a great focus of researchers [3]. Especially, metal oxide nanoparticles are drawing increasing attention in great numbers of applications. Various studies have centered on metal oxide nanoparticles (NPs) due to their electronic, specific optical and catalytic properties [4]. The metal nanoparticles are usually synthesized by diverse physical, chemical and biological methods. Among them chemical synthesis is widely prevailed which uses many inorganic and organic reducing agents. But, this method has

many disadvantages like toxic, expensive, high pressure and energy requirement, hard to separation and extremely dangerous. Therefore, improving of clean, nontoxic and eco-friendly green methods for synthesis of metal oxide nanoparticles have been arisen as best alternatives which has been reported current research [5]. In this study, the green synthesis of copper oxide nanoparticles (CuONPs) and characterisation were achieved by using *Myrtus communis* leaves extract as reducing agent and then they were used as an adsorbent for the removal of TB AGLF dye from aqueous solution.

II. MATERIAL AND METHODS

A. Preparation of *Myrtus Communis* Leaf Extract

Myrtus communis leaves collecting from Yenişehir Campus of Mersin University were twice with tap water in order to remove dirties, soil, etc. It was dried at room temperature and then in an oven at 105°C for 24 h until all the moisture was evaporated. The extract was prepared by boiling 100 g of dried *Myrtus communis* leaves in 500 mL of distilled water at 100 °C for 1 h, thereafter the extract was filtered and stored at +4 °C to use in the biosynthesis of CuONPs.

B. Biosynthesis of Copper Oxide Nanoparticles

For green synthesis of the CuONPs, 100 mL of 0.1 M CuSO₄ aqueous solution was added dropwise to 50 mL of *Myrtus communis* leaf extract (MCLE) and then the obtained solution was mixed at constant stirring rate and 130 °C temperature for 7h. As soon as the MCLE comes in to contact with the copper ions spontaneous, the blue color of copper ions changes to green color. After 15 min, the green mixture started changing to a brown suspended mixture, indicating the formation of copper oxide nanoparticles. The synthesized CuONPs precipitate was filtered out, washed with distilled water and dried at 130 °C for 6 h. Finally, CuONPs were stored in refrigerator at +4 °C for adsorption.

C. Batch Adsorption Studies

The adsorption experiments were conducted in 250 mL Erlenmeyer flasks in a thermostated water bath at constant temperature for 180 min. The dye solutions were prepared with deionized water. The solution pH values were adjusted by using 0.1 M HCl or 0.1 M NaOH solutions. The known amount of CuONPs was mixed with 100 mL of TB AGLF solution at the desired initial pH and TB AGLF concentration. The flasks were shaken in an agitation vessel at constant temperature for 180 min to achieve adsorption equilibrium. The samples at predetermined time intervals were taken and centrifuged at 3000 rev/min for 5.0 min. The residual dye concentration in the supernatant was analyzed at 610 nm by Chebios brand spectrophotometer.

D. Characterization Of Copper Oxide Nanoparticles

The characterization studies of the biosynthesized CuONPs were done by using X-ray diffractometry (XRD), Fourier transform infrared (FT-IR), Scanning electron microscopy (SEM) and EDX analysis methods.

III. RESULTS AND DISCUSSION

A. The Characterization of Biosynthesized CuONPs

Scanning electron microscopy (SEM) images of CuONPs before and after adsorption were presented in Figure 1a-b and the size and shape of CuONPs were analysed by using SEM images. The SEM images of CuONPs before adsorption showed that their surface were porous and spherical structure. It was observed that the pores of CuONPs after adsorption covered with dyestuff molecules. In addition, the average particle size from SEM images was observed in the range of 40-60 nm.

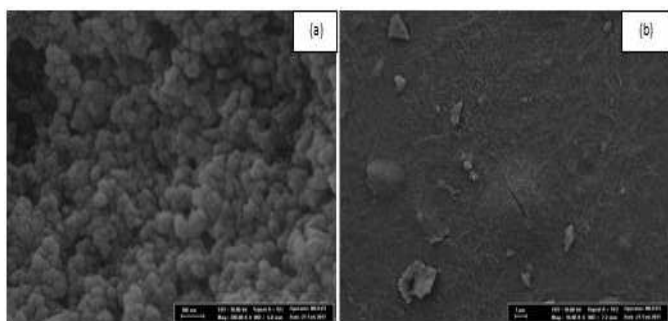


Figure 1. The SEM images of CuONPs a) before b) after adsorption

The EDX spectrums of CuONPs before and after adsorption were recorded to determine the elemental composition of the nanoparticle samples and were presented in Figure 2a-b. EDX analysis results indicated that CuONPs before adsorption have 36.34% Cu, 32.33% O, 30.15% C, 0.8% Cl, 0.32% Fe and 0.06% Mg. According to the results of elemental analysis; C, O, Fe and Mg elements was resulted from the plant extract. The elemental composition of CuONPs after adsorption was determine as 24.48% Cu, 24.72% O, 34.62% C, 7.46% S, 6.88% N and 3.9% Na. As a result, N, Na and S elements in CuONPs can be explained by the presence of the adsorbed dye molecules on CuONPs.

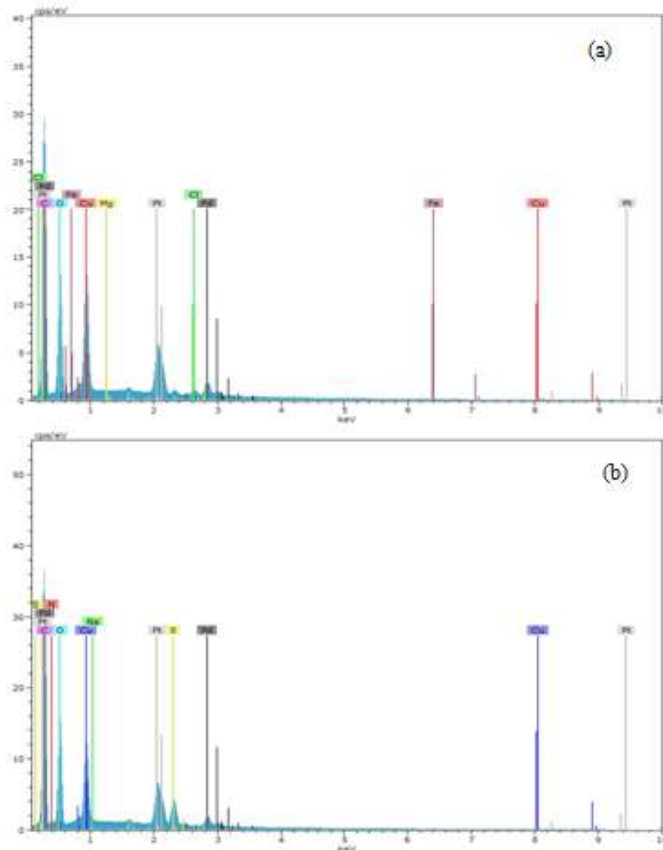


Figure 2. EDX analysis of CuONPs a) before b) after adsorption

The XRD analysis of CuONPs before and after adsorption were indicated in Figure 3a-b. XRD pattern of CuONPs was recorded peaks at 2θ angles of 35.46° , 38.63° , 53.50° , 58.20° , 66.11° , 68.30° and 75.24° which corresponded to the (0 0 2), (1 1 1), (0 2 0), (2 0 2), (1 1 3) and (0 0 4) crystal planes of a cubic lattice structure of CuONPs [6]. It can be said that the adsorption of TB AGLF dye on CuONPs was by physical adsorption. Because any differences from XRD patterns before and after adsorption for CuONPs were not observed.

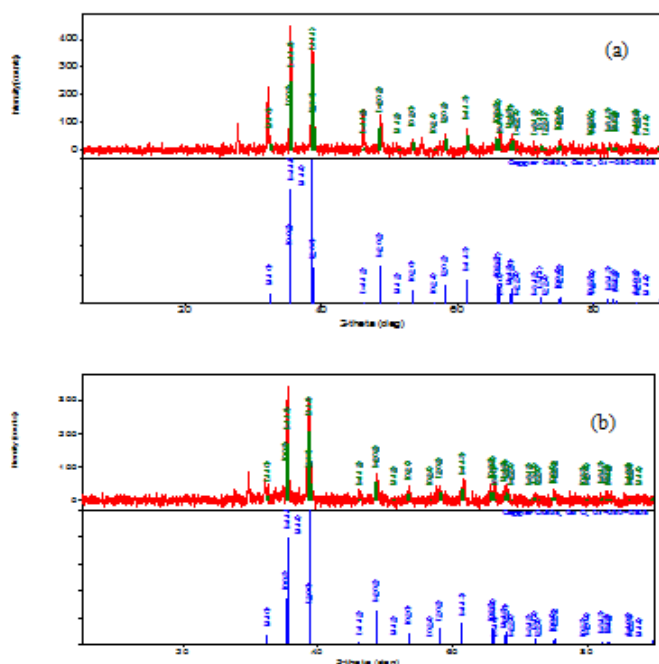


Figure 3. XRD patterns of CuONPs a) before b) after adsorption

The various absorption peaks were observed from FT-IR spectra of CuONPs before and after the adsorption, as can be seen from Figure 4a-b. From FT-IR spectra before adsorption, it was determined that the peaks in the 1075 cm^{-1} and 1230 cm^{-1} bands caused by the C = C aromatic ring and the C - H or C - O stretching vibrations of methyl, methylene and methoxy groups, respectively. These peaks show the presence of phenolic compounds in the leaf extract, which leads to the reduction of metal ions and the formation of nanoparticles. The observed peak at 803.1 cm^{-1} was originated from the M-O (M = Cu) stretching vibration of the CuO nanoparticles. In addition, the observed peaks at 616 cm^{-1} , 595 cm^{-1} and 474 cm^{-1} showed the presence of the stretching vibration of the Cu - O bond in the monoclinic CuO structure. The observed peaks at 1012 cm^{-1} and 1039 cm^{-1} in the FT-IR spectra after adsorption were determined to belong to C - O stretching of alcohols and the observed peaks at 1571 cm^{-1} and 931 cm^{-1} were indicated that they originated from the C = O stretching vibrations of the alcohol.



Figure 4. FT-IR spectra of CuONPs a) before b) after adsorption

B. The Effect of Environmental Conditions on the TB AGLF Adsorption onto CuONPs

The initial pH is one of the most important parameters influencing the removal process of dyes for water treatment as the charge of surface on adsorbent and dye molecules can be influenced by pH values in aqueous solution. The effect of initial pH on TB AGLF adsorption was examined by varying the pH from 5.0 to 10.0 at the initial TB AGLF concentration 100 mg/L , CuONPs dose 1.0 g/L , temperature 25°C and contact time 180 min . The effect of initial pH on TB AGLF adsorption is shown in Figure 5-a. From Figure 5-a, it was observed that the amounts of adsorbed TB AGLF per unit adsorbent mass at equilibrium did not change with the studied initial pH values. The wide range of pH was an advantage for the waste water treatment because the excess reagent was not use in the purification process. The optimum initial pH for the adsorption of TB AGLF on CuONPs was chosen as 7.0-8.0 which is the original pH value of the dye solution.

The effect of temperature on TB AGLF adsorption onto CuONPs was studied in the range of $25\text{--}55^\circ\text{C}$ at 100 mg/L initial TB AGLF concentration, 7.0- 8.0 initial pH, 1.0 g/L CuONPs concentration and 180 min contact time. The relationship between temperature and TB AGLF adsorption capacity of CuONPs was shown in Figure 5-b. For the TB AGLF dye, the adsorption capacity of CuONPs decrease slightly with increasing temperature, implying the exothermic nature of the adsorption process. This exothermic nature is beneficial to the practical application such as the river or other natural systems. The excess energy did not add to adsorption process to reach the desired purification. Therefore, the optimum temperature value was determined as 25°C for TB AGLF adsorption onto CuONPs.

The adsorbent dose and dye removal rate are economically very important parameters for industrial effluent treatment process. The effect of adsorbent concentration on TB AGLF adsorption onto CuONPs was studied for 0.5, 1.0, 2.0, and 3.0 g/L at initial pH value 7.0-8.0, 100 mg/L initial TB AGLF concentration, and 25°C temperature for 180 min contact time and the results was shown in Figure 5-c. As can be seen from Figure 5-c, the uptake capacity of CuONPs decreased from 173.3 to 32.6 mg/L whereas, the percentage removal increased from 88.13% to 94.62% with increasing from 0.5 g/L to 3.0 g/L of the CuONPs concentration. The aggregation of CuONPs at high adsorbent concentrations may result in a decrease in the active surface area and an increase in the diffusional path length, and so the lower adsorption capacities were observed at high adsorbent concentrations. As a consequence, the optimum adsorbent concentration for TBAGLF adsorption was determined to be 1.0 g/L .

In order to investigate the effect of initial TB AGLF concentration on percentage removal of TB AGLF and uptake capacity of CuONPs, the experiments were conducted by varying TB AGLF concentration from 50 mg/L to 3000 mg/L at initial pH 7.0– 8.0, CuONPs dose 1.0 g/L and temperature 25°C

for 180 min contact time. The obtained results are reported in Fig. 5-d.

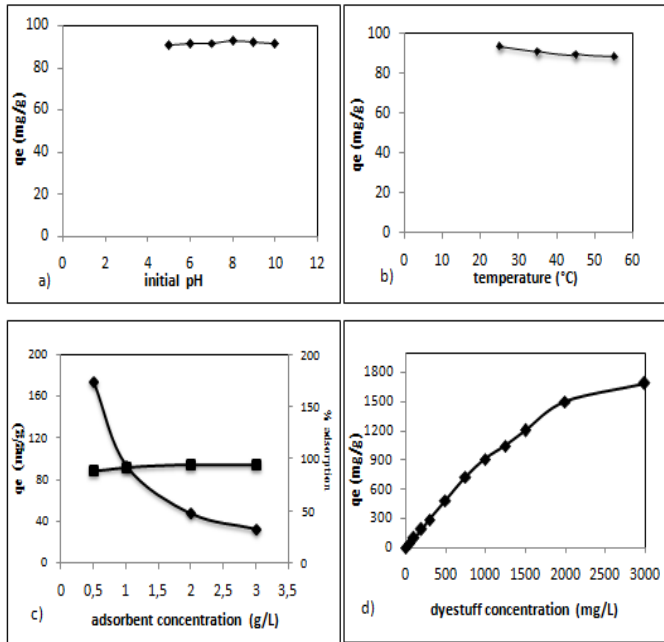


Figure 5. Effect of the environmental conditions on the adsorption of TBAGLF onto CuONPs

C. Equilibrium, Kinetic and Mass Transfer Modelling

Two isotherm models such as Langmuir isotherms and Freundlich isotherm were used to analyze the adsorption equilibrium of TB AGLF onto CuONPs. The Langmuir model showed the good linearity with high values of R^2 (Table I) which indicated that the adsorption was monolayer and adsorption energy was uniformly distributed over CuONPs surface. The R^2 values indicate that the Langmuir isotherm fitted the experimental data better than that of the Freundlich isotherm model at 25 °C. As a result, the adsorption of TB AGLF dye onto CuONPs was the monolayer uniform adsorption type. Langmuir and Freundlich isotherm models were given in equations (1) and (2):

$$\begin{aligned} \text{Langmuir isotherm} & ; 1/q_e = 1/Q^\circ b(1/C_e) + 1/Q^\circ \\ \text{Freundlich isotherm} & ; \ln q_e = \ln K_F + (1/n) \ln C_e \end{aligned} \quad (2)$$

Table 1. The isotherm model constants and regression coefficients (initial pH 7.0-8.0, CuONPs concentration 1.0 g/L, temperature 25 °C and contact time 180 min)

T (K)	Langmuir isotherm model			Freundlich isotherm model		
	Q°	b	R^2	K_F	$1/n$	R^2
298	3225.8	0.00145	0.999	9.94	1.3004	0.980

Q° (mg/g), b (L/mg), K_F [(mg/g)/(L/mg)^{1/n}]

Adsorption kinetics describe the residence time of adsorbate at the solution adsorbent interface which controls the rate of removal. Thus, the kinetic studies are essential to design a continuous system for the adsorption. In this study, the experimental adsorption data determined at different initial TB AGLF concentrations were used to evaluate the kinetics of TB AGLF adsorption on CuONPs. Both the linear forms of the pseudo-first order and the pseudo-second order kinetic models were employed and evaluated to define the kinetic behavior of the adsorption system. The calculated kinetic parameters and correlation coefficients (R^2) for these two models are given in Table 2. The pseudo-second order kinetic model showed better fit for TB AGLF adsorption on the CuONPs in the terms of correlation coefficient. Pseudo-first order and the pseudo-second order kinetic models were given in equations (3) and (4):

$$\text{Pseudo-first order; } [\log (q_e - q_t) = \log (q_e) - k_1 t / 2.303] \quad (3)$$

$$\text{Pseudo-second order; } [(t/q_t) = (1/q_e^2 \cdot k_2) + (t/q_e)] \quad (4)$$

The Weber-Morris model was used to evaluate the mass transfer effects in this adsorption process. To evaluate the diffusion mechanism between TB AGLF and CuONPs, an intraparticle diffusion model proposed by Weber-Morris ($q_t = K_i \cdot t^{0.5} + I$) was used and the calculated parameters were presented in Table 3. If Weber-Morris plot of q_t versus $t^{0.5}$ gives a straight line and pass through the origin, this means that only intraparticle diffusion controlled the adsorption process. On the other hand, the Weber-Morris plot can be linear and also has intercept value if the adsorption system follows both intraparticle and film diffusion. As understood from Table 3, both intraparticle and film diffusion were effective on TB AGLF-CuONPs adsorption process.

Table 2. Rate constants of kinetic models (k_1 , k_2)

C_0 (mg/L)	$q_{e,exp}$ (mg/g)	Pseudo first order			Pseudo second order		
		$q_{eq,cal1}$ (mg/g)	k_1 (min)	R^2	$q_{eq,cal2}$ (mg/g)	k_2 (g/mg.min)	R^2
50	43,83	22,33	0,03684	0.898	44,40	0,00702	0,999
100	93,33	51,52	0,02993	0.917	94,75	0,00238	0,999
200	185,55	110,91	0,03454	0.897	188,57	0,00113	0,998
300	284,44	131,82	0,03454	0.886	287,43	0,00113	0,999
500	485,00	168,42	0,02556	0.788	487,32	0,00086	0,999
750	693,33	256,44	0,02993	0.842	698,32	0,00061	0,998
1000	855,55	534,56	0,03454	0.767	858,36	0,00115	0,999
1250	1045,83	272,89	0,03454	0.815	1050,42	0,00081	0,999
1500	1165,27	281,19	0,02993	0.764	1169,59	0,00069	0,999
2000	1400,00	302,69	0,03224	0.749	1404,49	0,00074	0,999
3000	1627,77	368,12	0,03224	0.892	1633,98	0,00060	0,999

Table 3. Intraparticle diffusion coefficients (K_i), and the related regression coefficients (R^2)

$C_0(\text{mg/L})$	Weber-Morris Model		
	K_i	Intercept	R^2
50	0.956	31.83	0.98
100	2.864	64.68	0.99
200	5.283	118.7	0.99
300	11.4	174.7	0.99
500	22.78	299.6	0.98
750	30.43	433.5	0.98
1000	41.78	535.7	0.97
1250	56.52	678.3	0.99
1500	83.66	668.5	0.99
2000	58.17	654.6	0.99
3000	69.60	791.8	0.98

IV. CONCLUSION

The green synthesis of CuONPs was achieved by using MCLE as reducing agent. The physiochemical properties of green synthesized CuONPs were characterized by SEM, EDX, XRD and FTIR. The average particle size of the synthesized CuONPs by using MCLE was found in the range of 40-60 nm. The biosynthesized CuONPs were used as an adsorbent for batch adsorption of TB AGLF dye. The optimum adsorption conditions were determined to be initial pH 7.0–8.0, temperature 25 °C and adsorbent concentration 1.0 g/L. The adsorption equilibrium was described well by the Langmuir isotherm model with maximum adsorption capacity of 3225.8 mg/g at 25 °C. The intraparticle diffusion model and the pseudo-second order kinetic model were applied to the experimental data in order to describe the removal mechanism of TB AGLF by CuONPs. The pseudo-second order kinetic model described very well the

adsorption kinetics of TB AGLF dye. It was concluded that both intraparticle and film diffusion were effective on TB AGLF-CuONPs adsorption process. As a result, the biosynthesized CuONPs by using the leaf extract, as a known cheap source, can be used as an adsorbent with high capacity for the purification of the waste water involving dyes.

ACKNOWLEDGMENT

This study was supported by the Research Fund of Mersin University in Turkey with Project Number:2016-2-TP2-1805.

REFERENCES

- [1] Banerjee S., Dubey S., Gautam R. K., M.C. Chattopadhyay, Sharma Y.C., "Adsorption characteristics of alumina nanoparticles for the removal of hazardous dye, Orange G from aqueous solutions", Arabian Journal of Chemistry (2016)
- [2] D.K. Singh, D.K. Verma, Y. Singh and S.H. Hasan, "Preparation of CuO nanoparticles using Tamarindus indica pulp extract for removal of As(III): Optimization of adsorption process by ANN-GA", Journal of Environmental Chemical Engineering 5 (2017) 1302–1318
- [3] R. Sivaraj, Pattanathu K.S.M. Rahman, P. Rajiv, S. Narendhran and R. Venkatesh, "Biosynthesis and characterization of Acalypha indica mediated copper oxide nanoparticles and evaluation of its antimicrobial and anticancer activity", Molecular and Biomolecular Spectroscopy 129 (2014) 255–258
- [4] P. Falcaro, R. Ricco, A. Yazdi, I. Imaz, S. Furukawa, D. Maspoch, R. Ameloot, J.D. Evans, C.J. Doonan, "Application of metallic and metal oxidenanoparticles@MOFs", Coordin. Chem. Rev. 307 (2016) 237–254.
- [5] M. Maruthupandy, Y. Zuo, J.S. Chen, J.M. Song, H.L. Niu, C.J. Mao, S.Y. Zhang, Y.H. Shen, "Synthesis of metal oxide nanoparticles (CuO and ZnO NPs) via biological template and their optical sensor applications", Applied Surface Science 397 (2017) 167–174
- [6] Alaa Y. Ghidana, Tawfiq M. Al-Antarya, Akl M. Awwad, "Green synthesis of copper oxide nanoparticles using Punica granatumpels extract: Effect on green peach Aphid", Environmental Nanotechnology, Monitoring & Management 6 (2016) 95–98

Efficient Color Removal of Reactive Black 5 by UV/ZnO System in an Annular Photoreactor

Veyis SELEN

Gülbeyi Dursun

Department of Bioengineering

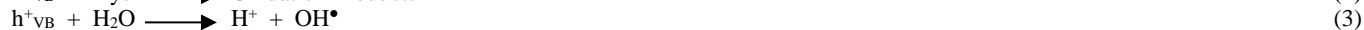
Department of Chemical Engineering

Firat University

Elazig, TURKEY

vselen@firat.edu.tr

Abstract— Advanced Oxidation Process (AOP), one of most efficient method for the degradation of dyes is the photocatalytic process. AOP including fenton, photo-fenton, UV/semiconductors and UV/O₃ have been recently studied extensively and seen as a promising technology to clean the toxic dye effluents [1]. Therefore, AOPs represent potential alternative methods able to decolorize and reduce to final products such as CO₂ and H₂O. Photo-catalysis using semiconductor zinc oxide (ZnO) is an alternative method and extensively provided itself to be the significantly better material for the purification because of its properties such as highly stable, cheap and capable of oxidation of a wide range of organic compounds into harmless compounds [2, 3]. A significant advantage of using heterogeneous photocatalysis, ZnO and TiO₂ which are based on the generation of very reactive species such as hydroxyl radicals (OH•) and others, is the total mineralization of organic dyes and organic compounds which results in CO₂, H₂O and mineral acids. ZnO as semiconductor used for the degradation of dyes is considered to proceed via the following general mechanism [4];



where, $h\nu$ is photon energy required to excite the semiconductor electron from valance band (VB) to conduction band (CB) region.

The photo-generated holes are capable of oxidizing the dye either directly (2) or indirectly by the production of adsorbed OH• radicals and via reactions (3) and (4). The photo-generated electrons on the surface of ZnO are able to reduce oxygen which is absorbed into the media with the feeding air to superoxide radical (5), which consequently react with the dye and then acting as a source of OH• radical to oxidize the dye. The dye is also directly reduced by the photo-generated electrons (7).

To increase the k_{la}, in the solution of dye in order to increase oxygen level in solution, the air is introduced to the reactor in a good manner. The introducing air into reactor improve degradation rate in many ways as diluting and decreasing the color intensity which increase penetration debt to enhance degradation rate with increasing OH• radicals.

In this study, the photocatalytic degradation of reactive dye, C.I. Reactive Black 5 (RB5), was investigated by using zinc oxide (ZnO) in aqueous solution under UV-C lamb in a batch aerated annular Photoreactor (Figure 1.). The effect of key operation parameters including photocatalyst loading (0-10.0 g/L), initial dye concentration (150-550 mg/L) and aeration rate (0.0-3.0 L/min) were determined on color removal in aqueous solution. The efficiency values of photocatalytic degradation process of the RB5 dye at 45 minutes reaction time were 100, 77.0, 62.4, 44.0 and 31.5 % for the initial dye

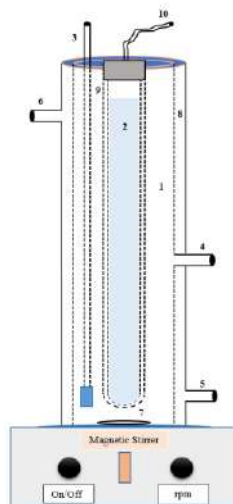


Figure 1. Illustration of annular photoreactor (1- Annular Reactor; 2- UV-C Lamb; 3- Air Feed; 4- Sampling Port; 5- Cooling Water In; 6- Cooling Water Out; 7- Magnetic Rod; 8- Cooling Jacket; 9- Lamp Shield; 10- Power Supply).

concentration values of 150, 250, 350, 450 and 550 mg/L respectively, at the conditions of 7.5 g/L ZnO; 2.0 L/min aeration rate; $\text{pH}_{\text{in}} = 5.6$ (natural pH of dye solution); 293 K reaction temperature; 1000 rpm mixing rate.

The result showed that the degradation of RB5 dye depended on initial dye concentration, catalyst loading and aeration rate as well. The further increase of catalyst loading, observed from the experiment started decreasing the color removal yield because of the decreasing of light intensity and thereby decreasing OH^\bullet radicals. The increasing of initial dye concentration decreased the color removal yield whereas increasing of aeration rate increased the color removal yield.

Keywords—component; Annular Photoreactor, Photocatalytic Degradation, Reactive Black 5, UV-C/ZnO.

REFERENCES

- [1] T.S. Natarajan, M. Thomas, K. Natarajan, H.C. Bajaj, R.J. Tayade, "Study on UV-LED/ TiO_2 process for degradation of Rhodamine B dye," Chemical Engineering Journal, vol. 169, pp. 126-134, 2011.
- [2] S.K. Kansal, N. Kaur, S. Singh, "Photocatalytic degradation of two commercial reactive dyes in aqueous phase using nanophotocatalysts," Nanoscale Research Letters, vol. 4, pp. 709-716, 2009.
- [3] E. Yassitepe, H.C. Yatmaz, C. Ozturk, K. Ozturk, C. Dursun, "Photocatalytic efficiency of ZnO plates in degradation of azo dye solutions," Journal of Photochemistry and Photobiology A: Chemistry, vol. 198, pp. 1-6, 2008.
- [4] M.A. Behnajady, N. Modirshahla, R. Hamzavi, "Kinetic study on photocatalytic degradation of CI Acid Yellow 23 by ZnO photocatalyst," Journal of Hazardous Materials, vol. 133, pp. 226-232, 2006.

Synthesis of Silver Particles Using Aloe Vera Extract and Their Characterization

Didem DEMİR, Gülşah Gül, Nimet Bölgen Karagülle
Chemical Engineering Department, Faculty of Engineering, University of Mersin,
Mersin, Turkey
nimetbolgen@yahoo.com

Abstract— *In recent years, there is a worldwide interest in developing a cost effective and environmental friendly process for synthesis of metal particles. The use of plant extracts for this purpose is potentially advantageous due to the ease of improvement, less biohazard and very short reaction time. Aloe vera (Aloe Barbadensis) is a shrubby, perennial succulent plant characterized by stemless large, thick, fleshy leaves having a sharp apex and a spiny margin. Since early times, Aloe vera has been traditionally used for the treatment of several skin cuts and burn abnormalities, because of its anti inflammatory, antiviral, antifungal and antibacterial properties.*

In the present study, young fresh aloe vera leafs were collected and their green extract was used for the synthesis of silver particles. 50 mL of aqueous extract was added to 500 mL of 0.001 M silver nitrate solution. The solution was allowed to react at room temperature and incubated in dark condition for 24hrs. The color of solution changed from yellow to dark Brown. The extract was analysed by Ultraviolet-Visible spectrophotometer (UV-Vis). The synthesized silver particles were characterized by Fourier Infra Red Spectroscopy (FTIR) and Dynamic Light Scattering (DLS). In DLS analysis, the size of the silver particles was found to be 169 nm. Since silver particles are known to have antibacterial properties, the submicron sized silver particles produced in this study can be potential candidates to be used in biomedical applications.

Keywords— *Silver, Particles, Aloe vera, Extract, Synthesis*

Eggshell Derived Nanohydroxyapatite Reinforced Chitosan Cryogel Biocomposites for Tissue Engineering Applications

Didem Demir¹, Seda Ceylan^{1,2}, Fatma Öfkeli¹, Duygu Şen¹, Nimet Bölgen Karagülle^{1,*}

¹ Mersin University, Engineering Faculty, Chemical Engineering Department, Mersin, Turkey

² Adana Science and Technology University, Bioengineering Department, Adana, Turkey

Abstract— Hydroxyapatite has a biocompatible, biodegradable and natural apatite characteristic to be used in biomedical applications such as bone tissue engineering. The objectives of this study were to synthesize hydroxyapatite from domestic waste eggshells which is utilized as pure calcium source; compare the properties of biosynthesized hydroxyapatite with commercially purchased hydroxyapatite; and produce biosynthesized hydroxyapatite reinforced chitosan cryogels for possible tissue engineering applications. Calcium oxide powders obtained after calcination of waste eggshells showed different particle sizes depending on calcination temperature. It was found that increased temperature of calcination led to the powders of smaller particle sizes. Structural changes at carbonate groups of calcined eggshell were determined by FTIR analysis. The effect of the biosynthesized hydroxyapatite on the morphology of chitosan cryogel biocomposites were determined. The changes in the chemical bond structure of the cryogels were analysed by FTIR and swelling behavior of produced chitosan cryogels was determined by swelling ratio tests.

Keywords— biosynthesis; eggshell; hydroxyapatite; chitosan; biocomposite scaffold; cryogel; tissue engineering.

*Corresponding Author: Nimet Bölgen Karagülle, Mersin University, Engineering Faculty, Chemical Engineering Department, 33343, Mersin, Turkey. E-mail: nimetbolgen@yahoo.com and nimet@mersin.edu.tr

I. INTRODUCTION

Hydroxyapatite (HAp, $\text{Ca}_{10}(\text{PO}_4)_6(\text{OH})_2$) exhibits excellent biocompatibility, biodegradability, osteoconductive and bioactive properties due to its chemically similar composition to the inorganic component of natural bone minerals [1]. HAp can be produced by chemical synthesis such as sol-gel method, hydrothermal method, sono-chemical synthesis, co-precipitation and mechanochemical method or by extraction from natural sources such as corals, sea shells, animal bones and eggshells [2]. The worldwide availability, unlimited supply, low cost, simple, inexpensive, economical, and efficient production are the advantages of obtaining HAp from natural

biological sources [3]. Eggshell is one of the major waste product of food industry, and it becomes useless after the use of egg contents and its derivatives [4]. Eggshell is composed of calcium carbonate (94%), organic matter (4%), calcium phosphate (1%) and magnesium carbonate (1%) [5]. In recent years, the combination of a polymeric matrice (especially made of a natural polymer) with a biocompatible, reinforcing and bioactive component like HAp has shown significant improvements as biomaterials for clinical applications [6]. In this study, we aimed to obtain biosynthesized HAp (bio-HAp) from waste egg shells and combine it with chitosan cryogel scaffolds. The chitosan used in this study was extracted from the blue crab, as demonstrated in our previous study [7]. The present study firstly demonstrates producing calcium oxide (CaO) powder from domestic waste eggshells (a cheap and widely available biological source in worldwide) by using a simple heat treatment process at different calcination temperatures. Then, describes the synthesis and characterization of nanometer scale bio-HAp from this CaO powder by co-precipitation method. The properties of synthesized CaO powders and bio-HAp was characterized by fourier transform infrared spectroscopy (FTIR) and dynamic light scattering (DLS) analysis. Finally, we combined bio-HAp with chitosan cryogels. The chemical structure and swelling behaviour of chitosan-HAp cryogels were demonstrated for possible tissue engineering applications.

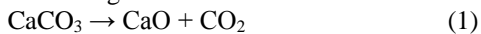
II. MATERIALS AND METHODS

A. Material

In this study, eggshells which were collected from domestic wastes were used as starting material for the synthesis of biosynthesized HAp (bio-HAp). Phosphoric acid was obtained from Merck, Germany. The commercial HAp (com-HAp) used for the comparison of the properties of bio-HAp was purchased from Sigma Aldrich, USA. Chitosan from blue crab shells were used for the production of cryogel scaffolds. Glutaraldehyde (25%, v/v) as the crosslinker was obtained from Merck, Germany. All solution preparations and washing steps were performed by using distilled water.

B. Preparation of Waste Eggshells and Synthesis of CaO

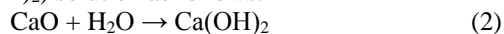
Waste eggshells were first washed with tap water to remove contaminants. The cleaned eggshells were washed with distilled water and dried at 105 °C for 4 hours. The pretreated eggshells were crushed, milled and sieved to a standart powder (500 µm sieve). For CaO synthesis, powder of eggshells were calcined in an ash furnace (Protherm, Plf 130/45, Turkey) at different temperatures (400, 600, 800 and 1000 °C) for 2 hours with a heating rate of 10 °C/min. During calcination, the eggshells were converted to calcium oxide by releasing carbon dioxide (CO₂) according to following reaction:



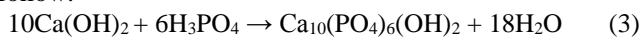
The CaO samples obtained from the eggshells were stored in an oven at 40 °C for further analysis.

C. Synthesis of Bio-HAP

Bio-HAP were prepared from CaO powders by co-precipitation method according to Kunjalukkal et al, 2015 [6]. The calcination temperature of 800 °C was selected in order to prepare CaO powders for certainty of the complete transformation of CaCO₃ to CaO based on TGA results. A stoichiometric amount of CaO powder (2 grams) were weighed and hydrolysed in 250 mL of distilled water to obtain calcium hydroxide (Ca(OH)₂) solution as follows:



Under continuous stirring at 1400 rpm, 1350 µL phosphoric acid solution was added drop by drop to the Ca(OH)₂ solution at 100 °C by using a magnetic stirrer. The expected reaction is as follow:



After the bubbling was finished, the mixed solution was kept on the same conditions for 2 h. The resulting solution was allowed to cool down to room temperature and the resulting precipitate was filtered out using filter paper. Wet sample was put in an oven at 40 °C for 24 h. The dried precipitate was then collected and stored.

D. Characterization of Synthesized CaO and Bio-HAP

Thermogravimetric analysis, TGA/DTG of waste eggshell was carried out using Perkin Elmer Pyris 1 TGA, ABD. A total of 7.5 mg of the sample was used and TGA curve was obtained from 40 °C to 1000 °C in nitrogen atmosphere with a heating rate of 10 °C/min. FTIR (Perkin Elmer, FTIR/FIR/NIR Spectrometer Frontier ATR, USA) was used to determine the functional groups and chemical compositions of the CaO powders synthesized by the calcination of waste eggshells at different temperatures and synthesized bio-HAP at selected calcination temperature. FTIR analysis were performed at a resolution of 4 cm⁻¹ in the wavelength range of 450-4000 cm⁻¹. For the characterization of particle size, the dynamic light scattering (DLS) (Malvern, Nano ZS90, England) was used to measure powder particle size distribution of synthesized CaO and bio-HAP samples. The samples were dispersed in acetic acid (100% purity, Glacial).

E. Production of Chitosan-HAP Cryogel Biocomposites

The chitosan-HAP cryogels were synthesized at different amounts of synthesized HAP by cryogelation method. Chitosan solution (3%, w/v) was prepared in acetic acid solution (6%, v/v) and mixed on a magnetic stirrer until solution was homogenous and clear. At the end of mixing, three different ratio of synthesized HAP (1:1, 1:2, 1:3, ratio of chitosan to HAP) was added to prepared chitosan solutions. 1 mL of GA solution (3%, v/v) was added to 2 mL of prepared chitosan-HAP solution. The whole solution was immediately poured into a 2 mL plastic syringe and transferred into the cryostat. The reaction mixture was incubated in the cryostat at -16 °C for 2 h. After this period the cryogels were stored in the fridge at same conditions for 24 h. After the reaction was completed, the frozen samples in the syringe molds were thawed to room temperature and washed several times to remove the unreacted reagents. The samples were lyophilized before characterization.

F. Characterization of Produced Chitosan-HAP Cryogel Biocomposites

The obtained cryogels' chemical structure was analysed by FTIR in the range of 450-4000 cm⁻¹, with automatic signal gain collected in 20 scans at a resolution of 4 cm⁻¹. To determine the swelling behavior of chitosan-HAP cryogels, the samples were dried at room temperature to a constant weight (W_D). Then, dried samples were immersed in distilled water to obtain swollen cryogels. The excess water on the surface of the cryogels was removed and the samples were weighed (W_S). Swelling ratio was calculated by the following equation:

$$\text{SR\%} = [(W_S - W_D) / (W_D)] * 100 \quad (4)$$

III. RESULTS AND DISCUSSION

A. Characterization of Synthesized CaO and Bio-HAP

FTIR analysis was carried out to determine the chemical composition of the waste eggshell and CaO powders synthesized after calcination of eggshells at different temperatures. Fig. 1 shows the FTIR spectra of the waste eggshell and CaO powders. The bands at between 873 and 1413 cm⁻¹ were attributed to C-O bond of carbonate (CO₃) groups of eggshell. However, the CO₃ ions disappeared from the structure at high temperatures (800 and 1000 °C) during heat treatment. The intensity of the O-H stretching band observed at 3642 cm⁻¹ wavelength is due to the O-H bond in Ca(OH)₂, which is formed during the adsorption of water by CaO [8]. The peak at 2981 cm⁻¹ is characteristics of free CO₂ due to the background of the measurement system or reaction process [9]. Presence of these characteristic bands is a proof of the CaO powder formed.

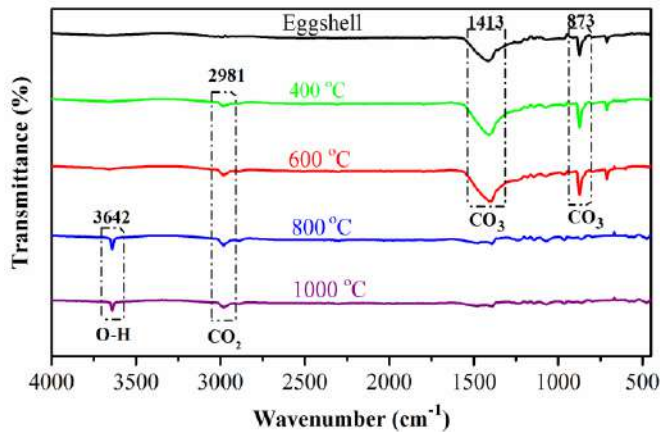


Fig. 1. FTIR analysis of waste eggshell and CaO powders synthesized at 400, 600, 800 and 1000 °C.

CaCO_3 , the main component of the eggshell, can completely decompose in CaO and CO_2 with the increase in calcination temperature [10]. In this study, eggshells were calcined in an ash furnace at 400, 600, 800 and 1000 °C, respectively to evaluate the effect of calcination temperature on formation of CaO. Thermal analysis of the waste eggshell was performed to determine the optimum calcination temperature (Fig. 2). The weight decrement during the heating process was determined by TGA. The CaO content in the eggshells were determined as about 49% (w/w). With the increase in temperature from 600 to 800 °C, a significant weight loss has occurred because of the CO_2 molecules moving up from the structure of eggshell. The CaCO_3 decomposes completely into CaO at a maximum temperature of 760 °C.

Beside the thermal analysis of waste eggshell, DLS analyser measurements were made to observe the effect of the calcination temperature on the particle size of the synthesized CaO. Fig. 3 shows the variation of CaO powder size as a function of calcination temperature of eggshells. It reveals that increasing the calcination temperature results in smaller size of CaO powder which was in close agreement with the [11]. At the calcination temperature of 800 the particle size was 103,5496 nm. The calcination temperature was chosen as 800 °C for the synthesis of bio-HAp.

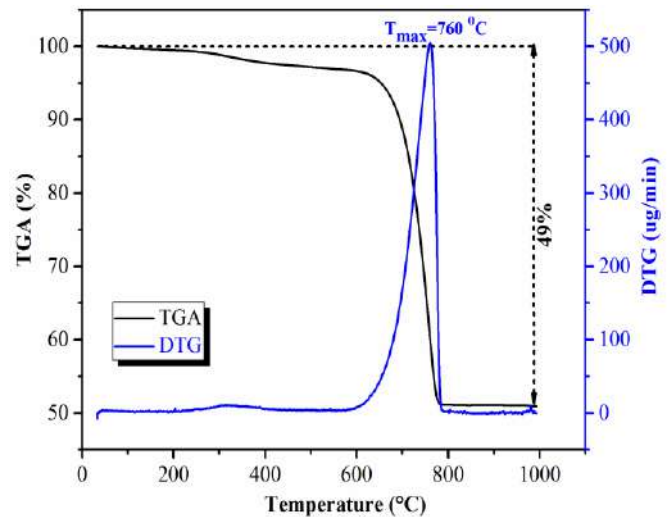


Fig. 1. TGA and DTG curves of waste eggshell

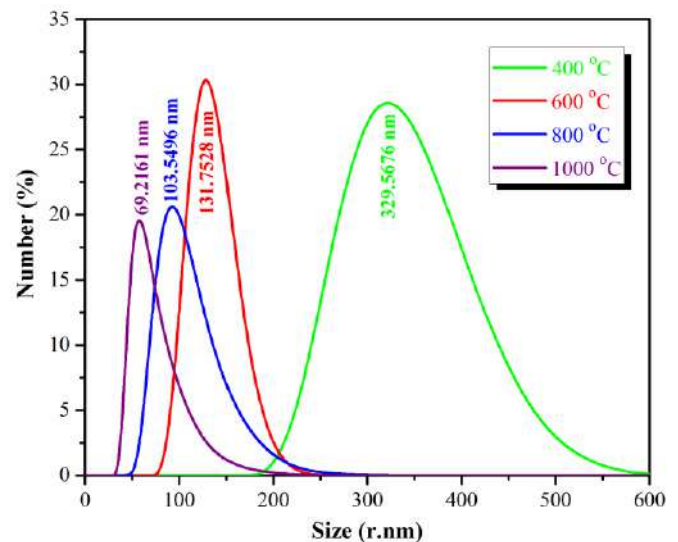


Fig. 2. Particle size distribution of CaO powders synthesized at 400, 600, 800 and 1000 °C.

B. Characterization of Bio-HAp

FTIR analysis was performed to compare the functional groups of bio-HAp and commercially purchased hydroxyapatite (com-HAp). The FTIR spectrum of the bio-HAp was chemically in good agreement with the spectrum of com-HAp and the FTIR spectrum reported by another study that demonstrated HAp powder synthesized from hen eggshells [12]. The band at 1027 cm^{-1} is the characteristic band of phosphate (PO_4) stretching vibration whereas the bands at 562 and 501 cm^{-1} are due to phosphate bending vibration [13]. According to spectral data, the absorption peak at 1412 cm^{-1} corresponds to the asymmetric stretching of carbonate ion substitution. FTIR spectra indicated that bio-HAp was successfully derived from CaO calcined at 800 °C.

The particle size distribution of bio-HAp and com-HAp samples was analysed (Fig. 5). The average size of bio-HAp was 33.08 nm while the size of com-HAp was 115.98 nm. The polydispersive index (PDI) of samples were 0.462 and 0.722, respectively. This PDI value showed that the synthesized sample was homogeneous and uniform in size [14]. Moreover, DLS analysis showed that the synthesized bio-HAp was in the nanometer size.

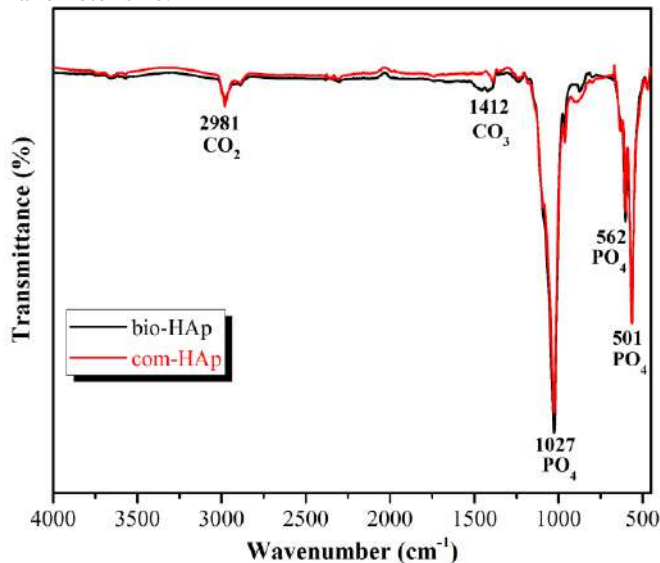


Fig. 3. FTIR analysis of com-HAp and bio-HAp

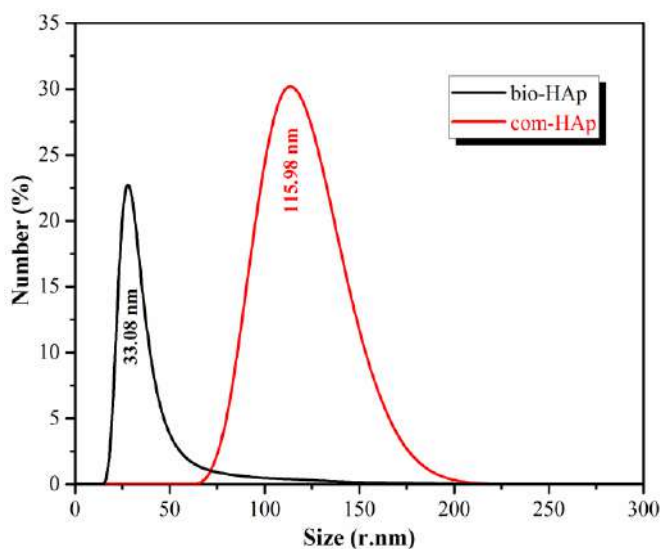


Fig. 4. Particle size distribution of com-HAp and bio-HAp

C. Characterization of Chitosan-HAp Cryogels

The ratio of bio-HAp to chitosan solution was varied in this study. The amount of bio-HAp affected the chemical, physical, mechanical, morphological and porous structure of cryogels.

Fig. 6 shows the photograph of chitosan-HAp cryogels after cryogelation reaction is completed (in wet form) and after lyophilization (in dry form). The colour of cryogels including bio-HAp were more opaque than the plain chitosan cryogel. Also with increasing the amount of bio-HAp in the chitosan cryogels, a more smooth and elastic surface was reached.

Furthermore, FTIR analysis demonstrated the functional groups of bio-HAp, interactions between bio-HAp and chitosan, crosslinking bonds between glutaraldehyde and chitosan. The FTIR spectra of the cryogels, as shown in Fig. 7, demonstrated bands corresponding to hydroxyl, phosphate and amine groups. The major absorbance bands of the spectra correspond to hydroxyapatite. Width of bands decreases with increasing bio-HAp content of cryogels [15]. With the increase in the amount of bio-HAp a sharp peak was observed at near by 1050 cm^{-1} . This peak shows the interaction of chitosan with the phosphate groups of bio-HAp [16]. The bands between $1550\text{--}1700\text{ cm}^{-1}$ are attributed to mode superposition of the hydroxyl group of bio-HAp and amide groups of chitosan [15]. The hydroxyapatite phosphate bending bands are at 562 cm^{-1} . The broad peak started at 3480 cm^{-1} , gradually decreased and became narrower with the increase in the amount of bio-HAp.

At the cryogelation step, chitosan-HAp cryogels with interconnected pores were obtained. Swelling ability of a cryogel is related with the highly porous and spongy morphology of the cryogels [7]. The swelling ratio results of the plain chitosan and chitosan-HAp cryogels are demonstrated in Fig. 8. Plain chitosan and all chitosan-HAp cryogels showed a swelling ratio higher than 3000% in the first 5 min. It was observed that as the amount of bio-HAp in the cryogels increased the swelling ratio decreased. The decrease may be due to the decrease in the pore size of the cryogels. As the amount of bio-HAp increased the pore walls of the cryogels were filled with more bio-HAp. Plain chitosan cryogel showed the highest swelling ratio (8660.43%) after 60 minutes of swelling time.

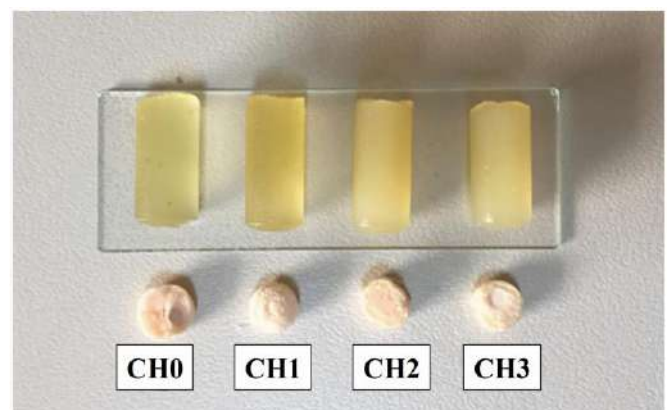


Fig. 6. Photograph of blank chitosan and chitosan-HAp cryogels in wet and dry form [CH0= plain chitosan. CH1=1:1, CH2= 1:2, CH3= 1:3 (chitosan:HAp)]

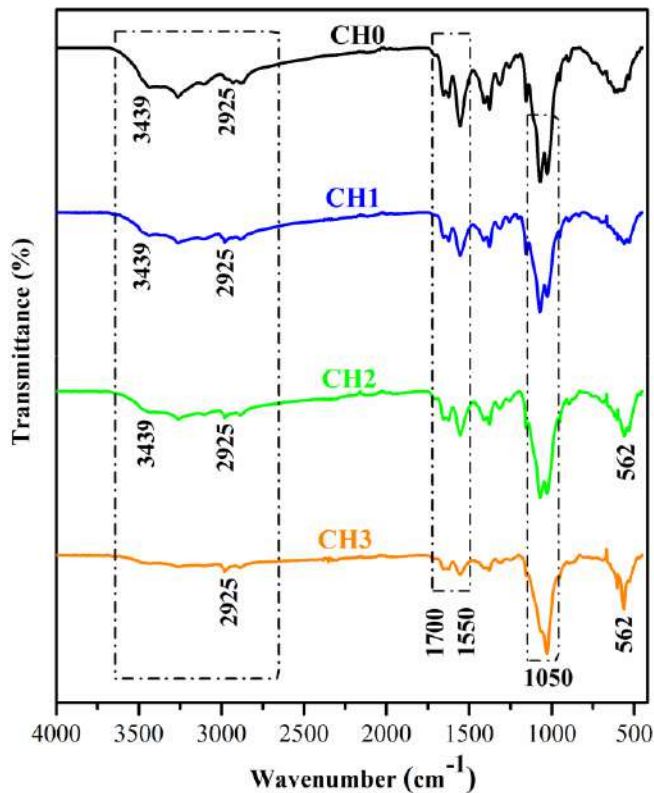


Fig. 7. FTIR analysis of plain chitosan and chitosan:bio-HAp cryogels

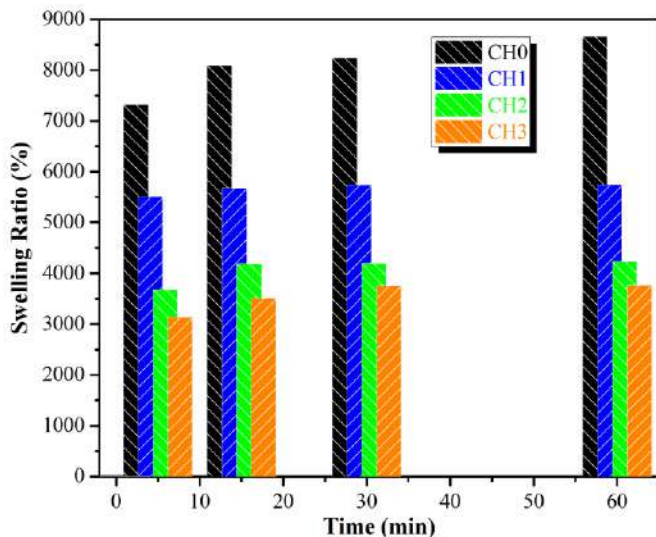


Fig. 8. Swelling ratio analysis of plain chitosan and chitosan-HAp cryogels

IV. CONCLUSION

CaO powder was produced by using domestic waste eggshells through a calcination process at different temperatures. Pure bio-HAp was synthesized by co-precipitation method using the CaO powder which was calcined at 800 °C. The particle size of the synthesized bio-HAp was measured as in nano scale. FTIR analysis showed the purity of bio-HAp. This process can lead to the development of a cost

effective biomaterial and can improve waste management in future. Chitosan cryogel scaffolds reinforced with bio-HAp were successfully produced for possible tissue engineering applications. Hence, from the results, it can be concluded that the synthesized bio-HAp can be economically produced from waste eggshells by a simple calcination and co-precipitation method for wide range of biomedical applications especially for tissue engineering. The bioHAp reinforced chitosan cryogel biocomposites can be potential scaffold candidates to be used in possible tissue regeneration.

Acknowledgement

The authors declare that no conflict of interest occurred in this work.

REFERENCES

- [1] H. Zhou, and J. Lee, "Nanoscale hydroxyapatite particles for bone tissue engineering," *Acta Biomater*, vol. 7, pp. 2769-2781, April 2011.
- [2] J. Brzezińska-Miecznik, K. Haberko, M. Sitarz, M. M. Bućko, and B. Macherzyńska, "Hydroxyapatite from animal bones-Extraction and properties," *Ceram Int*, vol. 41, pp. 4841-4846, December 2014.
- [3] T. Rasool, S. R. Ahmed, I. Ather, M. Sadia, R. Khan, and A.R. Jafri, "Synthesis and Characterization of hydroxyapatite using egg-shell," November 2015 [Digests IMECE 2015 Texas, p. 1-6, 2015].
- [4] S-C. Wu, H-C. Hsu, S-K. Hsu, Y-C. Chang, and W-F Ho, "Synthesis of hydroxyapatite from eggshell powders through ballmilling and heat treatment," *JASCERS*, vol. 4, pp. 85-90, December 2015.
- [5] A. Mittal, M. Teoti, R. K. Soni, and J. Mittal, "Applications of egg shell and egg shell membrane as adsorbents: A review," *J Mol Liq*, vol. 223, pp. 376-387, August 2016.
- [6] S. K. Padmanabhan, L. Salvatore, F. Gervaso, M. Catalano, A. Taurino, A. Sannino, and A. Licciulli, "Synthesis and characterization of collagen scaffolds reinforced by eggshell derived hydroxyapatite for tissue engineering," *J. Nanosci. Nanotechnol*, vol. 14, pp. 1-6, September 2015.
- [7] D. Demir, F. Öfkeli, S. Ceylan, and N. Bölgen Karagülle, "Extraction and characterization of chitin and chitosan from blue crab and synthesis of chitosan cryogel scaffolds," *JOTSCA*, vol 3, pp. 131-144, August 2016.
- [8] T. Wittoon., "Characterization of calcium oxide derived from waste eggshell and its application as CO₂ sorbent," *Ceram Int*, vol. 37, pp. 3291-3298, May 2011.
- [9] R. Choudhary, S. Koppala, and S. Swamiappan, " Bioactivity studies of calcium magnesium silicate prepared from eggshell waste by sol-gel combustion synthesis," *JASCERS*, in press.
- [10] S. Ummartyotin, and B. Tangnorawich, "Utilization of eggshell waste as raw material for synthesis of hydroxyapatite," *Colloid Polym Sci*, vol. 293, pp. 2477-2483, June 2015.
- [11] E. G. Mornani, P. Mosayebian, D. Dorraniana, and K. Behzad, "Effect of calcination temperature on the size and optical properties of synthesized ZnO nanoparticles," *J Ovonic Res*, vol. 12, pp. 75-80, April 2016.
- [12] G. Gergely, F. We'ber, I. Luka'cs, A. L. To'th, Z. E. Horva'th, J. Miha'ly, and C. Bala'zsi, "Preparation and characterization of hydroxyapatite from eggshell," *Ceram Int*, vol.36, pp. 803-806, October 2009.
- [13] B. Chaudhuri, B. Mondal, D. K. Modak, K. Pramanik, and B. K.Chaudhuri, " Preparation and characterization of nanocrystalline hydroxyapatite from egg shell and K₂HPO₄ solution," *Mater Lett*, vol. 97, pp. 148-150, January 2013.
- [14] M. S. M. Arsad, P. M. Lee, and L. K. Hung, "Morphology and particle size analysis of hydroxyapatite micro- and nano-particles," pp. 1030-1034, December 2010 [Digests CSSR 2010 Malaysia, 2010].
- [15] S. N. Danilchenko, O. V. Kalinkevich, M. V. Pogorelov, A. N. Kalinkevich, A. M. Sklyar, T. G. Kalinichenko, V. Y. Ilyashenko, V. V. Starikov, V. I. Bumeyster, V. Z. Sikora, L. F. Sukhodub, A. G. Mamalis,

S. N. Lavrynenko, and J. J. Ramsden, "Chitosan-hydroxyapatite composite biomaterials made by a one step co-precipitation method: preparation, characterization and in vivo tests," *J Chem Biol Phys Sci*, vol. 9, pp. 119-126, September 2009.

- [16] I. Manjubala, S. Scheler, J. Bossert, and K. D. Jandt, "Mineralisation of chitosan scaffolds with nano-apatite formation by double diffusion technique," *Acta Biomater*, vol. 2, pp. 75-84, September 2005.

Removal of Hexavalent Chromium from Aqueous Solution by Using Activated Carbon Prepared from Triple Mixture in a Fixed-bed Column

Ramazan ORHAN

Chemical Department, Faculty of Engineering,
University of Firat,
Elazığ, Turkey
rorhan@firat.edu.tr

Şeyma YÜKSEL

Firat University
Elazığ, Turkey,

Abstract— *In this study; removal of Cr(VI) from aqueous solution by using activated carbon prepared from apricot, peach stones and almond shell mixture was investigated in a fixed-bed column as a function of pH, initial Cr(VI) concentration and flow rate.*

In order to prepare the solutions used in the experiments, the stock solution of Cr(VI) (1000 mg/L) was prepared by dissolving K₂CrO₄ in distilled water. All working solutions of varying Cr(VI) concentrations (10, 20 and 40 mg/L) were obtained by diluting the stock solution with distilled water. pH adjustments were performed by using HNO₃ and NaOH solutions in different concentrations. All the reagents used in this study were of analytical grade. The fixed-bed column experiments were carried out in a glass column designed with an internal diameter of 0.8 and 22 cm in length having a cooling jacket. Activated carbon was placed into the column supported with glass wool from the top and bottom. Liquid samples were collected from the top of the column at 15 minute intervals until $C/C_0 \geq 0.95$. Cr(VI) concentration was then measured by using a spectrophotometer depending on diphenyl carbazide method. The performance of fixed-bed column adsorption is usually described through the concept of the breakthrough curve. The time for breakthrough appearance and the shape of the breakthrough curve are very important characteristics for determining the operation and the dynamic response of an adsorption column. The breakthrough curve is defined as the ratio of effluent metal concentration to inlet metal concentration (C/C_0) as a function of time or volume of effluent for a given bed height. It has been determined that the adsorption of Cr(VI) onto activated carbon is pH dependent. Although Cr(VI) adsorption yields increased with the decreasing pH, Cr(VI) began to reduce to Cr(III) oxidation stage under pH 3. Cr(VI) concentration decreased with this reduction but total chromium concentration began to increase. Therefore, pH of 3 was selected as most suitable pH for the adsorption of Cr(VI). The maximum bed capacities for the investigated flow rates of 2, 3 and 4 mL/min were found to be 9.95, 6.67 and 6.16 mg/g, respectively. When the initial Cr(VI) concentration was increased from 10 to 40 mg/L, the adsorption bed capacities increased from 6.67 to 11.77 mg/g.

The adsorption capacity was decreased with increasing the pH and flow rate but increased with the increasing influent Cr(VI) concentration. As the flow rate and initial Cr(VI) concentration increased, the breakthrough curve became steeper, the breakthrough time and adsorbed ion concentration decreased. The results indicates that the activated carbon prepared from triple mixture can be used as an effective and environmentally friendly adsorbent for the treatment of Cr(VI) ions in aqueous solutions.

Keywords— Cr(VI), Adsorption, Activated carbon, Almond shell, Apricot stone, Peach Stone

Effect Of Coating Time On ZnO Thin Film Photocatalyst Prepared By Sol–Gel Method

Hande Yılmaz

Ataturk University, Engineering Faculty

Erzurum, Turkey

handemylmz@gmail.com

Taner Tekin

Ataturk University, Engineering Faculty

Erzurum, Turkey

ttekin@atauni.edu.tr

Abstract—ZnO thin films deposited on glass substrate were prepared by dip-coating and studied different coating time for structural characterization and photo catalytic activity. The films were prepared by depositing different numbers of layers. The morphology, structure and resistivity of the thin films were measured by scanning electron microscopy, X-ray diffraction, and UV Spectrophotometer. The best photocatalytic activity obtained when the multilayer was 3.

Keywords— zinc oxide; photocatalyst; sol gel; dip-coating

I. INTRODUCTION

In recent years, nanomaterials have attracted much attention because of their excellent physical and chemical properties, large surface area and ability to interact with other materials. [1,2]. Zinc oxide (ZnO) semiconductors have properties such as easy availability, chemical stability, and strong oxidative capacity. Also the processing performance, crystallographic compatibility is high [3,4]. These properties make ZnO catalysts a simple and attractive solution to water pollution.

ZnO as a special photocatalyst has been achieve mineralization of a lot of organic dyes leading to the investigated in recent years also. Many kinds of nanostructured such as nanoparticle, nanotube, nonorod and thin film ZnO structures have been used for the photocatalytic degradation of pollutants such as textile dyes, organic waste and pesticides in water[5–6]. Some studies show that ZnO is a better catalyst than TiO₂ [7,8] because ZnO has a wide band gap (3.37 eV) and thus electron holes efficiency and mobility is higher. The most important feature of these catalysts is that visible light activities can be enhanced [9].

ZnO photocatalysts can be used in diffused forms immobilized on a substrate or powders [10]. Although more efficient results are obtained in slurry reactors there are two important restrictions [11] on its use. First, small particles can agglomerate to form large particles lead to reduce catalyst performance. Secondly, the separation and recovery of catalyst

from slurry is a difficult and costly process. Thus, many researchers have been prefer immobilized catalysts on a suitable support.

When a semiconductor irradiated with UV light, an electron in the valence band is excited into the conduction band. So that electrons are formed in conduction band and holes are formed in conduction band. These electron-hole pairs become radicals after various redox reactions. These radicals also effect the oxidation of organic substances and pollutants, the destruction of bacteria and viruses [12,13]

In the present work, ZnO thin films were prepared by the sol–gel technic and immobilized on surface by dip-coating method. Five different coatings were selected and thus thin films were obtained in different layers, 1 2 3 4 and 5. After each coating the samples were subjected to heat treatment for 10 minutes at 200 ° C. So that the layers are strengthened and the final film thickness is obtained.

II. METHOD

A. Preparation of sol-gel

Zinc acetate dihydrate) was used as the precursor and dissolved in the isopropanol with the molar ratio of zinc acetate is 0.4. DEA was also added dropwise with molar ratios ZnAc: DEA = 1: 1. DEA was used as a stabilizer. Solutions stirred at room temperature for 2 hours until a homogenous solution was formed.

B. Preparation of thin film

This solution was immobilized on glass substrates by applying several times the dip-coating technique. After each coating the samples were subjected to heat treatment for 10 minutes at 200 ° C. For 5 samples coating times choosen 10, 20, 30, 45 and 60 minute. Thin films consisting of 1 2 3 4 and 5 layers were obtained with this procedure. Finally, For the removal of organic residues and for the provision of crystallisation the multilayer films were annealed during 2,5 h at 500°C.

C. Characterization

Prepared samples were characterized by using X-ray diffraction (XRD) (Rigaku D/Max-2200). For surface structures and morphology analysis, scanning electron microscope (SEM) was used (FEI, Inspect S50). UV spectrophotometer (Shimadzu UV-2200, Japan) was used to test the photocatalytic activity of thin films. And also the transmittance of the film was analyzed by this spectrophotometer.

D. Photocatalytic degradation experiment

The photocatalytic efficiency of the prepared thin film photocatalyst were tested in batch reactor under UV lamb (Cole-Parmer 254 nm 44W/m²) irradiation source using Acid Red 27 as the pollutant. O₂ in the reaction was provided by sending air at a constant flow rate by a pump. The dye solution was prepared at 20 mg/l and filled in the 400 ml batch reactor. Samples were taken from the reactor every 15 minutes and analyzed.

III.RESULTS AND DISCUSSIONS

Effect of the coating time on ZnO layers on transmittance for photocatalytic activity. The transmittances of the thin films photocatalyst from 1 layer to 5 layers are shown in Fig1 Fig. 2 shows XRD patterns results for ZnO thin films at different thicknesses. 1 2 3 4 and 5 layers of samples are named from A to E in Fig. 2. As a result of the analysis, characteristic peaks of (100), (002) and (101) (102), (110) (103) and (004) planes were obtained. The result are in accordance with the standard XRD patterns of JCPDS 36-1451 data.

Fig. 3 shows the SEM images of the ZnO thin films prepared at different coating time. SEM images show that, thin films of ZnO is in network structure. According the results when the dip coating layer was 3, it gives the best transmittence. As shown in Fig. 3b, when the dip coating layer was 3 thin films have smooth and uniform surface and polycrystalline structure. The layers for this coating time do not clog the pores, thus obtained light trapping structure on surface. With this surface property, both sunlight reflections and photocatalytic efficiency can be increased. As shown in Fig. 3a, The ZnO crystals, when dip coating at 1 layer, combine on the surface like a island structure. As shown in Figure 3b, when the 3-layer coating is applied, the layer structure is formed to the layer by layer growth. So that the light trapping structure is formed. As shown in Figure 3c, when the 5 and over layers are coated, the granules are collected and maintained in one direction to reduce surface energy, then many dendritic crystals are formed and interconnected.

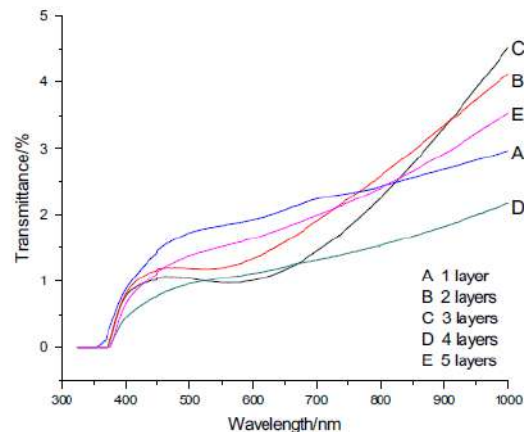


Fig 1. The transmittance curves of the multilayer thin films with different numbers of the coating times

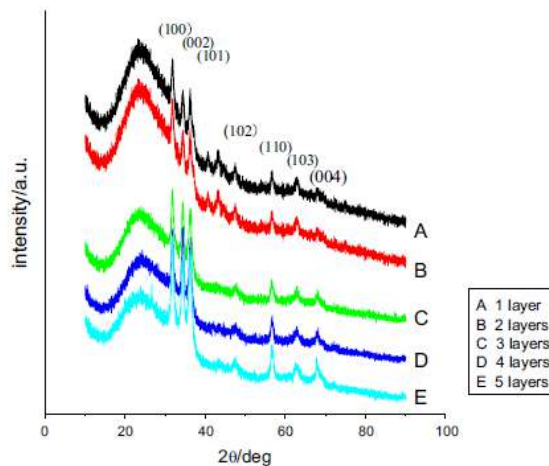


Fig. 2. XRD patterns of (A) 1 layer (B) 2 layers (C) 3 layers (D) 4 layers (E) 5 layers of ZnO thin film photocatalyst.

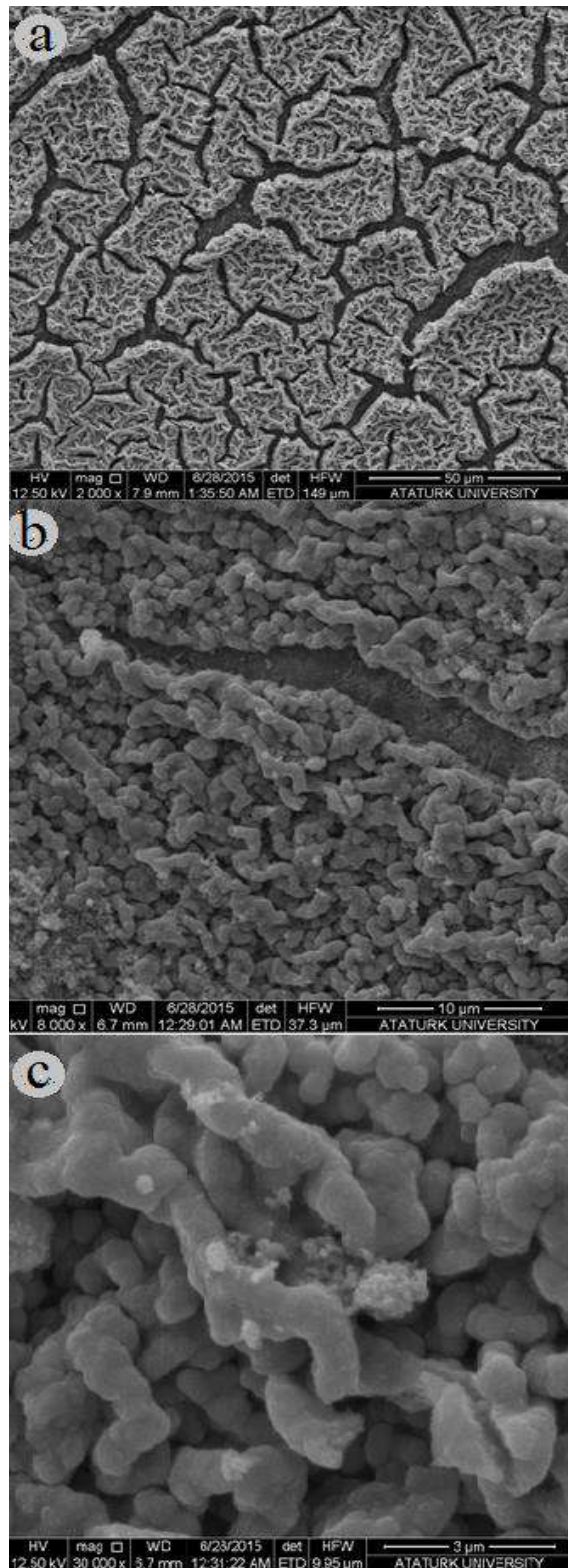


Fig. 3. SEM images of (a) 1 layer, (b) 3 layers, (c) 5 layers of ZnO thin film photocatalyst

REFERENCES

- [1] M. Helgesen, R. Sondergaard, F.C. Krebs, Advanced materials and process for polymer solar cell devices, *J. Mater. Chem.* 20 (2010) 36–60.
- [2] H. Zhu, Y. Mai, M. Wan, et al., Study of back reflectors for thin film silicon solar cells, *Thin Solid Films* 539 (2013) 284–289.
- [3] V. Smirnov, W. Böttler, J. Hüpkes, et al., ZnO based back reflectors with a wide range of surface morphologies for light trapping in i-p microcrystalline silicon solar cells, *Energy Procedia* 44 (2014) 223–228.
- [4] S. Fernández, A. Bollero, F.B. Naranjo, et al., Optimization of ZnO:Al based back reflectors for applications in thin film flexible solar cells, *Vacuum* 99 (2014) 56–61.
- [5] M. Rauscher, T. Salditt, H. Spohn, Small-angle X-ray scattering under grazing incidence: the cross section in the distorted-wave Born approximation, *Phys. Rev. B* 52 (1995) 16855–16863.
- [6] R. Li, S. Yabe, M. Yamashita, S. Momose, S. Yoshida, S. Yin, T. Sato, UV-shielding properties of zinc oxide-doped ceria fine powders derived via soft solution chemical routes, *Materials Chemistry and Physics* 75 (2002) 39–44.
- [7] Z. Wang, H.J. Li, Highly ordered zinc oxide nanotubes synthesized within the anodic aluminum oxide template, *Applied Physics A* 74 (2002) 201–203.
- [8] S. Lepoutre, B. Julián-López, C. Sanchez, H. Amenitsch, M. Linden, D. Grosso, Nanocasted mesoporous nanocrystalline ZnO thin films, *Journal of Materials Chemistry* 20 (2010) 537–542.
- [9] M. Miyauchi, A. Nakajima, T. Watanabe, K. Hashimoto, Photocatalysis and photoinduced hydrophilicity of various metal oxide thin films, *Chem. Mater.* 14 (2002) 2812–2816.
- [10] C. Wang, J. Zhao, X. Wang, B. Mai, G. Sheng, P. Peng, J. Fu, Preparation, characterization and photocatalytic activity of nano-sized ZnO/SnO₂ coupled photocatalysts, *Appl. Catal. B* 39 (2002) 269–279.
- [11] R.E. Marotti, C.D. Bojorge, E. Broitman, H.R. Cánepa, J.A. Badan, E.A. Dalchiale, A.J. Gellman, Characterization of ZnO and ZnO:Al thin films deposited by the sol-gel dip-coating technique, *Thin Solid Films* 517 (2008) 1077–1080.
- [12] L.-Y. Yang, S.-Y. Dong, J.-H. Sun, J.-L. Feng, Q.-H. Wu, S.-P. Sun, Microwave assisted preparation, characterization and photocatalytic properties of a dumbbell-shaped ZnO photocatalyst, *J. Hazard. Mater.* 179 (2010) 438–443.
- [13] G. Marci, V. Augugliaro, M.J. López-Muñoz, C. Martín, L. Palmisano, V. Rives, M. Schiavello, R.J.D. Tilley, A.M. Venezia, Preparation characterization and photocatalytic activity of polycrystalline ZnO/TiO₂ systems. 2. Surface, bulk characterization, and 4-nitrophenol photodegradation in liquid–solid regime, *J. Phys. Chem. B* 105 (2001) 1033–104.

FOOD ENGINEERING

ORAL SUBMISSIONS



Effects of Storage Time on Some Properties of Yogurt Cheeses

Çağla Özbek, Nuray Güzeler

Çukurova University, Agricultural Faculty, Food Engineering Department
Adana, Turkey
cglaayldrm@gmail.com

Abstract— In this research Yogurt cheeses which were produced by coagulation of milk by adding yogurt with different ratios (20%, 30%, 40%, 50%) were stored at $4\pm 1^\circ\text{C}$ for 90 days. Some physical, chemical and sensory properties of cheeses were analyzed while storage and the effects of storage on these properties were evaluated. For this reason pH, titration acidity, dry matter amount, fat content, protein content, salt content, curd firmness, water soluble nitrogen, ripening degree, 12% TCA soluble nitrogen, 5% PTA soluble nitrogen, casein nitrogen, proteose-peptone nitrogen, total free amino acid values, color and sensory analysis were performed. Titration acidity, dry matter content, fat content, salt content, water soluble nitrogen, ripening degree, 12% TCA soluble nitrogen, 5% PTA soluble nitrogen, proteose-peptone nitrogen, total free amino acids, a^* and b^* values of cheeses increased while pH, protein content, curd firmness, casein nitrogen, L^* values and sensory points of cheeses decreased during storage. The effects of storage time on titration acidity, protein content, salt content, water soluble nitrogen, ripening degree, 12% TCA soluble nitrogen, 5% PTA soluble nitrogen, casein nitrogen, proteose-peptone nitrogen, total free amino acids, a^* values, curd firmness, appearance, odor and taste properties of cheeses were significant ($p<0.05$). As a result of sensory analysis, the most desirable cheese was selected as cheese that contained 30% yogurt.

Keywords— Yogurt cheese; acid coagulation; storage effects

I. INTRODUCTION

Yogurt cheese is produced by adding yogurt to boiling milk, filtering the whey, keeping the curd in brine or grating of curd, mixing with salt and black cumin, pressing into pots and lastly keeping at cool places. The milk-yogurt ratio changes with production places and producers [1], [2], [3], [4]. This cheese type is not produced by industrially; it is generally produced in small scaled plants or domestically and is sold in local markets. The origin of Yogurt cheese which is generally produced in Hatay and Mersin (Tarsus) provinces is considered as Arabic countries such as Syria and Lebanon [5]. It is known that Yogurt cheeses are used in making of desserts such as “Künefe”, “Cheese Halva” and “Semolina Dessert with cheese” in Hatay province [6].

The cheeses which are similar with Yogurt cheeses are generally in the form of “Tulum” cheeses. “Ayaş Ovma” cheese which is produced by adding black cumin to “Cokelek” and pressing into the pots, “Antalya Çoban” cheese which is produced by boiling and filtering of buttermilk that is obtained

by butter production, adding salt and black cumin to it and pressing into the pots, “Erzincan Tulum” cheese which is produced by coagulating of milk by enzyme, pressing the curd, mixing with black cumin and pressing into the pots, “Hatay Carra” cheese which is produced by mixing with cokelek with black cumin and crushed cheese with black cumin and pressing them into the pots, “Mersin Köy” cheese which is produced by adding rennet and some yogurt to cow and ewe milks, boiling of them, pressing the curd and pressing into the drums, “Çerkez” cheese which is produced by coagulation of milk by using whey can be shown as examples to these cheeses [7], [8], [9], [10], [11], [12]. It is possible to obtain cheese which is similar with Yogurt cheese can be produced by coagulating milk by lemon juice or vinegar [3], [11].

II. MATERIAL AND METHOD

Milk was obtained from Cukurova University Faculty of Agriculture, Research and Application Farm Animal Husbandry Branch. Yogurt was produced from obtained milk. Black cumin and salt were supplied from markets. Plastic cans were supplied from Konya Şah Plastik plant.

The first step is yogurt production for the production of Yogurt cheese. For this purpose, raw cow milk was heat treated (at 95°C for 5 min) and it is cooled to inoculation temperature ($44\pm 1^\circ\text{C}$). 3% yogurt (w/w) was inoculated to milk and it was incubated at $44\pm 1^\circ\text{C}$ up to pH 4.7. When the pH reached to 4.7, obtained yogurt was stored at $4\pm 1^\circ\text{C}$ for one night. After yogurt production, raw cow milk was boiled for producing of cheese. 20%, 30%, 40% and 50% (w/w) yogurt additions were performed to boiling milk. Yogurt and milk were boiled together for 10 minutes and they were cooled to room temperature. The curd was taken to cloth bags and they were pressed for removing the whey. After 2-3 hours pressing, cheeses were grated and kneading with 2% salt (w/w) and 1.25% black cumin (w/w). Obtained cheese was pressed into plastic drums and some cloth pieces were placed on the mouth of the drums. They were kept at $4\pm 1^\circ\text{C}$ for 90 days.

The chemical, physical and sensory analyses were performed at Çukurova University Food Engineering Department Dairy Technology Laboratory. pH values and titration acidities were measured according to [13]. Dry matter amounts were determined according to [14], Fat amounts were determined according to [15], protein contents were measured according

to [16], salt amounts were determined according to [17]. Water soluble nitrogen (WSN) and ripening degrees of cheeses were determined according to [16]. 12% Trichloroacetic acid (TCA) soluble nitrogen values were determined according to [18]. 5% Phosphotungstic acid (PTA) soluble nitrogen values were measured according to [16]. Casein nitrogen and proteose-peptone nitrogen values were determined according to [19]. Total free amino acid values were measured according to [20], [21]. Color measurement was performed by using Minolta CR-400 color meter. Curd firmness of cheeses was

determined according to [22]. Sensory properties were evaluated according to [13].

III. RESULTS

Some chemical properties of Yogurt cheeses which were obtained by adding yogurt in different ratios are shown in Table 1. In the table, the cheese that contains 20% yogurt is called as A, 30% yogurt is called as B, 40% yogurt is called as C, 50% yogurt is called as D.

Table 1. Some chemical properties of Yogurt cheeses while storage

Properties	Storage time (day)	Cheeses			
		A	B	C	D
pH	1	5.44±0.27 ^K	5.55±0.08 ^K	5.25±0.14 ^K	4.86±0.21 ^K
	15	5.41±0.27 ^K	5.47±0.14 ^K	5.26±0.15 ^K	4.85±0.22 ^K
	45	5.03±0.20 ^K	5.29±0.16 ^K	5.03±0.14 ^K	4.79±0.32 ^K
	90	5.08±0.12 ^K	5.28±0.03 ^K	5.12±0.10 ^K	4.94±0.17 ^K
Titration Acidity (in terms of %Lactic acid)	1	0.65±0.28 ^K	0.52±0.11 ^{KL}	0.65±0.17 ^K	0.89±0.24 ^K
	15	0.67±0.30 ^K	0.57±0.14 ^{KL}	0.72±0.22 ^K	0.87±0.22 ^K
	45	0.94±0.33 ^K	0.76±0.11 ^K	0.91±0.18 ^K	1.17±0.16 ^K
	90	0.90±0.43 ^K	0.33±0.08 ^L	0.80±0.14 ^K	0.86±0.21 ^K
Dry matter amount (%)	1	45.21±2.22 ^K	50.02±2.41 ^K	48.92±3.85 ^K	47.98±3.51 ^K
	15	46.13±2.45 ^K	49.91±2.20 ^K	48.54±3.85 ^K	48.67±3.70 ^K
	45	45.87±0.91 ^K	49.41±2.45 ^K	50.70±3.55 ^K	49.13±2.27 ^K
	90	46.17±1.30 ^K	50.17±3.08 ^K	50.77±2.86 ^K	46.47±0.33 ^K
Fat (%)	1	14.33±1.36 ^K	18.83±1.46 ^K	16.00±1.28 ^K	17.66±0.88 ^K
	15	15.33±1.67 ^K	18.75±2.88 ^K	16.25±1.37 ^K	19.75±1.34 ^K
	45	16.50±0.66 ^K	14.83±2.38 ^K	16.75±0.22 ^K	19.16±1.32 ^K
	90	17.83±0.93 ^K	19.41±0.72 ^K	20.25±0.75 ^K	18.08±0.33 ^K
Protein (%)	1	28.40±1.76 ^K	28.98±0.82 ^K	30.49±2.52 ^K	27.51 ±1.24 ^K
	15	22.84±4.87 ^K	27.48±0.7 ^K	28.81±2.72 ^K	21.91 ±2.29 ^L
	45	25.42±1.45 ^K	28.77±2.50 ^K	31.66±7.66 ^K	25.22±1.50 ^{KL}
	90	24.06±1.96 ^K	26.74±1.81 ^K	27.85±1.49 ^K	24.07±0.90 ^{KL}
Salt (%)	1	1.61±0.43 ^K	1.14± 0.15 ^{KL}	1.03±0.15 ^K	1.26±0.04 ^K
	15	1.27±0.58 ^K	0.83 ±0.14 ^L	1.04±0.09 ^K	1.64±0.45 ^K
	45	1.94±0.90 ^K	1.42 ±0.09 ^K	1.69±0.22 ^K	1.71±0.20 ^K
	90	2.25±1.08 ^K	1.32± 0.23 ^{KL}	1.55±0.24 ^K	2.07±0.52 ^K

K, L: Values that are shown in the same column with different exponential letters are different in terms of $p < 0.05$ level of significance.

When the table is examined, it is possible to see that the effects of storage time on pH, dry matter content and fat content of cheeses were not found significant ($p > 0.05$). Titration acidity

of cheeses increased during storage and the effects of storage time were found significant on titration acidity values of B cheese ($p < 0.05$). The increase of the titration acidity of

cheeses during storage was reported by many researchers [23], [24], [25], [26], [27], [28], [29], [30], [31]. The protein contents of cheeses decreased during storage and these changes on D cheese were found significant ($p<0.05$). In many research it is reported that the protein content of cheeses decreased while storage [32], [33], [34], [35], [36].

Salt content of cheeses increased during storage and the effects of storage time were found statistically significant on salt contents of B cheese ($p<0.05$). The increase of the salt contents of cheeses during storage was reported by many researchers [37], [38], [39], [40], [41].

Table 2. Nitrogen fractions and total free amino acid values of Yogurt cheeses while storage

	Storage time (day)	Cheeses			
		A	B	C	D
Water Soluble Nitrogen (%)	1	0.17 \pm 0.01 ^K	0.21 \pm 0.01 ^L	0.22 \pm 0.04 ^K	0.11 \pm 0.01 ^L
	15	0.13 \pm 0.02 ^K	0.13 \pm 0.03 ^L	0.14 \pm 0.03 ^K	0.10 \pm 0.001 ^L
	45	0.23 \pm 0.08 ^K	0.50 \pm 0.23 ^{KL}	0.55 \pm 0.20 ^K	0.31 \pm 0.11 ^K
	90	0.31 \pm 0.07 ^K	0.68 \pm 0.05 ^K	0.50 \pm 0.16 ^K	0.28 \pm 0.02 ^{KL}
Ripening degree (%)	1	3.83 \pm 0.24 ^K	4.78 \pm 0.31 ^{LM}	4.65 \pm 0.98 ^{KL}	2.57 \pm 0.06 ^L
	15	4.52 \pm 1.55 ^K	3.00 \pm 0.68 ^M	3.27 \pm 0.52 ^L	3.01 \pm 0.33 ^L
	45	5.93 \pm 2.17 ^K	10.65 \pm 4.11 ^{KL}	10.59 \pm 2.97 ^{KL}	8.05 \pm 2.90 ^K
	90	8.09 \pm 1.36 ^K	16.36 \pm 0.23 ^K	11.21 \pm 3.22 ^K	7.39 \pm 0.48 ^{KL}
12% TCA soluble nitrogen (%)	1	0.02 \pm 0.01 ^{aK}	0.02 \pm 0.01 ^L	0.01 \pm 0.01 ^L	0.02 \pm 0.01 ^K
	15	0.02 \pm 0.01 ^K	0.02 \pm 0.01 ^L	0.02 \pm 0.01 ^{KL}	0.02 \pm 0.01 ^K
	45	0.12 \pm 0.06 ^K	0.17 \pm 0.08 ^K	0.15 \pm 0.07 ^{KL}	0.20 \pm 0.11 ^K
	90	0.10 \pm 0.02 ^K	0.13 \pm 0.01 ^{KL}	0.17 \pm 0.04 ^K	0.11 \pm 0.01 ^K
5% PTA soluble nitrogen (%)	1	0.06 \pm 0.01 ^L	0.06 \pm 0.01 ^K	0.07 \pm 0.01 ^L	0.05 \pm 0.01 ^L
	15	0.09 \pm 0.02 ^L	0.05 \pm 0.01 ^K	0.07 \pm 0.01 ^L	0.05 \pm 0.01 ^L
	45	0.14 \pm 0.01 ^K	0.10 \pm 0.03 ^K	0.13 \pm 0.01 ^K	0.09 \pm 0.02 ^{KL}
	90	0.08 \pm 0.01 ^L	0.10 \pm 0.02 ^K	0.13 \pm 0.01 ^K	0.15 \pm 0.01 ^K
Casein nitrogen (%)	1	4.28 \pm 0.26 ^K	4.32 \pm 0.12 ^K	4.55 \pm 0.37 ^K	4.20 \pm 0.18 ^K
	15	3.44 \pm 0.77 ^K	4.17 \pm 0.09 ^K	4.36 \pm 0.40 ^K	3.33 \pm 0.35 ^K
	45	3.74 \pm 0.22 ^K	4.00 \pm 0.23 ^{KL}	4.40 \pm 1.02 ^K	3.63 \pm 0.28 ^K
	90	3.45 \pm 0.23 ^K	3.50 \pm 0.23 ^L	3.86 \pm 0.08 ^K	3.49 \pm 0.11 ^K
Protease-peptone nitrogen (%)	1	0.14 \pm 0.01 ^K	0.19 \pm 0.01 ^L	0.20 \pm 0.05 ^K	0.08 \pm 0.01 ^{KL}
	15	0.10 \pm 0.02 ^K	0.10 \pm 0.03 ^L	0.12 \pm 0.03 ^K	0.07 \pm 0.01 ^L
	45	0.11 \pm 0.02 ^K	0.33 \pm 0.15 ^{KL}	0.40 \pm 0.15 ^K	0.10 \pm 0.03 ^{KL}
	90	0.21 \pm 0.05 ^K	0.55 \pm 0.04 ^K	0.32 \pm 0.11 ^K	0.16 \pm 0.02 ^K
Total free amino acid (mg Leu/100 ml)	1	1.31 \pm 0.56 ^L	1.44 \pm 0.62 ^L	1.30 \pm 0.81 ^L	0.50 \pm 0.24 ^L
	15	1.35 \pm 0.54 ^L	1.55 \pm 0.74 ^L	1.26 \pm 0.72 ^L	0.34 \pm 0.09 ^L
	45	2.13 \pm 0.63 ^{KL}	2.44 \pm 1.26 ^{KL}	2.47 \pm 0.93 ^{KL}	2.85 \pm 0.75 ^K
	90	4.08 \pm 0.83 ^K	4.31 \pm 0.20 ^K	4.04 \pm 0.26 ^K	3.14 \pm 0.80 ^K

K, L: Values that are shown in the same column with different exponential letters are different in terms of $p<0.05$ level of significance.

Water soluble nitrogen value is accepted as an indicator of proteolysis and ripening of cheeses. Low molecular weight fractions of nitrogen levels which are occurred by casein

hydrolysis may be expressed by water soluble nitrogen value [42]. In this research, water soluble nitrogen values of Yogurt cheeses continuously increased during storage and the effects

of storage time on these values of B and D cheeses were found statistically significant ($p<0.05$). Similarly in another research, it is reported that water soluble nitrogen value increased with time [43]. The changes of ripening degrees of cheeses with storage time were also found significant on B, C and D cheeses.

12% TCA soluble nitrogen values of cheeses increased during storage and the effects of storage time were found statistically significant ($p<0.05$) on 12% TCA soluble nitrogen values of B and C cheeses. Similar results were reported in many other researches [44], [45], [46], [47].

5% PTA soluble nitrogen values of cheeses increased during storage similar with 12% TCA soluble nitrogen values. These increases were statistically significant ($p<0.05$) on 5% PTA soluble nitrogen values of A, C and D cheeses. In some other researches it was reported that 5% PTA soluble nitrogen values of cheeses increased during storage, too [48], [49], [50], [51].

Casein nitrogen values of cheeses decreased during storage and the changes on casein nitrogen values of B cheese were found statistically significant ($p<0.05$). Many researchers reported that while storage casein nitrogen values of cheeses decreased [52], [27], [33].

Protease-peptone nitrogen values of cheeses increased during storage and the effects of storage time were found statistically significant ($p<0.05$) on protease-peptone nitrogen values of B and D cheeses. Similar results were reported in many other researches [53], [54], [55], [56].

Total free amino acid content of cheeses increased during storage and the effects of storage time were found statistically significant on total free amino acid contents of all cheeses ($p<0.05$). The increase of the total free amino acid contents of cheeses during storage were reported by many researchers [57], [58], [59], [60].

Table 3. Color values of Yogurt cheeses while storage

	Storage time (day)	Cheeses			
		A	B	C	D
L*	1	85.03±3.51 ^K	80.71±1.19 ^K	83.24±3.77 ^K	85.69±4.92 ^K
	15	86.69±1.11 ^K	80.36±0.67 ^K	83.96±2.91 ^K	86.52±3.35 ^K
	45	84.97±1.11 ^K	78.76±5.04 ^K	82.74±4.27 ^K	90.68±1.74 ^K
	90	83.23±2.27 ^K	77.69±2.49 ^K	80.30±6.98 ^K	83.93±3.95 ^K
a*	1	-2.86±0.28 ^K	-3.75±0.28 ^L	-3.58±0.38 ^K	-2.79±0.22 ^K
	15	-2.89±0.39 ^K	-3.95±0.08 ^L	-3.27±0.36 ^K	-2.93±0.42 ^K
	45	-2.89±0.45 ^K	-3.38±0.22 ^L	-3.33±0.56 ^K	-2.57±0.32 ^K
	90	-2.57±0.49 ^K	-1.94±0.56 ^K	-1.41±1.13 ^K	-2.32±0.30 ^K
b*	1	11.79±1.48 ^K	13.52±0.71 ^K	13.30±1.23 ^K	11.14±1.52 ^K
	15	13.21±2.23 ^K	16.51±0.36 ^K	14.59±1.32 ^K	14.33±1.39 ^K
	45	13.20±1.75 ^K	13.90±1.37 ^K	12.96±1.18 ^K	12.00±1.20 ^K
	90	14.05±2.31 ^K	15.68±2.05 ^K	13.69±1.92 ^K	15.57±1.56 ^K

K, L: Values that are shown in the same column with different exponential letters are different in terms of $p<0.05$ level of significance.

In the colorimetric analysis, L* value is expressed brightness (0-100), a* value is expressed from green to redness (-120-120), b* value is expressed from blue to yellow (-120-120) [61], [62]. According to the statistical analyses, the storage time had no significant effects on L* and b* values of cheeses. a* values of cheeses increased during storage and these changes were found significant ($p<0.05$). In the other researches, it was reported that a* values of cheeses increased during storage [63], [33].

Table 4. Curd firmness and sensory properties of Yogurt cheeses while storage

	Storage time (day)	Cheeses			
		A	B	C	D
Curd firmness (1/10 mm)	1	52.05±1.63 ^K	39.66±5.09 ^K	30.88 ±2.79 ^{KL}	31.77±8.29 ^K
	15	42.63±2.82 ^K	35.05±9.66 ^K	40.97±10.90 ^K	25.36±7.05 ^K
	45	30.83±5.70 ^L	26.16±1.82 ^K	19.87 ±4.90 ^L	24.50±8.59 ^K
	90	19.83±2.91 ^L	20.33±6.14 ^K	15.41 ±1.81 ^L	21.75±6.14 ^K
Appearance	1	16.90±0.77 ^K	18.52 ± 0.47 ^K	16.52±0.17 ^K	14.61±0.31 ^K
	15	17.80±1.07 ^K	17.90±0.20 ^{KL}	16.14±0.45 ^K	15.85±0.43 ^K
	45	16.90±1.20 ^K	16.19 ± 0.96 ^L	15.00±1.28 ^K	12.61±0.70 ^L
	90	16.19±0.83 ^K	17.71±0.28 ^{KL}	15.80±0.90 ^K	15.28±0.45 ^K
Texture and structure	1	25.23±0.88 ^K	29.09±2.37 ^K	27.14±1.79 ^K	23.76±2.35 ^K
	15	28.71±2.35 ^K	30.42±1.44 ^K	28.04±1.71 ^K	25.23±0.73 ^K
	45	27.61±2.12 ^K	26.52±2.55 ^K	24.38±2.51 ^K	21.23±1.52 ^K
	90	25.19±0.53 ^K	27.61±1.11 ^K	25.38±1.09 ^K	24.66±1.95 ^K
Odor	1	7.80±0.62 ^K	9.14±0.00 ^K	8.09±0.49 ^K	8.47±0.28 ^K
	15	9.09±0.49 ^K	9.33±0.41 ^K	8.71±0.14 ^K	8.09±0.84 ^K
	45	7.23±1.17 ^K	7.76±0.61 ^L	7.71±0.71 ^K	7.19±0.45 ^K
	90	7.09±0.31 ^K	6.71±0.16 ^L	8.04±0.46 ^K	7.02±1.21 ^K
Taste	1	27.14±1.54 ^{KL}	30.23 ± 2.26 ^K	27.66±1.67 ^K	25.52±2.55 ^K
	15	30.61 ± 1.93 ^K	30.00 ± 0.78 ^K	27.76±1.66 ^K	24.57±1.58 ^K
	45	20.00 ± 2.61 ^L	23.42±2.91 ^{KL}	23.28±2.52 ^K	19.90±1.74 ^K
	90	19.42 ± 3.86 ^L	19.90 ± 1.61 ^L	24.76±1.63 ^K	22.57±3.51 ^K

K, L: Values that are shown in the same column with different exponential letters are different in terms of $p < 0.05$ level of significance.

Curd firmness of cheeses increased during storage and the effects of storage time were found statistically significant on curd firmness of A and C cheeses ($p < 0.05$). The increase of the curd firmness of cheeses during storage was reported by many researchers [64], [65], [66], [67].

When the sensory properties of cheeses were evaluated, it was seen that the texture and structural properties of cheeses were not affected by storage time significantly ($p > 0.05$). Appearance properties of B and D cheeses, odor properties of B cheese and taste properties of A and B cheeses were affected significantly by storage time ($p < 0.05$). D cheese which contained the highest yogurt amount was selected as the least desired cheese. The most desired one was chosen as B cheese with 80.13 points and C (76.11), A (75.75) and D(69.16) cheeses followed it respectively.

IV. CONCLUSION

Yogurt cheese is a traditional cheese type which is produced by directly using of yogurt instead of common coagulators. It could not be found any scientific research about Yogurt cheese which is produced by this method and it could not be reached enough information about cheeses that are obtained by using yogurt. It is considered that they are important to determine the properties of traditional cheeses and to record them. For this reason, further researches are required in these subjects.

As a result of the research, the effects of storage time on titration acidity, protein content, salt content, water soluble nitrogen, ripening degree, 12% TCA soluble nitrogen, 5% PTA soluble nitrogen, casein nitrogen, protease-peptone nitrogen, total free amino acids, a^* values, curd firmness, appearance, odor and taste properties of cheeses were significant ($p < 0.05$) and according to the sensory analysis, the most desirable cheese was selected as cheese that contained 30% yogurt.

REFERENCES

- [1] Anonymous, "Ev Yapımı Peynir". <http://blog.milliyet.com.tr/AramaBlogger/ev-yapimi-peynir/Blog/?BlogNo=96562>, (Access date: 19.02.2017) 2008.
- [2] Anonymous, "Küp Peyniri". http://tr.wikipedia.org/wiki/K%C3%BCp_peyniri, (Access date: 19.02.2017) 2014a.
- [3] Anonymous, "Süt Kesiginden Çörekotlu Peynir Yapımı". <http://www.reitix.com/Makaleler/Sut-Kesiginden-Corekotlu-Peynir-Yapimi/ID=4091>, (Access date: 19.02.2017) 2014b.
- [4] Anonymous, "Akdeniz Bölgesi Yöresel Peynirleri". <http://acar.coolpage.biz/ak.html>, (Access date: 19.02.2017) 2015a.
- [5] Anonymous, "A Spicer Side of Rosh Hashana". <http://articles.latimes.com/2007/sep/12/food/fo-aleppo12>, (Access date: 19.02.2017) 2007.
- [6] Say, D., Çayır, M.S. and Güzeler, N., Yoghurt Cheese Production and Consumption Types. The 3rd International Symposium on "Traditional Foods from Adriatic to Caucasus", 01-04 October, Sarajevo, Bosnia and Herzegovina, s. 210, 2015.
- [7] Adam, R.C., Peynir. Ders Kitabı, Ege Üniversitesi Ziraat Fakültesi Yayınları, No:176, İzmir, s.57, 1974.
- [8] Kırdar, S.S., Burdur Yöresi Geleneksel Peynirleri: Çökelek Peyniri. I.Burdur Sempozyumu, 16-19 Kasım, Burdur, 1176-1179, 2005.
- [9] Durlu Özkaya, F. and Gün, İ., Anadolu'da Peynir Kültürü. 38.ICANAS, 10-15 Eylül, Ankara, 2: 485-507, 2007.
- [10] Şahin, K., Hatay Mutfak Kültürü ve Yemekleri. T.C. Hatay Valiliği, s.111-115, 2012.
- [11] Anonymous, "Evde Peynir Yapımı". <http://www.gimdes.org/evde-peynir-yapimi.html>, (Access date 19.02.2017), 2015b.
- [12] Anonymous, "Ovma Peyniri". <http://www.peynirrehberi.com/Ovma-Peyniri,PR-142.html>, (Access date: 19.02.2017), 2015c.
- [13] TSE, TS 591 Beyaz Peynir Standardı. Türk Standartları Enstitüsü. Necatibey Caddesi, 112. Bakanlıklar, Ankara. s.9, 2006.
- [14] IDF, Determination of the Total Solid Content (Cheese and Processed Cheese). IDF Standart 4A, Brussels: International Dairy Federation, 1982.
- [15] TSE, TS 3046 Peynirde Yağ Miktarı Tayini (Van Gulik Metodu). Türk Standartları Enstitüsü. Necatibey Caddesi, 112. Bakanlıklar, Ankara, s.4, 1978.
- [16] IDF, Milk Determination of Nitrogen Content. IDF 20B, International Dairy Federation: 41, Brussels, s. 12, 1993.
- [17] TOKB, Gıda Maddeleri Muayene ve Analiz Yöntemleri. TC Tarım Orman ve Köyişleri Bakanlığı, Gıda İşleri Genel Müdürlüğü, Genel Yayın No: 65, Ankara, s.796, 1983.
- [18] Polychroniadou, A., Michaelidou, A. and Paschaloudis, N., Effect of Time, Temperature and Extraction Method on the Trichloroacetic Acid-Soluble Nitrogen of Cheese. International Dairy Journal, 9: 559-568, 1999.
- [19] Argumosa, O.G., Carballo, C., Bernardo, A.O. and Martin, R., Chemical Characterisation of aSpanish Artisanal Goat Cheese. Microbiologie-Aliments-Nutrition, 10:69-76, 1992.
- [20] Doi, E., Daisuke, S., and Matoba, T., Modified Colorimetric Ninhydrin Methods for Peptidase Assay. Analytical Biochemistry, 118(1): 173-184, 1981.
- [21] Folkertsma, B. and Fox, P.F., Use of Cd-ninhydrin Reagent to Assess Proteolysis in Cheddar Cheese During Ripening. Journal of Dairy Research, 59(2): 21224, 1992.
- [22] Güven, M. and Konar, A., Keçi Sütünden Üretilen Yarı Sert Kadiz Peyniri Üretimi. Çukurova Üniversitesi Ziraat Fakültesi Dergisi, 11(4): 137-146, 1994.
- [23] De Souza, C.F.V., Dalla Rosa, T. and Ayub, M.A.Z., Changes in The Microbiological and Physicochemical Characteristics of Serrano Cheese During Manufacture and Ripening. Brazilian Journal of Microbiology, 34: 260-266, 2003.
- [24] Güven, M., and Tatar Görmez, P., Antimikrobiyal Madde Kullanımı ve Paketleme Materyalinin Kaşar Peynirinin Bazı Özellikleri Üzerine Etkisi. Gıda ve Yem Teknolojisi, 5: 3-11, 2004.
- [25] Tarakçı, Z. and Küçüköner, E., Changes on Physicochemical, Lipolysis and Proteolysis of Vacuum packed Turkish Kashar Cheese During Ripening. Journal Central European Agriculture, 7(3): 459-464, 2006.
- [26] Jasinska, M., Dmytrow, I. and Stradomski, A., Changes of Selected Quality Attributes of Edam Cheese With Various Fat Contents During Storage. Pol. J. Food Nutr. Sci, 57(1): 31-38, 2007.
- [27] Yaşar, K., Farklı Pıhtılaştırıcı Enzim Kullanımının ve Olgunlaşma Süresinin Kaşar Peynirinin Özellikleri Üzerine Etkisi. Çukurova Üniversitesi, Ziraat Fakültesi, Gıda Mühendisliği Bölümü, Adana, Doktora Tezi, s.134, 2007.
- [28] Uaboi-Egbenni, P.O., Okolie, P.N., Akintunde, T.I., Bisi-Johnson, O., Enwe, L. and Bessong, P.O., Proximate Analysis and Microbiological Quality of Cheese Produced from Raw Cow Milk Obtained from Fulani Settlement in Ogun State Nigeria, Using Lactic Acid Bacteria and Extract from Sodom Apple Leaf (*Calotropis procera*). Pakistan Journal of Nutrition, 9(9): 920-925, 2010.
- [29] Emirmustafoglu, A. and Coşkun, H., Keçi Sütü, İnek Sütü ve Bu Sütlerin Karışımından Yapılan Otlı Peynirlerde Olgunlaşma Boyunca Meydana Gelen Değişmeler. Gıda Dergisi, 37 (4): 211-218, 2012.
- [30] Talevski, G., Traditional Production of Beaten Cheese. Third International Scientific Symposium "Agrosym Jahorina 2012", s.524-528, 2012.
- [31] Zaharia, N.C., Research Regarding Accelerated Ripening of Pasta Filata Cheeses. The Annals of the University Dunarea de Jos of Galati Fascicle VI – Food Technology, 36(1): 26-38, 2012.
- [32] Yaygın, H. and Dabiri, K., İnek, Koyun, Keçi Sütleriyle Yapılan ve Farklı Sıcaklıklarda Olgunlaştırılan Kaşar Peynirlerinin Özellikleri Üzerinde Araştırmalar. E.Ü.Z.F. Dergisi, 26(1): 333-346, 1989.
- [33] Say, D., Haşlama Suyunun Tuz Konsantrasyonu ve Depolama Süresinin Kaşar Peynirinin Özellikleri Üzerine Etkileri. Çukurova Üniversitesi, Ziraat Fakültesi, Gıda Mühendisliği Bölümü, Adana, Doktora Tezi, s. 131, 2008.
- [34] Kara, R., Geleneksel Bir Peynir: Afyon Tulum Peynirinin Karakterizasyonu ve Deneysel Olarak İnoküle Edilen *Brucella abortus* ve *Brucella melitensis* Suşlarının Üreme ve Canlı Kalma Yeteneklerinin Araştırılması. Afyon Kocatepe Üniversitesi, Besin/Gıda Hijyeni Ve Teknolojisi Anabilim Dalı, Afyonkarahisar, Doktora Tezi, s.168, 2011.
- [35] Teshome, B.T., Emire, S.A. and Jha, Y.K., Bio-Chemical and Textural Changes in Pre-Ripening Stages During Manufacture of Cheddar Cheese from Different Blends of Doe and Ewe Milk. World Journal of Dairy & Food Sciences, 7(1): 49-53, 2012.
- [36] Tavakolipour, H., Matini, S., Pasdar, N. and Jalilzade, A., Monitoring The Chemical and Textural Changes During Ripening of Iranian White Cheese Made with Different Concentration of Glucono Delta Lactone. Animal Biology & Animal Husbandry International Journal of the Bioflux Society, 6 (2): 181-188, 2014.
- [37] Göllü, E. and Koçak, C., Kazein / Yağ Oranı Farklı Sütlerden İmal Edilen Beyaz Peynirlerin Bazı Nitelikleri Üzerine Araştırmalar. Doğa, TU. Veterinerlik ve Hayvancılık Dergisi 13 (3): 265-272, 1989.
- [38] Uraz, T., Yetişemeyen, A. and Atamer, M., Kurutulmuş Peyniraltı Suyunun Beyaz Peynir Yapımında Kullanma Olanakları Üzerine Bir Araştırma. Gıda Dergisi, 15(3): 137-143, 1990.
- [39] Şahan, N., Konar, A. and Kleeberger, A., Hidrojen Peroksit, Isıl İşlem Uygulamaları ve Olgunlaşma Süresinin Beyaz Peynirin Kimyasal Niteliğine Etkisi. Gıda Dergisi, 21(2): 109-117, 1996.
- [40] Saltan Evrensel, S., Yüksek, N. and Berberoğlu, S., Farklı Salamuralarda Olgunlaştırılan Beyaz Peynirlerin Fiziko-Kimyasal ve Mikrobiyolojik Özellikleri. Y.Y.Ü. Vet. Fak. Derg., 9(1-2): 51-56, 1998.

- [41] Sulejmani, E., Musliu, Z.H. and Srbinovska, S., Influence of Starter Culture, Temperature and Processing Technology on The Quality of Macedonian White Brined Cheese. *Biotechnology in Animal Husbandry* 30(4): 579-588, 2014.
- [42] Koçak, C., Aydinoglu, G. and Uslu, K., Ankara Piyasasında Satılan Dil Peynirlerinin Proteoliz Düzeyi Üzerinde Bir Araştırma. *Gıda Dergisi*, 22(4): 251-255, 1997.
- [43] Tuncel, N.B., Güneşer, O., Engin, B., Yaşar, K., Zorba, N.N. and Karagül-Yüceer, Y., Ezine Peyniri II. Olgunlaşma Süresince Proteoliz Düzeyi. *Gıda Dergisi*, 35(1): 1-6, 2008.
- [44] Kindstedt, P.S., Yun, J.J., Barbano, D. M. and Larose, K. L., Mozzarella Cheese: Impact of Coagulant Concentration on Chemical Composition, Proteolysis and Functional Properties. *J. Dairy Sci.* 78: 2591-1297, 1995.
- [45] Mutluer, U., Uygulanan Bazı Farklı İşlemlerin Sünme Peynirinin Özellikleri Üzerine Etkisi. Çukurova Üniversitesi Fen Bilimleri Enstitüsü, Gıda Mühendisliği Anabilim Dalı, Adana, Yüksek Lisans Tezi, s.76, 2007.
- [46] Sert, D., Ayar, A. and Akin, N., The Effects of Starter Culture on Chemical Composition, Microbiological and Sensory Characteristics of Turkish Kasar Cheese during Ripening. *Internet Journal of Food Safety*, 9: 7-13, 2007.
- [47] Sabanoğlu, S., Emmental Peynirinin Bazı Özellikleri Üzerine Bakır Kullanımının Etkisi. Pamukkale Üniversitesi Fen Bilimleri Enstitüsü, Gıda Mühendisliği Anabilim Dalı, Denizli, Yüksek Lisans Tezi, s. 78, 2010.
- [48] Kaminarides, S. E., Anifantakis, E. M. and Alichanidis, E., Ripening Changes in Kopanisti Cheese. *Journal of Dairy Research*, 57: 271-279, 1990.
- [49] Pavia, M., Trujillo, A. J., Guamis, B. and Ferragut, V., Proteolysis in Monchego-Type Cheese Salted by Brine Vacuum Impregnation. *Journal of Dairy Science*, 83: 1441-1447, 2000.
- [50] Gürsoy, A., Effect of Using Attenuated Lactic Starter Cultures on Lipolysis and Proteolysis in Low Fat Kaşar Cheese. *Tarım Bilimleri Dergisi*, 15 (3): 285-292, 2009.
- [51] Çakmakçı, S., Gurses, M. and Gundogdu, E., The Effect of Different Packaging Materials on Proteolysis, Sensory Scores and Gross Composition of Tulum Cheese. *African Journal of Biotechnology*, 10 (21): 4444-4449, 2011.
- [52] Hayaloğlu, A.A., Starter Olarak Kullanılan Bazı Lactococcus Suşlarının Beyaz Peynirlerin Özellikleri Üzerine Etkisi. Çukurova Üniversitesi Fen Bilimleri Enstitüsü, Adana, Doktora Tezi, 170 s, 2003.
- [53] Karaca, O. B., Mikrobiyolojik Kaynaklı Proteolitik ve Lipolitik Enzim Kullanımının Beyaz Peynirlerin Özellikleri ve Olgunlaşma Hızları Üzerine Etkileri. Çukurova Üniversitesi, Fen Bilimleri Enstitüsü, Gıda Mühendisliği Anabilim Dalı, Adana, Yüksek Lisans Tezi, s.102, 2000.
- [54] Özer, H.B., Atasoy, A.F. and Akin, M.S., Some Properties of Urfa Cheese (A Traditional White Brined Turkish Cheese) Produced From Bovine and Ovine Milks. *International Journal of Dairy Technology*, 55: 94-99, 2002.
- [55] Atasoy, F., Farklı Tür Sütlerden Yapılan Urfa Peynirlerinin Nitelikleri Üzerine Değişik Pastörizasyon Normlarının ve Starter Kültürlerinin Etkileri. Ankara Üniversitesi, Fen Bilimleri Enstitüsü, Süt Teknolojisi Anabilim Dalı, Ankara, Doktora Tezi, s.275, 2004.
- [56] Sert, D., Geleneksel Yöntemle Üretilen Tulum Peynirlerinde Kullanılan Sütün Orijinine Bağlı Olarak Olgunlaşma Esnasında Meydana Gelen Bazı Değişmelerin Belirlenmesi. Selçuk Üniversitesi Fen Bilimleri Enstitüsü, Gıda Mühendisliği Anabilim Dalı, Konya, Doktora Tezi, s. 234, 2011.
- [57] Fernandez-Garcia, E., Lopez-Fandino, R., Alonso, I. and Ramos, M., The Use of Lipolytic and Proteolytic Enzymes in the Manufacture of Manchego Type Cheese from Ovine and Bovine Milk. *Journal of Dairy Science*, 77(8): 2139-2149, 1994.
- [58] Kandarakis, I., Moatsou, G., Georgala, A. I. K., Kaminarides, S. and Anifantakis, E., Effect of Draining Temperature on the Biochemical Characteristics of Feta Cheese. *Food Chemistry*, 72: 369-378, 2001.
- [59] Awad, S., Texture and Flavour Development in Ras Cheese Made from Raw and Pasteurised Milk. *Food Chemistry*, 97: 394-400, 2006.
- [60] Özcan, T. and Vapur, U.E., Effect of Different Rennet Type on Physico-Chemical Properties and Bitterness in White Cheese. *International Journal of Environmental Science and Development*, 4(1): 71-75, 2013.
- [61] McGuire, R.G., Reporting of Objective Color Measurements. *Hort Science*, 27(12): 1254-1255, 1992.
- [62] Leon, K., Mery, D., Pedreschi, F. and Leon, J., Color Measurement in L* a* b* Units from RGB Digital Images. *Food Research International*, 39: 1084-1091, 2006.
- [63] Saldo, J., Sendra, E. and Guamis, B., Colour Changes During Ripening of High Pressure Treated Hard Carpine Cheese. *High Pressure Research*, 22 (3-4): 659-663, 2002.
- [64] Yildiz, F., Koçak, C., Karacabey, A. and Gürsel, A., Türkiye’de Kaliteli Salamura Beyaz Peynir Üretim Teknolojisinin Belirlenmesi. *Doğa, Tarım, Veterinerlik ve Hayvancılık Dergisi*, 13(3): 384-392, 1989.
- [65] Thapa, T.B. and Gupta, V.K., Changes in Sensoric and Rheological Characteristics During Storage of Processed Cheese Foods Prepared with Added Whey Protein Concentrates. *Indian Journal of Dairy Science*, 45: 140-145, 1992.
- [66] Kaya, S., Effect of Salt on Hardness and Whiteness of Gaziantep Cheese During Short-Term Brining. *J. Food Eng.* 52: 155-159, 2002.
- [67] Calvo, M.V., Castillo, I., Diaz-Barcos, V., Requena, T. and Fontecha, J., Effect of Hygienized Rennet Paste and A Defined Strain Starter on Proteolysis, Texture and Sensory Properties of Semi-Hard Goat Cheese. *Food Chem.* 102: 917-924, 2007.

The Effects of Storage Time on the Properties of Soft Cheeses That Was Produced By Sodium Caseinate Addition to Fat Enriched Milk

Nuray Güzeler, Fazaleh Mesgari, Çağla Özbek

Çukurova University, Agricultural Faculty, Food Engineering Department

Adana, Turkey

nsahan@cu.edu.tr

Abstract— In this research, cheeses which were produced by adding sodium caseinate to milk for condensation in 1.5%, 2.5% and 3.5% ratios were stored for 90 days at $4\pm1^{\circ}\text{C}$. The effects of storage time on cheese yields, pH, titration acidity, dry matter, fat in dry matter, total nitrogen, protein, protein in dry matter, salt, salt in dry matter, curd firmness, water soluble nitrogen, ripening degree, 12% TCA soluble nitrogen, 5% PTA soluble nitrogen, casein nitrogen, proteose-peptone nitrogen, total free amino acids, color and sensory properties were determined. According to the statistical analyses that were performed it was determined that the storage time had significant effects ($p<0.05$) on pH, titration acidity, dry matter content, protein content, salt content, water soluble nitrogen, ripening degree, 5% PTA soluble nitrogen, casein nitrogen, proteose-peptone nitrogen, total free amino acid values, curd firmness, L^* , a^* and b^* values of Soft cheeses. There was no significant effects of storage time on fat content and 12% TCA soluble nitrogen values of Soft cheeses ($p>0.05$). As a result of sensory analysis; the most liked cheese were selected as cheese with 3.5% sodium caseinate and cheeses with 2.5% and 1.5% sodium caseinate were followed it respectively.

Key words— Condensed milk; Cottage White cheese; sodium caseinat; storage period

I. INTRODUCTION

Sodium caseinate is defined as milk protein and it is generally used as emulsifier and stabilizer. It binds water and fat molecules and it makes fat globules smaller for making foods have good appearances [1]. It is commonly used in making of yogurt and cheese for increasing protein content, in preparing light products, in protein and lysine enrichment of breads and in sticking sauces and meat products together [2],[3]. It is possible to elongate the shelf life of the foods by using sodium caseinate [4]. The advantages of increasing dry matter amount of milk may be remarked as;

- The production method is industrially profitable,
- The cheeses that are produced by this method have higher yield than other cheese types,

- The obtained cheeses are more hygienic because of the simplicity of the production method,
- The obtained cheeses have more nutritional values because there is no loss of serum protein and minerals with whey removing by this method [5], [6].

II. MATERIAL AND METHOD

For the production of Soft cheeses that were produced by using sodium caseinate ratio in different ratios, raw cow milk was obtained by Kültürova plant. Danisco MA19LYO starter culture was supplied from Danisco. Microbial cheese yeast (*Rhizomucor miehei*) that was used as coagulating enzyme was obtained from DSM Food Specialties. Cheese powder that was used in production of Soft cheese was supplied from Enka Milk plant. Sodium caseinate was supplied from MBH Food plant and salt was provided from Unvertuz Ind. Plant. For packaging, 500 grams of plastic cheese bowls were supplied from IML Çağrı Packaging.

The production procedure of Soft cheese was started with fat standardization of raw cow milk to 18% fat content. After standardization, milk was pre-heated to $35-45^{\circ}\text{C}$ and dry matter standardization was performed. For this reason, sodium caseinate with different ratios (1.5%, 2.5%, 3.5%), 1.5% cheese powder and 2% salt were added to milk. It was homogenized at 65°C at 180 bar. Then it was pasteurized at 75°C for 10 minutes. It was cooled to inoculation temperature (42°C) and 1% starter culture and 0.15g/100kg rennet additions were performed. It was packaged and incubated at 42°C for 9-11 hours until pH reached to 4.7. After incubation, cheeses were stored at $4-8^{\circ}\text{C}$ for 90 days.

The chemical, physical and sensory analyses were performed at Çukurova University Food Engineering Department Dairy Technology Laboratory. pH values and titration acidities were measured according to [7]. Dry matter amounts were determined according to [8], Fat amounts were determined according to [9], protein contents were measured according to [10], salt amounts were determined according to

[11]. Water soluble nitrogen (WSN) and ripening degrees of cheeses were determined according to [10]. 12% Trichloroacetic acid (TCA) soluble nitrogen values were determined according to [12]. 5% Phosphotungstic acid (PTA) soluble nitrogen values were measured according to [10]. Casein nitrogen and proteose-peptone nitrogen values were determined according to [13]. Total free amino acid values were measured according to [14], [15]. Color measurement was performed by using Minolta CR-400 color meter. Curd firmness of cheeses were determined according to [16]. Sensory properties were evaluated according to [7].

Some chemical properties of soft cheeses which were obtained by adding sodium caseinate in different ratios are shown in Table I. In the table, the cheese that contains 1.5% sodium caseinate is called as A, 2.5% sodium caseinate is called as B, 3.5% sodium caseinate is called as C.

When the chemical properties of Soft cheeses were evaluated, it could be seen that pH values of cheeses decreased during storage. The effects of storage time were found statistically significant on pH values of all Soft cheeses ($p < 0.05$). It was reported that pH values of cheeses decreased with time in many researches [17],[18],[19],[20],[21],[22].

III. RESULTS

Table 1. Some chemical properties of Soft cheeses while storage

	Storage time (day)	Cheeses		
		A	B	C
pH	1	4.64 ± 0.01 ^M	4.60 ± 0.01 ^M	4.59 ± 0.01 ^M
	15	4.54 ± 0.01 ^{LM}	4.50 ± 0.01 ^L	4.50 ± 0.01 ^L
	45	4.47 ± 0.01 ^L	4.45 ± 0.00 ^L	4.43 ± 0.01 ^L
	90	4.27 ± 0.25 ^K	4.20 ± 0.00 ^K	4.09 ± 0.09 ^K
Titration Acidity (in terms of % Lactic acid)	1	1.16 ± 0.07 ^K	1.20 ± 0.01 ^K	1.22 ± 0.03 ^K
	15	1.23 ± 0.05 ^{KL}	1.32 ± 0.01 ^{KL}	1.34 ± 0.01 ^{KL}
	45	1.29 ± 0.02 ^{KL}	1.35 ± 0.02 ^{KL}	1.39 ± 0.01 ^{KL}
	90	1.60 ± 0.02 ^L	1.71 ± 0.00 ^L	1.79 ± 0.00 ^L
Dry matter amount (%)	1	24.96 ± 0.29 ^L	26.54 ± 0.22 ^M	27.03 ± 0.56 ^L
	15	25.05 ± 1.08 ^L	27.22 ± 1.13 ^{LM}	27.84 ± 0.25 ^L
	45	25.41 ± 0.83 ^L	27.98 ± 0.41 ^L	29.38 ± 0.64 ^K
	90	29.14 ± 0.93 ^K	29.55 ± 0.55 ^K	29.94 ± 0.18 ^K
Fat (%)	1	17.50 ± 0.50 ^K	17.33 ± 0.57 ^K	17.83 ± 0.76 ^K
	15	18.00 ± 0.50 ^K	18.16 ± 0.28 ^K	17.83 ± 1.04 ^K
	45	18.16 ± 0.76 ^K	18.16 ± 1.04 ^K	18.33 ± 0.57 ^K
	90	18.33 ± 1.15 ^K	18.66 ± 0.57 ^K	18.66 ± 0.28 ^K
Protein (%)	1	6.25 ± 0.81 ^M	6.51 ± 0.16 ^L	6.89 ± 0.19 ^{KL}
	15	5.87 ± 1.33 ^L	6.38 ± 1.01 ^{KL}	6.64 ± 0.06 ^{KL}
	45	5.68 ± 0.35 ^{KL}	6.19 ± 0.03 ^K	6.32 ± 0.06 ^K
	90	5.30 ± 0.20 ^K	6.06 ± 0.07 ^K	6.06 ± 0.01 ^K
Salt (%)	1	0.84 ± 0.03 ^M	0.78 ± 0.01 ^M	0.72 ± 0.04 ^N
	15	1.01 ± 0.08 ^L	0.92 ± 0.01 ^L	0.88 ± 0.03 ^M
	45	1.22 ± 0.04 ^K	1.13 ± 0.03 ^K	1.04 ± 0.02 ^L
	90	1.33 ± 0.08 ^K	1.19 ± 0.06 ^K	1.13 ± 0.01 ^K

K, L, M: Values that are shown in the same column with different exponential letters are different in terms of $p < 0.05$ level of significance.

Titration acidities of Soft cheeses increased unlike pH values during storage and the similar results were reported in some other researches in terms of increasing titration acidities of

cheeses [23], [24], [25], [26], [27], [28], [29], [30]. Storage time had statistically significant effects on titration acidities of all Soft cheeses ($p < 0.05$).

Table 2. Nitrogen fractions and total free amino acid values of Soft cheeses while storage

	Storage time (day)	Cheeses		
		A	B	C
Water Soluble Nitrogen (%)	1	0.06 ± 0.02 ^M	0.11 ± 0.00 ^N	0.12 ± 0.00 ^M
	15	0.09 ± 0.00 ^L	0.11 ± 0.00 ^M	0.13 ± 0.01 ^{LM}
	45	0.11 ± 0.00 ^{KL}	0.14 ± 0.00 ^L	0.14 ± 0.00 ^L
	90	0.12 ± 0.00 ^K	0.18 ± 0.00 ^K	0.19 ± 0.00 ^K
Ripening degree (%)	1	4.95 ± 0.00 ^K	8.20 ± 0.85 ^K	8.27 ± 0.62 ^K
	15	8.16 ± 2.42 ^K	9.73 ± 1.94 ^M	9.90 ± 1.64 ^{LM}
	45	9.93 ± 0.50 ^K	12.60 ± 0.04 ^M	12.18 ± 0.11 ^N
	90	14.10 ± 0.22 ^K	18.32 ± 0.11 ^L	18.43 ± 0.31 ^L
12% TCA soluble nitrogen (%)	1	0.03 ± 0.00 ^K	0.03 ± 0.00 ^K	0.03 ± 0.00 ^K
	15	0.02 ± 0.01 ^K	0.03 ± 0.00 ^K	0.03 ± 0.00 ^K
	45	0.02 ± 0.00 ^K	0.04 ± 0.00 ^K	0.04 ± 0.00 ^K
	90	0.03 ± 0.00 ^K	0.04 ± 0.00 ^K	0.04 ± 0.00 ^K
5% PTA soluble nitrogen (%)	1	0.05 ± 0.00 ^K	0.06 ± 0.00 ^{KL}	0.07 ± 0.00 ^{KL}
	15	0.06 ± 0.00 ^{KL}	0.05 ± 0.00 ^L	0.06 ± 0.00 ^L
	45	0.05 ± 0.01 ^K	0.05 ± 0.00 ^L	0.07 ± 0.00 ^{KL}
	90	0.06 ± 0.00 ^{KL}	0.07 ± 0.00 ^K	0.08 ± 0.00 ^K
Casein nitrogen (%)	1	1.15 ± 0.13 ^M	1.23 ± 0.00 ^K	1.33 ± 0.00 ^K
	15	1.06 ± 0.20 ^L	1.06 ± 0.00 ^L	1.15 ± 0.01 ^{KL}
	45	0.98 ± 0.05 ^K	0.96 ± 0.00 ^M	1.00 ± 0.00 ^L
	90	0.71 ± 0.03 ^K	0.80 ± 0.00 ^N	0.84 ± 0.00 ^M
Proteose-peptone nitrogen (%)	1	0.41 ± 0.12 ^M	0.54 ± 0.00 ^K	0.59 ± 0.00 ^K
	15	0.84 ± 0.22 ^L	0.92 ± 0.00 ^L	0.94 ± 0.00 ^{KL}
	45	1.13 ± 0.05 ^K	1.17 ± 0.00 ^{LM}	1.18 ± 0.00 ^L
	90	1.18 ± 0.03 ^K	1.21 ± 0.00 ^M	1.22 ± 0.00 ^L
Total free amino acid (mg Leu/100 ml)	1	0.43 ± 0.01 ^M	1.11 ± 0.01 ^M	1.80 ± 0.01 ^M
	15	0.44 ± 0.00 ^M	1.38 ± 0.01 ^{LM}	1.71 ± 0.02 ^N
	45	0.52 ± 0.04 ^L	1.64 ± 0.35 ^{KL}	1.95 ± 0.02 ^L
	90	0.69 ± 0.06 ^K	1.91 ± 0.15 ^K	2.10 ± 0.05 ^K

K, L, M: Values that are shown in the same column with different exponential letters are different in terms of $p < 0.05$ level of significance.

Dry matter amounts of Soft cheeses increased during storage and this increase was found statistically significant on all cheese types ($p < 0.05$). Increasing of dry matter amounts of

different cheeses by time was reported by many researchers [31], [32], [33], [34], [35], [36], [37], [38], [39]. The storage

time had no significant effect on fat contents of cheeses ($p>0.05$).

Soft cheeses' protein contents decreased during storage and similar decreases were reported by many researchers [40], [41], [42], [43]. The effects of storage time were found statistically significant on protein contents of all Soft cheeses ($p<0.05$).

Salt content of cheeses increased during storage and the effects of storage time were found statistically significant on salt contents of A, B and C cheeses ($p<0.05$). The increase of the salt contents of cheeses during storage was reported by many researchers [44], [18], [45], [2], [46], [47]. Nitrogen fractions and total free amino acid values of Soft cheeses during storage are given in Table II.

Water soluble nitrogen and ripening degrees of Soft cheeses increased during storage. These increases were reported by some researchers [2], [46]. The effects of storage time were found statistically significant on water soluble nitrogen values of all Soft cheeses and ripening degrees of B and C cheeses ($p<0.05$). There was no statistically significant effect on 12% TCA soluble nitrogen values of cheeses ($p>0.05$).

5% PTA soluble nitrogen values and proteose-peptone nitrogen values of cheeses increased during storage and the effects of storage time were found statistically significant on 5% PTA soluble nitrogen values and proteose-peptone nitrogen values of A, B and C cheeses ($p<0.05$). The increase of the 5% PTA soluble nitrogen values of cheeses during storage was reported by many researchers [48], [46], [49], [50]. Otherwise casein nitrogen values of cheeses decreased with time and this decrease was found statistically important ($p<0.05$). It was reported that casein nitrogen values increased during storage in many researches [51], [52], [2], [41]. Additionally the increase of the proteose-peptone nitrogen values of cheeses during storage was reported by many researchers [53], [52], [54], [55].

There were increases on total free amino acid values of Soft cheeses during storage and storage time affects total free amino acid values of all cheeses significantly ($p<0.05$). In some researches, it was reported that total free amino acid values of different cheeses increased while storage [54], [56]. The results of the color measurements are shown at the Table III.

Table 3. Color values of Soft cheeses while storage

	Storage time (day)	Cheeses		
		A	B	C
L*	1	96.00±0.26 ^K	93.79±3.74 ^{KL}	94.97±1.02 ^K
	15	95.89±0.31 ^K	96.08 ± 0.59 ^K	95.27±0.74 ^K
	45	95.23±0.76 ^K	92.74±0.26 ^{KL}	92.66±0.54 ^L
	90	91.98±1.34 ^L	90.98 ± 0.97 ^L	91.36±2.00 ^L
a*	1	-2.81 ±0.09 ^K	-2.81 ± 0.19 ^L	-2.68 ±0.15 ^{KL}
	15	-2.59 ±0.06 ^K	-2.98±0.03 ^{LM}	-2.42 ± 0.16 ^K
	45	-3.04±0.45 ^{KL}	-3.10 ±0.12 ^M	-3.18 ± 0.40 ^L
	90	-3.39 ±0.21 ^L	-2.43±0.07 ^K	-3.07±0.56 ^{KL}
b*	1	9.26 ± 0.18 ^L	9.78±0.11 ^K	8.51±0.46 ^K
	15	10.37±0.06 ^{KL}	9.95±0.15 ^K	8.34±0.56 ^K
	45	10.20±1.02 ^{KL}	9.93±0.51 ^K	9.73±0.87 ^K
	90	11.23 ± 1.07 ^K	9.64±0.39 ^K	9.48±1.11 ^K

K, L, M: Values that are shown in the same column with different exponential letters are different in terms of $p<0.05$ level of significance.

L* values of cheeses decreased during storage and the effects of storage time were found significant on L* values of all cheeses ($p<0.05$). Some other researchers reported that L* values of cheeses decreased with [57], [58], [59].

a* values of Soft cheeses increased while storage. Storage time had statistically significant ($p<0.05$) effects on a* values of all cheeses. It was reported that increasing of a* values was occurred with time [41], [58].

There were increases on b* values of Soft cheeses during storage and storage time affects b* values of C cheeses significantly ($p<0.05$). In a research, it was reported that b* values of different cheeses increased while storage [57]. The curd firmness and sensory properties of Soft cheeses are shown at Table IV.

Curd firmness of cheeses increased during storage and the effects of storage time were found statistically significant on

curd firmness of A, B and C cheeses ($p<0.05$). The increase of the curd firmness of cheeses during storage was reported by many researchers [2], [60], [61].

Table 4. Curd firmness and sensory properties of Soft cheeses while storage

	Storage time (day)	Cheeses		
		A	B	C
Curd firmness (1/10 mm)	1	304.00± 22.71 ^K	320.00 ± 5.00 ^K	329.00 ± 3.60 ^K
	15	266.00±35.53 ^{KL}	281.66±16.07 ^L	301.66 ± 8.50 ^L
	45	221.33±26.76 ^{LM}	240.33±11.23 ^M	251.33±12.22 ^M
	90	191.00 ± 6.00 ^M	199.00± 2.64 ^N	207.66 ± 4.04 ^N
Appearance	1	4.50±0.00	4.57±0.00	5.00±0.00
	15	4.57±0.00	4.28±0.00	4.92±0.00
	45	3.66±0.00	4.33±0.00	5.00±0.00
	90	-	-	-
Texture and structure	1	3.71±0.00	4.07±0.00	8.50±0.00
	15	3.85±0.00	4.14±0.00	8.57±0.00
	45	3.08±0.00	4.16±0.00	7.91±0.00
	90	-	-	-
Taste and Odor	1	5.00±0.00	5.00±0.00	9.85±0.00
	15	4.92±0.00	5.00±0.00	8.57±0.00
	45	5.00±0.00	5.00±0.00	7.66±0.00
	90	-	-	-

K, L, M: Values that are shown in the same column with different exponential letters are different in terms of $p<0.05$ level of significance.

Sensory analyses were performed on Soft cheeses at 1st, 15th and 45th days of the storage. It could not been performed at 90th day of the storage because of molding on the surface of the cheeses. When the sensory properties of cheeses were generally evaluated, it was determined that the most desired cheese was C cheese which contained the highest sodium caseinate ratio (3.5%) and B and A cheeses followed it respectively. According to obtained results, it was concluded that Soft cheeses should be consumed as fresh and sodium caseinate addition improved the sensory properties of Soft cheeses.

IV. CONCLUSION

It was determined that sodium caseinate addition affected the sensory properties of cheeses in a positive way. According to the results of the sensory analyses it was determined that the most desired cheese was cheese contained 3.5% sodium caseinate and the least desired one was cheese contained 1.5% sodium caseinate. The negativities that were happened on the taste and odor properties of Soft cheeses at the 45th days of the storage showed that the Soft cheeses should

be consumed as fresh. Molds and off-flavors were occurred on the surface of the cheeses at the 90th day of the storage.

As a result of the research it was determined that the storage time had significant effects ($p<0.05$) on pH, titration acidity, dry matter content, protein content, salt content, water soluble nitrogen, ripening degree, 5% PTA soluble nitrogen, casein nitrogen, proteose-peptone nitrogen, total free amino acid values, curd firmness, L*, a* and b* values of Soft cheeses.

REFERENCES

- [1] Erdoğan, Ö. and Ergün, Ö., Dana Jambon Üretiminde Sodyum Difosfat ve Sodyum Kazeinatın Çeşitli Kombinasyonlarda Kullanılması ve Bunların Ürünün Bazı Duyusal Olarak Algılanan Fiziksel Özelliklerine ve Bazı Kimyasal Özelliklerine Etkileri. KSÜ Fen ve Mühendislik Dergisi, 7(2):29-33, 2004.
- [2] Güven, M., Saydam, İ.B. and Karaca, O.B., Kazeinat Kullanımının Beyaz Peynir Randımanı ve Özellikleri Üzerine Etkileri. Gıda Dergisi, 31(4):187-194, 2006.
- [3] Anonymous, Sodyum Kazeinat. <http://www.sodyum.gen.tr/sodyum-kazeinat.html> (Access date: 24.02.2017), 2016.

- [4] Sarioğlu, T. and Öner, Z., Yenilebilir Filmlerin Kaşar Peynirinin Kaplanması Kullanılma Olanakları ve Peynir Kalitesi Üzerine Etkileri. *Gıda Dergisi*, 31(1):3-10, 2006.
- [5] Kelly, A.L., Huppertz, T. and Sheehan, J.J., Pre-Treatment of Cheese Milk: Principles and Developments. *Dairy Science and Technology* 88:549-572, 2008.
- [6] Mahdavi, A., Ehsani, M. and Mirzayee, M., Koyulaştırılmış Sütten Üretilen Peynir Yöntemiyle Süzme yoğurt Üretimi. Sabzevar Üniversitesi Gıda Mühendisliği Bölümü, Tahran, 2009.
- [7] TSE, TS 591 Beyaz Peynir Standardı. Türk Standartları Enstitüsü. Necatibey Caddesi, 112. Bakanlıklar, Ankara. s.9, 2006.
- [8] IDF, Determination of the Total Solid Content (Cheese and Processed Cheese). IDF Standart 4A, Brussels: International Dairy Federation, 1982.
- [9] TSE, TS 3046 Peynirde Yağ Miktarı Tayini (Van Gulik Metodu). Türk Standartları Enstitüsü. Necatibey Caddesi, 112. Bakanlıklar, Ankara, s.4, 1978.
- [10] IDF, Milk Determination of Nitrogen Content. IDF 20B, International Dairy Federation: 41, Brussels, s. 12, 1993.
- [11] TOKB, Gıda Maddeleri Muayene ve Analiz Yöntemleri. TC Tarım Orman ve Köyşleri Bakanlığı, Gıda İşleri Genel Müdürlüğü, Genel Yayın No: 65, Ankara, s.796, 1983.
- [12] Polychroniadou, A., Michaelidou, A. and Paschaloudis, N., Effect of Time, Temperature and Extraction Method on the Trichloroacetic Acid-Soluble Nitrogen of Cheese. *International Dairy Journal*, 9: 559-568, 1999.
- [13] Argumosa, O.G., Carballo, C., Bernardo, A.O. and Martin, R., Chemical Characterisation of a Spanish Artisanal Goat Cheese. *Microbiologie-Aliments-Nutrition*, 10:69-76, 1992.
- [14] Doi, E., Daisuke, S., and Matoba, T., Modified Colorimetric Ninhydrin Methods for Peptidase Assay. *Analytical Biochemistry*, 118(1): 173-184, 1981.
- [15] Folkertsma, B. and Fox, P.F., Use of Cd-ninhydrin Reagent to Assess Proteolysis in Cheddar Cheese During Cheese Ripening. *Journal of Dairy Research*, 59(2): 21224, 1992.
- [16] Güven, M. and Konar, A., Keçi Sütünden Üretilen Yarı Sert Kadız Peyniri Üretimi. Çukurova Üniversitesi Ziraat Fakültesi Dergisi, 11(4): 137-146, 1994.
- [17] Özdemir, C., and Demirci, M., Soğutulmuş Sütlerden Üretilen Kaşar Peynirlerine Sorbat Katılmasının Etkileri. T.Ü. Fen Bilimleri Enstitüsü, Doktora Tezi, s.91, 1997.
- [18] Saltan Evrensel, S., Yüksek, N. and Berberoğlu, S., Farklı Salamuralarda Olgunlaştırılan Beyaz Peynirlerin Fiziko-Kimyasal ve Mikrobiyolojik Özellikleri. *Y.Y.Ü. Vet. Fak. Derg.*, 9(1-2): 51-56, 1998.
- [19] Pastorino, A.J., Hansen, C.L. and McMahon, D.J., Effect of pH on the Chemical Composition and Structure Function Relationships of Cheddar Cheese. *Journal of Dairy Science*, 86(9):2751-60, 2003.
- [20] Najafi, M.N., Koocheki, A. and Mahdizadeh, M., Studies on the Effect of Starter Culture Concentration and Renneting pH on the Iranian Brine Cheese Yield. *American-Eurasian J. Agric. and Environ. Sci.*, 3(3): 325-332, 2008.
- [21] Hui, Y.H., Handbook of Food Science, Technology and Engineering. CRC Press, Volume 2, p.1000, 2006.
- [22] Moller, K.K., Effect of NaCl Content in Cheddar Cheese of Equal Moisture Content Manufacture and Metabolic Characteristics During Ripening. The 8th Cheese Symposium, Cork, 2011.
- [23] Tarakçı, Z. and Küçüköner, E., Changes on Physicochemical, Lipolysis and Proteolysis of Vacuum packed Turkish Kashar Cheese During Ripening. *Journal Central European Agriculture*, 7(3): 459-464, 2006.
- [24] Jasinska, M., Dmytrow, I. and Stradomski, A., Changes of Selected Quality Attributes of Edam Cheese With Various Fat Contents During Storage. *Pol. J. Food Nutr. Sci.*, 57(1): 31-38, 2007.
- [25] Perveen, K., Alabdulkarim, B. and Arzoo, S., Effect of Temperature on Shelf Life, Chemical and Microbiological Properties of Cream Cheese. *African Journal of Biotechnology*, 10(74):16929-16936, 2011.
- [26] Talevski, G., Traditional Production of Beaten Cheese. Third International Scientific Symposium "Agrosym Jahorina 2012", s.524-528, 2012.
- [27] Zaharia, N.C., Research Regarding Accelerated Ripening of Pasta Filata Cheeses. *The Annals of the University Dunarea de Jos of Galati Fascicle VI – Food Technology*, 36(1): 26-38, 2012.
- [28] Akarca, G., Çağlar, A. and Tomar, O., The Effects of Spicing on Quality of Mozzarella Cheese. *Mljekarstvo*, 66(2):112-121, 2016.
- [29] Regu, M., Yılma, Z. and Seifu, E., Effect of Garlic (*Allium sativum*) and Ginger (*Zingiber officinale*) Powder on Chemical Composition and Sensory Property of Ayib-Ethiopian Cottage Cheese. *International Food Research Journal*, 23(3):1226-1232, 2016.
- [30] Yagoub, A.H., Abdel Razig, K.A. and Abdalla, M.I., Effect of Different Levels of Palm Oil on the Compositional Quality of Mozzarella Cheese During Storage. *American Journal of Research Communication*, 4(4):97-112, 2016.
- [31] Verdier-Metz, L., Coulon, J.B. and Pradel, P., Relationship Between Milk Fat and Protein Contents and Cheese Yield. *Anim. Res.*, 50: 365–371, 2001.
- [32] Tarakçı, Z., The Effects of Packaging Materials and Filling Methods on Some Characteristics of Herby Cheese (Otlu Peynir). *Proceedings of European Congress of Chemical Engineering (ECCE-6)*, Copenhagen, 16-20 September, 2007.
- [33] Yaşar, K., Farklı Pıhtılaştırıcı Enzim Kullanımının ve Olgunlaşma Süresinin Kaşar Peynirinin Özellikleri Üzerine Etkisi. Çukurova Üniversitesi, Ziraat Fakültesi, Gıda Mühendisliği Bölümü, Adana, Doktora Tezi, s.134, 2007.
- [34] El-Owni, O.A.O. and Hamid, O.I.A., Effect of Storage Period on Weight Loss, Chemical Composition, Microbiological and Sensory Characteristics of Sudanese White Cheese (Gibna Bayda). *Pakistan Journal of Nutrition* 7 (1): 75-80, 2008.
- [35] Ali, A.M. and Abdel-Razig, K.A., Cholesterol Content of Mozzarella Cheese During Storage as Affected by Level of Milk Fat. *Pakistan Journal of Nutrition*, 10(1):65-70, 2011.
- [36] Vandenberghe, E., Choucharina, S., Luca, S., De Ketelaere, B., De Baerdemaeker, J. and Claes, J., Spatio-Temporal Changes of Physicochemical Parameters During Cheese Ripening. *Inside Food Symposium*, 9-12 April, Leuven, Belgium, 2013.
- [37] Elhaseen, H.A., Hamid, O.I.A. and El Owni, A.O., Effect of Lime and Grape Fruit Extract as Coagulants on Chemical Composition of Sudanese White Soft Cheese During Storage. *International Journal of Advanced Research in Biological Sciences*, 1(7):123-130, 2014.
- [38] Karaca, O.B. and Güven, M., Effect of Commercial Lipase and Protease Enzymes from Microbiological Sources on Properties of White Cheese. *Turkish Journal of Agricultural and Natural Sciences*, Special Issue: 1: 1080-1084, 2014.
- [39] Mushtaq, M., Gani, A., Shetty, P.H. and Ahmad, M., Himalayan Cheese (Kaları/Kradi): Effect of Different Storage Temperatures on Its Physicochemical, Microbiological and Antioxidant Properties. *Lebensmittel-Wissenschaft und-Technologie* 63(2), 2015.
- [40] Yaygın, H. and Dabiri, K., İnek, Koyun, Keçi Sütleriyle Yapılan ve Farklı Sıcaklıklarda Olgunlaştırılan Kaşar Peynirlerinin Özellikleri Üzerinde Araştırmalar. *E.Ü.Z.F. Dergisi*, 26(1): 333-346, 1989.
- [41] Say, D., Haşlama Suyunun Tuz Konsantrasyonu ve Depolama Süresinin Kaşar Peynirinin Özellikleri Üzerine Etkileri. Çukurova Üniversitesi, Ziraat Fakültesi, Gıda Mühendisliği Bölümü, Adana, Doktora Tezi, s. 131, 2008.
- [42] Alizadeh, M. and Shahab Lavasani, A.R., Effect of Different Types of Milk on Some Physicochemical and Sensory Characteristics of Iranian White Brined Cheese. *Annals of Biological Research*, 4 (10):67-70, 2013.
- [43] Tavakolipour, H., Matini, S., Pasdar, N. and Jalilzade, A., Monitoring The Chemical and Textural Changes During Ripening of Iranian White Cheese Made with Different Concentration of Glucono Delta Lactone. *Animal Biology & Animal Husbandry International Journal of the Bioflux Society*, 6 (2): 181-188, 2014.
- [44] Şahan, N., Konar, A. and Kleeberger, A., Hidrojen Peroksit, Isıl İşlem Uygulamaları ve Olgunlaşma Süresinin Beyaz Peynirin Kimyasal Niteliğine Etkisi. *Gıda Dergisi*, 21(2): 109-117, 1996.
- [45] Yüzbaşı, N. and Uraz, T., Glucono Delta Lactone (GDL)'ün Beyaz Peynir Üretiminde Kullanılması II. Starter Kültürü Katılmış*. *Tarım Bilimleri Dergisi*, 6(1):15-21, 2000.

- [46] Tuncel, N.B., Güneşer, O., Engin, B., Yaşar, K., Zorba, N.N. and Karagül-Yüceer, Y., Ezine Peyniri II. Olgunlaşma Süresince Proteoliz Düzeyi. *Gıda Dergisi*, 35(1): 1-6, 2008.
- [47] Sulejmani, E., Musliu, Z.H. and Srbinovska, S., Influence of Starter Culture, Temperature and Processing Technology on The Quality of Macedonian White Brined Cheese. *Biotechnology in Animal Husbandry* 30(4): 579-588, 2014.
- [48] Pavia, M., Trujillo, A. J., Guamis, B. and Ferragut, V., Proteolysis in Monchecho-Type Cheese Salted by Brine Vacuum Impregnation. *Journal of Dairy Science*, 83: 1441-1447, 2000.
- [49] Gürsoy, A., Effect of Using Attenuated Lactic Starter Cultures on Lipolysis and Proteolysis in Low Fat Kaşar Cheese. *Tarım Bilimleri Dergisi*, 15 (3): 285-292, 2009.
- [50] Çakmakçı, S., Gurses, M. and Gundoğdu, E., The Effect of Different Packaging Materials on Proteolysis, Sensory Scores and Gross Composition of Tulum Cheese. *African Journal of Biotechnology*, 10 (21): 4444-4449, 2011.
- [51] Hayaloğlu, A.A., Starter Olarak Kullanılan Bazı Lactococcus Suşlarının Beyaz Peynirlerin Özellikleri Üzerine Etkisi. Çukurova Üniversitesi Fen Bilimleri Enstitüsü, Adana, Doktora Tezi, 170 s, 2003.
- [52] Çürük, M., Kaşar Benzeri Peynirlerin Bazı Özellikleri Üzerine Eritme Tuzu Kullanımının ve Olgunlaşma Süresinin Etkileri. Çukurova Üniversitesi, Fen Bilimleri Enstitüsü, Gıda Mühendisliği Anabilim Dalı, Doktora Tezi, s.89, 2006.
- [53] Atasoy, F., Farklı Tür Sütlerden Yapılan Urfa Peynirlerinin Nitelikleri Üzerine Değişik Pastörizasyon Normlarının ve Starter Kültürlerinin Etkileri. Ankara Üniversitesi, Fen Bilimleri Enstitüsü, Süt Teknolojisi Anabilim Dalı, Ankara, Doktora Tezi, s.275, 2004.
- [54] Karaca, O. B., Mikrobiyolojik Kaynaklı Proteolitik ve Lipolitik Enzim Kullanımının Beyaz Peynirlerin Özellikleri ve Olgunlaşma Hızları Üzerine Etkileri. Çukurova Üniversitesi, Fen Bilimleri Enstitüsü, Gıda Mühendisliği Anabilim Dalı, Adana, Yüksek Lisans Tezi, s.102, 2000.
- [55] Sert, D., Geleneksel Yöntemle Üretilen Tulum Peynirlerinde Kullanılan Sütün Orijinine Bağlı Olarak Olgunlaşma Esnasında Meydana Gelen Bazı Değişmelerin Belirlenmesi. Selçuk Üniversitesi Fen Bilimleri Enstitüsü, Gıda Mühendisliği Anabilim Dalı, Konya, Doktora Tezi, s. 234, 2011.
- [56] Özcan, T. and Vapur, U.E., Effect of Different Rennet Type on Physico-Chemical Properties and Bitterness in White Cheese. *International Journal of Environmental Science and Development*, 4(1): 71-75, 2013.
- [57] Johnston, D.E. and Darcy, P.C., The Effects of High Pressure Treatment on Immature Mozzarella Cheese. *Milchwissenschaft*, 55(11): 617-620, 2000.
- [58] Saldo, J., Sendra, E. and Guamis, B., Colour Changes During Ripening of High Pressure Treated Hard Carpine Cheese. *High Pressure Research*, 22 (3-4): 659-663, 2002.
- [59] Shrivastava, S., Goyal, S. and Goyal, G.K., Effect of Modified Atmosphere Packaging on Colour Profile of Paneer Stored at 3±1°C. *Journal of Agriculture and Sustainability*, 3(2): 195-204, 2013.
- [60] Thapa, T.B. and Gupta, V.K., Changes in Sensoric and Rheological Characteristics During Storage of Processed Cheese Foods Prepared with Added Whey Protein Concentrates. *Indian Journal of Dairy Science*, 45: 140-145, 1992.
- [61] Calvo, M.V., Castillo, I., Diaz-Barcos, V., Requena, T. and Fontecha, J., Effect of Hygienized Rennet Paste and A Defined Strain Starter on Proteolysis, Texture and Sensory Properties of Semi-Hard Goat Cheese. *Food Chem.* 102: 917-924, 2007.

Modeling Moisture Change During Convection Cooking of Chicken Patties Using Comsol Multiphysics

Mehmet Utku BADAĞ

Faculty of Engineering
Department of Chemical Engineering
Yuzuncu Yil University
Van, Turkey
utkubadak@gmail.com

Neşe BADAĞ

Faculty of Engineering
Department of Food Engineering
Yuzuncu Yil University
Van, Turkey
nneşebadak@gmail.com

Suha Orçun MERT

Faculty of Engineering
Department of Chemical Engineering
Yuzuncu Yil University
Van, Turkey
orcunmert@gmail.com

Abstract— To enhance consumer comfort, many of today's food products are pre-prepared so they can be quickly reheated, for example in a microwave. There has been an important increase in the number of household microwave ovens in recent years. Microwave food processes offer many advantages such as short start up time, faster heating, high energy efficiency, space savings, precise process control, selective heating and foods with high nutritional quality. One of the industrial pre-inspection methods is air-convection cooking. During this cooking procedure moisture content of food products are changed. The moisture concentration in patty is also modified by COMSOL Multiphysics simulation. In terms of product quality, it is interesting to minimize the loss of moisture in the cooking line. In this context, cooking yield is the percentage of moisture in the patty after the cooking process. Moreover, the moisture concentration affects the temperature field by the loss of heat due to evaporation and also by changing the thermal conductivity of the patty [1].

Keywords— Heat change, Comsol multiphysics, Food processes modeling.

REFERENCES

- [1] H. Chen, B.P. Marks, and R.Y. Murphy, "Modeling Coupled Heat and Mass Transfer for Convection Cooking of Chicken Patties," J. Food Engineering, vol. 42, pp. 139–146, 1999.

Modeling Of Convection Cooking Of Chicken Patties Using Comsol Multiphysics

Neşe BADAĞ

Faculty of Engineering
Department of Food Engineering
Yuzuncu Yil University
Van, Turkey
nnesebadak@gmail.com

Mehmet Utku BADAĞ

Faculty of Engineering
Department of Chemical Engineering
Yuzuncu Yil University
Van, Turkey
utkubadak@gmail.com

Yusuf TUNÇTÜRK

Faculty of Engineering
Department of Food Engineering
Yuzuncu Yil University
Van, Turkey
yusuftuncturk@yyu.edu.tr

Abstract— *In the poultry sector, fully-cooked products are a rapidly growing part of total product sales, with pre-cooked, refrigerated products projected to account for 80% of the industry growth. Today many of food are precooked so they can be quickly reheated, for example in a microwave. One of the industrial pre-cooking methods is air-convection cooking method. For this reason, thermal processes for determining the safety, quality and safety of retail products are becoming increasingly important. The design and operation of these processes also affect the total cooking yield, which is an important economic parameter for the industry. In order to analyze and improve these processes, considerable previous study has focused on simulation of heat penetration in meat products under different thermal conditions. To predict heat penetration during thermal processing, heat transfer models have been widely employed for meat products. In these models COMSOL Multiphysics program can be used for this purpose. This model forms a time dependent model of convection cooking for a chicken patty and shows the increase in temperature within the patty relative to time [1].*

Keywords— *Heat change, Convection heating, Comsol multiphysics, Food processes modeling.*

REFERENCES

- [1] H. Chen, B.P. Marks, and R.Y. Murphy, "Modeling Coupled Heat and Mass Transfer for Convection Cooking of Chicken Patties," J. Food Engineering, vol. 42, pp. 139–146, 1999.

Changes in Some Quality Characteristics of Erzincan Tulum Cheeses Ripened in Goat's Skins and Plastic Barrels

Yusuf Çakır

Bingöl University, Food Engineering Department,
Bingöl, Turkey
yusufcakir_55@yahoo.com.tr

Songül Çakmakçı

Atatürk University, Food Engineering Department,
Erzurum, Turkey

cakmakci@atauni.edu.tr

Abstract— In Turkey, Erzincan Tulum (Şavak) cheese which is one of the most important cheese and in third place in terms of amount of production is produced from sheep's milk as original and traditional and ripened in the goat's skin bags. The cheese is our first cheese taken out a patent with the geographical sign. The economic significance and production of this cheese increases for the reasons of its originality having very high nutritional value, winning the appreciation of every segment of the consumers and being more expensive than butter.

In this research, ripened in goat's skin bags (Tulum) originally but nowadays in the cheese replaced by plastic barrels, were investigated the effect on some quality characteristics of packaging difference. Therefore, the Tulum cheeses produced traditionally from raw sheep's milk Dumlu (Erzurum) plateaus were ripened at $4\pm1^{\circ}\text{C}$ for 90 days pressed in the tulum and plastic barrels.

The cheeses pressed into the Tulum the dry matter, fat, fat in dry matter, total protein, total nitrogen, salt, salt in dry matter contents were found higher statistically significant according to the cheeses pressed into the plastic barrels at 90 d of ripening ($P<0.01$). Also, the value of ripening index in the Erzincan Tulum (Şavak) cheese samples pressed into the plastic barrels was found higher statistically significant according to the samples pressed into the Tulum ($P<0.01$). According to these results, it is more appropriate ripening in the Tulum in terms of nutritional value. In this study, will be make to contribute some results have been obtained for branding of this cheese as offered on behalf of the Tulum Cheese Festival and Elazığ Cheese Panel arrangement in Tulum Cheese Workshop by us.

Keywords— Erzincan Tulum (Şavak) cheese, Packaging material, Ripening, Cheese festival and panel

Effect of Using *Coriandrum sativum* L. on the Quality of Fresh White Cheese

Tamer TURGUT

Program of Food Technology
Ataturk University Erzurum Vocational School
Turkey

tturgut@atauni.edu.tr

Alper BARAN

Program of Food Quality, Control and Analysis
Ataturk University Erzurum Vocational School
Turkey

alper.baran@atauni.edu.tr

Ahmet ERDOĞAN

Department of Food Engineering
Ataturk University Agriculture Faculty
Turkey

aerdogan@atauni.edu.tr

Mehmet Cemal ADIGÜZEL

Department of Microbiology
Ataturk University Veterinary Faculty
Turkey

mcemal.adiguzel@atauni.edu.tr

Abstract— As an aromatic plant, *aşotu* (*Coriandrum sativum* L.) is an annual herb in the family of Apiaceae. All parts of the plant are edible, but the fresh leaves and dried seeds are the parts most traditionally used in cooking. The use of *Coriandrum sativum* L. in Erzurum is very common and it is used especially with ayran soup. In this study, the possibility of using *Coriandrum sativum* L. as an ingredient in white cheese was investigated.

Coriandrum sativum L was added to cheese by the rate of 2%, and microbiological analysis were made on the 1, 5, 10 and 14 days of ripening period at 4°C. According to the results, 2% level of *Coriandrum sativum* L. and storage time had a significant effects on the total viable count (TVC), lactic acid bacteria, *Streptococcus* counts and yeast-mould and Enterobacteriaceae counts ($p < 0.05$). Acidity, pH, analysis of the cheese samples were investigated on days 1, 5, 10, and 14 during storage at 4°C.

Keywords— White Cheese, *Coriandrum sativum* L, TVC, storage period

I. INTRODUCTION

Cultured dairy products especially cheeses are an important part of the diet of many societies. These dairy products, initially developed as a means to preserve milk also have desirable sensory characteristics [1]. More than 1000 varieties of cheese are produced around the world. In Turkey, 40–50 cheese varieties are known, but only three of them have national and economic value: Turkish White (its original name is Beyaz peynir), Kasar and Tulum cheeses [2]. In Turkey, although there are many traditional cheese varieties, their production is largely based in small-scale dairies and family farms. Recently, the industrial production of herby cheese has been introduced, and today this variety has gained nationwide popularity as well as being exported to Middle Eastern countries [3,4]. For thousands of years the cradle of diverse civilizations, and with a geography which lends itself to animal raising, Anatolia is

well endowed in terms of the variety of its cheeses. If at first impression it appears that Turkey does not possess a rich cheese culture, there are in fact more than 130 varieties of cheese to be found in Anatolia. The data in hand shows that, alongside several types of cheese such as White Cheese, Kaşar, Tulum, Lor and Çökelek which dominate the Turkish marketplace at large, there are to be found numerous varieties of cheese able to meet society's every requirement. Some of these are still produced in response to local preferences and needs, while others are now known and sold in many regions of the country [5].

Nonconventional oilseeds are being considered because their constituents have unique chemical properties and may augment the supply of edible oils. Interest in newer sources of edible oils has recently grown. Among the various seed oils, black cumin (*Nigella sativa* L.), coriander (*Coriandrum sativum* L.), and Niger (*Guizotia abyssinica* Cass.) are of particular interest because they may be utilized for the production of formulations containing phytochemicals with significant antioxidant properties and health benefits [6]. The aromatic proprieties of the fruits of coriander (*Coriandrum sativum* L.) and wild fennel [*Foeniculum vulgare* Miller var. *Vulgare* (Miller)], plants belonging to the family Apiaceae typical of the Mediterranean region, are exploited by the pharmaceutical industry to correct the flavor of medicines and, above all, of some laxatives of plant origin. In the case of fennel oil, an effect on the digestive processes has been ascertained; hence, it may exert an additive effect [7].

The objective of this study was to introduce the production of coriander herb cheese and reveal its microbiological properties and chemical composition.

II. MATERIAL AND METHODS

A. Milk and manufacture:

Milk used in the manufacture of cheese samples was obtained from the Atatürk University, Pilot Dairy Factory of Food Engineering, Erzurum, Turkey. The leaves used to manufacture cheese were obtained from Coriander plants in Erzurum, Turkey in the autumn. Rennet was obtained from the Mayasan, İstanbul, Turkey.

Cheeses were manufactured according to the standard procedure with a different modification [8]. Turkish white cheese, used as a control, and Turkish white cheese made using 2 % Coriandrum leaf were manufactured in the pilot dairy plant (Department of Food Engineering, Erzurum, Turkey).

All samples were stored at 4 ± 1 °C for up to 14 days. Analysis were conducted on the 1th, 5 th, 10th, and 14th days of the storage.

B. Microbiological analysis:

Total aerobic mesophilic bacteria, Lactic acid bacteria, Streptococcus count and Enterobacteriaceae counts were determined on the 1th, 5 th, 10th, and 14th days of the storage. Samples of cheese (10 g) were serially diluted (w/v) with saline solution (NaCl 0.85%) and homogenized for 1 min. Serial dilutions of the homogenates were prepared up to 10⁻⁵, then spread-plated (0.1 mL) in duplicate onto plates of MRS agar (de Man Rogosa Sharpe Agar, Merck) for the enumeration of Lactic acid bacteria (LAB) and M17 Agar (Merck) for Streptococcus. Inoculated plates were incubated anaerobically (Anaerocult C; Merck) at 30°C for 72 h for Lactobacilli and aerobically for Streptococcus at 30°C for 48 h. The counts of Lactobacilli were enumerated according to the method of Dave and Shah [9]. The counts of Streptococcus were enumerated according to the method of Harrigan [10]. For total viable bacteria (TVC), Plate Count Agar (PCA, Merck) was used and plates were aerobically incubated at 30 °C for 48 h. VRBD Agar (violet red bile dextrose, Merck) was used for Enterobacteriaceae and plates were anaerobically incubated at 30 °C for 48 h. Yeast and mould count were enumerated on PDA (Merck) after incubation at 23 °C for 5 days. [11]. Plates containing 25 to 250 colonies were enumerated and the colony forming units per gram (CFU/g) of the product was calculated.

C. Chemical analysis

Cheese samples were analyzed for salt according to the IDF standard method [12], fat content by Gerber method [13], moisture content [14]. The pH values of the yoghurt samples were determined by direct measurement with a digital microprocessor pH meter (Hanna Instruments 211, Romania) after calibration with pH 4.0 and 7.0 standard buffer. Titratable acidity (lactic acid, %) was determined by the titrating with 0.1 N NaOH using phenolphthalein indicator previously described by Kurt et al. [15] and expressed as a percentage of lactic acid. All analyses were performed in duplicate.

III. RESULTS AND DISCUSSION

Adding Coriandrum sativum L. had a few effect on pH and titratable values of samples. The results of mean values are presented in Table 1

	pH	Titrateable acidity (%)	TVC (log cfu/g)	LAB (log cfu/g)	Streptococcus counts (log cfu/g)
Storage time (days)					
1	6.15	0.21	5.17	4.844	5.04
5	6.20	0.24	5.21	4.837	4.967
10	6.19	0.27	5.27	4.948	5.497
14	6.21	0.25	5.26	4.891	5.518
Chesee samples					
C	6.18	0.24	5.26	5.102	5.74
2%	6.19	0.26	5.17	4.612	5.14

The pH value of the chesee samples was not significantly affected by adding of Coriandrum sativum L. The initial mean pH values of the control and containing C. sativum L. chesee were 6.22, and 6.265 respectively. At the end of 14 d, the values were 6.232, and 6.194. This results may have been due to the lack of starter cultures. Treatment also affected the titratable acidity of the chesee samples. During the storage period, titratable acidity of the samples increased slowly.

Coriandrum sativum L. treatment had a significant on TVC numbers. The highest average TVC count was in the control chesee samples while the lowest counts were in the Coriandrum sativum L. added samples. These results indicate that Coriandrum sativum L. may has an antimicrobial effect. But since the storage time is very short, telling a definite conclusion is difficult at this situation. Storage time also had effects on TVC number. (Table 1). TVC counts did not differ between the 10th and 14th days of storage. However, TVC counts increased slowly in samples during storage.

Coriandrum sativum L application affected viable counts of LAB and Streptococcus counts. Changes in the counts of number in during storage are presented in Table I. LAB numbers in control samples showed a more marked increase than treatment group during the storage period. The counts of LAB counts increased in regularly during the storage time.

IV. CONCLUSION

Adding Coriandrum sativum L application significantly affected the pH and acidity of cheese samples. Through this research, At this point, a step will be taken towards the

introduction of a new cheese to our regional cheese varieties and transfer to future generations.

REFERENCES

- [1] J. T.D. Boylston, C. G. Vinderola, H.B. Ghoddusi, and J. A. Reinheimer, "Incorporation of bifidobacteria into cheeses: challenges and rewards", (in eng), International Dairy Journal, vol14, no 5, pp. 375-387, 2004.
- [2] [2] A. A. Hayaloglu, M. Guven, and P. F. Fox, "Microbiological, biochemical and technological properties of Turkish White cheese 'Beyaz Peynir'", (in eng), International Dairy Journal, vol 12, no 8, pp 635-648, 2002,
- [3] [3] B. Ozer, F. Atasoy, and S. Akin, "Some properties of urfa cheese (a traditional white- brined Turkish cheese) produced from bovine and ovine milks", (in eng), International Journal of Dairy Technology, vol. 55, no 2, pp. 94-99, 2002.
- [4] [4] T. Turgut, A. Erdoğan, and M. Ataserver, "Karin Kaymağı Peynirinden İzole Edilen Laktobasillerin Tanımlanması", (in eng), Kafkas Üniversitesi Veteriner Fakültesi Dergisi, vol 18, no 2, 2012.
- [5] [5] U. Kamber, "Traditional Turkey Cheeses and their classification", (in eng), Van Veterinary Journal, vol. 26, no 3, 2015.
- [6] [6] M. F. Ramadan, L. W. Kroh, and J. T Mörsel, "Radical scavenging activity of black cumin (*Nigella sativa* L.), coriander (*Coriandrum sativum* L.), and niger (*Guizotia abyssinica* Cass.) crude seed oils and oil fractions", Journal of agricultural and food chemistry, vol 51 no 24, pp.6961-6969, 2003.
- [7] [7] P. Lo Cantore, N. S. Iacobellis, A. De Marco, F. Capasso, and F. Senatore, "Antibacterial activity of *Coriandrum sativum* L. and *Foeniculum vulgare* Miller var. *vulgare* (Miller) essential oils", (in eng), Journal of agricultural and food chemistry, vol 52, no26, pp. 7862-7866, 2004.
- [8] [8] A. Kasımoğlu, M. Göncüoğlu, and S. Akgün, "Probiotic white cheese with *Lactobacillus acidophilus*" (in eng), International Dairy Journal, vol 14, no 12, pp.1067-1073, 2004.
- [9] [9] R. Dave, and N.P Shah, "Viability of yoghurt and bacteria in yoghurts made from commercial starter cultures", (in eng), International Dairy Journal, vol.7, pp. 31-41, 1997.
- [10] [10] W.F. Harrigan, "Laboratory Methods in Food Microbiology," 3,d ed., Academic Press Inc, London, 1998.
- [11] [11] J. Baumgart, J. Firnhaber, and G. Spcher, "Mikrobiologische Untersuchung von Lebensmitteln", Hamburg, Germany: Behr's Verlag, 1993.
- [12] [12] International Dairy Federation (IDF) "Determination of salt content", Standard 12 B. Brussels: International Dairy Federation, 1988.
- [13] [13] M. Metin, and G. F. Öztürk, "Süt ve Mamülleri Analiz Yöntemleri", Ege Üniversitesi Yayınları, 7. Baskı, Bornova, İzmir.
- [14] [14] International Dairy Federation (IDF) Determination of dry matter in cheese and processed cheese, Standard 4. Brussels: International Dairy Federation ,1958.
- [15] [15] A. Kurt, S. Çakmakçı, and A. Çağlar, "Süt ve Mamulleri Muayene ve Analiz Metotları Rehberi",Atatürk Üniversitesi Ziraat Fak. Yayın No: 252/D, Turkey, 2007.

Textural Parameters and Ultrastructural Changes of Banana Which Applied to Osmotic Dehydration Pretreatment

Ferit AK*

Food Department,
Faculty of Engineering,
University of Munzur,
Tunceli, Turkey,
feritak@munzur.edu.tr

Alper GÜVEN

Food Department,
Faculty of Engineering,
University of Munzur,
Tunceli, Turkey,

Mükerrem KAYA

Food Department,
Faculty of Agriculture,
University of Atatürk,
Erzurum, Turkey,

Abstract–The aim of present study is to analyse the effect of osmotic dehydration pretreatment applied to the banana of Grand Nain type (*Musa Parasidiaca*) on the textural parameters and ultrastructural changes of this fruit. For this purpose, at the end of time periods as 0, 60, 120, 240, 360 and 480 minutes of 8 hours immersion time, the effect of 25%, 45%, 55% and 65% sucrose solution concentrations and 25°C, 35°C and 45°C immersion temperatures on banana slices has been studied. The samples have been examined by analyzing on scanning electron microscope with the aim of determining cellular structure and changes. Also the fruit slices have been evaluated by using Texture Analyzer instrument with the aim of detecting the texture profile analyse (TPA). During the osmotic dehydration process as associated with water loss and solid gain parameters, the increase in cohesiveness and elasticity values has been determined while there has been the decrease in textural values such as hardness, adhesiveness, chewiness and gumminess in TPA of fruit samples. While the effect of process time and temperature with solution concentration has found statically significant ($p<0.01$) on the values of hardness, gumminess and elasticity, it has been stood out that the effect of process temperature only has found statistically insignificant ($p>0.01$) on the values of cohesiveness and springiness of banana samples. It has been determined that there are ultrastructural changes generally such as collapse in the cells, dilatation in the intracellular spaces, deterioration in the cell segmentations and deformation in the cell's walls of the banana sample tissues. Unlike fresh control samples which are not subjected to any treatment, it has been stood out that starch molecules which are found largely in structure have gelatinized by swelling with increasing process temperature in these samples dried by the osmotic method. In conclusion, it has been determined that osmotic dehydration pretreatment is not sufficiently a effective method for the banana fruit.

Key Words– *Osmotic dehydration, texture, microscopic structure, banana.*

Various Animal Species Milk: Nutritional Value and Technological Properties

Songül Çakmakçı

Food Engineering Department, Atatürk University
Erzurum, Türkiye

Engin Gündoğdu

²Food Engineering Department, Gümüşhane University,
Gümüşhane, Türkiye

Abstract— According to FAO databases, the total World milk production accounted for 696 million tons of which approximately 83% was cow milk. Throughout the centuries, milk became a desirable and valuable food source. Different regions around the world have adapted the particular species common to their area for the purpose of producing milk. In many regions of the world buffalo milk is often used. The latest nutritional discovery is donkey milk, which is exceptionally similar to human milk in terms of protein composition. The majority of milk produced in the world undergoes processing, during which a variety of technological procedures occur. It is not only mainly related to cow milk, but also sheep, buffalo, goat, and camel milk. The most universal is cow milk and technological suitability of milk from other species is very diverse. The concentration of protein, mainly including casein, determines the technological suitability of milk. Currently, global milk production is dominated by 5 animal species: dairy cattle, buffalo, goats, sheep, and camels. The impact of factors altering the milk composition, such as breed, feeding system, stage of lactation and seasons. Cow milk is the most universal raw material for processing, which is reflected in the broadest spectrum of manufactured products. Sheep and buffalo milk, regarding their high content of protein, including casein, and fat, make a very good raw material for processing, especially cheesemaking. Camel milk also has valuable nutritional properties as it contains a high proportion of antibacterial substances and higher concentration of vitamin C in comparison to cow milk. The composition of goat milk allows using it as the raw material for dairy processing and also to some extent as a therapeutic product. The energy value of milk from various animal species is closely related to the concentration of certain compounds in dry matter, especially content of fat. The highest energy value is characteristic of sheep milk. In this review, this subject has been discussed.

Keywords— various animal species milk; nutritional properties; technological properties

I. INTRODUCTION

The milk of different ruminant species, which is consumed directly or as dairy products, has a profound importance for humans throughout their lives as being a source of macro- and micronutrients, and has a number of

active compounds having a significant role in both nutrition and health protection [1]. Because of being nutritionally essential food for humans and contains nearly all nutrients milk and milk products are recommended to consume an adequate amount for healthy lifestyle. In terms of fluid milk consumption, developed countries have changed the habits due to health concerns, aging of the population, increased education and income level factors [2]. Today, world milk production is provided from 5 animal species including dairy cattle, buffalo, goats, sheep, and camels. The major cow milk producers worldwide are The European Union (148.1million kg3), The United States of America (85.9million kg3), India (45.1million kg3), and Russia (32.3 million kg3) [3]. Milk consumption is fairly different between consumers as they prefer fluid, pasteurized, reconstituted for daily fresh milk requirement especially for the people living in big cities [4].

II. METHOD

1. NUTRITIONAL VALUE OF MILK

Milk composition of mammalian species varies widely with reference to genetic, physiological and nutritional factors and environmental conditions [5]. Milk from different species varies most notably regarding protein quality and concentration but also in the content of electrolytes, various carbohydrates and lipids [6]. Basic milk components are protein, fat, and lactose, breed, feeding system, stage of lactation, or time of year alter the composition of milk. Milk is a valuable source of vitamins, both water-soluble and fat-soluble ones [3]. The energy value of milk from various animal species is closely related to the concentration of certain compounds in dry matter, especially the amount of fat. The highest energy value is characteristic of sheep milk, cow milk, buffalo milk, camel milk, goat milk, donkey milk, and horse milk as respectively. The main component of milk, which has a major impact on its nutritional value and technological suitability, is protein. Milk proteins are a heterogeneous group consisting of casein complexes and whey protein fractions which have different from composition and properties [3]. Lipids are the most important components of milk in terms of cost, nutrition, physical and

sensory characteristics that impart to dairy products [7]. Fat which is the major substance for milk's energetic value makes a major contribution to the nutritional properties of milk, as well as to its technological suitability [8]. Milk is a considerable resource of products whose composition varies. Four components are dominant in quantitative terms: water, fat, protein and lactose; while the minor components are minerals, enzymes, vitamins, and dissolved gases [9]. Raw milk and raw milk products can lead to food-borne illness in humans. If these products are not pasteurized, alternative safety controls are required to ensure that they do not a public health risk.

2. VARIOUS ANIMAL SPECIES MILK

A. Cow Milk

The term "milk" being almost synonymous with cow milk in most people's minds. The literature mainly deals with cow milk, followed by goat and sheep milk. More than 80% of World milk production is cow's milk [10]. Cow's milk is the most used raw material in the variety of dairy products. Casein is the most important protein in milk, while the proportion of whey proteins is low. Content of whey proteins in cow milk is in the range of 0.55 to 0.70 [11]. Some studies have found that the majority of children with cow milk protein allergy synthesize antibodies predominantly against α -casein and β -lactoglobulin [12]. In cow milk the casein content is 86.01% of total protein [13]. The average diameter of milk fat globules in cow milk is 3.51 μm for cow milk (range of 0.92 to 15.75 μm) [14].

Cow milk accounted for 83 % of global milk production in 2010 [15]. Cow milk contains more protein and minerals, especially calcium and phosphorus, than human milk. This is because a young calf grows faster than a child. The protein in cow milk is of high-quality, containing a good balance of all the essential amino acids, including lysine. Many human diets are deficient in certain essential amino acids [10, 16]. Cow milk contains more protein than does human milk, but human milk contains more lactose, resulting in comparable energy contents. Cow milk and human milk differ in the amounts of various proteins they contain. Human milk does not contain β -lactoglobulin, one of the main proteins associated with cow milk allergy. Caseins can form leathery curds in the stomach and be difficult to digest. The casein content of cow milk varies between breeds and cheese makers often use milk from breeds with a higher κ -casein content in their milk [17]. Cow milk generally contains between 3 and 4 g of fat/100 g. Most milks consumed now contain a standardized fat content of around 3.5 g/100 g. Cow milk contains a higher proportion of saturated FA (SFA) than does human milk: 65–75 g/100 g total FAs, of which about 40 percent are C12:0–C16:0. Cow milk also has a high content of C18:0. The monounsaturated FA that is present in highest concentration in cow milk is C18:1 (oleic acid). The conjugated linoleic acid (CLA) content in cow milk is generally reported to vary from 0.1 to 2.2 g/100 g total FA depending on season, region, farming system and feeding,

and animal and breed [18]. Cow milk is mostly used in the production of drinking milk. Basic chemical composition of milk from various animal species was given in Table 1.

B. Goat Milk

Goats play an important role in livestock industry because of having adaptability to harsh climates which make them suitable for landless and marginal farmers. The contribution of goats for milk and milk products is high and contribute to rural economy and health. Goat milk has high amount of calcium, magnesium and phosphorus when compared cow and human milk [19]. Goat milk is a good source of vitamin A, niacin, thiamin, riboflavin, and pantothenic acid. However, it contains 5 times less vitamin B₁₂ and folic acid than cow milk does [3]. Goat milk is rich in terms of medium chain triglycerides (MCT) and proteins, and these MCT and proteins have unique health benefits. Goat milk having a soft curd may be an advantage for adult humans suffering from gastrointestinal disturbances and ulcers. Goat milk is important for prevention of cardiovascular disease, cancer, allergy and microorganism and used for stimulation of immunity. Goat milk is recommended for infants, old and convalescent people. Despite this fact, goat has remained neglected in research and development [19]. Goat milk production as commercially is more expensive due to lower productivity, seasonal variations and the need of bigger animal herds. Goat milk which is better digestibility alkalinity, buffering capacity and certain therapeutic values in medicine and human nutrition is different from cow milk [7]. The excellent digestibility of goat milk, the favorable composition of fatty acids and its content of bioactive compounds make suitable food in treating or preventing certain medical conditions [19]. The average diameter of milk fat globules in goat milk is 2.76 μm (range of 0.73 to 8.58 μm) [14]. Goat milk has a stronger flavor due to the liberation of short-chain fatty acids during rough handling, which give off a goaty smell. Goat milk is alkaline in nature because of higher protein content and, which is very useful for people with acidity problems, when compared with cow milk which is acidic. This alkalinity is due to the higher protein content and a different arrangement of phosphates [20]. Goat milk is mostly used in drinking milk and ice cream technology.

C. Sheep Milk

The sheep milk, regarding its high content of protein, including casein, and fat, make a very good raw material in the world is used for cheese manufacture [3, 16, 21]. While yoghurt is also produced in Turkey, fresh sheep milk is rarely consumed and in Greece [22]. Sheep milk is the richest in whey proteins (1.02 g/100 g), and also contains the highest concentration of casein (4.18 g/100 g) [23]. The main use for sheep in cheese making and is usually conducted 30 at farm level or in small local dairies, in particular in Mediterranean

and South-East European countries, although some big cheese factories can also be found, mainly in Western Europe. Over the past few years, the sheep milk dairy industry, along with the other agro food sectors, has considerably developed its production capacity by increasing the industrialization and automation of the processes. These changes are because of the definition of hygienic and sanitary standards at international level Codex Alimentarius and European Union Directives [24]. Dairy sheep farming comprise a crucial part of the national economy in many countries, especially in the Mediterranean and Middle East region [25], and are particularly well organized in France, Italy, Spain, and Greece [26]. The Mediterranean region produces 66% of the world's sheep milk and 18% of the world's goat milk. Of all the milk around the world produced by all species, sheep milk makes up about 1.5% and goat milk 2.0% in official statistics, although the actual usage is much higher due to the non-reporting of home consumption to the IDF (1996) [27]. Sheep's milk is mostly used in cheese and yoghurt technology.

Table 1. Proximate composition of cow, sheep, goat, buffalo milks (per 100 g of milk) [10].

Energy and component	Cow milk	Sheep milk	Goat milk	Buffalo milk
Energy (kcal)	62	100	66	99
Water (g)	87.8	82.1	87.7	83.2
Total protein (g)	3.3	5.6	3.4	4.0
Total fat (g)	3.3	6.4	3.9	7.5
Lactose (g)	4.7	5.1	4.4	4.4
Ash (g)	0.7	0.9	0.8	0.8
Minerals				
Calcium (mg)	112	190	118	191
Iron (mg)	0.1	0.1	0.3	0.2
Magnesium (mg)	11	18	14	12
Phosphorus (mg)	91	144	100.4	185
Zinc (mg)	0.4	0.6	0.3	0.5
Vitamins				
Retinol (µg)	35	64	45	69
Carotene (µg)	16	-	13	-
Vitamin A (µg)	37	64	48	69
Vitamin E (mg)	0.08	0.11	0.05	0.19
Riboflavin (mg)	0.20	0.34	0.13	0.11

D. Buffalo Milk

Buffalo milk which is produced 82 billion litres each year (12.5% of milk produced in the world), is the second most

produced milk in the world after cow's milk (84% with 551 billion litres) [28]. More than 91% of buffalo milk is produced in India (60%) and Pakistan (31%).

Buffalo milk has a rich compositional point of view between other milks. Especially fat constitutes the main fraction of buffalo milk and gives it a highly energetic and nutritive value. For example, the production of 1 kg of butter requires 14 kg of cow milk against 10 kg of buffalo milk. In many countries, buffalo milk is used for making traditional cheeses, such as mozzarella and ricotta in Italy, gemir in Iraq, paneer in India, domiati in Egypt, pecorino in Bulgaria, and pickled cheeses from the Middle- Eastern countries. Thus, buffalo milk is important due to its nutritional value for the countries that breed buffaloes. From this point, if the the knowledge of the specific physicochemical properties of buffalo milk fat globules are known these will give permit for dairy plants to improve their technological processes and to produce high quality products [29]. While buffalo milk over 50% is used for drinking milk in certain developing countries including India, Pakistan, Egypt and Nepal, it is almost exclusively used for mozzarella cheese production in italy [30]. There is an increasing research interest and investment in various countries for Buffalo milk because of its attractive nutrient content. Buffalo milk has a higher content of fat, crude protein, lactose, total solids, vitamins and minerals, which impart a rich flavour and taste, and make it a highly suitable ingredient for the manufacture of a wide variety of milk products, such as cheese, butter fat, ice cream, and yoghurt when compared with cow milk [30]. In Turkey, buffalo milk is widely used in making fat-rich milk products called "kaymak" [31].

E. Camel Milk

There are approximately 18 million camels in the world, 14 million of which are located in Africa and 4 million in Asia according to the FAO data (2008) [32]. In arid and semi-arid areas camels play a major role in supplying the population with milk [10]. One of the main components of the human diet in many parts of the world [33]. It contains all essential nutrients and a high biological value because of having the higher contents of antimicrobial factors such as lysozyme, lactoferrin and immunoglobulins [33]. Camels are well adapted to the harsh desert climate and can survive without drinking water for up to forty days and can produce a volume of milk well beyond the capacity of other domestic animals. A camel can yield 3,500 or more liters of milk during a lactation period which can extend for 18 months [4]. Camel milk is an important source of proteins for the people living in the arid lands of the world and is known for its medicinal properties as in several countries from the ex-Soviet Union and developing countries [34]. It is much more nutritious than that from cow milk due to its low fat and lactose contents, and higher in potassium, iron and vitamin C [35]. Camel milk contains 81.4-87% water, 1.2-6.4% milk fat, 2.15-4.90% protein, 1.63-2.76% casein, 0.65-0.80% whey protein, 2.90-5.80% lactose and 0.60-0.90% ash [32].

F. Donkey Milk

In the last decade, donkey's milk has a considerable scientific interest in Europe, especially because of its nutritional and functional ingredients. Because it is a suitable milk substitute for the infants who are not accessible of giving of human milk or in allergic reactions to cow's milk during the first months of life infants show [36]. The properties of milk differ from that one of other mammals in many ways that include important differences in nutritional value; moreover, its composition does not permit the production of cheese due to the high content of whey proteins that represent 35-50% of the nitrogen fractions [37]. The average milk production found 172.12 mL per milking with the average fat percentage of 0.33%, milk protein 1.55%, and lactose 6.28% [36]. Donkey's milk composition and its organoleptic characteristics are similar to human milk, especially with respect to the composition of proteins and lipids. It has low amounts of casein and β -lactoglobulin, and high concentrations of lysozyme which is essential to protect digestive system of children from various infections [36]. Enzymes in donkey milk have unique characteristics such as bactericidal property which makes donkey milk different from other mammals' milks and lysozym concentration in ass's milk is 4000 mg/L when compared to bovine milk [38]. Donkey milk has gained popularity due to its beneficial components.

G. Mare Milk

Mare's milk, is not only the most important nutritional resource for foals during the first months of life, but also the most important basic foodstuffs for the human populations in those areas of central Asia, where a lactic-alcoholic beverage called Koumiss is traditionally produced through fermentation [5]. Around 30 million people consume mare milk regularly throughout the world especially in areas of central Asia steppes: Turks, Bashkirs, Kazakhs, Kyrgyz, Mongols, Yakuts and Uzbeks. It is also one of the most important basic foodstuffs for the human populations [39]. Composition of mare milk is between human and cow milk and is suitable especially for the elderly, convalescents, and infants due to its nutritional characteristics. It is rich with whey protein, polyunsaturated fatty acids, vitamin C content, optimal Ca/P ratio and bioactive components [40, 41]. Also, It is sensitive for preservation and transformation processes. On the other hand the lactose content of mare's milk is similar to that of human milk and higher than that of cow's milk [40, 41]. From the early 20th century it was popular in Germany where it was delivered door to door. Now it is also back fashion in France, Belgium, Austria, and Holland. Mare milk contains high levels of vitamins and minerals, better digestibility and lower fat content than cow milk and that is why it is preferred by consumers who are conscious about health. Different breeds of dairy horses are used for mare milk production in the world and the composition of mare milk

are: dry matter: 9.3-11.6; protein: 1.5-2.8; fat: 0.5-2; laktoz: 5.8-7.0 g/100 g milk [42].

CONCLUSION

Milk is a valuable source of dietary energy, high-quality protein and fat. Bioavailability of some nutrients in milk, for example calcium, is high compared with that in other foods. Cow milk is the rawest material for processing in the World. Sheep and buffalo milk, regarding the high content of protein, especially casein, and also fat, make a very good raw material for processing, cheese and yogurt making. Goat milk was used for a wide range, such as consumption milk, and therapeutical product. Goat milk is mostly used in drinking milk and ice cream technology. Camel milk also has valuable nutritional properties as it contains a high proportion of antibacterial substances and higher concentration of vitamin C. Donkey milk has the most comparable protein composition with human milk. It is consumed predominantly in a nonprocessed form. Composition of mare milk is between human and cow milk and is suitable especially Koumiss making.

REFERENCES

- 1 L.S. Ceballos, E.R. Morales, G. de la Torre Adarve, J.D. Castro, L.P. Martínez, and M.R.S. Sampelayo, "Composition of goat and cow milk produced under similar conditions and analyzed by identical methodology", *J. Food Compos. Anal.*, 22(4), 322-329, 2009.
- 2 S.A. Hatirli, B. Ozkan, and A.R. Aktas, "Factors affecting fluid milk purchasing sources in Turkey", *Food Qual. Prefer.*, 15(6), 509-515, 2004.
- 3 J. Barłowska, M. Sz wajkowska, Z. Litwińczuk, and J. Król, "Nutritional value and technological suitability of milk from various animal species used for dairy production". *Compr. Rev. Food Sci. Food Saf.*, 10(6), 291-302, 2011.
- 4 M.S. Haddadin, S.I. Gammoh, and R.K. Robinson, "Seasonal variations in the chemical composition of camel milk in Jordan". *J. Dairy Res.* 75(01), 8-12, 2008.
- 5 M. Malacarne, F. Martuzzi, A. Summer, and P. Mariani, "Protein and fat composition of mare's milk: some nutritional remarks with reference to human and cow's milk", *Int. Dairy J.*, 12(11), 869-877, 2002.
- 6 E. D'auria, C. Agostoni, M. Giovannini, E. Riva, R. Zetterström, R. Fortin, G. Franco Greppi, L. Bonizzi, and P. Roncada, "Proteomic evaluation of milk from different mammalian species as a substitute for breast milk", *Acta Paediatrica*, 94(12), 1708-1713, 2005.
- 7 Y. Park, "Hypo-allergenic and therapeutic significance of goat milk", *Small Ruminant Res.*, 14(2), 151-159, 1994.
- 8 H.M. El-Zeini, "Microstructure, rheological and geometrical properties of fat globules of milk from different animal species". *Pol. J. Food Nutr. Sci.*, 15(2), 147, 2006.
- 9 M. Guetouache, B. Guessas, and S. Medjekal, "Composition and nutritional value of raw milk- Review", *IBSPR*, 2(10): 115-122, 2014.
- 10 R. Wijesina Bettoni, and B. Burlingame, "Milk and dairy product composition", in: *Milk and Dairy Product in Human Nutrition*, E. Muehlhoff, A. Bennett, and D. McMaon, Eds. FAO, Rome. E-ISBN 978-92-5-10 10786-8 (PDF), 2013, pp. 41-102.
- 11 H.Y. Guo, K. Pang, X.Y. Zhang, L. Zhao, S.W. Chen, M.L. Dong, F.Z. Ren, "Composition, physicochemical properties, nitrogen fraction

- distribution, and amino acid profile of donkey milk. *J. Dairy Sci.* 90(4):1635–1643, 2007.
- 12 F. Lara-Villoslada, M. Olivares, and J. Xaus, "The balance between caseins and whey proteins in cow's milk determines its allergenicity", *J. Dairy Sci.*, 88(5):1654–1660, 2005.
- 13 G. Boebe, G.L. Lindberg, A.E. Freeman, D.C. Beitz, "Short communication: composition of milk protein and milk fatty acids is stable for cows differing in genetic merit for milk production", *J. Dairy Sci.* 90(8):3955–3960, 2007.
- 14 R. Attaie, and R.L. Richter, "Size distribution of fat globules in goat milk", *J. Dairy Sci.*, 83(5):940–944, 2000.
- 15 FAOSTAT, "FAO statistical database". Available at: <http://faostat.fao.org/>. Accessed 21 September 2012.
- 16 M. J., "Süt Teknolojisi: Sütün Bileşimi ve İşlenmesi". Ege Üniv. Müh. Fak. Yay. No: 33, 1998.
- 17 V. Bonfatti, G. Di Martino, A. Cecchinato, L. Degano, and P. Carnier, "Effects of β -k-casein (CSN2-CSN3) haplotypes, β -lactoglobulin (BLG) genotypes, and detailed protein composition on coagulation properties of individual milk of Simmental cows", *J. Dairy Sci.*, 93(8): 3809–3817, 2010.
- 18 A. Elgersma, S. Tamminga, and G. Ellen, "Modifying milk composition through forage", *Anim. Feed Sci. Tech.*, 131(3–4): 207–225, 2006.
- 19 T. Zenebe, N. Ahmed, T. Kabeta, and G. Kebede, "Review on medicinal and nutritional values of goat milk", *Acad. J. Nutr.*, 3, 30–39, 2014.
- 20 J. Jandal, "Comparative aspects of goat and sheep milk". *Small Ruminant Res.*, 22(2), 177–185, 1996.
- 21 Y. Çakır, S. Çakmakçı, and A.A. Hayaloglu, "The effect of addition of black cumin (*Nigella sativa* L.) and ripening period on proteolysis, sensory properties and volatile profiles of Erzincan Tulum (Şavak) cheese made from raw Akkaraman sheep's milk". *Small Ruminant Res.*, 134: 65–73, 2016.
- 22 R. Bencini, and G. Pulina, "The quality of sheep milk: a review", *Anim. Prod. Sci.*, 37(4), 485–504, 1997.
- 23 C. Dario, D. Camicella, M. Dario, and G. Bufano, "Genetic polymorphism of β -lactoglobulin gene and effect on milk composition in Leccese sheep", *Small Ruminant Res.* 74(1–3):270–3, 2008.
- 24 Pirisi, A., A. Lauret, and J. Dubeuf, "Basic and incentive payments for goat and sheep milk in relation to quality", *Small Ruminant Res.*, 68(1), 167–178, 2007.
- 25 FAO, 2003. The yak (2nd ed.). Revised and enlarged by G. Wiener, H. Jianlin and L. Ruijun. RAP publication 2003/6 Bangkok, FAO Regional Office for Asia and the Pacific (RAP).
- 26 Y. Park, M. Juárez, M. Ramos, and G. Haenlein, "Physico-chemical characteristics of goat and sheep milk". *Small Ruminant Res.*, 68(1), 88–113, 2007.
- 27 A. Pandya, and K. Ghodke, "Goat and sheep milk products other than cheeses and yoghurt", *Small Ruminant Res.*, 68(1), 193–206, 2007.
- 28 IDF (International Dairy Federation), "The world dairy situation 2007". Bulletin No. 423.
- 29 O. Ménard, S. Ahmad, F. Rousseau, V. Briard-Bion, F. Gaucheron, and C. Lopez, "Buffalo vs. cow milk fat globules: Size distribution, zeta-potential, compositions in total fatty acids and in polar lipids from the milk fat globule membrane", *Food Chem.*, 120(2), 544–551, 2010.
- 30 B. -Z. Han, Y. Meng, M. Li, Y.-X. Yang, F.-Z. Ren, Q.-K. Zeng, and M.R. Nout, "A survey on the microbiological and chemical composition of buffalo milk in China". *Food Control*, 18(6), 742–746, 2007.
- 31 S. Çakmakçı, and A.A. Hayaloglu, "Evaluation of the chemical, microbiological and volatile aroma characteristics of İspir Kaymak, a traditional Turkish dairy product". *Int. J. Dairy Technol.*, 64(3): 444–450, 2011.
- 32 A. Brezovečki, M. Čagalj, Z.F. Dermitt, N. Mikulec, D.B. Ljoljić and N. Antunac, "Camel milk and milk products", *Mljekarstvo*, 65(2), 81–90, 2015.
- 33 E. Elagamy, "Effect of heat treatment on camel milk proteins with respect to antimicrobial factors: a comparison with cows' and buffalo milk proteins". *Food Chem.*, 68(2), 227–232, 2000.
- 34 G. Konuspayeva, B. Faye, and G. Loiseau, "The composition of camel milk: a meta-analysis of the literature data. *J. Food Compos. Anal.*, 22(2), 95–101, 2009.
- 35 M. Khaskheli, M. Arain, S. Chaudhry, A. Soomro, and T. Qureshi, "Physico-chemical quality of camel milk". *J. Agric. Soc. Sci.*, 2, 164–166, 2005.
- 36 A. Ivanković, J. Ramljak, I. Štulina, N. Antunac, I. Bašić, N. Kelava, and M. Konjačić, "Characteristics of the lactation, chemical composition milk hygiene quality of the Littoral-Dinaric ass". *Mljekarstvo*, 59(2), 107–113, 2009.
- 37 C. Chiavari, F. Coloretti, M. Nanni, E. Sorrentino, and L. Grazia, "Use of donkey's milk for a fermented beverage with *Lactobacilli*", *Lait* 85(6): 481–490, 2005.
- 38 X.-Y. Zhang, L. Zhao, L. Jiang, M.-L. Dong, and F.-Z. Ren, "The antimicrobial activity of donkey milk and its microflora changes during storage", *Food Control*, 19(12), 1191–1195, 2008.
- 39 K. Potočník, V. Gantner, K. Kuterovac, and A. Cividini, "Mare's milk: composition and protein fraction in comparison with different milk species". *Mljekarstvo*, 61(2), 107, 2011.
- 40 E. Marconi, and G. Panfili, "Chemical composition and nutritional properties of commercial products of mare milk powder", *J. Food Comp. Anal.*, 11(2), 178–187, 1998.
- 41 Q. Sheng, and X. Fang, "Bioactive components in mare milk", in *Bioactive Components in Milk and Dairy Products*, ed. Park Y.W., Wiley-Blackwell, pp. 195–213, 2009.
- 42 G. Solaroli, E. Pagliarini, and C. Peri, "Compositional and nutritional quality of mare's milk". *Ital. J. Food Sci.*, 4:323–333, 1993.

Molecular Methods in Food Microbiology

Şehriban UĞUZ
Food Engineering Department,
Faculty of Engineering,
University of Yüzüncü Yıl,
Van, Turkey
sehribanuguz@yyu.edu.tr

Seval ANDIÇ
Yüzüncü Yıl University
Van, Turkey

Abstract - Traditionally microbiological assessment for quality and safety of demands the foodstuffs enumeration and specific detection of pathogenic and spoilage microorganisms. Known testing methods consist of growth media and cultivation to enumerate and isolate cells of microorganisms from food samples. However, testing methods rely on cultivation are usually slow and give results after a few days. Also a lot of material and labour are used for this method. In recent decades, some non-traditional techniques named as molecular methods have been developed. Molecular techniques are applied for the detection and characterization of microorganisms in food products due to increasing demand for rapid results. Especially the polymerase chain reaction (PCR), detecting specific DNA or RNA for amplification processes constitutes based on method. Real time PCR, RFLP, DNA microarray assay, immunological techniques like ELISA are different molecular methods used for this purpose.

Key words: Molecular methods, PCR, food microbiology, food safety.

Recent advances in ultrasound and microwave assisted extraction of bioactive compounds from plant food processing by-products

Mehmet HAYTA

Food Engineering, Faculty of Engineering,
Erciyes University,
Kayseri, Turkey
mhayta@erciyes.edu.tr

Elif Meltem İŞÇİMEN

Food Engineering, Faculty of Engineering,
Erciyes University,
Kayseri, Turkey

Abstract—The food industry generate considerably huge amount of byproducts such as pomace, hull, peel, shells, seeds, stems, bran, etc., from a variety of sources which potentially lead environmental pollution. Therefore, there has been growing interest in valorization of byproducts through the extraction of bioactive compounds such as proteins, polysaccharides, fibres, flavor compounds, and phytochemicals, and using them in health promoting functional food and/or pharmaceutical formulations. Emerging “green” techniques, such as ultrasound-assisted extraction (UAE), microwave-assisted extraction (MAE), pressurized solvent extraction, supercritical fluid extraction, pulsed electric field extraction, and enzyme-assisted extraction has been considered as fast and efficient methods applicable for bioactive recovery from natural byproducts.

Novel techniques or the combination with conventional techniques might be employed as a pretreatment to increase the efficiency of extraction by improving cell-membrane permeability. UAE is simple and easy to scale up to the industrial level and MAE offers good recovery yields, and extractions are usually performed particularly fast. The principal objective of any extraction process is to obtain materials in higher yields while retaining the desired levels of bioactivity. However, the application of emerging techniques in industrial level still require further investigation and optimization researches, and represents a major step regarding the valorization of food processing byproducts. This presentation will cover an up-to-date review on the use of ultrasound and microwave assisted extraction processes to obtain functional bioactive compounds from plant based food byproducts.

Keywords— Ultrasound assisted extraction, microwave assisted extraction, bioactives, food byproducts

Evaluation of presence of Staphylococcus aureus and enterotoxigenic properties of isolates by multiplex PCR in meat samples offered for sale in Erzurum Province, Turkey

Alper BARAN

Program of Food Quality, Control and Analysis
Ataturk University Erzurum Vocational School
Turkey
alper.baran@atauni.edu.tr

Tamer TURGUT

Program of Food Technology
Ataturk University Erzurum Vocational School
Turkey
tturgut@atauni.edu.tr

Mehmet Cemal ADIGÜZEL

Department of Microbiology
Ataturk University Veterinary Faculty
Turkey
mcemal.adiguzel@atauni.edu.tr

Ahmet ERDOĞAN

Department of Food Engineering
Ataturk University Agriculture Faculty
Turkey
aerdogan@atauni.edu.tr

Abstract— In this study, it was aimed to determine the presence of *Staphylococcus aureus* (*S. aureus*) and the ability to enterotoxin production by molecular methods in meat samples (beef and chicken) obtained from different local markets in Erzurum. *Staphylococci* isolated from 54 different meat samples were identified as presumptive *S. aureus* using classical microbiological and biochemical methods. In the molecular evaluation of isolates, the presence of *S. aureus* was confirmed by detecting the *nuc* gene region and their toxigenic properties were revealed by detecting the enterotoxin A, B, C and D gene regions. *S. aureus* positive isolates were obtained in 15 (24%) of the analyzed meat samples. When evaluated according to the meat origin, *S. aureus* was detected in 6 (32%), 2 (13%) and 7 (63%) samples in drumstick, wing and beef, respectively. *S. aureus* strains which can produce the enterotoxin A were detected for all three meat types based on the multiplex PCR application for the determination of enterotoxigenic properties in the isolates.

Keywords— PCR; meat; *S. aureus* Introduction

I. INTRODUCTION

Staphylococcus genus are ubiquitous microorganisms which contain at least 40 species. They are Gram positive, non-spore, non-motile, facultative anaerobic and catalase positive microorganisms. They also form the part of the normal flora by living on the skin and mucous membranes of humans and animals. Bacteria in the *Staphylococcus* genus can cause to many diseases in humans, *Staphylococcus aureus* (*S. aureus*), which is included in this group, is known as an agent that causes more staff infections such as pneumonia, dermatitis, toxic shock syndrome, septicemia and food poisoning. *S. aureus*, resistant to high salt concentrations, has the ability to produce lecithinase, coagulase and thermonuclease [1]. Especially

enterotoxemia, which is caused by ingestion of enterotoxins produced by *S. aureus* which has enterotoxigenic properties, is a serious concern for public health. The data on outbreaks caused by this microorganism are very limited. As a result, toxication has a short duration and moderate symptoms. Despite the fact that this bacterium is susceptible to methods of control the growth of microorganisms on foods, especially high heat treatment applications, the toxins are resistant to heat treatments. Although many enterotoxin types that can be produced by *S. aureus* have been identified to date, toxemia is known to be caused mainly by types Enterotoxin A, B, C, D and E, which are classical enterotoxins. The enterotoxin production occurs in foods contaminated (i.e., poultry, meats, salads, eggs and products, pudding and pie) with *S. aureus* [2]. Nonspecific poisoning symptoms such as nausea, vomiting, stomach cramps, sweating, exhaustion and sometimes a decrease in body temperature occur with the consumption of these foods that contain enterotoxins. In addition, the presence of this microorganism in the food is considered as a sign of weak personnel hygiene.

Meat and meat products have a highly capacity of production and consumption in the world. These foods have a potential for outbreaks due to production under inappropriate conditions and contamination by food workers. Meat and meat products cause outbreaks a contaminant with pathogenic microorganisms such as *S. aureus*, mainly *Salmonella*, *Listeria*, *Escherichia*, *Campylobacter*, *Shigella*. *S. aureus* can proliferate and produce the toxins in contaminated meats that are kept on inappropriate conditions by food workers or self-contaminated [3]. There are many studies that were conducted in different countries in order to reveal the presence of *S. aureus* which can

produce enterotoxin. The aim of this study is to reveal the presence of *S. aureus* and ability of enterotoxin production of isolates by molecular methods in cattle and poultry meat offered for sale in Erzurum.

II. MATERIAL AND METHODS

A. Sampling and Analysis:

The samples were taken at local markets in Erzurum, Turkey and brought to laboratory under cold chain. Microbiological analyzes were conducted on the same day. The presence of *S. aureus* was studied on 54 different meat samples (drumstick, wing, beef). 10 g of meat sample was weighed into a stomacher bag and 90 ml of ¼ Ringer solution was added. Homogenization was then carried out for 2 min using a masticator. One mL was taken to make serial dilutions (100,10-1,10-2) from the homogenized sample.

B. Isolation and identification of *S. aureus*

0.1 mL of the homogenate from prepared each dilutions were planted onto mannitol-salt agar by spreading techniques. The plates were incubated for 24 hours at 37 °C. At the end of the incubation, yellow colonies with yellow zone were evaluated as presumptive staphylococcus. Presumptive colonies were subcultured on blood agar and then gram positive, catalase positive, oxidase negative and coagulase positive colonies were identified as presumptive *S. aureus* colonies. Subsequently, presumptive *S. aureus* was confirmed by PCR targeting the nuc gene region. *S. aureus* ATCC 29213 strain was used in this study as reference strain.

C. Extraction of DNA

For DNA extraction, the isolates were subcultured in tubes containing Brain Heart Infusion Broth (Oxoid, CM0225) and incubated at 37 °C for 18-24 hours in aerobic conditions. 0.1 mL of broth culture was taken into eppendorf tubes and centrifuged (Hettich Rottina 35R) for 30 secs at 16.000 g. Thereafter, the pellet was suspended in 50 µl of lysostaphin (Sigma-Aldrich, L7386) (100 µg/mL) and the suspension was allowed to incubate at 37 °C for 10 min. 50 µl proteinase K (Sigma-Aldrich, P2308) (100 µg/mL) and 150 µl buffer solution (10 mM Tris-HCl pH 8.3) were added to the cell suspension and incubated again at 37 °C for 10 min. Then, it was kept in boiling water bath for 5 minutes and at the end of this process it was immediately taken on ice and it was maintained at -20 °C until used for PCR.

D. PCR Protocol&Condition

PCR reactions were performed using a mixture (25 µl final volume) containing 1 µl of genomic DNA, 0.25 µl of each primer (nuc1a (5'-CCTGAAGCAAGTGCATTTACGA-3'); nuc1b (5'-CTTTAGCCAAGCCTTGACGAAGT-3')), 1.25 µl of dNTPs, 2.5 µl 10x PCR buffer, 1.5 µl of MgCl₂ and 0.2 µl of Taq DNA polymerase (Thermo Fisher Scientific) in a Biomeriux thermal cycler. Amplification conditions were given Table I. The presence of Enterotoxin A, B, C and D (SEA, SEB, SEC and SED) were performed according to Mehrotra et al.[4] by multiplex PCR method.

DNA amplification was carried out with the following protocol: initial denaturation at 95°C for 15 min, 35 cycles of amplification (denaturation at 91°C for 1 min, annealing at 60°C for 1 min, extension at 72 °C for 1 min) and final extension at 72 °C for 10 min in a (Bio-Rad Gel Doc XR System) system. PCR products were analysed on a 1% Agarose (Bio Basic Inc.) with 1 x Tris-acetate-EDTA buffer to see PCR products with 166 bp length [5].

E. Statistical analysis

One way ANOVA was used in the evaluation of the data by SPSS statistic programme.

III. RESULTS AND DISCUSSION

A total of 54 samples were examined. Presumptive *S. aureus* was isolated from 40 of the 54 samples. Isolates confirmed by species specific PCR (nuc gene) and 15 (27.8%) of them were determined as *S. aureus*. The results showed Table I. The PCR image of the analyzed samples was shown in Fig. 1.

Table 1 Number of meat samples positive for *S. aureus* and enterotoxigenic strain

Meat origin	Number of samples	N (%) of samples positive for <i>S.aureus</i>	N (%) of samples positive for enterotoxigenic strains of <i>S. aureus</i>
Drumstick	19	6 (32%)	1 (17%)
Wing	17	2 (13%)	1 (50%)
Beef	18	7 (63%)	1 (14%)

The contamination rate of beef with *S. aureus* was higher than chicken meats. Of the four different types of enterotoxins tested, only Enterotoxin A was detected in one drumstick, wing and beef sample.

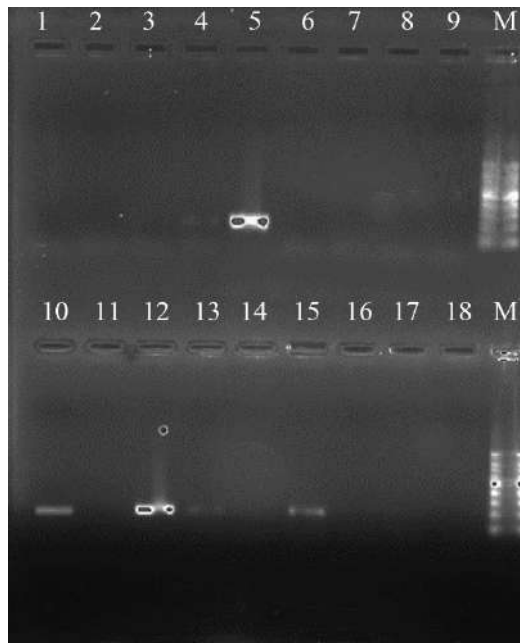


Figure 1 : Gel electrophoresis of PCR products, using primer for *nuc* gen: *S. aureus* ATCC 29213 (lanes 10), negative control (lanes 11), positive (lanes 5, 10, 12, 13 and 15) samples, and 100 bp DNA ladder (lanes M)

S. aureus, located in the natural habitat, contaminates the meats due to poor hygienic conditions during the processing, storage or sale of the meat. It was reported by Gündoğan and Ataol [6] that 10.7% of the minced meat samples were positive for *S. aureus*, however, they could not isolate from chicken samples. In another study, Gündoğan et al. [7] demonstrated that *S. aureus* was isolated from 80 (53.3%) of 150 meat and chicken samples. In this study, the presence of *S. aureus* was determined in chicken meats and beef at a rate 22.2%, 38.8%, respectively. Cıtaç and Duman [8] identified 195 isolates of staphylococci from a total of 105 chicken samples in Ankara and identified 92 (47%) of them as *S. aureus*. The results obtained from these studies are higher than our findings. Guven et al. [9] reported that they isolated the *S. aureus* at a rate of 68.4% in beef cattle and 55% in poultry meat samples. The reason for the emergence of this difference between the data, the meats served in the Erzurum region indicate that the contamination during transportation and sales are low. It is also believed that the sample numbers are different, which may cause these data to be different

All strains were analysed for the presence of several known staphylococcal enterotoxin (SE) genes (SEA, SEB, SEC and SED) determinants by PCR. Staphylococcal enterotoxin A (SEA) were detected in 3 out of 15 *S. aureus*. When *S. aureus* finds the appropriate conditions, it rapidly growth and can form one or several of the toxins A, B, C, D, E, G, H. Guven et al. [9] reported that they found the presence of enterotoxigenic *S. aureus* in 2 and 7, respectively, of isolates from beef and poultry by ELISA-based method. Gencay et al. [10] found that two chicken meat isolate out of 70 *S. aureus* strain were carried out

SEA gene. Omoe et al. [11] determined that 36 (11.7%) out of 146 *S. aureus* isolates had SEA genes. SEA in 77.8% and SEB in 10% of the food poisoning cases in the US have been reported [2]. Enterotoxin A is the most toxic of *S. aureus* enterotoxins. Enterotoxin B (SEB), on the other hand, is the most resistant to heat and is also used as a biological weapon [12]. It has been reported that SEA is produced mostly by human strains, and SEC and SED are produced by strains isolated from mammals [13]. Rosec and Gigaud [14] determined that the rate of the strains carrying SEG, SEH, SEI and SEJ genes was very higher (57%) than that of the strains classical enterotoxin genes (SEA, SEB, SEC, SED, and SEE). Aydin et al. [15] reported that they isolated enterotoxigenic *S. aureus* at 13 of a total of 115 meat samples. Of the isolated enterotoxigenic strains, four SEH (30.7%), one SEA (7.7%), SEL (7.7%) and SEP (7.7%) were found. In this study the data of SEA gene was similar to those found by Gencay et al. [10] and Omoe et al. [11], but differ from those found by Aydin et al. [15] and Rosec and Gigaud [14]. Different result may be due to the low number of samples. Also only classical enterotoxin genes have been determined in this study. These isolates are thought to be investigated for other enterotoxin genes in subsequent studies.

CONCLUSION

The presence of *S. aureus* in the meat samples presented on sale at the Erzurum local markets shows that this bacterium can easily be contaminating directly or indirectly at any stages of food production. Moreover, the isolation of strains capable of producing enterotoxin suggests that these foods may be a source of public health risk. Although the data on toxemia caused by *S. aureus* in Turkey is little, it is an important fact that higher value-added studies are needed.

Acknowledgment

This study was supported by Ataturk University Scientific Research Projects Office.

REFERENCES

- [1] J. E. Bennett, R. Dolin, and M. J. Blaser, Principles and practice of infectious diseases. New York: Elsevier Health Sciences, 2014.
- [2] N. Balaban and A. Rasooly, "Staphylococcal enterotoxins," (in English), International Journal Of Food Microbiology, vol. 61, no. 1, pp. 1-10, Oct 1 2000.
- [3] H. Tassew, A. Abdissa, G. Beyene, and S. Gebre-Selassie, "Microbial flora and food borne pathogens on minced meat and their susceptibility to antimicrobial agents," (in eng), Ethiop J Health Sci, vol. 20, no. 3, pp. 137-43, Nov 2010.
- [4] M. Mehrotra, G. Wang, and W. M. Johnson, "Multiplex PCR for detection of genes for Staphylococcus aureus enterotoxins, exfoliative toxins, toxic shock syndrome toxin 1, and methicillin resistance," (in eng), Journal Of Clinical Microbiology, Research Support, Non-U.S. Gov't vol. 38, no. 3, pp. 1032-5, Mar 2000.
- [5] H. U. Graber, M. G. Casey, J. Naskova, A. Steiner, and W. Schaeren, "Development of a highly sensitive and specific assay to detect Staphylococcus aureus in bovine mastitic milk," (in eng), Journal Of Dairy Science, Research Support, Non-U.S. Gov't vol. 90, no. 10, pp. 4661-9, Oct 2007.

- [6] N. Gundogan and O. Ataol, "Determination of biofilm production and DNase activity of *Staphylococcus aureus* and coagulase negative staphylococci isolated from meat samples," *Türk Hijyen ve Deneysel Biyoloji Dergisi*, vol. 69, no. 3, pp. 135-142, 2012.
- [7] N. Gundogan, S. Citak, N. Yucel, and A. Devren, "A note on the incidence and antibiotic resistance of *Staphylococcus aureus* isolated from meat and chicken samples," (in English), *Meat Science*, vol. 69, no. 4, pp. 807-810, Apr 2005.
- [8] S. Citak, O. Varlik, and N. Gundogan, "Slime production and DNase activity of *Staphylococci* isolated from raw milk," (in English), *Journal Of Food Safety*, vol. 23, no. 4, pp. 281-288, Dec 2003.
- [9] K. Guven, M. B. Mutlu, A. Gulbandilar, and P. Cakir, "Occurrence and characterization of *Staphylococcus aureus* isolated from meat and dairy products consumed in Turkey," *Journal Of Food Safety*, vol. 30, no. 1, pp. 196-212, 2010.
- [10] Y. E. Gencay, N. D. Ayaz, and A. Kasimoglu-Dogru, "Enterotoxin gene profiles of *Staphylococcus aureus* and other *Staphylococcal* isolates from various foods and food ingredients," *Erciyes Üniversitesi Veteriner Fakültesi Dergisi*, vol. 7, no. 2, pp. 75-80, 2010.
- [11] K. Omoe, M. Ishikawa, Y. Shimoda, D.-L. Hu, S. Ueda, and K. Shinagawa, "Detection of seg, seh, and sei genes in *Staphylococcus aureus* isolates and determination of the enterotoxin productivities of *S. aureus* isolates harboring seg, seh, or sei genes," *Journal Of Clinical Microbiology*, vol. 40, no. 3, pp. 857-862, 2002.
- [12] F. Kamarehei, E. A. Ghaemi, and T. Dadgar, "Prevalence of enterotoxin A and B genes in *Staphylococcus aureus* isolated from clinical samples and healthy carriers in Gorgan City, North of Iran," *Indian Journal Of Pathology And Microbiology*, vol. 56, no. 3, p. 265, 2013.
- [13] B. Boynukara, T. Gulhan, K. Gurturk, M. Alisarli, and E. Ogun, "Evolution of slime production by coagulase-negative staphylococci and enterotoxigenic characteristics of *Staphylococcus aureus* strains isolated from various human clinical specimens," *Journal Of Medical Microbiology*, vol. 56, no. 10, pp. 1296-1300, 2007.
- [14] J. Rosec and O. Gigaud, "Staphylococcal enterotoxin genes of classical and new types detected by PCR in France," *International Journal Of Food Microbiology*, vol. 77, no. 1, pp. 61-70, 2002.
- [15] A. Aydin, M. Sudagidan, and K. Muratoglu, "Prevalence of staphylococcal enterotoxins, toxin genes and genetic-relatedness of foodborne *Staphylococcus aureus* strains isolated in the Marmara Region of Turkey," *International Journal Of Food Microbiology*, vol. 148, no. 2, pp. 99-106, 2011.

Sensory quality and food composition of fish crackers made from *Oncorhynchus mykiss*

Nermin KARATON KUZGUN^a

Ayşe GÜREL İNANLI^b

^aPertek Sakine Genç Vocational School, Munzur
University Tunceli, Turkey
nerminkaraton@hotmail.com

^bFisheries Faculty, Firat University Elazığ, Turkey
agurelinanli@hotmail.com

Abstract—In this study, it was aimed to product of fish crackers *Oncorhynchus mykiss*. For the purpose of adding groups into the paste mixture, two different groups of crackers were occurred as A and B by adding fish meat at the rates of % 20 and % 30. Nutrient composition (moisture, raw protein, raw oil, raw ash, carbohydrate) and sensory quality of the samples that were acquired in the study were determined and the analyses were repeated for 3 times. Evaluating the data acquired as a result of chemical analyses in the study statistically; it was determined that the difference between these two groups was significant in terms of food composition ($p<0,05$). Additionally, energy values of the products were determined respectively as 349,12—348,41 Cal/100 g in the groups A and B. As a result of sensorial analyses which were conducted in this study; samples in the group A received the highest number of likes from the panelists among the products that were prepared experimentally.

Keywords—Fish cracker; *Oncorhynchus mykiss*; Food composition; Energy value, Sensory quality.

I. INTRODUCTION

In our contemporary world, in parallel to evolving life style, changes in eating habit have increased consumption of foods easy to carry and ready to eat. Food products such as crackers, treats, biscuits and chips are considered as low nutritious and imbalanced because they lack of some nutrition elements although their energy values are high (1; 2; 3; 4). Therefore, if snack foods are consumed frequently between meals this might result in excessive energy intake. It is considered that it would be worth to enrich these products with fish meat since they are consumed in large volumes today (1; 2; 3; 5; 6; 7).

The present study aims to investigate the effect of fish meat on chemical composition, energy values and sensorial characteristics of crackers in order to supply an alternative food, crackers containing meat of trout aquacultured in Turkey.

II. MATERIAL AND METHODS

Within this study, *Oncorhynchus mykiss* fishes with certain economic value were procured from fisheries in Pertek territory in the Keban Dam Lake. Fishes were transferred in insulated polyurethane carriage boxes with ice in them to the laboratory set in the Pertek Vocational College. Then, they were processed in the very same day. After fish fillets were prepared, they were rinsed with fresh water. Then, they were boiled in water for 10 minutes before grounding in blender.

A. Creation of Fish Crackers

Figure 1 exhibits flow chart of fish cracker process and Fish crackers are seen in Figure 2. As a result of these operations, 2 distinct groups were prepared and each operation was repeated for three times.

B. Chemical Analyzes

Moisture content was determined by drying the sample at 100 °C until constant weight was obtained. (8). Crude Protein was determined according to AOAC procedure with N-Protein analysis (9). In analysis of fat content, Soxhlet (Extraction) method was employed (10). The percentage of ash content was determined by means of crude ash burning method (9). Carbohydrate value was determined by subtracting total moisture, ash, protein and fat amount percentages found during analysis from 100 (11). Energy values were obtained by adding up energy values supplied by individual nutrition elements (11).

C. Sensory Analysis

Sensory analyses on samples were conducted by a group of panelist (n=40) aged 18-65. Each panelist sensorial examined cracker samples in terms of their colour, odour, flavour appearance and general acceptability (5—Very Good to 1—Very Bad) (12).

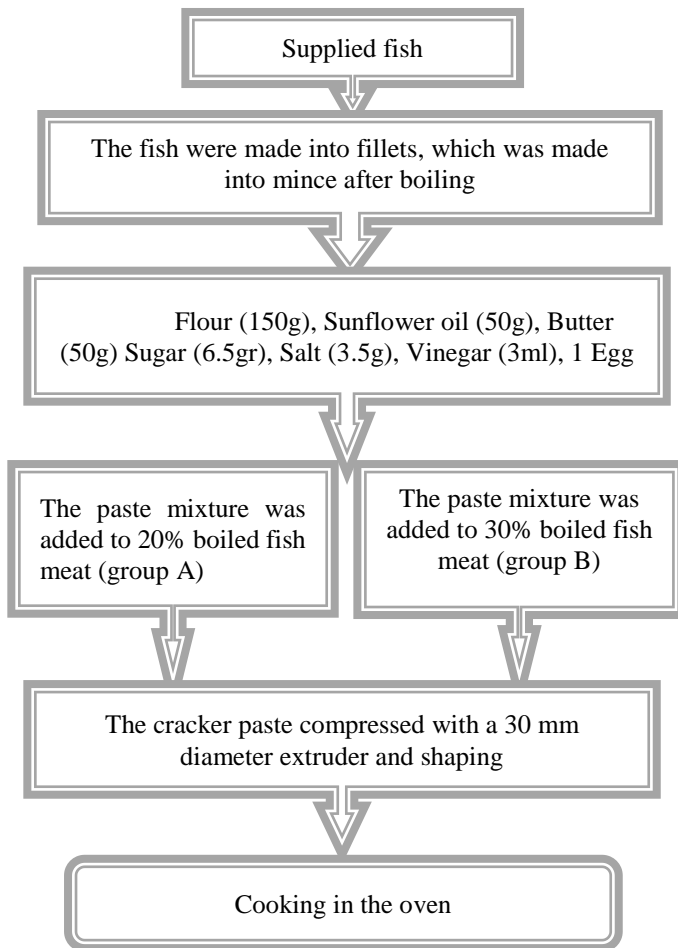


Figure 1. Flow chart of fish cracker process



Figure 2. Cracker Samples

III. RESULTS AND DISCUSSIONS

Table 1 exhibits chemical compositions of prepared samples. According to the Table 1, average moisture, protein, fat, ash, carbohydrate contents of fish meat ingredient of cracker samples were determined as follows $71 \pm 1.00\%$, $21.00 \pm 1.00\%$, $4.75 \pm 0.25\%$, $0.85 \pm 0.05\%$ and $2.25 \pm 0.15\%$, respectively. Table 1 exhibits moisture %, protein %, fat %, ash % and carbohydrate % amount of prepared cracker paste as they were containing fish meat in various proportions. Across these samples, statistically significant difference wasn't determined among groups in terms of moisture ($p > 0.05$). In parallel to these findings, Karaton Kuzgun (15) reported in their study conducted on *Luciobarbus esocinus* fillet that moisture, protein, fat and ash percentages were 71.27 ± 1.20 , 19.21 ± 1.78 , 7.75 ± 1.20 and 1.19 ± 0.28 , respectively. These values are also similar to our findings.

Of considered samples, whereas the highest protein amount was determined with the group B cracker and paste at 20.50 ± 0.50 and 13.50 ± 0.50 , respectively; the lowest amount was determined with group a cracker at 9.76 ± 0.23 (Table 1). Statistically significant difference was determined between samples in terms of protein amount ($p < 0.05$). Two groups displayed similarity in terms of fat amounts in cracker samples, others wasn't exhibited notable statistically significant difference among groups ($p > 0.05$) (Table 1). Whereas the highest ash percentage measured with crackers enriched with fish meat was estimated with group A at 2.80 ± 0.20 ; the lowest percentage was estimated with group B at 1.60 ± 0.10 . In terms of percentage of carbohydrate content of prepared fish cracker samples, it was estimated with group A and B at 40.90 ± 0.50 and 37.21 ± 0.05 , respectively. For paste samples, the same Carbohydrate value was estimated with group A and B at 11.50 ± 1.70 and 13.05 ± 0.15 , respectively (Table 1). In terms of ask content of samples, statistically significant difference wasn't determined among groups ($p > 0.05$). In the statistical analysis of cracker samples enriched with fish meat with respect to their carbohydrate content, the differences among groups were found significant ($p < 0.05$). In another study on cake paste, moisture, ash, fat and protein content percentages of mixture were

D. Statistical Analysis

In statistical analysis of acquired data within the scope of the present study, IBM SPSS®22 (SPSS Inc., Chicago, IL, USA) statistical package software was employed. The statistical significance of the difference among groups was investigated by means of variance analysis (ANOVA) ($p < 0.05$) (13).

reported as 58.32 ± 0.70 , 0.45 ± 0.02 , 2.58 ± 0.37 and 4.23 ± 0.50 , respectively. These findings are similar to our findings. However, fat and protein amounts were found to be lower than the values found in our study (16). This situation could be associated with the different proportions in paste mixture. As it could be seen from Table 1, sample crackers' moisture%, protein%, fat%, ash% and carbohydrate% values were measured at high levels as follows $7.50 \pm 0.50\%$ (B), $20.50 \pm 0.50\%$ (B), $32.31 \pm 0.31\%$ (A), $2.80 \pm 0.20\%$ (A) and $40.90 \pm 0.50\%$ (A), respectively. According to another study in the literature, amounts of constituents in per 100 g of substance were determined measured; and ash%, moisture%, protein%, fat% and carbohydrate% percentages were reported as 2.55, 10.00, 11.68, 6.74 and 69.08, respectively (4). In the same line, Yağmur et al. (2005)(17), measured nutrition values of biscuits and similar wheat products found available in the market. In these products, average moisture, protein fat, carbohydrate and

ash were determined as 5.54%, 6.48%, 18.49%, 68.43% and 1.08%, respectively. These findings displayed similarity with our findings.

As it was exhibited by Table 1, when 100 g. of each sample was analyzed on the basis of their energy values, group A and B samples were measured as 349.12 Cal/100 g and 348.41 Cal/100 g, respectively. The difference between groups was then found statistically significant in terms of energy value ($p < 0.05$). According to another study, the respective value was reported as 466 Cal/100 g for prepared biscuit and similar wheat products (17).

Table1. Food Composition of Cracker Samples

(%)	Fish Meat	Paste A	Paste B	A	B
Moisture	71.00 ± 1.00^d	45.00 ± 1.00^c	41.00 ± 1.00^b	6.50 ± 0.50^a	7.50 ± 0.50^a
Protein	21.00 ± 1.00^a	9.76 ± 0.23^d	13.50 ± 0.50^c	17.43 ± 0.43^b	20.50 ± 0.50^a
Fat	4.75 ± 0.25^a	31.81 ± 0.81^b	30.50 ± 0.50^b	32.31 ± 0.31^b	32.30 ± 0.30^b
Ash	0.85 ± 0.05^a	1.90 ± 0.10^{bc}	1.60 ± 0.10^b	2.80 ± 0.20^d	2.41 ± 0.19^{cd}
Carbohydrate	2.25 ± 0.15^a	11.50 ± 1.70^b	13.05 ± 0.15^b	40.90 ± 0.50^c	37.21 ± 0.05^d
Energy value	-	-	-	349,12	348,41

a,b,c,d: The difference between average values with different letters on the same column

Sample crackers were also evaluated by participants in terms of color, smell, taste, appearance and general like (Figure 2). Sample crackers were scored the same in two groups in terms of their color (5.00 ± 0.00) (Figure 3). When colors of samples were analyzed statistically, the differences among groups weren't found to be significant ($p > 0.05$). When cracker samples were evaluated by participants in terms of their smell, the highest score was given to samples from group A (4.50 ± 0.50), the lowest score was given to the samples from group B (3.25 ± 0.43) (Figure 3). In statistical analysis of samples for sensorial perception regarding their smells, it was revealed that differences among groups were found to be statistically significant ($p < 0.05$). As it was seen from Figure 3, in sensorial analysis of cracker samples for their tastes, whereas group A samples were given 4.50 ± 0.70 score, group B samples were given 4.00 ± 0.00 . It was also determined that the differences among groups weren't statistically significant in terms of taste sense ($p < 0.05$). As it was exhibited in Figure 3, when sample groups were evaluated by respondents for their appearance, the difference among groups weren't found to be statistically significant in terms of their appearance ($p > 0.05$). According to Figure 3, when samples were evaluated by respondents in terms of general acceptability, it was seen that the highest score

(4.75 ± 0.43) was given to group A; and the lowest score (4.00 ± 0.00) was given to group B. In statistical analysis of samples in terms of sensorial general acceptability, the differences among groups were found significant ($p < 0.05$). İzci ve Bilgin, (2015) (18), determined in their study conducted on cracker that general acceptability score of the cracker as 8.09 ± 0.25 . This value coincides with our findings.

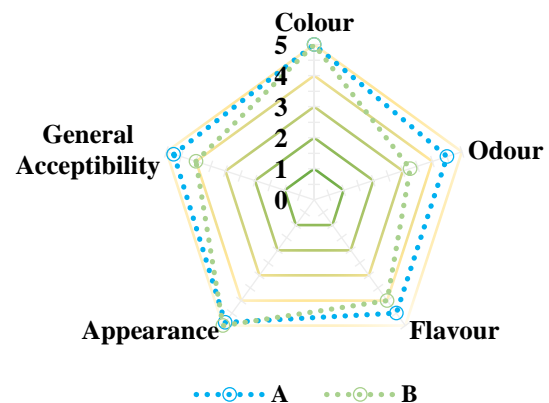


Figure 3. Sensory Change in Cracker Samples

IV. CONCLUSION

Finally, it was concluded that crackers could be added meat of fish species studied in this research so that nutritious values of crackers could be enhanced and variety of products could be enriched, which eventually makes significant contribution into country economy.

REFERENCES

- [1] Anon, (1995). Technical consultation on Food Fortification. Technology and Quality Control. Rome, Italy 22-23 November.
- [2] Egemen, A., (1986). 'Vitaminlerin Sağlığımızdaki Önemi' Konulu Sempozyum Notları, İzmir 119 s.
- [3] Karagözlü, C., Akbulut, N. ve Ömeroğlu, S., (2000). Zenginleştirilmiş Süt ve Süt Ürünleri, Süt Mikrobiyolojisi ve Katkı Maddeleri VI. Süt ve Süt Ürünleri Sempozyumu, Tebliğler Kitabı. Tekirdağ, 595.
- [4] Özer, E. A., (2007). Ekstrüzyon yöntemi ile besleyici değeri yüksek çerez tipi fonksiyonel bir ürün geliştirme gıda, Çukurova Üniversitesi, Doktora tezi.
- [5] Richardson, D.P., (1990). Food Fortification, Proceedings of the Nutrition Society. 49, 39-50.
- [6] Ekşi, A. ve Karadeniz, F., (1996). Gıda Zenginleştirme Yaklaşımı ve Türkiye'de Uygulama Olanağı. Beslenme ve Diyet Dergisi, 25 (2), 45-51.
- [7] Obatolu V.A. and Cole A.H., (2000). Functional Property of Complementary Blends of Soybean and Cowpea with Malted or Unmalted Maize. Food Chemistry (70), 147-153.
- [8] AOAC, (2002a). Moisture content. 950.46. Official Methods of Analysis (17th ed.). Association of Official Analytical Chemists. Gaithersburg, Maryland.
- [9] AOAC., (2002). Official Methods of Analysis of The Association of Official Analytical Chemists (17 th ed.) Association of Official Analytical Chemists, Gaithersburg, Maryland.
- [10] AOAC, (2002b). Fat content in meat. 960.39. Official Methods of Analysis (17th ed.). Association of Official Analytical Chemists, Gaithersburg, Maryland
- [11] Gibson R.S., (1990). Principles of Nutritional Assessment. Oxford University Press.
- [12] Altuğ Onoğur, T. ve Elmacı, Y., (2011). Gıdalarda Duyusal Değerlendirme, Sidas Medya, İzmir.
- [13] Özdamar, K., (2001). SPSS ile Biyoistatistik. Yayın no: 3,4. Baskı. Kaan Kitabevi, Eskişehir, 452.
- [14] Gürel İnanlı, A., Emir Çoban, Ö., Özpolat, E. ve Dartay, M., (2006). Bıyıklı balıktan yapılan balık kroketlerinin soğukta raf ömrünün belirlenmesi, (*Barbus esocinus*, Heckel, 1843) Su Ürünleri Mühendisleri Dergisi, 40-44.
- [15] Karaton Kuzgun, N., (2014). Farklı esansiyel yağlar ve kitosan ile hazırlanan filmlerle ambalajlanmış *Luciobarbus esocinus* filetoalarının 2±1°C'de raf ömrünün araştırılması, Doktora Tezi, 116.
- [16] Gürel İnanlı, A., Karaton N., and Emir Çoban Ö., 2011, Sensorial, chemical and microbiological quality of anchovy cake, African Journal of Biotechnology Vol. 10(48), pp. 9870-9874.
- [17] Yağmur C., Mazahreh A., Özer, E.A. 2005. Türkiye'de Üretilen Bazı Bisküvi ve Benzeri Tahıl Ürünlerinin Besin Değerleri (Protein, Yağ, Rutubet, Kül, Karbonhidrat ve Enerji Miktarları). Sendrom, 17(2), 76-80.
- [18] İzci L. ve Bilgin Ş., (2015). Sensory acceptability and fatty acid profile of fish crackers made from *Carassius gibelio*, Food Science and Technology, 35(4): 643-646.

Pekmez Powder Production by Spray Drying Technology with Niro Atomizer Type Pilot Drying Unit

Durmuş Sert

Necmettin Erbakan University,
Engineering and Architecture
Faculty
Konya, Turkey
dsert@konya.edu.tr

Emin Mercan

Bayburt University, Engineering
Faculty
Bayburt, Turkey
emercan@bayburt.edu.tr

Emrah Karakavuk

Munzur University, Engineering
Faculty
Tunceli, Turkey
ekarakavuk@tunceli.edu.tr

Abstract— Spray-drying, which has been used for commercial production of functional ingredients from several fruits and vegetables, has not yet been studied for grape juice processing. Pekmez, known also as evaporated grape juice, was spray dried in the laboratory type pilot drying unit to obtain pekmez powder. Because fruit juices could not be spray-dried in the drying unit without filler or carrier, maltodextrin which is frequently used as a filler and carrier, was used for this purpose. Therefore, pilot experiment was carried out with the mixture of grape pekmez and maltodextrin (as a carrier, 40-60% v/w).

Keywords— *Pekmez powder; spray drying; maltodextrin*

I. INTRODUCTION

Pekmez is one of the traditional food products in Turkey and it is commonly produced from grape and mulberry by concentration of juices up to 70–80 soluble dry matter content. Pekmez, consumed generally for breakfast [1], can also be produced from fruits containing high amounts of sugar like apple, carnob, plum, watermelon, apricot, sugar beet and fig [2, 3].

Pekmez is a concentrated and shelf-life extended form of grape juice formed by boiling without the addition of sugar or other food additives [4, 5, 6]. Therefore, it can be assumed as a natural food containing natural sugars such as glucose, galactose and minerals. The purpose of concentration is to extend the shelf-life by reducing the water content and to pasteurize the grape juice [5, 7, 8, 9, 10].

Pekmez is nutritious food. Average energy value is 280 kcal/100g (11). Specially, pekmez is rich in iron, phosphor, calcium, and potassium minerals (12). Pekmez is a natural source of energy due to its high carbohydrate content (65-68%). It contains valuable minerals such as calcium (0.084-0.086%) and iron (0.005-0.01%). The high iron content makes the product a recommended treat for anemia [13]. In addition, B1 and B2 vitamins add extra value to the product. This is of nutritional importance, especially for babies, children,

sportsmen and in situations demanding immediate energy [14, 15].

Pekmez is produced in low heat evaporation steps, commercially sold and commonly consumed in viscous liquid and solid forms. The color of the pekmez changes from dark brown to white depending on the processing conditions, concentration, types of bleaching agents, heat and mixing rate. The viscosity of pekmez increases with increasing solids concentration and decreasing temperature [16].

However, prolonged storage of pekmez causes problems related with some quality characteristics. Hydroxymethyl furfural (HMF) development is one of the most significant problems occurring during the pekmez storage. Tosun and Ustun [15] reported that HMF content of pekmez increased during prolonged storage period. In addition, the color of pekmez darkens during this period, because of maillard reaction. When excessive maillard browning is undesirable in food systems, it can be inhibited by drying process in which the moisture is decreased to very low levels [17]. HMF is one of the most widely used indices in nonenzymic browning studies on juices and fruit derivatives. Therefore, storage of pekmez as a dried form may be one of the useful ways to inhibit or delay excessive maillard browning, consequently decrease HMF development during the storage period. Another purpose of drying is to extend the shelf-life by reducing water content. In addition, storage of pekmez as a dried form will help to reduce storage costs. Spray drying is ideal for heat sensitive products such as maltodextrine, soup mixes and sugar-based foods. However, pekmez powder production by spray-drying technology is new and has not been applied yet in Turkey so far. Fig. 1 shows a flow diagram of pekmez powder processing operation. Pekmez powder is produced from pekmez by using spray drying, which is the most widely used industrial technology involving particle formation and drying. Like other heat sensitive liquid foods, pekmez can also be dried by the spray drying technology.

II. MATERIAL AND METHODS

A. Spray Drying

Spray drying involves the atomization of a liquid feedstock containing solids in solution, suspension or emulsion, and directing the resulting spray of droplets into a flow of hot drying air. Liquid feedstocks are not only just dried, but are also converted into powders having specific properties as determined by the atomization and drying conditions adopted, and also the drying chamber and plant layout selected. One of the most important reasons why spray drying has been adopted for producing powdered products is the ability of the technology to produce an end product continuously to a precise quality specification. The most commonly quoted specifications involve moisture content, solubility, bulk density, and hygroscopicity. The temperatures and drying conditions experienced by a droplet during drying have an important influence on the above powder properties [18, 19]. In the early stages of drying, the droplet has a free liquid surface and evaporation from this surface is rapid. The depletion of liquid will cause the solute to be more concentrated at the surface - this will depend on the speed of evaporation and the rate at which the liquid can be replenished from the interior of the droplet. Because of this increased concentration, solids will come out of solution at the surface of the droplet first, leading to the formation of a crust or skin around a hollow particle. The thickness of the crust will depend on the drying rate - high initial drying rates will lead to larger particles with thin shells and low density, whereas, low initial drying rates will lead to smaller particles with thick shells and high density. The presence of occluded or absorbed gases in the liquid feed is another possible mechanism for the formation of hollow, high porosity particles. In addition to the above particle formation processes, conditions should also be tailored to physical and chemical changes within the material itself [18, 19]. Spray drying of sugar-rich foods is difficult due to the presence of high content of sugars and organic acids. These compounds exhibit sticky behavior during spray drying. Stickiness is a term used to describe the phenomena of particle-particle cohesion and particle-wall adhesion in the spray drying process. Stickiness depends not only on the properties of materials but also on the inlet variables applied in a spray drying system. Deposition is another phenomenon in spray drying. It relates to the stickiness and the design of a dryer system. Theoretically, there should no deposition problem if the size of the dryer chamber is large enough. Because of the economic factors, the size of the dryer needs to be limited to a suitable range. Therefore, stickiness and deposition need to be solved by other methods rather than by using a very large dryer chamber.

Additives such as glucose syrups or maltodextrin have been used to produce physical changes in the product, consequently reducing the stickiness and wall deposition in spray drying. Glucose syrups have been used for blackcurrant [20] and

orange juice [21] and maltodextrin has been used for different sugar-rich foods such as orange [22], blackcurrant [23], honey [24] and tamarind [25]. The addition of these carriers into the feed improved the powder recovery. The fraction of additives in juices is normally in the range of 40–60% but higher fraction can also be used [26]. However, the required sensory quality of final products limits the amount of additives.

B. Pekmez Powder Production

To produce pekmez powder, pekmez produced from fresh grapes according to the traditional method was spray-dried by Niro atomizer laboratory type pilot drying unit in the plant of ENKA Dairy and Food Products Co., Konya, TURKEY, as in the process flow scheme diagrammed in the Fig. 1.

Pilot scale test was performed in Niro Atomizer pilot spray-drying unit with the capacity of 1-7 kg water evaporative per hour. The sprays were produced by rotary (wheel) energy (Fig. 2.). Evaporation of moisture from the pekmez droplets and formation of particles were performed under controlled temperature and airflow conditions. Pilot experiment was carried out with the mixture of grape pekmez and maltodextrin (as a carrier, 40-60% v/w).

Because fruit juices could not be spray dried in the drying unit without filler or carrier, maltodextrin which is frequently used as a filler and carrier, was used for this purpose. Maltodextrin addition prevents pekmez from becoming thicker and more adhesive to the processing equipment due to maillard reaction, which may also result in pumping problems. The drying step took 60 min. The temperature of inlet air was 200 °C and outlet air temperature did not exceed 70 °C. The air flow direction and particle trajectories were the same. At the end of processing, the pekmez powder having 96-97% of dry matter was packed with triple layered kraft paper pouches and stored in this way until analyses. To analyze physical and chemical properties of the pekmez powder properly, it was diluted with 30 % of distilled water.

C. Determination of Chemical and Physical Characteristics

Total and soluble dry matter, ash and pH values were determined according to the standard method of AOAC [27]. The pH was measured with a pH meter (pH 315i/SET WTW, Weilheim, Germany). Soluble dry matter was determined with an Abbe-Zeis refractometer at 21 °C and expressed as °Brix. Water activity measurements were performed with an AQUALAB apparatus (DECAGON Devices Inc., Model Series 3TE, USA). Pure water (1.000±0.003%) was used as standard for equipment calibration. Color measurement was performed using a Minolta Chroma Meter CR-400 (Minolta, Osaka, Japan).

The L*, a* and b* color measurements were determined according to the CIELab color space system, where L*

corresponds to light/dark chromaticity (changing from 0% dark to 100% light), a^* to green/red chromaticity (changing from -60% green to 60% red) and b^* to blue/yellow chromaticity (changing from -60% blue to 60% yellow). The instrument was calibrated with a white reference tile ($L^*=97.10$, $a^*=-4.88$, $b^*=7.04$) before the measurements. Color measurements were made 4 times, 1 on the middle and 3 on the different parts of the solutions.

III. RESULTS AND DISCUSSION

As shown in Table 1, diluted pekmez powder (DPP) produced from fresh grape contained similar total and soluble dry matter, ash content and pH value to those reported for mulberry and white grape pekmez [28, 29]. L^* , a^* and b^* values of DPP were measured as 50.68, +4.44 and +10.19, respectively. A high redness (a^*) value is not desired because it occurs as a result of excessive caramelization of sugars. A low redness (a^*) and high brightness (L^*) values indicate a good quality pekmez parameters [30]. In this study, DPP, which was regarded to be equivalent to pekmez showed high L^* values and low a^* values, being an indicative of good quality DPP product. Therefore, pekmez powder production process and obtained pekmez from DPP product could be regarded as a valid production method and product, which was free of problems with respect to the pekmez's physical and chemical quality parameters, mentioned above.

IV. CONCLUSION

Pilot-scale experiment proved the possibility of production of dried product, called pekmez powder whose diluted form (diluted pekmez powder, DPP) showed the similar physical and rheological characteristics to those reported for the pekmez in the literature. Therefore, process of pekmez powder production from pekmez by pilot type atomizer drying unit can be regarded as an acceptable production method, without modifying the fundamental pekmez's physical and quality parameters studied in this study, by this way, processing and storage of pekmez powder may be an alternative way to the processing of pekmez in the liquid form.

TABLE 1 The chemical and physical characteristics of DPP

Properties		DPP
Total dry matter		74.09 %
Soluble dry matter		69.43 °Brix
Ash		2.01 %
pH		5.37
a_w		0.852
Color	L^*	50.68
	a^*	+4.44
	b^*	+10.19

DPP, diluted pekmez powder.



Rotary atomizer, located in the center of the chamber roof. An air turbine drive operating from a six-bar compressed air source, supplies power to the atomizer wheel. A vaned atomizer wheel is used for non-abrasive feeds and an atomizer wheel with carbide bushings for atomizing abrasive feeds. Particles in the range 5-25 μ m are created.

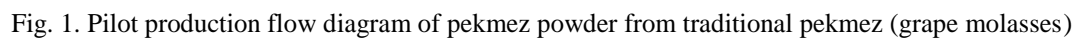


Co-current two-fluid nozzle, located also in the center of the chamber roof. The atomization is created by compressed air at a pressure of 0.5-2.0 bar. The feed and atomizing gas are passed separately to the nozzle head where the atomization takes place. Two-fluid nozzles have the advantage of handling more viscous feeds. The co-current mode is selected for drying heat sensitive products to fine particles in the range 5-25 μ m.



Fountain two-fluid nozzle, located in the cone of the drying chamber, spraying upwards. The fountain mode is selected to meet a more coarse and free-flowing powder specification. Often used for fine ceramics and other non-heat-sensitive products. The counter-current flow offers a dryer performance with excellent heat utilization and provides the longer powder residence time in the drying chamber required to complete the drying to larger particles in the range 15-80 μ m.

Fig. 2. Spray-drying-process (NIRO 2007)



REFERENCES

- [1] Alparslan M, Hayta M. 2002. Rheological and sensory properties of pekmez (grape molasses)/tahin (sesame paste) blends. *Journal of Food Engineering*, 54: 89-93.
- [2] Demirözü B, Sökmen M, Uçak A, Yılmaz H, Gülderen S. 2002. Variation of copper, iron, and zinc levels in pekmez products. *Bulletin Environmental Contamination and Toxicology*, 69: 330-334.
- [3] Üstün NS, Tosun I. 1997. Pekmezlerin bileşimi. *Gıda*, 22: 417-423.
- [4] Gökçen J, Ömeroğlu S, Ceritoğlu A. 1982. Üzümlerden elde edilen pekmez bulama, jöle, cevizli sucuk gibi tipik Türk gıda maddelerinin yapım yöntemlerinin geliştirilmesi olanaklarının araştırılması. TÜBİTAK, Marmara Bilimsel ve Endüstriyel Araştırma Ens. Gebze. Yay. No. 65.
- [5] Tekeli ST. 1965. Ziraat Sanatları. Ziraat Fak. Yay. 237, A.Ü.Basımevi.
- [6] Yazıcıoğlu T. 1967. Türkiye’de üzüm üretilmesi ve değerlendirilmesi. *Ziraat Fak. Yıllığı*, 17(2) 303-314.
- [7] Kaya A, Belibağlı KB. 2002. Rheology of solid Gaziantep Pekmez. *Journal of Food Engineering*. 54: 221-226.
- [8] Batu A, Yurdagel U. 1993. Değişik katkıların kullanımı ile beyaz katı üzüm pekmezi eldesi üzerine bir araştırma. *Gıda*, 18: 157-163.
- [9] Gökçe K, Çizmecı M. 1965. Pekmez. Tarım Bakanlığı Ziraat İşeri Genel Müdürlüğü Yayınları, A-109, Ankara.
- [10] Kayahan M. 1982. Üzüm şirasının pekmeze işlenmesinde meydana gelen terkip değişimleri üzerinde araştırmalar. Ankara Üniv. Ziraat Fak. Yay. No: 797.
- [11] Güven S, 1982. 3. Gıda Kongresi, Gıda Tekniği Derneği, Yayın No:4, 10-12 s, Ankara.
- [12] Eksi A, Artık N. 1984. Pestil İşleme Tekniği ve Kimyasal Bileşimi, 273-276 s, Ankara.
- [13] Öztürk BA, Öner MD. 1999. Production and Evaluation of Yogurt with Concentrated Grape Juice. *Journal of Food Engineering*. 64(3) 530-532.
- [14] Batu A. 1993. Kuru Üzüm ve Pekmezin İnsanlığı ve Beslenmesi Açısından Önemi. *Gıda*. 18(5) 303 307.
- [15] Tosun I, Üstün NS. 2003. Nonenzymic browning during storage of white hard grape pekmez (Zile pekmezi). *Food Chemistry*, 80: 441-443.
- [16] Ermurat Y. 2006. Carbonation of Evaporated Grape Syrup “Pekmez” Formulation and Production of Carbonated Evaporated Grape Syrup Pekmez Soft Drinks: Pekmez Gazoz, Pekmez Cola and Pekmez Limon, *Electron. J. Environ. Agric. Food Chem.*, 1221-1223.
- [17] Whistler RL, Daniel JR. 1985. Carbohydrates. In OR. Fennema (Ed.), *Food chemistry* (2nd ed., 69-137 s). New York: Marcel Dekker.
- [18] Oakley DE. 1997. Produce uniform particles by spray drying. *Chem. Eng. Prog.* 93(10) 48-54.
- [19] Masters K. 1997. Spray dryers. In *Industrial Drying of Foods*; Baker, CGJ, Ed.; Blackie Academic & Professional: NY, 90-114.
- [20] Zaleski J, Lipowska T, Kuszlik J. 1968. Spray drying of concentrated fruit juices. *Prace Instytutow I Laboratoriow Badawczych Przemysluspozywczego*, 18(4) 53.
- [21] Brennan JG, Herrera J, Jowitt R. 1971. A study of some of the factors affecting the spray drying of concentrated orange juice, on a laboratory scale. *Journal of Food Technology*, 6(September), 295-307.
- [22] Gupta AS. 1975. Spray drying of orange juice. US patent No. 4112130.
- [23] Bhandari BR, Senoussi A, Dumoulin ED, Lebert A. 1993. Spray drying of concentrated fruit juices. *Drying Technology*, 11: 1081-1092.
- [24] Bhandari BR, Datta N, Howes T. 1997. Problems associated with spray drying of sugar-rich foods. *Drying Technology*, 15: 671-684.
- [25] Truong V. 1994. Spray drying of tamarind concentrate and its quality evaluation. Master Thesis. Bangkok, Thailand: Asian Institute of Technology.
- [26] Masters K. 1994. Spray drying handbook. London: Longman Scientific & Technical.
- [27] AOAC, 1984. Official methods of analysis. 14th ed. Assoc. Official Anal. Chemists. Arlington VA.
- [28] Sengül M, Ertugay MF, Sengül M. 2005. Rheological, physical and chemical characteristics of mulberry pekmez. *Food Control*, 16: 73-76.
- [29] Yoğurtçu H, Kamışlı F. 2006. Determination of rheological properties of some pekmez samples in Turkey. *Journal of Food Engineering*, 77: 1064-1068.
- [30] Aksu I, Nas S. 1996. Dut pekmezi üretim tekniği ve çeşitli fiziksel-kimyasal özellikleri. *Gıda*, 21: 83-88.
- [31] NIRO. 2007. MOBILE MINOR™ Spray Dryer, www.niroinc.com (14.05.2007)

Organic matter-major-trace elements relationship of the Derindere–I area, from Dadaş Formation , Bismil, Diyarbakır, Southeastern Turkey

Dicle BAL AKKOCA(1)

¹Fırat University, Faculty of Engineering, Department of Geological Engineering. International Conference on Advances and Innovations in Engineering (ICAIE)

Elazığ, Turkey

e-mail: dbal@firat.edu.tr

Ümit IŞIK(2)

²Fırat University, Faculty of Engineering, Department of Geological Engineering. International Conference on Advances and Innovations in Engineering (ICAIE)

Elazığ, Turkey

umit.isik@hotmail.com

Abstract— The study area is located in the Derindere drill hole, around Bismil, Diyarbakır, southeast of Turkey. Investigated Early Silurian-Early Devonian organic rich Dadas Formation is one of the main source rocks for oil. Formation consists of grayish-green, organic-matter rich dark colored shales, limestones, mudstones and sandstones. Samples were collected from the Derindere drill hole. Element analysis of 20 representative samples were carried out, using ICP-AES for the determination of major and trace elements. 20 total organic carbon (TOC) analysis was performed by the pyrolysis method using the Rock-Eval 6 analyzer. Al_2O_3 , Fe_2O_3 , Na_2O , TiO_2 and Cr_2O_3 , Sc, Ba, Co, Cs, Ga, Hf, Rb, Nb, Ta, Th decrease at the between 3000-3020 m. showing lower detritic contribution at these levels. On the other hand CaO is higher at these levels show carbonate occurrences. Cu, Pb, Zn, As sulphophile elements are lower at the 3060. meter (Table 2), showing lower sulphide minerals at these level. TOC values increase between 2890–3070 meters. These variations in elements and TOC concentrations reflect changes in paleoclimate, paleoredox and paleoproductivity in Paleozoic sedimentation. The positive correlations between SiO_2 , Al_2O_3 , Cs, Ga, Nb, Rb, Ta, Th, Sc reflect silicates and, positive correlations between Cu, Pb, Zn, Ni show sulphide occurrences. Negative correlations of TOC and SiO_2 , Al_2O_3 , Fe_2O_3 reflect that these elements depend on silicates than organic materials. The correlations between Ga, Rb, Ta, Th and TOC show detritic silicate- organic material discriminations.

Keywords—organic matter; major element, trace element, Dadaş , Eastern Turkey

1. INTRODUCTION

In comparison to shales, black shales are enriched in both organic matter and some trace elements [1]. Element enrichment in shale is associated with the accumulation of

elements together with organic matter under anoxic conditions [2].

Paleozoic Dadaş Shales are exposed around Diyarbakır – Bismil in southeast Anatolia, and are deposited in the foreland area of south-east of Turkey [3]. Dadaş Shale is the Turkish equivalent of Silurian hot shales in the Middle East. and have been continued since 2011 by the Turkish National Petroleum Company (TPAO) and several international companies.

Geology and organic geochemical characteristics of the Dadaş Shales were investigated by [4], [5], [6], [7],[8]. However, the major and trace element geochemistry of these shales were not study. In this study, the concentrations of both major, trace elements and the organic matter element relations have been investigated in Derindere drill hole samples from Dadaş Formation.

I. GEOLOGICAL SETTING

The study area is located in the Derindere drill hole area around Bismil, Diyarbakır, southeast of Turkey (Fig. 1). The Formation around area is shown in Fig. 2. In the area, Miocene Şelmo Formation overlies the Early Silurian-Early Devonian Dadaş Shales.

The Dadaş Formation consists chiefly of shale, mudstone and sandstone starts with a grayish, green colored transgressive sequence deposited in a shelf environment and ends up with a regressive sequence [3], and divided into three members; with organic rich clastic rocks restricted to the lowermost part as Dadaş I and Dadaş II and uppermost part of Dadaş III (Fig.3). Dadaş-I member is comprised by carbonate-interlayered dark shales, Dadaş-II member is composed of sandstone-interbedded, banded, organic-matter rich dark shales and Dadaş-III member is comprised by shale, sandstone, dolomite and marl lithologies [6]. Derindere drill hole cut the Dadaş-I member.

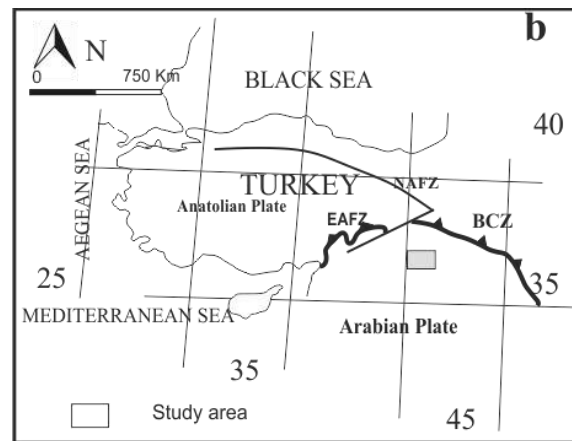


Figure 1. Location map of the study area

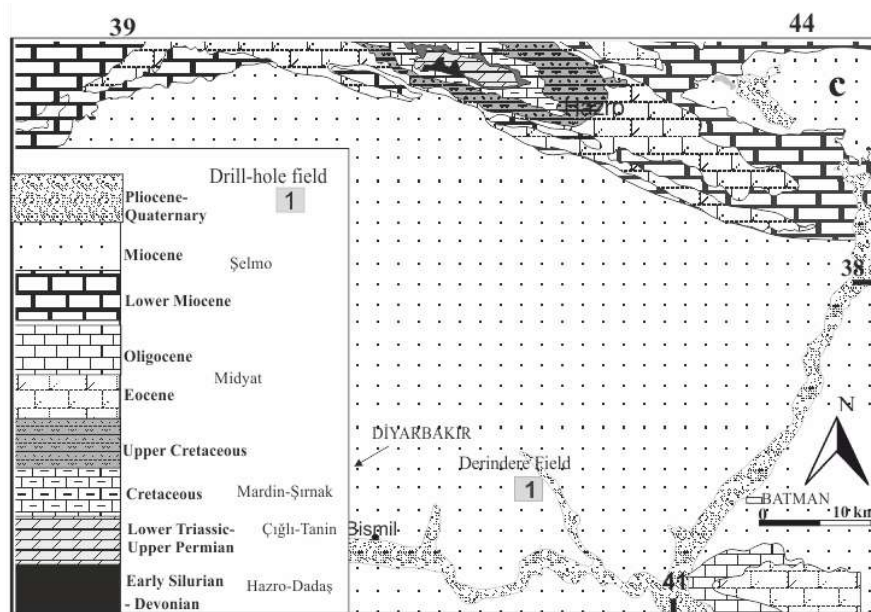


Figure 2. Geological map of the study area showing the locations of Derindere drill hole. Simplified from 1/500.000 scale geological map.

II. SAMPLING AND ANALYTICAL METHODS

Samples were collected from the Derindere drill hole (DDH). Element analysis of 20 representative samples were carried out at Acme Analytical Laboratories Ltd. (Canada), using ICP-AES for the determination of major and trace elements. Major elements are expressed as oxide percents (i.e. SiO_2 , Al_2O_3 , CaO , Cr_2O_3 , total Fe_2O_3 , K_2O , MgO , MnO , Na_2O , P_2O_5 and TiO_2). Other element concentrations are given in ppm. Loss on ignition was determined by weight difference after ignition at 1000 °C. In order to determine the relation between the elements and organic material, total organic carbon (TOC) analysis was performed. TOC (%) analysis was conducted at Geochemistry Laboratories of Turkish Petroleum Corporation (TPAO) by the pyrolysis method using the Rock-Eval 6 analyzer.

III. RESULTS and DISCUSSIONS

A. Geochemistry

Concentrations and average of major and trace elements of the Derindere drill hole samples are shown in Table 1. Al_2O_3 , Fe_2O_3 , Na_2O , TiO_2 and Cr_2O_3 elements depend on the detritic silicates [9]. In drill hole, these elements decrease at the between 3000-3020 m. levels. This shows that detritic contribution is lower at these levels. Sc, Ba, Co, Cs, Ga, Hf, Rb, Nb, Ta, Th are lower at levels also suggest this phenomena. CaO element is higher at the these levels show carbonate sedimentation (Table 1). On the other hand, Cu, Pb, Zn, As elements (sulphophile elements) are lower at the 3060. meter (Table 2)., showing lower sulphide minerals.

Formation	Member	Lithology	Explanations
Hazro			Shale Sandstone
Dadaş	III		Shale Siltstone Limestone
	II		Limestone band and gray shale
	I		Limestone Shale
Bedinan			Shale Sandstone Siltstone

Figure 3. Lithographic section of Dadaş Formation [3].

The Dadaş Shales were deposited in a shelf environment. These variations in element concentrations reflect deposition conditions and paleoclimate [10]. Detritic contribution shows mainly drier climatic conditions prevailed between 3000-3020 levels. There is a significant positive correlation with LOI and CaO ($r=0.96$) in all samples suggesting that carbonates play an important role on the LOI of the shale samples (Fig. 4). With the exception of MgO, CaO, P_2O_5 the major oxides show significant positive correlation with Al_2O_3 demonstrating that Al, K, Na and Ti sources are mainly from feldspar and clay minerals. However, CaO shows a negative correlation with SiO_2 , Al_2O_3 , K_2O and TiO_2 .

Ca is attached to carbonates and these negative correlations reflect the separation of carbonates and silicates. The positive correlations between SiO_2 , Al_2O_3 , Cs, Ga, Nb, Rb, Ta, Th, Sc reflect silicates (Table 4) and, positive correlation between Cu, Pb, Zn, Ni show sulphide occurrences (Fig. 5).

B. Organic Matter Content

The concentration of organic matter in a rock is typically evaluated by measurement of the TOC content. TOC values of the Dadaş Shales are shown in Table 5. TOC values increase between 2890–3070. meters. In generally, TOC content increase with the deep of Derindere drill-hole (Table 5, Fig. 6).

C. Elements -TOC Relationships in Derindere Drill-hole

Table 6 and Fig. 7 show correlations between TOC and some important elements. Negative correlations of TOC and SiO_2 , Al_2O_3 , Fe_2O_3 , show that these elements depend on silicates than organic elements. These elements are detritic in origin [11]. It is not present correlation between TOC and MgO, CaO, show that these elements depend on carbonates than organic materials.

There are no significant correlation present between TOC and Ga, Rb, Ta, Th which are detritic elements, also suggest detritic silicate - organic material discriminations. Mangan is an element sensitive to redox changes [2]. It is not present correlation between Mn and TOC can be explained by consumption in anoxic conditions. The association of P with the organic matter in coals has been established. P is associated with the organic material [12]. A positive correlation between TOC and P indicates the dependence of this element on the organic matter.

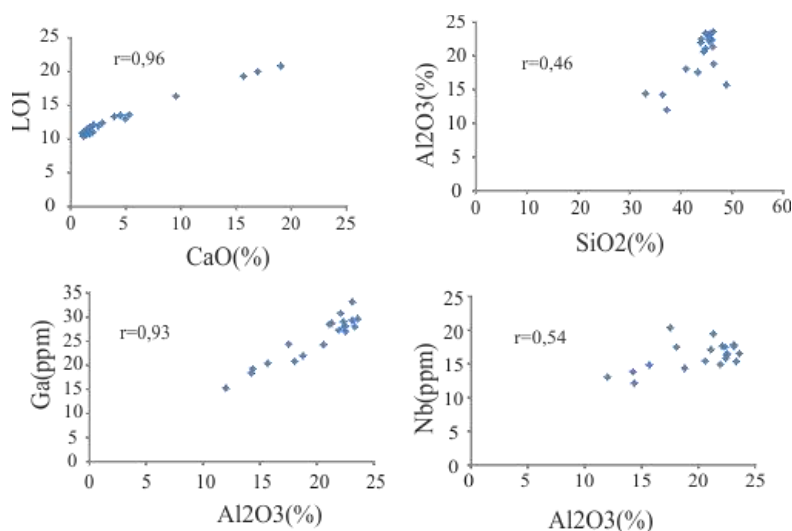


Figure 4. Some major oxide elements correlations ($P>0.05$)

Table 1. Major element contents of Derindere–drill hole samples. Average and standart deviation values are also given.

Sample N.	Major Oxides Elements (%)												Total
	SiO ₂	Al ₂ O ₃	Fe ₂ O ₃	MgO	CaO	Na ₂ O	K ₂ O	TiO ₂	P ₂ O ₅	MnO	Cr ₂ O ₃	LOI	
D2880	48.90	15.68	6.92	4.76	4.94	0.36	4.37	0.67	0.16	0.05	0.012	13.0	99.78
D2890	46.27	23.60	8.84	2.34	2.00	0.40	4.20	0.94	0.14	0.04	0.018	11.0	99.82
D2900	45.32	23.12	11.62	2.04	1.03	0.44	4.08	0.90	0.17	0.12	0.020	10.9	99.81
D2910	46.06	22.34	10.61	2.33	1.78	0.43	4.16	0.92	0.17	0.11	0.019	10.9	99.83
D2920	44.79	23.33	12.89	1.98	1.14	0.41	3.74	0.87	0.15	0.13	0.019	10.4	99.81
D2930	43.99	22.49	11.42	2.39	2.08	0.42	3.75	0.89	0.16	0.14	0.020	12.1	99.81
D2940	45.67	23.13	10.85	2.22	1.24	0.41	3.94	0.90	0.17	0.15	0.018	11.1	99.84
D2950	43.88	21.93	14.24	2.29	1.38	0.48	3.76	0.86	0.16	0.23	0.023	10.6	99.81
D2960	44.81	21.10	11.26	2.84	2.51	0.49	3.68	0.85	0.19	0.19	0.019	11.9	99.79
D2970	45.68	22.09	11.54	2.55	1.68	0.39	3.77	0.90	0.19	0.20	0.018	10.8	99.81
D2980	45.56	22.42	10.98	2.39	1.48	0.40	3.85	0.90	0.17	0.17	0.019	11.5	99.81
D2990	45.63	22.54	10.22	2.47	1.72	0.48	3.77	0.93	0.17	0.15	0.018	11.7	99.81
D3000	33.12	14.37	8.74	2.57	16.96	0.33	2.73	0.62	0.17	0.16	0.014	20.0	99.77
D3010	36.45	14.24	7.12	2.50	15.65	0.35	3.10	0.69	0.19	0.11	0.013	19.3	99.76
D3020	37.24	12.01	4.76	1.82	19.05	0.47	2.80	0.63	0.19	0.06	0.011	20.8	99.81
D3030	44.45	20.60	9.14	2.34	4.50	0.42	3.65	0.87	0.18	0.15	0.017	13.5	99.81
D3040	41.03	18.07	7.57	2.08	9.54	0.47	3.39	0.83	0.23	0.10	0.016	16.4	99.76
D3050	46.20	21.32	9.12	2.34	2.87	0.44	3.88	0.92	0.19	0.14	0.016	12.4	99.78
D3060	43.33	17.53	11.63	2.78	5.30	0.51	3.77	0.85	0.20	0.15	0.022	13.6	99.62
D3070	46.41	18.79	7.71	3.59	3.95	0.48	4.42	0.85	0.15	0.10	0.017	13.3	99.76
Average	43.74	20.04	9.86	2.53	5.04	0.43	3.74	0.84	0.18	0.13	0.02	13.26	99.79
St. Dev.	3.79	3.45	2.24	0.63	5.51	0.05	0.44	0.10	0.02	0.05	0.00	3.17	0.05

Table 2. Trace element contents of Derindere–drill hole samples. Average and standart deviation values are also given.

Sample N.	Trace Elements (ppm)								
	Ni	Sc	Ba	Co	Cs	Ga	Hf	Nb	Rb
D2880	43	14	407	20.0	4.5	20.4	3.9	14.8	107.9
D2890	47	21	289	26.1	6.6	29.6	3.2	16.5	148.1
D2900	52	21	290	25.4	7.6	29.3	2.9	17.8	159.8
D2910	54	20	363	23.3	6.8	29.0	2.9	17.5	147.7
D2920	56	20	315	22.7	7.0	28.0	2.3	15.3	147.9
D2930	57	20	320	21.8	7.0	28.1	2.4	16.3	154.1
D2940	54	21	339	23.7	8.0	33.1	2.3	17.6	179.9
D2950	60	20	327	24.7	7.1	27.3	2.3	14.9	159.5
D2960	54	19	446	23.7	7.8	28.5	2.4	17.1	163.0
D2970	51	20	392	23.2	8.0	30.8	2.7	17.6	174.7
D2980	56	20	375	23.4	7.5	27.9	2.5	15.8	167.0
D2990	52	20	357	23.6	7.2	27.0	2.5	16.5	165.7
D3000	43	13	439	17.7	5.3	19.3	2.0	12.1	115.0

<i>Table 2 cont. Sample N.</i>	<i>Ni</i>	<i>Sc</i>	<i>Ba</i>	<i>Co</i>	<i>Cs</i>	<i>Ga</i>	<i>Hf</i>	<i>Nb</i>	<i>Rb</i>
D3010	50	13	351	15.4	5.1	18.4	2.8	13.8	114.4
D3020	55	11	288	13.2	4.3	15.2	3.4	13.0	93.7
D3030	52	19	395	20.2	6.8	24.2	2.7	15.4	152.3
D3040	94	17	362	18.2	6.6	20.8	3.2	17.5	132.8
D3050	49	19	425	22.4	8.1	28.7	3.0	19.4	168.7
D3060	94	18	1441	22.9	7.6	24.4	3.3	20.3	147.5
D3070	70	19	577	16.2	7.5	22.0	4.0	14.3	151.5
Average	57.2	18.3	424.9	21.4	6.8	25.6	2.8	16.2	147.6
St. Dev.	13.5	2.9	242.3	3.4	1.1	4.6	0.5	2.0	22.8

Table 2 cont. Sample N.	<i>Sr</i>	<i>Ta</i>	<i>Th</i>	<i>U</i>	<i>V</i>	<i>W</i>	<i>Zr</i>	<i>Y</i>	<i>Cu</i>	<i>Pb</i>	<i>Zn</i>	<i>As</i>
D2880	158.9	1.1	13.4	3.4	119	1.9	144.0	28.1	40.9	12.3	29	9.0
D2890	152.5	1.2	14.1	2.5	162	4.7	113.8	29.7	29.0	13.6	238	8.7
D2900	157.4	1.2	13.6	1.9	165	8.8	101.5	31.3	30.2	19.2	155	10.7
D2910	154.9	1.2	14.4	2.2	156	2.5	103.5	33.7	31.8	10.2	74	8.5
D2920	118.3	1.1	13.4	1.7	177	2.7	84.7	29.2	37.9	9.5	86	8.8
D2930	125.2	1.2	13.2	2.1	166	7.5	85.1	27.9	35.7	9.8	88	8.9
D2940	156.5	1.3	14.6	2.3	152	1.8	84.2	34.3	25.1	10.7	84	10.0
D2950	138.0	1.0	14.2	1.8	184	2.8	81.4	29.8	32.1	8.3	92	11.1
D296	152.6	1.1	14.8	2.5	157	2.5	91.7	33.7	28.3	7.7	77	8.6
D2970	158.4	1.2	14.9	2.5	157	2.2	90.2	35.8	29.7	10.0	330	10.0
D2980	134.1	1.0	14.1	2.1	154	2.8	90.1	30.9	46.5	11.7	111	11.2
D2990	125.5	1.1	14.8	2.2	153	1.9	89.3	30.4	60.6	15.2	100	9.4
D3000	425.7	0.8	10.5	3.7	145	22.6	81.5	29.7	27.9	7.4	82	3.4
D3010	502.4	0.9	10.1	4.3	177	1.7	99.4	32.2	53.0	5.8	42	6.0
D3020	368.3	1.0	9.5	7.7	179	1.1	132.6	33.5	36.0	7.4	67	7.2
D3030	149.4	1.2	13.0	2.9	156	1.4	99.2	30.1	34.7	12.9	58	8.5
D3040	205.4	1.1	11.9	6.0	363	1.3	122.6	32.2	41.7	14.2	140	9.7
D3050	165.5	1.1	14.7	4.1	240	2.0	110.9	37.4	39.0	19.4	78	8.4
D3060	186.7	1.4	12.5	7.5	373	24.7	129.4	36.0	27.8	7.9	55	7.2
D3070	115.5	0.9	12.7	4.9	167	2.0	138.3	34.6	56.8	8.9	65	10.1
Average	192.56	1.11	13.22	3.42	185.10	4.95	103.67	32.03	37.24	11.11	102.55	8.77
St. Dev.	104.97	0.14	1.57	1.78	64.85	6.53	19.58	2.67	9.86	3.66	68.46	1.77

V, Ni, Cu, Pb, Zn, As are enriched in organic matter-rich rocks [13], [2], [14]. This explains the positive correlation of these elements with TOC (Table 6). U, Mo, also have positive

correlations with TOC, indicate that these elements are grouped with TOC. U and Mo is one of the most common and

highly enriched elements in black shales [11]. The positive correlation is present between Ba and TOC. Ba is often assumed to be an indicator for paleo-production [15]

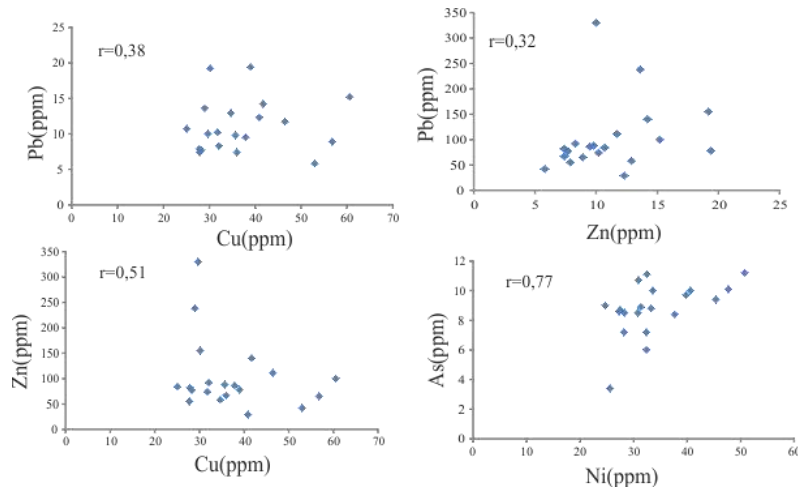


Figure 5. Some trace elements correlations ($P>0.05$)

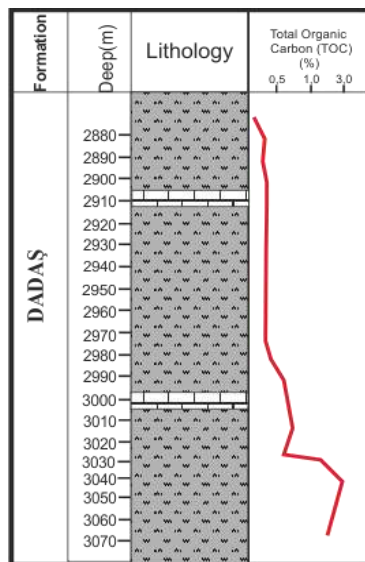


Figure 6. Total organic carbon (TOC) contents of samples in Derindere drill-hole

IV. CONCLUSION

Chemical compositions of analyzed samples of Derindere drill hole from Dadaş Formation have been used to deduce the following.

- 1) In study area, Miocene Şelmo Formation overlies the Early Silurian-Early Devonian Dadaş Shales. The Dadaş Formation is divided into three members; Dadaş I and Dadaş II and uppermost part of Dadaş III. Derindere drill hole cut the Dadaş-I member. The formation that consists chiefly of shale, mudstone and sandstone starts with a dark grayish, green colored
- 2) Transgressive sequence deposited in a shelf environment and ends up with a regressive sequence.
- 3) Detritic silicate contribution is lower, carbonate contribution is lower between 3000-3020, and sulphide minerals are lower at the 3060 meter.
- 4) TOC values increase between 2890–3070 meters and in generally, TOC content increase with the deep of Derindere drill-hole
- 5) The variations in detritic element concentrations and TOC contents reflect deposition conditions and paleoclimate. Lower detritic contribution shows drier climatic conditions prevailed in 3000-3020 levels than the other levels of drillhole.
- 6) The correlation analysis show the silicate, carbonate , sulphide discriminations.
- 7) It was shown that U, V, Ni, Cu, Pb, Zn, As , Ba show the enrichment with organic material content in Derindere drill-hole.

ACKNOWLEDGMENT

The financial support of the Firat University (Turkey) Scientific Research Projects Unit under FUBAP-MF.11.09 project number is gratefully acknowledged

Table 3 Major oxide element correlation coefficients .Significant correlations were noted .

	SiO ₂	Al ₂ O ₃	Fe ₂ O ₃	MgO	CaO	Na ₂ O	K ₂ O	TiO ₂	P ₂ O ₅	MnO	Cr ₂ O ₃
SiO ₂	1.00										
Al ₂ O ₃	0.46	1.00									
Fe ₂ O ₃	0.45	0.81	1.00								
MgO	0.43	-0.13	-0.09	1.00							
CaO	-0.91	-0.91	-0.76	-0.23	1.00						
Na ₂ O	0.29	0.24	0.30	-0.29	-0.30	1.00					
K ₂ O	0.96	0.68	0.47	0.51	-0.89	0.17	1.00				
TiO ₂	0.69	0.94	0.80	-0.24	-0.87	0.44	0.65	1.00			
P ₂ O ₅	-0.18	-0.04	0.16	-0.47	0.10	0.60	-0.31	0.21	1.00		
MnO	0.04	0.59	0.82	-0.31	-0.40	0.14	-0.01	0.55	0.37	1.00	
Cr ₂ O ₃	0.43	0.72	0.94	-0.17	-0.70	0.55	0.45	0.80	0.32	0.68	1.00

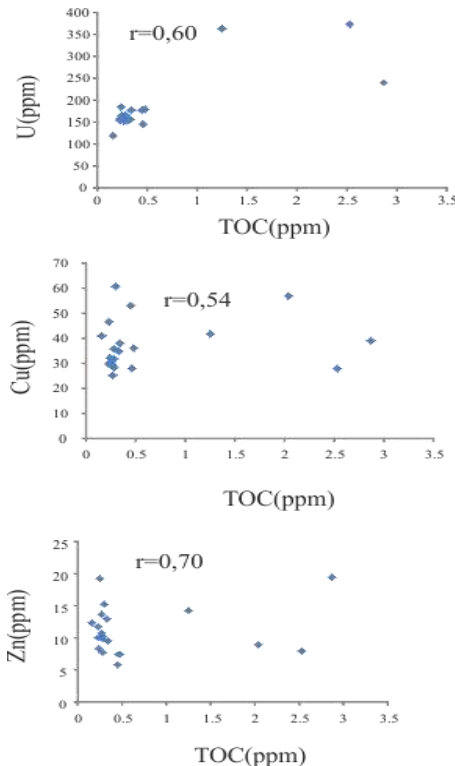


Figure 7 .Correlation coefficient between some trace elements and total carbon (TOC) in samples

REFERENCES

- [1] P.B. Wignall, "Black Shales", Clarendon Press:Oxford, U.K., 1994
- [2] S.E. Calvert, S. Mukherjee, R.J. Morris, "Trace-metals in fulvic and humic acids from modern organic-rich sediments", *Oceanologica Acta*, 8(2), 167-173, 1985.
- [3] N. Bozdoğan, O. Bayçelebi, R. Willink, "Paleozoic stratigraphy and petroleum potential of the Hazro area, S.E. Turkey", *The 7th Biannual Petroleum Congress of Turkey*, Ankara (Turkey), 117—130, 1987.
- [1] D. Perinçek, O. Duran, N. Bozdoğan, T. Çoruh, "Stratigraphy and paleo-geographical evolution of the autochthonous sedimentary rocks in the SE Turkey". *Ozan Sungurlu Symposium*, Ankara, (Turkey), 274-305, 1991.
- [2] O. Kavak and S. Toprak, "Organic geochemical and petrographic properties of Hazro Dadaş (Diyarbakır) coals", *Bulletin of the Mineral Research and Exploration Bulletin of MTA* 147, 91-113, 2013.
- [3] F. Özdemir, Ü.C. Ünlüoğlu, "Evaluation of hydrocarbon potential and stratigraphy of Gökici (Diyarbakır) structure", *Cukurova University Journal of the Faculty of Engineering and Architecture* 1, 127-141, 2013.
- [4] Ö. Bozkaya, H. Yalçın, H. Kozlu, "The mineralogy of Paleozoic rocks from the Amanos region. Turkey" *Geological Bulletin of Turkey*, 21, 1, 53-81, 2009.
- [5] M.C. Göncüoğlu, N., Turhan, "Geology of the Bitlis metamorphic belt", In: *Geology of the Taurus Belt*, (eds): O. Tekeli and M.C. Göncüoğlu, *Proceedings of the International Symposium on the Geology of the Taurus Belt*, Ankara (Turkey), 237-244, 1984.
- [6] B. Velde, "Clay minerals: a physico-chemical explanation of their occurrence", *Developments in Sedimentology*, vol. 40. Elsevier, New York, p.427, 1985.
- [7] S. E. Calvert, T. F., Pedersen "Geochemistry of recent oxic and anoxic marine sediments: Implications for the geological record". *Mar. Geol.* 113, 67–88, 1993.
- [8] H.J. Brumsack, "The trace metal content of recent organic carbon-rich sediments: implications for Cretaceous black shale formation", *Palaeogeogr., Palaeoclimatol., Palaeoecol.* 2006.
- [9] J.R. Hatch, J.S. Leventhal, "Relationship between inferred redox potential of the depositional environment and geochemistry of the Upper Pennsylvanian (Missourian) Stark Shale Member of the Dennis

- Limestone, Wabaunsee County, Kansas, USA”, Chem. Geol. 99: 65-82, 1992.
- [10] D.Z. Piper, C.M. Isaacs, “Minor elements in Quaternary sediments from the sea of Japan a record for surface-water productivity and intermediate-water redox conditions”, Geological Society of America Bulletin 107 (1), 54–67, 1995.
- [11] J. D. Vine, E. B. Tourtelot, “Geochemistry of black shale deposits---a summary report” Econ. Geol. 65, 253- 272, 1970.
- [12] B. Schmitz, “Barium, equatorial high productivity, and the northward wandering of the Indian Continent”, Paleoceanography, 2: 63—78, 1987.
- [13] E. D. Ingall, P. Van Cappellen, “Relation between sedimentation rate and burial of organic phosphorous and organic carbon in marine sediments”, Geochim. Cosmochim. Acta, 54, 373–386, 1990.
- [14] J. Mc Manus, W. M. Berelson, S. Severmann, R. L. Poulson, D. E. Hammond, G. P. Klinkhammer, C. Holm, “Molybdenum and uranium geochemistry in continental margin sediments: Paleoproxy potential”, Geochim. Cosmochim. Acta, 70, 4643 – 4662, 2006.
- [15] C.E. Piela, M., Lyle, F. Marcantonio, J. Baldauf, A.O. Lyle, “Paleoceanography, 27, 2, 2012.

Table 4 SiO₂, Al₂O₃ and Trace element correlation coefficients.

	SiO ₂	Al ₂ O ₃	Ni	Sc	Ba	Co	Cs	Ga	Hf	Nb	Rb	Sr	Ta	Th	U	V	W	Zr	Y
SiO ₂	1																		
Al ₂ O ₃	0.70	1.00																	
Ni	-0.04	-0.10	1.00																
Sc	0.72	0.97	0.07	1.00															
Ba	0.00	-0.21	0.63	-0.04	1.00														
Co	0.64	0.87	-0.11	0.84	0.01	1.00													
Cs	0.55	0.79	0.24	0.87	0.20	0.68	1.00												
Ga	0.66	0.93	-0.15	0.91	-0.11	0.90	0.82	1.00											
Hf	0.37	-0.38	0.29	-0.27	0.27	-0.37	-0.27	-0.42	1.00										
Nb	0.55	0.54	0.41	0.61	0.43	0.63	0.72	0.64	0.05	1.00									
Rb	0.62	0.88	0.03	0.91	0.02	0.76	0.96	0.90	-0.38	0.63	1.00								
Sr	-0.90	-0.79	-0.15	-0.83	-0.03	-0.68	-0.68	-0.70	-0.06	-0.54	-0.71	1.00							
Ta	0.54	0.49	0.28	0.54	0.36	0.59	0.47	0.58	0.05	0.81	0.46	-0.54	1.00						
Th	0.85	0.87	-0.16	0.85	-0.09	0.86	0.75	0.89	-0.20	0.61	0.85	-0.83	0.50	1.00					
U	-0.45	-0.76	0.58	-0.64	0.55	-0.67	-0.37	-0.70	0.57	-0.02	-0.57	0.45	-0.07	-0.67	1.00				
V	-0.15	-0.17	0.88	-0.05	0.63	-0.08	0.18	-0.17	0.24	0.52	-0.03	0.03	0.31	-0.20	0.65	1.00			
W	-0.40	-0.25	0.26	-0.17	0.68	0.04	-0.02	-0.14	-0.14	0.09	-0.15	0.26	0.10	-0.29	0.29	0.35	1.00		
Zr	0.13	-0.51	0.36	-0.40	0.36	-0.44	-0.36	-0.53	0.97	0.04	-0.50	0.04	0.04	-0.32	0.71	0.35	-0.02	1.00	
Y	0.06	-0.06	0.32	0.05	0.42	-0.07	0.43	0.13	0.24	0.52	0.28	0.03	0.22	0.11	0.44	0.41	0.02	0.25	1.00
Cu	0.04	-0.16	0.05	-0.15	-0.12	-0.39	-0.15	-0.35	0.30	-0.28	-0.12	0.05	-0.47	-0.14	0.09	-0.06	-0.38	0.22	-0.10
Pb	0.48	0.46	-0.10	0.43	-0.23	0.42	0.35	0.37	0.14	0.49	0.37	-0.44	0.30	0.45	-0.24	0.08	-0.21	0.08	0.03
Zn	0.19	0.42	-0.08	0.40	-0.21	0.41	0.34	0.45	-0.10	0.26	0.38	-0.21	0.23	0.35	-0.26	-0.04	-0.09	-0.20	0.12
Ni	0.21	0.23	0.22	0.28	-0.10	-0.06	0.40	0.11	0.06	0.06	0.41	-0.27	-0.23	0.20	-0.02	0.06	-0.38	-0.04	0.24
As	0.76	0.67	0.16	0.69	-0.22	0.51	0.56	0.56	0.11	0.38	0.63	-0.78	0.33	0.66	-0.41	-0.06	-0.55	-0.03	0.01

Table 4 continued

	<i>Mo</i>	<i>Cu</i>	<i>Pb</i>	<i>Zn</i>	<i>Ni</i>	<i>As</i>
<i>Mo</i>	1.0					
<i>Cu</i>	0.8	1.0				
<i>Pb</i>	0.3	0.38	1.0			
<i>Zn</i>	0.7	0.51	0.32	1.0		
<i>Ni</i>	0.9	0.8	0.3	0.8	1.0	
<i>As</i>	0.7	0.5	0.3	0.6	0.77	1

Table 5. TOC contents of Derindere drill-hole samples.

<i>TOC</i>	<i>D288</i>	<i>D2890</i>	<i>D2900</i>	<i>D291</i>	<i>D2920</i>	<i>D2930</i>	<i>D2940</i>	<i>D2950</i>	<i>D296</i>	<i>D2970</i>	<i>Average</i>	<i>St. Dev.</i>
	0.16	0.27	0.25	0.28	0.34	0.28	0.27	0.24	0.28	0.23	0.26	0.04
	<i>D2980</i>	<i>D2990</i>	<i>D3000</i>	<i>D3010</i>	<i>D3020</i>	<i>D3030</i>	<i>D3040</i>	<i>D3050</i>	<i>D3060</i>	<i>D3070</i>		
	0.23	0.3	0.46	0.45	0.48	0.33	1.25	2.87	2.53	2.04		

Table 6. Correlations coefficients between major and some trace elements and total organic carbon (TOC) ($P < 0.05$).

<i>TOC</i>	<i>SiO2</i>	<i>Al2O3</i>	<i>Fe2O3</i>	<i>MgO</i>	<i>CaO</i>	<i>Na2O</i>	<i>K2O</i>	<i>TiO2</i>	<i>P2O5</i>	<i>MnO</i>	<i>Cr2O3</i>
	-0.14	-0.18	-0.15	0.01	0.05	0.42	0.10	0.10	0.34	-0.05	0.04

Tablo 6 continued	<i>Ni</i>	<i>Sc</i>	<i>Ba</i>	<i>Co</i>	<i>Cs</i>	<i>Ga</i>	<i>Hf</i>	<i>Nb</i>	<i>Rb</i>
<i>TOC</i>	0.54	-0.03	0.64	-0.18	0.29	-0.14	0.44	0.43	0.07
	<i>Sn</i>	<i>Sr</i>	<i>Ta</i>	<i>Th</i>	<i>U</i>	<i>V</i>	<i>W</i>	<i>Zr</i>	<i>Y</i>
	-0.06	-0.04	0.08	-0.08	0.60	0.68	0.29	0.49	0.65

Tablo 6 continued	<i>Cu</i>	<i>Pb</i>	<i>Zn</i>	<i>Ni</i>	<i>As</i>
<i>TOC</i>	0.54	0.46	0.70	0.68	0.47